ICENS

3rd International Conference on Engineering and Natural Sciences

BOOK OF PROCEEDINGS 2017

Organized by

Partners

BOOK OF PROCEEDING OF THE
III INTERNATIONAL CONFERENCE ON ENGINEERING AND NATURAL SCIENCES (ICENS)

03-07 MAY 2017, BUDAPEST

Edited by

Prof. Dr. Özer Çınar

Published, 2017

info@icens.eu
www.icens.eu

info@icens.org

SCIENTIFIC COMMITTEE

1. Prof. Dr. Adisa Parić - University of Sarajevo
2. Prof. Dr. Ahmet Doğan – Yıldız Technical University
3. Prof. Dr. Aleksandar Dimitrov - Ss. Cyril and Methodius University
4. Prof. Dr. Anita Grozdanov - Ss. Cyril and Methodius University
5. Prof. Dr. Asif Šabanović – International University of Sarajevo
6. Prof. Dr. Cem Şensöğüt - Dumlupınar University
7. Prof. Dr. Christos Douligeris - University of Erlangen-Nurnberg
8. Prof. Dr. Dragutin T. Mihailović - University of Novi Sad
9. Prof. Dr. Falko Dressler - University of Paderborn - Germany
10. Prof. Dr. Harry Miller – International University of Sarajevo
11. Prof. Dr. Houssam Toutanji – Western Michigan University
12. Prof. Dr. Ian F. Akyıldız – Georgia Institute of Technology
13. Prof. Dr. İsmail Usta - Marmara University
14. Prof. Dr. Liljana Gavrilovska - Ss Cyril and Methodius University
15. Prof. Dr. Lukman Thalib - Qatar University
16. Prof. Dr. M. Asghar Fazel – University of Environment
17. Prof. Dr. Özer Çınar – Yıldız Technical University
18. Prof. Dr. Perica Paunovik - Ss. Cyril and Methodius University
19. Prof. Dr. Rifat Škrijelj – University of Sarajevo
20. Prof. Dr. Samir Đug, Faculty of Science Sarajevo
21. Prof. Dr. Tanju Karanfil – Clemson University
22. Prof. Dr. Ümit Alver – Karadeniz Technical University
23. Prof. Dr. Wolfgang Gerstacker - University of Erlangen-Nurnberg
24. Prof. Dr. Yılmaz Yıldırım - Bülent Ecevit University
25. Assoc. Prof. Dr. Izudin Dzafic - International University of Sarajevo
26. Assoc. Prof. Dr. Nusret Drešković - University of Sarajevo
27. Assoc. Prof. Dr. Senija Tahirovic - International University of Sarajevo
28. Assist. Prof. Dr. Fouzi Tabet - German Biomass Research Center
29. Assist. Prof. Dr. Haris Gavranovic - International University of Sarajevo
30. Assist. Prof. Dr. Muhamed Hadziabdic - International University of Sarajevo
31. Assist. Prof. Dr. Sasan Rabieh - Shahid Beheshti University
32. Assist. Prof. Dr. Ševkija Okerić - University of Sarajevo
33. Dr. Muhammet Uzun - RWTH Aachen University
34. Dr. Zsolt Hetesi - National University of Public Service, Budapest
35. Dr. Zsolt T. Németh - National University of Public Service, Budapest

ORGANIZATION COMMITTEE

Chairman of the Conference

Prof. Dr. Özer Çınar – Yıldız Technical University

Members of the Committee

Dr. Gábor Baranyai (Co-Chairman) – National University of Public Service, Hungary
Prof. Dr. Ahmet Dogan (Co-Chairman) – Yıldız Technical University
Prof. Dr. M. Asghar Fazel – University of Environment
Prof. Dr. Lukman Thalib - Qatar University
Assoc. Prof. Dr. Nusret Drešković - University of Sarajevo
Assoc. Prof. Dr. Samir Đug, Faculty of Science Sarajevo
Assist. Prof. Dr. Sasan Rabieh - Shahid Beheshti University
Teaching Asistant Amra Banda - University of Sarajevo
Teaching Asistant Amina Sivac - University of Sarajevo
Teaching Asistant Boris Avdic - University of Sarajevo
Senior Teaching Asistant Edin Hrelja - University of Sarajev

WELCOME TO ICENS 2017

On behalf of the organizing committee, we are pleased to announce that the 3rd International Conference on Engineering and Natural Sciences (ICENS 2017) will be held from May 3 to 7, 2017 in Budapest, Hungary. ICENS 2017 provides an ideal academic platform for researchers to present the latest research findings and describe emerging technologies, and directions in Engineering and Natural Sciences issues. The conference seeks to contribute to presenting novel research results in all aspects of Engineering and Natural Sciences.

The conference aims to bring together leading academic scientists, researchers and research scholars to exchange and share their experiences and research results about all aspects of Engineering and Natural Sciences. It also provides the premier interdisciplinary forum for scientists, engineers, and practitioners to present their latest research results, ideas, developments, and applications in all areas of Engineering and Natural Sciences. The conference will bring together leading academic scientists, researchers and scholars in the domain of interest from around the world.

The scientific program will focus on current advances in the research, production and use of Engineering and Natural Sciences with particular focus on their role in maintaining academic level in Engineering and Applied Sciences and elevating the science level.

The conference's goal will to provide a scientific forum for all international prestige scholars around the world and enable the interactive exchange of state-of-the-art knowledge. The conference will focus on evidence-based benefits proven in clinical trials and scientific experiments.

Best regards,

Prof. Dr.Özer ÇINAR

ICENS
III INTERNATIONAL CONFERENCE ON ENGINEERING AND NATURAL SCIENCE
3 - 7 May 2017 BUDAPEST

CONTENT	PAGE

USING DYNAMIC STIFFNESS METHOD

Process Analytical Technology To Optimize Performance Of Extrusion Process For uPVC Pipes

Abbas Al-Refaie[1]*, Raed Athamneh[2], Nour Bata[2]

Abstract

This paper aims at optimizing performance of the polyethylene extrusion process in plastic industry using the framework of Process Analytical Technology (PAT) utilizing fuzzy-neural approach. Two pipe's quality responses, weight, and thickness where chosen as both are main features of manufacturer interest. Initially, the individual moving range (I-MR) control charts are established for each response which illustrates that the process is incapable. Nine process factors are studied utilizing the L_{27} array. The fuzzy-neural approach is, therefore, proposed and then implemented to optimize process settings. Confirmation experiments are finally conducted at the combination of optimal factor settings. It is found that the estimated mean values for weight and thickness are close to their corresponding targets. Moreover, the estimated standard deviations for the pipe's weight and thickness at initial settings are reduced significantly using the optimal factor settings. As a result, the estimated process capability indices are significantly enhanced for both responses. The capability index of multiple processes is increased accordingly. In practice, the gained improvements by using the PAT framework will reduce quality and productivity costs significantly.

Keywords: PAT Framework, Extrusion Process, Process Capability, Multiple Responses

1. INTRODUCTION

Inexpensive raw materials, ease of processing, greater flexibility in the design of components, and attractive properties, the demand for plastic products has dramatically increased. In such products in order to meet customer expectations, manufacturers should continually optimize plastic manufacturing processes in a cost-effective manner [1-2]. Among the heavily-used plastic products is the Unplasticized Poly Vinyl Chloride (*uPVC*) pipe used in pressure and non-pressure applications; such as, transfer water, protection electrical, communications wires and other applications. The main manufacturing processes involved in producing *uPVC* pipes are the injection and extrusion processes. In order to cut huge quality costs, optimizing the performance of plastic process becomes a real challenge to product/process engineers.

1.1. Process Analytical Technology

Process Analytical Technology (PAT) is a system for designing, analyzing, and controlling plastic manufacturing through timely measurements of critical quality and performance attributes of raw and in-process materials and processes, to ensure final product quality [3-4]. The PAT's goal is to enhance the understanding and controlling of the manufacturing process to improve quality and efficiency. PAT framework in *uPVC* includes the steps shown in Fig. 1.

---

[1]* *Corresponding author: University of Jordan, Department of Industrial Engineering, Amman 11942.*
  abbas.alrefai@ju.edu.jo

[2]*Received master degree in Industrial Engineering from the University of Jordan.*
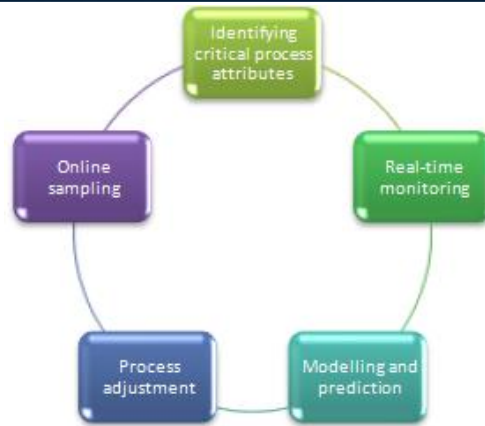
Fig.1. PAT framework

1.2. Fuzzy logic

Typically, the fuzzy logic principle is widely-applied to deal with vague and unsure information for optimizing performance using multiple quality characteristics [5]. The Mamdani systems in fuzzy logic involve mathematical expressions that have a linear function [6]. Generally, a fuzzy system shown in Fig. 2 includes the fuzzifier, fuzzy rules, and the defuzzifier that transforms the fuzzy input values into a comprehensive output measure [7].
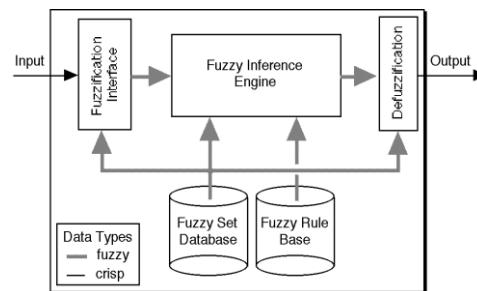
Fig. 2. A schematic of fuzzy logic system.

1.3. Artificial Neural Networks

The Artificial Neural Networks (ANNs) are soft computing techniques used to emulate some functions of the human behavior, by having a finite number of layers with different neurons being as the computing elements [8]. The most popular type of ANNs consists of input, hidden, and output layers. The input and output layers represent the nodes, and the hidden layer represents the relationship between the input and output layers. In ANNs, the Radial Basis Function Neural Network (RBFNN) shown in Fig. 3 can approximate the desired outputs predicted without a need to have a mathematical formula of the relationship among the outputs and the inputs [9].
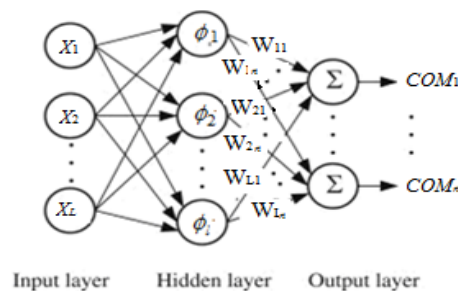
Fig. 3. Architecture of the RBFNN.

Previous research attempted to improve *uPVC* pipes' quality and enhance extrusion process's productivity. For example, Mu *et al*. [10] developed an optimization approach for processing design in the extrusion process of plastic profile with metal insert. Mamalis *et al*. [11] optimized processing parameters of Tube - extrusion of polymeric materials. This research utilizes the fuzzy logic and RBFNN techniques in the PAT framework to optimize the parameters of plastic extrusion process. Research results may contribute to reduce huge quality and production costs.

2. MATERIALS AND METHODS

The pipes' manufacturing line starts by mixing the raw material, which consists mainly of *uPVC* particles. Within the barrel, raw material is subjected to extremely high temperatures until it starts to melt. Depending on the type of thermoplastic, barrel temperatures can range between 400 and 530 degrees Fahrenheit. Once the molten plastic reaches the end of the barrel, it is forced through a screen pack and fed into the feed pipe that leads to the die, which is designed and built based on the dimensions desired in the pipe and the shrink rate of the type of plastic being used. After leaving the extrusion die, the pipe passes through precision sizing sleeves with an external vacuum. The puller or haul off is used to pull off the pipe through sizing and cooling operations. To expedite the cooling process, the newly formed plastic receives a sealed water bath. Once it has passed a certain length, it will trip a sensor (electric eye) triggering a cutting operation on the pipe. The cut is made by a cutter that moves forward at the rate of pipe extrusion to offset the motion of the pipe moving forward so that the end of the pipe will remain perpendicular to the pipe wall after it is cut. The PAT framework is then implemented as follows.

2.1. Identifying critical process attributes

The pipe quality can be described by several physical parameters; such as, accurate pipes weight and thickness. Pipe's average thickness and average weight are considered the most vital quality characteristics. Typically, the pipe is composed of PVC and additives, such as UV inhibitors, anti-oxidants, or colorants. Accurate pipe's weight for a homogeneous powder mixture ensures that each produced pipe contains sufficient amount of resin stated in the standards. The specification of the pipe's weight is 1666 ± 14 grams/meter. Thus, the average weight is considered as nominal-the-best (NTB) type. The thickness is also a significant measure to the uniformity of the pipe and the resulted defects; an accurate thickness is an indicator to a good surface finish. Therefore, pipe's thickness will be used as an indicator to measure if it can hold the pressure on its' inner wall and does not cause pipe's fracture. The specifications of the pipe's thickness are 3200 ± 200 Micrometer. The pipe thickness is measured using a Vernier caliper, while the pipe weight is measured using a weighing device.

2.2. Real-time monitoring

(a) Weight.   *(b) Thickness.*
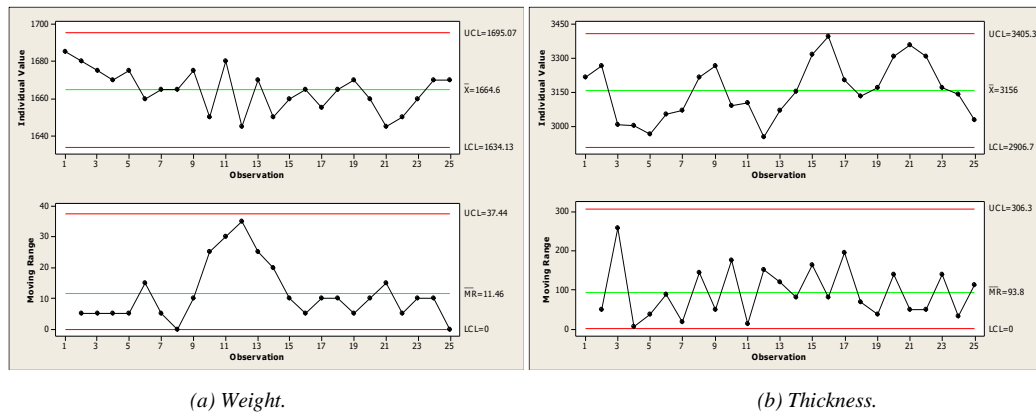
Fig. 4. The I-MR control charts at initial factor settings.

A control chart is one of the primary monitoring techniques of statistical Process control. A normality test for the current data is conducted before proceeding in establishing the control charts. The *p* values of 0.379 and 0.857 for the pipe's average weight and thickness respectively are displayed in Fig. 4, which confirms that the normal distribution is a satisfactory model for each response. The data is collected for the pipe's thickness and weight. *I-MR* control charts for the averages of pipe's weight and thickness are constructed and depicted in Fig. 9. In this figure, the calculated *LCL*, *CL*, and *UCL* values for *I* chart are 1634.13, 1664.6, and 1695.07 g/m, respectively, while their respective values for the *MR* chart are estimated 0.0, 11.46, and 37.44 g/m. For the average thickness, the *LCL*, *CL*, and *UCL* of the *I* chart are respectively calculated as 2906.7, 3156.0, and

3405.3 µm, while their values for the *MR* chart are estimated 0.0, 93.8, and 306.4 µm, respectively. Observing the *I-MR* charts, neither point falls beyond the control limits nor is a significant pattern observed within the control limits for both the pipe's average weight and thickness. Consequently, the *I-MR* charts are concluded in statistical control.

A vital part of an overall quality-improvement program is the process capability analysis by which the capability of a manufacturing process can be measured and assessed. The c_p is estimated as shown in Eq.(1).

$$\hat{C}_p = \frac{USL - LSL}{6\hat{\sigma}} \tag{1}$$

Furthermore, the actual process capability index C_{pk} attempts to take the target, *T*, into account. The actual capability index, C_{pk}, can be expressed mathematically by:

$$\hat{C}_{pk} = \min\left(\frac{USL - \hat{\mu}}{3\hat{\sigma}}, \frac{\hat{\mu} - LSL}{3\hat{\sigma}}\right) \tag{2}$$

A criterion for selecting an optimal design is known as $M\hat{C}_{pk}$ and is used as a capability measure for a process having multiple performance measures. $M\hat{C}_{pk}$ is a proposed system capability index for the process which is the geometric mean of performance measure $\hat{C}_{pk}$ values (Plante, 2001).

$$M\hat{C}_{pk} = \left(\prod_{i=1}^{m}\hat{C}_{pki}\right)^{1/m} \tag{3}$$

Where *m* is the number of quality characteristics. A summary of all the statistical data gathered in the measuring phase for both quality characteristics is listed in Table 1.

Table 1. Statistical summary for both quality responses.

Quality Response	LCL	CL	UCL	LSL	Target	USL	$\hat{\sigma}$	$\hat{C}_{pk}$	$M\hat{C}_{pk}$
Weight (gm)	1634.13	1664.60	1695.07	1652	1666	1680	10.16	0.41	0.51
Thickness (µm)	2906.70	3156.00	3405.30	3000	3200	3400	83.11	0.63	

2.3. Optimization and Prediction

The quality characteristics are the pipe's weight (WE, g/m) and pipe thickness (TH, µm). Both quality characteristics are the nominal-the-best (NTB) type responses. Based on technical knowledge, nine three-level process factors are studied. The appropriate array is the L_{27} orthogonal array shown in Table 2.

Table 2. The controllable factors and their levels.

Process factor	Level		
	1	2	3
x_1: T1	190	195	200
x_2: T2	180	185	190
x_3: T3	165	170	175
x_4: T4	165	170	175
x_5: T5	160	165	170
x_6: T6	170	175	180
x_7: T7	165	170	175
x_8: T8	225	230	235
x_9:	700	800	900

In the Taguchi method, the orthogonal array (OA) consists of columns that represent the controllable factors to be studied. While, the rows represent the combination of factor levels at which experiments are held. Let η_{ij} denotes the signal-to noise ratio for the jth response at experiment i calculated for the nominal-the-best (NTB) type response as:

$$\eta_i = -10\log[\bar{y}_i^2 / s_i^2] \; ; i = 1, ..., 27 \tag{4}$$

where $\bar{y}_i$ and s_i are the estimated average and standard deviation in experiment i of each response, respectively. In this research, nine three-level factors are considered, and thus the L_{27} array shown in Table 3 will be utilized for conducting experimental work. Each experiment is conducted at the combination of factor levels with two replicates. Then, the weight and thickness values are measured and listed in Table 4. Finally, the η_{ij} values are computed at experiment i for each response j; $i=1,\dots, 27$, $j=1,2$. The obtained results are also displayed in Table 3.

(a) Optimization of process settings

The two quality characteristics are converted into a single response using fuzzy logic. Its input variables are the η_{ij} values, whereas the *COMi* values are the output. The minimum and maximum values of η_{ij} for each quality characteristic are shown in Table 5. The fuzzy logic method is built by setting the inputs and output as shown in Fig. 5. The rules that represent the association between the input variables in the fuzzy model that are represented as η_{ij} for each quality characteristic and the output are setas shown in Table 6. Then the three fuzzy subsets are assigned to the output value (the COM value) as shown in Fig. 6.The output of the non-fuzzy value (the COM value) is calculated by using the COG Defuzzification method.

Table 3. The calculated η_{ij} values in the L_{27} array.

Exp. i	x_1	x_2	x_3	x_4	x_5	x_6	x_7	x_8	x_9	Wi_{11}	Wi_{12}	Ti_{21}	Ti_{22}	η_{i1}	η_{i2}	Mean Weight	Mean Thickness
1	1	1	1	1	1	1	1	1	1	1595.0	1606.0	3180.2	3182.3	46.27	66.62	3181.25	1600.5
2	1	1	2	1	2	2	2	2	2	1673.0	1667.0	3102.1	3104.2	51.90	66.57	3103.13	1670.00
3	1	1	3	1	3	3	3	3	3	1678.0	1675.0	3203.0	3197.0	57.96	57.55	3200.00	1676.5
4	1	2	1	2	1	1	1	2	2	1612.0	1613.0	3170.2	3173.6	67.16	62.51	3171.88	1612.5
5	1	2	2	2	2	2	2	3	3	1647.0	1642.0	3038.8	3042.5	53.35	61.40	3040.63	1644.5
6	1	2	3	2	3	3	3	1	1	1663.0	1657.0	2977.1	2979.2	51.85	66.21	2978.13	1660.00
7	1	3	1	3	1	1	1	3	3	1601.0	1609.0	2839.0	2836.0	49.06	62.53	2837.5	1605.00
8	1	3	2	3	2	2	2	1	1	1688.0	1692.0	3218.3	3213.0	55.53	58.60	3215.63	1690.00
9	1	3	3	3	3	3	3	2	2	1701.0	1699.0	3323.2	3333.1	61.60	53.58	3328.13	1700.00
10	2	1	1	3	1	2	3	1	2	1670.0	1675.0	3010.3	3008.5	53.50	67.28	3009.38	1672.5
11	2	1	2	3	2	3	1	2	3	1644.0	1646.0	3010.3	3008.5	61.31	67.28	3009.38	1645.00
12	2	1	3	3	3	1	2	3	1	1660.0	1665.0	3207.2	3199.1	53.45	54.91	3203.13	1662.50
13	2	2	1	1	1	2	3	2	3	1664.0	1666.0	3180.0	3182.5	61.42	65.10	3181.25	1665.00
14	2	2	2	1	2	3	1	3	1	1633.0	1637.0	3100.0	3112.5	55.24	50.92	3106.25	1635.00

15	2	2	3	1	3	1	2	1	2	1627.0	1623.0	2982.0	2993.0	55.19	51.69	2987.5	1625.00
16	2	3	1	2	1	2	3	3	1	1665.0	1670.0	3199.2	3182.1	53.47	48.41	3190.63	1667.50
17	2	3	2	2	2	3	1	1	2	1742.0	1738.0	3342.0	3358.0	55.78	49.43	3350.00	1740.00
18	2	3	3	2	3	1	2	2	3	1647.0	1648.0	3011.2	3026.3	67.35	49.03	3018.75	1647.50
19	3	1	1	2	1	3	2	1	3	1604.0	1606.0	2932.0	2930.5	61.10	68.83	2931.25	1605.00
20	3	1	2	2	2	1	3	2	1	1658.0	1652.0	3143.3	3144.2	51.82	73.87	3143.75	1655.00
21	3	1	3	2	3	2	1	3	2	1612.0	1608.0	2977.7	2966.1	55.11	51.15	2971.88	1610.00
22	3	2	1	3	1	3	2	2	1	1597.0	1583.0	2785.4	2789.6	44.12	59.45	2787.50	1590.00
23	3	2	2	3	2	1	3	3	2	1613.0	1617.0	2860.0	2865.0	55.13	58.17	2862.50	1615.00
24	3	2	3	3	3	2	1	1	3	1654.0	1646.0	3078.6	3065.1	49.30	50.18	3071.87	1650.00
25	3	3	1	1	1	3	2	3	2	1670.0	1675.0	3113.0	3112.0	53.50	72.87	3112.5	1672.50
26	3	3	2	1	2	1	3	1	3	1666.0	1674.0	3142.9	3144.6	49.40	68.35	3143.75	1670.00
27	3	3	3	1	3	2	1	2	1	1642.0	1648.0	3096.5	3091.0	51.77	58.01	3093.75	1645.00

Table 5. The max and min values of η_{ij}

Response	min η_{ij}	High (%)	Low (%)	max η_{ij}	High (%)	Low (%)
Weight (gm)	44.12	0	100	67.35	100	0
Thickness (μm)	48.41	0	100	73.87	100	0

Table 6. The fuzzy rules.

η_{ij}		COM
Weight	Thickness	
LOW	LOW	Low
LOW	HIGH	Medium
HIGH	LOW	Medium
HIGH	HIGH	High

a) MFs for weight   b) MFs for thickness.
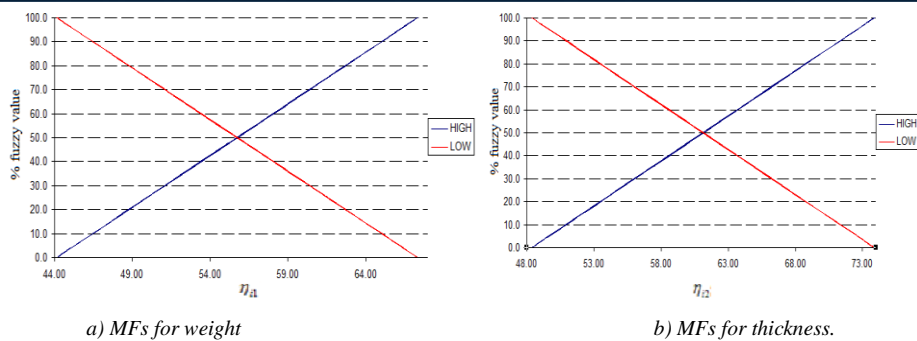
Fig. 5. Membership functions for quality responses.
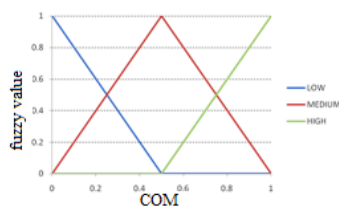
Fig. 6. Membership functions for the output.

The COM_i values obtained from fuzzy logic at each experiment are shown in Table 7.

Table 7. The COM_i values.

Exp. i	COM_i	Exp. i	COM_i	Exp. i	COM_i
1	0.482	10	0.522	19	0.624
2	0.507	11	0.617	20	0.528
3	0.493	12	0.432	21	0.435
4	0.577	13	0.586	22	0.420
5	0.483	14	0.436	23	0.473
6	0.504	15	0.438	24	0.339
7	0.465	16	0.410	25	0.540
8	0.480	17	0.439	26	0.501
9	0.495	18	0.500	27	0.438

Step 3: The complete data set for the COM value is generated using RBFNN by setting the orthogonal array as an input matrix and the COM values as an output matrix. The results are displays in Table 8.

Step 4: The COM averages are calculated at each factor level as shown in Table 9, where the combination of optimal factor levels is $x_{1(1)}x_{2(1)}x_{3(1)}\ x_{4(2)}x_{5(1)}\ x_{6(3)}\ x_{7(3)}\ x_{8(2)}\ x_{9(3)}$, which is identified by selecting the level that maximizes COM average for this factor.

(b) Response Prediction

The weight and thickness averages are predicted at the combination of optimal factor levels $x_{1(1)}x_{2(1)}x_{3(1)}x_{4(1)}x_{5(1)}x_{6(3)}x_{7(3)}x_{8(2)}x_{9(3)}$ and then the results are shown in Table 10. It is found that the predicted average weight at the optimal factor levels is 1720.2 ± 17.6 gm, while the predicted average thickness is 3188.515 ± 84 μm.

Table 8. The full data set for the com value.

Run no.	x_1	x_2	x_3	x_4	x_5	x_6	x_7	x_8	x_9	COM_i
1	1	1	1	1	1	1	1	1	1	0.4820
2	1	1	1	1	1	1	1	1	2	0.5127
3	1	1	1	1	1	1	1	1	3	0.5341
4	1	1	1	1	1	1	1	2	1	0.5124
5	1	1	1	1	1	1	1	2	2	0.5321
6	1	1	1	1	1	1	1	2	3	0.5385
.	.	.	.	.	.	.	.	.	.	.
19681	3	3	3	3	3	3	3	3	1	0.5332
19682	3	3	3	3	3	3	3	3	2	0.5324
19683	3	3	3	3	3	3	3	3	3	0.5332

Table 9. The COM averages for the full factorial design.

Factor	Level		
	1	2	3
x_1	0.529	0.521	0.527
x_2	0.531	0.523	0.526
x_3	0.531	0.526	0.525
x_4	0.528	0.522	0.524
x_5	0.531	0.526	0.525
x_6	0.521	0.526	0.529
x_7	0.524	0.526	0.529
x_8	0.522	0.528	0.526
x_9	0.525	0.526	0.531

Table 10. Anticipated improvements summary.

Response	Target	Initial settings $x_{1(1)}x_{2(1)}x_{3(2)} x_{4(2)}x_{5(3)}x_{6(2)}x_{7(2)}x_{8(2)} x_{9(1)}$	Predicted average ± 2× S $x_{1(1)}x_{2(1)}x_{3(1)}x_{4(1)}x_{5(1)}x_{6(3)}x_{7(3)}x_{8(2)}x_{9(3)}$
WE	1660	1615.138	1720.2 ± 17.6
TH	3200	2875.875	3188.515 ± 84

2.4. Process adjustment and online sampling

The process parameters are set at the combination of optimal factor settings. During operation, an online sampling is conducted and then the weight and thickness averages are measured. Fig. 7 displays the estimated capability indices for both responses. It is found that the injection process exhibits statistical control for both responses. Further, the $\hat{C}_{pk}$ value for the average pipe weight is increased from 0.41 to 1.06, while the $\hat{C}_{pk}$ value has been increased from 0.63 to 9.36.
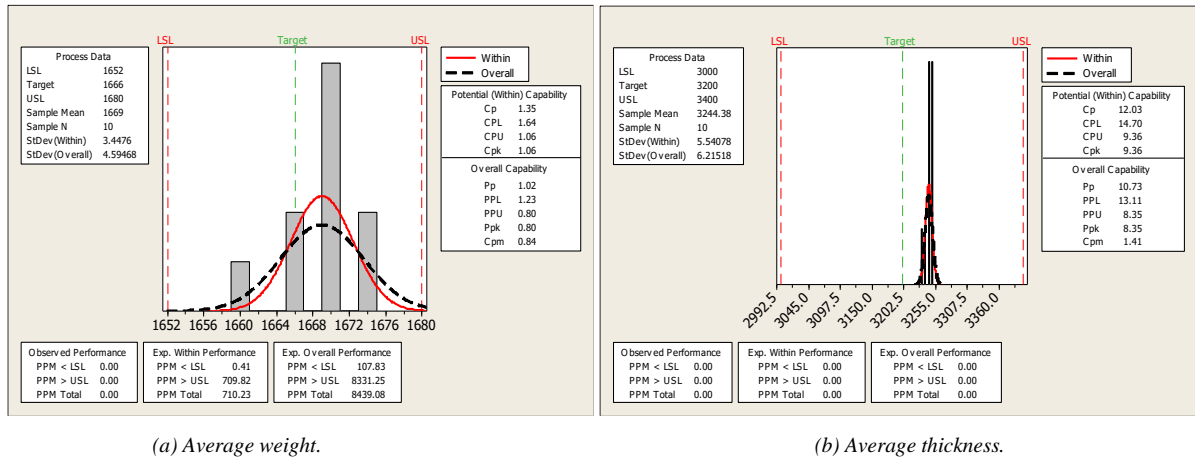
(a) Average weight.   *(b) Average thickness.*

Fig. 7. The estimated capability indices at optimal factor settings.

3. RESULTS AND DISCUSSION

The anticipated improvements in both responses are summarized in Table 11, where it is found that:

For the pipe's weight, the estimated mean, $\hat{\mu}$, at the combination of initial (optimal) factor settings is equal to 1664.6 (1669), which is close to the target weight value of 1666. The estimated standard deviation, $\hat{\sigma}$, at initial factor settings of 10.16 is reduced significantly to 3.45. As a result, the estimated process capability index, $\hat{C}_{pk}$, is significantly improved from 0.41 to 1.06.

For the pipe's thickness, the $\hat{\mu}$ at initial (optimal) factor settings is equal to 3156 (3244.4), which is close to the target weight value of 3200. Moreover, the $\hat{\sigma}$ at initial factor settings of 83.11 is reduced significantly to 5.54 using the optimal factor settings. Consequently, the estimated $\hat{C}_{pk}$ is significantly enhanced from 0.63 to 9.36.

Due to the improvement in individual capability indices, the multiple process capability index, MC_{pk}, index is increased from 0.51 to 3.15, which indicates that the process becomes highly capable for both quality responses concurrently.

Table 11. Comparison Summary.

Quality response	*LSL*	*T*	*USL*	Condition	$\hat{\mu}$	$\hat{\sigma}$	$\hat{C}_{pk}$
Average weight	1652	1666	1680	Initial	1664.6	10.16	0.41
				Online	1669	3.45	1.06
Average thickness	3000	3200	3400	Initial	3156	83.11	0.63
				Online	3244.4	5.54	9.36

4. CONCLUSİONS

This paper adopted the Process Analytical Technology (PAT) to improve the performance of extrusion process with two main quality responses; pipe's weight and thickness. The main findings of this research is that using Statistical Control Charts to assess process condition at the combination of factor settings demonstrates that the extrusion process is in control while the capability analysis shows poor process

performance. Thus, the L_{27} array is utilized to provide experimental design, the fuzzy-neural for identifying optimal factor settings and regression models to predict process performance. Confirmation experiments showed that the process means are close to target values of weight and thickness. Moreover, the estimated standard deviation of 10.16 for the pipe's weight at initial settings is reduced significantly to 3.45 at the optimal factor settings. For the pipe's thickness, the estimated standard deviation at initial settings of 83.11 is significantly reduced to 5.54 using optimal settings. As a result, the estimated process capability index is significantly enhanced from 0.41 to 1.06 for weight and it is significantly increased for thickness from 0.63 to 9.36. The multiple process capability index is increased from 0.51 to 3.15. The main conclusion drawn out of this research is that the gained improvements in extrusion process performance using PAT framework will result in significant savings in quality and production costs.

REFERENCES

[1] A. Al-Refaie and M-H. Li, "Optimizing the performance of plastic injection molding using weighted additive model in goal programming," *International Journal of Fuzzy System Applications*, vol. 22 (07), pp. 676-689, 2011.

[2] J-C Yu, X-X Chen, T-R Hung, F. Thibault, "Optimization of extrusion blow molding processes using soft computing and Taguchi's method," *Journal of Intelligent Manufacturing*, vol. 15(5): pp. 625-634, 2004.

[3] A. Al-Refaie, "Optimizing Multiple Quality Responses in the Taguchi Method Using Fuzzy Goal Programming: Modeling and Applications, " *International Journal of Intelligent Systems*, vol. 30(6): pp. 651-675, 2015.

[4] *CDER (Center for Drug Evaluation and Research), "Guidance for Industry: PAT- A Framework for Innovative Pharmaceutical Development, Manufacturing, and Quality Assurance, " US Department of Health and Human Services Food and Drug Administration, 2004.*

[5] K. Mandic, B.Delibasic, S.Knezevic, S. Benkovic, " Analysis of the financial parameters of Serbian banks through the application of the fuzzy AHP and TOPSIS methods," Economic Modeling, vol. 43, 30–37, 2014.

[6] J-H. Sun, Y-C. Fang, B-R. Hsueh, " Combining Taguchi with fuzzy method on extended optimal design of miniature zoom optics with liquid lens," *Optik*, vol. 123(19) , pp.1768– 1774, 2012.

[7] T. Tsai,"Improving the fine-pitch stencil printing capability using the Taguchi method and Taguchi fuzzy-based model", *Robotics and Computer-Integrated Manufacturing*, vol. 27, pp. 808–817, 2014.

[8] A. Marvuglia, A.Messineo, G. Nicolosi, " Coupling a neural network temperature predictor and a fuzzy logic controller to perform thermal Comfort regulation in an office building," *Building and Environment*, vol. 72, pp. 287-299, 2014.

[9] S.X. Chen, H.B. Gooi, M.Q. Wang, " Solar radiation forecast based on fuzzy logic and neural networks," *Renewable Energy*, vol. 60 , pp.195-201, 2013.

[10] Y Mu, G Zhao, X. Wu, " Optimization approach for processing design in the extrusion process of plastic profile with metal insert, " *e-Polymers*, 12(1), pp. 353- 366, 2013.

[11] A.G Mamalis, A.K Vortselas, G. Kouzilos, " Tube -extrusion of polymeric materials: optimization of processing parameters, " *Journal of Applied Polymer Science*, vol. 126(1), pp.186-193, 2012.

The Study of Genetic Diversity in Canola Cultivars of Kashmar-Iran Region

Seyed Habib Shojaei[1], Khodadad Mostafavi[2], Mir Sajjad Shojaei[1], Alireza Akbari[1], Seyede Mitra Sadati[1], Farnaz Farbakhsh[1]

Abstract

To study the genetic diversity in rapeseeds and agronomic traits, an experiment was conducted using multivariate statistical methods at Agricultural Research Station of Kashmar in 2012-2013.In this experiment, ten genotypes of rapeseed in a Randomized Complete Block designs with three replications were evaluated. The following traits were studied: seed yield, number of days to the fifty percent of flowering, plant height, number of pods on main stem, length of the pod, seed yield per plant, number of seed in pod, harvest index, weight of 100 seeds, number of pods on lateral branch, number of lateral branches. In analyzing the variance, differences between cultivars were significant. The average comparative revealed that the most valuable variety was Licord regarding to the traits while the least valuable variety was Opera. In stepwise regression, harvest index, grain yield per plant and number of pods per lateral branches were entering to model. Correlation analysis showed that the grain yield with the number of pods per lateral branches and seed yield per plant have positive and significant correlation. In the factor analysis, the first 5 components explained more than 83% of the variance in the data. In the first factor, seed yield and the number of pods per lateral branches were of the highest importance. The traits, seed yield per plant, and pod per main stem were of a great significance in the second factor. Moreover, in the third factor, plant height and the number of lateral branches were more important. In the fourth factor, plant height and one hundred seeds weight were of the highest variance. Finally, days to fifty percent of flowering and one hundred seeds weight were more important in fifth factor.

Keywords: *Rapeseed, Variance analysis, Regression, Correlation, Factor analysis*

1. INTRODUCTION

Canola is an edible plant of Cruciferea family and the Brassicaceae genus. A special feature of Canola seed (having 40 to 50 percent oil) and the plants compatibility to the climatic conditions in most parts of the country has led to the plants growing development as a hope for the country's needed oil production [13]. The high oil content of Canola seed as well as the combination of oils fatty acids of improved varieties, attracted most of the worlds in this oilseed [3].

Economically, Canola is the fifth plant after rice, wheat, maize, cotton and has the second place after soybeans in supplying oil. So that about 14.7% of the world's oil production has been allocated to it. World population growth and improving living standard increased Canola production for edible consumption. Also, creation of special cultivars caused by industrial, specific markets increases the cultivation of this plant. According to the fact that every Iranian's oil consumption has been estimated about 16 kilograms, so with a population of 70 million the amount of needed oil will be 1,120,000 tons, although among foods the highest level of dependency is related to the import of oil. In 1994, Canola cultivation began with the aim of achieving self-sufficiency in the country oil. From the beginning of Canola cultivation up to the years 2007-2008, a great deal of fluctuation in increasing or decreasing of the function has been seen [6]. The genetic control of the function is done in directly through physiological components which has a correlation with economical function. Although the function of agricultural plants has increased over the past years, but the morphogenetic process under laying this increase in performance have not been well understood [14]. If the sources of variability in function and its components are known, it may be a way to improve agricultural plant potential through modification or improvement of farm operations [4]. Unlike classical methods, multivariate methods and the internal structure of the data clearly show the most suitable statistical method for testing the

data [5]. By using multivariate statistical techniques that simultaneously consider multiple measurements, you can analyze genetic diversity based on morphological and biochemical data. Among the various, multivariate and statistical methods factor analysis is one of the most important and used ones [7,10].

Multivariate analysis, such as regression and factor analysis are used in order to interpret the relationships between attributes and grouping them based on these relations [15].

Factor analysis is used in reducing the number of variables to a number of hidden factors, identifying the major functional components, grouping traits based on the inter-relationships between them and exploring the genetic diversity [2].

The purpose of this study is to investigate the genetic diversity in different cultivars of canola and classify genotypes using a multivariate statistical method.

2. MATERIALS AND METHODS

To study the genetic diversity and agronomic performance using multivariate statistical methods, an experiment in the agricultural year of 2012-2013 was conducted at Agricultural Research Station of Kashmar. In this experiment, 10 genotypes of canola (Table 1) under normal irrigation conditions in a randomized complete block design (RCBD) with three replications were evaluated. Conventional tillage operations such as plowing land, land leveling, etc. are regularly conducted and after tillage, seed cultivation is going to be performed manually and carefully. Each experimental plot consists of four rows of two meter length and fifty centimeter apart from each other. The irrigation was done regularly and weeding operations were performed weekly and accurately and also the thinning operation was performed in the trifoliate stage of the plant. Before harvest, the plant height and the number of days to 50% flowering and then in order to avoid marginal errors, experimental plots were harvested from the middle two rows and data analysis was performed using SAS software.

Table 1. The name and the source of Canola genotypes evaluation in the experiment

Row	Genotype	Orijin	Row	Genotype	Orijin
1	Modena	Russia	6	Zarfam	Iran
2	Okapi	France	7	RGS003	German
3	Hyola401	Canada	8	SLM046	German
4	Licord	German	9	Sarigol	German
5	Opera	Sweden	10	Hyola308	Canada

3. RESULT AND DISCUSSION

The results of variance analysis showed that all traits were significantly different at the level of 0.01. Also in the variance analysis we found non-significant differences that represent equalization between blocks. The highest level of CV was related to the number of pods per lateral branches (20.76) and the lowest one was related to the number of the days to fifty percent flowering (5.79). Variance analysis results of investigated traits are presented in Table 2. The amount of the function of yield per square meter as a dependent variable to other traits was considered as an independent variable. The impression of ineffective or low impact traits can be removed with the help of stepwise regression and the traits which significantly justify the performance changes can be examined [1]. Stepwise regression results show that grain yield per plant, harvest index and the number of pods per lateral branches entered to the model. The regression results have been mentioned in table 3. Grain yield and grain yield per plant, harvest index and seed pods on lateral branches had a significant positive correlation. The number of days to 50% flowering with the number of pods per main stem and lateral branches had a significant, positive correlation but on the other hand with the plant height had a significant negative difference. Plant height was also significantly and positively correlated with the pod length. The number of pods per main stem and lateral pods according to the weight of a hundred seeds were in a positive and significant correlation. The correlation results showed that this trait is significantly and positively is correlated with pod length, seed per pod and the number of lateral branches. Grain yield per plant also has a significant correlation with harvest index and the number of pods per lateral branches. The Weight of hundred seeds and the number of seed pods and the number of seed pods lateral branches with the number of seed pods are in a positive and significant correlation. Finally, harvest index and the number of seeds per pod showed no correlation with any of the examined traits. The correlation table is presented in Table 4.

By using factor analysis and statistical method, we can explain a larger number of variables as smaller, independent factors [10]. It is one of the oldest, multivariate methods whose aim is to reduce the volume of data that is usually used to describe multivariate data. The utility of this method is at the highest level when there is a remarkable correlation between the main variables [9].

Factor analysis can complement the stepwise regression as well as providing information [2]. Also, factor analysis was used in this study in order to assess the diversity and distribution of genotypes and grouping them based on the examined characteristics and parameters and as a result, the first 5 factors cover more than 83% of the variance and regarding to factor matrix they have the highest level of functionality among other ones. In the first factor in the factor analysis, grain yield and the number of pods per lateral branches had the highest rates so it was named performance characteristics Factor. In the second factor, grain yield per plant and number pod per main stem had the highest rate and it was named grain yield per plant factor. Plant height and the number of lateral branches in the third factor had the highest rate and it was named quantitative characteristic factor and in the fourth factor, plant height and seed weight had the highest rate, which was named the Plant Factor. In the fifth factor, day traits to 50% flowering the weight of a hundred seeds had the highest level which was named phenological Factor. Factor analysis results are given in table 5.

Duncan ranking results of the varieties were used which are shown in Table 6. The result of average comparison indicated that Licord has the most desirability that other numbers according to the studied traits while Opera has the lowest one. Licord has the highest amount of seed functionality (760) and Opera has the lowest rate (246). Regarding to the trait of days to 50% flowering Okapi (166.6) has the most desirable varieties and SLM 046 (138.3) has the lowest rate. Also in terms of plant height opera has the most desirable varieties (139.4) and Okapi has the least desirable (100.4). According to the number of seed pods on the main stem Modena has the most favorable rate (55) and the most undervalued figure is Hyola 401 (26.4). In terms of length and the number of pods and seed yield, Licord has the highest value (respectively 6.83 and 20.6) and Modena (5.81) and Sarigol respectively have the lowest value (5.2). Hyola 401 number of seeds per pod has the highest (32.8) and Sarigol has the lowest rate (14.4). In terms of harvest index the highest and lowest rate respectively were related to Modena and Opera. The seed weight, the two varieties have ESLR & J (respectively, 0.23 and 0.24) had the lowest value relative to other varieties. In terms of the weight of a hundred seeds, RGS 003 and SLM 046 (respectively, 0.23 and 0.24) had the lowest value in comparison to other varieties. In terms of the number of pods per lateral branches and the number of the main pods, Licord has the highest rate (respectively 267.7 and 5.66) and in terms of number of pods per lateral branches and the number of main pods the lowest rate respectively is restricted to Opera (79.6) and Modena (2.66).

Table2- Analysis of variance for traits in Brassica napus.

S.O.V	df	Seed yield in square meter	Number of days to the 50% of flowering	Plant height	Number of pods on main stem	Length of the pods	Seed yield per plant	Number of seed in pod	Harvest index	Weight of 100 seeds	Number of pods on lateral branch	Number of lateral branches
Block	2	41147.82^{ns}	226.53^{ns}	6.92^{ns}	485.02^{ns}	0.3^{ns}	37.69^{ns}	85.29^{ns}	0.11^{ns}	0.005^{ns}	2299.23^{ns}	0.72^{ns}
Genotype	9	105079.87^{*}	227.78^{*}	399.42^{*}	314.38^{*}	0.5^{*}	84.37^{**}	116.06^{**}	0.19^{*}	0.16^{**}	11077^{**}	2.33^{**}
Error	18	35600.12	73.01	140.74	106.57	0.16	18.05	14.28	0.09	0.004	2481.9	0.63
C.V		28.56	5.79	9.9	25.68	6.32	24.17	14.55	29.2	17.28	30.76	20.85

*ns * and **: Non significant, significant at 5% and 1% levels, respectively.*

Table 3 - Stepwise regression analysis of traits in Brassica napus

Traits	Partial R Square	Model R Square	C(P)	Prob
Seed Yield Per Plant	0.73	0.73	21.3	<0.0003
Harvest Index	0.09	0.82	6.4	0.0006
Number of Pods on Lateral Branches	0.03	0.85	3.08	0.02

Table 4: Correlation coefficients between analysis traits in Brassica napus.

	X1	X2	X3	X4	X5	X6	X7	X8	X9	X10
Y: Seed yield in square meter	-0.01^{ns}	-0.06^{ns}	0.2^{ns}	0.09^{ns}	0.85^{**}	0.15^{ns}	0.65^{**}	-0.08^{ns}	0.47^{**}	0.14^{ns}
X1: Number of days to the 50% of flowering	1	-0.36^{ns}	0.49^{**}	-0.06^{ns}	-0.01^{ns}	-0.13^{ns}	-0.1^{ns}	0.02^{ns}	0.1^{ns}	0.31^{*}
X2:Plant height		1	0.28^{ns}	0.34^{*}	0.05^{ns}	-0.01^{ns}	-0.21^{ns}	0.24^{ns}	-0.02^{ns}	0.03^{ns}
X3:Number of pods on main stem			1	-0.28^{ns}	-0.09^{ns}	-0.22^{ns}	-0.001^{ns}	-0.35^{*}	0.44^{**}	0.28^{ns}
X4:Length of the pods				1	0.14^{ns}	0.34^{**}	-0.27^{ns}	-0.1^{ns}	0.14^{ns}	0.35^{*}
X5:Seed yield per plant					1	0.21^{ns}	0.43^{**}	0.02^{ns}	0.36^{*}	0.14^{ns}
X6:Number of seed in pod						1	-0.11^{ns}	0.27^{ns}	-0.02^{ns}	0.04^{ns}
X7:Harvest index							1	0.01^{ns}	0.14^{ns}	0.18^{ns}
X8:Weight of 100 seeds								1	-0.42^{**}	-0.28^{ns}
X9:Number of pods on lateral branch									1	0.6^{**}
X10:Number of lateral branches										1

ns, * and **: Non significant, significant at 5% and 1% levels, respectively.

Table 5- Factor analysis for traits in Brassica napus.

Traits	Factor 1	Factor 2	Factor 3	Factor 4	Factor 5
Seed yield in square meter	0.46	0.37	-0.1	-0.004	0.09
Number of days to 50% of flowering	0.18	-0.42	-0.1	0.01	0.64
Plant height	-0.14	0.25	0.36	0.49	-0.01
Number of pods on main stem	0.33	-0.39	-0.14	0.039	0.01
Length of the pods	0.06	0.11	0.58	0.025	0.18
Seed yield per plant	0.4	0.39	-0.01	0.03	0.26
Number of seed pod	0.02	0.21	0.33	-0.65	0.21
Harvest index	0.25	0.34	0.41	-0.031	0.13
Weight of 100 seeds	-0.25	0.22	-0.18	-0.46	0.52
Number of pods on lateral branch	0.46	-0.11	0.13	0.26	-0.34
Number of lateral branches	0.32	-0.24	0.37	0.89	0.06

Table 6- Comparision of treatments mean (Brassica napus varieties) by Duncan method

Genotype	Seed yield in square meter	Number days to the 50% of flowering	Plant height	Number of pods on main stem	Length of the pods	Seed yield per plant	Number of seed in pod	Harvest index	Weight of 100 seeds	Number of pods on lateral branch	Number of lateral1 branches
					Traits						
Modena	2.66C	193.8ABC	0.38A	0.91A	16 C	13.9AB	5.81B	55 A	118.9ABC	145.6BC	668 A
Okapi	3.44BC	86.3D	0.38A	0.88A	27 AB	14.1AB	5.88B	44.6ABCD	100.4C	166.6A	546 ABC
Hayola401	3.66BC	106.5CD	0.4A	0.24B	32.8A	7.06BC	6.66A	26.4D	113.6BC	143 BC	299 BC
Licord	5.66A	267.7A	0.37A	0.67AB	27.4AB	20.6A	6.83A	48.5ABC	122.06AB	152.3ABC	760 A
Opera	3.44BC	79.6D	0.45A	0.22B	25.6AB	8.5BC	8.86A	29.1CD	139.4A	145.6BC	207 C
Zarfam	3.66BC	147.3BCD	0.46A	0.71AB	25.6B	13.7AB	6.26AB	31.5BCD	130.3AB	142.3BC	535 ABC
RGS003	3.77BC	183.5ABC	0.23B	0.68AB	32.6A	8 BC	6.44AB	50.5AB	109.8BC	143 BC	449 ABC
SLM 046	4.2BC	190.2ABC	0.24B	0.67AB	26.13AB	12.73ABC	6.7A	35.4ABCD	125.2AB	138.3C	528 ABC
Sarigol	4.7AB	221.7AB	0.4A	0.37AB	14.4C	5.2C	6.39AB	48 ABC	109.5BC	157.3AB	246 C
Hayola308	2.8C	142 BCD	0.42A	0.8AB	13.9AB	20.3A	7.04A	32.6BCD	123.9AB	141.3BC	652 AB

4. CONCLUSİON

In the variance analysis, all of the studied traits found meaningful existences and it was figured out that there was a significant correlation between them. In stepwise regression analysis, three traits entered the model. In factor analysis, the first five ones covered 83% of variance and in terms of factor matrix they had more effects in comparison to other traits. Comparison analysis also suggested that Licord was the most valuable element while Opera was the least one.

REFERENCES

[1]. Agrama, H.A.S., 1996. Sequential path analysis of grain yield and its components in maize. Plant breeding. 115: 343 – 346
[2]. Azizi, F.,A.M. Rezaie. A.M. Mir mohammadi Meibodi. 2001 Evaluation of genetic and phenotypic variation and factor analysis on morphological traits in bean genotypes. Jurnal of science and technology in agriculture and natural sciense. Vol 5.3: 127 – 140
[3]. Cardoza, V., Stewart,C.N., 2003. Increased Agrobacterium – mediated transformation and rooting efficiencies in canola (*Brassica napus L.*) from hypocotyls segment explant. Plant cell Rep. 21: 599 – 604
[4]. Fraser, J.and G.W. Eaton. 1983. Apllication of yield component analysis to crop research field crop Abst. 36: 787 – 797
[5]. Gauch, H.G. 1982. Multivariate analysis in community ecology. 1st ed. Cambridge Univ. press London and New York.
[6]. Ghadami,N.2011.Planting and breeding of Canola (Planting , Harvest), education and cultivation Press.
[7]. Harman, H.H., 1976. Modern factor analysis. 3nded university of Chicago.376pp
[8]. Johnson, R.A. and Wichern, D.W. 1988. Applied multivariate statistical analysis. Prentice Hall U.S.A 33: 65 – 71
[9]. Moghaddam, M, Mohammadi, S. A, and Aghaee Sarbarze,M. 2010. Intoduction of multivariety Statistical method (Maneli Compilaton). Parivar Press. Tabriz.
[10]. Mohammadi,S.A.,P rasanna,B.M., 2003. Analysis of genetic diversity in crop plants salient statistical tool and considerations. Crop sic. 43: 1235 – 1248
[11]. Perkins,J.M. 1971. The principal component analysis of genotype – environment interaction and physical measure of the environment.
[12]. Roy , D. 2000. Plant breeding analysis and exploition of variation, Alpha science Internation Ltd.u.k
[13]. Shirani Rad,A.M, Dehshiri ,E. 2003. Canola guide (Planting , Harvest). Karaj. Planting education Press.
[14]. Tollenaar , M. 1991. Physiological basis of genetic improvement of maize hybrids is Ontario from 1959 to 1988 crop sci. 31: 119-124
[15]. Zeinali nezhad. Kh.A.,F. Mirlouhi., Gh. Nematzadeh., A.M.Rezaei. 2003. Genetic variation of some inheritance pools of Iranian rice based on morphological traits. Journal of sciense and technology in agriculture and natural sciense. Vol 4: 199 - 213

Environmental Impact Of A Phase Change Material Wall Covered With Novel Triple Glass

Yusuf Ali Kara[1], Aslıhan Kurnuc Seyhan[2]

Abstract

Solar thermal energy can be effectively stored in walls of a building by incorporating phase change materials (PCMs) within them. Plasterboards containing PCM can be used to absorb and store solar heat gains during daytime and release stored heat during nighttime. A wall fitted with plasterboards containing PCM is usually called a PCM wall. In this study, south facade of a test room was constructed using PCM walls covered with novel triple glass for heating the test room by means of solar thermal energy. Solar heat gains and environmental impact of the PCM wall were evaluated. The PCM wall reduced CO_2 emission from the test room. The reduction in CO_2 on a monthly basis varied in the range of 70% to %4 from October to March, and was 14% on an annual basis.

Keywords: *Phase change material (PCM); Greenhouse emissions; PCM wall*

1. INTRODUCTION

The amount of energy consumed in buildings is approximately 30–35% of the total energy consumption in Turkey, and a large portion of the energy consumed in buildings is used to meet the heating needs of the occupants. Therefore, considerable amounts of greenhouse gases are produced by district heating systems, causing both global warming and air pollution. Solar energy as a clean and renewable energy source can be used in buildings to reduce the emission released from building heating systems. Solar energy storage for heating and cooling of buildings requires an efficient thermal energy storage system. Latent heat storage in phase change materials (PCMs) is an efficient way to store energy because of its high energy storage density over a fairly narrow temperature range. Solar energy can be directly captured and stored in the building envelope by incorporating PCMs in a building's wall, ceiling, floor and window etc.

In this study, south facade of a test room in Erzurum, Turkey, was constructed using PCM walls consisted of brick wall, plasterboards including PCMs, and novel triple glass (NTG) for heating the test room with solar thermal energy. The outer surface of the brick walls were fitted with the plasterboards enhanced with encapsulated PCMs and covered with NTG. The plasterboards included Rubitherm® GR41 and GR35 as the PCM. The NTG was placed in front of the PCM walls to prevent overheating in the summer. The tests were conducted in outdoor conditions continuously for a one-year period in order to observe the performance of the PCM walls during both heating and cooling periods. In this paper, solar energy gain (SEG) provided by the PCM walls and the reduction in CO_2 emission as a result of using the PCM walls were calculated for the test room in the heating period, based on experimental data.

---

[1] Corresponding author: Department of Mechanical Engineering, Faculty of Engineering, Bursa Technical University, Bursa, Turkey, yusufali.kara@btu.edu.tr

[2] Department of Mechanical Engineering, Faculty of Engineering, Erzincan University, Erzincan, Turkey, akurnuc@erzincan.edu.tr

ICENS

III INTERNATIONAL CONFERENCE ON
ENGINEERING AND NATURAL SCIENCE
3 - 7 May 2017 BUDAPEST

NOMENCLATURE

Symbols			Subscripts	
E	Energy (J)		b	Boiler
$\dot{m}$	Mass flow rate (kg/s)		f	Fuel
a	Molar air-fuel ratio		g	Gain
C	Carbon		hl	Heat load
CO_2	Carbon dioxide		m	Monthly, Mean
H	Hydrogen		s	Stoichiometric
LHV	Lower heating value (kJ/N·m^3)		**Abbreviations**	
M	Molecular weight (kg/kmol)		NTG	Novel triple glass
m	Mass (kg)		PCM	Phase change material
n	Mole number		SEG	Solar energy gain
O	Oxygen		ST	Solar transmittance
Greek symbols				
ρ	Density (kg/m^3)			
ϕ	Fuel-air equivalence ratio			
η	Efficiency			

2. MATERİAL AND METHODS

2.1. Experimental work

The cross sections of the PCM walls consisted of insulation, brick, PCM plasterboards, an air gap, and novel triple glass (NTG). The middle layer of the glass in the NTG was the Prismasolar® glass [1] that transmits solar rays that have a lower angle of incidence and reflects solar rays that have a higher angle of incidence (Fig. 1). The incident angle of solar rays is lower in the winter and higher in the summer; therefore the majority of the sunlight incident on the NTG is transmitted in winter and reflected in summer by the Prismasolar® glass. Thus, the amount of thermal energy stored in the PCM plasters was lower in the summer and higher in the winter.

The heat load of a building can be defined as the energy requirement for maintaining the indoor air at a specific comfortable temperature, which is typically 20 °C. In order to determine the heat load of the test room, the test room was equipped with electrical heaters keeping the indoor air at comfortable temperature. The electrical heaters were considered a primary heating system, while the PCM walls were considered a secondary or assistant heating system for the test room.

During the experimentation period, the following parameters were measured and recorded with a data acquisition system: solar radiation before and after the NTG, the inner and outer surface temperatures of the NTG, the surface temperature of the PCM plasterboards, the air temperatures at the inlet and outlet of the gap, the indoor air temperature, the outdoor air temperature, the velocity of the circulation air, and the electric consumption of the heater. The recorded data were analyzed to determine the incident and the transmitted solar radiation, the SEG provided by the PCM walls, the heat load of the test room, and CO_2 emission from the test room. Further information about the description of the test room, the instrumentation, the energy evaluation, and the annual performance of the PCM walls can be found in the Refs. [2,3].

2.2. CO_2 Calculations

At low temperatures (T<1000 K), the overall combustion reaction for any equivalence ratio can be written [4]

$$C_\alpha H_\beta O_\gamma N_\delta + \frac{a_s}{\phi}\left(O_2 + 3.76 N_2\right) \rightarrow$$
$$n_1 CO_2 + n_2 H_2 O + n_3 N_2 + n_4 O_2 + n_5 CO + n_6 H_2 \tag{1}$$
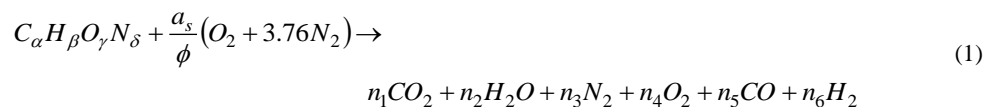
where n on the right-hand side of equation (1) denotes the mole number. This equation assumes that the combustion is complete and the disassociation of molecules is negligible at low temperatures (T<1000 K).

The combustion in the boilers of district heating systems usually occurs with an equivalence ratio less than unity $(\phi < 1)$ and at low temperatures (T<1000 K) because of the water-cooled combustion chamber.
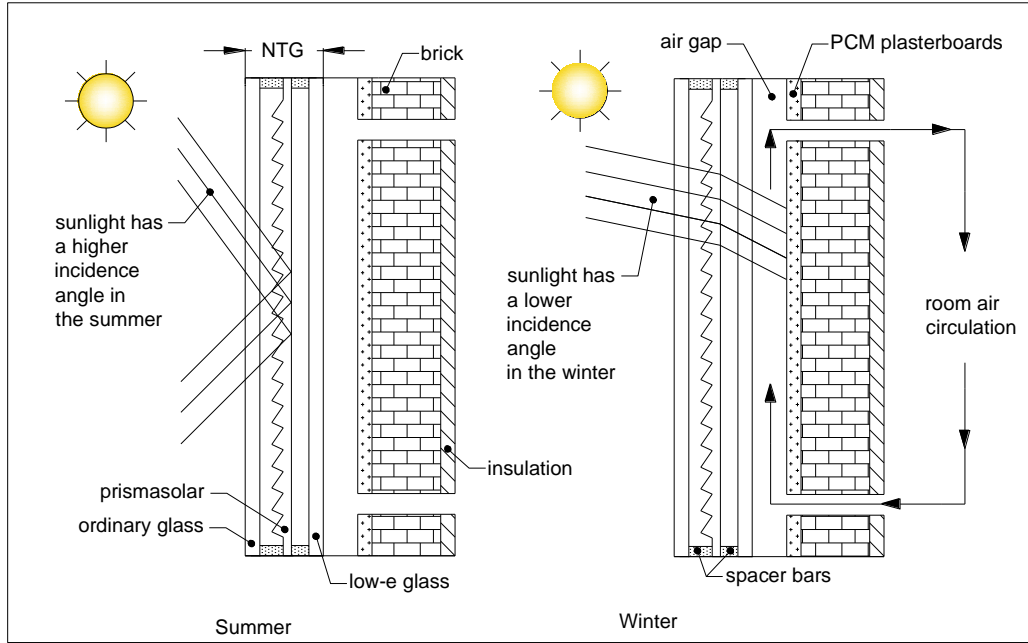
Figure 1. The working principle of the novel triple glass.

Therefore, it can be assumed that no CO and H_2 are produced for lean combustion ($\phi < 1$) at low temperatures, i.e. $n_5 = n_6 = 0$. In this case, the atom balance equations are sufficient to determine the product composition. The mole numbers of the products for $\phi < 1$ as follows:

$$n_1 = \alpha \tag{2}$$

$$n_2 = \frac{\beta}{2} \tag{3}$$

$$n_3 = \frac{\delta}{2} + 3.76\frac{a_s}{\phi} \tag{4}$$

$$n_4 = a_s\left(\frac{1}{\phi} - 1\right) \tag{5}$$

where a_s is the stoichiometric coefficient of air and is written

$$a_s = \alpha + \frac{\beta}{4} - \frac{\gamma}{2} \tag{6}$$

The mass of CO_2 (kg) emitted from the test room is written as follows:

$$m_{CO_2} = \frac{44(\rho_f)(n_1)(E_{hl,m} - \sum E_{g,m})}{(M_f)(\eta_b)(LHV)} \tag{7}$$

where ρ_f, M_f, and *LHV* are the density, molecular weight and lower heating value of the fuel, respectively, and η_b is the efficiency of the boiler. $E_{hl,m}$ is the heat load of the test room, and $\Sigma E_{g,m}$ is the total solar energy gained from the PCM walls.

3. RESULTS AND DISCUSSION

Natural gas was considered as the fuel for the CO_2 analysis. The chemical composition of the fuel on a volumetric basis was assumed to be 93% CH_4, 3% C_2H_6, 1.3% C_3H_8, 0.6% C_4H_{10}, 1% CO_2, and 1.1% N_2. α, β, γ and δ in equation (1) and the physical properties of the fuel such as the LHV and the density were calculated by assuming the fuel was an ideal gas mixture. The chemical formula of the fuel was determined to be $C_{1.063}H_{4.064}O_{0.02}N_{0.022}$. The lower heating value (LHV), the density $\left(\rho_f\right)$ and the molecular weight $\left(M_f\right)$ of the fuel were calculated as 34485 kJ/Nm³, 0.79 kg/Nm³ and 17,448 kg/kmol, respectively. The efficiency of the natural gas boiler was typically assumed to be 0.93.

The energy calculations were performed and the main energy balance of the test room is briefly shown in Fig. 2. Further information on energy analysis can be found in Refs. [2-3]. "Heat load of the test room" in Fig. 2 is energy requirement of the test room per month to maintain a comfortable indoor air temperature, "Total solar energy gain from PCM walls" is the total SEG provided by both of the PCM walls per month, and "Total solar energy incident on NTGs" is the total solar energy incident on the NTGs per month. The total SEG decreased in March and was zero in April and May because the solar transmittance (ST) decreased dramatically after March 21st [2].

The energy values given in Fig. 2 were used to calculate the CO_2 emissions (Fig. 3). Inserting the values of the "Heat load of the test room" and the "Total solar energy gain from PCM walls" (Fig. 2) into Eq. 7, the CO_2 emission labeled "with solar energy gain" in Fig. 3 was calculated. The emissions of CO_2 labeled as "with incident solar energy" and "without solar energy gain" in Fig. 3 were calculated by equating the $\Sigma E_{g,m}$ in Eq. 7 to the "Total solar energy incident on NTGs" and to zero, respectively. The CO_2 bars labeled "with incident solar energy" in Fig. 3 show the theoretical lower limit for the amount of CO_2 emitted from the test room, which was calculated for the theoretical case in which all of the solar energy incident on the NTGs was gained. The bars labeled "without solar energy gain" in Fig. 3 show the CO_2 emissions for the case in which no PCM walls were used at the south facade of the test room.

The reduction in CO_2 (Fig. 4) was calculated by subtracting the mass of CO_2 given by the "with solar energy gain" bars from the mass of CO_2 given by the "without solar energy gain" bars in Fig. 2. Considering the bars labeled "Based on solar energy gain" in Fig. 4, the PCM wall reduced the CO_2 emission by approximately 70% in October 2008, 41% in November 2008, 14% in December 2008, 9% in January 2009, 11% in February 2009, and 4% in March 2009. There was no reduction in April 2009 and May 2009 because there was no solar energy gain in those months, as shown in Fig. 2. The reduction of CO_2 on an annual basis was calculated as 14%. The bars labeled "Theoretical potential" in Fig. 4 show the CO_2 reduction for the theoretical case in which the total amount of solar energy incident on the NTGs was converted to solar energy gain. Because the overall conversion efficiency cannot be 100%, the bars labeled "Theoretical potential" only demonstrate the theoretical limit for CO_2 reduction. There would have been no CO_2 emissions in the months of October and November 2008 and April and May 2009 if the overall efficiency of the PCM wall had been 100%; the CO_2 reduction would have been over 40% for the remaining months.

4. CONCLUSION

A test room with PCM walls was built to determine the energy gain and the environmental impact of the PCM walls. The PCM walls are made of brick walls, plasterboards containing PCMs and novel triple glass. The thermal energy balance of the test room was determined to calculate the reduction in CO_2 emission due to the PCM walls.

Solar energy gains and CO_2 calculations based on the experimental data collected during the period from October 2008 to October 2009 indicated that the PCM walls reduced the CO_2 emission from the test room by 70% in October 2008, 41% in November 2008, 14% in December 2008, 9% in January 2009, 11% in February 2009, and 4% in March 2009. The average reduction in CO_2 was 14% on an annual basis.
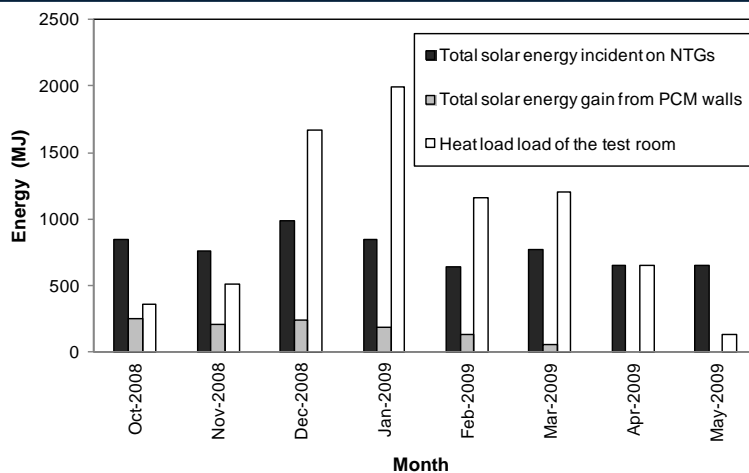
Figure 2. *The experimentally evaluated energy balance of the test room.*
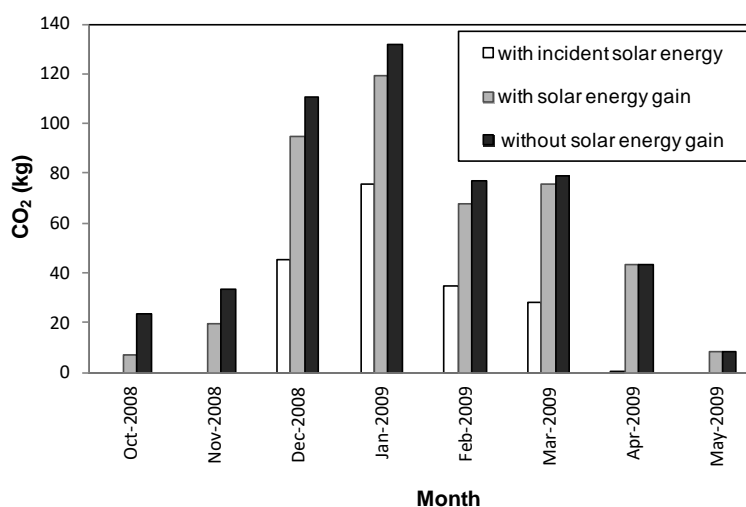
Figure 3. *The CO_2 emissions in (kg) emitted from the test room.*
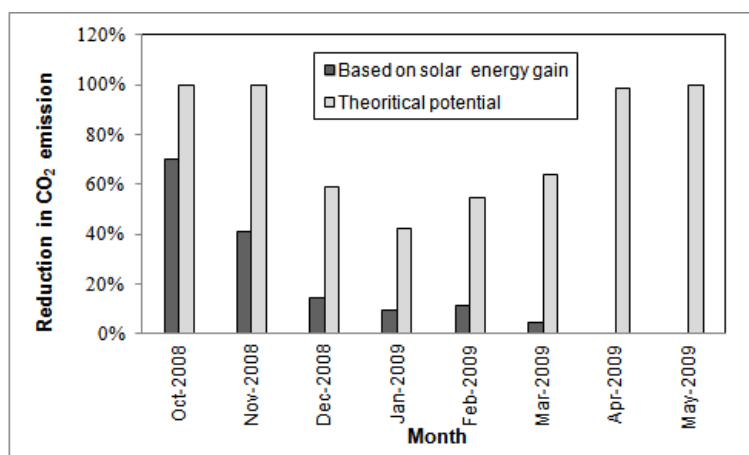
Figure 4. *The reduction in the CO_2 emitted from the test room.*

ACKNOWLEDGEMENT

REFERENCES

[1]   Regal Co., 2010 www.regal.com.tr.
[2]   Kara, YA, Kurnuc A. Performance of coupled novel triple glass and pcm wall in   the heating season: an experimental study. Solar Energy. 86: 2432–2442.
[3]   Kara, YA, Kurnuc A. Performance of Coupled Novel Triple Glazing Unit and PCM Wall. Applied Thermal Engineering. 2012;35:243-246.
[4]   Ferguson CR., Kirkpatrick AT. Internal combustion engines. Second ed. John Wiley.

Environmental Impact of Car Combustion Emissions in Braila, Romania

Mihaela Picu[1], Laurentiu Picu[1]

Abstract

Problem This paper analyses the variation of some parameters specific to air pollution due to road traffic in Braila, Romania.

Objective In this paper were made a complete analysis of some pollutants factors due to traffic, by filling in the data presented by the automatic stations which monitor the air quality with data obtained from air analysis in several major junctions in the city, directly at ground level, using portable equipment; in this way was revealed the importance of direct measurements at street level, where people or other traffic partners are moving, thus influencing directly the quality of life.

Research methods The concentrations variations of SO2, NO2, CO, and PM10 were studied. Measurements were made on 16h/day, 5day/week, between July 2015–July 2016. A complete analysis of pollutants due to traffic, by filling in the data presented by the automatic stations which monitor the air quality (at H1=17.5m) with data obtained from air analysis in several major junctions, directly at ground level (at H2=0m), using portable equipment.

Results and Conclusions From measurements it was observed a constant and high enough exceedance of legal limits for these parameters, for the major crossroads of the city, at ground level. It has been found that the legal concentration has been exceeded. The average values of the pollutants concentrations are: a) for H1, cmax is lower than the value "good" of specific index and b) for H2, cmax is higher than the value "good" of specific index (SO2: with 66,64%; NO2: with 110.04%; PM10: with 230.85%; CO: with 82.14%). This leads to the conclusion that each local administration should take measures to reduce traffic in those crowded areas.

Keywords: *Air Pollution, Road Traffic, Pollutants Concentration.*

1. INTRODUCTION

Braila is the 10th most populous city in Romania, with over 205,000 inhabitants and is the only amphitheatrically city in the world continuously inhabited for over 5000 years. Braila is 2 km away from a protected area (Balta Mica of Braila Natural Park) and 40 km away from a World Heritage Site: Danube Delta (Figure 1).

In Braila are around 70,000 vehicles, most of which are more than 10 years old to which we add trucks, minibuses and buses – these being also more than 10 years old. Because of this and because in Romania people do not ride the bike or use to its full capacity the public transport the cities are heavily polluted due to traffic. For these reasons, continuous supervision is required by monitoring specific parameters of air pollution caused by traffic in Braila ([1], [2]).

2. SPECIFIC OBJECTIVES

In this paper were made a complete analysis of some pollutants factors due to traffic, by filling in the data presented by the automatic stations which monitor the air quality with data obtained from air analysis in several major junctions in the city, directly at ground level, using portable equipment; in this way was revealed the importance of direct measurements at street level, where people or other traffic partners are moving, thus influencing directly the quality of life ([3], [4]).

---

[1] *"Dunarea de Jos" Unviersity, Galati, Romania, mihaelapicu@yahoo.com*

Figure 1. 1. The Balta Mică a Brăilei Natural Park is a protected area (natural park category V IUCN); 2. Danube Delta is World Heritage Site, UNESCO Biosphere Reserve. Danube Delta site is protected by the The Ramsar Convention on Wetlands (Id Ramsar: 521) as a wetland of international importance. http://whc.unesco.org/en/list/588
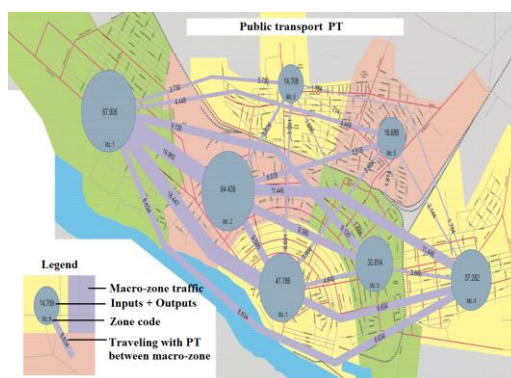
Figure 2. Braila: Public transport

3. MATERIALS AND METHODS

Figure 3. Macro-zone 4
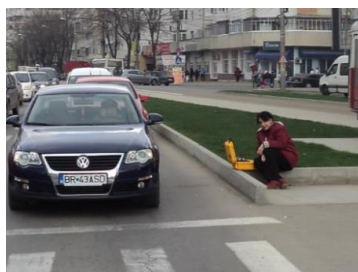
Figure 4. Car stopped at traffic light

These stations are equipped with automatic analysers that monitor air quality on-line and with these measured values the hourly and daily average are then calculated. These average values are transmitted every hour from the stations to the EPA servers (Environmental Protection Agency) in Braila and Bucharest ([5], [6]).

We analysed the changes in concentrations in the atmosphere for SO_2 [μg/m³], NO_2 [μg/m³], CO [mg/m³], and PM10 [μg/m³]. To study how these types of pollutants are affecting the quality of air, the variation of their concentrations was monitored over a period of 1 year.

Also, data on these pollutants were collected at ground level in the major junctions in Braila. These data are important because the pollutant emissions due to road traffic are released at street level, where the people and the other traffic partners are moving, thus directly affecting the quality of life ([7], [8]).

4. RESULTS AND DISCUSSION

Climatic parameters taken into consideration when studying the variation of the mentioned concentrations are: wind speed, temperature, humidity, pressure, solar radiation, noise ([9], [10]). Next we will exemplify just a few of the determinations:

4.1. Variation Of Average So_2 And No_2 Concentration During April 2016

By processing the gathered data it was obtained a polynomial dependence of the SO_2 on time (the error is within the allowable range). From this it appears that on April 11, 2016, the amount of SO_2 reached its peak of 79.2 μg/m³ air. The average value of SO_2 concentrations in April 2016 was 69.17μg/m³ air (Figure 5). By processing the gathered data it was obtained a polynomial dependence of the NO_2 on time (Figure 5). This shows that the NO_2 concentrations values did not remained constant having quite large variations. The average value of NO_2 concentrations in April 2012 was 50.81 μg/m³ air and the maximum was reached in April 5, 2016 - 56.31 μg/m³ air.
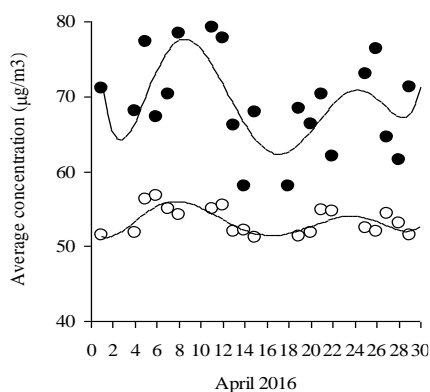
Figure 5. Variation of average pollutants concentration during April 2016 - (●) SO_2; (o) NO_2
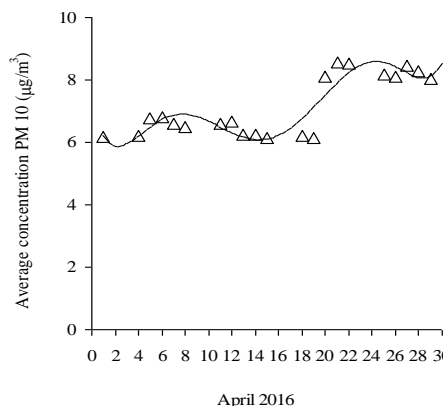
Figure 6. Variation of average PM 10 concentration during April 2016
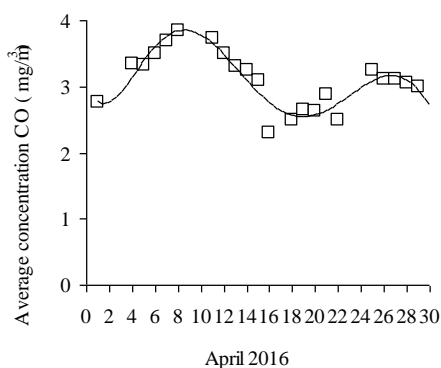
Figure 7. Variation of average CO concentration during April 2016

Table 1. The specific index corresponding polluant(according to Romanian laws)

SO2 (μg/m³)	NO2 (μg/m³)	PM 10 (μg/m³)	CO (mg/m³)	Specific index
0-49.(9)	0-49.(9)	0-9.(9)	0-2.(9)	excelent
50-74.(9)	50-99.(9)	10-19.(9)	3-4.(9)	very
75-124.(9)	100-139.(9)	20-29.(9)	5-6.(9)	good
125-349.(9)	140-199.(9)	30-49.(9)	7-9.(9)	medium
350-499.(9)	200-399.(9)	50-99.(9)	10-14.(9)	bad
>500	>400	>100	>15	very
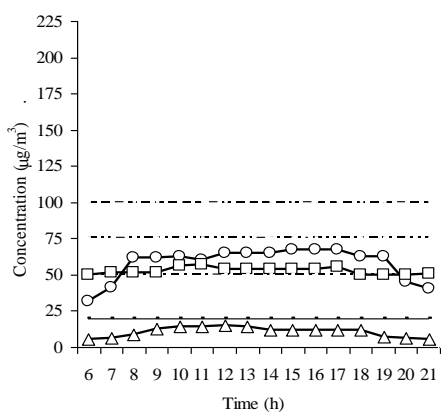
Figure 8. Variation of pollutants concentrations at H1 = 17.5 m

(━o━) SO2; (━□━) NO2; (━Δ━) PM10;

(━ ━) NO2 good=100μg/m3; (━ ⋯ ━) SO2 good=75μg/m3;

(━ ⋅ ━) SO2 very good=50μg/m3; (━▪━▪) PM10 good=20μg/m3

c (μg/m³)	min	max	average
SO₂	31.45 at 6⁰⁰	67.55 at 15⁰⁰	57.9538 "very good"
NO₂	50.01 at 6⁰⁰	55.40 at 17⁰⁰	52.7911 "very good"
PM 10	5.70 at 6⁰⁰	14.70 at 12⁰⁰	10.6650 "very good"
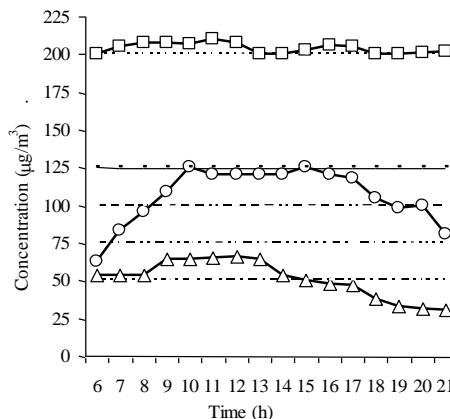
Figure 9. Variation of pollutants concentrations at H2 = 0 m

(━o━) SO2; (━□━) NO2; (━Δ━) PM10;

(⋯⋯⋯) NO2 bad=200μg/m3; (━▪━▪) SO2 medium=125μg/m3;

(━ ⋅ ━) PM10 bad=100μg/m3; (━ ⋯ ━) SO2 good=75μg/m3;

(━ ⋅ ━ ⋅ ━) SO2 very good=50μg/m3

c (μg/m³)	min	max	average
SO₂	62.90 at 6⁰⁰	124.98 at 15⁰⁰	106.45 - "good"
NO₂	200.01 at 6⁰⁰	210.04 at 11⁰⁰	203.939 - "bad"
PM 10	30.70 at 6⁰⁰	66.17 at 12⁰⁰	51.028 - "bad"
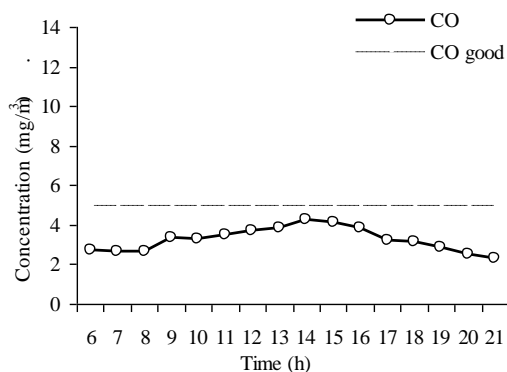
Figure 10. Variation of CO concentrations at H1 = 17.5 m

c (mg/m³)	min	max	average
CO	2.29 at 21⁰⁰	4.25 at 14⁰⁰	2.9113 "excelent"
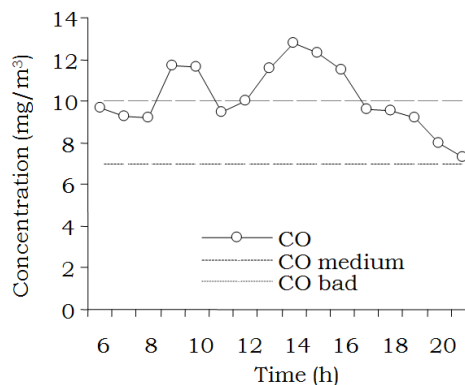
Figure 11. Variation of CO concentrations at H2 = 0 m

c (mg/m³)	min	max	average
CO	7.34 at 21⁰⁰	12.75 at 14⁰⁰	10.1680 "bad"

4.2. Variation Of Average Pm 10 Concentration During April 2016

The same thing I have got for PM (Figure 6). The average value of PM 10 concentrations in April 2012 was 50.81 μg/m³ air and the maximum was reached in April 21, 2016 - 8.55 μg/m³ air.
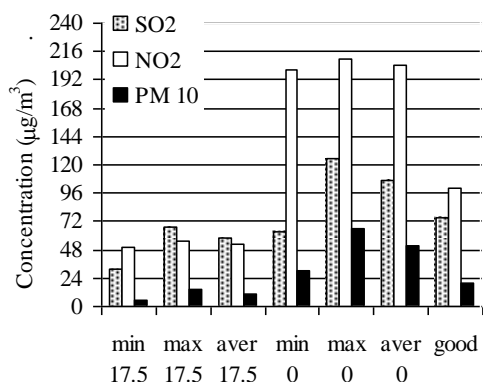
Figure 12 Variation of pollutants concentrations during
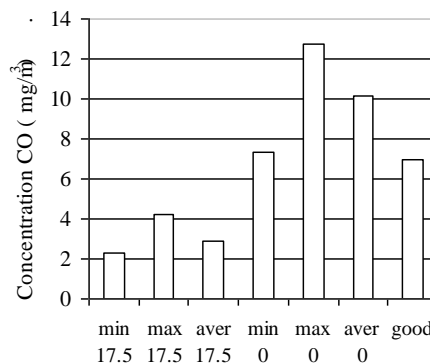
July 2015-July 2016

Figure 13 Variation of CO concentrations during

July 2015-July 2016

		min	max	average
H₁=17.5m	SO₂	31.45	67.55	57.9538 "very good"
	NO₂	50.01	55.40	52.7911 "very good"
	PM 10	5.70	14.70	10.6650 "very good"
H₂=0 m	SO₂	62.90	124.98	106.45 - "good"
	NO₂	200.01	210.04	203.939 - "bad"
	PM 10	30.70	66.17	51.028 - "bad"

		min	max	average
H₁ = 17.5m	CO	2.29	4.25	2.9113 - "excelent"
H₂ = 0 m	CO	7.34	12.75	10.1680 - "bad "

4.3. Variation Of Average Co Concentration During April 2016

In the same manner and for the same time we analyzed the concentration of CO; in Figure 7 is shown the variation of average CO concentration during April 2016. The average value of CO concentrations in April 2012 was 3.25 mg/m³ air and the maximum was reached in April 8, 2016 - 3.85 mg/m³ air.

4.4. The differences between the determinations achieved at 17.5 m and those made from 0m

Figures 8 and 10 show average values for pollutants analyzed on July 11, 2016. It finds that the readings at monitoring stations (at H_1 = 17.5 m) are assigned at specific index "very good" and "excellent" (Table 1).

Figures 9 and 11 show the average values for pollutants analyzed in the same day. It finds that the readings at ground level (H_2 = 0m), even in large intersections of the city, are included in the index specific "good" and "bad".

5. CONCLUSIONS

From measurements made over a period of 1 year in high traffic areas it was observed a constant and high enough exceedance of legal limits for the parameters that characterize air quality, for the major crossroads of the city, at ground level. During July 2015-July 2016, the average values of the concentrations are the following (Figure 12 and 13):

- for H_1=17.5 m, c_{max} is lower than the value "good" of specific index (SO_2: with 9.933%; NO_2: with 44.6%; PM10: with 26.5%; CO: with 39.28%).

- for H_2=0 m, c_{max} is higher than the value "good" of specific index (SO_2: with 66.64%; NO_2: with 110.04%; PM10: with 230.85%; CO: with 82.14%).

It is obvious that this topic is always of most acute importance. It undergoes changes from day to day and is under continuous surveillance. This leads to the conclusion that each local administration should take measures to reduce traffic in those crowded areas in order to improve the life quality of those living or passing through those areas.

ACKNOWLEDGEMENT

REFERENCES

[1]. N. Pérez, J. Pey, M. Cusack, C. Reche, X. Querol, A. Alastuey, „Variability of Particle Number, Black Carbon, and PM10, PM2.5, and PM1 Levels and Speciation: Influence of Road Traffic Emissions on Urban Air Quality", *Aerosol Science and Technology* , vol. 44, Issue 7, pp. 487-499, 2010.

[2]. G. Invernizzi, A. Ruprecht, R. Mazza, C. de Marco, G. Močnik, C. Sioutas, D. Westerdahl, „Measurement of Black Carbon Concentration as an Indicator of Air Quality Benefits of Traffic Restriction Policies within the Ecopass Zone in Milan, Italy", *Atmospheric Environment*, vol. 45, Issue 21, pp. 3522–3527, July 2011.

[3]. K. Fuks, S. Moebus, S. Hertel, A. Viehmann, M. Nonnemacher, "Long-Term Urban Particulate Air Pollution, Traffic Noise, and Arterial Blood Pressure", *Environmental Health Perspectives*; Research Triangle Park 119.12, pp.1706-11, Dec 2011.

[4]. S. Weichenthal, R. Kulka, A. Dubeau, C. Martin, D. Wang, et al., „Traffic-Related Air Pollution and Acute Changes in Heart Rate Variability and Respiratory Function in Urban Cyclists", *Environmental Health Perspectives*, Research Triangle Park 119.10, (Oct 2011): pp. 1373-1378.

[5]. *On ambient air quality and cleaner air for Europe,* **Directive 2008/50/EC of the European Parliament and of the Council of 21 May 2008**.

[6]. P. S. Kanaroglou, M. Jerrett, J. Morrison, B. Beckerman, M. A. Arain, N. L. Gilbert, J. R. Brook, „Establishing an air pollution monitoring network for intra-urban population exposure assessment: A location-allocation approach", *Atmospheric* Environment, Volume 39, Issue 13, pp. 2399–2409, April 2005.

[7]. M. Hatzopoulou, E.J. Miller, „Linking an activity-based travel demand model with traffic emission and dispersion models: Transport's contribution to air pollution in Toronto", *Transportation Research* Part D: Transport and Environment, Volume 15, Issue 6, pp. 315–325, August 2010.

[8]. P. Pant, R. M. Harrison, „Estimation of the contribution of road traffic emissions to particulate matter concentrations from field measurements: A review", *Atmospheric Environment*, Volume 77, pp. 78–97, October 2013.

[9]. M. Foraster, A. Deltell, X. Basagaña, M.Medina-Ramón, I. Aguilera, L. Bouso, M. Grau, H. C. Phuleria, M. Rivera, R. Slama, J. Sunyer, J. Targa, N. Künzli, „Local determinants of road traffic noise levels versus determinants of air pollution levels in a Mediterranean city", *Environmental Research*, vol. 111, Issue 1, pp. 177–183, Jan. 2011.

[10]. J. Mori, A. Sæbø, H. M. Hanslin, A. Teani, F. Ferrini, A. Fini, G. Burchi, „Deposition of traffic-related air pollutants on leaves of six evergreen shrub species during a Mediterranean summer season", Urban Forestry & Urban Greening, Volume 14, Issue 2, pp. 264–273, 2015.

Evaluation of Neural Network Based Prediction Techniques for Water Quality Assessment for Smart Cities

Gurkan Tına[1]*, Dogan Savran[2], Mehmet Kabakan[3]

Abstract

Smart cities use information and communication technologies to improve availability, quality, reliability, performance and interactivity of urban services. In addition, smart city technologies help to reduce costs and resource consumption and improve contact between citizens and municipalities/government. There is a great interest towards smart city technologies due to their technological, economic and environmental benefits. Water is essential for life, and on average, each person on Earth needs about 20 litres of clean and safe water a day to meet metabolic, hygienic, and domestic needs. Since the quality of our water is directly linked to the quality of our lives, water quality monitoring which can be defined as the sampling and analysis of water constituents and conditions is an essential process. However, the first step of water quality monitoring is the process of collecting a large number of samples; therefore, it takes time and costs money. Also, obtained results can be difficult to interpret. While developing smart city technologies to improve the quality of life of citizens, at the same time the goal should be to make smart city services and networks more autonomous and more sustainable. Accordingly, in this study, a wireless water quality network-based water quality monitoring system for smart cities is proposed. The proposed system collects water quality parameters at specified time-intervals and transfers them to the server. Then, the server periodically runs an artificial neural network-based estimator to predict groundwater quality. The periodic prediction of groundwater quality enables the authorities to take immediate actions for ensuring water quality. Compared to traditional water quality monitoring systems, the proposed system has the advantage of letting the authorities know the quality of their water resources beforehand. A set of performance evaluation studies presented in this paper proves the efficiency and accuracy of the proposed system.

Keywords: *Smart cities; groundwater quality; prediction; artificial neural network; wireless networking; rapid assessment.*

1. INTRODUCTION

Although it is difficult to precisely describe smart city concept due to the variety of technologies implemented under its label, a smart city can be described as a city where the existing networks and services are made more efficient with the use of information and communication technologies (ICTs) for the benefit of its inhabitants [1-3]. Smart cities rely on the application of a wide range of ICTs to communities and cities and ICTs embedded in government systems, and thereby transform life and working environments within the region [4, 5]. While smart city technologies are implemented to meet the demands of the citizens of the city, community involvement in the process is a must.

Water is a fundamental human need and each person needs at least 20 litres of clean and safe water a day for drinking, cooking, and keeping themselves clean. Polluted and/or contaminated water can be deadly. Although around 70% of the Earth's surface is water covered, almost 95% of it is saline [6]. Hence, preserving the quality of fresh water is highly important. Around 1 billion people have the lack of accessing to proper drinking water supplies and therefore around 1.8 million people die every year of diarrheal diseases. In addition, tens of millions of others are sickened by a host of water-related ailments. On the other hand, the deaths attributed to unsafe water, sanitation and hygiene [7] are easily preventable. In this regard, water quality assessment plays a key role in ensuring the access to safe water.

[1] Corresponding author: Trakya University, Department of Computer Programming, 22020, Edirne, Turkey. gurkantuna@trakya.edu.tr

[2] Trakya University, Department of Mapping and Cadastre, 22020, Edirne, Turkey. dogansavran@trakya.edu.tr

[3] Kabakan Mühendislik, Kesan, Turkey.

Water quality is determined by the assessment of physical, chemical, and biological classes of water quality indicators. For this purpose, all around the world, the authorities develop standards for water quality which set a limit to the highest concentrations of organic and inorganic chemicals, microbial pathogens, and radioactive elements that may affect the safety of drinking water supplied by public water systems [8]. Typical parameters for assessing drinking water quality are pH, Dissolved oxygen (DO), electrical conductivity (EC), nitrate, and turbidity [8, 9]. As stated by the existing directives [8-10], the maximum permissible limit for pH is 6.5-8.5 units, for DO is 5 mg/L, for EC is 2.5 mS/cm, and for nitrate is 10-50 mg/L.

Traditional water quality assessments are performed in two steps: analysis in the field and analysis at the laboratory [10, 11]. The latter allows performing more detailed analysis by means of sophisticated devices and computational approaches. However, this procedure is time-consuming and results in considerable delays. Furthermore, in many countries the water quality of lakes and reservoirs suffers from degradation due to contaminated inflows. This makes it necessary to take immediate decisions in order to provide the basis for an on-time warning of authorities and people. Hence, continuous water quality assessment through real-time monitoring systems is essential to ascertain the sources of pollutants and contaminants in order to take preventive measures [8-12].

In this paper, performance evaluation of different artificial intelligence based estimation techniques for groundwater quality assessment is performed. The data used in the performance evaluation study was periodically collected using portable water quality monitoring nodes with wireless interfaces and sent to the logging server. The nodes are equipped with detachable probes for typical water quality parameters such as pH, EC, DO, calcium, nitrate and temperature.

2. PROPOSED APPROACH AND EXPERIMENTAL SETUP

In the experimental setup realized in a water reservoir directly fed from a water-well, off-the-shelf sensor nodes [13] were used. Every 15 minutes, pH, EC, DO, calcium, nitrate and temperature values were measured and then sent to the logging server. A part of the dataset collected during the field tests is listed in Table 1. Since energy harvesting capability of the nodes was rather limited due to the lack of direct sunlight and even indoor harvesting was unavailable almost all the time [14], we set the measurement interval to 15 minutes to arrange the schedule of periodical visits and appropriate recharging schedules, normally the batteries inside the nodes had lasted at least 22 days; therefore, we recharged the nodes every 20 days, but the measurement interval can be adjusted to 10 minutes or even less in the presence of direct sunlight. The dataset collected by the nodes was the input of the proposed ANN-based water quality prediction approach.

ANNs are basically a group of statistical learning algorithms inspired by biological neural networks which consist of simple processing units with an inherent trend for storing experiential knowledge and making it available for use [15-19]. Beginning with an untrained ANN, a training pattern is presented to the input layer, the signals are passed through the network, and finally the output at the output layer is determined. At the end of the iteration called epoch, the outputs are compared to the desired values and any difference corresponds to an error. In ANNs, error is some scalar function of the connection weights, and because of this, the connection weights are adjusted to reduce the error. The error is at minimum when the network outputs match the target outputs.

In the proposed ANN-based prediction approach, three different techniques are used. The first technique is back propagation (BP) neural network. BP learning uses the gradient descent procedure to train the connection weights was used along with Levenberg-Marquardt algorithm, one of the most important optimization methods [20-23]. In the classical BP algorithm, Eq. (2) is used to estimate the entire error in the output layer for the pth sample pattern, and the error is minimized by means of the weights and biases using gradient descent (3). The structure of the multilayer ANN model developed in MATLAB [14, 25].

$$o_j = f(net_j) = f(x) \text{ then } net_j = \sum_{j}^{i} w_{ji} o_i + \theta_j \tag{1}$$

$$E_p = \frac{1}{2} \sum_{j \in out.} (t_{pj} - o_{pj})^2 \tag{2}$$

$$\left. \begin{array}{l} \delta_{pj} = (t_{pj} - o_{pj}) \\ \Delta_p w_{ji} = -\varepsilon(\dfrac{\partial E_p}{\partial w_{ji}}) \\ \Delta_p \theta_j = -\varepsilon(\dfrac{\partial E_p}{\partial \theta_j}) \end{array} \right\} \tag{3}$$

where i is neuron number, j is layer number, w_{ji} is weight, o_j is neuron output, t_{pj} represents target output, o_{pj} is actual output, δ_{pj} is error value in layer j, net_j is weighted sum, ε is learning rate, and θ_j is bias.

In the proposed ANN-based prediction approach, the second technique used is radial basis function neural network. Radial basis function neural networks which are implement to simplify their training by self-learning algorithm with gradient descent are function proximity models to provide a required input-output [26]. They have a trade-off between training quickness and performance [27]. Eq. (4) is used for radial basis function algorithm.

$$f(x_i) = \sum_{j=1}^{n} w_j \; \emptyset_{ij} (\|x_i - x_j\|) \qquad (4)$$

$$\emptyset_{ij}(r) = exp^{-(\frac{r^2}{2\sigma^2})} \qquad (5)$$

where i is neuron number, j is layer number, $\phi_{ij}(r)$ is activation function, x_i is input data, x_j is the center of Gaussian function, $r = \|x_i - x_j\|$ is Euclidean distance, σ is the radius of activation function.

In the proposed ANN-based prediction approach, the third technique used is the Elman neural network. Elman neural network which is a recursive network was originally proposed and applied by Elman in 1990 to a specific processing problem [28]. Elman neural network is generally preferred for its advantages in providing a required input-output pair [29]. The Elman network contradicts from conventional two-layer network in that the first layer has recurrent connection. Elman networks are two-layer BP networks with including a feedback connection from the output of the hidden layer to its input.

Table 1. Partial dataset of the water quality measurements

No	pH	Temperature	Calcium	Nitrate	Dissolved Oxygen	Electrical Conductivity
1	7,438389	15,9638	23,83103721	5,160355121	2,74544	314,45227
2	7,430459	15,97198	23,83276233	5,160240113	2,70548	284,08081
3	7,471235	15,97796	23,83586756	5,16185023	2,66446	248,17678
4	7,419829	15,97503	23,83678763	5,160815155	2,73864	259,56765
5	7,45001	15,97109	23,83437245	5,16116018	2,73424	254,06808
6	7,460981	15,9739	23,83379741	5,161792726	2,65754	253,35243
7	7,490957	15,97277	23,83402742	5,161217684	2,60835	250,09071
8	7,465527	15,96899	23,83494749	5,160182609	2,66953	250,73939
9	7,451138	15,9652	23,83448746	5,160240113	2,69234	248,59481
10	7,455068	15,97244	23,83483248	5,158457483	2,6881	243,13497
11	7,500151	15,96606	23,83460247	5,1600676	2,6859	229,61462
12	7,480566	15,97039	23,8392028	5,162022742	2,62106	242,40853
13	7,441704	15,9667	23,83540753	5,1600676	2,60887	236,72639
14	7,474858	15,95913	23,83437245	5,160700146	2,66018	231,51327
15	7,46563	15,96231	23,83621258	5,159435054	2,62021	228,46827
16	7,533716	15,96084	23,84173298	5,160642642	2,59661	211,68975
17	7,498408	15,95785	23,8364426	5,160297617	2,58534	219,54275
18	7,475576	15,95507	23,84230803	5,159205038	2,58061	212,98112
19	7,460811	15,95404	23,83690263	5,159780079	2,63496	208,97703
20	7,509551	15,95233	23,83655761	5,159262542	2,64277	208,05442

3. RESULTS AND DISCUSSION

In the training dataset, the goal was to present every group having its own central tendency toward a particular pattern and to represent the range of data to the ANN with noise included and by making it sure that statistical variation is represented adequately. In the performance evaluation study, we used the dataset collected at 120 minutes interval which consists of 207 rows and compared the performance of the three techniques. In this case, for all the techniques, 30 rows were used for testing and of 177 rows were used for training. The proposed system was tested with three different techniques: BP neural network, radial basis function neural network, and the Elman neural network. The predicted and measured values for the output (Nitrate) by BP neural network, radial basis function neural network, and the Elman neural network are shown in Figures. 1, 2 and 3, respectively. The network had 5 inputs, 2 hidden layers (including 15 and 14 neurons, respectively), and 1 output layer in BP neural network.

Figure 1. Result of BP Neural Network for 120 minutes interval
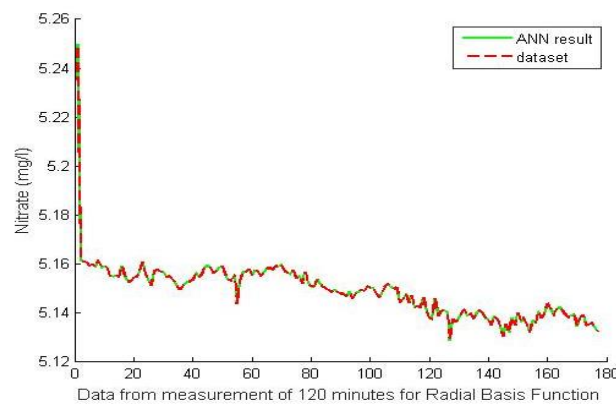
Figure 2. Result of Radial Basis Function Neural Network for 120 minutes interval
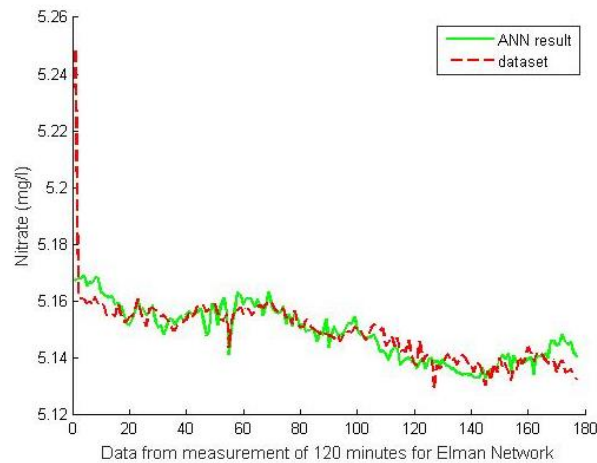
Figure 3. Result of Elman Neural Network for 120 minutes interval

When the performances of the three techniques were taken into consideration, it can be seen that although BP neural network converged more slowly and its training time was relatively long, its estimation performance was good. The Elman neural network completed its training step more quickly than the others but its estimation performance was the worst. However, Radial basis neural network obtained the highest accuracy when the same dataset was employed.

4. CONCLUSION

In smart cities, thanks to the integration of innovative ICTs, better public services are provided for citizens, resources are more efficiently used and impact on the environment is reduced. On the other hand, smart cities offer many other advantages since they involve advanced urban transport networks, safer public spaces, highly interactive and responsive city administration, services for the needs of ageing populations, more efficient ways to light and heat buildings, upgraded water supply, and waste disposal facilities.

Water is vital for human life. It directly or indirectly affects all facets of life. It is necessary to keep people' bodies and the environment healthy and should be valued and protected as the precious resource it is. Therefore, its quality must be periodically analyzed. Although traditional water quality monitoring systems enable the authorities to assess the quality of water resources, they do not enable to perform the estimation of water quality for near future projections.

To address this need, in this paper, a novel water quality assessment system which consists of a wireless groundwater quality monitoring network integrated and an artificial neural network-based estimator was presented. The proposed system provides real-time water quality data and predicts water quality parameters using three different artificial neural network algorithms, and in this way it allows the authorities to take immediate actions for improving groundwater quality. In addition, the proposed system is a valuable tool for smart homes and smart cities. The future work of this study consists of a set of field tests planned to be conducted in a district of Edirne, Turkey, displaying the predictions for water quality parameters in real-time through a web-based interface, and delivering the predictions to the residential customers by e-mail and SMS.

REFERENCES

[1].   A. Monzon, "Smart cities concept and challenges: Bases for the assessment of smartcity projects," in *Proc. 2015 International Conference on Smart Cities and Green ICT Systems (SMARTGREENS)*, 2015, pp. 1-11.

[2].   K. Su, J. Li, and H. Fu, "Smart city and the applications," in *Proc. 2011 International Conference on Electronics, Communications and Control (ICECC)*, 2011, pp. 1028-1031. doi: 10.1109/ICECC.2011.6066743

[3].   M. Angelidou, "Smart cities: A conjuncture of four forces," *Cities*, vol. 47, pp. 95-106, September 2015.

[4].   M. Deakin and H. A. Waer, "From Intelligent to Smart Cities," *Journal of Intelligent Buildings International*, vol. 3, no. 3, 2011. doi: 10.1080/17508975.2011.586671.

[5].   C. E. A. Mulligan and M. Olsson, "Architectural implications of smart city business models: an evolutionary perspective," *IEEE Communications Magazine*, vol. 51, no. 6, pp. 80-85, 2013. doi: 10.1109/MCOM.2013.6525599

[6].   (2016) How much water is there on, in, and above the earth? [Online]. Available at: http://ga.water.usgs.gov/edu/earthhowmuch.html

[7].   (2016) Facts and Figures on Water Quality and Health. [Online]. Available at: http://www.who.int/water sanitation health/facts_figures/en/index.html

[8].   (2016) Groundwater and drinking water, drinking water standards [Online]. Available at: http://www.epa.gov/safewater

[9].   *Directive 2000/60/EC of the European Parliament and of the Council of 23 October 2000 establishing a framework for Community action in the field of water policy, EC*, 2000.

[10]. (2016) National Water Information System: Web Interface. [Online]. Available: http://waterdata.usgs.gov/nwis/qw

[11]. B. Werner, "Automated Surface Monitoring Stations in Hamburg," in *Proc. AquaLife 2006 workshop*, 2006.

[12]. G. Tuna, B. Nefzi, O. Arkoc, and S. M. Potirakis, "Wireless Sensor Network-Based Water Quality Monitoring System," *Key Engineering Materials*, Vol. 605, pp. 47-50, 2014.

[13]. (2016) Libelium World. [Online]. Available at: http://www.libelium.com/libeliumworld/smart-water/

[14]. G. Tuna, V. C. Gungor, and K. Gulez, "Energy harvesting techniques for industrial wireless sensor networks," in *Industrial Wireless Sensor Networks: Applications, Protocols, Standards, and Products*, G. P. Hancke and V. C. Gungor, (Eds.), pp. 119-136, CRC Press, 2013.

[15]. Y. Kılıcaslan, G. Tuna, G. Gezer, K. Gulez, O. Arkoc, and S. M. Potirakis, "ANN-Based Estimation of Groundwater Quality Using a Wireless Water Quality Network," *International Journal of Distributed Sensor Networks*, Vol. 2014 (2014), Article ID 458329. http://dx.doi.org/10.1155/2014/458329

[16]. S. Haykin, *Neural networks and Learning Machines*, 3rd ed., Pearson International Edition, 2009.

[17]. S. Kumar, V. K. Bharti, K. B. Singh, and T. N. Singh, "Quality assessment of potable water in the town of Kolasib, Mizoram (India)," *Environmental Earth Sciences*, vol. 61, no. 1, pp. 115-121, 2010.

[18]. A. K. Verma and T. N. Singh, "Prediction of water quality from simple field parameters," *Environmental Earth Sciences*, vol. 69, no. 3, pp. 821-829, 2013. DOI: 10.1007/s12665-012-1967-6

[19]. B. Khalil, T.B.M.J. Ouardab, and A. St-Hilaire, "Estimation of water quality characteristics at ungauged sites using artificial neural networks and canonical correlation analysis," *Journal of Hydrology*, vol. 405, no.3-4, pp. 277-287, 2011.

[20]. F. Fazayeli, L. Wang, and W. Liu, "Back-Propagation with chaos," in *Proc. IEEE Int. Conference on Neural Networks & Signals Processing*, 2008, pp. 5-8.

[21]. K. Levenberg, "A method for the solution of certain non-linear problems in least squares," *Quarterly of Applied Mathematics*, vol. 2, pp. 164-168, 1944.

[22]. D. Marquardt, "An algorithm for least-squares estimation of nonlinear parameters," *SIAM Journal on Applied Mathematics*, vol. 11, no. 2, pp. 431-441, 1963.

[23]. A. Ranganathan, "The Levenberg-Marquardt Algorithm," Honda Research Institute, USA, 2004.

[24]. Z. Zhao, H. Xin, Y. Ren, and X. Guo, "Application and Comparison of BP Neural Network Algorithm in MATLAB," in *Proc. International Conference on Measuring Technology and Mechatronics Automation*, 2010, pp. 590-594.

[25]. (2016). Neural Network Toolbox—MATLAB. [Online]. Available at: http://www.mathworks.com/products/neural-network/

[26]. C. M. Bishop, *Neural Networks for Pattern Recognition*. Oxford, U.K.: Oxford Univ. Press, 1995

[27]. N. B. Karayiannis, "Gradient descent learning of radial basis neural networks," in *Proc. 1997 IEEE International Conference on Neural Networks*, 1997, vol. 3, pp. 1815-1820.

[28]. J. Elman, "Finding structure in time," *Cognitive Science*, vol. 14, no. 2, pp. 179-211, 1990.

[29]. Z. Liu, X. Wang, and J. Xu, "Prediction Technique for Water-Bloom in Lakes Based on Elman Network," in *Proc. the IEEE International Conference on Automation and Logistics*, 2009.

Route Assessment of Underground Tunnels Using Mobile Robots

Gurkan Tuna[1]*, Dogan Savran[2]

Abstract

Though archaeologists have a great desire to uncover ancient underground tunnels, it is a really tough work since most of those tunnels are narrow, typically measuring only around 60 cm in width, just enough to crawl through. Moreover, most underground ancient tunnels include storage chambers and small rooms in some places. Generally, those underground tunnels are very long, exploring and mapping those tunnels is not practical at all by using traditional approaches. In this paper, we propose a novel approach to assess the route of ancient underground tunnels. The proposed approach is based on the use of autonomous mobile robots and geodesic methods. In the proposed approach, the mobile robots are responsible for exploring and mapping of the route, and the geodesic methods are used to minimize mapping errors. A set of simulation studies is given to show the usability and efficiency of the proposed approach.

Keywords: *Route assessment; underground tunnels; route; surveying; mapping; mobile robots.*

1. INTRODUCTION

Since ancient underground tunnels are typically narrow and collapsed at some points, uncovering them requires great effort and lots of time in addition to a significant budget. Traditional approaches used in ground level are not valid options for underground tunnels. Hence, the use of mobile robots for this task seems a good and safe option. Because those tunnels may be long and it is not easy for a person to move inside them.

In this study, we propose the use of mobile robots to explore and map ancient underground tunnels. In our approach one or more mobile robots are responsible for exploring and mapping of the route of underground tunnels. However, instead of relying only on the mapping accuracy provided the robots, we incorporate GPS measurements into the mapping process and this way we reduce the mapping errors and deviations from the ground truth. We present the details and results of our simulation studies to show the usability and efficiency of the proposed approach.

2. PROPOSED APPROACH AND SIMULATION STUDY

In order for a mobile robot to complete a given task, the robot must be able to identify and control its own location in the environment [1, 2]. Thanks to the probabilistic approaches, a set of range measurements and control inputs enable the robot to calculate its pose [2]. One of the most commonly used probabilistic approaches is to model control inputs and observations of the robot using a Markov Chain. The Markov hypothesis states that past and future situations are conditionally independent of each other if the current state of the mobile robot is known [2]. In this approach, a mobile robot's motion model defines the robot position as a function of the previous exposure and control inputs. The observation model defines the robot's sensor measurements as a function of the robot's position and the cyclic position. The Extended Kalman Filter (EKF) is a way to use Bayesian estimation methods for robot localisation and mapping [2-4]. Mapping and localisation using landmarks found in the environment may rely on active beacons, e.g., radio, GPS and passive, e.g., visual, retro-reflective. The application of the EKF for Simultaneous Localisation and Mapping (SLAM) problem is fast, consistent and reliable under normal circumstances [5]. In the real world, the model used in the SLAM process can be adjusted to reduce and improve failures. In SLAM processes, sensors provide distance, bearing, or distance and bearing. While an exteroceptive sensor such as a Laser Range Finder (LRF) satisfies the requirements of most exploration and SLAM applications, in this study we incorporate measurements obtained using a Global Positioning System (GPS) receiver to reduce errors and

---

[1] *Corresponding author: Trakya University, Department of Computer Programming, 22020, Edirne, Turkey. gurkantuna@trakya.edu.tr*

[2] *Trakya University, Department of Mapping and Cadastre, 22020, Edirne, Turkey. dogansavran@trakya.edu.tr*

deviations from the ground truth. GPS is a satellite-based navigation system which provides users with proper equipment access to positioning information [6]. Sensors used in mobile robots have different characteristics in terms of noise, dimensionality of output, range, and frame of reference. For example, a Light Detection and Ranging (LIDAR) device provides three dimensional (3D) point clouds. But, vision-bearing only devices provide 2D rays in space. In terms of frame of reference, most sensors including LIDAR devices and vision-based sensors are in robot frame. GPS devices rely on earth centered coordinate frame. Finally, accelerometers/gyros are in inertial coordinate frame. In our approach, the robot's pose is simply estimated as follows.

Let $x_r = \begin{bmatrix} x \\ y \\ \theta \end{bmatrix}$ be initial robot pose, $u_{0:t} = \{u_0, u_1, \ldots, u_t\}$ be control inputs, $z_{1:t} = \{z_1, z_2, \ldots, z_t\}$ be observations, m be map features and landmarks, we obtain estimated robot pose shown in Figure 1. m consists of landmark positions parameterized as $\lfloor x \; y \; \theta \rfloor$ 3D locations. Positions of all of the landmarks the robot knows about are fused into the state vector so that both the positions and estimates of the current pose of the robot are stated in a single state vector.
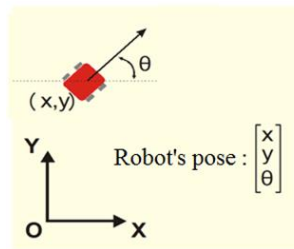
Figure 1. Estimated robot pose

SLAM has been heavily investigated in the last couple of decades and has become a foundation of mobile robotics. On the other hand, though the scale and quality of SLAM results have improved significantly, SLAM approaches may fall short in addressing the requirements of some scenarios. On the contrary, GPS is an extraordinarily useful source of localisation information and a proven technology; hence, the incorporation of GPS signals into SLAM processes is a promising approach since its potential benefits include increased scalability, increased robustness, and more importantly improved accuracy of localisation. Nevertheless, the noise characteristics are complex since they arise from many sources, some of which have large autocorrelation [7]. Therefore, to make appropriate use of the information, such incorporation requires the use of low-level system information and explicit models of the underlying system. The details of the approach we adopted can be found in [4, 7, 8].

Basically, in our approach, we have three types of observations; namely, landmark observations, orientation observations, and global distance observations. Each type of update of the EKF has well defined matrices; hence, multiple applications of update can be made straightforward. If a landmark is not observed over a long period of time, the estimate of that landmark's position becomes decorrelated from the current bias estimate. If the localisation estimate is dominated by beacon data, then repeated observations of a landmark in a short period of time causes the landmarks' localisation to become correlated with the bias terms of the beacons in use. However, if the same landmark is observed again after a significant time lapse, the beacon bias becomes decorrelated from the landmark position, allowing for a further reduction in uncertainty.

The results of our simulation studies, realized using MATLAB, are shown in Figures 2 (a), 2 (b), 3, 4, and 5, respectively. Figure 2 (a) shows the robot's real waypoint (ground truth), Figure 2 (b) shows the robot's estimated waypoint and observations carried out by the robot while following the estimated waypoint, Figure 3 shows the details of the observations and odometry, Figure 4 shows position uncertainty of the robot and finally Figure 5 shows comparative overall deviations of the robot from the ground truth (total simulation time 20 min). Although the observations carried out by the robot are very limited, the deviation of the robot is around 0.2 m. When we increase the number of observations, the deviation of the robot becomes much less. As shown in Figure 5, as expected, when GPS measurements are fed into the EKF process, the robot's localisation errors become less.
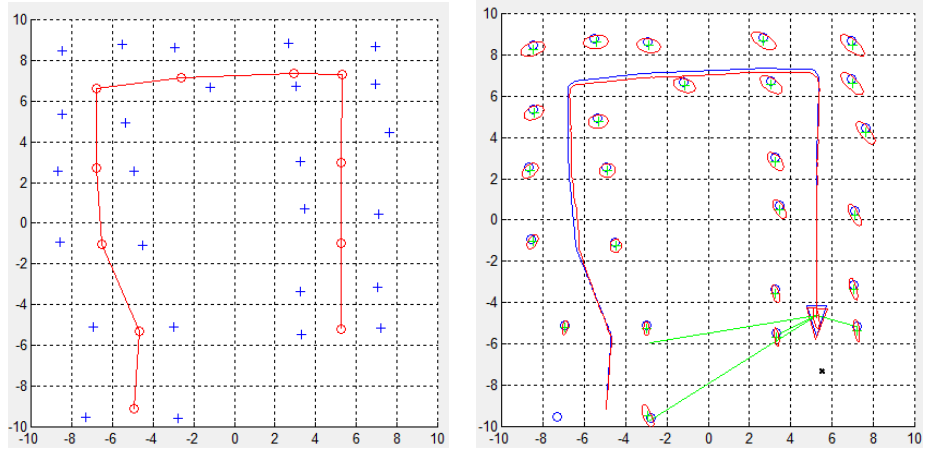
Figure 2 (a). The robot's waypoint,   *(b) Observations carried out by the robot*
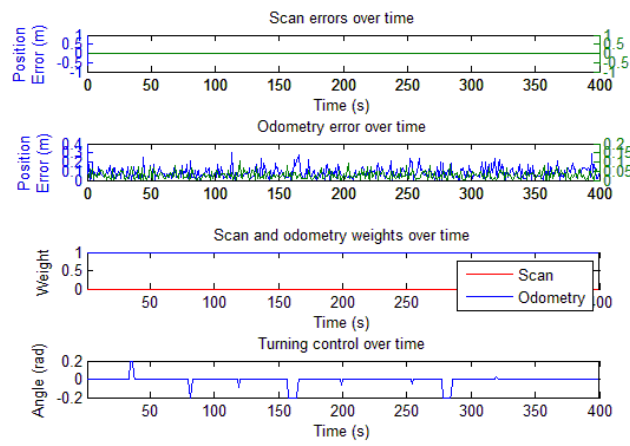
Figure 3. Details of the observations
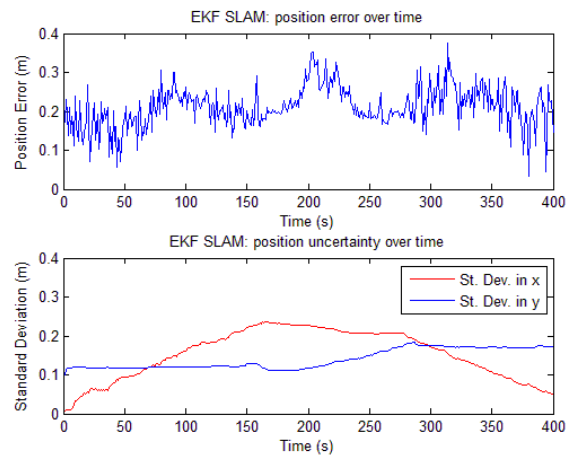
Figure 4. Position uncertainty of the robot
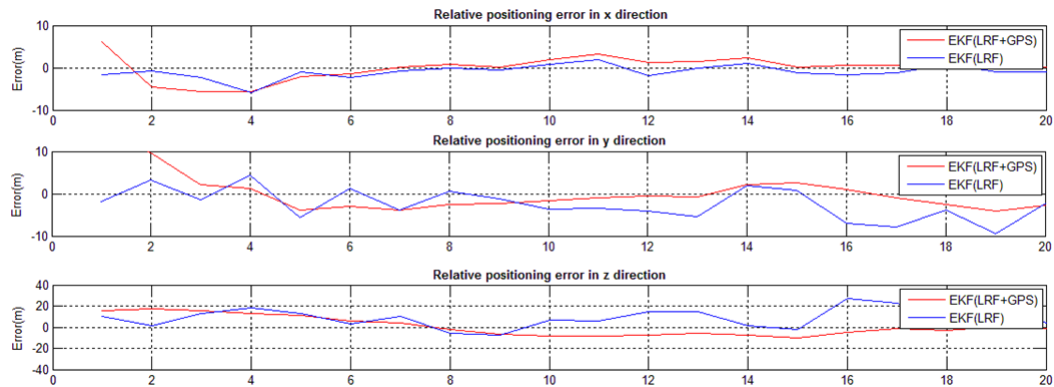
Figure 5. Comparative overall deviations of the robot from the ground truth (total simulation time 20 min)

3. CONCLUSION

Exploration and mapping of underground tunnels is very difficult since most of the tunnels are very long and narrow and it is very difficult for a human to move inside the tunnels. In this study, we proposed a novel approach to explore and map ancient underground tunnels. In the proposed approach, one or more mobile robots are used to explore and map the underground tunnels. Since GPS signals are not available inside the underground tunnels, GPS data received from handheld GPS receivers is provided to the mobile robots at predefined locations. Using the GPS data, the mapping errors are minimized and the accuracy of the overall process is increased. A set of simulation studies was given to show the usability and efficiency of the proposed approach. Although in real world applications there may be many problems and challenges that are not predicted in simulation studies, the simulation studies are important in terms of giving an idea about the feasibility of the proposed approach.

REFERENCES

[1]. I. J. Cox, "Blanche—an experiment in guidance and navigation of an autonomous robot vehicle," *IEEE Transactions on Robotics and Automation*, vol. 7, no. 2, pp. 193-204, 1991.
[2]. S. Thrun, W. Burgard, and D. Fox, *Probabilistic Robotics*, MIT Press: Cambridge, 2005.
[3]. R. E. Kalman, "A New Approach to Linear Filtering and Prediction Problems," *Journal of Basic Engineering*, pp. 35-45, 1960.
[4]. S. J. Julier and J. K. Uhlmann, "Unscented filtering and nonlinear estimation," in *Proc. the IEEE*, 2004, pp. 401-422.
[5]. J. Neira and J. D. Tardos, "Data association in stochastic mapping using the joint compatibility test," *IEEE Transactions on Robotics and Automation*, vol. 17, no. 6, pp. 890-897, 2001.
[6]. P. K. Enge, "The Global Positioning System: Signals, measurements, and performance," *International Journal of Wireless Information Networks*, vol. 1, no. 2, pp. 83-105, 1994. doi:10.1007/BF02106512
[7]. J. D. Carlson, "Mapping Large, Urban Environments with GPS-Aided SLAM," doctoral dissertation, tech. report CMU-RI-TR-10-27, Robotics Institute, Carnegie Mellon University, August, 2010.
[8]. S. J. Julier and J. K. Uhlmann, "A new extension of the Kalman Filter to nonlinear systems," in *Proc. International Symposium on Aerospace/Defense Sensing, Simulation and Controls*, Orlando, FL, 1997.

A NEW EMPIRICAL MODELS TO ESTIMATE GLOBAL SOLAR RADIATION FOR TURKEY

Nurullah Arslanoglu[1*]

Abstract

In this study, three different sunshine-based regression models are developed to estimate the monthly average daily global solar radiation on a horizontal surface for provinces in the different regions of Turkey by using the meteorological data from Turkish State Meteorological Services. These models are derived from Angstrom–Prescott linear regression model and its derivatives such as quadratic, cubic. To indicate the performance of the models, the statistical test methods of the coefficient of determination (R2), mean bias error (MBE), mean absolute bias error (MABE), root mean square error (RMSE) are used. Consequently, the empirical models can be used to predict solar energy in Turkey and nearby regions.

Keywords: *Global solar radiation, Regression models, Turkey*

1. INTRODUCTION

The global solar radiation is the fundamental energy source for our world such as designing and construction of solar energy-related system [1]. However, for many locations, solar radiation equipments are not readily available due to the cost, maintenance requirements of the solar measuring equipments, therefore posing the need to employ regression models of solar radiation based on meteorological data [2]. The first regression model developed for estimating monthly average daily global radiation was carried out by Angstrom [3]. In this empirical model, the sunshine duration data for estimating the global radiation were used. Most of the sunshine based empirical equations built to estimate the monthly average daily global solar radiation are of the Angstrom equation [4].In addition to difficulty of determination of clear sky global irradiance, Prescott [5] proposed extraterrestrial radiation intensity values instead of it [1]. Many types of models have been proposed to predict global solar radiation in the literature [1-7, 9, 10].

The values of the monthly average daily global radiation on a horizontal surface used in the present study were taken from Turkish State Meteorological Service in the periods between 1967 and 2015.The main objective of this study is: (i) to estimate the global solar radiation using sunshine duration based on Angstrom–Prescott method in Turkey.

2. ESTIMATION MODELS FOR GLOBAL SOLAR RADIATION

Many empirical models and correlations have been found in the literature, such as linear, quadratic and cubic regression models, to predict global solar radiation on a horizontal surface from observed the monthly average daily hours of bright sunshine and calculated extraterrestrial radiation and monthly average day length. The first model developed for estimating the monthly average daily global radiation is based on the method of Angstrom, Prescott[3;5]. The equation used in this model is;

$$\frac{H}{H_o} = a + b(n/N) \tag{1}$$

where H is the monthly average daily global radiation on horizontal surface, H_o is the monthly average daily extraterrestrial radiation on horizontal surface The ratio between observed monthly average daily sunshine duration (n) and monthly average day length (N) called as relative sunshine duration ratio, and a and b are the regression coefficients. The quadratic model is proposed by Akinoglu and Ecevit [6] and the related equation is;

$$\frac{H}{H_o} = a + b(n/N) + c\left(\frac{n}{N}\right)^2 \tag{2}$$

The cubic model is proposed by Bahel et al. [7] and the related model is;

$$\frac{H}{H_o} = a + b(n/N) + c\left(\frac{n}{N}\right)^2 + d\left(\frac{n}{N}\right)^3 \tag{3}$$

The monthly average daily extraterrestrial radiation on a horizontal surface (H_o) can be computed from the following equation [8];

$$H_o = \frac{24 \times 3600 G_{sc}}{\pi}\left[1 + 0.033\cos\left(\frac{360D}{365}\right)\right] \times \left[\cos\varphi\cos\delta\sin w_s + \frac{2\pi w_s}{360}\sin\varphi\sin\delta\right] \tag{4}$$

where G_{sc} is the solar constant (1367W/m^2), φ the latitude of the site, δ is the solar declination, w_s is the mean sunrise hour angle for the given month and D is the number of days of the year starting from first of January. The solar declination (δ) and the mean sunrise hour angle (w_s) can be calculated by Eqs. (5) and (6), respectively [8];

$$\delta = 23.45\sin\left[\frac{360(D+284)}{365}\right] \tag{5}$$

$$w_s = \cos^{-1}[-\tan(\delta)\tan(\varphi)] \tag{6}$$

The monthly average day length (N) can be calculated by following equation [8]:

$$N = \frac{2}{15}w_s \tag{7}$$

The regression constants (a, b, c and d) and R^2 of the three models obtained by the curve estimation technique, and have been reported in Table 1.

Table 1. Regression constants for provinces of Turkey

Location	Models	R^2	a	b	c	d
BURSA	Linear	95.4	0.2517	0.3643		
	Quadratic	95.7	0.2139	0.5303	-0.1660	
	Cubic	96.5	0.4482	-1.062	3.249	-2.318
MUGLA	Linear	96.4	0.2606	0.3860		
	Quadratic	98.6	0.1187	0.9315	-0.4823	
	Cubic	98.7	-0.0447	1.890	-2.269	1.063
KONYA	Linear	95.8	0.3396	0.3040		
	Quadratic	96.1	0.3041	0.4392	-0.1179	
	Cubic	96.2	0.2180	0.943	-1.042	0.536
ARTVİN	Linear	90	0.2993	0.4056		
	Quadratic	93.6	0.1892	1.022	-0.8042	
	Cubic	94.1	0.3713	-0.526	3.349	-3.547
SİİRT	Linear	95.2	0.3453	0.2722		
	Quadratic	96.1	0.2732	0.5342	-0.2153	
	Cubic	96.4	0.1250	1.362	-1.676	0.817
ANTALYA	Linear	81.1	0.2938	0.3611		
	Quadratic	81.1	0.2895	0.3738	-0.0091	
	Cubic	83.6	2.859	-11.22	17.13	-8.302
IGDIR	Linear	92.3	0.3223	0.2533		
	Quadratic	92.6	0.3050	0.3341	-0.0844	
	Cubic	92.7	0.2408	0.819	-1.191	0.782

2.1. Statistical performance evaluation

The MBE provides information on the long-term performance of the regression equations. The ideal value of MBE equals zero. MBE is expressed by [9]:

$$MBE = \frac{1}{k}\sum_{i=1}^{k}(H_c - H_m) \tag{8}$$

The MABE performs the absolute value of bias error. The ideal value of MABE is zero. MABE is given by [10]:

$$MABE = \frac{1}{k}\sum_{i=1}^{k}|H_c - H_m| \tag{9}$$

The RMSE provides information on the short-term performance of an regression models. The value of RMSE is zero in the ideal case. The RMSE may be calculated the following equation [10]:

$$RMSE = \left[\frac{1}{k}\sum_{i=1}^{k}(H_c - H_m)^2\right]^{1/2} \tag{10}$$

3. RESULTS AND DISCUSSION

The measured and calculated values of the monthly average daily global radiation for the seven main locations are performed in Fig. 1. As can be seen from figure, agreement between the values obtained from models and the measured data are good.
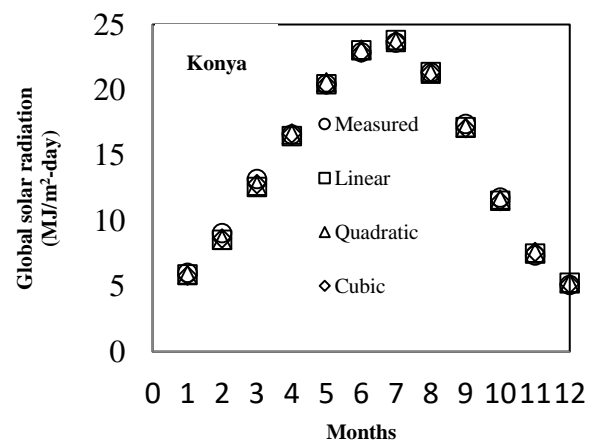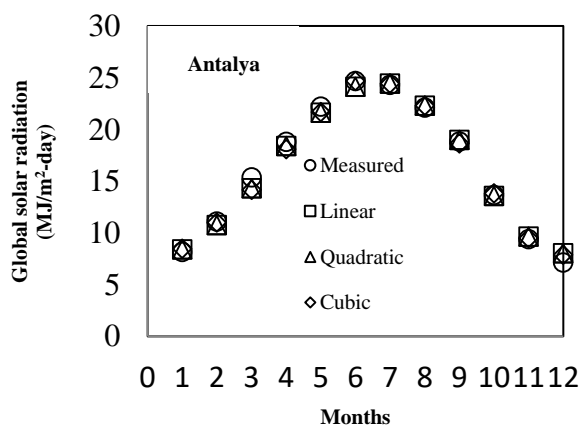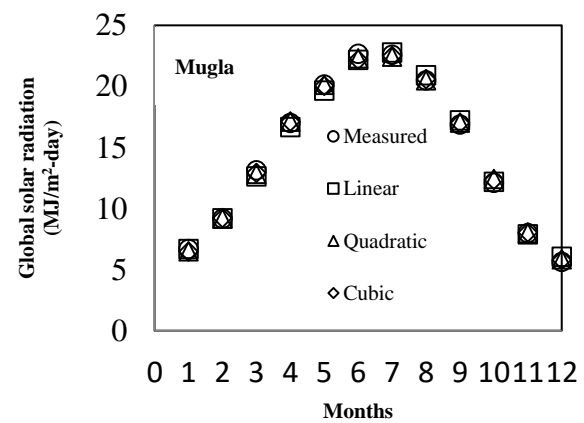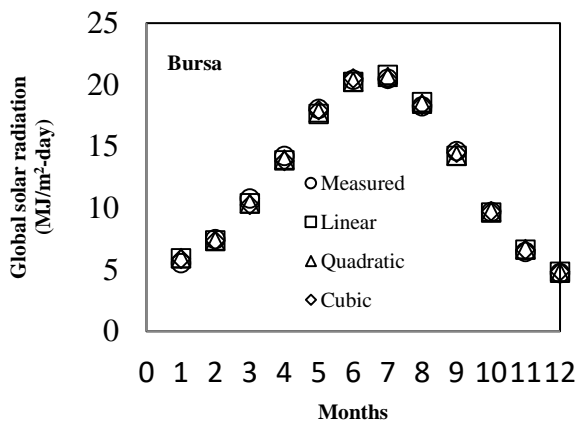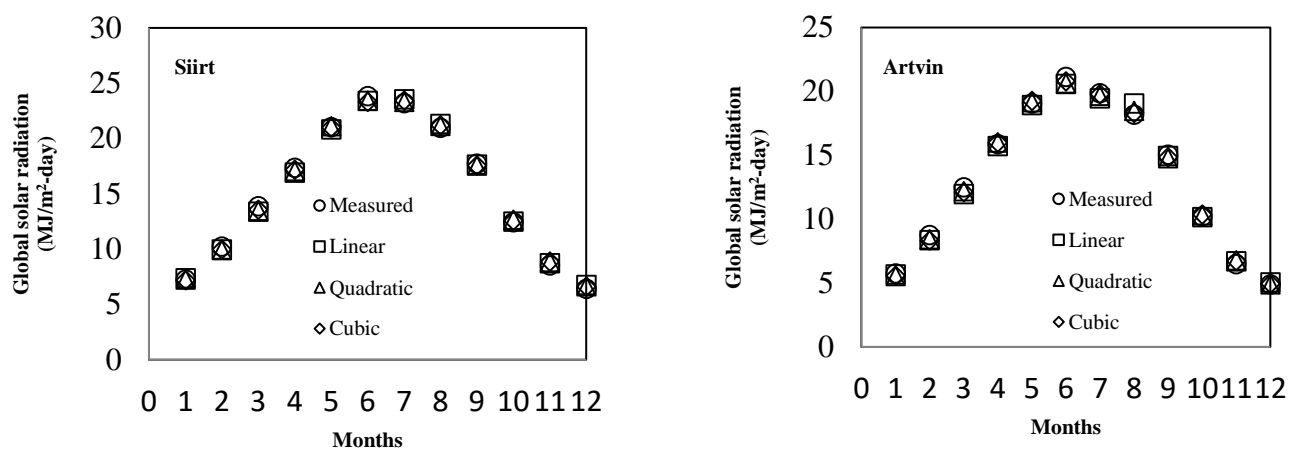
Fig 1.Measured and calculated values of monthly average daily global radiation over Turkey
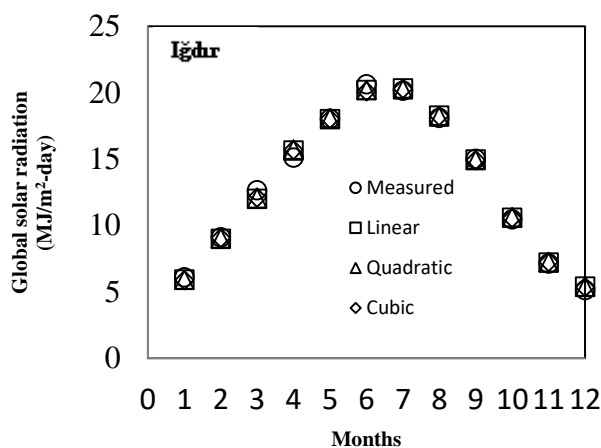
Fig.1.(continued)

For the seven locations studied, the following main results were obtained from the evaluation of the values presented for Turkey in Table 2.

Table 2. Statistical indicators of the regression models for stations.

	MODEL		
	1	2	3
Bursa			
MBE	-0.0518	-0.0495	-0.0406
MABE	0.2718	0.2295	0.1880
RMSE	0.3021	0.2595	0.2400
Mugla			
MBE	-0.0399	-0.0219	-0.0249
MABE	0.2840	0.1530	0.1690

RMSE	0.3389	0.1966	0.2050
Konya			
MBE	-0.0097	-0.0058	-0.0138
MABE	0.1655	0.1821	0.1946
RMSE	0.2383	0.2272	0.2353
Artvin			
MBE	-0.0390	-0.0239	-0.0098
MABE	0.2879	0.2349	0.2129
RMSE	0.3859	0.2609	0.2328
Siirt			
MBE	-0.0423	-0.0359	-0.0349
MABE	0.2777	0.2304	0.2285
RMSE	0.3124	0.2604	0.2650
Antalya			
MBE	-0.1030	-0.1033	-0.0974
MABE	0.4052	0.4037	0.3591
RMSE	0.5046	0.5039	0.4986
Igdır			
MBE	-0.0088	-0.0081	-0.0113
MABE	0.2339	0.2321	0.2325
RMSE	0.3039	0.3017	0.3042

For the province of Bursa: The best results for R2=0.965, MBE=-0.0406 MJ/m2-day, MABE=0.1880 MJ/m2-day, RMSE= 0.2400 MJ/m2-day are obtained from the cubic model. For the province of Mugla: The best result for R2=0.987 is obtained from the cubic model, while the computed lowest values for MBE= -0.0219 MJ/m2-day, MABE=0.1530 MJ/m2-day, RMSE= 0.1966 MJ/m2-day are obtained from the quadratic model. For the province of Konya: The computed lowest values of the MBE, RMSE are calculated as -0.0058 MJ/m2-day, 0.2272 MJ/m2-day respectively for quadratic model. The best results for R2=0.962 is obtained from the cubic model, while the lowest results for MABE=0.1655 MJ/m2-day is calculated from the linear model. For the province of Artvin: The best results for R2=0.941, MBE=-0.0098 MJ/m2-day, MABE=0.2129 MJ/m2-day, RMSE= 0.2328 MJ/m2-day are obtained from the cubic model. For the province of Siirt: The ideal values of the statistical analysis are obtained as -0.0349 MJ/m2-day (MBE), 0.2285 MJ/m2-day (MABE), 0. 0.964 (R2) with cubic model, 0.2604 MJ/m2-day (RMSE) with quadratic model. For the province of Antalya: The best results for R2=0.836, MBE=-0.0974 MJ/m2-day, MABE=0.3591 MJ/m2-day, RMSE= 0.4986 MJ/m2-day are obtained from the cubic model. For the province of Igdır: The required ideal values of the MBE, MABE, RMSE gained from quadratic regression model such as -0.0081 MJ/m2-day, 0.2321 MJ/m2-day, 0.3017 MJ/m2-day, respectively. The best result for R2=0.927 is obtained from the cubic model.

4. CONCLUSIONS

Three different sunshine-based regression models are developed to predict the monthly average daily global solar radiation on a horizontal surface for provinces in the different regions of Turkey. The main conclusions of this study can be summarized. According to R^2 values, the use of all models for Turkey is recommended. The statistical analyses (MBE, MABE, RMSE) indicate that all regression models have applicable over Turkey. This results also can be used the similar climatic conditions to predict monthly average daily global solar radiation. The accurate regression models can therefore be used to estimate solar energy in Turkey and nearby regions.

ACKNOWLEDGEMENT

REFERENCES

[1]. H. Duzen and H. Aydin, "Sunshine-based estimation of global solar radiation on horizontal surface at Lake Van region (Turkey)," *Energy Conversion and Management* vol. 58, pp.35–46, 2012.

[2]. M.H. Sonmete, C. Ertekin, H.O. Menges, H. Hacıseferogulları, F. Evrendilek, " Assessing monthly average solar radiation models: a comparative case study in Turkey," *Environ Monit Assess* , vol. 175, pp. 251–277, 2011.

[3]. A. Angstrom, "Solar and terrestrial radiation," *Quarterly Journal of Royal Meteorological Society,* vol. 50,pp. 121–125, 1924.

[4]. K. Bakirci, "Models of solar radiation with hours of bright sunshine: a review," *Renew Sustain Energy Rev*, vol.13, pp. 2580-2588, 2009.

[5]. J.A. Prescott, "Evaporation from water surface in relation to solar radiation," *Transactions of the Royal Society of Australia*, vol. 46, pp. 114–118,1940.

[6]. B.G. Akinoglu, and A. Ecevit, "A further comparison and discussion of sunshine based models to estimate global solar radiation," *Solar Energy, vol.* 15, pp.865–872 1990.

[7]. V. Bahel, H. Bakhsh, R. Srinivasan, "A correlation for estimation of global solar radiation," *Energy*, vol.12, pp.131–135, 1987.

[8]. A,Yigit and I. Atmaca, *Solar Energy (Güneş Enerjisi)* (Alfa-Aktüel Yayınları, Bursa, Turkey, 2010) (in Turkish).

[9]. K. Ulgen, A. Hepbasli, "Diffuse solar radiation estimation models for Turkey's big cities," *Energy Conversion and management*, vol. 50: pp.149-156, 2009.

[10]. K. Bakirci, "Correlation for estimation of daily global solar radiation with hours of bright sunshine in Turkey," *Energy*, vol.34, pp. 485-501, 2009.

AERODYNAMIC SHAPE IMPROVEMENT FOR FINES MAXIMIZATION OF TUAVS

Tugrul Oktay[1], Metin Uzun[2]

Abstract

The purpose of this conference article is to progress autonomous flight performance of a tactical unmanned aerial vehicle (i.e. TUAV) via using aerodynamic nosecone and tailcone shapes improvement both experimentally (i.e. using wind tunnel) and computationally (using CFD software). Aerodynamic performance criteria, i.e. maximum fines, of a scaled model of our autonomous TUAV named as Zanka-III manufactured in Erciyes University Faculty of Aeronautics and Astronautics Model Aircraft Laboratory is first examined in sub-sonic Wind Tunnel. Results found are validated using computational fluid dynamics software. Nosecone and tailcone of fuselage is reshaped in order to improve maximum fines of our TUAV Zanka-III by applying software. A novel scaled model using best data is then manufacture and placed in Wind Tunnel in order to validate software results with experimental results.

Keywords: *UAVs, Aerodynamics, Fines, Optimization.*

1. INTRODUCTION

For the last four and five decades *unmanned aerial vehicles* (UAVs) have been mostly benefited for military tasks and also in commercial requests because of the fact that they have several superiorties with respect to the old-style manned vehicles. These superiorties are having cheap manufacturing and operation, having flexible configuration for customer request and not risking the pilot's life on dangerous missions.

UAVs have also been used in aerial agriculture (e.g. crop monitoring and spraying), photography (i.e. film and video), coast guarding (i.e. coastline and see-lane), conservation (e.g. pollution and land monitoring), etc. for civilian purposes.

They have also been used for military operations. For instance, they have been used for navy (e.g. decoying missiles by the emission of artificial signatures and shadowing enemy fleets), army (e.g. reconnaissance and surveillance of enemy activity) and air force (i.e. radar system jamming and destruction and airfield base security). Many other UAV examples is examined in detail by [1].

The precise UAVs observed in this conference article is Tactical UAVs (i.e. TUAVs). TUAVs are heavier UAVs (from 50 kg to 1,500 kg) that operate at higher altitudes (from 3000 m to 12000 m) and are presently used principally to support military applications. Tactical UAVs can be categorized as: EN-TUAV (long endurance TUAV), LR-TUAV (long range TUAV), SR-TUAV (short range TUAV) and CR-TUAV (close range TUAV) [2]. Our TUAV is in the class of CR-TUAV.

In order to obtain better flight performance, several studies have been done for aerodynamic shape optimization (for instance, [3] to [7]). In [3] several nose cone shapes were applied in order to mininize drag such as elliptical nose, conical nose, bi-conical nose, spherically blunted tangent ogive nose. In [8] it is described the potential of the adjoint technique for aerodynamic shape optimization. In this way, drag reduction studies using optimization techniques for transonic flows have become important for literature. In [9,10] it has been conducted by comparing different angles of wing sweep in drag and noise reduction. Low wing sweep angle and increased wing height had lower induced drag. This has had a significant impact on the flight performance of the aircraft. In [11] it has been clearly found that winglet usage especially in UAVs has an important effect in reducing the drag force. The different winglets were first attached on the wing itself and compared by means of computational modeling for a wide range of angles of attack. Installing the optimized winglet, the results showed a significant improvement in the aerodynamic performance of UAV.

---

[1] *Erciyes University, Faculty of Aeronautics and Astronautics, Kayseri, Turkey, 38039, tugruloktay52@gmail.com.*

[2] *Corresponding author: Erciyes University, Faculty of Aeronautics and Astronautics, Kayseri, Turkey, 38039 m.uzun2010@gmail.com*

This is the *first conference article* examining aerodynamic shape improvement for Emax maximization of TUAVs. Moreover, Emax maximization is first time evaluated for both passively and actively morphing TUAVs.

2. SOME PROPERTIES OF OUR TUAV (ZANKA III)

In Figure 1 upper technical drawing and ground test photo of our TUAV are given respectively.
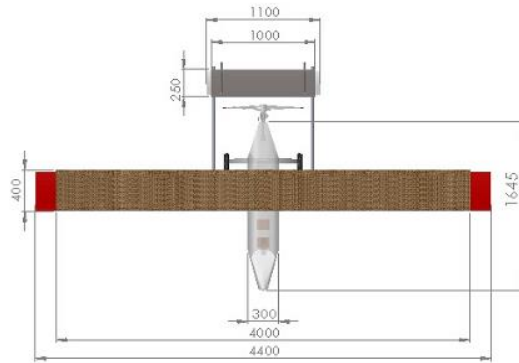
Figure1. a) Upper technical view   b) Ground test photo

Its wing span is 400 cm and chord length is 40 cm. After %10 morphing during flight, it may reach 440 cm. Its horizontal tail span is 100 cm and chord length is 25 cm and after %10 morphing it may reach 110 cm. Our TUAV's weight is 50 kg and it is able to carry 15 kg payload.

3. DIFFERENT GEOMETRY DESIGNS OF TUAV
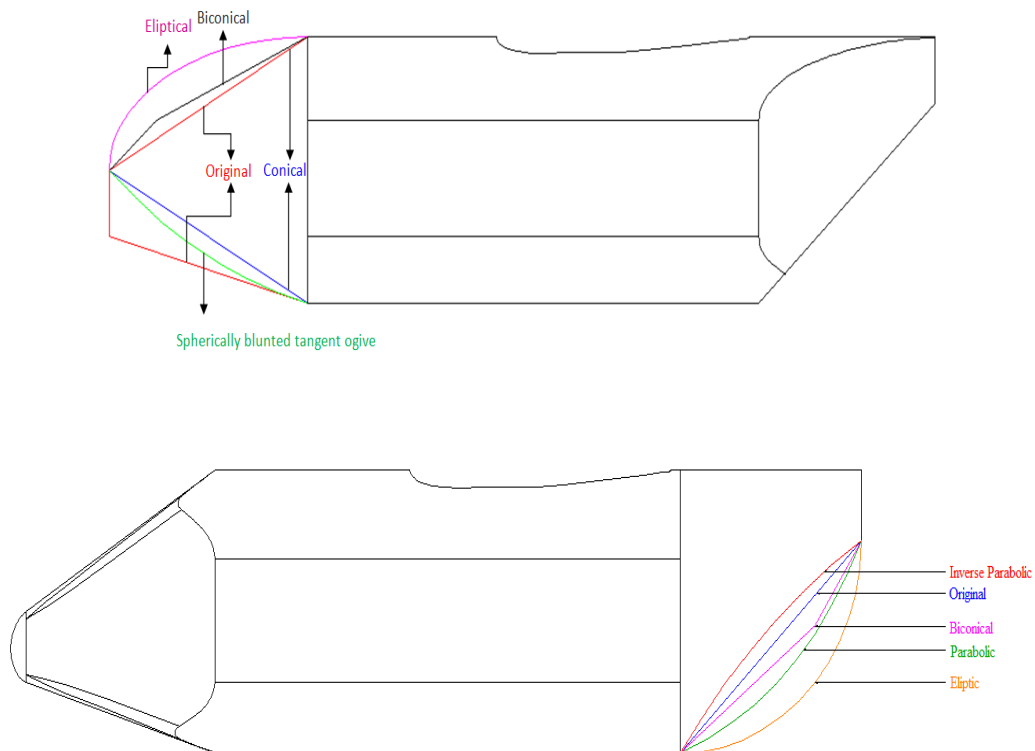
Figure 2. Display of curves obtained with equations

Figure 2 shows that how the different nose and tail cone designs of the TUAV are drawn and designed with the help of equations existing in the literature. As you can see, there is no change in the dimensions of the body of the TUAV. Only the curve of the line connecting the nose and tail cone to the body has been changed.

4. BOUNDARY CONDITIONS

Computational domain extended 15 lengths (C) upstream and downstream of the nose of the aircraft. Also 20C was applied from pressure outlet surface. Velocity inlet boundary condition was applied upstream and downstream with speed of 33.3 m/s. No-slip boundary condition are used at solid surfaces. Figure 3 illustrates all these setups for simulations.
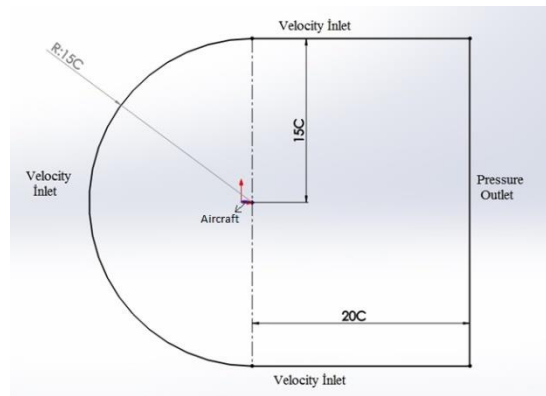
Figure 3. The dimensions and boundary conditions of the computational domain

Velocity components are defined for each angle of attack situation. The x component of velocity is calculated by x=33.3.cosα and y component of velocity is defined with y=33.3.sinα formula, where α is the angle of attack of the aircraft in degree unit.

5. GRID INDEPENDENCY STUDY

Used grid for simulations is generated by CFD Mesh program and all nose options with mesh are shown in figure 4 Patch Conforming / Sweeping method used. For eliminating of mesh effects, optimum mesh element number should be determined. Increasing of the element number provides more accurate results, but using more element increases solving time. For this reason grid independency study has been done with 100k, 400k, 1000k, 2400k, 6000k and 10000k elements. In figure 4 lift coefficient variation with different element numbers are given at 0 degree angle of attack. After 2400k elements number, lift coefficient value does not change a lot. So it can be said 2400k elements is enough for accurate results. Furthermore, convergence criteria was selected 10^{-6}. Approximately all analysis completed between 500-1000 iterations. Used computer has Intel(R) Xeon(R) CPU E5-1620-0 @ 3.60 GHz x64 bit and 8GB ram. Maximum analysis time for a simulation is 4 hours.
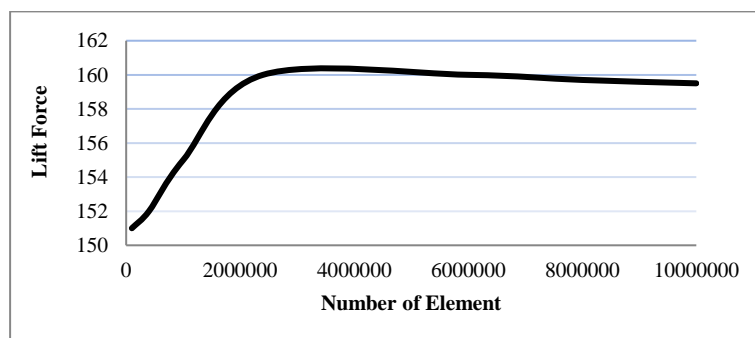
Figure 4. Variance of lift coefficient and number of elements

Table 1. Mesh Properties

MESH PROPERTIES	
Minimum Element Size	0.001 m
Number of Elements	2400000
Maximum Size	9.73 m
Maximum Face Size	4.86 m
Growth Rate	1.20
Curvature Normal Angle	18º
Mesh Method	Patch Conforming / Sweeping

Table 1 gives the mesh properties of the TUAV. Patch Conforming / Sweeping is selected as the mesh method and the smallest mesh element size is 1mm.

6. AERODYNAMIC SHAPE IMPROVEMENT

In this study a number of different nose and tail contour shapes have been investigated to improve rate of maximum fines (E_{max}). Nose and tail consecutive equations respectively are Elliptical, Bi-conical, Original, Conical, Spherically blunted tangent ogive and Tail cone equations and Inverse parabolic, Original, Bi-conical, Parabolic, Eliptical of TUAV. Table 1 gives the solidworks drawing, C_L and C_D graphs and E_{max} values for the original and optimized shapes. CFD and wind tunnel aerodynamic parameters of the original and optimized versions are given. Clearly, the results of RT and CFD are overlap. The fines values were 13.61 for the original shape but optimized to 14.87. So that the autonomous performance is approximately %9.25 increased.

Experimental and numerical studies to optimize the autonomous performance of the tuav aircraft were carried out in this article. The numerical section of the work is done in the CFD program. The initial and optimized miniature models of TUAV were produced in the Erciyes University Faculty of Aeronautics and Astronautics Model Aircraft Laboratory and experimental studies were carried out in sub-sonic Wind Tunnel to verify numerical data. Figure 5 shows the model images produced for the experimental studies.

Table.2. Optimization Results

	Original Nose Original Tail	Eliptical Nose Eliptical Tail
Solidworks Drawing		
Lift Coefficient Graph		
Drag Coefficient Graph		
E_{max}	**13.61**	**14.87**

a)Eliptical Nose and Tail   b)Initial Nose and Tail

Figure 5. Wind Tunnel Test
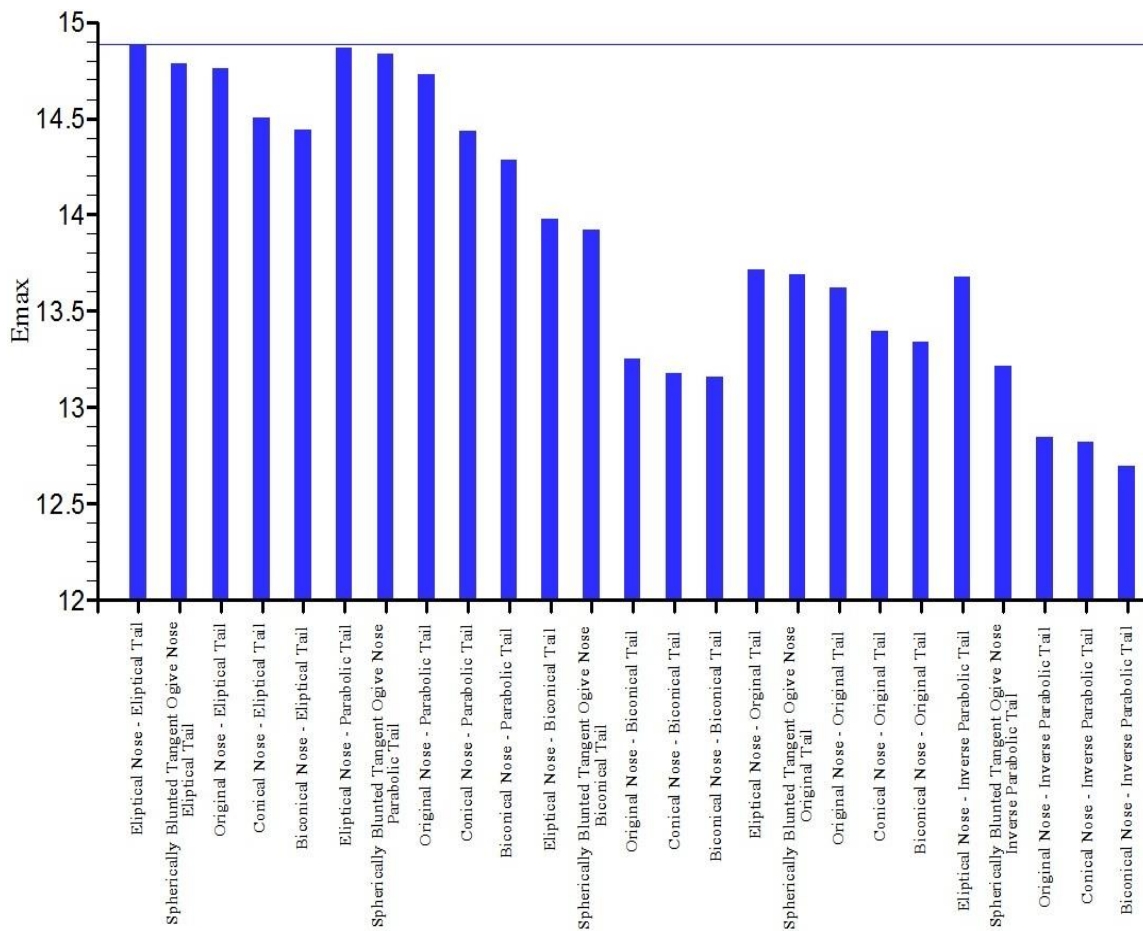
Figure 6. E_{max} comparison of 25 different configurations

In figure 6, the E_{max} values of 25 different configurations as comparative are presented. The nose and tail cones of the TUAV were changed 25 times to obtain new body designs that were different from each other. The E_{max} values of each design are visible. With the help of a line it is seen that the elliptical nose and the elliptical tail have the highest E_{max} value as 14,87. The E_{max} value of the original state of the TUAV is given as 13.61 in table 1. So that the aerial vehicle's autonomic performance increased by approximately 9.25%

7. CONCLUSIONS

In order to improve Emax value of our TUAV called as Zanka-III, aerodynamic nose and tail shape improvement both experimentally and computationally was applied. Aerodynamic performance criteria (i.e. maximum fines) of a scaled model of our autonomous TUAV called as Zanka-III produced in Erciyes University Faculty of Aeronautics and Astronautics Model Aircraft Laboratory was first observed in sub-sonic Wind Tunnel. Results obtained were validated using computational fluid dynamics (i.e. CFD) software. Nose and tail cone of fuselage was optimized in order to maximize maximum fines of our TUAV by using CFD software. A novel scaled model using optimum data was then produced and placed in Wind Tunnel in order to validate CFD results with experimental results. A significant improvement and increase (around %9.25) for the maximum value of fines is found via aerodynamic nose and tail shape improvement for a morphing TUAV.

ACKNOWLEDGEMENT

REFERENCES

[1]. H. Duzen and H. Aydin, "Sunshine-based estimation of global solar radiation on horizontal surface at Lake Van region (Turkey)," *Energy Conversion and Management* vol. 58, pp.35–46, 2012.
[2]. Austin, R., Unmanned aircraft systems, Wiley, 2010.
[3]. Bento, M. F., Unmanned aerial vehicles: An Overview. Working papers, 2008.
[4]. Xuetao, Z., UAV Design and Manufacture, BS Thesis, 2010.
[5]. Brezillon, J., Gauger, N.R., 2D and 3D aerodynamic shape optimization using the adjoint approach. Aerospace Science and Technology 8. (715–727), (2004).
[6]. Abbas, A., Vicente, J de., Valero, E., Aerodynamic technologies to improve aircraft performance. Aerospace Science and Technology 28. 100-132 (2013).
[7]. Kontogiannis, Spyridon G., Ekaterinaris, John A., Aerospace Science and Technology 29. 3339-350 (2013).
[8]. Panagiotou, P., Kaparos, P., Yakinthos, K., Aerospace Science and Technology 39. 190-205 (2014).
[9]. Brezillon, J., Gauger, N.R., 2D and 3D aerodynamic shape optimization using the adjoint approach. Aerospace Science and Technology 8. (715–727), (2004).
[10]. Abbas, A., Vicente, J de., Valero, E., Aerodynamic technologies to improve aircraft performance. Aerospace Science and Technology 28. 100-132 (2013).
[11]. Kontogiannis, Spyridon G., Ekaterinaris, John A., Design, performance evaluation and optimization of a UAV. Aerospace Science and Technology 29. 3339-350 (2013).
[12]. Panagiotou, P., Kaparos, P., Yakinthos, K., Winglet design and optimization for a MALE UAV using CFD. Aerospace Science and Technology 39. 190-205 (2014).

EFFECTS OF THE TOP PARTS OF SPORTS SOCK'S PARAMETERS ON PRESSURE ALONG WEARING TIME

Sertac Guney[1], İbrahim Ucgul[2]

Abstract

In this study, the relation between the top parts of sports sock's parameters and the pressure along wearing time was investigated to design and develop socks that provide wearing comfort. Body skin strain is an important factor affecting pressure comfort. There are three essential components required in meeting the skin strain: garment fit, garment slip and fabric strecth. This study aims to investigate the effects of structural mechanics of knitted fabrics on the amount of pressure generated on lower leg. Five sports sock (three high-calf socks and two mid-calf socks) made of polyamide, polyester and cotton including different amounts of elastane fibers and having different knits on lower leg section were selected from the market. We carried out friction and tensile tests on top parts of sports socks. When the top of socks are stretched to a certain extension, this induces stress relaxation and the pressure changes depending on wearing the socks. So we also measured the sock pressure along wearing time generated on lower leg by pressure sensors directly after wearing the sock and also until a certain stable pressure value along wearing time. Results show that the sock specimens having high tensions exerted high pressure values on lower leg but the fabric weight and friction coefficient are also important for the pressure applied on lower leg. We also investigated the pressure change along wearing time. This objective analysis of sports sock pressure is expected to help designing socks for better wearing comfort.

Keywords: *Pressure comfort, sports socks, wearing time, fabric structure*

1. INTRODUCTION

Socks are an important part of clothing in maintaining foot comfort. Therefore, pressure comfort parameters should not be ignored while designing functional socks, especially pressure on the top part of socks [1]. Degree of pressure produced by a garment is determined by complex interrelations between the following principle factors: the construction and fit of the garment, structure and physical properties of its materials, the size and shape of the body parts to which it is applied and the nature of the sports activity undertaken [2]. Dan et al. (2013) investigated the relationships between pressure and material properties of the top part of socks and established four indices which closely relate to pressure level; these are elastic coefficient of top part of socks, Poisson's ratio, elastic elongation and width of top part of socks [3]. Matsumoto et al. (2004) measured leg size, tensile properties and pressure values of the top of socks and found comfortable pressure values as 2.02+/- 0.29 kPa and investigated the feeling of pressure changes depending on wearing period [4]. Nakahashi et al. (1999) compared the pressures between front and back of lower leg and pointed out that comfortable value of pressure on the front part of a lower leg was lower than that on the back part [5].

2. EXPERIMENTAL

2.1. Materials

Five men's sports socks *(three high-calf socks and two mid-calf socks)* having different compositions and knit structures (Figure 1) were selected from the market.

---

[1]Corresponding author: Süleyman Demirel University ,Engineering Faculty, Textile Engineering Department, Isparta, Turkey sertacguney@sdu.edu.tr

[2]Süleyman Demirel University ,Engineering Faculty, Textile Engineering Department, Isparta, Turkey ibrahimucgul@sdu.edu.tr

Code	1	2	3
Knit Structure			
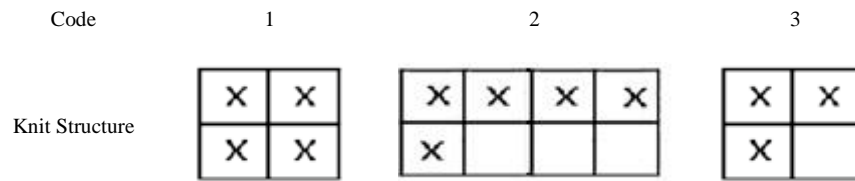
Figure 1. Sock knit structures [6]

Their physical and structural parameters were given in Table 1.

Table 1. Physical parameters of fabric samples

Fabric	Fiber Composition (%)	Stitch density loop/cm²	Mass per unit area (g/m2)	Thickness (mm)	Knit Structures
A	87/12/1% PA/PES/Elastane	44	1: 264 3: 160	1: 1.59 3: 1.67	
B	99/1% PA/Elastane	54	1: 325 2: 398 3: 279	1: 1.50 2: 2.40 3: 1.50	
C	96/3/1% PES/ Elastane/PA	60	1: 240 2: 280	1: 1.09 2: 1.50	
D	82/15/2/1 % Cotton/PES/Elastane/PA	96	1: 425 2: 479 3: 472	1: 1.32 2: 1.99 3: 1.93	
E	81/17/1/1% Cotton/PES/PA/Elastane	96	1: 422 3: 552	1: 1.43 3: 1.56	

Two types of socks were selected: high-calf socks and mid-calf socks The sizes of leg part for both types are shown in Table 2.

Table 2. The sizes of leg part for high-calf socks and mid-calf socks

Sock type	Fabric code	A (cm)	B (cm)	C (cm)	D (cm)
high-calf socks	A	44	10	10	11.5
	B	53	10.5	10	10
	C	46	10.5	2	10.5
mid-calf socks	D	22	8	2	8.5
	E	22	8.5	2	9
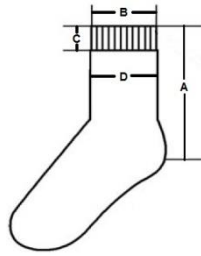
2.2. Methods

Each section having different structures on the lower leg part of socks were cut out and the tensile characteristics under extension rates corresponding to the girth of pressure sensor points were tested. Friction coefficients (static and dynamic) had been tested and calculated from the force-displacement graphics for each section for course direction according to ASTM D-1894 by using a Lloyd Tensile Tester (LR5K plus) in the previous study [6]. Dimensions of the cradle was 4.5 x 4.0 cm and test was carried out on the sample placed on a horizontal platform by movement of the cradle with a speed of 50 mm/min. Extra weights were used to obtain a normal force of 1,2 g/cm^2 by the cradle. The objective pressure of the tops was measured for subject sitting in a chair in a resting position by flexible pressure sensor system (Tekscan, USA). The sensors were kept on point of the front lower leg by using the clear plastic so that the pressure would be positioned at the exact point even with movement. The measurement points (P1-P2 for high-calf socks and P3-P4 for mid-calf socks) on the front lower leg were fixed for each of sock types. The girths of measurement points on lower leg are 39 cm of P1, 43 cm of P2, 32 cm of P3 and 26 cm of P4 (Figure 2). The socks showed different extension percentage on measurement points. so we tested the tensile characteristics of socks according to the extension percentage for each sock.
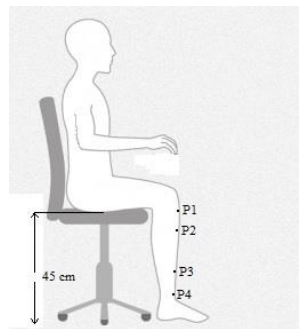
Figure 2. Pressure measurement points on the front lower leg

3. RESULTS AND DISCUSSION

Tension characteristics of knit structures on lower leg part of socks were tested. Figure 3 shows that knit structures exhibited different tension characteristics for each part of sock because of their different material compositions and constructions (stitch density, weight).
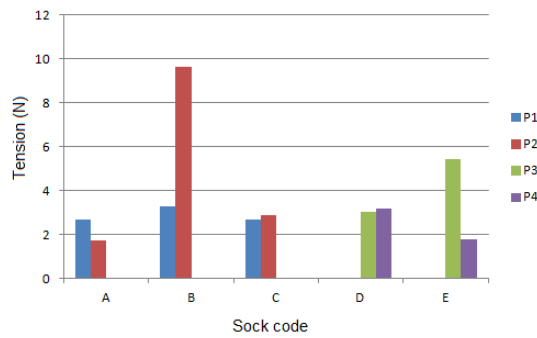
Figure 3. Tension characteristics of socks at measurement points (P1-P2-P3-P4)

Fabrics B.1 and E.3 showed higher tension values. Knit structures in all fabrics showed different friction and elastic characteristics (Table 2). The values for Fabric D.1 could not be measured because of inadequate fabric dimensions for the test [6].

Table 2. Friction and elastic characteristics of different socks parts [6]

Fabric Code/ Knit Structure	Static Friction Coefficient (S.D.)	Kinetic Friction Coefficient (S.D.)	Extension percentage (%) Tension (N) (S.D.)	Objective Pressure directly after wearing (gr/cm²)
A.1	0.493[b] (0.074)	0.482[b] (0.062)	on point P2: 87% 1.7109 (0.025)	on point P2: 35.81
A.3	0.241 (0.048)	0.208[a] (0.042)	on point P1: 95% 2.6646 (0.034)	on point P1: 22.92
B.1	0.225[a] (0.129)	0.312[a] (0.136)	on point P2: 115% 9.6184 (0.281)	on point P2: 58.61
B.3	0.372 (0.151)	0.368[b] (0.108)	on point P1: 86% 3.2829 (0.045)	on point P1: 29.30
C.1	0.302[a] (0.072)	0.293[a] (0.700)	on point P2: 105% 2.8874 (0.062)	on point P2: 130,26
C.2	0.447[ab] (0.090)	0.425[ab] (1.105)	on point P1: 86% 2.6980 (0.027)	on point P1: 52,09
D.1	-	-	on point P4: 53% 3.2073 (0.073)	on point P4: 29.30

D.3	0.302 (0.063)	0.246[a] (0.062)	on point P3: 100% 3.0571 (0.036)	on point P3: 35,81
E.1	0.297[a] (0.038)	0.227[a] (0.052)	on point P4: 44% 1.8014 (0.029)	on point P4: 22.78
E.3	0.354 (0.057)	0.264[ab] (0.063)	on point P3: 88% 5.4374 (0.096)	on point P3: 58,61

According to the results, kinetic friction coefficients can be ranked as 2>3>1 for all fabric types. Float stitches have negative effects on friction characteristics. So the knit structures 2 and 3 have higher kinetic friction coefficients (except for fabric code 1).The knit structure 3 has more repeated pattern and it gives an irregular fabric surface [6]. Fabrics gave different pressure values because of their physical differences (surface, weight, etc.). Tension value of fabric A.3 is higher than the value of fabric A.1. But the objective pressure value is not compatible with tension values. It may be explained by higher friction coefficients and higher weights. Fabric code E.3 has generally high friction coefficient, tension and weight so it generated higher pressure. Fabric C.1 generated the highest pressure on point P2. This may be because of stitch density and material composition. but it is not exactly clear to see the influences of materials on pressure values. PA and Cotton materials are smoother than PES. It is expected that socks with PES may exert much more pressure on body. We also investigated the pressure change along wearing time (300 s). The subject sat in an office chair (seat height of 45cm) in a resting posture and measurements were carried out immediately after and 300 s after putting on the socks. Figure 4 shows the pressure changes on points P1-P3 respectively. The pressure values gradually decreased with the course of time and became almost stable. It can be said that the fabric having high friction coefficient shows slow stress relaxation and slow pressure decreasing. the fabric having high tension shows immediate decreasing in pressure after wearing sock. Fabric A.3 has lower weight and stitch density so the pressure change occurred slower than the others.
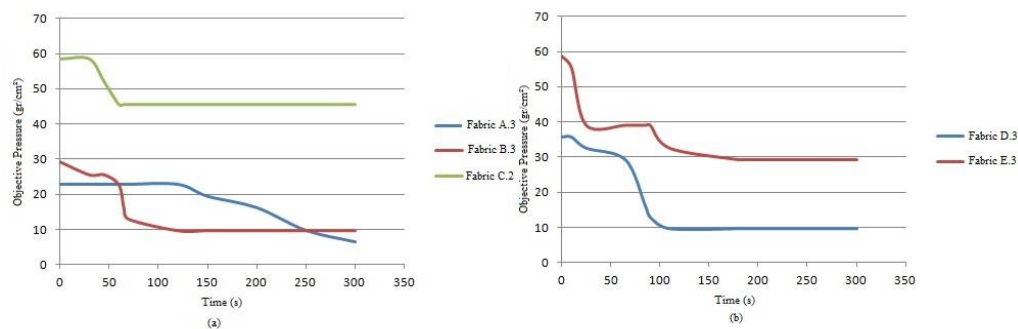
Figure 4. Objective pressure change along wearing time. (a) on point P1 (b) on point P3

4. CONCLUSIONS

In this study, we investigated the pressure changes for subject sitting in a chair in a resting posture and wearing sports socks. According to the results of the friction and pressure measurements carried out on sports socks produced from different materials and structures; tensile, friction characteristics and weight of fabrics have important effect on pressure generated on lower leg immediately after wearing and along wearing time. If a fabric has high friction and stretching resistance, high pressure value is likely to be exerted on the body, which could result in discomfort feeling. Also sock size is very important for easy to put on and desired shaping and comfort. During designing and developing the pressure comfort of the socks, we should take account of these parameters.

REFERENCES

[1]. Li, J., (2007). Study on the pressure comfort of the top part of socks, Shanghai, Donghua University.

[2]. [2].Troynikov, O., Ashayeri, E., Burton, M., Subic, A., Alam., F. and Marteau,S., (2010). Factors influencing the effectiveness of compression garments used in sports, Procedia Engineering 2, 2823-2829

[3]. Dan, R., Fan, X., Xu, L. and Zhang, M., (2013). Numerical simulation of the relationship between pressure and material properties of the top part of socks, The Jounal of The Textile Institute, 104(8), 844-851.

[4]. Tsujisaka, T., Azuma, Y., Matsumoto, Y. and Morooka, H., (2004). Comfort Pressure pf the Top Part of Men's Socks, Textile Research Journal, 74(7), 598-602.

[5]. Nakahashi, M., Morooka, H., Morooka, H., Hiraga, S. and Deguchi,J. (1999),, Effect of clothiing pressure on front and back of lower leg on compressive feeling, Journalof the Japan Research Assıciation for Textile End-use, Vol.40 (10), pp.661-668.

[6]. Güney, S., Akgünoglu, B. and Kaplan, S., (2016), Parameters affecting sports socks pressure and pressure prediction from tensile characteristics, 21st International Strutex, pp.61-66.

AN INVESTIGATION ON THE VALIDITY OF FABRIC OBJECTIVE MEASUREMENTS FOR VIRTUAL GARMENT SIMULATION

Sertac Guney[1], İbrahim Ucgul[2]

Abstract

Virtual garment simulation received much attention in the past decade, and the fashion industry has been attracted to use this brandnew tool in actual product development process to strengthen the collaboration along the supply chain and optimize the product time for market. But still there is some hesisation for the accuracy of the 3D virtual simulation results. To overcome this disadvantage, the 3D simulation systems should not only predict the garment shapes properly on a 3D fit avatar, but also accurately simulate the fabric behaviours. Nowadays software providers have begun to develope their own measuring devices to obtain the required textile parameter specific to their application. This study aims to analyse the accuracy of fabric objective measurements of commercial 3D virtual garment software's testing kit. Eleven strech knitted fabric made of polyamide, polyester and cotton including different amounts of elastane fibers were selected from sports garment producers. We carried out tensile tests and bending resistance test under standard laboratory condition and also used the software's testing kit to compare the extension, shear (bias extensibility) and bending measurements between objective fabric measurements and the derived parameters for the virtual garment simulation. Results showed that for extensibility, there was a good agreement between the two objective testing systems with the exception of a few specimens. Two testing systems use the same cantilever principle to measure the bending length under the fabrics own weight. But the results showed good agreement for some fabrics but not for all, because of the unsuitable dimensions of testing kit to get the right angle of 41.5˚.

Keywords: *Virtual simulation, fabric objective measurement, 3D simulation systems, textile parameters*

1. INTRODUCTION

Nowadays the textile and clothing producers have experienced a transformation into a high technology industry. 3D virtual garment simulation will play an important role within apparel product development in the future. The actual representation of a virtual garment is dependent on two factors, precise computational models and exact input of fabric parameters [1]. There are many advanced systems considering these factors on the market such as Optitex's 3D virtual clothing, Browzwear's V-stitcher and Lectra's Modaris 3D fit. Independent of the software utilised for the virtual simulation, all 3D virtual garment simulation software require the input of objective fabric measurements. Some software providers have developed their own measuring devices to obtain the required textile parameter specific to their application. Examples of these include Browzwear's fabric testing kit and Optitex's fabric testing utility. The fabric properties obtained vary depending on the system, but generally all devices include facilities for measuring tensile and bending properties. Other parameters such as surface properties, mass and thickness can be obtained either as part of the main testing process or extra testing instruments may be required [2]. Some researchers have investigated on the virtual simulation by inputing the fabric properties [2-4]. Jess (2013) faced some limitations within FAST measurement system for stretch fabrics. In this study, we carried out tensile tests and bending resistance test under standard laboratory condition to overcome these limitations and also used the Browzwear's V-stitcher Fabric Kit (FTK) to measure the required properties for the simulation.

[1] *Corresponding author: Süleyman Demirel University ,Engineering Faculty, Textile Engineering Department, Isparta, Turkey sertacguney@sdu.edu.tr*

[2] *Süleyman Demirel University ,Engineering Faculty, Textile Engineering Department, Isparta, Turkey ibrahimucgul@sdu.edu.tr*

1.1. Browzwear V-Stitcher Fabric Test Kit (Ftk)

The Browzwear fabric testing kit (Figure 1) is a single set of apparatus that measures three parameters, bending, tensile and shear; although other parameters (mass and fabric thickness) are required to enable the data to be input into the 3D virtual garment simulation. Bending is defined in the FTK manual as 'the amount of cloth resistance to folding when applying an external force on a cloth'. Warp and weft fabric specimens are prepared, each specimen is clamped at one end and fed through a metal clip. The fabric is pulled though the clip by moving the clamp, until the edge of the cloth is almost detached from the lower scale (bend scale). The lengths known as the distance (d) and curved length (l) are obtained (Figure 1), the height is fixed at 2.7cm. This is the similar as the cantilever principle.
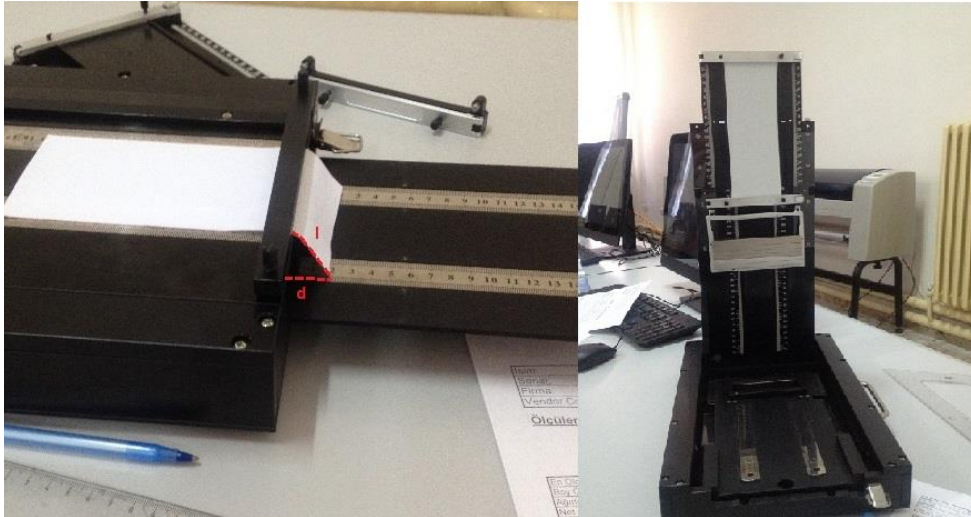
Figure 1. Browzwear V-stitcher Fabric Test Kit (FTK)

In tensile tests a series of 6 weights (50, 100, 200, 300, 450, 650g) are applied to a vertically mounted fabric in sequence (Figure 1). The fabric is clamped between two clips; the distance between the clips is measured. The top clip is then secured to a frame and the fabric is allowed to hang freely, a second measurement is recorded, a sequence of weights are then applied and the distance between the clips recorded manually using the mounted measuring device. This test is repeated for the weft, warp and bias of the fabric. Shear is measured by repeating the tensile procedure but the fabric sample is cut in the bias [5].

2. EXPERIMENTAL

2.1. Materials

Eleven strech knitted fabrics (having the same warp and weft knit structure) made of polyamide, polyester and cotton including different amounts of elastane fibers were provided from sports garment producers. Their physical and structural parameters of fabric specimens were given in Table 1.

Table 1. Physical and structural parameters of fabric specimens.

Fabric Code	Fibre Composition	Fabric Structure	Fabric Mass (g/m²)	Fabric Thickness (mm)
A	82% PES 18% Elastane	weft knitted	155	0.41
B	80% PES 20% Elastane	warp knitted	250	0.46
C	80% PA 20% Elastane	warp knitted	210	0.64
D	85% PA 15% Elastane	warp knitted	240	1.33
E	83% PES 17% Elastane	warp knitted	280	1.23

F	75% Cot 25% Elastane	weft knitted	200	0.49
G	80% PES 20% Elastane	weft knitted	300	0.59
H	82% PA 18% Elastane	warp knitted	180	0.57
I	84% PA 16% Elastane	warp knitted	180	0.49
J	80% PA 20% Elastane	warp knitted	240	0.65
K	85% PES 15% Elastane	warp knitted	230	0.48

2.2. Methods

All the fabric measurements has been conducted in accordance with each systems operating manual and sample size specification. The fabrics have been conditioned and all testing were performed in a standard laboratory environment. The analysis and discussion given in this paper are based on an explorative study to determine if fabric objective measuring results obtained from the two different testing systems are compatible.

3. RESULTS AND DISCUSSION

The Browzwear's fabric testing kit uses a simple strain gauges for measurement. Six weights (50, 100, 200, 300, 450, 650g) are hung from a vertically mounted sample and the user records the extensibility results. The tensile tests were carried out by using a Lloyd Tensile Tester (LR5K plus). In testing kit, we measured the tensile properties of specimens under a series of loads. A suitable extension was determined covering the range of both testing devices to enable a good comparison for fabric extensibility. We compared the tension values corresponding to the same extensions. The extensibility data for the eleven fabrics until 450g weight put indicated good agreement between two test systems with except for fabric B and J. The extensibility data under 650g weight showed good agreement for just fabric A and C. Figure 2 showed the tensions at the same extensions per each weight for fabric E.
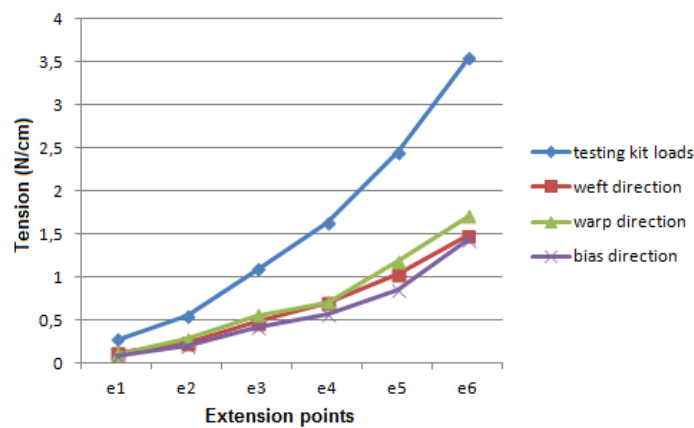
Figure 2. The tension values at the same extension points for Fabric E in weft, warp and bias directions

The tension values in Newton (N) from testing kit were not the same as the results from tensile tests. But the results from tensile tests were the same for ones corresponding to extension in testing kit for weft, warp and bias directions . This may be because of the different sample sizes used in two test systems.

For bending measurements; both testing systems use the cantilever principle to obtain the bending length under the fabric own weight. But because of the unsuitable dimensions of testing kit, it is not suitable to get the right angle of 41.5˚ that used in Peirce's cantilever tester (Figure 3) [6].
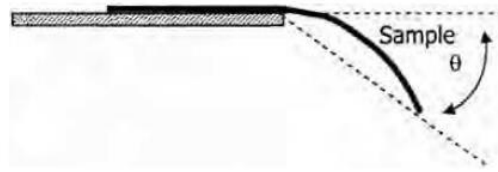
Figure 3. Peirce's cantilever tester

The height in testing kit is constant at 2.7 cm and to get the right angle 41.5°, the curved length (l) should be less than 3.604 cm. so it is not suitable to measure all fabric bending rigidity. Manuel calculation of the bending angles taken from Browzwear testing kit was shown in Table 2.

Table 2. The calculated bending angles of fabrics in testing kit

Fabric	Machine direction θ	Cross machine direction θ
A	39.27	40.54
B	41.30	37.66
C	32.20	37.30
D	43.94	30.00
E	45.80	35.09
F	23.57	38.90
G	30.00	38.90
H	15.01	15.01
I	20.12	24.39
J	23.57	34.05
K	11.06	11.06

The bending rigidity values (dyne*cm) from two testing systems were seen in Table 3. Results showed that the fabrics bending rigidity on machine direcion (A, D, E, H, I, J) measured from WIRA bending device have good agreement with the ones from Browzwear testing kit. Fabric F is supreme knit and showed curling. so it was not measured correctly in WIRA bending device because of its curling.

Table 3. The bending rigidity values from two testing systems

Fabric	WIRA Bending Device		Browzwear Testing Kit	
	Machine direction (dyne*cm)	Cross machine direction (dyne*cm)	Machine direction (dyne*cm)	Cross machine direction (dyne*cm)
A	21.04	18.29	21.57	21.57
B	25.49	67.72	100.19	111.53
C	10.96	47.04	58.42	32.86
D	32.57	60.21	35.42	115.28
E	70.24	128.25	70.39	187.97
F	1.30	4.40	71.15	20.69
G	6.60	40.71	96.26	37.32
H	7.43	3.05	8.01	8.01
I	21.24	7.74	19.53	15.44
J	53.76	10.32	49.27	24.12
K	12.00	9.89	5.77	5.77

4. CONCLUSIONS

In this study we compared the tensile and bending rigidity results of fabrics from two testing systems. Results showed that for extensibility, there was a good agreement between the two objective testing systems with the exception of a few specimens. Two testing systems use the same cantilever principle to measure the bending length under the fabrics own weight. The results showed good agreement for some fabrics but not for all, because of the unsuitable dimensions of testing kit to get the right angle of 41.5˚. It is expected that virtual garment simulation properly simulate the fabric behaviours for fabric A and E according to the results of tensile and bending rigidity in both testing system. In next study, we will simulate the sports garments by using these fabric measurements. And we will investigate the effects of the fabric objective measurement on virtual simulation. Software providers still introduce their own textile testing method to measure the fabric parameter but there should be standardization and also they should add some important parameters such as friction coefficient to approve the accuracy of the 3D virtual simulation results.

ACKNOWLEDGEMENT

REFERENCES

[1]. Luible, C. and Magnenat-Thalmann, N. (2007), "Suitability of standard fabric characterisation experiments for the use in virtual simulations", MIRA Lab, University of Geneva, Switzerland. Proceedings: Autex 2007 Conference, Tampere, Finland, June 2007.
[2]. Jess, P., (2013), Fabric objective measurements for commercial 3D virtual garment simulation, International Journal of Clothing Science and Technology, 25 (6). pp. 423-439.
[3]. Wu,Y.Y., Mok, P.Y., Kwok, Y.L., Fan, J.T. and Xin, J.H., (2011), An investigation on the validity of 3D clothing simulation for garment fit evaluation, International conference on Innovative Methods in Product Design, pp. 463-468.
[4]. Luible, C. and Magnenat-Thalmann, N.(2008), The simulation of cloth using accurate physical parameters, The tenth IASTED International Conference on Computer Graphics and Imaging, pp.123-128.
[5]. User manuel, FTK Handout_(2013)_For VS User. http://www.browzwear.com/products/v-stitcher
[6]. Ghosh, T.K. and Zhou, N., (2003), Characterization of fabric bending behaviour: A review of measurement principles, Indian Journal of Fibre&Textile Research, Vol.28, pp:471-476.

Mechanical Properties of Dissimilar 5754-H22/6082-T6 Aluminum Alloy Lap Joints by FSSW

Oguz Tuncel[1], Kurtulus Yigit[1], Mumin Tutar[1], Hakan Aydin[1]

Abstract

Friction stir spot welding (FSSW), which is a solid-state welding process, was generally used for joining lightweight alloys. The application of this process lies in the capacity to assemble alloys which are not easily weldable by the traditional processes especially aluminum alloys. In addition, demand for the joining of different materials is increasing day by day. Especially in the automotive industry, focusing on energy efficiency has made it necessary to combine different materials. The aim of this study is to evaluate the effect of welding parameters on the mechanical properties of dissimilar aluminum alloys (3 mm-thick AA5754-H22 and 3 mm-thick AA6082-T6 sheets) joints produced by FSSW. The rotational speed, dwell time and plunge depth were the parameters taken into consideration. In the experimental study, micro hardness tests and tensile shear tests of the FSSW joints were conducted.

Keywords: *Friction stir spot welding, 5754-H22/6082-T6, Dissimilar Welding, Mechanical Properties*

1. INTRODUCTION

Friction stir spot welding (FSSW) is an alternative joining technique for resistance spot welding (RSW) of Al alloys. FSSW is a solid state joining technique, was developed by Mazda Motor Corporation and Kawasaki Heavy Industries to lap join aluminum sheets. FSSW offers 90% energy saving and 40% equipment saving due to its minimal equipment requirement [1]. The advantages of FSSW relative to RSW are, no cracking problems, no porosity, higher joint strength, suitable for welding dissimilar materials[2]. FSSW process is a derivative of the friction stir welding (FSW) process, and the main difference is the type of the joint [3].

Welding process is performed using a non-consumable rotating tool. The two main functions of the welding tool are to produce friction heat and ensure the flow of material. FSSW process has three phases; plunging, stirring and drawing out. First phase of tool is spinning and slowly plunging into a weld spot until the shoulder contacts the top surface of the work piece and reaches the desire depth. Then in the stirring phase, the materials of the two work pieces mix together. In this phase the tool downward force and the tool rotation speed applied for a desired time to generate frictional heat and sheets soften. Then the heated and softened materials deforms plastically and the two work pieces are mixed together. In the last phase when the adequate penetration achieves, the tool retracts from weld area and solid state bonding is achieved between the surfaces of the upper and lower sheets[4], [5].

Fig. 1 shows a schematic illustration of the phases of FSSW process [6]. After the tool is retracted a keyhole is left. The cross section of the FSSW joint is divided into four regions, which are base material (BM), heat-affected zone (HAZ), thermo-mechanically affected zone (TMAZ), and stir zone. Two microstructural zones are created around the pin, namely, thermo-mechanically affected zone (TMAZ) in which the material was plastically deformed by the tool stirring action and stir zone (SZ) in which original grains appear to be replaced with fine grains of uniform size showing nominal dimension of a few μm. Besides these zones, heat affected zone (HAZ) where the material has undergone a thermal load that modified microstructure and mechanical properties. And a base material zone (BM) is found, in which no metallurgical modification is found due to the welding process[7],[8] . Choosing the wrong welding parameters leads to low weld strength and weld defects. Therefore, the welding parameters (tool rotational speed, dwell time, plunge depth and feed rate selection is very important for superior weld mechanical properties[9].
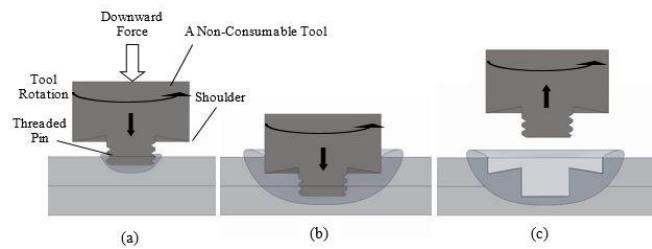
Figure 1. A schematic illustration of FSSW process (a) plunging; (b) stirring (dwell); (c) drawing out [6].

Many works have been carried out concerning FSSW of Al alloy base materials: Piccini et al[10] analyzed the influence of the tool penetration depth, as well as the relative position of the dissimilar aluminum alloys (AA5052-H32/AA6063-T6) in superimposed joints, on the conformation and mechanical properties of FSSW welded joints. They stated that, for all analyzed conditions micro hardness diminishes from BM towards SZ, reaching the minimum value in the HAZ, for all configurations. Jeon et al [11] investigated two typical aluminum alloys (5052-H32/6061-T6) were investigated. They showed that, the dissimilar 5052-H32 and 6061-T6 aluminum alloys were successfully joined with the selected FSSW parameters without visible superficial porosity or macroscopic defects. Buffa et al [12] studied the effect of tool geometry and main process parameters on the micro and macro mechanical properties of FSSWed joints of AA6082. They obtained the best mechanical performance from the cylindrical pin.

The demand for producing dissimilar light-weight materials is continuously increasing day by day due to their advantages. For this reason there is a need to study welding behavior of dissimilar aluminum alloys. In this study, 6082-T6 sheet and 5754-H22 sheet was FSSWed. In the experimental studies, micro hardness tests and tensile shear tests of the FSSW joints were conducted.

2. MATERIAL AND METHODS

In this study, FSSW was performed on 3 mm thick rolled sheets of 6082-T6 and 5754-H22 aluminum alloys. The chemical compositions and mechanical properties of these alloys are shown in Table 1 and 2 respectively.

Table 1. Chemical composition of 6082-T6 and 5754-H22 aluminum alloys used in this study (wt. %)

Alloy	Si	Fe	Cu	Mn	Mg	Cr	Zn	Ti	Ni	Ga	V	Al
6082-T6	0.9	0.44	0.08	0.54	0.7	0.03	0.04	0.04	-	-	-	Balance
5754-H22	0.4	0.4	0.1	0.5	3.6	0.3	0.2	0.15	0.05	0.05	0.05	Balance

Table 2. Mechanical properties of 6082-T6 and 5754-H22 aluminum alloys used in this study

Alloy	Ultimate Tensile Strength [MPa]	0.2% Proof Strength [MPa]	Elongation [%]
6082-T6	342	298	16
5754-H22	130	220-270	10-15

Samples were cut into pieces in dimensions of 100mm × 40mm to prepare the shear tensile test samples according to ANSI/AWS/SAE/D8.9-97 standard [13] (Figure 2). These pieces were friction stir spot welded in the overlapping configuration using a vertical CNC milling machine. A non-consumable tool made of H13 hot work tool steel, having a 10° concave shoulder of 15 mm in diameter was used for all welds. A threaded cylindrical pin used for the welds has a length 3 mm along with a right-hand screw of 0.8 mm pitch. (Figure 3). The welding tool was rotated in a clockwise direction during the welding process. Additionally, a specific clamping fixture for the work pieces was fabricated to ensure correct axial positions and obtain precise plunge depth values.
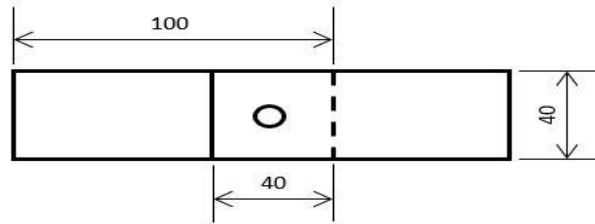
Figure 2. Welding sample installed as lapping joints for the shear-tensile test
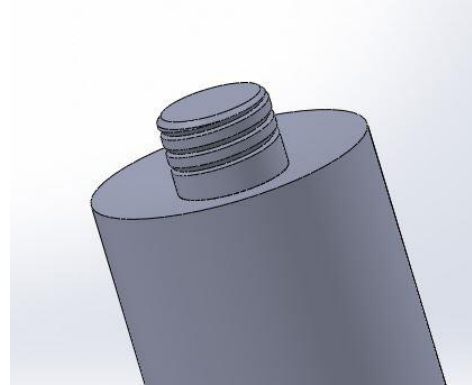
Figure 3. The welding tool used in this study.

An experimental design was created to determine the effect of dwell time and rotation speed. The welding parameters used in this study are listed in Table 3. The welded samples were carefully cross-sectioned through the weld center using a low speed precision cutting machine for macro structural examination and micro hardness measurements. Then, the cross-sectioned samples were mounted in Bakelite, and then ground manually using SiC emery papers. Subsequently, the samples were mirror polished successively through 1 µm and 0.3 µm diamond pastes on a polishing machine, and then washed and blow dried. Mirror-polished samples were characterized to obtain their cross-sectional morphology using a Nikon DIC microscope with a Clemex image analysis system after etching in a reagent with the following composition for 4 minutes: 5 ml hydrofluoric acid and 95 ml distilled water. The mechanical properties of the welds were evaluated through micro hardness measurements and tensile shear tests. Vickers micro hardness measurements were performed on the metallographic samples using a DUROLINE-M micro hardness tester with a 300-gram load for 20 seconds of dwell time, taking five readings and calculating an average value for each weld zone of the welded joints. In order to evaluate the mechanical strength of the welds, the lap shear tensile tests were carried out on a UTEST-7014 tensile testing machine, at room temperature and with a crosshead displacement speed of 5 mm/min. Two additional sheet pieces having a thickness equal to 3 mm were also fixed on the clamping sides of the tensile shear test samples in order to avoid the possible parasitic effects of the bending moment. The tensile lap-shear load for each weld was obtained by averaging five test results.

Table 3. Welding parameters used in this study

Sample	Rotational speed [rpm]	Plunge depth [mm]	Dwell Time [s]	Feed Rate [mm/min]
S1	1000	5	6	50
S2	2000	5	6	50
S3	2500	5	6	50
S4	1500	5	2	50
S5	1500	5	10	50
S6	1500	5	14	50

3. RESULTS AND DISCUSSION

To determine the quality of the FSSW joints of different sheets tensile shear tests were conducted. The results of the tensile shear tests are shown in Table 4. The highest tensile strength was found 6.4 kN for S1 sample. After the tensile test the effects of parameters were separately evaluated. Figure 4 shows the effect of rotational speed change on the tensile shear load. The tensile shear loads of joints decreased almost linearly with increasing rotational speed. The tensile shear load of the spot welded joints decreased approximately 23% when rotational speed was increased from 1000 rpm to 2500 rpm. Figure 5 shows the effect of dwell time change on the tensile shear load. The tensile shear loads of joints decreased almost linearly with increasing dwell time. The tensile shear load of the spot welded joints decreased approximately 12% when dwell time was increased from 2 s to 14 s. This decreases in tensile shear load of the spot welds can be primarily attributed to the increased of thermal softening in HAZ.

Table 4. The tensile properties of the dissimilar FSSW joints (average values)

Sample	Tensile Shear Load [kN]
S1	6.4
S2	5.05
S3	4.92
S4	5.82
S5	5.26
S6	5.14
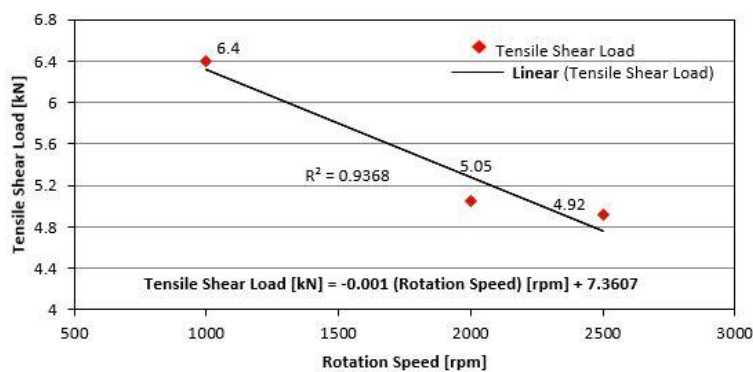
Figure 4. The effect of rotation speed on tensile shear load of a friction stir spot-welded AA6082-T6 joint for different materials
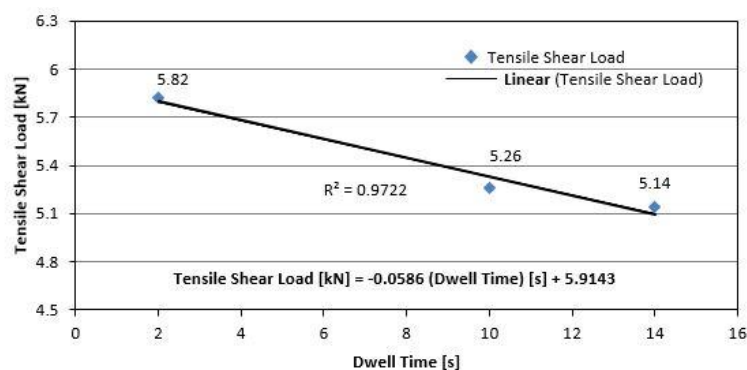
Figure 5. The effect of dwell speed on tensile shear load of a friction stir spot-welded AA6082-T6 joint for different materials

In order to examine the property variations across the welds, micro hardness measurements were performed for the different weld zones of the spot welds and the results are shown in Table 5. The average hardness of the BMs of 6082-T6 and 5754-H22 aluminum alloys was about 110 $HV_{0.3}$ and 67 $HV_{0.3}$, respectively. Comparing with the hardness of BMs of the alloys, the as-welded joints exhibited a hardness drop particularly in around the HAZ and TMAZ indicating that these regions have undergone an annealing process. On the other hand, the average hardness of the SZs was higher than that of 5754 BM and lower than that of 6082 BM. This suggests that the welding process was able to thoroughly mix the solid metals in the SZ originating from the 6082 and 5754 alloys. Except BM hardness of 6082-T6 aluminum alloy, peak hardness values for the weld zones were generally observed in the SZs of the joints. The effect of the rotation speed on the hardness of the weld zones of the dissimilar FSSW joints can be seen in Fig. 6. The average hardness values in the HAZ and TMAZ of 6082 side decreased almost linearly with increasing rotation speed, especially completely linearly in TMAZ. In addition, the rotational speed exhibited similar effect on the hardness of HAZ and TMAZ of 5754 side: The average hardness values in the HAZ and TMAZ of 6082 side decreased almost linearly with increasing dwell time especially completely linearly in HAZ. However, the average hardness values in the SZ increased almost linearly with increasing dwell time.

Table 5. Average micro hardness values ($HV_{0.3}$) of the distinct microstructural zones in the weld regions of the spot welds

Sample No	BM (6082)	HAZ (6082)	TMAZ (6082)	SZ	TMAZ (5754)	HAZ (5754)	BM (5754)
1	110	68	72	78	59	58	67
2	110	63	66	83	58	56	67
3	110	62	63	84	56	55	67
4	110	71	72	81	60	59	67
5	110	61	63	83	58	57	67
6	110	58	60	79	54	54	67
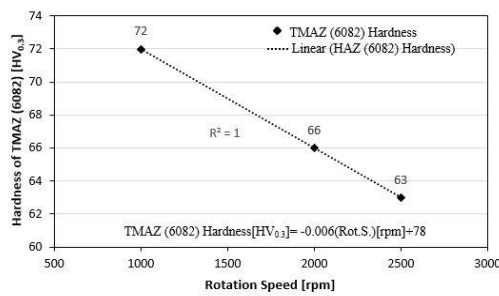
b)
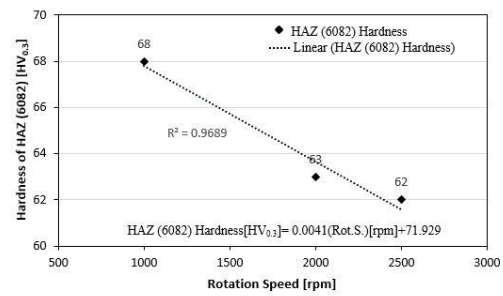
a)
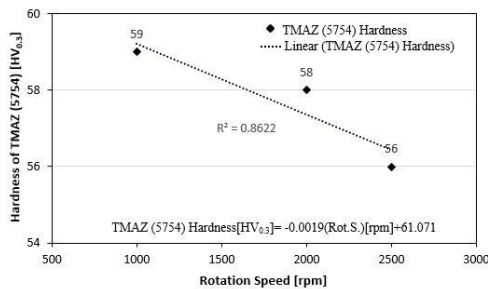
d)
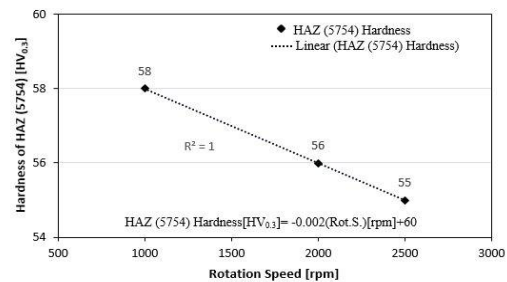
c)
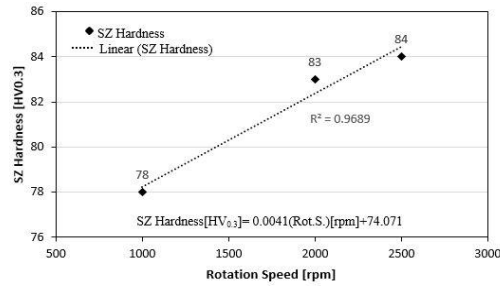
e)

Figure 6. Hardness of (a) HAZ (6082), (b) TMAZ (6082) (a) HAZ (6082), (c) HAZ (5754), (d) TMAZ (5754) and (e) SZ of the FSSW joints versus the rotational speed

The effect of the dwell time on the hardness of the weld zones of the dissimilar FSSW joints can be seen in Fig. 7. The average hardness values in the HAZ and TMAZ of 6082 side decreased almost linearly with increasing dwell time. In addition, the dwell time exhibited similar effect on the hardness of HAZ and TMAZ of 5754 side: The average hardness values in the HAZ and TMAZ decreased almost linearly with dwell time. The average hardness values in the SZ firstly increased then decreased with increasing dwell time. This may be associated with the grain coarsening in the SZ through the advanced dynamic recrystallization with the increased heat input.
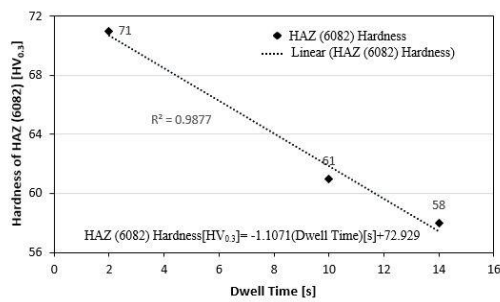
a)
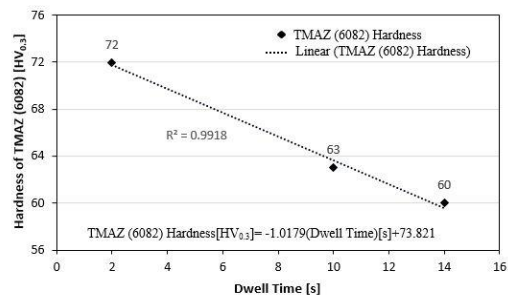
b)
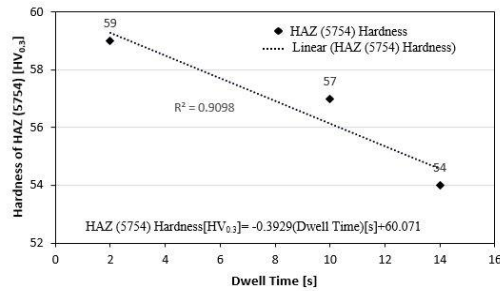
c)
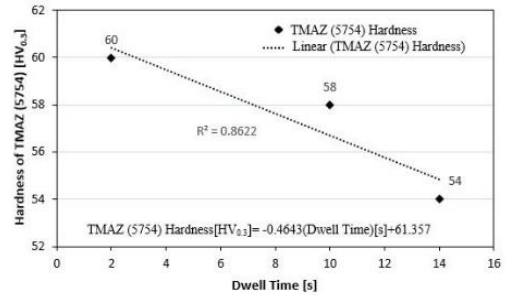
d)
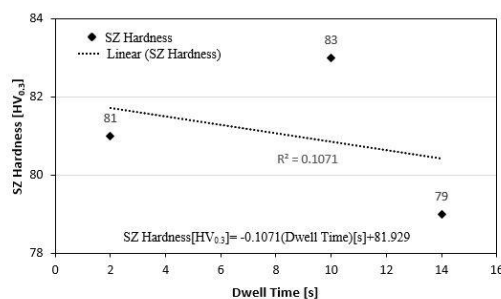
e)

Figure 7. Hardness of (a) HAZ (6082), (b) TMAZ (6082) (a) HAZ (6082), (c) HAZ (5754), (d) TMAZ (5754) and (e) SZ of the FSSW joints versus the dwell time

4. CONCLUSION

The present study was focused on the effect of the rotational speed and dwell time on the mechanical properties of dissimilar friction stir spot welds between 6082-T6 sheet and 5754-H22 aluminum alloys. Based on the experimental results reported earlier, the following major conclusions were derived.

- The highest tensile strength was found 6.4 kN for sample S1; experimental parameters; rotational speed: 1000 rpm, plunge depth: 5 mm, dwell time: 6s, feed rate: 50 mm/dk.
- As a result of experiment carried out, the most influential parameter was found rotation speed. The tensile shear load of the spot welded joints increased approximately 23% when rotation speed was increased from 1000 s to 2500 s.
- The tensile shear load of joints decreased almost linearly with increasing rotational speed and dwell time.
- Comparing with the hardness of BMs, the FSSW joints exhibited a hardness drop in the HAZ and TMAZ. The SZ hardness was higher than 5754 BM and lower than 6082 BM.
- The hardness values in the HAZ and TMAZ of 6082 side decreased almost linearly with increasing rotation speed. In addition, the rotational speed exhibited similar effect on the 5754 side decreased almost linearly with increasing rotation speed. On the other hand, the SZ hardness increased almost linearly with increasing rotation speed.
- The hardness values in the HAZ and TMAZ of 6082 side decreased almost linearly with increasing dwell time. In addition, the dwell time exhibited similar effect on the 5754 side decreased almost linearly with increasing dwell time. On the other hand the hardness values of SZ firstly increased with increasing dwell time from 2 s to 10 s then decreased with increasing dwell time from 10 s to 14 s.
- The lowest hardness values (around 54 $HV_{0.3}$) for the weld zone were observed in HAZ owing to the significantly over aging and grain coarsening due to frictional heat during welding process.

REFERENCES

[1]. D. Mitlin, V. Radmilovic, T. Pan, J. Chen, Z. Feng, and M. L. Santella, "Structure – properties relations in spot friction welded (also known as friction stir spot welded) 6111 aluminum," vol. 441, pp. 79–96, 2006.

[2]. Z. Li, Y. Yue, S. Ji, C. Peng, and L. Wang, "Optimal design of thread geometry and its performance in friction stir spot welding," *JMADE*, vol. 94, pp. 368–376, 2016.

[3]. H. Aydin, O. Tuncel, C. Yuce, M. Tutar, N. Yavuz, and A. Bayram, "Effect of rotational speed and dwell time on mechanical properties of dissimilar AA1050-AA3105 friction stir spot welded joints," *Mater. Test.*, vol. 56, no. 10, 2014.

[4]. A. Gerlich, P. Su, T. H. North, A. Gerlich, P. Su, and T. H. North, "Peak temperatures and microstructures in aluminium and magnesium alloy friction stir spot welds Peak temperatures and microstructures in aluminium and magnesium alloy friction stir spot welds," vol. 1718, no. February, 2017.

[5]. H. Badarinarayan, Q. Yang, and S. Zhu, "International Journal of Machine Tools & Manufacture Effect of tool geometry on static strength of friction stir spot-welded aluminum alloy," vol. 49, pp. 142–148, 2009.

[6]. M. Tutar, H. Aydin, C. Yuce, N. Yavuz, and A. Bayram, "The optimisation of process parameters for friction stir spot-welded AA3003-H12 aluminium alloy using a Taguchi orthogonal array," *J. Mater.*, vol. 63, pp. 789–797, 2014.

[7]. W. Yuan *et al.*, "Effect of tool design and process parameters on properties of Al alloy 6016 friction stir spot welds," *J. Mater. Process. Technol.*, vol. 211, no. 6, pp. 972–977, 2011.

[8]. G. D. Urso, "Thermo-mechanical characterization of friction stir spot welded AA6060 sheets : Experimental and FEM analysis," *J. Manuf. Process.*, vol. 17, pp. 108–119, 2015.

[9]. M. K. Bilici and A. I. Yükler, "Influence of tool geometry and process parameters on macrostructure and static strength in friction stir spot welded polyethylene sheets," *Mater. Des.*, vol. 33, no. 1, pp. 145–152, 2012.

[10]. J. M. Piccini and H. G. Svoboda, "Effect of the tool penetration depth in Friction Stir Spot Welding (FSSW) of dissimilar aluminum alloys," *Procedia Mater. Sci.*, vol. 8, pp. 868–877, 2015.

[11]. C. Jeon, S. Hong, Y. Kwon, H. Cho, and H. N. Han, "Material properties of friction stir spot welded joints of dissimilar aluminum alloys," *Trans. Nonferrous Met. Soc. China*, vol. 22, pp. s605–s613, 2012.

[12]. G. Buffa, P. Fanelli, L. Fratini, and F. Vivio, "Influence of joint geometry on micro and macro mechanical properties of friction stir spot welded joints," *Procedia Eng.*, vol. 81, no. October, pp. 2086–2091, 2014.

[13]. A. American and N. Standard, "Practices for Test Methods for Evaluating the Resistance Spot Welding Behavior Sheet Steel Recommended Practices for Test Methods for Evaluating the Resistance Spot Welding Behavior of," 2002.

MATLAB GUI Model for PV System Feasibility of a House Electricity Consumption in Turkey

Kubra Nur Akpınar[1], Ayse Ceyda Bilu [2,] Bedri Kekezoglu[2]

Abstract

In this study, feasibility analysis was done with a program that created a simulation model in the MATLAB GUI environment for the PV system installation in the production of electricity requirement of a house in Turkey conditions. The energy consumption is calculated through the data of the operating hours in a day and the number of running days in a year which entered by user. Once the panel and zone selection options have been specified, the program calculates the annual energy need for the house, the energy generated, the number of panels required to produce this energy, and the area required for system. Monthly energy distribution is shown graphically. Calculations are being revised for different panel number usage. In the economic analysis part, system cost, payback period and annual earnings are determined. PV system model, consumers will invest in renewable energy that will help to make the pre-feasibility and can be used as a decision-making mechanism.

Keywords: *Feasibility analysis, MATLAB GUI, Photovoltaic System, Payback Period, Renewable Energy*

1. INTRODUCTION

According to the definition of the International Energy Agency (IEA), renewable energy is defined as a type of energy that is constantly renewed and obtained from natural processes. According to this; solar energy, wind, biomass, biofuels, geothermal, hydraulic power, ocean resources and hydrogen energy obtained from natural sources are the energy sources that make up this concept [1]. Reducing foreign dependency since it is obtained from countries' own natural resources, being continuous as long as natural resources exist, lack of harms against the environment unlike fossil resources and the fact that it is safe are the reasons of preference of renewable energy. It helps economic development by creating new business areas in the country with the decrease of energy import [2].

In order to increase the use of our country's high renewable energy potential, green energy investments are being developed under the Renewable Energy Laws (REN). Wind and solar energy investments come to the forefront, based on the incentives and practices of these laws [3]. While wind energy is preferred for systems with great power, individuals throughout the world and especially in Germany produce their own energy by using solar energy without harming the environment by integrating PV panels into the roofs which are one of the smallest energy systems. Since this solar-generated energy has wave characteristic, it can be connected to the grid at times when the sun is insufficient and can take electricity from the interconnected system or use storage tools such as accumulator, battery, etc.

In this study, the feasibility of integrating the PV system into the dwellings of a 4-member family, like in many other developed countries, was realized with the MATLAB GUI program.

---

[1]*Corresponding author: Ondokuz Mayıs University, Department of Electrical Electronics Engineering, kubranur.birlik@omu.edu.tr*

[2]*Yıldız Technical University, Istanbul,Turkey. ayseceydabilu@gmail.com*

[2]*Yıldız Technical University, Istanbul,Turkey. bkekez@yildiz.edu.tr*

2. MATERIALS AND METHODS

In the created model, it is waited from the user to enter the data of electrical devices powers, operating hours of them in a day and number of day in a year to calculate the total energy need in a year. If user need more devices to specify the power that undefined in the program, he/she can use the option "other" labeled.

After the entering power of devices, the next step of the program is PV panel and location choices. User selects one of the PV panels from the popup menu to install the system with, then chooses the location where it will be installed. Yingli Solar PV panels were used for the program as panel options and three districts from Izmir; Cigli, Dikili and Menderes as location examples in this study. Later on, exchange rate of dollar/Turkish liras is defined with the value of the day, to calculate the sale price of the surplus energy.

Then the run button is clicked and the program shows the results. It calculates the annual energy need and, required area, setup cost, installed power, panel number required of the suitable PV system according to the energy need, and annual energy production, annual earning, depreciation time of the system and the graph of generated energy by month. If the user has a thought to install the system with different panel number from calculated by program, he/can specify a new one. The screen of the program as shown below (*Figure 1*), without entering any data.

Figure 1: First screen of the program

Solar energy data are taken from SEPA (Solar Energy Potential Atlas) for selected regions. In this study, by using the global radiation values of the Dikili district of İzmir province, energy reaching a house in that area were calculated. When we look at the one-year radiation distribution in the SEPA radiation bar graph *Figure 2*, it appears that the selected zone is suitable for solar energy investment.
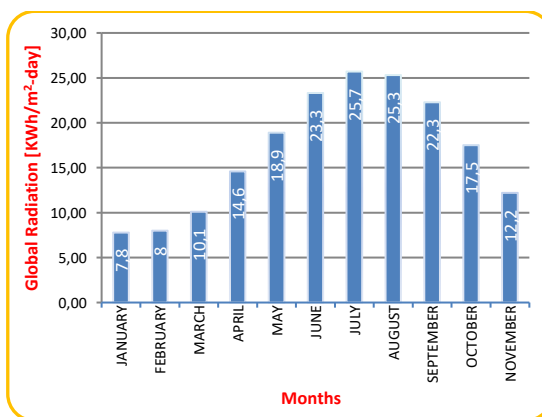
Figure 2: Izmir - Dikili Global Radiation Values [4]

69

Figure 3 shows air temperature data for selected regions, taken from the RETScreen program. RETScreen is a renewable energy feasibility program used by the Canadian government that supplies all atmospheric data from NASA. Detailed atmospheric solar data from the RETScreen program was also used in calculations to support global radiation data from SEPA for the selected region.
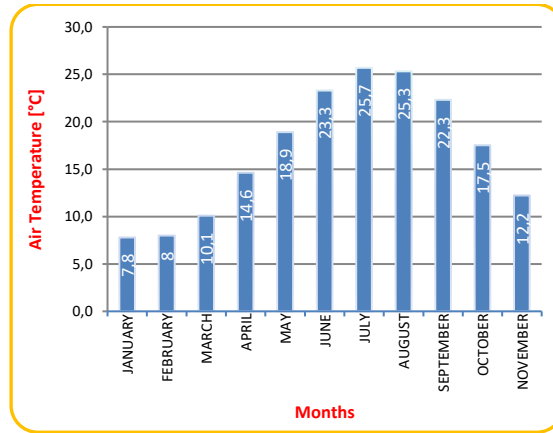
Figure 3:Air Temperature of Dikili [5]

3. MATHEMATICAL BACKGROUND

After providing the potential of solar energy and weather temperature data, the total solar energy, the required number of panels and the panel area is calculated. After the power of the annual energy requirement devices and the annual working hours are entered into the program as hours and days, with the multiplication and subsequent collection of the data of each device in itself, the number of panels required, is calculated by dividing the calculated energy requirement by the energy generated by one of the selected panels on the program in the selected region. The required space for the system setup is obtained by multiplying the selected panel by the required number of panels [6].

3.1. Calculation of Energy from the PV

NOCT (nominal cell operating temperature) is the cell temperature module with solar radiation of 0,8 kW/m^2, air temperature of 20°C and wind speed of 1 m/s [7]. Cell [°C], T_{air} [°C] is the cell temperature calculated from the air temperature. S is the solar radiation value [kW/m^2]. The cell temperature was calculated under PTC conditions (PVUSA Test Conditions - air temperature = 20°C, radiation S = 1 kW/m^2). P [kW] is PV panel power calculated using P_{mpp} (maximum power point) and κ [%/°C] (estimated power loss for each temperature value around 25°C) values. Annual solar energy E [MWh] is calculated by adding 10% operational cost loss, multiplying solar panel power with daily sun peak hour strike (solar peak hour/day).

$$T_{cell} = T_{air} + [(NOCT - 20°C)/0,8].S \tag{1}$$

$$P = P_{mpp}.[1 - \kappa.(T_{cell} - 25°C)] \tag{2}$$

$$E = P.\left(sun\ peak\ \frac{hour}{day}\right) * 365\ \frac{day}{year} * 0,9 \tag{3}$$

$$Panel\ Number = \frac{Daily\ Energy\ Demand}{(Power\ of\ a\ PV)*(Sunshine\ Duration)} \tag{4}$$

3.2. Economic analysis

As a result of calculating the annual energy requirement, the next step is economic analysis. The following formulas are used to calculate the annual earnings and payback period obtained from the PV system.

$$Payback\ Period = \frac{CAPEX[TL]}{Yearly\ Energy\ Produced[kWh]*0,40\left[\frac{TL}{kWh}\right]} \tag{5}$$

The system cost (CAPEX: Capital Expenditure) is calculated by multiplying the system installation cost, which is taken as 4500 TL per kilowatt, with the installed power.

4. CASE STUDY

In this study, the pre-feasibility analysis of a complete house for a four-person household in the case of the complete supply of energy from the PV system was carried out using the MATLAB GUI program. The investor calculates the annual energy consumption by entering the data of the power of each household electrical appliances, the working hours, and the number of days the appliances work for each year into the program. To supply the consumed energy from the PV system, panel options are selected as desired. Region selection is made for the planned system to be established. Finally, the current dollar parity is entered and the results are evaluated.

As an example, required data to calculate annual energy need for a family of four, electrical devices powers was entered by us as shown below *(Figure 4)*, YINGLI SOLAR YL200P-23b named PV model and Izmir-Dikili location was chosen and dollar parity value was typed as 3.7 for that day.

	Power [W]	Operating Time [h]	Number of Day
Refrigerator	1100	24	365
Washing Machine	2000	2	120
Dishwasher	1200	2	120
Oven	2500	1	75
TV	100	5	365
Computer	75	4	365
Lighting	90	5	365
Geyser	2000	1	365
Small House Appliances	500	1	100
Other	1000	2	120

Figure 4: Energy demand chart for each device

As output, the annual energy need and the optimum number of panels (53) required for the system are calculated. Accordingly, the area that needs investor, system installed power, annual generated energy, system cost, payback period, annual earnings and generated energy by month are calculated as shown below *(Figure 5)*. If the person planning to install the system wants to use with different number of panels, he/she can change the panel number (i.e. 70 panels) on the program and accordingly the results on the screen are updated *(Figure 6)*.
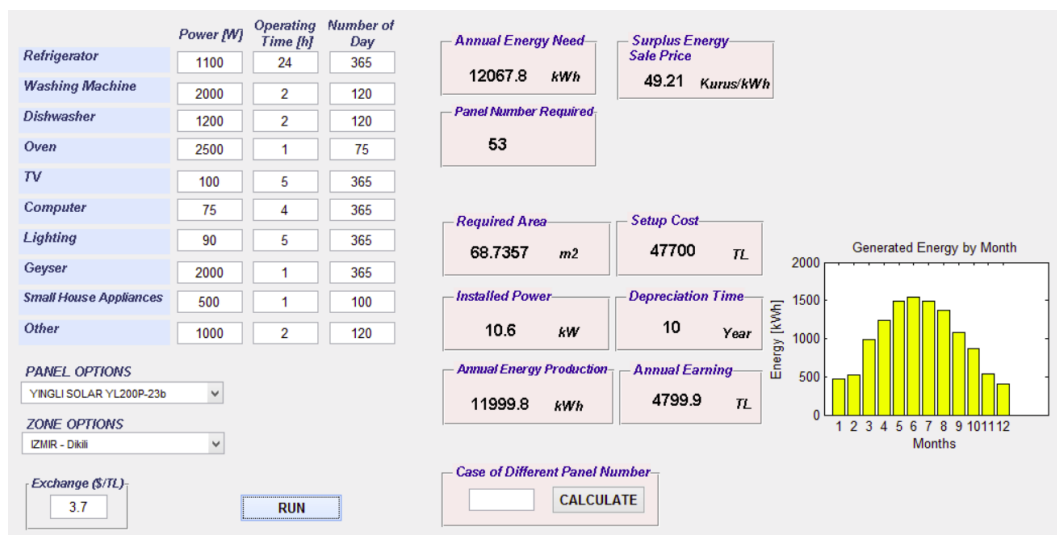
Figure 5: The results of the program according to defined example
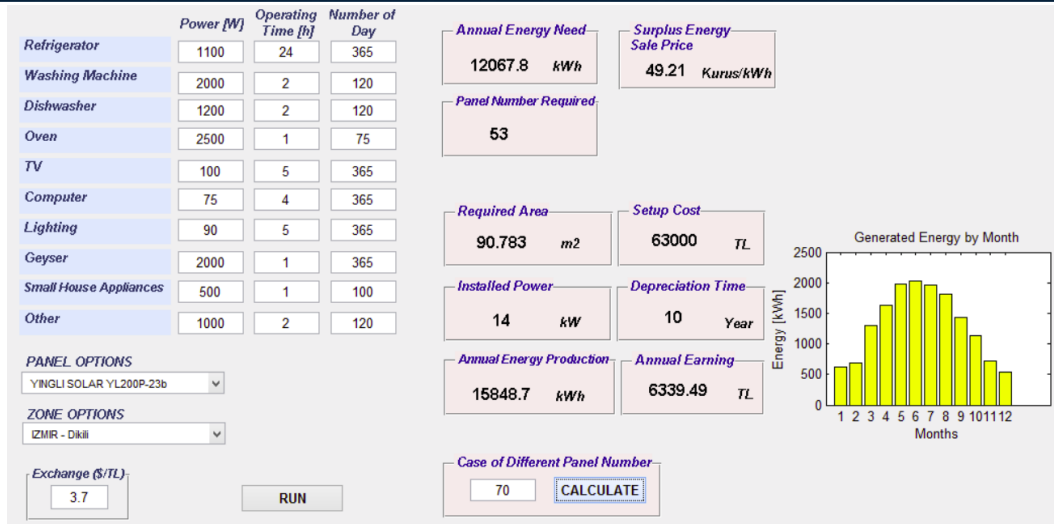
Figure 6: Screenshot of the program for the second case, with different panel number

5. CONCLUSIONS

In this paper, a MATLAB GUI program is created for calculate the annual energy production, component number, required area for producing this energy, payback period and installed power from PV panel. Calculations are based on a four-person household in the case of the complete energy supply from the PV system. Consumed energy is calculated through the data of the operating hours in a day and the number of running days in a year which entered by user. There are various PV panel and region options in the program. Monthly generated energy distribution is shown graphically. System cost, payback period and annual earnings are also calculated in the economic analysis part so that will help to make the pre-feasibility and can be used as a decision-making mechanism for investors.

REFERENCES

[1]. Karadag, C.;Gülsac, I.; Ersoz, A.; Calıskan, M.: "Cevre Dostu ve Temiz: Yenilenebilir Enerji Kaynakları", Bilim ve Teknik Dergisi, n.498, p.24-27, May 2009.
[2]. SimlaYasemin Ozkaya. 2004. Yenilenebilir Enerji Kaynakları. Uluslararası Ekonomik Sorunlar Dergisi, Retrieved August, 2004 from the World Wide Web: http://www.mfa.gov.tr/yenilenebilir-enerji-kaynaklari.tr.mfa
[3]. SimlaYasemin Ozkaya. 2004. Yenilenebilir Enerji Kaynakları. Uluslararası Ekonomik Sorunlar Dergisi, Retrieved August, 2004 from the World Wide Web: http://www.mfa.gov.tr/yenilenebilir-enerji-kaynaklari.tr.mfa
[4]. Retrieved March 2017, from http://www.eie.gov.tr/MyCalculator/pages/35.aspx
[5]. Retrieved March 2017, from http://www.retscreen.net/
[6]. Martin Kaltschmitt, Wolfgang Streicher, Andreas Wiese, Springer, 2007, Renewable energy: technology, economics, and environment. ISBN 3-540-70947-9, ISBN 978-3-540-70947-3, page 55
[7]. Gilbert M. Masters, 2004, Renewable and Efficient Electric Power Systems, United States of America, John Wiley & Sons, page 476

Accuracy Assessment of Kinematic PPP Using Various Online Services

Salih Alcay[1*], Huseyin Zahit Selvi[1]

Abstract

In recent years, in addition to the static mode, online services enhanced the capabilities of Precise Point Positioning (PPP) to provide kinematic mode. In this study, in order to assess the accuracy of the kinematic PPP, The Canadian Spatial Reference System Precise Point Positioning Service (CSRS-PPP) and the Magic Global Navigation Satellite System (MagicGNSS) were used. The raw data were taken from 5 IGS stations, located in different part of the world. Estimated coordinates were tested in terms of both accuracy and precision based on ITRF 2008 measurement epoch coordinates of the stations. The results indicate that centimeter accuracy and millimeter to centimeter precision can be achieved for horizontal components.

Keywords: *CSRS-PPP, IGS, ITRF, Kinematic PPP, MagicGNSS*

1. INTRODUCTION

Precise Point Positioning (PPP) is an absolute positioning technique which has increasing interest among the researchers in different study areas. It was first developed for using in static applications and has been studied extensively in the last decade [1]-[5]. Besides static PPP, with the development of final, near-real-time or real-time satellite orbit and clock products, kinematic PPP is being increasingly used in research and survey applications including airborne, marine, hydrographic survey, etc.[6]-[10].

Reference [8] presents a case study of kinematic PPP accuracy using different data configurations. Different online services are used for the processing. Results exhibits that kinematic PPP can achieve sub-decimeter level accuracy with respect to planimetric measurements and better than 20 cm for the altimetric measurements. Reference [9] evaluates the variability of kinematic PPP precision based on different observation types (single and dual frequency). Results prove the quality of dual-frequency observations over single frequency observations, where the improvement is more than 100%. Among the recent ones, Reference [10] examines the kinematic performance of online services in terms of positioning precision. GNSS data are used for hydrographic surveying. The results indicate that with 1s data, decimeter to meter precision can be achieved for horizontal and vertical coordinates.

In order to estimate kinematic coordinates, scientific software (Bernese and GIPSY-OASIS) and online PPP data processing services can be used. Currently, four online PPP data processing services provide kinematic data processing options. They are Automatic Precise Positioning Service (APPS) [11], Canadian Spatial Reference System Precise Point Positioning Service (CSRS-PPP) [12], GNSS Analysis and Positioning Software (GAPS) [13] and MagicGNSS [14]. Details about online services are given at the relevant web sites.

This study examines the performance of kinematic PPP in terms of both accuracy and precision using two different processing services (CSRS-PPP and MagicGNSS).

2. MATERIAL AND METHOD

In order to examine the performance of the kinematic PPP method, observation data of 5 IGS stations, located in different region, were used (Figure 1).

[1*] *Corresponding author: Necmettin Erbakan University, Geomatics Engineering Department Konya/ Turkey.* salcay@konya.edu.tr
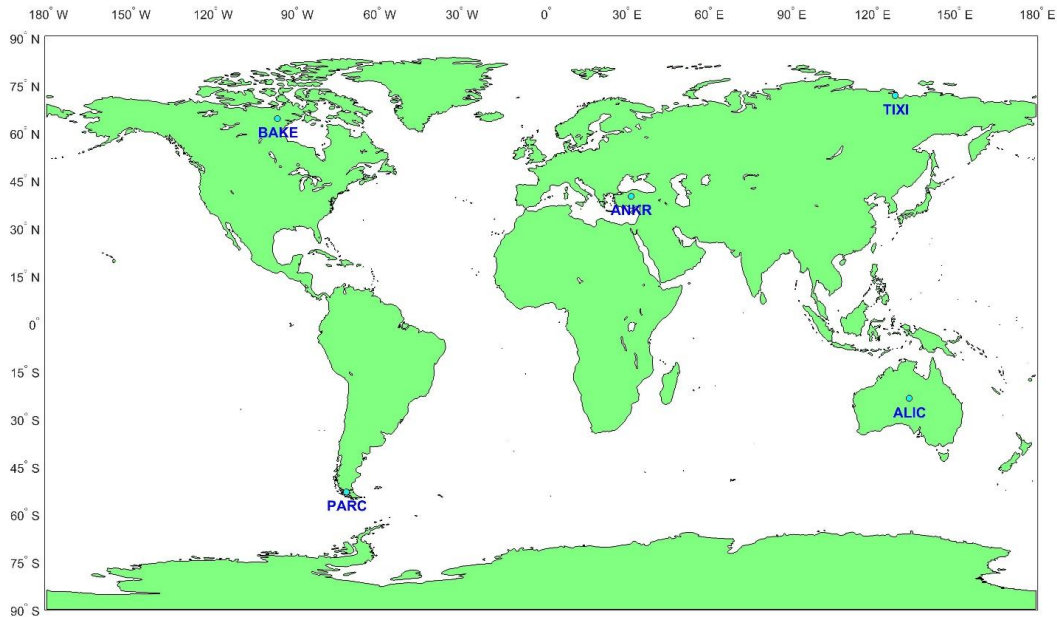
Figure 2. Regional location of the used IGS sites

Observation data were downloaded from the SOPAC website [15]. The data set cover from 01.01.2017 to 05.01.2017, with data recorded at 30 s interval. Using permanent stations are helpful to evaluate the kinematic PPP model and algorithm since its placement should eliminate signal loss and multipath problems. Only GPS data were used for this test. Besides the CSRS-PPP, MagicGNSS was used for the alternative kinematic solution.

3. RESULTS

In this study, kinematic PPP results including 5 daily observations were examined in terms of both accuracy and precision. Accuracy of the estimated kinematic PPP coordinates for each epoch were tested based on ITRF 2008 measurement epoch coordinates (true coordinates) of IGS stations, derived based on ITRF 2008 reference epoch coordinates and velocities. Differences between true coordinates and the estimated ones are given in figures 2-6. As depicted in figures, up (u) components are larger than the horizontal components of all stations. Similar results are observed corresponding to each day. In addition, figure 4 exhibits that both CSRS-PPP and MagicGNSS results corresponding to ANKR station, located in the mid-latitude region, are better than the results of other stations, located in the northern/southern hemisphere high latitude regions. Besides, CSRS-PPP results are generally better than the MagicGNSS results at all stations. Particularly in the northern hemisphere high latitude stations, some outliers are observed in the results of MagicGNSS (Figure 2, 3).
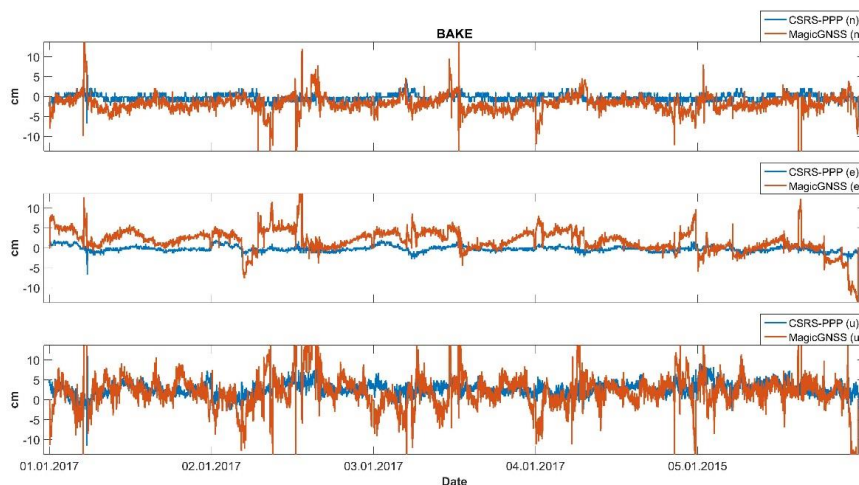
Figure 2. Differences between true and estimated coordinates at BAKE station
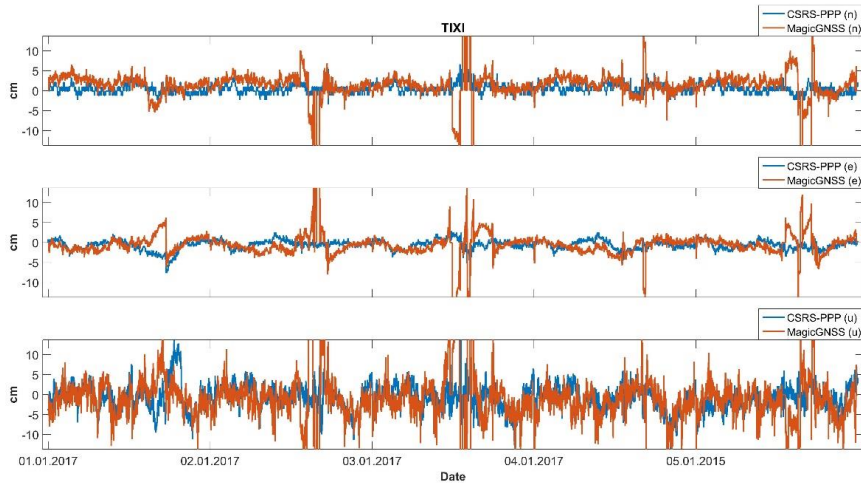
Figure 3. Differences between true and estimated coordinates at TIXI station

Figure 4. Differences between true and estimated coordinates at ANKR station
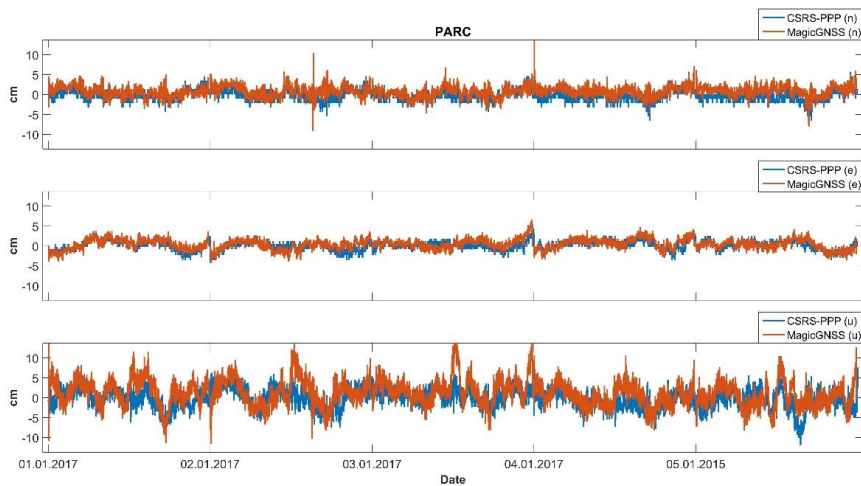
Figure 5. Differences between true and estimated coordinates at PARC station
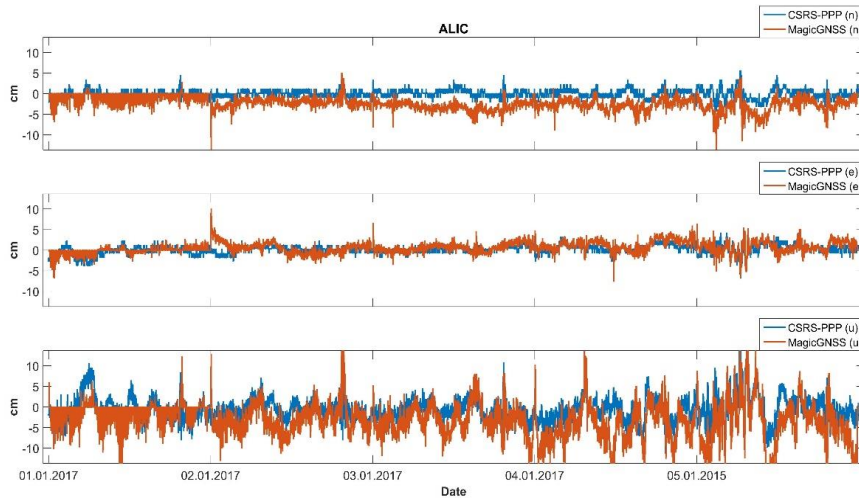
Figure 6. Differences between true and estimated coordinates at ALIC station

Besides the accuracy analysis, in an attempt to further enhance our evaluation in assessing the precision of the results, some statistical values, including standard deviation (std), maximum (max), minimum (min) and range, corresponding to the differences were computed and given in table 1.

Table 1. Statistical values of the differences

Stations		CSRS-PPP			MagicGNSS		
		n (cm)	e (cm)	u (cm)	n (cm)	e (cm)	u (cm)
BAKE	std	0.85	0.70	1.58	2.37	2.94	6.70
	max	7.70	2.10	12.00	19.80	18.90	68.50
	min	-6.80	-6.60	-11.50	-28.80	-13.60	-70.70
	range	14.50	8.70	23.50	48.60	32.50	139.20
TIXI	std	1.13	1.22	3.18	4.32	3.06	7.26
	max	7.70	2.90	19.90	38.80	22.40	63.50
	min	-5.70	-7.70	-17.20	-33.70	-20.50	-95.60
	range	13.40	10.60	37.10	72.50	42.90	159.10
ANKR	std	0.59	0.65	1.41	0.94	0.88	2.11
	max	1.30	3.20	7.00	3.20	4.10	11.60
	min	-3.10	-1.90	-3.90	-8.20	-4.80	-6.20
	range	4.40	5.10	10.90	11.40	8.90	17.80
PARC	std	1.30	1.19	2.44	1.36	1.32	3.32
	max	5.70	5.20	7.60	14.80	6.70	18.20
	min	-6.50	-4.20	-11.90	-9.10	-4.30	-11.50
	range	12.20	9.40	19.50	23.90	11.00	29.70
ALIC	std	1.00	1.13	3.02	1.52	1.43	4.53
	max	5.60	4.30	23.40	5.10	10.20	18.50
	min	-7.70	-6.90	-14.30	-15.10	-7.70	-25.50
	range	13.30	11.20	37.70	20.20	17.90	44.00

According to the table 1, while standard deviations are less than 1.30 cm for the horizontal and 3.18 cm for the vertical components corresponding to CSRS-PPP, less than 4.32 cm and 7.26 cm for the horizontal and vertical components of MagicGNSS results, respectively. In addition, according to the range values, ANKR results are better than the others for both CSRS-PPP and MagicGNSS.

4. CONCLUSIONS

In this study, positioning performance of kinematic PPP was investigated in terms of both accuracy and precision. 5 daily observations of 5 IGS stations were used. IGS stations were chosen in different regions. Processes were performed using CSRS-PPP and MagicGNSS online services. According to the CSRS-PPP results of all stations, it is possible to obtain better than 7.70 cm accuracy for the horizontal components and better than 23.40 cm accuracy for the vertical components. This condition can change according to the stations. For instance, it is possible to reach better than 3.20 cm and 7.00 cm accuracy at ANKR station for the horizontal and vertical components, respectively. In addition, standard deviations are smaller than 3.18 cm which indicates the precision of the results. Besides, MagicGNSS results are a little larger than the CSRS-PPP results.

ACKNOWLEDGEMENT

REFERENCES

[1]. C.O. Yigit, V. Gikas, S. Alcay, A. Ceylan, "Performance evaluation of short to long term GPS, GLONASS and GPS/GLONASS post-processed PPP," *Survey Review*, vol. 46(3), pp. 155-166, 2014.
[2]. R.M. Alkan, V. Ilci, I.M. Ozulu and M.H. Saka, "A Comparative study for accuracy assessment of PPP technique using GPS and GLONASS in Urban Areas," *Measurement*, vol. 69, pp. 1-8, 2015.
[3]. K. Huber, F. Heuberger, C. Abart, A. Karabatic, R. Weber, P. Berglez, "PPP: Precise Point Positioning – constrains and opportunities," *In Proc. FIG Working Week*, Sydney, Australia, 11– 16 April, 2012.
[4]. F. Moschas, A. Avallone, N. Moschonas, V. Saltogianni, S. Stiros, "Assessment of the accuracy of PPP for very-high-frequency dynamic, satellite positioning and earthquake modeling," *Geophysical Research Abstracts, EGU General Assembly,* 14, EGU2012–4289, 2013.
[5]. C. Rizos, V. Janssen, C. Roberts, T. Grinter, "GNSS: Precise Point Positioning PPP versus DGNSS". *Geomatics World* (October), 18–20, 2012.
[6]. M. Tsakiri, "GPS processing using online services," *J. Surv. Eng.,* 134(4): 115-125, 2008.
[7]. H. Landau, X. Chen, S. Klose, R. Leandro, U, Vollath, "Trimble's RTK and DGPS solutions in comparison with Precise Point Positioning". *International Association of Geodesy Symposia* 133: Observing our changing Earth, pp 615-623, 2009.
[8]. A. Martín, A.B. Anquela, J.L. Berné, M. Sanmartin, "Kinematic GNSS-PPP results from various software packages and raw data configurations," *Sci. Res. Essays,* vol. 7(3), pp 419–431, 2012.
[9]. A. Farah, "Accuracy Assessment Study for Kinematic GPS–PPP Using Single- and Dual-Frequency Observations with Various Software Packages," *Arab J Sci Eng.,* 40:2013–2019, 2015.
[10]. M. Berber, W. Wright, "Online kinematic GNSS data processing for small hydrographic surveys" *Ocean Engineering*, 112, 335–339, 2016.
[11]. APPS website. Available http://apps.gdgps.net/ (accessed 15.03.2017)
[12]. CSRS-PPP website. Available https://webapp.geod.nrcan.gc.ca/geod/tools-outils/ppp.php?locale=en (accessed 15.03.2017)
[13]. GAPS website. Available http://gaps.gge.unb.ca/submitadvanced.php (accessed 15.03.2017)
[14]. MagicGNSS website. Available https://magicgnss.gmv.com/ppp (accessed 15.03.2017)
[15]. SOPAC website. Available http://sopac.ucsd.edu/ (accessed 10.03.2017)

Scheduling the Unrelated Parallel Machines with a Common Server

Cagrı Sel[1], Alper Hamzadayı[2], Atabak Elmi[3]

Abstract

In this study, we address the unrelated parallel machines scheduling problem where the sequence dependent setup operations are performed by a common server. A mixed integer linear programming model is proposed to solve the problem. The model is tested by a randomly generated problem instance. As an overall remark, the model is capable of solving the small and/or medium sized illustrative examples optimally.

Keywords: *Unrelated parallel machines, A common server, Sequence dependent setup times, Mixed integer linear programming.*

1. INTRODUCTION

Production scheduling can be described by two terms, i.e. allocation and sequencing. The allocation is to assign the production resources to perform the operations. Sequencing is to order the operations based on their precedence relationships and technological constraints of the allocated resources. The decisions made on allocation and sequencing vary on the production environments, e.g. a single machine to perform the operations in which the allocation decisions can be ignored or a shop to be scheduled based on job flows. Hereby, several machines can also be positioned parallelly. The parallel machines are able to perform the same operations but in different processing times, so called unrelated parallel machines. The changeovers on each machine depends on the preceding operation, i.e. require sequence dependent setup times regarding to the previously processed job on that machine for each job. The servers required to perform the sequence dependent changeovers can be limited in modern manufacturing systems. In addition to the schedule of the unrelated parallel machines, the limited servers require a certain schedule allocating the servers to the sequence dependent setup operations. A common server is an industrial wide example of scheduling the unrelated parallel machines with sequence dependent setup time such as paper ranging from paper and textile industries to casting industry. In this study, we address the unrelated parallel machine scheduling with a common server to perform the sequence dependent changeovers. A mathematical model is formulated to solve the problem and the model is tested by an illustrative example. The problem and the mathematical model are the extension of on the identical parallel machine scheduling problem addressed by Hamzadayi & Yildiz (2017). The contribution of the research is the mathematical formulation to be used as a decision support model in real-life applications.

The remainder of the paper is organized as follows. In section 2, related literature is presented to position the study in the existing literature. The mathematical formulation is explained in section 3. The illustrative example is described and the results of the numerical analysis are presented in section 4. The conclusion section including the future research directions are given in Section 5.

2. LITERATURE REVIEW

In this section, we review the static scheduling problems where a known collection of jobs is processed on a set of machines. Each of the jobs has a pre-determined processing time in a certain operation sequences by technological constraints of the machines. The static problems address the parallel machine scheduling with a

[1] *Corresponding author: Karabuk University, Industrial Engineering Department, 78050, Karabuk, Turkey. cagrisel@karabuk.edu.tr*

[2] *Alper Hamzadayı, Yüzüncü Yıl University, Industrial Engineering Department, 65080, Van, Turkey. alperhamzadayi@yyu.edu.tr*

[3] *Atabak Elmi, Gaziantep University, Industrial Engineering Department, 27310, Gaziantep, Turkey. atabak.elmi@gantep.edu.tr*

common server. The preliminary research is focused on the scheduling of two parallel machines (e.g. Abdekhodaee and Wirth 2002; Hall et al, 2000; Koulamas, 1996). The scheduling of two identical parallel machines with a common server is NP-Hard (Kravchenko & Werner, 1997) and, the mathematical modelling is the well-known approach to solve the problems (Hasani et al., 2014a,b). The mathematical models are also introduced for the same problem for m parallel machines (e.g. Huang et al., 2010; Kim and Lee 2012) and shown to be strongly NP-hard (Hamzadayi & Yildiz, 2017). The research currently address on the identical machine scheduling in order not to increase the problem complexity in the literature, however there is still need for research on mathematical formulations accounting for the unrelated parallel machines.

3. MATHEMATICAL FORMULATION

A mixed integer linear programming formulation is proposed to solve the problem in line with Hamzadayi & Yildiz (2017). The extension is to revise the existing formulation with the unrelated parallel machine consideration, i.e. the standard processing time for job j depends on the machine m ($P_{jm} \mid j \in \{1, 2, \ldots, J\}, m \in \{1, 2, \ldots, M\}$). The decision variables and the corresponding parameters are extended with an additional sub-index. The notation (see Table 1.) and the mathematical formulation is given below;

Table 1. Notation of the mathematical formulation

Notation	Definition
Sets and indexes	
$j, j', j'' \in J$	Planned number of jobs to be produced on the machines
$m \in M$	Number of identical parallel machines
Parameters	
P_{jm}	Standard processing time for job j on the machine m
$D_{jj'}$	Sequence dependent setup time to process job j' after job j on the same machine
BM	A very large number
Decision variables	
$X_{jj'm}$	1 if job j is processed on machine m just before job j', 0 otherwise
$Z_{jj'}$	1 if server loads job j before job j', 0 otherwise
Y_{jm}	1 if machine m processes job j, 0 otherwise
S_j	The start time of job j
$C\max$	The completion time of all the jobs

Minimise $C\max$ $\qquad$ (1)

$$\sum_{m=1}^{M} Y_{j,m} = 1 \qquad (2)$$
$$j \in \{1, 2, \ldots, J\}$$

$$\sum_{j'=1}^{J} X_{j,j',m} \leq Y_{j,m} \qquad (3)$$

$$j \in \{1, 2, \ldots, J\}; m \in \{1, 2, \ldots, M\}$$

$$\sum_{j=1}^{J} X_{j,j',m} \leq Y_{j',m} \tag{4}$$

$$j' \in \{1, 2, \ldots, J\}; m \in \{1, 2, \ldots, M\}$$

$$X_{j,j,m} = 0 \tag{5}$$

$$j \in \{1, 2, \ldots, J\}; m \in \{1, 2, \ldots, M\}$$

$$1 + \sum_{j=1}^{J}\sum_{j'=1}^{J} X_{j,j',m} = \sum_{j=1}^{J} Y_{j,m} \tag{6}$$

$$m \in \{1, 2, \ldots, M\}$$

$$X_{j,j',m} \leq Z_{j,j'} \tag{7}$$

$$j, j' \in \{1, 2, \ldots, J\} \mid j \neq j'; m \in \{1, 2, \ldots, M\}$$

$$X_{j,j'',m} - BM \times (6 - Y_{j,m} - Y_{j',m} - Y_{j'',m} - Z_{j,j'} - Z_{j',j''} - Z_{j,j''}) \leq 0 \tag{8}$$

$$j, j', j'' \in \{1, 2, \ldots, J\} \mid j \neq j', j' \neq j'', j \neq j''; m \in \{1, 2, \ldots, M\}$$

$$S_j + BM \times (4 - Y_{j,m} - Y_{j',m} - Z_{j',j} - X_{j',j,m}) \geq S_{j'} + P_{j'm} + D_{j',j} \tag{9}$$

$$j, j' \in \{1, 2, \ldots, J\} \mid j \neq j'; m \in \{1, 2, \ldots, M\}$$

$$S_{j'} + BM \times (3 - Y_{j,m} - Y_{j',m'} - Z_{j,j'}) \geq S_j + (X_{j'',j',m'} \times D_{j'',j'}) \tag{10}$$

$$j, j', j'' \in \{1, 2, \ldots, J\} \mid j \neq j', j' \neq j'', j \neq j''; m, m' \in \{1, 2, \ldots, M\}$$

$$S_j + BM \times (2 - Y_{j,m} - Y_{j',m'} + Z_{j,j'}) \geq S_{j'} + (X_{j'',j,m} \times D_{j'',j}) \tag{11}$$

$$j, j', j'' \in \{1, 2, \ldots, J\} \mid j \neq j', j' \neq j'', j \neq j''; m, m' \in \{1, 2, \ldots, M\}$$

$$S_j + P_{jm} \leq C_{max} \tag{12}$$

$$j \in \{1, 2, \ldots, J\}, m \in \{1, 2, \ldots, M\}$$

4. ILLUSTRATIVE EXAMPLE

In this section, we provide a medium sized illustrative example to validate the mathematical formulation. The example includes 10 jobs to be processed on 4 non-identical machines. For the illustrative example, we generate random numbers. A uniform distribution UNIF(1,100) is used for the processing times of each job on the machines, see Table 3. A triangular distribution TRI(1,25,150) is used for the sequence dependent setup times, see Table 4.

Table 3. The processing times of the jobs (in minutes)

Machines/Jobs	1	2	3	4	5	6	7	8	9	10
1	7	90	37	81	6	32	17	17	40	87
2	49	48	52	56	83	62	26	71	76	6
3	85	49	7	24	48	81	73	36	73	71
4	51	32	23	66	96	82	56	49	16	62

Table 4. The sequence dependent setup times for the changeovers between the jobs (in minutes)

Jobs/Jobs	1	2	3	4	5	6	7	8	9	10
1	0	87	63	76	50	40	41	37	20	35
2	87	0	114	91	122	109	26	50	62	21
3	63	114	0	89	133	40	137	36	77	84
4	76	91	89	0	35	39	85	60	98	124
5	50	122	133	35	0	59	60	6	45	107
6	40	109	40	39	59	0	34	61	28	50
7	41	26	137	85	60	34	0	46	16	26
8	37	50	36	60	6	61	46	0	36	126
9	20	62	77	98	45	28	16	36	0	23
10	35	21	84	124	107	50	26	126	23	0

The MILP model is coded and run on the GAMS/Cplex 12.7.0.0 optimization software using IBM ILOG CPLEX 24.8.2 r59988 with the default parameter settings. The illustrative example has been solved within 6,282 CPU seconds. The analyse is conducted on a computer with an Intel Core i7-5600QM CPU @ 2.60GHz and 8 GB memory. As an overall remark, the model is capable of solving the small and/or medium sized illustrative example optimally. The resulting schedule is presented using the Gantt chart in Figure 1 and yields to 273 minutes of production makespan.

Schedule of	Scheduling horizon (time in minutes)																						
	10	20	30	40	50	60	70	80	90	100	110	120	130	140	150	160	170	180	190	200	210	220	230
Machine 1								Job1				Job9									Job7		
Machine 2						Job6										Job4							
Machine 3					Job3				Job8											Job5			
Machine 4	Job10																		Job2				
Server							Setup 3-8			Setup 1-9		Setup 6-4				Setup 10-2		S. 8-5	Setup 9-7				
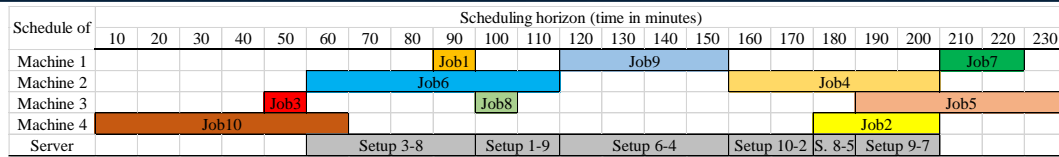
Figure 1. Gantt chart of the resulting optimal schedule

5. CONCLUSION

Scheduling of unrelated parallel machines is analogous with a variety of industries ranging from paper and textile industries to casting industry. Sequence dependent changeovers are encountered in the production stages including cutting, bending or molding operations. In case of servers for the changeovers are limited, only one setup operation can be allocated to a common server and, the common server causes inevitable delays of the production. In this study, we develop a decision support model to minimize the production makespan, i.e. total time needed to finish the daily production. The numerical analysis are made on a small and/or medium sized illustrative example and show the need for heuristic algorithms to overcome the complexity of the problem in large sized examples. Therefore, the future research directions might be on the enhancement of the computational performance. Developing constrictive heuristics or at least applying the well-known search algorithms such as bee optimization could be a way to solve the problem in a reasonable time. Besides, the dynamic and stochastic nature of the problem and so the rescheduling issues should not be neglected to be the more error prone problems.

REFERENCES

[1]. Abdekhodaee, A. H., & Wirth, A. (2002). Scheduling parallel machines with a single server: Some solvable cases and heuristics. Computers & Operations Research, 29, 295–315.
[2]. Hamzadayi, A., & Yildiz, G. (2017). Modeling and solving static m identical parallel machines scheduling problem with a common server and sequence dependent setup times. Computers & Industrial Engineering, 106, 287-298.
[3]. Hall, N. G., Potts, C. N., & Sriskandarajah, C. (2000). Parallel machine scheduling with a common server. Discrete Applied Mathematics, 102, 223–243.
[4]. Hasani, K., Kravchenko, S. A., & Werner, F. (2014a). Block models for scheduling jobs on two parallel machines with a single server. Computers & Operations Research, 41, 94–97.
[5]. Hasani, K., Kravchenko, S. A., & Werner, F. (2014b). Simulated annealing and genetic algorithms for the two-machine scheduling problem with a single server. International Journal of Production Research, 52(13), 3778–3792.
[6]. Huang, S. H., Cai, L., & Zhang, X. (2010). Parallel dedicated machine scheduling problem with sequence–dependent setups and a single server. Computers & Industrial Engineering, 58, 165–174.
[7]. Kim, M. Y., & Lee, Y. H. (2012). MIP models and hybrid algorithm for minimizing the makespan of parallel machines scheduling problem with a single server. Computers & Operations Research, 39(11), 2457–2468.
[8]. Koulamas, C. P. (1996). Scheduling two parallel semiautomatic machines to minimize machine interference. Computers & Operations Research, 23(10), 945–956.
[9]. Kravchenko, S. A., & Werner, F. (1997). Parallel machine scheduling problems with a single server. Mathematical and Computer Modelling, 26(12), 1–11.

Metaheuristic based optimization of tuned mass dampers on single degree of freedom structures subjected to near fault vibrations

Sinan Melih Nigdeli[1], Gebrail Bekdas[2], Aikerim Aydın[3]

Abstract

Near fault ground motions excitations have specific characteristics comparing to regular earthquake excitations. Near fault ground motions contain directivity pulses and flint steps in different directions and these excitations are the reason of more damages than regular excitations for structures. A successful method to reduce structural vibrations is the usage of tuned mass dampers. By using optimally tuned mass dampers, it will be possible to reduce vibrations resulting from earthquake excitations. In the present study, the optimization of tuned mass dampers are done for near fault excitations. During optimization, 6 different pulse like excitations are used. Three of these excitations are directivity pulses while the other ones are flint steps. The periods of excitations are 1.5s, 2.0s and 2.5s since near fault pulses have long period and big peak ground velocity around 200 m/s. The optimization objectives are related to maximum displacement of structure in time domain, the maximum stroke limitation of tuned mass damper and transfer function of the structure in frequency domain analyses. The iterative optimization process uses both time and frequency domain analyses of the structure. Three different metaheuristic algorithms are used in the methodology. These methods are harmony search algorithm, teaching learning based optimization and flower pollination algorithm which are inspired from musical performances, education process and reproduction of flowering plants, respectively. As the numerical investigation, three different single degree of freedom structures with periods 1.5s, 2.0s and 2.5s are investigated for optimum mass, period and damping ratio of a tuned mass damper positioned on the structure.

Keywords: *Metaheuristic algorithm, Near fault vibrations, Optimization, Tuned mass dampers.*

1. INTRODUCTION

The undesired responses of structures subjected to earthquake and strong winds can be reduced by using control systems. These control systems may be passive, active, semi-active or hybrid. As a passive control system, a tuned mass damper (TMD) can be used on top of the structures. There are several existing examples of using TMDs on structures. Examples include Taipei 101, Berlin TV Tower (Fig. 1), LAX theme Building and other high rise buildings, towers or bridges.

Especially, near fault ground motions are more dangerous than far fault motions because of significant impulsive motions; namely directivity pulse and flint step. These pulses have long period and big peak ground velocity (PGV). For that reason, these motions are dangerous for structures with long period. In several studies, these motions are formulized. The formulations of Makris [1] are the best equations which represent the behavior of motions. In order to use TMDs on structures in near fault regions, an optimum tuning is needed. In the documented methods, several formulations have been proposed [2-4], but these formulations may not be an exact solution for structures with inherent damping and effected by impulsive motions. For that reason, numerical algorithms are more suitable for the optimization problem. Especially, metaheuristic algorithms are effective on optimization [5-8].

---

[1] Corresponding author: İstanbul University, Department of Civil Engineering, 34320, Avcılar/İstanbul, Turkey. melihnig@istanbul.edu.tr

[2] İstanbul University, Department of Civil Engineering, İstanbul, Turkey, bekdas@istanbul.edu.tr

[3] İstanbul University, Department of Civil Engineering, İstanbul, Turkey, aykerimaydin@gmail.com

Figure 3. Berlin TV Tower

In this study, the optimization of TMDs positioned on the top of single degree of freedom (sdof) structures was investigated for near fault motions. During the optimization, three directivity pulses and three flint steps (with periods 1.5s, 2.0s and 2.5s and 200m/s PGV) are considered by using the equations of Makris [1]. Three different algorithms such as harmony search (HS), flower pollination algorithm (FPA) and teaching learning based optimization (TLBO) have been used.

2. MATERIALS AND METHODS

The aim of the optimization is to find design variables such as mass (m_d), period (T_d) and damping ratio (ξ_d) of TMD by considering the optimization objectives such as related with maximum displacement ($f_1(v)$), stroke capacity of TMD ($f_2(v)$) and maximum value of acceleration transfer function ($f_3(v)$). In the methodology, the design constants, excitations and solution ranges are defined. Then, initial solution matrix (V) is constructed with p sets of solutions (v_i for the ith solution) including randomly generated design variables from the defined solution range. The formulations of v_i, V, $f_1(v)$, $f_2(v)$ and $f_3(v)$ are given in Eqs.(1-5).

$$v_i = \begin{Bmatrix} m_{di} \\ T_{di} \\ \xi_{di} \end{Bmatrix} \quad i = 1,...., p \tag{1}$$

$$V = \begin{bmatrix} v_1 & v_2 & ... & v_i & ... & v_p \end{bmatrix} \tag{2}$$

$$f_1(v) = \max(\begin{vmatrix} x_1 & x_2 & ... & x_i & ... & x_N \end{vmatrix}) \leq x_{max} \tag{3}$$

$$f_2(v) = \frac{\max(|x_d - x_N|)_{withTMD}}{|x_N|_{withoutTMD}} \leq st\_\max \tag{4}$$

$$f_3(v) = \max(|TF_N(w)|)_{withTMD} \leq \max(|TF_N(w)|)_{withoutTMD} \tag{5}$$

In these equations, x_i are the displacement of ith story; x_{max} is a user defined value which is iteratively increased (0 is the initial value in current study); x_d is the total displacement of TMD; st_max is a user defined value for stroke limitation (2 in the current study); TF_N (w) is the acceleration transfer function which uses the Laplace transforms. After the generation of initial solution matrix, new solutions are produced according to the rules of the algorithms. The main comparisons factor is f1(v), but the function; f2(v) must be provided.

HS is music based algorithm developed by Geem et al. [9]. It imitates the musical performances in a musician tries to gain admiration of audience. FPA is a nature inspired algorithm and uses four rules proposed by Yang [10] including cross pollination, self-pollination, flower constancy and switch probability. TLBO developed by Rao et al. [11] imitates two phases of education such as teacher phase and learner phase in which self-education of students is considered. The details and formulation of the algorithms can be found in Reference [8].

3. RESULTS AND DISCUSSION

Three single degree of freedom structures with 5% inherent damping and periods 1.5s, 2.0s and 2.5s are investigated for an optimum TMD. The mass of structures are taken as a symbolic value (1kg). Three different cases of maximum damping was investigated. The maximum damping ratio is 0.2, 0.3 and 0.4 for cases 1, 2 and 3, respectively while the minimum bound is 0.01. The mass ratio of TMD was searched between 1% and 10% while T_d was optimized between 0.5 and 1.5 times of the period of main structure. For the structure with 2 s period, the maximum mass ratio is taken as 20% in order to obtain an effective control. The optimum results are shown in Table 1. The objective function and maximum acceleration values are presented in Tables 2-4 for HS, FPA and TLBO algorithms. The best solutions were obtained for TLBO algorithm. For the structure with 2.0s and 2.5s period, the optimum results are the same since the optimum damping ratio of TMD is within the ranges of case 1. For the structure with 1.5s period, the results are the same for cases 2 and 3. The time history plots of top story displacements of structures are given in Figs. 2-5 for TLBO algorithm.
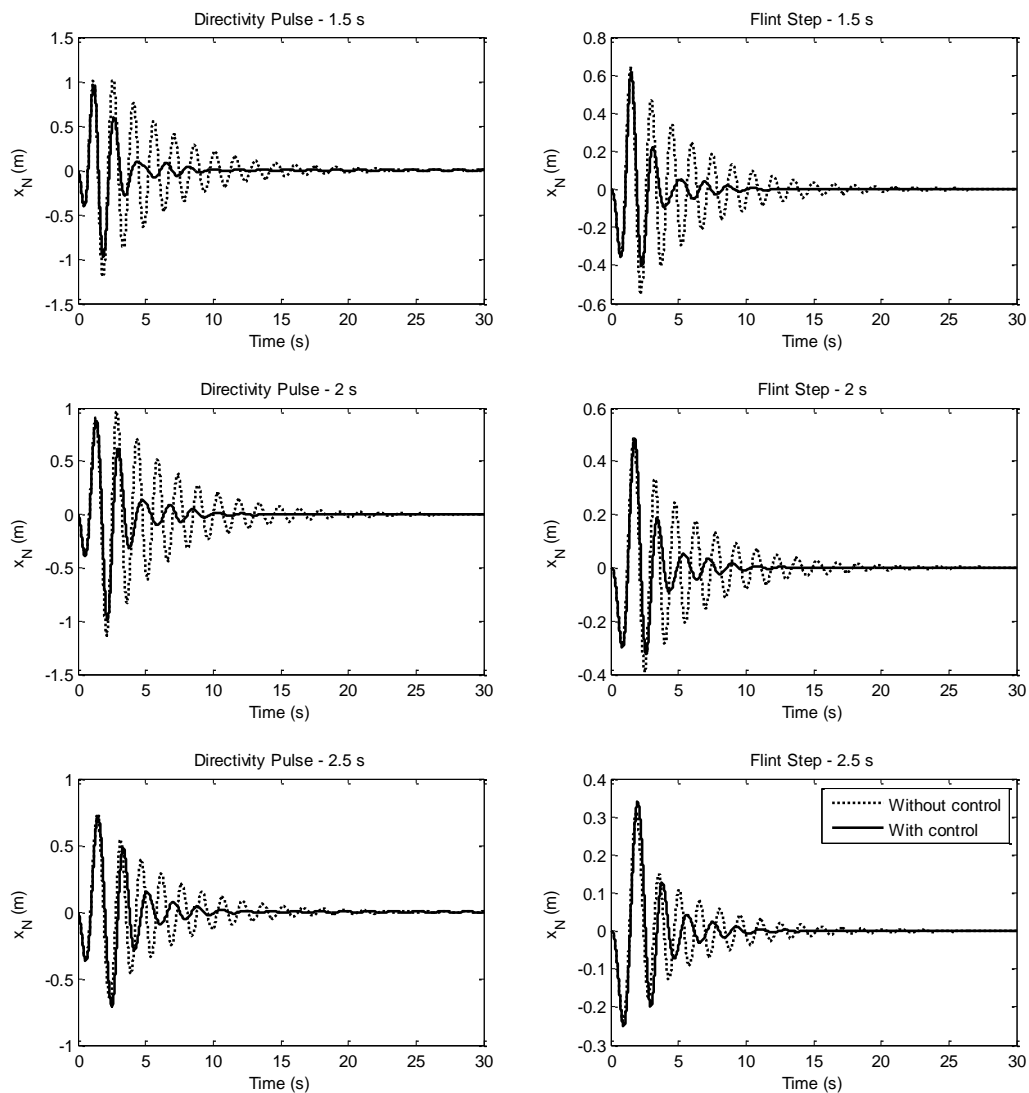
Figure 4. Time history plot for structure with 1.5s period (case 1)

Table 2. The optimum design variables

Case	Structure periods (s)	HS			FPA			TLBO		
		m_d (kg)	T_d(s)	ξ_d	m_d (kg)	T_d(s)	ξ_d	m_d (kg)	T_d(s)	ξ_d
1	1	0.100	1.597	0.190	0.100	1.653	0.200	0.100	1.653	0.200
	2	0.198	1.955	0.068	0.200	1.929	0.047	0.200	1.929	0.047
	3	0.099	2.170	0.055	0.100	2.150	0.047	0.100	2.071	0.018
2	1	0.098	1.738	0.229	0.100	1.753	0.231	0.100	1.753	0.231
	2	0.195	1.967	0.064	0.200	1.929	0.047	0.200	1.929	0.047
	3	0.099	2.070	0.024	0.100	2.071	0.018	0.100	2.071	0.018
3	1	0.099	1.729	0.227	0.100	1.753	0.231	0.100	1.753	0.231
	2	0.200	1.956	0.067	0.200	1.929	0.047	0.200	1.929	0.047
	3	0.098	2.178	0.059	0.100	2.071	0.018	0.100	2.071	0.018
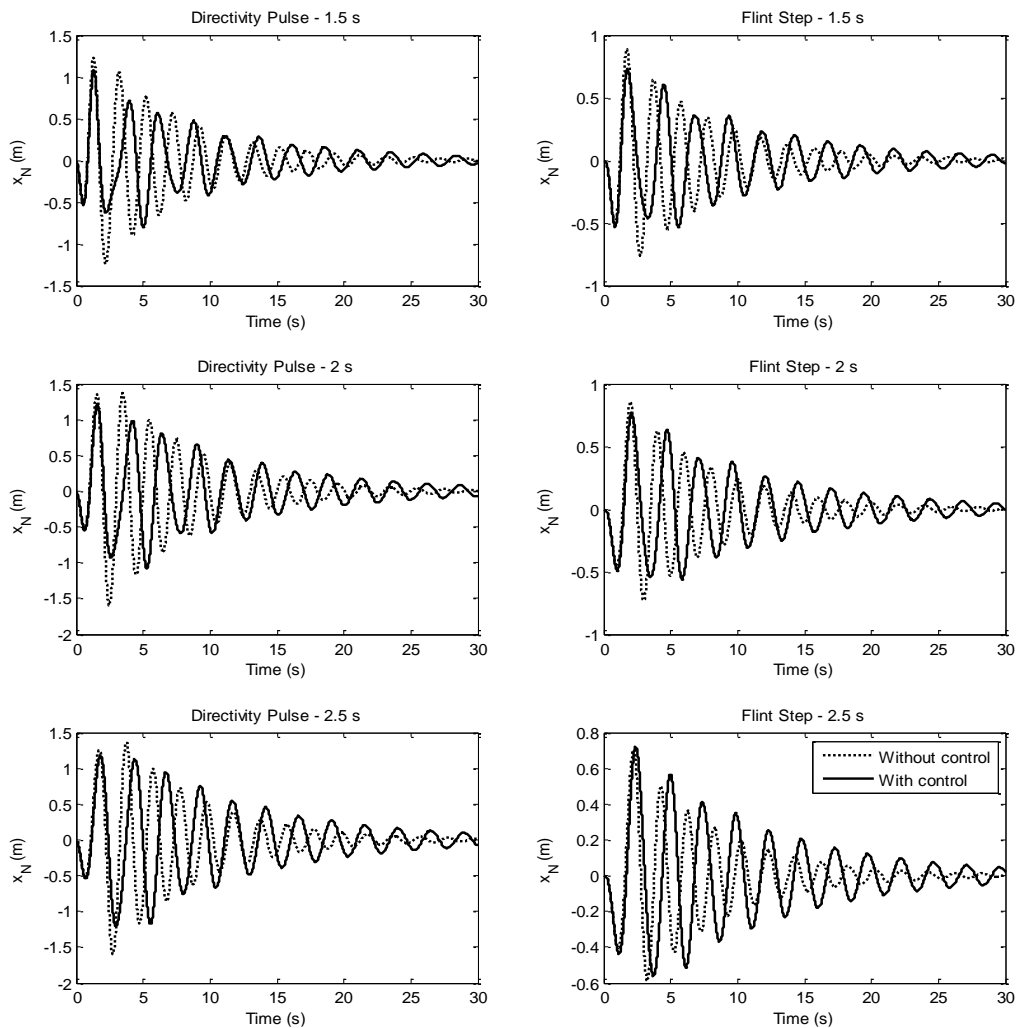
Figure 5. Time history plot for structure with 2.0s period
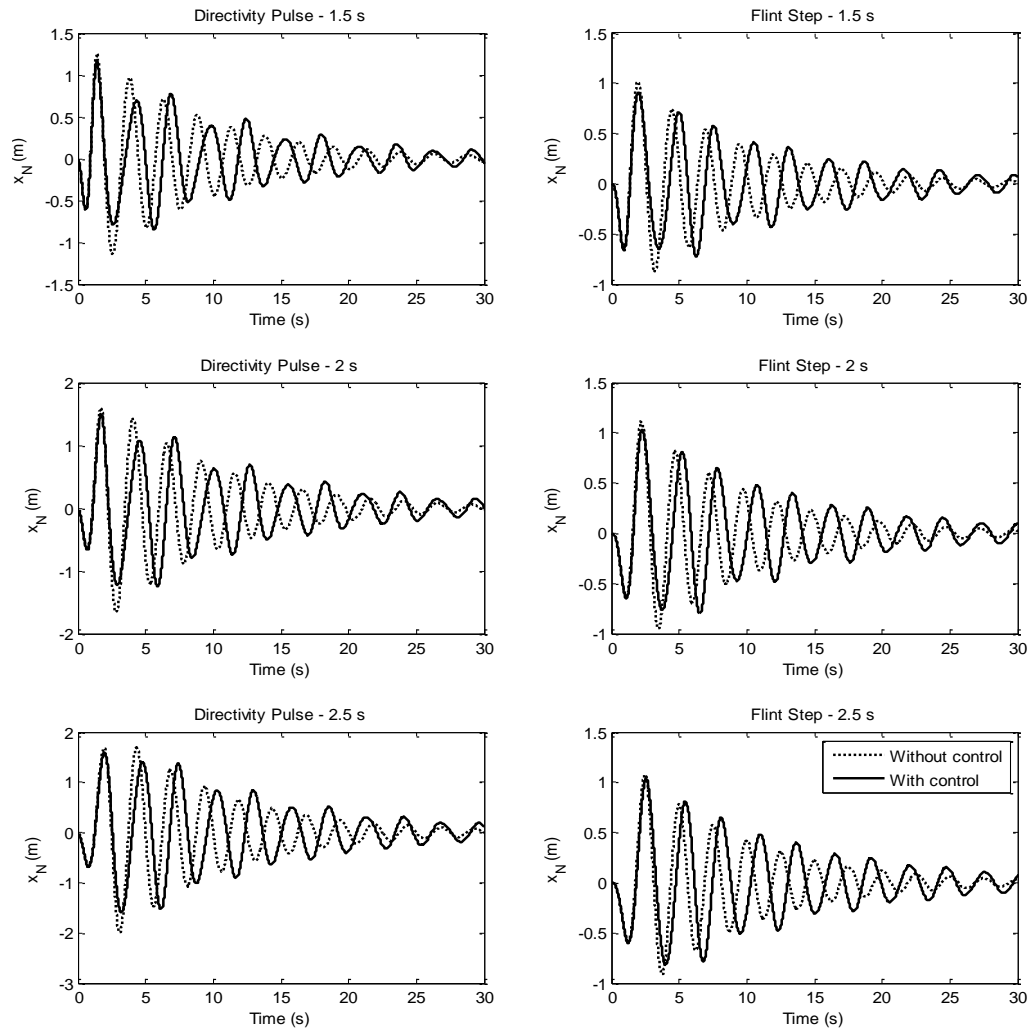
Figure 6. Time history plot for structure with 2.5s period

Table 3. The objective function values (HS)

Case	Structure periods (s)	$f_1(v)$		Maximum acceleration		$f_3(v)$		$f_2(v)$		Iteration
		With TMD	Without TMD	With TMD	Without TMD	With TMD	With TMD	Without TMD		
1	1	1.204	1.006	21.224	16.418	10.012	3.425	1.948	2184
	2	1.602	1.217	15.889	10.482	9.558	6.617	1.940	3304
	3	2.000	1.605	12.697	9.234	9.892	7.815	1.999	6373
2	1	1.204	0.998	21.224	17.033	10.012	3.882	1.994	4097
	2	1.602	1.217	15.889	10.544	9.558	6.667	1.995	1335
	3	2.000	1.604	12.697	9.109	9.892	9.760	1.967	1035
3	1	1.204	0.997	21.224	16.950	10.012	3.816	1.988	2618
	2	1.602	1.216	15.889	10.459	9.558	6.701	1.937	4062
	3	2.000	1.606	12.697	9.256	9.892	7.687	1.997	2675

4. CONCLUSIONS

The optimized TMDs are effective in reduction of structural displacements and accelerations. All algorithms are effective, but FPA and TLBO can find precise optimum solutions. The iteration number for the optimum values are nearly 2000 iterations. The reduction of maximum displacements are 17%, 25% and 20% for the structure with period 1.5s, 2.0s and 2.5s, respectively. For near fault motions, these values are good, but active control system may be more effective for impulsive motions. The cost, maintain, stability problem and energy consumption are big problems of the active systems comparing to passive control methods.

Table 4. The objective function values (TLBO)

	Structure periods (s)	$f_1(v)$		Maximum acceleration		$f_3(v)$		$f_2(v)$	Iteration
		With TMD	Without TMD	With TMD	Without TMD	With TMD	With TMD	Without TMD	
1	1	1.204	0.997	21.224	16.631	10.012	3.489	2.000	4180
	2	1.602	1.209	15.889	10.381	9.558	7.488	2.000	4480
	3	2.000	1.601	12.697	9.085	9.892	9.892	2.000	4750
2	1	1.204	0.994	21.224	17.014	10.012	3.909	2.000	4130
	2	1.602	1.209	15.889	10.381	9.558	7.488	2.000	5160
	3	2.000	1.601	12.697	9.085	9.892	9.892	2.000	6850
3	1	1.204	0.994	21.224	17.014	10.012	3.909	2.000	4010
	2	1.602	1.209	15.889	10.381	9.558	7.488	2.000	4990
	3	2.000	1.601	12.697	9.085	9.892	9.892	2.000	6850
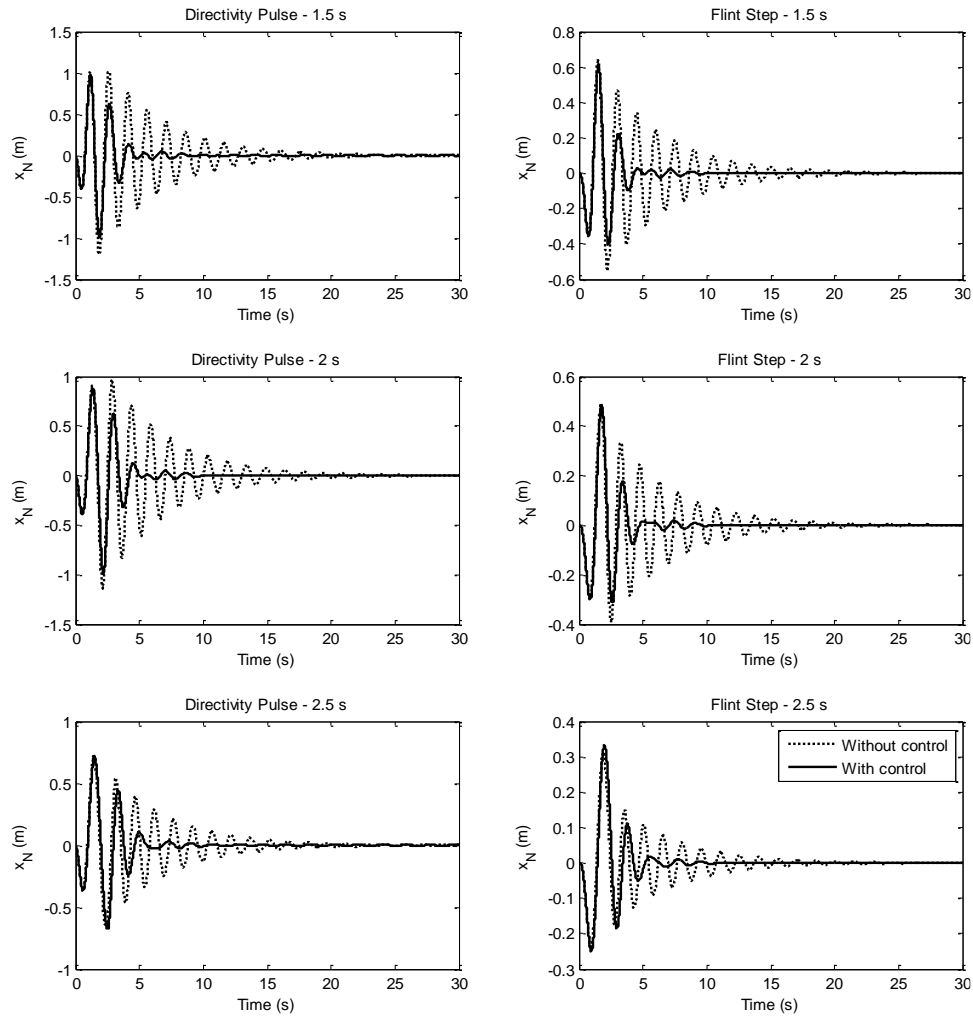
Figure 7. Time history plot for structure with 1.5s period (case 2-3)

Table 5. The objective function values (FPA)

Case	Structure periods (s)	$f_1(v)$		Maximum acceleration		$f_3(v)$	$f_2(v)$		Iteration
		With TMD	Without TMD	With TMD	Without TMD	With TMD	With TMD	Without TMD	
1	1	1.204	0.997	21.224	16.631	10.012	3.489	2.000	3465
	2	1.602	1.209	15.889	10.381	9.558	7.488	2.000	5045
	3	2.000	1.603	12.697	9.196	9.892	8.194	2.000	2620
2	1	1.204	0.994	21.224	17.014	10.012	3.909	2.000	4055
	2	1.602	1.209	15.889	10.381	9.558	7.488	2.000	4915
	3	2.000	1.601	12.697	9.085	9.892	9.892	2.000	7370
3	1	1.204	0.994	21.224	17.014	10.012	3.909	2.000	4020
	2	1.602	1.209	15.889	10.381	9.558	7.488	2.000	5090
	3	2.000	1.601	12.697	9.085	9.892	9.892	2.000	7290

REFERENCES

[1]. Makris, N., (1997). Rigidity-Plasticity-Viscosity: Can Electrorheological Dampers Protect Base-Isolated Structures From Near-Source Ground Motions? *Earthquake Engineering and Structural Dynamics,* 26, 571-591..

[2]. Den Hartog, J. P., (1947). Mechanical Vibrations. *McGraw-Hill,* New York..

[3]. Warburton, G.B., (1982). Optimum absorber parameters for various combinations of response and excitation parameters. *Earthquake Engineering and Structural Dynamics*, 10, 381–401..

[4]. Sadek, F., Mohraz, B., Taylor, A.W., Chung, R.M., (1997). A Method of Estimating The Parameters of Tuned Mass Dampers for Seismic Applications. *Earthquake Engineering and Structural Dynamics,* 26, 617–635.

[5]. Bekdas, G., Nigdeli, S.M., (2011). Estimating Optimum Parameters of Tuned Mass Dampers using Harmony Search. *Engineering Structures*, 33, 2716-2723.

[6]. Hadi, M.N.S., Arfiadi, Y., (1998). Optimum Design of Absorber for MDOF Structures. *Journal of Structural Engineering-ASCE,* 124, 1272–1280.

[7]. Bekdas, G., & Nigdeli, S. M., (2017). Metaheuristic Based Optimization of Tuned Mass Dampers Under Earthquake Excitation by Considering Soil-structure Interaction. *Soil Dynamics and Earthquake Engineering*, 92, 443-461.

[8]. Bekdas G, Nigdeli SM, Yang X-S, *Metaheuristic Based Optimization for Tuned Mass Dampers Using Frequency Domain Responses*. In: Harmony Search Algorithm. Advances in Intelligent Systems and Computing, vol 514, Del Ser J. (eds) Springer, pp. 271-279, 2017.

[9]. Geem, Z. W., Kim, J. H., & Loganathan, G. V. (2001). A new heuristic optimization algorithm: harmony search. *Simulation*, 76(2), 60-68.

[10]. Yang, X. S., (2012). Flower Pollination Algorithm for Global Optimization. *International Conference on Unconventional Computing and Natural Computation* (pp. 240-249), Springer Berlin Heidelberg.

[11]. Rao, R. V., Savsani, V. J., & Vakharia, D. P., (2011). Teaching–learning-Based Optimization: A Novel Method for Constrained Mechanical Design Optimization Problems. *Computer-Aided Design*, 43(3), 303-315.

BİOGRAPHY

Sinan Melih Nigdeli, Associative Professor, is researcher in Structural Control and Optimization at Istanbul University. He obtained his DPhil in Structural Engineering from Istanbul Technical University with a thesis subject of active structural control. He co-organized the 15th EU-ME Workshop: Metaheuristic and Engineering in Istanbul. In optimization and structural control, he organized several mini-symposiums or special sections in prestigious international events. He co-edited Metaheuristics and Optimization in Civil Engineering published by Springer in 2016 and he is one of the guest editors in 2017 special issue of KSCE Journal of Civil Engineering. He has authored more than 100 papers for journals and scientific events.

Gebrail Bekdas, Associative Professor, is researcher in Structural Control and Optimization at Istanbul University. He obtained his DPhil in Structural Engineering from Istanbul University with a thesis subject of design of cylindrical walls. He co-organized the 15th EU-ME Workshop: Metaheuristic and Engineering in Istanbul. In optimization, he organized several mini-symposiums or special sections in prestigious international events. He co-edited Metaheuristics and Optimization in Civil Engineering published by Springer in 2016 and he is one of the guest editors in 2017 special issue of KSCE Journal of Civil Engineering. He has authored more than 100 papers for journals and scientific events.

Aikerim Aydın, graduated from department of civil engineering in Kazakhstan. She is a Master of Science student in İstanbul University. Passive control of structure is the expertise and thesis subject of her.

The Effect Of The Consideration Of Slab Dimensions On Optimum Design Of Reinforced Concrete Beams

Sinan Melih Nigdeli[1], Gebrail Bekdas[2]

Abstract

In the design of reinforced concrete (RC) beams, the slab can be also considered as a part of the beam and a t-shaped cross section is considered. In the presented study, the optimum design of RC beams are investigated for different slab thickness values. Thus, the effect of the consideration of slab dimensions for the optimum design is investigated. In the optimization methodology, an iterative cost optimization process is proposed. The process contains the optimization of design variables such as the cross-section dimensions and amount of rebar of RC beams subjected to flexural moments. In order to find a precise optimum solution without trapping local optimums, a metaheuristic based method called harmony search is employed. The optimum values are chosen according to user selected range and the design constraints. The design constraints are generated according to ACI318- Building code requirements for structural concrete. By the increase of compressive force in the compressive section of the beam, the amount of the rebar shows a decreasing manner and this situation is effective on the optimum design and cost.

Keywords: *Metaheuristic algorithm, Frames, Optimization, Teaching learning based optimization.*

1. INTRODUCTION

In the design of reinforced concrete (RC) beams, the slab can be included in the compressive section of the beam in order to increase the force carried by the concrete. Thus, a T-shaped cross section is used and the flange width is calculated according to effective width by considering zero moment measures while the thickness of the flange is equal to the thickness of the slab. The consideration of a T-shaped section is effective on the economy in order to reduce the amount of rebar, especially in the compressive section.

In this paper, the optimum design of RC beams under flexural moments are presented for different thickness values of slab and the results are also compared with a rectangular section. The optimum design employs harmony search algorithm (HS) [1] and considers the rules of ACI318: Building code requirements for structural concrete [2] in the analyses.

Harmony search (HS) is a music inspired metaheuristic algorithm. Like genetic algorithm inspired form the evaluation theory [3] or ant colony optimization [4] inspired from the food search process of ants, HS inspired from musical performance in which a musician tries to find the best harmony in order to gain attention of the listeners. In this process, a well-known popular note can be played or it can be modified a little in order to adjust the level of admiration. Metaheuristic based methodologies are effective on the engineering problems and several good examples can be also found for optimization of RC members like beams [5-8], columns [9-10], frames [11-12] and retaining walls [13-14].

2. METHODOLOGY

The methodology of the optimization process can be explained in five steps. These steps are summarized in the flowchart given as Fig. 1.

---

[1] Corresponding author: İstanbul University, Department of Civil Engineering, 34320, Avcılar/İstanbul, Turkey. melihnig@istanbul.edu.tr

[2] İstanbul University, Department of Civil Engineering, İstanbul, Turkey, bekdas@istanbul.edu.tr
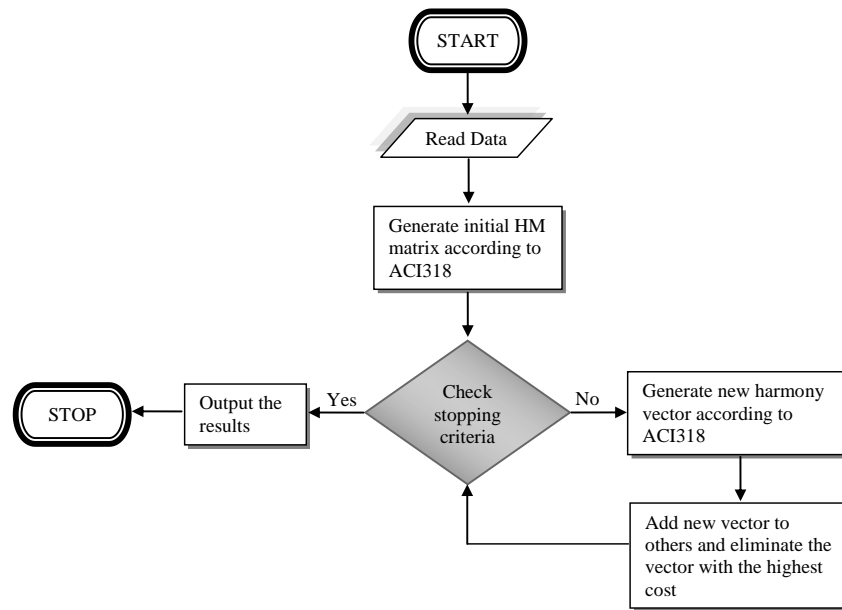
Figure 1. Flowchart of the methodology [7]

Step 1: Read Data

In this step, the design constants (given in Table 2 with the values used in numerical example), the ranges of design variables (values also given in Table 2) such as height (h) and width (b) of the beam, number (n_1, n_2, n_3 and n_4) and size (ϕ_1, ϕ_2, ϕ_3 and ϕ_4) of rebar, the algorithm parameters (HMS: harmony memory size, HMCR: harmony memory considering rate, PAR: pitch adjusting rate, values on Table 2) are defined. A T-shaped cross section which is optimized, is shown in Fig. 2.
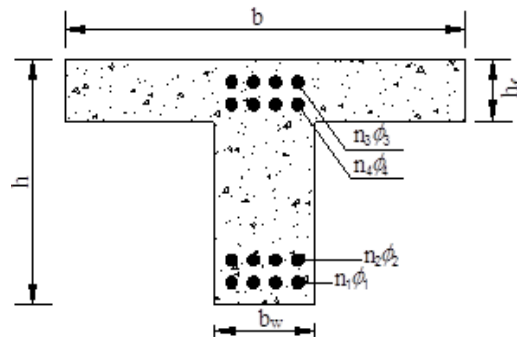
Figure 2. The T-shaped cross section

Step 2: Generate initial harmony memory (HM) matrix

In this step, initial solution vectors for design variables are randomly generated. This generation of vectors is done for HMS and the initial HM matrix is generated. In the generated values must provide the ACI-318 rules in the analyses.

Step 3: Generate a new harmony memory

After the generation of initial HM matrix, a new vector is generated in two ways. These two ways are chosen with possibility called HMCR. With HMCR possibility, a new solution is generated around existing solution by using a narrow range which is PAR times of the length of the initial solution range. The other way is to use the initial solution range in the generation of design variables. All dimension variables are rounded to values which are divisible to 50 mm and the diameters of rebar are even numbers for practical production in a construction yard.

Step 4: Elimination and update

If the newly generated solution is better than the worst existing solution, the solution is keep and the old one is eliminated. This comparison is done according to objective function which is the total material cost of unit meter.

Step 5: Check the stopping criteria

The methodology has various criteria for stopping of the iterative process given as step 3 and 4. The difference of the web width and height for different sets of solution must be smaller than 50 mm. Also, the difference in flexural moment strength and the required flexural moment capacity must be less than 0.5% of required. The required flexural moments are increased by dividing the values by 0.9 according to ACI-318. When these criteria are satisfied, the optimum results are output.

3. NUMERICAL EXAMPLE

The investigation is done for 4 cases of the slab thickness (h_f). In the first case, the section is rectangular ($h_f=0$). All numerical values used in the optimization are presented in Table 2. The required flexural moments are investigated for different values and the optimum results are given in Table 3.

Table 6. The design constants, ranges and parameters

Definition	Symbol	Unit	Value
Range of width section	b_{wmin}, b_{wmax}	mm	250-350
Range of height section	h_{min}, h_{max}	mm	300-500
Clear cover	cc	mm	35
Range of diameter of rebar	ϕ_{min}, ϕ_{max}	mm	10-30
Size of stirrups	ϕ_v	mm	10
Width of flange	b	mm	1000
Slab thickness	h_f	mm	0 (case 1) 100 (case 2) 120 (case 3) 140 (case 4)
Max. aggregate diameter	D_{max}	mm	16
Yield strength of steel	f_y	MPa	420
Comp. strength of concrete	f'_c	MPa	25
Elasticity modulus of steel	E_s	MPa	200000
Specific gravity of steel	γ_s	t/m^3	7.86
Specific gravity of concrete	γ_c	t/m^3	2.5
Cost of the concrete per m^3	C_c	\$/ m^3	40
Cost of the steel per ton	C_s	\$/ m^3	400
Harmony memory size	HMS	-	5
Harmony memory considering rate	HMCR	-	0.5
Pitch adjusting rate	PAR	-	0.5

Table 2. The optimum results

Objective Flexural Moment (kNm)		50	100	150	200	250	300	350	400	450	500
CASE 1	h (mm)	300	400	500	500	500	500	500	500	500	500
	b_w (mm)	250	250	250	250	250	250	250	300	350	350
	ϕ_1 (mm)	10	12	16	16	22	30	30	30	26	30
	ϕ_3 (mm)	30	16	12	14	10	10	10	10	20	22
	n_1	5	4	3	4	3	3	3	4	5	4
	n_3	0	0	0	0	0	3	0	4	2	3

	ϕ_2 (mm)	10	12	12	14	18	10	18	10	10	16
	ϕ_4 (mm)	24	14	16	30	16	18	30	18	10	20
	n_2	3	4	4	4	3	2	4	3	8	5
	n_4	0	0	0	0	0	0	0	0	3	0
	M_u (kNm)	55.96	112.00	172.26	222.77	280.42	343.99	393.37	451.50	501.01	572.40
	Cost ($/m)	4.95	6.81	8.28	9.41	10.91	12.80	14.74	16.48	19.87	22.44
CASE 2	h (mm)	350	350	350	400	450	500	500	500	500	500
	b_w (mm)	250	250	250	250	250	250	250	250	250	250
	ϕ_1 (mm)	10	12	16	16	18	24	24	28	20	24
	ϕ_3 (mm)	14	18	28	12	20	22	14	26	28	16
	n_1	2	3	3	4	3	2	2	2	4	3
	n_3	0	0	0	0	0	0	0	0	0	0
	ϕ_2 (mm)	10	10	10	10	14	12	12	14	14	22
	ϕ_4 (mm)	22	30	22	22	18	26	14	20	16	20
	n_2	2	3	4	2	2	2	4	2	3	2
	n_4	0	0	0	0	0	0	0	0	0	0
	M_u (kNm)	36.87	67.26	105.92	133.76	168.11	201.03	236.70	268.95	300.78	360.03
	Cost ($/m)	7.48	8.28	9.35	9.98	10.83	11.51	12.21	12.78	13.33	14.57
CASE 3	h (mm)	350	350	400	400	450	500	500	500	500	500
	b_w (mm)	250	250	250	250	250	250	250	250	250	250
	ϕ_1 (mm)	10	12	10	16	14	24	22	28	20	24
	ϕ_3 (mm)	30	10	16	30	28	14	14	24	12	16
	n_1	3	3	5	3	4	2	3	2	4	3
	n_3	0	0	0	0	0	0	0	0	0	0
	ϕ_2 (mm)	10	10	12	10	14	10	12	12	18	16
	ϕ_4 (mm)	28	14	14	14	10	26	28	22	30	22
	n_2	2	3	3	5	3	3	2	3	2	3
	n_4	0	0	0	0	0	0	0	0	0	0
	M_u (kNm)	46.53	67.26	100.25	134.76	167.74	202.63	243.10	273.86	307.64	337.39
	Cost ($/m)	8.32	8.88	9.87	10.69	11.44	12.14	12.84	13.48	14.08	14.68
CASE 4	h (mm)	350	350	350	400	450	500	500	500	500	500
	b_w (mm)	250	250	250	250	250	250	250	250	250	250
	ϕ_1 (mm)	12	12	12	14	18	16	18	24	24	26
	ϕ_3 (mm)	30	26	30	24	28	28	12	30	24	28
	n_1	2	3	4	4	3	4	4	3	3	3
	n_3	0	0	0	0	0	0	0	0	0	0
	ϕ_2 (mm)	10	10	12	16	12	12	14	10	16	16
	ϕ_4 (mm)	24	28	20	12	20	24	26	22	22	28
	n_2	2	3	4	2	3	3	2	2	2	2
	n_4	0	0	0	0	0	0	0	0	0	0
	M_u (kNm)	45.15	67.26	103.19	137.72	172.65	203.70	235.74	269.45	306.89	345.88
	Cost ($/m)	8.89	9.48	10.51	11.36	12.12	12.75	13.32	13.90	14.66	15.39

4. CONCLUSIONS

Generally, the rectangular design is economical for low flexural moment values as seen in the optimum results, but it must be noted that the optimum cost is only calculated by using $h_f=0$. In that case, the slab concrete cost is not taken in the consideration. Although the slab is not considered in case 1, the cost is more than other cases, if the required flexural moment is more than 250 kNm. The significant effect on the increase of the cost is because of the need for rebar in compressive section. According to the results, the thickness of the slab has no significant effect on the optimum cost, but the consideration of a T shaped design is important in optimization.

REFERENCES

[1]. Geem, Z. W., Kim, J. H., & Loganathan, G. V. (2001). A new heuristic optimization algorithm: harmony search. Simulation, 76(2), 60-68.
[2]. ACI 318M-05, Building code requirements for structural concrete and commentary, American Concrete Institute, 2005.
[3]. Goldberg, D.E. (1989), *Genetic algorithms in search, Optimization and machine learning*, Boston MA: Addison Wesley.
[4]. Dorigo, M., Maniezzo, V. and Colorni A (1996), "The ant system: Optimization by a colony of cooperating agents", *IEEE Transactions on Systems Man and Cybernet B*, **26**, 29–41.
[5]. Koumousis, V. K., Arsenis, S. J. (1998), "Genetic Algorithms in Optimal Detailed Design of Reinforced Concrete Members", Comput-Aided Civ. Inf., 13, 43-52.
[6]. Govindaraj, V., Ramasamy, J. V. (2005), "Optimum detailed design of reinforced concrete continuous beams using Genetic Algorithms", Comput. Struct., 84, 34–48.
[7]. Bekdas, G. and Nigdeli, S.M. (2012), "Cost optimization of T-shaped reinforced concrete beams under flexural effect according to ACI 318", In: 3rd European Conference of Civil Engineering, Paris, France.
[8]. Nigdeli, S. M., & Bekdas, G. (2016). Optimum design of RC continuous beams considering unfavourable live-load distributions. KSCE Journal of Civil Engineering, DOI: 10.1007/s12205-016-2045-5.
[9]. Rafiq, M. Y., Southcombe, C. (1998), "Genetic algorithms in optimal design and detailing of reinforced concrete biaxial columns supported by a declarative approach for capacity checking", Comput. Struct. 69, 443-457.
[10]. Nigdeli, S. M., Bekdas, G., Kim, S., & Geem, Z. W. (2015). A novel harmony search based optimization of reinforced concrete biaxially loaded columns.Structural Engineering and Mechanics, 54(6), 1097-1109.
[11]. Camp, C. V., Pezeshk, S., Hansson, H. (2003), "Flexural Design of Reinforced Concrete Frames Using a Genetic Algorithm", J Struct. Eng.-ASCE., 129, 105-11.
[12]. Govindaraj, V., Ramasamy, J. V. (2007), "Optimum detailed design of reinforced concrete frames using genetic algorithms", Eng. Optimiz., 39(4), 471–494.
[13]. Camp, C.V. and Akin, A. (2012), "Design of retaining walls using big bang–big crunch optimization", Journal of Structural Engineering, Vol.138, No.3, pp.438–448, DOI:10.1061/(ASCE)ST.1943-541X.0000461.
[14]. Temur, R, Bekdas, G. (2016), "Teaching learning-based optimization for design of cantilever retaining walls", Structural Engineering and Mechanics, Vol.57, No.4, pp.763-783, DOI: 10.12989/sem.2016.57.4.763.

BİOGRAPHY

Sinan Melih Nigdeli, Associative Professor, is researcher in Structural Control and Optimization at Istanbul University. He obtained his DPhil in Structural Engineering from Istanbul Technical University with a thesis subject of active structural control. He co-organized the 15th EU-ME Workshop: Metaheuristic and Engineering in Istanbul. In optimization and structural control, he organized several mini-symposiums or special sections in prestigious international events. He co-edited Metaheuristics and Optimization in Civil Engineering published by Springer in 2016 and he is one of the guest editors in 2017 special issue of KSCE Journal of Civil Engineering. He has authored more than 100 papers for journals and scientific events.

Gebrail Bekdas, Associative Professor, is researcher in Structural Control and Optimization at Istanbul University. He obtained his DPhil in Structural Engineering from Istanbul University with a thesis subject of design of cylindrical walls. He co-organized the 15th EU-ME Workshop: Metaheuristic and Engineering in Istanbul. In optimization, he organized several mini-symposiums or special sections in prestigious international events. He co-edited Metaheuristics and Optimization in Civil Engineering published by Springer in 2016 and he is one of the guest editors in 2017 special issue of KSCE Journal of Civil Engineering. He has authored more than 100 papers for journals and scientific events.

The Effect Of Cross-Section Dimension Limits In Optimum Design Of Reinforced Concrete Continuous Beams

Gebrail Bekdas[1], Sinan Melih Nigdeli[2]

Abstract

As known, steel and concrete are different types of materials in fracture. In order to express a ductile behavior, reinforced concrete elements must have less reinforcements from the situation in which concrete and steel rebar yields at the same time. There are two options if the maximum reinforcement area is exceeded. The first optimum is to use a doubly reinforced design, but this design may not be an economic choose since steel is a more expensive material than concrete. The other option is to use a bigger cross-section to enlarge the force in compressive section. In the present study, the optimum design of reinforced concrete (RC) continuous beams are investigated for different ranges of cross-section dimensions. Thus, it will be possible to see the effect of singly or doubly reinforced beams in economic design. For the investigations, a random search technique (RST) is used and the methodology considers the rules of ACI318 building code requirements for structural concrete, all live-load distribution patterns for unfavorable solution and detailed reinforcement design of rebars according to the market sizes.

Keywords: *Continuous beams, Metaheuristic algorithm, Optimum design, Reinforced concrete.*

1. INTRODUCTION

The only aim of an engineer is not to form a design. The design must provide safety conditions including several standards and cost efficiency. In that case, optimization is one of the vital tools of engineers. Especially in the design of composite structures, the existing of two types of materials in behavior is the reason of a nonlinear engineering problem if a ductile and a brittle materials are used. In reinforced concrete (RC) structures, a slender design must be done. In that case, the steel must yield before the concrete in order to prevent sudden and brittle fracture of concrete. For that reason, the maximum reinforcement must be also considered in the design. For the designs exceeding the maximum reinforcement area, two options are possible. The first option is to enlarge the concrete cross sectional size and the other option is to use additional reinforcements in the compressive section of the member. The first option looks like a better choice if the cost of the steel is considered, but architectural issues related to the use of individuals and esthetics may prevent the increase of the sizes of structural members.

In the present study, the optimum design of RC continuous beams is presented for different ranges of beam dimensions. In that case, the effect of doubly or singly reinforced design can be seen in optimum cost. To optimize RC members, numerical algorithm are a good option. By using numerical algorithms, it is possible to find an optimum design which is practical solution in construction at a construction yard. Several methodologies on RC beams [1-8], columns [9-11], frames [12-14] and retaining walls [15-17] have been proposed. In the present study, random search technique (RST) developed by Nigdeli and Bekdas is employed [8].

2. MATERIALS AND METHODS

RST method considers all possible live-load patterns and finds an optimum design for the most unfavorable condition. The optimization objective is the total cost of the continuous beam. Seven general constraints are considered in the optimum design and these constraints are related with the placement of rebars in order to sustain adherence, maximum reinforcement ratio for slender design, minimum longitudinal and shear

---

[1] Corresponding author: İstanbul University, Department of Civil Engineering, 34320, Avcılar/İstanbul, Turkey. *bekdas@istanbul.edu.tr*

[2] İstanbul University, Department of Civil Engineering, İstanbul, Turkey, *melihnig@istanbul.edu.tr*

reinforcements, shear force capacity, distance of stirrups and flexural moment capacity. The details of the methodology can be found in Reference [8] and the flowchart of the algorithm is shown as Fig.1.
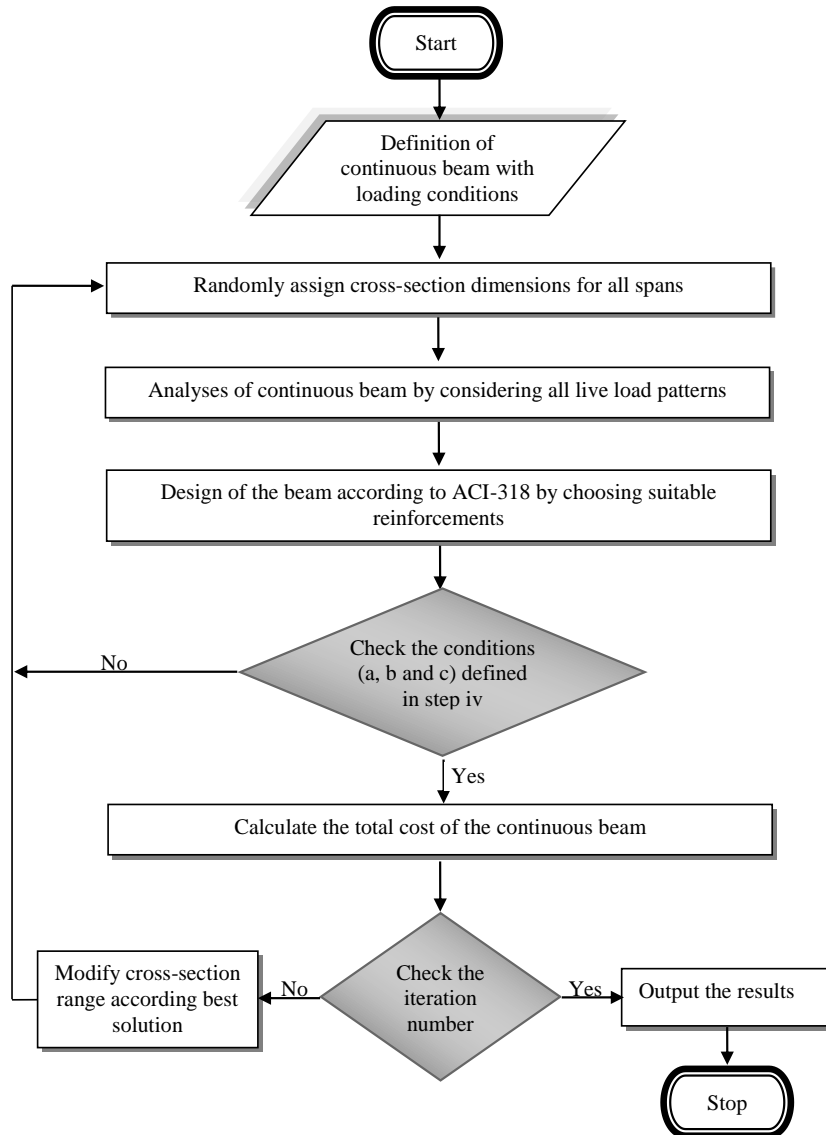
Figure 8. Flowchart of the RST [8]

The optimum design is done according to ACI318 (Building Code Requirements for Structural Concrete) [18]. The stopping conditions (a, b and c) are follows.

    a)   All constraints must be provided.

    b)   The area of rebars must be less than 5% more of the required one.

In doubly reinforced design, rebars in compressive section must be less than rebars in tensile section.

3. RESULTS AND DISCUSSION

In this paper, a two span RC continuous beam was optimized for 4 cases of cross section dimension limits shown in Table 1. The design constants are given in Table 2. The loading on the spans are trapezoidal distribute load as seen in Fig. 2. In the figure, also live load patterns are shown. The optimum results are given in Tables 3-6.

Table 7. The cross section dimension limits

Case Number	Lower and upper limits of Breadth (B) and Height (H)
1	250-300
2	250-350
3	250-400
4	250-500

Table 8. The design constants

Definition	Symbol	Unit	Value
Dead Load	D	kN/m	30
Live Load	L	kN/m	10
Clear cover	c_c	mm	30
Range of reinforcement	ϕ_l	mm	16-30
Range of shear reinforcement	ϕ_s	mm	8-14
Max. aggregate diameter	D_{max}	mm	16
Yield strength of steel	f_y	MPa	420
Comp. strength of concrete	f_c'	MPa	25
Elasticity modulus of steel	E_s	MPa	200000
Specific gravity of steel	γ_s	t/m^3	7.86
Specific gravity of concrete	γ_c	t/m^3	2.5
Cost of the concrete per m^3	C_c	\$	40
Cost of the steel per ton	C_s	\$	400
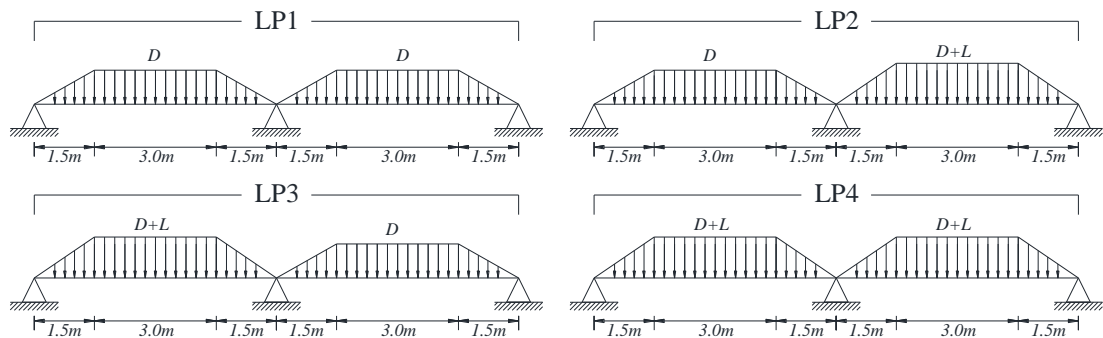
Figure 9. The live load patterns

Table 9. The optimum results for case 1

	First span	Middle support	Second span
Cross-section (B/H) (mm)	300/300	-	300/300
First line of compressive section	-	1Φ12+2Φ14	-
First line of tensile section	1Φ12+1Φ14+2Φ20+2Φ22	3Φ22+2Φ24	1Φ12+1Φ14+2Φ20+2Φ22
Stirrup steel diameter /distance (mm)	Φ8/120	-	Φ8/120
Optimum Cost (\$)		98.6938	

Table 4. The optimum results for case 2

	First span	Middle support	Second span
Cross-section (B/H) (mm)	250/350	-	250/350
First line of compressive section	-	1Φ10+1Φ10	-
First line of tensile section	1Φ16+2Φ18+1Φ20	1Φ22+3Φ24	1Φ16+2Φ18+1Φ20
Stirrup steel diameter /distance (mm)	Φ8/150	-	Φ8/150
Optimum Cost ($)		84.0452	

Table 5. The optimum results for case 3

	First span	Middle support	Second span
Cross-section (B/H) (mm)	260/400	-	260/400
First line of compressive section	-	-	-
First line of tensile section	2Φ12+1Φ14+1Φ24	2Φ20+2Φ22	2Φ12+1Φ14+1Φ24
Stirrup steel diameter /distance (mm)	Φ8/170	-	Φ8/170
Optimum Cost ($)		81.4234	

Table 6. The optimum results for case 4

	First span	Middle support	Second span
Cross-section (B/H) (mm)	250/410	-	250/410
First line of compressive section	-	-	-
First line of tensile section	1Φ14+2Φ16+1Φ18	3Φ24	1Φ14+2Φ16+1Φ18
Stirrup steel diameter /distance (mm)	Φ8/180	-	Φ8/180
Optimum Cost ($)		80.0726	

4. CONCLUSIONS

In the design example, doubly reinforced designs were found in case 1 and 2. In these cases, the optimum costs are significantly higher than the other cases. Especially, in case 1, both B and H values are at the upper bound of the solution range. Since the dimensions of the beam are small, the required stirrups are showing a significant increasing member and the distance between the stirrups is short. In case 2, the reduction of member and sizes of rebars can be clearly seen. The breadth of the beam is at the lower bound while the height is at the upper bound in order to increase the flexural moment bearing capacity. In case 3, the reduction of the cost can be clearly seen by not using rebars in compressive section of the member at the middle support, but the most economical case is 4. The optimum height of the beam is not at upper bound. In that case, this increase of the height of the beam is unnecessary after the value of 410 mm.

REFERENCES

[1]. Coello, C. C., Hernandez, F. S., Ferrera, F. A. (1997), "Optimal Design of Reinforced Concrete Beams Using Genetic Algorithms", Expert Syst. Appl., 12 101-108.
[2]. Koumousis, V. K., Arsenis, S. J. (1998), "Genetic Algorithms in Optimal Detailed Design of Reinforced Concrete Members", Comput-Aided Civ. Inf., 13, 43-52.
[3]. Govindaraj, V., Ramasamy, J. V. (2005), "Optimum detailed design of reinforced concrete continuous beams using Genetic Algorithms", Comput. Struct., 84, 34–48.
[4]. Fedghouche, F., Tiliouine, B. (2012), "Minimum cost design of reinforced concrete T-beams at ultimate loads using Eurocode2", Eng. Struct., 42, 43–50.
[5]. Leps, M., Sejnoha, M. (2003), "New approach to optimization of reinforced concrete beams", Comput. Struct., 81, 1957–1966.

[6]. Akin, A. and Saka, M.P. (2010), "Optimum Detailed Design of Reinforced Concrete Continuous Beams using the Harmony Search Algorithm", In: The Tenth International Conference on Computational Structures Technology", Stirlingshire, UK, Paper 131.

[7]. Bekdas, G. and Nigdeli, S.M. (2012), "Cost optimization of T-shaped reinforced concrete beams under flexural effect according to ACI 318", In: 3rd European Conference of Civil Engineering, Paris, France.

[8]. Nigdeli, S. M., & Bekdas, G. (2016). Optimum design of RC continuous beams considering unfavourable live-load distributions. KSCE Journal of Civil Engineering, DOI: 10.1007/s12205-016-2045-5.

[9]. Rafiq, M. Y., Southcombe, C. (1998), "Genetic algorithms in optimal design and detailing of reinforced concrete biaxial columns supported by a declarative approach for capacity checking", Comput. Struct. 69, 443-457.

[10]. Bekdas, G. and Nigdeli, S.M. (2014), "Optimization of slender reinforced concrete columns", In:85th Annual Meeting of the International Association of Applied Mathematics and Mechanics, Erlangen, Germany.

[11]. Nigdeli, S. M., Bekdas, G., Kim, S., & Geem, Z. W. (2015). A novel harmony search based optimization of reinforced concrete biaxially loaded columns.Structural Engineering and Mechanics, 54(6), 1097-1109.

[12]. Camp, C. V., Pezeshk, S., Hansson, H. (2003), "Flexural Design of Reinforced Concrete Frames Using a Genetic Algorithm", J Struct. Eng.-ASCE., 129, 105-11.

[13]. Govindaraj, V., Ramasamy, J. V. (2007), "Optimum detailed design of reinforced concrete frames using genetic algorithms", Eng. Optimiz., 39(4), 471–494.

[14]. Bekdas G., Nigdeli, S. M., Modified Harmony Search for Optimization of Reinforced Concrete Frames.In: Harmony Search Algorithm. Advances in Intelligent Systems and Computing, vol 514, Del Ser J. (eds) Springer, pp. 213-221, 2017

[15]. Camp, C.V. and Akin, A. (2012), "Design of retaining walls using big bang–big crunch optimization", Journal of Structural Engineering, Vol.138, No.3, pp.438–448, DOI:10.1061/(ASCE)ST.1943-541X.0000461.

[16]. Talatahari, S., Sheikholeslami, R., Shadfaran, M. and Pourbaba, M. (2012), "Optimum design of gravity retaining walls using charged system search algorithm", Mathematical Problems in Engineering, Article ID 301628, 1-10. DOI:10.1155/2012/301628

[17]. Temur, R, Bekdas, G. (2016), "Teaching learning-based optimization for design of cantilever retaining walls", Structural Engineering and Mechanics, Vol.57, No.4, pp.763-783, DOI: 10.12989/sem.2016.57.4.763

[18]. ACI 318M-05, Building code requirements for structural concrete and commentary, American Concrete Institute, 2005.

BIOGRAPHY

Sinan Melih Nigdeli, Associative Professor, is researcher in Structural Control and Optimization at Istanbul University. He obtained his DPhil in Structural Engineering from Istanbul Technical University with a thesis subject of active structural control. He co-organized the 15th EU-ME Workshop: Metaheuristic and Engineering in Istanbul. In optimization and structural control, he organized several mini-symposiums or special sections in prestigious international events. He co-edited Metaheuristics and Optimization in Civil Engineering published by Springer in 2016 and he is one of the guest editors in 2017 special issue of KSCE Journal of Civil Engineering. He has authored more than 100 papers for journals and scientific events.

Gebrail Bekdas, Associative Professor, is researcher in Structural Control and Optimization at Istanbul University. He obtained his DPhil in Structural Engineering from Istanbul University with a thesis subject of design of cylindrical walls. He co-organized the 15th EU-ME Workshop: Metaheuristic and Engineering in Istanbul. In optimization, he organized several mini-symposiums or special sections in prestigious international events. He co-edited Metaheuristics and Optimization in Civil Engineering published by Springer in 2016 and he is one of the guest editors in 2017 special issue of KSCE Journal of Civil Engineering. He has authored more than 100 papers for journals and scientific events.

Optimization Of Spans Of Multi-Story Frames Using Teaching Learning Based Optimization

Gebrail Bekdas[1], Sinan Melih Nigdeli[2], Aylin Ece Kayabekir[3]

Abstract

Optimization is a major issue of civil engineering since different goals (design, safety and economy) must be considered at the same time for an engineering design. In the present study, a methodology is presented for optimization of span lengths of frame structures for minimizing the stress of elements resulting from axial force and flexural moments. A metaheuristic based algorithm called teaching learning based optimization (TLBO) is employed in the presented methodology. The methodology can be explained in five steps. In the first step, the design constants and the ranges of design variables are defined. Then, the design variables are randomly generated within the selected range. The generation is done for several times and the number of total generations is equal to the population number representing the population of a class. In the third step, the teacher phase is started and the existing results are updated by using the best existing solution which represents the teacher. Then in the fourth step, the student phase is started and this phase is the imitation of the self-study of students. The existing solutions are used in the modification of the existing solutions. In the last step, the maximum iteration number is checked and the iterations will continue from the third step. The methodology is tested on multi-story frame structures in order to find the optimum lengths of spans.

Keywords: *Metaheuristic algorithm, Frames, Optimization, Teaching learning based optimization.*

1. INTRODUCTION

A safe and esthetic design is not the only need in an engineered product. The design must also have profits in mean of cost. In a civil engineering structures, the cost economy can be provided in two ways. The first way is to find the precise design of materials. In that case, the strength of a member will be close, but higher than required. If the system is statically determined (like Gerber beam) or rigidities of member are not too effective on the internal forces, the design variables can be mathematically found if there are no constraints. But, all engineering problems have constraints in the real world. Although, trusses are only under the effects of axial stresses and the only variables are the size of members, the existing of stress and displacement constraints for several cases generates an important optimization problem which is one of the oldest one, but still active in current research by using numerical algorithms based on metaheuristics [1-4]. Since reinforced concrete (RC) members contain more design variables (size of concrete and amount of rebar) and complex design constraints (generally for ductile design) than trusses, the optimization problem is challenging. Metaheuristic based methods have been used for cost optimization of RC beams [5-7], columns [8-10], frames [11-13] and retaining walls [14-16].

The second option is to find a topology design (or shape) in order to reduce the internal forces. The topology optimization of trusses has been investigated in several studies [17-18]. Also, the topology of frames was investigated by Pezeshk et al. [19].

In the present study, the optimum span lengths of frame structures are investigated. The structural models are multi story, but the results are also compared for structures with one story. A metaheuristic based method called teaching learning based optimization (TLBO) [20] is employed for the optimization problem. The algorithm is inspired by teaching and learning process of a class and the phases; namely teacher and learner phases are mathematically formalized for optimization.

---

[1] Corresponding author: İstanbul University, Department of Civil Engineering, 34320, Avcılar/İstanbul, Turkey. bekdas@istanbul.edu.tr

[2] İstanbul University, Department of Civil Engineering, İstanbul, Turkey, melihnig@istanbul.edu.tr

[3] İstanbul University, Department of Civil Engineering, İstanbul, Turkey, ecekayabekir@gmail.com

2. METHODOLOGY

The algorithm can be briefly explained in five steps as follows.

i. The design constraints and possible ranges of design variables are defined. The design variables are the coordinates of columns. Thus, the span lengths are optimized. For a fast logical optimization, design constraints are several inequalities of several design variables as seen in numerical example section.

ii. Then, initial solutions are randomly generated for several times. The number of generations is the population number. For all set of design variables, the extreme and minimum stresses of all members ($\sigma_{i,min,max}$ for ith member for i=1,2,...n: number of members) are calculated according to Eq. (1).

$$\sigma_{i,min,max} = \frac{N_i}{A_i} \mp \frac{M_i}{W_i}, \ (i = 1,2,....n) \tag{1}$$

N_i and M_i are internal forces, namely; axial force and flexural moment of ith member which have a W_i; section modulus and A_i; cross sectional area. The analyses are done according to the coded program for analyses and optimization. The internal forces are found by using the well-known stiffness method in structural analyses.

iii. In this step, the essential optimization starts with teacher phase, which is formulized as Eq. (2)

$$X_{new,i} = X_{old,i} + rand(0,1) \cdot (X_{teacher} - T_F \cdot X_{mean}) \quad for \ i = 1 \ to \ n \tag{2}$$

In this equation, a new design variables ($X_{new,i}$) is generated by updating the old one ($X_{old,i}$) by using $X_{teacher}$; the best existing solution, TF; a random integer number which is namely teaching factor and can only be 1 or 2, X_{mean}; mean of the design variables for all sets and rand(0,1); a random real number.

iv. After using teacher phase, the learner phase formulized as Eq. (3) is used.

$$X_{new,i} = \begin{cases} X_{old,i} + rand(0,1)(X_j - X_k) & if \ j^{th} \ \text{solution is better than } k^{th} \ \text{solution} \\ X_{old,i} + rand(0,1)(X_k - X_j) & if \ k^{th} \ \text{solution is better than } j^{th} \ \text{solution} \end{cases} \tag{3}$$

In this phase, two random solution (jth and kth) are used in modification.

v. The two explained phases are iteratively conducted until a defined iteration number

3. RESULTS AND DISCUSSION

In this paper, three numerical examples are compared. A three span frame structure is presented for one, two and three story for cases 1, 2 and 3, respectively as seen in Figs. 1-3. The design constants are given in Table 1. Also, the design constraints are as follows.

$$0 < X_1 < X_2 \tag{4}$$

$$X_1 < X_2 < L_{span} \tag{5}$$

Table 10. The design constants

Definition	Symbol	Unit	Value
Total length of span	L_{span}	m	15.0
Distributed load	q	kN/m^2	36.0
Elasticity modulus	E	MPa	200000
Breadth of the elements	b	m	0.4
Height of the elements	h	m	0.4
Length of column	L_{column}	m	3
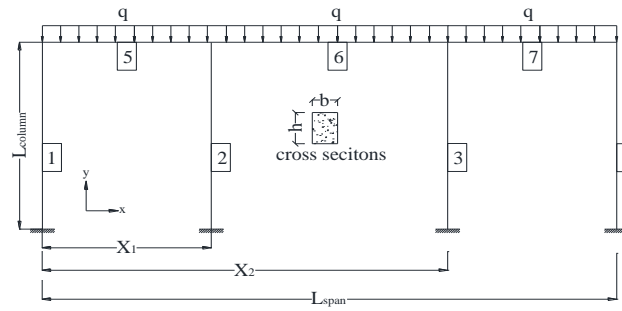
Figure 1. The numerical cases (case 1)
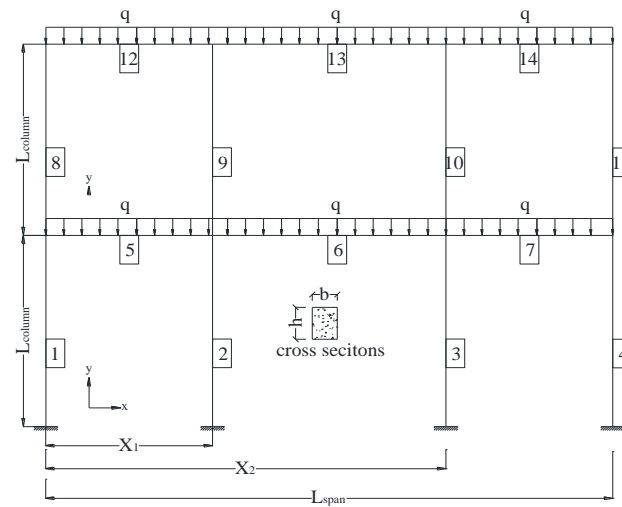
Figure 2. The numerical cases (case 2)
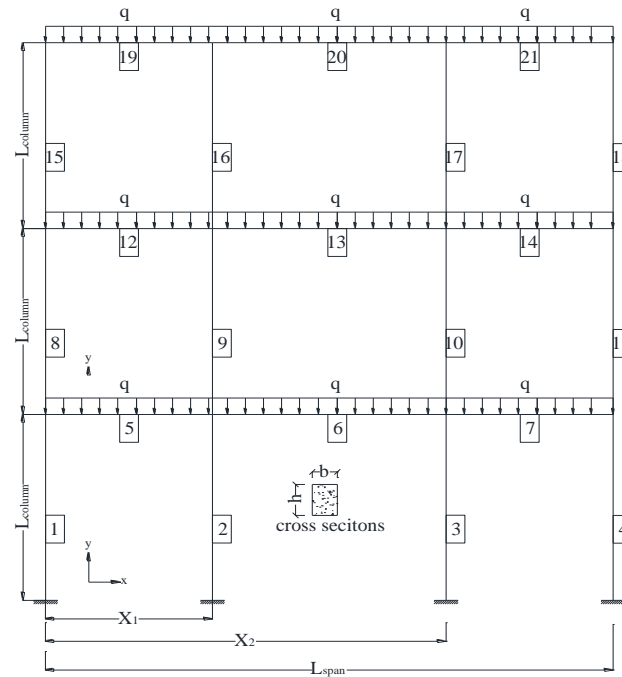
Figure 3. The numerical cases (case 3)

The optimum results are presented in Table 2. The number of population is taken as 30 in the analyses.

Table 2. The optimum design variables

	Case 1	Case 2	Case 3
X_1 (m)	4.85	4.9	4.95
X_2 (m)	10.15	10.10	10.05
$\max\lvert\sigma_{max}, \sigma_{min}\rvert$ (kN/m^2)	8015.5	7835.4	7722.3
Critical Member	6	12, 14	19, 21

4. CONCLUSIONS

The expected optimum solution is a symmetric one. The proposed method is effective in finding the exact optimum solution because all the optimum designs are symmetric. For the structures with multi stories, the maximum stress is showing a reducing trend. Also, the middle span length is decreasing a little and critical members is changing. For the single story structure, the middle beam (number 6) is critical, but for the multi-story structures; the critical member is the edge beams of the upper stories.

REFERENCES

[1]. C.V. Camp, M. Farshchin, Design of space trusses using modified teaching–learning based optimization, Engineering Structures 62–63 (2014) 87–97.

[2]. T. Dede, Y. Ayvaz, Combined size and shape optimization of structures with a new meta-heuristic algorithm, Applied Soft Computing 28 (2015) 250–258.

[3]. A. Kaveh, B. Mirzaei, A. Jafarvand, An improved magnetic charged system search for optimization of truss structures with continuous and discrete variables, Applied Soft Computing 28 (2015) 400-410.

[4]. Bekdas, G., Nigdeli, S. M., & Yang, X. S. (2015). Sizing optimization of truss structures using flower pollination algorithm. Applied Soft Computing, 37, 322-331.

[5]. Coello, C. C., Hernandez, F. S., Ferrera, F. A. (1997), "Optimal Design of Reinforced Concrete Beams Using Genetic Algorithms", Expert Syst. Appl., 12 101-108.

[6]. Bekdas, G. and Nigdeli, S.M. (2012), "Cost optimization of T-shaped reinforced concrete beams under flexural effect according to ACI 318", In: 3rd European Conference of Civil Engineering, Paris, France.

[7]. Nigdeli, S. M., & Bekdas, G. (2016). Optimum design of RC continuous beams considering unfavourable live-load distributions. KSCE Journal of Civil Engineering, DOI: 10.1007/s12205-016-2045-5.

[8]. Rafiq, M. Y., Southcombe, C. (1998), "Genetic algorithms in optimal design and detailing of reinforced concrete biaxial columns supported by a declarative approach for capacity checking", Comput. Struct. 69, 443-457.

[9]. Bekdas, G. and Nigdeli, S.M. (2014), "Optimization of slender reinforced concrete columns", In:85th Annual Meeting of the International Association of Applied Mathematics and Mechanics, Erlangen, Germany.

[10]. Nigdeli, S. M., Bekdas, G., Kim, S., & Geem, Z. W. (2015). A novel harmony search based optimization of reinforced concrete biaxially loaded columns. Structural Engineering and Mechanics, 54(6), 1097-1109.

[11]. Camp, C. V., Pezeshk, S., Hansson, H. (2003), "Flexural Design of Reinforced Concrete Frames Using a Genetic Algorithm", J Struct. Eng.-ASCE., 129, 105-11.

[12]. Govindaraj, V., Ramasamy, J. V. (2007), "Optimum detailed design of reinforced concrete frames using genetic algorithms", Eng. Optimiz., 39(4), 471–494.

[13]. Bekdas G., Nigdeli, S. M., Modified Harmony Search for Optimization of Reinforced Concrete Frames.In: Harmony Search Algorithm. Advances in Intelligent Systems and Computing, vol 514, Del Ser J. (eds) Springer, pp. 213-221, 2017

[14]. Camp, C.V. and Akin, A. (2012), Design of retaining walls using big bang–big crunch optimization, Journal of Structural Engineering, Vol.138, No.3, pp.438–448, DOI:10.1061/(ASCE)ST.1943-541X.0000461.

[15]. Talatahari, S., Sheikholeslami, R., Shadfaran, M. and Pourbaba, M. (2012), "Optimum design of gravity retaining walls using charged system search algorithm", Mathematical Problems in Engineering, Article ID 301628, 1-10. DOI:10.1155/2012/301628

[16]. Temur, R, Bekdas, G. (2016), Teaching learning-based optimization for design of cantilever retaining walls, Structural Engineering and Mechanics, Vol.57, No.4, pp.763-783, DOI: 10.12989/sem.2016.57.4.763

[17]. Mortazavi, Ali, and Vedat Togan. "Simultaneous size, shape, and topology optimization of truss structures using integrated particle swarm optimizer." Structural and Multidisciplinary Optimization 54.4 (2016): 715-736.

[18]. Savsani, Vimal J., Ghanshyam G. Tejani, and Vivek K. Patel. "Truss topology optimization with static and dynamic constraints using modified subpopulation teaching–learning-based optimization." *Engineering Optimization* 48.11 (2016): 1990-2006.

[19]. Pezeshk, S., Camp, C. V. and Chen, D. (2000), "Design of nonlinear framed structures using genetic optimization", *Journal of structural engineering*, Vol.126, No.3, pp.382-388, DOI:10.1061/(ASCE)0733-9445(2000)126:3(382).

[20]. Rao, Ravipudi V., Vimal J. Savsani, and D. P. Vakharia. "Teaching–learning-based optimization: a novel method for constrained mechanical design optimization problems." *Computer-Aided Design* 43.3 (2011): 303-315.

BIOGRAPHY

Gebrail Bekdas, Associative Professor, is researcher in Structural Control and Optimization at Istanbul University. He obtained his DPhil in Structural Engineering from Istanbul University with a thesis subject of design of cylindrical walls. He co-organized the 15th EU-ME Workshop: Metaheuristic and Engineering in Istanbul. In optimization, he organized several mini-symposiums or special sections in prestigious international events. He co-edited Metaheuristics and Optimization in Civil Engineering published by Springer in 2016 and he is one of the guest editors in 2017 special issue of KSCE Journal of Civil Engineering. He has authored more than 100 papers for journals and scientific events.

Sinan Melih Nigdeli, Associative Professor, is researcher in Structural Control and Optimization at Istanbul University. He obtained his DPhil in Structural Engineering from Istanbul Technical University with a thesis subject of active structural control. He co-organized the 15th EU-ME Workshop: Metaheuristic and Engineering in Istanbul. In optimization and structural control, he organized several mini-symposiums or special sections in prestigious international events. He co-edited Metaheuristics and Optimization in Civil Engineering published by Springer in 2016 and he is one of the guest editors in 2017 special issue of KSCE Journal of Civil Engineering. He has authored more than 100 papers for journals and scientific events.

Aylin Ece Kayabekir, is a student of civil engineering master program of İstanbul University. She is working on structural optimization. Up to now, the authored several papers about optimization of RC retaining walls, RC shear walls, frames, carbon fiber reinforced polymers and dynamic of structures interacting with soil in conference like 7th European conference of civil engineering, International science symposium 2016, 3rd International conference on engineering and natural science and International conference on civil and environmental engineering.

Newtonian Heating Effect on Radiative Casson Fluid Flow over Exponentially Stretching Sheet in Porous Media

Kartini Ahmad[1], Zaharah Wahid[2]

Abstract

This study focuses on a steady two-dimensional boundary layer flow and heat transfer of a Casson fluid over an exponentially stretching sheet which is embedded in a porous medium along with Newtonian heating and radiation effects. By imposing suitable similarity transformation, the partial differential equations are transformed into ordinary differential equations which are then solved numerically using the Keller-box method. The numerical solutions for the skin friction $-f''(0)$ and the surface temperature $\theta(0)$ are obtained for a few values of exponential parameter N, Casson fluid parameter β, permeability number κ, radiation parameter R, Prandtl number Pr and Biot number Bi. It is found that increasing N will decrease surface temperature and increase the skin friction coefficient. However, the imposition of the radiation towards the thermal flow rises the wall temperature.

Keywords: *Newtonian heating, boundary layer, numerical methods*

1. INTRODUCTION

In the last few decades, fluid flow and heat transfer in porous media has received great attention due to enormous engineering applications, such as geothermal systems, thermal insulation, metals processing, catalytic reactors, granular insulation, design of packed bed reactors, transpiration cooling, filtration etc. Tien and Vafai [1] described convective and radiative heat transfer in porous media, Hsieh et al. [2] presented nonsimilarity solutions for mixed convection from a vertical plate embedded in a porous medium for two surface heating conditions, i.e variable wall temperature and variable surface heat flux, Bakier and Gorla [3] investigated the effects of radiation and mixed convection from a horizontal plate in a saturated porous medium, and Tashtoush [4] presented a new analytical solution for the effects of viscous dissipation on mixed convection flow and heat transfer involving an isothermal vertical wall embedded in Darcy and non-Darcy porous media with uniform free stream velocity.

As stretching sheet plays an important role in determining the final product, many studies have been conducted to discuss the effects of stretching sheet in depth. The sheet can either be stretched linearly or nonlinearly. Khan and Sanjayanand [5] studied boundary layer flow of viscoelastic fluid in a porous medium over a porous quadratic stretching sheet; Kechil [6] considered flow and mass transfer of a chemically-reactive species over a nonlinearly stretching sheet in a porous medium, Mandal and Mukhopadhyay [7] carried out numerical analysis for the boundary layer flow and heat transfer towards an exponentially stretching porous sheet embedded in porous medium, and recently, Yadav and Sharma [8] investigated radiation effects on the MHD flow over an exponentially moving stretching sheet placed in a porous medium. An analytical solution for viscous and incompressible fluid towards an exponentially stretching porous sheet with surface heat flux in porous medium was solved by Ali et al. [9], and Sharma and Gupta [10] analysed MHD boundary layer flow and heat transfer of a viscous incompressible fluid oven an exponentially porous stretching sheet in the presence of thermal radiation, to name a few.

All the above mentioned works are limited to either prescribed surface temperature or prescribed surface heat flux. However, the effects where the heat transfer rate from the bounding surface with a finite heat capacity

---

[1] *Corresponding author: International Islamic University Malaysia, Department of Science in Engineering, Kulliyyah of Engineering, 50728 Gombak, Kuala Lumpur, Malaysia. kartini@iium.edu.my*

[2] *International Islamic University Malaysia, Department of Science in Engineering, Kulliyyah of Engineering, 50728 Gombak, Kuala Lumpur, Malaysia. zaharahwahid@iium.edu.my*

are proportional to the local surface temperature, also known as Newtonian heating, should also be considered due to its wide range of engineering applications, such as in heat exchangers where the conduction in a solid tube wall is greatly influenced by convection in the fluid flowing over it, convective flows set up where the bounding surface absorbs heat by solar radiation and for the conjugate heat transfer around fins where the conduction within the fin and convection in the fluid surrounding it must be simultaneously analysed in order to obtain vital design information [11]. Kasim et al. [12] carried out an investigation of the magnetic field effects on the mixed convection boundary layer flow of viscoelastic fluid past a sphere with Newtonian heating embedded in a porous medium and very recently, Lavanya et al. [13] studied the phenomenon of Newtonian heating under the application of uniform porous medium when heat generation and chemical reaction appear in the energy and volumetric species equations in the nanofluid flow and MHD convective boundary layer flow of Casson fluid over an exponentially inclined permeable stretching surface in the presence of thermal radiation and chemical reaction has been studied by Reddy [14].

To date, no study on radiative Casson fluid flow over exponentially stretching sheet in porous media with Newtonian heating has been reported. However, the study of radiative Casson fluid flow over exponentially stretching sheet in the presence of suction or blowing was conducted by Pramanik [15] and an investigation on unsteady free convection radiative Casson fluid flow past an exponentially accelerated infinite vertical plate with Newtonian heating has been done by Jain [16]. Hence, motivated by the work of Mandal and Mukhopadhyay [7] and Ishak [17], here we probe into the effects of Newtonian heating on radiative Casson fluid flow over exponentially stretching sheet in porous media.

2. PROBLEM FORMULATION

We investigate steady two-dimensional Casson fluid flow over stretching sheet embedded in porous medium with a non-uniform permeability κ_1. The flow is generated due to the sheet being stretched exponentially, with velocity $u_w = U_0 e^{Nx/L}$, where U_o is the reference velocity, L is the reference length and N is the exponential parameter. The sheet is heated due to Newtonian heating and the surrounding temperature is assumed as T_∞. Imposing the Boussinesq and boundary layer approximations, the motion of the flow with radiation effects are:

$$\frac{\partial u}{\partial x} + \frac{\partial v}{\partial y} = 0, \tag{1}$$

$$u\frac{\partial u}{\partial x} + v\frac{\partial u}{\partial y} = \upsilon\left(1+\frac{1}{\beta}\right)\frac{\partial^2 u}{\partial y^2} - \frac{\upsilon}{\kappa_1}u, \tag{2}$$

$$u\frac{\partial T}{\partial x} + v\frac{\partial T}{\partial y} = \frac{1}{\rho c_p}\left(k\frac{\partial^2 T}{\partial y^2} - \frac{\partial q_r}{\partial y}\right), \tag{3}$$

along with boundary conditions:

$$u = u_w, \quad v = 0, \quad \frac{\partial T}{\partial y} = -h_s T \ (\mathrm{NH}) \quad \text{at} \quad y = 0, \quad u \to 0, \quad T \to T_\infty \quad \text{as} \quad y \to \infty. \tag{4}$$

Here, u and v are the velocity components with respect to horizontal (x) and vertical (y)-axes, respectively. υ is the kinematic fluid viscosity, β is the non-Newtonian (Casson) fluid parameter, T is the fluid temperature, k is the thermal conductivity, ρ is the density of the fluid, c_p is the specific heat at constant pressure, q_r is the radiative heat flux given by the Rosseland approximation

$$q_r = -\frac{4\sigma^*}{3k^*}\frac{\partial T^4}{\partial y} \tag{5}$$

where σ^* and k^* is the Stefan-Boltzman constant and mean absorption, respectively and

$$T^4 = 4T_\infty^3 T - 3T_\infty^4. \tag{6}$$

Making use of (5) and (6) into (3), we get

$$u\frac{\partial T}{\partial x} + v\frac{\partial T}{\partial y} = \frac{1}{\rho c_p}\left(k + \frac{16\sigma^* T_\infty^3}{3k^*}\right)\frac{\partial^2 T}{\partial y^2}. \tag{7}$$

For the problem to have similarity solutions, it is assumed that the non-uniform permeability parameter is $\kappa_1 = 2\kappa_o e^{-Nx/L}$ and the heat transfer parameter for Newtonian heating $h_s = h_0 e^{Nx/2L}$, where κ_o and h_0 are constant.

To solve Eqs. (1) – (3) subject to (4), we apply the following transformation [7]:

$$u = U_o\, e^{Nx/L}\, f'(\eta), \quad v = -N\sqrt{\frac{\upsilon U_o}{2L}}\, e^{Nx/2L}\left[f(\eta)+\eta\, f'(\eta)\right], \quad \eta = \sqrt{\frac{U_o}{2\upsilon L}}\, e^{Nx/2L}\, y, \quad \theta(\eta)=\frac{T-T_\infty}{T_\infty}, \tag{8}$$

where η is the similarity variable, $f(\eta)$ and $\theta(\eta)$ are the dimensionless stream function and dimensionless temperature, respectively, and prime denotes differentiation with respect to η. Eqs. (1) is automatically satisfied and Eqs. (2) and (7) are reduced to

$$\left(1+\frac{1}{\beta}\right)f''' + N f\, f'' - 2Nf'^2 - \kappa f' = 0, \tag{9}$$

$$\left(1+\frac{4}{3}R\right)\theta'' + N\, Pr\, f\, \theta' = 0, \tag{10}$$

with boundary conditions

$$f(\eta)=0, \quad f'(\eta)=1, \quad \theta'(\eta)=-Bi\left[1+\theta(0)\right] \qquad \text{at} \quad \eta=0,$$
$$f'(\eta)\to 0, \quad \theta(\eta)\to 0 \qquad \text{as} \quad \eta\to\infty, \tag{11}$$

where prime denotes differentiation with respect to η, $\kappa = \dfrac{\upsilon L}{\kappa_o U_o}$ is the permeability number, $R = \dfrac{4\sigma^*}{k^*}\dfrac{T_\infty^3}{k}$ is the radiation number, $Pr = \dfrac{\mu c_p}{k}$ is the Prandtl number and $Bi = h_o\sqrt{\dfrac{2\upsilon L}{U_o}}$ is the conjugate parameter for the Newtonian heating.

3. RESULTS AND DISCUSSION

Using the method described by Cebeci and Bradshaw [18], we solved Eqs. (9) – (11) for a few values of Casson fluid parameter (β), permeability number (κ), exponential parameter (N), radiation parameter (R), Biot number (Bi) and Prandtl number. The impact of Bi and Pr are tabulated in the form of a table and all the graphical results obtained are limited to Biot number (Bi) = 0.5 and Prandtl number (Pr) = 7 (air). From an engineering point of view, there are two physical quantities of interest, i.e the skin friction coefficient and local Nusselt number, which can be found once the values of $-f''(0)$ and $\theta'(0)$ are obtained. However, the value of $\theta'(0)$ is gained from (11) after the value of $\theta(0)$ is known.

Table 1 presented the values obtained for $\theta(0)$ for various values of the Pr and Bi numbers for $R = 0$ and 1 respectively, with the absence of permeability number κ and when the flow is dominated by Newtonian fluid ($\beta = \infty$), taking into account $N = 1$. It is noticed that at a fixed R and Bi number, the increment of the Pr number decreases wall temperature. Due to Newtonian heating, it is clear that the surface temperature increases as Bi increases. The effects of radiation R also plays an important role by raising the surface temperature, as given by results tabulated in Table 1.

Table 11. Values of θ(0) when β = ∞, N = 1, κ = 0

R	Pr	Bi = 0.5	Bi = 1.5
0	7	0.371354	4.318261
	10	0.284579	1.980117
	100	0.069348	0.241469
1	7	0.803404	-
	10	0.561926	-
	100	0.112292	0.434291

The effects of κ for various values of N when $Bi = 0.5$ on the flow and thermal fields are depicted in Figures 1 and 2 respectively, taking into account both Newtonian ($\beta = \infty$) and non-Newtonian (Casson) fluid ($\beta \neq \infty$).

The presence of a porous medium causes higher restriction to the fluid, which results in higher shear stress at the surface. As such, the higher the permeability number κ is, the more resisted the flow motion will be. This in turn increases the skin friction $-f''(0)$, as can be seen in Figure 1. The same phenomenon occurs for the surface temperature $\theta(0)$ as κ increases. It should be pointed out that, the negative sign of $f''(0)$ is due to the surface, which exerts a dragging force on the fluid [7]. Also, as κ increases, an outstanding wall temperature is found to occur for $N = 1$ as compared to $N = 2$, where the variation of $\theta(0)$ is very small at $N = 2$. However, the impact of N is very much profound in the flow field compared to the thermal field as depicted in Figures 1 and 2, respectively. The effects of N is found to decrease surface temperature $\theta(0)$ and increase skin friction $-f''(0)$ at a fixed value of κ. As non-Newtonian fluid is concerned in this study, the Casson fluid is inferred to decrease both skin friction and surface temperature. On top of that, the imposition of R on the thermal field increases wall temperature and it is predictable that R does not influence the flow field due to the absence of this term in Eq. (9).
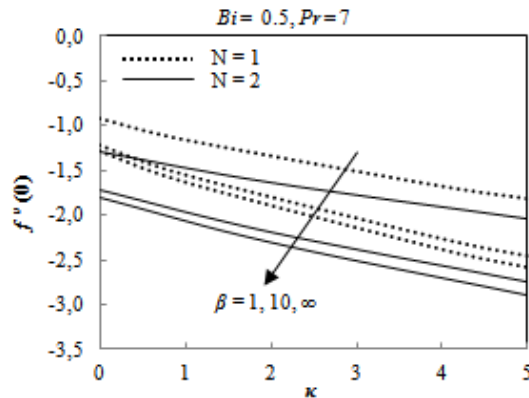
Figure 1. Skin friction coefficient $f''(0)$ for some values of κ, β and N when Bi = 0.5.
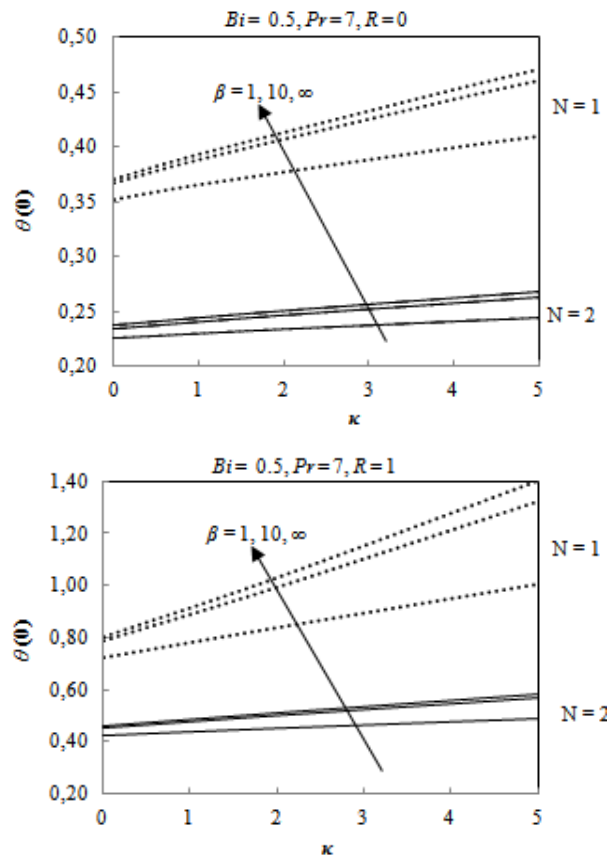
Figure 2. Surface temperature $\theta(0)$ for some values of κ, β, N when Bi = 0.5 and (a) R = 0 (b) R = 1

The velocity and temperature profiles for a few values of β, N and R when $\kappa = 1$ are depicted in Figures (3) and (4), respectively. Both velocity and temperature decrease with the increase of N, which leads to decrement of the boundary layer thickness. However, this scenario is very much remarkable in the formation of thermal boundary layer rather than the momentum boundary layer. As the surface was heated due to Newtonian heating, the initial temperature is $\theta(0)$ and slowly decreases to zero once it reaches 99% of the temperature from the inviscid fluid (see Figure 4). The initial values of $\theta(0)$ can be found in Figure 2 for some embedded parameters. It is also observed that the imposition of radiation R to the thermal flow increases surface temperature and, hence, thickens the thermal boundary layer.
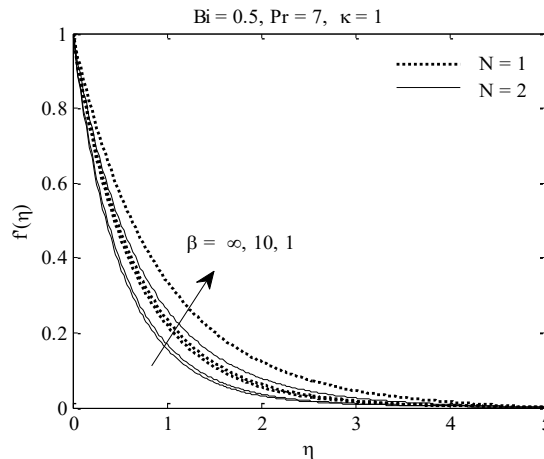
Figure 3. Velocity profiles $f'(\eta)$ for some values of β and N
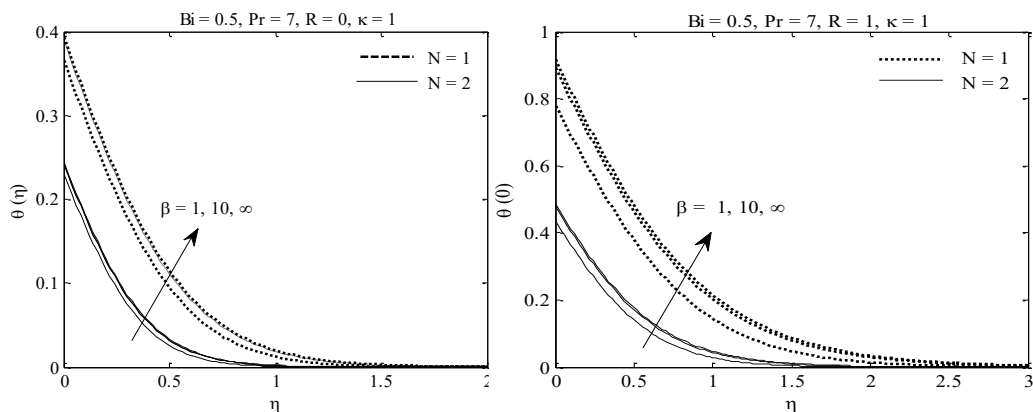
Figure 4. Temperature profiles $\theta(0)$ for some values of β, N and (a) $R = 0$ (b) $R = 1$

4. CONCLUSION

In this paper, we have studied numerically the two dimensional boundary layer flow of radiative Casson fluid over an exponentially stretching sheet embedded in porous media where the sheet is heated due to Newtonian heating. It is found that the skin friction coefficient and the surface temperature increase with the increase of the porosity parameter κ. The exponential stretching parameter N is found to increase the skin friction coefficient, however opposite trend is observed for the surface temperature. The imposition of radiation to the thermal flow gives higher temperature at the surface.

ACKNOWLEDGMENT

REFERENCES

[1]. C.L. Tien and K. Vafai, "Convective and radiative heat transfer in porous media," *Advances in Applied Mechanics*, vol. 27, pp. 225–281, 1989.

[2]. J.C Hsieh, T. S. Chen and B.F. Armaly, "Nonsimilarity solutions for mixed convection from vertical surfaces in porous media: variable surface temperature or heat flux," *International Journal of Heat and Mass Transfer,* vol 36, pp. 1485-1493, 1993.

[3]. A.Y. Bakier and R.S.R Gorla, "Thermal radiation effect on mixed convection from horizontal surfaces in saturated porous media," *Transport in porous media*, vol. 23, pp. 357-363, 1996.

[4]. B. Tashtoush, "Analytical solution for the effect of viscous dissipation on mixed convection in saturated porous media," *Transport in Porous Media,* vol. 41, pp. 197-209, 2000.

[5]. S. K. Khan and E. Sanjayanand, "Viscoelastic boundary layer MHD flow through a porous medium over a porous quadratic stretching sheet," *Archives of Mechanics,* vol. 56, pp. 191-204, 2004.

[6]. S.A. Kechil, "Flow and diffusion of chemically reactive species over a nonlinearly stretching sheet immersed in a porous medium," *Journal of Porous Media*, vol 12, pp. 1053 – 1063, 2009.

[7]. I.C. Mandal and S. Mukhopadhyay, "Heat transfer analysis for fluid over an exponentially stretching porous sheet with surface heat flux in porous media," *Ain Sham Engineering Journal,* vol. 4, pp. 103-110, 2013.

[8]. R.S. Yadav and P.R. Sharma, "Effects of radiation and viscous dissipation on MHD boundary layer flow due to an exponential moving stretching sheet in porous medium," *Asian Journal of Multidisciplinary Studies*, vol. 2, pp. 119-124, 2014.

[9]. A. Ali, H. Zaman, M.Z. Abidin and S.I.A. Shah, "Analytic solution for fluid flow over an exponentially stretching porous sheet with surface heat flux in porous medium by means of homotopy analysis method," *American Journal of Computational Mathematics*, vol. 5, pp. 224 - 238, 2015.

[10]. K. Sharma and G. Sumit, "Analytical study of MHD boundary layer flow and heat transfer towards a porous exponentially stretching sheet in presence of thermal radiation," *International Journal of Advances in Applied Mathematics and Mechanics,* vol. 4, pp. 1-10, 2016.

[11]. R.C. Chaudhary and J. Preeti, "An exact solution to the unsteady free-convection boundary-layer flow past an impulsively started vertical surface with Newtonian heating," *Journal of Engineering Physics and Thermophysics*, vol. 80, pp. 954-960, 2007.

[12]. A.R.M. Kasim, N.F. Muhammad, I. Anwar and S.Shafie, "MHD effect on convective boundary layer flow of a viscoelastic fluid embedded in porous medium with Newtonian heating," *Recent Advances in Mathematics*, ISBN: 978-1-61804-158-6, 2013.

[13]. M. Lavanya, M.S. Babu and G. V. Ramanaiah, "Heat transfer of nanofluid past an exponentially permeable stretching sheet with heat generation and Newtonian heating in a porous medium," *International Journal of Innovative Research and Development,* ISSN 2278–0211 5.1, 2016.

[14]. P.B.A. Reddy, "Magnetohydrodynamic flow of a Casson fluid over an exponentially inclined permeable stretching surface with thermal radiation and chemical reaction," *Ain Shams Engineering Journal,* vol. 7, pp. 593-602, 2016.

[15]. S. Pramanik, "Casson fluid flow and heat transfer past an exponentially porous stretching surface in presence of thermal radiation," *Ain Shams Engineering Journal*, vol. 5, pp. 205-212, 2014.

[16]. P. Jain, "Exact solutions for chemically reactive species in casson fluid past an exponentially accelerated surface with newtonian heating in the presence of thermal radiation," *International Journal of Engineering Research and General Science*, ISSN 2091-2730, 2015.

[17]. A. ISHAK, "MHD boundary layer flow due to an exponentially stretching sheet with radiation effect," *Sains Malaysiana*, vol. 40, pp. 391–395, 2011.

[18]. T. Cebeci and P. Bradshaw. *Physical and Computational Aspects of Convective Heat Transfer*, New York, USA: Springer, 1988.

A Roadmap for Data Driven Decision Making to Improve Quality

Onur Dogan[1]

Abstract

Many quality improvement programs including inspection, statistical process control, total quality control, zero defects, kaizen and lean six sigma, which is the most recognized, require collection and analysis of data to solve quality problems. With six sigma as a quality improvement program, the errors in the manufacturing are reduced to the error level of 3.4 parts per million and it is aimed to go to zero defect. With lean manufacturing, the lead-time is shortened and quality is improved by determining and eliminating all kinds of waste in the processes. Lean six sigma uses so called define-measure-analyze-improve-control (DMAIC) approach to reach six sigma quality levels, less than 3.4 part per million defectives, by reducing variations and wastes within processes. To achieve the goal depends on collection of data to attack quality problems.

Although many traditional data analysis tools can be used to develop quality of products and processes, now with industry 4.0, massive data sets collected through computerized systems should be mined with powerful data analysis methods. Data mining involves techniques used to produce meaningful results from data stacks. It is possible to make effective and quick decisions by utilizing these techniques in five steps of lean six. The use of data mining at every stage, especially in the measure and analyze stages, has critical importance to make powerful decisions.

The aim of this study is to provide a roadmap that allows companies that apply lean six sigma to make faster, more reliable and satisfied decisions with data. On the one hand, it will contribute to the manufacturing processes with lean six sigma by reducing the lead-time, producing better quality products; on the other hand, it will aid to make effective decisions using data mining techniques.

Keywords: *Data mining, Lean six sigma, Quality improvement*

1. INTRODUCTION

Today, producing quality products or services is vital for a company. Many competitors provide the same product or service. To improve quality depends on collection of a large volume of data and extraction useful information from it. Quality improvement programs such as inspection, statistical process control, total quality control, zero defects, kaizen and lean six sigma (LSS) collect data about quality problems to solve [1].

LSS emerged initially as different methods. Similarities and complementary features make it useful to use these two philosophies together. It has thus become a powerful and effective tool for sustainable operational outcomes. LSS is the most recognized quality improvement program. A combined program LSS includes of six sigma and lean manufacturing. Six sigma has been widely adopted as a discipline that use a systematic problem-solving approach and methodology in a variety of industries [2, 3]. Sigma is a statistical term for measuring how a given process deviates from perfection [4]. With six sigma, the errors in the manufacturing are reduced to the error level of 3.4 parts per million (ppm) and it is aimed to go to zero defect. Given the increasing customer expectations considerations, it is of great importance for successful companies. Six sigma asserts that this goal can be achieved if the variance in production is within a certain range.

Lean manufacturing aims to make production with value-creating operations by removing all kinds of activities that are worthless from the customer's point of view. The cost is reduced by determining and eliminating all kinds of waste and so, the lead-time is shortened. The difference between lean manufacturing and six sigma is to define the basic causes of waste in different ways. While lean manufacturing claims that wastes in the processes are due to non-value added activities to the final product, the six sigma argues that wastes come from the variation in the processes. However, the common goal of both is to create a production system that meets the customer expectations most effectively by producing quality products. Approximately

---

[1] *Corresponding author: Istanbul Technical University, Department of Industrial Engineering, 34367, Besiktas/İstanbul, Turkey. odogan@itu.edu.tr*

95% of LSS projects follow so-called define-measure-analyze-improve-control (DMAIC) approach [5] to reach six sigma quality levels, less than 3.4 part per million defectives. DMAIC is for available processes. If a new process is to be created, define-measure-analyze-design-verify (DMADV) cycle is used.

When looked at the output of LSS, it can be seen that the results are based on the data. Where data is available, the use of data mining is very natural. By data mining, decision makers gain time by identifying what is difficult to see at first sight. In addition, the accuracy is high because the decisions made are based on the data. The use of advanced analytical solutions, which are defined as multivariate statistical methods and machine learning algorithms, in DMAIC stages will be an indispensable tool for business decision makers.

Although many companies have adopted lean manufacturing and six sigma, few are satisfied with results [6]. Because quality problems contains data that are not easy to model or optimize. Knowledge discovery in databases (KDD), which includes data mining (DM), can be used to overcome quality and control problems [7]. Data or information is perceived as one of the factors of production of goods or services. This forces decision makers to store as much data as possible in order to avoid the risk of wrong decision. In era of industry 4.0, gathered massive data increase the risk. To prevent making wrong decision, data mining techniques are very useful. DM tasks such as clustering, association, prediction, classification helps to reach correct and optimum decisions in various stages of six sigma. In this study, a roadmap was created to obtain satisfied results using data.

2. LEAN SIX SIGMA METHODOLOGY

Lean Six Sigma (LSS) is a management philosophy that has resulted in two separate processes - the combination of "Lean" and "Six Sigma" processes. LSS provides standardization about both quality improvement and economic gain. On the other hand, it has a systematic effect in reducing waste and cost [8]. Lean Six Sigma has gained worldwide popularity, providing both output and quality-based improvements. This approach, which simplifies manufacturing processes and improves product quality with less than 3.4 ppm errors, has saved significant improvements and cost savings in many companies such as General Electric Co. [9], Dell Inc. [10] and Xerox Corp. [11].

Many of six sigma projects follow DMAIC cycle for the existing [12]. The Six Sigma system demonstrated by DMAIC is a structured method that helps solve existing problems, see future opportunities and manage projects. DMAIC has proven to be one of the most effective problem-solving methods used up to now, because it forces the teams to use the data to do the following [13].

- Verifying the nature and extent of the problem

- Describe the real causes of the problems

- Find solutions depending on causes

- Establish procedures to protect solutions even after the project is over

Some of six sigma projects use DMADV cycle, also known as design for six sigma, to create new processes. The steps DMA (Define, Measure and Analyze) are similar to DMAIC but not the same. DMADV was used for different purposes. For example, Chang et al. used to improve quality of product [14]. Chen et al. used improve the assembly efficiency of military products [15]. Table 1 summarizes steps of six sigma both DMAIC and DMADV cycles and gives some sample activities used in the steps.

3. DATA MINING OVERVIEW

Knowledge discovery in databases (KDD) is one of the methodologies for data mining. It was defined by Fayyad et al. as "the nontrivial process of identifying valid, novel, potentially useful [16]. They used the terms "knowledge discovery in databases" to denote whole process of turning data into valuable knowledge. Entire KDD process consists of five steps: data preparation, data preprocessing, data mining, pattern evaluation and then knowledge discovered in databases. It should be noted that data mining is only a part of the KDD process.

Table 1. Key steps of Six Sigma for existing and new processes

Phase	Descriptions	Sample activities
Define	Define the purpose and scope of the six sigma project	Define why the project should be done
		Define the targets, goals and scopes of project
		Define the customer requirements

Measure	Measure to determine the current situation	Select the output characteristics (the CTQs)[1]
		Assess the performance specifications
		Establish the initial process capability
Analyze	Analyze and determine the actual causes for process improvement	Analyze the current process performance
		Monitor the potential CTPs[2]
		Analyze what resources will be needed for improvement
Improve	Improve the process by eliminating wasteful causes, removing the problem or reducing the effects of the problem	Improve idea
		Identify optimal operating conditions
		Eliminate wastes
Control	Control the improved process performance	Determine the process capability (for CTPs[2])
		Implement the process controls
		Document what you have learned
Design	Design a new process in parallel with customer needs	Develop design to meet customer needs
		Design analyze model
Verify	Confirm the truth of designed model	Create a plan for full implementation
		Create metrics to keep it measured
		Validate to model

[1] CTQ: Critical to Quality: Element of a process or practice which has a direct impact on its perceived quality

[2] CTP: Critical to Process: The most important attributes for the process

Data mining (DM) techniques use the integrated data to cluster, predict, classify etc. through large amounts of data stored in databases using statistical and mathematical techniques [17]. They can be classified into two groups as descriptive and predictive [18].

3.1. Data Preparation

Data are usually available data sources such as databases, files, data warehouses. To start KDD, firstly data sources are integrated. Then, instances and variables are transformed into tabular format, taking place in rows and columns [19].

3.2. Data Preprocessing

Data is mainly redundant, incomplete and inconsistent [1]. Data preprocessing overcomes this kind of problems to develop data quality before mining. Some of data preprocessing tasks are data cleaning, data transformation, data reduction and discretization [19, 20, 21].

3.3. Data Mining

Data mining is considered the central step of the KDD process. DM is an exploratory data-analytic process that detects interesting, novel patterns within one or more data sets that are usually large [22]. Descriptive DM tasks includes clustering and association while predictive tasks consist of classification and prediction. KDD stages are described shortly. The most common types of data mining tasks that can be used in six sigma cycles:

- **Association** discovers some rules among data. It also named as association rule mining. It tries to find frequent items and generates interesting if-then rules [23].

- **Clustering** is a method of grouping data sets according to similarities between objects in same groups and dissimilarities between objects in other groups [24]. Unlike classification, the class label of each group is unknown. It calculates distances between data and group center and assigns the data into the nearest group.

- **Classification** aims to classify a data into predefined class. Like clustering, classification technique also uses distance-based algorithms. The class label of each group is known [25].

- **Prediction** associates a data to a quantitative variable and predicts the value of that variable [25].

3.4. Evaluation

Evaluation of DM results depends on comparing different DM techniques. The technique that gives the best result is chosen to interpret. To make optimum and correct decisions, it is clear that knowledge extracted from data sets should be evaluated and interpreted correctly [26].

3.5. Implementation

The final KDD step includes implementation of results obtained from evaluation stage to improve quality. To make structured and transparent decisions, some decision making constructs such as decision tables, decision maps atlases can be used.

4. THE SUGGESTED ROADMAP

The flow diagram showing LSS stages for existing (DMAIC) and new (DMADV) process can be seen in Figure 1. Define phase is almost similar in each cycle. Measure and Analyze phases have some differences but they can be considered similar. The differences are not remarkable. In existing process to make better decisions for improving quality, improve phase should be used and the process should be controlled. On the other hand, if process does not exist, to create a new process design phases should be used and designed process is validated.
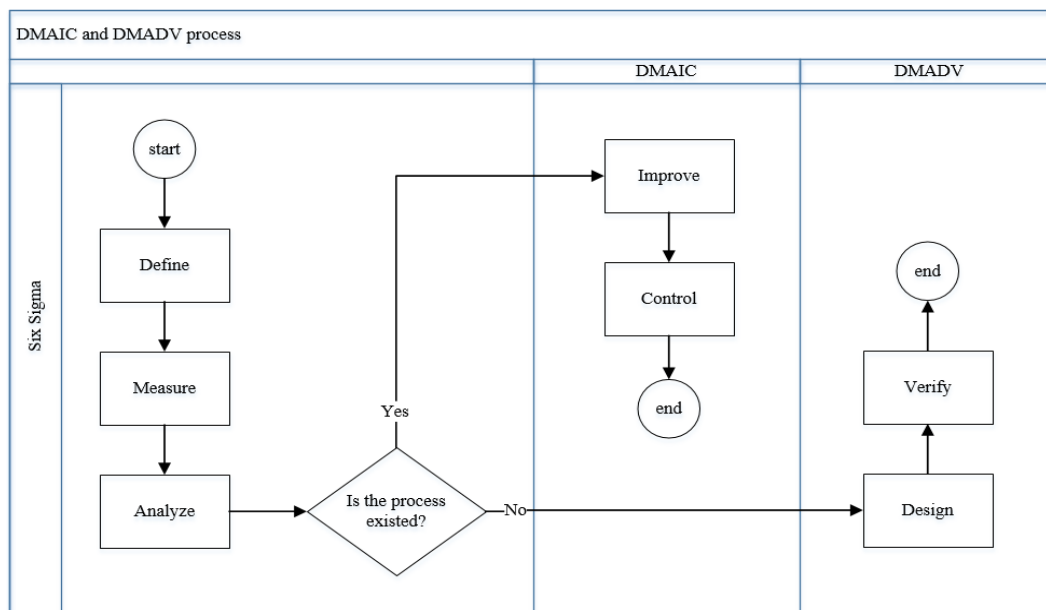
Figure 1. Six sigma stages for existing (DMAIC) and new (DMADV) process

Table 2 demonstrates some methods can be used in both DMAIC and DMADV cycles. Define phase requires to identify problems, process goals with respect to customer needs. One can use methods used in Define column in Table 2 for this stage. For example, in DMADV cycle, brainstorming is a useful tool to define potential problems. After definition of potential problems, using prioritization matrix or pareto analysis, it is decided that which problem(s) will be solve firstly. To determine process goal according to customer requirements, quality function deployment (QFD) may be useful [27]. Figure 2 indicates the suggested roadmap for the Define phase.

Table 2. Methods can be used in six sigma cycles

Define	Measure	Analyze	Improve	Control	Design	Verify
Brain storming	Tally chart	Correlation	TRIZ	Control diagram	QFD	Graphing
Prioritization matrix	Pareto analysis	T-test	Flow diagrams	Flow diagrams	DOE	Visualization
Matrix diagram	Descriptive statistics	Chi-square test	DOE	Standardization	Descriptive analysis[1]	Correlations
Pareto analysis	Z-test	F-test	Multivariate statistical	FMEA	Predictive analysis[2]	Causality
Process map	Process sigma	Hypothesis tests			Market basket analysis	Ratio rules
SIPOC diagram	ANOVA	SPC				FMEA
Nominal group technique		ANOVA				
Interrelationship diagram		Histogram				
QFD		Fishbone				
FMEA		Predictive analysis[2]				
Descriptive analysis[1]						

[1] Descriptive analysis includes some DM techniques such as summarization, clustering, association rule mining

[2] Predictive analysis includes some DM techniques such as regression, decision tree, neural network

SIPOC: Supplier, Inputs, Process, Outputs, Customers   ANOVA: Analysis of Variance

QFD: Quality Function Deployment   TRIZ: Theory of Inventive Problem Solving

FMEA: Failure Mode and Effects Analysis   DOE: Design of Experiments

SPC: Statistical Process Control
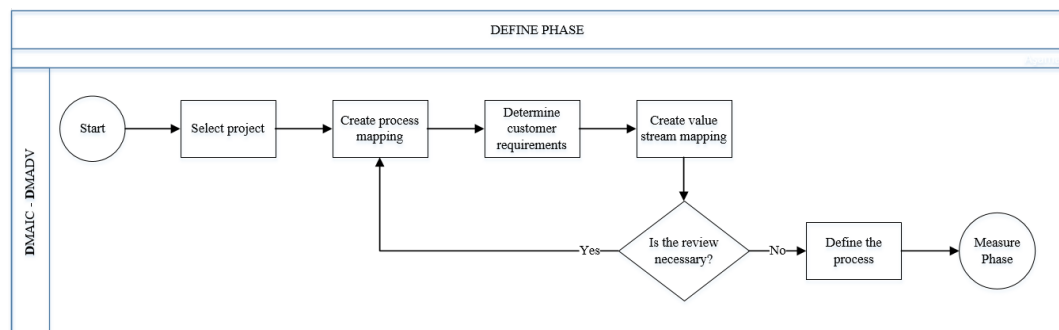
Figure 2. Define Phase

One of the goals of LSS is to eliminate variations in the process. In Measure phase, ANOVA can be identify the variation. Tally chart and descriptive statistics such as mean, variance and standard deviation can be used

to measure current situation of process. Figure 3 indicates the suggested roadmap for the Measure phase. Key variables inputs and outputs are determined as key variables. The phase includes first KDD steps, data preparations.

Data gathered in the Measure phase is used to analyze process. In this phase, relationship between dependent and independent variables can be found by regression analysis. Correlation explains relationship between variables. Figure 4 indicates the suggested roadmap for the Analyze phase. Process competence and process performance are analyzed using SPC in measure process performance step. Analyze data includes second KDD steps, data preprocessing.

Multivariate statistical methods such as clustering analysis and discriminant analysis can be used to improve the process. TRIZ for solving innovatively problems and DOE to find best parameters can be utilized. Figure 5 indicates the suggested roadmap for the Improve phase. The Analyze and Control phases include data mining step of KDD.
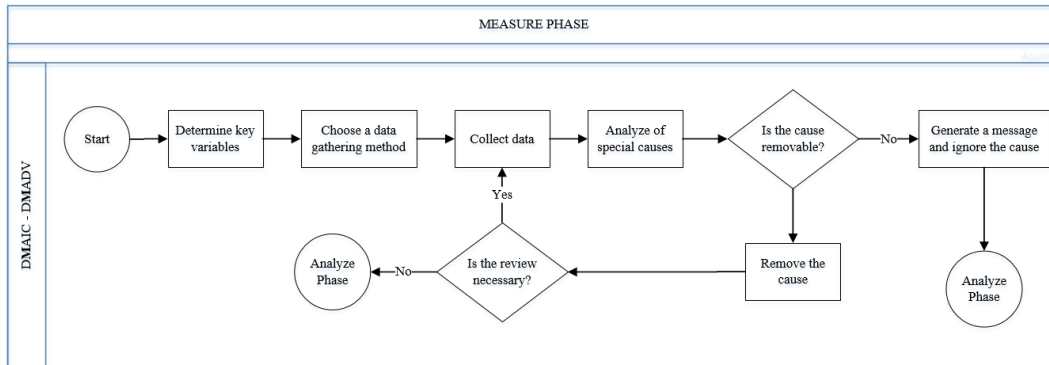
Figure 3. Measure Phase
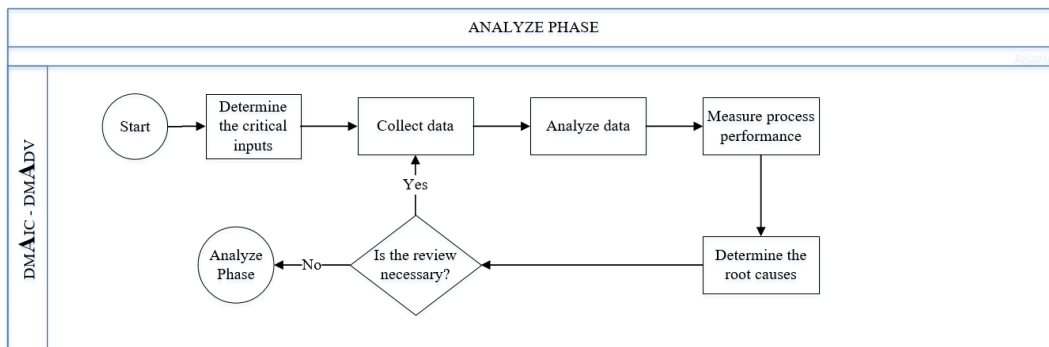
Figure 4. Analyze Phase
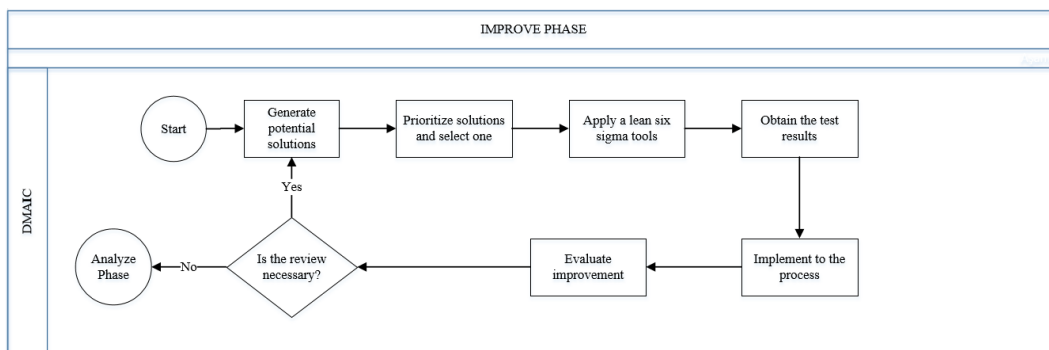
Figure 5. Improve Phase

In the control phase, FMEA to avoid potential risks and control diagrams to check whether the process is in control or not can be used. The phase includes fourth KDD steps, evaluation. . Figure 6 indicates the suggested roadmap for the Control phase.
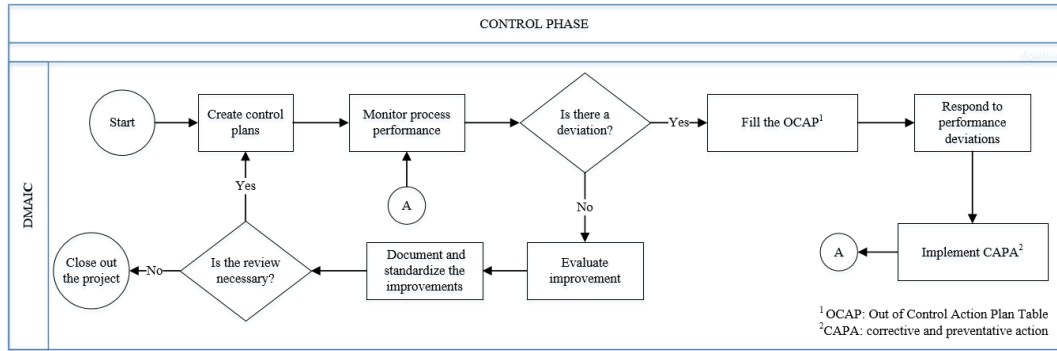
Figure 6. Control Phase

To create a new process, the Design phase can utilize QFD to consider customer requirements. Market basket analysis as a DM method identifies products and content that go well together Figure 7 indicates the suggested roadmap for the Design phase.
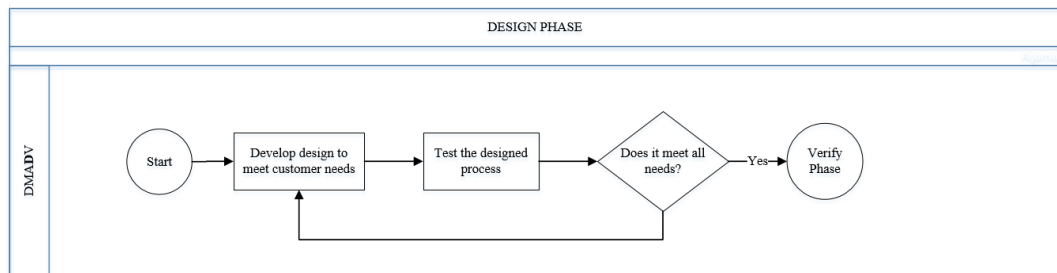
Figure 7. Design Phase

In the last step of DMADV cycle, some metrics are created to keep and a pilot run is developed to verify the new process. Results can be visualized using different methods mentioned in the Verify column in Table 2 to see whether there is any potential failures affecting quality.
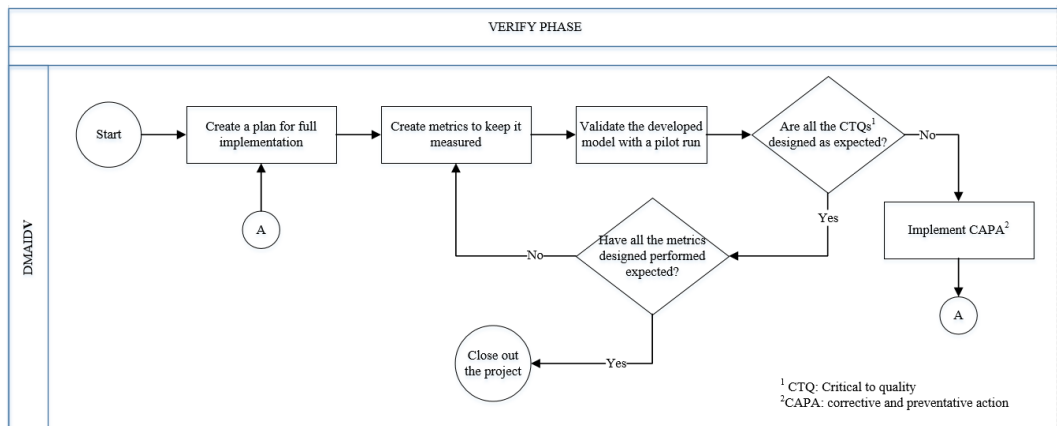
Figure 8. Verify Phase

5. CONCLUSION

There are various methods such as inspection, statistical process control, total quality control, zero defects, kaizen and lean six sigma to improve quality. In the study, lean six sigma is chosen to develop quality. It aims to reduce variations and wastes within processes using different techniques. Lean six sigma collects data to achieve the its goal. Data gathered should be analyzed to make optimum and correct decisions. There are some methodologies to analyze data systematically. Knowledge discovery in database is applied to overcome quality and control problems. Its steps are adapted to lean six sigma cycles, DMAIC (define-measure-analyze-improve-control) and DMADV (define-measure-analyze-design-verify). Each phases of the cycles contains various methods utilized collected data. They were shown in a table and flowcharts for each phases are drawn separately.

The aim of this study is to provide a roadmap that makes easier to make faster, more reliable and satisfied decisions with data for improving quality in processes.

REFERENCES

[1]. G. Koksal, I. Batmaz and M. C. Testik, "A review of data mining applications for quality improvement in manufacturing industry," *Expert Systems with Applications,* vol. 10, no. 38, p. 13448–13467, 2011.

[2]. Y.-H. Lee, K. G. Min, C. H. K. S. Chang and T. H. Choi, "Process improvement methodology based on multivariate statistical analysis methods," *Control Engineering Practice,* vol. 8, no. 12, pp. 945-961, 2004.

[3]. General Electric, "What is Six Sigma: the roadmap to customer impact?," 29 August 2016. [Online]. Available: http://www.ge.com/sixsigma/SixSigma.pdf.

[4]. Angoss Software Cooperation, "Key Performance Indicators, Six Sigma nad Data Mining," Canada, 2011.

[5]. A. Trnka, "Results of application data mining algorithms to (lean) six sigma methodology," *Annals of Faculty Engineering Hunedoara - Internationala Journal of Engineering,* 2012.

[6]. P. Guarraia, G. Carey, A. Corbett and K. Neuhaus, "Lean Six Sigma for manufacturing," Bain&Company, Los Angeles, 2008.

[7]. K. Yang and J. Trewn, Multivariate Statistical Methods in Quality Management, New York: McGraw-Hill, 2004.

[8]. J. D. Polk, "Lean Six Sigma, Innovation, and The Change Acceleration Process Can Work Together," *American College of Physician Executives,* vol. 37, no. 1, pp. 38-42, 2011.

[9]. General Electric Co., "The Roadmap to Customer Impact," [Online]. Available: http://www.ge.com/sixsigma/SixSigma.pdf. [Accessed 02 03 2017].

[10]. C. Lovin and T. Yaptangco, "Best Practices: Measuring the Success of Enterprise Testing," August 2006. [Online]. Available: http://www.dell.com/downloads/global/power/ps3q06-20060252-Yaptangco.pdf. [Accessed 02 03 2017].

[11]. Xerox Corp., "Lean Six Sigma Leads Xerox," August 2004. [Online]. Available: https://www.xerox.com/downloads/usa/en/n/nr_SixSigmaForumMag_2004_Aug.pdf. [Accessed 02 03 2017].

[12]. M. Kanakana, J. Pretorius and B. V. Wyk, "Lean six sigma framework to improve throughput rate," in *IEEE 17Th International Conference on Industrial Engineering and Engineering Management (IE&EM)*, Xiamen, China, 2010.

[13]. M. L. George, D. Rowlands and B. Kastle, What is Lean Six Sigma, New York: McGraw-Hill, 2004.

[14]. T. C. Chang, C. Huang and K. Chen, "An application of DMADV methodology for increasing the yield rate of CMOS camera," in *2th International conference on ISO 9000 & TQM*, Taichung, Taiwan, 2007.

[15]. Y. Cheng, The improvement of assembly efficiency of military product by Six-Sigma, NCUT Thesis Archive, Taiwan, 2005.

[16]. U. Fayyad, G. Piatetsky-Shapiro and P. Smyth, "The KDD process for extracting useful knowledge from volumes of data," *Communications of the ACM,* vol. 39, no. 11, pp. 27-34, 1996.

[17]. D. T. Larose, Discovering Knowledge in Data: An Introduction to Data Mining, John Wiley, 2005.

[18]. J. Han, M. Kamber and J. Pei, Data mining: Concepts and techniques, San Francisco: Morgan Kaufmann; 3 edition, 2011.

[19]. P. Giudici, Applied data mining: Statistical methods for business and industry, New York: John Wiley, 2003

[20]. D. Pyle, Data preparation for data mining, San Francisco: Morgan Kaufmann, 1999.

[21]. I. H. Witten, Data mining: Practical machine learning tools and techniques, Boston: Morgan Kaufman 2 edition, 2005.

[22]. P. Nadkarni, "Core Technologies: Data Mining and "Big Data"," in *Clinical Research Computing: A Practitioner's Handbook*, Cambridge, Academic Press, 2016, pp. 187-204.

[23]. D. J. Hand, H. Mannila and P. Smyth, Principles of data mining, Cambridge: MIT Press, 2001.

[24]. M. A. Rahman and M. Z. Islam, "A hybrid clustering technique combining a novel genetic algorithm with K-Means," *Knowledge-Based Systems,* vol. 71, no. 1, pp. 345-365, 2014.

[25]. D. Talia, P. Trunfio and F. Marozzo, "Introduction to Data Mining," in *Data Analysis in the Cloud Models, Techniques and Applications*, Amsterdam, Elsevier, 2016, pp. 1-25.

[26]. M. H. Dunham, Data mining introductory and advanced topics, New Jersey: Prentice Hall/Pearson Education, 2003.

[27]. O. Dogan and U. Cebeci, "A Methodology For New Product Development by Using QFD, FMEA and Its Application in Metal Plating Industry," in *Uluslararası Katılımlı 16. Üretim Araştırmaları Sempozyumu*, Istanbul, Turkey, 2016.

Analysis of Depth of Different Bodies Using Multi-Scale Wavelet Tomography

Fikret Dogru[1]

Abstract

In this study, the continuous wavelet transform was used for estimation of depths of buried different structures such as sphere, horizontal and vertical cylinder at different depths. Multi-scale wavelet tomography method is based on continuous wavelet transform was applied on theoretical gravity data. All the local maxima points in the result of continuous wavelet transform were combined thorough the line using Least-Squares Fitting method. The location where the lines merged in the new figure under the continuous wavelet transform gives depth of burried structure. The dilation value of wavelet transform turns into the depth values in the new figure. The theoretical anomalies of three different structures at different depths were used for testing the accuracy of this method and the depth values were obtained so close the true values. As a conclusion, this method gives a prior information about depth of buried structure without using inversion tehniques and this prior information could be used as an initial parameter in the other inversion methods.

Keywords: *Wavelet transform, tomography, inversion, buried structure*

1. INTRODUCTION

Wavelet transform and its multi-scale tomography application has been used in soo many fields by researchers for a long time. Saracco et al. ([1]) used multi-scale wavelet tomography to localize the buried magnetic structures. Mauri et al. ([2]) used multi-scale wavelet tomography on self-potential data to determine depth of hydrothermal systems. Guo et al. ([3]) used multi-scale wavelet tomography for edge detection. Georgiou and Kumar ([4]) used multi-scale wavelet analysis to signal processing.

In this study, multi-scale wavelet tomography was used to determine depth of buried structures which are sphere, vertical and horizontal cylinders. For this purpose, theoretical anomalies of three model were used to depth estimation. The depths were obtained very close to real values. Also same method was applied on the derivatives of anomalies and it is seen that the depth values were obtained much more closer than before.

2. METHODS

2.1. Wavelet Transform

The wavelet transform has contributed significantly in the study of many processes/signals in almost all areas of earth science. Different applications of wavelet transform have also shown its important role while dealing the complex behavior of real geophysical data. Wavelet transform can be given following formula;

$$\psi_{a,\tau}(t) = \frac{1}{\sqrt{a}} \psi\left(\frac{t-\tau}{a}\right) \qquad (a, \tau \; \epsilon \; R \; a > 0) \qquad (1)$$

where a is the dilation factor, τ is the translation factor and $\psi_{(a,\tau)}$ (t), is the mother wavelet depending on parameters a and τ ([5]).

In the wavelet transform, instead of holding constant time and frequency resolutions, both can be used as a variable to obtain multi-resolution analysis in the time-frequency domain. Thus, increases in the frequency shows improvement in time resolution. Likewise, decreases in frequency shows improvement in the frequency resolution.

---

[1] *Corresponding author:* Dokuz Eylul University, Department of Geophysical Engineering, 35160, Buca/İzmir, Turkey. *fikret.dogru@deu.edu.tr.*

Table 1. Relationship between frequency and resolution (Modified from Arı et al. [6]).

Frequencies/Resolutions	Time Resolutions	Frequency Resolutions
Low	Weak	Good
High	Good	Weak

2.2. Continuous Wavelet Transform

The continuous wavelet transform was developed as an alternative approach to the short time Fourier transform (STFT) to overcome the resolution problem. The wavelet analysis is done in a similar way to the STFT analysis, in the sense that the signal is multiplied with a function, similar to the window function in the STFT, and the transform is computed separately for different segments of the time-domain signal.

However, there are two main differences between the STFT and the CWT:

1. The Fourier transforms of the windowed signals are not taken, and therefore single peak will be seen corresponding to a sinusoid, i.e., negative frequencies are not computed.

2. The width of the window is changed as the transform is computed for every single spectral component, which is probably the most significant characteristic of the wavelet transform.

The continuous wavelet transform is defined as follows:

$$CWT_x^{\psi}(\tau, s) = \Psi_x^{\psi}(\tau, s) = \frac{1}{\sqrt{|s|}} \int x(t) \psi^* \left(\frac{t - \tau}{s} \right) dt \qquad (2)$$

the transformed signal is a function of two variables, *tau* (τ) and *s*, the translation and scale parameters, respectively. $\Psi_x^{\psi}(\tau, s)$ is the transforming function, and it is called the mother wavelet ([7]).

2.3. Multi-Scale Wavelet Tomography (MSWT)

In this study, complex gaussian wavelet (cgau1) was used for estimation of buried structure. Then wavelet modulus was calculated following formula:

$$mod = \sqrt{reel(coef(cwt))^2 + imag(coef(cwt))^2} \qquad (3)$$

where reel and imag are reel and imaginer parts of continuous wavelet transform. Lokal maximums were determined from coefficients of CWT. In addition, derivative of anomaly was calculated and then CWT was applied on this anomaly.

3. THEORETICAL STUDIES

In theoretical studies, the sphere, horizontal and vertical cylinder models were used at different depths. In first and second theoretical studies, the sphere and the horizontal cylinder models were used at 30 m depth. The three models, sphere, vertical and horizontal cylinder, were used together at different depths in the last theoretical study. CWT applied on these theoretical data and depths were determined succesfully. But depths could not determined well and the local maxima values could not seen from the structure which is in the middle in the three models study. Then the derivative of anomalies was investigated and the results shows that the derivative of anomaly made the clear to see of the middle body in the last example. Also the depths were determined very close to real value. The theoretical model formulas are following:

$$g_{sphere} = G \frac{4}{3} \pi \Delta p R^3 z / ((x - xo)^2 + z^2)^{3/2}$$
$$g_{hor} = G 2\pi \Delta p R^2 z / ((x - xo)^2 + z^2)$$
$$g_{ver} = G \pi \Delta p R^2 / ((x - xo)^2 + z^2)^{1/2}$$

where G is Gravitational constant, Δp is density contrast, R and z radius and depth of structure, xo is distance to center of body in x direction.
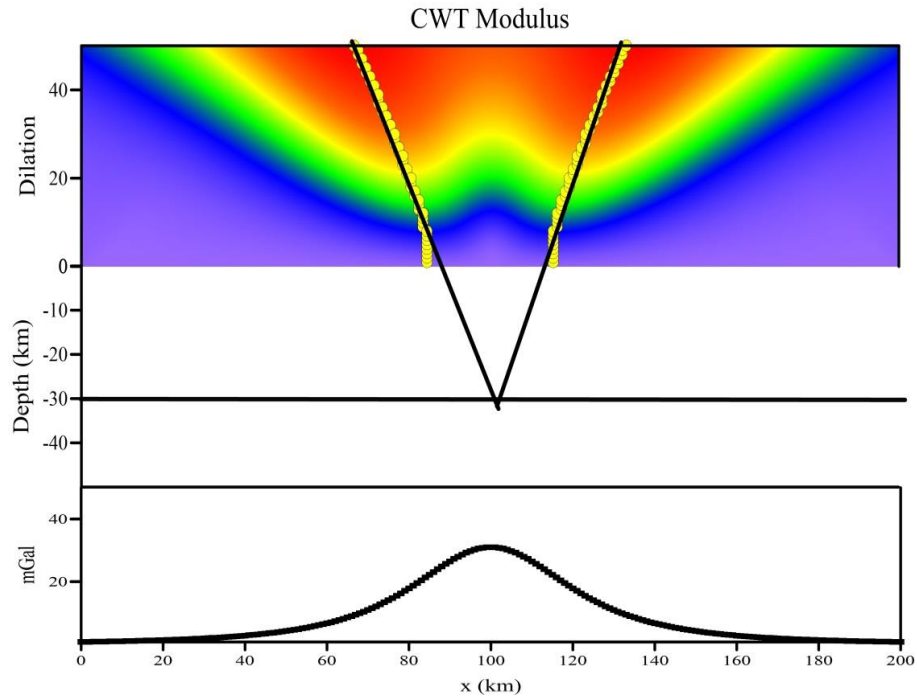
Figure 1. The result of CWT applied on anomaly.Top: CWT modulus,
Bottom: The theoretical sphere anomaly at 30 km depth, Middle: The depth of buried structure.
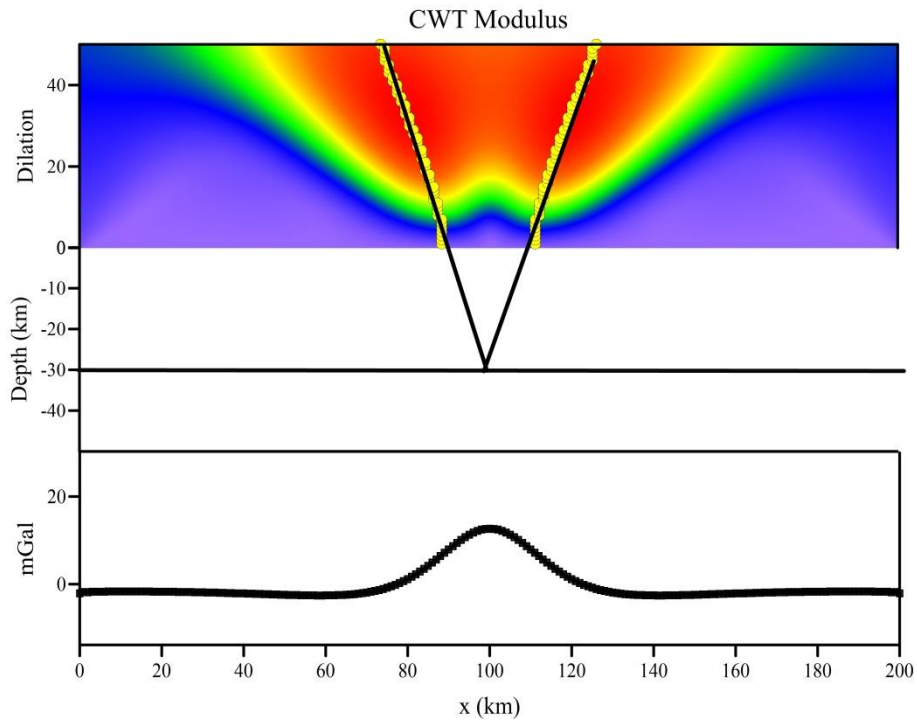
Figure 2. The result of CWT applied on derivative of anomaly. Top: CWT modulus,
Bottom: The derivative of theoretical sphere anomaly at 30 km depth, Middle: The depth of buried structure.

121
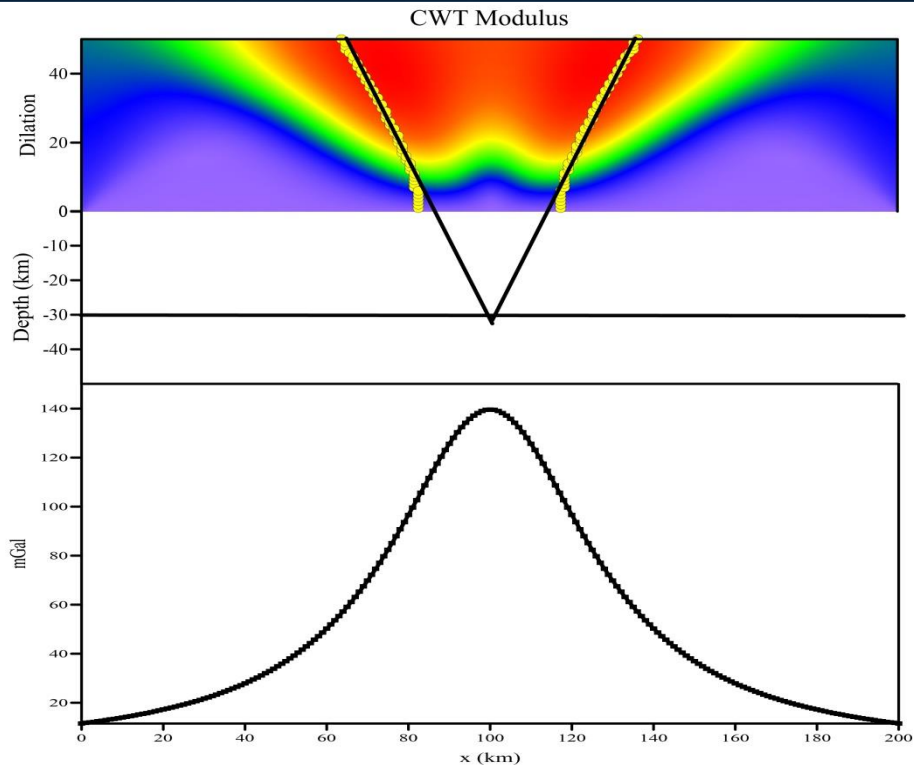
Figure 3. The result of CWT applied on anomaly. Top: CWT modulus,
Bottom: The theoretical horizontal cylinder anomaly at 30 km depth, Middle: The depth of buried structure.
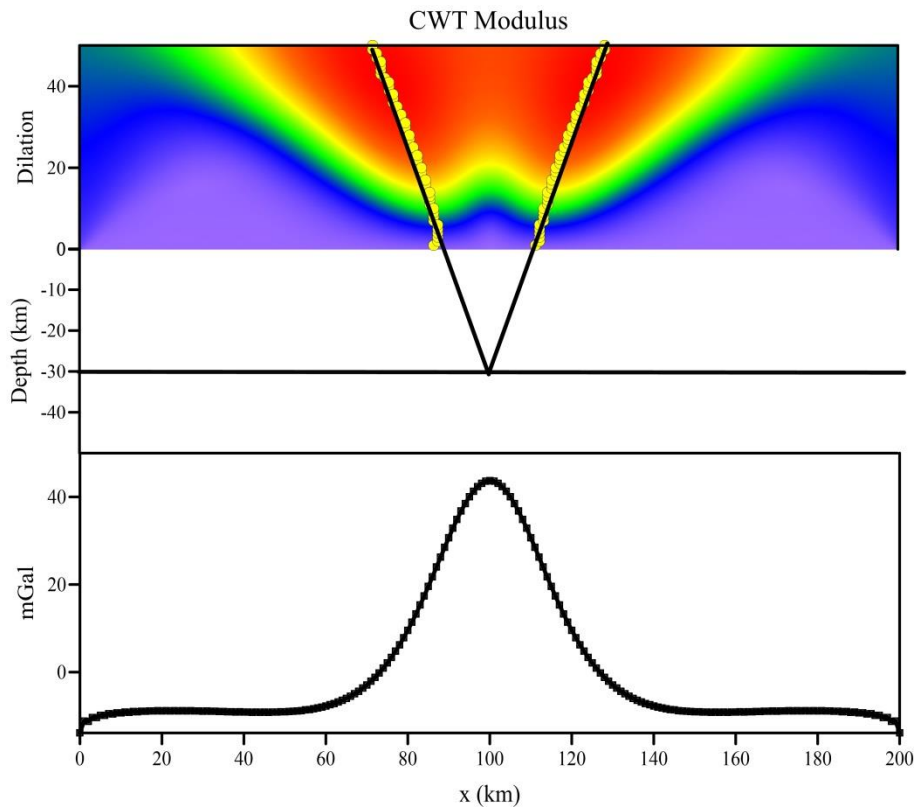
Figure 4. The result of CWT applied on derivative of anomaly. Top: CWT modulus, Bottom: The derivative of theoretical
horizontal cylinder anomaly at 30 km depth, Middle: The depth of buried structure.
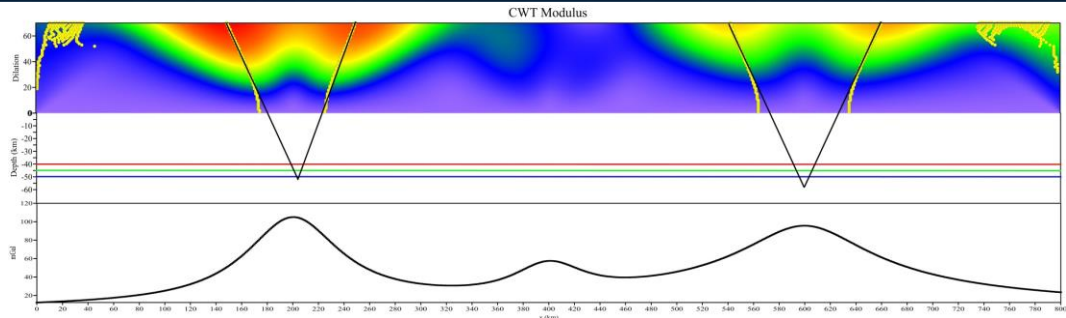
Figure 5. The result of CWT applied on anomaly. Top: CWT modulus, Bottom: The theoretical sphere, horizontal and vertical cylinder anomalies at 45 km, 40 km and 50 km depths respectively, Middle: The depths of buried structures.
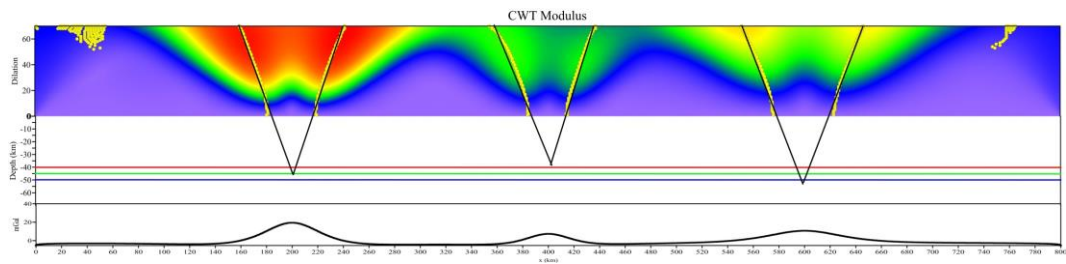
Figure 6. The result of CWT applied on anomaly. Top: CWT modulus, Bottom: The derivative of theoretical sphere, horizontal and vertical cylinder anomalies at 45 km, 40 km and 50 km depths respectively, Middle: The depths of buried structures.

4. CONCLUSIONS

The depths of buried bodies were determined succesfully using Multi-Scale Wavelet Tomogoraphy method. This method provides us the depths without using any inversion techniques. Theoretical examples shows that the result of depths was closer to the more accurate after applying MSWT to the derivation of anomaly.

The inversion techniques are used to determine the shape, the radius for identifiying the amount of mine. Preliminary estimation of parameters improve the result of inversion. If preliminary estimation is far from the real values, the result will be far from accurate result. So this method give an crucial preliminary parameter of depth so close thus the modelling of the reserve will be modelled much more akin to the real shape.

REFERENCES

[1].   Saracco, G., Moreau, F., Mathé, P.E., Hermitte, D. and Michel, J.M. Multiscale tomography of buried magnetic structures: its use in the localization and characterization of archaeological structures. Geophysical Journal International, 171(1), pp.87-103, 2007.
[2].   Mauri, G., Williams-Jones, G. and Saracco, G. Depth determinations of shallow hydrothermal systems by self-potential and multi-scale wavelet tomography. Journal of Volcanology and Geothermal Research, 191(3), pp.233-244, 2010.
[3].   Guo, F., Yang, Y., Chen, B. and Guo, L., 2010. A novel multi-scale edge detection technique based on wavelet analysis with application in multiphase flows. Powder Technology, 202(1), pp.171-177.
[4].   Foufoula-Georgiou, Efi, and Praveen Kumar, 2014 eds. Wavelets in geophysics. Vol. 4. Academic Press.
[5].   Mallat, S.G., 1989. A theory for multiresolution signal decomposition: the wavelet representation. IEEE transactions on pattern analysis and machine intelligence, 11(7), pp.674-693.
[6].   Arı, N., Ozen, S. ve Colak, O.H., 2008. Dalgacık teorisi wavelet MATLAB uygulamaları. Sıhhiye Ankara: Palme Yayıncılık.
[7].   Daubechies, I., 1992. Ten lectures on wavelets. Society for industrial and applied mathematics.

The Hollow Earth Phenomania and Its Some of Proofs

Fikret Dogru[1]

Abstract

The Earth has still changed since estimated 4.5 billion years with its unknowns. The phenomena such as the Hollow Earth, is discussed from the 15th century to the now. Some of scientists claimed that the earth has two part shells and and each shell has its own magnetic poles. Also they brought about that the arctic wars are all related to the conquer this entered area of hollows. Because they believe that ancient people, amazing creatures, giants and especially superior technology knowledge is in the Hollow Earth. In addition, there is so much documents, photos and films about a journey to the Earth's interior. Also we are witness to some incredible inventions that we could not imagine ten years ago and we are facing all of them. Is not it so weird that the technology development is so fast? Could the governments hide these all information? Because some of photos are from NASA in the 80's and statements of soldiers who are retired from army shows that there are hollows in the North and South Poles. In my personal research, I could not find any proof about hollows in the results of satellite gravity and Google Earth photos except new magnetic satellite that is called SWARM. It is seen in that photo, NASA is adjusting their satellites route from outside the hollows. Because these hollow areas have very low gravity values so satellites may be lose its trajectory. The hollows in the poles are obviously visible in the SWARM satellite route.

Keywords: *The Hollow Earth, NASA, Earth's interior, SWARM.*

1. INTRODUCTION

To date, we have explored less than 5 percent of the ocean. Much remains to be learned from exploring the mysteries of the deep. The ocean is the lifeblood of Earth, covering more than 70 percent of the planet's surface, driving weather, regulating temperature, and ultimately supporting all living organisms.

Yet for all of our reliance on the ocean, 95 percent of this realm remains unexplored, unsee, by human eyes. Also 86 percent of Earth's species still unkown ([1]).

Edmond Halley in 1692 put forth the idea of Earth consisting of a hollow shell about 800 km (500 mi) thick, two inner concentric shells and an innermost core. Atmospheres separate these shells, and each shell has its own magnetic poles. The spheres rotate at different speeds. Halley proposed this scheme in order to explain anomalous compass readings. He envisaged the atmosphere inside as luminous (and possibly inhabited) and speculated that escaping gas caused the Aurora Borealis ([2]).

Figure 1. A cross-sectional drawing of the planet Earth showing the "Interior World" of Atvatabar, from William R. Bradshaw's 1892 science-fiction novel 'The Goddess of Atvatabar' ([3]).

This is the one of the most interesting conspiracy theory, the Hollow Earth. Figure 1 shows a cross-sectional drawing of the planet Earth showing the "Interior World" of Atvatabar. I have personally read all about worldwide: Deep Underground Military Bases (D.U.M.B.)'s, Admiral Byrd's trip to the poles, Olaf Jansen's book, Dr. Nansen's and several other 19th century explorer's accounts of the land beyond the poles. The various witnesses are interested and surprisingly there is actually plenty of particular evidence pointing towards Hollow Earth theory (Fig. 2).
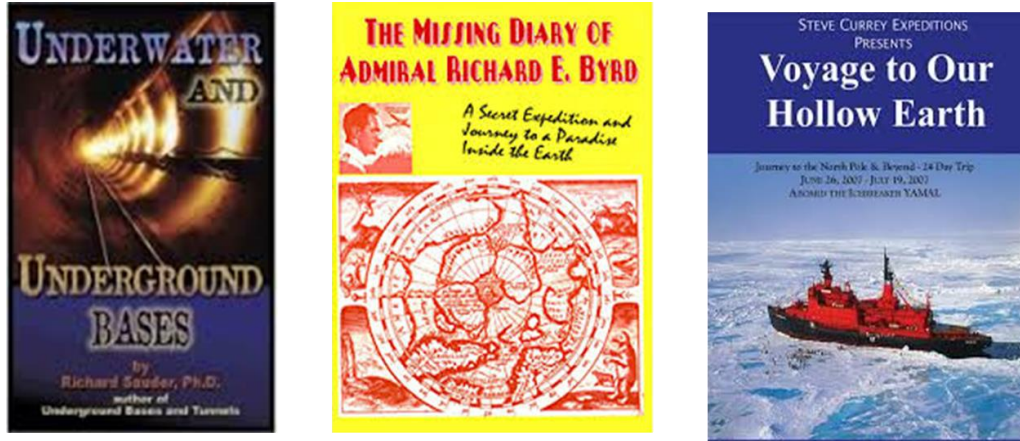
Figure 2. Books and a diary which are related to the Hollow Earth.

2. GAP IN THE EARTH

According to some researchers; the poles are no-fly zones and compasses start going haywire as soon as explorers sail/fly near them. During earthquakes the Earth behaves much more like a hollow body than a solid one, ringing like a bell with after-shocks spreading out like ripples in a pond. This behavior is indicative of a Hollow Earth and something which plate tectonics theory falls short of adequately explaining.
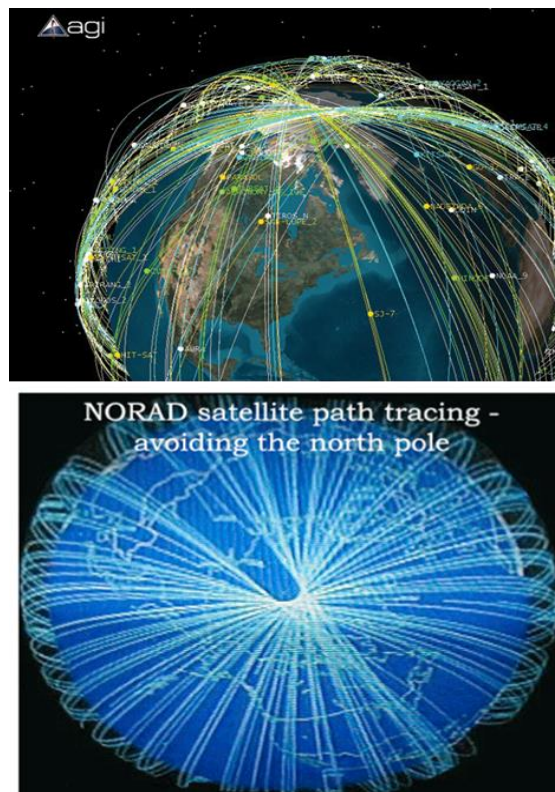
Figure 3. Orbits of AGI and NORAD satellites at the north pole ([4]).

In the early 19th century an American eccentric, John Cleves Symmes (1779-1829), sought funding for an expedition to enter the Earth through one of two 4,000-mile wide polar holes. Inside the Earth, he was convinced, a benevolent advanced civilization existed. Though an object of derision to most people, some took him seriously, and the idea of a hollow Earth was championed in a number of books throughout the rest of the century and right into the next ([5]).

B. Gardner published "A Journey to the Earth's Interior" in 1913 claiming that the inside of the Earth was hollow and housed a Sun; he also believed that the inside of the Earth could be reached through the north and south poles. More recently, the hollow Earth theory has been linked to Hitler and Nazi Germany. The Nazis were convinced of many occult beliefs and practices, including astrology, the prophecies of Nostradamus, and the hollow/inverted Earth theory or "hohlweltlehre.".

Admiral Richard E. Byrd of the United States Navy flew to the North Pole in 1926 and over the South Pole in 1929. But the official U.S. government release of Byrd's diary revealed erased records. His erased diary led to widespread allegations of a cover-up. A so-called "secret diary" of Admiral Byrd was later circulated among raw supporters of the hollow Earth theory. In that disputed diary, Byrd allegedly told of entering the interior of the earth and traveling over mountains with green vegetation. After crossing subterranean lakes and rivers, he discovered life resembling prehistoric animals. He eventually came across cities and a prosperous civilization in the hollow interior realm.

The North Pole legend regularly centers on a Norwegian sailor named Olaf Jansen. Jansen's sloop supposedly sailed through an entrance to the Earth's interior at the North Pole. For years he lived with the inhabitants of the Agharta Kingdom. According to the writer Ellie Crystal ([6]), Agartha is analogous to the Lost Eden or a sunken Atlantis, which still exists as a celebrated city that is said to reside in the Earth's core. Initiates guided by masters who are the spiritual leaders of humanity inhabit the inner realm. They do not meddle in the lives of humans that live above the surface. Nor is there any communication from them, alike to underworld spirits of the departed. However, the race of supermen and superwomen do occasionally come to the surface to oversee the development of the human race.

We've all heard tales of Nazis exploring the southern extremities of the globe and even setting up bases in Neuschwabenland. Some have also heard of Operation Highjump and Admiral Byrd's altercation with entrenched German forces that overpowered them with amazing flying craft." A video lately surfaced which supposedly shows "a 1944 map from the Third Reich detailing not only the direct passageway used by German U-boats to access this subterranean domain, but also a complete map of both hemispheres of the inner realm ([7]).

At the beginning of 1939, a Nazi submarine expedition explored a hitherto uncharted part of Antarctica. New Swabia (Neuschwabenland) is a cartographic name given to an area of Antarctica where a Nazi colony was allegedly established. (Rothschild Island is an island 39 kilometres long, mainly ice covered, also in Antarctica.) Rodney Cluff on his "Our Hollow Earth" website had a copy of a letter (with translation) supposedly sent from a Karl Unger that was aboard the U-boat 209 (commanded by Heinrich Brodda) saying that they had reached the inner realm.

A year after World War II ended, the U.S. Navy mounted Operation "High Jump," which according to different critics was basically an invasion of the Antarctic. The primary mission of Operation Highjump was for the United States to set up an Antarctic research base. However, some evaluators claimed that in 1947, Admiral Richard E. Byrd led 4,000 military troops from the U.S., Britain and Australia in an invasion against "former Nazi interests in Antarctica."

On March 5, 1947 the "El Mercurio" newspaper of Santiago, Chile, had a headline article "On Board the Mount Olympus on the High Seas" which quoted Byrd in an interview with Lee van Atta:

"Admiral Byrd declared today that it was imperative for the United States to initiate immediate defense measures against hostile regions. Furthermore, Byrd stated that he 'didn't want to frighten anyone unduly' but that it was 'a bitter reality that in case of a new war the continental United States would be attacked by flying objects which could fly from pole to pole at incredible speeds."

We may have another 'ocean' to add to the world map — only this one is hidden hundreds of miles beneath our planet's surface. A new study suggests that a hidden 'ocean' is nested in the Earth's mantle some 400 miles beneath North America. The hidden reservoir, apparently locked in a blue crystalline mineral called ringwoodite, may hold three times as much water that exists in all the world's surface oceans ([8]).

3. THE TIME IN THE EARTH INTERIOR

In physics, the "twin paradox" is a thought experiment where a person who makes a journey into space in a rocket will return home to find he or she has aged less than an identical twin that stayed on Earth. The same

could also be true with acceleration and deceleration when cruising the Earth's interior. Would a clock traveling into the Earth's interior lag behind a clock on the surface?

The idea of a hollow Earth appears in myths and legends of various cultures. Greek legend refers to a paradise region known as Hyperborea. According to legend, the people of Hyperborea enjoyed good health and lived 1000 years or longer without growing old. Chinese and Eskimo legends state that there is an opening in the North to a subterranean realm where an underground species resides. They believe the underground realm is a paradise and is where their ancestors came from. Eskimo legend also states that the underground paradise is a place of perpetual light where the sun never sets ([9]).

According to their stories, it is a land of peace and happiness with a mild climate, large lakes, tropical animals and no darkness. The Hopi Indians also have a legend that states they emerged from an underground realm within Earth. The legends also refer to snake people that resided underground ([9]).

4. SOME PHOTOS RELATED TO THIS ISSUE

Figure 4 shows the schematic display of the Hollow Earth such as tunnel entrances, lands, cities. Figure 5 and 6 are satellite photos and the entrances of Hollow Earth are seen clear. Also Figure 7 and Figure 8 shows the Free-air and Bouguer gravity anomalies which were taken from Arctic Gravity Project. The high anomaly values over the pole in the Free-air and Bouguer anomaly are odd because the area covered with approximately 4000 m ice. When the Free-air anomaly values become higher due to the elevation but Bouguer anomaly values should be lower. So there should be something complex structure than we know. In addition, the no fly zone is seen clear in the one of the latest satellite image (SWARM satellite) (Figure 9).
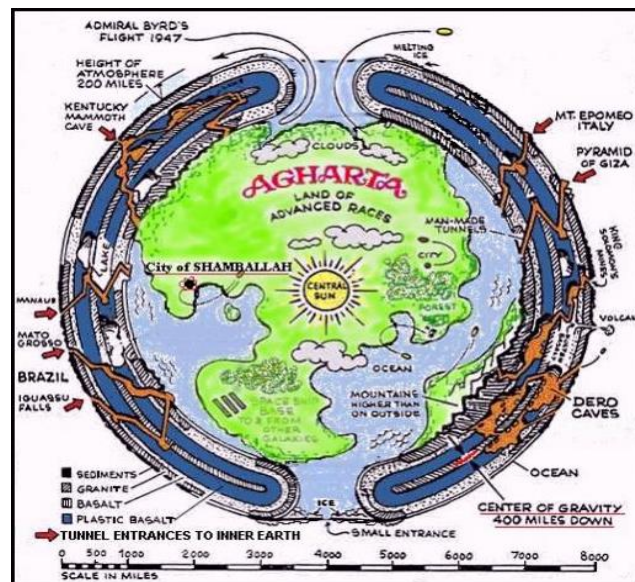
Figure 4. A schematic display of Hollow Earth ([10]).
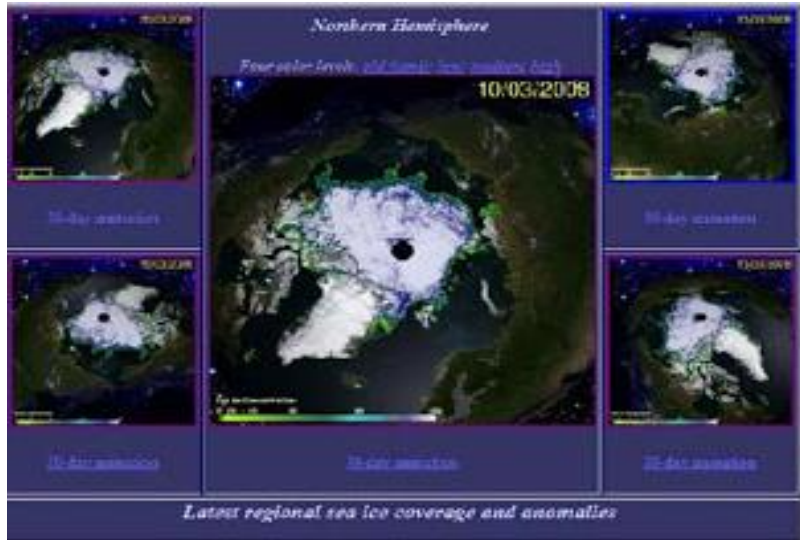
Figure 5. A satellite image of Northern Hemisphere and the hollow is seen clear([11]).
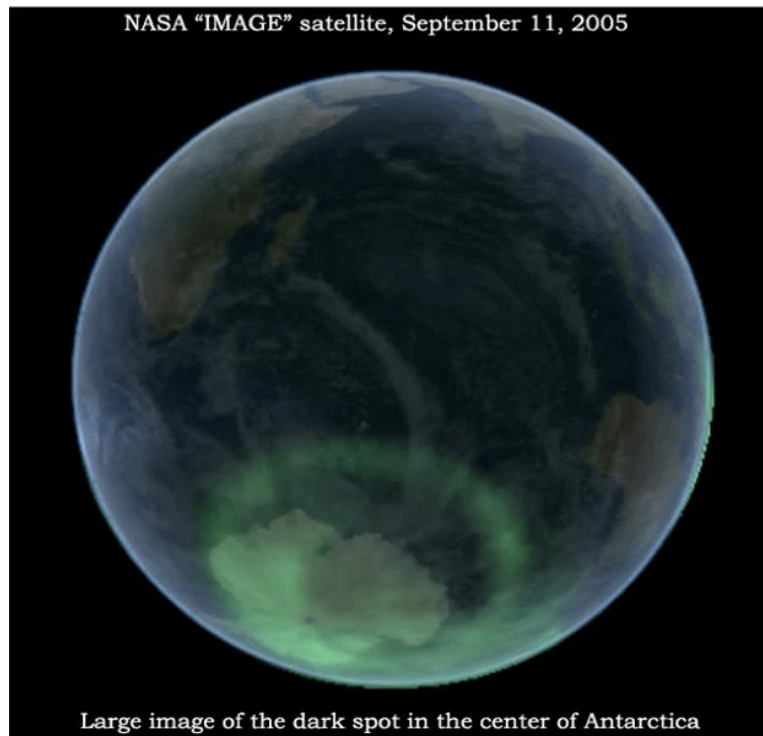
Figure 6. A satellite image of Southern Hemisphere ([12]).
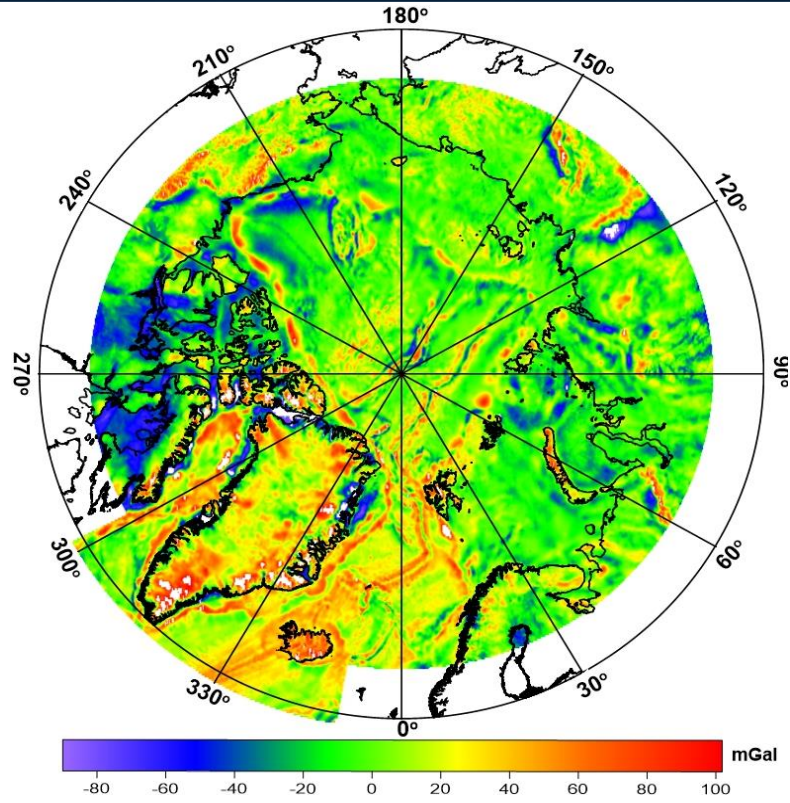
Figure 7. Free-air gravity anomaly of North pole ([13]).
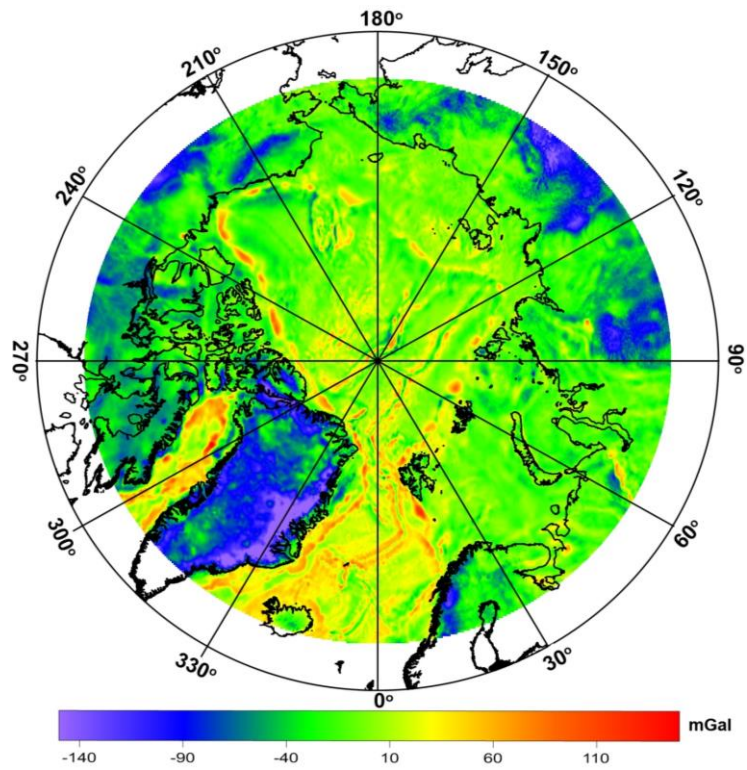
Figure 8. Bouguer gravity anomaly of North pole ([13]).
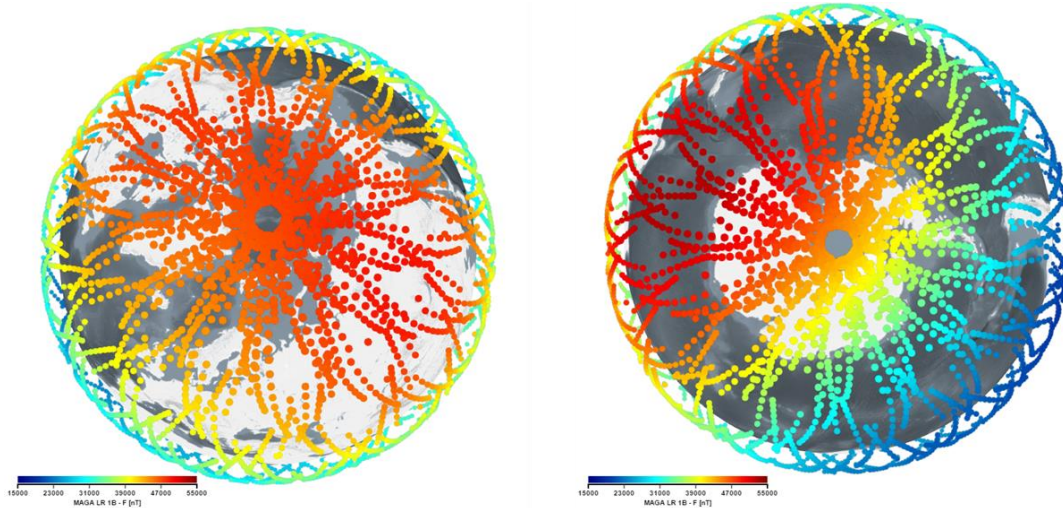
Figure 9. Display Orbits of SWARM satellite at North and South Pole ([14]).

5. CONCLUSION

As a conclusion, The Hollow Earth theory may be true or just fiction. If it is only fiction or not, nothing will change in our lives. Because if it is true, governments will hide it from the knowledge of mankind and we maintain our monotonous life as unaware pawns. When there is so much evidence, then still think that it is not is just ignore nothing else.

Consider the speed of development of the technology in 10 years, is this development normal? Not for me. There seems to be some agreement made with some.

In addition, there is so much subliminal messages in tv series and my idea is to familiarize people with something to be explained in the future. Finally you can not imagine and design something you have not seen.

REFERENCES

[1]. Saracco, G., Moreau, F., Mathé, P.E., Hermitte, D. and Michel, J.M. Multiscale tomography of buried magnetic structures: its use in the localization and characterization of archaeological structures. Geophysical Journal International, 171(1), pp.87-103, 2007.

[2]. J.R. Saurav, 2014, Have we explored our world completely?, https://www.quora.com/Have-we-explored-our-world-completely.

[3]. H. Edmond, 1692, An Account of the cause of the Change of the Variation of the Magnetic Needle; with an Hypothesis of the Structure of the Internal Parts of the Earth, Philosophical Transactions of Royal Society of London, No. 195, pp 563–578.

[4]. R. Bradshaw, 1892, The Goddess of Atvatabar: being the history of the discovery of the interior world, and conquest of Atvatabar.

[5]. URL: http://thegreaterpicture.com/hollow-earth.html.

[6]. J. C. Symmes, 1998-2014, "Hollow Earth Theory," HowStuffWorks.

[7]. URL: crystalinks.com

[8]. "Third Reich Maps of the Inner Earth", Subterranean Bases, 2012-2014, http://www.subterraneanbases.com/third-reich-maps-inner-earth/.

[9]. Sara Gates, 2014, "Hidden 'Ocean' Discovered Deep Underground Near Earth's Core", The Huffington Post.

[10]. Jason Carr, 2012, The Hollow Earth Part 1, http://www.theeventchronicle.com/study/hollow-earth-hidden-ocean/.

[11]. URL: http://www.telegraph.co.uk/culture/books/10961412/Hollow-Earth-conspiracy-theories-the-hole-truth.html.

[12]. URL: http://www.atlanteanconspiracy.com/2011/01/hollow-earth-evidence.html.

[13]. URL: http://www.viewzone.com/hollowearth.html.

[14]. URL: http://earth-info.nga.mil/GandG/wgs84/agp/readme.html

[15]. URL: https://vires.services/.

Internet of Things and Intelligent Systems in Digital Learning

Mahir Oner[1], Ceren Oner[1], Onur Dogan[2]

Abstract

Current global competition forces educational institutions to cope with the difficulties such as increasing costs and decreasing number of resources. Thus, educational institutions are prone to focus on value creation based activities and naturally, digital learning should be adopted more commonly in institutions, companies especially improving learning activities. Recently, value creation based education could be reached as the form of tracing, controlling, optimizing and autonomy of activities that is named as, Internet of Things in digital learning, the next generation of education. In this study, opportunities and threats of digital learning are explained within the concept of the relationship between big data analytics, smart platforms and teaching assistants, Internet of Things and cloud systems. Additionally, further improvements are outlined with respect to the developments in information systems.

Keywords: *Big Data Management, Digital Learning, Internet of Things,*

1. INTRODUCTION

Digital learning paradigms are becoming increasingly applied all over the world due to violent global competition of learning and teaching process and rapid changes in technology. In recent years, thanks to the communication improvements, practitioners have become more conscious about purchasing digital learning tools. Naturally, teacher-student desires are changing day by day -in other meaning, high expectations of students are emerged- and these changings force universities to be speedier to satisfy student requests with more qualified learning materials in acceptable prices. Furthermore, educational institutions and also employee focused companies have to be more flexible against the dynamism of continuous learning environment which increases uncertainties in terms of the effectiveness of critical learning parameters. Besides flexibility, this student oriented attitude helps organizations to take a chance about making more attractive tools but also brings pressure to take risks such as decreasing demand, learning material shocks, quality loses etc. Many organizations adopt themselves to this continuously changing environment only with technology based tools such as tablets, online learning etc. but generally they are not sufficient enough for detecting the effectiveness of learning and making adjustments according to these outcomes. In this concept, Internet of Things (IoT) in digital learning in terms of interaction between intelligent and communicative learning tools that enables self-organizing and centralized context for sustainable learning area.

The transformation process from hard copy materials to IoT is actualized by the improvements in both information technology and education. The first conversion is the entrance of computers in labs and second transformation is occurred after the penetration of internet. At the end of 2000s, automation and learning platforms are introduced and finally, cyber-physical systems that are the combination of digital and physical systems are being mentioned and digitalization of learning is emerged using smart and personalized platforms in educations.

The improvements in information technology also provide the infrastructure of digital learning. The initial development is the educational planning via digital platforms and the development is continued as the increasing usage of Internet and penetration of personal computers in daily life. The final complement in the digitalization is the consolidation of learning products with digital systems such as the integration of software and wireless devices with products and new educational models are appeared in order to maintain the fierce competence and value creation.

---

[1] *Istanbul Technical University, Department of Industrial Engineering, 34367, Besiktas/İstanbul, Turkey.* mahironer@itu.edu.tr, csalkin@itu.edu.tr

[2] *Corresponding author: Istanbul Technical University, Department of Industrial Engineering, 34367, Besiktas/İstanbul, Turkey.* odogan@itu.edu.tr

In this study, we focused on explaining advantageous, value creation aimed properties and critical issues of IoT for learning environment especially in academic and practical aspects. Additionally, opportunities and threats are defined for the operational perspective. The evaluation of intelligent cross linked devices (Cyber-Physical Systems) and digitalized control systems are actualized. Finally, some of the educational models, value creation networks and changes that should be adopted to organizations are briefly explained.

2. IOT AND PROPERTIES OF IOT

Internet of Things implies that the objects will be "smart" by the integration of microprocessors, embedded softwares, wireless connections and data storage units. In education, this smart connection enables intelligence in education in terms of monitoring, controlling, personalization and autonomy. Monitoring implies the reflection of the educational outcomes gathered from other educational activities and its own operations and giving warning according to the records from these reflections. Controlling denotes the educational management of capability of the definition of new functions to the education plan according to the specialized tasks. Finally, optimization provides utilizing artificial intelligence and predictive methods to improve overall system ability. Autonomy supports the combination of monitoring, optimization and controlling of the education in order to coordinate joint activities and self-organizing of the functions of the students.

Interoperability: The connection and communication of machines, devices, sensors, and people using Internet of Things (IoT) or Internet of People (IoP).

Information transparency: The accomplishment of information systems to create a virtual sample of the physical world by providing digital models with raw data. This requires the transformation of gathered data to knowledge using cloud computing, big data analytics etc.

Technical assistance: The integration of assistance systems using machine-machine interaction and human-machine interaction to support decision making and eliminating unpleasant, too exhausting, or unsafe actions using cyber physical systems in education.

Decentralized decision making: The autonomous decision making and interpretation ability with respect to conflicting goals of other systems [1]0.

The triggers that directly affect IoT are big data analytics, smart robots, augmented reality, additive production, cyber security, simulation, vertical and horizontal integration and cloud computing. The brief explanations are given in the following:

Big data analytics: In order to evaluate the data gathered from diversified sources, both inner and external sources, and obtaining knowledge from the raw data enable real time decision making, tracing and tracking decentralized services.

Smart Robots: Adaptive and flexible robots that are combined with the usage of artificial intelligence provides easier understanding of different products by recognizing the lower segments of each parts and this enables decreasing production costs, reducing education time and interaction time.

Augmented reality: Virtual and physical elements could be combined with each other such as smart wears (Google Glass etc.) to ensure decreasing the number of faults especially in tracing the education items.

Cloud computing: Data storage and data processing via cloud will be useful in the accessibility of processed data on request in anytime and anywhere. Additionally, sophisticated algorithms could be activated on cloud structure which provides easier data management and knowledge extraction.

Cyber security: Data transmission security is essential while connected machines and educational products are working together. The security infrastructure that provides reliable data interchange between virtual servers and connected devices via wireless network. Additionally, new user identification, access privilege and secure data storage could be available.

Simulation: Before the implementation of the personalized digital learning tools, analyzers should model the physical system and the model should be activated according to the changing conditions and different scenarios in order to evaluate the practicability of digital education project or tool and determine the optimum parameters of the system.

Vertical and horizontal integration: Vertical integration requires the intelligent cross-linking and digitalization of education units in different hierarchal levels within the organization. On the other hand, horizontal integration obtain entire value creation between organizations for enriching sustainable learning [2]. The horizontal and vertical integration enable real time data sharing, productivity in resource allocation, coherent working educational units and accurate planning which is crucial for connected devices.

Besides IoT has significant advantages, problems could be appeared in implementation stage. The most crucial issue is the expensiveness of the initial investments. Thus, governments should practice new stimulus packages for diversified sectors [3]. Additionally, first implementation could not be conducted if collaborators do not support the institutions in terms of both technically and financially. In this respect, risk analysis and expected outcomes should be carefully considered before making the investments. Additionally, qualified teachers are required especially monitoring and controlling the entire system operations. Governments should support training programs in order to simplify the implementation stage of IoT.

3. RECOMMENDER SYSTEMS AND BIG DATA MANAGEMENT

Recommender systems have been attracted due to the first papers published by Resnick et al. [4] and Shardanand and Maes [5]. The main idea in recommendation system is classifying users related to similarities and trying to find out the most appropriate choice among different alternatives in accordance to the users preferences [6]. Thus, recommendation systems has been used in many areas such as movie, news, book, learning style, product recommendations as well as task, content and document recommendation [7].

Over the last twenty years, researchers have investigated recommender systems in terms of two basic methodology: content based filtering which implies grouping related to similar items for offering new items in accordance with past preferences and collaborative filtering which infers finding the most convenient option depending on users' preferences in order to predict new users' preferences [8].

Most recent studies could be seen in the literature. Papers can be grouped according to the problem domain and additionally, methodology and specific points of the studies are given for understanding the originality of the research paper. As seen from the literature, most of the studies are focused on clustering issues for collaborative filtering and content based applications. Different tools of operations research such as genetic algorithm, MCDM and utility models are utilized in order to make correct user- item matching.

The most emphasized point in literature is the cold start problem that the recommendation system could not make any inferences due to the insufficient data especially for a new item is added to the system and data sparsity which reduces recommendation accuracy [10]. In order to solve these problems, hybrid models are preferred with the assistance of cloud computing and machine learning algorithms.

By the reason of innovations in information science and communication technologies, data generation began to appear in various types such as sound, graphic, word, picture, GPS data, entries in search engines etc. with petabytes and Exabyte which complicates data storage and data management for institutions. These data could be captured by RFID, wireless sensors, mobile devices, cameras and the data size has reached in massive amounts. For instance, 120000 tweets, 2 billion searches in Google, 277000 entries in Facebook arise per minute in Internet. The introduction to term "big data" is first declared by Michael Cox and David Ellsworth [11] in the article named as "Application-controlled demand paging for out-of-core visualization" appeared in Proceedings of the IEEE 8th conference on Visualization in 1997 and consequently, academic and practitioner based publications and reports were submitted dramatically. The reflection of this term in marketing and retailing presented not long after Cox and Ellsworth: Roger E. Bohn and James E. Short [12] published "How Much Information? 2009 Report on American Consumers" which emphasizes on the consumption of the size of the information is approximately 1.3 trillion hours, as almost 12 hours per day. Sum of the consumption reached to 3.6 Zettabytes and 10,845 trillion words, is equaled to 100,500 words and 34 gigabytes for an average person on an average day. In the World Economic Forum made in Davos, 2015 is selected as a "data driven" year that "big data" term will become widespread. This situation implies that both invaluable and "trash" data is accumulated and sorting out the data provides the advantage of extracting knowledge that will point out the misunderstandings. For instance, World Bank declared that $1.5M valued projects are ongoing and they recently finished 100 projects in various sectors and regions in order to find out valuable patterns of information.

According to Gartner Group [13], big data means "high velocity, high volume and high variety of information assets that require new forms of processing to enable enhanced decision making, insight discovery and process optimization". Therefore, big data consists of the terms listed below:

- Variety: Big data obtains diversified type of data collected from various resources. The data type could be text, graphic, picture, audio etc. and generally unstructured. The execution, auditability and summarization of data is necessary for realistic analysis.

- Volume: Amount of the data is another property of big data term. By the increasing of the data size, data becomes lower density such as tweets, clicks on a web page, geo data etc. Thus, data should be transformed in valuable data.

- Velocity: The interchange of the data required to be faster due to the real time data transfer as realized in IoT, mobile applications and mobile advertising. For example, location based mobile

advertising needs the combination of geo data and user preferences with time adjusted recommendations.

- Value: Effective data analysis is required for extracting knowledge from data. On the other hand, doing computations on huge amount of data for recognition patterns or predicting behavior is sometimes results misunderstanding of information caused by statistical sampling.

- Verification: Inconsistencies in data analysis are caused by irrelevant data usage. Thus, verification is actualized by using different data sources or analysis tools for making comparisons especially with real life cases. This provides the determination of unnecessary data and unproductive data analysis methods for future big data based analytics.

As Boyd and Crawford [14] mentioned, implementation of "big data" includes: (1) Technology: Minimizing computation time and maximizing algorithmic support to gather, analyze, link, and compare large data sets. (2) Integration: collecting necessary data and separating "trashes" from data warehouses. (3) Analysis: determination of patterns for economic, social, technical, and legal interpretations. From this point of view, this procedure is similar to the "known" data analysis processes except the computational time and separation unnecessary data from storages.

Methods that will be used in big data analytics studies should also be determined according to the properties listed below:

- Objective of the analysis: In order to decide the proper strategy that will be adopted in each group, organizational resources and environmental factors should be included in the big data analytics model.

- Sampling: Inadequate number of observations will lead to gathering meaningless information from the education transactions that will cause unproductive usage of education budget.

- Data type and source: The selection of big data analytics method highly specifies the purposed model. A priori segmentation (classification) is based on the selected variables and classifying learning needs according to these variables with a certain number of classes. Post hoc segmentation mainly applies clustering and the number of classes are not known before clustering. In dynamic classification, learning needs are generally segmented in alternative segments. Conjoint analysis is the other method that education needs are grouped with respect to the preferred types of education or services.

- Determination of variables: Geographic and economic variables are commonly used for grouping education activities On the other hand, product or service usage frequency, learning speed and preferences should also be considered for the determination of big data analytics method. Additionally, they should be combined with geographic and economic variables for identification of different education characteristics.

- Optimization techniques: For the data analysis, clustering, CHAID, multiple regression, discriminant analysis, latent class structure, ANN, SOM, metaheuristic methods such as genetic algorithm are preferred in literature. Hiziroglu [15] mentioned that previous studies demonstrated that hierarchical approaches could not deal with large data sets because of the partitioning ineffectiveness of dendrogram. To overcome this problem, hybrid methods should be applied large datasets especially hierarchical approaches with non-hierarchal approaches (K means) and association rule mining.

- Standardization and normalization: Different variables could have diversified number of data types. To make the calculations easily, standardization and normalization is necessary to implement.

- Validation: Execution with multiple times, cross validation, adopting completely different data to the purposed segmentation method, compactness (closeness of the elements in the same group) and separation (distance between different clusters) are critical measures for proving the validation of segmentation technique.

Big data implementation is generally assisted with an infrastructure such as Hadoop, MapReduce, Hive, HBase, MongoDB or Cassandra. Naturally, programming languages like Java, Linux, PHP is necessary before and after the big data solution adaptation. Additionally, while working with multiple data warehouses, NoSQL platform knowledge provides the advantage of the extension of clearing "trash" data in big data solution platform.   Among big data infrastructure solutions, MapReduce is a programming aspect that introduced by Google as data is separated with little parts for easy, parallel and quick pre-analysis and reduce is the combination of these extractions according to the learning logic. In order to cope with the enormous amount of unstructured data storage, ingestion, processing and filtering, Hodoop infrastructure is a promising solution introduced by Apache Software Developers and it was developed in Java and especially useful for

parallel processing. It is not working as a "data warehouse" because of interactive and iterative processing of business intelligence based operations in web or mobile platforms such as web log analysis, visitor behavior, text analyzing, search analysis by integrating machine learning approaches and data mining methods. In other words, Hadoop structure is useful for fast data loading, ETL, image processing and online data integration including distributed file systems YARN and Map Reduce platform. In Hadoop, YARN tool clusters resources according to the relation of obtained data. As a part of Hadoop framework, Map Reduce platform is similar to Google's solution. In addition to that Hadoop framework could be described as an "ecosystem" serving with diversified software packages as Apache Pig, Apache Hive, Apache HBase, Apache Phoenix, Apache Spark, Apache ZooKeeper, Cloudera Impala, Apache Flume, Apache Sqoop, Apache Oozie, and Apache Storm.

The dissemination of Bluetooth 4.0 supported devices such as Beacons will ensure the location determination in indoor locations. This situation provides the development of learning recommendation systems framework in terms of presenting special actions via mobile devices to the "smart" products. On the other hand, irrelevant offerings and wrong directions given automatically will affect customer attitude to the institutions in a negative way. Thus, recommendation intentional algorithms should be more personalized and speedy enough in computing the results.

4. RECOMMENDER SYSTEMS AND BIG DATA MANAGEMENT IN DIGITAL LEARNING

Besides IoT has significant advantages, some problems could be appeared in implementation stage. The most crucial issue is the expensiveness of the initial investments. Thus, governments should practice new stimulus packages for diversified sectors [3]. Additionally, first implementation could not be conducted if collaborators do not support the institutions in terms of both technically and financially. In this respect, risk analysis and net present values should be considered before making the investments. Additionally, qualified employees are required especially monitoring and controlling the entire system operations. Governments should support training programs in order to simplify the implementation stage of IoT.

Since increasing number of innovations in information technology and communication have being appeared, the intersection of statistics, data management and knowledge management has become more substantial especially in the applications of learning algorithms. While extracting information and patterns from large data sets, personalized learning systems should be adopted widely by establishing intelligent, self-organizing and self-learning systems [16]. The overall presentation of digital learning systems can be seen from Figure 1.
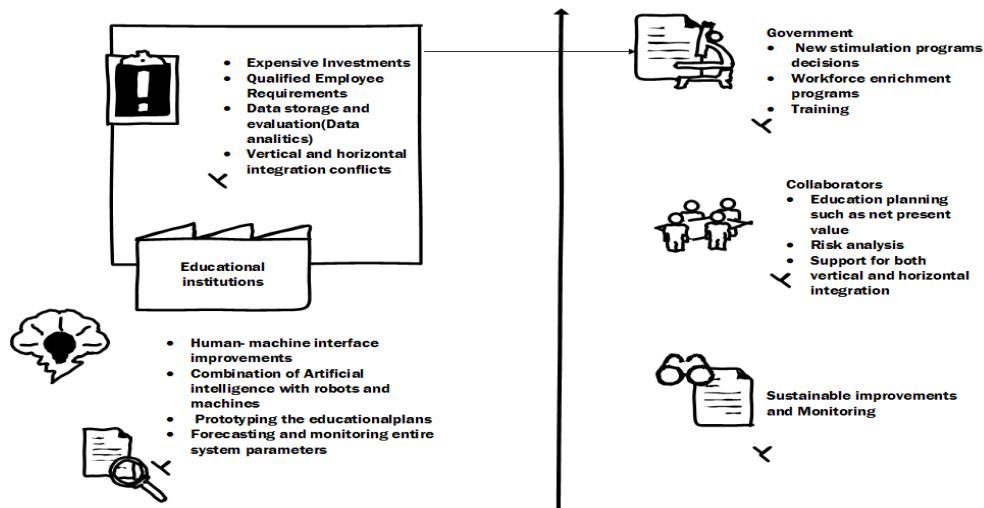
Figure 1. Issues and solutions of the issues appeared in IoT (Inspired from Berger [9])

5. CONCLUSION

In this study, we focused on explaining advantageous, value creation aimed properties and critical issues of IoT for education environment especially in academic and practical aspects. Additionally, opportunities and threats are defined for the operational perspective. The evaluation of intelligent cross linked machines (Cyber- Physical Systems), end-to-end engineering (educational product development) and digitalized control systems are actualized. Finally, some of the educational tools, value creation networks and changes that should be adopted to organizations and sectors are briefly explained.

REFERENCES

[1]. M. Hermann, T. Pentek and B. Otto, "Design Principles for Industrie 4.0 Scenarios: A Literature Review," in *49th Hawaii International Conference on System Sciences (HICSS)*, Hawaii, 2016.

[2]. Acatech, "Umsetzungsstrategie Industrie 4.0 Ergebnisbericht der Plattform Industrie 4.0," BITKOM, Frankfurt, 2015.

[3]. A. Ustundag, "Endüstri 4.0 ve Akıllı Sistemler," 29 04 2016. [Online]. Available: http://alpustundag.blogspot.com.tr/. [Accessed 04 07 2016].

[4]. P. Resnick, N. Iacovou, M. Suchak, P. Bergstrom and J. Riedl, "GroupLens: An Open Architecture for Collaborative Filtering of Netnews," *Proceedings of ACM 1994 Conference on Computer Supported Cooperative Work,* pp. 175-186, 199.

[5]. U. Shardanand and P. Maes, "Social information filtering: algorithms for automating "word of mouth".," *Proceedings of the SIGCHI Conference on Human Factors in Computing Systems ,* pp. 210-217, 1995.

[6]. J. Bobadilla, F. Ortega, A. Hernando and A. Gutierrez, "Recommender systems survey," *Knowledge-Based Systems,* vol. 46, p. 109–132, 2013.

[7]. D. H. Park, H. K. Kim, Y. Choi and J. K. Kim, "A literature review and classification of recommender systems research," *Expert Systems with Applications,* vol. 39, p. 10059–10072, 2012.

[8]. Y. Zhang and J. Jiao, "An associative classification-based recommendation system for personalization in B2C e-commerce applications," *Expert Systems with Applications,* vol. 33, p. 357–367, 2007.

[9]. R. Berger, "INDUSTRY 4.0: The new industrial revolution, How Europe will succeed," March 2014. [Online].Available:
https://www.rolandberger.com/publications/publication_pdf/roland_berger_tab_industry_4_0_20140403.pdf. [Accessed 18 04 2017].

[10]. L. B., K. Kolomvatsos and S. Hadjiefthymiades, "Facing the cold start problem in recommender systems," *Expert Systems with Applications,* vol. 41, no. 4, p. 2065–2073, 2014.

[11]. M. Cox and D. Ellsworth, "Application-controlled demand paging for out-of-core visualization," in *Proceedings of the 8th conference on Visualization '97*, Phoenix, Arizona, 1997.

[12]. R. Bohn and J. E. Short, "How Much Information? 2009 Report on American Consumers," Global Information Industry Center, San Diego, 2009.

[13]. Gartner Group, "Big Data," [Online]. Available: http://www.gartner.com/it-glossary/big-data. [Accessed 30 07 2016].

[14]. D. Boyd and K. Crawford, "Critical Questions For Big Data, Provocations for a cultural, technological, and scholarly phenomenon," *Information, Communication & Society,* vol. 15, no. 5, p. 662 –679, 2012.

[15]. A. Hiziroglu, "A neuro-fuzzy two-stage clustering approach to customer segmentation,," *Journal of Marketing Analytics,* vol. 1, no. 4, pp. 202-221, 2013.

[16]. E. Hüllermeier, "Fuzzy Sets in Machine Learning and Data Mining," *Applied Soft Computing,* vol. 11, pp. 1493-1505, 2011.

Examination of Matrakci Nasuh's Galata Miniature in terms of Cartography

Huseyin Zahit Selvi[1], Ilkay Bugdayci[1], Gaye Bekiroglu Keskin[1]

Abstract

The map has become very important role throughout the human life. Even during the Ottoman history, it is possible to encounter many products bearing map quality. In particular, the world map designed by Piri Reis is valuable in terms of quality even today. Although both lived in the same period, researchers had more interest to Piri Reis' maps than Matrakci Nasuh's miniatures. However, while the maps of Piri Reis in terms of marine cartography is crucial, Matrakci's miniatures are valuable in terms of landscape cartography. In this study, Galata miniature designed by Matrakci Nasuh, who drawn miniatures with his own style, examined in terms of cartography. In this context, landmarks such as mosque, tower, etc. in the miniature were compared with maps and Google Earth images obtained by today's technology. In addition, miniature was examined in terms of its geometric and topological accuracy. Results indicated that although geometrical accuracy of the miniature was poor, topological accuracy was good.

Keywords: *Historical Map; Matrakci Nasuh; Geometric Accuracy; Topologic Accuracy*

1. INTRODUCTION

Map production was important in Ottoman Empire. The Ottoman Empire, which had a very large landscape, needed products as a guide to determine its existing borders and to learn new places. As in other sciences, in the field of geography and cartography, the Ottomans produced important works.

Maps produced especially in the 16th century had an important place in Ottoman cartography. In particular, the world map designed by Piri Reis is valuable in terms of quality even today. Although both lived in the same period, researchers had more interest to Piri Reis' maps than Matrakci Nasuh's miniatures. Over 100 miniatures designed by Matrakci during the east and west expeditions should be evaluated in terms of city planning and cartography. The aim of this study is to examine Matrakci's Galata miniature in terms of cartography and to detect its importance as a map and city plan by determining the geometric and topological accuracy. In this context, Matrakci Nasuh's Galata miniature was compared with the Google Earth images produced with today's possibilities. Then, the miniature was evaluated with the MapAnalyst software used to determine the geometric accuracy of historical maps and examined in terms of geometric and topological accuracy. This paper is divided into five sections. Following the Introduction, the next section provides a brief overview of Matrakci's life. Used materials and methods are explained in the third part. Then, a detailed presentation of application is given. Finally, conclusions are shared in the last section.

2. MATRAKCI NASUH'S LIFE

Nasuh was born in Bosnia towards the end of the 15th century. It was taken to the Ottoman palace at a young age as a devshirmeh. He was educated in Enderun in the last years of Sultan II. Bayezid period (1481-1512) [1]. Matrakci Nasuh was one of the most interesting people of the 16th century as a historian, a swordsman, a mathematician, a calligrapher and an artist. Intensive military activities during the Kanuni period encouraged the writing of productive works in many disciplines. The most important work that described the expeditions of this period was Matrakci Nasuh's work titled Beyan-i Menâzil-i Sefer-i Irakayn-ı Sultan Suleyman Han or Mecmû'-ı Menâzil. In this book, he documented all ranges along the Kanuni's Iran expedition (1533-1536), that started from Istanbul and reached Baghdad over and again from here back to Istanbul, again over Tabriz. He gave important information about the landmarks of these regions with carefully drawn miniatures [2]. Nasuh's book, written in 1537, consists of 88 pages of text, 107 pages of miniature, 25 pages of miniature and text [1]. Miniatures such as Istanbul, Galata, Eskisehir, Adana and Erzurum were included in this book.

---

[1] *Corresponding author: Necmettin Erbakan University, Geomatics Engineering Department Konya/ Turkey. hzselvi@konya.edu.tr*

Matrakci Nasuh has two additional works bearing the same qualities as Mecmu-i Menazil. Nasuh described important places along the Kanuni's Second Hungarian Expedition (1542-1543) with the miniatures in the book of History-i Feth-i Siklos Estergon and Istol-Belgrad. There are 32 miniatures in this book. This book was completed in 1543. Another similar work of Nasuh was the work called Tarih-i Sultan Bayezid, which told about the expeditions of the 2. Beyazit period. Miniatures of the cities of Kili, Akkerman, İnebahtı, Muton and Gulek were included in this book. Distances between destinations were presented in miles [1]. It is thought that Matrakci was died in 1564 [3].

3. MATERIAL METHOD

3.1. Miniature

Miniature refers to painting made with watercolors to decorate handwritten books. Miniatures have their own characteristics. Some of these properties are objects do not close each other, the remaining objects are drawn on the top of the paper, and the size of the objects is determined according to their importance [4].

Paintings of landmark buildings such as mosques, tombs and palaces are very valuable in terms of the history of Turkish architecture in Matrakci's miniatures. On the other hand, the plants and animals seen in these miniatures give important information about the vegetation and lifestyle of those regions [5].

3.2. MapAnalyst

MapAnalyst is a software application for the accuracy analysis of old maps. Its main purpose is to compute distortion grids and other types of visualizations that illustrate the geometrical accuracy and distortion of old maps. MapAnalyst uses pairs of control points on an old map and on a new reference map. The control points are used to construct distortion grids, vectors of displacement, accuracy circles, and isolines of local scale and rotation. MapAnalyst also computes the old map's scale, rotation and statistical indicators[6-10]. In this study, the geometrical accuracy of miniatures was investigated with MapAnalyst software.

3.3. Method

In this study, first of all, the Google Earth image of the studied region was returned to the viewpoint of Matrakcı in order to examine Matrakcı's Galata miniature in terms of cartography. Then, with the help of clear historical details drawn by Matrakci, the historical places in the miniature were compared with their real positions in Google Earth. After this, with the help of MapAnalyst software, the locations of the obvious historical places on the miniature were geometrically compared with the current maps in order to investigate the geometric accuracy of the miniature.

4. APPLICATION

4.1. Map Accuracy

Map production based on original (classical or photogrammetric methods) measurements may be possible at large scales (1: 1000, 1: 5 000) or at the bottom of medium scales (1: 25 000) as applied in Turkey. Smaller scale maps are produced with cartographic generalization techniques by using larger scale maps [11]. Cartographic generalization is the process of changing the content of a map to a new map design in terms of geometric position, number of objects and format of representation [12]. As a result of such changes, the planimetric accuracy on the map is no longer preserved. However, in small-scale maps, it is expected that the spatial objects, especially called topological accuracy, should protect their relations with each other. A well-designed map should provide a metric and topological understanding of the objects [13].

4.2. Galata Miniature

Galata's miniature is in the book of Matrakci's Beyân-ı Menâzil-i Sefer-i Irakayn-ı Sultan Suleyman Han. The three sides of Galata are Bogazici, Halic and Kagithane River.

Galata Tower is shown with number 1 in miniature (Figure 1) and Google Earth (Figure 2). Rookies School is shown with number 3. In miniature, Rookies School appears to be in line with the Galata Tower but is actually outside the walls and somewhat behind. It is also seen that Rookies School, which is shown with number 3 in Google Earth, is located to the east of the Galata Tower. When the topological position and metric consistency with other constructions are examined, it is seen that the Galata Tower should be drawn a little further south-west.

1. Galata Tower
2. Tophane and Uskudar Pier
3. Rookies School
4. Uskudar
5. Bazaar
6. Eyup Sultan Mosque
7. Kagithane River
8. Maiden's Tower

Figure 10. Matrakci Nasuh's Galata miniature
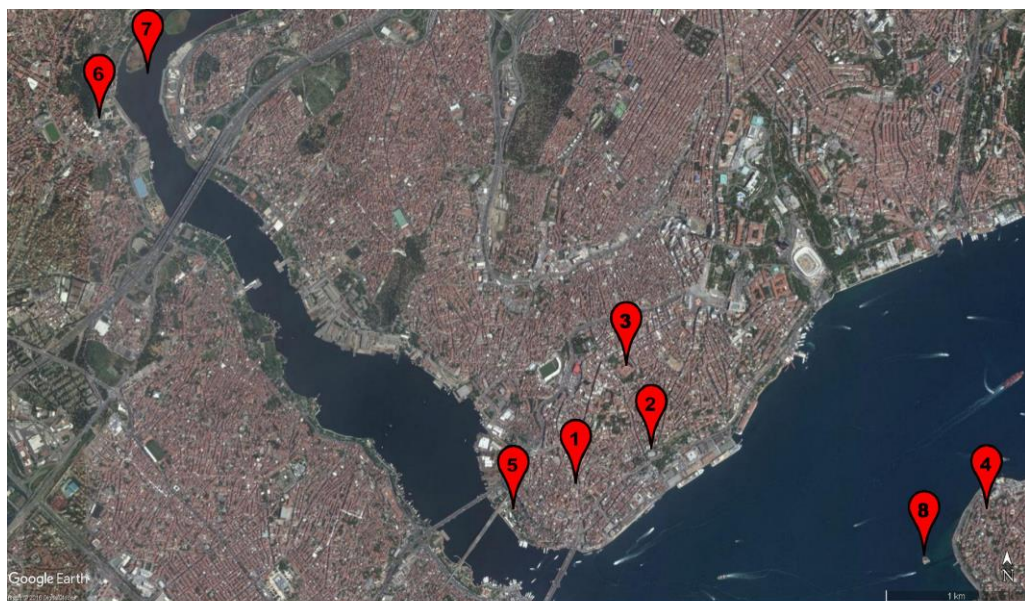
1. Galata Tower
2. Tophane and Uskudar Pier
3. Rookies School
4. Uskudar
5. Bazaar
6. Eyup Sultan Mosque
7. Kagithane River
8. Maiden's Tower

Figure 2. Galata in Google Earth

A pier lies from Tophane towards the sea. The Maiden's Tower and Uskudar are located just opposite to the Tophane. Tophane and Uskudar Pier, shown with number 2 in miniature (Figure 1) and Google Earth (Figure 2), is located at the bottom right of the page. Matrakci draws Tophane and Uskudar Pier in the southern part of the Rookies School. It is seen that Tophane and Uskudar Pier is also in the southern part of Rookies School in Google Earth. It is also compatible with other constructions.

Uskudar is shown with number 4 in miniature (Figure 1). The position of Uskudar in miniature is shown on the opposite side of Tophane. Uskudar is also on the opposite side of Tophane in Google Earth and it seems that Uskudar is depicted with accuracy close to perfection. The Bazaar, which is shown in miniature with number 5, is displayed outside and west of Galata walls. The position of Bazaar according to Google Earth is topologically harmonious.

The Eyup Sultan Mosque, which is shown with number 6 in miniature, is depicted on the opposite side of the Kagithane River. Although the location of Eyup Sultan in miniature is just opposite the Bazaar, it appears to be further north on Google Earth. It is thought that Matrakci found such a solution because of the narrowness of the drawing area and the desire to show the Eyup Sultan Mosque. It is seen that the Maiden's Tower, which is shown in miniature with number 8, is very well placed geometrically and topologically.

4.2.1. Investigation of Galata Miniature in terms of Planimetric Accuracy

In order to investigate the planimetric accuracy of the Galata miniature with the help of MapAnayst software, 5 points (Galata Tower,Tophane, Rookies School, Bazaar and Maiden's Tower) which can be selected clearly on Galata Miniature were chosen. Then, the correspondences of these points in the current map (Open Street Map) were determined and analyzed with the transformation parameters of Affine (6 parameters). As a result of the analysis, it was determined that the mean scale of the miniature was 1: 24000-1: 27000, the mean rotation angle was 320° (clockwise) from the north, and the average positioning error was 629 m. While considering the value of this rotation angle, It should not be forgotten that Matrakci drew a miniature from his own point of view, and he was not in the opinion of drawing north-up miniature. The locations of the selected points determined by the analysis are shown in Figure 3.
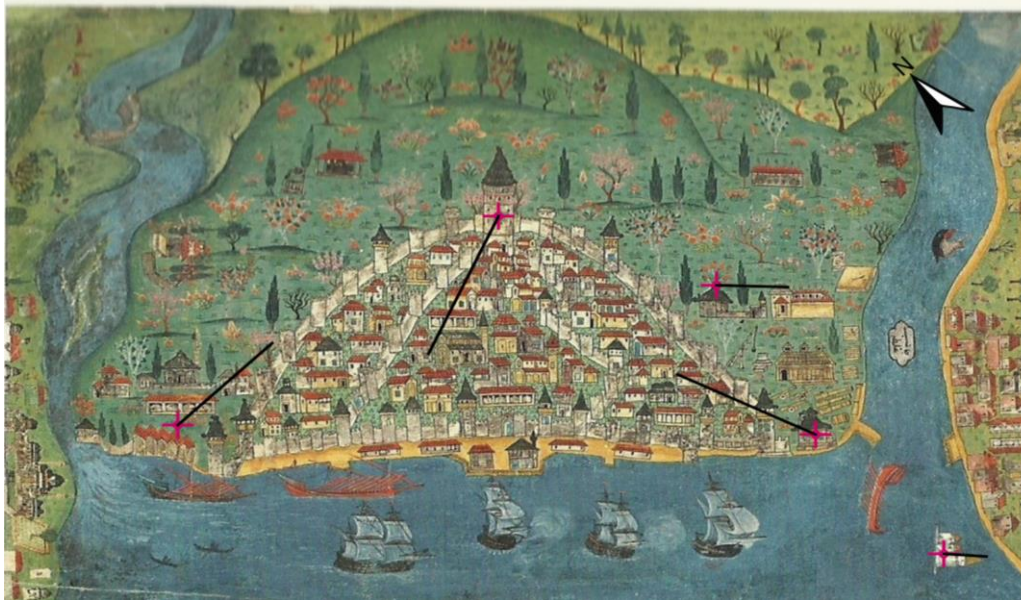
Figure 3. 4.2.1. Investigation of Galata Miniature in terms of planimetric accuracy

5. CONCLUSIONS

When Matrakci's Galata miniature is examined in term of cartography, it is possible to detect the deficiency of the miniature in terms of map quality. Because exact scale is not specified and required information such as coordinate is not determined. However, Matrakci represents objects according to importance is very meaningful in terms of cartography. In addition the chosen objects have been drawn to reflect their shapes and colors. Planimetric accuracy of Galata miniature was determined as 629 m. Considering the conditions of the period in which the miniature was made, this accuracy value is also quite good. Moreover, topological accuracy is more important than planimetric accuracy when working with a scale of 25000 or smaller. From this point of view, it is seen that the topological neighborhood relations in Matrakci's miniature are very compatible.

ACKNOWLEDGEMENT

REFERENCES

[1]. M. Onder, "Gecmisten Günümüze Resimlerle Türk Haritacılık Tarihi", Ankara, 2002, [in Turkish].

[2]. M. Ak, "Osmanlı'nın Gezginleri", İstanbul, 2006, [in Turkish].

[3]. D. Erkan, "Osmanlı Arastırmaları," n. 37, İstanbul, p.185,186,2011, [in Turkish].

[4]. I. Binark, "Türklerde Resim ve Minyatür Sanatı," İstanbul, p.272, 1978, [in Turkish].

[5]. H.G. Yurdaydın, "Beyan-ı Menazil-i Sefer-i Irakeyn," İstanbul, 2014, [in Turkish].

[6]. B. Jenny, "MapAnalyst – A Digital Tool for the Analysis of the Planimetric Accuracy of Historical Maps," *e-Perimetron*, 1(3), 239-245, 2016.

[7]. B. Jenny, A.Weber, L. Hurni, "Visualizing the Planimetric Accuracy of Historical Maps with MapAnalyst," *Cartographica*, 42(1), 89-94, 2007.

[8]. B. Jenny, "New Features in MapAnalyst," *e-Perimetron*, 5(3), 176-180, 2010.

[9]. B. Jenny, L. Hurni, "Studying Cartographic Heritage: Analysis and Visualization of Geometric Distortions", *Computers & Graphics*, 35(2), 402-411, 2011.

[10]. T. Gokgoz, B. Karahan, B. Kuzucu, "1878 Tarihli Davutpasa Haritasının Planimetrik Dogruluk Analizi", 6. *Uzaktan Algılama-CBS Sempozyumu (UZAL-CBS 2016),* 5-7 Ekim 2016, Adana, [in Turkish].

[11]. D. Ucar, N. Ulugtekin, "Kartografyaya Giris ders notu", s.46, 2006, [in Turkish].

[12]. K. Brassel, "Der Generalisierungsbegriff in der Kartographie und anderen Disziplinen", in Kartographisches Generalisieren, Schweizerische Gesellschaft für Kartographie, Zürich, 3-5, 1990.

[13]. W. Mackaness, D. Burghardt, C. Duchêne, "Map Generalisation: Fundamental to the Modelling and Understanding of Geographic Space", Chapter 1, *Abstracting Geographic Information in a Data Rich World* (edt. Dirk Burghardt Cécile Duchêne William Mackaness), 2014.

Determination of Appropriate Distribution Functions for the Wind Speed Data Using the R Language

İsmail KIRBAS[1]

Abstract

Accurate determination of the proper distribution and parameters of this distribution according to the wind characteristics of the zone is vital for wind energy investment. In determining a wind energy potential belonging to a region, meteorological wind speed measurements have a great proposition to take place within a certain statistical distribution. In our study, the wind speed data obtained from the metrology station within 1 year was evaluated and it was determined using the R language, which is an open source statistical programming language, which is better suited to distributions such as Weibull, gamma, lognormal and logistic. The Akaike Information Criterion and Schwarz-Bayesian Information Criterion (SBIC) scores were calculated as the performance parameters of the distributions and the distribution performances were compared graphically. While gamma and lognormal distributions have better results at low wind speeds, Weibull distribution achieves higher performance for higher wind speeds.

Keywords: *Gamma, Logistic, Lognormal, R Language, Statistical Distribution, Weibull, Wind Speed.*

1. INTRODUCTION

The use of renewable energy sources is increasing day by day in the production of electricity all over the world. Along with that, electricity generation from wind energy is getting more and more popular every day. The greatest difficulty of generating electricity from wind energy is the complexity of the dynamics that make up the wind and it is very difficult to predict in long term period [1]–[3].

Before the wind energy investments are made, it is necessary to make wind speed measurements related to the installation area. The long-term results obtained are analysed by using statistical methods. Weibull distribution is the most frequently used method in the analysis process. However, for places with low wind speeds, the success of the Weibull distribution remains relatively low [4]–[6].

In our study, wind speed measurements made by Antalya International Airport meteorological station between 2016 and 2017 were examined. The meteorological station records 30-min average wind speed data. However, the data obtained was converted into a 6-hour average in order to make the evaluation of the data easier. All operations on the wind data were performed using the R language and Rstudio software.

R programming language was originally written by Robert Gentleman and Ross Ihaka alumni members of the statistical department of the Auckland University in New Zealand. These two statisticians were influenced syllabically by S language which is written by Chambers, Becker and Wilson and the scheme language developed by Susman. Statisticians who have developed R language, have aimed to use open source software due to the high cost of licensing of other statistical package programs and software, and high cost of learning and teaching. Later R software developers from different parts of the world gave themselves the name "r core team". R software was published by "r core team" on 29 February 2000. Software that includes the open source code feature is used free of charge. R language is a generous medium for statistical calculations and graphs. It has the feature of data processing and storing and special operators that can be used in the calculations of data and especially matrices. It contains compatible and co-usable graphical tools that can be used for data analysis [7], [8].

---

[1] *Corresponding author: Mehmet Akif Ersoy University, Department of Computer Engineering, 15100,Istiklal Campus/Burdur, Turkey. ismailkirbas@mehmetakif.edu.tr*

The source code for R, which is part of the GNU project, is available under the GNU General Public License and is available for various operating systems. There are also various graphical user interfaces, although the R command uses a line interface. It provides a language and environment for data processing, classification, clustering, time-series analysis, classical statistical tests, linear and nonlinear modelling calculations and graphic display. Because it is open source, it is very prone to development [9].

In this study, gamma, log-normal and logistic distributions are used together with Weibull distribution which is widely used in the literature in determination of wind energy efficiency and they are graphically compared with Weibull distribution. In Figure 1, 6-hour average annual wind speed data is shown graphically. The data and the R codes used in this study can be accessed freely via the GitHub platform [10].

Wind Speed Time Series
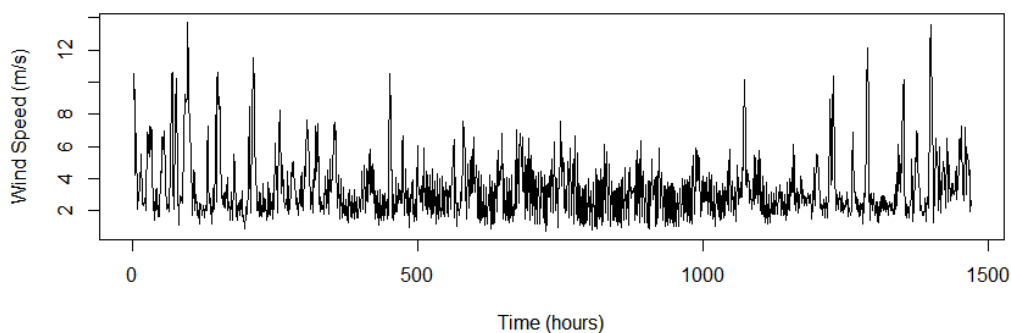
Figure 11. 6-hour average annual wind speed data from International Antalya Airport meteorological station.

Table 1 also gives some fundamental statistical information about collected data.

Table 1. Statistical results for wind speed data.

Statistical Calculation	Value
Average	3.3697
Standard Error Mean	0.0492
Standard Deviation	1.8858
Median	2.9200
Variance	3.5561
Skewness	1.7100
Kurtosis	3.8600
Range	12.980
Mode	2.4100
N for Mode	22
Maximum	13.720
Minimum	0.7400
Sum	4953.51
Quantity	1470

It is essential to use the correct statistical distribution model in assessing wind energy efficiency. In our study, firstly candidate models which are used in the literature have been determined in order to choose the best model. The comparative distributions were determined as Weibull, gamma, lognormal and logistic distributions. Since the Weibull distribution is the most commonly used model in wind energy analysis, the other models are compared one by one with the Weibull distribution. In the rest of our work, information about these distributions was given and mathematical and graphical comparisons were made using R language.

2. DISTRIBUTION MODELS

In this section, mathematical equations of Weibull, gamma, lognormal and logistic distributions are given and comparative performance ratios are graphically shown. In order to perform distribution analysis, fitdistrplus package is used in R language. In addition, ggplot and readr libraries are included for graphical drawings and reading data in csv format.

2.1. Weibull Distribution

The Weibull distribution, which is found by Professor Waloddi Weibull, has an important place in probability distributions. It is one of the most broadly used distributions in reliability analysis since it has the ability to characterize all the regions of the force curve. Weibull distribution is applied with two or three parameters according to the usage areas [11], [12]. Equation 1 gives Weibull probability distribution function with 3 parameters where γ is used for shape parameter, β for scale parameter and ω for location parameter.

$$f(x) = \frac{\gamma}{\beta}\left(\frac{x-\omega}{\beta}\right)^{\gamma-1} . exp\left(-\left(\frac{x-\omega}{\beta}\right)^{\gamma}\right), f(x) \geq 0, x \geq 0, \gamma > 0, \beta > 0, \omega \geq 0, \omega \leq x \leq \infty \qquad (1)$$

Two-parameter Weibull probability distribution is obtained by taking $\omega = 0$ as shown in Equation 2.

$$f(x) = \frac{\gamma}{\beta}\left(\frac{x}{\beta}\right)^{\gamma-1} . exp\left(-\left(\frac{x}{\beta}\right)^{\gamma}\right), \ f(x) \geq 0, x \geq 0, \ \gamma > 0, \ \beta > 0 \qquad (2)$$

This version of the Weibull distribution is used intensely, especially when information on wind distribution and variation in wind velocity are needed. The probability of this distribution is not symmetric but the skew is skewed and the distribution is indicated by shape and scale variables. The total likelihood of the area under this distribution equals to 1.

2.2. Gamma Distribution

In probability theory and statistical science, gamma distribution is a two-parameter continuous probability distribution. One of these parameters is the scale parameter θ; and the other is called the shape parameter k. If k is an integer, the gamma distribution represents the sum of random variables with k exponential distributions.

$$f(x; k, \theta) = x^{\alpha-1}\frac{e^{-x/\theta}}{\theta^k\Gamma(k)}, \ x > 0, \ k > 0, \ \theta > 0 \qquad (3)$$

Gamma probability distribution function is given in Equation 3 and cumulative gamma distribution function is shown in Equation 4.

$$F(x; k, \theta) = \int_0^x f(u; k, \theta)du = \frac{\gamma(k, x/\theta)}{\Gamma(k)} \qquad (4)$$

Empirical and theoretical comparison for Weibull and gamma distributions is shown in Figure 2. According to histogram graph in Figure 2, gamma distribution fits data better than Weibull distribution.
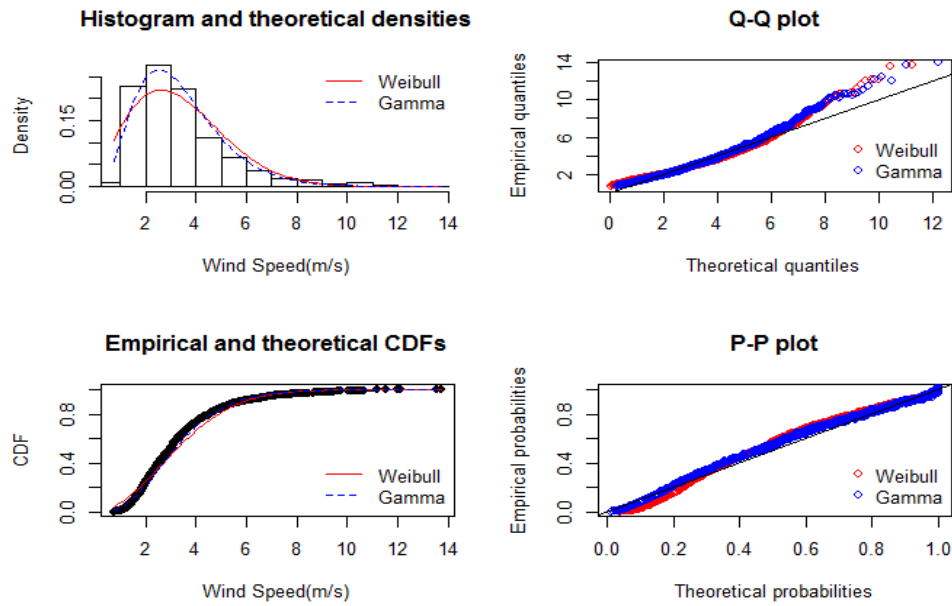
Figure 12. Empirical and theoretical comparison for Weibull and gamma distributions.

2.3. Log-Normal Distribution

Since the log-normal distribution can take many different forms, many data can be modelled by log-normal distribution. It is mainly used for economic production data and reliability analysis [13].

Log-normal probability distribution function is shown in Equation 5 and log-normal cumulative distribution function is located in Equation 6.

$$f(x) = \frac{1}{2\sigma} \cdot \frac{1}{\sqrt{2\pi}} exp\left[-\frac{(\ln x - \mu)^2}{2\sigma^2}\right], \ x \geq 0 \tag{5}$$

$$F(x) = P(X \leq x) = P(lnX \leq lnx) = \int_{-\infty}^{x} f(t)dt = \emptyset.\left(\frac{lnx}{\sigma\mu}\right) \tag{6}$$

Figure 3 depicts empirical and theoretical comparison for Weibull and lognormal distributions. According to histogram graph in Figure 3, lognormal distribution is more successful than Weibull distribution.

Histogram and theoretical densities

Q-Q plot

Empirical and theoretical CDFs

P-P plot
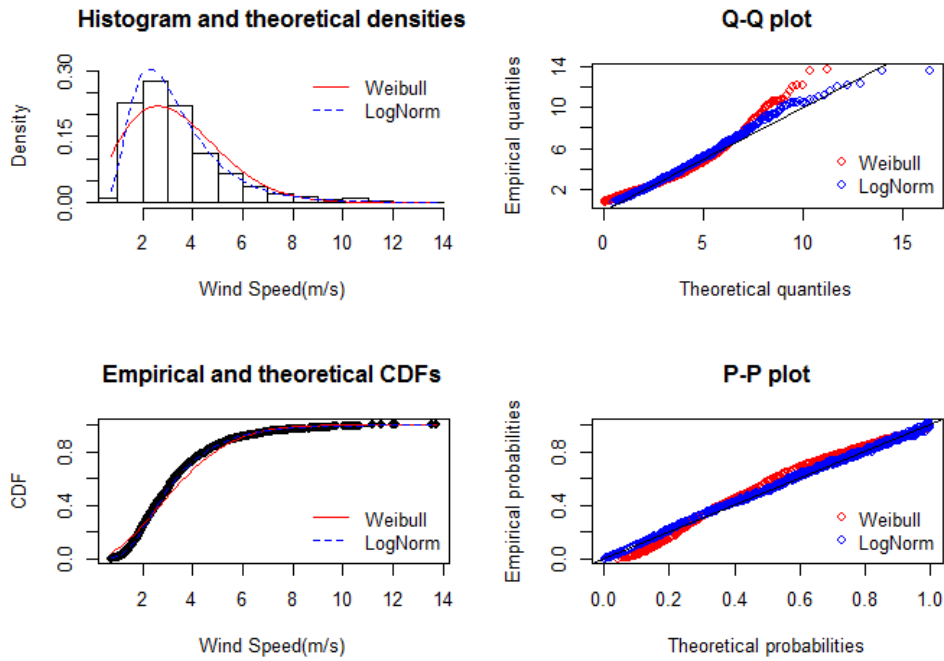
Figure 13. Empirical and theoretical comparison for Weibull and lognormal distributions.

2.4. Logistic Distribution

The logistic distribution function which is given in Equation 7 is a continuous probability distribution and also plays a role in the issues of feed-forward neural networks and logistic regression.

$$f(x;\ \mu, s) = \frac{e^{-\frac{x-\mu}{s}}}{s\left(1+e^{-\frac{x-\mu}{s}}\right)^2} = \frac{1}{4s} sech^2 \left(\frac{x-\mu}{2s}\right) \tag{7}$$

Cumulative distribution function can be seen in Equation 8 and, x is the random variable, μ is the mean, and s is a scale parameter proportional to the standard deviation.

$$F(x;\mu, s) = \frac{1}{1+e^{-\frac{x-\mu}{s}}} = \frac{1}{2} + \frac{1}{2} tanh \left(\frac{x-\mu}{2s}\right) \tag{8}$$

Figure 4 shows theoretical and empirical comparison for Weibull and logistic distributions. Graphical results show that the Weibull distribution is more successful than the logistic distribution.

Histogram and theoretical densities

Q-Q plot

Empirical and theoretical CDFs

P-P plot
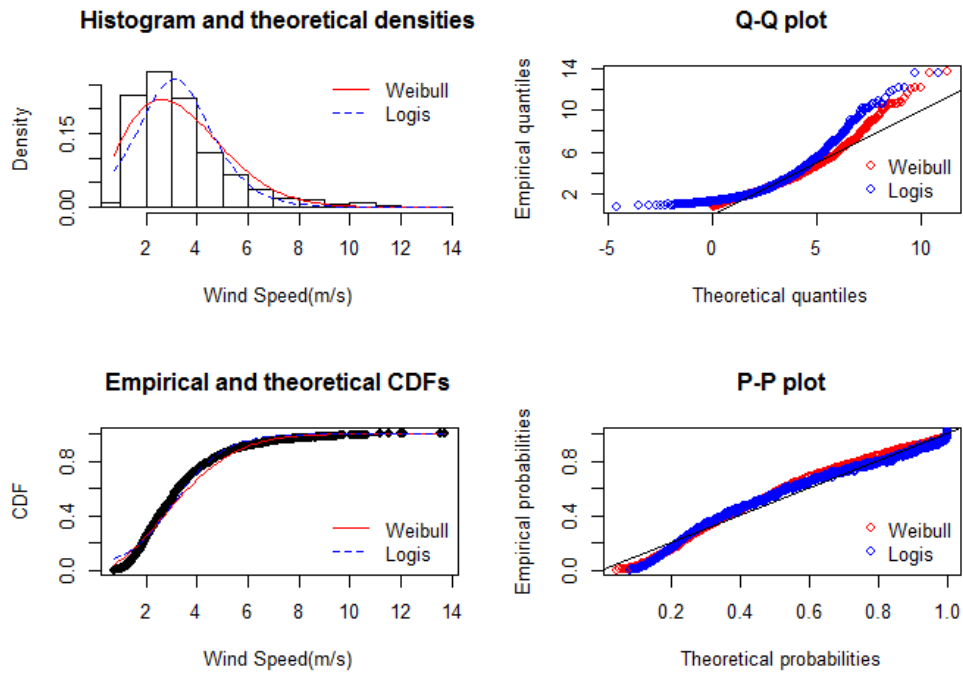
Figure 14. Empirical and theoretical comparison for Weibull and logistic distributions.

3. DISTRIBUTION EVALUATION

In literature, there are many statistical evaluation method to evaluate the developed models. In this study we choose Kolmogorov-Smirnov, Cramer-von Mises, Anderson-Darling, Akaike Information Criterion (AIC) and Schwarz-Bayesian Information Criterion (SBIC). Each model has been evaluated using the model evaluation methods given in Table 2 with the results obtained from the statistical model evaluations.

The Akaike information criterion (AIC) is a quality statistical relative model measure for a given set of data. When a collection of data models is given, the AIC relatively estimates each model quality. Therefore, the AIC provides a way to select the model. The Akaike criterion is based on information theory, the information given is the model data, the process is used to represent, and provides a relative estimation. Thus, the model's goodness of fit and model complexity can be understood. This criterion does not provide a model test for the null hypothesis test; If all candidate models are bad, they will not give any warning. The model with the lowest AIC value has the highest relative performance [2].

AIC value can be calculated using Equation 9 where k represents estimated number of parameters and L symbolize maximum value of the likelihood function for the model.

$$AIC = 2k - 2\ln(L) \tag{9}$$

The Bayesian Information Criterion (BIC) index imposes a penalty for increasing the number of parameters. Thus, it considers both the degree of statistical conformity and the number of parameters to be estimated. The BIC formula is given in Equation 10. Here, k denotes the number of parameters that are modelled, n represents the sample size, and finally L indicates the maximized log likelihood of the model.

$$SBIC = -2 \cdot \ln L + k \cdot \ln(n) \tag{10}$$

In Table 2, 4 different distribution models were compared according to 5 evaluation criteria and the best values were indicated as underlined.

Table 2. Distribution model evaluation results.

Metric	Weibull	Gamma	Logistic	LogNormal
Kolmogorov-Smirnov	0.0838	0.0581	0.0959	0.0292
Cramer-von Mises	3.736	1.581	2.942	0.224
Anderson-Darling	25.377	10.022	28.635	1.546
Akaike's Information Criterion	5661.043	5461.841	5841.270	5350.209
Bayesian Information Criterion	5671.629	5472.427	5851.856	5360.795

A histogram graph of 4 different distribution models is given in figure 5.
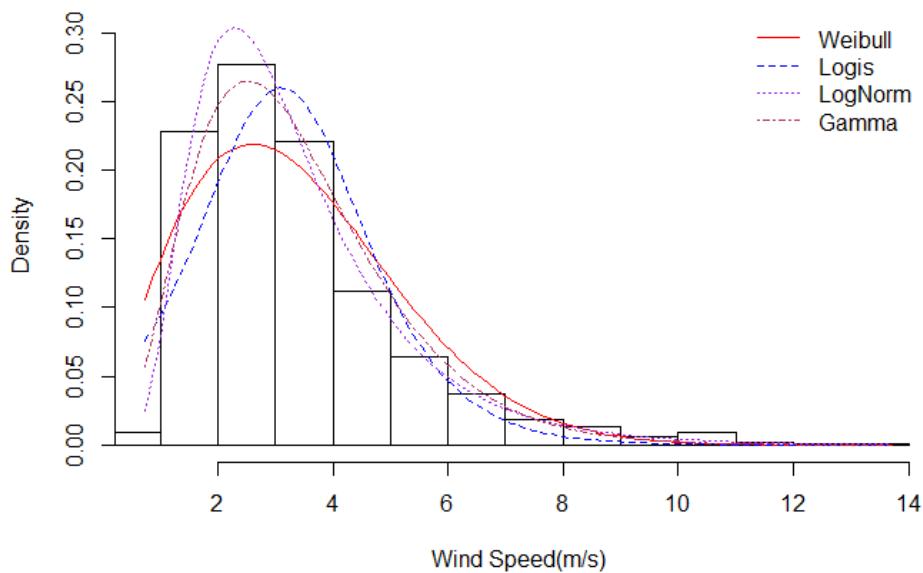
Figure 15. Graphical comparison of 4 different distribution models.

When model evaluation results in Table 2 and graphical representations in Figure 5 are evaluated together, it is seen that the most successful models for data used in the study are lognormal, gamma, Weibull and logistic distribution respectively.

4. CONCLUSION

In this study, four different distribution models were used when performing efficiency analysis before wind energy investment was made. 6-hour average wind speed data of the International Antalya Airport meteorological station was investigated as the case data. An open source software language, R, was used for statistical and graphical analysis.

The distribution models were compared according to 5 different evaluation criteria and their performance was evaluated in Table 2 and Figure 5 respectively. The results show that lognormal and gamma distributions give better results than the Weibull distribution widely used in the literature for low wind speeds. The logistic distribution has shown the worst performance.

REFERENCES

[1]. I. Kirbas and A. Kerem, "Short-Term Wind Speed Prediction Based on Artificial Neural Network Models," Meas. Control, vol. 49, no. 6, pp. 183–190, 2016.

[2]. A. Kerem, I. Kirbas, and A. Saygın, "Performance Analysis of Time Series Forecasting Models for Short Term Wind Speed Prediction," presented at the International Conference on Engineering and Natural Sciences (ICENS), 2016, pp. 2733–2739.

[3]. P. Bhattacharya and R. Bhattacharjee, "A Study On Weibull Dıstrıbutıon For Estimating The Parameters," J. Appl. Quant. Methods, vol. 5, no. 2, pp. 234–241, 2010.

[4]. M. Kurban, Y. M. Kantar, and F. O. Hocaoglu, "Weibull Dagılımı Kullanılarak Rüzgar Hız ve Güc Yogunluklarının İstatistiksel Analizi," Afyon Kocatepe Univ. J. Sci., vol. 7, no. 2, pp. 205–218.

[5]. W.-Y. Chang, "A Literature Review of Wind Forecasting Methods," J. Power Energy Eng., vol. 2, no. 4, pp. 161–168, 2014.

[6]. T. P. Chang, "Estimation of wind energy potential using different probability density functions," Appl. Energy, vol. 88, no. 5, pp. 1848–1856, 2011.

[7]. A. F. Ozdemir, E. Yıldıztepe, and M. Binar, "İstatistiksel Yazılım Gelistirme Ortamı: R," presented at the XII. Akademik Bilisim Konferansı, Mugla, 2010, vol. 1, pp. 375–379.

[8]. R Core Team, R: A Language and Environment for Statistical Computing. Vienna, Austria: R Foundation for Statistical Computing, 2014.

[9]. P. Dalgaard, Introductory statistics with R. Springer Science & Business Media, 2008.

[10]. İ. Kırbas, "Wind Speed Distribution Dataset and R Source Codes," GitHub Page, 23-Apr-2017. [Online]. Available: https://github.com/ismkir/windSpeedDistribution/. [Accessed: 24-Apr-2017].

[11]. O. Elitok, "Weibull Distributions and Its Applications," M. Sc. Thesis, Kırıkkale University Institute of Science and Technology, Kırıkkale, 2006.

[12]. D. Indhumathy, C. V. Seshaiah, and K. Sukkiramathi, "Estimation of Weibull Parameters for Wind speed calculation at Kanyakumari in India," Int. J. Innov. Res. Sci. Eng. Technol., vol. 3, no. 1, pp. 8340–8345, Jan. 2014.

[13]. A.-A. Bromideh, "Discriminating Between Weibull and Log-Normal Distributions Based on Kullback-Leibler Divergence," Istanb. Universitesi İktisat Fakültesi Ekonomi Ve Istat. Derg., no. 16, pp. 44–54, 2012.

BIOGRAPHY

İsmail KIRBAS,got his bachelors' degree in the Computer Education Department in Technical Education Faculty at Kocaeli University, Kocaeli/Turkey in 2000, his master degree in the Electronics and Computer Education at Kocaeli University in 2008, PhD degree in Electronics and Computer Education Department at Sakarya University in 2013. He is still an academic member of the Computer Engineering Department at Burdur Mehmet Akif Ersoy University. His major areas of interests are: Wireless Sensor Networks, Embedded Systems, Design of Experiments, Time Series Predictions and Mobile Programming.

A Review of Aerodynamic Shape Optimization

Tugrul Oktay[1], Metin Uzun[2]

Abstract

In this conference article a review of aerodynamic shape optimization is carried out in order to view performance of possible new aerodynamic shape optimization studies. The aim of this conference article is to determine different future aerodynamic shape optimization techniques for improvement of aerodynamic fines coefficient and flight performance. For this purpose, initially a brief definition and methods of aerodynamic shape optimization are mentioned. Then, different existing aerodynamic shape optimization types are classified and summarized. After, a brief summary of our previous shape optimization studies are listed. Finally, the results for future perspectives are presented.

Keywords: *Aerodynamics, Shape Optimization, Classification of Shapes.*

1. INTRODUCTION

First of all previous literature studies on wing aerodynamic redesign is followed. There are several studies for this purpose in the literature. For example, in [1] it was described the potential of the adjoint technique for aerodynamic shape optimization. In this way, drag reduction studies using optimization techniques for transonic flows have become important for literature. In [2] it used a morphing wing to increase the performance of a small unmanned air vehicle that was made of balsa wood ribs, a balsa torsion box and carbon-fiber spars. On the purpose of improving flight performance, the optimal wing shapes were obtained using an aerodynamic shape optimization code along with a structural morphing model. Aerodynamic, structural analysis and weight prediction were improved to design a morphing wing. In [3] it was studied about two types of technologies called as twisteron and the circulation controlled (CC) wing to provide efficient flight in the high and low speed condition. Their work present a method for decreasing the induced drag created on a CC wing by altering the blowing along the wing. In [4] it was conducted by comparing different angles of wing sweep in drag and noise reduction. Low wing sweep angle and increased wing height had lower induced drag. This has had a significant impact on the flight performance of the aircraft. In [5] it was carried out a numerical optimization to find out the potential of unconventional aircraft. It is focused on the affect of the flow nonlinearity on the aerodynamic design and induced drag of unconventional aircraft. In the methodology, a box wing, a c-tip blended wing body and a braced wing were used for optimizations.

Moreover, previous literature studies on body aerodynamic redesign is followed. For also body there are numerous studies for this purpose in the literature. For instance, in [6] it was presented a methodology for aerodynamic shape optimization in turbulent flow. This methodology is based on the three dimensional RANS equations. Constrained gradient-based optimization is applied using SNOPT. The results show that wing geometries in optimizations based on inviscid flow are deficient to on viscous analysis. In [7] it wasdescribed a new methodology using a Multi-objective Evolutionary Algortihms for aerodynamic and Radar Cross Section optimization of the wing body sections. The new method that involved the concepts of Hierarchical Topology, Asynchronous Evaluation is based on canonical evolution strategies . Analytical results indicated that this method can be a strong technique to obtain optimum airfoil geometries for unmanned air vehicles. In [8] it was described the general situation of an aerodynamic shape optimization method in different aircraft configurations (transonic and supersonic aircraft) including multiple design points, subject to geometric constraints. The Euler equations were used to determine the aerodynamic performance. The precision of the adjoint-based sensitivity information was investigated and compared by the finite difference method. In [9] it was presented a new method that can provide better performance for different missions to carry out multipoint high accuracy optimization of aircraft configurations. This method

is based on the CFD of a whole aircraft that has a detailed finite element model of the wing structure. In [10] it was studied the affect of the new methodologies on a blended wing airfoil structure. Their methodologies consists of six different studies. The initial concept is the twist-optimized baseline for all the optimizations. The mentioned studies are (Study 1) by adding airfoil shape variables, (Study 2) a trim constraint, (Study 3) a center of gravity point variable and static margin constraint, (Study 4) a bending moment constraint and (Study 5) planform design variables. The last one (Study 6) is multipoint optimization. These studies were finished using the Advanced Research Computing cluster.

Finally, previous literature studies on winglet aerodynamic design is followed. There are so many studies for this intention in the literature. For example, in [11] it was clearly found that winglet usage especially in UAVs has an important effect in reducing the drag force. The different winglets were first attached on the wing itself and compared by means of computational modeling for a wide range of angles of attack. Installing the optimized winglet, the results showed a significant improvement in the aerodynamic performance of UAV. In [12] it was investigated that large winglet and winglet flap mechanisms experimentally in large transport vehicles.

In this conference article a review of aerodynamic shape optimization is followed in order to view performance of possible new aerodynamic shape optimization studies. The aim of this conference article is to find different future aerodynamic shape optimization techniques for improvement of aerodynamic fines coefficient and flight performance. This is *one of rare studies existing in the literature* for research on novel aerodynamic shape optimization techniques.

2. AERODYNAMIC SHAPE OPTIMIZATION CLASSIFICATION

2.1. Wing Shape

Wing shape optimization is an important aeronautical application using more efficient and more efficient production of air vehicles. Shape optimizations significantly improve the flight performance of the aircraft and achieve simpler structures and minimize fuel consumption. In [1] it was described the potential of the adjoint technique for aerodynamic shape optimization. In this way, drag reduction studies using optimization techniques for transonic flows have become important for literature. Drag reduction of RAE2822 airfoil is introduced in transonic flow for validation. They studied on two test cases both called as "Aeroshape" to show the potential of the adjoint technique. First case is the 2D multi-point drag optimization under geometrical as well as physical constraints, and the second one is wing body optimization of a supersonic commercial aircraft. As a result, the efficiency of the adjoint technique was demonstrated for aerodynamic shape optimization of a supersonic aircraft in inviscid flow where a lot of CPU time has been saved compared to brute force approaches. In [2] it was used a morphing wing to increase the performance of a small unmanned air vehicle that was made of balsa wood ribs, a balsa torsion box and carbon-fiber spars. On the purpose of improving flight performance, the optimal wing shapes were obtained using an aerodynamic shape optimization code along with a structural morphing model. Aerodynamic, structural analysis and weight prediction were improved to design a morphing wing. At the result, their works show that least decreasing of wing drag up to 30% could be provided by morphing the wing. In [3] it was presented a method for decreasing the induced drag created on a CC wing by altering the blowing along the wing. The results of CFD study show that the more efficiency can be provided with the way of decreasing the induced drag on a CC wing. Blowing method showed an 11% improvement in induced drag and a 6.5% reduction in total drag. In [4] it was conducted by comparing different angles of wing sweep in drag and noise reduction. Low wing sweep angle and increased wing height had lower induced drag. This has had a significant impact on the flight performance of the aircraft. Firstly, linear aerodynamic performance and stability analysis was accomplished for the initial design. Then, the aerodynamic characteristics and efficiency of the airfoil section, the wing, and the full configuration were determined with CFD. In this work, aerodynamic efficiency optimization by wingspan is focused only on. The combination of improvements proposed and the increase of wingspan and AR, would lead to a greater range, an endurance increase and to a more economical and eco-friendly aircraft. In [5] it was carried out a numerical optimization to find out the potential of unconventional aircraft. It is focused on the effect of the flow nonlinearity on the aerodynamic design and induced drag of unconventional aircraft. In the methodology, a box wing, a c-tip blended wing body and a braced wing were used for optimizations. At the result, the box wing has 34.1%, C-tip blended wing body has 36.2%, and braced wing has 40.3% less induced drag than a similar to baseline tube and wing.

2.2. Body Shape
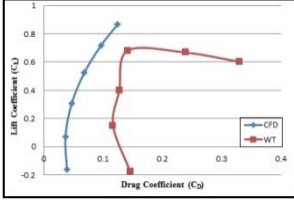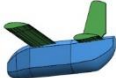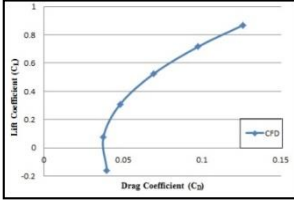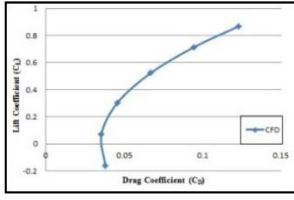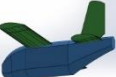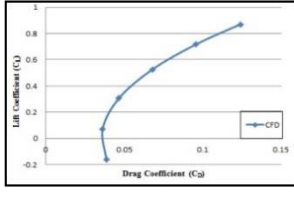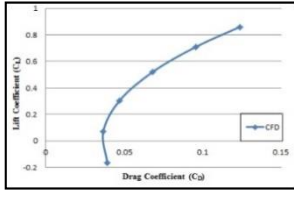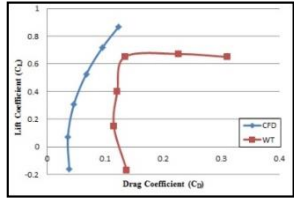
Body shape optimization studies are very important for the autonomous performance of air vehicles. Flight parameters such as aircraft resistance, fuel consumption and maximum range can be improved by using the different equations in the literature and due to the shape variations of the air gap on the nose, tail and other body elements. For instance in [6] it was presented a methodology for aerodynamic shape optimization in turbulent flow. This methodology is based on the three dimensional RANS equations. Constrained gradient-based optimization is applied using SNOPT. The results show that wing geometries in optimizations based on inviscid flow are deficient to on viscous analysis. This methodology also reduces wave drag and weight in order to have a minimal effect on wing structure. At last this method provided that could be able to accommodate major changes in the wing body. In [7] it was described a new methodology using a Multi-objective Evolutionary Algorithms for aerodynamic and Radar Cross Section optimization of the wing body sections. The new method that involved the concepts of Hierarchical Topology, Asynchronous Evaluation is based on canonical evolution strategies. Analytical results indicated that this method can be a strong technique to obtain optimum airfoil geometries for unmanned air vehicles. Also it can be seen from the results that the new method is efficient and produces optimal and Pareto non-dominated solutions. In [8] it was described the general situation of an aerodynamic shape optimization method in different aircraft configurations (transonic and supersonic aircraft) including multiple design points, subject to geometric constraints. The Euler equations were used to determine the aerodynamic performance. The precision of the adjoint-based sensitivity information was investigated and compared by the finite difference method. In computing the number of processors increases, the mesh becomes progressively smaller sections separately. The rate of surface region to volume rises and the parallel performance is degraded. In [9] it was presented a new method that can provide better performance for different missions to carry out multipoint high accuracy optimization of aircraft configurations. This method is based on the CFD of a whole aircraft that has a detailed finite element model of the wing structure. The results revealed that while the single-point optimization reduced the weighted average fuel burn by just 1.7%, the new method could reduce it by 6.6%. In [10] it was studied the affect of the new methodologies on a blended wing airfoil structure. Their methodologies consists of six different studies. The initial concept is the twist-optimized baseline for all the optimizations. The mentioned studies are (Study 1) by adding airfoil shape variables, (Study 2) a trim constraint, (Study 3) a center of gravity point variable and static margin constraint, (Study 4) a bending moment constraint and (Study 5) planform design variables. The last one (Study 6) is multipoint optimization. These studies were finished using the Advanced Research Computing cluster. Consequently, this study reveals that aerodynamic shape optimization could be advantageous for the design of BWB configurations. The optimal combination of wing twist, and airfoil reflex to obtain the lowest drag while satisfying trim, stability and structural constraints is not obvious, but numerical optimization can help designers find the best possible configuration.

2.3. Winglet Shape

The addition of winglets in air vehicles significantly reduces fuel consumption by increasing the carrying capacity by reducing the induced drag. Winglet design, is an important parameter in reducing the flow disturbances on the wing, prevent vortices due to pressure difference in aircraft wings. In [11] it was clearly found that winglet usage especially in UAVs has an important effect in reducing the drag force. The different winglets were first attached on the wing itself and compared by means of computational modeling for a wide range of angles of attack. Installing the optimized winglet, the results showed a significant improvement in the aerodynamic performance of UAV. In [12] it was investigated that large winglet and winglet flap mechanisms experimentally in large transport vehicles. İt is produced 1:32 models and the work was done at 7 degrees of attack angle and 0.5×10^6 Reynolds number. The aerodynamic parameters of different winglet types are placed on the trailing edge were investigated. The rotating winglet mechanisms create additional vortices. In [13] it was examined 3 different winglet configuration such as no Winglet, whitcomb Winglet, Optimized Winglet. Graphs of change of attack angle and cl / cd and root bending momentum graphs of winglet design investigated are given. Optimized winglet design increase endurance about %33.96 and Emax value %15.61. In [14] it was compared split winglet design with previously made winglets in sailplanes by numerical studying. Cross-country flight, making the positive impact on the flight performance is discussed in detail. The use of split winglet in has significantly increased cross country speed and decrease Sink Rate value. In [15] optimum design was tried to be achieved investigating the lift and drag forces of two different winglet designs. Examples of research done, without winglet, elliptical winglet 45^0, elliptical winglet 60^0, Semicircular winglet 45^0, Semicircular winglet 60^0. According to other winglet designs, elliptical winglet 45^0 was found that it has a higher lift force.
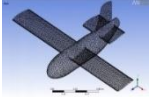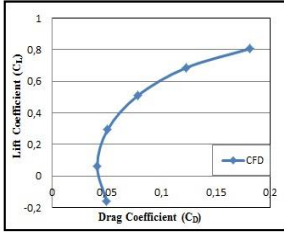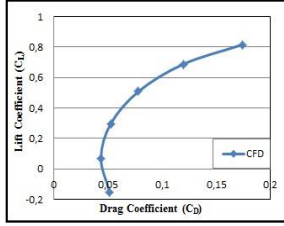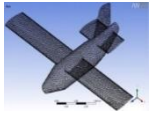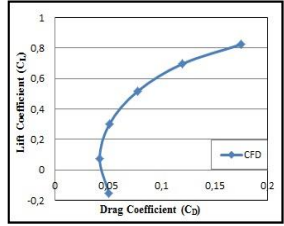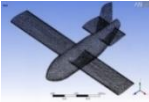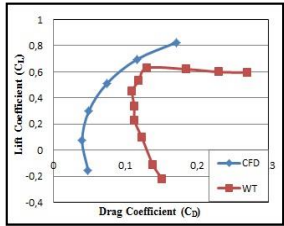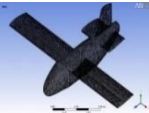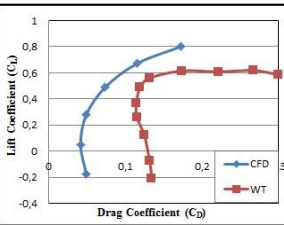
3. OUR STUDIES FOR AERODYNAMIC SHAPE OPTIMIZATION

Table 1. Optimization Results

Tailcone	CFD	C_L - C_D	E_{max}
Production Aircraft			7.72
Haack Series C=0.3			7,54
Parabolic			7.825
Inverse Parabolic			7.74
Elliptical			7.65
Conical			7.828

Different [16] tail cones have been obtained by using different equations in the literature to increase the autonomic performance of the aircraft. Studies are primarily in the CFD analysis program were obtained and numerical data for verification of the reduced models has also been tested in the wind tunnel. Aerodynamic parameters of different tail design designs for the aircraft were examined in Table 1 to improve flight performance. According to the initial design, it has been found that the value of Emax increases approximately 1.4%.

Table 2. Optimization Result

Nosecone	CFD	C_L - C_D	E_{max}
Elliptical			6.33
Conical			6.22
Bi-Conical			6.36
Spherically Blunted Tangent Ogive			6.54
Produced Aircraft			6.35

In [17] it was given for this nose shapes, Wind Tunnel (WT) and CFD results CFD drawings, and E_{max} values in Table 2. Aerodynamic parameters were obtained both numerically and experimentally. As can be seen easily from the table given the spherically blunted tangent ogive E_{max} value was the highest. Therefore, maximum durability and flight performance of the aircraft, approximately 3% of has improved.

4. CONCLUSIONS

In this conference article an evaluation of aerodynamic shape optimization was followed in order to view performance of possible new aerodynamic shape optimization studies. The purpose of this conference article was to decide different future aerodynamic shape optimization techniques for improvement of aerodynamic

fines coefficient and flight performance. After examining several approach and also one more evaluating our previous studies we decided that winglet is an opportunity to improve aerodynamic fines of our UAVs.

ACKNOWLEDGEMENT

REFERENCES

[1].   Brezillon, J., Gauger, N.R., 2D and 3D aerodynamic shape optimization using the adjoint approach. Aerospace Science and Technology 8. (715–727), (2004)

[2].   Gamboa, P., Vale, J., Lau, F. J. P. Suleman, A., Optimization of a Morphing Wing Based on Coupled Aerodynamic and Structural Constraints. AIAA Journal. Vol. 47, No. 9, September 2009.

[3].   Alley, N.R., Phillips, W.F., Minimizing Induced Drag with Spanwise Blowing Variation on a Circulation-Controlled Wing. Journal of Aircraft. Vol. 47, No. 6, November–December 2010.

[4].   Abbas, A., Vicente, J de. Valero, E., Aerodynamic technologies to improve aircraft performance. Aerospace Science and Technology 28. 100-132 (2013)

[5].   Gagnon,H., Zingg, D.W., Euler-Equation-Based Drag Minimization of Unconventional Aircraft Configurations. Journal Ofaırcraft. Vol. 53, No. 5, September-October 2016.

[6].   Osusky, L., Buckley, H., Reist,T., W. Zingg. D., Drag Minimization Based on the Navier–Stokes Equations Using a Newton–Krylov Approach. Aıaa Journal. Vol. 53, No. 6, June 2015.

[7].   Lee, D.S., Gonzalez, L.F., Srinivas, K., Periaux, J., Robust evolutionary algorithms for UAV/UCAV aerodynamic and RCS design optimisation. Computers & Fluids 37 (2008) 547–564.

[8].   Reuther, J. J., Rimllnger, M. J., Saunders, D., Constrained Multipoint Aerodynamic Shape Optimization Using an Adjoint Formulation and Parallel Computers, Part 2. Journal of Aircraft. Vol. 36, No. 1, January-February 1999.

[9].   Liem, R. P., Kenway, G. K. W., Martins, J. R. R. A., Multi-mission Aircraft Fuel-Burn Minimization via Multipoint Aerostructural Optimization. Aıaa Journal Vol. 53, No. 1, January 2015.

[10].   Lyu, Z., Martins, J. R. R. A., Aerodynamic Design Optimization Studies of a Blended-Wing-Body Aircraft. Journal of Aircraft. Vol. 51, No. 5, September–October 2014

[11].   Panagiotou, P., Kaparos, P., Yakinthos, K., Winglet design and optimization for a MALE UAV using CFD. Aerospace Science and Technology 39. 190-205 (2014)

[12].   Allen, A., Breitsamter., C., Transport Aircraft Wake Influenced by a Large Winglet and Winglet Flaps. Journal of Aircraft. Vol.45, No.2, March-April 2008.

[13].   Weierman, J., Jacob J. D., Winglet Design and Optimization for UAVs. 28th AIAA Applied Aerodynamics Conference. 28 June-1 July 2010, Chicago, Illinois.

[14].   Krebs, T., Bramesfeld, G., An Optimization Approach to Split-Winglet Design for Sailplanes. 54th AIAA Aerospace Sciences Meeting. 4-8 January 2016, San Diego, California, USA.

[15].   Azlin, M.A., Taib, C.F.M., Kasolang, S., Muhammad, F.H., CFD Analysis of Winglets at Low Subsonic Flow. Proceedings of the World Congress on Engineering, 2011, Vol I, WCE 2011, July 6 - 8, 2011, London, U.K.

[16].   Oktay, T., Uzun, M., Aerodynamic Tailcone Shape Optimization for Autonomous Navigation Performance Maximization of Morphing Aerial Robot. Engineering and Natural Science, 24-28 May 2016, Sarajevo, Bosnia and Herzegovina.

[17].   Oktay, T., Uzun, M., Yılmaz, İ., Konar, M., Aerodynamic Nose Shape Optimization for Performance Maximization of Morphing Autonomous Aerial Robot. Engineering and Natural Science, 24-28 May 2016, Sarajevo, Bosnia and Herzegovina.

Medicinal Plants Commonly Used in Anatolian Folk Medicine

Belgin Cosge Senkal[1], Cuneyt Cesur[1], Tansu Uskutoglu[1], Hulya DOGAN[2]*

Abstract

In times when medicine has not developed, the method people used to treat their diseases with their own special efforts is regarded as folk medicine. The public is constantly applying for various practices to treat existing diseases since ancient times. One of these practices is to make medicines from plants. Anatolia is a place where many peoples have settled and various civilizations have been established. For this reason, it has a rich culture and civilization. Also, folk medicine and medicines is a part of this richness. A large number of medicinal plants (Ecbalium elaterium, Sideritis sp., Salvia sp., Lauris nobilis, Malva neglecta, Tilia sp., Urtica dioica, Melissa officinalis, Foeniculum vulgare etc.) are used in Anatolian folk medicine. This wealth of Anatolia having more than ten thousand plant species diversity is of great importance for human health and treatment. Thousands of plant species that the medical aspect has not been discovered at present are held to promise great for diseases that are not yet treatable.

Keywords: *Folk medicine, medicinal plants, Anatolia*

1. INTRODUCTION

Anatolia is a piece of land where various civilizations was founded since ancient times. Therefore, Anatolia is a treasure of culture and civilization. An important part of this treasure is the folk medicine and folk remedies. The folk medicine is the whole of medical practices related to beliefs, traditions and value systems of societies [1].

Folk medicine is a part of cultural diversity which is the most characteristic feature of Anatolia. The effects of ancient Greek, Roman and Islamic civilizations are observed in traditional medical practices in Anatolia. In the formation of traditional Anatolian folk medicine, it became a great contribution of Turkish who came to Anatolia after 1071. The Turkish brought shaman cultures of Asian societies to Anatolia. Shamans served both as clergy and physicians in ancient Turkish societies. The shamans identified incest, dancing, and singing, illnesses caused by evil spirits, and then tried to treat them with their own primitive methods. Kutatgu Bilig and Divan-I Lugat-it Turk written in the 11th century mentioned folk physicians as "otacı", "efsuncu", and "idisci". The "ocaklar" where traditional treatment practices are made still exist in many parts of Anatolia [2].

As in the past, folk medicine and folk remedies also maintain their importance today. In the preparation of folk remedies, mostly local plants are used. In fact, there are some similarities between modern medicine's treatment and care techniques and folk medicine. As it is all over the world, plants known as medicinal plants have a growing use in the country in recent years.

2. MEDICINAL PLANT

A plant that carries bioactive substances or substances with therapeutic properties is called a medicinal plant [2]. The part or organ bearing bioactive substance of a medicinal plant is called as drug. Raw materials used in the production of herbal drugs. Leaves, flowers, shells, roots, rhizomes, tubers, bulbus, wood, seeds, fruits and whole plant parts of plants can be evaluated as drugs [2-4]. While all organs of some plants are available as drugs, only certain organs of some are suitable for use as drugs (Table 1).

---

[1] Corresponding author: Bozok University, Field Crops Department, Merkez/Yozgat, Turkey. bcosgesenkal@gmail.com*

[2] Bozok University, Vocation School of Technical Science-Yozgat/TURKEY

Table 12. Classification of the drugs according to the organs from which they are obtained

The name of drug	The example of plant
Flower (Flos)	safflower, linden, chamomile, saffron, jasmine
Fruit (Fructus)	anise, dill, jujube, black pepper, cumin, coriander, rosehip, fennel, vanilla
Seed (Semen)	fenugreek, nigella, mustard, poppy, coffee, cocoa, cardamom, mahalep cherry, sesame
Root (Radix)	ginseng, valerian, angelica, liquorice plant, ginseng, alkanet, angelica
Rhizoma (Rhizoma)	yellow gentian, galangal, madder, ginger, turmeric
Bark (Cortex)	cinnamon, tarragon
Tuber (Tuber) and Onion (Bulbus)	snowdrop, salep, garlic
Leaf (Folium)	sage, rosemary, tea, laurel, basil, ginkgo, thyme, mint

According to the World Health Organization report, about 21 000 of about 70 000 plants used worldwide for medical purposes are used in the pharmaceutical industry. In our country, only about 1000 of most naturally grown species are used for medical purposes. The number of plants registered in pharmacopoeia is more than 200 [3].

There are 1 251 genus and more than 12 000 species and subspecies taxa belonging to 174 families in Turkey Flora. Also, Turkey is the gene center of many plants. Because of the rich plant species and diversity of the flora, it has a great economical potential in terms of medicinal plants cultivated and collected from nature. According to the ethnobotanical studies carried out in Turkey; average 10-12% of the natural plant species growing around the local people are used for various purposes [5].

Plants are very important part of natural drug raw material resources. The well-known and widely used natural compounds derived from plants are quite a few. These include morphine, digoxin, papaverine, caffeine, atropine, quinidine, ergotamine and many other active ingredients [2,6].

3. MEDICINAL PLANTS COMMONLY USED IN ANATOLIAN FOLK MEDICINE

The most important source of natural medicines used in traditional treatment methods is plants. Today, although traditional treatment methods has decreased, it continues its existence. Some of these methods are scientifically accepted to be useful, and even studies in the field of scientific medicine make use of the data of folk medicine. The use of plants and medicines prepared for them in the treatment of many diseases has reached to present day in Anatolia, one of the first regions where human beings have settled down, and in the world. Approximately 500 plant species in Turkey are utilized in folk medicine or traditional medicine applications [2].

The plant used in the treatment of many diseases is either obtained from plants grown in its natural environment or from foods that are produced by the people themselves. The pictures of some medicinal plants used in the treatment of some diseases and collected from nature in Turkey and are presented in Figure 1. Some medical plants used in Anatolian folk medicine and their traditional use purposes are given in Table 2 [7,8].

Helichrysum sp.   *Salvia sp.*   *Achillea millefolium*

Crocus sp.   *Sideritis sp.*

Anthemis nobilis   *Papaver rhoeas*

Coriandrum sativum   *Hypericum sp.*

Figure 1. Pictures of some medicinal plants spreading in natural flora of Turkey

Table 2. Some of the most important medicinal and aromatic plants traditionally used for treatment in Turkey

Latin name	Turkish name	The purpose of traditional use
Polygonum bistorta	Kurtpencesi	Liver disease and cirrhosis treatment
Salvia officinalis	Tıbbi adacayı	Antiseptic and stimulant
Hypericum perforatum	Kantaron	Wound healing
Melissa officinalis	Ogulotu	Relaxing and diarrhea-cutting
Zingiber officinale	Zencefil	Against stomach pain and nausea
Cassia angustifolia	Sinameki	Correction of constipation and intestinal laxity
Ocinium bacilicum	Feslegen	
Thymus, *Origanum*, *Satureja* and *Thymbra* sp.	Kekik	Gastric, digestive aids, spasm remover, secretion enhancer, antioxidant, degasser and diuretic
Coriandrum sativum	Kisnis	
Cuminum cyminum	Kimyon	
Ecbalium elaterium	Acıkavun	Sinusitis treatment
Sideritis sp.	Dag cayı	Against the mouth
Lauris nobilis	Defne	Relaxing and digestive
Malva neglecta	Ebegumeci	Lung and respiratory disorders
Tilia sp.	Ihlamur	Against colds
Urtica dioica	Isırgan otu	Relieving rheumatism and arthralgia
Foeniculum vulgare	Rezene	Carminative and diuretic
Artemisia absinthium	Yavsan otu	Analgesic and anti-inflammatory
Matricaria chamomilla	Papatya	Relaxing, antiseptic and gastric
Slybum marianum	Deve dikeni	Hepatitis and liver ailments
Achillea millefolium	Civan percemi	Hemostatic
Tribulus terrestris	Demirdikeni	Heart and vascular disorders
Nigella sativa	Corekotu	Asthma and flu
Glycyrrhiza glabra	Meyan koku	Antitussive
Urginia maritima	Ada soganı	Cough and heart condition
Silybum marianum	Deve dikeni	Diuretic and appetizing
Althea officinalis	Hatmi	Expectorant
Cichorium intybus	Hindiba	Diuretic and liver diseases

4. CONCLUSIONS

Drugs prepared from many medical herbs that have been traditionally used for health purposes in Anatolia and the world for centuries are in the treatment of many diseases. This wealth of Anatolia having more than 10 000 plant species diversity is of great importance for human health and treatment. There are thousands of plant species and varieties that have not yet been explored for medical reasons. These plants offer great promise for diseases that are not yet treatable.

REFERENCES

[1]. O. Turkdogan, *Kültür ve saglık-hastalık sistemi*. MEB Yayınları:2213, İstanbul, Turkey: 1991.
[2]. H. Baydar, *Tıbbi ve Aromatik Bitkiler Bilimi ve Teknolojisi*. Süleyman Demirel Üniversitesi, Ziraat Fakültesi Yayın No:51, 2013, p. 303.
[3]. A Kaya, Tıbbi bitkiler ve etnobotanik calısmalar. Bitkilerle Tedavi sempozyumu, 5-6 Haziran 2010, Zeytinburnu, Bildiriler Kitabı, 2011, p. 11-18.
[4]. N. Arslan, B. Gurbuz and A. Gumuscu, *Tıbbi Bitkiler İsim Kılavuzu*. Ankara Üniversitesi Ziraat Fakültesi Yayın No:1530, 2002, p. 180.
[5]. N. Arslan, Endemik Tıbbi Bitkilerimiz. II. Tıbbi ve Aromatik Bitkiler Sempozyumu, 23-25 Eylül 2014, Yalova, Bildiriler Kitabı, 2014, p. 9-21.
[6]. S. Harput, Yeni ilac gelistirme calısmalarında tıbbi bitkiler. Bitkilerle Tedavi sempozyumu, 5-6 Haziran 2010, Zeytinburnu, Bildiriler Kitabı, 2011, p. 45-50.
[7]. N. Arslan, B. Gurbuz and A. Gumuscu, *Acıklamalı Tıbbi ve Aromatik Bitkiler Rehberi*. Ankara Üniversitesi, Ziraat Fakültesi Yayın No: 1620, 2005, p. 385.
[8]. A. Demirhan Erdemir, *Sifalı Bitkiler Dogal İlaclarla Geleneksel Tedaviler*. Alfa Yayınları, 2010, p.600.

Solar Heating of a Concrete Block

Ersan Guray[1]

Abstract

The amount of sun radiation varies with the time in the day referring to the geographical location on the earth at a specific date of a year. In this study, a numerical simulation is performed to observe the heat propagation in a concrete block which is exposed to daily solar radiation and convection under clear sky conditions. The location is chosen to be city of Mugla in Turkey at a usual summer day. A numerical scheme is developed with finite difference formulation and varying solar radiation is contributed into the calculations at each time step. Fully implicit equations are solved by Gauss-Seidell iteration. Temperature variation at the top and bottom surfaces is given at a figure.

Keywords: *solar radiation, concrete, heating, finite difference method*

1. INTRODUCTION

Heat propagates through a typical homogeneous medium with a constant diffusion rate. A temperature difference does not occur between any two points of the surface of the structure that is heated or cooled a certain period of time. In other words, whole surface will have a constant temperature in the case of a single homogeneous medium. This fact, although, is not really in consideration of engineering applications solely. However, the formation of temperature gradients on the surface, provides a great advantage in civil engineering applications. Subsurface cracks and voids occurrence can be detected by measurement of the temperature difference on the surface. Morely, the depth and the amount of the crack formation can be determined by the temperature contrasts on the surface. In this study, a numerical tool is developed to make analysis on heat propagation on the surface of a concrete slab.

2. FORMULATIONS

The concrete slab has a length of L in x direction and a height of H in y direction. Solar radiation and convection act on the top surface, however, the bottom surface is exerted only convection. The left and right sides of the layer is considered to be heat insulated.

Heat is transferred through the layer by conduction and the related equation of motion is given:

$$\rho c_p \frac{\partial T}{\partial t} = k \nabla^2 T \qquad (1)$$

Where ρ is the density, c_p is the specific heat, k is the heat transfer coefficient of the material. T denotes temperature variable as a function of position of any point, x,y and the time, t. $\nabla^2 = \frac{\partial^2}{\partial x^2} + \frac{\partial^2}{\partial y^2}$ is the laplacian operator.
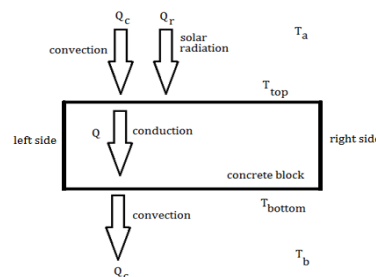
Figure 16. Model of the heat problem

[1] *Corresponding author: Mugla Sıtkı Kocman University, Faculty of Engineering, Department of Civil Engineering, Mugla, Turkey. ersan.guray@mu.edu.tr*

The equation of motion is subjected to the boundary conditions:

$$k\frac{\partial T_{top}}{\partial y} = Q_c + Q_r = h(T_a - T_{top}) + Q_r \quad \text{at the top surface} \tag{2}$$

$$k\frac{\partial T_{bottom}}{\partial y} = Q_c = h(T_{bottom} - T_b) \quad \text{at the bottom surface} \tag{3}$$

$$\frac{\partial T}{\partial x} = 0 \text{ at the left and right sides} \tag{4}$$

And for the convenience, the initial temperature distribution is given a function , f(x,y):

$$T(x, y, 0) = f(x, y) \tag{5}$$

2.1. Fully Implicit Finite Difference Scheme with Gauss Seidell Iteration

To use the finite difference formulation for the numerical approximation, the problem domain is discretized with a uniform grid, where the stepsizes in x and y directions are taken to be equal, Δx. Numbering started from the left bottom and driven in top surface direction and from left to right. Since the boundary conditions all consist of derivative terms, there exists virtual nodes out of the domain. Interior and boundary nodes satisfy the heat equation, implicit finite difference formula is written for them:

$$\frac{T_{i,j}^{k+1} - T_{i,j}^{k}}{\Delta t} = \frac{k}{\rho c_p} \frac{T_{i+1,j}^{k+1} + T_{i-1,j}^{k+1} + T_{i,j+1}^{k+1} + T_{i,j-1}^{k+1} - 4T_{i,j}^{k+1}}{\Delta x} \tag{6}$$

Where i and j denominate indices in x and y directions, k represents time index. Implicit formula is solved by Gauss Seidel iterations such that, where n is the iteration number:

$$T_{i,j}^{n+1} = \frac{T_{i,j}^{k} + \alpha(T_{i+1,j}^{n+1} + T_{i-1,j}^{n+1} + T_{i,j+1}^{n+1} + T_{i,j-1}^{n+1})}{1 + 4\alpha} \tag{7}$$

Where $= \frac{k\Delta t}{\rho c_p \Delta x}$. After a successive number of iterations, $max|T_{i,j}^{n+1} - T_{i,j}^{n}| \leq e$ where e is the tolerance error such that $T_{i,j}^{k+1} = T_{i,j}^{n+1}$ is set.

Top virtual nodes satisfy the boundary condition given in eq. It gives an approximation for the values at virtual nodes such that:

$$k\frac{T_{i,j+2}^{k+1} - T_{i,j}^{k+1}}{2\Delta x} = h(T_a^{k+1} - T_{i,j+1}^{k+1}) + Q_r^{k+1} \tag{8}$$

and

$$T_{i,j+2}^{k+1} = T_{i,j}^{k+1} + \frac{2\Delta x}{k}(h(T_a^{k+1} - T_{i,j+1}^{k+1}) + Q_r^{k+1}) \tag{9}$$

Virtual nodes at the bottom satisfy the boundary condition such that:

$$k\frac{T_{i,j}^{k+1} - T_{i,j+2}^{k+1}}{2\Delta x} = h(T_{i,j+1}^{k+1} - T_b^{k+1}) \tag{10}$$

and

$$T_{i,j}^{k+1} = T_{i,j+2}^{k+1} + \frac{2\Delta x}{k}h(T_a^{k+1} - T_{i,j+1}^{k+1}) \tag{11}$$

Where $T_{i,j+1}^{k+1}$ denotes for the boundary nodes at the current time step. At the side walls, heat isolated conditions are to be satisfied such that:

$$\frac{T_{i+1,j}^{k+1} - T_{i-1,j}^{k+1}}{2\Delta x} = 0 \tag{12}$$

and

$$T_{i-1,j}^{k+1} = T_{i+1,j}^{k+1} \text{ for the left side virtual nodes,} \tag{13}$$

$$T_{i+1,j}^{k+1} = T_{i-1,j}^{k+1} \text{ for the right side virtual nodes.} \tag{14}$$

While iterating the eq. the boundary conditions are applied at each iteration with the updated inner and boundary nodes' updated temperature values. Notice that nodes at the corners are not associated with someother nodes' information.

2.2. Solar Radiation Calculations

Solar radiation is a time dependent, unsteady function such that it must be determined at each time level depending on the geographic location, time of the year and the elevation of the place. Other than solar emitting, block's absorption depends on the blocks lateral and azimuthal orientation. In the absence of the atmosphere, the radiation is called extraterrestrial that the extraterrestrial radiation is:

$$I_S = I_{SC}\left(1 + 0.033\cos\frac{360n}{365}\right) \tag{15}$$

Where $I_{SC} = 1353\ W/m^2$ is the solar constant and n is the day of the year, for which $1 \leq n \leq 365$. The solar radiation incident on a horizontal plane is the normal incident solar radiation such that;

$$I_0 = I_S \cos\theta_z \tag{16}$$

θ_z is the angle of incidence of a beam radiation on a horizontal surface given as:

$$\cos\theta_z = \cos\varphi\cos\delta\cos\omega + \sin\varphi\sin\delta \tag{17}$$

Here, φ is the lattitude of the location, δ is the declination angle such that:

$$\delta = 23.45\sin\left(360\frac{n+284}{365}\right) \tag{18}$$

And ω is the hour angle, the angular displacement of the sun east or west of the local meridian due to rotation of the earth such that;

$$\omega = 15(T_{SOLAR} - 12) \tag{19}$$

Where T_{SOLAR} is the solar time and calculated by:

$$T_{SOLAR} = T_{ST} + (-4(L_{ST} - L_{LOC}) + E)/60 \tag{20}$$

T_{ST} is the standard time in terms of hours, L_{ST} is the standard meridian for the local time zone, L_{LOC} is the longitude of the location and E is a variable calculated by (Spencer,1971):

$$E = 229.2(0.000075 + 0.001868\cos B - 0.032077\sin B - 0.014615\cos 2B - 0.04089\sin 2B) \tag{21}$$

where $B = 360\,(n-1)/365$.

The scattering and absorption of solar radiation depends on not only the time but also the effects of atmosphere. Solar radiation incidence is multiplied with a transmittance variable, clear sky horizontal beam radiation is obtained such that:

$$I_{CS} = \tau I_0 \tag{22}$$

Where τ is the atmospheric transmittance for the beam radiation given as(Hottel, 1976):

$$\tau = a_0 + a_1 e^{(-k/\cos\theta_z)} \tag{23}$$

Here, a_0, a_1 and k are constants for standard atmosphere with 23 km visibility and calculated by the uncorrected constants, a_0^*, a_1^* and k^* given as $a_0^* = 0.4237 - 0.00821(6 - A)^2$,$a_1^* = 0.5055 - 0.00595(6.5 - A)^2$ and $k^* = 0.2711 - 0.01858(2.5 - A)^2$ where A is the altitude of the observer in kilometers. a_0, a_1 and k are determined by correction factors, r_0, r_1 and r_k determined from table given at (Hottel, 1976) as $a_0 = r_0 a_0^*$, $a_1 = r_1 a_1^*$ and $k = r_k k^*$.

3. AN OBSERVATION AT MUGLA PROVINCE

A case study is held in this part of the study. In Mugla, Turkey, the daily low temperature is 19.7 ^{0}C and the daily high temperature is 33.5 ^{0}C. (table), in July. If the temperature is considered to be typically halfway at 10 a.m and 10 p.m and the highest temperatures occur to be in the afternoon, a sinusoidal function to model the daily temperature variation versus seconds after midnight is to be:

$$T(t) = \frac{T_{max} - T_{min}}{2}\sin\left(\frac{2\pi}{period}(t - t_{av})\right) + \frac{T_{max} + T_{min}}{2} \tag{24}$$

then

$$T(t) = 6.9\sin\left(\frac{2\pi}{86400}(t - 36000)\right) + 26.6 \tag{25}$$

The ambient temperatures above and below the concrete block are assumed to be equal and obtained by the formula given. Maximum and minimum average temperature values are used to have a reference for constructing an average daily ambient temperature variation curve. Curve is set to be sinusoidal with a period

of 1 day or 86400 seconds ($period$) which starts at midnight(12 am) and the t_{av} is the time when the temperature is on the daily average.

Table 13. Temperature data records of Mugla. Data is provided by Meteorology Department of Turkey

MONTH	J	F	M	A	M	J	J	A	S	O	N	D
Max.Average Temperature(°C)	10	11	14.3	18.7	24.3	29.8	33.5	33.6	29.4	23	16.5	11.5
Average Minimum Temperature(°C)	1.6	1.9	3.6	6.9	11.2	16.1	19.7	19.7	15.2	10.1	5.7	3.2

The convection at the top and the bottom surfaces of the block is directly related with the wind speed close to the surfaces. The convective heat transfer coefficient of air is calculated from the empirical relationship:

$$h = 10.45 - v + 10\sqrt{v} \tag{26}$$

where v is the speed of the wind in terms of m/s. Here in this study, the convective heat coefficient is taken as $h = 20\ W/m^2K$ corresponding to a speed of wind of 1 m/s approximately.
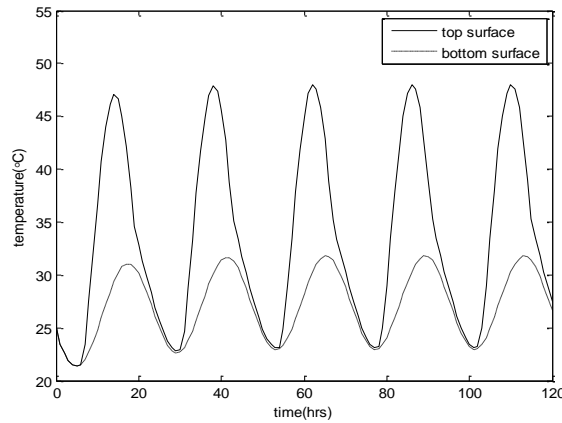
Figure 2. Temperature variation on the surfaces
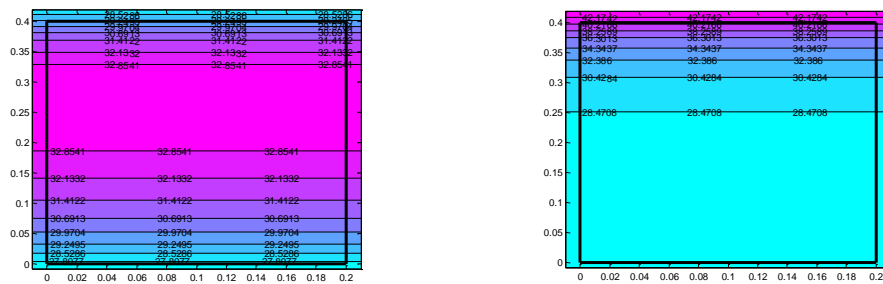
Figure 3. Midnight and noon temperature distributions

REFERENCES

[1]. John A. Duffie and William A. Beckman, Solar Engineering of Thermal Processes, 4th Edition, ISBN: 978-0-470-87366-3.
[2]. Spencer, J.W., Fourier Series Representation of the Position of the Sun, Search,2(5),172,1971.
[3]. McAdams W.H., Heat transmission, McGraw-Hill series in chemical engineering, Edition 3, Publisher McGraw-Hill, 1954.
[4]. Hottel, H.C., A Simple Model for Estimating the Transmittance of Direct Solar Radiation Through Clear Atmospheres, Solar Energy, 18,129,1976.

Investigation of Existing Coastal Problems of Bursa Province in the Sea of Marmara

Adem Akpınar[1], Recep Emre Cakmak[2], Halid Jafali[3]

Abstract

This study aims to investigate the status of existing coastal structures along the coastline of about 115 km along the Bursa Coast of Marmara Sea. It plans to investigate if there exist any problems associated with the structures, presenting those problems, and possible solutions to solve them. Within this goal, existing coastal structures and usage status of coastal area were examined and it was discovered that some applications put in place without proper planning contributed to some problems in coastal areas. Mainly, four types of coastal problems were determined along the Bursa coast. The first problem being the accumulation of sediments on one side of a structure and erosion on the other due to the structure interrupting longshore sediment transport. This case can be observed in coastal areas around Karacabey region where two fishing ports are located. The second problem noticed is the filling of harbors constructed without taking into account longshore sediment transport with sediments and therefore reaching a state where they can have no longer function. An example to this would be a harbor area built on the shore of Eskel. The third is interventions to coastal areas without regard to wave-structure interaction in the coastal zone. This problem was observed at Kucukkumla beach where erosion formed due to concrete block platforms built parallel to the coastline and on the beach which cause reflection problems. I-shaped groins perpendicular to the coast, formed with concrete blocks removed from these concrete platforms contributed to keeping the sand on the coast from eroding away, however, some of them were observed to be unnecessary. The fourth problem is the capsizing of boats due to agitation in fishing harbors. This is due to the construction of harbors without detailed analysis of winds and wind generated waves.

Keywords: Coastal Infrastructure, Coastal Problems, Lack of planning, Bursa coasts

1. STUDY AREA

The study area includes the coastal area of Bursa extending from Balikesir-Bursa province border in the west to the Bursa-Yalova province border on the northern coast of Gemlik Gulf in the Sea of Marmara (Figure 1). All the coastal structures existing along the coast of Bursa province were examined within a field study conducted for two days and information about the structures was collected. Based on all the information gathered and fieldwork, it was investigated whether there is any problem related to the coastal structures along the coast of Bursa province.

---

[1] Corresponding author: Uludag University, Department of Civil Engineering, 16059, Nilüfer/Bursa, Turkey. ademakpinar@uludag.edu.tr

[2] Uludag University, Department of Civil Engineering, 16059, Nilüfer/Bursa, Turkey. r.emre.cakmak@gmail.com

[3] Uludag University, Department of Civil Engineering, 16059, Nilüfer/Bursa, Turkey. halidjfone@gmail.com

Figure 17. Study area

2. RESULTS AND DISCUSSION

It is discovered that some applications put in place without proper planning contributed to some problems in coastal areas. Mainly, four types of coastal problems were determined along the Bursa coast:

(1) Accumulation of sediments on one side of a structure and erosion on the other due to the structure interrupting longshore sediment transport.

(2) Filling up of harbors constructed without taking into account longshore sediment transport therefore reaching a state where the harbors can no longer function.

(3) Carrying out construction activities on coastal areas without regard to the wave-structure interaction in the coastal zone.

(4) Capsizing of boats due to swash in fishing harbors.

The first problem is accumulation of sediments on one side of a structure and erosion on the other due to the structure interrupting longshore sediment transport. This situation is observed in coastal areas around Karacabey region (Kursunlu and Bayramdere shores) where two fishing ports are located. Figure 2 shows Kursunlu and Bayramdere regions of Bursa province and the representative wind and wave roses from the deep sea wave atlas [1]. A more detailed overview of both shorelines is presented in Figures 3 and 4 and two different shoreline lines are included in these figures to examine the annual changes of the shoreline. As can be seen in Figure 3, sediments brought by the Susurluk river on the eastern side of the Kursunlu fishing harbor are piled up. It is presumed that erosion took place on the west side of the harbor because of sediment transport blockage. In order to prevent this erosion and stabilize the coast, 6 I-type groins were erected along the shore in the region and as a result, no change in the coast line was witnessed over 2 years i.e. the coast became stable (Figure 3). In Figure 4, it is also seen that sediments brought by the Susurluk Stream to the Sea

piled on the eastern side of the Yenikoy fishing harbor and erosion occurred on the western side of the harbor because of of sediment transport blockage.
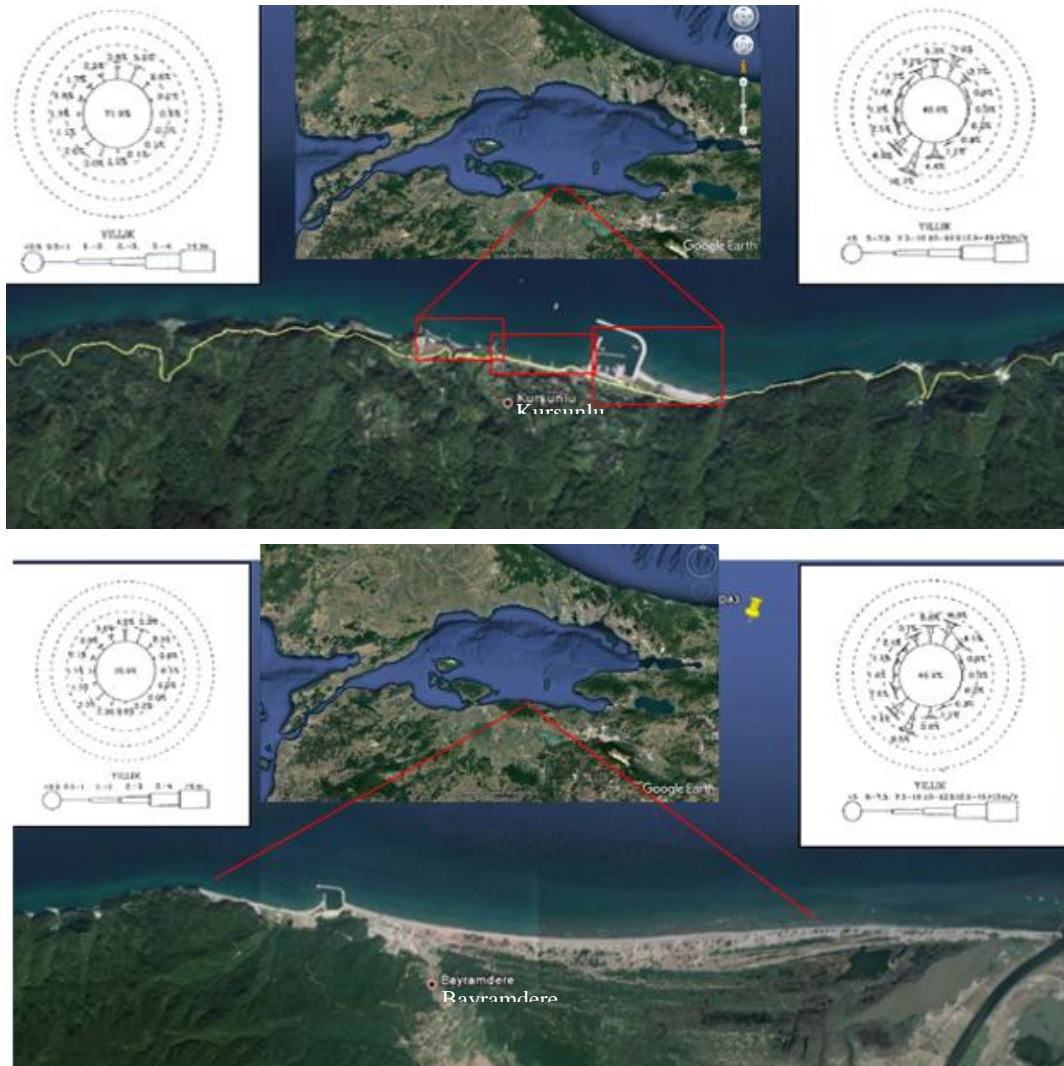
Figure 2. Kursunlu and Bayramdere regions of Bursa province and the representative wind and wave roses from the deep sea wave atlas [1]

Figure 3. Kursunlu fishing harbor, groins on the western part of Kursunlu fishing harbor and coastline for two years 2011 and 2013

Figure 4. Yenikoy fishing harbor, groins on the western part of Yenikoy fishing harbor and coastline for two years 2011 and 2013

The second problem is the filling up of harbors constructed without taking into account longshore sediment transport therefore reaching a state where the harbors can no longer function. An example to this would be a harbor area built on the shore of Eskel (Egerce) (Figure 5). A more detailed overview of problems in this area can be seen in Figure 6. It can be seen from this figure that a harbor on Eskel beach area got filled up with sediments. Some of the sediments that the Susurluk Stream brought to the Marmara Sea feeds this region. The harbor area built on the Eskel beach was built to form a sheltered area for the ships. However, this place is a trap that holds the sediments the river pours into the sea and waves carry to the east. As a result, the inside of the harbor has been filled to a considerable extent and the connection points of ships at the harbor are now covered in sand. Therefore, the fishing harbor is now nonfunctional.
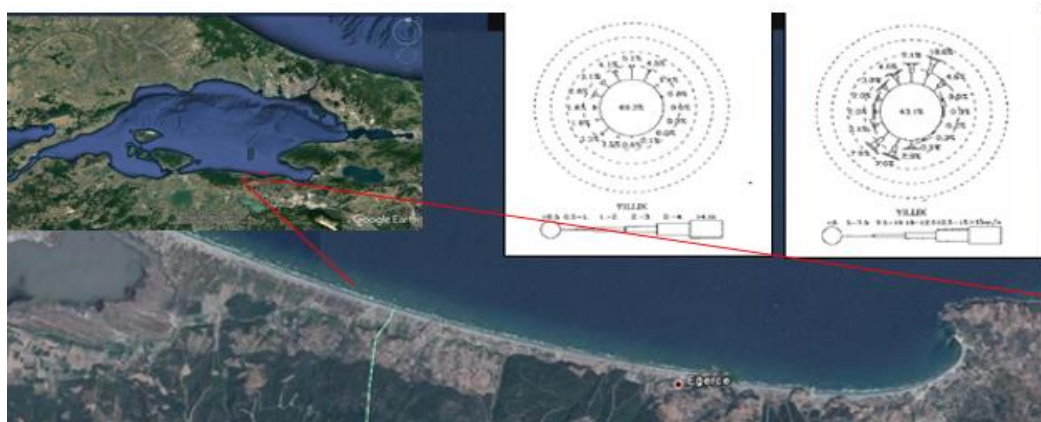
Figure 5. Location of Egerce and the representative wind and wave roses from the deep sea wave atlas [1]

Figure 6. Outlook of a fishing harbor on Eskel beach area filled with sediments

The third problem is carrying out construction activities on coastal areas without regard to the wave-structure interaction in the coastal zone. This problem was observed at Kucukkumla beach (Figure 7a). In this region, erosion formed due to concrete block platforms built on the beach parallel to the coastline and then concrete block groins built on the beach perpendicular to the coastline which cause reflection problems (Figure 7c and 7d). In some of the concrete I-type groins build towards the middle and north-west section of the shore, the sand retaining properties were observed visibly (Figure 7b and 7d), but in some cases they did not function. It has been observed that no intervention has been made beforehand in the south-eastern part of the coast, and as a result, there has not been a significant change in the coastline (Figure 7e). Finally, I-shaped groins perpendicular to the coast and made of concrete blocks removed from these concrete platforms contributed to keeping the sand on the coast from eroding away, however, some of them were observed to be unnecessary.
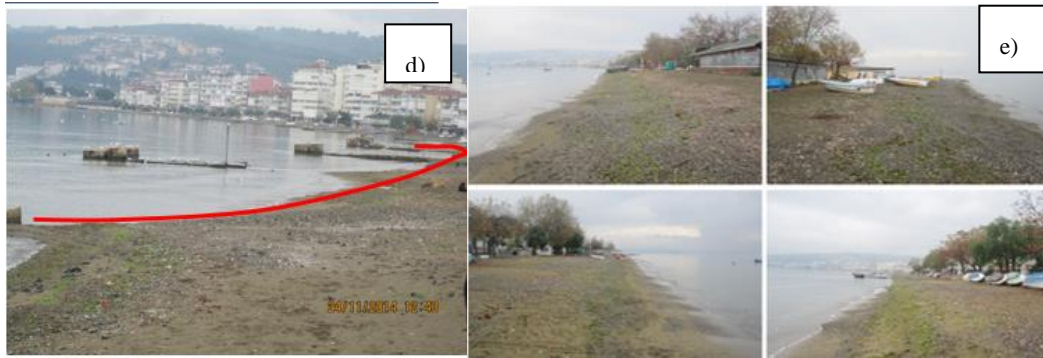
Figure 7. Outlook of Buyukkumla region and Kucukkumla beach, the region with groins and no groin and with accumulation and erosion

The fourth problem is the capsizing of boats due to swash in fishing harbors. This is due to the construction of harbors without detailed analysis of the winds and wind generated waves. The first example to the fourth problem is the Narlı fishing harbor (Figure 8a). Based on the position and the annual and seasonal wave climates (Figure 9) of the Narlı fishing harbor, the zone is sheltered only by the main breakwater. However, in the boatyards in harbor which extend to the east are out of the basin protected by the main breakwater. As a result, almost half of the area currently used for ship docking is exposed to waves coming from south and south-southeast directions in winter and summer. The second example to the fourth problem is the Gemlik fishing harbors (Figure 8b). The Gemlik fishing harbor is open to waves coming from the North-Northeast direction, which can be observed especially in the spring. In some cases these conditions cause agitation for some of the ships to due to fluctuation in these fishing harbors.
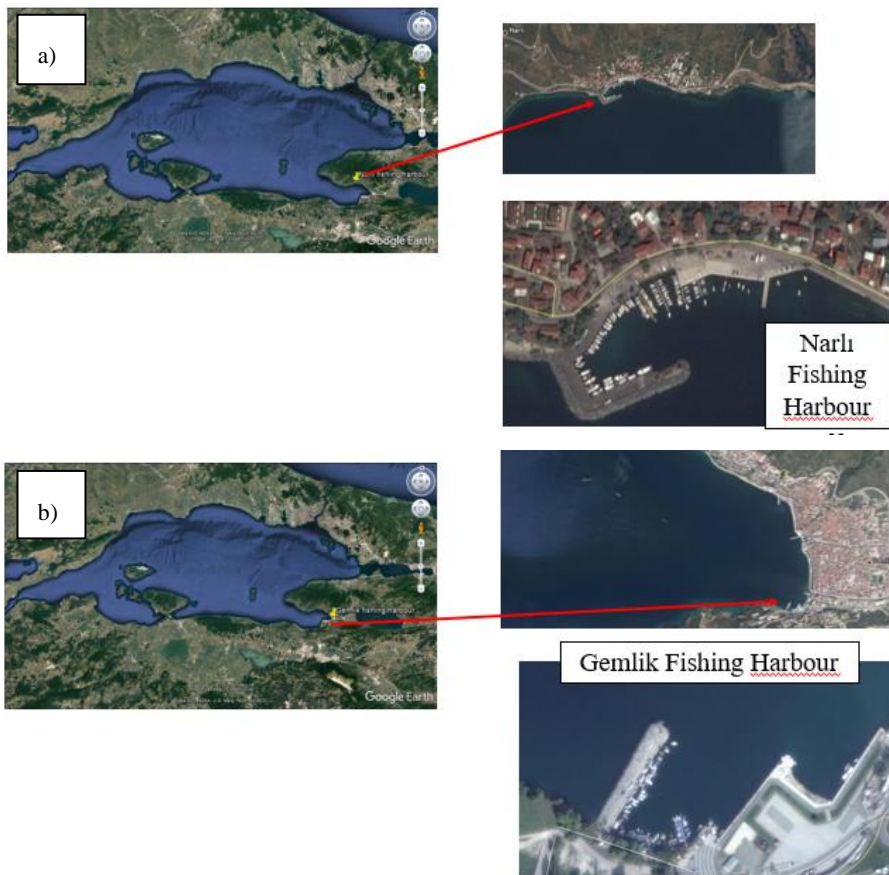
Figure 8. Outlook of Narlı and Gemlik Fishing Harbors

| Winter | Spring | Summer | Autumn |
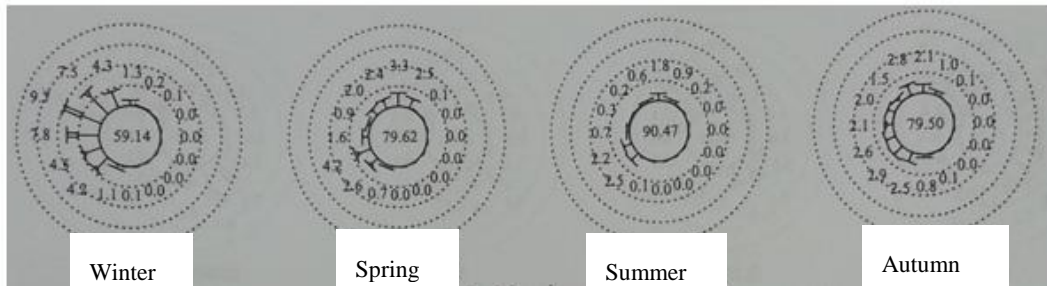
Figure 9. Seasonal wave roses at the closet grid points to the Narlı and Gemlik fishing harbors from deep water wave atlas [1]

3. CONCLUSION AND RECOMMENDATIONS

It is discovered that some applications put in place without proper planning contributed to some problems in coastal areas of Bursa, Turkey. Mainly, four types of coastal problems were determined along the Bursa coast. To solve these issues the following options for the specified problems should be taken into account:

1) In order to prevent beach erosion and probably increase sand levels on beaches along Bursa coasts, offshore breakwater or T-head groins or submerged breakwaters should be built.

For agitation/swash problem in the fishing harbors, additional secondary breakwaters and extension of the main breakwaters should be designed. Moreover, due to lack of appropriate wind and wave climate information which is needed in the design of all coastal structures and ports, an appropriate wind and wave atlas representing the coasts of Bursa should be produced.

REFERENCES

[1]. E. Ozhan, S. Abdalla, 2002. Wind and Deep Sea Wave Atlas for Turkey's Coasts, Turkish National Committee on Coastal Areas, MEDCOAST, Middle East Technical University, Ankara, Page 445.

Estimation of Projection Matrices from a Sparse Set of Feature Points for 3D Tree Reconstruction from Multiple Images

Štefan Kohek[1,2], Damjan Strnad[1], Borut Žalik[1], Simon Kolmanič[1]

Abstract

3D reconstruction of trees is an important task for tree analysis but the most affordable approach to capture real objects is with a camera. Although, there already exist methods for 3D reconstruction of trees from multiple photographs, they mostly handle only self-standing trees captured at narrow angles. In fact, dense feature detection and matching is in most cases the first step of the reconstruction, which requires a large set of features and high similarity between the individual pictures. Capturing trees in the orchard is in most cases possible only at wider angles between the individual pictures and with overlapping branches from other trees, which prevents reliable feature matching. We introduce a new approach for estimating projection matrices to produce 3D point clouds of trees from multiple photographs. By manually relating a smaller number of points on images to reference objects, we substitute the missing dense set of features. We assign to each image a projection matrix and minimize the projection error between the images and reference objects using simulated annealing. Thereby, we produce correct projection matrices for further steps in 3D reconstruction. Our approach is tested on a simple application for 3D reconstruction of trees to produce a 3D point cloud. We analyze convergence rates of the optimization and show that the proposed approach can produce feasible projection matrices from a sufficiently large set of feature points. In the future, this approach will be a part of a complete system for tree reconstruction and analysis.

Keywords: *3D reconstruction, simulated annealing, projection matrix*

1. INTRODUCTION

Reliable measurement of branches is important for successful examination of trees. However, manual measurement and examination of trees inside orchards is a tedious task, which is prone to errors and also requires extensive workforce. It is more preferable to capture real trees and perform examination on digitized trees inside the office. Therefore, numerous algorithms for automatic 3D reconstruction of trees have been developed. Many of them require special devices for tree capturing, e.g. terrestrial LIDAR [1] and Kinect [2], which are not widely deployed. On the other hand, cameras (e.g., on mobile phones) are the most affordable and widely adopted approach to capture real objects.

Pipelines for 3D reconstruction from images in most cases [3] consist of numerous steps: detecting feature points on a sequence of images, matching feature points between image pairs, camera calibration (i.e., pose estimation), and triangulation [4]. The biggest issue with this approach lies in the heavy dependence on detecting and matching feature points. Most commonly, SIFT [5] or SURF [6] are used for this task, but they require distinct features on images. When trying to perform 3D reconstruction of trees inside the orchards, we cannot easily produce enough distinct feature points because trees might be captured at wider angles, have repeating patterns, look quite similar and therefore lack distinct features. Overlapping trees in the orchards further aggravate the aforementioned problem.

3D tree reconstruction inside orchards is a problem which cannot be easily solved with the standard 3D reconstruction pipeline. Although numerous approaches for 3D reconstruction of trees from photographs were developed, many of them are designed mostly for convincing visualization or animation of reconstructed 3D models and therefore perform more coarse reconstruction [7, 8, 9, 10]. On the other hand, other more exact approaches [11, 12] have specific requirements, such as clear background, no overlapping trees, or smaller

---

[1] *University of Maribor, Faculty of Electrical Engineering and Computer Science, Smetanova ulica 17, 2000 Maribor, Slovenia*

[2] *Corresponding author: stefan.kohek@um.si*

recording angles. Because we cannot adhere to aforementioned requirements, we must use alternative approach for 3D reconstruction. In our case, an approach similar to voxel coloring [13] is used, which performs 3D reconstruction in inverse direction than ordinarily (i.e., with triangulation [3]) and it thus does not require matched feature points. On the other hand, it requires correct camera projection matrices in advance.

Evolutionary algorithms are useful tool for camera calibration when calculating intrinsic parameters [14] or even extrinsic parameters by considering relation between real 3D object with known coordinates and its occurrence on images [15]. However, considering solely relation between 3D object and its occurrence on images is not enough when 3D object covers only part of the image. In this case, the projective error on other parts of the image increases, which prevents correct 3D reconstruction.

In this work, we introduce new approach for estimating camera matrices which considers in addition to few correspondences between points on a known object and its occurrences on multiple images also correspondences between points on multiple images. We use simulated annealing [16] for calculating projection matrices because it requires only few parameters and is quite successful on various applications (e.g., automated tree pruning [17]). We show that consideration of direct relations between images lowers projective error and thus enables 3D reconstruction.

2. OVERVIEW OF THE METHOD

Automatic feature extraction and matching from our photographs is not reliable, therefore we provide alternative data for estimating matrices of images. We can easily provide just a set P of few corresponding points between neighbor images and reference object. Thus before recording, we place a unit cube inside the scene. After taking pictures, we manually match each vertex of the cube with its occurrence on all pictures. For each vertex p of the cube, we thus define its 3D coordinates $\mathbf{u}_p$ inside the scene and its 2D position $\mathbf{v}_{p,i}$ on each picture i. Additional data are provided by manually relating few tips of branches between the images. Therefore, we provide $\mathbf{v}_{p,i}$ for branch tips and thus match each point p on a branch tip between different pictures.

Our approach for estimating projection matrices is designed to consider input data which can be easily provided. To find 3×4 camera projection matrix $\mathbf{M}_i$ of each image i from a set of images I, two-step approach is used. In the first step, we calculate initial estimation of projection matrices, where relations between known object in 3D space and its projection in images are considered. Here, a draft approximation of metric reconstruction is obtained. In the second step, we refine matrices from the previous step by considering also the correspondences between points (tips of branches) on multiple images.

2.1. Initial projection matrix estimation

The objective of the first step is to find for each image i a coarse projection matrix for metric reconstruction. With simulated annealing [16], we calculate projection matrix $\mathbf{M}_i$ of picture i by minimizing for vertices $p \in P$ the distance between projection $\mathbf{M}_i$ of 3D point $\mathbf{u}_p$ and its 2D position $\mathbf{v}_{p,i}$ on the image i. Criteria/energy function of matrix $\mathbf{M}_i$ is:

$$f_1(\mathbf{M}_i) = \frac{\sum_{p \in P} g(\mathbf{M}_i, \mathbf{u}_p, \mathbf{v}_{p,i})}{\|P\|}, \tag{1}$$

where function $g(\mathbf{M}, \mathbf{u}, \mathbf{v})$ calculates distance between point $\mathbf{v}$ and projection $\mathbf{M}$ of point $\mathbf{u}$ (in pixels):

$$g(\mathbf{M}, \mathbf{u}, \mathbf{v}) = \left\| \mathbf{v} - \frac{(\mathbf{Mu})_{xy}}{(\mathbf{Mu})_z} \right\|. \tag{2}$$

The initial state of simulated annealing is for the first image a random matrix which has values in the range of a typical projection matrix:

$$\mathbf{M}_1 = \begin{bmatrix} 1000\,r_1 & r_2 & r_3 & 1000\,r_4 \\ r_5 & 1000\,r_6 & r_7 & 1000\,r_8 \\ 1000\,r_9 & 1000\,r_{10} & 1000\,r_{11} & r_{12} \end{bmatrix}. \tag{3}$$

Here, $r_i \in [0, 1]$ is a random number from the uniform distribution.

New candidate projection matrix $\mathbf{M}'_i$ is calculated from $\mathbf{M}_i$. One random element at row r and column c of matrix $\mathbf{M}_i$ is in each iteration of simulated annealing perturbed according to parameter F and current temperature T:

$$\mathbf{M}'_{i,r,c} = \mathbf{M}_{i,r,c} + TF\mathbf{M}_{i,r,c}(2r - 1). \tag{4}$$

Other elements are perturbed with probability C. If candidate $\mathbf{M}'_i$ is better solution than $\mathbf{M}_i$, it is accepted as the new state ($\mathbf{M}_i$), otherwise it is accepted with Metropolis criterion [18].

The best estimated projection matrix of image $i-1$ is used as the initial state of image i in order to speed up the estimation of subsequent matrices.

2.2. Final estimation of matrices

In this step, we refine matrices from the first step by considering also the correspondence between points on multiple images. With simulated annealing from the previous step we produce a set of projection matrices M. Initial state of simulated annealing is thus a set of matrices from the first step M={$\mathbf{M}_1, \ldots, \mathbf{M}_{\|I\|}$}. Criteria function for minimization in the second step is:

$$f_2(\mathrm{M}) = \frac{\sum_{i \in I} f_1(\mathbf{M}_i)}{2\|I\|} + \frac{\sum_{p \in P} \sum_{i \in I} g(\mathbf{M}_i, t(p, M), \mathbf{v}_{p,i})}{2\|P\|\|I\|}. \tag{5}$$

Here, function $t(p, M)$ calculates 3D position from correspondences $\mathbf{v}_p$ of point p by averaging triangulated positions between image-pairs [19].

Unlike the first step, each iteration of simulated annealing changes one random element of randomly chosen matrix. Other elements are perturbed with probability C.

3. RESULTS AND DISCUSSION

Our approach for estimating projection matrices was tested on a set of 8 orchard images (Figure 1) which are obtained synthetically from EduApple [21]. For each test we executed simulated annealing 10 times. At first, we estimated coarse projection matrix of the first image. Here, we used next parameters for simulated annealing: $T_0=1$, $F=0.5$, and $C=0$. Figure 2 displays convergence curves of median, highest, and lowest errors. Results indicate successful estimation as best solution had errors (i.e. average distance of pixels) smaller than 10 pixels.
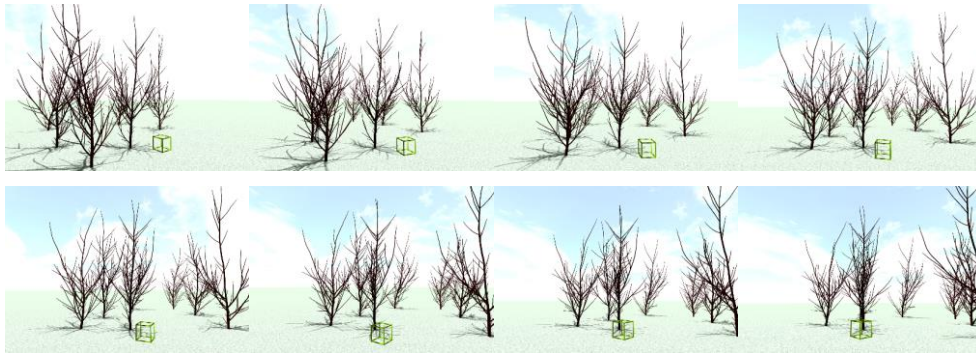
Figure 1. A sequence of images used in 3D reconstruction.

Figure 2. Convergence curves of initial projection matrix estimation (median/best/worst estimations).

The best solution of each estimation of $\mathbf{M}_i$ was used for each subsequent image (Figure 3). Here, the parameters of simulated annealing were: T_0=1, F=0.1, and C=0.5. For the first image, we again used previous estimation and lowered the error even further. The errors of other images were also significantly lowered from the initial estimation, although initial errors were not so high because projection matrices of consecutive images are already similar to final estimation.
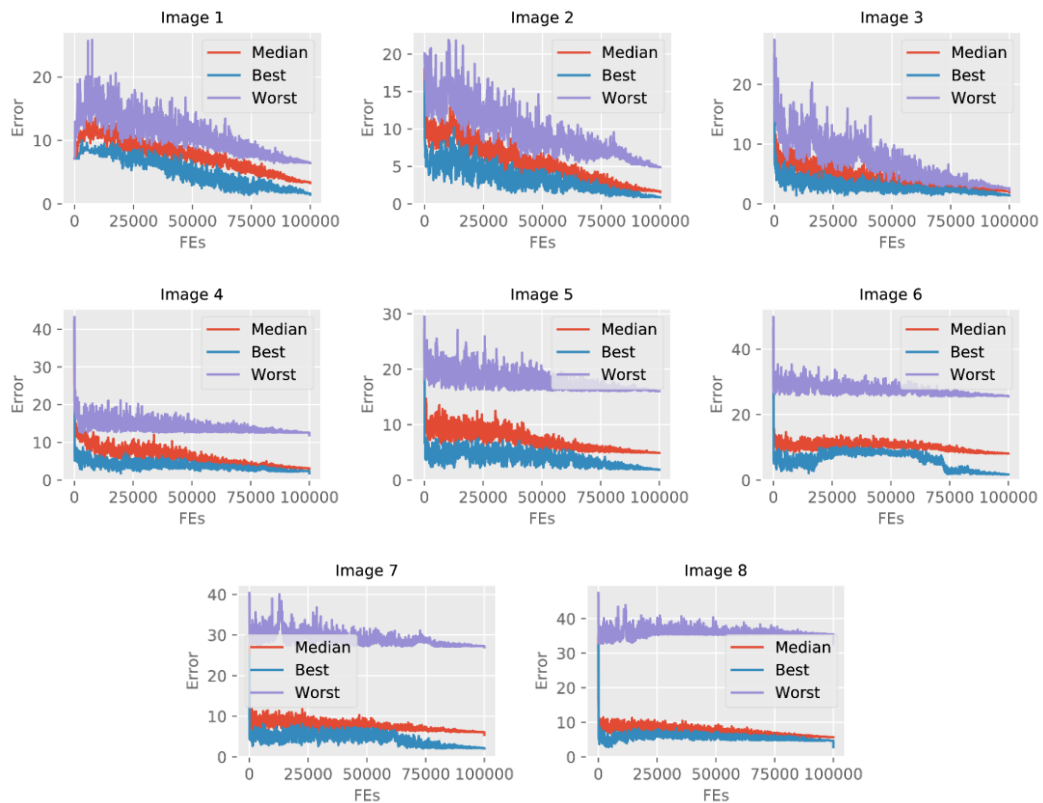
Figure 3. Convergence curves of initial estimation of all projection matrices (median/best/worst estimations).

Figure 4 shows convergence rates of the second step of matrix estimation. Here, we used next parameters: F=0.1, T_0=0.01, and C=0.05. Lower initial temperature was used because matrices were in most cases already

oriented towards the optimal solution. Smaller variations between best and worst estimation confirm the aforementioned fact. The final error was just few pixels, which enables further steps of 3D reconstruction. Here, we used resulting matrices for initial version of 3D reconstruction pipeline, which works similar to voxel coloring [13]. Figure 5 shows result of successful 3D reconstruction, where produced tree is similar to the tree at the cube (Figure 1).
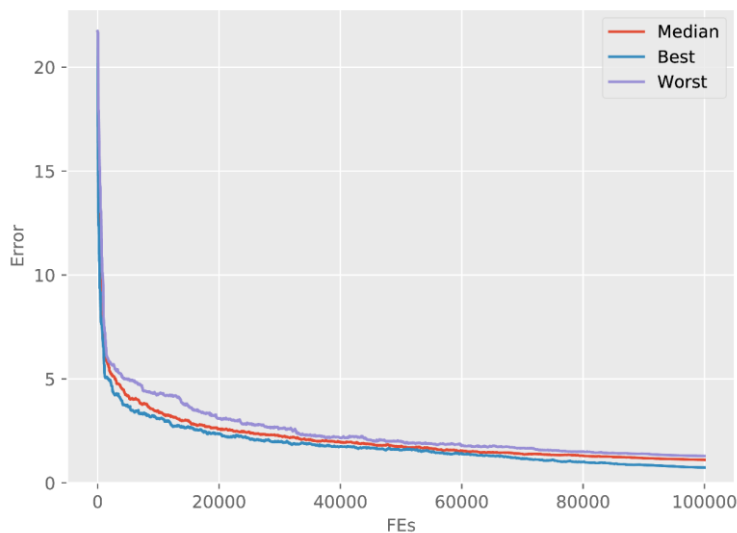
Figure 4. Convergence curves of final optimization of all eight matrices (median/best/worst estimations).
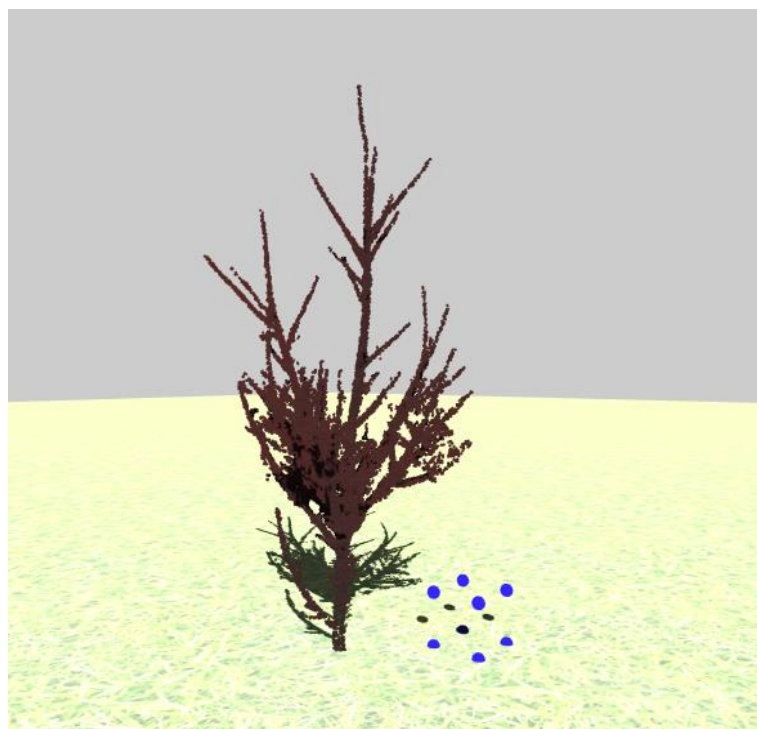
Figure 5. Resulting 3D structure of the reconstructed tree.

4. CONCLUSIONS

In this paper, we presented alternative approach for estimating projection matrices and show that two-step approach was able to correctly estimate projection matrices and enable further steps of 3D reconstruction. Simulated annealing supported steady convergence of our optimization problem. Initial estimation of projection matrices lowered complexity of the problem for the second step and thus increased estimation speed of final projection matrices. Finally, we have successfully produced 3D point cloud of simple tree from multiple images inside the orchards. 3D structure was similar to input images and thus appropriate for subsequent analyses.

In the future, we plan to develop a complete framework for tree reconstruction. Matching corresponding branches manually is tedious, therefore we want to automate this task to a greater extent. Simulated annealing in current version requires large number of criteria function evaluations. Therefore, we plan to increase convergence speed of the presented approach by tuning input parameters. Simulated annealing is also only one of the algorithms for global optimization. We plan to verify other algorithms for global optimization, e.g., DE [22] or jDE [23], or even multi-criteria optimization algorithms [24]. Finally, we plan to use our approach for further growth analysis.

ACKNOWLEDGEMENTS

REFERENCES

1. J. R. Rosell, J. Llorens, R. Sanz, J. Arno, M. Ribes-Dasi, J. Masip, A. Escolà, F. Camp, F. Solanelles, F. Gràcia, et al., "Obtaining the three-dimensional structure of tree orchards from remote 2d terrestrial lidar scanning," Agricultural and Forest Meteorology, vol. 149, no. 9, pp. 1505–1515, 2009.
2. N. M. Elfiky, S. A. Akbar, J. Sun, J. Park, and A. Kak, "Automation of dormant pruning in specialty crop production: An adaptive framework for automatic reconstruction and modeling of apple trees," in Proceedings of the IEEE Conference on Computer Vision and Pattern Recognition Workshops, pp. 65–73, 2015.
3. C. Li, J. Zheng, C. Dang, and H. Zhou, "A method of 3d reconstruction from image sequence," in Image and Signal Processing, 2009. CISP'09. 2nd International Congress on, pp. 1–5, IEEE, 2009.
4. R. I. Hartley and P. Sturm, "Triangulation," Computer vision and image understanding, vol. 68, no. 2, pp. 146–157, 1997.
5. D. G. Lowe, "Object recognition from local scale-invariant features," in Computer vision, 1999. The proceedings of the seventh IEEE international conference on, vol. 2, pp. 1150–1157, Ieee, 1999.
6. H. Bay, A. Ess, T. Tuytelaars, and L. Van Gool, "Speeded-up robust features (surf)," Computer vision and image understanding, vol. 110, no. 3, pp. 346–359, 2008.
7. P. Tan, G. Zeng, J. Wang, S. B. Kang, and L. Quan, "Image-based tree modeling," ACM Trans. Graph., vol. 26, 2007.
8. P. Tan, T. Fang, J. Xiao, P. Zhao, and L. Quan, "Single image tree modeling," ACM Trans. Graph., vol. 27, pp. 1081–1087, 2008.
9. B. Neubert, T. Franken, and O. Deussen, "Approximate image-based tree-modeling using particle flows," ACM Transactions on Graphics, vol. 26, no. 3, 2007.
10. A. Zamuda, J. Brest, B. Bošković, and V. Žumer, "Differential evolution for parameterized procedural woody plant models reconstruction," Applied Soft Computing, vol. 11, no. 8, pp. 4904–4912, 2011.
11. C. Wu, L. He, X. Du, S. Chen, and K. Ni, "3d reconstruction of chinese hickory tree for dynamics analysis," Biosystems Engineering, vol. 119, pp. 69 – 79, 2014.
12. D. Zhang, N. Xie, S. Liang, and J. Jia, "3D tree skeletonization from multiple images based on PyrLK optical flow," Pattern Recognition Letters, vol. 76, pp. 49 – 58, 2016. Special Issue on Skeletonization and its Application.
13. S. M. Seitz and C. R. Dyer, "Photorealistic scene reconstruction by voxel coloring," International Journal of Computer Vision, vol. 35, no. 2, pp. 151–173, 1999.
14. A. Whitehead and G. Roth, "Estimating intrinsic camera parameters from the fundamental matrix using an evolutionary approach," EURASIP Journal on Advances in Signal Processing, vol. 2004, no. 8, p. 412751, 2004.
15. Q. Ji and Y. Zhang, "Camera calibration with genetic algorithms," IEEE Transactions on Systems, Man, and Cybernetics-Part A: Systems and Humans, vol. 31, no. 2, pp. 120–130, 2001.
16. S. Kirkpatrick, C. D. Gelatt, M. P. Vecchi, et al., "Optimization by simulated annealing," science, vol. 220, no. 4598, pp. 671–680, 1983.
17. D. Strnad and Š. Kohek, "Novel discrete differential evolution methods for virtual tree pruning optimization," Soft Computing, pp. 1–13, 2015.
18. N. Metropolis, A. W. Rosenbluth, M. N. Rosenbluth, A. H. Teller, and E. Teller, "Equation of state calculations by fast computing machines," The journal of chemical physics, vol. 21, no. 6, pp. 1087–1092, 1953.
19. R. Hartley, R. Gupta, and T. Chang, "Stereo from uncalibrated cameras," in Computer Vision and Pattern Recognition, 1992. Proceedings CVPR'92., 1992 IEEE Computer Society Conference on, pp. 761–764, IEEE, 1992.

20. P. C. Schuur, "Classification of acceptance criteria for the simulated annealing algorithm," Mathematics of Operations Research, vol. 22, no. 2, pp. 266–275, 1997.
21. Š. Kohek, N. Guid, S. Tojnko, T. Unuk, and S. Kolmanič, "Eduapple: Interactive teaching tool for apple tree crown formation," HortTechnology, vol. 25, no. 2, pp. 238–246, 2015.
22. R. Storn and K. Price, "Differential evolution–a simple and efficient heuristic for global optimization over continuous spaces," Journal of global optimization, vol. 11, no. 4, pp. 341–359, 1997.
23. J. Brest, S. Greiner, B. Boskovic, M. Mernik, and V. Žumer, "Self-adapting control parameters in differential evolution: A comparative study on numerical benchmark problems," IEEE transactions on evolutionary computation, vol. 10, no. 6, pp. 646–657, 2006.
24. T. Robič and B. Filipič, "Demo: Differential evolution for multiobjective optimization," in International Conference on Evolutionary Multi-Criterion Optimization, pp. 520–533, Springer, 2005.

BIOGRAPHY

Štefan Kohek graduated in 2012 from Faculty of Electrical Engineering and Computer Science at University of Maribor with M. E. degree in computer science. Currently, he works as a teaching assistant in Laboratory for Geometric Modeling and Multimedia Algorithms at UM FERI. His research interests lie in the areas of parallel computing, computer graphics, tree growth simulation, and optimization techniques.

Creating A 3D Model on A Human Skeleton Using Kinect

Yusuf Uzun[1], Mehmet Bilban[2], Huseyin Arıkan[3]

Abstract

Moving 3D modeling is widely used in many areas such as cinema, gaming, robot control and training. Kinect is a system that can detect human movements and send them to computers. It was developed by Microsoft to play games for the Xbox game console and is being used over time for applications in other areas. Because of the new technology, there is a lack of application and the literature in this field. In this study, 3D model will be created on the human skeleton using Kinect and the generated model motion feature will be given.

Keywords: *kinect, skeleton, 3d modelling*

1. INTRODUCTION

Kinect or Project Natal is a device that allows you to play games without any controller and a line of motion sensing input devices by Microsoft for Xbox 360 and Xbox One video game consoles and Windows PCs [1]. Kinect is a camera with a depth sensor. The convenience Kinect provides here is for the human to perceive the joint points and transfer the arm movements towards the computerized environment. Depth sensing systems such as Kinect are among the current research topics in computer vision and image processing [2].

Due to the increasing importance of your visuals, it is getting harder drawing operations that performed manually in the fields as technology, construction and architecture. It has become inevitable to present drawing and Computer Aided Design (CAD) models on paper or computer applications in the form of augmented reality. Kinect is a technology that grows in this point in human - computer interaction [8].

Recently, computer vision systems using Kinect, which costs less than traditional 3D cameras, have begun to be developed [3].

In this study, 3d model will be put on human skeleton onto Windows Presentation Foundation (WPF) screen by programming previously designed 3D models in visual studio application. Here, the software provides an integrity by adding control steps to the modeling phase of a skeleton using the data it receives from the sensors on the Kinect.

The work was arranged as follows: In Section 2, materials and methods was explained. In Section 3, evaluations of the study were described. In Section 4, conclusions were presented.

2. MATERIALS AND METHODS

2.1. Kinect Mechanism

Kinect is a special purpose camera system developed by Microsoft that has the ability to detect motion, depth and audio. The hardware structure of the device includes RGB camera, infrared projector, depth sensor camera and sound sensor microphones. The version produced for Xbox 360 game consoles is called "Kinect for Xbox 360" and the version produced for commercial use is called "Kinect for Windows". The device view of the Kinect for Windows version is shown in Figure 1 [4].

---

[1] Corresponding author: Necmettin Erbakan University, Seydisehir Vocational School, 42370, Seydisehir/Konya, Turkey. yuzun@konya.edu.tr

[2] Necmettin Erbakan University, Seydisehir Vocational School, 42370, Seydisehir/Konya, Turkey. mbilban@konya.edu.tr

[3] Necmettin Erbakan University, Seydisehir Department of A.C. Engineering, 42370, Konya, Turkey. harikan@konya.edu.tr

Figure 1. Kinect for Windows [4]

Kinect's optical components consist of IR Emitter, IR Depth Sensor, color sensor, tilt motor and microphone array. Kinect optical components in Figure 2 are as shown.

Figure 2. Kinect optical components [5]

Where, IR Emitter is emits infrared light beams, IR Depth Sensor is reads the IR beams reflected back to the sensor, Color Sensor is to make capturing a color images possible. The tilt motor is the mechanism that gives the sensor the ability to move vertically, and a simple DC motor is formed. Kinect can be moved by (+/- 27) degrees using software. In the grate at the bottom portion of the Kinect is available 4 microphone. These microphones are arranged at regular intervals on the bottom of the Kinect to capture the best sound quality and the angle that the sound comes from [5].

Normal cameras collect light that jumps between objects in front. The camera turns this light into an image that resembles our own eyes. The Kinect, on the other hand, records the distance of the objects placed in front of it. Kinect uses infrared light to create a depth image that captures where things are, not what objects look like [6].

2.2. 3D Modeling of The Kinect Skeleton

Kinect forms the skeleton structure from 20 joint points as shown in Figure 3. Each joint datum belongs to a predefined body region in the Kinect coordinate space, which contains 3D coordinates and is shown as a time series. The Microsoft Kinect SDK and OpenNI libraries are available for real-time and advanced animations. Both of these libraries can track the 20 joins of the human skeleton.

The joint data representing the human limbs are updated with the depth image frames captured at specific time intervals without deteriorating the integrity of the Kinect skeletal structure. In order to adapt the 3D model to the motion capture data obtained by Kinect, the orientation information about the joints is needed in addition to the 3D coordinate information of the joint points [8].
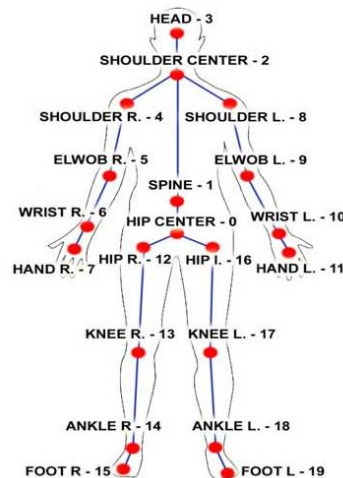
Figure 3. Joint points of the Kinect skeleton [7]

The 3d model to be used in this study will be designed in the IClone program. The IClone program is an interactive platform that allows you to create a model in the X, Y, and Z coordinate plane. The program is compatible with Kinect.

3. EVALUATION OF THE STUDY

In this study, the Kinect SDK application is loaded onto the computer and Kinect is connected to the computer via the USB cable. Kinect skeleton detection libraries are added to the project software. Once all the necessary configurations have been completed, Kinect will calculate the distance between the joints and detect the joint points on the human skeleton.

Control parameters of the mouse operations that correspond to human hand movements are added to the application. In this study, respectively 3D models to be put on human skeleton structure will be designed and 3D model covered will be done for perceived human skeleton structure. The movements of the human on the WPF screen will be captured and the 3D model worn on the skeleton will be adapted to these movements. Finally, a 3D model can be created that can make human-like movements on the real human image.

In the lower left corner of the pictures are shown the human skeletal structure that Kinect perceives. The operation steps of the application are shown in Figure 4.

Figure 4. Process steps of the application

Kinect actually seems to have three eyes. Two of them are in the middle, the third side is the side. This "third eye" determines how Kinect works. However, Kinect's third eye is actually an infrared projector. Kinect's infrared beam shines the rays of the form of infrared spots on the person in front of the projector. We can't see these points normally, but we can see using an IR camera.

In this study, we first identified the joint points on the human skeleton with Kinect. Using the program code we wrote, we combined these joint points with a line so that the human body would form. In this way we have created the human skeleton structure of Kinect corresponding to the human skeletal structure. Kinect's depth information acts like a 3D scanner to detect human movements.

In the IClone program, we designed all the joint regions corresponding to the Kinect skeleton of the 3D model separately. The model shown in Figure 5 was designed in the IClone program, and the model was given motion characteristics in the 3D plane. In the IClone program, we designed all the joint regions corresponding to the Kinect skeleton of the 3D model separately. We have acquired this 3D model motion feature that we have designed using sensor data from Kinect. In Figure 5, the movements of the dressed 3D model are shown on the human skeleton.

| (a) | (b) | (c) |
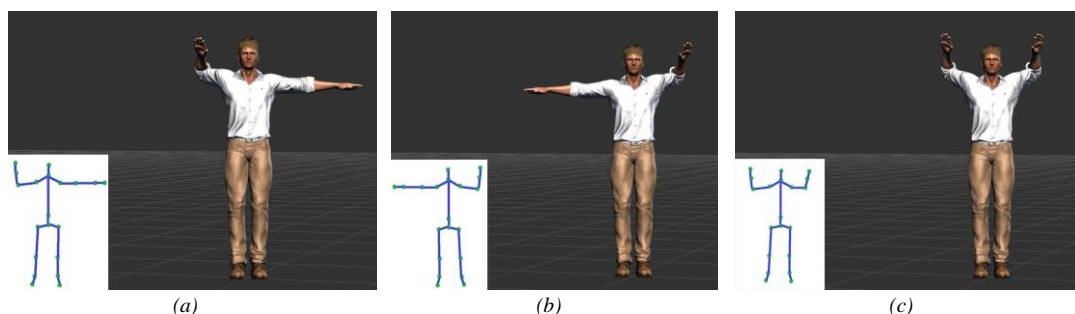
Figure 5. (a) right hand motion ,(b) left hand motion and (c) double hand motion

In Figure 5 (a), when we lift the right hand side up against the Kinect, the 3D model covered on the skeletal structure raises the right hand upwards. In Figure 5 (b), when we lift the left hand upwards, the 3D model covered on the skeletal structure raises the left hand upwards. In Figure 5 (c), when we lift the double elimination upwards, the 3D model clad on the skeletal structure lifts the double hand upwards.

4. CONCLUSIONS

In this study, an application was carried out to adapt 3D model designed in IClone application to human skeletal structure which Kinect created. With this study, a new application on Kinect has been realized. We have provided a road map for us to try Kinect on different platforms. We have seen that this new technology can be successfully used in different disciplines.

In this study, we have found that 3D image scanning, 3D animation and interactive training applications can be done easily with Kinect at low cost.

ACKNOWLEDGMENTS

REFERENCES

[1]. (2017) Wikipedia website [Online]. Available: https://en.wikipedia.org/wiki/Kinect
[2]. J. Han, L. Shao, D. Xu, and J. Shotton, "*Enhanced Computer Vision With Microsoft Kinect Sensor: A Review*," IEEE Trans. Cybern., 2013, vol. 43, no. 5, pp. 1318–1334, Oct.
[3]. Z. Zhang, "Microsoft Kinect sensor and its effect," IEEE Multimedia Mag., 2012, vol. 19, no. 2, pp. 4–10
[4]. (2017) Kinect camera [Online]. Available: http://www.xbox.com/en-US/ kinect/default.htm
[5]. (2017) Kinect for Windows Sensor Components [Online]. Available: https://msdn.microsoft.com/en-us/library/jj131033.aspx
[6]. G. Borenstein, *Making Things See*, O'Reily., 2012, p.416
[7]. J.A. Diego-Mas and J. Alcaide-Marzal, "*Using Kinect™ sensor in observational methods for assessing postures at work*", Applied Ergonomics ,2014, vol. 45, no. 4, pp. 976-985
[8]. (2010), A. Tasdelen, *Windows Presentatin Foundation*, Pusula Yayın Evi, 350s., İstanbul

BIOGRAPHY

Yusuf Uzun has been working as a full-time lecturer at Seydisehir Vocational High School from Konya Necmettin Erbakan University at the Turkey. He received his MSc in Computer Engineer from the Selcuk University of Konya. In his Master Thesis, he extracted rules with the machine learning algorithms and fuzzy logic over the medical data. Also, he received his Ph. D. in Computer Engineer from the Necmettin Erbakan University of Konya. He has been involved in research and development in the areas of metaheuristic methods, data mining, fuzzy logic and machine learning systems.

Mehmet Bilban has been working as a full-time lecturer at Seydisehir Vocational High School from Konya Necmettin Erbakan University at the Turkey. He received his MSc in Computer Science from the Gazi University of Ankara. He has been involved in research and development in the areas of Kinect, mobile software, and data mining.

Prof. Dr. Huseyin Arıkan was born in KONYA, Turkey, in 1967. He received the B.E. degree in mechanical engineering from the University of Selcuk, Konya, Turkey, in 1989, and the M.S. and Ph.D. degrees in mechanical engineering from the Institute of Science and Technology of University of Selcuk in 1993 and 2002, respectively. Since 2007, he has been with the Department of Mechanical Department, Seydisehir Vocational School, where he was an Assistant Professor. He has been with the Department of Mechanical Engineering, became an Associate Professor in Seydisehir Ahmet Cengiz Engineering Faculty in 2011. His current research interests include Materials science, fracture mechanics, machine design and polymer composites, metal matrix composites and structural analysis.

A Study on The Training of Disabled People Using Voice Control with Kinect

Yusuf Uzun[1], Mehmet Bilban[2], Huseyin Arıkan[3]

Abstract

Kinect is a system that can detect human movements and send them to computers. It was developed by Microsoft to play games for the Xbox game console and is being used over time for applications in other areas. Because of the new technology, there is a lack of application and the literature in this field. We can describe the term disability as a person that is restricted by some movements, senses, or functions due to injury, physical or mental discomfort. The obstacle may arise from congenital or acquired diseases or accidents. In this study, have been developed an application for using the training materials by disabled individuals using the Kinect device which is controlled by the sound.

Keywords: *kinect, voice control, disabled*

1. INTRODUCTION

The use of technology-supported learning materials in disability education plays an important role in increasing learning and quality of life. Kinect or Project Natal is a device that allows you to play games without any controller and a line of motion sensing input devices by Microsoft for Xbox 360 and Xbox One video game consoles and Windows PCs [1]. Kinect is a camera with a depth sensor. Kinect is a system that can be controlled only by body movements without any control means in the computer environment. The convenience Kinect provides here is for the human to perceive the joint points and transfer the arm movements towards the computerized environment. Depth sensing systems such as Kinect are among the current research topics in computer vision and image processing [2].

For to sustain the lives of persons with disabilities and can be a productive individuals in society must be made of a number of researches and regulations related to meeting educational, cultural, economic and social needs [3].

According to World Health Organization report, 10% of the population in developed countries and 12% of the population in developing countries is made up of disabled people [4]. The lived of approximately 600 million people with disabilities in the world and this numbers are expected to increase to time [5]. According to the Disability Survey 2002 conducted by the Turkey Statistical Institute and Department of Administration for Disabled People, 12.29% of the total population in Turkey will be disabled citizens. Approximately 8.5 million people with disabilities are consisting chronic illnesses 9.7%, 1.25% of orthopedic, mental 0.48%, speech and language 0.38%, hearing 0.37%, blind and visually impaired 0.6% [6].

In this study, models designed for the construction of a city with speech control of individuals with disabilities who can't fully use their hands have been carried on the numbered parcels on the WPF screen.

The work was arranged as follows: In Section 2, materials and methods was explained. In Section 3, evaluations of the study were described. In Section 4, conclusions were presented.

In this study, models designed for the construction of a city with speech control of individuals with disabilities who can't fully use their hands have been carried on the numbered parcels on the WPF screen.

[1] Necmettin Erbakan University, Seydisehir Vocational High School, 42370, Seydisehir/Konya, Turkey. yuzun@konya.edu.tr

[2]Necmettin Erbakan University, Seydisehir Vocational High School, 42370, Seydisehir/Konya, Turkey. mbilban@konya.edu.tr

[3] Corresponding author: Necmettin Erbakan University, Seydisehir Department of A.C. Engineering, 42370, Konya, Turkey. harikan@konya.edu.tr

The work was arranged as follows: In Section 2, materials and methods was explained. In Section 3, evaluations of the study were described. In Section 4, conclusions were presented.

2. MATERIALS AND METHODS

2.1. Kinect Mechanism

Kinect is a special purpose camera system developed by Microsoft that has the ability to detect motion, depth and audio. The hardware structure of the device includes RGB camera, infrared projector, depth sensor camera, and sound sensor microphones. The version produced for Xbox 360 game consoles is called "Kinect for Xbox 360" and the version produced for commercial use is called "Kinect for Windows". The device view of the Kinect for Windows version is shown in Figure 1 [7].

Figure 1. Kinect for Windows [7]

Kinect's optical components consist of IR Emitter, IR Depth Sensor, color sensor, tilt motor and microphone array. Kinect optical components in Figure 2 are as shown.
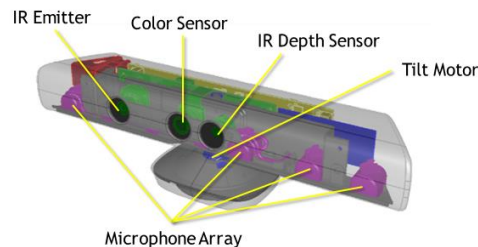
Figure 2. Kinect optical components [8]

Where, IR Emitter is emits infrared light beams, IR Depth Sensor is reads the IR beams reflected back to the sensor, Color Sensor is to make capturing a color images possible. The tilt motor is the mechanism that gives the sensor the ability to move vertically, and a simple DC motor is formed. Kinect can be moved by (+/- 27) degrees using software. In the grate at the bottom portion of the Kinect is available 4 microphone. These microphones are arranged at regular intervals on the bottom of the Kinect to capture the best sound quality and the angle that the sound comes from [8].

Kinect actually seems to have three eyes. Two of them are in the middle, the third side is the side. This "third eye" determines how Kinect works. However, Kinect's third eye is actually an infrared projector. Kinect's infrared beam shines the rays of the form of infrared spots on the person in front of the projector. We can't see these points normally, but we can see using an IR camera.

Normal cameras collect light that jumps between objects in front. The camera turns this light into an image that resembles our own eyes. The Kinect, on the other hand, records the distance of the objects placed in front of it. Kinect uses infrared light to create a depth image that captures where things are, not what objects look like [9].

2.2. Kinect Audio Control

Microsoft provides access to Kinect's microphone array to allow programs to spatially aware perceive of user sounds and other sounds. There are 4 microphones in the structure of Kinect. The Microsoft SDK accesses these microphones and can be used to find the difference between the sounds heard by each of the microphones to determine the direction in which the sound is coming from. This allows the creation of a volume control interface that allows simultaneous parse of multi-user voices. In addition, the SDK provides sophisticated tools for clearing the audio signal and achieving high-quality speech recognition when watching movies or playing games [9].

In Figure 3, Kinect's audio system is shown to be the sensing and working principle.
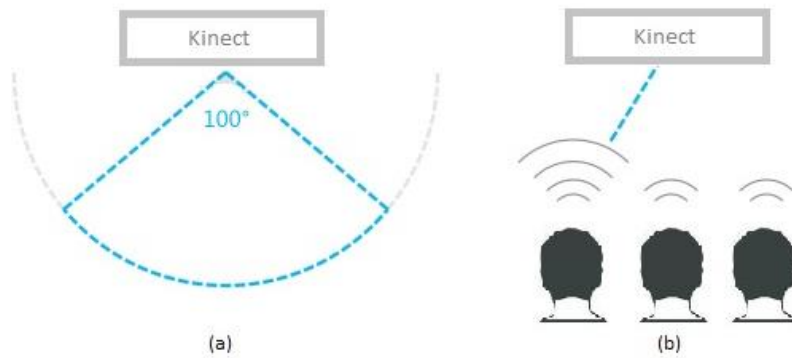
Figure 3. Kinect's sound detection principle

The sound input is detected at an angle of +50 and - 50 degrees from the center in front of the sensor. Here, Kinect detects the angle with the highest sound level and uses the microphone corresponding to that angle.

3. EVALUATION OF THE STUDY

In this study, models designed for the construction of a city with speech control of individuals with disabilities who can't fully use their hands have been carried on the numbered parcels on the WPF screen. Firstly, the Kinect SDK application is loaded onto the computer and Kinect is connected to the computer via the USB cable.

Since Kinect did not have a Turkish language library, a grammar library with Turkish words to be used in the first stage was created. The generated grammar library was transferred to the Kinect SDK to perform the voice recognition engine task. Then, a confidence coefficient between 0.4 and 0.8 was determined in the speech recognition process. If a confidence coefficient smaller than 0.4 is chosen, it is assumed that Kinect has performed an erroneous operation. If a confidence coefficient greater than 0.8 is selected, the user will be forced unnecessarily.

When the multi-feature is activated in the speech recognition process, it continues to listen for the next speech recognition process when it matches any word in the grammar. When the singular feature is activated, if there is a match with any word in our grammar, listening for the next speech recognition process is terminated.

The related feature in the Kinect SDK is activated to distinguish the user's voice from the background audio. The operation steps of the application are shown in Figure 4.
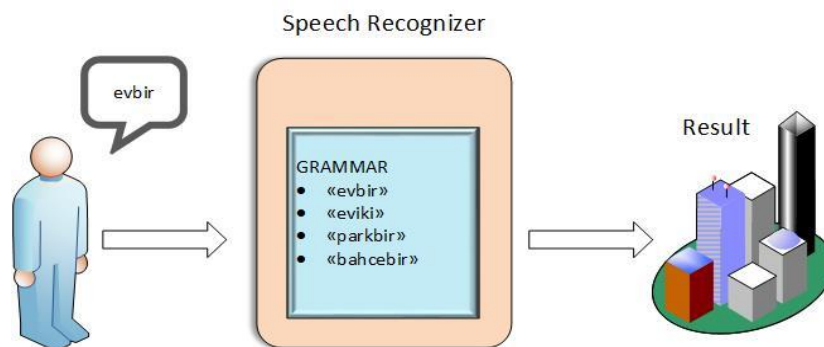
Figure 4. Process steps of the application

The operations performed in this study are as follows; firstly, the word that the user spoke with Kinect was transferred to the speech recognition program class included in the SDK. The transmitted word was compared with the words in the grammar library in the speech recognition class. If a matching word is found in the grammar library, the model corresponding to that word is selected and waits for us to talk about which parcel we will transfer. After the parcel information is spoken by the user, the selected model is placed on the relevant parcel.

In Figure 5 (a), the image at the start of the program is shown. In Figure 5 (b), the display of the placement of the models on the WPF screen with the speech control in Kinect is shown.

(a)   *(b)*

Figure 5. (a) The initial state of the program, (b) program working status

4. CONCLUSIONS

In talks with experts in the field; it is stated that if the technology of Kinect is integrated into special education environments, it will make a significant contribution to the learning of the students with disabilities. They also pointed out that technology can help students with mental disabilities to learn and comply with the pace, and to increase their motivation to learn permanently.

Because of the low cost of Kinect technology, special education institutions will be able to easily create the technical substructure of this technology. Since the use of Kinect technology is easy, it allows the trainers to adapt to the system comfortably.

In this study, it was observed that the perceptions and reactions of the disabilities to the models used increased positively. It has been observed that the use of Kinect has significantly increased motor skills. It also contributed positively to the development of linguistic skills.

ACKNOWLEDGEMENT

REFERENCES

[1]. (2017) Wikipedia website [Online]. Available: https://en.wikipedia.org/wiki/Kinect
[2]. J. Han, L. Shao, D. Xu, and J. Shotton, "*Enhanced Computer Vision with Microsoft Kinect Sensor: A Review*", IEEE Trans. Cybern., 2013, vol. 43, no. 5, pp. 1318–1334, Oct.
[3]. Y. Uzun, G. Tezel and H. Arıkan, "Engellilere Ait Verilerin Analizinde Veri Madenciligi Metodunun Kullanımı", Uluslararası Engelsiz Bilisim Kongresi, 2014
[4]. A. Bilgin and Et. Al., *"1 NoluSaglıkOcagıBolgesinde 18-58 YasEngellilikSıklıgıveEngelliligiBelirleyenEtmenler"*, SaglıktaYasamKalitesiSempozyumuOzetKitabı, İzmir, 2004
[5]. Oz-Veri, BasbakanlıkOzurlulerİdaresiBaskanlıgıHakemliSureliYayını, 2006, 75
[6]. Oz-Veri, BasbakanlıkOzurlulerİdaresiBaskanlıgıHakemliSureliYayını, 2006, 28
[7]. (2017) Kinect camera [Online]. Available: http://www.xbox.com/en-US/ kinect/default.htm
[8]. (2017) Kinect for Windows Sensor Components [Online]. Available: *https://msdn.microsoft.com/en-us/library/jj131033.aspx*.
[9]. G. Borenstein, *Making Things See*, O'Reily., 2012, p.416.

Compliance of university websites with modern web standards: The model of top 30 Turkish Universities

Abdurrahman Palalı[1], Huseyin Eldem[2], Ayse Eldem[3]

Abstract

The Internet and web sites has become a mandatory requirement for universities. With the increased usage of mobile devices and the emergence of new standards such as HTML5, universities changed their web pages. By using the Entrepreneurial and Innovative University Index of TUBITAK, this study compares the web accessibility, the HTML5 and mobile compliance of the university web sites. Also web page performance analyzes were conducted. Based on research results, some suggestions were given.

Keywords: *HTML5, Web accessibility, compliance, Turkish Universities*

1. INTRODUCTION

Web Accessibility is important for people with disabilities, but also important for low end devices such as IOT and mobile devices. Latest recommendation of World Wide Web Consortium's Web Content Accessibility Guidelines (WCAG 2.0) was published in December 2008 and a working draft for WCAG 2.1 was published in April 2017. But still in 2017 many sites are inadequate for WCAG 2.0 Accessibility that became a ISO standard.

There are already conducted studies on Web Accessibility. For example Irina C. and Ben S. [1] searched for 50 US state web sites, Abdulmohsen A., Ali A.and Pam M. [2] evaluated the accessibility of e-government web sites of Saudi Arabia and Oman, Joanne K., Dorothy Y. and Klus O. [3] searched for EU, Asian and African e-government web accessibility, Uthayasankar and Zahir [4] searched for UK e-government sites ad a recent study by Serhat [5] searched for 10 Turkish university web sites.

With standards such as HTML5 web sites getting more powerful and multimedia rich but also are getting bigger. Existing studies shows that web sites are growing. [6] As of April 15, the average website size has reached 2602 KB. This represents an increase of 50.7% (1726 KB) compared to the data of 3 years ago. While the largest part of the average website is generated by images with 1712 kb (65.8%), the html part only generated 50kb (1.9%). Yet another study [7] estimates that globally, there will be 4.1 billion total Internet users (52% of population) in 2020, up from 3.0 billion (40% of population) in 2015. This kind of growth makes compliance difficult.

2. METHOD

To pick universities, we used Entrepreneurial and Innovative University Index of TUBITAK from 2016. [8] By using automated tools we compared 30 of them. Our main tool is World Wide Web Consortium's Non document type version of markup validation service. [9] We also used their CSS Validation service. [10] Also we used HTTP Archive's tool [11] for checking web page size.

---

[1] *Corresponding author: Karamanoglu Mehmetbey University, Technical Sciences Vocational High school, 70100, Merkez/Karaman, Turkey. abdpalali@kmu.edu.tr*

[2] *Karamanoglu Mehmetbey University, Technical Sciences Vocational High school, 70100, Merkez/Karaman, Turkey. heldem@kmu.edu.tr*

[3] *Karamanoglu Mehmetbey University, Technical Sciences Vocational High school, 70100, Merkez/Karaman, Turkey. ayseeldem@kmu.edu.tr*

3. RESULTS

All the results are from April 15 2017.

Table 14. W3C Markup Validation

University	Number of	Number of
SABANCI UNİVERSİTESİ	11	13
ORTA DOGU TEKNİK UNİVERSİTESİ	10	13
İHSAN DOGRAMACI BİLKENT UNİVERSİTESİ	10	14
İSTANBUL TEKNİK UNİVERSİTESİ	29	30
BOGAZİCİ UNİVERSİTESİ	12	12
KOC UNİVERSİTESİ	16	17
GEBZE TEKNİK UNİVERSİTESİ	30	4
OZYEGİN UNİVERSİTESİ	x	x
İZMİR YUKSEK TEKNOLOJİ ENSTİTUSU	996	5
YILDIZ TEKNİK UNİVERSİTESİ	34	1
TOBB EKONOMİ VE TEKNOLOJİ	11	5
SELCUK UNİVERSİTESİ	76	8
EGE UNİVERSİTESİ	13	2
ERCİYES UNİVERSİTESİ	4	0
İSTANBUL SEHİR UNİVERSİTESİ	106	34
GAZİANTEP UNİVERSİTESİ	196	161
HACETTEPE UNİVERSİTESİ	77	44
CANKAYA UNİVERSİTESİ	299	32
ATILIM UNİVERSİTESİ	133	20
ANADOLU UNİVERSİTESİ	20	5
GAZİ UNİVERSİTESİ	43	0
ANKARA UNİVERSİTESİ	62	6
ABDULLAH GUL UNİVERSİTESİ	660	11
ULUDAG UNİVERSİTESİ	6	0
SAKARYA UNİVERSİTESİ	47	2
DOKUZ EYLUL UNİVERSİTESİ	45	6
YEDİTEPE UNİVERSİTESİ	69	17
CUKUROVA UNİVERSİTESİ	687	47
İZMİR EKONOMİ UNİVERSİTESİ	6	4
İSTANBUL UNİVERSİTESİ	9	0

Erciyes University web site has the lowest errors, Izmir High Technology Institute has the highest errors. Markup validation service was not worked for Ozyegin University. Table 3. Page Size Comparison

Table 2. W3C CSS Validation

University	Number of	Number of
SABANCI UNİVERSİTESİ	605	470
ORTA DOGU TEKNİK UNİVERSİTESİ	67	288
İHSAN DOGRAMACI BİLKENT UNİVERSİTESİ	37	178
İSTANBUL TEKNİK UNİVERSİTESİ	353	533
BOGAZİCİ UNİVERSİTESİ	1	43
KOC UNİVERSİTESİ	102	71

University	CSS Errors	Warnings
GEBZE TEKNİK ÜNİVERSİTESİ	55	165
OZYEGİN ÜNİVERSİTESİ	257	1388
İZMİR YUKSEK TEKNOLOJİ ENSTİTUSU	17	83
YILDIZ TEKNİK ÜNİVERSİTESİ	61	333
TOBB EKONOMİ VE TEKNOLOJİ	142	2190
SELCUK ÜNİVERSİTESİ	565	494
EGE ÜNİVERSİTESİ	x	x
ERCİYES ÜNİVERSİTESİ	162	308
İSTANBUL SEHİR ÜNİVERSİTESİ	7	42
GAZİANTEP ÜNİVERSİTESİ	6	100
HACETTEPE ÜNİVERSİTESİ	11	70
CANKAYA ÜNİVERSİTESİ	54	179
ATILIM ÜNİVERSİTESİ	60	60
ANADOLU ÜNİVERSİTESİ	26	659
GAZİ ÜNİVERSİTESİ	x	x
ANKARA ÜNİVERSİTESİ	725	755
ABDULLAH GUL ÜNİVERSİTESİ	176	1439
ULUDAG ÜNİVERSİTESİ	45	214
SAKARYA ÜNİVERSİTESİ	107	1016
DOKUZ EYLUL ÜNİVERSİTESİ	334	1159
YEDİTEPE ÜNİVERSİTESİ	1115	785
CUKUROVA ÜNİVERSİTESİ	6	20
İZMİR EKONOMİ ÜNİVERSİTESİ	219	317
İSTANBUL ÜNİVERSİTESİ	337	1406

Bogazici University web site has the lowest CSS errors, Yeditepe University has the highest errors. CSS validation service was not worked for Ege University.

Table 3. Page Size Comparison

University	HTML Size (KB)	Total Size (MB)
SABANCI ÜNİVERSİTESİ	58	4,59
ORTA DOGU TEKNİK ÜNİVERSİTESİ	16	1,92
İHSAN DOGRAMACI BİLKENT ÜNİVERSİTESİ	23	2,26
İSTANBUL TEKNİK ÜNİVERSİTESİ	336	8,71
BOGAZİCİ ÜNİVERSİTESİ	45	0,50
KOC ÜNİVERSİTESİ	11	2,40
GEBZE TEKNİK ÜNİVERSİTESİ	472	2,52
OZYEGİN ÜNİVERSİTESİ	38	3,88
İZMİR YUKSEK TEKNOLOJİ ENSTİTUSU	230	2,58
YILDIZ TEKNİK ÜNİVERSİTESİ	65	8,30
TOBB EKONOMİ VE TEKNOLOJİ ÜNİVERSİTESİ	53	7,53
SELCUK ÜNİVERSİTESİ	280	4,70
EGE ÜNİVERSİTESİ	25	1,47
ERCİYES ÜNİVERSİTESİ	428	11,35
İSTANBUL SEHİR ÜNİVERSİTESİ	18	0,64
GAZİANTEP ÜNİVERSİTESİ	75	11,93

HACETTEPE UNİVERSİTESİ	8	1,89
CANKAYA UNİVERSİTESİ	74	6,72
ATILIM UNİVERSİTESİ	29	5,06
ANADOLU UNİVERSİTESİ	10	1,76
GAZİ UNİVERSİTESİ	15	5,10
ANKARA UNİVERSİTESİ	18	2,02
ABDULLAH GUL UNİVERSİTESİ	433	50,31
ULUDAG UNİVERSİTESİ	65	9,77
SAKARYA UNİVERSİTESİ	88	8,42
DOKUZ EYLUL UNİVERSİTESİ	25	1,87
YEDİTEPE UNİVERSİTESİ	103	1,89
CUKUROVA UNİVERSİTESİ	148	5,06
İZMİR EKONOMİ UNİVERSİTESİ	59	5,60
İSTANBUL UNİVERSİTESİ	33	4,58

*Hacettepe University web site has the lowest HTML size, Gebze Teknik University has the highest HTML size. Bogazici University web site has the lowest total size, Abdullah Gul University has the highest total size.

4. CONCLUSION

According to Greenwood the home page is the first glimpse of the college for many prospective students.[12] Because of that a clean and more accessible web site is very important. %23,3 of this universities web pages has more than 100 markup errors and %46,6 of this universities web pages has more than 100 CSS errors . To reduce that web developers need to follow the guidelines carefully.

Also %43 of these sites are bigger than 5 MB. If a regular student visit the universities main page daily. It will cost 150 MB per month. To reduce that web developers need to use compression tools for images and minifiers for other files.

REFERENCES

[1]. Irina Ceaparu & Ben Shneiderman, (2002) "Improving Web-based Civic Information Access: A Case Study of the 50 US States", Technology and Society, 2002. (ISTAS'02). 2002 International Symposium on, Copyright 2002 IEEE, pp. 275-282.
[2]. Abdulmohsen Abanumy, Ali Al-Badi and Pam Mayhew,(2005) "e-Government Website Accessibility: In-Depth Evaluation of Saudi Arabia and Oman", The Electronic Journal of e-Government 3 (3), pp- 99-106.
[3]. Joanne M. Kuzma, Dorothy Yen, Klaus Oestreicher,(2009) "Global e-government Web Accessibility: An Empirical Examination of EU, Asian and African Sites", Second International Conference on Information and Communication Technologies and Accessibility, pp 1-6.
[4]. Uthayasankar Sivarajah, Zahir Irani,(2012) "Exploring the application of web 2.0 in e-government: A united kingdom context", tGovernment Workshop 2012 (tGov2012) May 8th - 9th, 2012 Business School, Brunel University, United Kingdom.
[5]. Serhat Kurt, (2016) "Accessibility of Turkish university Web sites" Universal Access in the Information Society doi:10.1007/s10209-016-0468-x
[6]. (2017) The HTTP Archive webpage. [Online]. Available: *http://httparchive.org/interesting.php?a=All&l=Apr%2015%202017*
[7]. *(2015) Cısco Visual Networking Index webpage. [Online]. Available: http://www.cisco.com/c/dam/m/en_us/solutions/service-provider/vni-forecast-highlights/pdf/Global_Device_Growth_Traffic_Profiles.pdf*
[8]. (2016) Entrepreneurial and Innovative University Index of TUBITAK webpage. [Online]. Available: https://www.tubitak.gov.tr/sites/default/files/2016_gyue_ilk50.pdf
[9]. (2017) The W3C Markup Validator webpage. [Online]. Available: https://validator.w3.org/nu/
[10]. (2017) The W3C CSS Validator webpage. [Online]. Available: https://jigsaw.w3.org/css-validator/
[11]. (2017) The HTTP Archive webpage. [Online]. Available: http://httparchive.org/websites.php
[12]. Greenwood, G. (2012). Examining the presence of social media of university Web sites. Journal of College Admission, Summer, 24-28.

BIOGRAPHY

Abdurrahman Palalı holds a Bachelors degree in Computer Systems and currently pursuing his Masters Program in Computer Animation and Game Technologies at Hacettepe University. His research interests include Graphic Programming and Game Design.

Huseyin Eldem holds a Master degree in Computer Engineering. His research interests include object based programming and web services.

Ayse Eldem holds a Ph.D. degree in Computer Engineering. Her research interests include data mining, image processing, dynamic web design.

Investigation of Heat Transfer with Laminar Pulsating Flow of Nanofluids in a tube using circular rings

Selma Akcay[1], Unal Akdag[2]

Abstract

In this study, the heat transfer characteristics and friction factor of nanofluids under pulsating inlet flow conditions in a tube with circular rings are investigated numerically. In investigations, the governing equations are solved along with boundary conditions using the finite volume approach (FVM) by SIMPLE algorithm. Firstly, the effects on heat transfer performance of different nanofluid types with varying particle volume fractions and Reynolds numbers under steady flow conditions are analyzed. Then, these nanofluids parameters are kept constant and the heat transfer performance under pulsating flow conditions of nanofluids are investigated. The average Nusselt number and friction factor are calculated for different, pulsating frequencies and amplitudes with a constant particle volume fraction of nanofluid at a fixed Reynolds number. The numerical results indicate that the heat transfer performance enhances with increase in particle volume fraction and Reynolds number in steady regime. It is observed that the heat transfer performance increases with increasing pulsating amplitude in pulsating nanofluid flow, and there is a slightly increase in pressure drop. The computed results reveal that there is a good potential in promoting the heat transfer enhancement by using the nanoparticles under pulsating flow in a tube with circular rings.The obtained results are given as function of dimensionless parameters.

Keywords: *Nanofluids, Pulsating flow, Circular ring, Heat transfer, Numerical study*

1. INTRODUCTION

Alternative ways have been investigated to enhance the heat transfer performance of thermal devices which used in cooling/heating systems, the most important of these is either the use of wavy channel surfaces [1]-[3] or the addition of turbulators such as ring, fin to improve the fluid mixture in the tubes [4]-[8]. These methods are known as passive heat transfer enhancement methods and their production is quite simple. The main purpose for design these devices is to minimize the flow resistance while improving the heat transfer performance. Flow and heat transfer with inserting fins, twisted tapes baffles and coil into a tube have been investigated numerically and experimentally by many researchers and with the results of this studies was reported that the turbulators inserted into tube have significant effect on the heat transfer enhancement [9]-[14].

Ozceyhan et al. [15], studied numerically the heat transfer performance in a tube using circular rings in the range of Reynolds number from 4475 to 43725 for five different spacings between the rings (p= d/2, d, 3d/2, 2d, 3d) and the results shown that the best heat transfer performance was obtained as 18% in p=3d for Re=15600.Gunes et al. [16], investigated experimentally heat transfer performance in a tube using coiled wire for three different pitch ratios (P/D=1, 2, 3) in turbulent flow and it reported that Nusselt number and friction factor increased with decreasing pitch ratio and Reynolds number. Sheikholeslami et al. [17], investigated experimentally the effects on heat transfer and friction factor of perforated helical turbulators for different values of open area ratio (0–0.0625), Reynolds number (6000–12000) and pitch ratio (1.83–5.83) and it declared that heat transfer performance and friction factor decreased with increase of open area ratio and pitch ratio. Keklicioglu and Ozceyhan [18], examined experimentally thermal performance of a tube with coiled-wire inserts installed with a separation from the tube wall with three different pitch-to-diameter ratios (P/D = 1, 2, and 3) for Reynolds numbers from 3429 to 26663. Experimental results were indicated the coiled-wire inserts enhanced significantly the thermal performance together with increase the friction factor when

---

[1] *Corresponding author: Selma Akcay; Institute of Science and Technology, Aksaray University, 68100 Aksaray, Turkey. selma.352@hotmail.com*

[2] *Unal Akdag: Mechanical Engineering Department, Aksaray University, 68100 Aksaray, Turkey. uakdag@gmail.com*

compared with a smooth tube and the highest heat transfer enhancement was found about 1.82 for the P/D = 1 at a Reynolds number of 3429.

Jasiński [19] presented a numerical study to investigate the thermal performance in a circular tube using ball turbulators in the range of Reynolds number from 10,000 to 300,000 for different ball diameters and different distance between the balls. The results indicated that the highest thermal performance (η= 1.22) was obtained with the smallest ball diameters and the greatest distance between the balls at increasing Reynolds numbers. Chingtuaythong et al.[20] investigated experimentally the heat transfer enhancement and friction factor in a tubular heat exchanger using V-shaped rings with four different ring-pitches ($R_P = P/D = 0.5$, 1.0, 1.5 and 2.0) and three ring blockage ratios ($R_B = e/D = 0.1$, 0.15 and 0.2)for $5000 \leq Re \leq 25,000$. Air as the working fluid was used. The experimental results shown that the increase in ring blockage ratio enhanced the heat transfer performance and friction loss but the increase in ring-pitch decreased the heat transfer. The highest thermal performance of the V-ring found as 1.63 at RB = 0.1 and RP = 1.0.Also, it was declared that using V rings acquired much higher heat transfer performance in comparison with other vortex-generation devices such as inclined rings, wire-coils and twisted tapes. Chang et al.[21], studied experimentally flow structures and thermal performance of the tubes fitted with swirl generator configured by twin and four spiky twist fins along a rod at Reynolds number of 750-70,000. The thermal performance factor achieved the higher laminar flow than turbulent flow. It observed that the thermal performance factor found higher values than turbulent flow in laminar flow.

Due to limited transport properties of base fluid, nano-sized particles are added to the base fluids to enhance the fluid transport properties. The use of nanofluids are increased the heat transfer performance of devices such as heat exchanger and electronic components. But the use of nanoparticles are increase the pressure drop due to create the flow resistance. Many researchers have carried out numerically and experimentally to improve the heat transfer performance of a tube with twisted tape insert using nanofluids for turbulent and laminar flow [22]-[25].

Azmi et al. [26], investigated numerically to improve the heat transfer performance of a tube with twisted tape insert using SiO_2 nanofluids for turbulent flow and it was reported that the heat transfer performance enhanced significantly compared to pure water. Yang et al [27], studied numerically turbulent heat transfer of nanofluids using single- and two-phase models in a three-dimensional arc rib-grooved channel with constant wall temperature. The numerical results shown that the average Nusselt number was affected from geometric parameters, nanofluids and Reynolds number. S. Eiamsa-Ard and K. Wongcharee [28], examined experimentally the heat transfer performance of TiO_2-water nanofluids for three different particle volume concentrations of 0.05%, 0.1% and 0.15% in the range of Reynolds number from 8,000 to 15,000 in wavy tubes using semi-circular wings tapes. The results shown that the heat transfer performance enhanced with increasing wing angle and the highest thermal performance of 1.98 was acquired at wing angle of 75°, particle volume concentration of 0.15% and Reynolds number of 8000.

The pulsating flow in a tube using turbulators can lead to enhance of fluid mixture and prevent to agglomeration of nanoparticles. There are very few studies examining the effect of pulsating flow on the heat transfer enhancement in a tube using turbulators. In the literature studies, the flow and heat transfer characteristics with nanofluids in a tube using turbulators were investigated but there is no a study examining the effects of pulsating flow with nanofluids on the flow and heat transfer characteristics in a tube using turbulators. In this study, the flow and heat transfer characteristics under laminar pulsating flow conditions with nanofluid in the tube using circular rings are analyzed. The effects of the nanofluid type, nanoparticle volume fraction, Reynolds number and pulsating parameters on heat transfer performance and friction factor are investigated.

2. NUMERICAL STUDY

2.1. Description of the Physical Domain and Governing Equations

Fig.1. shows the basic geometry of the tube with circular cross sectional rings used in the present study. The geometry considered in present study is similar to the geometry used by Ozceyhan et al.[15]. The circular rings are placed at a distance (a) of 0.6 mm from the tube wall. The ring diameter (d) and the distance between the ring axes (b) are of 1.2mm and 18 mm, respectively. The tube diameter (D) is 18 mm, the tube length (L) is of 108 mm. The problem is considered two dimensional and axis symmetric. All geometric parameters are kept constant.
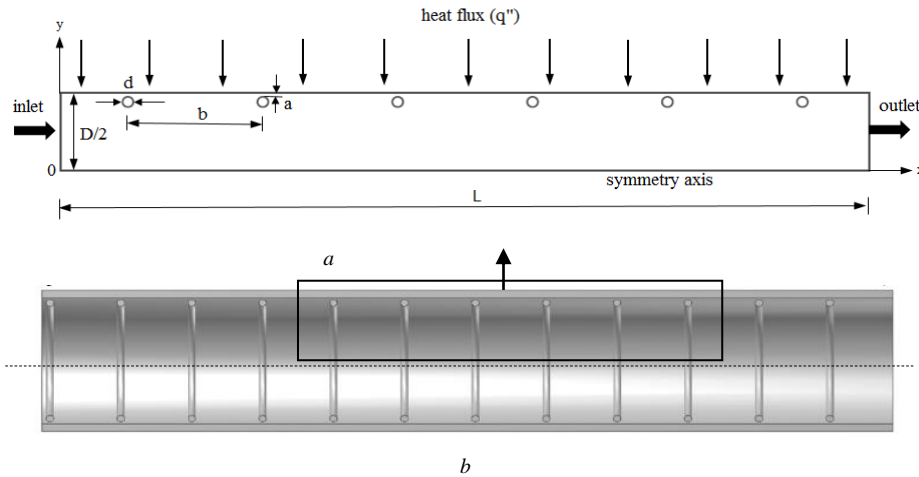
Fig.1. (a) The basic geometry of the tube with circular rings (b) symbolic representation of the present geometry

The nanofluid flow is assumed as a Newtonian fluid, fully developed, laminar, incompressible, two-dimensional, the single phase and steady. The mixture of water and nanoparticles is homogenous and enters the channel at the same flow and thermal conditions. Gravity and radiation heat transfer are negligible. Therefore the governing equations based on these assumptions are as follows:

$$\frac{\partial u_i}{\partial t} + \nabla(\rho u) = 0 \tag{1}$$

$$\frac{\partial u_i}{\partial t} + \frac{\partial(u_i u_j)}{\partial x_i} = -\frac{\partial p}{\partial x_i} + \frac{1}{Re}\nabla^2 u_j \tag{2}$$

$$\frac{\partial T}{\partial t} + u_i \frac{\partial T}{\partial x_i} = \frac{1}{Re\,Pr}\nabla^2 T \tag{3}$$

2.2. Numerical Method and Grid Testing

For the solutions of present problem are used the CFD code Fluent 6.3 [29]. A finite volume method is applied for discretizing the governing equations and they are solved by using the SIMPLE algorithm. The convergence criterion for energy equation and each variable is determined to be 10^{-6}. The different cell numbers are applied to the geometry and simulated by calculating the Nusselt number. The number of cells varied as 23562, 28454, 34580, 42128 and 50342 cell and it shown no much difference in the values of Nusselt number. Thus, the cell number of 34580 is chosen in present study to grid independent solution.

2.3. Physical Properties of the Nanofluids

Physical properties include thermal conductivity, viscosity, density and heat capacitance. By assuming the nanoparticles are well dispersed within the base fluid, the effective thermo-physical properties of the nanofluids can be evaluated using some classical appropriate formulas. The following equations are used in this study.

$$\rho_{nf} = (1-\varphi)\rho_{bf} + \varphi\rho_{pt} \tag{5}$$

$$C_{nf} = (1-\varphi)C_{bf} + \varphi C_{pt} \tag{6}$$

$$k_{nf} = \frac{k_{np} + 2k_{bf} - 2\varphi(k_{bf} - 2k_{np})}{k_{np} + 2k_{bf} + 2\varphi(k_{bf} - 2k_{np})} \tag{7}$$

$$\mu_{nf} = \mu_{bf}(1+1.25\varphi) \tag{8}$$

where the subscript *nf*, *pt* and *bf* indicate the nanofluid, the nanoparticle and base fluids, respectively. Different equations applied in literature studies are tested especially to calculate thermal conductivity,

viscosity and heat capacitance values from thermo-physical properties of the nanofluids. It was observed that there was not so much changed values of this thermo-physical properties [30]-[32].

3. RESULTS AND DISCUSSION

The present numerical study is validated by comparing with the obtained results of Ozceyhan et al. [15]. A similar geometry is simulated for purpose of validating this study. Nusselt numbers are calculated in the range of $4475 \leq Re \leq 43725$ using standard k-ε turbulence model for a smooth circular tube in the simulations. In Fig. 2 is shown the comparison between the two sets of results that a good agreement has been found.
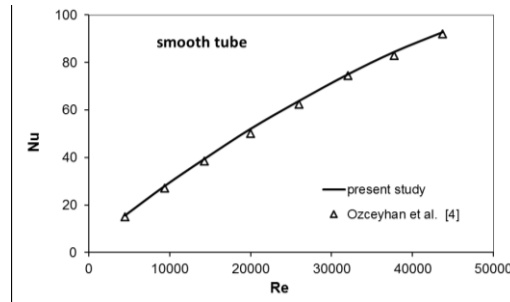
Figure 2.Verification of present study with reference [4]

In this study, the heat transfer mechanism and friction factor are examined as two steps. The steady flow of nanofluids in the first step, the pulsating flow of the nanofluids in the second step are investigated.

Firstly, the effects on heat transfer performance and friction factor of different nanofluid types with varying particle volume fractions and Reynolds numbers under steady flow conditions in the tube with circular rings are analyzed. The investigations are performed with three different nanofluid type as Al_2O_3, CuO and SiO_2, for varying nanoparticle volume fractions (φ=1%, 2%, 3%) in the range of Reynolds number from 20 to 500. Water is used as the working fluid. The numerical solution parameters is given in Table.1 for steady flow of nanofluids. At the tube inlet for steady flow, parabolic velocity profile $[U_r=2U_m(1-(r/R)^2)]$ is defined to keep the hydrodynamic entrance length to be reasonably short. Geometric parameters are kept constant for all cases. The Nusselt number and friction factor are calculated for different nanofluid types, particle volume fractions and Reynolds numbers. The type of nanofluid and volume fraction of nanoparticle that provide the best heat transfer performance at tested Reynolds numbers are determined.

Table 15. The numerical solution parameters for nanofluid flow

Nanofluid	Volume fraction: (φ %)	Reynolds Number: *Re*
Al_2O_3- water	1, 2, 3	20, 50, 100, 200, 500
CuO-water	1, 2, 3	20, 50, 100, 200, 500
SiO_2-water	1, 2, 3	20, 50, 100, 200, 500

The fluids enters the tube with uniform temperature T_o=293K. At the inlet of tube is defined "velocity inlet" boundary condition for steady flow of nanofluids. At the outlet of tube is performed "outflow" boundary condition. The constant heat flux condition is applied for all tube walls. The tube walls are kept at a uniform heat flux (q") of 3000 W/m². At the tube walls are used the usual no-slip boundary conditions. For these boundary conditions, Nusselt number and friction factor are calculated.

The Nusselt numbers are calculated for different case studies of nanofluids. For this purpose, the heat transfer coefficient, *h (W/m²K)*and Nusselt number and are defined as:

$$h = \frac{q''}{(T_w - T_b)} \tag{9}$$

where, T_w is wall temperature of tube and T_b is the bulk fluid temperature in the tube.

$$Nu_{nf} = \frac{hD}{k_{nf}} \tag{10}$$

The effectiveness of the heat transfer is obtained by the heat transfer performance ε, which is defined by Eq. (11).

$$\varepsilon = \frac{Nu_{nf}}{Nu_w}$$ (11)

Where Nu_{nf} is Nusselt number for nanofluids, Nu_w is Nusselt number for pure water. Thus a value of ε over 1.0 denotes enhanced heat transfer.

The circular rings and particle concentration contributes to a significant increase in the shear stress because of the interaction and collision among particles, fluid and the flow passage surfaces. It has been clearly known in the literature that the addition of nanoparticles into a base fluid has produced an adverse effect on the wall shear stress. Because the nanofluids have a higher viscosity value in comparison with base fluids. For the evaluation of pressure drop in present tube with circular rings, the relative skin friction ratio is defined as $r=f_{nf}/f_w$. Where f_{nf} is the friction for nanofluid and the f_w is the friction for pure water.

In Figure 3 is shown the variation of heat transfer performance (a) and friction ratio (b) with varying Reynolds number and particle volume fraction for Al_2O_3-water nanofluid. It is observed that Reynolds number and particle volume fraction affected the heat transfer performance. The heat transfer enhances with a slight increase in friction ratio while Reynolds number and particle volume fraction increase. The maximum heat transfer performance and friction ratio are found of 1.084 and 1.14 at Re=500 and $\varphi=3\%$, for Al_2O_3-water nanofluid, respectively.

In Figure 4 is demonstrated the variation of heat transfer performance (a) and friction ratio (b) with varying Reynolds number and particle volume fraction for CuO-water nanofluid. The heat transfer performance increases as Reynolds number and particle volume fraction increase. But the friction factor is slightly affected from nanoparticle volume fraction. The maximum heat transfer performance and friction ratio are found of 1.082. and 1.079 at Re=500 and $\varphi=3\%$, for CuO-water nanofluid, respectively.
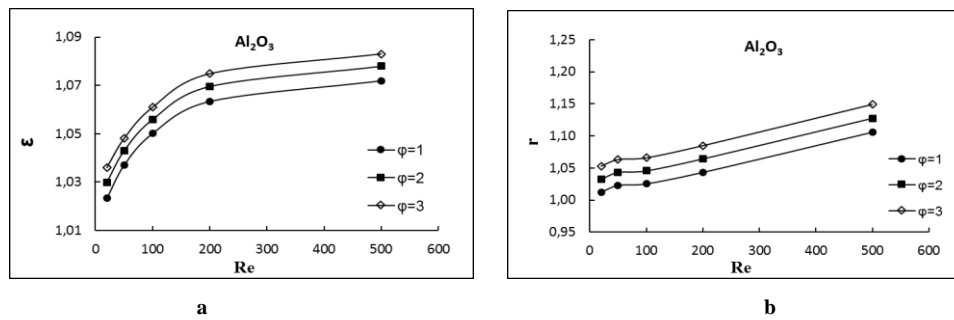
Figure 3. (a)The heat transfer performance and (b) friction ratio varyingforAl₂O₃–water nanofluid.
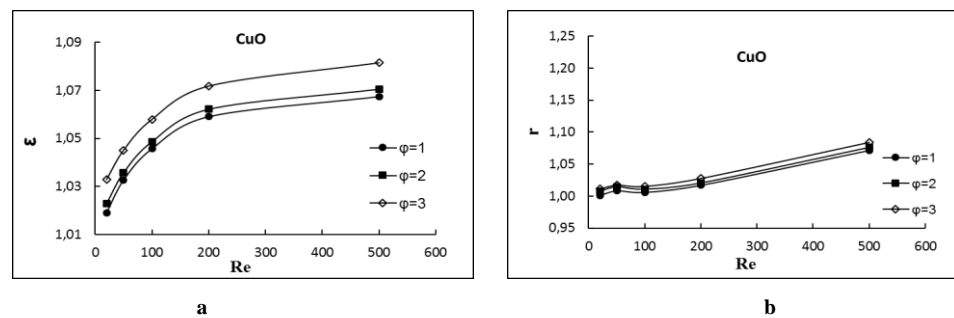
Figure 4. (a) The heat transfer performance and (b) friction ratio varying for CuO-water nanofluid.
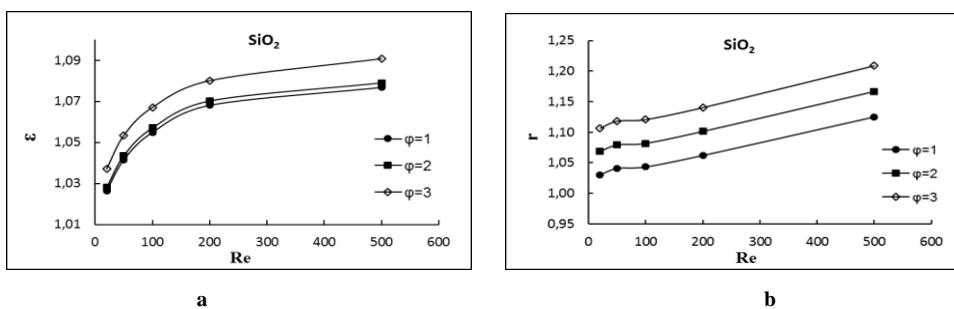
Figure 5. (a)The heat transfer performance and (b) friction ratio varyingforSiO₂–water nanofluid.

In Figure 5 is shown the variation of heat transfer performance (a) and friction ratio (b) with varying Reynolds number and particle volume fraction for SiO_2-water nanofluid. The heat transfer performance increases as Reynolds number and particle volume fraction increase. But the friction factor is significantly affected from nanoparticle volume fraction. The maximum heat transfer performance and friction ratio are found of 1.095. and 1.20 at Re=500 and φ=3%, for SiO_2-water nanofluid, respectively.

In the second step, these nanofluid parameters that provided the best heat transfer performance are kept constant and the heat transfer performance under pulsating flow conditions of nanofluid is investigated. Numerical results indicated that the best heat transfer performance is obtained at Re=500 and φ=3%, for SiO_2-water nanofluid in all the studied cases. The time-average Nusselt number and friction factor are calculated for varying pulsating frequencies and pulsating amplitudes with a specific nanofluid type, particle volume fraction and Reynolds number. In Table 2. is given the numerical solution parameters for pulsating flow of nanofluid.

At the tube inlet, the velocity profile is found by adding the uniform velocity profile with a sinusoidal pulsation for unsteady solutions. The sinusoidal pulsating velocity profile is given by;

$$u_{in} = U_0 \left[1 + A_0 \, sin(\omega t) \right] \tag{12}$$

where A_o is the non-dimensional amplitude ($A_o = x_m/D_h$), ω is the angular velocity and the non-dimensional frequency is defined as the Strouhal number, where $St = fL/U$ and $f = \omega/2\pi$ are the angular frequency. Other boundary conditions are accepted to be the same as the boundary conditions considered for steady flow.

Table 2. The numerical solution parameters for pulsating flow

Nanofluid	Volume fraction: (φ %)	Reynolds number: Re	Pulsating amplitude: Ao	Pulsating frequency: St
SiO_2-water	3	500	1, 2, 3	1, 2, 3, 4

Pulsating frequency and pulsating amplitude are more important parameters in the convection heat transfer of pulsating flow. The periodic flow occurred due to the pulsating parameters in the tube and heat transfer is achieved periodically. Therefore, the heat transfer calculations are achieved to over a cycle. To explain how the mechanisms behave over a cycle, phase angles have been used and presented by "τ=ωt". The 2π radian or 360° indicates a cycle. The results are evaluated after the system achieved fully time periodic state.

In this way, the temporal and time-averaged values of cycle and space-averaged Nusselt numbers are presented for different case studies. For this purpose, time-averaged Nusselt and space-averaged Nusselt numbers are combined with each other and the total or cycle averaged Nusselt number is defined as:

$$Nu_p = \frac{1}{\tau L} \int_0^L \int_0^\tau Nu(x,t)\,dt\,dx \tag{13}$$

Where, τ is dimensionless time period of the cycle, L is the heated length of the tube. The effectiveness of the heat transfer for pulsating flow of nanofluids is obtained by the heat transfer performance ε_p, which is defined by Eq. (14).

$$\varepsilon_p = \frac{Nu_p}{Nu_{nf}} \tag{14}$$

a   b
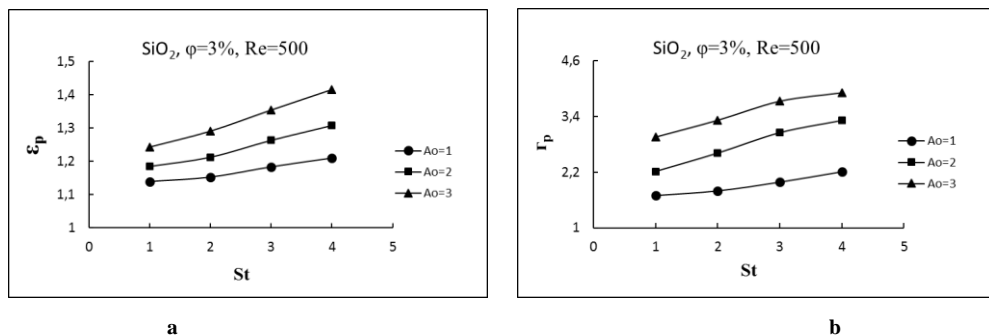
Figure 6. (a) The heat transfer performance and (b)friction ratio varying for pulsating flow of SiO$_2$–water nanofluid.

Where Nu_p is cycle-averaged Nusselt number), Nu_{nf} is Nusselt number for nanofluid. For the pulsating flow of nanofluid in present tube with circular rings, the relative skin friction ratio is defined as $r_p = f_p/f_{nf}$. Where f_p is the friction for pulsating flow of nanofluid and the f_{nf} is the friction for nanofluid.

In Figure 6 is shown the variation of heat transfer performance (a) and friction ratio (b) with pulsating flow of SiO$_2$-water nanofluid at a fixed Reynolds number (Re=500) and particle volume fraction (φ=3%). The heat transfer performance and friction ratio for pulsating flow of nanofluid increase as Strouhal number and pulsating amplitude increase according to the steady flow case of nanofluid. The increasing of amplitude and frequency are increased the fluctuation effect in the flow and as a result of this the friction is increasing. In addition, the pulsating flow in a tube has an advantage to prevent the sedimentation of nanoparticles in the nanofluids suspensions. The maximum heat transfer performance and friction ratio are obtained of 1.42 and 3.91 at Re=500 and φ=3%, for pulsating flow of SiO$_2$-water nanofluid, respectively.

The numerical results shown that the heat transfer performance improves under steady flow by using nanofluids in the tube with circular rings. It observed that the heat transfer performance increases with increasing pulsating parameters in pulsating flow of nanofluids, but there is an increase in friction factor. The numerical results show that there is a good potential in promoting the thermal performance improvement by using the nanoparticles under pulsating flow in the tube with circular rings.

4. CONCLUSIONS

In this study, the effect of nanofluids on heat transfer in the tube with circular rings under laminar pulsating inlet flow conditions is investigated by using control volume based CFD solver. It also friction factor is presented and discussed. Firstly, the effects on heat transfer performance and friction factor of different nanofluid types under steady flow conditions are analyzed. The heat transfer performance and friction factor are effected nanoparticle type, particle volume fraction and Reynolds number. The results indicated that the best heat transfer performance is found at Re=500 and φ=3, for SiO$_2$-water nanofluid in all the studied cases. Then, the heat transfer performance under pulsating flow of nanofluids are investigated. The maximum heat transfer performance and friction ratio are obtained of 1.42 and 3.91 at Re=500 and φ=3, for pulsating flow of SiO$_2$-water nanofluid, respectively.As a result, pulsating flow of nanofluids plays a considerable role on flow structure and thermal fields in the tube with circular rings, which may lead to heat transfer enhancement.

REFERENCES

[1]. U.Akdag, S.Akcay, and D.Demiral, "Heat transfer enhancement with laminar pulsating nanofluid flow in a wavy channel", *Int. Commun. Heat Mass Transfer*, vol. 59, pp. 17–23, 2014.

[2]. M. Khoshvaght-Aliabadi, M. Sahamiyan, M. Hesampour, and O. Sartipzadeh, "Experimental study on cooling performance of sinusoidal‑wavy minichannel heat sink", *Applied Thermal Engineering*, vol. 92, pp. 50‑61,2016.

[3]. M. Akbarzadeh, S. Rashidi, and J.A. Esfahani, "Influences of corrugation profiles on entropy generation, heat transfer, pressure drop, and performance in a wavy channel", *Applied Thermal Engineering*, vol. 116, pp. 278–291, 2017.

[4]. P.R.Chandra, V.R.Alexander, andJ.C.Han, "Heat transfer and friction behavior in rectangular channels with varying number of ribbed walls",*Int. J. Heat and Mass Transf.*, vol. 46, pp. 481–495, 2003.

[5]. P.Promvonge, andS.Eiamsa-ard,"Heat transfer and turbulent flow friction in a circular tube fitted with conical-nozzle turbulators",*Int Commun Heat Mass Transf.*,vol. 34, pp. 72–82, 2007.

[6]. V.Kongkaitpaiboon, K. Nanan, andS.Eiamsa-ard,"Experimental investigation of convective heat transfer and pressure loss in a round tube fitted with circular-ring turbulators". *Int Commun Heat Mass Transf.*, vol. 37, pp. 568–574, 2010.

[7]. G. Pathipakka, and P. Sivashanmugam, "Heat transfer behaviour of nanofluids in a uniformly heated circular tube fitted with helical inserts in laminar flow", *Superlatt. Microstruct.*, vol. 47, issue 2, pp.349–360, 2010.

[8]. G.Tanda, " Effect of rib spacing on heat transfer and friction in a rectangular channel with 45° angled rib turbulator on one/two walls",*Int. J. Heat Mass Transf.*, vol. 54, pp. 1081–1090, 2011.

[9]. P. Promvonge, C. Khanoknaiyakarn, S. Kwankaomeng, and C. Thianpong, "Thermal behavior in solar air heater channel fitted with combined rib and delta-winglet", *Int. Commun. Heat Mass Transf.,*vol. 38,pp. 749–756, 2011.

[10]. A. García, J.P. Solano, P.G. Vicente, and A. Viedma, "The influence of artificial roughness shape on heat transfer enhancement: Corrugated tubes, dimpled tubes and wire coils", *Appl. Therm. Eng.*, vol. 35, pp. 196–201, 2012.

[11]. S. Skullong, S. Kwankaomeng, C. Thianpong, and P. Promvonge, "Thermal performance of turbulent flow in a solar air heater channel with rib-groove turbulators", *Int. Commun. Heat Mass Transf.*, vol. 50, pp. 34–43, 2014.

[12]. T. Alam, R.P.Saini, and J.S.Saini,"Use of turbulators for heat transfer augmentation in an air duct—a review", *Renew Energy*, vol. 62, pp. 689–715, 2014.

[13]. S. Tamna, Y. Kaewkohkiat, S. Skullong, and P. Promvonge, "Heat transfer enhancement in tubular heat exchanger with double V-ribbed twisted-tapes", *Case Studies in Thermal Engineering*, vol. 7, pp. 14–24,March 2016.

[14]. A. Saysroy, and S. Eiamsa-ard, "Periodically fully-developed heat and fluid flow behaviors in a turbulent tube flow with square-cut twisted tape inserts", *Applied Thermal Engineering,*vol. 112, pp. 895–910, February 2017.

[15]. V. Ozceyhan, S. Gunes, O. Buyukalaca, and N. Altuntop, "Heat transfer enhancement in a tube using circular cross sectional rings separated from wall", *Applied Energy*, vol. 85, pp. 988–1001, 2008.

[16]. S. Gunes, V. Ozceyhan, O. Buyukalaca, "The experimental investigation of heat transfer and pressure drop in a tube with coiled wire inserts placed separately from the tube wall", *Applied Thermal Engineering*, vol. 30, pp. 1719-1725,2010.

[17]. M. Sheikholeslami, M. Gorji-Bandpy, and D.D. Ganji, "Effect of discontinuous helical turbulators on heat transfer characteristics of double pipe water to air heat exchanger", *Energy Conversion and Management,* vol. 118, pp. 75–87, June 2016.

[18]. O. Keklikcioglu and V. Ozceyhan, "Experimental investigation on heat transfer enhancement of a tube with coiled-wire inserts installed with a separation from the tube wall", *International Communications in Heat and Mass Transfer,* vol. 78, pp. 88–94, November 2016.

[19]. P. B. Jasiński, "Numerical study of thermo-hydraulic characteristics in a circular tube with ball turbulators. Part 3: Thermal performance analysis", *International Journal of Heat and Mass Transfer*, vol. 107, pp. 1138–1147,April 2017

[20]. W. Chingtuaythong, P. Promvonge , C. Thianpong, and M. Pimsarn, "Heat transfer characterization in a tubular heat exchanger with V-shaped rings", *Applied Thermal Engineering*, vol. 110, pp. 1164–1171, January 2017.

[21]. S. W. Chang, K. C. Yu, K. C. Huang, Thermal performances of tubular flows enhanced by twin and four spiky twisted fins on rod, Applied Thermal Engineering, Volume 112, 5 February 2017, Pages 45–60.

[22]. K.V. Sharma, L.S. Sundar, and P.K. Sarma, "Estimation of heat transfer coefficient and friction factor in the transition flow with low volume concentration of Al_2O_3 nanofluid flowing in a circular tube and with twisted tape insert, Int. Commun. Heat Mass Transfer 36 (2009) 503–507.

[23]. L.S. Sundar, and K.V. Sharma, "Turbulent heat transfer and friction factor of Al_2O_3 nanofluid in circular tube with twisted tape inserts", *Int. J. Heat Mass Transfer*, vol. 53, pp.1409–1416, 2010.

[24]. M. Chandrasekar, S. Suresh, and A.C. Bose, "Experimental studies on heat transfer and friction factor characteristics of Al_2O_3/water nanofluid in a circular pipe under laminar flow with wire coil inserts", *Expt. Thermal Fluid Sci*. vol. 34, issue 2, pp.122–130, 2010.

[25]. L. S. Sundar, N.T. R. Kumar, M.T. Naik, and K.V. Sharma, "Effect of full length twisted tape inserts on heat transfer and friction factor enhancement with Fe_3O_4 magnetic nanofluid inside a plain tube: An experimental study", *International Journal of Heat and Mass Transfer*, vol. 55, pp.2761–2768, 2012.

[26]. W.H.Azmi, K.V. Sharma, P.K. Sarma, R. Mamat, S. Anuar and L. S. Sundar, "Numerical validation of experimental heat transfer coefficient with SiO_2 nanofluid flowing in a tube with twisted tape inserts", *Appl. Therm. Eng*. vol. 73, pp.296–306, 2014.

[27]. Y. Yang, H. Tang, B. Zeng and M. Jian, "Numerical simulation and optimization of turbulent nanofluids in a three-dimensional arc rib-grooved channel", *Numerical Heat Transfer, Part A: Applications, An International Journal of Computation and Methodology*, vol. 70, issue 8, pp. 831-846,2016.

[28]. S. Eiamsa-Ard and K. Wongcharee, "Experimental study of TiO_2-water nanofluid flow in corrugated tubes mounted with semi-circular wing tapes", *Heat Transfer Engineering*, http://dx.doi.org/10.1080/01457632.2017.1280277.

[29]. Fluent 6.3. FLUENT user's guide. Fluent, Inc., Lebanon, NH. 03766, USA, 2006.

[30]. A.A.Minea, "Effect of microtube length on heat transfer enhancement of a water/Al2O3 nanofluid at high Reynolds numbers", *Int. J. Heat Mass Transfer*, vol. 62, pp. 22–30, 2013.

[31]. B.C.Pak and Y.I.Cho, "Hydrodynamic and heat transfer study of dispersed fluids with submicron metallic oxide particles", *Experimental Heat Transfer*, vol. 11, issue (2), pp. 151–170, 1998.

[32]. S.Kakac, A.Pramuanjaroenkij, "Review of convective heat transfer enhancement with nanofluids*", Int. J. Heat Mass Transfer*, vol. 52, pp. 3187–3196, 2009.

Selma Akcay, She was born in 1975 in Kayseri. In 2000, she completed the Department of Mechanical Engineering at Erciyes University, Turkey. She graduated from Aksaray University, Institute of Science and Technology in 2015. She is working as a Mechanical Engineer at Kayseri Provincial Health Directory. Heat transfer, pulsating flow, computational fluid dynamics, nanofluids and microflow topics are of interest.

Unal Akdag, He was born in 1970 in Aksaray. In 1992, he completed the Department of Mechanical Engineering at Erciyes University,Turkey. He graduated from Nigde University in 1997 with a Master's degree in Institute of Science and Technology, in 2005 with Istanbul Technical University, Institute of Science Mechanical Engineering and Energy Program Doctorate. In 2006, he was a scholarship researcher at Texas A & M University (USA). He is working as a Professor at Aksaray University, Mechanical Engineering Department. Heat and mass transfer, heat transfer in oscillating/pulsating flow, computational fluid dynamics, nanofluids and microflow topics are of interest.

The Removal of Phenol by Electro-Oxidation Process Using Graphene Cathode

Erhan Gengec[1], Nevin Atalay Gengec[2], Merve Anac[3], Mehmet Kobya[4]

Abstract

In this study, a graphene (G) cathode for electro-oxidation process was produced by four main steps; (I) production of graphite oxide, (II) sonication of graphite oxide to graphene oxide (GO), (III) GO films fabrication with a thickness of about 8.7 μm by filtration of a measured amount of GO dispersion, and (IV) a direct thermal annealing process of GO film at 1100 ºC. The structure and properties of G cathode were determined with XRD, SEM, and four probe methods. The fabricated G cathode and a piece of Platine as anode were used in treatment of model pollutants (phenol). The effects of pH, current density, operating time, and phenol concentration were evaluated on treatment efficiencies. The results showed that the produced graphene cathode has a huge potential for treatment of wastewater. The maximum removal efficiencies for 50, 100, 200 and 300 mg/L of phenol were obtained respectively as 95.6 %, 87.8 %, 56.9 % and 18.1 % at the 100 mA/cm^2, 180 min., pH 5 and 4.0 g/L Na$_2$SO$_4$.

Keywords: *Electro oxidation; Graphene Cathode, Phenol*

1. INTRODUCTION

The most basic goal in wastewater treatment is to obtain the highest treatment efficiencies without generating any secondary waste at the cheapest cost. To this end, electrochemical treatment techniques are emerging as an important alternative. Electrocoagulation (EC), electrooxidation (EO), and electro-fenton (EF) are the most promising in the electrochemical treatment systems. Electrooxidation (EO) have presented a lot of advantages: (I) oxidation of pollutant up to their mineralization or the less toxic by-products when compared with coagulation, membrane, filtration, and adsorption processes, (II) low oxidation time requirements, non-sensitivity to toxic and non-biodegradable material, and no sludge problem in contrast with biological oxidation processes, and (III) environmental compatibility because the addition of chemical reagents is not required (except of electrolyte or catalyst addition in a low amount). EO can be categorized as direct and indirect oxidation. In direct oxidation processes, EO may occur by (I) direct oxidation of pollutants on anode surface, and (II) oxidation of water on anode's surface to produce hydroxyl radicals, and degradation of pollutants by hydroxyl radicals. In indirect oxidation processes (mediated oxidation), oxidizing reagents such as chlorine, hypochlorous acid, hypochlorite, hydrogen peroxide, ozone are formed at electrodes surface and then, destroy pollutants in wastewater[1–4]. In the EO processes the selection of electrode is a key point because EO processes carry out on electrode surface as summarized above. Therefore, in this study, a novel graphene cathode was fabricated and used for treatment of the model pollutant, phenol. As known, graphene has presented extraordinary physical, mechanical, thermal, and electrical properties [5]. Moreover, the graphene related works are increasing day by day due to numerous applications such as nanoelectronics, sensors, transistors, solar cell, ultracapacitors, conducting polymer composites, adsorbents, and electrodes [6].

We studied the production of graphene cathode via the thermal annealing of graphene oxide film at 1100 C and reported the removal of phenol via the G cathode in electro oxidation process. The effect of pH (3-10), current density (10-100 mA/cm^2), operation time(0-180 min), electrolyte concentration (0.3-2.0 g/L), and phenol concentration (50-300 mg/L) on treatment efficiencies were evaluated during electrooxidation.

[1] *Corresponding author: Department of Environmental Protection; Kocaeli University; Kocaeli; Turkey . erhan.gengec@kocaeli.edu.tr*

[2] *Department of Environmental Protection; Kocaeli University; Kocaeli; Turkey . atalay_nevin@hotmail.com*

[3] *Department of Environmental Protection; Kocaeli University; Kocaeli; Turkey . mrve.anc@gmail.com*

[4] *Department of Environmental Engineering; Gebze Technical University; Gebze; Turkey, kobya@gte.edu.tr*

2. MATERIALS AND METHODS

2.1. Reagents and apparatus

Sulphuric acid (98 %), ortho-phosphoric acid (85 %), and hydrochloric acid (35 were purchased from Merck. Graphite powder ($< 20\,\mu m$), Anodisc membrane filter (47 mm in diameter, 0.2 μm pore size, Whatman), and all the other chemicals were purchased from Sigma Aldrich and used without further purification.

2.2. Graphene Cathode Fabrication

In this study, graphite oxide (GO) was synthesized from graphite powder by Torr method [5] as reported in literature. A 9:1 mixture of concentrated H_2SO_4/H_3PO_4 (360:40 mL) was added to a mixture of graphite powder (3.0 g,) and $KMnO_4$ (18.0 g), producing a slight exotherm to 35-40 °C. The reaction was then heated to 50 °C and stirred for 24 h. The reaction was cooled to room temperature and 30% H_2O_2 (3 mL) was added in ice bath. Then, the mixture was centrifuged (3000 rpm for 30 min), and the supernatant was decanted away. The remaining solid material was then washed twice in succession with 200 mL of water, 200 mL of 30% HCl, and 200 mL of ethanol. The resulting suspension was dried at 60 °C and thus graphite oxide power was obtained. GO dispersion was obtained by ultrasonication (100W, KUDOS) of the prepared graphite oxide powder in deionize water (1 mg/mL) and centrifugated at 3000 rpm for 30 min to remove non-exfoliated materials[7]. After sonication process, turbidity and density of obtained dispersion (GO) were determined respectively as 28.5 NTU by turbidity meter and 0.75 mg/mL by pycnometer. Then, GO films were fabricated by vacuum assisted filtration of 100 ml GO dispersion through an anodisc membrane filter. The resulting GO films were stored in a desiccator before use. Finally, fabrication of G was carried out at 1100 ºC from GO film under Argon flow of 0.3 L/min (STF13/130, Protherm Furnaces, Turkey).

X-ray diffraction (XRD) of the prepared GO and G films were performed on a Bruker D8 Advance diffractometer using a Cu tube as X-ray source (λ Cu, K α = 1.54A°) a tube voltage of 40 kV, and a current of 40 mA. The morphology of the GO and G films were characterized by scanning electronic microscopy (SEM) using a Philips XL 30 SFEG microscope. Resistance values of the GO and G films were determined by four probe method.

2.3. Electro oxidation (EO) set-up and procedure

EO experiments were carried out at room temperature in a 500 mL undivided cylindrical glass cell equipped with two electrodes. A DC power supply (Lambda Electronique, USA) was used at galvanostatic mode. The prepared graphene electrode (9 cm^2) as cathode and a Platine (0.5 cm^2) as anode electrode were used. The distance between electrodes was arranged as 3 cm. The 250 mL aqueous phenol solution was filled to the reactor. pH of solution was adjusted by 1 M H_2SO_4 and NaOH and magnetically stirred at 300 rpm. Na_2SO_4 was used as electrolyte for increased the conductivity of solution. Phenol concentrations in samples were determined with Agilent 1260 Infinity HPLC with a UV detector at 280 nm. A 250 mm long C-18 capillary column (Eclipse XDB, Agilent) with an internal diameter of 4.6 mm was used to separate compounds. A 88:12 v/v mixture of ultra-pure water+acetic acid (1%): methanol was used as a mobile phase. Flow rate was set to 0.8 mL/min. The R^2 value of regression line, which was obtained by measuring diluted series of phenol from stock solution of 1000 mg/L were 0.9992.

(a)   *(b)*
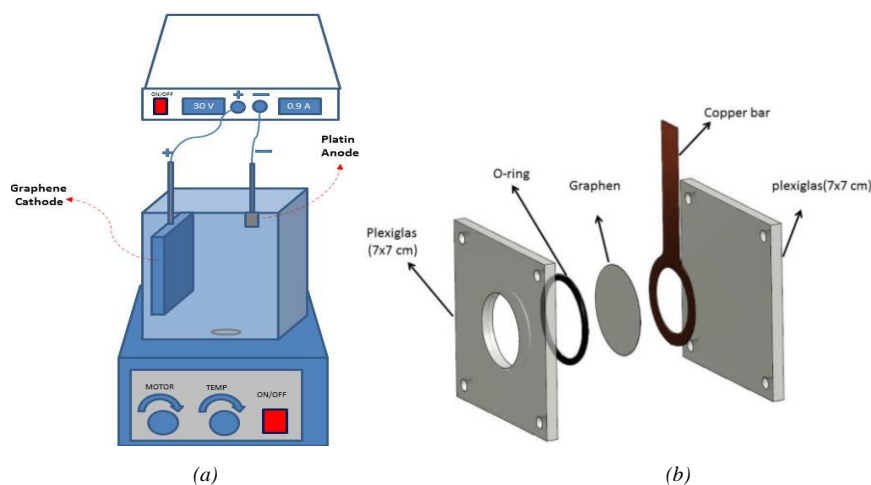
Figure 2.1 EO Reactor (a) and graphene cathode (b).

3. RESULTS AND DISCUSSION

3.1. Characterization of electrode

The graphene oxide is obtained by exfoliation of graphite oxide. Generally, the most commonly used method for exfoliation is sonication and thermal methods. On the other hand, the difference between graphene oxide and graphene is that the graphene is free from functional groups present in the graphite oxide. Thus, in this study, a reduction process was applied following the ultrasonication process. The selected reduction method in this study is thermal reduction at 1100 ºC. The thermal reduction is generally carried out at a temperature of 1000-1200 ºC. In the first few hundred degrees C of the thermal reduction process, the water of the material is completely removed. As the reduction process is carried out under an inert gas (N_2, H_2, Ar), functional groups such as carboxyl from graphene oxide are reduced when it reached to high temperatures. One of the greatest advantages of thermal reduction is contribution of the thermal reduction to the exfoliation. For these reasons, while the thickness of the material decreases during thermal reduction (loss of functional groups and loss of water), the distance between the layers increases. On the other hand, the biggest disadvantage of thermal reduction is the difficulties in practice.

To confirm production of G and GO films X-ray diffraction (XRD) and Scanning Electron Microscope were used. As seen in Fig 3.1, diffraction peaks at $\theta = 11.66º$ and $24.8º$ were recorded for XRD patterns of graphene oxide and graphene films, respectively.
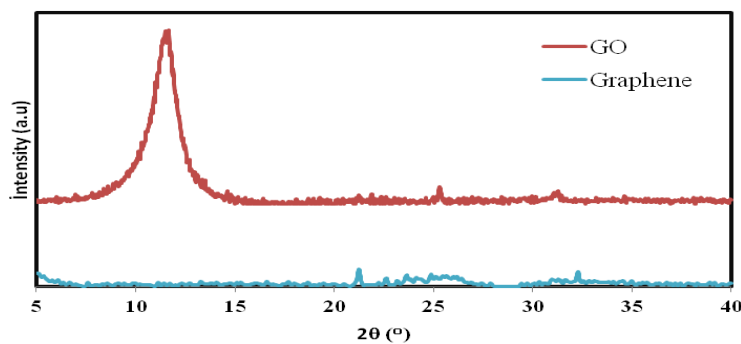
Figure 3.1 XRD patterns of GO and graphene film.

As a matter of fact, according to literature [8], peaks in XRD patterns of G and GO films are almost $2\theta = 10-11º$ and $23-25º$, respectively and for this reason our results are compatible with the literature. Furthermore, XRD results give important information about the interlayer spacing of the materials which is about proportional to the degree of oxidation.

The interlayer spacing for GO and graphene films were measured as 0.75 and 0.34 nm, respectively. In literature it is reported that when the interlayer spacing of GO varies between 0.7-0.8 nm, that of graphene varies between 0.3-0.4 nm[5]. These results are in harmony with ours. As mentioned above the results showed that the most of the interlayer water molecules and oxygen-containing groups on the plane could be removed with the thermal reduction process.

Digital and SEM images of the GO and G films are given in Figure 3.2. The area of the GO and G films were almost 17 cm^2 and the color of dark brown GO films converted to gray with thermal reduction. Both GO and G films were flexible and foldable without deformation
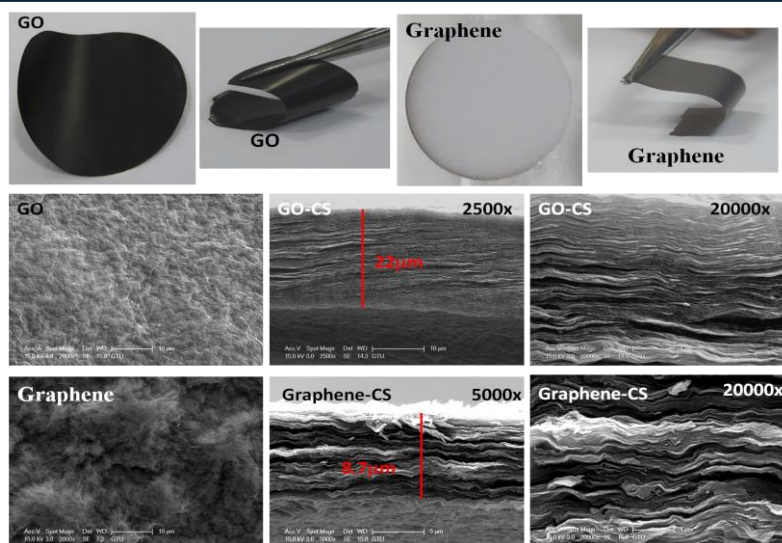
Figure 3.2 SEM images on surface and cross-section (CS) of the produced GO and G films.

From SEM cross-section images, layered structures for both GO and G films are seen and an overall thickness of GO and graphene films were 22, and 8.7 μm , respectively. As seen in SEM images (Figure 1.2), the surface roughness of graphene films was higher than that of GO. This phenomena could be explained as removal of oxygen-containing functional group and molecules of water intercalated in the spacing between the GO layers upon reduction[8].

3.2. Effect of variables on the dye removals

It is known that the main parameters affecting the treatment efficiency in the electrooxidation process are the pH, the current density and the operating time. However, the optimum values of these parameters in wastewater treatment may vary depending on the characterization of the waste water (pH, pollutant species, affinity of pollutants, etc.) and the type of electrode (carbon fiber, graphite, BDD etc.). Thus, the effects of pH (3-10), current density (10-100 mA/cm^2), operation time (0-180 min), and phenol concentration (50-300 mg/L) were evaluated during EO in this study.

Since 1882 it is known that hydrogen peroxide can be formed in aqueous NaOH by cathodic reduction of dissolved oxygen with high surface area carbon electrodes. A number of researchers have been deal with the electro generation of alkaline hydrogen peroxide solutions using carbon-based cathodes in present of pure oxygen or air. More recently, the electro generation of H_2O_2 in the acid medium has been applied to the removal of waste water (Eqn 1). [9].

$$O_2 + 2H^+ + 2e \rightarrow H_2O_2 \tag{1}$$

The removal efficiencies for phenol were measured respectively as 24.55, 19.62, 21.05, 22.26, 20.39, 20.08, and 24.36 % for pH of 3.0, 4.0, 5.0, 6.0, 7.0, 8.5, and 10.0 in this study. The results showed that the removal efficiencies were higher when the pH was acidic and basic, as expected as. Although the removal efficiencies were higher at the two extremes points (pH 3 and 10) of the studied pH range, the yield at pH 5, the solution's natural pH value, was rather close to them. For this reason, the studies in the following sections were conducted at pH of 5.0.
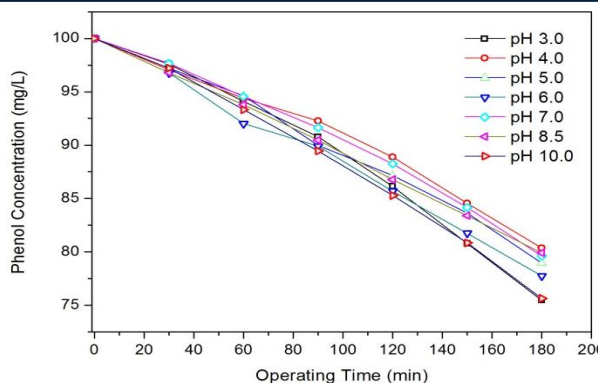
Figure 3.3 The effect of pH on removal efficiencies of phenol (2 g/L Na$_2$SO4, 100 mg/L of phenol and 10 mA/cm^2).

On the other hand, among operating parameters, current density and operating time are important operational parameters for the removal of pollutants. Generally, the increased current density and operation time improved the removal efficiencies. The reason of this situation can be explained as reduction of oxygen and the generation of hydrogen peroxide at the cathode (Eqn 1). As seen in Fig.1.3, the removal efficiencies improved from 25.40 % to 87.85 % when the current density increased from 25 to 100 mA/cm^2 during 180 min. In addition, at the all current densities, the efficiencies of the treatment increased by increased amount of peroxide produced in cathode, due to the increased operating time.
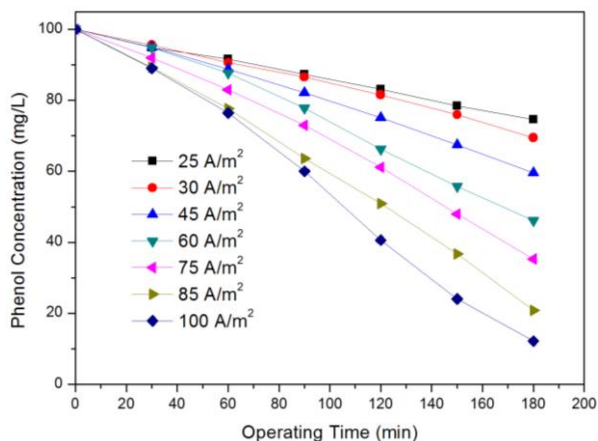
Figure 3.4 The effect of current density and time on removal efficiencies of phenol (pH=5.0, 2 g/L Na$_2$SO4, and 100 mg/L of phenol).

In this study, the studied concentrations of phenols (50-300 mg/L) were determined by taking into account the concentrations of phenol in real wastewaters [10]. The final concentrations of phenol were measured as 6.0, 12.15, 86.27 and 245.62 mg/L for 50, 100, 200 and 300 mg/L of initial phenol concentrations at pH of 5.0, 2 gr/L of Na$_2$SO4, 180 min. and 100 mA/cm^2.
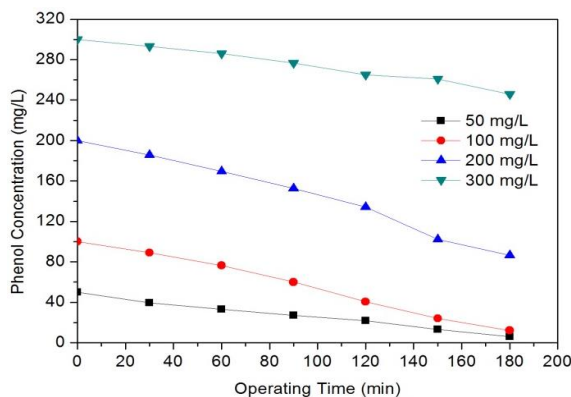
Figure 3.5 The effect of phenol concentration on removal efficiencies (pH=5.0, 2 gr/L Na$_2$SO4, 10 mA/cm^2).

4. CONCLUSIONS

In this study, a graphene cathode was produced by a direct thermal annealing process at 1100 ºC from graphite oxide film. The structure and properties of cathode were characterized with XRD and SEM. The maximum removal efficiencies for 50, 100, 200 and 300 mg/L of phenol were obtained as 95.6 %, 87.8 %, 56.9 % and 18.1 % at the 100 mA/cm^2, 180 min., pH 5 and 2.0 g/L Na$_2$SO$_4$. The results showed that the most effective parameters in EO studies performed with a graphene cathode were current density and operating time.

ACKNOWLEDGMENT

REFERENCES

[1]. O. Scialdone, Electrochemical oxidation of organic pollutants in water at metal oxide electrodes: A simple theoretical model including direct and indirect oxidation processes at the anodic surface, Electrochim. Acta. 54 (2009) 6140–6147. doi:10.1016/j.electacta.2009.05.066.

[2]. H. Särkkä, A. Bhatnagar, M. Sillanpää, Recent developments of electro-oxidation in water treatment - A review, J. Electroanal. Chem. 754 (2015) 46–56. doi:10.1016/j.jelechem.2015.06.016.

[3]. C.A. Martínez-Huitle, S. Ferro, Electrochemical oxidation of organic pollutants for the wastewater treatment: direct and indirect processes., Chem. Soc. Rev. 35 (2006) 1324–40. doi:10.1039/b517632h.

[4]. G. Chen, Electrochemical technologies in wastewater treatment, 38 (2004) 11–41. doi:10.1016/j.seppur.2003.10.006.

[5]. D.C. Marcano, D. V Kosynkin, J.M. Berlin, A. Sinitskii, Z.Z. Sun, A. Slesarev, et al., Improved Synthesis of Graphene Oxide, ACS Nano. 4 (2010) 4806–4814. doi:10.1021/nn1006368.

[6]. T.X.H. Le, M. Bechelany, S. Lacour, N. Oturan, M.A. Oturan, M. Cretin, High removal efficiency of dye pollutants by electron-Fenton process using a graphene based cathode, Carbon N. Y. 94 (2015) 1003–1011. doi:10.1016/j.carbon.2015.07.086.

[7]. E. Ghoniem, S. Mori, A. Abdel-moniem, Low-cost fl exible supercapacitors based on laser reduced graphene oxide supported on polyethylene terephthalate substrate, J. Power Sources. 324 (2016) 272–281. doi:10.1016/j.jpowsour.2016.05.069.

[8]. C. Valles, J.D. Nunez, A.M. Benito, W.K. Maser, Flexible conductive graphene paper obtained by direct and gentle annealing of graphene oxide paper, 0 (2011). doi:10.1016/j.carbon.2011.09.042.

[9]. C. Comninellis, G. Chen, G. Comninellis, Christos ... Chen, Electrochemistry for the Environment, Springer New York Dordrecht Heidelberg London, 2010. doi:DOI 10.1007/978-0-387-68318-8.

[10]. Y. Yavuz, A.S. Koparal, Electrochemical oxidation of phenol in a parallel plate reactor using ruthenium mixed metal oxide electrode., J. Hazard. Mater. 136 (2006) 296–302. doi:10.1016/j.jhazmat.2005.12.018.

Treatment of Acid Orange 7 dye by Electro-Fenton: Optimization through Response Surface Methodology

Erhan Gengec[1], Mehmet Kobya[2], Burak Durmus[3]

Abstract

In this study, electro-fenton process parameters such as current density, operation time, concentration of Fe^{2+} and electrolyte (Na_2SO_4) were optimized at the treatment of acid orange dyes by response surface methodology. The treatment system designed by placing the carbon felt ($25\ cm^2$) as the anode and the platinum plate ($0.5\ cm^2$) as the cathode in an un-divided Plexiglas reactor ($0.5\ l$) was run at batch mode. When air was supplied to the system, the determined amount of iron and electrolyte was added and then the treatment was carried out by applying a potential with a DC power supply. The obtained experimental results were of a fairly high degree of conformity with quadratic model results. R^2 correlation coefficients (94.79%) for the dye removal efficiencies showed a high significance of the model. Furthermore, the Prob>F values from the ANOVA was less than 0.05 showed that the model was considered to be statistically significant. The optimum process conditions for removal efficiencies of dye was found as 96.26% at 96.49 min, 15 mA/cm², 30mM of electrolyte concentration and 0.20 mM of Fe^{2+} concentration. These results showed that RSM is a convenient way to minimize operating costs in order to optimize operating conditions and maximize dye removal efficiency and the Electro-Fenton treatment was a suitable process for the treatment of wastewater.

Keywords: Electro-Fenton; Carbon Soft Felt; Acid Orange 7

1. INTRODUCTION

Increased attention of human about the protection of natural sources has caused limitation of wastewater charge standards. Due to wastewater charge standards limited, nowadays, researchers focus on advanced oxidation processes (AOPs) in the treatment of industrial wastewater for the removal of non-biodegradable and/or toxic pollutants. Among AOPs, electrochemical advance oxidation processes (EAOPs) come into prominence because of some advantages such as easy operating, providing the high removal efficiencies, no sensitive against toxic pollutants and less or no sludge production. EAOPs can be categorized as indirect and direct oxidation processes. Direct oxidation (anodic oxidation) realizes on the surface of anode electrode and is very effective for treatment of wastewater. However, generally used anode electrode such as boron-doped diamond and metal composite electrodes (Ti/Ru-Ir-Sn-Sb) are expensive and hard-accessible. On the other hand, indirect oxidation processes realize via both anode and cathode electrode. Generally, when indirect oxidation carries out at anode, oxidants like chlorine, hypochlorous acid and hypochlorite are formed. On the other hand, in cathode electrode, two electron reduction of oxygen forms the hydrogen peroxide in acidic conditions (Eqn. 1)[1].

$$O_2 + 2H^+ + 2e^- \rightarrow H_2O_2 \tag{1}$$
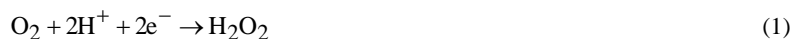
Actually, hydrogen peroxide is not a very effective oxidant. However, adding Fe^{2+} in the presence of hydrogen peroxide encourages the formation of hydroxyl radicals which is the one of the most important and effective radicals in wastewater treatment. The formation of hydroxyl radicals during electrochemical processes by an electron transfer between H_2O_2 and Fe^{2+} was called as electro-fenton (Eqn. 2) [1–4].

---

[1]Corresponding author: Department of Environmental Protection; Kocaeli University; Kocaeli; Turkey . erhan.gengec@kocaeli.edu.tr

[2] Department of Environmental Engineering; Gebze Technical University; Gebze; Turkey, kobya@gte.edu.tr

[3] Department of Environmental Protection; Kocaeli University; Kocaeli; Turkey, b.durmus53@gmail.com

$$Fe^{2+}(aq) + H_2O_2(l) \rightarrow Fe^{3+}(aq) + HO^{\bullet}(aq) + OH^-(aq) \tag{2}$$
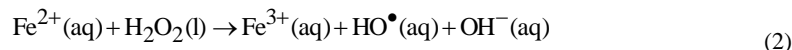
Electro-Fenton processes have many advantages, such as the use of non-toxic reagents, the relatively low production of sludge, in situ production of peroxide and the safety of technology [5,6]. Furthermore, cheap and easy accessible electrodes such as graphite felt, carbon felt, carbon-polytetrafluoroethylene (PTFE), graphite-PTFE, graphite, reticulated vitreous carbon (RVC), activated carbon fiber (ACF), Pt flakes, carbon sponge and stainless steel [6] are probably the most of the important advantage of EF. The performance of EF reactions depends on a lot of process parameters such as pH, current density, electrode type, operation time, concentration of Fe^{2+} and electrolyte. Thus, determination of optimum experimental conditions is necessary for high removal efficiencies and low operation cost. Determination of optimum experimental conditions by conventional methods, which can define one-factor-at-a-time, is time-consuming and does not combine the impacts of all involved factors. Statistical experimental design methods have been applied to chemical processes such as EF to overcome these deficiencies. Response Surface Methodology (RSM), a combination of mathematical and statistical techniques, is widely preferred in order to improve and optimization of parameters[7,8].

This study deals with the optimization of the operation parameters (current density, operation time, concentration of Fe^{2+} and electrolyte (Na_2SO_4)) by RSM for treatment of acid orange model dye by electro-fenton.

2. MATERIALS AND METHODS

2.1. Experimental set-up and procedure

EF experiments were carried out at room temperature in a 600 mL undivided cylindrical glass cell equipped with two electrodes. A soft carbon felt (25 cm^2, Sigratherm® GFA 5) as cathode and a piece of platine (0.5 cm^2) as anode electrode were used and the distance between electrodes was 3 cm. Undivided cylindrical glass cell (Fig. 1) was filled with the 500 mL aqueous solution of AO7 (0.05 mM). The concentration of AO7 was identified according to literature [9] and we noted that the selected concentration was high compared to that commonly found in textile effluents (10^{-4} to 10^{-6} M). Na_2SO_4 as supporting electrolyte and $FeSO_4.7H_2O$ as the catalyst were added into the solution and the pH of solution was adjusted to 3 with 1 M H_2SO_4. Solution was magnetically stirred at 300 rpm.
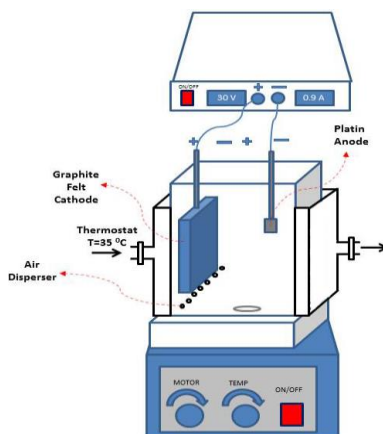
Figure 1.1 A schematic diagram of the experimental set up.

A DC power supply (Lambda Electronique, USA) was used at galvanostatic mode. Continuous saturation of O_2 at atmospheric pressure was ensured by bubbling air. At the end of the experiments, samples were taken and subsequently filtered through a 1.6 μm Whatman glass microfiber to remove iron species. Dye concentrations of the solutions were measured using a UV–vis spectrophotometer at 485 nm (Perkin-Elmer 550 SE).

2.2. Experimental design and data analysis

The Design Expert 8.0.4 software (trial version) for the statistical design of experiments and data analysis was used. The four most important operating variables: operating time (min, x_1), current density (A/m^2, x_2), electrolyte concentration (mM, x_3) and Fe^{2+} concentration (mM, x_4) were optimized. Their range and levels were shown in Tables 1.1.

Table 1.1 Process parameters and their levels for electro-fenton

Factor	Variables	Range of actual and coded variables				
		-2	-1	0	+1	+2
x_1	Operating Time (min)	60	90	120	150	180
x_2	Current Density (A/m^2)	7.5	15	22.5	30	37.5
x_3	Electrolyte Concentration (mM)	20	30	40	50	60
x_4	Fe^{2+} Concentration (mM)	0.05	0.20	0.35	0.50	0.65

3. RESULTS AND DISCUSSION

3.1. Statistical analysis

RSM is one of the most used optimization processes. RSM uses an experimental design such as the Central Composite Design (CCD) to fit a model by least squares technique [7]. Optimization processes can be summarized in three steps as; (1) performing statistically designed experiments, (2) the coefficient estimating in a mathematical model, and the response predicting and (3) checking the validity of the model. CCD in the form of a 2^3 full factorial design with six additional experimental trials as replicates of the central point showed in Tables 3.1.1.

Table 3.1.1 CCD of the experimental variables

	Time	Current Density	Electrolyte	Catalyst	Dye Removal
	(x_1 , min)	(x_2 , A/m^2)	(x_3 , Na$_2$SO$_4$, mM)	(x_4 , FeSO$_4$, mM)	(%)
1	60.0	22.5	40.0	0.35	91.2
2	150.0	30.0	50.0	0.50	97.6
3	150.0	30.0	30.0	0.50	96.9
4	150.0	15.0	50.0	0.20	95.0
5	90.0	30.0	30.0	0.50	96.2
6	180.0	22.5	40.0	0.35	95.2
7	120.0	22.5	40.0	0.35	97.5
8	120.0	7.5	40.0	0.35	96.0
9	150.0	15.0	50.0	0.50	94.4
10	90.0	15.0	50.0	0.50	93.0
11	90.0	15.0	50.0	0.20	93.1
12	120.0	22.5	40.0	0.65	97.1
13	90.0	15.0	30.0	0.50	94.0
14	120.0	37.5	40.0	0.35	98.6
15	120.0	22.5	40.0	0.35	96.8
16	120.0	22.5	60.0	0.35	94.1
17	120.0	22.50	20.0	0.35	96.4
18	120.0	22.50	40.0	0.05	97.4
19	150.0	30.00	30.0	0.20	98.2
20	120.0	22.50	40.0	0.35	97.4
21	90.0	30.00	50.0	0.50	96.9
22	120.0	22.50	40.0	0.35	98.2
23	90.0	30.00	50.0	0.20	96.7
24	150.0	15.00	30.0	0.50	97.2
25	90.0	15.00	30.0	0.20	95.8
26	150.0	15.00	30.0	0.20	98.2

27	120.0	22.50	40.0	0.35	97.5
28	90.0	30.00	30.0	0.20	97.5
29	120.0	22.50	40.0	0.35	97.5
30	150.0	30.00	50.0	0.20	98.2

Analysis of variance (ANOVA) was used to obtain the interaction between the process variables and the responses. The quality of the fit polynomial model was expressed by R^2, and its statistical significance was checked by the Fisher F-test. Model terms were evaluated by the P value (probability) with 95% confidence level (Tables 3.1.2).

Table 3.1.2 ANOVA results for the EF process

Source	Sum of Squares	df	Mean Square	F Value	p-value Prob > F	
Model	91.3314	14	6.523671	19.49805	< 0.0001	Significant
x_1	17.35362	1	17.35362	51.86678	< 0.0001	Significant
x_2	21.52621	1	21.52621	64.33788	< 0.0001	Significant
x_3	7.727101	1	7.727101	23.09488	0.0002	Significant
x_4	2.259569	1	2.259569	6.753435	0.0201	Significant
$x_1 x_2$	1.70311	1	1.70311	5.090282	0.0394	Significant
$x_1 x_3$	0.1186	1	0.1186	0.354474	0.5605	Not significant
$x_1 x_4$	0.027456	1	0.027456	0.082062	0.7784	Not significant
$x_2 x_3$	6.532218	1	6.532218	19.5236	0.0005	Significant
$x_2 x_4$	0.020617	1	0.020617	0.061621	0.8073	Not significant
$x_3 x_4$	1.121734	1	1.121734	3.352657	0.0870	Not significant
x_1^2	27.4306	1	27.4306	81.98503	< 0.0001	Significant
x_2^2	0.020428	1	0.020428	0.061055	0.8082	Not significant
x_3^2	6.487068	1	6.487068	19.38865	0.0005	Significant
x_4^2	0.007223	1	0.007223	0.021589	0.8851	Not significant
Residual	5.01871	15	0.334581			
Lack of Fit	3.991693	10	0.399169	1.943344	0.2400	not significant
Pure Error	1.027016	5	0.205403			
Cor. Total	96.35011	29				
SD	0.578					
Mean	96.324					
C.V. %	0.601					
PRESS	24.471					
R^2	0.948					
Adj. R^2	0.900					
Pred R^2	0.746					
AP	18.83					

SD: Standard Deviation, CV: Coefficient of Variance, PRESS: Predicted Residual Error sum of squares, AP: Adequate Precision, P: Probability of Error.

The F-statistics value was calculated as 19.49 % for dye removal and this value indicated that model was significant. Moreover, the large F-values indicated that most of the variation in the response could be explained by the regression model. On the other hand, If the ANOVA Prob> F values were lower than 0.05, the model was considered statistically significant. In this study, values of Prob>F were <0.0001 for model. As shown in Table 3.1.2, value of coefficient of variance (CV) was 0.601% for dye removal. The CV as the ratio of the standard error of estimate to the mean value of the observed response (as a percentage) was a measure of reproducibility of the model. CV was considered to be reproducible when it is not greater than 10%. The adequate precision (AP) measures the signal to noise ratio and AP was compared for the range of the predicted values at the design points to the average prediction error. The AP values greater than 4 indicated an adequate signal for all response. Therefore, the quadratic model could be used to navigate the design space. A high value of R^2 (>0.94) showed that the model could explain the response successfully (Fig. 3.1). Actual values were the measured response data for a particular run, and the predicted values were evaluated from the model and generated by using the approximating functions. It was seen in Fig. 3.1. that the data points lay close to the diagonal line and the developed model was adequate for the prediction of each response.
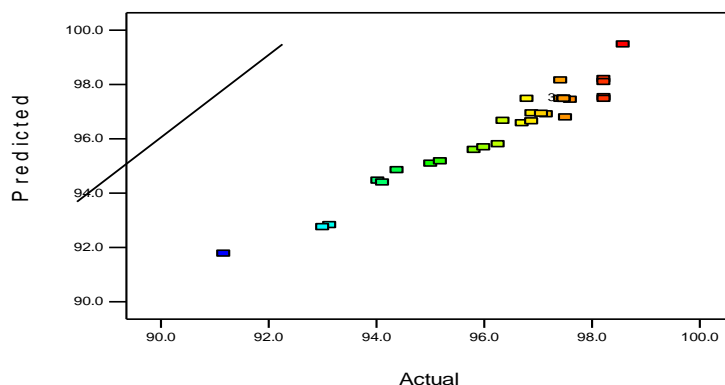
Figure 3.1 Comparisons of predicted and experimental values.

3.2. Effect of variables on the dye removal

The effects of x_1, x_2, x_3 and x_4 on dye removal efficiency were investigated and determined using approximating functions (Eqn. 2). A positive and negative signs in front of the terms refer to a synergistic effect and antagonistic effect, respectively.

$$\text{Dye Removal}(\%) = +97.48 + 0.85\,x_1 + 0.95\,x_2 \quad 0.57\,x_3 \quad 0.31\,x_4 \quad 0.33\,x_1x_2 \quad 0.086\,x_1x_3$$
$$0.041\,x_1x_4 + 0.64\,x_2x_3 + 0.036\,x_2x_4 + 0.26\,x_3x_4 \quad 1.00\,x_1^2 + 0.027\,x_2^2 \quad 0.49\,x_3^2 + 0.016\,x_4^2 \tag{3}$$

Among operating parameters, current density and operating time are important operational parameters for the decolourization, and cost of the treatment processes. As seen in Fig 3.2.a, increasing operating time (x_1) and current density (x_2) contributed noticeably to removal efficiency of dye.
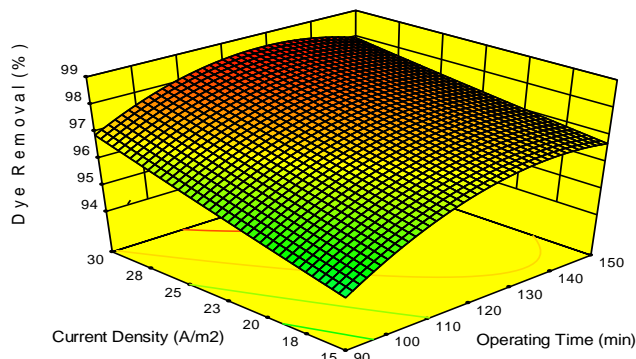
(a)
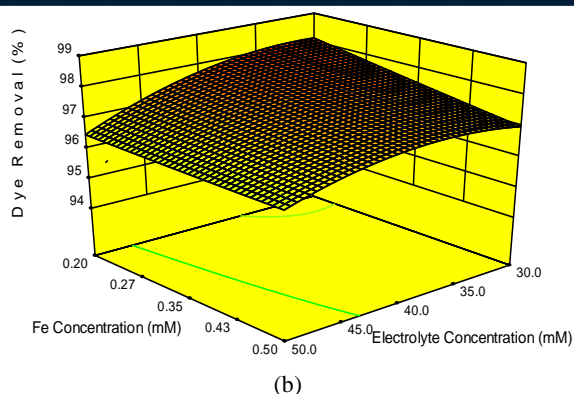
Figure 3.2. Effects of the variables on removal efficiencies.

The applied current density and operation time are the driving force for the reduction of oxygen, and provide the generation of hydrogen peroxide at the cathode (Eqn. 1). High current and long operation time increases the production rate of hydrogen peroxide. The forming hydrogen peroxide increases the number of hydroxyl radicals in the electrolyte medium which are highly reactive and responsible for the degradation [6].

It was observed that the treatment efficiencies increased depending on the reduction of the iron concentration, one of the operating parameters, from 0.20 mM to 0.50 mM, in the studying range. It is well-known that excess ferrous ions could consume the hydroxyl radicals and affect the extent of degradation. Similarly, the increase in electrolyte concentration also reduced the efficiency of treatment (Fig 3.2.b). On the other hand, increase in electrolyte concentration reduced the solution resistance and the voltage between the electrodes.

4. CONCLUSIONS

As a result, the removal efficiencies of dye at the optimum process conditions, 96.6 min, 15 mA/cm^2, 30mM of electrolyte concentration, and 0.20 mM of Fe^{2+} concentration, was found as 96.2%. These results showed that RSM was a suitable method to optimize the operating conditions and maximize the dye removal efficiency while keeping the operating costs to minimal and the electro-Fenton process was an appropriate process for treatment of wastewater.

REFERENCES

[1]. H. Särkkä, A. Bhatnagar, M. Sillanpää, Recent developments of electro-oxidation in water treatment - A review, J. Electroanal. Chem. 754 (2015) 46–56. doi:10.1016/j.jelechem.2015.06.016.

[2]. W. Wu, Z.-H. Huang, T.-T. Lim, Recent development of mixed metal oxide anodes for electrochemical oxidation of organic pollutants in water, Appl. Catal. A Gen. 480 (2014) 58–78. doi:http://dx.doi.org/10.1016/j.apcata.2014.04.035.

[3]. E. Brillas, J. Casado, Aniline degradation by Electro-Fenton® and peroxi-coagulation processes using a flow reactor for wastewater treatment, Chemosphere. 47 (2002) 241–248. doi:10.1016/S0045-6535(01)00221-1.

[4]. E. Brillas, I. Sires, M.A. Oturan, Electro-fenton process and related electrochemical technologies based on fenton's reaction chemistry, Chem. Rev. 109 (2009) 6570–6631. doi:10.1021/cr900136g.

[5]. A. Fernandes, M.J. Pacheco, L. Ciríaco, A. Lopes, Review on the electrochemical processes for the treatment of sanitary landfill leachates: Present and future, Appl. Catal. B Environ. 176–177 (2015) 183–200. doi:10.1016/j.apcatb.2015.03.052.

[6]. P. V. Nidheesh, R. Gandhimathi, Trends in electro-Fenton process for water and wastewater treatment: An overview, Desalination. 299 (2012) 1–15. doi:10.1016/j.desal.2012.05.011.

[7]. A. Fernandes, M.J. Pacheco, L. Ciríaco, A. Lopes, Review on the electrochemical processes for the treatment of sanitary landfill leachates: Present and future, Appl. Catal. B Environ. 176–177 (2015) 183–200. doi:10.1016/j.apcatb.2015.03.052.

[8]. P. V. Nidheesh, R. Gandhimathi, Trends in electro-Fenton process for water and wastewater treatment: An overview, Desalination. 299 (2012) 1–15. doi:10.1016/j.desal.2012.05.011.

[9]. E. Gengec, M. Kobya, E. Demirbas, A. Akyol, K. Oktor, Optimization of baker's yeast wastewater using response surface methodology by electrocoagulation, Desalination. 286 (2012) 200–209. doi:10.1016/j.desal.2011.11.023.

[10]. E. Gengec, U. Ozdemir, B. Ozbay, I. Ozbay, S. Veli, Optimizing dye adsorption onto a waste-derived (modified charcoal ash) adsorbent using box-behnken and central composite design procedures, Water, Air, Soil Pollut. 224 (2013) 1751. doi:10.1007/s11270-013-1751-6.

The Effect of Production Conditions on the Structural and Physical Properties of the Graphene; a potential electrode

Nevin Atalay Gengec[1], *Erhan Gengec*[2], *Mehmet Kobya*[3]

Abstract

The purpose of this study was to investigate the effect of production conditions on structural and physical properties of the graphene films. Therefore, graphite oxide was synthesized by three different methods (Hummers, modified Hummers and improved Hummers methods) as reported in literature, and then graphene oxide (GO) dispersion was obtained by ultrasonication of the graphite oxide in water. Finally, GO films were produced by filtration at different dispersion volumes (33, 50, 80, and 120 mL) of GO, and conductive thin graphene films were fabricated a direct thermal annealing process of GO films through at different temperature (700 and 1100 ºC). Structural analysis and physical properties of the prepared GO and graphene films were determined by SEM, digital Avometer and XRD. XRD results showed that GO was successfully produced with the three methods. However, the improved Hummers method was selected for the synthesis method due to high oxidation degree and reaction yields. The cross-section SEM images indicated that GO and graphene films have a layered structure. GO and graphene films were flexible and foldable without deformation. During our studies, it concluded that the reduction degree, conductivity, and the surface roughness of graphene films increased with increasing of the thermal annealing temperature and decreasing of dispersion volumes. Furthermore, it was clear that the increasing of the thermal annealing temperature contributed the exfoliation of the graphene films. Our results were supported that the produced low rough and conductive graphene films might had an important potential as an electrode.

Keywords: *Graphene, Graphene oxide, Filtration, Thermal annealing, Thick film*

1. INTRODUCTION

Recently, Graphene, a two-dimensional carbon honeycomb nanostructure, has become popular in various application aspects due to its extraordinary physical, mechanical, thermal, and electrical properties[1]. Its unusual properties make it highly attractive for numerous applications such as nanoelectronics, sensors, transistors, solar cell, ultracapacitors, conducting polymer composites, adsorbents, and electrodes [2–4]. A graphene film could be prepared by four steps: (I) the oxidation of graphite, (II) the exfoliation of graphite oxide by thermic or ultrasonic processes, (III) the reduction of graphene oxide by chemical, thermal, and chemical+thermal processes, (IV) preparation of films using different methods such as dip coating, casting, filtration, spray coating, and chemical vapor deposition (CVD) [9,11].

Nowadays, graphite oxide synthesis, which is the first of this four step graphene film synthesis, is realized by three main methods (the Brodie[6], Staudenmaier[7], and Hummers methods[5])[8]. The Hummers method is generally considered the best among others [9]. In addition, a modification of the Hummers method has improved the oxidation degree, and thus, the method increases its utility. [10]. For this reason, graphene oxides were synthesized by the above three methods. Then, the most effective method was selected among these three methods and GO films were produced by filtering the GO in different dispersion volumes. Finally, conductive thin graphene films were fabricated by direct thermal annealing of GO films at different temperatures. Thus, the potential of the graphene films as electrodes has been investigated. In addition, these investigations were supported by examining the structural analysis and physical properties of GO and graphene films.

[1] Corresponding author: University of Kocaeli, Department of Environmental Protection, 41275, Izmit, Kocaeli, Turkey, atalay_nevin@hotmail.com

[2] University of Kocaeli, Department of Environmental Protection, 41275, Izmit, Kocaeli, Turkey, erhan.gengec@kocaeli.edu.tr

[3] Gebze Institute of Technology, Department of Environmental Engineering, 41400, Gebze, Turkey, kobya@gtu.edu.tr

2. MATERIALS AND METHODS

Sulphuric acid (98 %), ortho-phosphoric acid (85 %), and hydrochloric acid (35 were purchased from Merck. Graphite powder (< 20μm, synthetic), Anodisc membrane filter (47 mm in diameter, 0.2 μm pore size, Whatman), and all the other chemicals were purchased from Sigma Aldrich and used without further purification. Graphite oxide was synthesized from graphite powder by oxidation using the Hummers method [5], modified Hummers method [12], and improved Hummers method [13] as reported in literature [13]. GO dispersion was obtained by ultrasonication (100W, KUDOS) of the prepared graphite oxide powder in deionize water (1 mg/mL) for 2 days followed by centrifugation at 3000 rpm for 30 min to remove non exfoliated materials. A final concentration, turbidity, and density of exfoliated GO determined by solid analysis, turbidity meter, and picnometer as 0.75 mg/mL, 28.5 NTU, and 0.99 g/mL, respectively.

GO films was fabricated by vacuum assisted filtration of a measured amount of GO dispersion (33-120 mL) through an Anodisc membrane filter followed by air drying and peeling from the filter. The resulting GO films were stored in a desiccator before use. The thickness of GO films determined by micrometer measurements is about 10-30 μm. The reductions of GO films were realized in a furnace providing inert atmosphere (STF13/130, Protherm Furnaces, Turkey). Different thermal annealing temperatures (700 and 1100 ºC) under Argon flow of 0.1 L/min were applied to reduce the functional groups of GO films.

X-ray diffraction (XRD) of the prepared graphene and GO films was performed on a Bruker D8 Advance diffractometer using a Cu tube as X-ray source (λCu Kα = 1.54A°) a tube voltage of 40 kV, and a current of 40 mA. The morphology of the graphene and GO films was characterized by scanning electronic microscopy (SEM) using a Philips XL 30 SFEG microscope. Resistance values of the graphene and GO films were determined by ovameter.

3. RESULT AND DISCUSSION

3.1. Graphite Oxide and Graphene Oxide Synthesize and Characterization

Graphite oxide was synthesized by oxidation using Hummers (HGO) [5], modified Hummers (MGO) [12], and improved Hummers (IGO) [13] methods as in the literature (Figure 1). Reaction yields of synthesized graphite oxide were calculated gravimetrically. The IGO method had higher reaction yield (32 %) than the HGO (26 %) and MGO (19 %) methods.
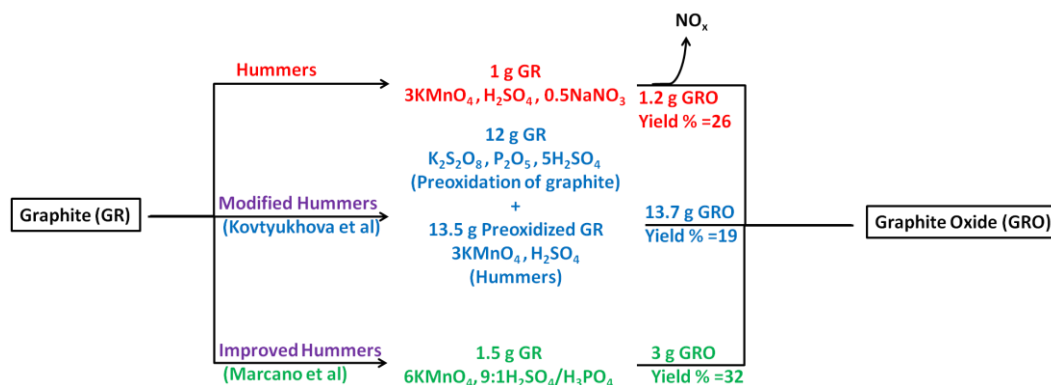
Figure 1: Representation of graphite oxide synthesis using the Hummers and modified Hummers methods. Graphite (GR); Graphite Oxide (GRO).

Graphene oxide (GO) dispersion was prepared by ultrasonication of graphite oxide synthesized with three different methods. Then, GO powders were obtained by drying of GO dispersion at 35 °C. X-ray diffraction (XRD) patterns of GO powders prepared according to Hummers, improved Hummers, and modified Hummers methods presented a diffraction peak 2θ= 11.68º, 11.66º, and 9.76º, respectively (Figure 2). According to literature [14], XRD patterns of graphite and GO are almost 2θ= 27º, 10-11º, respectively. Our results are compatible with the literature. The interlayer spaces for HGO, IGO, MGO were 0.74, 0.75, and 0.88 nm. The materials interlayer spacing measured by XRD is proportional with degree of oxidation [13]. Although the oxidation degree of MGO is higher than HGO and IGO, the reaction yield of MGO is lower than others. Also, considered the interlaying spacing, the oxidation degrees of HGO and IGO are almost the same. For this reason, it was decided to use graphite oxide obtained by the IGO method in the subsequent sections of the study.
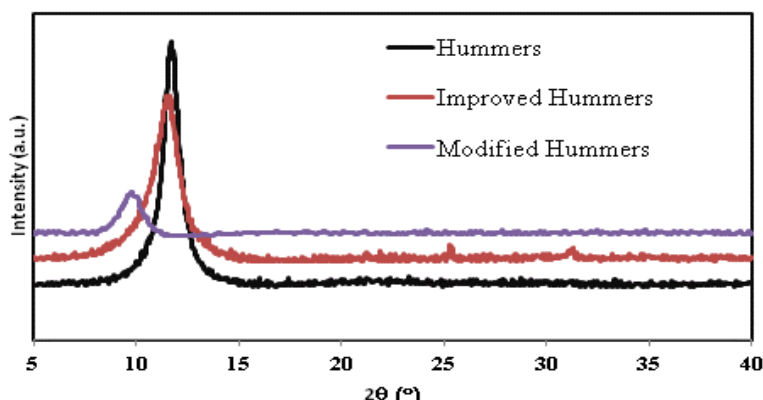
Figure 2: XRD patterns of GO powders synthesized by Hummers, improved Hummers, and modified Hummers methods.

3.2. Production of Thick Graphene Oxide and Graphene Films and Characterization

Thin GO films were fabricated by vacuum assisted filtration of the various volumes (33, 50, 80, and 120 mL) of GO dispersion. The flexible conductive thin graphene films were obtained by the thermal reduction of prepared GO films at 700 and 1100 ºC. Digital images of the GO and graphene films are given in Figure 3. The area of the GO and graphene films were measured as almost 17 cm^2 and dark brown color of GO films converted to gray during thermal reduction process. After reduction, it was observed that both GO and graphene films were flexible and foldable without deformation (Figure 4).
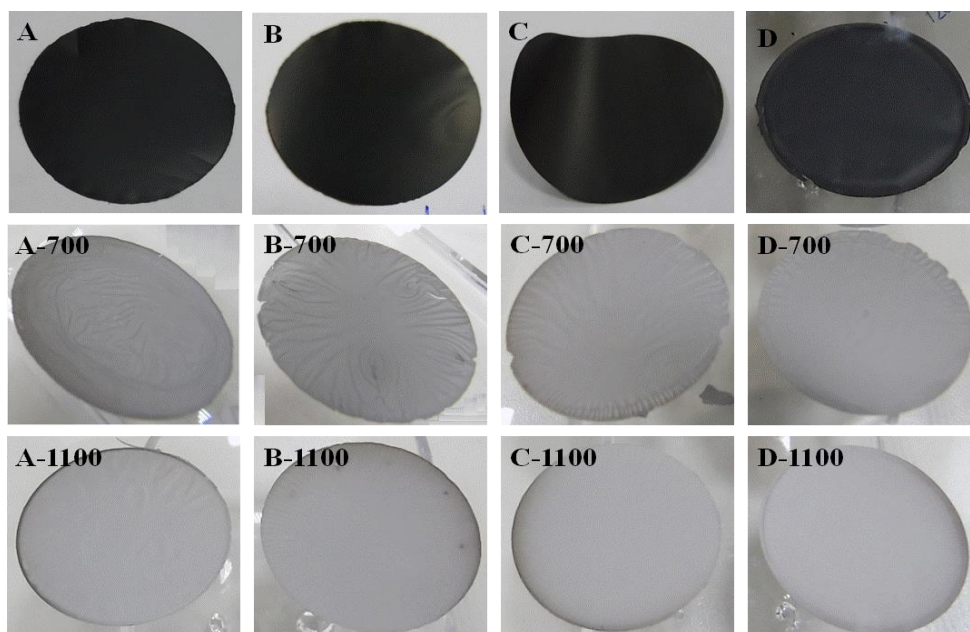
Figure 3: Camera pictures of produced GO films by filtration at the various volume of GO dispersions and prepared graphene films by thermal annealing process at 700, and 1100 ºC. While A, B, C, and D codes in photographs represent the prepared from 33, 50, 80, and 120 mL GO dispersions of this films, 700 and 1100 codes represent the thermal annealing temperatures .

Film thicknesses determined from SEM and micrometer measurements for GO and graphene films were given in Table 1. As seen in Table 1, the film thickness and resistance values of GO and graphene films increased with the increased of GO dispersions volumes. The film thicknesses were reduced by about 2-3 times with the thermal annealing of GO films due to the removal of oxygen-containing functional groups and molecules of water intercalated in the spacing between layers [14]. Addition, film thicknesses are reduced due to the loss of oxygen functional groups caused by an increase in thermal annealing temperature (700 to 1100 ºC) [14]. While GO films are almost insulator due to contain large sp^2 domain sizes that are interrupted by sp^3

bonds due to the presence of oxygen, the reduced GO films with thermal annealing process are conductive. The reason of the conductivity cause from the removal of oxygen-containing functional groups from the GO film enhancing the connectivity among the graphitic domains by formation of new sp^2 clusters [14]. Resistance values that varied inversely with conductivity showed that the resistance values of graphene films reduced approximately 20 times with the increase of the thermal annealing temperature from 700 to 1100 °C (Table 1).

Table 1: The film thickness and resistance values of GO and graphene films obtained from various amount of GO dispersions.

	Sample Codes	Filtered GO dispersion volume (mL)	Thermal annealing temperature (ºC)	Thickness (μm)	Resistance (Ω)
GO	A	33	NOT DONE	18	N.A.
	B	50	NOT DONE	22	N.A.
	C	80	NOT DONE	34	N.A.
	D	120	NOT DONE	50	N.A.
Graphene-700	A-700	33	700	10	680
	B-700	50	700	12	1100
	C-700	80	700	18	1720
	D-700	120	700	29	2340
Graphene-1100	A-1100	33	1100	6	30
	B-1100	50	1100	9	58
	C-1100	80	1100	16	77
	D-1100	120	1100	24	112

The surface and cross-section morphology of the GO films, and the reduced graphene at 700, and 1100 ºC were observed by SEM (Figure 4). From these cross-section images, layered structures for both GO and graphene films were observed and an overall thickness of GO, graphene-700 and graphene-1100 films prepared from 50 mL GO dispersion were measured respectively as 22, 11.7, and 8.7 μm. In addition, the surface morphology of the graphene and GO films varied depending on the thermal annealing temperature and the film thickness. As can be seen from the SEM images (Figure 4), the surface roughness of graphene films has increased by increased the thermal annealing temperature. Also, the film thickness and graphene films were rougher than GO. The roughness were caused from the removal of oxygen-containing functional groups and molecules of water intercalated in the spacing between the GO layers upon reduction [14].
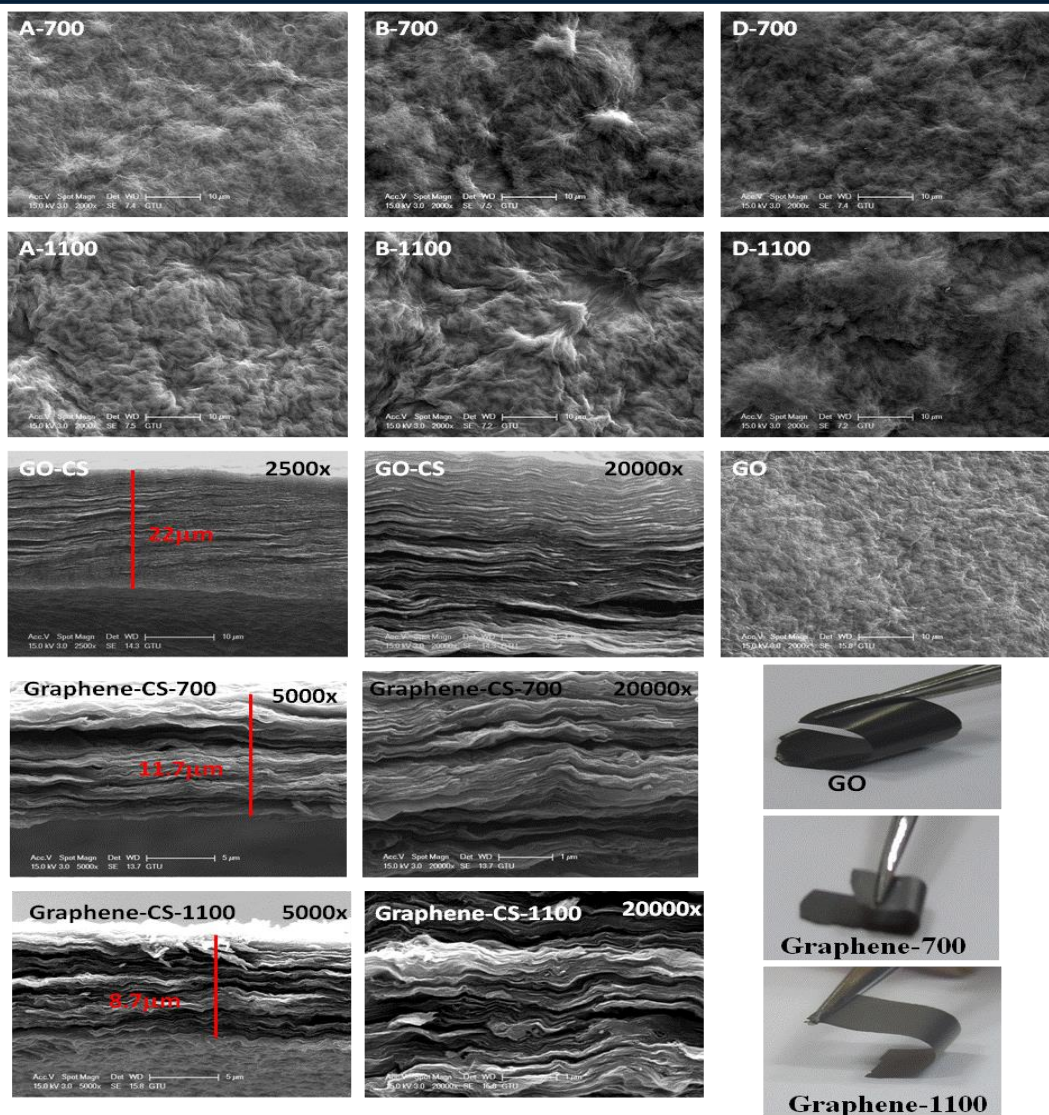
Figure 4: SEM images on surface and cross-section of the produced GO and graphene films. Folded images of GO and graphene films (prepared through thermal annealing at 700 and 1100 ºC). While A, B, and D codes in photographs represent the prepared from 33, 50, and 120 mL GO dispersions of this films, 700 and 1100 codes represent the thermal annealing temperatures. CS: cross-section.

XRD diffractions of prepared GO and graphene films are depicted in Figure 5. The XRD pattern of graphite oxide powder presented a diffraction peak at $2\theta = 10.72^{\circ}$, indicating a larger interlayer spacing (0.84 nm) than that typical of the starting bulk graphite ($2\theta = 27^{\circ}$, corresponding to 0.34 nm). The presence of functional groups on GO sheet surfaces, and molecules of water cause the larger interlayer spacing.
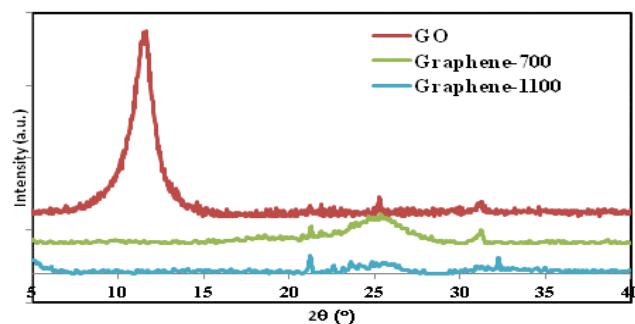
Figure 5: XRD patterns of GO, graphene-700, and Graphene 1100 films prepared from 50 mL GO dispersion. 700 and 1100 codes represent the thermal annealing temperatures.

4. CONCLUSION

Graphite oxide was synthesized with three different methods and one of them, the improved Hummers method, was selected as the synthesis method due to high oxidation degree and reaction yields.

The flexible conductive graphene films which have different reduction degree, roughness and thickness were fabricated by thermal annealing of graphene oxide films (GO) which prepared by filtration.

GO film thickness was adjusted with GO dispersions volumes. The conductivity of graphene films has been increased with increasing of the thermal annealing temperature. Furthermore, the surface roughness of the graphene has been increased by increasing the thermal annealing temperature and the film thickness. GO and graphene films have a layered structure and the interlayer spacing increase with the increasing of thermal annealing temperature. In this study, a fabrication route for flexible conductive graphene films was presented which is easy-fabrication, cost-effective, and environmentally friendly. It is obvious; this film has important potential for using as an electrode in electrooxidation of wastewater.

ACKNOWLEDGMENTS

REFERENCES

[1]. C. Lee, X. Wei, J.W. Kysar, J. Hone, Measurement of the elastic properties and intrinsic strength of monolayer graphene., Science. 321 (2008) 385–388. doi:10.1126/science.1157996.

[2]. D. Li, M.B. Müller, S. Gilje, R.B. Kaner, G.G. Wallace, Processable aqueous dispersions of graphene nanosheets., Nat. Nanotechnol. 3 (2008) 101–5. doi:10.1038/nnano.2007.451.

[3]. Y. Li, Q. Du, T. Liu, J. Sun, Y. Jiao, Y. Xia, et al., Equilibrium, kinetic and thermodynamic studies on the adsorption of phenol onto graphene, Mater. Res. Bull. 47 (2012) 1898–1904. doi:10.1016/j.materresbull.2012.04.021.

[4]. T.X.H. Le, M. Bechelany, S. Lacour, N. Oturan, M.A. Oturan, M. Cretin, High removal efficiency of dye pollutants by electron-Fenton process using a graphene based cathode, Carbon N. Y. 94 (2015) 1003–1011. doi:10.1016/j.carbon.2015.07.086.

[5]. J. William S. Hummers, R.E. Offeman, Preparation of Graphitic Oxide, J. Am. Chem. Soc. 80 (1958) 1339. doi:10.1021/ja01539a017.

[6]. B. Brodie, Sur le poids atomique du graphite, Ann. Chim. Phys. 59 (1860) 466–472.

[7]. L. Staudenmaier, Verfahren zur Darstellung der Graphitsäure, Berichte Der Dtsch. Chem. Gesellschaft. 31 (1898) 1481–1487.

[8]. H. Hu, C.C.K. Allan, J. Li, Y. Kong, X. Wang, J.H. Xin, et al., Multifunctional organically modified graphene with super-hydrophobicity, Nano Res. 7 (2014) 418–433. doi:10.1007/s12274-014-0408-0.

[9]. S. Stankovich, D. a. Dikin, R.D. Piner, K. a. Kohlhaas, A. Kleinhammes, Y. Jia, et al., Synthesis of graphene-based nanosheets via chemical reduction of exfoliated graphite oxide, Carbon N. Y. 45 (2007) 1558–1565. doi:10.1016/j.carbon.2007.02.034.

[10]. S. Park, K.-S. Lee, G. Bozoklu, W. Cai, S.T. Nguyen, R.S. Ruoff, Graphene oxide papers modified by divalent ions-enhancing mechanical properties via chemical cross-linking., ACS Nano. 2 (2008) 572–578. doi:10.1021/nn700349a.

[11]. Y. Xu, K. Sheng, C. Li, G. Shi, Highly conductive chemically converted graphene prepared from mildly oxidized graphene oxide, J. Mater. Chem. 21 (2011) 7376. doi:10.1039/c1jm10768b.

[12]. N.I. Kovtyukhova, P.J. Ollivier, B.R. Martin, T.E. Mallouk, S. a. Chizhik, E. V. Buzaneva, et al., Layer-by-Layer Assembly of Ultrathin Composite Films from Micron-Sized Graphite Oxide Sheets and Polycations, Chem. Mater. 11 (1999) 771–778. doi:10.1021/cm981085u.

[13]. D.C. Marcano, D. V Kosynkin, J.M. Berlin, A. Sinitskii, Z.Z. Sun, A. Slesarev, et al., Improved Synthesis of Graphene Oxide, ACS Nano. 4 (2010) 4806–4814. doi:10.1021/nn1006368.

[14]. C. Valles, J.D. Nunez, A.M. Benito, W.K. Maser, Flexible conductive graphene paper obtained by direct and gentle annealing of graphene oxide paper, 0 (2011). doi:10.1016/j.carbon.2011.09.042.

Fractional Order Controller Design for a DC Motor

Huseyin Oktay ERKOL[1]

Abstract

In this study, an integer order PID and a fractional order PID controller are designed for achieving high performance and made a performance comparison between them. The controllers are designed as speed controller for a DC motor and simulated by the MATLAB program. The integer order PID is the conventional form of the PID controller and widely used in industry and commercial systems by help of its acceptable performance. On the other hand, a fractional order PID has more degrees of freedom. An integer order PID has three parameters (Kp, Ki, Kd) and a fractional order PID has two additional parameters (mu and delta) that effect the controller characteristic. Fractional order PID has better time and frequency response due to the additional parameters. In addition to this advantage, it has also a disadvantage about the tuning processes. It has five parameters to tune and finding the optimum values is more difficult than the integer order PID with the three parameters. Artificial bee colony algorithm, one of the popular optimization algorithms, is used to overcome this problem. Both of the controllers are tuned identically by the Artificial Bee Colony algorithm. The Integral Absolute Error function is used as the objective function. The study shows that the fractional order PID controller has less overshoot and short settling time than the integer order PID controller.

Keywords: *Fractional order PID, Artificial Bee Colony, DC motor, speed control*

1. INTRODUCTION

There are many control techniques successfully applied to many problems in literature. Fuzzy logic, linear quadratic regulator, back stepping control and proportional-integral-derivative (PID) are some of the popular techniques [1]–[3]. PID controllers are widely used in industry due to its simple structure and acceptable performance. Conventional PIDs (integer order PIDs) are based on integer order integral and differential operators but the fractional calculus describes the real systems better then integral calculus. A fractional order controller can have better performance than an integer order controller. Thus, a fractional order PID (FOPID) and an integer order PID is compared in this study. A PID has three coefficients and a FOPID has two extra parameters so it has five adjustable parameters. It has better time and frequency response due to the additional parameters.

Tuning a controller is an important problem. There are no any methods that guarantee finding the optimum parameters that have critical effects on the controller characteristic. There are many method for tuning the optimum parameters or one of the optimum ones for controllers in literature and bio inspired optimization algorithms are popular choices due to their problem independent structure [4]. Particle Swarm Optimization, Genetic Algorithm and Artificial Bee Colony algorithm (ABC) are some of them.

In this study, an integer order PID and a FOPID controller designed for the speed control of a DC motor. DC motor is a popular system for studying control theory [5]. Many basic or modern techniques have been used to control a DC motor. ABC algorithm is preferred to tune the designed controllers. An objective function is required to use an optimization algorithm and the Integral Absolute Error function is used. The study shows that the FOPID controller has better performance. It has less overshoot and short settling time when compared to the integer order PID controller.

---

[1] Corresponding author: Karabuk University, Department of Mechatronics Engineering, 78100, Karabuk, Turkey. oktayerkol@karabuk.edu.tr

2. MATERIALS AND METHODS

2.1. DC Motor Model

One of the widely used actuator in control systems is the DC motor. It provides rotary motion and many rotational or linear motion can be achieved using it. It has simple structure and it can be controlled by the input voltage. A DC motor has two basic inputs; one of them is the voltage applied to its electrical circuit and the second one is the torque applied on its rotor. The equivalent model of the motor used in this study is given in Figure 18. R is the armature resistance, L is the armature inductance, V_a is the armature voltage and V_k is the supply voltage. They are parts of the electrical circuit. J is the inertia of the motor, b is the coefficient of frictional force, w is the angular velocity of the rotor and T is the torque applied to the rotor. All of these parameters are about the mechanical parts of the system.
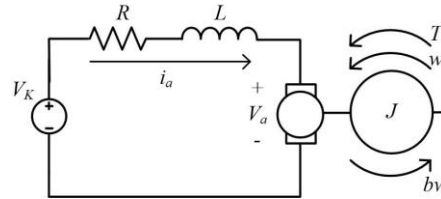
Figure 18 Equivalent circuit of the DC motor

The differential equations of the system are given in equation 1 and equation 2. Using these equations, state-space model of the motor is achieved and it is simulated by MATLAB program. The used motor parameters are given in Table 16.

$$J\frac{dw}{dt} + bw = Ki_a - T \tag{1}$$

$$L\frac{di_a}{dt} + Ri_a = V_a - Kw \tag{2}$$

Table 16. Motor parameters

Parameter	Value
R	2 Ohm
L	0.5 H
K	0.1
b	0.2 N.m/rad/s
J	0.02 kg.m^2
w	- rad/s
i	- ampere
T	- Nm

2.2. Controller Structure

In this study, an integer order PID and a fractional order PID (FOPID) controller designed for the speed control of a DC motor and the performances of the controllers are compared. The structure of an integer order PID in frequency domain is given in equation 3. This is the conventional form of the PID controller. The structure of fractional order PID is given in equation 4. The difference between them is the orders of "s". If the order of "s" is equals to 1, it is called as integer order PID. The structure of the controller changes if the order of "s" is fractional. Integer order PID has three coefficients and the fractional order PID has five coefficients that affect the characteristics and performance of the controller. The structure of the fractional order PID is given in equation 4.

$$CI(s) = K_p + K_d s + \frac{K_i}{s} \tag{3}$$

$$CF(s) = K_p + K_d s^\mu + \frac{K_i}{s^\delta} \tag{4}$$

The control scheme for the speed control of the motor is given in Figure 19. The error "e" is equals to the difference between the reference speed and the measured speed of the motor. The controller produces a motor voltage value (Vref) using the error and the driver drives the motor producing the required voltage. The new measured speed is used to calculate the new error.
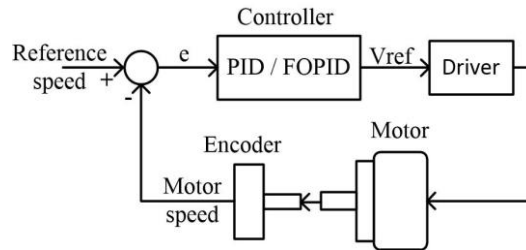
Figure 19 The control scheme

2.3. Optimization of the Controller

Optimization is finding the best parameters for a system. It is mathematically a maximization or minimization problem. There are many different methods for optimization in literature. Nature inspired algorithms are getting much popular day to day. Genetic Algorithm, Ant Colony Algorithm and Particle Swarm Algorithm are same popular ones [6]. In this study the Artificial Bee Colony (ABC) algorithm is used for the optimization due to its robustness and high performance.

Bees live in groups and they have a system to find and manage the food sources. There are three types of bees in a colony. Employed bees collect foods from a known source. Scout bees search randomly new food sources and they inform the onlooker bees about the position, quality and quantity of the food sources. Onlooker bees choose one of the food sources due to the information given by the scout bees and they go to the food source to collect. ABC algorithm is inspired form this systematic behavior of the bee colonies and applied successfully to many problems [7].

An objective function must be determined to use an optimization algorithm. It can be found many objective functions to optimize a PID controller in literature. In this study, the Integral Absolute Error (IAE) function is used for optimization. The function is given in equation 5. The error (e) is the difference between the system output and the reference value. Detailed information can be found in [8].

$$IAE = \int |e| \, dt \tag{5}$$

3. RESULTS AND DISCUSSION

Optimizations of the designed controllers are made by the ABC algorithm. It is run 10 times for each controller and the best results are compared. The K_p, K_d and K_i parameters are bounded between 0-500 and the μ and δ are bounded between 0-1. The optimum parameters found for each controller is given in Table 17.

Table 17. Optimum controller parameters

Coefficients of PID	Value
K_n	493.04
K_d	22.51
K_i	60.84
Coefficients of	**Value**
K_n	253.60
K_d	10.76
K_i	62.14
μ	0.794
δ	0.933

The simulation results made by the MATLAB are given below. Figure 20 shows the motor speed. The reference speed is 200rpm. The settling time of the integer order PID controlled system is 0.398s and it has a 0.7% steady-state error. The maximum speed of integer order PID controlled system is 202.5rpm and it has a 1.25% maximum overshoot. The FOPID controlled system has better performance. It has no overshoot and its settling time is 0.368s. It has a shorter settling time than the integer order PID controlled system. It has also 0.35% steady-state error. The motor current graphs are also given in Figure 21. As seen as the current graph of the FOPID controlled system has less oscillation.
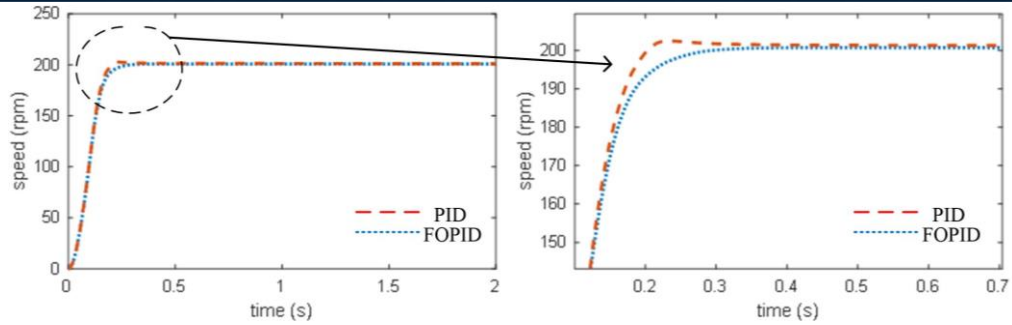
Figure 20 The speed graphs of the motor
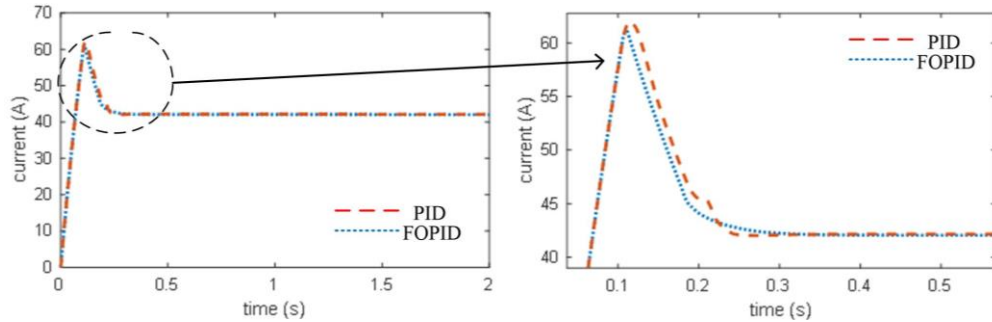
Figure 21 The current graphs of the motor

4. CONCLUSIONS

In this study an integer order PID controller and a FOPID controller are designed as speed controller and a performance comparison is made. Optimizations of the designed controllers are made by the Artificial Bee Colony algorithm and the Integral Absolute Error function is used as the objective function. All studies are made by simulations using the MATLAB program. The results show that the FOPID controller has better performance than the integer order PID. The FOPID controller has no overshoot and short settling time. It has also small K_p coefficient. Integer order PID has overshoot and longer settling time.

REFERENCES

[1]. O. Montiel, R. Sepulveda, P. Melin, O. Castillo, M. A. Porta, and I. M. Meza, "Performance of a Simple Tuned Fuzzy Controller and a PID Controller on a DC Motor," in *2007 IEEE Symposium on Foundations of Computational Intelligence*, 2007, pp. 531–537.
[2]. M. Keshmiri, A. Jahromi, A. Mohebbi, A. Mohammad, and W.-F. Xie, "Modeling and Control of Ball and Beam System Using Model Based and Non-Model Based Control Approaches," *Int. J. Smart Sens. Intell. Syst.*, vol. 5, no. 1, pp. 14–35, 2012.
[3]. F. Chen, W. Lei, K. Zhang, G. Tao, and B. Jiang, "A Novel Nonlinear Resilient Control for a Quadrotor UAV via Backstepping Control and Nonlinear Disturbance Observer," *Nonlinear Dyn.*, vol. 85, no. 2, pp. 1–15, 2016.
[4]. S. Binitha and S. S. Sathya, "A Survey of Bio Inspired Optimization Algorithms," *Int. J. Soft Comput. Eng.*, vol. 2, no. 2, pp. 137–151, 2012.
[5]. M. R. Khan, A. A. Khan, and U. Ghazali, "Speed Control of DC Motor Under Varying Load Using PID Controller," *Int. J. Eng.*, vol. 9, no. 3, pp. 38–48, 2015.
[6]. C. A. Coello Coello and M. Reyes-Sierra, "Multi-Objective Particle Swarm Optimizers: A Survey of the State-of-the-Art," *Int. J. Comput. Intell. Res.*, vol. 2, no. 3, pp. 287–308, 2006.
[7]. D. Karaboga, B. Gorkemli, C. Ozturk, and N. Karaboga, "A Comprehensive Survey: Artificial Bee Colony (ABC) Algorithm and Applications," *Artif. Intell. Rev.*, vol. 42, no. 1, pp. 21–57, 2014.
[8]. M. Kishnani, S. Pareek, and R. Gupta, "Optimal Tuning of DC Motor via Simulated Annealing," in *International Conference on Advances in Engineering & Technology Research (ICAETR - 2014)*, 2014, pp. 1–5.

Analysis of Textile and Clothing Trade between Turkey and Major Asian Countries

Seher Kanat[1], Turan Atılgan[2]

Abstract

Textile and clothing sector is one of the leading sectors which constitute a basis for development in many developed or developing countries. This situation is also valid for Turkey. The industrialization effort of the sector, which has begun with Sumerbank, is improved and its efficiency is increased in time. Turkish textile and clothing sector, which is a pioneer and competitive sector, has always been placed near the top during 1980s and 1990s. It has played a significant role in export oriented development model, which has begun in 1980s and in customs union with European Union in 1996. Although the sector is one of the Turkey's most competitive sectors, it is faced with intense competition of Asian countries during the recent years. Production costs play a significant role in this competition.

In this study, textile and clothing trade between Turkey and major Asian countries is analyzed and suggestions are made. Also, alternatives are offered in order to preserve and improve the efficiency of the sector, which has significant contributions to Turkish economy, against Asian counties in national and international fields.

Keywords: *Asian countries, textile and clothing sector, foreign trade, competitiveness*

1. GLOBAL TEXTILE AND CLOTHING TRADE

Textile and clothing sector is a longstanding sector due to the irreplaceable and fundamental place of clothing and ornamentation in human life. The sector, which has improved its structure and properties in the course of time, has protected its importance and played significant roles in industrialization and development processes of numerous countries. Besides, many developed countries preserve their positions in the sector and continue to exist as global players. In this context, textile and clothing trade proceeds on its way as an important partner of global trade.

Table 1. Global textile and clothing export figures by years and their shares within the total global export [1,2]

	2010	2011	2012	2013	2014	2015
Total global export (billion $)	15.301	18.338	18.496	18.952	19.005	16.489
Annual change (%)	-	19,85	0,86	2,47	0,28	-13,24
Global clothing export (million $)	354.151	418.523	421.554	462.005	490.168	453.894
Annual change (%)	-	18,18	0,72	9,60	6,10	-7,40
Share of clothing (%)	2,31	2,28	2,28	2,44	2,58	2,75
Global textile export (million $)	252.138	293.844	283.430	303.503	313.621	290.519
Annual change (%)	-	16,54	-3,54	7,08	3,33	-7,37
Share of textile (%)	1,65	1,60	1,53	1,60	1,65	1,76

If the alterations of global textile and clothing exports over the years are analyzed, it can be seen that both sectors' export figures and shares within the global exports have increased until 2015 (Table 1). Although their shares within the global exports are increased in 2015, their total export figures are decreased. Similarly, global textile and clothing import figures and shares have also increased until 2015 (Table 2). Their shares within the global imports are increased in 2015. However, their total import figures are decreased. This situation can be explained with the global trade slowdown, which is occurred in the first half of 2015.

If the leading textile and clothing exporters of the world are analyzed, it can be seen that China has been placed on the top both in textile and clothing throughout the years (Table 3 and 5). China has increased its textile exports 41,5% within 6 years whereas it has increased its clothing exports 34% during the same period.

---

[1]*Corresponding author: Ege University, Department of Textile Engineering, 35100, Bornova/İzmir, Turkey, seher.kanat@ege.edu.tr*

[2]*Ege University, Department of Textile Engineering, 35100, Bornova/İzmir, Turkey, turan.atilgan@ege.edu.tr*

China is followed by European Union, India, USA, Turkey, South Korea, Taiwan, Hong Kong, Pakistan and Japan respectively in textile exports; whereas it is followed by European Union, Bangladesh, Vietnam, Hong Kong, India, Turkey, Indonesia, USA and Cambodia respectively in clothing exports. As it can be seen, Asian countries have an overwhelming superiority both in textile and clothing exports. Also, Turkey is ranked at the fifth place in textile exports, whereas it is ranked at the seventh place in clothing exports. Turkey has increased its textile exports 22% within 6 years whereas it has increased its clothing exports 18,5% during the same period.

Table 2. Global textile and clothing import figures by years and their shares within the total global import [1,2]

	2010	**2011**	**2012**	**2013**	**2014**	**2015**
Total global import (billion $)	15.511	18.503	18.705	19.018	19.101	16.743
Annual change (%)	-	19,29	1,09	1,67	0,44	-12,34
Global clothing import (million $)	369.420	436.641	441.710	481.113	525.239	498.525
Annual change (%)	-	18,20	1,16	8,92	9,17	-5,09
Share of clothing (%)	2,38	2,36	2,36	2,53	2,75	2,98
Global textile import (million $)	267.117	311.276	300.658	323.661	335.559	308.108
Annual change (%)	-	16,53	-3,41	7,65	3,68	-8,18
Share of textile (%)	1,72	1,68	1,61	1,70	1,76	1,84

Table 3. Leading textile exporters of the world (million $) [1,2]

	2010	**2011**	**2012**	**2013**	**2014**	**2015**
China	76.871	94.411	95.499	106.624	111.726	108.817
EU (28)	68.003	77.137	69.727	72.264	75.122	64.627
India	12.833	15.340	15.348	17.417	18.339	17.289
USA	12.169	13.852	13.479	13.934	14.368	13.761
Turkey	8.964	10.772	11.054	12.149	12.516	10.952
South Korea	10.968	12.369	11.970	12.043	11.909	10.646
Taiwan	9.719	11.016	10.293	10.217	10.264	9.678
Hong Kong	11.307	11.283	10.546	10.714	9.785	9.106
Pakistan	7.848	9.082	8.705	9.341	9.077	8.232
Japan	7.086	8.034	7.818	6.842	6.678	6.164

Table 4. Leading textile importers of the world (million $) [1,2]

	2010	**2011**	**2012**	**2013**	**2014**	**2015**
EU (28)	74.424	85.211	75.029	78.713	83.546	73.409
USA	23.376	25.359	25.948	27.057	28.268	29.562
China	17.679	18.901	19.810	21.563	20.249	18.977
Vietnam	7.042	8.702	9.075	10.633	12.069	13.288
Hong Kong	11.265	11.049	10.364	10.411	9.358	8.521
Japan	7.197	9.195	9.009	8.752	8.888	8.178
Bangladesh	4.471	6.610	5.480	5.947	6.778	7.023
Mexico	5.150	5.859	6.003	6.180	6.408	6.528
Turkey	6.540	7.557	6.441	6.789	7.117	6.232
Indonesia	4.216	5.654	5.570	5.788	5.814	5.709

Table 5. Leading clothing exporters of the world (million $) [1,2]

	2010	**2011**	**2012**	**2013**	**2014**	**2015**
China	129.820	153.774	159.754	177.530	186.704	174.082
EU (28)	100.695	117.407	109.852	118.639	127.519	112.265
Bangladesh	14.855	19.214	19.788	23.501	24.584	26.603
Vietnam	10.390	13.149	14.443	17.148	20.174	23.463
Hong Kong	24.049	24.505	22.573	21.922	20.510	18.416
India	11.229	14.672	13.928	15.542	17.742	18.254
Turkey	12.760	13.948	14.290	15.393	16.668	15.121
Indonesia	6.820	8.045	7.524	7.692	7.670	7.593
USA	4.692	5.241	5.606	5.861	6.103	6.073
Cambodia	3.041	3.995	4.294	5.025	5.339	5.938

Table 6. Leading clothing importers of the world (million $) [1,2]

	2010	**2011**	**2012**	**2013**	**2014**	**2015**
EU (28)	167.498	191.798	174.526	183.192	199.657	180.316
USA	81.939	8.8584	87.971	91.040	93.192	96.919
Japan	26.874	32.945	33.976	33.626	31.149	28.581
Hong Kong	16.645	17.248	16.338	16.448	16.173	14.902
Canada	8.314	9.526	9.371	9.950	10.082	9.895
South Korea	4.443	6.110	6.267	7.535	8.472	8.512
Australia	4.832	5.838	6.080	6.257	6.524	6.602
China	2.518	4.012	4.525	5.339	6.129	6.544
Switzerland	5.288	6.139	5.721	5.904	6.131	5.614

Russia	7.541	9.238	9.245	9.014	8.513	5.589

European Union (28) takes the first place within the leading textile and clothing importers of the world (Table 4 and 6). European Union has decreased its textile imports 1,4% within 6 years whereas it has increased its clothing imports 7,6% during the same period. European Union is followed by USA, China, Vietnam, Hong Kong, Japan, Bangladesh, Mexico, Turkey and Indonesia respectively in textile imports; whereas it is followed by USA, Japan, Hong Kong, Canada, South Korea, Australia, China, Switzerland and Russia respectively in clothing imports. Asian countries also have an overwhelming superiority in textile imports. However, the superiority in clothing imports is taken over by the developed countries.

2. THE PURPOSE, METHOD AND FINDINGS OF THE RESEARCH

The superiority of Asian countries in textile and clothing exports has been continuing for many years. Besides, they are the leading textile importers of the world. Therefore, their importance and shares within the global textile and clothing trade are blindingly obvious. Turkey is also ranked at the fifth place in textile exports, whereas it is ranked at the seventh place in clothing exports. Thus, Asian countries are the biggest rivals and potential customers of Turkey, which maintains its importance and place in global textile and clothing trade. This study aims to analyze textile and clothing trade between Turkey and major Asian countries. In accordance with the aim of the research, the leading Asian textile and clothing exporters of the world (Bangladesh, Vietnam, China, Indonesia, Cambodia, India and Hong Kong) are chosen as the countries which will be investigated. The textile and clothing imports and exports between these countries and Turkey are found in binary forms according to HS classification and summarized in tables. Besides, shares of textile and clothing exports and imports within total exports and imports are also given in tables. Data are obtained from Trademap database and total textile and clothing export and import figures and their shares within total exports and imports are calculated according to these data. The explanations of HS classification codes are given in Table 7.

Table 7. HS classification code explanations [3]

50-Silk
51-Wool, fine or coarse animal hair; horsehair yarn and woven fabric
52-Cotton
53-Other vegetable textile fibers; paper yarn and woven fabrics of paper yarn
54-Man-made filaments
55-Man-made staple fibers
56-Wadding, felt and nonwovens; special yarns; twine, cordage, ropes and cables
57-Carpets and other textile floor coverings
58-Special woven fabrics; tufted textile fabrics; lace; tapestries; trimmings; embroidery
59-Impregnated, coated, covered or laminated textile fabrics
60-Knitted or crocheted fabrics
61-Apparel and clothing accessories, knitted or crocheted
62-Apparel and clothing accessories, not knitted or crocheted
63-Other made-up textile articles; sets; worn clothing and worn textile articles; rags

Turkey's textile exports to Bangladesh have increased eleven times within seven years (2010-2016) (Table 8). Turkish clothing enterprises have invested in Bangladesh during the recent years in order to provide cost advantage and they import their raw materials from Turkey. Therefore, this export increase can be explained by this situation. Turkey's textile export shares within total exports have increased from 4% to 28% within seven years. Besides, Turkey's clothing exports to Bangladesh have increased fifty one times during the same period whereas their shares from the total exports have increased from 0,01% to 0,31%. Cotton and man-made staple fibers are the mostly increased items within textile exports whereas woven apparel and clothing accessories are the mostly increased items within clothing exports. On the other hand, Turkey's textile imports from Bangladesh have increased 12,5% within seven years whereas its clothing imports have approximately increased 1% (Table 9). Turkey's textile import shares within total imports have increased from 21% to 23% whereas clothing import shares within total imports have decreased to 75% from 77%. Man-made staple fibers and impregnated, coated, covered or laminated textile fabrics are the mostly increased items within textile imports whereas woven apparel and clothing accessories are the mostly increased items within clothing imports. Although Turkey's textile and clothing exports to Bangladesh have increased in recent years, trade deficits have occurred both in Turkey's textile and clothing trades with Bangladesh.

Turkey's textile exports to Vietnam have increased six times within seven years (2010-2016) (Table 10). Turkey's textile export shares within total exports have increased from 8% to 20% within seven years. Besides, Turkey's clothing exports to Vietnam have increased four times during the same period whereas their shares within total exports have increased from 0,08% to 0,15%. Cotton, man-made staple fibers and man-made filaments are the mostly increased items within textile exports whereas woven apparel and clothing accessories are the mostly increased items within clothing exports. On the other hand, Turkey's textile imports from Vietnam have decreased 22% within seven years whereas its clothing imports have

increased 13% (Table 11). Turkey's textile import shares within total imports have decreased to 13% from 38% whereas clothing import shares within total imports have decreased to 4,5% from 9%. Cotton is the mostly increased item within textile imports whereas other made-up textile articles are the mostly increased items within clothing imports. Although Turkey's textile and clothing exports to Vietnam have increased in recent years, trade deficits have occurred both in Turkey's textile and clothing trades with Vietnam.

Table 8. Turkey's textile and clothing exports to Bangladesh (Thousand US Dollar) [4]

	2010	2011	2012	2013	2014	2015	2016
Total exports	169.540	132.200	214.168	195.536	148.511	199.890	263.955
50	46	0	70	0	44	17	0
51	19	87	191	249	345	92	264
52	4.351	2.980	19.994	14.489	31.786	42.826	59.621
53	0	0	0	0	0	69	0
54	266	477	1.216	743	867	901	982
55	514	614	673	494	4.743	6.600	6.366
56	49	60	39	55	257	202	613
57	848	1.076	1.414	1.885	2.247	2.629	3.657
58	298	848	663	931	1.558	2.207	1.423
59	132	98	324	754	717	596	1.088
60	17	95	289	379	692	1.508	977
Total textile exports	6.540	6.335	24.873	19.979	43.256	57.647	74.991
Share of textile exports within total exports	3,86	4,79	11,61	10,22	29,13	28,84	28,41
61	12	33	3	4	54	10	255
62	0	136	681	291	132	122	544
63	4	4	10	45	11	96	17
Total clothing exports	16	173	694	340	197	228	816
Share of clothing exports within total exports	0,01	0,13	0,32	0,17	0,13	0,11	0,31

Table 9. Turkey's textile and clothing imports from Bangladesh (Thousand US Dollar) [4]

	2010	2011	2012	2013	2014	2015	2016
Total imports	844.661	895.967	766.376	1.004.419	1.028.728	995.970	881.039
50	0	0	0	0	0	0	0
51	0	0	0	0	0	0	0
52	356	4.792	1.505	1.001	3.948	1.202	1.302
53	176.156	179.508	189.399	183.555	206.387	197.123	183.787
54	1.296	301	1.236	2.296	6.147	4.986	4.387
55	3	3.039	12.045	6.492	6.472	5.859	8.804
56	70	345	94	98	170	280	114
57	724	977	1.791	1.191	1.800	617	570
58	134	109	5	24	194	47	10
59	3	0	0	0	0	306	1.466
60	0	0	1	1	4.823	3.523	718
Total textile imports	178.742	189.071	206.076	194.658	229.941	213.943	201.158
Share of textile imports within total imports	21,16	21,10	26,89	19,38	22,35	21,48	22,83
61	342.726	313.880	186.108	238.260	214.339	191.479	159.230
62	305.103	370.183	350.428	541.979	552.691	559.886	493.231
63	4.927	7.855	4.566	5.125	5.337	3.799	5.566
Total clothing imports	652.756	691.918	541.102	785.364	772.367	755.164	658.027
Share of clothing imports within total imports	77,28	77,23	70,61	78,19	75,08	75,82	74,69

Table 10. Turkey's textile and clothing exports to Vietnam (Thousand US Dollar) [4]

	2010	2011	2012	2013	2014	2015	2016
Total exports	106.209	100.090	90.104	107.299	168.145	155.449	234.123
50	0	0	0	0	0	0	0
51	1.192	1.346	763	1.046	1.581	896	1.306
52	3.231	8.899	8.910	17.469	18.589	24.464	27.241
53	5	1	28	66	40	210	259
54	244	814	2.623	1.528	1.906	2.855	4.870
55	2.520	8.021	4.308	5.145	8.428	8.255	9.931
56	203	1.024	1.188	368	700	457	451
57	0	54	60	78	249	209	455
58	104	94	88	79	141	265	382
59	31	216	242	281	432	98	108
60	544	178	516	692	1.236	958	949
Total textile exports	8.074	20.647	18.726	26.752	33.302	38.667	45.952
Share of textile exports within total exports	7,60	20,63	20,78	24,93	19,81	24,87	19,63
61	16	27	107	100	114	96	98

225

62	6	29	48	51	47	117	178
63	61	21	62	45	33	43	71
Total clothing exports	83	77	217	196	194	256	347
Share of clothing exports within total exports	0,08	0,08	0,24	0,18	0,12	0,16	0,15

Turkey's textile exports to China have increased 19% within seven years (2010-2016) (Table 12). Turkey's textile export shares within total exports have increased from 5% to 6% within seven years. Besides, Turkey's clothing exports to China have increased two times during the same period whereas their shares within total exports have increased from 1% to 3%. Cotton, man-made staple fibers, impregnated, coated, covered or laminated textile fabrics and knitted or crocheted fabrics are the mostly increased items within textile exports whereas woven and knitted apparel and clothing accessories are the mostly increased items within clothing exports. On the other hand, Turkey's textile imports from China have increased 8% within seven years whereas its clothing imports have decreased 13% (Table 13). Turkey's textile import shares within total imports have decreased to 6% from 9% whereas clothing import shares within total imports have decreased to 3% from 5%. Man-made filament fibers and special woven fabrics are the mostly increased items within textile imports whereas other made-up textile articles are the mostly increased items within clothing imports. Although Turkey's textile and clothing exports to China have increased in recent years, enormous trade deficits have occurred both in Turkey's textile and clothing trades with China.

Table 11. Turkey's textile and clothing imports from Vietnam (Thousand US Dollar) [4]

	2010	2011	2012	2013	2014	2015	2016
Total imports	751.327	1.009.484	1.213.957	1.666.812	2.009.894	1.756.262	1.735.872
50	0	2	0	0	0	160	0
51	0	26	0	0	0	2	0
52	28.496	19.300	25.493	25.690	60.419	50.071	79.763
53	0	0	0	0	25	0	0
54	142.809	197.264	190.147	176.511	191.738	134.122	95.215
55	109.035	161.774	217.148	191.045	83.529	61.729	40.006
56	121	431	1	609	801	371	189
57	0	0	0	0	0	2	2
58	1.193	1.750	1.774	1.617	1.824	2.104	2.820
59	5.631	2.301	2.445	1.489	5.306	7.465	5.397
60	536	1.734	2.548	1.156	161	93	80
Total textile imports	287.821	384.582	439.556	398.117	343.803	256.119	223.472
Share of textile imports within total imports	38,31	38,10	36,21	23,88	17,11	14,58	12,87
61	16.756	21.820	17.043	20.956	26.484	23.505	23.637
62	50.431	64.291	41.100	47.826	58.146	51.829	50.541
63	2.521	3.847	3.542	4.319	4.608	4.596	4.380
Total clothing imports	69.708	89.958	61.685	73.101	89.238	79.930	78.558
Share of clothing imports within total imports	9,28	8,91	5,08	4,39	4,44	4,55	4,53

Table 12. Turkey's textile and clothing exports to China (Thousand US Dollar) [4]

	2010	2011	2012	2013	2014	2015	2016
Total exports	2.259.785	2.466.316	2.833.255	3.600.865	2.861.052	2.414.932	2.329.371
50	345	249	275	148	16	70	502
51	18.143	27.274	25.266	33.362	42.307	32.003	15.712
52	24.766	41.513	40.970	68.623	40.079	33.838	40.871
53	335	181	101	317	373	430	544
54	4.764	4.002	4.836	10.405	12.233	11.326	10.006
55	55.026	58.121	63.335	63.579	32.388	53.756	24.543
56	1.994	3.176	3.801	2.138	1.958	1.321	742
57	7.113	18.679	30.234	46.636	50.502	28.473	24.632
58	2.519	2.486	3.213	2.738	3.920	2.757	2.531
59	3.944	3.742	2.341	4.450	7.175	12.200	20.395
60	838	2.326	2.175	2.461	3.143	2.598	2.558
Total textile exports	119.787	161.749	176.547	234.857	194.094	178.772	143.036
Share of textile exports within total exports	5,30	6,56	6,23	6,52	6,78	7,40	6,14
61	7.606	13.633	14.777	15.140	19.507	24.626	33.360
62	6.494	11.718	18.219	23.540	18.250	17.000	20.540
63	15.489	25.878	15.458	17.440	14.829	8.759	7.027
Total clothing exports	29.589	51.229	48.454	56.120	52.586	50.385	60.927
Share of clothing exports within total exports	1,31	2,08	1,71	1,56	1,84	2,09	2,62

Table 13. Turkey's textile and clothing imports from China (Thousand US Dollar) [4]

	2010	2011	2012	2013	2014	2015	2016

Total imports	17.180.806	21.693.336	21.295.242	24.685.885	24.918.224	24.873.452	25.440.454
50	26.097	31.273	24.938	33.600	35.436	31.228	27.023
51	107.263	158.134	128.011	102.643	109.283	73.416	58.562
52	350.076	408.403	207.100	293.953	251.180	138.648	114.747
53	21.605	29.436	41.902	48.800	44.564	34.486	30.057
54	360.148	462.253	554.659	547.482	578.394	534.762	635.080
55	268.618	405.916	350.112	230.154	308.814	238.615	279.695
56	49.193	63.534	27.301	29.158	41.151	30.828	31.059
57	45.946	39.228	35.433	37.002	32.193	22.610	11.886
58	43.061	49.695	64.356	87.874	112.718	98.942	99.874
59	102.749	140.511	121.983	139.270	165.694	134.988	124.706
60	155.758	281.617	182.741	231.170	256.697	245.650	236.481
Total textile imports	1.530.514	2.070.000	1.738.536	1.781.106	1.936.124	1.584.173	1.649.170
Share of textile imports within total imports	8,91	9,54	8,16	7,22	7,77	6,37	6,48
61	309.767	344.803	281.564	266.433	267.508	229.314	208.429
62	577.824	748.303	521.082	563.140	560.742	523.634	512.925
63	56.319	79.119	58.309	65.730	77.913	89.869	96.009
Total clothing imports	943.910	1.172.225	860.955	895.303	906.163	842.817	817.363
Share of clothing imports within total imports	5,49	5,40	4,04	3,63	3,64	3,39	3,21

Turkey's textile exports to Indonesia have increased two times within seven years (2010-2016) (Table 14). Turkey's textile export shares within total exports have increased from 8% to 17% within seven years. Besides, Turkey's clothing exports to Indonesia have increased nine times during the same period whereas their shares within total exports have increased from 0,29% to 2,60%. Cotton, man-made filament fibers, carpets and other textile floor coverings are the mostly increased items within textile exports whereas woven and knitted apparel and clothing accessories are the mostly increased items within clothing exports. On the other hand, Turkey's textile imports from Indonesia have increased 15% within seven years whereas its clothing imports have decreased 19% (Table 15). Turkey's textile import shares within total imports have increased from 37% to 44% whereas clothing import shares within total imports have decreased to 2,21% from 2,63%. Wadding, felt and nonwovens; special yarns; twine, cordage, ropes and cables; carpets and other textile floor coverings; impregnated, coated, covered or laminated textile fabrics are the mostly increased items within textile imports whereas knitted apparel and clothing accessories are the mostly increased items within clothing imports. Although Turkey's textile and clothing exports to Indonesia have increased in recent years, trade deficits have occurred both in Turkey's textile and clothing trades with Indonesia.

Table 14. Turkey's textile and clothing exports to Indonesia (Thousand US Dollar) [4]

	2010	**2011**	**2012**	**2013**	**2014**	**2015**	**2016**
Total exports	250.732	307.971	243.621	230.995	227.583	207.001	253.901
50	0	0	0	0	0	0	0
51	292	536	276	635	138	556	124
52	4.493	7.520	10.159	3.947	5.057	6.977	16.613
53	277	1	48	14	0	124	190
54	1.861	1.633	896	2.638	6.422	4.219	7.737
55	6.725	6.106	2.451	1.861	3.719	5.133	5.359
56	289	156	160	226	236	155	299
57	3.614	5.330	6.040	6.810	5.593	4.661	10.193
58	244	143	106	213	19	106	432
59	1.570	4.206	6.904	2.488	1.873	33	2.636
60	686	1.504	1.067	396	622	279	427
Total textile exports	20.051	27.135	28.107	19.228	23.679	22.243	44.010
Share of textile exports within total exports	8,00	8,81	11,54	8,32	10,40	10,75	17,33
61	92	105	435	742	873	849	1.718
62	71	183	451	2.585	2.763	1.101	4.699
63	559	472	48	157	106	101	178
Total clothing exports	722	760	934	3.484	3.742	2.051	6.595
Share of clothing exports within total exports	0,29	0,25	0,38	1,51	1,64	0,99	2,60

Table 15. Turkey's textile and clothing imports from Indonesia (Thousand US Dollar) [4]

	2010	2011	2012	2013	2014	2015	2016
Total imports	1.476.659	1.931.717	1.795.778	1.989.683	2.043.492	1.638.245	1.424.722
50	0	0	0	0	1	0	0
51	0	0	0	0	0	0	0
52	32.292	24.500	17.236	17.535	23.244	14.921	13.796
53	2	103	0	3	11	4	0
54	212.696	288.945	346.843	296.396	312.300	255.566	229.443
55	298.508	333.562	268.389	351.033	413.785	421.482	379.370
56	1.021	1.431	1.035	1.023	207	927	2.198
57	6	37	284	119	33	43	61
58	2.685	3.103	2.372	1.638	2.125	1.426	2.028
59	328	122	202	1.297	459	4.450	1.307
60	337	482	347	686	234	274	452
Total textile imports	547.875	652.285	636.708	669.730	752.399	699.093	628.655
Share of textile imports within total imports	37,10	33,77	35,46	33,66	36,82	42,67	44,12
61	13.019	15.886	13.674	13.274	13.397	14.904	16.019
62	25.232	31.854	20.904	17.930	17.039	15.457	15.041
63	644	754	743	1.080	723	321	426
Total clothing imports	38.895	48.494	35.321	32.284	31.159	30.682	31.486
Share of clothing imports within total imports	2,63	2,51	1,97	1,62	1,52	1,87	2,21

Turkey's textile exports to Cambodia have increased one hundred thirty nine times within seven years (2010-2016) (Table 16). Turkey's textile export shares within total exports have increased from 0,80% to 35% within seven years. Besides, Turkey's clothing exports to Cambodia have decreased seven and half times during the same period whereas their shares within total exports have decreased to 0,03% from 0,67%. Cotton, special woven fabrics and knitted or crocheted fabrics are the mostly increased items within textile exports whereas knitted apparel and clothing accessories are the mostly decreased items within clothing exports. On the other hand, Turkey's textile imports from Cambodia have increased twelve times within seven years whereas its clothing imports have increased four times (Table 17). Turkey's textile import shares within total imports have increased from 0,10% to 0,46% whereas clothing import shares within total imports have increased from 60% to 84%. Man-made staple fibers are the mostly increased items within textile imports whereas all imported clothing items are increased tremendously. Although Turkey's textile exports to Cambodia have increased in recent years, its clothing exports have decreased. Therefore, trade surpluses have occurred in Turkey's textile trade with Cambodia whereas enormous trade deficits have occurred in Turkey's clothing trade with Cambodia.

Table 16. Turkey's textile and clothing exports to Cambodia (Thousand US Dollar) [4]

	2010	2011	2012	2013	2014	2015	2016
Total exports	4.490	3.916	5.200	10.839	11.615	13.667	14.177
50	0	0	0	0	0	0	0
51	0	0	0	0	24	20	0
52	9	0	250	2.812	980	4.885	4.673
53	0	0	0	2	0	0	0
54	0	1	0	1	140	1	2
55	9	5	150	705	105	92	78
56	0	1	0	0	3	7	5
57	17	0	0	1	0	1	53
58	1	13	46	55	3	101	79
59	0	0	18	0	0	0	0
60	0	0	30	28	0	173	125
Total textile exports	36	20	494	3.604	1.255	5.280	5.015
Share of textile exports within total exports	0,80	0,51	9,50	33,25	10,80	38,63	35,37
61	25	0	0	0	3	0	0
62	0	58	5	8	0	2	0
63	5	0	0	10	0	1	4
Total clothing exports	30	58	5	18	3	3	4
Share of clothing exports within total exports	0,67	1,48	0,10	0,17	0,03	0,02	0,03

Table 17. Turkey's textile and clothing imports from Cambodia (Thousand US Dollar) [4]

	2010	2011	2012	2013	2014	2015	2016
Total imports	27.981	45.843	53.768	76.420	112.810	94.745	77.217
50	0	0	0	0	0	0	0
51	0	0	0	0	0	0	0
52	26	0	0	0	0	0	0
53	3	0	0	0	0	0	0
54	0	0	0	0	0	0	0
55	0	0	0	0	0	0	353
56	0	0	0	0	0	0	0
57	0	0	0	0	0	0	0
58	0	0	0	0	0	0	0
59	0	0	0	1	0	0	0
60	0	0	0	0	0	1	0
Total textile imports	29	0	0	1	0	1	353
Share of textile imports within total imports	0,10	0,00	0,00	0,00	0,00	0,00	0,46
61	12.114	20.014	21.915	31.921	56.674	49.167	41.482
62	4.601	7.472	12.194	31.391	37.339	34.500	23.220
63	0	0	1	6	207	274	53
Total clothing imports	16.715	27.486	34.110	63.318	94.220	83.941	64.755
Share of clothing imports within total imports	59,74	59,96	63,44	82,86	83,52	88,60	83,86

Table 18. Turkey's textile and clothing exports to India (Thousand US Dollar) [4]

	2010	2011	2012	2013	2014	2015	2016
Total exports	606.835	756.082	791.720	586.927	586.589	650.319	652.018
50	111	87	43	149	33	178	14
51	4.733	4.879	5.426	7.415	5.458	3.317	4.308
52	17.370	17.057	12.884	9.656	5.260	6.740	9.693
53	30	142	81	184	124	26	308
54	2.006	3.224	2.797	3.614	3.510	3.615	3.497
55	1.950	3.164	1.217	4.389	1.899	1.760	3.435
56	1.161	1.783	2.411	1.255	1.423	1.661	4.269
57	4.208	5.316	5.473	6.549	7.997	7.623	6.948
58	746	930	703	1.103	802	774	787
59	2.080	2.629	1.947	1.994	1.865	1.361	1.257
60	170	363	384	729	710	377	137
Total textile exports	34.565	39.574	33.366	37.037	29.081	27.432	48.032
Share of textile exports within total exports	5,70	5,23	4,21	6,31	4,96	4,22	7,37
61	558	704	979	1.514	1.568	1.723	3.070
62	1.170	1.858	1.450	2.425	2.120	2.286	2.427
63	544	928	527	1.137	864	1.583	1.545
Total clothing exports	2.272	3.490	2.956	5.076	4.552	5.592	7.042
Share of clothing exports within total exports	0,37	0,46	0,37	0,86	0,78	0,86	1,08

Table 19. Turkey's textile and clothing imports from India (Thousand US Dollar) [4]

	2010	2011	2012	2013	2014	2015	2016
Total imports	3.409.938	6.498.651	5.843.638	6.367.791	6.898.577	5.613.570	5.757.156
50	3.256	3.866	1.913	1.864	1.579	1.380	1.084
51	4.689	4.916	4.680	1.099	1.779	2.684	1.369
52	271.555	189.572	67.177	127.926	191.683	61.711	98.788
53	34.699	22.066	15.973	3.163	4.196	2.824	3.896
54	128.599	188.260	281.552	281.094	379.140	355.392	344.539
55	232.674	282.973	232.085	245.118	234.683	228.778	219.845
56	9.110	6.934	11.619	24.961	22.738	23.092	10.536
57	54.128	63.225	57.656	56.379	55.773	23.554	10.191
58	20.568	23.142	14.103	10.424	11.597	8.187	5.890
59	697	983	1.234	903	1.477	874	1.582
60	2.093	15.139	64	333	840	57	40
Total textile imports	762.068	801.076	688.056	753.264	905.485	708.533	697.760
Share of textile imports within total imports	22,35	12,33	11,77	11,83	13,13	12,62	12,12
61	48.481	54.163	27.683	30.085	37.097	33.879	26.314
62	98.391	115.906	68.271	70.988	71.234	61.120	47.292
63	12.363	10.152	9.227	13.289	12.711	10.956	12.558
Total clothing imports	159.235	180.221	105.181	114.362	121.042	105.955	86.164
Share of clothing imports within total imports	4,67	2,77	1,80	1,80	1,75	1,89	1,50

Turkey's textile exports to India have increased 39% within seven years (2010-2016) (Table 18). Turkey's textile export shares within total exports have increased from 6% to 7% within seven years. Besides, Turkey's

clothing exports to India have increased three times during the same period whereas their shares within total exports have increased from 0,37% to 1,08%. Man-made staple fibers, man-made filament fibers, wadding, felt and nonwovens; special yarns; twine, cordage, ropes and cables; carpets and other textile floor coverings are the mostly increased items within textile exports whereas all exported clothing items are increased tremendously. On the other hand, Turkey's textile imports from India have decreased 8% within seven years whereas its clothing imports have decreased 46% (Table 19). Turkey's textile import shares within total imports have decreased to 12% from 22% whereas clothing import shares within total imports have decreased to 1,5% from 4,67%. Cotton, other vegetable textile fibers; paper yarn and woven fabrics of paper yarn; carpets and other textile floor coverings; impregnated, coated, covered or laminated textile fabrics and knitted or crocheted fabrics are the mostly decreased items within textile imports whereas knitted and woven apparel and clothing accessories are the mostly decreased items within clothing imports. Turkey's textile and clothing exports to India have increased in recent years whereas its imports have decreased. In spite of this situation, enormous trade deficits have occurred both in Turkey's textile and clothing trades with India.

Table 20. Turkey's textile and clothing exports to Hong Kong (Thousand US Dollar) [4]

	2010	2011	2012	2013	2014	2015	2016
Total exports	247.541	425.636	337.239	420.350	439.472	345.319	400.253
50	114	12	21	4	0	39	62
51	4.728	4.370	2.900	1.635	1.514	1.019	927
52	27.311	40.052	57.242	64.539	63.463	56.098	41.628
53	391	224	293	130	215	261	314
54	3.415	4.026	4.264	5.626	4.575	4.520	4.494
55	5.404	16.426	10.446	4.948	5.536	4.306	3.282
56	183	325	273	68	26	42	214
57	158	946	493	261	295	426	241
58	5.140	5.984	5.748	6.380	4.380	3.014	2.589
59	268	167	185	1.546	322	576	1.217
60	2.117	3.614	2.523	2.546	2.144	1.770	1.758
Total textile exports	49.229	76.146	84.388	87.683	82.470	72.071	56.726
Share of textile exports within total exports	19,89	17,89	25,02	20,86	18,77	20,87	14,17
61	9.648	15.471	19.699	18.391	17.549	15.081	16.281
62	10.343	13.711	14.920	12.640	9.954	6.960	9.974
63	861	1.580	1.111	883	449	468	704
Total clothing exports	20.852	30.762	35.730	31.914	27.952	22.509	26.959
Share of clothing exports within total exports	8,42	7,23	10,59	7,59	6,36	6,52	6,74

Table 21. Turkey's textile and clothing imports from Hong Kong (Thousand US Dollar) [4]

	2010	2011	2012	2013	2014	2015	2016
Total imports	118.246	99.809	111.857	97.305	94.979	81.296	126.488
50	214	14	4	223	38	1	0
51	44	4	0	98	31	13	76
52	1.137	357	1.428	308	572	595	361
53	13	138	0	3	0	0	0
54	274	49	156	109	50	68	18
55	82	95	111	890	689	2.884	76
56	266	87	123	78	73	66	86
57	2	2	4	9	0	0	4
58	4.007	3.547	4.082	3.593	4.213	3.497	4.372
59	159	99	42	91	23	34	38
60	167	190	194	62	164	218	149
Total textile imports	6.365	4.582	6.144	5.464	5.853	7.376	5.180
Share of textile imports within total imports	5,38	4,59	5,49	5,62	6,16	9,07	4,10
61	1.938	1.993	1.052	798	660	350	448
62	1.467	2.274	1.518	1.989	1.077	980	393
63	15	22	41	53	20	196	85
Total clothing imports	3.420	4.289	2.611	2.840	1.757	1.526	926
Share of clothing imports within total imports	2,89	4,30	2,33	2,92	1,85	1,88	0,73

Turkey's textile exports to Hong Kong have increased 15% within seven years (2010-2016) (Table 20). Turkey's textile export shares within total exports have decreased to 14% from 20% within seven years. Besides, Turkey's clothing exports to Hong Kong have increased 29% during the same period whereas their shares within total exports have decreased to 7% from 8%. Cotton, man-made filament fibers, impregnated, coated, covered or laminated textile fabrics are the mostly increased items within textile exports whereas

knitted apparel and clothing accessories are the mostly increased items within clothing exports. On the other hand, Turkey's textile imports from Hong Kong have decreased 19% within seven years whereas its clothing imports have decreased 73% (Table 21). Turkey's textile import shares within total imports have decreased to 4% from 5% whereas clothing import shares within total imports have decreased to 1% from 3%. Silk, cotton, man-made filament fibers, wadding, felt and nonwovens; special yarns; twine, cordage, ropes and cables are the mostly decreased items within textile imports whereas knitted and woven apparel and clothing accessories are the mostly decreased items within clothing imports. Turkey's textile and clothing exports to Hong Kong have increased in recent years whereas its imports have decreased. Therefore, enormous trade surpluses have occurred both in Turkey's textile and clothing trades with Hong Kong.

3. RESULTS, GENERAL EVALUATION AND SUGGESTIONS

Seven Asian countries, which have significant shares within global textile and clothing trades, are included in this research. These countries have increased their shares within global textile and clothing trades in recent years. These countries are both existing and potential rivals of Turkish textile and clothing sectors; which are the leading and significant exporters of Turkish economy. Besides, these sectors have foreign trade surpluses. If the obtained research data are analyzed, it can be seen that these countries have very low shares in Turkey's textile and clothing exports (4,24% and %0,084 respectively according to 2016 data) whereas their shares within Turkish textile and clothing imports (45% and 64,5% respectively according to 2016 data) are tremendously high. This data indicates that Turkey have enormous trade deficits (-2,988 billion dollar in textiles and -1,594 billion dollar in clothing) in textile and clothing trade with these countries. Turkey is a net textile and clothing importer from five countries (Bangladesh, Vietnam, China, Indonesia and India) whereas it is a net textile exporter to Cambodia. Moreover, it is a net textile and clothing exporter to Hong Kong. These countries efficiencies within textile and clothing trade are rapidly increased and become settled. Besides, their effects on the textile and clothing trade between Turkey and themselves are increased. Therefore, Turkey has difficulties while competing against these countries. Turkey has been recently implementing anti-dumping duties to some of these countries. However, this implementation can't be able to prevent these difficulties; it only restricts the difficulty increment. These countries have several overwhelming superiorities in international textile and clothing trades. These superiorities can be summarized as; production cost advantages, energy cost advantages, tax advantages, financing cost advantages and government incentive advantages.

Turkish textile and clothing enterprises hardly compete with these countries, which have serious cost advantages, on the basis of same products. Productivity increments can slightly contribute to this difference. Therefore, Turkish textile and clothing enterprises can compete with their rivals via innovative products, design and quality and speed increments. In addition to these they should improve their own retail chains, trademarks and branded products. Besides, Turkish government should increase its increments in terms of production costs. In this context, it should support enterprises in terms of energy costs, taxes, social security premiums and suitable financial sources.

REFERENCES

[1]. World Trade Organization Statistics Database, Time Series on International Trade, Available: http://stat.wto.org/StatisticalProgram/WSDBStatProgramHome.aspx?Language=E (Access Date: April 2017)
[2]. World Trade Organization World Trade Statistical Review 2016, 165 p., Available: https://www.wto.org/english/res_e/statis_e/wts2016_e/wts16_toc_e.htm (Access Date: April 2017)
[3]. Harmonized System (HS) Classification Code Explanations, Available: http://www.foreign-trade.com/reference/hscode.htm (Access Date: April 2017)
[4]. International Trade Center, Trademap – Trade Statistics for International Business Development, Available: http://www.trademap.org/Index.aspx (Access Date: April 2017)

Measurement of Turkish Textile and Clothing Enterprises' Export Efficiencies with Data Envelopment Analysis

Turan Atılgan[1], Seher Kanat[2]

Abstract

Textile and clothing sector constitutes the second biggest item of Turkish exportation after automotive sector. Besides, sector is the biggest sector of the country in terms of net added-value creation. The sector is the most competitive Turkish sector in international trade due to its export success. Moreover, brand value of the country and textile and clothing enterprises are increased due to the sector's international trade success. The performance and success of the sector; which approximately constitutes 18% of Turkish exportation, 9% of gross domestic product and 22% of manufacturing industry employment; seriously affect the performance of national economy. Therefore, a cause and effect relationship between them is established.

In this study, export efficiencies of textile and clothing enterprises, which are quoted on Borsa İstanbul, in 2016 are measured with data envelopment analysis which is one of the most significant techniques that are used in efficiency measurement. Besides; suggestions are made about the factors that should be observed and the strategies that would be implemented by the enterprises.

Keywords: *Data envelopment analysis, textile and clothing sector, efficiency, textile and clothing exportation*

1. EFFICIENCY CONCEPT AND DATA ENVELOPMENT ANALYSIS

Efficiency is the degree of an achievement for an aim to which an activity, movement or behavior is directed [1]. In other words, it is the degree of achievement for predetermined goals.

Efficiency is an evaluation criterion, which indicates the sufficient or efficient utilization of labor, raw material, auxiliary materials and other inputs in accordance with the determined enterprise goals. Efficiency can be calculated with the below formula [1]:

$$Efficiency = \frac{Standard\ performance}{Actual\ (real) performance} \qquad (1)$$

Efficiency ratio must be equal to one in order to obtain efficient or sufficient performance. If the efficiency ratio is below one, it means that the activity isn't actualized as it is required [1]. The efficiency is measured via different techniques, where many factors are effective. Data envelopment analysis is one of these efficiency measurement techniques.

Data envelopment analysis is a widely practiced method used for performance benchmarking and comparison and the first application of this technique was performed over the public sector. It is currently a method applicable in many fields [2]. Data envelopment analysis is a non-parametric programming technique to measure the relative efficiency of peer decision making units using multiple inputs to generate multiple outputs. Data envelopment analysis considers n decision making units to be evaluated, where each decision making units consumes varying amounts of m different inputs to produce s different outputs. The relative efficiency of a decision making unit is defined as the ratio of its total weighted output to its total weighted input. In mathematical programming terms, this ratio, which is to be maximized, forms the objective function for the particular decision making unit being evaluated. A set of normalizing constraints is required to reflect the condition that the output to input ratio of every decision making unit be less than or equal to unity [3].

[1]Corresponding author: Ege University, Department of Textile Engineering, 35100, Bornova/İzmir, Turkey, turan.atilgan@ege.edu.tr

[2]Ege University, Department of Textile Engineering, 35100, Bornova/İzmir, Turkey, seher.kanat@ege.edu.tr

The mathematical programming problem is then represented as;

$$\max E_{jo} = \frac{\sum_r u_r y_{rj_0}}{\sum_i v_i x_{ij_0}} \qquad (2)$$

subject to

$$\frac{\sum_r u_r y_{rj}}{\sum_i v_i x_{ij}} \leq 1, j = 1, \ldots, j_0, \ldots, n \qquad (3)$$

$$u_r, v_i \geq \varepsilon > 0, r = 1, \ldots, s; i = 1, \ldots, m \qquad (4)$$

where Ej_0 is the efficiency score of the evaluated decision making unit (j_0), u_r is the weight assigned to output r, v_i is the assigned to input i, y_{rj} denotes amount of output r produced by the jth decision making unit, x_{ij} denotes amount of input i used by the jth decision making unit and $\mathcal{E}$ is an infinitesimal positive number. A decision making unit attains a relative efficiency rating of 1 only when comparisons with other decision making units do not provide evidence of inefficiency in the use of any input or output. Data envelopment analysis identifies the most favorable set of weights for each decision making units and it enables to dichotomize the decision making units into two categories as efficient and inefficient [3].

It is necessary for the decision units to be analyzed to have similar functions focusing on the same objective and to operate under the same market circumstances. It is also imperative for all units in the group to be identical in terms of the factors identifying their efficiencies, excluding unit size and intensity. In addition, all inputs and outputs should be represented by positive numbers and there should be no null input or output. Data envelopment analysis compares the production units, considered to be identical, to identify the best observation as efficiency frontier. Other observations are assessed by reference to this frontier. The inefficiency level and its roots and causes in every decision unit are identifiable by use of this technique. This provides insights for the executives and top administrators on how to decide with respect to the increase in the amount of inputs and/or decrease in the amount of outputs. DEA models are analyzed in two separate groups: input-oriented and output-oriented [2].

In an input-orientation model (input minimization) desired output is produced with minimum inputs. This model s preferred when output is given and inputs are flexible. On the other hand, in an output orientation model (output maximization) efforts are made to maximize the output with given inputs. The choice of the model depends on the available flexibility either with the inputs or outputs [4]. In the literature there are many researches, which have used data envelopment analysis for efficiency measurement. Therefore, the ones, which include textile, are going to be summarized.

One of these researches aims to examine the technical, pure technical and scale efficiencies of profitability of textile companies in Turkey for 2007. The profitability efficiency scores of textile sector in 2007 are evaluated by using data envelopment analysis. The result of analyze shows that efficiency score of textile sector is low [5].

Another study aims to examine the efficiencies of textile enterprises' exports in Eskisehir Organized Industrial Zone (which is located in Turkey) during the period 2008-2009 by using data envelopment analysis. The study analyzes 5 enterprises as a decision making units by applying two data envelopment analysis models. The results show that, Sarar Textile is efficient based on the two models [2].

In other research, efficiencies of eight textile enterprises, which operate in home textile area, are measured by data envelopment analysis. Three outputs (turnover, profit before tax, export revenue) and three inputs (net assets, equity capital, number of employees) are used. According to the obtained results, four enterprises are determined as efficient [6].

Another research aims to evaluate the export efficiency of textile and clothing enterprises listed in the 2012 Istanbul Chamber of Industry 500 report. The export efficiencies of 30 textile and clothing enterprises with complete data for 2012 are evaluated with data envelopment analysis and analytic hierarchy process. Output-oriented data envelopment analysis method is applied using four input variables (number of employees, net assets, number of exporting countries and export experience) and one output variable (export sales) to determine enterprise export efficiency levels. Based on the analysis results, four enterprises are identified as efficient units [7].

2. THE PURPOSE, MATERIAL AND METHOD OF THE RESEARCH

The research aims to measure the export efficiencies of textile and clothing enterprises, which are quoted on Borsa İstanbul, in 2016. Besides; suggestions are made about the factors that should be observed and the strategies that would be implemented by the enterprises. In accordance with the aim of the research, data envelopment analysis is chosen as a method. The material of the research consists of 20 textile and clothing enterprises, which are quoted on Borsa İstanbul and whose data can be obtained.

Employee numbers, total assets, turnover and number of countries to which exports are actualized, are used as inputs whereas export revenue is utilized as output within the constituted linear programming model. All data belongs to 2016. The inputs, output and decision making units (enterprises) of the research are demonstrated in Table 1. Linear programming models are constituted for all decision making units and they are solved with DEAP Version 2.1 program [8]. Input orientated, Multi-Stage, CRS (The constant returns to scale model) model is used as data envelopment method.

Table 1. Data of textile and clothing enterprises [9]

Enterprise Name	Output	Inputs			
	Export Revenue (TL)	Employee Numbers	Total Assets (TL)	Turnover (TL)	Country Numbers[*]
Akın Textile	117.176.000	484	468.814.448	175.818.540	31
Arsan Textile	15.471.500	1.107	296.026.452	140.593.167	9
Bilici Yatırım	15.849.332	536	224.316.067	81.757.104	20
Birko	2.516.445	419	186.609.315	95.157.526	6
Birlik Mensucat	711.973	25	73.985.665	15.273.580	3
Bossa	160.981.142	1.834	718.931.761	361.200.233	51
Dagi	257.004	362	152.343.488	71.869.179	16
Hateks	109.378.122	1.150	352.608.946	125.789.228	45
Karsu	32.155.898	453	223.629.461	142.942.404	30
Kordsa	624.547.736	3.782	2.543.674.117	1.908.345.131	42
Luks Kadife	12.396.542	160	133.177.410	27.835.001	6
Menderes	514.218.847	3.791	838.511.692	645.115.929	38
Rodrigo	2.928.890	46	16.880.924	9.018.021	6
Soktas	96.062.215	1.361	567.662.425	275.308.924	50
Yatas	41.556.691	1.909	348.602.809	502.323.499	31
Yunsa	166.982.461	1.271	255.172.371	247.008.760	52
Vakko	1.286.363	1.681	442.656.163	520.383.120	5
Aksa	776.140.000	1.245	2.632.970.000	1.954.385.000	50
Sasa	471.120.000	1.241	1.032.187.000	1.182.909.000	50
Sanko Pazarlama	2.089.935	85	436.257.845	869.893.806	10

[*]*Number of countries to which exports are actualized*

3. FINDINGS OF THE RESEARCH

Export efficiency scores which are obtained with data envelopment analysis are demonstrated in Table 2. As it is mentioned in the literature part; if efficiency score is equal to one, the enterprise is efficient. The enterprise becomes less efficient as the score lowers down one. According to this, 6 textile and clothing enterprises (Akın Textile, Hateks, Menderes, Yunsa, Aksa and Sasa) are efficient in terms of export. Potential improvement table is constituted for inefficient decision making units (Table 3). Reference enterprises are chosen for each of the inefficient enterprises in order to make them efficient and the input reduction ratios are obtained according to these references.

Table 2. Export efficiency scores of textile and clothing enterprises

Enterprise Name	Export Efficiencies	Enterprise Name	Export Efficiencies
Akın Textile	1.000	Luks Kadife	0.563
Arsan Textile	0.138	Menderes	1.000
Bilici Yatırım	0.239	Rodrigo	0.425
Birko	0.038	Soktas	0.460
Birlik Mensucat	0.089	Yatas	0.191
Bossa	0.584	Yunsa	1.000
Dagi	0.005	Vakko	0.017
Hateks	1.000	Aksa	1.000
Karsu	0.367	Sasa	1.000
Kordsa	0.958	Sanko Pazarlama	0.039

Table 3. Potential improvement table for inefficient decision making units

Enterprise Name	Reference Set	Factors		Actualized (Real)	Target	Potential Improvement (%)
Arsan Textile	Hateks Menderes	Output	Export Revenue	15471500	15471500	0
		Inputs	Employee Numbers	1107	114	-90
			Total Assets	296026452	25687712	-91
			Turnover	140593167	19379732	-86
			Country Numbers[*]	9	1	-89
Bilici Yatırım	Hateks Menderes	Output	Export Revenue	15849332	15849332	0
		Inputs	Employee Numbers	536	127	-76

234

Company	References		Metric			
			Total Assets	224316067	31469735	-86
			Turnover	81757104	19514836	-76
			Country Numbers[*]	20	2	-90
		Output	Export Revenue	2516445	2516445	0
Birko	Menderes Akın Textile Aksa		Employee Numbers	419	16	-96
		Inputs	Total Assets	186609315	5229869	-97
			Turnover	95157526	3619491	-96
			Country Numbers[*]	6	1	-83
		Output	Export Revenue	711973	711973	0
Birlik Mensucat	Akın Textile Aksa		Employee Numbers	25	2	-92
		Inputs	Total Assets	73985665	2675489	-96
			Turnover	15273580	1357703	-91
			Country Numbers[*]	3	1	-67
		Output	Export Revenue	160981142	160981142	0
Bossa	Menderes Akın Textile		Employee Numbers	1834	1070	-42
		Inputs	Total Assets	718931761	347676221	-52
			Turnover	361200233	210796065	-42
			Country Numbers[*]	51	19	-63
		Output	Export Revenue	257004	257004	0
Dagi	Menderes Akın Textile		Employee Numbers	362	2	-99
		Inputs	Total Assets	152343488	562285	-100
			Turnover	71869179	337282	-100
			Country Numbers[*]	16	1	-94
		Output	Export Revenue	32155898	32155898	0
Karsu	Menderes Akın Textile Sasa		Employee Numbers	453	166	-63
		Inputs	Total Assets	223629461	82129911	-63
			Turnover	142942404	52496870	-63
			Country Numbers[*]	30	5	-83
		Output	Export Revenue	624547736	624547736	0
Kordsa	Aksa		Employee Numbers	3782	1002	-74
		Inputs	Total Assets	2543674117	2118709836	-17
			Turnover	1908345131	1572663085	-18
			Country Numbers[*]	42	40	-5
		Output	Export Revenue	12396542	12396542	0
Luks Kadife	Menderes Akın Textile		Employee Numbers	160	90	-44
		Inputs	Total Assets	133177410	21230413	-84
			Turnover	27835001	15657550	-44
			Country Numbers[*]	6	1	-83
		Output	Export Revenue	2928890	2928890	0
Rodrigo	Menderes Akın Textile		Employee Numbers	46	19	-59
		Inputs	Total Assets	16880924	6278345	-63
			Turnover	9018021	3830317	-58
			Country Numbers[*]	6	1	-83
		Output	Export Revenue	96062215	96062215	0
Soktas	Akın Textile Menderes		Employee Numbers	1361	626	-54
		Inputs	Total Assets	567662425	216430352	-62
			Turnover	275308924	126717998	-54
			Country Numbers[*]	50	12	-76
		Output	Export Revenue	41556691	41556691	0
Yatas	Menderes Yunsa		Employee Numbers	1909	309	-84
		Inputs	Total Assets	348602809	66536177	-81
			Turnover	502323499	54827438	-89
			Country Numbers[*]	31	6	-81
		Output	Export Revenue	1286363	1286363	0
Vakko	Aksa		Employee Numbers	1681	2	-100
		Inputs	Total Assets	442656163	4363845	-99
			Turnover	520383120	3239168	-99
			Country Numbers[*]	5	1	-80
		Output	Export Revenue	2089935	2089935	0
Sanko Pazarlama	Aksa		Employee Numbers	85	3	-96
		Inputs	Total Assets	436257845	7089875	-98
			Turnover	869893806	5262629	-99
			Country Numbers[*]	10	1	-90

*Number of countries to which exports are actualized

Hateks and Menderes Textile are chosen as references for Arsan Textile, which is one of the inefficient enterprises in terms of export. Reference enterprises are suggested by DEAP program which constitutes and solves the linear programming models. Arsan Textile should decrease its employee number by 90%, total assets by 91%, turnover by 86% and country numbers (number of countries to which exports are actualized)

by 89% in order to be efficient. In other words, Arsan Textile can reach this export revenue with fewer employees (-90%), fewer assets (-91%), fewer turnover (-86%) and fewer countries (-89%).

Bilici Yatırım, which is one of the inefficient enterprises in terms of export, should decrease its employee number by 76%, total assets by 86%, turnover by 76% and country numbers (number of countries to which exports are actualized) by 90% according to its reference enterprises (Hateks and Menderes) in order to be efficient. Birko Textile can reach the same export revenue with fewer employees (-96%), fewer assets (-97%), fewer turnover (-96%) and fewer countries (-83%). Menderes, Akın Textile and Aksa are chosen as references for Birko Textile.

Birlik Mensucat, which is one of the inefficient enterprises in terms of export, should decrease its employee number by 92%, total assets by 96%, turnover by 91% and country numbers (number of countries to which exports are actualized) by 67% according to its reference enterprises (Akın Textile and Sasa) in order to be efficient. Bossa can reach the same export revenue with fewer employees (-42%), fewer assets (-52%), fewer turnover (-42%) and fewer countries (-63%). Menderes and Akın Textile are chosen as references for Bossa.

Dagi, which is one of the inefficient enterprises in terms of export, should decrease its employee number by 99%, total assets by 100%, turnover by 100% and country numbers (number of countries to which exports are actualized) by 94% according to its reference enterprises (Menderes and Akın Textile) in order to be efficient. Karsu Textile can reach the same export revenue with fewer employees (-63%), fewer assets (-63%), fewer turnover (-63%) and fewer countries (-83%). Menderes, Akın Textile and Sasa are chosen as references for Karsu Textile.

Kordsa, which is one of the inefficient enterprises in terms of export, should decrease its employee number by 74%, total assets by 17%, turnover by 18% and country numbers (number of countries to which exports are actualized) by 5% according to its reference enterprise (Aksa) in order to be efficient. Luks Kadife can reach the same export revenue with fewer employees (-44%), fewer assets (-84%), fewer turnover (-44%) and fewer countries (-83%). Menderes and Akın Textile are chosen as references for Luks Kadife.

Rodrigo, which is one of the inefficient enterprises in terms of export, should decrease its employee number by 59%, total assets by 63%, turnover by 58% and country numbers (number of countries to which exports are actualized) by 83% according to its reference enterprises (Menderes and Akın Textile) in order to be efficient. Soktas can reach the same export revenue with fewer employees (-54%), fewer assets (-62%), fewer turnover (-54%) and fewer countries (-76%). Akın Textile and Menderes are chosen as references for Soktas.

Yatas, which is one of the inefficient enterprises in terms of export, should decrease its employee number by 84%, total assets by 81%, turnover by 89% and country numbers (number of countries to which exports are actualized) by 81% according to its reference enterprises (Menderes and Yunsa) in order to be efficient. Vakko can reach the same export revenue with fewer employees (-100%), fewer assets (-99%), fewer turnover (-99%) and fewer countries (-80%). Aksa is chosen as a reference for Vakko. Sanko Pazarlama, which is one of the inefficient enterprises in terms of export, should decrease its employee number by 96%, total assets by 98%, turnover by 99% and country numbers (number of countries to which exports are actualized) by 90% according to its reference enterprise (Aksa) in order to be efficient.

4. RESULTS AND SUGGESTIONS

Textile and clothing sector, which is the second biggest exporter of Turkey, also possesses a significant efficiency within the economy. There are approximately sixty thousand enterprises in the sector at different sizes and ten thousand of them are exporters. Besides, 403 enterprises are quoted on Borsa İstanbul in 2016 and 26 of them are textile and clothing enterprises. 20 of these enterprises are incorporated into the research. When their export efficiency results are evaluated generally, it can be seen that only 6 of them are efficient. 14 of them are inefficient in terms of export, due to different reasons. Inefficient enterprises' export shares within their total turnovers are very low.

Three of these textile and clothing enterprises operate in home textile field. Two of these enterprises (Menderes and Hateks) are efficient whereas one (Yatas) of them is inefficient in terms of export. Yatas's export revenue only takes 8% share from its turnover. Also, it focuses on domestic market and makes sales over its own retail chain with its own trademark. These can be indicated as the most important reasons of being inefficient. On the other hand, two efficient home textile enterprises focus on export and work for international organizational customers. Similarly, three clothing enterprises are included in the research. All of them are inefficient in terms of export because they focus on domestic markets and make sales over their own retail chains with their own trademarks. All these enterprises should constitute their own retail chains in international markets in order to obtain export efficiency and increase their brand values.

When the export efficiencies of 20 textile and clothing enterprises are evaluated generally, these suggestions can be made for 14 inefficient enterprises:

1. Inefficient enterprises, whose export shares are low within their total turnovers, should increase their export shares in order to minimize their risks and succeed in national and international competition. Their export shares should be approximately at 50%.

2. Enterprise managers should canalize towards institutionalization and should take serious steps about this issue.

3. They should canalize towards high value-added products. Therefore, they can be successful in international markets as well as being able to increase their profitability due to the increasing unit export prices.

4. They should deeply penetrate into international markets where they operate. Thus, they can improve their brand awareness and customer portfolios.

5. They should give great importance to international fairs and activities due to the significance of marketing within the international markets.

6. Customer relations are both important in domestic market and international markets. Therefore, enterprises should give great importance to customer relations in order to increase their export efficiencies.

REFERENCES

[1].   Dogan M., 2006, Business Economy and Management, Birlesik Matbaacılık, İzmir, 526 p. (in Turkish).
[2].   Yenilmez F., Girginer N., 2012, Assessing export performance of textile companies in Eskisehir organized industrial zone by use of data envelopment analysis, *Tekstil ve Konfeksiyon*, Vol.22, No.1, p:12-17.
[3].   Karsak E.E., Karadayı M.A., 2017, Imprecise DEA framework for evaluating health-care performance of districts, *Kybernetes*, Vol.46, No.4, p:706-727.
[4].   Sahoo B.K., 2016, Ownership, size and efficiency: evidence from software companies in India, *Benchmarking: An International Journal*, Vol.23, No.2, p:313-328.
[5].   Kayalı C. A., Evaluating the financial profitability efficiencies of textile companies in 2007, *Tekstil ve Konfeksiyon*, Vol.17, No. 1, p: 3-8 (in Turkish).
[6].   Gülsevin N., Atılgan T., 2006, Determining enterprise efficiency with data envelopment analysis and an application in home textile area, *Tekstil Maraton*, Vol.16, No.86, p:74-79 (in Turkish).
[7].   Ozturk O., Girginer N., 2015, The export efficiency of Turkish textile and apparel firms: an investigation employing data envelopment analysis and analytic hierarchy process methods, *Tekstil ve Konfeksiyon*, Vol.25, No.1, p:10-23.
[8].   Coelli T., DEAP Version 2.1 (Data Envelopment Analysis Computer Program), Centre for Efficiency and Productivity Analysis, Available: http://www.uq.edu.au/economics/cepa/deap.php (Access Date: April 2017)
[9].   Public Disclosure Platform, Enterprise Notifications, Annual Financial Reports and Annual Activity Reports, Available: https://www.kap.org.tr/tr/bildirim-sorgu (Access Date: April 2017) (in Turkish).

A Review of Emerging Optical Access Solutions for Broadband Access

Nisa Nacar Cıkan[1], Murat Aksoy[1]

Abstract

Bandwidth demand for optical access technologies is growing. In this paper, solutions for increasing bandwidth demand is reviewed and Passive Optical Networks is found as a solution for bandwidth hungry applications. Passive Optical Network Types are compared in terms of cost and bandwidth. Wavelength Division Multiplexing Passive Optical Networks(WDM-PONs) allow much higher bandwidth and show promise for future broadband applications. We especially presented WDM-PONs technologies with different aspects.

Keywords: *Optical Access Networks, TDM, WDM, PON*

1. INTRODUCTION

There is increasing huge demand on bandwidth hungry applications, exponential growth in Internet traffic, which require broader bandwidth usage for per user. Some of the broadband multimedia applications are video-on-demand, high definition television(HDTV), multi-party videoconferencing, online gaming and many others[1]. These multimedia digital services are highly bandwidth intensive, and require underlying Access network infrastructures that are capable of supporting the very high-speed data transmission rates that are needed[1, 2]. Thus, there is a need to move from conventional broadband Access Technologies (such as xDSL networks) to next generation optical access networks.

Digital Subscriber Lines(DSL) are used as communication services[3]. DSL divided into two standards as asymmetric digital subscriber loop(ADSL), and very high speed digital subscriber line(VDSL). DSL use copper infrastructure that is already deployed and this removes investment cost. However, DSL is not an option for future Access solution, since the copper based is not provide high speeds[1]. DSL is limited by data rates and distance when compared with future Access networks. The limits of different types of digital subscriber lines are given in Table 1. Optical fibers have been suggested as a novel solution to limitations of copper-based access networks[4].

In this study, optical broadband access technologies focusing mainly on passive optical networks(PONs) are presented and discussed in terms of architecture, cost effective, reliability, latency and vs. It is widely accepted that Passive Optical Networks are the most promising, cost-effective, and high-performance access solutions[5]

2. ACCESS NETWORK TECHNOLOGIES

Main types of Access Technologies are summarized in this section. The types of Access Technologies[6] are explained in this section.

2.1. Digital Subscriber Line(DSL)

DSL is used to transmit digital data over telephone lines. DSL is mainly divided into two categories as asymmetric digital subscriber loop(ADSL) and very high speed digital subscriber loop(VDSL).

2.2. Hybrid Fiber Coaxial(HFC)

It is deployed current Access technology which uses video distribution and the Internet for data transfer.

---

[1]*Cukurova University, Electrical& Electronics Engineering Department, 01330, Sarıcam/Adana, Turkey.* ncikan@cu.edu.tr , aksoy@cu.edu.tr

2.3. Wireless Fidelity(Wi-Fi)

Wi-Fi network based on IEEE 802.11 standard.

2.4. Worldwide Interoperability for Microwave Access(WIMAX)

WIMAX network based on IEEE 802.16 standard form as a part of wireless access deployment.

2.5. The Fiber-to-the-X(FTTX)

FTTX infrastructure architectures, where X can be replaced as ranging from the Cabinet, distribution point, home and building depending on how close is the optical fiber terminated to the end-user. FTTX is a solution for broadband Access and the strongest and promising competitor amongst all currently deployed Access Technologies and is a good substitute to copper in new generation networks[7]. It offers many advantages as the low power loss, small weight, small size, longer transmission distances and immunity to electromagnetic interference.

Table 18. Comparison of bandwidth and reach for popular access technologies

Service	Medium	Downstream(Mbps)	Upstream(Mbps)	Max Reach(km)
ADSL	Twisted pair	8	0.896	5.5
ADSL2	Twisted pair	25	3.8	5.5
VDSL1	Twisted pair	50	30	1.5
VDSL2	Twisted pair	100	30	0.5
HFC	Coaxial cable	40	9	25
Wi-Fi	Free space	54	54	0.1
WiMAX	Free space	134	134	5
BPON	Fiber	1244	622	20
GPON	Fiber	2488	1244	20
EPON	Fiber	1250	1250	20

3. TYPES OF FTTX

FTTX networks are classified as Passive Optical Network (PON) or Active Optical Network(AON).

3.1. Active Optical Network

Active Optical Network utilizes electrically powered equipment like routers, Ethernet switch or switch aggregator. Electrically powered equipment causes more power consuming. The one advantage is subscribers have a dedicated optical strand but this requires more fiber and higher cost. The other advantage is active optical networks can cover long distances as a range to about 100 km.

3.2. Passive Optical Network

A Passive Optical Network does not have electrically powered equipment and use optical splitters to separate and collect optical signals. In this case, subscribers share fiber optic strands for a portion of the network and this causes slowing down of the transmission speed and latency. Thus, the amount of fiber and central Office equipment is reduced in PON.   The advantage of passive optical network is power required only at the ends. The limitation of PON is fiber cable runs of up to 20 km[8]. A PON is a very good solution for access networks. PON uses a point-to-multipoint(PTMP) topology. PON consists of an optical line terminal(OLT) at the service provider's central Office(CO) and a number of optical network units(ONUs) near end user side.
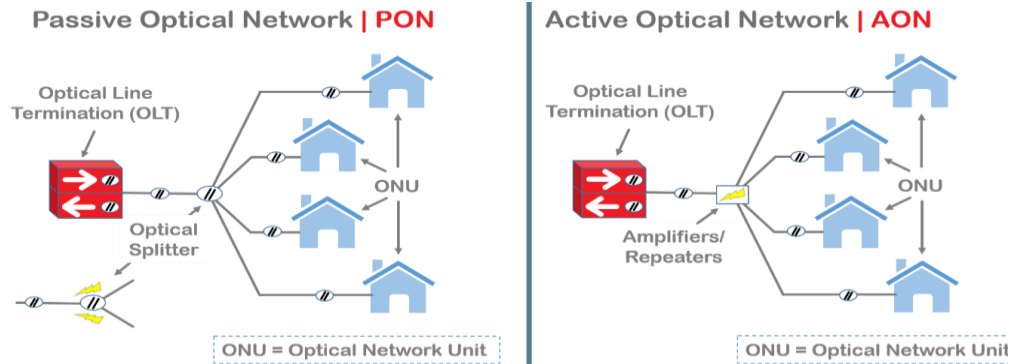
Figure 22. Schematic of Passive and Active Optical Networks[9]

4. PASSIVE OPTICAL NETWORK TYPES AND MULTIPLEXING TECHNIQUES

Passive optical networks offer point to multi-point(P2MP) network which is emerging development of broadband access network. In PON, the central office(CO) is connected to users by using one wavelength channel in the downstream direction [from optical line terminal(OLT) to optical network unit(ONU)], and another wavelength channel in the upstream direction (form OLT to ONU at central office)[10]. The main five types of passive optical networks are explained in this section. The OLT and ONUs process data according to the used technique.

4.1. Time Division Multiplexed Passive Optical Network

Time-division multiplexed passive optical networks (TDM-PON) are widely deployed worldwide to satisfy the traffic demand in access networks[11]. It works as the whole bandwidth is available to all the users and they can transmit and receive their data as assigned time slots.
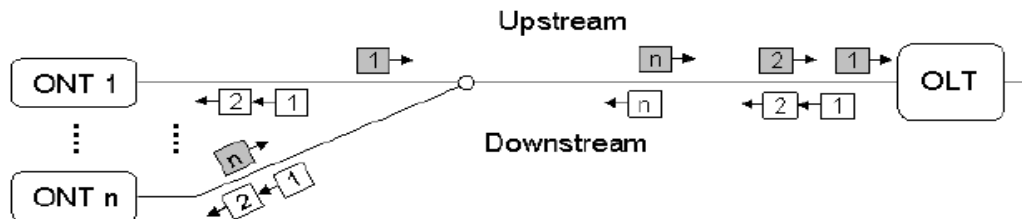
Figure 2. Schematic view of TDM-PON[12]

A particular time window is dictated by OLT for each ONU. This means that only a single upstream wavelength is needed, which lowers the cost as a universal type of ONU can be employed in every site[13]. There are currently three main PON standards which are shown in Table 2. BPON and GPON are authenticated by International Telecommunications Union(ITU) and EPON is authenticated by Institute of Electrical and Electronic Engineering(IEEE). Standardized versions of TDM PONs are EPON, BPON and GPON.

1. Broadband Passive Optical Network(BPON): BPON is a TDM based multiplexing system and first developed by the Full Service Access Network(FSAN) group, using Asynchronous Transfer Mode (ATM). The first BPON released in 1998. BPON supports 622 Mbps for downstream(DS) and 155 Mbps for upstream traffic. Final version of BPON supports speeds up to 1244 Mbps for downstream and 622 Mbps for upstream[14]

2. Gigabit Passive Optical Network (GPON): Gigabit passive optical network is TDM based multiplexing system and developed by FSAN. It is defined in the ITU-T PON standard and first released in 2003[15]. GPON transmission provides symmetric downstream and upstream   rates up to 2488 Mbps and asymmetric rates are 2488 Mbps for downstream and 1244 Mbps for upstream traffic[15]. The split ratio can be up to 1:128. Difference of GPON from EPON is to use Generic Encapsulation Mode(GEM) as a transportation mechanism[16].

3. Ethernet Passive Optical Network(EPON): Ethernet passive optical network is based on Ethernet Protocol and is an IEEE standard. It uses 802.3ah standard and is a competitor to GPON. EPON offers symmetrical rates up to 1.25 Gbps in both downstream and upstream traffic and split ratio up to 1:64[15, 17].

The explained all three PON standards are optically similar and they all use a single fiber, in which 1310 nm-centered band is used for upstream data, the 1490 nm-centered band is used for downstream traffic[15]. Although TDM-PON utilizes the bandwidth of fiber efficiently, it has limitations in increased transmission speeds, difficulty in burst synchronization, low security, dynamic bandwidth allocation(DBA) requirement and inaccurate ranging[18-20]

4.2. Code Division Multiple Access Passive Optical Network

The concept of Code Division Multiple Access PON(CDMA-PON) was proposed in optical communication in the late 1980s. In this technique, the network resources are shared among users that are assigned a code instead of a time-slot as in TDM or a wavelength as in WDM[21]. Downlink channels, from OLT to ONUs, are spectrum spread, combined, and then provided to an LD modulation part[22]. After transmission, the signal is split at a splitter and spread at a receiver side. Since only one laser diode(LD) is used for the downlink, no optical beat noise exists. However, in the uplink case, each ONU uses its own LD whose wavelength is not unique unlike in WDM-PON. As in the TDM-PON case, since it uses an optical power splitter at the remote network(RN), it suffers the same power-insertion-loss penalty[22].

4.3. Subcarrier Multiplexing Passive Optical Network

Subcarrier multiplexing passive optical network(SCM-PON) access enables point-to-point connectivity and one dedicated electrical subcarrier for each ONU is used, and it allows multiple users to share the same optical channel and its corresponding components[23]. As in the TDM case, an optical-power splitter can be used at the RN location[22]. SCM is found less sensitive to fiber dispersion because the dispersion penalty is determined by the width of the baseband of each individual signal channel when compared to conventional high speed TDM systems[24].Compared to the conventional WDM systems, it has better optical spectral efficiency because much narrower channel spacing is allowed[24].

4.4. Optical Frequency Division Multiplexing Passive Optical Network

Optical frequency division multiplexing passive optical network(OFDM-PON) has shown its usefulness for next generation PON[25-32] and long reach(LR) hybrid wavelength division multiplexed(WDM)/ time division multiplexed(TDM) PON[25, 33, 34]. It has a strong tolerance to the fiber chromatic dispersion, and this feature is very important to PON and LR-PON since these networks usually cannot be fully dispersion compensated[25]. The main disadvantages of OFDM are its high peak to average power ratio and its sensitivity to phase noise and frequency offset[35].

4.5. Wavelength Division Multiplexing Passive Optical Network

There is need to employ separate wavelength channels as downstream and upstream directions to increase the bandwidth of the Passive Optical Networks by employing wavelength division multiplexing(WDM)[36]. Such a PON is known as a WDM-PON[36]. Among other passive optical network types, the wavelength dimension may be exploited to (i) increase network capacity, (ii) improve network scalability by accommodating more end users and (iii) separate services[21].
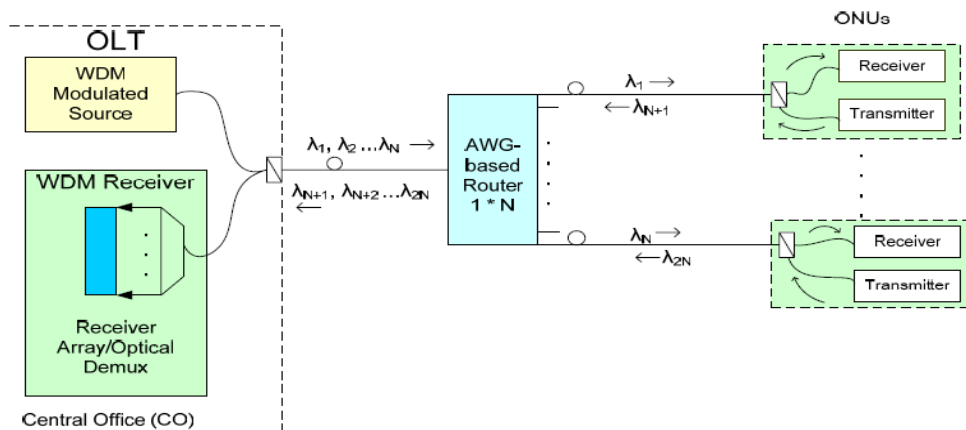
Figure 3. Simple WDM-PON architecture[36]

As already noted, standard PONs (i.e. BPON, GPON and EPON) utilize single wavelengths for data communication. In particular, 1310 nm is used for upstream communication, whereas 1490 nm is used in the downstream direction[15]. Thus the bandwidth in these two wavelengths is inherently shared between all end-users. It is evident that the full bandwidth capacity of fibers is not utilized in such schemes. In contrast, in a WDM-PON each uses a dedicated separate wavelength to communicate with the appropriate OLT. In this way, a point-to-point connection is established between each ONU and the OLT, resulting in a dedicated communication channel for each end user, and hence a dedicated fixed bandwidth[15]. Although WDM-PON has many advantages, the one disadvantage is high cost of requirement equipment. There is a way to lower the such kind of cost, mostly by addressing the need for expensive broadband light sources[37]. Colorless optical network unit(ONU) has been suggested as a solution to cost effect of passive optical networks[38-42].
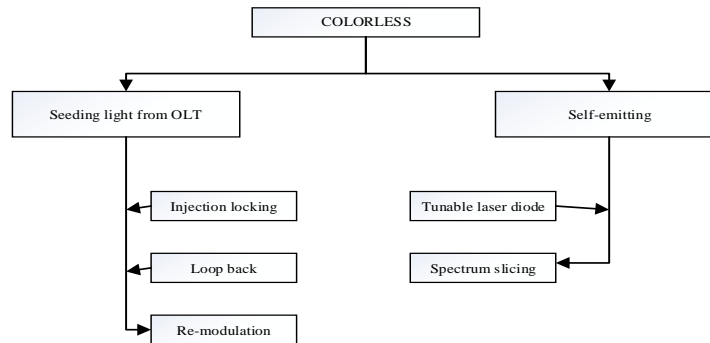
Figure 4. Categories of colorless scheme[43]

The most popular two approaches for colorless ONU are:

1. Tunable Laser: The most traditional way to have a nonspecific wavelength ONU is to install a tunable laser diode as a light source[41]. Tunable laser as a light source provides sufficient scalability to the network. In this scheme direct laser modulation is not used and external modulation scheme is preferred. From another point of view, the cost of the tunable laser diode as a component is high, even if the performance of this scheme is considered the best, whereby the performance of this scheme can reach up to 10 Gbps[38, 41].

2. Based on Loop Back the Seed Light: Seeding scheme is based on modulating the seed light received from the OLT and sends it back as upstream signal from ONU. At optical network unit side, WDM divides the received signal and the received downstream signal is demodulated and upstream signal is modulated. In ONU side, Reflective Semiconductor Optical Amplifier(RSOA) can be the amplifier and the modulator is electro-absorption modulator (EAM)[41]. Some researches use RSOA as a modulator due to its low cost[44-47]. Recently the most popular research subject for low cost and long reach solution is offered as self-seeding reflective semiconductor optical amplifier(SS-RSOA)[48-50].

CONCLUSION

In this paper, optical network Access Technologies are reviewed and analyzed. Fiber based Access networks provide significantly better performance than copper networks and support the increasing demands for high speed connections. The offered architectures are differing in terms of the technical perspective, the bandwidth for per user, especially the cost and number of subscribers. Currently many researches are ongoing to provide cost efficient, large bandwidth with low latency to the subscribers. One of the most promising candidate among next generation passive optical network is hybrid of time and wavelength division multiplexing technique. WDM-PON provides bandwidth scalability, quality of service and support of emerging traffic patterns required by video and broadcast standards. The bottleneck of WDM-PON is to be high cost. Recently, many research studies have been done to find a cost effective solution. Using the technique of self-seeding reflective semiconductor optical amplifier is a perfect candidate at optical network unit to remove the high cost problem.

REFERENCES

[1]. P. Chochliouros, G. A. Heliotis, I. P. Chochliouros, and G. A. Heliotis, *Optical Access Networks and Advanced Photonics: Technologies and Deployment Strategies*. Information Science Reference - Imprint of: IGI Publishing, 2009, p. 380.

[2]. C. Hellberg, D. Greene, and T. Boyes, *Broadband Network Architectures: Designing and Deploying Triple-Play Services*. Prentice Hall PTR, 2007.

[3]. T. Starr, P. Silverman, and S. Thomas, *DSL Advances*. Pearson Education, 2002, p. 512.

[4]. P. E. Green, *Fiber to the Home: The New Empowerment*. Wiley-Interscience, 2005.

[5]. L. Gutierrez, P. Garfias, M. De Andrade, C. Cervello-Pastor, and S. Sallent, "Next Generation Optical Access Networks: from TDM to WDM," in *Trends in Telecommunications Technologies*: InTech, 2010.

[6]. S. Bindhaiq *et al.*, "Recent development on time and wavelength-division multiplexed passive optical network (TWDM-PON) for next-generation passive optical network stage 2 (NG-PON2)," *Optical Switching and Networking,* vol. 15, pp. 53-66, 1// 2015.

[7]. G. Kramer and G. Pesavento, "Ethernet passive optical network (EPON): building a next-generation optical access network," *IEEE Communications Magazine,* vol. 40, no. 2, pp. 66-73, 2002.

[8]. G. Shen, R. S. Tucker, and C. J. Chae, "Fixed Mobile Convergence Architectures for Broadband Access: Integration of EPON and WiMAX [Topics in Optical Communications]," *IEEE Communications Magazine,* vol. 45, no. 8, pp. 44-50, 2007.

[9]. Hymax. (2015). *Passive and Active Optical Networks-What is the difference*. Available: http://www.hymax.co.za/passive-and-active-optical-networks-what-is-the-difference/

[10]. S. Sarkar, S. Dixit, and B. Mukherjee, "Hybrid Wireless-Optical Broadband-Access Network (WOBAN): A Review of Relevant Challenges," *Journal of Lightwave Technology,* vol. 25, no. 11, pp. 3329-3340, 2007.

[11]. C. Xia *et al.*, "Time-division-multiplexed few-mode passive optical network," *Optics Express,* vol. 23, no. 2, pp. 1151-1158, 2015/01/26 2015.

[12]. B. Skubic, B. Chen, C. Jiajia, J. Ahmed, and L. Wosinska, "Improved scheme for estimating T-CONT bandwidth demand in status reporting DBA for NG-PON," in *2009 Asia Communications and Photonics conference and Exhibition (ACP)*, 2009, vol. 2009-Supplement, pp. 1-6.

[13]. G. A. H. Ioannis P.Chochliouros, Anastasia S. Spiliopoulou, "An Introduction to Optical Access Networks:Technological Overview and Regulatory Issues for Large-Scale Deployment," in *Networking and Telecommunications: Concepts, Methodologies, Tools, and Applications*, I. R. M. Association, Ed.: Information Science Reference, 2010.

[14]. ITU-T. (2005). *Broadband Optical Access Systems Based on Passive Optical Networks (PON)*. Available: https://www.itu.int/rec/T-REC-G.983.1-200501-I/en

[15]. I. R. M. Association, *Networking and Telecommunications: Concepts, Methodologies, Tools, and Applications*. Information Science Reference, 2010.

[16]. I. E. Consortium, *Annual Review of Communications* (no. v. 59). International Engineering Consortium, 2007.

[17]. J. C. K. G.Pesavento, T. Koyama. IEEE Acccess Standards,802.3 ah GE-PON Status [Online]. Available: http://www.itu.int/itudoc/itu-t/workshop/optical/s3amp03.html.

[18]. C. Zhang, K. Qiu, and B. Xu, "Passive optical networks based on optical CDMA: Design and system analysis," *Chinese Science Bulletin,* journal article vol. 52, no. 1, pp. 118-126, 2007.

[19]. K. Ohara *et al.*, "Traffic Analysis of Ethernet-PON in FTTH Trial Service," in *Optical Fiber Communication Conference*, Atlanta, Georgia, 2003, p. ThAA2: Optical Society of America.

[20]. C. M. Assi, Y. Yinghua, D. Sudhir, and M. A. Ali, "Dynamic bandwidth allocation for quality-of-service over Ethernet PONs," *IEEE Journal on Selected Areas in Communications,* vol. 21, no. 9, pp. 1467-1477, 2003.

[21]. H. Ghafouri-Shiraz and M. M. Karbassian, *Optical CDMA Networks: Principles, Analysis and Applications*. Wiley, 2012.

[22]. C. H. Lee, W. V. Sorin, and B. Y. Kim, "Fiber to the Home Using a PON Infrastructure," *Journal of Lightwave Technology,* vol. 24, no. 12, pp. 4568-4583, 2006.

[23]. W. Shieh and I. Djordjevic, *OFDM for Optical Communications*. Elsevier Science, 2009.

[24]. R. C. Dorf, *Broadcasting and Optical Communication Technology*. CRC Press, 2006.

[25]. C. W. Chow, C. H. Yeh, C. H. Wang, C. L. Wu, S. Chi, and C. Lin, "Studies of OFDM signal for broadband optical access networks," *IEEE Journal on Selected Areas in Communications,* vol. 28, no. 6, pp. 800-807, 2010.

[26]. T. Duong, N. Genay, A. Pizzinat, B. Charbonnier, P. Chanclou, and C. Kazmierski, "Low cost Multi Band-OFDM for remote modulation of colourless ONU in hybrid WDM/TDM-PON architecture," in *33rd European Conference and Exhibition of Optical Communication*, 2007, pp. 1-2.

[27]. D. Qian, N. Cvijetic, J. Hu, and T. Wang, "108 Gb/s OFDMA-PON With Polarization Multiplexing and Direct Detection," *Journal of Lightwave Technology,* vol. 28, no. 4, pp. 484-493, 2010.

[28]. C. W. Chow, C. H. Yeh, C. H. Wang, F. Y. Shih, and S. Chi, "Rayleigh Backscattering Performance of OFDM-QAM in Carrier Distributed Passive Optical Networks," *IEEE Photonics Technology Letters,* vol. 20, no. 22, pp. 1848-1850, 2008.

[29]. C. W. Chow, C. H. Yeh, C. H. Wang, F. Y. Shih, and S. Chi, "Signal Remodulation of OFDM-QAM for Long Reach Carrier Distributed Passive Optical Networks," *IEEE Photonics Technology Letters,* vol. 21, no. 11, pp. 715-717, 2009.

[30]. M. F. Huang, J. Yu, D. Qian, N. Cvijetic, and G. K. Chang, "Lightwave centralized WDM-OFDM-PON network employing cost-effective directly modulated laser," in *2009 Conference on Optical Fiber Communication - incudes post deadline papers*, 2009, pp. 1-3.

[31]. A. Chowdhury, H. C. Chien, M. F. Huang, J. Yu, and G. K. Chang, "Rayleigh Backscattering Noise-Eliminated 115-km Long-Reach Bidirectional Centralized WDM-PON With 10-Gb/s DPSK Downstream and Remodulated 2.5-Gb/s OCS-SCM Upstream Signal," *IEEE Photonics Technology Letters,* vol. 20, no. 24, pp. 2081-2083, 2008.

[32]. L. Chen *et al.*, "A Novel Scheme for Seamless Integration of ROF With Centralized Lightwave OFDM-WDM-PON System," *Journal of Lightwave Technology,* vol. 27, no. 14, pp. 2786-2791, 2009.

[33]. C. W. Chow, C. H. Yeh, C. H. Wang, F. Y. Shih, Y. M. Lin, and S. Chi, "Demonstration of high spectral efficient OFDM-QAM long reach passive optical network," in *2008 34th European Conference on Optical Communication*, 2008, pp. 1-2.

[34]. C.-W. Chow, C.-H. Yeh, C.-H. Wang, F.-Y. Shih, C.-L. Pan, and S. Chi, "WDM extended reach passive optical networks using OFDM-QAM," *Optics Express,* vol. 16, no. 16, pp. 12096-12101, 2008/08/04 2008.

[35]. J. Armstrong, "OFDM for Optical Communications," *Journal of Lightwave Technology,* vol. 27, no. 3, pp. 189-204, 2009.

[36]. A. Banerjee *et al.*, "Wavelength-division-multiplexed passive optical network (WDM-PON) technologiesfor broadband access: a review [Invited]," *Journal of Optical Networking,* vol. 4, no. 11, pp. 737-758, 2005/11/01 2005.

[37]. S. S. Wagner and H. Kobrinski, "WDM applications in broadband telecommunication networks," *IEEE Communications Magazine,* vol. 27, no. 3, pp. 22-30, 1989.

[38]. C. H. Lee, "Colorless optical sources for WDM-PON," in *2009 Conference on Lasers & Electro Optics & The Pacific Rim Conference on Lasers and Electro-Optics*, 2009, pp. 1-2.

[39]. K. Iwatsuki and J. i. Kani, "Applications and Technical Issues of Wavelength-Division Multiplexing Passive Optical Networks With Colorless Optical Network Units [Invited]," *IEEE/OSA Journal of Optical Communications and Networking,* vol. 1, no. 4, pp. C17-C24, 2009.

[40]. G. Berrettini *et al.*, "Colorless WDM-PON performance improvement exploiting a Service-ONU for multiwavelength distribution," in *2009 Conference on Optical Fiber Communication - incudes post deadline papers*, 2009, pp. 1-3.

[41]. M. S. A.-R. a. F.Shaltami, "Principles and Issues of Colorless WDM-PON," *Australian Journal of Basic&Applied Sciences,* vol. 7, 2013.

[42]. M. S. S. Ab-Rahman, Farhat M., "Colorless and sourceless optical network units in passive optical networks," *Journal of Theoretical and Applied Information Technology,* vol. 75, no. 3, pp. 293-300, 2015.

[43]. M. S. S. Ab-Rahman, Farhat M., "Principles and Issues of Colorless WDM-PON," *Australian Journal of Basic & Applied Sciences,* vol. 7, no. 12, p. 294, 2013.

[44]. C.-H. Yeh, H. C. Chien, and S. Chi, "Cost-Effective Colorless RSOA-Based WDM-PON with 2.5 Gbit/s Uplink Signal," in *Optical Fiber Communication Conference/National Fiber Optic Engineers Conference*, San Diego, California, 2008, p. JWA95: Optical Society of America.

[45]. S.-q. G. Fu-mei Sun, Pan Zhuang, Ming Lei, Wen Liu, "SOA as colorless transmitters for bidirectional WDM PON," presented at the International Conference on Computer, Mechatronics, Control and Electronic Engineering(CMCE), 2010.

[46]. E. Kehayas *et al.*, "All-optical carrier recovery with periodic optical filtering for wavelength reuse in RSOA-based colorless optical network units in full-duplex 10Gbps WDM-PONs," in *2010 Conference on Optical Fiber Communication (OFC/NFOEC), collocated National Fiber Optic Engineers Conference*, 2010, pp. 1-3.

[47]. J. Soo-Yong, K. Tae-Young, H. Seung Heon, L. Gap Youl, K. Kilhun, and C. S. Park, "Colorless upstream transmission using remote self-injection locked reflective SOA for WDM-PON," in *OECC/ACOFT 2008 - Joint Conference of the Opto-Electronics and Communications Conference and the Australian Conference on Optical Fibre Technology*, 2008, pp. 1-2.

[48]. A. Maho *et al.*, "Demystification of the Self-Seeded WDM Access," *Journal of Lightwave Technology,* vol. 34, no. 2, pp. 776-782, 2016.

[49]. T. Diallo, A. Pizzinat, F. Saliou, P. Chanclou, G. Simon, and C. Aupetit-Berthelemot, "Self-Seeded DWDM Solution for Fronthaul Links in Centralized-Radio Access Network," *Journal of Lightwave Technology,* vol. 34, no. 21, pp. 4965-4971, 2016.

[50]. P. Parolari *et al.*, "10-Gb/s Operation of a Colorless Self-Seeded Transmitter Over More Than 70 km of SSMF," *IEEE Photonics Technology Letters,* vol. 26, no. 6, pp. 599-602, 2014.

Wave Energy Potential in and around Sinop

Bilal Bingolbali[1], Halid Jafali[2], Adem Akpınar[3]*

Abstract

Being one of the renewable energy resources, wave energy has high potential and low negative impact on the environment, especially in coastal regions. For the selection of an appropriate location for wave energy exploitation, wave energy potential is computed based on the wave characteristics. Due to lack of, or inadequate measurements of such data, these parameters are estimated using the third generation wave hindcast models. On this basis, we aim to develop a nested grid system based on a third generation wave hindcast model SWAN (Simulating WAves Nearshore) for modeling of wave characteristics and to describe the existence and variability of wave energy in the southwestern part of the Black Sea within the TUBITAK Project [1]. The present study summarizes wave energy potential in and around Sinop, which has hot spot areas i.e. areas with high wave energy, based on 31-year long-term wave hindcast results obtained from this nested grid system. Here, spatial distribution maps of the monthly, seasonal, and annual average wave energy are presented and statistical analysis of wave energy in the selected locations is investigated. Furthermore, wave energy resource is characterized in terms of sea state parameters i.e. significant wave heights, wave periods and mean directions for selecting the most appropriate wave energy converters in the selected site.

Keywords: *Wave Energy, Spatial Distribution, Statistical Analysis, Sinop*

1. INTRODUCTION

As recommended by the Kyoto protocol, decreasing the amount of gases that have negative impact on the environment is very significant. In order to meet this goal, the currently available renewable energy sources have to be improved and innovative steps have to be taken to come up with novel sources. Wave energy is one of the novel sources of energy and it is very promising in a way that; it is more predictable and has high energy density per meter. In addition, wave energy is also environmental friendly since it produces zero emissions. Wave energy potential of in a specific area is computed based on wave characteristics (e.g. significant wave height H_{m0} and wave energy period T_{m-10}). Data of such characteristics is scarce in most cases, therefore, wave hindcast models are adopted to generated simulated data, in our case a third-generation model was used. The aim was to develop a nested grid system based on a third generation wave hindcast model SWAN (Simulating WAves Nearshore). The model would simulate wave characteristics and in this way, help describe the existence and variability of wave energy in the southwestern part of the Black Sea within the TUBITAK Project [1]. In line with this, the present study summarizes wave energy potential in and around Sinop based on 31-year long-term wave hindcast results obtained from this nested grid system. Monthly, seasonal, and annual average wave energy spatial distribution maps are given and statistical analysis of wave energy in selected locations is investigated. Wave energy resource is characterized in terms of sea state parameters that include significant wave heights, wave periods and mean directions that act as reference when choosing the most suitable wave energy converter to be diploid in an area.

2. STUDY AREA

The shoreline of Sinop and its vicinity in the central region of the southern coast of the Black sea (Figure 1).

[1] *Uludag University, Department of Civil Engineering, 16059, Nilüfer/Bursa, Turkey. arda_bilal_49@hotmail.com*

[2] *Uludag University, Department of Civil Engineering, 16059, Nilüfer/Bursa, Turkey. halidjfone@gmail.com*

[3*] *Corresponding author: Uludag University, Department of Civil Engineering, 16059, Nilüfer/Bursa, Turkey. ademakpinar@uludag.edu.tr*
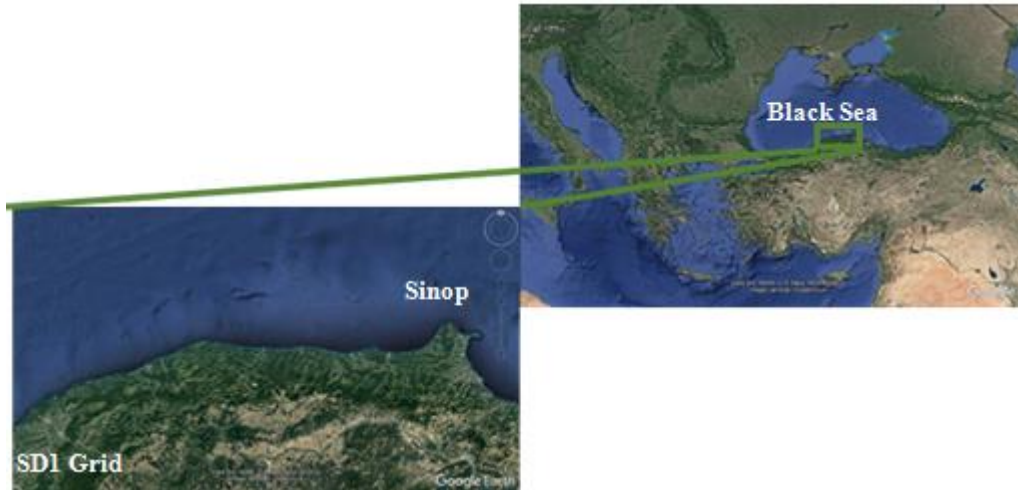
Figure 23. Study area

3. MODEL DETAILS

Long-term temporal and spatial variation of wave energy potential in the middle part of the southern coast of the Black sea at Sinop and surrounding areas is studied based on results determined from an established, developed, calibrated and verified model set over a nested grid system (Figure 2). For this, the establishment, calibration and verification of the main domain has been performed beforehand and all details are given in Akpınar et al [2]. In addition, initial results and model setting details connected with the establishment, development and calibration of the nested grid system as a whole are described in Akpınar et al. [3].
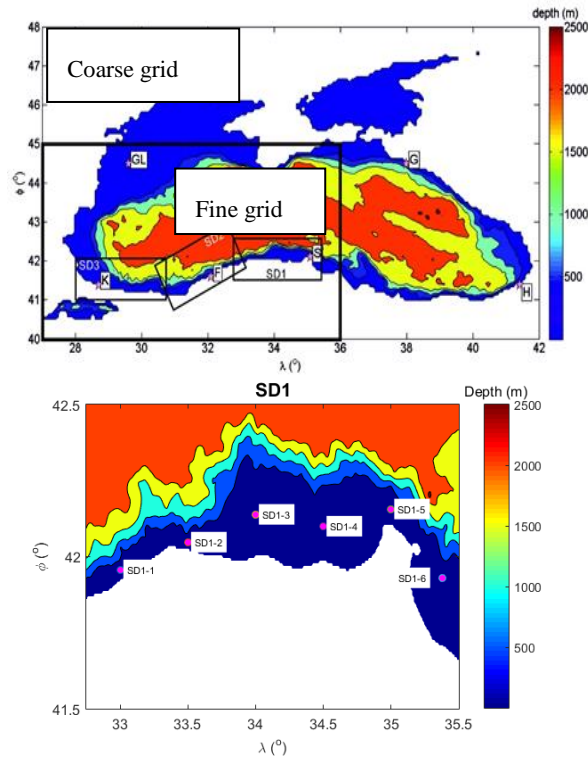
Figure 2. Configuration of Nested Grid model (Coarse grid, Fine grid, and three sub-grids) (in the upper panel), bathymetry of Sinop sub-grid and locations studied

4. RESULTS AND DISCUSSION

After model setup, development, calibration and validation, 31-year long term simulations for SD1 sub-grid (around Sinop) were carried out to correctly assess wave energy potential for middle part of the south western coasts of the Black Sea. Some integral parameters of wind waves were collected. In this area, wave energy potential and its variability were computed and quantified based on these integral parameters (H_{m0} and T_{m-10}). The first result regarding wave energy potential in and around Sinop is spatial distribution maps of monthly, seasonal, and annual mean of the average wave energy flux during 1979 – 2009 (Figure 3 and 4).
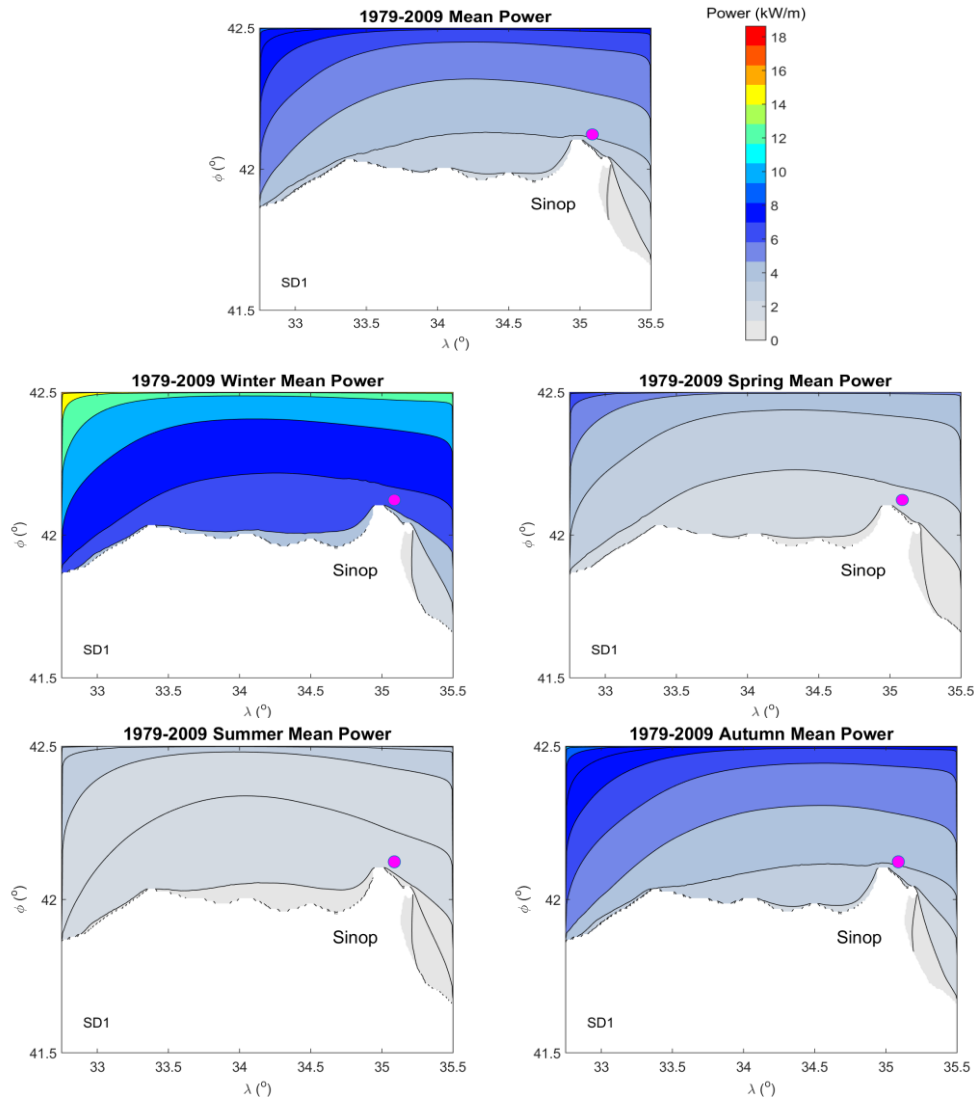
Figure 3. Spatial distribution maps of seasonal and annual means of the average wave energy flux during 1979–2009

The maximum average wave energy value along the coastal line is about 4 kW/m according to the mean distribution map (upper panel in Figure 3) obtained based on the entire data for 31 years of wave energy potential around Sinop. It is also seen that this value can reach 9 kW/m offshore towards the corners. This grid was seasonally sorted for a period of 31 years in a 10 minute temporal resolution, and spatial distribution maps of average wave energy flux for each season were derived. Winter season represents December, January and February; spring season: March, April and May, summer season: June, July and August; and autumn season: September, October and November. According to the seasonal mean wave energy distribution maps, it is seen that the most energetic season is winter and the least energetic is summer. It has also been determined that the map of the average wave energy flux based on the whole data is very close to the map of the autumn season. An average wave energy flux of 6 kW/m was estimated along the coastal strip during the winter season. From the coast to offshore and towards the corner points of the grid, the average wave energy flux was estimated to be 14 kW / m, especially on the western side.
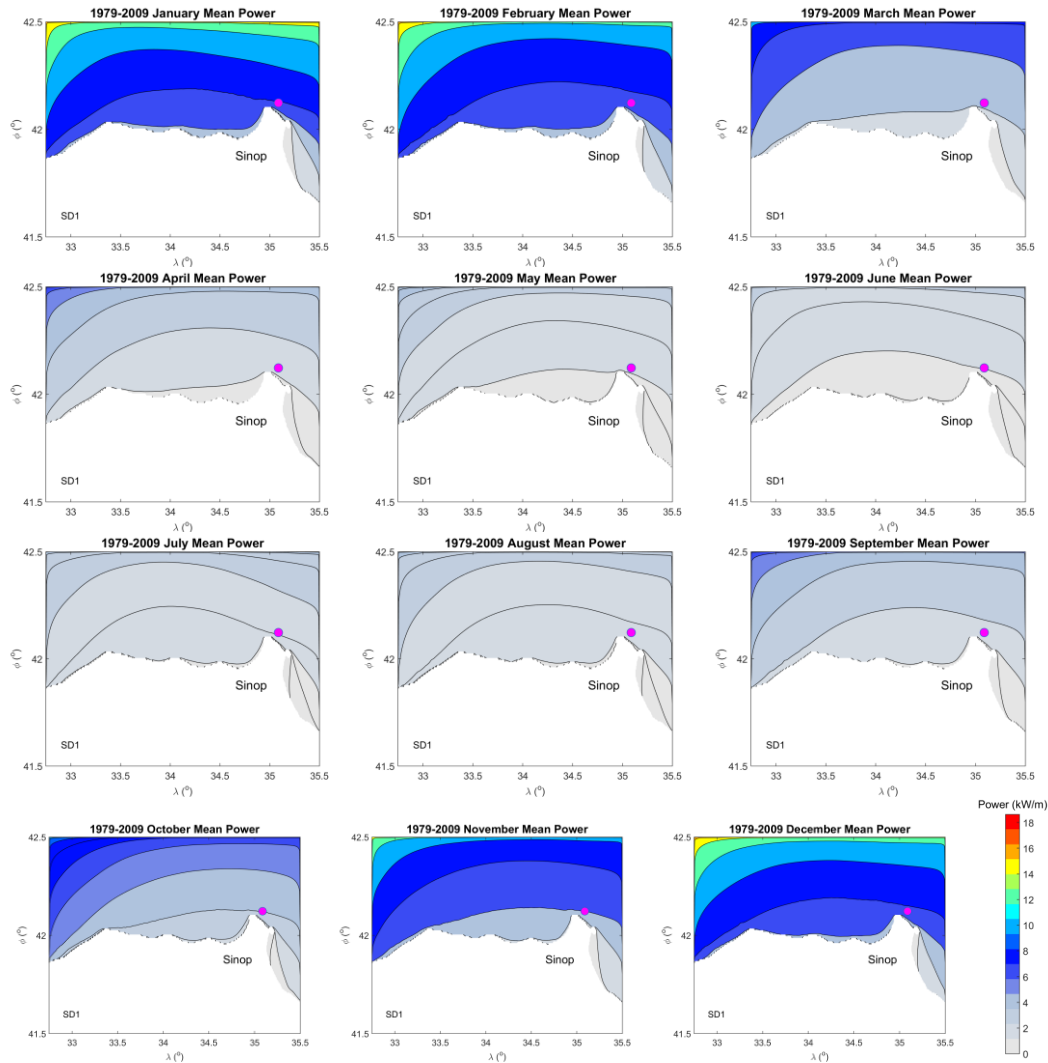
Figure 4. Spatial distribution maps of monthly means of the average wave energy flux during 1979 – 2009

Estimated data obtained over 31 years are extracted monthly and monthly average wave energy flux is calculated for each month. It is seen from the monthly distributions of average wave energy flux maps in Figure 4 that the most energetic months are December, January and February and that the lowest energy months are June, July and August. Monthly average spatial distribution maps provide similar characteristics to their seasonal average spatial distribution maps. There is an average wave energy flux of 6 kW/m along the coastal strip excluding the east of Sinop in winter months. This value increases to 14 kW/m offshore. After annual, seasonal and monthly spatial distribution maps of the mean wave energy flux of Sinop and its surrounding areas were determined, a statistical analysis was conducted for two stations along the coastal strip, one on the east and one on the west coast. This was done in order to examine the temporal variation of the long-term wave energy potential and the following were determined:

✓ Annual and seasonal wave power roses (Figure 5),

✓ Annual average wave energy flux for different H_{m0} and T_{m-10} during 1979 – 2009 (Figure 6),

✓ Annual average wave energy flux for different H_{m0} and Dir during 1979 – 2009 (Figure 7),

✓ Annual changes and linear trend of average wave energy flux during 1979 – 2009 (Figure 8).
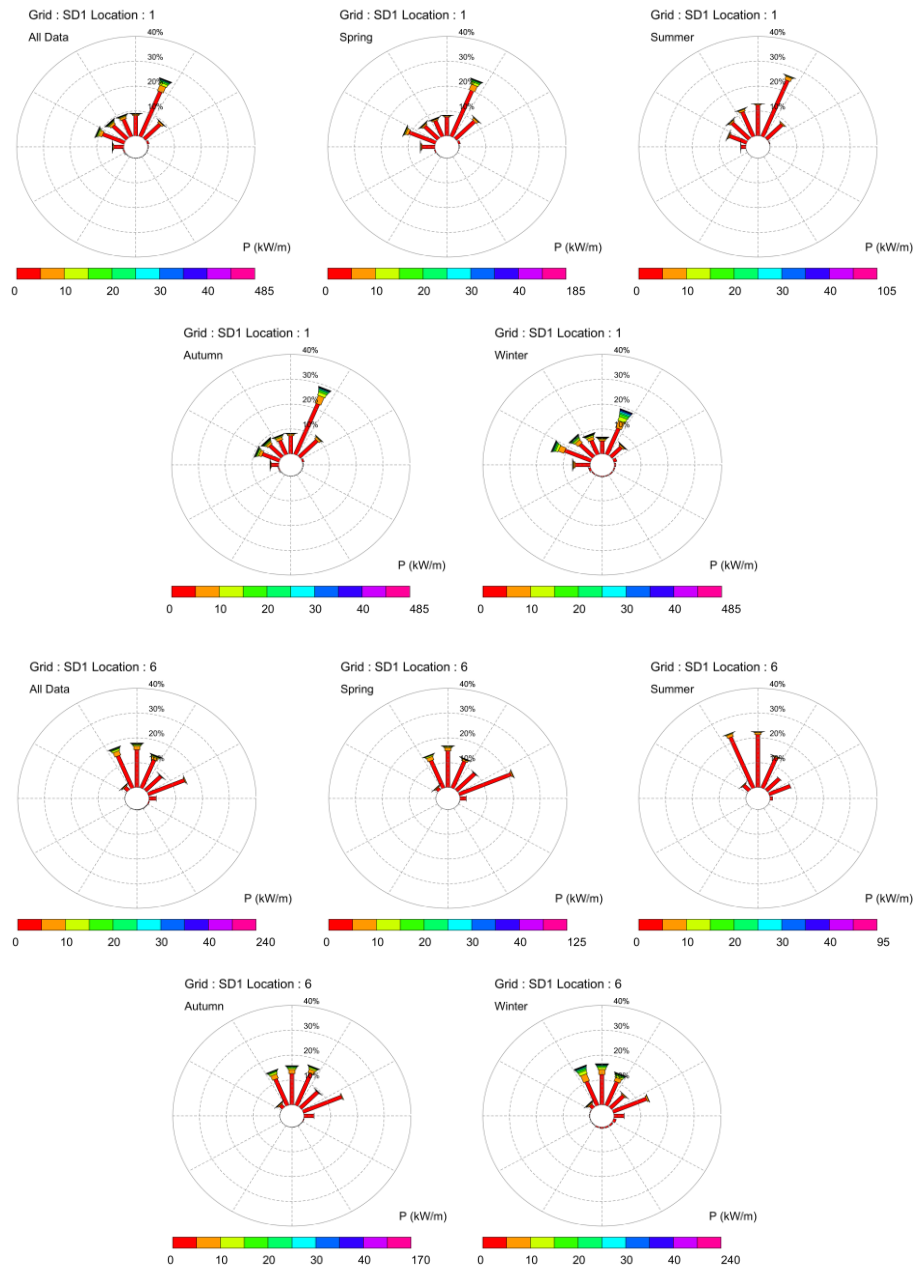
Figure 5. Annual and seasonal wave power roses for locations 1 and 6 in SD1 grid (Sinop).
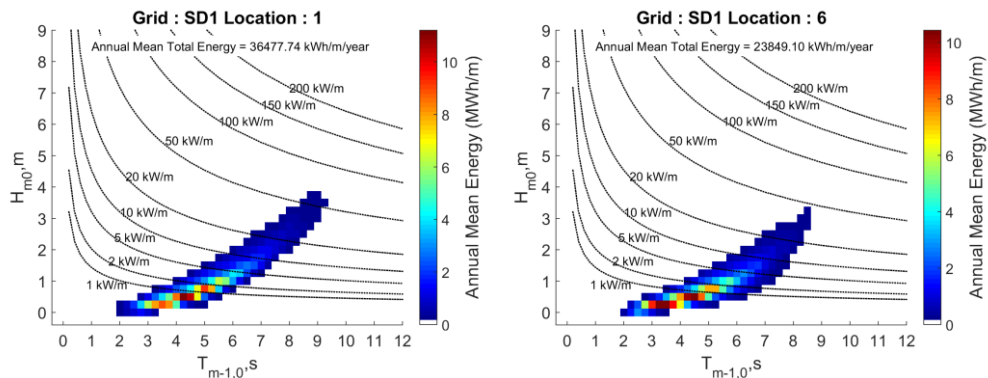
Figure 6. Annual average wave energy flux for different H_{m0} and T_{m-10} during 1979 – 2009 for locations 1 and 6
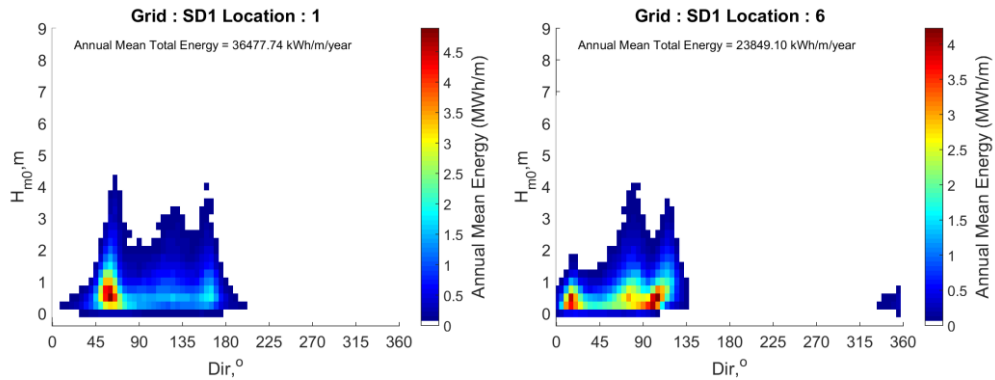
Figure 7. Annual average wave energy flux for different H_{m0} and Dir during 1979 – 2009 for locations 1 and 6 in SD1 grid
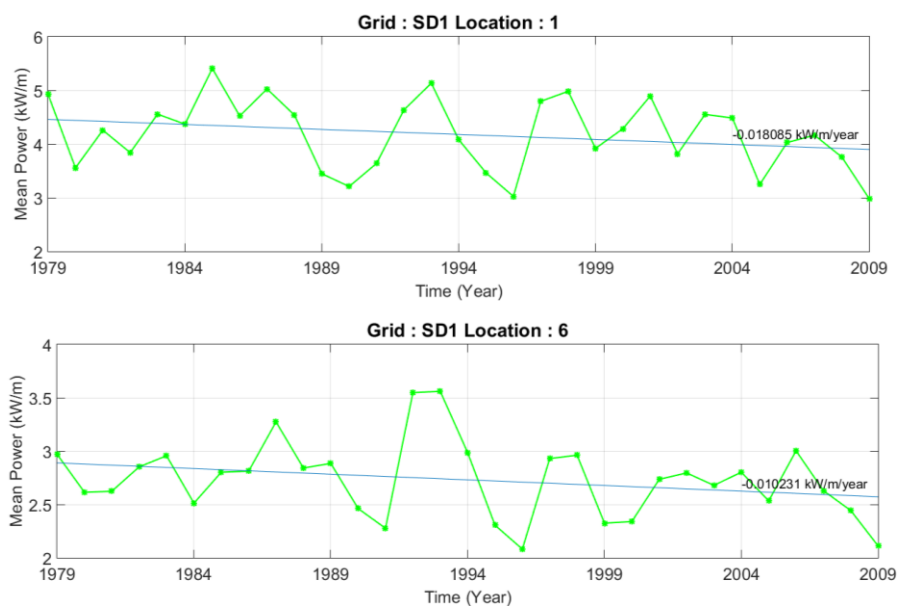
Figure 8. Annual changes and linear trend of average wave energy flux during 1979 – 2009 for locations 1 and 6 in SD1 grid (Sinop)

According to the wave power rose obtained based on the entire data, and wave energy roses for each season in Figure 5, it can be seen that the waves that will generate the wave power at a selected station in the west coast of the grid originate from the west (W) and northeast (NE). On the east coast station, it is understood that in all the roses, the dominant waves come from the east (E) and northeast (NE) sectors.

Based on the annual average energy variation graph (Figure 6) defined for different intervals of significant wave height and wave energy period, the maximum average wave energy flux is between 0.5 – 1.5 m of significant wave height and 3 – 6 s wave period at the station on the western shoreline. On the eastern shore, the maximum energy flux is observed for significant wave height between 0.5 – 1 m and period between 2.5 – 5.5 s. The average annual total energy at location 1 is 36.5 MWh/m and 23.9 MWh / m at location 6. As seen here, the energy on the western side is higher than that of the eastern side.

The variation graph of average wave energy flux (Figure 7) versus different wave height and average wave direction shows the highest energy at location 1 is in waves of 0.5 - 1.5 m in height and between 45º – 80º in direction. At location 6, the highest energy is between 0.5 – 1 m wave height and between 5º – 22.5º as well as 67.5º – 112.5º direction. Figure 8 presents annual changes and the linear trend of the average wave energy flux over 31 years at the two locations. As can be seen from this figure, there is a decreasing trend at both stations in variations of annual average wave energy flux. However, it should be noted here that no trend test has been conducted on the trend. Moreover, the linear trend value is also very close to zero.

For a more detailed analysis of the average wave energy potential based on the stations, hourly, monthly and seasonal variations in average wave energy flux in the 6 stations selected in this sub-grid are obtained and

shown in Figure 9. From these graphs, the wave energy potential is high during the day between 12:00 - 19:00. Location 6 on the eastern part of the grid has the lowest energy potential.
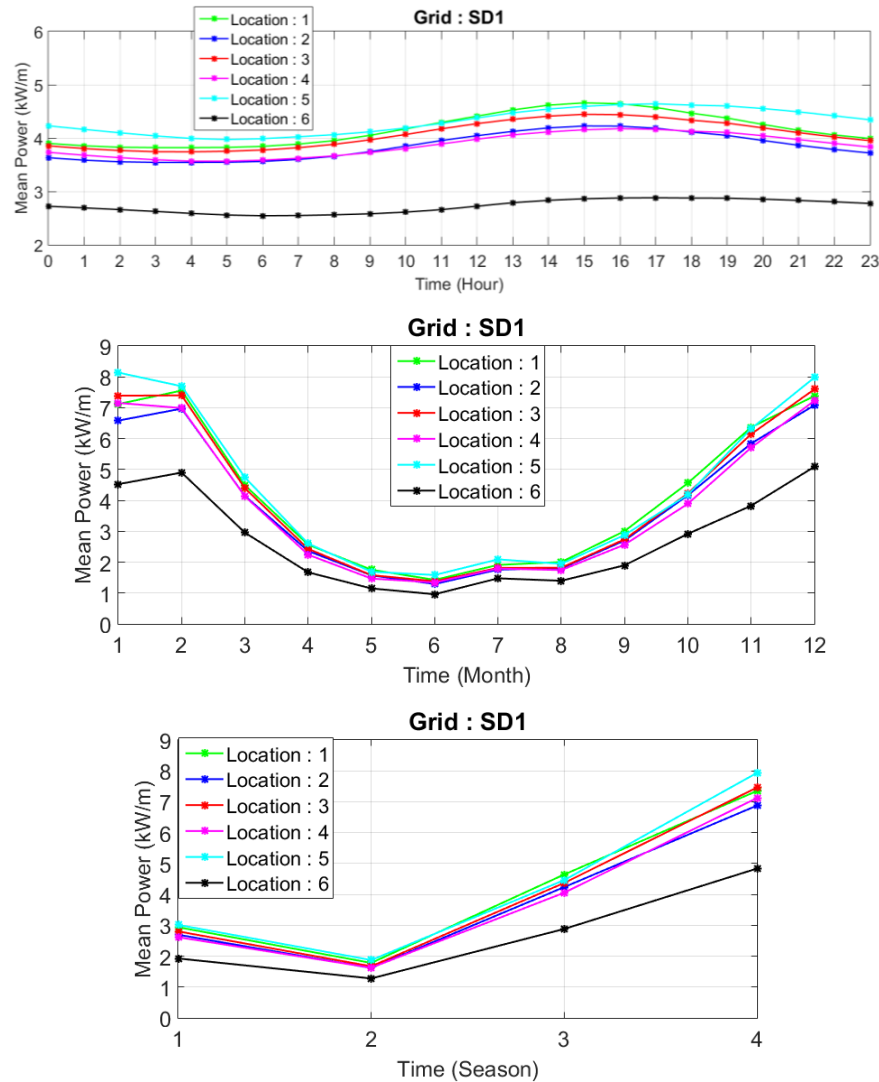
Figure 9. Hourly, monthly, and seasonal average wave energy flux for different locations during 1979 – 2009 in SD1 grid (Sinop).

ACKNOWLEDGMENT

REFERENCES

[1]. A. Akpınar, S. Bekiroglu, G.Ph. Van Vledder, B. Bingolbali, H. Jafali, *Temporal and Spatial Analysis of Wave Energy Potential Along the Southern west Coasts of the Black Sea*, Project Number: 214M436, TUBITAK Project, 2015 (In Progress).

[2]. A. Akpınar, B. Bingolbali, G.Ph. Van Vledder, "Wind and wave characteristics in the Black Sea based on the SWAN wave model forced with the CFSR winds", Ocean Engineering, vol. 126, pp. 276-298, 2016.

[3]. A. Akpınar, B. Bingolbali, H. Jafali, "Wave Hindcasting for Wave Energy Assessments in the Black Sea", in Proc. ICENS2016, 2016, paper 29, p. 14.

Indoor Air Quality Monitoring System Using Raspberry Pi for Energy Efficiency in Classrooms

Deniz BALTA[1], Nesibe YALCIN[2], Ahmet OZMEN[1]*

Abstract

Indoor air pollution has become a serious issue for people health. Indoor air quality monitoring systems help detecting unhealthy and low comfort levels to control and improve the air quality. This paper discusses a monitoring system that gives real-time information about indoor air quality of university classrooms. The system collects online data from CO2 meters that are installed to the target classrooms along with embedded systems (Raspberry PI) and presents information over the web interface. Air quality parameters such as CO2 concentration, temperature and humidity are gathered from different locations simultaneously. The data collected from the nodes are transmitted to the web server and database server. The results are displayed on web for connected clients. The system is developed using cost effective embedded hardware that has advantage of low-power consumption.

Keywords: *Indoor Air Quality; Monitoring; Raspberry Pi; Web Based Information System; Energy Efficiency*

1. INTRODUCTION

People spend more than 90% of their time in indoor environment. So important of monitoring indoor air quality (IAQ) issue increases day by day.   Because air quality has major influence on the health, productivity, focusing and comfort of people [1, 2]. Recently, indoor air quality monitoring studies asserts that CO_2 is an essential pollutant and its concentration is acceptable indicator while determining the air quality [3, 4]. Fraction of population most susceptible to potential health hazards deriving from poor IAQ are teenager and children. For example, Students spend at least 30% their weekdays in the classrooms of school buildings in Turkey. So indoor air quality is very important for their health. Each student can be thought a source of pollutant in a closed place. When considering course durations, student number, classroom's volume and ventilation rate, indoor air quality may come to dangerous levels. The air quality monitoring system must be detect indoor air quality changes and warn users for opening/closing windows or ventilation system. This is important for improving the performance of studying and learning. In some studies, it has been determined that if CO_2 level is higher than 1000 ppm, decision-making performance decreases moderately and if CO_2 level is higher than 2500 ppm, it decreases significantly [5, 6]. Other studies in the literature also show that IAQ influences school academic performance and attendance [7], memory and focus [8] and error rate [9].

In order to enhance the environmental monitoring technology, the technologies of sensor network and monitoring system were improved in many studies [10,11,12]. The data from sensor node were transmitted to the back end server through the sensor network, are analyzed in there and the results are informed to the monitoring part for checking whether they exceed the values. In [13], a low-cost environment monitoring system is presented. Raspberry Pi, Arduino and XBee are used in the system designed as wireless sensor network. Integration of gateway node of wireless sensor network, database server and web server into one Raspberry Pi board is an advantage to the system. In [14], two types of WLAN- Ad Hoc architecture and AP infrastructure network are suggested for air quality monitoring. They says that the Ad Hoc structure is better solution for monitoring air quality, because it requires less components and thus less power. Wi-Fi has

---

[1] *Corresponding author: Sakarya University, Department of Computer Engineering, 54187, Serdivan/Sakarya, Turkey. ddural@sakarya.edu.tr*

[2] *Bilecik Seyh Edebali University, Department of Computer Engineering, 11230, Merkez/Bilecik, Turkey. nesibe.yalcin@bilecik.edu.tr*

[1]*Sakarya University, Department of Computer Engineering, 54187, Serdivan/Sakarya, Turkey.ozmen@sakarya.edu.tr*

weaknesses that allowed communication distance shorter and it may get more interference because there are many WLANs in real world. According to experiments of [15], real time monitoring on air quality is essential because, many factors may affect air quality and it may change constantly. Then, selection of sensor types is very important for energy efficiency during design. Because gas sensors for air quality monitoring consumes a lot of power.

In this study, we present a web based IAQ monitoring system developed using CO2 meter, Raspberry Pi, database and web servers. Such a design has advantage of low-cost, easy build and easy maintain, less component as compared to other studies [10,12,16]. The main goal is to assess good IAQ in terms of comfort and healthy conditions in school buildings by avoiding unnecessary ventilation and high-energy consumption. To achieve the goal, a web based IAQ monitoring system has been developed to analyze and improve IAQ in the buildings. Using a web based information system, the data provided by sensor network is published. Then, users who can be alerted about the poor air conditions in the classrooms access the results. Developed system can be used to help head of faculty to analyze extended amount of experimental data and the bad influence of the indoor air quality on the learning of the students. Thus, he contributes to keeping the maximum of learning by giving importance to ventilation in classrooms.

2. OVERALL SYSTEM ARCHITECTURE

The aim of the study is to adapt indoor air quality by providing instant information on CO_2 concentration, temperature and humidity levels in a class. Thus, it is aimed to keep the CO_2 level in the class below a certain value and to avoid the humidity of the indoor air being too dry or moldy. Because this situation is very influential on the learning performance of the students.

The system is developed in three parts, sensing network, server and clients. The overall system architecture is shown in Figure 1. Firstly, CO_2 gas is sensed by AZ77535 CO_2 meter and the data is transmitted periodically to the sink node, which is a single board computer Raspberry Pi 3 via a RS232 to USB port.

Sampling rate for data collection is set as 1 second; however, an average value is calculated for 10 minutes data and this average value is transferred and presented at the front end.
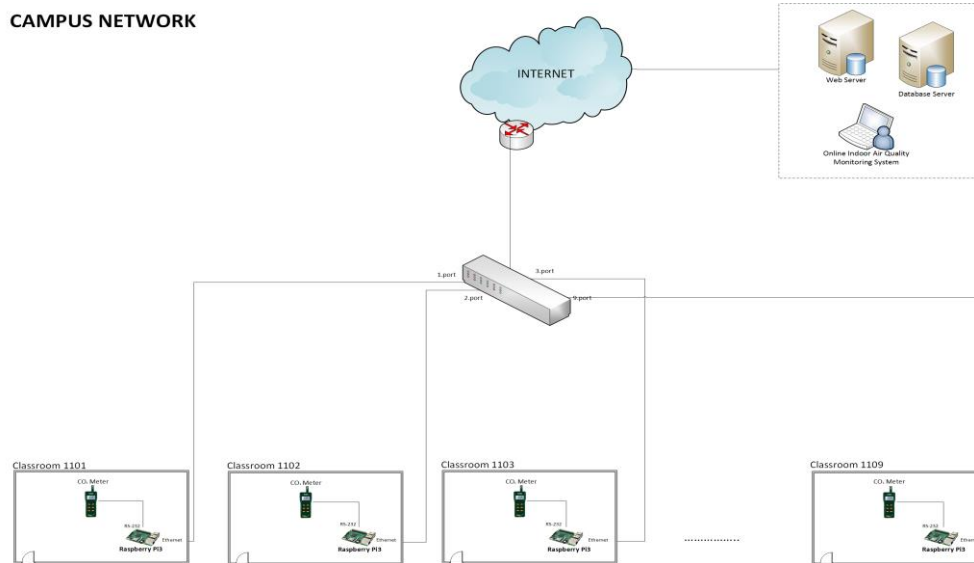
Figure. 1. Overall the system architecture

A middleware software on the sink nodes does the buffering, average calculation and sending the data to the web server. A sink node forwards the data to the server by using Ethernet ports in the classrooms. The TCP raw packets from each classroom go to the servers in the internet environment via the switch and router in the building. The server (www.csogr.sakarya.edu.tr) holds both web server and database server. Therefore, it stores the data received in every 10 minutes in MYSQL database, performs the analysis and provides IAQ information through web server. Finally, a client can observes the results from the web interface real-time graphics or access the monthly or weekly statistical data from anywhere.

3. DESIGN OF HARDWARE AND SOFTWARE COMPONENTS

3.1. Design of Sink Node

In this research, we developed networked sink nodes using AZ Inst. 77535 CO_2/Temp/RH Meter for measurement and Raspberry Pi 3 for data collecting and gateway application in network. The hardware components that are used in design are shown in Figure 2.

To increase the flexibility and interoperability of the implemented architecture a coordinator based on Raspberry Pi 3 Model B that is a low power single computer based on Raspbian Linux operating system is considered. It offers less complexity and more affordable solutions for monitoring. The CPU on board is a 64-bit quad-core ARM processor with 1.2 GHz clock speed. It also has 1 GB RAM and Micro SD card slot for storage, a HDMI port and 4 USB Ports, and 40 GPIO pins to communicate peripheral devices. It supports many operating systems such as Debian, Windows etc. A monitor, keyboard and mouse can be connected to Raspberry Pi 3 through USB and HDMI ports. So it can be used like a desktop computer. Also using Ethernet port or Wi-Fi adapter it can be connected to the internet. Raspberry Pi makes a perfect choice for implementing our system for its cheap pricing, low power consumption, containing a processor, graphical unit and many more. It provides us Ethernet output port, which is advantageous to our system. By this way remote access management via SSH could be provided by giving IP address to the device and the data could be transferred to the central server over the internet.

The device brand used for measurements is "AZ Instrument 77535 CO_2/Temp./RH Meter", and it is capable of reading CO_2 concentration, air temperature and relative humidity with a measuring range of 0 ~ 9999 ppm CO_2; accuracy 30 ppm + %5 of the reading (0 ~5000 ppm). It has self-calibration property that calibrates itself before any measurement process begins. Therefore, there was no need for calibration during the measurements in the study. The device shows the measurement data at its small LCD screen or outputs via RS-232 port. For continuous measurements, a piece of software is developed to run on Rapsberry Pi for logging the data from RS-232 and converting to Ethernet packets. This software is intermediate layer between CO_2 meter and database. It collects measurement data from CO_2 meter and inserts them into the MYSQL database, and is programmed in C# using Mono Develop in Ubuntu Mate.

Figure. 2. Raspberry Pi 3 Model B and AZ Instrument 77535 CO2/Temp./RH Meter

3.2. Design of Web Application

Web application implemented with ASP.NET, is used to visualize classrooms' measurement data in dynamic real time charts. The web interface in the system can be used for three different purposes. Real-time data graphs can be viewed, all measurement data can be downloaded in excel file for statistical analysis and system configuration can be provided. Users can also monitor the classroom's indoor CO_2 value updates in real time using real time display utility. The CO_2 meter, which is placed in the area where the students are heavily located, makes a measurement in seconds. By default, the measurement period is set to 10 minutes in the system. However, in order not to lose the data in this time interval and to obtain more realistic information, the average of 10 minutes measurement data is taken and monitored in the system. A user can configure the system by updating the periods for graphical display of the data.

If the limit value is exceeded during the measurements, the system warns the user about the indoor air quality. The threshold for classrooms' CO_2 concentration is 1000 ppm or 1800 mg/m^3 set by Environmental Protection Agency (EPA) [17] and American Society of Heating, Refrigerating and Air-Conditioning Engineers (ASHRAE) [18].

4. EXPERIMENTAL RESULTS

In this study, the building of Computer Engineering Department of Sakarya University in Turkey is selected for development and testing. In this experiment, we use a medium size classroom which volume is 190 m3 as a test location. The classrooms are naturally ventilated and have three windows (the dimensions of a window, 1.1 m × 1.3 m) and one interior door (2.05 m × 0.9 m). The total number of students in the classrooms varies according to the course schedule of the computer-engineering department.

Web interfaces of the IAQ monitoring system were assists the users to monitor the system through the internet. The web interfacing as shown in Figure 3. In the web page, CO_2 concentration in parts per million (ppm) unit, temperature and humidity level can be monitored. There are graphical graphs that show the average measurements for every 10 minutes.

During monitoring, the maximum levels of CO_2 were largely above 1000 ppm, commonly used as a warning threshold limit for acceptable air quality in terms of comfort. As you can see in the Figure 4, classes are held between 12: 30-13: 30 and the classroom rank is approximately 45 students. From the current measurements, the concentration CO_2 gas for the classroom is above the acceptable limit that is recommended by EPA. For example, the concentration of CO_2 gas in classroom is in the range of 1200-2450 ppm. Temperature and humidity level inside the classroom is above the maximum limit of the standard. The range is between 26.1-29.2 oC and 33.6-39.2%, respectively.
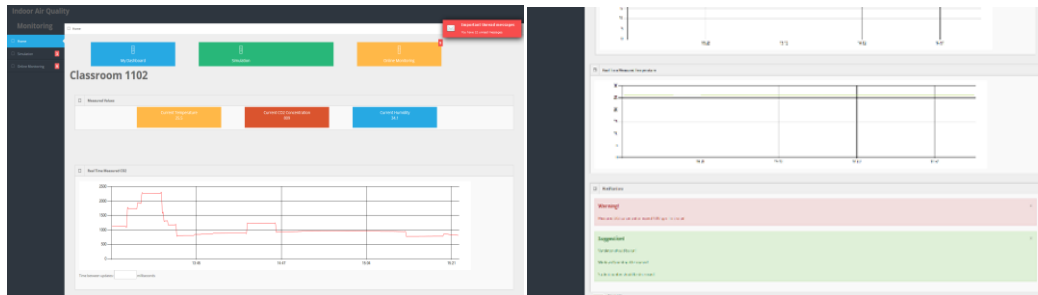
Figure 3. Web interface of the proposed system for indoor air quality monitoring

Between 13:30 and 14:00 hours, some students left the classroom during the break and windows/door are opened and the classroom is ventilated for a while. Thus, the level of measurement in the class has dropped considerably. Nevertheless, it did not reach the targeted levels. According to the observation, the IAQ that monitored by the proposed system is not within the acceptable limit and standard for health and safe environment for the students and lecturer.

The level of air quality always is effected by size of classroom, bad air sources/materials, number of people and airflow etc. When there is insufficient ventilation in the classrooms, the best behaviors to keep the level of CO_2 at the appropriate values are to open the windows between the two courses, open a window or door during the course for airflow, and leave the classroom during the break. Otherwise, unnecessary air conditioning ventilation system will be operated to clean the bad air in the environment or to reduce the class temperature. However, the real-time monitoring system will be the trigger for instant intervention in bad weather in the classroom. In this way, unnecessary energy consumption can be avoided and the widespread use of such technologies will contribute to environmental energy efficiency improvement.
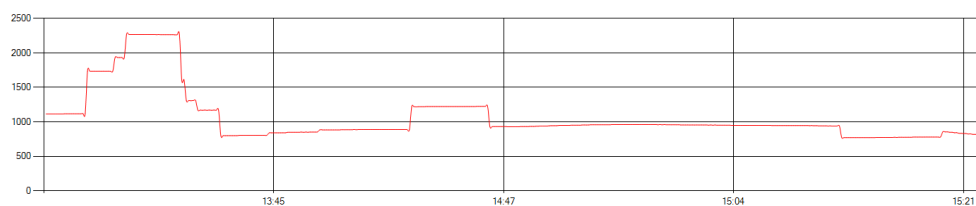
a)
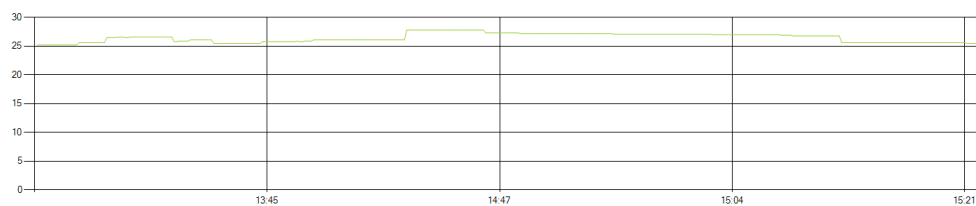
b)
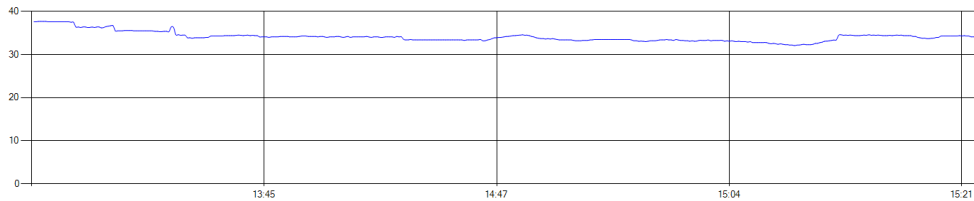
c)

Figure 4. a) Sample real time CO_2 concentration; b) humidity level; c) temperature level

5. CONCLUSION

In this paper, we have presented an indoor air quality monitoring system using Raspberry PI and AZ Instrument 77535 CO_2/Temp./RH Meter, database, web server and a number of software packages. A graphical user interface was developed to support data presentation and warning generation such as web site. The information that allows to users to know classroom's situation about risk condition for students health can be accessed from instant location. In addition, system ability can be improved by integrating Raspberry with other hardware components. The system has many useful characteristics such as, low-cost compact, easy build, easy maintain. Since the use of such a monitoring system will control the level of comfort in the classrooms regularly, it contributes to the development of environment energy efficiency.

REFERENCES

[1]. Rabl A, Spadaro J. Public health impact of air pollution and implications for the energy system. Annual Review of Energy and the Environment 2000; 25:601–628.
[2]. Guo H, Lee SC, Chan LY, Li WM. Risk assessment of exposure to volatile organic compounds in different indoor environments. Environmental Research 2004; 94(1):57–66.
[3]. Satish U, Mendel MJ, Shekhar K, Hotchi T, Sullivan D, Streufert S, Fisk WJ. Is CO2 an indoor pollutant? Direct effects of low-to-moderate CO2 concentrations on human decision-making performance. Nviron Health Persp 2012; 120: 1671-1677.
[4]. Persily AK. Evaluating Building IAQ and Ventilation with Indoor Carbon Dioxide. ASHRAE Tran 1997; 103: 4072(1-12).
[5]. Fisk WJ, et al. Higher Levels of CO2 May Diminish Decision Making Performance. REHVA Journal, 2013; 63.
[6]. Satish U, et al. Is CO2 an indoor pollutant? Direct effects of low-to-moderate CO2 concentrations on human decision-making performance. Environmental Health Perspectives, 2012; 120, 1671-7.
[7]. Mendell MJ, Heath GA. Do indoor pollutants and thermal conditions in schools influence student performance? A critical review of the literature. Indoor Air, 2005; 15, 27-52.
[8]. Bako-Biro Z, Clements-Croome DJ, Kochhar N, Awbi HB, Williams MJ. Ventilation rates in schools and pupils performance. Building and Environment, 2012; 48, 215-223.
[9]. Twardella D, et al. Effect of classroom air quality on students' concentration: results of a cluster-randomized cross-over experimental study. Indoor Air, 2012; 22, 378-87.
[10]. Abraham S, Li X. A cost effective wireless sensor network system for indoor air quality monitoring application. The 9th ınternational conference on future network and communications, Procedia computer science 2014; 34:165-171.
[11]. Saad SM, et al. Indoor air quality monitoring system using wireless sensor network with web interface. International conference on electrical, electronics and system engineering. 2013; 60-64.
[12]. Marchetti N, et al. A campus sustainability initiative: indoor air quality monitoring in classrooms. XVIII AISEM annual conference, IEEE, 2015.
[13]. Ferdoush S, Li X. Wireless sensor network system design using Rapsberry Pi and Ardunio for environmental monitoring applications. Procedia Computer Science 2014; 34, 103-110.
[14]. Postolache OA, Pereira JMD, Girao PMBS, Smart sensor network for air quality monitoring applications. IEEE Trans. Instrum. Meas., 2009; 58, 3253–3262
[15]. Kim J, Chu CH, Shin SM. ISSAQ: An integrated sensing system for real-time indoor air quality monitoring. IEEE Sensors Journal, 2014; 14, 4230-4244.
[16]. Peng IH, Chu YY, Kong CY, Su YS. Implementation of indoor VOC air pollution monitoring system with sensor network. IEEE 7th international conference on complex, intelligent and software intensive systems. 2013; 639-643.
[17]. Introduction to indoor air quality. A reference manual. Washington, D.C.: U.s. Environmental Protection Agency, EPA/400/3-91/003.
[18]. American Society of Heating, Refrigerating and Air-conditioning Engineers, Inc. (ASHREA), standard 62-2001, Ventilation for acceptable Indoor air quality. Atlanta.

Evaluation of Vibration Spectral Values of a Rolling-Element Bearing Used in a Vehicle Inspection Station

Selman Kulac[1], Suat Sarıdemir[2]

Abstract

Most of the machines used in the industry have rotating parts. The rotating parts are usually mounted on the machine with the rolling bearing. Bearings have an important and critical role because they are constantly working under loads. Bearings of vehicle brake testers used in vehicle inspection stations are an important example for bearings operating under constantly varying loads. Because vehicles with different weights are subjected to vehicle brake tests. In this study, the vibration characteristics of a specific bearing of a vehicle brake test device were examined at specific time intervals. Vibration measurements were made at intervals of 15 days. It has been observed that the sum of peak values above the determined threshold values of the vehicle brake tester rolling bearing in frequency domain increases depending on time intervals.

Keywords: *Rolling-element bearing, vibration measurements, frequency analysis*

1. INTRODUCTION

There are many factors directly affecting braking performance, such as vehicle weight, drum or disc construction, center and wheel cylinders, brake hydraulic circuit and brake hydraulics, tires, suspension system, mechanical components of the brake system and road conditions. Vehicle braking systems are controlled at certain intervals because of their decisive importance in vehicle safety. The effectiveness of the vehicle brakes is determined on the actual vehicle with the vehicle braking tester. Brake drums used in vehicle brake testers are assembled with ball bearings. Brake drums used in vehicle brake testers are assembled with rolling element bearings. Rolling Element Bearings commonly used in machines directly influence the machine's dynamic performance, operating accuracy, reliability and service life of all equipment. The most popular way to detect characteristic frequencies of ball bearings is to use the vibration measurement of the rolling element bearing advanced signal processing techniques. The Fast Fourier Transform (FFT) is the natural choice to retrieve frequency features from measured stationary time-domain data [1]. It is stated in the literature that vibration measurement methods are used in determining bearings life and faults.

Fault detection and diagnosis for a class of rolling-element bearings using signal-based methods were investigated by Yang et al. [1]. The auto correlation analysis on the FFT transformed signals with an aim to distinguish the faults in the bearings was accomplished by Mingetal [2]. In [3], vibration analysis techniques and explored their capabilities, advantages and disadvantages were examined in monitoring rolling element bearings. In [4], FFT of intrinsic mode functions (IMFs), from Hilbert–Huang Transform (HHT) process was incorporated to utilize efficiency of Hilbert transform (HT) in frequency domain. In [5], local surface defects in radial ball bearings were studied experimentally through the vibration analysis method. For this purpose, first artificial local defects on the running surface of the ball bearing (inner and outer ring) are made and resulting radial shaft vibrations were recorded. In [6], the vibration monitoring and analysis case studies were presented and examined in machineries that were running in real operating conditions. Failures formed on the machineries in the course of time were determined in its early stage by the spectral analysis.

---

[1] *Corresponding author: Duzce University, Faculty of Engineering, Department of Electrical - Electronics Engineering, 81620, Duzce, Turkey. selmankulac@duzce.edu.tr*

[2] *Duzce University, Faculty of Technology, Department of Manufacturing Engineering, 81620, Duzce, Turkey. suatsaridemir@duzce.edu.tr*

In this study, the vibration characteristic of a specific bearing of a vehicle brake test device were examined at specific time intervals. The sum of peak values above the determined threshold values of the vehicle brake tester rolling bearing in frequency domain were analyzed depending on time.

2. MATERIALS AND METHODS

In this section, an experimental setup used for this study is explained. Experiments were carried out at the TUVTURK Duzce vehicle inspection station at intervals of 15 days. A total of 3 measurements were made. Between the first measurement and the second measurement intervals, the 1921 vehicles were tested by vehicle brake test device. Between the second measurement and the third measurement interval, the 1349 vehicles were tested from the vehicle brake test device. The experimental setup is schematically shown in Fig. 1. Also the picture of the experiment setup is shown in Figure 2.
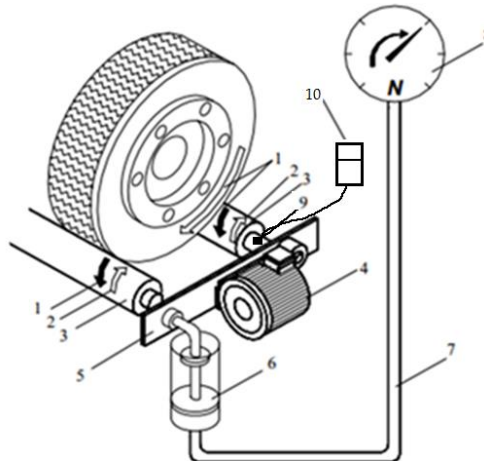
1.Braking torque 2. Rotating torque 3. Coupling pair 4. Transmission electric motor 5. Moment line 6. Hydraulic force measuring box 7. Hydraulic piping 8. Brake force indicator 9. Accelerometer 10. Data acquisition device

Figure 1. Schematic view of the experimental setup[7]

Figure 2.The picture of the experiment setup

Vibration measurement data was obtained with a four-channel VIBROTEST 80 model data acquisition device capable of FFT analysis with three-axis piezoelectric acceleration measurement. The device has a software and hardware system from Bruel & Kjaer. The data were analyzed by filtering at 6400 resolution with Hanning filtering method. The specific bearing of a vehicle brake test device vibration data were obtained with a Bruel & Kjaer 4527 piezoelectric accelerometer. The accelerometer is mounted on the bearing with glue. The properties of the triaxial accelerometer are given in Table 2.

Table 2. Accelerometer technical specifications

Accelerometer technical specifications	
Accelerometer Type	Bruel & Kjaer 4527
Frequency Range	0.3 - 10000 Hz
Sensitivity	10 mV / g
Temperature Measurement Range	-60 - 180 ºC
Weight	6 gram
Electrical Connection	1-4 28 UNF
Resonance Frequency	30 kHz

Experiments were carried out when the vehicle brake test device's drum were rotating under load and unloaded conditions. The brake drums were run with electrical motor when the vehicle brake test device was in the unloaded position. The drums were rotated by the vehicle wheel when the vehicle brake test device was run under load condition. The drum rotating speed is 7 kilometers per hour. The frequency domains analysis using FFT (Fast Fourier Transform) was done in MATLAB. The obtained figures are given below.
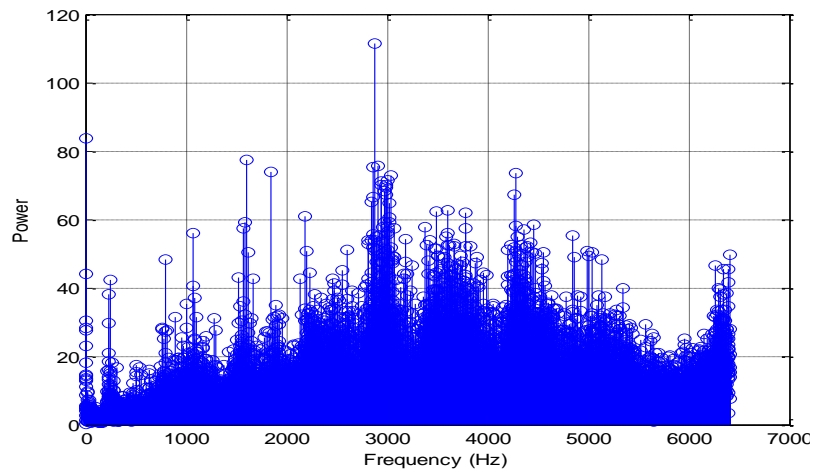
Figure 3. Frequency spectrum of rolling-element bearing vibration signal at unloaded condition for first measurement
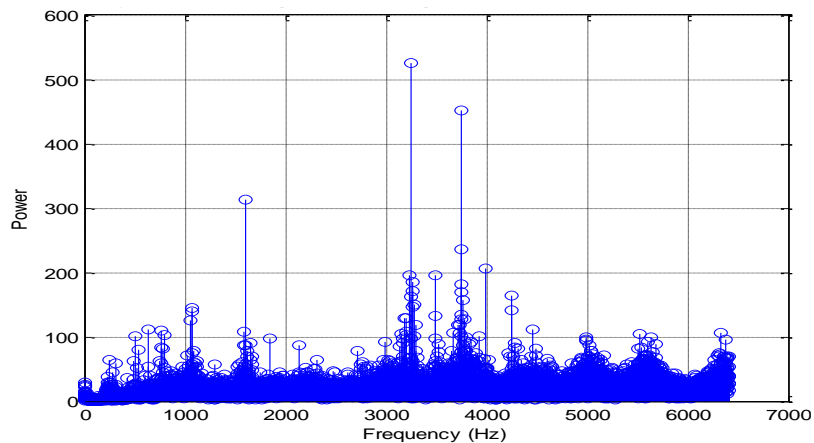
Figure 4. Frequency spectrum of rolling-element bearing vibration signal at loaded condition for first measurement
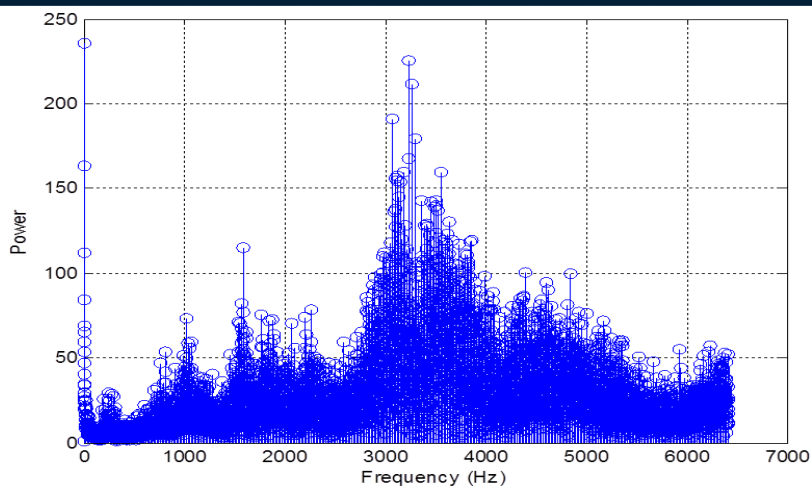
Figure 5. Frequency spectrum of rolling-element bearing vibration signal at unloaded condition for second measurement
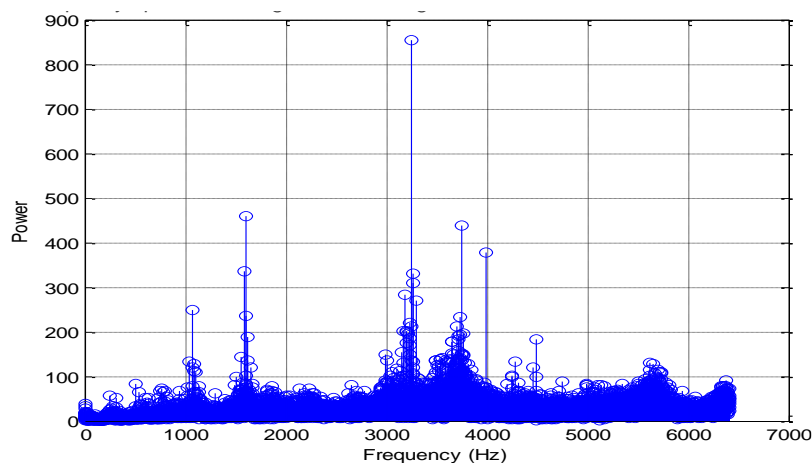
Figure 6. Frequency spectrum of rolling-element bearing vibration signal at loaded condition for second measurement
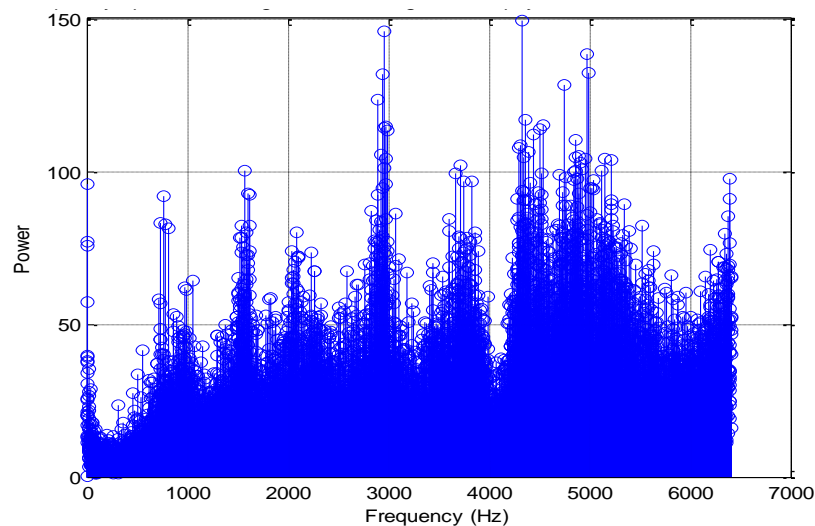
Figure 7. Frequency spectrum of rolling-element bearing vibration signal at unloaded condition for third measurement
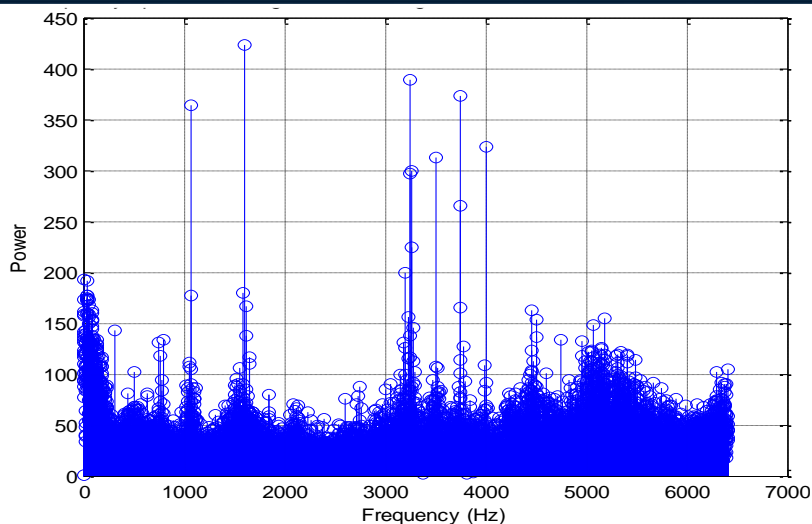
Figure 8. Frequency spectrum of rolling-element bearing vibration signal at loaded condition for third measurement

3. RESULTS AND DISCUSSIONS

Sum of peak amplitude values over the threshold values of 100 and 150 has been calculated from the specific bearing of the vehicle brake test device vibration values under loaded and unloaded conditions. It is also seen in Table 3 that as the time passes, sum of peak amplitude values of specific bearing of the vehicle brake test device increases.

Table 3. Results

Measurement Number (Unloaded)	Sum of peak amplitude values over the threshold value of 100
First measurement	111,5
Second measurement	12438
Third measurement	3725

Measurement Number (Loaded)	Sum of peak amplitude values over the threshold value of 100
First measurement	6982
Second measurement	19580
Third measurement	29415

Measurement Number (Unloaded)	Sum of peak amplitude values over the threshold value of 150
First measurement	0
Second measurement	2315
Third measurement	0

Measurement Number (Loaded)	Sum of peak amplitude values over the threshold value of 150
First measurement	3316
Second measurement	8449
Third measurement	8793

4. CONCLUSIONS

In this study, the vibration characteristics of a specific bearing of the vehicle brake test device were examined. Frequency spectrums of the specific bearing of the vehicle brake test device vibration signals have been obtained at 15 day intervals. The experiments were carried out with loaded and unloaded conditions for 7 kilometers per hour drum rotating speed. It is shown that sum of peak amplitude values of a specific bearing of the vehicle brake test device increases depending on passed time for loaded and unloaded drum conditions over the threshold value of 100. Also sum of peak amplitude values of a specific bearing of a vehicle brake test device increased depending on time intervals for only loaded drum conditions over the threshold value of 150.

ACKNOWLEDGMENT

REFERENCES

[1]. Zhenyu Yang, Uffe C. Merrild, Morten T. Runge, Gerulf Pedersen, Hakon Børsting, ''A Study of Rolling-Element Bearing Fault Diagnosis Using Motor's Vibration and Current Signatures'', Proceedings of the 7th IFAC Symposium on Fault Detection, Supervision and Safety of Technical Processes, Barcelona, Spain, June 30 - July 3, 2009.
[2]. Ming AB, Qin ZY, Zhang W, Chu FL, ''Spectrum auto-correlation analysis and its application to fault diagnosis of Rolling element bearings'', Mech. Syst. Signal Process,41(1),141–54, 2013.
[3]. Adel Boudiaf, Abederrazek Djebala, Hocine Bendjma, Adel Balaska, Amine Dahane, ''A Summary of Vibration Analysis Techniques for Fault Detection and Diagnosis in Bearing'', 8th International Conference on Modelling, Identification and Control (ICMIC-2016) Algiers, Algeria- November 15-17, 2016.
[4]. V.K. Rai, A.R. Mohanty, ''Bearing fault diagnosis using FFT of intrinsic mode functions in Hilbert–Huang transform'', Mechanical Systems and Signal Processing, 21, 2607–2615, 2007.
[5]. Hakan Arslan, Ersan Aslan, Nizami Aktürk, ''Investigation Of Vibrations Due To Ball Bearing Defects'', J. Fac. Eng. Arch. Gazi Univ., 21(3), 541-552, 2006.
[6]. Sadettin Orhan, Nizami Akturk , Veli Celik, ''Vibration monitoring for defect diagnosis of rolling element bearings as a predictive maintenance tool: Comprehensive case studies'', NDT&E International, 39, 293–298, 2006.

Power Spectral Ratio Analysis of a Single-Cylinder Diesel Engine Vibration When B50 Diesel-Biodiesel Fuel Blend Used

Selman Kulac[1], Suat Sarıdemir[2]

Abstract

Emissions from petroleum-based fuels used in vehicles pollute the atmosphere. However, the limited availability of world oil reserves accelerated the works on alternative fuels. Biodiesel, one of the alternative and renewable fuels, can be produced from vegetable and waste frying oils. One of the factors causes vibration in internal combustion engines is the combustion characteristic of the fuel. In this study, standard diesel fuel and biodiesel fuel were mixed 50% by volume and B50 fuel was obtained. Frequency spectrums of engine vibration signals have been obtained for the single-cylinder diesel engine operating under full load conditions when B50 diesel-biodiesel fuel blend. The experiments were carried out at engine speeds of 1500, 2000, 2500, 3000 and 3500 rpm. It was seen that as the engine rpm increases, the ratio of the power of high frequency components of vibration signals decreases.

Keywords: *Biodiesel, vibration, engine, frequency analysis, power ratio of frequency components*

1. INTRODUCTION

Global warming is increasing. The largest part of global warming is from vehicles we use. Taking measures against to this danger threatening our world makes the countries think. For this reason, renewable energy sources have been gaining importance and researches have also been increasing rapidly in these areas. In this context, it is important to obtain electrical energy from the sun and wind, and the use of this energy in electric vehicles is an example of reducing the use of fossil fuels. However, it seems that it will take some time for spreading of only electrically powered vehicles with the required efficiencies. For this reason, in order to reduce fossil fuel consumption, biodiesel has been started to be preferred.

Although biodiesel fuels are derived from vegetable and animal wastes, they come to the forefront with the fact that they have a combustion characteristic close to diesel fuel. However, when engine performance and lifetime are taken into account, solutions for diesel and biodiesel mixtures continue to be explored.

Some indicators for the engine performance and lifetime can give a lead and one of them is engine vibration signals. It has been concluded that vibration signals should be observed in terms of engine performance and lifetime. In [1], for example, vibrations of a six-cylinder motor have been investigated and in [2] the effects of vibration on an agricultural machine engine have been examined. It has also been shown that for a normal diesel engine, fault diagnosis can be done with the vibration signals in terms of time and frequency domains [3]. In [4], it is stated that vibration diagnosis can be performed by using blind source separation technique based on fuel. In another study, an RMS and SVM-based approach to vibration signals was proposed at the point of detection of fault of the turbo pump, an important part of the liquid rocket motor [5].

In this study, a vibration analysis was carried out using diesel biodiesel fuel blend. In particular, the ratio of high frequency components against to the total vibration signal power has been examined for the different engine speeds.

---

[1] Corresponding author: Duzce University, Faculty of Engineering, Department of Electrical - Electronics Engineering, 81620, Duzce, Turkey. selmankulac@duzce.edu.tr

[2] Duzce University, Faculty of Technology, Department of Manufacturing Engineering, 81620, Duzce, Turkey. suatsaridemir@duzce.edu.tr

2. MATERIALS AND METHODS

In this section, an experimental setup used for this study is explained. Engine vibration signals based on measurements have been taken with single-cylinder engine according to varying engine speeds with this experimental setup.

Biodiesel fuel is produced from waste vegetable oils by transesterification method in accordance with TS EN 14214 standards. Biodiesel fuel (B0) was mixed with standard diesel fuel by volume 50% just before the experiments. A direct-injection, 4-stroke, single-cylinder air-cooled diesel engine and an electric dynamometer capable of absorbing 15 kW of power were used in the experiments. The specifications of the test engine are given in Table 1. The experimental setup is schematically shown in Fig. 1.

Table 1. Technical specifications of the test engine.

Technical specifications	
Number of Cvlinders	1
Course Volume	395 cc
Compression Ratio	18:1
Cooling system	Air cooled
Maximum engine speed	3600 rpm
Injector opening pressure	200 bar
Maximum Engine Load	2200 rpm (21 Nm)
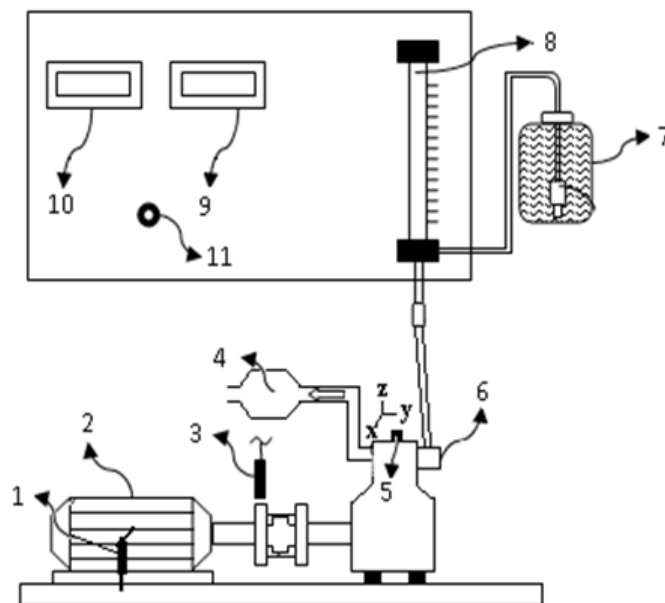
1. Load cell 2. Electric dynamometer 3. Speed sensor 4.Exhaust 5. Accelerometer (3 axis) 6. Fuel pump

7. Fuel tank 8. Fuel measuring burette 9. Speed indicator 10. Torque indicator 11.Load key

Figure 1. Schematic view of the experimental setup.

Vibration measurement data was obtained with a four-channel VIBROTEST 80 model data acquisition device capable of FFT analysis with three-axis piezoelectric acceleration measurement. The device has a software and hardware system from Bruel & Kjaer. The data were analyzed by filtering at 6400 resolution with Hanning filtering method. Vibration data up to 5 kHz were taken during 1.28 seconds in experiments. The motor vibration data were obtained with a Bruel & Kjaer 4527 piezoelectric accelerometer. The accelerometer is mounted on the cylinder head with screws. Figure 1 shows the axis of the accelerometer in the horizontal (x-Ch1), axial (y-Ch2) and vertical (z-Ch3) axes. The properties of the triaxial accelerometer are given in Table 2.

Table 2. Accelerometer technical specifications.

Accelerometer technical specifications	
Accelerometer Type	Bruel & Kjaer 4527
Frequency Range	0.3 - 10000 Hz
Sensitivity	10 mV / g
Temperature Measurement Range	-60 - 180 ºC
Weight	6 gram
Electrical Connection	1-4 28 UNF
Resonance Frequency	30 kHz

On this experimental setup, engine vibration signals based on measurements taken with single-cylinder engines according to varying engine speeds when B50 Fuel Blend used are presented in frequency domains using FFT (Fast Fourier Transform) in MATLAB in figures below.
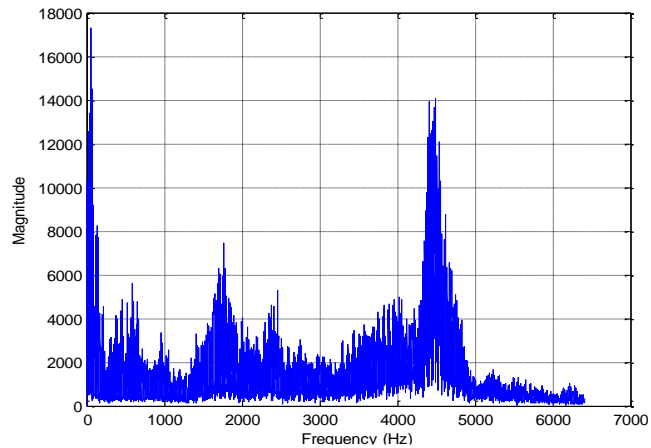
Figure 2. Frequency spectrum of engine vibration signal at 1500 RPM when B50 Fuel Blend used.
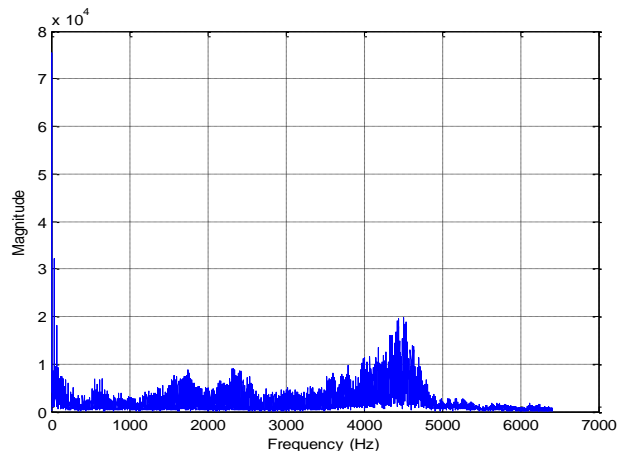
Figure 3. Frequency spectrum of engine vibration signal at 2000 RPM when B50 Fuel Blend used.
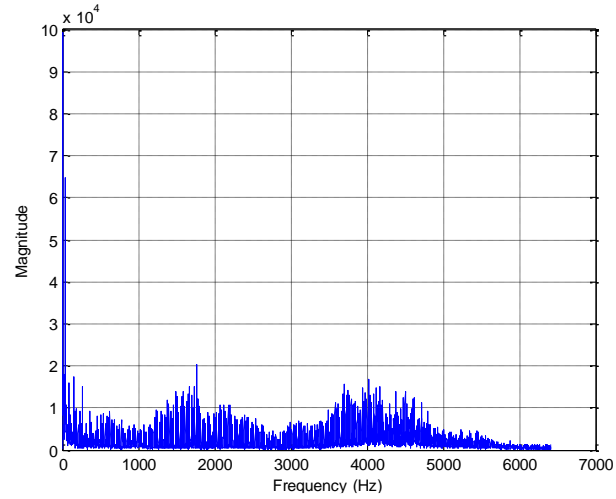
Figure 4. Frequency spectrum of engine vibration signal at 2500 RPM when B50 Fuel Blend used.
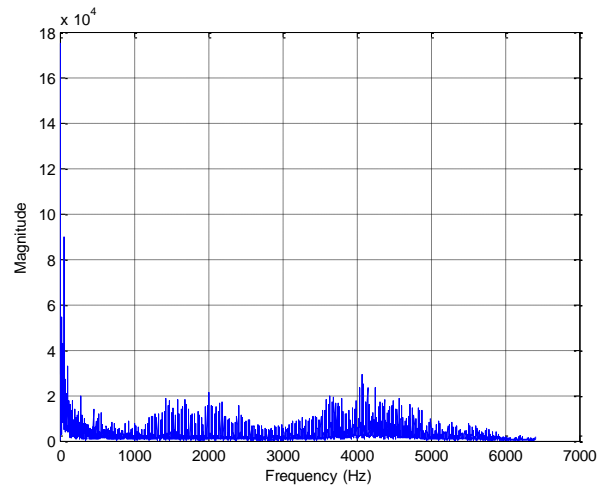
Figure 5. Frequency spectrum of engine vibration signal at 3000 RPM when B50 Fuel Blend used.
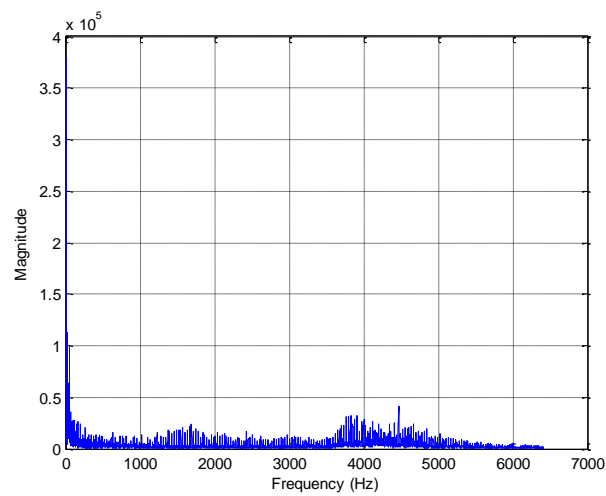
Figure 6. Frequency spectrum of engine vibration signal at 3500 RPM when B50 Fuel Blend used.

266

3. RESULTS AND DISCUSSIONS

It is accepted that the frequency spectral values of engine vibration signals above the 960 Hz are high frequency components. The power of high frequency spectral values has been calculated and the power of all spectral components has also been calculated at engine speeds of 1500, 2000, 2500, 3000 and 3500 rpm under full load conditions when B50 diesel-biodiesel fuel blend. The ratio between them gives us the ratio of the power of high frequency components against to the total vibration signal power.

It is also seen in Table 3 that as the engine rpm increases, the ratio of the power of high frequency components of vibration signals decreases.

Table 3. Results

B50	High Frequency Power Ratio
1500 RPM	0.811493178818379
2000 RPM	0.046764625445704
2500 RPM	0.013407889075201
3000 RPM	0.001792864076474
3500 RPM	0.000514060494921

4. CONCLUSIONS

In this study, standard diesel fuel and biodiesel fuel were mixed 50% by volume and B50 fuel was obtained. Frequency spectrums of engine vibration signals have been obtained for the single-cylinder diesel engine operating under full load conditions when B50 diesel-biodiesel fuel blend. The experiments were carried out at engine speeds of 1500, 2000, 2500, 3000 and 3500 rpm. It is shown that as the engine rpm increases, the ratio of the power of high frequency components of vibration signals decreases.

ACKNOWLEDGMENT

REFERENCES

[1]. Taghizadeh-Alisaraei A, Ghobadian B, Tavakoli-Hashjin T, Mohtasebi SS, 2012, ''Vibration analysis of a diesel engine using biodiesel and petrodiesel fuel blends'', Fuel;102: 414–422

[2]. Heidary B, Hassan-Beygi SR, Ghobadian B, Taghizadeh A, 2013, ''Vibration analysis of a small diesel engine using diesel-biodiesel fuel blends'', Agric. Eng. Int. CIGR Journal;15(3),117-126

[3]. C. Jin, W. Zhao, Z. Liu, and J. Lee, "A vibration-based approach for diesel engine fault diagnosis," *2014 International Conference on Prognostics and Health Management*, Cheney, WA, 2014, pp. 1-9.

[4]. Y. Chang and Y. Hu, "Vibration diagnosis study about the marine diesel engine based on BSS," *2010 2nd International Conference on Signal Processing Systems*, Dalian, 2010, pp. V3-196-V3-200.

[5]. T. Hong and H. Li, "Turbopump fault detection algorithm based on protruding frequency components RMS and SVM," *2013 IEEE International Conference on Mechatronics and Automation*, Takamatsu, 2013, pp. 1311-1316.

Elimination Of Harmonics With Using Passive Filters In Power System

Mustafa YAGCI[1], Orhun DOS[2]

Abstract

The current and voltage should be 50 Hz and very similar with the sine graph in power system. The harmonics cause to distortions at the current and voltage forms. Because of this case the quality of the electrical energy decreases and the malfunctions begin. In this study; a model of the electrical systems which includes harmonics has been simulated with MATLAB/SIMULINK. The types of passive filter have applied to this system. The effects of these filters have investigated. The results were analyzed and the most efficient filter type was determined for the designed system.

Keywords: *Passive filters, harmonics, power systems, matlab/simulink*

1. INTRODUCTION

The main reason of using filters is elimination to the distortion that is occurred due to waveform disturbances[1]. Also we need to use filters for technical and economical reasons. Harmonic filters should design separately for each installation[2].

The basic approach to designing filters can be summarized as follows:

- The magnitudes of harmonic currents to be filtered are determined.
- The inductance value to provide the desired setting is determined.
- Check the filter response, including the effect of tolerances on capacitor and inductance values.
- Continuously checks the voltage peaks on the capacitor at fundamental and harmonic frequencies.
- Check for adverse interactions between the system and filter.

Passive filters consist of inductive, capacitive and resistive elements for controlling harmonics. These types of filters are cheaper than commonly used filters and other harmonic solutions[3].

2. MATERIAL AND METHOD

2.1. Parallel Passive Filters

In parallel passive filters, the purpose is to connect this circuit to the power system by calculating the L, C values to resonance for the harmonic frequency to be eliminated[4].

Separate resonance arms must be created for each harmonic frequency and these arms must be connected to the power system. Since it is not an optimum solution to create a separate resonance line for each harmonic component, only a resonance line should be formed for high harmonic frequencies with amplitude values. For non-high harmonic frequencies it would be sufficient to create a single resonance line that would reduce their effectiveness [5].

Passive filters can cause dangerous problems in the power system. Before designing, the properties of the system and the response of the system to these elements should be well known.

---

[1] *Corresponding author: Necmettin Erbakan University, Department of Electrical and Electronics Engineering, Meram/Konya, Turkey. myagci@konya.edu.tr*

[2] *Necmettin Erbakan University, Institute of Science, Meram/Konya, Turkey. orhun.dos@gmail.com*

In this study, two different types of parallel passive filters will be examined. These are;

- Single-tuned (bandpass) filters,
- Double-tuned filters,

2.1.1. Single-Tuned (Bandpass) Filters

Single-tuned (bandpass) filters create a short-circuit path for a single frequency harmonic current, allowing this current to be deflected[6]. Single-tuned filters consist of series R-L-C[7]. A single tuned filter example is shown in Figure 1.
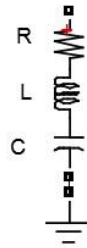
Figure 1. Single-Tuned Parallel Passive Filter.

Filter impedance of harmonic frequencies other than the fundamental frequency and the harmonic frequency set by the single-tuned filter;

$$Z = Z_T = R + j(X_L - X_C) = R + j(2.\pi.f_n.L - \frac{1}{2.\pi.f_n.C}) \tag{1}$$

The working principle of this filter is to provide the resonance of the filter at the desired harmonic frequency to achieve Xl = Xc condition. In this case, the filter impedance (the impedance at the harmonic frequency being set);

$$Z_{T_0} = R \tag{2}$$

That is, the filter shows the minimum impedance value for the set frequency and the set frequency harmonic flows to the ground.

Since the single-tuned filter operates according to the series resonance principle, the Xl = Xc condition is sought for in these filters. These Xl and Xc values should be selected according to the system. When single tuned filters are applied to the system, the capacities at the filter, the fundamental frequency of the system and the frequencies outside the set harmonic frequency are affected by the compensation in the system.

Therefore, while the filter is being calculated, the capacity to be used in the filter should be determined at the value that will compensate for the system's need for compensation. Finally, with this value, the inductance value in the resonance should be calculated. These calculations should be done in the following order.

First of all, the reactive power requirement of the system should determine [8]. To do so,

$$Q = P(\tan_{\theta 1} - \tan_{\theta 2}) \tag{3}$$

After the calculated compensation power, the capacitive reactance of the capacitor which should be connected to the system from the formula should be determined.

$$X_c = \frac{U^2}{Q} \tag{4}$$

The capacitive reactance value that should be connected to the system should be distributed proportionally to the single-tuned filters. Then, The XL value corresponding to Xc for each filter stage should be calculated. In this case, the capacity should be divided equally by the number of each single harmonic filter line.

$$C = C_1 = C_2 = C_3 = C_n = \frac{1}{2.\pi.f.X_c} \tag{5}$$

The calculation of the inductor size is performed as follows;

$$L = \frac{1}{4.\pi^2.f_n^2.C_n}$$

(6)

Finally a small (100Ω) resistor value should be added to the circuit to create the internal resistance of the single-tuned filter. On the non-linear load side has got R=100Ω and C=1uF.

Designed as an example harmonics source and its is generated harmonics elimination has modelled below with using Matlab/Simulink;
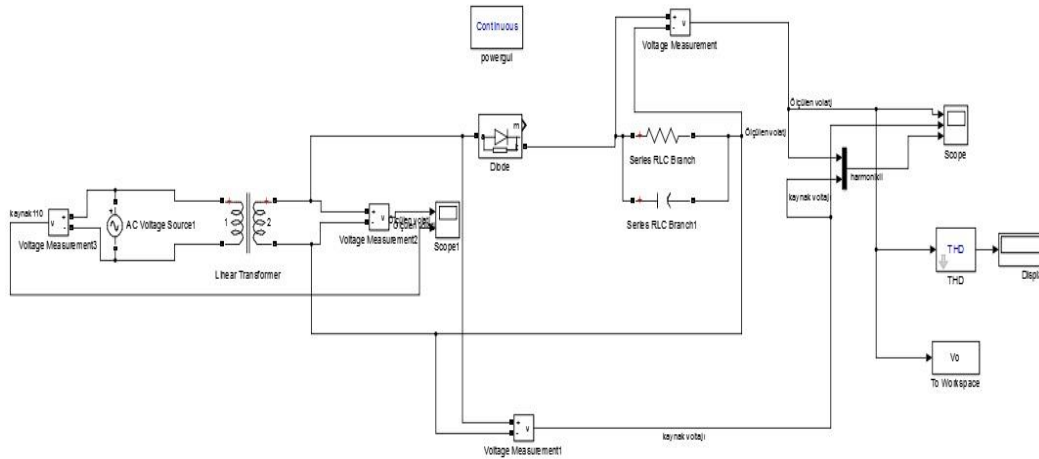
Figure 2. Created Harmonic Circuit Model

In this modelling parameters of the transformer are as below;
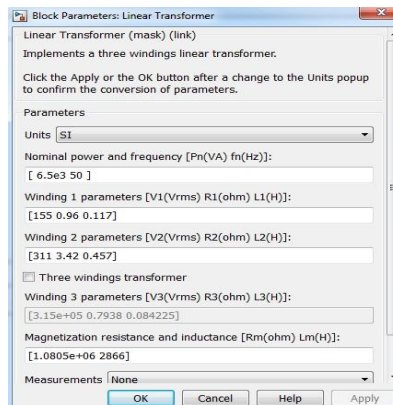
Figure 3. Parameters of Transformer.

After this modelling, Fast Fourier Transform (FFT) is performed. The signals that have occurred according to this transform is as below;
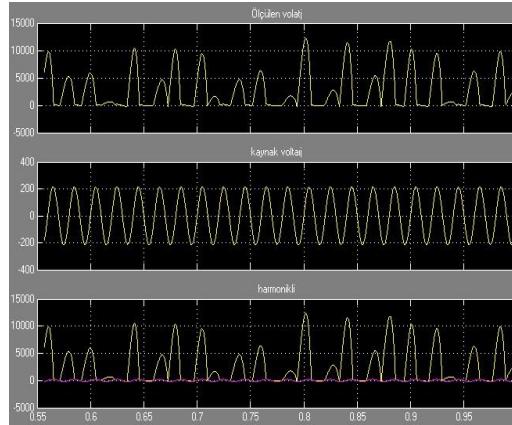
Figure 4. Measured Voltage Curves.

The result of FFT for this circuit is as below;
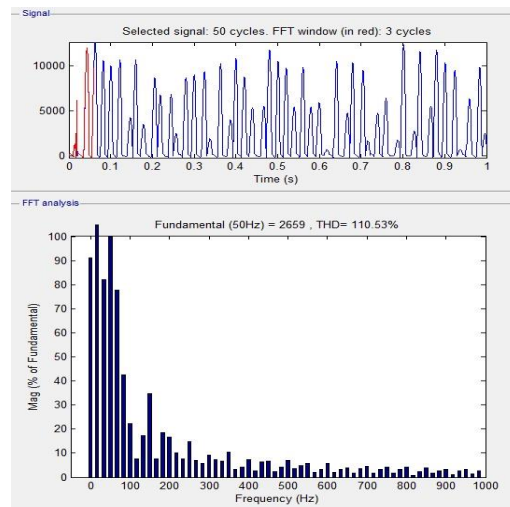
Figure 5. The Result of FFT.

For the harmonic filters to be designed, it is enough to select the compensation power of the system 10MVAR. For this system, it is considered sufficient to take the resistance value R = 100Ω in a single-tuned filter consisting of one parallel arm. This small resistance will create internal resistance of the filter.

Single-tuned harmonic filter is shown in the following model;
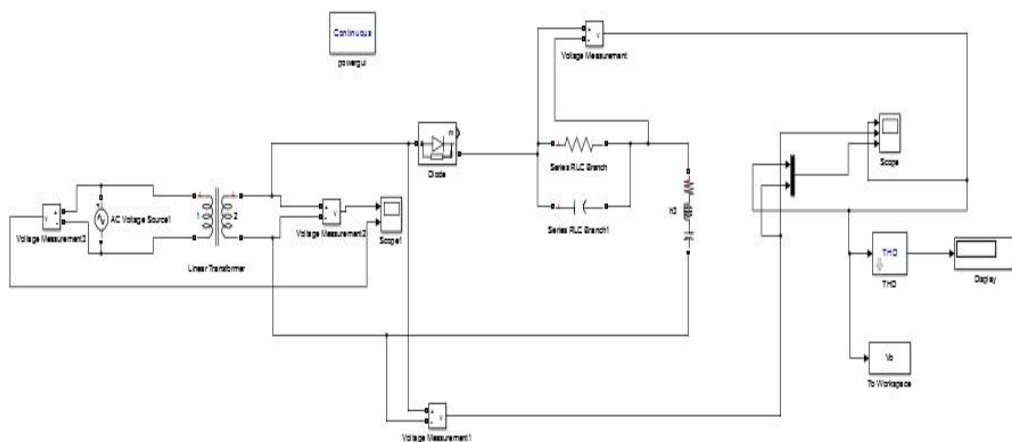
Figure 6. Created Harmonic Circuit Model for H3.

The voltage graphs after single-tuned harmonic filter is added to the system are as below;

271
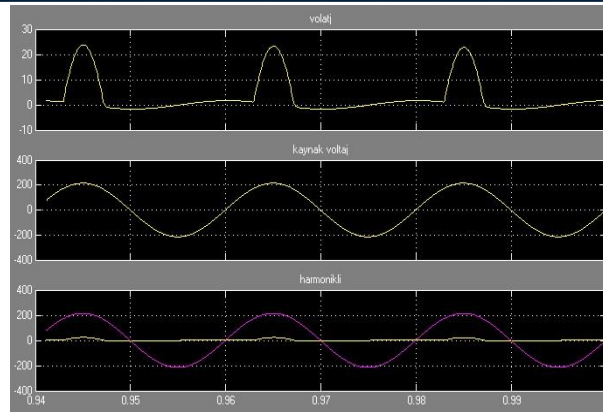
Figure 7. Measured Voltage Curves.

The result of FFT for this circuit is as below;
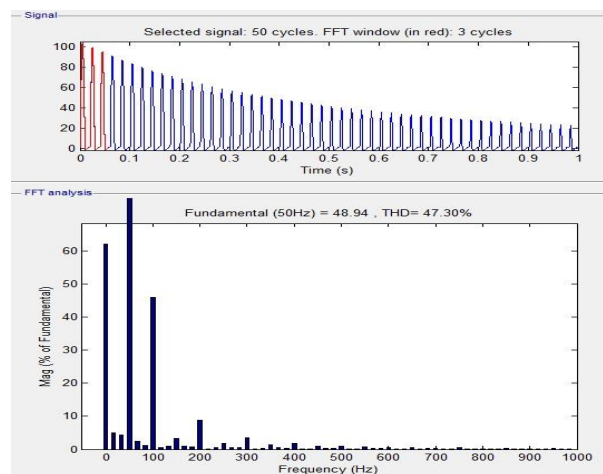
Figure 8. The Result of FFT.

The harmonics that are occurred in this circuit are shown as table below;

	H3	H5	H7	H9	H11	H13
Unfiltered(%)	34.62	14.63	10.31	6.83	5.84	4.05
Filtered(%)	3.26	1.90	1.30	0.96	0.72	0.56

As can be seen, the harmonic distortions on the nonlinear circuit elements of harmonic loads produced by a harmonic source are reduced to a minimum level. According to international standards, low voltage harmonics are allowed to be at most 3%. In accordance with these conditions, we have made harmonic reduction at a sufficient level with a single tuned filter.

2.1.2 Double-Tuned Filters

The equivalent impedance of the double tuned filter is the same as the equivalent impedance of the two single tuned filters. The double tuned filter can eliminate two different harmonics. According to single-tuned filters, the low power loss of the fundamental frequency is the most important feature of these filters. There are two different resonance points of the double-tuned filter, due to it consist of two single tuned filters. It is possible to design with three and four tuned filters, but they are not used due to adjustment difficulties[9].
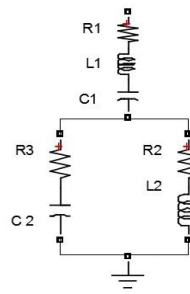
Figure 9. Double-Tuned Filter.

The relationship between the double-tuned filter components is as below:
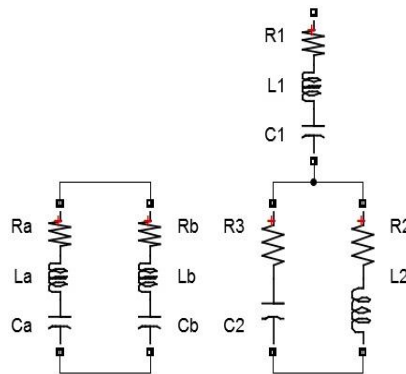
Figure 10. Parameters of Double-Tuned Filter.

$$C_1 = C_a + C_b \tag{7}$$

$$C_2 = \frac{C_a . C_b . (C_a + C_b) . (L_a + L_b)^2}{(L_a . C_a - L_b . C_b)} \tag{8}$$

$$L_1 = \frac{L_a . L_b}{L_a + L_b} \tag{9}$$

$$L_2 = \frac{(L_a . C_a - L_b . C_b)^2}{(C_a + C_b)^2 . (L_a + L_b)} \tag{10}$$

As a result of these calculated values, the double tuned filter modeled in Matlap / Simulink as below;
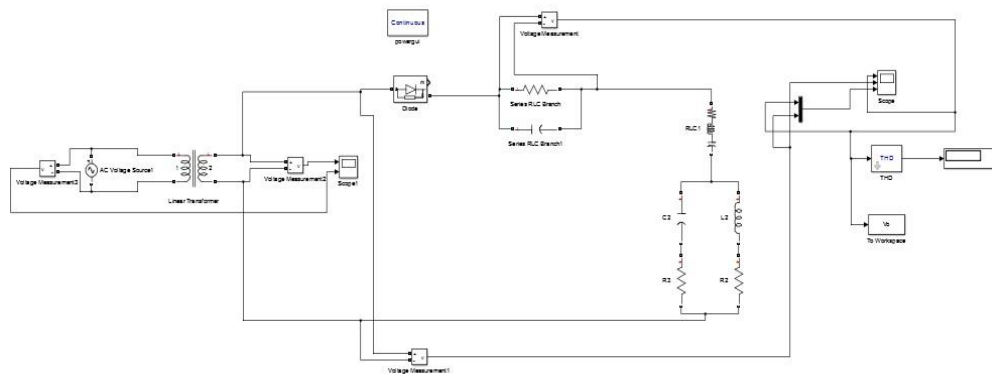
Figure 11. Created Harmonic Circuit Model for H3 and H5.

The voltage graphs that appear after adding the double-tuned harmonic filter to the system are as below;
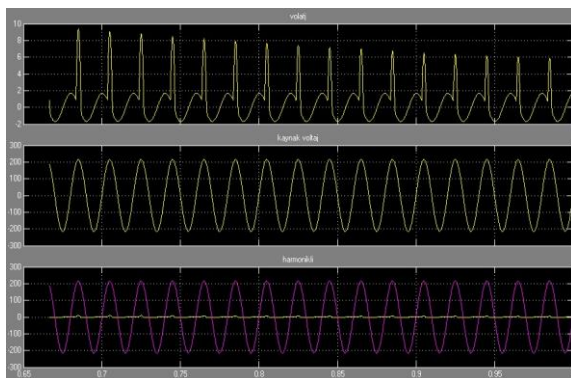
Figure 12. Measured Voltage Curves.

The result of FFT for this circuit is as below;
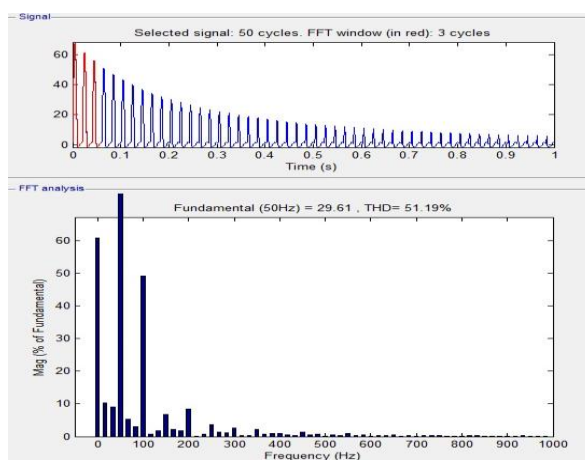
Figure 13. The Result of FFT.

The harmonics that are occurred in this circuit are shown as table below;

	H3	H5	H7	H9	H11	H13
Unfiltered(%)	34.62	14.63	10.31	6.83	5.84	4.05
Filtered(%)	6.74	3.65	2.22	1.38	0.84	0.48

The final measurements of the harmonics according to the applied filters are as in the following table;

	H3	H5	H7	H9	H11	H13
Unfiltered(%)	34.62	14.63	10.31	6.83	5.84	4.05
Single Tuned Filtered for H3(%)	3.26	1.90	1.30	0.96	0.72	0.56
Double-Tuned Filter for H3 and H5	6.74	3.65	2.22	1.38	0.84	0.48

3. RESULTS AND DISCUSSION

The advantages of single-tuned filters are:

• If there is no resistance added on demand, the losses are very small.

• Shows an impedance close to zero to the harmonic current for the set harmonic frequency.

- Multiple filters can be used in parallel for more than one harmonic current to be filtered.

The disadvantages of single-tuned filters are:

• Due to its precise construction calculations, it is very sensitive to variations in the value of the elements that make up the filter. This problem can be solved with additional capacitor and resistance values.

• Single-tuned filters can only be used on systems with nonlinear loads that have fixed power. Because the capacitances above are not variable, the capacitors will remain on when the inductive loads in the system are removed, so overcompensation can occur in this case.

The disadvantage of the double-tuned filter is that it operates erratically in high voltage applications.

4. CONCLUSION

The excusable harmonic distortion is %3 for low voltage harmonic standards at power systems. All the efforts for elimination to harmonics aim to keep down the voltage harmonics under %3. In this study we have investigated how harmonics were affected from the single-tuned passive filter and double-tuned passive filter. One of the most imported harmonic order is third harmonic due to we aim to eliminate successfully to this harmonic level. For this purpose several modellings have performed on Matlab/Simulink. As can be seen on the result of modellings, the harmonic distortions that are shown on the nonlinear circuit elements of harmonic loads produced by a harmonic source are reduced at a high rate. According to the performed modelling results, the single-tuned passive filter is more efficient than dual-tuned passive filter on the modellings that we have constituted on Matlab/Simulink.

ACKNOWLEDGEMENT

REFERENCES

[1]. Acarkan B, "Harmonic efficiency and harmonic analysis of office equipment" Yıldız Technical University, Doctoral Thesis, 2006.
[2]. Leszek S. and Czarnecki F. "The effect of the design method on efficiency of resonant harmonic filters" IEEE Transactions on power delivery, Vol.20, No.1, 2005.
[3]. Dugan R. "Electrical Power Systems Quality", Second Edition.
[4]. Kocatepe C., Uzunoglu M., Yumurtacı R., "Harmonics in power plants", Istanbul, 2003.
[5]. Sucu M. "Computer aided modeling and simulation of harmonics filtering in electrical power system" Marmara University ,Master Thesis, 2003.
[6]. Zhao Y, "Optimal planning of harmonic filters on distribution system by chance constrained programming" Electric Power Systems Research 68, pp149-156, 2004.
[7]. Tuncalp K, "The usage of passive filtered compensation for filtering harmonics occurred in electric energy systems and simulations steps" Journal of Politechnic, Vol:9,No:4,pp263-269, 2006
[8]. Arrilaga J. and Watson N. "Power System Harmonics", England, 2003.
[9]. Bilge M. "Elimination of harmonics by passive filter in power plant" Kahramanmaras University, Master Thesis, 2008.

BIOGRAPHY

Mustafa YAGCI was born in Konya, Turkey, in 1963. He received the BS degree from Marmara University, Istanbul, Turkey, in 1984, the MS degree from Gazi University, Ankara, Turkey, in 1994 and the PhD degree from Selcuk University, Konya, Turkey, in 2005. He is currently Assistant Professor in the Electrical and Electronics Engineering Department of Necmettin Erbakan University, Turkey. His research interests include electrical machines and driving circuits, harmonics of transformers, power electronics and photovoltaic power plants. He is author or co-author of several papers published in scientific journals or conference proceedings.

DETERMINATION EFFECT OF LIQUID GLASS ON COLOR CHANGING ON WOOD MATERIALS STAINED BY INDIGO (*Isatis tinctoria* L.) EXTRACTS

Osman GOKTAS[1], Sezil ALİYAZICIOGLU[1], Mehmet YENİOCAK[1]*, Mehmet COLAK[1], Mehmet UGURLU[2], Ertan OZEN[1]

Abstract

The aim of this study is to develop durable natural colorants and liquid glass for the surface of wooden products and determine the color resistance of this stain to UV light irradiation. Natural dyestuff was extracted from Indigo (lsatis tinctoria L.) by boiling method and mordent with ferrous sulphate, aluminum sulphate, and vinegar mixes. Scots pine (Pinus sylvestris L.), chesnut (Castanea sativa Mill.) and mahogany (Khaya ivorensis) wood specimen were used for the study. After treatment with stain, wood test samples were exposed to UV irradiation for the periods of 50, 100 and 150 hours. The results showed that the color change values for all wood specimens stained with Indigo extract and liquid glass dyestuff had a better performance compared to synthetic colorants. However, liquid glass was not precisely effective on color stability on some samples.

Keywords: *Indigo, Natural coloration, Liquid glass, UV weathering, Color change*

1. INTRODUCTION

Wood is an organic, hygroscopic and anisotropic material. Its thermal, acoustic, electrical, mechanical, aesthetic, working, etc. properties are very suitable to use it for buildings, furniture and a range of wooden products. It is easy to repair and maintain the damaged wood. However, wood has some disadvantages too. It changes shape, and it is suitable for discoloration, it can be decayed by biotic agents as fungi, bacteria and insects; and abiotic agents as sun, wind, water, certain chemicals and fire [1]. For protecting wooden products against to these disadvantages, many materials developed and applied on it. For the purpose of aesthetic and protection, many stain, coatings and paints are used. Generally, these synthetic materials contain "Volatile Organic Compounds" (VOCs) [2], [3], [4]. VOCs are a large group of chemicals that are found in many products we use to build and maintain our homes. These chemicals defines as typical solvents, they are aliphatic hydrocarbons, ethyl acetate, glycol ethers, and acetone. "Volatile" means that these chemicals evaporate or can easily get into the air at room temperature. "Organic" means these chemicals are carbon based. For manufacturing paints and stains, some types of solvents are used. The term "chemical emissions" refers to VOCs as they evaporate into the air from products [5]. Unfortunately, these VOCs are hazardous for people and environment. For short-term exposure, they can appear as eye, nose, and throat irritation, headaches, nausea/vomiting, dizziness, worsening of asthma symptoms. Additionally, for chronic exposures, they can be cause of cancer, liver, kidney and central nervous system damage. It has been determined that these solvents can cause miscarriages of pregnant womenbirth defects and children's learning disabilities [6].It is stated that kids are more affected by VOC's since they have relatively higher respiratory rate, not established immune system, are closer to the ground, breathe more by mouth and not by nose. Therefore, children don't benefit from the advantage of nose filtering which is critical due to the fact that chemicals entering the body by high pulse rate diffuse to the tissues faster [7].

Recent resurgence in research and development on natural dye production and application is observed due to increasing popularity of more natural lifestyle based on naturally sustainable goods [8].

---

[1]* *Corresponding author: Mugla Sitki Kocman University, Faculty of Tecnology, Department of Woodworking Industrial Engineering. 48000 Mugla/Turkey. myeniocak@mu.edu.tr*

[2] *Mugla Sitki Kocman University, Faculty of Science, Department of Chemistry, 48000 Mugla / Turkey.*

Recently international awareness of environment, ecology and pollution control created an upsurge on the interest of people to use more environmentally products and due to increasing popularity of more natural lifestyle based on naturally sustainable goods [8].

Research into new natural dyes sources along with eco-friendly, robust and cost-effective technologies for their processing and application have greatly aided in widening the scope of natural dyes in various traditional and advanced application disciplines [9]. Natural dyes derived from flora and fauna are believed to be safe because of their non-toxic, non-carcinogenic and biodegradable nature [10]. For this reason, the importance of the protection and staining wood material by natural sources is gaining importance day by day.

Goktas et al. investigated the development of environmentally friendly wood stains derived from laurel (Laurus nobilis L.) [11], walnut shell (Juglans regia) [12], saffron (Crocus sativus L.) [13], madder root (Rubia tinctorium L.) [14], oleander (Nerium Oleander L.) [15], extract and determined the color stability of the stains when exposed to ultra-violet (UV) light irradiation. Their results showed that the extract provided some color stability after UV irradiation.

Indigo (lsatis tinctoria L.) refers both to the blue pigment used as a dye and to indigo plants of the genus Indigofera. Indigo dye has been used for thousands of years by civilizations all over the world to dye fabric [16,] [17]. Natural indigo has a high proportion of impurities such as indirubins that give beautiful color variations and it is environmentally friendly. There is no need for harmful chemicals in a fermentation vat. It has been the most famous and most widely used natural dye throughout history and still used for cotton, silk, wool, feathers, basket canes, willow, leather, mother of pearl buttons, and paper [17].

In this study, we have focused on the coloring wood material by Indigo extract+liquid glass and determined color changing after UV weathering. Our theory was that, liquid glass could enhance the color stability of natural dye on wood materials. Therefore, the research question of the study was "how effect the liquid glass on color chancing against to UV weathering".

2. MATERIAL AND METHOD

2.1. Wood materials

As wood material, Scots pine (*Pinus sylvestris* L.), chesnut (*Castanea sativa* Mill.)) and mahogany (*Khaya ivorensis*) wood specimens were used for the study. The wood test samples were prepared in accordance with TS 2470 standard [18]. The samples prepared for UV weathering tests in dimensions of 150×75×5 mm were kept under suitable temperature (20 ± 2°C) and suitable moisture (moisture of ±12% and relative humidity of ±65%) conditions until they became air-dried, in order to achieve the moisture value in furniture used under interior area conditions in accordance with TS 2471 standard [19].

2.2. Plant material and Mordant agents

In this study, for natural pigments, Indigo (lsatis tinctoria L.) was chosen and provided from domestic market (Turkey). In addition to creating affinity between dye and wood fiber, the use of mordants also change the hue of certain dyes [9]. Different mordants used with the same dye may darken, brighten or drastically alter the final color of the dyed wood sample. Mordant agents ferrous sulphate ($Fe_2(SO_4)_3 7H_2O$), aluminum sulphate ($Al_2(SO_4)_3.18H_2O$) were provided from Kimetsan Co. and vinegar was purchased from Fersan Co. A synthetic dye (woodtex - Kayalar kimya Co./Turkey) has been used for comparison to natural dyes.

2.3. Preparation of dyestuff

A weighed amount of dry plant material was extracted with distilled water in a bath (Elmasonic X-tra 150 H). In the standard procedure the mass ratio of plant material to the volume of liquid was 1:20; extraction was performed for approximately 180 min. at 45 °C. Due to the rather high liquor ratio, some manual stirring was sufficient to distribute the plant material in the liquid during the extraction period. Volume loss due to evaporation was compensated by the addition of water at the end of the extraction period to obtain the initial volume.

Aqueous solutions were mordanted by adding ferrous sulphate ($Fe_2(SO_4)_3.7H_2O$) 3%, aluminum sulphate ($KAl_2(SO_4)_3.18H_2O$) 5%, and grape vinegar 10% in order to stabilize the color of dyes extracted, to ensure it to hang on the applied material (to increase retention amount), and to create color options. After mordanting, liquid glass added to mordanted aqueous with 20% (w/w).

2.4. Dyeing test samples

All air-dried wood specimens were placed into the dye bath container according to their mordants and plant types. For treatment procedures, immersion method has been applied for 60 min and at 45 °C. Any extra

solution left on the specimens was removed with a clean cloth. Specimens were then left to dry at 20±3 °C in a vertical position.

2.5. Accelerated weathering test

Operation of accelerated weathering device is composed of two periods. Weathering process was performed by operating the device for 4 h in the condensation stage, and for 8 h in UV period. The average irradiance was about 330 nm at 50 percent relative humidity and 20 °C. Specimens were directly exposed to UV light at a distance of 20 cm and an angle of 90E [20]. Five replicate samples treated with each stain solution and untreated controls were run for the randomly selected irradiation times of 0 (no irradiation), 50 hours, 100 hours, and 150 hours The color of the samples was measured after each irradiation period.

2.6. Color measurements

In order to determine the color change after cold check tests, the colors of the coated parts were identified prior to exposure by using Konica Minolta CR–10, a portable color reader device. Color measurements were performed on each sample due to the non-homogenous color structure of the wooden material in four measures. The identified color values were classified according to the coordinates Commission International de I'Eclaireage-CIELAB 1976 set in ISO 2470 standards (Figure 1). The obtained colors were indicated with numerical values of L, a, and b. Here, "L" indicates lightness from 0% (black) and 100% (white), "a" from green (-a) to red (+a), and "b" from blue (-b) to yellow (+b). Coated sample pieces were subjected to color measure prior to exposureto cold check and stated as "color values prior to cold check".

2.7. Determination of color change values

 Color changes due to accelerated weathering were calculated with the following formulas in accordance with ISO 2470 standards.

$$\Delta L^* = L^*_f - L^*_i \tag{1}$$

$$\Delta a^* = a^*_f - a^*_i \tag{2}$$

$$\Delta b^* = b^*_f - b^*_i \tag{3}$$

$$\Delta E^* = \sqrt{\Delta L^{*2} + \Delta a^{*2} + \Delta b^{*2}} \tag{4}$$

Here; ΔL^*, Δa^* ve Δb^* are the changes occurring between the initial state (i) and final state (f) of the colors. ΔE^*, indicates total changes of the colors occurring in the directions of L, a, and b. Here, the highest value shows the highest color change.
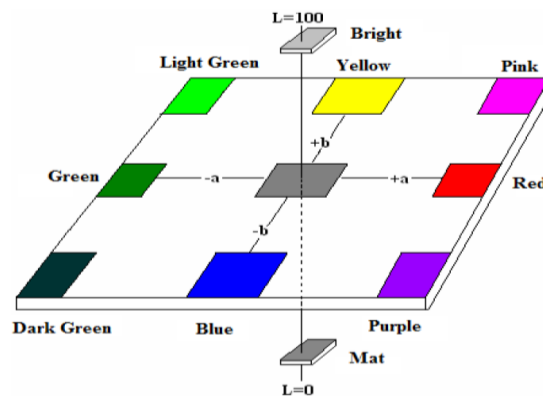
Figure 1. CIELAB–76 color system.

3. RESULTS AND DISCUSSION

Color changes values occurring on Scots pine, chestnut (*Castanea sativa Mill.*) and mahogany wood test samples that were stained with indigo+ liquid glass and mordant mixes extracts, and exposed to UV application for 50, 100, and 150 h are numerically represented in Tables 1, 2 and 3.

Positive values of ΔL^* show whitening, and negative values of ΔL^* indicate the color turning grey. Positive values of Δa^* indicate reddening of the colors, and negative values of Δa^* show a shift towards green.

Positive values of Δb^* represent yellowing in color, and negative values of Δb^* represent the color turning blue.

According to the results, all wood specimens exposed to UV radiation for all the exposure periods generally showed negative values of ΔL^*. This was attributed to chemical changes which occurred, especially in lignin, due to photo-degradation resulting from UV exposure and, consequently, to a darkening of color on the wood [21], [22]. The high negative values of ΔL^* indicate the sensitivity of that wood type against UV radiation and the surface quality [23].

In general, it is realized that color changes occurs quickly in 50 h periods; nevertheless, a less changes occurred in following periods. The first part of the color change process is because of the formation of chromophoric groups as carbonyl and carboxyl groups resulting mainly from degradation of α-carbonyl, biphenyl and ring-conjugated double bond structures in lignin and moving the extractives towards to wood surface from inside of wood [24], [25]. Relatively more quick change is reported even if the wood material is exposed to UV light in external environment for short period or under accelerated weathering [25], [23].

Table 1. Color Change values UV application for 150 h for dyed test sample of Scots pine (Pinus sylvestris L.)

Wood type	Dye extract		After dyeing (before UV)				After 50 h UV				After 100 h UV				After 150 h UV			
			ΔL^*	Δa^*	Δb^*	ΔE^*	ΔL^*	Δa^*	Δb^*	ΔE^*	ΔL^*	Δa^*	Δb^*	ΔE^*	ΔL^*	Δa^*	Δb^*	ΔE^*
Scots pine (*Pinus sylvestris L.*)	Liquid glass	Control	-8,93	-3,99	-3,62	10,43	-19,95	5,51	10,62	23,26	-24,98	7,79	9,96	28,00	-27,42	9,37	9,13	30,38
		Indigo + Ferrous	31,40	-1,86	-61,76	69,31	16,81	2,13	-56,88	59,35	13,79	2,47	-57,96	59,63	10,09	2,62	-60,14	61,04
		Indigo +Alum	26,09	-11,49	-87,53	92,06	14,10	-3,54	-75,30	76,69	12,88	-2,73	-74,81	75,96	11,38	-1,11	-73,93	74,81
		Indigo +Vinegar	-22,18	-8,22	-18,79	30,21	-32,47	-3,03	-2,81	32,73	-36,27	-0,63	-2,78	36,38	-37,38	1,01	-2,61	37,48
	Without liquid glass	Control	20,02	-8,80	-84,50	87,28	13,75	-7,66	-72,43	74,12	10,67	-4,66	-70,81	71,76	8,64	-3,10	-71,64	72,23
		Indigo + Ferrous	-32,76	-11,89	24,35	42,51	-42,15	-7,42	-16,29	45,79	-46,48	-6,75	-18,22	50,38	-48,62	-6,18	-19,31	52,68
		Indigo +Alum	57,18	-7,12	-36,22	68,06	44,14	4,07	-19,63	48,48	40,76	5,57	-20,53	45,98	39,05	6,86	-20,80	44,77
		Indigo +Vinegar	50,00	-12,96	-6,61	52,07	43,23	-8,61	10,64	45,35	40,72	-5,46	12,76	43,02	39,07	-3,44	13,02	41,33
	Synthetic		51,97	26,05	35,85	68,30	49,39	26,75	35,71	66,56	47,81	26,34	35,24	64,44	48,25	26,74	34,41	65,02

The best color stability (ΔE^* 30,38) of scots pine wood attained with indigo + liquid glass for control (without mordant) after 150 h of exposure. The biggest color change was seen on scots pine species dyed with indigo + liquid glass and alum mordant mixes.

Table 2. Color Change values UV application for 150 h for dyed test sample of Chestnut (Castanea sativa Mill)

Wood type	Dye extract		After dyeing (before UV)				After 50 h UV				After 100 h UV				After 150 h UV			
			ΔL*	Δa*	Δb*	ΔE*	ΔL*	Δa*	Δb*	ΔE*	ΔL*	Δa*	Δb*	ΔE*	ΔL*	Δa*	Δb*	ΔE*
Chestnut (*Castanea sativa* Mill)	Liquid glass	Control	16,99	-5,39	-73,25	75,39	13,91	-2,65	-65,33	66,84	10,63	-2,80	-66,70	67,60	9,32	-1,76	-67,48	68,14
		Indigo + Ferrous	-41,86	-9,21	-28,25	51,33	-41,70	-10,00	-18,67	46,77	41,44	-9,77	-17,10	45,88	42,05	-9,35	-17,15	46,37
		Indigo +Alum	63,08	-5,78	-21,66	66,95	91,09	2,27	-7,23	91,40	48,12	4,32	-7,78	48,94	47,58	4,86	-7,59	48,43
		Indigo +Vinegar	39,32	-7,75	-5,90	40,51	30,11	-4,80	5,11	30,91	33,05	-4,60	6,45	33,99	32,81	-3,65	7,02	33,75
	Without liquid glass	Control	-6,89	-5,00	-4,78	9,76	-16,52	1,09	10,57	19,64	-20,34	2,16	8,70	22,23	-20,76	3,02	8,99	22,82
		Indigo + Ferrous	9,00	0,30	-76,57	77,10	12,38	-1,66	-65,69	66,87	13,12	-1,26	-63,33	64,69	12,71	-1,02	-63,16	64,43
		Indigo +Alum	33,06	-6,59	-71,01	78,61	22,60	-0,23	-55,34	59,78	21,62	1,38	-53,80	58,00	20,49	2,50	-53,80	57,62
		Indigo +Vinegar	-21,34	-10,03	-18,00	29,66	25,55	-7,09	-2,62	26,64	27,04	-5,18	-1,08	27,55	28,33	-4,53	-1,46	28,73
	Synthetic		51,76	19,45	32,04	63,91	49,30	21,55	31,98	62,59	47,66	21,44	30,59	60,55	48,12	22,14	31,37	61,56

When we look at the color changes on chestnut wood species the lowest change value (ΔE^* 22, 82) observed with control group (indigo-without mordant, without mordant) group, and the biggest change value (ΔE^* 68,14) acquired from the application of indigo+liquid glass (without mordant) mixes.

Table 3. Color Change values UV application for 150 h for dyed test sample of mahogany (Khaya Ivorensis)

Wood type	Dye extract		After dyeing (before UV)				After 50 h UV				After 100 h UV				After 150 h UV			
			ΔL*	Δa*	Δb*	ΔE*	ΔL*	Δa*	Δb*	ΔE*	ΔL*	Δa*	Δb*	ΔE*	ΔL*	Δa*	Δb*	ΔE*
Mahogany (*Khaya Ivorensis*)	Liquid glass	Control	-3,74	-2,76	-2,23	5,16	-14,38	0,77	-2,27	14,58	-15,29	-1,21	-4,27	15,92	-15,03	-2,28	-5,00	16,00
		Indigo + Ferrous	12,64	-0,81	-44,51	46,28	7,99	1,45	-43,05	43,81	7,14	1,17	-43,67	44,27	5,83	0,96	-44,34	44,73
		Indigo +Alum	16,27	1,37	-43,40	46,37	7,52	6,32	-42,11	43,24	6,79	5,99	-43,06	44,00	5,97	6,38	-45,22	46,06
		Indigo +Vinegar	-9,69	-9,68	-9,50	16,67	-19,68	-5,04	-6,81	21,43	-21,24	-5,89	-8,57	23,65	-21,48	-5,48	-8,78	23,84
	Without liquid glass	Control	19,11	0,17	-45,14	49,02	14,20	3,50	-42,73	45,16	10,68	4,37	-43,97	45,46	9,65	3,83	-44,86	46,05
		Indigo + Ferrous	-18,28	-17,34	-18,72	31,39	21,17	15,96	16,56	31,26	23,46	15,91	17,45	33,29	-23,24	16,19	-18,28	33,71
		Indigo +Alum	40,88	6,69	-20,12	46,05	28,52	11,62	-21,52	37,57	29,14	10,64	-22,31	38,21	28,66	10,67	-22,36	37,88
		Indigo +Vinegar	35,89	2,76	8,38	36,96	28,96	8,27	9,69	31,64	29,16	7,47	8,62	31,31	29,65	6,72	8,00	31,44

Synthetic	39,59	18,51	21,33	48,63	36,26	19,33	19,02	45,28	35,73	17,95	17,71	43,73	35,98	18,24	17,97	44,16

The lowest color change value (ΔE^* 16,00) is obtained from the application of control (without mordant) on mahogany wood species, and the highest color change value (ΔE^* 46,06) from the application of indigo + liquid glass and aluminum sulphate mixes.

Generally all wood species have got darken color with indigo + liquid glass and mordant mixes. These changes may be explained with interaction of metal mordants ions and wood components. Metal mordant have been pointed out as the reason for color stability. Because metal ions, promotes free radical formation of wood components even when they are exposed to light [25], [23]. The stabilization of lignin by ferrous was reported to occur through the formation of complex [18].

The reason for the differences between wood types may be due to the differences of chemical composition of the wood types, and interaction of indigo and mordant mixes extract compounds with wood component, resulting in the different photo-degradation effects of UV irradiation. [25] reported that higher color changes were found in samples having higher lignin content. Lignin is the compound absorbing UV of 80 to 95% among the three main components of wood [21]. Besides, generally soft woods have 2-10% more lignin than hard woods [26].Lignin has aromatic, phenolic and carboxylic groups that absorb rays of different energy levels. Although cellulose is not sensitive to UV light of wavelengths longer than 340 nm [25].

Nevertheless, the roughness of color stabilized wood is complex phenomenon because anisotropic and heterogeneous material. Several factors, such as anatomical differences, growing characteristics, machining properties, pre-treatments (e.g. steaming, drying, etc.), can affect the color stability [26]. In addition, the treatments parameters as treatment time, percentage of dyer materials, application temperature and percentage of mordant may be effect the color stability.

4. CONCLUSIONS

This study is carried out in order to develop natural surface dyestuffs extracted from indigo as an alternative to synthetic based dyestuffs, and to determine the influence of liquid glass on color change performances of application of such dyes on wood types under conditions exposed to UV for 50, 100, and 150 h. Generally, natural dyes color changing values were better than the synthetic dyes. This result is satisfactory for using natural dyes as alternative colorants.

Liquid glass could not be entirely effective on color changing stability. This was an unexpected result. May be the reason was the application method of liquid glass as mixed form with other dyestuff to on wood samples. We guess that if liquid glass could have applied on wood samples after dyeing as coating layer, it would be more effective.

Between mordant types, vinegar mordant applications provided the best color changing with (ΔE^* 32,76), ferrous mordant was second with (ΔE^* 50,49), and alum was the third with (ΔE^* 51,59), based on average value on all types of wood. When we compared the types of mordant, the performance of vinegar was satisfactory. Even though, alum and ferrous sulphate are considered safest among metallic salt mordants [27], [28] considering environmental concerns, use of biomordants in place of metallic salt mordants is also advised [29]. Metal mordants observed with the highest color changing. Therefore, metal mordants should be avoided, especially for moist or wet environments, or it can be preferred in places of the color change may be omitted. Thus, a 100% natural dyestuff and mordant is possible for wood surfaces.

Natural dyes have been getting more important due to their advantages. Our further work will be focus on the use of various natural dyes and mordants in the production of wooden product, especially child furniture and wooden houses. Turkey has the potential of approximately 150 dye plants, and does not benefit there sufficiently [30]. Therefore, more economical and eco-friendly compared to synthetic dyes, wood paints may be developed.

REFERENCES

[1]. Kultur, https://www.kultur.gov.tr/EN,98769/wood-as-a-building-material-its-benefits-and-disadvantages, Date of access: 12 01.2017.

[2]. Salthammer, A. Schwarz, F. Fuhrmann, Emission of reactive compounds and secondary products from wood-based furniture coatings, Atmospheric Environment 33 (1998) 75-84.

[3]. WHO, World Health Organization: 1987. Air Quality Guidelines for Europe, European Series No: 23, WHO Regional Office for Europe, Copenhagen, pp. 91–104.

[4]. Ucgun, I., Ozdemir N., Metintas M., Metintas S., Erginel, S., Kolsuz, M. 1998. "Prevalence of occupational asthma among automobile and furniture painters in the center of Eskisehir (Turkey): the effects of atopy and smoking habits on occupational asthma". Allergy 53(11): 1096-100.

[5]. Greenguard, (http://greenguard.org/en/indoorAirQuality/iaq_chemicals.aspx). Date of access: 07, 06, 2016

[6]. Wolfe, L. "Is it safe to paint or be around paint fumes during pregnancy?" www.babycenter.com, Date of access: 18.06.2015.

[7]. Dalsan, www.dalsan.com.tr, Date of access:18.06.2015.

[8]. Grifoni, D., Bacci, L., Zipoli, G., Albanese, L., Sabatini, F., 2011. The role of natural dyes in the UV protection of fabrics made of vegetable fibres. Dyes Pigm. 91, 279-285.

[9]. Shahid, M., Islam, S., & Mohammad, F. (2013). Recent advancements in natural dye applications: a review. *Journal of Cleaner Production, 53*, 310–331.

[10]. M.H. Mirjalili, E. Moyano, M. Bonfill, R.M. Cusido, J. Palazon, Overexpression of the Arabidopsis thaliana squalene synthase gene in Withania coagulans hairy root cultures. Biologia plantarum. 55(2) (2011) 357-360.

[11]. O. Goktas, M.E. Duru, M. Yeniocak, E. Ozen, Determination of the color stability of an environmentally friendly wood stain derived from laurel (Laurus nobilis L.) leaf extracts under UV exposure, For. Prod. J. 58(1/2) (2008a) 77-80.

[12]. O. Goktas, E. Baysal, E. Ozen, R. Mammadov, M. E. Duru, Decay resistance and color stability of wood treated with Juglans regia extract, Wood Res. 53(3) (2008b) 27-36.

[13]. O. Goktas, E. Ozen, M.E. Duru, M. H. Alma, Determination of the color stability of an environmentally-friendly wood stain from saffron (Crocus sativus L.) extracts under UV exposure, Wood Res. 54(4) (2009c) 111-118.

[14]. O. Goktas, E. Ozen, E. Baysal, R. Mammadov, M.H. Alma, A. Sonmez, Color stability of wood treated with madder root (Rubia tinctorium L.) extract after lightfastness test, Wood Res. 54(1) (2009a) 37-44.

[15]. O. Goktas, E. Ozen, M. E. Duru, R. Mammadov, Determination of the color stability of an environmentally-friendly wood stain derived from oleander (*Nerium Oleander* L.) leaf extracts under UV exposure, Wood Res. 54(2) (2009b) 63-72.

[16]. Comlekcioglu, N. L. Efe, S. Karaman. Extraction of Indigo from Some Isatis species and Dyeing Standardization Using Low-technology Methods Braz. arch. biol. technol. vol.58 no.1 Curitiba Jan./Feb. 2015).

[17]. Wildcolours (http://www.wildcolours.co.uk/html/why_indigo.html, erisim tarihi:23.02.2017)

[18]. TS 2470, Wood-Sampling Methods and General Requirements for Physical and Mechanical Tests, TSE (2005) Ankara.

[19]. TS 2471 Wood, Determination of Moisture Content for Physical and Mechanical Tests, TSE (2005) Ankara.

[20]. D.P. Kamdem, S. Grelier, Surface roughness and color change of copper amine and UV absorber-treated red maple (Acer rubrum) exposed to artificial ultraviolet light, Holzforschung, 56(5) (2002) 473-478.

[21]. H. Peker, A. Atılgan, H. Ulusoy, O. Goktas, Usage opportunities of the natural dye extracted from acorn (Quercus ithaburensis Decaisne) in the furniture industry upper surface treatment, Int. J. Phys. Sci. 7(40) (2012) 5552-5558.

[22]. E. Ozen, M. Yeniocak, M. Colak, O. Goktas, I Koca, Colorability of wood material with Punica granatum and Morus nigra extracts, BioRes. 9(2) (2014) 2797-2807.

[23]. W.C. Feist, D.N.S. Hon, Chemistry of weathering and protection, Adv. Chem. Ser. 207 (1984) 401-451.

[24]. S.Y. Lin, K.P. Kringstad, Photosensitive groups in lignin and lignin model compounds Tappi. 53(1970) 658–663

[25]. D.N.S. Hon, W.C. Feist, Hydroperoxidation in photoirradiated wood surfaces Wood Fiber Sci. 24(1992) 448–455.

[26]. Tereza, C.M.P.; Santos, K.O.; Rubim, J.C. 2004. A spectrocolorimetric study on the effect of ultraviolet irradiation of four tropical hardwoods. Bioresource technology 93: 37-42.

[27]. Savvidis, G., Zarkogianni, M., Karanikas, E., Lazaridis, N., Nikolaidis, N., Tsatsaroni, E., 2013. Digital and conventional printing and dyeing with the natural dye annatto: optimisation and standardisation processes to meet future demands. Color. Technol. 129, 55e63.

[28]. Zarkogianni, M., Mikropoulou, E., Varella, E., Tsatsaroni, E., 2011. Colour and fastness of natural dyes: revival of traditional dyeing techniques. Color. Technol. 127, 18e27.

[29]. Prabhu, K.H., Teli, M.D., 2011. Eco-dyeing using Tamarindus indica L.seed coat tannin as a natural mordant for textiles with antibacterial activity. J. Saudi Chem. Soc.

[30]. H.H. Mert, Y. Dogan, S. Baslar, Some plants used in natural dyes obtained, Ecology, 4(5) (1992) 14-17.

INVESTIGATION EFFECT OF LIQUID GLASS ON LEACHING PERFORMANCE OF WOOD MATERIALS STAINED BY POMEGRANATE SKIN (*Punica granatum L.*) EXTRACTS

Osman GOKTAS[1], Sevil YENİOCAK[1], Mehmet YENİOCAK[1], Mehmet UGURLU[2], Mehmet COLAK1, Ertan OZEN[1]

Abstract

The aim of this study is to develop durable natural colorant and liquid glass for the surface of wooden products and determine their desorption performance by leaching method. For this purpose, natural colorant was extracted from pomegranate skin (Punica garnatum L.) by boiling method and mordant with ferrous sulfate ($Fe_2(SO_4)_3.7H_2O$), aluminum sulfate ($KAl_2(SO_4)_3.18H_2O$), and vinegar (CH_3COOH). Wooden blocks were prepared from chestnut (Castanea sativa Mill.), mahogany (Khaya Ivorensis) and Scots pine (Pinus sylvestris L.). Deeping method was utilized for application of the dyestuff on the wood blocks. Leaching test application conditions included temperature (22 °C), pH (3, 7, and 11) and agitating speed (120 rpm). The results showed that the leaching performance of some tested samples increased by % 57.06 due to liquid glass.

Keywords: *Natural dye, Pomegranate skin (Punica granatum L.), Liquid glass, Leaching*

1. INTRODUCTION

Beside a lot of advantages of wood, it has some disadvantages too. It changes shape, and it is suitable for discoloration, it can be decayed by biotic agents as fungi, bacteria and insects; and abiotic agents as sun, wind, water, certain chemicals and fire [1]. For the purpose of aesthetic and protection, many stain, coatings and paints are used. Generally, these synthetic materials contain "Volatile Organic Compounds" (VOCs) [2, 3 and 4] and preservatives. "Volatile" means that these chemicals evaporate or can easily get into the air at room temperature. "Organic" means these chemicals are carbon based. The term "chemical emissions" refers to VOCs as they evaporate into the air from products [5]. Unfortunately, these VOCs are hazardous for people and environment. For short-term exposure, they can appear as eye, nose, and throat irritation, headaches, nausea/vomiting, dizziness, worsening of asthma symptoms. Additionally, for chronic exposures, they can be cause of cancer, liver, kidney and central nervous system damage.

It has been determined that these solvents can cause miscarriages of pregnant womenbirth defects and children's learning disabilities [6]. It is stated that kids are more affected by VOC's since they have relatively higher respiratory rate, not established immune system, are closer to the ground, breathe more by mouth and not by nose. Therefore, children don't benefit from the advantage of nose filtering which is critical due to the fact that chemicals entering the body by high pulse rate diffuse to the tissues faster [7].

Recently international awareness of environment, ecology and pollution control created an upsurge on the interest of people to use more environmentally products. Natural dyes derived from flora and fauna are believed to be safe because of their non-toxic, non-carcinogenic and biodegradable nature [8]. For this reason, the importance of the protection wood material by natural sources is gaining importance day by day [2, 9].

---

[1] *Corresponding author: Mugla Sitki Kocman University, Faculty of Tecnology, Department of Woodworking Industrial Engineering. 48000 Mugla/Turkey. myeniocak@mu.edu.tr*

[2] *Mugla Sitki Kocman University, Faculty of Science, Department of Chemistry, 48000 Mugla / Turkey.*

Goktas *et al.* [10] investigated the development of environmentally friendly wood stains derived from laurel (*Laurus nobilis* L.), oleander (*Nerium Oleander* L.) [11], madder root (*Rubia tinctorium* L.) [12], walnut shell (*Juglans regia)* Goktas *et al.* [13] extract and determined the color stability of the stains when exposed to ultra-violet (UV) light irradiation. Their results showed that the extract provided some color stability after UV irradiation. Goktas *et al*. [14] used walnut husk on wood materials and investigated the leaching performance of natural dye. Result showed that, generally aluminum sulfate and ferrous sulfate performed well desorption were reduced desorption on all wood species surfaces.

Pomegranate skin is a source of natural dye. This dye is high in tannin (19 to 26%), therefore it works particularly well with cotton and other plant fibres. You will get yellow fawn when using pomegranate without a mordant and golden yellows with a mordant. With the addition of iron, you will get mossy greens, greys and blacks. You can over-dye it with indigo to make beautiful dark greens. Pomegranate rinds (skin) are popular for contact dyeing. Each pomegranate has a tough, leathery skin or rind, basically yellow, more or less overlaid with light or deep pink or rich red [15].

In this study, we have focused on the coloring wood material by pomegranate skin (*Punica garnatum* L.) extract+liquid glass and determined effect of liquid glass on leaching performance. Our theory was that, liquid glass could enhance the leaching performance of natural dye on wood materials. Because liquid glass is a strong hydrophobic material. Therefore, the research question of the study was "how effect the liquid glass on leaching performance against to leaching test".

2. MATERIAL AND METHOD

2.1. Material

In this study, wood was prepared from chestnut (*Castanea sativa* Mill.), mahogany (*Khaya Ivorensis*) and Scots pine (*Pinus sylvestris* L.). Plant dyestuff was extracted from pomegranate skin (*Punica garnatum* L.) by boiling method and mordant with ferrous sulfate ($Fe_2(SO_4)_3.7H_2O$), aluminum sulfate ($KAl_2(SO_4)_3.18H_2O$), and vinegar (CH_3COOH).

2.2. Method

2.2.1. Preparing wood blocks

Test samples prepared for leaching tests, accordig to TS 4176 [16]. Test sample has been prepared 19x19x19 mm measure and stored in climate cabinet at 20 ± 2 °C temperature and $65 \pm 5\%$ relative humidity.

2.2.2. Dye material

In this study, the plant was pomegranate skin (*Punica garnatum* L.) and dried in shade and ground. Plant particles mixed with distilled water having a 20/1 ratio and extracted in a bath (45 °C, 180 minutes, Elmasonic X-tra 150 H). Diminishing evaporation of water is brought to the initial level by the addition of water.

2.2.3. Dyeing of the wood

The extraction is filtered with filter paper for separated from solid particles. Table 1 showed that the proportions of mordant agents. Wood samples completely immersed in a bath during 60 min and 45 °C temperature. At the end of time wood samples surface cleaned with a cloth and allowed to dry at room temperature in an upright position.

Table 1. Dye solution + mordant mixture ratios

Extracts	Mordant	Mixture (%)
Pomegranate skin extract	Control	0
	Ferrous sulfate	3
	Alum	5
	vinegar	10

2.2.4. Leaching test

Firstly maximum wave length determined of each solution in UV spectrophotometer for to use as reference point for absorbance. Two samples from each group were placed into Erlenmeyer flask in 250 ml distilled water. Erlenmeyer flasks placed into rinsing bath shaken during 120 minutes. In 5, 15, 30, 45, 60, 75, 90, 120 minutes some water was taken to get absorbance inside, in reference of maximum wave length of each colorant. Leaching test application conditions included temperature (22 °C), pH (3, 7, and 11) and agitating speed (120 rpm).

3. RESULTS

UV spectrophotometer used in the leaching tests. Maximum wavelength and color intensity between wavelengths was determined for walnut husk and mordanting concentrations (Table 3).

Table 3. Wavelength of dye

Type of Dye	Max. wavelength (nm)
Control (%100 *pomegranate*)	299
Pomegranate+liquid glass	306
Pomegranate+ Ferrous sulfate	255
Pomegranate+ Ferrous sulfate+ liquid glass	273
Pomegranate+ Alum	360
Pomegranate+ Alum + liquid glass	275
Pomegranate+ vinegar	204
Pomegranate+ vinegar+ liquid glass	289

3.1. Leaching data of chestnut

When examined Table 4, leaching data of chestnut at pH: 3, the pomegranate + liquid glass mixture leaching data is minimum (0,531 abs), and maximum leaching (3,467 abs) observed for vinegar without liquid glass. At pH: 7, again the pomegranate + liquid glass mixture leaching data is minimum (0,536 abs), and maximum leaching (3,826 abs) observed for vinegar without liquid glass. For pH: 11, the pomegranate + liquid glass and ferrous mixture leaching data is minimum (0,675 abs), and maximum leaching (4,00 abs) observed for vinegar + without liquid glass.

Table 4. Leaching data (abs) of chestnut at 22 ºC and 120 rpm

		Dye extract	Mordant	5	15	30	60	75	90	120
Chestnut	pH 3	Without liquid glass	Control	0.196	0.445	0.556	0.686	0.749	0.785	0.884
			Ferrous	0.209	0.264	0.344	0.462	0.513	0.563	0.649
			Alum	0.122	0.155	0.177	0.213	0.226	0.228	0.244
			Vinegar	1.483	2.162	2.616	3.058	3.249	3.448	3.467
		Liquid glass	Control	0.292	0.304	0.365	0.428	0.474	0.479	0.531
			Ferrous	0.382	0.428	0.488	0.586	0.629	0.673	0.739
			Alum	0.336	0.498	0.654	0.851	0.917	0.966	1.102
			Vinegar	0.554	0.723	0.903	1.089	1.185	1.250	1.394
	pH 7	Without liquid glass	Control	0.282	0.454	0.562	0.772	0.812	0.908	0.988
			Ferrous	0.054	0.123	0.187	0.289	0.343	0.380	0.456
			Alum	0.114	0.166	0.171	0.197	0.198	0.204	0.206
			Vinegar	1.838	2.391	2.809	3.091	3.455	3.579	3.826
		Liquid glass	Control	0.084	0.256	0.334	0.424	0.484	0.508	0.571
			Ferrous	0.138	0.193	0.274	0.366	0.414	0.449	0.536
			Alum	0.319	0.445	0.561	0.703	0.769	0.819	0.904
			Vinegar	0.328	0.496	0.664	0.894	0.982	1.043	1.188
	pH 11	Without liquid glass	Control	1.210	1.470	1.691	2.084	2.177	2.211	2.438

				Ferrous	0,308	0,376	0,469	0,547	0,605	0,612	0,675
				Alum	0,197	0,253	0,337	0,485	0,526	0,588	0,684
				Vinegar	1,274	1,992	2,603	3,072	3,334	3,551	4,000
		Liquid glass		Control	1,025	1,136	1,148	1,693	1,942	2,065	2,258
				Ferrous	0,601	0,721	0,853	0,957	1,030	1,047	1,136
				Alum	0,571	0,631	0,692	0,753	0,784	0,803	0,855
				Vinegar	1,070	1,583	1,979	2,359	2,616	2,621	2,891

3.2. Leaching data of mahogany

Leaching data of mahogany are given in the Table 5. According to results, leaching data of mahogany at pH: 3, the pomegranate + liquid glass mixture leaching data is minimum (0,253 abs), and maximum leaching (1,700abs) observed for vinegar without liquid glass. At pH: 7, again the pomegranate + liquid glass mixture leaching data is minimum (0,222 abs), and maximum leaching (1,853 abs) observed for vinegar without liquid glass. For pH: 11, the pomegranate + liquid glass and ferrous mixture leaching data is minimum (0,447 abs), and maximum leaching (1,914 abs) observed for vinegar + without liquid glass.

Table 5. Leaching data (abs) of mahogany at 22 ºC and 120 rpm

		Dye extract	Mordant	Leaching time (min)						
				5	15	30	60	75	90	120
mahogany	pH 3	Without liquid glass	Control	0,124	0,315	0,378	0,442	0,461	0,473	0,511
			Ferrous	0,200	0,238	0,267	0,328	0,339	0,359	0,391
			Alum	0,800	0,930	1,101	1,119	1,123	1,128	1,132
			Vinegar	0,834	1,052	1,239	1,451	1,535	1,610	1,700
		Liquid glass	Control	0,226	0,230	0,234	0,242	0,246	0,250	0,253
			Ferrous	0,323	0,326	0,326	0,334	0,340	0,347	0,347
			Alum	0,197	0,240	0,281	0,328	0,334	0,346	0,368
			Vinegar	0,409	0,465	0,491	0,519	0,539	0,547	0,560
	pH 7	Without liquid glass	Control	0,230	0,273	0,323	0,384	0,405	0,426	0,452
			Ferrous	0,012	0,034	0,053	0,081	0,094	0,104	0,123
			Alum	0,036	0,081	0,082	0,090	0,088	0,089	0,093
			Vinegar	1,029	1,264	1,401	1,621	1,713	1,717	1,853
		Liquid glass	Control	0,034	0,149	0,174	0,187	0,198	0,208	0,222
			Ferrous	0,124	0,147	0,170	0,199	0,207	0,222	0,237
			Alum	0,154	0,179	0,202	0,227	0,232	0,246	0,262
			Vinegar	0,199	0,242	0,283	0,331	0,345	0,359	0,381
	pH 11	Without liquid glass	Control	0,683	0,836	0,758	1,061	1,073	1,089	1,123
			Ferrous	0,179	0,196	0,222	0,253	0,270	0,270	0,295
			Alum	0,127	0,175	0,242	0,327	0,339	0,357	0,397
			Vinegar	0,875	1,157	1,393	1,619	1,735	1,798	1,914
		Liquid glass	Control	0,591	0,673	0,726	0,761	0,778	0,798	0,810
			Ferrous	0,417	0,430	0,444	0,458	0,464	0,465	0,477
			Alum	0,417	0,428	0,444	0,455	0,467	0,468	0,478
			Vinegar	0,567	0,694	0,792	0,877	0,908	0,915	0,961

3.3. Leaching data of Scots pine

Leaching data of Scots pine is given in the Table 6. According to results, leaching data of mahogany at pH: 3, the pomegranate + alum + without liquid glass mixture leaching data is minimum (0,181 abs), and maximum leaching (0,988 abs) observed for vinegar without liquid glass. At pH: 7, again the pomegranate + without liquid glass + ferrous mixture leaching data is minimum (0,300 abs), and maximum leaching (2,745 abs)

observed for vinegar without liquid glass. For pH: 11, the pomegranate + without liquid glass and alum mixture leaching data is minimum (0,157 abs), and maximum leaching (3,015 abs) observed for vinegar + without liquid glass.

Table 6. Leaching data (abs) of Scots pine at 22 °C and 120 rpm

| | | Dye extract | Mordant | Leaching time (min) | | | | | | |
				5	15	30	60	75	90	120
Scots pine	pH 3	Without liquid glass	Control	0,164	0,416	0,525	0,655	0,706	0,750	0,826
			Ferrous	0,207	0,253	0,290	0,375	0,395	0,423	0,471
			Alum	0,086	0,102	0,119	0,146	0,153	0,159	0,181
			Vinegar	0,988	1,343	1,461	2,055	2,141	2,264	0,988
		Liquid glass	Control	0,262	0,293	0,346	0,414	0,446	0,465	0,498
			Ferrous	0,329	0,370	0,404	0,472	0,487	0,512	0,534
			Alum	0,263	0,389	0,515	0,685	0,734	0,786	0,263
			Vinegar	0,33	0,437	0,561	0,668	0,740	0,762	0,825
	pH 7	Without liquid glass	Control	0,269	0,374	0,511	0,662	0,720	0,757	0,839
			Ferrous	0,060	0,098	0,173	0,258	0,234	0,270	0,300
			Alum	0,030	0,049	0,058	0,077	0,085	0,088	0,096
			Vinegar	1,403	1,820	1,994	2,347	2,491	2,521	2,745
		Liquid glass	Control	0,050	0,173	0,214	0,253	0,267	0,288	0,306
			Ferrous	0,131	0,166	0,212	0,274	0,310	0,332	0,379
			Alum	0,182	0,238	0,29	0,376	0,400	0,429	0,463
			Vinegar	0,213	0,317	0,418	0,543	0,589	0,635	0,710
	pH 11	Without liquid glass	Control	1,498	1,911	2,169	2,613	2,650	2,394	2,801
			Ferrous	0,401	0,472	0,574	0,719	0,766	0,821	0,892
			Alum	0,091	0,107	0,123	0,140	0,144	0,157	0,157
			Vinegar	1,089	1,618	1,983	2,523	2,694	2,694	3,015
		Liquid glass	Control	0,911	1,244	1,443	1,656	1,717	1,772	1,872
			Ferrous	0,462	0,539	0,602	0,666	0,696	0,729	0,766
			Alum	0,442	0,471	0,500	0,544	0,548	0,574	0,593
			Vinegar	0,629	0,939	1,187	1,468	1,581	1,639	1,752

4. CONCLUSIONS

Leaching test application conditions included temperature (22 °C), pH (3, 7, and 11) and agitating speed (120 rpm). For general evaluation, liquid glass, increased the leaching performance by 35.72% based on samples without liquid glass. The best performance gained on Scots pine at pH: 7 by 57,06 % and the least level was observed on chestnut at pH:11 by 4,90.

The leaching performance of liquid glass by 35,72 %, cannot meet our whole expectations. It is well known that dying processes depend highly on pH because of the high sensitivity of functional groups on wood surfaces to hydrogen and hydroxyl ions. The observed higher dying performance at the low pHs can be attributed to be active sites over surface on Scots pine. Silicon oxides in liquid glass can ionize as follows in acidic and alkaline conditions [17]:

$$-SiOH_2^+ \xrightarrow{\ H^+\ } -SiO_2 \xrightarrow{\ OH^-\ } Si(OH)_{-2} \xrightarrow{\quad} -SiO^- + H_2O$$

Pozitive changed surface in acidic medium   Negative changed surface in alkaline medium
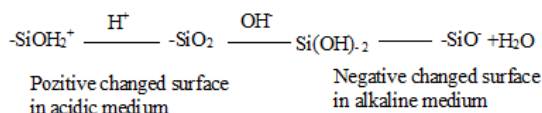
According to results of leaching, generally seen that is a partial decrease in wash values at low pH, whereas the values pretty higher at high pH. The best leaching values seen at pH:7. The low efficiency in the low pH range can be explained by the fact that the surface is covered with the maximum amount of protons and that the positive ion metal salts used as the mordant are not sufficiently bonded to the surface. It is generally seen that there is a partial decrease in wash values at low pH, whereas these values are much higher at high pH.

It is thought to result of the inability to obtain sufficient efficiency in the high pH range due to poor interaction with the dye molecules because of the electro negativity of the liquid glass adhered to the surface. The best leaching performance at pH 7.0 can be attributed by the binding of mordants to the functional groups in the wood material, followed by a negative charge of the liquid glass on this surface, behind by better binding of the dye to these functional groups.

For mordant type, there are not clear evidences about mordants contribution to leaching performance. Especially performance of vinegar that treated without liquid glass is the lowest. However, the samples mordant by vinegar and liquid glass increased leaching performance by 58,75 % when compared to vinegar mordant and without liquid glass. In addition to the low pH value, the weak acid vinegar (acetic acid) solution can be associated with the affinity of the functionalized groups to adhere to the wood surface, resulting in adhesion of the hydrogen ion releasing prototypes to the wood surface and as a result adversely affecting adhesion. Because of this, in wet environments, without additional protection measures, vinegar is not very effective mordant against to leaching for pomegranate dyes on wood materials.

Average of leaching performances of wood types are respectively; mahogany (0,532 abs), scots pine (0,762 abs) and chestnut (1,00) abs. The leachability depends on chemical properties and the extractives which includes of wood species. Chemical composition and extractives are affected how chemical bonding is strong between wood material and plant extraction. According to results chemical bonding is stronger between mahogany and pomegranate skin than other wood species. As a results, When we evaluate the general effect of pH degree on leaching performance, It was observed that pH 7 (0,544 abs) and pH 3(0,579 abs) nearly the same for leaching process, but pH 11 (1,163 abs) is least effective.

ACKNOWLEDGMENT

REFERENCES

[1]. Kultur, www.kultur.gov.tr, 2017 Date of access: 12 01.2017
[2]. Salthammer T., Bednarek, M., Fuhrmann, F., Funaki, R., Tanabe, S.I., Formation of organic indoor air pollutants by UV-curing chemistry. Journal of Photochemistry and Photobiology A: Chemistry. 152: 1-9, (2002).
[3]. WHO, World Health Organization: 1987. Air Quality Guidelines for Europe, European Series No: 23, WHO Regional Office for Europe, Copenhagen, pp. 91–104.
[4]. Ucgun, I., Ozdemir N., Metintas M., Metintas S., Erginel, S., Kolsuz, M. 1998. "Prevalence of occupational asthma among automobile and furniture painters in the center of Eskisehir (Turkey): the effects of atopy and smoking habits on occupational asthma". Allergy 53(11): 1096-100.
[5]. Greenguard, (http://greenguard.org/en/indoorAirQuality/iaq_chemicals.aspx). Date of access: 07, 06, 2016
[6]. Wolfe, L. "Is it safe to paint or be around paint fumes during pregnancy?" www.babycenter.com, Date of access: 18.06.2015.
[7]. Dalsan, www.dalsan.com.tr, Date of access:18.06.2015.
[8]. R Bhuyan and C N Saikia. Extraction and identification of colour components from the barks ofMimusops elengi and Terminalia arjuna and evaluation of their dyeing characteristics on wool. Indian Journal of Fibre & Textile Research Vol 29-December 2004-pp 470-476
[9]. Bechtold T., Ali, A.M.A., Mussak, R., Natural dyes for textile dyeing: A comparison of methods to assess the quality of Canadian golden rod plant material. Dyes and Pigments. 75, 287-29, (2007).
[10]. Goktas, O., E. M. Duru, M. Yeniocak, E. Ozen. Determination of the color stability of an environmentally friendly wood stain derived from laurel (*Laurus nobilis* L.) leaf extracts under UV exposure. *Forest Products Journal 58 (1/2):77-80,(2008).*
[11]. Goktas, O., E. Ozen, M. E. Duru, R. Mammadov,. Determination of the Color Stability of An Envıironmentally-Friendly Wood Stain Derived From Oleander (*Nerium oleander* L.) Leave Extracts Under Uv Exposure. Wood Research, 54(2): 63-72 (2009).
[12]. Goktas, O., E. Ozen, E. Baysal, R. Mammadov, H. Alma, A. Sonmez. Color Stability of Wood Treated with Madder Root (*Rubia tinctorium* L.) Extract After Lightfastness Test. Wood Research, 54(1): 37-44 (2009)
[13]. O. Goktas, E. Baysal, E. Ozen, R. Mammadov, M. E. Duru, Decay resistance and color stability of wood treated with *Juglans regia* extract, Wood Res. 53(3) (2008) 27-36.
[14]. Goktas, O., M. Yeniocak, M. Ugurlu, E. Ozen, M. Colak, S. Yeniocak, Investigation of Leaching Performance of Wood Materials Colored with Walnut Husk" CBU Journal of Science, Vol 11, No 3, 391-400. (2015)
[15]. Folkfibers 2017, http://www.folkfibers.com. pomegranates, reach time:14.03.2017.
[16]. TS 4176, 1984. Wood - Sampling Sample Trees and Long for Determination Of Physical and Mechanical Properties of Wood in Homogeneous Stands.TSE, Ankara.
[17]. Ugurlu M., Gurses A., Yalcın M. and Dogar C., Removal of Phenolic and Lignin Compounds from Bleached Kraft Mill Effluent by Fly Ash and Sepiolite, Adsorption 11: 87–97, 2005.

A Feedback Loop Model of Interaction Between Soil Characteristics and Vegetation in Afforestation Simulator ForestMAS

Damjan Strnad[1], Štefan Kohek1, Simon Kolmanič1, Borut Žalik1

Abstract

The application ForestMAS is a combined simulation/visualization tool that allows the users to foresee landscape changes due to spontaneous afforestation following the abandonment of land cultivation, natural disasters, or clear-cuts. The core mechanism of forest development simulation is the algorithm for interaction among trees competing for resources such as light, water, and nutrients. In this paper we present the extension of existing reference growth model with the sub model of interaction between the plant and the growing site, which reflects the natural process of species communities to adapt to imperfect growth conditions and adjust them by affecting certain properties of the soil such as acidity and nitrogen content. The importance of such feedback loop between a plant and its surroundings is to improve the plant's own chances as well as to suppress those of the competition. In the paper we describe the effects of this mechanism on simulation results with respect to the obtained forest composition. We evaluate the suitability of the extended model by comparing the simulation results to those of the reference model and validating them against long-term historical record data from a forest fire site in northern Slovenia.

Keywords: *feedback loop, forest growth simulation, ForestMAS, secondary succession*

1. INTRODUCTION

Spontaneous afforestation is a natural process that occurs in areas affected by forest fire, clear-cuts, and abandoned farmland. Forest restoration in such regions happens by ways of secondary succession. The recolonization of damaged areas is normally started by pioneering tree species and bushes, which are gradually supplanted by shade tolerant species originally present in the area. Because this is a slow process that takes many decades before settling to an equilibrium, several simulators of forest growth have been developed in the past [1]-[5]. The original aim of such tools was to evaluate the growth of economically important species, but has later moved to other environmental and ecological goals. ForestMAS is our recently developed secondary succession simulator with integrated high quality forest visualization (Figure 1), which aims to support a variety of forest management functions [6]. One of main ForestMAS objectives is to evaluate forest composition and biodiversity dynamics at different stages of its re-establishment.

The core mechanism of forest development simulation is the algorithm for interaction among trees competing for resources such as light, water, and nutrients. The competitive advantage of individual plant depends on congruence between its resource requirements and corresponding conditions at the growth site. In this paper we describe an extension of ForestMAS, by which we introduce a simple feedback loop model that changes soil properties within ecological neighborhoods of plants. We compare the results obtained from original and extended model with respect to forest composition and biodiversity index values. We validate them against long-term historical record data from a forest fire site in northern Slovenia.

Figure 24. Visualization of simulation results in ForestMAS.

2. MATERIALS AND METHODS

In this section we first describe in necessary detail the part of ForestMAS simulation model that is affected by the proposed extension, followed by the explanation of the feedback loop model itself.

2.1. ForestMAS tree competition model

In ForestMAS, plant requirements are defined using Ellenberg indicator values (EIV) for the following five growth resources: temperature (E_T), light (E_L), moisture (E_F), soil pH (E_R), and soil nitrogen content (E_N). Each indicator value denotes ideally amount of resource, which is expressed linguistically on a scale with 10 levels [7]. The last level on every scale denotes plant's complete tolerance to the state of corresponding resource. In order to be used in calculation of congruence with terrain conditions, EIV values are normalized to interval [0,1]. We will denote the normalized values by $\hat{E}$.

The simulated terrain area is divided into rectangular patches with dimension 10-by-10 meters. For each patch the level of a resource is sampled from the available map (pH, nitrogen and elevation dependent temperature conditions) or approximated by offline computation (direct sun exposure for light and water run-off simulation for moisture). All resource availability values are also normalized to interval [0,1] with respect to possible extremes. The normalized resource values on the patch will be denoted by $\hat{T}$ in the rest of the paper.

To determine individuals directly competing for resources, ForestMAS uses plants' ecological radii of influence, which are species dependent and proportional to tree height. When ecological radii of two trees intersect, the weaker of them will become suppressed and eventually die with some probability. The strength of a plant is expressed by its vigor value, whose main component is growth potential that depends directly on congruence between plant requirements and growth conditions on its patch. The value of congruence P between the demands of species s and actual conditions on patch p with respect to resource E is calculated as:

$$P(E(s), p) = \begin{cases} 1 - \left| \hat{T}(p) - \hat{E}(s) \right|, & 0 \leq \hat{E}(s) < 1 \\ 1, & \hat{E}(s) = 1 \end{cases} \tag{1}$$

The actual growth potential of tree i with age a_i that belongs to species s and grows on patch p is then calculated as [6]:

$$w_i(a_i, p, s) = \frac{2 \prod_{x \in \{L,T,F,R,N\}} P(E_x(s),p) + P(a_i,s)}{3},$$

where $P(a_i, s)$ is age-dependent survival probability of the tree. $\qquad$ (2)

2.2. Feedback loop model

Existence of feedback loops between stand structures and growth conditions allows resilience to disturbances and returns to stable equilibria [8]. Such feedback loops encompass the effects of forest composition on soil

pH, nitrogen storage, and water availability related to varying nutrient deposition and uptake [9]. Some of these effects have been incorporated into forest simulation models such as LINKAGES [10].

In reality, the processes governed by plant-soil feedback loops are extremely complex. Modeling them veraciously would require large amounts of detailed data about plant-soil interactions, which is not available. In this paper, we describe a simplified feedback loop model integrated into the ForestMAS simulator, which works by changing terrain patch properties towards each species' ideal conditions in proportion to its localized presence and domination. The latter is determined as a proportion f of growth potential belonging to trees of species s with respect to total accumulated potential on patch p:

$$f(p,s) = \frac{\sum_{i \in (p,s)} w_i(a_i, p, s)}{\sum_{j \in p} w_j(a_j, p, s_j)} \tag{3}$$

Here, the sum in the numerator runs over all individuals on patch p that belong to species s, while in the denominator the sum components are filtered only with respect to the patch. The accumulated effect on soil value $\hat{T}$ of patch p is then obtained as:

$$\Delta \hat{T}(p) = \alpha \cdot \sum_s f(p,s)\big(\hat{E}(s) - \hat{T}(p)\big) \tag{4}$$

where α is a feedback loop strength parameter that can be adjusted together with other simulation parameters.

The proposed model does not separate positive (growth inducing) and negative (growth inhibiting) cycles of natural feedback loops, but rather approximates their fused effect through improved resilience of suppressed intolerant species and ecosystem saturation with respect to dominant and/or tolerant species.

3. RESULTS AND DISCUSSION

We have compared the forest composition obtained from the original and feedback simulation model against the historical reference data for a forest fire recovery site Mozirska Požganija located in northern Slovenia [11]. The recorded data are available for years 31, 38, and 56 of forest recuperation. The simulation involved 11 species with significant presence in the area. The rest of the details can be found in the paper about ForestMAS [6].

To calculate the error of simulated forest composition at some time point, we use the sum of absolute differences between predicted and actual species' shares:

$$Err = \sum_s |obs_s - sim_s|, \tag{5}$$

where obs_s and sim_s denote the fraction belonging to species s in the observed and simulated forest compositions, respectively. We further compare the values of Simpson biodiversity index, which is calculated as:

$$S = \sum_s sim_s{}^2 \tag{6}$$

and analogously for the observed proportions.

Figure 2 shows the mean sum of error for years 31, 38, and 56 obtained from 30 simulation runs for different values of α, where the baseline $\alpha=0$ is equivalent to using the original model. It can be observed that the best fit was achieved for values of α between 0.008 and 0.014, where the relative reduction of fit error with respect to the baseline is 15-20 %.
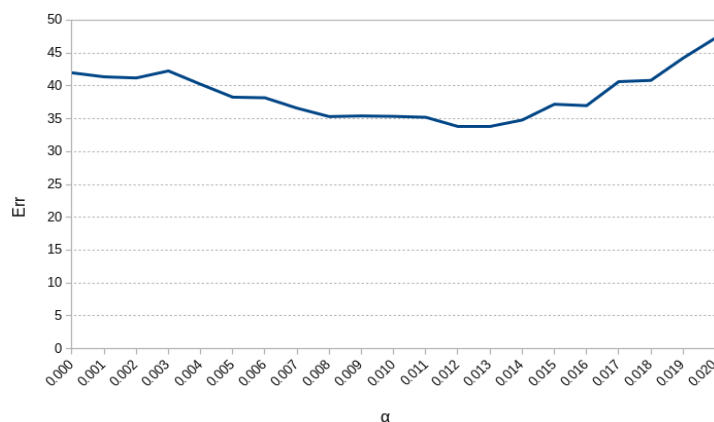
Figure 25. Sum of absolute differences between observed and simulated forest composition for years 31, 38, and 56 with respect to different values of feedback loop strength α; the case α=0 is baseline model without the feedback loop.

Figure 3 illustrates forest composition dynamics for the baseline and the best fitting feedback model.
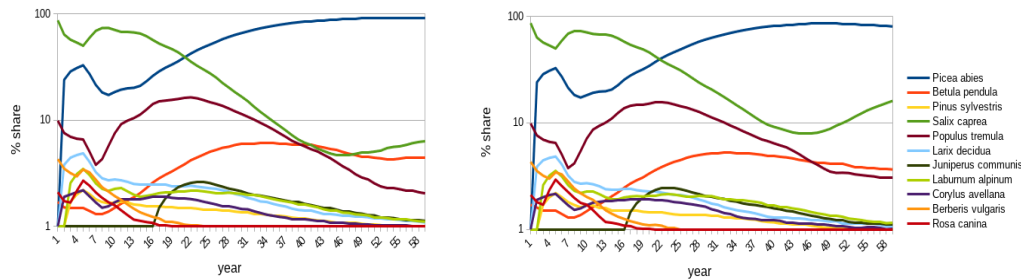
Figure 26. Forest composition dynamics through 60 years of simulation for the model without feedback loop (left) and the model with feedback loop and α=0.012 (right). The vertical axis uses logarithmic scale to emphasize changes in minor species.

The values of Simpson biodiversity index for relevant time points in the observation period are collected in Table 1. The preservation of higher proportions of minority species in the feedback model is reflected in biodiversity values that are closer to the observed ground truth for years 38 and 56.

Table 19. Values of Simpson biodiversity index for observed and simulated forest compositions at three time points

Year	Observed	Simulated with α=0	Simulated with α=0.012
31	0.476	0.487	0.461
38	0.582	0.668	0.630
56	0.652	0.815	0.686

4. CONCLUSIONS

In the paper, we have described a simple model of plant-soil feedback loop effects added to the ForestMAS secondary succession simulator. We have shown that by using the feedback model we can improve the fit to observed historical data with respect to forest composition and biodiversity indices. Although the proposed approach is based on simplifying assumptions that do not directly model highly complex processes in true forest ecosystems, the results encourage further research in this direction.

ACKNOWLEDGMENT

REFERENCES

[1]. R. Leemans and I. C. Prentice, *FORSKA – a general forest succession model*, Meddelanden Från Växtbiologiska Institutionen, 1989.
[2]. D. L. Urban, *A versatile model to simulate forest pattern: a user's guide to ZELIG version 1.0*, University of Virginia, Charlottesville, Virginia, 1990.
[3]. S. W. Pacala, C. D. Canham, and J. A. Silander Jr., *Forest models defined by field measurements: I. the design of a northeastern forest simulator*, Canadian Journal of Forest Research, 23(10):1980–1988, 1993.
[4]. H. K. M. Bugmann, *A simplified forest model to study species composition along climate gradients*, Ecology, 77(7):2055–2074, 1996.
[5]. H. Pretzsch, P. Biber, and J. Ďurský, *The single tree-based stand simulator SILVA: construction, application and evaluation*, Forest ecology and management, 162(1):3–21, 2002.
[6]. S. Kolmanič, N. Guid, and J. Diaci, *ForestMAS – a single tree based secondary succession model employing Ellenberg indicator values*, Ecological Modelling, 279:100–113, 2014.
[7]. H. Ellenberg, H. E. Weber, R. Düll, V. Wirth, W. Werner, and D. Paulißen, *Zeigerwerte von Pflanzen in Mitteleuropa*, Scripta Geobotanica 18, 1992.
[8]. H. Pretzsch, *Forest Dynamics, Growth and Yield: From Measurement to Model*, Berlin, Germany: Springer-Verlag, 2009.
[9]. J. G. Ehrenfeld, B. Ravit, and K. Elgersma, *Feedback in the plant-soil system,* Annual Review of Environment and Resources 30, 75-115, 2005.
[10]. W. M. Post and J. Pastor, *Linkages – an individual-based forest ecosystem model*, Climatic change 34(2):253–261, 1996.
[11]. M. Lekše, *The development of pioneer forest in the reserve Mozirska Požganija*, graduation thesis, University of Ljubljana, Biotechnical faculty, in Slovene, 2007.

Gap Regeneration Simulation Employing Ellenberg Ecological Values and Realistic Real-time Forest Visualization

Simon Kolmanič[1,2], Štefan Kohek[1]

Abstract

Gap dynamics is important part of forests regeneration process. The gaps are generated in the forest canopy when one or more canopy trees die or are removed by the forest managers to induce natural regeneration. The gaps are then slowly closed by younger trees. Gaps involved in forest regeneration are small and their effect on the surrounding is limited. That changes when gaps are created by natural disturbances or the human intervention by clear-cut logging. These gaps are much larger and can considerably influence their surroundings. Therefore it is important to predict the course of gap regeneration or be even in control of it by employing different forest tending actions. Currently forest managers still use decade old or even older forest management systems with limited forest visualisation capabilities. In order to visualize forests and thus efficiently present simulation results to all interested parties stand-alone visualization systems are used together with all their limitations. In this article we present a good alternative to these systems, a simulator ForestMASa, based on Ellenberg ecological values with integrated realistic forest visualization. Ellenberg ecological values give the system the necessary flexibility to include any plant species important for the gap regeneration and thus gap regeneration results true to reality. Beside usual statistical outputs the simulation results in ForestMASa are presented as realistic areal and close-up images, which present the simulation results on simple and understandable way.

Keywords: *Ellenberg ecological values, forests regeneration, forest visualization, gap dynamics, simulation.*

1. INTRODUCTION

In the forest canopy the gap is generated when one or more canopy trees die, whether by natural causes (e.g. old age, storms, tornados, etc.) or human intervention (e.g. clear-cutting and selective logging). Gaps are gradually filled with younger trees. Gaps therefore play an important role in forest regeneration. The process of gap generation and closing is termed gap dynamics and is closely related with practical forest applications like forest conservation practice and natural regeneration [1], [2]. Gaps, however, represent the disturbance in the normal socio-economic function of the forest. The larger is the gap area, the greater is the disturbance of the forest function. Despite many methods for gap areas measuring, all researcher agree that gaps involved in forest regeneration are usually not larger than 0.5 ha and have therefore little influence on forest stand dynamics. If gaps are generated by natural disturbances like wildfires, ice storms or bark beetle outbreaks, however, the areas they occupy are of much larger sizes. In order to restore forest functions as soon as possible appropriate forest management actions have to be performed. To better understand gap dynamics, in order to perform more efficient forest management, the forest growth models have been developed very early. The main concern of the researchers at that time were the forest products [3]. Consequently, all forest models were concentrated on this forest role, while the environmental dimensions of forests were neglected. The trees in these models were described with a lot of parameters that could be obtained only with the long-time observations. Therefore, only tree species important for the forestry were included. The main focus in the results was on forest composition, tree mortality and biomass production. The forest stands were displayed in schematic manner [4].

As the environmental functionality of the forests grew in importance, the forest management became more interdisciplinary. To make the simulation results available also to related ecosystem management specialists

---

---

such as hydrologists, botanists, and ecologists, more sophisticated forest and countryside visualization was needed. Stand-alone forest visualization systems were created to match this need. Many of the forest management systems of that time are still in use today [5] (e.g. Landscape Management System (LMS) with Stand Visualization System (SVS) and Environmental Visualization System (EnVision), Forest Vegetation Simulator (FVS) [6]). Besides the fact, that the used graphics does not meet today's standards, the main disadvantage of separated visualization from the simulation was user inability to interact with the model. In this article we will demonstrate, that computers are already capable enough to incorporate realistic forest visualization with secondary succession model. We developed and used such a simulator, named ForestMASa in order to predict course of gap regeneration. This problem become very important in Slovenia since 2014, when large parts of forests were devastated by severe ice storm, followed by bark beetles outbreaks. Since the ownership of these forests is very fragmented, the simulation results had also to be understandable to the number of non-experts, therefore a sophisticated forest visualization was required.

2. MATERIALS AND METHODS

In this article we are interested in gaps, caused by extraordinary events or by human intervention e.g. clear-cut logging, with strong influence on the surrounding ecosystem. The course of gap regeneration determine the remaining trees, capable of seed generation in the gap area or in immediate vicinity of it. Therefore the positions of the seed trees have to be part of the gap regeneration model along with gap geometry and the positions of the stumps of removed trees in order to simulate the stump sprouting process. We extended existing secondary succession model ForestMAS [7], rather than develop a new one from scratch in order to omit the errors, associated with the new model development. The resulting gap regeneration simulator ForestMASa was at the end equipped additionally with powerful real time forest visualization. In the following, the needed extension are described.

2.1. Secondary succession model

As the basis of our gap regeneration simulator we used single tree based secondary succession model ForestMAS [7]. The main advantage of this model is the use of Ellenberg ecological values for defining the needs of the trees and other Central European plants. This gives the model needed flexibility to include various species needed in the early phases of the secondary succession. Ellenberg ecological values (EV) provide simple ordinal classes where plants are ranked according to their requirements for soil acidity (EV_A), nutrients (EV_N), soil humidity (EV_M), temperature (EV_T), light (EV_L), continentality, and soil salt content. The last two indicators are not important for the reliability of simulation results and were therefore omitted in the ForestMAS model. The indicators contain values on a 10-point scale, where the last point, tagged by the value x, indicates that the given indicator has no influence. Each plant in the Ellenberg classification is thus described by a set of five numbers, expressing the average plant requirements along seven fundamental gradients. Some of the indicators were used also in simulators SILVA [8] and ForClim [9]. The plant needs are compared with the conditions on growing site and on the basis of matching between these two, the actual plant vigour is determined.

Each of the trees occupy certain area, which grows with tree's height. Many authors call those area an ecological neighbourhood of the tree. Early individual based models used Voronoi diagrams to represent the ecological neighbourhoods, but were later replaced by a circles to improve the performance. When two ecological neighbourhoods intersect, the vigours of both trees are compared and one with smaller vigour becomes suppressed and dies eventually. The main data source for terrain data represent digital terrain model (DTM). With its help the light conditions, temperature, and soil moisture are calculated, while soil acidity and nutrition availability are estimated from digital soil database. All these parameters are easy to obtain, but they are not enough for reliable simulation. Certain species specific data have to be considered as well, e.g. maximum tree age and height, mast years, tree maturity age, etc., which are results of long-term observations of several researchers.

In order to ensure the necessary efficiency of the simulator, the above mentioned data were organized in special data structure, presented in Figure 1. Since the terrain data represent the bulk of input data, they play a central role in the data structure. The terrain is divided into a regular square net of dimension 10 x 10 metres. Each cell contains five terrain parameters, described above, and the list of vegetation located on it. Vegetation is sorted according to species it belongs to. Individual tree contains specific data e.g. its height and age, its position, actual vigour, and neighbouring radius, defining ecological neighbourhood. Other data concerning the whole species are stored separately to omit redundancy.

ECOSYSTEM DATA STRUCTURE
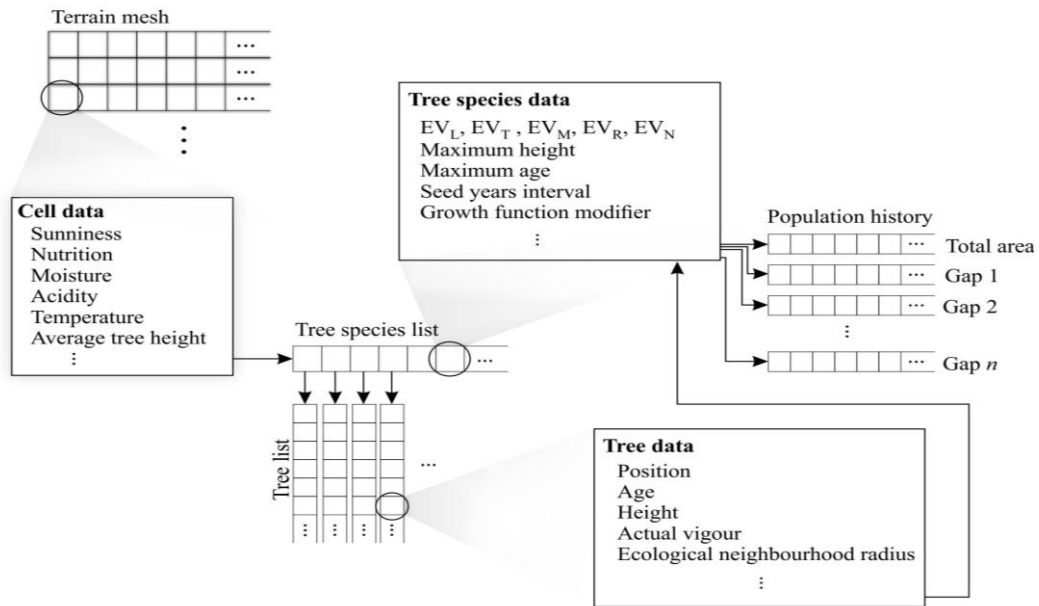
Figure 1. Data management in gap regeneration simulator, ensuring its efficiency.

The important part of simulation results represent statistical reports. In order to collect statistical data, forest history is recorded for the entire simulation area as well as for each of gaps, respectively. On account of this history, the reports of forest composition dynamics can be generated again, either for entire simulation area, or for each of the gaps. For each of the tree species in simulation the current height and age distributions are collected together with the population size history. Since the relations between forest dynamics and biodiversity is becoming increasingly important, the Simpson [10] and Shannon [11] biodiversity indexes are calculated and then displayed for the duration of entire simulation in a form of history graph.

2.1.1. Tree competition, mortality, and tree reproduction

The actual tree vigour depends on the matching between the tree needs, described by Ellenberg values, and condition on the growing site, which is calculated by:

$$P(E_x(s), \mathbf{p}_i) = \begin{cases} 1 - |T_x(\mathbf{p}_i) - E_x(s)|, & 0 \le \hat{E}_x(s) < 1 \\ 1, & \hat{E}_x(s) = 1 \end{cases} \tag{1}$$

where $T_x(\mathbf{p}_i)$ represents terrain's properties at the given tree location, $E_x(s)$. L - light, T - temperature, F - moisture, R - soil pH, and N - nutrients, are species specific tree requirements described by EVs, while $\hat{E}_x$ are normalized EVs ($\hat{E}_x = E_x / 10$).

The actual tree vigour $v(a_i, \mathbf{p}_i, s)$ is calculated at each simulation cycle, corresponding to one simulation year by the next formulae:

$$v(a_i, \mathbf{p}_i, s) = \gamma(s)\xi(a_i, \mathbf{p}_i, s)(2\prod_{x \in \{L,T,F,R,N\}} P(E_x(s), \mathbf{p}_i) + P(a_i, s))/3 \tag{2}$$

where $\mathbf{p}_i$ is the tree location, $\gamma(s)$ and $\xi(a_i, \mathbf{p}_i, s)$ are dumping factors according to the maximum age the tree can reach and the current tree height, respectively [7]. $P(a_i, s)$ is the survival probability, based on the tree age, which was modelled with the assumption that all trees are initially weak and vulnerable even if the site conditions are perfect. Over the time, the plants become stronger and more resilient. On account of these facts the survival probability changes accordingly throughout the tree lifespan. As we mentioned already, when the ecological neighbourhood circle of a tree is intersecting with one of its neighbour, the actual vigour are compared and the tree with the smaller vigour becomes suppressed, which means it can die with the probability, defined by a random number from the interval [0, 1 - $v(a_i, \mathbf{p}_i, s)$]. Since this operation is repeated in each cycle, the suppressed tree will die eventually. This operation corresponds to the stress related mortality. The tree can also die if the growing place conditions deviate much from the tree needs for one or more indicator. The death probability in this case amounts to 0.5 % and also corresponds to stress-related

mortality. Beside this the tree can die with 0.1 % probability on account of unexpected events, which corresponds to background mortality.

The tree that survives the competition and mortality process and has reached the maturity age contributes in reproduction process. Each tree generates amount of seed which depends on the tree vigour and mast year [12]. In mast year considerably, up to five times, more seed is produced by the tree as in-between. In the model, we modelled only a small percentage of seed, generated by real trees. The seed which not germinate are not of importance for the simulation since they do not influence the competition process and can be omitted. Therefore all seeds, produced by trees in the model also germinate and form new seedlings. The seeds are then dispersed in the neighbourhood where the distance to the parent tree depends on the seed weight.

2.1.2. Realistic forest visualization

By forest visualization we distinguish between the forest visualization on the scale of the landscape and the forest visualization in the immediate vicinity to the camera. In the first case the trees are represented with the billboard textures. In order to improve the impression of the realism, the shadows are used, which give the trees in the forest three-dimensional look, see Figure 2a. On this scale a few hundred hectares large areas can be visualized in the real time and give user the ability to fly over the landscape in real time.

a)   *b)*
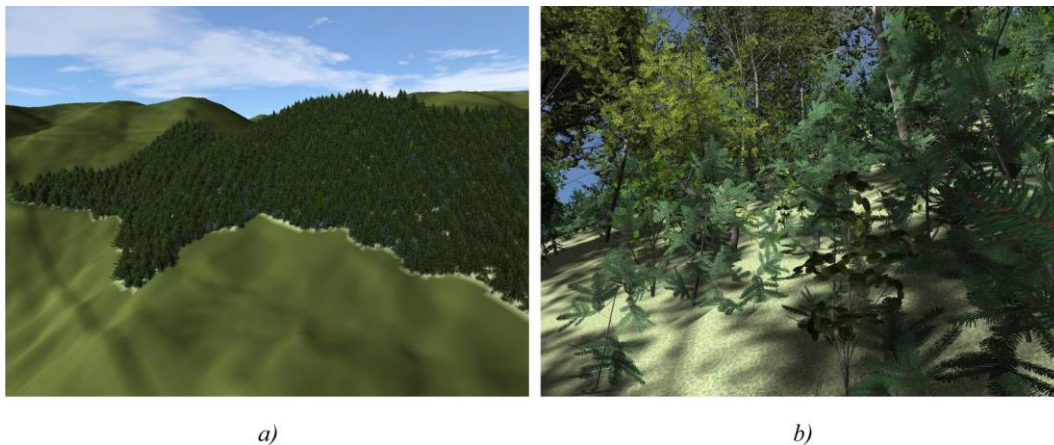
Figure 2. Forest visualization a) on the landscape level, b) in immediate vicinity to the camera.

Billboard tree visualization gives poor results for trees close to camera. Procedural trees, based on self-organizing growth, are used instead [13]. The tree synthesis parameters are species-specific and are defined by the user in order to mimic real trees on the best possible way (see Figure 2b). The trees are generated on graphic processing unit (GPU) and are capable to visualize deciduous and conifer trees, and even some types of shrubs. This method enables the generation of 40.000 highly-detailed trees in less than 10 seconds. After the trees are generated, they can be displayed instantly. Since this is still not enough for real time visualization, we combined the procedural trees with the billboard representation to achieve the desired effect (see Figure 4e). With the procedural trees in immediate vicinity of the camera and billboard trees further away, the real-time walk through the realistic looking forest can be achieved. During forest walk-through the user can also interact with the trees in the model and remove individual trees, which corresponds to selective logging.

In order to study the spreading of interesting tree species through the forest stand, the tree species can be displayed separately. In this way the observation of the changes in the species population is much easier and the conclusion drawn from the simulation results more accurate.

2.2. Gap creation

A gap creation is an integral part of gap regeneration model. In order to create a gap, forest growth simulation has to be paused. After that user has to input gap geometry, optionally he/she can also insert the seed trees types and locations and/or locations of tree stumps. Gap borders are defined by the polygon, therefore the task to determine, which terrain cells are included in the gap area, translates to problem of polygon rasterization and point in polygon problem. In order to solve these problems, the winding number algorithm has been used [14]. With successfully finding the gap interior all vegetation is cleared. If provided, the seed trees can then

be inserted into the gap area. If stumps locations are given, then stumps are converted into trees according to the tree species tendency to stump sprouting. While the seed trees are excluded from the competition and mortality processes, the trees formed from stumps behave like any regular trees in the model.

a)   b)
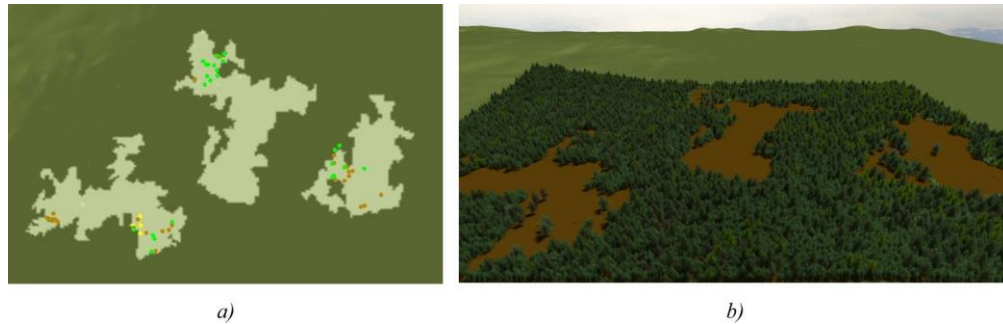
Figure 3. Gap creation a) Shapes of three distinct gaps of total size of 51.2 ha with a seed tree positions, b) Gap areas cut out from the forest with seed trees put to their place.

Gaps data can whether be real, like those in the Figure 3a, or they can be imaginary, as a part of a forest management scenarios. The gaps in Figure 3a for example were the consequence of massive bark beetle outbreak near town Kočevje in Slovenija in 2003, where Spruce trees were so badly damaged that they had to be removed completely to stop the bark beetle spreading. In Figure 3b the same gaps in the virtual forest are visible along with the observed seed trees.

3. RESULTS AND DISCUSION

ForestMAS model was validated on the regeneration of 82 ha area of Mozirska Požganija. Today this is a natural reserve, but in 1950 this area was devastated by wildfire, that destroyed the majority of vegetation located there. About 30 years later 23 permanent research plots were established on the area, which provided valuable long term data to compare to [7].

However, the gap regeneration simulator was developed with the aim, to provide the answer, whether or not a given gap will close in a specified time frame, usually within 30 years. Since this is the time not covered by the data from Mozirska Požganija, we compared simulation results with the observation data of early stage of secondary succession on the abandoned agricultural land in Haloze region and gap regeneration of three gaps, already presented in Figure 3a in management unit Vrbovec near town Kočevje, all Slovenia. In all cases the simulation results followed the observed data, although in Haloze observed population size in first five years was something larger than in simulation, but in later years the population sizes matched, too. In all cases the population sizes were increasing rapidly and reached their maximum in about 20 years after the simulation start. In following years the population drop can be observed and after 100 years the stable population was reached. Together with the population size the forest composition was changing as well. If the trend of changes in the population size was common on all sites, the forest compositions vary significantly, but again at the beginning the pioneer species dominated on the growing sites, but later on, they were usually replaced by the climax tree species that dominated in the remaining parts of the forest.
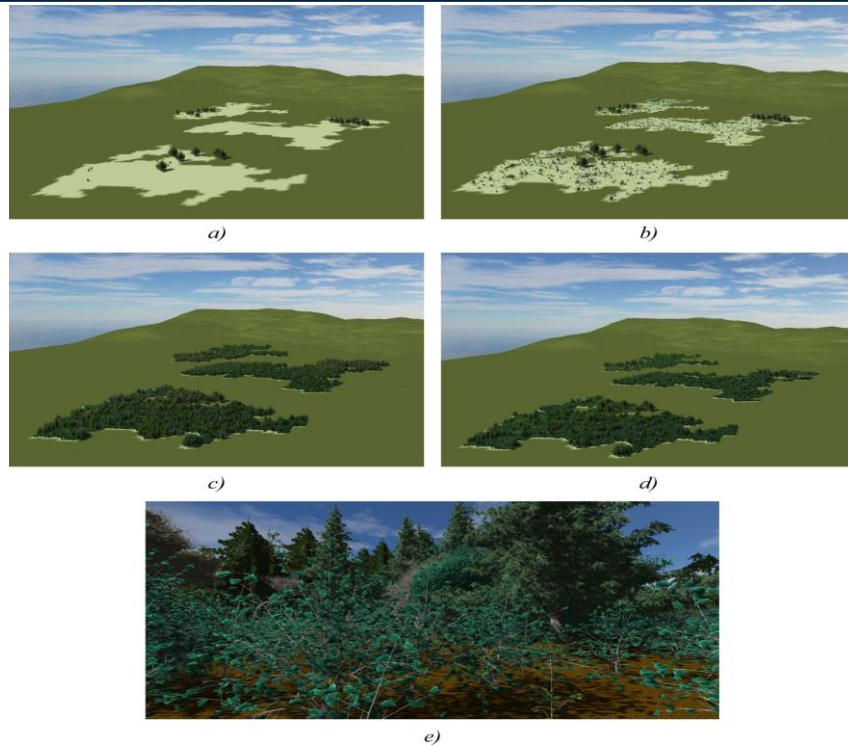
Figure 4. Gap regeneration simulation: a) Starting gaps with seed trees, b) Gaps after 10 years since regeneration start, c) 30 years after regeneration start, d) 50 years since the begin of regeneration, e) Close-up view on gap vegetation 15 years after regeneration begin.

If we want to visually follow the changes in the gap vegetation, the surrounding forest can be irritating. Therefore only the gaps and their content can be displayed while the seed from the surrounding forest is described by the cumulative distribution function. Such is also the case in Figure 4, where the starting situation (Figure 4a) and course of gap regeneration can be seen after 10, 30, and 50 years (Figures 4b, 4c, and 4d). For more in-depth forest dynamics analysis and result interpretation, however, the statistical reports can be used. In Figure 5 three reports can be visible, the forest composition history (Figure 5a), current height distribution for Norway spruce (Figure 5b), and the history of Simpson biodiversity index for 50 years of gap regeneration (Figure 5c). Together with the species visualization filter and schematic forest visualization, the detailed insight into the regeneration process can be achieved more easily. With the close-up forest visualization the changes on the micro locations can be followed, which is a new feature in forest management systems but particularly useful for the owners of small forest areas with limited knowledge of forestry.
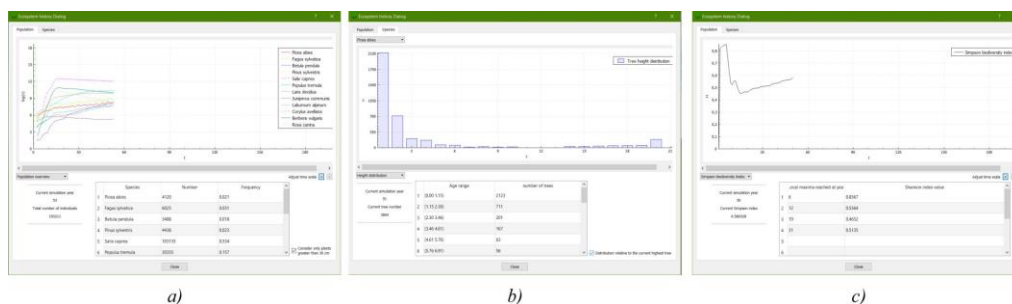
Figure 5. Different statistical reports, giving better insight in the course of gap regeneration, a) forest composition history, b) Current height distribution for selected tree species, d) Simpson biodiversity index history.

4. CONCLUSION

In this article, we presented a powerful gap regeneration simulator ForestMASa with capability to generate realistic areal and close-up imagery. With the use of GPU generated trees the real-time walk through the forest are possible, with possibility of performing basic forest management functions. Currently only selective

logging is enabled in the future, however, we will extend this function with the possibility to selective plant trees. This will enable the forest managers to develop and test new forest tending measures more efficiently.

On the example of the gap regeneration simulator we demonstrated, that today's computers are capable enough for sophisticated real time visualization to become an integral part of new generation forest management software. Such software may bring together wider range of different ecosystem management specialists than ever before. As the consequence our knowledge about different ecological forest functions may grow, which can in turn help to preserve them for the future.

ACKNOWLEDGMENT

REFERENCES

[1]. S. Yamamoto and N. Nishimura, "Canopy gap formation and replacement pattern of major tree species among developmental stages of beech (Fagus crenata) stands, Japan," *Plant Ecol.*, vol. 140, no. 2, pp. 167–176, 1999.
[2]. S.-I. Yamamoto, "Forest gap dynamics and tree regeneration," *J. For. Res.*, vol. 5, no. 4, pp. 223–229, 2000.
[3]. D. B. Botkin, J. F. Janak, and J. R. Wallis, "Some ecological consequences of a computer model of forest growth," *J. Ecol.*, pp. 849–872, 1972.
[4]. H. Bugmann, "A review of forest gap models," *Clim. Change*, vol. 51, no. 3–4, pp. 259–305, 2001.
[5]. D. Coffin and W. Lauenroth, "A gap dynamics simulation model of succession in a semiarid grassland," *Ecol. Model.*, vol. 49, no. 3, pp. 229–266, 1990.
[6]. U. Berger, C. Piou, K. Schiffers, and V. Grimm, "Competition among plants: concepts, individual-based modelling approaches, and a proposal for a future research strategy," *Perspect. Plant Ecol. Evol. Syst.*, vol. 9, no. 3, pp. 121–135, 2008.
[7]. T. Czárán, *Spatiotemporal models of population and community dynamics*, vol. 21. Springer Science & Business Media, 1998.
[8]. E. Fuhrer, "Forest functions, ecosystem stability and management," *For. Ecol. Manag.*, vol. 132, no. 1, pp. 29–38, 2000.
[9]. R. A. Monserud, R. W. Haynes, and A. C. Johnson, *Compatible forest management*, vol. 8. Springer Science & Business Media, 2013.
[10]. N. L. Crookston and G. E. Dixon, "The forest vegetation simulator: a review of its structure, content, and applications," *Comput. Electron. Agric.*, vol. 49, no. 1, pp. 60–80, 2005.
[11]. S. Kolmanič, N. Guid, and J. Diaci, "ForestMAS–A single tree based secondary succession model employing Ellenberg indicator values," *Ecol. Model.*, vol. 279, pp. 100–113, 2014.
[12]. H. Pretzsch, P. Biber, and J. Ďurský, "The single tree-based stand simulator SILVA: construction, application and evaluation," *For. Ecol. Manag.*, vol. 162, no. 1, pp. 3–21, 2002.
[13]. H. K. Bugmann, "A simplified forest model to study species composition along climate gradients," *Ecology*, vol. 77, no. 7, pp. 2055–2074, 1996.
[14]. E. H. Simpson, "Measurement of diversity.," *Nature*, 1949.
[15]. C.-W. Shannon and W. Weaver, "W (1949) The mathematical Theory of Communication," *Press UoI Ed.*, 1948.
[16]. D. Kelly, "The evolutionary ecology of mast seeding," *Trends Ecol. Evol.*, vol. 9, no. 12, pp. 465–470, 1994.
[17]. Š. Kohek and D. Strnad, "Interactive synthesis of self-organizing tree models on the GPU," *Computing*, vol. 97, no. 2, pp. 145–169, 2015.
[18]. K. Hormann and A. Agathos, "The point in polygon problem for arbitrary polygons," *Comput. Geom.*, vol. 20, no. 3, pp. 131–144, 2001.

BIOGRAPHY

Simon Kolmanič received his M.Sc. and Ph.D. in 1999 and 2005 in Computer Science from the Faculty of Electrical Engineering and Computer Science, University of Maribor, where he is currently assistant professor. His research and teaching activities focus on computer graphics and animation, algorithms and data structures, modelling and simulation, and computer-supported teaching.

Numerical Investigation of Hot Ultrasonic Assisted Turning of Titanium Alloy

M.Alper Sofuoğlu[1], Fatih Hayati Çakır[2], M.Cemal Kuşhan[1], Sezan Orak[1], Selim Gürgen[2]*

Abstract

Titanium alloys exhibit superior properties such as high strength-to-weight ratio and corrosion resistance but these alloys possess poor machinability. To overcome this disadvantage, new machining methods (Ultrasonic Assisted Machining, Hot Machining etc.) are developed. Hot Ultrasonic Assisted Turning (HUAT) is a new machining method which changes the cutting system between tool and workpiece therefore reduced cutting forces and better surface finish for workpiece are obtained. In this study, 2D finite element (FE) analysis was carried out to investigate the effects of HUAT for titanium alloys. It was confirmed that HUAT technique reduces cutting forces and effective stress significantly but cutting temperature increases compared to conventional turning.

Keywords: *Finite element modelling; hot ultrasonic assisted machining; titanium alloys; ultrasonic assisted machining; hot machining*

1. INTRODUCTION

In recent years, titanium alloys have wide range of applications in automotive, aerospace and biomedical sectors. The reason is that these alloys are light in weight and they have high strength, fatigue and corrosion resistance. However, machining of these materials is very difficult due to their low thermal conductivity. Therefore, conventional machining methods cause low dimensional accuracy and undesired surface roughness. In addition, these alloys can react with cutting tools [1].

Machining of workpiece with the aid of a heat source is called hot machining. External heat sources such as gas torch, furnace preheating, induction heating, electric current heating, plasma and laser heating are most commonly used methods. In early studies of hot machining, ceramic materials are preheated between room temperature and 1400°C. Also, steel products and titanium alloys are preheated from room temperature to 600°C, and Inconel products are preheated from room temperature to 550°C. The results show that preheating of workpiece has a positive impact on tool life, surface roughness, cutting force and machining cost [2-6].

Ultrasonic assisted turning (UAT) is a non-conventional machining technique by applying vibrations to cutting tool at high frequency (20 kHz) and low amplitude (15-20 microns). Using this machining method, cutting forces and surface roughness are reduced. Also, tool wear is reduced and dimensional accuracy is improved. UAT is effective at low cutting speeds, when cutting speed increases, the process outputs (surface roughness, tool wear, cutting force etc.) approaches the outputs of conventional turning operations [7-9].

Hot ultrasonic assisted turning (HUAT) is a new hybrid machining method which is developed in recent years. The method consists of a combination of hot turning (HT) and UAT. In this method, the disadvantage of UAT at high cutting speeds can be eliminated. An early study showed that surface roughness and cutting force are decreased by using HUAT [10].

In this study, HUAT and HT methods are investigated for Ti6Al4V. Both methods are compared with conventional turning (CT) and UAT. In the second part of the study, finite element simulation of HT and HUAT is given. The third section shows the results of finite element simulations. In the last section, conclusions and recommendations are given.

---

[1] *Corresponding Author: Department of Mechanical Engineering, Eskişehir Osmangazi University, Eskişehir, 26480, Turkey, asofuoglu @ ogu.edu.tr.*

[2] *Vocational School of Transportation, Anadolu University, Eskişehir, 26470, Turkey.*

2. FE SIMULATION OF HT AND HUAT

Simulations were performed by using DEFORM 2D software. The number of elements used in the simulations was about 3000 for the cutting tool and 5000 for the workpiece. Because of the remeshing, the number of elements was increased to 6000 for workpiece. A previous study was used to compare the results with UAT and CT [11]. Details of the modeling was given in previous study [11]. Ti6Al4V was used as workpiece material. Dimensions of the workpiece were 3 mm in length and 1 mm in width. Plain strain conditions were applied. FE simulations were performed for four different cutting speeds (10, 20, 30 and 40 m/min) and three different cutting temperatures (20°C, 250°C and 500°C). Ultrasonic vibration was also applied with 20 kHz frequency and 20 μm amplitude. The vibration was applied in the direction of cutting speed. Depth of cut was 0.1 mm and simulations were performed in dry cutting conditions. Table 1 represents the machining conditions of the FE simulations. Fig. 1 shows a screenshot in FE simulation.
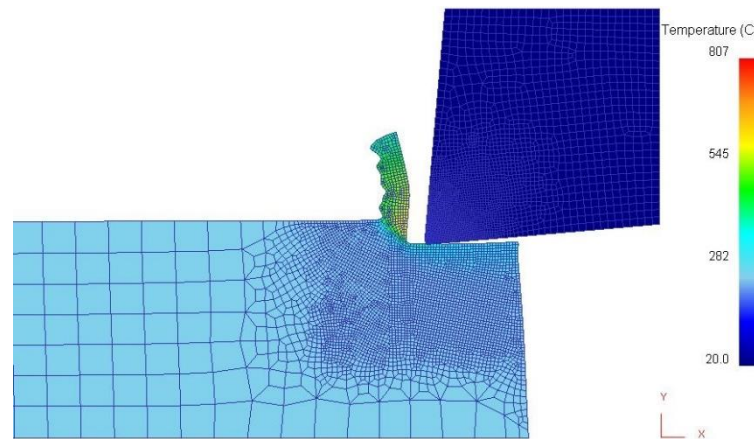
Fig. 1. Screenshot of FE simulation of HUAT

Cutting tool (DNMG 150608 KC 9225) was assumed to be rigid in the simulations. Material of the cutting tool was chosen as non-coated tungsten carbide (WC) and the only thermal calculation for the tool was activated.

Table 1. Machining conditions

Machining Condition	Temperature (°C)	Ultrasonic vibration
CT [11]	20	-
UAT [11]	20	+
HT	250	-
HT	500	-
HUAT	250	+
HUAT	500	+

Johnson-Cook (JC) material model was used in the simulations. The equations of stress and temperature for JC model are given in Eq.1-2. Material parameters used in the simulations for Ti6Al4V alloy are given in Table 2. Values of the parameters were taken from the study performed by Lee [12].

$$\sigma = \left(A + B\varepsilon^n\right)\left(1 + C\ln\left(\frac{\dot{\varepsilon}}{\dot{\varepsilon}_0}\right)\right)\left(1 - T^*\right)^m \tag{1}$$

$$T^* = \frac{\left(T - T_{room}\right)}{\left(T_{melt} - T_{room}\right)} \tag{2}$$

$\dot{\varepsilon}_0$: reference plastic strain rate

$\dot{\varepsilon}$: plastic strain rate

n: strain rate sensitivity of the material

T_{room}: room temperature

T_{melt}: melting temperature of the material

A, B, C, m: material constants

Table 2. Constants of JC Model suggested for Ti-6Al-4V alloy [12]

A	B	C	n	m	$\dot{\varepsilon}_0$
724.7	683.1	0035	0.47	1	2000 s^{-1}

Fracture criterion has considerable effect on the chip separation therefore Cockcroft & Latham fracture criterion was chosen for the simulations. Similar to materials toughness, fracture limit changes with the temperature. At higher temperatures, continuous chip formation is observed.

3. RESULTS AND DISCUSSION

3.1. Cutting Force Prediction

Improving cutting performance has many aspects. One of the most common approaches is to observe cutting forces. Cutting force results for different machining conditions are presented in Fig.2. The results of the numerical simulation indicate that heating workpiece and applying ultrasonic vibration decrease average cutting force. Simulation results of 30 m/min cutting speed show that at 250°C, cutting force reduction is about 10% and at 500°C, it is nearly 15% compared to CT. One of the most significant advantages of UAT method is the effect of the average cutting forces. At the same conditions, effect of UAT at room temperatures reduces average cutting forces about 35% compared to CT. HUAT at 250°C and 500°C lowers cutting forces about 42% and 57%, respectively compared to CT. HUAT decreases average cutting forces and this hybrid approach is much more efficient compared to the other techniques. According to the numerical results, the lowest cutting force is obtained in HUAT at 500°C. HUAT at 250°C produces promising results therefore heating of workpiece may not be necessary and probably not cost effective at higher temperatures (500°C).
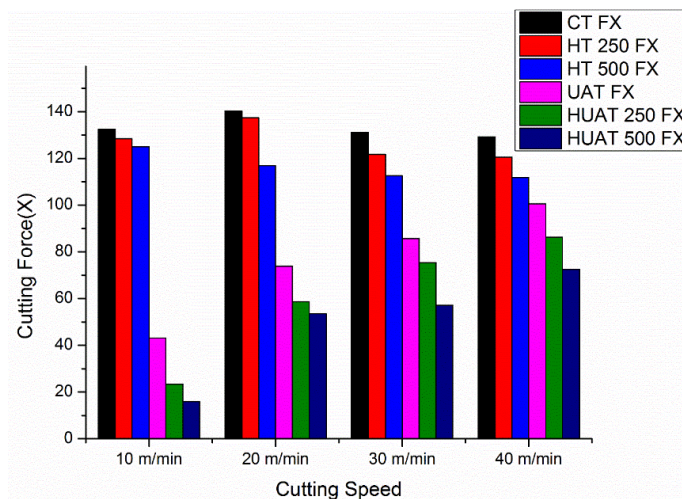
Fig. 2. Average load data for various cutting speeds

3.2. Cutting Temperature

Numerical results show that maximum cutting temperature in HUAT process is slightly higher compared to HT. Fig.3 shows the results of thermal analyses for different cutting conditions.

HT 250°C   HUAT 250°C

HT 500°C   HUAT 500°C
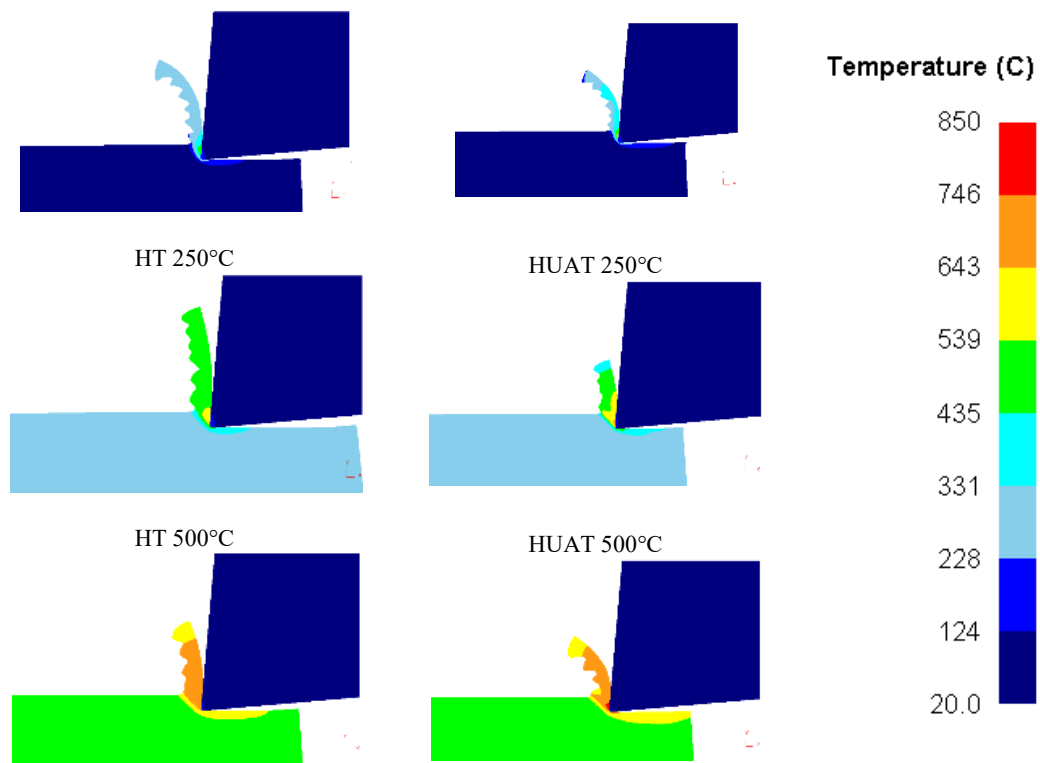
Fig. 3. Temperature distributions in the cutting zone (Cutting speed: 30 m/min)

In HT at 500°C, maximum cutting temperature is nearly 700°C, whereas it is about 800°C in HUAT at 500°C. Applying additional heat increases cutting zone temperature. In HT at 250°C, maximum cutting temperature is nearly 600°C, whereas in HUAT at 500°C, it is about 700°C. Maximum temperatures in the simulations of CT and UAT are about 513°C and 670°C, respectively. In UAT, the maximum cutting temperature increases compared to CT.

3.3. Effective Stresses in the Process Zone

The calculated distributions of effective stresses in the cutting regions of the Ti6Al4V are shown in Fig.4. These stresses are taken at UAT penetration stage because in UAT, stress distribution is changed during each vibration cycle. Maximum effective stress decreases by the increase in temperature as expected. The average levels of the effective stress in the cutting region in HUAT and HT are lower than UAT and CT. Maximum effective stresses in the simulations of CT, HT at 250°C, HT at 500°C are 1300 MPa, 985 MPa, 800 MPa, respectively, whereas in UAT, UAT at 250°C, HUAT at 500°C are 1260 MPa, 995 MPa, 795 MPa, respectively. There are similar findings from previous studies [10].
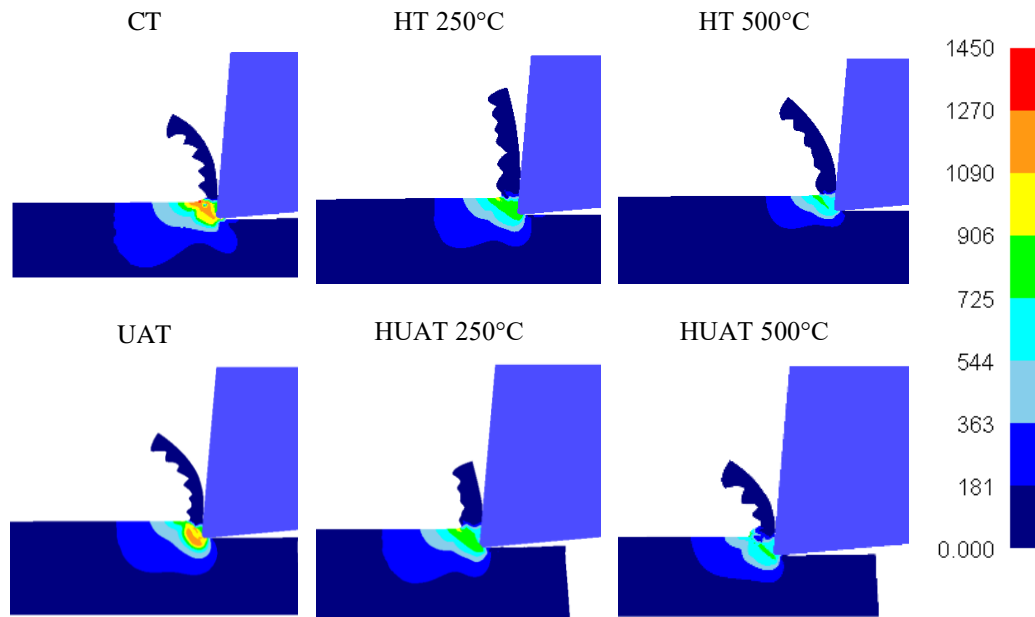
Fig. 4. Effective stresses (MPa) (Cutting speed: 30 m/min)

4. CONCLUSION

In this study, HT and HUAT processes were modeled by FE. The results of simulations demonstrate that HUAT technique reduces average cutting forces significantly but maximum cutting temperature increases compared to the other techniques. Increasing workpiece temperature lowers its yield strength and decreases cutting forces. Reduced cutting forces have many advantages on machining operations. However, lower tool life is obtained because of high cutting temperature. Heat treatments might be applied for cutting tools to avoid increased tool wear. In UAT, reduction of cutting forces is obtained by reducing the tool-workpiece contact area. Furthermore, in HT, thermal softening of workpiece results in reduction in the cutting forces. The average levels of the effective stress in the cutting region in HUAT were lower than UAT and CT. HUAT is much more effective than CT, UAT and HT. Integrating ultrasonic vibrations and heat supply improves machinability of Ti6Al4V. Developed numerical model is useful to understand the effects of process parameters.

ACKNOWLEDGEMENT

REFERENCES

[1]. C. R. Dandekar, Y. C. Shin, J. Barnes, "Machinability improvement of titanium alloy (Ti–6Al–4V) via LAM and hybrid machining", *International Journal of Machine Tools and Manufacture* 50/2,174-182, 2010.

[2]. L.Ozler, A. İnan, C. Ozel, "Theoretical And Experimental Determination Of Tool Life In Hot Machining Of Austenitic Manganese Steel", *International Journal Of Machine Tools And Manufacture* 41/2,163-172, 2001.

[3]. P.A Rebro, Y.C. Shin, F.P. Incropera, "Desing Of Operating Conditions For Crackfree Laser- Assisted Machinig Of Mullite", *International Journal Of Machine Tools And Manufacture* 44/7-8, 677-694, 2004.

[4]. M.C. Anderson, Y. C. Shin, "Laser-Assisted Machining Of An Austenitic Stainless Steel: P550", *J. Engineering Manufacture* 220/12, 2055-2067, 2006.

[5]. T. Ozel, F. Pfefferkorn, "Pulsed Laser Assisted Micromilling For Die/Mold Manufacturing", *ASME 2007 International Manufacturing Science and Engineering Conference*, 337-342, 2007.

[6]. F.E. Pfefferkorn, S. Lei, Y. Jeon, G. Haddad, "A Metric For Defining The Energy Efficiency Of Thermally Assisted Machining", *International Journal Of Machine Tools & Manufacture* 49/5, 357–365, 2009.

[7]. V.I Babitsky, A.V Mitrofanov, V.V Silberschmidt, "Ultrasonically assisted turning of aviation materials: simulations and experimental study", *Ultrasonics* 42/1-9, 81-86, 2004.

[8]. A. Maurotto, R. Muhammad, A. Roy, V. V. Silberschmidt, "Enhanced ultrasonically assisted turning of a β-titanium alloy", *Ultrasonics* 53/7, 1242-1250, 2013.

[9]. M.J. Nategh, H. Razavi, A. Abdullah, "Analytical modeling and experimental investigation of ultrasonic-vibration assisted oblique turning, part I: Kinematics analysis", *International Journal of Mechanical Sciences*, 63/1, 1-11, 2012.

[10]. R. Muhammad, A.Maurotto, M.Demiral, A.Roy, V. V. Silberschmidt, "Thermally enhanced ultrasonically assisted machining of Ti alloy", *CIRP Journal of Manufacturing Science and Technology* 7/2, 159-167, 2014.

[11]. F. H. Cakir, S. Gurgen, M. A. Sofuoglu, O. N. Celik, and M. C. Kushan, "Finite Element Modeling of Ultrasonic Assisted Turning of Ti6Al4V Alloy", *Procedia - Soc. Behav. Sci.*195, 2839–2848, 2015.

[12]. W.S. Lee and C.F. Lin, "High-temperature deformation behaviour of Ti6Al4V alloy evaluated by high strain-rate compression tests," *J. Mater. Process. Technol.* 75/1–3, 127–136, 1998.

4 bit Flash Analog to Digital Converter

Nisa Nacar Cıkan[1], Murat Aksoy[1]

Abstract

Digital Signal Processing has advantages over analog processing. Improving technology has provided the most of the signal processing work can be done in digital domain. Analog to digital converters(ADCs) convert analog signals to digital processing. Flash Analog to digital converter is a type of ADCs that may able to make conversion of analog to digital process very fast. In this paper, a design of a four bits Flash Analog to Digital Converter using 180 nm CMOS is studied. It has been simulated for different speeds starting from 5 Gs/s up to 40 Gs/s. Simulation results of a 4-bit ADC for 10 Gs/s is demonstrated the best performance.

Keywords: *Analog to digital converter, Flash, CMOS*

1. INTRODUCTION

Analog to digital conversion everywhere around us. ADCs have function from a tiny electronic device to medical imaging and satellites. Whether you are making a phone call, taking pictures, browsing the internet or even when doing the laundry, it is necessary to convert analog signals to digital form due to processing them in the analog domain is too complex [1-2]. ADCs are also important part of many systems on chip applications. The most common types of ADCs are Flash, Successive Approximation, Delta-Sigma, Pipeline and Folding Interpolation [2-5]. High speed, low power, low voltage and high resolution are becoming more important to ADC designs as the length of transistors shrinks [6-7]. Therefore, it is crucial to understand how ADCs work, which ADC is right for our application and how we can compare and evaluate their performances [7].

A variety of ADCs with different architectures, resolutions, sampling rates, power consumptions, and operating temperature ranges are available. Flash ADC is known as the fastest due to its parallel architecture and ideal for large bandwidth applications. Hence, it has been widely studied [6-8]. Because of the parallel architecture of Flash ADC, all conversions are done in one cycle with many comparators. Flash analog to digital converters are thus fastest for analog to digital signal conversion. However, power consumption and large chip area required for the implementation of flash converters have practical limits at higher resolution. CMOS technology helps to design power saving systems [9]. Flash ADC requires $2^n - 1$ comparators for an n bit A/D converter. Complexity increases with increasing number of bits at Flash ADC.

In this study, four bits Flash ADC is designed by using CMOS 180 nm technology in Advanced Design System(ADS). Encoder and comparator are modified to get better digitized outputs and to prevent delays. As an input signal, sinus and ramp signals are applied and both applied signals are compared.

2. FLASH ANALOG TO DIGITAL CONVERTER

Flash ADC design composed of comparators and an encoder. Encoder design requires to design of many logic gates. Following parts explain the design and simulation results in detail.

2.1. Theory of Flash ADC

Flash ADC also called parallel analog to digital converter. It consists of a series of comparators, each one comparing the input signal to a unique reference voltage. Comparator outputs, calculated as $2^4 - 1$ and equals to 15, connect to the inputs of encoder circuit, which produce binary output as bit one to bit four. Flash ADCs are ideal for applications requiring very large bandwidth; however, they typically consume more power than other ADC architectures and generally limited to 8-bit resolution [10].

---

[1] *Cukurova University, Electrical& Electronics Engineering Department, 01330, Sarıcam/Adana, Turkey. ncikan@cu.edu.tr , aksoy@cu.edu.tr*

The performance of the parallel ADC depends on the ability to sample the input without jitter. There are two approaches that have been used on parallel or flash ADCs. The first is to use a sample-and-hold at the input. The disadvantage of this approach is that the sampling time of the sample-and-hold circuit may not be small enough. The second approach is to use clocked comparators. It is extremely important that all comparators are clocked simultaneously to avoid jitter, which reduces the resolution at high speeds. And the offset voltage of the comparators also is clocked simultaneously to avoid jitter, which reduces the resolution at high speeds. In this design, clocked comparators are used [11].

2.2. Nyquist-Shannon's Sampling Theorem

According to Shannon's or Nyquist Sampling Theorem, the sampling rate must be at least twice the maximum frequency present in the signal. Analog to digital converter technology implements the usual quantized Shannon representation: the signal is uniformly sampled at or above the Nyquist rate [12]. The minimum sampling frequency f_{sample} must be greater than twice the highest frequency component of the original signal f_{signal}

$$f_{sample} \geq 2 \times f_{signal}$$

2.3. Comparator Theory

The maximum sampling speed of a Flash ADC is directly related to the maximum operating speed of the comparators. Therefore, the design of the comparators usually determines both the sampling speed and the power consumption of the ADC [13].

The comparator that we used in this design compares input voltage and reference voltage and switches its output to indicate which is larger.

2.4. Encoder Theory

Encoder is a circuit that converts information from one format or code to another. Encoders are combinational logic circuits and they are opposite of decoders. Encoders accept one or multiple inputs and generate a multibit output code [14]. Logic gates are crucial components for an encoder design. We have designed and simulated Inverter, Or, And, Nor gates to set the Encoder design up. In our design encoder helps to convert 15 comparator outputs of Flash ADC to the 4 bits as bit1, bit2, bit 3 and bit 4.
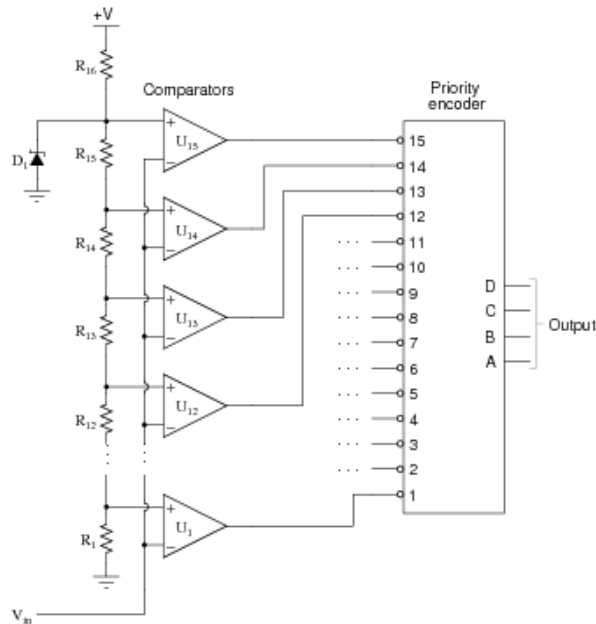
Figure 1. Encoder Design Sample [15]

Reference voltage is divided into 15 levels with the help of resistor ladder diagram. For each comparator, input voltage is compared with reference voltage and generates thermometer code,which is converted to binary or other code by the following encoder.

3. DESIGN AND SIMULATIONS

A comparator is a circuit that has binary output. Comparator compares two voltages or currents. In our design; it compares input and reference voltages and switches its output to indicate which is larger. If Vin is bigger than Vref than output is logic "1" otherwise output is logic "0". We used sin wave as a input and DC voltage as a reference voltage and compared these two voltages. We also changed reference voltage to negative dc voltage and ramp voltage and demonstrated the simulation results below:

Single Comparator Design:
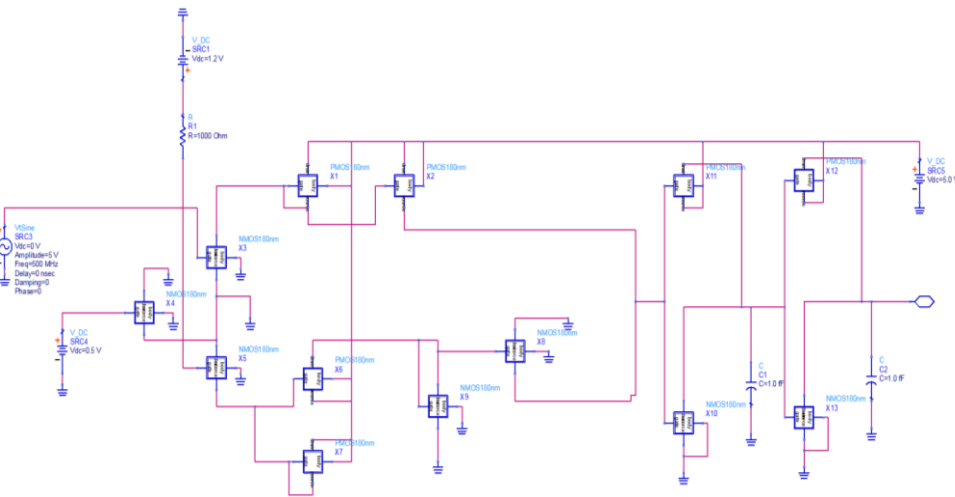
Figure 27. Single Comparator [16].

Encoder Design for Four Bits:
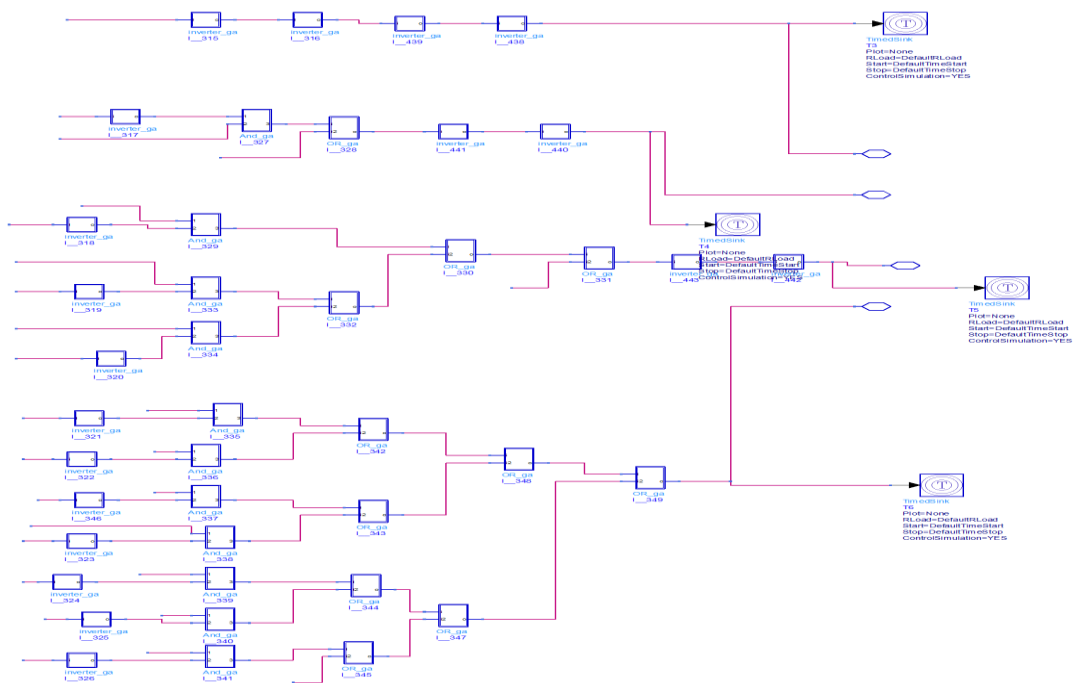
Figure 2. Single Comparator

Four bits flash ADC design:
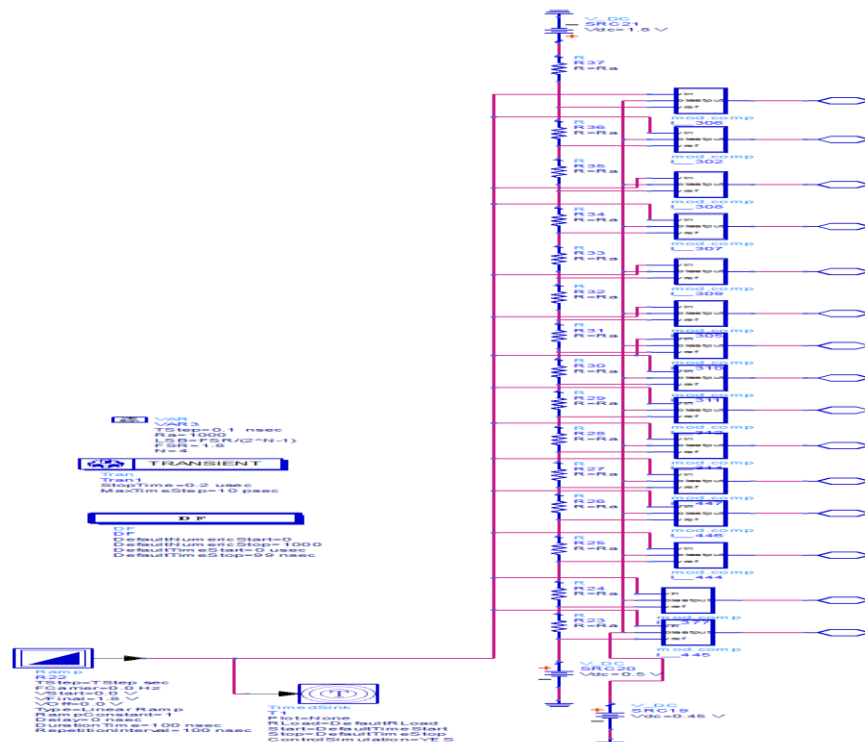
Figure 3. Four Bits Flash ADC Design

Simulation Results:

    A.   **For applied Ramp Signal**

At 5 Gs/s Applied Ramp Signal and follows with four bits outputs as bit 4 to bit 1 in order.
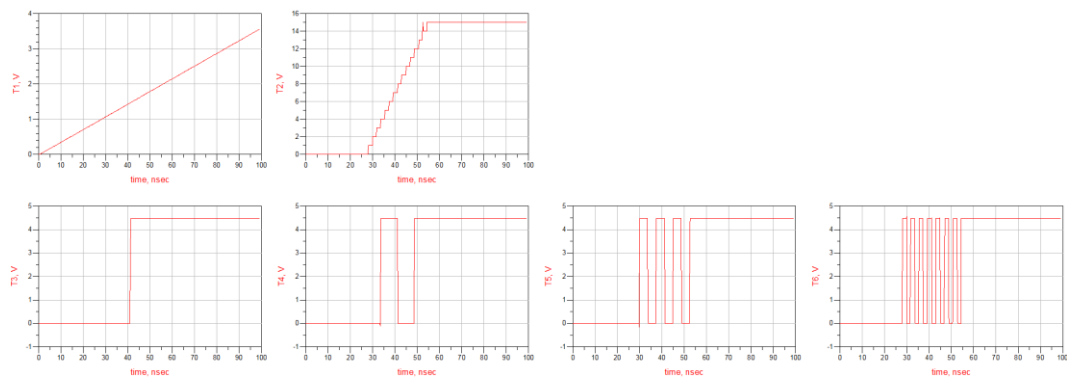
Comparator Outputs at 5 Gs/s:

We have made modification on comparator modification on comparator and gained very good digitized comparator outputs. If these comparator outputs are compared with reference paper comparator outputs, we may able to observe that we had much better and digitized results. Set of fifteen comparators shown in figure below, clearly depicts the desired step changes.
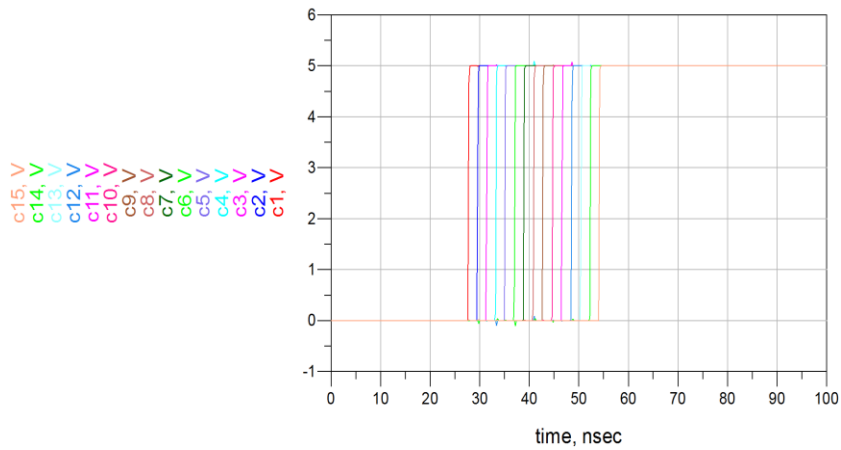
At 10 Gs/s Applied Ramp Signal and follows with four bits outputs as bit 1 to bit 4 in order.
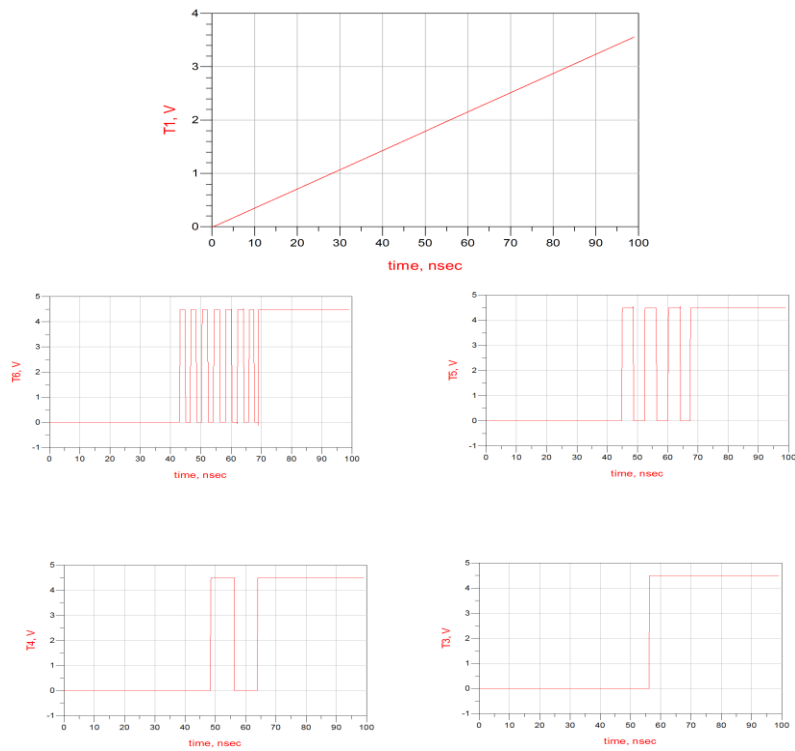
Comparator Outputs at 10 Gs/s:
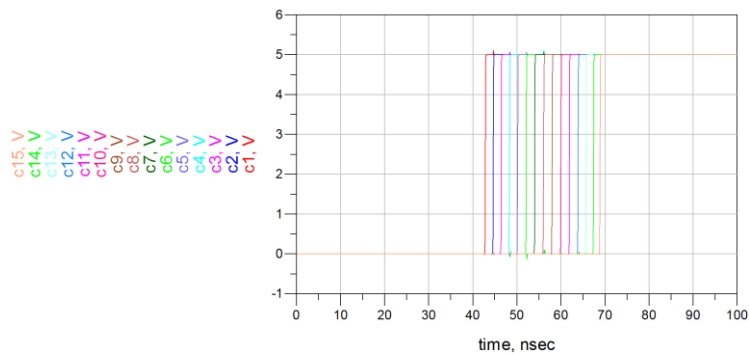
A. For applied Sinus Signal

At 10 Gs/s Applied Sinus Signal and follows with four bits outputs as bit 1 to bit 4 in order.
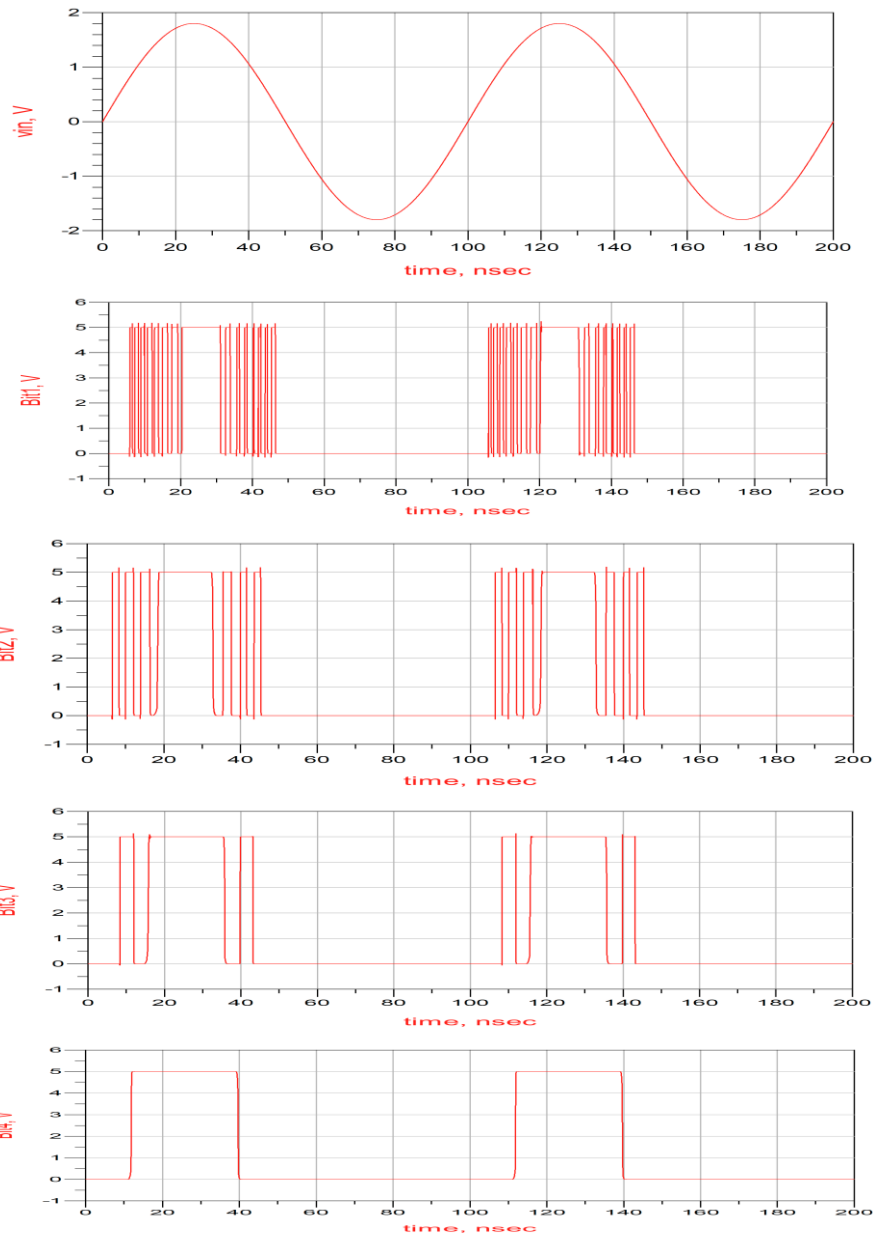
4. CONCLUSION

In this paper, the design and simulation results for four bits Flash ADC using 180nm CMOS have been presented. CMOS technology has good speed to power ratio compared to other logic types. Flash ADC is generally limited the 8 bits and the design we have provided can be extended to higher resolutions for future works. We have used Ramp and Sinus signals as inputs and observed that for higher frequencies and bit numbers, signal distortions are increased.

ACKNOWLEDGMENT

REFERENCES

[1]. M. Figueiredo, J. Goes, and G. Evans, *Reference-Free CMOS Pipeline Analog-to-Digital Converters*. New York, NY: Springer New York, 2013.

[2]. B. Le, T. W. Rondeau, J. H. Reed, and C. W. Bostian, "Analog-to-digital converters," IEEE Signal Processing Magazine, vol. 22, no. 6, pp. 69–77, 2005.

[3]. R. H. Walden, "Analog-to-digital converter survey and analysis," IEEE Journal on selected areas in communications, vol. 17, no. 4, pp. 539–550, 1999.

[4]. M. J. M. Pelgrom, *Analog-to-Digital Conversion*. Dordrecht: Springer Netherlands, 2010.

[5]. J. Cazes and G. W. Ewing, Eds., *Ewing's analytical instrumentation handbook*, 3rd ed. New York: Marcel Dekker, 2005.

[6]. M. O. Shaker, S. Gosh, and M. A. Bayoumi, "A 1-GS/s 6-bit flash ADC in 90 nm CMOS," in *2009 52nd IEEE International Midwest Symposium on Circuits and Systems*, 2009, pp. 144–147.

[7]. N. Nacar Cikan, M. Aksoy, "Analog to Digital Converter Evaluation Using Figure of Merits(FOM) in Industrial Applications," in 2016 *IEEE European Modelling Symposium* ,2016, pp.

[8]. S. Park and M. P. Flynn, "Design techniques for high performance CMOS flash analog-to-digital converters," in *Proceedings of the 2005 European Conference on Circuit Theory and Design, 2005.*, 2005, vol. 1, pp. I–131.

[9]. Chun-Cheng Huang and Jieh-Tsorng Wu, "A background comparator calibration technique for flash analog-to-digital converters," *IEEE Transactions on Circuits and Systems I: Regular Papers*, vol. 52, no. 9, pp. 1732–1740, Sep. 2005.

[10]. Baljit Singh and Praveen Kumar (2009), "Characterization analysis of a High speed, Low Resolution ADC based on simulation results for different resolutions", International conference on information and multimedia technology, pp533 – 537.

[11]. N. Nacar Cikan, M. Aksoy, "A 10-Gs/s 3 bit Flash ADC in 180 nm CMOS ," in *International Engineering Science and Educatio Conferance* ,2016, pp.1008-1014.

[12]. E. J. Candes and M. B. Wakin, "An Introduction To Compressive Sampling," *IEEE Signal Processing Magazine,* vol. 25, no. 2, pp. 21-30, 2008.

[13]. P. Sunghyun and M. P. Flynn, "Design techniques for high performance CMOS flash analog-to-digital converters," in *Proceedings of the 2005 European Conference on Circuit Theory and Design, 2005.*, 2005, vol. 1, pp. I/131-I/134 vol. 1.

[14]. L. E. Frenzel, *Crash Course in Digital Technology*. United States of America, 1997, p. 195.

[15]. https://www.allaboutcircuits.com/worksheets/analog-to-digital-conversion/.

[16]. Advanced Design System(ADS) 2011.

The Annual Energy Consumption Comparison by means of Energy Savings of a Two Story Flat and a Regular Flat That are Located in the same Building in Ankara During Winter

Nalan Kalkan[1], Murat Korkmaz[2]

Abstract

Due to increasing population in country, house construction is also in rise. House construction not only should satisfy the need of housing but also should aid people meet their energy consumption expenses in reasonable amounts especially during winter in order to maintain a standard of living. The housing preferences of people vary by their need of area of use. Our country is 70% to 80% foreign-dependent by means of providing fuel/natural gas that is needed to heat housings. Because of that reason it becomes an obligation to conserve energy and there are regulations on energy efficiency in our country. The aim of this study is to evaluate the energy consumptions of a loftdoublex (LD) and a regular flat (RF) which are in the same building in October, November, December 2015 and January, February, March 2016 by means of energy saving and propose suggestions on energy saving and efficiency.

Keywords: *Energy savings, The annual energy consumption, Heating*

1. INTRODUCTION

Construction industry is still leading sector in Turkey's industry. People have been building housing and dwelling in order to meet their residential needs. These housing that they built has undergone some changes according to changing life standards, varying technical, social and cultural methodologies. As a result of these external factors they eventually become what they are now. Residences are built in two types such as garden houses and apartment flats. Garden houses are constructed as one story, two story (dublex), three story (triplex) and four story (fourlex) depeding on the needs. First instances of apartments and flats were first introduced after the Edict of Gulhane which was declared in 1839 in Ottoman Empire followed by designs such as loft doublex (which is a two story flat with an entrance in apartment's top floor),[1] and reverse doublex (which is a two story flat with an entrance in apartment's first floor) that are still seen in today's architecture. In the recent period; the construction industry which is offering not only functionality but also hedonic sense, provides a wide range of product scale to an area that is changing constantly and has customers that are getting harder to satisfy. Consequently; residences, practical homes consisting of one bedroom and one living room (which is called studio flat), smart homes that are socially better (public socialising areas and sport areas), more luxurious (caring about green fields, gardens) , more functional (parking lot, laundry areas, private security services), villas that are constructed at rural areas out of town have gained their places in the market thanks to variation phenomenon [2].

The types of housing that are mentioned above have different construction methods and versions. Due to the fact that they differ, their heating, cooling and air conditioning needs vary too which is resulting in using different types of energy sources. Energy demand in Turkey is in rise on these areas day by day. In order to meet the energy demand, Turkey is highly dependent on external sources and it is a well-known fact that this situation comes with a high risk. Concurrently, when greenhouse gas emission values in Turkey are examined it is observed that "energy density" and "carbon density" rates are relatively higher compared to developed

[1]*Corresponding author: Hacettepe University, Polatlı Vocational School of Technical Sciences, 06909, Sincan/Ankara, Turkey. nkalkan@hacettepe.edu.tr*

[2]*Second author, Hacettepe University, Polatlı Vocational School of Technical Sciences, 06909, Sincan/Ankara, Turkey.mkorkmaz@hacettepe.edu.tr*

countries [3]. These rates point out the importance of energy efficient approach and Turkey needs to decrease its energy consumption.

Construction industry has a large percentage of share in industry-specific energy distribution of Turkey as it is in the rest of the world. A large extent of the energy that is consumed in buildings is also sacrificed to climatization and air-conditioning in order to maintain a comfort zone of its residents. Hence, it is vital to design energy efficient constructions and improve current buildings to become energy efficient to solve problems in energy and environmental area [4].

On the other hand; heating and cooling calculations of the residences vary by climate conditions, residential area, direction of the housing, isolation properties of housing, air-conditioning system that is used etc [5]. Especially, isolation material and its properties affect the expenses of heating systems and their initial investment costs largely [6]. Although central heating mechanisms are used in order to maintain energy efficiency and energy savings in the buildings that are constructed recently, it is observed that people tend to prefer personallised heating systems which they specify and determine the consumption according to their needs [7]. In those personal heating systems, combi boilers that are able to provide both heating water and tap water to be used daily [8].

Despite the fact that all heating conditions are the same, the "loft doublex" housing that people are more fond of lately can differ in expenses by means of heating/cooling and thermal comfort when compared to regular flat.

In this study, a "loft doublex" (LD) and a regular flat (RF) which are in the same apartment building and in the same direction with the same properties in Ankara/Turkey in October, November, December 2015 and January,February, March 2016 are compared, examined and suggestions are made by means of energy consumption, energy savings and efficiency.

2. MATERIAL AND METHOD

2.1. Material

The study covers the examination of two housing which are located in Ankara province Etimesgut district that are in the same building pointing at north-east direction with different areas in size. One of the residences is a regular mid floor flat while the other is "loft doublex". Both residences that are used in this examination have different brand condensing combi boilers. The flat in the mid floor is using a combi boiler with capacity of 24 KW. The loft doublex is using a combi boiler with capacity of 35 KW. The heating installation on both residences are collector(mobile) heating systems. The apartment building that is used in this examination has partial jacketing.

2.2. Method

The research conducted is comparing the annual energy consumption values of regular flat and loft doublex in October, November, December 2015 and January, February, March 2016 which are provided by Ankara Baskent Gas compnay. Next, other values that could come up in energy consumption are also examined. Energy consumption values of the residences are evaluated by means of energy savings and efficiency. As a result of evaluation, predictions and recommendations are made related to energy saving and efficiency.

3. RESULTS AND DISCUSSION

In Figure.1 the monthly energy consumption of regular mid floor flat (RF) and loft doublex (LD) is shown. Both energy consumption amounts include energy needed to acquire hot water and gas required to cook. It is observed that the energy consumption of RF is higher than LD in November, December 2015 and January 2016. On contrary, it is seen that the monthly energy consumption values of LD is higher than RF in October 2015 and February, March 2016.
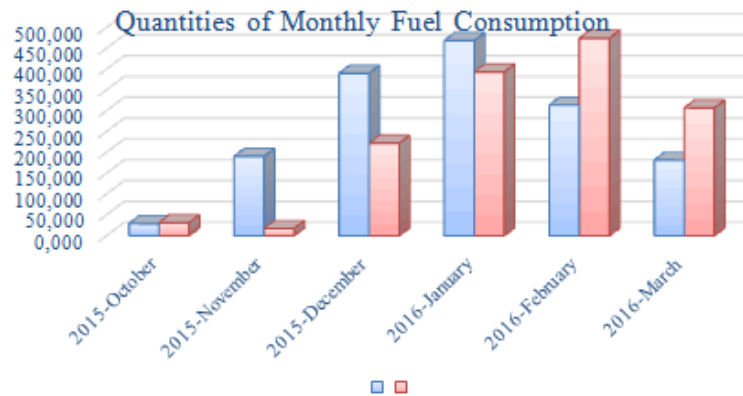
Figure 1. Monthly fuel consumption values

The total annual fuel consumption values of both RF and LD can be seen in Figure.2. When these values are observed it is seen that RF has higher values of consumption compared to LD annually.
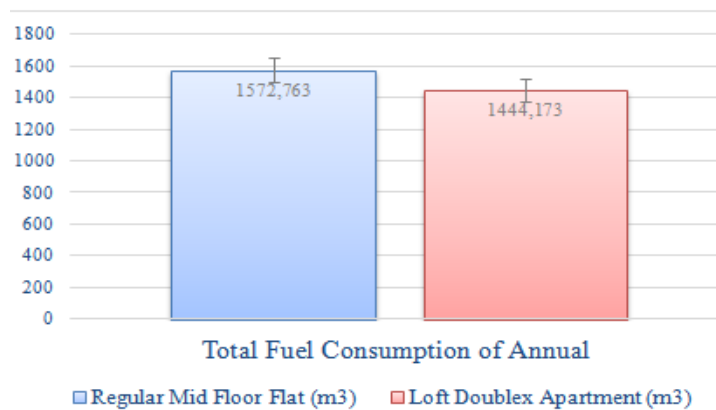
Figure 2. Annual total fuel consumption

When both Figure.1 and Figure.2 is taken into account; even though LD has higher usage area of 240m^2 than the RF's usage are of 140m^2, RF has reached higher consumption amounts than LD. This situation can be explained that; while there are 4 residents in RF, LD has 2 residents. All rooms in RF are used as living space which results in the obligation of heating all of its rooms while the two residents in LD are not using heating in 2 unused rooms and terrace. The total area that is being heated in RF is larger than the area being heated in LD. Besides, 3 of 4 residents of RF is currently not working on a regular job due to that they are spending most of their times inside so that all of its rooms are being heated during the entire day. All of 2 residents of LD are going to work on regular basis so they prefer to use heating on certain time intervals of the day. Moreover, the average age of residents in RF is higher than the average age of residents in LD. Therefore, it can be said that when the average of age increases the energy consumption also increases accordingly.

The flats below and above RF are currently empty and not being heated. Flat below LD is also empty and isolation material that is used and place to isolate on its roof is inadequate. Besides, the jacketing in the building is insufficient especially there is no isolation in its wide yard. These negativities affect the energy costs of both flats badly and resulting in poor comfort levels.

4. CONCLUSIONS

In this study, contrary to being expected that the LD would have higher energy consumption values, the RF has higher energy consumption than LD. The annual total fuel consumption of the RF and LD are calculated as 1572.763 m^3 and 1444.173 m^3 accordingly (Figure.2). The reasons to this can be explained by means of demographic factors and other factors as follows:

- The average age of the residents in RF is higher than the average age of the residents that live in LD so the need of heating is higher in RF due to this.

- The fact that most of the residents of RF are not going to work in a daily basis so that this flat needs to be heated continuously while the residents of LD are going to work every day which limits the need of heating to certain hour intervals.

- Due to having 4 residents, all rooms in RF are being used actively and all of its rooms are being heated while LD has only some of its rooms that are being heated.

- Having more residents than the LD causes increased hot water usage and energy needed to cook in RF.

When the reasons mentioned above are also taken into account in personal heating systems; residences can be heated according to preferences of their residents by means of their needs, when they want to use it in desired heat values. If we compare central heating systems and personal heating systems, those factors are considered as advantageous and reason for preference.

When two flats are examined by means of energy savings, both flats needs to acquire energy performance certificate and complete the isolation of the places that are lack isolation system as soon as possible. The heating systems in the building should be inspected, reviewed and by doing feasibility study they should switch to heat cost allocator system. Thus, it will force every flat in every floor to get heated in order to meet expected comfort levels.

REFERENCES

[1]. *Mutdogan, S., Türkiye'de cok katlı konut olusum sürecinin İstanbul ornegi üzerinden incelenmesi, Sosyolojik Arastırmalar E-Dergisi 7 Nisan 2014.*

[2]. *Yıldırım, F.,Türkiye'de ikamet amaclı konut pazarının makroekonomik degiskenler ile iliskisi, İstanbul Ticaret Üniversitesi Social Sciences Research Journal, Volume 2, Issue 1, 12-18 (March 2013), ISSN: 2147-5237 12.*

[3]. *Dünya Enerji Konseyi Türk Milli Komitesi, "Enerji Raporu 2011", 2011.*

[4]. *Dilara, S., Gül, M., vd,.Türkiye'nin farklı iklim bolgelerinde bir konut binasının enerji etkin iyilestirilmesi, 11. Ulusal Tesisat Mühendisligi Kongresi – 17/20 Nisan 2013/İzmir 921.*

[5]. *A. Türkeri, 2007, Bireysel ve merkezi ısıtma sistemlerinin tanıtımı ve karsılastırılması, VIII. Ulusal Tesisat Mühendisligi Dergisi, Sanayide Konutlarda Dogalgaz Semineri, İzmir, TURKEY.*

[6]. *Recknagel, H., Sprenger, E., Schramek E.R., 2000, Taschenbuch für heizung und klimatechnik, oldenbourg verlag*

[7]. *T. Tetik, 2011, Dogalgaz yakıtlı bireysel ısıtma sisteminin enerji ve ekserji Analizi, Hitit Üniversitesi Fen Bilimleri Enstitüsü, Corum, TURKEY.*

[8]. *R. Kücükcalı, 2005, Merkezi ve bireysel sistemlerde enerji tüketimi, VII. Ulusal Tesisat Mühendisligi Dergisi, İzmir, TURKEY.*

BIOGRAPHY

Nalan Kalkan: She was born in Eskisehir in 1962. She completed his primary and secondary education in Eskisehir.She studied Architecture at Eskisehir Vocational High School. Gazi University Technical Education Faculty Department of Building Education finished. Gazi University Graduate School of Natural and Applied Sciences Graduate and Ph.D. The MSc thesis is "Selection of Technology in Housing Construction for Low Revenues". Ph.D. thesis "Reinforcement of Plane Girder Reversed Loading Wall with Sprayed Concrete". He started his career at Hacettepe University Vocational School of Construction Technology Program and continues his life at the same school. She continues to teach at other units of Hacettepe University. She is working in the areas of reinforced concrete, static, building installations, professional computing, reinforced concrete project, architectural project, cost analysis, survey restoration, educational sciences.

Murat Korkmaz: He was born in 1980 in Ankara. He completed his primary and secondary education in Ankara. He studied at Ankara High School. Gazi University Technical Education Faculty Mechanical Education Department of Installation Training finished. Graduated from Gazi University Graduate School of Natural and Applied Sciences. He is currently continuing his Ph.D. Education in the Energy Systems Engineering Program of the Karabuk University Graduate School of Natural and Applied Sciences. Master thesis "Experimental Investigation of Absorbent Plates in Different Profiles in Planar Solar Collectors". Hacettepe University Polatlı Technical Sciences Vocational School Gas and Plumbing Technology Program is started in the same school is continuing to work life. He continues to teach at other units of Hacettepe University. Heating, cooling, natural gas, energy efficiency and air conditioning, educational sciences.

Determination of Pozzolanic Activity for Using Natural Zeolite Analcime in Sustainability Additive Cement Products

Yasemin Akgun [1]

Abstract

It is known that the cement industry is responsible for 5-8% of world CO_2 emissions and also for intensive energy consumption. For this reason, cement productions need to sustainability studies. Mineral admixtures added to cement as partial replacement material enable to sustainable blended cement productions due to used less amount of cement. Mineral admixtures with pozzolanic property are also preferred in terms of increasing cement performances. This situation corresponds to improved performance of cement and concrete products as well as saving energy, reducing world CO_2 emissions. In recent years, the cement industry has been using natural zeolites extensively as pozzolanic materials. Analcime is known as second valuable zeolite mineral after from clinoptilolite in natural zeolite groups The aim of this study is to determinate the pozzolanic properties of analcime and to investigate whether it has potential availability in sustainable blended cement production. The clinoptilolite was used with comparison purpose in this study. Blaine values, densities, chemical composions, pozzolanic activities, mineralogical structures of analcime and clinoptilolite which are subject of study were determined. Accordance with TS 25, which contains pozzolan conformity criterias, 7-days average compressive strength values of lime-pozzolan mixture samples were determined. The datas obtained shown that, the 7-days average compressive strengths of lime-zeolite (pozzolan) blended samples are 9.02 MPa for clinoptilolite and 6.3 MPa for analcime. The total content of $SiO_2 + Al_2O_3 + Fe_2O_3$ was 77.3% for clinoptilolite and 73.16% for analcime. Accordingly, analcime which is a natural zeolite satisfies to puzolan conformity criterias in TS 25 has the potential to be an alternative to clinoptilolite which is more widely used in cement productions.

Keywords: *Analcime, clinoptilolite, pozzolanic activity, zeolite.*

1. INTRODUCTION

Cement is a construction material that needs to sustainability studies due to the decrease of non-renewable energy resources and the increase of CO_2 emissions in the world. The easiest solution in sustainability studies is to produce blended cement by using pozzolans. Nowadays, the use of pozzolans which are substituted by cement has become very popular. The use of portland cement in a lesser amount leads to less energy consumption and less CO_2 emissions. Thus, more environmentalist, energy saving, economical and sustainable cement productions can be possible. Also, the pozzolans with high activity affect positively to performances of mortar/concrete.

Pozzolans are defined as materials with silica and alumina. They have either any or very low binding property on their own. But, in the fine grained state, they are capable of exhibiting hydraulic binding when combined with calcium hydroxide in hydrous medium. Pozzolanic activity is defined as how much can provide reacting with slaked lime and water of pozzolanic materials and how much binding it can provide [1].

In other words, pozzolanic activity can be defined as the ability to react with $Ca(OH)_2$ of active silica which is in the pozzolan. At the end of this reaction the amount of portlandite ($Ca(OH)_2$) is reduced, calcium silicate hydrate (CSH) is increased [2]. To determine the pozzolanic activity, various chemical and mechanical experiments were included in the standards [3,4,5]. With chemical experiments, silica and $Ca(OH)_2$ are determined qualitatively and quantitatively. In mechanical experiments, it is determined whether pozzolans have active silica by determining flexural and compressive strengths of mortars produced with pozzolans mixed with lime or cement [6].

---

[1] Corresponding author: Ordu University, Department of Renewable Energy, 52200, Ordu, Turkey. yakgun@odu.edu.tr

It is known that, zeolites have used as pozzolanic additives in mortar and concrete productions. The natural zeolites formed by the alteration of the vitric pyroclastic deposits are more reactive materials than the fly ash and furnace slags between mineral additives [7]. Zeolites contribute to the formation of cement-like hydrated products during the hydration of cement and to $Ca(OH)_2$ consumption occurred during the hydration process. So, zeolites improve performances of mortar/concrete [8]. Analcime is known as second valuable zeolite mineral after from clinoptilolite in natural zeolite groups. Analcime is a feldspathite mineral with a very large amount of hydrated sodium aluminosilicate $(Na (AlSi_2O_6) .H_2O)$ in its structure. The clinoptilolite is a natural zeolitic mineral species with chemical formula (Na_3K_3) $(Al_6Si_{30}O_{72})$ $24H_2O$, which is rich in silica and contains alkali and earth alkaline cations [9].

Despite the large number of studies on pozzolanic activity of clinoptilolite in the literature, studies on that of analcime are very limited [10,11]. This study has been carried out in order to provide actively using of local and natural resources that could contribute to the sustainability of cement. The use of such natural additives with optimum values may be possible with scientific research outputs. So, the aim of this study is to determinate the puzolanic properties of analcime and to investigate whether it has potential availability in sustainable blended cement production. The clinoptilolite was used with comparison purpose in this study.

2. MATERIALS AND METHODS

2.1. Materials

In experimental studies, the clinoptilolite and analcime which are natural zeolite minerals were used as replaced material by cement. The analcime and clinoptilolite were obtained from Ordu/Persembe and Manisa/Gordes regions in Turkey, respectively. The two different natural zeolite samples were obtained by grinding from zeolite rocks in a ball mill. As a fineness parameter, in accordance with ASTM C430 [12] material percentage passing from 45-μm was used. In pozzolanic activity tests, CEN standard sand which has preferably round granulated and characterized by a natural silica sand content of at least 98% silica dioxide according to TS EN 196-1 [13] standard was used. In lime-pozzolan mixtures, slaked lime $(Ca(OH)_2)$ as specified in TS 25 [5] was used. In the production of the samples, water which does not contain organic matter and mineral salts which may be harmful were used.

2.2. Methods

The specific surface, density, chemical composition, mineralogical structure of the materials used as pozzolan have an important effect on pozzolanic activity. The following methods were used for the determination of these parameters effected on pozzolanic activity of natural zeolites used in the study. Additionally, the determination method of pozzolanic activities of natural zeolites was mechanical experiment method which is determined by average compressive strengths of lime-pozzolan mortars.

Firstly, the physical properties of the natural zeolites were determined. The densities were determined according to TS EN 197-1 [14]. The specific surface (Blaine) were determined according to TS EN 196-6 [15]. X-Ray Diffraction (XRD) Analysis was performed to determine the chemical composition of natural zeolites. SEM views were also obtained using a Scanning Electron Microscope. The mineralogical structures of natural zeolites were determined by using XRD analysis. And then, the pozzolanic activities of natural zeolites were determined according to TS 25.

2.3. Preparation of the Samples and Tests on Pozzolanic Activity

In TS 25, the pozzolanic activity test is defined as a characteristic determined in terms compressive strength of the mortar obtained by mixing natural pozzolan which is grinded at a certain fineness with water, standard sand and calcium hydroxide $(CaOH_2)$. The amounts of materials required to prepare three test samples for tests on pozzolanic activity are given in Table 1. The moulds of the prepared samples were covered with a glass plate to prevent evaporation. The samples were allowed to stand at room temperature for 24 hours (23 ± 2) ° C. And then, they were left for 6 days in an drying oven at 55 ± 2 ° C without removing the moulds. The samples removed from the oven were left to cool until the room temperature reached. Finally, the compressive strengths of samples were performed in accordance with TS EN 196-1.

Table 1. The amounts of materials for tests on pozzolanic activity

	TS 25	The amounts for tests	
		Clinoptilolite	Analcime
Slaked lime (CaOH₂)	150gr	150gr	150gr
Pozzolan	2x150x(density of pozzolan /density of CaOH₂) (gr)	2x150x(2.11/2.15)= 294.42gr	2x150x(2.28/2.15)= 318.14gr
Standard sand	1350gr	1350gr	1350gr
Water	0.5x (150+pozzolan) (gr)	0.5x(150+294.42) =222.21gr	0.5x(150+318.14) = 234.07gr

3. RESULTS AND DISCUSSION

3.1. The Physical Properties, Chemical Compositions and Pozzolanic Activities of Zeolites

The physical properties, chemical compositions and pozzolanic activity values of natural zeolites are given Table 2. XRD diffraction patterns of zeolites are given Figure 1 and Figure 2.

Table 2. The Physical properties, chemical compositions and pozzolanic activity values of natural zeolites

Chemical composition	Clinoptilolite (wt.%)	Analcime (wt.%)	Physical properties		
SiO_2	64.70	46.71		Clinoptilolite	Analcime
Al_2O_3	11.21	17.24	Density, (g/cm³)	2.11	2.28
Fe_2O_3	1.38	9.21	Specific surface (Blaine) (cm²/g)	4079	4780
CaO	2.08	3.03	Pozzolanic activity values		
MgO	0.79	5.29	TS 25 limit values	Clinoptilolite	Analcime
Na_2O	0.38	4.84	Lime-pozzolan mix. 7 day comp. strength>4MPa	9.02MPa	6.30MPa
K_2O	3.78	4.08	$SiO_2+Al_2O_3+Fe_2O_3$ wt. content >%70	%77.30	%73.16
Loss of ignition	11.80	7.00			

According to Table 2. In TS 25, one of the conformity criterias for pozzolans is the 7 day compressive strength of samples prepared with lime-natural pozzolan mixture. The limit value of the compressive strength is at least 4 MPa. In experimental studies performed for clinoptilolite and analcime, the average compressive strength values for the lime-zeolite (pozzolan) mixture samples were determined as 9.02MPa and 6.30MPa, respectively. It has also been emphasized that the sum of SiO_2 + Al2O₃ + Fe₂O₃ in TS 25 should be at least 70% by mass. The value of this total was found to be 77.3% for clinoptilolite and 73.16% for analcime. At the same time, the specific surfaces of the pozzolans should be greater than 3000 cm²/gr. The specific surfaces of the pozzolans which is used in this study were found to be 4079 cm²/gr for clinoptilolite and 4780 cm²/gr for analcime. In the pozzolanic activity tests. Because of the specific surfaces of natural zeolites were below of portland cement fineness, the reaction which is between pozzolan and lime was increased. It is thought that, this situation was lead to an increment at the value of pozzolanic activity. These values show that the zeolites used in the study have an usability potential as a pozzolan.
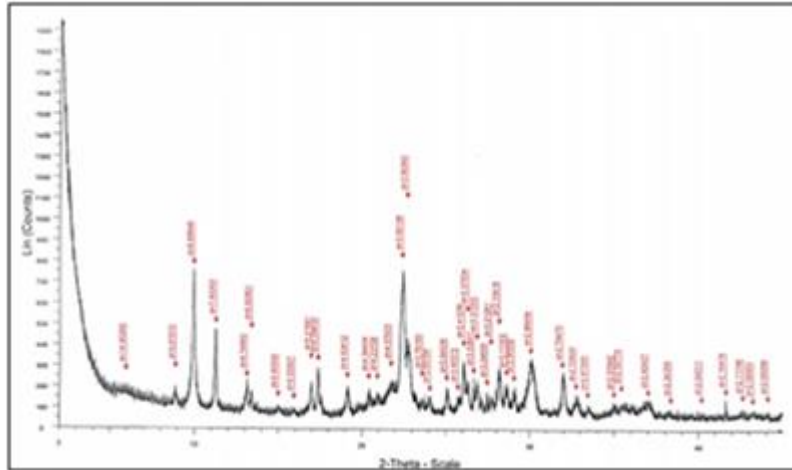
Figure 1. XRD diffraction patterns of clinoptilolite sample
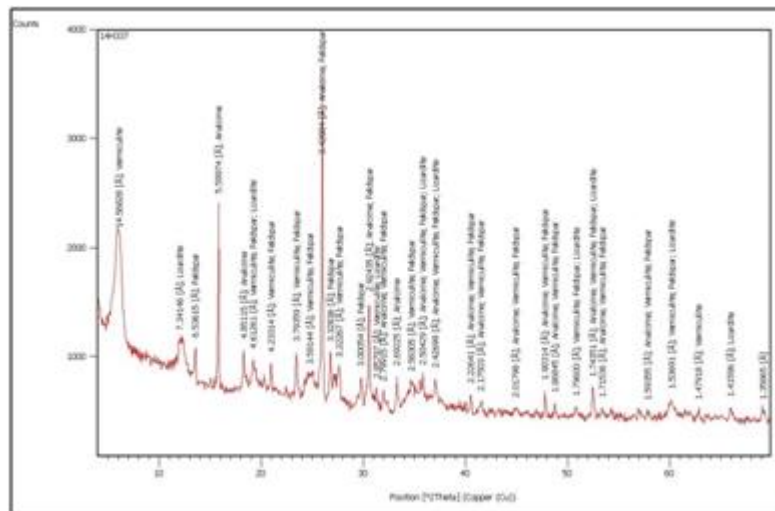
Figure 2. XRD diffraction patterns of analcime sample

3.2. Mineralogical Structures of Zeolites

According to the mineral modal ratios at the mineralogical composition results determined by the X-ray diffraction analysis (XRD) of the clinoptilolite sample, the sample is characterized by zeolite industrial raw material. The modal-mineralogical composition identified as the result of the XRD analysis of the sample is given below. The ratio of clinoptilolite in the sample is 80-85% (Figure 3). As other minerals; Opal-CT is in a certain ratio, illite mica, quartz and feldspat are low ratios. SEM views obtained using a Scanning Electron Microscope of clinoptilolite were determined with analysis result reports performed by Gordes Zeolite Company.

- Clinoptilolite (Silicate–Zeolite Group Mineral) (%80-85)

- Opal-CT (Opal-Critobalite/Tridimite) (Silicate-Silica Group Mineral) (10-15%)

- Quartz (Silicate-Silica Group Mineral (% <2)

- Feldspat (Na and K-Felspat) (Silicate-Feldspat Group Mineral) (% <2)

- İllit-Mica (Silicate-Clay-Mica Group Mineral) (% <5)

The analcime rock is a vitric tuff and consists of glass splinters and crystal components. The glass splinters are converted to zeolite and chlorite, which are heavily altered. Cryptocrystalline silica formations are present in the binder material. The crystalline components are heavily fragmented augite (pyroxene) and very little biotite. Opaque minerals are found in less than 5% of the rock (Figure 4).

SEM views of analcime were determined by Mineralogy and Petrography Laboratory of General Directorate Of Mineral Research And Explorations. The clinoptilolite and analcime samples confirm the national and international standards required for zeolite applications.

Figure 3. SEM view of clinoptilolite sample
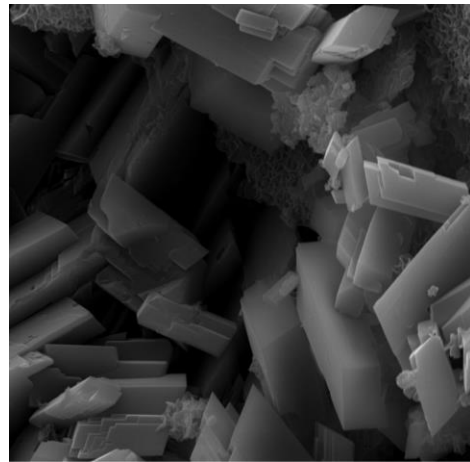
Figure 4. SEM view of analcime sample

When the SEM views of the two zeolites are examined, it is understood that the clinoptilolite and analcime zeolites are in a crystal structure. It is thought that, despite crystal structures of natural zeolites, the reason of exhibit pozzolanic activity is the may be reaction with Ca (OH) $_2$ of free silica and alumina components as a result of dissolution at certain scale of the crystal structure in high pH environment.There are some studies in the literature about the dissolution of crystalline structures in low or high pH environments of natural zeolites [16,17].

4. CONCLUSIONS

1) It has been determined that both natural zeolites (clinoptilolite and analcime) used in the study have potential to be used in sustainable blended cement productions. Due to their favorable qualities such as silica-alumina contents, pozzolanic activity values, low densities, high specific surfaces, glassy structures of rocks and mineralogical structures.

2) The 7-days average compressive strength values of lime-pozzolan mixtures for clinoptilolite and analcime determined by pozzolanic activity tests accordance with TS 25 were 9.02 MPa and 6.30 MPa respectively. Accordingly, the determined compressive strengths are satisfied by TS 25 limit values.

3) The total SiO_2, Al_2O_3 and Fe_2O_3 contents of the natural zeolites used in the study are similar to some pozzolanic materials used in the cement industry. The value of this total was found to be 77.3% for clinoptilolite and 73.16% for analcime. The determined total content values are satisfied by TS 25 limit values.

4) In the result of this study conducted to determinate the puzolanic activity of analcime and to investigate whether it has potential availability in sustainable blended cement production. It is thought that analcime which is the second valuable mineral of natural zeolites may be an alternative to clinoptilolite, which is more widely used in the construction industry. It is also thought that energy-saving, economical and environment-friendly solutions will be obtained due to using less portland cement in cement production. But, it should not be forgotten that, this result may become more certainty after tests for strength and durability on analcimes which will be obtained from different regions.

REFERENCES

[1]. Erdogan, T. Y., Beton, METU Press, Ankara, 757s., 2013.
[2]. Massazza F., "Pozzolanic Cement", Cement and Concrete Composites, v:15, pp: 185-214, 1993.

[3]. ASTM C 311, Standard test methods for sampling and testing fly ash or natural pozzolans for use a mineral admixture in portland-cement concrete, Annual book of ASTM standards, 1994.

[4]. TS EN 450, Fly ash for concrete - Part 1: Definition, specifications and conformity criteria, Turkish Standarts Institute, Ankara, 2013.

[5]. TS 25, Natural pozzolan (trass) for use in cement and concrete - Definitions, requirements and conformity criteria, Turkish Standarts Institute, Ankara, 2008.

[6]. Kılınckale F.M., "Cesitli puzolanların puzolanik aktivitesi ve bu puzolanlarla üretilen harcların dayanımı", Chamber of Civil Engineers, Journal of Technical, pp: 1217-1229, 1996.

[7]. Chan SYN, Ji X. Comparative study of the initial surface absorption and chloride diffusion of high performance zeolite, silica fume and PFA concretes. Cem Concr Compos. 1999; 21:293–300.

[8]. Trnı´k, A., Scheinherrova´, L., Medved, I., Cˇ erny, R., "Simultaneous DSC and TG analysis of high-performance concrete containing natural zeolite as a supplementary cementitious material", J Therm. Anal. Calorim., 121:67–73, 2015.

[9]. Kumbasar, I., Silika mineralleri, Press of Istanbul Technical University, Istanbul, 1977.

[10]. Yazıcıoglu, O.F., "Investigation of usability as pozzolanic additive material of natural zeolite (analcime) in sustainable productions of cement and Concrete industry", MSc. Thesis, University of Ordu, Institute for Graduate Studies in Science and Technology, Department of Renewable Energy, 85p, 2016.

[11]. Akgün, Y., Yazıcıoglu, O.F.," The effect of two different natural zeolite additions on the abrasion resistance of cement mortar", Ordu University, Journal of Science and Technology, Vol:6, No: 1, 94-104, 2016.

[12]. ASTM C 430, Test method for fineness of hydraulic cement by the 45-µm (No. 325) sieve, American Society for Testing and Materials, United States of America, 2005.

[13]. TS EN 196-1, Methods of testing cement - Part 1: Determination of strength, Turkish Standarts Institute, Ankara, 2016.

[14]. TS EN 197-1, Cement – Part 1: Composition, specification and conformity criteria for common cements, Turkish Standarts Institute, Ankara, 2012.

[15]. TS 196-6, Methods of testing cement - Part 6: Determination of fineness, Turkish Standarts Institute, Ankara, 2010.

[16]. Yamamoto, S., Sugiyama, S. , Matsuoka, O., Kohmura, K., Honda, T., Banno, Y., Nozoye, H., Dissolution of Zeolite in Acidic and Alkaline Aqueous Solutions As Revealed by AFM Imaging, Journal of Physical Chemistry 100, pp:18474-18472, 1996.

[17]. Cizmek, A., Subotic, B., Smit, I., Tonejc, A., Aiello, R., Crea, F., Nastro, A., Dissolution of high-silica zeolites in alkaline solutions II. Dissolution of 'activated' silicate-1 and ZSM-5 with different aluminum content, Microporous Materials 8, pp:159-169, 1997.

Water Budget and Water Quality of Akgol Lake Sensitive Basin

Rabia Koklu[1], Emrah Dogan[2]

Abstract

The aim of this study is to propose a solution for Akgol (Sakarya) Lake, which is at risk from water budget and water quality due to seasonal water reductions and human activities around it. For this aim, the water budget and water quality of the Akgol Lake sub-basin, which is in the sensitive water masses class in Sakarya Basin, were evaluated. Firstly evaporation-precipitation values were obtained from the Sakarya Provincial Meteorological Affairs Directorate. Samples were taken for a period of 3 months from the 3 tributaries and drainage channel. While the samples were taken, flow measurements were made in the channels and the water level fluctuations was determined simultaneously. Some of the water quality parameters that cause eutrophication in the lake and its tributaries have been measured. In addition, lake water budget was determined by using rainfall and evaporation data, flow measurements and water fluctuations. According to the results of the study, to ensure a healthy continuity of life cycle and ecology of the Akgol Lake Basin, it is necessary to control point and diffuse pollutants, regulation of water level and to determine the protection status of the basin.

Keywords: *Water Budget, Water Quality, Sensitive Basin, Akgol Lake (Sakarya)*

1. INTRODUCTION

The lakes used for different purposes such as drinking, use and agricultural irrigation are being damaged in quality and quantity as they are used as a receiving medium for industrial wastes, agricultural wastes and urban wastes. Since the intense pollution in the lakes prevents us from benefiting from these sources, it is necessary to protect water resources from pollution.

Big Akgol located between the borders of Karasu and Ferizli districts bound to Sakarya, is formed by tectonic activity and the set brought by the alluviums of Sakarya River. The lake, which is of special importance as the natural resource of the event, is a delicate lake under the threat of a great pollution and consequently the useful areas of use are rapidly restrained. Due to the fact that it is a shallow lake, its surroundings are completely surrounded by agricultural areas, it is surrounded by a large-scale canal and many small drainage channels opened by farmers, and the drainage door is used to drain water from the grounds, Akgol's water level is constantly falling and its water quality is deteriorating. According to the results of measurements made in 2001, the water quality was determined as the IVth and the trophic level in the lake was found to be eutrophic [1]. Between May 2003 and April 2004, the trophic level was calculated as C = 18.5 and the lake found to be highly eutrophic according to the yearly yield. This rate is better between June and August. In the Big Akgol, this ratio was found to be 36. Considering the phytoplankton species and densities that this ratio and the lake contain, it is determined that Big Akgol is in hypereutrophic level [2]. Due to water extraction and high evaporation, aquatic plants can reach the water surface, especially in the summer months. This process not only deeply affects the stability of the lake aquatic ecosystem, but also accelerates the depletion of the lake's life.

In this study, it was aimed to determine the effect of lake water budget and water quality on the lake by calculating the effect of evaporation, rainfall, and rainfall amount on the water level of Akgol to keep the lake water level at optimum level due to decrease of water level.

---

[1] Corresponding author: Department of Environmental Engineering, Sakarya University, 56180 Sakarya, Turkey. rkoklu@sakarya.edu.tr

[2] Department of Civil Engineering, Sakarya University, 56180 Sakarya, Turkey, dogan@sakarya.edu.tr

2. MATERIAL AND METHODS

2.1. Study Area

Big Akgol is located between Karasu and Ferizli district boundaries of Sakarya province. Golkent, Adatepe, Bakırlı, and Karasu districts in the north of the city of Ferizli are the borders of the Konacik settlements and the Big Akgol is in the status of the Nature Protection Area. It lies 4-5 km from the Black Sea and lies between 41 ° 01 'northern latitudes and 30 ° 33' east longitudes. The lake, which is 39 km from Sakarya city center and 13 km away from the center of Ferizli district, is the result of a tectonic activity and is the result of a set of alluvial deposits of the Sakarya River alluvium. Since the area where the lake is located was far away from the Sakarya River, alluvials survived without being drowned, so that Akgol came to an edge as a pond [3]. Its surface area is 3.5 km^2 and its maximum depth is 5 m [4]. The average height at sea level is 60 m. Big Akgol location map and lake characteristics are shown in Figure 1 and Table 1, respectively. Agricultural fertilizer wastes and sediment flow reaching the lake due to very intensive agriculture around the lake increased the intensity of eutrophication in the lake. The three canals connected to Big Akgol Lake constitute the most important source of nitrogen and phosphorus in the lake with their agricultural and domestic waste loads. Also, septic leak waters from some settlement areas around it are another pollutant for the lake. Since no measures have been taken in order to prevent eutrophication in the lake, excessive algal growth is seen every summer. Water quality in Akgol is determined by water budget.

Figure 1. Big Akgol Location MAP

2.2. Station and Parameters

The samples were taken at regular intervals from nine points, from the Kulak, Park and Kusca channels feeding the birds, from the points where the channels are mixed with the lake, from the point of intersection, from the middle point and from the exit channel. Coordinates of the stations are given in Table 1.

Table 1. Coordinates of the stations

	Stations	N	W
A	Kusca Canal Inflow	41° 2'4.87"	30°33'28.09"
B	Park Canal Inflow	41° 2'0.69"	30°33'32.05"
C	Kulak Canal Inflow	41° 2'4.33"	30°33'42.79"
D	Level Measurement Point	41° 2'14.59"	30°33'42.02"
E	Middle Point	41° 2'40.84"	30°33'48.30"
F	Kusca Canal	41° 1'52.56"	30°33'12.19"
G	Park Canal	41° 1'53.94"	30°33'28.59"
H	Kulak Canal	41° 1'54.05"	30°34'6.06"
I	Outflow	41° 3'43.48"	30°36'8.05"

pH, temperatures (T, 0C), electrical conductivity (EC, mohm/cm), dissolved oxygen (DO, mg L-1), 5-days ammonia nitrogen (NH4–N, mg L-1), nitrate nitrogen (NO3–N, mg L-1), nitrite nitrogen (NO2–N, mg L-1), Total Phosphorus (TP, mg L-1), were analyzed by using standard methods.

2.3. Water Quality

Water quality classes of the parameters to SWQM Directive are shown in Table 2. Water quality classes were determined using conventional classification method. All calculation was applied according to SWQM Directive and the parameters were grouped for their classes [5].

Table 2. Water Quality Classes in SWQM Directive (Turkiye)

Water Quality Parameters	Water Quality Classes			
	I	II	III	IV
Genereal Conditions				
Temp. (ºC)	≤ 25	≤ 25	≤ 30	> 30
pH	6.5-8.5	6.5-8.5	6.0-9.0	6.0-9.0
EC (µS/cm)	< 400	400-1000	1001-3000	> 3000
Group A				
DO (mg O_2/L)	> 8	6-8	3-6	< 3
Group B				
NH_4^+-N (mg/L)	< 0.2	0.2-1	1-2	> 2
NO_2^--N (mg/L)	< 0.01	0,06	0.12	> 0.3
NO_3^--N (mg/L)	< 5	5-10	10-20	> 20
TP (mg/L)	< 0.03	0.16	0.65	> 0.65

2.4. Water Budget

The principle of conservation of mass leads to the equation of continuity (water balance, water budget) which shows that there is neither water nor water in any part of the hydrological cycle. In this equation;

X: the amount of water entering the considered hydrological system,

Y: the amount of water from the system at the unit time,

S: is the amount of water accumulated in the system (Lake Displacement) (Figure 2.)
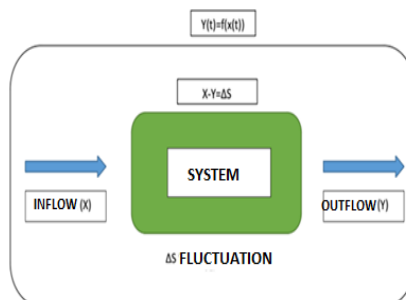
Figure 2. Mass Balance

3. RESULTS

Water quality of Kulak canal is IInd class according to general condition and oxygenation parameters and IIIrd class according to nutrient parameters. According to the general condition parameters of Kusca canal is IInd class, Ist class according to oxygenation parameters and IIIrd class according according to nutrient parameters. Park Canal is IInd class and IVth class according to general condition, oxygenation parameters and nutrient parameters respectively.

Since the rivers feeding the lake especially include the domestic wastewaters of the Kusca and Park Canal, Golkent districts that are not connected to the infrastructure and the polluters from the livestock activities in the vicinity, the quality of the water is particularly important in terms of nutrient parameters IIIrd and IVth class. Especially high nitrite concentration according to the measurement results indicates that there is continuous domestic wastewater entry into the streams.

The high phosphorus parameter also indicates domestic and agricultural pollution. Water quality on the lake is IIIrd class according to general condition, oxygenation and nutrient parameters. According to general condition, nutrient parameters and oxygenation parameters in the middle point, water quality is determined as IIIrd and I[st] class respectively. Observations from the measurement points on the lake clearly show that the side tides feeding the lake, the residential areas around the lake, and the agricultural lands have a negative effect on the water quality of the lake. Especially, when the tributaries and lakes are monitored together, it can be said that the water quality of the tributaries determines the water quality of the lake. Although the

general conditions and oxygenation parameters were not high, the nitrogen components were also found to be high in the lake measurements, and this was due to the water quality has found to be IIIrd class. As the nitrogen components and phosphorus are high, it will cause eutrophication in the lake, so pollution intrusion must be prevented as soon as possible.

Table 3. Obtained Water Quality Classes for SWQM Directive (Turkiye)

	Kulak Canal			Park Canal			Kusca Canal		
	Mean	WQC	WQC	Mean	WQC	WQC	Mean	WQC	WQC
Temp. (ºC)	14.37	I		11.65	I		14.1	I	
pH	7.81	I		8.05	I		8.2	I	
EC (µs/cm)	658.72	II		530.15	II		481.65	II	
DO %	57.52	II		60.25	II		121.05	I	
DO (mg/L)	5.87	II	III	6.29	II	IV	12.27	I	III
NH$_4$ (mg/L)	0.81	II		0.89	II		0.74	II	
NO$_2$ (mg/L)	0.28	III		0.31	IV		0.21	III	
NO$_3$ (mg/L)	0.44	I		1.16	I		0.49	I	
TP (mg/L)	0.26	III		0.84	IV		0.09	II	

	Level Meas. Point			Middle Point			Outflow		
	Mean	WQC	WQC	Mean	WQC	WQC	Mean	WQC	WQC
Temp. (ºC)	18.30	I		18.03	I		18.70	I	
pH	8.72	III		8.72	III		8.20	I	
EC (µS/cm)	334.10	I		338.57	I		356.07	I	
DO %	103.40	I		96.80	I		86.20	II	
DO (mg/L)	9.79	I	III	9.26	I	III	8.13	I	III
NH$_4$ (mg/L)	0.83	III		0.57	III		0.59	II	
NO$_2$ (mg/L)	0.29	III		0.20	III		0.21	III	
NO$_3$ (mg/L)	0.07	I		0.10	I		0.09	I	
TP (mg/L)	0.11	III		0.18	III		0.24	III	

	Kulak Canal Inflow			Kusca Canal Inflow			Park Canal Inflow		
	Mean	WQC	WQC	Mean	WQC	WQC	Mean	WQC	WQC
Temp. (ºC)	18.77	I		18.73	I		21.60	I	
pH	8.78	III		8.58	III		8.75	III	
EC (µS/cm)	348.50	I		350.90	I		398.60	I	
DO %	107.27	I		102.37	I		112.35	I	
DO (mg/L)	10.07	I	III	9.58	I	III	9.89	I	III
NH$_4$ (mg/L)	0.56	III		0.56	II		0.08	II	
NO$_2$ (mg/L)	0.28	III		0.20	III		0.02	II	
NO$_3$ (mg/L)	0.06	I		0.10	I		0.11	I	
TP (mg/L)	0.11	II		0.12	II		0.16	II	

Table 4. Water budget

	24.03.2016	28.04.2016	Mean	Inflow (hm³)	Outflow (hm³)	ΔS
Lake Volume (hm³)	4.065	3.774				-0.291
Area (km²)	4.247	3.860	4.054			
Outflow (m³/s)	0.478	0.143	0.311	0	0.800	-0.800
Stream Inflow (m³/s)	0.083	0.045	0.064	0.167	0	0.167
Precipitation (mm)	68.600	49.000	61.730	0.250	0	0.250
Evaporation (mm)	0	116.000	108.260	0	0.440	-0.439
Infiltration (hm³)				0.535		0.535

Δs = Inflow (Precipitation+ Stream Inflow+Infiltration) - (Outflow+Evaporation)

-0.291 = 0.250 + 0.167 + X - 0.805 – 0.439

X = 0.535 hm³

Infiltration = 0.206 m³/s

The value of infiltration is found by means of the mass method using the rainfall and evaporation data and the flow measurements of the lake entering and falling from the lake based on the water budget calculations. According to the measurements, the water level in the lake has decreased to 2.39 m. The Lake total volume is decreased by 0.291 hm^3. The total monthly infiltration value was found to be 0.535 hm^3. Despite being fed by infiltration from the lake underground, serious decreases in water level are observed. It can be argued that the reason for this is the uncontrolled drainage canal and drainage cover.

4. CONCLUSIONS

The water level falls in Akgol as a result of the surroundings being completely surrounded by agricultural areas, a large-scale canal for the protection of agricultural land from floods and numerous small drainage channels opened by farmers, and the drainage door being used for drainage. In the summer months due to water evacuation and high evaporation, aquatic plants can reach the water surface. This process not only deeply affects the stability of the lake aquatic ecosystem, but also accelerates the depletion of the lake's life. For this reason, the key solution is to control point and diffuse pollutants, regulation of water level and protection status of the basin in order to ensure a healthy continuity of life cycle and ecology of Akgol and Akgol Basin.

REFERENCES

[1]. B. Sengorür, A. Demirel, Determination of Eutrophication and Water Quality Class in Akgol (Golkent-Sakarya), Journal of SAU Institute of Science, Vol.6-3, 2002.
[2]. S. P. Akyüz, Y.A. Morkoyunlu, E. Soylu, Büyük Akgol (Sakarya) Phytoplankton Composition and Seasonal Changes, Journal of SDÜ Egirdir Water Products Faculty, 2015.
[3]. Alluvial Morphology of T. Bilgin, Adapazarı Plain and Sapanca, and Geomorphological Evolution in the Quaternary, Istanbul University, Literature Faculty Publications, No. 2572, 199 pp., Istanbul, 1984.
[4]. H. İnandık, The Lakes of Turkey (Morphological and Hydrological Properties), İstanbul University Publication no: 11-55, Geography Institute Publication no: 44, 1961.
[5]. TC. Ministry of Forestry and Water Affairs, General Directorate of Water Management, Surface Water Quality Regulation, 15 April 2015.
[6]. TR Ministry of Forestry and Water Works, General Directorate of Water Management, Measurement of Bathymeters of Lake in Sakarya Basin, Design of Inventory Works and Final Report of Design of Lake Landscapes, Ankara 2014

Evaluation of Total Phosphorus Loads in the Eastern Black Sea Basin

Nail Erdogan[1], Rabia Koklu[2], Bulent Sengorur[2], Selma Ayaz[1],Yakup Karaaslan[3]

Abstract

In this study, it is aimed to estimate the total phosphorus (TP) pollution loads which can reach to the water environment from point and diffuse pollutant sources in Eastern Black Sea Basin. Within the scope of the study, information on the urban wastewater infrastructure and solid waste management status of all the settlements over 2000 inhabitants in the basin was obtained. In addition, information about the individual industries that constitute the priority in terms of pollution load for the basin and the environmental infrastructure of all Organize Industrial Zones in the activity was collected. In this context, information and coordinates were obtained about the urban and industrial wastewater treatment plant discharge points, direct discharge points, deep sea discharge points and regular/irregular solid waste sites. Using the obtained data, basin population was estimated between 2017 and 2040 and TP loads were determined. According to the results, the highest values in the study area in terms of TP load were obtained in Ordu-Giresun and Trabzon waters. As a result of the estimations, the decrease in the TP loads from 2017 to 2040 was observed.

Keywords: *Total Phosphorus Load, Pollution Sources, Eastern Black Sea Basin*

1. INTRODUCTION

Increasing world population and water demands in different sectors are creating serious pressures on water resources. Water resources are threatened by dispersed pollutants, especially from agricultural activities, as well as domestic and industrial activities.

Eastern Black Sea Basin is one of the 25 hydrological basins in Turkey (Figure 1). Watershed management studies are carried out by subdivision of hydrological basins. In the approach taken by TUBITAK MAM, the micro basins previously determined for the Eastern Black Sea basin with shallow waters are divided into 4 sub-basins, taking into account administrative restrictions for administrative purposes among them, including Ordu-Giresun waters, Harsit waters, Trabzon waters and Rize-Artvin waters [1].

The total area of the Eastern Black Sea Basin is 2284439 ha according to the CORINE classification; including artificial areas, agricultural areas, forests and semi-natural areas, wetlands and surface waters. The ratio of the basin projection area to the projection of Turkey is 2.92% [1]. It is observed that the studies on the basin scale are not enough and at the same time all the pollution load sources are not studied. This study aimed to determine the phosphorus pollution loads from point and non-point sources in Eastern Black Sea Basin chosen as pilot basin. In the calculations of pollution load, it is necessary to apply detailed and complex watershed models which require time, cost and many data especially for non-point sources.

However, a generic approach has been developed in this study that will be more practical and able to be applied to all basins. In this context, urban and industrial wastewaters and landfills were investigated as point pollution sources; agricultural and livestock activities, land use, septic tank and solid waste irregular landfills were investigated as non-point pollution sources.

---

[1] *TÜBİTAK-MRC Environment Institute, Gebze-Kocaeli, TURKEY*

[2] *Corresponding author: Department of Environmental Engineering, Sakarya University, 56180 Sakarya, Turkey. rkoklu@sakarya.edu.tr*

[3] *The Ministry of Forestry and Waters Affairs Ankara, TURKEY*
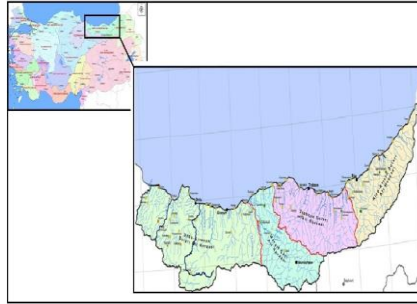
Figure 1. 25 hydraulic basins in Turkey and Eastern Black Sea Basin [1]

2. MATERIAL AND METHODS

2.1. Population Prediction

For the settlements within the scope of the study, urban / rural, summer / winter and equivalent based population prediction scenarios were established up to 2040. Among these scenarios, the population estimate that best reflects the basin structure is chosen. Population estimations were made with "decreasing rapid geometric increase method" on the basis of the cities located in the basin by taking account the 1975-2016 people, urban and rural distinction, summer and winter differences. According to this calculation method, it is assumed that the rate of population growth over time will decrease and will form an "s" curve on the graph [1].

2.2. Point Pollution Sources

Point pollution loads have been investigated as urban and industrial wastewater and solid waste landfill leachate. In the study, urban pollution loads and wastewater discharges from villages with a population of more than 2000 were calculated. In the calculations, the points included in the Wastewater Treatment Facilities Technical Procedures Declaration [2] have been taken into consideration. These values were also added to the leachate entering the wastewater collection system from the groundwater. Total wastewater flow per person was calculated by increased 50% in 2017, 40% in 2020, 35% in 2030 and 30% in 2040. The pollution load arising from the settlement sites examined was considered as point pollution in the places where sewerage network was located and non-point pollution in places where there was no sewage network. The point urban pollution load is discharged directly to the basin or after being removed in WTP depending on whether it is WTP or not. In the calculations, the population ratio of the sewer network in the settlements is taken into account. In addition, urban pollution loads have been increased by 10% for domestic wastewaters originating from the industry.

In the Eastern Black Sea Basin, pollutant load calculations made from industrial facilities were made while the pollutant load limit values determined in the discharge standards of the related industry in the Water Pollution Control Regulation (WPCR) [3] were taken into consideration by multiplying them by a certain safety coefficient, depending on whether or not the industrial facilities are environmental permitting documents. For facilities that do not have environmental permit documents, the load calculations have been carried out from the view that the limit values given here will be obtained in the case of 15% treatment for TP. Facilities within the watershed discharging the waters to the receiving center were considered to be in the basin, and those discharging to the sea were considered to be outside the watershed. The value found for the flow and pollution load values arising from the facilities that are not accessed to the dataset is multiplied by a specified safety factor (10%). Industrial plants that are only domestic wastewater are not included in the industrial load calculations, as they are accounted for in domestic pollutant load calculations. Ratios based on literature data have been used for cases in which the concentration of one or more of the polluters that are bidding for the relevant sub-sector in WPCR is not significant [4-5]. When calculations are made, 2017 year flow values of the basin industries are used. It is accepted that the yearly flow rates in 2017 and the distribution of the river to the basin and Black Sea will remain the same until 2040.

When pollutant load calculations are made, it is assumed that there will be differences on the treatment efficiencies for several years. For this reason, the discharge limits of WPCR are multiplied by coefficients that vary with years. These coefficients are given in Table 1.

Table 1. Used treatment yield coefficients according to years [6]

Years	Coefficients	Explanation
2017	20% more of the WPCR discharge limits (x1,2)	To stay on the safe side
2020	Same as WPCR discharge limits (x1,0)	Improved WTP performance
2030	90% of WPCR discharge limit (x0,9)	Improved WTP performance
2040	80% of WPCR discharge limit (x0,8)	Improved WTP performance

In the calculation of the point pollution load due to solid wastes for the Eastern Black Sea Basin, all municipalities are preferably included in proposed or new waste disposal units; closure and rehabilitation of existing irregular landfills; establishment of new regional sanitary landfills and other waste management facilities; (50%) collected from rehabilitated irregular landfills, pre-treatment of leachate from existing and new sanitary landfill sites, and subsequent treatment of urban WTPs by transporting or linking to urban sewerage network were considered. Calculations were made taking into account the approaches included in the Solid Waste Master Plan (SWMP) [7] and the Waste Management Action Plan [8]. The annual mean rainfall heights are utilized in the calculation of the leach water streams for the current irregular landfills. For this purpose, meteorological bulletin records specific to the province have been used since 1975 from the General Directorate of Meteorology (GDM).

2.3. Non-Point Pollution Sources

The non-point pollution loads are scattered around and it is difficult to determine and measure the movement and behavior of the earth until it reaches water mass. For this reason, the following methodology has been used in this study rather than the application of detailed and complex watershed models requiring time, cost and many data for non-point sources. Phosphorus sources of pollution in the basin are listed as agricultural activities, animal husbandry, land use, irregular solid waste disposal sites and septic tank. The applied methodology is determined by the land use CORINE system database. The unit loads of each pollution source were selected from the ranges specified in the literature. Unit loads, as is known, depend on climatic conditions, soil characteristics, population tendency, agricultural pattern and applications. The amounts of pollutant loads are calculated according to the unit loads given in Table 2.

Table 2. Unit loads used to calculate the non-point loads according to the activities [1]

Land use	TP (kg/ha.year)
Rural area	0.90
Forests	0.05
Meadow and pasture	0.1
Urban area	0.50
Farming	**TP (kg/ton.day)**
Cattle ($\approx$ 500 kg)	0.1
Small bow ($\approx$ 45 kg)	0.06
Poultry ($\approx$ 2 kg)	0.22
Agricultural activities	**TP (-)**
(By region)	2.5%
Solid waste leachate	**TP (mg/L)**
(According to the adjacent rainfall)	10

Non-point pollutants reach the receiving environment with complicated transportation and transformation routes depending on meteorological, climatic, geographical and geological conditions. For this reason, it is accepted that some of the pollution will reach the surface water. The values obtained from literature [9-16] related to these quantities are given in Table 3.

Table 3. Percentage of Non-point pollution sources reaching the surface water

Non-point pollution sources	Reaching the surface water (%) TP
Agricultural activities	2.5
Farming	2.5
Septic tanks	70

3. RESULTS

As a result of the calculations, it is expected that the total population of settlements with municipalities above the 2000 population of the basin in 2040 will be 3113779. Urban pollution loads calculated from the population constitute 99% of the point TP load generated in the basin. Urban origin pollution followed by industrial pollution (1%). Figure 2 shows the change of point TP load with respect to years. As can be seen, almost all of the point TP loads in the sub-basins are due to urban wastewater. After the planned WTPs are set up, the urban TP load is reduced and the point TP load due to the solid waste leaking water after the establishment of the solid waste landfill is markedly increased. It is considered that point source pollutants originating from solid waste leachate will be treated in their own structures or in urban WTPs. The TP load of industrial origin decreases partially after 2030. This decrease is related to the establishment of WTP in industrial facilities and the improvement of the character of the wastewater by revising existing WTP facilities. The evaluation of point TP loads on the basis of years is given in Figure 3. The point phosphorus loads detected in the Ordu-Giresun Waters (204 tons / year) and Trabzon Waters (186 tons / year) sub-basins are relatively higher. This is related to the sub-basin population.
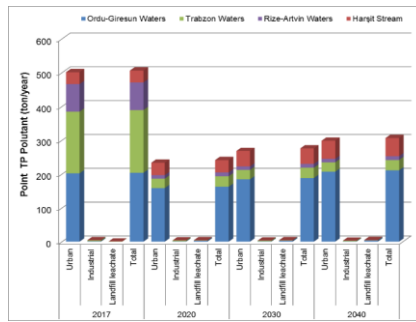
Figure 2. Distribution of point TP loads by years
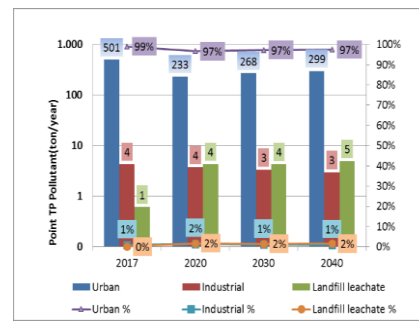
Figure 3. Change of point TP loads by years in sub-basin

When the Eastern Black Sea basin evaluated according to sources non-point TP loads, maximum TP loads stems from livestock activities (33%), followed by, respectively, septic use (29%), land use (20%), agricultural activities (16%) and solid waste leak waters (2%). The highest non-point TP value comes from the Ordu-Giresun sub-basin (224 tones / year). Trabzon Waters (136 tones/year), Rize-Artvin Waters (76 tons / year) and Harsit Stream (57 tones / year) are followed by this sub-basin respectively. The distribution of the non-point TP loads is given in Figure 5.
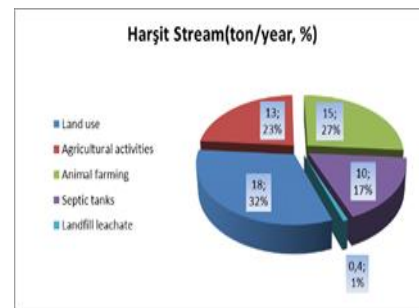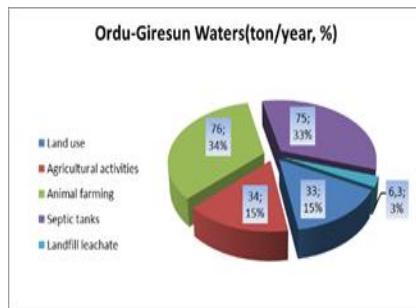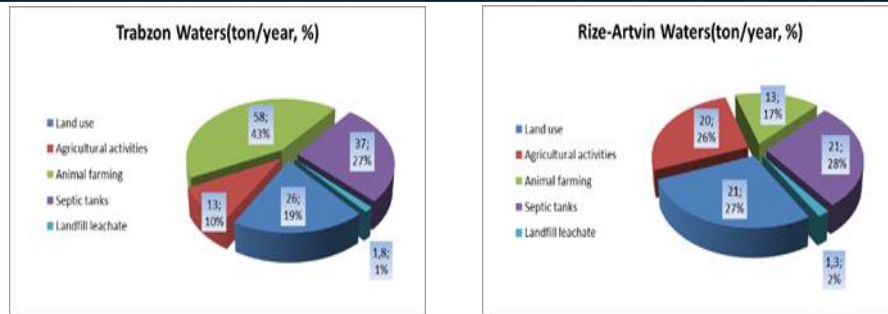
It is seen that point pollution loads from urban areas, industrial facilities and solid waste are compared with non-pollution loads in the Eastern Black Sea Basin, point and non-point pollution have approximately equal share in the total. The ratio of the point charges to the total load for 2017 is 51% based on the TP parameter. The highest phosphorus load in the basin is due to the Ordu-Giresun waters (43%) and Trabzon waters (32%) sub-basins (Figure 5).
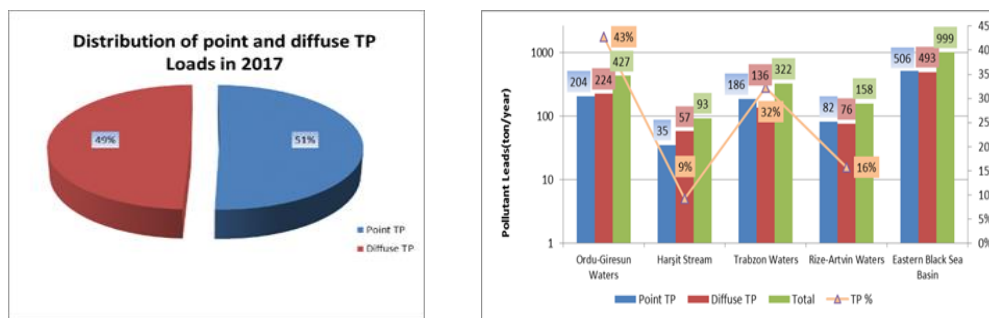
Figure 5. Eastern Black Sea Basin point and non-point TP loads distribution in 2017

4. CONCLUSION

In the light of the information presented above it is envisaged that the generic approach used gives an idea as to the sources of pollution and that its outcomes can draw road maps for decision makers. Even if it is possible to reduce point and diffuse pollutant sources, it is not possible to prevent them completely. With protective measures, loads can be reduced at a certain rate. It is expected that urban settlements will improve with the assumption that all settlements with municipal organization have WTP. The reduction in pollutant load from industrial plants is achieved through the establishment of WTP at industrial plants and the revision of existing AATs. In the future, it is expected that the non-point pollution will be controlled by the increase of organic agriculture and good agricultural practices, the decrease of fertilizer use, the increase of animal husbandry activities and the continuation as livestock breeding in farms.

Leachate, which appears to be the source of pollution in the present case, is expected to reduce both the amount and the pollutant concentration considerably with regular solid waste landfills that have been rapidly constructed in recent years.

REFERENCES

[1]. S. Ayaz and N. Erdogan, *Project for the Preparation of Watershed Conservation Action Plans Final Report of Eastern Black Sea Basin*, TUBITAK MAM Environment and Cleaner Production Institute, Gebze, Turkey, 2013.
[2]. *Wastewater Treatment Facilities Technical Procedures*, TR. Ministry of Environment and Urbanization Legislation, Ankara, Turkey, 2010.
[3]. *Water Pollution Control Regulation*, TR. Ministry of Environment and Urbanization Legislation, Ankara, Turkey, 2004.
[4]. İ. Oztürk, *Big İstanbul Drinking water Project II Melen System Master Melen Basin Integrated Protection and Water Management Master Plan*, Final Report, ITU, Istanbul, Turkey, 2008.
[5]. *Project for the Preparation of Watershed Protection Action Plans for 11 Watersheds,* TUBITAK MAM Environment and Cleaner Production Institute, Gebze, Turkey, 2010.
[6]. S. Ayaz and N. Erdogan, *Burdur Basin Final Report*, TUBITAK MAM Environment and Cleaner Production Institute, Gebze, Turkey, 2010.

[7]. *Solid Waste Master Plan*, TR Ministry of Environment and Forestry General Directorate of Environmental Management, Ankara, Turkey, 2006.

[8]. *Waste Management Action Plan*, TR Ministry of Environment and Forestry General Directorate of Environmental Management, Ankara, Turkey, 2008.

[9]. S. Dahl and B. Kurtar, *Environmental Situation, Working Paper, No: 21, Omerli and Elmalı Environmental Protection Project - Feasibility Report, Omerli and Elmalı Joint Venture*, 1.1-5.10, Turkey, 1993.

[10]. FAO, *Organic Agriculture, Environment and Food Security, Food and Agriculture Organization of the United Nations*, Edited by Scialabba, N., and Hatam, C., Rome, Italy, 2002.

[11]. S. Ayaz , N. Erdogan, H. Gürsoy, E. Atasoy, C. Aydoner, İ. Oztürk, N. Cicek, L. Akca, *Solid Waste Storage Areas Detection of Pollutants from Leaking Waters, Case Study: Burdur Basin*, 3rd National Solid Waste Management Congress, 7-10 September 2011, TRNC.

[12]. D. Ozalp, *Determination of Polluted Sources and Management Recommendations in the Eastern Black Sea Basin*, Master Thesis, Supervisor: Prof. Dr. Aysegül Tanık, ITU, Institute of Science and Technology, 2009.

[13]. İ. Ozturk, A. Ozabalı, İ. Karakaya, K. Ericyel, *Tersakan Basin Integrated Protection Action Plan, Amasya Special Provincial Administration Directorate*, Biosfer Consultancy and Engineering Ltd., Volume I, II, 2009 .

[14]. M. Stolze, A. Piorr, A. Haring, S. Dabbert, *The Environmental Impacts of Organic Farming in Europe*, 6, Stuttgart, University of Stuttgart-Hohenheim, Germany, 2000 .

[15]. A. Witness, *Integrated Watershed Management*, Lecture Notes, ITU Environmental Engineering, 2007.

[16]. B. Yontar, *Determination of Pollutant Sources and Management Recommendations in the Aras Basin*, Master Thesis, Supervisor: Prof. Dr. Aysegül Tanık, ITU Institute of Science and Technology, Istanbul, 2009.

Influence of Tool Pin Profile on Mechanical Properties of 6082-T6 Friction Stir Spot Welds

Hakan Aydin[1], Oguz Tuncel[1], Mumin Tutar[1], Ali Bayram[1]

Abstract

Friction stir spot welding (FSSW) is a recent trend of joining lightweight sheet metals such as aluminum alloys. FSSW is a solid-state welding technique which uses a rotating tool consisting of a shoulder and a pin. The welding tool has two principal functions, which are producing frictional heating and material flow. The welding tool pin profile plays a major role in obtaining desirable weld. Therefore, the present study is performed on AA6082-T6 Al alloy to investigate the effect of pin profile on mechanical properties. In FSSW technique two different tools with the same shoulder diameter and concave shape but different pin profile, which are threaded cylindrical pin and threaded conical pin were used in this study. Also, dwell time was varied to determine the effect of the process parameter on lap-shear separation load. Tensile shear tests were carried out to find the weld static strength. From the experiments, the effects of pin profile and dwell time on FSSW formation and joint strength was determined.

Keywords: *Friction stir spot welding, 6082-T6, Tool Pin Profile, Mechanical Properties*

1. INTRODUCTION

Decreases in global sources make the production of lighter and environmentally friendly vehicles compulsory especially in the automotive industry. For this reason, high strength aluminum alloys have begun to replace with conventional steel.[1] The joining of metal sheets is an important challenge for better welding quality. Resistance spot welding (RSW) is suitable method for automation and high welding quality which is commonly used in joining of metal sheets. However, the application of the RSW to lightweight metals results in material melting, porosity, hydrogen cracking and shorter electrode tip life. Friction stir spot welding (FSSW) is a solid state welding method. It is seen as a competing technology to traditional methods (RSW and riveting)[2], [3].

FSSW is a novel method in which a specially designed rotating cylindrical tool with varying geometry and a probe pin plunge into the sheets. Heat input and the plastically deformed material made the solid state welding thanks to the rotating tool. Inappropriate welding parameter (rotational speed, dwell time, plunge depth, feed rate) and tool geometry (pin diameter, pin length, pin angle, pin profile shoulder diameter, shoulder angle) selection results in low mechanical strength and welding errors. For this reason, the welding parameters and tool specifications should be selected properly.[4], [5],[6]. In FSSW different welding zones (stir zone (SZ), thermo mechanically affected zone (TMAZ), heat affected zone (HAZ), base material (BM) and hook) generally are observed [7]. Hook is a characteristic feature for FSSW which is formed with upward bending of the sheet interface because of tool penetration into the bottom sheet. Tool geometry significantly affects the hook geometry and so static strength of FSSW. For this reason it is important to understand how pin profile and processing parameters affect hook formation, hook geometry and weld mechanical properties[8], [9].

Many works have been carried out concerning FSSW of Al alloy base materials: Babu et al [10] conducted the experiment in a heat treatable aluminium alloy in T4 and T6 conditions, with and without Alclad layers. Also they showed the effect of bond width and height on mechanical properties. Maximizing bond width and minimizing hook height is a good basis for process optimization. Badarinarayan et al [11] studied the effect of tool geometry on the key welding geometric features such as hook height, effective top sheet thickness and stir zone size and their effect on weld strength. High welding strength is obtained in welds made with concave tool. Also, they stated that stir zone size does not seem to play a significant role in this aspect but instead the

effective top sheet thickness is an important geometric feature that must be considered. Rao et al [12] carried out an investigation to quantify the influence of welding parameters on FSSW of a rare-earth containing ZEK100 Mg alloy. They showed that macro sections of FSSW with a large upper effective sheet thickness and a small hook height were found to have the highest lap-shear strength. And they reported that an increase in tool rotation speed resulted in lower hardness measurements, larger hook height, smaller effective sheet thickness and hook width.

In the present study, the test were conducted using lap-shear specimens of FSSWed AA6082-T6 aluminum alloy. The mechanical properties of FSSWed joints have been highlighted using tensile shear test and the effect of process parameters (dwell time and tool pin profile) on tensile shear load was investigated. Two different pin profiles (cylindrical and conical) were considered. Weld geometric features such as hook height, hook width and effective top sheet thickness were monitored and their effect on the static strength of FSSW's were discussed.

2. MATERIAL AND METHODS

In this study, FSSW was performed on 3 mm thick AA6082-T6 aluminum alloy sheets. The chemical composition and mechanical properties of AA6082-T6 aluminum alloy sheet used in this study are listed in Table 1 and 2, respectively.

Table 1. Chemical composition of AA6082-T6 aluminum alloy used in this study (wt. %)

Si	Fe	Cu	Mn	Mg	Cr	Zn	Ti	Al
0.9	0.44	0.08	0.54	0.7	0.03	0.04	0.04	Balance

Table 2. Mechanical properties of AA6082-T6 aluminum alloys used in this study

Ultimate Tensile Strength [MPa]	0.2% Proof Strength [MPa]	Elongation [%]
342	298	16

Samples were cut into pieces in dimensions of 100 mm × 40 mm to prepare the shear tensile test samples according to ANSI/AWS/SAE/D8.9-97 standard [13](Figure 1). These pieces were friction stir spot welded in the overlapping configuration using a vertical CNC milling machine. A non-consumable tool made of H13 hot work tool steel, having a $10°$ concave shoulder of 15 mm in diameter was used for all welds. Two different pin (threaded cylindrical pin and threated conical pin) used for the welds have a length 3.5 mm along with a right-hand screw of 0.8 mm pitch (Figure 2). The welding tool was rotated in a clockwise direction during the welding process. Additionally, a specific clamping fixture for the work pieces was fabricated to ensure correct axial positions and obtain precise plunge depth values.
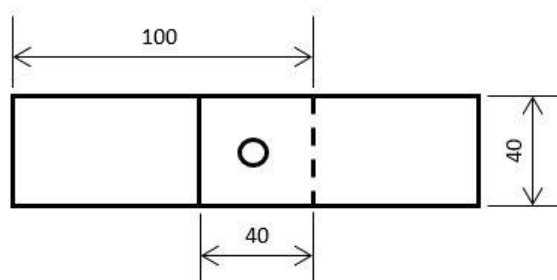
Figure 1. Welding sample installed as lapping joints for the shear-tensile test
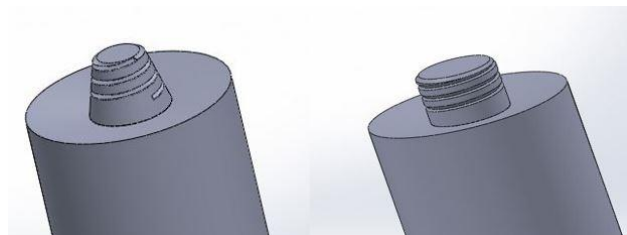
Figure 2. The welding tools used in this study.

An experimental design was created to determine the effect of dwell time. The welding parameters used in this study are listed in Table 3. The welded samples were carefully cross-sectioned through the weld center using a low speed precision cutting machine for macro structural examination and hook observations. Then, the cross-sectioned samples were mounted in Bakelite, and then ground manually using SiC emery papers. Subsequently, the samples were mirror polished successively through 1 µm and 0.3 µm diamond pastes on a polishing machine, and then washed and blow dried. Mirror-polished samples were characterized to obtain their cross-sectional morphology using a Nikon DIC microscope with a Clemex image analysis system after etching in a reagent with the following composition for 4 minutes: 5 ml hydrofluoric acid and 95 ml distilled water. The mechanical properties of the welds were evaluated through tensile shear tests. In order to evaluate the mechanical strength of the welds, the lap shear tensile tests were carried out on a UTEST-7014 tensile testing machine, at room temperature and with a crosshead displacement speed of 5 mm/min. Two additional sheet pieces having a thickness equal to 3 mm were also fixed on the clamping sides of the tensile shear test samples in order to avoid the possible parasitic effects of the bending moment. The tensile lap-shear load for each weld was obtained by averaging five test results.

Table 3. Welding parameters used in this study

Sample	Rotational speed [rpm]	Plunge depth [mm]	Dwell Time [s]	Feed Rate [mm/min]
S1	1500	5	2	50
S2	1500	5	4	50
S3	1500	5	7	50
S4	1500	5	9	50
S5	1500	5	11	50

3. RESULTS AND DISCUSSION

To determine the quality of the FSSW joints of AA6082-T6 sheets for different pin profiles tensile shear tests were conducted. The results of the tensile shear tests are shown in Table 4. The highest tensile strength was found 6.99 kN for S3 sample. After the tensile test the effects of pin profile were separately evaluated. Figure 3 shows the effect of dwell time change on the tensile shear load for cylindrical pin. The tensile shear load of joints firstly increased then decreased with increasing dwell time. The tensile shear load of the spot welded joints increased approximately 17% when dwell time was increased from 2 s to 7 s. This increase can be associated with fully bonded section size. It should also be noted that the tensile shear load of the spot welds decreased above dwell time of 7s. Figure 4 shows the effect of dwell time change on the tensile shear load for conical pin. The tensile shear loads of joints increased almost linearly with increasing dwell time. The tensile shear load of the spot welded joints increased approximately 69% when dwell time was increased from 2 s to 11 s. This increase can be attributed to larger fully bonded section size and larger hook width. When comparing different pin profile, welds made with cylindrical pin yielded higher static strength than conical pin at same welding parameters. And the dwell time has higher effect on tensile shear load for conical pin.

Table 4. Tensile shear load values of the friction stir spot welded joints (average values)

Sample	Tensile Shear Load (Cylindrical Pin)[kN]	Tensile Shear Load (Conical Pin)[kN]
S1	5.96	3.2
S2	6.15	3.44
S3	6.99	3.98
S4	6.7	4.84
S5	6.67	5.41
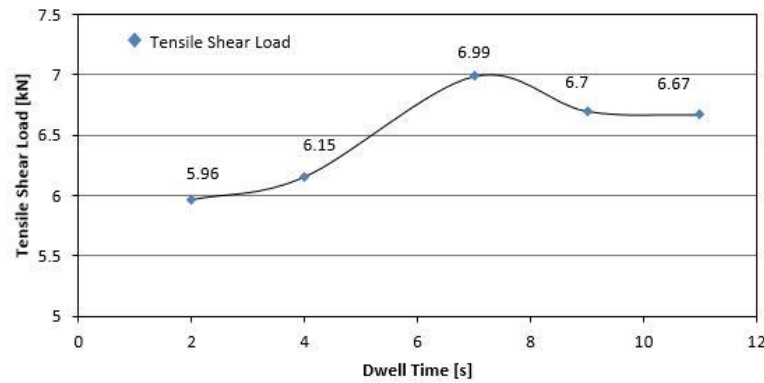
Figure 3. The effect of dwell time on tensile shear load of a friction stir spot-welded AA6082-T6 joint for cylindrical tool
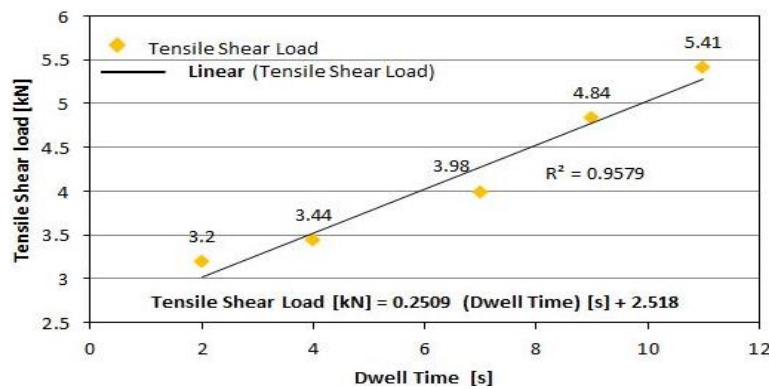
Figure 4. The effect of dwell time on tensile shear load of a friction stir spot-welded AA6082-T6 joint for conical tool

The effect of dwell time on hook shape (Hook Height, Hook Width and Effective Top Sheet Thickness) on a friction stir spot-welded AA6082-T6 joint for different pin geometries are shown in Table 5. Figure 5 and Figure 6 compares the hook shape of welds made with 2 different pin profile: cylindrical and conical under the same weld process conditions. Figure 5 shows the hook shape comparison of welds made with cylindrical pin. Higher dwell time resulted in larger bonded section size and larger hook width due to the higher heat input. Any significant difference in hook height was not observed with the increase of dwell time. Figure 6 shows the hook shape comparison of welds made with conical pin. Higher dwell time resulted in larger bonded section size and larger hook width due to the higher heat input. Any significant difference in hook height was not observed with the increase of dwell time. When comparing different pin profile, welds made with cylindrical have larger hook width and hook height than conical pin at same welding parameters. A correlation could not established between top effective sheet thicknesses and mechanical properties.

Table 5. Hook measurement results for cylindrical and conical pins

Sample	HookWidth (HW) (Cylindrical Pin)[μm]	HookWidth (HW) (Conical Pin)[μm]	HookHeight (HH) (Cylindrical Pin) [μm]	HookHeight (HH) (Conical Pin) [μm]	Effective Sheet Thickness (T_{eff}) (Cylindrical Pin) [μm]	Effective Sheet Thickness (T_{eff}) (Conical Pin) [μm]
S1	1165	708	1799	575	848	2060
S5	2156	955	1758	665	467	1868
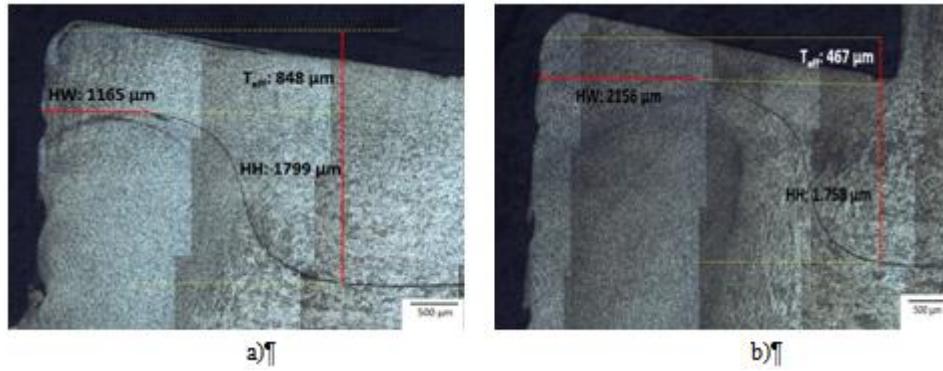
Figure 5. The effect of dwell time on hook shape of a friction stir spot-welded AA6082-T6 joint for cylindrical pin:

a) S1 Sample (2s), b) S5 Sample (11s). (HH: Hook Height, HW: Hook Width, $T_{eff:}$ Effective Top Sheet Thickness)
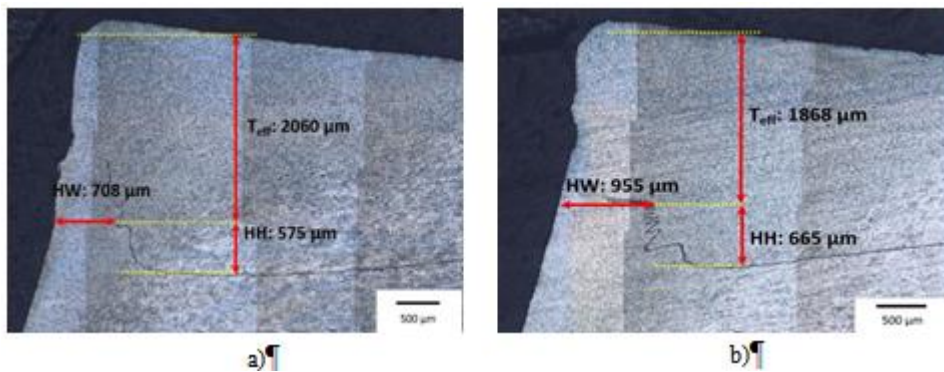
Figure 6. The effect of dwell time on hook shape of a friction stir spot-welded AA6082-T6 joint for conical pin:

a) S1 Sample (2s), b) S5 Sample (11s). (HH: Hook Height, HW: Hook Width, $T_{eff:}$ Effective Top Sheet Thickness)

4. CONCLUSION

The effect of pin geometry and dwell time on the hook formation and tensile shear load of friction stir spot welded 6082-T6 aluminum alloy was investigated. The following conclusions were made:

- When comparing 2 different pin profiles, welds made with cylindrical pin has higher tensile shear load than conical pin at same welding parameters.
- The highest tensile strength was found 6.99 kN for cylindrical pin; experimental parameters; rotational speed: 1500 rpm, plunge depth: 5 mm, dwell time: 7s, feed rate 50 mm/min.
- The tensile shear loads of joints increased with increasing dwell time from 2s to 7s then the tensile shear load of the spot welds decreased above dwell time of 7s for cylindrical pin.
- The tensile shear loads of joints increased almost linearly with increasing dwell time from 2s to 11s for conical pin.
- When comparing different tool pin profiles, welds made with cylindrical pin showed larger hook width, higher hook height and lower effective top sheet thickness than conical pin.

Higher dwell time resulted in larger bonded section size and larger hook width due to the higher heat input for cylindrical and conical pin. Hook width played a significant role on tensile shear load. However, hook height and effective top sheet thickness were not effective on tensile shear load.

REFERENCES

[1]. H. Badarinarayan, Q. Yang, and S. Zhu, "Effect of tool geometry on static strength of friction stir spot-welded aluminum alloy," *Int. J. Mach. Tools Manuf.*, vol. 49, no. 2, pp. 142–148, 2009.

[2]. M. Tutar, H. Aydin, C. Yuce, N. Yavuz, and A. Bayram, "The optimisation of process parameters for friction stir spot-welded AA3003-H12 aluminium alloy using a Taguchi orthogonal array," *J. Mater.*, vol. 63, pp. 789–797, 2014.

[3]. T. Rosendo *et al.*, "Mechanical and microstructural investigation of friction spot welded AA6181-T4 aluminium alloy," *Mater. Des.*, vol. 32, no. 3, pp. 1094–1100, 2011.

[4]. M. K. Bilici and A. I. Yükler, "Influence of tool geometry and process parameters on macrostructure and static strength in friction stir spot welded polyethylene sheets," *Mater. Des.*, vol. 33, no. 1, pp. 145–152, 2012.

[5]. H. Aydin, O. Tuncel, C. Yuce, M. Tutar, N. Yavuz, and A. Bayram, "Effect of rotational speed and dwell time on mechanical properties of dissimilar AA1050-AA3105 friction stir spot welded joints," *Mater. Test.*, vol. 56, no. 10, 2014.

[6]. W. Yuan *et al.*, "Effect of tool design and process parameters on properties of Al alloy 6016 friction stir spot welds," *J. Mater. Process. Technol.*, vol. 211, no. 6, pp. 972–977, 2011.

[7]. G. Buffa, P. Fanelli, L. Fratini, and F. Vivio, "Influence of joint geometry on micro and macro mechanical properties of friction stir spot welded joints," *Procedia Eng.*, vol. 81, no. October, pp. 2086–2091, 2014.

[8]. Y. H. Yin, N. Sun, T. H. North, and S. S. Hu, "Journal of Materials Processing Technology Hook formation and mechanical properties in AZ31 friction stir spot welds," vol. 210, pp. 2062–2070, 2010.

[9]. J. Y. Cao, M. Wang, L. Kong, and L. J. Guo, "Journal of Materials Processing Technology Hook formation and mechanical properties of friction spot welding in alloy 6061-T6," vol. 230, pp. 254–262, 2016.

[10]. S. Babu, V. S. Sankar, G. D. J. Ram, P. V Venkitakrishnan, G. M. Reddy, and K. P. Rao, "Microstructures and Mechanical Properties of Friction Stir Spot Welded Aluminum Alloy AA2014," vol. 22, no. January 2013, pp. 71–84, 2014.

[11]. H. Badarinarayan, Y. Shi, X. Li, and K. Okamoto, "Effect of tool geometry on hook formation and static strength of friction stir spot welded aluminum 5754-O sheets," *Int. J. Mach. Tools Manuf.*, vol. 49, no. 11, pp. 814–823, 2009.

[12]. H. M. Rao *et al.*, "Friction stir spot welding of rare-earth containing ZEK100 magnesium alloy sheets," *Mater. Des.*, vol. 56, pp. 750–754, 2014.

[13]. A. American and N. Standard, "Practices for Test Methods for Evaluating the Resistance Spot Welding Behavior Sheet Steel Recommended Practices for Test Methods for Evaluating the Resistance Spot Welding Behavior of," 2002.

Free Vibration Analysis of Multi-span Timoshenko Beams on Elastic Foundation Using Dynamic Stiffness Method

Baran Bozyigit[1], Yusuf Yesilce[2]

Abstract

In this study, the exact first five natural frequencies of three-span Timoshenko beams on Winkler foundation are calculated using dynamic stiffness formulation. Different elastic foundation spring constants and different beam cross-sections are used to reflect their effects on natural frequencies. Moreover, the natural frequencies are also calculated via structural analysis software SAP2000 and tabulated with exact results. It is seen that the influence of elastic foundation spring stiffness in inner span is high in comparison with outer spans. The cross-section of the beam plays an important role on natural frequencies of multi-span Timoshenko beams on Winkler foundation.

Keywords: *Dynamic stiffness, free vibration, multi-span Timoshenko beam, Winkler foundation*

1. INTRODUCTION

The calculation of exact natural frequencies of beams is of great interest to researchers for a long time. In the recent years, free vibration analyses of different types of beams with various loading conditions are performed using different methods [1-5]. The vibration problem of beams on elastic foundations can be encountered especially in civil engineering and mechanical engineering applications. The elastic foundations are modeled using elastic springs. The effects of elastic foundation can be important for beams or beam assembly structures. Thus, there are numerous studies about different foundation models carrying various types of beams and structures [6-10]. The dynamic stiffness method (DSM) is an effective method for calculating exact natural frequencies of beams or beam like structures as the method uses the exact shape functions. Vibration analyses of many types of beams and plates are performed by using DSM in recent years [11-17].

In this study, free vibration analysis of three-span simply supported beams on Winkler foundation is performed using DSM. Timoshenko Beam Theory (TBT) which considers shear deformation and rotational inertia is used. In the numerical analysis, different spring stiffness values for spans are selected to reveal the effect of elastic foundation on natural frequencies. To reflect the importance of beam geometry, several analyses are completed for different beam geometries. SAP2000 is a well known and widely used structural analysis software worldwide. Thus, SAP2000 is used to obtain natural frequencies of beams on Winkler foundation and the results are compared with exact values.

2. MODEL AND FORMULATION

The mathematical model of three-span Timoshenko beam on Winkler foundation can be seen in Figure 1. Here, x and y represents the axes, k_{s1}, k_{s2} and k_{s3} are Winkler foundation spring stiffnesses, L is the span length, b is width of the beam and h is the height of the beam.

---

[1] Corresponding author: Dokuz Eylul University, Department of Civil Engineering, 35160, Buca/Izmir, Turkey.

baran.bozyigit@deu.edu.tr

[2] Dokuz Eylul University, Department of Civil Engineering, 35160, Buca/Izmir, Turkey. yusuf.yesilce@deu.edu.tr
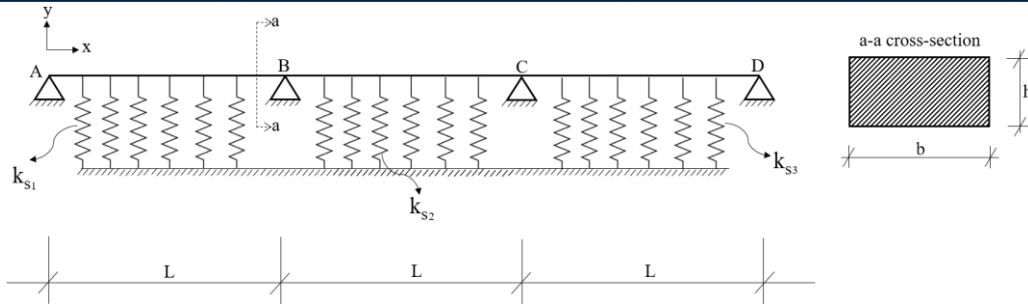
Three-span Timoshenko beam on Winkler foundation

Let the denomination of span AB as 1, span BC as 2 and span CD as 3.

The assumptions listed below are considered to clarify and simplificate the analysis procedure:

1) The beam is constructed by using an isotropic and homogenous material.

2) The cross-section of the beam is uniform.

3) The beam behaves linear and elastic.

4) The damping is neglected.

5) The foundation springs are linear and distributed along the beam length.

The governing equations of motion of vibrating Timoshenko beam resting on Winkler foundation are given as follows:

$$\frac{AG}{\bar{k}}\left(\frac{\partial^2 y_n(x,t)}{\partial x^2} - \frac{\partial \theta_n(x,t)}{\partial x}\right) - \bar{m}\frac{\partial^2 y_n(x,t)}{\partial t^2} - k_{sn}y_n(x,t) = 0$$

$$EI\frac{\partial^2 \theta_n(x,t)}{\partial x^2} - \bar{m}\frac{I}{A}\frac{\partial^2 \theta_n(x,t)}{\partial t^2} + \frac{AG}{\bar{k}}\left(\frac{\partial y_n(x,t)}{\partial x} - \theta_n(x,t)\right) = 0$$

(1)

In Eq. (1), A is cross-sectional area, I is area moment of inertia, G is shear modulus, E is Young's modulus, $\bar{k}$ is shear coefficient, $\bar{m}$ is mass per unit length. $y_n(x,t)$ and $\theta_n(x,t)$ are n th beam span's deflection function and rotation function, respectively (n=1, 2, 3).

If the motion of the beam is harmonic and separation of variables method is applied, the following equation is obtained:

$$\frac{AG}{\bar{k}L^2}\frac{d^2 y_n(z)}{dz^2} - \frac{AG}{\bar{k}L}\frac{d\theta_n(z)}{dz} + \bar{m}\omega^2 y_n(z) - k_{sn}y_n(z) = 0$$

$$\frac{EI}{L^2}\frac{d^2 \theta_n(z)}{dz^2} + \frac{AG}{\bar{k}L}\frac{dy_n(z)}{dz} + \left(\frac{\bar{m}I\omega^2}{A} - \frac{AG}{\bar{k}}\right)\theta_n(z) = 0$$

(2)

where z=x/L and ω is natural frequency.

The solution is assumed as:

$$y_n(z) = \left\{\bar{C}\right\}_n e^{isz}$$

$$\theta_n(z) = \left\{\bar{D}\right\}_n e^{isz}$$

(3)

Substituting Eq.(3) into Eq.(2), yn(z) and θn(z) functions are given in Eq.(4) and Eq. (5), respectively.

$$y_n(z) = (\bar{C}_{n1}e^{is_{n1}z} + \bar{C}_{n2}e^{is_{n2}z} + \bar{C}_{n3}e^{is_{n3}z} + \bar{C}_{n4}e^{is_{n4}z})$$

(4)

$$\theta_n(z) = (K_{n1}\bar{C}_{n1}e^{is_{n1}z} + K_{n2}\bar{C}_{n2}e^{is_{n2}z} + K_{n3}\bar{C}_{n3}e^{is_{n3}z} + K_{n4}\bar{C}_{n4}e^{is_{n4}z})$$

(5)

where $K_{nm} = \dfrac{-\left(\dfrac{AG}{\bar{k}L^2}\right) + \left(m\omega^2\right) - k_{sn}}{\left(\dfrac{AG}{\bar{k}L^2}\right) is_j}$; m=1,2,3,4; j=1,2,3,4

The bending moment function and shear force function are defined in Eq.(6) and Eq.(7), respectively.

$$M_n(z) = \frac{EI}{L}\frac{d\theta_n(z)}{dz} \tag{6}$$

$$Q_n(z) = \frac{AG}{\bar{k}L}\frac{dy_n(z)}{dz} - \frac{AG}{\bar{k}}\theta_n(z) \tag{7}$$

3. DYNAMIC STIFFNESS METHOD (DSM) FOR CALCULATING NATURAL FREQUENCIES

DSM is a technique that can be used for calculating exact natural frequencies using exact mode shapes. First of all, the dynamic stiffness matrix should be obtained. The dynamic stiffness matrix can be constructed by using end displacements and end forces of beam. The vector of end displacements of beam and the vector of coefficients are given in Eqs. (8) and (9), respectively.

$$\delta_n = [\, y_{n0} \quad \theta_{n0} \quad y_{n1} \quad \theta_{n1}\,]^T \tag{8}$$

$$\bar{C}_n = [\, \bar{C}_{n1} \quad \bar{C}_{n2} \quad \bar{C}_{n3} \quad \bar{C}_{n4}\,]^T \tag{9}$$

where $y_{n0} = y_n(z=0), \theta_{n0} = \theta_n(z=0), y_{n1} = y_n(z=1), \theta_{n1} = \theta_n(z=1)$

Eqs. (8) and (9) can be rewritten in the form below:

$$\begin{bmatrix} y_{n0} \\ \theta_{n0} \\ y_{n1} \\ \theta_{n1} \end{bmatrix} = \begin{bmatrix} 1 & 1 & 1 & 1 \\ K_{n1} & K_{n2} & K_{n3} & K_{n4} \\ e^{is_{n1}} & e^{is_{n2}} & e^{is_{n3}} & e^{is_{n4}} \\ K_{n1}e^{is_{n1}} & K_{n2}e^{is_{n2}} & K_{n3}e^{is_{n3}} & K_{n4}e^{is_{n4}} \end{bmatrix} \begin{bmatrix} \bar{C}_{n1} \\ \bar{C}_{n2} \\ \bar{C}_{n3} \\ \bar{C}_{n4} \end{bmatrix} \tag{10}$$

The closed form of Eq. (10) is given in Eq. (11):

$$\delta_n = \Delta_n \bar{C}_n \tag{11}$$

where $\Delta_n = \begin{bmatrix} 1 & 1 & 1 & 1 \\ K_{n1} & K_{n2} & K_{n3} & K_{n4} \\ e^{is_{n1}} & e^{is_{n2}} & e^{is_{n3}} & e^{is_{n4}} \\ K_{n1}e^{is_{n1}} & K_{n2}e^{is_{n2}} & K_{n3}e^{is_{n3}} & K_{n4}e^{is_{n4}} \end{bmatrix}$

The end forces of the beam is given in vector form in Eq. (12):

$$F = [\, Q_{n0} \quad M_{n0} \quad Q_{n1} \quad M_{n1}\,]^T \tag{12}$$

where $Q_{n0} = Q_n(z=0), M_{n0} = M_n(z=0), Q_{n1} = Q_n(z=1), M_{n1} = M_n(z=1)$

Eqs. (12) and (9) can be written in the following form:

$$\begin{bmatrix} Q_{n0} \\ M_{n0} \\ Q_{n1} \\ M_{n1} \end{bmatrix} = \begin{bmatrix} \lambda_1 & \lambda_2 & \lambda_3 & \lambda_4 \\ \Lambda_1 & \Lambda_2 & \Lambda_3 & \Lambda_4 \\ -\lambda_1 e^{is_{n1}} & -\lambda_2 e^{is_{n2}} & -\lambda_3 e^{is_{n3}} & -\lambda_4 e^{is_{n4}} \\ -\Lambda_1 e^{is_{n1}} & -\Lambda_2 e^{is_{n2}} & -\Lambda_3 e^{is_{n3}} & -\Lambda_4 e^{is_{n4}} \end{bmatrix} \begin{bmatrix} \bar{C}_{n1} \\ \bar{C}_{n2} \\ \bar{C}_{n3} \\ \bar{C}_{n4} \end{bmatrix} \tag{13}$$

where $\lambda_j = \dfrac{AG}{\bar{k}L}is_{nj} - \dfrac{AG}{\bar{k}}K_{nj}; \Lambda_j = \dfrac{EI}{L}is_{nj}K_{nj}; j = 1,2,3,4$

The closed form of Eq. (13) can be written as:

$$F_n = \kappa_n \bar{C}_n \qquad (14)$$

where $\kappa_n = \begin{bmatrix} \lambda_1 & \lambda_2 & \lambda_3 & \lambda_4 \\ \Lambda_1 & \Lambda_2 & \Lambda_3 & \Lambda_4 \\ -\lambda_1 e^{is_{n1}} & -\lambda_2 e^{is_{n2}} & -\lambda_3 e^{is_{n3}} & -\lambda_4 e^{is_{n4}} \\ -\Lambda_1 e^{is_{n1}} & -\Lambda_2 e^{is_{n2}} & -\Lambda_3 e^{is_{n3}} & -\Lambda_4 e^{is_{n4}} \end{bmatrix}$

Eqs.(11) and (14) are used to construct the dynamic stiffness matrix of the n th span of the Timoshenko beam on elastic foundation.

$$F_n = \kappa_n \Delta_n^{-1} \bar{C}_n \qquad (15)$$

In Eq.(15), $\kappa_n \Delta_n^{-1}$ represents the dynamic stiffness matrix of the n th span. The natural frequencies of the beam are calculated by equating the determinant of assembly of $\kappa_1 \Delta_1^{-1}, \kappa_2 \Delta_2^{-1}$ and $\kappa_3 \Delta_3^{-1}$ to zero. It should be noted that the related rows and columns of dynamic stiffness matrix of the beam are erased according to boundary conditions.

4. NUMERICAL ANALYSIS AND DISCUSSION

A three-span Timoshenko beam on Winkler foundation is used for numerical analysis with the following properties: $E=2\times10^7$ kN/m², $G=7692308$ kN/m², $\bar{k}=1.2$, $\rho=25$ kN/m³, $L=6$ m, b=1 m.

The boundary conditions are same for each span and given below.

$y_n(z=0)=0, M_n(z=0)=0, y_n(z=1)=0, M_n(z=1)=0$

The analyses are performed for constant k_{s2} and k_{s3} with varying k_{s1}, constant k_{s1} and k_{s3} with varying k_{s2}, constant spring stiffnesses with various beam height values. The first five natural frequencies of the beam are presented in Tables (1-3). It should be noted that SAP2000 results are obtained by dividing spans into 1 cm segments for accuracy.

Table.1. First five natural frequencies (h=0.75 m, k_{s2}=10000 kN/m, k_{s3}=10000 kN/m)

Natural Frequency (Hz)	k_{s1} (kN/m)									
	5000		10000		15000		20000		25000	
	DSM	SAP2000	DSM	SAP2000	DSM	SAP2000	DSM	SAP2000	DSM	SAP2000
1st Mode	28.0633	27.9550	28.4933	28.3837	28.8479	28.737	29.1383	29.026	29.3761	29.263
2nd Mode	34.2849	34.1590	34.7388	34.6111	35.2293	35.100	35.7462	35.615	36.2791	36.146
3rd Mode	47.7167	47.5440	47.8373	47.6645	47.9680	47.795	48.1097	47.936	48.2637	48.089
4th Mode	97.9198	98.8130	98.0322	98.9265	98.1410	99.036	98.2463	99.142	98.3481	99.245
5th Mode	108.2491	109.1420	108.3922	109.2864	108.5373	109.433	108.6843	109.582	108.8329	109.732

Table.2. First five natural frequencies (h=0.75 m, k_{s1}=10000 kN/m, k_{s3}=10000 kN/m)

Natural Frequency (Hz)	k_{s2} (kN/m)									
	5000		10000		15000		20000		25000	
	DSM	SAP2000	DSM	SAP2000	DSM	SAP2000	DSM	SAP2000	DSM	SAP2000
1st Mode	28.0891	27.9805	28.4933	28.3837	28.8707	28.7591	29.2232	29.1088	29.5528	29.4346
2nd Mode	34.7134	34.5983	34.7388	34.6111	34.7642	34.624	34.7894	34.6364	34.8145	34.6488
3rd Mode	47.3841	47.2243	47.8373	47.6645	48.2986	48.1141	48.7671	48.5716	49.2421	49.0365
4th Mode	97.9209	98.8141	98.0322	98.9265	98.1421	99.0373	98.2505	99.1466	98.3576	99.2545
5th Mode	108.3738	109.2747	108.3922	109.2864	108.4108	109.2981	108.4295	109.3099	108.448	109.3218

Table.3. First five natural frequencies ($k_{s1}= k_{s2}= k_{s3}=10000$ kN/m)

Natural Frequency (Hz)	h(m)									
	0.55		0.65		0.75		0.85		0.95	
	DSM	SAP2000	DSM	SAP2000	DSM	SAP2000	DSM	SAP2000	DSM	SAP2000
1st Mode	23.5876	23.4357	25.8912	25.7561	28.4933	28.3837	31.2525	31.1793	34.0842	34.0593
2nd Mode	27.9915	27.8159	31.2701	31.1127	34.7388	34.6111	38.2623	38.1773	41.7629	41.7336
3rd Mode	37.6891	37.4618	42.8127	42.5751	47.8373	47.6645	52.7395	52.6141	57.4279	57.3597
4th Mode	75.5356	75.6747	87.0604	87.5351	98.0322	98.9265	108.3847	109.7625	118.095	119.9983
5th Mode	84.3307	84.4696	96.7702	97.2515	108.3922	109.2864	119.1587	120.5124	129.078	130.9151

It is seen from Table 1 that, the natural frequencies are increased with increasing spring stiffness of an outer span of three-span beam. Table 2 shows that there is also an augmentation in natural frequencies when the spring stiffness of middle span is increased. There is no significant difference between the particular increment of spring stiffness of middle span and an outer span on natural frequencies. Table 3 reveals that the natural frequencies are increased due to increasing beam height and higher modes are more sensitive to this effect.
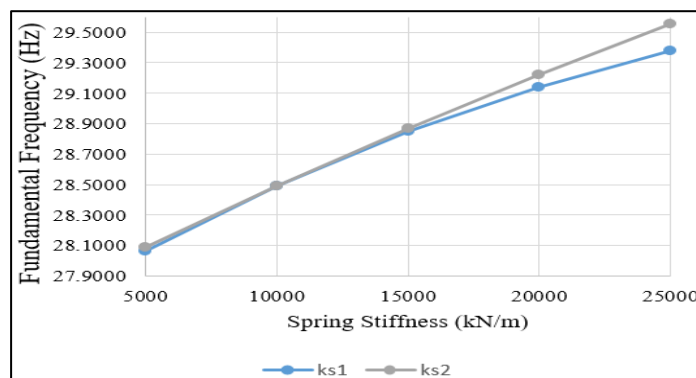
Figure.2. Fundamental frequencies for different k_{s1} and k_{s2} values

Figure 2 implies that fundamental frequency of three-span Timoshenko beam on Winkler foundation is more sensitive to spring stiffness of middle span in comparison with outer span especially for high stiffness values. Figure 3 represents the variation of first three natural frequencies with different beam height values.
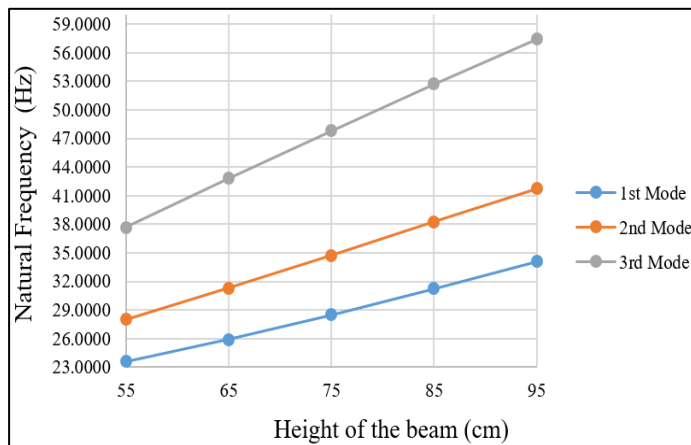
Figure.3. First three natural frequencies for different h values ($k_{s1}=k_{s2}=k_{s3}=10000$ kN/m)

5. CONCLUSIONS

The first five exact natural frequencies of three-span Timoshenko beams on Winkler foundation are obtained using dynamic stiffness approach. The spring stiffnesses of middle span is more effective than outer span. Different beam height values are used in the numerical analysis and effects on natural frequencies are observed. SAP2000 provides fairly well results when segment number increased sufficiently. The DSM can be used for calculating exact natural frequencies of multi-span Timoshenko beams on elastic foundation with different support conditions and foundation models.

REFERENCES

[1]. Y. Yesilce, "Determination of Natural Frequencies and Mode Shapes of Axially Moving Timoshenko Beams with Different Boundary Conditions using Differential Transform Method", *Advances in Vibration Engineering*, vol. 12, pp. 89-108, 2013.

[2]. W. R Chen, "Parametric studies on bending vibration of axially-loaded twisted Timoshenko beams with locally distributed Kelvin–Voigt damping", *International Journal of Mechanical Sciences*, vol. 88, pp. 61-70, 2016.

[3]. S. G. Kelly, C. Nicely, "Free vibrations of a Series of Beams Connected by Viscoelastic Layers", *Advances in Acoustics and Vibration*, Article ID 976841, 8 pages, 2015.

[4]. G. Tan, W. Wang , Y. Jiao, "Flexural Free Vibrations of Multistep Nonuniform Beams", *Advances in Acoustics and Vibration*, Article ID 7314280, 12 pages, 2016.

[5]. B. R. Goncalves, A. Karttunen, J. Romanoff, J. N. Reddy, "Buckling and free vibration of shear-flexible sandwich beams using a couple-stress-based finite element", *Composite Structures*, vol. 165, pp. 233-241, 2017.

[6]. T. M. Wang, J. E. Stephens, "Natural frequencies of Timoshenko beams on Pasternak foundations", *Journal of Sound and Vibration*, Vol. 51(2), pp. 149-155, 1977.

[7]. S. Y. Lee, Y. H. Kou, F. Y. Lin, "Stability of a Timoshenko beam resting on a Winkler elastic foundation", *Journal of Sound and Vibration*, vol. 153(2), pp. 193-202, 1992.

[8]. M. A. De Rosa, "Free vibrations of Timoshenko beams on two-parameter elastic foundation". *Computers & Structures*, vol. 57(1), pp. 151-156, 1995.

[9]. A. S. Kanani, H. Niknam, A. R. Ohadi, M. M. Aghdam, "Effect of nonlinear elastic foundation on large amplitude free and forced vibration of functionally graded beam", *Composite Structures*, vol. 115, pp. 60-68, 2014.

[10]. M. Aslami, P. A. Akimov, "Analytical solution for beams with multipoint boundary conditions on two-parameter elastic foundations", *Archives of Civil and Mechanical Engineering*, vol. 16(4), pp. 668-677, 2016.

[11]. J. R. Banerjee, "Dynamic Stiffness Formulation for Structural Elements: A General Approach", *Computers&Structures*, vol. 63, pp. 101-103, 1997.

[12]. L. Jun, H. Hongxing, H. Rongying, "Dynamic stiffness analysis for free vibrations of axially loaded laminated composite beams", *Computers and Structures*, vol. 84, pp. 87-98, 2008.

[13]. L. Bao-hui, G. Hang-shan, Z. Hong-bo, L. Yong-shou, Y. Zhou-feng, "Free vibration analysis of multi-span pipe conveying fluid with dynamic stiffness method", *Nuclear Engineering and Design*, vol. 241, pp. 666-671, 2011.

[14]. J. R. Banerjee, "Free vibration of beams carrying spring-mass systems - A dynamic stiffness approach", *Computers and Structures*, vol. 104-105, pp. 21-26, 2012.

[15]. J. R. Banerjee, D. R. Jackson, "Free vibration of a rotating tapered Rayleigh beam: A dynamic stiffness method of solution", *Computers and Structures*, vol. 124, pp. 11-20, 2013.

[16]. H. Su, J. R. Banerjee, "Development of dynamic stiffness method for free vibration of functionally graded Timoshenko beams", *Computers and Structures*, vol. 147, pp. 107-116, 2015.

[17]. B. Bozyigit, Y. Yesilce, "Dynamic stiffness approach and differential transformation for free vibration analysis of a moving Reddy-Bickford beam", *Structural Engineering and Mechanics*, vol. 58(5), pp. 847-868, 2016.

Effects Of Paraffin Application, Heat Treatment, And Densification Process On Some Physical And Biological Properties Of Scotch Pine Wood

Mesut Yalcın[1], Halil İbrahim Sahin[1], Huseyin Pelit[2], Caglar Akcay[1]

Abstract

The aim of this study was to determine on the some physical and biological properties of paraffin applicated, heat treated, and densification process. In the study, three different process were applied: heat treatment at 180^0C, hot paraffin application and densification at hot press temperatures. At the end of procedures, the physical properties such as anti-shrinkage efficiency and water absorption, as well as activity against Coriolus versicolor and Coniophora puteana wood destroying fungi were determined. The results shown that, while the anti-shrinkage efficiency was carried out higher than 80% until water immersion for 8 hours in paraffine applications, It was obtained lower than after this time. It can be seen that heat treatment and densification in paraffin-free specimens gave effective results on both fungal species. However, with paraffin application, efficacy against fungi has been variable. With the heat treatment application at 180^0C, the weight loss was increased compared to the control samples, while the weight loss was the lowest value in densification samples with hot press.

Keywords: *Heat treatment, Densification, Paraffine aplication, Fungal activitiy, Water absorption*

1. INTRODUCTION

Although wood materials have many important advantages in usage places, they have significant disadvantages. The major disadvantages in usage area are that they are not sufficiently resistant to biological factors in the natural form and that they can not adequately protect the dimensional stability in humidity environments. These disadvantages shorten the life span as they cause technical problems in the places of use.

Many methods have been developed in the past to gain the dimensional stability of wooden materials. In addition to the superficial or in-depth application of various water-repellent chemical substances, various modification methods are at the forefront of methods applied to provide dimensional stability. Heat treatment, acetylation, etc. are important modification methods applied in recent years.

Wooden materials can be destroyed when exposed to biological factors such as various fungi and insects at appropriate places of use. There are a variety of mechanical and chemical methods that have been developed and used against these factors for many years. Today, one of the most preferred methods is the preservation of various woods by impregnation with various preservatives. However, many of these chemical substances disrupt the natural order of nature and may even pose a threat to the environment and to life. For this reason, the use of some of these chemicals has been limited or even banned in recent years (Kartal et al. 2006).

Paraffin is a harmless chemical for plants and animals. In addition to having many uses, it is also used to impart water repellent activity to materials by virtue of having a hydrophobic structure. Today, they are used to protect wood from biodegradation by impregnating wood materials (Esteves, 2014).

High temperature applications can change the color of the wood material; improve its biological strength and dimensional stability. However, the mechanical properties of wood diminishes and changes the chemical structure of wood (Yalcin and Sahin 2015). In a study conducted, the effects of heat treatment on some physical, mechanical and chemical properties of redwood were investigated and significant reductions in all

---

[1] *Corresponding author : Duzce University, Forest Faculty Department of Forest Industry Engineering, Duzce, Turkey. mesutyalcin@duzce.edu.tr*

[2] *Duzce University, Faculty of Technology, Department of Wood Products Industrial Engineering, Duzce, Turkey*

the physical properties of redwood were determined depending on the heat treatment time and temperature (Ates et al., 2009). In a study using ash wood, the biological resistance of wood is also increased due to the increased heat treatment temperature (Yalcin and Sahin 2015).

2. MATERIAL AND METHOD

2.1. Wood samples

In this study, scotch pine (*Pinus sylvestris* L. sapwood was used for test samples. The wood samples were cut to 5 cm long, 2.5 cm wide, and 1.5 cm thickness according to the TS 5563 EN 113,1996 standards with minor modifications in sample size. All specimens were conditioned at 20 ^{0}C and 65 % RH for 3 weeks.

2.2. 2.2. Paraffin treatment, heat treatment and densification

The solid paraffin was heated to a temperature of 70 ^{0}C to make it liquid. The samples were weighed (W_{unP}) then placed in a desiccator and vacuum applied at 600 mmHG for 20 minutes. The liquid paraffin was added in the desiccator and waited for 10 minutes for impregnation. The surface of test samples were cleaned from the paraffin residues. After one week, the test samples were reweighed (WP) and the weight gain amounts (WPG) were determined according to the following formula.

$$WPG (\%) = [(W_P - W_{unP})/W_{unP}] \times 100 \tag{1}$$

After impregnation, the two groups of samples were heated to 180°C for 2 h. Impregnated samples were thermo-mechanically densified with a hydraulic press machine, the capability of pressure and temperature control. The densification process was carried out at target compression ratios of 20% with temperatures of 185°C. After densification processes the samples were taken from the press machine and cooled to room.

Table 1. Experimental groups and weight gain values

Group	Application	Process	Weight increase (%)
A Group		Control	-
B Group	Without Wax	Heat treatment at 180 °C	-
C Group		%25 densification at heat press	-
D Group		180 °C + %25 densification at heat press	-
E Group		Control	83,42
F Group	Waxed	Heat treatment at 180 °C	25,27
G Group		%25 densification at heat press	84,26
H Group		180 °C + %25 densification at heat press	25,95

2.3. Water absorption (WA) and Water Repellent Effectiveness (WRE)

Wood specimens were placed in glass containers filled with distilled water. The specimens were placed separately and horizontally in the containers with stainless steel mesh over the specimens. The water was replaced daily during the test. The specimens were first oven-dried at 103°C and then weighed. The specimens were weighed after 2, 4, 8, 24, 48, 72, and 168 h of immersion and water absorption (*WA*) was calculated as an index of bulking efficiency according to the formula below:

$$WA(\%) = [(W_2 - W_1)/W_1] \times 100 \tag{2}$$

where W_2 is the weight of the water-saturated specimen and W_1 is the weight of the oven-dried specimen. In addition to the WA values, the Water Repellent Effectiveness (WRE) values were calculated using following equation:

$$WRE (\%) = [(WA_1 - WA_2)/ WA_1] \times 100 \tag{3}$$

where WA_1 is water absorption of non-paraffine specimen and WA_2 is water absorption of paraffine specimen.

2.4. Decay Tests

Decay tests were carried out in Wood Preservation Laboratory of Duzce University according to EN 113 (1996). Test samples were dried at 60 °C for 24 h and weighed to determine their oven-dried weighets before decay test. The treated and untreated wood blocks were sterilized at 110 °C for 20 minute. The samples were then exposed values to the white rot fungus *Corillous versicolor*, the brown rot fungi *Coniophora puteana* fungi cultered on 3.7% Malt Extract Agar (MEA) medium. All tests samples were transferred to the petri dishes and incubated at 24 + 2^{0}C with 75% relative humidity (RH) for 12 weeks. At the and of the exposure time, the samples were clened of the fungal mycelia and weighed their oven-dried weighets after decay test for calculate the percentage of mass.

3. RESULT AND DISCUSTION

3.1. Density and Water Absorption

The weight gain ratios resulting from paraffin treatment differed. A higher weight gain was observed, especially in the samples subjected to control and compression. In heat treatment applications, weight gains were lower than others (Table 1). This is due to the effect of heat, the paraffin, which is found in the wood after the heat treatment, becomes liquid again and moves away from the wood. In addition, there is also the effect of thermal degradation which is the result of heat treatment (Sahin 2013, Esteves et al 2014),

The density values and the water absorption values for different water absorption times are given in Table 2. Increases in water absorption rates were detected in all treatments due to the increase in the immersion time in the water. The highest water absorption rates of the paraffinized and non-paraffinized applications were determined in the hot press compaction experiments (groups C and G).

Table 2. Density and water absorption values of the experimental samples

Group	Density	Water absorption rate (%)						
		2 h	4h	8h	24h	48h	72h	168h
A Group	0,548	29,63	35,44	39,57	44,93	52,00	58,21	69,48
B Group	0,54	21,38	29,58	36,32	43,17	49,28	55,21	64,93
C Group	0,547	61,45	64,88	67,13	71,26	78,06	82,89	90,95
D Group	0,543	44,97	58,57	64,20	69,91	76,15	80,78	87,78
E Group	0,976	1,5	2	2,76	4,9	6,86	8,17	12,24
F Group	0,685	3,21	4,48	6,15	11,44	19,16	24,65	37,40
G Group	0,986	3,50	4,61	6,76	15,12	40,59	54,97	63,98
H Group	0,706	2,44	3,71	5,58	14,88	39,59	51,97	64,04

The heat treatment applied before the densification showed an effect of reducing the water absorption rate of the test specimens. In unwaxed test samples, the lowest water absorption rate was obtained in heat treatment (group B). Paraffin application to experimental specimens caused considerable decreases in water absorption rates while significant increases were seen in density values. Lesar and Humar (2010) treated beech (*Fagus sylvatica*) and Norway spruce (*Picea abies*) with 5 different fat solutions and found significant reductions in water absorption and fungal destruction

The water absorption rates of the paraffinized test samples in 2 hours of water ranged from 1.5 to 3.5% and these values were found to be 21.4 to 61.5% in the without paraffin control samples. The highest density values after the paraffin application were obtained in groups E and G without heat treatment (0,976 and 0,986 g / cm3). Esteves et al. (2014) reported that the paraffin treatment increased the density of the *Pinus pinaster*.

The water repellent efficacy value (SDI) refers to the reduction in water absorption rates of treated test samples according to control samples. For this purpose, the arithmetic mean values of SIE values of the test specimens suspended in water for various periods after different treatment procedures are given in Table 3.

Table 3. Water repellent activity values of the experimental specimens

Group	Water repellent activity						
	2h	4h	8h	24h	48h	72h	168h
E Group	94,94	94,36	93,03	89,09	86,81	85,96	82,38
F Group	84,99	84,84	83,07	73,51	61,12	55,35	42,39
G Group	94,30	92,89	89,94	78,79	48,01	33,69	29,65
H Group	94,57	93,67	91,30	78,71	48,01	35,67	27,04

Significant increases were observed in water-repellent activity values resulting from paraffin application. In particular, paraffin-treated test specimens have water-repellent activity values of more than 80% obtained during 2, 4 and 8 h of water retention. The highest water repellency activity values were obtained only in paraffin-treated test samples (group E). The water repellency activity values of these samples were obtained as 89.5% on average in all water waits. Paraffin application gave better results than heat treatment and compression processes. This has also been expressed in previous studies (Esteves et al., 2014). The lowest water repellent activity values were determined in the test samples with hot press compression (group G and H). Water retention efficiency values of the samples belonging to these groups were obtained by 29.7% and 27%, respectively, during long waiting periods. Significant reductions in the water repellent activity values of the samples belonging to groups G and H have been determined, especially after 24 hours of immersion in water. In addition, water repellent activity values of all experimental groups showed a decrease depending on the immersion time in water.

3.2. Fungi Test

Findings about the effects of paraffin impregnation, heat treatment and press applications on wood decaying fungi are seen in Table 4. According to the findings obtained, the highest weight losses were determined in the control samples in the unwaxed samples. It was determined that the highest weight losses were obtained in 170 °C heat treated and not densificated samples.

In general, paraffin administration has resulted in reductions in the mean weight loss caused by both fungi species (*Coriolus versicolor* and *Coniophora puteana*) That is, paraffin application increases the resistance of chambers to fungi. In some studies it has been reported that some impregnated chemicals used in conjunction with paraffin give effective results against wood-fungus fungi (Lesar et al., (2009).) In other studies, it has been reported that paraffin application reduced the moisture content of the wood and thus decreased the rot fungus (Lesar and Humar (2010). Paraffin application has been shown to give very effective results in destructive termites in woods (Scholz et al. (2010; Esteves, 2014).

It is seen that heat treatment application has little resistance to fungi alone. However, it has been found that the application of hot pressing together with the heat treatment significantly increases the resistance to fungi in both unwaxed and waxed samples.

Densification with hot press seems to increase resistance to fungi in waxed specimens. However, it has been determined that this resistance alone is sufficient for densification.

Table 4: Mean waight loss of samples

Heat treatment tempreature (⁰C)	Press tempreature (⁰C)	Mean weight loss (%)			
		without wax		waxed	
		Coriolus versicolor	*Coniophora puteana*	*Coriolus versicolor*	*Coniophora puteana*
Control		21.4	20.5	7.0	3.8
170	0	19.7	13.9	14.2	5.2
0	185	16.1	12	1.8	0.9
170	185	8.5	8.4	5.0	1.3

4. CONCLUSİON

The paraffin-impregnated Scotch pine woods caused significant increases in density and water repellency when compared to the untreated samples, while significant reductions in water absorption rates were found. The water absorption rates of only the wax treated Scotch pine woods gave better results than the densfication and heat treatments. The highest water absorption rates were obtained when the untreated scotch pine woods were densficated.

The paraffin application provided effective protection against both white rot and brown rot fungus. The alone heat treatment application has little effect on the durability of wood against fungi. However, if heat treatment and densification were applied together, the resistance against decay increased considerably.

REFERENCES

[1]. Ates S., Akyıldız M.H. and Ozdemir H. (2009). Effects of heat treatment on Calabrian pine (*Pinus brutia* Ten.) wood, *BioResources*, 4 (3): 1032-1043.
[2]. Esteves B., Nunes, L., Domingos, I. and Pereira, H. (2014). Improvement of termite resistance, dimensional stability and mechanical properties of pine wood by paraffin impregnation, *European Journal of Wood and Wood Products*, 72 (5): 609-615.
[3]. Kartal, NS, Engur O, Kose C.2006. Environmental Problems Of Wood Preservatives And Preservative Treated Wood Use. İstanbul Universitesi Orman Fakultesi Dergisi, B, 56(1).
[4]. Lesar B. and Humar M. (2010). Use of wax emulsions for improvement of wood durability and sorption properties, *European Journal of Wood and Wood Products*, 69: 231–238.
[5]. Scholz G, Militz H, Gasco´n-Garrido P, Ibiza-Palacios MS, Oliver-Villanueva JV, Peters BC, Fitzgerald CJ (2010) Improved termite resistance of wood by wax impregnation. Int Biodeterior Biodegrad 64:688–693
[6]. Sahin, H.İ. (2013). Isıl islemin dogal ve plantasyon ormanlarında yetisen disbudak (*Fraxinus angustifolia* Vahl.) odunlarının bazı teknolojik ozelliklerine etkisi, *Doktora Tezi*, Duzce Üniversitesi, Düzce (Turkish).
[7]. Yalcin, M. and Sahin H.I. (2015). Changes in the chemical structure and decay resistance of heat-treated narrow-leaved ash wood, *Maderas. Ciencia y tecnología,* 17(2): 435-446.

PREPARATION OF WASTE MANAGEMENT PLAN AT UNIVERSITIES AND IMPLEMENTATION OF WASTE MANAGEMENT

Hande Atasoy[1], Asude Ates[2]

Abstract

The high diversity and high amounts of wastes generated in areas such as industrial establishments, universities, hospitals, etc., make it very difficult to follow these wastes. Disruptions in the follow-up process cause the wastes that can be recovered to be lost by subjecting them to disposal / landfilling and also the natural resource usage, energy and raw material savings cannot be applied. For this reason, it is necessary to establish a system for waste collection in areas where collective life is led. Waste management is the process of separation of the wastes at their sources and its collection, temporary storage, recycling, transport, disposal and controls after disposal operations. This process starting from the formation of the wastes continues until the final disposal of the wastes. With the waste management to be implemented, it is aimed to reduce the amount of waste sent to regular storage or recycling operations by increasing producer responsibility. The waste management planned to be implemented at the Sakarya University is aimed at defining the generated wastes, collecting them separately at their sources, leading awareness raising activities through personnel-student trainings, sending wastes to disposal/recycling and keeping records. With this study, the wastes at the Sakarya University have been classified as solid wastes, package wastes, non-hazardous wastes, hazardous wastes and special wastes. With this classification, the waste management plan is being prepared by evaluating what kind of waste is generated by which departments or faculties. It has been determined that the package wastes and domestic solid wastes are more common than other types of wastes and that the hazardous wastes generated at the university are mostly from laboratories where experimental works are conducted. With this plan prepared after the determinations, a waste management implementation will be launched and thus, the wastes to be generated will be foreseen and assessed. Depending on the type of wastes generated, agreements will be concluded with the appropriate recycling / disposal companies and appropriate waste recycling / disposal methods will be determined. With this implementation planned at the university, it is aimed at separating the waste at its source and determining the appropriate recycling/disposal methods.

Keywords: *Waste management, university, hazardous wastes, non-hazardous wastes, recycling*

1. INTRODUCTION

Waste is all kind of material that has been used, is not wanted anymore, and constitute harm for environment. All kinds of materials, the useful time of which is expired and required to be thrown away from the environment that we live are defined as wastes. Waste Management Regulation dated 02.04.2015 and No.29314 has been issued in order to determine the general procedures and principles to ensure the management without harming the environment and human health from the formation to the disposal of the wastes and the provisions of the regulation are executed by the Ministry of Environment and Urbanization and all wastes are evaluated within the scope of this regulation. Waste producers are liable to take the required measures in order to reduce the waste production to minimum, and to collect the wastes separately and store them temporarily.

Sakarya University is involved in the definition of the waste producer and is liable to provide all of the waste producer liabilies included in the legislation. Waste producers must prepare a waste management plan for wastes and the prevention and reduction of the produced wastes and they must submit it to the provincial

---

[1] Corresponding author: Sakarya University, Department of Environmental Engineering, 54055,Serdivan/Sakarya, Turkey. atasoyhande@hotmail.com

[2] Sakarya University, Department of Environmental Engineering, 54055,Serdivan/Sakarya, Turkey. aates@sakarya.edu.tr

directorate and have the plan approved. Within this scope a Waste Management Plan is being prepared within structure of Sakarya University the waste characteristics and waste types of the University are determined in line with the conducted studies. With this study, the wastes formed at Sakarya University are classified under 5 titles as solid wastes, packaging wastes, non-hazardous wastes, hazardous wastes and special wastes.

2. MATERIALAND METHODS

2.1. Waste Types and Management Methods According to Waste Types

However the waste management is the basic regulation for all wastes, different regulations and communiques are included in the legislation for special wastes, packaging wastes and non-hazardous wastes. Within this scope, any types of wastes occurred and likely to occur in the area are evaluated according to waste management regulation and other related regulation-notification information.

2.1.1. Mixed Municipal Wastes

The mixed municipal wastes, which occur at university, are accumulated in 5 liters of plastic boxes in the rooms of instructors, in 15-20 liter plastic boxes inside the building and at floors and in 800 liters of galvanized containers in the common areas outside the building and these are transfered to municipal waste disposal facility by being collected at regular intervals by garbage collection vehicles. When considered that the solid waste boxes accumulated in waste bins in interior areas are 50% full everyday and that the solid wastes' density is 90 m^3/kg on daily basis, it is estimated that everyday average of 930 kg mixed municipal wastes occur in interior areas and when considered that the containers outside (common areas outside the building) are 50% full everyday and that the solid waste density is 130 m^3/kg, it is estimated that that average of 2 tons of mixed municipal wastes occur in exterior areas on daily basis. According to these evaluations, it is foreseen that an average of 3 tons of mixed municipal waste at the university on daily basis. The collection of mixed municipal wastes is not a problem within the scope of collection points and vehicle provision, although the collection of other waste types together with municipal waste increases the daily tonnage and causes the waste possible to be recycled to be sent to storage facility.

2.1.2. Special Wastes

These wastes are the wastes, which have special importance and legally remain out of domestic solid wastes, required to be collected, transported, processed and disposed with different methods according to the proper conditions stated in their regulations.

2.1.2.1   Medical Wastes

It is essential not to mix the medical wastes with other wastes such as hazardous, non-hazardous, municipal or packaging wastes. At the university, there is a medico-social center, in which instant diagnoses and interventions are made in case of an emergencies, and the medical wastes, that occur in the medico social center and the faculty of health sciences, are collected in medical waste boxes. As stated in Article 10 of the Medical Waste Control Regulation, the medical wastes are classified under two titles as wastes with cutting and puncturing features and the other medical wastes. Separately than other medical wastes, the wastes with cutting and puncturing features must be collected in a sealed, plastic box which is resistant to puncturing, tearing, breaking and exploding, and these collecting containers shall be filled to the maximum at the rate of ¾ and certainly shall not be tightened or opened after the containers are filled. The accumulated medical wastes are transfered to the authority competent for the medical waste collection and sterilization.

2.1.2.2   Waste Batteries

Waste battery manufacturers are liable to provide the collecting boxes or containers containing the words "Waste Battery" and "Waste Batteries Only" to be put at the collection points at the facilities as free of charge and to transport the waste batteries or have them transported to the storage areas by ensuring the filled boxes or containers to be collected.

Waste batteries occur from the electronic equipments in the rooms and departments of the instructors and the areas, in which battery wastes are intense, will be determined and the waste batteries will be ensured to be accumulated in the collecting boxes to be provided by the Portable Battery Manufacturers and Importers Association and they shall be ensured to be sent to this association which is authorized within the scope of this regulation.

2.1.2.3 Electronical Wastes

Waste electrical and electronic items defines all the components, elements and consumables of the items included in the categories defined in Annex-1/A of the Waste Electrical and Electronic Items Control Regulation dated 22.05.2012 and No.28300 in accordance with the waste definition in the Waste Management Regulation. The wastes occurred due to maintenance-repair-replacement operations of the technical equipments used at the university, and those, the life span of which are filled from the fluorescent lamps used for lighting in the interior areas of the university such as classrooms, mezzanines, laboratories, rooms of the instructors, are within the coverage of electronic wastes such as floor lamps, floors, These wastes shall be sent to the licensed recycling company to be recycled/disposed.

2.1.2.4 Waste Vegetable Oils

Vegetable oils and used frying oils compatible with the definition of waste in the Waste Management Regulation are the wastes included within this scope. Waste vegetable oils and the wastes occur due to treatment of these oils are forbidden to be stored, transport so that this will cause pollution of environment, to be drained into groundwater, sewage, through surface waters and into soil by drainage systems directly or indirectly and to be burnt causing air pollution by exceeding the limit values determined by the current regulations. It is essential to collect the vegetable waste oils separately at the source and stored appropriately. For this reason, waste oils, which occur in the kitchens of the university are collected in appropriate sealed containers and sent to licensed recycling companies.

During the waste management process, the occurence situations of the waste vegetable oils in the canteens will be examined and containers will be provided to be used to accumulate the oils and then the evaluation and reduction works will be started over the accumulated amounts.

2.1.3. Packaging Wastes

Packaging wastes can be collected at specific locations within the university separately as paper-cardboard and plastic packaging wastes and these can be collected as mixed packaging wastes at specific locations or they are evaluated as mixed municipal wastes, for this reason their quantities cannot be foreseen in the first stage. However, in the characterization study conducted in 2012 by the university it is estimated that an average of 2 tons of packaging waste occurred. One of the targets determined in the waste management to be sustained at the university is to increase the diversity of packaging wastes at all locations and to collect them separately in metal and glass containers particularly in canteens.

2.1.4. Hazardous Wastes

Hazardous wastes; is a general name given to all of flammable, burning, cancerogenic, explosive, irritating and toxic wastes, which are dangerous for the environment and human. Hazardous wastes means the wastes, which have one or more of the hazardous properties listed in Annex-3/A of the Waste Management Regulation and have a (*) mark next to their six-digit waste code in Annex-4. Non-hazardous waste producers can store their wastes in the facility for maximum six months by taking the necessary measures until the recycling process.

The studies performed in the laboratories, which are located in the faculties, are evaluated and the wastes, which occurred and likely to occur within the scope of the performed processes, and their codes that are determined and given in Table 1. Appropriate containers shall be provided by considering the diversity and density of wastes for separate collection of these wastes and these shall be sent to the licensed recycling company, with which agreement shall be conducted after determining the appropriate waste codes.

Table:1 Codes of Hazardous Wastes, which Occurred and will Probably Occur in Laboratories.

06 01 01*	Sulfuric acid and sulfurous acid
06 01 02*	Hydrochloric acid
06 01 03*	Hydrofluoric acid
06 01 04*	Phosphoric and phosphorous acid
06 01 05*	Nitric acid and nitric acid
06 01 06*	Other acids
06 02 01*	Calcium hydroxide
06 02 03*	Ammonium hydroxide

06 02 04*	Sodium and potassium hydroxide
06 02 05*	Other bases
06 03 13*	Solid salts and solutions containing heavy metals
07 01 08*	Other bottom sediment and reaction residues
07 01 01*	Water based washing liquids and main solvents
07 01 03*	Halogenated organic solvents, washing liquids and main
15 01 10*	Packaging materials containing the residues of hazardous
15 01 11*	Metallic packages containing hazardous porous solid
15 02 02*	Absorbents contaminated with hazardous materials, filter
16 05 06*	Laboratory chemicals consisting of hazardous materials
16 03 03*	Inorganic wastes containing hazardous materials
16 03 05*	Organic wastes containing hazardous materials

Waste print toners, which will occur due to the maintenance of office processes and photocopy machines, other than those specified in Table 1 shall be sent to the licensed recycling company, with which an agreement will be made, by determining the appropriate waste codes.

2.1.5. Non-hazardous Wastes

The wastes, which do not adversely affect the health of the environment or human, are insoluble, in combustable, do not react physically or chemically, non-biodegradable, or do not affect the substances it contacts so that they will harm the environment or human life, are defined as non-hazardous wastes. According to the Communique on Recycling of Specific Non-Hazardous Wastes dated 17.06.2011 and No.27967, the wastes, which are not marked with a (*) mark in ANNEX-IV of the Waste Management Regulation, are indicated as non-hazardous wastes. Non-hazardous waste producers are able to store their wastes within the facility for maximum one year by taking the necessary measures until recycling process. Within the scope of maintenance, repair and construction activities conducted within the structure of Sakarya University, the scrap metals, wood, glass, plastic wastes are determined as wastes which densely occurred and likely to occur. These wastes and other non-hazardous wastes to be determined shall be sent to the licensed recycling company, with which an agreement will be made.

3. FINDINGS AND DISCUSSION

In the evaluations and surveys conducted, it was determined that there are densely domestic and packaging wastes at the university and that the quantities of non-hazardous wastes are less than other types of wastes. These proportional distinctions could not be made clear due to the mixed collection of non-hazardous wastes, packaging wastes and domestic solid wastes. In addition, since the study was performed by taking the hazardous wastes occurred and likely to occur into consideration, the proportional transitions indicated in graph 1 have been created.
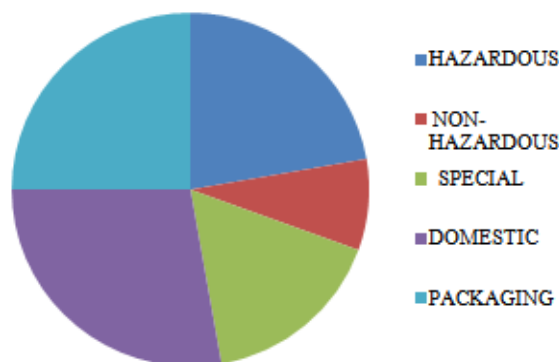

Figure 1: Percent distribution of waste types and amount of occurance

As a result of the studies conducted, it is stated that the the population, which the municipalities in our country provide service, constitutes 80% of the total population according to the data related to the year 2008. When the data of the Turkish Statistical Institute (TUIK) is examined, it is seen that the annual amount of waste collected is 24 million tons. When it is assumpted that municipalities are providing service to the whole population, it is calculated that this figure will be 30 million tons annually when the whole population is multiplied with 1.15 kg waste for each person for each day, and that this figure will be 42 million tons in 2030 with population growth. In Graphic 2 the amount of waste is shown according to years. When this study is evaluated, it is foreseen that the amount of solid waste will increase every passing year by accelerating along with the population increase and the consumption rate, and this increase will affect also the universities, at which the collective life is continued, in the same way. For this reason, the value of waste management practices increases every year. The organizations, which initiate the process will overcome the problems, which they will encounter, more easily than the other organizations and they will be the parties the least affected by the problems that may occur as a result of the planless nesses.
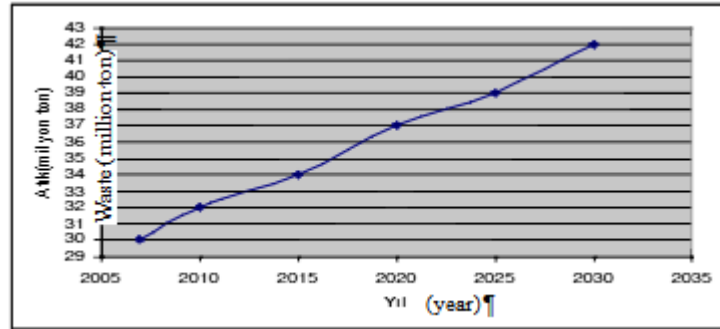
Figure 2: Waste Quantities By Years (EUROSTAT, 2010)

According to the European Statistical Office, 40% of domestic wastes is disposed by being stored, 23% of them by being recycled, 20% of them by being burnt and 17% by composting method. It is possible to say that as a result of the recycling and recovery of packaging wastes and as a result of decomposition of decomposable wastes in storage facilities, the rate of the regular storage method decreases rapidly compared to previous years, and that the burning has increased and the recycling and recovery has highly increased in the wastage.

As the importance of the recycling processes increases, the waste stock market also has taken its place in the economy. According to data of the European Statistical Office, the value of wastes in Europe compared to 2008 is given in graphic 3. According to this, the value of plastic is the highest with 350 Euro per ton, on the other hand the value of glass is the lowest with 50 Euro per ton. When it is evaluated within this scope, along with the waste management and the recovery of the wastes to be made, it is also possible to contribute to the economy.
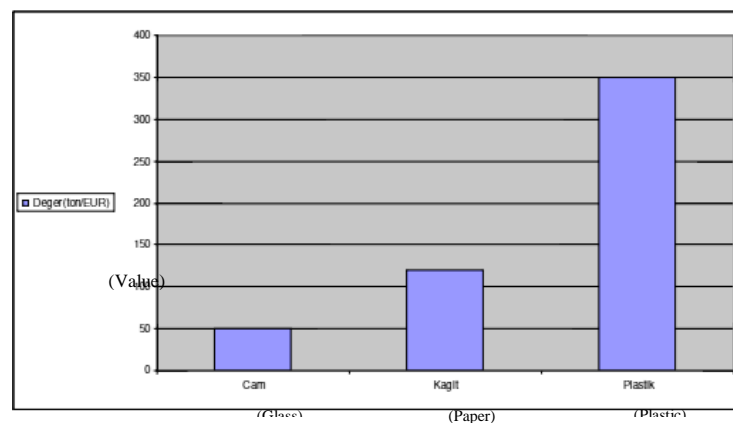
Figure 3: Values of recyclable wastes in Europe compared to the year 2008 (EUROSTAT, 2010)

In Turkey, around 20 million tons of wastes are produced annually by the manufacturing industry, and 1.12 million tons of which are hazardous wastes. Unfortunately, the data related to hazardous waste is limited to those, which come from the manufacturing industry. For this reason, there is not a healthy data flow about the types and quantities of hazardous wastes occur at universities. For the hazardous wastes to be manufactured, the first 5 rows in the list are taken by the base metal industry, chemical industry, food and beverage

production, petroleum and coal activities, and motor-vehicle production and maintenance. According to the data of Ministry of Environment and Forestry shown in Graphic 4, 3.5% of hazardous wastes are burnt for disposal and energy recovery purposes.
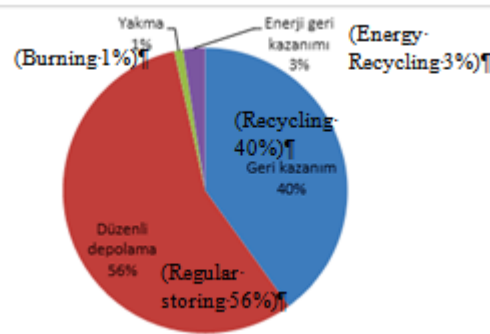
Figure 4: Disposal rates for hazardous solid waste (Ministry of Environment and Forestry 2009)

Hazardous wastes and special wastes shall be collected separately according to the occurance points and sent to the licensed recycling companies subjected to appropriate recovery/disposal processes. The percentage ratios shall be determined more clearly by providing the data rates by means of keeping records during the transfers, and the solutions to follow for mitigation studies to be determined.

4. RESULTS

Waste types were determined with the waste diversity and waste management study conducted at Sakarya University and the data were collected in order to prepare the waste management plan. With the waste management plan to be created, the waste management process planned to be established at the university shall be started. Within the scope of this process, agreements shall be made with the licensed companies for installations of waste accumulation intermediate stations and temporary waste storage area in compliance with the regulation. In the direction of the determinations, the quantity densities of the waste types shall be determined according to the departments-faculties and the relevant collecting boxes shall be provided for efficient collection. In order to sustain these activities, a waste management operation scheme has been established as indicated in graphic 5.
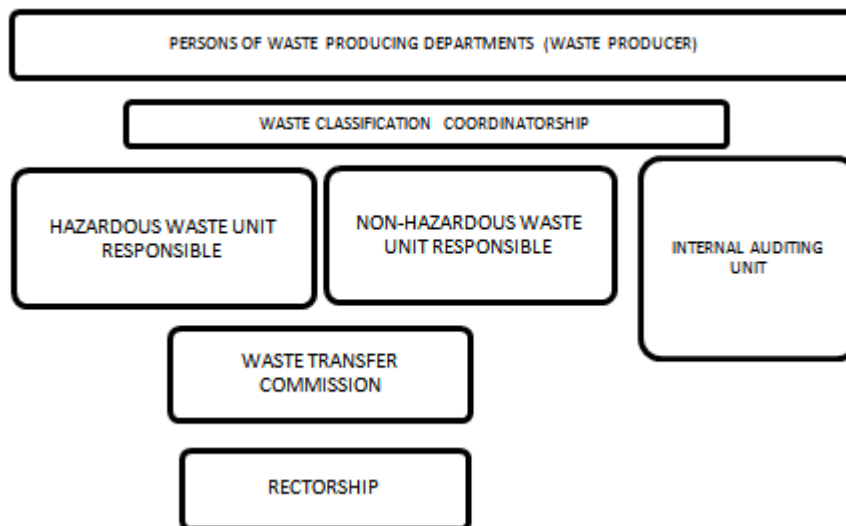
Figure 5:Waste Management Operation Scheme

All the wastes, that will occur as a result of the activities performed in the units within the responsibility of Sakarya University, shall be classified by the administrative staff working in the waste classification coordinator ship to be established. Waste analyzes to be carried out within the scope of classification procedures shall also be carried out by this unit. The wastes to be classified shall be transferred to the relevant waste unit responsible for the waste disposal operations and the necessary informings shall be made. Waste unit responsibles shall ensure the occurred wastes to be stored for appropriate periods of time (maximum 6 months for hazardous wastes in temporary storage facility, on the other hand maximum 1 year for non-hazardous wastes, excluding medical wastes) specified in the regulation.

It shall also ensure the waste to be reacted with each other to be stored separately and shall be responsible for the safety, control, maintenance, and clean-up procedures of the waste storage facilities. The waste transfer commission to be established shall prepare the waste labeling in accordance with the codes determined by carrying out the appropriate waste code study.

In addition, the licensed firm shall conduct its works, follow the waste market and collect the transfer proposals, and shall submit the most appropriate transfer proposals to the Rectorate office. The final decisions shall be made by the Rectorate office and the cycle shall be completed by auditing the all units by internal audit unit within the scope of the process.

Within the scope of this study, budget preparations shall be made by making appropriate location determinations and financing studies related to the waste storage facilities. Waste transfer stations and final storage areas shall be established at the university. Layout plans of waste storage facilities shall be prepared according to the determined basic waste codes and waste characteristics.

The waste management plan to be completed within the structure of Sakarya University and the waste management works started to be operated shall be monitored for 6 months of period. Within the scope of the determinations, informative works shall be made towards the concerned persons and trainings v be performed. With the completion of this process, Sakarya University's waste management process is targeted to be started to implement effectively and to ensure it to sustain.

REFERENCES

[1].   Waste Management Regulation, 02.04.2015.
[2].   Regulation on the Control of Waste Batteries and Accumulators, 31.08.2004.
[3].   Regulation on the Control of Medical Waste, 25.01.2017.
[4].   Regulation on the Control of Vegetable Wastes, 06.06.2015.
[5].   Comminique on Recycling of Certain Non-Hazardous Wastes, 17.06.2011.
[6].   Süheyla Duran, Sümeyye Akdemir, Sakarya University Esentepe Campus Waste Characterization and Waste Management Study, Dissertation, Sakarya University Engineering Faculty Environment Engineering Department, Sakarya,2012.
[7].   Emine Rana Battal, Integrated Solid Waste Management Turkey Implementation, Master's Thesis, T.R. Gebze High Technology Institute of Engineering and Science, Major of Environment Engineering, Gebze, 2011.
[8].   Gülcin Tıglı, Hazardous Wastes Occuring at Universities: Specific to Ege University, Master's Thesis, Ege University Institute of Science,İzmir,2013

RAILWAY VEHICLE MANUFACTURING COMPANY INTEGRATED MANAGEMENT SYSTEM (ISO 9001, ISO 14001, OHSAS 18001) APPLICATION

Asude ATES[1], Serap GUNAY[2]

Abstract

Rising competitive conditions make the control necessary to control companies? risksin every area. Producing a qualitative product or giving a quality service is not enough for the companies, besides they should give respect to natural environment, the society and obtain a safe and healthy work environment for their workers. By this way, companies can improve their prestige in the sector. Applying Quality, Environment, Occupational Health and Safety Management Systems is the best way to have a control in those three different management areas. However, the difficulties encountered by organizations vary over the years, the activities in the supply chain become more complex in parallel with globalization, changes in the way businesses conduct business, increased expectations of customers and all parties involved, facilitating access to information and making the voice of today's society stronger. In this context, the ISO 9001 Quality Management System and ISO 14001 environmental management standards was published by ISO in September 2015. Ensure that management systems are integrated into the new revision in conjunction with the establishment of different and multiple management systems to ease the annex SL structure a draft that was created to make it attractive, more than one management system provides an opportunity for new concepts to overcome between. In this research, integrated quality, environment, occupational health and safety management systems are investigated with a railway vehicle production firm example. Quality, Environment and Occupational Health & Safety Management Systems necessary for their studies and to revise the influence of the sector have been revealed by research.

Keywords: *İntegrated Management System, Annex SL, ISO 14001:2015 And ISO 9001:2015 Revision*

1. INTRODUCTION

In the world of information, technology and communication societies experiencing major advances and new developments in the field of competition has led to an economic race each day. To survive in the current world order in all sectors of production of goods and services appropriate to customer needs and expectations by providing can be achieved. This will only be possible through the implementation of Integrated Management Systems that target all stages from start-up to start-up, production, marketing and after sales services. It is now accepted that the sources of our ever-shrinking world are not infinite, that the environmental effects of our products and activities are not local and regional but global. This consciousness has brought along the need for environmental influences to be controlled by market forces rather than legal practices. In addition to meeting the expectations and needs of today's consumers at the highest level, today's consumers are demanding respect and respect for the neighborhood and the world they live in, and questioning this on the market. These developments have revealed the need for management systems that will enable businesses to control their interactions with the environment and to continuously improve their environmental performance and success. One of the most important human resource problems encountered in enterprises is that employees do not have a safe and healthy work environment. To ensure that the remediation measures are carried out effectively and that the expected benefits derive from the enterprise strategy adopted by an organization, it is recommended to use appropriate remediation measures and tools and remedies that help to accurately assess remediation results. Employees need to carry out planned and

---

[1] *Corresponding author: Sakarya University, Department of Environmental Engineering, 54055,Serdivan/Sakarya, Turkey. aates@sakarya.edu.tr*

[2] *Sakarya University, Department of Environmental Engineering, 54055,Serdivan/Sakarya, Turkey. serap.gunay1@ogr.sakarya.edu.tr*

systematic work on occupational health and safety in order to achieve better competition conditions. Standards such as ISO 9001 and ISO 14001 have focused on quality and environmental management, while ISO 18001 has emerged as a separate standard for the provision of occupational health and safety in enterprises and continuous improvement and protection, and the human resources of enterprises are important in terms of ensuring quality efficiency and continuity.

2. INTEGRATED MANAGEMENT SYSTEM

In the context of globalization, competition conditions first brought about the quality management system of ISO 9000. This standard, in short, contains the conditions that must be met in a workplace to satisfy the customer. ISO 9000 has attracted worldwide attention and has become an international identity. ISO 9001 is applied in different organizations all over the world [4]. Organizations with this certificate can trust each other and trade easily. However, the quality management system does not cover work safety and environmental aspects of production. The OHSAS 18001 and ISO 14001 standards fill this gap; In other words, it integrates the quality management system. Our production or service we offer to the market; If we want to satisfy our customers, minimize the number of business accidents and pollute the environment, we need to consider these three management systems. The commitment of the staff and management personnel of the companies is of great importance after the adoption of the standards [6]. ISO 9000, customer orientation, OHSAS 18001, employee orientation, ISO 14001, environmental awareness. All three together, increase our competitiveness and ensure the profitability of our organization. Nowadays, quality management system, safety management system, environmental management system, each organization at the same time social responsibility.

2.1. Advantages of Integrated Management System for Companies

In this period, most companies are looking for integrated approaches to quality, environment, health and safety issues. Between the increasing adoptions of standards together with this integration (integration) the most practical step will be thrown on a prospective basis.

An integrated management system;

- Reduces documentation costs by visibly reducing repetitions and time savings.

- Removes conflicting responsibilities.

- Education and development are facilitated.

- Communication is easy.

- Applications are optimized.

- The integration of management systems makes it easier to focus on the most important issues in a company.

- It can be shaped according to the needs of the organization; two or four systems can be integrated.

- It is a management system that brings integrity to the concepts of quality, environment and work safety related to business.

- Allows the requirements of the relevant standards to be met within the framework of the bureaucratic remote and process approach by reducing the documentation to a minimum.

- Allows a reversal of a visible decline in the costs of companies [7].

3. REVISION OF ISO 9001, ISO 14001 AND OHSAS 18001

The International Standardization Organization (ISO) monitors standards every five years, revises them in line with needs and makes them useful for interested parties. The challenges that organizations face vary over the years, in line with globalization, the need to revise their operations in the supply chain to become more complex, to change the way businesses do business, to increase the expectations of customers and all parties involved, to facilitate access to information and to strengthen the voice of today's society. The ISO 14001 Environmental Management System standard, which was published by ISO in September 2015, was published by Turkish Standards Institution in January 2016 as Turkish Standard (TS EN ISO 14001: 2015) [8]. The revision of OHSAS 18001 has not yet been realized and will be revised in accordance with Quality and Environmental Management systems.

3.1. ISO 9001:2015 and ISO 14001:2015 Revision Differences

- High level of adoption of the structure [9],

- There is a clear requirement for a risk-based approach to promote a better understanding and implementation of the process approach [9],

- There are fewer rules and conditions [9],

- Less emphasis on documents [9],

- Increased applicability for services [9],

- There is a condition for defining the limits of the quality management system [9],

- Emphasis on institutional structure [9],

- Increased emphasis on leadership [9],

- Greater emphasis on achieving desired outcomes to enhance customer satisfaction [9],

- Determination of environmental conditions for the design and development processes of the product or service [9].

In particular, the 2015 edition emphasizes risk-based thinking that is clearly built into the entire management system. Risk-based thinking can be considered a positive aspect of risk. Acceptance of this term can increase customer confidence and satisfaction and ensure consistency of quality goods and services. In general, this new version aims to provide a more satisfying application and not just specific products, but also service-oriented [10].

3.2. Annex SL

For many years, ISO has set the standard for many management systems, ranging from quality and environment to information security, business continuity management and record management. Despite the common elements of the standards, the ISO management system standards are published in many different ways and structures. This lack of common structure causes some confusion and difficulties in the implementation phase. These confusion and difficulties led to the adoption of the Annex SL in ISO standards.

Initially established to coordinate compliance between ISO 9001 and ISO 14001, the Annex SL has been implemented for all management standards. Annex SL, a structure created to facilitate the integration of different management systems and make it easier and more attractive to establish multiple management systems, provides an opportunity to overcome new concepts among multiple management systems.

Annex SL was originally designed as ISO Guide 83, previously known as Annex SL, with the latest modifications. As all newly published management system standards will be in this structure, revisions of existing standards will be made according to this structure.

Annex SL is applicable to all management standards such as ISO standards, Public Specification Requirements (PAS) and Technical Specifications (TS). All standards, including the new ISO 45001 as well as the revised ISO 9001 and ISO 14001, will be based on the High Level Structure of the Annex SL.

3.2.1. High Level Structure

High Level Structure has been established with Annex SL, ie the main item numbers and titles can not be changed in the standard.

High Level Structure a structure consisting of 10 items and the items are as follows:

- Article 1: Scope [12]

- Article 2: Normative References [12]

- Article 3: Terms and Definitions [12]

- Article 4: Context of The Organization [12]

- Article 5: Leadership [12]

- Article 6: Planning [12]

- Article 7: Support [12]

- Article 8: Operation [12]

- Article 9: Performance Evaluation [12]

- Article 10: Improvement [12]

4. INTEGRATED MANAGEMENT SYSTEM APPLICATION

The applications of Integrated Quality, Environment and Occupational Health and Safety Management Systems have been applied in the scope of High Level Structure in a railway vehicle manufacturing company.

Article 1 - Scope:

The desired results from the Integrated Management System are stated.

Article 2 - Normative References:

Reference standards publications are included.

Article 3 - Terms and Definitions:

The Integrated Management System terms and definitions are detailed. Within the scope of this article, some of the newly added terms are as follows:

1) Compliance Obligations: An organization that must comply with legal requirements, and you have to comply with that or any other that chooses to comply with legal requirements (mandatory requirements, voluntary commitments).

2) Documented Information: Ready information for the control and maintenance of the establishment and the environment in which this area is located.

3) Life Cycle: A product or service; from purchasing raw material, consecutive and interlinked stages from production to final disposal or from natural sources (life cycle stages, raw materials, design, manufacturing, transportation/Delivery, use, processing and final disposal end-of-life).

4) Indicator: Operations, management, and representation of the conditions of a measurable condition or status.

5) Related Parties: A decision or activity can affect or be affected by them yourself, or them the person or organization who might be affected (such as customers, communities, suppliers, regulators, civil society organizations, investors and employees).

6) Risk: The effect of uncertainty.

7) Performance: The process required to determine the value.

Article 4 - Context of The Organization:

Article 4, consists of four sub-items:

1) 4.1. Understanding the Organization and Its Context: Within this article, internal issues (personnel, salaries, resources, etc.) and external issues (climate, suppliers, customers, etc.) have been identified that affect the objectives of the establishment, its strategic direction and the competence of the Integrated Management System to achieve the desired results.

2) 4.2. Understanding the Needs and Expectations of Interested Parties: The needs and expectations of the related parties have been determined (contracts, complaints, praise), legal conditions have been determined within the scope of the activity of the organization, and compliance has been checked.

3) 4.3. Determining the Scope of the Integrated Management System: The Integrated Management System and defined the boundaries of the organization's internal and external issues, compliance obligations, within the framework of the scope of products and services has been identified.

4) 4.4. Integrated Management System: Inputs required for processes and projected outputs are determined.

Article 5 - Leadership:

Article 5, contains three sub-articles:

1) 5.1. Leadership and Commitment: An integrated policy has been established by the senior management, duties, powers and responsibilities have been determined and information has been given to ensure that all personnel are involved in the system. In this context, authorized personnel

have been given and supported, and the process approach and risk-based thinking have been encouraged.

2) 5.2. Integrated Policy: Establishment of an Integrated Management System policy in line with its activities, objectives and content, objectives, compliance obligations and continuous improvement.

3) 5.3. Organizational Roles, Responsibilities and Authorities: By senior management roles, responsibilities and authorities are defined and communicated to the person concerned.

Article 6 - Planning:

Article 6, contains three sub-clauses:

1) 6.1. Actions to Address Risks and Opportunities:

6.1.1. Activities for Risks and Opportunities: Using the PUKO Cycle shown in Figure (1), the risks for the purpose and activities of the foundation were identified and decisions were made on how to improve these risks.

Figure 28. PUKO Cycle

6.1.2. Environmental Aspects: Environmental aspects and environmental effects have been identified in line with the activities of the organization.

6.1.3. Compliance Obligations: Compliance obligations that need to fit into the organization has identified and documented knowledge.

6.1.4. Planning of Activities: Reducing the need for corrective action by determining what risks are, who, how and when they should be addressed.

2) 6.2. Integrated Management System Objectives and Planning to Achieve Them:

6.2.1. Targets: Measurable, traceable management system targets that are compatible with the Integrated Management System have been identified..

6.2.2. Planning Activities to Achieve Targets: Resource requirements are set for goals, when and how they are planned and how the results will be assessed.

3) 6.3. Planning of Changes: It has been determined how the plan should be planned if changes are required in the Integrated Management System of the establishment.

Article 7 - Support:

Article 7, contains five sub-clauses:

1) 7.1. Resources: Top management, commitment and planning after the establishment of management systems, maintenance is determined necessary resources for continuous improvement.

2) 7.2. Competence: The activities of the organization which will affect persons with the necessary qualifications (education, experience, etc.) to assess whether is appropriate and inappropriate subjects, the actions taken and the effectiveness of actions was evaluated.

3) 7.3. Awareness: The organization's Integrated Management System the duties and responsibilities of the persons involved in situations that do not comply with requirements are not fulfilled, and the compliance obligations in the absence of current significant environmental aspects and potential environmental impacts, etc.) awareness provided.

4) 7.4. Communication: Created internal and external communication of the Integrated Management System processes for their communication needs (the subject of communication, when to communicate, how to communicate with whom communication can be established) were determined.

5) 7.5. Documented Information: Depending on the size of the organization's activities and processes the information that should be documented (Integrated Management System Policy, environmental aspects, monitoring and measuring results, Management Review results of corrective action results, etc.) defined and have been established.

Article 8 - Operation:

This article is within the scope of the Integrated Management System requirements have been given. Planned and unwanted change (emergency etc.) all process of criteria and control methods necessary to manage (emergency intervention, administrative controls, etc.) besides, both supplied from outside, and processes within the institution are discussed.

Article 9 - Performance Evaluation:

Article 9, consists of three sub-items:

1) 9.1. Monitoring, Measurement, Analysis and Evaluation: The organization's activities within the scope of monitoring, measurement, analysis and evaluation conditions (product control, customer satisfaction, device calibration period, etc.) assessment methods, period, Designated and effectiveness have been evaluated.

2) 9.2. Internal Audit: With regard to the Integrated Management System, the organization has developed and implemented an auditing program including its own requirements, requirements of the standard, frequency, methods, responsibilities, planning and reporting. Audit programs and results are reported in a sustainable manner.

3) 9.3. Management Review: Top management of the continuous compliance with the Integrated Management System, is reviewing at regular intervals to ensure the accuracy and effectiveness. The revised status of the task from reviewing the previous management of the topics, the Integrated Management System concerning internal and changes in foreign issues, not compliant and corrective actions, monitoring and measuring results, test results, continuous improvement opportunities, decisions on all of the requirements for the necessary changes in the Integrated Management System .

Article 10 - Improvement:

Article 10, consists of two sub-items:

1) 10.1. Nonconformity and Corrective Action: In case of nonconformities arising under this article, nonconformities have been analyzed and their causes examined. Corrective actions have been made in accordance with these nonconformities and nonconformities have been eliminated by checking the conformity with the effects of nonconformities.

2) 10.2. Continual improvement: Within the scope of this article, the organization constantly improves the compliance with the integrated management system by analyzing the correctness, effectiveness and adequacy.

5. RESULTS

Thanks to the High Level Structure applied to the railway vehicle manufacturing company, the following effects have been observed:

- The Quality, Environment and Occupational Health and Safety Management Systems have increased in terms of coherence and harmony.

- Within the framework of the same basic text and common terms has created a unifying structure.

- With the inclusion of employees in the system, the implementation of the system has become easier.

- Incorporation of environmental issues into business strategies has created opportunities for sustainability.

- Financial advantages are provided through efficient use of resources.

- The need for documentation has decreased.

- Improved environmental performance has reduced unnecessary expenses for the organization.

- Integrated management system provides a competitive advantage.

REFERENCES

[1]. A. Górny, Management Systems in Production Engineering, 3, 106-111 (2014).

[2]. M. Dudek-Burlikowska, J. of Achievements in Materials and Manufacturing Engineering, 45(1), 89-102 (2011).

[3]. D.H. Stamatis, *Failure Mode and Effect Analysis. FMEA from Theory to Execution, 2nd edition*, (ASQ Quality Press, Milwaukee 2003).

[4]. A. Hamrol, *Quality management with examples* (Wydawnictwo Naukowe PWN, Warszawa 2005).

[5]. *H. T. Ingason,* "*Best Project Management Practices in the Implementation of an ISO 9001 Quality Management System",* ScienceDirect, 2016, p.193.

[6]. C. T. Albulescuab, A. Drăghicia, G. Magdolna Fistisa, A. Trusculescua, "*Does ISO 9001 Quality Certification Influence Labor Productivity in EU-27?",* ScienceDirect, 2016, p.285.

[7]. J. G. Sanz-Calcedoa,*, A.G. Gonzáleza, O. Lópeza, D.R. Salgadob, I. Camberob, J.M. Herrerab," *Analysis on integrated management of the quality, environment and safety on the industrial projects",* The Manufacturing Engineering Society International Conference, MESIC 2015.

[8]. (2017) Turkish Standards Institute (TSE) website. [Online]. Available: http://www.tse.org.tr/

[9]. (2017) International Organization for Standardization (ISO) website. [Online]. Available: http:// www.iso.org/

[10]. C. Chen, K. Anchecta, Y. Lee, J. J. Dahlgaard, *A Stepwise Iso-Based Tqm Implementation Approach Using Iso 9001:2015,* Management and Production Engineering Review, 2016, p.71.

[11]. Avacert Akademi Training Document.

The Investigation of Tool Life on Processing Open Internal Threads by Rolling and Cutting in Ti6Al4V Alloy

Gultekin UZUN[1], İhsan KORKUT[2]

Abstract

Requirements for durable and light materials have gradually increased in especially medical, electronic, computer, aviation and space industries. Titanium and its alloys have met a great portion of these expectations because of high durability, heat and corrosion resistance they had. Ti6Al4V alloy has the biggest share among these alloys. While titanium allow is maintaining its strength under too high temperatures formed during process, cutting tool may loss its strength under these high temperature and pressure. The increase in development amount has increased tool/chips section temperature and cutting force falling into tool/chips contact area and decreased tool life rapidly. In this study, tapping was carried out the holes formed on Ti-6Al-4V alloy using different types of taps (coated and uncoated taps, oblique mouth taps, rolling taps) and different levels of cutting parameters. Cutting performances of the taps was determined depending on cutting tool wear and screw quality were occurred during tapping operations.

Keywords: *Internal thread rolling, Tapping, Tool Life, Ti-6Al-4V*

1. INTRODUCTION

Titanium and its alloys are preferred owing to their high strength, thermal resistance and corrosion resistance [1-3]. The high temperature occurred between tool/chip and tool/work piece during machining Ti-6Al-4V alloys causes many problems [4-5]. Titanium alloy which has low thermal conductivity even shows resistance to arisen elevated temperatures during machining, cutting tools can show strength reduction at high temperatures and high pressure [6-7]. Because of their soft matrix microstructure, titanium alloys harden swiftly during machining. Some reasons (such as tendency of reacting with cutting tool material at high temperatures and cohere to the cutting tool edge) effect process efficiency significantly [8-10]. Riberiro [11], stated that it is necessary to searching optimum cutting conditions, because there is always a problem during machining this material no matter which classical method is used. Tap selection is really important for threading operation in machining. The right choice of tap and required parameters (cutting speed, revolutions per minute, feed rate and cutting geometry, coolant etc.) effect the quality of composed thread and production economy. Threading processing time takes 22% of total machining time in machinery industry [12]. Arising unintended consequences effect this process even more adversely. Occurred high torque value during threading operation with tap causes backlash (springback) and turning difficulties. These results lead to break the tap [13]. These problems can be seen during production. The competition in industry and higher efficiency create the need of higher qualified thread [14]. Rolled thread manufacturing forms the thread by crushing the material, instead of cutting thread manufacturing which forms the thread by pulling off the material.

This process is done cold. In the beginning of this process, the cylindrical material diameter which will be rolled is smaller than the thread major diameter. Forcing the rolled part to cold yielding makes the material stronger and more durable. In this operation, there is no chip forming, no material loss, material only change its place. Roll taps open internal threads without chip formation [15]. The events occurring between cutting tool and material is more complex during tapering process than the other cutting tools. The occurred high torque value (momentum) during tapering on titanium material was shown as the main reason on a study

---

which is about the reasons and the solutions of the failure of cutting tool during tapering deep holes with small diameter taps [13]. It is estimated that titanium materials elasticity caused high frictional resistance between cutting tool and material, and it caused high torque value. Another study investigated the effects of cutting fluid on notch and flank wears occurred on M10 HSS straight fluted uncoated tap during thread cutting. Consequently, the lowest cutting torque value was determined on dry cutting conditions [16]. Mechanical properties such as hardness, abrasive wear resistance and friction coefficient determined by using M8 tap and other taps different coated on stainless steel. It is emphasized that TiCN coated tap has shown great abrasive and adhesive wear resistance [17]. S.C. Veldhuis and his friends were investigated the effects of ultra-thin fluorine mixed cutting fluid on wear between tool/work piece during tapering operations and they were observed that the friction coefficient was reduced 18% [18]. During machining beta type titanium alloy which is known as one of hard-to-machine materials, it was emphasized that CBN coated taps are better than classic coated taps in terms of tool life and tapping strength [19]. Kayır was exhibited in his studies that the small drill hole diameters increase the torque value during tapering on AA5083, in the contrary case, reduce the torque value. It is stated that the most effective force is cutting torque value on tap failure and increasing cutting torque value forces to failure the tap more at small hole diameters [20, 21]. Some models were developed by using many variables for tapering process. It is stated that these models can be used with experimentally examined [22, 23].

2. MATERIAL AND METHOD

2.1. Test Sample

During the experiments, Ti-6Al-4V (α+β-Ti alloy) was used which has the most usage area between titanium alloys in the industry. The usage of this alloy is 45% in industrial applications. The most important properties of Ti-6Al-4V alloy are high corrosion resistance, hardness and durability. The materials chemical components are given in Table 1. The dimensions of test samples are 100x80x15 mm.

Table 1. The chemical components of Ti-6Al-4V alloy.

Chemical Components							
Al	V	Fe	O	N	H	C	Ti
5.9%	4.00%	0.09%	0.14%	0.01%	0.002%	0.01%	Equilibrium quantity

2.2. Cutting Tool and Machining Tool

In the experiments, it was decided that opening standard metric threads which are used in manufacturing industry and M8x1.25 size was grounded. Straight fluted with spiral point taps and roll taps were used which were advised. In this study, the experiments were carried out with coated (TiAlN) and uncoated two different tapping types. Tap forms and some properties of taps were given in Table 2.

Table 2. Tap forms and types.

Leading Screw Size	Tap Forms	Point type	Helical Flute	Material	Abbreviation
M8x1,25	Form B Cutting	Spiral R15	Straight	HSS-E	SFSP
	Form C Rolling	Straight	None	HSS-E	TR

For creating tapping hole diameter, carbide drills were used in two different diameters. For cutting tapping 6.8 mm diameter drills, for rolling tapping 7.4 mm diameter drills were used. The experiments were carried out in wet cutting condition. 20% emulsion cutting fluid were used in wet cutting condition. During the experiments, CNC machines cooling system were used for cutting fluid and it was vaporized on cutting tool and work piece.

The experiments were carried out on Johnford VMC-550 branded CNC vertical machining center. Possible stagger was prevented by sending the tap to the same coordinates without changing the work piece position after sample drilled on CNC vertical machining center. Because of not having the rigid tapping option on CNC milling machine, the experiments were carried out by using tapping head and secured tap holder.

2.3. Cutting Conditions, Cutting Parameters and Measuring the Tool Life

In this study, four different cutting speeds (2, 3, 4 and 5 m/min) and 1.25 mm/rev feed rate were used. Cutting speeds were determined as a result of preliminary tests by considering the studies have done in literature and cutting tool catalogues.

The wear of the cutting tools and coherent materials were displayed during the study by zooming 50x on AM413ZT Polarized Digital Microscope. After the experiments, EDX analysis were carried out by displaying the cutting tools on SEM device.

3. TEST RESULTS AND DISCUSSION

3.1. Evaluation of Tool Life

Tool life experiments were carried out in wet conditions with two different taps. For each tap, maximum 750 mm machining distance were determined as upper limit and experiment was ended. The built-up edge and wear of the cutting tools on cuts were commented with displaying SEM images after tool life experiments.
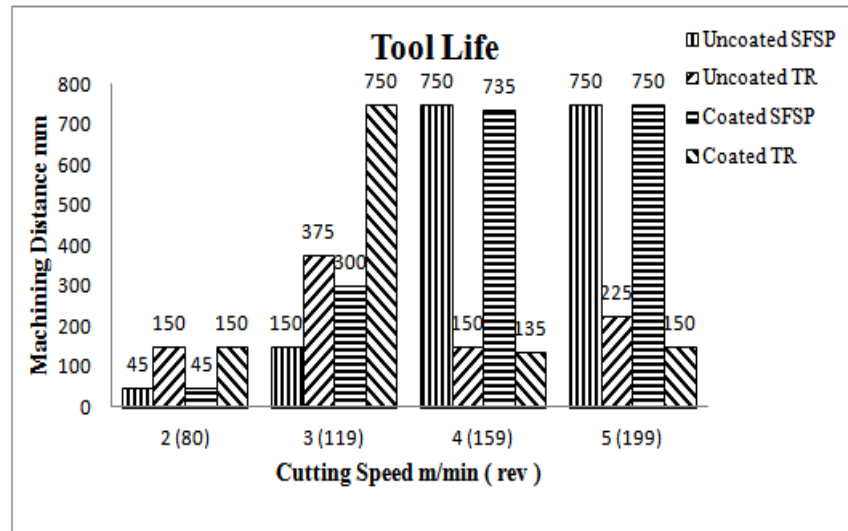

Figure 1. Tool life graphic depending on cutting speed.

Examining Figure 1, increasing cutting speed increases the tool life of uncoated SFSP cutting tool. The lowest tool life results were seen at 2 m/min cutting speed and the highest tool life results were seen at 4 and 5 m/min cutting speeds. As a result of uncoated SFSP cutting tools tool life experiments, it was determined that there were some fractions on cutting tool after 3 holes at 2 m/min cutting speed (Figure 2.a). Built-up edge formations after 150 mm machining distance at 3 m/min cutting speed (Figure 2.b) are close to built-up edge formations after 750 mm machining distance at 4 and 5 m/min cutting speeds (Figure 2.c and Figure 3.d).

In Figure 1, the best tool life for uncoated TR cutting tool were determined after 375 mm machining distance at 3 m/min cutting speed. Second best result were determined after 225 mm machining distance at 5 m/min. The tool life of uncoated TR cutting tool was determined after 150 mm machining distance at 2 and 4 m/min cutting speeds. In figure 3, when tool images were examined as a result of uncoated TR cutting tools tool life experiments, the built-up edge ratio on cutting tools can be said as the determinant cause of tool life [25-27].

The increase of the amount of built-up edge effects cutting tools tapping property inversely and caused entrapments. In Figure 3, EDX analysis shows the built-up edge on cutting tool frankly.

In Figure 2 and Figure 3, it was determined that SFSP cutting tool showed longer tool life than TR cutting tool by evaluating tool life in terms of uncoated cutting tools. The leading causes of this situation can be shown as SFSP cutting tool threads by chip removing and chip evacuation is easy. While threading operation with plastic deformation perform, higher friction generation and more built-up edge formation can be shown as the reason of short tool life [25-27]. The crushing behavior of TR cutting tool caused more built-up edge formations and more cutting tool compactions. SEM images and EDX analysis show clearly that the material compacted with plastering on cutting tool and formed a proper layer.
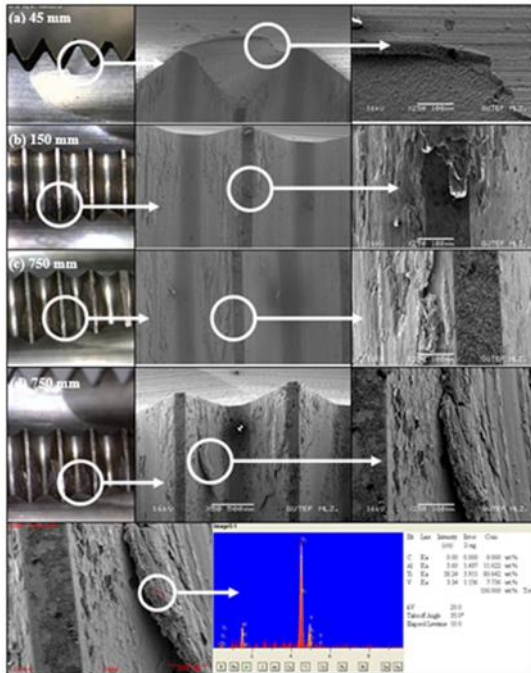
Figure 2. EDX analysis and SEM images of uncoated SFSP cutting tools after tool life experiments at (a) 2, (b) 3, (c) 4 and (d) 5 m/min cutting speeds
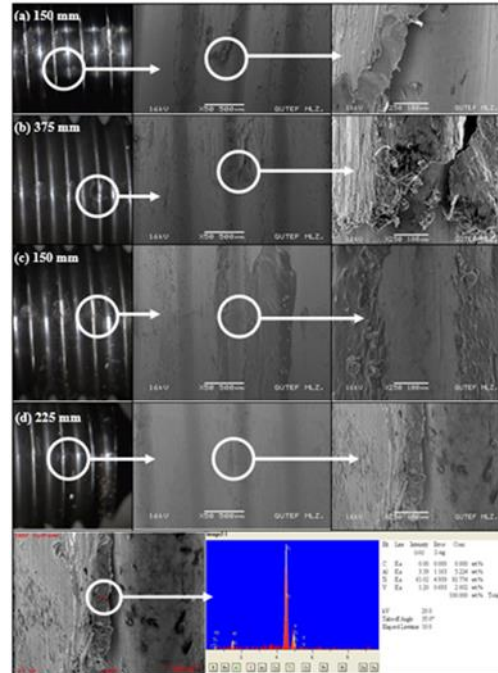
Figure 3. EDX analysis and SEM images of uncoated TR cutting tools after tool life experiments at (a) 2, (b) 3, (c) 4 and (d) 5 m/min cutting speeds

Tool life increases with changing the cutting speed from 2 m/min to 3 m/min on uncoated TR cutting tool, tool life value showed a falling tendency at 4 m/min and tool life showed an increasing tendency at the highest cutting speed (Figure 1). The best tool life performance was determined after 375 mm machining distance at 3 m/min cutting speed.

It was seen that the tool life was extended with the increase of cutting speed on coated SFSP cutting tool (Figure 1). The best tool life was determined at 5 m/min cutting speed. Built-up edge was decreased with the increase of cutting speed (Figure 4). Besides, increasing cutting speed eased cutting process with increasing the heat at cutting zone. The shortest tool life was determined after 45 mm machining distance at 2 m/min cutting speed for coated SFSP cutting tool. The longest tool life was determined after 750 mm machining distance at 5 m/min cutting speed.

In Figure 4, as seen after the tool life experiments results of coated SFSP cutting tools, there is some fractures on the cutting tool after 45 mm machining distance at 2 m/min cutting speed (Figure 4.a) and cutting tool completes its life. The built-up edge on the tool caused fracture by compacting after 300 mm machining distance at 3 m/min cutting speed (Figure 4.b). Tool life was measured after 735 mm machining distance at 4 m/min cutting speed (Figure 4.c) and after 750 mm machining distance at 5 m/min cutting speed (Figure 4.d). Built-up edge can be shown as the leading cause of the compaction of cutting tool during machining. The increase of cutting speed retards the built-up edge formation and extends tool life is clearly seen on Figure 4. This situation can be explained as increasing cutting speed increases the heat in cutting zone and causes less built-up edge formations [28].

In Figure 1, the longest tool life was determined after 750 mm machining distance at 3 m/min cutting speed for coated TR cutting tool. The shortest tool life was seen after 135 mm machining distance at 4 m/min cutting speed. The tool life was determined after 150 mm machining distance at both 2 m/min and 5 m/min cutting speeds. When analyzed Figure 5, it is seen that the built-up edge formation causes cutting tool compaction. More built-up edge formation can be clearly seen after 135 mm machining distance at 4 m/min cutting speed and after 150 mm machining distance at 5 m/min cutting speed (Figure 5.d). Especially, it can be said that built-up edge formations are not only at cutting zone, spread all across on tap and causes compactions.

Evaluating the tool life from the point of coated cutting tools, it was determined that SFSP cutting tool showed better tool life performance than TR cutting tool. It can be said that TR cutting tool showed better tool life performance at low cutting speeds. The leading causes of this result can be shown as SFSP cutting tool threads with chip removing, also coating and spiral point ease chip evacuation. Crushing behavior of TR cutting tool causes more built-up edge formation and caused compaction of the cutting tool.
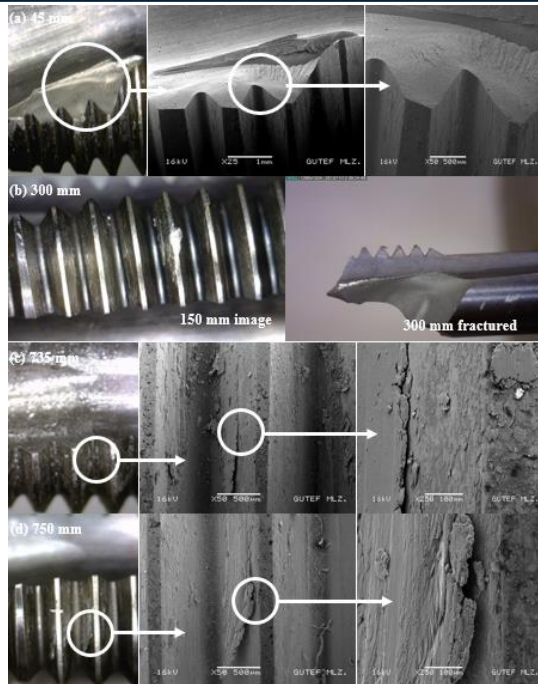
Figure 4. SEM images of coated SFSP cutting tools after tool life experiments at (a) 2, (b) 3, (c) 4 and (d) 5 m/min cutting speeds
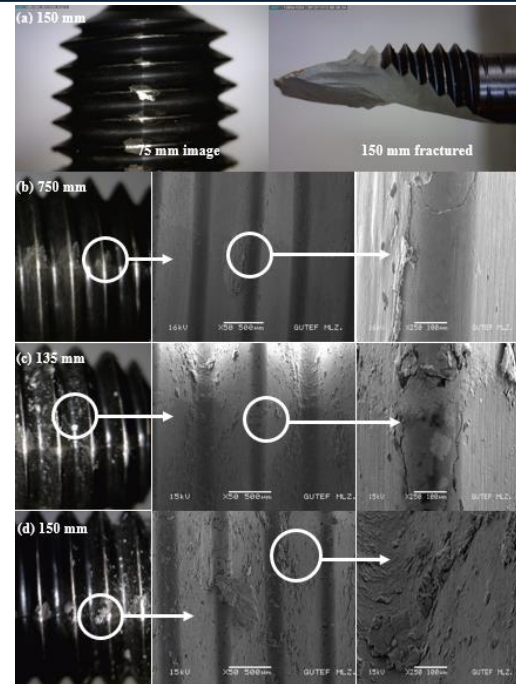
Figure 5. SEM images of coated TR cutting tools after tool life experiments at (a) 2, (b) 3, (c) 4 and (d) 5 m/min cutting speeds

3.2. Evaluation of Tolerances

Because of tool life experiments were performed with two different SFSP and TR cutting tool in wet conditions, cutting tool measurements were evaluated by based on these cutting tools. These cutting tools major diameters (max. 6,912 mm – min 6,647 mm) and minor diameters (8 mm) were measured according to 6H tolerance (DIN 336) and interpreted with graphics [24].

When examining Figure 6 for SFSP and TR cutting tools, it was determined that major diameter measurements were in tolerance range for both cutting tool types. Minimum major diameter values in tolerance range were measured on threads which were opened with coated SFSP cutting tool. Maximum major diameter values in tolerance range were measured on threads which were opened with coated TR cutting tool at 4 m/min and 5 m/min cutting speeds. Maximum major diameter value in tolerance range was measured on the thread which was opened with uncoated TR cutting tool at 3 m/min cutting speed. Maximum major diameter value in tolerance range was measured on the thread which was opened with uncoated SFSP cutting tool at 2 m/min cutting speed.
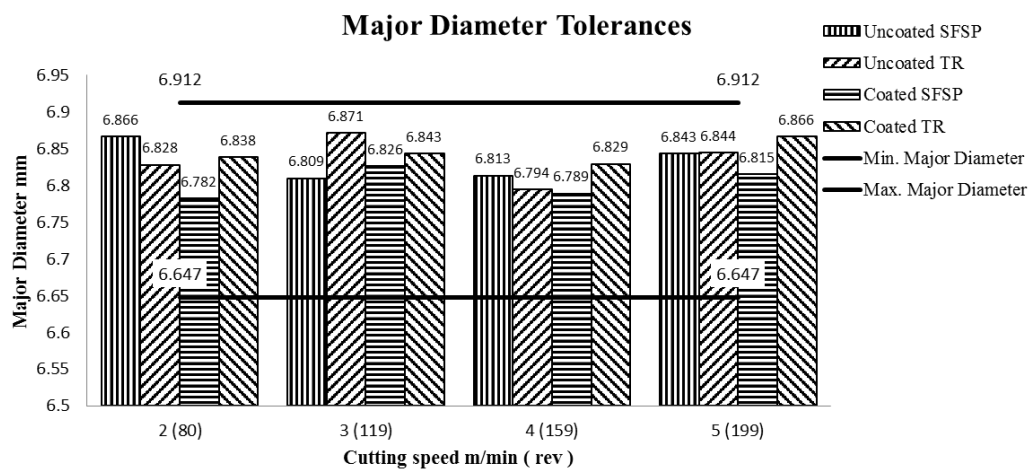
Figure 6. Major diameters tolerance graphic.

Minor Diameter Tolerances
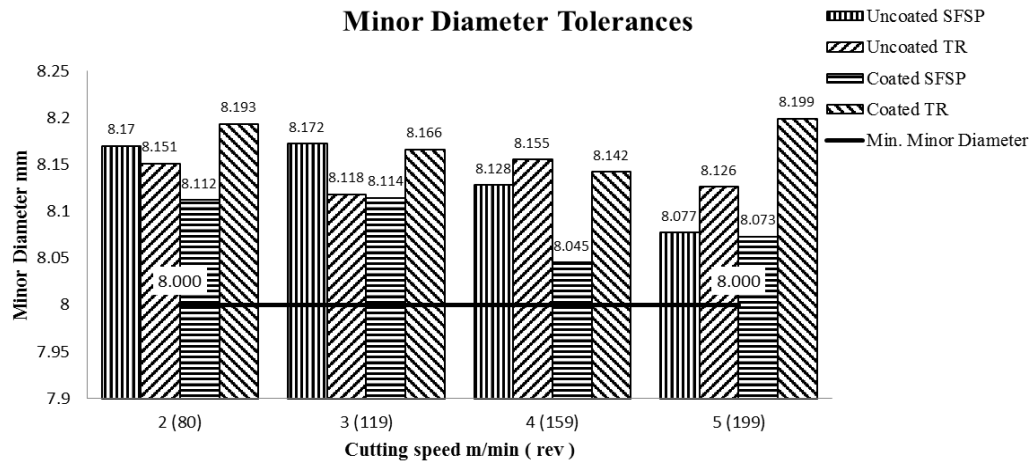
Figure 7. Minor diameter tolerance graphic.

When examining Figure 7 for SFSP and TR cutting tools, it was determined that minor diameter measurements were higher than the tolerance range for both cutting tool types. Minimum minor diameter values were measured on threads which were opened with coated SFSP cutting tool at all cutting speeds. Maximum minor diameter values were measured on threads which were opened with coated TR cutting tool at 2 m/min and 5 m/min cutting speeds. Maximum minor diameter value was measured on the thread which was opened with uncoated SFSP cutting tool at 3 m/min cutting speed. Maximum minor diameter value was measured on the thread which was opened with uncoated TR cutting tool at 4 m/min cutting speed.

Evaluating Figure 6 and Figure 7 in general, it was determined that the threads suit the tolerance values. In terms of uncoated cutting tools, it was determined that SFSP cutting tool tolerance values were higher than TR cutting tool at 2 m/min and 3 m/min cutting speeds. However, this situation was exact opposite at 4 m/min and 5 m/min cutting speeds. When evaluate Figure 7 in terms of coated cutting tools, it was determined that TR cutting tool tolerance values were higher than SFSP cutting tool at all cutting speeds. It can be said that both cutting tool types can be used on threading operation.

4. RESULTS

In this study, threading experiments were carried on Ti-6Al-4V titanium alloy by tapping. The effects of coating technology on cutting tool, cutting speed and wet cutting conditions on tool life were studied. The results can be summarized as:

- The most important factor effecting tool life is determined as built-up edge formations occurred by chip and material on cuts.

- In wet conditions, SFSP cutting tools showed better performance in terms of tool life among all coated and uncoated cutting tools.

- Especially at high cuttings speeds, SFSP cutting tools showed better performance than TR cutting tools in terms of tool life. On the contrary, it was seen that TR cutting tools superior at low cutting speeds.

- Evaluating SFSP and TR cutting tools in terms of tolerances, it was observed that both cutting tool types were given good results.

ACKNOWLEDGEMENT

REFERENCES

[1]. Nabhani, F.,"Machining of Aerospace Titanium Alloys", Robotics and Computer Integrated Manufacturing, volume 17, pages 99–106, 2001.
[2]. Ezugwu, E.O., Wang, Z.M., "Titanium alloys and Their Machinability–a review", Journal of Materials Processing Technology, volume 68, pages 262–274, 1997.

[3]. Ensarioglu, C., Cakır, M.C., "Titanyum ve Alasımlarının İslenebilirlik Etüdü", Mühendis ve Makine, cilt 46, sayı 546, sayfa 1-7, 2005.

[4]. Kishawy, H.A., Wilcox, J., "Tool wear and chip formation during hard turning with self – propelled rotary tools", International Journal of Machine Tools and Manufacture, volume 43, pages 433–439, 2003.

[5]. Schueller, J.K., Tlusty, J., Smith, S., Leigh, E., "Advanced machining techniques on titanium rotor parts", American Helicopter Society, Virginia, pages: 1-7, 2000.

[6]. Nabhani, F., "Wear Mechanisms of Ultra – Hard cutting tools materials", Journal of Materials Processing Technology, volume115, pages 402–412, 2001.

[7]. Haron, C.H. C., Jawaid, A., "The effect of machining on surface integrity of titanium alloy Ti6Al4V", Journal of Materials Processing Technology, volume 166, pages 188–192, 2005.

[8]. Jawaid, A., Che Haron, C.H., Abdullah, A., "Tool wear characteristics in turning of titanium alloy Ti–6246", Journal of Materials Processing Technology, volume 92 – 93, pages 329 – 334, 1999.

[9]. Benes J., 2007. "Cool Tips for Cutting Titanium", http://www.americanmachinist.com/304/Issue/Article/False/77297/.

[10]. Kitagawa, T., Kubo, A., Maekawa, K., "Temperature and wear of cutting tools in high–speed machining of Inconel 718 and Ti6Al6V2Sn", Wear, volume 202 (2), pages 142–148, 1997.

[11]. Riberiro, M.V., Moreira, M.R.V., Ferreira, J.R., "Optimization of titanium alloy (6Al4V) machining", Journal Of Materials Processing Technology, volume 143–144, 458–463, 2003.

[12]. Uzun G., Korkut İ., "The effect of cryogenic treatment on tapping" The International Journal of Advanced Manufacturing Technology, volume 67 Pages 857-864, 2013.

[13]. Kuo, K., "Experimental İnvestigation Of Ultrasonic Vibration-Assisted Tapping", Journal of Materials Processing Technology, volume 192–193, pages 306–311, 2007.

[14]. Li, W., Li, D., Ni, J., "Diagnosis of Tapping Process Using Spindle Motor Current" International Journal of Machine Tools & Manufacture, volume 43, pages 73–79, 2003.

[15]. Ay İ., Demircioglu T.K. "Kesme ve Ovalama Yolu ile Cıvata-Vida Disi İmalat Yontemlerinin Kıyaslanması" Makina Magazin Dergisi, sayı: 10, sayfa 64-67, 2005.

[16]. Cao T., Sutherland J. W., "Investigation of thread tapping load characteristics throughmechanistics modeling and experimentation" International Journal of Machine Tools & Manufacture, volume 42, pages. 1527–1538, 2002.

[17]. Reiter A.E., Brunner B., Ante M., Rechberger J., "Investigation of several PVD coatings for blind hole tappingin austenitic stainless steel", Surface & Coatings Technology, volume 200, Pages 5532–5541, 2006.

[18]. Veldhuis S.C., Dosbaeva G.K., Benga G., "Application of ultra-thin fluorine-content lubricating films to reduce tool/workpiece adhesive interaction during thread-cutting operations", International Journal of Machine Tools and Manufacture, volume 47, Pages 521–528, 2007.

[19]. Jin M., Watanabe S., Miyake S., Murakawa M., "Trial fabrication and cutting performance of c-BN-coated taps", Surface and Coatings Technology, volumes 133–134, pages 443-447, 2000.

[20]. Kayır Y., "Kılavuz kesici takımları ile AA5083 malzemesine vida acılmasında matkap delik capının kesme kuvvetlerine etkisi", Gazi Üniv. Müh. Mim. Fak. Der., cilt 25, sayı 4, sayfa 671-679, 2010.

[21]. Kayır Y., "Kılavuz kesici takımları ile AISI 1050 celigine vida acılmasında matkap delik capının kesme kuvvetleri ve momente etkisi" Uludag Üniversitesi Mühendislik-Mimarlık Fakültesi Dergisi, cilt 15, sayı 1, sayfa 99-111, 2010.

[22]. Armarego E.J.A., Chen M. N.P., "Predictive Cutting Models for the Forces and Torque in Machine Tapping with Straight Flute Taps" Department of Mechanical and Manufacturing Engineering, 2000, The University of Melbourne, Australia.

[23]. Dogra A. P. S., Kapoor S. G., Devor R. E., "Mechanistic Model for Tapping Process with Emphasis on Process Faults and Hole Geometry" Journal of Manufacturing Science and Engineering, volume 124, pages 18-25, 2002.

[24]. Gühring Kesici Takım Firması, "Teknik Bilgiler", 2011. http://www.guhring.com.tr/Upload/Document/document_3c5f4d55a196484184ceedddb32a1341.pdf, sayfa 1570-1603.

[25]. Yakup Turgut, Hanifi Cinici, Ismail Sahin, Tayfun Fındık "Study of cutting force and surface roughness in milling of Al/SiC metal matrix composites" Scientific Research and Essays, volume 6-10, pages 2056-2062, 2011.

[26]. Mustafa Günay, Alaattin Kacal, Yakup Turgut "Optimization of Machining Parameters in Milling of Ti-6Al-4V Alloy Using Taguchi Method" e-Journal of New World Sciences Academy Engineering Sciences, volume 6-1, pages 428-440, 2011.

[27]. İhsan KORKUT, Kadir YAVUZ, Yakup TURGUT "An experimental investigation into the machinability of GGG70 grade spheroidal graphite cast iron" Indian Journal of Engineering Materials Sciences, volume 16, pages 123-127, 2009.

[28]. Gültekin UZUN, İbrahim CİFTCİ "C 5140 Celiginin Mekanik Ozelliklerinin Takım Asınması ve Kesme Kuvvetlerine Etkisinin İncelenmesi" Politeknik Dergisi, Cilt: 15, Sayı:1, sayfa: 29-34, 2012.

ANTIOXIDANT ACTIVITIES OF TOTAL ANTHOCYANINS EXTRACTED FROM SWEET CHERRY CULTIVARS

Fatih Sonmez*[1], Zuhal Gunesli[2], A.Ali Berber[2], Nurcan Berber[3], Taki Demir[3]

Abstract

Sweet cherry (Prunus avium) belongs to Rosales order, Rosasea family, Prunoidea subfamily and Prunus genus. This fruit, which can conveniently be grown in mild climate zones, is widely used in a variety of areas such as fruit juice industry, table consumption, cake and jam production In this study, total anthocyanins were extracted from seven sweet cherry cultivars ('Z0900', 'Stella', 'Bing', 'Karakiraz', 'Noble', 'Beyaz Anadolu', and 'Berriyessa') grown in Sakarya, Turkey and DPPH activities were evaluated. Among them, The highest total anthocyanins amount was in the 'Noble' cultivar (331 mg/100 g), however; 'Berriyessa' and 'Stella' (DPPH% = 78.55 and 75.56, respectively) had the highest value for antioxidant activity.

Keywords: *Anthocyanin, Antioxidant, Extraction, Sweet Cherry.*

1. INTRODUCTION

Sweet cherry (Prunus avium) belongs to Rosales order, Rosasea family, Prunoidea subfamily and Prunus genus. This fruit, which can conveniently be grown in mild climate zones, is widely used in a variety of areas such as fruit juice industry, table consumption, cake and jam production [1]. Hence, it has a high market value and demand potential. Fruits are considered a natural source of antioxidants including polyphenols and anthocyanins. These compounds can reduce the risk of degenerative diseases caused by oxidative stress, such as cancer, cardiovascular disease and stroke. Red fruits, including sweet cherries, are rich in these types of compounds (2). Sweet cherry cultivars, known throughout the world, are used for both table consumption and processed products [2].

In this study, total anthocyanins were extracted from seven sweet cherry cultivars ('Z0900', 'Stella', 'Bing', 'Karakiraz', 'Noble', 'Beyaz Anadolu', and 'Berriyessa') grown in Sakarya, Turkey and DPPH activities were evaluated.

2. MATERIALS AND METHODS

2.1. Materials

The sweet cherry samples were analyzed in an appropriate stage of maturity. The samples (0.5 kg) were packed in plastic bags, frozen and kept at -18°C before extraction of anthocyanins. All chemicals and solvents used in analysis were obtained from Sigma Aldrich and Merck.

2.2. Extraction of total anthocyanins

Seeds of deep-frozen cherry samples were separated by hand. Cherry samples (about 100 g) were blended twice with 250 ml of methanol acidified with 1.0 N HCl (85:15, v/v) for 2 min in a Waring blender. Extract

---

[1]* *Corresponding author: Sakarya University, Department of Chemistry, 54100, Serdivan/Sakarya, Turkey. fsonmez@sakarya.edu.tr*

[2] *Canakkale Onsekiz Mart University, Saglik Hizmetleri Vocational High Scholl, Canakkale, Turkey. aberber@comu.edu.tr*

[3] *Sakarya University, Pamukova Vocational High Scholl, Pamukova/Sakarya, Turkey. tdemir@sakarya.edu.tr*

was filtered under vacuum on a Buchner funnel using Whatman No. 1 paper . Filtrate was concentrated to a small volume at 40°C using rotary evaporator under vacuum for purification of total anthocyanins.

2.3. Purification and measurement of total anthocyanins

The anthocyanins were purified according to the methodology of Zhang et al [3]. The filtrate containing sugars, organic acids, polyphenolics and anthocyanins etc. were loaded onto an Amberlite XAD-7 resin column. Firstly, it was washed with distilled water (about 1000 ml) to remove sugars, acids and other water-soluble compounds and then washed with ethyl acetate (about 500 ml) to remove polyphenolics compounds. Finally, total anthocyanins were recovered with methanol containing 0.1% trifluoroacetic acid (v/v). This acidified methanol fraction was combined and evaporated under vacuum to dryness and weighed on GX-300 balance. Of total anthocyanins 20 mg was dissolved with 0.1% TFA-MeOH (v/v) and submitted to spectrophotometric analysis (200 - 600 nm) using a UV-Vis spectrophotometer. All measurements were taken in duplicate.

2.4. DPPH assay

The measurement of the DPPH radical scavenging activity was performed according to methodology described by Brand-Williams et al [4].

3. RESULTS AND DISCUSSION

Total anthocyanins amounts of sweet cherry cultivars were between 91 and 331 mg/100 g (Table 1). The highest total anthocyanins amount was in the 'Noble' cultivar (331 mg/100 g), followed by the 'Z900' (215 mg/100 g) and 'Karakiraz' (210 mg/100 g). The lowest total anthocyanins amount was recorded in the 'Stella' cultivar (91 mg/100 g).

The results in Table 1 indicated that all of the sweet cherry cultivars exhibited antioxidant activity. Among them, 'Berriyessa' and 'Stella' (DPPH% = 78.55 and 75.56, respectively) had the highest value for antioxidant activity and significantly better activity than the other cultivars.

Table 1. Total anthocyanins amounts and antioxidant activity in local sweet cherry cultivars

Sample No	Sweet Cherry Cultivars	Total anthocyanins amounts (mg/100 g)	DPPH (%)[a]
N1	Stella	91	75.56 ±
N2	Z0900 (Ziraat)	215	23.38± 1.08
N3	Bing	126	37.35± 1.54
N4	Noble	331	28.16± 0.96
N5	Beyaz Anadolu	181	39.12± 1.21
N6	Berriyessa	107	78.55± 5.37
N7	Karakiraz	210	69.12± 3.49

[a] *DPPH % represent the means ± S.E.M. of three parallel measurements ($p < 0.05$).*

The any relationships or connection were not observed between the total anthocyanins amounts and %DPPH. We think that these differences are due to the sweet cherry genotypes and genetic variations.

4. CONCLUSION

In conclusion, total anthocyanins were extracted from seven sweet cherry cultivars ('Z0900', 'Stella', 'Bing', 'Karakiraz', 'Noble', 'Beyaz Anadolu', and 'Berriyessa') grown in Sakarya, Turkey. Their antioxidant activities were evaluated. The highest total anthocyanins amount was in the 'Noble' cultivar (331 mg/100 g), however; **'Berriyessa'** and '**Stella**' (%DPPH = 78.55 and 75.56, respectively) had the highest value for antioxidant activity. These results have revealed that there is no any relation between antioxidant activity and anthocyanin amount in sweet cherry cultivars.

ACKNOWLEDGMENTS

REFERENCES

[1] V.Usenik, J.Fabcic, and F. Stampar, "Sugars, organic acids, phenolic composition and antioxidant activity of sweet cherry (Prunus avium L.)," *Food Chemistry*, vol. 107, pp. 185-192, Oct. 2008.

[2] T. Demir, "Determination of carotenoid, organic acid and sugar content in some sweet cherry cultivars grown in Sakarya, Turkey," *Journal of Food, Agriculture & Environment*, vol. 11, pp. 73-75, Sep. 2013.

[3] Z. Zhang, P. Xuequn, C. Yang, Z. Ji, and Y. Jiang, "Purification and structural analysis of anthocyanins from litchi pericarp," *Food Chemistry*, vol. 84, pp. 601–604, Jan. 2004.

[4] W. Brand-Williams, M.E. Cuvelier, and C. Berset, "Use of a free radical method to evaluate antioxidant activity," *Lebenson Wiss Technology*, vol. 28, pp. 25-30, Aug. 1995.

Synthesis and Anticholinesterase Activity of Eugenol Derivatives

Belma Zengin KURT[1], Fatih SONMEZ[2]*, Mustafa KUCUKISLAMOGLU[2]

Abstract

Alzheimer's disease (AD) is a progressive neurodegenerative disease and the most common form of dementia that affects aged people. Acetylcholinesterase is a hydrolase involved in the termination of impulse transmission at cholinergic synapses by rapid hydrolysis of the neurotransmitter ACh in the central and peripheral nervous system. Eugenol (4-allyl-2-methoxyphenol) is a phytochemical compound isolated from many medicinal herbs, such as Syzigium aromaticum, Ocimum Sanctum. It is known that eugenol has been widely used as an aroma substance in food and cosmetic products and in the pharmaceutical sector. In this paper, a series of 14 novel eugenol substituted carbamate derivatives (2a-n) was synthesized and their inhibitory activities on AChE and BuChE were evaluated. Among them, 4-allyl-2-methoxyphenyl(3,4-dichlorophenyl)carbamate (2j) exhibited the strongest inhibition against AChE with an IC_{50} value of 71.60 µM, which was minimum 3-fold more than that of eugenol (IC_{50} = >200 µM).

Keywords: *Acetylcholinesterase, Butyrylcholinesterase, Carbamate, Eugenol.*

1. INTRODUCTION

Alzheimer's disease (AD) is a progressive neurodegenerative disease and the most common form of dementia that affects aged people [1]. Acetylcholinesterase (AChE; EC 3.1.1.7) is a hydrolase involved in the termination of impulse transmission at cholinergic synapses by rapid hydrolysis of the neurotransmitter ACh in the central and peripheral nervous system. AChE inhibitors (AChEI) inhibit the hydrolysis of ACh improving both the level and of duration of neurotransmitter [2]. Another cholinesterase, butyrylcholinesterase (BuChE; EC 3.1.1.8), primarily localized in plasma, liver and muscle tissues, able of hydrolyzing ACh and other acylcholines differs from AChE for tissue distribution and sensitivity to substrates and inhibitors [3]. AChE inhibitors such as galantamine, rivastigmine, and donepezil are the main stay drugs for the clinical management of AD in the early to moderate stage [4].

Many plants and their components have acted an important role in conventional implementation of medicine to raise the cognitive purpose and to reduce other signs of AD [5,6]. Due to their small molecular size and lipophilicity, volatile constituents of essential oils and liberated volatile aglycones from glycosides are likely to readily cross the blood–brain barrier [6]. Eugenol (4-allyl-2-methoxyphenol) is a phytochemical compound isolated from many medicinal herbs, such as *Syzigium aromaticum, Ocimum Sanctum* [7]. It is known that eugenol has been widely used as an aroma substance in food and cosmetic products and in the pharmaceutical sector [8]. It has also been found to possess various pharmalogical and biological properties, such as antioxidant, antiviral, antifungal, antitumor, anti-inflammatory and antibacterial activities [9-11]. In this study, a series of 14 eugenol derivatives (**2a-n**) was synthesized and their inhibitory effects on AChE and BuChE were evaluated. Structure-activity relationship was also investigated.

2. MATERIALS AND METHODS

2.1. Synthesis of eugenol derivatives

Eugenol (1 mmol) was dissolved in CH_2Cl_2, then Et_3N (1.25 mmol) and isocyanate derivatives (1.25 mmol) were added to the solution, respectively. The mixture was refluxed for overnight, cooled and washed with water. The organic layer was dried over Na_2SO_4, and concentrated in vacuo.

[1]   Bezmialem Vakif University, Department of Pharmaceutical Chemistry, Fatih/Istanbul, Turkey. BZengin@bezmialem.edu.tr

[2]   Corresponding author: Sakarya University, Department of Chemistry, 54100, Serdivan/Sakarya, Turkey. fsonmez@sakarya.edu.tr

2.2. Anticholinesterase activity assays

Acetyl- (AChE) and butyryl-cholinesterase (BuChE) inhibitory activities of the synthesized compounds were determined according to Ellman's method [12]. The IC_{50} was determined by constructing an absorbance and/or inhibition (%) curve and examining the effect of five different concentrations. IC_{50} values were calculated for a given antagonist by determining the concentration needed to inhibit half of the maximum biological response of the agonist. The substrates of the reaction were acetylthiocholine iodide and butyrylthiocholine iodide. 5,5'-dithio-bis(2-nitrobenzoic) acid (DTNB) was used to measure anticholinesterase activity. Stock solutions of the compounds and galanthamine in methanol were prepared at a concentration of 4000 µg/mL. Aliquots of 150 µL of 100 mM phosphate buffer (pH 8.0), 10 µL of sample solution and 20 µL AChE (2.476×10^{-4} U/µL) (or 3.1813×10^{-4} U/µL BuChE) solution were mixed and incubated for 15 min at 25ºC. 10 µL of DTNB solution was prepared by adding 2.0 mL of pH 7.0 and 4.0 mL of pH 8.0 phosphate buffers to a mixture of 1.0 mL of 16 mg/mL DTNB and 7.5 mg/mL $NaHCO_3$ in pH 7.0 phosphate buffers. The reaction was initiated by the addition of 10 µL (7.1 mM) acetylthiocholine iodide (or 0.79 mM butyrylthiocholine iodide). In this method, the activity was measured by following the yellow colour produced as a result of the thio anion produced by reacting the enzymatic hydrolysis of the substrate with DTNB. Also, methanol was used as a control solvent. The hydrolysis of the substrates was monitored using a BioTek Power Wave XS at 412 nm.An easy way to comply with the symposium paper formatting requirements is to use this document as a template and simply type your text into it.

3. RESULTS AND DISCUSSION

The synthetic procedures to obtain the target compounds 2a-n are depicted in Scheme 1.
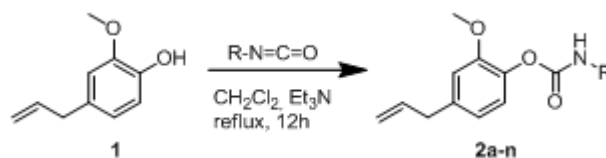
Figure 1. Synthesis of novel eugenol derivatives

The IC_{50} values for AChE and BuChE inhibitions are summarized in Table 1. Most of the synthesized eugenol-carbamate derivatives (**2a-n**) showed significantly higher inhibition activity than eugenol against both ChEs. IC_{50} values against AChE ranges from 71.60 µM to >200 µM. Compound **2j** exhibited the strongest inhibition against AChE with an IC_{50} value of 71.60 µM, which was 3-fold more than that of eugenol (IC_{50} = >200 µM). Furthermore, most of the synthesized carbamate derivatives exhibited better AChE inhibition (IC_{50} = 71.60 µM – >200 µM) than eugenol, by 1-3 fold. All the synthesized compounds inhibited BuChE. IC_{50} values against BuChE ranges from 0.58 µM to 15.14 µM. Compound **2e** exhibited the strongest inhibition against BuChE with an IC_{50} value of 0.58 µM, which was >345-fold more than that of eugenol (IC_{50} = >200 µM), 31-fold more than that of galanthamine (IC_{50} = 18.13 µM), and almost 2-fold more than that of rivastigmine (IC_{50} = 1.08 µM).

Table 1. In vitro inhibition IC_{50} values (µM) of 2a-n for AChE and BuChE.

Compound	R	AChE (IC_{50},µM)[a]	BuChE (IC_{50},µM)[a]
Eugenol (1)	-	>200	>200
2a	Cyclopentyl	>200	2.78±0.254
2b	Cyclohexyl	>200	1.56±0.195
2c	Cyclohexyl-methyl	>200	1.11±0.021
2d	Cycloheptyl	>200	0.97±0.011
2e	**3-Methoxyphenyl**	73.95±1.141	**0.58±0.012**
2f	4-Methoxyphenyl	155.55±1.112	4.48±0.417
2g	3-Fluorophenyl	191.28±1.555	12.89±1.823
2h	4-Fluorophenyl	>200	15.14±1.914
2i	4-Chlorophenyl	>200	4.66±0.554
2j	**3,4-di-Chlorophenyl**	**71.60±0.985**	5.36±0.144
2k	4-Bromophenyl	143.11±1.223	2.25±0.569
2l	3-Nitrophenyl	113.12±1.336	2.48±0.653

2m	3-Trifluoromethyl-phenyl	133.9±1.584	3.57±0.584
2n	4- Trifluoromethyl-phenyl	179.49±1.952	4.68±0.130
Galantamine	-	2.05±0.011	18.13±0.457
Rivastigmine	-	12.40±1.011	1.08±0.251

[a] IC_{50} values represent the means ± S.E.M. of three parallel measurements ($p < 0.05$).

4. CONCLUSION

A series of 14 novel eugenol substituted carbamate derivatives (**2a-n**) was synthesized and their inhibitory activities on AChE and BuChE were evaluated. Among them, **2j** exhibited the strongest inhibition against AChE with an IC_{50} value of 71.60 µM, which was 3-fold more than that of eugenol (IC_{50} = >200 µM). Additionally, **2e** exhibited the strongest inhibition against BuChE with an IC_{50} value of 0.58 µM, >345-fold more than that of eugenol (IC_{50} = >200 µM), 31-fold more than that of galantamine (IC_{50} = 18.13 µM), and almost 2-fold more than that of rivastigmine (IC_{50} = 1.08 µM). Generally, the presence of carbamate moiety at the eugenol increased the both ChEs inhibition. This finding can provide guidance for researches to design new efficient ChEs inhibitors in the future works. The SAR revealed that the inhibitory activity of the synthesized compounds could also be affected by the type and position of the halogen and electron-donating and electron-withdrawing substituents on the phenyl ring. Overall these derivatives could be recommended as new chemotypes to develop new ChEIs for the treatment of AD disease by suitably modulating the substitution pattern also in the perspective of multifunctional anti AD agents.

ACKNOWLEDGMENTS

REFERENCES

[1] P. M. Ruiz, L. Rubio, E. G. Palomero, I. Dorronsoro, M. M. Millan, R. Valenzuela, P. Usan, C. de Austria, M. Bartolini, V. Andrisano, A. B. Chanal, M. Orozco, F. J. Luque, M. Medina, and A. Martinez, "Design, synthesis, and biological evaluation of dual binding site acetylcholinesterase inhibitors: New disease-modifying agents for alzheimer's disease," *J. Med. Chem.*, vol. 48, pp. 7223-7233, Oct. 2005.

[2] M. Citron, "Strategies for disease modification in Alzheimer's disease," *Nat. Rev. Neurosci.*, vol. 5, pp. 677-685, Sep. 2004.

[3] Z. P. Wu, X. W. Wu, T. Shen, Y. P. Li, X. Cheng, L. Q. Gu, Z. S. Huang, and L. K. An, "Synthesis and acetylcholinesterase and butyrylcholinesterase inhibitory activities of 7-alkoxyl substituted indolizinoquinoline-5,12-dione derivatives," *Arch. Pharm. Chem. Life Sci.*, vol. 345, pp. 175–184, Mar. 2012.

[4] M. Catto, L. Pisani, F. Leonetti, O. Nicolotti, P. Pesce, A. Stefanachi, S. Cellamare, and A. Carotti, "Design, synthesis and biological evaluation of coumarin alkylamines as potent and selective dual binding site inhibitors of acetylcholinesterase," *Bioorg. Med. Chem.*, vol. 21, pp. 146–152, Jan. 2013.

[5] M. J. Balunas, and A. D. Kinghorn, "Drug discovery from medicinal plants," *Life Sci.*, vol. 78 pp. 431–441, Dec. 2005.

[6] M. Jukic, O. Politeo, M. Maksimovic, M. Milos and M. Milos, "In Vitro Acetylcholinesterase Inhibitory Properties of Thymol, Carvacrol and their Derivatives Thymoquinone and Thymohydroquinone," *Phytother. Res.*, vol. 21, pp. 259–261, Mar. 2007.

[7] J. Mastelic, I. Jerkovic, I. Blazevic, M. P. Blazi, S. Borovic, I. I. Bace, V. Smrecki, N. Zarkovic, K. B. Kostic, D. V. Topic, and N. Muller, "Comparative study on the antioxidant and biological activities of carvacrol, thymol, and eugenol derivatives," *J. Agric. Food Chem.*, vol. 56, pp. 3989-3996, May 2008.

[8] H. Sadeghian, S. M. Seyedi, M. R. Saberi, Z. Arghiani, and M. Riazi, "Design and synthesis of eugenol derivatives, as potent 15-lipoxygenase inhibitors," *Bioorg. Med. Chem.*, vol. 16, pp. 890-901, Jan. 2008.

[9] J. D. Barbosa, V. B. Silva, P. B. Alves, G. Gumina, R. L. Santos, D. P. Sousa, and S. C. Cavalcanti, "Structure–activity relationships of eugenol derivatives against Aedes aegypti (Diptera: Culicidae) larvae," *Pest Manag. Sci.*, vol. 68, pp. 1478-1483, Jun. 2012.

[10] N. Chaibakhsh, M. Basri, S. H. M. Anuar, M. B. A. Rahman, and M. Rezayee, "Optimization of enzymatic synthesis of eugenol ester using statistical approaches," *Biocatal. Agric. Biotechnol.*, vol. 1, pp. 226-231, Jul. 2012.

[11] G. D. Yadav, and A. R. Yadav, "Insight into esterification of eugenol to eugenol benzoate using a solid super acidic modified zirconia catalyst UDCaT-5," *Chem. Eng. J.*, vol. 192, pp. 146-155, Jun. 2012.

[12] G. L. Ellman, K. D. Courtney, V. Andres, R. M. Featherstone, "A new and rapid colorimetric determination of acetylcholinesterase activity," *Biochem. Pharmacol.*, vol. 7, pp. 88–95, Jul. 1961.

Effects of SiO$_2$/Water Nanofluid Flow in a Square Cross-Sectioned Curved Duct

Kamil Arslan[1]*, Recep Ekiciler[1]

Abstract

Forced convection SiO$_2$/water nanofluid flow and heat transfer was numerically performed in 180-degree curved duct with square cross-section under steady and laminar flow conditions. Dean number was changed from 102 to 898. All the surface of curved duct was exposed to uniform and constant heat flux of 15000 W/m^2. Nanoparticle volume fractions was ranged from 1.0% to 4.0%. Average Nusselt number and average Darcy friction factor were determined for each nanoparticle volume fractions. Velocity and temperature profiles and secondary flows were analyzed in detail.

Keywords: *Laminar forced convection, Dean number, SiO$_2$/water nanofluid, Square cross-sectioned curved duct*

1. INTRODUCTION

Conventional heat transfer fluids such as water, oil and ethylene glycol has a low thermal conductivity. So, using conventional fluids limit the performance and compactness of heat exchangers and cooling devices. The new heat transfer fluids, nanofluids, having high thermal conductivity are capable to eliminate this effect. Nanofluids are a new kind of heat transfer fluids containing a small quantity of nano-sized particles (generally less than 100 nm) that are uniformly and stably suspended in a liquid. The dispersion of a small number of solid nanoparticles in conventional fluids remarkably changes their thermal conductivity. Compared to the existing techniques for enhancing heat transfer, the nanofluids show a superior potential for increasing heat transfer rates in a variety of cases. In fact, Maxwell (1873) firstly suggested adding solid particles for increasing of thermal properties [1]. But, S. Choi firstly studied about nanofluids at 1995 [2]. Lee et al. [3] have proved that oxide ceramic nanofluids consisting of CuO or Al$_2$O$_3$ nanoparticles in water or ethylene glycol exhibit enhanced thermal conductivity. A maximum increase in thermal conductivity of approximately 20% was observed in that study, having 4.0% vol. CuO nanoparticles with mean diameter 35 nm dispersed in ethylene glycol. But larger nanoparticles with an average diameter of 40 nm led to an increase of less than 10%. As nanofluids are rather new, relatively few theoretical and experimental studies have been reported on convective heat transfer coefficients in confined flows. Park and Cho [4] and Xuan and Li [5] obtained experimental results on convective heat transfer for laminar and turbulent flow of nanofluids inside a tube. They produced the first empirical correlations for the Nusselt number using Cu/water, TiO$_2$/water and Al$_2$O$_3$/water nanofluids. The results indicate a remarkable increase in heat transfer performance over the base fluid for the same Reynolds number. To increase of heat transfer can apply lots of geometries. When compared the curved ducts with straight ducts, curved ducts have more pressure losses. However, curved ducts are widely used in industrial concerning heat and mass transfer devices. The applications areas of curved ducts are heat exchanger, turbomachines, air condition systems, centrifugal pumps, rocket engines and gas turbines [6]. Flow and heat transfer in curved duct has more complicated system than straight duct. Therefore, analytical study is nearly impossible [7]. Accordingly, experimental and numerically studies on curved duct are the other alternative investigations. In literature reviews, there have been various experimental and numerical study about laminar flow in curved duct at uniform surface temperature and uniform heat flux boundary condition. Facao and Oliveira [7] used rectangular cross-sectioned curved duct and obtained Nusselt number changed with Dean number. It is found that Nusselt number is higher than at straight duct. Sturgis and Mudauer [8] investigated heat transfer enhancement using rectangular cross-sectioned curved duct. In this study, duct curvature radiuses were changed. Working fluid was air. It is found that increasing of duct curvature radius, convection heat transfer coefficient also increased. Fang Liu [9] studied the effects of geometries on heat transfer enhancement of thermal fluids in curved duct. There are a few studies about heat transfer enhancement using of nanofluids at curved ducts.

---

[1]Corresponding author: Karabük University, Faculty of Engineering, Mechanical Engineering Department, 78050, Karabük, Turkey. kamilarslan@karabuk.edu.tr

Akbarinia et al. [10] carried out numerical study of laminar mixed convection of a nanofluid in horizontal curved tubes. It is found that increasing the buoyancy forces causes to reduce the skin friction and free convection has a negative effect on the heat transfer enhancement in the presence of centrifugal force. Heat transfer coefficients were determined with SiO_2 nanoparticle in base liquid water at various concentrations. Ghaffari et al. [11] investigated numerically turbulent mixed convection heat transfer flow of Al_2O_3/water nanofluid in a horizontal curved tube. They performed the study using two phase mixture model. They analysed the effects of nanoparticle volume fractions on heat transfer. It was obtained from the numerical results that the nanoparticle volume fraction improves the Nusselt number.

The objective of this paper is to study effect of SiO_2/water nanofluid on flow and heat transfer characteristics for different Dean numbers and different nanoparticle volume fractions in 180-degree square cross-sectioned curved duct. The average Nusselt number and average Darcy friction factor are presented and discussed. Also, velocity and temperature distributions are given for varying nanoparticle volume fraction and the Reynolds number.

2. PROBLEM DESCRIPTION AND GOVERNING EQUATIONS

Nanofluid flow in 180-degree square cross-sectioned 3D curved duct was modelled in this study. SiO_2/water nanofluid was used for working fluid. Particle size is 20 nm. ANSYS 15.0 was used to obtain numerical results. Geometry of curved duct is shown in Figure 1. Curvature radius was R=60 mm and length of the one edge of square duct was 10 mm.
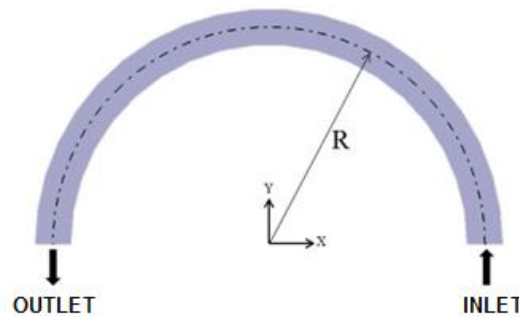
Figure 1. Schematic diagram of horizontal curved duct

Continuity, momentum and energy equations are given below for steady-state, incompressible, laminar flow condition in Eq (1) – (3), respectively.

$$\vec{\nabla}.\vec{V} = 0 \tag{1}$$

$$\rho \frac{D\vec{V}}{Dt} = -\Delta p + \mu \nabla^2 \vec{V} \tag{2}$$

$$\rho c_p \frac{DT}{Dt} = k \nabla^2 T \tag{3}$$

The properties of density, specific heat, viscosity and thermal conductivity of nanofluids have been calculated as given below, respectively [12]:

$$\rho_{nf} = (1-\varphi)\rho_w + \varphi \rho_p \tag{4}$$

$$c_{nf} = \frac{(1-\varphi)(\rho c)_w + \varphi(\rho c)_p}{(1-\varphi)\rho_w + \varphi \rho_p} \tag{5}$$

$$\mu_{nf} = \mu_w \left(1 + \frac{\phi}{100}\right)^{11.3} \left(1 + \frac{T_{nf}}{70}\right)^{-0.038} \left(1 + \frac{d_p}{170}\right)^{-0.061} \tag{6}$$

$$k_{nf} = k_w 0.8938 \left(1 + \frac{\phi}{100}\right)^{1.37} \left(1 + \frac{T_{nf}}{70}\right)^{0.2777} \left(1 + \frac{d_p}{150}\right)^{-0.0336} \left(\frac{\alpha_p}{\alpha_w}\right)^{0.01737} \tag{7}$$

The average Nusselt number (*Nu*), average Darcy friction factor (*f*) and Dean number (*De*) are determined by:

$$Nu = \frac{hD_h}{k} \qquad (8)$$

$$f = \frac{(-dp/dx)D_h}{\rho U_m^{\,2}/2} \qquad (9)$$

$$De = Re\sqrt{\frac{D_h}{R}} \qquad (10)$$

The average heat transfer coefficient was also calculated with Eq.(11).

$$h = \rho U_m A_c c_p (T_{mo} - T_{mi})/A_s(T_w - T_m) \qquad (11)$$

All of the duct's walls were heated by uniform heat flux of 15000 W/m^2 and no-slip condition was applied for nanofluid flow. Inlet temperature of fluid flow was 300 K. The nonafluid enters the duct with uniform velocity. At the outlet of the duct, taking the pressure as atmospheric pressure condition. The following assumptions were adopted for this numerical study: (i) Both heat transfer and fluid flow in duct are in three-dimensional and steady-state; (ii) fluid flow is under incompressible and laminar flow conditions; (iii) the physical properties of nanofluid, such as density, specific heat, thermal conductivity and viscosity are taken as temperature independent; (iv) negligible buoyancy effect, viscous dissipation and radiation heat transfer; and (v) the base fluid and the nanoparticles are in thermal equilibrium.

3. NUMERICAL PROCEDURE

In the computations, the finite-volume method based commercial CFD software Ansys Fluent 15.0 was used to perform the numerical calculations by solving the governing equations along with the boundary conditions. The convection terms in mass, momentum and energy equations were discretized using a second order upwind scheme. The standard scheme was employed for discretization of pressure and the SIMPLE algorithm was used for pressure-velocity coupling. The Green-Gauss cell based method was applied for discretization of the momentum and energy equations. To obtain the convergence, each equation for mass, momentum, and energy were iterated until the residual falls below 1×10^{-6}. No convergence problems were observed during the calculations. The hexahedral mesh distribution was used for the curved duct having square cross-section. The numbers of mesh points or control volumes were increased close to wall of the duct to enhance the resolution and accuracy as given in Figure 2.
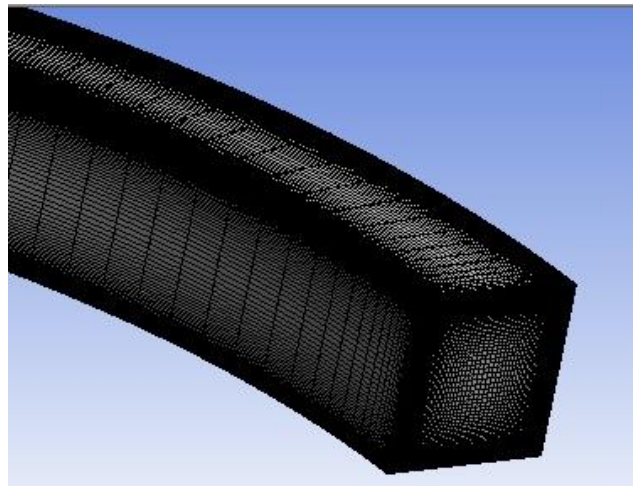
Figure 2. Mesh distribution of the computational domain

The mesh independence study was performed for the curved duct by refining the mesh number until the variation in both average Nusselt number and average Darcy friction factor are less than 0.1%. To obtain the optimum mesh number, a grid independence study was conducted using thirteen different mesh numbers changing from 5×10^2 to 1.255×10^6 for De=898. Changing of average Nusselt number and average Darcy friction factor values with mesh number for pure water flow is given in Figure 3 as an illustration. It was observed that a further refinement of mesh number from 4×10^5 to 1.25×10^6, the changing of average Nusselt number and average Darcy friction factor is negligible. If Figure 3 is observed, optimum mesh number with minimum computational time and maximum accuracy can be seen approximately at 4×10^5.
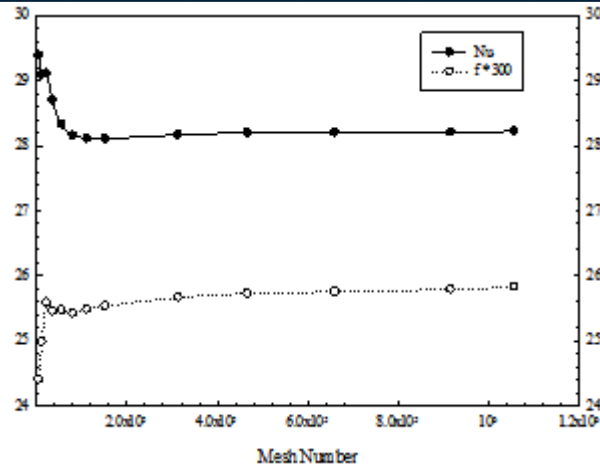
Figure 3. Variation of average Nusselt number and average Darcy friction factor with mesh number for pure water at De=898

To understand the accuracy of the numerical simulation, values of average Nusselt numbers of pure water obtained from numerical calculations were compared with experimental data given by Dravid et al. [13] and Kalb and Sieder [14]. The comparison can be seen in Figure 4. The results obtained by present study are good agreement with the correlations proposed from studies.
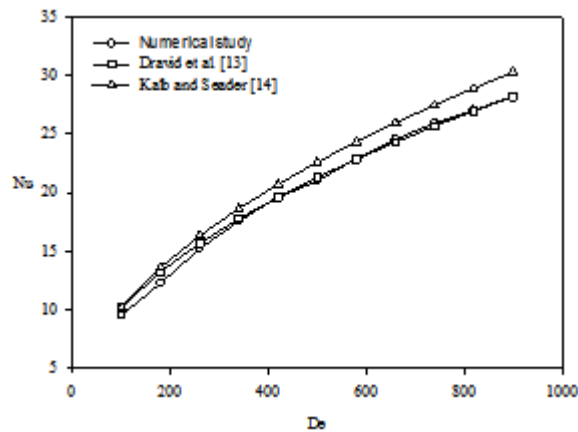
Figure 4. Comparison of average Nusselt number of the present study with experimental data given in the literature for pure water

4. RESULTS AND DISCUSSIONS

Laminar forced convection in a curved duct having square cross-sectioned was numerically investigated in this study. Figure 5 is presented to understand the effect of nanoparticles volume fractions on average Nusselt number. As can be seen Figure 5, average Nusselt number increases with increasing nanoparticle volume fractions. Also, average Nusselt number increases with increasing Dean number. The highest average Nusselt number was obtained at 4.0% nanoparticle volume fraction and the highest Dean number. This result is attributed that adding nanoparticles increases viscosity of nanofluid which enhances the random and irregular movement. Pure water has the lowest average Nusselt number.
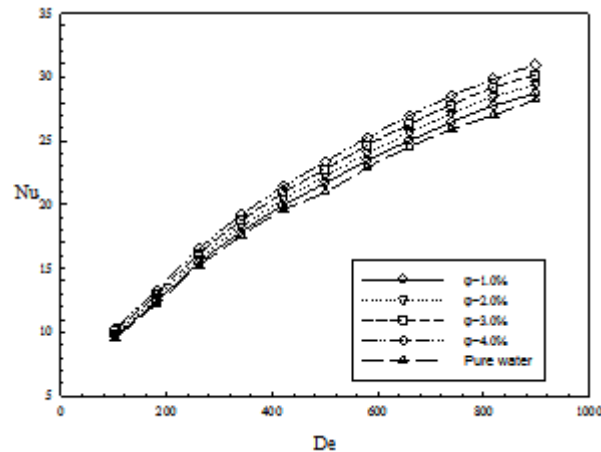
Figure 5. Variation of average Nusselt number with Dean number for different nanoparticle volume fractions of SiO_2/water nanofluid

Figure 6 shows the changing of average Darcy friction factor with nanoparticle volume fractions and Dean numbers. It can be noticed that average Darcy friction factor is not affected from changing of nanoparticle volume fractions. This is the most important advantage of SiO_2/water nanofluid flow for reducing pumping power. Also, average Darcy friction factor decreases with increasing Dean number.
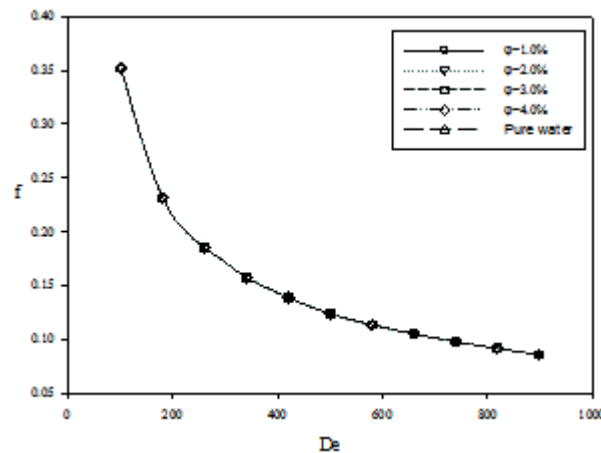
Figure 6. Variation of average Darcy friction factor with Dean number for different nanoparticle volume fractions of SiO_2/water nanofluid

Figure 7 shows that variation of temperature with nanoparticle volume fractions at the duct outlet for De=500. It can be revealed that temperature distributions are symmetric. The outer wall of the curved duct has lower temperature magnitude compared to the inner wall because of the highest flow velocity magnitude at the outer wall. Flow velocity of the outer wall is high according to flow velocity of the inner wall. Also, increasing of nanoparticle volume fractions slightly effects the temperature distribution of the inner wall.

Figure 8 shows that variation of velocity streamlines with nanoparticle volume fractions at the duct outlet for De=500. It was obtained that velocity distribution is symmetric and secondary flows occur at the outer wall. As nanoparticle volume fraction increases, the velocity magnitude at the outer wall increases.

Figure 9 shows that the temperature distribution at the duct outlet for different Dean numbers and 4.0% nanoparticle volume fraction of SiO_2/water nanofluid. It was revealed that Dean number significantly effects the temperature distribution in the duct. Also, temperature magnitude decreases with increasing Dean number.

Figure 10 shows that the velocity streamlines at the duct outlet for different Dean numbers and 4.0% nanoparticle volume fraction of SiO_2/water nanofluid. It was obtained that Dean number significantly effects the velocity distributions, too. At De=102, there is a secondary flow which has one center. However, at De=500, there are a lot of secondary flows. On the other hand, at De=898, there is no secondary flow. Also, velocity magnitude increases with increasing Dean number.

Figure 7. Temperature distribution at the duct outlet for different nanoparticle volume fractions of SiO₂/water nanofluid at De=500 for nanoparticle volume fraction of (a) 1.0%, (b) 2.0%, (c) 3.0%, (d) 4.0%

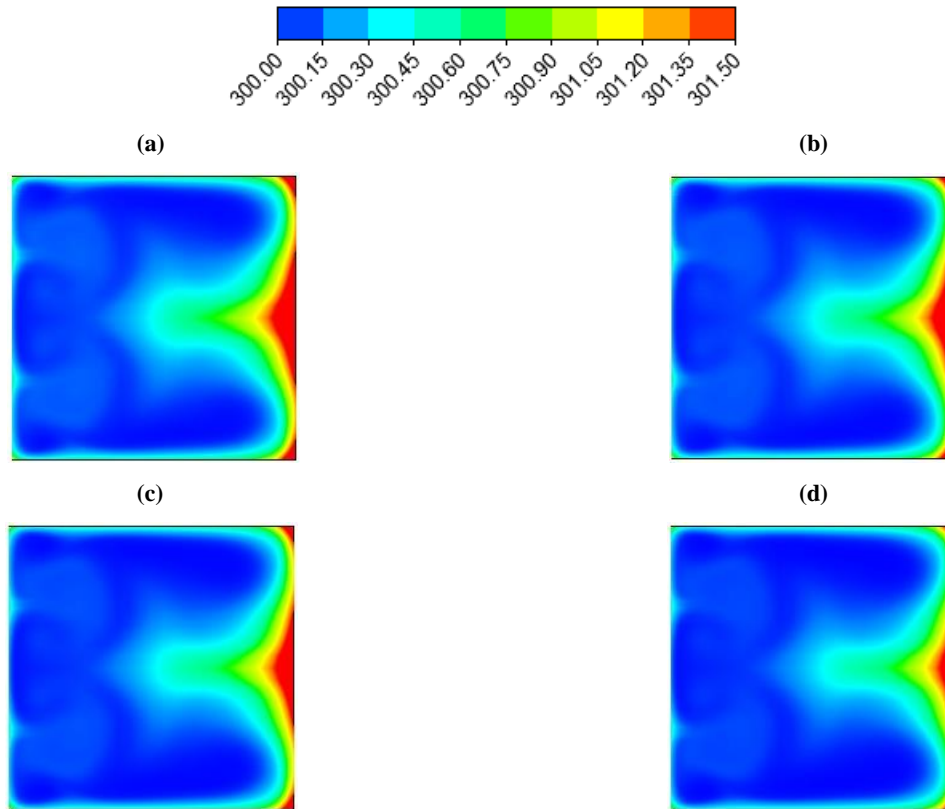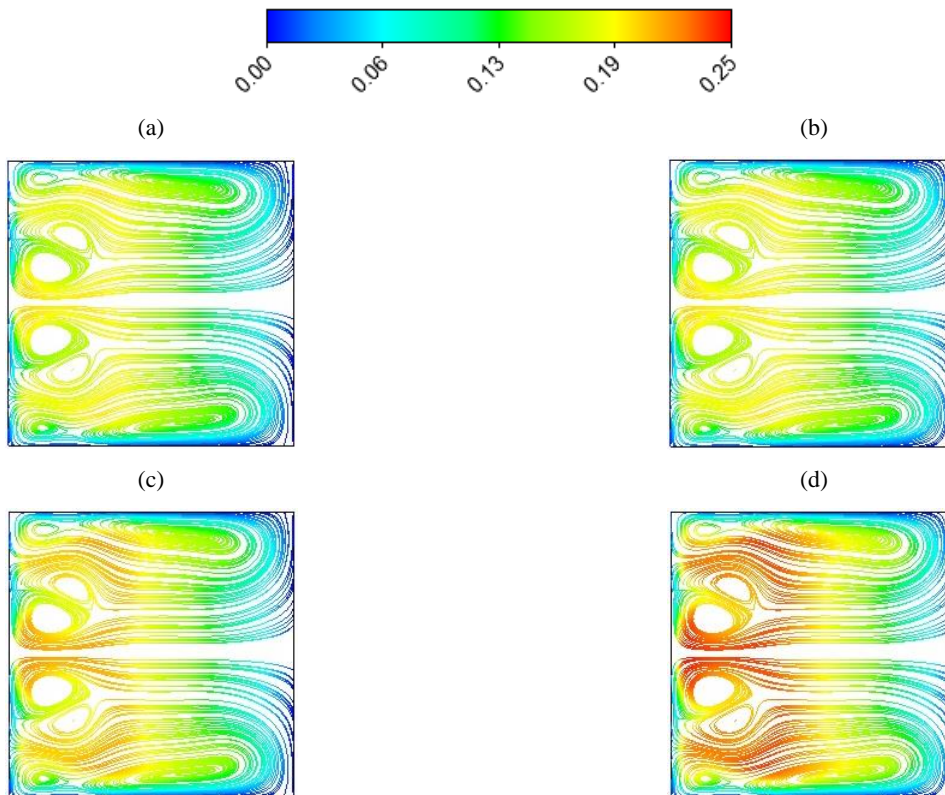*Figure 8. Velocity streamlines at the duct outlet for different nanoparticle volume fractions of SiO₂/water nanofluid at De=500 for nanoparticle volume fraction of (a) 1.0%, (b) 2.0%, (c) 3.0%, (d) 4.0%*

(a)   (b)   (c)
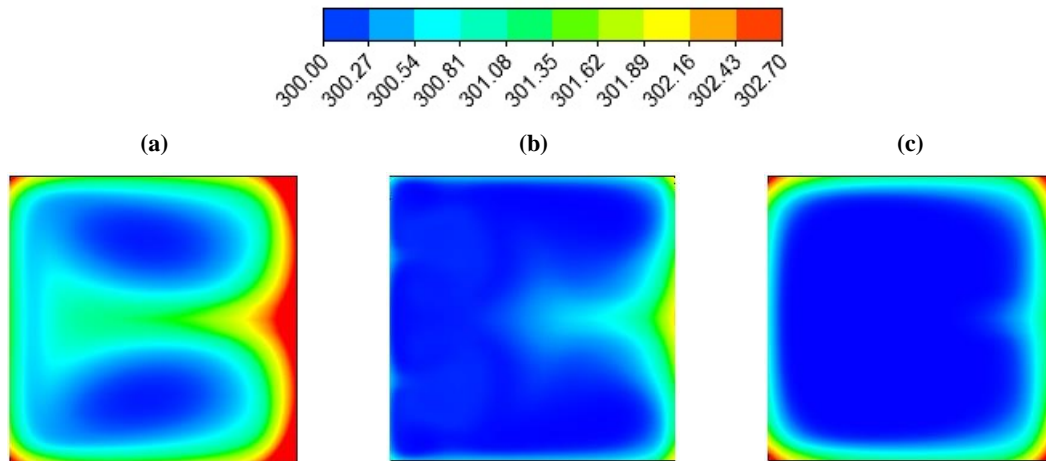
Figure 9. Temperature distribution at the duct outlet for 4.0% nanoparticle volume fraction of SiO₂/water nanofluid at (a) De=102, (b) De=500, (c) De=898

(a)   (b)   (c)
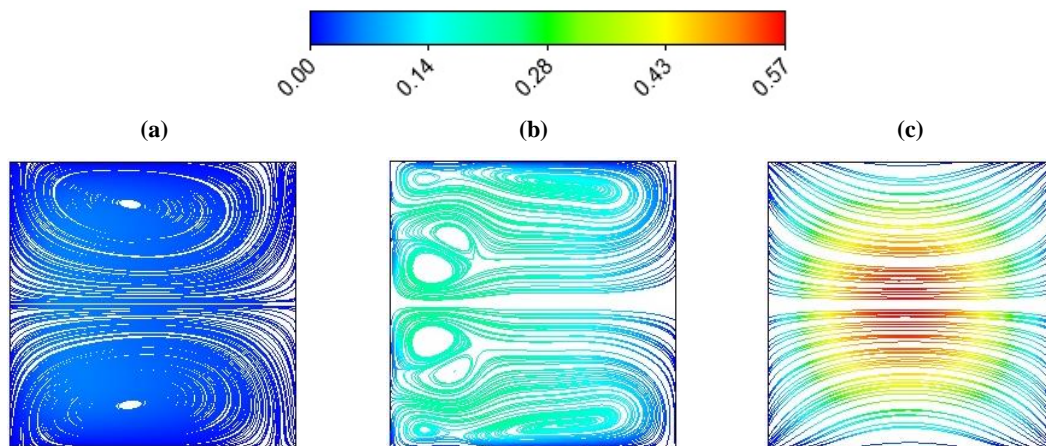
Figure 10. Velocity streamlines at the duct outlet for 4.0% nanoparticle volume fraction of SiO₂/water nanofluid at: (a) De=102, (b) De=500, (c) De=898

5. CONCLUSIONS

Numerical simulation of steady state laminar forced convection flow and heat transfer in a 3D square cross-sectioned curved duct using SiO_2/water nanofluid is presented in this study. Effect of different Dean numbers and the nanoparticle volume fractions on fluid flow and heat transfer were investigated. It was noticed from the numerical simulation results that adding SiO_2 nanoparticle inside the pure water enhances the heat transfer. The average Nusselt number increases with increasing the Dean number and nanoparticle volume fractions. Also, Darcy friction factor decreases with increasing Reynolds number. There is no effect of changing of nanoparticle volume fractions on average Darcy friction factor.

ACKNOWLEDGMENTS

REFERENCES

[1]. H. A. Mohammed, G. Bhaskaran, N. H. Shuaib, and R. Saidur, "Heat transfer and fluid flow characteristics in microchannels heat exchanger using nanofluids: a review", *Renewable and Sustainable Energy Rev.*, vol. 15, pp. 1502-1512, 2011.

[2]. S. U. S. Choi, "Enhancing thermal conductivity of fluids with nanoparticles", in: D.A. Singer, H.P. Wang (Eds.), *Development and Applications of Non- Newtonian Flows*, ASME, New York, pp. 99-105, 1995.

[3]. S. Lee, S. U. S. Choi, S. Li, and J.A. Eastman, "Measuring thermal conductivity of fluids containing oxide nanoparticles", *ASME J. Heat Transfer,* vol. 121, pp. 280-288, 1999.

[4]. B. C. Pak, and Y. I. Cho, "Hydrodynamic and heat transfer study of dispersed fluids with submicron metallic oxide particles", *Exp. Heat Transfer*, vol. 11, pp. 151-170, 1998.

[5]. Y. Xuan, and Q. Li, "Heat transfer enhancement of nanofluids", *Int. J. Heat Fluid Flow*, vol. 21, pp. 58-64, 2000.

[6]. M. S. Islam, and N. R. Mondal, "Effects of curvature on unsteady solutions through a curved square duct flow", *5th BSME International Conference on Thermal Engineering*, vol. 56, pp. 217-224, 2013.

[7]. J. Facao, and A. C. Oliviera, "Modelling laminar heat transfer in a curved rectangular duct with computational fluid dynamics code", *J.Heat Transfer,* vol. 48, pp. 165-177, 2005.

[8]. J. C. Sturgis, and I. Mudawar, "Single-phase heat transfer enhancement in a curved, rectangular channel subjected to concave heating", *Int. J. Heat and Mass Transfer*, vol. 42, pp. 1255-1272, 1999.

[9]. L. Fang, "Effects of geometries on heat transfer enhancement of thermal fluids in curved ducts", *Appl. Therm. Eng.,* vol. 90, pp. 590-595, 2015.

[10]. A. Akbarinia, and A. Behzadmehr, "Numerical study of laminar mixed convection of a nanofluid in horizontal curved tubes", *Appl. Therm. Eng.,* vol. 207, pp. 1327-1337, 2007.

[11]. O. Ghaffari, A. Behzadmehr, and H. Ajam, "Turbulent mixed convection of a nanofluid in a horizontal curved tube using a two-phase approach", *Int. Commun. Heat and Mass Transfer*, vol. 37, pp. 1551–1558, 2010.

[12]. W. H. Azmi, K. V. Sharma, P. K. Sarma, R. Mamat, and G. Najafi, "Heat transfer and friction factor of water based TiO_2 and SiO_2 nanofluids under turbulent flow in a tube", *Int. Commun. Heat and Mass Transfer*, vol. 59 pp. 30-38, 2014.

[13]. A. N. Dravid, K. A. Smith, and E. W. Merrill, "Effect of secondary fluid on laminar flow heat transfer in helical coiled tubes", *AICHE J.,* vol. 17, pp. 1114-1122, 1971.

[14]. C. E. Kalb, and J. D. Seader, "Fully developed viscous-flow heat transfer in curved circular tubes with uniform wall temperature", *AICHE J.,* vol. 20, pp. 340-346, 1974.

The Optimization of Tool Wear of Carbide End Mills Using Taguchi Method in Machining Carbon Fiber Reinforced Composite Materials

Selcuk YAGMUR[1], Yafes CAVUS [2], Ramazan CAKIROGLU[3], Ulvi SEKER[1]

Abstract

Carbon fiber reinforced composite materials are widely used in aviation and aerospace industries due to their low density, high strength, high corrosion resistance, low thermal expansion coefficient characteristics. In this study, the optimization of tool wear of four cutting edges coated carbide end mills which were used for peripheral milling on carbon fiber reinforced composites (CFRP) were investigated using Taguchi method. Two different cutting speeds (400 and 450 m/min), four different cutting tools (TiAlN coated without chip breaker (G1), TiAlN coated with chip breaker (G2), AlCrN coated with chip breaker (G3) and diamond coated (G4)) and constant feed rate (1270mm/min) were used as cutting parameters. The experiments were carried by using Taguchi L8 orthogonal experimental setup. By the help of Taguchi method, 450 m/min (cutting condition was 1270 mm/min constant feed rate with machining G4 tool) were determined as optimum cutting parameter by using experimental results. Moreover, the most effective operational parameter on tool wear was determined as cutting tool under the favor of analysis of variance (ANOVA).

Keywords: *CFRP, Carbide End Mills, Machining, Taguchi, ANOVA*

1. INTRODUCTION

As a result of advanced technology of our times, traditional materials have started failing in satisfaction of needs. Thus, the importance of material science has increased and the field of material engineering has been segmented into other sub-fields of science. Some of these fields are; ceramics, metals, nonmetals, polymers and composite materials. Especially composite materials have gained importance recently, and composite materials in different structures are being used in various areas. Weight reduction may be achieved by 60-80% when composite materials are used instead of steel, and by 20-50% when they are used instead of aluminum. Composite materials appear as preferred materials for many engineering applications today. This may be explained by weight advantages and energy savings in our era where energy is increasingly a problem [1].

In addition to the advantages of composite materials, they also have disadvantages such as difficulty of production. It is more difficult to machine fiber-reinforced composite materials which seem to be indispensable materials of current technology in different sectors. Difficulties experienced in machining composite materials have led researchers to be interested in studies on composite materials. However, the subject of tool wear in machining composite materials is not seen frequently in studies [2, 3]. Generally, the subject focused on researchers has been delamination that takes place during machining of composite materials. Researchers frequently studied delamination that takes place during machining processes for different composite materials [4-8]. Moreover, frequently studied issues in the literature include cutting forces that occur during machining of carbon fiber reinforced composite materials and the quality of machined surfaces [9-15]. This study investigated tool wears that occurred as a result of peripheral milling of carbon fiber composite materials by four different carbide end-mills. Optimization of cutting parameters over drill tip temperature drilling was investigated with Taguchi method [16-17]. The study analyzed the optimization of drilling parameters using Taguchi method in drilling AISI 316 steel by using PVD one-layer and multi-layer HSS drills [18]. Mohan et al. studied the effects of cutting parameters on cutting forces and moments during drilling of a glass fiber reinforced composite material. In the study, they optimized cutting parameters for glass fiber reinforced composite materials using Taguchi optimization methodology [20].

---

[1] XXXXXX

In peripheral milling of the carbon fiber reinforced composite material, this study optimized the tool wear that occurred as a result of using four-cutting edges carbide end-mills, four different end-mills, fixed feed rate and two different cutting speed parameters, by utilizing Taguchi method.

2. MATERIAL AND METHOD

The carbon fiber reinforced composite materials are used frequently in the aviation sector. These materials were produced by Odak Kompozit Teknolojileri Inc. in compliance with material properties used in the aviation sector. The materials were produced as prepreg using 245 gr/m^2 2x2 3K twill carbon fiber and Huntsman XU3508 resin system. The prepreg material was laid into a glass surface with 0º and 45º fiber angles symmetrically, and plates were obtained using the method of vacuum bagging. The plates were cured at 120º C temperature for 4 hours. After obtaining a sufficient amount of prepreg material, the material was cut into the desired dimensions. 80 layers of reinforcing material were used for 20 mm plates. In the twill weaving, carbon fibers form a weave in the directions of 0º and 90º. Thus, layering angles were chosen only as 0º and 45º.An easy way to comply with the symposium paper formatting requirements is to use this document as a template and simply type your text into it.

Four different carbide end-mills were used in the experiments. These were defined as Geometry 1, Geometry 2, Geometry 3 and Geometry 4, and shown in charts as G1, G2, G3 and G4. Table 2.1 shows the properties of the cutting tools used in the experiments. Among these G1, G2 and G3 had a single direction helices, while G4 had a two-directional helix.

Table 2.1. Properties of the cutting tools used in the experiments

Cutting Tool	Coating	Friction Coefficient	Hardness Hv	Diameter (mm)	Number of Cutting edges	Helix Angle (Degree)	Helix Height (mm)	Cutting Tool Length (mm)
G1/no Chip Breaker	TiAlN	0,35	3300	10	4	30	21	73
G2/with Chip Breaker	TiAlN	0,35	3300	10	4	30	21	73
G3/ with Chip Breaker	AlCrN-Based	0,25-0,35	3200	10	4	38	21	73
G4/Rigt Left Helix	Diamond	0,01	10000	10	4	19	35	73

The machining experiments were conducted using the CNC vertical machining center (Johnford VMC-550) whose technical properties are given in Table 2.2. Figure 2.1 shows the schematic representation of the experimental setup used in this study.

Table 2.2. Technical properties of the CNC Machine used in the experiments

Machine power	5 KW
Max. Revolutions	6000 rev/min
Axis Length (x, y, z)	600, 500, 600 mm
Precision	0,001 mm
Operating system	Fanuc

Figure 2.1. Schematic representation of experimental setup

High cutting speeds are needed to machining of composite materials. As the highest rate of revolution for the CNC machine 6000 rev/min. It was decided to use a spindle speeder. was connected to the spindle of the CNC machine revolution rate of spindle was increased to 4.8 times the original maximum rate.
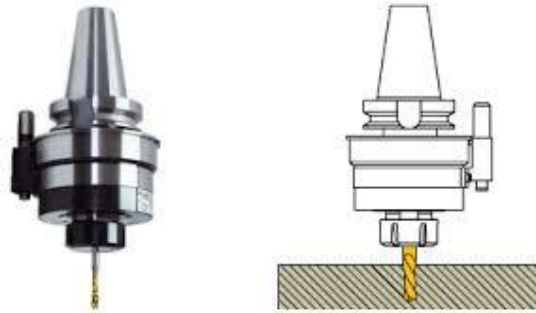
Figure 2.2. Spindle speeder

Table 2.3. Technical properties of the spindle speeder

Power (KW)	Axial force (N)	Turning Ratio	Weight (kg)	Max. Revolution (rev/min)
1,7	380	1:4,8	3,8	30 000

A Dino Lite digital camera was used to measure the wear that occurred in the cutting tools after the experiments. The photos were taken by 60X zooming with this camera. The plots were formed by using the measurements taken from the photos.

3. DISCUSSION AND CONCLUSION

The values obtained after the experiments conducted by using four different cutting tools and two different cutting speeds are given in Table 3.1. Figure 3.1 shows the changes in the tool wear values measured at the end of the experiments based on cutting speed and tool geometry.

Table 3.1. Outputs of the experimental study based on the inputs

Number	Cutting Speed (m/min)	Feed Rate (mm/min)	Cutting Tool	Tool Wear (mm)
2	400		G1	0,222
3	450			0,242
5	400		G2	0,160
6	450	1270		0,137
8	400		G3	0,145
9	450			0,167
11	400		G4	0,065
12	450			0,027

Figure 3.1. The change in tool wear based on cutting speed and tool geometry

Tool wear was measured separately for four cutting edges in each cutting tool used in the experiments, and the arithmetic average of the results taken from four cutting edges was accepted as the wear amount in each cutting tool. Figure 3.1 shows the changes in the tool wear values measured at the end of the experiments based on cutting speed and tool geometry. Accordingly, it was seen that the tool wear decreased along with increased cutting speed in G2 and G4, while it was the opposite case for G1 and G3. Considering the tool wear amounts in all tool geometries, flank wears took place in side surfaces of the cutting edges as a result of abrasive wearing. It was seen that this wear varied based on the type of coating and the friction coefficient of the coating. It was observed that tool wear increased in G1 with the increase in cutting speed, while it decreased with the increase in cutting speed in G2, which had the same helix angles but was different only in terms of chip breaker. Tool wear increased in G3 as the cutting speed increased. While G4 provided the lowest values of tool wear, it was found that tool wear decreased in increased cutting speeds.
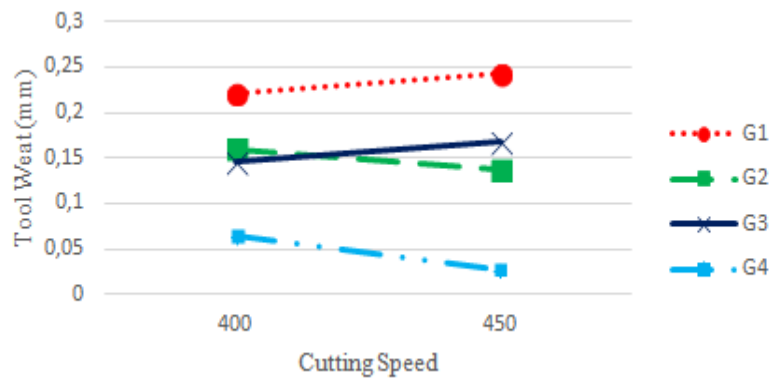
3.1. Analysis of the Results Using Taguchi Method

The tool wear values obtained as a result of the experimental setup carried out in compliance with the Taguchi L8 orthogonal order are converted to Signal/Noise ratios and expressed in decibels (dB). Tool wear and Signal/Noise ratios are given in Table 3.1.

Table 3.1 Experiments results based on Taguchi L8 Experiment Design and S/N ratios

Number	A (Cutting Tool)	B (Cutting Speed)	C (Feed Rate)	Wa Experiment (µm)	S/N (dB)
1	G1	400		0,222	13,0729
2	G1	450		0,242	12,3237
3	G2	400		0,160	15,9176
4	G2	450	1270	0,137	17,2656
5	G3	400		0,145	16,7726
6	G3	450		0,167	15,5457
7	G4	400		0,065	23,7417
8	G4	450		0,027	31,3727

The S/N ratio considers both mean values and variation. While the signal factor represents the actual value obtained from the system, the noise value represents the factors that are not considered in experimental design but are influential on the results of the experiment. The sources of noise are all variables that lead to deviation from the final targeted value. In this optimization process, there is a function that is suitable for 3 different purposes which is known as the Taguchi loss function and also expressed as the Signal/noise ratio (S/N) function. Accordingly, among the equations based on the objective being "the best is minimum", "the best is maximum" and "the best is nominal", the equation on "the best is minimum (Eq. 3.1) was used to calculate S/N ratios and the results are given in Table 3.1.

$$\eta = -10\log\left(\frac{1}{n}\sum_{i-1}^{n} y_i^2\right)$$

(3.1)

In the equations, y_i: performance response, i: observation value, n: the number of tests in a trial. The plot shoving the S/N change of the tool wear based on the parameters used in the peripheral milling experiments is given in Figure 4. According to the graphical depiction of the S/N rates shown in Figure 4, the experimental combination for minimum tool wear is G4 (A4) as the cutting tool, and 450 (B2) as the cutting speed.
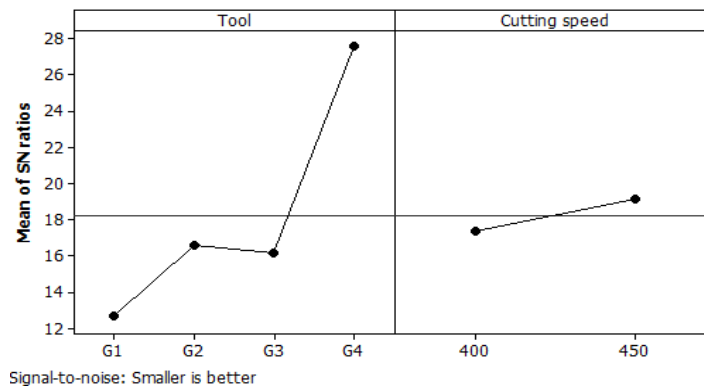
Figure 4: The plot of S/N ratios for tool wear

3.2. Analyzing the parameters with ANOVA

Eight different experiments were conducted in peripheral milling of carbon fiber reinforced composite materials with four cutting edge carbide end-mills, four different end-mills, constant feed rate and two different cutting speeds, and different tool wear values were measured in each experiment. Analysis of variance is used to determine whether these differences are entirely coincidental or based on factors, and find the effect of each factor. Analysis of variance results for tool wear are provided in Table 6.3.

Table 6.3. ANOVA results based on tool wear values

	Cutting Parameters	Freedom of degree	SS	MS	F	P	Efficiency (%)
A	Cutting	3	249.135	83.045	9.99	0.045	80.02
C	Cutting	1	6.13	6.13	0.74	0.454	0
Residual		3	24.928	8.309			17,08
Total		7	280.193				100

The maximum value of F obtained among the values that are found by calculating the sum of the squares of each factor separately, shows the most influential factor in tool wear. As seen in Table 6.2, it was found that cutting tool was the most influential factor in tool wear by 80.02%.

3.3. Verification tests and results

After estimation of the parameters that would provide optimal results based on Taguchi method, verification experiments are conducted as the final step in optimization and the accuracy of the performed optimization is checked. For the tool wear we previously determined, the reliability of the results was tested by taking the average of verification experiment results obtained by three control experiments using "A4B2" parameters. In obtaining the best tool wear values based on this, optimized cutting parameters are given in Table 3.2.

Table 3.2. Optimal values for tool wear

	Initial cutting parameters	Optimal cutting parameters	
		Prediction	Experimental
Level	A2B2	A4B2	A4B2
Tool Wear	0.132	0.043625	0.025
S/N Ratio (dB)	17.5885	28,4326	32,0411
Improvement of S/N ratio		14.4526 dB	
Prediction error (dB)		3.6085	

Using the A4B2 cutting parameters we determined as a result of Taguchi optimization, 3 verification experiments were conducted and the success of the optimization was tested. The tool wear value obtained with the verification experiments was measured as (Wa) 0.075 mm. Therefore, the tool wear value obtained in the initial experiments (0.132 mm) was improved by 82% after the optimization. It was seen that the tool wear value was successfully reduced by the Taguchi optimization technique.

4. INTERPRETATION OF THE RESULTS

Peripheral milling of Carbon Fiber Reinforced Composites (CFRP) was experimentally investigated using four different cutting tools (four-cutting edges carbide end-mills: TiAlN-coated without chip breaker, Geometry 1 (G1); TiAlN-coated with chip breaker Geometry 2 (G2); AlCrN-coated with chip breaker Geometry 3 (G3); and diamond-coated Geometry 4 (G4)). The study used two different cutting speeds (400 and 450 m/min), and a constant feed rate (1270 mm/min). The following results were obtained in the analysis of the data gathered in this study;

• The optimal result among the tool wear values was obtained with a 450 m/min cutting speed and using the cutting tool G4.

• While increasing the cutting speed led to an increase in tool wear in tools coded G1 and G3, it led to a decrease in tool wear in tools G2 and G4.

• The highest tool wear values were found in the experiments conducted with the tool coded G1, while the lowest values were found in the experiments conducted with G4.

• The tools G2 and G3 showed similar performances in terms of tool wear values.

• As a result of the analysis by using Taguchi method, the optimal parameter levels (A4B2) for tool wear were found as diamond-coated geometry, and a cutting speed value of 450 m/min.

ACKNOWLEDGMENT

REFERENCES

[1]. Ersoy, M.S. (2005). Lif Takviyeli Polimerik Kompozit Malzeme Tasarımı, Yüksek Lisans Tezi, Kahramanmaras Sütcü İmam Üniversitesi Fen Bilimleri Enstitüsü, Kahramanmaras, 5-18.
[2]. Park, K. H., Beal, A., Kwon, P., & Lantrip, J. (2011). Tool wear in drilling of composite/titanium stacks using carbide and polycrystalline diamond tools.Wear, 271(11), 2826-2835.
[3]. Ciftci, I., Turker, M., Seker, U. (2004). CBN cutting tool wear during machining of particulate reinforced MMCs. Wear, 257(9), 1041-1046.
[4]. Urban, N. A. (2001) Analysis Of Machining Quality in Edge Trimming of Carbon Fiber Reinforced Composite, Kerala University B. Tech, İndia.
[5]. Davim, J. P., & Reis, P. (2005). Damage and dimensional precision on milling carbon fiber-reinforced plastics using design experiments. Journal of materials processing technology, 160(2), 160-167.
[6]. Bayraktar, S. (2011). Karbon elyaf takviyeli polimer kompozit malzemelerin frezeleme isleminde islenebilirliginin deneysel arastırılması, Yüksek Lisans Tezi, Gazi Üniversitesi Fen Bilimleri Enstitüsü, Ankara, 35-55.
[7]. Rawat, S., Attia, H. (2009). Wear mechanisms and tool life management of WC–Co drills during dry high speed drilling of woven carbon fibre composites. Wear, 267(5), 1022-1030.
[8]. Celik, A., Lazoglu, I., Kara, A., Kara, F. (2015). Investigation on the performance of SiAlON ceramic drills on aerospace grade CFRP composites. Journal of Materials Processing Technology, 223, 39-47.
[9]. Jenarthanan, M. P., Jeyapaul. R. (2013). Machinability study of carbon fibre reinforced polymer (CFRP) composites using design of experiment technique, Pigment & Resin Technology, 35-44.
[10]. Rusinek, R. (2010). Cutting process of composite materials:An experimental study, International Journal of Non-Linear Mechanics 45, 458-462.
[11]. Sorrentino, L., Turchetta, S. (2011) Milling of Carbon Fiber-Reinforced Plastics: Analysis of Cutting Forces and Surface Roughness, 18th Internatıonal Conference On Composıte Materıals, Korea.
[12]. Chatelain, J. F., Zaghbani, I., Monier, J. (2012). Effect of Ply Orientation on Roughness for the Trimming Process of CFRP Laminates. C. World Academy of Science, Engineering and Technology, 68, 1204-1210.
[13]. Hosokawa, A., Hirose, N., Ueda, T., Furumoto, T. (2014). High-quality machining of CFRP with high helix end mill. CIRP Annals-Manufacturing Technology, 63(1), 89-92.
[14]. Denkena, B., Boehnke, D., Dege, J. H. (2008). Helical milling of CFRP–titanium layer compounds. CIRP Journal of manufacturing Science and Technology, 1(2), 64-69.
[15]. Bayraktar, S., Turgut, Y. (2016) Investigation Of Cutting Forces And Surface Roughness In Milling Of Carbon Fiber Reinforced Polymer Composite Material. Materiali in Tehnologije / Materials and Technology, 4 (in press).
[16]. Cakıroglu, R., Acır, A., "Optimization of cutting parameters on drill bit temperature in drilling by Taguchi method" Measurement, 2013, s. 3525-3531.

[17]. Cakiroglu, Ramazan, and A. C. I. R. Adem. "Al2014 Malzemesinin Delinmesinde Takım Talas Ara Yüzey Sıcaklıkları Ve Kesme Kuvvetinin Taguchı Metodu İle Optimizasyonu." Makine Teknolojileri Elektronik Dergisi 10.2 (2013): 73-86.

[18]. Kıvak, T., Samtas, G., Cicek, A., "Taguchi method based optimisation of drilling parameters in drilling of AISI 316 steel with PVD monolayer and multilayer coated HSS drills" Measurement, 2012, s.1547-1557.

[19]. Mohan, N.S., Ramachandra, A, Kulkarni, S.M., "Influence of process parameters on cutting force and torque during of glass-fiber polyester reinforced composites", Composite Structures, 2005.

Influence of Opening Ratio and Position in Infill Wall on Constitutive Law of Equivalent Compression Strut

Onur Ozturkoglu[1], Taner Ucar[2]

Abstract

Infill walls are widely used in any building to create a separation between spaces intended for different purposes. In general, partial openings exist in infill wall with different opening ratio and position due to architectural considerations, functional needs and aesthetic concerns. In current practice, buildings are considered as bare frames ignoring infills and openings. However, infill walls and partial openings may significantly affect the seismic behavior of structures. Equivalent compression strut model is frequently used in modelling of infill walls for structural analysis. Accordingly, the force-displacement (F–D) relationship of equivalent compression strut is quite important in nonlinear analysis of infilled frames. In particular, opening sizes and position are essential parameters in order to properly constitute F–D relationship of infill wall with openings simulated by means of an equivalent compression strut. In this study, F–D relationship of equivalent compression strut is determined for different opening ratios and positions in infill wall considering three different F–D relationship models available in the literature. The maximum strength of equivalent compression strut and the corresponding displacement, the compression cracking force and the corresponding displacement, the residual strength and the axial compressive stiffness of the strut are compared and discussed for different constitutive F–D laws. It is found that force values of F–D relationships decrease as opening ratio increases. However, displacement values are not generally effected by opening ratio or position. Furthermore, openings upon the diagonal are more influential on F–D relationships of equivalent compression strut in comparison to other opening positions.

Keywords: *Infill wall with openings, opening ratio and position, force-displacement relationship, equivalent compression strut.*

1. INTRODUCTION

In current design practice the presence of infill walls is generally neglected due to the complex composite behavior of the bounding frame and the infill wall, and the lack of a rational design procedure for masonry infilled buildings. However, the field observations after destructive earthquakes clearly illustrate that infill walls may have significant influence on seismic performance of structures by drastically altering the strength and stiffness characteristics, as well as the expected failure mechanism. Therefore, neglecting the infill walls in practical structural analysis and design may lead to a substantial inaccuracy in estimating the seismic response of infilled structures in terms of both capacity and earthquake demand.

Numerical simulation of infill walls is essential to understand and evaluate the possible effects of infill walls on global seismic response of infilled structures during major seismic events. Accordingly, during the last decades, extensive experimental investigations and analytical studies have been performed to properly model the contribution of infill [1]–[13]. On the basis of available research works, the fundamental idea to incorporate the infill wall in numerical models is generally oriented at micro- and macro-modelling techniques. Although infill walls can be simulated more adequately using micro-models, this type of modelling technique generally requires more computational effort and found to be impractical for the analysis of three dimensional structures [9], [14]. Meanwhile, macro-models exhibit significant advantages by providing reasonable accuracy and efficiency in simulating the contribution of infill. Among these, the concept of single or multiple compressive equivalent diagonal struts has by far been the most favored one [7],[8], [10]–[18].

Estimation of nonlinear strength and stiffness characteristics of the infill during the inelastic response is the preliminary issue to be considered in nonlinear analysis. In this sense, it is essential to constitute realistic force–displacement relationships capable of representing the nonlinear behavior of the equivalent strut, which is not an easy task. Therefore, many different proposals have been made for determining the stiffness and strength characteristics of infill wall and several nonlinear constitutive F–D laws composed of three or four segments and mainly developed for solid infill walls are available in the literature [19]–[24]. The presence of prevalent openings, such as windows and doors, may possibly effect the adopted constitutive parameters causing a discontinuous load path within the infill wall. Furthermore, the variability of percentage and position of the opening reveals an important uncertainty in determination of the characteristic parameters assumed in the constitutive model.

Three different constitutive models all of which enable simulating infill walls by means of a single equivalent strut are considered. The influence of the opening in terms of both percentage and position is taken into consideration by using the derived stiffness reduction factors. The variation of stiffness reduction factor as a function of opening percentage for different positions of opening is obtained from finite element analysis considering infill wall-frame interaction. The modified F–D relationship models are constituted for specific opening percentages considering three different positions of opening as upon the diagonal, above the diagonal and under the diagonal. The stiffness and strength parameters calculated in the horizontal direction are precisely transformed to the direction of the equivalent diagonal. In order to investigate the influence of the infill wall opening percentage and the opening position on the constitutive law, the characteristic parameters assumed in constitutive models of the compressive equivalent diagonal strut in terms of strength, stiffness and displacement are compared for the reference F–D relationships.

2. STIFFNESS REDUCTION FACTORS FOR INFILL WALLS WITH OPENINGS

In order to account for the possible effects of openings on stiffness and strength of infill wall, stiffness reduction factors (k) varying between 0 (bare frame) and 1 (fully infilled frame) are introduced. Stiffness reduction factors are originally developed considering the position and the percentage of the opening within the infill wall. Infill walls are widely simulated by two-dimensional finite elements since their thickness is smaller in comparison to the length and the height. Accordingly, a modelling technique of plane finite elements is implemented to simulate infill wall. Dimension of finite elements (i.e. small pieces of shell elements) are accurately selected and openings within the wall are easily provided by erasing the related finite elements. The mutual interaction of the bounding frame and the masonry panel is modeled by means of gap elements that can only transform axial compression. The stiffness of gap element is determined as:

$$K_g = \frac{t_w \cdot a_w \cdot E_{me}}{r_w} \tag{1}$$

where t_w and E_{me} are the thickness and the elastic modulus of the infill wall, and a_w and r_w are the width and the length of the compressive equivalent diagonal strut, respectively. The implemented modelling technique is shown in Figure 1.
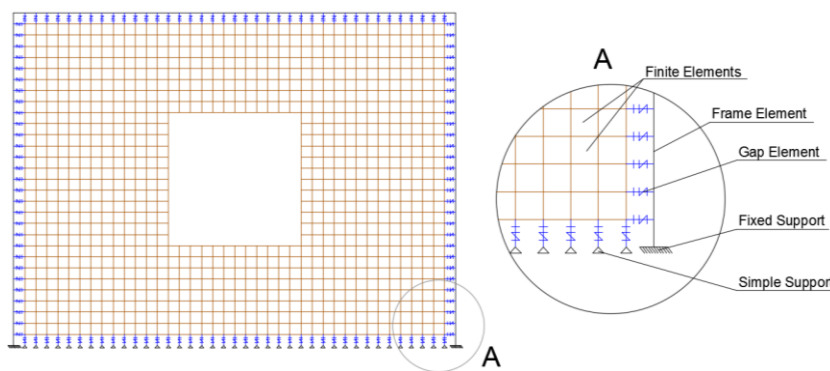
Figure 1. Modelling of the bounding frame, the infill wall and the interaction

Having completed the analytical model, a finite element analysis is conducted in elastic region for monotonic loading in order to determine stiffness reduction factors of infill walls with openings. Firstly, the lateral stiffness of one-story one-bay bare frame (k_{bare}) subjected to a horizontal load at the top level is obtained by dividing the applied load (P) to the lateral top displacement of the bare frame (Δ_{bare}). Then, applying the same procedure for a fully infilled frame yields the lateral stiffness of the fully infilled one (k_{full}). Finally, openings are provided within the infill wall and the lateral stiffness of partially infilled frame (k_{part}) is calculated. Figure 2 describes the procedure used to determine the lateral stiffness one-story one-bay infilled frame with openings.
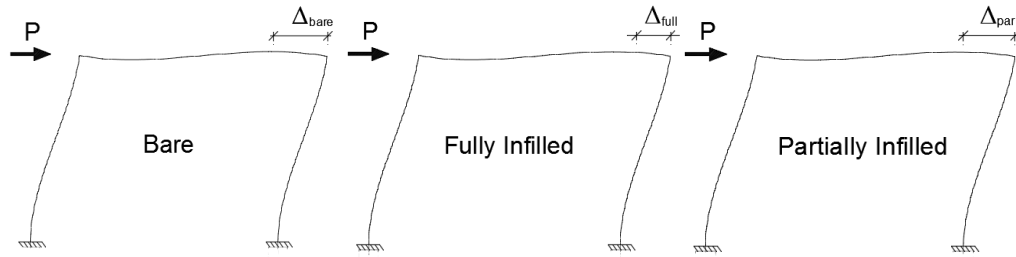
Figure 2. Determination of lateral stiffness of frames

The following equations yield the lateral stiffness of solid masonry infill panel ($k_{full,i}$) and the lateral stiffness of infill panel with openings ($k_{part,i}$), respectively:

$$k_{full,i} = k_{full} - k_{bare} \tag{2}$$

$$k_{part,i} = k_{part} - k_{bare} \tag{3}$$

Consequently, the stiffness reduction factor (k) accounting for the effect of the opening on the stiffness is obtained as the ratio of the lateral stiffness of infill wall with opening to the lateral stiffness of solid infill wall:

$$k = \frac{k_{part,i}}{k_{full,i}} \tag{4}$$

3. CONSTITUTIVE MODELLING OF INFILL WALLS

Infill walls with or without openings can significantly alter the seismic performance of structures by contributing to lateral resistance, interacting with the bounding frame and leading to different failure mechanisms expected for bare structures. In the field of nonlinear seismic analysis, the method of the compressive equivalent diagonal strut is widely used to simulate the behavior of infill panels since nonlinear micro-modelling technique requires high computational effort. The main problem containing large uncertainties is how to determine the F–D envelopes and hysteretic behavior of the diagonals. The following multi-linear constitutive models (i.e. F–D envelopes) which provide the simulation of infill wall by means of a single equivalent diagonal strut are adopted as a reference in the present study.

3.1. *The Constitutive Law Proposed by Panagiotakos and Fardis*

The constitutive model proposed by Panagiatakos and Fardis is composed of four segments [20]. The slope of the first branch, i.e. the initial shear stiffness of the uncracked panel (K_1), is specified as:

$$K_1 = \frac{G_w \cdot L_{in} \cdot t_w}{H_{in}} \tag{5}$$

where G_w is the shear modulus of the wall, L_{in} and H_{in} are the length and the height of the infill, respectively, and t_w is the thickness of the wall.

The yielding force (F_y) corresponding to the first cracking of infill wall (i.e. the cracking force) is associated with the tensile strength of the infill (f_{tp}) obtained from the diagonal compression test and is determined using the following equation:

$$F_y = f_{tp} \cdot L_{in} \cdot t_w \tag{6}$$

The second branch corresponds to the formation of a diagonal compressive path within the infill wall. Accordingly, the axial stiffness of the compressive equivalent diagonal strut (K_2) is:

$$K_2 = \frac{E_{me} \cdot t_w \cdot a_w}{r_w} \tag{7}$$

The ratio between the maximum force (F_m) and the cracking force is assumed to be 1.3. The displacement corresponding to the maximum force can easily be determined as:

$$\delta_m = \delta_y + \frac{F_m - F_y}{K_2} \tag{8}$$

where δ_y is the displacement at the cracking point.

The stiffness of the third branch representing the softening of the infill panel is assumed to range within $0.005 \cdot K_1 \leq K_3 \leq 0.1 \cdot K_1$. The residual force ($F_r$) is assumed $0.05 \cdot F_y \leq F_r \leq 0.1 \cdot F_y$ whereas the corresponding displacement (δ_r) is calculated as:

$$\delta_r = \delta_m + \frac{F_m - F_r}{K_3} \tag{9}$$

The fourth branch characterized by a constant residual strength describes the ultimate state of the infill wall. The F–D relationship of Panagiotakos and Fardis is shown in Figure 3 (a).

3.2. The Constitutive Law Proposed by Dolsek and Fajfar

A three-linear F–D envelope for the diagonal strut representing the masonry infill based on the results of some experimental tests is proposed by Dolsek and Fajfar [22]. The initial stiffness of the infill (K_1) is calculated according to Eq. (5). The strength of the infill (F_m) is determined as follows:

$$F_m = 0.818 \cdot \frac{L_{in} \cdot t_w \cdot f_{tp}}{C_I} \cdot \left(1 + \sqrt{C_I{}^2 + 1}\right) \tag{10}$$

where C_I is estimated by:

$$C_I = 1.925 \cdot \frac{L_{in}}{H_{in}} \tag{11}$$

The cracking force (F_y) is assumed to be $0.6 \cdot F_m$. The story drift corresponding to the maximum force (D_m) is 0.2% in case of solid infill panel, 0.15% in case of window opening and 0.10% in case of door opening. The ratio between the story drift at collapse of the infill panel and that at the maximum force is arbitrarily assumed as 5 (Figure 3 (b)).

For the F–D envelope of the diagonal strut, both the initial stiffness and the strength in horizontal direction have to be transformed to the direction of the diagonal, as well as in the constitutive relationship proposed by Panagiotakos and Fardis.

3.3. The Constitutive Law Proposed by Tsai and Huang

A multi-linear constitutive F–D law is used to simulate the nonlinear behavior of the compressive equivalent diagonal strut. The compressive strength of the infill (R_m) is evaluated through the following equation:

$$R_m = a_w \cdot t_w \cdot f'_{m90} \tag{12}$$

where f'_{m90} is the horizontal expected strength of the infill panel and is assumed to be 65% of the compressive strength of the infill (f'_m) which is estimated in terms of the compressive strength of bricks (f_b) and the mortar strength (f_j) as follows [2]:

$$f'_m = 0.63 \cdot f_b{}^{0.49} \cdot f_j{}^{0.32} \tag{13}$$

The displacement corresponding to the compressive strength of the infill is:

$$\Delta_m = \varepsilon'_m \cdot r_w \tag{14}$$

where ε'_m is the strain corresponding to the maximum compressive strength and is estimated by:

$$\varepsilon'_m = \frac{0.27}{f_j{}^{0.25}} \cdot \frac{f'_m}{E_{me}{}^{0.7}} \tag{15}$$

The cracking force (R_y) is given by:

$$R_y = \frac{R_m - \alpha \cdot K_1 \cdot \Delta_m}{1 - \alpha} \tag{16}$$

The post-stiffness ratio (α) is assumed as 0.2. The displacement at the cracking (Δ_y) can be calculated as:

$$\Delta_y = \frac{R_y}{K_1} \tag{17}$$

Finally, the residual strength of the diagonal strut (R_r) is assumed to 30% of the cracking force. The model of Tsai and Huang, and the main involved parameters are shown in Figure 3 (c).
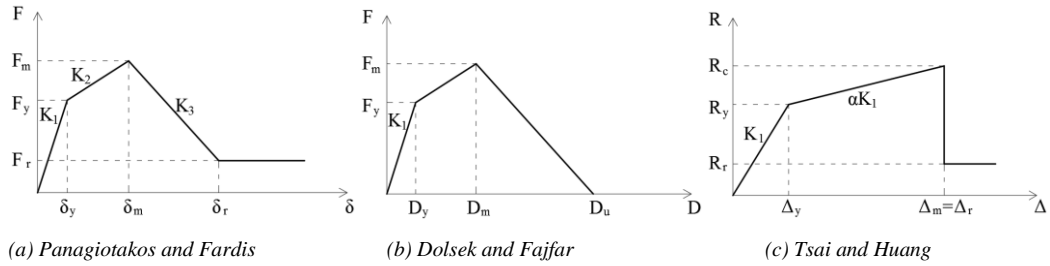
(a) Panagiotakos and Fardis *(b) Dolsek and Fajfar* *(c) Tsai and Huang*

Figure 3. The adopted constitutive models

4. CASE STUDY

In order to investigate the possible influence of opening percentage and position within the infill wall on the relevant parameters of the constitutive model of the compressive equivalent diagonal strut, one-story one-bay reinforced concrete (RC) frame is considered. The bay length is 5 m and the story height is 3 m. Rectangular beams and square columns are considered in the design. Rectangular beam dimensions are 25x50 cm and square columns dimensions are 40x40 cm. The compressive strength of concrete is assumed to be 20 MPa. The masonry infill consists of hollow bricks with a thickness of $t_w = 200$ mm. The elastic modulus of infill wall is calculated as $E_{me} = 1661$ MPa considering the stress–strain relations of brick infill and mortar [2]. Three different positions of window opening as opening upon the diagonal, opening above the diagonal and opening under the diagonal, and three opening percentages (the area of the opening to the total area of infill) as 22%, 32% and 45% are considered. The typical layout of the openings is shown in Figure 4.
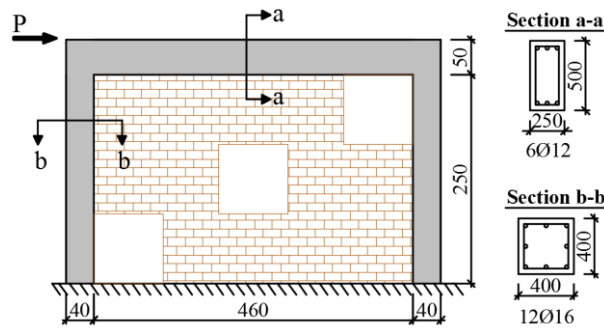
Figure 4. Layout of the openings within the wall and the bounding RC frame.

4.1. Stiffness Reduction Factors

The influence of the opening in terms of both percentage and position is taken into consideration by means of stiffness reduction factors. The variation of stiffness reduction factor as a function of opening percentage for different positions of opening is obtained from finite element analysis considering infill wall-frame interaction. The finite element analysis is conducted in the elastic region for the monotonic loading using the structural analysis tool SAP2000 [25]. Figure 5 shows the derived stiffness reduction factor of infilled frame with openings in relation to opening percentage for three different positions of opening. One can easily obtain the stiffness reduction factors entering in this graph. The stiffness reduction factors determined for the opening positions and percentages considered in this study are presented in Table 1.
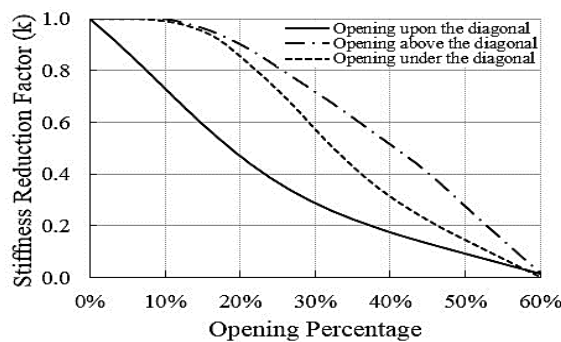
Figure 5. Variation of stiffness reduction factor in relation to opening percentage

Table 20. Stiffness reduction factors

Opening percentage (%)	Position of the opening		
	Upon the diagonal	Above the diagonal	Under the diagonal
22	0.43	0.88	0.82
32	0.26	0.68	0.52
45	0.13	0.41	0.22

With reference to Figure 5, it can be concluded that stiffness reduction factors of all opening positions decrease as opening percentage increases. However, the position of opening substantially effects the variation of the stiffness reduction factor with respect to opening percentage. Opening upon the diagonal is more influential on reducing the stiffness of the infill wall, since it gives smaller stiffness reduction factors. This position of opening significantly reduces the stiffness even in case of small opening percentages. On the other hand, opening above the diagonal is the least influential position. For opening percentages smaller than 18 both opening positions above the diagonal and under the diagonal have the same influence on stiffness of infill and for opening percentages small than 10, the presence of the opening may be neglected for those positions of the opening. On the contrary, the contribution of the infill wall with opening can be ignored regardless of the position in case infill wall opening ratio exceeds 60%.

4.2. The Modified Constitutive Relationships

Since the influence of the opening in terms of both percentage and position is taken into consideration by using the stiffness reduction factors of the study, strength and stiffness parameters of the constitutive F–D law are conveniently reduced. Accordingly, modified F–D relationships reflecting the influence of the opening are constituted for infill walls with openings. The additional necessary parameters to constitute the reference F–D relationships are taken as $G_w = 664.4$ MPa, $f_{tp} = 0.36$ MPa and $f'_{m90} = 3.02$ MPa. The width of the compressive equivalent diagonal strut is calculated as $a_w = 637$ mm for the infill wall without opening [26]. In order to properly investigate the influence of opening percentage and position on the constitutive law of the compressive equivalent diagonal strut, stiffness and strength parameters applied to the horizontal direction in the models of Panagiotakos and Fardis, and Dolsek and Fajfar are transformed to the direction of the diagonal. Accordingly, summarized in Table 2 are the constitutive parameters of the diagonal strut.

Table 2. Constitutive parameters of the diagonal strut

Opening position	Opening percentage	R_y (kN)	Δ_y (mm)	R_m (kN)	Δ_m (mm)	R_r (kN)	Δ_u (mm)
Panagiotakos and Fardis							
Fully infilled	0%	377	1.19	490	3.99	38	18.27
Upon the diagonal strut	22%	164	1.19	213	3.99	16	18.27
	32%	97	1.19	126	3.99	10	18.27
	45%	49	1.19	64	3.99	5	18.27
Above the diagonal strut	22%	330	1.19	429	3.99	33	18.27
	32%	254	1.19	331	3.99	25	18.27
	45%	153	1.19	198	3.99	15	18.27
Under the diagonal strut	22%	308	1.19	400	3.99	31	18.27
	32%	196	1.19	255	3.99	20	18.27
	45%	83	1.19	108	3.99	8	18.27
Dolsek and Fajfar							
Fully infilled	0%	245	0.77	408	4.39	-	21.96
Upon the diagonal strut	22%	106	0.77	177	3.29	-	16.47
	32%	63	0.77	105	3.29	-	16.47
	45%	32	0.77	53	3.29	-	16.47
Above the diagonal strut	22%	214	0.77	357	3.29	-	16.47
	32%	165	0.77	275	3.29	-	16.47
	45%	99	0.77	165	3.29	-	16.47

Under the diagonal strut	22%	200	0.77	333	3.29	-	16.47
	32%	127	0.77	212	3.29	-	16.47
	45%	54	0.77	90	3.29	-	16.47
Tsai and Huang							
Fully infilled	0%	294	7.28	385	18.54	88	-
Upon the diagonal strut	22%	128	7.28	168	18.54	38	-
	32%	76	7.28	99	18.54	23	-
	45%	38	7.28	50	18.54	12	-
Above the diagonal strut	22%	258	7.28	337	18.54	77	-
	32%	199	7.28	260	18.54	60	-
	45%	119	7.28	156	18.54	36	-
Under the diagonal strut	22%	240	7.28	314	18.54	72	-
	32%	153	7.28	201	18.54	46	-
	45%	65	7.28	85	18.54	19	-

The values of constitutive parameters in terms of both strength and stiffness decrease with increasing infill wall opening ratio in all the constitutive models. The highest strength and stiffness values are obtained when the opening is considered above the diagonal and the smallest ones are calculated for the central opening. The cracking and the maximum force values of the Panagiotakos and Fardis constitutive law are relatively higher than those values of the other two models. Although its higher strength, the cracking force of the constitutive law proposed by Fardis and Fajfar is smaller than the cracking force of the Tsai and Huang constitutive law. The initial stifness of the constitutive F–D laws of Panagiotakos and Fardis and Dolsek and Fajfar is equal while the initial stiffness of Tsai and Huang constitutive relationship is quite low. Accordingly, larger displacements are obtained in the case of the model of Tsai and Huang. K_2 stiffness of the Dolsek and Fajfar constitutive law is 60% higher than K_2 stiffness of the Panagiotakos and Fardis model, while the stiffness of the softening branch of the two model is almost the same. Displacement corresponding to the cracking point is not influenced by the infill wall opening ratio and the opening position. The displacement corresponding to the maximum force and the ultimate displacement of the infill panel with opening are found to be smaller than those values of the solid panel in the case of Dolsek and Fajfar constitutive law. However, the infill wall opening ratio does not affect these displacements. On the other hand, the constitutive displacements of the other two models do not change according to the infill wall opening ratio and the opening position.

In Figure 6, the F–D relationships obtained for the opening position upon the diagonal, which is found to be the most influential opening position, using the constitutive parameters of Table 2 is plotted.

(a) Panagiotakos and Fardis   *(b) Dolsek and Fajfar*   *(c) Tsai and Huang*
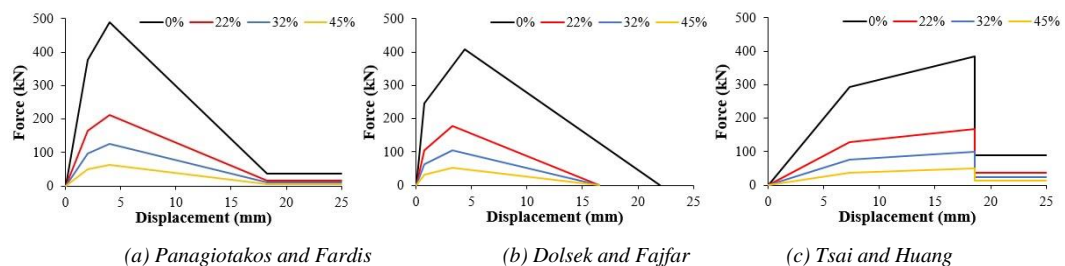
Figure 6. F–D relationships for the opening position upon the diagonal strut.

5. CONCLUSIONS

The results of the study demonstrate that the stiffness and strength values of the constitutive relationships decrease as the opening ratio increases and the position of the opening has a substantial influence on those values. However, the displacements are not affected by the infill wall opening ratio and the opening position expect the displacement corresponding to the strength of the infill in the case of the constitutive law proposed by Dolsek and Fajfar. A relatively large displacement at the cracking point of the infill wall is obtained in the case of the Tsai and Huang constitutive law, while the cracking displacements of the other two models show quite close agreement. Although the constitutive law of Dolsek and Fajfar yields relatively smaller ultimate displacement, the ultimate displacements of the considered models agree quite well. Openings upon the

diagonal are found to be more influential on the constitutive parameters of the considered F–D relationships of the compressive equivalent diagonal strut.

Considering the complexity of adopting a simple yet realistic constitutive law for masonry infill walls, it can be concluded that the agreement between the characteristic parameters of the different constitutive models is quite reasonable.

REFERENCES

[1]. K. M. Mosalam, R. N. White, and P. Gergely, "Static response of infilled frames usıng quasi-static experimentation," *Journal of Structural Engineering*, vol. 123(11), pp. 1462–1469, 1997.
[2]. H. B. Kaushik, D. C. Rai, and S. K. Jain, "Stress-strain characteristics of clay brick masonry under uniaxial compression," *Journal of Materials in Civil Engineering*, vol. 19(9), pp. 728–739, 2007.
[3]. D. J. Kakaletsis, and C. G. Karayannis, "Experimental investigation of infilled reinforced concrete frames with opening," *ACI Structural Journal*, vol. 106(2), pp. 132–141, 2009.
[4]. P. G. Asteris, D. J. Kakaletsis, C. Z. Chrysostomou, and E. E. Smyrou, "Failure modes of in-filled frames," *Electronic Journal of Structural Engineering*, vol. 11(1), pp. 11–20, 2011.
[5]. S. M. M. Emami, and M. Mohammadi, "Influence of vertical load on in-plane behavior of masonry infilled steel frames," *Earthquakes and Structures*, vol. 11(4), pp. 609-627, 2016.
[6]. M. Bolhassani, A. A. Hamid, C. Johnson, and A. E. Schultz, "Shear strength expression for partially grouted masonry walls," *Engineering Structures*, vol. 127, pp. 475-494, 2016.
[7]. M. Dolsek, and P. Fajfar, "Mathematical modelling of an infilled RC frame structure based on the results of pseudo-dynamic tests," *Earthquake Engineering and Structural Dynamics*, vol. 31(6), pp. 1215–1230, 2002.
[8]. G. Mondal, and S. K. Jain, "Lateral stiffness of masonry infilled reinforced concrete (RC) frames with central opening," *Earthquake Spectra*, vol. 24(3), pp. 701–723, 2008.
[9]. E. Smyrou, C. Blandon, S. Antoniou, R. Pinho, and F. Crisafulli, "Implementation and verification of a masonry panel model for nonlinear dynamic analysis of infilled RC frames," *Bulletin of Earthquake Engineering*, vol. 9(5), pp. 1519–1534, 2011.
[10]. A. Fiore, F. Porco, D. Raffaele, and G. Uva,. "About the influence of the infill panels over the collapse mechanisms actived under pushover analyses: Two case studies," *Soil Dynamics and Earthquake Engineering*, vol. 39, pp. 11–22, 2012.
[11]. E. Martinelli, C. Lima, and G. D. Stefano, "A simplified procedure for nonlinear static analysis of masonry infilled RC frames," *Engineering Structures*, vol. 101, pp. 591–608, 2015.
[12]. P. G. Asteris, C. C. Repapis, A. K. Tsaris, F. D. Trapani, and L. Cavaleri, "Parameters affecting the fundamental period of infilled RC frame structures," *Earthquakes and Structures*, vol. 9(5), pp. 999–1028, 2015.
[13]. O. Ozturkoglu, T. Ucar, and Y. Yesilce, "Effect of masonry infill walls with openings on nonlinear response of reinforced concrete frames," *Earthquakes and Structures*, vol. 12(3), pp. 333–347, 2017.
[14]. G. Uva, D. Raffaele, F. Porco, and A. Fiore, "On the role of equivalent strut models in the seismic assessment of infilled RC buildings," *Engineering Structures*, vol. 42, pp. 83–94, 2012.
[15]. A. Madan, A. M. Reinborn, J. B. Mander, and R. E. Valles, "Modeling of masonry infill panels for structural analysis," *Journal of Structural Engineering*, vol. 123(10), pp. 1295–1307, 1997.
[16]. P. Ricci, G. M. Verderame, and G. Manfredi, "Analytical investigation of elastic period of infilled RC MRF buildings," *Engineering Structures*, vol. 33(2), pp. 308–319, 2011.
[17]. G. Uva, F. Porco, and A. Fiore, "Appraisal of masonry infill walls effect in the seismic response of RC framed buildings: A case study," *Engineering Structures*, vol. 34, pp. 514–526, 2012.
[18]. M. Ercolino, P. Ricci, G. Magliulo, and G.M Verderame, "Influence of infill panels on an irregular RC building designed according to seismic code," *Earthquakes and Structures*, vol. 10(2), pp. 261–291, 2016.
[19]. S. H. Bertoldi, L. D. Decanini, and C. Gavarini, "Telai tamponati soggetti ad azioni sismiche, un modello semplificato: confronto sperimentale e numeric," in *Proc. Atti del 6° Convegno Nazionale L'ingegneria Sismica in Italia*, Perugia, Italy, 1993.
[20]. T. B. Panagiotakos, and M. N. Fardis, "Proposed nonlinear strut models for infill panels," University of Patras, Greece, 1st Year Progress Report of HCM-PREC8 Project, 1994.
[21]. K. B. Hanoglu, "Fiber reinforced plastic overlay retrofit of hollow clay tile masonry infilled reinforced concrete frames," PhD Thesis, Bogazici University, Istanbul, Turkey, 2002.
[22]. M. Dolsek, and P. Fajfar, "The effect of masonry infills on the seismic response of a four-storey reinforced concrete frame-a deterministic assessment," *Engineering Structures*, vol. 30(7), pp. 1991–2001, 2008.
[23]. H. Rodrigues, H. Varum, and A. Costa, "Simplified macro-model for infill masonry panels," *Journal of Earthquake Engineering*, vol. 14(3), pp. 390-416, 2010.
[24]. M. H. Tsai, and T. C. Huang, "Numerical investigation on the progressive collapse resistance of an RC building with brick infills under column loss," *World Academy of Science, Engineering and Technology*, vol. 58, pp. 946–953, 2011.
[25]. *SAP2000 Integrated Structural Analysis and Design Software, Ver.16.0.0*, Computer and Structures Inc., USA, 2016.
[26]. *Prestandard and Commentary for the Seismic Rehabilitation of Buildings (FEMA 356)*, Federal Emergency Management Agency, Washington, D.C., 2000.

COAL DUST EXPLOSIONS IN MINING – CAUSES, FORMATIONS AND PRECAUTIONS TO BE TAKEN

Ozer Oren[1], Cem Sensogut[2]

Abstract

There are taking place many work related accidents each year resulting mostly and unfortunately in fatalities due to mining which can be listed as one of the riskiest sector in the world. Coal dust explosion resembles itself as one of the most serious problems encountered in mining. The most catastrophic and deadly mining accident recorded so far in the world occurred in China in 1942 due to gas and coal dust explosions leaving behind a total death of 1549 miners. Additionally, mining accidents took place in Zonguldak which is the only bituminous coal district were mostly caused by the coal dust and methane explosions during the course of mining history in Turkey. In the present work, the causes and the mechanism of coal dust explosions will be given in detail. In addition, the minimization of risk factors or the precautions to tackle the problem of coal dust explosions will be explained in the light of previous works.

Keywords: *Coal, Coal Mining, Coal Dust Explosions, Precautions*

1. INTRODUCTION

From the beginning of mankind to the day-to-day, minerals have played a key role in the vital continuity of life, along with the necessity for food and shelter. Increasing demand for advancing technology and a more comfortable life has led to the use of minerals on many industrial sites and in particular the raw materials of today's energy tools. Energy, as one of the most important inputs for essential functions in society, industrial, residential, transportation and information processing technologies are emerging as an indispensable element in the sub-sectors. Today, energy actors that are consumed on the world make up the headings such as oil, natural gas, coal, nuclear, hydroelectric and solar energy. In other words, it is possible to say that the coal has a significant share among these instruments and that it will become even more important in the near future. When the global energy consumption rates of 2015 are examined (Figure 1); it is seen that the coal is the most critical energy source after petroleum with a percentage of %29. When it is looked at the situation in the scale of Turkey; according to the data of 2014, coal received second order with %29.2 after natural gas (Figure 2) [1].

The production of coal which has such an important place in the world energy supply, is now achieved in deeper seams. Along with the increased depth, the pressure on the coal seams and the temperature values in the working area are also increasing. In addition, as a result of widespread mechanized production in the field, the coal particle size is also seriously decreasing. Due to such factors, the occurrence of occupational accidents, especially gas and coal explosions, seems likely in the future. Because of the mentioned hazards, it is of great importance to know the mechanism of coal dust explosions and to formulate immediate precautions against dust explosions by the mine executive people.

[1] *Dumlupinar University, Department of Mining Engineering, 43270, Kütahya, Turkey, ozer.oren@dpu.edu.tr*

[2] *Corresponding author, Dumlupinar University, Department of Mining Engineering, 43270, Kütahya, Turkey, cem.sensogut@dpu.edu.tr*
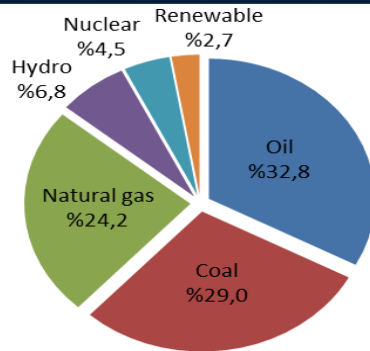
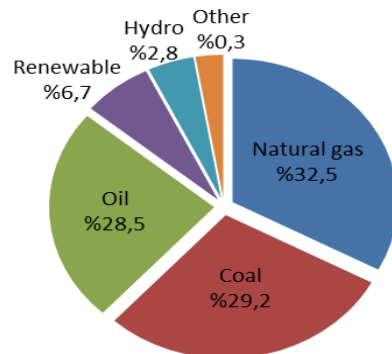*Figure 1. Global primary energy consumption rates in 2015*

Figure 2. Primary energy consumption rates in Turkey for the year 2014

2. COAL DUST AND ITS FORMATION

As a result of the activities carried out during the production in the mining sector, serious amount of dust may occur. These dusts can cause critical health problems, especially in coal mines, as well as in mine workers' respiratory tracts. In general; the main sources of dust problem in mine enterprises are as follows [2]:

- Drilling works,
- Blasting works,
- Removal of loose material after blasting,
- Works carried out by shearers,
- Crushing works,
- Friction of drums,
- Loading or unloading works,
- Backfilling of excavated spaces (especially pneumatic packing),
- Roof collapsing of old workings,
- Use of stone dust to prevent the spread of explosions and to take measures against coal dust explosion,
- Disruption of face or pillar break-up due to high overburden pressure,
- Extension of the roadway section,
- Supporting works,
- Hauling works.

The dusts resulting from the activities mentioned above are collected on the surfaces of the roadways and the supporting elements. A vortex occurring due to the effect of an inappropriate airflow can cause coal dust to explode. Factors affecting dust formation in mines can be listed as follows [3];

- Properties of the mineral extracted,
- Condition of the mineral strata (more dust is produced in the production of vertical seams than in others),
- Production method,
- Loosening technique used during the production (by hand, pressurized water, pressurized gas or blasting),
- Loading or unloading method,
- Hauling system.

3. COAL DUST EXPLOSION AND FACTORS AFFECTING EXPLOSION

There is an ambiguity about the term of "coal dust". In fact, the question is that how finely coal must be called as dust. Some researchers use the distinction of the point whether it can be carried to considerable distances by air flow movements. On the other hand, coal that will pass under 149 µm is frequently accepted as representing mine dust [4]. The amount of coal dust depends both on the physical characteristics of the coal, as well as on the structural and geological features of the seam [5]. Dust can be found at high amounts on the surfaces of the roadways. Although these dusts are of a flammable nature, they do not have sufficient properties for dust explosions initially. The normal combustion triangle turns into a mechanism called the pentagon when the dust is present in the environment (Figure 3) [6].
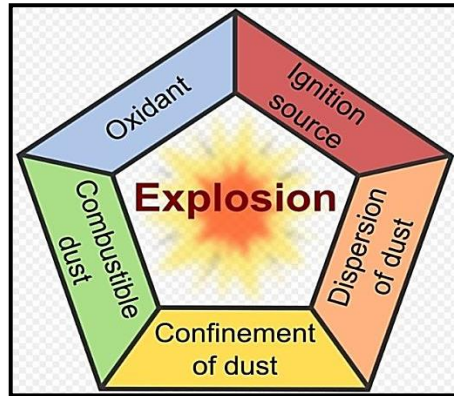

Figure 3. Dust explosion pentagon

As a general consensus, in order for a coal dust explosion to take place, the dust must be able to suspend in the air and react with an igniting element. In underground conditions, the two most important circumstances for this special requirement are methane explosions and drilling and blasting operations. The high temperature and expanding gases formed in the explosions remove the dust located on the surfaces by the effect of the waves. The cloud of dust that has become suspended in the air can be ignited as a result of the combustion of methane. In the same way, drilling and blasting operations for underground production also cause collapsed coal dust to vortex in the air. If the explosive element used does not have the necessary safety standards, it can allow the dust to ignite [7].

The coal dust explosions show a slow progression from 60 to 100 m from the beginning of the ignition point. The intensity, speed, and dynamic pressure of explosions continue to increase, depending on the distance travelled from the explosion source. While the weakest explosion has a flame speed of 30 m/s and a dynamic pressure of 1 Kpa, in severe explosions these values can reach up to 1000 m/s and up to 1700 KPa. The flame speed, corresponding to the full explosion of coal dust, theoretically increases to 2000 m/s, with the observed flame velocities reaching up to 200 m/s. The development of the coal dust explosion is shown in Figure 4. [8].
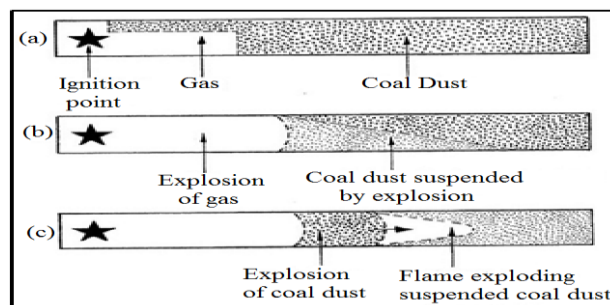
Figure 4. Development of Coal dust explosion.

Explosion of coal dusts and the severity of explosion define some factors such as the chemical content of the dust, particle size distribution, concentration, and the presence of an explosive gas, distribution of the coal dust in the working area, ignition source and environmental conditions [9]. Along with the effect of more than one factor on the explosion of coal dust, these factors can be classified under two headings as internal and external factors [5].

Table 1. Internal and external factors affecting coal dust explosion

Internal Factors	External Factors
Volatile matter content	Dust distribution
Coal dust particle size	Turbulence
Coal dust concentration	Ignition source
Moisture content	O_2 gas presence
CH$_4$ gas presence	Temperature
	Pressure

All the factors given in Table 1 affect the coal dust explosions at different levels. As the particle size of the dust becomes smaller, the surface area in contact with the air increases and the risk of ignition also increases. It is accepted that coal with a high volatile content is more liable to coal dust explosion. The increase in moisture reduces the risk of coal dust explosion. In addition, the presence of any gas that can be found even in small quantities in the air can cause dust explosion as well [10].

4. PREVENTION OF COAL DUST EXPLOSIONS

Different methods and applications have been used for years in the name of coal mining to prevent the explosion of coal dust causing many mortal and injured accidents. Basically, when examined, the basis of these methods is to prevent the accumulation of dust or to reduce the accumulated dust concentration below a certain threshold value.

The actions to be taken to prevent dust explosions may be explained with the following stages [7]:

• Preventing dust formation, accumulation and mixing with the air,
• Preventing the dust from flaming,
• Preventing the development of dust explosion,
• Stopping the dust explosion from jumping to different parts of the mine.

The whole of the measures mentioned under these main headings is tried to be passed on with some specific applications in itself. Generally, in order to prevent the formation of dust, water barrier operations in the underground mine contribute to the suppression of the dust in a large area. However, continuously water usage is not an efficient method due to the fact that this process increases the temperature of the mine air, causes over barrier costs and causes various diseases [9]. Adding stone dust to the coal dust in addition to the water barriers is also a method used to prevent the flaming of the precipitated coal dust. The main purpose of this process is to reduce the explosive level of the coal dust by adding different kinds of materials into the accumulated dust. While some stone dusts such as limestone, dolomite, gypsum, clay stone and anhydrite are used for this aim, they may cause some problems especially as they easily absorb moisture. Therefore, olein, stearin and aged acids, such as tar and resin oil additives are added to the stone dust mixtures to avoid this situation [9, 11].

Injecting an inert gas into the region of the coal dust is also effective in reducing the explosion property. It is stated that nitrogen, oxygen and carbon dioxide gases can be used as inert gas [5].

When the cases of coal dust explosion in the past periods are examined, it is seen that most of them occur after the explosion of the methane gas and air mixture. Therefore, all the precautions to be taken in the context of the methane explosions indirectly are a measure for the coal dust explosion. In particular, it is important to select an optimal level of ventilation plan in order to ensure that the dust does not reach the flammability limits.

If the explosion cannot be prevented in spite of all the measures taken, the only thing to do is to minimize the impact level of the explosion. For this reason, stone dust and water barriers are used for the purpose of preventing the explosion from spreading to other locations of the mine. The working principle of these two systems is as simple as that the containers made of materials such as plastic or pvc filled with stone dust or water are rolled over by the effect of pressure wave in front of the explosion flame, to extinguish the flame and to stop the explosion [11]. Previous experiences have shown that it is optimal for barriers to be at a distance of 100 m from the working face of the mine. It is also stated that while the distance of 200 m is expressed as a limit value, a barrier at a distance of 40 m carries risk [2]. Figures 5 and 6 show stone dust and water barriers in general [8].
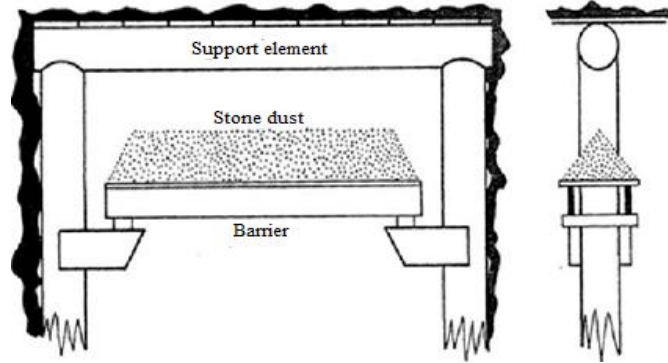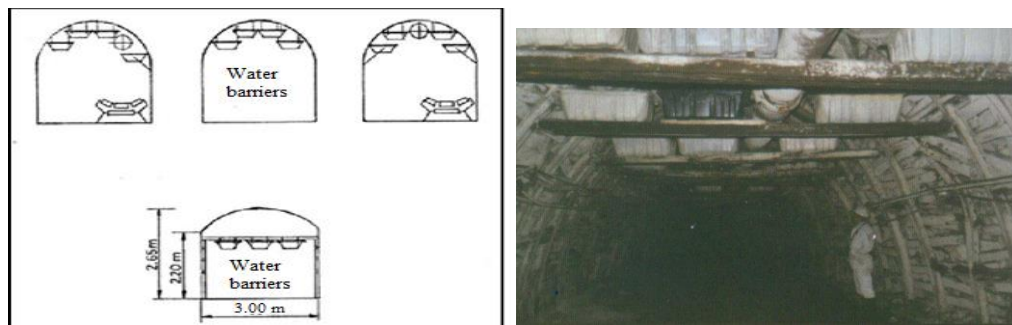
Figure 5. Stone dust barriers.

Figure 6. Application of water barriers.

3. RESULTS

Parallel to the growing population on Earth, it is a doubtless reality that the energy demand will rise to higher levels. Depending on the recent technological developments, it is seen that different alternative energy sources are being used. However, due to lack of infrastructure, higher initial investment costs and lower energy efficiency, the desired capacities are still not reached. Nevertheless, coal, an indispensable raw material for human being for centuries, continues to be popular due to the experience and knowledge of the past. In order to be able to overcome the painful disasters that both exist in Turkey and in different regions of the world, coal-related production policies should be based on occupational health and safety issues. Particularly, it is very important to take the necessary precautions against all kinds of risks that may arise and to be evaluated separately for different processes such as production, transportation and ventilation starting from the project phase of the mine, especially in the initial stage of the explosion of methane gas and coal dust. In addition, recent technological developments should be followed carefully and it will be useful to form necessary consciousness in order to increase the usage of stone dust or water barriers activated through electronic sensors and detectors.

REFERENCES

[1].   Turkish Petroleum, Crude Oil and Natural Gas Report, May 2016.

[2].   Ergün, A.R., Gas and Dust Explosions in Underground Mines and Precautions, Thesis for Occupational Health and Safety Experts, 2007.

[3].   Oztürk, M., Investigation of Dust Problems Occurring During the Coal Production in Gokler Lignite District, MSc Thesis, Dumlupinar University, 2012.

[4].   Rice, G.S., Frazer, J.C.W., Larsen, A., Haas, F., Scholz, C., The Exposibility of Coal Dust, Department of the Interior United States Geological Survey, Bulletin 425, 1910, p.183.

[5].   Yıldırım, O.S., Sarac, S., Determination of Explosibility Characteristics of Coal Dust and 20 lt Explosion Chamber, 10th Turkish Coal Congress, pp355-364, May 1996.

[6].   Sensogüt, C., Assessment of the Explosibility of Industrial Dusts and Wastes in the Light of Occupational Health and Safety, Occupational Health and Safety Symposium in Mines, pp 345-354, December 2015.

[7].   Didari, V., Coal Dust Explosion, Journal of Turkish Mining Engineers Chamber, 24/4, December 1985.

[8].   Ediz İ. G. & Yuvka S., Lecture Notes of Mine Ventilation, Dumlupinar University, Mining Engineering Department, Kütahya 2011.

[9]. Güyagüler, T., Komür Tozu Patlamalarında Tas Tozu Barajları, Türkiye 4. Komür Kongresi, Zonguldak 1984.

[10]. Üstünkol, S., G,yagüler, T., Ocak Havasının Etüdü, Gaz ve Komür Tozu Patlamaları, Ani Metan Püskürmeleri, Türkiye Madencilik Bilimsel ve Teknik 5. Kongresi, Subat 1977.

[11]. Didari V., Komür Tozu Patlamalarına Karsı Onlemler, Madencilik, 25/1, Mart 1986.

UNDERGROUND COAL MINING IN TURKEY – WESTERN LIGNITE CORPORATION CASE

Cem Sensogut[1], Ozer Oren[2]

Abstract

The main target of coal mining is to exploit the coal reserves from the depth of underground economically. The coal, which is the primary input for many sectors due to possessing energy in its form, has been the important area of interest for positive science for centuries. The coal reserves, which have been extracted since the historical ages, maintain its presence nowadays in the depth of ground where mostly underground mining can only be practised. This current state is unfortunately valid both for Turkey and for many countries in the entire world.

In the present work, brief information about the coal reserves found in the world and particularly in Turkey together with the underground coal mining activities was given. Additionally a specific enlightenment was made for the Western Lignite Corporation (WLC) which is a subsidiary of Turkish Coal Board.

Keywords: *Coal, Coal Mining, Underground Coal Mining*

1. INTRODUCTION

The growing demand of the people in the world in parallel with the acceleration in their population for the better living standards bring up the increase in the necessity of basic goods in our life. Therefore, the request to the minerals which are the main articles of daily used materials increased and will continue to increase with the same ratio. Many minerals especially coal gained more importance with the commencing of its usage in steam ships and trains after the industrial revolution in 18. Century. The coal primarily used for heating purposes has become an inseparable part of the industry for years. Coal mining begun with exploiting the coal beds near the surface in small scales at 2. Century (AD) [1] has now become possible to produce coal from very deep seams by the help of recent improvements occurred in technology.

Coal beds near surface have now reached the point of exhaustion in Turkey as well as in the world. Therefore, the coal is nowadays produced by the underground activities in many countries. This situation is generally similar in Turkey.

2. COAL IN THE WORLD

2.1. Coal Reserves in the World

World Energy Council's reports for the year 2013 [2], [3] shows that the total coal reserves of the world in 2011 were 892 Bt. The most wide-spread fossil fuel in the world is coal and it exists more than 80 countries The territorial dispersion of these resources can be seen in Figure 1 [2]. Additionally, 403 Bt of these resources are anthracite and bituminous coal while 288 Bt and 201 Bt are sub-bituminous coal and lignite respectively. While Figure 2 illustrates the territorial distribution of world coal production between the years 1971 and 2015, Figure 3 shows the regional shares of world coal production for the years 1973 and 2015 [4].

---

[1] Corresponding author: Dumlupinar University, Department of Mining Engineering, 43270, Kütahya, Turkey. cem.sensogut@dpu.edu.tr

[2] Dumlupinar University, Department of Mining Engineering, 43270, Kütahya, Turkey, ozer.oren@dpu.edu.tr
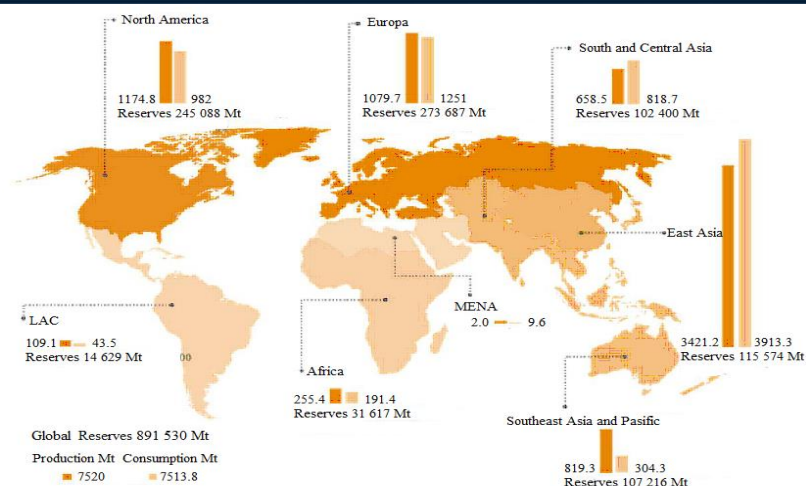
Figure 1. Territorial Distribution of World Coal Resources
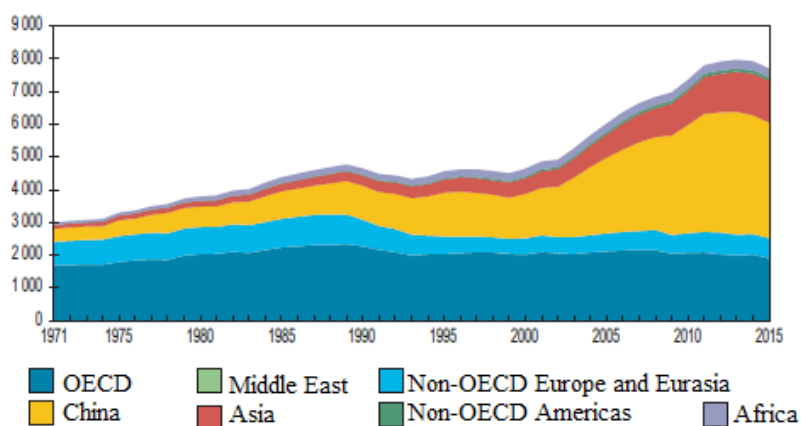
Figure 2. Territorial Distribution of World Coal Production between 1971 and 2015
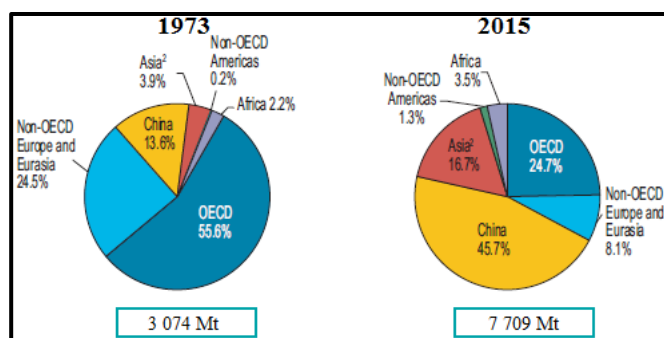
Figure 3. Regional Shares of World Coal Production for the Years 1973 and 2015

2.2. World Coal Production

The year 2015 was recorded as the most declined year with a value of 3,6% for the world coal production [5]. In addition, the top 12 countries with the most coal production rate for the years 2013 to 2015 in the world are given in Table 1. The People's Republic of China takes place as the first in the list with a production amount of 3538 Mt.

Table 1. The First 12 Countries in the World's Coal Production for the years 2013 to 2015.

Country	Coal Production (million tons)		
	2013	2014	2015
People's Republic of China	3749	3651	3538
United States of America	904	916	820
India	610	668	764
Australia	459	491	471
Indonesia	488	471	387
Federation of Russia	328	335	349
South Africa	256	253	248
Germany	191	187	186
Poland	143	137	136
Kazakhstan	120	115	107
Colombia	85	89	86
Canada	69	69	62

2.3. World Coal Consumption

The highest 12 countries with the most coal consumption rate in the world for the years 2013 to 2015 are listed in Table 2 [5]. For the last two years (2014-2015), a consecutive decrease was experienced in the People's Republic of China.

Table 2. The First 12 Countries in the World's Coal Consumption for the years 2013 to 2015.

Country	Coal Consumption (million tons)		
	2013	2014	2015
People's Republic of China	3992	3876	3732
India	808	914	990
United States of America	837	835	730
Germany	245	233	232
Federation of Russia	207	199	207
Japan	190	191	190
South Africa	191	187	179
Poland	137	130	131
South Korea	126	130	130
Australia	122	116	118
Kazakhstan	90	93	87
Turkey	83	94	78

3. COAL IN TURKEY

In spite of having extremely low natural gas and oil sources, Turkey has almost doubled its coal reserves by the exploration works in order to minimize external dependency since 2004. However, the coal production rate in Turkey has been dropping while the tendency for the importation of coal has been increasing since the year 2007 [6]. The increase in the energy demand in Turkey between the years 1990 and 2012 became 127%. On the contrary, only 30% of the energy consumption was met by the coal fired power stations. 68% of the coal consumed in Turkey is utilized in power stations while 16,8%, 9,7% and the remaining part are used in industry, agriculture and heating purposes respectively.

3.1. Coal Resources

The latest data proves that Turkey has almost 1,3 Bt of bituminous coal (Table 3) and 14,2 Bt lignite reserves (Table 4) [6]-[9] . These amount of coal form 1,7% of proven and operable world's coal reserves. Additionally, Turkey comes as the 20th in the world's list with 7,1% lignite sources.

Table 3. Coal Reserves of Subsidiaries of Turkish Bituminous Coal Board (May 2015)

Corporation	Total Reserves (tons)
Armutcuk	32.381.296
Kozlu	156.008.103
Uzulmez	303.668.492
Karadon	410.215.535
Amasra	406.255.377
Total	1.308.528.803

Table 4. Lignite Reserves of Turkish Enterprises (end of 2014)

Establishments	Total Reserves (tons)
Electricity Production Inc. of Turkey	7.585.327.000
Turkish Coal Board	3.665.043.000
Mineral Research & Exploration Institute of Turkey	1.213.113.000
Private Sector (After 2013)	1.749.921.000
Total	14.213.404.000

3.2. Coal Production in Turkey

Marketable coal production in Turkey extremely decreased (15,5%) in 2013 in a comparison with the previous year and was realized as 60,4 Mt (57,5 Mt lignite, 2 Mt bituminous coal, 0,9 Mt asphaltite) [3], [10]. In Figure 4, the cities in which coal mining activities take place in Turkey can be seen.

Figure 4. Coal Mining Locations in Turkey

410

3.3. Coal Consumption in Turkey

The total coal consumed in Turkey was 83 Mt in 2013 including the bituminous coal consumption of 28,2 Mt. The reduction compared with the previous year was almost 16,6% [3], [10].

4. UNDERGROUND COAL MINING IN TURKEY

Coal mining activities take place in many locations in Turkey. Almost all bituminous coal resources of Turkey are extracted by means of underground workings. In addition, the most of higher quality lignite reserves have also begun to be exploited from underground collieries recently due to the exhaustion of lignite sources near the surface. A big scale of produced coal is utilized in power stations to generate electricity. There are approximately 180 underground lignite mines in Turkey. Distinctive examples of these workings are situated in districts such as Soma (Manisa), Tuncbilek (Kutahya), Gediz (Kutahya), Cayirhan (Ankara), Dursunbey (Balikesir), Suluova (Amasya), Ermenek (Karaman).

4.1. Western Lignite Corporation (WLC)

More or less 4,6% of Turkish lignite reserves are located in Tuncbilek, Kutahya. 7,5% of annual coal production of Turkey is realized by WLC (a subsidiary of Turkish Coal Board) actively working since 1940 [11]. 80% of the produced coal is met by open pit mining activities while the remaining is provided by Omerler Underground Colliery operating since 1985. There are two coal enrichment plants and three packaging facilities in the district presently. In Figure 5, the location of Omerler Underground Colliery (Tuncbilek) is presented.

Figure 5. Location of WLC

The average thickness and inclination of coal stamp in Omerler underground Colliery are 8 m and 10º respectively. After the coal was exploited in a mechanized way by using coal plough at the faces in the top section between the years 1956 and 1961, the faces were mechanized by the drum shearer seen in Figure 6 until the working problems encountered in the seam were faced. Therefore, the coal was extracted by only classical methods during the years 1985 and 1997. After the year 1997, operations were carried out by means of both classical and mechanized ways. The coal extraction in Omerler underground Colliery has been realized by only mechanized means since 2013. The coal specifications of run-off-mine coal are given in Table 5. In addition, a representative illustration of the coal stamp can be seen in Figure 7. As seen from the figure, the coal is separated into five sections between hanging and foot walls by A, B, C and yellow clay bands.

Table 5. Run-off-mine coal specifications produced at Omerler Underground Colliery

Specifications	Value
Moisture (%)	14-16
Ash (%)	40-42
Volatile Matter (%)	25-30
Fixed Carbon (%)	18-20
Total Sulphur (%)	1,5-2
Lower Calorific Value (Kcal/Kg)	2000-2500
In situ Coal Density (ton/m³)	1,5
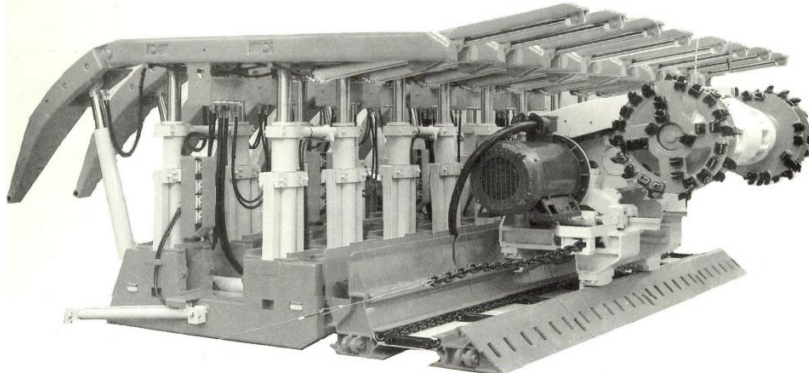
Figure 6. Drum Shearer previously used in Western Lignite Corporation.
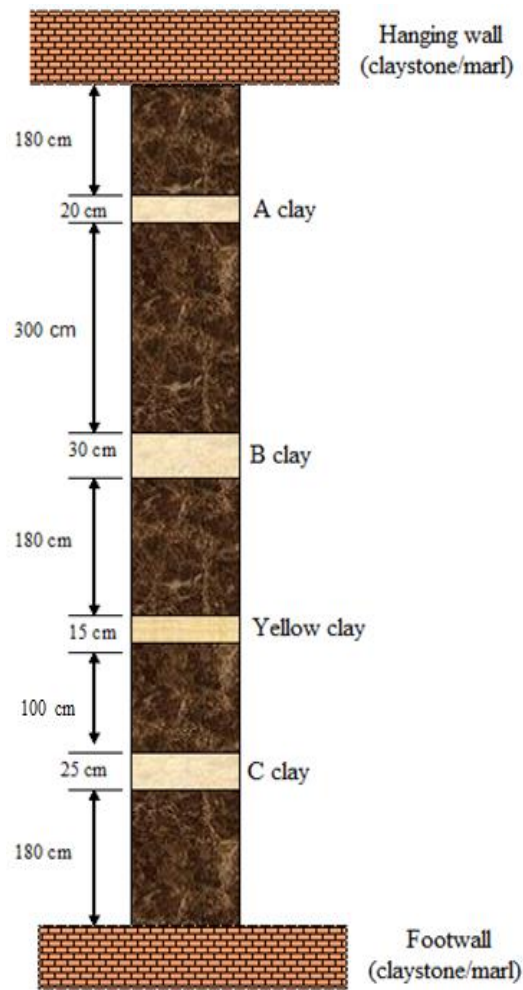
Figure 7. A Representative Illustration of Coal Stamp in Omerler Underground Colliery.

4.2. Mechanized Coal Production at Omerler Underground Colliery

Coal production in Omerler Underground Colliery has been proceeding as fully mechanized at the Panel A (Figure 8) since 2013. The amount of lignite produced in the years 2014 and 2015 at the 5th Working Face of the Panel A were 377.592 and 323.642 tons respectively while 307.904 tons of lignite were extracted at the 2nd Working Face of the same panel. In this system, 3 to 3,5 meters part of the coal is cut from the face by means of double drum shearer and the remaining upper part of the coal is gained through the caved area and hauled by the second armored chain conveyor located under the rear part of the shields (Figure 9).
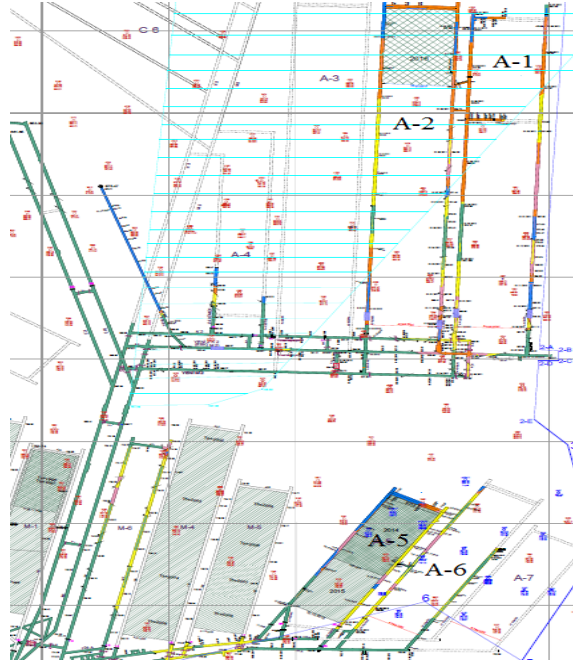
Figure 8. The Panel A at Omerler Underground Colliery.
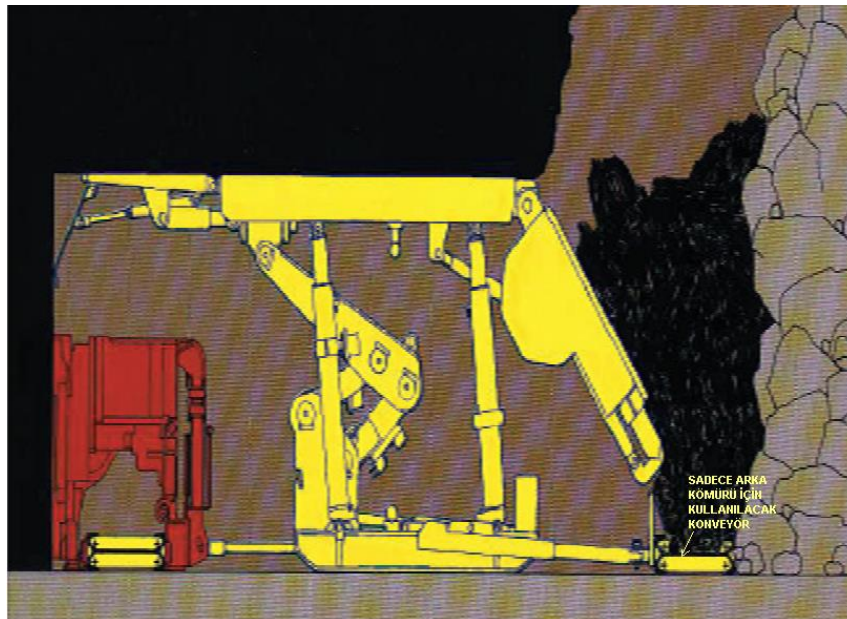
Figure 9. Mechanized Shield System with two Armoured Chain Conveyors

5. RESULTS

Coal production in Turkey and the world seems to keep its importance for a long time in spite of the existence of the alternative energy sources. However, the coal extracted from the sources near the surface for years are diminishing. This situation causes the open pit mining to lose its feasibility. Therefore, underground coal mining has to be carried out economically to meet the demand for now and for the near future in spite of all difficulties encountered in parallel with the improvements occurring in the technology. On the other hand, all precautions from the perspective of occupational health and safety have to be taken and a special care should be given specifically in underground coal mining.

REFERENCES

[1]. Smith, A.V.H. (1997), "Provenance of Coals from Roman Sites in England and Wales", Britannia, Vol. 28, pp297-324.

[2]. World Energy Council, 2013 Survey.

[3]. Coal Sector Report of Turkish Coal Board concerning Lignite (in Turkish), May 2015.

[4]. Keyword Energy Statistics, International Energy Agency 2016, https://www.iea.org/publications/freepublications/publication/KeyWorld2016.pdf

[5]. Global Energy Statistical Yearbook 2016, https://yearbook.enerdata.net/

[6]. Energy Policies of IEA Countries, Turkey 2016 Review

[7]. Turkish Coal Board Activity Report (2014), (in Turkish) 2015 Ankara

[8]. Turkish Hard Coal Board Annual Report (2014), May 2015, http://www.taskomuru.gov.tr

[9]. General Directorate of Mining Affairs of Turkey, Ministry of Energy and Natural Resources of Turkey, MIGEM-*17 March 2015*

[10]. Ministry of Energy and Natural Resources of Turkey, 2015a. *2013* General Energy Balancing Table

[11]. http://www.gli.gov.tr/faaliyet.html.

Implementation of Controller Area Network (CAN) and ZigBee Protocol for Precision Farming Application

İlker Unal[1], Salih Sozer[1], Onder Kabas[1], Mehmet Topakcı[2]

Abstract

In precision agriculture technology, real-time data acquisition that comes from the different sensors and automation is very important to specify the characteristics of the machine, soil and plant. WSN (Wireless Sensor Network) is a major technology that drives the development of precision agriculture. Sensor networks are used to provide integration of the variability such as temporal, spatial and predictive and the determination of the optimal agricultural management options. Recently, wireless sensor networks have been used to communicate between sensors and the central control unit. Wireless sensor networks are preferred due to the advantages such as cost, size, power, flexibility and deliverability, compared to wired sensor networks. However, many sensors that use in agricultural production may not be able to control as completely wireless. In this study, some wireless sensor network technologies were surveyed. In addition, a sample agricultural sensor network model that is created by the integration of the CAN (Controller Area Network) known as ISO 11783 and ZigBee wireless sensor network was designed. Finally, the data flow within designed network model between CAN data frame and the ZigBee data frame was described.

Keywords: *Wireless sensor networks, ZigBee, ISO 11783*

1. INTRODUCTION

Precision agriculture demands intensive field data acquisition, which is usually done as machines perform field operations. However, more frequent data acquisition and interpretation can be the key to understanding productivity variability. Wireless sensor networks are a new technology that can provide processed real-time field data from sensors physically distributed in the field [1]. A wireless sensor network is a collection of sensor nodes organized into a cooperative environment. Each sensor node is capable sensing physical parameters like atmospheric pressure, temperature, humidity, etc. and also capable of processing the sensed data. The nodes communicate wirelessly and often self-organize after being deployed in a working environment [2]. Recent advances about Wireless Sensor Technologies offer vast opportunities for research and development. This is the consequence of the decreasing costs of ownership, the engineering of increasingly smaller sensing devices and the achievements in radio frequency technology and digital circuits [3].

The wired networks provide a secure and faster means of connectivity, but the need of mobility, i.e. anywhere, anytime and anyone access is tilting the network users towards wireless technology [4]. Also, wired networks provide a fixed service, whereas the core value of wireless networks is mobility in all its forms. Wireless networks support communications while in motion. Wireless networks provide ubiquitous coverage, while a wired network only provides service where there is a plug. Wireless networks offer flexibility in choosing and changing service location, while wired networks require cable rerouting to change location [5].

Nowadays, agriculture requires new monitoring and control equipment, embedded and distributed systems for agricultural tractors and implements. These systems are composed of several devices like sensors, actuators, control elements and supervision and control units, all of them intercommunicating in real time [6]. At present, the wired communication between the tractors and the electronic systems on the connected machines is provided by the CANBUS network, which is also known ISO 11783 standard. However, when the developments in agricultural wireless sensor technology are taken into account, these sensors need to be

---

[1] XXX

[2] YYY

adapted to the existing CAN system. The integration of CAN bus and wireless sensing systems is used to solve problems in agricultural automation systems.

In this context, the integrated use of wireless sensor networks with advantages such as cost, size, power, flexibility and mobile communication with the advantages of the existing wired network system with reliability, robustness and fast data transmission will provide important contributions to the automation of agricultural machines. In this paper, information about the ZigBee and CAN was given. In addition, a sample agricultural sensor network model that is created by the integration of the CAN and ZigBee wireless sensor network has been proposed. The goal of this paper is to produce a network processing node for a rapidly, deployable, easily reconfigurable monitoring and controlling solutions for agricultural mechanization systems.

1.1. Wireless Sensor Networks

A WSN is a system comprised of radio frequency (RF) transceivers, sensors, microcontrollers and power sources [7]. Wireless communication in industrial automation is mostly based on standardized technologies, such as the IEEE 802.11 [8] and IEEE 802.15 standard families [9], also designated as Wireless Local Area Networks (WLAN) and Wireless Personal Area Networks (WPAN). In fact, the IEEE 802.11-based standards offer high data rates in the order of tens of Mbit/s and ranges up to tens/hundreds of meters, while the IEEE 802.15-based standards only supports data rates of hundreds of kbit/s to several Mbits/s with ranges from a few meters up to hundreds of meters. However, to provide greater data rate and range, IEEE 802.11 technology consumes a greater energy budget that can limit the benefits obtained by wireless communications [10]. Power consumption is thus a major concern for WSN and we therefore focus on the IEEE 802.15-based standards, and particularly on the IEEE 802.15.1 [11] and IEEE 802.15.4 [12] standard, within the scope of this work. All wireless network models that also describe power consumption, data transmission speed, and cost were given in Figure 1.
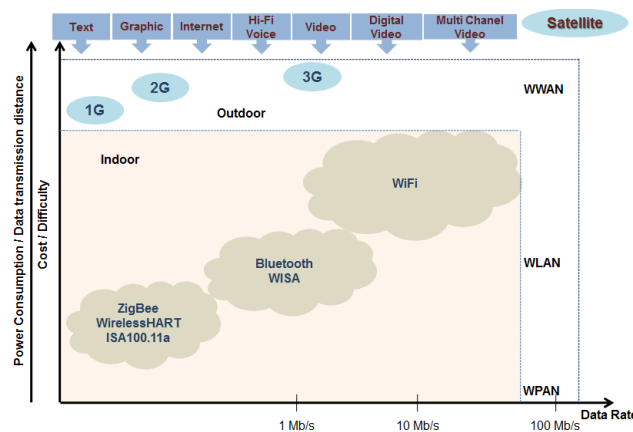

Figure 29. Wireless network models

1.2. ZigBee

ZigBee is a standard that defines a set of communication protocols for low-data-rate short-range wireless networking. The ZigBee Alliance is an association of companies working together to develop standards (and products) for reliable, cost-effective, low-power wireless networking. ZigBee technology will probably be embedded in a wide range of products and applications across consumer, commercial, industrial and government markets worldwide [13]. ZigBee builds upon the IEEE 802.15.4 standard [14] which defines the physical and MAC layers for low cost, low rate personal area networks. ZigBee defines the network layer specifications for star, tree and peer-to-peer network topologies and provides a framework for application programming in the application layer. The IEEE 802.15.4 standard [14] defines the characteristics of the physical and MAC layers for Low-Rate Wireless Personal Area Networks (LR-WPAN). The advantages of an LR-WPAN is ease of installation, reliable data transfer, short-range operation, extremely low cost, and a reasonable battery life, while maintaining a simple and flexible protocol stack.

ZigBee-compliant products operate in unlicensed bands worldwide, including 2.4GHz (global), 902 to 928MHz (Americas), and 868MHz (Europe). Raw data throughput rates of 250Kbps can be achieved at 2.4GHz (16 channels), 40Kbps at 915MHz (10 channels), and 20Kbps at 868MHz (1 channel). The transmission distance is expected to range from 10 to 75m, depending on power output and environmental characteristics. Like Wi-Fi, ZigBee uses direct-sequence spread spectrum in the 2.4GHz band, with offset-

quadrature phase-shift keying modulation. Channel width is 2MHz with 5MHz channel spacing. The 868 and 900MHz bands also use direct-sequence spread spectrum, but with binary-phase-shift keying modulation.

The ZigBee standard is based on the two defined IEEE 802.15.4 device classes including Full-Function Device (FFD) and Reduced-Function Device (RFD) and proposes three different types of devices: ZigBee coordinator, ZigBee router and ZigBee end devices (Figure 2). A unique FFD ZigBee coordinator manages the network by supervising the network formation as well as information storage, and bridges it with others ZigBee networks. The ZigBee routers are complementary to the network manager and also FFD devices with additional routing capabilities, responsible for linking group of devices and supporting multi-hop communications. ZigBee end devices are either RFD or FFD. They transmit the collected sensor or actuator data to a unique FFD including router or coordinator functionality.
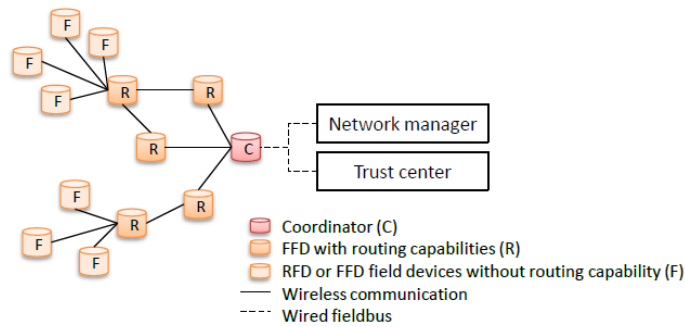

Figure 2. Wireless network models

1.3. CAN

The CAN protocol was developed by the automotive industry, to support the communication of on-board equipment, in trucks and buses. Its good acceptance caused its adoption as a standard by SAE (Society of Automotive Engineers), and, later, by the ISO (International Organization for Standardization). The CAN protocol was designed at first to be used in vehicle applications, so it is very suitable for use in agricultural tractors and implements (now it is also being used in factory automation) [15]. A single cable with two wires is used to link all modules and extensive error detection and correction allows it to operate reliably in the agricultural environment. The bit rate of the CAN protocol can reach 1Mbit/Sec, the maximum bus length being 40m with a minimum of 10cm between nodes. Greater distances can be reached by slowing the bit rate. In a CAN network, there is no need for a master to be polling slave nodes. Instead, any node can choose to talk at any instant, and simultaneous accesses are resolved by message priority. The data carried in each message can be up to 8 bytes long, which is sufficient for most control and data messages [16]. Besides the data field, each message contains an identifier field that indicates the type of information carried in the data, like position, velocity, seed count, etc. This field can also be used to indicate the priority and the source and destination addresses of the nodes involved. However, the standard specifies how the information is exchanged with no regard to the format and type of information. Also, it does not describe the physical characteristics of the cables and connectors. Various protocols were thus created based on CAN, including the proposed ISO 11783, which is about to become a standard. The ISO 11783 proposal specifies a serial network for communication and control of agricultural vehicles (tractors) and its implements. An ISO 11783 network can have several segments, connected by bridges. The tractor segment links devices such as controllers for engine, transmission, brakes and lights of the tractor. One or more segments in the implements link the implement devices one to each other, and to the tractor. The reason for having a separate tractor segment is to protect the tractor electronics. The structure of a typical CAN line was shown in Figure 3.
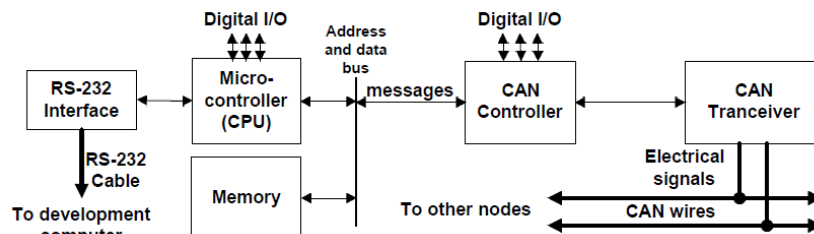

Figure 3. The structure of a typical CAN line

2. PROPOSED AGRICULTURAL SENSOR NETWORK MODEL

In this study, a CAN-ZigBee based agricultural sensor network model was designed for data collection using tractors and variable rate applications. In addition, the data flow between the sensors and actuators used in agriculture and the central computer on the tractor is explained. The sensors and actuators are connected to the ZigBee sensor module. And, collected data from the ZigBee sensor module is sent to ZigBee coordinator via CAN Bus. The ZigBee coordinator sends data which come from the wireless sensor modules to the central computer vice versa. The central computer can also be a central control unit in the tractor bus system or a portable computer with a CAN connection. The proposed agricultural ZigBee coordinator module and the block diagram of the ZigBee sensor module are shown in Figure 4.
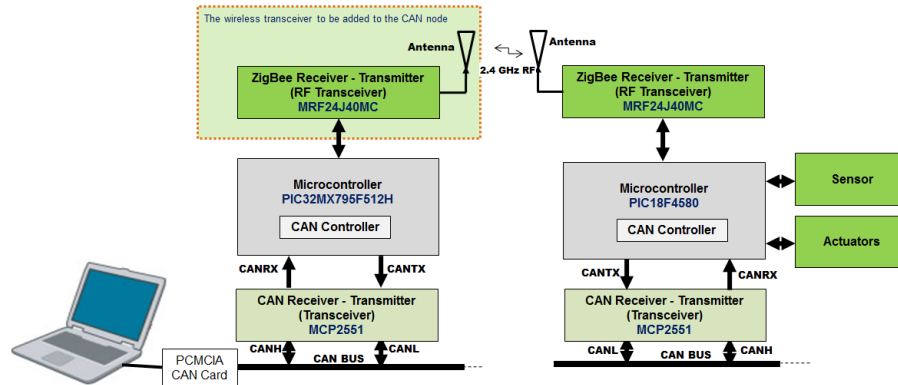

Figure 4. Agricultural ZigBee coordinator and sensor modules

In ZigBee networks, three elements are used as coordinator, router and the end device (sensor) depending on the network topology. If the star topology is to be used in the network system, the router may not be used in the network. The designed agricultural sensor network model is designed by using the star topology. A ZigBee coordinator module with CAN connection must be designed for CAN-ZigBee based agricultural sensor network. The coordinator module is connected to the tractor CANBUS system with cable. Wired and wireless sensors are used in agricultural operations. For this reason, a separate sensor module must be designed for each sensor in the designed system. Designed sensor modules should be formed as an end device. The proposed agricultural sensor network model is shown in Figure 5.
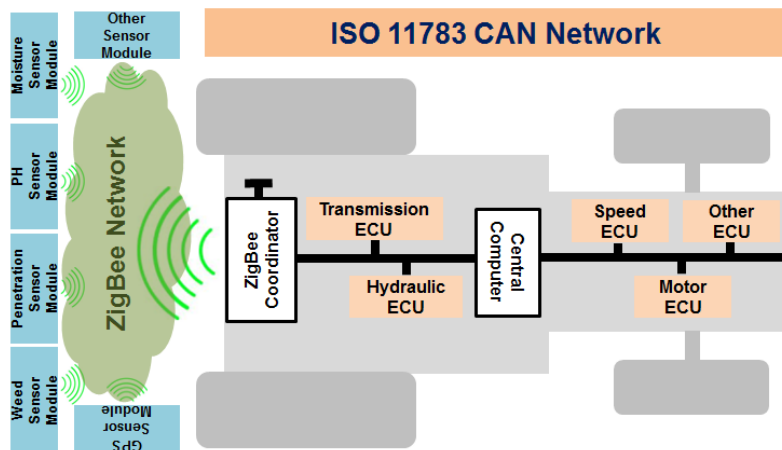
Figure 5. Proposed agricultural sensor network model.

3. PROPOSED CAN-ZIGBEE MESSAGE FRAME

The ZigBee sensor modules send the collected sensor data to the ZigBee coordinator with the ZigBee data packets of IEEE 802.15.4 standard. A standard ZigBee data frame is shown in Figure 6. The size of the data packet is maximum 127 bytes and this value can be decreased according to the status of some variable fields. The most important area in the data packet is the addressing field. In ZigBee networks, 65536 nodes as maximum can be created based on the topology of the installed system. Up to 240 sensor modules can be placed in each node [17]. Each node has a 16bit PAN ID. All devices in a ZigBee network are assigned a single PAN ID. If there is only one node in the installed network, the network number is 0 (0x0000). The destination and source addresses in the data packet describe MAC (Media Access Control) addresses of the

sender and receiver modules. This address is a 48-bit number that allows the modules in the network to recognize each other. The ZigBee network is an address-based communication environment.

1016 Bit (127 Byte)							
16 Bit	8 Bit	16 Bit	0 - 64 Bit	16 Bit	0 - 64 Bit	0 - 816 Bit	16 Bit
FCF	DSN	Destination PAN ID	Destination Address	Source PAN ID	Source Address	Data Field	FCS

Figure 6. ZigBee data frame

The CAN communication protocol is a contention-based serial communication. As an access method, the CAN uses CSMMCR, Carrier Sense Multiple Access with Collision Resolution. The CAN although serial in nature is unlike many serial communication protocols; it contains no information relating to the destination or source addresses. Instead, the message contains an identifier which indicates. The identifier is not only used to identify the message, but also used in the arbitration mechanism. The CAN associates a priority with each message to be sent and uses a special arbitration mechanism to ensure that the highest priority message is the one transmitted. Broadcast to all nodes is inherent in this system and therefore data will be consistent in that either none or all of the nodes will receive the message. In other words, any node can have access to the bus for transmission of messages or any number of the nodes can receive and simultaneously act upon the same message [18]. The data frame contains information to synchronize, to identify, to control and to save the data flow in addition to the user data. The CAN data frame is shown in Figure 7.

128 Bit (16 Byte)						
1 Bit	32 Bit	6 Bit	0 - 64 Bit	16 Bit	2 Bit	7 Bit
SOF	Identifier Field	Control Field	Data Field	CRC	ACK	EOF

Figure 7. CAN data frame

The standard ZigBee and CAN message structures need to be redefined to match each other so that the message traffic within the designed agricultural sensor network can be edited. For this reason, the proposed ZigBee - CAN data packet transmission to the agricultural sensor network is shown in Figure 8.
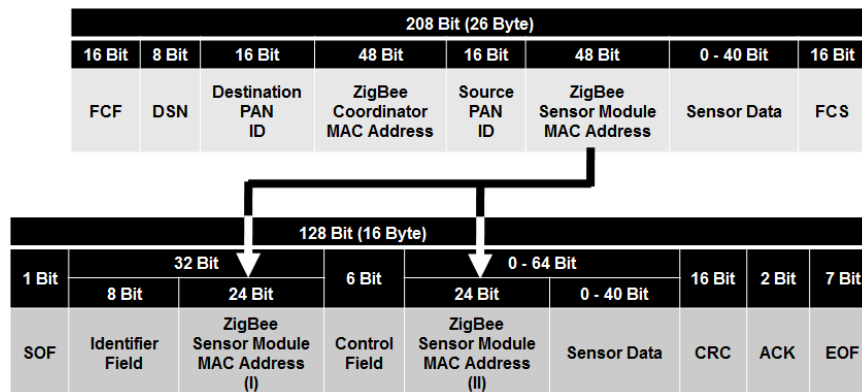
Figure 7. ZigBee-CAN data frame transition

The designed agricultural network model consists of one node according to the "star" topology. For this reason, the target and source PAN ID numbers in the ZigBee message structure must be the same. The purpose of the network model is to send the instantaneous data collected by the sensors to the ZigBee coordinator module. For this reason, the destination address in the standard ZigBee message structure must be the MAC address of the ZigBee coordinator module, and the source address must be the MAC address of the ZigBee sensor module. Sending a message by the sensor module will be sent to the central computer by the coordinator via CAN line. However, the main problem is that the ZigBee message is addressed-based and the CAN message is a message-based. There is no MAC address of the sender or receiver of the CAN message.

To remove this problem, the 48-bit MAC address of the sensor module in the ZigBee message is split into two parts. The first 24 bits in the CAN message are embedded in the last 24 bits of the 29-bit identifier field. The last 24 bits in the CAN message are embedded in the first 24 bits of the 64-bit sensor data field in the CAN message. After all, the sensor data length in the ZigBee message and the sensor data length in the CAN message is 40 bits. For this reason, the sensor module must be designed to send 40 bit sensor data.

4. CONCLUSION

In recently, wireless sensor networks are highly interested, due to reliability, flexibility, cost efficiency and especially low power consumption. This work proposes the implementation of ZigBee and CAN for monitoring and controlling the agricultural sensor parameters. In the agricultural machinery, there is a wired CAN network known as the ISO 11783 standard. Hence, the agricultural sensor networks must not completely redesign wirelessly. It must be integrated in the existing wired system. For this reason, a CAN-based ZigBee agricultural sensor network model has been proposed. The data traffic in the proposed network model was explained.

REFERENCES

[1]. A. Camilli., C.E. Cugnasca, A.M. Saraiva, A.R. Hirakawa, and P.L.P. Correa. "From Wireless sensor to field mapping: Anatomy of an application for precision agriculture". *Computers and Electronics in Agriculture*, vol. 58, pp. 25–36, 2007.
[2]. S. Attar, and K.N. Sudhakar. "Real-Time Monitoring Of Agricultural Activities Using Wireless Sensor Network". *International Journal of Science and Research (IJSR)*, vol. 4(5), pp. 2843-2846, 2015.
[3]. L. Ruiz-Garcia, L. Lunadei, P. Barreiro, and I. Robla. "A Review of Wireless Sensor Technologies and Applications in Agriculture and Food Industry: State of the Art and Current Trends.". *Sensors*, vol. 9, pp. 4728-4750, 2009.
[4]. R.K. Bansal, V. Gupta, and R. Malhotra. "Performance Analysis of Wired and Wireless LAN Using Soft Computing Techniques- A Review". *Global Journal of Computer Science and Technology*, vol. 10, pp. 67-71, 2010.
[5]. W. Lehr, and J. Chapin. "On the convergence of wired and wireless access network architectures". *Information Economics and Policy*, vol. 22, pp. 33-41, 2010.
[6]. C. Strauss, C.E. Cugnasca, A.M. Saraiva, and A.R. Hirakawa. "Application of the CAN and ISO 11783 protocols to a Planter Monitor," *In: 3th InternationaL Multiconference on Circuits, Systems, communications and Computers-IMACS/IEEE*, 1999, p. 211.
[7]. I. Akyildiz, W. Su, Y. Sankarasubramaniam, and E. Cayirci. "A survey on sensor networks". *IEEE Commun. Mag,* vol. 40, pp. 102–114, 2002.
[8]. IEEE Computer Society. IEEE Standard for Information Technology, Telecommunications and Information Exchange between Systems, Local and Metropolitan Area Networks, Specific Requirements, Part 11: Wireless LAN Medium Access Control (MAC) and Physical Layer (PHY) Specifications, 2007.
[9]. A. Willig, K. Matheus, and A. Wolisz. "Wireless Technology in Industrial Networks". *Proceedings of the IEEE*, vol. 93, pp. 1130–1151, 2005.
[10]. D. Christin, P.S. Mogre, and M. Hollick. "Survey on Wireless Sensor Network Technologies for Industrial Automation: The Security and Quality of Service Perspectives". *Future Internet*, vol. 2, pp. 96-125, 2010.
[11]. IEEE Computer Society. IEEE Standard for Information Technology, Telecommunications and Information Exchange between Systems, Local and Metropolitan Area Networks, Specific Requirements, Part 15.1: Wireless Medium Access Control (MAC) and Physical Layer (PHY) Specifications for Wireless Personal Area Networks (WPANS), 2002.
[12]. IEEE Computer Society. IEEE Standard for Information Technology, Telecommunications and Information Exchange between Systems, Local and Metropolitan Area Networks, Specific Requirements, Part 15.4: Wireless Medium Access Control (MAC) and Physical Layer (PHY) Specifications for Low Rate Wireless Personal Area Networks (LR-WPANs), 2007.
[13]. P. Baronti, P. Pillai, V.W. Chook, S. Chessa, A. Gotta, and Y.F. Hu. "Wireless Sensor Networks: A Survey on the State of the Art and the 802.15.4 and ZigBee Standards". *Computer Communications*, vol. 30, pp. 1655–1695, 2007.
[14]. Institute of Electrical and Electronics Engineers, Inc., IEEE Std. 802.15.4-2003 ''Wireless Medium Access Control (MAC) and Physical Layer (PHY) Specifications for Low Rate Wireless Personal Area Networks (LR-WPANs), New York, IEEE Press. October 1, 2003.
[15]. M.J. Darr, T.S. Stombaugh, J.K. Ward, and M.D. Montross. "Development of a Controller Area Network Based Handheld Data Acquisition System for Identity Preservation." ASAE Paper No. 031103. Annual International Meeting, 2003.
[16]. W. Lawrenz. World-wide Status of CAN- Present and Future. proc. ICC'95 2. *International CAN conference*, 1995, p. 12.
[17]. A. Elahi, and A. Gschwender, A. *ZigBee Wireless Sensor and Control Network*. Upper Saddle River, New Jersey, Prentice Hall, 2009.
[18]. H. Ekiz, A. Kutlu, and M.D. Baba. "Performance Analysis of a CAN / CAN Bridge," *International Conference on Network Protocols (ICNP '96)*, 1996, p. 181.

Investigation of the Criteria Taken into Account in the Selection of Subcontracting Workshop of Apparel Companies

Mahmut Kayar[1], Oyku Ceren Bulur[2]

Abstract

Companies have to develop new methods and techniques to take place, to protect this place and to be able to stand in a competitive environment. Companies have to leave their old habits to survive in these changing expectations and competition area. Previously companies were trying to control all the production process but nowadays they are producing their all or some goods by outsourcing. Outsourcing is making all or a part of production of another company according to main company's priority and principal cause. Outsourcing method is often used in ready to wear sector, like in the all other sectors. Apparel companies take in consideration some factors when deploying business to subcontracting workshops. The most prominent of these factors can be listed as cost, quality and delivery time. In this study; firstly, general information about outsourcing method are explained. After that information which obtains as a result of a survey which was done in apparel companies will be appreciated.

Keywords: *Apparel, outsourcing, subcontracting, multi-criteria decision making*

1. INTRDODUCTION

Outsourcing is a management technique that dates back to old times when handled as a type of flexible production under the title of taking in home job. Generally, it spread during 1970's economic crisis [1].

Lexical meaning of outsourcing is described as the work or the cut that the tailor makes to shape the fabric according to a certain size and model. In the broadest meaning, outsourcing is defined as the manufacturing work that is done in accordance with the wishes and directives of the employer by someone else [2].

Outsourcing according to Halbach's definition; is an agreement between two manufacturing units; with reference to this, one of the parties (subcontract workshop) supplies the products (part or the final product) to the other party (main company) within determined period and conditions [3].

The high labour cost keeps the enterprises in labour intensive apparel industry from making production investments. As a result, apparel companies have to make all or part of the production outside their companies [4].

Companies prefer to gain some of their own functions from an outsource firm to be a better company as an advantage. In addition, some of these functions have high edit value. Another reason of working without source is the fast exchange of design and technology [5].

The most important reason for the decision of outsourcing usage is cost effectiveness [6]. Labour cost is very high in cost of product in apparel sector. Because of this reason, to compete with price is very difficult. As a result of this, outsourcing is a very useful method in apparel companies to lowing costs, being faster and to make better quality products [4].

The reasons of outsource use can be reviewed under the two headings as internal and external factors. One of these two headings "external factors" can be named as global factors and changes that affect all the enterprises in the world. The second reason that directs the enterprises to choose outsourcing practice is

---

[1] *Corresponding author: Marmara University, Department of Textile Engineering, 34722, Kadıköy/İstanbul, Turkey. mkayar@marmara.edu.tr*

[2] *Penti Clothing Trade inc., İstanbul, Turkey, oykucerenbulur@gmail.com*

"internal factors". As a result of internal system changes and its effects, enterprises may prefer outsourcing practice [7].

Please find reasons of outsource benefit application below.

External Factors

- Social Changes
- Technological Changes
- Economic Changes
- Cultural Changes
- Globalization
- Quick Change
- Increase of Competition [7],[8].

Internal Factors

- Increasing Flexibility
- Concentration to Basic Skills (Core Activities)
- Successful Entrepreneurship
- Non-Control Functions
- Process Renewal
- Wide and Flexible Weld Pool
- Redistribution of Resources
- Resource Transfer
- Saving time
- Increasing Productivity
- Tracking Technological Innovations
- Reduce Risks
- Increment Quality
- Reduction
- Cost Reduction
- Capacity Overflow [6], [9] - [13].

Outsourcing is a type of manufacturing of a company's whole or a part of production by another company within the framework of the company that gives the job to the subcontracting manufacturer. There are two types of companies in this production relationship, namely the ordering company and the subcontracting company that is responsible for order fulfilment, and these companies are related to each other with different scopes. [14].

Whereas subcontracting manufacturers are independent production enterprises that manufacture and produce the parts in accordance with the recommendation and working technique of the company that gives the job to the contractor, return the parts to the company and does not sell the company's products to someone else [1].

Especially the companies which have wide product range and produce and sell in high quantities work with many workshops of different characteristics. This, in turn, results in the need of work distribution to the workshops according to a specific system.

When job distribution is made according to multi-criteria decision making methods, each workshop's score is taken as basis according to the factors mentioned in below basis. A scientific path is followed to decide on the basis of the factor scores of each factor and the factor weight. This, in turn allows them to choose the best option or make an objective decision about choosing the good.

Choosing the best alternative is a though job for the decision makers. Decision makers are supposed to choose the most appropriate alternative among the ones that have different goals and sometimes among the alternatives that contradict with each other. Therefore, most of the decision makers apply Multi Criteria Decision Making Methods when they face such problems. "Multi Criteria Decision Making" means choosing the one with highest priority among the others, in other words, brief evaluation, sorting and choosing [15].

There are several factors that are taken into account in job distribution to subcontract workshops. These factors can be listed as follows.

- Quality: refers to the production quality of the sub-contracting workshop.
- Deadline: refers to the performance of the workshop in terms of having accomplished the production within required period of time.
- Price: refers to the workshop's production cost for the work/product that will be produced.

422

- Production Capacity of the Workshop: refers to the daily/monthly/annual production capacity of the sub-contracting workshop.
- Distance from the workshop to the company: refers to the distance from the sub-contracting workshop to the main company.
- Ordonnance – Physical Condition: refers to the tidiness and physical efficiency of the workshop.
- Communication Capability: refer to the communication capability of the workshop authorities and whether the communication related to the production is healthy.
- Technological Equipment: refers to the technological equipment of the machinery the workshop has.
- Business follow-up: refers to the fact whether the workshop follows up the business in accordance with the main company's requirements, production related defects or missing materials or not.
- Financial Situation: refers to the fact whether the workshop has sufficient financial power to carry out the production requested by the main company [16].

Although all the parameters listed above are taken into account for job distribution to subcontract workshops, the weight of each may differ from each other. For some companies, the production capacity of the subcontract workshop is important whereas for another company cost-efficient production or production finish within the deadline is more important. Therefore, evaluating the weight of above parameters and making the job distribution accordingly is essential.

In this study, factors that are taken into account for job distribution to subcontracting workshop in garment industry and the factor weight of each one are investigated.

2. MATERIALS AND METHODS

In this research, a survey is conducted among the first 500 companies in garment industry which are determined each year by Istanbul Chamber of Commerce. Survey results analysed and evaluated with SPSS programme.

In the scope of the research, 15 apparel companies that use outsourcing method were asked about the factors that apparel companies consider when distributing job to subcontracting workshops.

3. RESULTS AND DISCUSSIONS

Table 1 gives the results of the factors that apparel companies consider when distributing job to subcontracting workshops.

Table 1. The factors that apparel companies consider when distributing job to subcontracting workshops.

	Number of companies	
Factors	Yes	No
Quality	15	-
Deadline	15	
Price	15	-
Production Capacity of the workshop	15	-
Distance from the workshop to the	8	7
Ordonnance – Physical Condition	11	4
Communication Capability	8	7
Technological Equipment	8	7
Business Follow-up	10	5
Financial Situation	10	5

As can be seen from above table, all companies consider quality, deadline, price and capacity when distributing the job to the subcontracting workshops. The other factors that are taken into account are ordonnance, business follow-up, financial situation, distance from the workshop to the main company, communication capability and technological equipment respectively.

According to the research results, the weight of each factor for garment enterprises are given in below respectively.

Table 2. Frequency table based on the criteria considered in choosing the subcontractor workshop and their weights (Quality).

Quality	Frequency	Percent	Valid Percent
10 – 19 %	2	13,3	13,3
20 – 29 %	**5**	**33,3**	**33,3**
30 – 39 %	4	26,7	26,7
40 – 49 %	1	6,7	6,7
50 – 60 %	3	20,00	20,00
Total	15	100,0	100,0

Based on these results, it can be said that the weight of the quality criterion considered in the selection of the workshop is 20-29% according to the majority of the enterprises participating in the survey.

Table 3. Frequency table based on the Criteria Considered in Choosing the Subcontractor Workshop and Their Weights (Deadline).

Deadline	Frequency	Percent	Valid Percent
5 – 9 %	3	20,0	20,0
10 – 14 %	3	20,0	20,0
15 – 19 %	2	13,3	13,3
20 – 24 %	**5**	**33,3**	**33,3**
25 – 30 %	2	13,3	13,3
Total	15	100,0	100,0

When Table 3 is examined, it can be said that the weight of the deadline criterion considered in the selection of the workshop is 20-24% according to the majority of the enterprises participating in the survey.

Table 4. Frequency table based on the Criteria Considered in Choosing the Subcontractor Workshop and Their Weights (Price).

Price	Frequency	Percent	Valid Percent
5 – 13 %	4	26,7	26,7
14 – 22 %	**6**	**40,0**	**40,0**
23 – 31 %	3	20,0	20,0
41 – 50 %	2	13,3	13,3
Total	15	100,0	100,0

Based on the answers of this question; it can be said that the weight of the price criterion considered in the selection of the workshop is 14-22% according to the majority of the enterprises participating in the survey.

Table 5. Frequency table based on the Criteria Considered in Choosing the Subcontractor Workshop and Their Weights (Production Capacity of the Workshop).

Production Capacity of the Workshop	Frequency	Percent	Valid Percent
5 – 8 %	5	33,3	33,3
9 – 12 %	**7**	**46,7**	**46,7**
13 – 16 %	1	6,7	6,7
17 – 20 %	1	6,7	6,7
21 – 25 %	1	6,7	6,7
Total	15	100,0	100,0

When Table 5 is examined, it can be said that according to 46,7% of the participating enterprises weight factor of the capacity criterion is between 9-12%.

Table 6. Frequency table based on the Criteria Considered in Choosing the Subcontractor Workshop and Their Weights (Distance from the workshop to the company).

Distance from the workshop to the company	Frequency	Percent	Valid Percent
1 – 2.5 %	2	13,3	25,0
4,2 – 5,7 %	1	6,7	12,5
5,8 – 7,3 %	1	6,7	12,5
7,4 – 9 %	**4**	**26,7**	**50,0**
Total	8	53,3	100,0
Missing System	7	46,7	
Total	15	100,0	

Based on these results, it can be said that according to 50% of the participating enterprises weight factor of the distance criterion is between 7,4-9%.

Table 7. Frequency table based on the Criteria Considered in Choosing the Subcontractor Workshop and Their Weights (Ordonnance – Physical Condition).

Ordonnance – Physical Condition	Frequency	Percent	Valid Percent
3 – 5,3 %	**5**	**33,3**	**45,5**
5,4 – 7,7 %	1	6,7	9,1
7,8 – 10,1 %	4	26,7	36,4
12,6 – 15 %	1	6,7	9,1
Total	11	73,3	100,0
Missing System	4	26,7	
Total	15	100,0	

When Table 7 is examined, it can be said that according to majority of % 45,5 of the participating enterprises weight factor of the ordonnance criterion is between 3-5,3%.

Table 8. Frequency table based on the Criteria Considered in Choosing the Subcontractor Workshop and Their Weights (Communication Capability)

Communication Capability	Frequency	Percent	Valid Percent
1 – 1.9 %	1	6,7	12,5
2 – 2,9 %	1	6,7	12,5
3 – 3,9 %	1	6,7	12,5
5 - 6 %	**5**	**33,3**	**62,5**
Total	8	53,3	100,0
Missing System	7	46,7	
Total	15	100,0	

Based on these results, it can be said that according to majority of % 62,5 of the participating enterprises weight factor of the communication capability criterion is between 5-6%.

Table 9. Frequency table based on the Criteria Considered in Choosing the Subcontractor Workshop and Their Weights (Technological Equipment)

Technological Equipment	Frequency	Percent	Valid Percent
2 – 3,3 %	2	13,3	25,0
3,4 – 4,7 %	**3**	**20**	**37,5**
4,8 – 6,1 %	1	6,7	12,5
6,2 – 7,5 %	1	6,7	12,5
7,6 - 9 %	1	6,7	12,5
Total	8	53,3	100,0
Missing System	7	46,7	
Total	15	100,0	

When Table 9 is examined, it can be said that according to majority of % 37,5 of the participating enterprises weight factor of the technological equipment criterion is between % 3,4-4,7.

Table 10. Frequency table based on the Criteria Considered in Choosing the Subcontractor Workshop and Their Weights (Business Follow-up)

Business Follow-up	Frequency	Percent	Valid Percent
2 – 3,5 %	1	6,7	10,0
3,6 – 5,1 %	**7**	**46,7**	**70,0**
6,8 – 8,3 %	1	6,7	10,0
8,4 – 10 %	1	6,7	10,0
Total	10	66,7	100,0
Missing System	5	33,3	
Total	15	100,0	

Based on these results, it can be said that according to majority of 70% of the participating enterprises weight factor of the business follow-up criterion is between 3,6-5,1%.

Table 11. Frequency table based on the Criteria Considered in Choosing the Subcontractor Workshop and Their Weights (Financial Situation).

Financial Situation	Frequency	Percent	Valid Percent
3 – 4,7 %	1	6,7	10,0
6,6 – 8,3 %	**7**	**46,7**	**70,0**
8,4 – 10,1 %	1	6,7	10,0
10,2 – 12 %	1	6,7	10,0
Total	10	66,7	100,0
Missing System	5	33,3	
Total	15	100,0	

When Table 11 is examined, it can be said that according to majority of % 70 of the participating enterprises weight factor of the financial situation criterion is between % 6,6-8,3.

The highest factor weights determined by the apparel companies for each factor in the context of the above explanations are summarized in the table below.

Table 12. The factors' weights that apparel companies consider when distributing job to subcontracting workshops.

Factors	Factor weights (%)
Quality	20-29
Deadline	20-24
Price	14-22
Production Capacity of the workshop	9-12
Distance from the workshop to the company	7,4-9
Financial situation	6,6-8,3
Communication Capability	5-6
Ordonnance – Physical Condition	3-5,3
Business Follow-up	3,6-5,1
Technological equipment	3,4-4,7

As can be seen from Table 12, the factors of quality, deadline, price and production capacity taken into consideration by all enterprises have the highest factor weights.

4. CONCLUSION

When the research results are examined, it is seen that quality, deadline and price come first in the criteria that garment enterprises consider when distributing work to sub-contracting workshops. Again, according to this research, factors have different factor weights, hence is seen that the quality, deadline and price skills of the sub-contracting workshop are more important when job distribution is done. Especially for enterprises that work with many workshops, it is important to determine the factors and factor weights that are important for them in job distribution to the workshops in order to benefit in the best way from the contract manufacturing technique.

This will ensure that decisions are made more accurately in job distribution. The use of multi-criteria decision-making methods in job distribution will also be a driving force for contract workshops to develop themselves. Thus, the main company and the sub-contracting workshop will gain mutual benefits.

ACKNOWLEDGMENT

REFERENCES

[1] M. Kayar. "Fason Uretim Yontemi ve Fason Üretim Yontemi Uygulamalarını Ortaya Cıkaran Nedenler*"*, in *Proc. UMES-07, Ulusal Teknik Egitim Mühendislik ve Egitim Bilimleri Genc Arastırmacılar Sempozyumu*, 2007, vol. 1. p. 466-469.
[2] İktisadi Kalkınma Vakfı; "Milletlerarası Fason İmalatı İle İlgili Mevzuat Ve Sorunlar", *İ.K.V. Yayınları*, vol. 63, 1974.
[3] J. Axel. Halback, *Multinational Enterprises and Subcontracting in the Third World: A Study of Inter- Industrial Linkages*, International Labour Office, 1988.
[4] M. Kayar. "Hazır Giyim İsletmelerinde Fason Organizasyon Departmanının Yeri Onemi ve İslevi," in *Proc. UMES-07, Ulusal Teknik Egitim Mühendislik ve Egitim Bilimleri Genc Arastırmacılar Sempozyumu,* 2007, vol. 1. p. 497-500.
[5] J. B. Quin, *Intelligent Enterprise*, the Free Press, New York: A Division of Simon & Schuster Inc, 1992.
[6] M. C. Lacity and R.A. Hirschheim, *Information System Outsourcing*, New York, USA: John Wiley & Sons, Inc, 1993.
[7] F. Anaral "Cok Kriterli Karar Verme Yontemi ile Yazılım Gelistirme Metodolojisi Gelistirme Secimi", MSc Thesis, İstanbul Technical University, Institute of Pure and Applied Sciences, İstanbul, Turkey, 2012.
[8] N. Yılmaz. "Dıs Kaynak Kullanımı (Outsourcing) ve Hastanelerde Dıs Kaynak Kullanımı", MSc Thesis, Beykent University, Institute of Social Sciences, İstanbul, Turkey, 2013.
[9] O. F. Karayel, "Temel Yetenek Ve Dıs Kaynak Kullanımı, İstanbul Tekstilkent Ornegi, MSc, Sakarya University, Institute of Social Sciences, Sakarya, Turkey, 2006.

[10] M. Ozgün, "Kalite Artırıcı Bir Strateji Olarak Dıs kaynaklardan Yararlanma ve Lojistik Hizmet Saglayıcı Firmalar Üzerine Bir Arastırma", MSc Thesis, Beykent University, Institute of Social Sciences, İstanbul, Turkey, 2006.

[11] A. Kuru, " Entegre Yonetim Sistemlerinde Cok Kriterli Karar Verme Tekniklerinin Kullanımına Yonelik Yaklasımlar ve Uygulamalar", PHd Thesis, Marmara University, Institute of Social Sciences, İstanbul, Turkey, 2011.

[12] S. Kanat, "Hazır Giyim Sektoründe Outsourcıng (Dıs Kaynak Kullanımı) Uygulamaları Ve Isletme Performansına Etkisi" – MSc Thesis, Ege University, Institute of Pure and Applied Sciences, İzmir, Turkey, 2007.

[13] M. Kayar. "An Investigation of the Relation between Using Outsourcing and Capacity Utilisation Rate for Apparel Companies," in *Proc. International Symposium on Engineering and Architectural Sciences of Balkan, Caucasus and Turkic Republics,* 2009, p.214-220.

[14] T. Kuyumcu, "İsletmeler Arasında Fason Üretim İliskileri", *İ.K.V. Dergisi*, vol. 70, 1989.

[15] Y. Kaya. (2004) Cok Amaclı Karar Verme Yontemlerinden TOPSIS ve ELECTRE Yontemlerinin Karsılastırılması. Available: www.hho.edu.tr/.../YILMAZ%20KAYA/YILMAZ%20KAYA%20%5BWORD%5D.pdf.

[16] M.A. Reyhan, "Hazır Giyim İsletmelerinde Fason Kesimhane Seciminde Topsis Yonteminin Uygulanması", MSc Thesis, İstanbul Kültür University, Institute of Social Sciences, İstanbul, Turkey, 2010.

BIOGRAPHY

Mahmut KAYAR has a PhD in textile technology (Marmara University; 2009). He is a full assistant professor at Marmara University, Faculty of Technology, Department of Textile Engineering. He has worked on many projects about clothing technology. He has produced many articles concerning assembly line balancing, ultrasonic sewing, productivity on apparel companies, composites etc. Adress: Marmara University, Faculty of Technology, Department of Textile Engineering, 34722 Goztepe-İstanbul, Turkey. E-mail: mkayar@marmara.edu.tr.

Relation between Sink Marks Formation and Rib Dimension on Plastic Parts

Omer BAYRAKTAR[1], Abdulmecit GULDAS[1], Mustafa GOKTAS[2], Mesut DUZGUN[3]

Abstract

In this study, the optimization of rib dimensions on plastic parts to prevent sink mark during molding has been investigated. Ribs are used for improving strength without increase in thickness of parts on design of plastic parts. Sink marks occur due to the non-uniform thickness distribution on the plastic parts. Quantitative analyzes were carried out to determine the relationship between rib dimensions and sink mark formation. The effects of rib parameters such as rib thickness, rib height, and corner radius on the formation of sink mark were investigated. As a result of these analyzes, it was determined that the most effective parameter in the formation of sink marks was the rib thickness. Besides, it has been determined that the corner radius parameter is more effective than the rib height.

Keywords*: Sink marks, Plastic part design, Ribs, Strength of plastic parts.*

1. INTRODUCTION

Ribs are used to increase the mechanical strength of plastic parts. This method is widely preferred because it increases the strength without increasing the use of plastic materials [1]. However, when rib sizes are not properly determined, sink marks appear on the surface of the plastic part. In plastic injection molding, the melting plastic material expands and shrinking occurs during cooling. Whenever plastic parts are designed, care should be taken to keep the wall thickness as constant as possible in all areas. Otherwise, different shrinking events will occur in areas with different thicknesses. Sink marks usually occur at the places where the plastic part wall thickness distribution is deteriorated, in the ribs, the bolt channel and the nail head. Because there is more mass in these regions, more shrinkage occurs here compared to others. As a result, sink marks occur on nearby surfaces. Sink marks reduce the visual quality of plastic parts if they occur on visible surfaces in plastic parts.

Various methods have been investigated to prevent the formation of sink marks. Attempts have been made to identify suitable process parameters in order to minimize the formation of sink marks [2-5]. There are many processes affecting the plastic injection molding process such as melt temperature, mold temperature, holding pressure, holding time, and cooling process. The increase in the holding pressure, and the decrease in the melt and the mold temperatures reduce the formation of sink marks. Models based on process parameters have been developed to be used in design and production of parts [6-8]. Thanks to these models, sink marks that may occur have been tried to be predicted. Moreover, by making the cooling process more effective, sinks around the ribs have been tried to be reduced [9]. It is aimed to solidify and harden the surface where the sink will occur before it occurs. With internal gas assisted injection molding, the mass of the material at the rib base was reduced to prevent shrinkage. External gas-assisted injection molding has been used to improve shrinkage prevention and cooling [10,11]. By studying the perceptibility of the shrinkage amount, the acceptability of sink marks at certain levels has been investigated [12-15]. In order to prevent bending and torsion in low-profile plastic parts, rib geometry with different types and placement that minimizes sink marks have been researched [4,16-20]. In addition, the side surfaces of the ribs are angled so that they can be easily removed from the mold, similar to the surfaces of the plastic parts being angled. To reduce notch effect, the ribs are rounded on the rib base. In this study, the effect of rib width, rib height and base roundness on sink mark formation was quantitatively investigated. Filling and packing analyzes were carried out with a

---

[1] *Corresponding author: Gazi University, Department of Manufacturing Engineering, 06500Teknikokullar/Ankara, Turkey.*
   omerbayraktar@gazi.edu.tr

[2] *Gazi University Technical Sciences Junior technical college Ankara /TURKEY*

[3] *XXXYYYZZZ*

plastic part designed for this purpose. Filling and packing analyzes were performed with Moldflow software [21]. The effect of different sizes of rib sections on sink mark formation has been compared.

2. MATERIAL AND METHODS

In order to perform the filling and packing analyzes, a plastic part with t = 2 mm thickness with perpendicular ribs with respect to each other was determined. The dimensions of the piece are 40 mm, 40 mm and 2 mm (Figure 1). On the surface opposite the surface of the ribs, sink marks are expected to form along the rib extension.
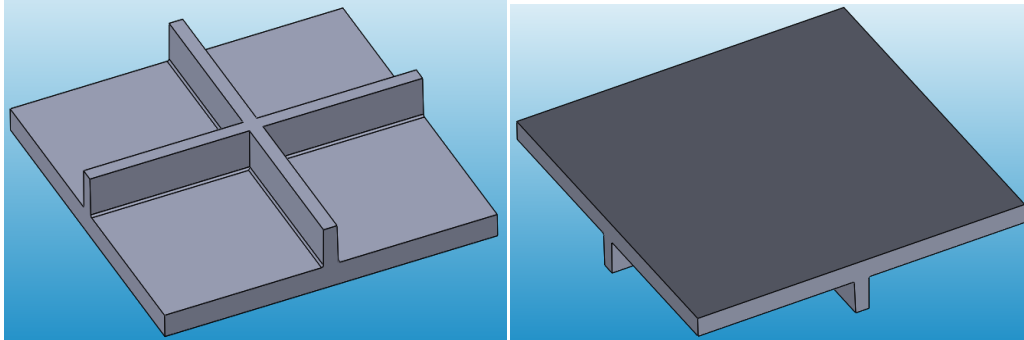

Figure 1. Plastic part, and the surface on which the sink marks will for.

Side surfaces of the ribs are angled to be a=1° so that the plastic part can be easily removed from the mold. The corners are rounded at the rib base (Figure 2). For numerical analyzes 0.4 mm, 0.7 mm and 1.225 mm rib widths (w) are used. For rib height (h) 2mm, 3.5mm, 6.125mm and 10.72mm values are used. The values used for the base corner radius (r) are 0.001mm 0.178mm 0.54mm and 1.6mm.
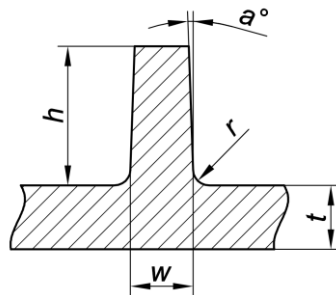

Figure 2.Rib dimension.

MoldFlow Insight 2016 commercial software was used for filling and packing analysis. Polyproplen (PP) Shell PM6100 was used as plastic material. Tetrahedral type cells were used as mesh members. Global edge size is specified as 0.3 mm-0.6 mm. about 80000 members were used in the analyses. Injection temperature used in the analysis is 230°C and mold temperature is 50°C. Injection pressure is 80MPa. holding time is 10s. In the filling analysis, the entry point was provided from the side surface of the plastic part (Figure 3).
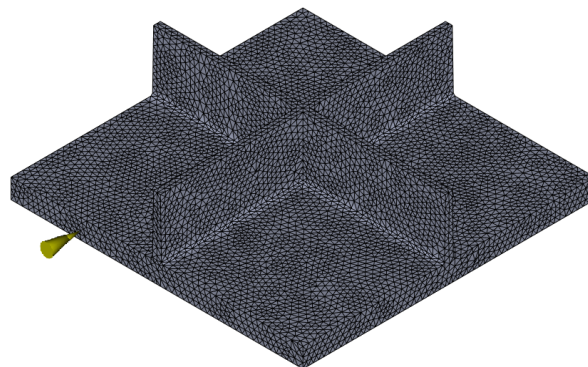

Figure 3. Material entry point

3. RESULTS AND DISCUSSION

Filling and packing analyzes of the plastic part were performed with the determined process parameters. Sink marks were observed in the analysis results. As expected, sink marks occurred on the opposite surface alongside the ribs (Figure 4). 48 analyzes were performed with different rib thickness, rib height and base corner radii values. Mean values were obtained with the values obtained from the sink mark regions formed as a result of the analyses made. Mean values are shown in Figure 5, Figure 6 and Figure 7. According to the analysis results, depth of sink mark increases as rib height, rib width, and base corner radius increase.
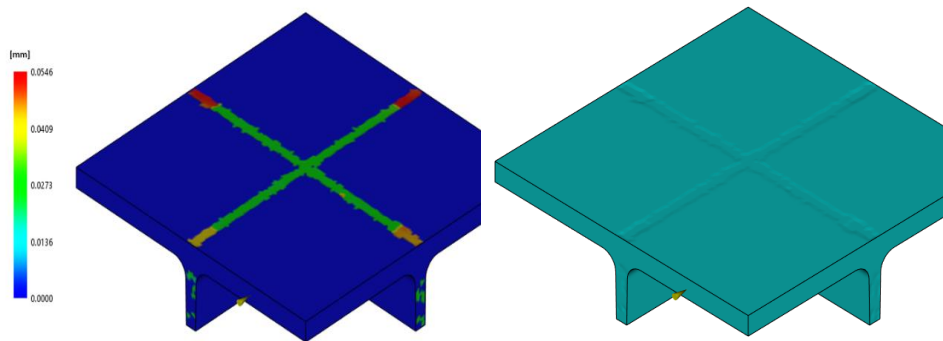

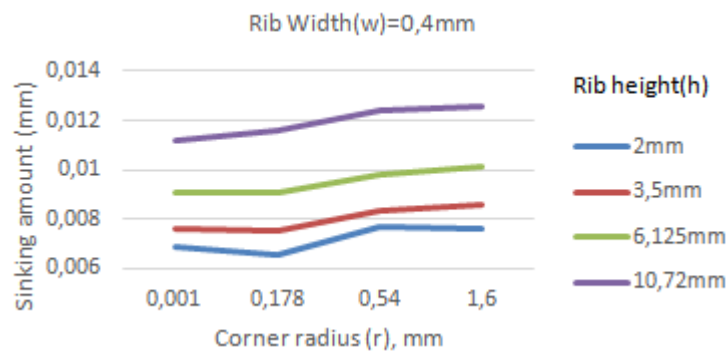*Figure 4. Sink mark distribution (left), shaded view (right).*

Figure 5. Sinking amounts (Rib width w=0.4mm).

Figure 6. Sinking amounts (Rib width w=0.7mm)

Rib Width (w)=1,225mm

Figure 7. Sinking amounts (Rib width w=1.225mm)

The most effective parameter on the depth of sink is the rib width. When rib thickness increased from 0.2t to 0.6t, sink depth increased approximately 3 times. Rib height is more effective than base corner radius. While rib height increased from t to 5t, sink depth only increased 1.5 times. There was a 1.1 times increment in depth of sink mark at the 0.8t value of the base radius.

4. CONCLUSION

Quantitative analyzes were carried out to investigate the effects of rib dimensions on the formation of sink marks. Analyses were performed with Moldflow software, and the results of the sink marks were examined. Rib dimensions were changed while process parameters were kept constant. The effects of Rib Width, Rib Height and Base Corner Radius were investigated. It was found that the most effective dimension on the depth of sink marks is the rib width. Base corner radius has a lower effect compared to rib height.

REFERENCES

[1]   Malloy, R., "Plastic Part Design for Injection Molding An Introduction", Hanser Publication.
[2]   Zhilian, Z., Bo, J., "Optimal Process Design of Shrinkage and Sink Marks in Injection Molding", Journal of Wuhan University of Technology-Mater. Sci. Ed., 22 404-407, (2007).
[3]   Pacher, G.A., Gruber, D.P., Berger, G.R., Friesenbichler, W., "Influence of Process Settings on The Topography Of Sink Marks", Advances in Plastics Technology - Conference Papers, 31, (2013), Gliwice, Polen.
[4]   Erzurumlu, T., Ozcelik, B., "Minimization of warpage and sink index in injection-molded thermoplastic parts using Taguchi optimization method", Materials and Design 27 853–861 (2006).
[5]   Shen, C., Wang, L., Cao, W., Qian, L., "Investigation of the Effect of Molding Variables on Sink Marks of Plastic Injection Molded Parts Using Taguchi DOE Technique", Polymer-Plastics Technology and Engineering, 46 219–225, (2007).
[6]   Mathivanan, D., Parthasarathy, N.S., "Prediction of sink depths using nonlinear modeling of injection molding variables", Int J Adv Manuf Technol 43 654–663, (2009)

[7]   Altan, M., "Reducing shrinkage in injection moldings via the Taguchi, ANOVA and neural network methods", Materials and Design 31 599–604, (2010)

[8]   Mathivanan, D., Parthasarathy, N.S., "Sink-mark minimization in injection molding through response surface regression modeling and genetic algorithm", Int. J. Adv. Manuf. Technol., 45 867–874, (2009)

[9]   Manaf, A. R. A., Zawawi, M. Z., Adly, N. Z. I., "Thin Walled Part Warping Overcoming by Honeycomb Ribs Design", Advanced Materials Research, Vol. 903, pp. 181-186, (2014)

[10]   Yang, S.Y., Huang, F.Z., Lıau, W.N., "A Study of Rib Geometry for Gas-Assisted Injection Molding", Polymer Engineering and Science, 36 23 2824-2831, (1996)

[11]   Wang,X., Zhao, G., Wang, G., "Research on the reduction of sink mark and warpage of the molded part in rapid heat cycle molding process", Materials and Design 47 779–792 (2013)

[12]   Gruber, D.P., Macher, J., Haba, D., Berger, G.R., Pacher, G.A., Friesenbichler, W., "Measurement of the visual perceptibility of sink marks on injection molding parts by a new fast processing model", Polymer Testing 33 7–12, (2014)

[13]   Macher, J., Gruber, D.P., Altenbuchner, T., Pacher, G.A., Berger,G.R., Friesenbichler, W., "Detection of visually perceptible sink marks on high gloss injection molded parts by phase measuring deflectometry", Polymer Testing 34 42–48 (2014)

[14]   Gruber, D.P., Berger, G.R., Pacher, G.A., Friesenbichler, W., "Novel approach to the measurement of the visual perceptibility of sink marks on injection molding parts", Polymer Testing 30 651–656 (2011)

[15] Macher, J., Gruber, D.P., Altenbuchner, T., Pacher, G.A., Berger, G.R., Friesenbichler, W., "A novel sink mark model for high gloss injection molded parts e Correlation of deflectometric and topographic measurements", Polymer Testing 39 12-19, (2014)

[16] Wang, L., Li, Q., Shen, C., Lu, S., "Effects of Process Parameters and Two-Way Interactions on Sink Mark Depth of Injection Molded Parts by Using the Design of Experiment Method", Polymer-Plastics Technology and Engineering, 47 30–35, (2008)

[17] Güldas, A., Goktas, M., Bayraktar, O., Khakzad F., "Optimization of Rib Geometry for Plastic Parts", ICENS 2016 International Conference on Engineering and Natural Science May 24-28, 2016 Sarajevo, Bosnia and Herzegovina

[18] Lam, Y. C., Santhikumar, S., "Automated rib location and optimization for plate structures", Struct. Multidiscip. O., 25 1, 35–45, (2003)

[19] Mathivanan, D., Nouby, M., Vidhya, R., "Minimization of sink mark defects in injection molding process – Taguchi approach", Int. Journal of Eng., Science and Technology, Vol. 2 2, 13-22,(2010)

[20] Guo, W., Hua, L., Mao, H., "Minimization of sink mark depth in injection-molded thermoplastic through design of experiments and genetic algorithm", Int J Adv Manuf Technol 72 365–375, (2014)

[21] Autodesk, MoldFlow Insight, 2016. http://www.autodesk.com.

Examination of Wire Electrical Discharge Machining of AISI S1 (60WCrV8) Cold Work Tool Steel

Omer BAYRAKTAR[1], Abdulmecit GULDAS[1], Mustafa GOKTAS[2]

Abstract

Wire electro-discharge machining (WEDM) is a competitive machining method for cutting hard and conductive materials with electrical sparks. In WEDM, materials were machined roughly in first cutting operation and finished by one or several cutting operations. However, rough cutting process is used as finishing operation sometimes. Using this process as finishing operation makes very difficult to estimate the surface characteristics. Therefore, the effort in obtaining desired surface properties depends on correct selection of the machining parameters. In this study, the effects of machining parameters, such as pulse on time (T_{ON}), pulse off time (T_{OFF}) and peak current (I_P) on surface roughness (R_a), material removal rate (MRR) and the wear of wire electrode have been evaluated. Based on the result of obtained data, analysis of variance (ANOVA) was performed for determining the most effective parameter on MRR and Ra.

Keywords: *Wire electrical discharge machining, material removal rate, surface roughness, analysis of variance.*

1. INTRODUCTION

Cold work tool steels are highly alloyed type of steels in comparison with conventional standard steels. AISI S1, which is in this steel group, having properties such as high hardness, toughness and wear resistance and used in heavy duty blanking and forming dies, punches, chisels, shear blades, slitter knives, cold striking dies, cold extrusion tools, coining dies, master hobs. It is very difficult to carry out the processes like turning, milling and drilling on the hardened materials. Machining of such hard materials with traditional methods causes severe damage on the cutting tools [1]-[2]. Non-traditional techniques are being applied to prevent the difficulties encountered during machining of such materials with traditional methods.

Wire electric discharge machining (WEDM) process is a non-traditional manufacturing manufacturing process which is often used in the machining of conductive materials. The material can be easily processed regardless of its level of hardness as long as it has electrical conductivity [3]. The material processed through WEDM become a final product generally after it is roughly cut and its degree of surface roughness is brought to the desired level with a secondary cutting process. However, rough cutting is sometimes used as the last operation depending on the application area, properties and machining costs of the product. It is highly important to obtain a high degree of surface roughness (Ra) and material removal rate based on the cutting parameters in rough cutting processes. Therefore, it is of critical importance to specify the machining parameters in order to reach optimum level machining performance.

Patil [4] et al. have worked on determination of material removal rate in wire electro-discharge machining of metal matrix composites. silicon carbide particulate reinforced aluminum matrix was machined using WEDM process. Their results show that material removal rate not only depends strongly on pulse on time but also thermo-physical properties such as coefficient of thermal expansion, thermal diffusivity and melting point temperature etc. Ramakrishnan [5] et al. developed an Artificial Neural Network(ANN) models to predict the best cutting parameters of wire electro-discharge machining (WEDM) process to predict the MRR and surface roughness. They were selected Inconel 718 as work material to conduct experiments. Analysis of variance (ANOVA) was employed to identify the level of importance of the machining parameters on the multiple performance characteristics. According to their findings the developed ANN models could predict

---

the performance characteristics of WEDM process accurately. Singh [6] et.al. have investigated the effect of process parameters on MRR and surface roughness in WEDM. Their experiment was conducted on P20 Tool Steel and brass wire of 0.25mm diameter was used. According to their findings MRR increased with increasing pulse on time, while increase in pulse off time decreased MRR. The value of surface roughness increased with increasing pulse on time, Peak current and wire feed rate, but decreased as the increasing pulse off time, servo voltage and wire tension. Their finding also indicated that wire tension and wire feed rate has small effect on material removal rate.

In the present work, wire electric discharge machining of AISI S1 Tool Steel have been studied. The effect of parameters like current, pulse on time and pulse off time on surface roughness, material removal rate and wear of wire electrode have been evaluated. Analysis of variance (ANOVA) was also employed to identify the level of importance of the machining parameters on the MRR and Ra.

2. EXPERIMENTAL WORK

2.1. Specimen Materials

The AISI S1 (1.2550) cold work tool steel (hardened 60 HRC) which made by Dorrenberg Edelstahl was selected to be machined with one main cut. The specimen for the research is prepared as plates of 15mm thick. The chemical composition of work piece material is shown in Table 1.

Table 1. Chemical composition of AISI S1 experimental work piece (wt%).

C	Si	Mn	P	S	Cr	W	V
0.6	0.74	0.33	0.012	0.007	1.01	1.88	0.16

2.2. Experimental Details

Brass wire electrode (SUNCUT brand, with a tensile strength of 900 N/mm^2) with a diameter of 0.25mm was used as electrode. The specimens were machined using WEDM under rough cutting pass. Deionized water was used as the dielectric fluid in the current investigation. The experiments (Fig 1) were performed using a Mitsubishi 1200MV-S Advance WEDM machine. The machining parameters (Table 2), including peak current (I_P), pulse on time (T_{ON}) and pulse off time (T_{OFF}) were selected to investigate the effect on machining performance. The other machining parameters were kept constant (Table 3).The machining parameter levels were selected based on no wire breakage conditions for the maximum T_{on}, minimum T_{off} and Maximum I_P with.

Table 2. Machining parameters for WEDM

Parameter	Values			Unit
I_P	4	6	8	Ampere
T_{ON}	6	11	16	μs
T_{OFF}	2	6	10	μs
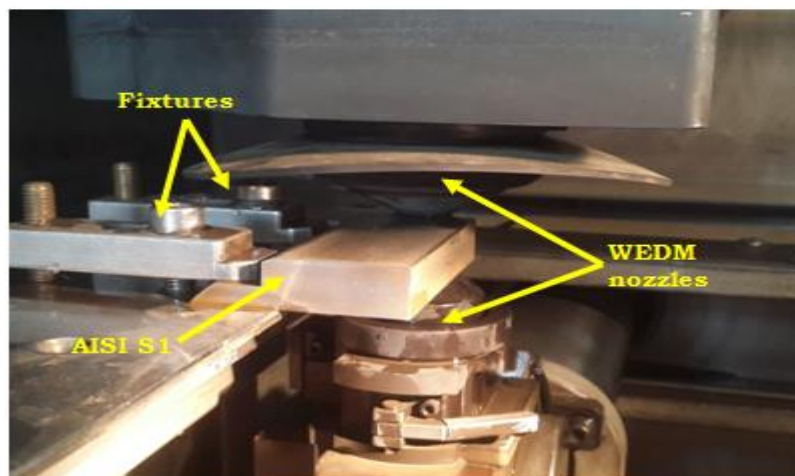
Figure 1. WEDM experimental setup.

Table 3. Constant machining parameters

Parameter	Values	Description
V_0	4 V	Open-circuit voltage
V_G	50 V	Servo voltage
WT	10 N	Wire tension
WS	10 m/min	Wire speed
LQ	14 kgf/cm^2	Liquid quantity
SA	5	Stabilizer A
SB	6	Stabilizer B
SC	7	Stabilizer C
SE	4	Stabilizer E

2.3. Measurement

The surface roughness was measured with a stylus-based profilometer (Mitutoyo SJ-201). The average surface roughness, which was commonly used in the manufacturing industry, was chosen for the current study. Machined surface roughness was measured with a total travel length of 5mm. The average surface roughness was calculated using five different measurement averages under the same cutting conditions. The cutting speed was calculated from the machine time and cutting length by monitoring the WEDM machine monitor. Data The MRR was calculated by equation;

$$MRR \; (mm^3/min \;) = V_c \times b \times h \tag{1}$$

where V_c is the cutting rate (mm/min); b is width of the cut (mm); and h is the depth of the job (mm). Wear of electrode wire was measured by weighed of one meter long eroded wire, to the nearest 0.0001 g. The measurement of electrode wear was carried out on three different samples with a five meters long under the same cutting conditions. The measured values of Ra, MRR and Wire electrode wear for the current investigation are listed in Table 4.

Table 4. Experimental plan and results

Exp. No.	Factor Assignment			R_a (µm)	MRR (mm^3.min^1)	Wire electrode
	T_{ON} (µm)	T_{OFF} (µm)	I_P (A)			
1.	6	2	4	2.508	4.75	0.80
2.	6	2	6	2.310	7.98	1.40
3.	6	2	8	2.773	12.29	2.19
4.	6	6	4	2.463	2.32	0.36
5.	6	6	6	2.155	4.45	0.82
6.	6	6	8	2.499	7.68	1.44
7.	6	10	4	2.358	1.26	0.13
8.	6	10	6	2.142	2.41	0.36
9.	6	10	8	2.315	4.30	0.85
10.	11	2	4	2.649	8.70	1.80
11.	11	2	6	2.443	13.97	2.60
12.	11	2	8	2.612	21.16	4.18
13.	11	6	4	2.542	4.70	1.04
14.	11	6	6	2.132	8.26	1.67
15.	11	6	8	2.698	14.34	3.42
16.	11	10	4	2.349	2.55	0.55
17.	11	10	6	2.027	4.57	0.96
18.	11	10	8	2.573	8.22	1.84
19.	16	2	4	2.834	16.72	3.24
20.	16	2	6	2.475	21.44	4.30
21.	16	2	8	2.985	29.97	7.04
22.	16	6	4	2.558	10.19	2.51
23.	16	6	6	2.209	18.37	3.06

24.	16	6	8	2.976	22.65	5.17
25.	16	10	4	2.770	5.30	1.36
26.	16	10	6	2.390	10.54	2.33
27.	16	10	8	2.830	13.97	3.24

2.4. Analysis Of Variance (ANOVA)

In order to evaluate the effect of cutting parameters of WEDM process in terms of cutting performance such as surface roughness, MRR and wire electrode wear, ANOVA with a confidence interval of 95% was performed. The ANOVA results are given separately in Table 5. MINITAB software version 17 was used to perform ANOVA.

Table 5. Results of ANOVA for Ra, MRR, wire electrode wear

	Factors	Degrees of freedom	Sum of squares	F-Test	P	Percent Contribution (%)
R_a	I_P	2	0.92181	41,45	0,000	53
	T_{ON}	2	0,39000	17,53	0,000	22
	T_{OFF}	2	0,20138	9,05	0,002	12
	Error	20	0,22242			13
	Total	26	1,73560			100
	I_P	2	0,92181	41,45	0,000	53
	S = 0,105455 R-Sq = 87,19% R-Sq(adj) = 83,34%					
MRR	I_P	2	585,08	58,73	0,000	41
	T_{ON}	2	391,02	39,25	0,000	28
	T_{OFF}	2	339,71	34,10	0,000	24
	Error	20	99,61			7
	Total	26	1415,42			100
	I_P	2				
	S = 2,23175 R-Sq = 92,96% R-Sq(adj) = 90,85%					
Wire electrode wear	I_P	2	32,106	53,63	0,000	46
	T_{ON}	2	14,099	23,55	0,000	20
	T_{OFF}	2	17,872	29,85	0,000	26
	Error	20	5,987			9
	Total	26	70,063			100
	I_P	2				
	S = 0,547108 R-Sq = 91,46% R-Sq(adj) = 88,89%					

3. RESULTS AND DISCUSSION

3.1. Effect Of Process Parameters On Material Removal Rate

Material removal rate is a very important parameter that determines the speed of production in WEDM. If the material removal rate is high, the production will be less costly. As indicated in Figure 2, MMR increases as the pulse on time increases and decreases as the pulse off time increases. This is related to the duration of erosion as active T_{ON} and closed T_{OFF}. Moreover, we can also see that MRR increases as the amount of current increases. The amount of peak current, which is the magnitude of energy that will induce the erosion, directly affects MRR. The generation of heat increases with an increase in T_{ON} and ampere. However, in order to prevent breakages in the wires, which heavily affects the manufacturig time in WEDM, $T_{ON,}$ T_{OFF}, and current must be selected properly [6]. Maximum MRR has been detected as 29.97mm^3.min^{-1} in a case which the pulse on time was 16, pulse off time was 2 at 8 amperes and the minimum MRR has been detected as 1.26mm^3.min^{-1} in a case which the pulse on time was 6, pull off time was 10 at 4 current. This information shows that an incorrect selection of parameters will significantly increase the manufacturing time.
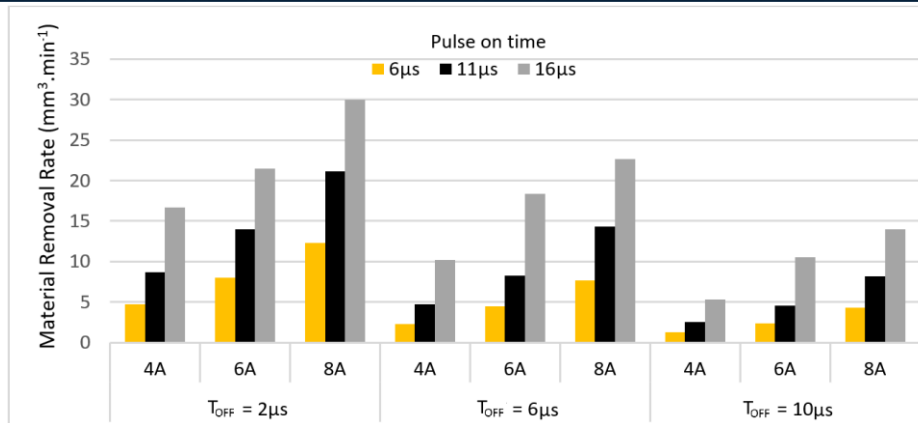
Figure 2. Change in material removal rate depending on pulse on time, pulse of time and peak current.

3.2. Effect Of Process Parameters On Surface Roughness

Degree of surface roughness is an important quality parameter, which is an significant factor in industrial production. In WEDM, random spark excursions produce many crater on the surface of the material. Therefore, the degree of surface roughness substantially depends on the sizes of craters produced by sparks. In this study, the effect of parameters used for AISI S2 steel on the degree of surface roughness are given in Figure 3. As can be seen in the table, an increase in pulse on time increases the degree of surface roughness in general because as the pulse on time increases more electrolyte output is produced and thus, the surface roughness increases. The degree of surface roughness decreases with increase in pulse off time, since produced electrolyte output and released heat increases during the pulse off time. Many studies in the literature also observed that the degree of roughness increases with an increase of current in the ampere [5][6][7]. However, in this study, the degree of surface roughness decreased with the rise of ampere from 4 to 6, and increased again at 8 ampere. This may be caused by reshaping of molten material by discharge energy that is dependent on the current. As it can be observed in Figure 4, resolidified surface can get a more round shape with the increase of heat in the environment caused by an increase in the current. Yet, with the operating current at 8 ampere, larger craters are produced on the surface of workpiece through the molten material hitting the surface.
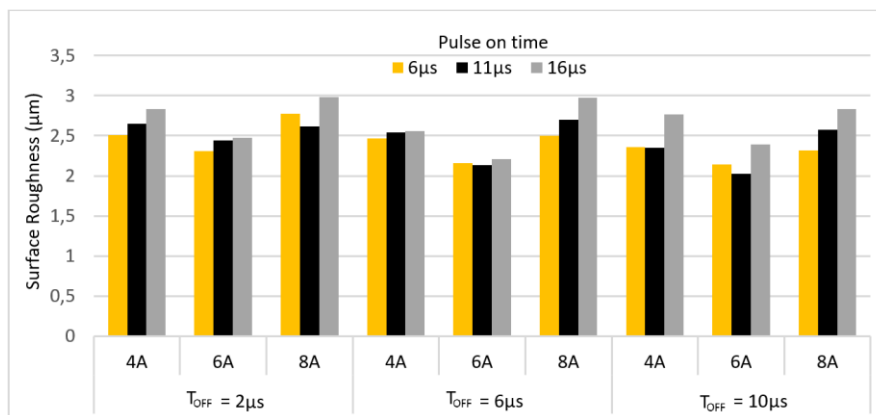

Figure 3. Change in surface roughness depending on pulse on time, pulse of time and peak current.

3.3. Evaluation Of The Results of ANOVA

According to the ANOVA results, while the sum of squares represents 87% of Ra, it represents approximately 92% of the MRR and the wire wear. The most effective parameter on the surface roughness has been detected as the current with 53%, followed by TON with 22% and TOFF with 12%. The most effective parameter on MRR was the current parameter with 41% contribution, followed by TON with 28% and TOFF with 28%, respectively. As the analysis wear of wire indicated, the most effective parameter on wire wear has been found to be the current value with 46%, followed by TON with 26% and TOFF with 20%. Considering the ANOVA, the most effective parameter on the results has been determined as the current in the ampere.

4. CONCLUSION

This study was conducted on the machining of AISI S1 steel by using different parameters like pulse on time, pulse off time and the current through wire electric discharge machining technique. The results of machining were evaluated in terms of MRR, Ra and electrolyte depreciation. The results are presented below for the interested researchers:

•MRR increases with current and pulse time increase, and MRR decreases with pulse off time increase.

•The degree of surface roughness generally decreases as the pulse off time increases, and increases as the pulse on time increases. However, an optimum value has been detected for the current.

•The amount of wire wear increases as the current and pulse on time increase, and decreases as the pulse off time increases.

•According to obtained ANOVA data, the most effective parameter for MRR, Ra and Wear of wire has been detected as the current value.
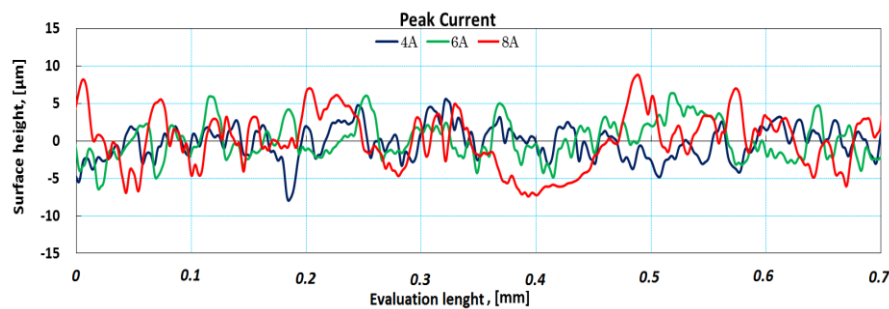

Figure 4. Comparison of surface roughness profile, for the T_{OFF} 6, T_{ON} 16.

4.1. Effect Of Process Parameters On Wear Of Wire Electrode

Wire breakage occurs due to the decrease in tensile strength of the brass wire through thermal softening and wear of wire electrode. For this reason, the amount of depreciation is an important parameter in wire electric discharge machining. Figure 5 shows the amount of wear amount of a one meter long wire. As can be also seen in the figure, since high peak currents and high values of pulse on time produce higher spark energy and the wire is long time exposed to this high energy, the amount of wear is higher. The increase in pulse off time depending on the current causes shorter exposure to the spark energy. As a result, the increase in pulse off time decreased the amount of depreciation in the wire.
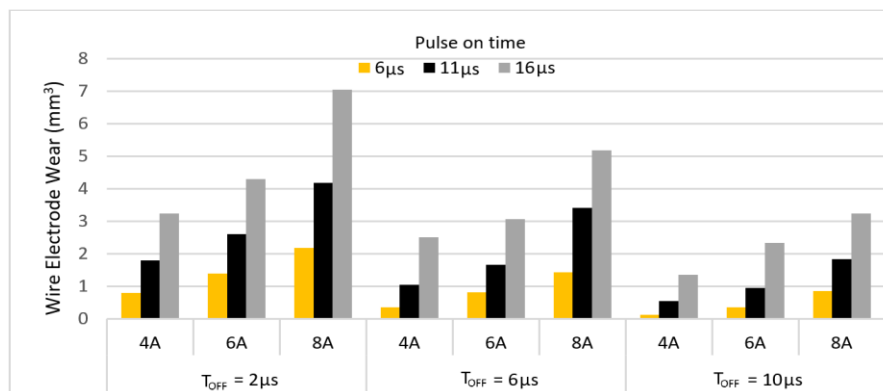

Figure x3. Change in wire wear depending on pulse on time, pulse of time and current.

REFERENCES

[1]   Y. B. Guo, W. Li, and I. S. Jawahir, "Surface Integrıty Characterızatıon And Predıctıon In Machınıng Of Hardened And Dıffıcult-To-Machıne Alloys: A State-Of-Art Research Revıew And Analysıs," *Mach. Sci. Technol.*, vol. 13, no. 4, pp. 437–470, Nov. 2009.

[2] Y. Cheng, H. Hu, S. Sun, and Z. Yin, "Experimental study on the cutting performance of microwave sintered Al2O3/TiC ceramic tool in the machining of hardened steel," *Int. J. Refract. Met. Hard Mater.*, vol. 55, pp. 39–46, 2016.

[3] P. Fonda, K. Nakamoto, A. Heidari, H.-A. Yang, D. A. Horsley, L. Lin, and K. Yamazaki, "A study on the optimal fabrication method for micro-scale gyroscopes using a hybrid process consisting of electric discharge machining, chemical etching or micro-mechanical milling," *CIRP Ann. - Manuf. Technol.*, vol. 62, no. 1, pp. 183–186, 2013.

[4] N. G. Patil and P. K. Brahmankar, "Determination of material removal rate in wire electro-discharge machining of metal matrix composites using dimensional analysis," *Int. J. Adv. Manuf. Technol.*, vol. 51, no. 5–8, pp. 599–610, Nov. 2010.

[5] R. Ramakrishnan and L. Karunamoorthy, "Modeling and multi-response optimization of Inconel 718 on machining of CNC WEDM process," *J. Mater. Process. Technol.*, vol. 207, no. 1, pp. 343–349, 2008.

[6] J. Singh and S. Sharma, "Effects of Process Parameters on Material Removal Rate and Surface Roughness in WEDM of P20 Tool Steel," *J. Multidiscip. Curr. Res. Int. J. Multidiscip. Curr. Res.*, vol. 1, 2013.

[7] I. Maher, A. A. D. Sarhan, M. M. Barzani, and M. Hamdi, "Increasing the productivity of the wire-cut electrical discharge machine associated with sustainable production," *J. Clean. Prod.*, vol. 108, pp. 247–255, 2015.

[8] R. Chalisgaonkar and J. Kumar, "Investigation of the machining parameters and integrity of the work and wire surfaces after finish cut WEDM of commercially pure titanium," *J. Brazilian Soc. Mech. Sci. Eng.*, 2016.

Estimation of Total Catch for Pikeperch (Sander lucioperca) and Common Carp (Cyprinus carpio) in Seyhan Dam Lake and Comparison with the Turkish Statistical Institute Data

Caner Enver Oyurt[1] *, Volkan Barış Kiyaga[1], Meltem Manasırlı[1],Dursun Avsar[1]

Abstract

The academic community claimed that the fisheries statistics of Turkish Statistical Institute (TUIK) did not reflect the actual production. However, this suspicion is often based on individual observations. So far, there is no qualitative data on this. In this study, the total amount of pikeperch and common carp caught in Seyhan Dam Lake in 2007 and 2008 was estimated and the data obtained were compared with those of TUIK's statistics. Therefore, the accuracy of the concerns of the fisheries scientists has been tested. In order to calculate the required data, the amount of fish caught by 20 fishing boats in a fishing season was used. The amount of fish caught by fishing boats in subsample was obtained from the merchants. Results showed that the amount of pikeperch caught from this lake in 2007 and 2008 was 62 and 37 tons, respectively. The amount of carp caught in the same years was 88 and 180 tons, respectively. This shows that the amount of pikeperch caught in lake has reduced by almost half in a year. On the contrary, the amount of carp caught doubled in a year. As a result, significant similarities were found between the data obtained in this study and the TUIK statistics.

Keywords: *Common Carp, Pikeperch, Total Catch, TUIK, Statistics*

1. INTRODUCTION

Fishery statistics of Turkish Statistical Institute have always been controversial. In particular, the fisheries scientists have claimed that these statistics do not reflect the correct total annual landing. This claim is usually based on personal observations and there is no quantitative data to show how accurate this claim.

Seyhan Dam Lake built in 1956. A large number of pikeperch (*Sander lucioperca*) and common carp (*Cyprinus carpio*) juveniles were released in this lake between 1971 and 1980. Over time, a fleet of 80 fishing boats which caught especially these two species whose population density increase rapidly was formed. This fishing fleet was catching with completely gill nets and trammel nets.

The economic relationship between the fishermen and merchants in the Seyhan Dam Lake is recorded in the ledger. Every day for a week, the fish caught by the fisherman is weighed and recorded in their ledger. At the end of a week, the fisherman takes his money for this ledger. Therefore, the records on the ledger are very trustworthy [1]. But it is very difficult to reach these ledgers. Merchants are reluctant to give these ledgers to the authorities because of concerns such as taxes. However, ledgers belonging to 20 boats showing the amount of fish caught in 2007 and 2008 were given us for academic study. Using these ledgers, the amount of pikeperch and common carp caught in Seyhan Dam Lake in 2007 and 2008 was determined. The results obtained are compared with the data published by the TUIK for these years. Thus, it has been tried to show how much the claims of the academic community reflect the truth.

---

[1] *Corresponding author: Cukurova University, Faculty of Fisheries, Balcalı Campus, Sarıcam/Adana, 01330, TURKEY, cozyurt@cu.edu.tr*

2. MATERIAL AND METHOD

Ledgers of 20 fishing boats catching in Seyhan Dam were used to determine the total amount of catching pikeperch and carp. The method proposed by Bingel [2] and FAO [3] was used to determine the total catch of the fleet. According to this method;

$$\bar{y} = \sum_i^n \frac{y_i}{n} \tag{1}$$

$$Y = N * y \tag{2}$$

$$v(Y) = N^2 * v(y) \tag{3}$$

$$S_y = \sqrt{v(Y)} \tag{4}$$

$$cv(Y) = {S_y}/{Y} \tag{5}$$

$$cv(Y) = {S_y}/{Y} \tag{6}$$

In these equations; $\bar{y}$ =mean catch by a fishing boat at a season, Y =total catch (landing), N = number of fishing boats in fleet, n =number of fishing boats in subsample y_i = amount of fish caught by i. fishing boat at a fishing season, $v(Y)$ =variance of the total catch, $v(y)$ =variance of subsample, S_y =standard error of the total catch and $cv(Y)$ = coefficient of variation of total catch.

3. RESULTS AND DISCUSSION

TUIK's fishery statistics are published for all the lakes and ponds in Adana and there are 11 dam lake and ponds in this city. Most of them are engaged in commercial fishing activities. For this reason, it is not possible to compare the data obtained from the Seyhan Dam Lake with TUIK statistics. However, pikeperch is only found in Seyhan Dam Lake in Adana. Therefore, this is the only water source that the pikeperch has been caught. For this reason, TUIK's statistics can be compared with pikeperch total catch determined in this study.

In 2007 and 2008, the amount of pikeperch and carp caught by 20 fishing boats forming sub-samples are shown in Table 1 and Table 2, respectively. Official statistics published by TUIK are also shown in Table 3.

According to the obtained data, the amount of pikeperch and common carp caught in Seyhan Dam Lake in 2007 is 59.20 and 88 tons, respectively. For the same year, the production of pikeperch and common carp determined by TUIK is 62 and 438 tons, respectively. In 2008, the amount of pikeperch and carp caught from this dam lake was determined as 36.80 and 180 tons respectively. For this year, according to the official statistics given by TUIK, the amount of pikeperch and carp caught in Adana is 37 and 428 tons, respectively. This data shows that the amount of pikeperch caught in the dam lake decreased by about half a year.

For 2007, the amount of catching pikeperch (59.20 tons) determined in this study is very close to TUIK's statistics (62 tons). There is a similar situation in 2008. The amount of caught the pikeperch was determined in this study (36.8 tons) and TUIK statistic (37 tons) are very close. Another important point is that the amount of pikeperch caught has fallen by half as, reflected in the TUIK's data. This suggests that the TUIK's statistics reflect the correct production values. But, in TUIK statistics, the amount of pikeperch caught for 2013 and 2014 is given as 20 and 25 tons, respectively. In these two years, commercial fishing was completely over at Seyhan Dam Lake. In the other word, pikeperch was not caught. Where did these values come from?

Table 1. The amount of pikeperch and common carp caught by 20 fishing boats in 2007 and total catch

No	Name of Boats	Pikeperch		Common carp	
		Catch (ton) y_i	$y_i{}^2$	Catch (ton) y_i	$y_i{}^2$
1	Adem	1,23	1,52	1.90	3.59
2	Arıcı	0,17	0,03	2.43	5.88
3	Cabbar	0,42	0,18	1.09	1.18
4	Cafer	0,95	0,90	0.26	0.07
5	Cemil	0,29	0,08	1.79	3.20
6	Cengiz	0,81	0,65	2.12	4.51
7	Cumali	0,16	0,01	0.79	0.62

No	Name of Boats	Catch (ton) y_i	$y_i{}^2$	Catch (ton) y_i	$y_i{}^2$
8	Ceko	0,86	0,72	2.13	4.52
9	Cetin	1,17	1,36	0.66	0.44
10	Depbo	0,10	0,01	1.08	1.16
11	Dogan	1,79	3,19	1.32	1.73
12	Eniste	0,51	0,26	0.31	0.10
13	Eyüp	0,26	0,07	0.16	0.03
14	Hamdi	0,29	0,09	0.53	0.28
15	Hasan	1,54	2,36	0.28	0.08
16	Hoca	0,86	0,73	1.52	2.30
17	Naim	0,03	0,001	2.08	4.31
18	Osman	0,46	0,21	0.19	0.04
19	Tahir	1,18	1,38	1.05	1.11
20	Yigit	1,73	2,98	0.35	0.12

N=80 n=20	$\sum y_i = 14.81$	$\sum y_i{}^2 = 16.83$	$\sum y_i = 22.01$	$\sum y_i{}^2 = 35.25$
	$\bar{y}_{pike} = 0.74\ Y_{pike} = 59.20\ v(Y) = 74.4$ $S_y = 8.63\ cv(Y) = 0.15$		$\bar{y}_{carp} = 1.10\ Y_{carp} = 88\ v(Y) = 139.2$ $S_y = 11.80\ cv(Y) = 0.13$	
$Y_{total} = Y_{pike} + Y_{carp}$	$Y_t = 59.20 + 88$ $Y_t = 147.2\ ton$			

Table 2. . The amount of pikeperch and common carp caught by 20 fishing boats in 2008

No	Name of Boats	Pikeperch		Common carp	
		Catch (ton) y_i	$y_i{}^2$	Catch (ton) y_i	$y_i{}^2$
1	Adem	1.20	1.43	3.35	11.20
2	Arıcı	0.07	0.004	2.80	7.83
3	Cabbar	0.21	0.05	1.94	3.76
4	Cafer	1.10	1.20	1.34	1.80
5	Cemil	0.24	0.06	2.25	5.04
6	Cengiz	0.49	0.24	2.74	7.51
7	Cumali	0.19	0.03	3.05	9.32
8	Ceko	0.43	0.19	2.63	6.89
9	Cetin	0.97	0.95	2.13	4.57
10	Depbo	0.006	0,00004	2.85	8.14
11	Dogan	0.59	0.35	2.72	7.40
12	Eniste	0.25	0.06	0.45	0.20
13	Hasan	0.25	0.06	1.17	1.36
14	Hoca	0.49	0.24	2.57	6.51
15	Rıdvan	0,38	0.14	2.56	6.55
16	Selo	0.57	0,32	1.73	3.00
17	Suphi	0	0	1.83	3.23
18	Sahin	0.26	0.07	2.45	5.99
19	Tahir	0.52	0.27	1.86	3.46
20	Yigit	1.04	1.08	2.86	8.21

N=80 n=20	$\sum y_i = 9.25$ $\sum y_{i^2} = 6.75$	$\sum y_i = 45.25$ $\sum y_{i^2} = 121.09$
	$\bar{y}_{pike} = 0.46$ $Y_{pike} = 36.80$	$\bar{y}_{carp} = 2.26$ $Y = 180.80$
	$v(Y) = 31.2$ $S_y = 5.59$	$v(Y) = 122.4$ $S_y = 11.06$
	$cv(Y) = 0.15$	$cv(Y) = 0.061$
$Y_t = Y_{pike} + Y_{carp}$	$Y_t = 36.99 + 180.80$ $Y_t = 217.79\ ton$	

For common carp, similarity between the amount of catching obtained in this study and TUIK's statistics cannot be expected. Because, carp is caught in many lakes and ponds in Adana. Therefore, the TUIK's statistics on common carp should be higher than the amount of common carp caught in this lake determined in this study. In fact, the carp statistics (438 tons) given by TUIK in 2007 are 5 times higher than the amount of common carp (88 tons) caught in Seyhan Dam Lake. This ratio is 2.4 times higher than that of 2008. In 2008, the amount of common carp caught from Seyhan Dam Lake increased by 2 times compared to the previous year. However, there has not been much change in TUIK's statistics. This may have been due to a reduction in the amount of common carp caught from the other inland water sources in Adana.

Table 3. Official statistics published by TUIK for pikeperch and common carp in Adana

Year	Catch (ton)	
	Pikeperch	Common carp
2000	13	410
2001	14	398
2002	23	412
2003	22	449
2004	26	441
2005	83	447
2006	73	412
2007	**62**	**438**
2008	**37**	**428**
2009	35	384
2010	37	396
2011	39	368,7
2012	35	395
2013	20	300
2014	25	295
2015	20	270

4. CONCLUSION

The results obtained in this study show that the production of pikeperch in 2007 and 2008 is correct in TUIK's statistics. By implication, it can be concluded that the concerns of fisheries scientists are not very accurate, at least for the fishery statistics of the TUIK's inland waters.

REFERENCES

[1] C. E. Ozyurt and D. Avsar, "Seyhan Baraj Golü Balıkcılıgındaki Yeni Gelismeler Üzerine Bir Degerlendirme," *Ege Üniversitesi Su Ürünleri Dergisi*, 20 (1-2), pp. 199-204, 2003.
[2] F. Bingel, *Balık popülasyonlarının incelenmesi*. Baki Kitap Evi, Adana, Turkey: 2002.
[3] FAO, *The collection of catch and effort statistics*. FAO Fish Circular, Rome, Italy: 1980.

Is It Possible to Prevent the Collapse of Fish Stocks by the Evaluating Simple Overfishing Indicators? An example: Seyhan Dam Lake.

Caner Enver Ozyurt[1], Volkan Barıs Kiyaga1, Meltem Manasırlı[1], Dursun Avsar[1]

Abstract

Due to the collapse of fish stocks, commercial fishery at Seyhan Dam Lake is completely over in 2013. As a result, both financial and social problems have been experienced. In this study, it was evaluated whether it would be prevented the collapse of the pikeperch (Sander lucioperca) stock by following simple overfishing indicators. For this, the data of the sampling performed in Seyhan Dam Lake in 2008 was used. Catching was carried out with gillnets with 20-22 and 24 mm mesh size. With the data obtained; length distribution, length at first maturity, length-weight relationship, optimum length, optimum size and mega-spawner size were determined. Using these results, an assessment was made on the status of the pikeperch stock in terms of overfishing. For this species, length at first maturity, optimum length, optimum size and the lower limit of mega-spawner were determined as 26cm, 34cm, 30-38cm and 42cm respectively. It was also found that if fishermen would have used 32-34 mm mesh size instead of 20-22 mm, even if they caught the same number of fish, the biomass would have increased 58 times.

Keywords: *Mega Spawner, Maturity, Optimum Size, Overfishing, Pikeperch*

1. INTRODUCTION

Seyhan Dam Lake built in 1956 for irrigation, flood prevention and energy production has a surface area of 6800 hectares, a maximum depth of 45 meters and an altitude of 67m. The lake, which is located on the subtropical climatic zone, is mesotrophic [1]. A large number of juvenile *Sander lucioperca* (Linnaeus, 1758) was released in this dam lake between 1971 and 1973. Over time, a fleet of 80 fishing boats which catch especially this species whose population density increased rapidly was formed. This fishing fleet was catching with completely gill and trammel nets. However, the fishermen complained that their incomes could not even afford to their cost after a while. When it came to 2012, commercial fishing is completely over in the lake. As a result, many fishing boats were discarded and many people had to look for different jobs.

In global fisheries, there is increasing evidence that natural stocks consume are much faster than they can regenerate themselves [2], [3], [4]. In order to solve this problem, fishery researchers have developed increasingly complex stock management models over the past century. However, in terms of legislators and law enforcement, social and political issues can take precedence over scientific data. The complexity of scientific methods makes them more difficult to be taken into account. For this reason, Froese [5] has suggested that overfishing be pursued with simpler and clearer indicators in order to avoid stock collapse.

There are three indicators proposed by Froese [5] for the protection of stocks and monitoring of overfishing: a) The proportion of mature individuals in catch is 100%. b) The proportion of individuals of optimum size in catch is 100%. c) The proportion of mega-spawner in catch is 0%. Froese defined the optimum length as a slightly larger length than the length at first maturity and the optimum size as the optimum length ± 10% and researcher stated that 10% bigger size of the upper limit of the optimum size can be regarded as mega-spawner.

Experimental studies have not been conducted on the condition of stocks in Seyhan Dam Lake. Therefore, it is a rough estimate to say that the fishing activity on the Seyhan Dam Lake is over due to overfishing. In this study, experimental samplings were carried out in Seyhan Dam Lake and the condition of pikeperch stock was evaluated in terms of overfishing parameters mentioned above.

[1] *Corresponding author: Cukurova University, Faculty of Fisheries, Balcalı Campus, Sarıcam/Adana, 01330, TURKEY, cozyurt@cu.edu.tr*

2. MATERIAL AND METHOD

This study was carried out in the Seyhan Dam Lake in 2008 (Figure 1). Gillnets with the same technical characteristics as those used in commercial fishing were used in the samples (mesh size: 20, 22, 24 mm (knot to knot)). The obtained samples were brought to the faculty laboratories and the total length (mm) and weight with the sensitivity of 0.01 gr of each individual were measured. Later, fish were dissected and sex determination was made with the naked eye. With the help of the obtained data; length distribution of the stock, length-weight relationship, length at first maturity, optimum size, mega-spawner length and their proportion in catch were calculated.
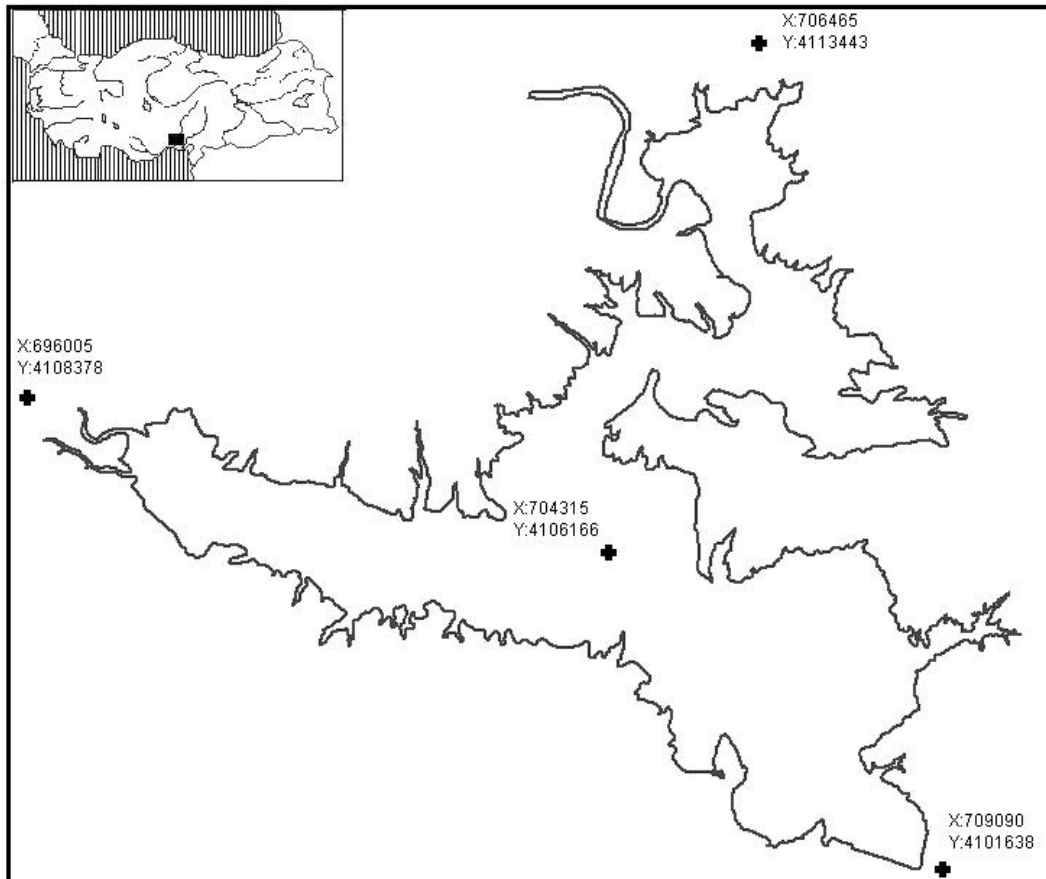
Figure 1. Sehan Dam Lake (UTM Zone 36 North)

The functional length-weight relationship given by Ricker [6] was used for the estimation of the biomass. The size group in which the individuals in the stock reached 50% sexual maturity was accepted as length at first maturity [7]. For the calculation of this size group, a two-stage (mature and immature) scale was used. In the months when gonadal development was observed, female and male individuals were divided into two groups, mature and immature for each length group. Therefore, the sexual maturity rate was obtained according to the lenght group. This data was then fit using the logistic function, $M(L)=1/1+e^{a-b*L}$ [8]. The length at first maturity was calculated by the equation $M(L_{50})=a/b$. The size 8 cm larger than the length at first maturity was considered as the optimum length. Optimum lengths of about ±10% were considered as the optimum size. The length 10% larger than the upper limit of the optimal size was considered as the lower limit of the mega spawner size [5].

3. RESULTS AND DISCUSSION

A total of 819 individuals were caught during the study and 458 of these individuals female, 349 male and 12 juvenile.

Sexual maturity rates by length for females and males were fitted with logistic functions (Figure 2; female: $y = {1}/{1 + (e^{5.2854-0.2004*l})}$; male: $y = {1}/{1 + (e^{5.6047-0.2236*l})}$. According to these functions,

length at first maturity of female and male were determined as 26.4 and 25.13cm, respectively. For the entire stock, the length at first maturity was accepted as 26cm. The length-weight relationship for female, male and entire stock was shown in Figure 3 (female: $y = 0.0108x^{2.8912}$; male: $y = 0.0123x^{2.8527}$; entire stock $y = 0.0115x^{2.8734}$)
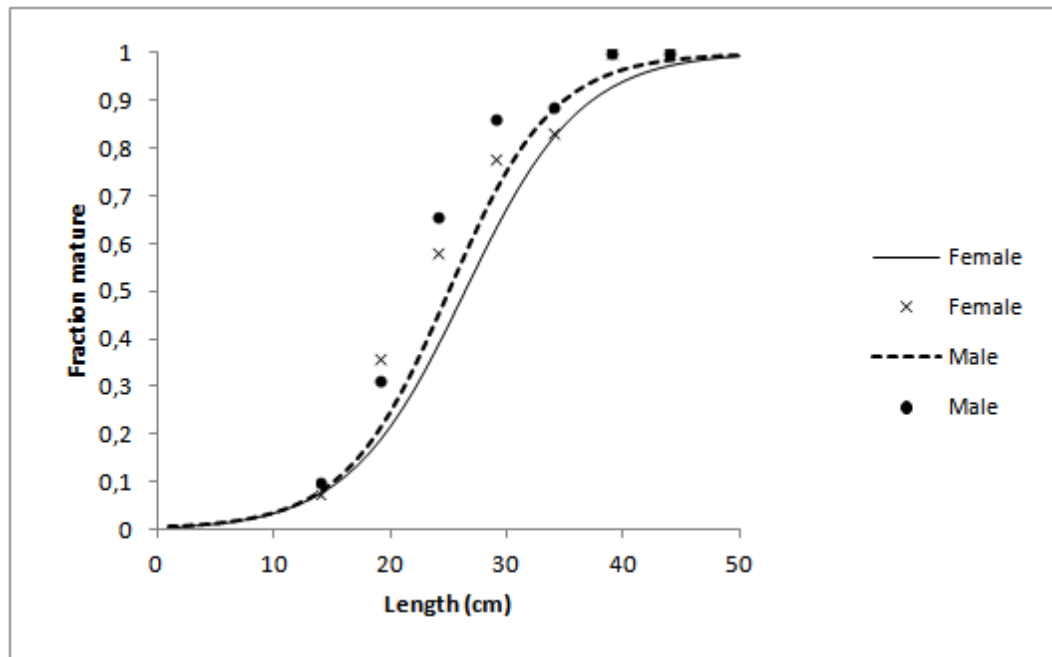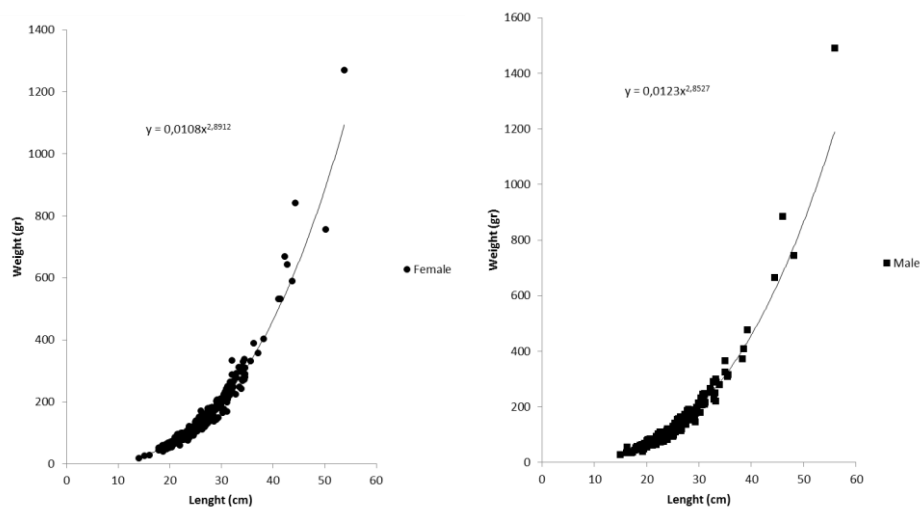

Figure 2. Proportion of mature individuals according to length

Optimum length was determined as 34cm (8cm more than the length at first maturity). Accordingly, the optimum size was accepted as 30-38cm. About 10% more than the upper limit of the optimum size (42cm) was defined as the lower limit of the mega-spawner size (Figure 4). The data obtained showed that 54% of the biomass of caught individuals was mature, 46% immature and 28% in optimum size. As number of individuals, it was found that 32% of the individuals caught were mature, 68% immature and only 16% the optimum size. The mega-spawner ratio in catch was determined as 1.58%.

Froese [5] stated that for protection of stock size, all individuals in the catch should be in mature and optimum size. Furthermore, the researcher stated that if the mega-spawner ratio in stock is between 30-40%, the age and length distribution of the stock is healthy, but if this ratio is less than 20%, there may be a problem. From the point of view of these simple overfishing indicators, it is possible to say that the pikeperch stock in Seyhan Dam Lake is under overfishing pressure.
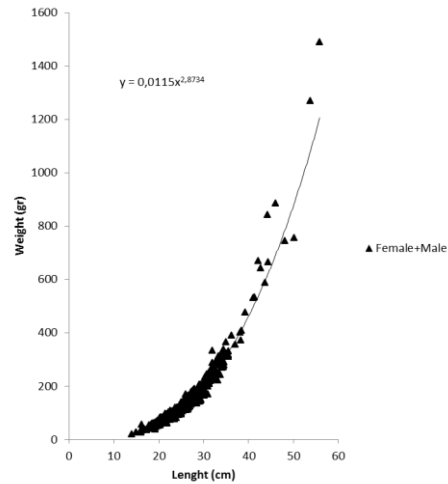
Figure 3. Length-Weight relationship

The proportion of immature individuals in catch was over 60%, which should be 0%. The mega-spawner rate that should be at least 30% was only 1.58%. In the face of this situation, it is inevitable that the pikeperch stock would collapse. Indeed, five years after this work (2013), the commercial fishery activity in the lake was completely stopped. At the Seyhan Dam Lake, fishermen used a 32 mm and 34 mm mesh size to catch pikeperch in the late 1990s [9]. However, at the end of the 2000s, it was observed that fishermen used 20 and 24 mm mesh size [9]. In fact, this change in mesh size clearly shows that fishermen were beginning to catch smaller and smaller fish. If the fishermen had used a 32-34 mm mesh size, how would have been the size distribution of the pikeperch catch? Unfortunately, this information was not available from past studies. However, the selectivity factor of gillnet used in the pikeperch catch was determined as 10.58 [10]. According to this selectivity factor, the optimum lengths for gillnet with mesh sizes of 32 and 34 mm are 33.8 and 35.9 cm, respectively. If these mesh sizes had been used, the length distribution of the catch pikeperch would have been shown in Figure 4. According to this length distribution, it is understood that all of the caught fish would have been mature and 70% of the captured individuals of optimal size (Figure 4). In fact, these values are quite consistent with the ratios proposed by Froese [5]. In addition, biomass was found to be increased by 58 times, even if the same number of fish were caught when using 32 and 34 mm mesh instead of 22-24 mm mesh size. This would mean that fishermen would earn more income. In fact, in these conditions, the stock should have not been collapse. So why did the fishermen narrow the mesh size of the nets they used? There were almost no fishing pressures at Seyhan Dam Lake in the early 1970's, but by the 1990's the number of boats reached 80. It seems that the fishing power applied in this area has exceeded the ability of stock to replenish itself. As a result of the decline of large individuals, fishermen with income anxiety have narrowed their net mesh size in order to catch smaller individuals. This situation caused the stock to collapse. In fact, the problem was that the fishing power was high (number of boats, number of nets vs.).
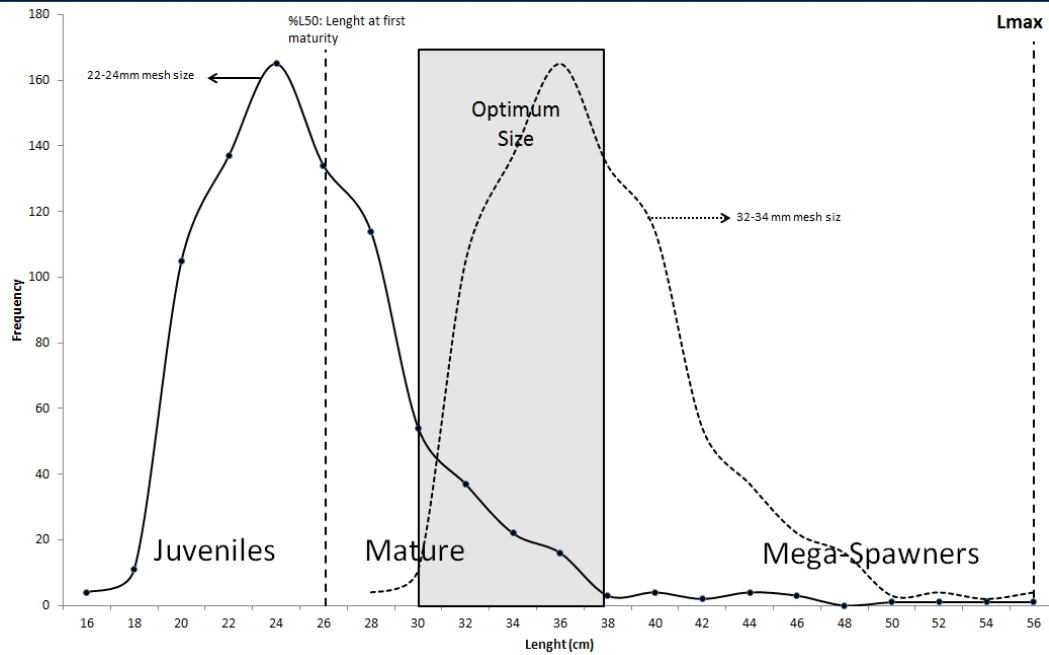
Figure 4. Length frequencies for different mesh size

4. CONCLUSION

If the simple overfishing indicators suggested by Froese [5] had been followed, could have been prevent the collapse of the pikeperch stock? Despite some weaknesses, this seems possible. If deterioration in overfishing indicators had been noticed, simple measures could have been applied. For example, new fishing boats might not have been licensed. So the number of boats had not reached 80. In addition, the number of nets to be used on a fishing boat could have been limited.

REFERENCES

[19]. F. Cevik,, M. Z. L. Goksu, O. B. Derici, and O. Fındık, "An assessment of metal pollution in surface sediments of Seyhan dam by using enrichment factor, geoaccumulation index and statistical analyses," *Environmental Monitoring and Assessment*, vol. 152(1), pp. 309-317, 2009.

[20]. D. Pauly, V. Christensen, J. Dalsgaard, R. Froese and F. Torres, "Fishing down marine food webs," *Science*, vol. 279(5352), pp. 860-863, 1998.

[21]. Y. Sadovy, "The threat of fishing to highly fecund fishes," *Journal of Fish Biology*, vol. 59(sA), pp 90-108, 2001.

[22]. V. Christensen, S. Guenette, J.J. Heymans, C. J. Walters, R. Watson, D. Zeller, and D. Pauly, "Hundred-year decline of North Atlantic predatory fishes," *Fish and fisheries*, vol. 4(1), pp. 1-24, 2003.

[23]. R. Froese, "Keep it simple: three indicators to deal with overfishing," *Fish and fisheries*, vol. 5(1), pp. 86-91, 2004.

[24]. W.E. Ricker, "Computation and interpretation of biological statistics of fish populations," *Bulletin of the Fisheries Research Board of Canada*, (191) 382p, 2016.

[25]. D. Avsar, *Balıkcılık biyolojisi ve popülasyon dinamigi*, Akademisyen Kitapevi, Adana, Turkey: 289, 2016.

[26]. M. King, *Fisheries biology, assessment and management*, Fishing News Books, Oxford: England.

[27]. C. E. Ozyurt, "Seyhan Baraj Golü Sazan (*Cyprinus carpio* Linnaeus, 1758) ve Sudakları (*Sander lucioperca* Bogustkaya & Naseka, 1996) İcin Uygun Ag Goz Genisliginin Belirlenmesi" Cukurova Üniversitesi Fen Bilimleri Enstitüsü Su Ürünleri Anabilim Dalı, Yüksek Lisans Tezi, Adana, 68s.

[28]. C. E. Ozyurt, V. B. Kiyaga, S. Mavruk and E. Akamca, "Spawning, Maturity Length and Size Selectivity for Pikeperch (*Sander lucioperca*) in Seyhan Dam Lake," *Journal of Animal and Veterinary Advances*, vol. 10(4), pp. 545-551, 2011.

A Simple Battery Management System Design for an Electrical Vehicle

Emre Akarslan[1], Said Mahmut Cınar[2], Fatih Onur Hocaoglu[3], Fatih Serttas[4]

Abstract

Electrical vehicles get more importance day by day due to some reasons such as increased environmental awareness, reduced fossil sources and travelling costs etc. One of the most important components of such kind of vehicles is the battery management system (BMS). In this study a simple battery management system designed for an electrical vehicle is presented. In this design some important parameters of the battery such as currents, voltages and temperatures are measured. These values are collected and evaluated via an Arduino based BMS. System informs the diver continuously about these values. In the electrical car studied, Lead-Acid batteries are used. In case of an imbalance on battery modules, a passive balancing strategy is realized. In this strategy, higher charged battery is discharged via a discharge resistor to equalize the voltage levels of the batteries. The control unit discharges the higher charged battery until a certain level, switches off the discharge resistor and allows the charge procedure to continue normally. The performance of the BMS is presented and discussed.

Keywords: *Battery Management System, Passive Balancing, Arduino Controller*

1. INTRODUCTION

Electrical vehicle is vehicles that is propelled by one or more electric motors and provide needed energy from the battery. There are different kind of batteries and each of them has own characteristics. To keep the battery safe and to benefit from it efficiently, battery management system (BMS) is employed. The BMS checks single-cell voltages, current and temperatures in a battery pack to guarantee compliance with cell limits. When a cell exceeds the so-called safe operating area (SOA), the BMS limits the power, or shuts down the system completely before an uncontrollable state is obtained [1]. The goals of BMS are to maximize the run-time per discharge cycle, as well as the number of life cycles attainable for the life of the battery [2,3]. There are a lot of studies on battery management design in the literature.

[4] propose a BMS that uses an active charge equalization technique based on a dc/dc converter topology. The technique achieves cell balancing of batteries in a stack in terms of both voltage and charge as the pack is being charged/discharged and in idle periods to maximize the energy and reliability of stack operation. In [5] a typical BMS block diagram using various functional blocks is presented. The state of charge (SOC) estimation has been implemented using Coulomb counting and open-circuit voltage methods, thereby eliminating the limitation of the stand-alone Coulomb counting method. [2] propose a BMS that estimates the critical characteristics of the battery (such as SOC, SOH, and RUL) using a data-driven approach. The estimation procedure is based on a modified Randles circuit model consisting of resistors, a capacitor, the Warburg impedance for electrochemical impedance spectroscopy test data, and a lumped parameter model for hybrid pulse power characterization test data. They show that proposed framework provides a systematic way for estimating relevant battery characteristics with a high-degree of accuracy. [6] presents an efficient power converter (based on a switched-inductor ladder topology), instrumentation, and an embedded control platform that can provide both active balancing and real-time diagnostic capability through electrochemical impedance spectroscopy. A digital proportional-integral controller enforces sinusoidal reference signals from a direct digital synthesizer, enabling the power converter to perturb the cells and extract their impedance. Experimental results showed balancing converter efficiency of 95%.

---

[1] Corresponding author: Afyon Kocatepe University, Department of Electrical Engineering, Afyonkarahisar, Turkey. e.akarslan@gmail.com.

[2] Afyon Kocatepe University, Department of Electrical Engineering, Afyonkarahisar, Turkey, smcinar@gmail.com

[3] Afyon Kocatepe University, Department of Electrical Engineering, Afyonkarahisar, Turkey, fohocaoglu@gmail.com

[4] Afyon Kocatepe University, Department of Electrical Engineering, Afyonkarahisar, Turkey, serttasf@gmail.com

n [7], a design flow from a high-level requirements definition to an actual hardware implementation, using design automation approaches such as verification, synthesis and optimization are presented. Here, graph-based models and algorithms from the domain of formal verification are applied to prove the system properties and are extended to enable synthesis of optimized and correct-by-construction active balancing circuit architectures. [8] presents the design and realization of a wireless lithium-ion battery management system. This system is composed of feedback circuits, a microcontroller, pulse-width modulated (PWM) boost circuits, a boost/buck converter, a wireless monitoring system. The microcontroller could automatically regulate the PWM signal to change the charging and discharging rates of the boost/buck converter. The BMS provides wireless transmission to monitor the charging and discharging status of battery. In [9] a new framework which can accommodate a control-oriented model of a balancing system while maintaining the same measured input and output as an equivalent circuit model is proposed. This allows for model-based design of the balancing control system and other battery management system functions such as state estimation. A model based controller is designed for one balancing system to show how the framework can be used to generate less heat while removing imbalance at the same rate.

In this study, a simple battery management system is designed. In this design current, voltage and temperature parameters are measured and evaluated by a microcontroller. A passive balancing strategy is adopted and stone resistances are employed to discharge the overloaded battery cell to the level of others. The battery management system is tested on a battery pack including 6 Lead-acid batteries connected in series.

2. BATTERY MANAGEMENT SYSTEMS

A battery management system is needed to keep the battery safe and to benefit from it efficiently. Actually the BMS has two main tasks; monitoring some parameters which are important for manage the battery pack such as voltage, current, temperature etc. and controlling the system against the overcharge, high temperature, unbalancing situations etc. Voltage, current and temperature are critic parameters due to they may be reporting a problem in the battery pack. Voltage is one of the important parameters. In both charging and discharging regime, the voltage value of the each battery and battery pack should keep in a certain limit. In charging, on a specified upper limit charging should be ended and in discharging, on a lower limit the load should be deactivated to protect the battery from deep charge. The battery current variate in a certain interval during the driving process. Major changes from this range are the sign of a fault. Furthermore, high current values cause increase on temperature and temperature is a big problem for some types of batteries. Therefore, observing the battery parameters is crucial.

Another important mission of the BMS is to protect the battery cells from unbalancing conditions. The cell capacity variance becomes more and more significant over lifetime due to internal factors (such as capacity degradation, impedance increase) and external factors (such as operation conditions and temperature). This cell imbalance results in two major problems: first of all, it reduces the effective discharge time. In fact, the battery management system (BMS) cuts off the whole battery once the first cell reaches the minimal voltage limitation even though other cells are still usable. Thus, a portion of energy remains unusable in the battery pack [10]. Especially for lithium based batteries, unbalancing conditions between the battery cells cause big problems such as explosion. There are two main balancing method; active and passive balancing. The passive balancing circuit uses balancing resistors to dissipate some energy of high-charged (strong) cells, whereas the active balancing circuit uses energy carriers to transfer energy from strong cells to low-charged (weak) cells. The circuit for passive balancing is very simple and can be implemented at low cost, but the circuit generates heat, and the time required to balance the battery (balancing time) is relatively long [11]. A simple block diagram of a BMS is shown in Figure 1.
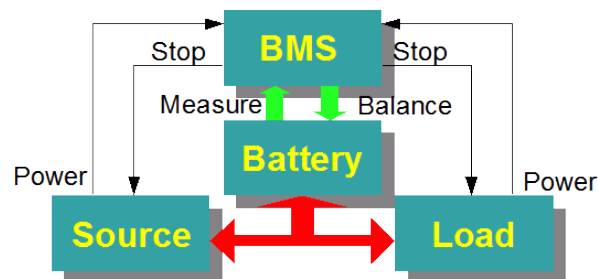

Figure 1. A simple block diagram of a BMS [12]

451

3. DESIGNED BMS AND EXPERIMENTAL RESULTS

In this study, a BMS is designed for an electrical vehicle produced in Afyon Kocatepe University Laboratories. The energy demand of this vehicle is met by the battery pack consisting of the series connection of 6 units 12V lead-acid batteries. The first mission of the designed BMS is measurements. To measure the voltages, an isolated measurement method is considered and ACPL is employed as voltage sensor. The voltage of each battery is measured, separately and sent to the controller for evaluation. A current sensor belong to ACS series is used for current measurement. The temperatures of the batteries are sensed by LM35 temperature sensors. All of the measured parameters are evaluated by the control unit and it is decided what to do. In case of high values in current and temperature in driving process, the driver is warned by activating the warning lamps and the display. If the observed higher than a certain value, control unit deactivates the load to protect system. Arduino Mega micro-controller is used in control unit of this study.

The use of the passive balancing system in the designed BMS is decided. The shunting resistor strategy is used for passive balancing. This strategy is based on removing the excess energy from the higher voltage cell(s) by bypassing the current of the highest cell(s) and wait to until the lower voltage cell(s) to be in the same level [13]. 10 Ω stone resistors are selected as shunting resistors. The picture of the designed BMS on the electrical vehicle is shown in Figure 2. The voltage measurement modules measures the voltage values of each battery in the battery pack send sent the values to control unit. Control unit is evaluated the values and in case of determining the unbalancing, activates the related stone resistor. In this way, the control unit discharges the overloaded battery through the stone resistor until the battery voltage are equalized. Unbalancing status is determined by following equation;

$$V_{max} > V_{avarage} + 50mV \qquad [1]$$

where;

$$V_{avarage} = \frac{V_1 + V_2 + \cdots + V_n}{n} \qquad [2]$$

Figure 2. The picture of the designed BMS on the electrical vehicle

The control unit deactivates the related discharge resistor when the voltage of the battery reaches the average voltage value. To test the designed system in laboratory environment, a voltage imbalance was created between the battery cells by loading one cell more than others. Later, the cell voltages are measured as follow: " 12.35, 12.22, 12.19, 12.20, 12.21, 12.17". In this case, the average value is calculated as 12.23 V and if the maximum cell voltage is bigger than 12.28 V (12.23V + 50mV), BMS will switch on the discharge resistor. As seen Figure 3, BMS switches on the discharge resistor of the Battery 1 (terminal voltage 12.35V). The discharge continues until the terminal voltage of the Battery 1 drops to average voltage value.
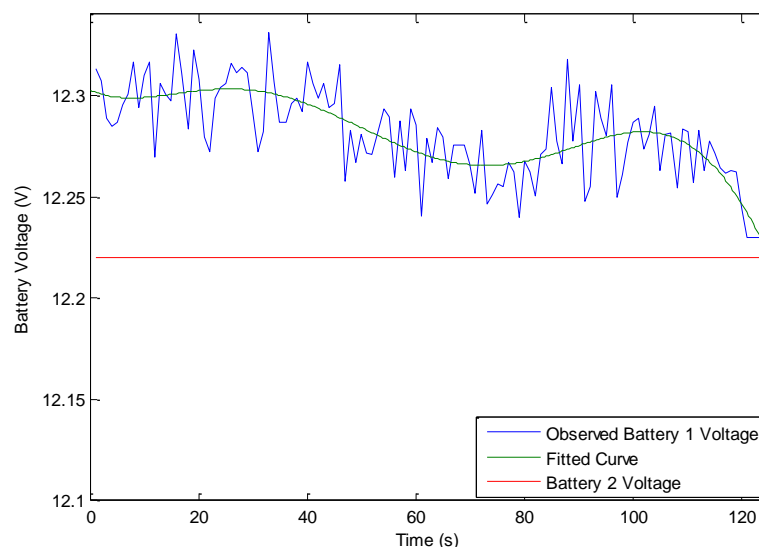
Figure 3. Change of the voltage after the discharge resistor switch on.

The control unit, controls the voltage balance according to Eq. 1 and Eq. 2, continuously, and in case of any imbalance, switch on the related discharge resistor. In the test, the battery cell is discharged more than 100 mV. However, in real time applications, the load value to be discharged will be much lower because the system will immediately switch on in case of any imbalance.

4. CONCLUSION

In the presented study a simple battery management system design for an electrical vehicle is implemented. Arduino is selected as controller for the battery management system. To test the performance of the system: current, temperature and voltage parameters are measured. A passive balancing schema is designed for balancing and in case of any imbalance on battery voltages in charging process; the more loaded battery is discharged via discharge resistor. Experiments show that, the battery management system observe the related parameters and provides load balancing by performing its task successfully when needed. The active balancing system will be investigated and the performance of this system will be compared with the passive system, as a future work.

ACKNOWLEDGeMENT

REFERENCES

[1]   C. Campestrini, M. F. Horsche, I. Zilberman, T. Heil, T. Zimmermann and A. Jossen, "Validation and benchmark methods for battery management system functionalities: State of charge estimation algorithms", Journal of Energy Storage, vol. 7, pp. 38–51, 2016.

[2]   B. Pattipati, C. Sankavaram, and K. R. Pattipati, "System Identification and Estimation Framework for Pivotal Automotive Battery Management System Characteristics", IEEE Transactions on Systems, Man, and Cybernetics—Part C: Applications and Reviews, Vol. 41, No. 6, pp. 869-884, November 2011.

[3]   E. Bordeaux, "Portable Power Management—A Holistic Perspective," Intersil Corp., 2002.

[4]   S. Yarlagadda, T. T. Hartley and I. Husain, "A Battery Management System Using an Active Charge Equalization Technique Based on a DC/DC Converter Topology", IEEE Transactions on Industry Applications, Vol. 49, No. 6, pp. 2720-2729, November/December 2013.

[5]   K. W. E. Cheng, B. P. Divakar, H. Wu, K. Ding, and H. F. Ho, "Battery-Management System (BMS) and SOC Development for Electrical Vehicles", IEEE Transactions on Vehicular Technology, Vol. 60, No. 1, pp. 76-88, January 2011.

[6]   E. Din, C. Schaef, K. Moffat and J. T. Stauth, "A Scalable Active Battery Management System With Embedded Real-Time Electrochemical Impedance Spectroscopy", IEEE Transactions on Power Electronics, Vol. 32, No. 7, pp. 5688-5698, July 2017.

[7]   S. Steinhorst and M. Lukasiewycz, "Formal Approaches to Design of Active Cell Balancing Architectures in Battery Management Systems", ICCAD '16, November 07-10, 2016, Austin, TX, USA.

[8] C. W. Wang, L. J. Lu, Z. X. Chi and J. L. You, "A novel structural design of wireless lithium-ion battery management system (BMS) by using pulse width modulation method for charging and discharging", Proceedings of the IEEE International Conference on Advanced Materials for Science and Engineering IEEE-ICAMSE 2016 - Meen, Prior & Lam (Eds), pp. 204-206, 2016.

[9] T. Bruen, J. Marco and M. Gama, "Model Based Design of Balancing Systems for Electric Vehicle Battery Packs", IFAC-PapersOnLine vol. 48-15, pp. 395–402, 2015.

[10] N. Bouchhima, M. Schnierle, S. Schulte, K. P. Birke, "Active model-based balancing strategy for self-reconfigurable batteries", Journal of Power Sources, vol. 322, pp. 129-137, 2016.

[11] K. M. Lee, Y. C. Chung, C. H. Sung, and B. Kang, "Active Cell Balancing of Li-Ion Batteries Using LC Series Resonant Circuit", IEEE Transactions on Industrial Electronics, Vol. 62, No. 9, pp. 5491-5501, September 2015.

[12] http://lithiumate.elithion.com.

[13] M. Daowd, N. Omar, P. V. D. Bossche, J. V. Mierlo, "Passive and Active Battery Balancing comparison based on MATLAB Simulation", Vehicle Power and Propulsion Conference (VPPC), 6-9 Sept. 2011, IEEE.

BIOGRAPHY

Emre Akarslan was born in Afyonkarahisar, Turkey, in 1980. He received the B.S. degree in electrical and electronics engineering from the Selcuk University, Konya, Turkey in 2004 and M.S. degree in electrical education from Afyon Kocatepe University, Afyonkarahisar, Turkey. He received the Ph.D. degree in electrical and electronics engineering from Osmangazi University, Eskisehir, Turkey, in 2014. He is an Assistant Professor with the electrical engineering department of Afyon Kocatepe University since 2017.

Said Mahmut Cınar is an Assist. Professor in Electrical Engineering Dept. at the Afyon Kocatepe University. He completed his B.S. in Electrical Engineering at the Kocaeli University in 2003. He got his M.S. in the Electrical Education Department at the University of Afyon Kocatepe in 2007. He received his Ph.D. in Electronic and Computer Education Department at Sakarya University, Turkey in 2011. His work focuses on applications of Energy efficiency, Data acquisition, Automation technologies, Renewable energy resources, Power Electronics, and microcontroller based embedded design.

Fatih O. Hocaoglu was born in Afyonkarahisar, Turkey, in 1979. He received the B.S. degree in electrical and electronics engineering from the Pamukkale University, Denizli, Turkey in 2002 and the Ph.D. degree in electrical and electronics engineering from Anadolu University, Eskisehir, Turkey, in 2008. From 2002 to 2008 and from 2008 to 2011 he was a Research Assistant with the Anadolu University and Afyon Kocatepe University, respectively. He was an Assistant Professor with the Electrical Engineering department from 2011 to 2014. He is Associate Professor with the electrical engineering department of Afyon Kocatepe University since 2014. He is head of the Electrical Engineering Department since 2011. His research interests include solar energy, wind energy, hybrid energy systems, electrical installations and electrical vehicles he holds a patent

Fatih Serttas was born in Afyonkarahisar, Turkey, in 1989. He received the B.S degree in Electrical and Electronics Engineering from the Pamukkale University, Denizli, Turkey in 2011 and the MSc degree in Electrical Engineering Renewable Energy Systems from Afyon Kocatepe University in 2015. He is still PhD student (PhD Candidate) in Electrical Engineering from Afyon Kocatepe and Pamukkale University joint PhD program. He is Research Assistant in Afyon Kocatepe University since 2012. His research interests include solar energy, high voltage techniques, power systems and electrical vehicles.

Solar Radiation Modeling with Adaptive Approach

Emre Akarslan[1], Fatih Onur Hocaoglu[2]

Abstract

The unsustainable formation of fossil fuels, increase the interest on different resources and this leads to greater emphasis on clean resources. Solar energy is one of the popular sources among the renewables. Electricity generation from PV panels directly related to the solar radiation value measured on surface of the panel. Modeling of solar radiation is important due to manage the integration of different sources to the grid. In this study, previously developed Adaptive Approach method is used for modeling the solar radiation values. This method combines linear prediction filter method with an empiric approach. Linear prediction filter used in this study utilize the current value of the solar radiation to predict next hour's solar radiation value while the empiric model utilize from the current value of the solar radiation and the deviation on extraterrestrial radiation. One year solar radiation data belong to Van region is used in this study. The accuracies of the forecasting results are compared and discussed.

Keywords: *Solar Radiation Forecasting, Adaptive Approach, Empiric Model, Linear Prediction Filter*

1. INTRODUCTION

The best solutions for alternative energy sources, such as some of the solar energy and photovoltaic (PV) systems are rapidly gaining acceptance [1]. In order to integrate the electricity generated by solar energy into the grid, solar irradiation must be reasonably well forecasted, where deviations of the forecasted value from the actual measured value involve significant costs [2]. Several methods are used before for solar radiation forecasting. [3] used the combination of unsupervised k-means clustering algorithm and artificial neural networks (ANN) for hourly global horizontal solar radiation forecasting. They show that the combination of these models provide better results. In [2] a univariate Dynamic Harmonic Regression model set up in a State Space framework for short-term solar irradiation forecasting is proposed. This method is based on the frequency domain and provides a fast automatic identification and estimation procedure. Their results show that the Dynamic Harmonic Regression achieves the lowest relative Root Mean Squared Error for a forecast horizon of 24 h ahead. In [1] neural networks to predict solar radiation is used. They categorized the review under three major performance schemes such as delay, number of neurons and activation function for establishment of neural network architecture.

[4] applied Support Vector Regression (SVR), Gradient Boosted Regression (GBR), Random Forest Regression (RFR) as well as a hybrid method to combine them to downscale and improve 3-h accumulated radiation forecasts provided by Numerical Weather Prediction (NWP) systems for seven locations in Spain. They showed that Machine Learning methods are quite effective. In [5] a novel solar radiation forecasting method based on a novel game theoretic self-organizing map (GTSOM) is proposed. They compared the proposed method with that of the K-means and the original SOM. They show that comparison demonstrates the superior performance of the proposed approach. [6] used satellite data to improve solar radiation forecasting with Bayesian Artificial Neural Networks. They show that forecasting skills are improved by including exogenous inputs to the model by using global horizontal solar irradiance satellite data from surrounding area.

In [7] linear prediction filter approach for hourly solar radiation forecasting is proposed. In this approach solar radiation time series is converted to 2-D image and this new form of the data provide better understanding about the seasonal and daily behavior of the solar data. The optimum filter coefficients are determined by scanning image with a filter template. [8] improved the linear prediction approach by

---

developing multi-dimensional filter templates. In their method, the images obtained from different time series such as temperature, extraterrestrial and solar radiation data etc. are linked each other with filter templates. This method provides utilize from different parameters for solar radiation forecasting and up to 40% improvement is achieved as per to linear prediction filter approach. In [9] a novel adaptive approach (NAA) for solar radiation forecasting is proposed. This approach integrates an empiric model to linear prediction filter approach to improve the prediction accuracy. The solar radiation data are predicted using different methods for different weather condition cases. Two different strategies are used to decide the prediction method. Seasons and clearness index values are employed to select the forecasting method. The results show that the accuracy of the forecast is considerably improved using proposed adaptive prediction approach.

In this paper, the adaptive approach method which is developed previously [9], is employed to determine next hour solar radiation values. The clearness index values are used to determine the forecasting method. If the clearness index value is greater than a specified value, linear prediction filters otherwise an empirical model is used. The solar radiation data belong to Van region is used to test the performance of the adaptive approach method. The organization of the paper is as follows. The data used for this study are described in Section 2. The adaptive approach method is explained in Section 3. The experimental results are illustrated in Section 4. Finally, conclusions are explained in Section 5.

2. DATA USED

In this study, solar radiation data belong to Van region of Turkey is used. Van region has a good insolation characteristic as seen in Fig. 1. The solar radiation data belong to Van region is taken from the Turkish State Meteorological Service (DMI). The variation in the solar irradiance value over a 1-year period from 2014 is shown in Figure 2. The extraterrestrial irradiance is the intensity of the sun at the top of the Earth's atmosphere [8,10]. Therefore, the actual measured data on the earth's surface must be less than the extraterrestrial irradiance. The extraterrestrial irradiance can be calculated as follow:

$$I_s = CSin(\varphi)/24R^2 \tag{1}$$

where I_s is the total radiation falling on the atmosphere; C is the solar constant assumed to be 1367 (W/m^2); and R is the solar radius vector (assumed to be 1). Then the solar elevation angle is calculated by using following equation:

$$sin(\varphi) = sin(L)sin(D) + cos(L)\cos(D)\cos(h) \tag{2}$$

Here, L is the latitude of the location, D is the declination angle of the sun, and h is the solar hour angle.
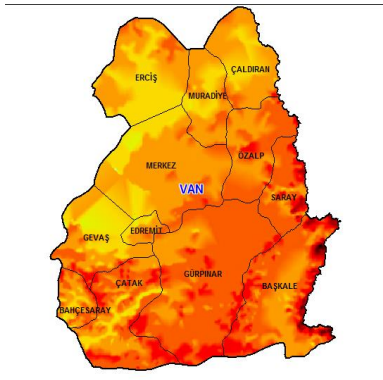

Figure 1. The insolation map of the Van region

Forecasting model is selected by using clearness index values. These values are calculated by dividing solar radiation value to extraterrestrial radiation value for each hour [11] as seen in Eq. 3:

$$K_t = I/I_0 \tag{3}$$

Here, K_t, I and I_0 represent the clearness index, solar radiation and extraterrestrial radiation, respectively.
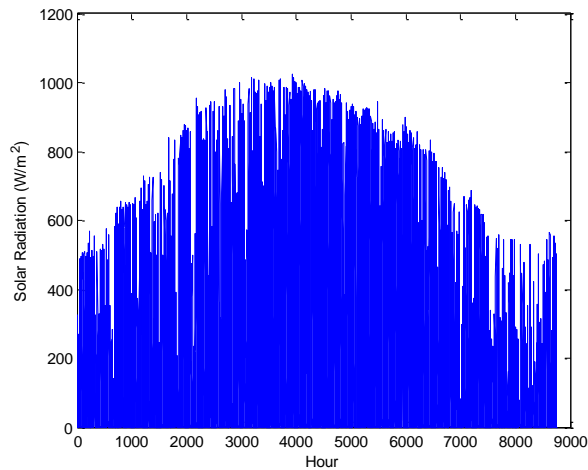
Figure 2. Variation of the solar radiation data over a 1-year period

3. ADAPTIVE APPROACH METHOD

The adaptive approach method includes combination of linear prediction filters and an empiric model. For a better understanding, linear prediction filter and empiric model used are explained in this section. Linear prediction filters for solar radiation forecasting are firstly introduced by [7]. In this approach solar radiation time series is converted to 2-D image. This image provides better understanding of seasonal and daily behavior of solar radiation. Furthermore, image processing techniques can be applied to this data after conversion. Linear prediction filter scan overall image and optimum filter coefficients which will be used for prediction are determined. In this study, filter template which use the actual data to predict one hour later data is used. Consider the 2-D linear prediction filter as follow:

$$Z_{i,j} \qquad Z_{i,j+1} = ? \tag{4}$$

The prediction pixel was determined by using past pixels with the following formula:

$$\check{Z}_{i,j+1} = Z_{i,j}.a_1 \tag{5}$$

i,j and $Z_{i,j}$ are identify the row and column number of the pixel and the pixel value, respectively. In 2-D linear filter approach, the estimation $\hat{Z}_{i+1,j+1}$ is considered as a linear combination of past samples. After calculated prediction error for each (i,j) coordinates, the energy of total prediction error is calculated with Eq. 6:

$$\varepsilon = \sum_{i=2}^{m} \sum_{j=2}^{n} \varepsilon_{i,j}^{2} \tag{6}$$

where m and n identify the size of image. By equating to zero the derivative of this function, the filter coefficients which minimize the Eq. 6 are obtained and the solution yields the following equation:

$$\begin{bmatrix} R_{11} & R_{12} & R_{13} \\ R_{21} & R_{22} & R_{23} \\ R_{31} & R_{32} & R_{33} \end{bmatrix} \begin{bmatrix} a_1 \\ a_2 \\ a_3 \end{bmatrix} = \begin{bmatrix} r_1 \\ r_2 \\ r_3 \end{bmatrix} \tag{7}$$

where R_{ij} is the correlation value between the past values, a_i is the linear filter coefficients and r_k is the correlation between the past and predicted pixel.

2-D linear prediction filters have a good forecasting performance but this approach good at linear data. The solar radiation data generally nonlinear due to weather conditions such as rain, wind, cloud etc. To overcome this weakness, an empiric model can be integrated to the linear prediction filters [9]. The empiric model used in the adaptive approach method is as follow:

$$S(t+1) = S(t) + (E(t+1) - E(t)) \tag{8}$$

457

In this empiric approach, the next hour solar radiation value is calculated by summing the solar radiation with the difference of actual and next hour extraterrestrial radiation. In the integration strategy, clearness index value is employed to decide which method will be used in prediction. Clearness index value is the ratio of solar radiation to the extraterrestrial radiation in a certain time and formulated with Eq. 3. In the used strategy, if the clearness index value is smaller than 0.5, the next hour solar radiation value is predicted by empiric model otherwise; the linear prediction filters are employed.

4. EXPERIMENTAL RESULTS

In this study adaptive approach method is used for hourly solar radiation forecasting. In this paper clearness index value is employed to decide combining strategy of adaptive approach method. The solar radiation data belong to Van region of Turkey is used to test this method. Van region has a good insolation characteristic. The Root Mean Square Error (RMSE) and Mean Bias Error (MBE) assessment criteria are used to evaluate the performance of adaptive approach method. The RMSE is a commonly used measure of the differences between the values extracted by a forecasting model and the observed values. The value of RMSE provides information on the short term performance [12]. The MBE provides information in the long term performance of the correlations by allowing a comparison of the actual deviation between predicted and measured values term by term. The MBE is used to describe whether a model over-(positive value) or under-(negative value) predicts the observation and has the same units as the measured variable-parameter. The ideal value of MBE is 'zero' [12,13]. To illustrate the performance of the adaptive approach method, experimental results with Liner Prediction filter and adaptive approach method are compared in Table 1.

Table 1. Experimental Results on solar radiation data of Van region, Turkey

	RMSE (W/m^2)	MBE (W/m^2)
Linear Prediction Filter	104.23	8.97
Adaptive Approach Method	76.08	11.76

As seen in Table 1, adaptive approach method outperforms the Linear Prediction Filter according to RMSE criteria. Nearly 25% improvement on prediction performance is achieved by using adaptive approach method. MBE result with adaptive approach bigger than the linear prediction filter. This means adaptive approach method over predicts the observation and these predictions are generally greater than linear prediction filter's. However, overall estimations with adaptive approach method are better than the linear prediction filter. The correlations between the observed and predicted values are shown in Figure 3.
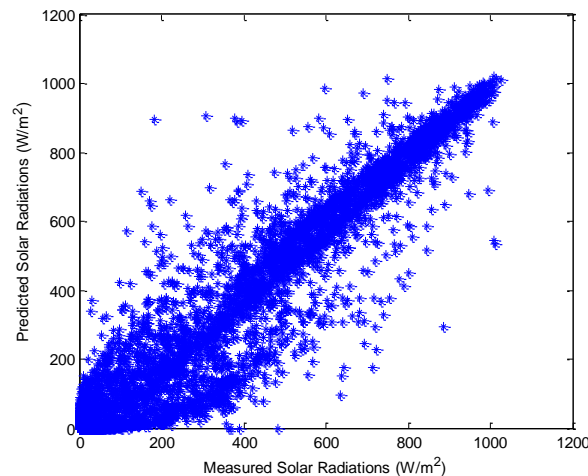

Figure 3. Correlations between the observed and predicted data.

As seen in Figure 3, the predicted values are correlated with the observed values of solar radiation. The prediction results are closely matching observed data along the diagonal axis. The slope of the fit nearly 45^0 and scatter is so narrow. These indicate a good prediction performance. Figure 4 illustrates the mesh plot of the prediction error. The error pixels are almost uncorrelated with each other. The uncorrelated samples indicate that the prediction almost totally exploits the predictable part of the data. Therefore, the model works with very good accuracy.
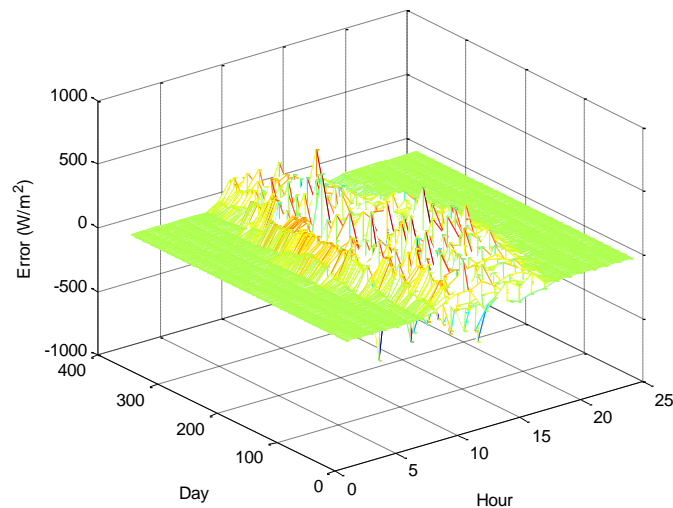
Figure 4. Mesh plot of the prediction error with adaptive approach method.

5. CONCLUSION

The adaptive approach method is used in this study for hourly solar radiation modeling. adaptive approach method, combines linear prediction filter and an empiric model to improve the prediction performance. The selection of the model is managed by using actual clearness index value. The solar radiation data used in this study belongs to Van region of Turkey and measure in 1 year period from 1st Jan to 31th Dec 2014. To test the performance of the adaptive approach method, results are compared to results obtained with linear prediction filters. The experimental results show that the adaptive approach method outperforms the linear filter approach. The performance of different combining strategies with different filter templates and empiric models can be investigated as a future work.

REFERENCES

[1]. K. Benmouiza and A. Cheknane, "Forecasting hourly global solar radiation using hybrid k-means and nonlinear autoregressive neural network models," Energy Convers. Manag., vol. 75, pp. 561–569, Nov. 2013.

[2]. J. R. Trapero, N. Kourentzes, and A. Martin, "Short-term solar irradiation forecasting based on Dynamic Harmonic Regression," Energy, vol. 84, pp. 289–295, May 2015.

[3]. Y. Kashyap, A. Bansal, and A. K. Sao, "Solar radiation forecasting with multiple parameters neural networks," Renew. Sustain. Energy Rev., vol. 49, pp. 825–835, Sep. 2015.

[4]. Y. Gala, Á. Fernández, J. Díaz, and J. R. Dorronsoro, "Hybrid machine learning forecasting of solar radiation values," Neurocomputing, vol. 176, pp. 48–59, May 2015.

[5]. M. Ghayekhloo, M. Ghofrani, M. B. Menhaj, and R. Azimi, "A novel clustering approach for short-term solar radiation forecasting," Sol. Energy, vol. 122, pp. 1371–1383, Dec. 2015.

[6]. L. Mazorra Aguiar, B. Pereira, M. David, F. Díaz, and P. Lauret, "Use of satellite data to improve solar radiation forecasting with Bayesian Artificial Neural Networks," Sol. Energy, vol. 122, pp. 1309–1324, Dec. 2015.

[7]. F. O. Hocaoglu, O. N. Gerek, and M. Kurban, "Hourly solar radiation forecasting using optimal coefficient 2-D linear filters and feed-forward neural networks," Sol. Energy, vol. 82, no. 8, pp. 714–726, Aug. 2008.

[8]. E. Akarslan, F. O. Hocaoglu, and R. Edizkan, "A novel M-D (multi-dimensional) linear prediction filter approach for hourly solar radiation forecasting," Energy, vol. 73, pp. 978–986, Aug. 2014.

[9]. E. Akarslan and F. O. Hocaoglu, "A novel adaptive approach for hourly solar radiation forecasting," Renew. Energy, vol. 87, pp. 628–633, Mar. 2016.

[10]. R. G. Allen, "Environmental, and E. Water Resources Institute," Task Comm. Stand. Ref. ASCE Stand. Ref. evapotranspiration equation. Reston, Va. Am. Soc. Civ. Eng., 2005.

[11]. N. Z. Al-Rawahi, Y. H. Zurigat, and N. A. Al-Azri, "Prediction of hourly solar radiation on horizontal and inclined surfaces for Muscat/Oman," J. Eng. Res., vol. 8, no. 2, pp. 19–31, 2011.

[12]. P. T. Nastos, A. G. Paliatsos, K. V. Koukouletsos, I. K. Larissi, and K. P. Moustris, "Artificial neural networks modeling for forecasting the maximum daily total precipitation at Athens, Greece," Atmos. Res., vol. 144, pp. 141–150, Jul. 2014.

[13]. K. P. Moustris, I. C. Ziomas, and A. G. Paliatsos, "3-Day-Ahead Forecasting of Regional Pollution Index for the Pollutants NO2, CO, SO2, and O3 Using Artificial Neural Networks in Athens, Greece," Water, Air, Soil Pollut., vol. 209, no. 1–4, pp. 29–43, Aug. 2009.

BIYOGRAPHY

Emre Akarslan was born in Afyonkarahisar, Turkey, in 1980. He received the B.S. degree in electrical and electronics engineering from the Selcuk University, Konya, Turkey in 2004 and M.S. degree in electrical education from Afyon Kocatepe University, Afyonkarahisar, Turkey. He received the Ph.D. degree in electrical and electronics engineering from Osmangazi University, Eskisehir, Turkey, in 2014. He is an Assistant Professor with the electrical engineering department of Afyon Kocatepe University since 2017.

Fatih O. Hocaoglu was born in Afyonkarahisar, Turkey, in 1979. He received the B.S. degree in electrical and electronics engineering from the Pamukkale University, Denizli, Turkey in 2002 and the Ph.D. degree in electrical and electronics engineering from Anadolu University, Eskisehir, Turkey, in 2008. From 2002 to 2008 and from 2008 to 2011 he was a Research Assistant with the Anadolu University and Afyon Kocatepe University, respectively. He was an Assistant Professor with the Electrical Engineering department from 2011 to 2014. He is Associate Professor with the electrical engineering department of Afyon Kocatepe University since 2014. He is head of the Electrical Engineering Department since 2011. His research interests include solar energy, wind energy, hybrid energy systems, electrical installations and electrical vehicles he holds a patent.

The Investigation of Rock Mass Characteristics of the Caglayan Dam Reservoir Area (Western Anatolia) by *Using Geophysical Parameters*

Tumay Kadakci Koca[1], Aykut Tuncel[2], Mehmet Yalcın Koca[1]

Abstract

Geophysical methods are commonly used to solve geological, geotechnical and environmental problems. Investigation of the dynamic properties of rock masses and water table level in a dam site is one of these problems. In this study, an electrical resistivity tomography (ERT) survey was performed to investigate the water table level and geological units were evaluated in terms of being foundation rock for Caglayan Dam in Manisa city (Western Anatolia). Dynamic elasticity modulus, poisson's ratio, shear modulus and lame constant were identified for the carbonate and clastic sedimentary rocks. The resistivity data were acquired along 3 profiles by a Wenner-Schlumberger electrode array and were processed by a tomographic inversion technique. Geologic units up to a depth of 24 m were clearly revealed by the electrical resistivity imaging and the results were compared with the multichannel analysis of surface waves (MASW) data along 6 profiles and logs from two drillholes.

Resistivity values of the layers were defined between 15 Ωm and 750 Ωm at P1 and P2 profiles. Resistivity values at P3 profile are changing about 15 Ωm and 250 Ωm and well correlated with the high resistivity values derived from 2D resistivity models. Each profile demonstrates a high resistivity top layer and low resistive zones following the depth of 10 m are found. Low resistivity values are associated with high water and clay content of the sediments. Water table level indicates that once the water is retained in the reservoir, it may be discharged towards the permeable layers on the left and right banks of the dam structure. As a consequence, seepage problems may arise in the left and right banks. Dynamic elastic constants of the rock mass were calculated from the P and S-wave velocities derived from MASW method along six profiles. The amount of settlements will be lower than the permissible settlement (12 mm) beneath the dam structure due to the favourable dynamic elastic properties of the sedimentary rocks.

Keywords: *Borehole Logging, Dam, ERT, MASW, Seepage*

1. INTRODUCTION

The geological investigation of Caglayan Dam site is important since active faults are predominant in the region, in addition the Neogene aged sedimentary rocks are unconsolidated and weak rocks. Caglayan Dam is located in approximately 22 km southeast of Akhisar village (Figure 1). A dam site is evaluated mainly in terms of embankment and bank stabilities, bearing capacity and settlement of the foundation, seepage and permeability. In this study, geophysical methods such as electrical resistivity tomography (ERT) and multichannel analysis of surface waves (MASW) methods were used in order to determine the variation of water table level and geotechnical parameters of the rock mass, respectively. In addition, different geological layers and zones were identified.

ERT method was used as a practical and cheap tool for examining lithological units in a dam site, landslides and embedded geological structures in previous studies ([1]-[4]).

Electrical resistivity (or conductivity), which is an easy geophysical parameter to measure in the field, exhibits a wide range of values in nature, from 1 ohm.m in clay or contaminated soil to more than 104 ohm.m in rocks like limestone or granite ([5]). Recent developments in the data acquisition have led to multi

---

electrode resistivity equipment and interpretation of the data in the form of electrical resistivity tomography (ERT). Electrical resistivity tomography has various applications in the landslides studies, groundwater explorations, investigations in waste disposal areas, defining physical properties of soil and detection of faults ([6]).
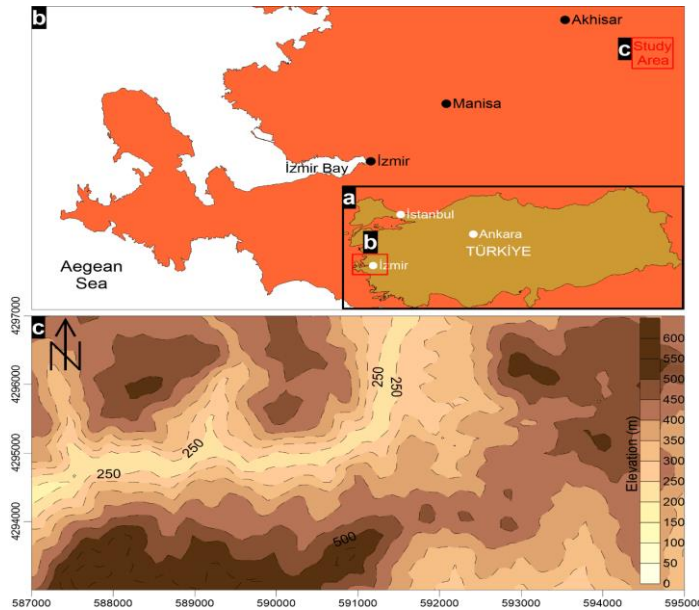

Figure 1. Location of the study area

2. GEOLOGY OF THE STUDY AREA

The youngest to oldest geological units in the study area are alluvium and talus, Kucukderbent Formation, Yenikoy Formation, Gocek Formation and the metamorphic rocks of Menderes Massif, respectively ([7]-[13]). The observed landslides in the study area and the maximum ground water level when the water is retained in the dam are also mapped (Figure 2).

Alluvium and talus are consisting of, clay that derived from basement unit, silt, sand and block sized materials.

Kucukderbent Formation majorly comprises calcareous shale, thin bedded limestone, mudstone and minor clastics and tuffaceous unit. Coal layer at the study area is overlaid by this formation.

Hamit member of Yenikoy Formation dominantly includes sandstone and fewer conglomerate, mudstone and claystone. Hamit member of this formation which has total thickness of 75 meters was widely spread northern part of the Hamit-Cıtak boundary. Limestone in Hamit member includes fresh water algae which indicates the lacustrine environment.

Ilıcak member of Gocek Formation mainly comprises non-compacted conglomerate, cross-bedded sandstone and limestone with algae. Gocek formation was unconformably overlaid by Yenikoy Formation.

E-W trending normal faults which forms the valley were identified. Similarly to the tectonics of Aegean region, NE-SW trending thrust faults and NW-SE trending normal faults were determined as well.

The geological units were defined in boreholes (BH-11, 4, 18, 34, 35) and correlated with the MASW profiles. As a result, the first 17 m from the ground level is composed of alluvium and embedded rock block underlained by breccia zone. Below this zone, Neogene aged, highly fractured sedimentary rocks are encountered and unconformably overlying the basement rock metamorphics of Menderes Massif.

Field discontinuity survey was performed in order to define bedding planes, joint sets and foliations. As a result, the sedimentary rock mass is defined to be highly fractured and an anticline axis is assumed to be intersecting the stream bed due to the compressional regime.
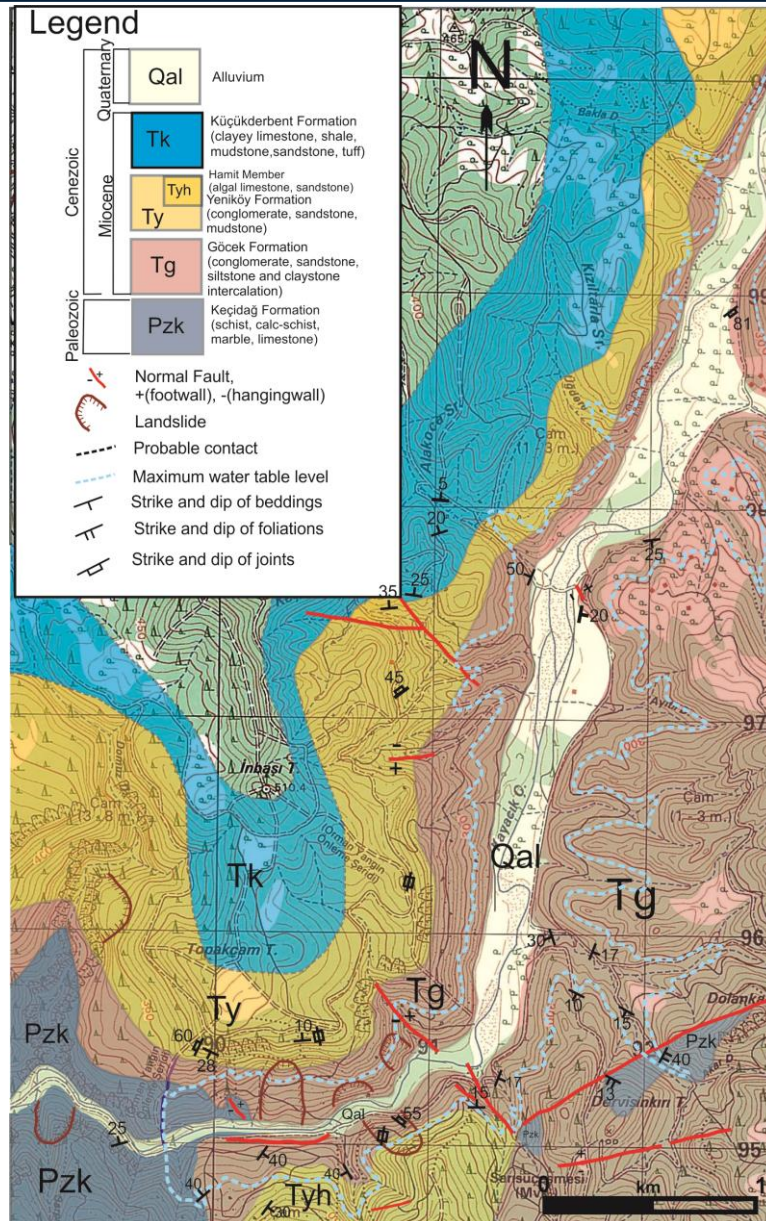
Figure 2. Geological map of the study area

2.1. Geophysical Investigations

Revealing the resistivity distribution in the subsurface may help identifying structural features, fluid content and sub- surface fluid movement. As a result of the developments in multielectrode resistivity equipment and data acquisition technique, the electrical imaging has become a standard tool in near-surface geophysical surveys. The main components of the system are a multicore cable, a switching unit and a resistivity meter ([14]). The method is based on recording electrical potential difference between two certain electrodes generated by current injected by means of other two certain electrodes.

Two-dimensional electrical imaging surveys were performed along the three profiles (the profiles 1–3) in the different sections of the study area. The profiles are located both in upstream and downstream area and overlapping with the MASW profiles (Figure 3).
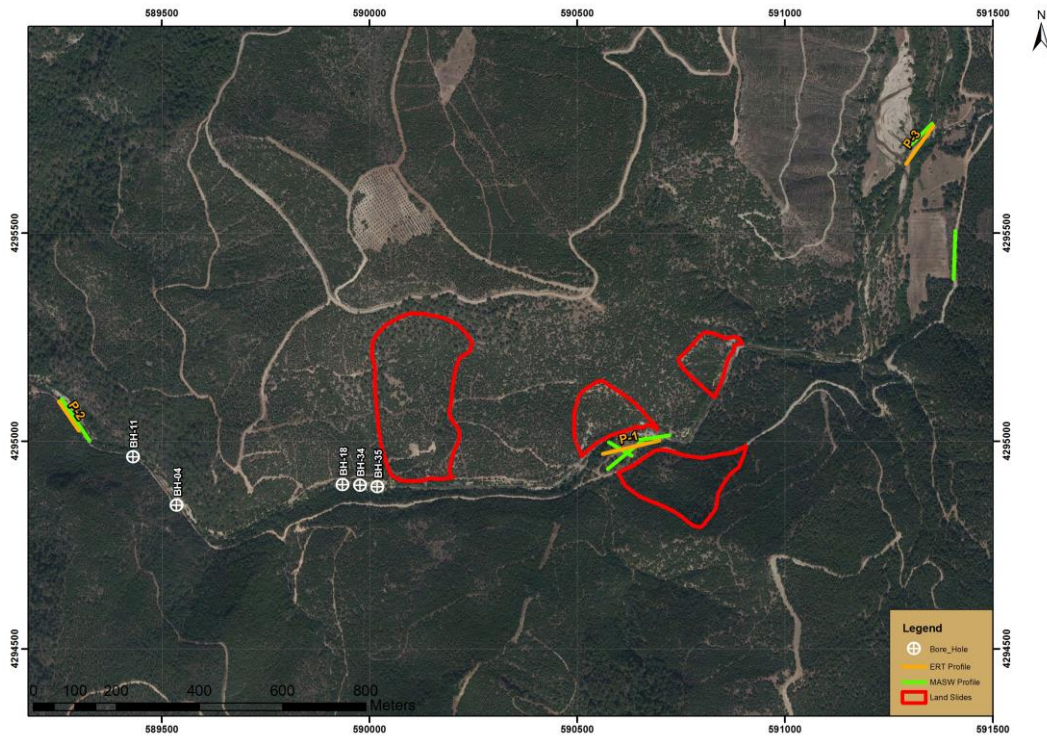
Figure 3. Illustration of MASW and ERT profiles, pre-failed slopes and boreholes.

The system was composed of two multicore cables, each having 30 take-outs, a manual switching unit and a resistivity meter. The profile lengths were variable. P1 profile was about 140 m, P2 profile was about 84 m and P3 was about 112 m. Data acquisition was performed by a Wenner–Schlumberger array using a 29-electrode cable with changing (5 m for P1, 3 m for P2 and 4 m for P3) electrode spacing.

The measured apparent resistivity data were inverted using the smoothness-constrained least-squares inversion method of the Res2Dinv software ([15]). This method attempts to find the subsurface resistivity by trying to fit the measured and calculated data in an iterative manner. The Jacobian matrix was recalculated for all iteration steps and a homogeneous half-space, which is derived from the averaged value of the apparent resistivities, was used for the initial model.

The ground water levels in drillholes BH-11, BH-4, BH-18, BH-34, and BH-35 are 17.9 m, 30,65 m, 9.90 m, 9.8 m, and 11.45 m respectively. These are well correlated with the estimated ground water levels from ERT method (Figure 4).
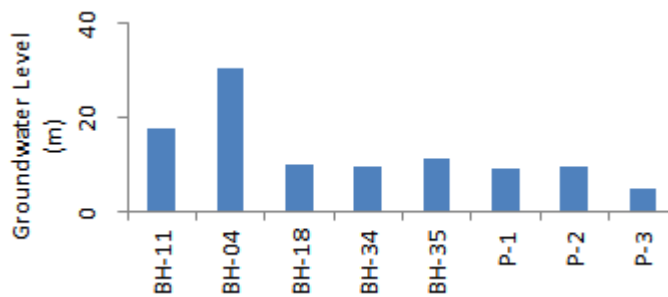
Figure 4. Groundwater level defined in boreholes and ERT profiles

2.2. Geotechnical Parameters

Rock mass consists of discontinuities which control the strength and stability. However, rock material is intact and thus generally does not involve the inhomogeneities which are present in the rock mass. Thus, laboratory testing of rock materials give overestimated values of strength and elastic constants. In the case of laboratory testing, rock mass can be classified by rock mass classification systems such as RMR, Q and GSI. In order to directly estimate the geotechnical parameters of the rock mass, seismic wave velocities derived

from geophysical methods are commonly used. The geotechnical parameters such as density (ρ), modulus of elasticity (E), shear modulus (G), Poisson's ratio (υ), Lamé parameter (λ) and bulk modulus (K) were calculated from the weighted mean P and S- wave velocities for different geological layers obtained from MASW method and represent the rock mass (Table 1). MASW profiles are presented in [16]. The soil and rock were distinguished according to the threshold value of 700 m/s for shear wave velocity. S-wave velocities lower than the threshold value represents soil and the higher ones represent rock mass.

Table 1. Geotechnical parameters of the rock masses in the dam site

Vp (m/s)	Vs (m/s)	γ (g/cm^3)	E (MPa)	G (MPa)	μ	λ (MPa)	K (MPa)	Description
1694,70	454,02	2,03	1223,64	418,67	0,46	4995,86	5274,98	Alluvium+embedded rock blocks
1888,34	585,40	2,16	2146,21	741,69	0,45	6234,12	6728,58	Breccia zone subjected to rock failures
1998,00	763,90	2,31	3818,44	1349,85	0,41	6534,58	7434,48	Fractured limestone, conglomerate, sandstone and intercalations
2270,71	972,63	2,46	6451,27	2324,53	0,39	8020,54	9570,23	Metamorphic rocks belonging to Menderes Massif (schist and marble intercalations)

Bearing capacity and settlement investigation the foundation rock of the dam body is beyond the scope of this study. However, when the upper 17 m part of the ground profile which includes alluvium and breccia zone (soil) is excavated, the foundation rock beneath that depth is favourable for dam site if only there are no seepage problems.

3. RESULTS AND DISCUSSION

Water saturation degree of geological units has almost no effect on the S-wave velocities. Besides, electrical resistivity values mainly depend on water saturation. Therefore, ERT was used to define the water table level. MASW data were evaluated to distinguish the lithological units and determine the geotechnical parameters belonging to these units.

According to the obtained resistive tomography results, there is a very low resistivity layer after about 5-10 meters of depth for 3 profiles. It can be said that the water content of this layer is high and water table level is taking place after this limit. As the water table level is at 5 to 10 m depth below the stream bed and the orientation of bedding planes, it can be interpreted that the stream bed discharges towards the right and left banks of the reservoir area. The estimated ground water levels based on the ERT results are well matches with the drillhole data.

According to the ERT results, the resistivity values of P1 and P3 profiles are changing in the vertical direction and the geological units are horizontally layered. On the contrary, lateral changes are observed around 50 meters on the P2 profile where the upper layers are sharply interrupted by a relatively low resistivity body (Figure 5). It can be assumed that the difference is caused by rock blocks with high resistivity embedded in alluvium. The coarse grained talus is also frequently encountered in the study area. Rock blocks covered partly by alluvium were defined also in MASW model.
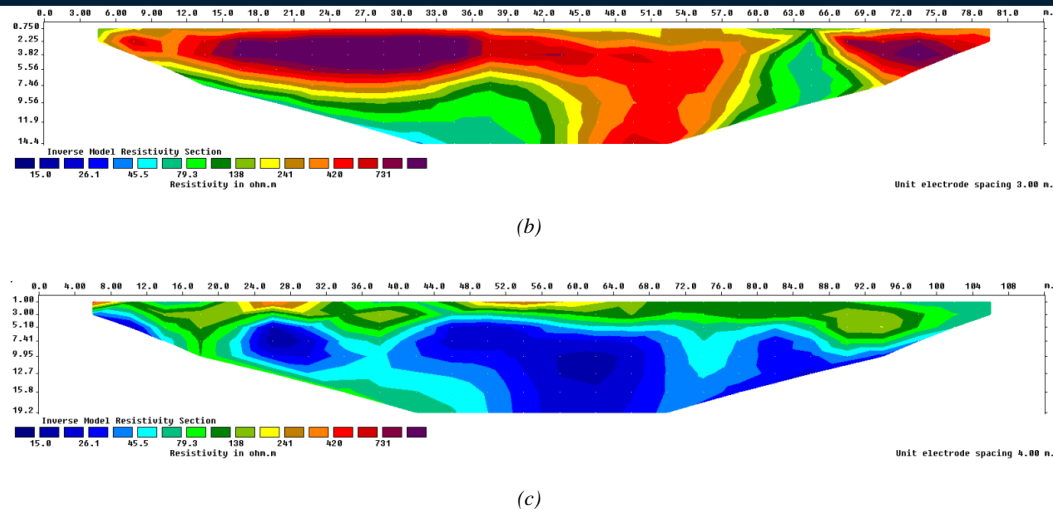

(a)

(b)

(c)
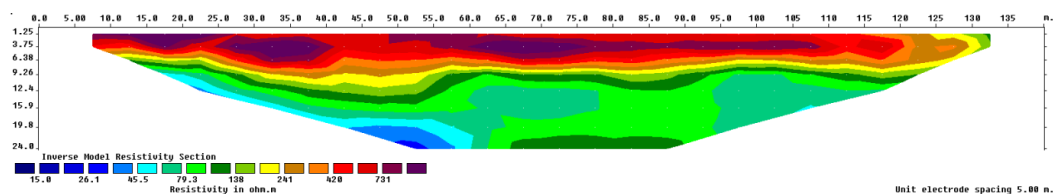
Figure 5. Electrical resistivity tomography results for a) P1 profile, b) P2 profile, c) P3 profile

Geotechnical parameters calculated from P and S-wave velocities obtained from MASW method indicates that if the soil (alluvium and breccia zone) is excavated beneath the dam axis, the rock basement has favourable elastic properties in terms of bearing capacity. The main problem in the dam site will be seepage from left and right banks of the reservoir area according to the discontinuity measurements and water table level derived from ERT method.

REFERENCES

[1]. V. Naudet, M. Lazzari, A. Perrone, A. Loperte, S. Piscitelli, V. Lapenna, "Integrated geophysical and geomorphological approach to investigate the snowmelt-triggered landslide of Bosco Piccolo village (Basilicata, southern Italy)", *Engineering Geology*, 98, 156–167, 2008.

[2]. N.S. Isık, M. Ozer, M. Orhan, F. Adil, "A case study of using electrical resistivity in landslide investigation: The park of Yıldırım Beyazıt (Etimesgut-Ankara)", *Earthsciences*, 33 (3), 283-293, 2012, (in Turkish).

[3]. O. Uyanik, O. Cakmak, E. Algül, M. Gürbüz, A. Okumus, "Haydarlı baraj alanının elektrik ozdirenc ve jeolojik ozellikleri", *Geophysics*, 16, 43-53, 2012, (in Turkish).

[4]. M. A. Berge, "Electrical resistivity tomography investigations on a paleoseismological trenching study", *Journal of Applied Geophysics*, 109, 162–174, 2014.

[5]. J. Reynolds, *An Introduction to Applied and Environmental Geophysics*, Ed. Wiley, John and Sons, Inc., 1997.

[6]. D. W. Steeples, "Engineering and environmental geophysics at the millennium", *Geophysics*, 66, 31–35, 2001.

[7]. Akdeniz, N., "Geology of Akhisar-Golmarmara-Gordes-Sındırgı" PhD Thesis, İstanbul University, p.254, İstanbul, 1985, (in Turkish).

[8]. Kılıc, A.M., "Stratigraphy of Lower Mesozoic sediments of Akhisar (Manisa) region", MSc Thesis, Cumhuriyet University, pp.70, Sivas, 1997, (in Turkish).

[9]. Konak, N., "A general review of Menderes Massif Menderes", 47. Turkey Geological Congress, Ankara, pp. 126, 1994, (in Turkish).

[10]. Yagmurlu, F., "Geology and coal potential of the Neogene sediments in the east of Akhisar", PhD Thesis, Dokuz Eylül University, Institute of Natural and Applied Sciences, pp.217, İzmir, 1983, (in Turkish).

[11]. Yagmurlu, F., Baykal, H., "Fundamental geological properties of Gordes Dam and its surrounding", *Geological Bulletin of Turkey*, vol. 32/1-2, pp. 1-7, Ankara, 1989, (in Turkish).

[12]. Yagmurlu, F., Karayigit, A.İ., "Petrographical properties of Cıtak (Akhisar) lignites", in *Turkey 4. Coal Congress, TMMOB*, pp. 111-122, 1984, (in Turkish).

[13]. Emre,T., "Geology and tectonics of Gediz Graben", *Turkish Journal of Earth Sciences*, vol. 5,pp. 171-185, 1996.

[14]. D.H. Griffiths, R.D. Barker, "Two-dimensional resistivity imaging and modelling in areas of complex geology", *Journal of Applied Geophysics*, 29, 211–226, 1993.

[15]. Loke, M.H., Barker, R.D., "Rapid least-squares inversion of apparent resistivity pseudo sections by a quasi-Newtonmethod", *Geophysical Prospecting*, 44, 131–152, 1996.

[16]. T. Kadakci Koca, A. Tuncel, M.Y. Koca, "Comparison of the Borehole Logs Drilled in Caglayan Dam Reservoir Area and In-Situ Seismic Velocities," in *Proc. ICENS*, 2016, pp. 1352-1359.

Performance of Grasshopper Optimization Algorithm and Other Swarm Based Methods on Benchmark Functions

Umit Can[1], Bilal Alatas[2]

Abstract

The real world optimization problems have high dimensions and complexity. The traditional classical optimization technique does not solve current complicated problems. However, at that point to overcome this obstacle the novel metaheuristic algorithms have been developed and proposed. Due to the advantages of these metaheuristic techniques they are getting more strong and famous. These popular techniques provide an acceptable solution within an acceptable time. There is still a gap at the point of finding the best metaheuristic optimization algorithm for all types of problems and state of the art techniques or new types of current algorithms are being developed for this reason. Grasshopper Optimization Algorithm (GOA) is the most current metaheuristic algorithm that has been proposed in 2017 and it has been inspired behavior of grasshopper swarms in the nature. This paper has demonstrated the GOA using in optimization and search problems. The detailed properties of GOA have been shown and GOA's operators have been explained for leading optimization process. In addition to that, the results for benchmark functions obtained from GOA and other swarm based optimization algorithms have been compared and analyzed. GOA is the most recent metaheuristic algorithm and there is only one work in the related area. GOA revealed an impressive and robust optimization way solving in many complicated optimization problems. The obtained results are very promising and hopeful for many future studies.

Keywords: *Global Optimization, Metaheuristic Algorithms, Grasshopper Optimization Algorithm, Swarm Intelligence*

1. INTRODUCTION

The process of finding the best values for the variables of a particular problem to minimize or maximize an objective function is called optimization [1]. Classical optimization algorithms are inefficient to the solving of high dimensions and complex problems. Therefore, metaheuristic algorithms have been developed. Heuristic algorithms find the possible solutions of problem instead of searching and evaluating all solutions. They do not guarantee the best solution, so that they can be considered as algorithms to find solutions.

Metaheuristic algorithms tries to find the best solution and they can be apply to the various problem in a simple way. In addition to that metaheuristic algorithms are flexible and they can accommodate changes in the objective function. Generally they focuses to find quality solutions. Metaheuristic algorithms are preferred in highly nonlinear and multimodal real-world optimizations with various complex constraints and different conflicting objectives [2]. Although there are many successful search and optimization algorithms and techniques in the literature; design, development, and implementation of new techniques is an important task under the philosophy of improvement in the scientific field and always searching to design better. The best algorithm that gives the best results for all the problems has not yet been designed, that is why constantly new artificial intelligence optimization algorithms are proposed or some efficient additions or modifications have been performed to the existing algorithms [3].

Sometimes individuals who cannot do anything alone can exhibit very smart behavior when they act collectively. Individuals belonging to a community are encouraged to learn from the behavior of the best Individual or from their own experience. As a tool for solving the problems they will face in the future. For example, when one of the individuals who make a living tract senses a danger, it reacts to that danger. And this reaction allows the individual to move in the herd and behave in a common way against the danger. Lots

[1] *Munzur University, Department of Computer Engineering, 62000, Tunceli,, Turkey. ucan@munzur.edu.tr*

[2] *Firat University, Department of Software Engineering, 23119, Elazig, Turkey, balatas@firat.edu.tr*

of creatures Observations of these movements in the herd-based optimization algorithms have been developed [3]. Lots of swarm based algorithms have been proposed by the scientist. Some of them are: Firefly Bug Algorithm (FBA), Firefly Herd Optimization (FHO), Ant Colony Optimization (ACO), Particle Swarm Optimization (PSO), Artificial Fishery Algorithm (AFO), Bacterial Food Search Optimization Algorithm (BFSO), Grey Wolf Algorithm (GWO), Cat Swarm Optimization (CSO), Whale Optimization Algorithm (WOA) and Grasshopper Optimization Algorithm (GOA).

In this paper, GOA is introduced and this method has been compared with different swarm based metaheuristic method for benchmark functions. In section 2, GOA is demonstrated in detailed. The used benchmark functions have been shortly described in Section 3. Comparative results obtained from Grasshopper Optimization [1], Grey Wolf Optimization [4] and Whale Optimization algorithms [5] for Sphere and Rastrigin benchmark functions have been shown in Section 4. Finally, some conclusions are given in Section 5.

2. GRASSHOPPER OPTIMIZATION ALGORITHM

Swarm intelligence (SI) is an important category of optimization methods. SI is the property of a system whereby the collective behaviors of agents that interact locally with their environment cause coherent functional global patterns to emerge. Different from evolutionary algorithms (EAs), SI algorithms are inspired from simple behaviors and self-organizing interaction among agents, such as ant colonies foraging, bird flocking, animal herding, bacterial growth, honey bees, fish schooling, and so on [6].

One of the insect species that migrate as a swarm is a grasshopper. They are famous for their passing large distances to find food. The main characteristic of the swarm in the larval phase is slow movement and small steps of the grasshoppers. In contrast, long- range and abrupt movement is the essential feature of the swarm in adulthood. Food source seeking is another important characteristic of the swarming of grasshoppers. As discussed in the introduction, nature-inspired algorithms logically divide the search process into two tendencies: exploration and exploitation. In exploration, the search agents are encouraged to move abruptly, while they tend to move locally during exploitation. These two functions, as well as target seeking, are performed by grasshoppers naturally. Therefore, if we find a way to mathematically model this behavior, we can design a new nature-inspired algorithm [1]. The pseudo code of GOA is given in Figure 1.

Initialize the swarm $X_i(i = 1,2, ... , n)$

Initialize cmax, cmin, and maximum number of iterations

Calculate the fitness of each search agent

T=the best search agent

while(*I < Max number of iterations*)

    Update c using Eq.(2.8)

  for *each search agent*

      Normalize the distances between grasshoppers in [1,4]

      Update the position of the current search agent by the equation (2.7)

      Bring the current search agent back if it goes outside the boundaries

     end for

    Update T if there is a better solution

    I=I+1

end while

Return T

Figure 1. The pseudo code of GOA

3. BENCHMARK FUNCTIONS

Well-defined benchmark functions which are based on mathematical functions can be used as objective functions to measure and test the performance of optimization methods. The nature, complexity and other

properties of these benchmark functions can be easily obtained from their definitions. The difficulty levels of most benchmark functions are adjustable by setting their parameters [7]. In this study, the selected benchmark function are Sphere and Rastrigin functions. The first selected benchmark function Shepe is continuous, differentiable, separable, scalable, and multimodal. However, Rastrigin function is a typical example of non-linear multimodal function. Below in Table 1 the selected benchmark functions have been demonstrated.

Table 1. Benchmark functions

Function Name	Definition	Interval	Characteristic
Sphere	$f_1(x) = \sum_{i=1}^{n} x_i^2$	$-100 \leq x_i \leq +100$	Uni-modal
Rastrigin	$f_2(x) = 10n + \sum_{i=1}^{n} x_i^2 - 10cos(2\pi x_i)$	$5.12 \leq x_i \leq 5.12$	Multi-modal

The graphs of benchmark functions with two variables have been shown in Figure 2 and Figure 3 respectively.
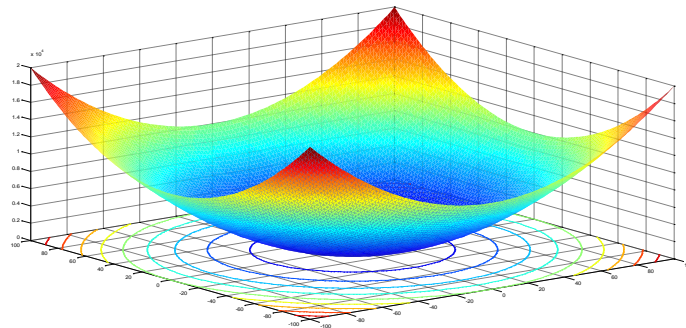
Figure 2. Sphere function with two variables
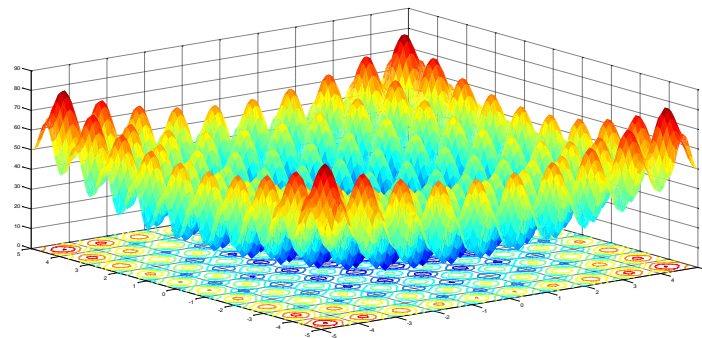
Figure 3. Rastrigin function with two variables

4. EXPERIMENTAL RESULTS

In this study to measure the performance of the newest metaheuristic algorithms GOA, two other swarm based algorithms GWO and WOA have been selected. At first GOA, GWO, and WOA have been applied to benchmark functions. Parameters of these algorithms adjusted as same value except initial population number. For Sphere function the dimensions have been selected as 5. Then maximum iteration number has been decided as 500. In addition to that lower bound (lb) and upper bound (ub) of these algorithms have been selected same number as lb=-100 and ub=100. During the process for comparison the initial population size has been changed as 10, 20, 30, 40, 50, 70, and 100 respectively. At last both algorithms have been run 10 times. The result of experiments provide use to measure the sensitivity of algorithms in different size of population numbers. Below in Table 2, Table 3, and Table 4 the results for sphere function have been demonstrated.

Table 2. Sphere results for population size 10, 20

Pop.Size	10			20		
	GOA	GWO	WOA	GOA	GWO	WOA
Best	3.96E-05	4.65E-50	**1.12E-62**	1.42E-04	**2.83E-77**	8.66E-77
Mean	1.03E-03	**3.01E-46**	3.60E-45	1.03E-03	**1.66E-73**	5.11E-67
Worst	5.55E-01	3.00E-45	3.60E-44	4.19E-03	1.27E-72	5.03E-66

Table 3. Sphere results for population size 30, 40

Pop.Size	30			40		
	GOA	GWO	WOA	GOA	GWO	WOA
Best	6.20E-05	**2.31E-99**	8.33E-91	2.20E-04	**1.73E-108**	1.18E-97
Mean	2.03E-04	**3.66E-90**	2.63E-79	5.96E-04	**5.77E-104**	3.72E-85
Worst	1.04E-04	3.65E-89	2.54E-78	1.71E-03	5.66E-103	3.72E-84

Table 4. Sphere results for population size 50, 70, and 100

Pop.Size	50			70			100		
	GOA	GWO	WOA	GOA	GWO	WOA	GOA	GWO	WOA
Best	1.38E-04	**7.30E-123**	5.72E-101	9.29E-06	**1.52E-142**	1.11E-108	4.59E-05	**1.49E-156**	1.42E-112
Mean	3.12E-04	**3.30E-114**	8.54E-90	9.16E-04	**3.55E-132**	1.05E-98	1.01E-03	**1.34E-146**	4.49E-107
Worst	6.34E-04	3.27E-113	8.52E-89	1.36E-03	2.86E-131	4.99E-97	1.55E-03	1.34E-145	7.02E-107

It can be easily seen that except population size 10, in all initial population size GWO result are better than WOA and GOA results. With the increasing of population size the sensitivity of GOA didn't changed more. In contrary, algorithm GWO and WOA has given huge changes when population size of algorithms changed.

For Rastrigin function the dimensions of GOA, GWO and WOA have been selected as 5. Then maximum iteration number is decided as 500. In addition to that lower bound (*lb*) and upper bound (*ub*) of these algorithms have been selected same number as *lb*=-100 and *u*b=100. During the process for comparison the initial population size has been changed as 10, 20, 30, 40, 50, 70, and 100 respectively. At last both algorithms have been run 10 times. The result of experiments provide use to measure the sensitivity of algorithms in different size of population numbers. Below in Table 5, Table 6 and Table 7 the results for Rastrigin function have been demonstrated.

The results disclosed that WOA function is better than the GWO and GOA functions for the Rastrigin function. However, WOA and GWO algorithms had very close results. In Sphere benchmark test GOA has showed little changes with the population increasing. On the other hand, in Rastrigin test GOA shows big changes with the population increasing.

Table 5. Rastrigin results for population size 10 and 20

Pop. Size	10			20		
	GOA	GWO	WOA	GOA	GWO	WOA
Best	26.3782	**1.42E-10**	**0**	15.1724	15.1724	0
Mean	52.0738	3.247	**2.26483**	37.5648	375.648	**0**
Worst	76.9756	1.9338	7.3813	53.3481	53.3431	0

Table 6. Rastrigin results for population size 30 and 40

Pop.Size	30			40		
	GOA	GWO	WOA	GOA	GWO	WOA
Best	6.0593	**0**	**0**	2.9859	**0**	**0**
Mean	21.1186	**0**	**0**	13.8203	**0**	**0**
Worst	49.7101	0	0	54.794	0	**0**

Table 7. Rastrigin results for population size 50, 70, and 100

Pop. Size	50			70			100		
	GOA	GWO	WOA	GOA	GWO	WOA	GOA	GWO	WOA
Best	6.5271	**0**	**0**	2.556	**0**	**0**	2.0851	**0**	**0**
Mean	20.2623	**0**	**0**	20.5790	**0**	**0**	16.0062	**0**	**0**
Worst	42.1083	0	0	32.4511	0	0	32.0234	0	**0**

5. CONCLUSIONS

In this paper, the newest metaheuristic method Grasshopper Optimization Algorithm has been compared with Grey Wolf Optimization and Whale Optimization algorithms. The unimodal and multimodal benchmark functions have been used to test sensitivity of these algorithms. Dimensions, upper and lower bounds of functions and maximum iteration number of algorithms have been taken as same values. Only the population size of algorithms has been changed. According to the results Grey Wolf Optimization algorithm has been showed better sensitivity then Grasshopper Optimization and Whale Optimization algorithms. Increasing of initial population number has not effected on Grasshopper Optimization Algorithm performance significantly. However, Grey Wolf Optimization algorithm and Whale Optimization have shown significantly changes.

Grasshopper Optimization, Grey Wolf Optimization and Whale Optimization algorithms are newest algorithms and they can be developed in variety areas for future studies.

REFERENCES

[1]. Saremi, Shahrzad, Seyedali Mirjalili, and Andrew Lewis. "Grasshopper optimization algorithm: Theory and application." Advances in Engineering Software 105 (2017): 30-47.
[2]. Kiziloluk, Soner, and Bilal Alatas. "Automatic Mining of Numerical Classification Rules with Parliamentary Optimization Algorithm." Advances in Electrical And Computer Engineering 15.4 (2015): 17-24.
[3]. Akyol, Sinem, and Bilal Alatas. "Güncel Sürü Zekası Optamizasyon Algoritmaları." Nevsehir Bilim ve Teknoloji Dergisi 1.1 (2012).
[4]. Mirjalili, Seyedali, Seyed Mohammad Mirjalili, and Andrew Lewis. "Grey wolf optimizer." Advances in Engineering Software 69 (2014): 46-61.
[5]. Mirjalili, Seyedali, and Andrew Lewis. "The whale optimization algorithm." Advances in Engineering Software 95 (2016): 51-67.
[6]. Mavrovouniotis, Michalis, Changhe Li, and Shengxiang Yang. "A survey of swarm intelligence for dynamic optimization: algorithms and applications." Swarm and Evolutionary Computation (2017).
[7]. Alatas, Bilal. "Chaotic bee colony algorithms for global numerical optimization." Expert Systems with Applications 37.8 (2010): 5682-5687*FLEXChip Signal Processor (MC68175/D)*, Motorola, 1996.

Performance Comparisons of Current Metaheuristic Algorithms on Unconstrained Optimization Problems

Umit Can[1], Bilal Alatas[2]

Abstract

Optimization is the process of searching for the optimal solution. Analytical, enumeration, and heuristic methods can be used for global optimization tasks. A metaheuristic is a higher level heuristic that may provide a sufficiently good solution to any optimization problem. In this paper; seven of newest metaheuristic algorithms namely, Ant Lion Optimization, Dragonfly Algorithm, Grey Wolf Optimization, Moth-Flame Optimization, Multi-Verse Optimizer, Sine Cosine Algorithm, and Whale Optimization Algorithm have been tested on unconstrained benchmark optimization problems and their performances have been reported. Some of these algorithms are based on swarm while some are based on biology and mathematics. Performance analysis of these novel search and optimization algorithms satisfying equal conditions on benchmark functions for the first time has given important information about their behavior on uni-modal and multi-modal optimization problems. These algorithms have been recently proposed and many new versions of them may be proposed in future for efficient results in many different types of search and optimization problems.

Keywords: *Metaheuristic Algorithms, Global Optimization, Performance*

1. INTRODUCTION

Optimization is the process of searching for the optimal solution. Analytical, enumeration, and heuristic methods can be used for optimization task. Heuristic refers to experience-based techniques for problem-solving and learning. Heuristics are problem-dependent and designed only for the solution of a specific problem. A metaheuristic is a higher level heuristic that may provide a sufficiently good solution to any optimization problem [1]. Metaheuristic algorithms are simple to implement and faster than the classical calculus based optimization algorithms, they are capable of achieving good approximation to the global optimum, and they are robust to problem changes.

Metaheuristics are recently getting stronger and increasing their popularity due to their advantages. They are used extensively in various fields such as management, computer, engineering due to advantages such as not having difficult mathematical models to set up, good computing powers, and requiring no change on the interested problems like classical algorithms. Their modified new versions or novel metaheuristic algorithms are still proposed due to the absence of the most efficient method for all types of problems.

There are many metaheuristic optimization methods that are based on biology, physics swarm, sociology, music, chemistry, sports, mathematics and plants. In this paper, seven of newest metaheuristic algorithms namely, Ant Lion Optimization (ALO) [2], Dragonfly Algorithm (DA) [3], Grey Wolf Optimization (GWO) [4], Moth-Flame Optimization (MFO) [5], Multi-Verse Optimizer (MVO) [6], Sine Cosine Algorithm (SCA) [7], and Whale Optimization Algorithm (WOA) [8] have been tested on unconstrained benchmark optimization problems and their performances have been reported.

Organization of this paper has been as follows: Section 2 gives brief explanations of the current algorithms with pseudo-codes. Section 3 gives the experimental results obtained from these metaheuristic algorithms on unconstrained benchmark optimization problems. Section 4 concludes the paper along with future research directions.

[1] *Munzur University, Department of Computer Engineering, 62000, Tunceli,, Turkey. ucan@munzur.edu.tr*

[2] *Firat University, Department of Software Engineering, 23119, Elazig, Turkey, balatas@firat.edu.tr*

2. CURRENT METAHEURISTIC ALGORITHMS

In the past decades, various metaheuristic intelligence optimization algorithms have been proposed to solve complex search and optimization problems. These algorithms have shown an outstanding performance on the problems. Hence, while many researchers have focused in adapting them on different problems or to improve their performances, some researchers have proposed novel algorithms inspired from biology, swarm, physics, and etc.

ALO is a nature-inspired algorithm mimicking the hunting behavior of antlions in nature [2]. ALO is implemented in five main steps: random walks of ants, building pits, entrapment of ants, catching preys, and lastly rebuilding pits. Pseudo-code of ALO is depicted in Figure 1.

```
Initialize problem parameters
Initialize algorithm parameters
Initialize the first population of ants and ant lions
Determine the best ant lion and assume it as the elite
While termination criteria not satisfied
For each ant
Select and ant lion with roulette wheel method
Create a random walk normalize it
Update the position of ant

End For

Compute the fitness of all ants

Replace an ant lion with its corresponding fitter ant

Update elite if ant lion becomes fitter than the elite

End While

Return elite
```

Figure 1. Pseudo-code of ALO

DA is inspired from the static and dynamic swarming behaviors of dragonflies in nature [3]. Two essential phases in optimization, namely exploration and exploitation, are designed by modelling the social interaction of dragonflies in navigating, searching for foods, and avoiding enemies when swarming dynamically or statistically [3]. Pseudo-code of DA is shown in Figure 2.

```
Initialize problem parameters
Initialize algorithm parameters
Initialize swarm of dragonflies, the initial velocity vector, food source, and enemy.
Compute fitness function
While termination criteria not satisfied
Update the food source and enemy
For each dragonfly
Compute the Euclidean distance of each dragonfly with other members in the swarm and select the number of neighbors
Based on the number of neighbors, update the velocity and position vectors

End For

End While

Return best food source
```

Figure 2. Pseudo-code of DA

GWO mimics the leadership hierarchy and hunting mechanism of gray wolves in nature [4]. GWO has three main steps of hunting, searching for prey, encircling prey, and attacking prey. Pseudo-code of GWO is shown in Figure 3.

```
Initialize problem parameters
Initialize algorithm parameters
Initialize the initial positions of grey wolves
Initialize the vectors for mathematically modelling encircling behavior
Compute the fitness of each grey wolf
Get the first three best wolves
While termination criteria not satisfied
For each search agent
Update the position of the current grey wolf

End For

Update the vectors

Compute the fitness of all grey wolves

Update the first three best wolves

End While

Return grey wolf with the first maximum fitness
```

Figure 3. Pseudo-code of GWO

MFO is inspired from navigation method of moths in nature called transverse orientation [5]. Spiral flying path of moths around artificial lights (flames) has been mathematically modeled in MFO. Main steps of this algorithm is demonstrated in Figure 4.

```
Initialize problem parameters
Initialize algorithm parameters
Initialize the initial positions of moths
Compute the fitness
While termination criteria not satisfied
For each moth
Update positions
Compute the fitness
End While
Return the best flame
```

Figure 4. Pseudo-code of MFO

MVO is a novel search and optimization algorithm main inspirations of which are based on three concepts in cosmology: white hole, black hole, and wormhole [6]. The mathematical models of these three concepts are developed to perform exploration, exploitation, and local search, in optimization respectively. Main steps MVO is demonstrated in Figure 5.

```
Initialize problem parameters
Initialize algorithm parameters
Initialize galaxy
While termination criteria not satisfied
Apply Black/White Hole mechanism
Apply Wormholes mechanism
End While
Return best universe position
```

Figure 5. Pseudo-code of MVO

SCA is an interesting math inspired search and optimization algorithm and uses mathematical model based on sine and cosine functions. SCA adaptively balances the exploration and exploitation phases in optimization quickly [7]. Main steps SCA is demonstrated in Figure 6.

Initialize problem parameters
Initialize algorithm parameters
Initialize search agents
While *termination criteria not satisfied*
Compute the fitness
Update the next position region between solution and destination, parameters that tells how far the movement should be towards or outwards the destination, random weight for destination, and value controlling switches between sine and cosine component.
Update the positions
End While

Return *best result*

Figure 6. Pseudo-code of SCA

WOA is inspired from the bubble-net hunting strategy [8]. The mathematical model of WOA is based on encircling prey, bubble net hunting, and searching the prey. Main steps WOA is demonstrated in Figure 7.

Initialize problem parameters
Initialize algorithm parameters
Initialize search agents
Compute the fitness of all search agents
While *termination criteria not satisfied*
Encircle prey
Bubble net hunt
Search the prey
Compute the fitness
End While
Return *best result*

Figure 7. Pseudo-code of WOA

3. EXPERIMENTAL RESULTS

To evaluate the performance of these seven current metaheuristic algorithm, two benchmark test functions with different characteristics have been used. These benchmark functions are frequently used to evaluate and compare the characteristics of optimization algorithms in terms of convergence, precision, robustness, and general performance. The nature, complexity, and other properties of these benchmark functions can be easily obtained from their definitions and the difficulty levels of these benchmark functions can be adjusted by changing their dimension and interval parameters [9]. The selected benchmark functions and their properties have been demonstrated in Table 1. The dimensions (n) for all benchmark functions have been determined as 10. Chung Reynolds function is a unimodal function with less complexity and it can be used to evaluate the converging behaviors of algorithms [10]. Griewank function is a multi-modal function with many local optima and it can be used to test the global search ability of the optimization algorithms in avoiding premature convergence [11]. Rastrigin function is highly multimodal, but locations of the minima are regularly distributed. Their graphs with two dimensions have been shown in Figure 8, Figure 9, and Figure 10.

Table 1. Benchmark functions

Function No	Function Name	Definition	Interval	Characteristics
1	Chung Reynolds	$f_1(x) = \left(\sum_{i=1}^{n} x_i^2 \right)^2$	$-100 \leq x_i \leq 100$	Unimodal
2	Griewank	$f_2(x) = 1 + \frac{1}{4000} \sum_{i=1}^{n} x_i^2 - \prod_{i=1}^{n} \cos(\frac{x_i}{\sqrt{i}})$	$-600 \leq x_i \leq 600$	Multi-modal
3	Rastrigin	$f_3(x) = 10 \times n + \sum_{i=1}^{n} x_i^2 - 10\cos(2\pi x_i)$	$-5 \leq x_i \leq 5$	Multi-modal

The performances of algorithms have been tested on Chung Reynolds function with 10 dimensions. Initial population size of all algorithms is selected as 30 and maximum iteration number for termination criteria is determined as 100. All algorithm parameters have been selected as their original values. All algorithms have been run 10 times. The results obtained from this problem have been demonstrated in Table 2. From these results, it can be concluded that WOA is the best algorithm within this unimodal problem. GWO is the second best algorithm.

The performances of algorithms have been tested on Griewank function with 10 dimensions. Initial population size of all algorithms is selected as 30 and maximum iteration number for termination criteria is determined as 100. All algorithm parameters have been selected as their original values. All algorithms have been run 10 times. The results obtained from this problem have been demonstrated in Table 3. From these results, it can be concluded that WOA is the best algorithm within this multi-modal problem. GWO is the second best algorithm.

The performances of algorithms have also been tested on another multi-modal problem, namely Rastrigin function, with 10 dimensions. Initial population size of all algorithms is selected as 30 and maximum iteration number for termination criteria is determined as 100. All algorithm parameters have been selected as their original values. All algorithms have been run 10 times. The results obtained from this problem have been demonstrated in Table 3. From these results, it can be concluded that again, WOA is the best algorithm within this multi-modal problem. GWO is the second best algorithm.
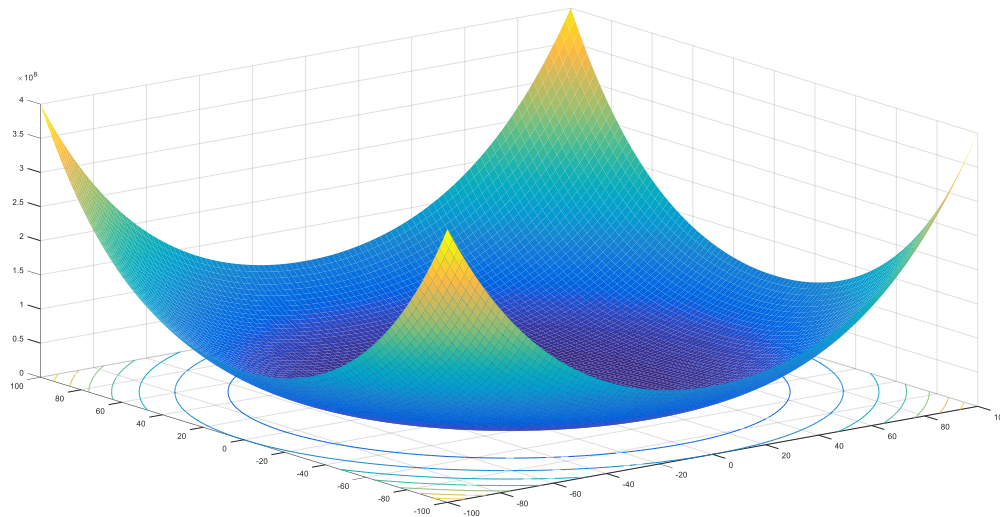
Figure 8. Chung Reynolds function with two variables
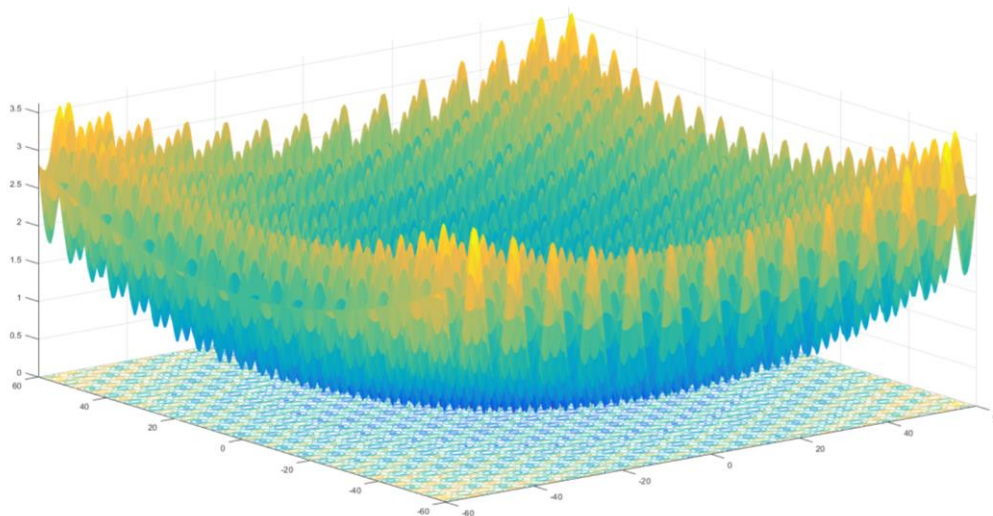
Figure 9. Griewank function with two variables

476
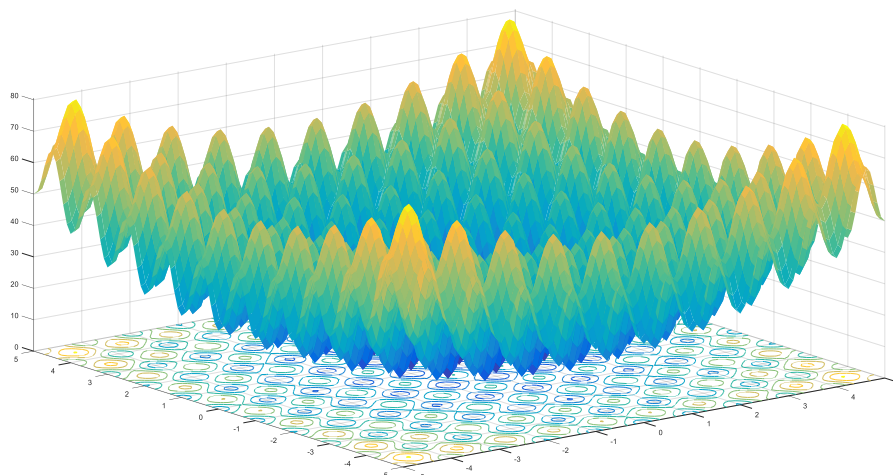
Figure 9. Rastrigin function with two variables

Table 2. Performances of algorithms on Chung Reynolds function

Algorithm	Mean optimum
ALO	0.3793
DA	50.2239
GWO	8.3804e-18
MFO	88.5679
MVO	0.0478
SCA	0.2782
WOA	2.7393e-28

Table 3. Performances of algorithms on Griewank function

Algorithm	Mean optimum
ALO	0.0913
DA	0.9221
GWO	0.0319e-4
MFO	1.0425
MVO	0.6848
SCA	1.0809
WOA	5.4877e-7

Table 4. Performances of algorithms on Rastrigin function

Algorithm	Mean optimum
ALO	22.9145
DA	42.7102
GWO	4.4678
MFO	15.5878
MVO	33.9496
SCA	47.6633
WOA	1.0747e-06

4. CONCLUSIONS

In this paper, performances of current metaheuristic search and optimization methods have been tested and seven new algorithms, namely Ant Lion Optimization, Dragonfly Algorithm, Grey Wolf Optimization, Moth-Flame Optimization, Multi-Verse Optimizer, Sine Cosine Algorithm, and Whale Optimization Algorithm have been selected for this goal. They have been executed on unconstrained unimodal and multimodal benchmark optimization problems. According to the obtained results, WOA is the best algorithm and GWO is the second best algorithm within both unimodal and multimodal problems.

These algorithms are very new computational methods and they can be improved in many ways. More validation studies should be performed to discover the capabilities of these algorithms in dealing with the search and optimization problems. There are positive challenges in terms of efficiency and best possible use of these algorithms.

REFERENCES

[1]. Du, Ke-Lin, and M. N. S. Swamy. Search and Optimization by Metaheuristics. Springer, 2016.
[2]. Mirjalili, Seyedali. (2015). the ant lion optimizer. Advances in Engineering Software. 83. 80-98.
[3]. Mirjalili, S. (2016). Dragonfly algorithm: a new meta-heuristic optimization technique for solving single-objective, discrete, and multi-objective problems. Neural Computing and Applications, 27(4), 1053-1073.
[4]. Mirjalili, S., Mirjalili, S. M., & Lewis, A. (2014). Grey wolf optimizer. Advances in Engineering Software, 69, 46-61.
[5]. Mirjalili, S. (2015). Moth-flame optimization algorithm: A novel nature-inspired heuristic paradigm. Knowledge-Based Systems, 89, 228-249.
[6]. Mirjalili, S. M., & Hatamlou, A. (2016). Multi-verse optimizer: a nature-inspired algorithm for global optimization. Neural Computing and Applications, 27(2), 495-513.
[7]. Mirjalili, S. (2016). SCA: a sine cosine algorithm for solving optimization problems. Knowledge-Based Systems, 96, 120-133.
[8]. Mirjalili, S., Lewis, A. (2016). The whale optimization algorithm. Advances in Engineering Software, 95, 51-67.
[9]. B. Alatas, E. Akin, A. B. Ozer, "Chaos Embedded Particle Swarm Optimization Algorithms", Chaos, Solitons & Fractals, vol. 40, pp. 1715-1734, 2009.
[10]. (2017) C. J. Chung, R. G. Reynolds, "CAEP: An Evolution-Based Tool for Real-Valued Function Optimization Using Cultural Algorithms", International Journal on Artificial Intelligence Tool, 7(3), 239-291, 1998.
[11]. (2017) Geatbx: Examples of Objective functions. Available: http://www.pg.gda.pl/mkwies/dyd/geadocu/fcnfun8.html.

Surface Properties of Styrene Maleic Anhydride (SMA) Composites Filled with Thermally Treated Wood Flour

Mustafa ZOR[1]*, Douglas J. GARDNER[2], Nadir AYRILMIS[3]

Abstract

The main objective of the present study was to evaluate the effect of thermal treatment on the surface properties of heat treated wood flour filled styrene maleic anhydride (SMA) composites. SMA is an engineering polymer in the automotive for interior and exterior construction applications by injection molding and thermoforming. The heat-treatment of the pine wood was performed at 212 °C for 8 h. The SMA polymer was filled with untreated or thermally treated wood flour from 0 to 50 wt%. After the extrusion process by twin screw extruder, the specimens were produced by injection molding machine. The surface roughness values of the filled polypropylene composites increased with increasing with heat treated loading filler. Similarly, the wettability of heat treated wood flour SMA composites increased with increasing content of the wood flour.

Keywords: *Wood Thermoplastic Composite, Heat Treatment, Wettability, Surface Roughness*

1. INTRODUCTION

It is well known that wood materials have been used by the plastics industry as inexpensive filler to enhance durability, strength and stiffness of thermoplastic and to reduce raw material costs. Wood plastic composites (WPC) consist initially of thermoplastic polymers and wood due to an improved complication in processing and formulations caused to development of WPC. Therefore, WPC development has followed previous work on synthetic fibers and filler such as glass, carbon, boron, aramid, and mineral fillers.

Styrene maleic anhydride (SMA) copolymer is a thermoplastic polymer obtained by the copolymerization of styrene and maleic anhydride monomers and can be preferred as heat stabilizer, coupling agent and compatibilizer. The SMA is an engineering polymer in the automotive for interior and exterior construction applications by injection molding and thermoforming. It can also improve the reaction and adhesion between polymer and fillers in the composite industry (1-3). When compared to conventional wood based composites, such as medium density fiberboard (MDF) and particleboard (PB), is quite limited to interior and exterior applications (moist application) due to the having strong ability to absorb water. Despite the hygroscopic nature of natural fibers, the hydrophobic thermoplastic matrix decelerates the uptake of water, and durability of WPCs has significantly been improved when compared with used decking (4-6). However, WPCs absorb moisture because of the hydrophilic properties of the wood filler, and water uptake results in reduction in mechanical properties, dimensional in stability and susceptibility to biological attack (7-9).

Thermal modification improves the durability of wood (10-12). Previous studies reported that thermal modification reduce wood's hygroscopicity, increase the degree of crystallinity of cellulose, and improve dimensional stability and resistance to fungal degradation (13-18). Several wood researchers have used heat treatment to improve wood properties (19), increased mass loss and color changes (20), and decreased some mechanical properties, as well as the wettability of wood (21). Wettability is crucial for good adhesion in wood bonding and to establish contact between molecules of wood and adhesive (22). The wettability of wood can be characterized by contact angle analysis. This analysis is very significant to define the adhesive and coating properties of wood and wood based composite surfaces (23). There is no information on surface properties of the SMA containing different amounts of thermally treated wood flour. The main objective of

---

[1]* Corresponding author: mustafa.zor@beun.edu.tr *Furniture and Decoration Programme, Caycuma Vocational School, University of Bulent Ecevit, Zonguldak, TURKEY.*

[2] *School of Forest Resources, Advanced Structures and Composite Center, University of Maine, Orono, ME, USA.*

[3] *Department of Wood Mechanics and Technology, Forestry Faculty, University of Istanbul, Istanbul, TURKEY.*

the present study was to evaluate the effect of thermal treatment on the surface properties of heat treated wood flour filled SMA composites.

2. EXPERIMENTAL

2.1. Materials

The SMA (XIRAN® SE700) was supplied by Poyscope Polymer, USA. It has a density of 1.08 g/cm^3 (Maleic anhydride contents 10% wt., melt flow 22 g/10min at 240°C/10.0 kg). The eastern white pine (*Pinus strobus* L.) was used as fillers in this study were kindly supplied by Wicks Lumber in Pittsfield, ME, USA.

2.2. Heat Treatment

Pine wood samples were cut from the sapwood of a radial board of eastern white pine (*Pinus strobus* L.). Cubic samples with 360 mm x 20 mm x 20 mm were cut with clear faces, kept in a conditioned room at 20ºC and 50% relative humidity for 3 weeks and weighed afterwards. The heat treatment was made in an oven heated by electric coils located in the walls and with exhaustion of the heated gases by natural convection through an opening in the oven wall. The heat-treatment of the pine wood was performed at 212 ºC for 8 h. The treatment started by putting the samples at ambient temperature in the oven. The time to reach the treatment temperature was about 60 min. After heat treatment, the solid wood board samples were removed from the oven and ground in a grinder. Wood flour of pine greater than 60 mesh was used as raw materials to prepare the wood flour/SMA composites. Untreated samples were used as the control.

2.3. Sample Preparation

The untreated wood flour, heat treated wood flour and SMA were dried to a moisture content of less than one percent using an oven at 105°C for 16-h. The matrix polymer, SMA, was mixed with the untreated wood flour, or heat treated wood flour. The compounding was conducted with a Brabender Prep-mixer equipped with a bowl mixer and the process temperature was measured in real time. The temperature was set at 230°C and rotor speed at 60 rpm. The untreated wood flour, heat treated wood flour were added to the mixer when the polymer appeared well melted. Mixing was done for 15 min until the torque stabilized. The SMA–wood flour compounds were granulated using a lab-scale grinder. The ground particles were dried in an oven at 105°C for 16 h before being injection molded into ASTM test specimens. All materials were injection molded using a barrel temperature of 230°C mold temperature of 230°C injection pressure of 2500 psi. The compositions of the composites are shown in Table 1.

Table 1. Composition of SMA, untreated and heat treated composites.

SMA (wt%)	Untreated wood-UT (wt%)	Heat treated wood-T (wt%)
100	-	-
90	10	-
80	20	-
70	30	-
60	40	-
50	50	-
90	-	10
80	-	20
70	-	30
60	-	40
50	-	50

2.4. Determination of Contact Angle (Wettability)

An imaging system was used to measure contact angle of water droplets for the prepared specimens. Contact angle measurement was done in 15-s intervals from 0 to 45 s for wetting behavior. For convenient observation, image profiles on each test specimen exposed at 15 s were measured to reveal its isotropic

behavior. For contact angle, six water droplets on each specimen were observed along and across the grain direction, respectively. The images were captured using the video camera. All captured images were then stored as image files and measured using **SigmaScan® software** (Figure 1.).
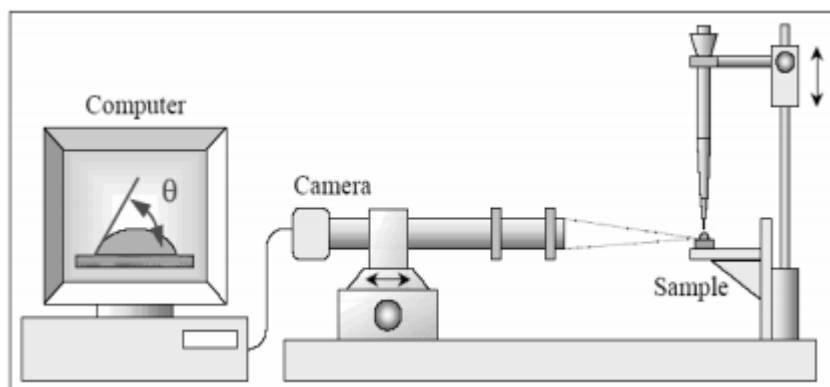

Figure 1. Scheme of Contact Angle Determination Device

2.5. Determination of Surface Roughness

Three roughness parameters characterized by ISO 4287 standard (1997), respectively, average roughness (R_a), mean peak-to-valley height (R_z) and maximum peak-to-valley height (R_y) were considered to evaluate the surface properties of the wood filled SMA composites. The surface properties roughness parameters were calculated from the digital information.

3. RESULTS AND DISCUSSION

3.1. Wettability

As shown in Table 2, the wettability of the wood flour SMA composites significantly increased with increasing loading filler. The samples containing the 50T (81,11° for 15 s)had the highest wettability, while the lowest wettability was found for samples containing the 20UT (50,69° for 15 s) among the all groups. The contact angle of the composites was significantly affected by increasing the wood flour loading content. This is expected because wood flour is a hydrophilic porous due to the presence of cellulose and hemicellulose polymers that are rich in functional groups such as hydroxyls, which readily interact with water molecules by hydrogen bonding associated with the SMA matrix has a hydrophilic nature and polar. Decreasing hydroxyl groups on the fiber surface as a function of the heat-treatment, hydrogen-bonding sites for water molecules decreased on the SMA composite surface. This resulted in a higher contact angle value for the specimens.

The surface activity of wood decreases the wettability of the wood. During the thermal modification process, the surface inactivation occurs. Surface inactivation is defined as a heat-induced change in the wood structure resulting in a loss of bonding ability (24). Northcott et al. (25) confirmed that inactivation induced by heat treatment resulted in a decrease of the absorptivity of the wood. The effect occurs much more quickly at higher temperatures. An inactivated wood surface does not bond well with adhesives, because the inactivation process reduces the ability of an adhesive to properly wet, flow, penetrate and cure (26). A similar result was found in the present study. As the amount of the heat treat wood content in the wood/SMA composition, the wettability of the composites decreased, in other words contact angle values increased.
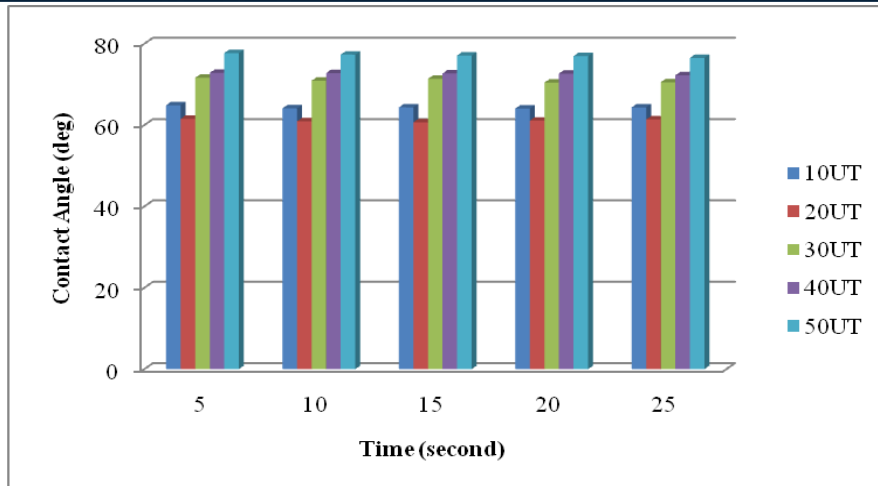
Figure 2. Effect of the wood flour loading on the wettability values of the wood flour SMA composites (UT: untreated wood SMA composite, T: treated wood SMA composite)
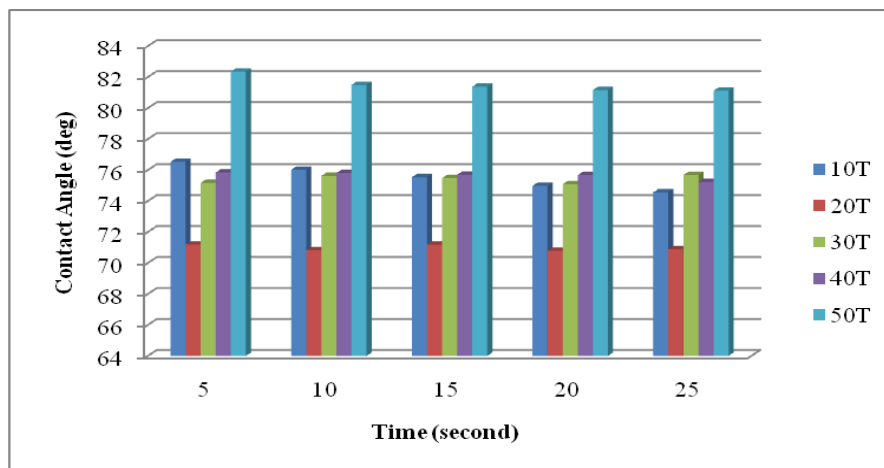
Figure 3. Effect of the loading flour on the wettability values of the heat treated wood flour SMA composites (UT: untreated wood SMA composite, T: treated wood SMA composite)

The wettability values of the wood flour SMA composites increased with increasing with heat treated wood flour. The samples containing the 20T had the highest wettability, while the lowest wettability was found for the samples containing the 50T (in Table 2).

Table 2. Contact angle values between groups and diffence (%).

Group Name	Contact Angle (deg at 15 s)	Difference (%)
10UT	64,36 (0,78)	17,35
10T	75,53 (0,32)	
20UT	60,69 (0,34)	17,26
20T	71,17(0,19)	
30UT	71,38 (0,26)	5,73
30T	75,47 (0,24)	
40UT	72,69 (0,28)	4,12
40T	75,69 (0,52)	
50UT	77,13(0,24)	5,50
50T	81,11 (0,49)	

*Values in parentheses are standard deviations.

482

3.2. Surface roughness

The surface roughness of wood flour SMA composite samples was significantly affected by heat treatment. Significant differences among the wood flour SMA composites were determined ($p < 0.05$) according to the ANOVA statistical analysis (Table 3.). Homogeneity groups were determined individually for *Ra, Ry, and Rz* by Duncan's multiply range test.

The surface roughness of the samples significantly increased with increasing with loading filler and heat treatment. As the amount of the heat-treated wood content in the composites, the roughness values increased. The 10UT samples had the lowest average roughness with an Ra value of 0,94 (µm), while the highest roughness with an Ra value of 2,74 (µm) was found in the samples containing 50T. For example, when the heat treatment content from 30 wt-% to 50 wt-%, longitudinal direction average *Ra, Ry, and Rz* values of the samples increased by 16,10%, 15,94%, and 13,73%, transversal direction average *Ra, Ry, and Rz* values of the samples increased by 32,95%, 37,90%, and 34,59%, respectively (Table 3.).

The increases in the surface roughness of the wood flour/SMA composites containing the heat treatment were mainly attributed to increasing volume percentages of the loading filler used in the experiments. The increment in the surface roughness could be due to the fact thermal degradation of wood starts at 100 °C, while above 200 °C, structural damage, a change in the compounds making up the wood, and the production of degradation products in the gas phase occur. At above 140 °C, dehydration reactions commence, causing a decreasing the hydroxyl content; this increases the surface roughness with increasing temperature (27).

Table 3. Effect of the wood flour loading and heat treatment on the surface roughness (Ra, Ry, and Rz) values of the wood flour SMA composites.

Group Name	Surface roughness parameters (µm)						Composite density (g.cm⁻³)
	longitudinal direction			transversal direction			
	Ra	Ry	Rz	Ra	Ry	Rz	
10UT	0,94(A)	5,94(A)	4,20(A)	1,85(ABC)	10,69(ABCDE)	7,78(ABC)	1,06
10T	1,88(AB)	7,85(BC)	5,78(ABC)	1,28(ABC)	8,28(ABC)	5,74(ABC)	1,08
20UT	1,20(AB)	8,34(ABC)	5,30(AB)	1,44(ABC)	9,77(ABCD)	6,42(ABC)	1,10
20T	1,95(ABC)	11,95(ABCDE)	7,98(ABC)	2,50(BC)	15,67(CDE)	10,15(BC)	1,11
30UT	1,54(ABC)	9,79(ABCD)	6,80(ABC)	1,65(ABC)	11,13(ABCDE)	7,32(ABC)	1,13
30T	2,36(ABC)	14,68(BCDE)	9,61(ABC)	1,76(ABC)	11,74(ABCDE)	7,85(ABC)	1,12
40UT	1,58(ABC)	10,98(ABCDE)	6,95(ABC)	1,74(ABC)	12,07(ABCDE)	7,61(ABC)	1,15
40T	2,04(ABC)	12,6(ABCDE)	8,29(ABC)	1,85(ABC)	12,3(ABCDE)	8,01(ABC)	1,14
50UT	2,72(C)	17,97(E)	11,30(C)	2,34(ABC)	17,34(DE)	10,47(BC)	1,17
50T	2,74(C)	17,02(DE)	10,93(BC)	2,34(ABC)	16,19(DE)	10,70(BC)	1,16

4. CONCLUSIONS

These preliminary findings indicated that the surface characteristics properties of the heat treated woof filled SMA composites were significantly affected by the thermal treatment of the wood fibers. The results of the present study have shown that the surface roughness values of wood flour SMA composites increased with increasing with heat treated wood flour. Wettability strength between the untreated and treated wood filled SMA composites were negatively affected by the thermal treatment of the fibers. It can be included that decreasing in the hydroxyl groups on the fibers resulted in a lower wettability on the composite surface. Wettability and surface roughness of the composites can provide good information on their ability to bond. Further studies should monitor the contact angles for longer time periods to attain a better understanding of the effect of the treatment variables on the surface quality of the heat treated wood filled SMA composites.

ACKNOWLEDGEMENT

REFERENCES

[1] Bledzki, A. K.; Sperber, V. E.; Faruk, O., (2002).Rapra Review Reports, Vol.13, No. 8.

[2] Sperber, V. E., 2002. Fourth International Wood and Natural Fiber Composites Symposium, April 10-11, Kassel, Germany.Riedel, U.; Nickel, J., (2003). Seventh International Conference on Wood fi ber-Plastic Composites, May 19-20, Madison, Wisconsin, USA.

[3] Clemons, C.M. and Ibach, R.E. (2004). The effects of processing method and moisture history on the laboratory fungal resistance of wood-HDPE composites, Forest Prod J, 54, 50-57.

[4] Morrell, J.; Stark, N.M.; Pendleton, D.E.; Mcdonald, A.G. (2006): Durability of woodplastic composites. Wood Design Focus 16, 7e10.

[5] Lomelí-Ramírez, M.G.; Ochoa-Ruiz, H.G.; Fuentes-Talavera, F.J.; García-Enriquez, S.; Cerpa-Gallegos, M.A.; Silva-Guzmán, J.A. (2009): Evaluation of accelerated decay of wood plastic composites by Xylophagus fungi. International Biodeterioration & Biodegradation 63, 1030e1035.

[6] Joseph, P.; Rabello, M.S.; Mattoso, L.; Joseph, K.; Thomas, S. (2002): Environmental effects on the degradation behaviour of sisal fiber reinforced polypropylene composites. Composites Science and Technology 62, 1357e1372.

[7] Espert, A.; Vilaplana, F.; Karlsson, S. (2004): Comparison of water absorption in natural cellulosic fibres from wood and one-year crops in polypropylene composites and its influence on their mechanical properties. Composites Part A: Applied Science and Manufacturing 35, 1267e1276.

[8] Schirp, A.; Wolcott, M.P. (2005): Influence of fungal decay and moisture absorption on mechanical properties of extruded wood-plastic composites. Wood and Fiber Science 37, 643e652.

[9] Hill, C. A. S. (2006). Wood Modification: Chemical, Thermal and Other Processes, John Wiley & Sons Ltd. West Susses, England.

[10] Rowell, R.M. (2007): Chemical modification of wood. In: Handbook of Engineering Biopolymers Homopolymers, Blends and Composites. Eds. Fakirov, S., Bhattacharyya, D. Carl Hanser Verlag, Munich. pp. 673-691.

[11] N. Ayrilmis, S. Jarusombuti, V. Fueangvivat, and P. Bauchongkol, Polym. Degrad. Stab., 2011, 96, 818.

[12] Bhuiyan TR, Hirai N, Sobue N (2000) Changes of crystallinity in wood cellulose by heat treatment under dried and moist conditions. J Wood Sci 46:431–436.

[13] Kandem D., Pizzi, A and Jermannaud, A. 2002. Durability of heat-treated wood. Holz Roh-Werkst. 60, 1-6.

[14] Rowell, R.M.; Ibach, E.R.; McSweeny, J.; Nilsson, T. Understanding decay resistance, dimensional stability and strength changes in heat treated and acetylated wood. Wood Mater. Sci. Eng. 2009, 1,14–22.

[15] Stanzl-Tschegg S, Beikircher W, Loidl D (2009) Comparison of mechanical properties of thermally modified wood at growth ring and cell wall level by means of instrumented indentation tests. Holzforschung 63(4):443–448.

[16] Windeisen E., Strobel, C. and Wegener, G. 2007.Chemical changes during the production of thermos-treated beech wood. Wood Sci Technol. 41, 523-536.

[17] Pfriem A, Zauer M, Wagenfu¨hr A (2010) Alteration of the unsteady sorption behaviour of maple (Acer pseudoplatanus L.) and spruce (Picea abies (L.) Karst.) due to thermal modification. Holzforschung 64(2):235–241.

[18] Hillis WE (1984) High temperature and chemical effects on wood stability. Part 1: general considerations. Wood Sci Technol 18:281–293.

[19] Hakkou M, Pe´trissans M, Ge´rardin P, Zoulalian A (2006) Investigations of the reasons for fungal durability of heat-treated beech wood. Polym Degrad Stabil 91:393–397.

[20] Esteves, B., and Pereira, H. M.,. Wood modification by heat treatment: A review, Bioresources, 2009, 4(1), 370-404.

[21] Wood Handbook, 2010: Forest Products Laboratory,United States Department of Agriculture Forest Service,Madison, Wisconsin.

[22] Petrissams, M., Gerardin, P. Elbakali, D., and Serraj,M. 2003. Wettability of heat-treated wood, Holzforschung 57, 301-307.

[23] Trougton, G.E., Chow, S.Z. (1971): Migration of fatty acids to white spruce veneer surface during drying: Relevance to theories of inactivation – Wood Science, No 3, 129-133.

[24] Northcott, P.L. W. V. Hancock, and H. G. M. Colbeck. 1962. Water relations in phenolic (plywood) bonds. Forest Prod. J. 12(10):478-486.

[25] USDA (1999) Wood Handbook. Wood as an Engineering Material - Madison, WI, United States Department of Agriculture Forest Service, Forest Products Laboratory, 463p.

[26] Budakci M, Ilce A.C., Korkut D.S., Gürleyen T. Evaluating the surface roughness of heat treated wood cut with different circular saws. Bioresurces 2011;6(4): 4247-4258.

The Effects of Nanosilica on Charpy Impact Behavior of Glass/Epoxy Fiber Reinforced Composite Laminates

Omer Yavuz Bozkurt[1], Ozkan Ozbek[2], Atban Rafea Abdo[3]

Abstract

Desire to improve the efficiency of composite materials for engineering applications has led to the use of nano-sized additives or fillers such as nanoclay, nanosilica, nano-graphene, carbon nanotubes. The effect of nanoparticle inclusion on mechanical properties of fiber reinforced composite materials has been investigated by many researchers and crucial effects have been reported in several papers. In this work, the effects of nanosilica content on the low velocity impact behaviors of glass/epoxy fiber reinforced composite laminates are determined using Charpy impact tests. The composite laminates are fabricated via hand lay-up followed by hot press molding. The nanosilica particles with different weight percentages are dispersed in epoxy resins using mechanical stirring. The absorbed impact energy values of flatwise-unnotched and edgewise-notched beam specimens, and impact damages are analyzed as a measure of impact behavior. The results show that the incorporation of nanosilica particles have significant effects on the Charpy impact behavior.

Keywords: *Charpy Impact, Glass Fiber, Nanosilica*

1. INTRODUCTION

In the past few decades, fiber reinforced composite materials have become promising materials in aerospace, automotive, marine and defense industries due to their outstanding performance-to-weight ratio, better damping characteristics, good fatigue resistance, high resistance to corrosion when compared to conventional engineering materials. However, they have low intensity on the impact behavior because its brittle characteristics. Heavier design, so reduction in strength of the materials, may be necessary to satisfy requirement of the system safety. One of the techniques to improve the impact damage resistance of fiber reinforced polymer composites are the addition of small amounts of nanoparticles into the matrix of composites.

Desire to improve the efficiency of composite materials for engineering applications has led to the use of nano-sized additives or fillers such as nanoclay, nanosilica, nano-graphene, carbon nanotubes. The effect of nanoparticle inclusion on mechanical properties of fiber reinforced composite materials has been investigated by many researchers and crucial effects have been reported in several papers [1]. Nano silica particle is the one of the common nanoparticles used in literature studies to improve behaviors of fiber reinforced composite materials. Due to better mechanical properties, nanosilica inclusion in polymer composite has been used in many areas such as automotive, electronics, aerospace industries [2-3].

Several studies related to nanosilica incorporation on polymer based composite materials are present in the literature. Kuzmin et al. [4] conducted a study related to surface modification of basalt fibers by coating the fibers with nanosilica particles. 23% increase in tensile strength was obtained from the sample having 0.1 wt.% nanosilica inclusion when compared to non-coated fibers. Different weight percentages of nano silica particles were considered as between the 0.1 wt.% and 1 wt.%. Huang and Tsai [5] researched the effect of nanosilica and rubber particles on the vibration and damping behavior of E-glass fiber reinforced composite

---

[1] *Gaziantep University, Department of Mechanical Engineering, 27310, Sehitkamil/Gaziantep, Turkey, oybozkurt@gantep.edu.tr.*

[2] *Corresponding author: Gaziantep University, Department of Mechanical Engineering, 27310, Sehitkamil/Gaziantep, Turkey. ozkanozbek@gantep.edu.tr.*

[3] *Ministry of Industry and Minerals, The State Company for Textile Industries and Leather Cotton Factory, Anbar, Iraq, yaatban@yahoo.com.*

laminates. The samples having different stacking sequences and nanoparticle incorporation in epoxy component were prepared and the obtained results were compared with the pure ones. Zeng et al. [6] examined the fracture toughness characteristics of carbon fibre/epoxy laminates by adding the nanosilica and rubber particles. The highest improvement comparing to sample without nanoparticle was obtained from 10 wt.% rubber addition as 2.5 times. Nanosilica incorporation showed the 20-30% increase in fracture toughness. Manjunatha et al. [7] investigated the tensile fatigue behavior of glass fibre reinforced epoxy composites having 10 wt.% nanosilica particles. Fatigue life of samples having nanosilica was improved with three or four times compared to pure samples. Kang et al. [8] derived an advanced proof material for body armor materials. Kevlar fiber reinforced composites were prepared with incorporation of the fumed silica. Kevlar/silica composite fabric exposed to quasi-static stab testing and impact tests. The samples having silica particles showed the better results than pure ones. Rosso et al. [9] employed the well-dispersed silica nanocomposites for tensile and fracture tests. The author indicated that the addition of ratio of 5% silica nanoparticles from the total volume of composite material could be developed the stiffness and facture energy at the range from 20% to 140%. Zamanian et al. [10] noticed that the mechanical characteristics of an epoxy resin have been improved drastically by the addition of silica nanoparticles with various sizes, the best improvements being approached with the smaller nanoparticles.

In this work, the effects of nanosilica content on the low velocity impact behaviors of glass/epoxy fiber reinforced composite laminates are determined using Charpy impact tests. The nanosilica particles with different weight percentages are dispersed in epoxy. Absorbed impact energy values of beam specimens, and impact toughness are analyzed as a measure of impact behavior.

2. MATERIALS & METHODS

Plain weave E-glass fabrics having 202 g/m^2 areal density, epoxy resin (MOMENTIVE-MGS L285) and hardener (MOMENTIVE-MGS H285) were purchased from DOST Chemical Industrial Raw Materials Industry, Turkey. Nanosilica particles having average particular dimension, specific surface area, mass density and high purity as 15 nm, 300 m^2/g, 0.05 g/cm^3, 99.5%, respectively, were supplied by Grafen Chemical Industries, Turkey. Firstly, epoxy resin/nanosilica mixtures were prepared in a beaker according to different weight percentages of nanosilica particles as 0.5, 1.0, 1.5, 2.0 and 3.0. The mixture were blended by mechanical stirring to provide homogeneous mixture. Then, hardener was added to mixture in the weight ratio of mixture/hardener as 100: 40 and stirred again.

Step by step representation of fabrication procedure are given in Fig. 1a. Hand layup technique, shown in Fig. 1b, was conducted to obtain composite laminates. For this purpose, a thin release agent and a layer of glass fabric were placed on the below mold plate. Then, resin mixture was applied on the fabric layer with a help of brush. Afterwards, second fabric layer was placed and resin mixture was applied, respectively. This process was repeated until twelve layers were stacked. Lastly, top mold plate was deposited on the wet fabric layers. After finishing the preparation of combination of resin mixture and fabric layers, curing process was performed as shown in Fig. 1c in a hot press. Charpy impact test specimens were cut on the mini CNC machine. All this procedure was applied for each nanosilica content of 0.5%, 1%, 1.5%, 2% and 3%.
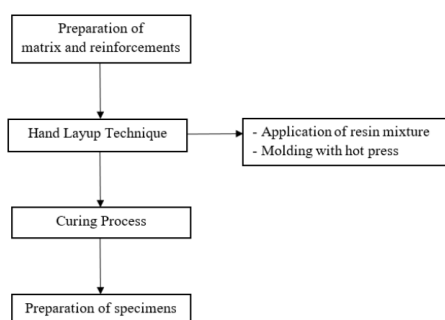
(a)   *(b)*
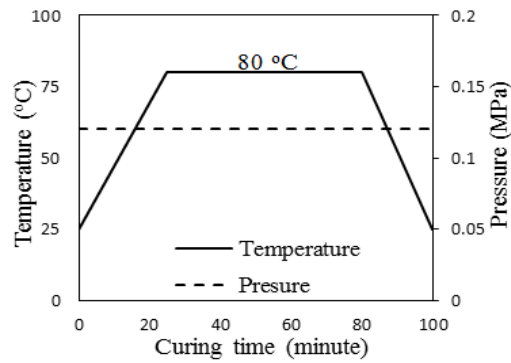
(c)

Figure 1. Fabrication Process; a) step by step representation of fabrication, b) hand layup technique, c) curing process.

Charpy impact tests were conducted by Koger 3/70 Charpy impact test machine, which is shown in Fig. 2 and Fig.3, for determining the impact behavior of composite laminates having nanosilica particles. The specimens with dimensions of 55 mm x 10 mm were prepared in accordance with ISO 179/92 standard [12]. Notched and unnotched specimens were exposed to edgewise and flatwise impact loading, respectively. Five specimens were tested for each configuration. All experiments carried out at standard room temperature.

Absorbed impact energy and impact toughness for each specimen are determined by following equation (1) and (2);

$$E = E_a - E_b \qquad\qquad (1)$$

$$a_{cu} = E \,/\, (bh) \qquad\qquad (2)$$

where, E, E_a, E_b, a_{cu}, b and h represents the absorbed impact energy, potential energy of the weighted pendulum before and after impact, impact toughness, width and thickness of the specimen.
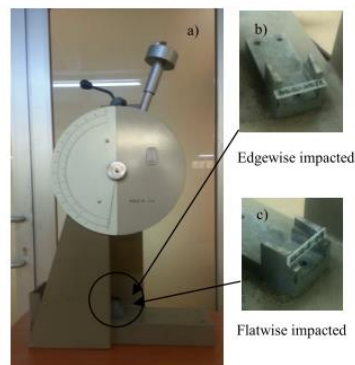
Figure 2. Koger 3/70 Charpy impact tester; a) the calibrated dial on the impact tester, b) edgewise impacted notched test specimen, c) flatwise impacted unnotched test specimen.
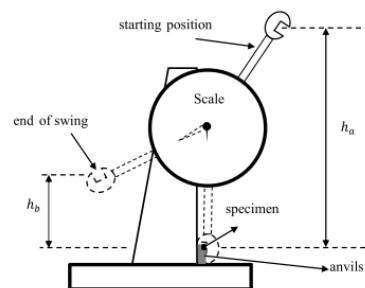
Figure 3. Schematic illustration of Charpy impact test.

3. RESULTS & DISCUSSIONS

The Charpy impact test was performed to observe effects of nanosilica inclusion of the impact behavior of glass/epoxy fiber reinforced composite laminates.

The impact energy and impact toughness values for edgewise (notched) were plotted versus nanosilica contents in Fig. 4 and Fig. 5. GFRE means the pure epoxy laminates that has no addition of silica particles in all figures. For the edgewise specimens, the maximum impact energy and toughness values are obtained from the specimen having 1.5% nanosilica inclusion as 3.34 J and 156.84 kJ/m^2. All silica particles inclusions have the increase comparing to pure one. The results for impact energy and toughness give an idea that there is an improvement trend up to 1.5% and afterwards decreasing trend happens. This can be related to some agglomerations resulted with a weak interfacial adhesion between the matrix and nanoparticles.
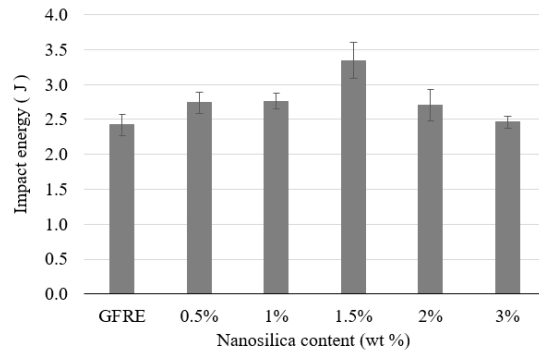
Figure 4. Impact energy of edgewise-notched impacted with respect to nanosilica content.
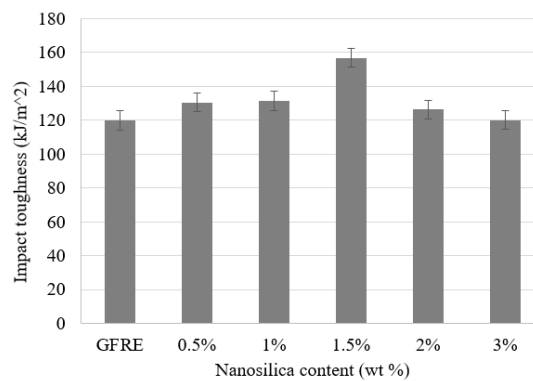
Figure 5. Impact toughness of edgewise-notched impacted with respect to nanosilica content.
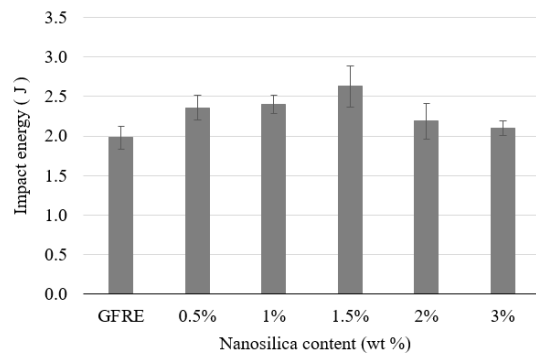
Figure 6. Impact energy of flatwise-unnotched impacted with respect to nanosilica content.
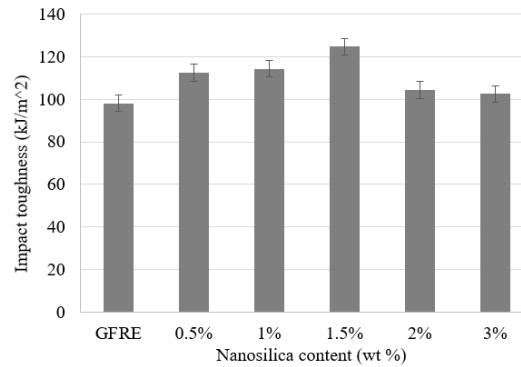
Figure 7. Impact toughness of flatwise-unnotched impacted with respect to nanosilica content.

The Figures 6. and 7. represents the impact energy and toughness results that belong the flatwise (unnotched) specimens. For the results belong the flatwise specimens, they have similar fashion with the edgewise results. The best improvement are obtained from the 1.5% nanosilica incorporation again as 2.63 J and 124.67 kJ/m^2. At this point, 32.8% and 27.1% increase in impact energy and toughness are ensured against to pure ones. In the literature, several similar results were reported for the decreasing trend after a certain value of nanoparticle inclusion [11].

4. CONCLUSIONS

In this study, the effects of nanosilica inclusion on the impact behavior of glass/epoxy fiber reinforced composite laminates were investigated by conducting Charpy impact tests. For each nanosilica content, five specimens as notched and unnotched were exposed to edgewise and flatwise impact loading. Impact energy and impact toughness results were obtained and compared to specimens having pure epoxy matrix. 38.02%, 30.86% for edgewise-notched specimens and 32.83%, 27.1% for flatwise-unnotched specimens increase in impact energy and toughness were obtained from the test results. The best improvements were achieved on the addition of 1.5 wt.% nanosilica inclusion for both situations. Also, all addition of nanosilica weight percentages gave the improvements compared to pure ones.

As seen in the results, nanosilica addition in the matrix the crucial effects on the impact behavior of the fiber reinforced composite laminates even the usage of very small amounts. It can be recommended in the engineering applications.

REFERENCES

[1]. M. Jawaid, A. el Kacem Qaiss, R. Bouhfid, "Nanoclay Reinforced Polymer Composites: Natural Fibre/Nanoclay Hybrid Composites," *Springer*, 2016.

[2]. A. Moisala, Q. Li, I. A. Kinloch, A. H. Windle, "Thermal and electrical conductivity of single- and multi-walled carbon nanotube-epoxy composites," *Composite science and technology*, 66(10), pp. 1285-1288, 2006.

[3]. R. Goyal, M. Sharma, U. K. Amberiya, "Innovative nano composite materials and applications in automobiles," *International Journal of Engineering Research and Technology*, 3(1), 2014.

[4]. K. L. Kuzmin, I. A. Timoshkin, S. I. Gutnikov, E. S. Zhukovskaya, Y. V. Lipatov, B. I. Lazoryak, "Effect of silane/nano-silica on the mechanical properties of basalt fiber reinforced epoxy composites," *Composite Interfaces*, 24(1), pp. 13-34, 2017.

[5]. C. Y. Huang & J. L. Tsai, "Characterizing vibration damping response of composite laminates containing silica nanoparticles and rubber particles," *Journal of Composite Materials*, 49(5), pp. 545-557, 2015.

[6]. Y. Zeng, H. Y. Liu, Y. W. Mai, X. S. Du, "Improving interlaminar fracture toughness of carbon fibre/epoxy laminates by incorporation of nano-particles," *Composite Part B: Engineering*, 43(1), pp. 90-94, 2012.

[7]. C. M. Manjunatha, A. C. Taylor, A. J. Kinloch, S. Sprenger, "The tensile and fatigue behaviour of a silica nanoparticle-modified glass fibre reinforced epoxy composite," *Composite Science and Technology*, 70(1), pp. 193-196, 2010.

[8]. T. J. Kang, K. H. Hong, M. R. Yoo, "Preparation and properties of fumed silica/Kevlar composite fabrics for application of stab resistant material," *Fibers and Polymers*, 11(5), pp. 719-724, 2010.

[9]. P. Rosso, L. Ye, S. Sprenger, "A toughened epoxy resin by silica nanoparticle reinforcement," *Journal of Applied Polymer Science*, 100(3), pp. 1849-1855, 2006.

[10]. M. Zamanian, M. Mortezaei, B. Salehnia, J. E. Jam, "Fracture toughness of epoxy polymer modified with nanosilica particles: Particle size effect," *Engineering Fracture Mechanics*, 97, pp. 193-206, 2013.

[11]. J. K. Pandey, K. R. Reddy, A. K. Mohanty, M. Misra, "Handbook of Polymer nanocomposites. Processing, Performance and Application Volume A: Layered Silicates," *Germany: Springer-Verlag Berlin Heidelberg*, 2014.

[12]. ISO, EN. "179: 72." Plastics -- Determination of Charpy impact properties -- Part 1: Non-instrumented impact test.

The Finite Element Analysis and Geometry Improvements of Some Structural Parts of a Diesel Forklift Truck

Omer Yavuz Bozkurt[1], İhsan Cihan Dai[2], Ozkan Ozbek[3]

Abstract

In this work, static analyses of structural parts of a diesel forklift were performed using Finite Element Method and possible modifications based on the original geometry of parts were utilized with respect to stress distributions at critical region to improve reliability of the forklift design. The analyses were carried out according to standard regulations related with the examined parts. The structural parts of forklift such as chassis and head guard were analysed under compulsion loading conditions. The improvements in relevant parts were demonstrated by the comparison of stress values of original and modified geometries. The finite element analyses were carried out using MSC SimXpert Nastran Finite Element software package.

Keywords: *Finite element analysis, forklift, Msc SimXpert Nastran*

1. INTRODUCTION

Forklift is a relatively small industrial vehicle used to carry industrial goods in a short distances by two power-operated forks at the front. It is also called as a lift truck, a fork truck, or a forklift truck. A forklift can be used in numerous places such as; warehouses, factories, farms, shipping yards, construction sites, supermarkets, and much more. Several different forklift models are found in literature. They can be categorized based on their design, i.e. capabilities, size and methods of operation.

The tests or testing steps are one of the most important and necessary part of a design procedure. Several tests must be performed to develop a new product. Due to requirement of long time durations and production of a prototype, destructive and non-destructive physical tests are generally expensive and adversely affect the product's time to enter the market. In today's world, computer simulations are carried out to improve the efficiency of design procedures in terms of cost and time by reducing or eliminating the need of physical tests. Finite element method (FEM) is the most widely used numerical analysis method in the computer simulations. The FEM does not require a physical prototype production and it can be used to analyse any parts/components of the whole system under certain operating conditions. Also, it permits improvements in the reliability of product by changing the design according to the results of analysis.

In the literature, there are several articles on the open literature associated with the finite element analysis of forklifts. Bhagat et al. [1] developed the CAD model of a translation carriage for reach truck and performed the static analyse of it under various loading and boundary conditions using finite element analysis in ANSYS environment. Doci et al. [2] examined the structural behaviours of forklift under dynamic loadings and specified the parameters that affect the dynamic behaviours of forklift. Meshram [3] developed 3D models for the forklift mast with a change in geometry to perform of structural analysis using finite element method. Also, in terms of stress distribution, the performance of structural steel and gray cast iron were compared using the same boundary conditions. Rane et al. [4] carried out topology optimization technique for the design of forklift chassis to reduce the weight without changing the working conditions of forklift. Cline [5] conducted fatigue analysis of forklift forks applying loads at two different positions; centred and offset. Miralbes et al. [6] designed the crane gibs and pallet box lock for a forklift truck using finite element analysis.

[1] Gaziantep University, Department of Mechanical Engineering, 27310, Sehitkamil/Gaziantep, Turkey. oybozkurt@gantep.edu.tr

[2] Sanko Machine, ARGE Department, Sahinbey/Gaziantep, Turkey, i.cihandai@gmail.com

[3] Corresponding author: Gaziantep University, Department of Mechanical Engineering, 27310, Sehitkamil/Gaziantep, Turkey ozkanozbek@gantep.edu.tr

The boundary conditions were provided according to the forklift truck regulations. Stoychev and Chankov [7] proposed a dynamic model to investigate the stresses for the lifting installation of a forklift truck. Todorov et al. [8] constructed a virtual design of a forklift transmission module and improved it by executing thermal and structural analysis with finite element method.

In this paper, some of the mechanical construction parts of a diesel forklift with three ton capacity is analysed using finite element method and geometry changes on 3D solid model of these forklift construction parts are applied to improve the reliability of design by reducing stress values at critical sections.

2. GEOMETRICAL VIEW AND TECHNICAL PARAMETERS

General view of the diesel forklift marked with major parts is shown in Fig. 1 and some of its technical parameters such as carrying capacity, dimensions, engine power and driving speed are presented in Table 1.
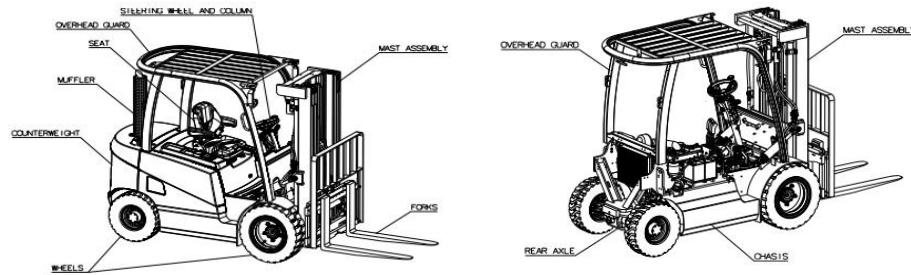
Figure 1. General view of a diesel forklift

Table 21. Diesel forklift technical parameters

Power unit	Diesel
Carrying capacity/load	3000 kg
Load centre	500 mm
Wheel base	1720 mm
Weight	4500 kg
Tilt angle, mast/fork carriage forwards	6°
Tilt angle, mast/fork carriage backwards	10°
Lift height	3230 mm
Overall length	3757 mm
Fork thickness	45 mm
Fork width	100 mm
Fork length	1000 mm
Fork carriage DIN 15173	2A
Turning radius	2400 mm
Driving speed with load	18.2 km/h
Driving speed without load	19.5 km/h
Engine Power	35,5 kW @ 2400 rpm

3. ANALYSIS OF CHASSIS

The chassis is the main supporting structure of the forklift truck which all other components are attached. The 3D solid model for the chassis of forklift truck is shown in Fig. 2. The calculations of external loads are carried out using static loading, rigid connection member and linear-elastic material behaviour assumptions.
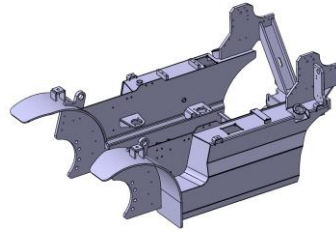
Figure 2. The 3D solid model of forklift chassis

The maximum lifting capacity of forklift truck were analysed as 3000 kg. According to the ISO 3691-1:2011 standard, the structural components of the truck and its attachments shall carry the static load of 1.33×3000 kg. It is the rated capacity at standard lift height and standard load centre distance with respect to the information on the capacity plate.

The various loads acting on the chassis are shown in Fig. 3. The forces of tilt cylinders (F_1), total weight of cabin with seat, bonnet and operator (F_2), total weight of counterweight and muffler (F_3), weight of radiator (F_4), total weight of rear axle with wheels (F_5), and total weight of engine with transmission (F_6) are calculated as 93.227 kN, 2.943 kN, 17.462 kN, 0.294 kN, 1.589 kN and 7.700 kN, respectively.
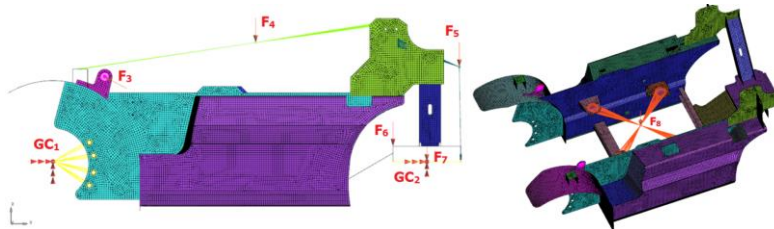
Figure 3. Loads acting on chassis.

The forces of tilt cylinders were examined using loading process of mast assembly at standard lift height under overload condition. The free body diagram of mast assembly is shown in Fig. 4. The mass of mast assembly is 1000 kg. The W_1 and W_2 are the weights of pay load and mast assembly, respectively, and are calculated as $W_1 = 39.142$ kN, $W_2 = 9.81$ kN.
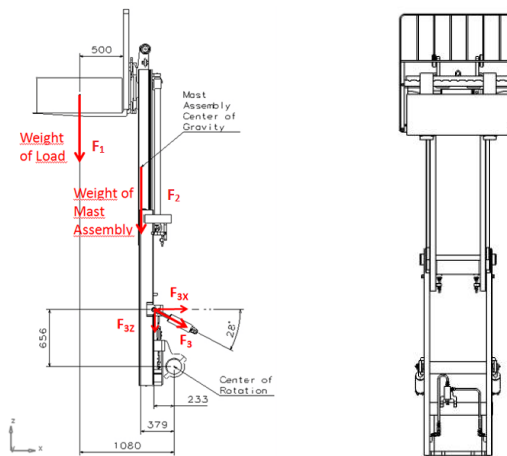
Figure 4. Free body diagram of mast assembly at standard lift height under overload condition.

The solid model, shown in Fig. 2, is meshed with 57289 elements in SimXpert Structure Analysis program. The finite element model of chassis is shown in Fig. 5. The chassis is made of St52-3 and the mechanical properties of St52-3 are given in Table 2.

492
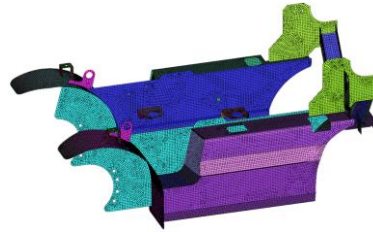
Figure 5. Finite element model of chassis

Shifting too much weight can raise the rear wheels and the boundary conditions GC1 and GC2, shown in Fig. 3, are defined by considering this possibility. GC1 shows the rotation of chassis according to axle centre of front wheels. All degrees of freedom except the rotation about y axis is restrained. GC2 includes three rotational constraints (angular along the x-, y-, and z-axis) and two translational constraints (linear along the x- and y-axis).

Table 2. The mechanical properties of St52-3

Material	St52-3
Yield Stress (MPa)	355
Ultimate Stress (MPa)	530
Poisson's Ratio	0.3
Young's Modulus (GPa)	210

The analysis of chassis is carried out in case of overload and standard lifting height, and the results are shown in Fig. 6. It is shown that the maximum von Mises stress is calculated as 257 MPa at the connection bracket of tilt cylinders. The resulting stress is below the yield stress value of St52-3 material. So, there is no plastic deformation on this bracket. However, a stress concentration is shown and a design revision in geometry of bracket can be done to reduce stress values.
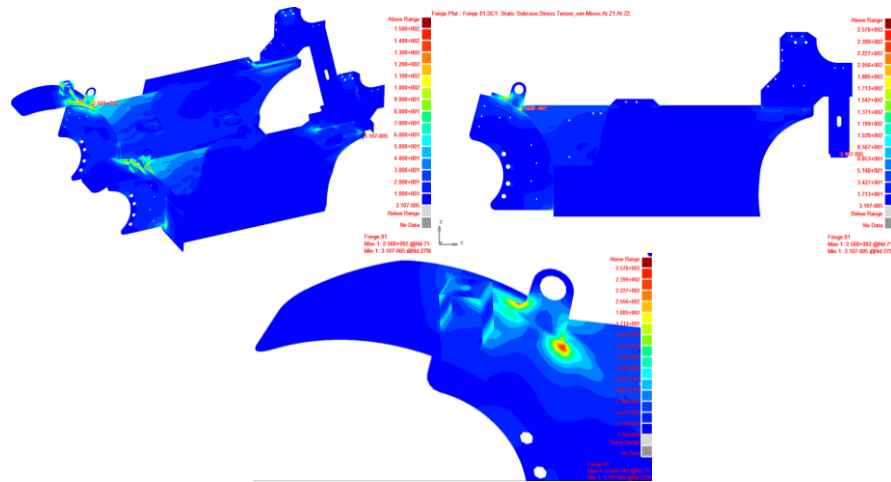
Figure 6. The FEA results of chassis. (a) Isometric view of chassis fem result; (b) Side view of chassis fem result; (c) Maximum Von Mises Stress in Tilt Cylinder Connection Bracket

The front and rear tips of connection bracket show 232 MPa and 257 MPa for the magnitude of von Mises stress. These tip points are marked as A and B, respectively. Two new geometry is designed to improve reliability of connection bracket by reducing stress values. Finite element analysis of chassis have been performed for the new connection bracket designs and the results in terms of von Mises stress distribution are shown in Fig. 7. The first design revision in geometry made possible to reduce maximum von Mises stress to 214 MPa from 257 MPa and second one was reduced to 136 MPa. The von Mises stress comparisons of original and revised geometries of connection bracket is given in Table 3. As seen in Table 3, the factor of safety with respect to connection bracket design was increased from 1.38 to 2.08.
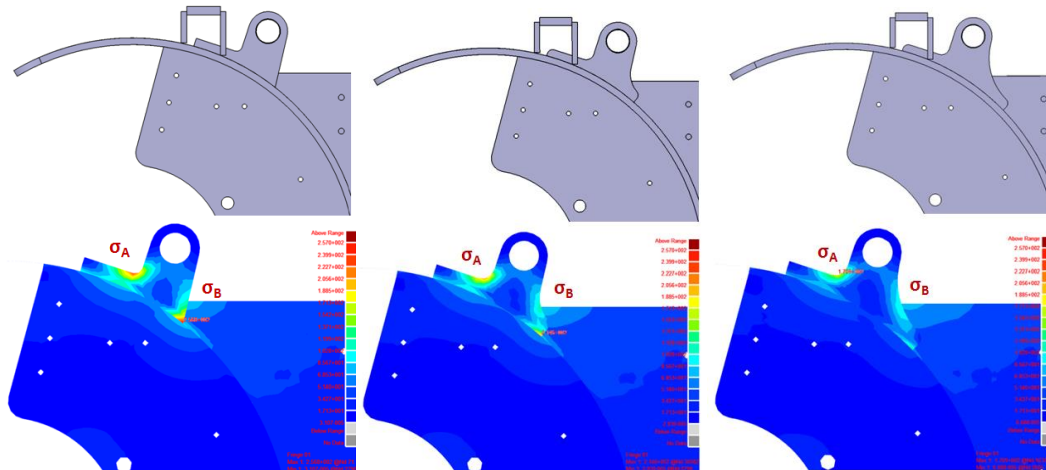
Figure 7. a) The original connection bracket, b) First revision of connection bracket, c) Second revision of connection bracket

Table 3. Comparison of von misses stresses of tilt cylinder connection bracket

Von Mises Stress	Original	Revision-1	Revision-2
σ_A (MPa)	232	206	171
σ_B (MPa)	257	214	136
Factor of Safety	1.38	1.66	2.08

4. ANALYSIS OF HEAD GUARD

The forklift trucks can be very dangerous. Serious or fatal injuries from forklift incidents, especially for roll-overs, can be happened for the forklift operators. The forklift manufacturers have formal responsibility for designing forklifts with protective structures that guard forklift operators under certain conditions. In this section, ROPS (Roll-over protective structures) test of forklift truck was simulated using finite element analysis. The simulation was carried out in accordance to EN ISO 3471 standard. Solid model of head guard and seated operator are given in Fig. 8. The model of seated operator is prepared as described in EN ISO 3411 standard and it is positioned to the sit point.
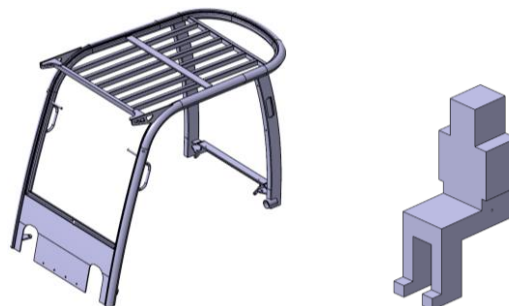
Figure 8. a) Forklift Head Guard Solid Model b) Seated Operator

In the ROPS analysis, the material of head guard was identified as St52-3. The stress values can exceed the yield value according to ROPS analysis. Therefore, the ROPS analysis of head guard is solved as a nonlinear analysis. Stress-strain values of St52-3 material are shown in Fig. 9.

The applied load and energy of the load shall be met at least a certain level in the ROPS test. The stress values can be over the yield stress value to satisfy this requirement and due to this possibility ROPS analysis was performed as nonlinear analysis. The amount of required lateral, vertical and longitudinal loads which are formulated in relation to the weight of forklift are given in EN ISO 3471 standard. The weight of the forklift was presented in Table 1. According to EN ISO 3471 standard, forklift truck is classified in the wheeled

earth-moving machine category, and the lateral load, lateral load energy, vertical load and longitudinal load are calculated as follows:

$$F_{lateral} = 6 \times M = 6 \times 4500 = 27 \text{ kN}$$

$$E_{Lateral} = 12500 \times [(M \div 10000)]^{1,25} = 12500 \times [(4500 \div 10000)]\wedge 1.25 = 4.607 \text{ kJ}$$

$$F_{vertical} = 19.6 \times M = 19.6 \times 4500 = 88.2 \text{ kN}$$

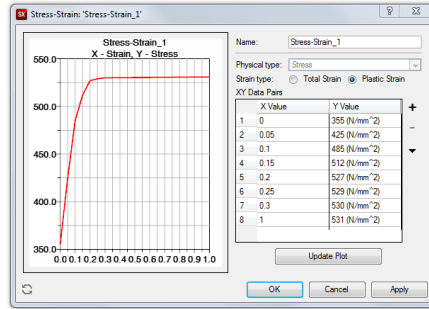$$F_{longitudinal} = 4.8 \times M = 4.8 \times 4500 = 21.6 \text{ kN}$$

Figure 9. Stress-strain values of St 52-3 material

The finite element model of head guard, shown in Fig. 10, has been formed from the solid model presented in Fig. 8. It has 22909 elements and in general consists of quadrilateral elements. The load distribution devices used for the load application was also modelled with solid mesh.

Figure 10. Finite Element Model of Head Guard

The prescribed boundary conditions and applied loads on the head guard for the lateral, vertical and longitudinal loadings are shown in Fig. 11. The load distribution devices for the loading procedures are also shown in Fig. 11. The lateral force, $F_{lateral}$, vertical force, $F_{vertical}$, and longitudinal force, $F_{longitudinal}$, were calculated as 27 kN, 88.2 kN and 21.6 kN, respectively. FC_1, FC_2, FC_3, FC_4, FC_5, FC_6, FC_7, FC_8, FC_9, FC_{10}, FC_{11} and FC_{12} show that all degrees of freedom for connection parts of the head guard are restrained.
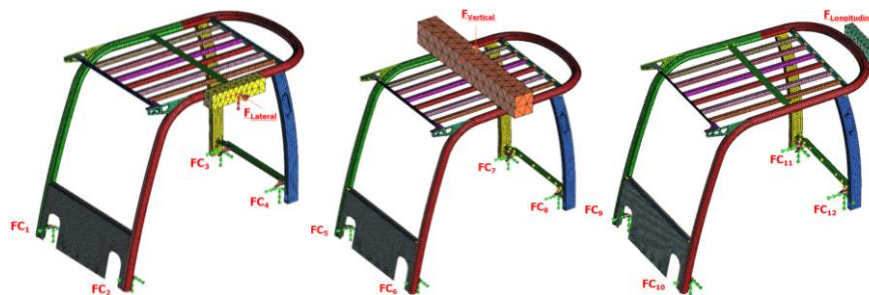
Figure 11. Loading Cases of Head Guard. (a)$F_{lateral}$ force, FC_1, FC_2, FC_3 and FC_4 Fixed Constraints; (b) $F_{vertical}$ force, FC_5, FC_6, FC_7 and FC_8 Fixed Constraints; (c) $F_{longitudinal}$ force, FC_9, FC_{10}, FC_{11} and FC_{12} Fixed Constraints

The lateral loading procedure was carried out using the load distribution device. At the end of the lateral loading, maximum stress value was measured as 411 MPa. Maximum deformation was measured as 87 mm. During the loading, head guard didn't enter to the seated operator area, but it has a permanent deformation. FEM results of lateral loading are shown in Fig. 12 and load-displacement curve is given in Fig. 13.
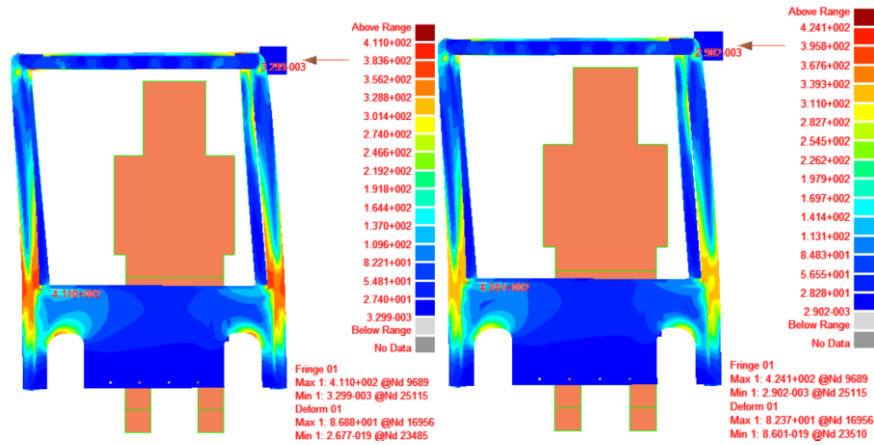
Figure 12. FEM results of Lateral Loading (a)Maximum Loading; (b) Load Removed
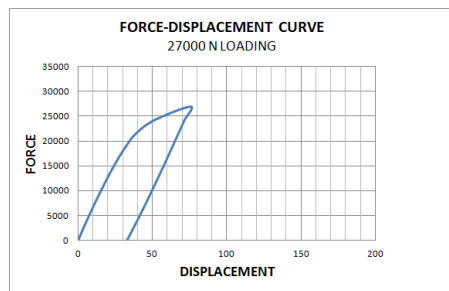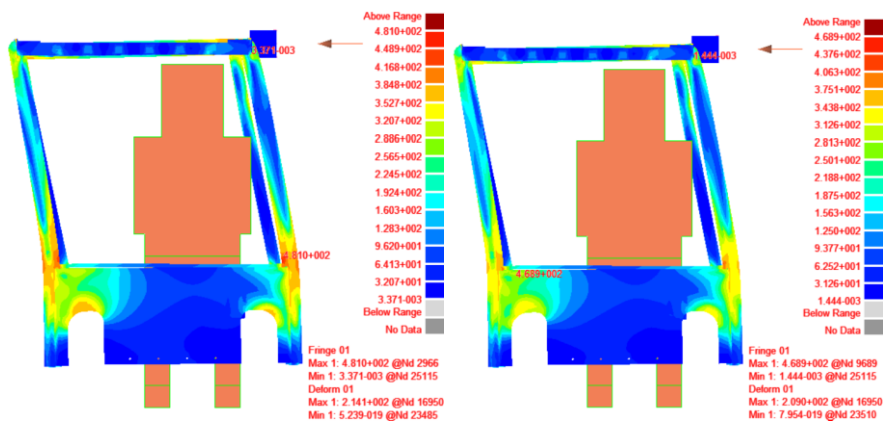

Figure 13. Force-Displacement curve under the application of 27 kN load

During the loading period, the head guard structure was permanently deformed but not in the operator area defined according to the specified standards. With the 1373 J energy generated by applying load of 27 kN, the energy requirement of 4607 J defined in the ROPS standard was not met. For this reason, a load of 32 kN was applied by increasing the amount of load to meet the energy requirement, and the energy requirement of the ROPS standard was met by the 4758 J energy output. The maximum tensile value obtained at 32 kN loading was 481 MPa and the maximum deformation value at force application point was determined as 189.5 mm. The results of the finite element method obtained from lateral load of 32 kN are shown in Fig. 14. The load-displacement curve graph is shown in Fig. 15. During the loading period, the head guard did not enter the operator area.

Figure 14. FEM results of Lateral Loading (a)Maximum Loading; (b) Load Removed
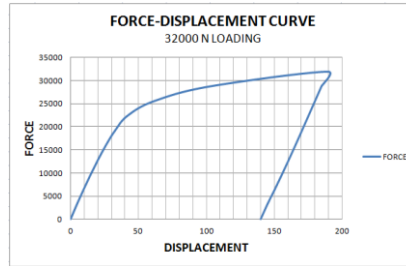
Figure 15. Force-Displacement curve under the application of 32 kN load

Vertical loading was carried out using the long load distribution device from the cabin. At the end of the vertical loading, maximum stress value was measured as 359 MPa. Maximum deformation was measured as 7.8 mm. During the loading, head guard didn't enter to the seated operator area. Head guard has a permanent deformation, no cracks have occurred in the cabin. FEM results of vertical loading was shown in Fig. 16.
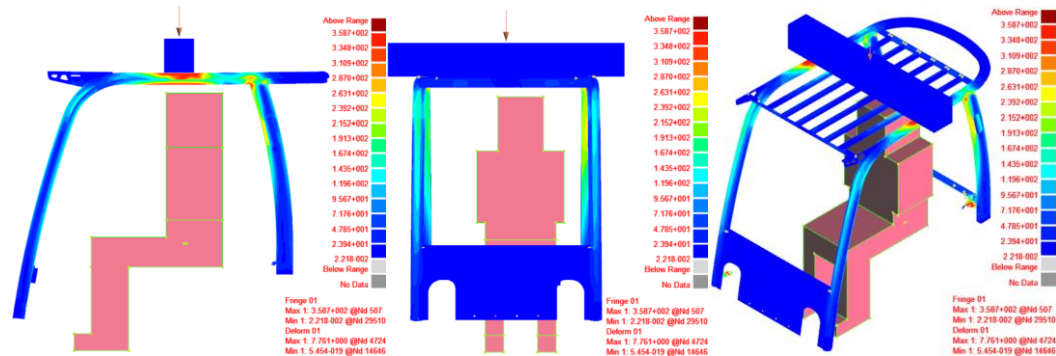

Figure 16. FEM results of Vertical Loading (a) Isometric view of fem result; (b) Front view of fem result; (c) Side view of fem result

Longitudinal loading was carried out using the load distribution device. At the end of the longitudinal loading, maximum stress value was measured as 354 MPa. Maximum deformation was measured as 17 mm. During the loading, head guard didn't enter to the seated operator area. Head guard has no permanent deformation, no cracks have occurred in the cabin. FEM results of longitudinal loading was shown in Fig. 17.
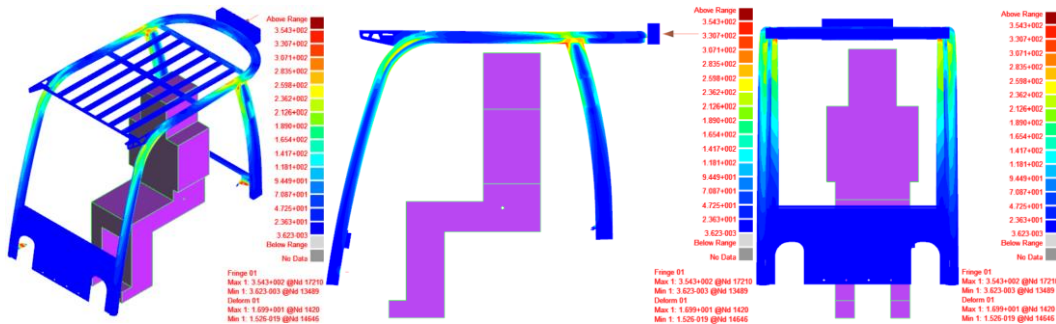

Figure 17. FEM results of Longitudinal Loading (a) Isometric view of fem result; (b) Front view of fem result; (c) Side view of fem result

5. CONCLUSIONS

In this study, static analysis of some structural parts such as chassis, head guard of a diesel forklift truck was performed by using finite element method. Critical regions with high stress values were determined according to the analysis results and design geometries were changed to reduce stresses in there. The analysis results that belong the original models and modified models were compared. The analysis of modified models with new geometries showed that the reliability of the design was improved by lower stresses. For operator safety, the maximum stress and deformation values that can occur in overload and overturn situations are determined by finite element analysis. The maximum lateral, vertical and longitudinal force values that can be applied to the head guard and their application forms are determined according to EN ISO 3471 standard. According to the results of deformation under these loads; the head guard was subjected to permanent deformation, but this deformation was observed to have no adverse effect on the safety of the operator of the truck.

REFERENCES

[1]. V. K. Bhagat, P. A. Wankhade, P. P. Gosh, "Development and structural analysis of translation carriage for reach truck," *International Journal of Applied Research in Mechanical Engineering*, 2(2), pp. 93-99, 2012.

[2]. I. Doci and V. Imeri, "Dynamic analysis of forklift during load lifting using modelling and simulations," *International Journal of Current Engineering and Technology*, 3(2), pp. 342-347, 2013.

[3]. A. T. Meshram, "Finite element mast assembly of material handling equipment," *International Journal of Technology*, 3(1), pp. 50-55, 2013.

[4]. S. B. Rane, H. Shirodkar, P. S. Reddy, "Finite element analysis and optimization of a forklift chassis," *Altair Technology Conference*, 1, pp. 1-6, 2013.

[5]. K. Cline, "Failure of a high-capacity forklift fork," *Microscopy Society of America*, 10.S02, pp. 776-777, 2004.

[6]. R. Miralbes, H. Malon, L. Castejon, "Design of accessories for the coupling in forklift trucks: Crane gibs and pallet box lock," *Selected Proceedings from the 15th International Congress on Project Engineering*, pp. 233-246, 2011.

[7]. G. Stoychev and E. Chankov, "Investigation of dynamic stresses in a forklift truck lifting installation," *Machine Design*, pp. 75-80, 2009.

[8]. G. Todorov, M. Ivanov, K. Kamberov, Sv. Stoev, "Design and virtual prototyping of a forklift transmission module," pp. 37-40, 2011.

Effects of Four Different Soil Tillage Systems on Fuel Consumption, Labor Requirements, Field Capacity and Working Time in West Mediterranean in Turkey (Part 2)

Onder KABAS[1], İlker UNAL, K. Cagatay SELVI, Salih SOZER

Abstract

The study presents comparison of four soil tillage systems in maize, during two summer seasons (2012 and 2013) under Mediterranean area conditions (South of Turkey) at the Bati Akdeniz Agricultural Research Institute, Antalya, Turkiye to determine the effect of four tillage systems. Tillage systems were: (T1) conventional tillage "Plough + disc harrowing + float + pneumatic seeding machine", (T2) reduced tillage I "rotovator + float + pneumatic seeding machine", (T3) reduced tillage II "rotary tiller combination + pneumatic seeding machine" and (T4) no tillage "seeding by direct seeding machine" on the soil physical properties in the area. In this study, the highest field capacity in all the systems was achieved under the no tillage (T4) tillage system and the highest field working time was found in conversation tillage and the lowest value was determined in the no tillage system. The highest fuel consumption was measured in conventional system (T1) whereas the lowest value was found in no tillage system (T4) as 35.37 l ha-1 and 8.78 ha-1, respectively, the highest labor requirements was determined in conventional system (T1) as 6.87 h ha-1 and the lowest value was found in no tillage system (T4) as 1.62 h ha-1.

Keywords: *Consumption, Maize, Mediterreanen*

1. INTRODUCTION

Maize (Zea mays L.) is one of the important cereal crops of Turkey. The rank is third in cultivated area and production after wheat and barley [1]. Conventional tillage practices in corn production in Turkey are more common according to other tillage practices. The most energy consuming part in plant production, concerning the fuel consumption is tillage [2]. In addition, the high cost of energy today forces farmers to find alternative economic tillage methods [3]. The technology of soil tillage in maize production is mainly conventional based on ploughing as primary tillage operation which is requires 75% of the total energy consumed before seed-time [4] and disc harrowing as secondary tillage operation or seedbed preparation. This tillage technology is, on one hand, the most expensive, complicated, organizationally slow, with high fuel consumption (At intensive production 220-240 kg of diesel fuel is consumed per hectare) and labor requirement, and, in the other one, ecologically unfavorable [5]. Economic production and sustainable agriculture are in getting attention improvement in product quality, reduction in production inputs, conservation the natural resources, and environmental awareness gain importance [3]. It is important to minimize energy inputs in terms of sustainable agriculture and for this reason; good management of soils will become increasingly important in the coming years [6]. On the other hand, mechanization of agricultural operations and use of modern machinery such as multi-task machines and direct drill planters can reduce energy consumption per ton of yield of crop, and results in lower cost of production, labor requirements ([7], [8]), soil conservation and environmental protection [9]. The use of modern machines and the reasons for sustainable agriculture are seen to be in many respects, especially in terms of conservation of natural resources and reduction of inputs.

Basically there are numerous possibilities for minimizing costs. Potentials can be exploited by changing cropping methods [10]. For example, moving away from ploughing could lead to a reduction of approximately 50 to 70 % in power and energy use. Depending on the soil type and the exact method of cultivating stubbles and seeding operations, corresponding fuel savings would range from 20 to 50 l/ha [11].

---

[1] XXYYZZ

A researcher worked on the effect of using multi-task machines and they reported that reduced tillage resulted in 55% less fuel consumption than the max. tillage, without a significant difference in the yield of crop [12]. Similarly, reported that in comparison three tillage methods (max. tillage, reduced tillage, and no-tillage). Results showed that max. tillage system (59.33 l/ha)) was more than three time greatest than no-tillage (14.33 l/ha) according to fuel consumption values [8]. Many researchers also indicated that ecological and economical benefits which can be achieved by using conservation tillage systems instead of conventional for example: ([13], [14], [5], [2], [15]).

The General objectives of this study were determining of different tillage systems effects on fuel consumption and labour requirement in West Mediterranean region in Turkey. Also the effect of tillage systems influence on field capacity and filed working time.

2. MATERIAL AND METHODS

2.1. Work area and Soil

This study was conducted at the West Mediterranean Agricultural Research Institute, Antalya, Turkey, during two summer seasons (2012 and 2013). The soil in the experiment field was a silty with pH of 7.5 and organic matter content of 1.8%. The results of soil analyses were given Table 1.

Table1. The result of soil analyses

Soil properties of Analysed	Results
pH (1:2.5)	7.5
Lime (%)	19.6
EC micromhos/cm (25°C)	195
Sand (%)	21
Clay (%)	33
Silty (%)	46
Organic matter (%)	1.8
P ppm	16
K ppm	250
Ca ppm	4585
Mg ppm	409

The average weather conditions in Antalya region during growing seasons such as annual temperatures and sunshine duration etc. were shown in Table 2.

Table 2. Average climate dates on a long-term at the site of experimentation (30 years)

	May	June	July	August	Sept.	October
Temperature (°C)	20.4	25.4	28.4	28.1	24.7	19.8
The highest Temperature (°C)	25.9	31.3	34.4	34.3	31.3	26.7
The lowest Temperature (°C)	14.8	19.4	22.5	22.4	19.1	14.9
Sunshine duration (hour)	9.5	11.4	11.5	11.3	9.5	8.0
Number of rainy days	5.0	2.4	0.7	0.5	1.7	5.4
Rainfall (kg/m²)	29.3	7.1	3.3	1.6	11.0	74.8

The experiments, which were begun in June 2012 and finished 2014 during two summer seasons compared four tillage systems (conventional tillage (T_1), reduced tillage I (T_2), reduced tillage II (T_3) and no tillage (T_4)) for maize (Zea mays L.) production following a wheat-maize rotation. The standard cultural practices for cultivation of Maize (such as irrigation and fertilizing) recommended by Bati Mediterranean Agricultural Research Institute; other than treatments, were followed throughout the growing seasons.

The experiment was established as a randomized block design with three replications. Plots were 5 m wide (four rows) and 25 m long with an inter row spacing of 0.7 m distance.

2.2. Soil Tillage Systems

Tillage systems were shown in Table 3 and the specifications of tools used in the experiment were given Table 4.

Table 3. Soil tillage methods utilized in experiments

Tillage systems	Tillage operations
T1 (conventional tillage)	Plough(25-30 cm) + disc harrowing + float + pneumatic seeding machine
T2 (reduced tillage I)	Rotovator + float + pneumatic seeding machine
T3 (reduced tillage II)	Rotary tiller combination + pneumatic seeding machine
T4 (no tillage)	Seeding by direct seeding machine

For the conventional tillage method, the soil was first ploughed with five bottom moldboard ploughs. After plowing, the field was harrowed with disc harrow and leveled with float. In the reduced tillage method I, soil was prepared for seeding with only one pass of soil tillage, float and pneumatic seeding machine. In the reduced tillage method II, soil was prepared for seeding with only one pass of soil tillage with rotary tiller combination and then pneumatic seeding machine. For the direct seeding application, seeding was applied without tillage. Massey Ferguson 5400 (Engine Power 105 HP) tractor was used in the experiments.

Table 4. The specification of the tools used in experiment

Tools	Working width (mm)	Working depth (mm)	Average speed (km h^{-1})
Plough	1500	300	5.5
Disc harrowing	2200	150	6.5
Rotovator	2000	220	6
Rotary tiller combination	2500	200	2.8
Float	3000	–	7
Seeding machine	2800	40-50	6.3
Direct seeding machine	2800	40-50	5.6

2.3. Investigations and Data Collection

At the start and the end of operations on each plot, the amount of fuel consumption was measured using a magnaugt M0512 fuel consumption meter which is $\pm$ 1% measurement accuracy and -10°C to 80 °C operating temperature. The operation time was also registered. The labor requirement was determined by measuring the time for finishing single tillage operation at each plot of the known area (125 m^2). The data examined with Kolmogorov-Smirnov One Sample Test for Normality and with Levene Test for homogeneity of variance, result showed that the data normally distributed (P>0.05) and variances were equal (P>0.05). According to this, Randomized bloc design was used to analyze the data. Year was used as bloc and it found statistically insignificant (P>0.05) and bloc was removed from the model. To compare the means LSD test was used.

3. RESULTS AND DISCUSSION

Average values of fuel consumption and labor requirements field capacity and working time for each tillage method are given in Table 5.

Table 5. The specification of the tools used in experiment

	T_1	T_2	T_3	T_4	CV	LSD	
Fuel Consumption (L/ha)	35.37	21.31	18.71	8.78	2.250	1.062	***
Labor requirements (h/ha)	6.87	4.32	2.27	1.62	5.205	0.356	**
Field capacity (ha/h)	0.32	0.87	0.55	1.40	4.315	0.312	**
Field working time (h/ha)	7.61	5.32	3.13	2.44	5.321	0.156	**

**: $P<0.01$; ***: $P<0.001$

The highest fuel consumption 35.37 L ha^{-1} was observed in T1 tillage whereas the lowest value 8.78 L ha^{-1} was found in the T4 method, requiring fuel consumption more than four times higher than T4 method. This observation is supported by [16], [17], [8].

Similarly, the labor requirements (6.87 h ha^{-1}) and field working time (7.61 h ha^{-1}) were as the highest in T1 and the lowest (1.62 h ha^{-1} and 2.44 h ha^{-1}) in T4 respectively. Labor requirements and field working time of T1 tillage method around three times more higher compared to the conservation soil tillage application. According to many scientific sources that are relevant to this topic, conservation tillage practices provide significantly more labor savings compared to traditional tillage applications. This difference in fuel consumption, labor requirements and field working time are due to the larger number of tilling operations associated with the T1 tillage method. Comparing the conventional and no-tillage systems in the production of maize in Croatia, [18] showed that large-scale possibility of labor requirement savings (up to 80%) due to the use of no-till system.

On the other hand, when examined at the values of field capacity, as a normally, the field capacity value of the T1 application (0.32 61 h ha^{-1}) was the lowest while the T4 (1.40 61 h ha^{-1}) was highest.

4. CONCLUSION

This study showed that deciding and choosing the appropriate tillage method is main factor especially in the fuel consumption reduction programs in agriculture. Inappropriate tillage application can waste significant amounts of fuel and also labor requirements. The conservation implements showed positive performances, in terms of reduced demand of labor and fuel consumption. This study examined the effect of four different tillage practices on fuel consumption, labor requirements, field capacity and working time in West Mediterranean in Turkey. According to our results:

1. Conventional tillage method (T1) "Plough + disc harrowing + float + pneumatic seeding machine" had the highest fuel consumption and lowest field capacity as compared to the other tillage methods.

2. No tillage "seeding by direct seeding machine" T4 method had the lowest fuel consumption with maximum field capacity. The conventional method (T1) requires four times more fuel consumption and again approximately four times labor requirements comparing the T4 method.

3. No tillage method at the same time had the lowest field working time than the other tillage methods. We concluded that under the agro-climatic conditions of West Mediterranean in Turkey, the No tillage method can be recommended and easily applied for fuel consumption and labor requirements.

REFERENCES

[1]   O. Kabas, and K.C. Selvi, "Yield components of maize (zea mays l.) under different conservation tillage systems in west Mediterranean in Turkey (part 1)," *International Symposium. ISB-INMATEH 2016*. Romania. Pages. 2016, 41-44.

[2]   Z.I. Mileusnic, D.V. Petrovic, and M.S Devic, "Comparison of tillage systems according to fuel consumption," *Energy*, vol 35, pp. 221–228, 2010.

[3]   A. Sessiz, A. Alp, and S. Gürsoy, "Conservation and conventional tillage methods on Selected soil physical properties and corn (zea mays l.) Yield and quality under cropping system in Turkey," *Bulgarian Journal of Agricultural Science*, vol 16(5), pp.597-608, 2010.

[4]   A.Tabatabaeefar, H. Emamzadeh, M.G. Varnamkhasti, R. Rahimizadeh, and M. Karimi, "Comparison of energy of tillage systems in wheat production," Energy, vol 34, pp. 41–45, 2009.

[5]   D. Filipović, S. Košutić, and Z. Gospodarić, "Influence of different soil tillage systems on fuel Consumption, labour requirement and yield in maize and Winter wheat production," *Agriculture*, vol 10(2), pp. 17-23, 2004.

[6]   P.J. White, J.W. Crawford, M.C.D. Alvarez, and R.G. Moreno, Soil management for sustainable agriculture," *Applied and Environmental Soil Science,* vol 2012, pp. 1-3, 2012.

[7]   W.L. Hargrove (1990) Role of conservation tillage in sustainable agriculture, conservation tillage for agriculture. [Online]. Available, http://www.ag.auburn.edu/auxiliary/nsdl/scasc/Proceedings/1990/Hargrove.pdf.

[8]   A. Akbarni, and F. Farhani, "Study of fuel consumption in three tillage methods," *Res. Agr. Eng.,* vol 60(4), pp. 142–147, 2014.

[9]   M. Paula, T. Rusu, L. Paulette, M. Buta, I. Oroian, A. Odagiu, D. Clapa, and S. Cosma, "Reducing Energy Consumption and Soil Conservation by Tillage System," *ProEnvironment*, vol 6, pp. 164 – 170, 2013.

[10]   S. Dutzi, "The effects of various tillage and sowing systems on energy input and crop production parameters," *Landtechnick,* vol 63(6), pp. 338-340, 2008.

[11]   K. Koller, *Soil Tillage in Agroecosystems. Techniques of Soil Tillage. Chapter 1*. Washington, USA, CRC Press, 2003.

[12]   E. Bonari, M. Mazzoncini, and A. Peruzzi, "Effects of conventional and minimum tillage on winter oilseed rape (Brassica napus L.) in a sandy soil," *Soil & Tillage Research*, vol 33, pp. 91–108, 1995.

[13]   L. Malicki, J. Nowicki, and Z. Szwejkovski, "Soil and crop responses to soil tillage systems: a Polish perspective," *Soil & Tillage Research*, vol 43, pp. 65-80, 1997.

[14]   S. Kosutic, D. Filipovic, and Z. Gospodaric, "Maize and winter wheat production with different soil tillage systems on silty loam," *Agricultural and food science in Finland*, vol 10, pp. 81-90, 2001.

[15]   R.Fanigliulo, M. Biocca, and D. Pochi, "Effects of six primary tillage implements on energy inputs and residue cover in Central Italy," *Journal of Agricultural Engineering,* vol 47(3), pp.177-180, 2016.

[16]   Z. Gozübüyük, İ., Oztürk, O. Demir, and A. Celik, "Comparison of Verious tillage-seeding systems for sunflower Production in terms of some operating parameters," *Journal of Agricultural Machinery Science*, vol 6(4), pp. 253-259, 2010.

[17]   E. Šarauskis, S. Buragiene, K. Romaneckas, A. Sakalauskas, A. Jasinskas, E. Vaiciukevicius and D. Karayel, "Working time, fuel consumption and economic analysis of diferent tillage and sowing systems in Lithuania," *11th International Scientific Conference Engineering for Rural Development,*2012, p. 52.

[18]   R. Zimmer, B. Miloš, Z. Milaković, and Ž. Kržek, "Comparison of conventional and notillage in maize production," *Proceedings of the 25th International Symposium "Actual Tasks on Agricultural Engineering",* Opatija, Croatia, 1997, p.155.

GEOGRAPHY OF WORLD ORGANIC VITICULTURE

Atilla CAKIR[1]*, Ezgi DOGAN[1] Alperen MERAL[2]

ABSTRACT

The first activities in organic viticulture date back to the 1950s when in Switzerland and Germany the first pioneers made great efforts to apply the basic principles of organic agriculture to viticulture. Since then, organic viticulture has developed dynamically in many countries.

The developments related to organic wine has begun in the 1970s, the first meeting in 1977, from Germany, Switzerland and France are regulated by organic wine producers in Germany.

While the world of organic grape fields is 87 577 ha in 2004, in 2013 it increases three fold and the value is 311 595 ha. That area of the world, grapes (6.8 million hectares) accountsfor 4.6%.

European continent is ranked first with 90% field of vie won the basis of organic grapes. Other continents in order in Asia, North America, South America, Australia, Africa and Antarctica.

The most important grape producing countries in the world: Spain, France, Italy, China, Turkey have retained the same time in order to organic grape fields in 2013. The largest organic grape of Spainis 83.922 ha., 67 937 ha of Italy. France is 64 610 ha, in addition to a considerable proportion of organic grape fields in China and Turkey are available.

Keywords: *Organic Viticulture, Grape, Wine, World*

1. INTRODUCTION

The rapid growth of the world population and the rapid development of industrialization have brought many problems together. It has been shown that the use of fertilizer inputs in agriculture has negative effects on human and environmental health [1]. In the past, people's population, knowledge, needs and desires have increased; Scientific and technological developments in all areas, after the initial cave life has created a modern society of today's needs [2] Agricultural practices, which are also defined as traditional (conventional) agriculture, have resulted in increased agricultural production to a certain point, but environmental pollution has occurred and natural balance has been destroyed.

In addition, drug residues and synthetic mineral fertilizers, which are used in agricultural products, are mixed with the underground waters and brought to the potable waters, have started to threaten human health and life [3]. The harmful effects of chemicals that are used in plant protection is often disclosed by determination of pesticide residues. However, there is no focus on the pollutants in the atmosphere, especially lead, cadmium and copper [4]. In many countries of the world, pesticides poisoning can sometimes result in disasters. Unfortunately, In 1984, 20,000 people were poisoned in a chemical drug factory in India, and at least 2500 people were killed. After 1970, it was found that the use of insecticide in the rice cultivation, which is called "green revolution" in Asia, resulted in a 27% increase in mortality rate in males [5]. In the face of the aforementioned problems, producers and consumers in many countries, especially those with high income levels and developed countries, have started to produce clean products that do not harm the natural balance, pollute the environment and do not cause toxic effect (poison effect) in humans and other living things.The production system realized for this purpose is called "Ecological Agriculture". In addition, "Ecological Agriculture", "Biological Agriculture" and "Organic Agriculture" are used synonymously in different countries of the world.

Among the organic agricultural products that are increasing rapidly all over the world, the traditional products of the countries usually come to the forefront. For example,tea in India milk and dairy products in Denmark, meat and meat products in Argentina, bananas in middle America and African countries, dates in Tunisia,

[1] **Corresponding Author: Bingol University, Faculty of Agriculture, Horticulture, 12000/BİNGOL cakiratilla@gmail.com*

[2] *Bingol University, Faculty of Agriculture, Landscape Architecture, 12000/BİNGOL*

olive oil, dried fruits in Turkey. Parallel to these, organic viniculture has become increasingly important in many countries, especially in wine grapes. Organic viticulture is currently in its infancy in most of the countries outside Europe, and the organic vineyards are still small. The demand for traditionally produced wines is an obstacle to turning the vineyards of producers into organic farming [6].In Turkey, which has come to the fore in raisins export product of organic viticulture.

1.1. Organic Agriculture In the World

According to 2013 data, 43.0 million hectares of organic farming is done in the world. When the collection sites (41.9 million hectares) from the country are taken into account, this figure is about 85 million hectares. When the distribution of organic agriculture by area is considered (Figure 1), the first order is about 17.3 million hectares. It is seen that the area is occupied by Oceania. It is observed that Europe is followed by Europe with an area of 11.5 million hectares, South America with an area of 6.6 million hectares, Asia with an area of 3.4 million hectares, North America with an area of 3.0 million hectares, and the African continent with an area of 1.2 million hectares.
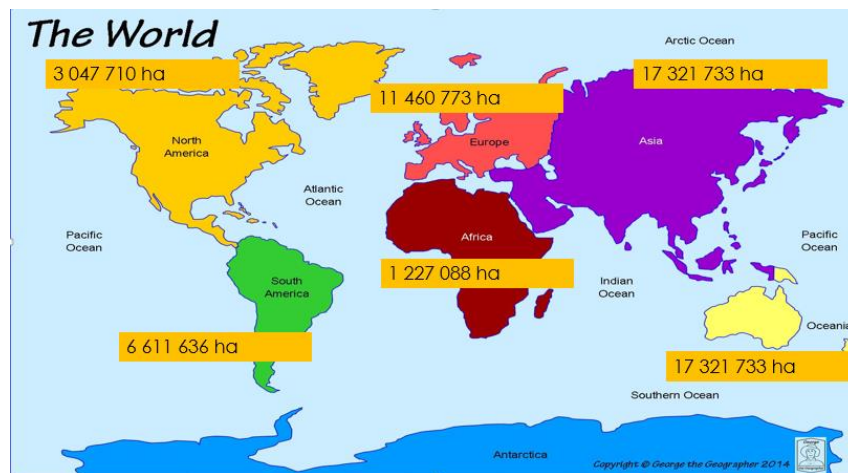
Figure 1. World Organic Farming Areas (Source: FIBL 2013). [7]

While the number of countries that collected organic farming data in the world in 2000 was 86, this figure reached 156 in 2008 and 160 in 2009. In 2013, this number has reached 162.Oceania has an area of 40% organic farming all over the World. Europe has drawn a growing parabola over the last few years, keeping the world organic agriculture for about a quarter of it; Latin America is followed by 15%. The Asian continent ranks 4th with an 8% share, followed by North America with a share of 7%.The share of the African continent in the last place in total organic farming areas in the world is about 3% (Table 1)

Table 1. Organic area on the basis of continents

Continents	Organic Area (ha)	Total organic farming areas in the world according to regions (%)
Africa	1 227.088	2.8
Asia	3 425.939	8.0
European	11 460.773	26.6
Latin America	6 611.636	15.3
North America	3 047.710	7.1
Australia	17 321.733	40.2
Total	**43 091.113**	**100**

1.1.1. World Organıc Agrıcultural Manufacturers

According to data from the year 2013, 1.988 million producers are engaged in organic agriculture in the world. In Europe, there are 334 877 (17%) producers in Africa, 574 129 (29%) in Africa, 730 244 (36%) in Asia, 319 459 (16%) in Latin America, 16 393 (1%) in North America, And Oceania 22 997 (1%) organic farming by the farmer (Figure 2).
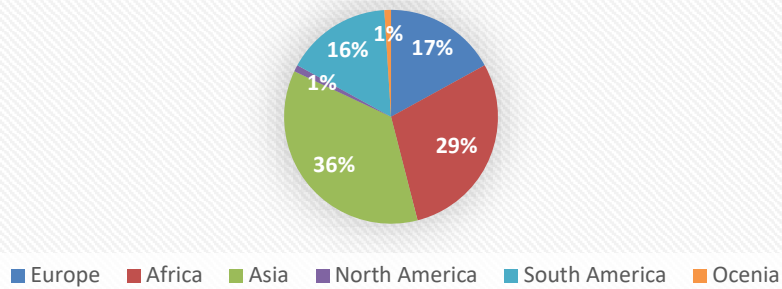
Figure 2. Producers rates in the continent

1.2. ORGANIC AGRICULTURE IN TURKEY

Organic agriculture in our country started with organic exports of dried grapes and dried figs from our traditional export products in the 1984-1985 season, and showed a rapid development in the following years, approaching 250 products on the basis of raw material according to 2008 data. The number of products shows a steady increase with the processed products obtained from these raw materials. Most of the organic certified products produced are exported to developed countries, mainly EU countries, USA and Japan. Turkey is still the leading country in the dry and dried fruit market, which helped to develop organic agriculture in the beginning. Also in recent years supportive policies and the interest of ecological products on the internal march of the efforts of civilian organizations have been increasing. However, the number of organic producers receiving individual certifications outside the projects is very low, the support given to the producers is inadequate and the establishment of a system based on a contract similar to the external market has not resulted in the desired improvement in the domestic market. When our country is evaluated according to vegetative production regions, it should be taken into consideration that geographical regions and provincial boundaries do not always coincide. In this chapter, although certain parts of some illusions are geographically located within a region due to provincial accumulation of statistical data, they are located within the region where most of the provinces are included.

Table 2. Total and organic farming areas of our country by region

Regions	Real Area (ha)	Total Area (ha)
Ege	18 071	39 216
Dogu Anadolu	17 605	19 651
Guneydogu Anadolu	9 245	9 881
Karadeniz	8 134	88 328
Marmara	4 835	5 774
Akdeniz	3 008	26 500
İc Anadolu	2 144	2 439
Total	63 042	191 791

Sources: Gıda, Tarım ve Hayvancılık Bakanlıgı [9]

Figure 3. Turkey's organic farming areas by region

The Aegean region is the most important region in organic agriculture because organic agriculture is the first shade to be established in our country and it is the center of raisin and fig production which is one of the most important items in organic production and export. It is in the first place in terms of real production area (Table 2, Figure 3).

1.2.1. Organıc Agrıcultural Manufacturers In Turkey

The number of producers, which was 12 428 in 2002, showed a continuous increase until 2010. According to 2010 data, the number of organic producers was 42 097 and the number increased to 42 460 in 2011 when including transitional products.

Table 3. Organic agriculture in Turkey

Years	Number of Products (Number)	Number of Farmers (Number)	Area (Hectare)	Production (Ton)
2005	205	14 401	203 811	421 934
2006	203	14 256	192 789	458 095
2007	201	16 276	174 283	568 128
2008	247	14 926	166 883	530 224
2009	212	35 565	501 641	983 715
2010	216	42 097	510 033	1 343 737
2011	225	42 460	614 618	1 659 543
2012	204	54 635	702 909	1 750 127
2013	213	60 797	769 014	1 620 466
2014	208	71 472	842 216	1 642 235

Sources: Gıda, Tarım ve Hayvancılık Bakanlıgı [9]

Although the number of organic farming products in Turkey has been changed until 2005-2014, the number of farmers has increased fivefold, although it has not increased significantly. Production increased to 1,642 235 tons depending on the increase in the area (Table 3).

1.2.2. Productıon Areas

The production area, which was approximately 90 000 ha in 2002, has increased by 5 times in 2012 and reached 510 033 ha. As in the case of producer numbers, production sites tend to fluctuate in general for some years.

1.3. ORGANIC VITICULTURE IN THE WORLD

The first activities relate In the late 1970s in Germany, they made great efforts to apply the basic principles of the first voluntary organic vineyard to organic viniculture began at the end of the 1970s. In Germany in 1977; the first meeting was conducted with organic wine producers from Switzerland France and Germany [10]. The inadequacy of information about organic viniculture limits the spread of organic vine cultivation . Many traditional wine producers have little knowledge of organic viticulture. The Organic Producer Association is not yet able to provide adequate expertise in organic viniculture in many countries [11]. The organic product market has become rapidly developing sector all over the world. Currently, the European Union, USA and Japan are the biggest markets.With an annual growth rate of 20-30%, it is estimated that the world trade volume will increase from 10 billion dollars to 100 billion dollars within the next 10 years [3].Organic viniculture has become increasingly important in many countries where wine grapes are grown.The demand for traditionally produced wines is an obstacle to turning farmers' ties into organic farming [6].In 2004, the first batches have been received and until 2012 the organic grape production area has increased by more than 3 times. There has been an increase of more than 9% from 2012 to 2013 (Figure 4).
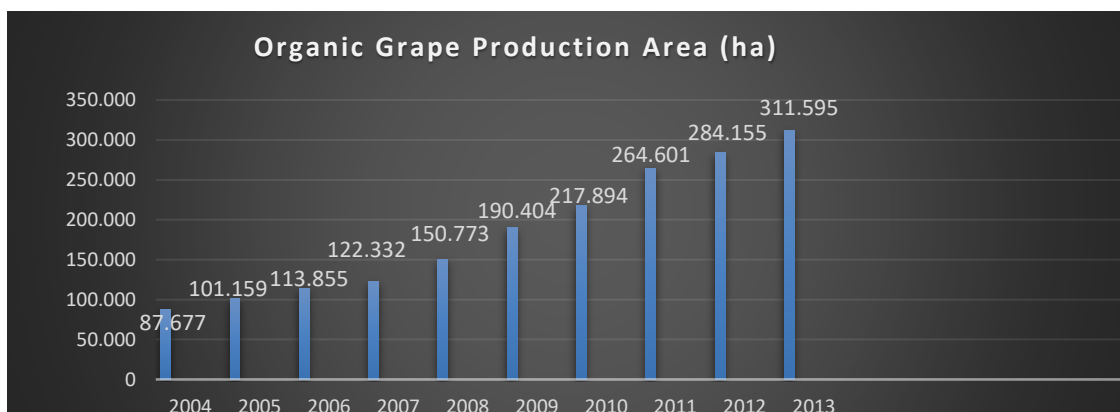
Figure 4. 2004-2013 World Organic Grape Production Area

311 595 hectares of organic vineyards are grown in the world. This figure represents 4.6% of the total grape production area in the world (6.8 million hectares [12]). All organic grapes produced are important not only in wine but also in dried grapes and table grapes in many important countries, especially in Turkey. The five most important producer countries in the world, Spain, France, Italy, China, and Turkey, are the countries that have the best food for organic viniculture in 2013. Spain, Italy and France, with the largest organic grape fields, each produce more than 60,000 hectares of organic grape. European organic grape production area has a 90% slope all over the world, and organic viniculture is done in 258 348 ha area. It is followed by Asia with 21 482 ha area, North America with 15 994 ha area, Latin America with 12 064 ha area, Oceania with 2 782 ha, Africa with 925 ha area (Figure 5).
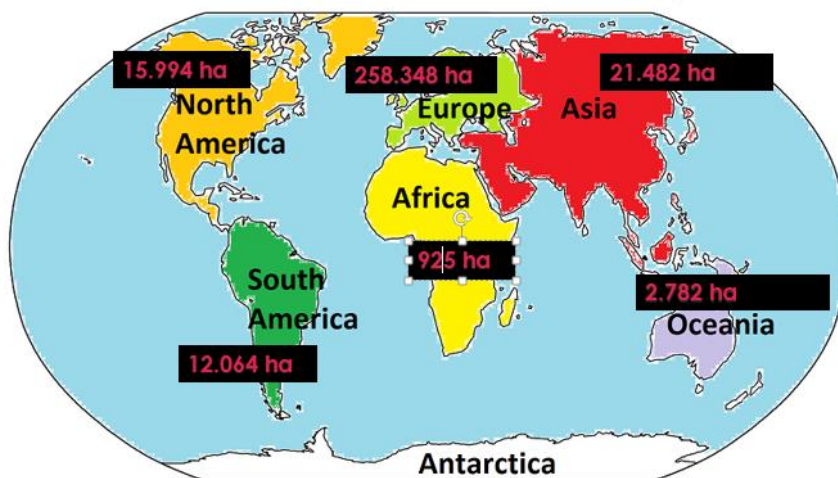

Figure 5. Organic grape production areas on the basis of continents

When the countries of the continents are examined on the basis of Europe, Spain is the country with the largest production area in the world with 83 932 hectares. Italy is the second country with 67 937 hectares, while France is the third country with 64 610 hectares of organic grapes (Table 4). China is the most important production area of Asia. With 19 194 ha organic grape fields, China accounts for about 89% of the entire Asian continent. With an area of 1 316 ha, Iran is the second most important country of Asia-Pacific. Located in North America, USA 15 is the most important producer country with an area of organic grapes of 647 ha. With 290 ha of area, Mexico is the number one manufacturer in the world. Argentina is the most important country in the sense of 4 139 ha area and the organic bond area of Latin America. Chile is another important country with an area of 3 595 ha. Organic viniculture is carried out in 2,500 hectares of New Zealand, a country in the Oceania continent. The countries that can be considered important in Africa are Algeria and South Africa (Figure 6).

Table 4. Areas of organic viniculture on the basis of countries

Countries	Organic Area (ha)	Share in Organic Areas
İspanya	83 932	% 8.9
France	64 610	% 8.5
İtaly	47 937	% 9.8
China	19 174	% 3.2
America	15 647	% 4.0
Turkey	8 418	% 1.8
Germany	7 100	% 7.1

Source: FAOSTAT 2012 [12]

Figure 6. Organic viniculture area on the basis of countries (ha) [12]

1.3.1. Organıc Vıtıculture In Turkey

Organic grape production in our country is around 25 thousand tons (for 2010 year data). Organic grape production, which tended to decline from 2001 to 2003, has increased in the following years. Since the beginning of organic production in the province of Manisa, most of the grape production takes place in this area. As seen in the 2010 data, Manisa is the first with about 15 000 tonnes of production.İzmir, which is the other important city in organic grape production, has about 5.5 tons of production.

Figure 7. Organic grape production quantities by illicit basis in Turkey [9]

2. CONCLUSION

As in organic production, organic viniculture is not a complete system, but a movement. Problems arise in soil treatment and crop protection applications.Lastly, health problems and deaths, which are based on the consumption of foodstuffs that use chemicals, are a matter of debate.People who care about their health, who have an allergic mind, find it suitable for their taste, and even seek chThe best indicator of this is the fact that in developed countries organic farming and its products are becoming more and more frequentange, tend to organic products. World organic viniculture and product design, especially the shape of the evaluation of grapes and market conditions are seen to be shaped.For example, in many European countries organic wines have come to the forefront and organic raisin production has become even more prominent in our country.

REFERENCES

[1]   Akgüngor, S., 1996., Türkiye'de Ekolojik Yontemlerle Üretilen Cekirdeksiz Kuru Üzümün Verimi, Maliyeti, Pazarlanması: Salihli ve Kemalpasa Ornegi, Ege Üniversitesi Ziraat Fakültesi Tarım Ekonomisi Bolümü, Can Ofset, Nisan 1996., İzmir.

[2]   İlter, E.,Onogur, E., Hakerler, H., Ayan, R., Altındisli, A.,Madanlar, N.,Yagmur, E., 1999., «Ege 103 Bagcılıkta Organik Tarım Bolgesinde Ekolojik ve Geleneksel Yontemlerle Cekirdeksiz Yas ve Kuru Üzüm Üretimi Üzerinde Mukayeseli Bir Arastırma,» *Bildiri Ozetleri*, 21-23 Haziran 1999.,İzmir, Türkiye,

[3]   Aksoy, U., Altındisli, A., 1999., Dünya'da ve Türkiye'de Ekolojik Tarım Ürünleri Üretimi, İhracatı ve Gelistirme Olanakları, İstanbul Ticaret Odası, İstanbul.

[4]   Baydar, N.G., Anlı, E., Akkurt, M. 2000., Tarımsal Savasımda Kullanılan Kimyasalların Üzüm ve Sarap Kalitesi ile Saraplarda Bazı Agır Metal İcerikleri Üzerine Etkileri, *Gıda Teknolojisi Dergisi,* cilt 25, no. 6, pp. 449-457.

[5]   Tuncer, C., Akca, İ., Saruhan, İ. 2000., İnsektisitlerin Cevre Kirliligine Etkileri, Tarım ve Koy İsleri Bakanlıgı Samsun İl Müdürlügü, 26-28 Eylül 2000., Samsun.

[6]   Kose , B., Odabas, F. 2005., Bagcılıkta Organik Tarım, cilt 20, no. 3, pp. 96-104.

[7]   «FIBL,» 2013., Available: http://www.fibl.org/en/themes/organic-farming-statistics.html. [Erisildi: 9. 11. 2016].

[8]   Frick, V., Bonn, K., 2015., The World of Organic Agriculture, Statistics and Emerging Trends, Available: http://www.organic-world.net/. [Erisildi: 15.11.2016].

[9]   Anonim 2014, Türkiye Organik Tarım Stratejik Planı (2012-2016),Gıda Tarım ve Hayvancılık Bakanlıgı Bitkisel Üretim Genel Müdürlügü, 2016.

[10]   Willer, H.,Urs Meier., 2000., «Organic Viticulture in Europe,» Convention Centre Basel,Stiftung Oekologie &Landbau, Bad Duerkheim., 25-26 Agustos 2000.

[11]   Geier, B.,Hofmann , U., Willer, H., 2000., «Organic Viticulture World-Wide,» Basel, 2000.

[12]   FAO, 2012.,Available: http://www.fao.org/faostat/en/#data [Erisildi : 16.12.2016]

Investigation Of The Effect Of Cutting Parameters With Artificial Neural Networks In Machining

Ramazan CAKIROGLU[1], Selcuk YAGMUR[2], Adem ACIR[2],Yakup TURGUT[2], Ulvi SEKER[2]

Abstract

In this study, a model was developed by using artificial neural networks (ANN) method to reduce the effect of machining parameters on the measurement accuracy of the Al 7075 material under dry cutting conditions. Drilling experiments were carried out using four different cutting speeds (170, 200, 230 and 260 m / min), three different feed amounts (0.1, 0.2 and 0.3 mm / rev) and two different cutting tools (uncoated and TiN / TiAl / TiCN coated). For each cutting tool, 8 pieces of experimental learning data and 4 pieces of testing data were performed in the model with ANN. In ANN model the 2-5-6-1 for the uncoated tool and the 2-4-5-1 for the coated tool were determined as the most suitable network structures. As a result of the study, it is seen that the estimations made with ANN are quite close to the results obtained from the experiments.

Keywords: Al7075, Machining parameters, Drilling, Artificial Neural Networks (ANN)

1. INTRODUCTION

Drilling is one of the most important machining processes and comprises about one-third of the machining process. This process is usually used as a last step in chip removal process. Although modern machining methods are being developed in the manufacturing industry, conventional drilling is still the most widely used machining method due to reasons such as economics and simple applicability [1].

The main purpose is to obtain a hole element with a desired diameter within certain tolerances in the hole drilling with the drill. The diameter obtained in drilled holes is usually larger than the nominal diameter. In the drilling process, the implementation of process, the stability of the fastening elements used, the rigidity, the overall state of the machine tool and in particular cutting edge geometry of drill affects the dimension accuracy of the obtained hole. It is also extremely important in parameters such as cutting speed and feed rate. From the literature review, it appears that the researchers generally consider the hole quality as a whole.

Kannan et al. carry out application of artificial neural network modelling for machining parameters optimization in drilling operation [2]. Meral et al. investigated multi-regression method the effect of drilling parameters on hole quality during drilling of AISI 1050 steel[3]. Cicek et al. examined the effects of deep cryogenic processing on cutting forces, hole diameters and tool life [4]. These studies show that the effect of the cutting parameters on the hole quality is usually investigated experimentally. In some studies, it has been determined that the machining output is analyzed using various mathematical modeling methods [5-16].

In this study, the effects of cutting parameters on deviation from the diameter (ovality) were investigated during drilling of the Al 7075 material with coated and uncoated tools. Besides, the experimental results was compared with results obtained using mathematical model which was developed for the ovality with artificial neural network.

2. METHOD

In the experiments, AA7075 alloy in diameter of 25 mm and length of 25 mm was used as workpiece material. The chemical composition of the material used in the experiments is given in Table 1.

Table 1. Chemical composition of the workpiece material (AA 7075) (% weight).

Si	Fe	Cu	Mn	Mg	Cr	Zn	Ti	Al
0.257	0.397	3.392	0.653	0.446	0.099	0.002	0.012	94.71

In the drilling process, the diameter of 14 mm uncoated solid carbide and multilayer coated (TiN/ TiAlN / TiCN) carbide drills were used as cutting tool. The mechanical and thermal properties of the drills used in the tests are given in Table 2.

Table 2. The mechanical and thermal properties of the drills

	K25 grade (Uncoated)	P25 grade (Coated)
Density (gr/cm3)	14,6	12,6
Compression strength (MPa)	5000	4600
Elasticity module (GPa)	590	550
Poisson ratio	0,22	0,22
Thermal conductivity (W/mK)	70	45
Coefficient of thermal expansion (106/K)	5,6	6,7

Four cutting speeds (170, 200, 230 and 260 m / min) and three feed rates (0.1, 0.2 and 0.3 mm/rev) were determined as cutting parameters. Drilling tests were carried out at Johnford VMC-550 CNC vertical machining center. The Coordinate Measuring Device (CMM) was used to determine the diameter of holes after drilling experiments.

3. ARTIFICIAL NEURAL NETWORKS

Artificial neural-network (ANN) is a computational model for prediction in the system performance and analysis. ANN can be used as alternative methods to simplicity and fast calculations in the engineering fields [17-18]. ANN network structure is consisting of layers and nodes. Nodes are also known as neurons. The ANN network structure with layers and nodes is given in Fig. 5. As shown in Fig. 5, the ANN network structure consists of three layers which are the input layer, hidden layer and output layer. The network structure has two nodes in the input layer, j nodes in the first hidden layer, k nodes in the second hidden layer, l nodes in the mth hidden layer and one nodes in the output layer [19]. Two nodes for the input layer stand for the two decision values of the case study which are cutting speed (V_c) and feed rate (f). One nodes for the output layer stands for the predicted ovality values. When considering that a back-propagation (BP) network is applied at the mth hidden layer with j and k nodes for each hidden layer, the network structure given in Fig. 5 could be defined as a 2–j–k–1 structure.
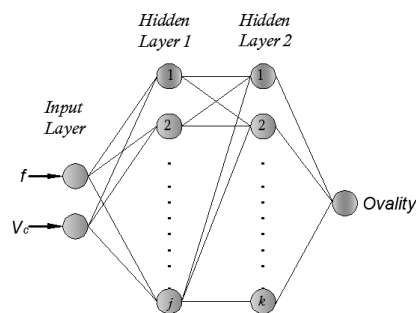
Figure 5. Example illustration of the ANN network structure with layers and nodes

The back-propagation (BP) algorithm is one of the most powerful learning algorithms in neural-networks. Each connection links between neurons on available layers in the ANN is called a weight vector (w) [17-18]. The BP with Levenberg–Marquardt (LM) algorithm is commonly used and has a wide acceptance in the ANN. The back propagation neural network with LM in the ANN has been described in Refs [17-21]. In this study, the ANN model was developed with two neurons in the input layer and one neurons in the output layer to estimate of ovality at different V_c and f. The ANN model the 2-5-6-1 for the uncoated tool and the 2-4-5-1 for the coated tool network structures were performed as shown in Fig. 6. The normalization values were given in Table 4.
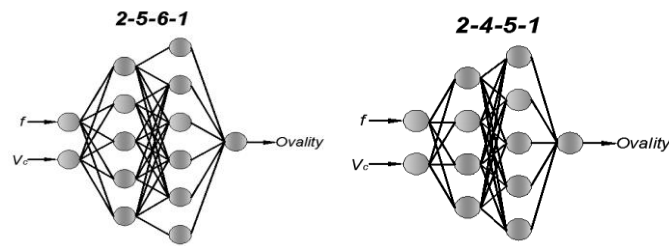
Figure 6. Network structure models with various hidden layers

Table 4. Parameter values used for normalization in the drill process

Symbol	Machining Parameter	Levels		
		1	2	3
A	Tool	Uncoated	Coated	
B	Feed rate, f (mm/rev)	0.1	0.2	0.3
C	Cutting Speed, V_c(m/min)	170	200	230

The normalization for inputs and outputs is done in the ranges between -1 and +1. The values of the operation conditions (ANN inputs) and ovality (ANN targets) were normalized. ANN model used for the performance prediction was prepared in "PHYTICA" toolbox software with back propagation neural network based on Levenberg–Marquardt algorithm. The equations used in back propagation algorithm with LM are mentioned below[22]:

Hidden layer calculations:

$$net_i = \sum x_i w_{ij} \tag{1}$$

$$y_i = f(net_i)$$

Output layer calculations:

$$net_k = \sum y_i w_{jk}$$

$$o_k = f(net_k) \tag{2}$$

where, xi are the input data, yi are the results obtained from layer 1 and ok are the results of layer 2.

Transfer function:

The fermi transfer function has been used for both hidden and output layers in calculation:

$$F_i = \frac{1}{1 + e^{-4(NET_i - 0.5)}} \tag{3}$$

The ANN model was performed through two stages: training stage and testing stage. A training ovality data was a group of matched input and output patterns used for training the networks. The measuring ovality data was used to train the ANN and it can precisely predict the ovality. Therefore, the training network model was tested with random selected experimental data to predict output in the testing stage.

The root-mean-square error (RMSE), the minimum error level of the mean absolute percentage (MAPE), and absolute fraction of variance (R^2) used in this paper for neural networks analyses as described in Refs. [20-21] are below:

$$RMSE = \sqrt{\frac{\sum_{m=1}^{n} (y_{pre,m} - t_{mea,m})^2}{n}} \tag{4}$$

$$MAPE = \frac{1}{n}\sum_{j}\left[\frac{t_{mea,m} - y_{pre,m}}{t_{mea,m}}\right]x100 \quad (5)$$

$$R^2 = 1 - \frac{\sum_{m=1}^{n}(y_{pre,m} - t_{mea,m})^2}{\sum_{m=1}^{n}(t_{mea,m})^2} \quad (6)$$

where n is the number of data patterns, $y_{pre,m}$, $t_{mea,m}$ indicate the predicted value and the measured value respectively of one data point m.

4. EXPERIMENTAL RESULTS AND DISCUSSION

The deviation values obtained as a result of the experiments based on the cutting parameters and drill type are given Table 3. Figures 3 and 4 shows the variations of deviation from the diameter depending on the coating application and cutting speed.

Table 3. Diameter values obtained by experimental inputs

No	Tool	Feed Rate (mm/rev)	Cutting Speed (m/min)	Diameter
1	Uncoated	0,1	170	14,039
2	Uncoated	0,1	200	14,041
3	Uncoated	0,1	230	14,050
4	Uncoated	0,1	260	14,013
5	Uncoated	0,2	170	14,029
6	Uncoated	0,2	200	14,033
7	Uncoated	0,2	230	14,001
8	Uncoated	0,2	260	14,002
9	Uncoated	0,3	170	14,002
10	Uncoated	0,3	200	14,021
11	Uncoated	0,3	230	14,031
12	Uncoated	0,3	260	14,035
13	Coated	0,1	170	14,001
14	Coated	0,1	200	14,006
15	Coated	0,1	230	14,032
16	Coated	0,1	260	14,002
17	Coated	0,2	170	14,034
18	Coated	0,2	200	14,052
19	Coated	0,2	230	14,010
20	Coated	0,2	260	14,020
21	Coated	0,3	170	14,071
22	Coated	0,3	200	14,035
23	Coated	0,3	230	14,040
24	Coated	0,3	260	14,114

When the graphics in Figure 3 are examined, it is shown that the increase in cutting speed led to generally a positive effect on the deviation for uncoated tools. One of the biggest problems encountered in machining of Al 7075 alloy is the chip formation of built-up edge (BUE). The increase in cutting speed increases the cutting zone temperature, and this situation prevents chip with BUE. For this reason, the increased cutting speed led to positive effect on the deviation. It can be also concluded from the graph that the increased feed rate has negative effect the obtained diameter values. This result can be attributed to increase in chip volume being removed per unit time with the increased feed rate.
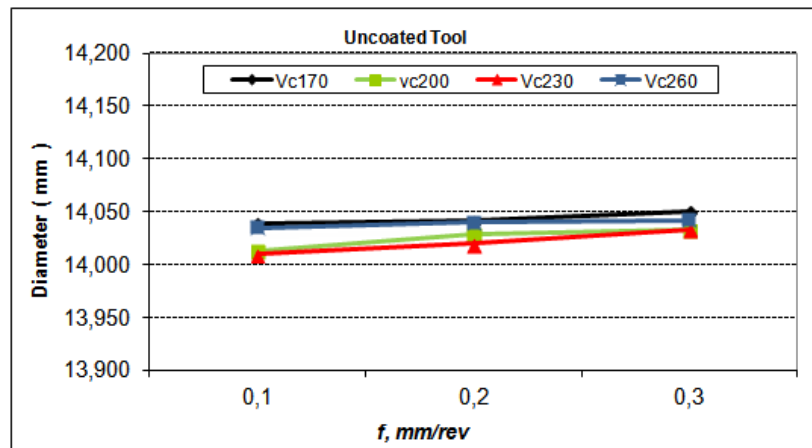
Figure 3. Change of the diamater according to cutting parameters for uncoated tools.

The graph given in Fig. 4 shows that the variation of diameter value has different trend according to cutting parameters. It can said that increased cutting speeds negatively affect the deviation from diameter unlike uncoated tools. The low coefficient of friction of the coated tools prevents the chip formation with built-up edge by easily removing the chips due to decreasing in tool-chip contact time. In this case, the axial deviation of the tool resulted from the machine/tool vibrations which is change depending on increased in cutting speed increased. However, the highest diameter value was obtained at the maximum cutting speed of 260 m/min. The peeling of the coating was became when the cutting speed was increased to the maximum value, and so the tool wear has increased. For this reason, the highest diameter value was obtained at above mentioned cutting speed. Similarly, the feed rate adversely effected the deviation from diameter for the coated tools.
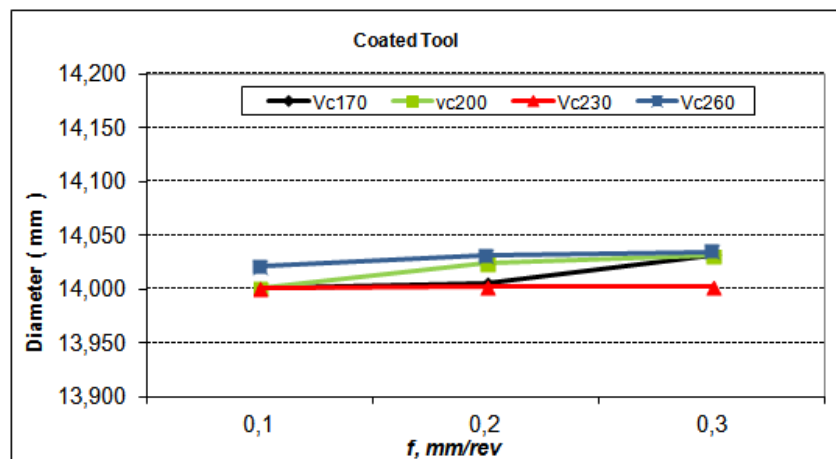
Figure 4. Change of the diamater according to cutting parameters for coated tools.

4.1. ANN Modelling of Experimental Results

The ovality values resulting from the drilling of AA 7075 material with coated and uncoated tools were compared with the ovality values calculated by the YSA modelling. In the YSA model developed for this purpose, back-propagation learning algorithm of multilayer feed forward neural network was used. In the ANN analysis, 70% of the total experimental data were used to train the network and remaining 15% was

used to test the validation of the network. In the scope of the study, a separate ANN model has been developed for uncoated and coated tools depending on the feed rate (f) and cutting speed (Vc). Eight of the 12 deviation values for each tool were used for the training and 4 were used for the testing. By using Pythia software, suitable network structures were determined according to 2 inputs (f, Vc) and 1 output (ovality) values depending on them. In the ANN modeling of the ovality, 2-5-6-1 for the uncoated tool and 2-4-5-1 for the coated tool were chosen as appropriate network structures. Comparison of the experimental data and the testing/training ANN model results for different numbers of nodes in the hidden layer were given in Table 5. The best results for ovality were obtained with different hidden layer structures. The weight values between the input layer, hidden layer and output layers for ovality were illustrated in Table 6-7. Mathematical equations derived from the best of ANN models for the ovality were given in Eqs. (7) and (8). The Eqs. (7) and (8) can be helped in the ovality calculations without the need for any experimental work.

$$Ovality_{Kaplamasız} = (1 + \exp(-4*(-0.22775*F_6 - 1.89396*F_7 + 0.619392*F_8 + 2.912923*F_9 \\ - 2.33076*F_{10} - 0.67737*F_{11} - 0.5)))^{-1} \quad \text{......(7)}$$

$$Ovalitiy_{Kaplamalı} = (1 + \exp(-4*(0.560795*F_5 - 2.47135*F_6 + 2.102803*F_7 \\ - 1.64967*F_8 + 0.770739*F_9 - 0.5)))^{-1} \quad \text{...........................(8)}$$

Table 5. Experimental and ANN results for ovality

No	Tool	Feed Rate (mm/rev)	Cutting Speed (m/min)	Actual Diameter	Predicted Diameter
1	Un Coated	0,1	170	14,039	14,039
2	Un Coated	0,1	200	14,041	14,05
3	Un Coated	0,1	230	14,050	14,05
4	Un Coated	0,1	260	14,013	14,013
5	Un Coated	0,2	170	14,029	14,011
6	Un Coated	0,2	200	14,033	14,033
7	Un Coated	0,2	230	14,001	14,001
8	Un Coated	0,2	260	14,002	14,001
9	Un Coated	0,3	170	14,002	14,002
10	Un Coated	0,3	200	14,021	14,021
11	Un Coated	0,3	230	14,031	14,047
12	Un Coated	0,3	260	14,035	14,035
13	Coated	0,1	170	14,001	14,003
14	Coated	0,1	200	14,006	14,012
15	Coated	0,1	230	14,032	14,019
16	Coated	0,1	260	14,002	14,004
17	Coated	0,2	170	14,034	14,036
18	Coated	0,2	200	14,052	14,031
19	Coated	0,2	230	14,010	14,031
20	Coated	0,2	260	14,020	14,002
21	Coated	0,3	170	14,071	14,044
22	Coated	0,3	200	14,035	14,022
23	Coated	0,3	230	14,040	14,034
24	Coated	0,3	260	14,114	14,034

Comparison of experimental values and values predicted by ANN for testing and training sets of the ovality were illustrated in Figs. 7 and 8. However, the best predicted ANN model were determined with obtained R^2 values and R^2 values were very close to 1. The statistical RMSE, R^2 and MAPE values for training and testing data's were given to performances analysis of the ANN models as shown in Table 8. It can be seen that R^2 values were computed for uncoated tool with 2-5-6-1 ANN model whereas, the R^2 values for coated tool were found with 2-4-5-1 ANN model as shown in Table 8. In the best ANN model developed for uncoated tool prediction, R^2 values were calculated as 0.999999 and 0.999999 for testing and training, respectively. On the other hand, R^2 values were calculated as 0.999999 and 0.999998 for testing and training, respectively, in the best ANN model developed for coated tool. Also, RMSE values for uncoated tool were calculated as 0.000706 and 0.000634whereas; these values for coated tool were computed as 0.000349 and 0.000990 for testing and training, respectively. MAPE values for uncoated tool were obtained as 0.093556 and 0.093556 whereas; these values for coated tool were calculated as 0.038340 and 0.089623 for testing and training, respectively as shown in Table 8.

Table 6. Weights among layers for uncoated tools

$$NET_{j(1-5)} = w_{1j} * f + w_{2j} * V_c$$

j	w_{1j}	w_{2j}
	Weights values between input and first hidden layers	
1	-1,64671	-0,48092
2	2,748284	-1,98975
3	-1,39601	1,167687
4	1,135534	-2,1264
5	-4,9782	2,424163

$$NET_{j(6-11)} = w_{1j} * F_1 + w_{2j} * F_2 + w_{3j} * F_3 + w_{4j} * F_4 + w_{5j} * F_5$$

k	w_{1k}	w_{2k}	w_{3k}	w_{4k}	w_{5k}
	Weights values between first hidden layers				
6	-0,5018	-0,25886	-1,00113	-0,47488	0,144287
7	-1,54246	-0,39431	0,507134	0,927992	-0,42815
8	0,895673	1,941614	-0,51109	2,073571	1,506268
9	3,138327	0,363399	-3,86451	-1,24723	3,388992
10	-0,84547	-0,30489	1,733653	-0,74733	-1,59619
11	-0,75151	0,012581	-1,02578	0,320643	-0,95456

Table 7. Weights among layers for coated tools

$$NET_{j(1-4)} = w_{1j} * f + w_{2j} * Vc$$

j	$\mathbf{w_{1j}}$	$\mathbf{w_{2j}}$		

Weights values between input and first hidden layers

j	$\mathbf{w_{1j}}$	$\mathbf{w_{2j}}$
1	0,494769	0,796078
2	-0,78731	-1,21477
3	1,274992	-1,00706
4	2,996709	-2,32053

$$NET_{j(5-9)} = w_{1j} * F_1 + w_{2j} * F_2 + w_{3j} * F_3 + w_{4j} * F_4$$

k	$\mathbf{w_{1k}}$	$\mathbf{w_{2k}}$	$\mathbf{w_{3k}}$	$\mathbf{w_{4k}}$

Weights values between first hidden layers

k	$\mathbf{w_{1k}}$	$\mathbf{w_{2k}}$	$\mathbf{w_{3k}}$	$\mathbf{w_{4k}}$
5	-0,11483	-0,89091	-0,0354	1,034822
6	0,959291	0,175011	1,178142	-1,90906
7	2,148122	-0,68075	-1,90777	-0,66238
8	0,534252	0,882762	0,156553	-0,44234
9	-0,50209	-0,59042	1,648906	-0,77583

Table 8. Statistical results of the a) testing data and b) training data for uncoated tools and coated tools

	RMSE	R2	MAPE
2-5-6-1	0.000706[a]	0.999999[a]	0.093556[a]
Uncoated tool	0.000634[b]	0.999999[b]	0.093556[b]
2-4-5-1	0.000349[a]	0.999999[a]	0.038340[a]
Coated tool	0.000990[b]	0.999998[b]	0.089623[b]

Figure 7. Comparison of predicted results with actual results for uncoated in testing ANN models.

518
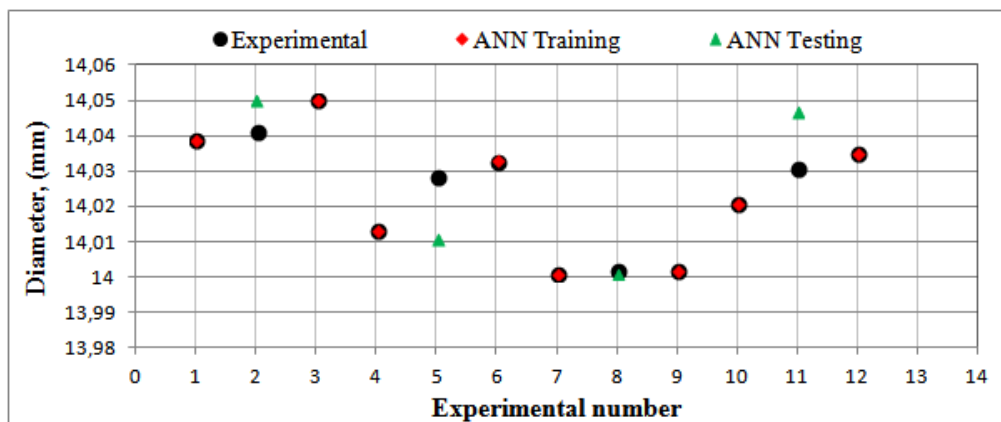
Figure 8. Comparison of predicted results with actual results for coated in testing ANN models
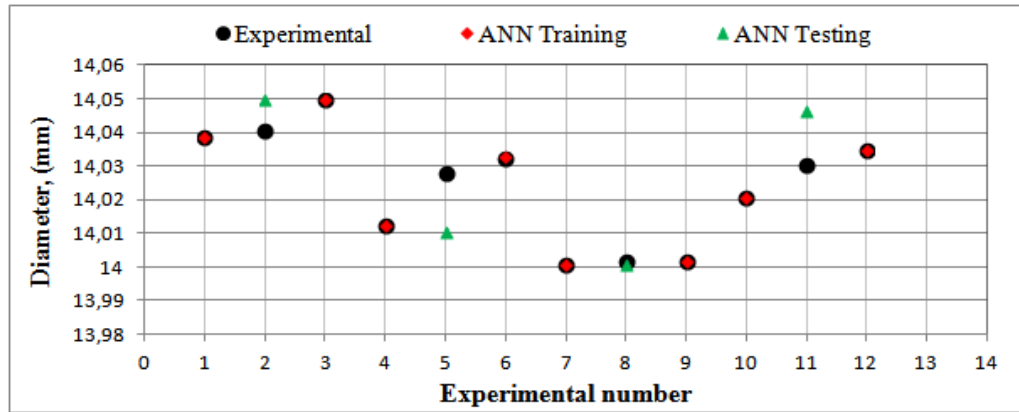
5. CONCLUSIONS

In this study, the ovality occurred at the drilling of AA7075 material uncoated and coated drills was evaluated, the obtained results was summarized as follows.

- The diameter of the hole was bigger than the nominal diameter for all conditions when the deviations from diameter have been considered.
- It was seen that the increase in cutting speed provided values closer to the nominal diameter with uncoated tools. The result closest to the nominal diameter in the coated tools was found at a cutting speed of 230 m/min
- In all experiments, it was seen that the increased feed rate increased the ovality value.
- It was obtained that the best of these models has given 2-5-6-1 and 2-4-5-1 ANN model in prediction of ovality.
- It was found that there was agreement between experimental data and predicted values for uncoated tool ($R^2 = 0.999999$) and uncoated tool ($R^2 = 0.999999$).

REFERENCES

[1]. Tonshoff, H.L., Spintig, W., Konig, W., Neises, A., "Machining of Holes D evelopments in Drilling Techonolgy", *Annals of the CIRP*, 43 : 551-560 (1994).

[2]. Kannan, T. Deepan Bharathi, B. Suresh Kumar, and N. Baskar. "Application of artificial neural network modeling for machining parameters optimization in drilling operation." Procedia Materials Science 5 (2014): 2242-2249.

[3]. Meral, G., Dilipak, H., & Sarıkaya, M. (2011). AISI 1050 Malzemenin delinmesinde delme parametrelerinin delik kalitesi üzerindeki etkisinin coklu regresyon metoduyla modellenmesi.

[4]. Cicek, A., Kıvak, T., Turgut, Y., Uygur, İ., & Ekici, E. (2011). Derin kriyojenik islemin kesme kuvvetleri, delik capları ve takım omrü üzerine etkileri. In 6th International Advanced Technologies Symposium (IATS'11), Elazıg (pp. 33-36).

[5]. Günay, M., and Yücel,E., "Application of Taguchi method for determining optimum surface roughness in turning of high-alloy white cast iron." Measurement 46.2 (2013): 913-919.

[6]. Yagmur, S., Acır, A., Seker, U. (2013). AISI 1050 Celiginin Delinmesinde Kesme Parametrelerinin ve Kaplama Uygulamasının Daireselikten Sapma (Ovalite) Üzerindeki Etkilerinin Arastırılması. Politeknik Dergisi, 16(3).

[7]. Kıvak, T., Inconel 718'in Delinebilirliginin Arastırılması, Yüksek Lisans Tezi, Gazi Üniversitesi Fen Bilimleri Enstitüsü, Ankara, (2007).

[8]. Cakıroglu, R., and Acır. A., "Optimization of cutting parameters on drill bit temperature in drilling by Taguchi method." Measurement 46.9 (2013): 3525-3531.

[9]. Pirtini, M., & Lazoglu, I. (2005). Forces and hole quality in drilling. International journal of machine tools and Manufacture, 45(11), 1271-1281.

[10]. Yücel, E., and Günay M., "Modelling and optimization of the cutting conditions in hard turning of high-alloy white cast iron (Ni-Hard)." Proceedings of the Institution of Mechanical Engineers, Part C: Journal of Mechanical Engineering Science 227.10 (2013): 2280-2290.

[11]. Wu, C. L. (1996). Statistical analysis of the effects of feed, speed, and wear on hole quality in drilling. Journal of Manufacturing Science and Engineering, 118, 367.

[12]. Akıncıoglu, S., Mendi, F., Cicek, A., Akıncıoglu, G. (2013). ANN-based prediction of surface and hole quality in drilling of AISI D2 cold work tool steel. The International Journal of Advanced Manufacturing Technology, 68(1-4), 197-207.

[13]. Giasin, K., Hodzic, A., Phadnis, V., Ayvar-Soberanis, S. (2016). Assessment of cutting forces and hole quality in drilling Al2024 aluminium alloy: experimental and finite element study. The International Journal of Advanced Manufacturing Technology, 87(5-8), 2041-2061.

[14]. Sharif, S., & Rahim, E. A. (2007). Performance of coated-and uncoated-carbide tools when drilling titanium alloy—Ti–6Al4V. Journal of Materials Processing Technology, 185(1), 72-76.

[15]. Korkut, I., Acır, A., and Boy, M., "Application of regression and artificial neural network analysis in modelling of tool–chip interface temperature in machining." Expert Systems with Applications 38.9 (2011): 11651-11656.

[16]. Sahin, İ., "Yapay Sinir Agları İle Al/Sic Kompozit Malzemenin Yüzey Pürüzlülüğünün Tahmini." Gazi Üniversitesi Mühendislik-Mimarlık Fakültesi Dergisi 29.1 (2014).

[17]. M.T. Hagan, H.B. Demuth, M.H. Beale: Neural Network Design, PWS Publishing, Boston, 1996.

[18]. Haykin S., Neural networks, a comprehensive foundation. New Jersey: Prentice 697 Hall. 1994.

[19]. Zain A.M., Haron, H., Sharif S., Prediction of surface roughness in the end milling machining using Artificial Neural Network, Expert Systems with Applications, 37, 1755–1768, 2010.

[20]. T.H. Martin, B.M. Mohammed: Training feed forward networks with the Marquardt algorithm. IEEE Trans. Neural Netw.,; 5 (6): 989–994, 1994.

[21]. R. Battiti: First and second-order methods for learning: between steepest descent and Newton's method, Neural Comput., 1992; 4:141–166.

[22]. Mohanraj M., Jayaraj S. and Muraleedharan C., Exergy analysis of direct expansion solar-assisted heat pumps using artificial neural Networks, Int. J. Energy Res.; 33:1005–1020, 2009.

Optimization of Drilling Conditions for Surface Roughness in Drilling of CFRP Composite Laminates

Mustafa GUNAY[1], Oguz GUN[2], Nafiz YASAR[3], Ramazan OZMEN[1]

Abstract

The thermo-mechanical formations occurred in drilling of the carbon fiber reinforced polymer composite materials, which change depending on their physical and mechanical properties and cutting conditions, indirectly affect the hole quality. On the other hand, surface roughness is one of the important factors when considering for hole quality in drilling of CFRP composite laminates. For these reasons, it is necessary to be selective in drilling of CFRP in terms of cutting tool material and drilling parameters such as cutting speed, feed rate, etc. In this study, the influences of drilling parameters on the average surface roughness (Ra) which have been formed during drilling of CFRP composite laminates with three different drill qualities (uncoated and coated WC drills) were examined. The highest surface roughness was obtained with uncoated WC drill while the lowest surface roughness was obtained with diamond coated WC drill. The interactive influences of drilling conditions on Ra were determined by analysis of variance (ANOVA) with 95% confidence level, and drill quality was stated as the most significant parameter on them. Finally, a Taguchi optimization study was performed based on "the-smaller-the-better" approach and then confirmation experiment was conducted. The results showed that the optimum conditions for better surface roughness were determined as drill quality of diamond coated drill, cutting speed of 100 m/min and feed rate of 0.05 mm/rev according to analysis of signal-to-noise ratios.

Keywords: *CFRP; Drilling; Surface Roughness; Optimization*

1. INTRODUCTION

Nowadays, using of carbon fiber reinforced polymer (CFRP) composite materials is becoming gradually widespread for manufacturing of numerous components in aerospace, automotive, marine, sport and biological equipment due to their higher specific strength, rigidity, fatigue and corrosion resistance and lower thermal strain than metallic materials [1,2]. CFRP composite laminates are commonly used components recently in hybrid composite constructions in regard to their excellent mechanical properties [3]. The composite materials are usually manufactured in near-net-shape to ensure excellent assembly performance. Accordingly, in order to supply quality and dimensional tolerance in assembly are required to secondary machining processes like milling, drilling, trimming etc. [4-6]. For instance, thousands of drilling operations are done in manufacturing of structural components in airplane [7,8]. However, heterogeneous structure of composites leads various difficulties during machining such as excessive temperature, tool wear, fiber pull-out, and so delamination undesired surface quality [3,9]. Especially, by unsuitable cutting parameters are chosen, serious cavity and cracks of the matrix and the interface occur easily with the removal of fiber owing to excessive cutting forces during chip formation [10]. Failure types of the fiber and matrix under cutting forces are still not clearly understood in machining of CFRP materials [11]. In addition, these cracks lead to the support disappearance of the matrix to fibers easily, so fibers cannot be cut off due to withdrawing [7].

The above mentioned situations are mainly reasons for surface damages, burr and peel-up or push-up delamination in drilling process. In the literature today, the fundamental research on the machinability of CFRP composite material by conventional or unconventional machining process still is a vital issue in modern manufacturing.

The surface roughness indicates the irregularity level on the machined surface. Thus, surface roughness is a very important factor in a drilled hole, because mechanisms of creep, wear, fatigue and corrosion depend on

---

surface roughness for metallic materials. Similarly, surface roughness is one of the surface integrity criteria for all parts manufactured by machining process and also is an important parameter to analysis of hole quality in drilling of CFRP composite laminates. On the other hand, the combination of low thermal conductivity of matrix, heterogeneity and anisotropy of CFRP composite layers cause their poor machinability, and so poor surface integrity. The occurrence and intensity of both delamination and surface roughness depend mostly on thrust force and torque occurred during drilling operation [7-12]. Mohan et al. indicated that the most important parameters in drilling of GFRP composites are cutting speed and material thickness for entry delamination, feed rate and material thickness for exit delamination according to their experimental and numerical studies [13]. El-Sonbaty et al. determined that cutting speed has negligible effect on thrust force, but torque values increase with increasing cutting speed [14]. In addition, the drill diameter, the drill materials and geometry, types of chip formation during drilling process have significant effects on the quality and integrity of the drilled holes. Karnik et al. emphasized that delamination factor is proportional with cutting speed and feed rate, similarly remarked that delamination increases with carbide drills having high point of angles [15]. İsmail et al. indicated that an increase in feed rate and thrust force caused an increase in delamination and surface roughness of CFRP composite at moderated cutting speed. The authors also stated that the minimum surface roughness and delamination factor was obtained at a low feed rate, moderate high cutting speed and a small drill diameter [12]. Consequently, for machining desired precision of the CFRP composite material are need to optimization of machining parameters such as drill geometry, cutting speed and feed rate etc., especially. For these reasons, this study focused on determine of optimum drilling conditions with regard to surface roughness in drilling of CFRP composite laminates through Taguchi and analysis of variance (ANOVA) method.

2. MATERIAL and METHOD

Carbon fibre reinforced polymer (CFRP) composite laminates were used as workpiece material in drilling experiments. The workpiece was produced as woven composite lamina from 40 layers of carbon fibre epoxy prepreg in configuration 245 g/m^2 2x2 Twill HS (3K) 0º/90º. Finally, CFRP laminates were manufactured at 10 mm thickness by compressing with vacuum were placed into furnace and a temperature of 120°C was applied to the system by four hours.

Drilling experiments were carried out on a CNC vertical machining centre according to Taguchi method in dry machining conditions. For this purpose, feed rate (f), cutting speed (V) and drill quality (T) were chosen as factors to apply Taguchi's L$_{27}$ orthogonal array in drilling of CFRP. The levels of these factors were determined by considering tool manufacturer's recommendations and researches on drilling of CFRP composites in literature. Tungsten carbide drills (uncoated, TiAlN coated and diamond coated) used as cutting tools were produced by Karcan. Drills have a diameter of 5 mm, drill point angle of 130º, helical angle of 30° and geometry of two cutting edges. Drilling parameters and their levels are given in Table 1.

Table 1. Factors and their levels

Factors	Leve1	Level2	Level3
Drill quality (T)	Uncoated	TiAlN coated	Diamond coated
Cutting speed (V)	60	100	140
Feed rate (f)	0.05	0.1	0.15

CNC vertical machining centre used in the experiments has a maximum spindle speed of 6000 rev/min. Therefore, suitable spindle speeds matching the appropriate cutting speeds were obtained using spindle speeder. The average surface roughness (*Ra*) on hole surfaces were measured as parallel to the drill direction with Mahr Perthometer M300 device. Five surface roughness measurements were performed for each hole surfaces with a cut-off length of 0.25 mm and sampling length of 1.75 mm according to ISO 4288 standard. The surface damages were displayed by scanning electron microscope (SEM) in order to investigate the effects of drilling parameters and drill quality for hole surface. The drilled holes were sectioned into two halves using a diamond saw to utilize a sectional view of the hole surface to prepare samples for SEM examination.

Drilling operations were repeated three times and evaluations were done by taking arithmetic mean of surface roughness. In the light of experimental results, the effects of factors on surface roughness were determined by analysis of variance (ANOVA) with 95% confidence level. Finally, drilling parameters for average surface roughness were optimized based on Taguchi method. Therefore, the-smaller-the-better approach were applied due to desire of minimum average surface roughness (*Ra*) which is selected as performance characteristic in drilling experiments. The drilling parameters giving optimum average surface roughness were determined in optimization study according to *S/N* ratio. *S/N* ratios for the smaller-the-better quality characteristic is calculated by the following equation [16].

$$S/N = -10 \cdot \log\left(\frac{1}{n} \cdot \sum_{i=1}^{n} y_i^2\right) \tag{1}$$

Where, y_i is the i_{th} measure of the experimental results in a run and n gives the number of measurements in each experiment. The function '-log' is a monotonically decreasing one, it means that we should maximize the *S/N* ratio. Statistical analyses and optimization studies were performed by Minitab software.

3. RESULTS and DISCUSSION

3.1. Evaluation of Surface Roughness

Surface roughness is one of the criteria of the surface integrity for all parts manufactured by machining process and also is an significant parameter to investigate of the hole quality in drilling of CFRP composite laminates. In this study, the average surface roughness (*Ra*) obtained in drilling of CFRP and their *S/N* ratios calculated by Eq. (1) are given in Table 2. Variation of surface roughness depending on drill quality and drilling parameters is shown in Figure 1.

Table 2. Experimental results and S/N ratios.

Exp. No	Drill quality	Cutting speed	Feed rate	Surface roughness	S/N ratio
1	1	60	0.05	0.45	6.9357
2	1	60	0.1	0.89	1.0122
3	1	60	0.15	1.03	-0.2567
4	1	100	0.05	0.74	2.6153
5	1	100	0.1	1.05	-0.4237
6	1	100	0.15	1.35	-2.6066
7	1	140	0.05	0.75	2.4987
8	1	140	0.1	0.99	0.0872
9	1	140	0.15	1.25	-1.9382
10	2	60	0.05	0.91	0.8191
11	2	60	0.1	1.02	-0.172
12	2	60	0.15	1.08	-0.6684
13	2	100	0.05	1.12	-0.9843
14	2	100	0.1	1.14	-1.1381
15	2	100	0.15	1.19	-1.5109
16	2	140	0.05	1.16	-1.2891
17	2	140	0.1	1.2	-1.5836
18	2	140	0.15	1.25	-1.9382
19	3	60	0.05	0.35	9.1186
20	3	60	0.1	0.43	7.3306
21	3	60	0.15	0.76	2.3837
22	3	100	0.05	0.49	6.1960
23	3	100	0.1	0.56	5.0362
24	3	100	0.15	0.86	1.3100
25	3	140	0.05	0.39	8.1787
26	3	140	0.1	0.52	5.6799
27	3	140	0.15	0.88	1.1103

Average surface roughness (*Ra*) were demonstrated similar tendencies for each drill quality according to drilling parameters when examining Figure 1. Surface roughness obtained in drilling process increased with increasing feed rate for drill quality at all cutting speed, as can be expected. Meanwhile, the lowest *Ra* values were determined in the lowest feed rate and cutting speed for all drill quality. It is possible to conclude that the surface damages are minimized with the adhesion of matrix material to the hole surfaces as a result of chip formation occurred like ploughing in low deformation rates (seen Fig. 2a). In addition, surface roughness increased with increasing cutting speed from 60 m/min to 100 m/min, subsequently roughness inclined to decrease. This is mostly originated from the incomplete cutting of fibers and their removal from the matrix with the increasing cutting speed and/or the surface damages on drilled hole occurred as a result of matrix-fiber debonding as mentioned in recent studies [2, 17].
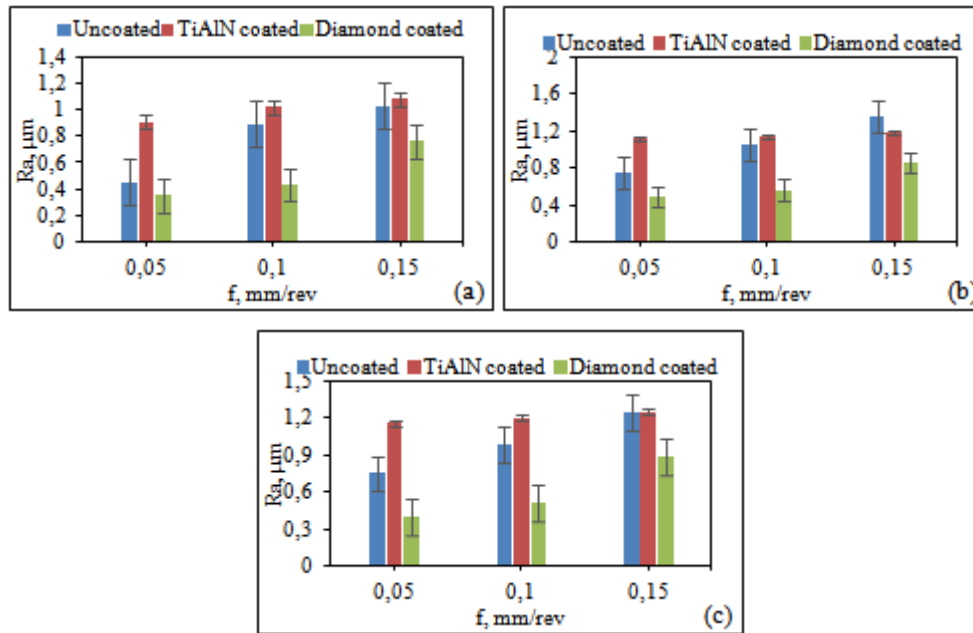
Figure 1. Ra variation for WC drills, a)V=60/min, b)V=100 m/min, c)V=140 m/min

The lowest *Ra* was measured as 0.35 µm with diamond coated WC drill at feed rate of 0.05 mm/rev and cutting speed of 60 m/min. The lower surface roughness obtained for diamond coated WC drill can be attributed to low coefficient of friction according to other drill quality. The highest *Ra* value was obtained as 1.35 µm with uncoated WC drill at feed rate of 0.15 mm/rev and cutting speed of 100 m/min. These results partly were supported by formation of fiber pull-out and fiber fragmentation (seen Fig. 2b), in drilling with high cutting speed and feed rate as can be mentioned in Refs. [9, 17]. Besides, matrix-fiber debonding occurred owing to increasing cutting temperature in higher cutting speed caused matrix debris and voids, thereby resulted in poorer surface roughness.
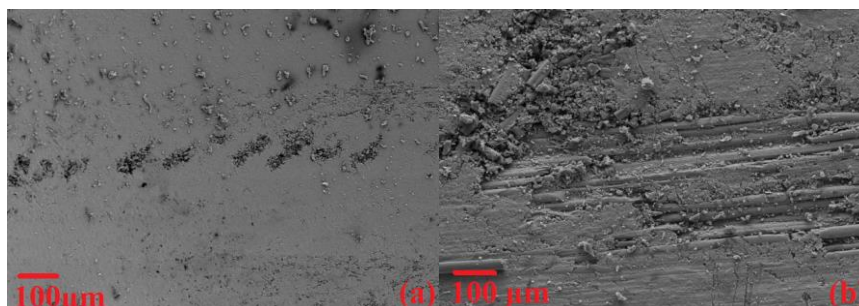
Figure 2. SEM micrographs of the hole surface; a) 200x magnification, b) 1000x magnification

Table 3. ANOVA results for surface roughness

Factor	DF	SS	MS	F	P	%PCR
T	2	175.885	87.9423	226.16	0.000	55.42
V	2	21.336	10.6679	27.44	0.000	6.72
f	2	81.139	40.5694	104.33	0.000	25.57
T*V	4	2.466	0.6165	1.59	0.268	0.78
T*f	4	30.898	7.7246	19.87	0.000	9.73
V*f	4	2.532	0.6330	1.63	0.258	0.8
Error	8	3.111	0.3888			0.98
Total	26	317.366				100

Moreover, surface roughness or surface damages is an important factor for performance in service conditions of structural part manufactured from CFRP composite laminates along with delamination. In this regard, it is believed that determining the influences of drilling parameters is very meaningful by analysis of variance (ANOVA) as a result of drilling experiments. The drill quality (T) is the most important parameter affecting the surface roughness with a PCR of 55.42%, as can be seen from Table 3. The other statistically significant parameters on the surface roughness are feed rate (f), cutting speed (V) and interaction between drill quality and feed rate (T*f) with PCR of 25.57%, 6.72% and 9.73%, respectively.

3.2. Optimization of Drilling Parameters

The final stage of Taguchi method is optimization study for surface roughness as quality characteristic. The highest *S/N* ratio shows the optimum level of factors according to "the-smaller-the-better" approach. The *S/N* ratios of factors calculated via experimental results of *Ra* are given in Table 4. The optimum levels for smallest surface roughness according to *S/N* ratios were determined as T3 (Diamond coated WC), V1 (cutting speed of 60 m/min) and f1 (feed rate of 0.05 mm/rev). As can be also seen from Table 4 that drill quality is the most important factor on *Ra* when considering difference (Δ) between the maximum and minimum values of *S/N* ratios.

Table 4. Response table of S/N ratios for Ra

Factors	Level 1	Level 2	Level 3	Δ
Drill quality (T)	0.8804	-0.9406	5.1494*	6.09
Cutting speed (V)	2.9448*	0.9438	1.2007	2.001
Feed rate (f)	3.7877*	1.7588	-0.4572	4.2449
*Optimum levels of factors				

The *S/N* ratio for drilling experiment result performed at optimal levels was calculated with Eq. (2) to forecast the mean for the improvement conditions. Eq. (1) which is the expression of calculated surface roughness (*Ra*) is derived from Eq. (3).

$$\eta_G = \bar{\eta}_G + (\bar{T}_o - \bar{\eta}_G) + (Vo - \bar{\eta}_G) + (fo - \bar{\eta}_G) \tag{2}$$

$$Ra_{cal} = 10^{-\eta_G/20} \tag{3}$$

Where, η_G is the *S/N* ratio calculated at optimal level of factors (dB), $\bar{\eta}_G$ is the mean *S/N* ratio of all parameters (dB), $\bar{T}_O$, $\bar{V}_O$ and $\bar{f}_O$ are the mean S/N ratio once drill quality, cutting speed and feed rate are at optimum levels, and Ra_{cal} is the calculated roughness value. Consequently, η_G and Ra_{cal} for optimum drilling parameters were determined as 9.5479 dB and 0.33 μm, respectively. Finally, confirmation experiments were done by using the optimum drilling parameters after the determination of these factors for *Ra* and thus dependability of the optimization has been confirmed. The drilling experiments conducted by considering the confidence interval (*CI*) calculated from Eqn. (4) and (5) [18].

$$CI = \sqrt{F_{\alpha,(1,\nu_e)}V_e\left(\frac{1}{\eta_{eff}} + \frac{1}{r}\right)} \qquad (4)$$

$$\eta_{eff} = \frac{N}{1+\nu_T} \qquad (5)$$

Where; $F_{\alpha(1,\nu e)}$ is the F-ratio at the 95 % significance level, α is the importance level, ν_e is the degree of freedom of the error, Ve is the error variance, n_{eff} is the effective number of replications, r is the number of replications for the verification test. In Equation 5, N is the total number of experiments and ν_T is the total of the degree of freedom for factors. Surface roughness obtained with the confirmation experiment (Ra_{exp}), calculated surface roughness (Ra_{cal}), and *S/N* ratios (η_{exp}, η_{cal}) for *Ra* are given by comparing between experimental results and calculated values (Table 5). Table 5 displays differences between confirmation experiment results and calculated values and their *S/N* ratios obtained by using Eqn. 2 and 3. As can be seen from the Table, a difference of 1.0588 dB is under the confidence interval of 1.5779 dB for surface roughness. Thus, the optimum drilling parameters for average surface roughness were approved as confident.

Table 5. Comparison of experiment results and calculated values

Confirmation exp.		Calculated value		Difference	
Ra_{exp} (µm)	η_{exp} (dB)	Ra_{cal} (µm)	η_{cal} (dB)	Ra_{exp}-Ra_{cal}	η_{exp}-η_{cal}
0.37	8.4891	0.33	9.5479	0.04	1.0588

4. CONCLUSIONS

The optimization and influences of drilling parameters on the surface roughness in drilling of CFRP composite laminates with uncoated and coated WC drills are determined by Taguchi method and ANOVA analysis. The results are summarized below:

- The calculate results obtained from Taguchi's experiment design are compatible with the confirmation experiments within the 95% confidence interval. Here, it is possible to say that the design of experiment with Taguchi method is usable to define optimum drilling parameters for surface roughness.

- The optimum parameters in terms of surface roughness in drilling CFRP laminate was determined as diamond coated WC drill, cutting speed of 60 m/min and federate of 0.05 mm/rev.

- The drill quality (T) is the most important parameter affecting the surface roughness with a PCR of 55.42% under the drilling conditions, as can be seen from ANOVA results.

ACKNOWLEDGEMENT

REFERENCES

[1]. Soutis, C., *Fibre reinforced composites in aircraft construction*. Progress in Aerospace Sciences 41(2) 143–51, 2005.
[2]. Eneyew, E.D., Ramulu, M., *Experimental study of surface quality and damage when drilling unidirectional CFRP composites*. J Mater Res Technol. 3(4), 354–362, 2014.
[3]. Liu, D., Tang, Y., Cong W.L., *A review of mechanical drilling for composite laminates*. Composite Structures 94(4), 1265–79, 2012.
[4]. Faraz, A., Biermann,D., Weinert, K., *Cutting edge rounding: An innovative tool wear criterion in drilling CFRP composite laminates*. International Journal of Machine Tools and Manufacture 49, 1185-1196, 2009.
[5]. Karpat, Y., Deger, B., Bahtiyar, O., *Drilling thick fabric woven CFRP laminates with double point angle drills*. Journal of Materials Processing Technology 212, 2117-2127, 2012.
[6]. Zitoune, R., Krishnaraj, V., Collombet, F., Le Roux, S., *Experimental and numerical analysis on drilling of carbon fibre reinforced plastic and aluminium stacks*. Composite Structures 146, 148–158, 2016.
[7]. Sheikh-Ahmad J.Y., *Machining of polymer composites*. New York, Springer, 2009.
[8]. Fan, Y., Zhang, L., *New development of extra-large composite aircraft components application technology*. Advanced of Aircraft Manufacture Technology 30(3) 534-543, 2009.
[9]. Xu, J., Mkaddem, A., Mansori, M., *Recent advances in drilling hybrid FRP/Ti composite: A state-of-the-art review*. Composite Structures 135, 316-338, 2016.
[10]. Jia Z.Y., Su Y.L., Niu B., Zhang B.Y., Wang F.J., *The interaction between the cutting force and induced sub-surface damage in machining of carbon fiber-reinforced plastics*. J Reinf Plast Compos, 35, 712–26, 2016.
[11]. Su, Y., Jia, Z., Niu, B., Bi, G., *Size effect of depth of cut on chip formation mechanism in machining of CFRP*, Composite Structures 164, 316–327, 2017.

[12]. Ismail, S.O., Dhakal, H.N., Popov, I., Beaugrand, J., *Comprehensive study on machinability of sustainable and conventional fibre reinforced polymer composites*. Engineering Science and Technology, an International Journal 19, 2043-2052, 2016.

[13]. Mohan, N.S., Kulkarni, S.M., Ramachandra, A., *Delamination analysis in drilling process of glassfiber reinforced plastic (GFRP) composite materials*. Journal of Materials Processing Technology 186, 265-271, 2007.

[14]. El-Sonbaty, I., Khashaba, U.A., Machaly, T., *Factors affecting the machinability of GFR/epoxy composites*. Composite Structures 63(3-4), 329-338, 2004.

[15]. Karnik, S.R., Gaitonde, V.N., Rubio, J.C., Correia, A.E., Abrao, A.M., Davim, J.P., *Delamination analysis in high speed drilling of carbon fiber reinforced plastics (CFRP) using artifical neural network model*. Materials and Design, 29, 1768-1776, 2008.

[16]. Gunay, M., Korkmaz, M.E., *Optimization of Honing Parameters for Renewal of Cylinder Liners*. GU J Sci 30(1), 111-119, 2017.

[17]. Ashrafi, S.A., Miller, P.W., Wandro, K.M., Kim, D., *Characterization and effects of fiber pull-outs in hole quality of carbon fiber reinforced plastics composite*. Materials 9, 828, 2016.

[18]. Gunay, M., *Optimization with Taguchi method of cutting parameters and tool nose radius in machining of AISI 316L steel*. Journal of Faculty Engineering Architecture of Gazi University 28(3), 437-444, 2013.

Optimization of Cutting Parameters in Hard Turning of AISI H10A Steel under Minimum Quantity Lubrication

Mustafa GUNAY[1], Halil DEMİR[2], Mehmet Erdi KORKMAZ[1], Ramazan CAKIROGLU[3]*

Abstract

In this study, influences of cutting parameters in hard turning of hot work tool steel by applying minimum quantity lubrication (MQL) were investigated and optimized by using Taguchi methodology. Firstly, the machinability experiments on hardened AISI H10A hot work tool steel with CBN inserts were performed under the MQL condition. The experiments were carried out by Taguchi's L9 orthogonal array. The machinability of AISI H10A steel were evaluated in terms of average surface roughness (Ra) and main cutting force (Fc). The analysis of variance (ANOVA) was applied to determine the effects of cutting parameters (cutting speed, feed rate and depth of cut) on surface roughness and cutting force. It was observed that surface roughness and cutting force increased with increasing feed rate and depth of cut in machining by applying MQL with uncoated CBN inserts. Depth of cut was determined as the most important parameter on surface roughness with 66.57% PCR while feed rate was determined on cutting force with 50.68% PCR. On the other hand, optimum cutting parameters for surface roughness and cutting force were found at different levels as a result of Taguchi optimization.

Keywords: AISI H10A; MQL; Optimization; Cutting Force; Surface Roughness.

1. INTRODUCTION

Hot work tool steels having high temperature strength, high toughness and resistance to thermal fatigue and shock are preferred frequently in many industrial applications. The chromium hot work steels are widely used for extrusion of aluminum, die casting of light metals and steel forging applications [1]. On the other hand, these steels due to chemical composition, microstructure, inclusions and thermo-mechanical properties are difficult to machine. When the die is subjected to heat treatment, some distortion usually occurs. Thus, machining allowance is left on the die prior to hardening in order to overcome these negativities as well as to ensure measurement and surface integrity. It is possible to adjust the die after the hardening and tempering by finish machining processes such as grinding, hard machining, etc.

Hard turning are mainly concentrated on the tool materials cost and the effect of the cutting conditions on machinability criteria. The machining of hardened steels using cubic boron nitride and ceramic tool are commonly known as a best replacement instead of grinding in order to reduce the tooling time and machining cost, keep off the lubrication [2]. Also, it is very difficult to develop a comprehensive model with related to any machinability criteria involving all machining conditions due to contain many factors. The machinability criteria such as cutting forces, surface roughness, tool life, dimensional accuracy can be significantly affected by machining parameters, mechanical properties of workpiece material, rigidity of machine tools, tool material and coolant technique [3,4].

The control of the machinability criteria can be primarily provided by choosing appropriate values of cutting speed, feed rate and depth of cut in hard turning [5]. However, unsuitable cutting parameters have negative effects on the machining outputs such as machining time, cost. In this context, design of experiment and analysis for machining process, then optimization of machining output is great importance with regards to decrease machining cost [6]. Also, some scientists observed that there is a disagreement between the researchers in terms of the use of coolants or lubricants in hard turning. Thus, it is required to identify eco-friendly alternatives to conventional cutting fluids during hard turning as can be specified in many

---

investigations [7]. Recently, scientists used nanoparticles in conventional lubricants owing to its remarkable improvement in thermo-mechanical, and heat transfer capabilities, decrease the friction coefficient and wear effect to enhance the efficiency and reliability of machine tools [8].

Newly, there are performed numerous experimental and statistical studies which are based on design and analysis of experiment methods to determine the effects of cutting conditions on machinability criteria. Aouici et al. conducted response surface methodology (RSM) in hard turning of DIN 1.2343 steel with CBN tool in order to obtain mathematical models for the cutting forces and surface roughness. They specified that the depth of cut and workpiece hardness are the most important factor on cutting forces while the feed rate and workpiece hardness have the most significant for surface roughness [9]. Boy et al. addressed on optimizing the cutting conditions to minimize the surface roughness, inner-diameter error and roundness in bearing rings produced by hard turning of AISI 52100 steel with coated CBN insert. The analysis of variance results indicated that the feed rate is the main factor for the surface roughness while the cutting speed is the major factor for the roundness and inner-diameter error [10]. Kacal investigated the cutting performance of ceramic insert in terms of surface roughness and tool wear in turning of hardened PMD 23 steel with three different cutting speeds, feed rates and depth of cuts. The experimental results indicated that feed rate is the most significant factor affecting Ra followed by depth of cut [11]. Islam investigated the surface roughness and dimensional accuracy properties (diameter error and circularity) via dry, wet and minimum quantity lubrication turning processes applied to different materials. The author indicated that surface roughness and dimensional values are affected by different cooling methods and the best result is obtained with MQL application [12]. Sarıkaya and Gullu focused on the use of the Taguchi based grey relation analysis to optimize the MQL process parameters such as cutting fluid, flow rate and cutting speed in terms of tool wear forms and surface roughness during the turning of Haynes 25 super alloy. According to the ANOVA results, the contribution percentage of process parameters were found as the cutting fluid, fluid flow rate and cutting speed, respectively [13]. Paul et al. examined parameters of minimum fluid application for minimizing surface roughness, flank wear, cutting force, tool vibration and cutting temperature in machining of AISI 4340 steel. The authors emphasized that tool vibration reduced in hard turning with minimal fluid application and the better cutting performance was provided as compared with dry turning and wet turning where a commercial cutting fluid was applied at a rate of 5 l/min [14]. Mia et al. investigated surface roughness during turning of hardened steel of 600 BHN with uncoated carbide tool under MQL application. The researchers stated that the cutting speed is insignificant factor surface roughness while feed rate is important factor for roughness [15].

2. MATERIAL AND METHOD

2.1. Material and Equipment

The workpiece material was used AISI H10A tool steel with the following chemical composition: 0.32% C; 0.40% Mn; 2.75% Co; 2.95% Cr; 2.8% Mo; 0.55% V and balance Fe. The material is a hot work tool steel having high toughness, high thermal shock resistant and high wear resistance in high temperatures. The hardness of AISI H10A workpiece was increased to 54-55 HRC with vacuumed hardening method. CNGA120404 coded uncoated CBN (KB1610) inserts and PCLNR 2525M12 coded tool holder produced by Kenna Metal Company were used in hard turning experiments. Hard turning experiments were carried out on Johnford TC 35 CNC having 20 HP motor under minimum quantity lubricant (MQL) cutting condition. UFB20-Basic cooling system branded SKF was preferred as MQL applicator. The Lubri-Oil was used as lubricant type because of AISI H10A steel. It was decided after preliminary experiments used MQL that the flow rate should be 16.25 ml/min.

The main cutting force (Fc) and average surface roughness (Ra) were considered on as the machinability criteria of AISI H10A steel. The cutting forces were measured by using Kistler 9257B type piezoelectric dynamometer during turning of workpiece material. Mahr Perthometer M1 type roughness device was used to measure surface roughness in hard turning experiments. The surface roughness values were taken into account in evaluating the roughness of machined surface. The experiments were repeated two times and evaluations were done by taking arithmetic mean of surface roughness.

2.2. Experimental Design and Optimization

The cutting parameters directly effecting machinability criteria were determined in experimental design according to Taguchi method. For this purpose, three factors were chosen as depth of cut (a), feed rate (f) and cutting speed (V) (seen Table 1). The levels of these parameters were preferred by reference to the recommendation of cutting tool firm and researches on hard turning. Taguchi L9 orthogonal array was used for experimental design in terms of the factor and levels. Moreover, the experiments conducted with uncoated CBN tools were performed in MQL cutting condition.

Table 1. Factors and their levels

Factors	Unit	Level 1	Level 2	Level 3
Depth of cut (a)	mm	0.1	0.2	0.3
Feed rate (f)	mm/rev	0.05	0.1	0.15
Cutting speed (V)	m/min	100	150	200

In the light of experimental results, the effects of factors on the main cutting force (*Fc*) and average surface roughness (*Ra*) were determined by analysis of variance (ANOVA) with 95% confidence level. Finally, cutting parameters for *Fc* and *Ra* were optimized based on Taguchi method. Therefore, the-smaller-the-better approach were applied due to desire of minimum Fc and Ra which is selected as performance characteristic in hard turning experiments. The cutting parameters giving optimum cutting force and surface roughness were determined in optimization study according to *S/N* ratio. The *S/N* ratios for the-smaller-the-better approach is calculated as follows [16].

$$S/N = -10 \cdot \log\left(\frac{1}{n} \cdot \sum_{i=1}^{n} y_i^2\right) \tag{1}$$

Here, y_i is the i_{th} measure of the experimental results in a run and *n* gives the number of measurements in each experiment. The function '-log' is a monotonically decreasing one, it means that we should maximize the *S/N* ratio. Statistical analyses and optimization studies were performed by Minitab software.

3. RESULTS AND DISCUSSION

3.1. Evaluation of Experimental Results

The variations of main cutting force and surface roughness values obtained with uncoated CBN tools in MQL cutting condition are given in separate graphs. Variations of Fc and Ra depending on feed rate (f), cutting speed (V) and depth of cut (a) are shown in Figure 1 and 2, respectively.
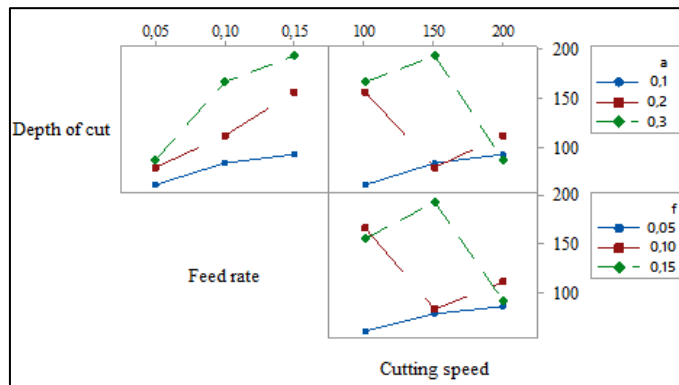
Figure 1. Variations of Fc in MQL cutting condition.

As can be seen from Figure 1, it was observed that main cutting force (*Fc*) generally increase with increasing feed rate and depth of cut. It was attracted from Figure 1 that the force values have irregularities in terms of cutting speed-depth of cut and cutting speed-feed rate interactions. This can be attributed with design of experiment that distribution of cutting speed is complicated in L9 orthogonal array. The lowest surface roughness value was obtained as 62.73 N with feed rate of 0.05 mm/rev, cutting depth of 0.1 mm and cutting speed of 100 m/min in MQL cutting condition with uncoated CBN inserts.

Average surface roughness (*Ra*) values increase with increasing feed rate and depth of cut (seen Fig.2). In a similar way, it was determined that *Ra* values does not decrease with increasing cutting speed because of hybrid experimental design. The lowest surface roughness value was obtained as 0.139 μm with the lowest feed rate, depth of cut and cutting speed in MQL cutting conditions with uncoated CBN inserts. The highest surface roughness was obtained as 0.36 μm with feed rate of 0.15 mm/rev, depth of cut of 0.3 mm and cutting speed of 150 m/min.
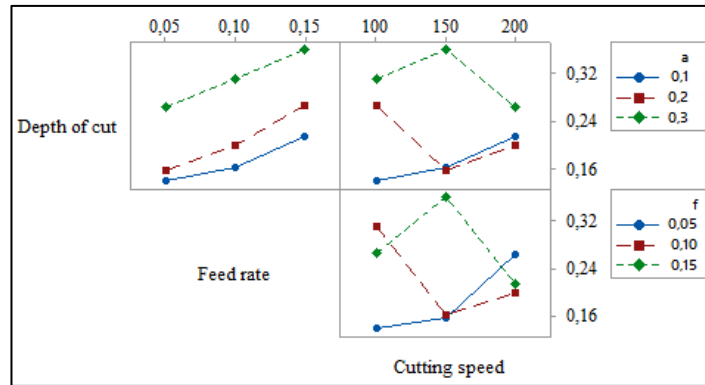
Figure 2. Variations of Ra in MQL cutting condition.

ANOVA was performed to determine the effectiveness of cutting parameters on main cutting force and average surface roughness during machining with uncoated CBN insert of AISI H10A hot work tool steel under minimum quantity lubrication (MQL) cutting environment. The results of ANOVA analysis of the cutting force and the surface roughness are presented in Tables 2 and 3, respectively.

Table 2. ANOVA results for cutting force

Factor	DF	SS	MS	F-ratio	P-value	PCR (%)
Depth of cut	2	39.1134	19.5567	114.24	0.009	43.27
Feed rate	2	45.7484	22.8742	133.62	0.007	50.68
Cutting speed	2	4.3925	2.1962	12.83	0.072	4.52
Residual error	2	0.3424	0.1712			1.53
Total	8	89.5966				100

DF: Degrees of freedom; SS: Sequential sum of squares; MS: Mean sum of squares

Table 3. ANOVA results for surface roughness

Factor	DF	SS	MS	F-ratio	P-value	PCR (%)
Depth of cut	2	44.2369	22.1185	201.57	0.005	66.57
Feed rate	2	20.7335	10.3668	94.47	0.000	31.03
Cutting speed	2	0.9312	0.4656	4.24	0.191	1.08
Residual error	2	0.2195	0.1097			1.32
Total	8	66.1211				100

DF: Degrees of freedom; SS: Sequential sum of squares; MS: Mean sum of squares

P value should be lower than 0.05 in 95% confidence level in order to determine that any parameter acting on the cutting force or surface roughness is effective on their. The feed rate (f) was the most important parameter affecting the cutting force with a PCR of 50.68% while the most significant parameter for surface roughness was obtained as depth of cut (a) with a PCR of 66.57%, as can be seen from Table 2 and 3. The other statistically significant parameters on *Fc* and *Ra* are depth of cut and feed rate with PCR of 43.27% and 31.03%, respectively.

3.2. Optimization with Taguchi Method

The main cutting force and surface roughness values were obtained as a result of hard turning experiments performed based on the Taguchi L$_9$ orthogonal array. According to Taguchi method, the experimental results have been transformed into *S/N* ratios to measure the quality characteristics diverging from the desired value. The *S/N* ratio is the ratio of the mean (signal) to the standard deviation (noise). In the present study, *S/N* ratio

is calculated as the logarithmic transformation of the loss function by using the-smaller-the-better approach as minimum values of *Fc* and *Ra* is required. The experimental results and *S/N* ratios is calculated by using Eq. (1) for *Fc* and *Ra* are shown in Table 4.

The mean values of *S/N* ratios (η) of the factors for each of the levels were determined by Equation (1). Figure 3 and Figure 4 shows the graphic of the η values for main cutting force and surface roughness, respectively. Regardless of category of the performance characteristics, a maximum η value corresponds to a better performance according to Taguchi method. Therefore, the optimal level of the cutting parameters is the level with the maximum η value. As can be observed from Figure 3 that the optimum cutting parameters for main cutting force were: a1 (0.1 mm), f1 (0.05 mm/rev) and V3 (200 m/min). Figure 4 also displayed that, the optimum cutting parameters for surface roughness were obtained as a1 (0.1 mm), f1 (0.05 mm/rev) and V2 (150 m/min).

Table 4. Experimental results based on L₉ orthogonal array and their S/N ratios.

Exp. no	Depth of cut (a)	Feed rate (f)	Cutting speed (V)	*Ra* (μ)	*S/N* (dB)	*Fc* (N)	*S/N* (dB)
1	0.1	0.05	100	0.139	17.1397	62.73	-35.9495
2	0.1	0.1	150	0.16	15.9176	84.01	-38.4866
3	0.1	0.15	200	0.212	13.4732	93.08	-39.3771
4	0.2	0.05	150	0.155	16.1933	79.88	-38.0488
5	0.2	0.1	200	0.198	14.0667	112.22	-41.0014
6	0.2	0.15	100	0.267	11.4697	157.24	-43.9313
7	0.3	0.05	200	0.263	11.6008	87.54	-38.8441
8	0.3	0.1	100	0.31	10.1727	166.78	-44.4429
9	0.3	0.15	150	0.36	8.8739	193.62	-45.7390
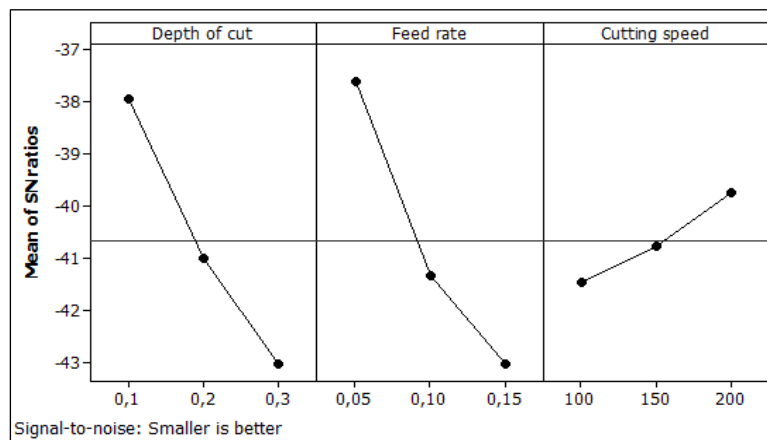
Figure 3. Main effect plot for S/N ratios of Fc
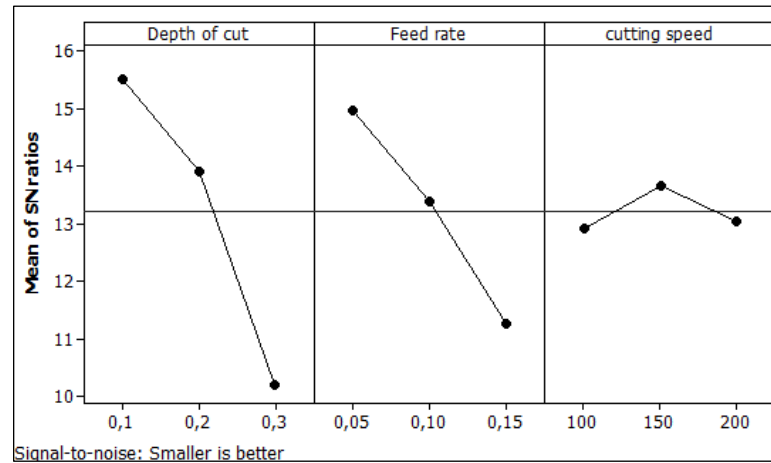
Figure 4. Main effect plot for S/N ratios of Ra

In the last stage of Taguchi method after the estimation of the optimum parameters, confirmation experiments are performed to display the accuracy of the optimization and to determine the improvement grade. Hence, the *S/N* ratio of performance characteristic for the experiments conducted at optimum parameters are calculated by using equation (2). Equation (1), which is the expression for performance characteristic, can be derived from by equation (3).

$$\eta_G = \bar{\eta}_G + (\bar{T}_o - \bar{\eta}_G) + (Vo - \bar{\eta}_G) + (fo - \bar{\eta}_G) \tag{2}$$

$$Fc, Ra = 10^{-\eta_G/20} \tag{3}$$

Here, η_G is the *S/N* ratio calculated at optimal level of factors (dB), $\bar{\eta}_G$ is the mean *S/N* ratio of all parameters (dB), $\bar{T}_O$, $\bar{V}_O$ and $\bar{f}_O$ are the mean S/N ratio once depth of cut, feed rate and cutting speed are at optimum levels, *Fc* and *Ra* are the calculated cutting force and surface roughness value, respectively. Consequently, comparison of predicted and experimental results for main cutting force and average surface roughness are given in Table 5 and Table 6, respectively.

Table 5. Results of confirmation experiments for main cutting force

	Initial cutting parameters	Optimal cutting parameters	
		Prediction	Experimental
Level	a2f1V2	a1f1V3	a1f1V3
Main cutting force, (N)	79.88	50.09	53.81
S/N ratio (dB)	-38.0488	-33.9965	-34.6172
Improvement of S/N ratio		3.4316 dB	
Prediction error (dB)		0.6207	

Table 6. Results of confirmation experiments for surface roughness

	Initial cutting parameters	Optimal cutting parameters	
		Prediction	Experimental
Level	a2f1V2	a1f1V2	a1f1V2
Surface roughness, (μm)	0.155	0.122	0.132
S/N ratio (dB)	16.1933	17.7259	17.5885
Improvement of S/N ratio		1.3952 dB	
Prediction error (dB)		0.1374	

The confirmation experiments results showed that prediction error became 0.6207 dB for the main cutting force and 0.1374 dB for the average surface roughness. It has been confirmed that the cutting force and surface roughness can be reduced significantly with Taguchi optimization, as a result of the machinability research on hardened AISI H10A hot work tool steel with uncoated CBN cutting tools and minimum quantity lubrication (MQL) cutting environment. Considering the differences between the predicted results for the cutting force and the surface roughness with the results of confirmation experiments, it was concluded that a remarkable success has been achieved by Taguchi method.

4. CONCLUSIONS

In this study, machinability experiments on hardened AISI H10A hot work tool steel with uncoated CBN inserts were performed under minimum quantity lubrication (MQL) condition. The effects of cutting parameters (feed rate, depth of cut and cutting speed) on the *Fc* and *Ra* were analyzed according to Taguchi experimental design. Obtained results were summarized below

- It was determined that *Fc* and *Ra* increased with increasing depth of cut and feed rate in MQL cutting conditions and this situation was referred to increasing chip cross-section with increasing feed rate and depth of cut.

- In the optimization of the cutting parameters for the cutting force by the Taguchi method, cutting depth of 0.1 mm, feed rate of 0.05 mm/rev and cutting speed of 200 m/min were found to be optimum conditions.

- In the optimization performed for the surface roughness, cutting depth of 0.1 mm, feed rate of 0.05 mm/rev and cutting speed of 150 m/min were found to be optimum conditions.

- MQL application is strongly recommended in order to increase efficiency in hard turning processes on account of the above-mentioned evaluations.

REFERENCES

[1] Shivpuri, R., *Dies and die materials for hot forging*. ASM Handbook, Metalworking: Bulk Forming, USA, 2005.
[2] Meddour, I., Yallese, M.A., Khattabi, R., Elbah, M., Boulanouar, L., *Investigation and modeling of cutting forces and surface roughness when hard turning of AISI 52100 steel with mixed ceramic tool: cutting conditions optimization.* Int J Adv Manuf Technol. 77, 1387–1399, 2015.
[3] Ozel, T. Hsu, T.K., Zeren, E., *Effects of cutting edge geometry, workpiece hardness, feed rate and cutting speed on surface roughness and forces in finish turning of hardened AISI H13 steel*. Int J Adv Manuf Technol. 25, 262–269, 2005.
[4] Stahl, J.E., *Metal Cutting-Theories and models*, Lund University in cooperation with Seco Tools AB, Lund/Fagersta, Sweden, 2012.
[5] Yücel, E., Günay, M., *Modelling and optimization of the cutting conditions in hard turning of high-alloy white cast iron (Ni-Hard)*. Proc IMechE Part C: J Mech Eng Sci. 227(10), 2280-2290, 2013.
[6] Yurtkuran, H., Korkmaz, M.E., Günay, M., *Modelling and Optimization of the Surface Roughness in High Speed Hard Turning with Coated and Uncoated CBN Insert*. Gazi Uni J Sci. 29(4), 987-995, 2016.
[7] Chinchanikar, S., Choudhury, S.K., *Machining of hardened steel-Experimental investigations, performance modeling and cooling techniques: A review*. Int J Mach Tools Manuf. 89, 95–109, 2015.
[8] Sidik, N.A.C., Samion, S., Ghaderian, J., Yazid, M.N.A.W.M., *Recent progress on the application of nanofluids in minimum quantity lubrication machining: A review*. Int J Heat Mass Transf. 108, 79–89, 2017.
[9] Aouici, H., Yallese, M.A., Chaoui, K., Mabrouki, T., Rigal, J.F., *Analysis of surface roughness and cutting force components in hard turning with CBN tool: prediction model and cutting conditions optimization*. Measurement 45, 344–353, 2012.
[10] Boy, M., Ciftci, I., Gunay, M., Ozhan, F., *Application of the taguchi method to optimize the cutting conditions in hard turning of a ring bore*. Materials and Technology 49 (5), 765–772, 2015.
[11] Kacal, A., *Investigation of Cutting Performance of the Ceramic Inserts in Terms of the Surface Roughness and Tool Wear at Turning of PMD 23 Steel*. Applied Mechanics and Materials 686, 10-16, 2014.
[12] Islam, M.N., *Effect of additional factors on dimensional accuracy and surface finish of turned parts*. Machining Science and Technology 17, 145–162, 2013.
[13] Sarıkaya, M., Güllü, A., *Multi-response optimization of minimum quantity lubrication parameters using Taguchi-based grey relational analysis in turning of difficult-to-cut alloy Haynes 25*. Journal of Cleaner Production 91, 347-357, 2015.

[14]   Paul, P.S., Varadarajan, A.S., Gnanadurai, R.R., *Study on the influence of fluid application parameters on tool vibration and cutting performance during turning of hardened steel*. Engineering Science and Technology, an International Journal 19, 241-253, 2016.

[15]   Mia, M., Razi, M.H., Ahmad, I., Mostafa, R., Rahman, S.M.S., Ahmed, D.H., Dey, P.R., Dhar, N.R., *Effect of time-controlled MQL pulsing on surface roughness in hard turning by statistical analysis and artificial neural network*. Int J Adv Manuf Technol. 1-13, 2017.

[16]   Günay, M., *Optimization with Taguchi method of cutting parameters and tool nose radius in machining of AISI 316L steel*. Journal of Faculty Engineering Architecture of Gazi University 28(3), 437-444, 2013.

Post-seismic Deformation of Aegean Sea Earthquake (24 May 2014, M_w= 6.9)

Ayca Cırmık[1]*, Oya Pamukcu[1]

Abstract

After the major earthquakes, post-seismic deformation may keeps on for a long time and additionally, affects the great scales of fields. The afterslip, pore fluid motion and the viscoelastic loosening in the lower crust and upper mantle may cause the post-seismic deformation. A great amount of changes on the stress field near faults are occurred during the post-seismic movements respect to the stress changes related with the co-seismic movements. Besides, respect to the co-seismic effects, the effects of post-seismic movements on the faults may reach to faraway. The viscoelastic loosening may keep on long time and effects on tectonic deformation at active fault zones with the effects of the major earthquakes. These deformation zones can be monitored with the help of Global Navigation Satellite System (GNSS) observations. In this study, GNSS solutions were performed for Aegean Sea earthquake which occurred in 24 May 2014 (Mw= 6.9) and affected in the Aegean and Marmara regions. In the applications, the GNSS stations of Continuously Operating Reference Stations-Turkey (CORS-TR) IPSA (Marmara Region) and CESM (Aegean Region) which locate in the northern and southern sides of the earthquake epicentre, respectively were used. The Eurasia fixed frame solutions were investigated for 12 days which include pre-seismic and post-seismic periods. Therefore, the co-seismic and post-seismic deformations were observed in the time series. As a result of this study, the large scale deformation was determined in the time-series at the date of earthquake. This result is observed at two different region stations; IPSA and CESM, so it can be said that this earthquake affected on the huge area.

Keywords: *Post-Seismic Deformation, Gnss, Aegean Sea Earthquake*

1. INTRODUCTION

The post-seismic deformation occurs with the effects of the viscoelastic loosening (relaxation) mechanism, afterslip mechanism and pore fluid motion and its effect can be seen in the great areas and keeps going for a long time ([1]). The post-seismic movements cause greater stress changes on the stress field near the faults respect to the stress changes caused by the co-seismic movements ([2, 3, 4, 5]) and the post-seismic movements which caused by the major earthquakes can affect the faults located faraway wherein the co-seismic movements can be remissible ([6, 7, 8, 9]).

A great amount of changes on the stress field near faults are occurred during the post-seismic movements respect to the stress changes related with the co-seismic movements. Besides, respect to the co-seismic effects, the effects of post-seismic movements on the faults may reach to faraway. The viscoelastic loosening may keep on long time and effects on tectonic deformation at active fault zones with the effects of the major earthquakes.

In recent years, Global Navigation Satellite System (GNSS) observations are used for creating the crustal deformation models ([10], [11]). The strain concentration is non stable condition and is related to the viscous flow in the lower crust and upper mantle which occurred with the effect of the major earthquakes. There are some inconsistencies between the estimations of the fault slip rates derived from gological data and geodetic data. The slip rates which were obtained by the geological data along Garlock fault and Mojave segment of the San Andreas Fault ([12]) were found two times higher than the slip rates which were obtained by the geodetic data ([13], [14]). On the other hand, the dextral slip rate, which was obtained by GNSS data across the southern Mojave section, was found two times higher than the geologic slip rates along the fault line over the region ([15]).

The shear stresses are occurred in the lower lithosphere during a major earthquake and the lithosphere is tried to be equilibrated in stages related with the rheological features of the lower crust and upper mantle ([16]).

[1]* Corresponding author: Dokuz Eylul University, Engineering Faculty, Department of Geophysical Engineering, 35160, Buca/Izmir, Turkey, ayca.yurdakul@deu.edu.tr.

Some rheological models were presented for investigating the effects of varied rheological structures; a model with a weak lower crust and a strong upper mantle ([2], [17], [18]), opposite of the first model ([19]) and the combining of the first and the second models ([20], [21]).

Therefore, the deformation types (elastic, plastic, viscoelastic) of the tectonic structures, when a large earthquake occurs, depend on the rheological regimes of the affected area. In this study, we investigated the postseismic effects of large earthquake (M = 6.9) which was effective in the Aegean and Marmara regions and occurred in Aegean Sea, near to Gokceada (Imbros) Island at 24th May 2014 by using GNSS data(Figure 1). Therefore, the GNSS stations of Continuously Operating Reference Stations-Turkey (CORS-TR) IPSA (Marmara Region) and CESM (Aegean Region) which locate in the northern and southern sides of the earthquake epicentre respectively were used.
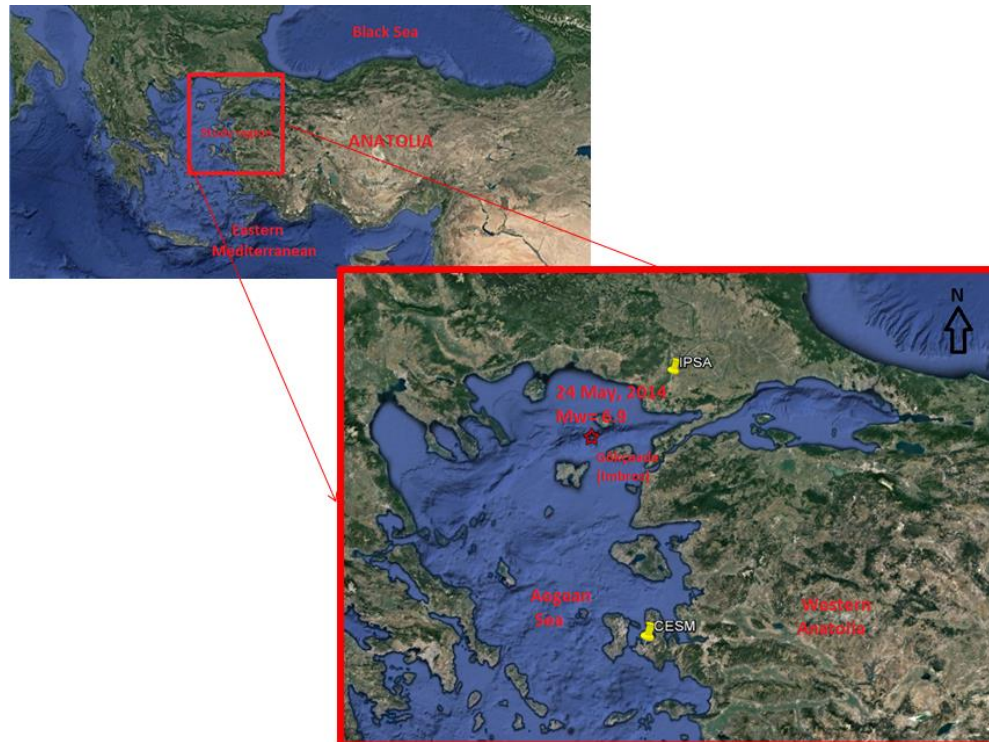
Figure 1. The location of study region and GNSS stations. The red star represents the epicenter of the earthquake.

2. APPLICATIONS

In order to define time series, 9 IGS (International GNSS Service) were chosen to circulate the network area. For defining Eurasia fixed reference frame; ISTA, TUBI (Turkey), ZECK (Russia), NICO (Cyprus), MIKL (Ukraine), GLSV (Ukraine), BUCU (Romania), PENC (Hungary), WTZR (Germany) and MATE (Italy) were chosen as IGS stations (Figure 2). The GNSS data of 13 days which include pre-seismic, co-seismic and post-seismic movements were proceed by using ITRF 2008 (International Terrestrial Reference Frame) relative to Eurasia fixed frame. The GAMIT/GLOBK software ([22]) was used to process the GNSS data. Therefore, the time-series which represent the horizontal (North and East component) and vertical movements (Up component) of CESM and IPSA were created (Figure 3 and Figure 4).

Figure 2. The locations of the IGS stations. The red circles represent the IGS stations which were used in this study.
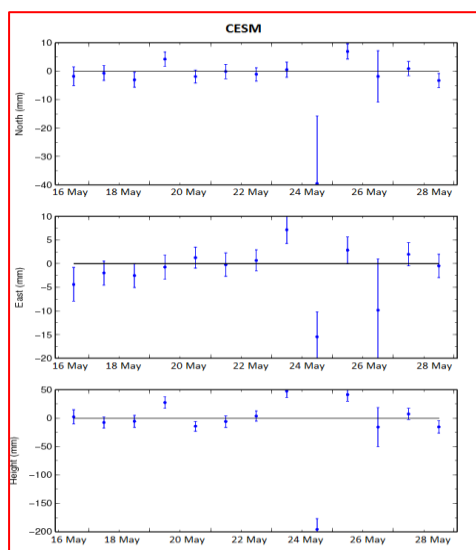
Figure 3. Time series of CESM station.
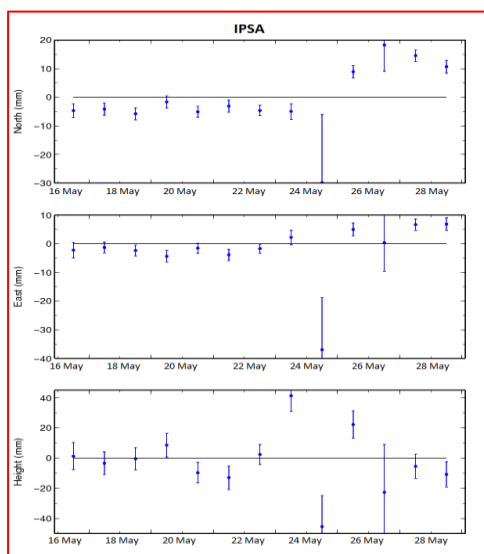
Figure 4. Time series of IPSA station.

3. RESULTS AND DISCUSSION

In this study, the Eurasia fixed frame solutions were investigated for 13 days which include pre-seismic, co-sesimic and post-seismic periods. Therefore, the co-seismic and post-seismic deformation were observed in the time series in Figure 3 and Figure 4. As a result of this study, the large scale deformation was determined in the time-series at the date of earthquake (24 May, 2014). This result is observed at two different region stations; IPSA and CESM, so it can be said that this earthquake affected on the huge area.

REFERENCES

[1]   W. Thatcher and F.F. Pollitz, "Temporal evolution of continental lithospheric strength in actively deforming regions", *GSA Today,* vol. 18, pp. 4–11, 2008.

[2]   A.M. Freed and J. Lin, "Delayed triggering of the 1999 Hector Mine earthquake by viscoelastic stress transfer", *Nature*, vol. 411, pp. 180–183, 2001.

[3]   P.A. Rydelek and I.S. Sacks, "Migration of large earthquakes along the San Jacinto fault; stress diffusion from the 1857 Fort Tejon earthquake", *Geophys. Res. Lett.,* vol. 28, pp. 3079–3082, 2001.

[4]   J. Chery, S. Carretier and J.F. Ritz, "Postseismic stress transfer explains time clustering of large earthquakes in Mongolia", *Earth Planet. Sci. Lett.,* vol. 194, pp. 277–286, 2001.

[5]   E. Casarotti, A. Piersanti, F.P. Lucente and E. Boschi, "Global postseismic stress diffusion and fault interaction at long distances", *Earth Planet. Sci. Lett.,* vol. 191, pp. 75–84, 2001.

[6]   F. Pollitz, R. Bürgmann, and B. Romanowicz, "Viscosity of oceanic asthenosphere inferred from remote triggering earthquakes", *Science*, vol. 280, pp. 1245–1249, 1998.

[7]   A.M. Freed and J. Lin, "Accelerated stress build up on the southern San Andreas Fault and surrounding regions caused by Mojave Desert earthquakes", Geology, vol. 30 (6), pp. 571–574, 2002.

[8]   S.S. Nalbant and J. McCloskey, "Stress evolution before and after the 2008Wenchuan, China earthquake", *Earth Planet. Sci. Lett.,* vol. 307, pp. 222–232, 2011.

[9]   F. Sunbul, S.S. Nalbant, N.M. Simão and S. Steacy, "Investigating viscoelastic postseismic deformation due to large earthquakes in East Anatolia, Turkey", *Journal of Geodynamics*, vol. 94–95, pp. 50–58, 2016.

[10] K.M. Johnson and J. Fukuda, "New methods for estimating the spatial distribution of locked asperities and stress driven inter seismic creep on faults with application to the San Francisco Bay area, California", *J. Geophys. Res.,* vol. 115, B12, 2010.

[11] R. Chuang and K. Johnson, "Reconciling geologic and geodetic model fault slip-rate discrepancies in Southern California: consideration of non steady mantle flow and lower crustal fault creep", *Geology,* vol. 39, pp. 627–630, 2011

[12] A. Matmon, D.P. Schwartz, R. Finkel, S. Clemmens, and T. Hanks, "Dating offset fans along the Mojave section of the San Andreas fault using cosmogenic ^{26}Al and ^{10}Be", *Geol. Soc. Am. Bull.,* vol. 117, pp. 795–807, 2005.

[13] B. Meade and B. Hager, "Viscoelastic deformation for a clustered earthquake cycle", *Geophys. Res. Lett.,* vol. 31, L10610, 2004.

[14] P. Bird, "Long-term fault slip rates, distributed deformation rates, and forecast of seismicity from joint fitting of community geologic, geodetic, and stress direction data sets", *J. Geophys. Res.,* vol. 114, B11403, 2009.

[15] M. Oskin, L. Perg, E. Shelef, M. Strane, E. Gurney, B. Singer and X. Zhang, "Elevated shear zone loading rate during an earthquake cluster in eastern California", *Geology,* vol. 36, pp. 507–510, 2008.

[16] D.P. Hill, F.F. Pollitz and C. Newhall, "Earthquake–volcano interactions", *Phys. Today*, vol. 55, pp. 41–47, 2002.

[17] F.F. Pollitz and I.S. Sacks, "Stress triggering of the 1999 Hector Mine earthquake by transient deformation following the 1992 Landers earthquake", *Bull. Seismol. Soc. Am.,* vol. 92, pp. 1487–1496, 2002.

[18] F.F. Pollitz, P. Banerjee, K. Grijalva, B. Nagarajan and R. Bürgmann, "Effect of 3D viscoelastic structure on post siesmic relaxation from the M = 9.2 Sumatra earthquake", *Geophys. J. Int.,* vol. 172, pp. 189–204, 2008.

[19] Y. Zeng, "Viscoelastic stress-triggering of the 1999 Hector Mine Earthquake by the 1992 Landers Earthquake", *Geophys. Res. Lett.,* vol. 28, pp. 3007-3010, 2001.

[20] F. Lorenzo-Martin, F. Roth and R.J. Wang, "Elastic and inelastic triggering of earthquakes in the North Anatolian Fault zone", *Tectonophysics,* vol. 424 (3–4), pp. 271–289, 2006.

[21] S.S. Nalbant, S. Steacy, and J. McCloskey, "Stress transfer relations among the earthquakes that occurred in Kerman province, southern Iran since 1981", *Geophys. J. Int.,* vol. 167 (1), pp. 309–318, 2006.

[22] T.A Herring, R.W. King, M.A. Floyd and S.C. McClusky, "Introduction to GAMIT/GLOBK, Release 10.6", Massachusetts Institute of Technology, Cambridge, 2015.

Heat Treatment Application Methods and Effects of Heat Treatment on Some Wood Properties

Halil İbrahim SAHİN[1]

Abstract

This study examined the heat treatment methods commonly used in Europe, and changes in some wood properties during heat treatment were investigated. Wood materials can be deteriorated because of many factors, containing fungal activity, insects, and high humidity conditions. For this reason, different methods have been developed to decrease this disadvantage for many years. One of these methods involves thermal treatments. Heat treatment technology is applied commercially using five different methods in Europe. These methods are ThermoWood in Finland, Plato Wood in the Netherlands, Bois Perdure and Rectification in France, and Oil Heat Treatment in Germany. All of the processes use timber and treatment temperatures between 160℃ and 260℃, but they differ in terms of process conditions, such as the presence of a shielding gas such as nitrogen or steam, humid or dry processes, use of oils, etc. The heat treatment of wood changes its chemical composition by degrading cell wall compounds and extractives. Furthermore, the decrease of equilibrium moisture of wood due to heat treatments leads to an improvement of wood dimensional stability. The swelling decreased between 50% and 80% for beech, poplar, pine, spruce, and birch with treatments at temperatures between 180 to 200℃ in inert gas atmosphere. Although physical properties improve, mechanical properties of wood decrease during thermal treatment at high temperatures. Wood becomes darker, wettability and thermal conductivity decrease, and finishing and the gluing process need special attention.

Keywords: *Dimensional stability, heat treatment, methods, thermal conductivity, wettability, wood properties*

1. INTRODUCTION

Wood materials can be deteriorated because of many factors, containing fungal activity, insects, and high humidity conditions. For this reason, different methods have been developed to decrease this disadvantage for many years. One of these methods involves thermal treatments. Wood modification can be defined has a process that improves the properties of wood, producing a new material that when disposed at the end of the product life cycle doesn't present an environmental hazard any greater than unmodified wood [1], [2].

The purpose of thermal wood modification is to obtain the products of improved dimensional stability, decay resistance and durability. During thermal modification, the most thermally unstable of wood polymeric components begin to degrade inside the cell wall (primarily hemicelluloses and in later stages also cellulose) resulting in the production of furan compounds, such as furfural and hydroxymethilfurfural [3]. At high temperatures, the links inside the lignin complex are degraded. This phase of increased lignin reactivity is characterized by the production of various condensation reactions between aldehyde and lignin, as well as by self condensation of lignin [4].

Some changes occur in technological properties of materials such as iron, glass, ceramic treated with high temperature and certain durations. Metals harden, the fragility of glass differs, and ceramic turns into harder materials. A similar situation occurs in wood. Some changes occur in the physical and mechanical properties of wood treated with high temperature. Some physical properties of wood are modified to be useful for use. It shows less swelling and shrinkage, and the percentage of equilibrium moisture content decreases. But the mechanical properties of wood decreased. Especially impact bending strength reasonably decreases [5].

It has been observed that when submitted to heat treatment at high temperature, the kinetics of humidity absorption is noticeably modified resulting in a major reduction of the volume retraction and a lowering till a

---

[1] Corresponding author: Duzce University, Department of Forest Industry Engineering, 81620, Konuralp/Düzce, Turkey. halilibrahimsahin@duzce.edu.tr

certain extent of some mechanical properties depending on the treatment applied [6]. Improved durability results from the combination of two factors induced by thermal treatment:

- A noticeable reduction of moisture absorption. Rot fungi need a minimum of 20% of humidity to develop.
- Elimination of some of the nutrients required by wood rotting fungi.

It should be noted that heat treatment induces chemical modifications in the wood which darken original color over the whole material [6].

In most of the publications on the heat treatment of wood, reference is made to improved dimensional stability and increased resistance to fungi, though also to negative changes in the wood's characteristics. The high temperatures during treatment increase the brittleness and the formation of cracks, in particular. Spotted surfaces due to exudation of rosin and low UV resistance of the heat-related brown hue also prove to be problematic during practical use of the wood. More recent investigations point to a lower resistance to fungi of heat-treated wood in contact with soil than suggested by earlier findings [7-10].

More recently the interest in heat treatment processes has been renewed. According to literature [3] this renewed interest is due to the declining production of durable timber, to the increasing demand for sustainable building materials, to the deforestation of especially sub-tropical forests, and to the increased introduction of governmental restrictive regulations reducing the use of toxic chemicals [2].

Usually softwoods are treated more strongly and are used in constructions which need moisture protection, for example in outdoor constructions. Hardwoods are treated more lightly and usually the most important property is the color or good surface quality. Heat treated hardwoods are used indoors, for example in kitchen furniture, paneling and parquets [11].

In recent years the heat treatment industrial processes have been developed successfully in Europe. These processes use air steam, nitrogen or oil as the heat transfer. Heat treatment technology is applied commercially using five different methods in Europe. These methods include the ThermoWood (Finland) and Dutch Plato Wood (Netherlands) using steam, Bois Perdure and Rectification (France) using nitrogen, and Oil Heat Treatment (Germany) using oil [2], [12-15].

2. HEAT TREATMENT METHODS

2.1. ThermoWood (Finland)

The process used for the Finnish treatment method can be divided into three different steps (Fig 1).

I. Step: temperature increase;

Wood temperature is raised rapidly using heat and steam to a level of around 100 °C. Thereafter the temperature is increased steadily to 130 °C. Raw material can be green of pre-dried wood. Steam is used to prevent cracking of the wood. It also affects the chemical changes taking place in the wood. Moisture content reduces to nearly zero.

II. Step: actual thermal modification;

During actual thermal modification phase the temperature is increased to a level of 185-215 °C. Temperature depends on the desired treatment class. When the target level has been reached, the temperature remains constant 2-3 hours. Steam is used to prevent the wood from burning in high temperatures and it also affects to the chemical changes in the wood.

III. Step: cooling and re-conditioning;

The temperature is reduced by using water spraying as cooling media. Conditioning and re-moisturing takes place to bring the wood moisture content to a level of 4-6 percent [16], [17].
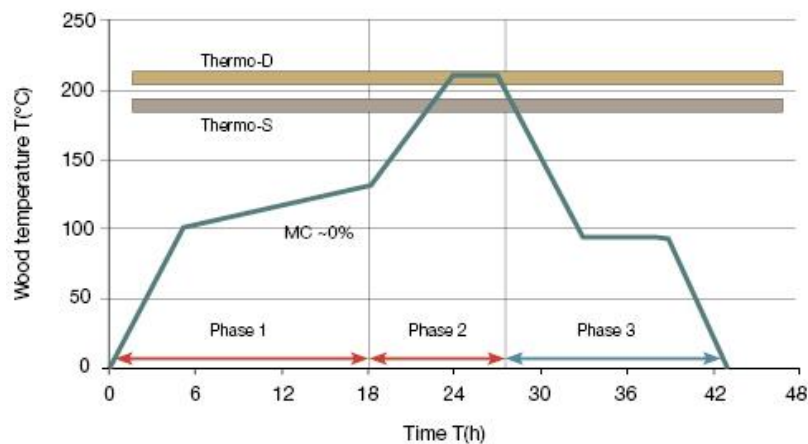
Figure 1. ThermoWood production diagram.

2.2. Plato Wood (Netherlands)

Recent efforts on thermal treatment of wood have lead to the development of several treatment processes previously or presently introduced to the European market. This has resulted in the development of processes in Finland [18], in France [19] and PLATO®-wood in the Netherlands. In the Netherlands a production plant was built and started its production in summer 2000. This plant is designed to treat initially 50.000 m^3.

The PLATO-process uses different steps of treatment and combines successively a hydrothermolysis step with a dry curing step. The impact of the hydrothermolysis in the PLATO-treatment results in the occurrence of different chemical transformations. One aim of this 2-step process is the use of the presence of abundant moisture in the woody cell wall during the hydrothermolysis. This provokes an increased reactivity of the cell wall components under comparable low temperature. In order to reach a selective degree of depolymerisation of the hemicellulose during the hydrothermolysis, relative mild conditions can be applied to limit unwanted side reactions, which can influence the mechanical properties negatively [20].

The PLATO-process [13] principally consists of two stages with an intermediate drying operation. In the first step (hydrothermolysis) of the process, green or air dried wood, is treated at temperatures typically between 160 °C-190 °C under increased pressure (super atmospheric pressure). A conventional wood drying process is used to dry the treated wood to a low moisture content (ca.10%). In the second step (curing) the dry intermediate product is heated again to temperatures typically between 170 °C - 190 °C [21].

The process time is depending on the wood species used, the thickness, form of wood etc., and looks in general:

1. thermolysis 4-5 hours
2. drying step 3-5 days
3. curing step 14-16 hours
4. conditioning 2-3 days

Depending on wood species and thickness of the material, these times can be shorter as well. The heating medium can be steam or heated air [21].

2.3. Retification and Bois Perdure (France)

Retification (Retified wood) has been developed by Ecole des Mines de Saint-Etienne and operating licences and patents have been acquired by the Company NOW (New Option Wood) (Also known as RETITECH). The process consists in starting from wood previously dried around 12 % in humidity and to heat slowly in a specific chamber up to 210 – 240°C in a nitrogen atmosphere with less than 2 % in oxygen. The Industrial oven has been developed by the Company Four et Brûleurs REY, near Saint-Etienne. Three Industrial Units are already in operation with a capacity of 3500 m³/year for each corresponding to a heat chamber of 8 m³ [6].

The second Process is named "Le Bois Perdure" and the oven has been developed by the Company BCI-MBS. Instead of starting from dry wood such a process allows to use fresh wood. The first step of the process consists in an artificial drying in the oven. Then the wood is heated up to 230°C under steam atmosphere (steam generated from the water of the wood).

In both cases there is a compromise between durability and mechanical properties-higher the temperature, better the durability and lower some mechanical properties as strength to rupture. The treated wood at 230 –

542

240°C is much more durable but can loose up to 40 % in Modulus of rupture and is more brittle. At 210°C, the material, depending upon the species, can be less brittle with mechanical characteristics close to the original values but the durability could be improved only slightly. It means that the heat treatment shall be adjusted in terms of rate of heating, duration of treatment and maximum temperature to reach according to the application on usage. The processes are very sensitive to slight changes in temperature which shall be controlled with accuracy. For example, in the Retification Process it has been observed and published recently that 230°C corresponds to a define modification of the lignin leading probably to crosslinking. Under such a temperature the treated wood does not show the same behavior, in terms of durability, that at a temperature above 230°C [6].

2.4. Oil Heat Treatment (Germany)

The principle design of the plant can be seen from Fig. 2.
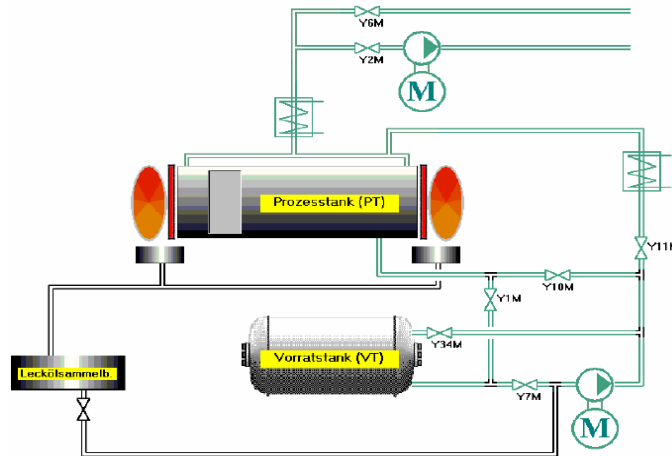
Fig. 2. *Principle design of the plant. designed by MENZ HOLZ Germany [9].*

The process is performed in a closed process vessel (PT). After loading the process vessel (PT) with wood, hot oil is pumped from the stock vessel (VT) into the process vessel (PT) where the hot oil is kept at high temperatures circulating around the wood. Before unloading the process vessel (PT) the hot oil is pumped back into the stock vessel (VT).

To obtain maximum durability and minimum oil consumption the process is operated at 220°C. To obtain maximum durability and maximum strength temperatures between 180°C and 200°C are used plus a controlled oil uptake. It proved to be necessary to keep the desired process temperature (for example 220°C) for 2-4 hours in the middle of the wooden pieces to be treated. Additional time for heating up and cooling down is necessary, depending on the dimension of the wood. Fig. 2 gives an example of the a heating up phase for logs with a cross section of 90 mm by 90 mm. Typical process duration for a whole treatment cycle (including heating up and cooling down) for logs with a cross section of 100 mm x 100 mm and length of 4 meters is 18 hours. The heating medium is crude vegetable oil. For example rape seed, linseed oil or sunflower oil. The oil serves for both, fast and equal transfer of heat to the wood, providing the same heat-conditions all over the whole vessel perfect separation of oxygen from wood [9].

3. EFFECTS OF HEAT TREATMENT ON WOOD PROPERTIES

3.1. Effect on Chemical Properties of Wood

The heat treatment of wood changes its chemical composition by degrading cell wall compounds and extractives. The chemical changes due to heating depend on the duration and temperature of the treatment, the temperature being the main factor [22]. For low temperatures between 20-150°C, the wood dries, beginning with the loss of free water and finishing with bound water. At 180-250°C, the temperature range commonly used for heat treatments, wood undergoes important chemical transformations, and at temperatures above 250°C starts the carbonization processes with formation of CO_2 and other pyrolysis products [2].

The incurred chemical changes have a positive effect on the decrease in hydrofility of the treated material. Boonstra and Tjeerdsma [23] reported decrease in wood hygroscopicity during thermal treatments is the result of:

- depolymerization of carbohydrates (especially hemicelluloses), which results in the decrease in the number of free hydroxyl groups,
- increasing the share of crystal zone in the cellulose where hydroxyl groups are not readily available,
- further cross linking of the lignin, by which the availability of hydroxyl groups is additionally decreased [24].

The hemicelluloses are the first structural compounds to be thermally affected, even at low temperatures. The degradation starts by deacetylation, and the released acetic acid acts as a depolymerization catalyst that further increases polysaccharide decomposition [25], [26]. For example, the content of pentosans of pine wood treated for 7 hours at 130ºC decreased from 11% to 9.1% [27]. Acid catalyzed degradation leads to the formation of formaldehyde, furfural, and other aldehydes [2], [25].

Cellulose is less affected by the heat treatments, probably because of its crystalline nature. Bourgois and Guyonnet [22] studied the treatment of pine wood at 260ºC, in an atmosphere without oxygen, did not alter cellulose significantly. Cellulose crystallinity increases due to degradation of amorphous cellulose, as reported earlier, resulting in an decreased accessibility of hydroxyl groups to water molecules [28, 23], which contributes to a decrease of equilibrium moisture content, in addition to the major effect caused by the degradation of hemicelluloses.

Lignin of *Pinus pinaster* increased from 28% to 41%, 54%, and 84%, respectively for 0.5, 1, and 4 hours at 260ºC [22]. It should be noted that the lignin determined using the standard methods in heat-treated wood samples is probably not a pure lignin, since several authors suggested polycondensation reactions with other cell Wall components, resulting in further cross-linking, contribute to the increase in apparent lignin content [2], [23], [29]. Despite the increase on the percentage of lignin there are also indications that lignin starts to degrade in the beginning of the treatment but at a lower rate than polysaccharides, as reported by some authors [29].

Most of the extractives disappear or degrade during the heat treatment, especially the most volatile, but new compounds that can be extracted from wood appear, resulting from the degradation of cell wall structural components. Esteves et al. [29] reported that despite the fact that most of the original extractives disappeared from the wood with heat treatment, the extractive content increased substantially with the mass loss, followed by a decrease. The major increase was due to water and ethanol extractives as a result of polysaccharide degradation [2].

3.2. Effect on Some Physical and Mechanical Properties of Wood

The positive influence of thermal wood modification on the decrease in hydrofility, swelling and shrinkage of treated wood was confirmed by numerous researches [30-32]. As opposed to these positive effects, thermal wood modification causes the decrease in most mechanical properties of wood. The two crucial factors affecting the final quality of treated wood are temperature and time [17], [24], [33].

During the heat treatment process, the organic acid coming from hemicelluloses creates an acidic environment which is combined with high temperature to break down the lignin-polysaccharide linkages in the wood structure, and makes wood from a hygroscopic material become a hydrophobic material [28]. Water absorption of the wood after the heat treatment is reduced because a large number of hydroxyl groups (-OH) of the carbon-hydrogen compounds decrease [34]. Specifically, the wood density decreases but the dimensional stability improves through the analysis of water uptake and volume swelling of the treated wood [35].

The decrease of equilibrium moisture of wood due to heat treatments leads to an improvement of wood dimensional stability. The increase in dimensional stability for heat-treated wood is mainly due to the decrease of wood hygroscopicity in view of the chemical changes at high temperatures. Dirol and Guyonnet [14] reported that the dimensional stability can be the result of the formation of polymers from sugars that are less hygroscopic than the hemicelluloses from which they derive.

One of the main heat-treated wood limitations is the decrease of mechanical strength, making this wood unsuitable for most structural applications. Two of the most affected mechanical properties by the heat treatment are the resistance to bending in static and dynamic tests (impact bending). The reduction depends on wood species and process conditions. The modulus of elasticity (MOE) seems to increase for softer treatments and decrease for more severe treatments. Results reported with steam heat-treated pine and ash wood showed a small increase until about 4% mass loss, followed by a decrease for higher mass losses. With the same treatment conditions, heating time, and temperature, the reduction of modulus of elasticity was higher for the treatment in air, and relationship prevailed also when comparing at constant mass loss. [2], [36], [37].

Poncsak et al. [33] conducted research with heat-treated birch and showed a reduction of bending strength with increasing treatment temperature, especially above 200 ºC. The authors also mention a slight hardness

increase. Shi et al. [17] studied the mechanical behavior of Quebec wood species heat-treated using the Thermowood process and concluded that the modulus of rupture decreased between 0% and 49% for heat-treated spruce, pine, fir, and aspen, while for birch the modulus increased slightly (6%) after the heat treatment.

The reasons for the changes on mechanical properties have been extensively discussed by researchers. The degradation of hemicelluloses has been proposed as the major factor for the loss of mechanical strength, affecting especially bending and tensile strength, but also the crystallization of amorphous cellulose might play an important role. Polycondensation reactions of lignin, resulting in cross-linking, are mentioned as having a positive impact mainly in the longitudinal direction. The lower equilibrium moisture content might affect positively the strength properties of heat-treated wood, but this effect is superseded by the degradation of the chemical compounds [2].

4. RESULTS AND DISCUSSION

Some of heat treatment processes are in installation, and others are already in full production. Several wood species are used, with different process conditions, depending on species and the final use of the product. All of the processes use sawn wood and treatment temperatures between 160ºC and 260ºC, but they differ in terms of process conditions, such as the presence of a shielding gas such as nitrogen or steam, humid or dry processes, use of oils, etc.

All modification treatments have in common that solid wood is subjected to temperatures close to or above 200°C for several hours in an atmosphere with low oxygen content. By this thermal modification some mechanical properties are reduced but the dimensional stability and the biological durability of wood is increased without adding outside chemicals / biocides to the wood. Therefore thermally modified wood is discussed as a new material for several applications.

Heat treatment changes the chemical composition of wood, leading to mass loss. Hemicelluloses are the most affected compounds. The degradation starts by deacetylation, and the released acetic acid acts as a depolymerization catalyst, which further increases polysaccharide decomposition. Cellulose is more resistant to heat, which is attributable mainly to the crystalline fraction. Cellulose crystallinity increases due to degradation of amorphous cellulose. In lignin polycondensation reactions with other cell wall components, resulting in further crosslinking, contribute to an apparent increase in lignin content. The downside of the treatment is the degradation of mechanical properties. The effect on MOE is small, whereas static and dynamic bending strength and tensile strength decrease. The degradation of hemicelluloses has been identified as the major factor for the loss of mechanical strength, but also the crystallization of amorphous cellulose might play an important role. Wood becomes darker, wettability and thermal conductivity decrease, and finishing and the gluing process need special attention.

REFERENCES

[1]. C.A.S. Hill, *Wood Modification: Chemical Thermal and Other Processes*, John Wiley & Sons Pres, Germany, 2006.
[2]. B. Esteves and H. Pereira, "Wood modification by heat treatment: A review", *BioResources*, vol. 4, no.1, pp. 370-404, 2009.
[3]. R.M. Rowell, E.R. Ibach, J. McSweeny and T. Nilsson, "Understanding decay resistance, dimensional stability and strength changes in heat treated and acetylated wood", *Wood Material Science and Engineering,* vol. 1, pp. 14–22, (2009).
[4]. B.F. Tjeerdsma, P. Swager, B.J. Horstman, B.W, Holleboom and W.J. Homan, "Process development of treatment of wood with modified hot oil", In: Proceedings (Eds H. Militz, CAS Hill) of the "Second European Conference on Wood Modification", 6-7 October 2005, Gottingen, Germany, pp. 186-197, 2005.
[5]. B.C. Bal, ve F.T. Efe, "Isıl islemin kayin (*Fagus orientalis* L.) odununun sok direnci üzerine etkilerinin incelenmesi", *1st International Conference on Engineering Technology and Applied Sciences*, Afyon Kocatepe University, Turkey 21-22 April 2016, pp. 1-7, 2016.
[6]. M. Vernois, "Heat treatment in France", P*roceedings of Seminar, Production and development of heat treated wood in Europe*, November 2000, Helsinki, Stockholm, Oslo, 2000.
[7]. S. Jämsä and P. Viitaniemi, "Heat treatment of wood, Better durability without chemicals", *Nordiske Trebeskyttelsesdager*, pp. 47-51, 1998.
[8]. A.O. Rapp, M. Sailer and M.Westin, "Innovative Holzvergütung-neue Einsatzbereiche für Holz", *In: Proceedings of the Dreiländer-Holztagung*, Luzern-Switzerland, 2000.
[9]. A.O. Rapp and M. Sailer, "Heat treatment in Germany", *Proceedings of Seminar, Production and Development of Heat Treated Wood in Europe*, November 2000, Helsinki, Stokholm, Oslo, 2000.
[10]. M. Boonstra, "A two-stage thermal modification of wood", Ph.D. Thesis in Applied Biological Sciences: Soil and Forest management, Henry Poincaré University-Nancy, France, 2008.

[11]. T. Syrjänen and K. Oy, "Production and classification of heat treated wood in Finland", COST ACTION E22 Environmental Optimization of Wood Protection, *Proceedings of Special Seminar held in Antibes*, France, 9 February 2001, pp. 9-17, 2001.

[12]. T. Syrjänen and E. Kangas, "Heat treated timber in Finland", *The international research group on wood preservation*, IRG/WP 00–40158, IRG Secretariat, Stockholm, Sweden, 2000.

[13]. M.J. Boonstra, B.F. Tjeerdsma and H.A.C. Groeneveld. "Thermal modification of non-durable wood species. 1. The PLATO technology: thermal modification of wood", *International Research Group on Wood Preservation*, Document no. IRG/WP 98- 40123, 1998.

[14]. D. Dirol and R. Guyonnet "The improvement of wood durability by retification process", *The international research group on wood preservation,* IRG/WP 93–40015, IRG Secretariat, Stockholm, Sweden,1993.

[15]. A.O. Rapp and M. Sailer, "Oil heat treatment of wood in Germany – State of the art. In: Review on heat treatments of wood", COST Action E22, Environmental optimisation of wood protection. *Proceedings of the special seminar held in Antibes*, France, on 9 February 2001, Forestry and Forestry Products, France, 2001.

[16]. D. Aydemir, "The effect of heat treatment on some physical, mechanic and technological properties of Uludag fir (*Abies bornmülleriana* mattf.) and hornbeam (*Carpinus betulus* L.) woods", *Master Thesis*, Zonguldak Karaelmas Üniversitesi, 2007.

[17]. J. Shi, D. Kocaefe and J. Zhang, "Mechanical behaviour of Quebec wood species heat treated using thermowood process", *Holz als Roh-und Werkstoff*, vol. 65, no. 4, pp. 255-259, 2007.

[18]. H.A. Viitanen, S. Jamsa, L.M. Paajanen, A.J. Nurmi and P. Viitaniemi, "The effect of heat treatment on the properties of spruce", *International Research Group on Wood Preservation*, IRG/WP 94-40032, Nusa Dua, Bali-Indonesia, 1994.

[19]. J.J. Weiland and R. Guyonnet. *Retifiziertes Holz*, 16. Verdichter Holzbau in Europa, 1997.

[20]. B.F. Tjeerdsma, M. Boonstra and H. Militz, "Thermal modification of non-durable wood species, 2. Improved wood properties of thermally treated wood. *International Research Group on Wood Preservation*, Document no. IRG/WP 98-40124, 1998.

[21]. H. Militz and B.Tjeerdsma, "Heat treatment of wood by the Plato-process": *Proceedings of Seminar, Production and Development of Heat Treated Wood in Europe*, November 2000, Helsinki, Stokholm, Oslo, 2000.

[22]. J. Bourgois and R. Guyonnet, "Characterisation and analysis of torrefied wood", *Wood Science and Technology*, vol. 22, pp. 143-155, 1988.

[23]. M.J. Boonstra, and B. Tjeerdsma, "Chemical analysis of heat treated softwoods", *Holz Roh- Werkst,* vol. 64, pp. 204-211. 2006.

[24]. V. Zdravković, A. Lovrić and B. Stanković, "Dimensional stability of plywood panels made from thermally modified poplar veneers in the conditions of variable air humidity", *Drvna Industrija,* vol. 64, no. 3, pp. 175-181, 2013.

[25]. B. Tjeerdsma, M. Boonstra, A. Pizzi, P. Tekely and H. Militz, "Characterisation of thermaly modified wood: Molecular reasons for wood performance improvement", *Holz Roh-Werkst*, vol. 56, pp. 149-153, 1998.

[26]. M. Nuopponen, T. Vuorinen, S. Jamsä and P. Viitaniemi, "Thermal modifications in softwood studied by FT-IR and UV resonance Raman spectroscopies", *Journal of Wood Chemistry and Technology*, vol. 24, pp. 13-26, 2004.

[27]. G. Potutkin and L. Shirayena, "Changes in chemical components of wood during high temperature drying", *Izvestiya Vysshikh Uchebnykh Zavedenii. Matematika*, vol. 18, pp. 127-129, 1975.

[28]. H, Wikberg and S. Maunu, "Characterisation of thermally modified hard- and softwoods by 13C CPMAS NMR", *Carbohydrate Polymers,* vol. 58, pp. 461-466, 2004.

[29]. B. Esteves, J. Graca and H. Pereira, "Extractive composition and summative chemical analysis of thermally treated eucalypt wood", *Holzforschung*, vol. 62, 344-351, 2008.

[30]. D. Kocaefe, J.L. Shi, D.Q. Yang and M. Bouzara, "Mechanical properties, dimensional stability, and mold resistance of heat-treated jack pine and aspen", *Forest Products Journal*, vol. 58, no. 6, pp. 88-93, 2008.

[31]. C. Yongjian, L. Jianxiong H. Rongfeng, and J. Jiang, "Increased dimensional stability of Chinese fir through steam-heat treatment", *European Journal of Wood and Wood Products*, vol. 70, no. 4, pp. 441-444, July 2012.

[32]. T. Sinković, S. Govorčin and T. Sedlar, "Comparison of physical properties of untreated and heat treated beech and hornbeam", *Drvna Industrija*, vol. 62, no. 4, pp. 283-290, 2011.

[33]. S. Poncsak, D. Kocaefe, M. Bouazara and A. Pichette, "Effect of high temperature treatment on the mechanical properties of birch (*Betula papyrifera*)", *Wood Science and Technology*, vol. 40, pp. 647-663, 2006.

[34]. T. Nakano and J. Miyazaki, "Surface fractal dimensionality and hygroscopicity for heated wood", *Holzforschung*, vol. 57, pp. 289-294, 2003.

[35]. T.V. Chu, "Improvement of dimensional stability of Acacia mangium wood by heat treatment: A case study of Vietnam", *Journal of Forest Science*, Vol. 29, No. 2, pp. 109-115, May, 2013.

[36]. B. Esteves, A. Velez Marques, I. Domingos and H. Pereira, "Influence of steam heating on the properties of pine (*Pinus pinaster*) and eucalypt (*Eucalyptus globulus*) wood", *Wood Science and Technology,* vol. 41, pp. 193-207, 2007.

[37]. H.İ. Sahin, "Effect of heat treatment on some technological properties of ash (*Fraxinus angustifolia* Vahl.) wood grown in natural and plantation forests", *Ph.D. Thesis*, Duzce University, Duzce, 2013.

Comparison Of Cutting Forces In Drilling Of Hot And Cold Work Tool Steels

İsmail Tekaut[1], Selcuk YAGMUR[1], Halil Demir [2], Ulvi SEKER[1]

Abstract

Carbon fiber reinforced composite materials are widely used in aviation and aerospace industries due to their low density, high strength, high corrosion resistance, low thermal expansion coefficient characteristics. In this study, the optimization of tool wear of four flute coated carbide end mills which were used for peripheral milling on carbon fiber reinforced composites (CFRC) were investigated using Taguchi method. Two different cutting speeds (400 and 450 m/min), four different cutting tools (TiAlN coated without chip breaker (G1), TiAlN coated with chip breaker (G2), AlCrN coated with chip breaker (G3) and diamond coated (G4)) and constant feed rate (1270mm/min) were used as cutting parameters. The experiments were carried by using Taguchi L8 orthogonal experimental setup. By the help of Taguchi method, 450 m/min (cutting condition was 1270 mm/min constant feed rate with machining G4 tool) were determined as optimum cutting parameter by using experimental results. Moreover, the most effective operational parameter on tool wear was determined as cutting tool under the favor of analysis of variance (ANOVA).

Key Words: *Drilling, AISI H13, AISI D2, Cutting Forces*

1. INTRODUCTION

The properties that distinguish tool steels is the variation of the material's hardness by operational temperature and the material's tempering temperature [1]. Hot work tool steels do not exhibit any reduction in hardness at high temperatures (500-600°C) and under high mechanical loads. Cold work tool steels are used for machining and forming workpieces functioning under an operational temperature below 200ºC [2]. In drilling these two materials with distinct properties, it is important to know appropriate cutting tools and cutting parameters. Properties of the workpiece such as its metallurgy, chemistry, mechanics, heat treatment, additives, internal residues and thickness of the hard layer on the surface affect the workability of the material [3]. Current studies in the literature focus on measuring cutting forces and cutting parameters in the process of drilling materials with different properties and chemistry. It was found that magnitude of shear forces is correlated with the material's microstructure and the feed rate. They found that as the feed rate increases, thrust force increases as well. They further found that increase in cutting speed causes a decrease in cutting forces. They also observed better hole quality and less wear at low cutting forces [4, 8, 9, 10, 11, 12, 13, 14, 15, 16, 18]. Hence, in this study, AISI H13 and AISI D2 steels (AlCrN monolayer) with different properties were drilled with multilayer solid helical carbide drills under same cutting conditions to measure cutting forces with respect to cutting parameters and compare them by material.

2. MATERIAL AND METHOD

Microstructures of AISI H13 and AISI D2 steels employed in the experiments are shown in Fig. 1, and their chemical compositions are presented in Table 1. For hardness measurements of materials, hardness of 10 test samples for each type was measured and averaged. As a result of these measurements, it was found that hardness value of AISI H13 steel and the AISI D2 steel is 90 HRB (184 HB) and 96 HRB (225 HB) respectively. In the experiments, a drilling procedure was applied to solid samples. Each test sample was ground to have an outer diameter of be 25 mm, and sample length was set to 35 mm to allow drilling at 3D standards. In the study, coated (AlCrN monolayer) multilayer solid helical carbide drills with a diameter of 14mm at DIN 6537 K standard were employed, and fixed cutting tool/ rotating workpiece methodology was chosen.

---

[1] *Technical Science Vocational School, Gazi University, Turkey,*
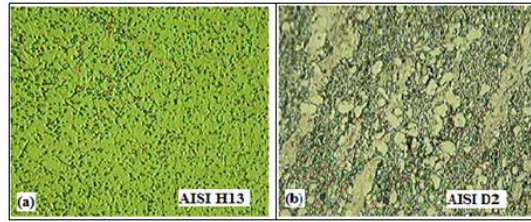
Figure 1. Microsturcture of the materials

Cutting parameters were determined by choosing an initial value within the cutting parameters range recommended for the drills selected in the manufacturer's catalogue (KARCAN). To respect the requirement that minimum four different cutting speeds should be selected for each cutting condition specified in life test standards, the initial value of 60 m/min was reproduced according to the ISO standard for Geometric Sequences of Standard Numbers (R10, R20 and R40). Four different cutting speeds (60, 75, 90, 108 m/min) and three different feed rates (0.15, 0.20 and 0.25 rpm) selected at foregoing conditions were used in the experiments. Experiments were carried out at Johnford VMC-550 CNC vertical machining centre located at the Gazi University's Technical Education Faculty, Department of Mechanics, Sub-department of Machining. In order to experimentally determine cutting forces and moments, a quartz crystal based *Kistler 9272* type dynamometer and a *Kistler Type 5070* amplifier capable of simultaneously measuring three cutting force components (Fx, Fy, Fz) and moment (Mz) were used. The values measured were digitized on the software DynoWare. The testing apparatus used in the experiment and position of the drill-workpiece are shown in Figure 2.

Table.1. Chemical composition of AISI H13 and AISI D2 steels

AISI H13 % Weight	C	Si	Mn	P	S	Cr	Mo	Ni
	0.418	1.08	0.348	0.017	0.001	5.12	1.36	0.044
Al	Co	Cu	Nb	Ti	V	W	Wd	Fe
0.037	≥ 0.01	0.018	0.006	0.009	1.09	<0.01	<0.001	90.455
AISI D2 % Weight	C	Si	Mn	P	S	Cr	Mo	Ni
	1.58	0.435	0.459	0.028	0.011	11.467	0.88	0.092
Al	Co	Cu	Nb	Ti	V	W	Wd	Fe
0.001	0.011	0.037	0.008	0.003	0.84	0.058	0.03	84.092
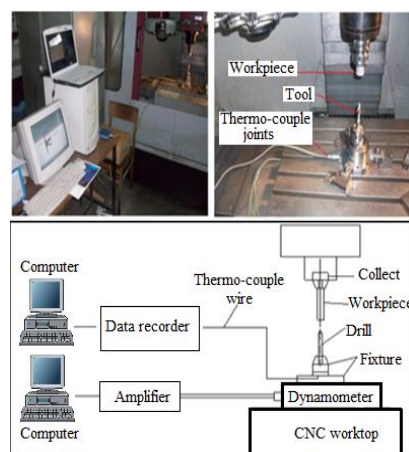
Figure 2. Testing Apparatus.

3. RESULTS AND DISCUSSION

In the study, thrust force, cutting force and moment values obtained during drilling of AISI H13 and AISI D2 steels with coated carbide drills at various combinations of cutting parameters were plotted and collectively provided in Figure 3. The graphs reveal that an increase in feed rate leads to increase in thrust forces and moment values in the entire process of drilling AISI H13 and AISI D2 steels (see, Figure 3.a-Figure 3.c). This is attributed to the fact that drill cutting edges move faster along the hole axis in unit time as driven by the increase in feed rate, and further to increased machining volume in unit time. The drill consumes more energy to move faster along the hole axis and generates more thrust force to fulfil the machining demand. And a higher cutting force is consumed to perform a heavier machining, culminating in larger moments [4, 6, 7, 8]. Having evaluated the graphs in Figures 3.a-3c with respect to cutting speed, it is obvious that increase in cutting speed leads to a decrease in both feed rates and moment values in all cutting operations. This may be attributed to the fact that coated drills exhibit high performance due to the characteristics of the coating material. High strength of coated drills to abrasion ensures a usual typical machining process, and thanks to low friction coefficient, machining facilitated by increase in cutting speed leads to reduction in thrust forces. Furthermore, increased cutting speed rises temperature, and due to less thermal conductivity of the drill coating material, increased temperature is shared between the workpiece and the chip, resulting in deformation of the workpiece with less force [5,18]. Thus, reduction in thrust forces and cutting forces driven by the increase in cutting speed leads to reduction in moment values.
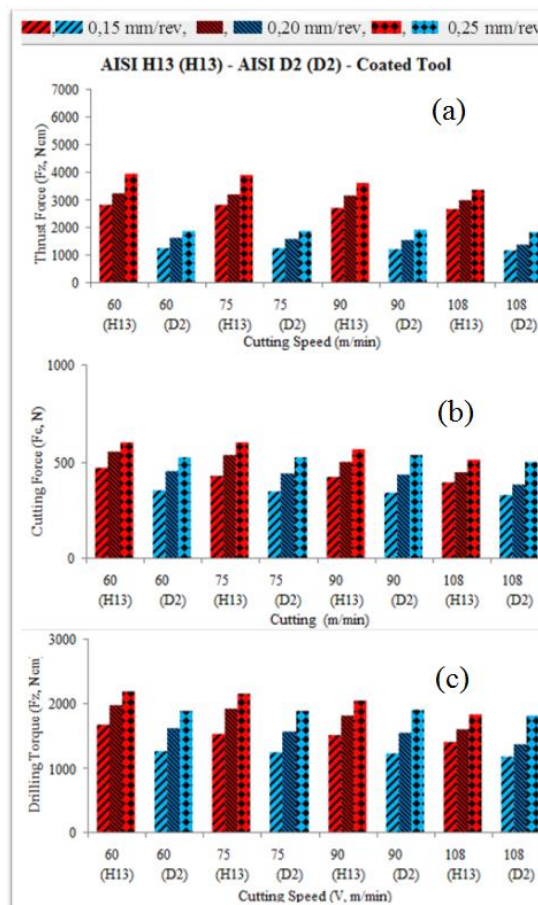
Figure 3. Comparison of cutting forces for AISI H13 and AISI D2 steels.

Having evaluated the graphs in Figure 3.a-Figure 3.c with respect to the workpiece, it is obvious that thrust forces, cutting forces and moments obtained during the drilling of AISI H13 steel with coated drills are higher than for the procedure applied to the AISI D2 steel. This may be explained with the structural differences of steels. The structural differences of AISI H13 and AISI D2 steels result from their alloy content as well as carbide formation and distribution induced by varied heat treatment applied to these steels during manufacturing [2]. Since carbon, sulphur and magnesium content of the AISI H13 steel is less than that found

in AISI D2 steel (see, Table 1), and since carbide distributions are more homogeneous, denser and finer than for the AISI D2 steel, plastic deformation of steel demands more force [5, 8, 9, 10]. For this reason, it is naturally expected that thrust forces, cutting forces and moments generated during machining of of the AISI H13 steel are higher than for the AISI D2 steel.

4. CONCLUSIONS

Cutting forces formed during the drilling of AISI H31 and AISI D2 materials with coated drills were compared with respect to increase in cutting speed and feed rate.

The following results were obtained with this study:

- Feed rate in drilling increases machining yield in unit time and correspondingly the cutting forces.
- Increase in cutting speed causes reduction in cutting forces due to faster machining and lower deformation force required for machining.
- Thrust forces, cutting forces and moments obtained during the drilling of AISI H13 steel are higher than for the AISI D2 steel. It is believed that this is due to more homogeneous carbide distribution within the microstructure of the AISI H13 steel compared to AISI D2 steels, and due to different thermal treatments applied.

REFERENCES

[1] Smith, W.F., "Materials Science and Engineering", Literatur Publishing, Translated by Nihat G.Kınıkoglu, Yıldız Technical University Publications, Istanbul, 451-547(2001).
[2] Kocak, H., "Tool Steels Handbook, 7th Edition", Ofset Matbaacılık Ltd. Sti., Istanbul, 32-83(2006).
[3] Cakır, M.C., "Principles of Modern Machining, I '', Vipas A.S., Bursa, 205- 302 (1999).
[4] Yagmur, S., "An experimental study of temperature generated with respect to cutting parameters in drilling operations", Master Thesis, Gazi University, Institute of Science, Ankara,42-100 (2011).
[5] Sandvik Coromant, "Modern Metal Cutting", Sandvik Endustriyel Mamüller Sanayi Ve Ticaret A.S., Istanbul, 2-61 (1994).
[6] Cakır, A., "Studying cutting parameters during drilling of Al 7075 and Al 6013 Aluminium materials'', Master Thesis, G.U. Institute of Science, Ankara, 22-37 (2009).
[7] Mendi, F., ''Theories and Calculations for Machine Tools, 2nd Edition'', Gazi Bookstore, Ankara, 155-167 (2006).
[8] Kalidas, S., DeVor, R.E., and Kapoor, S.G., "Experimental investigation of the effect of drill coating on hole quality under and wet drilling conditions", Surface and Coatings Technology, 148:117-128 (2001).
[9] Dorr, J., Mertens, T., Engering, G., and Lahres, M., "In-situ' temperature measurement to determine the machining potential of different tool coatings", Surface and Coatings Technology, 174: 389–392(2003).
[10] Cakıroglu, R., and Acır, A., " Taguchi optimization method of tool chip interface temperature depending on cutting parameters in drilling the A12014 material",Machine Technologies E-Journal,10:73-86(2013).
[11] Ertunc, H.M., and Sevim, İ., "Studies for observing wears on cutting tools", Journal of P.U. Engineering Sciences, 7:55-62(2001).
[12] Bosheh, S.S., Mativenga, P.T., "White layer formation in hard turning of H13 tool steel at high cutting speeds using CBN tooling", Int. Journal of Machine Tools and Manufacture, 46:225-233 (2006).
[13] Usta, M., "Investigating cutting forces and heat effect generated during drilling operations with lathe machine tools",Master Thesis, G.U. Institute of Science, Ankara, 100-145 (2010).
[14] İsbilir, O., and Ghassemieha, E., "Finite element analysis of drilling of titanium alloy", Procedia Engineering, 10:1877-1882 (2011).
[15] Soylu, A.,"Design and manufacturing of a drilling dynamometer & analysing thrust force and turning moment for the HSS-1040 material pair", Selcuk University, Institute of Science, Konya, 66-70 (2007).
[16] Kıvak, T., and Seker, U., "Effect of coating material and cutting conditions on cutting forces in drilling the Ti-6Al-4V alloy", International Iron & Steel Symposium, Karabük, April 02-04 (2012).
[17] Ozkul, İ., Buldum, B.B., and Akkurt, A.,"Modelling by regression analysis the effect of cutting parameters on cutting forces and surface quality in drilling Dievar hot work tool steel",Journal of Pamukkale University, Engineering Sciences,19 (1): 1-9 (2013).
[18] Trent E.M.,"Metal Cutting", Butterworths Pres, London (1989).

ISOSTATIC EFFECTS OF DAM LOADS AND EARTHQUAKES

Oya PAMUKCU[1]

Abstract

It is argued that the occupancy level and the discharge of the dams cause the earthquakes around the dams. The reason is that during these functions of the dam, the gravitational state of the natural medium and its isostatic conditions are affected. Up to now, the mediums which are under this effect are thought to have not caused very high magnitude earthquakes. Therefore, isostatic earthquakes did not come to the forefront much. However, the local seismic triggering function caused by dam loads can speed up the process of the earthquakes occurrence , which would be caused by a strike-slip or vertical-slip fault at the end of the tension. In addition, seismogravitational forces which are occurred in the charge and discharge stages of the dam, mass interaction, pressure induced around the dam, pre-existing pressure interaction and many geological, hydrological source may be one of the reasons for seismicity. The rate of increase in water level affecting gravitational isostasy, duration of the water charging to dam, the maximum water level of the dam can be affected the earthquake frequency. As a result, isostatic earthquakes can not reach big events, but when considered together with the triggering event, they can contribute to major earthquakes. Within the scope of this information, in this study, relations between Seferihisar and Tahtalı dams's data in Izmir (Turkey) and earthquakes which were around the dams were investigated. For this purpose, the dam water-month, water filled volume-month and earthquake number-month graphs were established. Depending on the region and coordinates studied, the effects of dams on the isostatic structure, their role in the seismic interaction, and state of gravitational interactions of faults around the dam were examined.

Keywords: *Dam Loads, Isostasy, Gravity, Earthquake*

1. INTRODUCTION

While the dams are discharged (Figure 1), the earth is in the natural isostatic balance. On the contrary, in a loaded dam, massive effect of tons of cubic meters of water load and its distribution underground is formed (Figure 2). Gravity is affected by the massive effect of water and the change in load distribution. The gravity time-series relation with water storage of dams tried to explain in some studies ([1]). Dam reservoirs are filled rapidly with the alluvial substance carried by streams and cause siltation to occur. Besides, mass movements and erosion are the other factors that increase siltation in dam reservoirs. Blasting operations that are performed during the construction of the dam cause vibrations which destroy the slope stability and increases the openings of fractures. Thus, these slopes which gain a loose character during dam construction get saturated as the dam restores water and finally mass movements and the intensity of erosion increases and also deformation around the dam structure takes place ([2]). In recent years, the deformation of a reservoir fields have been explored with different methods (etc. [3]). They found horizontal displacements around the reservoir area for different water level. These displacements are caused by local or regional soil or water loads such as dams. Because of the dams which are over the streams in deltaic regions, the material carried by streams accumulates in dam reservoirs. Besides, these materials are occupied by the sea and by the erosive activities of water flows and waves. The deltaic features scale with the magnitude of a river's discharge and the sediment load delivered by the river ([4]). The global ocean volume (eustasy), more regional earth-surface load changes (isostasy), sediment supply, and compaction of the deposited sediment affect to the coastline of a delta [4].

---

[1] *Dokuz Eylul University, Engineering Faculty, Department of Geophysical Engineering, 35160, Tinaztepe Campus, Buca, İzmir, TURKEY, oya.pamukcu@deu.edu.tr*

Figure 1. The view of the unloaded dam.

Figure 2. The view of the loaded dam.

The construction of a dam on rock foundation (with its water reservoir) causes redistribution of the stress field, and affects the state of mechanical and hydrogeologic properties of the rock mass beneath the dam. The rock stresses are affected by gravitational, tectonic, terrestrial stresses and also isostatic compensations etc. ([5]). The changes in seismic activities are closely related to the filling of large basins and the alteration of isostasy. The physical reasons of the seismic activities which were caused by loading of dams were studied by ([6], [7], [8]). Within the scope of this information, in this study, the relations between the data of Seferihisar and Tahtalı dams in İzmir (Turkey) and earthquakes occurred around the dams were investigated. For this purpose, the dams water-month, water filled volume-month and number of earthquakes-month graphs were established.

2. APPLICATIONS

As for the application part; it was investigated to what extent Seferihisar and Tahtalı dams affect the regional isostasy in a time-dependent manner. For this purpose, the beginning year of construction of Tahtalı (1986) and Seferhisar (1987) dams were taken as basis (Figure 3). All the earthquakes that occurred in those regions with a magnitude of 1-9 before and after these dates were examined without any limitation of focal depths. Earthquakes obtained from United States Geological Service (USGS) (Figure 4)

(a)

(b)

Figure 3. Pictures of (a) Tahtalı Dam (b) Seferihisar Dam

(a)   *(b)*

(c)   *(d)*
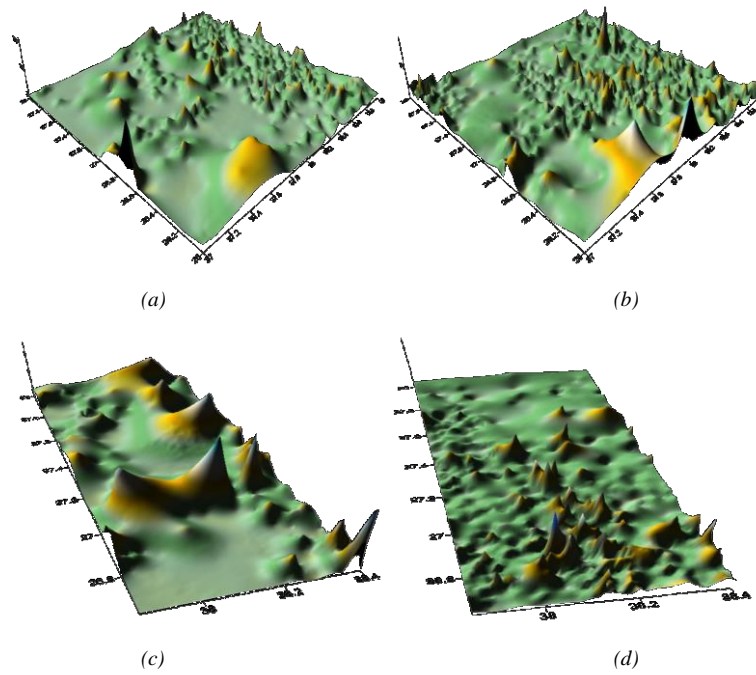
Figure 4. 3D focal depth graphs of earthquakes occurred around Tahtalı dam (a) away from 100 km between 1970-1986 years (before the construction of the dam) (b) away from 100 km between 1996-2006 years (after the construction of the dam) (c) closer than 100 km between 1970-1986 years (before the construction of the dam) (d) closer than 100 km between 1996-2006 years (after the construction of the dam).

(a)   *(b)*
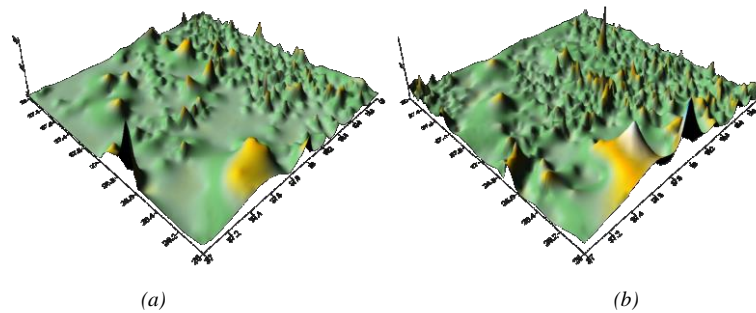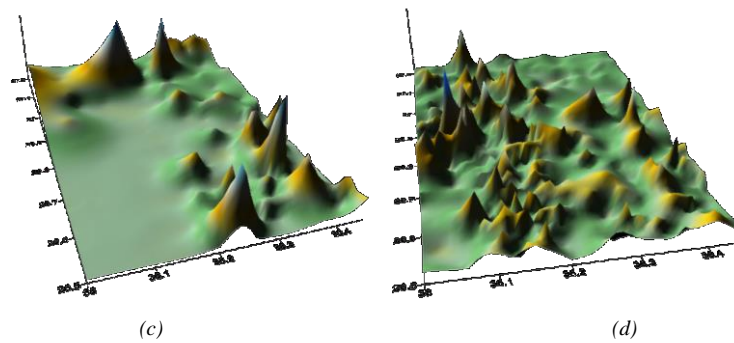
Figure 5. 3D focal depth graphs of earthquakes occurred around Seferihisar dam (a) away from 100 km between 1970-1986 years (before the construction of the dam) (b) away from 100 km between 1996-2006 years (after the construction of the dam) (c) closer than 100 km between 1970-1986 years (before the construction of the dam) (d) closer than 100 km between 1996-2006 years (after the construction of the dam).

ACKNOWLEDGMENT

REFERENCES

[19]. O. Francis, M. Van Camp, T.V. Dam, R. Warnant and M. Hendrickx, "Indication of the uplift of the Ardenne in long-term gravity variations in Membach (Belgium)". *Geophysical Journal International*, 158(1), 346-352, 2004.

[20]. E.M. Sonmez, "The Negative Impacts of Dams on Envıronment and Their Samples in Turkey", *Gaziantep University Journal of Social Sciences*, 11(1):213 -231, 2012.

[21]. H. Wang, H.T. Hsu and Y.Z. Zhu,. "Prediction of surface horizontal displacements, and gravity and tilt changes caused by filling the Three Gorges Reservoir". *Journal of Geodesy*, 76(2), 105-114, 2002.

[22]. J.P.M. Syvitski, "Deltas at risk". *Sustainability Science*, 3(1), 23-32,2008.

[23]. B. Amadei and O. Stephansson, *Rock stress and its measurement*. Springer Science and Business Media, 1997.

[24]. H.K. Gupta and B.K. Rastogi, *Dams and earthquakes*. *In Developments in geotechnical engineering* (No. 11). Elsevier Scientific Pub. Co., 1976.

[25]. D.W. Simpson, "Seismicity changes associated with reservoir loading". *Engineering Geology*, 10(2-4), 123-150, 1976.

[26]. H.K. Gupta, "A review of recent studies of triggered earthquakes by artificial water reservoirs with special emphasis on earthquakes in Koyna, India". *Earth-Science Reviews*, 58(3), 279-310, 2002.

[27]. O. Pamukcu, T. Gonenc, A. Cirmik, P. Sindirgi, I. Kaftan, and O. Akdemir 2015. "Investigation of vertical mass changes in the south of Izmir (Turkey) by monitoring microgravity and GPS/GNSS methods". *Journal of Earth System Science*, 124(1), 137-148, 2015.

REGIONAL ORGANIC AGRICULTURE IN TURKEY

Isıl SARAC[1]*, Ezgi DOGAN[2]

ABSTRACT

Organic farming, industrial agriculture based on high input use, revealed the face of negative consequences in terms of human health, economy and environment aims to protect the ecological balance. All kinds of vegetable products, animal products and aqua product to be produced according to organic farming methods of the inputs used in the production or supply allows. Forest and delivered in accordance with organic farming principles of natural areas, processing, packaging, labeling, storage, transport, marketing, control, aimed at certification and audit is an agricultural system that accepts the use of modern agricultural production techniques that do not harm the environment and human health.

In this study; that organic agriculture in Turkey, the situation has been examined by region. The socio-economic structure and natural richness of Turkey carries the potential to become one of the world's most important centers of organic farming too. Turkey with a total area of 1.066 million tons and the amount of 660,807.40 hectares has significant potential for organic agriculture. Be introduced first in the Aegean region of organic agricultural activities in our country, to be in Izmir, the majority of processing facilities and of manufactured products due to be exported from the port of Izmir major part of the organization team, inspection and certification companies, such as organic farming sector in almost all organizations headquarters in Izmir It is located. Initially dry and dried fruit to help the development of organic farming, Turkey has an important position in the organic cotton market.

Keywords: *Turkey, organic , organic farming*

1. INTRODUCTION

The rapidly increasing population growth in the world has also contributed to nutritional concerns. The concern about finding adequate nutrition has put a heavy pressure on the agriculture sector. Chemical fertilizers and agrochemicals have been rapidly spreading and the world has taken important steps to increase crop production.

The process has led to concerns about the negative effects of human health on the methods and materials used in such processes. Both the intensive irrigation activities and the effects of chemical fertilizers and agricultural chemicals on the environment and resources have begun to be investigated. It has been understood that modern farming methods cause many problems such as erosion, salting, pollution of water resources, damage of flora and animal existence, and chemical and drug residues in food affect human and animal health (Kırımhan, 2005: 47).

There has been a development called "Green Revolution" in order to meet the nutritional needs of the growing population. This revolution has been caused by the use of agricultural chemicals, chemical fertilizers and excess water in order to get products at the highest capacity from the restricted area. In serious terms agricultural production has increased markedly thanks to the green revolution. When it came to the 1970s, the effects of environmental health on human health began to be investigated and discussed. It has been shown that misused agricultural chemicals and chemical fertilizers harm human health and some agricultural medicines are prohibited.

The green revolution, seen as a savior, has left behind serious side effects such as environmental pollution. Soils are polluted and water resources are beginning to decline rapidly. The coming of organic agriculture has also been a result of these effects.

The protection of ecological balance against the adverse consequences of industrial agriculture based on high input use of human agriculture, economy and environment, the production of inputs to be used with all types

---

[1] *University of Bingöl, Ziraat Fakültesi, Bitki Koruma Bölümü Bingöl,Türkiye *saracsaracisil@hotmail.com.*

[2] University of Bingöl, Ziraat Fakültesi, Bahce Bitkileri Bölümü Bingöl,Türkiye *ezgidgn23@gmail.com.*

of plant, animal and aquatic products in accordance with the organic farming method or the production of organic, Registered and certified as a production method which aims at the processing, packing, labeling, storage, transport, marketing, control, certification and inspection in accordance with agricultural principles and using modern agricultural production techniques which do not harm the environment and human health. Agricultural system. The use of synthetic chemical fertilizers, medicines and hormones is not appropriate in the ecological agriculture system, which aims to maintain the natural balance that is the result of misapplications based on the best use of resources. The main objective of organic farming is to be able to provide a healthy production in the life cycle between soil-plant-animal and human.

1.1. Certification in organic farming

A farmer who makes organic produce must be certified by an international inspection company. Organic agriculture is the highest level of traceability and reliability in agricultural production systems. Control and certification are compulsory at every stage of production from farm to field according to all national and international standards regarding organic agriculture. For this reason, control and certification are an important step in gaining consumer awareness and trust in organic agriculture. The certification of organic products is the procedure for establishing compliance with the existing organic farming standards of that product and is divided into two parts: control and certification. It begins with an entrepreneur applying for an organic product certification process control and certification body. The entrepreneur (farmer, processor, packager, marketer) applies to the establishment of information and documentation which fully describes all the activities and the project to be carried out. The certification body evaluates this application and rejects the application without any activity in cases where it is impossible to certify. (The amount of land, crooks, products, storage, packaging units, address, land history) The acceptance of the application by the certification body does not guarantee a certification. After the evaluation of physical controls and control results, the certification is mentioned. After the application is made, the control and certification firm signs a contract with the entrepreneur to sign a contract on which standards to produce. A control program is prepared according to all steps in the production and the risks at this stage and the controller is assigned. At least once a year the control is specified in the regulation. However, this number can be increased by evaluating the risks related to product and production, and unaware checks are also made. In case of nonconformity, contract can be canceled.

Analyzes are made according to the identified risks or in case of doubt, and sometimes random sampling is possible. Regarding the items to be analyzed, the materials used in conventional production, the materials that can be used in storage and transportation, and the risk of contamination are taken into consideration. Based on organic farming cultural practices (rotation, conservation of soil fertility, no use of synthetic fertilizers) is a healthy agriculture and organic crop is a result of this system. Chemical residue analysis is not a goal in this agricultural system. As a result of the control data, it is a simple metric that ensures a precise result, especially in risky and suspicious situations. Because it is not possible to say that a product is organic according to the result of chemical analysis. Residues may not occur, many pesticides can not be detected by analysis. There may be contamination from transit or from a pre-start use of the transitional period. This risk is quite high especially because there are very small parcels in Turkey. Analyzes are carried out in accredited laboratories according to ISO-17025 standards and results are only accepted in these laboratories. The controllers are preparing a report as a result of the checks made. The report is reviewed and it is determined whether the activity will receive a certificate. The decision is sent to the entrepreneur together with the report. The 'Organic Farming Entrepreneur Certificate' entrepreneur is awarded one year when the specified conditions for certification are fulfilled. Product certificates are issued for organic products. In terms of traceability of the product certificate; The name and code number of the inspection and certification body, the address, the certificate number, the product name and the characteristic, the certification status, the product quantity, the harvest year, the production year, the source of the product, the contract number, Party number. Control and settling processes have to be renewed every year of organic production.

1.2. Second Semester (1994-2002)

In the second period, some legal regulations were made at the level of regulation and organic farming activities were carried out through various "committees". A regulation with the name "Production of Ecological Methods of Plant and Animal Products" numbered 22145 dated December 24, 1994 was published. Thanks to this regulation, for the first time, organic agriculture activities in Turkey have started to be carried out under the supervision of the Ministry of Agriculture and Rural Affairs. The "Regulation on the Principles and Implementation of Organic Agriculture" entered into force in order to harmonize with the changes in the EU legislation and to make changes in the said regulation and to encompass the organic animal husbandry and aquaculture of 24812 dated 11 July 2002.

1.3. Third Term (2003-2008)

Organic Farming Law No. 5262 has been published in the Official Gazette dated December 3, 2004 and numbered 25659 with the aim of bringing the activities in the organic agriculture sector to a legal basis. Provisions have been made for strengthening the legal regulations in the organic agriculture regulations as well as for forming the basis for the duties and responsibilities of the parties and penal sanctions and for the production, consumption and inspection of organic products. The Regulation on the Principles and Implementation of Organic Agriculture, which is based on this law, has been published in the Official Gazette dated June 10, 2005 and numbered 25841. This regulation; Organic Agriculture No. 2092/91 was prepared in line with the EU Council Regulation and on the list of "Third Countries Exporting Organic Products to the EU". Exported and marketed organic agricultural products in varieties and quantities sought in the outer market were made possible by this regulation. With the adoption of additional amendments to EU legislation, the Regulation amending various articles of Organic Agriculture Principles and Implementation Regulation published in the Official Gazette dated 17 October 2006 and numbered 26322 entered into force. The organic farming legislation in Turkey consists of the "Organic Farming Law" and the "Regulation on the Principles and Implementation of Organic Farming" which shows the implementation of this law. In addition to this, the Ministry (GDHR) General Information is also available.

1.4. Fourth semester (2009 and later)

In the fourth period, as already mentioned, EU legislation no 2092/91 on organic agriculture was abolished from 1 January 2009, and directives 834/2007 and 889/2008 entered into force. "Regulation on the Principles and Implementation of Organic Agriculture" in compliance with EU legislation was implemented with the regulation published in Official Gazette No. 27676 dated 18 August 2010. A number of amendments have been made to the regulations in this date with the regulations published in the Official Gazette No. 28076 dated 6 October 2011 and the regulations published in the Official Gazette dated 14 August 2012 and numbered 28384. Logo criteria to be used in organic products; Produce and sell organic agricultural products or articles according to the current regulation; Use the logo samples specified in the regulation in their packaging. Colors to be used in logs; Green, blue, black and white. Products that do not contain these logos are prohibited from being submitted to the internal market organically, making advertisements and promotions, or applying for patents. The authority to use the tag belongs to the GDDI. This logo is made available to authorized organizations in raw materials, semi-finished or finished agricultural organic production materials produced according to the provisions of the current regulation. No organic product logos are used in the transition process products. The logo should be Turkish in the organic products presented to the inner market. Logarithms should not be larger than 20 mm in diameter and 40 mm in diameter. Colors and tones outside of the given colors should not be used.

The existing organic agriculture legislation in Turkey has been harmonized with EU legislation. Thus, the EU has assessed Turkey in the category of the country that fully implements the last directive in organic agriculture.

1.5. Development of Organic Agriculture and Turkey

With the advent of the negative effects of convective agriculture, the agriculture sector has been looking for alternatives. At the beginning of the 1900's, pioneering groups in Europe, beginning with the use of chemicals in agriculture, laid the foundation for organic farming by showing different perspectives on the concept of soil fertility (Aksoy, 2001). All of this basic and post-work activities aimed at steadily promoting the development of organic agriculture around the world, the preparation of standards and regulations, and the integration of organic farming movements under one roof. For this purpose the International Federation of Organic Farming Movements (IFOAM) was founded in 1972 as a Germany based organization. Worldwide trade of organic products has improved in the 1980s and has continued to increase in the 1990s.

Organic agriculture in Turkey began with the 1984-1985 season when raisins and figs were produced and exported organically in general export products. It has also made rapid progress in the following years. In Turkey, organic agriculture is contracted specifically for organic production for the outer market. Organic products for the internal market have started in recent years with the opening of organic retailers of large markets and companies selling organic products in big cities. Thus, organic products are introduced to the consumer.

1.6. Organic Agriculture in Turkey

Organic agriculture is developing in Turkey according to the period of 2002-2014. During the first 7 years of the 13-year period, the price of organic products has risen by 150% to 247%, an increase of 64.6%. However, between 2008 and 2014, the organic product category fell by 15.7% to 208. The number of farmers, which was 12,428 in 2002, increased to 83,751 in 2014 with an increase of 83%. The area where plant organic crops

were cultivated was 57.365 ha in 2002 and 88% in 491.977 ha in 2014. Respectively. The natural harvest area increased by 0.91% from 32.462 ha to 350.239 ha. Total production area increased by 90% from 89,827 ha to 842,216 ha. In addition, a continuous increase in the amount of production has also been observed. While the total amount of organic crop production was 310,125 tons in 2002, it increased by 80% to 1,620,466 tons in 2014.

Table 1. General Organic Farming Plant Production Data (Including Transition Process)

Years	Number of products	Number of farmers	Cultivation Area (hectare)	Natural Total Area (hectare)	Total Production Area (hectare)	Production Amount (tonnes)
2002	150	12.428	57.365	32.462	89.827	310.125
2003	179	14.798	73.368	40.253	113.621	323.981
2004	174	12.751	108.598	100.975	209.573	377.616
2005	205	14.401	93.134	110.677	203.811	421.934
2006	203	14.256	100.275	92.514	192.789	458.095
2007	201	16.276	124.263	50.020	174.283	568.128
2008	247	14.926	109.387	57.496	166.883	530.224
2009	212	35.565	325.831	175.810	501.641	983.715
2010	216	42.097	383.782	126.251	510.033	1.343.737
2011	225	42.460	442.581	172.037	614.618	1.659.543
2012	204	54.635	523.627	179.282	702.909	1.750.126
2013	213	60.797	461.395	307.619	769.014	1.620.466
2014	208	71.472	491.977	350.239	842.216	1.642.235

Source: Republıc Of Turkey Mınıstry Of Food, Agrıculture And Lıvestock.

Table 2. Organic Agriculture Crop Production Data According to Some (2014).

City	Farmer number	Area (hectare)	Production (tonnes)
Adana	170,00	2.268,92	18.699,20
Adıyaman	94,00	446,90	2.333,02
Afyon	248,00	1.088,34	7.777,99
Agrı	1.473,00	29.401,78	85.151,59
Amasya	8,00	1.207,08	131,82
Ankara	34,00	2.132	8.585,54
Antalya	39,00	12.421,07	3.188,01
Artvin	548,00	1.186,49	4.205,43
Aydın	4.231,00	21.694,65	80.300,16
Aksaray	1,00	0,61	0,56
Bartın	11,00	1.001,18	14,55
Balıkesir	71,00	831,59	1.874,92
Batman	13,00	662,75	1.769,53
Bayburt	113,00	1.283,26	6.134,90
Bilecik	60,00	93,64	1.801,15
Bitlis	371,00	6.388,14	20.033,23
Bolu	8,00	94,41	125,63

Burdur	60,00	158,93	707,97
Bursa	108,00	927,22	4.992,65
Canakkale	334,00	2.100,87	8.246,36
Cankırı	80,00	88,88	577,10
Corum	20,00	987,54	73,30
Denizli	119,00	550,93	2.665,04
Diyarbakır	224,00	801,51	2.790,36
Düzce	91,00	382,94	953,43
Edirne	1,00	30,00	2,70
Elazıg	5,00	47,11	111,40
Erzincan	223,00	3.186,54	10.582,88
Erzurum	2.929,00	32.828,33	132.317,77
Eskisehir	8,00	85,12	473,62
Gaziantep	69,00	2.036,60	3.989,89
Giresun	16,00	76,81	127,00
Gümüshane	33,00	429,32	2.695,62
Hakkari	14,00	32,30	94,05
Hatay	25,00	929,67	2.335,71
Igdır	4,00	46,82	869,10
Isparta	117,00	740,65	3.151,86
İstanbul	19,00	152,37	1.434,69
İzmir	1.161,00	144.005,77	50.282,61
K.maras	10,00	82,25	15,50
Karabük	2,00	9,04	49,01
Karaman	72,00	135,56	1.014,30
Kars	3.345,00	38.181,64	89.898,26
Kastamonu	240,00	80.675,32	6.123,58
Kayseri	6,00	79,81	88,41
Kırıkkale	5,00	3,62	40,29
Kırklareli	5,00	123,12	508,91
Kırsehir	2,00	23,49	155,01
Kilis	129,00	1.359,12	1.821,71
Kocaeli	5,00	249,51	165,01
Konya	449,00	822,52	9.162,85
Kütahya	34,00	724,85	991,56
Malatya	530,00	4.272,02	7.499,07
Manisa	1.178,00	7.297,90	45.020,68
Mardin	34,00	1.081,26	3.326,65
Mersin	211,00	100.800,76	19.370,34
Mugla	141,00	10.708,44	2.799,95
Mus	2.626,00	28.828,80	89.712,61
Nevsehir	2,00	14,17	172,68

Nigde	277,00	1.916,68	19.844,32
Ordu	429,00	1.988,34	4.412,04
Osmaniye	1,00	100,00	10,00
Rize	1.409,00	1.282,00	2.618,69
Sakarya	29,00	147,64	537,39
Samsun	622,00	2.285,86	5.650,43
Sinop	1,00	1.160,00	405,00
Sivas	513,00	8.617,55	27.960,20
Sanlı Urfa	231,00	10.661,52	42.649,93
Tekirdag	4,00	85,46	426,32
Tokat	153,00	1.564,21	6.074,70
Trabzon	257,00	361,71	706,43
Tunceli	88,00	584,94	1.919,77
Usak	47,00	148,28	202,85
Van	6.339,00	78.205,88	195.396,97
Yalova	4,00	14,19	318,47
Yozgat	2,00	102,91	107,86
Zonguldak	878,00	1.779,21	2.758,01

Source: Republıc Of Turkey Mınıstry Of Food, Agrıculture And Lıvestock

Table 3. Organic Agriculture Crop Production According to Regions (2014)

Regions	Farmer number	Area (hectare)	Production(tonnes)
Southeastern Anatolia	794	17,049,08	58,708,09
Aegean	7040	86,219,16	190,040,84
Central Anatolia	941	5,522,637	68,519,77
Eastern Anatolia	16474	192,062,52	548,435,104
Mediterranean	633	27,502,25	47,479,24
Black Sea	4291	96,568,64	39,054,14
Marmara	636	4,740,21	19,522,65

Source: Republıc Of Turkey Mınıstry Of Food, Agrıculture And Lıvestock

2. RESULT

Turkey's territory is historically hosted by agricultural activitie have done. Even Turkey partly covers the first agricultural areas in the world. 1980's among the most important resources of the Turkish economy until the ages, agricultural products was coming. Even though the weight of agriculture in the country's economy has decreased, today, agricultural activities are continuing at full speed. Turkey offers ideal conditions for agricultural activities in terms of geographical conditions. Coexistence of different climatic conditions, with a diversity of natural and cultural diversity with different ecosystems. Organic agriculture in Turkey began in 1980s with the request of European companies and It has increased in general to daylight. Aegean Region, Southeast Anatolia and East Anatolia regions are the first regions in terms of organic agricultural activities.

bAs of 2014, 30,809 farmers have realized production of 972,134 tons in 430,485 hectares. Organic herbal production in Turkey is mostly export-oriented and the demand on the domestic market is low. Despite its proximity to Europe, which is one of the most important markets, organic production in Turkey is inadequate and the production volume is insufficient.

REFERENCES

[1] Anonymous 2016a, Organik Tarımın Esasları Ve Uygulanmasına İliskin Yonetmelik (http://mevzuat.basbakanlık.gov.tr/Metin.Aspx?MevzuatKod=7.5.14217&MevzuatIliski=0&sourceXmlSearch=tar%C4%B1m). [Erisim Tarihi:11.12.2016].

[2] Anonymous 2016b, Organik Tarım Kanunu, (http://www.mevzuat.gov.tr/MevzuatMetin/1.5.5262-20100311.pdf).[Erisim Tarihi: 15.12.2016].

[3] Aksoy, U. -Tüzel, Y., -Altındisli, A. -Can, H. Z. -Onogur, E. -Anac, D. -Okur, B. -Cicekli, M.-Sayan, Y. -Kırkpınar, F. -Kenanoglu, B. Z. -Celik, S. -Arın, L. -Er, C. -Ozkan, C. -Ozenc, D.B., 2005, Organik (=Ekolojik, Biyolojik) Tarım Uygulamaları, Türkiye.

[4] Aksoy, U., 2001, "Ekolojik Tarım: Genel Bir Bakıs", Türkiye 2.Ekolojik Tarım Sempozyumu, 14-16 Kasım 2001, Antalya, s.3-11.

[5] BILEN, E., Dünya ve Türkiyede Organik Tarım. İmak Ofset, 2012. p. 8-37.

[6] ETO, Organik Tarım Girdileri, http://www.eto.org.tr [Erisim Tarihi:25/02/2017].

[7] Gıda, Tarım Ve Hayvancılık Bakanlıgı 2016,Organik Tarım Mahsulleri Üretim Verileri, http://www.tarim.gov.tr [Erisim Tarihi: 18.12.2016].

[8] Goney, S., 1987, Türkiye Ziraatinin Cografi Esasları I, İstanbul Ü. Yay. No:2600, Cografya Bölümü Yay. No:110, İstanbul.

[9] Gündüz, M. -Koc, D., 2001, "Türkiye'de Organik Tarım Ürünleri İhracatının Dünü, Bugünü ve Gelecegi", Türkiye 2. Ekolojik Tarım Sempozyumu, 14-16 Kasım 2001, Antalya, s.30-36.

[10] Ziraat Mühendisligi VI. Teknik Kongresi Bildirileri, Organik Tarım Esasları, 3-7 Ocak, 2005, Ankara, s. 291-314.

A Research on Agglomeration of Fine Coal with Different Oils

SelmaDuzyol[1]*, Seher Uzel[1], Hilal Celahir[1]

Abstract

Coal is enriched mostly with gravity methods because of the difference in its density with the gangue mineral. A large quantity of fine particles occurs during the preparation for both production and enrichment processes. Unfortunately, it is not possible to recover economically the fine sized coal due to the ineffectiveness of gravity forces occurring on these particles. Therefore, they are mostly discharged as wastes and cause a large amount of economic loss and environmental problems. Despite the oil agglomeration method allows the acquisition of fine and ultrafine mineral particles from the solution, it is not preferred remarkably because of the high prices of oil. In this study, the possibilities of enriching the fine coal with oil agglomeration technique by using different oils were investigated. For this purpose, the agglomeration experiments were performed using kerosene, mineral oil and domestic waste oil and the results were comparatively given. According to these test results, the domestic waste oil has been found to be as successful as the others. It may also be stated that the use of domestic waste oil for this purpose could also generate economic and environmental benefits.

Keywords: *Coal, Oil Agglomeration, Oil, Waste Oil.*

1. INTRODUCTION

The increase of mechanization in the coal mining methods has brought about the augmentation of the amount of fine sized coal. Due to rise of mining costs, the acquisition of these coals has become compulsory both economically and environmentally. Despite flotation is a method which mostly applied for beneficiation of fine particles, it is not effective under a certain size of mineral. Although oil agglomeration is another process which is influential on the recovery of very fine particles, the economic side of this method is discussable due to the high amount of oil consumption (the weight of used oil is about 10-50% of the processed coal [1]). However, this method has major advantages such as high efficiency and selectivity, less effectiveness of clay, ash and oxidation, simplicity of applying and the products with low moisture [2], [3].The oil agglomeration method is based on the wetting of particles with oil in the suspension. The oil coated particles come together and become agglomerates in large size with proper mixing [4], [5].

The oil agglomeration of Zonguldak bituminous coal was investigated by researchers using kerosene [6], [7], diesel oil [8], heptane, pentane, toluene and hexane [9] and it was also stated that this method would be very economic if the reduction in oil consumption and the increase in recovery of oil can be achieved [10].Therefore, in this study, the success of oil such as kerosene, mineral oil and domestic waste oil in the agglomeration process was evaluated in the light of various parameters and the findings are presented comparatively.

2. MATERIAL AND METHOD

2.1. Material

In this study, bituminous coal obtained from Karadon region (Zonguldak, Turkey) was used in the oil agglomeration experiments. The coal was ground under 53 microns using a ceramic ball mill. The ash content of the feed was determined as to be 13.8%. A 75 micron sieve was chosen as a test criterion. Three types of oil such as kerosene, mineral oil and domestic waste oil were selected for the tests.

---

[1]*Corresponding author: Selcuk University, Department of Mining Engineering,42075, Selcuklu/Konya, Turkey. selmad@selcuk.edu.tr*

2.2. Method

Oil agglomeration experiments were carried out in a 400 ml volume of glass cell with four barriers. These barriers were attached onto interior surface of the cell in order to increase collision of coal particles. The coal sample, weighed in a certain amount, is thoroughly mixed with 100 ml of distilled water and then 300 ml of water is also added. Two stages of agitation were performed between the coal sample and water due to the high level of hydrophobicity that the coal sample has for a good dispersion, oil was added into the suspension and the system was stopped after the sufficient agglomeration time period. Then, the slurry was poured onto the test sieve. The agglomerates composed from the agglomeration test were separated by washing away from the non-agglomerated portion with tap water. When the agglomerated parts remained on the test sieve, the non-agglomerated parts passed under the sieve with water. After the washing process, the agglomerates were dried in an oven at pre-determined temperature of 105 ºC and then weighed at room temperature. At the end, the ash analysis was performed on the agglomerates. The success of the agglomeration experiments were interpreted by the Combustible Recovery (CR). The CR was calculated by following equation.

$$CR\% = \frac{A(100 - A_{ash})}{F(100 - F_{ash})} * 100 \qquad (1)$$

Where, A; the percentage of agglomerate, F; the percentage of feed, A_{ash}; the ash content of agglomerates, F_{ash}; the ash content of feed.

3. RESULTS AND DISCUSSIONS

3.1. Effect of oil amount

The effect of oil concentration on the agglomeration was investigated for three types of oil. The mixing velocity was kept constant at 1000 rpm. 5 grams of coal sample were agglomerated with oil for a period of 5 minutes. The obtained results from three oil samples were presented in Fig 1. It is clear from the Figure 1, when the oil concentration was increased, the CR% of obtained agglomerated was also increased. However, in the experiments in which the amount of oil was further increased, the agglomerates obtained became sticky paste form. Similar behaviour was seen in the previous experiments [11], [12]. Therefore, the optimum oil amount was selected as to be 1 ml for kerosene and mineral oil and 2 ml for waste oil.
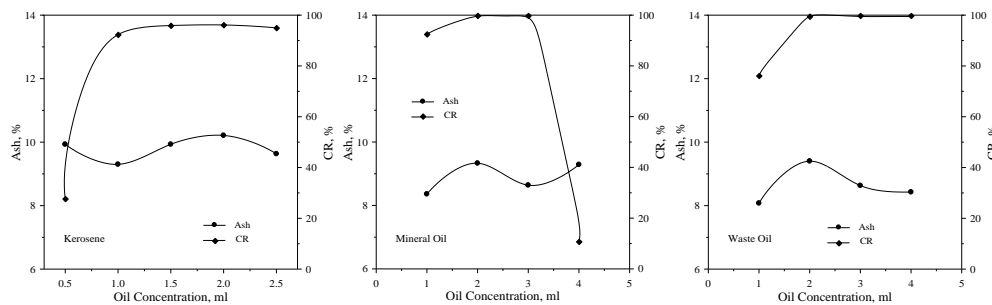
Figure 1. The variation of ash content and CR of agglomerates with oil concentration.

3.2. Effect of Agglomeration Time

The agglomeration time is one of the important parameters to realize a successful agglomeration. Agglomerates cannot be obtained if not enough time is allowed. Therefore, the optimum agglomeration times for kerosene, mineral oil and waste oil were also investigated. The amount of oil was kept constant as to be 1 ml for kerosene and mineral oil and 2 ml for waste oil. The acquired results were given in Figure 2. The optimum agglomeration time was determined as to be 5 min for kerosene and 2 min for mineral oil and waste oil. In addition it is to be said that the results obtained with waste oil are much more successful than expected. Especially by the use of waste oil, the shape and size of the gained agglomerates were more spherical and bigger than the others (Figure 3).
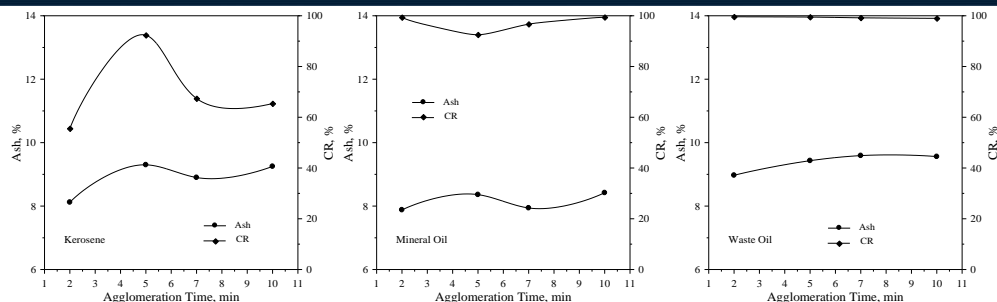
Figure 2. The variation of ash content and CR of agglomerates with agglomeration time

kerosene   mineral oil   waste oil
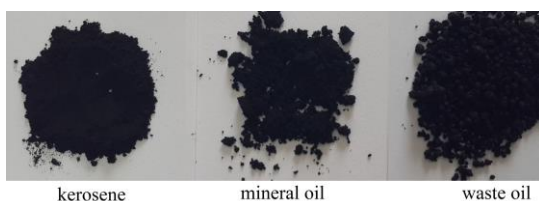
Figure 3. The obtained agglomerates by using kerosene, mineral oil and domestic waste oil.

3.3. The Oil Agglomeration Performance of Domestic Waste Oil

The results ascertained with waste oil are quite successful. Therefore, the experimental studies were continued in this respect. In the following stage, the agglomeration tests were carried out by increasing the amount of coal. For this purpose 2 ml waste oil was used for each 5 g of coal and the test results are given in Table 1. From the Table 1, the ash contents of the agglomerates were found to vary between 8.6% and 9.2% and the CR% values were found as close as to the value of almost 100%. Furthermore, the spherical shape of the agglomerates obtained were not deteriorated (Figure 4).

Table 1.The ash content and CR values of agglomerates

Coal Amount	Ash (%)	CR (%)
5	8.9	99.8
10	9.2	99.6
15	8.6	99.8
20	8.6	99.7
25	8.6	99.6
30	8.7	99.8
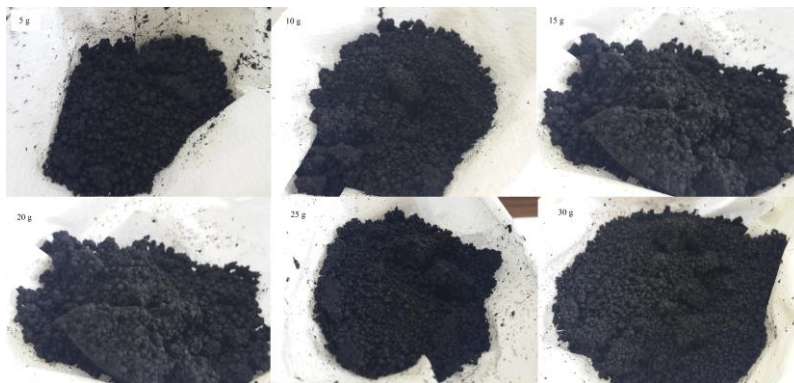
Figure 4. The agglomerates gained from the agglomeration tests by using domestic waste oil (5-30 grams of coal).

4. CONCLUSIONS

In this study, the behaviour of oil agglomeration of bituminous coal was investigated by using kerosene, mineral oil and domestic waste oil. The ash content of coal is 13.8%. The results obtained for all three types of oils are quite successful. The most important finding determined from this study is that the domestic waste oil brings about very successful results in oil agglomeration of bituminous coal. Therefore, the usage of this kind of oils in agglomeration will disclose two major benefits. The first one, significant energy loss will be prevented economically. The second one is that the environmental problems due to the waste oil will be avoided.

REFERENCES

[1]. H. Hacıfazlıoglu, "AzdavayKomürününYag Aglomerasyonu ve Bazı Onemli Calısma Parametrelerinin Etkilerinin Belirlenmesi", Madencilik, vol. 47, No. 4, pp. 3-11, 2008.
[2]. R. H. Yoon, *Advanced Coal Cleaning, Coal Preparation Book*, Part: 2, J. W. Leonard and B. C. Hardince, Eds., 1991.
[3]. A. Yamık, Y. İ. Tosun and N.Günes, "Komürden Külün ve Kükürdün Arındırılması", Türkiye 9. Komür Kongresi, Zonguldak, pp. 201-210, 1994.
[4]. C. E. Capes, "Principles and Applications of Size Enlargement in Liquid Systems", Fine Particles Processing, AIME, Vol.2, pp. 1442-1462, 1980.
[5]. C. E. Capes and K. A. Jonasson, "Application of Oil-Water of Coals in Beneficiation," Interfacial Phenomena in Coal Technology, Surfactant Science Series, v.32. 1988.
[6]. İ. Ünal, Z. Aktas andA. Olcay, "Bitümlü Komür ve Linyitin Yag Aglomerasyonu", Türkiye 12. Komür Kongresi Bildiriler Kitabı, Zonguldak, 2000.
[7]. Y. Cebeci, U. Ulusoy and S.Simsek, "Investigation of The Effect of Agglomeration Time, pH and Various Salts on The Cleaning of Zonguldak Bituminous Coal by Oil Agglomeration", Fuel, vol. 81, pp.1131-1137, 2002.
[8]. Z. Aktas, "Some Factors Affecting Spherical Oil Agglomeration Performance of Coal Fines", International Journal of Mineral Processing, vol. 65, pp. 177-190, 2002.
[9]. N. Gence, "Coal Recovery from Bituminous Coal by Aggloflotation with Petroleum Oils", Fuel, vol. 85, pp. 1138-1142. 2006.
[10]. E. K.Aksay, V.Arslan, H.Polat, "Toz Komürlerin Zenginlestirilmesinde Yag Aglomerasyonu Yontemive Yenilikler", İstanbul Yerbilimleri Dergisi, vol. 23, pp. 97-108, 2010.
[11]. S. Duzyol, "The effect of hydrophobicity and surface tension on wettability based process in mineral processing", pH.D Thesis (in Turkish), Konya, p.158, 2009.
[12]. S. Duzyol and C. Sensogut, "Investigation of the oil agglomeration of Eskiceltek lignites in Turkey". Proceedings of 14th International Multidisciplinary Scientific GeoConference& EXPO, SGEM, 3, pp. 889-896, 2014.

BIOGRAPHY

Selma Düzyol is an Associated Professor in the Mining Engineering Department at Selcuk University where she has been a faculty member since 2001. Duzyol completed her undergraduate and Ph.D. studies at Selcuk University. Her research interests lie in the area of mineral processing. In recent years, she has focused on the recovery of ultrafine sized coal. In addition, she has improved herself on the occupational health and safety in recent years.

Investigation of Optimal Sedimentation of Marble Wastewater

Selma Duzyol[1]*, Samet Yucel[1], Sadettin Kayhan[1], Yasin Kara[1]

Abstract

Natural stones are one of the oldest construction materials that can be processed commercially following their extraction from nature. The Turkish natural stone sector has an important place in the world natural stone market. Marble production processes consist of cutting, washing, wiping and polishing steps. As a result of these processes, a large amount of process wastewater, especially rich in solid particles, is formed. Physico-chemical methods are widely used in the treatment of these wastewaters. In the present work, the treatment of marble wastewater obtained from a private company was investigated by the use of various polymers (1858U as an anionic, N100 as a non-ionic and SPP365 as a cationic). In order to reach the best sedimentation results, the flocculation experiments were carried out with different polymer combinations to examine the process parameters such as pH, polymer concentration, stirring speed and time. The results for all type of polymers from the sedimentation tests were obtained for pH, polymer concentration, stirring speed and time as 6.6, 2 mg/L, 200 rpm and 3 min., respectively. In addition, the different polymer combinations were also evaluated and the best consequent was acquired from the N100 and 1858U dual combination as to be 3.6 nephelometric turbidity unit (NTU).

Keywords: *Marble Wastewater, Sedimentation, Polymer.*

1. INTRODUCTION

Turkey has become one of the 10 biggest leader natural stone producers in recent years due to the different colours and quality of Turkish marbles. The annual natural stone production of Turkey is about 11.5 million tones and the capacity of the handling plants is approximately 6.5 million m^2 [1]. Almost all of the production is realized by the private sector. When the consecutive processes such as cutting, washing, wiping and polishing are performed, the large amount of waste water is formed. 50-150 m^3 process water is used for medium marble production plant and the loss of water is about 20% [2]. This process water contains solid particles and some polymer based chemicals are used to settle these particles. Therefore, the reuse of process water is made possible by this way. If the water has larger particles, serious problems come out with polishing, and clogging [3]. Therefore it is important to investigate the sedimentation of particles in waste water of plants. In general, the synthetic polymers having especially anionic characters are used for the treatment of marble waste waters [4].

The main objective of this paper is to determinate the optimal sedimentation conditions of marble waste water by using different types of polymers. In addition, some parameters known to affect the sedimentation such as pH, polymer concentration, stirring speed and time are considered and the sequential addition of polymers is also debated.

2. MATERIAL AND METHOD

2.1. Material

In this paper, some sedimentation experiments under the various conditions were carried out on the marble wastewater obtained from a private marble processing plant. The solid concentration and the turbidity of waste water were measured as to be 2.44% and 17.512 NTU, respectively. The Hatch brand portable turbidimeter (2100p model) was used for this purpose. The 250 cm^3 volume of the suspension was poured into the measuring cylinder and the change of turbidity value was pursued with time. Due to the certain amount of liquid was taken from the solution for turbidity measurements; each test was performed

---
[1]* *Corresponding author: Selcuk University, Department of Mining Engineering, 42075, Selcuklu / Konya, Turkey. selmad@selcuk.edu.tr.*

independently so as to avoid the alteration of concentration and volume of suspension in time. The time dependent variation of solution turbidity was given in Figure 1.
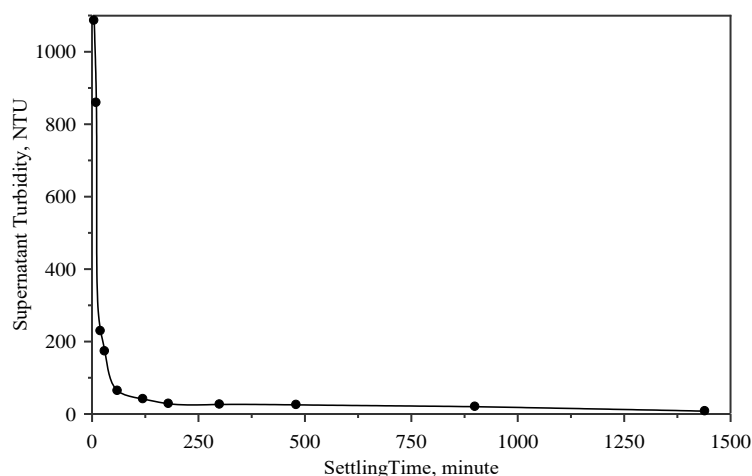
Figure 1. Time dependent solution turbidity of marble wastewater.

When the sedimentation curve of suspension having the 17.512 NTU of beginning turbidity was examined, it was observed that the turbidity values were 859 NTU and 7.6 NTU after 10 minutes and 24 hours, respectively without polymer. When considering the working conditions are excessive and consumed water is also high in the marble cutting plant, the long sedimentation time introduce both waste of time and economic loss. Accordingly, it is important to establish the appropriate conditions so as to reduce the sedimentation time and polymer addition for reaching maximum sedimentation rate. For this purpose, three types of polymer were selected for the sedimentation experiments. The properties of polymers were given in Table 1. The polymers concentrations used for tests were 0.01% (w/w). The 0.1 gram of polymer was dissolved in a 100 ml volume of distilled water and then the solution was diluted 10 times.

Table 1. The properties of polymers used in sedimentation tests.

Name	Type	Appearance	Charge	Molecular Weight
1858U	anionic	powder-white	medium	medium
N100	non-ionic	powder-white	none	high
SPP365	cationic	powder-white	high	high

2.2. Method

The suspension was stirred throughout the experiments to stay homogeneous and hinder the hanging particles settling. The 250 ml volume of solution taken from this suspension was filled into the cell and stirred at 500 rpm for 1 minute in order to obtain uniformity. Then, 1 minute after the pH regulation the polymer was added into the suspension and mixed for 2 minutes. Thereafter, the mixing rate was regulated to minimum (33 rpm) and the suspension was continued stirred for 1 minute in order to cluster particles and grow the particle sizes. At the end, the system was stopped and the solution was taken into the 250 ml volume of measuring cylinder. After the cylinder was reversed carefully for ten times, it was placed to the flat surface for settling at 10 minutes. At the end of the settling, a certain amount of supernatant (approx. 30 ml) was taken from the solution for the turbidity measurements. The sedimentation rate was calculated by following equation.

$$\text{Sedimentation Rate } \% = 100 * (T_0 - T_f)/T_0 \tag{1}$$

Where, T_0; the turbidity value of suspension after 10 minute settling time without polymer (859 NTU), T_f; the turbidity value of suspension after the experiments.

3. RESULTS AND DISCUSSIONS

3.1. Effect of pH

The pH of the suspension has major effect especially when using the charged polymers in sedimentation process. Therefore, the effect of pH on the sedimentation was investigated for three types of polymer and obtained results were given in Figure 2. The 1 ml (0.4 mg/L) volume of polymer was used for each test.

Additionally, the stirring speed and time was 200 rpm and 2 minutes, respectively. From the Figure 2, it was obvious that, the maximum sedimentation rate was reached for three types of the polymer at the 6.6 of pH value. The suspension become more stables due to the repulsive of particles each other when the pH value increases and therefore, the sedimentation decreases [5], [6].
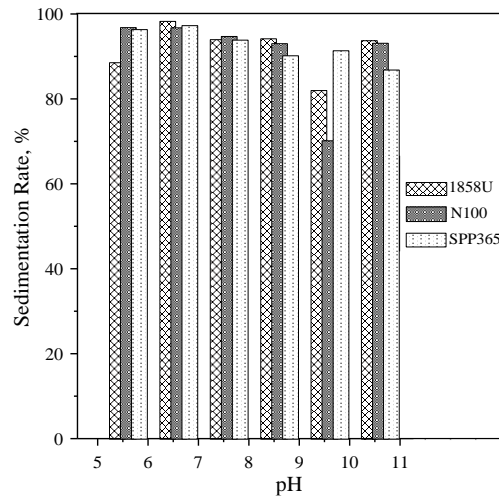
Figure 2. The sedimentation of marble wastewater with pH.

3.2. Effect of Polymer Concentration

Figure 3 shows the sedimentation results gained various polymer concentrations. The stirring speed, time and pH were constant as to be 200 rpm, 2 minutes and 6.6, respectively. The sedimentation rate was enhanced with the increasing polymer concentrations. It is known that, the polymers have less effective at low amounts. Their sedimentation ability can be seen more specifically when their addition reached at least cover the half of the particle surface [7], [8]. When the polymer amount augmented from 0.2 mg/L to 0.4 mg/L, the sedimentation rates were raised up 40%, 33% and 18% for 1858U, N100 and SPP365 polymers, respectively. In addition, the best sedimentation results were obtained at 2 mg/L polymer concentrations. For all types of polymer, the achieved sedimentation was over the 98% at this concentration value. Tasdemir and Erdem [9] were stated similar results for synthetic wastewater containing suspended particles.
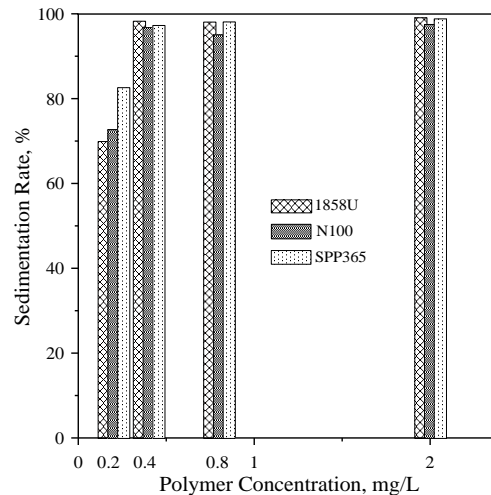
Figure 3. The sedimentation of marble wastewater with polymer concentration.

3.3. Effect of Stirring Speed and Time

The stirring of suspension is necessary for reaching best sedimentation by encountering of particles with each other. Therefore, the optimum conditions for velocity and time should be provided [10]. In order to determine the appropriate stirring speed, the sedimentation experiments were conducted by using the 2 mg/L polymer concentration for 100, 200 and 300 rpm of mixing velocities. The findings were given in Figure 4. From the Figure 4, it was observed that the sedimentation results obtained at all speeds were close to each other, but as

the mixing speed was increased, the sedimentation was decreased. The reason for that the forces holding the particles together was broken up at high speeds and increase the turbidity of the suspension, resulting in a decrease in sedimentation. The optimum stirring speed was determined as to be 200 rpm for all types of polymers. The results of the tests determined for the stirring time were also given in Figure 5. When the results were examined, over 98% of the sedimentation was achieved for all three polymers.
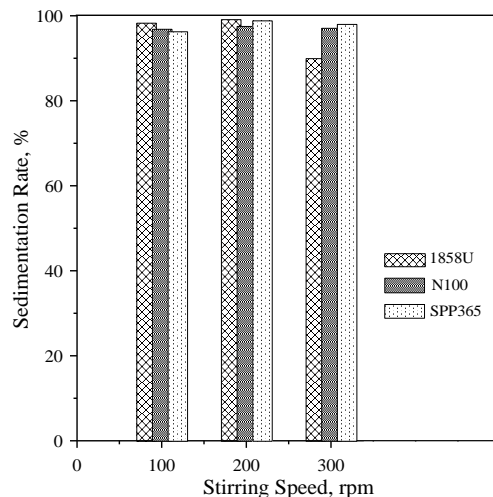
Figure 4. The sedimentation of marble wastewater with various speeds.
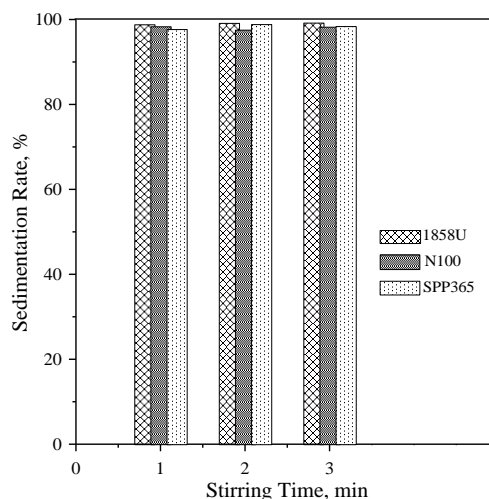
Figure 5. The sedimentation of marble wastewater with various stirring times.

3.4. Dual Combination of Polymers

Although the polymers themselves are highly effective in sedimentation processes, the synergistic effect of the simultaneous and sequential usage of advanced dewatering processes is known [10]. For this reason, various polymer combinations were investigated in this part of the study and the reached sedimentation values were compared (Figure 6). The polymer concentration, pH, stirring speed and time were constant as to be 2 mg/L, 6.6, 200 rpm and 2 minutes, respectively in the experiments. Although some combinations (1858U+N100 and SPP365+1858U) revealed the acceptable sedimentation results, the best conclusion of %99.6 was reached from the N100+1858U combination. The turbidity values from the dual combinations were also given in Table 2 separately. It was found that, not only the sequential addition of anionic and cationic polymers but also the mixture of anionic and non-ionic polymers disclosed an improvement in the sedimentation process [11], [12], [13].
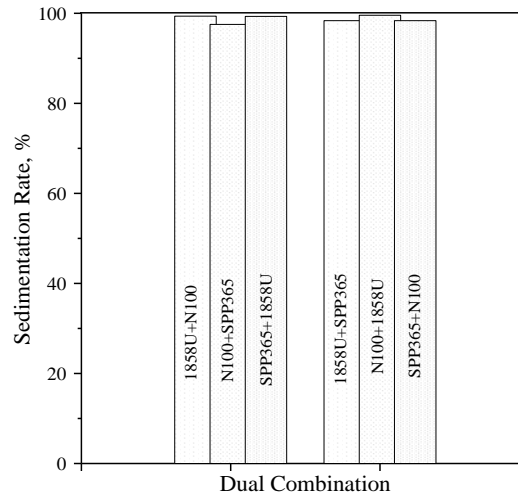
Figure 5. The sedimentation of marble wastewater with various polymer combinations.

Table 2. Turbidity values obtained from dual combination of polymers

Dual	Turbidity	Sedimentation (%)
1858U+N100	5.4	99.4
N100+SPP365	21.1	97.5
SPP365+1858U	5.7	99.3
1858U+SPP365	13.9	98.4
N100+1858U	3.6	99.6
SPP365+N100	13.8	98.4

4. CONCLUSIONS

The following results were disclosed in the sedimentation experiments of the wastewater obtained from the marble cutting plant containing fine particles;

- The initial turbidity of the suspension was 17,532 NTU and the turbidity after 10 minutes of free precipitation was 859 NTU.
- The optimum pH value was determined as 6.6 and over %97 of sedimentation was reached at this pH value.
- As the concentration of the used polymers was increased, the sedimentation rate was also increased and the highest sedimentation was reached at the concentration of 2 mg /L.
- Stirring speed and time were determined to be optimum as 200 rpm and 3 minutes.
- When 1858U and N100 polymers were used sequentially, a favourable sedimentation result was achieved.
- It is known that anionic and non-ionic polymers are very effective in sedimentation of the suspension of marble dust. However, it should also be said that sedimentation with cationic polymer SPP365 was also quite successful.

REFERENCES

[1]. Natural Stone Sector Report, Republic of Turkey Ministry of Economy, 2016.
[2]. M. Kavaklı, "Mermer İsletme Tesisleri Proses Atık Sularının Ozellikleri, Arıtılması ve Kontrolu" in *Proc. MERSEM'2003*, 2003, 313-326.
[3]. H. Acar, "Mermer İsleme Tesisi İcin Atık Su Arıtma Sistemi Kurulması ve İsletilmesinde Dikkat Edilmesi Gereken Hususlar", in *Proc. MERSEM'2001*, 2001, 289-296.
[4]. B. Ersoy, "Mermer İsleme Tesisi Atık Su Arıtımında Kullanılan Flokulantların Tanıtımı, in *Proc. MERSEM'2003*, 2003, 449–462.
[5]. J. Gergory, Particles in water: Properties and Process, University College London, UK, 2005.

[6]. J. Bratby, "Coagulation and Flocculation in Water and Wastewater Treatment", London, UK: IWA Publishing, 2006.

[7]. Hogg R. Flocculation and dewatering, *Int. J. Miner. Process.,* vol. 58, pp. 223–236, 2000.

[8]. P. Somasundaran, and K. K. Das, *Flocculation and Selective Flocculation,- An Overview*, S. Atak, G. Onal and M.S. Celik, Eds., in Innovations in Mineral and Coal Processing, AA. Balkema /Rotterdam /Brookfield; 1998.

[9]. T. Tasdemir and V. Erdem, "Flokulasyon Yontemi İle Atıksudan Askıda Tanelerin Giderimi", Eskisehir Osmangazi Universitesi Muhendislik Mimarlık Fakultesi Dergisi, vol: 23, No:1, pp. 109-121, 2010.

[10]. J. Gregory and S. Barany, Adsorption and flocculation by polymers and polymer mixtures, *Advances in Colloid and Interface Science*, vol. 169, pp. 1–12, 2011.

[11]. S. Barany, M. L. Meszaros, and J. Skvarla, Effect of polyelectrolyte mixtures on the electrokinetic potential and kinetics of flocculation of clay mineral particles, *Colloids and Surfaces A: Physicochemical and Engineering Aspects*, vol. 383, pp. 48-55, 2011.

[12]. L. Ringqvist and P. Igsell, Dual polymer system in peat dewatering, *Energy Fuels,* vol. 8, pp. 953-959, 1994.

[13]. Y. Zhu, X. Tan and Q. Liu, Dual Polymer Flocculants for Mature Fine Tailings Dewatering, *Canadian Journal of Chemical Engineering*, vol. 95, pp. 1-8, 2016.

BIOGRAPHY

Selma Duzyol is an Associated Professor in the Mining Engineering Department at Selcuk University where she has been a faculty member since 2001. Duzyol completed her undergraduate and Ph.D. studies at Selcuk University. Her research interests lie in the area of mineral processing. In recent years, she has focused on the recovery of ultrafine sized coal. In addition, she has improved herself on the occupational health and safety in recent years.

Stability of Embankment Built on the Slope

Askın Ozocak[1], Ertan Bol , Sedat Sert

Abstract

In this study, the stability of embankments built on a slope has been investigated. Embankment of 3 to 11 m height was placed on the soil surface of %10-30 slope. Slopes formed by the embankment are around 45 degrees. Embankment was constructed as a three step benches. After the construction, partial collapses occurred in the benches and tension cracks formed on the surface. The region is exposed to short period of intensive or long period of continuous rainfall.

In the study area, 6 rotary drilling studies were carried out. It is understood that the environment is composed of gravel and clayey units. Gravels are round and spherical in shape indicates that this region is dominated by stream beds in the geological past. In order to determine the parameters shear box tests were carried out in the laboratory. Soil layers with different shear resistance were considered when the boundaries of the layers are determined for the analyzes to be performed.

Earthquake forces were required to take part in the solutions due to the proximity of the region to the North Anatolian Fault. Stability analyzes pursued on all sections with different software have considered both earthquake conditions and different water pressures. The same solutions for the parameters used for the analyzes were also made with the Plaxis 2D software based on the finite element method. The number of security decreases as the groundwater level increases with the existing embankment, in all earthquake solutions it is less than 1. The rock fill (berm) system placed in the toe to play the role of increasing the passive resistance against slipping in order to ensure the safety of the area. Structural arrangements are proposed such as ditches, which will allow drainage without reaching the potential water supply.

Keywords: *Slope Stability, Embankment, Earthquake, Pore Water Pressure*

1. INTRODUCTION

In this study, stability of an embankment built on the slope has been investigated and sugestions have been given for providing the slope stability. 10-30% of the ground surface with natural inclination was filled up to 11 meters height on the heel. A sports filed and tribune platform is being planned on the embankment surface. The investigation area has an area of approximately 37500 m^2. The slope where the embankment is formed has a slope of about 45°. Within the scope of the study, land investigations and drilling studies were carried out. Laboratory data were submitted for final geological and geotechnical evaluations and precautions to be taken to get rid of the effects of the mass movements that might come into play.

According to field obsevations there are natural cuts at the north-eastern of the embankment. This figure shows that the environment is composed of gravelly and clayey units. Gravel particles are circular and spherical so it points out that this region dominated by stream beds in past geological period. (Sekil 1).

The filling is constructed in the form of three stepped palms. The width of the steps are about 5.0 meters and the height is about 4.0 meters at its highest point. It has been seen that the partial slips in the steps have been occured. It has been understood that these movements occur during the time of heavy rainfall when the environment becomes saturated. On the other hand, tension cracks appeared on the surface of the steps which are the news of a movement that may come again (Figure 2). It has also been seen that some slippings existed at the some steps.

Figure 1. A view of a section of the natural soil stratums

Figure 2. (a)Tension cracks appeared on the steps (b)Slippings existed at the steps

2. SITE INVESTIGATIONS

Six borehole were dirilled at different points in the investigation area (Figure 3). $SPTN_{30}$ impact numbers were determined in the drillings and disturbed samples were taken from the every 1.5 meters. The results of the standard penetration tests carried out during the drilling are shown in the Figure 4. The depth of the natural soil has become shallow near the eastern and north eastern parts of the study area.The depths of entry into the natural soil layer are presented in the Table 1. From here it is understood that the thickness of embankment is in the range of 3 to 15 meters. In addition, filling thickness increases as in the area goes through to west and southwest.
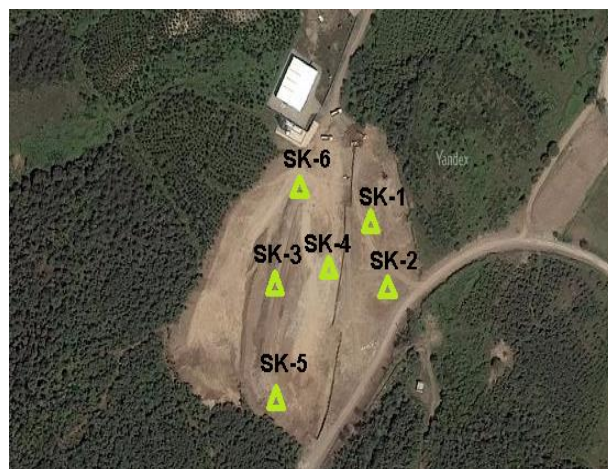
Figure 3. Borehole locations.
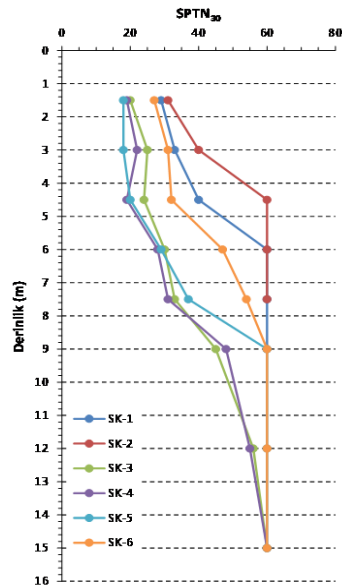
Figure 4. In-situ SPTN30 values.

Table 1. Natural soil layer and gwt depths.

BH No	Natural soil layer depths (m)	GWT
1	6.00	-
2	3.00	-
3	15.00	-
4	9.00	-
5	9.00	-
6	9.00	-

The cross-sections shown by the shape of the soil profiles with the drilling data have been obtained. According to this, in all sections there are clay-schist layers (yellow areas) in the upper part and filling layers (green areas) in the lower part representing the soil profiles (Figure 5). Different shear resistance are considered when the boundaries of the layers are determined.
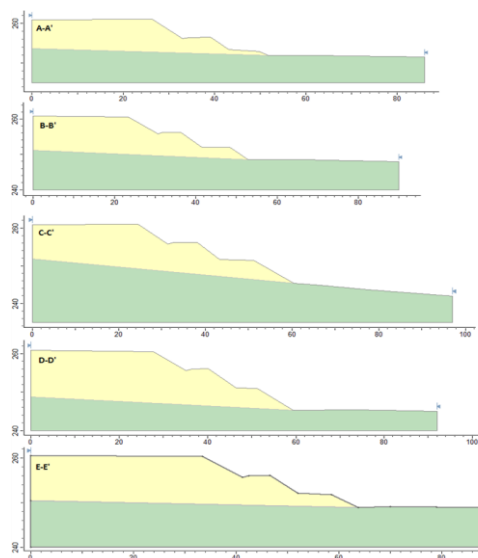
Figure 5. Analysed soil sections.

3. LABORATORY STUDY

Classification tests were carried out on the disturbed and undisturbed samples taken by drilling and soil classes were determined according to TS1500 in Geotechnical Laboratory odf Sakarya University. Physical test results are shown in the Table 2. Filling material representing the upper part of the study area is composed mostly of gravelly silty and clayey sands. The natural soils called as pieced shale in the drilling logs are symbolized as uniform gravel. It is understood that these rounded and spherical gravel particles structure are of serpentine origin.

Table 2. Physical soil properties

BH	z (m)	Color	w_n	w_L	w_P	I_P	I_L	% FC	% Gravel	% Sand	Class
1	2.50	kKY	25	46	21	25	0.16	41	28	31	**SC**
1	3.00	YGB	9	NP	NP	NP	-	1	2	97	**GP**
1	6.00	YKB	12	NP	NP	NP	-	0	99	1	**GP**
2	1.50	YGB	10	NP	NP	NP	-	1	95	4	**GP**
2	3.00	YGB	10	NP	NP	NP	-	1	97	2	**GP**
2	6.00	YGB	20	NP	NP	NP	-	0	100	0	**GP**
3	2.50	KY	19	46	19	27	0.01	57	25	18	**CI**
3	3.00	kKY	23	63	30	33	-0.18	35	23	42	**SC**
3	6.00	kKY	25	61	32	29	-0.26	57	11	32	**MH**
3	9.00	kKY	27	**55**	24	31	0.11	56	12	32	**CH**
3	12.00	KY	26	47	27	20	-0.07	42	12	46	**SM**
3	15.00	YG	7	NP	NP	NP	-	0	100	0	**GP**
4	1.50	kKG	18	56	21	35	-0.09	42	31	27	**GC**
4	2.50	YK	37	39	29	10	0.75	46	12	42	**SM**
4	4.50	kKG	34	53	26	27	0.30	45	0	55	**SC**
4	7.50	kK	32	40	21	19	0.56	42	28	30	**SC**
4	11.00	KY	33	48	19	29	0.47	89	0	11	CI
4	12.00	KG	24	61	23	38	0.03	42	30	28	**GC**
4	13.50	YG	2	NP	NP	NP	-	1	98	1	**GP**
5	2.50	KY	25	49	23	26	0.10	35	29	36	**SC**
5	3.00	KS	39	38	25	13	1.09	33	42	25	**GM**
5	6.00	K	32	42	24	19	0.47	27	38	35	**GC**
5	9.00	GY	11	NP	NP	NP	-	1	98	1	**GP**
5	11.00	K	34	54	19	35	0.41	69	16	15	**CH**
5	15.00	GY	5	NP	NP	NP	-	1	97	2	**GP**
6	1.50	kYG	24	52	29	23	-0.21	30	29	41	**SM**
6	2.50	YK	21	45	20	25	0.02	40	27	33	**SC**
6	4.50	kYG	31	49	33	16	-0.17	64	14	22	**MI**
6	9.00	YG	7	NP	NP	NP	-	0	100	0	**GP**
6	15.00	kYG	5	NP	NP	NP	-	0	100	0	**GP**

a: light, k: dark, K: brown, Y: green, G: gray, B: beige, S: black

The shear-box and triaxial test results on undisturbed samples are summarized in the Table 3 and Table 4. These data were used for stability analyzes.

Table 3. Results of shear box tests.

BH No	Depth (m)	e	$\rho(kN/m^3)$	S_r (%)	c (kPa)	ϕ (°)
SK-1	2.50-3.00	0.91	18.13	93.21	6	27
SK-3	2.50-3.00	0.86	18.39	94.26	42	13
SK-4	2.50-3.00	0.97	18.78	100.00	34	27
SK-5	2.50-3.00	0.81	19.23	100.00	13	32
SK-6	2.50-3.00	0.72	19.65	100.00	69	24
SK-4	11.00	0.88	18.47	97.75	0	33

Table 4. Results of triaxial tests

BH No	Depth (m)	e	(kN/m^3)	S_r (%)	c (kPa)	(°)	c' (kPa)	'(°)
SK-4	2.50-3.00	1.04	18.04	98.97	4	25	0	31

4. STABILITY ANALYZES

According to the laboratory tests, it was found that the cohesion on the average of 30 kPa and the shear resistance angle of 25° were appropriate. According to the experimental study on the sample representing the natural environment, it is found that this environment is uncohesive in drainage conditions and the slip resistance angle is about 33°. There is no definite conclusion in the literature about the choice of the horizontal earthquake (seismic) coefficient in the landslide analyzes. However, Table 5 summarizes the values that some researchers have suggested in this regard. Horizontal earthquake acceleration coefficient was taken as $k_h = 0.15$ and 0.20 in the landslide analyzes for the study area.

Table 5. Recommended horizontal seismic coefficients (Melo&Sunil, 2004)

Horizontal seismic coefficient, k_h	Explanation	
0.05-0.15	USA	
0.12-0.25	Japan	
0.10	Severe Earthquakes	
0.20	Violent Earthquakes	Terzaghi (1950)
0.30	Catastrophic Earthquakes	
0.10-0.20	GS>1.15	Seed (1979)
0.10	Major Earthquakes	Corps of Engineers (1982)
0.15	Great Earthquakes	
PHA/3-PHA/2	FS>1.0	Marcuson (1983)
PHA/2	FS>1.0	Hynes-Grifin (1984)
FS=Factor of safety, PHA= Peak horizontal acceleration, g		

Both the earthquake condition and the different water pressures are taken into consideration in the stability analyzes performed for all sections. A summary of all the analysis results is presented in the Table 6. Factors of safety corresponding to different values of the pore water pressures ($r_u = 0.10$, 0.20, 0.30 and 0.40) are shown for static and dynamic ($k_h = 0.15$ and 0.20) cases. Values in which the factors of safety decrease to critical situations (FS <1.00) are marked with yellow dyed and bold font.

Table 6. Factors of safety in the stability analysis

	A-A'			B-B'			C-C'			D-D'			E-E'		
r_u	Static	k_h	k_h	Static	k_h 0.15	k_h 0.20	Static	k_h 0.15	k_h 0.20	Static	k_h 0.15	k_h 0.20	Static	k_h 0.15	k_h 0.20
0.0	2.81	1.84	1.64	2.48	1.68	1.49	2.22	1.51	1.36	2.06	1.45	1.32	2.62	1.75	1.57
0.1	2.58	1.67	1.48	2.27	1.52	1.36	2.02	1.37	1.23	1.88	1.32	1.20	2.40	1.59	1.42
0.2	2.34	1.50	1.34	2.05	1.36	1.22	1.82	1.22	1.10	1.70	1.19	1.07	2.17	1.43	1.28
0.3	2.08	1.33	1.19	1.82	1.20	1.07	1.60	1.07	0.96	1.52	1.05	0.95	1.93	1.27	1.13
0.4	1.82	1.16	1.03	1.65	1.03	0.96	1.39	0.92	0.82	1.32	0.91	0.82	1.67	1.10	0.98

In the Figure 6 the factors of safety numbers corresponding to the different pore water pressures are graphically displayed for static and earthquake situations. Pore water pressure values have a significant effect on slope safety. Drying in the profile increases the factorof safety in static conditions. However, it is found that there is a safety problem in the sections where the pore water pressure is increased and the filling thickness is higher in earthquake situations.
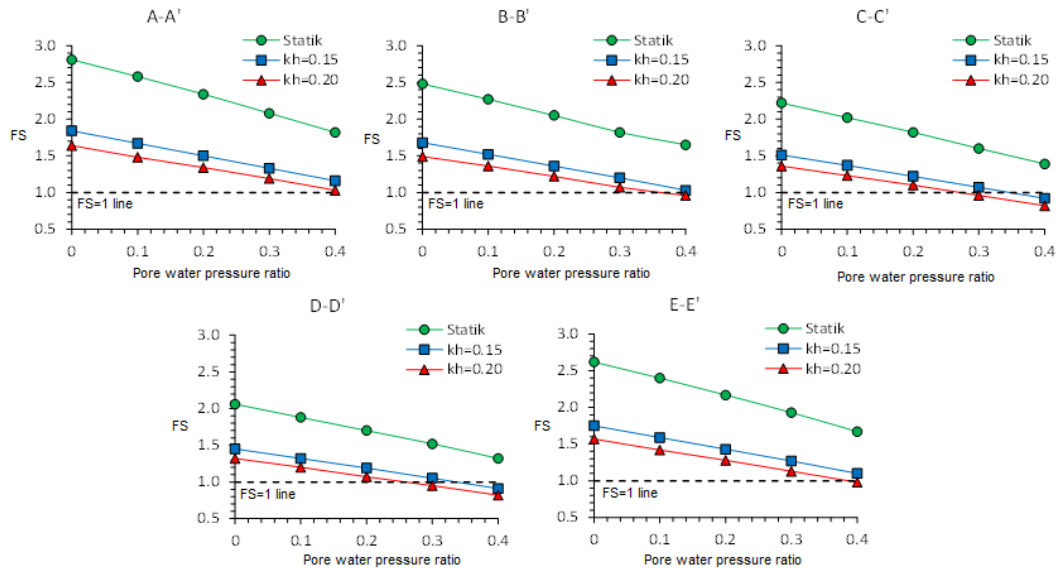
Figure 6. Variation of FS's with different earthquake and pore water pressure conditions

Increasing pore water pressures in C-C 'and D-D' sections, where the fill height is maximum, reduce safety critical levels even in static conditions. This situation can be understood when the calculated results of the cross sections are taken as k_h=0.20 and r_u=0.30 (Figure 7 and 8).
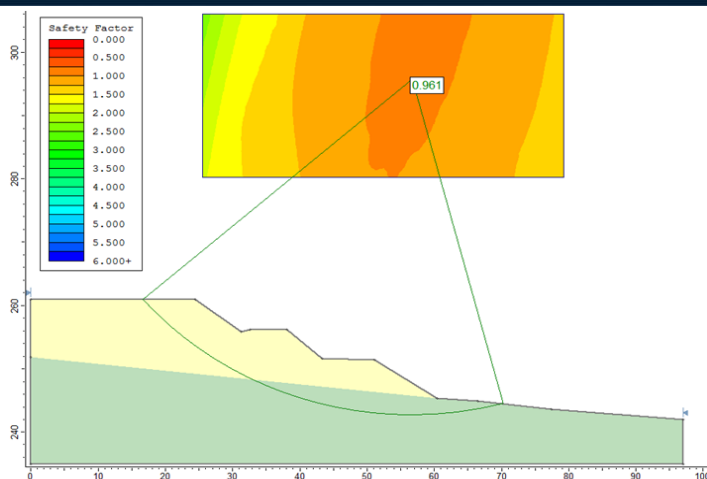
Figure 7. Stability Analysis of C-C' section (kₕ=0.20 and rᵤ=0.30).
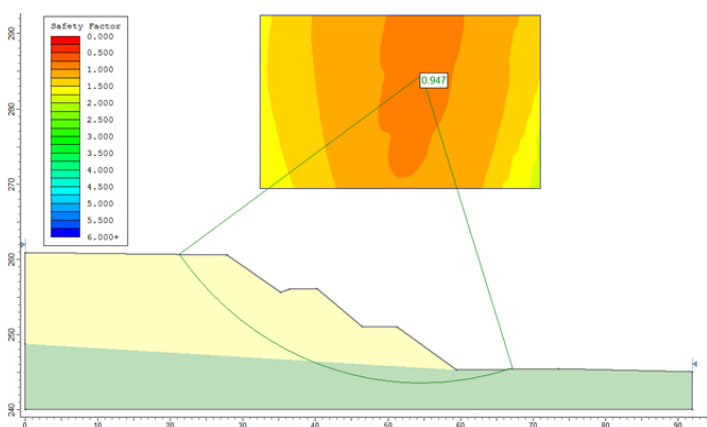
Figure 8. Stability Analysis of C-C' section (kₕ=0.20 and rᵤ=0.30).

The same solutions for the parameters used for the analysis were also made with the Plaxis 2D software based on the finite element method. Selected soil parameters for different units in these analyzes are shown in Table 7.

Table 7. Soil parameters used in Plaxis 2D analysis

Name	Embankment	Natural Soil	Berm
Material Model	Hardening soil	Hardening soil	Hardening soil
Material Type	Drained	Drained	Drained
ρ_n (kN/m³)	18.84	18.47	23
ρ_d (kN/m³)	19	20	23
$E_{50}'^{ref}; E'$ (kPa)	5000	10000	30000
$E_{oed}'^{ref}$ (kPa)	5000	10000	30000
$E_{ur}'^{ref}$ (kPa)	15000	30000	90000
m	0.8	0.7	0.5
c' (kPa)	30	1	5
ϕ' (°)	25	33	40

ψ (°)	0	3	10
P_{ref}	100	100	100
$\upsilon'_{ur}; \upsilon'$	0.2	0.2	0.2
OCR	2	2	2
R_f	0.9	0.9	0.9
Tension strength(kPa)	0	0	0

The effect of groundwater on stability was investigated in plaxis solutions. One of the most critical sections for this was the C-C 'section where analyzes were performed for different groundwater levels. Sections showing different GWT states used in the analyzes are presented in Figure 9. In these sections, Model 1 shows the dry state, and Model 6 shows the case where GWT is maximum in the fill.
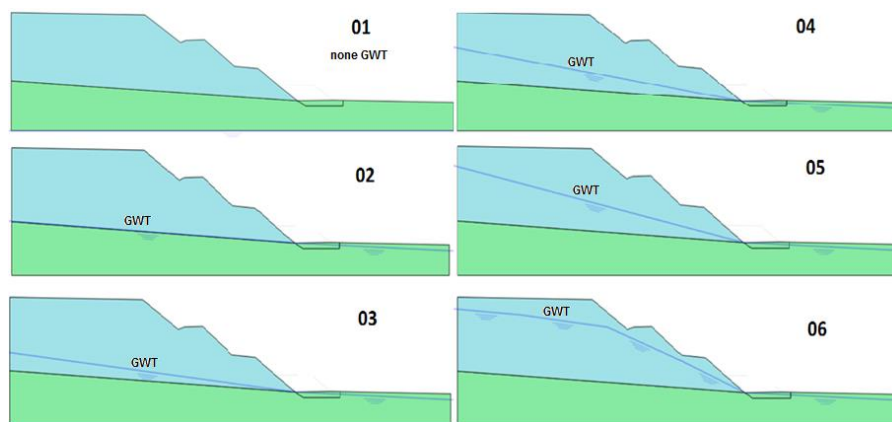
Figure 9. Different GWT states that have been resolved at C-C 'section (drained solution).

Table 8 shows the factors of safety numbers obtained with Plaxis software solutions. As the ground water table increases, factor of safety decreases, and it is smaller than 1 in the models of 5 and 6. It is understood that safety will be provided if berm is used as a precaution.

Table 8. Factors of safety numbers in plaxis 2D analysis

Model	With Berm	No Berm
1	2.01	2.36
2	1.79	2.07
3	1.69	1.94
4	1.25	1.77
5	0.86	1.63
6	0.76	1.56

Figure 10 shows the Plaxis solution of Model 2. In this section GWT is modeled parallel to the natural ground surface. In this case, the developing pore water pressure profile is given in the figure. The solution was carried out under drainage and static conditions. Factor of safety was 1.79. Loading on heel, in an other saying the berm solutions ensures safety in the cross sections.
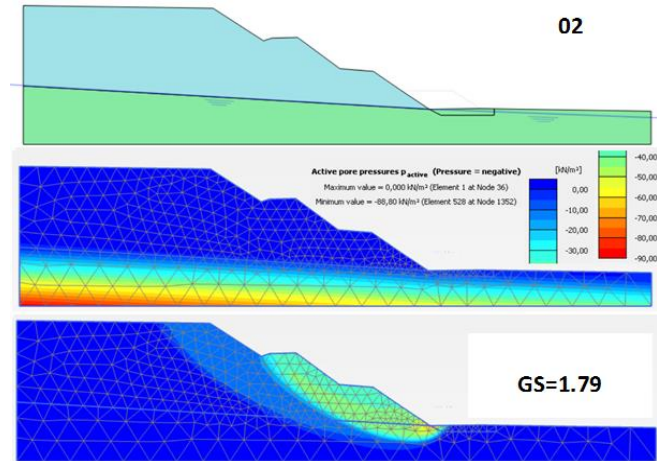
Figure 10. Plaxis solution results in Model 2 drainage and static conditions.

5. EVALUATION

It is understood that in stability analyzes run with different softwares above, the embankment provides safety in static and dry conditions. However, in the field observations, the presence of local failures was observed in the filling steps. This is declared to be the result of extreme precipitation, mass movements at different scales in the region are frequently confronted. For this reason, even though groundwater is not reported at the time of drilling, it is evident that GWT will increase for filling occasionally due to the climatic conditions, or the saturation will go down from the surface. In such cases, it is necessary to safely maintain the stability of the embankment. As can be seen from the sections above, analyzes have been conducted according to varying groundwater conditions. At the same time, due to the proximity of the region to the North Anatolian Fault, earthquake forces were required to take part in the solutions. In addition, the pressure increase of the pore water brings the stability of the system to a critical state. Hence, different options can be provided to ensure the safety of the system in situations where both the earthquake and the pore water pressures are maximum. Jet-grout, micro-pile or passive resistance enhancing rock filler (BERM) options in the heel can be considered. Here, it is thought that the rock filling (berm) placed in the heel will play an increasing role in the passive resistance against slipping (Figıre 11). At the same time, the rock filling material will allow easy drainage of the water that accumulates in the system.
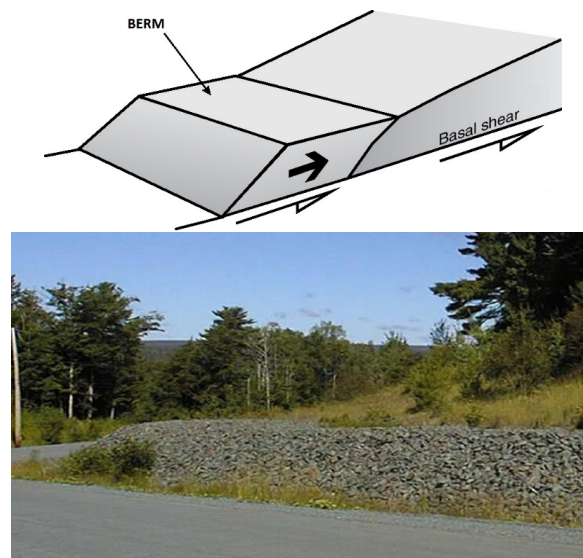
Figure 11. Berm application on the heel

The application can be constructed in various ways. It is possible to build by compressing the coarse rock filling material with the inclination of about 40 degrees. However, the mass can also be raised as a gabion retaining wall (Figure 12). In this system, the rockfill material is placed modularly into pre-prepared corrosion resistant wire cages and stacked at the desired height. The system will still provide drainage and will be more stable.

Figure 12. Gabion application with rock filler

Stability analyzes were repeated by placing berm in the C-C 'and D-D' sections which have the highest critical values in the working area. Table 9 summarizes the results of all analyzes performed in these sections. It can be understood as a result that safety can be increased even under various conditions of earthquake pressures.

Table 9. Summary of stability analysis results

r_u	C-C'			D-D'		
	Static	$k_h=0.15$	$k_h=0.20$	Static	$k_h=0.15$	$k_h=0.20$
0.00	2.08	1.59	1.43	2.02	1.57	1.43
0.10	2.08	1.45	1.29	2.02	1.45	1.30
0.20	1.99	1.30	1.15	1.96	1.30	1.17
0.30	1.76	1.14	1.01	1.74	1.16	1.03

With berm application (Figure 13), the factor of safety increases to 1.01 in the section C-C' with high filler thickness representing the most critical parts of the fill and increases to 1.03 in the section D-D' for $k_h=0.2$ and $r_u=0.3$ (Figure 14 and 15). In this case the slope of the steps forming the filling is seen to be appropriate. However, since the filler material contains fine grains in a considerable proportion, superfluous flows with precipitation will occur. Slope surfaces must be protected in order to avoid this situation. To avoid this situation slopes can be coated with geocells and head ditches can be formed the bottom of the steps. Figure 16 shows a typical geocell example and its application.
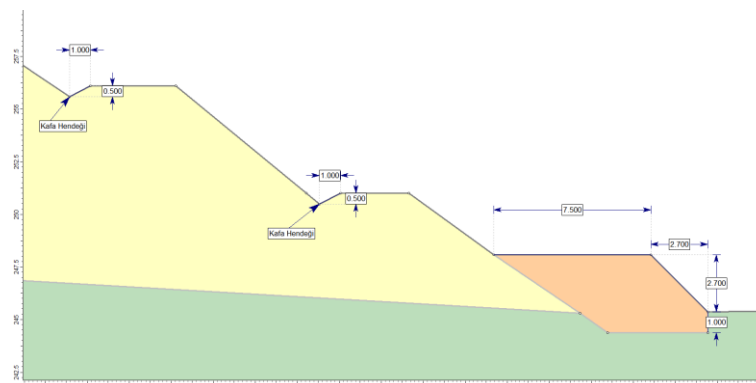
Figure 13. The location and dimensions of the berm and head trenches recommended for the D-D' section.
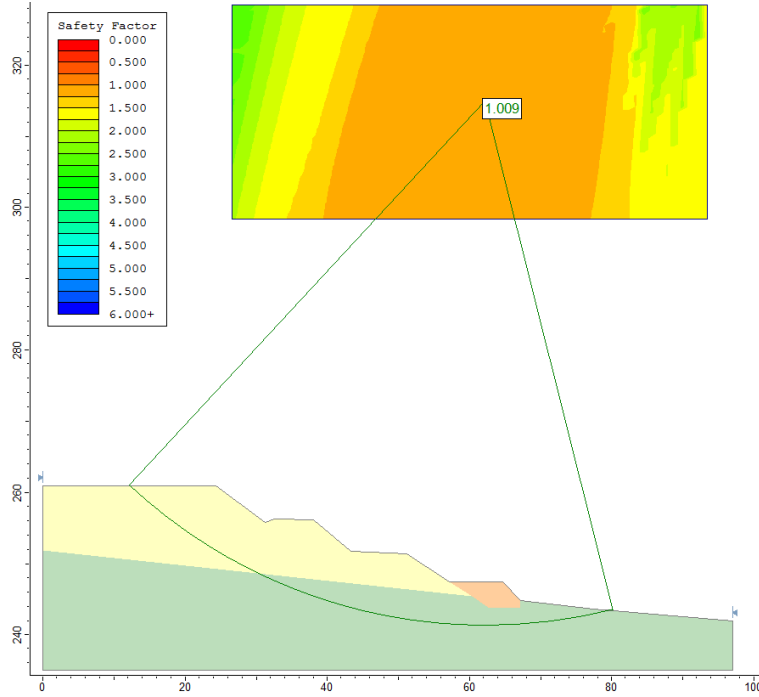
Figure 14. Stability analysis in C-C' section with berm (k_h=0.20 ve r_u=0.30).
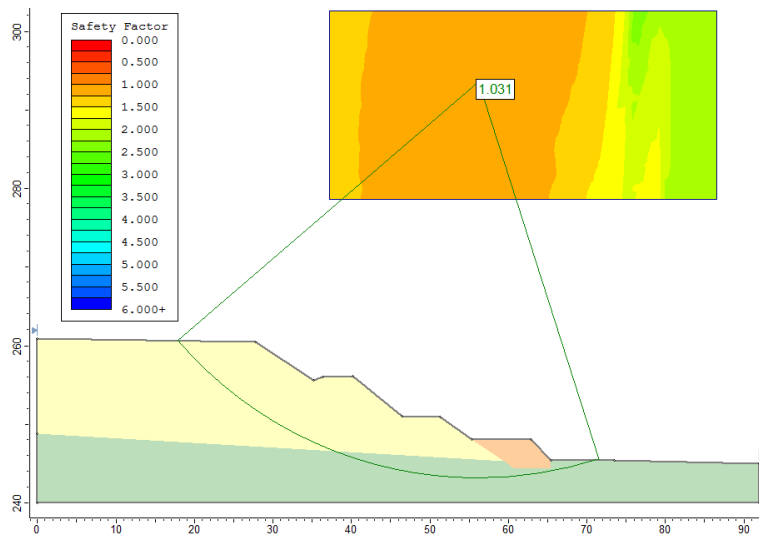
Figure 15. Stability analysis in D-D' section with berm (k_h=0.20 ve r_u=0.30)

Figure 16. Slope surface protection with geocell material

582

6. CONCLUSIONS

Pore water pressure value has a significant effect on the stability of the slope. Drying increases the factor of safety and increasing of the pore water pressure brings the stability to the critical state. Different options may be offered to increase the stability at either earthquake or high pore water pressure conditions. Jet-grout, micro-pile and berm (rock fill) options can be considered. Rock fill material (berm) placed over the heel plays role to increase the slope stability. At the same time rock fill material can provide the drainage of the accumulating water. It is possible to place the berm material with the slope of 40 degrees. Moreover this mass can be raised as a gabion retaining structure. In critical section the factors of safety get values higher than 1, under 0.3 pore water pressure ratio and 0.2 horizantal earthquake acceleration factor with berm application. Slopes of the steps of the existing fill seem appropriate. But filling material has high ratio of fines content so superficial flowing will occur because of the precipitation. To avoid this situation slopes can be coated with geocells and head ditches can be formed the bottom of the steps.

REFERENCES

[1]. Corps of Engineers. *Slope Stability Manual EM-1110-2-1902*. Washington, D. C.:Department of the Army, Office of the Chief of Engineers, 1982.
[2]. Marcuson WF, Franklin AG. *Seismic Design, Analysis, and Remedial Measures to Improve the Stability of Existing Earth Dams - Corps of Engineers Approach*, in Seismic Design of Embankments and Caverns, T.R. Howard, Ed., New York, ASCE, 1983.
[3]. Melo, C. and Sunil, S. *Seismic Coefficients For Pseudostatic Slope Analysis*. 13th World Conference on Earthquake Engineering, Vancouver, B.C.,Canada, Paper No. 369, August 1-6, 2004.
[4]. Hynes-Griffin ME., Franklin AG. *Rationalizing the seismic coefficient method*. U.S. Army Corps of Engineers Waterways Experiment Station, Vicksburg, Mississippi, MiscellaneousPaper GL-84-13, 21 pp, 1984.
[5]. Terzaghi K. *Mechanisms of Landslides*. Engineering Geology (Berkeley) Volume, Geological Society of America, 1950.
[6]. Seed HB. *Considerations in the earthquake-resistant design of earth and rockfill dams*. Géotechnique, Vol. 29, No. 3, pp. 215-263, 1979.

Design and Implementation of FPGA-Based Relation Matrix Similarity Unit for Color Images

Ismail Koyuncu[1], Ferzan Katırcıoglu[2]

Abstract

The similarity image processing is defined as a two-dimensional gray level image that obtained using three-dimensional color properties. Because of its parallel processing capability, FPGA chips are widely used in the image processing field which requires high processing volume. In this study, a high-speed FPGA-based similarity image unit design based on the relation matrix has been implemented to transform of two-dimensional similarity images of color images. In the present study, firstly, a similarity image has been obtained by using color image on Matlab. Processing time and visual results obtained from the study have been presented. In addition, a similarity image unit design based on the relation matrix in the 32-bit IEEE 754 1985 floating-point number standard the FPGA has been implemented using the Xilinx ISE simulation program with the VHDL language. Performance results from Matlab and FPGA-based designs have been compared. The maximum operating frequency of the FPGA-based similarity image unit is 90 MHz. The presented FPGA-based unit can produce 42 thousand results in 1 second. In the future studies, FPGA-based high-speed edge detection, filtering, and segmentation can be performed using this study presented.

Keywords: *Color Image Processing; Similarity Image; Relation Matrix; FPGA.*

1. INTRODUCTION

The correlation examining the characteristic of uniformity between the stimulants is defined as similarity. The situations where similar objects are classified or similar groups are differentiated are frequently encountered in every period of life. Therefore, the measurement of similarity is a very important instrument to find the degree of similarity between two groups or two objects [1]. Similarity image can be defined as the gray level image achieved by using the color features of pixels. Achieved as a result of the analysis of color difference values between pixels, the black-and-white image performs the operation of converting the three-dimensional image information at color space into two-dimensional features [2]. Regarding the image processing studies, first, the similarity feature of adjacent pixels of color images was calculated with the fuzzy logic rules [1]. In another study, the values of each pixel in the color image were calculated by using the similarity relation matrix and normalized to the greatest grey level [3]. On the similarity image achieved through the same method, by using the region growing algorithm, segmentation was realized with the similarity relation of the color image pixels [4]. Differently from the color image applications, the automatic segmentation algorithm grounding on the similarity of adjacent pixels based on refraction in medical images was suggested [5]. In another study, the reversible image storage method based on histogram shifting was suggested for medical images. The similarity of the adjacent pixels on images was researched by using assumption technique and the residual histogram method was used for the envisaged errors of the main computer image in order to store the hidden data on the diagram proposed [6]. Another study suggested the super-pixel algorithm that uses similarities of pixels and that adapts k-means clustering approach in order to efficiently produce super pixels [7]. The second section of this study briefly mentions the similarity method based on relation matrix for color images. The third section presents the design of FPGA-based similarity unit and the chip usage statistics. The fourth section includes the results obtained from the implementation of the proposed similarity method in Matlab environment. In the fifth section, the results of the FPGA-based similarity unit are interpreted. And the last section provides the evaluations related to the both methods.

---

[1]*Corresponding author: Afyon Kocatepe University, Faculty of Technology, Department of Electrical-Electronics Engineering, Afyon, Turkey. ismailkoyuncu@aku.edu.tr.*

[2]*University of Duzce, Duzce Vocational High School, City Center Campus, 81100, Duzce, TURKEY, ferzankatircioglu@duzce.edu.tr.*

2. SIMILARITY IMAGE BASED ON RELATION MATRIX FOR COLOR IMAGES

Similarity image is the black-and-white grey image having the feature information between colors achieved as a result of the analysis of color difference values between pixels, and it performs the operation of converting the three-dimensional image information at color space into two-dimensional features. On the color images, first, a mask panning operation of 3x3 is performed [8]. The purpose of the operations performed for the central pixel within the panning mask is to achieve the relation matrix as well as to find the mean value of this matrix and to write this mean value to the address where there is the central pixel on the similarity image. In this context, it is required first to find distances between pixels within mask in order to achieve the relation matrix. The distance between pixels is defined as the geometrical difference between colors of two pixels. When it is assumed that there are two pixels as *i* and *j* within the mask, the distance between two pixels as $P_i(R_i,G_i,B_i)$ and $P_j(R_j,G_j,B_j)$ is determined by using the following Euclidean distance [9].

$$d_{ij} = \sqrt{(R_i - R_j)^2 + (G_i - G_j)^2 + (B_i - B_j)^2} \tag{1}$$

In the equation (1), dij is the distance between pixels, and Ri, Gi and Bi means RGB values of i pixel and Rj, Gj and Bj means RGB values of j pixel. In order for dij distance values between pixels to meet the operability condition, they should have some features such as symmetry and non-negativity [10]. The exponential function in the equation (2) has been used to calculate the similarity value of the two pixels [11]. For this reason, the distribution range of similarity measurement varies by (0.1). It is concluded that the two pixels are not similar if the value obtained from this function is near-zero, and that they are similar if the value is near-one [1].

$$S_{(i,j)} = exp^{(-\frac{d_{ij}}{D})} \tag{2}$$

In the equation (2), *D* value is the normalization coefficient and the results achieved can be graded by assigning 32, 64, 128 and 255 values. 9 pixels within the mask create a 9x9 similarity relation matrix among themselves and with their adjacent, and the relevant similarity relation matrix is provided in the equation (3).

$$\begin{bmatrix} S(1.1) & \cdots & S(1.9) \\ \ldots & \ldots & \ldots \\ S(9.1) & \cdots & S(9.9) \end{bmatrix} \tag{3}$$

The arithmetic mean of the relation matrix provided above in the equation (3) is calculated and the similarity value to be included within the similarity image for central pixel is calculated according to the equation (4).

$$S_{center} = \frac{1}{81} * \sum_{i=1}^{9} \sum_{j=1}^{9} S_{ij} \tag{4}$$

This value obtained is assigned to the newly created similarity image by considering the address of the central pixel on the real image and the mask panning is realized for the next operation. This operation is continued until the similarity value of the last pixel in the lower-right corner of the real image is found.

3. FPGA-BASED SIMILARITY UNIT FOR COLOR IMAGES

FPGA chips have certain features as they can be reprogrammed and they can process parallel signal [12, 13]. In this study, a similarity image unit has been designed for color images on FPGA. The design prepared has been coded of 32-bit IEEE 754-1985 floating point number and by using VHDL. The top-level block diagram of the FPGA-based similarity image unit designed is provided in Figure 1. The FPGA-based similarity unit operates as a pipeline. The unit input has 1-bit Start and Clk signals and 6 data input signals of 32 bits. The unit output has Sim_out having the result value of 32-bit unit, and 1-bit Ready signal indicating that this signal is generated. The designed FPGA-based unit generates first Sim_out value, after 2135 clock cycles following its receipt of the first Start signal and required input signals, and then Ready signal becomes "1".
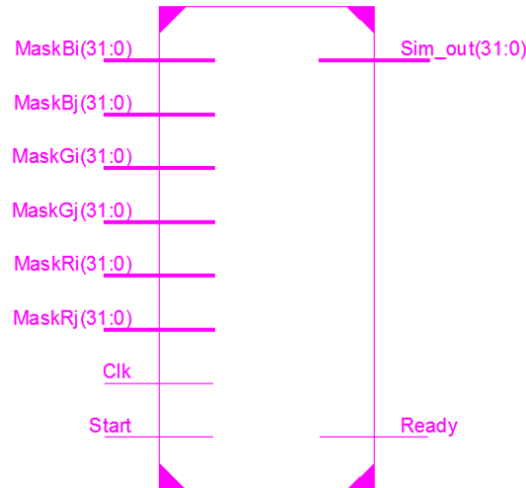
Figure 1. Top-level block diagram of the FPGA-based similarity image unit

The second level block diagram of the FPGA-based similarity image unit is provided in Figure 2. The modules used within the unit such as adder, subtractor, multiplier and divider have been created by using the design instrument Xilinx ISE. On the system, first Mask(R/G/B)i values received when Start signal becomes "1" are subtracted from Mask(R/G/B)j values and this value is squared. Then, this signal value is added and its square root is calculated. In this study, the square root value calculated is divided by -D value of the floating point number standard and is sent to the exponential operation module and then each 81 operation results are added. The value added is divided by 81-value of the floating point number standard and multiplied by 255-value of the floating point number standard, and Sim_out signal value is achieved. At that moment, Ready signal value becomes "1". When the unit does not generate new Sim_out values, it sends Ready "0" value.
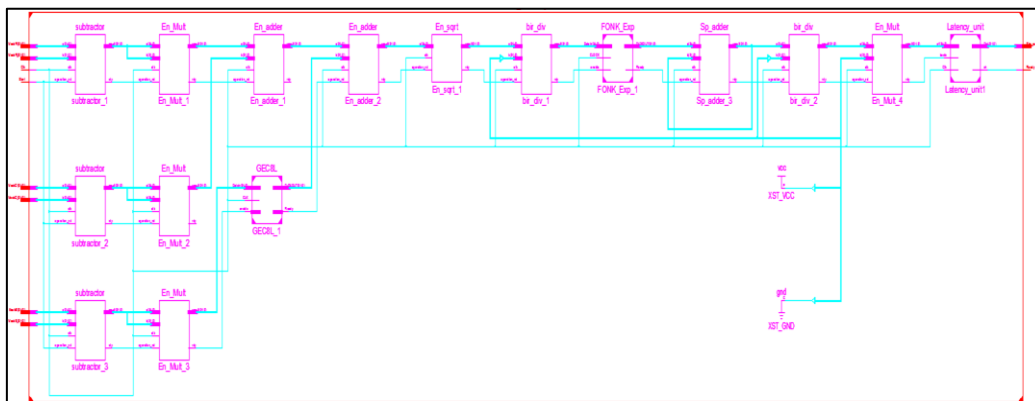
Figure 2. Second level block diagram of the FPGA-based similarity image unit

4. SIMILARITY IMAGE RESULTS IN MATLAB ENVIRONMENT

The house and water color images in Figure 3 used in the study are 256x256 pixels and of jpeg format. They have been implemented with Matlab version in the computer having specifications of Intel(R) Core(TM) i5-4200U CPU 1.60 GHz 2.30 GHz processor, 6-GB RAM and 64-bit Operating System. Each has been achieved for the normalization values of 32, 64, 128 and 255 D. Duration of achievement for each different D normalization similarity image and Top Signal Ratio (TSR), determining the similarity between the original image and the similarity image, have been taken into consideration. In Figure 4, it can be observed that when D normalization coefficient is higher, the brightness of the image is also higher.

On TABLE I, it is concluded from the lower TSR value that the real image becomes more distant when D value is higher. The increase of D value has also slightly increased the duration. The transition from the color image to the similarity image has taken a long time of 91 seconds in average.

TABLE 1. Sımılarıty Image TSR ve Operatıng Tımes.

	D	TSR_R	TSR_G	TSR_B	Time (s)
Home	32	16.757	15.164	15.639	87.774
	64	14.918	13.145	13.533	90.285
	128	13.649	11.942	12.283	90.770
	255	12.866	11.236	11.563	90.295
Water	32	10.433	11.911	8.228	90.990
	64	9.639	10.804	7.447	91.211
	128	9.063	10.001	6.917	91.699
	255	8.676	9.471	6.575	91.632
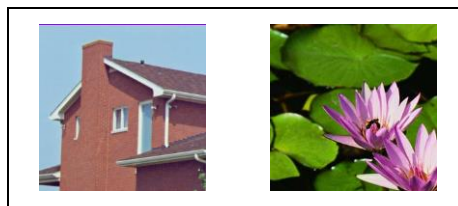
Figure 3. House and water images used in the study

| a. House D=32 | b. House D=64 | c. House D=128 | d. House D=255 |
| e. Water D=32 | f. Water D=64 | g. Water D=128 | h. Water D=255 |
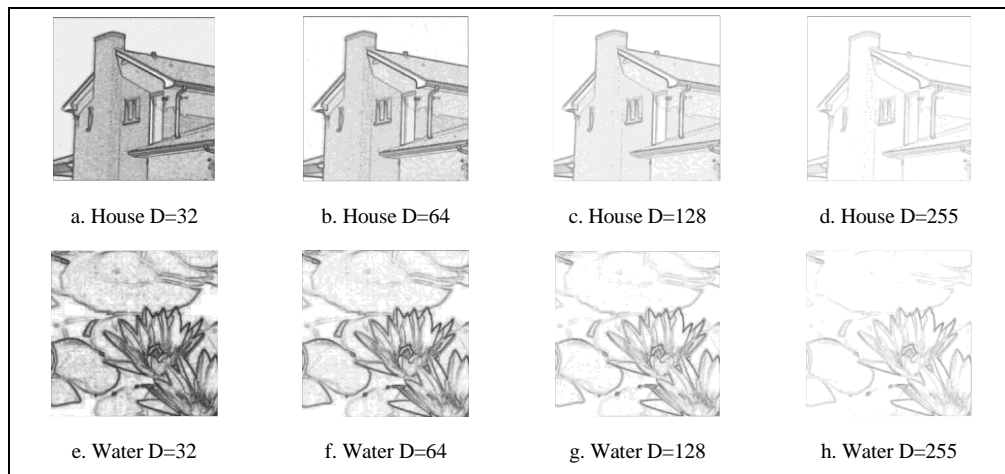
Figure 4. Similarity images

5. TEST RESULTS OF FPGA-BASED SIMILARITY UNIT

In this study, the FPGA-based similarity unit for color images provided in the third section have been synthesized for Virtex-6 chip family (device: XC6VLX240T, package: FF784, speed: -3) by using Xilinx ISE 14-1 Project Navigator Design Tools (X-ISE-DT). Following the synthesizing operation, the Place and Route (P&R) operation has been realized. The FPGA chip source usage rates achieved following the P&R operation and the unit's lowest operating period as ns are presented in TABLE II. The highest operating frequency of the FPGA-based unit is 90,246 MHz. For the purpose of testing the designed unit, the testbench file has been created by using X-ISE-DT. During the test period of the unit, the sample data set has been taken from the house image values on Matlab provided in the fourth section. The unit has been tested by coding the values taken in the floating point number standard in the testbench file created. Figure 5 presents the test results for the similarity unit implemented by using X-ISE-DT on FPGA. Although the unit is in the 32-bit floating point number format, it has been showed in the hexadecimal number standard on the X-ISE-DT simulator in order to perform the operations in an easier way during the test phase of the design. The FPGA-based similarity unit can calculate the operation of achieving the similarity image from the house image provided in the study within 1,538 seconds.

TABLE 2. FPGA Chıp Statıstıcs of The Sımılarıty Image Unıt.

Virtex-6 FPGA chip	Number of Slice Register	Number of Shift Register	Number of Slice LUT	Number of Occupied Slice	Number of IOB	Minimum Period (ns)	Processing Time of Similarity Image Unit (s)
Used	8,611	460	9,978	2,940	227	11.081	1.538
Rate of Used (%)	2	1	6	7	56		
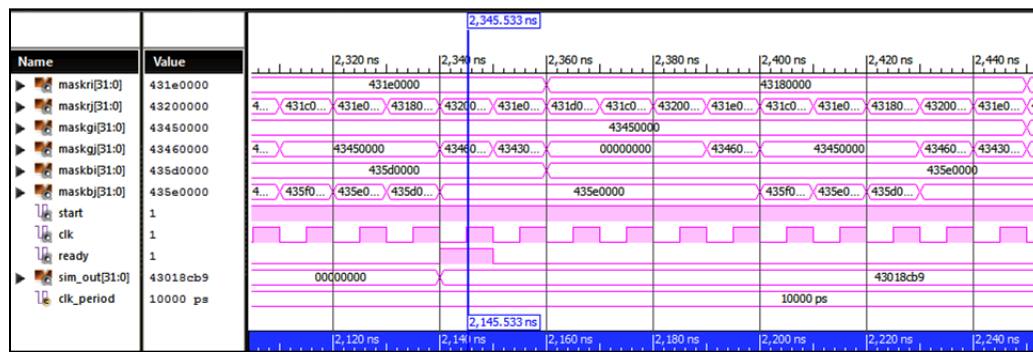
Figure 5. ISE Simulator results of FPGA-based similarity unit

6. CONCLUSIONS

In this study, the high-speed FPGA-based similarity image unit grounding on relation matrix has been designed with the purpose of converting color images into two-dimensional similarity images. For this purpose, the similarity image has been achieved by using the color image on Matlab and the similarity image based on relation matrix has been achieved by using FPGA-based Xilinx ISE simulation program. According to the results obtained, while the duration of operation for the similarity application on the Matlab-based house image is 87,774 seconds, the duration of operation for the same image is 1,538 seconds on the FPGA-based unit. The FPGA-based similarity image unit has provided a quite high acceleration gain compared to the Matlab-based application. The FPGA-based similarity unit presented in this study forms a basis for real-time and high-speed image processing applications intended to be realized in the future. In future studies, FPGA-based high-speed edging, filtering and segmentation applications may be realized by using the unit presented in this study.

ACKNOWLEDGMENT

REFERENCES

[1]. R. Demirci,"Rule-based automatic segmentation of color images", Int.J. *Electronics and Communication (AEu)*, 60: 435-442, 2006.

[2]. F. Katircioglu, "Segmentation of color images based on relation matrix and edge detection" ,Master of Science , Dept. Electrical Education, Duzce Universtiy, Duzce, Turkey, 2007.

[3]. R. Demirci, *"*Similarity relation matrix-based color edge detection", *AEU-international journal of electronics and communications,* 61(7): 469-477, 2007.

[4]. R. Demirci and F. Katircioglu,"Segmentation of color images based on relation matrix", *Signal Processing and Communications Applications, SIU 2007 IEEE 15th*, Eskisehir, 2007.

[5]. P. Tsai, Y. C. Hu and H. L. Yeh, "Reversible image hiding scheme using predictive coding and histogram shifting",*Signal Processing*, 89(6): 1129-1143, 2009.

[6]. R. Achanta, A. Shaji, K. Smith, A. Lucchi, P. Fua,. and S.Susstrunk, "SLIC superpixels compared to state-of-the-art superpixel methods",*IEEE transactions on pattern analysis and machine intelligence,* 34(11): 2274-2282, 2012.

[7]. O. E. Celikalca, R. Demirci, and C. Elmas, "Renkli goruntulerin uc boyutlu histogram yardımıyla ayrıstırılması",*İleri Teknoloji Bilimleri Dergisi,* 3(1): 38-44.

[8]. G. Borgefors, "Distancetransformations in digitalimages",*Computervision, graphics, andimageprocessing,* 34(3): 344-371, 1986.

[9]. H. F. Tombak, "Cok degiskenli analizlerde kullanılan uzaklık ve benzerlik olcutlerinin kullanım yerleri uzerine uygulamalı bir calısma", Hacettepe Universitesi Saglık Bilimler Enstitusu, Ankara, 73, Turkey, 1996.

[10]. M. Jourlin and J. C. Pinoli, "A model for logarithmic image processing", *Journal of microscopy,* 149(1): 21-35, 1998.

[11]. R. M. Tong, "Analysis of fuzzy control algorithms using the relation matrix",*International Journal of Man-Machine Studies*, 8(6): 679-686, 1976.

[12]. I Koyuncu, A.T Ozcerit, and I. Pehlivan, "Implementation of FPGA-based real time novel chaotic oscillator", *Nonlinear Dynamics*, 77(1-2): 49-59, 2014.

[13]. İ. Koyuncu, and A. T. Ozcerit. "The design and realization of a new high speed FPGA-based chaotic true random number generator", *Computers & Electrical Engineering*, 58: 203-214, (2017).

Application of Linear Stochastic Models for Drought Forecasting

Ulker Guner Bacanlı[1]

Abstract

Drought is a global phenomenon. Many different measures are used to determine drought. Drought forecasting plays an important role in the planning and management of water resource systems. The models can be used from generating data to planning, design of hydraulic structures. In this study is the investigation of the meteorological drought in Eskısehır city in Central Anatolian Region in Turkey. In the presented study, the Standard Precipitation Index are investigated. For this purpose, long term precipitation observations of Eskisehir station by The Turkish State Meteorological Service (DMİ) are evaluated. In the presented study, stochastic models are established to forecast the 12 monthly SPI drought index of Eskısehır Station. For establishment of models, 12 SPI which were observed between 1960 and 2014. Linear autoregressive [AR(1) and AR(2)] which are mostly used in hydrology were investigated. Autocorrelation function [ACF], minimum residual variance [Min Var(e)], Akaike Information Criterion [AIC], Modified Akaike Information Criterion [AICC] and final prediction error [FPE] for testing the goodness of fit model identification in time series modelling were evaluated. The 12 monthly SPI drought index of Eskısehır Station showed that the linear autoregressive moving average AR(2) model is the most appropriate model among the competing models.

Keywords: *Drought, Standardized Precipitation Index (SPI)Linear Autoregressive Models, Time Series Modeling, Diagnostic Checking.*

1. INTRODUCTION

Drought is a slow-moving natural hazard. Wilhite and Glantz (1985) have defined the four types of drought in order to consider a set of decisions. They are meteorological drought, hydrological drought, agricultural drought and socio-economic drought. The three categories are referred as environmental droughts, and the last categories is considered as water resources systems droughts [1], [2].

Many indices are used to identify drought. Most of the indices which used commonly Palmer Drought Severity Index (PDSI), Standard Precipitation Index (SPI), Crop Moisture Index (CMI), developed by researchers, have been proposed to monitor current drought conditions. Palmer presented a drought index in 1965 [3]. McKee et al. presented the Standard Precipitation Index which to have several advantages over the PDSI. SPI is based on precipitation and calculated on various timescales. The frequencies of drought events are consistent, because the SPI is normally distributed [4]. SPI is determined the precipitation deficit for multiple time scales.

It is important to evaluate of annual and monthly time scales. The stochastic models are applied to simulate and forecast the SPI series. Misra and Desa (2005) used linear statistical (ARIMA and SARIMA) models to forecast droughts in Kansabat river of India [5]. Nirmala and Sundaram (2010) and Durdu (2010) used ARIMA and SARIMA models [6]. Durdu developed linear stochastic models for forecasting droughts in Turkey using SPI series as drought index [7]. Moreira et al. (2015) assessed drought cycles in SPI time series using a Fourier analysis in Portugal [8]. Salahi et al. (2016) was modeled of precipitation and future droughts using stochastic time series and standardized precipitation ındex(SPI) in Mashhad plain, Iran [9].

In this study, firstly, monthly precipitation were analyzed for the period 1960-2014. Linear regression analysis of monthly precipitation for Eskisehir was made. Secondly, drought in Eskisehir was assessed with Standardized Precipitation Index (SPI). The SPI values were calculated on 3, 6, 9, 12 and 24 months time scale conditions. Finally, Standardized Precipitation Index (SPI) time series is addressed by means of linear autoregressive models (AR).

---

[1] *Corresponding author: Pamukkale University, Department of Civil Engineering, 20020 Denizli, Turkey. ugbacanli@pau.edu.tr.*

2. DATA

In the presented study, long term between 1960 and 2014 precipitation observations of Eskisehir city station by The Turkish State Meteorological Service (DMİ) are evaluated. Eskisehir is a city in northwestern Turkey. The province covers an area of 2,678 km^2 (Figure 1) [10].
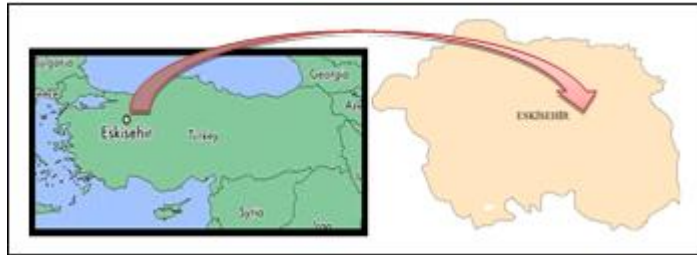
Figure 1. Eskisehir Map

3. METHODS

3.1. Standardized Precıpıtatıon Index (SPI)

McKee et al. (1993) developed the SPI to quantify precipitation deficits on time scales. SPI estimation is long term precipitation data. SPI is obtained by dividing the difference between precipitation and mean to standard deviation in a specific duration [4].

$$SPI = \frac{x_i - \bar{x}_i}{\sigma} \tag{1}$$

The SPI is produced by standardizing the probability of observed precipitation for any duration [11], [12]. The calculation of SPI is complex. The SPI index classes are shown in the Table 1.

Table 1. Classification According to SPI Values

SPI value	Class
>=2	Extremely wet (**EW**)
1.5 to 1.99	Very wet (**VW**)
1.0 to 1.49	Moderately wet (**MW**)
-0.99 to 0.99	Near normal (**NN**)
-1 to -1.49	Moderately dry (**MD**)
-1.5 to -1.99	Severely dry (**SD**)
<=-2	Extremely dry (**ED**)

3.2. Linear Autoregressive Models

Common term of Markov models can be defined as:

$$x_t = \mu + \sum_{j=1}^{p} \phi_j (x_{t-j} - \mu) + \varepsilon_t \tag{2}$$

In which, xi : flow of i. th year, j: autoregressive coefficients (model parameters), ε_i : a normally distributed variable which constituted an independent process, m : order of model. m th order Markov model means which the flow of any year is attached to previous m year flows [13].

3.3. Test of Goodness of Fit

Minimum Residual Variance test of the model suitability is the calculation of Var(e) value where:

$$e = X_{Si} - X_{Mi} \tag{3}$$

X$_{Si}$ is observed data; X$_{Mi}$ is estimated data for each model. Minimum Var(e) value assists for deciding the suitable model [14].

Another method which testing the model suitability is Akaike Information Criterion (AIC). Akaike Information Criterion (AIC) proposed by Akaike in 1974 is the mathematical formulation, which considers the principle of parsimony [15]. So as to compare among computing ARMA models, Akaike recommends

$$AIC(p,q) = N \ln(\hat{\sigma}_\varepsilon^2) + 2(p+q) \qquad (4)$$

where N is the sample size and   is the maximum likelihood estimate of the residual variance; k is the number of distribution parameters (k = p+q); p is α coefficient number; q is θ coefficient number. The model, which gives the minimum AIC number, is the one to be selected.

Hurvich and Tsai (1989) used the Kullback-Leibler information with its unbiased estimators and Modified Akaike Information Criterion (AICC). The modified criterion is expressed as:

$$AICC(p,q) = N * \ln(\hat{\sigma}_\varepsilon^2) + \left(\frac{2(p+q+1)*N}{N-p-q-2} \right) \qquad (5)$$

The model which gives the minimum AICC (min AICC) number is the one to be selected [16].

An alternative procedure for order determination in AR modelling is the Final Prediction Error Criterion (FPE) due to Akaike (1974), the basic idea of which is very simple. The FPE criterion is defined as:

$$FPE(p) = \hat{\sigma}_\varepsilon^2 \frac{N+p}{N-p} \qquad (6)$$

where N is the sample size; is the maximum likelihood estimate of the residual varince; and p is the number of autoregressive (AR) coefficient.

The model which gives the minimum FPE (min FPE) number is the one to be selected.

Various procedures described by Akaike have been proposed to modify the criterion in order to obtain a consistent estimator and to find a field of application. All criteria [AIC, AICC] proposed by Akaike are asymptotically equivalent [15, 16, 17].

4. RESULTS

4.1. Precipitation Analysis

Monthly precipitation were analyzed for the period 1960-2014 (Figure 2). Linear analysis was made of the value of total annual and monthly precipitation. Significant trend aren't found for annual precipitation in Eskisehir.
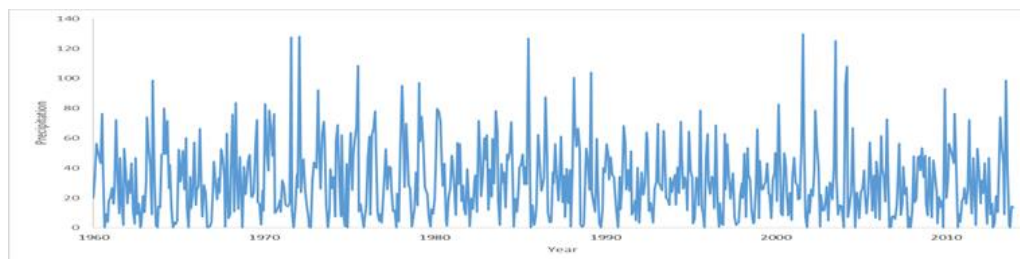
Figure 2. Monthly precipitation for the study area.

Linear regression analysis of monthly precipitation for Eskisehir was made. Table 2 are given slope, correlation coefficient. According to Linear Regression statistically significant (%5 risk), it was found that the monthly precipitation trend is decrease in May. But, It was found that the monthly precipitation trend is increase in October. But statistically significant trend are not found for another.

Table 2. Monthly Linear regresion analysis results of precipitation for Eskisehir

Month	a	b	R^2	Month	a	b	R^2
January	-97,35	0,06	0,003	July	-357,30	0,20	0,011
February	760,15	-0,36	0,044	August	305,01	-0,14	0,005
March	405,24	-0,18	0,010	September	-267,25	0,14	0,018
April	588,96	-0,28	0,049	October	-619,55	0,32	0,177
May	1023,60	-0,50	0,120	November	447,87	-0,22	0,046
June	121,00	-0,04	0,001	December	-329,96	0,18	0,016

4.2. Standard Precipitation Index Analysis Assessment

The SPI values were calculated on 3, 6, 9, 12 and 24 month time scale conditions. The graphs of Eskisehir are plotted as Figure 3. On 24 month time scales, the important droughts also occurred in 1962-1964, 1965-1968, 1991-1994, 2005-2010 in Eskisehir. The extreme drought was observed in 1967, 1998, 2008 year. As it can be seen from Figure 3 in the short time period (as 3 months) drought is more frequent but shorter, and as the period increases the duration of drought also increases but frequency decreases. Winter droughts are beginning to occur in the class of "severe" in the recent year. In the shorter periods, for example 3-6 months, the duration of wet or dry periods of SPI values are shorter (Figure 3). In longer periods the duration of wet or dry periods are longer (Figure 3). These situations can be expanded in different approaches according to different water users.

The relative frequencies of SPI values for 3, 6, 9, 12 and 24 month time period for Eskisehir are given in Table 3. Moderate degree drought distribution varies between 7 % and 9 % for the periods of 3-24 months. Severe degree drought distribution varies between 3 % and 5 % for the periods of 3-24 months. Extremely level drought distribution varies between 3 % and 4 % for the periods of 3-24 months. Normal distribution varies between 65 % and 68 % for the periods of 3-24 months. Moderate degree wet distribution varies between 9 % and 13 % for the periods of 3-24 months. Very degree wet distribution varies between 3 % and 6 % for the periods of 3-24 months. Extremely level wet distribution varies between 0 % and 2 % for the periods of 3-24 months.

Table 3. The relative frequencies of Eskisehir city SPI values for 3, 6, 9, 12 and 24 months time period

	3 Month	6 Month	9 Month	12 Month	24 Month
EW	0,02	0,01	0,01	0,00	0,00
VW	0,06	0,06	0,05	0,06	0,03
MW	0,09	0,12	0,11	0,10	0,13
NN	0,68	0,65	0,67	0,67	0,68
MD	0,09	0,09	0,07	0,09	0,07
SD	0,03	0,05	0,05	0,04	0,05
ED	0,03	0,03	0,04	0,04	0,05
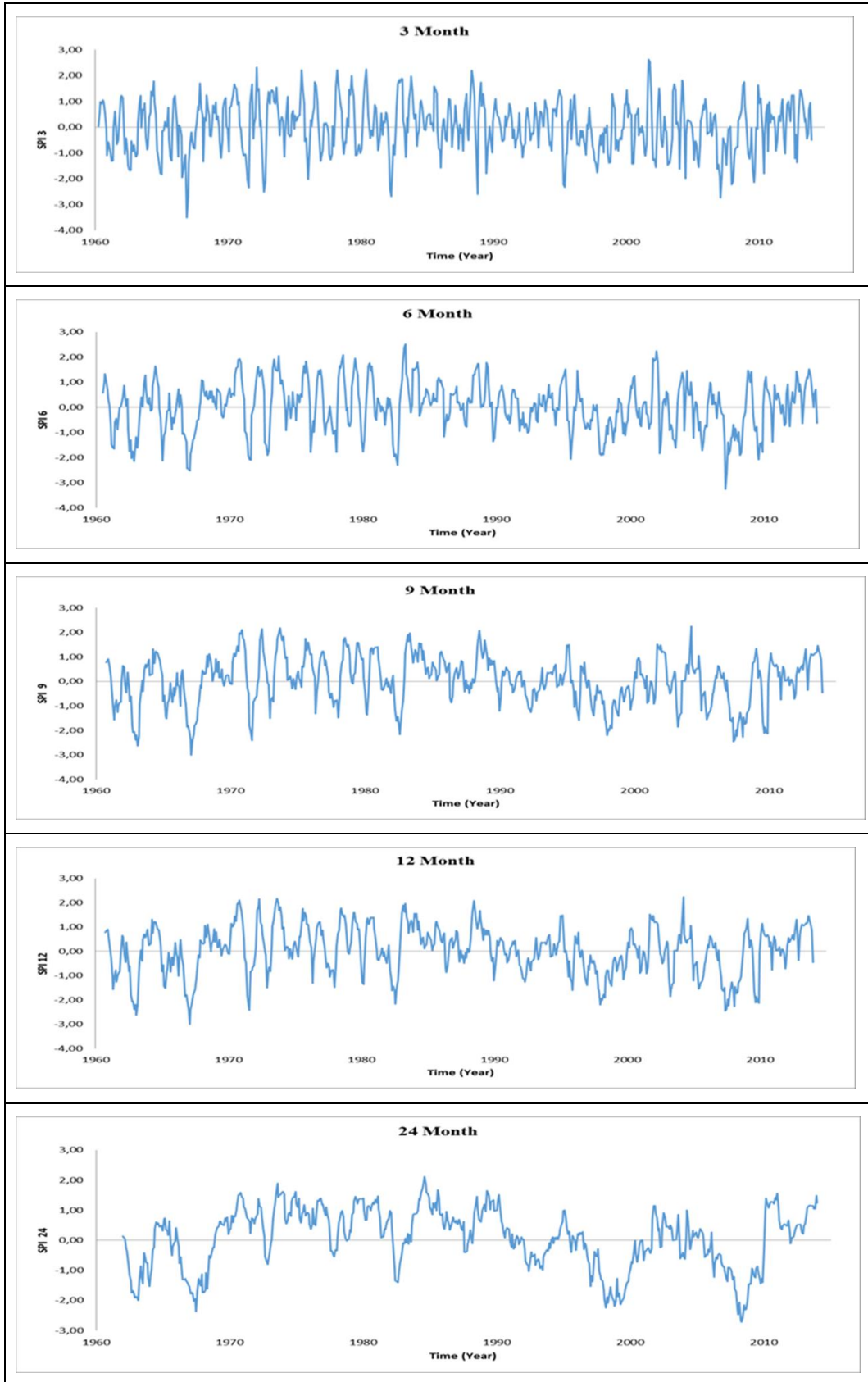
Figure 3. SPI values of Eskisehir city for 3, 6, 9, 12 and 24 months period

4.3. Time Series Analysis Assesment

The precise model parameters are never known in the determination stage of the mathematical models of a hydrological time series. Therefore, they must be estimated from limited observed data. The deduced population model is only an approximation. Consequently, the most important issue in stochastic hydrology is to define the model with the best fit between various models [1].

In the this study, results of 12 monthly SPI drought index of Eskısehır Station at 55 years length (1960-2014) are modeled. The consequences of test of goodness of fit are summarized in Table 4 and Table 5. The statistical properties of observed data have demonstrated that the probability distribution can be acceptable as Normal Distribution. The results confirmed that AR(2) can be selected as the best fit model for evaluations for all models (Table 5).

Table 4. The parameters of models for 12 monthly SPI series of Eskisehir

	AR1	AR2
α_1	0,9114	0,9571
α_2		-0,0509

Table 5. The results of goodness of fit for 12 monthly SPI series of Eskisehir

	Evaluations for AR type models
VAR(e)	AR(2)
AIC	AR(2)
AICC	AR(2)
FPE	AR(2)

5. CONCLUSIONS

In this study was to analyze annual and monthly precipitation in Eskisehir, Turkey for the minimum 55 yearly period. For this analyses were used Linear Regression method. Significant trend aren't found for annual precipitation. It was found that the monthly precipitation trend is decrease in May. But, It was found that the monthly precipitation trend is increase in October. But statistically significant (%5 risk) trend are not found for another month.

The SPI values were calculated on 3, 6, 9, 12 and 24 month time scale conditions. The extreme drought was observed in 1967, 1998, 2008 year. In the short time period (as 3 months) drought is more frequent but shorter, and as the period increases the duration of drought also increases but frequency decreases. The total relative frequencies of the drought vary between 15 % and 17 % for the periods of 3, 6, 9, 12 and 24 months in all cities.

Standardized Precipitation Index (SPI) time series is modelled by means of linear autoregressive models (AR).

The results of test of goodness of fit are showed results for 12 SPI data. AR(2) is the best for all investigated models by Var(e), AIC, AICC and FPE. Var(e), AIC, AICC and FPE criterion have different advantages and disadvantages depending on the data length. Hence, it can be said that the new criterion must be investigated for the test of goodness of fit for stochastic modeling.

Further study should be focused on improving the precision of the model forecasting, and on studying the types of droughts described by the SPI series with different time scales. It is needed to establish a drought center with researchers from different disciplines for decreasing the drought influences, taking precautions and continuous monitoring.

ACKNOWLEDGMENT

REFERENCES

[1].   D. A. Wilhite and M. Glantz, Understanding: the Drought Phenomenon: The Role of Definitions. Water International 10(3):111-120, 1985.

[2].   D.A. Wilhite, *Drought as a Natural Hazard: Concepts and Definitions (Chapter 1).* In: D.A. Wilhite (Ed.), Drought: A Global Assessment. Hazards and Disasters: A Series of Definitive Major Works, edited by A.Z. Keller. Routledge Publishers, London, UK, 2000.

[3].   W. C. Palmer, Meteorological Drought. Research Paper No.45. Washington, DC: US Weather Bureau, 1965.

[4].   T. B. McKee, N. J. Doesken, J. Kleist, The relationship of drought frequency and duration to time steps. *8th Conference on Applied Climatology, January 17–22* 1993. 179–184 pp., Anaheim, California.

[5].   A. K. Mishra, V. P. Singh, A review of drought concepts. Journal of Hydrology 391: 202-216, 2010.

[6].   M. Nirmala and S.M. Sundaram, A Seasonal Arima Model for forecasting monthly rainfall in Tamilnadu. National Journal on Advances in Building Sciences and Mechanics, 1(2), 43–47, 2010.

[7].   O. F. Durdu, Application of linear stochastic models for drought forecasting in the Buyuk Menderes river basin, Western Turkey. Stochastic Environmental Research and Risk Assessment, 24(8), 1145–1162, 2010.

[8].   E.E. Moreira, D.S. Martins and L.S. Pereira, Assessing drought cycles in SPI time series using a Fourier analysis. Natural Hazards Earth System Sciences, 15, 571–585, 2015.

[9].   B. Salahi, A. Nohegar and M. Behrouzi, The Modeling of Precipitation and Future Droughts of Mashhad Plain using Stochastic Time Series and Standardized Precipitation Index (SPI). Int. J. Environ. Res., 10(4):625-636, Autumn, 2016.

[10]. DMI (State Meteorological Service)   http://www.dmi.gov.tr/files/en-US/climateof turkey.pdf , Last Access : November 2009.

[11]. Y. Zhang, W. Cai, Q. Chen, Y. Yao, K. Liu, Analysis of Changes in Precipitation and Drought in Aksu River Basin, Northwest China. Advances in Meteorology. doi.org/10.1155/2015/215840, 2015.

[12]. P. Ganguli and M. J. Reddy, Evaluation of trends and multivariate frequency analysis of droughts in three meteorological subdivisions of western India. International Journal of Climatology 34/3: 911-928, 2014.

[13]. M. Bayazıt, Statistical Methods in Hydrology (in Turkish). İstanbul, İTU, 1981.

[14]. J.D. Salas, J.W. Delleur, V. Yevjevich and W.L. Lane, Applied Modeling Of Hydrologic Time Series, Littleton: Water Resources Publications (First Printing 1980), 484 p., 1985.

[15]. H. Akaike, A New Look at the Statistical Identification Model Identification. IEEE Transactions on Automatic Control, 19: 716-723., 1974.

[16]. P.J. Brockwell, and R.A. Davis, Introduction to time series and forecasting, New York: Springer, 2002.

[17]. J. Fan and Q. Yao, Nonlinear Time Series: Nonparametric and Parametric Methods, New York: Springer Series in Sttistics, 2003.

INVESTIGATION OF SIVAS-DIVRIGI MINE LOCATION USING MAGNETIC DATA

Cagatay PAMUKCU[1], Oya PAMUKCU[2], Fikret DOGRU[2]

Abstract

Edge detection and edge enhancement techniques have been used interpreting potential field data to investigate edges of subsurface structures. There have been various edge detection applications to magnetic data in geophysics such as analytic signal, total horizontal derivative, theta angle, tilt angle etc. In this study, the magnetic anomaly of Sivas-Divrigi mining area was selected because of importance of this area in terms of high-grade iron ore reserves. The mentioned method was applied on field data and the location of iron ore was revealed. Also radial average power spectrum method was applied on magnetic data to determine average depths of sediments and iron ore reserve. As a result, tilt angle and theta map methods gave a good agreement for determination of the structure location in field study.

Keywords: *Magnetic, Geophysics, Mining, Tilt Angle*

1. INTRODUCTION

In this study, the magnetic anomaly of Sivas-Divrigi mining area was selected because of importance of this area in terms of high-grade iron ore reserves. The edge detection methods were applied on field data and the location of iron ore was revealed. Also, radial average power spectrum method was applied on magnetic data to determine average depths of sediments and iron ore reserve. Natural resources in the vicinity of Sivas compose an important potential of Turkey from the aspects of reserve quantity, grade and diversity. In this region; the most important metallic mines are iron, gold, chrome, lead-zinc and manganese while the most important industrial minerals are marble, gypsum, kaolin, limestone, halite, asbest and cement raw materials. In addition, energy raw materials such as lignite and geothermal fluids are also found in this city.

Three main tectonic units exist in the vicinity of Sivas, in which the study area is also located. They are Pontide Tectonic Zone, North Anatolia Ophiolite Zone and Taurus Tectonic Zone, respectively ([1]). The magmatic rocks which are observed around Divrigi, Yıldızdagı, Karacayır and Kosedagı, are rift tectonism products of arc tectonism, collision or after collision ([2]). The rift tectonism was played an important role to occur important metal mines in Sivas region. The ore is mainly magnetite, hematite and limonite but secondarily, pyrite and chalcopyrite veinlets are also encountered. The mean grade value of the ore body is nearly 55%.

In geophysical methods, succesful results are obtained using magnetic methods such as these ore area because of high magnetic susseptibility of iron ore. In this study, the radially averaged power spectrum method was applied on this magnetic anomaly of high magnetic susseptibility iron ore area in Sivas and its surroundings. The application results were compared with tilt angle (TA), theta map (TM), total horizontal derivative (THDR), analitic signal (AS) method results ([3]).

2. APPLICATIONS

Radial average amplitude spectrum is used to extract sediment and iron ore depth information in magnetic anomaly. The most important feature of the radial average power spectrum is that it shows the correct fractions at different slopes in the different radial wave number (k_r) order. In general, the correct parts corresponding to small radial wave numbers are represented by deep local sources, the medium-sized wave numbers are represented by shallow sources and the high-wave numbers are represented by noise in the data ([4], [5]). The depth of each equivalent layer is calculated as follows:

---

[1]

$$h = \frac{B\,(k r_1) - B(k r_2)}{4\pi(k r_2 - k r_1)}$$

Where kr_1 and kr_2 are the start and end radial wave numbers of the superposed line and $B(kr_1)$ and $B(kr_2)$ are the radial average natural logarithmic power spectrum values corresponding to these wave numbers ([6]).

The Radial average amplitude spectrum was used on ground magnetic data (Figure 1 and Figure 2). The magnetic values changes between 1000 - 23000 nT. The depth values were obtained 37 m for sediment and 77 m for iron ore.
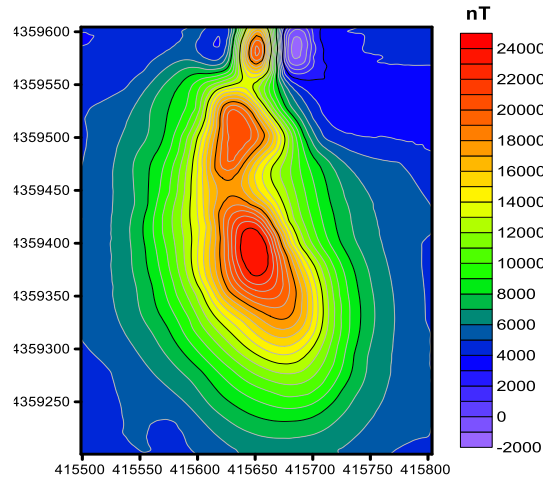
Figure 1. The magnetic map of Sivas Divrigi iron ore area.
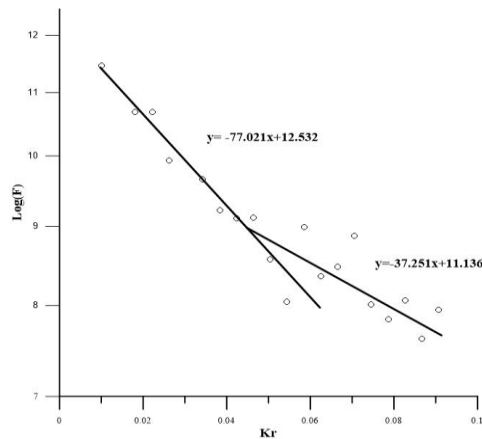
Figure 2. Radially averaged power spectrum result of magnetic data.

3. RESULTS

The average depths of sediment and iron ore were computed using radially averaged power spectrum and average ~37 m, ~77 m depth values obtained for sediment and iron ore respectively. This depth result are coherent with the known drilling information in the study area ([7]). Within the field studies ([3]); THDR, AS, TA and TM methods were applied to magnetic map depicted in Figure 3, which belongs to a iron ore deposit located in Sivas-Divrigi.
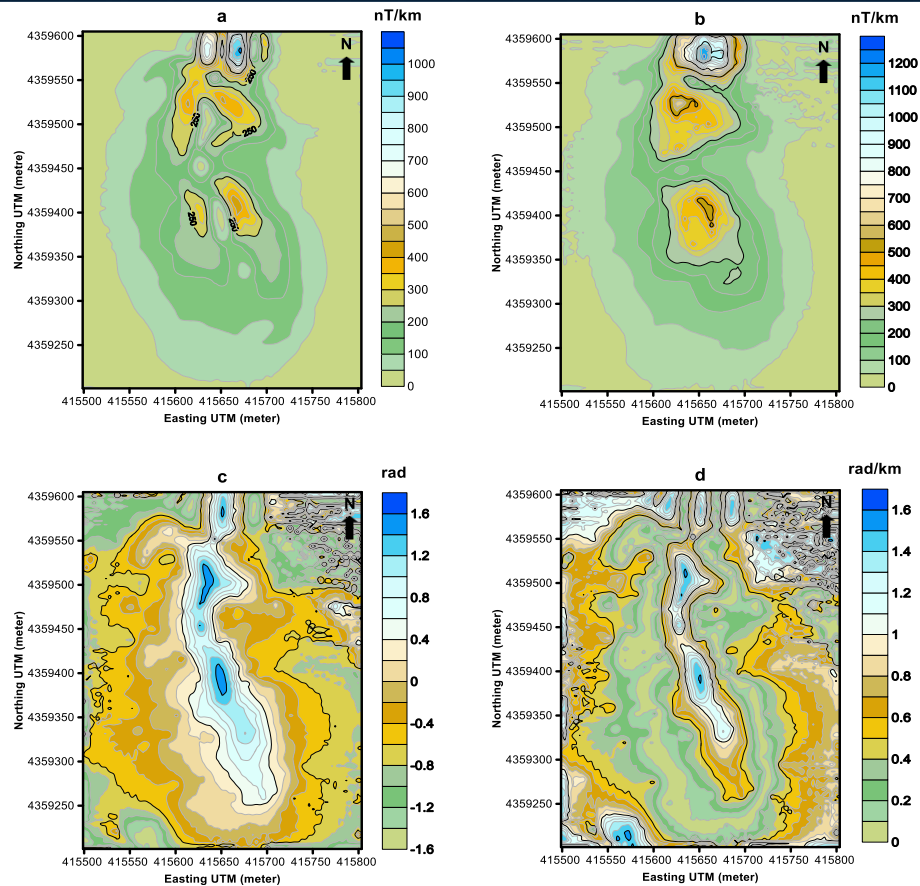
Figure 3. Results of edge detection filters on field study a) THDR, b) AS, c) Tilt, d) Theta map (revised from [3]).

When the results are investigated together, 3 different iron ore bodies are existent at the mine site. The maximum depth is at this elevation in the field obtained from magnetic data depending on the profile length. In case the data length is incerased more, the lower levels of the iron ore can also be studied.

ACKNOWLEDGMENT

REFERENCES

[1]. N.İ. Cetin, "Geology and petrology of Mursal (Sivas-Divrigi) magmatic rocks". M. Sc. Thesis, Ankara University, Ankara, 2007.

[2]. A. Yılmaz," Geodynamic Evolution of Sivas Basin "Symposium of Iron Beds Developing with Ophiolite-Granitoid Relationship, Sivas, D. Boztug, T. Ozer and N. Otlu (Ed), Proceedings, 66-82.1998.

[3]. F. Dogru, O. Pamukcu, C. Pamukcu, "Determination of Mine Location by Using Edge Detection Methods: A Case Study of Sivas-Divrigi". *Earth*, 5(4), 56-61, 2016.

[4]. A. Spector and F:S: Grant " Statistical models for interpreting aeromagnetic data". *Geophysics*, 35(2), 293-302, 1970.

[5]. R.S. Pawlowski, "Green's equivalent-layer concept in gravity band-pass filter design". *Geophysics*, 59(1), 69-76, 1994.

[6]. B. Oruc and T. Sonmez, "The rheological structure of the lithosphere in the Eastern Marmara region, Turkey". *Journal of Asian Earth Sciences,* 2017.

[7]. Z. Demirkıran and B. Kahraman, "The geology of Taslıtepe Plaser and Drilling Studies", Report. 2009.

STRESS ANALYSING WITH GRAVITY DATA

Oya PAMUKCU[1]

Abstract

Geodynamic movements are a consequence of gravitational mass forces acting on the solid mantle and crust. Gravitational forces cause to increase of pressure with the effect of depth increasing. The rocks must carry the weight of the rising covering together with the depth. Static equilibrium is not possible with absolutely increasing pressure because there are horizontal differences in the gravitational mass forces within the earth. Horizontal variations of the gravitational mass force produce different stresses that control the relative movements associated with plate tectonics. It is possible to obtain stresses by going out of the gravity anomalies. In this study, for the application of this method, gravity anomalies of two theoretical cube models were calculated, which had different depths and densities. Using gravity values, the horizontal tectonic stresses of medium were determined.

Keywords: *Tectonic Stress, Gravity, Geodynamic.*

1. INTRODUCTION

Geodynamic movements are a consequence of gravitational mass forces acting on the solid mantle and crust. Gravitational forces cause to increase of pressure with the effect of depth increasing. The rocks must carry the weight of the rising covering together with the depth. Static equilibrium is not possible with absolutely increasing pressure because there are horizontal differences in the gravitational mass forces within the earth. Horizontal variations of the gravitational mass force produce different stresses that control the relative movements associated with plate tectonics. It is possible to obtain stresses by going out of the gravity anomalies. The rocks must support the weight of the overburden that increases pressure with depth. The pressure creates gravitational forces. These are caused by horizontal variations in density. These variations produce the differential stresses that drive the relative motions associated with plate tectonics ([1]).

In this study, using [1] and [2] techniques, the tectonic stress values obtained from gravity data for a theoretical application. For this, stress distribution analysis was carried out by two cube models. Tectonic stress model presented by two cube models.

2. APPLICATIONS

The horizontal force F_m, on a section of continental block can be defined as,

$$F_m = \int_0^b p_L dy = \rho_m g \int_0^b y dy = \frac{1}{2} \rho_m g b^2 \tag{1}$$

here ρ_m is mantle density, P_L is lithostatic pressure, g is gravity acceleration, b is the block thickness. In the next step, the stress distribution of this block should be found by using static balance of force ([1] and [2]) as,

$$\sigma_{xx} = -\frac{1}{2} gh\Delta\rho \frac{\rho_c}{\rho_m} \tag{2}$$

where h is the thickness of the continent, ρ_c is density of the crust and ρ_m is the density of the mantle. The Bouguer gravity anomaly is calculated by ([3])

$$\Delta g_z = -2\pi hG\Delta\rho \tag{3}$$

G is the gravitation constant. If $\Delta\rho$ in Eq. (1) is combine with Eq. (2).

---

[1] *Dokuz Eylul University, Engineering Faculty, Department of Geophysical Engineering, 35160, Tinaztepe Campus, Buca, İzmir, TURKEY, oya.pamukcu@deu.edu.tr.*

$$\sigma_{xx} = \frac{g\,\rho_{(x,y)}}{4\pi G \rho_{(m)}}\Delta g_{(z)} \tag{4}$$

Eq. (4) gives a way to estimate the horizontal tectonic stress from the gravity anomaly.

In this study, the gravity anomalies of two theoretical cube models were calculated ([4]), which had different depths and densities (Figure 1 and Figure 2). Using gravity values, the horizontal tectonic stresses of medium were determined by Eq.2, Eq.3 and Eq.4 (Figure 3).
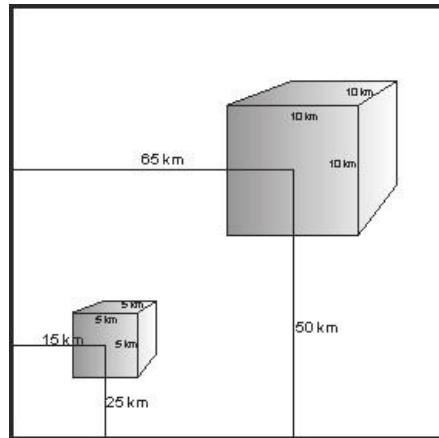
Figure 1. Calculated gravity anomaly using the cube models0.
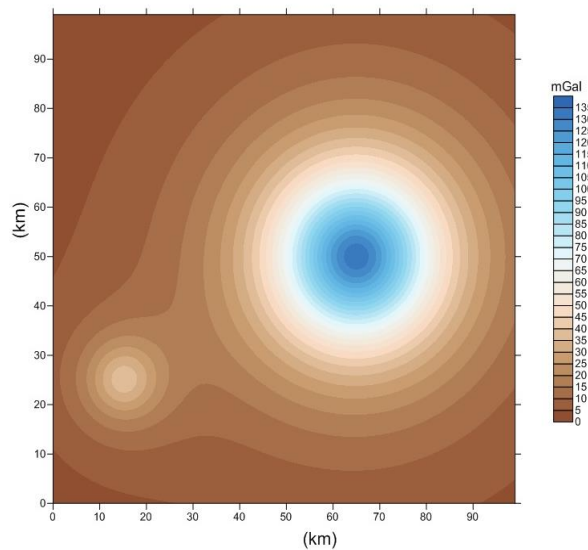
Figure 2. The gravity anomalies of models in Figure 1.
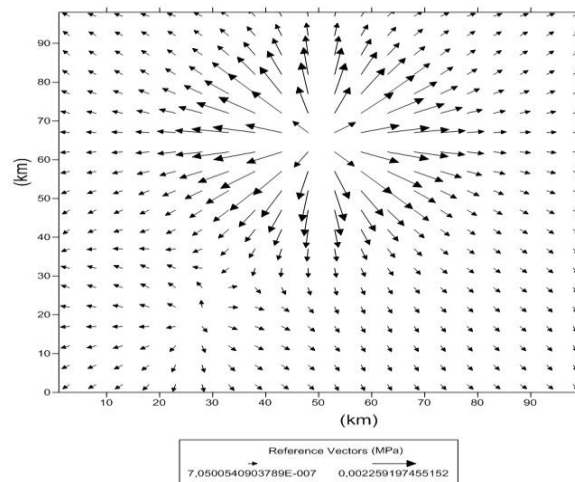
Figure 3. The horizontal tectonic stresses were obtained by the gravity anomalies of the models.

3. RESULTS

Within the scope of this study, a theoretical application was done to obtain gravity tension. For this, two cube models were created. Then, the stress distribution was calculated by using gravity anomaly (Figure 3) and density difference values. The regions in which the variation of the vectors is clearly observed are the cube models (Figure 4). As a result, the theoretical study of the calculation of the horizontal stress from the gravity values was successfully carried out.
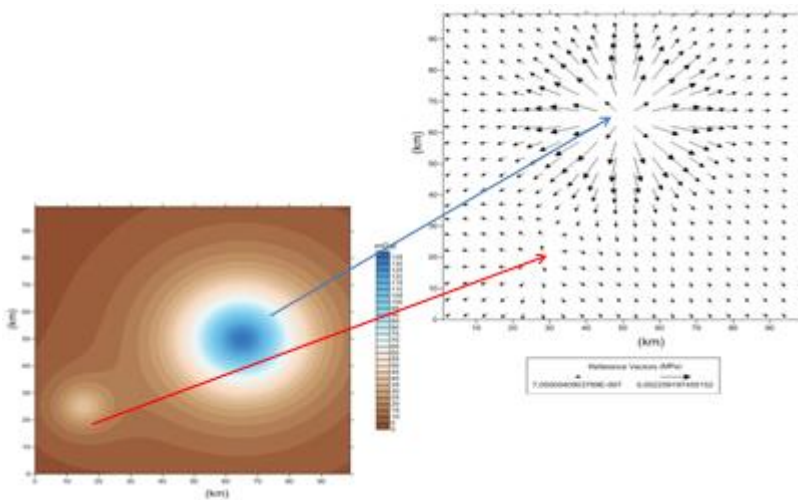
Figure 4. The gravity anomalies and the horizontal tectonic stresses of the models.

ACKNOWLEDGMENT

REFERENCES

[8]. D.L. Turcotte and G. Schubert. Geodynamics: Applications of continuum physics to geological problems, 450 pp, 1982.

[9]. C. Xu, H. Wang, Z.C., Luo, J.S. Ning and H.L. Liu. "Multilayer stress from gravity and its tectonic implications in urban active fault zone: A case study in Shenzhen, South China". *Journal of Applied Geophysics*,114, 174-182, 2015

[10]. W.A. Heiskanen and H. Moritz, "Physical geodesy". *Bulletin Géodésique* (1946-1975), 86(1), 491-492, 1967.

[11]. F.S. Grant and G.F. West, Interpretation theory in applied geophysics, 1965.

Comparative Properties of Polyolefin Fibers in Dyeing with Microwave Heating and Conventional Methods

Burcu Yılmaz Sahinbaskan[1], Mujgan Naycı Duman[2], Dilara Kocak[3]

Abstract

In this work, 100% isotactic polypropylene (iPP) fibers, 100% linear low-density polyethylene (LLDPE) polymer fibers and polymer blends obtained from different proportions of these polymer fibers with elastomer of ethylene-vinyl acetate (EVA) [80/19/1 % iPP/LLDPE/EVA, 80/19/1 % LLDPE/iPP/EVA, 60/30/10% iPP/LLDPE/EVA and 60/30/10% LLDPE/iPP/EVA] were dyed with conventional and microwave heating methods. The coloristic and mechanical properties of dyed fibers were investigated. The results show that the proportion of up to 10% EVA in polymer blends has good coloristic and mechanical properties for both dyeing methods. Using microwave energy for dyeing has provided a saving in almost 90% of time.

Keywords: *Polyolefin Fibers; Polymer Blends; Microwave Energy; Ethylene Vinyl Acetate Elastomer*

1. INTRODUCTION

The microwave energy can be used an alternative heating method to conventional processes for pre-treatment, dyeing, finishing, drying, fixation, surface modification and grafting processes of textile materials. The energy of microwave photons is quite low compared with the chemical bond energies. Microwaves do not change the electronic configuration of atoms and directly affect the molecular structure of a compound. The materials that absorb microwave energy are being heated effectively, fast and uniform. The direct dyeing of cotton, reactive dyeing of flax and disperse dyeing of synthetic fibres with microwave energy have been investigated in several research works. Use of microwave heating is enhanced the hydrophilicity, dyeability and color fastness properties of textiles, reduced the process time and provided energy savings [1-4].

In the industry, polypropylene fibers are increasingly being used, while they are light, inexpensive and have good thermal stability [5].

The polypropylene/linear low-density polyethylene blends can be used for technical, home and medical textiles. The melting point of branched linear low-density polyethylene is low. For the textile technology, it is suitable for stick with many of the polymer in the high temperature. Various fibre blends were prepared for improve the dyeability of polyolefin fibres such as polypropylene/polyethylene terephthalate, polyamide/polyamide 6, polypropylene/ polyamide 6, polypropylene/polyethylene etc [6-19].

In this research work, 100% isotactic polypropylene (iPP) fibers, 100% linear low-density polyethylene (LLDPE) polymer fibers and polymer blends obtained from different proportions of these polymer fibers with elastomer of ethylene-vinyl acetate (EVA) [80/19/1 % iPP/LLDPE/EVA, 80/19/1 % LLDPE/iPP/EVA, 60/30/10% iPP/LLDPE/EVA and 60/30/10% LLDPE/iPP/EVA] were dyed with conventional and microwave heating methods. The coloristic and mechanical properties of dyed fibers were investigated.

---

[1] *Corresponding author: Marmara University, Department of Textile Engineering, 34722, Göztepe/İstanbul, Turkey. burcuyilmaz@marmara.edu.tr.*

[2,3] *Marmara University, Department of Textile Engineering, 34722, Göztepe/İstanbul, Turkey. mnayci@marun.edu.tr, dkocak@marmara.edu.tr.*

2. EXPERIMENTAL

2.1. The Aim of The Research

The aim of this research is to dye fibers produced from 100% isotactic polypropylene (iPP), 100% linear low density polyethylene (LLDPE) and different proportions of these polymers with an elastomer of ethylene-vinyl acetate (EVA).

2.2. Fibers

Throughout this experimental work, 100% iPP, 100% LLDPE, 80/19/1 iPP/LLDPE/EVA, 60/30/10 iPP/LLDPE/EVA, 80/19/1 LLDPE/iPP/EVA and 60/30/10 LLDPE/iPP/EVA. Granule fibers of polymer blends were prepared using a twin-screw extruder at a screw speed of 170 rpm, temperature range of 170-245 °C, and head pressure of 21 bars. The granular materials were then used to melt spin fibers using the conditions summarized in Table 1. Melt flow index (MFI), density, tensile strength, and elongation values of the fiber samples are in given Table 2. MFI values of polymer blends were obtained from melt indexer at 230°C and 2160 g load. Tensile test specimens were prepared from the fibers.

Table 22. Production condition of polymer blends.

Parameter	Value
Temperature	180-200 °C
Extruder pressure	50 bar
Pump rotation	80 rev/min
Spinning ratio	1:3
Velocity of first spinning mill	300 rev/min
Velocity of second spinning mill	900 rev/min
Winging speed	183.7 m/min
Lineer density of single fiber	20dtex
Number of spinneret	40x2
Diameter of spinneret	0.4 mm

Table 23. Material properties.

Material	MFI (g/10 min)	Density	Tensile Strenght	Elongation (%)
iPP	35	S (mm)	S (mm)	S (mm)
LLDPE	50	7.5	7.5	7.5
EVA	35-45	5.5	5.5	5.5

2.3. Dyes and Chemicals

Sarapol 349 U (CHT) was used as a carrier. C.I. Disperse Blue 79 (monoazo) was used fort he sample dyeing. A non-ionic surfactant Perlavin OSV (Dr.Petry) and sodium carbonate (Merck) were used for washing process of dyed fibers.

2.4. Dyeing Methods

All dyeing prosess were carried out under atmospheric conditions with conventional and microwave heating with C.I. Disperse Blue 79. 1.5 g samples were used for each dyeing. 1% owf depth of shade dye and 1 g/L carrier were added to the dye bath with a liquar ratio 50:1. The conventional dyeing process was initiated at

30°C. The dye bath temperature was than increased at 98°C at a heating rate of 2°C/min and kept at this temperature for 45 minutes. Finally, the bath has been cooled and the dyed fibers were removed from dye bath. The dyed fibers were washed, and then rinsed with cold water. 2 g/L Perlavin OSV and 0.5 g/L sodium carbonate have been added to the washing bath in washing process; and the process was carried out at 75 °C for 15 minutes with a liquor ratio of 25:1. The total conventional dyeing process took 79 minutes, including the time for heating up the dyebath.

The dyeing with the help of microwave heating were carried out in a microwave oven (White Westing house, model KM06VF2W) with a maximum output power of 700 W and operating at 2450 MHz. The dyebath in a glass beaker was placed into the microwave oven and processed at 30°C. The energy level of the oven was adjusted to medium level (460 W). The temperature was raised and kept at 98°C for 3 minutes. Then, the energy level of the oven was shifted to low level (120 W) for 5 minutes. The dyebath in the glass beaker was taken out of the oven and cooled down to 60°C in the room conditions. The cooled sample was removed from the dyebath, washed as described fort he method in the conventional method, and then rinsed with cold water. The total processing time, including heating up the dyebath, was 8 minutes for the dyeing with the help of microwave heating method.

2.5. Equipment and Standards Used for The Tests

The reflectance values of dyed fibers were measured using Datacolor SF600+ spectrophotometer with specular included mode LAV (6.6 mm) viewing aperture. The color (CIELab) values of these fibers were calculated using D65 illuminant and 10° standard observer values. The CMC 2:1 Color Differences Formula was used to find and express the color differences. For fastness test, the Light Fastness Tester *(James H.Heal)* and the Wash Fastness Tester [Gyrowash] *(James H.Heal)* were used.

The light and washing fastness tests were carried out in accordance with the methods described in ISO 105-B02 and ISO 105-C06 (A1S test conditions; 40°C temperature, 30 min, and 10 steel balls), respectively. The dyed fibers were exposed to the light for 100 hours.

The tensile strenght tests of the fibers were carried out using Instron 4411 testing machine according to the ASTM D 2256 standard (10 mm/min speed).

3. RESULTS

3.1. Color Measurement Results of Dyed Fibers

The CIELab values and color differences of dyed fibers are given in Table 3. All the dyed fibers with microwave heating are darker than the dyed fibers with conventional method.

Table 3. The CIELab values and color differences of dyed fibers.

Fibers	Method[a]	CIELab Values					Color Differences[b] $\Delta E_{CMC (2:1)}$
		L^*	a^*	b^*	C^*	$h°$	
100% iPP	C	72.29	-1.36	-7.83	7.95	260.15	3.28
	M	67.13	-1.37	-10.67	10.76	262.68	
100% LLDPE	C	71.65	-1.24	-8.02	8.12	261.21	3.96
	M	68.01	-3.11	-11.48	11.89	254.84	
80/19/1 % iPP/LLDPE/EVA	C	62.13	-1.37	-10.67	10.76	262.68	7.75
	M	54.88	-3.12	-19.34	19.59	260.84	
80/19/1 % LLDPE/iPP/EVA	C	58.50	-3.25	-18.66	18.94	260.12	4.64
	M	49.20	-1.29	-20.78	20.82	266.45	
60/30/10% iPP/LLDPE/EVA	C	34.86	-0.54	-26.37	26.38	268.83	1.78
	M	31.73	-0.57	-26.03	26.04	268.75	
60/30/10 % LLDPE/iPP/EVA	C	37.87	-0.56	-28.09	28.10	268.86	3.45
	M	31.76	-0.26	-26.09	26.09	269.43	

a C: Conventional, M: Microwave; b Conventionally dyed samples were taken as 'standard'.

3.2. Color Fastness Dyed Results of Dyed Fibers

The light and washing fastness test results are summarized in Table 4. The light fastness of the fibers dyed with microwave heating method is quite good (5) when compared with those fibers dyed with conventional method. The color change (CC) values of all fibers after the washing fastness tests are found as 4-5 and the staining test results of adjust multifibers are found as ¾-5 greyscale ratings.

Table 4. Color fastness test results of dyed fibers.

Fibers	Method[a]	Light Fastness	Washing Fastness[c]						
			CC	CA	Co	PA	PES	PAN	Wo
100% iPP	C	3	5	4	4/5	4	3/4	5	4/5
	M	5	5	4	4/5	4	3/4	5	4/5
100% LLDPE	C	3	5	4	4/5	4	3/4	5	4/5
	M	5	5	4	4/5	4	3/4	5	4/5
80/19/1 % iPP/LLDPE/EVA	C	3	5	4	4/5	4	3/4	5	4/5
	M	5	5	4	4/5	4	3/4	5	4/5
80/19/1 % LLDPE/iPP/EVA	C	2	4/5	4/5	4/5	4	3/4	5	4
	M	5	4/5	4/5	4/5	4	3/4	5	4
60/30/10% iPP/LLDPE/EVA	C	3	5	4	4/5	4	3/4	5	4/5
	M	5	5	4	4/5	4	3/4	5	4/5
60/30/10 % LLDPE/iPP/EVA	C	2	4/5	4/5	4/5	4	3/4	5	4
	M	5	4/5	4/5	4/5	4	3/4	5	4

c CC: color change, CA: cellulose acetate, Co: cotton, PA: polyamide (nylon 6.6), PES: polyester (Terylene),

PA: polyamide (Nylon 6.6), PAN: acrylic (Courtelle), Wo: wool

3.3. Mechanical Properties of Fibers

The tensile strength, elongation and young modules values of the fibers, obtained from the samples before and after dyeing, are given in Figure 1-3, respectively.
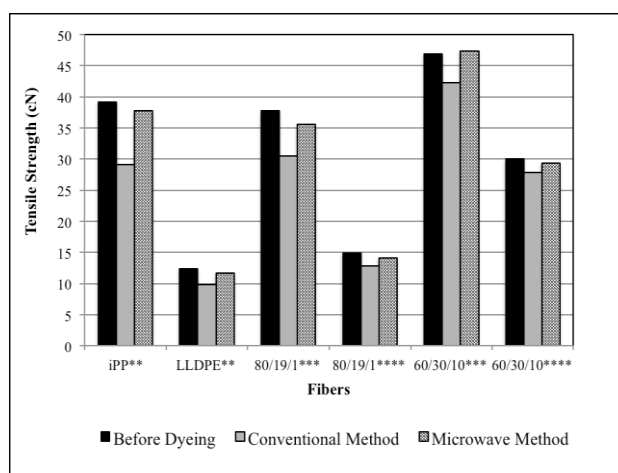
Figure 30. Tensile strength (cN) values of fibres before and after dyeing

([**] 100%, [***]iPP/LLDPE/EVA, [****]LLDPE/iPP/EVA).

The tensile strength, elongation and young modules values of the fibers dyed with microwave heating method are higher than the values of the fibers dyed with conventional method. For most fiber compositions, the difference in tensile strength and Young's modulus between the undyed fiber and dyed fibers with microwave heating method are not significant. There have been minimal changes in the molecular chain structure of the polymers processed with microwave heating method because of shorter process time.
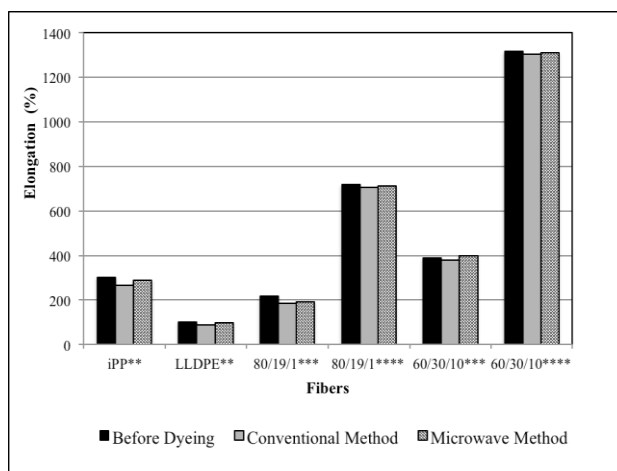
Figure 2. The change on elongation (%) of fibers before and after dyeing

*(** 100%, ***iPP/LLDPE/EVA, ****LLDPE/iPP/EVA).*

The results show that increasing the EVA content amount increased the mechanical properties of the fibers. This is caused by the orientation of the molecular chains of the fibers occurred during the spinning.
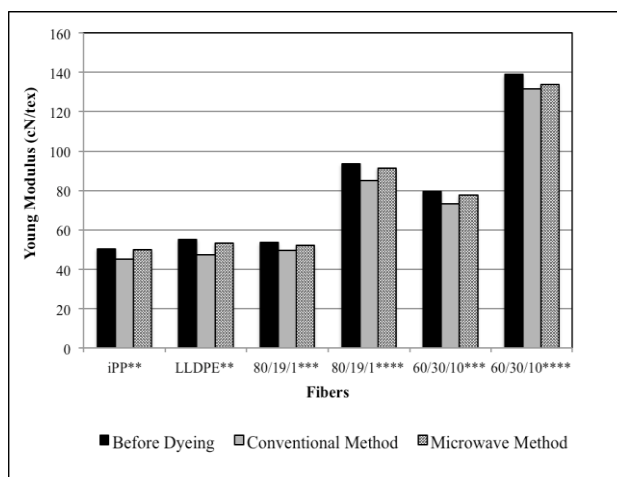
Figure 3. The change on young modulus (cN/tex) of fibers before and after dyeing

*(** 100%, ***iPP/LLDPE/EVA, ****LLDPE/iPP/EVA).*

Generally, different proportions of iPP and LLDPE polymer blends with addition of different amount of EVA can be used as industrial polymers.

4. CONCLUSION

The following advantages of microwave heating compared with conventional method can be reached through the results of this experimental work.

- The high proportion of EVA improved the coloristic and mechanical properties of the polyolefin blends.

- The color fastness values to light in presence of microwave heating improved from 2 to 5. The washing fastness results were adequate.

- Including heating up the dye bath, the total dyeing time was 79 minutes for conventional method and 8 minutes for microwave heating. The dyeing with microwave heating process was about shorter than conventional dyeing process. This means that almost 90% of time and a great amount of energy have been saved.

REFERENCES

[1]. E. Oner, Y. Buyukakıncı and N. Sokmen, "Microwave-assisted dyeing of poly (butyleneterephthalate) fabrics with disperse dyes", *Color Technol,* vol.129 (2), pp125-130, 2013.

[2]. Y. Büyükakıncı, Y., B. Oktem, B., N. Sokmen and E. Oner, "Exhaust dyeing of polypropylene". In: Paper presented at the 5th International Istanbul Textile Conference, Istanbul, Turkey, 19-21 May 2005.

[3]. Y. Büyükakıncı, N. Sokmen and E. Oner, "Microwave assisted exhaust dyeing of polypropylene", In: Paper presented at the 4th Centrel European Conference, Liberec, Czech Republic, 7-9 September 2005.

[4]. Y. Büyükakıncı, N. Sokmen and E. Oner, "Improving the dyeability of polyolefin fibres by microwave heating", *Industria Textila*,vol. 65(1), pp.228-232, 2014.

[5]. Ahmed M. Polypropylene fibers-science and technology, New York, Elsevier, 1982.

[6]. J. Jang J and W.S. Go, "Continuous photografting of HEMA onto polypropylene fabrics with benzophenone photoinitiator", *Fibers Polym*, vol. 9(4), pp. 375-379, 2008.

[7]. N. Yaman, E., Ozdogan, N. Seventekin and H. Ayhan, "Plasma treatment of polypropylene fabric for improved dyeability with soluble textile dyestuff", *Appl Surf Sci*, vol. 255(15), pp.6764-6770, 2009.

[8]. L. Toshniwal L, Q. Fan and S.C. Ugbolue, "Dyeable polypropylene fibers via nanotechnology", *J Appl Polym Sci* , vol. 106(1), pp. 706-711, 2007.

[9]. W. Xu and C. Yang, "Hydrolysis and dyeing of polyester fabric using microwave irradiation", *Color Technol*, vol.118(5), pp.211-214 2002.

[10]. T. Biswal, R. Samal and P.K. Sahoo, "Co (III) complex mediated microwaveassisted synthesis of PAN", *J Appl Polym Sci*, 117(3), pp.1837–1842, 2010.

[11]. L. Li, Y. Yeping, L. Yu and Y. Fang, "Rapid N-phthaloylation of chitosan by microwave irradiation", *Carboh Polym*, vol. 57(1), pp. 97-100, 2004.

[12]. R.L., Shogren and A. Biswas A, "Preparation of watersoluble and water-swellable starch acetates using microwave heating", *Carboh Polym*, vol.64 (1), pp.16-21, 2006.

[13]. K. Haggag, "Fixation of pad-dyeing on cotton using microwave heating", *Am Dyestuff Rep*, pp. 26-30, 1990.

[14]. K.F. Elgert and C. Hoffmann, "Abschaben von polyestergewebe mit mikrowellenheizung", *Melliand Textilberichte*, vol.3, pp.174-178, 1995.

[15]. S. Soo Kim, S. Gyung Leem, H. Do Ghim, J. Ho Kim and W. Seok Lyoo, "Microwave heat dyeing of polyester fabric", *Fibers and Polym*, vol. 4(4), pp. 204 -209, 2003.

[16]. A. Ozerdam, I. Tarakcıoglu and A. Ozgüney, "The use of microwave energy for the fixating of reactive printed cotton fabrics", *J Text and App*, vol. 18(4), pp. 289-296, 2008.

[17]. D.R. Keshwani, J.J. Cheng, J.C. Burns, L. Li and V. "Chiang Microwave pre-treatment of switch grass toenhance enzymatic hydrolysis", In: Paper Presented at Proceedings of the ASABE Annual International Meeting, No. 077127. 35, pp. 1239-1247, 2007.

[18]. W.T. Son, D.W. Lee, J.H. Park and S.K. Lim,"Poly(ethylene-co-vinyl acetate) blends with phenoxy", *J Appl Polym Sci*, vol.73(2), pp. 227-236, 1999.

[19]. A. Ujhelyiov, E. Bolhova, J. Oravkinova, R. Tiňo and A. Marcinčin, "Kinetics of dyeing process of blend polypropylene/polyester fibres with disperse dye", *Dyes and Pigmt*, vol. 72(2), pp. 212-216, 2007.

BIOGRAPHY

Burcu Yılmaz Sahinbaskan has a PhD in textile technology (Marmara University; 2010). She is a full associate professor at Marmara University, Faculty of Technology, Department of Textile Engineering. She has worked on many projects about dyeing of textile materials using ecofriendly methods and color measument. She has produced many articles concerning natural dyes, effect of enzymatic treatments on textile materials and dyeing of cellulosic fibers and its blends in one-bath. Adress: Marmara University, Faculty of Technology, Department of Textile Engineering, 34722 Goztepe-İstanbul, Turkey. E-mail: burcuyilmaz@marmara.edu.tr.

Determination of Pre-combustion Chamber Design for a Stratified Charge Natural Gas Engine

Mehmet Cakır[1],Halil İbrahim Sonmez[2]

Abstract

The fuel efficiency of the engine is investigated intensely by researchers. Less fuel consumption for the same engine running hours is wanted by engine users. The engines operate principally as otto or diesel cycles. Although diesel cycle is advantageous at partial loads over otto cycle, it is disadvantageous at full load. Especially, diesel cycle is more efficiency at partial loads than otto. Therefore, otto principle running engines can be run like to diesel cycle at partial loads with stratified charge combustion chamber. The stratified charge in combustion engine means that rich mixture is formed around spark plug, lean mixture is formed other zone.

This study is about a new combustion chamber design for a stratified charged natural gas engine. Therefore, a small pre-chamber on the cylinder cover has designed to stratified charge in-cylinder. The engine has three valves. These are exhaust valve, main and auxiliary intake valves. Main and auxiliary valves operate simultaneously. While the rich mixture is taken from the auxiliary valve into pre-chamber, air or lean mixture is taken from main valve. Thus, the stratified charge is formed in-cylinder. Cylinder heads that is produced will be assembled to research engine. In result of the experimental tests, it will be obtained most ideal design for stratified charge natural gas engine. This paper aims to announce preliminary designs.

Keywords: *Combustion Engine Design, Natural Gas Engine, Stratified Charge.*

1. INTRODUCTION

In recent years, the reduction of fuel consumption and the increase of engines effective efficiency have been investigated by researchers. Engine users want less fuel consumption due to increase the engine efficiency.

Internal combustion engines are operated in two forms which are known spark ignition and compression ignition. In Spark ignition (Otto engine), air-fuel mixture is taken into the cylinder and ignition is provided by a spark plug. On the other hand for compression ignition (Diesel engine), the air is taken into the cylinder and combustion is achieved by spraying fuel to the compressed air.

Lean mixture combustion is performed in order to reduce the fuel consumption. Lean burn occurs when excess air is introduced into the engine along with the fuel [1]. Lean mixture limit is defined and can be increased by increasing the in-cylinder turbulence [2,3]. However, this situation decreases combustion efficiency due to the ignition problem of the air-fuel mixture. In order to overcome the disadvantages of the lean mixture, the charge in the cylinder must be stratified. The stratified charge in engine is formed by concentrating a rich mixture near the spark plug. This allows for higher compression ratios without knock, and leaner air/fuel ratio than in conventional internal combustion engines. The rich mixture near the spark plug easily ignites and smoothly burns. An internal combustion engine can be converted to a stratified charge engine by combustion pre-chamber. Pre-mixed natural gas engines are being more widely used in the vehicle, marine and power plant fields [4]. Pre-chamber contains rich mixture and the other chamber contains lean mixture. There is the rich mixture around the spark plug and lean mixture in the other region. The engine may run on a much leaner overall air/fuel ratio, using stratified charge.

---

[1] Corresponding author: Yildiz Technical University, Department of Marine Engineering Operations, 34349, Besiktas/İstanbul, Turkey. mecakir@yildiz.edu.tr.

[2] Yüzüncü Yıl University, Department of Marine Engineering Operations, Van, Turkey, hisonmez@yildiz.edu.tr.

In this study, a new combustion chamber has considered for a stratified charged natural gas engine. Therefore, a small pre-chamber on the cylinder head has designed to stratified charge in-cylinder. This paper aims to announce preliminary designs.

2. EXPERIMENTAL APPARATUS AND METHOD

An internal combustion engine can be converted to a stratified charge engine by combustion pre-chamber. The engine can run on a much leaner overall air-fuel ratio using stratified charge.

The setup consists of measurement devices and research engine connected to eddy current type dynamometer for loading. Research engine is single cylinder, water cooled, 4 stroke, 87.5 mm bore and 110 mm stroke length. Original cylinder head is given in Figure 1 that consists of coolant, intake and exhaust passages. Also, original combustion chamber cross section shows that it is consist of piston bowl, cylinder head and liner surface. It is given in Figure 2.
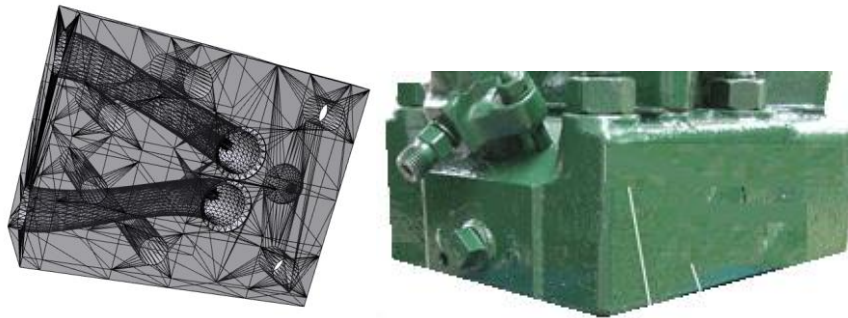
Figure1. Original cylinder head and drawing
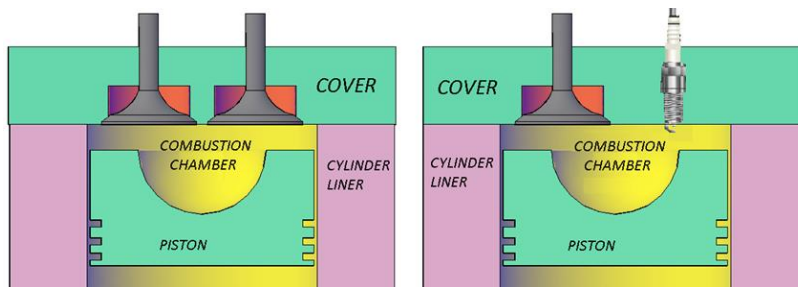
Figure 2. Research engine combustion chamber view

A small pre-chamber on the cylinder head has considered to stratified charge in combustion chamber.

Original engine has 661 cc stroke volume and 58 cc combustion chamber volume. According to literature, optimum compression rate can be selected a value between 8 and 12 for natural gas combustion. Pre-chamber volume approximately can be determined 20-30% of clearance volume [5,6]. As it is shown in Figure 2, piston bowl that a part of combustion chamber is 34 cc. Designed pre-chamber of natural gas engine nearly has determined 25% of clearance volume. Thus, combustion pre-chamber volume;

Prechamber volume = Clearance volume · 0.25

Prechamber volume = 58 cc · 0.25 = 14.5 cc

The combustion pre-chamber is connect to main chamber by a throat. According to 14.5 cc volume, sphere diameter has determined as 30 mm. Pre-combustion chamber cross section demonstrates in Figure 3.
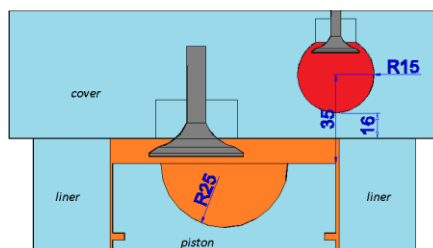
Figure 3. Pre-combustion chamber location

The orange section shows the main combustion chamber, the red section shows the pre-chamber. The combustion pre-chamber is designed in a spherical form in diameter 30 mm. It is located to 35 mm distance above from the piston edge. The combustion pre-chamber has an auxiliary intake valve, spark plug and the throat that connects main and pre-chamber.

Main and auxiliary valves operate simultaneously. While the rich mixture is taken from the auxiliary valve into pre-chamber, lean mixture is taken from main valve. Thus, the stratified charge is formed in-cylinder. The combustion process to main chamber from the pre-chamber by the throat. The throat dimensions and angles will be product changing in different models. Figure 4 illustrates these models.
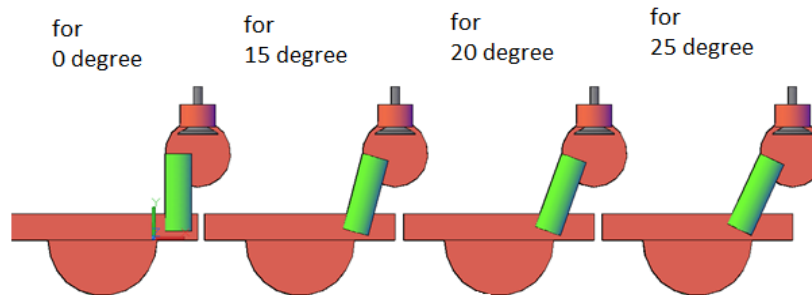
Figure 4. The appearance of different throat angles

Engine performance studies will be carried out by cylinder heads have 15-20 and 25 angles and aimed to determine the best angle from the performance data. Finally, an example view of the combustion pre-chamber is given in Figure 5.
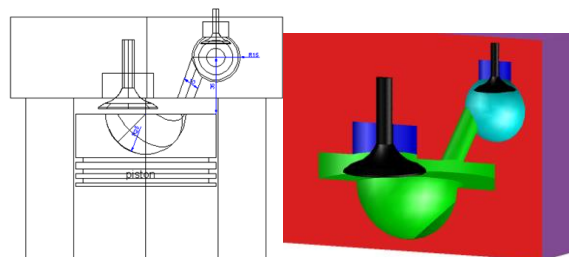
Figure 5. The combustion chamber project and 3D cross section appearance

3. RESULTS

Results of calculations show that ratio of orifice radius which is connecting the main combustion chamber and the combustion pre-chamber must be taken as 5-6 mm. According to design calculations and determined model, it was passed to the production stage for cylinder head.

Firstly, cylinder head was produced by casting method. It is shows in Figure 6 that, cylinder head was produced from the aluminum as two parts.

Figure 6. Two parts cylinder head

Pre-chamber is designed to be divided into two. Then, the machining of the big part of the cylinder head was completed by turning, milling and drilling that it is given in Figure 7.
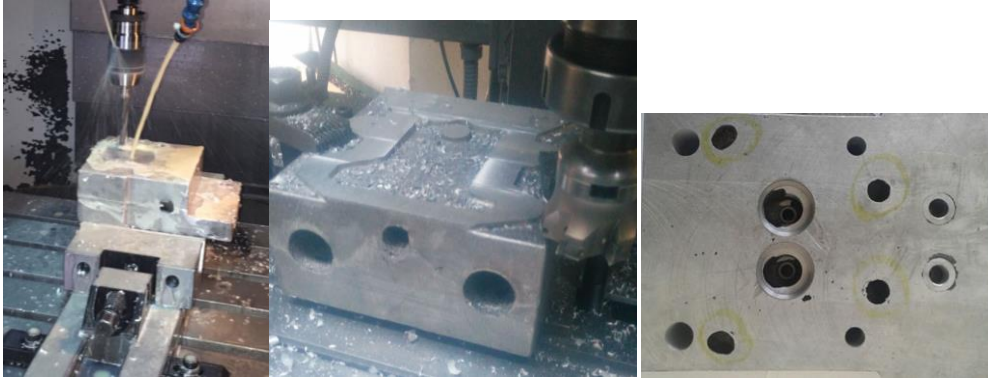
Figure 7. Machining of cylinder head.

In Figure 7, with the milling done on the entire cylinder head, the cylinder head is made smoothened and free from waste parts. The holes of the water channels seen at the bottom of the cylinder head are processed appropriately. The processed cylinder head is shown in Figure 8.
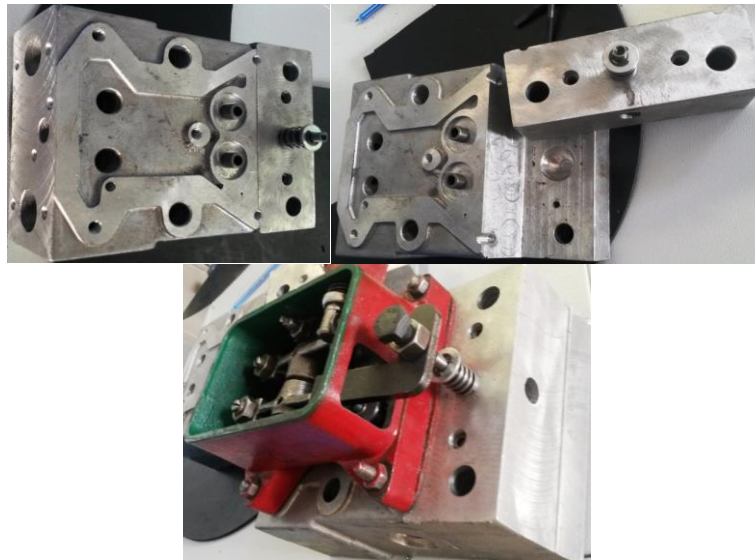
Figure 7. Final situation of combustion pre-chambered cylinder.

It seems from the Figure 8 that, the coolant, intake and exhaust passages have been produced by processing. All faults and surface roughness which are caused by casting cavities have been removed. All screw holes are opened, the part of the combustion pre-chamber is assembled with the main body and the cylinder head is ready for use.

4. COCLUSION

This study is about a new combustion chamber design for a stratified charged natural gas engine. Therefore, a small pre-chamber on the cylinder head has designed to stratified charge in-cylinder. Cylinder heads were produced successfully for stratified charge natural gas engine.

The engine has three valves. These are exhaust valve, main and auxiliary intake valves. Main and auxiliary valves operate simultaneously. While the rich mixture is taken from the auxiliary valve into pre-chamber, air or lean mixture is taken from main valve. Thus, the stratified charge is formed in-cylinder.This paper aims to announce preliminary designs.

Finally, cylinder heads have been produced for 6 different designs. Throat diameters are 10 and 12 mm, throat angles are 15, 20 and 25 degrees. Six different cylinder heads will be assembled to research engine, and engine performance tests will be carried out respectively. In result of the experimental tests, it will be obtained most ideal design for stratified charge natural gas engine.

REFERENCES

[1]. Keith Packham, Lean-burn engine technology increases efficiency, reduces NOx emissions, Power topic 7009, Technical information from Cummins Power Generation, 2007.
[2]. Ferran A. Ayala, Michael D. Gerty, John B. Heywood, Effects of combustion phasing, relative air-fuel ratio, compression ratio, and load on SI engine efficiency, (2006) SAE Paper 2006-01-0229
[3]. Xun Shen, Yahui Zhang, Tielong Shen, Chanyut Khajorntraidet, Spark advance self-optimization with knock probability threshold for lean-burn operation mode of SI engine, Energy, Volume 122, 2017, Pages 1–10.
[4]. Li-Ping Yang, En-Zhe Song, Shun-Liang Ding, Richard J. Brown, Norbert Marwan, Xiu-Zhen Ma, Analysis of the dynamic characteristics of combustion instabilities in a pre-mixed lean-burn natural gas engine, Applied Energy, 183, 2006, Pages 746-759.
[5]. Gupta H.N., Fundamentals of internal combustion engine. PHI Leaning Private Limited, Second print, 2006, New Delhi.
[6]. Willard W. Pulkrabek, Engineering Fundamentals of the Internal Combustion Engine, Prentice Hall, 1997, New Jersey.

BIOGRAPHY

Mehmet CAKIR graduated from Department of Mechanical Engineering at Suleyman Demirel University with PhD degree in 2013. His PhD research project was about investigation of single cylinder internal combustion engine performance by using boronized cylinder liner. In addition, he is involved in projects supported by TUBİTAK. Mehmet CAKIR is still working as the Assistant Professor in the Naval Architecture and Maritime Faculty, Yildiz Technical University, Istanbul.

Halil İbrahim SONMEZ graduated from Naval Architecture and Marine Engineering at Yildiz Technical University with BSc. Degree in 2012. He is appointed to Research Assistant at Yuzuncu Yil University. In Same year, he has started to study in Yildiz Technical University. He is still working as a Researcher in Department of Marine Engineering Operations, Yildiz Technical University.

The Wear Behaviour Borided Cast Iron Cylinder Liner on a Running Diesel Engine

Mehmet Cakır[1], İsmail Hakkı Akcay[2]

Abstract

This work aims to investigate wear effects of borided cast iron cylinder liner on a running diesel engine. With this regard, cast iron cylinder liner was borided using powder box-boronizing technique at 780 °C for 4 hours. The boronizing thickness and microstructure were defined as 25 µm. Borided surfaces hardness of cylinder liner was increased from 330 HV to 1380 HV. Single cylinder diesel engine was operated for 150 hours both cylinder liners (original and borided). Then, the engine was separated into parts. The microstructural analyses of worn surfaces were examined by SEM and X-ray diffraction, especially at the top dead center area of cylinder liner. As a result of, the abrasive wear deeply formed axial scratches have been observed on the surface of Top Dead Point vicinity (TDC) of the original liner. The same section of the borided liner has been not observed any plastic deformation. Only, little plastering damages were observed on surface morphology. Besides, crushing shaped plastic deformation is formed on the borided liner surface. In this case, it is interpreted that graphite on the surface were crushed and plastered on borided surface. Because, it was seen that borided layer were exactly protected and proved by XRD analysis.

Keywords: *Cylinder Liner Wearing, Boronizing, Engine Tribology.*

1. INTRODUCTION

In the recent years, the researches on designs of engine performance-enhancing has been focused because the increment in crude oil price, the reduction in the liquid fuel reserves and their detrimental effects, the increase in energy requirement day by day. Best method for increase engine efficiency is reduced of mechanical losses in engine. In internal combustion engines, about 15% of the fuel energy is consumed as mechanical losses. Approximately, half of mechanical losses are spent in process between the piston ring and cylinder liner surface [1-4]. Therefore, if mechanical losses in an internal combustion engine can be reduced about 10%, fuel efficiency could be increased about 1.5-2.5% [5-7].

Reciprocating engines have a piston assembly that compost of piston, piston rings, cylinder liner surface, connecting rod and crank shaft. The piston moves linearly between two dead centers under the influence of combustion pressure. Piston rings disposed on the piston is in contact with the surface of cylinder liner. This process can be named as piston ring-liner friction.

The study of relationships of the cylinder liner and piston ring for optimal engine life has attracted much attention in the last decade. The piston rings-liner wear and friction is considerably important in terms of engine efficiency. Particularly, upper dead center wears are effective to combustion pressure losses and uniformly lubrication regimes. The studies of piston ring-liner wear and friction have been investigated with simulate tribology tests and engine performance experiments. A lot of researchers have investigated to cylinder liner wear using firing engine tests [8-12]. Particularly, it can be said that cylinder liner wear is maximum at the top ring reversal point because of the tribological effects, high gas temperature and contact pressure [9, 10]. Wear on TDC area is very important in terms of compression pressure losses, lubrication regime and consumption in determining effective engine efficiency. For example, the metal-to-metal contact between cylinder liner and piston rings is the result of poor lubrication leads to higher wear [13]. In addition, Henein et al. (1998) reported that intense wear rate at upper dead center of liner occurred throughout the first hour in engine operation [9]. Ma et al. (2002) determined that abrasion wear of cylinder liner was formed as piston at TDC during engine break-in [14].

---

[1] *Corresponding author: Yildiz Technical University, Department of Marine Engineering Operations, 34349, Besiktas/İstanbul, Turkey. mecakir@yildiz.edu.tr.*

[2] *Suleyman Demirel University, Department of Mechanical Engineering, Isparta, Turkey, ismailakcay@sdu.edu.tr.*

Grabon et al. (2010) studied the effect of surface texture on cylinder liner wear. They reported that the effect of the number of processes on the coefficient of friction is small. They determined optimum values of the 3D extension of the roughness profile parameter (0.4–0.7 µm) and the friction coefficient was founded to be minimal in these values [15].

Dimkovski et al. (2011) investigated that develop algorithm for segmentation and quantification of plateau honing grooves and axial scratches. They estimated their modifications from 3D interference measurements taken at bottom, middle and TDC areas of a run cylinder liner surface. They determined that the axial scratches are densest in the TDC and about the same size as the plateau grooves in all three areas. But, they showed to formed only few scratches in the bottom region. Additionally, the plateau grooves in the top region clearly decreases and the deep groove interrupt and coverage are lowest in the top region, and the groove height and distance between grooves spread mostly [2].

The objective of this paper investigates wear effects of borided cast iron cylinder liner on a fire running diesel engine. Experiments were conducted on a single cylinder diesel engine for the duration of 150 hours. The original liner and borided liner engine was operated respectively. Then, the cylinder liner was removed from the engine and was sliced for analysis. The microstructural analyses of worn surfaces were examined by SEM and X-ray diffraction, especially at the top dead center area of cylinder liner.

2. EXPERIMENTAL APPLICATION

This work aims to investigate wear effects of borided cast iron cylinder liner on a running diesel engine. With this regard, cast iron cylinder liner was borided using powder box-boronizing technique at 780 °C for 4 hours. Then, single cylinder diesel engine was operated for 150 hours both cylinder liners (original and borided).

A single cylinder, air cooled and four stroke diesel engine given Table 1 was coupled to a hydraulic dynamometer. The engine loads were measurement with Torqsense trademark RWT 310 type. The experimental setup is given in Figure 1.
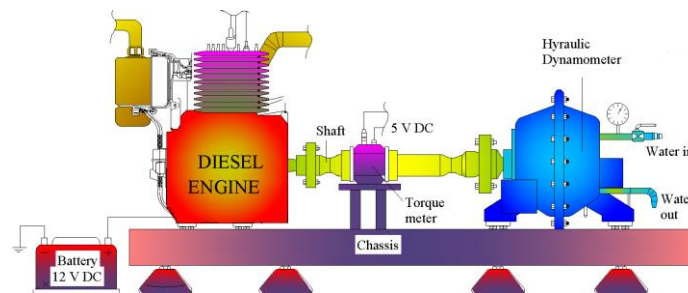
Figure 1. Schematic layout of the experimental setup

Cylinder liner of engine was boronized with pack-boronizing method using commercial Ekabor® 2 powder. The boronizing treatment was carried out in a furnace at 780°C for 4 hours by pack-boronizing method. The chemical composition of the cylinder liner used in the experiments was given in Table 1.

Table 1. The chemical composition of the cylinder liner %

C	Si	S	P	Mn	Ni	Cr	Mo	Cu	Fe
3,22	1,87	0,03	0,24	0,75	0,03	0,2	0,005	0,49	93,17

After engine operations, the cylinder liner was dismantled from the engine and it was sliced for analysis. The microstructural analyses of worn surfaces were examined by SEM and X-ray diffraction, especially at the top dead center area of cylinder liner. The analysed surface is illustrated in Figure 2.

Figure 2. Prepared sample for microstructural analysis.

3. RESULTS AND DISCUSSION

In result of microstructural analysis, the boronizing thickness and microstructure were defined as 25 µm. Borided surfaces hardness of cylinder liner was increased from 330 HV to 1380 HV. In Addition, the surface of cylinder liner became harder, smoother and evolved into a porous structural as a result of boronizing.

Topographic surface was formed a new shepe at the end of the borided process. It is very upright distinction, vanished the roughness of the surface. Fe$_2$B spherical particles were formed on the surface and the surface turned into topography porous surface.

In figure 3 is shown that amount of silisium on the original cylinder liner surface has not changed after the engine was operated. But, deep stratches were formed on the surface. It can be seen in the figure 3 that surface consist of iron, silisium and carbon.

Prior to engine operation Original Cylinder Liner Surface (0,002mm² area)				The engine after running for 150 hours Original Cylinder Liner Surface (0.002mm² area)			
Element	Net	unn. C [wt.-%]	AtomC [at.-%]	Element	Net	unn. C [wt.-%]	AtomC [at.-%]
Carbon	2129	2,47	10,37	Carbon	1941	5,45	20,83
Silikon	3415	1,89	3,40	Silikon	1510	1,93	3,16
Iron	47437	95,33	86,23	Iron	18718	92,37	76
	Total	99,7 %			Total	99,8 %	
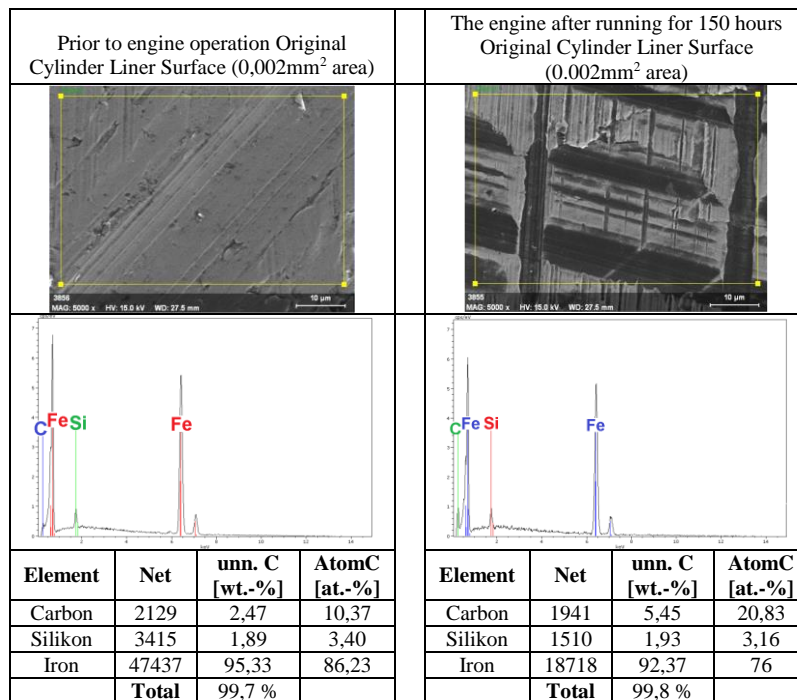
Figure 3. Original cylinder liner surface XRD.

But, after the boronizing treatment, figure 4 is seen that cast iron surface consist of carbon and iron. Here, it was seen that there is no silisium. Because, it is thougt that the boron atoms pushed the silisium inward. After engine was operated for 150 hours, it was still seen that on the surface is no silisium. This situation proves that no wear on the surface.

Prior to engine operation Borided Cylinder Liner Surface (0,002mm² area)		The engine after running for 150 hours Borided Cylinder Liner Surface (0.002mm² area)	

Element	Net	unn. C [wt.-%]	AtomC [at.-%]		Element	Net	unn. C [wt.-%]	AtomC [at.-%]
Carbon	2783	5,03	18,82		Carbon	2663	4,27	17,06
Iron	28134	100,86	81,18		Iron	33479	96,49	82,94
	Total	105,9 %				Total	100,8 %	
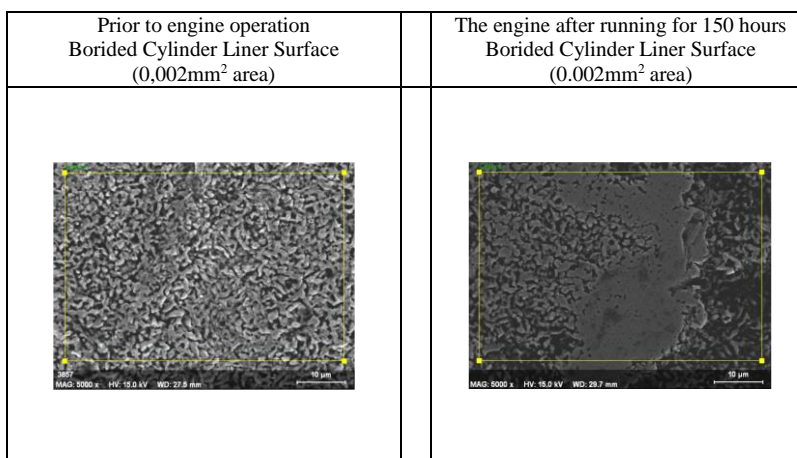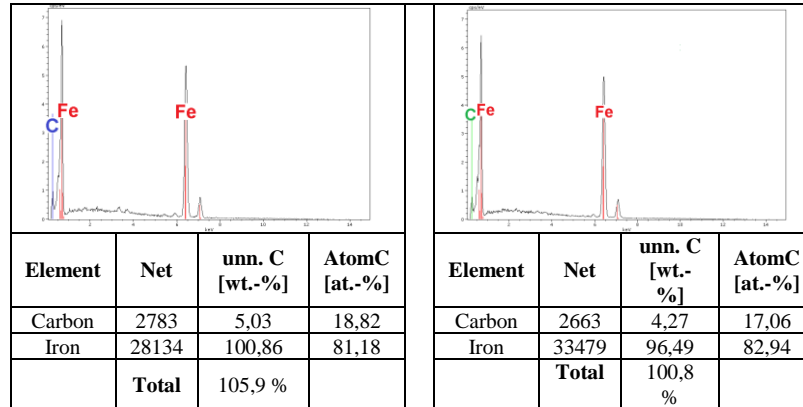
Figure 4. Borided cylinder liner surface XRD.

4. COCLUSION

This work is about to investigate wear effects of borided cast iron cylinder liner on a running diesel engine. With this regard, cast iron cylinder liner was borided using powder box-boronizing technique at 780 °C for 4 hours. Single cylinder diesel engine was operated for 150 hours both cylinder liners (original and borided).

In conclusion, boronizing treatment successfully is performed about 25 μm thickness. Wear and friction resistant of cylinder liner surface has been decreased by boronizing grey cast iron. The surface of cylinder liner has become harder, smoother, and evolved into a porous structure. Therefore, the service life of liner can be increased by a significant amount with this treatment.

ACKNOWLEDGMENT

REFERENCES

[1]. Bolander N. W., Steenwyk B. D., Sadeghi F. and Gerber G.R.,. Lubrication regime transitions at the piston ring-cylinder liner interface, Proc. IMechE Part J: Engineering Tribology, 2005, 219:19–31.
[2]. Dimkovski Z, Anderberg C, Ohlsson R, Rosén B G. Characterization of worn cylinder liner surfaces by segmentation of honing and wear scratches. Wear; 2011; 271: 548–552.
[3]. Johansson S, Nilssona P H, Ohlssonb R, Rosénc B G. Experimental Friction Evaluation of Cylinder Liner/Piston Ring Contact. Wear; 2011; 271: 625–633.
[4]. Kim M. Friction Force Measurement and Analysis of the Rotating Liner Engine. The University of Texas, Thesis of Doctorate; 2005; 196: Austin.
[5]. Andersson B. S., Company perspectives in vehicle tribology – Volvo, 17thLeeds-Lyon Symposium on Tribology - Vehicle Tribology, Tribology Ser., 1991,18:503–506.
[6]. Mishra P. C., Rahnejat H. and King P. D., Tribology of The Ring-BoreConjunction Subject to A Mixed Regime of Lubrication, Proc. IMechE PartC: J. Mechanical Engineering Science, 2009, 223, 987–998.
[7]. Spencer A., Optimizing Surface Texture for Combustion Engine Cylinder Liners, Lulea University of Technology, Licentiate Thesis, 2010, 104p.
[8]. Gara L., Zou Q., Sangeorzan B. P., Barber G., C., McCormick H. E., Mekari M. H., 2010. Wear measurement of the cylinder liner of a single cylinder diesel engine using a replication method, Wear 268, 558–564.
[9]. Henein N. A., Ma Z., Huang S., Bryzik W., Glidewell J., In Situ Wear Measuring Technique in Engine Cylinders, Tribology Transactions, 1998, 41:4, 579–585.
[10]. Ma Z., Henein N. A., Bryzik W., Glidewell J., Break-In Liner Wear and Piston Ring Assembly Friction in a Spark-Ignited Engine, Tribology Transactions, 1998, 41:4, 497 – 504.
[11]. Shuster M., Mahler F., Metallurgical and Metrological Examinations of the Cylinder Liner-Piston Ring Surfaces after Heavy Duty Diesel Engine Testing, Tribology Transactions, 42:1, 1999, 116-125.
[12]. Tamminen J., Sandstroma C. E., Andersson P., Influence of Load on the Tribological Conditions in Piston Ring and Cylinder Liner Contacts in a Medium-Speed Diesel Engine, Tribology International 39, 2006, 1643–1652.
[13]. Srivastava D. K., Agarwal A. K., Kumar J., Effect of liner surface properties on wear and friction in a non-firing engine simulator, Materials and Design, 28, 2007, 1632–1640.
[14]. Ma Z., Henein N. A., Bryzik W., Glidewell J., Cylinder Liner Surface Analysis During SI Engine Break-In, 2002, 45:3, 397-403.
[15]. Grabon W., Pawlus P., Sep J., Tribological characteristics of one-process and two-process cylinder liner honed surfaces under reciprocating sliding conditions, Tribology International 43, 2010, 1882–1892.

BIOGRAPHY

Mehmet CAKIR graduated from Department of Mechanical Engineering at Suleyman Demirel University with PhD degree in 2013. His PhD research project was about investigation of single cylinder internal combustion engine performance by using boronized cylinder liner. In addition, he is involved in projects supported by TUBİTAK. Mehmet CAKIR is still working as the Assistant Professor in the Naval Architecture and Maritime Faculty, Yildiz Technical University, Istanbul.

İsmail Hakkı AKCAY graduated from Department of Mechanical Engineering at Selcuk University with PhD degree in 1991. He is appointed to Assistant Professor at Akdeniz University. He has started to study in Suleyman Demirel University in 1992. He is still working as a Professor Doctor in Department of Machine Engineering, Suleyman Demirel University.

Dyeing of Polyamide Fabric with *Rubia tinctorium* L. Using Different Mordants

Burcu Yılmaz Sahinbaskan[1], Anıl Goksu[2], Mahmure Ustun Ozgur[3]

Abstract

Rubia tinctorium L. have been used for dyeing of textile materials such as wool, silk and cotton in many parts of the world since ancient times. In this experimental work, unmordanted and mordanted polyamide fabric samples were dyed with Rubia tinctorium L. Unmordanted samples were dyed at pH 5 and 9. Other samples were mordanted with potassium aluminium sulphate, silver nitrate and tannic acid before dyeing process, respectively. Colour differences and fastness properties of dyed fabrics were investigated and compared with each other. Finally, mordanted fabric samples were dyed successfully dark colours. Adequate results in colour fastness to perspiration and rubbing (+4) were obtained.

Keywords: *Polyamide Fabric, Rubia Tinctorium l., Mordant*

1. INTRODUCTION

Natural dyeing of textiles is as old as the history of weaving. Madder (*Rubia tinctorium* L.) is one of the most important dye plant used to produce fast red. It has been used from 3500-4000 BC to the present for red dyeing. Their roots have been used for dyeing textile materials such as protein fibers and cotton in many parts of the worlds since ancient times. *Rubia tinctorium* L. plants contain alizarin, pseudopurpurin, musjistin etc. as effective dyes. It was used for cotton dyeing in India as red dye until the beginning of the 18th century. In 1868, German chemist Gerber was found chemical formula of alizarin, which was the basic substance of madder. Alizarin was produced in large quantity after 1868 and became an important dye in the world [1-2].

Dyeing of protein fibers with natural dyes is an alternative process to synthetic dyes for environmentally friendly. When tannic acid and metal salts were used together for dyeing of protein fibers with natural colourants, the allergens were removed on fiber and some fastness properties of the textiles were improved. In various dyeing methods by using buffer solution at pH 4 for 1 hour and 100 °C, mixture of some selected metal salts and tannic acid were found effective [3-6].

Silk fabrics could be dyed with madder and another natural dye in the same bath to apply various procedures. Use of madder and walloon oak extracts together in the same bath was improved the washing fastness properties [7-8].

In other research work in the technical literature, dyeing of polyester and polyamide fabrics with curcumin and saffron was studied. Fabrics were pretreated with UV/ozone for different periods of time range from 5 to 120 minutes. This research show that the increment of the affinity of the studied synthetic fabrics towards natural dyes [9].

Nowadays, natural dyeing of textiles with *Rubia tinctorium* L. is supported as European Union Projects [1].

In this experimental work, *Rubia tinctorium* L. was applied as a natural dye with five different dyeing methods. Unmordanted samples were dyed at pH 5 and 9. Other samples were mordanted with potassium aluminium sulphate, silver nitrate and tannic acid. The effects of acidic and alkaline conditions of dye bath and three different mordants on dyeing for polyamide fabric were studied. Colour differences and fastness properties on rubbing and perspiration of dyed fabrics were investigated and compared with each other.

---

[1] *Corresponding author: Marmara University, Faculty of Technology, Department of Textile Engineering, 34722, Kadıköy/İstanbul, Turkey. burcuyilmaz@marmara.edu.tr.*

[2,3] *Yildiz Technical University, Faculty of Art and Science, Department of Chemistry, 34220, Davutpasa/İstanbul, Turkey. mozgur@yildiz.edu.tr.*

2. EXPERIMENTAL WORK

2.1. Fabric

100 % polyamide knitted fabric (118 g/m^2) was used for dyeing.

2.2. Natural Dye And chemicals

The sourse of natural dye (*Rubia tinctorium* L.) was purchased from the local market. Mordants of potassium aluminium sulphate (KAl $(SO_4)_2.12H_2O$), silver nitrate ($AgNO_3$) and tannic acid ($C_{76}H_{52}O_{46}$) were used in the study.

All the mordants being used, acetic acid (CH_3COOH) and sodium carbonate (Na_2CO_3) were analytical purity and products of Merck. Distillate water was used for preparation of the solutions.

Figure 31. Rubia tinctorium L. [1](Photographer: R. Karadag).

Dyeing was carried out laboratory scale dyeing machine (Roaches). The reflectance values of the dyed fabric samples were measured by X-rite Color i7 Benchtop Spectrophotometer with specular included mode. The colour values of the samples were calculated D65 illuminant/10° observer values. The $CMC_{(2:1)}$ Colour Differences Formula was used to express the colour differences.

The rubbing and perspiration of dyed fabrics were determined according to ISO 105-X12 and ISO 105-E04 standards, respectively.

2.3. Dyeing Methods

Method 1: 10 g *Rubia tinctorium* L. and 500 mL water were boiled for 1h and filtered through Whatman No 42 filter paper.10 g fabric samples were dyed with 90 mL filtered solution with pH 5 at 100 °C for 1h. The dyed samples were rinsed and dried at oven.

Method 2: 10 g *Rubia tinctorium* L. and 500 mL water were boiled for 1h and filtered through Whatman No 42 filter paper.10 g fabric sample was dyed with 90 mL of filtered solution with pH 9 at 100 °C for 1h. The dyed samples were rinsed and dried at oven.

Method 3: 10 g *Rubia tinctorium* L., 500 mL water and 2 g/L KAl $(SO_4)_2.12H_2O$ were boiled for 1h and filtered through Whatman No 42 filter paper. 10 g fabric sample was dyed with 90 mL of filtered solution at 100 °C for 1h. The dyed samples were rinsed and dried at oven.

Method 4: 10 g *Rubia tinctorium* L., 500 mL water and 2 g/L $AgNO_3$ were boiled for 1h and filtered through Whatman No 42 filter paper. 10 g fabric sample was dyed with 90 mL of filtered solution at 100 °C for 1h. The dyed samples were rinsed and dried at oven.

Method 5: 10 g *Rubia tinctorium* L., 500 mL water and 2 g/L $C_{76}H_{52}O_{46}$ were boiled for 1h and filtered through Whatman No 42 filter paper. 10 g fabric sample was dyed with 90 mL of filtered solution at 100 °C for 1h. The dyed samples were rinsed and dried at oven.

3. RESULTS

The colouristic and fastness properties of unmordanted/mordanted and dyed samples were evaluated and compared with dyed sample according to Method 1. Dyed fabric samples with five different methods were shown in Table 1.

Table 1. Dyed fabric samples

Methods			Samples
Method 1	Unmordanted	pH 5	
Method 2		pH 9	
Method 3	Mordanted	KAl $(SO_4)_2.12H_2O$	
Method 4		$AgNO_3$	
Method 5		$C_{76}H_{52}O_{46}$	

The CIELab values and colour differences ($\Delta E_{CMC(2:1)}$) of the dyed polyamide fabrics with *Rubia tinctorium* L. are summarized in Table 2 and 3.

Table 2. CIELab values of the dyed polyamide fabrics

Dyed Fabrics	L^*	a^*	b^*	C^*	h°
Method 1	41.47	7.87	-4.19	8.92	331.97
Method 2	48.63	7.32	-4.11	8.39	330.71
Method 3	73.62	7.36	10.98	13.23	56.16
Method 4	41.26	2.09	6.32	6.66	71.68
Method 5	40.08	5.64	11.49	12.80	63.86

The dyed fabric at pH 9 (Method 2) is lighter (ΔL^*= 7.16), less red (Δa^*= -0.55), less yellow (Δb^*= 0.08), and slightly less saturated (ΔC^*= -0.52). The colour difference ($\Delta E^*_{CMC(2:1)}$) is 3.68.

The mordanted with alum and dyed fabric sample (Method 3) is more lighter (ΔL^*= 32.15), slightly less red (Δa^*= -0.51), more yellow (Δb^*= 15.17) and more saturated (ΔC^*= 4.30). The colour difference ($\Delta E^*_{CMC(2:1)}$) is 23.87.

The mordanted with silver nitrate and dyed sample (Method 4) is slightly darker (ΔL^*= -0.21), redder (Δa^*= -5.78), more yellow (Δb^*= 10.51) and less saturated (ΔC^*= -2.26). The colour difference ($\Delta E^*_{CMC(2:1)}$) is 13.86.

The mordanted with tannic acid and dyed sample (Method 5) is darker (ΔL^*= -1.39), red (Δa^*= -2.23), more yellow (Δb^*= 15.68) more saturated. The colour difference ($\Delta E^*_{CMC(2:1)}$) is 18.21.

Table 3. Colour differences of the dyed polyamide fabrics.

Dyed Fabrics	ΔL^*	Δa^*	Δb^*	ΔC^*	ΔH^*	$\Delta E^*_{CMC(2:1)}$
Method 2	7.16	-0.55	0.08	-0.52	0.19	3.68
Method 3	32.15	-0.51	15.17	4.30	14.56	23.87
Method 4	-0.21	-5.78	10.51	-2.26	11.78	13.86
Method 5	-1.39	-2.23	15.68	3.88	15.35	18.21

*The dyed fabric sample at pH 5 (Method 1) was taken as 'standard'

All the unmordanted fabrics and mordanted fabrics with $AgNO_3$ and $C_{76}H_{52}O_{46}$ are dyed dark colours. Generally, mordanted with dyed fabric samples $C_{76}H_{52}O_{46}$ by Method 5 are also darker than the dyed samples by other methods.

Table 4. Rubbing and perspiration fastness test results of the dyed fabrics

Methods	Colour Fastness			
	Rubbing Fastness		Perspiration Fastness	
	Dry	Wet	Alkaline	Acidic
Method 1	5	5	5	5
Method 2	5	5	4-5	5
Method 3	4-5	5	4-5	5
Method 4	3	4-5	5	5
Method 5	5	5	4-5	4-5

In addition to colour properties results, the dry/wet rubbing and alkaline/acidic perspiration fastness tests were found to be quite good (4+ grey scale ratings).

4. CONCLUSION

Polyamide fabrics were successfully dyed with *Rubia tinctorium* L. The type of mordant used in the dyeing was found to be effective on the obtained colours. Alum should be used for obtained light colours with Method 3. For dark colours, fabrics should be dyed at pH 5 or silver nitrate and tannic acid should be applied as mordant salts. The colour fastness to rubbing and perspiration results of the all dyed fabrics were adequate. *Rubia tinctorium* L. may be alternative source of synthetic dyes as a natural dye for dyeing of polyamide. The antibacterial properties of these dyed fabric samples will be carried out in further investigations.

ACKNOWLEDGMENT

REFERENCES

[1]. R. Karadag, *History of Madder,* 2007.
[2]. R. Karadag and T. Yurdun, Dyestuff and colour analyses of the Seljuk carpets in Konya Ethnography Museum, Studies in Conservation, 2010, 55 (2) 178-183.
[3]. J. Lee, *Natural Dyes*, 19, 2005.
[4]. W. Chen, T. Koyama, K. Hanabusa and H. Shirai, "Preparation and antibacterial activity of silk fibroin fiber containing metal complexes", *Sen-i Gakkaishi*, 1995, 51 (4), 176-180.

[5].   G. Gumrukcu and M. Ustun Ozgur, "Effect of tannic acid and metal salts on dyeing of woolen fabrics with red onion (*Allium cepa* L.) ", Asian Journal of Chemistry, 2011, 23 (4), 1459-1466.

[6].   M. Üstün Ozgür, Z. Ogütgen Acıkgoz, G. Gümrükcü and B. Yılmaz Sahinbaskan, "Woolen fabric dyeing with *Punica granatum* L. rind using different mordants", Asian Journal of Chemistry, 2013, 25 (4), 1956-1964.

[7].   O. Deveoglu, B. Yılmaz Sahinbaskan, E. Torgan and R. Karadag, Investigation on colour, fastness properties and HPLC-DAD analysis of silk fibers dyed with *Rubia tinctorium* L. and *Quercus ithaburensis* Decaisene, Coloration Technology, 2012, 128 (5), 364-370.

[8].   O. Deveoglu, B. Yılmaz Sahinbaskan, E. Torgan and R. Karadag, Examination on RP-HPLC, colour and fastness properties of dyed silk fabrics with madder (Rubia tinctorium) and walloom oak (Quercus ithaburensis), Dyes in History and Archaelogy (DHA 30), 28-29, Derby/UK, 12-15 October 2011.

[9].   K. Elnagar, T.A. Elmaaty and S. Raouf, Dyeing of polyester and polyamide synthetic fabrics with natural dyes using ecofriendly technique, Journal of Textile, 2014, Article ID 363079, 8 pages.

BIOGRAPHY

Burcu Yılmaz Sahinbaskan has a PhD in textile technology (Marmara University; 2010). She is a full associate professor at Marmara University, Faculty of Technology, Department of Textile Engineering. She has worked on many projects about dyeing of textile materials using ecofriendly methods and colour measument. She has produced many articles concerning natural dyes, effect of enzymatic treatments on textile materials and dyeing of cellulosic fibers and its blends in one-bath. Adress: Marmara University, Faculty of Technology, Department of Textile Engineering, 34722 Goztepe-İstanbul, Turkey. E-mail: burcuyilmaz@marmara.edu.tr

An Example with Microsoft Kinect: City Modeling with Kinect

Mehmet Bilban[1], Yusuf Uzun[2], Huseyin Arıkan[3]

Abstract

Kinect is a system that can detect human movements and send them to computers. It was developed by Microsoft to play games for the Xbox game console and is being used over time for applications in other areas. Because of the new technology, there is a lack of application and the literature in this field. In this study , the user's hand movements were detected by Kinect and is done the modeling of the city by drag and drop method by accessing shapes that was designed in the WPF screen.

Keywords: *Kinect, Modelling, Wpf Screen*

1. INTRODUCTION

Kinect or Project Natal is a device that allows you to play games without any controller and a line of motion sensing input devices by Microsoft for Xbox 360 and Xbox One video game consoles and Windows PCs [1]. Kinect is a camera with a depth sensor. The convenience Kinect provides here is for the human to perceive the joint points and transfer the arm movements towards the computerized environment. Depth sensing systems such as Kinect are among the current research topics in computer vision and image processing [2].

Due to the increasing importance of your visuals, it is getting harder drawing operations that performed manually in the fields as technology, construction and architecture. It has become inevitable to present drawing and Computer Aided Design (CAD) models on paper or computer applications in the form of augmented reality. Kinect is a technology that grows in this point in human - computer interaction [8].

Recently, computer vision systems using Kinect, which costs less than traditional 3D cameras, have begun to be developed [3].

In this study, it is aimed to model a city by dragging and dropping onto Windows Presentation Foundation (WPF) screen by programming previously designed 3D models in visual studio application. Here, the software provides an integrity by adding control steps to the modeling phase of a city using the data it receives from the sensors on the Kinect.

The work was arranged as follows: In Section 2, materials and methods was explained. In Section 3, evaluations of the study were described. In Section 4, conclusions were presented.

2. MATERIALS AND METHODS

2.1. Kinect Mechanism

Kinect is a special purpose camera system developed by Microsoft that has the ability to detect motion, depth and audio. The hardware structure of the device includes RGB camera, infrared projector, depth sensor camera and sound sensor microphones. The version produced for Xbox 360 game consoles is called "Kinect for Xbox 360" and the version produced for commercial use is called "Kinect for Windows". The device view of the Kinect for Windows version is shown in Figure 1 [4].

[1] Corresponding author: Necmettin Erbakan University, Seydisehir Vocational High School, 42370, Seydisehir/Konya, Turkey. mbilban@konya.edu.tr.

[2]Necmettin Erbakan University, Seydisehir Vocational High School, 42370, Seydisehir/Konya, Turkey. yuzun@konya.edu.tr

[3]Necmettin Erbakan University, Seydisehir Department of A.C. Engineering, 42370, Konya, Turkey. harikan@selcuk.edu.tr

Figure 1. Kinect for Windows [4]

Kinect's optical components consist of IR Emitter, IR Depth Sensor, color sensor, tilt motor and microphone array. Kinect optical components in Figure 2 are as shown.
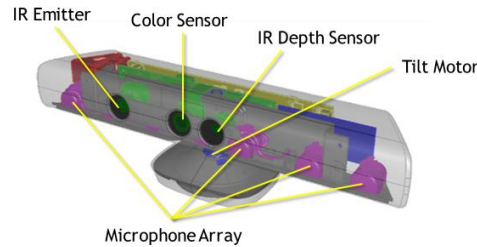
Figure 2. Kinect optical components [5]

Where, IR Emitter is emits infrared light beams, IR Depth Sensor is reads the IR beams reflected back to the sensor, Color Sensor is to make capturing a color images possible. The tilt motor is the mechanism that gives the sensor the ability to move vertically, and a simple DC motor is formed. Kinect can be moved by (+/- 27) degrees using software. The grate at the bottom portion of the Kinect 4 microphone is available. These microphones are arranged at regular intervals on the bottom of the Kinect to capture the best sound quality and the angle that the sound comes from [5].

Normal cameras collect light that jumps between objects in front. The camera turns this light into an image that resembles our own eyes. The Kinect, on the other hand, records the distance of the objects placed in front of it. Kinect uses infrared light to create a depth image that captures where things are, not what objects look like [6].

2.2. The Kinect Skeletal Structure

Kinect forms the skeleton structure from 20 joint points as shown in Figure 3. Each joint datum belongs to a predefined body region in the Kinect coordinate space, which contains 3D coordinates and is shown as a time series. The Microsoft Kinect SDK and OpenNI libraries are available for real-time and advanced animations. Both of these libraries can track the 20 joins of the human skeleton.
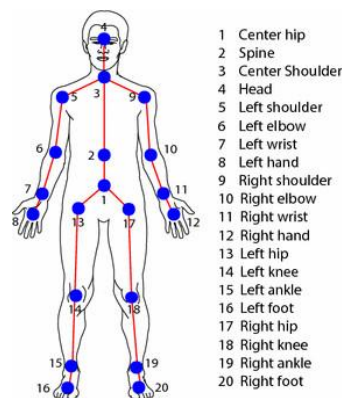
Figure 3. Joint points of the Kinect skeleton [7]

The joint data representing the human limbs are updated with the depth image frames captured at specific time intervals without deteriorating the integrity of the Kinect skeletal structure. In order to adapt the 3D model to the motion capture data obtained by Kinect, the orientation information about the joints is needed in addition to the 3D coordinate information of the joint points [8].

3. EVALUATION OF THE STUDY

In this study, the Kinect SDK application is loaded onto the computer and Kinect is connected to the computer via the USB cable. Kinect skeleton detection libraries are added to the project software. Once all the necessary configurations have been completed, Kinect will calculate the distance between the joints and detect the joint points on the human skeleton.

Control parameters of the mouse operations that correspond to human hand movements are added to the application. In this study, human skeleton is detected by Kinect. Using the mouse movements corresponding to human hand movements, the models are moved onto the WPF screen by drag and drop. The operation steps of working are shown in Figure 4.

Figure 4. Process steps of the application

Kinect actually seems to have three eyes. Two of them are in the middle, the third side is the side. This "third eye" determines how Kinect works. However, Kinect's third eye is actually an infrared projector. Kinect's infrared beam shines the rays of the form of infrared spots on the person in front of the projector. We can't see these points normally, but we can see using an IR camera.

In this study, we first identified the joint points on the human skeleton with Kinect. Using the program code we wrote, we combined these joint points with a line so that the human body would form. In this way we have created the human skeleton structure of Kinect corresponding to the human skeletal structure. Kinect's depth information acts like a 3D scanner to detect human movements.

The model shown in Figure 5 (a) was designed in the WPF screen, and the model was given motion characteristics in the XY plane. We have acquired this drag-drop motion feature that we have designed using sensor data from Kinect. In Figure 5 (a), the city model are shown on WPF screen.
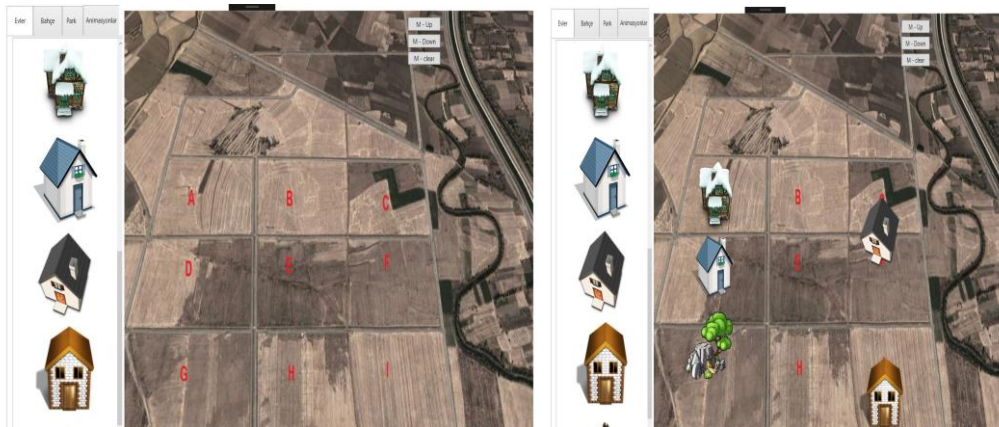
Figure 5. (a).Our city modeling designed   (b).Our city modeling application with Kinect

In Figure 5 (b), is shown the application interface we use to model the city using Kinect. The hand and arm movements of the user correspond to the mouse movement defined if it has a value less than 45 cm according to the value of the angle made by the shoulder sense. The user's hand and arm movements correspond to a double click in the mouse operation when the angle of the shoulder is greater than 45 cm.

4. CONCLUSIONS

In this study, human skeletal data detected by Kinect to correspond to mouse movement has been configured and a city modeling was carried out using hand movements. With this work, a new application on Kinect has

been realized. We have provided a road map for us to try Kinect on different platforms. We have seen that this new technology can be successfully used in different disciplines.

In this study, we have found that city planning, park-garden planning, interior and exterior architectural design can be done easily with Kinect at low cost. Using this work, we can make an analysis and calculations easier by preparing an interactive prototype in the planning of a city. The problems that will arise afterwards from traditional design problems are determined in advance by this application, and we can save time and cost in the project.

ACKNOWLEDGMENTS

REFERENCES

[1]. (2017) Wikipedia website [Online]. Available: https://en.wikipedia.org/wiki/Kinect.
[2]. J. Han, L. Shao, D. Xu, and J. Shotton, "*Enhanced Computer Vision with Microsoft Kinect Sensor: A Review*", IEEE Trans. Cybern., 2013, vol. 43, no. 5, pp. 1318–1334, Oct.
[3]. Z. Zhang, "Microsoft Kinect sensor and its effect", IEEE Multimedia Mag., 2012, vol. 19, no. 2, pp. 4–10
[4]. (2017) Kinect camera [Online]. Available: http://www.xbox.com/en-US/ kinect/default.htm.
[5]. (2017) Kinect for Windows Sensor Components [Online]. Available: https://msdn.microsoft.com/en-us/library/jj131033.aspx.
[6]. G. Borenstein, *Making Things See*, O'Reily., 2012, p.416.
[7]. S. Motiian, P. Pergami, K. Guffey, C.A. Mancinelli and G. Doretto, "*Automated extraction and validation of children's gait parameters with the Kinect*", Biomedical Engineering Online, 2015, 14:112, pp 1-32.
[8]. (2010), A. Tasdelen, *Windows Presentatin Foundation*, Pusula Yayın Evi, 350s., İstanbul.

BIOGRAPHY
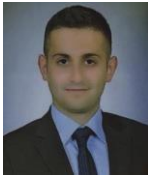
Mehmet Bilban has been working as a full-time lecturer at Seydisehir Vocational High School from Konya Necmettin Erbakan University at the Turkey. He received his MSc in Computer Science from the Gazi University of Ankara. He has been involved in research and development in the areas of kinect, mobile software, and data mining.

Yusuf Uzun has been working as a full-time lecturer at Seydisehir Vocational High School from Konya Necmettin Erbakan University at the Turkey. He received his MSc in Computer Engineer from the Selcuk University of Konya. In his Master Thesis, he extracted rules with the machine learning algorithms and fuzzy logic over the medical data. Also, he received his Ph. D. in Computer Engineer from the Necmettin Erbakan University of Konya. He has been involved in research and development in the areas of metaheuristic methods, data mining, fuzzy logic and machine learning systems.

Prof. Dr. Huseyin Arıkan was born in KONYA, Turkey, in 1967. He received the B.E. degree in mechanical engineering from the University of Selcuk, Konya, Turkey, in 1989, and the M.S. and Ph.D. degrees in mechanical engineering from the Institute of Science and Technology of University of Selcuk in 1993 and 2002, respectively. Since 2007, he has been with the Department of Mechanical Department, Seydisehir Vocational School, where he was an Assistant Professor. he has been with the Department of Mechanical Engineering, became an Associate Professor in Seydisehir Ahmet Cengiz Engineering Faculty in 2011. His current research interests include Materials science, fracture mechanics, machine design and polymer composites, metal matrix composites and structural analysis.

Adaptive General Relativity Search Algorithm for Global Optimization

Sinem AKYOL[1], Bilal ALATAS[2]

Abstract

Concepts, rules, and events in various field have been considered and modelled as novel efficient search and optimization methods with extremely effective exploration capabilities in many cases, which are able to outperform existing classical and computational intelligence based optimization methods within different types of search spaces. General Relativity Search (GRS) is one of the most current physics based computational intelligence optimization algorithm. GRS is very new and there is only one work about GRS. In this work, Adaptive General Relativity Search Algorithm (AGRSA) has been proposed by dynamically adjusting the parameters of GRS to prevent premature convergence, local solutions, and provide excellent quality of final results for the first time. AGRSA has been tested on unimodal and multimodal benchmark optimization problems and promising results have been obtained. The proposed AGRSA in this paper can be used as a new global optimization method in many complex problems.

Keywords: *General Relativity Search, Global Optimization, Dynamic Parameter Adjusting*

1. INTRODUCTION

Due to growing complexity of real-world optimization problems, better optimization algorithms are always needed. Generally, computational intelligence algorithms have good performances, however in some cases, the complexity of problems is so high that even existing methods are unable to achieve satisfactory solution in a reasonable runtime [1]. However, there are still some possibilities to invent new computational intelligence approaches [2].

Computational intelligence search and optimization algorithms can be categorized as biology, physics, swarm, sociology, music, chemistry, sports, mathematics, and plants based according to the inspiration source. General Relativity Search (GRS) is one of the newest physics based computational intelligence search and optimization algorithm and there is only one work about this method [3, 4]. This work is the first attempt to enhance its efficiency in handling search and optimization problems. The goal is to enhance the search ability of GRS and to increase the accuracy and speed by preventing premature convergence and stuck in local solutions.

This paper has been organized as follows: Section 2 gives brief explanations of GRS. Section 3 introduces the Adaptive General Relativity Search Algorithm (AGRSA) proposed in this study. Section 4 gives the experimental results obtained from GRS and AGRSA on unconstrained benchmark optimization problems. Section 5 concludes the paper along with future research directions.

2. GENERAL RELATIVITY SEARCH

General Relativity Theory (GRT) is the geometric theory of gravitation in modern physics developed by Einstein [5]. Technically, GRT is a theory of gravitation whose defining feature is its use of the Einstein field equations [6]. The solutions of the field equations are metric tensors which define the topology of the space time and how objects move inertially [7].

GRS is a novel population based computational intelligence algorithm and inspired by GRT. Particles are considered as search agents position of particles are used as candidate solutions. Position components of the particles are represented as a tensor and they change in each step of iterations. Particles move toward the best position on geodesics trajectories based on their energy–momentum. A position where particles find the least

physical action is considered as the best position. Based on GRT, particles have conserved masses and move along geodesic trajectories in a curved space. A particle with greater energy–momentum yields greater gravitational field [3]. Therefore, it has more effect on creating gravitational field and forming geodesic trajectories in the curved space. Step length and step direction for updating the particles are separately computed using particles velocity and geodesics, respectively. Velocity of particles is obtained by their energy–momentums. Any particle obtains different mass and energy from previous stage. According to physical action principle, a population of particles goes to the position with minimum action [3].

Based on these explanations, the analogy between GRT and a population based algorithm can be summarized as shown in Table 1. The pseudo-code of GRS is depicted in Figure 1.Gutter (from left) = 10 mm

Table 1. Analogy between GRT and optimization

GRT	Optimization
Particles	Search agents
Tensor	Decision variable
Position of particles	Candidate solution
Position with the least physical action	The best solution
Action	Objective function
Geodesic trajectories in a curved space	Search space

1. *Generate a random initial tensors for population of particles,*
2. *Divide initial tensor to some subspaces uniformly,*
3. *Calculate Action (cost function) for all particles,*
4. *Assign ratio of kinetic energy to the mass energy conversion for each particle,*
5. *Calculate velocity of particles,*
6. *Compute step length of motion for particles,*
7. *Compute step direction for particles,*
8. *Update position of particles,*
9. *Perform mutation operation for number of S particles with worst positions using Einstein's equation,*
10. *Repeat steps (3) to (9) until the termination criteria is satisfied,*
11. *End.*

Figure 1. Pseudo-code of GRS

3. ADAPTIVE GENERAL RELATIVITY SEARCH ALGORITHM (AGRSA)

In general relativity, total energy can be expressed as the sum of rest mass energy and kinetic energy as in Eq. (1).

$$m\gamma c^2 = E_k + mc^2 \tag{1}$$

where m is the particle mass, c is the speed of light, E_k is the kinetic energy and γ is Lorentz transformation coefficient. Initially, the ratio of kinetic energy to the rest mass energy is defined as in Eq. (2).

$$\xi = \frac{E_k}{mc^2} \tag{2}$$

ξ has been introduced in t-th iteration for the i-th test particle in s-th subspace as used in energy conversion ratio equation of GRS as in Eq. (3).

$$\xi_i(t) = \frac{I_{rand} - n}{n-1} GM_1 + \frac{1 - I_{rand}}{n-1} GM_2 \tag{3}$$

I_{rand} is a randomly selected index of one of the positions in s-th subspace. In step length computation step of GRS, GM_1 and GM_2 are called as geometry coefficients of spacetime which specify the rate of energy conversion. In GRS their values have been selected as 0.99 and 0.01 respectively. In AGRSA their values have been adaptively computed. In the first iterations GM_1 is started from 0.99 and decreased with later iterations as in Eq. (4) and GM_2 is started from 0.01 and increased in later iteration as in Eq. (5). In these

equations, iteration is the current iteration and $iter_{max}$ is the maximum iteration determined as termination criterion.

$$GM_1(iteration) = \left(-1 * \frac{iteration^{100}}{iter_{max}^{100}}\right) + 1 \qquad (4)$$

$$GM_2(iteration) = \left(1 * \frac{iteration^{100}}{iter_{max}^{100}}\right) \qquad (5)$$

All other steps are same with GRS.

SI units are strongly recommended. If non-SI units must be used, SI equivalents (or conversion factors) must also be given.

4. EXPERIMENTAL RESULTS

There are many benchmark functions to test the success of the algorithms. The selected benchmark functions and their characteristics are shown in Table 2. In this table, UM represent the unimodal, MM represents multimodal type and D is dimension. Graphics of Sphere function and Ackley function with two dimensions have been demonstrated in Figure 2 and Figure 3 respectively.

Table 2. Selected benchmark functions

Functions	Lower and Upper Limits	Min	D	Type	Equation
f_1–**Sphere**	[-100, 100]	0	30	UM	$\sum_{i=1}^{n} x_i^2$
f_2–**Ackley**	[-32, 32]	0	30	MM	$-20\exp\left(-0.2\sqrt{\frac{1}{n}\sum_{i=1}^{n} x_i}\right)$ $-\exp\left(\frac{1}{n}\sqrt{\frac{1}{n}\sum_{i=1}^{n}\cos(2\pi x_i)}\right) + 20 + e$
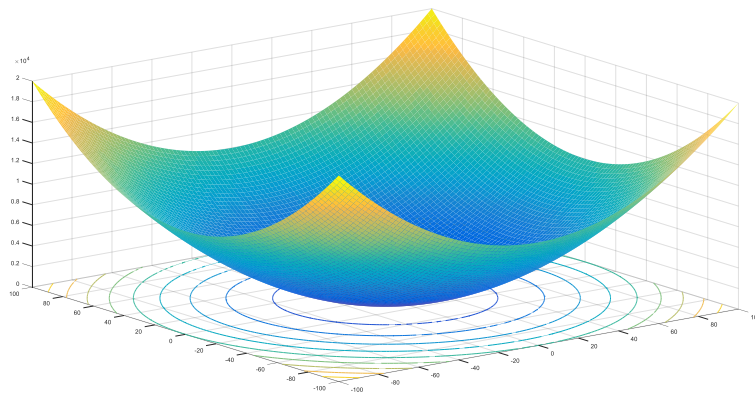
Figure 2. Sphere function with two dimensions
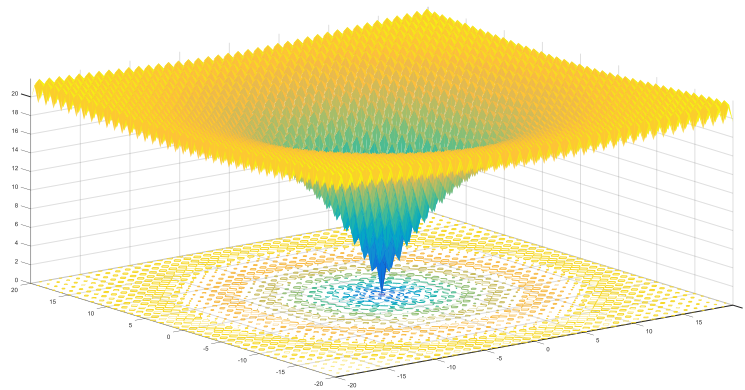
Figure 3. Ackley function with two dimensions

GRS and proposed AGRSA have been run 10 times for each benchmark function specified in Table 2. The number of search agents has been selected as 100 and maximum iteration number has been selected as 1000 for two algorithms. Table 3 presents the results obtained from two algorithms within Sphere function. Mean convergence graphics of AGRSA and GRS for Sphere function have been depicted in Figure 4 and Figure 5 respectively. Better results of AGRSA can be seen from this table and figures.

Table 3. Obtained results within Sphere function

Ex. No	AGRSA	GRS
1	7.1191e-08	3.3064e-06
2	3.4451e-08	4.4912e-08
3	2.8365e-07	6.6669e-07
4	2.6098e-07	4.0628e-04
5	4.2720e-06	2.4885e-06
6	7.1246e-08	4.5763e-07
7	3.0993e-08	1.4208e-07
8	2.1353e-07	1.2474e-05
9	5.8750e-06	3.7461e-05
10	5.9466e-06	5.4289e-05
Mean	1.71e-06	5.18e-05
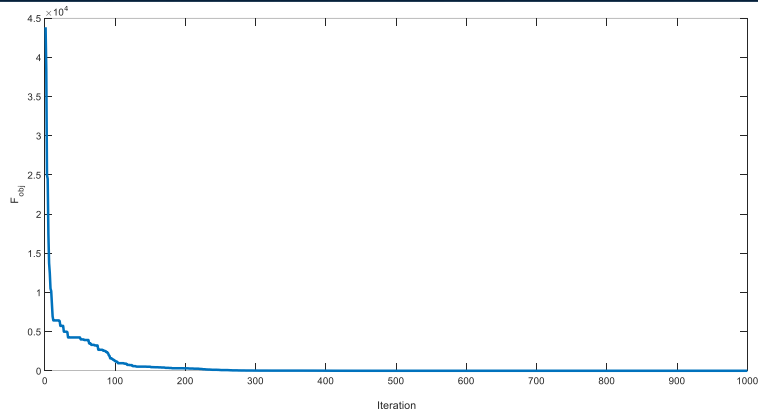
Figure 4. Mean convergence graphics of AGRSA for Sphere function
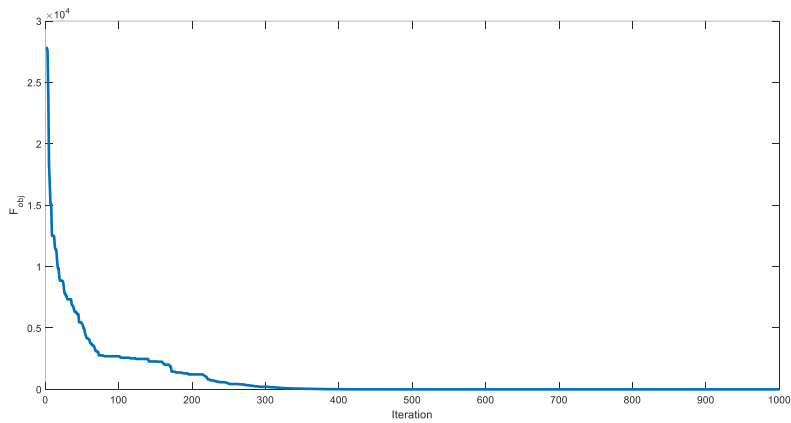
Figure 5. Mean convergence graphics of GRS for Sphere function

Table 4 presents the results obtained from AGRSA and GRS within Ackley function. Mean convergence graphics of AGRSA and GRS for Ackley function have been depicted in Figure 6 and Figure 7 respectively. According to these obtained results, AGRSA is better than GRS within this multimodal benchmark functions.

Table 4. Obtained results within Ackley function

Ex. No	AGRSA	GRS
1	1.099435503792989e-05	5.395302852102546e-04
2	6.026597245512022e-05	4.221340350669678e-04
3	7.969507259453224e-06	0.001642863473074
4	7.038233670275673e-05	0.001082251942290
5	4.674189663678163e-05	7.361079024166273e-04
6	5.661909254772723e-05	8.814749151619949e-04
7	2.372325192201430e-05	6.435195461707011e-04
8	7.896958789110897e-06	0.003138319193408
9	7.856682733820009e-05	0.001562091317596
10	5.712367790255968e-05	0.0078
Mean	4.20e-05	1.84e-03

632
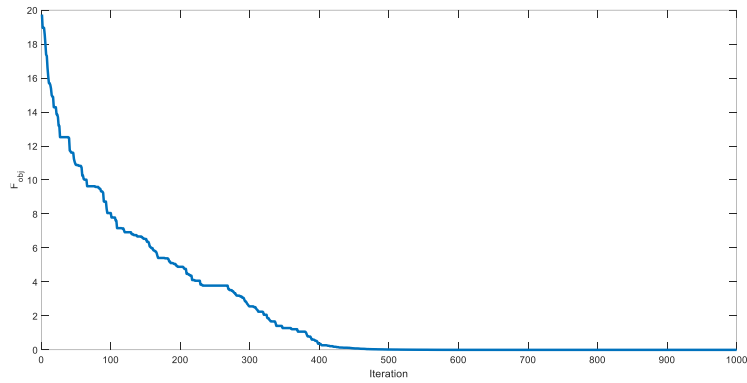
Figure 6. Mean convergence graphics of AGRSA for Ackley function
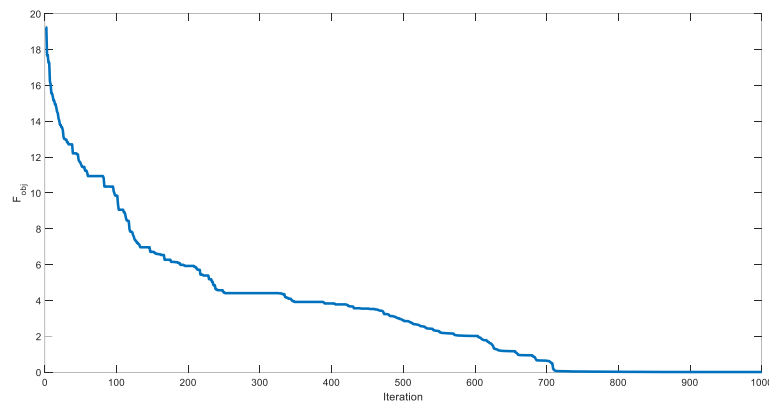
Figure 7. Mean convergence graphics of GRS for Ackley function

5. CONCLUSIONS

GRS is one of the most recent physics based general purposed computational serch and optimization method and there is only one work about GRS. In this work, Adaptive General Relativity Search Algorithm (AGRSA) has been proposed by dynamically adjusting the geometry coefficient parameters of GRS to prevent premature convergence, local solutions, and provide excellent quality of final results for the first time. According to the experimental results promising results have been obtained from AGRSA on unimodal and multimodal benchmark optimization problems. The proposed AGRSA in this paper can be used as a new global optimization method in many complex problems. Different adaptive methods can also be embedded to the original GRS to increase the performance within different types of search and optimization problems.

REFERENCES

[1]. A. Askarzadeh, A. Rezazadeh, *A new heuristic optimization algorithm for modeling of Proton Exchange Membrane Fuel Cell: Bird Mating Optimizer*, International Journal of Energy Research, vol. 37, 196–1204, 2013.
[2]. S. Akyol, B. Alatas, *Plant Intelligence based Metaheuristic Optimization Algorithms,* Artificial Intelligence Review, vol. 47(7), 417-462, 2017.
[3]. H. Beiranvand, E. Rokrok, *General Relativity Search Algorithm: A Global Optimization Approach*, International Journal of Computational Intelligence and Applications, vol. 14(3), 1550017, 2015.
[4]. A. Kumar, G. Srungavarapu, H. Beiranvand, E. Rokrok, *A Novel Approach for Automatic Generation Control of Multi Area Power Systems with Nonlinearity using General Relativity Search Algorithm.* 2016 IEEE Annual India Conference (INDICON), 1-6, 2016.
[5]. A. Einstein, *Relativity: The Special and General Theory* (Translation 1920), New York: H. Holt and Company, 1916.
[6]. J. Stewart, *Advanced General Relativity,* Cambridge University Press, 1994.
[7]. A. S. Eddington, *Space*, *Time and Gravitation*, Cambridge University Press, 1987.

Dragonfly Algorithm for Constrained Engineering Design Optimization Problems

Sinem AKYOL[1], Bilal ALATAS[2]

Abstract

Metaheuristics algorithms can give optimal solutions for large dimensional optimization problems in acceptable time. In recent years, it has been getting stronger and getting more popular every day. The dragonfly algorithm is one of the most current computational intelligence algorithms based on swarm intelligence. It has been inspired by the dynamic and static swarming behaviors of the dragonflies in nature. In static swarm, the dragonflies create small groups and fly back and forth in a small field to hunt other flying prey, while in dynamic swarm a massive number of dragonflies create swarm to migrate long distances in one direction. The algorithm has five parameters to control cohesion, attraction (towards food sources), separation, alignment, and distraction (outwards enemies) of individuals in the swarm. In this paper, dragonfly algorithm is introduced and performance is tested for constrained real engineering optimization problems. Experimental results show that the performance of this new algorithm is promising. Algorithm can be successfully applied in many complex real world search and optimization problems.

Keywords: *Dragonfly algorithm, swarm intelligence, metaheuristic algorithms, global optimization*

1. INTRODUCTION

Metaheuristic algorithms are used as a simple approach to solution of search or optimization problems, and in recent years they have become stronger and more popular every day. These algorithms, which can be used effectively in most places, have many advantages. Particularly concurrently, different types of decision variables offer objective solutions and general solution strategies where probability can be applied in the case of constraints. The solution strategies do not depend on the type of the objective function and the type of constraints and the type of variables used in problem modeling. It is also not dependent on the type of solution space, the number of decision variables, and the number of constraints. The system does not need well-defined mathematical models that are difficult to set up for the model and objective function, and sometimes cannot be used because the solution time cost is very high. The computational power of these algorithms is good, that is, they do not need computation time at extreme levels. Transformations and adaptations are easy. Another advantage is that they start to search for solutions within large scale combinational and nonlinear problems from more than one point and give effective results. These algorithms, as in the classical algorithms, do not require some assumptions that can be difficult to validate in a solution for the problem. It also does not require any modification to the problem of interest as in conventional algorithms. They adapt themselves to solve different kinds of problems. Due to these advantages, metaheuristic algorithms are widely used in management, computer science, engineering, etc., and new versions are proposed [1, 2].

General purposed metaheuristic methods are generally classified in different groups like swarm based, social based, music based, sports based, chemistry based, and etc. Swarm-based algorithms are inspired by the ability of animals such as birds, fish, and wolves to adapt to their environments by applying an "information sharing" approach, to find rich food sources and to avoid hunting. Artificial bee colony (ABC) [3], Particle swarm optimization (PSO) [4], Firefly algorithm (FA) [5], Ant colony optimization (ACO) [6] are the most well-known swarm-based metaheuristic-based optimization algorithms [1, 2].

There are about 3000 species of dragonfly insects in the world, and they have two largely turning points, larvae and adults. They are metamorphosed to become adults when they spend a large part of their lives as larvae. These little hunters, hunting almost all the other little insects in the world, have unique and rare

---

[1] *Corresponding author: Munzur University, Department of Computer Engineering, 62000, Tunceli, Turkey. sakyol@munzur.edu.tr*

[2] *Fırat University, Department of Software Engineering, 23119, Elazığ, Turkey. balatas@firat.edu.tr*

swarming behavior. Dragonflies are only gathering for hunting and immigration purposes. Static (feeding) swarm is called collectors for hunting purposes, while those gathered for immigration are called dynamic (migratory) swarm.

In the static swarm, dragonflies fly back and forth in small groups to hunt other flying animals such as mosquitoes and butterflies. In the dynamic swarm, a large number of dragonflies fly collectively in one direction at long distances. Dragonfly Algorithm's (DA) main source of inspiration is the static and dynamic swarm behaviors of dragonflies. The static swarm flies to different areas by creating small groups. On the other hand, the dynamic swarm migrates in a larger range [7].

In this work, the DA has been introduced and the comparative results obtained from other well-known swarm-based algorithms for constrained engineering design optimization problems have been presented. In Section 2, DA has been explained. Section 3 defines the constrained engineering design optimization problems used for comparisons. Section 4 presents the experimental results and finally Section 5 concludes the paper along with future research directions.

2. DRAGONFLY ALGORTIHM (DA)

It is thought that the behaviors of the swarms follow three primitive principles: separation, which means avoiding static collisions with other individuals in the neighborhood of individuals; alignment, indicating the speed matching of the other individuals in the neighborhood; and cohesion, indicating the tendency of individuals toward the center of convergence mass. The main purpose of the survivors is to survive. That is why, all the individuals in the swarm should be directed to the source of food and distribute the enemies outward. According to these behaviors, individuals have five main factors in updating the position, and mathematical modeling of each is as follows:

The mathematical model of the separation is defined as in Eq. (1).

$$S_i = -\sum_{j=1}^{N} X - X_j \tag{1}$$

where X is the position of the current individual, X_j is the position of the j-th neighbor, and N is the number of neighboring individuals [7].

The mathematical model of the alignment is defined as in Eq. (2).

$$A_i = \frac{\sum_{j=1}^{N} V_j}{N} \tag{2}$$

where V_j represents the speed of the j-th neighbor.

The mathematical model of the cohesion is defined as in Eq. (3).

$$C_i = \frac{\sum_{j=1}^{N} X_j}{N} - X \tag{3}$$

where X is the position of the current individual, X_j is the position of the j-th neighbor, and N is the number of neighboring individuals [7].

The mathematical model of the attraction towards a food source is defined as in Eq. (4).

$$F_i = X^+ - X \tag{4}$$

where X is the position of the current individual, and X^+ is the position of the food source.

The mathematical model of the distraction outwards an enemy is defined as in Eq. (5).

$$E_i = X^- + X \tag{5}$$

where X is the position of the current individual, and X^- is the position of the enemy [7].

The behavior of dragonflies is considered as combination of these five mathematical models. The step (ΔX) and the position (X) vectors are considered to update the position of the artificial dragonflies in a search space and to simulate their movement. The step vector indicates the direction of dragonfly movement and is defined as in Eq. (6).

$$\Delta X_{t+1} = (sS_i + aA_i + cC_i + fF_i + eE_i) + w\Delta X_t \qquad (6)$$

where s denotes the separation weight, S_i denotes the separation of the i-th individual; a is the alignment weight, A_i is the alignment of the i-th individual; c denotes cohesion weight, C_i denotes the cohesion of the i-th individual; f is the food weight, F_i is the food source of i-th individual; e indicates the enemy factor, E_i indicates the enemy position of the i-th individual; w is inertia weight, and t is iteration counter. Once the step vector has been calculated, the position vector is updated as in Eq. (7).

$$X_{t+1} = X_t + \Delta X_{t+1} \qquad (7)$$

t is the current iteration [7].

Different exploration and exploitative behaviors can be obtained during optimization through separation, alignment, cohesion, food, and enemy weights. Due to the importance of the neighborhoods of the dragonflies, it is assumed that each artificial dragonfly has a certain radius neighborhood.

Dragonflies in static and dynamic swarm can show differences in separation, alignment, cohesion, search for food, and removal of the enemy. For example, dragonflies tend to align their flight while maintaining proper separation and cohesion in the dynamic swarm. In static swarm, cohesion is too high to attack prey, while alignments are very low. For this reason, the weights with low alignment and high cohesion are specified when exploiting the search area, and the weights with high alignment and low cohesion are specified when exploring the search area. The radius of the neighborhoods is increased proportionally to the number of iterations for transition between exploration and exploitation. Another way to balance exploration and exploitation is to adapt the drifting factors (s, a, c, f, e, and w) during optimization [7].

In order to guarantee that dragonflies converge during optimization, their weights are changed adaptively in the transition from exploration to exploitation of the search area. In addition, the neighborhood area has been enlarged to allow the swarm to become a group in the final stage of optimization for converging to global optimization. The food source and the enemy are selected from the best and worst solutions available up to now.

Artificial dragonflies need to fly around the search area using a random walk (Lèvy flight) when there are no adjacent solutions to improve their randomness, their stochastic behaviors and their explorations. In this case, the position of the dragonflies is updated as in Eq. (8).

$$X_{t+1} = X_t + L\grave{e}vy(d) \times X_t \qquad (8)$$

Here t is the current iteration and d is the dimension of the position vector [7].

Lèvy flight is calculated as in Eq. (9).

$$L\grave{e}vy(x) = 0.01 \times \frac{r_1 \times \sigma}{|r_2|^{\frac{1}{\beta}}} \qquad (9)$$

where r_1 and r_2 are two random numbers in the range [0,1], β is a constant and σ is calculated as in Eq. (10).

$$\sigma = \left(\frac{\Gamma(1+\beta) \times \sin\left(\frac{\pi\beta}{2}\right)}{\Gamma\left(\frac{1+\beta}{2}\right) \times \beta \times 2^{\left(\frac{\beta-1}{2}\right)}} \right)^{\frac{1}{\beta}} \qquad (10)$$

where $\Gamma(x) = (x-1)!$. The pseudo code of DA is shown in Figure 1.

```
Dragonfly Algorithm

Initialize a population of n dragonflies Xᵢ (I=1, 2, ..., n)
Initialize step vectors ΔXᵢ (I=1, 2, ..., n)
While the end condition is not satisfied
            Calculate the objective values of all dragonflies
            Update the food source and enemy
            Update w, s, a, c, f, and e
            Calculate S, A, C, F, and E using Equation (1) to (5)
            Update neighboring radius
            if a dragonfly has at least one neighboring dragonfly
                    Update velocity vector using Equation (6)
                    Update position vector using Equation (7)
            else
                    Update position vector using Equation (8)
            end if
            Check and correct the new positions based on the boundaries of variables
end while
```

Figure 1. Pseudo code of DA

3. CONSTRAINED ENGINEERING DESIGN OPTIMIZATION PROBLEMS

In real world applications, most optimization problems are subject to different constraints. Such problems are known as constrained optimization problems. A constrained optimization problem is defined as the finding of a parameter vector that minimizes an objective function that is subject to inequality and / or equality constraints. In this work, welded-beam design problem and tension / compression spring problem are used from the most well-known constrained engineering problems.

3.1. Welded-Beam Design Optimization Problem

The aim of this problem is to obtain a welded beam design with minimum cost under certain constraints. Figure 2 represents a welded beam structure consisting of the beam A and the weld needed to hold this beam to object B. The problem consists of four design variables (x_1, x_2, x_3, and x_4). In Figure 2, the weld size is represented by h, (x_1); weld connection length is represented by l, (x_2); beam width is represented by t, (x_3); beam truncation is represented by b, (x4). The objective function of the problem and the constraints are given in Table 1.
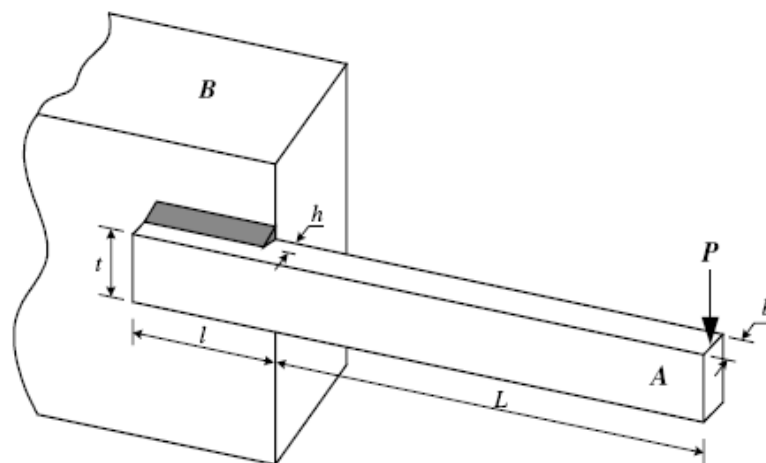
Figure 2. Welded beam design problem

III INTERNATIONAL CONFERENCE ON
ENGINEERING AND NATURAL SCIENCE
3 - 7 May 2017 BUDAPEST

Table 1. Welded-beam design problem

Problem: Welded beam design optimization problem	
Objective function	$f(x) = 1.10471x_2x_1^2 + 0.04811x_3x_4(14 + x_2)$
Subject to:	$g_1(x) = \tau(X) - 13600 \leq 0$
	$g_2(x) = \sigma(X) - 30000 \leq 0$
	$g_3(x) = x_1 - x_4 \leq 0$
	$g_4(x) = 0.10471x_1^2 + 0.04811x_3x_4(14 + x_2) - 5 \leq 0$
	$g_5(x) = 0.125 - x_1 \leq 0$
	$g_6(x) = \delta(X) - 0.25 \leq 0$
	$g_7(x) = 6000 - P_c(X) \leq 0$
where:	$\tau(X) = \sqrt{a^2 + 2ab(x_2/2R) + b^2}$
	$a = \frac{6000}{\sqrt{2}x_1x_2}$ $b = \frac{6000(14\frac{x_2}{2})R}{2\sqrt{2}x_1x_2\left[\frac{x_2^2}{12}+\left(\frac{x_1+x_3}{2}\right)^2\right]}$ $R = \sqrt{\frac{x_2^2}{4}+\left(\frac{x_1+x_3}{2}\right)^2}$
	$\sigma(X) = \frac{504000}{x_4x_3^2}$ $\delta(X) = \frac{65856000}{(30\times10^6)x_4x_3^2}$
	$P_c(X) = \frac{4.013(30\times10^6)}{196}\sqrt{\frac{x_3^2x_4^6}{36}\left[1 + \left(x_3\frac{\sqrt{\frac{30\times10^6}{4(12\times10^6)}}}{28}\right)\right]}$
With boundary conditions $0.1 \leq x_1 \leq 2, 0.1 \leq x_2 \leq 10, 0.1 \leq x_3 \leq 10$ and $0.1 \leq x_4 \leq 2$	

3.2. Tension-Compression Spring Design Optimization Problem

The purpose of the spring design problem, which is another well-known engineering problem, is to create a spring design with a minimum weight. The problem consists of three design variables (x_1, x_2, x_3) and four constraints (g_1, g_2, g_3, g_4). In Figure 3, the wire diameter is represented by d, (x_1); average coil diameter is represented by D, (x_2); the number of active rolls is represented by N, (x_3). The objective function of the problem and its constraints are given in Table 2.
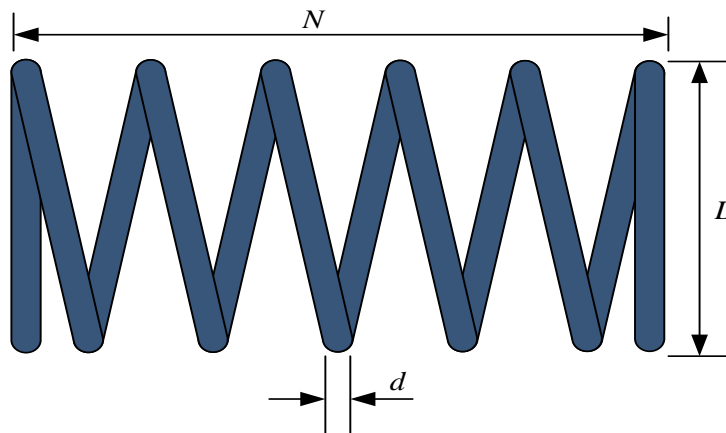
Figure 3. Tension/compression spring design problem

Table 2. Tension/compression spring design optimization problem

Problem: Tension/compression spring design optimization problem	
Objective function	$f(x) = (x_3 + 2)x_2 x_1^2$
Subject to:	$g_1(x) = 1 - \dfrac{x_2^3 x_3}{71785 x_1^4} \leq 0$
	$g_2(x) = \dfrac{4x_2^2 - x_1 x_2}{12566 x_2 x_1^3 - x_1^4} - \dfrac{1}{5108 x_1^2} \leq 0$
	$g_3(x) = 1 - \dfrac{140.45 x_1}{x_2^2 x_3} \leq 0$
	$g_4(x) = \dfrac{x_1 + x_2}{1.5} - 1 \leq 0$

With boundary conditions $0.05 \leq x_1 \leq 2, 0.25 \leq x_2 \leq 1.3$ and $2 \leq x_3 \leq 15$

4. EXPERIMENTAL RESULTS

In this work, it is aimed to measure the performance of the DA on constrained problems by selecting some real life engineering problems. The performance of the proposed method is compared with the results obtained by the PSO and ABC algorithms in order to better understand the effectiveness of the developed method. In order to make a fair comparison, the number of populations is selected as 50 and the number of iterations is selected 1000. In addition, three methods were run 30 times in order to ensure decisive and stable results.

The results obtained from DA's 30 runs for the welded-beam design optimization problem are shown in Table 3. x_1, x_2, x_3, and x_4 are four design variables, $f(x)$ is the objective function value. The best, worst and mean results and standard deviation for welded-beam design optimization problem obtained from DA, PSO, and ABC algorithms are shown in Table 4. According to this table, it is seen that DA has the best result and has better results in the mean than the PSO and ABC algorithms.

Table 3. The results obtained from DA's 30 runs for the welded-beam design optimization problem

	x_1	x_2	x_3	x_4	$f(x)$
1	0.15091	5.1897	9.0859	0.20548	1.8542
2	0.2036	3.4785	9.1358	0.2053	1.7365
3	0.187659	3.58859	10	0.201381	1.8437
4	0.20099	3.3664	9.6071	0.20305	1.78
5	0.20117	3.3677	9.5899	0.20314	1.7783
6	0.19707	3.5994	9.2046	0.20491	1.7514
7	0.195138	3.36918	10	0.201381	1.8245
8	0.1923	3.7357	9.1534	0.20515	1.7549
9	0.17415	4.3035	9.047	0.20568	1.7828
10	0.190094	3.47572	10	0.201381	1.8319
11	0.20241	3.3919	9.4434	0.20385	1.7642
12	0.19746	3.481	9.4961	0.20361	1.776
13	0.19494	3.604	9.3217	0.20435	1.7646
14	0.18847	3.8158	9.1956	0.2051	1.7663
15	0.182023	3.69231	10	0.201381	1.8492

16	0.20259	3.5037	9.1278	0.20528	1.7368
17	0.2006	3.5825	9.0416	0.20571	1.7325
18	0.17322	4.2586	9.1987	0.20493	1.7971
19	0.20047	3.25021	10	0.201388	1.8156
20	0.199156	3.28219	10	0.201381	1.8182
21	0.19811	3.6244	9.081	0.20551	1.7395
22	0.19434	3.7217	9.0814	0.20551	1.7464
23	0.18953	3.6408	9.5661	0.20323	1.7945
24	0.19036	3.7775	9.1713	0.20507	1.7598
25	0.20343	3.4822	9.1462	0.20519	1.7376
26	0.20592	3.4603	9.0526	0.20592	1.728
27	0.18068	4.1001	9.0468	0.20568	1.7682
28	0.187622	3.53831	10	0.201381	1.8368
29	0.18148	4.0765	9.0468	0.20604	1.7693
30	0.19907	3.5092	9.3202	0.20436	1.758

Table 4. The best, worst and mean results for welded-beam design optimization problem obtained from DA, PSO, and ABC algorithms

	DA	PSO	ABC
Best	1.72800	2.38098	1.80240
Worst	1.85420	2.64644	1.94540
Mean	1.77989	2.43620	1.86690
Standard Deviation	0.038084143983927	0.055608866601583	0.036445334438016

The results obtained from DA's 30 runs for the tension/spring design optimization problem are shown in Table 5. x_1, x_2, and x_3 are three design variables, $f(x)$ is the objective function value. The best, worst, and mean results and standard deviation for tension/spring design optimization problem obtained from DA, PSO, and ABC algorithms are shown in Table 6. According to this table, it is seen that DA has the best result and has better results in terms of mean than the PSO and ABC algorithms.

Table 5. The results obtained from DA's 30 runs for the tension/spring design optimization problem

	x_1	x_2	x_3	$f(x)$
1	0.05	0.316156	14.1975	0.012802
2	0.05	0.310414	15	0.013193
3	0.05	0.317265	14.0491	0.01273
4	0.052819	0.38275	9.9645	0.012776
5	0.056214	0.47566	6.6607	0.013018
6	0.05	0.314465	14.4277	0.012915
7	0.057628	0.51713	5.728	0.013272
8	0.05	0.317425	14.0278	0.012719
9	0.059788	0.58467	4.5894	0.013772

10	0.051456	0.350244	11.7129	0.012717
11	0.05612	0.47297	6.7295	0.013003
12	0.05	0.316747	14.1181	0.012763
13	0.05	0.315984	14.2207	0.012814
14	0.05	0.314468	14.4273	0.012915
15	0.05	0.316618	14.1354	0.012772
16	0.0520168	0.364654	10.8384	0.012667
17	0.0515397	0.353112	11.5044	0.012667
18	0.05	0.317371	14.035	0.012723
19	0.05311	0.39187	9.491	0.012701
20	0.05	0.317378	14.0341	0.012722
21	0.05545	0.45413	7.2462	0.01291
22	0.05	0.317352	14.0375	0.012724
23	0.05368	0.40582	8.9184	0.012768
24	0.057379	0.5097	5.8766	0.013218
25	0.05	0.31729	14.0458	0.012728
26	0.05	0.317279	14.0472	0.012729
27	0.05	0.310468	14.9921	0.013189
28	0.05	0.317424	14.0279	0.012719
29	0.053511	0.40216	9.0496	0.012724
30	0.05	0.3174	14.0312	0.012721

Table 6. The best, worst and mean results for tension/spring design optimization problem obtained from DA, PSO, and ABC algorithms.

	DA	PSO	ABC
Best	0.012667	0.012930	0.012917
Worst	0.013772	0.019850	0.013318
Mean	0.012868	0.015351	0.013134
Standard	0.00024520760380852	0.0017316194333828	0.00010960256834813

5. CONCLUSIONS

New metaheuristic algorithms are proposed and will continue to be proposed in the future as there is no best-yielding algorithm for all problems and researches always want to find the best. In this study DA, which is one of the most current swarm based search and optimization algorithm, is explained in detail and is tested in real-life engineering problems which are welded-beam design optimization and tension/spring design optimization problems. The obtained results are compared with the results obtained from PSO and ABC algorithms. According to this, it is observed that DA provides better results than these two most well-known algorithms, even though DA has recently been proposed and no parameters or other adjustments have not been made.

In future works, DA can be used effectively on many real-world problems. In addition, new search strategies and self-adapting approaches can be suggested to increase DA's search power and accuracy. Multi-objective, distributed, and parallel versions of the algorithm can be seen as future studies.

REFERENCES

[1] B. Alatas, ACROA: "Artificial Chemical Reaction Optimization Algorithm for Global Optimization," Expert Systems with Applications, vol. 38(10), pp. 13170-13180, 2011.

[2] S. Akyol, B. Alatas, "Fizik Tabanlı En Güncel Yapay Zekâ Algoritması "Elektromanyetik Alan Optimizasyonu"nun Performansının İncelenmesi," in 1st International Conference on Engineering Technology and Applied Sciences Afyon Kocatepe University, Turkey 21-22 April 2016, p. 670-676.

[3] B. Basturk, D. Karaboga, "An Artificial Bee Colony (ABC) Algorithm for Numeric Function Optimization," in Proceedings of the IEEE Swarm Intelligence Symposium 2006, Indianapolis, Indiana, USA, 12–14 May 2006.

[4] J.Kennedy, R. Eberhart, "Particle Swarm Optimization," in IEEE International Conference on Neural Networks, vol. 4, pp. 1942–1945, 1995.

[5] X. S. Yang, "Nature-Inspired Metaheuristic Algorithms," Luniver Press, 2008.

[6] A. Colorni, M. Dorigo, V. Maniezzo, "Distributed Optimization by Ant Colonies," in The 1st European Conference on Artificial Life, Paris, France, p. 134–142, 1991.

[7] S. Mirjalili, "Dragonfly Algorithm: A New Meta-Heuristic Optimization Technique for Solving Single-Objective, Discrete, and Multi-Objective Problems," Neural Computing and Applications, vol. 27(4), pp. 1053-1073, 2016.

BIOGRAPHY

Sinem Akyol: She received her BSc in Computer Engineering from Ege University, Turkey in 2009. She completed her MSc in Electrical and Electronics Engineering at Munzur University. At present she is pursuing Ph. D. in Computer Engineering, Firat University, Turkey. She is a Research Assistant in the Department of Computer Engineering at the Munzur University. Her research interests include social network analysis, data mining, and metaheuristic optimization.

Bilal Alatas: He received his B.S., M.S., and Ph.D. degrees from Firat University. His research interests include artificial intelligence, data mining, and metaheuristic computation. Dr. Alatas has published over 50 papers in many well-known international journals and proceedings of refereed conference since 2001. He has been editor of nine international journals and reviewer of twenty international journals.

The Heat Production and Definition of P-Wave (V_p) Velocities

Ayca Cırmık[1]

Abstract

The magnetic minerals in the crust which represent ferromagnetic features turn to paramagnetic minerals with the effect of the temperature increasing within increasing of the depth. This depth is called as Curie point depth (CPD) where the magnetic minerals lose their magnetism under that depth point. CPD values which are obtained by applying the magnetic spectral methods to the magnetic data represent the bottom of magnetic structures. In determining the depths of magnetic sources, a relation is defined between the spectrum and depths of the magnetic anomalies and during this application the spatial data is converted to frequency domain. Therefore, the CPD is a significant value for predicting the locations of the thermal structures of the crust. Additionally, the CPD values include information about the crustal radiogenic heat production by taking account the corruptions of the radioactive elements. There is an empiric relation between the radiogenic heat production and the P-wave (V_p) seismic velocities and with the help of this relationship V_p values of the region are obtained. Defining the V_p values is a very significant case for clarifying the locations of new possible geothermal regions. In this study, the applications related with determining the seismic velocities by using the heat productions which obtained from the CPD values is presented.

Keywords: *Curie point depth, heat production, seismic velocity (V_p)*

1. INTRODUCTION

The Curie point depth (CPD) is a significant value since under that value; the crustal minerals which represent ferromagnetic features lose their magnetism and change to paramagnetic features related to the temperature increasing. The regions which have shallow CPD values are related with the thin crust and geothermal and volcanic structures ([1]). CPD values which are used for determining the thermal structure of the crust ([2], [3], [4], [5], [6], [7], [1], [8]) are estimated from aeromagnetic anomaly data by using the magnetic spectral method ([2], [9]). A relationship between the power spectrum of magnetic anomalies and the depth of the magnetic sources is given with this method. In this method, firstly, the Curie depths (z_b) are calculated by using the equation,

$$z_b = 2z_0 - z_t \tag{1}$$

here, z_t is the depth to the top of the magnetic source and z_0 is the depth to the centre of the magnetic source. Then, the thermal gradient (*grad T*, $\partial T/\partial z$) values are obtained by dividing the Curie temperature (580º C) value to the CPD values given as,

$$grad\ T = \frac{-580^{\circ}\ C}{CPD\ (z_b)} \tag{2}$$

There is an inverse relationship between the heat flow values and CPD values. In the other words, if the heat flow values are high in a region, it means that this region has shallow CPD values, conversely, if the heat flow values are low, the region is related with deep CPD values ([1], [8]). The heat flow (q_0) values are estimated by ([10], [11]).

$$q_0 = grad\ T * k \tag{3}$$

this equation and here k is the thermal conductivity.

The decay of the heat production elements (Uranium−238 (238U), Uranium−235 (235U), Thorium−232 (232Th), and Potassium−40 (40K)) is the source of the great part of the crustal radiogenic heat production.

[1] *Dokuz Eylul University, Engineering Faculty, Department of Geophysical Engineering, 35160, Buca/Izmir, Turkey.*

Corresponding author: ayca.yurdakul@deu.edu.tr

An exponential decay model ([12]), which is dependent to the depth, provides the radiogenic heat production of the continental crust and the the radiogenic heat production (A) is calculated as the function of depth (*A(z)*) by:

$$A(z) = A_0 \exp\left(\frac{-z}{D}\right) \tag{4}$$

this equation. Here, A_0 is the radiogenic heat production rate at the Earth surface, z is CPD values, and D is the radiogenic scaling depth ([13]).

There is an empirical relationship between the seismic velocity (V_p, km/sn) and heat production (A, Wm^{-3}) ([14], [15]) as,

$$\ln A = 12.6 - 2.17\, V_p \tag{5}$$

By this equation the V_p values, which present the significant case for clarifying the locations of new possible geothermal regions, are estimated. There is an inverse relationship between the V_p values and the heat production (A). Therefore, in a region which contains crystalline elements while V_p values are increasing, the heat production is decreasing ([16]).

In this study, Eastern Anatolia (Turkey) (Figure 1) is chosen as the study area and its heat production and V_p values were calculated by using CPD values.

2. APPLICATION

Eastern Anatolia has a complicated tectonic mechanism with the effect of the collision between Eurasian and Arabian plates. In the previous studies (eg. [17], [18], [19], [20], [21], [22], [1], [23]) the properties of the lithosphere of Eastern Anatolia were investigated. The CPD values (Figure 2) were calculated by using aeromagnetic data of Directorate of Mineral Research and Exploration of Turkey (MTA) and thermal structures of the region were determined in the previous study ([1]). In this study, the P-wave velocities of the region which give information about the location of the possible geothermal sources were calculated by using CPD values of Eastern Anatolia (Figure 2).

Firstly, the thermal gradient of the region was calculated by using Eq. (2) with the CDP values ([1]) and the Curie temperature of the domain which is assummed as 580ºC. As the second step, the heat flow values of the study area were calculated by using Eq. (3) with these thermal gradient values and the thermal conductivity (k) which is assummed as 1.127 W/m ºC (Figure 3). Then, the the heat production (A) values for each of estimated Curie depths were obtained by assuming the coefficient D as 10 km ([13], [24]) and surface radiogenic heat production rate coefficient, A_0 of 1.5 µWm^{-3} ([25]) with Eq. (4). Finally, the V_p values of Eastern Anatolia (Figure 4) were calculated with the help of heat production (A) values with Eq. (5).

Figure 1.The location of the study area (Eastern Anatolia) (this image was created by using Google earth V 6.2.2.6613, http://www.earth.google.com).
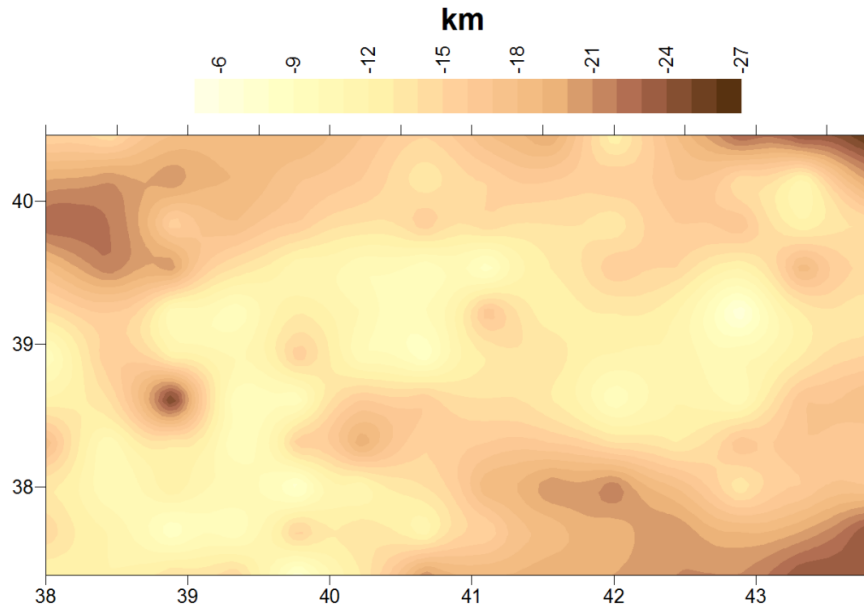
Figure 2. Curie Depth Point map of Eastern Anatolia (revised from [1])
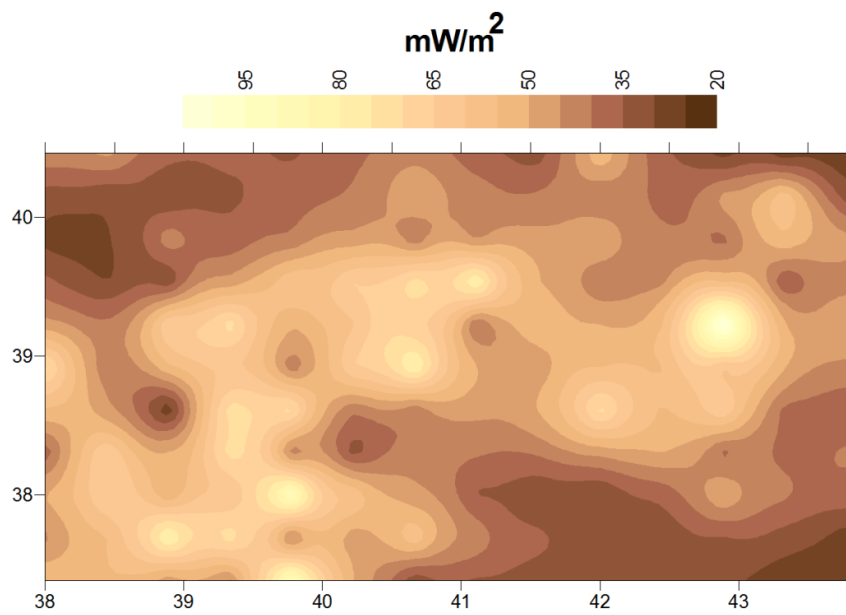
Figure 3. Heat flow map of Eastern Anatolia.
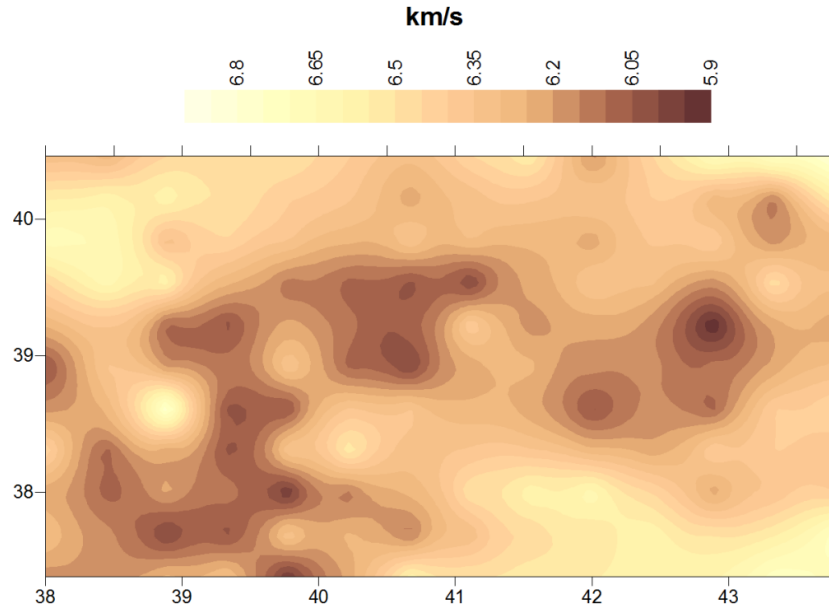
Figure 4. The V_p values distribution of Eastern Anatolia.

3. RESULTS

In this study, the geothermal gradient, the heat flow, the heat production and V_p values of Eastern Anatolia were calculated with the help of CDP values. The CPD values are in the range between 6 km and 26 km. It is known that the shallow Curie point depths and high heat flow values are associated with volcanic and geothermal areas crustal thinning ([26]). The CPD values are shallower than the Moho depth, it is possible to suggest that the magnetic sources in the study area are located at the upper crust ([1]). The heat flow values in the study area vary from 25.140 to 108.94 mW/m^2 .It is seen from heat flow and seismic velocities maps, the high heat flow regions usually have low seismic velocities.

ACKNOWLEDGEMENT

REFERENCES

[1] O. Pamukcu, Z. Akcıg, M. Hisarlı and S. Tosun, "Curie Point Depths and Heat Flow of Eastern Anatolia (Turkey)", Energy Sources, Part A: Recovery, Utilization, and Environmental Effects, vol. 36(24), pp. 2699-2706, 2014.

[2] Y., Okubo, J. R. Graf, R. O. Hansen, K. Ogawa, and H. Tsu, "Curie point depths of the Island of Kyushu and surrounding areas, Japan", *Geophysics,* vol. 53, pp. 481–494, 1985.

[3] A. Ates, F. Bilim, A. Buyuksarac, "Curie point depth investigation of central Anatolia, Turkey", *Pure Appl. Geophys.,* vol. 162, pp. 357–371, 2005.

[4] F. Bilim, "Investigation into the tectonic lineaments and thermal structure of Kutahya-Denizli region western Anatolia, from using aeromagnetic, gravity and seismological data", *Phys. Earth Planet. Inter*, vol. 165, pp. 135–146, 2007.

[5] F. Bilim, "Investigation of the Galatian volcanic complex in the northern central Turkey using potential field data", *Phys. Earth Planet. Inter.*, vol. 185, pp. 36–43, 2011.

[6] S. Saleh, M. Salk and O. Pamukcu, "Estimating Curie depth and heat flow map for northern Red Sea rift of Egypt and its surroundings, from aeromagnetic data", *Pure Appl. Geophys,* vol. 170, pp. 863–885, 2013.

[7] G.E. Obande, K.M. Lawal and L.A. Ahmed, "Spectral analysis of aeromagnetic data for geothermal investigation of Wikki Warm Spring, North-east Nigeria", *Geothermics,* vol. 50, pp. 85–90, 2014.

[8] F. Bilim, T. Akay, A. Aydemir and S. Kosaroglu, "Curie point depth, heat-flow and radiogenic heat production deduced from the spectral analysis of the aeromagnetic data for geothermal investigation on the Menderes Massif and the Aegean Region, western Turkey", *Geothermics*, vol. 60, pp. 44-57, 2016.

[9] A. Spector and F.S. Grant, "Statistical models for interpretation aeromagnetic data", *Geophysics,* vol. 35, pp. 293–302, 1970.

[10] D.L. Turcotte and G. Schubert, "Geodynamics: Applications of Continuum Physics to Geological Problems", John Wiley, New York, pp. 450, 1982.

[11] I.M. Artemieva and W.D. Money, "Thermal thickness and evolution of Precambrian lithosphere", *J. Geophys. Res.*, vol.106, pp. 16387–16414, 2001.

[12] A.H. Lachenbruch, "Crustal temperature and heat production: implication of the linear heat flow relationship", *J. Geophys. Res.,* vol.75, pp. 3291–3300, 1970.

[13] A.H. Lachenbruch, "Preliminary geothermal model of the Sierra Nevada", *J.Geophys. Res.,* vol. 73, pp. 6977–6989, 1968.

[14] L. Rybach and G. Buntebarth, "Relationship between the petrophysical properties density, seismic velocity, heat generation and mineralogical constitution", *Earth Planet. Sci. Lett.,* vol. 57, pp. 367–376, 1982.

[15] L. Rybach and G. Buntebarth, "The variation of heat generation, density and seismic velocity with rock type in the continental crust", *Tectonophysics,* vol. 103, pp. 309–344, 1984.

[16] L. Rybach, "The relationship between seismic velocity and radioactive heat production in crustal rocks: an exponential law", *Pure Appl. Geophys.,* vol. 117, pp. 75–82, 1978, 1979.

[17] Y. Rotstein, and A. L. Kafka, "Seismotectonics of the southern boundary of Anatolia, eastern Mediterranean region: Subduction, collision, and arc jumping", *J. Geophys. Res.,* vol. 87 pp. 7694–7706, 1982.

[18] D. McKenzie, "Active tectonics of the Mediterranean region", Geophys. J. R. Astro. Soc., vol. 30 pp. 109–185, 1972.

[19] E. Zor, E. Sandvol, C. Gürbüz, N. Türkelli, D., Seber, and M. Barazangi, "The crustal structure of the East Anatolian plateau (Turkey) from receiver functions", *Geophys. Res. Lett.,* vol. 30(24), 2003.

[20] A. M. C. Sengor, S. Ozeren, T. Genc, and E. Zor, "East Anatolian high plateau as a mantle-supported, north-south shortened domal structure", *Geophys. Res. Lett.,* vol. 30(24), 2003.

[21] M. Keskin, "Magma generation by slab steepening and breakoff beneath a subduction-accretion complex: An alternative model for collision-related volcanism in Eastern Anatolia, Turkey", *Geophys. Res. Lett.,* vol. 30(24), 2003.

[22] O. A. Pamukcu, Z. Akcıg, S. Demirbas and E. Zor, "Investigation of crustal thickness in eastern Anatolia using gravity, magnetic and topographic data", *Pure Appl. Geophys.*, vol. 164, pp. 2345–2358, 2007.

[23] O. Pamukcu, T. Gonenc, A. Y. Cırmık, S. Demirbas and S. Tosun, "Vertical and horizontal analysis of crustal structure in Eastern Anatolia Region", *Bulletin of The Mineral Research and Exploration*, vol. 151, pp. 217-229, 2015.

[24] C. Jaupart, "On the average amount and vertical distribution of radioactivity in the continental crust". In: Burrus, J. (Ed.), Thermal Modeling in Sedimentary Basins, Editions Technip, Paris, pp. 33–47, 1986.

[25] M. Springer, "Interpretation of heat-flow density in the Central Andes", Tectonophysics, vol. 306, pp. 377–395, 1999.

[26] A. Tanaka, Y. Okubo and O. Matsubayashi, "Curie point depth based on spectrum analysis of the magnetic anomaly data in east and southeast Asia", Tectonophysics, vol. 306, pp. 461–470, 1999.

Concrete Strength and Rebar Diameter Effects on Bond Behavior in Bending: Hinged Beam Test

Mehmet Emin Arslan[1], Talha Arslan[2]

Abstract

As it is known, RC construction owes its existence bond between concrete and steel rebar. Although there are many studies carried out on bond strength, this event has not yet been clarified due to its complexity. For this reason, in the current study, bond behavior between concrete and rebar was investigated in bending on hinged beam specimens produced with four different concrete strengths and □10, □12 and □14 rebar diameter by using 100 mm development length. In experimental study, totally 12 hinged beam specimens produced by using concretes with 250 kg, 300 kg, 400 kg and 500 kg cement dosage were tested. Tests result showed that strength of concrete and rebar diameter significantly affect bond behavior of concrete and rebar. While the maximum tensile stresses increased with increased concrete strength, the slips of the rebars from concrete decreased. In addition, reached maximum tensile stresses of rebar in the hinged beam specimens produced with 250 kg, 300 kg, 400 kg and 500 kg cement dosage increased for the same diameter and development length by 5-34%, 13-29%, 8-26%, respectively.

Keywords: *Bond strength, concrete strength, rebar diameter, hinged beam test.*

1. INTRODUCTION

Bond strength is one of the key properties in order to mention about a composite material known as RC structures. RC construction owes its existence to fully bond between concrete and rebar. Bond strength is defined shear stresses constitute connection between concrete and steel rebar [1]-[4]. It is necessary to have a suitable development length to ensure full bond strength. The appropriate development length can be expressed as the length that does not create a significant slip on rebar when the rebar reaches its yield strength. In order to avoid a significant decrease in bond between concrete and rebar throughout the life of the building, necessary precautions should be taken considering the factors that adversely affect bend strength.

Several types of experiments have been developed to determine the parameters affecting the bond strength. The most widely used of these experiments is pull-out test. Deficiencies of pull-out test are local compressive stresses at supports, thick concrete cover and absence of shear force vertical to the rebar. For these reasons, it does not represent entirely the bond behavior of flexural members. Thus, beam tests have been developed to determine more correctly bond behavior of flexural members. Hinged Beam Test (HBT) is one of the bending tests [1], [2], [5]-[14]. In this study, the bond behavior of beam specimens produced using different concretes with different dosages (250, 300, 400 and 500 kg) and rebars ($\Phi10$, $\Phi12$, $\Phi14$) with fixed development length (100 mm) are experimentally investigated under bending by using hinged beam test.

2. MATERIALS AND METHODS

In this study CEM-I 42,5 R Portland cement were used for producing of concrete. Hinged beam specimens were produced using 250, 300, 400 and 500 kg cement dosage with 0.60 constant W/C ratio. Mixture proportions of concretes are given in Table 1. Mean Compressive and splitting tensile strength values of concretes obtained from 150 mm cubic samples and some mechanical properties of rebars used for the tests are given in Table 2 and Table 3, respectively.

---

[1] Corresponding author: Duzce University, Department of Civil Engineering, 81620, Duzce, Turkey. mehmeteminarslan@duzce.edu.tr.

[2] Duzce University, Department of Civil Engineering, 81620, Duzce, Turkey. arstlh@hotmail.com.

Table 1. Mixture proportions of concretes

"Cement Dosage (kg)	Amount of aggregates (kg/m3)		Saturation water (kg/m³)	Mixing water (kg/m³)	Cement (kg/m³)	Superplasticizer (kg/m³)
	Sieve sizes (mm)					
	0–4,0	4,0–12,0				
250 Doz	793	1191	19.85	150	250	2.5
300 Doz	736	1105	18.42	180	300	3.0
400 Doz	648	972	16.20	240	400	4.0
500 Doz	550	816	13.67	300	500	5.0

Table 2. Some mechanical properties of concretes

Concrete Dosage (kg/m³)	Mean compressive Strength (MPa)	Splitting tensile strength (MPa)
250	32,10	5,908
300	34,53	6,15
400	42,49	6,556
500	50,42	6,114

Table 3. Some mechanical properties of steel rebars

Rebar Diameter (mm)	Mean Yield Strength (MPa)	Mean Tensile Strength (MPa)	Yield Strain (%)	Ultimate Strain (%)
10	509	595	1,19	13
12	442	575	1,28	16
14	487	640	1,33	18

The hinged beam test specimens were produced in accordance with the BS 4449:2005 standard [15]. Dimensions of the test specimens and loading set up of the hinged beam test were given in Figure 1. Also reinforcement details of the beam specimens are given in Figure 2. As seen from the figure, longitudinal reinforcements and stirrups were placed in the beam specimens. The reason of using of these reinforcements is to prevent flexural and shear cracks or kept them at acceptable level.
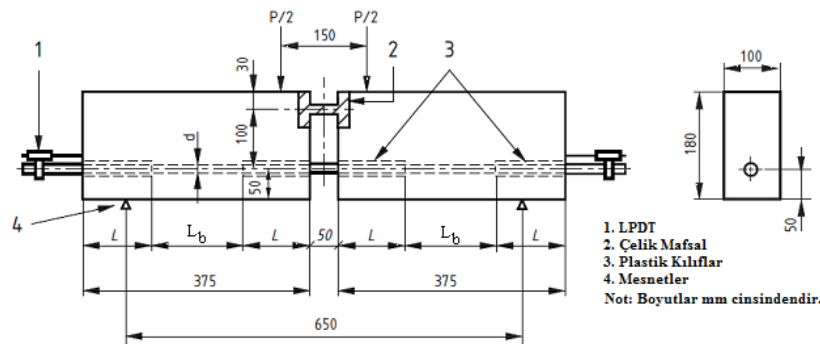
Figure 1. Dimensions of the test specimens and loading set up.
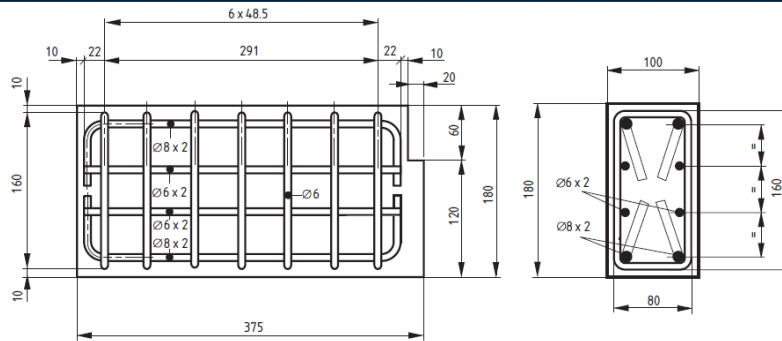
Figure 2. Reinforcement details of the beam specimens

The vertical loads were automatically applied to the test beams at a speed of 0.5 kN/s with a 600 kN capacity hydraulic piston. Hinged beam specimens were placed on one fixed and one movable supports and loaded in the mid-span vertically. Applied loads were determined by a Loadcell. Linear Potentiometric Displacement Transducers (LPDTs) with a sensitivity of 0.013 mm were used to measure the amount of slips of rebars at both ends of the beam specimens. A scene from the Hinged Beam Test is given in Figure 3. In the middle part of the beam specimens, a steel hinge is placed in order to more precisely determine the force on rebar.

Figure 3. Hinged Beam Test

3. RESULTS AND DISCUSSION

Labeling of the test specimens are explained in Figure 4. Hinged beam test results of specimens produced using 250, 300, 400 and 500 kg cement dosage and 10 mm, 12 mm and 14 mm rebar diameter with 100 constant development length are given in Figure 5.
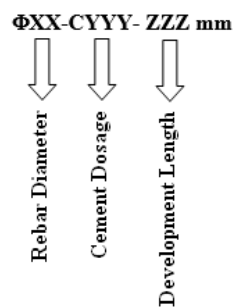
Figure 4. Hinged beam test specimen labeling
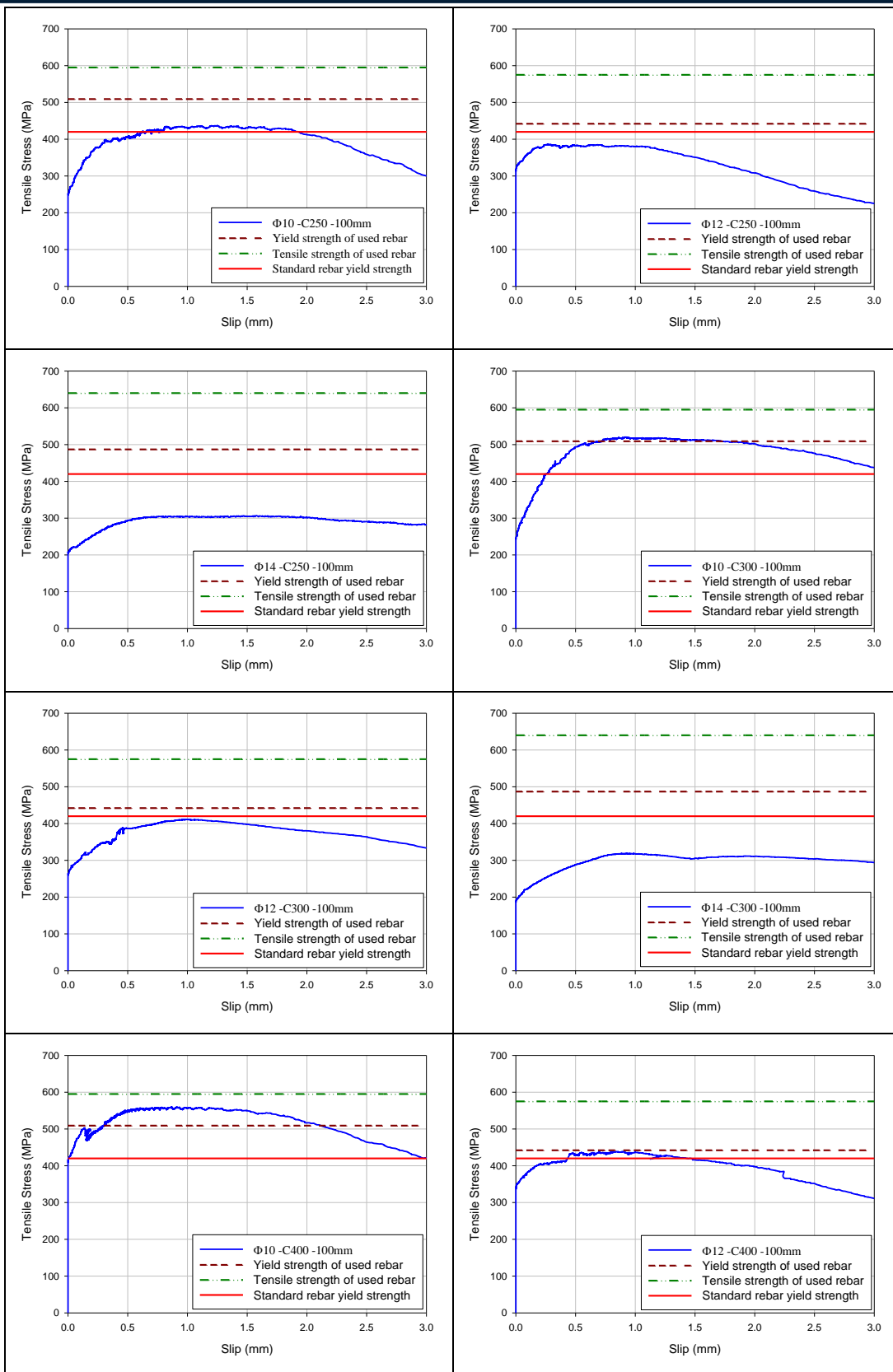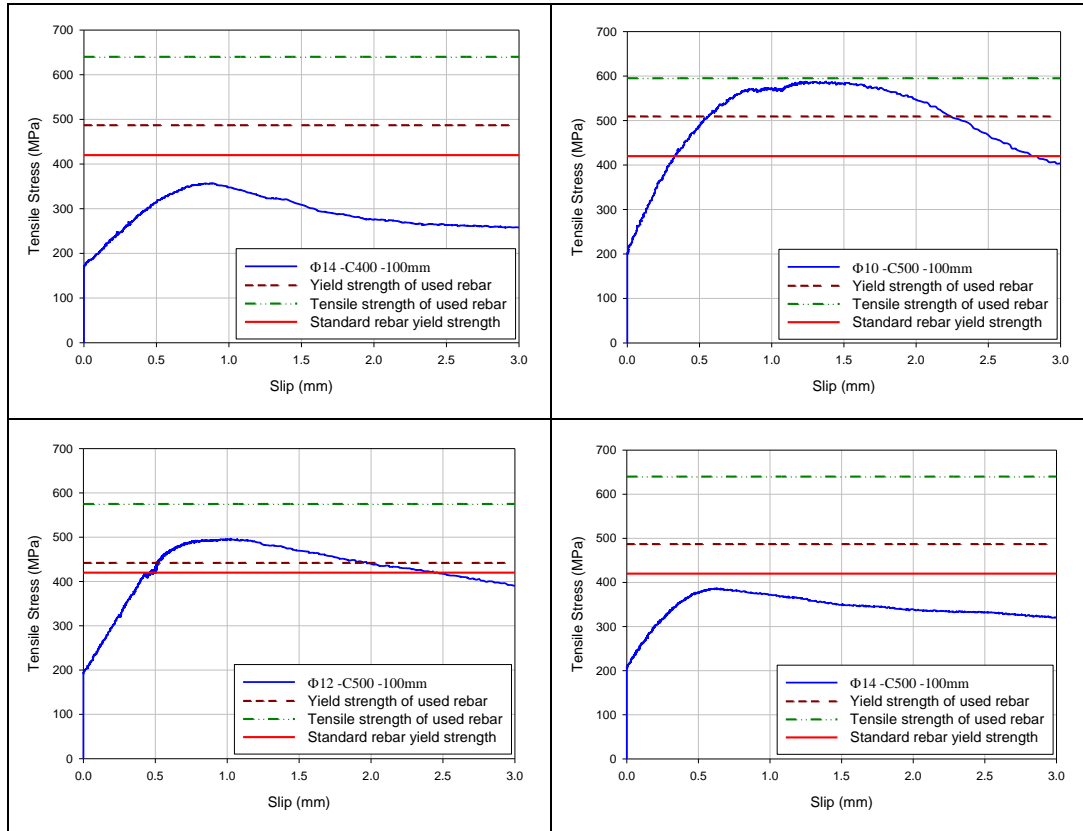
Figure 5. Hinged beam test results

Findings obtained from hinged beam test are discussed under two headings below. The first one is the effect of compressive strength of concrete, and the other is the effect of rebar diameter on the bond behavior between concrete and steel rebar.

3.1. Effects of concrete strength on bond behavior

Tensile stress-slip curves of hinged beam test specimens labeled as Φ10-C250-100mm, Φ10-C300-100mm, Φ10-C400-100mm and Φ10-C500-100mm are illustrated in Figure 6. As seen from the figure, as the concrete strength increases, the bond strength for the same diameter and development length also increases. The bond between concrete and rebar rapidly disappeared under increasing loads without reaching yield strength for specimen Φ10-C250-100mm. This result shows that the 100 mm development length is insufficient for concrete produced using 250 kg cement dosage and the Φ10 rebar. Reached maximum tensile stress and corresponding slip value are 437 MPa and 1.248 mm, respectively. Rebar reached yield stress for Φ10-C300-100mm specimen. In addition, reached maximum tensile stress and slip values are 520 MPa and 0.911 mm. Yield stress was reached with 0.193 mm slip for Φ10-C400-100mm beam specimen. Maximum tensile stress and corresponding slip values are 558 MPa and 0.753 mm. For Φ10-C500-100mm test specimen, yield stress is reached as well. Maximum tensile stress reached is 587 MPa and almost tensile strength of Φ10 rebar. The findings show that, bond strength increases between 5% and 34% with increased cement dosages for specimens prepared using Φ10 rebar and 100mm development length.
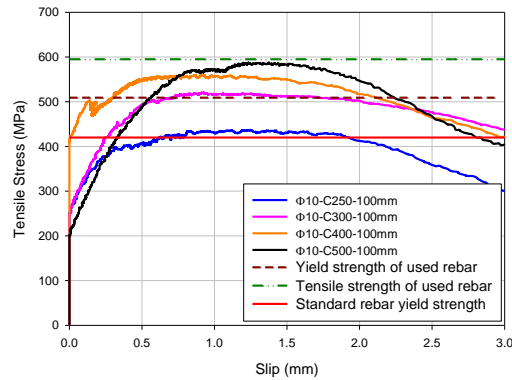
Figure 6. Φ10-(C250-C300-C400-C500)-100mm hinged beam test specimen

Tensile stress-slip curves of hinged beam test specimens labeled as Φ12-C250-100mm, Φ12-C300-100mm, Φ12-C400-100mm and Φ12-C500-100mm are illustrated in Figure 7. As seen from the figure, as the concrete strength increases, the bond strength for the same diameter and development length also increases. The bond between concrete and rebar rapidly disappeared under increasing loads without reaching yield strength for specimen Φ12-C250-100mm. This result shows that the 100 mm development length is insufficient for concrete produced using 250 kg cement dosage and the Φ12 rebar. Reached maximum tensile stress and corresponding slip value are 385 MPa and 0.270 mm, respectively. Rebar didn't reach yield stress for Φ10-C300-100mm specimen. In addition, reached maximum tensile stress and slip values are 411 MPa and 1.00 mm. Yield stress wasn't reached for Φ12-C400-100mm beam specimen, as well. Maximum tensile stress and corresponding slip values are 438 MPa and 0.843 mm. For Φ12-C500-100mm test specimen, rebar reached yield stress. Maximum tensile stress reached is 496 MPa and corresponding slip value is 1.023 mm. The findings show that, bond strength increases between 13% and 29% with increased cement dosages for specimens prepared using Φ12 rebar and 100mm development length.
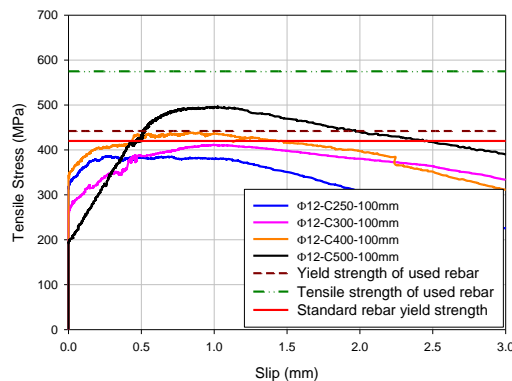
Figure 7. Φ12-(C250-C300-C400-C500)-100mm hinged beam test specimen

Tensile stress-slip curves of hinged beam test specimens labeled as Φ14-C250-100mm, Φ14-C300-100mm, Φ14-C400-100mm and Φ14-C500-100mm are illustrated in Figure 8. As seen from the figure, as the concrete strength increases, the bond strength for the same diameter and development length also increases. The bond between concrete and rebar rapidly disappeared under increasing loads without reaching yield strength for all the specimen with Φ14 rebar. The findings show that, bond strength increases between 8% and 26% with increased cement dosages for specimens prepared using Φ14 rebar and 100mm development length.
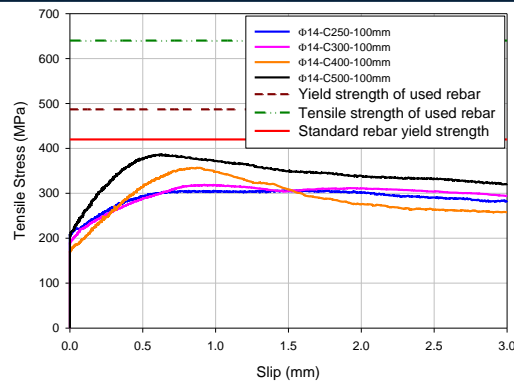
Figure 8. Φ14-(C250-C300-C400-C500)-100mm hinged beam test specimen.

As seen from the figures, as the concrete strength increases, the bond strength also increases for all rebar diameters. This may be explained by the decrease of void with increasing in the amount of cement in the concrete. The maximum stresses obtained for 100 mm development length at different rebar diameters and dosages are given in Figure 9.
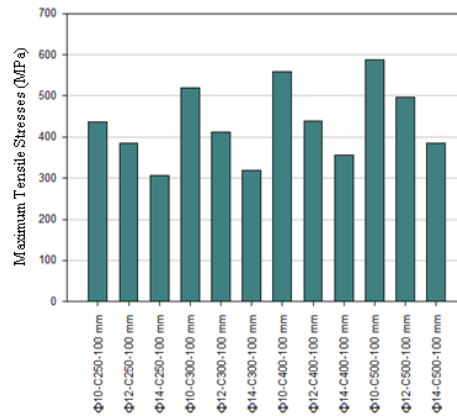
Figure 9. Maximum tensile stresses for all the hinged beam test specimens

4. CONLUSIONS

Some of the results obtained by evaluating the findings of the hinged beam tests carried out on the beam test specimens produced using different cement dosage and rebar diameters are summarized below.

- Increase in concrete compressive strength significantly increased bond strength between concrete and rebar. These increments change from 5% to 34% for □10, from 13% to 29% for □12 and from 8% to 26% for □14 with increasing cement dosage. On the other hand, slip values decreased at the same tensile stresses for each rebar diameter.

- When bond behaviors of different diameters are evaluated for the same development length, the bond strengths of large diameter rebars are seen to be very low compared to small diameters. So that while yield strength was achieved for all specimens of concrete except □10-C250-100mm for □10, it is only reached for □12-C500-100mm for □12. None of the specimens produced using different dosages with □14 rebar reached yield strength.

REFERENCES

[1] Yeih W., Chang J.J. ve Tsai C.L. "Enhancement of the Bond Strength of Epoxy Coated Steel by the Addition of Fly Ash", Cement & Concrete Composites , no. 26, pp. 310-321, 2004.
[2] Arslan Mehmet Emin, Durmus Ahmet (2011). Investigation of bond behavior between lightweight aggregate concrete and steel rebar using bending test. Computers & concrete, 8(4), 465-472.
[3] Arda, T. S. (1968) Betonarmede Aderans Konusunda Bir Derleme, 1. Baskı, İ.T.Ü. Matbaası, İstanbul, Türkiye.
[4] Arslan, M. E. (2007) Egilmede Tasıyıcı Hafif Beton-Donatı Aderansının Geleneksel Beton-Donatı Aderansıyla Karsılastırmalı Olarak İncelenmesi, Yüksek Lisans Tezi, K.T.Ü., Trabzon.

[5]   Ersoy, U. ve Ozcebe, G. (2001) Betonarme: Temel İlkeler TS-500-2000 ve Türk Deprem Yonetmeligine (1998) Gore Hesap, Genisletilmis Yeni Baskı, Evrim Yayınevi, İstanbul, Türkiye.

[6]   Dahil, H. (2001) Yüksek Performanslı Beton-Donatı Aderansının Geleneksel Beton-Donatı Aderansıyla Karsılastırmalı Olarak İncelenmesi, Yüksek Lisans Tezi, K.T.Ü., Trabzon.

[7]   Hüsem, M. ve Durmus A. (1995) Hafif Beton-Donatı Aderansının Geleneksel Beton Donatı Aderansıyla Karsılastırılmalı Olarak İncelenmesi, Türkiye İnsaat Mühendisligi XIII. Teknik Kongresi Bildiriler Kitabı, İstanbul, s. 341–354

[8]   Kankam, C. K., "Bond Strength of Reinforcing Steel Bars Milled From Scrap Metals", no. 25, pp. 231-240, 2004.

[9]   MacGregor, J. G., "Reinforced Concrete : Mechanics and Desing", Third Edition, New Jersey: Prentice Hall, 1997.

[10] El-Hawary, M. M., "Evaluation of Bond Strength of Epoxy-Coated Bars in Concrete Exposed to Marine Environment", Construction and Building Materials, no. 13, pp. 357-362, 1999.

[11] H. S. Arel, "Degisik Parametlerin Beton ile Celik Donatı Aderansına Etkisi", Ege Üniversitesi, Fen Bilimleri Enstitüsü, Doktora Tezi, 2012.

[12] A. Benli, "Kendiliginden sıkısan betondaki donatı aderansının deneysel ve sayısal olarak incelenmesi", Fırat Üniversitesi,Fen Bilimleri Enstitüsü,Doktora Tezi, 2007.

[13] A. Beycioglu, "Kendiliginden Yerlesen Betonlarda Beton İle Donatı Aderansı İliskisinin Arastırılması", Gazi Üniversitesi, Fen Bilimleri Enstitüsü, Doktora Tezi, 2013.

[14] Guneyisi, E., Gesoglu, M. and Ipek, S. (2013), "Effect of steel fiber addition and aspect ratio on bond strength of cold-bonded fly ash lightweight aggregate concretes", Constr. Build. Mater., 47, 358-365.

[15] BS 4449:2005+A2:2009 (2009), Steel for the reinforcement of concrete: Weldable reinforcing steel: Bar, coil and decoiled product, London.

VARIATIONS in SEED NUTRIENT CONTENT of DIFFERENT BITTER VETCH (*VICIA ERVILIA* WILLD.) LINES

Mahmut Kaplan[1], Kagan Kokten[2], Mehmet Fatih Yilmaz[3], Halit Tutar[2], Hasan Kale[1]

Abstract

The present study was conducted to compare feed quality parameters of 14 different forage bitter vetch genotypes. Experiments were carried out in randomized block design with 3 replications under Bingol conditions. A analyses (crude protein, acid detergent fiber, neutral detergent fiber, crude ash, dry matter digestibility, dry matter intake and relative feed value) were carried out to determine the chemical composition of bitter vetch grains.

Results revealed different outcomes with regard to chemical compositions of bitter vetch seeds (P<0.01). ADF ratios varied between 6.32-9.79%, NDF ratios between 17.94-28.45%, crude protein contents between 22.96-37.01%, crude ash contents between 2.55-3.26%, dry matter digestibility ratio between 81.28-83.98%, dry matter intakes between 4.22-6.69% and relative feed values between 268.40-435.53. It was concluded that Line 17 was prominent with crude protein, Line 3 with ADF and NDF ratios, dry matter intake and relative feed value.

Keywords: *Bitter vetch, ADF, NDF, crude protein, relative feed value*

1. INTRODUCTION

Legumes are used for livestock grazing, for dry hat and silage yields [1] and most of the time used in feed rations because of high protein, energy, mineral and vitamin content of kernels [2]. Bitter vetch is an abstinent plant and can easily be grown over poor sites where the other crops are not sufficiently grown, or over the stony and hilly sites with low lime contents [3]. It is a short plant with low mass yields but has high kernel yields in dry climates. Therefore, it is a common crop in dry regions [4]. In case the drought-resistant high yield species are breeded and supplied to farmers, bitter vetch cultivated lands may rapidly increase [5].

The chemical composition of the feeds and the identification of energy and digestible nutrients are important in determining the differences between feeds [6]. Nutritive quality is classified by crude protein, acid detergent fiber and neutral detergent fiber. Low acid detergent fiber and neutral detergent fiber values result in high digestible dry matter digestibility, dry matter intake and relative feed value. The ratios of these parameters directly influence feed quality [7].

Bitter vetch is a high quality forage source for livestock. Therefore, the present study was conducted to determine nutritive values of bitter vetch lines.

2. MATERIAL AND METHOD

In present study, chemical characterization of 14 bitter vetch lines supplied from International Center for Agricultural Research in the Dry Areas (ICARDA) (6), Diyarbakır and Mardin (3) Ankara University (5) were carried out. Experiments were carried out over field crops experimental fields of Bingol University Agricultural Faculty during the year 2014. Experiments were conducted in split plots experimental design with three replications. Plot size was 4 x 1.8 m and total 7.2 m². Based on soil analysis, during sowing, 3

---

[1] *Corresponding Author: Department of Field Crops, Faculty of Agriculture, University of Erciyes, Kayseri, Turkey mahmutkaplan5@hotmail.com*

[2] *Department of Field Crops, Faculty of Agriculture, University of Bingöl, Bingöl, Turkey*

[3] *East Mediterranean Transitional Zone Agricultural Research of Institute, Kahramanmaras, Turkey*

kg/da N and 6 kg/da P$_2$O$_5$ were applied to soil as fertilizer. Seeds were sown at the beginning of April of both years and harvested in the middle of July.

Experimental soils at 0-30 were classified as loam. Soils had low lime and unsaline, were moderate in potassium and phosphorus, poor in organic matter and were slightly acidic. Averages temperature values of experimental year was 20.4 °C, total precipitation was 282.2 mm and relative humidity was %45.0. Long term period Averages temperature, total precipitation and relative humidity were 18.1 °C, 366 mm and %48.8 respectively.

Bitter vetch samples were ground in a mill with 1 mm sieve and made ready for chemical analyses. Crude ash content of bitter vetch line seeds was determined through ashing them at 550 °C for 8 hours in an ash oven [8]. Nitrogen (N) content was determined by Kjeldahl method and crude protein ratio was calculated by using the formula of N x 6.25 [8]. NDF with [9], and ADF with [10] by using ANKOM 200 Fiber Analyzer (ANKOM Technology Corp. Fairport, NY, USA).

Relative feed value (RFV) of bitter vetch seeds is calculated from the estimates of dry matter digestibility (DDM) and dry matter intake (DMI) [11].

DMD % = 88.9 - (0.779 x ADF %); DMI % of BW = 120 / NDF %; RFV = (DDM % x DMI %) /1.29

Analyses results were subjected to variance analysis with SAS [12] software. Differences between mean values were tested by LSD multiple range test. Biplot analysis was done to explain the correlations between chemical composition and lines by the method of [13].

3. RESULTS AND DISCUSSION

Acid detergent fiber (ADF) and neutral detergent fiber (NDF) ratios of bitter vetch lines are respectively presented in Figure 1 and 2. Highly significant differences were observed in ADF and NDF (p<0.01). The greatest ADF ratio (9.79%) was obtained from 2795 line and it was followed by Line14 (9.47%) genotype which was placed in the same statistical group. The lowest ADF ratio (6.32%) was obtained from 2802 line. The greatest NDF ratio were obtained from 2801 (28.45%) and Line14 (28.25%) lines and the lowest NDF ratio were obtained from Line3 (17.94%) and 2798 (18.41%) lines. Low ADF and NDF values are desired in livestock feeds since these materials harden the digestion and decrease the feed quality. ADF and NDF ratios of the current study were similar to the values of [14], [15], [16].
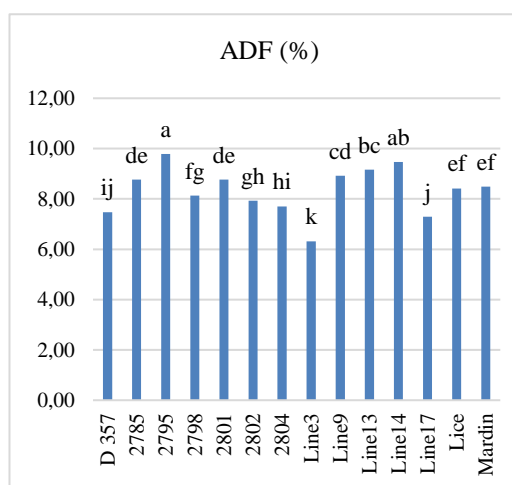
Figure 1. *Acid Detergent Fiber (ADF) Ratio of Bitter Vetch Lines (p≤0.01)*
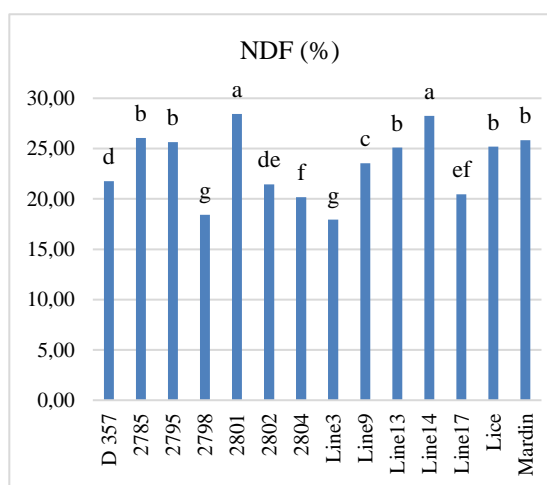
Figure 2. *Neutral Detergent Fiber (NDF) Ratio of Bitter Vetch Lines (p≤0.01)*

Crude protein and crude ash contents of bitter vetch seeds are respectively presented in Figure 3 and 4. Highly significant differences were observed in crude protein and crude ash contents (p<0.01). The lowest crude protein content was observed in 2785 with 22.96% and the greatest crude protein content in Line17 with 37.01%. Crude ash content varied between 2.55-3.26%. The lowest crude ash content was obtained from 2802 and the highest crude ash content from Line14. High-protein kernels are low-cost sources for ruminants [17], [18]. Beside high protein content exists in bitter vetch kernels [19], [20], [18] and it should be taken into consideration in breeding studies. Crude protein contents were also similar to the findings of [21], [18], [22], [16], [23]. Crude ash contents were lower than the value Sadeghi et al. (2009) but similar to the finding [24].
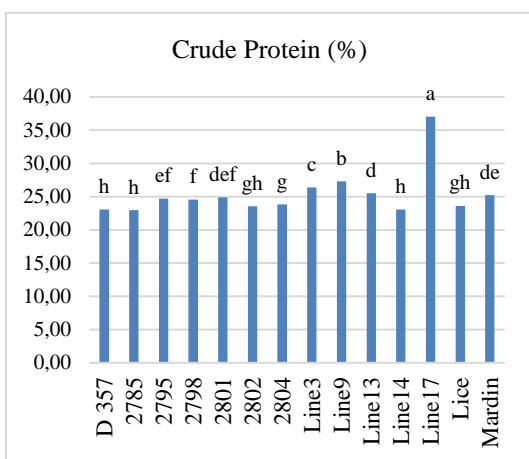
Figure 3. *Crude Protein Content of Bitter Vetch Lines (p≤0.01)*
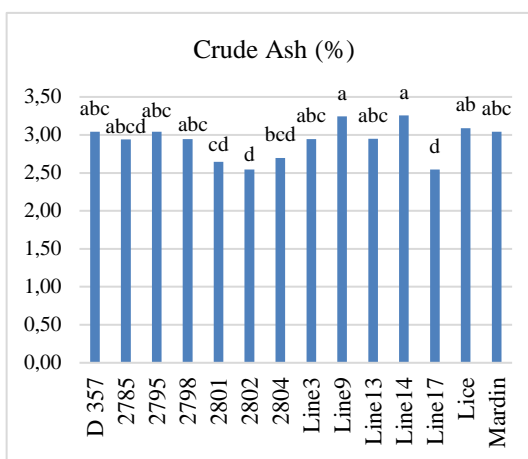
Figure 4. *Crude Ash Content of Bitter Vetch Lines (p≤0.01)*

Dry matter digestibility and dry matter intake of bitter vetch lines are respectively presented in Figure 5 and 6. Highly significant differences were observed in dry matter digestibility and dry matter intake (p<0.01). The greatest dry matter digestibility (83.98%) was obtained from Line3 lines and the lowest dry matter digestibility (81.28%) was obtained from 2795 line. The greatest dry matter intake (6.69%) was obtained from Line3 lines and the lowest dry matter intake were obtained from 2801 line (4.22%).
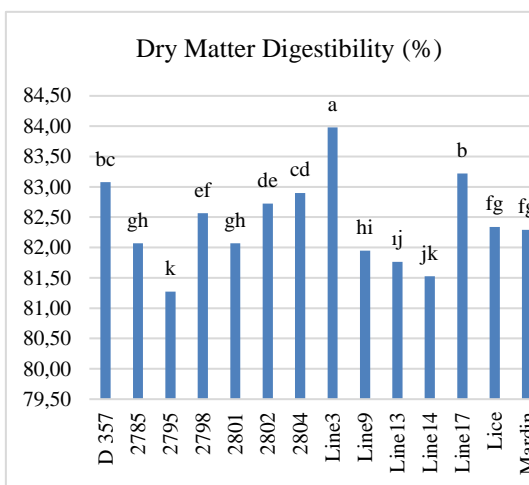
Figure 5. *Dry Matter Digestibility (DMD) of Bitter Vetch Lines (p≤0.01)*
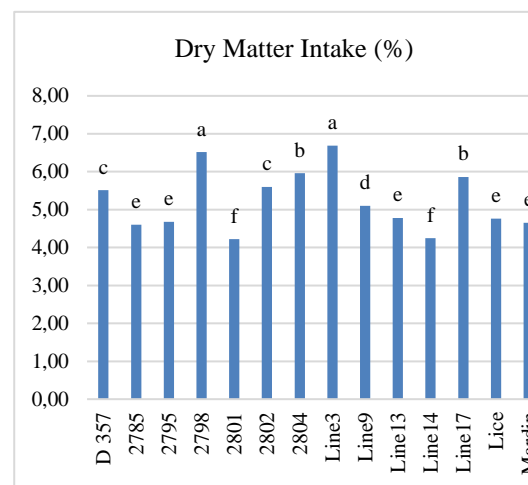
Figure 6. *Dry Matter Intake (DMI) of Bitter Vetch Lines (p≤0.01)*

Relative feed values of bitter vetch lines are presented in Figure 7. Highly significant differences were observed in relative feed values (p<0.01). The greatest relative feed value was observed in Line3 with 435.53 and the lowest relative feed value in line 2801 with 268.40. Biplot analysis explained 85.07% of total variation (PC1 69.61% and PC2 15.46%) (Figure 8). While crude protein and crude ash had high separation capacity, ADF, NDF, DMD, DMI and RFV had medium separation capacity for bitter vetch lines. Of the investigated parameters, ADF and NDF formed a group, DMD, DMI and RFV formed another group. Line17 was prominent with CP parameter, Line3 with DMI, RFV and DMD, Line 14 and 2795 with ADF and NDF. Although GGT biplot analysis is used for the analysis of multi-environmental experiments, it is also used for the analysis of all two-way data. With these data, characteristics of the genotypes can easily be compared. Several researchers used biplot analysis to compare various characteristics of genotypes [25], [26], [27], [28]. Since the cosine of angle between the vectors of any two characteristics almost estimates the correlation

coefficient between these two characteristics, biplot can reliably be used to visualize the relationships between the characteristics [28].
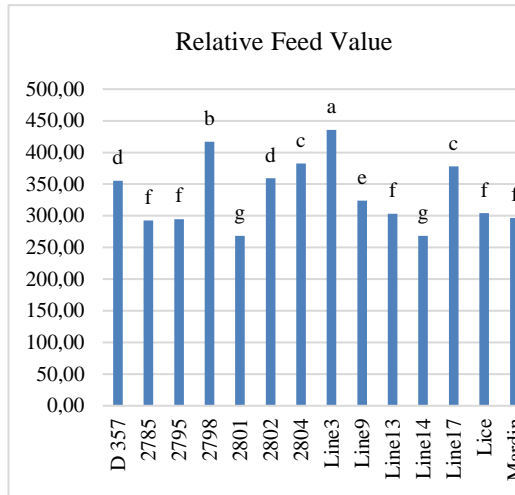
Figure 7. *Relative Feed Value (RFV) of Bitter Vetch Lines (p≤0.01)*
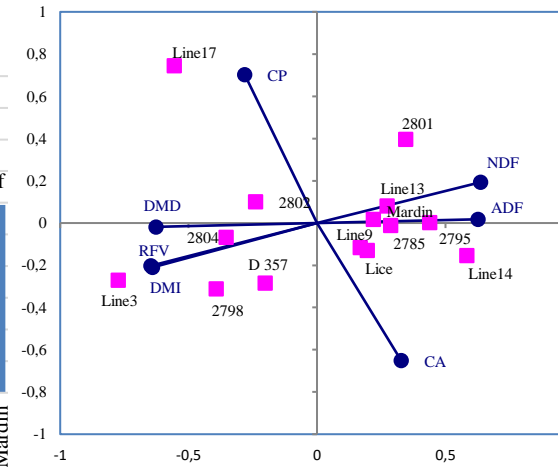
Figure 8. *The Biplot of Bitter Vetch Line for nutritive value parameters*

4. CONCLUSION

Bitter vetch is a significant feed source for livestock raised in dry and semi-dry regions. The bitter vetch lines investigated in present study yielded quite well-results. All bitter vetch lines can reliably be cultivated for animal feeding. The Line17 were found to be prominent with regard to high crude protein content. Line3 with higher DDM, DMI and RFV and low ADF and NDF in bitter vetch lines.

ACKNOWLEDGEMENTS

REFERENCES

[1] Berhane G., Eik L.O., Effect of vetch (*Vicia sativa*) hay supplementation to Begait and Abergelle goats in northern Ethiopia. I. Milk yield and composition. Small Rumin. Res. 64, 241–246, 2006.

[2] Lalles J.P. 1993. Nutritional and antinutritional aspects of soyabean and field pea proteins used in veal calf production: A review. Livestock Production Sci., 34: 181-202.

[3] Ayan I., Acar Z., Basaran U., Asci O.O., Mut H., Determination of forage and grain yields of some *Vicia ervilia* L. lines in Samsun ecological conditions. J. Fac. Agric. OMU 21, 318–322, 2006.

[4] Ekiz H., Ozkaynak İ., Türkiye'de yetistirilen bazı burcak (*Vicia ervilia* (L.) Willd.) cesitlerinin onemli morfolojik, biyolojik ve tarımsal karakterleri üzerinde arastırmalar. Ankara Üniversitesi Fen Bilimleri Enstitüsü, Yayın No: TB: 5, Ankara, 1984.

[5] Ekiz H., Secilmis burcak (*Vicia ervilia* (L.) Willd.) hatlarının kısa dayanıklılığı ile tohum verimi ve bazı bitkisel ozellikleri. Türkiye 3. Cayır-Mera ve Yembitkileri Kongresi, p: 246-252, Erzurum, 1996.

[6] Canbolat O. Karaman S., Comparison of in Vitro Gas Production, Organic Matter Digestibility, Relative Feed Value and Metabolizable Energy Contents of Some Legume Forages. Tarım Bilimleri Dergisi 15(2): 188-195, 2009.

[7] Kaplan, M., Baran, O., Ünlükara, A., Kale, H., Arslan, M., Kara, K., Buyukkiliz Beyzi, S., Konca, Y., Ulas, A., The Effects of Different Nitrogen Doses and Irrigation Levels on Yield, Nutritive Value, Fermentation and Gas Production of Corn Silage. Turkish Journal of Field Crops. 2(1): 100-108, 2016.

[8] AOAC., Official Methods of Analysis. 15th ed. Association of Official Analytical Chemists, Washington, DC.US, 1990.

[9] Van Soest P.J. and Wine R.H., The use of detergents in the analysis of fibrous feeds. IV. Determination of plant cell wall constituents. Journal of the Association of Official Analytical Chemists**,** 50, 50-55,1967.

[10] Van Soest P.J., The use of detergents in the analysis of fibre feeds. II. A rapid method for the determination of fibre and lignin. Journal of the Association of Official Analytical Chemists, 46, 829-835, 1963.

[11] Rohweder, D.A., Barnes, R.F. and Jorgensen, N., Proposed hay grading standards based on laboratory analyses for evaluating quality. Journal of Animal Science. 47: 747-759, 1978.
[12] SAS, SAS User's Guide: Statistic. Statistical Analysis Systems Institute Inc., Cary, NC, 1999.
[13] Yan W, Kang MS., GGE-Biplot Analysis: a graphical tool for breeders. Geneticists and agronomists. CRD Press, Boca Raton, 2003.
[14] Ramos-Morales E., Sanz-Sampelayo M.R., Molina-Alcaide E., Nutritive evaluation of legume seeds for ruminant feeding. Journal of Animal Physiology and Animal Nutrition, 94: 55–64, 2008.
[15] Sadeghi GH, Mohammadi L, Ibrahim SA, Gruber KJ: Use of bitter vetch (*Vicia ervilia*) as a feed ingredient for poultry. Worlds Poult Sci J, 65, 51-64, 2009.
[16] Reisi K., Zamani F., Vatankhah M., Rahimiyan Y., Effect of raw and soaked bitter vetch (*Vicia ervilia*) seeds as replacement protein source of cotton seed meal on performance and carcass characteristics of lori-bakhtiari fattening ram lambs. Global Veterinaria 7 (4): 405-410, 2011.
[17] Haddad S.G., Bitter vetch grains as a substitute for soybean meal for growing lambs. Livest. Sci. 99, 221–225, 2006.
[18] Sadeghi G.H., Mohammadi L., Ibrahim S.A., Gruber K.J., Use of bitter vetch (*Vicia ervilia*) as a feed ingredient for poultry. Worlds Poult Sci J, 65, 51-64, 2009a.
[19] Aletor V.A., Goodchild A.V., Abd El-Moneim A.M., Nutritional and anti-nutritional characteristics of selectedViciagenotypes. Anim. Feed Sci. Technol. 47, 125–139, 1994.
[20] Berger J.D., Robertson L.D., Cooks P.S., Agricultural potential of Mediterranean grain and forage legumes: 2) Anti-nutritional factor concentrations in the genus *Vicia*. Genet. Res. Crop Evol. 50, 201–212, 2003.
[21] Canpolat O., Bayram G., Comparison of *in vitro* gas production parameters, organic matter digestibility and metabolizable energy contents of some legume grains. Journal of Agricultural Faculty of Uludag University, 21 (1): 31-42, 2007.
[22] Sadeghi G.H., Pourreza J., Samei A., Rahmani H., Chemical composition and some anti-nutrient content of raw and processed bitter vetch (*Vicia ervilia*) seed for use as feeding stuff in poultry diet. Trop Anim Health Prod, 41:85-93, 2009b.
[23] Seifdavati J., Taghizadeh A., Effect of moist heat on *in vitro* gas production parameters of some of legume seeds. Journal of Petroleum and Gas Exploration Research. 2(4): 061-068, 2012.
[24] Sadeghi GH, Pourreza J., Serum proteins and some biochemical parameters in broiler chickens fed with raw and treated bitter vetch grains. Pakistan J Bio Sci, 9, 977-981, 2007.
[25] Akcura M., The relationships of some traits in Turkish winter bread wheat landraces. Turk J Agric For, 35: 115-125, 2011.
[26] Kokten K., Kaplan M., Hatipoglu R., Saruhan V., Cinar S., Nutritive Value of Mediterranean Shrubs. Journal of Animal and Plant Scıences, 22: 88-194, 2012.
[27] Akcura M., Kokten K., Gocmen Akcacık A., Aydogan S., Pattern Analysis of Turkish Bread Wheat Landraces and Cultivars for Grain and Flour Quality. Turk J Field Crops, 21(1), 120-130, 2016.
[28] Akcura M., Kokten K., Variations in Grain Mineral Concentrations of Turkish Wheat Landraces Germplasm. Quality Assurance and Safety of Crops & Foods, in press, 2016.

COMPARISON OF FEED QUALITY PARAMETERS OF NARBON VETCH (*VICIA NARBONENSIS* L.) LINES AND CULTIVARS

Mahmut Kaplan[1], Kagan Kokten[2], Mehmet Fatih Yilmaz[3], Yusuf Murat Kardes[1], Halit Tutar[2]

Abstract

Feed quality parameters of narbon vetch lines and cultivars were investigated in this study under Bingol Provincial conditions during the year 2015. A total of 9 different narbon vetch (Vicia narbonensis L.) lines and cultivars were used as the plant material of the study. Experiments were carried out in randomized blocks design with 3 replications. Effects of genotypes on grain feed quality were found to be highly significant (P<0.01).

Considering the results of experiments, crude protein ratios varied between 27.71-32.80%, crude ash ratios between 2.85-3.65%, acid detergent fiber (ADF) ratios between 11.11-16.12%, neutral detergent fiber (NDF) ratios between 25.27-36.09%. Dry matter digestibility (DMD) varied between 76.34-80.25%, dry matter intake (DMI) between 3.33-4.75% and relative feed value (RFV) between198.90-286.18. The line SEL 2382 was prominent with low ADF and high DDM, line SEL 2470 with low NDF and high DMI, Karakaya cultivar with high crude protein and line 103 2389 with high RFV.

Keywords: *Narbon vetch, genotype, crude protein, relative feed value*

1. INTRODUCTION

Legumes seeds are rich in protein, energy and some minerals and vitamins and mostly used as a source of protein for human and animal nutrition in developing and developed countries [1]. Narbon vetch is high seed yield potential, drought tolerance and cold resistance vetch. Narbon vetch could be used for grain as source for livestock feed [2].

Identification of feed quality parameters are too important in determining the differences between feed materials [3]. So landrace, line and cultural crops should be investigated with regard to not only yield parameters but also feed quality. The present study was conducted to investigate chemical composition of narbon vetch lines and cultivars.

2. MATERIAL AND METHOD

Six different narbon vetch lines and three narbon vetch cultivars were used as the plant material of this study. Experiments were carried out over field crops experimental fields of Bingol University Agricultural Faculty during the growing seasons in 2014 year. The seeds were sown at the beginning of April. Plot size was 5 x 1.2 m and row spacing was 20 cm. Experiments were conducted randomized blocks design with three replications. During sowing, 4 kg da^{-1} N and 10 kg da^{-1} P$_2$O$_5$ were applied as fertilizer. Narbon vetch cultivars and lines were harvested in the seeds hardening time.

Narbon vetch seeds were dried in an oven at 70 °C at 48 hour. Dried narbon vetch seeds were grinded in a hand mill with 1 mm screen and ready for chemical analyses. Crude ash analyses of narbon vetch line seeds

---

[1] *Corresponding Author: Department of Field Crops, Faculty of Agriculture, University of Erciyes, Kayseri, Turkey mahmutkaplan5@hotmail.com.*

[2] *Department of Field Crops, Faculty of Agriculture, University of Bingöl, Bingöl, Turkey.*

[3] *East Mediterranean Transitional Zone Agricultural Research of Institute, Kahramanmaras, Turkey.*

---

were performed through ashing them at 550 °C for 8 hours in an ash oven [12]. Nitrogen (N) content was determined by Kjeldahl method and crude protein ratio was calculated by using the formula of N x 6.25 [12]. NDF with [4] and ADF with [5] by using ANKOM 200 Fiber Analyzer (ANKOM Technology Corp. Fairport, NY, USA).

Relative feed value (RFV) of narbon vetch cultivars and lines seeds is calculated from the estimates of dry matter digestibility (DDM) and dry matter intake (DMI) [6].

DMD % = 88.9 - (0.779 x ADF %); DMI % of BW = 120 / NDF %; RFV = (DDM % x DMI %) /1.29

Narbon vetch chemical analyses results were subjected to variance analyses with SAS [7] statistical software. LSD multiple range test was employed to compare the treatment means. Biplot analysis was done to explain the correlations between chemical composition and lines by the method of [8].

3. RESULTS AND DISCUSSION

ADF and NDF ratios which are the cell wall components narbon vetch lines and cultivars are respectively presented in Figure 1 and 2. Highly significant differences were observed in ADF and NDF ratios (p<0.01). ADF and NDF ratios respectively varied between 11.11-16.12% and 25.27-36.09%. The lowest ADF ratio was obtained from SEL 2382 line and the lowest NDF ratio was obtained from SEL 2470 line. The greatest ADF ratio was obtained from Halilbey cultivar and the greatest NDF ratio was obtained from SEL 2379 line. ADF ratios were also similar to the findings of [3], [9], [10]. NDF ratios were higher than the value [3], [9] but similar to the values of [10]. Increasing ADF and NDF ratios complicates the digestion and reduces crude protein content, metabolic energy and digestible organic matter quantities [11].

Figure 1. *Acid Detergent Fiber (ADF) Ratio of Narbon Vetch Lines and Cultivars (p≤0.01)*

Figure 2. *Neutral Detergent Fiber (NDF) Ratio of Narbon Vetch Lines and Cultivars (p≤0.01)*
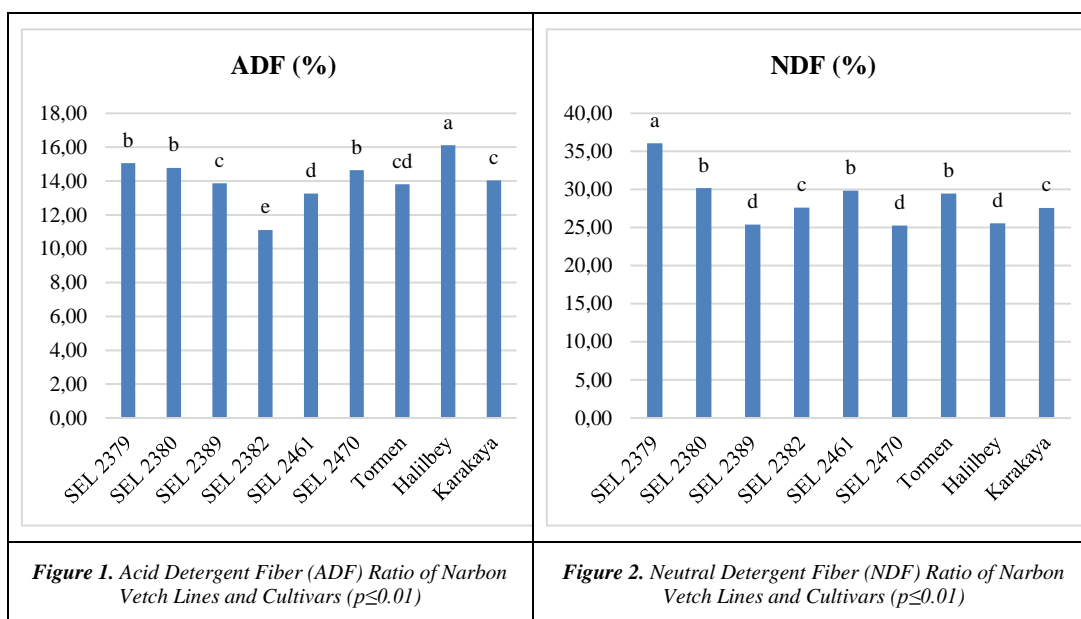
Crude protein and crude ash contents of narbon vetch lines and cultivars are respectively presented in Figure 3 and 4. Highly significant differences were observed in crude protein and ash (p<0.01). The greatest crude protein content (32.80%) was obtained from Karakaya cultivar and it was followed by SEL 2470 (9.47%) line which was placed in the same. The lowest crude protein content were obtained from SEL 2461 (27.71%). The greatest crude ash content (3.65%) was obtained from SEL 2461 line and the lowest crude ash content were obtained from SEL 2382 line (2.85%). Crude protein and ash content of the current study were similar to the values of [9], [10], [3], [13] reported that the differences in protein contents of plant species were mostly due to differences in their genetic characteristics, ripening periods, temperature and fertilization conditions.

Crude Protein (%)
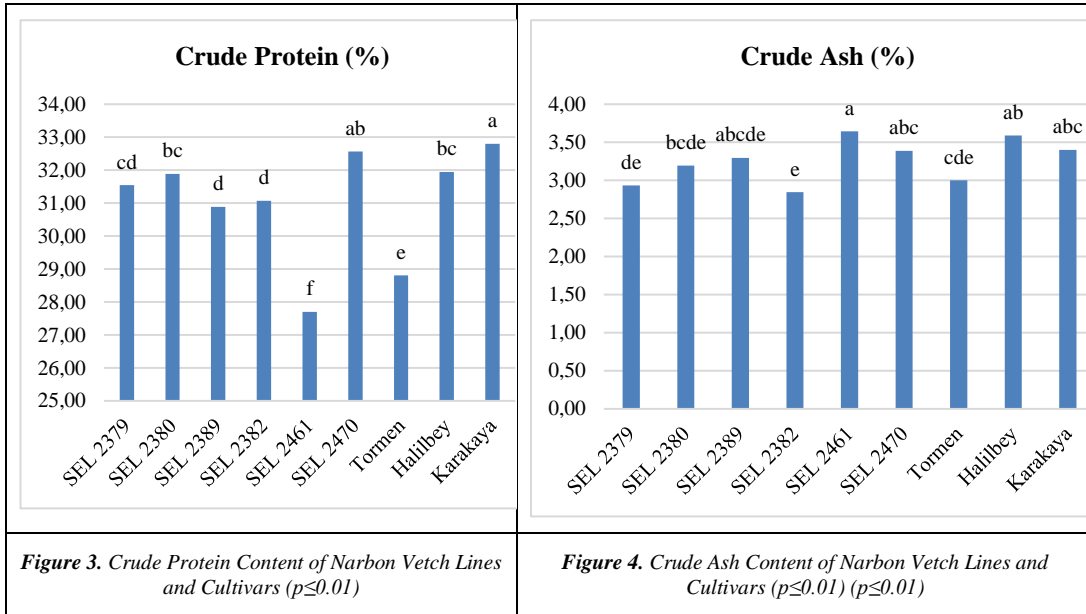
Crude Ash (%)

Figure 3. *Crude Protein Content of Narbon Vetch Lines and Cultivars (p≤0.01)*

Figure 4. *Crude Ash Content of Narbon Vetch Lines and Cultivars (p≤0.01) (p≤0.01)*

Dry matter digestibility and dry matter intake ratio of narbon vetch lines and cultivars are respectively presented in Figure 5 and 6. Highly significant differences were observed in dry matter digestibility and dry matter intake ratios (p<0.01). The lowest dry matter digestibility ratio was observed in Halilbey cultivar with 76.34% and the greatest crude protein content in SEL 2382 with 80.25%. Dry matter intake ratio varied between 3.33-4.75%. The lowest dry matter intake ratio was obtained from SEL 2379 line and the highest dry matter intake ratio from SEL 2470 line.

Dry Matter Digestibility (%)
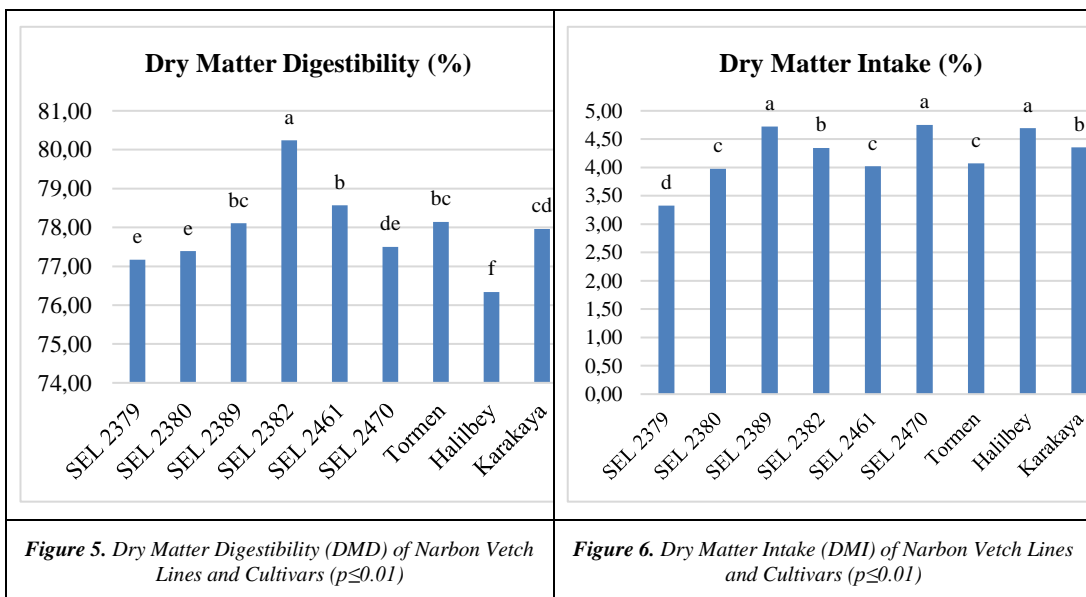
Dry Matter Intake (%)

Figure 5. *Dry Matter Digestibility (DMD) of Narbon Vetch Lines and Cultivars (p≤0.01)*

Figure 6. *Dry Matter Intake (DMI) of Narbon Vetch Lines and Cultivars (p≤0.01)*

Relative feed value of narbon vetch lines and cultivars are presented in Figure 7. Highly significant differences were observed in relative feed value (p<0.01). The greatest relative feed value (286.18) was obtained from SEL 2389 line and the lowest relative feed value (198.90) was obtained from SEL 2379 line. Biplot is presented in Figure 8. PC1 represented 47.29% and PC2 34.03% of total variations (81.32%) in investigated traits. While ADF, CP and CA formed a group, DMI and RFV formed another group over Biplot. While ADF, NDF, DMD, DMI and RFV had high separation capacity, CP and CA had quite low separation capacity. SEL 2379 was found to prominent with NDF, Karakaya, SEL 2475 and Halilbey with crude protein, SEL 2382 with DMD and SEL 2389 with RFV.

Although GGT biplot analysis is used for the analysis of multi-environmental experiments, it is also used for the analysis of all two-way data. With these data, characteristics of the genotypes can easily be compared. Several researchers used biplot analysis to compare various characteristics of genotypes [14], [15], [16]. Since the cosine of angle between the vectors of any two characteristics almost estimates the correlation coefficient between these two characteristics, biplot can reliably be used to visualize the relationships between the characteristics [16].

Figure 7. *Relative Feed Value (RFV) of Narbon Vetch Lines and Cultivars (p≤0.01)*

Figure 8. *The Biplot of Narbon Vetch Lines and Cultivars for Nutritive Value Parameters*
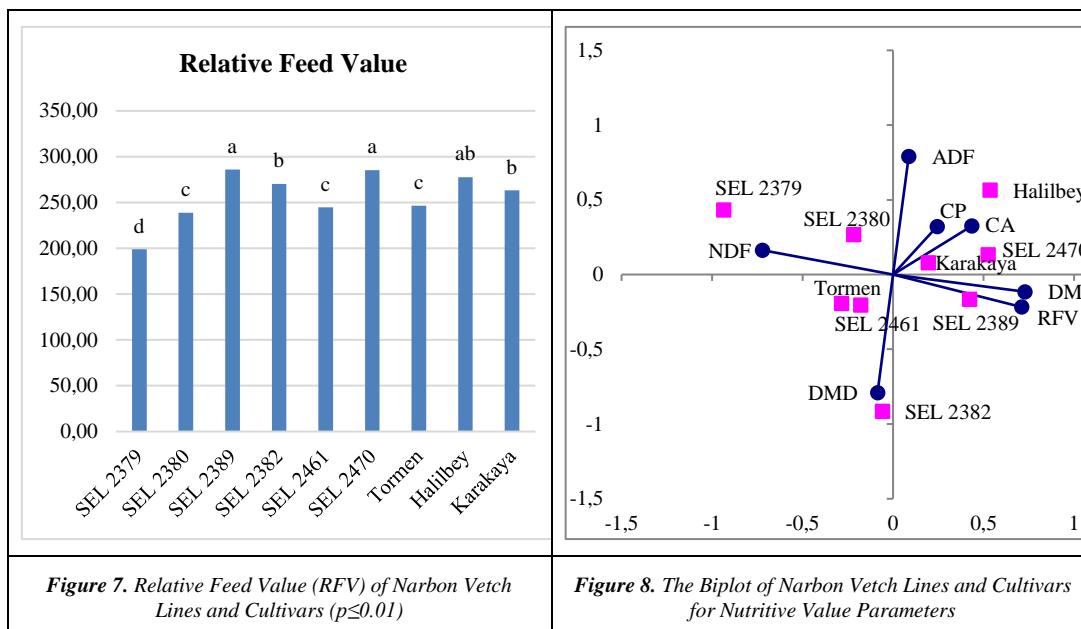
4. CONCLUSION

This study investigated chemical composition in different narbon vetch cultivars and lines. All narbon vetch lines and cultivars seed had height nutritional quality values. The Karakaya cultivar was found to be considerable with regard to high crude protein content, SEL 2382 with lower ADF, SEL 2470 with lower NDF and SEL 2389 with higher relative feed value. However these results obtained in the this study should be supported by *in vivo* feeding experiments.

ACKNOWLEDGEMENTS

REFERENCES

[1] Kaya, İ., Yalcın, S., Baklagil Tane Yemleri ve Ruminant Rasyonlarında Kullanımı. Lalahan Hayvansal Arastırma Enstitüsü Dergisi, 39(1): 101-114, 1999.

[2] Abd El Moneim A. M., Narbon Vetch (*Vicia narbonensis* L.): A Potential Feed Legume Crop for Dry Areas in West Asia. Journal of Agronomy and Crop Science, 169(5): 347–353, 1992.

[3] Canbolat O. Bayram G., Bazı Baklagil Danelerinin *in vitro* Gaz Üretim Parametreleri, Sindirilebilir Organik Madde ve Metabolik Enerji İçeriklerinin Karsılastırılması. U. Ü. Ziraat Fakültesi Dergisi, 21(1): 31-42, 2007.

[4] Van Soest P.J. and Wine R.H., The use of detergents in the analysis of fibrous feeds. IV. Determination of plant cell wall constituents. Journal of the Association of Official Analytical Chemists, 50, 50-55, 1967.

[5] Van Soest P.J., The use of detergents in the analysis of fibre feeds. II. A rapid method for the determination of fibre and lignin. Journal of the Association of Official Analytical Chemists, 46, 829-835, 1963.

[6] Rohweder, D.A., Barnes, R.F. and Jorgensen, N., Proposed hay grading standards based on laboratory analyses for evaluating quality. Journal of Animal Science. 47: 747-759, 1978.

[7] SAS, SAS User's Guide: Statistic. Statistical Analysis Systems Institute Inc., Cary, NC, 1999.

[8] Yan W, Kang MS., GGE-Biplot Analysis: a graphical tool for breeders. Geneticists and agronomists. CRD Press, Boca Raton, 2003.

[9] Hadjipanayiotou, M., Chemical composition, digestibility and in situ degradability of narbon vetch grain and straw grown in a Mediterranean region. INRA, EDP Sciences. Ann. Zootech. 49: 474-478, 2000.

[10] Hadjipanayiotou, M. and S. Economides. 2001. Chemical composition, in situ degradability and amino acid composition of protein supplements fed to livestock and poultry in Cyprus. Livestock Research for Rural Development 13: 6, 2001.

[11] Kaplan M., Kamalak A., Kasra A.A., Güven I., Effect of maturity stages on potential nutritive value, methane production and condensed tannin content of *Sanguisorba minor* Hay. Kafkas Univ Vet Fak Derg.20: 445-449, 2014.

[12] Association of Official Analytical Chemists (AOAC)., Official Method of Analysis. 15th. ed. Washington, DC. USA. pp 66-88, 1990.

[13] Ball, D.M., Collins, M., Lacefield, G.D., Martin, N.P., Mertens, D.A., Olson, K.E., Putnam, D.H., Undersander, D.J., Wolf, M.W., Understanding forage quality. American Farm Bureau Federation Publication 1-01, Park Ridge, IL, 2001.

[14] Kokten K., Kaplan M., Hatipoglu R., Saruhan V., Cinar S., Nutritive Value of Mediterranean Shrubs. Journal of Animal and Plant Sciences, 22: 88-194, 2012.

[15] Akcura M., Kokten K., Gocmen Akcacık A., Aydogan S., Pattern Analysis of Turkish Bread Wheat Landraces and Cultivars for Grain and Flour Quality. Turk J Field Crops, 21(1), 120-130, 2016.

[16] Akcura M., Kokten K.,Variations in Grain Mineral Concentrations of Turkish Wheat Landraces Germplasm. Quality Assurance and Safety of Crops & Foods, in press, 2016.

Numerical Investigation Of Single And Repeated Impacts For Foam Core Sandwich Structures

Umut CALISKAN[1], M. Kemal APALAK[2]

Abstract

Single and repeated impact behaviors of sandwich structures which are used in for various purposes in engineering structures such that they can absorb the impact energy induced by foreign objects were examined. In general, sandwich structures are constructed with a thicker flexible core between stiff, strong and thin face-sheets. Adhesive bonding is an effective joining technique and has been widely applied in various industries. Compared to other joining methods such as welding, adhesive bonding is relatively easier to perform and does not require excessive enterprise costs. The foam core sandwich structure is subjected by a mass at one time in single impact, but sometimes multiple impact load can occur simultaneously and/or non-simultaneously. Single and repeated impact loads were conducted for the different impact energy levels. Abaqus/Expiclit finite element package programme was used for the numerical simulations. Plates and adhesive were used as aluminum 6061-T6 and Araldite 2015 in numerical analysis, respectively and foam core was used as PVC foam. The variations of the contact force, kinetic energy histories and the deflection of the central impact region were investigated under single and repeated low velocity impact loads.

Keywords: *Repeated Impact, Foam Core Sandwich Structure, Nonlinear Finite Element Method*

1. INTRODUCTION

Sandwich structures based on strong, stiff skins bonded to a low-density core material are used widely in high-performance applications such as, aerospace industries, automotive, civil engineering and transportation industry due to their high in-plane and flexural stiffness, good acoustic and thermal insulation, high energy absorption capability, very good corrosion resistance [1-3]. Adhesive technology offers adhesives with high impact strength so that adhesively bonded joints can serve safely under an impact load for a short period. Impact mechanism develops strongly with surface conditions, and becomes more apparent on the metal surface whereas the damage may initiate inside the composite materials, such as along interfaces between the layers rather than on the surface of the composite material. Therefore, the prediction of the initiation and propagation of the damages in the composite materials needs various damage models to be considered. Low velocity impacts are considered as the most dangerous situations because of the difficulties to detect the damages. After an impact, a large reduction in the mechanical performance may occur. Thus, a good understanding of indentation, impact response and repeated impact response are necessary in order to predict and assess their residual strengths. Structures under repeated impacts are usually applied in engineering such as the landing gears of carrier-based aircrafts, excavator movable arms, rock crushers and firing system of artilleries. At these situations, high strain rate and accumulated plastic deformation are two significant features that increase the risk of failure. Hence, it is extremely essential to predict the residual life, i.e., the number of impacts to failure [4]. Xia and Wu [5] studied low velocity impact response of foam core sandwich composites in conjunction with various facing composed of glass, carbon, carbon/Kevlar hybrid and Kevlar fabric by using RTM process for three energy levels. Their results showed that the foam core with Kevlar facing were optimal for the peak load at load versus time plot. Wang et all. [6] studied the impact response of sandwich panels with different core materials. Their sandwich panels were made of aluminum face-sheets with five different cores such as low density balsa wood, high density balsa wood, cork, polypropylene honeycomb and polystyrene foam. The impact properties of sandwich panels with the five different cores were compared in terms of contact force, energy absorption, depth of indentation, overall bending deflection.

---

[1] *Corresponding author: Erciyes University, Department of Mechanical Engineering, 38039, Melikgazi/Kayseri, Turkey. ucaliskan@erciyes.edu.tr.*

[2] *Erciyes University, Department of Mechanical Engineering, 38039, Melikgazi/Kayseri, Turkey. apalakmk@erciyes.edu.tr.*

Their numerical model was carried out using the finite element software LS-Dyna. Their results showed that the core material was found to be very important in the target deformation, energy absorption, damage mechanism and penetration resistance of the sandwich panel. J. Aurrekoetxea et all. [7] investigated the repeated impact behaviour of self-reinforced polypropylene composite. Plastic deformation of the tape was the dominant mechanism, and the resulting penetration mode was a highly localised "star"-shaped hole. Damage and perforation thresholds are 5 J and 31.4 J respectively. Impact fatigue life exceeds 500 impact events up to 13 J, but drops sharply for 14 J. Strain-hardening was the origin of the trend of peak load increased and plastic deformation decreased with impact events. As a result of, the amount of energy absorbed by each impact was reduced. Zhou et al. [8] investigated the perforation resistance of foam-based sandwich panels with experimental and numerical techniques. The effect of oblique loading and an aqueous support on sandwich panels were studied. The perforation resistance of the plain foams and their sandwich panels was strongly dependent on the properties of the foam core. At intermediate and higher densities, the crosslinked PVC foams and their associated sandwich panels offered a superior perforation resistance to their linear PVC counterparts. It was shown that sandwich panels impacted in an aqueous environment exhibit a lower perforation resistance than tested in air.

2. MATERIAL AND METHODS

2.1. Finite Element Model

The low velocity impact behavior of sandwich panel was studied using ABAQUS/Explicit [9]. The impact behavior was investigated for single and multiple impact under four impact energy levels of 15, 30, 45 and 60 J. Aluminum plates were in dimension of 125x125x1 mm, foam core material was in dimension of 125x125x10 mm and were bonded using an epoxy based adhesive (Araldite 2015) in dimension of 125x125x0.2 mm. The face-sheets were modeled as an elasto-plastic material. The foam core was modeled as crushable foam material. The stress and strain curves of Aluminum (Al-6061 T6) and foam material (Expanded polystyrene) are shown in Figure 1 and the mechanical properties of sandwich panel components are listed in Table 1.

Table1. Mechanical properties of sandwich panel components.

Material	Al 6061 T6	Araldite 2015	EPS50
Density (kg/m^3)	2780	1450	50
Poisson's ratio	0.3	0.36	
Young's modulus	69	1.16	0
Yield stress (Mpa	275	24.7	-

Face-sheet material..   Face-sheet material.
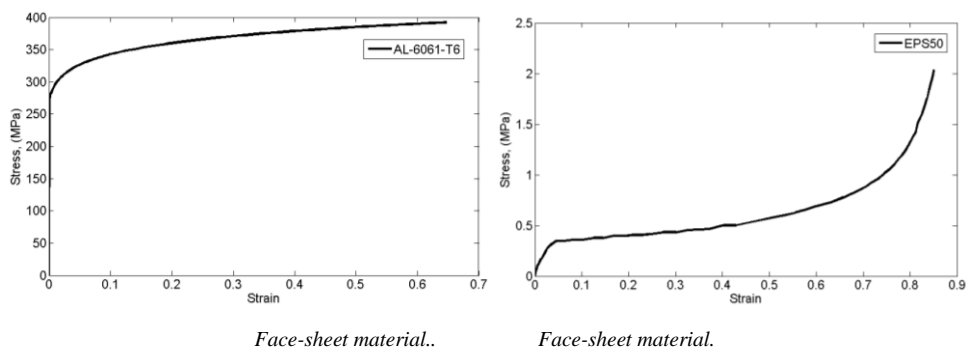
Figure 1. Stress-Strain curves of (a) Al 6061-T6 and (b) Expanded polystyrene foam.

The impactor was modeled as a rigid body behavior. The encastered boundary condition was applied to the sandwich panel. Both face-sheets and core foam were modeled using a three-dimensional solid finite element with three degrees of freedom at each node (C3D8R). The hourglass control was also used for the finite elements of core material as another option to avoid excessive element distortions and calculate numerical integrations accurately. The mechanical contact between the impactor, sandwich panel and impactor was simulated by the GENERAL CONTACT ALGORITHM in Abaqus/Explicit [9]. The adhesive layer between the face-sheets and core foam is simulated by means of the cohesive zone approach. The interfacial adhesive failure was modeled through this cohesive zone layer between the face-sheets and foam core. The cohesive

parameters of the epoxy adhesive were given in Table 2 [10] and a three-dimensional cohesive element (COH3D8) was used to model the cohesive response of the adhesive layer. The nominal traction stress vector t, with the components: t_n^0, t_s^0 and t_t^0, which represent the normal and the two shear tractions, respectively. G_n and G_s are the areas under the CZM laws in tension and shear. The cohesive thickness was taken as 0.2 mm for the adhesive layer. The finite element model of sandwich panel was shown in Figure 2.

Table 1: Cohesive parameters of adhesive Araldite 2015 used in CZM

Property	Araldite 2015
E (GPa)	1.85
G (GPa)	0.56
t_n^0 (MPa)	21.63
t_s^0 (MPa)	17.9
G_n^0 (N/mm)	0.43
G_s^0 (N/mm)	4.70
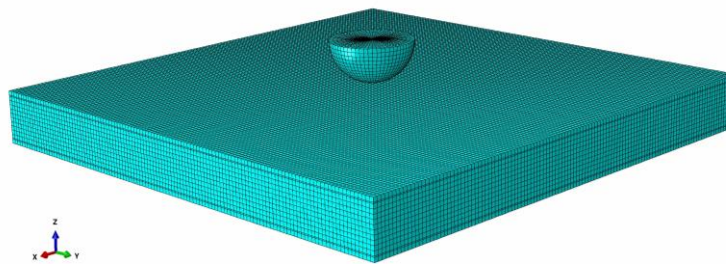
Figure 2. The Finite element model.

3. RESULTS ANAD DISCUSSION

Impact test were performed for impact energies of 15, 30, 45 and 60 J, respectively. The impactor was spheral tip geometry of 20 mm in diameter, and 5.045 kg of a mass. The effect of the single and multiple impact was investigated the sandwich panel. The temporal variations of the contact force and the permanent deflections at the top and bottom surfaces were determined for impact energy levels of 15, 30, 45 and 60 J, respectively. The kinetic energies were evaluated to determine the energy absorption capability of structures. The specimen thickness is 12.5 mm for the all specimens. The permanent deflections were evaluated at the top surface of upper face-sheet (u_U) and the bottom surface of the lower face-sheet (u_L) in order the determine the energy absorption capability of the specimens. Figure 3 shows the effect of single and repeated impact on the central transverse deflection of the central impact region for the impact energy levels of 15, 30, 45 and 60 J, respectively. As the impact energy is increased, the central permanent deflections are increased. The central permanent deflections were predicted as 5.6, 8.5, 10.5, and 12.3 mm at the top surface (u_U) and 0, 1.2, 1.8 and 2.3 mm at the bottom surface (u_L) and the after-impact thicknesses (Δ) were evaluated were 6.6, 4.9, 3.5 and 2.2 mm under impact energies of 15, 30, 45 and 60 J for single impact tests, respectively.

Repeated impact	Single impact	Repeated impact	Single impact
u_U=4,5 mm u_L=0 mm Δ=7,7 mm	u_U=5,6 mm u_L=0 mm Δ=6,6 mm	u_U=7,1 mm u_L=0 mm Δ=5,1 mm	u_U=8,5 mm u_L=1,2 mm Δ=4,9 mm
5J+5J+5J	15J	10J+10J+10J	30J

U_U=9,2 mm U_L=1,3 mm Δ=4,3 mm	U_U=10,5 mm U_L=1,8 mm Δ=3,5 mm	U_U=10,8 mm U_L=1,9 mm Δ=3,3 mm	U_U=12,3 mm U_L=2,3 mm Δ=2,2 mm
15J+15J+15J	45J	20J+20J+20J	60J
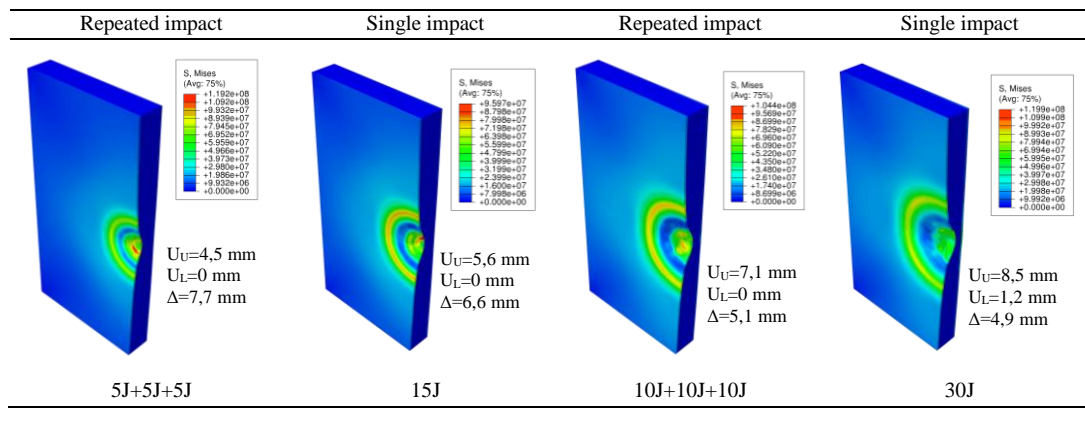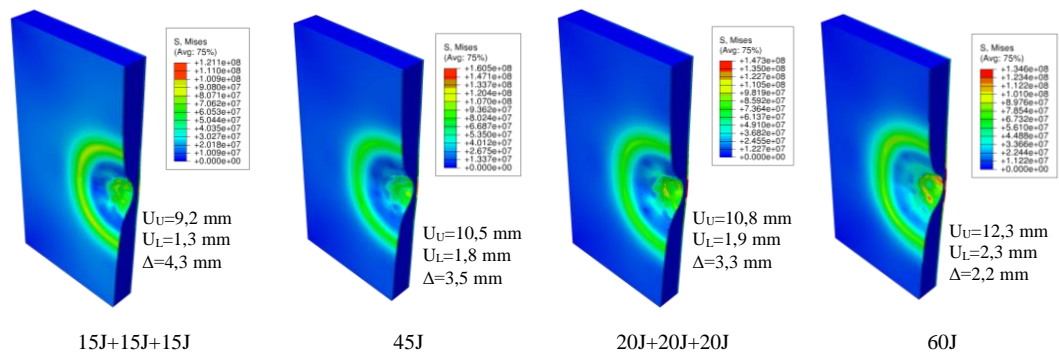
Figure 3. The effect of the single and repeated impact on the stress distribution, permanent deflections and after-impact thickness of the central impact region for the impact energy levels of 15, 30, 45 and 60J.

As the repeated impacts analyses are considered, repeated impact energy is 5 J (three times) for the total impact energy of 15 J and for the total impact energy of 30 J, repeated impact energy is 10 J, for the total impact energy of 45 J, repeated impact energy is 15 J, for the total impact energy of 60 J, repeated impact energy is 20 J. The central permanent deflections were measured as 4.5, 7.1, 9.2, and 10.8 mm at the top surface (u_U) and 0, 0, 1.3 and 1.9 mm at the bottom surface (u_L) and the after-impact thicknesses (Δ) were evaluated were 7.7, 5.1, 4.3 and 3.3 mm under impact energies of 15, 30, 45 and 60 J for repeated impact tests, respectively. The central permanent deflections of both upper and lower face-sheets for single impact tests is higher than repeated impact tests ones, and also after-impact thicknesses under single impact loads are lower than repeated impact tests ones.

E= 15 J   *E= 30 J*

E= 45 J   *E= 60 J*
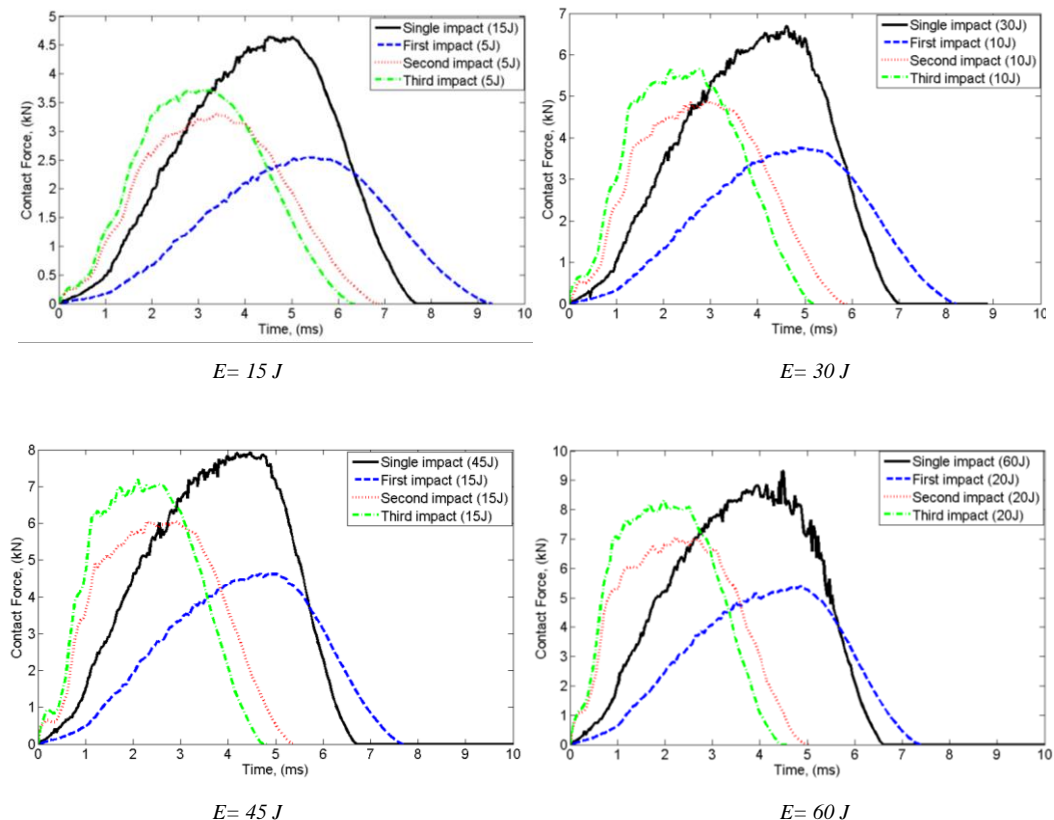
Figure 4. The effect of the single and repeated impact on the variation of contact force for the impact energy levels of 15, 30, 45 and 60J

Figure 4 shows the effect of the single and repeated impact on the temporal variations of the contact force under present impact energies, respectively. The peak contact forces are measured as 4.6, 6.9, 8 and 9.1 kN

under the impact energy levels of 15, 30, 45 and 60 J for a single impact test, respectively, and the corresponding peak contact times are nearly same for all specimens as nearly 4.8 ms. The impact analyses are completed in the total contact times of 7.8, 7, 6.8 and 6.5 ms. As the repeated impacts analyses are considered, repeated impact energy is 5 J (three times) for the total impact energy of 15 J and for the total impact energy of 30 J, repeated impact energy is 10 J, for the total impact energy of 45 J, repeated impact energy is 15 J, for the total impact energy of 60 J, repeated impact energy is 20 J. As the first impact energy level 15 J is considered, peak contact forces are measured as 2.5, 3 and 3.6 kN for the first, second and third impact (5J), respectively. The repeated impact tests are completed in the total contact times of 9.1, 5.2 and 4.8 ms. As the impact energy level of 30 J is considered, the peak contact forces are measured as 3.5, 4.9 and 5.8 kN for the first, second and third impact (10 J), respectively. The repeated impact analyses are completed in the total contact times of 8, 6 and 5.1 ms. As the impact energy level of 45 J is considered, the peak contact forces are measured as 4.5, 6 and 7.1 kN for the first, second and third impact (15 J), respectively. The repeated impact analyses are completed in the total contact times of 7.6, 5.1 and 4.9 ms. As the impact energy level of 60 J is considered, the peak contact forces are measured as 5, 7 and 8.2 kN for the first, second and third impact (20 J), respectively. The repeated impact analyses are completed in the total contact times of 7.1, 5 and 4.5 ms. As the impact energy is increased, peak contact forces are increased and total contact durations are decreased for all specimens. Peak contact force levels for single impact are higher than repeated impact. Peak contact force levels are gradually increased caused by strain hardening effect for same energy levels in the repeated impact analyses. Figure 4 shows the the effect of the single and repeated impact on the kinetic energy histories under present impact energies, respectively. Impact energies of 15, 30, 45 and 60 J for the single impact are reduced to kinetic energy levels of 4, 5, 7 and 9 J, respectively; thus, the impact energies are dissipated by 73, 76, 84 and 85%, respectively. Impact energy of 15, 30,45 and 60 J for the repeated impact analyses (5, 10, 15, 20 J) are reduced to kinetic energy levels of 9, 15, 18 and 22 J, respectively. As the impact energy is increased, the capability of the absorbing energy is incereased. Impact energy absorbtion capability under single impact analyses is better than under repeated impact analyses. The capability of the energy absorbing are gradually decreased caused by strain hardening effect for same energy levels in the repeated impact analyses.
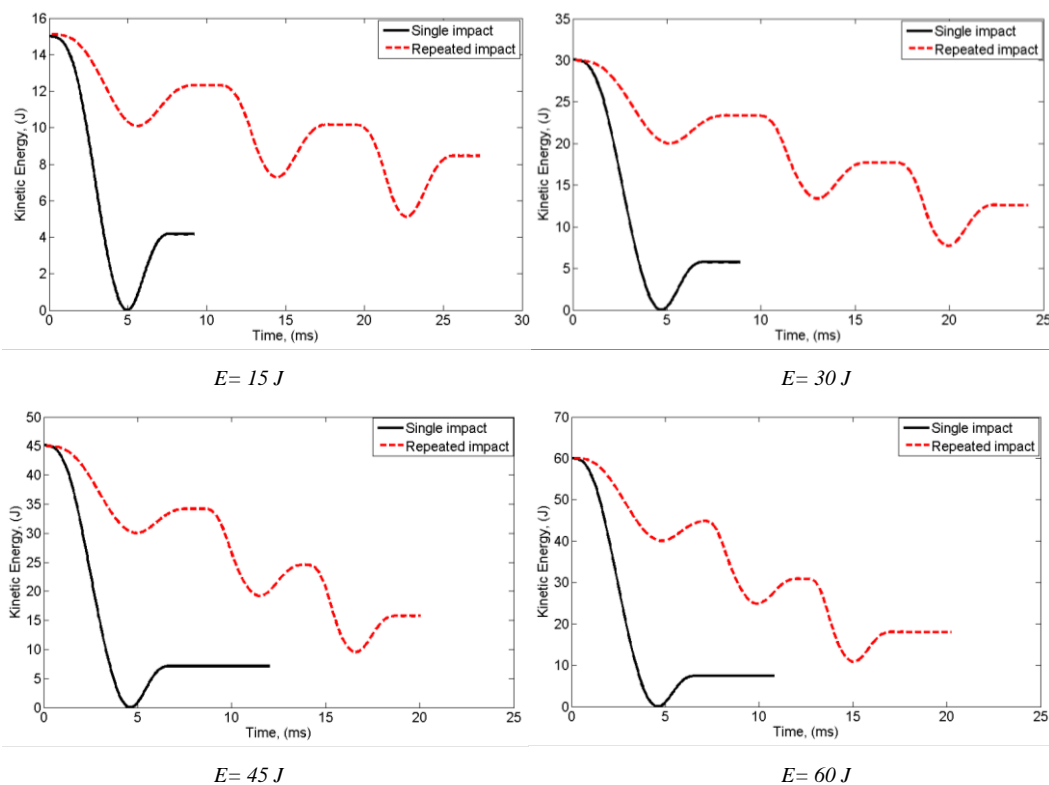
Figure 5. The effect of the single and repeated impact on the kinetic energy histories for the impact energy levels of 15, 30, 45 and 60J.

4. CONCLUSION

This study presented the single and repeated impact response of sandwich panel for various impact energies. The temporal variation of contact forces, kinetic energy histories and the permanent deflections at the top surface of plate assesses for the impact energies of 15, 30, 45 and 60 J. Strain hardening effect for the repeated impact analyses is appeared pretty much. Specimens have less permanent deflection in the repeated impact anayses than single impact anaylses. Peak contact force levels for the single impact are higher than the repeated impact. The capability of the impact energy absorbtion for the single impact analyses is better than in the repeated impact analyses due to strain hardening effect.

REFERENCES

[8]. V. Rizov, *"Non-linear indentation behavior of foam core sandwich composite materials—A 2D approach"*, *Computational Materials Science,* vol. 35, pp. 107-115, 2006.

[9]. P.M. Schubel, J.J. Luo, I.M. Daniel, *"Low velocity impact behavior of composite sandwich panels"*, *Composites Part A: Applied Science and Manufacturing*, Vol. 36, pp. 1389 – 1396, 2005.

[10]. L. Torre, J. Kenny, "Impact testing and simulation of composite sandwich structures for civil transportation", Composite Structures, vol. 50, pp.257 – 267, 2000.

[11]. L. Li, L. Sun, *"Experimental and numerical investigations of crack behavior and life prediction of 18Cr2Ni4WA steel subjected to repeated impact loading", Engineering Failure Analysis*, vol. 65, pp. 11-25 July 2016.

[12]. F. Xia, X. Wu, *"Work on Low-velocity Impact Properties of Foam Sandwich Composites with Various Face Sheets", Journal of Reinforced Plastics and Composites*, Vol. 29, pp. 1045-1054, 2010.

[13]. H. Wang, K. R. Ramakrishnan, K. Shankar, *Experimental study of the medium velocity impact response of sandwich panels with different cores", Materials & Design*, vol. 99, pp. 68-82, 2016.

[14]. J. Aurrekoetxea, M. Sarrionandia, M. Mateos, L. Aretxabaleta, *"Repeated low energy impact behaviour of self-reinforced polypropylene composites", Polymer Testing*, vol. 30, pp. 216-221, April 2011.

[15]. J. Zhou, M. Z. Hassan, Z. Guan and W. J. Cantwell, *"The low velocity impact response of foam-based sandwich panels", Composites Science and Technology,* vol. 72, pp. 1781-1790, July 2012.

[16]. ABAQUS/Explicit (Version 6.14), User's manual, Finite Element Software. Available from: http://www.simulia.com.

[17]. R. Campilho, M. Banea, J. Neto, L. da Silva, *"Modelling adhesive joints with cohesive zone models: effect of the cohesive law shape of the adhesive layer"*, *International Journal of Adhesion and Adhesives*, vol. 56, pp. 44:48, 2013.

Low Velocity Impact Response On Steel Sandwich Panels: An Experimental And Numerical Study

Umut CALISKAN[1], M. Kemal APALAK[2]

Abstract

This study presents a numerical and experimental investigation on low velocity impact response of steel sandwich panels with expanded polystyrene foam (EPS) core. Sandwich structures based on strong, stiff skins bonded to a low density core material are used widely in high-performance applications such as, aerospace industries, automotive, civil engineering and transportation industry due to their high in-plane and flexural stiffness, good acoustic and thermal insulation, high energy absorption capability, very good corrosion resistance. The effect of impact energy levels was investigated on the impact energy absorption of the panel. The dynamic response of the panels was predicted using the finite element analysis package ABAQUS/Explicit. The material and geometrical nonlinearities were considered and the foam material was modeled as a crushable foam material. The cohesive response of the adhesive interface was modeled using the cohesive zone model. The temporal variations of contact force, kinetic energy histories and central permanent deflections were compared for different impact energies experimentally and numerically. The peak contact force levels and central permanent deflections are increased with increasing the impact energies. The numerical simulations were found to be in good agreement with the experimental results.

Keywords: *Low Velocity Impact, Foam Core Sandwich Structure, Explicit Finite Element Method.*

1. INTRODUCTION

Sandwich structures, consisting of a low-density core, between two thin and stiff face-sheets have been increasingly used in applications requiring high flexural rigidity, buckling resistance, and energy absorption and bending stiffness. The face-sheet materials are usually aluminium or fibre reinforced polymers whereas the core material is woods, expanded metals, polymer and metal foams, and polymers and metal honeycombs. Composite sandwich structures are used widely in high-performance applications such as, aerospace industries, marine industries, automotive, civil engineering and transportation industry due to their high in-plane and flexural stiffness and good acoustic and thermal insulation, high energy absorption capability, very good corrosion resistance [1-4]. Flores-Johnson and Li [5] studied indentation of sandwich panels with carbon fibre-reinforced polymer face sheets and polymeric foam core. Both nose shape and foam core density have large influence on the indentation at failure and damage area and also C-scan images showed that these results. They observed a dependency of the indentation load on the supporting condition. They also found that the difference in indentation resistance between the sandwich panel and its corresponding core material depends on the core density. Singh et al. [6] investigated a damage evolution study of E-glass/epoxy composite under low velocity impact. Glass Fiber Reinforced Polymer composite is a popular material system that can be used in vehicles and is able to meet requirements in torsion, bending and crash. During the service of the components made of composite there is possible mass impact (stone and debris) which is considered as Low Velocity Impact (LVI). They compared two damage models and finally exponential model was used for low velocity impact simulations. They calculated material softening parameter m for different element sizes. Simulations were performed for low velocity impact of glass epoxy plate having two configurations i.e. unidirectional and crossply. They had good agreement between the predicted and measured strain was obtained. Lopes et al. [7] investigated low velocity impact damage resistance on dispersed stacking sequence laminates using the explicit finite element method. Their constitutive models which take into account the physical progressive failure behaviour of fibres, matrix, and interfaces between plies were implemented in an

---

explicit finite element method and used in the simulation of low-velocity impact events on composite laminates. They compared experimental results with those of their numerical model with 24-ply laminate specimens. Their simulations showed that the energy dissipated through delaminations was higher for the their alternative configuration specimens than for the baseline within the 9-30 J impact energy range.

2. MATERIAL AND METHODS

2.1. Specimen Preparation And Low Velocity Impact Test

The sandwich panel specimens consist of two face-sheets, core material and adhesive layers for bonding the face-sheet with core material. The face-sheets were manufactured from steel St-37 plates in dimension of 1x170x170 mm. The core material was expanded polystyrene (EPS) foam with diemsion of 20 mm, and density of 20 kg/m^3. The face-sheets and core material were joined using two components adhesive (ARALDITE 2015). Before applying adhesive, the bonding surfaces were cleaned by using ethanol (C_2H_6O) which is so effective on the cleaning of impurities and dirt affecting the bonding quality of two plates. Figure 1 shows sandwich panel and beam components samples.
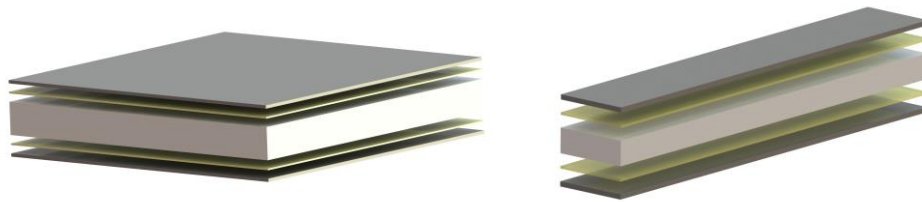
Figure 1. Sandwich panel and beam components.

In order to get a uniform adhesive layer between face-sheets and core material without air bubbles as possible, a uniform pressure was applied to adhesive layer between face-sheets. A bonding apparatus was designed and manufactured (Figure 2). The apparatus surfaces contacting with the face-sheet surfaces were operated sensitively. The upper and lower parts of bonding apparatus can be joined by bolts. The thickness-jigs were also produced for keeping the thickness of the adhesive layer at 0.2 mm.

Figure 2. Application adhesive and bonding apparatus

The two-components adhesive, Araldite 2015, needs an average curing time of 48-72 hours at room temperature. Therefore, all specimens, after the adhesive was applied, were left to a curing time of 72 hours at room temperature. During the bonding process the adhesive was first rolled up by a hoe on to the face-sheet bonding surface, and then the sandwich structure was pressed between the upper and lower parts of the apparatus so that the air bubbles could be removed as possible and to achieve a better adhesion. The low-speed impact tests of the sandwich specimens were performed via Fractovis Plus lowvelocity impact test equipment (Figure 3). The pre-specimens having unsatisfactory bonding quality were used in a series of preliminary tests and the optimal impact conditions were provided considering the temporal variation of contact force. Low velocity impact tests were repeated at least twice for each of all sandwich configurations at the impact energies of 25, 50 ,75 and 100 J. An impactor having a diameter of 20 mm, a mass of 5.045 kg and semi-cylindrical edge geometry was used.

Figure 3. Low velocity impact test system.

2.2. Finite Element Model

The low velocity impact behavior of sandwich panel was studied using ABAQUS/Explicit [8]. The impact behavior was investigated for impact under four impact energy levels of 25, 50, 75 and 100 J. Steel plates were in dimension of 170x170x1 mm, foam core material was in dimension of 170x170x20 mm and were bonded using an epoxy based adhesive (Araldite 2015) in dimension of 170x170x0.2 mm. The face-sheets were modeled as an elasto-plastic material. The foam core was modeled as crushable foam material. The stress and strain curves of Steel (St37) and foam material (Expanded polystyrene) are shown in Figure 4 and the mechanical properties of sandwich panel components are listed in Table 1.

Table1. Mechanical properties of sandwich panel components

Material	St-37	Araldite 2015	EPS20
Density (kg/m^3)	7860	1450	20
Poisson's ratio	0.3	0.36	0
Young's modulus (GPa)	210	1.16	0.011
Yield stress (Mpa)	310	24.7	-

Face-sheet material   *Foam core material*
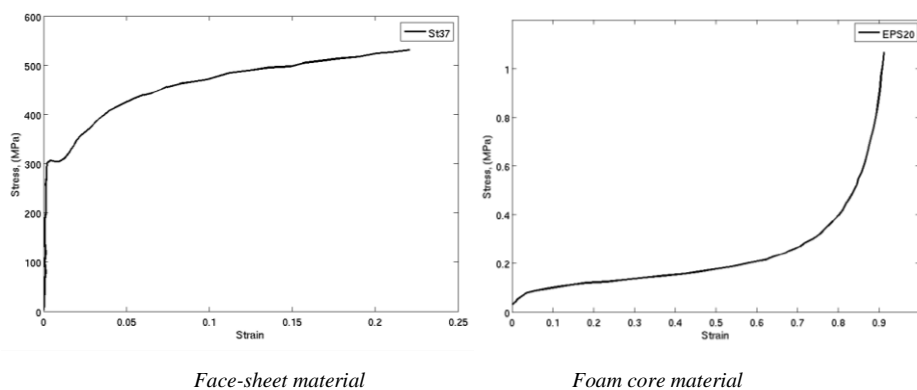
Figure 4. Stress-Strain curves of (a) St-37 and (b) Expanded polystyrene foam

The impactor was modeled as a rigid body behavior. Both face-sheets and core foam were modeled using a three-dimensional solid finite element with three degrees of freedom at each node (C3D8R). The hourglass control was also used for the finite elements of core material as another option to avoid excessive element distortions and calculate numerical integrations accurately. The mechanical contact between the impactor,

sandwich panel and impactor was simulated by the GENERAL CONTACT ALGORITHM in Abaqus/Explicit [8]. The adhesive layer between the face-sheets and core foam is simulated by means of the cohesive zone approach. The interfacial adhesive failure was modeled through this cohesive zone layer between the face-sheets and foam core. The cohesive parameters of the epoxy adhesive were given in Table 2 [9] and a three-dimensional cohesive element (COH3D8) was used to model the cohesive response of the adhesive layer. The nominal traction stress vector t, with the components: t_n^0, t_s^0 and t_t^0, which represent the normal and the two shear tractions, respectively. G_n and G_s are the areas under the CZM laws in tension and shear. The cohesive thickness was taken as 0.2 mm for the adhesive layer. The finite element model of sandwich panel was shown in Figure 5.

Table 2: Cohesive parameters of adhesive Araldite 2015 used in CZM

Property	Araldite 2015
E (GPa)	1.85
G (GPa)	0.56
t_n^0 (MPa)	21.63
t_s^0 (MPa)	17.9
G_n^0 (N/mm)	0.43
G_s^0 (N/mm)	4.70
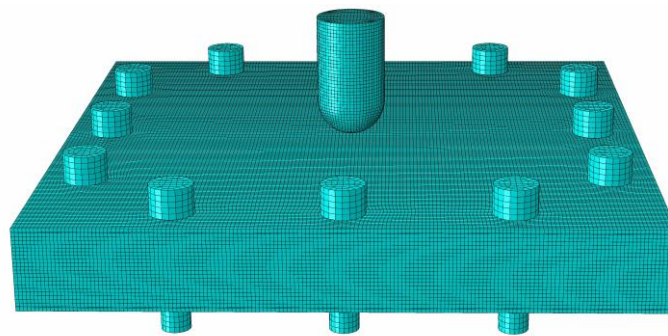
Figure 5. The Finite element model

3. RESULTS ANAD DISCUSSION

Impact analyses were performed for impact energies of 25, 50, 75 and 100 J, respectively. The impactor was spheral tip geometry of 20 mm in diameter, and 5.045 kg of a mass. The temporal variations of the contact force were determined for present impact energies, respectively. The kinetic energies were evaluated to determine the energy absorption capability of structures. The sandwich panel thickness is 22 mm for the all specimens. Figure 6 compares the predicted and experimental temporal variations of the contact force histories under present impact energies, respectively. The contact force levels are increased with increasing impact energy, whereas the total contact durations are decreased. The predicted and experimental contact force histories exhibit similar trends. The predicted and experimental peak contact forces are about 5, 7, 9 and 10 kN under the impact energy levels of 25, 50, 75 and 100 J, and the corresponding peak contact times are 6 ms.

Figure 7 compares the predicted and experimental temporal variations of kinetic energies for the different impact energies. As the impact energy is increased the penetration times decrease for all specimens. The predicted and experimental kinetic energy histories are similar for present impact energies. Figure 8 compares the temporal variations of the contact force versus the central transverse deflection for present impact energies, respectively. Increasing the impact energy results in evident increase in both the predicted and experimental contact force levels and in the central permanent deflections. the experimental contact force levels and permanent central deflections increase with increasing impact energy, and the experimental contact force–central deflection diagrams cover a larger area with increasing impact energy. Figure 9 compares the predicted and experimental deformed geometry of impacted specimens for present impact energies, respectively. The predicted and experimental deformed shapes are similar.

a) 25 J *b) 50 J*

c) 75 J *d) 100 J*
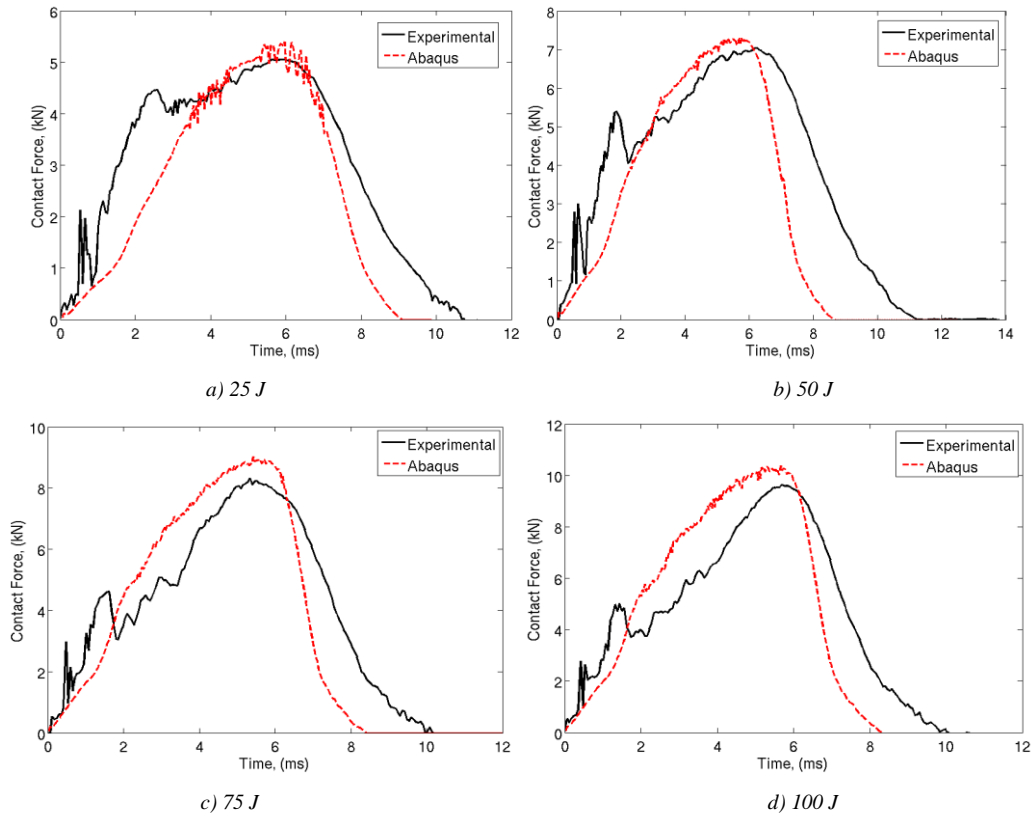
Figure 6. The contact force histories for the impact energies of a) 25, b) 50, c) 75 and d) 100 J

a) 25 J *b) 50 J*

c) 75 J *d) 100 J*
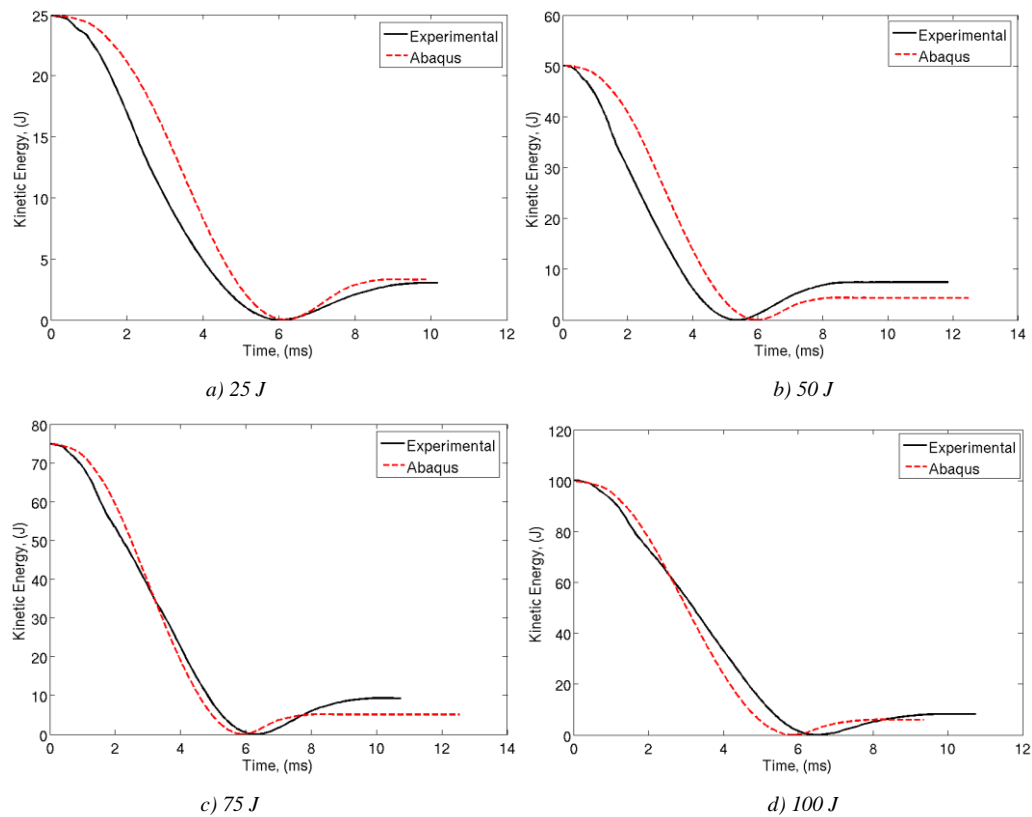
Figure 7. The kinetic energy histories for the impact energies of a) 25, b) 50, c) 75 and d) 100 J
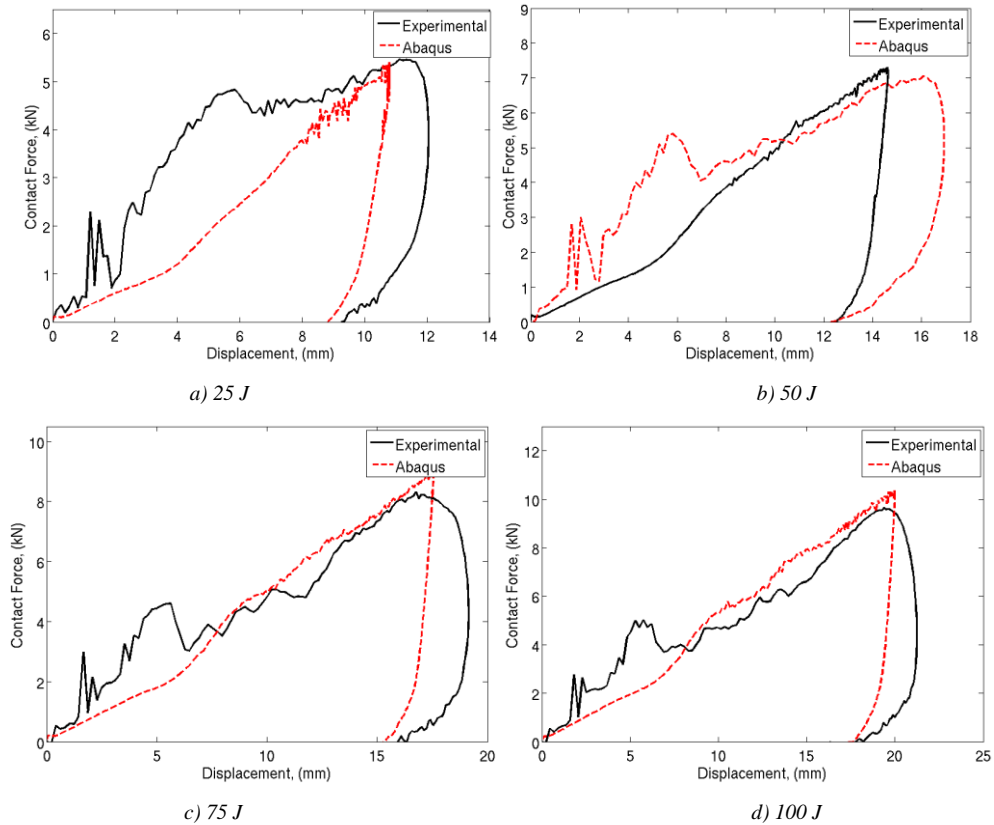
Figure 8. The contact force versus displacement histories for the impact energies of a) 25, b) 50, c) 75 and d) 100 J

| a) 25 J | b) 50 J | c) 75 J | d) 100 J |
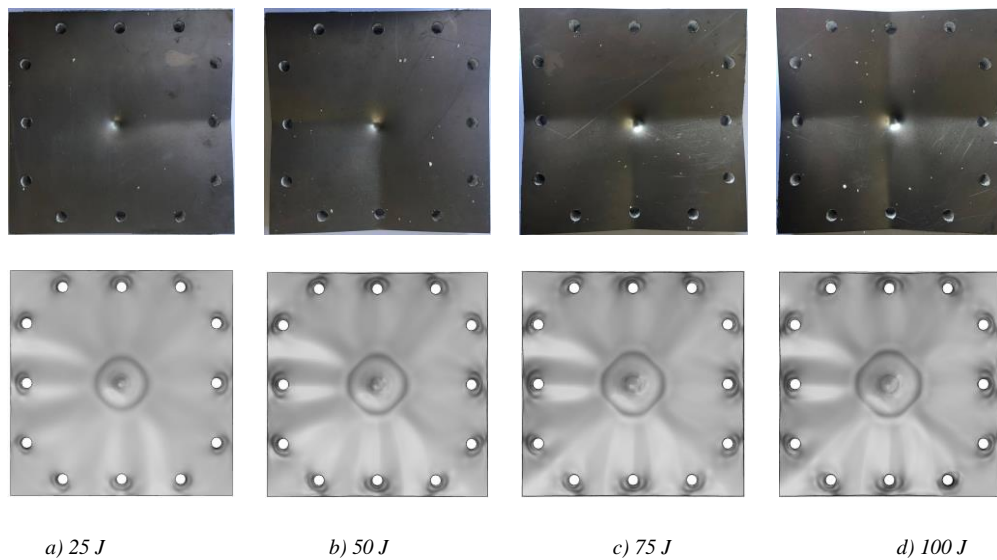
Figure 9. The predicted and experimental deformed shapes.

4. CONCLUSION

This study presented the impact response of EPS foam core sandwich panels of various impact energies experimentally and numerically. The temporal variation of contact force, kinetic energy histories and contact force versus vertical displacement of sandwich panels assessed for the impact energies of 25, 50, 75 and 100 J. Cohesive zone model (CZM) implemented simulations to model adhesive layer. As the impact energy is

increased, the peak contact force levels, the capability of energy absorption and central permanent displacement increased. Foam core materials supply geometrical continuity and absorb impact energy. The temporal variations of the contact force, kinetic energy and the permanent central deflections of the sandwich panels are in good agreement.

REFERENCES

[1] P. M. Schubel, J. Luo, and I. M. Daniel, *"Low velocity impact behavior of composite sandwich panels"*. *Composites Part A: Applied Science and Manufacturing*, 36(10):1389 – 1396, 2005.

[2] L. Torre and J.M. Kenny, *"Impact testing and simulation of composite sandwich structures for civil transportation"*, *Composite Structures*, 50(3):257 – 267, 2000.

[3] J. Yu, E. Wang, J. Li, and Z. Zheng, *"Static and low-velocity impact behavior of sandwich beams with closed-cell aluminum-foam core in three-point bending"*, *International Journal of Impact Engineering*, 35(8):885 – 894, 2008.

[4] V. Rizov, A. Shipsha, and D. Zenkert, "*Indentation study of foam core sandwich composite panels"*, *Composite Structures*, 69(1):95 – 102, 2005.

[5] E. A. Flores-Johnson and Q. M. Li, "*Experimental study of the indentation of sandwich panels with carbon fibre-reinforced polymer face sheets and polymeric foam core"*, *Composite: Part B*, vol. 42, pp. 1212-1219, March 2011.

[6] H. Singh, K. K. Namala, P. Mahajan, "*A damage evolution study of E-glass/epoxy composite under low velocity impact"*, *Composites Part B, vol. 76, pp. 235-248, Feb 2015*.

[7] C.S. Lopes, P.P. Camanho , Z. Gürdal, P. Maimí, and E.V. González, "*Low-velocity impact damage on dispersed stacking sequence laminates. Part II: Numerical simulations"*, *Composites Science and Technology*, vol. 69, pp. 937-947, Feb 2009.

[8] ABAQUS/Explicit (Version 6.14), User's manual, Finite Element Software. Available from: http://www.simulia.com.

[9] R. Campilho, M. Banea, J. Neto, L. da Silva, "*Modelling adhesive joints with cohesive zone models: effect of the cohesive law shape of the adhesive layer"*, *International Journal of Adhesion and Adhesives*, vol. 56, pp. 44:48, 2013.

The Pointed Arch Formations in 16th Century Istanbul Mosques

Ali Naci Ozyalvac[1], Pınar Ozyalvac[2]

Abstract

This study is an analytical review of arches as the key architectural element in traditional structures specially pointed arches in Mimar Sinan mosques in İstanbul. 19 mosques have been examined using architectural surveys, onsite measurements. Arches are classified according to their locations; interior, narthex, court and facades. The categorical properties like preferred types, places of use and grouping features are discussed and considered together with quantities like span, height, centers of intrados for understanding geometric formation principles of arches. Thus, new types were found like 1:7, 1:9, 1:11 beside known types like (1:5) pencî arches and statistics like where and which conditions they were shown has been revealed. It has also been possible to compare buildings over used arch types that make up the form repertoires of the designer in selected works. It has been revealed that pointed arches have been classified and arranged to provide speed and convenience in design and construction process as dominant stylistic determinant and founder of traditional construction systems.

Keywords: *Ottoman Architecture, Mimar Sinan, Pointed Arches, Istanbul Mosques.*

1. INTRODUCTION

An arch is a curvilinear structure used to span a space [1] and defined as an arc-shaped piece of structure [2] that its ends sit on these pillars or feet to cover an opening between two columns or two feet. The arch that is an important supporting element used in traditional construction systems has been developed in case that the size of the space to be span is bigger than the size of the parts the material, in other words, because of the necessity of spanning the large openings with small pieces [3] [4]. As a curvilinear bearing element that basically works only when pressing and transfers the loads on it to the two end bearers, the main function of the arch is to empty the wall section underneath. It is also one of the important architectural elements that determines the architectural styles with arch form. For example, style ogival / arc en ogive / croiseed'ogive for gothic style are used in the same sense. While art history research focused on the form of the arch, a classification was often made on the intrados profile and similar features were mentioned for certain periods.

The Ottomans moved architecture to an advanced point by developing the architectural elements and design principles that were used until its time and while doing this, testing of new design methods has been possible with arch architecture in order to cover larger openings. Ottoman architecture emerged with the use of most of the previously known arch forms and decoration techniques in new syntheses has used this element in a certain order and in a way that exhibits an inclusive approach in the direction of its own preferences.

It was seen that bricks, stone / brick alternatives and stone arches were used in the Ottoman period, starting from the first period structures. The use of bricks was made independent of the rubble wall masonry during the foundation years. Although there are opinions that it was used as decorative in Central Asia and India, the emergence of the pointed type is often associated with the Islamic world [5] [6]. It was the criterion to foreground the bearing nature of the ogive. The reason for the use of a pointed arch to cover large openings is that this type of the ogive gives less horizontal opening force. For the same reason, the semi-circular arch with large horizontal thrust was used in the places with secondary presets bearing less load. In addition to fulfilling the structural function of the arch in Ottoman architecture, its decorative use was also common thanks to the forms of the elements forming the arch or the side-by-side arrangement of more than one arch. In Ottoman architecture, arches were used so as to form a group by coming together in doors, in windows or in porticos.

---

[1] Corresponding author: Necmettin Erbakan University, Faculty of Engineering and Architecture, Department of Architecture, Konya / Turkey. aozyalvac@konya.edu.tr

[2] Necmettin Erbakan University, Faculty of Social Sciences and Humanities, Department of History, Konya / Turkey

(1:3) Ratio pointed arch (Rise / Span) (y/a) = 0,64

(1:3T) Ratio arch with tangential upper sections (Rise / Span) (y/a) = 0,48

(1:5) Ratio pointed (pencî) arch (Rise / Span) (y/a) = 0,59

(1:5T) Ratio pencî arch with tangential upper sections (y/a) = 0,52

(1:9) Ratio two centered pointed arch (Rise / Span) (y/a) = 0,55

(1:4,5T) Ratio pencî arch with tangential upper sections (y/a) = 0,51
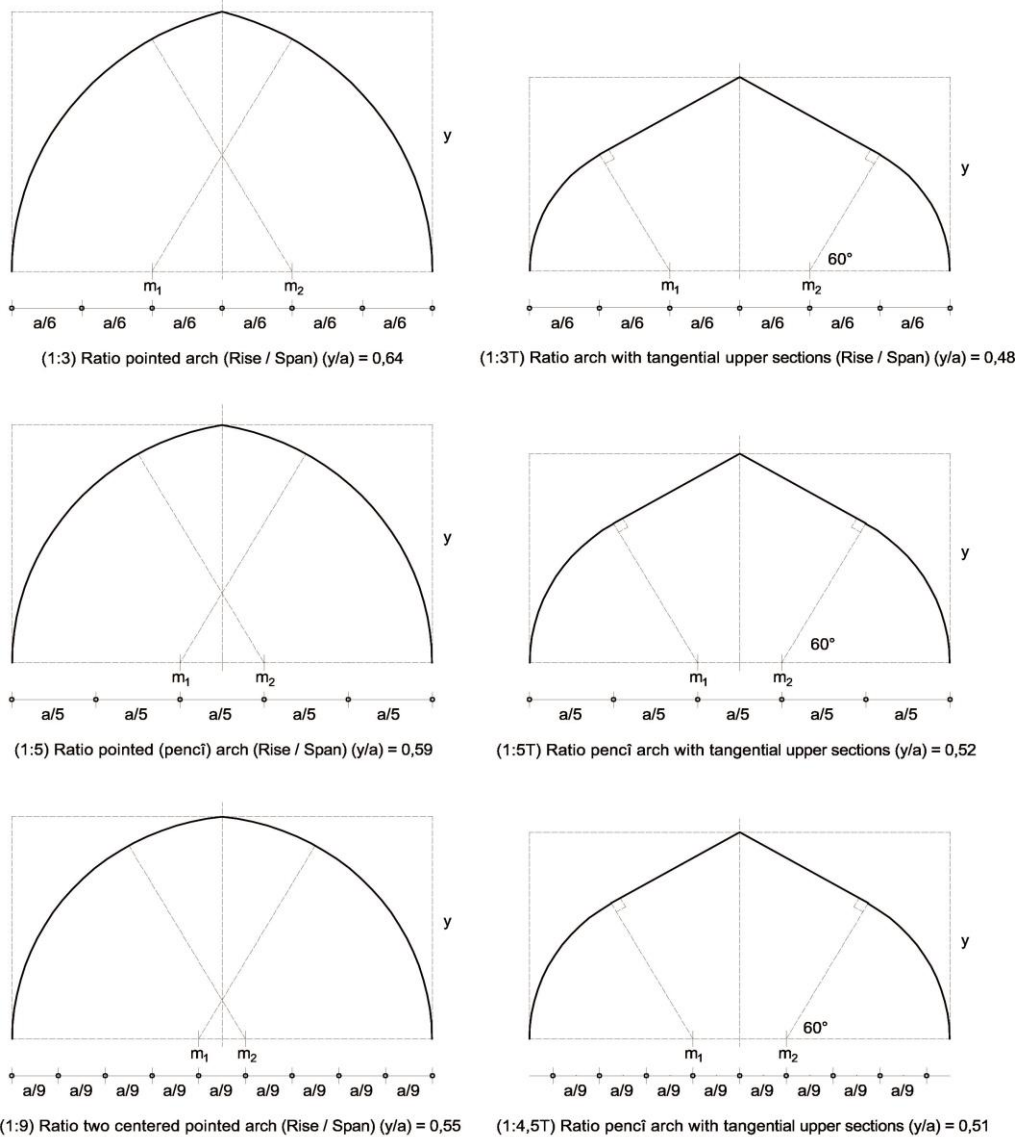
Figure 32. Pointed arch formations according to different centers by division of span

2. MATERIALS AND METHODS

The question that the design of the pointed arches used in the classical era of Ottoman architecture depends on which variables constitutes the subject of this study. In addition to many studies in which the arch that participates in structural fiction as part of the bearing system was examined within the scope of the style, several types of the arches that is a subspecies are mentioned depending on the position of the centers located by division of span. However, up to now, no research has been conducted on how many types were used in the constructions depending on the location and size. For the first time in this study, a research carried out on 19 mosques that were built in Istanbul during the period of Sinan The Architect based on the building surveys prepared by using recently developed techniques and the question that the design of the pointed arches depends on which variables, the location and utilization rates of two centered, tangent, three and four centered arches formed by division of space were discussed.

3. RESULTS AND DISCUSSION

There are 21 different types of the pointed arches in terms of distance between centers / span. The types used in the arches with tangents are grouped as 9 types. A total of 32 different arch types together with round (semicircular) arches were determined to be used. The arch types mentioned here are derivatives of two centered and few types depending on the division of span in terms of their structure as top-tangible varieties of the same type. The arches formed by drawing the arcs starting from the far ends of the span from the points

found through the division of the spring line are the pointed arches. Both cases are possible for tangent arches and the high arches drawn on 60° arcs from far ends are tudor-like and arches drawn on 60° arcs from near ends are can be named as drop pointed arches with tangential tops.

Table 24. Varieties of pointed arches found in examined mosques

Name of the Mosque	Type of the pointed arches (distance between centers / span)	Score
Fatih Nisancı Mehmet Pasa (1589)	1:5, 1:5T	2
Silivrikapı Hadım İbrahim Pasa (1551)	1:5, 1:5T, 1:6T, OT	4
Topkapı Gazi Kara Ahmet Pasa (1560)	1:5, 1:6, 1:8, 1:4,5, 1:4,5T	5
Kadırga Sokullu Mehmet Pasa (1572)	1:5,5, 1:9, 1:5, 1:5T, 1:6,5	5
Kasımpasa Piyale Pasa (1573)	1:7, 1:5,5, 1:6, 1:9, 1:5, OT	6
Haseki Hurrem Sultan (1538)	1:4T, 1:2,5T, 1:5, OT, 1:4, 1:7T	6
Karagumruk Mesih Mehmet Pasa (1586)	1:9, 1:13, 1:5, 1:5,5, 1:3T, 1:5T	6
Uskudar Mihrimah Sultan (1547)	1:11, 1:5, 1:6, 1:7, OT, 1:9, 1:4	7
Sehzade Mehmet (1548)	1:6, 1:5, 1:5,5, 1:7, 1:6T, 1:4,5, OT	7
Uskudar Semsi Ahmet Pasa (1580)	1:2,5, 1:5,5, 1:5, 1:1,5, OT, 1:5T, 1:2,5T	7
Suleymaniye (1557)	1:11, 1:5, 1:7, 1:6, 1:5T, 1:5,5, 1:4, 1:3	8
Fındıklı Molla Celebi (1562)	1:5, 1:2,5, 1:11, 1:2, 1:8, 1:9, 1:4,5, 1:11T	8
Uskudar Atik Valide (1579)	1:6,5, 1:13, 1:5,5, 1:11, 1:5, 1:3,5, 1:7, 1:9	8
Fatih Bâli Pasa (1546)	1:9, 1:6, 1:5, O, 1:11, 1:15, 1:13, 1:2,25, 1:4,5	9
Eminonu Rustem Pasa (1561)	1:10, 1:7, 1:5, 1:5T, 1:9, OT, 1:3T, 1:11, 1:3,5	9
Tophane Kılıc Ali Pasa (1581)	1:15, 1:5, O, 1:7, 1:3, 1:6, 1:4,5, 1:11, 1:9	9
Edirnekapı Mihrimah Sultan (1566)	1:15, 1:9, 1:20, 1:10, 1:7, 1:5,5, 1:6, 1:11T, 1:4, 1:4,5, 1:3,5	11
Eyup Zal Mahmut Pasa (1577)	1:25, 1:11, 1:7, 1:3, 1:3,5, 1:3T, 1:6, 1:5, 1:10, 1:13, 1:5,5	11
Azapkapı Sokullu Mehmet Pasa (1578)	1:15, O, 1:10, 1:5, 1:9, 1:6, 1:6T, 1:9T, 1:8, 1:3T, 1:4,5T	11

Considering the distribution of the 315 arches examined in the interior, the narthex, the court of porches and the facades according to the type in total, it was seen that there were 105 pencî arches with (1:5) ratio and more preferred than other types with 33.3% usage percentage. It was followed by 24 pointed arches with (1:9) ratio and 7.62% usage percentage. The one with (1:7) ratio was used in 20 places and had a weight of 6.35% in total. There are 19 arches with (1:5,5) ratio and these ranked as fourth with 6.03% usage rate and followed immediately by 17 five centered tangent ogives (1:5T) with 5.40% usage rate. As you can see, it was

determined that the types with (1:5), (1:9), (1:7), (1:5,5), (1:4,5), (1:11) and (1:5T) ratios distinguished in total, and pencî (1:5) tangent arches and the semicircular arches with top tangents were more preferred.

When we look at the proportions of the 159 arch types found to be used interiors in the examined mosques, it was seen that there are 65 pencî arches with (1:5) ratio and these ranked as first with 40.8% usage rate. The 159 different types and sizes of arches were collected under 25 types. 18 of them were two centered pointed, 6 were pointed with top tangent and 1 was semicircular. Other types of arch that were more common were 11 arches with (1:9) ratio and 6.92% usage rate and 11 arches with (1:11) ratio and 6.92% usage rate. And these were followed by 10 pencî type tangent arches (1:5T) with (1:7) ratio and 6.29% usage rate; 8 five centered tangent ogives (1:5T) with (1:5,5) ratio and 5.03% usage rate. 82.3% of the arches used indoors were the pointed types and it was found that pencî arch with top tangent (1:5T) ratio (with 5.03% usage rate) was preferred over the others.

79 (89.7%) of the 88 arches examined from the arches located in the court and the narthex were the two centered pointed arches. 4 of the 9 tangent ogives were round tangent ogives and the others were the tangent ogives with (1:5), (1:2,5) and (1:3) ratios. 24 five centered arch with (1:5) ratio and 27.27% usage rate were the most preferred ogive. 11 ogives with (1:5) ratio had 12.50% weight; 10 ogives with (1:9) ratio had 11.36% weight; 9 ogives with (1:4,5) ratio had 10.23% weight; and 6 ogives with (1:7) ratio had 6.82% weight.

Table 25. Pointed arches found in the narthex and the courtyards

Pointed Arches found in the narthex and the courtyard	(OT)	(1:13)	(1:15)	(1:7)	(1:4,5)	(1:5,5)	(1:5T)	(1:5)	(1:8)	(1:9)	(1:10)	(1:3,5)	(1:6)
Haseki Hurrem Sultan Mosque (1538)	■												
Fatih Bâli Pasa Mosque (1546)		■	■										
Uskudar Mihrimah Sultan Mosque (1547)				■									
Sehzade Mehmet Mosque (1548)					■	■							
Silivrikapı Hadım İbr. Pasa M. (1551)							■						
Suleymaniye Mosque (1557)								■					
Topkapı Kara Ahmet Pasa M. (1560)								■	■				
Eminonu Rustem Pasa Mosque (1561)										■			
Fındıklı Molla Celebi Mosque (1562)					■					■	■		
Edirnekapı Mihrimah Sultan M. (1566)			■							■			
Kadırga Sokullu Mehmet Pasa M. (1572)								■					
Eyup Zal Mahmut Pasa M. (1577)			■	■		■					■		
Uskudar Atik Valide Mosque (1579)				■				■				■	
Tophane Kılıc Ali Pasa Mosque (1581)													■

Mesih Mehmet Pasa M. (1586)		▪										
Fatih Nisancı Mehmet Pasa M. (1589)							▪					

When we look at the distribution of arches in 66 different types and sizes examined on the facades, 7 different tangent ogives and 9 different arches as well as semicircular arches were found to be used. 16 pencî arches with (1:5) ratio and 24.24% usage rate ranked as first. 7 tangential types with (1:3T) had 10.61% weight, 6 with (1:4,5) ratio and 6 (1:5T) had 9.09% weight. The arches with (1:3), (1:4), (1:9), (1:11) ratios and the semicircular and tangent semicircular types were in the same number. Their usage rate was 4.55%. It was seen that the two most common types of arches were have top tangent parts here, as well as more high types were used compared to the arches used interiors, narthex and court (like 1:3T, 1:4,5 and 1:5T).

Table 26. Arches over the niches created by wall buttresses (Interior).

Arches over the niches created by wall buttresses (Interior)	(1:9)	(1:11)	(1:5)	(1:7)	(1:6T)	(1:10)	(1:20)	(1:4)	(1:6)	(1:5,5)
Fatih Bâli Pasa Mosque (1546)	▪	▪								
Sehzade Mehmet Mosque (1548)		▪	▪	▪	▪					
Suleymaniye Mosque (1557)			▪							
Fındıklı Molla Celebi Mosque (1562)		▪								
Edirnekapı Mihrimah Sultan Mosque (1566)						▪	▪			
Uskudar Atik Valide Mosque (1579)		▪	▪							
Azapkapı Sokullu Mehmet Pasa M. (1578)			▪					▪	▪	
Kadırga Sokullu Mehmet Pasa M. (1572)	▪									▪
Karagumruk Mesih Mehmet Pasa M. (1586)	▪									
Fatih Nisancı Mehmet Pasa Mosque (1589)			▪							
Uskudar Mihrimah Sultan Mosque (1547)			▪							
Eyup Zal Mahmut Pasa Mosque (1577)		▪							▪	

Regarding the opening sequence of the arches found to be used interiors, the greatest arches carrying the dome of Suleymaniye Mosque ranked as first with an opening of 23.25 m and 21.59 m (about a 30 zira' long). Then these are followed by the arches of Edirnekapi Mihrimah Sultan Mosque with 18.45 m (24.5 zira'); the arches of Sehzadebasi Mosque with 16.50 m (22 zira'); the arches of Zal Mahmut Pasha Mosque with 12.42 m (16.5 zira'); the arches of Kılıc Ali Pasha Mosque with 11.35 m (15 zira'); Fatih Bâli Pasha and Uskudar Mihrimah Sultan Mosques with 11.10 m (14.5 zira'). 9 of the first 18 arches with big span are in Suleymaniye Mosque. It is observed here that the structures with the four supported baldachin schemes are highlighted. When we look at the types of the arches mentioned, it is seen that the pointed arch types like (1:11), (1:15) are common. Given the opening sequence in the court and narthex of porches, Sehzadebasi Mosque is seen to include 5 of the first 10 arches with arches between 7.34 and 6.80 m. While Edirnekapi Mihrimah Sultan Mosque with 6.66 m and Topkapi Kara Ahmet Pasha Mosque with 6.85 m rank as the top of the list, it is revealed that the first 20 of the arches with big spans are found in these 4 buildings including Suleymaniye Mosque.

Table 27. Relieving arches on the rectangular windows of ground floor

Relieving arches on the rectangular windows (ground floor)	(1:5)	(1:7)	(1:5T)	(1:6T)	(1:9)	(1:3T)	(1:4,5T)	(1:6)
Eminonu Rustem Pasa Mosque (1561)	■	■						
Fındıklı Molla Celebi Mosque (1562)	■							
Uskudar Semsi Ahmet Pasa Mosque (1580)	■							
Tophane Kılıc Ali Pasa Mosque (1581)		■						
Karagumruk Mesih Mehmet Pasa Mosque (1586)	■		■					
Fatih Nisancı Mehmet Pasa Mosque (1589)	■							
Suleymaniye Mosque (1557)	■							
Fatih Bâli Pasa Mosque (1546)	■							
Silivrikapı Hadım İbrahim Pasa Mosque (1551)				■				
Edirnekapı Mihrimah Sultan Mosque (1566)		■			■			■
Kasımpasa Piyale Pasa Mosque (1573)	■							
Eyup Zal Mahmut Pasa Mosque (1577)						■		
Azapkapı Sokullu Mehmet Pasa Mosque (1578)				■		■	■	

When we look at the diversity of arch types used in constructions; the mosques in which high level of diversity was observed among 19 mosques are Edirnekapi Mihrimah Sultan Mosque, Eyup Zal Mahmut Pasha Mosque and Azapkapi Sokullu Mehmet Pasha Mosque with 11 different types. Edirnekapı Mihrimah Sultan Mosque is also interesting because it has no pencî type pointed arch with (1:5) ratio in the interiors, narthex, court and facades. These three buildings are followed by Fatih Bâli Pasha, Eminonu Rustem Pasha and Tophane Kilic Ali Pasha Mosques with 9 arch types. It is possible to say that the scale and complexity of the structure are not directly related to the type and diversity of the arches observed. The number of arches observed in a single-domed structure such as the Bâli Pasha Mosque may be more than in many large mosques. Among these constructions, Tophane Kilic Ali Pasha Mosque draws attention in terms of not having any tangenteial pointed arches. It is observed that the types such as (1:5), (1:9), (1:7), (1:11) intensively used in total in all three structures are common. In addition, the use of the semicircular ones in the interiors was only encountered in two places (Kilic Ali Pasha and Azapkapi Sokullu Mehmet Pasha Mosques). The three and four centered pointed arches found in the facades of Fatih Bâli Pasha Mosque and in the court of porches of Eminonu Rustem Pasha Mosque were encountered as the ones of a kind. It is also interesting that Suleymaniye Mosque with arches in 43 different types and sizes among the structures most detailed examined here can be able to be reduced to 8 arch types. The use of both pointed and tangential types of the the same ratios as (1:6) ratio in Sehzadebasi Mosque and the (1:2,5) ratio in Semsi Ahmet Pasha Mosque together on the basis of the structure are examples of the reductionist approach observed in many buildings. Fatih Nisanci Mehmet Mosque draws attention as it was built by using only 2 different arch types (both of them have 1:5 ratio) among all the structures. 15 of the 22 different types and sizes of arches examined in terms of structure are pencî (1:5) type.

Regarding whether there is a relationship between the places they are used on the buildings and the types; for example, when viewed in terms of greatest arches, the mosques with a free-standing plan type give comparable results if the arches are grouped according to the plan schemes of the structures. Azapkapi Sokullu Mosque with (1:15) ratio, Mesih Mehmet Pasha Mosque with (1:9) ratio, Nisanci Mehmet Pasha Mosque with (1:5) ratio, Rustem Pasha Mosque with (1:7) and (1:10) ratio have 8-supported baldachin schemes. The same arches in Suleymaniye Mosque with (1:11) ratio, in Edirnekapı Mihrimah Sultan Mosque with (1:15) ratio, in Sehzadebasi Mosque with (1:5) and (1:6) ratios, Kilic Ali Pasha Mosque with (1:15) ratio, Uskudar Mihrimah Sultan Mosque with (1:11) ratio and Zal Mahmut Pasha Mosque with (1:25) and

(1:11) ratios have 4-supported baldachin schemes and it is observed that the arches have declined in this group where the space has grown.

When we look at the diversity of the types of the arches connected the upper surfaces of the buttresses spilled from the wall according to the location in where these were used in the interiors, it was seen that the ones with (1:5), (1:9) and (1:11) ratios were used more intensely than other types in the interiors where the appearance is important and that hardly ever of the tangential types were preferred here. When looking at the distribution of relieving arches on the windows with marble jamb with rectangular space especially located on the ground floor by types in terms of structure, it was seen that pencî arch with (1:5) ratio was the only type used in the relieving arches on the windows on many buildings and followed by the ogives with (1:7) and (1:9) ratios. For other constructions, diverse types were used in a way that will be consistent in itself. For example, (1:3T) type which is found in many windows of the facades of Zal Mahmut Pasha Mosque is also found on the columns supporting the gathering-place, the court of porches and madrasah units in the interiors. The pencî arch never used at Edirnekapı Mihrimah Sultan Mosque, intensively used types were the ogives with (1:7) and (1:9) ratios as in the relieving arches. It is understood that the arch types, one of the basic elements that constitute the form repertoire that structures have, were handled separately for each structure, however, fewer types were preferred in the locations where the appearance is important such as the narthex of porches, spaces on the facades and above the wall buttress. When we look at the types of arches found in the narthex of porches, it was seen that only one type of arch was used in the porches, between the columns, and between the columns and body walls in Suleymaniye, Kilic Ali Pasha, Rustem Pasha, Uskudar Mihrimah Sultan, Kadirga Sokullu, Mesih Mehmet Pasha and Nisanci Mehmet Pasha Mosques. It was also observed that (1:5) and (1:9) and types with similar height / opening ratio to these two types such as (1:4.5), (1:5.5), (1:8), (1:7) as (1:10) were used.

Table 28. Suspended arches (interior)

Suspended Arches (Interior)	(1:11)	(1:5)	(1:6)	(1:10)	(1:7)	(1:15)	(1:5,5)	(1:25)	(O)	(1:6,5)	(1:9)
Uskudar Mihrimah Sultan Mosque (1547)	■										
Sehzade Mehmet Mosque (1548)		■	■								
Suleymaniye Mosque (1557)	■										
Eminonu Rustem Pasa Mosque (1561)				■	■						
Fındıklı Molla Celebi Mosque (1562)		■									
Edirnekapı Mihrimah Sultan Mosque (1566)						■					
Kadırga Sokullu Mehmet Pasa M. (1572)							■				
Kasımpasa Piyale Pasa Mosque (1573)					■						
Eyup Zal Mahmut Pasa Mosque (1577)	■							■			
Azapkapı Sokullu Mehmet Pasa M. (1578)						■			■		
Uskudar Atik Valide Mosque (1579)										■	
Tophane Kılıc Ali Pasa Mosque (1581)					■						
Karagumruk Mesih Mehmet Pasa M. (1586)											■
Fatih Nisancı Mehmet Pasa Mosque (1589)		■									

4. CONCLUSIONS

After the preliminary investigations, examination of the types found in the mosques built by Sinan The Architect, the locations in where these were used and their prevalence ratings were determined as the subject of this study. Within the scope of the study, 19 mosques built in the period of Sinan The Architect in Istanbul were examined. The arches were examined in three groups: arches used in the interiors, arches used in the narthex and court of porches, and arches used in the facades. It is seen that 315 different arches were used when repeating arches in a total of 19 buildings are sifted. 295 of these 315 arches are the pointed arches, 8 are the semicircular and 48 are the pointed arches with tangential upper sections. When we look at the places where 315 arches were used, it was seen that 159 of these were used in the interiors, 88 in the narthex and courts, and 68 in the facades. Although the fact that the arch type representing the classical period architecture are the tangential and pencî type pointed arches obtained by dividing the openning by five is frequently repeated, when we look at the structures, first of all it is seen that the most of the arches were not tangential, as well as it is seen that the arches with different ratios such as (1:3), (1:7), (1:9), (1:11), (1:13) were used in the places such as tops of doors and windows, porches, suspended arches in addition to the type obtained by dividing the opening by five (there are centers with a deviation of 1:10 from center).

REFERENCES

[1]. M. Sozen and U. Tanyeli, *Sanat Kavram ve Terimleri Sozlügü*, İstanbul, Türkiye: Remzi Kitabevi,1986.
[2]. D. Hasol, *Ansiklopedik Mimarlık Sozlügü,* İstanbul, Türkiye: Yapı Endüstri Merkezi Yayınları, 1975.
[3]. A. Batur, *Osmanlı Camilerinde Kemer, Strüktür - Bicim İliskisi Üzerine Bir Deneme (1300-1730),* İstanbul, Türkiye: İTÜ Mimarlık Fakültesi Matbaası, 1974.
[4]. D. Kuban, *Mimarlık Kavramları*, İstanbul, Türkiye: İTÜ Matbaası, 1973.
[5]. R. Saoud, *The Arch That Never Sleeps*, UK: FSTC Limited, 2002.
[6]. D. Hill, *Islamic Science and Engineering*, Edinburgh, UK: Edinburgh University Press, 1993.

On the Parametric Design and Analysis of Industrial Dye Mixing Machines

Hatice Cansu Ayaz[1], Zeki Kıral[2]

Abstract

Industrial dye mixing machines are widely used in dye industry, but their analyses on determining the structural design, mixing impeller geometries, mixing performances and the power requirements are not generally performed in scientific quality. The aim of this study is to propose a practical method for the industry related to the design process of the dye mixing machines. In the scope this study, a Visual Basic API code is developed for parametric design of the impeller model in SolidWorks and then flow analyses are conducted with SolidWorks Flow Simulation software. With the help of the flow analyses, velocity values around the impeller and moment/torque values required for mixing operation are determined. This study is carried out for different RPM's. And the velocity values obtained from analysis and the calculated values theoretically are quite close. Torque values increase with the increased rotational speed as expected.

Keywords: *API, Flow analysis, Impeller model, Parametric design.*

1. INTRODUCTION

Mixing can be explained as a preparation work of mixture which occurs two or more mixing elements. Homogeneity of the mixture composition is very important because grade of homogeneity determines the success of the mixture. Therefore, it is very important to choose the right mixer equipment. The mixers are separated from each other according to the following criteria: The type of current they create in the blended material, shaft's velocity and viscosity of the mixture. Mixing machines are used in industries, especially; food, pharmaceutical, paper, dye, plastics, ceramic, rubber as in [1].

Impellers are an essential part of mixing equipment and the studies on mixing equipment particularly concentrate on impeller zone. The purpose of mixing impellers is to transfer the energy provided by the motor to the product in the most efficient way in order to produce the desired effect. Each mixing impeller type converts the energy given to it in a different way. A hydrofoil converts most of the energy into motion of the product and very little into shear. A three bladed propeller will convert more of the energy into shear than the hydrofoil but still mostly produces motion. The axial flow turbines and radial flow turbines devote a higher ratio to shear and a dispersion blade is almost completely devoted to shear production as in [2].

There are literally hundreds of impeller types in commercial use. Determination of the most effective impeller should be based on the understanding of process requirements and knowledge of physical properties. Impellers can be grouped as turbines for low to medium viscosity fluids and close-clearance impellers for high viscosity fluids. Turbine impellers are further characterized based on flow patterns, as axial flow and radial flow. Recent developments in the impeller technology have been focused on increasing axial flow at reduced shear. These impellers use a hydrofoil blade profile for efficient and more streamlined pumping. There are also many specialty impeller designs developed for specific process needs as in [3].

There are four types of turbine impellers, which are characterized by the flow patterns and level of shear they create: axial flow, radial flow, hydrofoil, and high shear impellers. They have the widest use in low and medium viscosity liquid applications, solids suspension, liquid–liquid emulsification, and gas dispersion. Turbine impellers can have blades varying from 2 to 12 in number. Two blades are normally unstable mechanically, while it is difficult to install more than six blades on a hub. Axial flow impellers generally have three or four blades, and radial flow impellers are designed with six blades needs as in [3].

[1]*Dokuz Eylül University, The Graduate School of Natural and Applied Sciences, Department of Mechatronics Engineering, 35000, Tınaztepe-Buca/İzmir, Turkey. cansu.ayaz@deu.edu.tr*

[2]*Corresponding author: Dokuz Eylül University, Faculty of Engineering, Department of Mechanical Engineering, 35000, Tınaztepe-Buca/İzmir, Turkey. zeki.kiral@deu.edu.tr*

Axial flow impellers cause the tank fluid to flow parallel to the impeller's axis of rotation while radial flow impellers cause the tank fluid to flow perpendicular to the impeller's axis of rotation as in [4]. Figure 1 shows the flow circulation.
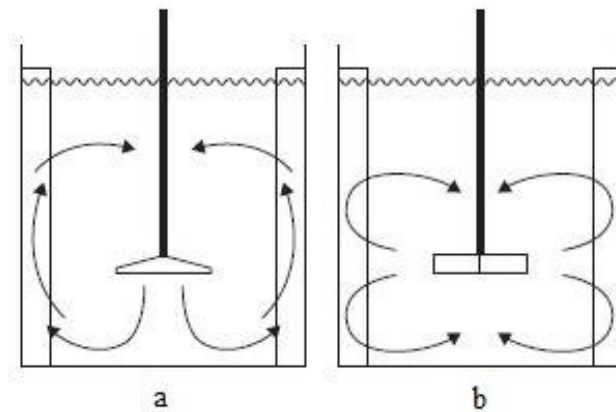
Figure 1.(a)Purely axial flow with a hydrofoil (b)Double circulation loops with a radial impeller, as in [5]

The aim of this study is the calculation of the required power at different RPM's for dispersion type impeller. Also, velocity values are investigated.

1.1. Dispersion Type Impeller

They are radial type of impeller. Dispersion blades rotate at high RPMs to facilitate the quick impartation of solids at a fine grind. The liquid contacts the blade and moves outward to flow over the teeth and break the agglomerations into increasingly smaller particles. Typically used in paints and inks, high shear mixer blades are now being used in a variety of industries for increased efficiency as in [6]. Dispersion type impeller can be seen in Figure 2.
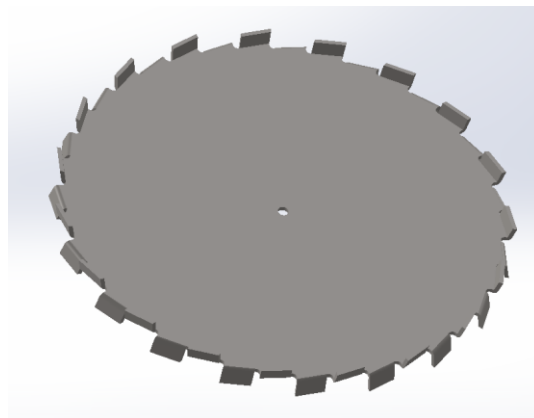
Figure 2.Dispersion type impeller

There are several researches about parametric design and mixing machines. Halkacı and Yigit [7] examined parametric design with SolidWorks® and Excel program. They designed solid model of fixed roller bearings and developed a program. Shahin [8] studied about feature-based design. He observed two feature modeling: Synthesis and destructive modeling and two principal techniques: Generative and variant design methods. Yuxia and Wei [9] studied about parametric design of straight bevel gears based on SolidWorks. The Visual Basic program was developed for the parametric design. Each control point was determined in Cartesian Coordinate System. Bodein et al. [10] proposed explicit integrated (reference) modeling for complex parts modeling in parametric CAD system. The modeling time is used to demonstrate the effectiveness of the study. Lad and Rao [11] aimed to develop software application for product design. They used SolidWorks application programming interface (API) for CAD model updating by automating repetitive tasks. They studied on Winding Machine and they developed a program using Visual Basic language. Camba et al. [12] examined three major modeling methodologies: horizontal modeling, explicit reference modeling, and resilient modeling by using three industrial CAD models with different levels of complexity designed with SolidWorks®.

Alnak et al. [13] investigated numerically the effects of impeller blade's geometries on the mixture. The using method contained solving three dimensional Navier-Stokes equations with Fluent software. Their research showed that the radial impeller structure had the best mixing effects when examined the velocity and turbulence kinetic energy distribution. Vakili and Esfahany [14] used three-compartment model to study non-homogeneity of mixing in a fully baffled stirred tank. They used multiple reference frame (MRF) technique for calculations.

In this study, dispersion type impeller is designed parametrically and then analysed with SolidWorks Flow Simulation software. Also some information about the power requirement is given.

2. PARAMETRIC DESIGN

In traditional CAD systems, geometric modeling is performed by the exact specifications of geometry. Dimensions are derived from the geometry. Designers are required to know beforehand the precise dimensions of the geometry, and changes are difficult once these are entered into systems. However, in the product development cycle, several design changes are typically needed before the full requirements for functionality, manufacturability and quality of a design are met. Parametric design allows designers to make modifications to existing designs by changing parameter values, thus making it possible for them to create shapes without knowing precisely how they will be configured in the final design as in [15].

The designer changes the parameters in the parametric model to search for different alternative solutions to the problem at hand. The parametric model responds to the changes by adapting or reconfiguring to the new values of the parameters without erasing or redrawing as in [16].

2.1. Constraints

There is a need in the Computer-Aided Design (CAD) community to standardize the classification and specification of geometric constraints. While the representation of solid models is now well developed and established in the literature, in solid modeling kernels and in exchange standards, the representation and exchange of geometric constraints is still evolving as in [17].

A parametric design change cannot be accomplished only with dimensional changes of a model. Modeling errors can be avoided by the help of the constraints as in [18].

2.2. Application Programming Interface (API) of SolidWorks

Modern design has made life so easier by reducing time wastage and maintaining proper usage of resources. By using SolidWorks and Visual Basic, products having the same mechanical characteristics and shapes, the corresponding entity model library can be created through parametric design. This can improve design efficiency and simplify design work as in [19].

Application programming interface is a tool to write a code in a programming language within another application. As a result, a direct integration between different applications can be developed as in [20].

Using the API, model files created in SolidWorks can be manipulated directly inside of a control program such as Excel and the resulting altered parameters can be returned for further review as in [21].

2.3. Phases of the Design

Some API functions are shown below. These functions have to be used in Visual Basic programming language in the first lines, because they are connection commands between the SolidWorks and the Visual Basic program. These commands allow us to open SolidWorks interface.

Set swApp = GetObject(, "sldworks.application")

Set Part = swApp.NewDocument("part.prtdot", 0, 0, 0)

Set Part = swApp.ActiveDoc

After connecting two programs each other, a plane must be selected to open a sketch. During the sketch creation process, constraints and dimensions must be identified. Because with the help of them, a fully-defined sketch can be created. If these relations don't be used, then part can be deteriorated after making some changing in the solid part. After making a fully-defined sketch, part can be created by extruding the sketch. During this design process, Part.FeatureManager.FeatureFillet3 command was used for making radius and Part.FeatureManager.FeatureCircularPattern4 command was used for making a pattern in the part to create the impeller blades. Part.FeatureManager.InsertRefPlane command was used for creating a new plane and then inserting a sketch on it.

When the form loads in Visual Basic program, firstly, the text file which includes all parameters about the design is read. With the help of this file, parameters can be changed according the existing conditions and requirements.

3. POWER REQUIREMENT

Reynolds number is the ratio of inertial forces to viscous forces. It indicates whether the flow at the impeller is laminar, turbulent, or transitional.

Power number is the ratio imposed forces to inertial forces, which relates power to impeller and fluid characteristics. Power number decreases with an increase in Reynolds number as seen in Figure 3.

$$Re = \frac{\rho n D^2}{\mu} \tag{1}$$

$$N_p = 32.372 Re^{-0.5675} \tag{2}$$

With the help of these equations, mixer power is calculated.

$$P = N_p \rho n^3 D^5 \tag{3}$$

Re: Reynolds number

ρ: Fluid density (kg/m3)

n: Rotational speed (rev/s)

D: Impeller diameter (m)

μ: Dynamic viscosity (Pa.s)

N_p: Power number

P: Impeller power (W)
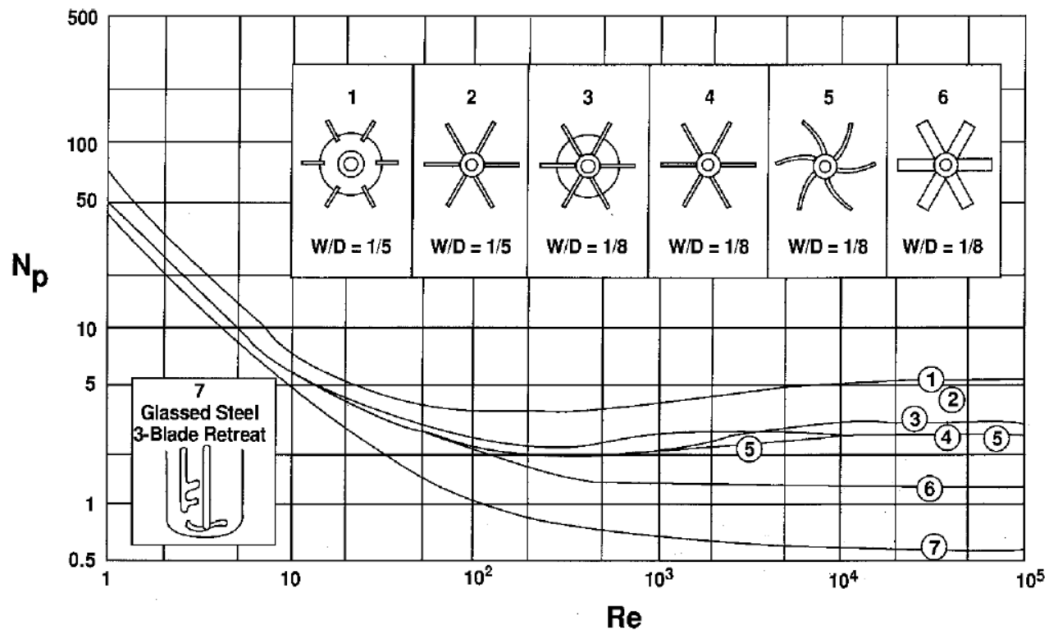
Figure 3.Power number versus impeller Reynolds number for seven different impellers as in [3]

Figure 3 shows the relationship between N_p and Re for seven different impellers. It is important to recognize that at Re<100, the conditions become laminar flow; and mixing quality, obtained using these impellers, becomes extremely poor. Under such conditions, impellers designed for laminar flow conditions are recommended as in [3].

While Figure 3 provides the power number data in a wide range of Re, the information should not be used below an impeller Reynolds number of 1000. The flow regimes are laminar flow below the Reynolds number of 10, transition between Reynolds numbers of 10 and 104, and turbulent above the Reynolds number of 104. The functionality between Np and Re can be described as follows as in [3]:

$N_p \propto Re^{-1}$ in the laminar regime and power depends greatly on viscosity.

690

N_p = constant in turbulent regime (Re > 10 000) and is independent of liquid viscosity.

N_p changes slightly in the transitional regime (100 < Re < 10 000).

4. FLOW ANALYSIS AND RESULTS

Flow analysis is essential for virtual testing and prediction of systems behavior. Fluid flow analysis is used to improve the design and the performance of the system. For the preparation of the flow analysis at SolidWorks® Flow Simulation software, rotational area and control volume were defined as shown in Figure 4 and Figure 5.

Figure 4.Rotational area
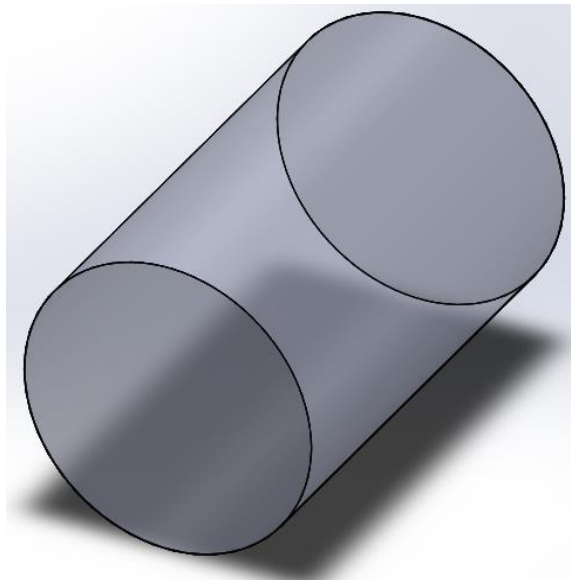
Figure 5.Control volume

Dimensions between the impeller and the control volume are shown in Figure 6. Before the analysis of the system, all parts must be assembled as shown in Figure 6.
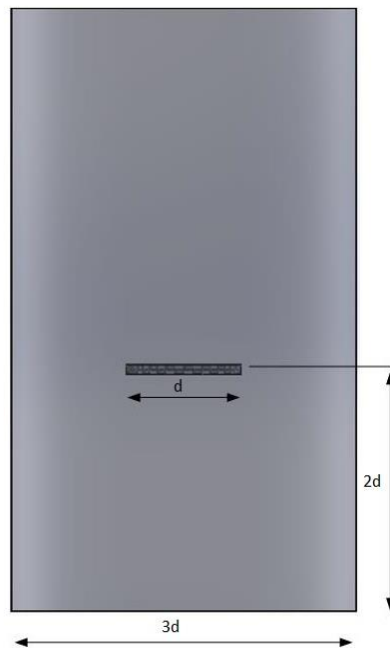
Figure 6.Dimensions between the impeller and the control volume

The dye should be defined within the control volume. Environmental pressure must be defined top surface of the control volume which represents the tank in the system. Because in real system, only the top surface of the tank is open. The other surfaces of the control volume are defined as ideal wall. The rotational speed is defined by selecting the rotational area. Then, goals must be defined. In this study, velocity profile around the impeller and moment/torque values required for mixing operation are determined. After defining of these detailed data for the analysis, program can be run. Figure 7 shows the preparation phase of the system for the analysis.
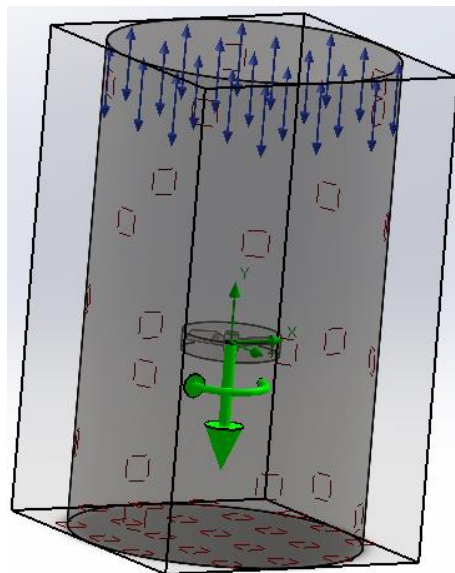
Figure 7.Preparation for the analysis

The following results were obtained for the 538mm diameter. Table 1 shows the results which obtained from SolidWorks Flow Simulation software. Figure 8 shows the impeller power – rotational speed relation for dispersion type impeller. In Table 1, GGmax represents velocity results and GGTy represents torque values on y-axis for the impeller at the SolidWorks Flow Simulation.

Table 1.Results for different RPM's

	100 rpm	200 rpm	300 rpm	400 rpm	500 rpm	600 rpm	700 rpm	800 rpm
ω [rad/s]	10,4719	20,9439	31,4159	41,8879	52,3599	62,8319	73,3038	83,7758
v [m/s]	2,8169	5,6340	8,4500	11,2680	14,0840	16,9020	19,7190	22,5360
GGmax [m/s]	2,7850	5,5690	8,3540	11,1390	13,9230	16,7080	19,4930	22,2770
GGTy [Nm]	5,015	12,278	20,332	28,680	38,484	49,171	58,828	69,893
P [W]	52,517	257,150	638,749	1201,345	2015,018	3089,505	4312,318	5855,342
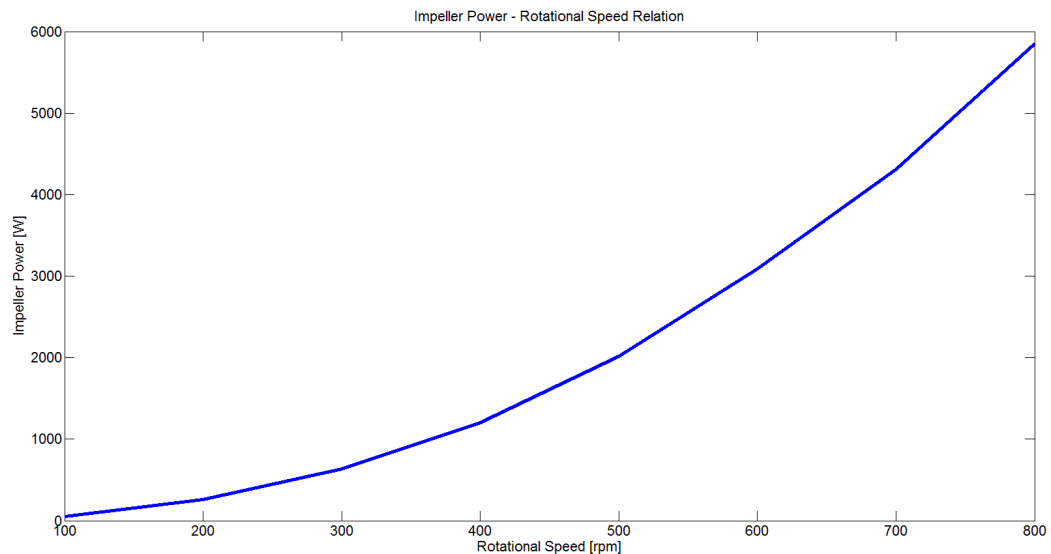
Figure 8.Impeller power – rotational speed relation

As seen in Table 1, the theoretical velocity values and the simulation results are quite close each other. It shows the accuracy of the results. Torque values increase with the increased rotational speed as expected. In Figure 8, the parabolic increase can be seen between the impeller power and rotational speed.

5. CONCLUSIONS

This study is carried out for different impeller rotational speeds. The theoretical velocity values and the simulation results are quite close each other. It shows the accuracy of the results. The required torque values increase with the increased rotational speed as expected. The impeller power increase parabolically depends on the increased rotational speed.

REFERENCES

[1]. Oren, "Karıştırma ve karıştırıcılar, kullanım alanları ve hesaplama yontemleri," M. Eng. thesis, Yıldız Technical University, Istanbul, Turkey, 2006.
[2]. (2017) The mixerdirect website. [Online]. Available: http://www.mixerdirect.com/impellers.html
[3]. R. R. Hemrajani, and G. B. Tatterson, *Handbook of Industrial Mixing Science and Practice,* Hoboken, USA: John Wiley & Sons, 2004.
[4]. H. S. Fogler, and M. N. Gürmen. (2008) impeller webpage on UMICH. [Online]. Available: http://www.umich.edu/~elements/01chap/html/reactors/mixing/impeller.htm
[5]. S. M. Kresta, and D. S. Dickey, *Advances in Industrial Mixing: A Companion to the Handbook of Industrial Mixing,* Hoboken, USA: John Wiley & Sons, 2016.
[6]. (2017) The mixerdirect website. [Online]. Available: http://www.mixerdirect.com/impellers/high-shear/dispersion-blade.html
[7]. H. S. Halkacı, and O. Yigit, "Parametrik tasarım ve SolidWorks CAD programı ile bir uygulama," *http://www1.mmo.org.tr/resimler/dosya_ekler/5b41fac0361d157_ek.pdf*, n.d..
[8]. T. M. Shahin, "Feature-based design - an overview," *Computer-Aided Design and Applications*, vol. 5, pp. 639–653, 2008.

[9]. S. Yuxia, and Z. Wei, "Parametric design of straight bevel gears based on SolidWorks," in *The 2nd International Conference on Computer Application and System Modeling*, 2012.

[10]. Y. Bodein, B. Rose, and E. Caillaud, "Explicit reference modeling methodology in parametric CAD system," *Computers in Industry*, vol. 65, pp. 136–147, 2014.

[11]. A. C. Lad, and A. S. Rao, "Explicit Design and drawing automation using SolidWorks application programming interface," *International Journal of Emerging Engineering Research and Technology*, vol. 2, pp. 157–167, 2014.

[12]. J. D. Camba, M. Contero, and P. Company, "Parametric CAD modeling: An analysis of strategies for design reusability," *Computer-Aided Design*, vol. 74, pp. 18–31, 2016.

[13]. D. E. Alnak, A. Oztürk, A. Pınarbası, and C. Ozalp, "Karıştırıcı tanklarda farklı kanat yapılarının sayısal yontemlerle incelenmesi," in *IV. Ege Enerji Sempozyumu*, 2008.

[14]. M. H. Vakili, and M. N. Esfahany, "CFD analysis of turbulence in a baffled stirred tank, a three-compartment model," *Chemical Engineering Science*, vol. 64, pp. 351–362, 2009.

[15]. J. Y. Lee, and K. Kim, "Geometric reasoning for knowledge-based parametric design using graph representation," *Computer-Aided Design*, vol. 28, pp. 831–841, 1996.

[16]. C. R. B. Hernandez, "Thinking parametric design: introducing parametric Gaudi," *Design Studies*, vol. 27, pp. 309–324, 2006.

[17]. B. Bettig, and J. Shah, "Derivation of a standard set of geometric constraints for parametric modeling and data exchange," *Computer-Aided Design*, vol. 33, pp. 17–33, 2001.

[18]. S. Myung, and S. Han, "Knowledge-based parametric design of mechanical products based on configuration design method," *Expert Systems with Applications*, vol. 21, pp. 99–107, 2001.

[19]. A. Titus, and X. Bin, "Secondary development of SolidWorks for standard components based on database," *International Journal of Science and Research*, vol. 2, pp. 162–164, 2013.

[20]. U. Farhan, S. O'Brien, and M. Tolouei Rad, "SolidWorks secondary development with Visual Basic 6 for an automated modular fixture assembly approach," *International Journal of Engineering*, vol. 6, pp. 290–304, 2012.

[21]. S. P. Prince, R. G. Ryan, and T. Mincer, T "Common API: using Visual Basic to communicate between engineering design and analytical software tools, "*Age*, vol. 10, 2005.

BIOGRAPHY

Hatice Cansu Ayaz received the bachelor degree in Mechatronics Enginnering from Kocaeli University in 2012 and in Mechanical Engineering from Kocaeli University in 2013. Now, she is doing M.Sc. in The Graduate School of Natural and Applied Sciences Department of Mechatronics Engineering, Dokuz Eylul University. She works as a research assistant at İzmir Katip Celebi University. Her current research interests include parametric design, computer aided engineering, flow analysis and mechatronics.

Dr. Zeki Kıral is working as a professor at Dokuz Eylul University, Faculty of Engineering, Department of Mechanical Engineering. He received his PhD in Mechanical Engineering department from Dokuz Eylul University in 2002. Dr. Kıral's teaching and research interests are computer aided engineering, system dynamics, control, mechanical vibrations, and mechatronics.

Levelized Cost Analysis of Solar Energy Plants

Yasin UST[1], Seyfullah DEDE[2]

Abstract

In our world, tendency to use renewable energy is increasing due to the reduction of fossil fuel reserves and climate changes. The using of renewable energy for electric generation will become widespread with decrease in the levelized cost of renewable electric energy. According to Bloomberg New Energy reports, the levelized cost of solar (PV) energy plants for electric generation will pass the levelized cost of fossil fuel based plants and wind plants for electric generation in 2030s.Because of this, Turkish government wants to nationalize the PV panels and equipments production, assembly works and O&M works according to 2023 energy vision. This work contains the levelized cost analysis of 500 kW PV plant for 3 suitable location in Turkey according to government supports. The results show that, the feasibility of this plant is really bad due to high interest rates, high costs and low efficiency of domestic panels & inverters. Government supports should be increased and investment rates should be decreased.

Keywords: *Renewable Energy, LCOE , Solar PV*

1. INTRODUCTION

1.1. Global Overview of the Renewable Energy

Renewable power generating capacity saw its largest annual increase ever in 2015, with an estimated 147 GW of renewable capacity added. Total global capacity was up almost 9% over 2014, reached 1712 GW at year's end. Wind and solar PV both saw record additions together making up about 77% of all renewable power capacity added in 2015. Also, hydropower capacity increased by 2.7%, accounting for approximately 19% of additions. By the end of 2015, renewables provided an estimated 23.7% of all electricity generated [2].
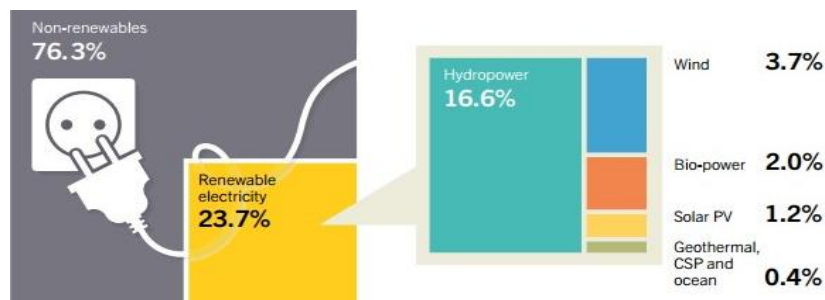
Figure 33. Estimated Renewable Energy Share of Global Electricity Production, End–2015 [5]

By the end of 2015, the top countries for total installed renewable electricity capacity continued to be China, the United States, Brasil, Germany and Canada. Considering only non-hydro capacity, the top countries were China, the United States and Germany; they were followed by Japan, India, Italy and Spain.

---

[1] *Corresponding author: Yildiz Technical University, Department of Naval Architecture and Marine Engineering, 34349, Besiktas/İstanbul, Turkey. yust@yildiz.edu.tr*

[2] *Yildiz Technical University, Department of Naval Architecture and Marine Engineering, 34349, Besiktas/İstanbul, Turkey. seyfullahdd@gmail.com*

Table 29. Renewable Electric Power Global Capacity, Top Regions/Countries, 2015 [2]

	Global	EU-28	BRICS[1]	China	United States	Germany	Japan	India	Italy	Spain
TECHNOLOGY	GW			GW						
Bio-power	106	36	31	10.3	16.7	7.1	4.8	5.6	4.1	1
Geothermal power	13.2	1	0.1	~0	3.6	~0	0.5	0	0.9	0
Hydropower	1,064	126	484	296	80	5.6	22	47	18	17
Ocean power	0.5	0.3	~0	~0	0	0	0	0	0	~0
Solar PV	227	95	50	44	26	40	34	5.2	18.9	5.4
Concentrating solar thermal power (CSP)	4.8	2.3	0.4	~0	1.7	~0	0	0.2	~0	2.3
Wind power	433	142	180	145	74	45	3	25	9	23

1.2. Overview of the Renewable Energy in Turkey

Turkey is a foreign-dependent country about primary energy nearly 75%. Also, 98.6% of natural gas, 93% of petrol and 92% of coil are imported. This situation can leads to the price fluctuation. So that, foreign-source dependency must be reduced for the reliable economic growth [4].

According to data from the Turkish ministry of energy, the electricity generation capacity from the solar energy is 380 million kWh/year [4].

BNEF analysis shows that, in 2030, 47% of the electricity will be generated from renewable sources. According to BNEF's estimates installed solar energy capacity will reach up to 24 GW [4].

1.3. The Future of Global Solar Energy Market

Up to 2040, estimates shows that renewable energy will constitute of 60% of electricity capacity added, 65% of energy investments. Solar energy will share 35% of electricity capacity added and 30% of energy investments [1].
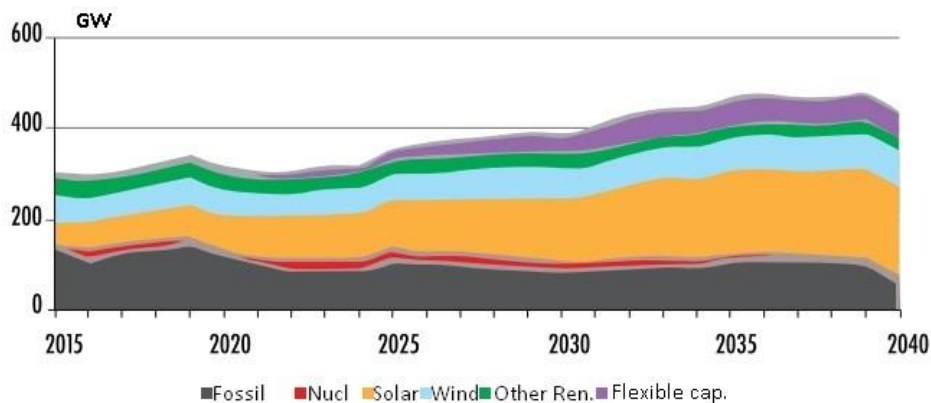
Figure 34. Annual electricity generation capacity increase [1]

According to the global electricity generation estimates, solar energy will share 26% of total global electricity generation capacity up to 2040. It means that, 24% capacity increase in solar energy between 2012 and 2040 [1].

1.4. The Future of Solar Energy Market in Turkey

According to the General Directorate of Renewable Energy, the average annual radiation in Turkey is 2,640 hours per year and the average solar radiation received is 1311 kWh∕m^2 per year [3].

Turkey's abundant source of solar power is a well-known. Despite this abundance, Turkey has not utilized solar energy efficiently until recently, and requires significant investment. Electricity demand of Turkey increase nearly 10% every year. Technical potential of solar energy in Turkey is nearly 190 TWh/year. It means that, Turkey has a potential to meet 75% of electricity demand with solar energy [3].
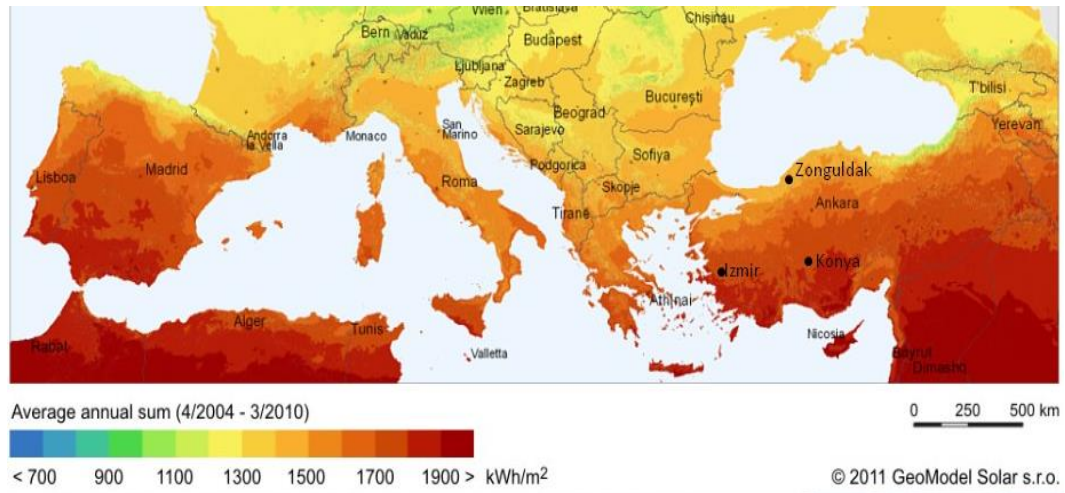
Figure 35. Solar energy potential map [8]

This figure shows that solar energy potential of some countries. Turkey has a greater potential than many countries, but some of them generate more electricity from solar power.
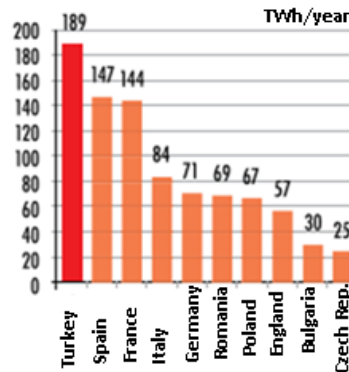
Figure 36. Theoretical solar energy potentials of some countries [1]

1.5. Cost of Medium-Sized and Large-Sized Solar PV Projects in Turkey

Government is encouraging the domestic production with incentives which provide the impulse for growth. Feed-in tariff for a period of ten years price of 13.3 USD cent / kWh for solar power plants. Local equipment bonus for a period of five years, if domestically manufactured mechanical and/or electromechanical equipment is used in the generation facility. With government incentives and local equipment bonus this price could reach up to 200 USD cent / kWh. Local equipment bonus information are shown in the graph below. Government gives the higher bonus for PV cells production. Details about feed-in tariff and local equipment bonus are given in this table.

Table 30.Feed-in-tariff and local equipment bonus prices for solar PV [3]

Feed-in-tariff and Local Equipment Bonus Prices for Solar PV	
Locally manufactured component	**Bonus (USD cent/kWh)**
PV panel integration and production	0.8
PV Modules	1.3
PV Module Cells	3.5
Inverter	0.6
Material which focuses radiation on PV Module	0.5
Total	**13.3 + 6.7 = 20**

In Turkey, generation facilities which capacities over 1 MW, license cost must be added to initial investment. Even if there is no license cost, the levelized cost of solar energy will be still high due to low rates of return. This graph shows levelized cost of energy for some countries which is between 0.59-0.73 TL/kWh for Turkey [1].
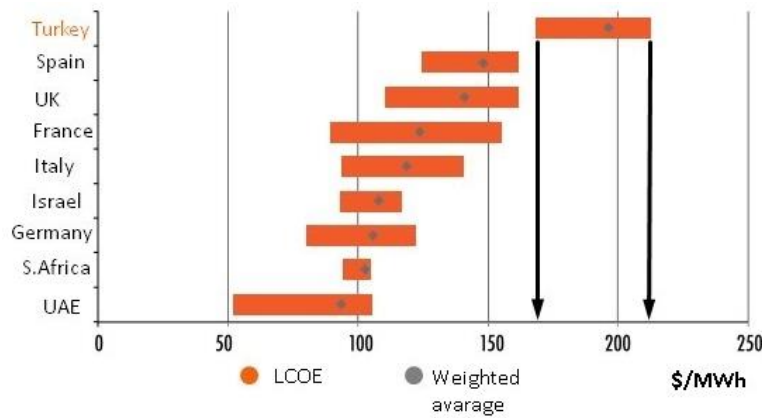
Figure 37.Estimated LCOE for some countries [1]

Even if there is no license cost, levelized cost of electricity continue to rank second among all the countries in the region after Spain due to the credit cost and low return for equity investor [1].

The cost reduction in solar PV is faster than other renewables. Probably, up to 2030 the cheapest way of electricity generation will be solar PV at a cost of 59 $/MWh. This decrease will be came true with decrease in equipment costs and return expectations. According to government target and incentive applications, 6.3 GW installed solar PV capacity is expected until 2023. 70% of new installations in Turkey will be solar PV facilities and will exceed 40 GW in the period 2030-2040 [1].

2. MATERIALS AND METHODS

2.1. Determining the Initial Investment Cost and O&M Cost

The analysis were made for 3 cities in Turkey and some assumptions were made. Some parameters using in analyses are shown in the table below.

Table 31. Parameters used in the analyses

Parameters	
System Capacity	500 kW
System Losses	15%
PV Efficiency	15%
Annual PV Efficiency Loss	1%
System Lifetime	25 Year
Required Area	10000 m^2
Electricity Sales Prices	0.46 - 0.54 - 0.7 TL/kWh
Equity Capital Ratio	100%
Electricity Sales Ratio	100%
Interest Ratios	5%, 8%, 11%
Exemption From Tax	100%
O&M Costs Annual Escalation	3%
1 $=3.5TL	

First of all, required and suitable system elements are selected for 500 kW capacity. Technical features of these elements are similar to the domestic productions. Such as panel and inverter efficiency, elements economic life, etc.

The required area for this system is nearly 10000 m^2. The status of the geographical area is the other effective parameter on cost. The cost of the construction area is different for each city .Also, on this study we assume that the location of the generation facility is close to the energy transmission line.

Electricity sales prices are determined according to government supports and local equipment bonus. For the first 5 operation years, these prices are taken as 0.46 , 0.54 , 0.7 TL/kWh , for the remaining 20 years which are taken as 0.46 TL/kWh. Interest rates which are assumed to be 11%, 8%, 5%. Electricity sales ratio and equity capital ratio were taken as 100%.

O&M cost of the 500 kW system is minimum 35,000 TL per year. Also, worker salary is 25,000 TL per year. Escalation rate is assumed to be 3% per year [5].

Initial investment cost of each city are detailed in the table below.

Table 32.Initial investment costs

Quantity	Type	Unit Price	Unit of Currency	Price (TL)		
				Zonguldak	**İzmir**	**Konya**
2,000	Polycrystal Panel	0. 60 $/W	dollar	300,000	300,000	300,000
25	Inverter	0. 14 $/W	dollar	70,000	70,000	70,000
	"	0. 14 $/W	dollar	70,000	70,000	70,000
1	One Way Counter		tl	100	100	100
1	Up-down Counter		tl	900	900	900
1,200 m	Galvanized Cable Channel	14 TL/m	tl	16,800	16,800	16,800
4,200 m	Solar Cable	2 TL/m	tl	8,400	8,400	8,400
1	Lightning Rod		tl	7,000	7,000	7,000
	P.T.L &Transformer		tl	130,000	130,000	130,000
400 m	Barbed Wire	35 TL/m	tl	14,000	14,000	14,000
	Security Eq.		tl	20,000	20,000	20,000
1	Admin. Building		tl	20,000	20,000	20,000
	Land Regulation		tl	80,000	80,000	80,000
	Lighting		tl	15,000	15,000	15,000
	Shipping		tl	18,000	18,000	18,000
	Workmanship Accommodation Food		tl	80,000	80,000	80,000
	Ssi Premium		tl	50,000	50,000	50,000
	extras		tl	50,000	50,000	50,000

Project Cost		tl	20,000	20,000	20,000
Planning Permission		tl	15,000	15,000	15,000
Certification Cost		tl	10,000	10,000	10,000
Land Value	$15\ TL/m^2$	tl	150,000	500,000	35,000
1\$=3.5TL	Total Investment Cost (TL)		*2,245,200*	*2,595,200*	*2,445,200*

2.2. Estimating Annual Grid Feed-in value on PC Program

Secondly, on the PV-Sol program the system was simulated according to the real technical features of the elements. The energy supplied to the network was estimated with climate estimates for some cities which are Zonguldak, Konya, Izmir. Grid feed-in values of these cities are given table below. The annual grid feed-in decrease is taken as 1%.

Table 33.Estimating annual grid feed-in and system loses values (kWh)

	ZONGULDAK	IZMIR	KONYA
Global PV radiation (kWh)	4.58E+06	6.62E+06	5.26E+06
%15, 03 PV eff.	-3.89E+06	-5.63E+06	-4.47E+06
Rated PV Energy (kWh)	6.88E+05	9.95E+05	7.91E+05
Module-specific Partial Shading	-1.35E+04	-1.31E+04	-1.42E+04
Low-light performance	-3.43E+04	-3.00E+04	-3.31E+04
Deviation from the nominal module temperature	-1.87E+04	-5.13E+04	-2.28E+04
Diodes	-3.10E+02	-6.47E+02	-6.40E+01
Mismatch (Manufacturer Information)	-1.24E+04	-1.80E+04	-1.44E+04
Mismatch (Manufacturer Information)	-1.65E+03	-2.46E+03	-1.76E+03
PV Energy (DC) without inverter regulation	6.08E+05	8.80E+05	7.05E+05
Regulation Losses	-2.04E+03	-1.16E+03	-1.71E+03
PV energy (DC) (kWh)	6.05E+05	8.79E+05	7.03E+05
Energy at the Inverter Input (kWh)	6.05E+05	8.79E+05	7.03E+05
Input voltage deviates	-5.21E+02	-1.10E+03	-8.07E+02
DC/AC Conversion	-1.56E+04	-1.93E+04	-1.66E+04
Stand-by Consumption	-3.12E+02	-2.80E+02	-2.78E+02
Total Cable Losses	-5.89E+03	-8.58E+03	-6.86E+03
Grid Feed-in (kWh)	5.83E+05	8.50E+05	6.79E+05

2.3. Levelized Cost of Energy Method

Electricity sales revenues and escalated O&M costs are adjusted to the present value according to the interest rates. Construction time is not considered in this calculations because it's a short period.

The total cost of the system from construction date to the end of the lifetime is calculated with Eq. (1) [7].

$$C_{PW} = \sum_{t=-1}^{n}(C_T(t)(1+r)^{-t}) \tag{1}$$

where ($C_T(t)$) is sum of the annual costs, (r) is interest ratio, (n) is lifetime, (L) is construction time. The ratio between the result of the Eq. (1) and the total electricity generation gives the levelized cost of energy. It means that the sale price of electricity must be bigger than the result of Eq. (2) [7].

$$g = \frac{\sum_{t=-L}^{n} C_T(t)(1+r)^{-t}}{\sum_{t=0}^{n} E(t)(1+r)^{-t}} \tag{2}$$

where ($C_T(t)$) is sum of the annual costs, (r) is interest ratio, (n) is lifetime, (L) is construction time, (E(t)) is annual electricity generation.

3. RESULTS AND DISCUSSION

Cash flow graphs for each city are shown below. Long depreciation times are obtained due to the high interest ratios and low sale prices. The shortest depreciation time will be obtained if 0.7 TL/kWh sales price and 5% interest rate are selected. For 5% interest rate these period is 14 years for Konya, 10 years for Izmir and 17 years for Zonguldak. For 8% interest rate these period is 17 years for Konya, 11 years for Izmir and 20 years for Zonguldak.

(a)   Cash Flow (S.P.=0.7 TL)/ Konya

(b)   Cash Flow (S.P.=0.7 TL/kWh) / Izmir
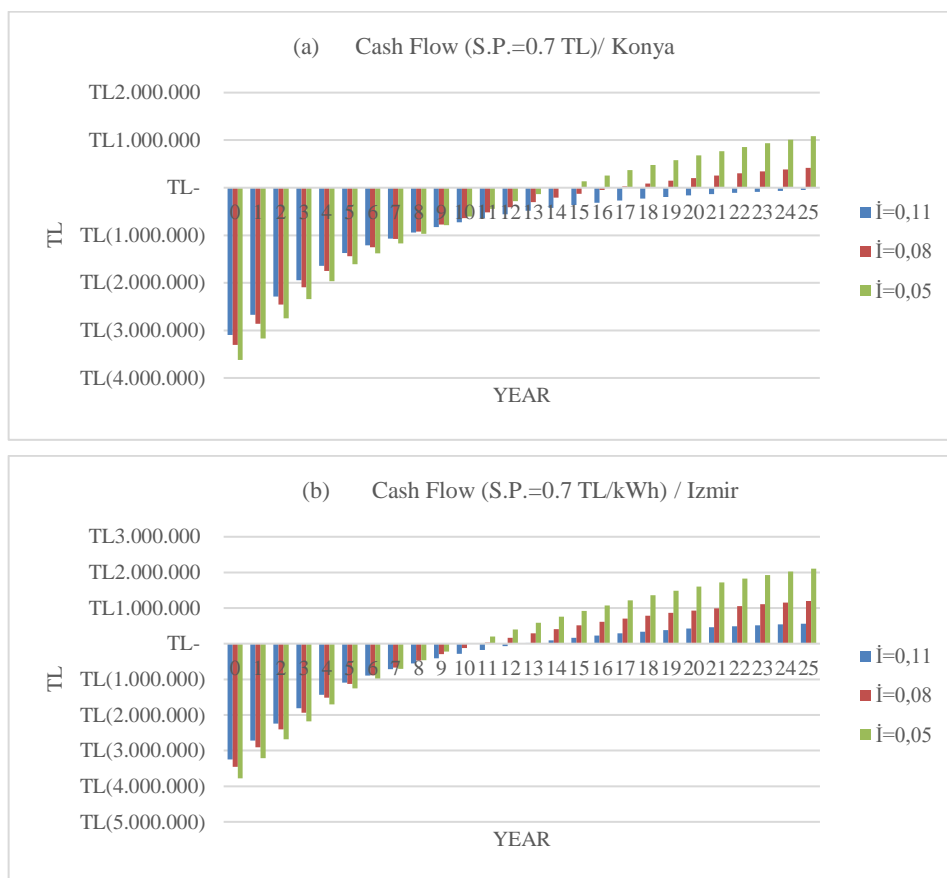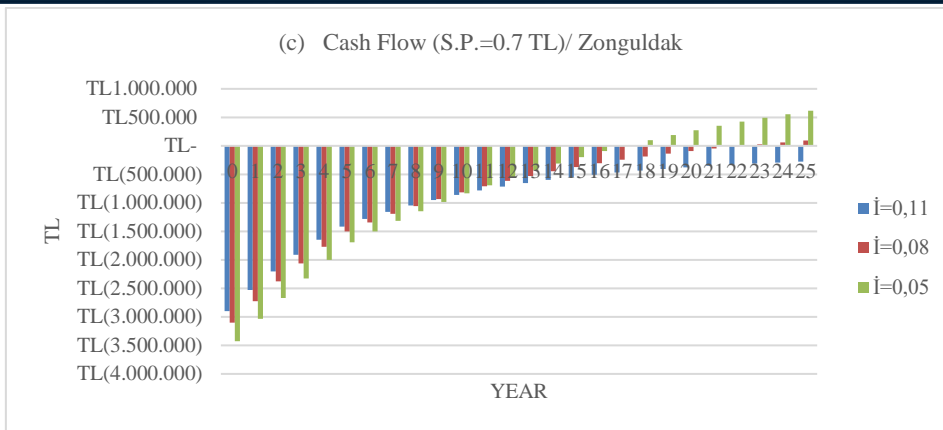
Figure 38. (a), (b), (c) Cash flow graphs [6]

Levelized cost of solar energy is calculated for each city showed the table below. The lowest LCOE is obtained for 5% interest ratio. Izmir is best option than the other cities. These results we obtained are close to the indicated values in some references (0.59-0.73 TL/kWh) [1]. Low profits are obtained at the end of the 25 years due to the low government supports and high equipment costs.

Table 34. Calculated LCOE for some interest rates (TL/kWh) [6]

	i= 11%	i= 8%	i= 5%
Izmir	0.489	0.415	0.349
Konya	0.583	0.496	0.419
Zonguldak	0.635	0.543	0.460

This figure show that levelized capital and o&m costs of solar energy for each city. Also, while annual electricity generation increase, levelized capital costs decrease.
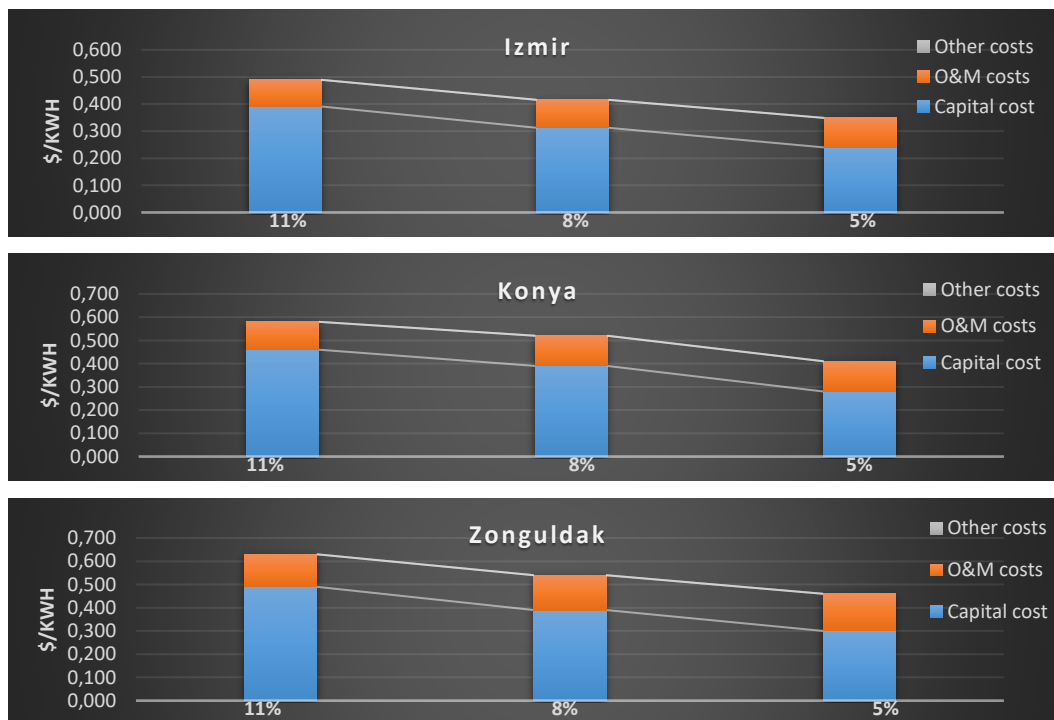
Figure 39.Capital and o&m cost for each cities

4. CONCLUSIONS

According to the result obtained from this study, electricity generation costs from solar PV are far from being a feasible in Turkey. This result supports to the LCOE calculations made for Turkey in some sources. Levelized cost of solar PV must be decreased to obtain more feasible results. Feed-in tariff period or local equipment bonus period should be extended. Government support for domestic producers should be increased. Interest rates should be reduced to the reasonable values. Research and development works in domestic organizations and technical universities should be supported to increase local equipments efficiencies and to decrease local equipments costs.

ACKNOWLEDGMENT

REFERENCES

[1]. *Today and Tomorrow of the Solar Energy: Inferences for Turke*y, Zorlu Energy. Istanbul, Turkey, 2016.
[2]. *Renewables Global Status Report.* REN21. Paris, France.
[3]. *Renewable Energy & Environmental Technologies*, Republic of Turkey Prime Ministry Investment Support and Promotion Agency (ISPAT), Istanbul, Turkey, Nov. 2013 [Online] Available: http://www.invest.gov.tr/en-US/Documents/.
[4]. *Turkey's Renewable Power,* WWF-Turkey , Istanbul, Turkey, 2014.
[5]. *Budgeting for Solar Pv Plant Operations & Maintenance: Practices and Pricing*, Electric Power Research Institute, California, USA, Dec. 2015.
[6]. U. Yasin, D. Seyfullah, *"Levelized Cost Analysis of PV Plants in Turkey''*, Istanbul, Turkey, Dec. 2016.
[7]. S. Bahri, A. Nejat, "Energy Cost'', Istanbul, Turkey , 1994
[8]. This figure available : http://www.solargis.info.

Cappuccino Effect on Intermediate Fuel Oil (IFO) Bunkering Operations

Yasin UST[1], Veysi BASHAN[2]

Abstract

In maritime and shipping industry the term of bunkering is commonly described as supplying IFO, MGO etc. fuels to tanks. The speed of the ship and the deadweight tonnage which are related with specific fuel-oil consumption determines the capacity and number of bunker tanks. Typical capacities of ship's bunker tank vary from 300 cubic meters to 5000 cubic meters. This means that if ship's main engine power demand increases the fuel-oil consumption will also increase and bunkering will be needed despite the big bunker tank capacities. Thus, ships are occasionally needed to be supplied with fuel. Ships complain about 'Cappuccino Effect' which fundamentally can be defined as frothing/bubbling caused by air and/or solvent blown through the fuel transfer pipes. In this study, 'Cappuccino Effect' and the sources of this problem have been introduced and some experimental investigation of air and solvent penetration to fuel has been analyzed and the amount of frothed fuel has been calculated by changing the percentages of solvent. Precautions for neutralizing Cappuccino Effect have been discussed and some advices have been given.

Keywords: *Cappuccino Effect; Fuel Bunkering; Fuel Frothing; Fuel Bubbling.*

1. INTRODUCTION

As a fact, transportation of goods by ships is the cheapest way in the world. Generally, the biggest cost of operating a ship is fuel. So, the fuels used in the ships should be cheap. Viscosity is the main characteristic to classify fuel oils. As the viscosity increases, the quality and price of the fuel decreases. Therefore, vessels use high viscous fuels. The most commonly used cheap fuels at ships are Intermediate Fuel Oil (IFO) 380 Centistokes (cSt) and IFO 180 cSt. Although ships have large fuel tanks they often have to buy fuel because they travel a long distance carrying too much load. It is often claimed that fuel suppliers, use many dubious practices during a typical bunkering operation. During bunkering, suppliers can apply tricky ways to gain unfair profit. Ships complain about 'Cappuccino Effect' which fundamentally can be defined as frothing/bubbling caused by air and/or solvent blown through the fuel transfer pipes [1]. Cappuccino effect can be clearly seen from Figure 1 and fuel oil without Cappuccino Effect is shown in Figure 2. It is often asked why the flow meter cannot detect the air being penetrated in the system. Because, most flow meters in use today are of either the wrong type or the wrong size. In other words; they are not technologically advanced. All the standard flow meters will only measure the volume of throughput and not the actual mass of fuel being delivered. As a result, when air/solvent penetrated into fuel transfer pipe the flow meter will register it as volume. Multi-phase fluids lead to measurement errors because of center of mass motion that is why Coriolis flowmeters must be in use with their high accuracy [2].

---

[1] Corresponding author: Yildiz Technical University, Department of Naval Architecture and Marine Engineering, 34349, Besiktas/İstanbul, Turkey. *yust@yildiz.edu.tr*

[2] Yildiz Technical University, Department of Naval Architecture and Marine Engineering, 34349, Besiktas/İstanbul, Turkey. *vbashan@yildiz.edu.tr*

Figure 1. Fuel oil in a double bottom tank displaying frothing with the cappuccino effect [3]

Figure 2. Fuel oil without cappuccino effect [3]

Especially, at purchase of high amount of fuel, it is crucial to make calculations accurately. Miscalculations during the fuel transfer process can cause conflicts, even financial losses. Because of fuel barges may have a lot of ways to hide fuel on their vessel; for example, hidden compartments, using of "magic pipes", non-class approved sounding tables etc. Before and after delivery measuring barge's fuel tanks is so important [1]. Ship fuels are stored in storage tanks, settling tanks and service tanks. The amount of fuel in the tanks is measured by the sounding meter which is shown in Figure 3. Sounding is the height between the surface height of the liquid fuel in the tank and the bottom of the tank.

Figure 3. Image of sounding meter [4].

Ullage; is the height of the empty part between the liquid fuel surface in the tank and the tank ceiling. Ullage is usually taken to be easy to measure when the liquid in the tank is too dense and the tank fullness is too much. This method can be seen from Figure 4. The shape of a fuel tank may not be always prismatic and the sounding pipe may not come straight down due to the geometry of the tank. That is why the volume may not be directly proportional to the level in the tanks. Thus, these level values measured by sounding or ullage must be converted to cubic meters by means of sounding tables prepared by shipyard. Sounding tables are tables that accurately prepared by shipyard according to tank geometry. The volume conversion must be done according to these tables. In addition, trim caused by the level difference between fore and aft of the ship and heeling caused by the leaning of the ship to port side or starboard side; changes the fuel level for the same amount of fuel. These corrections should also be done.
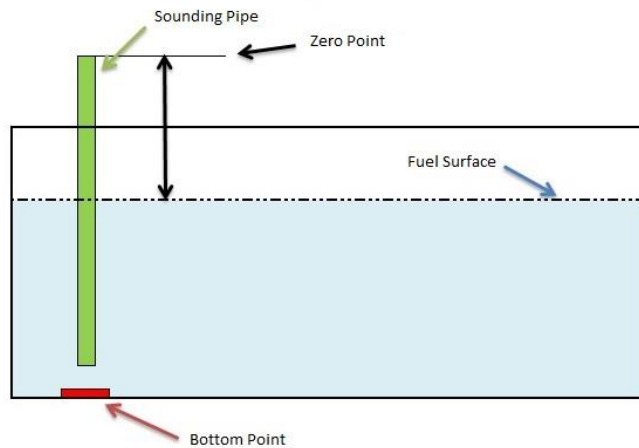
Figure 4. Calculation of fuel level with ullage method

2. MATERIALS AND METHODS

There are a lot of important points to be aware of when bunkering fuel. Marine fuels are nearly always sold by weight (mass) but delivered by volume [5]. Thus, all of receipt papers must be signed according to the volume. Duty engineer –mostly 3rd engineer – must never sign for weight if there is a doubt about the fuel density. A small miscalculation caused by the density of fuel can cause loss of thousand dollars. Supposing that shipping company has a fleet of 10 vessels and each of vessels approximately bunkering 1000 m^3 fuel each month. The damage caused by miscalculation is shown in the Table 1. with a simple way.

Table 1. Economical effect of miscalculation of IFO 380 density.

Average IFO Cost (USD/MT)	371
Bunker per month x 10 vessels	10.000 m^3
Density of IFO fuel @15°C (SDN)	0.9895 ton/m^3
Density of IFO fuel @15°C (Real value)	0.9861 ton/m^3
Differential between Real and Supplier's Delivery Note (SDN)	0.0034
Loss per vessel per month	3.4 ton
Economical Loss per vessel per month	1261.4 $
Fleet economical loss per month	12614 $
Fleet economical loss per year	151368 $

Likewise, many ships have been reported that thermometer is heated to create a bubble effect to prevent the correct registering of the IFO temperature. Table 2. Shows calculation of the commercial loss while actual temperature of IFO is 50 °C and declared temperature of IFO is 40 °C.

Table 2. Calculation of IFO weight with respect to temperature

Amount (m³)	Density @15°C (g/ml)	Temperature (°C)	Volume Correction Factor (ASTM Table-54B)	Gross Standard Volume (m³) @ 15°C	Weight (MT)
1000	0.9861	50	0.99821	998.21	984.33
1000	0.9861	40	0.99872	998.72	984.72

The difference is 0.39 MT. When 10 vessels buy 1000 m³ IFO per month with average cost of 371 usd/mt the commercial loss of fleet will reach up to 17362 \$/year.

2.1. Understanding Suspicious Cappuccino Bunkers

Duty engineer and Chief engineer on board must be well aware of some important points such as pressure, temperature, noise, smell etc. If there is sign of froth on the surface of the fuel in the barge tanks, excessive bubbles on the sounding tape prior to during and after bunkering, lower delivery transfer pressure and rates than agreed, suspicious noises from bunker barge, fluctuations of fuel transfer manifold gauge pressure, ship's crew and surveyor – if available- need to be alerted [6].

2.2. Precautions for Cappuccino Effect

To minimize the risk of being exposed to Cappuccino Effect the following points should be considered by Ship's Duty and Chief Engineer, respectively.

- All fuel tanks should be sounded including slop tanks and the sounding records should be signed by both Barge's Master and Ship's Chief Engineer.

- If air in the fuel oil is found or suspected, the vessel should wait for the air to escape after bunkering has been completed. The length of time depends on the viscosity and temperature of the fuel oil, as well as the size of the entrapped bubbles. The process will be quicker in tropical waters, but very small air bubbles in high viscosity fuels in cold climates may take up to two days to dissipate before accurate soundings can be taken [3].

- For calculating fuel oil density accurately, the temperature of fuel oil should be measured before bunkering [7].

- The draughts of the bunker barge should be taken before bunkering and on completion together with the Barge Master in order to compare the change in displacement with the quantity of fuel oil delivered [8].

- The mass of air must be negligible, ship owners should not pay for air that has intentionally or unintentionally found its way into the fuel. Coriolis mass flow technology is well-suited to HFO applications, particularly bunkering, where customer billing is based on mass [9].

- Blowing of fuel pipeline must only be permitted at the end of bunkering.

- Definite records of times, soundings, amounts, temperatures, densities and other key data ought to be kept up on the off chance that they are required in case of a disputes.

3. RESULTS AND DISCUSSION

An experimental study has been done for frothing IFO380 by using solvent and air. Specification of IFO380 used is given at Table 3.

Table 3. Marine fuel oil type IFO380 analysis report

Characteristics	Method	Limit	Result
Density 15 °C (kg/m³)	ISO 3675	991	991
Viscosity at 50 °C (cSt)	ISO 3104	380	338.7
Flash Point (Min) (°C)	ISO 2719	60	70
Ash Content (% m/m)	ISO 6245	0.15	0.053

Water Content (% v/v)	ISO 3733	0.5	0.1
Sulphur (% m/m)	ISO 8754	3.5	2.18
Vanadium (mg/kg)	ISO 14597	300	143
Aluminum + Silicon (mg/kg)	ISO 10478	80	29
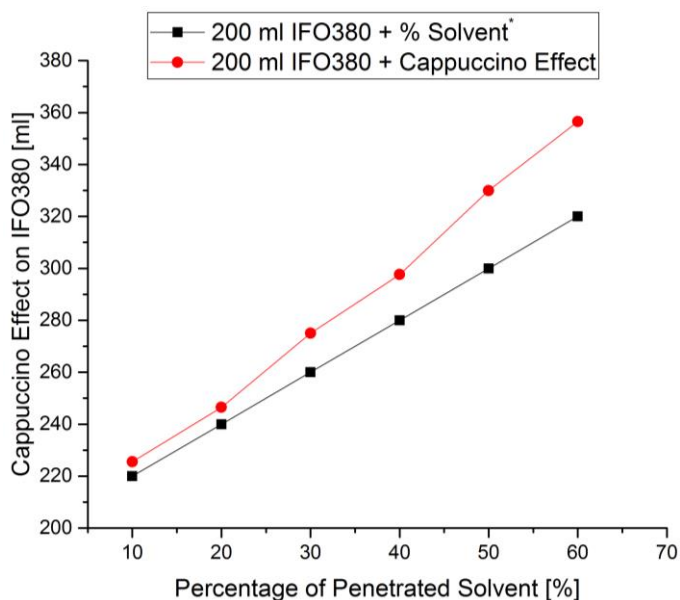
Figure 5. IFO380 frothing because of cappuccino effect

200 ml IFO380 were placed in the beaker. %10 percent frother solvent (20 ml) added into the beaker and 3 bar air injected into it by compressor blowgun. After nearly 30 minutes duration, cappuccino effect on IFO380 revealed. The percentage of frother solvent* is increased and cappuccino effect has been shown at Figure 5 in terms of different percentages of frother solvent*.

Figure 6. Frothing after air and frother solvent penetration to the IFO380*

Figure 6 shows bubbling and frothing of IFO380 while 100 ml frother solvent added to 200 ml IFO380 and 3 bar air injection for 5 minutes.
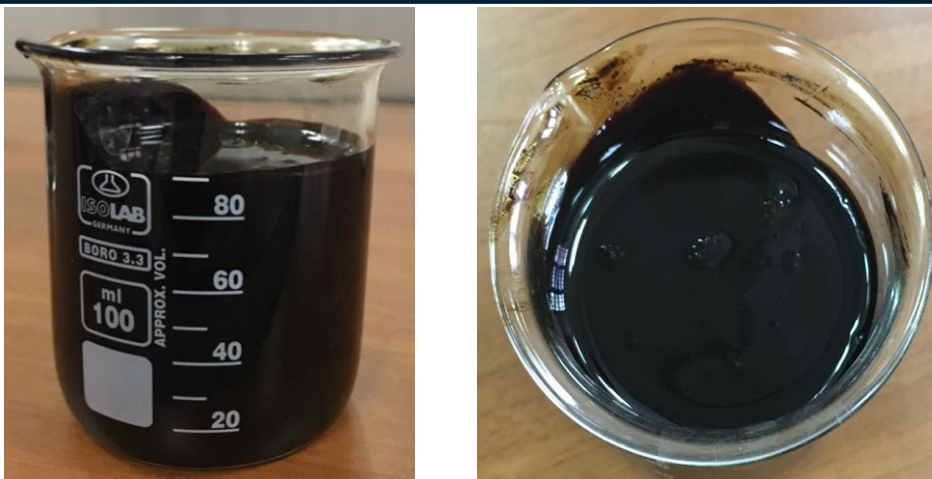
Figure 7. Neutralizing after solvent** penetration to the IFO380

Figure 7 shows effect of degreaser solvent** which helps to neutralizing of cappuccino effect.
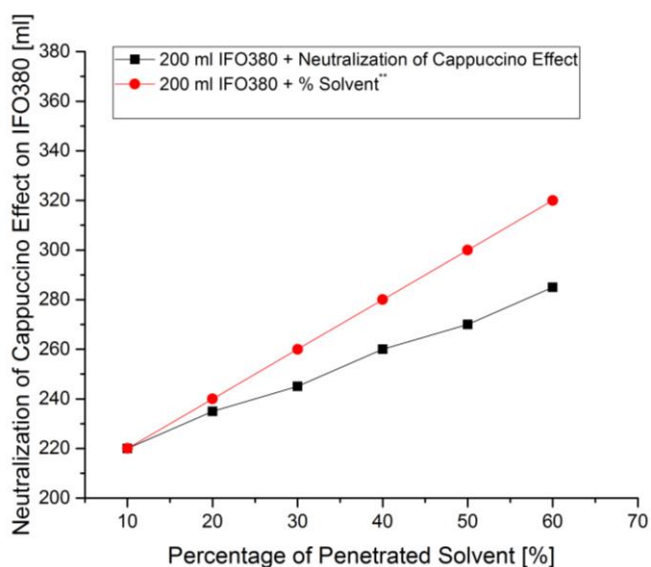
*Figure 8. Effect of degreaser solvent** for neutralizing cappuccino effect*

200 ml IFO380 were placed in the beaker. First scenario, %10 percent degreaser solvent (20 ml) added into the beaker. Approximately after 2 hours duration, neutralization of cappuccino effect on IFO380 revealed. Then, the percentage of degreaser solvent is increased and neutralization of cappuccino effect is shown at Figure 8 for different percentages of degreaser solvent**.

4. CONCLUSION

'Cappuccino Effect' and the sources of this problem have been introduced and some experimental investigation of air and solvent penetration to fuel has been analyzed and the amount of frothed fuel has been calculated by changing the percentages of solvent. It can clearly be seen that as the amount of frother solvent* and air penetrated to fuel increases, the Cappuccino Effect of the fuel increases. Similarly, as the amount of degreaser solvent** increases, neutralizing of frothing/bubbling effect increases. In addition, economic losses caused by miscalculation of density and mismeasurement of temperature has been calculated. Finally, some advices has been given to prevent Cappuccino Effect. It is crucial and necessary to take the recommended measures to ensure that the ships do not suffer economic damage.

REFERENCES

[1]   "13 Malpractices In Bunkering Operations Seafarers Should Be Aware Of," *Marine Insight*, 23-Oct-2014.
[2]   N. T. Basse, "A review of the theory of Coriolis flowmeter measurement errors due to entrained particles," *Flow Measurement and Instrumentation*, vol. 37, pp. 107–118, Jun. 2014.
[3]   "Loss Prevention Bulletin - Bunker Disputes - The 'Cappuccino Effect' | West of England P&I." (2017) [Online]. Available: http://www.westpandi.com/Publications/News/Archive/Loss-Prevention-Bulletin---Bunkering---The-Cappuccino-Effect/.
[4]   "Oil gauging tapes | Canepa & Campi - Life Saving Equipment." (2017) [Online]. Available: http://www.canepaecampi.com/product/oil-gauging-tapes/.
[5]   "General Terms and Conditions for the Sale of Marine Fuels." (2017) [Online]. Available: www.chemoil.com/Documents/Marinefuel-sales-generalterms.pdf+&cd=1&hl=tr&ct=clnk&gl=tr.
[6]   (2017) K. Chinoy, "PETRO INSPECT GROUP," *avagroup*. [Online]. Available: https://www.ava-marinegroup.com.
[7]   Md. Moynul Islam, "Marine Fuel Oil and Fuel Oil Bunkering Procedure," (2017) [Online]. Available: https://www.slideshare.net/moynulbd/loss-prevention-in-bunkering.
[8]   "CE Delft." (2017) [Online]. Available: http://www.cedelft.eu/publicatie/monitoring_of_bunker_fuel_consumption/1353.
[9]   J. Weinstein and David Ashley Hayes, "Micro Motion White Paper." (2017) Emerson Process Managment. [Online].Available: http://www2.emersonprocess.com/siteadmincenter/PM%20Marine%20Tank%20Management%20Documents/Marine-Fuel-Management-WP-001204.pdf

A Novel Breaker Kit Design for Continuous Chip Breaking in Turning Operations

Bahattin YILMAZ [1], Sener KARABULUT [2], Abdulkadir GULLU [3]

Abstract

Turning operation is one of the most commonly used machining methods. Continuous chip formation is one of the encountered problems in turning operations. Continuous chip formation endangers operator safety, machine safety and surface quality. Hence, continuous chip formation affects the operational efficiency adversely. In this field, there are many studies about chip breaking but such as Inconel 718 super alloy, some material chips could not be broken with existing methods. In this study, a chip breaker kit design was performed. The efficiency of the kit was experimentally investigated with four different cutting speeds, four different feed rates and four different cutting depths. Taguchi L16 experimental setup was used. As a result of the experiments, continuous chipping was successfully broken in all conditions. The effect of the chip breaker on cutting tools was studied. As a consequence of the studies, there was not seen any negative effect of the chip breaker on cutting tools. The chip breaker kit revealed an excellent performance.

Keywords:

1. INTRODUCTION

The method of machining has gained advantages of other production methods as it allows shaping a very diverse set of materials easily, achieving complex geometries, easily creating desired levels of dimensions and surface tolerances, and development of novel and genuine cutters for different machining conditions [1]. However, suitable cutting conditions and an efficient cutting environment should be provided for an ideal machining process [2].

Effective control of chipping is required for an efficient operation of cutting during a turning process. Continuous chipping is one of the cases that affect machinability negatively. In turning operations, continuous chipping disrupts the integrity of the work piece, as well as threatening the safety of the operator. Effective control of chipping is necessary for CNC machines or automated production systems. This is because any kind of error in chipping control will lead to reduction of operation efficiency as it will be required to stop the machine frequently. Therefore, chip breakers of different forms are widely used to obtain discontinuous chippings with purposes of efficiency and safety of the cutting process [3].

A chip breaker is a bump added to the chipping surface of the tool or a canal opened in the tool surface in various geometries. A chip breaker improves chipping breakability by reducing chipping bending radius, and increases operational efficiency by helping chipping control. Additionally, it may reduce cutting resistance and improve tool life-span and quality of the work piece [4]. Despite all these advantages, in order to develop a new cutting tool with a chip breaker, in addition to molding, sintering, grinding and coating, it is necessary to conduct long-term and high cost studies that include different analyses of the products [5].

Many studies have demonstrated that chip breaker geometries are inadequate in breaking the chipping in high-ductility materials. This case became more apparent especially in ductile materials such as superalloys [6]. The ductile and single-crystal structure of the material Inconel 718 leads to continuous chipping formation and this chipping cannot be broken using classical methods [7]. This made it necessary to develop alternate methods to break the chipping. In order to break chipping, it is necessary to increase feed rate and

---

[1] *Corresponding author: Gazi University, Faculty of Technology, Department of Manufacturing Engineering, 06500, Teknikokullar/Ankara, Turkey. bahattinyilmaz@gazi.edu.tr*

[2] *Hacettepe University, Department of Mechanical Program,06935,Ankara, Turkey. senerkarabulut@hacettepe.edu.tr*

[3] *Gazi University, Faculty of Technology, Department of Manufacturing Engineering, 06500, Teknikokullar/Ankara, Turkey. agullu@gazi.edu.tr*

cutting depth, while decreasing cutting speed. However, changing cutting conditions leads to negative effects on tool life-span and surface quality in machining various kinds of materials [8].

In Ezugwu's study, high pressure coolant was used to break continuous chipping and reduce cutting temperatures. As a result of the study, it was found that chipping may only be broken under a high pressure value such as 203 bar [9]. Colak turned the material Inconel 718 using a high-pressure jet cooler. As a result of the experiments, they stated that high-pressure cooling has positive effects on tool life-span and chipping may be broken under a pressure of 300 bar [10]. Kim and Kweun designed a special chip breaker apparatus to prevent occurrence of continuous chipping. This apparatus was designed to be able to break chipping in different directions of flow. They reported that chip breaking is more successful in low cutting speeds [11]. M. Nakamura, Y. Mitani et al. designed a special tool chuck. This tool chuck they designed was aimed for breaking chipping via movement of oscillation. In all machining conditions tested with this apparatus, chipping was broken. As a result of the oscillation during the cutting process, surface roughness increased [12]. Shane, Hong and Woo-Cheol provided a special design to increase machining efficiency and break chipping. In the designed system, liquid nitrogen (LN2) was applied to the cutting area. With the help of the correctly places apparatus, effective cooling and chip breaking were achieved [13]. Gullu and Karabulut designed a new breaker to break the continuous chipping that arises during machining of Inconel 718. It was seen that chipping was effectively broken in all machining conditions with the help of the breaker apparatus placed on the tool chuck. It was reported that temperatures dropped and surface quality was not disrupted with the help of the breaker apparatus [8].

In scope of this study, an inexpensive, practical, highly feasible and industrial chip breaker apparatus was designed in order to be able to break continuous chipping. The chipping was successfully broken with the designed breaker apparatus.

2. EXPERIMENTAL METHODS

2.1. Design Criteria

Considering the existing studies on breaking continuous chipping, it may be seen that the problem has not been efficiently solved yet. It was observed that methods developed for solution affected work piece quality (such as surface smoothness) negatively, required high costs, had low applicability or failed to effectively break the chipping.

It was aimed that the breaker apparatus developed in this study would be a product with high efficiency and applicability. Therefore, product development studies were conducted for designing a Dynamic Chip Breaker. The following main principles were determined for the design to satisfy expectations.

- An inexpensive method that will not increase costs,
- Applicability in CNC and classical machines,
- Fast and practical functioning,
- No disadvantages in operation due to dimensions and characteristics, and
- Easiness of usage and high feasibility.

2.2. Design Stages

This study aimed a high-feasibility apparatus by developing a Chip Breaker Apparatus. In initial studies in line with this purpose, it was aimed that the new breaker would be air-actuated and it would be saved from its bulky structure and extra energy needs. It was also expected that a more effective cooling process would take place in an air-actuated chip breaker.

The breaker apparatus designed as a result of analyses consists of a main body that surrounds the tool chuck and is able to move on the tool chuck, and a carrier arm with both sliding and circular joints that connects the breaker apparatus to this body. The circular joint between the breaker and the arm allows the breaker to move circularly, and makes it possible to adjust the position and easily change parts.

The breaker apparatus consists of a small air chamber and a breaker gear. There is an actuation gear in the air chamber. The air hits this gear and leads to a rotation movement. The breaker gear on the same shaft as the actuation gear is activated this way. The leaving air leads to evacuation of the broken chipping and cooling of the cutting area.
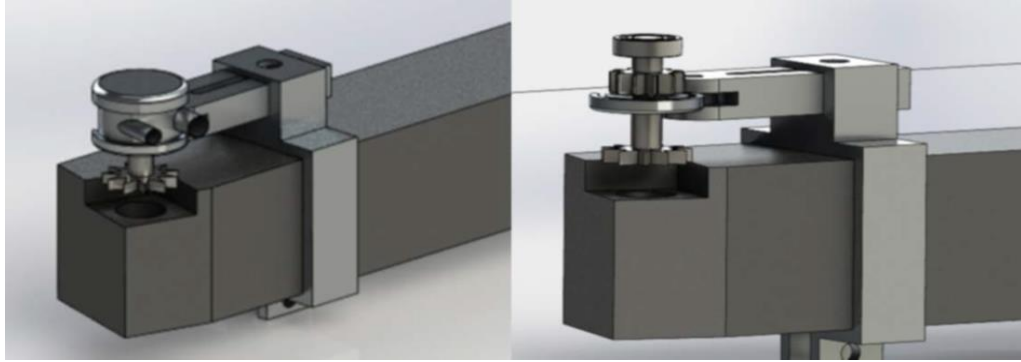
Figure 40. Chip Breaker Design

With this air-actuated breaker apparatus, the continuous chipping obtained in the pilot experiments with AISI 304 stainless steel were broken in all cutting conditions successfully. However, the air-actuated breaker apparatus was not able to produce the torque and power necessary to break the continuous chipping that occurred during the machining of Inconel 718. Therefore, the improvements on the design continued.

In the new design, a DC motor was used to actuate the breaker and this motor was placed inside the tool chuck. The power received from the motor was transferred to the breaker box. With the help of the gears inside the breaker box, the desired levels of revolutions and torque were transferred to the breaker gear. More effective and successful breaking was achieved with this system.
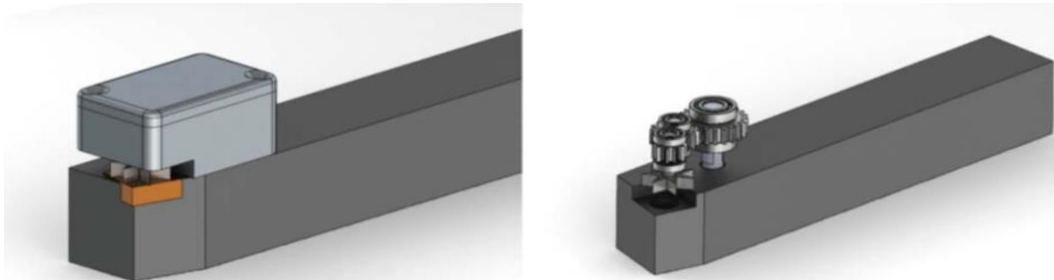
Figure 41. Chip Breaker Design

2.3. Material and Cutting Conditions

The experiments used a positively angled ISCAR tool chuck with the code SSBC R 25x25 M12 ISO. As the cutting tool, a SCMT 12 04 08 MM carbide cutting tip with 4μm PVD TiAlN-TiN coating was used as it was recommended for Inconel 718 by the firm Sandvik.

The cutting parameters used in the experiments were determined considering TS 10329 (ISO 3685) and the values provided in the cutting tool catalogue of the firm Sandvik. A chipping depth of a=0.8, 1.0, 1.3 and 1.7 mm, a feed rate of f = 0.10, 0.13, 0.17 and 0.22 mm/rev, and a cutting speed of 25, 35, 50 and 70 m/min were chosen and the experiments were carried out. Based on the Taguchi L_{16} experimental design, four different cutting speeds, feed rates and chipping depths were used in the experiments.

Table 35. The parameters used in the experiments

Number of	Cutting Speed	Feed Rate (f)	Cutting Depth
1	25	0.10	0.8
2	35	0.13	0.8
3	50	0.17	0.8
4	70	0.22	0.8
5	25	0.13	1.0
6	35	0.10	1.0
7	50	0.22	1.0

8	70	0.17	1.0
9	25	0.17	1.3
10	35	0.22	1.3
11	50	0.10	1.3
12	70	0.13	1.3
13	25	0.22	1.7
14	35	0.17	1.7
15	50	0.13	1.7
16	70	0.10	1.7

The machining experiments were conducted using the industry-type Johnford TC35 CNC turning bench located in the Laboratory of the Department of Manufacturing Engineering, Faculty of Technology, Gazi University.
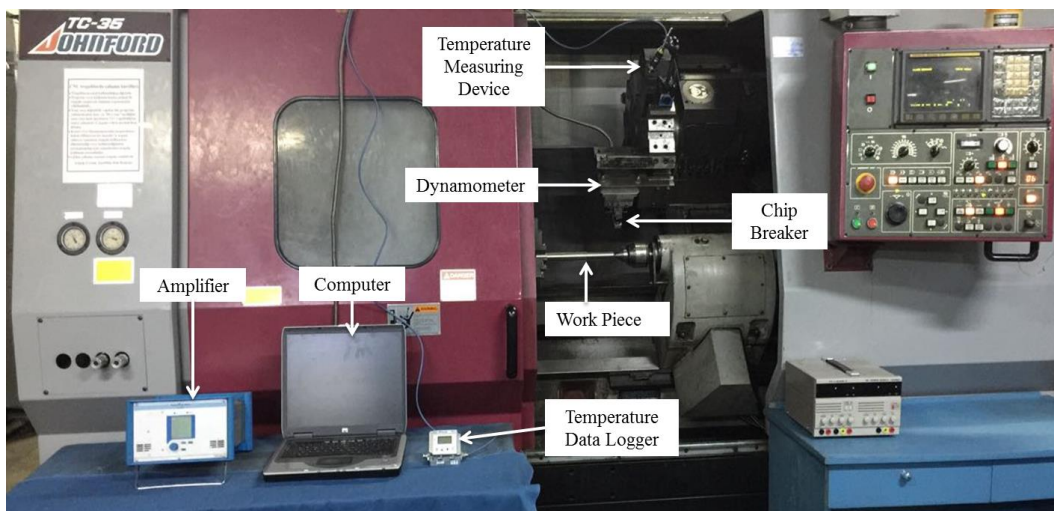
Figure 42. Experimental Setup

The material used in the experiments was Inconel 718, which is a nickel-based superalloy. The material has a density of 8.470 kg/dm³, and brinell hardness of 388 HBS. The Inconel 718 material used in the machining experiments had dimensions of Ø50x400 mm. Table 2 and Table 3 show the chemical and mechanical properties of the material used.

Table 36. Chemical composition of the Inconel 718 sample (weight %)

C	Mn	Si	Cr	Ni	Co	Mo	Cb+Ta	Ti	Al	Fe
0.020	0.04	0.06	17.83	53.53	0.23	3.04	5.34	0.98	0.56	18.40

Table 37. Mechanical characteristics of Inconel 718

Hardness (HB)	Yield Strength (MPa)	Tensile Strength (MPa)	Elongation (%5 d)
388	1375	1170	23.3

3. RESULTS AND DISCUSSION

3.1. The Chip-Breaking Effect of the Breaker Apparatus

In order to see the effectiveness of the breaker apparatus, experiments were conducted both in absence and in presence of the apparatus. As a result of the experiments, it was seen that different types of continuous chipping occurred in all cutting conditions. The breaker apparatus broke all the chipping.

During the machining of the superalloy Inconel 718, it was seen that the chipping left in white heat, the heat was transferred to the cutting tip as the chipping flew out, the cutting tip overheated and was worn out too quickly. Removal of the chipping by breaking provided significant benefits in terms of overheating.

During the experiments, it was seen that the continuous chipping that occurred in low revolutions (1200 rev/min) did not break. With increased breaker revolution (3500 rev/min), the chipping was broken in chipping depths of 1.3 mm or higher. However, the chipping continuously flew in chipping depths of 1 mm or lower. The ideal revolution rate for the breaker was determined as 9000 rev/min and all chippings that occurred in these conditions were effectively broken.

The images of the chippings obtained in the experiments are given in Figure 4. It was seen that the type of chipping that occurred in all cutting parameters was continuous chipping. This continuous chipping was removed with the help of the chip cutting apparatus. High-step spiral chipping formation was observed in the chipping depth of 0.8 mm. The breakability of the chipping increased under high cutting speeds and feed rates. Under these conditions, it was observed that the chipping was broken by being tangled around or hitting bench components.
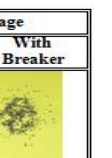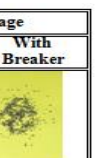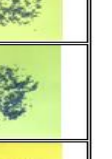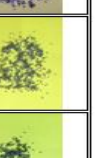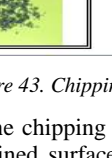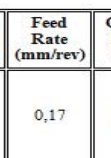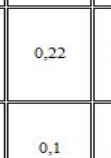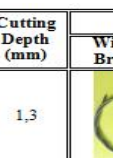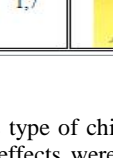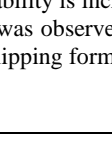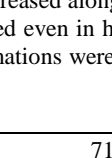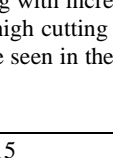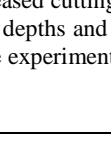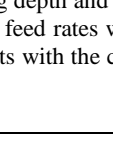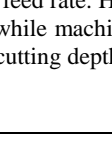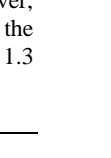
Cutting Speed (m/min)	Feed Rate (mm/rev)	Cutting Depth (mm)	Chip Image		Cutting Speed (m/min)	Feed Rate (mm/rev)	Cutting Depth (mm)	Chip Image	
			Without Breaker	With Breaker				Without Breaker	With Breaker
25	0,1	0,8			25	0,17	1,3		
35	0,13	0,8			35	0,22	1,3		
50	0,17	0,8			50	0,1	1,3		
70	0,22	0,8			70	0,13	1,3		
25	0,13	1			25	0,22	1,7		
35	0,1	1			35	0,17	1,7		
50	0,22	1			50	0,13	1,7		
70	0,17	1			70	0,1	1,7		

Figure 43. Chipping breaking effect

Tangled chipping formation was seen in the chipping depth of 1 mm. This type of chipping affects surface quality negatively by scratching the machined surface. Tangled chipping effects were minimized with the help of the chip breaker apparatus.

It is known that chipping breakability is increased along with increased cutting depth and feed rate. However, continuous chipping formation was observed even in high cutting depths and feed rates while machining the Inconel 718 material. Similar chipping formations were seen in the experiments with the cutting depths of 1.3

mm and 1.7 mm. In these conditions, the length of the chipping that elongated without breaking reached up to 3-5 m. These chippings were also easily broken with the help of the chip breaker.

SEM photographs were taken regarding the chippings obtained in the experiments. The SEM photographs provided information about chipping breaking, chipping formation and chipping surfaces.
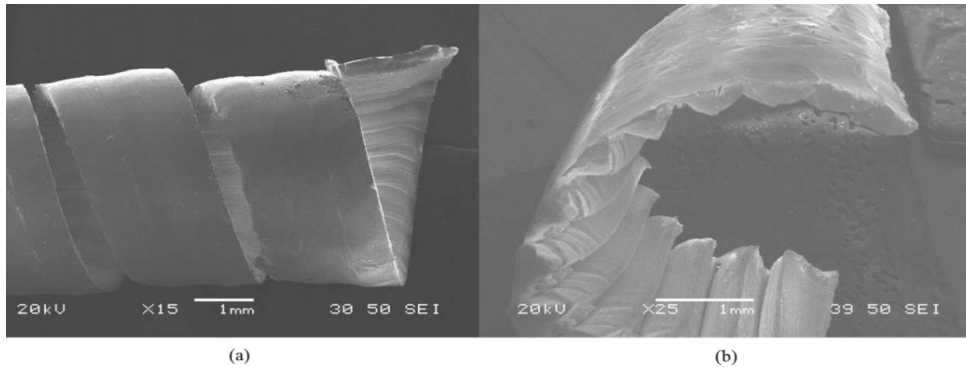
Figure 44. SEM image of the formed chipping (a) without chip breaker (b) with chip breaker

Figure 5 shows SEM images of the experiments conducted under the conditions of 25 m/min feed rate, 0.22 mm/rev cutting speed and 1.7 mm chipping depth. Due to the effects of the chip breaker apparatus, it was seen that the saw tooth appearance induced on the chipping was more noticeable. The breaker apparatus changed the chipping bending radius. It is thought that this change led to breaking of the chipping and made the saw tooth appearance more noticeable by increasing the chipping's accumulation rate [12].

3.2. Cutting Tool Images

Cutting tool efficiency is at the top of the most important parameters that affect costs and determine operational efficiency in cutting operations. The effects of the cutting apparatus on the tool are important for revealing its effects on the efficiency of the process. The tools were compared between experiment that used the breaker apparatus and those that did not, and the effects of the cutting apparatus were demonstrated.
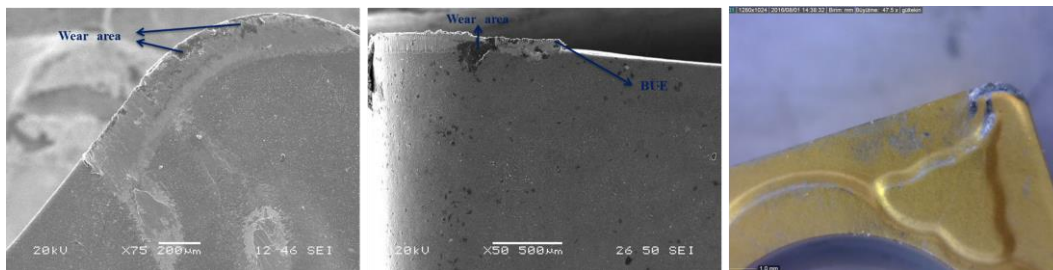
Figure 45. Cutting tool image from the Experiment No. 6 which was conducted without the breaker

Figure 6 shows SEM images of the experiment conducted without the breaker under the conditions of 35 m/min feed rate, 0.1 mm/rev cutting speed and 1 mm chipping depth. As a result of the cutting operations, a few cracks and side BUE formations were observed on the cutting tool. EDS images were taken to more correctly analyze the formations on the tool.
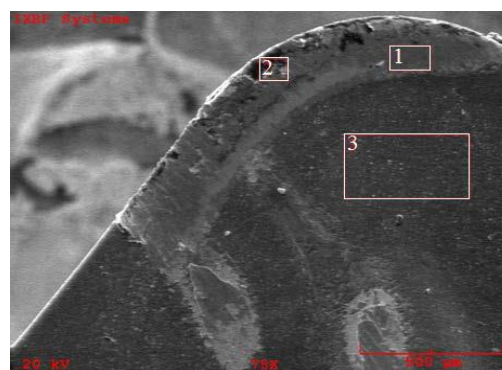
Figure 46. EDS regions on the tool

EDS data were taken from three regions for analysis. It was seen that the densest materials in Region 1 were nickel (39.2%) and chromium (14.8%). The density of chromium and nickel in this region showed that some parts were collected from the work piece. In Region 2, in addition to nickel (23.9%), there was a high amount of carbon (17.8%). The wear in the tool increased the carbon density in this part. It was seen that there was a high amount of titanium in Region 3, which was explained by the coating on the tool.
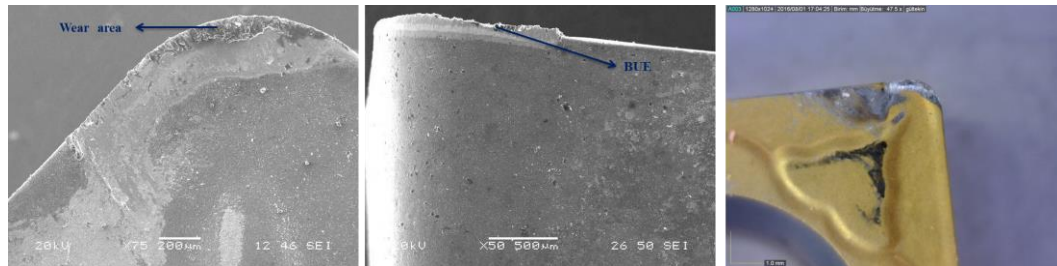
Figure 47. Cutting tool image of the Experiment No. 6 conducted using the breaker

Similar wear characteristics were also seen in the experiment that was conducted using the chip breaker. There was wear in the tip of the tool, while there was BUE formation in the side surface. Similarly, again, three EDSs were taken from this tool.
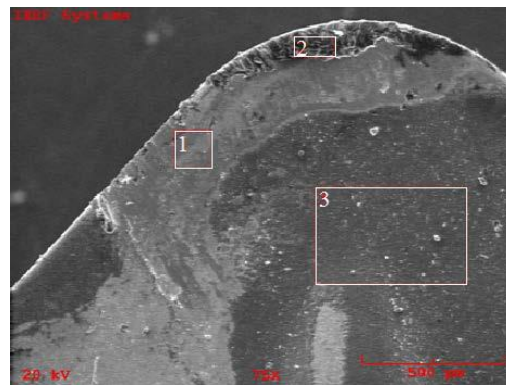
Figure 48. EDS regions on the tool

In Region 1 that we expected BUE formation, there was a high nickel and chromium presence. This supported BUE formation. In Region 2, there was a high carbon presence due to fractures and cracks. As in the case of the previous tool, Region 3 had dense titanium presence. Similar wear and BUE formation was seen in both tools. This shows that the chip breaker apparatus does not have a harmful effect on the cutting tool.

4. CONCLUSIONS

- It was seen that continuous chipping is an undesirable chipping type for cutting operations in terms of many aspects.

- An air-actuated breaker was designed, and it was seen that this design is not able to break the chipping of the material Inconel 718.

- The new breaker actuated by a DC motor successfully broke the chipping in all conditions.

- It was determined that the ideal revolution rate for the breaker was 9000 rev/min.

- As a result of the experiments, it was found that continuous chipping formed in all conditions, the chipping length reached up to 3-5 m, and these chippings were effectively broken.

- Different chipping formations were seen under different cutting parameters. In 1 mm cutting depth, tangle chipping was observed, which has negative effects on the surface.

- Similar cutting tool characteristics were seen in the experiments with and without the breaker. The breaker apparatus did not have a negative effect on the tools.

- Considering the analyzed data, the breaker apparatus performed its duties effectively and efficiently.

REFERENCES

[1]. M. P. Groover, Fundamentals Of Modern Manufacturing- Materials, Processes And Systems, Prentice-Hall Inc., New Jersey, 1996.

[2]. E.P. DeGarmo, J.T. Black and R.A. Kohser, Materials and Processes in Manufacturing, Prentice-Hall Inc., New Jersey, 533-600, 2013.

[3]. M.C. Shaw, Metal Cutting Principles, 2nd ed. Oxford University Press, New York, 2005.

[4]. İ., Tekayut, M. Gunay, and U. Seker, "Tornalama İslemlerinde Talas Kırıcı Formunun ve Kesme Parametrelerinin Taguchi Yontemiyle Optimizasyonu" 6th International Advanced Technologies Symposium (IATS'11), Elazıg, Turkey, 16-18 May 2011.

[5]. H.G. Kim, J.H. Sim and H.J. Kweon, "Performance evaluation of chip breaker utilizing neural network", Journal of Materials Processing Technology, 209, 647–656, 2009.

[6]. A. Avanessian, "An Analysis of The Effect of 3-D Groove Insert Design on Chip Breaking Chart", A Thesis Submitted to the Faculty of Worcester Polytechnic Institute, January, 2005.

[7]. B. Yılmaz, "Pnomatik Tahrikli Dinamik Talas Kırıcı Tasarımı ve İsleme Parametrelerine Etkilerinin Arastırılması", Yuksek Lisans Tezi, Gazi Universitesi Fen Bilimleri Enstitusu, Ankara, 2016.

[8]. A. Gullu, and S. Karabulut, "Dynamic Chip Breaker Design for Inconel 718 Using Positive Angle Tool Holder," Materials and Manufacturing Processes, 23, 852–857, 2008.

[9]. E. O. Ezugwu and J. Bonney, "Effect Of High- Pressure Coolant Supply when Machining Nickel-Base, Inconel 718, Alloy with Coated Carbide Tools," Journal of Materials Processing Technology, 153–154, 1045–1050, 2004.

[10]. O. Colak, "Investigation on machining performance of Inconel 718 under high pressure cooling conditions", Stroj. Vestnik/Journal Mech. Eng, 58 683–690, 2012.

[11]. J.D. Kim and O.D. Kweun, "A Chip-Breaking System for Mild Steel in Turning," *Int. J. Mach. Tools Manufacture.,* 607-617, 1997.

[12]. M. Nakamura, Y. Mitani, S. Asakura and T. Shibuya, "The Development of Chip Parting Processing Technology Oscillatory Feed Cutting," JSAE Review 21: 555-559, 2000.

[13]. Y.H. Shane, I. Markus and J. Woo-cheol, "New Cooling Approach and Tool Lifimprovement in Cryogenic Machining of Titanium Alloy Ti-6Al-4V," International Journal of Machine Tools & Manufacture, 41, 2245-2260, 2001.

Investigation of Cutting Force and Temperature Effect of Chip Breaker Used During Turning of Inconel 718 Material

Bahattin YILMAZ [1], Sener KARABULUT [2], Abdulkadir GULLU [3]

Abstract

The continuous chip formation which occur during turning operations decreases the precision of the work piece and threats the operator's safety. Continuous chip formation stops the operation on CNC machines and causes various damages on the hardware. All these situations reduce the machining efficiency and raise the importance of chip controlling. Therefore, in the terms of chip controlling, obtaining short chip becomes crucial. In this study, chip breaking of Inconel 718 super alloy material was aimed. Inconel 718 super alloy chip formation cannot be broken with conventional methods. In accordance with this purpose, a novel chip breaker apparatus was designed and its efficiency tested with experimental studies. Taguchi L16 test model was used in the experiments with four different cutting speeds, four different feed rates and four different cutting depths. Cutting forces and cutting zone temperatures were evaluated. The obtained data from the experiments were interpreted with the aid of ANOVA. It is seen that the chip breaker apparatus affects positively on cutting forces and temperature. Short chip formation was obtained in all cutting parameters.

Keywords:

1. INTRODUCTION

Machining operations can be divided into three main groups: turning, milling and drilling. In particular, the use of turning operations in the manufacturing industry is very common. Turning operations are complex operations due to the variability of the interrupt parameters [1].

An efficient turning operation is possible with ideal cutting conditions. The parameters affecting cost in machining operations are power and tool life. Determination of the power consumed during cutting is possible by measuring the cutting forces. The reduction of cutting forces indicates that power consumption is reduced and is a desired condition [2,3].

98% of the energy used during machining is converted into heat. The high temperatures created during cutting reduce tool life, resulting in hot work, which threatens work safety and degrades the dimensional accuracy of the workpiece due to thermal expansion. For all these reasons it is intended to keep the temperature under control during cutting operations [4].

Continuous chipping is a type of chipping formed by processing ductile materials with appropriate cutting parameters [3]. Continuous chipping flowing without breaking during turning is not desirable due to reasons such as work safety, control problems during automatic operation, deterioration of surface quality, damage to countertop equipment, etc. [5].

These negative features of continuous chipping have led cutting tool firms and scientific researchers to design and develop chip breaker forms. Operator safety, good surface and required power reduction have been achieved by providing effective chip control through the use of chip-breaking cutting tools [6]. However, cutting tools with chip breaker geometry have increased tool costs [4,7]. In addition, despite the improvements in the chip breaker forms, it is not possible to break the chips of some ductile materials. When

---

[1] *Corresponding author: Gazi University, Faculty of Technology, Department of Manufacturing Engineering, 06500, Teknikokullar/Ankara, Turkey. bahattinyilmaz@gazi.edu.tr*

[2] *Hacettepe University, Department of Mechanical Program,06935,Ankara, Turkey. senerkarabulut@hacettepe.edu.tr*

[3] *Gazi University, Faculty of Technology, Department of Manufacturing Engineering, 06500, Teknikokullar/Ankara, Turkey. agullu@gazi.edu.tr*

Inconel 718 material is processed, continuous long chips that cannot be cracked are obtained. Already hard machining of nickel alloyed material has been hardened by continuous chipping problem.

This has prompted researchers to develop different solutions. In the studies carried out, breakage of continuous chips with high-pressure coolers was investigated. In a study by Ezugwu the chip was broken under pressure of 203 bar [8]. Colak has reached a high pressure of 300 bar [9]. These high pressures have increased processing costs. Another solution developed to break the chips is to break the chips with the help of a crusher. A lot of work has been done in this area. M. Nakamura designed the swing motion device to break the chip, but determined that chip breaks the surface quality [10]. Shane, Hong and Woo-cheol have broken the chip with the apparatus they designed, but the apparatus has increased the processing cost [11]. With the system designed by Gullu and Karabulut, when the chip was broken successfully, problems were encountered in terms of applicability of the system [12].

In this study, a new breaker apparatus design was carried out to break the continuous chips formed during the turning operation. The productivity of the breaker was determined by measuring the cutting forces and the cutting zone temperature. As a result of the tests, continuous chipping was found to break efficiently. Positive effects of breaker on the cutting force and temperature were determined.

2. EXPERIMENTAL METHODS

2.1. The Breaker Apparatus

The apparatus, which is designed to break the chip effectively, is fixed with a screw connection on the tool holder. It is aimed to break the chip by transferring the breaker wheel with the breaker gear system driven by the DC motor placed in the tool holder. The operating conditions of the apparatus were set at 9000 rev / min at 15V and 3.5A. Experimental studies have shown that when the distance between tool-breaker is 0.2 mm and the distance between work-breaker is 2.5 mm, chip breaks successfully.
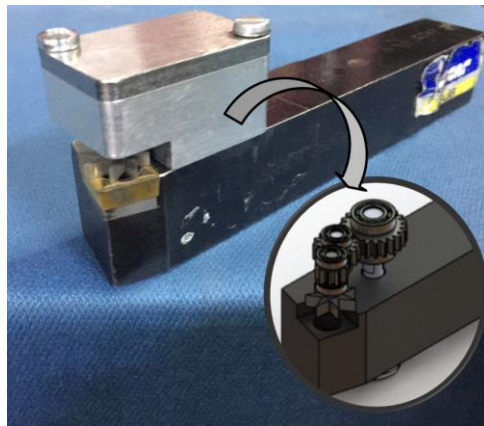
Figure 49. Chip breaker apparatus

2.2. Material and Method

During the tests, Inconel 718 material was used from nickel-based super alloys. The chemical composition and mechanical properties of the material are given in Table 1 and Table 2.

Table 38. Chemical composition of the Inconel 718 sample (weight %)

C	Mn	Si	Cr	Ni	Co	Mo	Cb+Ta	Ti	Al	Fe
0.020	0.04	0.06	17.83	53.53	0.23	3.04	5.34	0.98	0.56	18.40

Table 39. Mechanical characteristics of Inconel 718

Hardness (HB)	Yield Strength (MPa)	Tensile Strength (MPa)	Elongation (%5 d_0)
388	1375	1170	23.3

SSBC R 25x25 M12 ISO code, ISCAR brand tool holder was used during the experimental works. PVD TiAlN-TiN coated SCMT 12 04 08 MM carbide insert is used as the cutting tool. Cutting tools have been recommended by the Sandvik firm for super alloys.

Figure 50. Cutter tool and tool holder

Cutting parameters are determined according to the values recommended by Sandvik and ISO 3685 standards. Experiments were carried out by determining four parameters for each variable according to the Taguchi L16 test model. In cutting, cutting speeds of 25, 35, 50 and 70 m / min were selected as feed rates, 0.10, 0.13, 0.17 and 0.22 mm / rev were selected as feed rates and 0.8, 1.0, 1.3 and 1.7 mm as chip depth.

Table 40. The parameters used in the experiments

Number of	Cutting Speed (V)	Feed Rate (f)	Cutting Depth (a)
1	25	0.10	0.8
2	35	0.13	0.8
3	50	0.17	0.8
4	70	0.22	0.8
5	25	0.13	1.0
6	35	0.10	1.0
7	50	0.22	1.0
8	70	0.17	1.0
9	25	0.17	1.3
10	35	0.22	1.3
11	50	0.10	1.3
12	70	0.13	1.3
13	25	0.22	1.7
14	35	0.17	1.7
15	50	0.13	1.7
16	70	0.10	1.7

Experiments were carried out on Johnford TC35 industrial CNC lathe, which is located in Gazi University Faculty of Technology Department of Manufacturing Engineering.

The cutting forces generated during the tests were measured using a KISTLER 9257A type piezoelectric dynamometer. DynoWare Type 2825Ai-2 program was used to convert the force data to graph.

The heat released during the machining chip removal process is measured with the RAYTEK MI3 brand infrared measuring thermometer. The temperature measuring device, which focused on the starting point of the chip, measured during the cutting time.
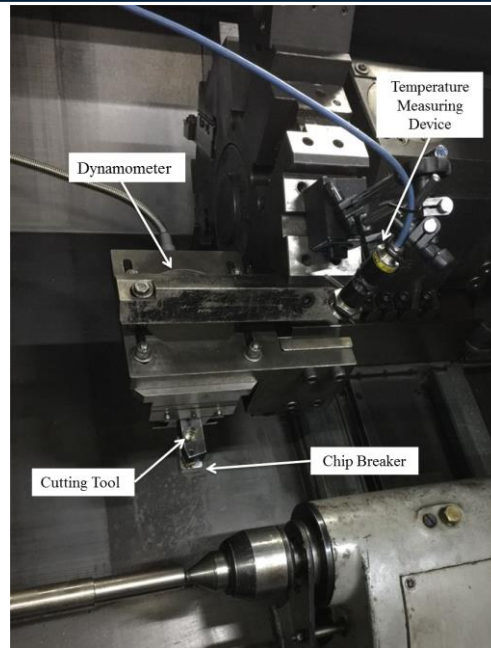
Figure 51. Working system

3. RESULTS AND DISCUSSION

3.1. Evaluation of Cutting Force

The force values measured for each experiment are presented graphically in Figure 4. The effect of the breaker on the cutting forces is comparatively determined. Similar force generation tendencies were observed in both experimental groups using chip breaking device and without breaker and near force values were obtained.
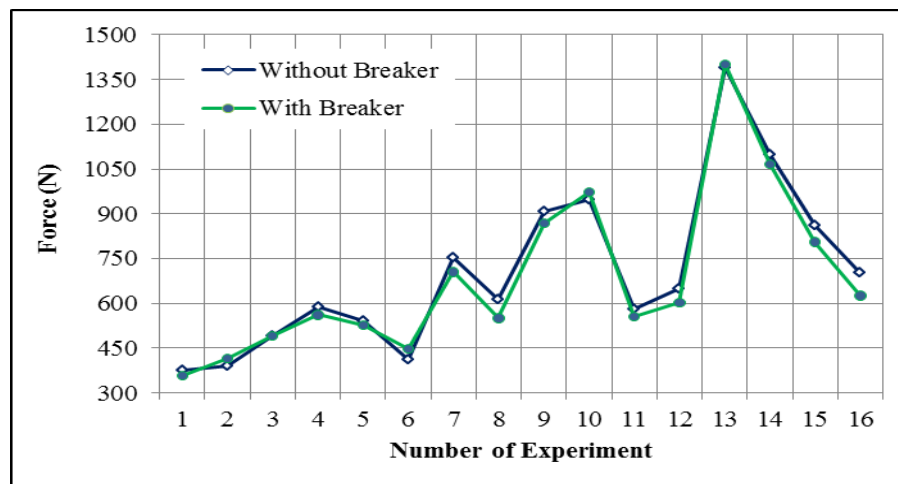
Figure 52. Comparison of cutting forces

It was observed that the developed chip breaker improved the cutting forces by 3% to 11%. The removal of the chip by cutting off the additional chip loads that have formed on the tool has been removed.

The variation of cutting forces according to cutting parameters was derived by ANOVA studies and tried to be explained with Main Effect graph.
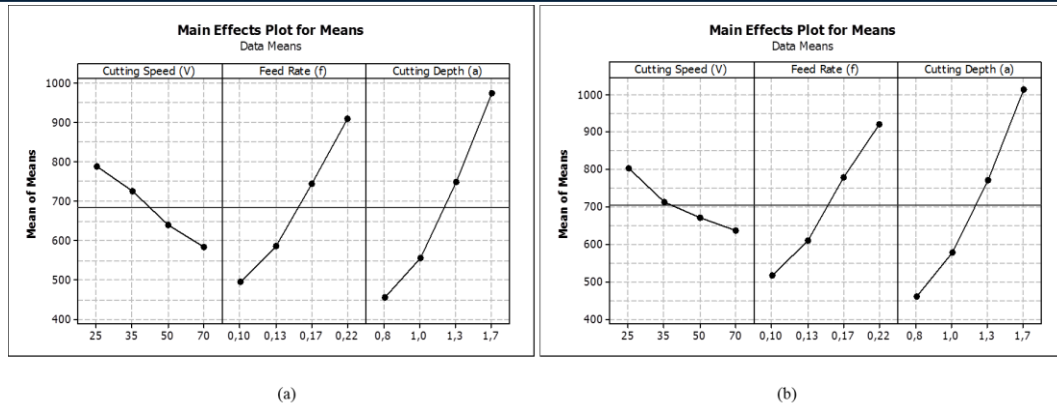
Figure 53. Average effect graph derived for forces (a) Experiments used chip breakers (b) Experiments without chip breakers

When the graphs obtained separately for the cutting conditions with chip breaker and without breaker are examined, it is seen that the cutting forces variety according to the cutting parameters are similar. A decrease in cutting forces was observed with increasing cutting speeds. Decreasing the cutting forces with increasing cutting speeds is explained by the decrease in the contact area of the cutting tool cutting surface due to the temperature increase and partly the decrease of the sliding resistance in the flow region [3,13]. In addition, the friction values at the tool-chip interface decrease with increasing temperature, which is a positive result [14]. On the contrary, in the case of increasing feed rate and chip depth, an exact opposite situation was observed and the increase of these two parameters has increased the forces. As the advance rate increases, the amount of chips raised per unit cycle also increases, so that the forces are also increased with increasing feed rate [3]. With increased chip depth, the tool-to-chip contact length increases, and this increases the area of the cutting plane, thus increasing the strength [2, 3].

From the point of view of force formation, Figure 6 shows that chip depth and feed rate are the most effective parameters in experiments made on crushed and unbreakable conditions.

Signal / Noise graphics help to determine the ideal cutting conditions for forces. When the Signal / Noise graphics designed for the smallest and best methods with breaker and without breaker conditions were examined the ideal cutting parameters were found to be 70 m / min for the cutting speed, 0,10 mm / rev for the feed rate and 0,8 mm for the depth of cut for both groups of experiments.
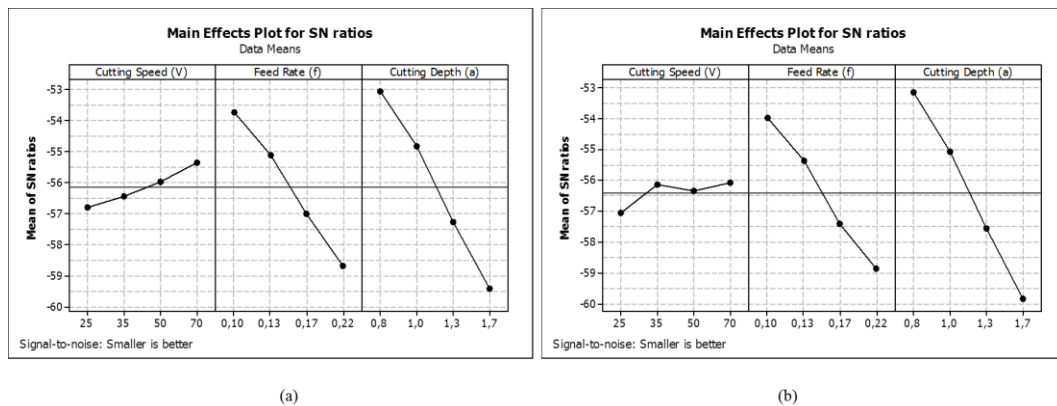
Figure 54. Signal Noise graph derived for forces (a) Experiments used chip breaker (b) Experiments without chip breaker

3.2. Evaluation of Temperature Data

For each experiment carried out with breaker and without breaker, the temperature was measured during the same cutting cycle. The graphic created by the temperature data as a result of the measurements is presented in Figure 7. When the graph is examined, lower temperature values are measured in all of the experiments made with the breaker. It is known that as much as 80% of the heat generated during cutting is thrown by chipping. It is estimated that the air flow caused by the machining effectively by the breaker and the turning of the chip breaker wheel at a certain speed is also effective in decreasing the temperature.

When examining the test data, it is seen that dynamic chip breaker gives an advantage of up to 15% in all experiments.
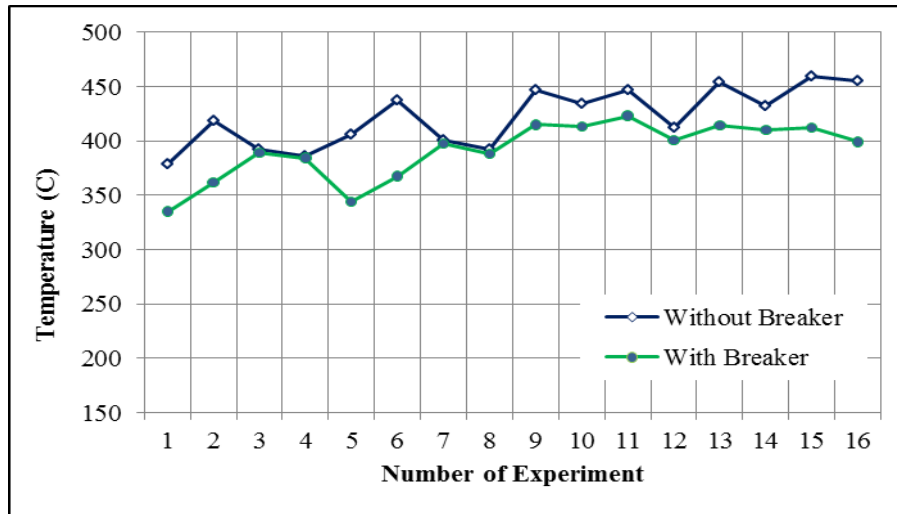
Figure 55. Comparison of temperature values

The main effect graphs are used to explain the effect of the cutting parameters on the temperature .
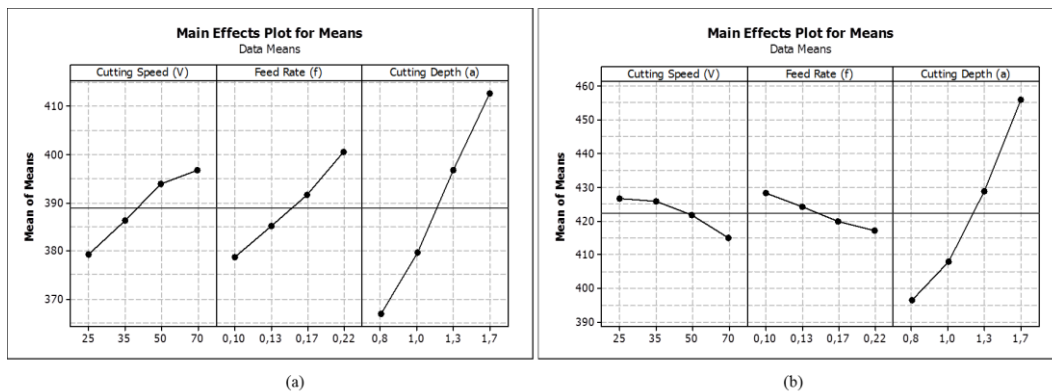
Figure 56. Average effect plot derived for temperature value (a) Experiments used chip breaker (b) Experiments without chip breaker

Experiments carried out by using chip breakers show that the temperature increases with increasing cutting parameters. As the amount of deformed material increased with increasing cutting speed and feed rate, the increase of the advance increased the temperature values. Similarly, with increased chip depth, temperatures have increased. The temperature value also increased due to the amount of deformation increasing with chip depth.

Experiments without chip breaker showed a decrease in temperature with increasing cutting speed and progress ratio. Failure to remove the continuous chipping from the cutting zone results in higher temperatures at low cutting speed and feed rate values. At increased cutting speeds and feed rates, the chip was not broken but flowed away from the cutting zone. Refraction of the chips is reflected as a decrease in temperature.

For the resulting temperature, when Signal / Noise graphics that are designed according to the smallest is the best method are examined it was determined that the ideal cutting parameters were a cutting speed of 25 m / min, a feed rate of 0,10 mm / rev and a chip depth of 0,8 mm in the experiments made with chip breaking device. In the case of work without a breaker, the optimum cutting parameters were found to be cutting speed 70 m / min, feed rate 0.22 mm / rev and chip depth 0.8 mm. In the changing ideal conditions, continuous chipping was also effected.
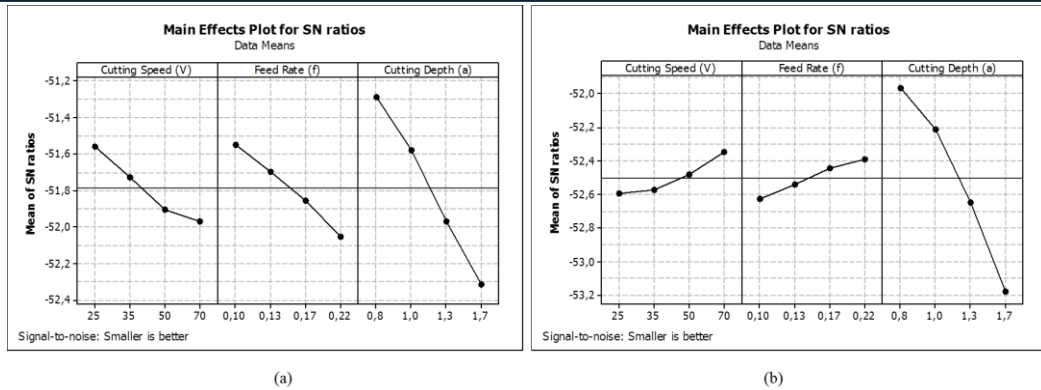
Figure 57. Signal noise figure derived for temperature value (a) Experiments used chip breaker (b) Experiments without chip breaker

3.3. Evaluation of Chip Images

In the experimental studies made, continuous chip formation was observed in all of the experiments without using the breaker. In all of the experimental groups where the chip breaker apparatus was used, it was determined that the continuous chip was broken effectively.

It is known that the high cutting depth, high feed rate and low cutting speed of the chip increase the friability. In these parameters, where the fracture of the chip is the highest, chip saws obtained as a result of the tests performed with chip breaker and without chip breaker are given in Figure 10.

Figure 58. Chip image of test parameters 14

As seen in Figure 10, continuous chipping formation of 3 m in length was observed in non-breaker experiments at a cutting speed of 35 m / min, a feed rate of 0.17 mm / rev and a depth of 1.7 mm. In the experiments with breaker carried out under the same cutting parameters, the chip was found to be broken effectively.
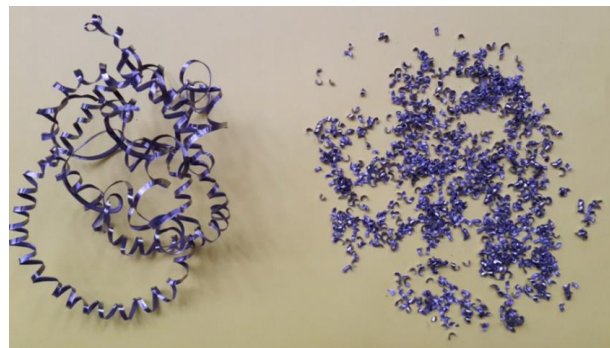
Figure 59. Chip visual of test parameters 6

Turbulent chipping structure which is formed in the experiments by using cutting depth 35 m / min, feed rate 0.10 mm / rev and 1 mm chip depth conditions is seen in the Figure 11. Low chip depths and turbulent chippings formed under low feed conditions negatively affected surface quality. In the same cutting conditions, it was seen that the chip was broken successfully in the experiments using the breaker.

In terms of chip fragility, the breaker has demonstrated a successful performance.

4. CONCLUSIONS

• The chip breaker has been found to break the chips effectively under all conditions.

• The most effective parameter for temperature values has been found to be chip depth.

• It has been determined that temperature values increase with increasing cutting speed, feed rate and chip depth.

• It has been seen that the continuous chipping reduce cutting efficiency by keeping the temperature in the cutting zone.

• Breaker apparatus provided an improvement up to 15% on the temperature.

• Increased cutting speeds have been shown to reduce forces.

• It is determined that cutting forces are increased with increased feed rate and chip depth.

• It has been determined that the progress rate and chip depth are the most effective parameters in terms of forces.

• An improvement of 3 - 11% on the forces was achieved with the breaker.

• It has been determined that the breaker has positive effects on cutting forces and temperatures.

REFERENCES

[14]. H. A. Yanda, G. Jaharah, C. H. C. Haron, "Effect of rake angle on stress, strain and temperature on the edge of carbide cutting tool in orthogonal cutting using fem simulation", *ITB J. Eng. Sci.,* 42 (2), 179-194. 2010.

[15]. Y. Ozcatalbas, "Muhendislik Malzemelerinin İslenebilirligi", Yüksek Lisans Ders Notu, Gazi Üniversitesi, Ankara, 2014.

[16]. U. Seker, "Kesici Takım Tasarımı", Ders Notu, Gazi Üniversitesi Teknoloji Fakültesi, Ankara, 22-45. 2008.

[17]. M. P. Groover, *Fundamentals Of Modern Manufacturing- Materials, Processes And Systems*, Prentice-Hall Inc., New Jersey, 1996.

[18]. B. Yılmaz, S. Karabulut ve A. Güllü, "AISI 304 Paslanmaz Celigin Tornalanması Esnasında Kullanılan Dinamik Talas Kırıcının Yüzey Pürüzlülügü Üzerine Etkilerinin Arastırılması" *7. Uluslararası Talaslı İmalat Sempozyumu (UTİS, 2016)*, İstanbul, 3-5 Kasım, 2016.

[19]. I.S. Jawahir, "Asurvey and Future Predictions For the Use Of Chip Breaking In Unmanned System", *Journal of Advenced Manufacturing Technology*, 3(4), 87-104. 1988.

[20]. H.G. Kim, J.H. Sim and H.J. Kweon, "Performance evaluation of chip breaker utilizing neural network", *Journal of Materials Processing Technology*, 209, 647–656, 2009.

[21]. E. O. Ezugwu and J. Bonney, "Effect Of High- Pressure Coolant Supply when Machining Nickel-Base, Inconel 718, Alloy with Coated Carbide Tools," *Journal of Materials Processing Technology*, 153–154, 1045–1050, 2004.

[22]. O. Colak, "Investigation on machining performance of Inconel 718 under high pressure cooling conditions", *Stroj. Vestnik/Journal Mech. Eng*, 58 683–690, 2012.

[23]. M. Nakamura, Y. Mitani, S. Asakura and T. Shibuya, "The Development of Chip Parting Processing Technology Oscillatory Feed Cutting," *JSAE Review* 21: 555-559, 2000.

[24]. Y.H. Shane, I. Markus and J. Woo-cheol, "New Cooling Approach and Tool Lifimprovement in Cryogenic Machining of Titanium Alloy Ti-6Al-4V," *International Journal of Machine Tools & Manufacture*, 41, 2245-2260, 2001.

[25]. A. Güllü, and S. Karabulut, "Dynamic Chip Breaker Design for Inconel 718 Using Positive Angle Tool Holder," *Materials and Manufacturing Processes*, 23, 852–857, 2008.

[26]. W. Chen, "Cutting forces and surface finish when machining medium hardness steel using CBN tools", *International Journal of Machine Tools & Manufacture*, vol. 40, pp. 445-466. 2000.

[27]. J. Zhao, X. Ai and Z. Li, "Finite element analysis of cutting forces in high speed machininig", *Materials Science Forum*, vol. 532-533, pp. 753-756, 2006.

Thermodynamic Analyses and Comparison of Various Geothermal Power Plant Configurations

Hasan Ozcan[1], Mutlu Tekir[2]

Abstract

Geothermal energy is one of the most abundant renewable and clean energy forms and its use sıgnıfıcantly ıncreases by exploration of new sources. In this research three geothermal power configurations are examined, namely a single flash cycle, a double flash cycle, and a binary geothermal system with organic Rankine cycle using R600a. Energy and exergy analyses of all configurations are examined using Engineering Equation Solver (EES) software package, furthermore the results are compared and highest efficient cycle is chosen between these there configurations. Both energy and exergy efficiencies of the binary cycle is superior than those of the single and double flash options at both with and without reinjection of the geothermal fluid.

Keywords: *Geothermal Energy, Flash System, Reinjection, R600a.*

1. INTRODUCTION

The world is facing an increasing demand for energy. To meet this demand, fossil fuels still take an important place. However the carbon emissions from fossil fuels threaten the eco system increasingly day by day and it is culpable for global warming. In order to reduce energy problems and conserve the environment, carbon emissions must be lowered. To achieve this aim, many researches has been studied to utilize renewable energy and waste heat to generate power [1],[2]. Among renewable energy sources, geothermal energy is the most liable and the most available, because it isn't dependent on weather conditions. During the past 20 years, several thermodynamic cycles have been introduced and studied [3].

Temperatures of available geothermal water range between 353K and 623K. The quality of a geothermal resource related to their specific exergy. Dry vapor is fed into the turbine directly in high quality resources of which the temperature is above 450K. However below 450K is low or medium quality resource binary power cycles are being used. Thermal energy of the geothermal water is transferred to a working fluid [4].

Aali et al. [5] in their study developed binary geothermal system working with R141b and then compared with single flash and double flash systems. Likewise Pambudi et. al. [6] investigated double flash system instead of an existed single flash power plant. They found that power output of a proposed double flash system would increase 20% compared to the existing single flash system. Manente et al. [7] studied single and dual pressure layouts of Organic Rankine Cycles, and compared these output gains at various geothermal water temperatures.

Zhao and Wang [8] studied combined flash-binary geothermal system. They researched Organic Rankine Cycle subsystem with R123 and did parametric study of flash pressure, ORC turbine inlet pressure and temperature. Yılmaz et. al. [9] researched combines flash-binary geothermal system, and they used the work output to produce hydrogen. Also they analyzed the system exergoeconomically. Zeyghami [10] investigated suitable working fluid for the combined flash-binary geothermal power cycle. Performances of thirty different working fluids which are environmental friendly refrigerants and hydrocarbons were compared for the cases using geothermal water of which temperature ranges between 150 and 200 ºC. Shokati et. al. [11] researched the double flash system and the single flash, Organic Rankine Cycle combined systems and compared them both thermodynamically and exergoeconomically. They found that first law and exergic efficiency is higher in combined cycle, but minimum unit cost of the produced power is lower in the double flash system.

[1] Corresponding author: Karabük University, Department of Mechanical Engineering, 78050, Karabük, Turkey. hasanozcan@karabuk.edu.tr

[2] Karabük University, Department of Mechanical Engineering, 78050, Karabük, Turkey. mutlutekir@karabuk.edu.tr

Geothermal energy is the least expensive renewable energy source and abundant. In this study single flash, double flash, and binary geothermal plant configurations are examined by energy and exergy efficiencies that are solved relevant equations by EES software.

2. SYSTEMS DESCRIPTION

In geothermal power plants geothermal water should be reinjected into the well after using its energy in the plant. In geothermal wells steam or hot pressurized water is produced, so to utilize this energy Rankine cycle is needed to be used. Today three main technologies are used to utilize energy from geothermal systems: Dry steam power plants, Flash steam power plants, Binary power plants. Dry steam geothermal systems use high temperature, vapor dominant reservoirs. Steam from the well directly passes through turbine unit. Flash geothermal systems are used if the geothermal well produces liquid dominant mixture. In single flash system the mixture from the well is separated into liquid and gas phases in a separator, and vapor is sent to the turbine to utilize energy [12].
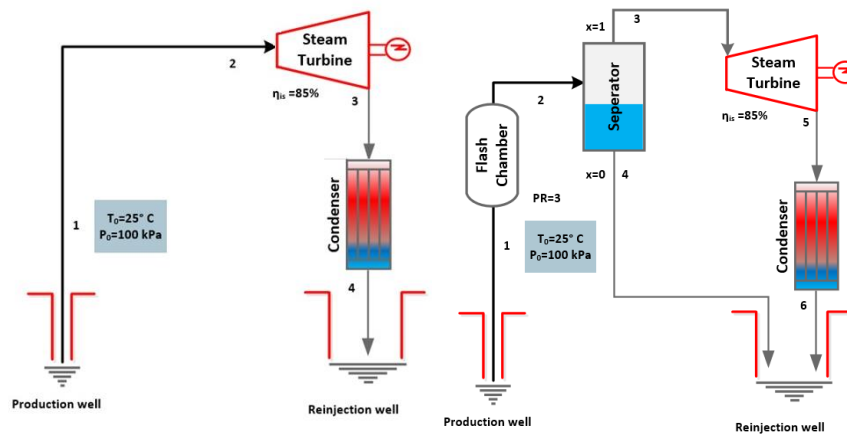
Figure 1. Schematics of the dry steam system (at left) and the single-flash system (at right) with input data.

In double flash system water at the first separator goes into the flash chamber. Produced low pressure vapor is separated second time, and sent to the low pressure turbine. Because of more energy utilization, double flash systems obtain more power. Binary systems are used if the water temperature in the reservoir is below 150ºC. In these plants the second working fluid, other than the geothermal water, crosses a closed cycle, and receives energy from the geothermal water through heat exchanger. This closed system generally is Kalina or Organic Rankine Cycle [12].
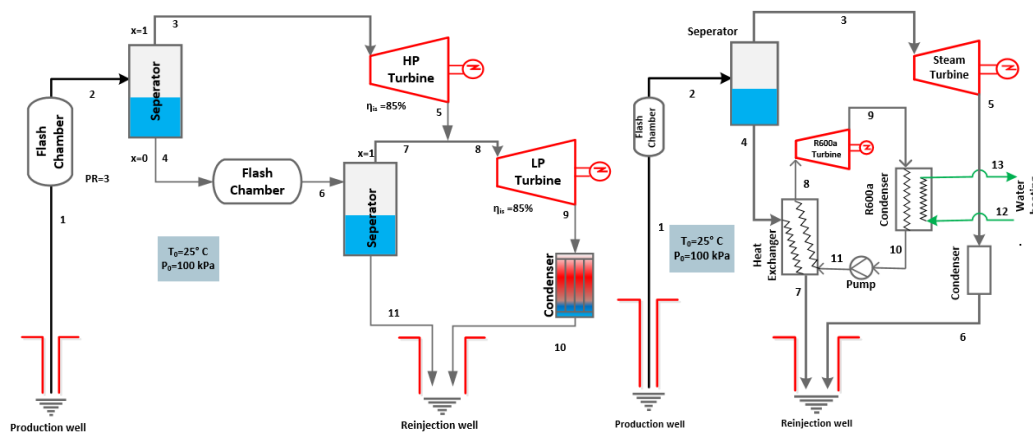
Figure 2. Schematics of the double-flash system (at left) and the combined flash-binary geothermal system (at right) with input data.

3. ANALYSES AND ASSESSMENT

The mass, energy, entropy and exergy balances are required in the first step of the exergy analysis to determine the heat input/output, entropy generation rate, exergy destructions, and energy and exergy efficiencies. The mass balance equation for a steady-state condition is as follows;

$$\sum \dot{m}_{in} = \sum \dot{m}_{out} + \frac{dm_{CV}}{dt} \tag{1}$$

where the second definition at the right side is cancelled when the flow is steady. Energy balance of a system can be defined by considering all forms of energy within a system;

$$\Delta E_{sys} = m\Delta e_{sys} = m\left[\left(u_{out} + \frac{1}{2}v_{out}^2 + gz_{out}\right) - \left(u_{in} + \frac{1}{2}v_{in}^2 + gz_{in}\right)\right] \tag{2}$$

where u stands for internal energy, v is velocity of the corresponding flow, g is gravity and z is height. Energy of a non-flowing thermodynamic system is defined as;

$$e = u + \frac{1}{2}v^2 + gz \tag{3}$$

Total energy of a flowing matter can be defined as sum of non-flow energy and flow work;

$$\theta = e + Pv \tag{4}$$

Energy balance of an open system can now be defined as follows;

$$\sum_{in} \dot{m}\theta + \sum \dot{Q}_{in} + \sum \dot{W}_{in} = \sum_{out} \dot{m}\theta + \sum \dot{Q}_{out} + \sum \dot{W}_{out} + \left[\frac{d(me)}{dt}\right]_{sys} \tag{5}$$

where the fourth definition at the right side is cancelled when the flow is steady. When kinetic and potential energies are cancelled, the sum of internal energy and the flow work correspond to enthalpy of the individual stream. Entropy balance of an open system can be expressed in rate form as sum of entropy input and generated entropy, and is equal to sum of entropy of output and change of control volume entropy as follows;

$$\sum \dot{S}_{in} + \dot{S}_{gen} = \sum \dot{S}_{out} + \frac{dS_{sys}}{dt} \tag{6}$$

If there is heat transfer across the boundary of a control volume, then the balance equation becomes;

$$\sum_{in} \dot{m}s + \sum_{in} \int \frac{d\dot{Q}}{T} + \dot{S}_{gen} = \sum_{out} \dot{m}s + \sum_{out} \int \frac{d\dot{Q}}{T} + \left[\frac{d(S)}{dt}\right]_{CV} \tag{7}$$

Above equation can be further simplified by considering a steady and adiabatic process;

$$\sum_{in} \dot{m}s + \dot{S}_{gen} = \sum_{out} \dot{m}s \tag{8}$$

Exergy of a non-flow system is sum of all forms of exergy, and flow exergy is sum of non-flow exergy and flow work as expressed below;

$$Ex_{nf} = Ex_{ph} + Ex_{kin} + Ex_{pot} + Ex_{ch} \tag{9}$$

$$Ex_{nf} + (P - P_0)V \tag{10}$$

Physical exergy of any stream is expressed as;

$$Ex_{ph} = (U - U_0) + P_0(V - V_0) - T_0(S - S_0) \tag{11}$$

Here, U, V, and S are internal energy, volume, and entropy of a closed system, respectively. Kinetic and potential energies are associated directly with work, which remains the same in exergy definition as expressed in energy balance definitions. For a control volume, exergy balance of a system can now be expressed as;

$$\sum_{in}\left[\dot{W} + \dot{m}ex + \dot{E}x^Q\right] = \sum_{in}\left[\dot{W} + \dot{m}ex + \dot{E}x^Q\right] + \frac{dEx}{dt} - \frac{P_0(dV_{CV})}{dt} + \dot{E}x_d \tag{12}$$

Ex_d is the exergy destruction and it's associated with the entropy generation rate as follows;

$$\dot{E}x_d = T_0\dot{S}_{gen} \tag{13}$$

Thermal exergy is associated with the corresponding heat transfer;

$$\dot{E}x^Q = \left(1 - \frac{T_0}{T}\right)\dot{Q} \tag{14}$$

It should be noted that the second and the third definitions in Eq. 12 are cancelled when the system is steady flow. One can now perform efficiency assessments based on energy and exergy of any system by simply considering inputs and outputs to and from the system. Energy and exergy efficiencies are expressed in a general form as follows:

$$\eta_{en} = \frac{Useful\ output}{Total\ input} \tag{15}$$

$$\eta_{ex} = \frac{Ex_{useful}}{Ex_{in}} = 1 - \frac{\dot{Ex}_d}{Ex_{in}} \qquad\qquad (16)$$

Further efficiency definitions can be made by considering geothermal plants with and without reinjection. If reinjection is present, the total energy and exergy input for energy production is considered as the difference between the fluid from the well and the reinjected geothermal fluid. Without reinjection, the total input is taken solely as the geothermal fluid extracted from the injection well. Table 1 summarizes the assumed data for all studied systems.

Table 1. Input data for the studied configurations

	Input data	Unit	Value
Single Flash Cycles	Geothermal fluid temperature	°C	220
	Geothermal fluid mass flow rate	kg/s	200
	Turbine outlet pressure	kPa	10
	Turbine isentropic efficiency	-	0.85
	Flash chamber pressure ratio	-	3
Double Flash Cycle	Geothermal fluid temperature	°C	220
	Geothermal fluid mass flow rate	kg/s	200
	Turbine outlet pressure	kPa	10
	Turbine isentropic efficiency	-	0.85
	Flash chamber pressure ratio	-	2
Binary Cycle	Approach temperature	°C	10
	R600a condenser effectiveness	-	0.85
	Water heating	°C	15 to 60

4. RESULTS AND DISCUSSION

For the given schematics of the problem, state point information of all plant configurations are given in Tables 2-4. Here, tables suggest a significant decrease in the exergy content of the reinjected fluid starting from single flash to binary cycle. This is due to high rate of geothermal energy utilization at double flash and binary configurations, which is expected that these cycles are expected to be more efficient.

Table 2. State point information for the single flash geothermal plant.

State	$\dot{m}$ (kg/s)	T (C)	P (kPa)	h (kJ/kg)	s (kJ/kgK)	x (-)	ex (kJ/kg)	$\dot{Ex}$ (kW)
0	N/A	25	100	104.8	0.3669	Liquid	0	0
1	200	220	2318	943.5	2.518	0	197.8	39558
2	200	169	772.6	943.5	2.549	0.11	188.3	37667
3	177.7	169	772.6	2767	6.674	1	783	17440
4	22.27	169	772.6	714.9	2.032	0	113.8	20227
5	22.27	45.82	10	2212	6.982	0.84	135.6	3021
6	200	45.82	10	191.8	0.6493	0	2.857	63.64

Table 3. State point information for the double flash geothermal plant.

State	m (kg/s)	T (C)	P (kPa)	h (kJ/kg)	s(kJ/kgK)	x (-)	ex (kJ/kg)	$\dot{Ex}$ (kW)

0	N/A	25	100	104.8	0.3669	Liquid	0	0
1	200	220	2318	943.5	2.518	0	197.8	39558
2	200	186.4	1159	943.5	2.532	0.07623	193.5	38699
3	15.25	186.4	1159	2783	6.535	1	840.3	12810
4	184.8	186.4	1159	791.7	2.202	0	140.1	25889
5	15.25	157.5	579.5	2673	6.58	0.9605	716.2	10919
6	184.8	157.5	579.5	791.7	2.213	0.0607	136.9	25285
7	11.22	157.5	579.5	2755	6.772	1	741.7	8318
8	26.46	157.5	579.5	2708	6.661	0.9772	727	19237
9	26.46	45.82	10	2199	6.943	0.8392	134.8	3567
10	26.46	45.82	10	191.8	0.6493	0	2.857	75.6
11	173.5	157.5	579.5	664.8	1.918	0	97.77	16968

Table 4. State point information for the binary geothermal plant.

State	Ref	m (kg/s)	T (C)	P (kPa)	h (kJ/kg)	s(kJ/kgK)	x (-)	ex (kJ/kg)	$\dot{E}x$ (kW)
0	Water	NA	25	100	104.8	0.3669	NA	0	0
00	R600a	NA	25	100	599	2.515	NA	0	0
1	Water	200	220	2318	943.5	2.518	0	197.8	39558
2	Water	200	169	772.6	943.5	2.549	0.1114	188.3	37667
3	Water	22.27	169	772.6	2767	6.674	1	783	17440
4	Water	177.7	169	772.6	714.9	2.032	0	113.8	20227
5	Water	22.27	45.82	10	2212	6.982	0.8445	135.6	3021
6	Water	22.27	45.82	10	191.8	0.6493	0	2.857	63.64
7	Water	177.7	45.4	772.6	190.8	0.6435	0	3.508	623.4
8	R600a	150	159	2700	814.1	2.688	sh	163.8	24573
9	R600a	150	104	450	738.8	2.723	sh	77.87	11683
10	R600a	150	33.84	450	281.4	1.279	0	50.9	7637
11	R600a	150	35.4	2700	286.3	1.281	cl	55.09	8266
12	Water	309.9	15	110	63.02	0.2242	cl	0.7062	218.9
13	Water	309.9	60	110	251.2	0.8311	Cl	8.053	2496

* cl: compressed liquid, sh: superheated

Considering the inpust data and base case studies, it is easy to calculate efficiencies based on the equations given in Eqs. (15) and (16). For the single flash cycle, the energy and exergy efficiencies without regeneration are;

$$\eta_{en} = \frac{\dot{W}_{tur}}{\dot{E}_1} = \frac{12378\ kW}{200\ kgs^{-1}x943.5\ kJkg^{-1}} = 6.56\% \tag{17}$$

$$\eta_{ex} = \frac{\dot{W}_{tur}}{\dot{E}x_1} = \frac{12378\ kW}{39558\ kW} = 31.29\% \tag{18}$$

The energy and exergy efficiencies with regeneration are;

$$\eta_{en} = \frac{\dot{W}_{tur}}{\dot{E}_1-\dot{E}_4-\dot{E}_6} = \frac{12378\ kW}{200\ kgs^{-1}x943.5\ kJkg^{-1}-177.7\ kgs^{-1}x714.9\ kJkg^{-1}-22.27\ kgs^{-1}x191.8\ kJkg^{-1}} = 21.58\% \tag{19}$$

$$\eta_{ex} = \frac{\dot{W}_{tur}}{\dot{E}x_1-\dot{E}x_1-\dot{E}x_1} = \frac{12378\ kW}{(39558-20227-63.64)kW} = 64.24\% \tag{20}$$

For the double flash cycle, the energy and exergy efficiencies without regeneration are;

$$\eta_{en} = \frac{\dot{W}_{tur}}{\dot{E}_1} = \frac{15137\ kW}{200\ kgs^{-1}x943.5\ kJkg^{-1}} = 8.02\% \tag{21}$$

$$\eta_{ex} = \frac{\dot{W}_{tur}}{\dot{E}x_1} = \frac{15137\ kW}{39558\ kW} = 38.27\% \tag{22}$$

The energy and exergy efficiencies with regeneration are;

$$\eta_{en} = \frac{\dot{W}_{tur}}{\dot{E}_1-\dot{E}_{10}-\dot{E}_{11}} = \frac{15137\ kW}{200\ kgs^{-1}x943.5\ kJkg^{-1}-173.5\ kgs^{-1}x664.8\ kJkg^{-1}-26.46\ kgs^{-1}x191.8\ kJkg^{-1}} = 22.18\% \tag{23}$$

$$\eta_{ex} = \frac{\dot{W}_{tur}}{\dot{E}x_1-\dot{E}x_{10}-\dot{E}x_{11}} = \frac{12378\ kW}{(39558-16968-75.6)kW} = 67.23\% \tag{24}$$

Finally for the binary cycle energy and exergy efficiencies can be defined as;

$$\eta_{en} = \frac{\dot{W}_{net}+\dot{Q}_{RWH}}{\dot{E}_1} = \frac{22940\ kW+58328\ kW}{200\ kgs^{-1}x943.5\ kJkg^{-1}} = 43.07\% \tag{25}$$

$$\eta_{ex} = \frac{\dot{W}_{tur}+\dot{E}x_{RWH}}{\dot{E}x_1} = \frac{22940\ kW+2277\ kW}{39558\ kW} = 63.75\% \tag{26}$$

The energy and exergy efficiencies with regeneration are;

$$\eta_{en} = \frac{\dot{W}_{tur}+\dot{Q}_{RWH}}{\dot{E}_1-\dot{E}_{10}-\dot{E}_{11}} = \frac{22940\ kW+58328\ kW}{188702\ kW-38177\ kW} = 53.99\% \tag{27}$$

$$\eta_{ex} = \frac{\dot{W}_{tur}+\dot{E}x_{RWH}}{\dot{E}x_1-\dot{E}x_7-\dot{E}x_6} = \frac{22940\ kW+2277\ kW}{(39558-623.4-63.64)kW} = 63.76\% \tag{28}$$

It should be noted that the efficiency measures with regeneration is more meaningful since the unused energy is reinjected to the well for future use. The exergy content of unused liquid at state 4 is significant. Therefore, multi flash options are expected to be more efficient than those of the single flash configuration. Pressure ratio is one of the main input of the system where it has influencing effect on system performances. A parametric illustration presented in Figure 3 depicts that increased pressure ratio is favorable for enhanced energy and exergy efficiencies without reinjection while it decreases the exergy efficiency for both efficiency definitions made considering reinjection.

Compared to the single flash geothermal power plant configuration, both energy and exergy efficiencies are significantly increased by just utilizing the unused stream (*state 4* in single flash operation). A triple flash option is expected to enhance both energy and exergy efficiencies. The multiple flash plants are configured to utilize the excess geothermal energy and more feasible options than that of the conventional single flash plants. Figure 4 represents that, the pressure ratio effect is proportional to that of the single flash configuration, where both efficiencies are showing the same trend.
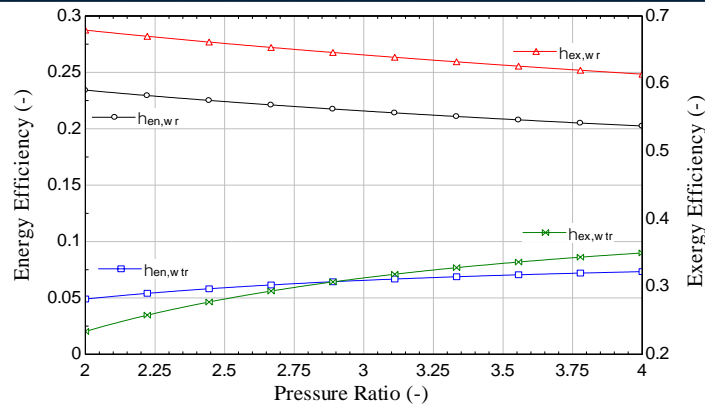
Figure. 3 Pressure ratio effect on energy and exergy efficiencies in single flash system.
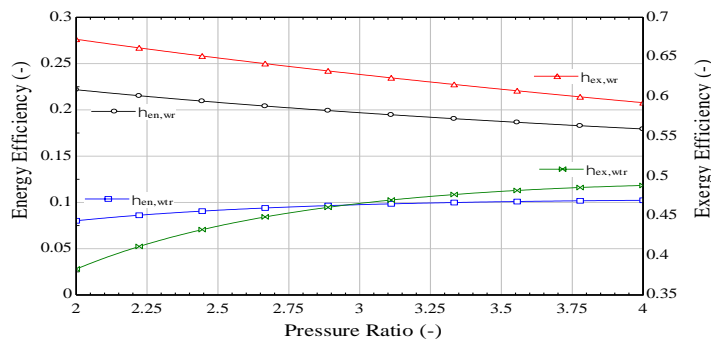
Figure 4. Pressure ratio effect on energy and exergy efficiencies in double flash system.
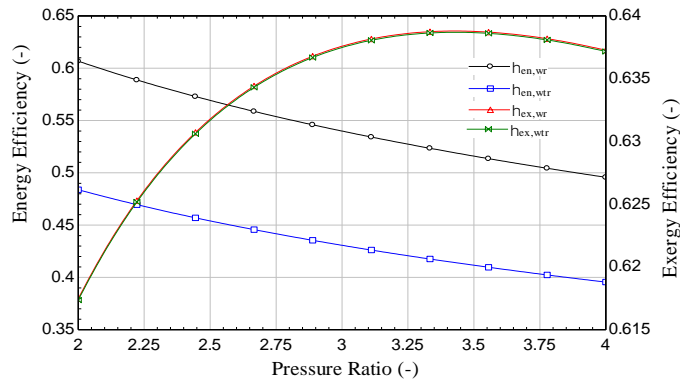
Figure 5. Pressure ratio effect on energy and exergy efficiencies in double flash system.

A parametric study is also conducted for the binary cycle by again varying the pressure ratio in the flash chamber. A tremendous amount of energy is recovered by the co-generation in the ORC condenser, resulting in enhanced energy and exergy performances. Here, it should be noted that exergy content of the reinjected fluid is very small in this configuration that does not make much difference in exergy efficiencies at with and without reinjection definitions.

A significant increase in the energy efficiency with regeneration is obtained due to decreased input energy content while this change is almost negligible for the exergy efficiency. This is due to very low exergy content of the reinjected streams that may be interpreted as a very successful energy conversion is accomplished with this cogeneration plant. Figure 6 represents the superiority of the cogeneration plant. Even though the cogeneration option wouldn't be considered, the net power production is also superior to those of single and double flash configurations. In terms of exergy efficiencies with reinjection, all configurations represent similar exergy efficiencies. This proves the qualitative assessment capability of exergy analysis, which does not only consider the quantitative amounts of energy forms, also their quality is taken into account.
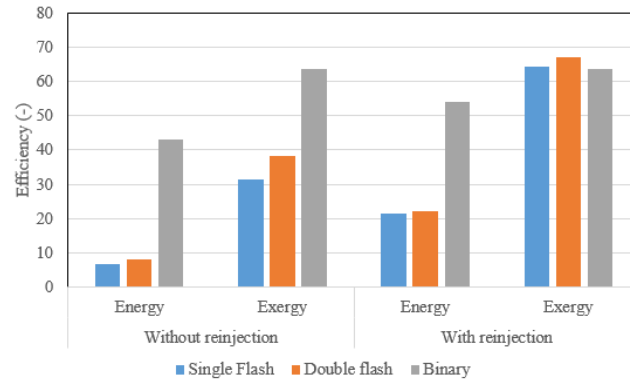
Figure 6. Comparison of geothermal power configurations.

5. CONCLUSION

In this study energy and exergy efficiencies of single flash, double flash, and binary geothermal power systems are investigated and compared. Efficiencies of single and double flash systems with reinjection decrease with increasing pressure ratio, on the other hand, efficiencies of single and double flash systems without reinjection increase with increasing pressure ratio. Combined flash and binary geothermal system with and without reinjection has same exergy efficiency values due to very low energy content of reinjected geothermal water. Among all configurations, combined flash and binary geothermal system with ORC subsystem using R600a has the highest energy and exergy efficiencies. Further parametric studies can also be applied for optimized configurations.

REFERENCES

[1]. Syed, H., Qureshi, S. R., Khan, W. A., Exergetic and Energetic Analysis of Power Generation from Geothermal Resources in Pakistan, Proceedings World Geothermal Congress 2015, Melbourne, Australia, 19-25 April 2015.

[2]. Akbari, M., Mahmoudi, S. M. S., Yari, M., Rosen, M. A., Energy and Exergy Analyses of a New Combined Cycle for Producing Electricity and Desalinated Water Using Geothermal Energy, Sustainability, Vol. 6, pp. 1796-1820, 2014.

[3]. Shi, X., Che, D., A Combined Power Cycle Utilizing Low-Temperature Waste Heat and LNG Cold Energy, Energy Conversion Management, Vol. 50, pp. 567–575, 2009.

[4]. Heberle, F., Brüggemann, D., Exergy Based Fluid Selection for a Geothermal Organic Rankine Cycle for Combined Heat and Power Generation, Applied Thermal Engineering, Vol. 30, pp. 1326-1332, 2010.

[5]. Aali, A., Pourmahmoud, N., Zare, V., Exergoeconomic Analysis and Multi-Objective Optimization of a Novel Combined Flash-Binary Cycle for Sabalan Geothermal Power Plant in Iran, Energy Conversion and Management, Vol. 143, pp. 377–390, 2017.

[6]. Pambudi, N. A., Itoi, R., Jalilinasrabady, S., Jaelani, K., Performance Improvement of a Single-Flash Geothermal Power Plant in Dieng, Indonesia, upon Conversion to a Double-Flash System Using Thermodynamic Analysis, Renewable Energy, Vol. 80, pp. 424-431, 2015.

[7]. Manente, G., Lazzaretto, A., Bonamico, E., Design Guidelines for the Choice between Single and Dual Pressure Layouts in Organic Rankine Cycle (ORC) Systems, Energy, Vol. 123, pp. 413-431, 2017.

[8]. Zhao, Y., Wang, J., Exergoeconomic Analysis and Optimization of a Flash-Binary Geothermal Power System, Applied Energy, Vol. 179, pp. 159–170, 2016.

[9]. Yilmaz, C., Kanoglu, M., Abusoglu, A., Exergetic Cost Evaluation of Hydrogen Production Powered by Combined Flash-Binary Geothermal Power Plant, International Journal of Hydrogen Energy, Vol. 40, pp. 14021-14030, 2015.

[10]. Zeyghami, M., Performance Analysis and Binary Working Fluid Selection of Combined Flash-Binary Geothermal Cycle, Energy, Vol. 88, pp. 765-774, 2015.

[11]. Shokati, N., Ranjbar, F., Yari, M., Comparative and Parametric Study of Double Flash and Single Flash/ORC Combined Cycles Based on Exergoeconomic Criteria, Applied Thermal Engineering, Vol. 91, pp. 479-495, 2015.

[12]. Melikoglu, M., Geothermal Energy in Turkey and Around The World: A Review of the Literature and an Analysis Based on Turkey's Vision 2023 Energy Targets, Renewable and Sustainable Energy Reviews, Vol. 76, pp. 485–492, 2017.

Probabilistic Approach to Solar Radiation Modelling

Fatih Onur HOCAOGLU[1], Fatih SERTTAS[2]

Abstract

Solar radiation prediction and modeling techniques have an important place in solar energy engineering. There are numerous studies in the literature for estimating and modeling solar energy. Many of these studies anticipate future data, taking into account the history of data and other related meteorological parameters. In this study on the other hand, it is aimed to propose an alternative but successful model for solar radiation. For this aim the data is converted into states with Markov chain approach and then to model the behavior of data state transition probabilities are calculated. Consequently, modeled data behaviors are transformed into a system that generates data using a proposed algorithm. The proposed modeling method was tested on hourly measured and recorded solar radiation data at the main campus of Afyon Kocatepe University. Successful modeling results are obtained and the results are discussed.

Keywords: *Solar Energy, Probabilistic Modeling, Forecasting.*

1. INTRODUCTION

Solar energy studies and investments are increasing day by day in many countries. Turkey has a great solar potential in terms of the location in the world. In today's competitive and dynamic environment, energy supply, demand and prices become increasingly volatile and unpredictable. More and more decision-making processes in the energy industry require a comprehensive view of the uncertain future. Many decision makers rely on probability estimates to measure these uncertainties rather than point estimates. Afyonkarahisar province is also a city with a solar radiation potential above the average of the country [1]. Investors have realized this potential and have increased solar energy investments in the city. One of the feasibility studies that needs to be done before these investments is modeling solar radiation.

Chu et Coimbra (2017) apply the short-term probabilistic estimation methods directly on the normal radiation [2]. By using the probabilistic distribution function and the k-nearest neighbors' technique, they make successful estimations for different weather conditions. Voyant et al. (2017) compare machine learning methods in predicting solar radiation [3]. They also explain that probabilistic estimation gives successful results in their study of the probabilistic Markov chain and Bayesian classification. Grantham et al. (2016) propose a new data-centric method to generate the full intelligent intensity of solar radiation based on nonparametric preloading [4]. New pre-emptive statistical communities shows that Mildura is useful for a probable one-hour forecast in Australia. David et al. (2016) evaluate the performance of two commonly used combinations of linear models (ARMA and GARCH) to provide estimates of solar radiation probability [5]. In addition, a recursive estimate of the model parameters is established to provide a framework that can be easily implemented in the operational context.

Hong et al. (2016) compare the current methods of recent years with 581 participants from 61 countries in the probabilistic energy estimation [6]. They publish the successful results of probabilistic modeling on solar and wind energy issues. The Markov method which is one of the probabilistic processes, is a method used in the wind speed modelling [7] - [9]. A Markov chain contains sequences of random variables. The Markov property only requires serial dependency between adjacent states. For this reason, it can be used to describe systems involving a chain of related events (states). The important feature here is that: The next state of a Markov process is independent only from other states outside the current state. In the literature, different Markov processes are called "Markov chains". However, the term has also been defined as a process with a distinct set of time periods (i.e., discrete-time Markov chain (DTMC)). However, some authors use the same

terminology to specify a continuous timely Markov chain without explicit declaration [10]. Except for a hybrid model available in the literature [11], no solar radiation estimation has been found using only a model based on the Markov chain.

In this study, hourly measured solar radiation data in Afyon Kocatepe University Solar and Wind Energy Research and Application convert into states. According to this states, state transition probability matrix is formed with Markovian process. To generate solar radiation estimation data, cumulative matrix is formed and synthetic solar radiation data is occurred. The aim of this cumulative matrix is choosing the data which has state transition probability. The statistical values of the results of the developed model is compared with the realistic state model formed by measured data.

2. MARKOV CHAIN

Markov (or Markovian) chain of the mathematics is a stochastic process which has the Markov property. Markov property is a random process usually defined as memoryless. This means, the next state is only depending on the actual state not the past states. There can be many applications of the Markov chains as a statistical model of the real world processes.

Markov chain term specifies the order of random variables that progress through a process that defines serial dependency between adjacent Markov properties only (eg, a "chain"). This can be used to describe systems that follow a chain of related events; the events depend only on the current state of the system. The equation of the Markov chain is shown in Equation 1.

$$P(X_{n+1} = j | X_0 = i_0, \dots, X_{n-1} = i_{n-1}, X_n = i)$$

$$P(X_{n+1} = j | X_n = i) = p_{ij}(n) \tag{1}$$

In these equations, $i, j \in S$ and $n \geq 0$, $p_{ij}(n)$ is the transition probability at the n step. The probability of transition p_{ij} is the probability of transition to state j from state i to the state of the next trial j (current state). A Markov chain is an almost memoryless chain. The transition probabilities $p_{ij}(n)$ in step n are placed in a matrix according to Eq. 2 as the columns in the present case and the cases in the future are the columns. Equation 3 also refers to the sum of elements in a row. All possibilities have to have a sum of 1.

$$p(n) = \left[p_{ij}(n) \right]_{i,j \in S} \tag{2}$$

$$\sum_{j \in S} p_{ij}(n) = 1 \tag{3}$$

3. SOLAR RADIATION DATA

In Afyon Kocatepe University Solar and Wind Applications Research Center, global solar radiation data is always recorded in every 10 minutes. The recorded minutely solar radiation data is converted into hourly average data. Therefore, for a year, there are 8760 (365 x 24) solar radiation data. The measured global solar radiation data is represented in Figure 1. As seen on the graphic in Figure 1 solar radiation values ranges from 0 to 1050 W/m².
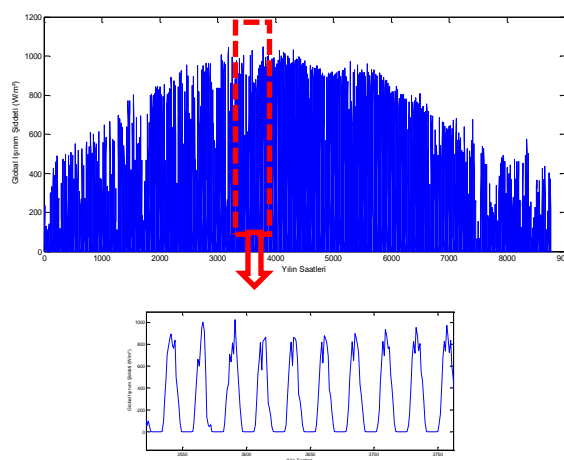
Figure 60. One yearSolar Radiation for Afyonkarahisar

Since these data values are very diverse and have decimal values, it is not possible to reproduce the exact same value of each value. Therefore, the data is converted into situations at regular intervals. Using the Markov chain from the transformed data, a matrix of state transition probabilities is established. This matrix is a square matrix based on the number of cases, depending on the possibilities of going to one another. It is expected that the density in the matrix, in other words, the high transition probabilities, would be close to the diagonal values, and after the studies, this prediction is confirmed as shown in Fig. 2. This proves that the radiation values do not change very rapidly.

4. MATERIALS AND METHODS

4.1. State Transition Probability Matrix

As shown in Table 1, The matrix of state transition probabilities is formed from the states of Afyonkarahisar province solar radiation values as shown in Table 1. In Figure 2, the distribution of the data is presented in 3D.
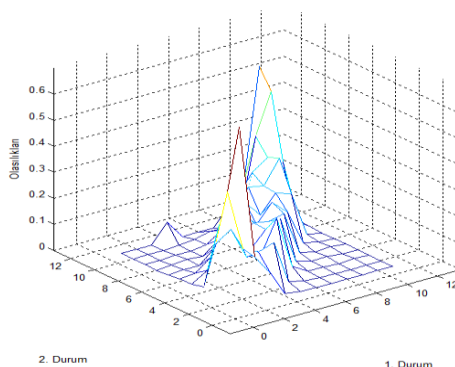
Figure 2. State Transition Probability Matrix

Table 1. State Transition Probability Matrix as a Number Values

States	1.	2	3	4	5	6	7	8	9	10	11
1	0,7	0,2	0,1	0,0	0,0	0,0	0,0	0,0	0,0	0,0	0,0
2	0,4	0,2	0,2	0,2	0,0	0,0	0,0	0,0	0,0	0,0	0,0
3	0,2	0,2	0,1	0,1	0,2	0,0	0,0	0,0	0,0	0,0	0,0
4	0,0	0,2	0,2	0,1	0,2	0,2	0,0	0,0	0,0	0,0	0,0
5	0,0	0,0	0,2	0,2	0,2	0,2	0,2	0,0	0,0	0,0	0,0
6	0,0	0,0	0,1	0,2	0,2	0,1	0,2	0,1	0,0	0,0	0,0
7	0,0	0,0	0,0	0,1	0,2	0,2	0,1	0,2	0,2	0,0	0,0
8	0,0	0,0	0,0	0,0	0,1	0,2	0,2	0,2	0,3	0,0	0,0
9	0,0	0,0	0,0	0,0	0,0	0,0	0,2	0,2	0,3	0,2	0,0
10	0,0	0,0	0,0	0,0	0,0	0,0	0,0	0,1	0,3	0,5	0,0
11	0,0	0,0	0,0	0,1	0,0	0,0	0,0	0,1	0,1	0,6	0,1

4.2. Cumulative Matrix

The cumulative matrix is formed by progressing to the right of each line of the state transition probabilities matrix. The purpose of creating this matrix is to select values that are only probable when making predictions. The 3D plot showing the values of the matrix is given in Figure 3.
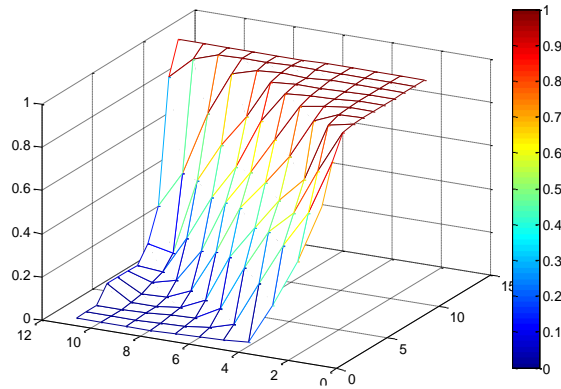
Figure 3. Cumulative Distribution Matrix

4.3. Prediction (Synthetic Data Generation) Algorithm

The prediction algorithm uses the following basic steps.

- Set initial state value.

- Get this value as the row value of the cumulative matrix.

- Randomly generate a number value. (0 to 1)

- Retrieve the value corresponding to the first largest of the number values as the estimate value.

- Save this value as a new vector light state data and assign it as the new starting state.

5. RESULTS AND DISCUSSION

In this study, Markov based probabilistic method is developed and used to model global solar radiation data. Comparison of the predicted and measured state data is shown in Figure 4. The standard deviation, variance, mean value and RMSE value of the data are given in Table 2.
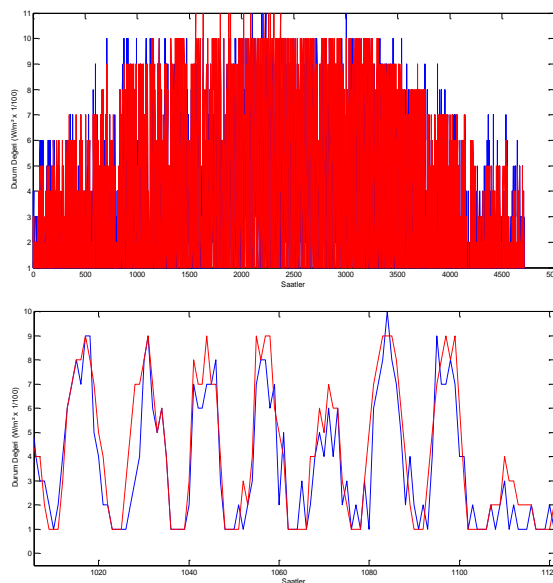
Figure 4. The Comparison of the Data Sequence of the States

In examination of the prediction results depicted in Figure 4, it is clear that event the stochasticity of the data is modelled accurately by the help of proposed methodology.

Table 2. The Comparison of the Statistical Values of Measured and Modelled Data

	Measured States	Modelling States
Standard Deviation	2,9104	2,6526
Variance	8.4705	7.0363
Mean Value	4,1674	3,7167
RMSE (For States)	1,28 (%11,63)	

It is also clear from the comparison of basic statistics of the modelled and measured data that proposed methodology is a good tool with considerable accuracy and can be adopted and used for modelling solar radiation data measured from any region in the world.

6. CONCLUSION

In solar radiation modeling and prediction, probabilistic modeling methods are used in a way that is believed to be correct. The basis of this work was modeling based on Markov processes. Modeling is based on the matrix of transition probabilities between states. The problem is that when the data is generated, the highest probability is not selected and the generated data repeats itself. For this reason, data production has been carried out randomly within the possibilities. The modeling method based on the matrix of state transition probabilities might be improved by adding different parameters in future studies.

ACKNOWLEDGMENT

REFERENCES

[1] "Yenilenebilir Enerji Genel Müdürlügü - Günes Atlası." [Online]. Available: http://www.eie.gov.tr/MyCalculator/pages/3.aspx. [Accessed: 14-Feb-2017].

[2] C. Voyant, G. Notton, S. Kalogirou, M.-L. Nivet, C. Paoli, F. Motte, and A. Fouilloy, "Machine learning methods for solar radiation forecasting: A review," Renew. Energy, vol. 105, pp. 569–582, 2017.

[3] R. Špicar and M. Januška, "Use of Monte Carlo Modified Markov Chains in Capacity Planning," Procedia Eng., vol. 100, pp. 953–959, 2015.

[4] T. Hong, P. Pinson, S. Fan, H. Zareipour, A. Troccoli, and R. J. Hyndman, "Probabilistic energy forecasting: Global Energy Forecasting Competition 2014 and beyond," International Journal of Forecasting, vol. 32, no. 3. pp. 896–913, 2016.

[5] F. O. Hocaoglu, O. N. Gerek, and M. Kurban, "A novel wind speed modeling approach using atmospheric pressure observations and hidden Markov models," 2010.

[6] F. O. Hocaoglu and F. Serttas, "A novel hybrid (Mycielski-Markov) model for hourly solar radiation forecasting," Renew. Energy, 2016.

[7] A. Grantham, Y. R. Gel, and J. Boland, "Nonparametric short-term probabilistic forecasting for solar radiation," Sol. Energy, vol. 133, pp. 465–475, 2016.

[8] S. P. Evans and P. D. Clausen, "Modelling of turbulent wind flow using the embedded Markov chain method," Renew. Energy, vol. 81, pp. 671–678, 2015.

[9] M. David, F. Ramahatana, P. J. Trombe, and P. Lauret, "Probabilistic forecasting of the solar irradiance with recursive ARMA and GARCH models," Sol. Energy, vol. 133, pp. 55–72, 2016.

[10] Y. Chu and C. F. M. Coimbra, "Short-term probabilistic forecasts for Direct Normal Irradiance," Renew. Energy, vol. 101, pp. 526–536, 2017.

BIOGRAPHY

Fatih O. Hocaoglu was born in Afyonkarahisar, Turkey, in 1979. He received the B.S. degree in electrical and electronics engineering from the Pamukkale University, Denizli, Turkey in 2002 and the Ph.D. degree in electrical and electronics engineering from Anadolu University, Eskisehir, Turkey, in 2008. From 2002 to 2008 and from 2008 to 2011 he was a Research Assistant with the Anadolu University and Afyon Kocatepe University, respectively. He is currently an Associate Professor with the electrical engineering department of Afyon Kocatepe University since 2014. He is head of the Electrical Engineering Department since 2011. His research interests include solar energy, wind energy, hybrid energy systems, electrical installations and electrical vehicles where he holds a patent related on his research field.

Fatih Serttas was born in Afyonkarahisar, Turkey, in 1989. He received the B.S degree in Electrical and Electronics Engineering from the Pamukkale University, Denizli, Turkey in 2011 and the MSc degree in Electrical Engineering Renewable Energy Systems from Afyon Kocatepe University in 2015. He is still PhD student (PhD Candidate) in Electrical Engineering from Afyon Kocatepe and Pamukkale University joint PhD program. He is Research Assistant in Afyon Kocatepe University since 2012. His research interests include solar energy, high voltage techniques, power systems and electrical vehicles.

An Examination on Smart Grid Projects in the World

Emre Akarslan[1], Fatih Onur Hocaoglu[2]

Abstract

It is expected that energy will be the most important problem of the word in the near future. Moreover by the increasing demand on energy and reducing fossil fuel sources, energy efficiency is get more attractive issue for researchers. Smart grids became very popular in recent year. Smart grid has more efficiency than the conventional electricity networks. This new structure provides to maximize distributed energy resources integration. Furthermore it allows the consumer's participation in the overall electricity network. With this technology, the integration of renewable energy sources to the network will increase and this will reduce demand on fossil fuels. On the other hand, usage of advanced control strategy will increase reliability and will reduce the leakage losses. In the 2015-2019 strategic plan of energy ministry of republic of Turkey, it is indicated that energy efficiency is an important topic. To achieve a good efficiency, conventional electricity networks should be converted to smart grids. In this study, the smart grid applications of several countries in the world but especially in Europe are investigated. To this end, Portuguese smart distribution system examined and especially InovCity project is analyzed. Smart grid strategies for Salzburg, Austria are investigated and the Smart Grid Model Region Salzburg project which has goal of gathering several smart grid applications in an integrated system is examined. Moreover the Olympic Peninsula Project of American Energy Department and Model City of Mannheim (MOMA) project of Germany is investigated. Finally, the Italian smart grid pilot projects are evaluated. After the investigation of the existing projects, a roadmap to convert the conventional electrical distribution system of Turkey to smart grids is presented.

Keywords: *Smart Grid; Pilot Projects; Electric distribution*

1. INTRODUCTION

Energy is at the top of the list about the major problems of the future. Increasing energy needs by the growing technology getting more importance day by day. Therefore, the integration of different sources to grid and effective management of the electricity network is a hot topic in energy area. Recently, smart grids are replaced with the conventional distribution systems for the effective usage of energy sources. Whilst there is no universal definition of what makes an electricity distribution grid "smart" [1]. One of the definitions is that "the Smart Grid is the concept of modernizing the electric grid. The Smart Grid comprises everything related to the electric system in between any point of generation and any point of consumption" [2]. However generally, it can be defined as "electricity networks that can intelligently integrate the behavior and actions of all users connected to it (generators, consumers and those that do both) in order to efficiently deliver sustainable, economic and secure electricity supplies" [3,4]. Smart grids take into account the consumer and producer side of system, network technologies, real time measurement systems, sensors and communication networks. To characterize the Smart Grids, there are certain components such as: efficient management of supply, two-way communication between the producer and consumer, use of IT technology to respond to and manage demand and ensuring safe and secure electricity distribution [5].

Across the world many vendors, policy-makers and utilities have already implementing smart technologies into their transmission, distribution and customer systems, based on several factors such as implementing legislative and regulatory policy, realizing operational efficiencies and creating customer value. Smart Grid value realization by utility customers and society at large is, in part, linked to the pace of technology implementation that enables a secure, smart and fully connected electric grid [2].

---

[1] Corresponding author: Afyon Kocatepe University, Department of Electrical Engineering, 03200, Afyonkarahisar, Turkey. e.akarslan@gmail.com

[2] Afyon Kocatepe University, Department of Electrical Engineering, 03200, Afyonkarahisar, Turkey. fohocaoglu@gmail.com

Nowadays, smart grids became a very important area of interest in the world since the consumers now have opportunity to generate their own electricity. However it is very difficult to convert conventional networks into smart grid networks. To encounter these difficulties, several strategies must be followed and similar smart grid systems must be examined before conversion. Hence, in this study, some smart grid projects of several countries are investigated and the situation of Turkey is examined. Possible answers to "what can be done in Turkey" question are discussed. The organization of the paper is as follows: The literature overview is given in Section 2. Some sample smart grid projects are presented in Section 3. The situation of Turkey in terms of smart grid development and needs are explained in Section 4. Finally conclusions are presented in Section 5.

2. LITERATURE OVERVIEW

Smart grids represent an important evolution in the design and operation of electrical systems because they integrate automation solutions, different optimizations, process improvement, monitoring and control, the integration of multiple sources of energy (renewable) and the development of new products and services. This integration is already being implemented in several countries via communication infrastructure systems, open standards and information technology [6]. Therefore there are a lot of studies describing the implementation of smart grid projects in different countries in the literature. In this section some of them are reviewed:

Acharjee (2013) discussed the present power situation of India and summarized potential energy options. The effects of smart grid development on social, economic and power sectors were investigated. Main barriers and possible solutions of problems to implement smart grid projects in India were presented. The recent initiatives taken by the Government of India related to smart grids were described and step by step implementation strategy of smart grid was suggested [7]. In another study, Galo et al. (2014), proposed a strategy to select electrical systems to carry out in smart grids in Brazil by applying the Delphi method based on technical, financial and human resources and environmental applications. The creation of a priority factor to determine the order of smart grid deployment to achieve the best cost benefit in electrical systems was investigated [6]. In a recent study, Lopez et al. (2015) presented the communications architecture and technologies which are deployed in the field, analyzing how they fit some specific Smart Grid communications requirement. They described the pilot itself along with the services which are currently been delivered as well as with the foreseen ones [8]. Delfanti et al. (2014) described the Smart Grid experiment developed by A.S.SE.M. (a Distribution System Operator of Central Italy) on its distribution grid. They provided some innovative features such as; increase in the reliability of Loss of Mains protections by transfer trip messages, logic selectivity between protections, centralized voltage control, real-time monitoring and control of generation [9]. Crispim et al. (2014) investigated the smart grid experiences in UK, Italy and Portugal. They described the risks and difficulties of implementation within an established network and presented EU policy response and three different approaches by regulators in the UK, Italy and Portugal [10].

Cardenas et al. (2014) prepared a literature survey on smart grid distribution. They concluded that consumer participation is going to play a key role in the near future as it requires developing a new business model with the inclusion of self-generation and selling-back of excess capacity to the utility company [11]. Yuan et al. (2014) investigated the smart grid structures and development of it in China. They analyzed the policy, pilot projects and achievements and researched on barriers of developing smart grids. They concluded that the main institutional barrier to development of smart grids is lack of clear national strategy [12]. On the other hand, Connor et al. (2014) investigated the policy and regulation for smart grids in the United Kingdom. The different policy elements of what will be required for energy delivery in the UK to become smarter were considered in their study. They determined some needs for development of smart grids which required changes in policy and regulation [4].

Olivieri et al. (2014) presented the results of the design phase of project on integration of distributed photovoltaic power generation into the smart grid in the city of Parintins, Brazil. They gave a brief description of the system design, technical data, telecommunication network structure and the smart metering and billing system of the first smart grid implementation in Brazil [13]. Gouveia et al. (2015) presented a study about development and implementation of Portuguese smart distribution system. They focused on major implementations of smart grid projects in Portugal that resulted from a close collaboration between academia and industry. A laboratory infrastructure implemented to be used as a real test bed and a pilot deployed in a large city are introduced in this study [14]. Zucker et al. (2011) studied on Smart Grid Model Region Salzburg (SGMS) project which has the goal of aggregating different smart grid applications in an integrated system and to implement flagship projects in the real environment, considering problems of daily business and addressing specific customer needs [15]. In a recent study, Coppo et al. (2015) focused on Italian smart grid pilot projects. They gave a brief description of the projects and add information about the selection criteria which allowed identifying the benefits of the system stakeholders. Additionally, the procedure used to define a regulatory environment suited for smart grids was described [16]. Kienesberger et al. (2011) presented a holistic view on the information in a Smart Grid and an approach for the design of a comprehensive information platform fostering integration, user acceptance and profitability of Smart Grids.

Privacy and security challenges were reviewed and methods for reaching encouraging solutions were proposed [17].

3. SAMPLE SMART GRID PROJECTS IN THE WORLD

The solution of the challenges such as reducing carbon emissions and losses inherent to the distribution and transmission process of the traditional grid is seems to be the concept of Smart Grid. This new concept provides efficient distribution of energy, use of renewable resources to generate electricity, participation of the consumers in the process by generating and/or conserving energy, feedback to consumers, observe real-time consumption via smart meters, etc. [11]. These benefits of the smart grids canalize the scientists and engineers to study on this area. In this paper, only brief explanation of these projects is examined to learn what is happening in the world in terms of smart grids. and right-justified.

3.1. InovCity Project of Portuguese

There are two important national smart grid projects in the Portuguese such as InovGrid and REIVE. The REIVE project aims to develop a technological framework to integrate the Electric Vehicles to Portuguese distribution system. The main purpose of the InovGrid project is to develop an advanced metering system and provide a number of functionalities for the distribution grid with the necessary intelligence to tackle the paradigm change in the electricity industry [14]. This project focuses on micro-generation management and control in low voltage grids and provides to customers the necessary conditions to access new services. One of the major achievements accomplished in the InovGrid project is the real implementation of a Smart Grid infrastructure in the Portuguese municipality of Évora, which is designated as InovCity where devices, functionalities and the control architecture were tested in a real-world scenario, providing both a test bed and a demonstration site. [14]. InovCity is developed as a larger scale concept to further evaluate technologies and functionalities, test the interoperability, better understand the mechanisms related to cost benefits analysis [10]. One of the main objectives in InovCity is to provide the participation of customers in energy efficiency programs, through the change of energy usage behaviors. The smart metering infrastructure plays a critical role in making customers aware of their expenditures. The customers have possibility to monitor their energy consumption and receive energy efficiency advices from distribution system [14]. Portugal's Distribution System Operator installed 31,000 smart meters and 340 Distribution Transformer Controller within the InovCity project [10]. Fig. 1 summarizes the benefits of the InovGrid and InovCity projects.
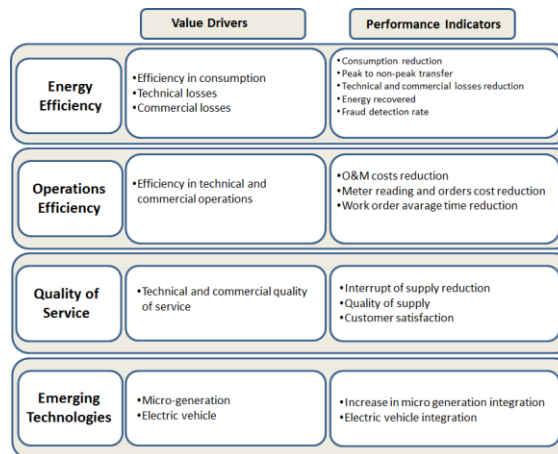
Figure 1. InovGrid and InovCity benefits [10].

In terms of energy efficiency, encouraging results are obtained in Portuguese. If the energy consumption observed in the project compare with the nearby municipality with the similar socioeconomic and climatic conditions, nearly 4% reduction in consumption was achieved for first year.

3.2. Smart Grid Model Region Salzburg Project of Austria

In 2009 Salzburg AG and its partners successfully submitted a bundle of projects in the third tender of "New Energies 2020", funded by the Austrian Climate and Energy Fund (KLI.EN), for the research, development and demonstration of intelligent networks and the integrated concept with the vision of an intelligent "Smart Infrastructure" that could protect resources. The Smart Grid Model Region Salzburg (SGMS) is supported by an interdisciplinary team of energy industry (Salzburg AG), housing industry (Salzburg Wohnbau), industry (Siemens AG, Fichtner) and top-class research partners (Austrian Institute of Technology, TU Vienna, CURE) [15]. The aim of the model region program is to combine several Smart Grid implementations and

issues (integration of renewables, smart metering, e-mobility, etc.) into an integrated system. Different applications are developed and analyzed in R&D projects in order to be field-tested and proved in real life demonstration projects [17]. SMGS project includes some projects such as Consumer to Grid (C2G) project, Building to Grid (B2G), Vehicle to Grid (V2G) Interfaces Project, Smart Heat Networks project, Smart Synergy project. C2G and B2G projects are related with the role of customers and buildings. It is aimed to optimize energy efficiency and affect customer behavior in a positive way. The V2G Interfaces project focuses on concepts for interaction portals for E-Mobility customers in the SGMS and offers a concrete implementation plan. Smart Synergy project, allows the creation of cost efficient Information and Communication Technology infrastructures [15]. The roadmap of the SGMS is shown in Fig. 2.
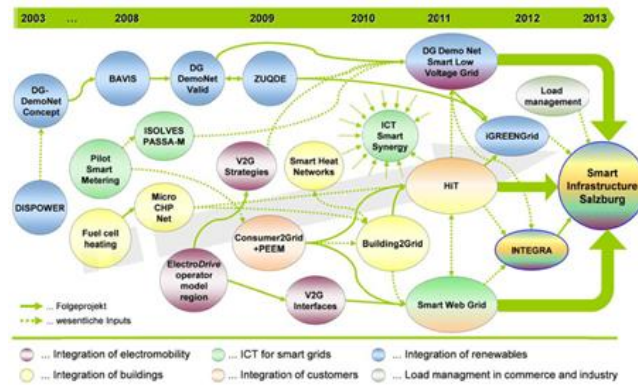
Figure 2. Roadmap of the SGMS [15]

3.3. Olympic Peninsula Project of America

The Olympic Peninsula Project is one of the two major Pacific Northwest GridWise Testbed demonstrations designed to show that advanced information-based technologies can increase asset utilization and reliability of the power grid in support of the national GridWise agenda [18]. This project started in 2005 and finished in March 2007. A total 120 residential, commercial and industrial customers take place in this project. [19]. Three electric power providers, BPA, Public Utility District (PUD) #1 of Clallam County, and the City of Port Angeles, provided the Olympic Peninsula Project with residential, commercial, and municipal test sites. Several other collaborators, specifically IBM's Watson Research Laboratory and Invensys Controls, provided valuable products and in-kind project support [18]. Three contract opportunities presented to the residential experimental group. A "shadow bill system" is designed via internet while the participants continue to take normal electrical bill. Customers which pay for the total cost of consumption according to normal bill, pay with virtual funds which are given them every 3 months. Savings of customers (virtual funds) are transferred to the next period and paid in cash to them at the end. In this project, participants can arrange their home profiles and they set the system which responds to demand with respect to tariffs. A reduction on electrical charge in the virtual feeders is provided by this way [19]. Some results are achieved in this project as follow;

- The project successfully managed a feeder and it is imposed feeder constraint for an entire year using these innovative technologies.

- Peak load reduction was successfully accomplished.

- Internet-based communications performed well for the control of distributed resources.

- Automation was particularly helpful for obtaining consistent responses from supply and demand resources [18].

3.4. Model City of Mannheim (MOMA) project of Germany

Germany is an important country in terms of renewable energy generation. It is planned that to provide 20% of energy generation renewable sources, 20% reduction on CO_2 emission, 20% reduction on energy consumption in scope of Horizon 2020 in Germany [20]. Therefore, governments develop some projects to achieve these objectives. In 2006, to provide the simultaneously consumption of the generated energy, a new tariff is started to use with a slogan "wash with sun". Then virtual power plant application is started and in this application all renewable sources are managed as a single power plant. Another phase of this project is using smart meters at homes. In 2009, smart grid project is started to implement in six different cities and government decided to determine appropriate project according to results. The electric distribution company MVV take support of Germany government with the project Model City of Mannheim (MOMA) [20]. This project includes e-energy exchange, smart homes, electrical transport, virtual power plant, storage systems

and two way communication systems [21]. The basic assumption of the system is consider it as a leaf of tree and produce energy as needed or a bit more and consume it, locally. Whereby loses will be reduced and a problem in any part of the system will not affect the whole system. Furthermore, through the energy butler software located at homes, it is provided that if the tariff is suitable, electricity need will provide from the grid otherwise home will use own energy production [20].

3.5. Telegestore Smart Grid Project of Italy

Italy is the country that firstly started to study on smart grids with the Telegestore Project which started at 2000 and finished at 2005. 27 million meters replaced with remotely readable smart meters in scope of this project [22]. There are a lot of pilot smart grid projects in Italy such as ENEL Telegestore, ASSM Tolentino, Carpinone, Deval-PS Villeneuve, A2A, etc. Telegestore project is considered as first smart grid project of the world with the features such as usage of smart meters, precise measurement, and communication functions and data management. The cost of the project is about 21billion Euro but the project is expected to gain 500 million euros per annum. More than 7000 employees were worked in this project and installation of 2,000 meters per day was carried out. The use of the multiphase meter which allows for two way communication and provides transferring the electricity produced from renewable energy sources to the grid was activated after 2006 [23]. The benefits of the project for customers can be summarized as invoices on real consumption, remote contract management, tailored tariff (possibility of select different daily, weekly, monthly or seasonal tariff), saving in billing etc. One of the most important benefits for electric power system is reduction on commercial and technical losses. Peak shaving, energy efficiency and CO_2 reduction are considered the other benefits of the project [24]. The system architecture of Telegestore project is shown in Fig. 3.
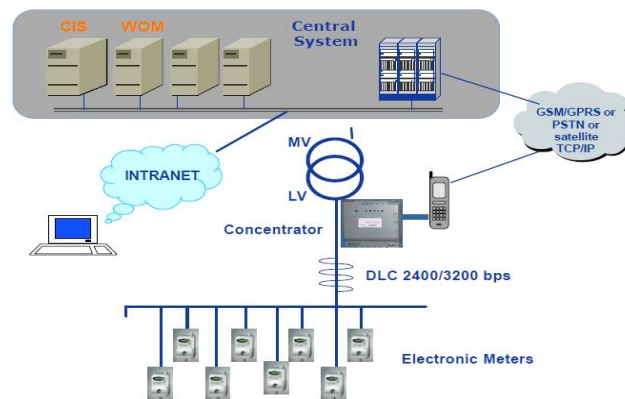
Figure 3. The system architecture of Telegestore Project [25].

4. WHAT IS HAPPENING IN TURKEY

At the end of the 2014, the installed capacity of the Turkey is almost reached 70000 MW [26]. However, it can be said that Turkey import almost half of the electricity need. According to Turkey Statistic Agency (TUIK) data, about 40% of the electricity need obtained from natural gas plant and natural gas is imported. These statistics show that energy and efficiency is very important topic for Turkey. In recent years, Turkey government pays attention to renewable sources and this result with an increase on energy production from renewables. The installed capacity of the wind and solar power plant reached about 4000 MW and 14 MW, respectively [27]. In energy ministry strategic plan, it is aimed that the installed capacity of the wind and solar power plant are increased to 10000 MW and 3000 MW. The leakage and losses rate will be reduced from 15.4 to 10 until 2019. To achieve these developments, the conventional distribution grid should be converted to modern smart grids. Conversion from conventional distribution grid to smart grids by gradually is a subject in both energy ministry strategic plan (2013-2020) and energy efficiency strategy document (2012-2023).

If the development process of the smart grids in the world is investigated, the common point is to start the process with a pilot project. This provides to see the difficulty and barriers in the process and calculate the cost and benefits. The results of the project will help the rearrange the process and determine the optimum way to evolution. When the smart grid pilot projects are analyzed, it is obvious that there are some common points. However there are some different issues due to countries' own needs. Therefore each country should develop its own project to determine a road map. It is thought that the first step of the conversion from conventional distribution grid to smart grids is to develop a pilot project. By this way an optimum road map can be determined for Turkey. The second step should be regulations and incentives. There are already some incentives about the renewables and the statistics show that these incentives showed an impact. For example in 2014 the installed capacity of wind energy power plant increased 27% compared to pre [27]. There are some regulations to convert to smart grids but the regulations should rearrange according to pilot projects

results to make easier the process. The third step should be starting the use of smart meters. To manage a system, it is necessary to observe it and collect data. Therefore, the smart meters are one of the most important parts of smart grids. According to [28] smart meters should have at a minimum microcomputer, memory and communication units. These devices should have both the narrow space (GSM/GPRS, PLC, etc.) and wide area (ZigBee, Wi-Fi, etc.) communication modules. In energy efficiency strategy document, it is obviously specified that to monitor the consumption, efficiency and savings as well as to reduce the consumption in peak hours will be provided by establishing "smart meter-home consumption control structure". In the other step smart electrical sockets can be designed and power unit of the home devices should be controlled by smart meters. In Spain, the electric distributions firms have to replace exist meters with smart ones without any cost to customers due to law which is available since 2008 [25].

Communication is one of the important parts of the smart grids. The fault at anywhere of the power line should be determined immediately and should be notified to the relevant units. Furthermore, the communication from power line with the local distribution grid should be provided. The remote observation and control of the power line communication components should be ensured. Electrical cars are important for smart grids. In future, it is expected that the most of the vehicle will be electrical. Therefore they need to be considered in design of smart grids. Electrical vehicle charge stations should be constructed and the effects of these stations to the grid should be considered to keep the stability and safety of the grid. Likewise, local electricity producers are important for smart grid structures due to the consumption of the electricity where it produced will reduce the losses of the line. Government should encourage the local electricity producers especially, which use renewable sources.

5. CONCLUSION

In this study, some smart grid pilot projects all over the world are examined. The differences and common points in these projects are investigated and a road map for Turkey is proposed. Firstly, it is obvious that some regulations and laws are needed to force the companies about the study on smart grids. However, all country has different conditions and it is proposed that every country should determine its own way by applying pilot projects. It is necessary to determine the steps to convert conventional grid to smart grid in Turkey. Due to the results of previous papers examined herein, needs should be determined and regulations should be rearranged. Since smart grids are so important for Turkey due to limited energy sources, Turkey should not lag behind of this technology.

REFERENCES

[1]. S. Hall, and T. J. Foxon "Values in the Smart Grid: The co-evolving political economy of smart distribution", Energy Policy, 74, 600-609, 2014.
[2]. IEC Smart Grid Standardization Roadmap, SMB Smart Grid Strategic Group (SG3), June 2010; Edition 1.0
[3]. European technology platform smart grids. Strategic deployment document for Europe's electricity networks of the future. Brussels; 2010.
[4]. P.M. Connor, P.E. Baker, D. Xenias, N. Balta-Ozkan, C.J. Axon and L. Cipcigan, "Policy and regulation for smart grids in the United Kingdom", Renewable and Sustainable Energy Reviews, 40, 269-286, 2014.
[5]. D. Xenias et al., "Scenarios for the development of Smart Grids in the UK: Literature review", Working Paper, January 2014: REF UKERC/WP/ES/2014/001.
[6]. J.J.M. Galo, M.N.Q. Macedo, L.A.L. Almeida, A.C.C. Lima, "Criteria for smart grid deployment in Brazil by applying the Delphi method", Energy, 70, 605-611, 2014.
[7]. P. Acharjee, "Strategy and implementation of Smart Grids in India", Energy Strategy Reviews, 1, 193-204, 2013.
[8]. G. Lopez, J.I. Moreno, H. Amaris, F. Salazar, "Paving the road toward Smart Grids through large-scale advanced metering infrastructures", Electric Power Systems Research, 120, 194–205, 2014.
[9]. M. Delfanti, E. Fasciolo, V. Olivieri, M. Pozzi, "A2A project: A practical implementation of smart grids in the urban area of Milan", Electric Power Systems Research, 120, 2-19, 2015.
[10]. J. Crispim, J. Braz, R. Castro, J. Esteves, "Smart Grids in the EU with smart regulation: Experiences from the UK, Italy and Portugal", Utilities Policy, 31, 85-93, 2014.
[11]. J.A. Cardenas, L. Gemoets, J.H.A. Rosas, R. Sarfi, "A literature survey on Smart Grid distribution: an analytical approach", Journal of Cleaner Production, 65, 202-216, 2014.
[12]. J. Yuan, J. Shen, L. Pan, C. Zhao, J. Kang, "Smart grids in China", Renewable and Sustainable Energy Reviews, 37, 896-906, 2014.
[13]. M.M.A. Olivieri et al. "Distributed generation in the smart grid – case study of Parintins", Energy Procedia, 57, 197-206, 2013.
[14]. C. Gouveia, D. Rua, F.J. Soares, C. Moreira, P.G. Matos, J.A. Pecas Lopes, "Development and implementation of Portuguese smart distribution system", Electric Power Systems Research, 120, 150-162, 2015.
[15]. G. Zucker, F. Kupzog, D. Reiter, "Smart Grids Strategy for Salzburg, Austria", 21st International Conference on Electricity Distribution, 6-9 June 2011, Paper 0787.
[16]. M. Coppo, P. Pelacchi, F. Pilo, G. Pisano, G.G. Soma, R. Turri, "The Italian smart grid pilot projects: Selection and assessment of the test beds for the regulation of smart electricity distribution", Electric Power Systems Research, 120, 136-149, 2015.

[17]. G. Kienesberger, M. Meisel, A. Adegbite, "A Comprehensive Information Platform for the Smart Grid", IEEE Africon 2011, Zambia.

[18]. Pacific Northwest GridWise™ Test bed Demonstration Projects, Part I. Olympic Peninsula Project, October 2007.

[19]. http://www.dektmk.org.tr/pdf/enerji_kongresi_11/39.pdf

[20]. http://www.solar-academy.com/menuis/Smart-Grid-Akilli-Sebekeler-Hakkinda174337.pdf

[21]. http://www.gridinnovation-on-line.eu/Articles/Library/Model-City-Mannheim-Moma.kl

[22]. http://www.emo.org.tr/ekler/a4d6c5a3223642b_ek.pdf

[23]. http://www.emo.org.tr/ekler/b790c8dde17d8bf_ek.pdf

[24]. http://www.aneel.gov.br/arquivos/pdf/enel-fabio_borghese.pdf

[25]. http://www.ieee-isplc.org/2007/docs/keynotes/rogai.pdf

[26]. http://www.enerjiatlasi.com/haber/elektrik-kurulu-gucu-2014-te-8-61-artti

[27]. http://enerjienstitusu.com/2015/02/11/turkiyenin-ruzgar-enerjisi-kapasitesi-2014te-yuzde-27-artti/

[28]. M. Akcin, B.B. Alagoz, C. Keles, A. Karabiber, A. Kaygusuz, "Dağıtık control ile akıllı sebekelerde genis-alan yonetimi ve gelecege donük projeksiyonlar", SAU J.Sci., 17(3), 457-470, 2013.

BIOGRAPHY

Emre Akarslan was born in Afyonkarahisar, Turkey, in 1980. He received the B.S. degree in electrical and electronics engineering from the Selcuk University, Konya, Turkey in 2004 and M.S. degree in electrical education from Afyon Kocatepe University, Afyonkarahisar, Turkey. He received the Ph.D. degree in electrical and electronics engineering from Osmangazi University, Eskisehir, Turkey, in 2014. He is an Assistant Professor with the electrical engineering department of Afyon Kocatepe University since 2017.

Fatih O. Hocaoglu was born in Afyonkarahisar, Turkey, in 1979. He received the B.S. degree in electrical and electronics engineering from the Pamukkale University, Denizli, Turkey in 2002 and the Ph.D. degree in electrical and electronics engineering from Anadolu University, Eskisehir, Turkey, in 2008. From 2002 to 2008 and from 2008 to 2011 he was a Research Assistant with the Anadolu University and Afyon Kocatepe University, respectively. He was an Assistant Professor with the Electrical Engineering department from 2011 to 2014. He is Associate Professor with the electrical engineering department of Afyon Kocatepe University since 2014. He is head of the Electrical Engineering Department since 2011. His research interests include solar energy, wind energy, hybrid energy systems, electrical installations and electrical vehicles he holds a patent.

EFFECTS of SOWING TIME on HERBAGE YIELD and QUALITY of LUPINE

Kagan Kokten[1], Mahmut Kaplan[2], Ersel Tal[2], Halit Tutar[1] Mevlut Akcura[3]

Abstract

The present study was conducted to investigate the effects of different sowing times on herbage yield and quality of lupine. Experiments were conducted for two years in 2014-2015 with four different sowing dates (1 April, 15 April, 1 May and 15 May) in randomized blocks design with three replications. Effects of sowing date on herbage yield and quality of lupine were found to be highly significant (P<0.01). While the years did not have significant effects on green and dry herbage yields, effects of years on plant height were found to be significant (P<0.05), and the effects on chemical composition were found to be highly significant (P<0.01).

The greatest plant height, crude protein yield, green herbage yield, dry herbage yield and crude ash contents were observed in the first sowing date and the lowest values of the same parameters were observed in the fourth sowing date. The greatest crude protein content was observed in the fourth sowing date and the lowest value was seen in the first sowing date. The greatest ADF and NDF ratios were seen in the third sowing date and the lowest values were observed in the fourth sowing date. The greatest digestible dry matter, dry matter intake and relative feed value were observed in the fourth sowing date and the lowest values were seen in the third sowing date. Considering the yield and quality values, the first sowing was considered as the best sowing date for lupine.

Key words: *Lupine, sowing time, yield, quality, relative feed value*

1. INTRODUCTION

Lupines are widely produced in many countries around the world and are used in different fields. In areas where soybeans, pods, chickpeas, lentils and other leguminous seeds do not usually grow, lupines show good adaptation [1]. It is reported that there are about 200 species known in the world and some species began to be cultivated 3000 years ago [2], [3].

In our country, lupine plants are known by names such as "ak lupen, beyaz lupen, delicebakla, gavurbaklası, yahudibaklası, kurtbaklası, mısırbaklası, termis, tirmis, ak acıbakla, beyaz acıbakla and termiye". Three species of lupine is important when one annual plant; Blue lupine, yellow lupine and white lupine [4]. The total production and marketing amount of lupine plant in Turkey is very small compared to other agricultural products. The reasons for this are; in terms of climate and soil requirements do not have the large areas, the lack of processing and use of technology and our country is not sufficiently known [5]. The lupine plant, which is generally used as an animal feed, is also consumed as a snack in a few cities such as Konya [6].

Lupine is a plant with 2-3 times more protein than grains. It is also rich in vitamins, minerals, calcium and iron [7]. Although soybean is in the first order in terms of plant protein production, it can compete with soybean if the production and yield of the lupine is increased by high protein content (28-47.6%) [8], [9]. With this study, it was aimed to determine the appropriate sowing time in the Bingol conditions of the lupine grown for the purpose of yield.

---

[1] Corresponding author: Department of Field Crops, Faculty of Agriculture, University of Erciyes, Kayseri, Turkey
kahafe1974@yahoo.com

[2] *Department of Field Crops, Faculty of Agriculture, University of Bingol, Bingol, Turkey*

[3] *Field Crops Department, Agricultural Faculty, Onsekiz Mart University, Canakkale, Turkey*

2. MATERIAL AND METHOD

The trial was conducted at the Research and Application Center of the Agricultural Faculty of Bingol University in 2014 and 2015. In the study, a livestock supplied from a farm in Konya was used as plant material. When examining the climate data of the study month; while the mean temperature was 20.4 ºC, total rainfall was 282.2 mm and mean relative humidity was 45.0% in the growing period of 2014, these values were 19.2 ºC, 251.8 mm and 42.9% respectively in the growing period of 2015. According to the average for long-terms, average temperature during vegetation was 18.1 ºC, total rainfall was 366 mm and average relative humidity was 48.8%. As a result, it can be said that the years 2014 and 2015 of Bingol province are less rainy, moist and warmer than the long-terms [10]. Soil samples taken from different points in the area where the experiment was conducted and from 0-30 cm depth were analyzed in the Soil-Plant Analysis Laboratory of the Agricultural Faculty of Bingol University. According to the analysis results; the experimental area was found to have a loamy soil area (43.81% saturation), no salinity (0.0066%), and the soil pH was slightly acidic (6.37). Organic matter (1.26%), lime content (0.15%) and potassium content (24.45 kg/da) were low and phosphorus content (7.91 kg/da) was found to be moderate. The trial was set up for two years with three replications, according to the design of random blocks. Sowing operations; it was made by hand with 30 cm row spacing and 4 rows in 1.2 m x 5 m = 6 m^2 parcels with 65 seeds per square meter on 1 April, 15 April, 1 May and 15 May. Before sowing in trial; DAP (18-46-0) compound fertilizer was given as 3.6 kg/da pure nitrogen and 9.2 kg/da pure phosphorous fertilizer. In the experiment, the weed was cleaned manually. Lupines were harvested during the flowering period. After drying in the samples was completed, the samples were prepared by chemical analysis by grinding mill with 1 mm mesh. Crude protein and crude ash analyzes were carried out by the methods described in [11]. The analysis of elements such as NDF and ADF, which make up the cell wall, was carried out by Van Soest and Wine [12] and Van Soest [13] respectively. It was found by calculating dry matter digestibility (DMD), dry matter intake (DMI) and relative feed values (RFV). The following formulas are used in calculations [14].

DMD= 88.9 - (0.779 x ADF)

DMI= 120 /NDF

RFV= (DMD x DMI) / 1.29

The results obtained from the research were subjected to analysis of variance using SAS [15] program. The difference between the averages found was significant by Duncan test.

3. RESULTS AND DISCUSSION

Mean values for the effect of sowing time on the yield and quality characteristics of the lupine are given in Tables 1, 2, 3 and 4. Sowing times were statistically significant at the 1% level in terms of all the features examined. Years of statistical significance were found to be very important at 1% level of significance in terms of all characteristics except green herbage and hay yield.

When Table 1 is examined; it can be seen that the statistically significant differences between the planting lengths of different sowing times were obtained from sowing on April 1 with 49.9 cm of the highest plant length and sowing on May 15 with the lowest plant length of 27.5 cm. In terms of years, it was determined that the highest plant height was obtained from sowing in 2014 with 38.3 cm. When we look at the yield of green herbage, it is determined that there is not a statistical difference in terms of years, and that there are significant differences in terms of sowing time. It has been determined that the highest green yield is obtained from cultivations made on April 1 at 720.0 kg/da. While hay yields did not differ statistically for years such as green herbage yields, statistically significant differences were found in terms of planting times. The highest hay yield was determined from plantations made on April 1 with 195.4 kg/da.

The values we obtained about the plant height of the lupus were determined by [16] was lower than the values obtained as 55.7-91.7 cm, it is similar to the values obtained by [6] as 28-69 cm. In the study conducted in the Konya ecological conditions, green grass yield was 1628-3121 kg/da [4], in the study conducted in Tekirdag ecological conditions as 1875-3157 kg/da [17] and in Odemis ecological conditions as 2193-8448 kg/da [16]. The values of green grass yield obtained without research were found to be lower than the findings reported by other researchers. On the other hand, hay yield values obtained from different studies were found to be 1100 kg/da [18], in Konya conditions as 293-529 kg/da [4], in Odemis conditions as 288-1057 kg/da [16] and in Tekirdag conditions as 8-86 kg/da [17]. It can be argued that the difference between the study and the other research we make is due to the differences in the types used or the soil and climate factors on which the studies are conducted. In a study on the planting time of the lupine, it was reported that early sowing plants had higher plant height and other characteristics affecting fertility than late sowing [19].

Table 1. *Mean values of plant height, green and dry yields of lupine at different planting times*

Sowing Time	Plant Height (cm)			Green Herbage Yield (kg/da)			Dry Hay Yield (kg/da)		
	2014	2015	Mean	2014	2015	Mean	2014	2015	Mean
1 April	54.3	45.5	49.9 a[**]	733.3	706.7	720.0 a[**]	203.9	187.0	195.4 a[**]
15 April	41.8	43.3	42.5 b	515.6	741.8	493.7 b	86.1	85.7	85.8 b
1 May	29.5	28.0	28.7 c	243.1	222.2	232.7 c	35.5	34.7	35.1 c
15 May	27.5	27.4	27.5 c	123.3	160.9	142.1 d	19.0	23.0	21.0 d
Mean	38.3 A[**]	36.0 B		403.8	390.4		86.1	82.6	

*** p<0.01*

Table 2. *Mean values of crude protein ratio, crude protein yield and crude ash ratio of lupine at different planting times*

Sowing Time	Crude Protein Ratio (%)			Crude Protein Yield (kg/da)			Crude Ash Ratio (%)		
	2014	2015	Mean	2014	2015	Mean	2014	2015	Mean
1 April	22.0	16.0	19.0 d[**]	44.8	30.0	37.4 a[**]	9.9	7.5	8.7 b[**]
15 April	25.1	22.9	24.0 c	21.7	19.6	20.6 b	10.4	8.2	9.3 b
1 May	27.0	24.7	25.9 b	9.6	8.6	9.1 c	10.7	7.0	8.8 b
15 May	28.9	30.4	29.6 a	5.5	7.0	6.2 d	10.5	11.5	11.0 a
Mean	25.8 A[**]	23.5 B		20.4 A[**]	16.3 B		10.4 A[**]	8.5 B	

*** p<0.01*

When we examine Table 2; the difference in crude protein ratio, crude protein yield and crude ash ratio of the lupine at different years and sowing times is statistically significant, The highest crude protein and crude ash ratios (29.6% and 11.0%, respectively) were obtained from sowing on May 15, while the highest crude protein yield was obtained from sowing on April 15 with 37.4 kg/da. In terms of years, the highest crude protein ratio, crude protein yield and crude ash ratio were found to be obtained from sowing in 2014 (25.8%, 20.4 kg/da and 10.4%, respectively).

When we look at Table 3; it is seen that there are very important differences between the lows of different years and sowing times statistically between ADF, NDF and DMD rates. The highest ADF rate was obtained from sowing on May 1 with 33.3%, while the lowest ADF rate was obtained from sowing on May 15 with 27.8%. The highest NDF rate was obtained from sowing done on 1 May with 39.0%, followed by sowing done on April 1 (37.8%) in statistically the same group. The lowest NDF rate was obtained from sowing made on April 15 with 35.0%. The highest rate of DMD was obtained from sowing on May 1 with 67.3%, followed by sowing on April 15 (66.2%), statistically in the same group. The lowest DMD rate was obtained from sowing on May 1 with 62.9%. There was a statistically significant difference between Lupine ADF, NDF and DMD rates over the years. ADF and NDF ratios were found to be higher in the first year and the DMD rate was higher in the second year.

Table 3. *Mean values of ADF, NDF and DMD ratios of lupine at different planting times*

Sowing Time	ADF Ratio (%)			NDF Ratio (%)			DMD Ratio (%)		
	2014	2015	Mean	2014	2015	Mean	2014	2015	Mean
1 April	32.9	28.5	30.7 b[**]	40.7	34.8	37.8 a[**]	63.3	66.7	65.0 b[**]

15 April	32.3	26.0	**29.2 c**	39.4	30.7	**35.0 b**	63.7	68.6	**66.2 a**
1 May	33.6	33.1	**33.3 a**	38.3	39.7	**39.0 a**	62.7	63.1	**62.9 c**
15 May	29.0	26.5	**27.8 c**	44.5	27.4	**36.0 b**	66.3	68.3	**67.3 a**
Mean	**32.0 A**[**]	**28.5 B**		**40.7 A**[**]	**33.2 B**		**64.0 B**[**]	**66.7 A**	

$**\ p<0.01$

Table 4. *Mean values of dry matter intake and relative feed values of lupine plants at different sowing times*

Sowing Time	DMI Ratio (%)			RFV		
	2014	**2015**	**Mean**	**2014**	**2015**	**Mean**
1 April	3.0	3.4	**3.2 b**[**]	144.6	178.3	**161.4 b**[**]
15 April	3.1	3.9	**3.5 a**	150.6	208.3	**179.5 a**
1 May	3.1	3.0	**3.1 b**	153.1	147.9	**150.5 c**
15 May	2.7	4.4	**3.5 a**	138.6	231.4	**185.0 a**
Mean	**3.0 B**[**]	**3.7 A**		**146.7 B**[**]	**191.5 A**	

$**\ p<0.01$

When Table 4 is examined, It is seen that the lupine at different years and sowing times have statistically significant differences between the DMI rate and RFV values. The highest rate of DMI was obtained from sowing on April 15 and May 15 with 3.5%, the lowest DMI rate was obtained from sowing on May 1 with 3.1%. It is seen that the highest RFV value was obtained from sowing done on May 15 with 185.0, followed by sowing made on April 15th (179.5) statistically in the same group. The lowest RFV value was obtained from sowing on May 1 with 150.5. Lupine has a statistically significant difference between years in terms of DMI and RFV values and it is found that the second year has higher values than the first year.

4. CONCLUSION

In this experiment made in Bingol ecological conditions; plant height, green herbage and hay yield were determined to be high because the plants extended the vegetation period with early sowing. Therefore, according to the results obtained from the experiment, it has been determined that the lupine in Bingol and similar ecologic areas should be done early enough to avoid damage from the spring colds.

REFERENCES

[1] Blanco, G.O., Genetic Variability of Tarwi (*Lupinus mutabilis* Sweet.) Agricultural and Nutritional Aspects of Lupines (34-49) Lima, Cuzco, Peru, 1980.

[2] Smit, D., Lupinus Een geslacht van zonan bidders. Groei and Bloei, 1996(7): 36-39, 1996.

[3] Yaltırık, F. ve Efe, A., System of Herbaceous Plants. İstanbul University, Faculty of Forestry Publication No:10, İstanbul, II. Printing, 518 s, 1996.

[4] Mülayim, M. and Semercioz, B.S., A study on the morphological, biological and agricultural characteristics of some varieties (*Lupinus albus* L.) local varieties made in Konya. S.Ü. Agr. Fac. Journal, Konya 1992.

[5] Kayserilioglu, R., Konya region Lupine (Aci Bakla-Termiye) production. T.C. Ministry of Public Works and Settlement. D.S.I. IV Regional Directorate. Konya, 1990.

[6] Mülayim, M., ve Acar, R.,Lupins and Some Other Legumes. In: Forage plants, Leguminous forage crops Volume II, R.Avcıoglu, R.Hatipoglu, Y.Karadag (eds.), 453-462 pp., T.C. Ministry of Agriculture and Welfare General Directorate of Agricultural Production and Development, İzmir 2009.

[7] Yorgancılar, M., Atalay, E., Babaoglu, M., Mineral content of inedible top seeds (Lupine = *Lupinus albus* L.). Selcuk Agriculture and Food Science Journal, 23 (50): 10-15, 2009.

[8] Williams, W., Studies on the development of lupins for oil and protein, Euphytica 28: 481-488, 1979.

[9]   Sator, C., In vitro Breeding of Lupins. Perspectives for Peas and Lupins as Protein Crops. (R Thomson and R Casey, eds.) In Proc. Int. Symp. Protein Production from Legumes in Europe, Sorrento, Italy pp. 79-87, 1983.

[10]   Anonymous, Bingol Provincial Meteorological Data, Bingol Provincial Meteorological Directorate 2015.

[11]   AOAC, Official Method of Analysis. Association of official analytical chemists 15th. edition, pp.66-88, 1990.

[12]   Van Soest PJ, Wine RH, The Use of Detergents in The Analysis of Fibrous Feeds. IV. Determination of Plant Celi Wall Constituents. JAOAC, 50: 50-55, 1967.

[13]   Van Soest PJ, The Use of Detergents in the Analysis of Fibrous Feeds. II. A rapid method for the determination of fiber and lignin. JAOAC. 46, 829-835, 1963.

[14]   Morrison, J.A., Hay and Pasture Management. Chapter 8. Extension Educator, Crop Systems Rockford Extension Center 2003.

[15]   SAS,SA S User's Guide: Statistic. Statistical Analysis Systems Institute Inc., Cary, NC 1999.

[16]   Okuyucu, F., Kır, B., Akdemir, H., Okuyucu, B.R., Baygın, M., Odemis Kosullarında Bazı Ak Acı (*Lupinus albus* L.), Sarı Tatlı (*Lupinus luteus* L.) ve Mavi Tatlı (*Lupinus angustifolius* L.) Lüpen Cesitlerinin Verim Ve Yem İcerikleri Üzerine Bir Arastırma, Ege Üniv. Ziraat Fak. Derg., 41 (3):89-98, 2004.

[17]   Orak, A., Tuna, M., Effect of Different Row Spaces on Some Yield and Yield Components of *Lupinus* sp. Ecotypes. Tekirdag University, Agricultural Faculty Publications 216, Research Publication Number: 83, Tekirdag 1994.

[18]   Romer, P., Genetische und Physiologische Untersuchungen an *Lupinus mutabilis*, Dissertation, Universitat Giessen 1990.

[19]   Karagüzel, O., Baktır, İ., Cakmakcı, S., Ortacesme, V., Aydınoglu, B., Atik, M., Effect of growing environment and planting time on growth and flowering characteristics of native *Lupinus varius* of South Anatolia. Journal of Agricultural Faculty of Akdeniz University, 16(2):187-197, 2003.

EFFECTS of SOWING TIME on HERBAGE YIELD and QUALITY of BLACK CHICKPEA

Kagan Kokten[1]*, Mahmut Kaplan[2], Hava Seyma Yilmaz[3], Mevlut Akcura[4], Halit Tutar[2]

Abstract

The present study was conducted to investigate the effects of different sowing times on herbage yield and quality characteristics of black chickpeas in terms of animal feeding. For this purpose, experiments were conducted for two years in 2014 and 2015 with four different sowing dates (1 April, 15 April, 1 May and 15 May) in randomized blocks design with three replications. Effects of sowing date on plant high, herbage yield, hay yield, crude protein ratio, crude protein yield and crude ash ratio of black chickpeas were found to be highly significant (P<0.01), neutral detergent fiber (NDF) and dry matter intake (DMI) of black chickpeas were found to be significant (P<0.05). But acid detergent fiber (ADF), dry matter digestibility (DMD) and relative feed value (RFV) of black chickpeas were not found significant.

Considering the results of two-year experiments, plant heights varied between 28.2-32.7 cm, green herbage yield between 56.6-375.9 kg/da, dry herbage yield between 11.2-98.4 kg/da, crude protein yield between 1.8-13.7 kg/da, crude protein ratio between 13.6-16.3%, crude ash between 9.3-11.3%, ADF ratio between 29.4-30.9%, NDF ratio between 36.5-38.5%, DMM ratio between 64.8-66.0%, DMI ratio between 3.1-3.3% and RFV between 159.1-168.4. Considering the yield and quality values, the first sowing was considered as the best sowing date for black chickpeas.

Key words: *Black Chickpeas, Sowing Date, Yield, Chemical Composition, Relative Feed Value*

1. INTRODUCTION

Although animal proteins have a very important place in human nutrition, per capita consumption of animal protein in our country is much lower than developed countries. We are at a lower level in terms of the production of animal products, although we are not in a good place in terms of animal existence among the countries of the world. The most important reasons for the low yields in our animals are poor quality of the feeds fed to animals and inadequate cultivation of forage crops.

In the world, chickpea, which is especially adapted to the arid regions of the Middle East [1], [2] is used not only as a human nutrition but also as a source of energy and protein in animals [3]. There are many factors that influence the feed values of feed plants. One of them is sowing time. Especially in arid areas, this is more important.

Most of the agricultural areas in our country are arid and semi-arid regions. In these regions, the amount of feed produced by meadow and pasture areas is very low and the number of bears that can be trained is very small. One of the plants that can be successfully cultivated in such areas is black chickpea. On the surface of black chickpeas, crude protein is high (21.06%) and ADF and NDF ratios are very low (14.04% and 21.63% respectively) [4]. With this study, it was aimed to determine the appropriate sowing time of black chickpea in Bingol conditions.

---

[1] **Corresponding author: Department of Field Crops, Faculty of Agriculture, University of Bingol, Bingol, Turkey*

kahafe1974@yahoo.com

[2] *Department of Field Crops, Faculty of Agriculture, University of Erciyes, Kayseri, Turkey*

[3] *Department of Horticulture, Faculty of Agriculture, University of Kahramanmaras Sutcu Imam, Kahramanmaras, Turkey*

[4] *Field Crops Department, Agricultural Faculty, Onsekiz Mart University, Canakkale, Turkey*

2. MATERIAL AND METHOD

The trial was conducted at the Research and Application Center of the Agricultural Faculty of Bingol University in 2014 and 2015. Black chickpea obtained from GAP International Agricultural Research and Education Center Directorate was used as plant material in the research. When examining the climate data of the study month, while the mean temperature was 20.4 ℃, total rainfall was 282.2 mm and mean relative humidity was 45.0% in the growing period of 2014, these values were 19.2 ℃, 251.8 mm and 42.9% respectively in the growing period of 2015. According to the average for long-terms, average temperature during vegetation was 18.1 ℃, total rainfall was 366 mm and average relative humidity was 48.8%. As a result, it can be said that the years 2014 and 2015 of Bingol province are less wet and humid and warmer than the long-terms [5]. Soil specimens taken from different points of the area where the experiment was conducted and from 0-30 cm depth were analyzed in the Soil-Plant Analysis Laboratory of the Agricultural Faculty of Bingol University. According to the analysis results; the experimental area was found to have a loamy soil area (43.81% saturation), no salinity (0.0066%), and the soil pH was slightly acidic (6.37). Organic matter (1.26%), lime content (0.15%) and potassium content (24.45 kg/da) were low and phosphorus content (7.91 kg/da) was found to be moderate. The trial was set up for two years with three replications, according to the randomized blocks design. Sowing operations; it was made by hand with 30 cm row spacing and 4 rows in 1.2 m x 5 m = 6 m^2 parcels with 65 seeds per square meter on 1 April, 15 April, 1 May and 15 May. Before sowing in trial; DAP (18-46-0) compound fertilizer was given as 3.6 kg/da pure nitrogen and 9.2 kg/da pure phosphorus fertilizer. In the experiment, the weed was cleaned manually. Black chickpeas were harvested in the flowering stage. After drying in the samples was completed, the feed samples were prepared by chemical analysis by grinding mill with 1 mm mesh. Crude protein and crude ash analyzes were carried out by the methods described in [6]. The analysis of elements such as NDF and ADF, which make up the cell wall, was carried out by Van Soest and Wine [7] and Van Soest [8] respectively. It was found by calculating digestible dry matter (DMD), dry matter intake (DMI) and relative feed values (RFV). The following formulas are used in calculations [9].

DMD= 88.9 - (0.779 x ADF)

DMI= 120 /NDF

RFV= (DMD x DMI) / 1.29

The results obtained from the research were subjected to analysis of variance using SAS [10] program. The difference between the averages found was significant by Duncan test.

3. RESULTS AND DISCUSSION

Mean values for the effect of sowing time on the quality and yield of black chickpea were given in Tables 1, 2, 3 and 4. While ADF, DMD and RFV values are statistically insignificant in terms of the features examined, the NDF and DMI ratios are statistically significant at 5% level and all other features are statistically significant at 1% level. For years, green herbage yield, crude protein ratio, crude protein yield and crude ash ratio were statistically significant at 1% level and the first year has a higher value than the second year.

When Table 1 is examined; It is observed that the statues of the black chickpea at different sowing times are statistically significant differences and that the highest plant height is obtained from sowing done on April 1 with 32.7 cm and this is done statistically on April 15th in the same group. It has been determined that there is no statistical difference between years in terms of plant length of black chickpea. There were significant differences between both years and planting times in terms of green herbage yields. The highest green herbage yield was obtained from April 1 sowing with 375.9 kg/da in terms of sowing times, while in terms of years the highest green herbage yield was determined with 267.1 kg/da from sowing in 2014. When we look at hay yields, it is determined that there is not a statistical difference in terms of years and that there are significant differences in terms of sowing time as statistically. It was determined that the highest dry matter yield was obtained from cultivations carried out on April 1 with 98.4 kg/da.

In regions with arid and semi-arid climates, the most important stress factors for plants growing due to rainfall conditions are water and temperature. Plants grown in these regions cannot show sufficient plant height and biomass production in case of water scarcity [11]. While there was no study of plant height and yield of black chickpea, [12] reported that, as the sowing time in chickpeas is delayed, it causes a decrease in plant height and herb yield, especially. Another researcher, [13], reported that green herbage and hay yield decreased with the delay of sowing time. Some studies have reported that late planting shortens the growth period of crops and therefore results in a decrease in yield [14], [15]. However, it is stated that plants that have a longer growing period in the field [16], [17], [18] and are not exposed to water stress have more leaf number per unit area [19], [20] leaf size and thus higher yield. The delay of sowing time leads to a lower formation of over-ground biomass and thus to a decrease in productivity [21].

Table 1. *Mean values of plant height, green herbage and dry yields of black chickpea plants at different sowing times*

Sowing Time	Plant Height (cm)			Green Herbage Yield (kg/da)			Dry Yield (kg/da)		
	2014	2015	Mean	2014	2015	Mean	2014	2015	Mean
1 April	34.1	31.2	32.7 a[**]	447.3	304.4	375.9 a[**]	101.3	95.4	98.4 a[**]
15 April	33.4	30.2	31.8 a	353.8	246.7	300.2 b	83.7	83.9	83.8 b
1 May	28.1	28.3	28.2 b	208.9	189.3	199.1 c	71.9	63.1	67.5 c
15 May	27.7	31.2	29.4 b	58.3	54.9	56.6 d	12.0	10.3	11.2 d
Mean	30.8	30.2		267.1 A[**]	198.8 B		67.2	63.2	

** p<0.01; * p<0.05

Table 2. *Mean values of crude protein ratio, crude protein yield and crude ash ratio of black chickpea plant at different sowing times*

Sowing Time	Crude Protein Ratio (%)			Crude Protein Yield (kg/da)			Crude v (%)		
	2014	2015	Mean	2014	2015	Mean	2014	2015	Mean
1 April	15.6	11.7	13.6 c[**]	15.8	11.1	13.5 a[**]	11.4	7.3	9.3 c[**]
15 April	18.3	14.3	16.3 a	15.3	12.0	13.7 a	13.6	9.1	11.3 a
1 May	15.6	15.7	15.7 b	11.2	9.9	10.6 b	12.1	8.9	10.5 b
15 May	15.2	17.2	16.2 a	1.8	1.8	1.8 c	11.6	10.6	11.1 a
Mean	16.2 A[**]	14.7 B		11.0 A[**]	8.7 B		12.2 A[**]	9.0 B	

** p<0.01; * p<0.05

When we examine Table 2; the difference in crude protein ratio, crude protein yield and crude ash ratio of black chickpea at different years and sowing times is statistically significant, the highest crude protein ratio, crude protein yield and crude ash ratio (16.3%, 13.7 kg/da and 11.3%, respectively) were obtained from sowing on April 15. In terms of years, the highest values were obtained from cultivations made in 2014 (16.2%, 11.0 kg/da and 12.2% respectively).

When we look at Table 3; there is no statistically significant difference between ADF and DMD ratios of black chickpea at different sowing times, NDF ratios are statistically significant. It was observed that the highest NDF ratio was obtained from sowing on 1 May with 38.5%, followed by sowing on April 1 and May 15 (38.4% and 37.0% respectively) in the same group statistically. The lowest NDF rate was found to be 36.5% on April 15 sowing. There was no statistically significant difference between years in terms of ADF, NDF and DMD ratios of black chickpea.

Table 3. *Mean values of ADF, NDF and DMD rates of black chickpea plant at different sowing times*

Sowing Time	ADF Rate (%)			NDF Rate (%)			DMD Rate (%)		
	2014	2015	Mean	2014	2015	Mean	2014	2015	Mean
1 April	31.2	27.6	29.4	39.2	37.7	38.4 a[*]	64.6	67.4	66.0
15 April	31.5	28.1	29.8	37.3	35.6	36.5 b	64.4	67.0	65.7
1 May	29.3	30.2	29.7	37.9	39.1	38.5 a	66.1	65.3	65.7
15 May	29.9	31.9	30.9	36.1	37.9	37.0 ab	65.6	64.1	64.8
Mean	30.4	29.5		37.6	37.6		65.2	66.0	

** p<0.01; * p<0.05

Table 4. *Mean values of dry matter intake and relative feed values of black chickpea plant at different sowing times*

Sowing Time	DMI Rate (%)			RFV		
	2014	2015	Mean	2014	2015	Mean
1 April	3.1	3.2	**3.1 b***	153.6	166.4	**160.0**
15 April	3.2	3.4	**3.3 a**	161.5	175.2	**168.4**
1 May	3.2	3.1	**3.1 b**	162.7	155.5	**159.1**
15 May	3.3	3.2	**3.2 ab**	168.9	157.3	**163.1**
Mean	**3.2**	**3.2**		**161.7**	**163.6**	

** p<0.01; * p<0.05

When Table 4 is examined, there is no statistically significant difference between the NYD values of black chickpea at different sowing times, DMI ratios are statistically significant at 5% level. It is observed that the highest DMI rate is obtained from the cultivation done on 15 April with 3.3%, followed by the cultivation on 15 May, which is statistically the same group (3.2%). The lowest DMI rate was found to be 3.1% at 1 April and 1 May. There was no statistically significant difference between years in terms of DMI and RFV values of black chickpea.

Due to the late wintering of the cultivars in the Bingol ecology with terrestrial climate, significant decreases in plant height, green weed and hay yields of black chickpeas were observed due to the increasing temperature and decreasing rainfall amounts. However, higher yields were obtained in early sowing. Considering that plant length is in linear relationship with dry matter rate, it can be concluded that planting should be done early in order to avoid loss of yield and quality. According to the results of the research, as the sowing time progressed, the yield of green grass, hay and crude protein decreased and the rate of NDF decreased and the proportion of crude protein increased slightly. Therefore, in Bingol and similar ecologies, the result was that the time of sowing of black chickpea should be done as early as possible in the spring.

REFERENCES

[1] Singh P., Influence of water-deficits on phenology, growth and dry-matter allocation in chickpea (*Cicer arietinum*). Field Crops Research, 28: 1-15, 1991.
[2] Saxena S., Micropropagation of adult plants of two bamboo species: Dendrocalamus Longispathus Kurz and Bambusa Vulgaris Schrader, Ph.D. Thesis, University of Delhi, 1993.
[3] Bampidis VA., Christodoulou V., "Chickpeas (*Cicer arietinum* L.) in animal nutrition: A review". Animal Feed Science and Technology, 168: 1-20, 2011.
[4] Kaplan M., Kokten K., Yılmaz SH., Arslan M., Kale H., Bozkurt S., Temizgül R., Effect of sowing time on grass, grain and cutting quality and quality characteristics in black chickpea (*Cicer arietinum* L.), 11. Field Crops Congress, 7-10 September 2015, Canakkale, 322-325, 2015.
[5] Anonymous, Bingol Provincial Meteorological Data, Bingol Provincial Meteorological Directorate, 2015.
[6] AOAC, Official Method of Analysis. Association of official analytical chemists 15th.edition, pp.66-88, 1990.
[7] Van Soest PJ, Wine RH, The Use of Detergents in the Analysis of Fibrous Feeds. IV. Determination of Plant Cell Wall Constituents. JAOAC, 50:50-55, 1967.
[8] Van Soest PJ, The Use of Detergents in the Analysis of Fibrous Feeds. II. A rapid method for the determination of fiber and lignin. JAOAC. 46, 829-835, 1963.
[9] Morrison JA, Hay and Pasture Management. Chapter 8. Extension Educator, Crop Systems Rockford Extension Center, 2003.
[10] SAS, SA S User's Guide: Statistic. Statistical Analysis Systems Institute Inc., Cary, NC, 1999.
[11] Taner S., Investigation of inheritance values using some physiological and morphological parameters in tolerant and sensitive genotypes of bread wheat. PhD Thesis, Selcuk University Institute of Science and Technology, Konya, 2011.
[12] Akdag C, Ütebay H, Düzdemir O, A study on the effects of nitrogen and phosphorus doses on yield and some other properties in chickpea (*C. arietinum*). Journal of Agricultural Faculty of Gaziosmanpasa University,12:110-121, 1995.
[13] Hakyemez BH., 2006. Effects of sowing time on herbage and seed yield in common vetch (*Vicia sativa* L.), Journal of Agricultural Faculty of Uludag University, 20: 47-55, 2006.
[14] Naceur MB., Daily M and Selmi M., Effect of water deficiency during different growth stages of wheat on soil different growth stages of wheat on soil humidity, plant physiology and yield components. Medit, 10: 63-60, 1999.
[15] Noferesti M., Effect planting date on yield and yield components of forage corn as second cultivation in Birjand, Iran region. M.Sc. Thesis on Agriculture, Islamic Azad University, Birjand Branch, Iran, 2006.

[16] Muldoon JF., Daynard TB., Duinen BV and Tollenaar M., Comparisons among rates of appearance of leaf tips, collars and leaf area in maize (*Zea mays* L.). Maydica. 29: 109-120, 1984.

[17] Dennis RE., Maize for Grain in Arizona. University of Arizona Cooperative Extension Tucson, 1996.

[18] Modarrres AM., Hamilton RI., Dwyer LM., Dijak M and Smith DL., Leafy reduced-stature maize for short season environments: population density and planting pattern effect on hybrid performance. Maydica, 43: 227-234, 1998.

[19] Al-Doori SA., 2011. A study of the importance of sowing dates and plant density affecting some rapeseed cultivars (*Brassica napus* L.). College of Basic Education Researchers Journal, 11: 615-632.

[20] Camoglu G., Genc L and Asık S., 2011. Effect of water stress on physiological and morphological parameters in sweet corn (*Zea mays saccharata* Sturt), Journal of Agricultural Faculty of Ege University, 48: 141-149.

[21] Temel S., Yıldız V., Kır AE., 2015. The effect of different planting dates on leaf area index in some common vetch varieties. International Journal of Agricultural and Wildlife Sciences, 1(2): 85-93.

The Seismic Behavior of High Rise Building Subjected to Far Field Ground Motions

Fikrat ALMAHDI[1], Adem DOGANGUN [2]

Abstract

In line with the modern trend toward high rise buildings, the needs to understand and evaluate the seismic response of this type of structure became an urgent demand. The effect of earthquake on high rise building has got high priority in current researches. Many studies addressed the seismic response of high rise structures when subjected to ground motions, Moreover the effect of seismic parameters of different types of ground motions on the seismic response have been searched. This paper aims to investigate the effect of far field ground motions on the seismic response of high rise building. A 55-story RC building was taken as a case study to carry out linear time history analysis with 3 sets of far field ground motions. The study concluded that far field ground motions have significant effect on the inter story drift. Therefore attention must be paid for far field ground motion effects on seismic response high rise building.

Keywords: *High rise building, Far field ground motion.*

1. INTRODUCTION

Nowadays, the world is seeing a massive revolution in the construction of high rise buildings (HRBs), for example at the time of this writing the Number of skyscrapers in Hong Kong is 1302, in New York city 722, in Istanbul 143,.. etc [1]. The particularity of high rise building such as functional requirements, high occupancy level, modeling of real behavior under different types of loads and acceptance criteria demands working on new guidelines to put up proper recommendations that meet this particular requirements. The structural behavior of high rise building subjected to different levels of seismic hazard has got a high priority among researchers. The seismic response of high rise building subjected to near fault ground motions (NFGM) has been investigated in depth and the characteristics of NFGM have been addressed, Studies revealed that NFGM produces a greater structural response than other type of ground motion records and should have significant attention in the case of (HRBs) especially for resonance phenomena [2-5]. Other researches presented a comparison between the effect of near fault and far fault ground motions including the characteristics of each type of ground motion [6]. Far field ground motion is characterized by low frequency motif, low peak acceleration but long duration, which means that it is possible to resonate the high rise building and cause failure of it [7].

This paper aims to investigate the seismic response of high rise building subjected to far field ground motions. 3 sets of far field ground motions were considered as caseloads to carry out linear time history analysis under Service-level Earthquake having a mean return period of 43 years (50% exceedance probability in 30 years) of 55 stories RC building. The seismic response results were evaluated such as inter story drift. The study concluded that far field ground motions resulted in significant value of inter story drift. Therefore, the impact of far field ground motions on the seismic response of some high rise building may be significant.

2. FAR FIELD GROUND MOTIONS

To carry out the time history analysis, 3 sets of far field ground motions were selected as agreed with Turkish Code Provisions-TEC2007 [8]. The maximum results from the 3 sets will adopted. The ground motions were selected in accordance with recommendations stated in FEMA695 and PEER initiative of high rise building [9,10,11]. Some properties of three far field ground motion records are given in Table 1.

Table 1: Summary of far field ground motion records. PEER, NGA_Flatfile, [11]

ID No	Record Sequence Number	source fault type	Earthquake Name	Station Name	Earthquake Magnitude	Epi. D (km)	Joyner-Boore Dist. (km)	Campbell R Dist. (km)	PGA (g)	PGV (cm/sec)	PGD (cm)
				Far field ground motions							
1	1148	strike-slip	Kocaeli, Turkey	Arcelik	7.51	53.68	10.56	13.52	0.1741	28.45	25.84
2	1161	strike-slip	Kocaeli, Turkey	Gebze	7.51	47.03	7.57	10.98	0.1833	38.30	33.69
3	1602	strike-slip	Duzce, Turkey	Bolu	7.14	41.27	12.02	12.41	0.7662	59.68	17.69

The response spectra of the used ground motions were obtained using SeismoSignal2016 software [12]. The elastic displacement response spectra for far field ground motions in *x* and *y* directions are presented in Fig.1 and Fig.2 respectively.
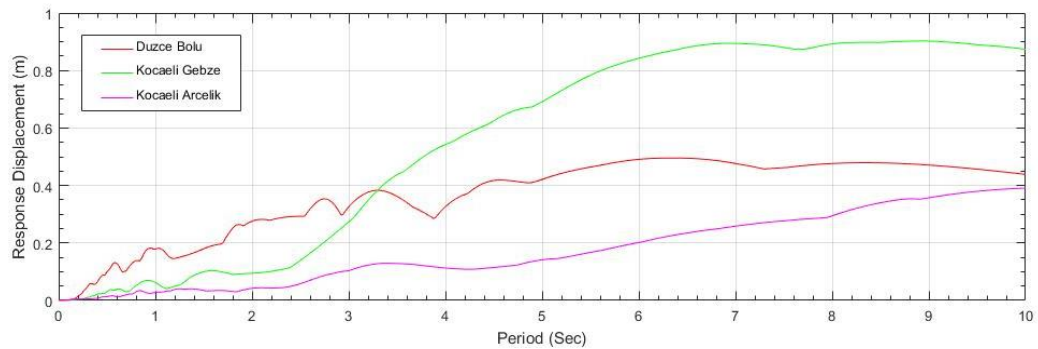
Figure 1: Elastic displacement response spectrum of far field ground motion in x direction 5% damping ratio.
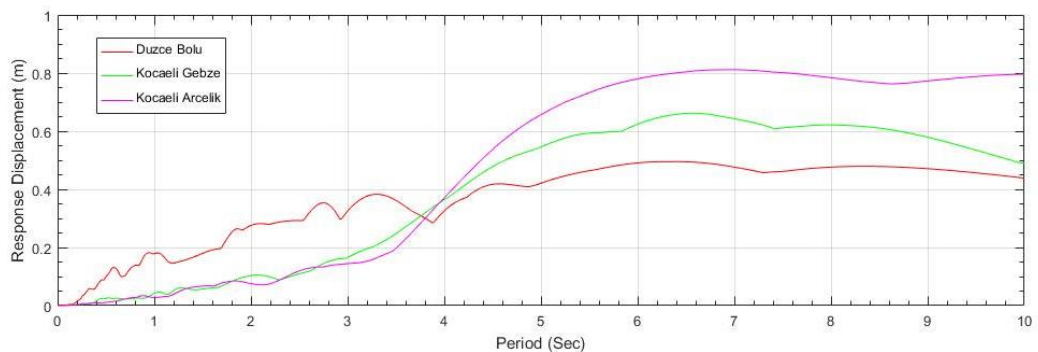
Figure 2: Elastic displacement response spectrum of far field ground motion in y direction 5% damping ratio.

3. CASE STUDY OF 55- STORY RC BUILDING

An RC building consists of 55 stories was taken as a case study. The RC building consists of 50 similar stories above the ground level and a podium of 5 stories. the typical story height is 3.5 m. the total height of the tower is 192.5m. The floor area of similar story is 780 m2. The floor area of podium story is 2700 m2. The lateral force-resisting system consists of a core wall and four shear walls along the x- direction, both of the core and 4 shear walls continue through the podium to the foundation level, in addition to exterior

basement walls around the perimeter of the 5-story podium. At ground level, a back stay diaphragm exists to transfer loads to the exterior basement walls. Typical plan for tower levels, basement levels, 2D elevation view and 3D view of the tower are presented in Figures 3-5.
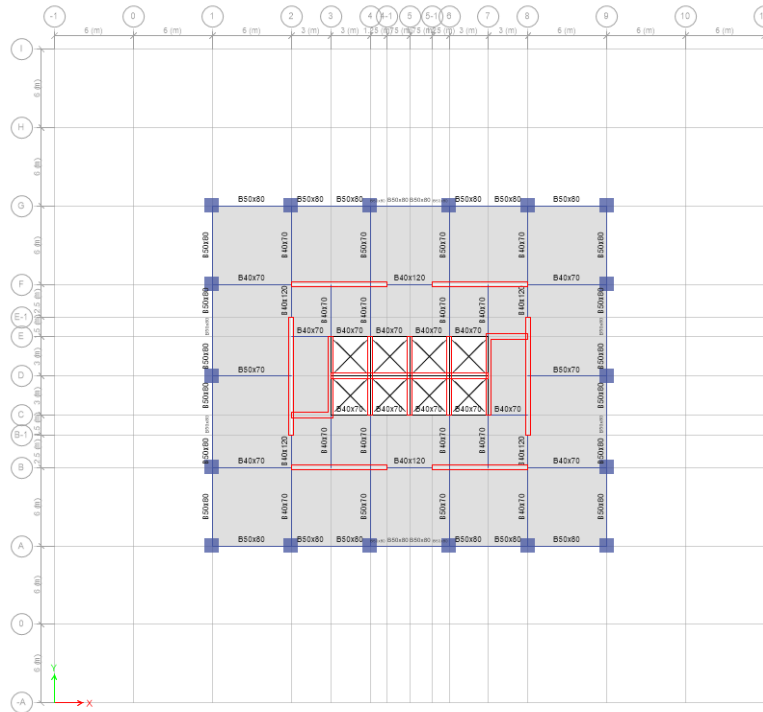
Figure 3: Typical story plan view of the case study.
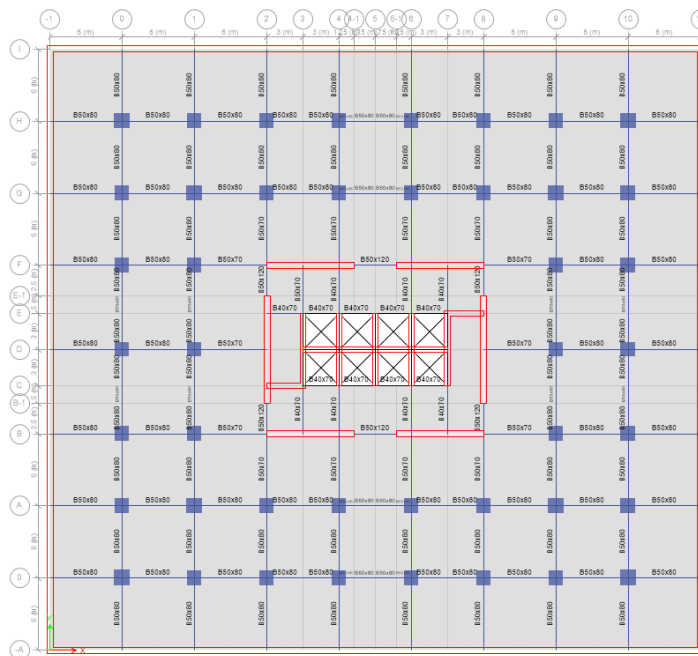
Figure 4: plan view of 5- story podium of the case study.
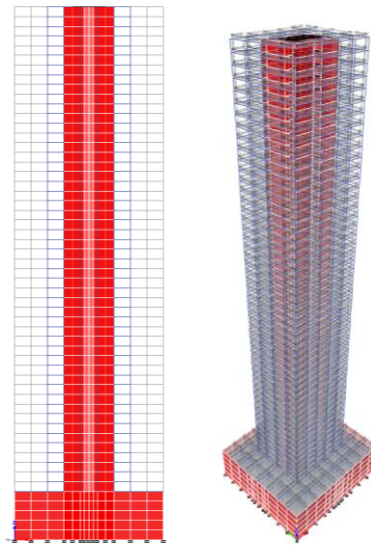
Figure 5: 2D Elevation and 3D- view of the case study.

3.1. Linear Time History Analysis:

A linear time history analysis under Service-level Earthquake having a mean return period of 43 years (50% exceedance probability in 30 years) was carried out used 3 sets of far field ground motions. The ground motions were scaled by time domain method to match the Turkish Response Spectrum of 5% damping ratio [13]. The first modal shape of the tall building is along the x-direction with time period of 5.82 sec., the second modal shape is in y- direction with time period of 4.157 sec., the third modal shape is torsion mode with time period of 3.995 sec. Time History analysis was carried out considering 3D model by ETABS v16.1.0. [14].

3.1.1. Evaluation of seismic response:

The ratio of inter story drift is considered as an important factor to evaluate and understand the structural behavior of high rise building [15]. Figs. 6 and 7 show the maximum and minimum inter story drift ratios resulted from far field ground motions in x and y directions respectively.
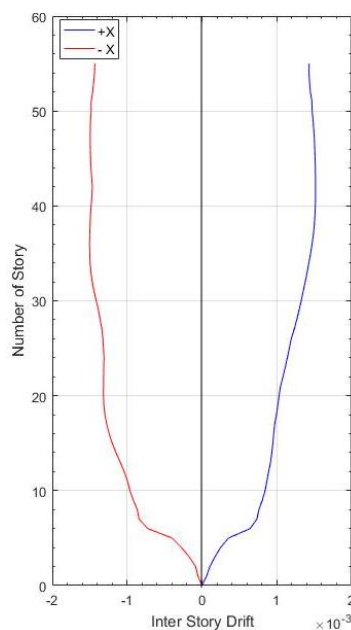
Figure 6: Inter story drift along x direction.
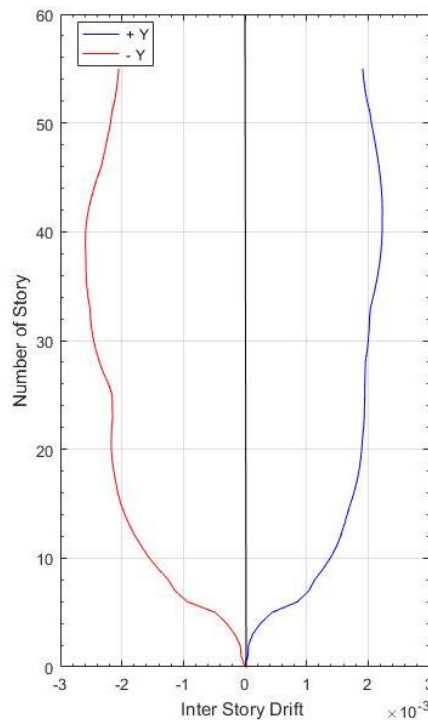
Figure 7: Inter story drift along y direction.

4. RESULTS AND DISCUSSION:

A linear time history analysis under Service-Level Earthquake having a mean return period of 43 years was carried out, Table 2 shows the maximum and minimum inter story drift ratios under the far field ground motions. The far field ground motions resulted in equal maximum and minimum inter story drift in x direction, but in different story level. The max and min. inter story drift ratio in x direction was 15% at the hight of 76% H_{total} and 65% H_{total} respectivily. Meanwhile, The max. and min. inter story drift ratio in y direction was 22% at the hight of 76% H_{total} and 26% at the hight of 71% H_{total}.

Table 2: Inter story drift ratios from far field ground motions.

	+ direction	- direction
Inter story drift ratios for x direction	0.15	0.15
Floor No.	42nd	36th
Inter story drift ratios for y direction	0.22	0.26
Floor No.	42nd	39th

5. CONCLUSION

In this study a linear time history analysis with 3 sets of far field ground motions under Service-level Earthquake having a mean return period of 43 years was carried out on a case study of 55-story RC high rise building. Inter story drifts increase extensively between 5-10 floors after the basal floors. There was a relative decrease after 40th floor.

The study concluded that far field ground motions resulted in a value of inter story drift ratio equal to 26% along which demands the necessity to consider the impact of far field ground motions on the seismic response of high rise building. This study is a preleminary study to invistigate the behavior of high rise building subjected to far field ground motions, more case studies and different parameters will be considered, a comparison between the structural response to far filed and near field ground motions will be conducted.

REFERENCES

[1] The emporis website. [Online]. Available: https://www.emporis.com/statistics/most-skyscraper-cities-worldwide.

[2] Ching Tung Huang, Shi- Shuenn Chen, Near field characteristics and engineering implication of the 1999 Chi-Chi Earthquake, Earthquake Engineering and Engineering Seismology, Vol:2, No. 1, March 2000, PP.23-41.

[3] Masumi Yamada, Anna H. Olsen, and Thomas H. Heaton, Statistical features of short-period and long-period near-source ground motions, Bulletin of the Seismological Society of America, Vol. 99, No. 6, pp. 3264–3274, December 2009.

[4] Karin Harnaes Hoel, Bjorn Thomas Svendsen, The effects of near-fault earthquakes on a high-rise structure in The Oslo Area, Department of Structural Engineering, Faculty of Engineering Science and Technology, NTNU - The Norwegian University of Science and Technology, June 2012.

[5] Ali Saffar, Fayaz R. Rofooei, Collapse capacity assessment of regular tall buildings under pulse like near field ground motions, 7th International Conference on Seismology & Earthquake Engineering, 18-21 May 2015.

[6] Anil K. Chopra and Chatpan Chintanapakdee, Comparing response of SDF systems to near-fault and far-fault earthquake motions in the context of spectral regions, Earthquake Engineering and Structural Dynamics. 2001.

[7] Jianping Han, Ming Chen, Seismic performance investigation on out-of-code high-rise building under near-fault and far-field ground motion, 2016 International Conference on Power Engineering & Energy, Environment (PEEE 2016).

[8] TEC 2007, Specification for Buildings to be Built in Seismic Zones, Ministry of Public Works and Settlement, Government of Republic of Turkey.

[9] Marshall Lew, Farzad Naeim, Martin B. Hudson and Boris O. Korin, Challenges in specifying ground motions for design of tall buildings in high seismic regions of the United States, The 14th World Conference on Earthquake Engineering October 12-17, 2008, Beijing, China.

[10] Quantification of Building Seismic Performance Factors, *FEMA P695 / June 2009.*

[11] Pacific earthquake engineering research center. Tall buildings initiative. [Oline]. Available: http://peer.berkeley.edu/tbi/.

[12] SeismoSoft.2017. SeismoSignal2016—A computer program for for the processing of strong-motion data. [online]. Available from www.seismosoft.com. [Official release of 06/04/2016].

[13] Yasin M. FAHJAN, Selection and scaling of real earthquake accelerograms to fit the Turkish Design Spectra, Teknik Dergi Vol. 19, No. 3 July 2008.

[14] Computer & Structures, INC. ETABS 2016, V16.1.0 - the ultimate integrated software package for the structural analysis and design of buildings. [online]. Available from www.csiamerica.com.

[15]   Zhou & G.B. Bu, K.N. Li, Calculation Methods for Inter-Story Drifts of Building Structures, 15th world conference on earthquake engineering (15 WCEE), 2012.

Comparison of Different Analytical Models of Infilled RC Frame

M. Omer Timuragaoglu[1], Adem Dogangun[2], Ramazan Livaoglu[3]

Abstract

Seismic performance of infilled reinforced concrete (RC) frame has been investigated by several researchers and become one of the most studied topic in the last five decades. However, the effect of infill wall is still not included in calculations because of fast degradation of strength, stiffness and energy dissipation capacity although the contribution of infill walls to initial stiffness, total strength and energy dissipation capacity of frame is expressed by different researchers and emerged in several different academic researches. In the present study, the influence of infill wall is investigated by using a commonly used analytical method; equivalent compressive strut. For this reason, a full scaled, one bay and one storey gas concrete infilled RC frame and a bare frame, representing weak sides of existing buildings widely used in Turkey, is produced and tested experimentally under lateral cyclic loading. Furthermore, in analytical models, three different strut models (one, two and three strut) are used to take into account the effects of wall on the RC frame and to compare the effectiveness of one and multi-strut models. Mander model for confined concrete is used to present stress strain relation of RC, whereas a tetra linear relationship is used in modeling of struts to represent the nonlinear behavior of infill wall. The analytical and experimental results are compared considering strength and stiffness of system. The analytical studies demonstrate that single equivalent strut model is a simple and effective way of representing global behavior of infilled RC frames. Additionally, using multi strut instead of one will only cause small variations in initial stiffness and strength of the system.

Keywords: *Equivalent compressive strut; Infill wall; Reinforced concrete*

1. INTRODUCTION

Seismic performance of infilled Reinforced Concrete (RC) framed structures has been gained much attention for more than half a century. The contradiction between researchers is to include the effects of infill wall in structural analysis or not. This is an ongoing debate. Researchers of agreeing with including infills in analysis come up with the influence of infill on strength, stiffness and energy dissipation capacity of RC frame, whereas the supporters of excluding infill in analysis argued that these properties have temporary influence on system and right after the crack occurred in infill, its effects are decreased with increased lateral force. However, although an observable degradation is seen in the strength, stiffness and energy dissipation capacity of the system, the enhancements of infill wall on the global system is an undeniable fact. However, the contradiction is still going on due to the fact that infilled RC frame behavior depends on several parameters.

Several analytical and experimental studies have been conducted in order to understand the seismic behavior of infilled frames. First, Reference [1] suggested to model the infill wall replacing with an equivalent diagonal strut. Afterwards, Reference [2], based on diagonal strut model, proposed an equation to specify the width of the equivalent diagonal strut. Reference [3], by taking into account strength and rigidity decrease in infill wall, suggested six strut model to predict the reaction of infilled frame under seismic loads in which only three struts are active in analysis. Reference [4], by proposing three-strut model, presented a simple method of estimating the stiffness and the lateral load capacity of concrete masonry-infilled steel frames (CMISFs) failing in corner crushing mode, as well as the internal forces in the steel frame members. Reference [5] suggested a new macro model to represent the influence of infill wall on the frame. The compressive and shear of the wall is taken into account separately by using two compressive strut and a shear spring. Reference [6] developed an analytical model based on the commonly used equivalent tie and strut approach in which the envelope properties of the strut are determined based on test data to define idealized

---

multi linear load-deformation relations of infill panel with openings. Reference [7] present a general review of the different macromodels used for the analysis of infilled frames by pointing out the advantages and disadvantages of each macro model and by indicating practical recommendations for the implementation of the different models. Recently, Reference [8] provided a large literature review including modeling techniques developed in the last decades, going from refined nonlinear FE micromodel approaches to simplified equivalent single or multiple strut macromodels. Reference [9] discussed the mechanical behavior of infilled frames under in-plane lateral loading and an analytical law considering the effects of vertical loads on the characteristics of pin-jointed diagonal strut. Reference [10] proposed an analytical expression, taking into account the effects of opening and vertical load, for the determination of the equivalent strut width considering extensive numerical finite element models. More recently, Reference [11], for seismic assessment of infilled frame structures, proposed an alternative macro-element approach. A multi-storey plane frame prototype is investigated and results are compared with a commonly used single-strut model.

In the present study, the influence of gas concrete infill wall on RC frame is investigated using macromodeling technique in which infill wall is replaced by a compression-only equivalent strut. In the analysis, one, two and three struts are used to represent the behavior of infill wall. The experimental test and analytical results are compared with each other. Since the experimental campaign of this study is done earlier by [12], only the results will be presented here together with analytical results.

2. MODELING OF INFILLED FRAME

Although RC is comprised of two different materials, it is modeled as a homogeneous material in analysis. Mander model, widely used in literature in order to represent stress-strain relationship for confined concrete, is used in FEA. Detailed explanation of analytical model of concrete can be found in literature [13].

A tetra linear relationship, proposed by [14], is used in FEA to represent the nonlinear behavior of infill wall. Reference [14], based on cyclic experimental tests on frames with brick infill panels, defined a simplified tetra linear relationship as shown in Figure 1. The branches describe the shear behavior of the infill panel, detachment of frame-infill (formation of strut), softening response after the displacement S_m, and a final constant residual resistance (generally introduced to improve numerical stability). The determination of parameters necessary to define the different branches of strut curve can be found in the mentioned paper.
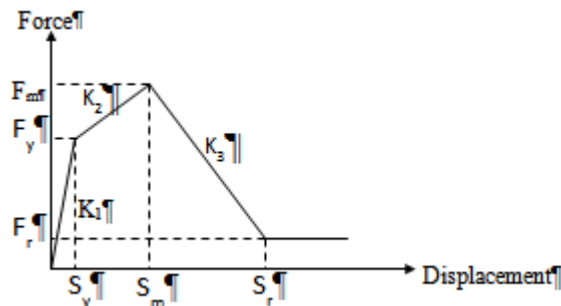
Figure 1. Force- displacement relationship for strut model (Panagiotakos and Fardis, 1996)

Multi-point constraints (MPCs), which is available in nonlinear FEA software [15], allow constraints to be imposed between different degrees of freedom of the model. MPC type pin provides a pinned joint between two nodes. This MPC makes the global displacements equal but leaves the rotations, if they exist, independent of each other. On the other hand, MPC beam provides a rigid beam between two nodes to constrain the displacement and rotation at the first node to the displacement and rotation at the second node, corresponding to the presence of a rigid beam between the two nodes. At first glance, MPC type pin constraint seems to be suitable for our model. But, both constraints gave proximate results while MPC type pin has ended suddenly in the quarter of the analysis. For this reason, MPC type beam is used in the analysis.

The base of the frame is modeled as fixed and there is no gravity load on the frame. The force applied to a surface corresponding to the height of the beam. Compression struts are modeled as linear beam elements with the same material properties and thickness of infill wall. Material and geometric properties of struts used in the analysis are given in Table 1. In this table, E_m specifies elasticity modulus of infill wall, f_{tp} defines the shear strength of the panel, t is the thickness of infill wall, w width of the diagonal strut and Z_h is the contact length between wall and surrounding frame.

Table 1. Material and geometric properties of struts

Infill type	E_m (MPa)	f_{tp} (MPa)	t (mm)	w (mm)	Z_h (mm)
Gas concrete	1000	0.15	200	$d_m/4=800$	1200

3. COMPARISON OF EXPERIMENTAL AND ANALYTICAL RESULTS

In this study, a full scale bare frame and one bay-one storey gas concrete infilled RC frame systems are modeled and analyzed under lateral loading using Finite Element Method (FEM). The experimental studies of this paper was done earlier by [12] as a doctorate dissertation. Three different equivalent strut approaches are used to evaluate the efficiency of the strut models. These models are one, two and three strut models.

The comparison of experimental test and numerical analysis results of force-displacement curve of bare and gas concrete infilled frame is given in Fig. 2a and 2b, respectively. As can be seen from the figure, both the initial stiffness and ultimate base shear of test results is captured well in numerical analysis of bare and infilled frame. For bare frame, the ultimate base shear in experimental test and numerical analysis have values of 74.6kN and 77.03kN. The difference between test and FEA results is approximately 3.3%. The lateral displacement and storey drift ratio corresponding to maximum experimental base shear is about 45mm and 2.1%, respectively while it is 48mm and 2.15% for numerical analysis results. The ultimate load, in gas concrete infilled frame, is 133.2kN and achieved at a displacement of 24.2mm and drift of 1.1%.
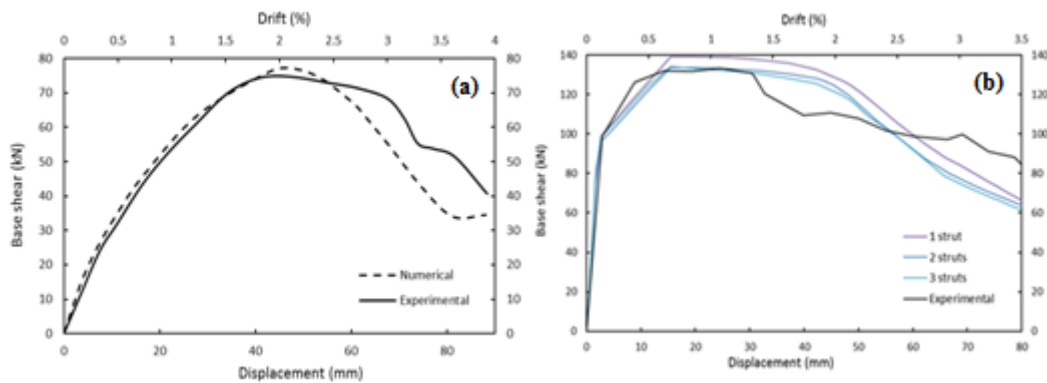
Figure 2. Comparison of experimental and analytical results for (a) bare frame (b) gas concrete infilled frame

The failure of the system contains of one or two simple failure types generally occur in frame or infill wall. It is rather hard to estimate the failure type which can happen in infilled RC frames because it depends on various parameters such as stiffness of frame or wall, their components, dimensions, mechanical properties etc. The failure types observed in frames from both experimental test and FEA results for gas concrete infilled system are shown in Figure 3. Initiation of damage of FEA results of one, two and three strut model analysis is shown in Figure 3b, c and d. It is obviously seen from the figure that plastic hinges (FF mode) formed in beam-column joints in experimental test are also formed in strut models while the formation is best observed in multi-strut models. Furthermore, in two-strut analysis result, only columns are damaged at the beginning of the analysis due to the configuration of strut on columns.
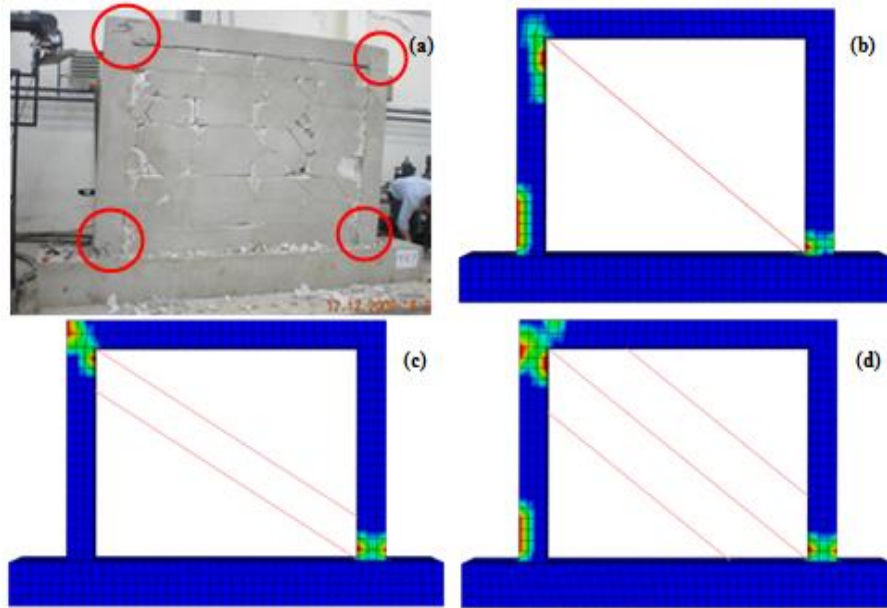
Figure 3. Comparison of experimental and analytical damages in gas concrete infilled frame

4. CONCLUSIONS

In this paper, the efficiency of different equivalent compression only strut models are compared. Three different strut configurations are used in models to understand the efficiency of strut models. These are one, two and three strut models.

The experimental results of bare and infilled frames showed that infill wall, when added to frame, reduces both lateral displacement and drift ratio of system at ultimate load, whereas it increases initial stiffness and strength capacity of system.

By comparing the analytical results of one, two and three strut models, it can be concluded that three strut model gives the best results in term of damage associated with surrounding frame while damages occurred only in leeward and windward columns in two strut model. Additionally, in one strut model, the global behavior of infilled frame is also captured.

Finally, it must be noted that the equivalent strut approach is valid only for infill walls without openings. Thus, equivalent strut method for infill walls with openings should be investigated experimentally and analytically.

REFERENCES

[1]. Polyakov, S. V. 1960. *On the interaction between masonry filler walls and enclosing frame when loading in the plane of the wall*. Translation in earthquake engineering, Earthquake Engineering Research Institute (EERI), San Francisco.

[2]. Holmes, M. 1961. "Steel Frames with Brickwork and Concrete Infilling," Proceedings of the Institution of Civil Engineers, 1961, London, Part 2, 19, 473-478.

[3]. Chrysostomou, C. Z., Gergely, P., and Abel, J. F. 1992. "Non-linear seismic response of infilled steel frame*s,"* Proceedings of 10th World Conference on Earthquake Engineering, 1992, Madrid, Spain.

[4]. El-Dakhakhni, W.W, Elgaaly, M. and Hamid, A.A. 2003. Three strut model for concrete masonry-infilled steel frames. ASCE, Journal of Structural Engineering, 129(2), 177-185.

[5]. Crisafulli, F. J. and Carr, A. J. 2007. Proposed macro-model for the analysis of infilled frame structures. Bull NZ Soc. Earthquake Engineering, 40(2), 69–77.

[6]. Kakaletsis, D. 2009. Analytical modeling of masonry infills with openings. Structural Engineering and Mechanics. 31(4), 423-437.

[7]. Asteris, P.G., Antoniou, S.T., Sophianopoulos, D.S., and Chrysostomou, C.Z. 2011. Mathematical macromodeling of infilled frames: State of the art. Journal of Structural Engineering, 137(12), 1508-1517.

[8]. Di Trapani, F. Macaluso, G. Cavaleri, L. and Papia, M. 2015. Masonry infills and RC frames interaction: literature overview and state of the art of macromodeling approach. European Journal of Environmental and Civil Engineering, 19(9), 1059-1095.

[9]. Campione, G., Cavaleri, L., Macaluso, G., Amato, G., & Di Trapani, F. (2015). Evaluation of infilled frames: an updated in-plane-stiffness macro-model considering the effects of vertical loads. Bulletin of Earthquake Engineering, 13(8), 2265-2281.

[10]. Asteris, P. G., Cavaleri, L., Di Trapani, F., & Sarhosis, V. (2016). A macro-modelling approach for the analysis of infilled frame structures considering the effects of openings and vertical loads. Structure and Infrastructure Engineering, 12(5), 551-566.

[11]. Pantò, B., Caliò, I., & Lourenco, P. B. (2017) Seismic safety evaluation of reinforced concrete masonry infilled frames using macro modelling approach. Bulletin of Earthquake Engineering, 1-25.

[12]. Arslan, M.E. 2013. Deprem kumasıyla güclendirilen cevrimsel yük etkisindeki dolgu duvarlı betonarme cercevelerin davranıslarının deneysel ve teorik olarak incelenmesi. Doctorate dissertation, Karadeniz Technical University, Trabzon (In Turkish).

[13]. Mander, J.B., Priestley, M.J.N. and Park, R. 1988. Theoretical stress-strain model for confined concrete. Journal of structural engineering, 114(8), 1804-1826.

[14]. Panagiotakos, T. B., and Fardis, M. N. (1996). Seismic response of infilled RC frames structures. In 11th world conference on earthquake engineering (pp. 23-28).

[15]. Abaqus 2013. ABAQUS Documentation, Dassault Systèmes, Providence, RI, USA.

An Investigation of Intelligent and Conventional Maximum Power Point Tracking Techniques for Uniform Atmospheric Conditions

Ekrem Kandemir[1,2], Numan Sabit Cetin[2], Selim Borekci[3]

Abstract

In recent years, power generation from photovoltaic (PV) system has received great attention compared to other renewable sources. Due to nonlinear characteristics of PV cells, the maximum allowable power level from PV panel changes with atmospheric parameters which are solar irradiance and temperature. In this context, maximum power point tracking (MPPT) algorithms are essential to maximize the output power of PV panel for any solar irradiance and temperature values. In the literature, various MPPT techniques have been studied to deliver maximum power from PV systems. Hence, this study discusses intelligent control techniques, which are called fuzzy logic controller (FLC) and neural network controller (NNC), and compares efficiency performance and convergence speed to conventional perturb & observe (P&O) and incremental conductance (Inc. Cond.) tracking techniques for MPPT of PV system..

In this paper, 150W PV panel model is investigated for different atmospheric conditions in MATLAB. Results of simulation show that NNC based and FLC based MPPTs have 4.66% better tracking accuracy than conventional P&O and Inc. Cond. under standard test condition (STC). NNC based MPPT has best iteration response rate among the other MPPTs under uniform atmospheric conditions. Therefore, the NNC based MPPT presents best superior quality in terms of efficiency and convergence speed for PV systems among the other MPPTs.

Keywords: *PV Model, Maximum Power Point Tracking, Perturb & Observe, Incremental Conductance, Fuzzy Logic Control, Neural Network Control*

1. INTRODUCTION

For a long term and sustainable supply of energy, it is essential to exploit and utilize the renewable sources at a much larger scale [1]. Compared to other renewable sources, photovoltaic energy (PV) has proven to be more pollution – free, noise – free and has limitless source of energy [2]. In addition, PV power has commonly used for industrial, commercial, residential and military purposes [3]. However, PV power is environment dependent such as solar irradiance and ambient temperature because of nonlinear electrical characteristics of PV cells. The development for improving the efficiency of the PV system is still a challenging field of research and the maximization of extracted PV power from PV systems is a matter concern as its conversion efficiency is low [4], [5].

In general, PV panels have only one maximum power point (MPP) on its power – voltage curve where PV panel produces its maximum power under uniform solar irradiance condition and this point changes with solar irradiance and temperature [6]. The position of MPP on the corresponding power – voltage curve varies depending on solar irradiance, temperature and also electrical load. Therefore, to make the PV power generation efficient, a capable maximum power point tracking (MPPT) techniques are used to estimate and to track the actual MPP against any environmental parameters changes such as solar irradiance and temperature [7].

---

[1] *Corresponding author: TUBITAK National Observatory, Research & Development Department, 07058, Antalya, Turkey, ekrem.kandemir@tubitak.gov.tr.*

[2] *Ege University, Solar Energy Institute, 35100, Izmir, Turkey, numan.sabit.cetin@ege.edu.tr.*

[3] *Akdeniz University, Electrical – Electronics Engineering Department, 07058, Antalya, Turkey, sborekci@akdeniz.edu.tr.*

Numerous MPPT techniques have been investigated in the literature such as Perturb & Observe (P&O), incremental conductance (Inc. Cond.), fuzzy logic controller (FLC) and neural network (NN) [1], [3], [8], [9]. The quality of an MPPT technique is evaluated in terms of its complexity, cost, tracking speed, accuracy and number of sensors required for its implementation [10]. Because of being simplicity and easy to implement, P&O and Inc Cond. MPPT techniques, which are known as a few of conventional MPPTs, are ones of the most preferred algorithms in the literature. Although, these methods present some drawbacks in its design such as convergence and oscillation problems around MPP region. To remove these drawbacks and enhance the performance of PV panels, intelligent or soft – computing MPPTs such as fuzzy logic and/or neural network based techniques are widely preferred in the literature [11].

In this paper, conventional MPPTs such as P&O and Inc. Cond. and intelligent MPPTs such as FLC and NN based MPPTs are investigated and compared in terms of tracking accuracy and convergence speed. Related analysis and simulation results are discussed separately for each MPPT technique and comparison tables for conventional and intelligent MPPTs are provided in detail.

2. PV CELL AND EQUIVALENT CIRCUIT MODEL

PV cells are the main components of the PV systems and they consist of p – n junction semi – conductor materials that sunlight exposure causes to release electrons around a closed circuit. Typically, they are modelled either as single diode or double diode equivalent circuits but single diode model is more preferred because of simplicity and easy to implement [11], [12].
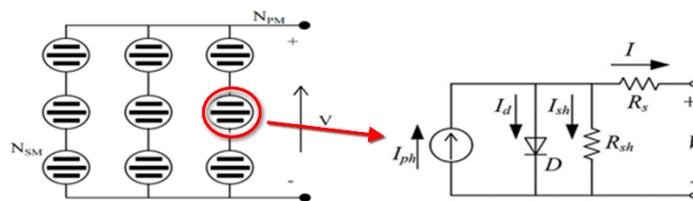
Figure 61. PV panel and single diode circuit model of a PV cell [11]

PV panel consists of several series and/or parallel connected PV cells in order to generate higher level electrical power. Figure 1 depicts single diode equivalent circuit model of a PV cell, which transforms directly sunlight into electrical current.

The output current of the PV cell can be expressed in Eq. (1) as,

$$I = I_{ph} - I_o \left(e^{\frac{q(V+R_sI)}{AkT}} - 1 \right) - \frac{V+R_sI}{R_{sh}} \tag{1}$$

where I and V represent PV cell output current and voltage. R_s and R_{sh} are the PV cell series and shunt resistances respectively. I_{ph} is the PV cell photo current, I_o is the diode saturation current, A is the diode quality factor ($\cong 1.2$), k is Boltzmann's constant (1.38×10^{-23} J/K) and T is the PV cell temperature in kelvins [6].

By solving Eq. (1) or using equivalent circuit model as shown in Figure 1, electrical characteristic curve of the related PV panel can be obtained for any environment condition in the simulations, MATLAB i.e. During uniform environment conditions where the solar irradiance is equally distributed among the PV panels, only single maximum power point is available in the PV panel's power – voltage curve as shown in Figure 2. And this MPP point changes with solar irradiance and temperature [6]. As shown in Figure 2, PV panel power is almost proportionally with the variation of solar irradiance. Hence, when solar irradiance increases, the maximum PV panel power also increases. In addition, the variation of temperature affects PV panel power inversely that PV power increases if temperature decreases.
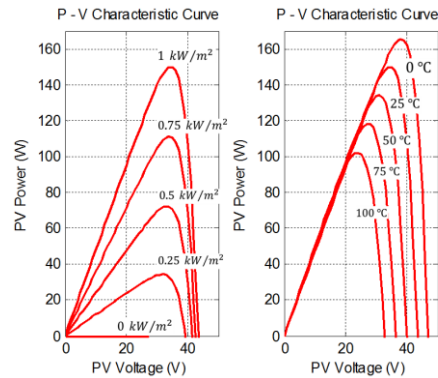
Figure 2. Voltage and power curves of PV panel for different solar irradiance and temperature conditions [6].

3. CONVENTIONAL AND INTELLIGENT MPPT TECHNIQUES

PV cells and panels operates on different power level depended on different environment condition and electrical load. Because of that, generation of maximum power is not guaranteed at all electrical loads [13]. Hence, MPPTs provide to ensure that at any environmental condition, i.e. any solar irradiance or temperature, maximum achievable power is extracted from PV system [12].

The MPPTs can be classified in many different groups depending on several parameters i.e. MPPT strategy, tracking speed, complexity, PV panel dependency, etc. In general, MPPT techniques are classified into two types [6]:

- Conventional techniques,
- Intelligent techniques.

The most popular conventional techniques are perturb & observe (P&O) and incremental conductance (Inc. Cond.) in the literature. These algorithms are widely used in commercial products due to their simplicity and robustness. On the other hand intelligent MPPTs such as fuzzy logic control (FLC) and neural network (NN) tend to be more versatile, efficiency and better steady state performance [1].

3.1. Perturb & Observe (P&O) Technique

This technique is commonly preferred by the researchers to implement MPPT operation for the PV systems because of simplicity and exhibiting enough convergence accuracy. In this technique, a perturbation is applied to PV panel voltage and PV panel output power is observed. The aim of this technique is to adjust PV panel voltage to the voltage of MPP of PV panel (V_{mpp}) to extract maximum power from the PV panel for the actual environment condition. This is done by applying small and constant perturbation to the PV voltage a step by step. After each perturbation, the output PV power variation (dP) is observed according to the variation of the PV voltage (dV) [5]. If the sign of (dP/dV) is positive, the actual point is in the left side of the MPP and the PV voltage should be increased to reach MPP; else the sign of (dP/dV) is negative, the actual point is in the right side of MPP and the PV voltage should be decreased to reach MPP [6]. This process is performed until (dP/dV) equals to zero. This mechanism is also defined as below.

$$\frac{dP}{dV} = 0 \Rightarrow at\ MPP \tag{2}$$

$$\frac{dP}{dV} > 0 \Rightarrow Left\ Side\ of\ MPP \tag{3}$$

$$\frac{dP}{dV} < 0 \Rightarrow Right\ Side\ of\ MPP \tag{4}$$

The disadvantage of this method is that at vicinity of MPP, it oscillates around MPP and this causes steady state error. Low values of perturbation size reduces steady state error at the cost of reduction in tracking speed [12]. In addition, this technique sometimes fails to track the MPP under rapid changing environment conditions.

3.2. Incremental Conductance (Inc. Cond.) Technique

This technique basically uses similar way but different relationship of PV characteristic curve from P&O technique to determine MPP. In this method, derivative of PV current and PV voltage are used to determine the movement of the actual operating point [6]. After each perturbation of PV voltage, the output PV current

is observed to determine MPP. If the $(\Delta I/\Delta V)$ is greater than negative sign of the actual PV conductance value, the actual point is in the left side of MPP and the PV voltage should be increased to reach MPP; else the $(\Delta I/\Delta V)$ is lower than the negative sign of actual PV conductance value, the PV voltage should be increased. And this process is performed until the $(\Delta I/\Delta V)$ equals to negative sign of the actual PV conductance value. This mechanism is also defined as below.

$$\frac{\Delta I}{\Delta V} = -\frac{I}{V} \Rightarrow at \ MPP \tag{5}$$

$$\frac{\Delta I}{\Delta V} > -\frac{I}{V} \Rightarrow Left \ Side \ of \ MPP \tag{6}$$

$$\frac{\Delta I}{\Delta V} < -\frac{I}{V} \Rightarrow Right \ Side \ of \ MPP \tag{7}$$

As the tracking of MPP is done rapidly it helps to overcome the disadvantage of the P&O technique which fails to track the MPP control under fast varying conditions and it can be easily implemented in a simple microcontroller [6], [7]. The main disadvantage of this technique is its perturbation size, which causes oscillations and steady state error around MPP, and complexity.

3.3. Fuzzy Logic Control (FLC) Based Technique

Fuzzy logic control (FLC) based MPPT is one of the most used intelligent method to perform MPPT task for any PV system in any environment condition [4], [14]. FLC is operated by using membership functions instead of mathematical model. It consists of three stages: fuzzification, fuzzy inference engine, rule tables and defuzzification as shown in Figure 3.
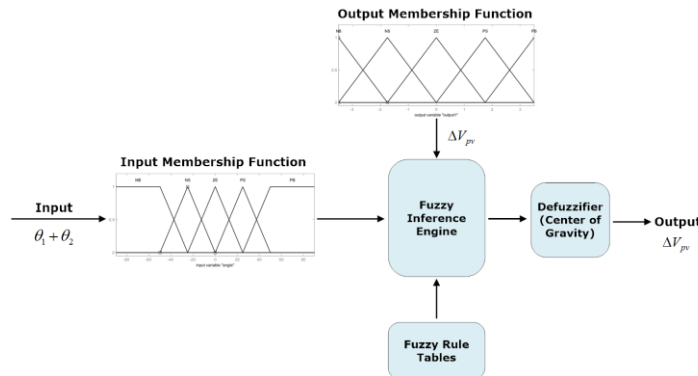
Figure 3. Block diagram of the FLC based MPPT
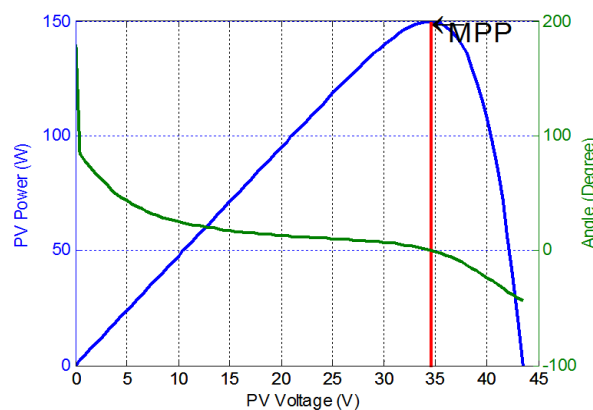
Figure 4. PV power – voltage and the angle ($\theta_1 + \theta_2$) MPPT relation for the proposed FLC based MPPT

In the proposed FLC system, the input of FLC is sum of angle conductance and angle of increment conductance. The input variables are expressed in Eq. (8) and the MPPT determination condition is illustrated in Figure 4.

$$\theta_1 + \theta_2 = \tan^{-1}\left(\frac{dI_{pv}}{dV_{pv}}\right) + \tan^{-1}\left(\frac{I_{pv}}{V_{pv}}\right) = 0° \tag{8}$$

During fuzzification process, input variables are converted into some defined linguistic variables according to chosen membership functions. For that purpose, the linguistic variables of the input are defined as NB (Negative Big), NS (Negative Small), ZE (Zero), PS (Positive Small) and PB (Positive Big). In fuzzy inference stage, the linguistic variables get manipulated based on the fuzzy rule base which defines the behavior of the controller as shown in Figure 5. In the defuzzification process, the FLC output is converted to a numerical value from the linguistic variable using membership function for the output [7].

$\theta_1 + \theta_2$	NB	NS	ZE	PS	PB
ΔV_{pv}	NB	NS	ZE	PS	PB
Region Area	Region 1		Region 2	Region 3	
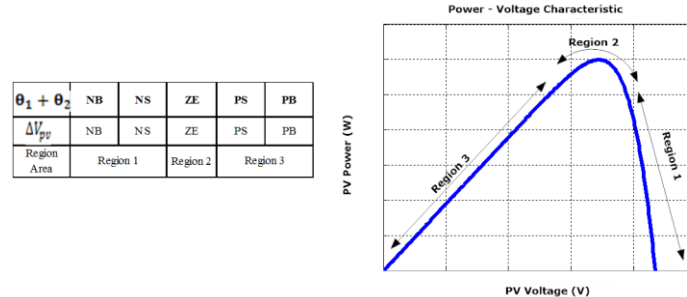
Figure 5. Fuzzy rule table and MPPT process in inference stage of the proposed FLC

The main advantages of FLCs are: no requirement of exact mathematical model of system to implement, capable of working with indefinite inputs, ability of handling non – linearity, fast and accurate convergence and tracking efficiency etc. The main disadvantages are: necessary to be tuned periodically, more complex structure, dependency to system and requiring prior knowledge of the behavior of PV system [5], [7], [12].

3.4. Neural Network (NN) Based Technique

The neural networks (NN) are becoming popular for system identification and non – linear system modelling applications. This technique is used to solve the difficult problems using parameter approximation. In recent days, NN control techniques are rising incrementally for the optimization and MPPT application of renewable power systems instead of conventional techniques [7], [9].

For MPPT operation, multi – layer feed forward neural network structure is commonly preferred and this NN structure consists of three layers: input, hidden and output layers as shown in Figure 6.
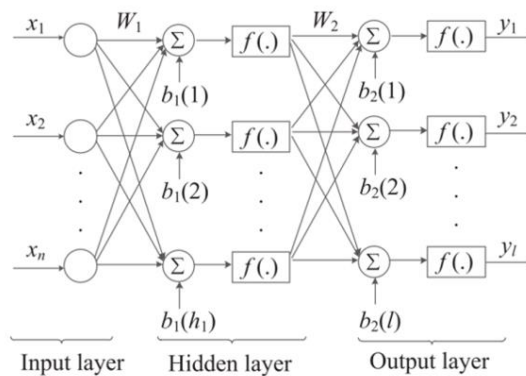
Figure 6. Architecture of multi-layer feed forward neural network [15].

The input layer receives input environmental data such as solar irradiance and temperature; second layer called as hidden layer contains 10 hidden neurons to estimate MPP value and sends to third layer. The third layer called as output layer contains single neuron to provide output to system. For MPPT purpose, 104 training data including MPP values for different solar irradiance and temperature values are applied 1000 times to train the designed NN structure. In addition, 10 different validation data, which also contains MPP values for different solar irradiance and temperature values, are used to verify and analyze performance of the trained neural network. After training the neural network 1000 times with the training data, the error of the neural network is approx. 1.5×10^{-4} according to the verification data. The performance analysis of the neural network is shown in Figure 7.
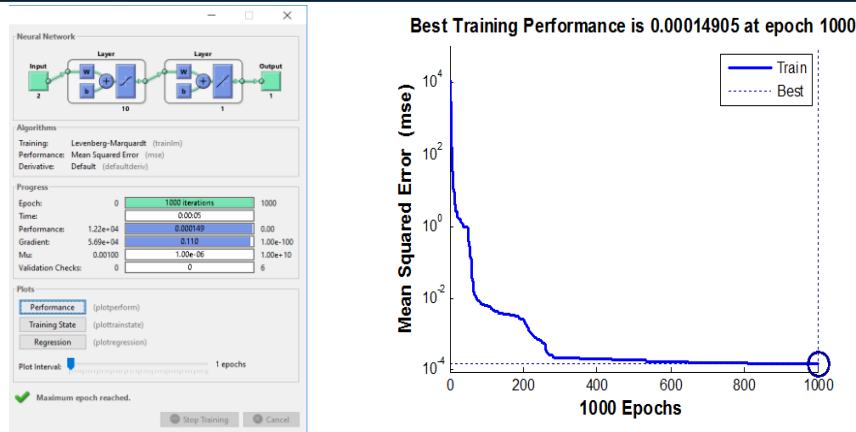
Figure 7. (a) Training result of the designed neural network (b) Performance result and error of the neural network

The main advantage of NN based MPPT technique is that it can provide satisfactory tracking accuracy of MPP and higher convergence speed without the exact information of the model parameters. However, its disadvantage is that it has to be specifically trained for the PV system on which it has to be implemented. In addition, the neural network requires to train in regular intervals of time to ensure accurate and efficient tracking of MPP when considering that the electrical characteristic of PV panel is time varying [5].

4. COMPARISON RESULTS OF CONVENTIONAL AND INTELLIGENT MPPTS

This study investigates a comparison between conventional P&O and Inc. Cond. MPPTs and intelligent FLC and NN based MPPTs in MATLAB. The performance of P&O, Inc. Cond. MPPT techniques with 3.5 V derivation parameter, fuzzy logic and neural network based MPPT techniques performance results are given in Figure 8 for standard test condition (1 kW⁄m², 25℃).
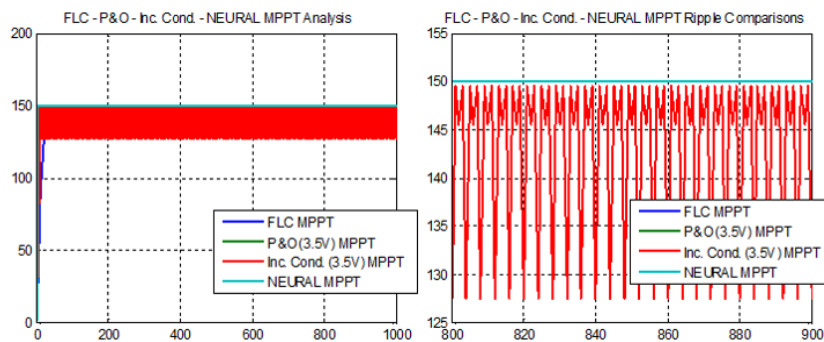
Figure 8. Conventional and intelligent MPPTs simulation results for standard test condition (1 kW⁄m², 25℃)

As shown in Figure 8, intelligent FLC and NN based MPPTs are 4.66% more efficient than conventional P&O and Inc. Cond. MPPTs. Especially, neural network based MPPT has best iteration rate and also tracking accuracy among the other MPPTs. The conventional MPPTs have 4.45 times faster convergence speed but 4.66 % less tracking accuracy than FLC based MPPT due to oscillations around MPP. The overall simulation results in terms of iteration rate and tracking accuracy performance are given in Table 1.

Table 1. Comparison results for conventional and intelligent MPPTs at standard test condition (1 kW⁄m², 25℃)

MPPT Type	MPPT Technique	Iteration Rate	MPP Power (W)	Tracking Accuracy (%)
Conventional	P&O (3.5 V)	11	142.988	95.33 %
	Inc. Cond. (3.5 V)	11	142.988	95.33 %
Intelligent	Fuzzy Logic Control	49	149.987	99.99 %
	Neural Network	2	149.987	99.99 %

To observe tracking accuracy and convergence speed for different environment condition, the following simulation results are discussed for different solar irradiance values (1, 0.8, 0.6, 0.4 kW/m^2) at a constant temperature (30℃) in Figure 9. The intelligent MPPTs have better tracking accuracy than conventional ones for different solar irradiance values due to no oscillations around MPP for fuzzy logic and neural network based MPPTs. According to the simulation results, neural network based MPPT technique is better than conventional MPPTs in terms of tracking efficiency and convergence speed and also faster than fuzzy logic based MPPT for standard and different environment conditions.
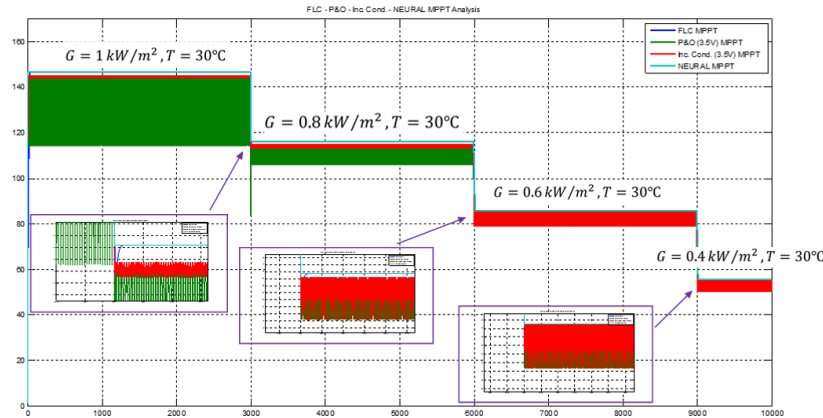
Figure 9. PV output power for conventional and intelligent MPPTs for different environment condition

Additionally, a characteristic comparison table in terms of panel dependency, tuning, tracking rate, complexity and required inputs for conventional and intelligent MPPT types, which are discussed in this paper, is presented in Table 2.

Table 2. Characteristic comparison for the MPPT techniques

MPPT Technique	PV Panel Dependency	Periodic Tuning	Tracking Rate	Complexity	Required Inputs
P&O	No	No	Variable	Low	Current, Voltage
Inc. Cond.	No	No	Variable	Moderate	Current, Voltage
Fuzzy Logic Control	Yes	Yes	High	High	Variable
Neural Network	Yes	Yes	High	Very High	Variable

Although, intelligent MPPTs are more difficult to implement and require additional PV panel information and periodic tuning; they have more efficient, robust and higher tracking rate features than conventional MPPTs.

5. CONCLUSIONS

In the last decade, PV energy generation has become one of the most used renewable energy choice instead of the fossil fuels. Compared to the other renewable sources, PV energy is more environmentally friendly, noise-free, low-cost and readily available universally. Hence, power generation from PV systems becomes important issue for the researchers. Due to non-linear characteristics of PV cells, the maximum allowable power level of PV systems is dependent on atmospheric parameters such as solar irradiance and temperature. Therefore, maximum power point tracking has turned out to be compulsory task to make energy conversion efficiently for the PV systems.

In this study, conventional P&O, Inc. Cond., intelligent FLC and NN based MPPT techniques performances are investigated and compared in terms of tracking efficiency and convergence speed for 150W PV panel under uniform environment conditions in MATLAB. According to the simulation results, intelligent MPPTs increased tracking efficiency 4.66% compared to the conventional MPPTs for the examined PV panel. Especially, NN based MPPT have best tracking and convergence performances among the other MPPTs. In addition, a characteristic comparison table for the investigated conventional and intelligent MPPT techniques is provided in this paper.

REFERENCES

[1]   J. Ahmed and Z. Salam, "A Modified P&O Maximum Power Point Tracking Method With Reduced Steady-State Oscillation and Improved Tracking Efficiency," IEEE Trans. Sustain. Energy, vol. 7, no. 4, pp. 1506–1515, Oct. 2016.

[2]   A. B. . Bahgat, N. . Helwa, G. . Ahamd, and E. . El Shenawy, "Estimation of the maximum power and normal operating power of a photovoltaic module by neural networks," 2004.

[3]   J.-K. Shiau, Y.-C. Wei, and B.-C. Chen, "A Study on the Fuzzy-Logic-Based Solar Power MPPT Algorithms Using Different Fuzzy Input Variables," Algorithms, vol. 8, no. 2, pp. 100–127, Apr. 2015.

[4]   P. Takun, S. Kaitwanidvilai, and C. Jettanasen, "Maximum Power Point Tracking using Fuzzy Logic Control for Photovoltaic Systems," in Proceedings of the International MultiConference of Engineers and Computer Scientists, 2011.

[5]   A. Gupta, Y. K. Chauhan, and R. K. Pachauri, "A comparative investigation of maximum power point tracking methods for solar PV system," Sol. Energy, vol. 136, pp. 236–253, 2016.

[6]   E. Kandemir, N. S. Cetin, and S. Borekci, "A comprehensive overview of maximum power extraction methods for PV systems," Renew. Sustain. Energy Rev., vol. 78, pp. 93–112, 2017.

[7]   S. Saravanan and N. Ramesh Babu, "Maximum power point tracking algorithms for photovoltaic system – A review," Renew. Sustain. Energy Rev., vol. 57, pp. 192–204, 2016.

[8]   M. A. G. de Brito, L. Galotto, L. P. Sampaio, G. de A. e Melo, and C. A. Canesin, "Evaluation of the Main MPPT Techniques for Photovoltaic Applications," IEEE Trans. Ind. Electron., vol. 60, no. 3, pp. 1156–1167, Mar. 2013.

[9]   K. Karabacak and N. Cetin, "Artificial neural networks for controlling wind–PV power systems: A review," Renew. Sustain. Energy Rev., vol. 29, pp. 804–827, Jan. 2014.

[10]   D. Gonzalez Montoya, C. A. Ramos Paja, and R. Giral, "Maximum power point tracking of photovoltaic systems based on the sliding mode control of the module admittance," Electr. Power Syst. Res., vol. 136, pp. 125–134, 2016.

[11]   E. Kandemir, N. S. Cetin, and S. Borekci, "A Comparison of Perturb & Observe and Fuzzy-Logic Based MPPT Methods for Uniform Environment Conditions," Period. Eng. Nat. Sci., vol. 5, no. 1, pp. 16–23, 2017.

[12]   A. R. Jordehi, "Maximum power point tracking in photovoltaic (PV) systems: A review of different approaches," Renew. Sustain. Energy Rev., vol. 65, pp. 1127–1138, 2016.

[13]   S. Borekci, E. Kandemir, and A. Kircay, "A Simpler Single-Phase Single-Stage Grid-Connected PV System with Maximum Power Point Tracking Controller," Elektron. ir Elektrotechnika, vol. 21, no. 4, pp. 44–49, Aug. 2015.

[14]   C. S. Chiu, "T-S Fuzzy Maximum Power Point Tracking Control of Solar Power Generation Systems," IEEE Transactions on Energy Conversion, vol. 25, no. 4. pp. 1123–1132, 2010.

[15]   L. L. Jiang, D. R. Nayanasiri, D. L. Maskell, and D. M. Vilathgamuwa, "A hybrid maximum power point tracking for partially shaded photovoltaic systems in the tropics," Renew. Energy, vol. 76, pp. 53–65, 2015

A Vehicle Routing Problem on Evacuation of Akkuyu Nuclear Power Station in Turkey

Sevban A. Tuzcuoglu[1], Cagrı Sel[2]

Abstract

Decreasing underground resources and the petroleum reserve force countries to search for new energy resources. Because of the changes in the ecological balance and the need for long-term energy sources, countries has been focused recently on renewable energy and nuclear energy. Although the nuclear energy meets the need for long-term energy sources, it probably carries some risks. Fukushima nuclear disaster, consecutive to the earthquake and tsunami that hit Japan on Mach 2011, is a recent event of a large disaster. In addition to at least 2 employees died and 40 people hurt in Fukushima, 200 thousand people are evacuated from the disaster areas. Humans and animals have still been affected by the radiation leakage[1][2]. In this study, we consider the evacuation of people from the disaster areas in case of a radioactive leakage or a possible hazard. A mixed-integer linear programming model is proposed to solve the problem. The implementation of the model to Akkuyu power station, which will be activated in Turkey 2023, is illustrated as a case study.

Keywords: *Disaster and Emergency Management, Plan of Evacuation, Logistics, Vehile Routing, Mixed Integer Programming*

1. INTRODUCTION

People need for energy from the beginning of the world. Besides all of the need of heating, lighting and eating, energy is necessary for products and technologies making people's life easier either. Those needs have been provided from fossil fuels (oil, coal, natural gas) for such a long time. But along with latest researches introduce that those fossil fuels effect the Earth a lot. The most distinct effect is carbon dioxide emission. The population increases the energy requirement and the carbon dioxide emission's rate. Global warming and climatic changes have been a result of using fossil fuels.

160 countries entered into a Kyoto Agreement which is about decreasing greenhouse gases emission (carbon dioxide, methane, nitrogen oxide, sulphur hexafluoride) and hydrofluorocarbon, perfluoro carbon within United Nations Framework Convention on Climate Change (UNFCCC). According to the agreement, countries promise decreasing known gases emission by determined under match [3]. Countries have begun to research new energy resources which is more fruitful and long-lived for gases decrease negative effect to Earth. Therefore, wind turbines, solar systems and nuclear power plants (NPPs) have been the center of interest recently.

Even if nuclear systems are fruitful and long-lived, radiation leakage possibility should be considered before when something goes wrong. The worst disaster is Chernobly nuclear accident which occurred at 26 April 1986. Hundreds of thousands of people were affected and the effects have been continuing since when it occurred [4].

The energy need of Turkey will be double in 2023. To meet the need, Turkey is interested in NPPs besides the hydroelectric stations. The recent NPPs call third generation NPPs which means safer and the new technology. The NPPs with four reactors are built in Akkuyu/Gulnar/MERSIN and it will be finished by 2023. During building of Akkuyu NPP or after, an emergency might occur. In case of any emergency, people should be evacuated from the area that NPP is planted. The people who is living around Akkuyu (within 20 km diameters) and is working at the company, are planned to be evacuated. The people must be picked up and taken to a safe region which is far at least 20 km from Akkuyu. In Figure 1, there are evacuation points which are blue and a safe point which is orange and, Akkuyu NPP point which is red. The number of the

people who must be evacuated is thousands therefore, the number of vehicles, routes, capacity of vehicles become a challenging problem. The problem is defined as vehicle routing problem [5] [6] and a mixed-integer linear programming model is proposed to solve the problem.

Figure 1. Evacuation areas and the safe point

In the following section, we present a literature review. In the third section, the the problem is described and the mathematical model is introduced. In the fourth section. In the fifth section, the case study is presented. In the last section, the results are discussed and the future research directions are indicated.

2. LITERATURE RESEARCH

Emergency and humanitarian relief logistics have caught the attention of the world recently. With increasing population, disasters and emergency situations might cause more loss of lives. Before any emergency or disaster occur, researchers should create several disaster scenarios to response quickly and active. Rawls and Turnquist suggest a mathematical model to tackle with the hurricanes in USA [7]. The model focus on the planning of inventory and transportation network under uncertainty. Afshar suggests a capacity constrained mathematical model. The model is proposed to control the multi-commodity flow and determine the number of vehiclesalong the supply chain [8]. Doyen et al. provide a mathematical model in a similar way but the model considers service points which are depot of commodity [9]. Balcik and Beamon suggest a mathematical model accounting for two-commodities of distribution points and network of transportation within a coverage zone. The coverage zone provides a priority to the people closer to distribution point than others [10].

The vehicle routing problems are NP-hard problems [11]. Travelling salesman problem, distribution problems and reverse logistic problems are examples of the vehicle routing problems. Guvez suggests a mathematical model which is on the reverse logistics case encountered in Kirikkale / TURKEY. The model considers recycling and picking medical wastes. This model is similar to our case study. Guvez solves that problem and finds active routes with the minimum cost [12]. Kula and his friends create scenario of Istanbul earthquake and for region of Bakirkoy, they suggest a mathematical model which considers routing of ambulances. The model is a mixed-integer programming model. They find the match between injured people and the convenient hospital [13]. For further information, readers could also lead the research Caunhye et al. [14].

3. PROBLEM DESCRIPTION

Akkuyu NPP in Mersin / TURKEY will be finished in 2023. The plan is to operate with 3500 people. These are the people who will be living around the Akkuyu NPP. Within 20 km diameter away from the Akkuyu NPP, there are 16 evacuation points as Aydincik, Hacibahattin, Eskiyoruk, Bozagac, Delikkaya, Kayrak, Cavuslar, Hirmanli, Isikli, Akdere, Yesilovacik, Kocasli, Yanisl, Sipahili, Buyukeceli and campus of Akkuyu NPP. Including employees' families (supposing each family have 4 people), there will be 31,850 people is to be evaluated in case of an emergency issue. The safe point is Silifke which is nearest region.

The evacuation is a competition against time. The most important point is transportation of people to safe point in minimum time.

Capacity-constrained problems are basic of vehicle routing problems. The main situations are;

1. Demands are determined, known and infrangible,

2. Distances of between clients and depots are known and fixed,

3. Vehicles are standard, limitless, have a capacity. Its capacities are known and they stand-by and wait for service.

In that case, as $V \in \{0, ...,N\}$ is set of nodes, capacity-constrained vehicle routing problem provides;

1. Total demand of clients don't go over the limit of capacity of each vehicles on the each routes

2. At least a vehicle must go to each client at least one time,

3. Each route is over wherever it starts.

The mathematical model is introduced below in line with Clarke and Wright [15].

3.1. Mathematical Model

$$min \quad \sum_{i \in N} \sum_{j \in N} c_{ij} x_{ij} \tag{1}$$

Subject to

$$\sum_{i \in N} x_{ij} = 1 \qquad\qquad j \in N_0 \tag{2}$$

$$\sum_{j \in N} x_{ij} = 1 \qquad\qquad i \in N_0 \tag{3}$$

$$\sum_{i \in N} x_{i0} = M \tag{4}$$

$$\sum_{j \in N} x_{0j} = M \tag{5}$$

$$x_{ij} \in \{0, 1\}, \qquad\qquad i, j \in N \tag{6}$$

$$M > 0, tms \tag{7}$$

$$u_i - u_j + C x_{ij} \leq C - d_j \qquad (\forall i \neq j, i, j \in N_0) \tag{8}$$

$$d_i \leq u_i \leq C \qquad (\forall i \in N_0) \quad (\forall u_i \geq 0) \tag{9}$$

where

x_{ij}:   1 if arc (i, j) is used and 0 otherwise, integer variable, $(\forall i, j \in N_0)$

M: number of route, integer variable

N: set of nodes ($0,...,N$)

N_0:   set of points ($1,...,N$)

c_{ij}:   time to travel between demand point i and j

d_i: demand of point i

C: capacity of each vehicles

The constraints are as follows; Equation (1) is to minimize the cost (distance or time) function, Equation (2-3). are the routing constraints. Equation (4-5) provide the number of vehicles allocated for the defined route. Equation (6) provides integrality and non-negativity constraints. Equation (8-9) eliminate the sub-tours and restrict the vehicle capacity.

4. CASE STUDY

We referenced Turkey Statistical Institute's report which belongs to 2016. According to the report, there are 31,850 people living around the Akkuyu NPP within 20 km diameter. This average population can be changed because the season. Also, after the construction of Akkuyu NPP, there will be 3,500 employees living in the area with their family. In case of people living in the corresponding area demands, several busses with the capacity 50 people can be used for the evacuation. Table 1. shows the demand points (districts) and the number of demands (population).

Table 1.Demand points and number of demands

Districts	Population
Delikkaya	400
Cavuslar	500
Bozagac	150
Eskiyorük	500
Hacıbahattin	350
Aydıncık	11,000
Kayrak	700
Sipahili	400
Kocaslı	100
Yanıslı	200
Büyükeceli	1,750
Hırmanlı	300
Yesilovacık	3,000
Isıklı	2,500
Akdere	2,000
Akkuyu	12,000
Total	**35,850**

5. CONCLUSION AND FUTURE RESEARCH

Nowadays, researchers have been trying to create scenario for how to respond before when nuclear disasters occur. In our study, 31,850 people will be evacuated from Akkuyu NPP to a safety point. We are recently working on data collection and experimental studies. The one limitation of the study might be to evacuate the Akkuyu NPP using a single safety point. The possible extension of the study can be tackle with the case with more than one safety point. Sinop NPP will be built in the future, which might be also an addition to our study.

ACKNOWLEDGMENT

BIOGRAPHY

Sevban Abdullah Tuzcuoglu is graduated from Industrial Engineering Department of Sakarya University / TURKEY in 2013. Recently, he is a master student at Industrial Engineering Department of Karabuk University / TURKEY. His ongoing research for the master thesis is in the field of Emergency and Disaster Management.

REFERENCES

[1]. World Nuclear News (March 12, 2011). "Battle to stabilise earthquake reactors". World Nuclear News. http://www.world-nuclear-news.org/RS_Battle_to_stabilise_earthquake_reactors_1203111.html
[2]. TEPCO (March 12,2011) "Press Releases" http://web.archive.org/web/20150123081359/http:/www.tepco.co.jp/en/press/corp-com/release/11031233-e.html

[3]. Akkuyu Nuclear Power Plant Co. "*Environmental Impact Assessment (EIA)*", p. 18-19. 2011.

[4]. International Atomic Energy Agency of Wien. *"ENVIRONMENTAL CONSEQUENCES OF THE CHERNOBYL ACCIDENT AND THEIR REMEDIATION: TWENTY YEARS OF EXPERIENCE"*. p. 180, 2006.

[5]. Güvez, H., Dege, M., & Eren, T. "*Kırıkkale'de Arac Rotalama Problemi ile Tıbbi Atıkların Toplanması*". International Journal of Engineering, 4(1), 41-45. 2012.

[6]. Ozdamar, L., Ekinci, E., & Kücükyazici, B. "*Emergency logistics planning in natural disasters. Annals of operations research*" 129(1), 217-245. 2004.

[7]. Barbarosoglu, G., L. Ozdamar, A. Cevik. *" An interactive approach for hierarchical analysis of helicopter logistics in disaster relief operations"*. Eur. J. Oper. Res. 140(1) 118–133, 2002.

[8]. Afshar, A., & Haghani, A. Modeling integrated supply chain logistics in real-time large-scale disaster relief operations. Socio-Economic Planning Sciences, 46(4), 327-338, 2012.

[9]. Doyen, A., Aras, N., & Barbarosoglu, G. "*A two-echelon stochastic facility location model for humanitarian relief logistics.*" Optimization Letters, 6(6), 1123-1145. 2012.

[10]. Balcik, B., & Beamon, B. M."*Facility location in humanitarian relief.International*" Journal of Logistics, 11(2), 101-121. 2008.

[11]. Toth, P., & Vigo, D. "*The vehicle routing problem, volume 9 of SIAM Monographs on Discrete Mathematics and Applications*". SIAM, Philadelphia, PA. 2002.

[12]. Güvez, H., Dege, M., & Eren, T. "*Kırıkkale'de Arac Rotalama Problemi ile Tıbbi Atıkların Toplanması*". International Journal of Engineering, 4(1), 41-45. 2012.

[13]. Kula, U., Tozanli, O., & Tarakcio, S. Emergency vehicle routing in disaster response operations. In *POMS 23rd Annual Conference, Chicago (April 20-23)*. 2012.

[14]. Caunhye, A. M., Nie, X., & Pokharel, S. "*Optimization models in emergency logistics: A literature review.*" Socio-economic planning sciences, 46(1), 4-13. 2012.

[15]. Clarke, G., & Wright, J. W. "*Scheduling of vehicles from a central depot to a number of delivery points. Operations research*", 12(4), 568-581. 1964.

Numerical Modelling of the In-Plane Loaded Homogenized Masonry Walls

Sedat Komurcu[1], Abdullah Gedikli[2]

Abstract

Masonry structures are one of the oldest structures in the world and have a considerable place among all the structures. Modelling of the masonry structures has become a significant requirement to evaluate the strengths of existing masonry structures and to build modern masonry structures. In this study, in-plane behaviors of the walls which constituting masonry structures are numerically modelled and analyzed. The homogenization technique is applied to obtain the material parameters used in the models. Unreinforced solid masonry wall and masonry wall with an opening are analyzed. The propagations of the cracks which may occur under the in-plane loads on the walls are investigated numerically. Fracture mechanisms occurring in the walls under the effect of in-plane loads are determined as a result of the analyzes. Results were compared with the experimental studies in the literature and it was seen that the results obtained in the numerical study were compatible with the experiments in the literature.

Keywords: *Crack, Fracture, Homogenization, Masonry*

1. INTRODUCTION

Masonry is a composite material that consist of units and mortar. It is necessary to model and analyze the masonry structures to understand them which exposed to many natural hazards especially earthquakes and to construct safe and modern masonry structures. There are several modelling techniques for modelling of walls constituting the masonry structures. Homogenous modelling techniques are suitable and widespread techniques reflecting general masonry behavior. In this study, nonlinear behaviors of walls under the effect of in-plane loads are numerically modelled and analyzed. The homogenization technique is used to model the masonry walls with their composite structures. Masonry walls were modelled and analyzed to determine the fracture mechanisms of the walls. In addition, in-plane behaviors of unreinforced masonry walls were analyzed numerically.

There are many studies about homogenous modelling of masonry structures. Researches have worked for producing homogenous damage models for masonry structures. The effects of in-plane effects on the masonry walls have been investigated by many scientists. Masonry units and mortar are modelled as a single material in the macro modelling technique. The macro modelling technique was studied in [1] and [2]. Researches were created orthotropic damage models in studies [3] and [4]. Lourenco worked on computational modelling of masonry structures using macro modelling technique [5]. Oller were studied on the numerical modelling of masonry walls [6]. Masonry panel wall behavior was studied in [7] and numerical study about strength of masonry was presented in [8]. Macro modelling is a significant modelling method for masonry structures and studies have continued to model masonry walls with homogeneous techniques.

2. HOMOGENIZATION OF MASONRY WALLS

Modelling of the masonry walls is a special issue because of the different characteristics of masonry units and mortar. There are various techniques to characterize structural behavior of masonry. Masonry structures can be generally modelled as heterogeneous and homogeneous models. Macro modelling technique is known as homogeneous modelling technique. Masonry units (brick, stone etc.) and mortar are represented as a single material with homogenization of masonry wall parts. The homogenous modelling procedure is shown in Figure 1. A composite structure is produced after the homogenization process.

---

[1] Corresponding author: İstanbul Technical University, Department of Civil Engineering, 34469, Sariyer/Istanbul, Turkey. komurcus@itu.edu.tr

[2] İstanbul Technical University, Department of Civil Engineering, 34469, Sariyer/Istanbul, Turkey, gedikliab@itu.edu.tr
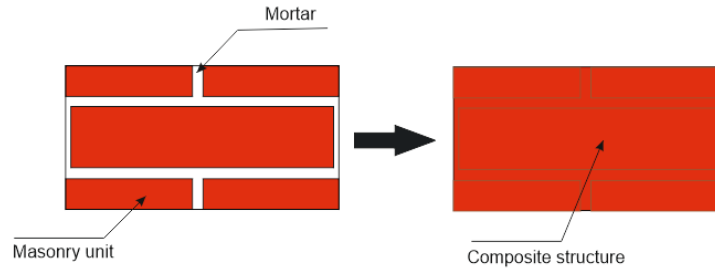
Figure 62 . Macro modelling procedure

Masonry walls are composite structures that can be homogenized using advanced techniques according to the macro modelling technique. It is beneficial to use masonry wall parts which periodically repeat themselves on the wall to model the masonry walls by homogenization. Some periodically repeated masonry wall parts that can be used for homogenization are shown in Figure 2. All the numbered wall parts in Figure 2 is called as elementary wall parts.
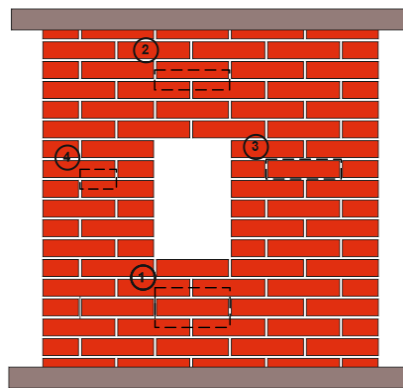
Figure 2 . Determination of periodically repeated elementary wall parts

Elementary wall parts are shown in Figure 3. These elementary wall parts can be used to determine material parameters of the masonry wall using in numerical analysis.
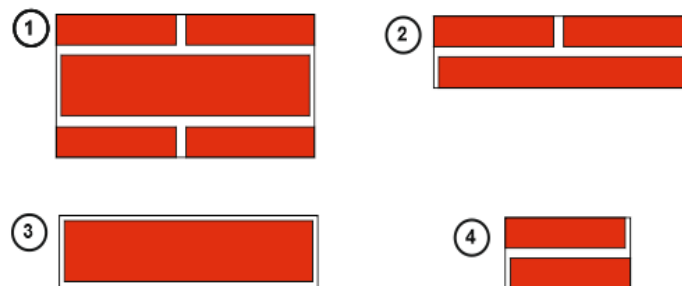
Figure 3 . Elementary wall parts

Homogenization procedure is applicated on an elementary wall part. Application of the homogenization technique is shown in Figure 4. There are two different directions to applicate homogenization because of orthotropic structure of the masonry walls. Elementary wall part can be divided as continuous parts both vertical and horizontal directions. Finally, a composite structure is obtained at the end of the homogenization procedure.
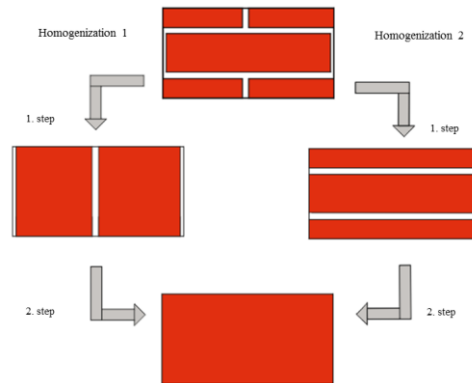
Figure 4 . Application of the homogenization technique

3. FINITE ELEMENT MODELS OF HOMOGENIZED MASONRY WALLS

In this study, finite element analysis was performed in ANSYS software by using homogenization technique on unreinforced masonry walls without and with an opening. Experimental studies were used to build numerical models in the literature [9], [10]. The periodically repeated masonry wall part used in the analysis and the masonry unit using in the wall are shown in Figure 5.
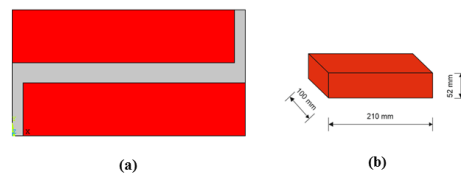
Figure 5 . (a) Elementary wall part (b) Masonry unit

Elementary wall part was divided to slices as shown in Figure 6.
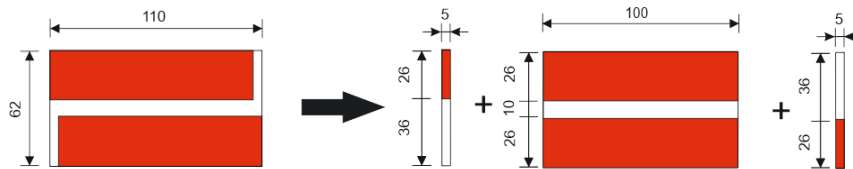
Figure 6 . Slicing of the elementary wall part

All the material units in the slices which obtain from the masonry elementary wall part can be considered as elastic springs as shown in Figure 7.
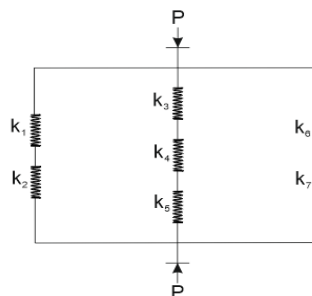
Figure 7 . Spring representation of the elementary wall part

The modulus of elasticity of the wall was calculated in Equation 1 according to use spring constants which represents the rigidity of the material units.

$$E_v = \frac{k_v L_v}{A_v} = \frac{648537 x 62}{11000} = 3655 \, MPa \tag{1}$$

SOLID 65 finite element in the ANSYS software was used for the finite element analysis. This element has 8 node points and each node point has 3 displacement degree of freedom in x, y and z directions. It can show collapse mechanisms both tensile and compression. Brittle materials can be modelled such as rock, stone, brick, concrete etc. This element is suitable for modelling of nonlinear behavior of structures and cracks can be determined in the structure. The structure of the SOLID 65 element is shown in Figure 8.
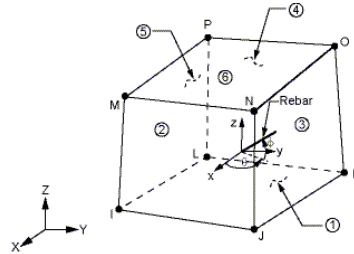
Figure 8 . SOLID 65 element.

Concrete material is used for the nonlinear analysis on the masonry walls. Crack distribution on the wall under in-plane loading can be determined with this material model. Material parameters used in the models are shown in Table 1. Wall material parameters were obtained with homogenization of the masonry wall and were implemented to the macro finite element model.

Table 41. Material properties.

Material	Modulus of Elasticity	Poisson's Ratio	Tensile Strength [MPa]	Compressive Strength [MPa]
Brick	16700	0,15	2	10,5
Mortar	780	0,15	0,25	3
Wall (Homogenous)	3655	0,15	0,25	9

In the numerical analysis, the Willam-Warnke fracture hypothesis is used for nonlinear behavior of the masonry wall. Willam-Warnke hypothesis is a suitable hypothesis for materials having different compressive strength and tensile strength such as masonry materials. The wall is loaded in two steps. In the first load step, the wall was loaded with a vertical pressure of 0.3 MPa to top nodes of the wall. In the second load step, horizontal displacement is given to the top nodes of the walls. The first load step is implemented by dividing by 10 equal sub-steps. The second load step is divided into 40 sub-steps.

3.1. Masonry Wall without Opening

In ANSYS software the geometry of the masonry wall was created by using the macro modelling technique. Masonry units and mortar were produced as a single material. Figure 9 shows the geometry and loading for the masonry wall without opening.
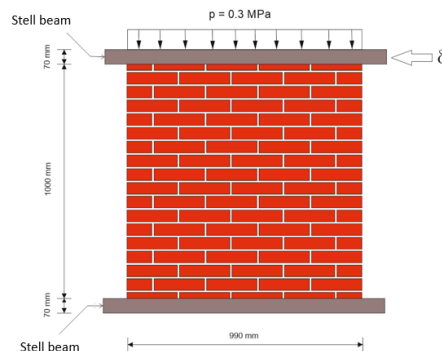
Figure 9 . Masonry wall geometry and loading.

Total displacement at the end of the 1. load step, minimum principal stresses at the end of the 1. load step, minimum principal stresses at δ=1, total displacement at δ=1mm and shear stresses at δ=1mm are shown in Figure 10. Continuous stress distribution is determined between the bricks and mortar.
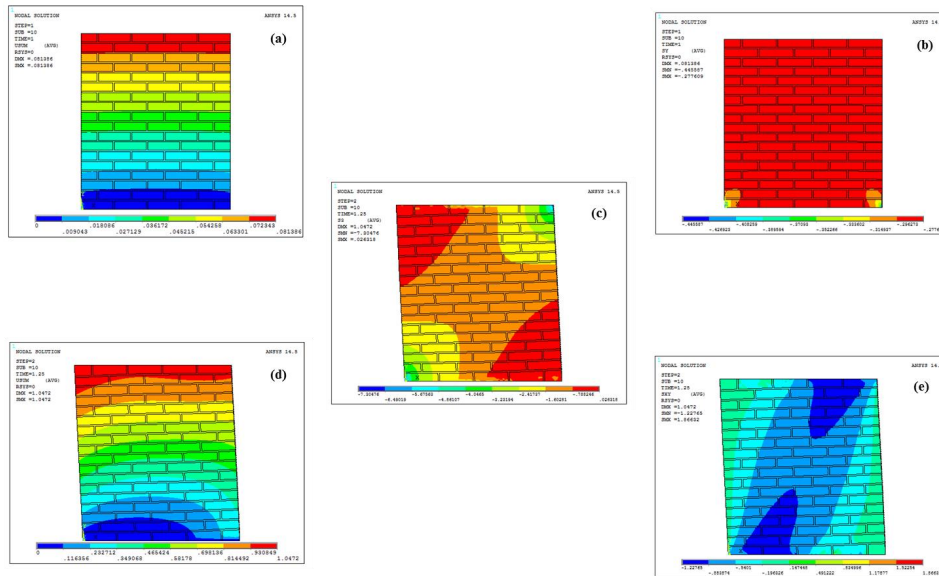
Figure 10 . Masonry without opening: (a) total displacement at the end of the 1. load step, (b) minimum principal stresses at the end of the 1. load step, (c) minimum principal stresses at δ=1, (d) total displacement at δ=1mm, (d) shear stresses at δ=1mm

The crack distribution of the unreinforced masonry wall from δ=0.1 mm to δ=1 mm is given in Figure 11. Continuous cracks are obtained with the macro modelling technique according to finite element analysis.
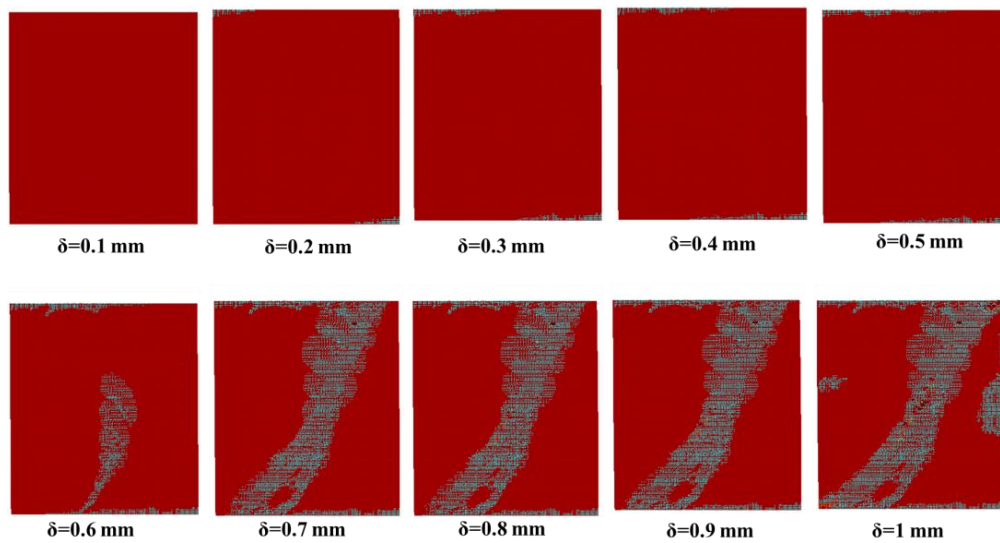
Figure 11 . Crack distributions for masonry wall without opening

It is seen that the cracks first started from the upper left and lower right corners of the wall. Next, diagonal cracks occurred on the wall.

3.2. Masonry Wall with an Opening

Second homogenization example worked on the masonry wall with an opening. Figure 12 shows the geometry and loading for the masonry wall with an opening.
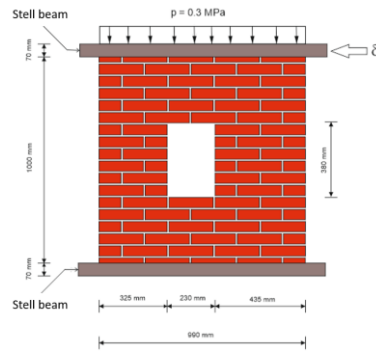
Figure 12 . Masonry wall with an opening geometry and loading

Total displacement at the end of the 1. load step, minimum principal stresses at the end of the 1. load step, minimum principal stresses at δ=1, total displacement at δ=1mm and shear stresses at δ=1mm according to finite element analysis are shown in Figure 13.
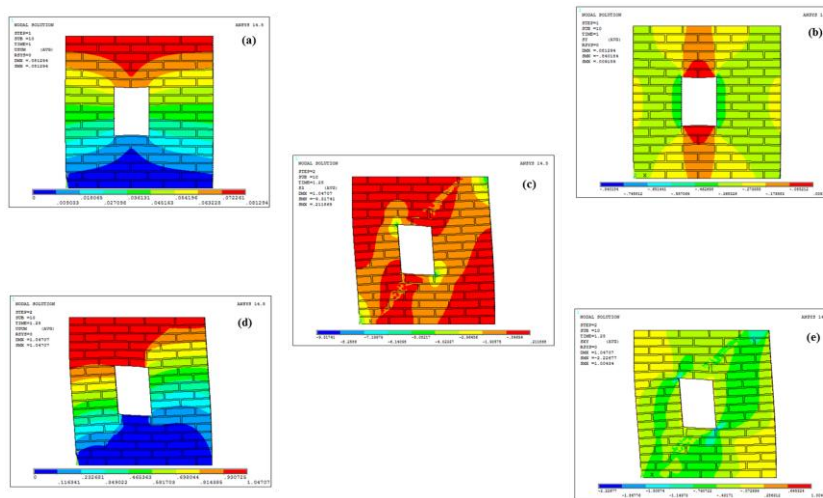
Figure 13 . Masonry with opening: (a) total displacement at the end of the 1. load step, (b) minimum principal stresses at the end of the 1. load step, (c) minimum principal stresses at δ=1, (d) total displacement at δ=1mm, (d) shear stresses at δ=1mm

The crack distributions of the unreinforced masonry wall with an opening are given from δ=0.1 mm to δ=1 mm in Figure 14.
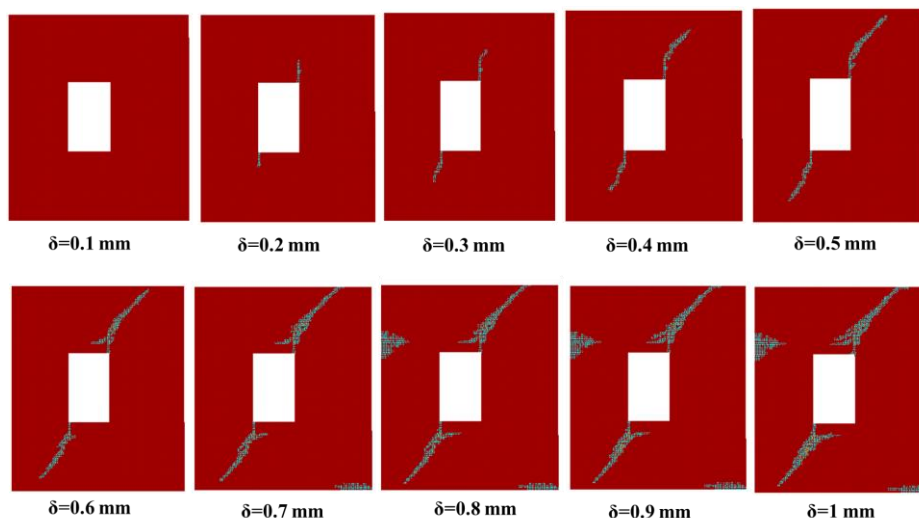
Figure 14 . Crack distributions for masonry wall with opening

It is seen that the cracks first started from the lower left and upper right corners of the gap in the wall. In addition to the diagonal cracks on the wall, cracks are formed in the lower right part of the wall and in line with the upper left part of the opening. Finally, diagonal cracks spread to the left lower and right upper portions of the wall. And horizontal cracks spread towards to upper left and lower right corner of the wall. Finally, failure mechanism of the masonry wall with an opening idealized as four rigid blocks connected by four joints.

4. RESULTS AND DISCUSSION

In this study, unreinforced masonry walls without and with an opening were modelled and analyzed using finite element method. Crack distributions were investigated step by step on the walls. The reason of the cracks can be explained in terms of internal effects. Figure 15 (a) shows the reasons of the cracks on the unreinforced masonry wall. Firstly, horizontal cracks that occur in the upper left and lower right parts of the wall shown with number (1) are tensile or shear cracks. Secondly, the cracks that occur in the upper right and lower left parts of the wall shown with number (2) are compressive cracks. Next, the diagonal cracks that occur in the middle region of the wall are represented by number (3) are caused by multiple influences.
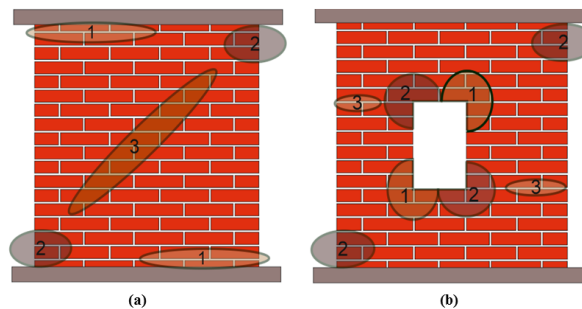
Figure 15 . The reasons of the cracks on the masonry walls

Figure 15 (b) shows the reasons of the cracks on the unreinforced masonry wall with an opening. The cracks formed in the upper right and left lower corners of the gap shown with number (1) are tensile cracks. The cracks in the lower left and upper right corners of the wall and the cracks in the lower right and left upper corners of the opening shown with number (2) are pressure cracks. Horizontal cracks started from the edge of the wall and continue towards the opening shown with number (3) are shear cracks.

Horizontal displacement of the top of the wall and horizontal reaction force of the wall diagrams of the two wall models are shown in Figure 16. It is seen that the masonry wall without opening has higher strength than the masonry wall with opening. But, masonry wall with an opening represents more ductile behavior than the masonry wall without opening.
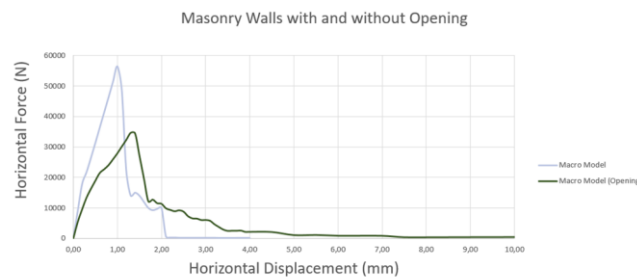
Figure 16 . Load – displacement curves of the masonry wall models after the analysis

5. CONCLUSION

The modelling technique, the material model and the fracture hypothesis form a combination for the modelling of the masonry walls. In homogenous modelling technique, single material parameters are used as an average property for masonry unit and mortar. Continuous cracks can be obtained with using homogenization technique on the walls. The strength of a masonry wall with an opening is dramatically at a lower level than masonry wall without opening but masonry wall with an opening represents more ductile behavior.

REFERENCES

[1]. R.D. Quinteros, S. Oller, L.G. Nallim, "Nonlinear homogenization techniques to solve masonry structures problems," *Composite Structures.,* vol. 94, pp. 724–730, 2012.

[2]. H.O. Koksal, B. Doran, A.O. Kuruscu, A. Kocak, "Elastoplastic finite element analysis of masonry shear walls," *KSCE Journal of Civil Engineering.,* vol. 20, pp. 784-791, 2016.

[3]. L. Pela, M. Cervera, P. Roca, "An orthotropic damage model for the analysis of masonry structures," *Construction and Building Materials.*, vol 41, pp. 957-967, 2012.

[4]. P.B. Lourenco, "An Orthotropic Continuum Model for The Analysis of Masonry Structures," The Netherlands, TU Delft, Report 03-21-1-31-27, 1995.

[5]. Lourenco, "Computational Strategies for Masonry Structures" Doctoral dissertation, Delft University of Technology, The Netherlands, 1996.

[6]. S. Oller, *Numerical Simulation of Mechanical Behavior of Composite Materials,* Barcelona, Spain, Springer, 2014.

[7]. A.Th. Vermeltfoort, T.M.J. Raijmakers, "Deformation controlled meso shear tests on masonry piers," The Netherlands: Building and Construction Research, Eindhoven, Report B-92-1156, TNO-BOUWrrU, 1992.

[8]. A.Th. Vermeltfoort, T.M.J. Raijmakers, "Deformation controlled meso shear tests on masonry piers," The Netherlands: Building and Construction Research, Eindhoven, Report B-92-1156, TNO-BOUWrrU Part 2 Draft report, 1993.

[9]. L. Berto, A. Saetta, R. Scotta, R. Vitaliani, "Shear behaviour of masonry panel: parametric FE analyses," *International Journal of Solids and Structures.,* vol. 41 pp. 4383–4405, 2004.

[10]. A. Drougkas, P. Roca, C. Molins, "Numerical prediction of the behavior, strength and elasticity of masonry in compression," *Engineering Structures.*, vol 90, pp. 15–28, 2015.

Macro and Micro Modelling of the Unreinforced Masonry Shear Walls

Sedat Komurcu[1], Abdullah Gedikli[2]

Abstract

Masonry structures are constructed by joining masonry units (brick, stone, marble etc.) with mortar. Various methods are used for modelling of masonry walls of the structures. Micro modelling and Macro modelling are two diverse modelling techniques. In this study, these two modelling strategies are analyzed on a solid unreinforced masonry shear wall numerically. The models are implemented in ANSYS software to simulate the structural behavior of a tested wall in literature. The homogenization technique is applied to obtain the material parameters used in the macro model. Brick and mortar are modelled separately in the micro model. Stresses occurring in the walls under the effect of in-plane loads are investigated. The propagations of the cracks on the walls are analyzed numerically. The results obtained in the micro modelling and macro modelling are in consistent with the experimental study in the literature. However, macro modelling and micro modelling represent strictly disparate behavior in the material identification, and crack propagations.

Keywords: *Crack, Macro, Masonry, Micro*

1. INTRODUCTION

Masonry structures are the first structures of the history and have a significant place among all the structures. There are many masonry monumental structures in the world such as buildings, palaces, bridges and towers. Modelling of the masonry structures has become a significant requirement to evaluate the strengths of existing masonry structures and to build modern masonry structures. Modelling of the masonry walls is a challenging issue because of their composite structures. There are several modelling techniques for modelling of walls constituting the masonry structures. Macro modelling and micro modelling are two different technique for modelling of masonry structures. In this study, the macro modelling and micro modelling techniques are investigated on the masonry walls. Masonry walls are modelled and analyzed to determine the fracture mechanisms of the walls. In-plane behaviors of unreinforced masonry walls are analyzed numerically.

Engineers and architects have worked to determine the in-plane effects on the masonry walls throughout the history. The effects of tension, pressure and shear on the masonry walls have been investigated by many scientists. The researchers used macro and micro modelling techniques to model the masonry walls. Masonry units and mortar are modelled as a single material in the macro modelling technique. The macro modelling technique was studied in [1] and [2]. Masonry units, mortar and interfaces are modelled separately in the micro modelling technique. The micro modelling technique was used in studies [3] and [4]. Lourenco made extensive work on modelling masonry structures using micro and macro modelling techniques [5], [6]. Oller were studied on the numerical modelling of masonry walls [7]. Many scientists have continued to model masonry walls.

2. MACRO AND MICRO MODELLING

The main goal in modelling is to produce a model that behaves close to the real structure. The modelling of the masonry walls requires more care than other constructions because of the different characteristics of the masonry units and mortar. Various methods are used in the modelling of masonry structures. Masonry structures can be generally modelled as heterogeneous and homogeneous models. Detailed micro and simplified micro models are heterogeneous models. Macro modelling technique is known as homogeneous modelling technique. The modelling techniques diagram is shown in Figure 1.

---

[1] Corresponding author: İstanbul Technical University, Department of Civil Engineering, 34469, Sariyer/Istanbul, Turkey. komurcus@itu.edu.tr.

[2] İstanbul Technical University, Department of Civil Engineering, 34469, Sariyer/Istanbul, Turkey, gedikliab@itu.edu.tr.
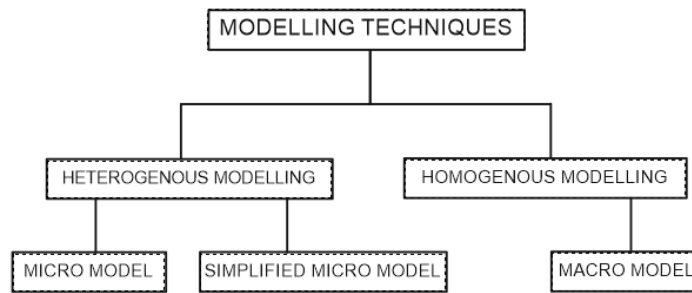
Figure 63 . Modelling techniques for masonry walls

2.1. Macro Modelling

In macro modelling technique, masonry units (bricks, stone units), and the mortar between them are modelled as a single material. Application of the macro modelling technique is shown in Figure 2. Masonry walls are composite structures that can be homogenized using advanced techniques according to the macro modelling technique. It is beneficial to use elementary masonry wall parts which periodically repeat themselves on the wall in order to model the masonry walls by homogenization.
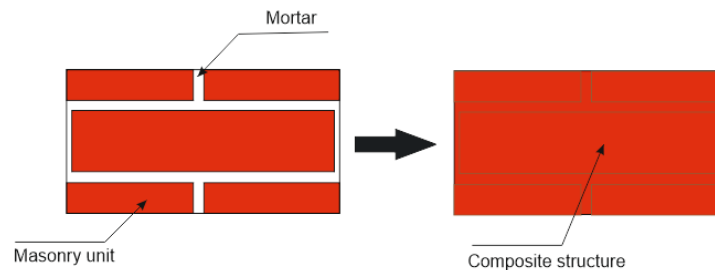
Figure 2 . Macro modelling procedure

2.2. Micro Modelling

In micro technique, masonry units (brick, stone, etc.) and the mortar are modelled separately. Interfaces in the joining areas of these elements can be also included in the model. The micro modelling is shown in Figure 3. Although modelling of structures with micro modelling technique is a detailed process, local behavior of the structures can be investigated wit this technique.
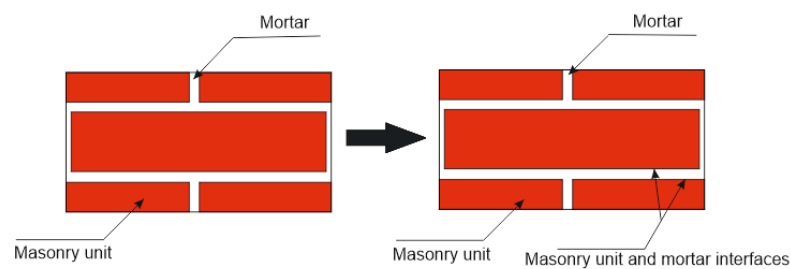
Figure 3 . Micro modelling procedure

3. FINITE ELEMENT MODELS OF MASONRY WALLS

In this study, finite element analysis was performed by using micro and macro modelling techniques on unreinforced masonry walls. Experimental study was used in the literature for numerical analysis [8]. The geometry of the masonry wall and the masonry unit using at the wall are shown in Figure 4. The wall is loaded in two steps. In the first load step, the wall was loaded with a vertical pressure of 0.3 MPa to top nodes of the wall. In the second load step, horizontal displacement are given to the top nodes of the walls. The first load step is implemented by dividing by 10 equal sub-steps. The second load step is divided into 40 sub-steps.
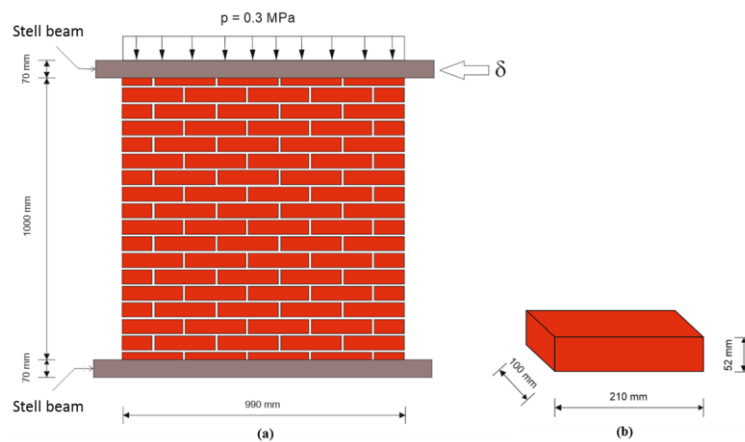
Figure 4 . (a) Masonry wall geometry (b) masonry unit used in the wall.

SOLID 65 finite element in the ANSYS software was used for the finite element analysis. This element has 8 node points and each node point has 3 displacement degree of freedom in x, y and z directions. It can show collapse mechanisms both tensile and compression. Brittle materials can be modelled such as rock, stone, brick, concrete etc. This element is suitable for modelling of nonlinear behavior of structures and cracks can be determined in the structure. The structure of the SOLID 65 element is shown in Figure 5.
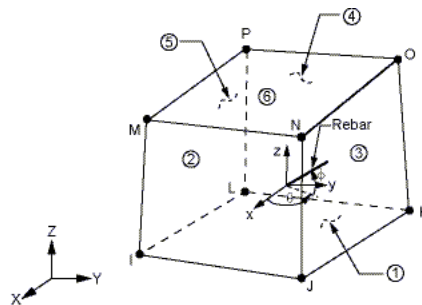
Figure 5 . SOLID 65 element

Concrete material is used for the nonlinear analysis on the masonry walls. Typical Stress-strain curve of the concrete material is shown in Figure 6. Crack distribution on the wall under in-plane loading can be determined with this material model.
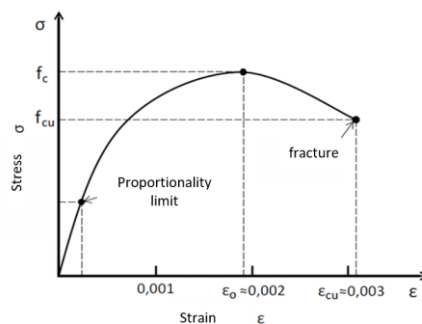
Figure 6 . Typical stress-strain diagram of the Concrete material

Material parameters used in the models are shown in Table 1. Brick and mortar material parameters were implemented to micro finite element model. But, wall material parameters were obtained with homogenization of the masonry wall and were implemented to the macro finite element model.

Table 42. Material properties

792

Material	Modulus of Elasticity	Poisson's Ratio	Tensile Strength [MPa]	Compressive Strength [MPa]
Brick (Micro)	16700	0,15	2	10,5
Mortar (Micro)	780	0,15	0,25	3
Wall (Macro)	3655	0,15	0,25	9

In the numerical analysis, the Willam-Warnke fracture hypothesis is used for nonlinear behavior of the masonry wall. Three-dimensional fracture surface and two-dimensional fracture surface for Willam-Warnke hypothesis is shown in Figure 7. Willam-Warnke hypothesis is a suitable hypothesis for materials having different compressive strength and tensile strength such as masonry materials. Masonry materials usually have high compressive strength and low tensile strength.
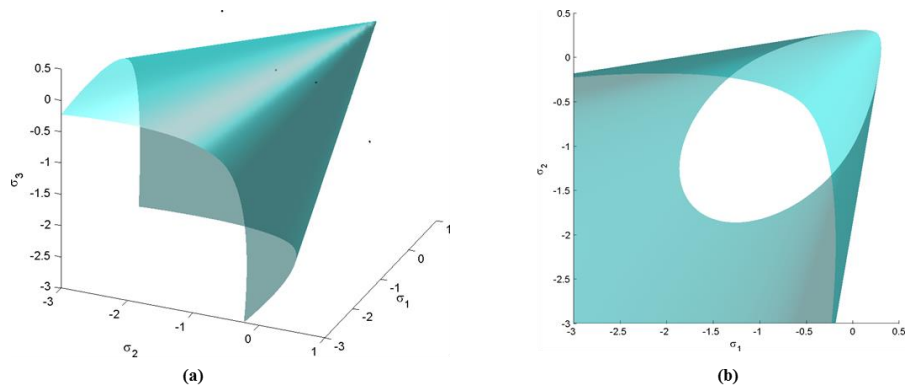
Figure 7 . Willam-Warnke fracture surfaces: (a) Three dimensional space (b) Two dimensional plane

3.1. Macro Finite Element Model

In ANSYS software the geometry of the masonry wall was created by using the macro modelling technique. Masonry units and mortar were produced as a single material. Figure 8 shows the geometry and the finite element mesh of the masonry macro model. Refined mesh distribution was used in the models to investigate the crack distributions well.
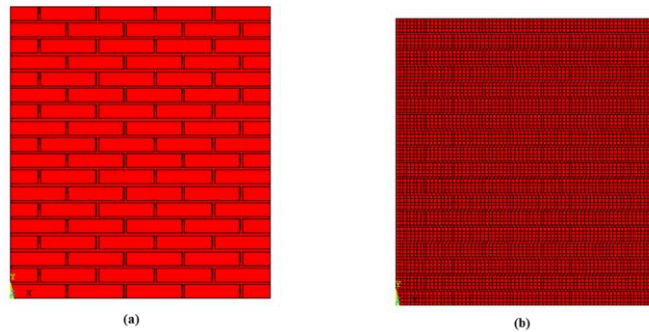
Figure 8 . (a) Geometry of the wall (b) finite element mesh of the masonry macro model

Total displacement at the end of the 1. load step, minimum principal stresses at the end of the 1. load step, minimum principal stresses at $\delta=1$, total displacement at $\delta=1$mm and shear stresses at $\delta=1$mm are shown in Figure 9. Continuous stress distribution is determined between the bricks and mortar.
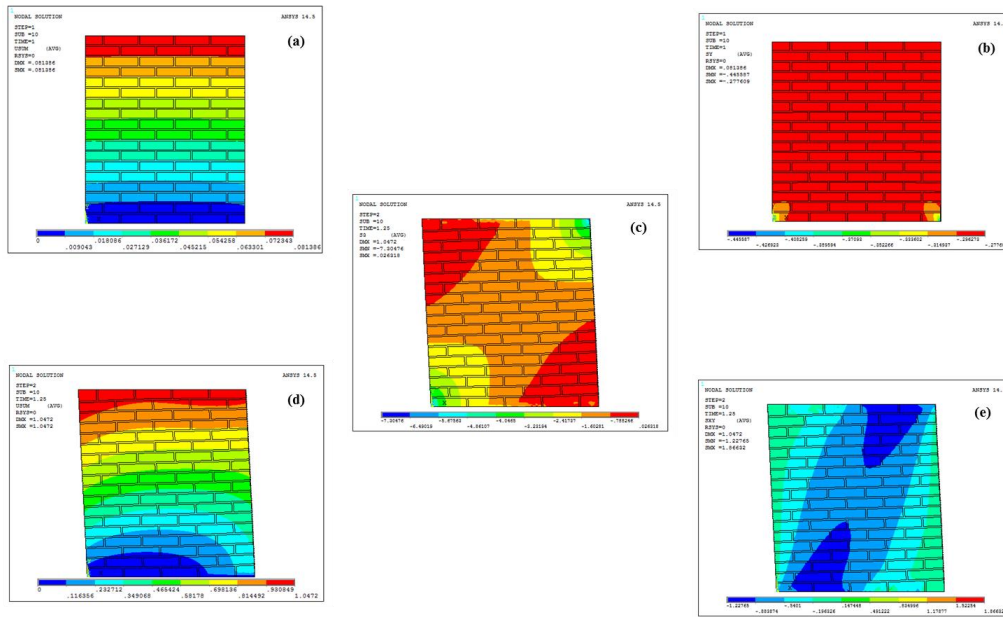
Figure 9 . Macro model: (a) total displacement at the end of the 1. Load step, (b) minimum principal stresses at the end of the 1. Load step, (c) minimum principal stresses at δ=1, (d) total displacement at δ=1mm, (d) shear stresses at δ=1mm

The crack distribution of the unreinforced masonry wall from δ=0.1 mm to δ=1 mm is given in Figure 10. Continuous cracks are obtained with the macro modelling technique according to finite element analysis.
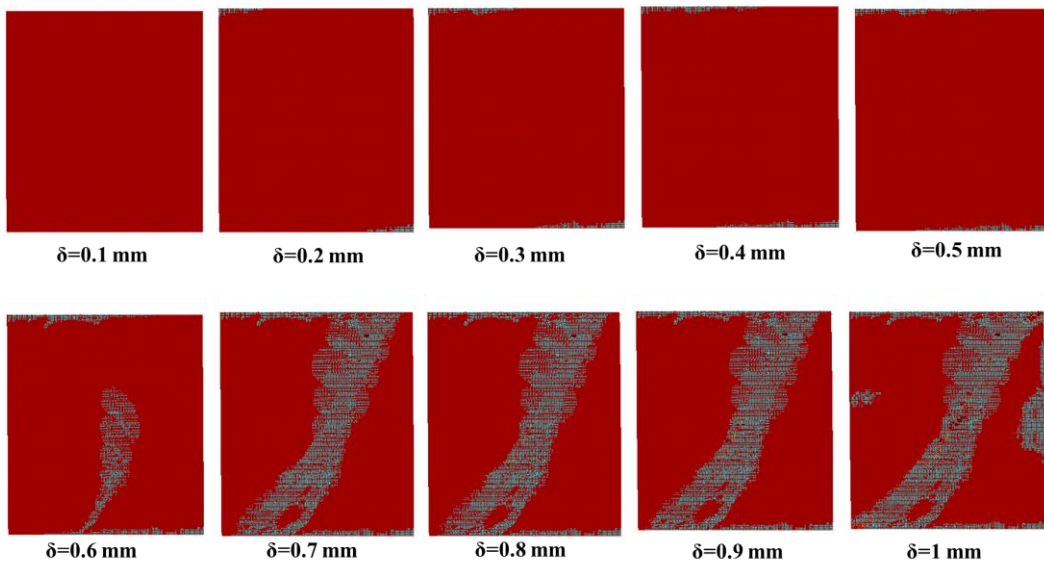
Figure 10 . Crack distribution at the end of the macro modelling

It is seen that the cracks first started from the upper left and lower right corners of the wall. Next, diagonal cracks occur on the wall.

3.2. Micro Finite Element Model

Geometry of the model and finite element mesh were produced with the micro modelling technique. In this technique bricks and mortar are modelled separately. The same mesh distribution was used with the macro model. Figure 11 indicates the geometry and the finite element mesh of the micro model.
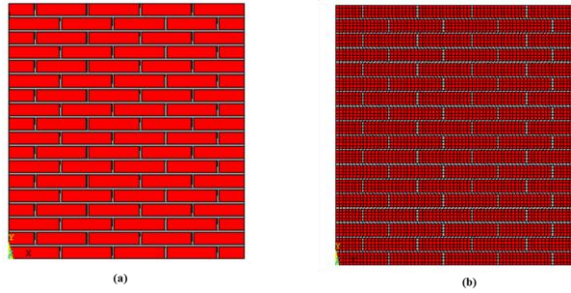
Figure 11 . (a) Geometry of the wall (b) finite element mesh of the masonry micro model

Total displacement at the end of the 1. load step, minimum principal stresses at the end of the 1. load step, minimum principal stresses at δ=1, total displacement at δ=1mm and shear stresses at δ=1mm according to finite element analysis are shown in Figure 12.
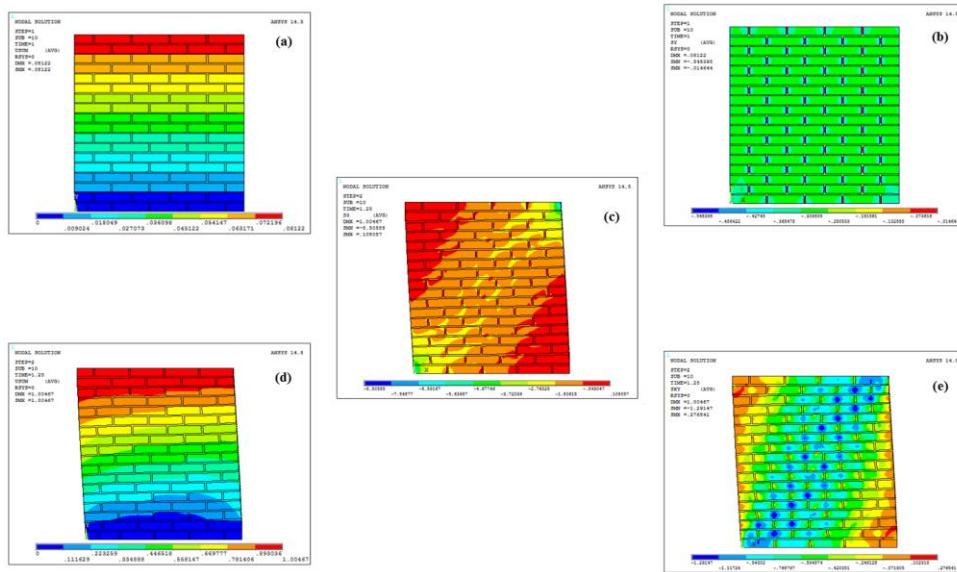
Figure 12 . Micro model: (a) total displacement at the end of the 1. Load step, (b) minimum principal stresses at the end of the 1. Load step, (c) minimum principal stresses at δ=1, (d) total displacement at δ=1mm, (d) shear stresses at δ=1mm

The crack distributions of the unreinforced masonry wall are given from δ=0.1 mm to δ=1 mm in Figure 13.

δ=0.1 mm   δ=0.2 mm   δ=0.3 mm   δ=0.4 mm   δ=0.5 mm

δ=0.6 mm   δ=0.7 mm   δ=0.8 mm   δ=0.9 mm   δ=1 mm
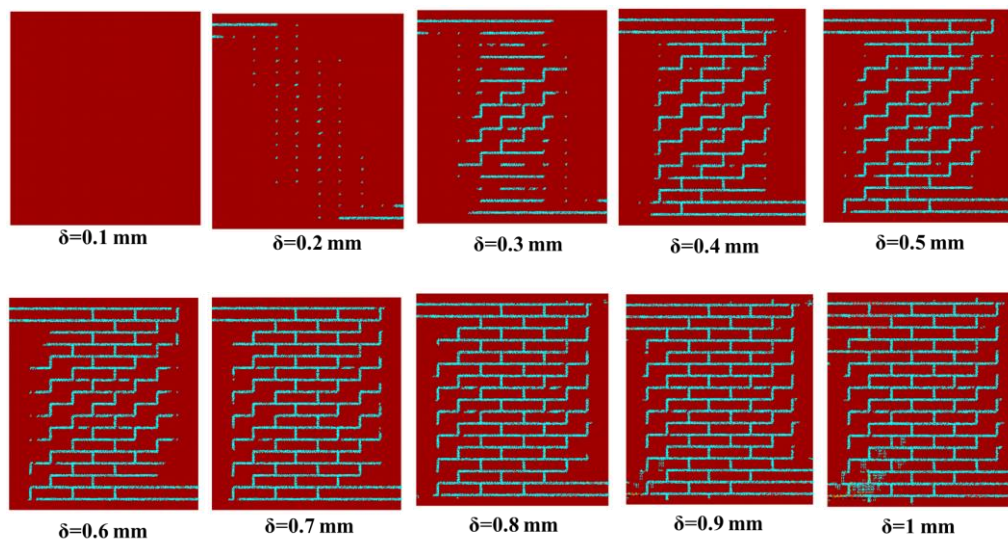
Figure 13 . Crack distribution at the end of the micro modelling

It is seen that the cracks first started from the upper left and lower right corners of the wall. Next, cracks in the mortar areas spread all over the wall because of low tensile strength of the mortar areas.

4. RESULTS AND DISCUSSION

In this study, an unreinforced masonry wall was modelled and analyzed using finite element method. Stresses and strains on the wall were determined after the analysis. In addition, the cracks were investigated step by step. The reason of the cracks can be explained in terms of internal effects. Figure 14 shows the reasons of the cracks on the unreinforced masonry wall. Firstly, horizontal cracks that occur in the upper left and lower right parts of the wall shown with number (1) are tensile or shear cracks. Secondly, the cracks that occur in the upper right and lower left parts of the wall shown with number (2) are compressive cracks. Next, the diagonal cracks that occur in the middle region of the wall are represented by number (3) are caused by multiple influences.
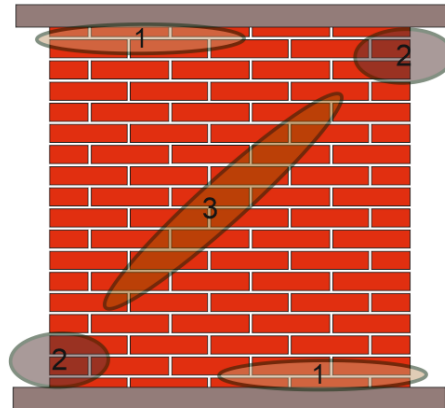
Figure 14 . The reasons of the cracks on the masonry wall

Horizontal displacement of the top of the wall and horizontal reaction force of the wall diagram is shown in Figure 15. There are four different diagrams in the figure. Two of them shows numerical analysis and the other two diagrams shows the experimental results in the literature. It is seen that, the models have similar behavior until reaching the wall collapse state but the concrete material suddenly lost its strength in numerical analysis.

Figure 15 . Load – displacement curves of the wall after the analysis

5. CONCLUSION

In micro modelling technique, masonry unit and mortar material properties are added to each model separately. However, single material parameters are used as an average property for masonry unit and mortar in macro modelling technique. In addition, the walls modelled by macro and micro methods represent consistent results with the experimental work, but does not fully reflect the post-peak behavior due to the concrete material property. While the micro modelling technique is suitable for small scale structures, the macro modelling technique is suitable for large-scale structures. Because the micro modelling technique requires more time, effort and computer capacity. Discrete cracks occur with using micro modelling technique. However, continuous cracks can be investigated with using macro modelling technique. Studies have been continued to model and analyze masonry walls.

REFERENCES

[1]. R.D. Quinteros, S. Oller, L.G. Nallim, "Nonlinear homogenization techniques to solve masonry structures problems," *Composite Structures.,* vol. 94, pp. 724–730, 2012.

[2]. H.O. Koksal, B. Doran, A.O. Kuruscu, A. Kocak, "Elastoplastic finite element analysis of masonry shear walls," *KSCE Journal of Civil Engineering.,* vol. 20, pp. 784-791, 2016.

[3]. J. Idris, M. Al Heib, T. Verdel, "Masonry Joints Mechanical Behavior Evolution in Built Tunnels," *Tunneling and Underground Space Technology,* vol. 24, pp. 617-626. 2009.

[4]. M. Bolhassani, A.A. Hamid, A.C.W. Lau, F. Moon, "Simplified micro modelling of partially grouted masonry assemblages," *Construction and Building Materials,* vol. 83, pp. 159-173 September 2015.

[5]. Lourenco, "Computational Strategies For Masonry Structures" Doctoral dissertation, Delft University of Technology, The Netherlands, 1996.

[6]. P.B. Lourenco, J.G. Rots, J. Blaauwendraad, "Two Approaches for the Analysis of Masonry Structures: Micro and Macro-Modelling," *Heron,* vol. 40, 1995.

[7]. S. Oller, *Numerical Simulation of Mechanical Behavior of Composite Materials,* Barcelona, Spain, Springer, 2014.

[8]. A.Th. Vermeltfoort, T.M.J. Raijmakers, "Deformation controlled meso shear tests on masonry piers," The Netherlands: Building and Construction Research, Eindhoven, Report B-92-1156, TNO-BOUWrrU, 1992.

Investigation And Statistical Analysis Of Cutting Force In Machining Of Az91 Magnesium Alloy

Omer Asal[1], Hakan Dilipak[2], Faruk Mullaahmetoglu[3]

Abstract

Magnesium is a material with a high risk of ignition at high temperatures. In this study, AZ91 Magnesium alloy is machined in the CNC lathe with different cutting parameters. The effects of cutting parameters on cutting force are investigated. The experiments were carried out under dry cutting conditions at the constant cutting speed (512 m/min) with uncoated tools. Experiments have been performed by chip removing with the three different cutting depths (1, 2 and 3 mm) and the three different feed rate (0.1 , 0.2 and 0.3 mm/rev) from cylindrical material of a diameter of 92 mm and a length of 300 mm. The variance analysis was practiced on the test results and the effect ratios of the cutting parameters were determined. Regression analysis was made to obtain the model. As a result, it was determined that cutting depth is a more effective parameter on the cutting force.

Keywords: *AZ91, Magnesium Alloys, Machinability, Cutting Force, Regression Analysis, ANOVA*

1. INTRODUCTION

In today's technology, among the desirable characteristics of the materials, the materials have to be light and durable. Magnesium has a density of 1.74 g / cm^3 and Magnesium is 35% lighter than aluminum and melts at low temperature. Magnesium alloys do not have as much resistance as aluminum alloys. However, specific strength ratios are higher than aluminum. Consequently, magnesium alloys are used in machinery such as hand tools, air tools and vehicles where lightness is important [1, 2].

Magnesium, the lightest metal known, exhibits excellent machinability and the most important machinability characteristics are low cutting forces, good surface quality and easy chip flow. Magnesium alloys also do not show a difference in machinability in themselves. Although magnesium alloy parts are produced close to the last shape with many molding techniques, often chip removing operations are carried out through magnesium. Chip removing operations can be done on low-capacity conventional machines as well as on high-capacity CNC machines. Low cutting pressures and high thermal conductivity ensure rapid heat dissipation. Thus, the cutting tool life is extended and the tool changing times are shortened [1, 3].

Magnesium and its alloys are used in many fields, especially in the field of automotive, with its low density and easy shaping properties. Therefore, the researches focus on the properties of magnesium alloys [1,3]. Magnesium alloys, which are one of the easiest metals for machinability, are produced close to the last with many molding techniques, but often require machining operations. Magnesium alloys do not show a difference in machinability in themselves. Although magnesium is preferred primarily for lightness in designs, it has a great advantage for high volume production due to its good workability properties [1, 3]. In this study of Kusdemir, he applied different alloying to improve the properties and microstructures of the magnesium alloy [4]. In Unal's study, he worked on improving the casting properties of AZ91 series of advanced magnesium alloys [5]. In the study of Mohd and his colleagues, they have found improvement of their machinability with increasing temperature ratios of magnesium alloys of AZ, ZK, WE [17]. In different studies, researchers have investigated the effects of adding of elements such as Ca, Sr, Sn, Si, Y, Pb to AZ91 [7-10].

---

[1] Corresponding author, Ömer Asal: Gazi University, Department of Manufacturing Engineering, Teknikokullar/Ankara, Turkey omerasal@gazi.edu.tr.

[2] Hakan Dilipak: Gazi University, Department of Manufacturing Engineering, Teknikokullar/Ankara, Turkey hdilipak@gazi.edu.tr.

[3] Faruk Mullaahmetoglu, Gazi University, farukmulla@hotmail.com.

In this work, AZ91 magnesium alloy is machined on the CNC lathe. In the experiments, the cutting speed was kept constant and 3 cutting depths and 3 different feed rates were used as cutting parameters. The effects on the cutting forces of cutting parameters were investigated. The results of the experiments were evaluated and variance analysis and regression analysis were performed.

2. MATERIAL AND METHOD

2.1. The Experimental and Cutting Parameters

AZ91 magnesium alloy specimens were used as test materials for machinability experiments. These materials are manufactured from pressure casting and have a diameter of 92 mm and a length of 300 mm. The chemical composition of the AZ91D magnesium alloy is given in Table 1.

Table 1. Chemical composition of AZ91D magnesium alloy (%)

Heat No	Al	Zn	Mn	Fe	Si	Cu	Ni	Mg
523	8.8	0.68	0.18	0.003	0.017	0.0021	0.00061	Balance
Requirement	8.5-9.5	0.45-0.90	0.17-0.40	Max 0.004	Max 0.08	Max 0.025	Max 0.001	Balance

Machinability experiments were carried out under dry cutting conditions at the CNC lathe at Gazi University Faculty of Technology Manufacturing Engineering laboratory.in accordance with ISO 3685 (turning items-lifetime test) standard and experiment conditions. In the experiments, "Johnford TC-35" industrial CNC lathe with FANUC control unit was used. Experiments were carried out at constant cutting speed (512 m/min), three different feed velocities (0.1 mm/rev, 0.2 mm/rev, 0.3 mm/rev) and three different cutting depths (1, 2 and 3 mm). A new cutting tool was used in each experiment. Uncoated carbide cutting tools were used as the cutting tool and a total of 9 experiments were carried out. The Experimental setup is shown in Figure 1. The experimental parameters are given in Table 2.
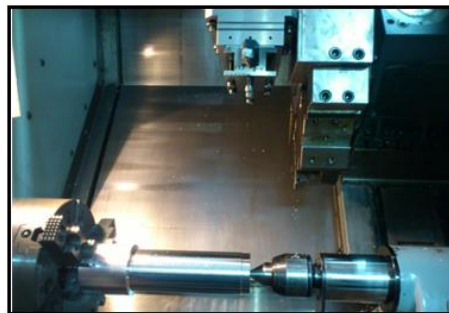
Figure 1. The specimen and experimental setup prepared for experiments.

Table 2. The experimental parameters.

Experimental	Cutting depth (mm)	Feed rate (mm/rev)
1	1	0.1
2	1	0.2
3	1	0.3
4	2	0.1
5	2	0.2
6	2	0.3
7	3	0.1
8	3	0.2
9	3	0.3

2.2. The Tool Holder and the Cutting Tools

In the experiments, the tool holder which has Walter mark with code "DSBNR2525M12" was supplied and used. The geometric properties and measurements of the cutting tool holder are given in Figure 2.
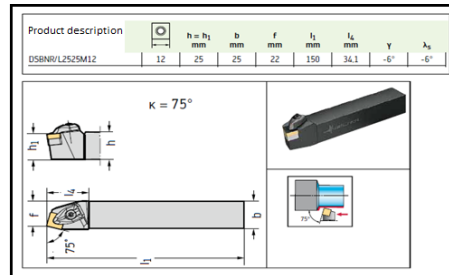
Figure 2. The geometric shape and dimensions of the tool holder used in the machinability experiments

In the experiments, the cutting tool which has Walter mark with uncoated and code "SNMG120412-NRT WS10" was used. ISO codes, structure and geometrical properties and technical information of the cutting tools are given in Figure 3.
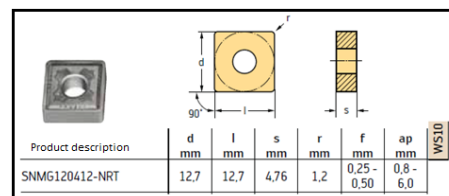
Figure 3. Cutting tool geometry and technical information of uncoated carbide insert

2.3. Measurement of the Cutting Force

The three force components occurring during chip removal; "KISTLER 9257B" type piezoelectric dynamometer which can measure the main cutting force Fz (Fc), the feed force Fx (Ff) and the radial force Fy (Fr) is used. And this dynamometer is connected to a signal amplifier (Multichannel Charge Amplifier) "KISTLER Type 5019". And the cutting forces were sent to the computer via RS-232C interface cable and graphics were obtained with the help of the program "DynoWareType2825A1-2". An image taken during the creation of graphics is given in Figure 4.
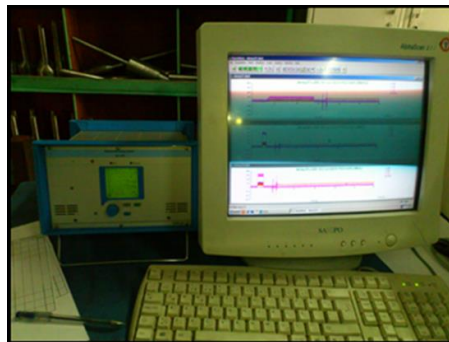
Figure 4. "KISTLER Type 5019" signals amplifier and computer equipment

The values obtained in each experiment were calculated by Dyno Ware Type program in Newton and the averages of the values were taken. The main cutting force Fz (Fc), the feed force Fx (Ff) and the radial force Fy (Fr) are determined. The test setup in which the cutting experiments are performed is given in Figure 5.
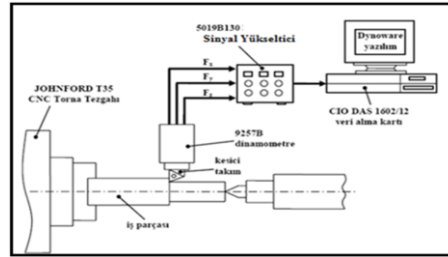
Figure 5. Experimental setup for cutting experiments

3. EXPERIMENTAL RESULTS AND DISCUSSION

Chip removing processing from the casting samples manufactured of AZ91 magnesium alloy were carried out in the CNC lathe. WS10 cutting tools were used for chip removing operations and a total of 9 tests were performed. The cutting forces generated during chip removing are measured and the cutting forces values are given in Table 3.

Table 3. The cutting force values (The Cutting speed 512 m/min)

Experiment Number	Cutting depth a (mm)	Feed rate f (mm/rev)	Cutting Forces (N)		
			Fc	Fr	Ff
1	1	0,1	94,22	43,76	40,29
2		0,2	136,09	58,88	47,96
3		0,3	170,58	66,63	52,59
4	2	0,1	152,04	51,76	68,41
5		0,2	229,32	71,21	88,19
6		0,3	289,55	88,09	99,01
7	3	0,1	219,91	80,88	123,2
8		0,2	325,45	99,74	142,8
9		0,3	404,31	104,6	140,2

In this study, When the shear forces are evaluated, the main cutting force of the highest force values due to the cutting mechanism is taken into account. Looking at the cutting forces obtained (Table 3), it is seen that the radial force (Fr) and the feed force (Ff) are close to each other. The main force (Fc) appears to be about three times or more of these two force values (Fr and Ff).

As the radial force creates deflection on the workpiece and the tool, it also affects the rigidity negatively. The radial force values are also increasing due to increasing values of the cutting speed, cutting depth and cutting speed and it is observed in significant changes in the three compositions of the cutting force due to the growth of section of the chip [11,12].

The most important factor determining the main cutting force is the section area of the chip created by the feed rate. It is therefore expected that the cutting forces increase with the increase in the feed rate. Due to the increase in the feed rate, there was an upward tendency in the main cutting force. The reason for this is the increased section area of the chip due to increasing the feed rate. In order to reduce the main cutting force, the feed rate value must be reduced. In studies done in the literature, it shows that the feed rate directly affects the cutting force [13]. The experimental carrying out at the cutting speed of 512 m / min using WS10 cutting tool of AZ91 magnesium alloy, the variation of the feed rate over the main cutting force is plotted as the graph in Figure 6 and the variation of the chip depth on the cutting force is plotted as the graph in Figure 7.
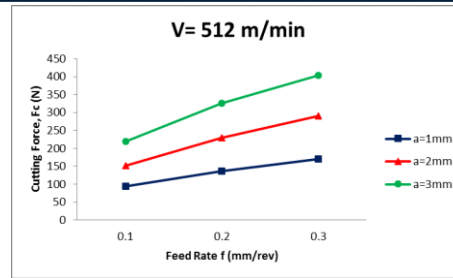
Figure 6. At the cutting speed of 512 m / min, the feed rate - cutting force graph
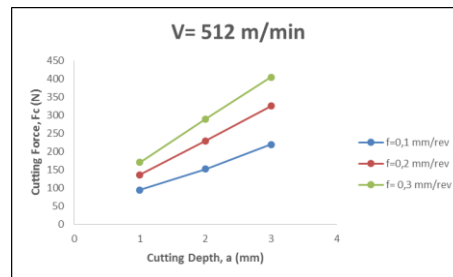
Figure 7. At the cutting speed of 512 m / min, the cutting depth - cutting force graph cutting depth

When Figure 6 and Figure 7 are examined, at the constant cutting speed of 512 m / min, the smallest cutting force was 94.22 N in cutting carrying out with WS10 cutting tool at a cutting depth of 1 mm and a feedrate of 0.1 mm / rev. With increasing 200% of the cutting depth and the feed rate, at the cutting depth of 2 mm and the feed rate of 0.2 mm / rev, the change in cutting force is increased to 229.32 N by approximately 250% during cutting with WS10 cutting tool. The highest cutting forces, on the other hand, increasing 300% of the cutting depth and feed rate, at the cutting depth of 3 mm and a cutting speed of 0.3 mm / rev in the cutting with WS10 cutting tool, it is observed that it increased to 404,31 N increasing by about 425%.

3.1. Statistical Analysis of the Cutting Force Results

The analysis of variance was performed to determine of the effect on the cutting force of the cutting depth and the feed rate. For statistical analysis, the factors which are cutting depth (a) and feed rate (f) were investigated the effects on the response variable which is the cutting force (Fc). Table 4 shows the ANOVA table determining the effect on the "Fc" response variable of "a" and "f" factors is determined.

Table 4. Response variable "Fc" for factors "a", "f" in ANOVA system.

Source	DF	Seq SS	Adj SS	Adj MS	F	P	PD
Cutting depth	2	50197	50197	25099	33,85	0,003	%62,95
Feed rate	2	26582	26582	13271	17,92	0,010	%33,33
Error	4	2966	2966	742			%3,72
Total	8	79745					%100
S = 7,2312 R-Sq = 96,28 R-Sq(adj) = 92,56%							
DF: Degree of Freedom, SS: Sum of squares, P:Meaningfulnes<0,05, PD: Percent distribution							

According to the results of variance analysis given to the Table 4, at the 95% confidence interval, the most effective parameter on the cutting forces was found to be cutting depth with 62.95% and feed rate with 33.33%. The regression analysis result for the cutting force, the statistical model constant and the coefficient values of the variables are given in the Table 5.

Table 5. The statistical model constant and the coefficient values

Term	Coefficient	Standard Coefficient	T	P
Constant	-91,076	27,3867	-3,32554	0,016
a	91,463	9,3028	9,83181	0,000
f	663,783	93,0280	7,13531	0,000

When the effects of factors are examined, similar to the results of analysis of variance, it appeared that the cutting force was the largest effective cutting depth (a) among the independent variables. The mathematical formula has been developed taking into account the effects of the independent variables (a and f) on the cutting force.

$$F_c = -91,0756 + 91,4633 \times a + 663,783 \times f \qquad (1)$$

4. RESULTS

The parameters affecting the cutting force results obtained from the experimental results were determined and the mathematical model was developed. It has been determined that the obtained models can be used at the 95% confidence level.

The results obtained from the models show that the error amount is small and the results are close to the experimental results.

- It has been found that the cutting depth and the feed rate affect the cutting force.
- It has been determined that the parameter that has the greatest effect on cutting force is cutting depth.
- The cutting force values increased as the cutting depth increased.
- The cutting force values increased as the feed rate increased.

ACKNOWLEDGMENT

REFERENCES

[1]. M. M. Avedesian and H. Baker, ASM Speciality Handbook, Magnesium and Magnesium Alloys, ASM International Materials Park, United States of America. 1999.
[2]. K. Kandemir and A.C. Can, "Otomotiv Endustrisi İcin Magnezyum Alasımlarının Kullanım Potansiyeli", Pamukkale Universitesi Mühendislik Fakültesi, Mühendislik Bilimleri Dergisi, 9 (1) 37-45, 2003.
[3]. F. Mert, "Magnezyum Alasımlarının İslenmesi", 3. Ulusal Talaslı İmalat Sempozyumu, Ankara, Türkiye, 04-05 Ekim, 282-288, 2012.
[4]. H. Kusdemir, "AZ91 magnezyum alasımının korozyon davranısları üzerine ilave alasım elementlerinin etkisi", Yüksek lisans Tezi, Karabük Üniversitesi Fen Bilimleri Enstitüsü, Karabük, 2008.
[5]. M. Ünal, "Magnezyum Alasımlarının Doküm Ozelliklerinin İncelenmesi", Doktora Tezi, Gazi Üniversitesi Fen Bilimleri Enstitüsü, Ankara, 2008.
[6]. H.R. Mohd, M. Norhamidi and A. B. Bakar, "A Review Of Workability Of Wrought Magnesium Alloys", Advanced Manufacturing Research Group, Malaysia, 2009.
[7]. M. Ünal, E. Koc, Y. Türena, F. Gül and E. Candan, 5. Uluslararası İleri Teknolojiler Sempozyumu (IATS'09), , Karabük, Türkiye, 2009.
[8]. J. Zhang, X. Niu, X. Qiu, K. Liu, C. Nan, D. Tang and J. Meng, "Effect of yttrium-rich misch metal on the microstructures, mechanical properties and corrosion behavior of die cast AZ91 alloy", Journal of Alloys and Compounds, 471, 322–330, 2009.
[9]. E. Koc, M. Ünal, Y. Türen and E. Candan, "AZ91 Magnezyum Alasımının Doküm ve Mekanik Ozelliklerine Kalay Elementinin Etkisi", 5. Uluslararası Ileri Teknolojiler Sempozyumu (IATS'09), Karabük, Türkiye, 2009.
[10]. H. Kinji, S. Hidetoshi, T. Yorinobu and H. Kenji, "Effects of Ca and Sr addition on mechanical properties of a castAZ91 magnesium alloy at room and elevated temperature", Materials Science and Engineering A, 403, 276–280, 2005.

[11]. "Modern metal cutting – A practical handbook", English Edition, Sandvik Coromant, Sweden, 1-3: 35-120, 1994.

[12]. L. Cizek, A. Hanus, M. Sozanska, T. Tanski and L. Pawlica, "Structure Characteristics of Magnesium Alloys With Admixture of Aluminium, Silicon and Zirconium Acta Metallurgica Slovaca", 13: 531-538, 2007.

[13]. J.D. Majumdar and I. Manna, "A Mathematical Model to Predict the Thermal History and Microstructure Developed in Laser Surface Alloying", Laser. Eng.,20, pp: 171-190, 2002.

Investigation And Statistical Analysis Of Surface Roughness In Turning Of AZ91 Materials

Omer Asal [1], Hakan Dilipak [2], Faruk Mullaahmetoglu [3]

Abstract

Magnesium and its alloys have very good machinability. In this work, it have been investigated that affecting of the feed rates and cutting speeds values on the surface roughness. For this purpose, Walter CNMG 120412-NRT WS10 uncoated tools have been used as cutting tools. The experiments were carried out at CNC lathe and under dry cutting conditions. The chip removal was carried out at a constant cutting depth of 2 mm. Three cutting speeds (200, 320 and 512 m / min) and three different feed rate (01, - 0.2 and 0.3 mm / dev) as cutting parameters were specified. For the test results, the variance analysis was performed so that the effect ratios of the parameters were determined. Regression analysis was performed to obtain the model. As a result, it was determined that the feed rate on the surface roughness is the most effective parameter.

Keywords: AZ91, Magnesium Alloys, Machinability, Surface Roughness, Regression Analysis, Anova

1. INTRODUCTION

In today's industry, companies are demanding materials that are light and have good mechanical properties. Magnesium and its alloys have become a preferred material because of the density being 1.74 gr / cm and the strength being almost the same as aluminum (200-250 MPa). Magnesium is the lightest metal used in structural applications [1]. Magnesium alloys have high strength, low density, good machinability, etc. properties. Magnesium alloys with low melting temperature and good weldability, it has a wide range of usage in electronics, aircraft and aviation industry, especially in automotive industry.

Magnesium is not only the known lightest metal but also has good machinability. During the shaping of magnesium with machining, the cutting forces are low, the surface quality is good and the chip flow is easy. At the same time, when magnesium is machined, the cutting forces are low, the surface quality is good and the chip flow is easy. Magnesium alloys also have similar machinability properties. Magnesium alloy parts are subjected to machining operations. Magnesium has low cutting pressures and high thermal conductivity and provides rapid heat dissipation. At this time, the tool life is extended and the tool change times are shortened [2, 3].

Magnesium and its alloys have been applied in various fields, due to its low density and easy forming properties. So it is generally seen that studies aimed to improve the mechanical properties of magnesium alloys [4]. The studies have been carried out to examine the mechanical properties by improving mechanical properties of AZ91 alloy [5, 6]. At the same time the studies were carried out to determine of the machinability of AZ91 added different alloying elements [1, 5, 6, 7]. The aluminum added to the AZ series magnesium alloy was investigated for its effect on machinability [7]. In the study carried out by Narita et al, it has been determined that very good surface quality is achieved by cutting at high speeds of the magnesium alloys [8]. Uzun and his colleagues, Al matrix and MgO reinforced composite materials have been produced at 5%, 10% and 15% reinforced-volume (T-H) ratios and they have made machinability experiments with carbide and coated carbide inserts. Friemuth and Winkler, they were investigated chip formation by turning

---

[1] *Corresponding author, Ömer Asal: Gazi University, Department of Manufacturing Engineering, Teknikokullar/Ankara, Turkey omerasal@gazi.edu.tr*

[2] *Hakan Dilipak: Gazi University, Department of Manufacturing Engineering, Teknikokullar/Ankara, Turkey hdilipak@gazi.edu.tr*

[3] *Faruk Mullaahmetoglu, Gazi University, farukmulla@hotmail.com*

with high speed cutting speed to improve the machinability of magnesium and its alloys [10]. Akyüz has worked on machinability characteristics during turning of AZ series alloys [11]. Tonshoff and Winkler investigated the effect of tool coating on the machinability of magnesium [12].

In this study, the machinability of AZ91 magnesium alloy has been investigated. For this purpose, the cutting depth was kept constant and nine experiments have been carried out by using three different cutting speeds and three different feed values. The effects on the surface roughness of the experiments parameters were investigated. The experiments were carried out on a CNC lathe. The variance analysis and the regression analysis were performed on the experiments results.

2. MATERIAL METHOD

2.1. The experiments Materials and the Cutting Parameters

In experiments, there have been used AZ91 magnesium alloy experiments materials in size 92x300 mm manufactured from pressure casting. The chemical composition of the AZ91D magnesium alloy which is used as experimental materials is given in Table 1.

Table 43. The chemical composition of the AZ91D (%)

Heat No	Al	Zn	Mn	Fe	Si	Cu	Ni	Mg
523	8.8	0.68	0.18	0.003	0.017	0.0021	0.00061	Balance
Requirement	8.5-9.5	0.45-0.90	0.17-0.40	Max 0.004	Max 0.08	Max 0.025	Max 0.001	Balance

Machinability experiments were carried out under the conditions of dry cutting on the CNC lathe in accordance with ISO 3685 standard (turning inserts - life test) and experiments conditions at Gazi University Faculty of Technology Manufacturing Engineering laboratory. "Johnford TC-35" industrial CNC lathe with FANUC control unit was used in the experiments. Experiments were carried out at the constant cutting depth (2 mm), three different cutting speed (200 m/min, 320 m/min, 512 m/min) and three different feed rate (0.1 mm/rev, 0.2 mm/rev, 0.3 mm/rev). A new cutting tool was used in each experiment. Uncoated carbide cutting tools were used as the cutting tool and a total of 9 experiments were carried out. The Experimental setup is shown in Figure 1. The experimental parameters are given in Table 2.
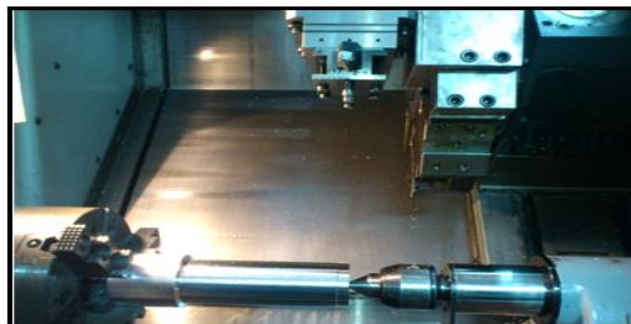
Figure 64. The specimen and experimental setup prepared for experiments

Table 44. The experimental parameters

Experimental Number	Cutting Speed (m/min)	Feed rate (mm/rev)
1	200	0.1
2	200	0.2
3	200	0.3

4	320	0.1
5	320	0.2
6	320	0.3
7	512	0.1
8	512	0.2
9	512	0.3

2.2. The Tool Holder and the Cutting Tools

In the experiments, the tool holder which has Walter mark with code "DSBNR2525M12" was supplied and used. The geometric properties and sizes of the cutting tool holder are given in Figure 2.
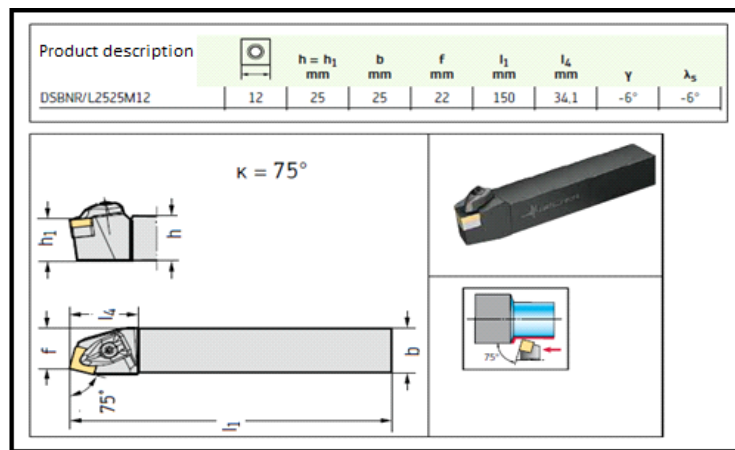
Figure 65. The geometric shape and sizes of the tool holder used in the machinability experiments

In the experiments, the cutting tool which has Walter mark with uncoated and code "SNMG120412-NRT WS10" was used. ISO codes, structure and geometrical properties and technical information of the cutting tools are given in Figure 3.
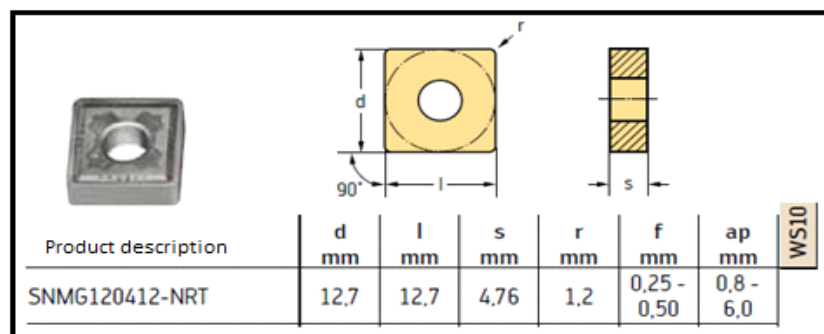
Figure 66. Cutting tool geometry and technical information of uncoated carbide insert

2.3. Measuring of the Surface Roughness

Surface roughness measurements were made with the "Mahr" brand of Perthometer M1, which is located in the CNC laboratory of Manufacturing Engineering Department of Gazi University Faculty of Technology, with the surface roughness measuring device which is used on the table and has printable property.

The surface roughness measurements carrying out on the treated surfaces of the experimental materials, the measuring ranges chosen as 5.6 mm as parallel to the axis of the experimental material and after each measurement, the experimental material was rotated 120 ° about its own axis and measured from three different surfaces.

The measuring processing were carried out in accordance with ISO 4288 (TS 6212) (Geometrical product specifications (gps) - surface texture: profile method - rules and procedures for the assessment of surface texture). The sampling length (λ) and the measuring length (L) have been taken in accordance with this standard. The average surface roughness (Ra) values were determined by taking arithmetic mean of the three values obtained as a result of the surface roughness measurements. The image of the "Mahr" brand Perthometer M1 type which is the surface roughness meter device is shown in Figure 4.

Figure 67. "Mahr" brand Perthometer M1 type surface roughness meter used in measurements

3. EXPERIMENTAL RESULTS AND DISCUSSION

The nine experiments were performed to investigate the surface roughness of AZ91 magnesium alloy. The mmeasurements were made in three different areas on the machined surface obtained by removing the chips with each cutting tool and average surface roughness values were determined by taking the arithmetic mean. The measured average surface roughness (Ra) values are given in Table 3.

Table 45. The value of surface roughness (the constant cutting depth 2 mm)

Experimental Number	Cutting Speed (m/min)	Feed Rate f (mm/rev)	Surface Roughness Ra (µm)
1		0,1	0,506
2	200	0,2	1,091
3		0,3	2,931
4		0,1	0,469
5	320	0,2	1,480
6		0,3	2,630
7		0,1	0,675
8	512	0,2	1,465
9		0,3	2,471

In experiments the chip removing from the AZ91 magnesium alloy by using WS10 cutting tools at the constant cutting depth of 2 mm, the variation on the surface roughness (Ra) of the feed rate (f) is shown as the graph in Figure 5. And the variation on the surface roughness (Ra) of the cutting speed (V) is shown also graphically in Figure 6.
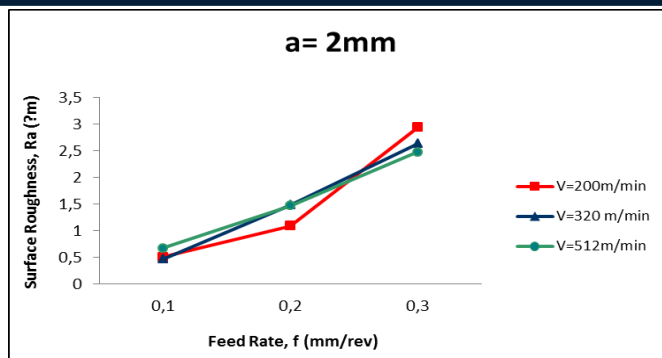
Figure 68. The graph of the feed rate – the surface roughness in the constant cutting depth 2 mm
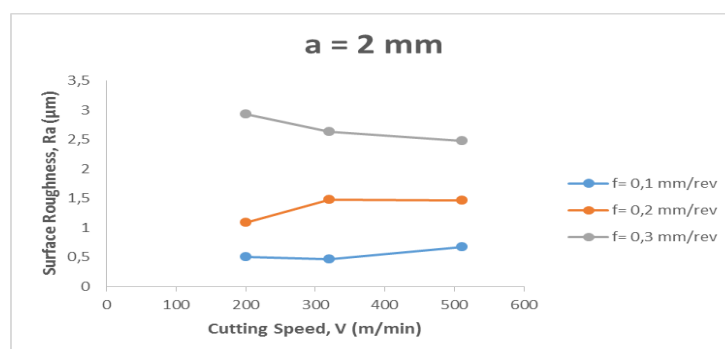
Figure 69. The graph of the cutting speed – the surface roughness in the constant cutting depth 2 mm

When investigating the average surface roughness values obtained in the constant cutting depth 2 mm, it is seen that the surface roughness value increases with increasing of the feed rate (Figure 5 and Figure 6). The lowest the average surface roughness value was determined as 0.409 µm at the cutting speed 320 m / min and the feed rate 0.1 mm / rev. And the highest surface roughness value was realized as 2.630 at the cutting speed 320 m / min and the feed rate 0.3 mm / rev.

An increasing relationship was found between the values of the feed rate and the average surface roughness values. However, the shear rate changes have no effect on the surface roughness.

3.1. Statistical Analysis of the Surface Roughness Results

Variance analysis was performed to determine the effect on the surface roughness of the cutting speed and the feed rate. For statistical analyzes, it were investigated the effects on variability in the response variable the surface roughness (Ra) of the factors the cutting speed (V) and feed rate (f). The table 4 is shown the ANOVA table showing the effect on the Ra response variable of V and f factors.

Table 46. Response variable "Ra" for factors "f", "V" in ANOVA system.

Source	DF	Seq SS	Adj SS	Adj MS	F	P	PD
Feed rate	2	6,9340	6,9340	3,4670	60,51	0,001	%96,78
Cutting speed	2	0,0012	0,0012	0,0006	0,01	0,990	%0,02
Error	4	0,2292	0,2292	0,0573			%3,2
Total	8	7,1643					%100

S = 0,239365   R-Sq = 96,80   R-Sq(adj) = 93,60%

DF: Degree of Freedom, SS: Sum of squares, P:Meaningfulnes<0,05, PD: Percent distribution

According to the results of variance analysis given to the Table 4, at the 95% confidence interval, it has been determined that the cutting speed has no effect on the surface roughness while the feed rate on the surface roughness is an effective parameter. The effect of the rate of progress on the surface roughness value was found to be 96.78%.

The regression analysis result for the surface toughness, the statistical model constant and the coefficient values of the variables are given in the table 5.

Table 47. The statistical model constant and the coefficient values

Term	Coefficient	Standard Coefficient	T	P
Constant	-0,6329	0,31303	-2,0219	0,090
f	10,6378	1,01860	10,4436	0,000
V	0,0001	0,00065	0,1326	0,899

When the effects of factors are examined, similar to the results of analysis of variance, it is seen that the feed is an effective parameter on the surface roughness. However, it has been determined that the cutting speed is not an effective parameter on the surface roughness. The mathematical formula has been developed taking into account the effects of the independent variables (f and V) on the surface roughness.

$$Ra = -0,632926 + 10,6378 \times f + 0,00000858096 \times V \qquad (1)$$

4. RESULTS

The parameters affecting the surface roughness results obtained from the experimental results were determined and the mathematical model was developed. It has been determined that the obtained models can be used at the 95% confidence level.

The results obtained from the models show that the error amount is small and the results are close to the experimental results.

The feed rate have been found to be a very effective parameter on the surface roughness.

It has been determined that the cutting speed is not an effective parameter on the surface roughness.

The surface roughness values increased as the feed rate value increased.

The change in feed rate values did not affect the surface roughness values.

ACKNOWLEDGEMENTS

REFERENCES

[1]. M. Akgün, G. Ozger, and H. B. Ulas, "Evaluation of machinability of cast az91 magnesium alloys in terms of surface roughness", Erciyes Üniversitesi Fen Bilimleri Enstitüsü Dergisi, 30(5):323-328, 2014.
[2]. F. Mert, "Magnezyum Alasımlarının İslenmesi", 3. Ulusal Talaslı İmalat Sempozyumu, Ankara, Türkiye, 04-05 Ekim, 282-288, 2012.
[3]. M. M. Avedesian and H. Baker, ASM Speciality Handbook, Magnesium and Magnesium Alloys, ASM International Materials Park, United States of America. 1999.
[4]. K. Kandemir and A.C. Can, "Otomotiv Endüstrisi İcin Magnezyum Alasımlarının Kullanım Potansiyeli", Pamukkale Üniversitesi Mühendislik Fakültesi, Mühendislik Bilimleri Dergisi, 9 (1) 37-45, 2003.
[5]. M. Ünal, "Magnezyum Alasımlarının Doküm Ozelliklerinin İncelenmesi", Doktora Tezi, Gazi Üniversitesi Fen Bilimleri Enstitüsü, Ankara, 2008.
[6]. N. Saklakoglu, Y. Ercayhan, "AZ91 Magnezyum Alasımının Metalurjik Ozelliklerine Kadmiyum Elementinin Etkisi" II. Ulusal Tasarım- İmalat ve Analiz Kongresi (TİMAK) 11-12 Kasım, Balıkesir, 2010.
[7]. B. Akyüz, "Influence of Al content on machinability of AZ series Mg alloys" Transactions of Nonferrous Metals Society Of China, 23: 2243-2249, 2013.

[8]. G. Uzun, M. Pul, R. Calın and U. Seker, "Al Matrisli MGO Takviyeli Kompozitlerin Farklı Kesici Uclarla Tornalanmasında Kesme Hızının Asınma Davranısına Etkilerinin İncelenmesi" 3. Ulusal Talaslı İmalat Sempozyumu, 04-05 Ekim, Ankara, Türkiye, 2012.

[9]. T. Friemuth, J. Winkler, "Machining of Magnesium Workpieces", Adv. Eng. Mater, 1 (3–4) 183–186, 1999.

[10]. B. Akyuz, "İnflence of Al content on machinability of AZ series Mg alloys", Metals Soc. China, 23 2243–2249, 2013.

[11]. H.K. Tonshoff, J. Winkler, "The influence of tool coatings in machining of magnesium", 1997 Surface & Coatings Technology, Germany, pp. 610-616, 1997.

The Effect Of Material Pairs On The Axial Force, Traverse Force And Temperature In The Friction Stir Welding Process

Musa BİLGİN[1], Sener KARABULUT[2], Ahmet OZDEMİR[3]

Abstract

In this study, the axial force, the traverse force and the friction temperature were investigated during the friction stir welding of aluminum alloy 7075 and magnesium alloys. For this purpose, Al 7075-T6 and magnesium alloys (AZ91 D and AZ 31 B) were combined by using friction stir welding under constant spindle speed of 1400 rev/min and welding speed of 25 mm/min. Visual inspection and penetrants tests were performed to investigate the weld quality of the joined materials. Nondestructive evaluation results indicated that an acceptable welding quality was achieved in the friction stir welding of the same materials while the noteworthy welding quality was not obtained during the dissimilar friction stir welding of aluminum and magnesium alloys. A smoother weld surface was obtained in the FSW of similar. The experimental results are also depicted that the axial force, traverse force and temperatures are affected by the mechanical properties of the experimental specimens.

Keywords: *Al Alloy; Mg Alloys, FSW, Force, Temperature*

1. INTRODUCTION

It is required to weld the different metals due to the economic and technical factors in today's institution [1]. Especially, it will have been provided that the advantages from the lightness in the products with joining the light metals such as Al and Mg safely are used. However, it is very difficult to make the welding of different metals due to the differences in their mechanic, physical and metallurgical properties with the classical fusion welding method [2].

Friction Stir Welding (FSW) is a solid-state welding method which would successfully do the welding of high-strength Al alloys and the different metals that it is difficult to join them by the classical fusion welding methods [3, 4]. The solidification and liquefaction cleavage due to non-emergence of molten metal in the FSW method, the loss of porosity alloy elements can be prevented with the vaporization. It is commonly used in welding aluminum alloys and other mild metals with these advantages [5].

The main concept of FSW method is very simple. The rotating tool which is designed especially with the roll pin and shoulder gets on throughout the submerging and welding line into the sheet metal or plates which are reclined against each other [Figure 1]. The friction which occurs between the mixer edge with the rotating and traverse movements with the workpiece make the heat input on the field where the mixer edge has an effect. The calescent material softens, it changes shape as plastic and a joining process occurs without the distortion in the case of the high-quality solid state due to the tool's compression force [6, 8].

---

[1] Corresponding author: Hacettepe University, Baskent **Organized Industrial Zone** Technical Sciences Vocational Schools, 06909, Sincan / Ankara, Turkey. musabilgin@hacettepe.edu.tr.

[2] Hacettepe University, **Ankara Chamber of Industry 1st Organized Industrial Zone Vocational School**, 06935, Sincan / Ankara, Turkey. senerkarabulut@hacettepe.edu.tr.

[3] Gazi University, Department of Manufacturing Engineering , 06500, Yenimahalle / Ankara, Turkey. ahmetoz@gazi.edu.tr
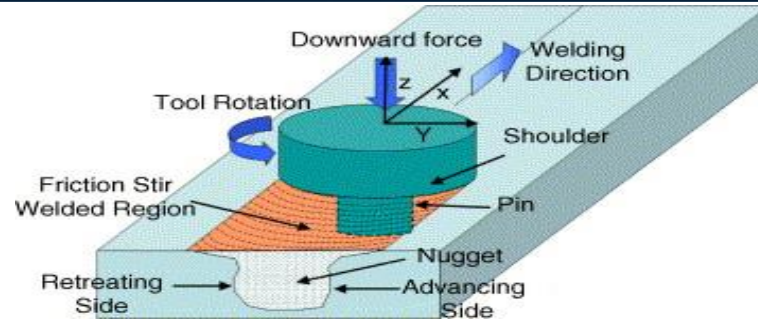
Figure 1. The Schematic Drawing of FSW Method [6].

The response variables [axial force, traverse force, heat input etc.] which are affected from the primary control parameters [welding speed, spindle speed, diameter of tool and diameter of pin etc.] in the method of FSW can be measured during the joining. These response variables effect on the properties of joining area. The quality of next joining can be increased as the response variables which occur during the processing are followed and interpreted [9].

As the heat input affects directly in the materials' ductility in the method of FSW, it is one of the most important response parameters in the welding of different materials [10]. The temperature should be at the range of 0, 6-0, 8 times of the material's melting point in the method of FSW [11]. The heat source is a tool to make the rotating and traverse motions in the method of FSW. The heat source is the friction heat and the deformation heat in the method of FSW [12].

The decreasing of heat input can cause the results such that the materials aren't mixed well, the gaps in the welding area occur. Moreover, the decreasing of spindle speed to decrease the heat input decreases the strength as it causes the distribution of Mg_2Al_3 and $Mg_{17}Al_{12}$ intermetallic compounds in a bad way which occurs in joining Al-Mg alloys [13,14]. As the increase in the welding speed to decrease the heat input causes to join two pieces with the low mixing, the tensile strength of samples decreases [15].

The excessive heat input affects negatively especially on the mechanical properties of the high-strength Al alloys in the welding field [16, 17]. The layer thickness of Mg_2Al_3 and $Mg_{17}Al_{12}$ intermetallic compounds which occur in parallel with the increase of heat input in joining Al-Mg alloys with FSW increases also. The tensile strength decreases substantially due to the declination of mechanical locking because of the increase in the intermetallic compounds' thickness, and to the fractures from the intermetallic compounds [18, 19, 20].

The high immersion force is necessary in order to soften the material sufficiently in terms of providing a perfect joining in the method of FSW [8, 21]. Moreover, it has a key role for the perfect joining that these forces are kept at the certain intervals [7].

In this study, Al alloy (7075 T6) and Mg Alloys (AZ 31 B and AZ 91 D) were joined as the same type and dissimilar of materials in the spindle speed of 1400 rev/min and at 25 mm/min welding speeds. After the joinings are controlled by the visual inspection and penetrant test, the effects of material couples on the axial force, traverse force and heat occurrence were reviewed.

2. MATERIAL AND METHOD

Al (7075 T6) which was generated by the method of extrusion and Mg (AZ 91 D and AZ 31 B) which was generated by the method of hot rolling were prepared at the dimensions of 100 mm x 100 mm x 3 mm onto the plate blocks. The processing of joining was done by the combination which was given at the following Table 1. The chemical content of materials was given at Table 2.

Table 1. The experiment ranking

Experiment No	The material couple		Experiment No	The material couple	
	Advancing Side	Retreating Side		Advancing Side	Retreating Side
1	7075 T6	7075 T6	4	AZ 31 B	AZ 91 D
2	AZ 31 B	AZ 31 B	5	AZ 31 B	7075 T6
3	AZ 91 D	AZ 91 D	6	AZ 91 D	7075 T6

Table 2. The Materials' Chemical Contents

Material	Al	Mg	Zn	Mn	Si	Fe	Cu	Ni	Ti	Cr	Sn	Be
7075 T6	The rest	2,65	5,80	0,30	0,40	0,50	1,81	---	0,20	0,22	---	---
AZ 91 D	9	The rest	0,76	0,29	0,012	0,0007	0,0018	0,0008	---	---	0,07	0,00098
AZ 31 B	3,25	The rest	1	0,4	0,17	0,003	0,0007	0,0008	---	---	---	---

The processing of joining was done with the stable spindle speed (1400 rev/min), the stable welding speed (25 mm/min) , the stable tool angle (0) and without offset from mixer tool weld line. The processing of joining was done on Taksan FU 400x1600 V/2 vertical milling machine, the measurement of Force was done with Kistler type 9272 dynamometre, and the measurement of temperature was done by Ratek M13 Contant-free temperature measurement device. DynoWare software was used for the measurement and assessment of dynamometre values. The image of testing apparatus was given at Figure 2.
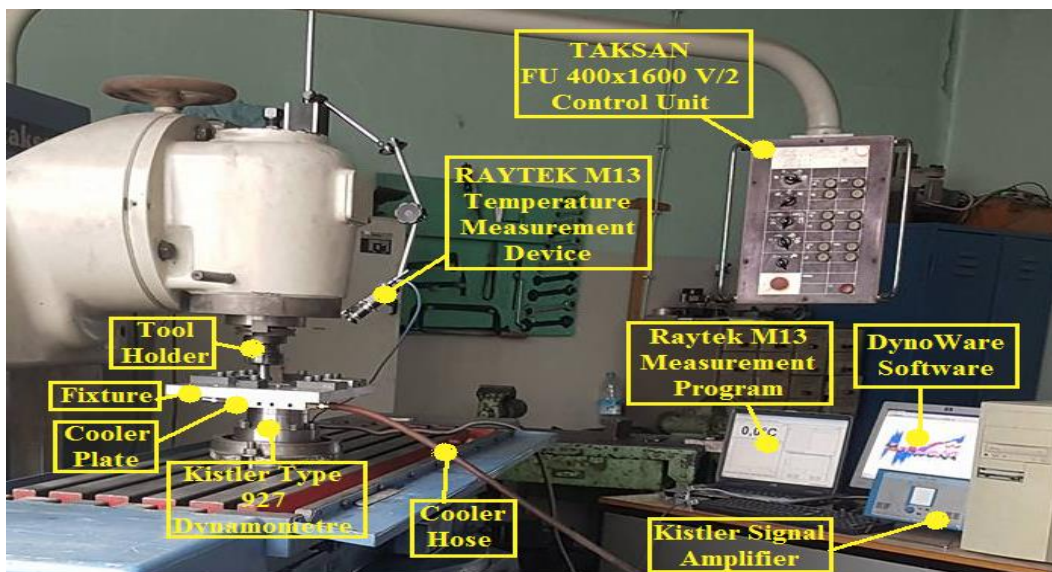
Figure 2. The Test Apparatus

The tool roll pin which is used in the processing of FSW has got the cambered triangular profile. The diameter of circle which touches slightly from the corners of triangle is 6.2 mm, the cambered radius is 5.4 mm, the length of roll pin is 2.8 mm and the diameter of shoulder is 18.6 mm. The top view of tool was given at Figure 3. Mixer tool is made from 3343 high speed steel. Heat treating hardness value is done in 62 HRc.

Figure 3. FSW tool top view

3. RESULTS AND DISCUSSION

The penetrant test was done for those which had the positive visual inspection of samples which were obtained as a result of the experiments which were done (Figure 4).

Exp. no	Inspection Method	Top View of The Plate Joined by The FSW Method
1	Visual Inspection	
	Penetrant Test	
2	Visual Inspection	
	Penetrant Test	
3	Visual Inspection	
	Penetrant Test	
4	Visual Inspection	
	Penetrant Test	
5	Visual Inspection	
6	Visual Inspection	

Figure 4. Visual Inspection and Penetrant Test of Samples

Although there was a joining on the weld root for the joining of different metals as a result of visual inspection, an open channel occurred on the top surface, and a successful welding to join Al-Mg alloys couldn't be obtained. This case is thought to arise from that the plastic flow doesn't occur with the demanded quality as Mg alloys become deformed in more difficult way than Al alloys especially for the low heat input [13]. The formation of open channel which doesn't occur in the joining of the same-type materials causes a great problem to join the dissimilar materials.

When the penetrant test to join the same-type materials was reviewed, the defects occurred on the points where the tool immerged into the plates especially to join AZ 91 D – AZ 91 D and 7075 T6 -7075 T6. As the waiting period of these defect is kept brief after the first entry, the gaps are caused with the mixing field from that the plastic deformation doesn't occur at the demanded level on the base that the sufficient temperature isn't gotten. The defects which occur in the mixing field and on the border of main material arise from the occurrence of burrs in penetrant test.

The graph which indicates the traverse force (Fx) and the axial force (Fz) which occur in the joining of the same-type materials and the dissimilar materials during the processing of FSW was given at Table 2 and the it was given by the order of designated experiments at Figure 5.
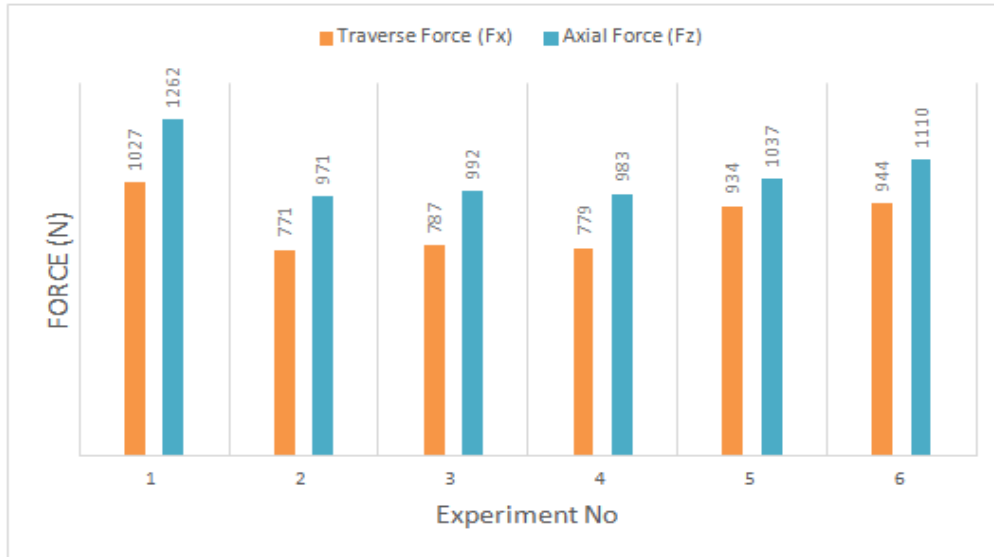
Figure 5. The traverse force (Fx) and the axial force (Fz) which occur to join the same-type and dissimilar materials.

When the axial force and traverse force are reviewed, the highest values occur in the joining of 7075 T6-7075 T6 , the lowest forces occur in the joining of AZ 31 B- AZ 31 B. When Al alloys and Mg alloys are compared, this case arises from that it has a higher flow resistance as the strength is too much at the high temperatures [22].

When the joining of the different Al and Mg alloys with the joining of the same-type materials is reviewed, the forces occur much more than Mg alloys and the less than Al alloys. This case arises from the Mg_2Al_3 and $Mg_{17}Al_{12}$ intermetallic compounds in the hard structure which occur in the joining of Al-Mg alloys.

The occurrence of temperature in the joining of the same-type materials and the dissimilar materials during the processing of FSW was given at Figure 6.

Figure 6: The occurrence of temperature in the joining of the same-type and dissimilar materials.

When Al alloy (7075-T6) is compared with Mg alloys (AZ 91 D and AZ 431 B) under the same conditions, the higher heat input occurs. The reasons of high heat input for Al alloys are:

- Al alloys generates the higher temperature than Mg alloys with the friction [23].
- Al aİloys' rigidity and strength at the high temperatures are the higher one. This case causes that Al alloys have the higher flow resistance and so, it causes the occurrence of higher temperatures [22].
- Al alloys' surface-centered cubic structure has much more activated sliding plane for the deformation than Mg allots' firm-order hexagonal structure. Thus, when Al is compared with Mg, it can be more deformed one and much more heat occurs [13, 21].

The lower heat occurrence in the joining of Al alloy with Mg alloys than the joining of Al alloys;

- Mg_2Al_3 and $Mg_{17}Al_{12}$ intermetallic compounds occur in the mixing field in the joining of Al Mg alloys. These liquid films cause the sliding of tool as they enter between the tool and material in the mixing field, and as its result, the heat which occurs with the friction decreases [13].

4. CONCLUSİONS

It is seen in the review of the visual inspection and penetrant test that the same-type materials were joined successfully. However, it is necessary to do the radiographic inspection and macro-structure analysis for the review of weld's internal structure.

The root of weld to join the dissimilar materials was successfully done but the open channel occurred.

The material strength is the determinant in the occurrence of heat input and also, the forces.

The heat and forces which occurred in the joining of Al alloys with FSW are much more than the heat and forces which occurred in the joining of Mg alloys.

It arises from the occurrence of low temperature that the dissimilar materials couldn't be joined at the demanded level, with the manner that the long length of tool pin prevented the increasing of compression force.

ACKNOWLEDGMENT

REFERENCES

[1]. K. P. Mehta and V. J. Badheka, "Effects of tilt angle on the properties of dissimilar friction stir welding copper to aluminum", Materials and Manufacturing Processes, vol. 31, pp. 255–263, 2016.
[2]. K. P. Mehta and V. J.Badheka, "A review on dissimilar friction stir welding of copper to aluminum: process, properties and variants", Materials and Manufacturing Processes, vol.31, pp. 233–254, 2016.
[3]. P. Sinha, S. Muthukumaran, S. Mukherjee, "Analysis of first mode of metal transfer in friction stir welded plates by image processing technique", J. Mater. Process. Technol. vol. 197, pp. 17–21, 2008.
[4]. M. Sued, D. Pons, J. Lavroff, E. Wong, "Design features for bobbin friction stir welding tools: development of a conceptual model linking the underlying physics to the production process", Mater. Des., vol. 54, pp. 632–643, 2014.
[5]. A. Arora, M. Mehta, A. De and T. DebRoy, "Load bearing capacity of tool pin during friction stir welding", Int J Adv Manuf Technol, vol. 61, pp.911–920, 2012.
[6]. R.S. Mishra and Z.Y. Ma, "Friction stir welding and processing", Material Science and Engineering R, vol.50, pp. 1–78, 2005.
[7]. S. Xu, "Microstructure analysis and solid mechanics modeling of friction stir welding", PhD Thesis, Department of Mechanical Engineering College of Engineering & Information Technology, University of South Carolina, 2003.
[8]. H. Uzun, R. Yılmaz ve F. Fındık, "Alüminyum Alasımları icin Süper Birlestirme Yontemi: Sürtünme Karıstırma Kaynak Teknigi ve Uygulamaları", Metal Dünyası, vol.118, pp. 75-82, 2003.
[9]. R. Kumar, K. Singh, S. Pandey, "Process forces and heat input as function of process parameters in AA5083 friction stir welds", Trans. Nonferrous Met. Soc., vol. 22, pp.288 – 298, 2012.
[10]. Y. K. Yang, H. Dong and S. Kou, "Liquation tendency and liquid-film formation in friction stir spot welding", Welding Journal, vol. 87 (8), pp. 202-211, 2008.
[11]. Edt. J. Paulo Davim, " Modern Manufacturing Engineering", Springer International Publishing, eBook ISBN 978-3-319-20152-8.
[12]. M. Z. H. Khandkar, J. A. Khan and A. P. Reynolds "Prediction of temperature distribution and thermal history during friction stir welding: input torque based model", Science and Technology of Welding and Joining, vol. 8 (3), pp. 165-174, 2003.

[13]. V. Fırouzdor and S. Kou, "Al-to-Mg friction stir welding: effect of positions of Al and Mg with respect to the welding tool", The *Welding Journal,* vol. 88, pp. 213-224, 2009.

[14]. S.H.C. Park, Y.S. Sato, H. Kokawa H, "Microstructural evolution and its effect on Hall-Petch relationship in friction stir welding of thixomolded Mg alloy AZ91", Mater Sci., vol. 38, pp. 4379-4383, 2003.

[15]. J.P. Bergmann, R. Schuerer and K. Ritter, "Friction stir welding of tailored blanks of aluminum and magnesium alloys", Key Engineering Materials , vol. 549, pp. 492-499, 2013.

[16]. J.H. Yan, M.A. Sutton, A.P. Reynolds, "Process–structure–property relationships for nugget and heat affected zone regions of AA2524–T351 friction stir welds", Sci. Technol.Weld.Join.,vol. 10(6), pp. 725–736, 2005.

[17]. T. Long, W. Tang, A. P. Reynolds, "Process response parameter relationships in aluminum alloy friction stir welds", Sci.Technol.Weld.Join., vol.12, pp.311 – 17, 2007.

[18]. J. Yan, Z. Xu, Z. Li, L. Li and S. Yang, "Microstructure characteristics and performance of dissimilar welds between magnesium alloy and aluminum formed by friction stirring" Scripta Materialia, vol. 53, pp. 585–589, 2005.

[19]. P. Venkateswaran and A. P. Reynolds, "Factors affecting the properties of friction stir welds between aluminum and magnesium alloys", Mater Sci. Eng. A, vol.545, pp.26–37, 2012.

[20]. N. Yamamoto, J. Liao, S. Watanabe and K. Nakata, "Effect of ıntermetallic compound layer on tensile strength of dissimilar friction-stir weld of a high strength mg alloy and al alloy" Materials Transactions, vol. 50(12), pp.2833-2838, 2009.

[21]. M. Azizieh, A. S. Alavijeh, M. Abbasi, Z. Balak and H. S. Kim, "Mechanical properties and microstructural evaluation of AA1100 to AZ31 dissimilar friction stir welds", Materials Chemistry and Physics, vol.170, pp.251-260, 2016.

[22]. X. Cao and M. Jahazi, "Friction stir welding of dissimilar AA 2024-T3 to AZ31B-H24 alloys", Materials Science Forum, vol. 638-642, pp.3661-3666, 2010.

[23]. R. Zettler, A. Augusto, M. da Silva, S. Rodrigues, A. Blanco and J. F. dos Santos, "Dissimilar Al to Mg alloy friction stir welds", Advanced Engineering Materials, vol. 8(5), pp. 415-421, 2006.

BIOGRAPHY

MUSA BİLGİN received his M.Sc. in Mechanical Education from the Gazi University of Turkey in 2012. He is currently Ph.D. student in Manufacturing Engineering from the same university and a lecturer in Baskent **Organized Industrial Zone** Technical Sciences Vocational Schools from the Hacettepe University. His research interests include mechanical design and manufacturing.

The Effect Of The Process Parameters On The Axial Force and Traverse Force In The Friction Stir Welding Of Al 7075 T6 and AZ91D

Musa BİLGİN[1], Sener KARABULUT[2], Ahmet OZDEMİR[3], Yunus KAYIR[4]

Abstract

In this study, an experimental study was conducted to investigate the effect of process parameters such as feed rate and spindle speed on the axial force and traverse forces in the Friction Stir Welding of Al 7075 – T6 and AZ 91 D. FSW process was carried out to join the 3 mm thick sheets Al 7075 and AZ 91 D. It is investigated to combine the Al7075 and AZ 91 D magnesium alloys by friction stir welding method using three different spindle speeds of 900, 1120 and 1400 rev/min and four different feed rates of 16, 25, 31.5, 40 mm/min at constant tool with a lead angle of 0°. Kistler multicomponent dynamometer type 9272 was used for the axial force measurements. The experiments were performed three times on the same process parameters and evaluated the axial and traverse forces on the influence of the better solid state welding conditions. Experimental results showed that the axial and feed forces were decreased with increasing spindle speed and reducing feed rates.

Keywords: *Friction Stir Welding, Axial Force, Traverse Force, AZ 91 D, 7075 T6*

1. INTRODUCTION

Al alloys are one of the light metals used in manufacturing sector. Usage of Mg alloys increases day by day because they are lighter than Al alloys. Important weight gain will be obtained by using of two metal alloys in common structures in order to lighten the vehicles especially. One of the most important obstacles of using two metals in common structures is the problem of welding. Friction Stir Welding (FSW) which is a solid state welding process was developed by TWI in 1991 [1]. Researchers have performed many studies on welding of Al-Mg alloys with this method and studies still continue [2-9].

FSW method is described as three-stage: immersion, waiting and progression stages. In immersion stage, tool is slowly immersed by deepening party line between two materials that will be welded. When tool reaches the necessary depth, it is kept in this position through 5-20 h which is called waiting stage. The aim of this stage is to soften the material part of tool. In progression stage, tool moves across the party line of two plates and performs welding [10].

In FSW method, rectilinear and rotational motion of tool simultaneously cause to have forces on tool [11-13]. Independent variables such as tool design, workpiece and tool material, rotational speed of tool, welding speed, immersion depth and tool angle significantly affects forces created during the operation [14,15]. Force which is created during FSW process and affects tool is showed in Figure 1.

[1] *Corresponding author: Hacettepe University, Baskent **Organized Industrial Zone** Technical Sciences Vocational Schools, 06909, Sincan / Ankara, Turkey. musabilgin@hacettepe.edu.tr*

[2] *Hacettepe University, **Ankara Chamber of Industry 1st Organized Industrial Zone Vocational School**, 06935, Sincan / Ankara, Turkey. senerkarabulut@hacettepe.edu.tr*

[3] *Gazi University, Department of Manufacturing Engineering , 06500, Yenimahalle / Ankara, Turkey. ahmetoz@gazi.edu.tr*

[4] *Gazi University, Department of Manufacturing Engineering , 06500, Yenimahalle / Ankara, Turkey. ykayır@gazi.edu.tr*
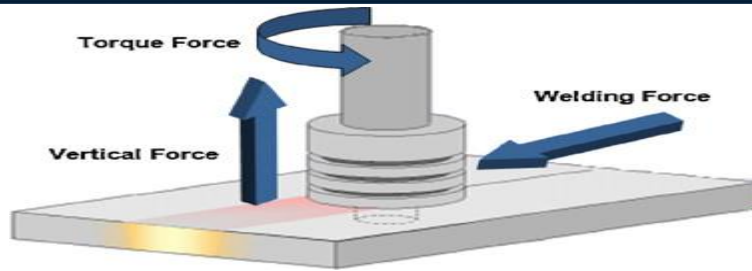
Figure 1. Forces created in FSW process [10]

In FSW method, while high immersion force is needed to soften tool in order to have a perfect welding [16-18], keeping of the other forces created at a certain intervals has a key role for perfect welding [14, 15]. In FSW method, traverse and axial force of optimization of process parameter have critical importance [19 -22].

Prediction, following and controlling of FSW forces provide many advantages [14, 15] as follows:

- Optimized tool design;
- Tool life estimation;
- Optimized binding mechanism design;
- Bonding strength estimation;
- More quality welding;
- Welding with high strength;
- Choosing of proper welding machine [23]

These advantages that provide optimization of forces lower cost and increase productivity [10].

In this study, effects of feedrate and spindle speeds in welding of Mg alloy (AZ 91 D) and Al alloy (7075 T6) with FSW method on axial force and traverse force have been analyzed.

2. MATERIALS AND METHODS

In this study, as shown in Figure 2, plates that will be welded are prepared as 100 x 100 x 3 mm size. AZ 91 D magnesium plate and AA 7075 –T6 aluminum plate are positioned in advancing (A.S.) and retreating side (R.S) respectively and fixed side by side without any space between them. Chemical compositions of AA7075-T6 plate produced with extrusion method and AZ 91 D plate produced with hot rolling method are given in Table 1 and Table 2 respectively.
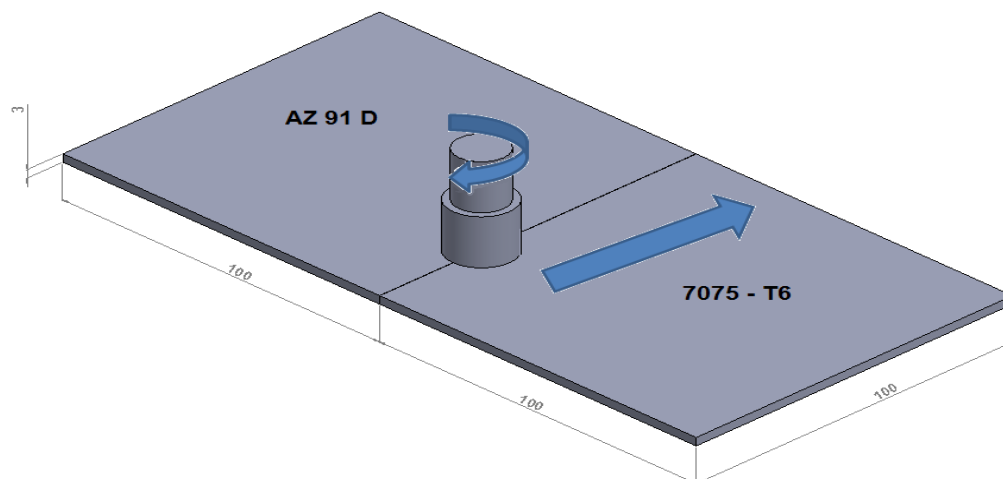
Figure 2. Positioning of plates

Table 1. Chemical composition of 7075 – T6

Chemical composition (%)								
Mg	Zn	Mn	Si	Fe	Ti	Cu	Cr	Al
2,65	5,80	0,30	0,40	0,50	0,20	1,81	0,22	The rest

Table 2. Chemical composition of AZ 91 D

Chemical composition (%)									
Al	Zn	Mn	Cu	Si	Fe	Sn	Be	Ni	Mg
9	0,76	0,29	0,0018	0,012	0,0007	0,07	0,00098	0,0008	The rest

Welding operation is carried out in Taksan FU 400x1600 V/2 vertical milling machine and force measure is performed in Kistler type 9272 dynamometer (Figure 3).

Figure 3. Kistler Type 9272 dynamometer

Air cooler plate is placed between dynamometer and bonding die to avoid measuring errors because of heat showed up during operation. Schematic representation of testing apparatus is shown in Figure 4. Also, the condition of test setup placed milling table is seen in Figure 5. DynoWare software is used for measuring of dynamometer values.
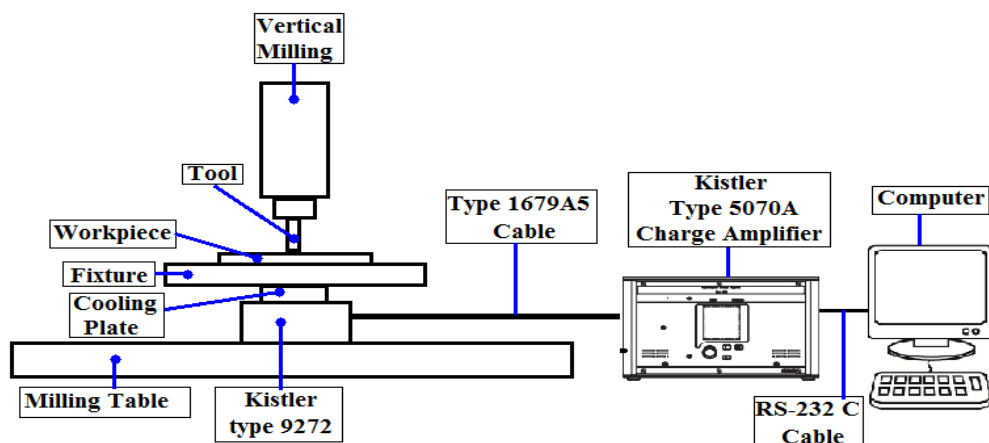
Figure 4. Schematic representation of testing apparatus

Figure 5. Reassemble of testing apparatus on milling table

In welding operation, mixer tool that has convex triangular profile is used. Technical picture of tool is given in Figure 6. Mixer tool is made from 3343 high speed steel. Heat treating hardness value is done in 62 HRc.
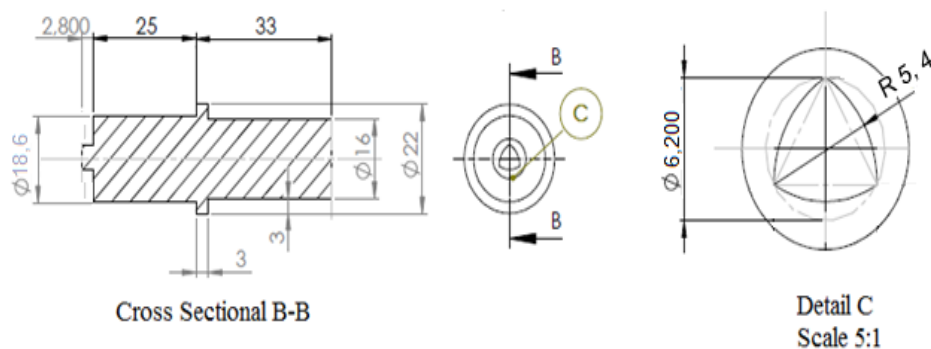

Figure 6. Technical picture of mixer tool

Welding operations is strained in tool angle (0°), 4 different rates of propagation (16, 25, 31.5, 40 mm/min), 3 different spindle speeds (900, 1120, 1400 revs/min) and without offset from mixer tool weld line. Maximum force created during operation is considered in evaluation of traverse force and axial force values

3. RESULTS AND DISCUSSION

Heat input is affected by not choosing of combination of feed rate and spindle speeds. While spindle speeds and heat formation are directly related (w), welding speed (v) and heat formation have inverse relationship. The equality between heat input and feedrate and spindle speeds is given as follows [24].

$$\frac{w}{v} \propto Heat\ Input \tag{1}$$

Heat input has an important effect on traverse force because plastic deformation of material will be easier with the increase of heat input. Changing of traverse force (Fx) formed by changing of feedrate and spindle speeds is shown in Figure 7.

	16	25	31,5	40
900 rev/dak	590	1095,4	2004,6	3708,5
1120 rev/dak	521,1	954,3	1651	2879
1400 rev/dak	572,1	944	1397	1985
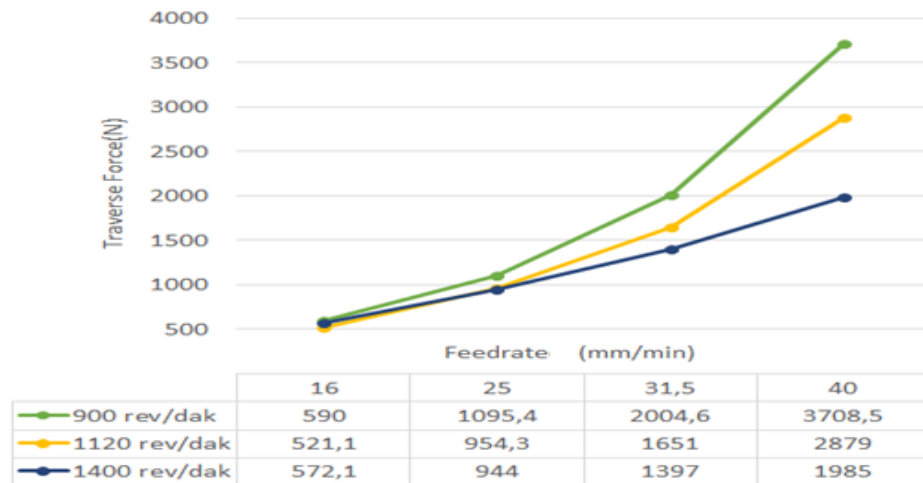
Figure 7. Effects of feed rate and spindle speeds on traverse force (Fx)

While the lowest traverse force in 1120 revs/min and 16 mm/min operation parameter is 590 N, the highest traverse force in 900 revs/min and 40 mm/min feedrate is 3708,50 N.

Substantial increase in traverse force with increase of feedrate is remarkable. The relation between increase of spindle speeds and traverse force has inverse proportion. In addition, it is seen that effect of feedrate on Fx is more than effect of spindle speeds on it.

The significant change in traverse force with change of feedrate occurs in 900 revs/min spindle speeds with increase of %86,66 by increasing of feedrate from 16 mm/min to 25 mm/min.

The significant change in traverse force with change of spindle speeds occurs in 40 mm/min feedrate with decrease of %31,05 by increasing of spindle speeds from 1120 revs/min to 1400 revs/min.

Also, when exchange ratio of feedrate and Fx force in 900 revs/min and 1400 revs/min spindle speeds is examined, change of feedrate affects Fx force less in high speed. Therefore, it is thought that heat created with friction is created more with rotation of shoulder of tool on plates in unit of time because material easily undergoes plastic deformation.

Axial force provides pin part of tool to immerge material. In addition to that, it provides heat formation by creating frictional force between tool shoulder and material surface. Keeping of force fixed during welding provides quality welding.

Axial force should be enough for full penetration in mixing area. While inadequate axial force causes deformed material to flow vertical direction improperly, high immersion force causes deformed material to slim. As a result, it causes material to burr by getting out from shoulder part of tool [25].

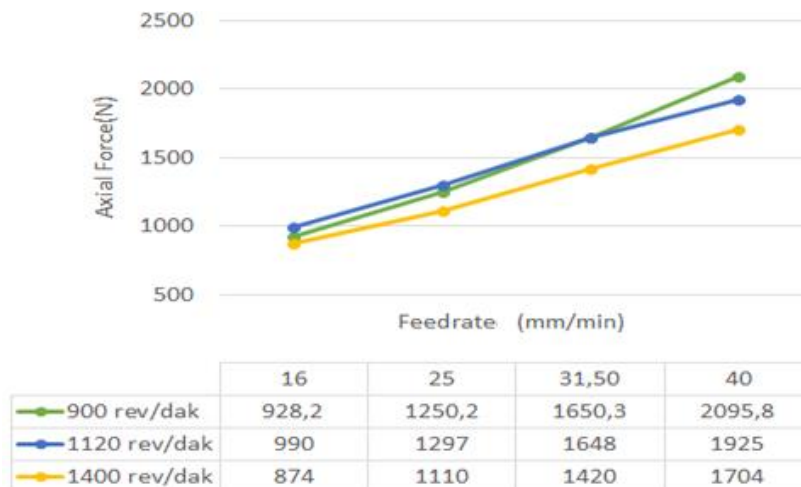Change of feedrate and spindle speeds and change of axial force are given in Figure 8.

	16	25	31,50	40
900 rev/dak	928,2	1250,2	1650,3	2095,8
1120 rev/dak	990	1297	1648	1925
1400 rev/dak	874	1110	1420	1704

Figure 8: Effect of feedrate and spindle speeds on axial force.

Axial force is dependent variable consisted of a combination of independent variables (feed rate; revolution; pin length, pin diameter; shoulder diameter etc.) Independent variables that affect axial force mostly are pin length and shoulder diameter. Pressure area expands with increase of shoulder diameter and immersion depth increases with lessening of pin length and then axial force increases.

The highest axial force will occur in 900 revs/min spindle speeds and 40mm/min feedrate as 2095, 83 N. The lowest feedrate will occur in 1400 revs/min and 16 mm/min rates of propagation as 874 N.

The significant change in axial force with change of feedrate occurs in 900 revs/min spindle speeds with increase of %34,69 by increasing of feedrate from 16 mm/min to 25 mm/min.

The significant change in traverse force with change of spindle speeds occurs in 25 mm/min feedrate with decrease of %14,4 by increasing of spindle speeds from 1120 revs/min to 1400 revs/min.

As a result of welding, weld qualities is not reached as desired level. An example of combined plates is given in Figure 9.
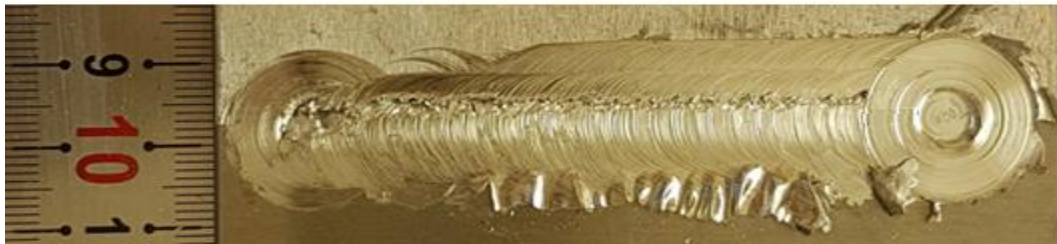
Figure 9 Welding of AZ 91 D (A.S.) and AA 7075 T6 (R.S.) in the condition of 900 revs/min, 25 mm/min

Desired level of welding is not achieved because enough axial force for welding is not applied because of long pin size of mixer tool.

4. CONCLUSIONS

- The most significant parameter was the feed rate of the mixer tool on the traverse force and the revolution per minute of the spindle is exhibited an insignificant effect on the traverse force.
- Traverse force and axial force decreased with the increasing revolution per minute of spindle and increased with increasing feed rate of the mixer tool.
- Desired level of welding quality could not be achieved due to the inadequate axial force because of the long pin size of mixer tool.
- The traverse force (Fx) was more affected at lower feed rates and lower spindle speeds compared to the higher spindle speeds

ACKNOWLEDGMENT

REFERENCES

[1]. W. Thomas, E. Nicholas, J. Needham, M. Murch, P. Temple-Smith and C. Dawes C., "Friction stir butt welding", *International Patent No.* PCT/GB92/02203, *GB Patent No.* 9125978.8, 1991, **U.S**. *Patent No*. 5,460,317, 1995.
[2]. A. Kostka, R. S. Coelho, J. Dos Santos and A.R. Pyzalla, "Microstructure of friction stir welding of aluminium alloy to magnesium alloy", *Scr. Mater.*, vol. 60(11), pp. 953–956, 2009.
[3]. J. Mohammadi, Y. Behnamian, A. Mostafaei, H. Izadi, T. Saeid, A. H. Kokabi and A. P. Gerlich, "Friction stir welding joint of dissimilar materials between AZ31B magnesium and 6061 aluminum alloys: Microstructure studies and mechanical characterizations" *Materials Characterization,* vol. 101, pp.189–207, 2015.
[4]. B. Fu, G. Qin, F. Li, X. Meng, J. Zhang and C. Wu, "Friction stir welding process of dissimilar metals of 6061-T6aluminum alloy to AZ31B magnesium alloy", *Journal of Materials Processing Technology*, 218:38–47, 2015
[5]. P. Venkateswaran and A. P. Reynolds, "Factors affecting the properties of friction stir welds between aluminum and magnesium alloys", *Mater Sci. Eng.* **A**, vol. 545, pp.26–37, 2012.
[6]. Y. Zhao, Z. Lu, K. Yan and L. Huang, "Microstructural characterizations and mechanical properties in underwater friction stir welding of aluminum and magnesium dissimilar alloys", *Materials and Design,* vol. 65, pp.675–681, 2015.
[7]. C. B. Jagadeesha, "Dissimilar friction stir welding between aluminum alloy and magnesium alloy at a low rotational speed", *Materials Science & Engineering A,* vol. 616, pp.55–62, 2014.

[8]. S. Malarvizhi and V. Balasubramanian, "Influences of tool shoulder diameter to plate thickness ratio (D/T) on stir zone formation and tensile properties of friction stir welded dissimilar joints of AA6061 aluminum–AZ31B magnesium alloys", *Materials and Design,* vol. 40, pp. 453–460, 2012.

[9]. A. Masoudıan, A. Tahaeı, A. Shakıba, F. Sharıfıanjazı and J. A. Mohandesı, "Microstructure and mechanical properties of friction stir weld of dissimilar AZ31-O magnesium alloy to 6061-T6 aluminum alloy" Trans. Nonferrous Met. Soc. China, vol. 24, pp.1317−1322, 2014.

[10]. D. Trimble, J. Monaghan, G.E. O'Donnell, " Force generation during friction stir welding of AA2024-T3", *CIRP Annals - Manufacturing Technology*, vol. 61, pp. 9–12, 2012.

[11]. C. D. Sorensen and A. L. Stahl, "Experimental measurement of load distribution on friction stir weld pin tools", *Metall. Mater. Trans. B*, vol. 38B, pp. 451–459, 2007.

[12]. M. Mehta, A. Arora, A. De and T. DebRoy, "Tool geometry for friction stir welding-optimum shoulder diameter", *Metall. Mater. Trans. A,* vol. 42A (9), pp. 2716–2722, 2011.

[13]. A. Arora, M. Mehta, A. De and T. DebRoy, "Load bearing capacity of tool pin during friction stir welding", *Inter. J. Adv. Manuf. Technol.*, vol. 61, pp. 911–920, 2012.

[14]. R. Nandan, G. G. Roy, T. Debroy, "Numerical simulation of three-dimensional heat transfer and plastic flow during friction stir welding" , *Metall .Mater. Trans. A*., vol. 37(4), pp. 1247–1259, 2006.

[15]. H. H. Cho, S. T. Hong, J. H. Roh, H. S. Choi, S. H. Kang, R. J. Steel, H. N. Han, "Three-dimensional numerical and experimental investigation on friction stir welding processes of ferritic stainless steel", *Acta Mater.,* vol. 61(7), pp. 2649–2661, 2013.

[16]. M. Mehta, K.Chatterjee, A.De, "Monitoring torque and traverse force in friction stir welding from input electrical signatures of driving motors", *Sci.Technol. Weld.Join*., vol. 18(3), pp. 191–197, 2013.

[17]. H.Su, C.S.Wu, A.Pittner, M.Rethmeier, "Simultaneous measurement of tool torque, traverse force and axial force in friction stir welding", *J.Manuf.Process*., vol. 15(4), pp. 495–500, 2013.

[18]. R. Rai, A. De, H. K. D. H. Bhadeshia, T. DebRoy, "Review: friction stir welding tools", *Sci. Technol. Weld. Join.,* vol. 16(4), pp. 325–342, 2011

[19]. H. B. Schmidt, J. H. Hattel, "Thermal modeling of friction stir welding", *Scripta Mater,;* vol.58(5), pp. 332–337, 2008.

[20]. H. Schmidt, J. Hattel, J. Wert, "An analytical model for the heat generation in friction stir welding", *Model Simul. Mater. Sci. Eng.,* vol. 12(1), pp.143–157, 2004.

[21]. M. Z. H. Khandkar, J. A. Khan, A. P. Reynolds, "Prediction of temperature distribution and thermal history during friction stir welding: input torque based model", *SciTechnol Weld Joining*, vol. 8(3), pp. 165–174, 2003

[22]. K. J. Colligan, R. S. Mishra, "A conceptual model for the process variables related to heat generation in friction stir welding of aluminum", *Scripta Mater*, vol. 58(5), pp.327–331, 2008.

[23]. P. Shahi and M. Barmouz, "Force and torque in friction stir welding", *Advances in Friction Stir Welding and Processing*, Woodhead Publishing, pp. 459 – 498, 2014.

[24]. Pourahmad P. and Abbası M., "Materials flow and phase transformation in friction stir welding of Al 6013/Mg", *Trans. Nonferrous Met. Soc. China*, vol. 23, pp. 1253−1261, 2013 .

[25]. Mehta K. P. and Badheka V. J., "A review on dissimilar friction stir welding of copper to aluminum: process, properties and variants", *Materials and Manufacturing Processes,* vol. 31, pp. 233–254, 2016.

BIOGRAPHY

MUSA BİLGİN received his M.Sc. in Mechanical Education from the Gazi University of Turkey in 2012. He is currently Ph.D. student in Manufacturing Engineering from the same university and a lecturer Baskent **Organized Industrial Zone** Technical Sciences Vocational Schools from the Hacettepe University. His research interests include mechanical design and manufacturing.

Structural Analysis and Fatigue Life Prediction of a Universal Joint with Finite Element Method

Murat Ozsoy[1], Neslihan Ozsoy[2]

Abstract

Universal joints are one of the most important parts of driveshaft systems. Generally they connect two shafts transmit power and motion. So they should be designed carefully. In this study a M27-a type U joint was discussed is a part of 1310 series drive shaft system. First manual calculations were done. Then a finite element analysis was performed and they both were compared to find a deviation between manual calculations and finite element analysis results. After static analysis, a fatigue analysis was performed for prediction of fatigue life of U joint. Both of the results showed that U joint is durable at working conditions.

Keywords: *Drive Shaft, Universal Joint, Structural Analysis, Fatigue Life, Finite Element Method*

1. INTRODUCTION

Drive shaft is a component that transmit motion, power or both at misalignment but intersecting axis situations. They are consist of several parts such as shafts, yokes, universal joints (cardan joints), etc. They have a wide range of usage where power or motion transmit needed in industry. Generally, most usage is at automotive industry for having a mass production.

U joint also named cardan cross, universal joint, cardan cross or Hooke joint, has a critical task at a drive shaft assembly, like connection one shaft to another. So they are exposed to torsion, bending or shear loads in single or together. They can be used under high speed and heavy load conditions. Because of having an important task in a drive shaft system they must be designed at high precision.

Traditionally strength calculations are done manually by hand at design stage. But with the developing technology, computers are started to be widely used for calculations in the design process because of market needs. Like time, reducing workmanship cost, etc. Today they are several commercial computer codes for performing static, dynamic, structural, fatigue et al at industrial and academic studies by finite element method (FEM).

Before starting the study, a literature search was carried out, in terms of giving information about the way to be followed. It was seen that many researchers studied about optimization, finite element simulation, fatigue life prediction of universal joints and drive shafts. Hummel and Chassapis [1] researched on the design of the universal joints. Ozsoy and Firat [2] made a static structural analysis and fatigue life prediction of a M83 type U joint by finite element method. Avrigean and Pascu [3] studied on the cardan cross using experimental and Analytical method. They made manual calculations then performed some structural analysis with finite element method with their 3D mathematical model. Finally, they verified their simulation results with an experimental study. Zivkovic and Ivanovic [4] studied the effect of geometry on the stress distribution of cross shaft. They changed a round radius at necklage and repeated their calculations by finite element method. Then compared stress distribution results depending on the necklage radius changes. Marudachalam and Kanthavel [5] studied about optimization of shaft design under fatigue loading using Goodman method. Rathi and Mandavgade [6] studied FEM analysis of universal joint of TATA 407. They performed finite element analysis and obtained stress distribution of the model. Chaudhry and Krishan [7] studied on weight reduction of universal joint with finite element analysis. Bayrakceken and Tasgetiren [8] made a research on failure in

---

[1] *Corresponding author: Sakarya University, Department of Mechanical Engineering, 54187, Serdivan/Sakarya, Turkey. ozsoy@sakarya.edu.tr.*

Sakarya University, Department of Mechanical Engineering, 54187, Serdivan/Sakarya, Turkey. nerken@sakarya.edu.tr.

the power transmission system on vehicles. They were studied about fracture analysis of drive shaft and universal joint yoke.

2. U JOINT GEOMETRIC MODEL AND MANUAL CALCULATIONS

In this study a M27-A type U joint (Manufactured by Demireller Kardan A.S) is a part of 1310 series drive shaft system was discussed used at SUV vehicle jeep wrangler jk. This vehicle has a maximum power of 213 kW at 6400 rpm. So all manual calculations and computer simulations with finite element method done at these criteria.

2.1. Geometric model of U joint

Geometric model was created at PTC Creo Parametric 4.0 as shown in figure 1. Solid model consist of body and four trunnions. Technical details of U joint are given in table 1.Figure2 shows a piece of driveshaft assembly U joint used.
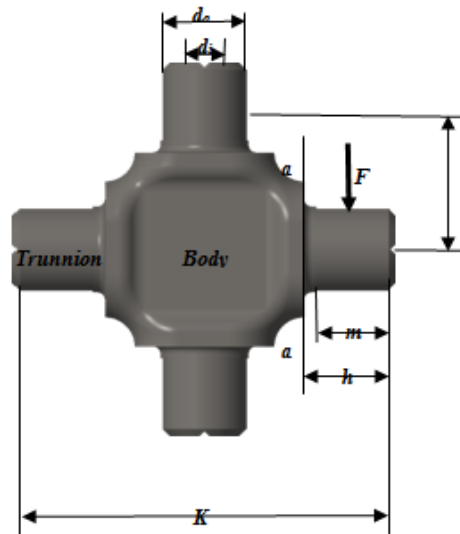
Figure 70. Technical details of M27-a type U Joint and place of force effected
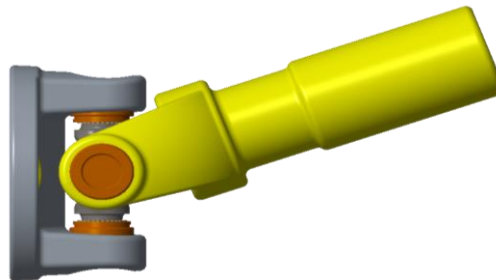
Figure 2. A piece of driveshaft assembly U joint used.

Table 48. Technical details of U joint

Symbol	Dimension
K	74
R	29.5
h	17
m	14.5
d_i	6
d_0	16.85

2.2. Manual Calculations

All of the moment calculations were done according to a-a section critical area. Bending and shear stresses occur at the muff of the cardan joint. Firstly the torque should be calculated with the help of equation 1 below.

$$M_{tmax} = 9550 * \frac{P}{n} = 9550 * \frac{213}{6400} = 317.836 \; Nm \tag{1}$$

$$F = \frac{M_{tmax}}{2 * R} = \frac{317.836 * 10^3}{59.5} \cong 5342 \; N$$

$$l = h - \frac{m}{2} = 17 - \frac{14.5}{2} = 9.75 \; mm \tag{2}$$

Bending Stress;

$$\sigma_{bending} = \frac{M}{W_b} = \frac{32*F*l}{\pi*\left(\frac{d_0^4-d_i^4}{d_0}\right)} = \frac{32*5342*9.75}{\pi*\left(\frac{16.85^4-6^4}{16.85}\right)} \cong 113 \; MPa \tag{3}$$

Finally; for finding real bending stress, the solution must be multiplied by theoretical stress concentration factor.

$$\sigma_{bReal} = K_t * \sigma_{bending} = 1.5 * 113 = 169.5 \; MPa \tag{5}$$

2.3. Mathematical Model

After creating geometric model at PTC Creo Parametric 4.0, some simplifications were done to decrease solution time and creating a closest mathematical model to the real part. So only trunnion part of the model was taken into account. During the mathematical model creation ANSYS Workbench commercial software was used. First model was created at PTC Creo then transferred to the Ansys Workbench software. 3D Solid 186 tetrahedral element type was used for generating mesh. At last a mesh was consisted from 2114177 nodes and 587181 elements (fig.3). Universal joint was made from 16MnCr5 steel. Second step of the FEM analysis was applying material properties of the model. In this study there are two types of analysis static structural and fatigue life. So fatigue life data was needed near of the mechanical properties of 16MnCr5. Material properties can be seen at the table 2 below.

Table 2. Mechanical properties of 16MnCr5

Name	Magnitude
Tensile Strength	900 MPa
Yield Strength	600 MPa
Elasticity Modulus	210 GPa
Poisson Ratio	0.3
Density	7.850 kg/m^3

Figure 3. Mesh of the mathematical model.

After structural analysis a fatigue life analysis would be performed so there is a need of S-N (Stress-Cycle) diagram of 16 MnCr5.
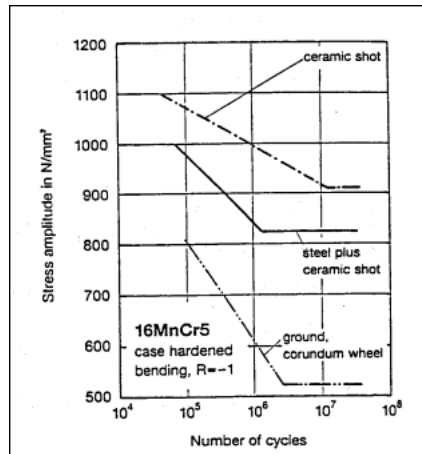

Figure 4. Fatigue data of 16MnCr5 [9]

Next step was defining boundary conditions and applying loads on the mathematical model. The model was fixed supported from the place of intersection of body and trunnion. Then a force was inserted as 5.358 N which had been calculated before. Boundary conditions and loading can be seen at the figure 5.
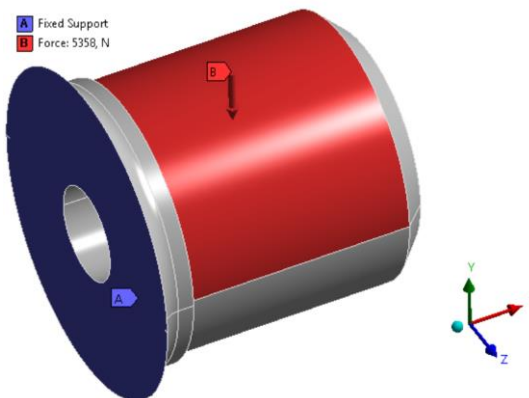

Figure 5. Boundary conditions and loading of mathematical model.

After defining boundary conditions and loading, the results that would be examined after the solution should be determined. So Von-Misses stress, total deformation, static safety factor and fatigue tool were inserted. A fatigue analysis would be performed under conditions of fully revised. Soderberg criteria would be used to control the safety factor and fatigue life. Then the mathematical model was ready to solve. Next step was solution.

3. RESULTS OF THE FINITE ELEMENT ANALYSIS AND DISCUSSION

After solution, maximum stress occurred at the neck of trunnion. Maximum stress was 183.5 MPa (fig.6). Maximum deformation was 0.00968 mm at the front side of the trunnion (fig.7). Static safety factor was min 3.27 (fig. 8). Infinite life was obtained according to the given stress values at fully reversed loading conditions. That means this u joints had not have a plastic deformation under 183.5 MPa loading before $5x10^6$ cycles. Finally a fatigue safety factor was determined as 2.72 (fig. 9).
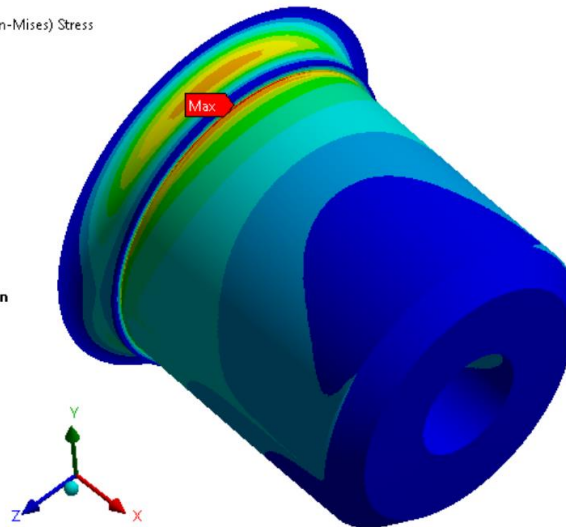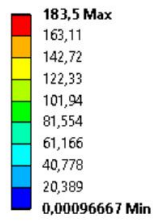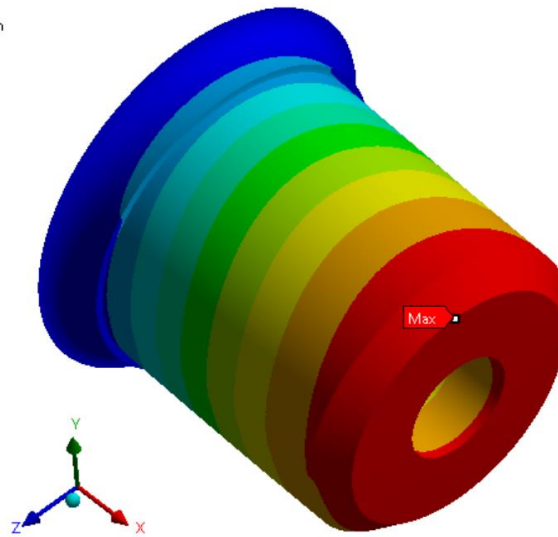
Figure 6. Maximum stress.
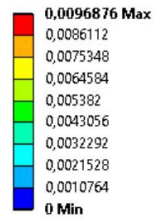
Figure 7. Maximum deformation.

B: Static Structural
Safety Factor
Type: Safety Factor
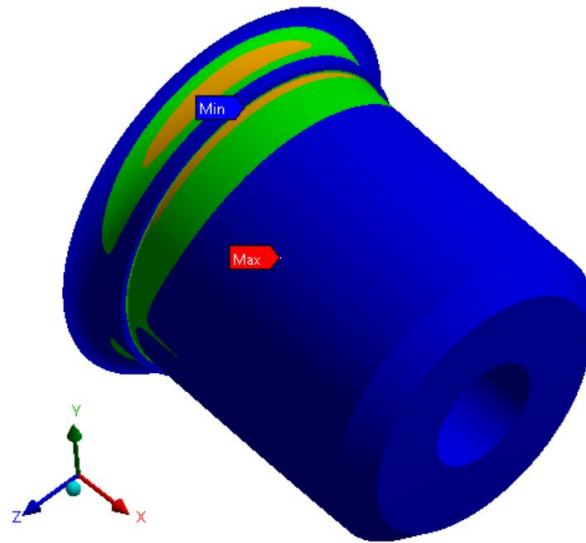Time: 1

15 Max
10
3,2698 Min
0
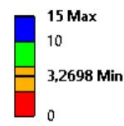
Figure 8. Static safety factor

B: Static Structural
Safety Factor
Type: Safety Factor
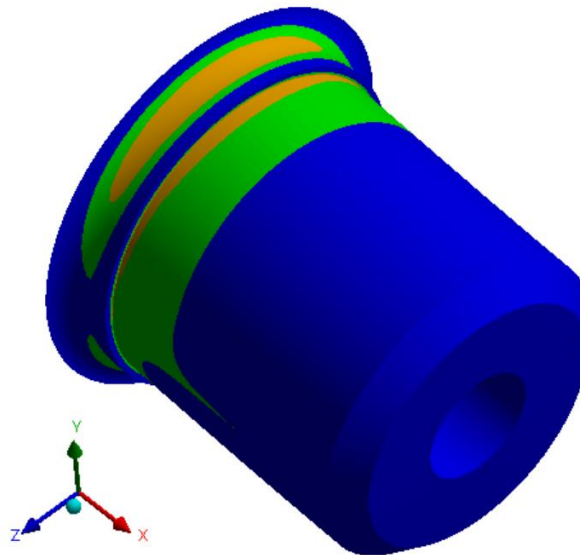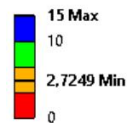Time: 0

15 Max
10
2,7249 Min
0

Figure 9. Fatigue safety factor

At the manual calculations section, maximum stress was calculated as 169.5 MPa. On the other hand maximum stress was obtained as 183.5 MPa by FEM analysis. There is a deviation between two results. This can be calculated as follows;

$$Deviation \% = \frac{\sigma_{fea} - \sigma_{manual}}{\sigma_{fea}} * 100 = \frac{183.5 - 169.5}{183.5} * 100 = 7.6 \% \qquad (6)$$

4. CONCLUSION

U joints are important parts of drive shaft systems. Therefore they must be examined very carefully before manufacturing. In this study an M 27 type U joint a part of 1310 drive shaft system was discussed whether it was safe under maximum working torque of 318 Nm. Both results of manual calculations and FEM analysis showed that the U joint had been durable under these working conditions. There was a 7.6 % deviation between manual calculations and FEM analysis results. It was an acceptable value for this type of analysis. In

the future it is planned to make the experimental work of this U joint to verify all results. When this task is completed, nothing will be missing in the study.

ACKNOWLEDGMENT

REFERENCES

[1]. Hummel, R.S, Chassapis, C., "Configuration design and optimization of universal joints", Mechanism and Machine Theory, vol. 33(5), pp. 479-490, 1998.
[2]. Ozsoy, M., Firat, M., "Computer aided structural analysis and fatigue life prediction of a cardan joint", European Journal of Science & Technology, vol. 8(1), pp. 50-52, 2016.
[3]. Avrigean, E., Pascu, M. "Study of cardan cross using the experimental and analytical method", Procedia Engineering. Vol. 100, pp. 499-504, 2014.
[4]. Zivkovic, K., Ivanovic, L., "The effect of geometry on the stress distribution of cross shaft", in Proc. The 7th International conference research and development of mechanical elements and systems, p. 245-252, 2011.
[5]. Marudachalam, D., Kanthavel K., Krishnaraj R.," Optimization of shaft design under fatigue loading using Goodman method", International Journal of Scientific & Engineering Research, vol 2(8), pp. 1-5, 2011.
[6]. Rathin, V., Mandavgade, K., "FEM analysis of universal joint of TATA 407," in Proc. ICETET 09 , p.98-103, 2009.
[7]. Chaudhry, S., Bansal, A., Krishan, G., "Finite element analysis and weight reduction of universal joint using CAE tools", International Journal of Engineering Research&Technology, vol. 3(10), pp. 1137-1139.
[8]. Bayrakceken, H., Tasgetiren, S., Yavuz, I., "Two cases of failure in the power transmission system on vehicles: A universal joint yoke and a drive shaft", Engineering Failure Analysis, Vol. 14, pp.716-724, 2007.
[9]. Sollich, A., Wohlfahrt, H., " Optimization of the fatigue strength of heat treated steels as a consequence of an optimum state of the surface and of subsurface layers after shot peening" , in Proc. 6th. International Conference on Shot Peening, p. 251-262, 1996.

BIOGRAPHY

Murat Ozsoy is a Assistant Professor of Mechanical Engineering at University of Sakarya in Turkey. He received his BSc degree in Mechanical Engineering from University of Balıkesir in 1996. He also received her MSc (1998) and PhD (2005) degrees in Mechanical Engineering at Institute of Natural Sciences at University of Sakarya. Her research fields are: Machine Elements, CAD, CAM, CAE, Fatigue.

Taguchi Optimization of Tribological Properties of Carbon Fiber Reinforced Epoxy Composites

Neslihan Ozsoy[1], Murat Ozsoy[1], Abdullah Mimaroglu[1]

Abstract

Dry tribological performance of carbon fiber reinforced epoxy (CFRE) composites are reported in this paper. Composites were fabricated by hand lay up method in three different orientations 0˚, 90˚,[0˚/90˚] according to the ASTM standard. Experiments were designed according to Taguchi method and conducted with pin on disk test apparatus against a steel disk (60 HRC) for a constant distance (1000 m) and under different loading conditions. Signal to noise ratio and analysis of variance (ANOVA) were used to investigate the influence of parameters on the wear rate and coefficient of friction. The results showed that performance of composites effected by load mostly.

Keywords: *Taguchi, ANOVA, Carbon fiber, wear*

1. INTRODUCTION

The fiber reinforced polymeric composites are the most rapidly growing class of materials, due to their good combination of high specific strength and modulus. They are widely used for a variety of engineering applications. The importance of tribological properties convinced many researchers to study the friction and wear behavior and to improve the wear resistance of polymeric composites. For fiber reinforced polymer matrix composites the process of material removal in dry sliding condition is dominated by four wear mechanisms, viz., matrix wear, fiber sliding wear, fiber fracture and interfacial debonding [1].

Many researchers have studied about the effects of fiber orientation and composite microstructure details on the friction and wear behavior of polymers and polymeric composites [2-9].Dhieb et all, investigated the friction and wear of bulk epoxy and unidirectional carbon fiber reinforced epoxy composite under reciprocating sliding against either alumina or stainless steel balls in ambient air [3]. Suresha et all invesigated the dry sliding wear and two-body abrasive wear behaviour of graphite filled carbon fabric reinforced epoxy composites and they conducted sliding wear experiments using a pin-on-disc wear tester under dry contact condition [4].

Experimental working for tribological properties needs to spend too much time so it is hard. Taguchi method is usefull to avoid this. Many researchers used this method [10-14]. Taguchi is one of the technique which reduces the experiment numbers and helps to predict results. The plan of experiments is generated in Taguchi method by the use of standard orthogonal arrays. The experimental results are then analysed by using analysis of mean and analysis of variance (ANOVA) of the influencing factors.

In the present work it is purposed to manufacture carbon fiber reinforced epoxy composites and investigate tribological properties of CFRE composites. Also it is aimed to plan wear experiments by Taguchi method and analyse results with ANOVA.

2. EXPERIMENTAL DETAILS

In this work the materials used for composite were unidirectional carbon fiber as reinforcement and epoxy as matrix material.

---

[1] *Corresponding author: University of Sakarya, Department of Mechanical Engineering, Sakarya Üniversitesi Esentepe Kampüsü 54187 Serdivan / Sakarya, Turkey, nerken@sakarya.edu.tr.*

Composites were manufactured by hand lay up prosess. Fabric was cut into squares 20x20cm^2. Epoxy resin (MGS L285) was mixed with hardener (HGS L285) in mass ratio of 100/40 as recommended by supplier.

Firstly wax was applied to the surface in order to seperate composite easily from the surface after curing. 0° or 90° orientation of fiber laid out and epoxy was poured over each layer. Layers were compressed with a roll to free air bubbles. This process was repeated until producing required thickness. Composites were cured at room temperature for 24 hours. After that 6x6x3 mm^3 specimens cutted from cured composite sheet and then they were glued to metal pin for tribological tets.

A pin on disc wear testing machine was used to define the dry sliding wear properties of composites according to ASTM G99-95 [15] standards. The wear specimen (pin) was 30 mm height. The initial weight of the specimen was measured using an electronic balance machine with accuracy of 0,0001 g. During the test pin was pressed against the counter part EN19 steel disc with hardness of 60 HRC by applying the load (20, 30, 40 N). After running through a fixed sliding distance of 1000 m, the specimens were removed, cleaned with acetone, dried and weighted to determine the weight loss due to wear. The difference in the weight measured before and after test gave the sliding wear of the composite specimen. The density of the specimens were measured and then the sliding wear of the composite was calculated according to equation 1 where Δm difference in mass, ρ is density and d is the sliding distance.

$$\text{Wear rate} = \frac{\Delta m}{\rho d} \qquad\qquad (1)$$

Dry sliding wear tests were performed with three parameters: applied load, sliding speed and orientation of fiber layers. According to the rule that degree of freedom for an orthogonal array should be greater than or equal to sum of those wear parameters, a L9 orthogonal array which has 9 rows and 3 columns was selected.

Table 1. Process parameters with their values at three levels

Level	A: Load (N)	B: Sliding speed (m/s)	C: Orientation of fiber layers
1	20	0.6	0°
2	30	0.8	90°
3	40	1	0°/90°

The process variables are given in table 1. The response variables to be studied were wear rate and coefficient of friction.The experiments were conducted based on the run order generated by Taguchi model and the results were obtained. The analysis of the experimental data were carried out using MINITAB 15 software, which is specially used for DOE applications. The experimental results were transformed into signal- to- noise (S/N) ratios. S/N ratio is defined as the ratio of the mean of the

signal to the standart deviation of the noise. The S/N ratio indicates the degree of the predictable performance of a product or process in the presence of noise factors. Process parameter settings with the highest S/N ratio always yield the optimum quality with minimum variance. The S/N ratio for wear rate and coefficient of friction using 'smaller the better' characteristic, which can be calculated as logarithmic transformation of the loss function, is given as:

$$S/N = -10\log[\frac{1}{n(\sum y^2)}] \qquad\qquad (2)$$

Where y is the observed data (wear rate or coefficient of friction) and n is the number of observations [16].

3. RESULTS AND DISCUSSION

The aim of this study is to find the important factors and combination of factors influencing the process to achieve the minimum wear rate and coefficient of friction. By the way, experiments were developed based on an orthogonal array. Taguchi recommends analyzing the S/N ratio using approach that includes plotting the effects and defining the significant factors. The results of experiments and signal/noise ratios of the wear tests of carbon fiber reinforced epoxy composites are shown in table 2.

Table 2. Results of L9 orthogonal array for carbon fiber reinforced epoxy composites

Experiment number	Load(N)	Sliding speed(m/s)	Orientation of fiber layers	Wear rate (mm³/m)	Coefficient of friction	S/N ratio of wear rate (dB)	S/N ratio of coefficient of friction (dB)
1	20	0.6	0	0.000225	0.296	72.956	10.556
2	20	0.8	90	0.00015	0.388	76.478	8.205
3	20	1	0/90	0.000412	0.341	67.702	9.334
4	30	0.6	90	0.0006	0.355	64.436	8.983
5	30	0.8	0/90	0.000659	0.396	63.622	8.026
6	30	1	0	0.000525	0.401	65.596	7.933
7	40	0.6	0/90	0.001648	0.433	55.660	7.258
8	40	0.8	0	0.000779	0.482	62.169	6.323
9	40	1	90	0.000981	0.529	60.166	5.530

Table 3 shows S/N ratio results for the wear rate. Wear rate mostly affected by load, orientation and sliding speed respectively.

Table 3. Table of S/N ratio results for the wear rate

Level	Load	Sliding speed	Orientation
1	72.38	64.35	66.91
2	64.55	67.42	67.03
3	59.33	64.49	62.33
Delta	13.05	3.07	4.70
Rank	1	3	2

S/N ratio results for the coefficient of friction are shown in table 4. It can be seen that load is the dominant parameter, sliding speed is the second parameter and orientation is third parameter effect the coefficient of friction.

Table 4. Table of S/N ratio results for the coefficient of friction

Level	Load	Sliding speed	Orientation
1	9.365	8.933	1.414
2	8.314	7.519	7.573
3	6.371	7.599	8.206
Delta	2.995	1.414	0.698
Rank	1	3	2

Main effects plot for SN ratios can be seen in figure 1 and 2. As the load increase S/N ratio decrease and both coefficient of friction and wear rate increase. Optimum levels 20 N as load, 0.8 m/s as sliding speed and 90° as orientation for wear rate, on the other side 20 N as load, 0.6 m/s as sliding speed and 0° as orientation are optimum levels for coefficient of friction. That means combination of factors $A_1B_2C_2$ for wear rate and $A_1B_1C_1$ for coefficient of friction offer the best results.
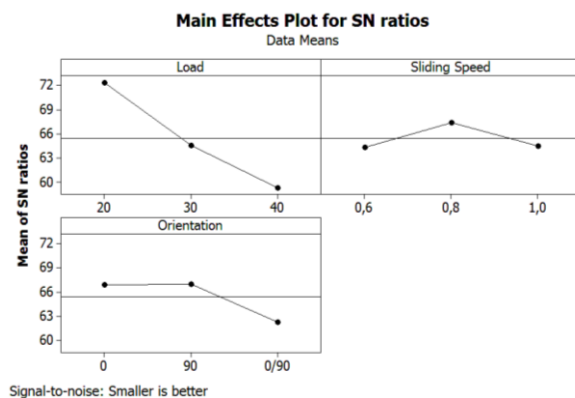
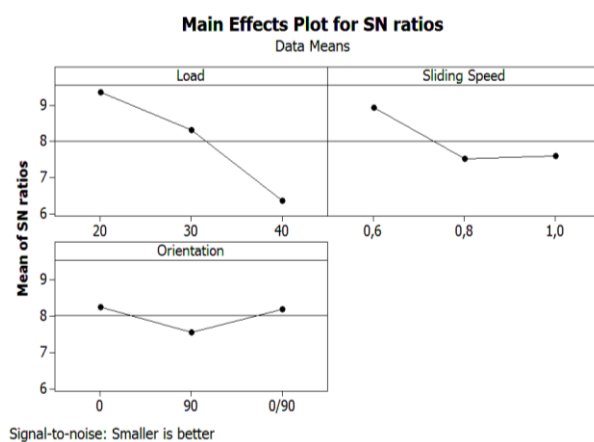*Figure 1. Main effects plot for SN ratios on wear rate*

Figure 2. Main effects plot for SN ratios on coefficient of friction.

3.1. Analysis of Variance and Effects of Factors

In order to observe statistical significance of factors like load, sliding speed, orientation on coefficient of friction and wear rate, Analysis of variance (ANOVA) was performed with MINITAB 15. This analysis was made for a level of confidence 90%. Analysis of variance results of wear rates and coefficient of friction of experiments are shown in table 5 and 6 respectively. The last columns of the tables show the effect % of parameters.

Table 5. ANOVA results of wear rate.

Source	DF	Seq SS	Adj SS	Adj MS	F	Contribution %
Load	2	0.0000012	0.0000012	0.0000006	21.08	75
Sliding speed	2	0.0000001	0.0000001	0.0000001	2.41	6.25
Orientation	2	0.0000003	0.0000003	0.0000001	4.88	18.75
Error	2	0.0000001	0.0000001	0.0000000		0
Total	8	0.0000016				

ANOVA results of wear rate indicate that load was the dominant parameter with a ratio of 75%. Orientation was the second with a ratio of 18.75 and the last one was the sliding speed with a ratio of 6.25%.

Table 6. ANOVA results of coefficient of friction

Source	DF	Seq SS	Adj SS	Adj MS	F	Contribution %
Load	2	0.0307316	0.0307316	0.0153658	73.93	75.3
Sliding speed	2	0.0075559	0.0075559	0.0037779	18.18	18.3
Orientation	2	0.0021050	0.0021050	0.0010525	5.06	5.15
Error	2	0.0004157	0.0004157	0.0002078		1.25
Total	8	0.0408081	0.0408081			

According to the ANOVA results of coefficient of friction, load was the first parameter affected the performance of composite with a ratio of 75.3%, sliding speed was the second parameter with a ratio of 18.3% and the orientation was the last one with a parameter of 5.15%.

3.2. Confirmation Tests

Results of signal to noise analysis showed that optimum parameters for the wear rate had been $A_1B_2C_2$ and $A_1B_1C_1$ for the coefficient of friction. In order to check the optimal parameter, a set of experiments were conducted. Experimental and predicted results were compared and error was calculated as confirmation. Predicted S/N ratio of wear rate calculated by equation 3 and predicted S/N ratio of coefficient of friction calculated by equation 4 below. In these equations $\hat{\eta}$ is the predicted average S/N ratio, $\overline{T}$ is the total experimental average and $\overline{A_1}$, $\overline{B_1}$, $\overline{B_2}$, $\overline{C_1}$, $\overline{C_2}$ are the average responses of factors. The error ratios are acceptable according to the confirmation test results shown in table 7.

$$\hat{\eta} = \overline{T} + (\overline{A_1} - \overline{T}) + (\overline{B_2} - \overline{T}) + (\overline{C_2} - \overline{T}) \tag{3}$$

$$\hat{\eta} = \overline{T} + (\overline{A_1} - \overline{T}) + (\overline{B_1} - \overline{T}) + (\overline{C_1} - \overline{T}) \tag{4}$$

Table 7. Confirmation test results

Level	S/N ratio of wear rate (dB)			S/N ratio of coefficient of friction (dB)		
	$A_1B_2C_2$			$A_1B_1C_1$		
	Predicted	Experimental	Error %	Predicted	Experimental	Error %
	75.987	77	1.315	10.535	10.556	0.2

3.3. Surface Morphology

Figure 3 shows the images of worn surfaces of Scanning Electron Microscope (SEM) for 0/90, 0 and 90 orientated composites. Figure 3 shows deformation of fibers in the sliding direction. The most severe wear is seen in composites in the 90 direction. It may be due to faults occurred during to manufacturing of composites or environmental conditions during the tests. Also it is known that fibers show weak performances as orientated 90˚.
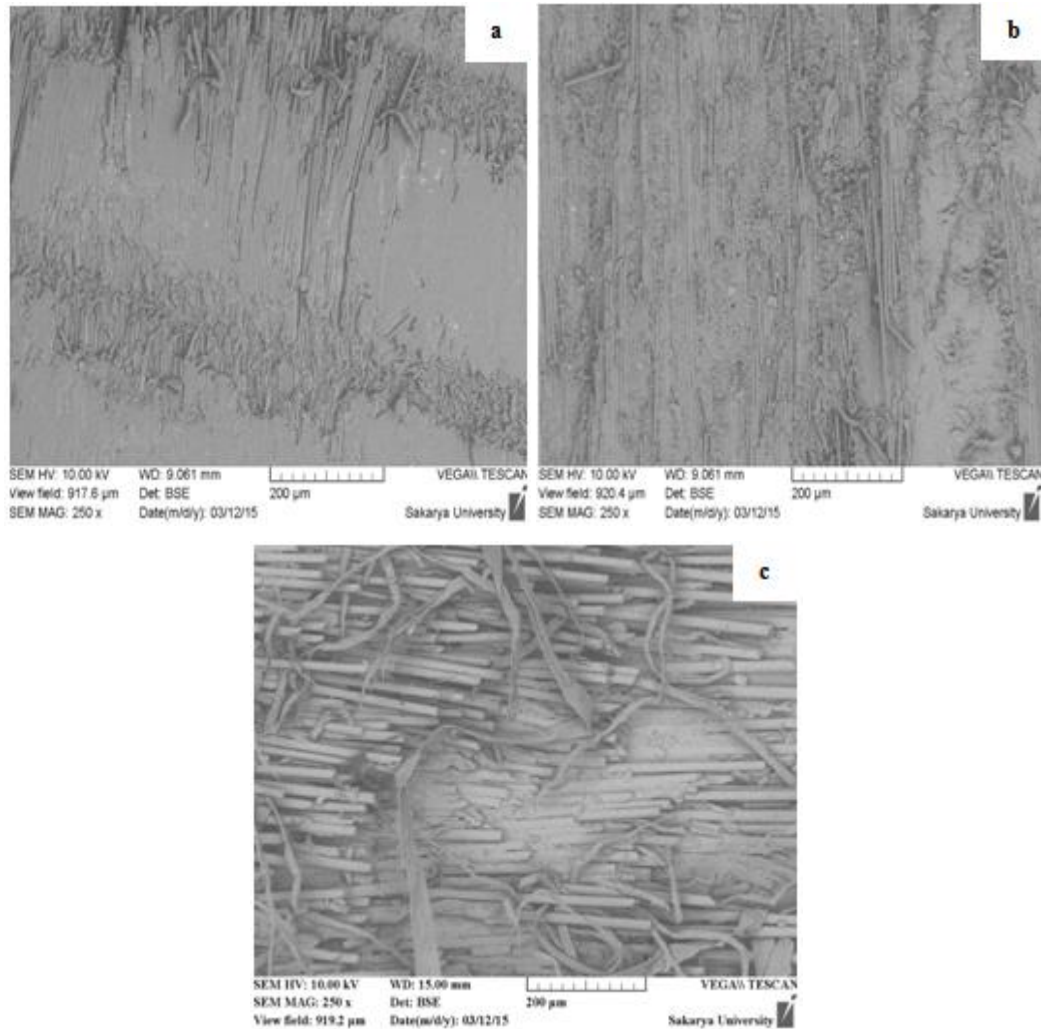
Figure 3. Scanning electron microscope of (a) 0/90, (b) 0, (c) 90 orientated composites

4. CONCLUSIONS

After the tests and analysis of the test results, main conclusions are given:

- The dominant parameter is found from ANOVA table. Applied load have most influence on the increase of wear and coefficient of friction respectively.

- Taguchi analysis indicates that combination of factors $A_1B_2C_2$ and $A_1B_1C_1$ offer minimum wear rate and coefficient of friction. Confirmation tests prove the accuracy of this.

- Images of worn surfaces of SEM show deformation of fibers in the sliding direction. Worn surface features show matrix and fiber debris, fiber–matrix debonding, fiber breakage and fiber removal.

ACKNOWLEDGMENT

REFERENCES

[1]. K. Friedrich, Z. Lu, A. M. Hager, "Recent advances in polymer composites tribology", Wear, vol. 190, pp.139–44, 1995.
[2]. B. Suresha , K. S. Kumar , S.Seetharamu, P.Sampath Kumaran, " Friction and dry sliding wear behavior of carbon and glass fabric reinforced vinyl ester composites", Tribology International, vol.43, pp. 602-609, 2009.

[3]. H. Dhieb , J.G. Buijnsters , F. Eddoumy , J.P. Celis, "Surface damage of unidirectional carbon fiber reinforced epoxy composites under reciprocating sliding in ambient air", Composites Science and Technology, vol. 71, pp.1769–1776, 2011.

[4]. B. Suresha, Siddaramaiah, Kishore, S. Seetharamu, P. Sampath Kumaran, "Investigations on the influence of graphite filler on dry sliding wear and abrasive wear behaviour of carbon fabric reinforced epoxy composites", Wear, vol. 267, pp. 1405-1414, 2009.

[5]. J.Schon, "Coefficient of friction and wear of a carbon fiber epoxy matrix composite", Wear, vol. 257, pp. 395-457, 2004.

[6]. B. Suresha, G. Chandramohan, "Effect of Normal Load and Sliding Velocity on Friction and Wear Behavior of Carbon Fiber Reinforced Epoxy Composites", Journal of Reinforced Plastics and Composites, vol. 26, No. 16, pp. 1695-1703, 2007.

[7]. N. Mohan, S. Natarajan , S.P. KumareshBabu, "Abrasive wear behaviour of hard powders filled glass fabric–epoxy hybrid composites", Materials and Design, no. 32, pp. 1704-1709, 2011.

[8]. R. Md. Nasir and M. Mu'az Azizan, "Adhesion and Friction of E-Glass Fiber-reinforced Epoxy Composites for Tribo-applications", Journal of Thermoplastic Composite Materials, vol. 24, pp. 861-874, 2011.

[9]. B.F. Yousif , N.S.M.El-Tayeb, "Wear characteristics of thermoset composite under high stress three-body abrasive", Tribology International", vol.43, pp. 2365–2371, 2010.

[10]. M. S. Kumar, N. Raju, P. S. Sampath, U. Vivek, " Tribological analysis of nano clay/epoxy/glass fiber by using Taguchi's technique", Materials and Design, vol.70, pp. 1-9, 2015.

[11]. A. Pattanaik, M. P. Satpathy, S. C. Mishra, "Dry sliding wear behavior of epoxy fly ash composite with Taguchi optimization", Engineering Science and Technology, an International Journal, vol.19, pp. 710-716, 2016.

[12]. S.Biswas , A. Satapathy, "A comparative study on erosion characteristics of red mud filled bamboo–epoxy and glass–epoxy composites", Materials and Design, vol. 31, pp. 1752-1767, 2010.

[13]. Siddhartha, K. Gupta, "Mechanical and abrasive wear characterization of bidirectional and chopped E-glass fiber reinforced composite materials", Materials and Design, vol. 35, pp.467-479, 2012.

[14]. S Basavarajappa and G Chandramohan, "Wear studies on metal matrix composites: a Taguchi approach", J. Mater. Sci. Technol. vol. 21, no. 6, pp. 845-850, 2005.

[15]. Standard Test Method for Wear Testing with a Pin-on-Disk Apparatus, ASTM G99-95, 2010.

[16]. N. Ozsoy, M. Ozsoy. A. Mimaroglu," Influence of parameters on tribological behaviour of E-glass fiber reinforced epoxy composites", Acta Physica Polonica A, vol. 128, no. 2-B, pp. 55-58, 2015.

BIOGRAPHY

Neslihan Ozsoy is a research asistant of Mechanical Engineering at University of Sakarya in Turkey. She received her BSc degree in Mechanical Engineering from University of Sakarya in 2006. She also received her MSc (2008) and PhD (2015) degrees in Mechanical Engineering at Institute of Natural Sciences at University of Sakarya. Her research fields are: tribology, mechanics, composites.

A Numerical Investigation on Deformation Behaviors of Energy Absorbers for Passenger Coaches

Ramazan OZMEN[1*], Mustafa GUNAY[1]

Abstract

Thin-walled structures is used commonly as energy absorbers at the front and back of the coaches. These parts should be designed to minimize the damage to the vehicle and prevent the passengers from fatality and/or injury by absorbing the collision energy in railway transportation. In this paper, deformation behaviors of tube like structures with truncated cone under the axial impact load were investigated by means of finite element analysis (FEA). The energy absorbers having tube like structures were modelled at the same weight and have three different wall thickness and taper angle. As a result of FEA, the performances of straight and truncated cone type energy absorbers were compared in terms of energy absorption capacities and an optimization study was done to determine the effects of thickness and taper angle on energy absorbing performances of the members. The analysis of variance in 95% confidence level was applied in order to determine the effects of design parameters on total efficiency (TE). Besides, optimum design parameters for TE were determined by using Taguchi optimization methodology. Thickness was found as the most significant parameter on total efficiency with 60.52% percentage contribution ratio according to ANOVA results.

Keywords: *Coach, Energy absorption, Finite element analysis, HSLA steel*

1. INTRODUCTION

In railway transport, collision zones have been developed in front and rear of the car to damp the collision energy to prevent catastrophic events such as accidental death and injury. During the accident the kinetic energy is consumed in a controlled manner by way of these collision zones to preserve the integrity of the passengers and the occupied areas [1][2].

In order to absorb impact energy, thin-walled tube-like components are generally used as energy absorbing members in vehicles such as cars, planes and trains etc. The static and dynamic axial impact behaviors of these members with different cross sections (circular, rectangular etc.) were examined by means of several experimental and theoretical studies and certain theoretical expressions were suggested according to the cross sectional properties [3].

Energy absorption capabilities and axial impact behaviors of thin-walled tubes depend on many factors such as material properties [4], member geometry [5], impact velocity [6], applied boundary conditions [7], and forming history [8]. These studies have revealed that the hardening characteristics and strain rate sensivity of the material are significant effects on the collision behavior of the energy absorber [4]. On the other hand, it was stated that the stress-strain relationship of the material has an important place in the numerical simulation of the collision events in which the large deformations occurs [9].

In some studies, trigger structures like holes and groves have been utilized to provide a controlled deformation and to increase energy absorption. One of the most important features of this trigger mechanism is to reduce

the initial peak force generated during the impact [10]. And also, aluminum foams and honeycomb structures were placed inside the energy absorber to increase the energy absorption capability of the member [11].

The primary energy absorber is one of the crucial structure in the passenger wagon that is designed for the collapse of impact energy. The current primary energy absorber is comprised of two tube like structures in the form of square cross section. Holes are drilled on the member to improve energy absorption capability and the two members are joined to each other using welded intermediate diaphragm like members [12].

---

[1]* Corresponding author: Karabük University, Engineering Faculty, 78050, Karabük/Turkey, mgunay@karabuk.edu.tr.

In this study, the deformation behaviors of tube like structures in the form of straight and truncated cone members were investigated by means of finite element analysis method. The investigated members have same weight and length and different wall thicknesses.

At the end of the study, the axial deformation performances of straight and truncated cone members were compared. An optimization study was done to determine the effects of thickness and taper angle on energy absorbing performances of the members.

The above mentioned situations are mainly reasons for surface damages, burr and peel-up or push-up delamination in drilling process. In the literature today, the fundamental research on the machinability of CFRP composite material by conventional or unconventional machining process still is a vital issue in modern manufacturing.

2. MATERIAL AND METHOD

2.1. Material Model And Design Parameters

High-strength low alloy (HSLA) or micro alloyed steels present a yield strength of 340–420 MPa and ultimate tensile strength of 410–510 MPa, while their uniform elongation ranges between 10 and 25%. Consequently, HSLA steels generally require 25–30% more power to form due to of their higher strength and toughness, for example compared to carbon steels [13]. Thus, the steels are commonly used in trucks, construction equipment, off-highway vehicles, mining equipment, and heavy-duty vehicles for constructing chassis components, buckets and grader blades [14]. In the light of this knowledge, the HSLA 350 steel was chosen as material in the axial collision analysis of the energy absorbers or members used in the passenger coach. The design parameters for energy absorbers was selected as thickness (T) and taper angle (Ta), but the weights of circular section absorbers was kept as constant. The following design parameters were used for the finite element analyses; thickness of 4, 6 and 8 mm, taper angles of 0, 1.5 and 3 degree. In order to achieve the same weight value, the cross section of the absorber is increased as the thickness is decreased, and the member cross section is decreased as the thickness is increased.

In the analysis, the mass and speed values of the impacting wall, which was modelled for the axial deformation of the structure in the form of the tube, were taken from the experiments applied to the existing energy absorber used in passenger coaches [15]. The method and material properties used during modelling are given below. In the axial collision analysis of the energy absorbers made of HSLA 350 material, stress strain diagrams of the material were used depending on the strain rate. The stress-strain diagram of the HSLA-350 high strength steel, depending on the deformation rate, is given in Figure 1.
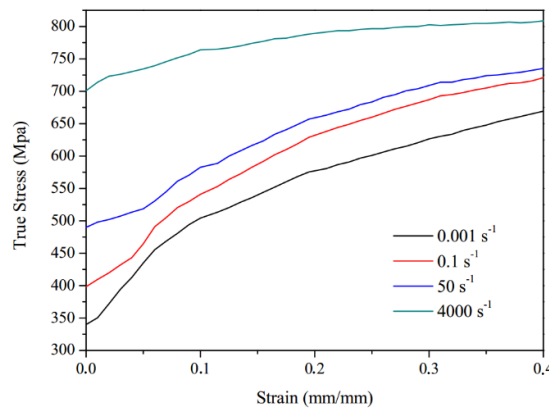

Figure 71 Stress-strain diagram of HSLA-350 steel [6]

In LS-DYNA, these stress-strain values were defined using the Type-24 material model. This material model is defined as a piecewise linear isotropic elastic-plastic material model. In Type-24 material model, the effect of strain rate is achieved by Cowper-Symonds equation. In this equation the yield stress is multiplied by the factor given below [16]. In the equation (1), σ_d, σ_s, $\dot{\varepsilon}$, D and p are dynamic yield stress, yield stress, deformation rate and Cowper-Symonds material constants, respectively.

$$\sigma_d = \sigma_y \left[1 + (\dot{\varepsilon}/D)^{1/p} \right] \tag{1}$$

2.2. Finite Element Model

In this study, the deformation behaviors of thin-walled tubes under axial load were examined by the software of LS-DYNA. When describing the boundary conditions in the finite element model, existing installation conditions were considered. Under existing conditions, one end of one energy absorbing member free and the other is welded to the frame of the CEM (Crash Energy Management) system. For this reason, all the degrees of freedom of the base nodes of the modelled member were restricted and no boundary conditions were applied to the ceiling nodes. The impacting body was modeled with a rigid plate with a mass of 2500 kg and a velocity of 21 m/s. The finite element model of the energy absorber used in the analyses is given in Fig. 2.
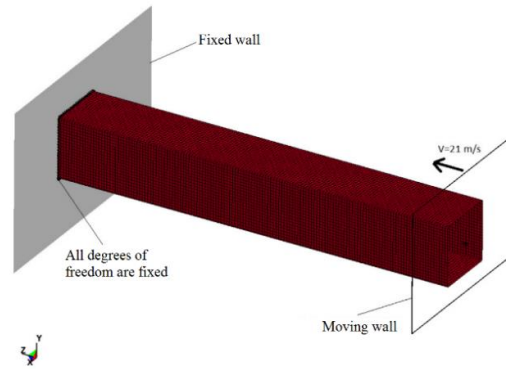

Figure 72 Finite element model of energy absorber.

The automatic contact option was used to prevent the folding surfaces from penetrating into each other during deformation, and the friction coefficient was taken as 0.25 for dynamic and static conditions. In addition, the friction coefficient for the friction between the moving rigid plate and the tube was also taken as 0.25. Belytscho-Tsay shell elements with six degrees of freedom for each node and five integration points along the thickness was chosen for meshing the tube because of frequently used element type in the collision analysis for giving short solution times and approximate value assignments [9]. Consequently, the mesh size used in the analyses was chosen to be about twice the thickness value used for each energy absorber according to Ref [10].

3. RESULTS AND DISCUSSION

In this section, axial deformation behaviors of straight and truncated (with angles of 1,5° and 3°) tube-like structures under dynamic loading conditions were investigated.

For truncated and straight circular cross-section members, rigid wall force-displacement graph is given in Figure 3, the mean force-displacement and absorbed energy displacement graphs are given in Figure 4. The deformation patterns of straight and truncated (with angle of 1,5°) members with wall thicknesses of 4 and 6 mm are given in Figure 5.

It is seen from Figure 7 that; the local maximum and minimum force values are comprised during the formation of the folds in the axial deformation of the energy absorbing members. In the formation of the first fold the rigid wall force value reaches its maximum and then decreases suddenly. During the formation of the second and subsequent folds, the force fluctuates between the local maximum and minimum values.

Al Galib and Limam [17] emphasized this situation that, the initial force required to form the first fold of the member should be high because there is no deformation at the beginning of the tube. When the formation of the first fold, deformations occur in the member and that these deformations reduce the subsequent peak forces.

If the member has the capability to absorb the current impact energy, the force value reaches zero at the rigid wall force-displacement graph. Otherwise, the member loses its energy absorbing ability and starts to behave like a rigid body.
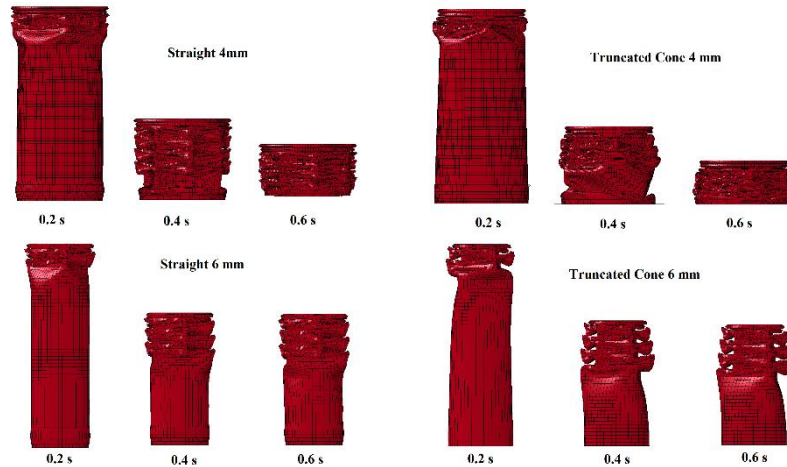
Figure 73 Deformation states of straight and truncated cone members with respect to time

When the rigid plate wall force - displacement graph is examined (Fig. 3), it is seen that the rigid wall force increases again towards the end of the analysis due to the loss of energy absorbing ability of members with 4 mm thickness.
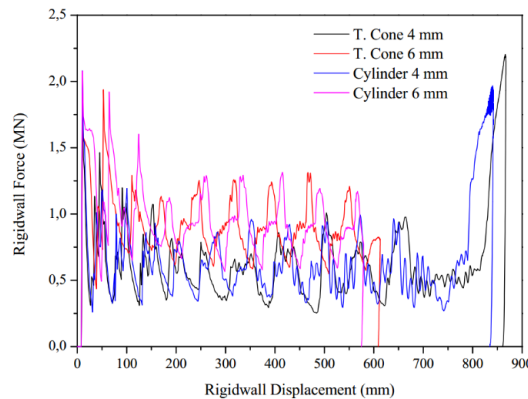

Figure 74 Rigid wall force-displacement graph of square and circular cross-section members
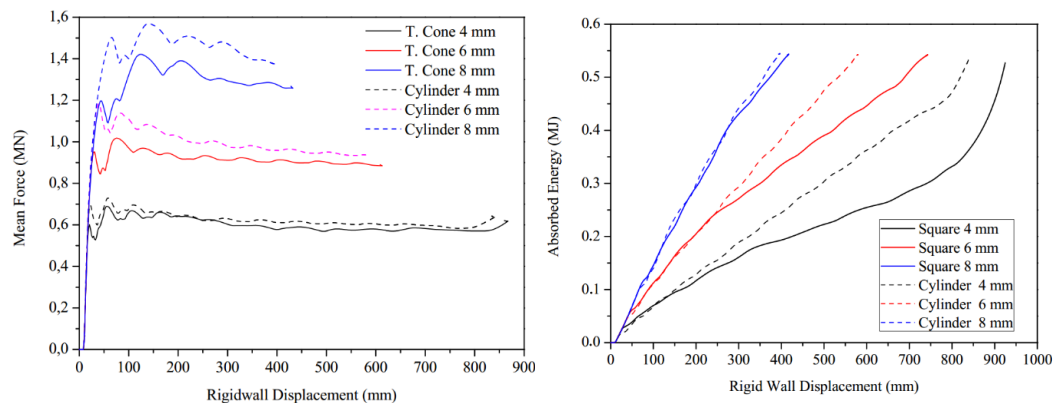

Figure 75 Mean force-displacement and absorbed energy-displacement graph of 1.5° tapered and non-tapered circular members

According to the average deformation force-rigid plate displacement graph (Fig. 4), it is seen that the average deformation force is increases as the thickness increases because a rigid structure is obtained at the same member weight. Though the weight is the same, the member becomes more rigid as the thickness increases.

In this study, axial deformation behaviors of equally weighted members were examined, hence the cross-sectional dimensions change with increasing thickness. Even though the thickness and the cross-sectional properties of the members change, the amount of material required for plastic deformation remains the same.

In this case, the increase of the average deformation force is due to the increase of the full plastic bending moment($M_0 = \sigma_0 h^2/4$) required for buckling when the thickness increases.

From the figure 4, when a comparison is made between straight and truncated members, it is seen that the average deformation force values of straight members are higher than those with truncated members with the same wall thicknesses.

The amount of maximum deformation and the change in initial peak force with respect to thickness and taper angle for the members in the form of straight and truncated cone are given in Figure 5.
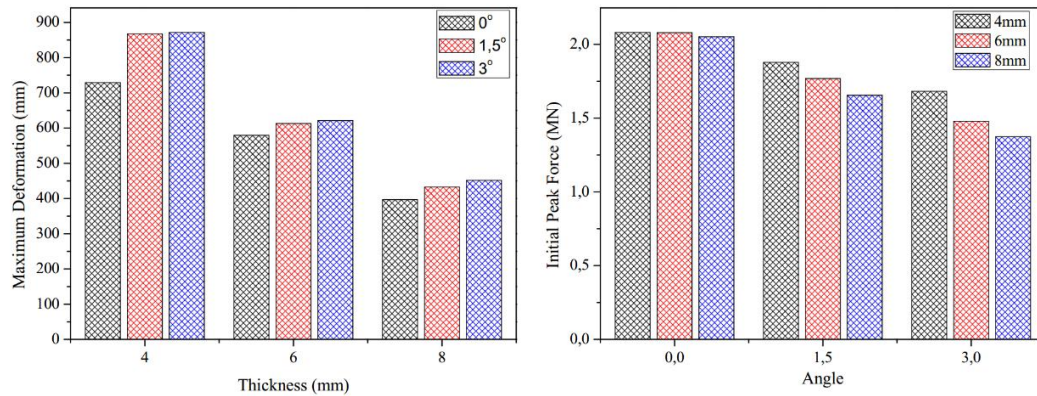

Figure 76-The effect of taper angle on maximum deformation of the member and initial peak force

From the Figure 5, the amount of maximum deformation decreases as the thickness of the member increases. When the effect of the taper angle on the maximum deformation is examined for the same thickness elements, the amount of maximum deformation increases as the taper angle of the member increases.

The low initial peak force is desirable feature for energy absorbing members. Therefore, when the change of the first peak force with the taper angle is examined, it is seen that as the taper angle increases, the initial peak force decreases. The reduction in the initial peak force is very small for the straight elements, but this reduction is more pronounced for the truncated elements. The cross-sectional area of the member is decreased to provide the same weight as the thickness of the element increased. From the initial peak force vs angle graph, the initial peak force decreases even if the thickness of the member increases.

3.1. Optimization Procedure

The effect levels of design parameters on TE were determined according to experimental results with %95 confidence level of analysis of variance (Table 1). The F-ratios and their PCR values have been considered to identify the significance levels of the design parameters. Table 1 shows that the most effective parameter is thickness of energy absorber with PCR of 60.52%. The taper angle is secondary important with PCR of 29.01% on the total efficiency according to ANOVA results.

Table 49 ANOVA for S/N ratios for total efficiency

Source	DF	SS	MS	F-ratio	%PCR
T	2	8.109	4.0546	11.56	60.52
Ta	2	3.887	1.9434	5.54	29.01
Error	4	1.403	0.3507		10.47
Total	8	13.399			100

3.2. Optimization Of Design Parameters

Design parameters for energy absorbers were optimized based on Taguchi method. Therefore, the-larger-the-better approach were applied due to desire of maximum total efficiency (T_E) which is determined as performance characteristic in finite element modelling. The design parameters giving optimum total efficiency value were determined in optimization study according to S/N ratio [18]. In the Eq. (2), *n* and *y* shows the number of simulations and performance characteristic, respectively.

$$\frac{S}{N} = -10 \log \left(\frac{1}{n} \sum_{i=1}^{n} \frac{1}{y_i^2} \right) \tag{2}$$

The total efficiency which is calculated with the data obtained from finite element analysis and S/N ratios are given in Table 2. Statistical analyses and optimization studies were performed via Minitab 15 software.

Table 50 FE simulation results and S/N ratios

Exp. No	T	Ta	T_E	S/N
1	4	0	0.215605	-13.3268
2	4	1.5	0.233029	-12.6518
3	4	3	0.247227	-12.1381
4	6	0	0.267511	-11.4532
5	6	1.5	0.283052	-10.9627
6	6	3	0.366202	-8.72558
7	8	0	0.257682	-11.7783
8	8	1.5	0.257676	-11.7785
9	8	3	0.270111	-11.0534

S/N ratios of parameters are considered in Taguchi optimization method. The highest S/N ratio shows the optimum level of parameters according to "smaller is better" approach. S/N ratios calculated via simulation results of total efficiency are shown in main effect plot (Fig. 3). Also, the variation of S/N ratios according to parameters is given in Table 3. It was shown that thickness is the most important thickness on T_E when examining the main effect plots in Fig. 3 and the difference (Δ) between maximum and minimum values of S/N ratios in Table 2. The optimum levels for minimum T_E according to S/N ratios were determined as T2, Ta3.
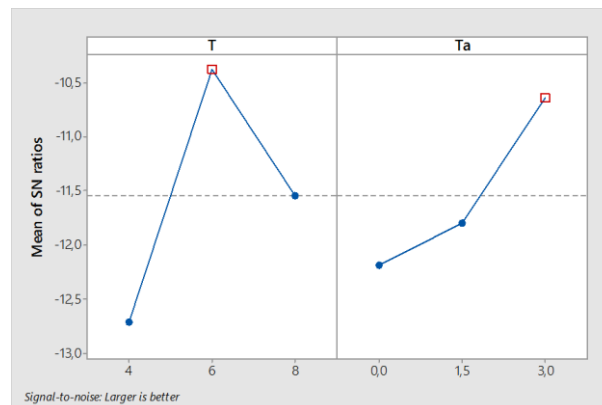

Figure 77 The main effect plot for SN ratio of total efficiency

Table 3. Response table of S/N ratios for total efficiency

Parameter	S/N ratios			
	Level 1	*Level 2*	*Level 3*	*Δ*
Thickness	-12.71	-10.38*	-11.54	2.33
Taper angle	-12.19	-11.8	-10.64*	1.55
*Optimum levels of parameters				

Average of FE simulation results performed at optimal levels are evaluated by Eq. (3) to forecast the mean for the improvement conditions. Eq. (1) which is the expression of calculated total efficiency (TE) is derived from Eq. (4).

$$\eta_G = \bar{\eta}_G + (\bar{T}_O - \bar{\eta}_G) + (Ta_O - \bar{\eta}_G) \tag{3}$$

$$TE_{cal} = 10^{-\eta_G/20} \tag{4}$$

Where, η_G is the S/N ratio calculated at optimal level of factors (dB), $\overline{\eta_G}$ is the mean S/N ratio of all parameters (dB), $\overline{A_0}$ and $\overline{B_0}$ are the mean S/N ratio once thickness and taper angle are at optimum levels, and

TE_{cal} is the calculated value. Consequently, η_G and TE_{cal} for optimum design parameters were determined as -9.4785 dB and 0.3358, respectively. Lastly, confirmation experiments with FE modelling were done by using the optimum design parameters after the determination of these factors for TE and thus reliability of the optimization has been confirmed. The FE simulations conducted by considering the confidence interval (CI) calculated from Eqn. (5) and (6) [19].

$$CI = \sqrt{F_{\alpha,(1,v_e)} V_e \left(\frac{1}{n_{eff}} + \frac{1}{r}\right)} \tag{5}$$

$$n_{eff} = \frac{N}{1 + v_T} \tag{6}$$

Where; $F_{\alpha,(1,v_e)}$ is the F-ratio at the 95 % significance level, α is the importance level, v_e is the degree of freedom of the error, Ve is the error variance, n_{eff} is the effective number of replications, r is the number of replications for the verification test. In Equation 6, N is the total number of experiments and v_T is the total main factor of the degree of freedom. Total efficiency obtained with FE simulation (TE_{exp}), calculated total efficiency (TE_{cal}), and S/N ratios (η_{exp}, η_{cal}) for TE are given by comparing between simulation results and calculated values (Table 5). Table 5 shows differences between confirmation experiment results and calculated values and their S/N ratios obtained by using Eqn. 2 and 3. As can be seen from the Table, a difference of 0.7529 dB is under the confidence interval of 1.6893 dB for total efficiency. Thus, the optimum levels of design parameters for total efficiency were approved as confident.

Table 5. *Comparison of simulation results and calculated values*

Simulation results		Calculated value		Difference	
TE_{exp} (μm)	η_{exp} (dB)	TE_{cal} (μm)	η_{cal} (dB)	TE_{exp}-TE_{cal}	η_{exp}-η_{cal}
0.3662	-8.7256	0.3358	-9.4785	0.0304	0.7529

4. CONCLUSIONS

In this study, the axial deformation behaviors of the energy absorbing members in the form of straight and truncated (with angles of 1,5° and 3°) tubes were investigated under the impact force acting on the existing primary energy absorbing member.

In the study, deformation performances were compared with the condition that the weight and length of the energy absorbing members were the same. As a result of comparison, it was found that the average deformation force values of straight members are higher than those with truncated members with the same wall thicknesses. When the thickness of the member is increased, the average deformation force increased due to the increase of the full plastic bending moment required for buckling. Though the weight is the same, the member becomes more rigid as the thickness increases.

When the effects of thickness and taper angle of the member on the amount of maximum deformation and initial peak force were investigated, it was seen that, the amount of maximum deformation decreases as the thickness of the member increases and increases as the taper angle of the member increases for the same thickness elements. The low initial peak force is desirable feature for energy absorbing members. Therefore, when the change of the first peak force with the taper angle is examined, it is seen that as the taper angle increases, the initial peak force decreases.

In the study, design parameters for energy absorbers were optimized based on Taguchi method. Therefore, the-smaller-the-better approach were applied due to desire of maximum total efficiency (T_E) which is determined as performance characteristic of the member. The design parameters giving optimum total efficiency value were determined in optimization study according to S/N ratio. According to optimization study, the optimum energy absorbing member was determined as a truncated member with the 6mm thickness and taper angle of 1,5°. The effects of taper angle and thickness on total crush efficiency of the member calculated as 10.38 % and 10.64 % respectively.

REFERENCES

[1]   E. Martinez, D. Tyrell, R. Rancatore, R. Stringfellow, and G. Amar, "A crush zone design for an existing passenger rail cab car," in *Proceedings of 2005 ASME International Mechanical Engineering Congress & Exposition*, 2004, pp. 85–94.

[2] K. Jacobsen, D. Tyrell, and B. Perlman, "Impact Tests of Crash Energy Management Passenger Rail Cars: Analysis and Structural Measurements," in *ASME 2004 International Mechanical Engineering Congress and Exposition*, 2004, pp. 97–105.

[3] W. Abramowicz and N. Jones, "Dynamic progressive buckling of circular and square tubes," *Int. J. Impact Eng.*, vol. 4, no. 4, pp. 243–270, 1986.

[4] S. Simunovic, J. Shaw, and G. a Aramayo, "Material Modeling Effects on Impact Deformation of Ultralight Steel Auto Body," *SAE Tech. Pap.*, no. 724, 2000.

[5] A. A. Nia and J. H. Hamedani, "Comparative analysis of energy absorption and deformations of thin walled tubes with various section geometries," *Thin-Walled Struct.*, vol. 48, no. 12, pp. 946–954, 2010.

[6] M. Langseth, O. S. Hopperstad, and T. Berstad, "Crashworthiness of aluminium extrusions: validation of numerical simulation, effect of mass ratio and impact velocity," *Int. J. Impact Eng.*, vol. 22, no. 9–10, pp. 829–854, 1999.

[7] A. Tasdemirci, "The effect of tube end constraining on the axial crushing behavior of an aluminum tube," *Mater. Des.*, vol. 29, no. 10, pp. 1992–2001, 2008.

[8] R. Gümrük and S. Karadeniz, "The influences of the residual forming data on the quasi-static axial crash response of a top-hat section," *Int. J. Mech. Sci.*, vol. 51, no. 5, pp. 350–362, 2009.

[9] R. Gümrük and S. Karadeniz, "A numerical study of the influence of bump type triggers on the axial crushing of top hat thin-walled sections," *Thin-Walled Struct.*, vol. 46, no. 10, pp. 1094–1106, 2008.

[10] G. Chen, X. M. Chen, and M. F. Shi, "Experimental and Numerical Studies of Crash Trigger Sensitivity in Frontal Impact," *SAE Tech. Pap.*, no. 724, 2005.

[11] A. G. Hanssen, M. Langseth, and O. S. Hopperstad, "Static and dynamic crushing of circular aluminium extrusions with aluminium foam filler," *Int. J. Impact Eng.*, vol. 24, no. 5, pp. 475–507, 2000.

[12] G. Mayville, R. A., Rancatore, R. J., Stringfellow, R. G., Amar, "Repair of Budd Pioneer Coach Car Crush Zones," Cambridge, MA, 2007.

[13] D. A. Skobir, "High-strength low-alloy (HSLA) steels," *Mater. Technol.*, vol. 45, no. 4, pp. 295–301, 2011.

[14] J. Patel, C. Klinkenberg, and K. Hulka, "Hot rolled HSLA strip steels for automotive and construction applications," *Niobium Sci. Technol.*, no. Grade 100, pp. 647–674, 2001.

[15] R. Mayville, A. D. Little, K. Johnson, and P. Engineering, "The Development of a Rail Passenger Coach Car Crush Zone," in *Proceedings of the 2003 IEEE/ASME Joint Rail Conference*, 2003, pp. 1–8.

[16] J. O. Hallquist, *LS-DYNA users manual*. Livermore, California: Livemore Software Technology Corporation, 1998.

[17] D. Al Galib and A. Limam, "Experimental and numerical investigation of static and dynamic axial crushing of circular aluminum tubes," *Thin-Walled Struct.*, vol. 42, no. 8, pp. 1103–1137, 2004.

[18] G. Taguchi, S. Chowdhury, Y. Wu, Taguchi's Quality Engineering Handbook, John Wiley & Sons, Inc., New Jersey, USA, 2005.

[19] M. Günay, M.E. Korkmaz, *Optimization of Honing Parameters for Renewal of Cylinder Liners*. GU J Sci 30(1), 111-119, 2017.

Entropy Generation Analysis for a Tube with Equilateral Triangle Cross Sectioned Coiled-Wire Inserts Installed with a Separation from the Tube Wall

Orhan Keklikcioglu[1], Toygun Dagdevir[2],Veysel Ozceyhan[3]

Abstract

This paper presents an experimental investigation on the entropy generation induced by turbulent forced convection in a circular tube with coiled-wire inserts. The wire inserts are manufactured with an equilateral triangular cross-section to destruct the boundary layer effectively. The triangle side length of e=6 mm was chosen for the experiment. The coiled-wire inserts installed with 1 and 2 mm separation from the inner tube wall and coiled with three different pitch-to-diameter ratios: P/D= 1, P/D= 2 and P/D= 3. A specific method was employed to coil the wires so that an edge of the triangle was oriented to face the incoming air flow. A uniform heat flux was applied to the outer surface of the tube. Experiments were performed for a range of Reynolds numbers from 3429 to 26,663. The experimental results indicated that the coiled-wire inserts led to a significant increase in both the heat transfer rate and friction factor over the smooth tube based on coil pitches and clearance. The reduction of entropy generation rates were obtained with using coiled-wire at low Reynolds numbers.

Keywords: *Entropy generation, heat transfer, pressure drop, coiled wire*

1. INTRODUCTION

Heat transfer enhancement is a process of increase the heat transfer rate or thermo-hydraulic performance by using different methods. These methods are used a diverse range of heat transfer applications in thermal systems. Design parameter of thermal systems relates with not only heat transfer enhancement but also the amount of power input and in the systems. Therefore, the determining of the optimal consistence between the heat transfer rate and requirement of power input becomes main purpose of the design evaluations of a thermal systems. Entropy generation minimization has been conducted by many researchers to determine the optimal model of the thermal systems. There are several investigations on entropy generation and heat transfer analyses of thermal systems.

Siavashi et al. [1] numerically studied the effect of different source shapes and configurations on fluid flow, heat and mass transfer for steady double-diffusive natural convection of two-phase flow through a square enclosure filled with a fluid-saturated porous medium. Also, entropy generation analysis was conducted in terms of the thermal, the viscous and the solutal entropy generation. They reported that the case (a) was the optimum model, as a result of low entropy generation. Das and Basak [2] investigated the entropy generation rate during natural convection in the square and triangular cavities subjected to discrete solar heating from the side walls. As a result, the lowest entropy generation obtained for the case 4 but this case has not been defined thermally efficient system because of the low heat transfer rate. Eger et al. [3] carried out a numerical study of entropy generation relying on canonical configuration for improve the heat transfer process in a alternator system. Gord et al. [4] investigated the optimal geometry and operational conditions of helically coiled heat exchangers for both laminar and turbulent flows. It was concluded that optimize the performance of this type of heat exchanger based on the lowest rate of entropy generation were determined. Vishal Anand [5] studied entropy generation analyses of flow of nanofluids in a tube immersed in an isothermal external fluid. It was concluded that the entropy generation rate decreased due to increasing of heat transfer.

---

[1] Corresponding author: Erciyes University, Department of Mechanical Engineering, 38039, Melikgazi/Kayseri, Turkey. keklikcioglu@erciyes.edu.tr.

[2] Erciyes University, Department of Mechanical Engineering, 38039, Melikgazi/Kayseri, Turkey, toygun@erciyes.edu.tr.

[3] Erciyes University, Department of Mechanical Engineering, 38039, Melikgazi/Kayseri, Turkey, ozceyhan@erciyes.edu.tr.

Ghanbarpour and Khodabandeh [6] carried out entropy generation analysis of cylindrical heat pipe using nanofluid. The results revealed that the entropy generation in heat pipes decreased when nanofluids were used as working fluids instead of basefluid. Ko and Wu [7] analysed the entropy generation induced by turbulent forced convection in a curved rectangular duct with external heating by numerical methods. Huminic and Huminic [8] studied the heat transfer and entropy generation inside a helically coiled tube in tube heat exchanger in laminar flow regime using two different types of nanofluids. The increase of nanoparticles volume concentration leads to the reduction of the entropy generation. Ventsislav Zimparov [9] conducted an experimental investigation on heat transfer enhancement and entropy generation of three start spirally corrugated tubes with a twisted tape. Yakut et al. [10] studied the performance characteristics of conical ring turbulators were determined by means of the entropy generation minimization method. It was observed that the conical rings are thermodynamically advantageous up to 8000 Reynolds number with respect to entropy generation. Another investigation of Yakut and Sahin [11] effect of coiled wire inserts on heat transfer enhancement and the entropy generation rate were investigated. Ching Chang Cho [12] investigated the heat transfer performance and entropy generation of natural convection in a partially heated wavy wall square cavity filled with Al2O3-water nanofluid. According to the results entropy generation decreased with increasing volume fraction.

From the literature cited above, several passive techniques have been applied in thermal systems to investigate the heat transfer and entropy generation rate. On the other hand, no study has been presented on entropy generation analysis for a tube with equilateral triangle cross sectioned coiled wire inserts. In present study, the coiled wire inserts were located into the experiment tube separately from the inner wall to improve heat transfer efficiency via disturbing the laminar sublayerexperımental method.

2. EXPERIMENTAL METHOD

2.1. Experimental Apparatus

The test tube has 56 mm inner diameter (D1), 60 mm outer diameter (D2), and 2 mm thickness. The details of test tube fitted with coiled wire insert are shown in Fig.1.
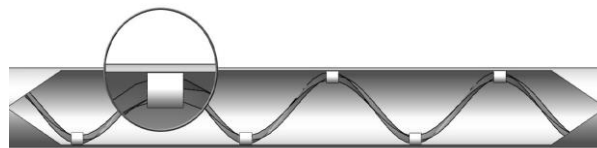

Figure 78. The equilateral triangle cross section coiled-wire inserted in a tube with a separation from the inner wall of the tube.

All tests were carried out with experimental equipments as shown in Fig. 2. The experimental apparatus consisted of a calming tube to improve the hydrodynamics of the air flow and a heated tube (the test section), in length of 6000 mm and 2600 mm, respectively.
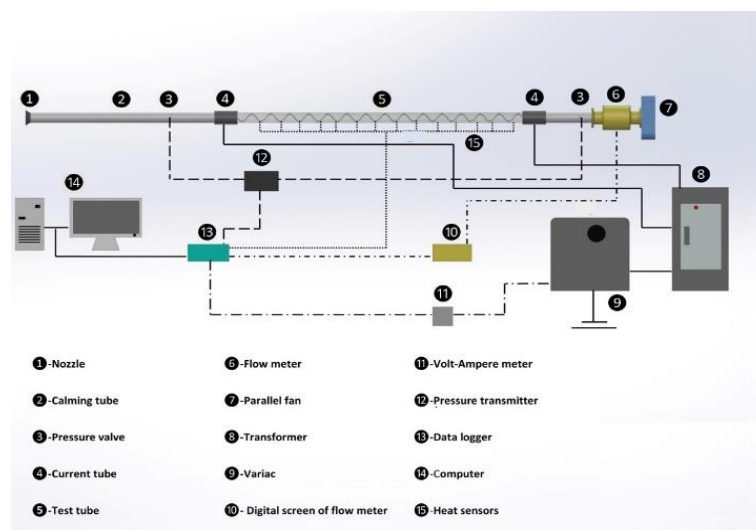

Figure 2. The details of experimental apparatus.

The test tube was subjugated uniform heat flux that was supplied by a variac transformer. The external surface of the heated tube was well insulated with glass wool to prevent the convective heat loss. Twenty six piece sensors were placed periodically on the outer surface of the heated tube to measure the temperatures. Also, the inlet and the outlet temperatures of the bulk air were measured by two different sensors at certain points. The sensors measure the temperatures within ±0.2 °C accuracy rating according to the calibration test result. A blower that has the power of 3 kW is used to vacuum air into the test section and the blower is controlled by an inverter. To establish the pressure drop, a differential pressure gauge was used. The volumetric flow rate was determined by using flow meter in to the flow field.

Different flow rate and electrical power values were tested in the experiments. The numeric data of temperature, the decrease of pressure, volumetric flow rate of the bulk air and electrical output were saved by a data logger and transmitted the computer via the data logger after the system reached the steady state condition. The experiments were carried out at the Reynolds number ranges from 3429 to 26,663. The Nusselt and Reynolds numbers, friction factor, heat transfer enhancement and the other data of the system were calculated by using software in the FORTRAN language.

2.2. Calculation Of Heat Transfer And Friction Factor

The heat given by the air from the test tube is calculated by;

$$Q_{air} = mC_{p,air}(T_0 - T_i) = \Delta VI - Q_{loss} \tag{1}$$

As a consequence, the heat flux subjected on to the experiment tube can be described as:

$$q = \frac{Q_{air}}{\pi D_2 L} \tag{2}$$

The coefficient of local heat transfer for the experiment tube is represented as;

$$h(x) = \frac{q}{T_{iw}(x) - T_b(x)} \tag{3}$$

In Eq.3, and represent the local inner wall temperature of the heated test tube and local bulk temperature of the fluid, respectively.

The local Nusselt Numbers were acquired by Eq.4,

$$Nu(x) = \frac{h(x)D}{k} \tag{4}$$

For the air, the Reynolds number is

$$Re = \frac{UD}{\nu} \tag{5}$$

The friction factor, f is calculated as follows, for the fully developed isothermal flow;

$$f = \frac{\Delta P}{\frac{1}{2}\rho.U^2 \frac{L}{D}} \tag{6}$$

where U represents the mean fluid velocity in the tube.

The heat transfer rate and friction factor of the smooth tube and tube fitted with coiled wire inserts are evaluated under the same pumping power as below [13];

$$(\dot{V}\Delta P)_s = (\dot{V}\Delta P)_c \tag{7}$$

$$(f\,Re^3)_s = (f\,Re^3)_c \tag{8}$$

$$Re_s = Re_c(f_c / f_s)^{1/3} \tag{9}$$

The enhancement efficiency is presented as follows [13]:

$$\eta = \frac{h_c}{h_s}\bigg|_{pp} = \frac{Nu_c}{Nu_s}\bigg|_{pp} = \left(\frac{Nu_c}{Nu_s}\right)\left(\frac{f_s}{f_c}\right)^{1/3}$$

(10)

2.3. Entropy Generation Analyses

The entropy generation rate for fluid flow is given [14, 15] by:

$$\dot{S'}_{gen} = \frac{q'^2}{\pi k T^2 Nu} + \frac{32 m^3}{\rho^2 T}\frac{f}{D^5}$$

(11)

where T, cp and ρ bulk properties. The Eq. 11 derived for for a straight tube and can be applied tube with coiled wire inserts. The first term of the equation is the contribution made by heat transfer, while the second term is the contribution due to fluid friction:

$$\dot{S'}_{gen} = \dot{S'}_{gen,\Delta T} + \dot{S'}_{gen,\Delta P}$$

(12)

The entropy generation number (Ns) is defined as the proportion of entropy generation rate by rough tube to the entropy generation rate in smooth tube [16],

$$N_s = \dot{S'}_{gen,r} / \dot{S'}_{gen,s}$$

(13)

Heat transfer augmentation techniques with Ns <1 are thermodynamically advantageous, because these techniques both enhance the heat transfer rate and reduce the degree of irreversibility of the unit's performance [16].

3. EXPERIMENTAL RESULTS

3.1. Validation Method

In this present work, in order to demonstrate the accuracy of the experimental results on Nusselt number and friction factor in smooth tube were compared with equations of Gnielinski [17] and Petukhov [18], as shown in Figs. 3 and 4, respectively. Both Nusselt number and friction factor values were validated in the turbulance flow conditions.
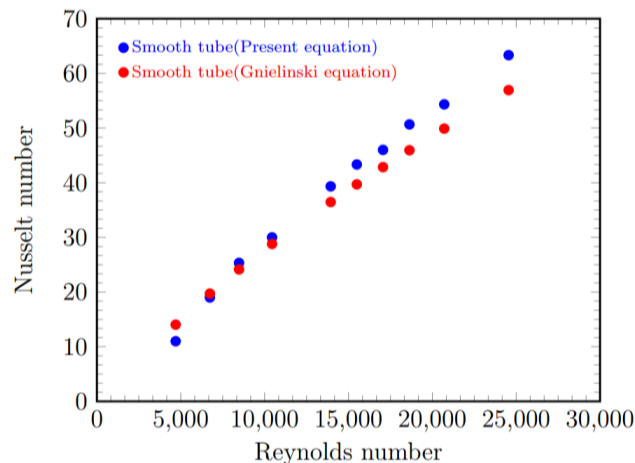

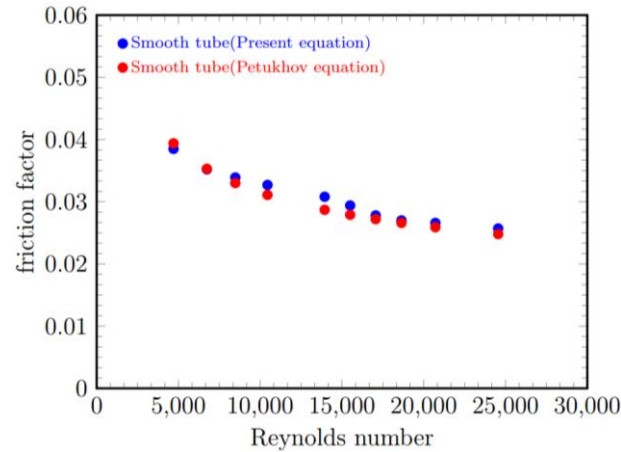Figure 3. Validation of Nusselt number in the smooth tube.

Figure 4. Validation of friction factor in the smooth tube.

As shown in figures, Nusselt number and friction factor values coincide with the previous equations.

3.2. The evaluation Of Entropy Generation

Thermal performance of the tube with the coiled-wire inserts placed into the flow region is related with the Nusselt number and friction factor . The coiled-wire inserts in the tube cause not only an increase in Nusselt number but also an increase in the friction factor. Therefore, the conversion of the Nusselt number and the friction factor should be investigated. In Figs. 5 and 6, the variation in the Nusselt number and friction factor are presented for all configurations.
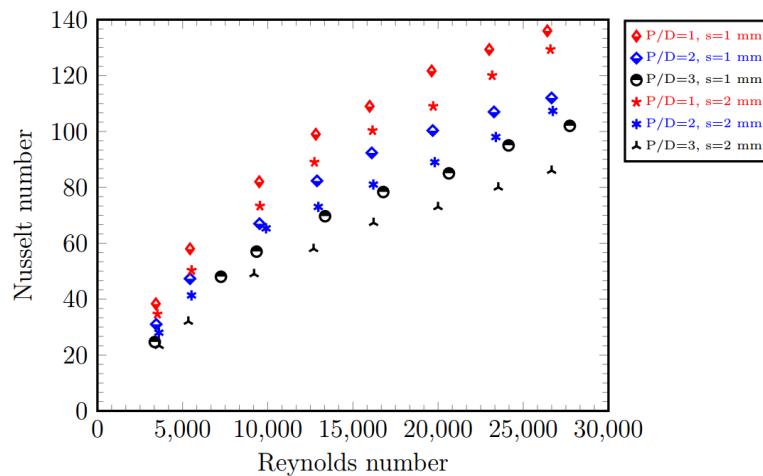

Figure 5. Variation of Nusselt number versus Reynolds number for all configurations.

Figure 5 depicts the Nusselt number increases with increasing Reynolds number and decreasing the distance between the coiled-wire inserts and inner wall of the tube. It can be understood from the experimental results compared between clearance of 1 mm and 2 mm that the coiled-wire inserts destruct the laminar boundary layer effectively when the clearance decreases. Comparison between the models at the same pitch ratio and different clearances shows the Nusselt number is in the range 83–94% higher than the s = 2 mm model depending on the Reynolds number.
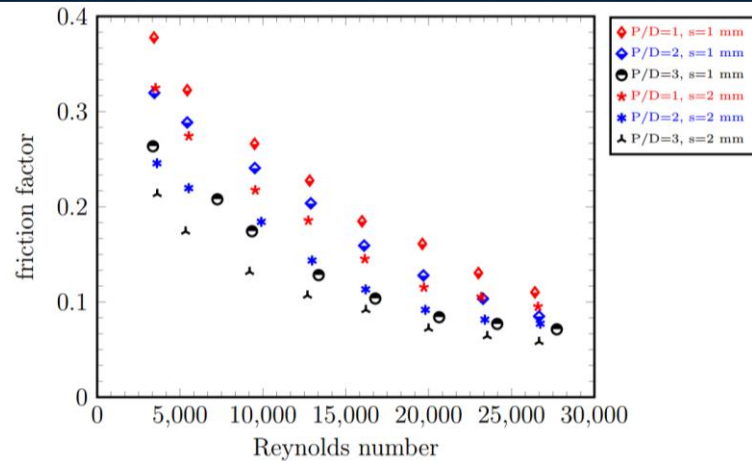
Figure 6. Variation of friction factor versus Reynolds number for all configurations.

It is clear from the Fig. 6 that the use of coiled-wire inserts caused a significant increase in friction factor. The friction factors for the P/D = 3, s = 1 mm model at different Reynolds numbers are higher than for the P/D = 3, s = 2 mm model in the range of 79–87%.

In the thermal systems entropy is generated from heat transfer caused by temperature difference and fluid friction. Heat transfer enhancement techniques, especially passive methods increase the heat transfer rate but they also increase the friction factor. The primal aim of this study evaluate methods of enhancement of heat transfer based on entropy generation theorem. Entropy generation number values versus Reynolds number for different configurations presented in Figs. 7, 8.
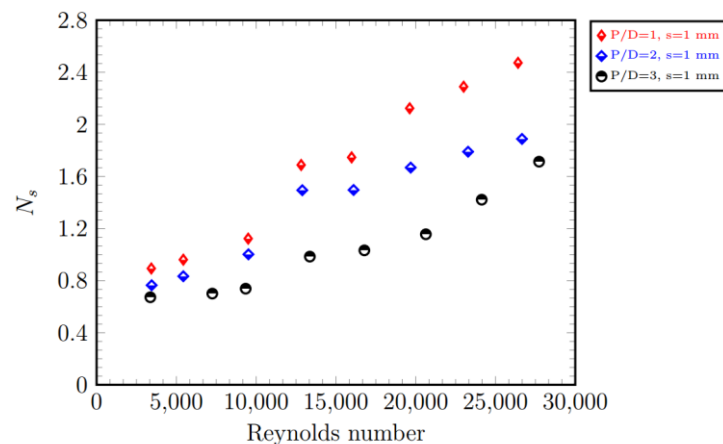

Figure 7. Variation of entropy generation number versus Reynolds number s=1 mm.

Figure 7 represents the comparison of the entropy generation number for the various Reynolds number for s=1 mm clearance with three different pitch ratios at a constant side length. The entropy generation rate shows ascending trend with the increment of Reynolds number. The highest entropy generation rate achieved for the model of P/D=1, s=1 mm at Reynolds number of 26,663. In order to determine an advantageous thermal system entropy generation number should be lower than unity. In the Figure 7, entropy generation numbers above unity for Reynolds number higher than 15,000.
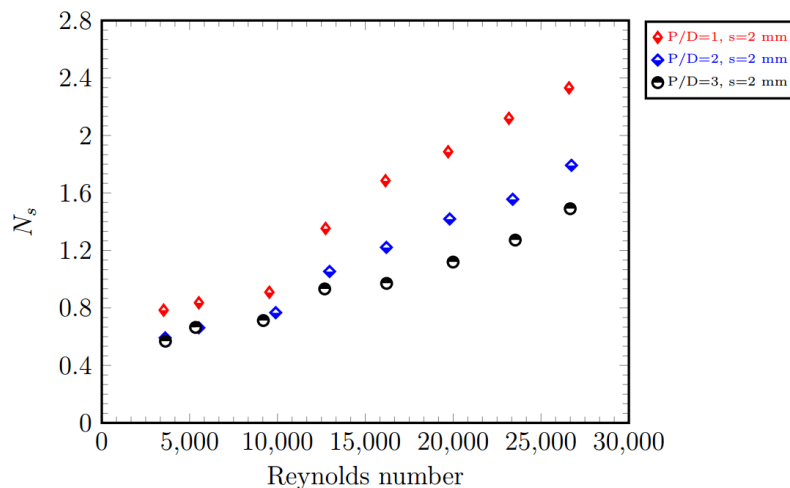
Figure 8. Variation of entropy generation number versus Reynolds number for s=2 mm.

Figure 8 represents the entropy generation number for the various Reynolds number for s=2 mm clearance with three different pitch ratios at a constant side length. Entropy generation number decreases with increasing pitch ratio. Entropy generation numbers remain under unity before Reynolds number of 15,000. The lowest entropy generation number of 0.568 observed for P/D=3 model at lowest Reynolds number as expected.

4. CONCLUSIONS

The investigations were conducted for a range of Reynolds numbers from 3429 to 26,663. The triangle side length of 6 mm was chosen for the experiments. The coiled-wire inserts installed with 1 mm and 2 mm separations from the inner tube wall and coiled with three different pitch-to-diameter ratios: P/D= 1, P/D= 2 and P/D= 3. The experimental results revealed that entropy generation number increases with increasing of Reynolds number and decreases with increasing pitch ratio. It was also obtained that separation has significant effect on entropy generation number. Due to the frictional forces and irriversibilities entropy generation rate state above unity after 15,000 Reynolds number. Negative effect of friction factor was also observed at decreasing pitch ratio, frictional forces overcomed the heat transfer effect when pitch ratio decreased. The lower seperation configuration's entropy generation numbers were higher than the other models. Especially at low Reynolds numbers, the system achieves lower entropy generation number, making a more compact and efficiency heat exchanger possible. The lowest entropy generation number of 0.568 occurs for the tube-and-insert combination with s=2 mm and P/D=3 at lowest Reynolds number.

REFERENCES

[1]. M. Siavashi, V. Bordbar, P. Rahnama, Heat transfer and entropy generation study of non-darcy double-diffusive natural convection in inclined porous enclosures with different source configurations, *Applied Thermal Engineering,* vol. 110, pp. 1462 -1475, 2017.

[2]. D. Das, T. Basak, Role of distributed/discrete solar heaters for the entropy generation studies in the square and triangular cavities during natural convection, *Applied Thermal Engineering*, vol. 113, pp. 1514-1535, 2017.

[3]. T. Eger, T. Bol, L. Darczy, G. Janiga, R. Schroth, D. Thvenin, Numerical investigations of entropy generation to analyze and improve heat transfer processes in electric machines, *International Journal of Heat and Mass Transfer*, vol. 102, pp. 1199 – 1208, 2016.

[4]. M. Farzaneh-Gord, H. Ameri, A. Arabkoohsar, Tube-in-tube helical heat exchangers performance optimization by entropy generation minimization approach, *Applied Thermal Engineering*, vol. 108, pp. 1279 – 1287, 2016.

[5]. Vishal Anand, Entropy generation analysis of laminar flow of a nanofluid in a circular tube immersed in an isothermal external fluid, *Energy*, Vol. 93, pp. 154-164, 2015.

[6]. Morteza Ghanbarpour, Rahmatollah Khodabandeh, Entropy generation analysis of cylindrical heat pipe using nanofluid, *Thermochimica Acta*, vol. 610, pp. 37-46, 2015.

[7]. T.H. Ko, C.P. Wu, A numerical study on entropy generation induced by turbulent forced convection in curved rectangular ducts with various aspect ratios, *International Communications in Heat and Mass Transfer*, vol. 36, pp. 25-31, 2009.

[8]. Gabriela Huminic, Angel Huminic, Heat transfer and entropy generation analyses of nanofluids in helically coiled tube-in-tube heat exchangers, *International Communications in Heat and Mass Transfer*, vol. 71, pp. 118-125, 2016.

[9]. Ventsislav Zimparov, Enhancement of heat transfer by a combination of three-start spirally corrugated tubes with a twisted tape, *International Journal of Heat and Mass Transfer*, vol. 44, pp. 551-574, 2001.

[10]. Kenan Yakut, Bayram Sahin, Suat Canbazoglu, Performance and flow-induced vibration characteristics for conical-ring turbulators, *Applied Energy*, vol.79, pp. 65-76, 2004.

[11]. Kenan Yakut, Bayram Sahin, The effects of vortex characteristics on performance of coiled wire turbulators used for heat transfer augmentation, *Applied Thermal Engineering*, vol. 24, pp. 2427-2438, 2004.

[12]. Ching-Chang Cho, Heat transfer and entropy generation of natural convection in nanofluid-filled square cavity with partially-heated wavy surface, *International Journal of Heat and Mass Transfer*, vol. 77, pp. 818–827, 2014.

[13]. [13] R.L. Webb, Performance evaluation criteria for use of enhanced heat transfer surfaces in heat exchanger design, *International Journal of Heat and Mass Transfer*, vol. 24, pp. 715-26, 1981.

[14]. A. Bejan, Entropy Generation Minimization, *CRC Press*, 1976.

[15]. A. Bejan, Thermodynamic optimization of geometry in engineering flow systems*, Energy An International Journal*, vol. 1, pp. 269-277, 2001.

[16]. Ventsislav D. Zimparov, Nikolai L. Vulchanov, Performance evaluation criteria for enhanced heat transfer surfaces, *International Journal of Heat and Mass Transfer*, vol. 37, pp. 1807-1816, 1994.

[17]. V. Gnielinski, New equations for heat and mass transfer in turbulent pipe flow and channel flow, *Int. Chem. Eng.*, vol. 16, pp. 359-368, 1976.

[18]. B.S. Petukhov, Heat transfer in turbulent pipe flow with variable physical properties, J. P. Harnett (Eds.), *Advances in Heat Transfer*, Academic Press, New York, vol. 6, pp. 504-564, 1970.

Study Of Laser Induced Micro-Hole Configuration In Order To Exploit Mechanical Interlocking Effect On Adhesive Bonding

Mustafa Ozgur Bora[1]*, Erhan Akman[1], Onur Coban[1], Belgin Genc Oztoprak[1], Arif Demir[2]

Abstract

There are many different techniques to improve the adhesion between carbon fiber reinforced plastics (CFRP) which are used in aircraft primary structures. One of the most common techniques is the specific surface structuring of the joining partners in order to obtain mechanical interlocking. In this study laser induced surface structuring effect on adhesion strength of carbon-epoxy composites was investigated by single lap shear tests. Micro-holes were created by CO_2 laser treatment with different configurations in x and y axis for the best mechanical interlocking effect on adhesive bonding. Different micro-hole configured CFRP composite partners were adhesively bonded for single lap shear tests. Single lap shear adhesion tests were conducted according to ASTM D5868-01 standard with 60 kN DARTEC universal test machine. Single lap shear tests showed that micro-hole structuring has significant effect on mechanical interlocking for adhesive bonding of CFRP composites.

Keywords: *Adhesive bonding, Carbon fiber reinforced plastics, Laser surface structuring, Mechanical Interlocking*

1. INTRODUCTION

Carbon fibre reinforced plastic (CFRP) composites have attracted considerable interest from a number of different industrial sectors but primary from the aerospace sector. Aircraft manufacturers, such as Boeing and Airbus, see the potential benefits of using CFRP composites due to its superior mechanical properties over its metallic alternatives. Their low density, high strength and high stiffness to weight ratio make them a suitable candidate for many aerospace applications [1]. Achieving high joint quality to meet the needs of engineering applications is always a challenging process for researchers [2]. From all the available joining techniques such as bolting, riveting, welding, etc. to join two composite materials, the preferred joining technique for polymer composite materials remains adhesive bonding [3]. The joining of composite structures by adhesive bonding, without using fasteners, is a promising method to reduce aircraft cost and weight. Adhesive bonding also brings several technical advantages such as the avoidance of detrimental stress concentrations and the avoidance of fiber cuts associated with the drilling of holes for introducing fasteners [4]. Adhesives are extensively used to bond components in many fields where structures are subject to high stress levels in service. Adhesive bonding distributes stresses over the whole bonded region and therefore stress concentrations are less likely to occur than in conventional fastening techniques (bolted, riveted, or welded) [5]. However, the manufacture procedure, in particular, the preparation of surfaces to adhesive, is also another parameter with significant influence on the mechanical resistance of adhesive joints. A good surface treatment involves several steps: elimination of contaminants; oxidized layers and low-molecular-weight species; improved wetting of low energy surfaces; chemical modifications (introduction of polar chemical groups and/or coupling agents onto the surface) and increase in surface roughness giving rise to improved mechanical interlocking [6]. These surface treatments are generally effective to some extent but have their own limitations.

---

[1] *Corresponding author: Aircraft Material Research and Development Laboratory, Faculty of Aeronautics and Astronautics, Kocaeli University, Kocaeli, Turkey, E-mail: ozgur_bora@yahoo.com, ozgur.bora@kocaeli.edu.tr*

[2] *Department of Physics, Kocaeli University, Kocaeli, Turkey*

A meanwhile qualified procedure in the aerospace is the use of a CO_2 laser for the removal / activation of release agent residues on CFRP surfaces before painting. The application of the same laser technique, as a surface treatment method for structural adhesive bonding can be under consideration. The degree of treatment of the carbon fibres depend very much on the laser systems and treatment conditions [7]. A very interesting application of surface structuring is the ability to develop new composite materials by employing micro mechanical interlocking. From literature survey, Baburaj et al. [8] studied mechanical interlocking on the titanium surfaces with developing process of micro-coulumn array generation by laser processing. Due to micro coulumn arrays on the titanium surface the surface area and the surface roughness were increased. By this way, shear strength of the adhesive bonded sample was improved. Kim and Lee [9] investigated the effects of loading mode and mechanical interlocking on the adhesion strength of metal-polymer interfaces. Mechanical interlocking was obtained by creating craters and pores in rough metal for penetrating the polymer into these craters and pores. The results showed that the amount of molecular dissipation of the polymer was determined by the interface geometry of the metal-polymer bonding, thus the adhesion strength of a metal-polymer interface was controlled by the interaction of the two principal adhesion mechanisms, the adsorption and mechanical interlocking.

From the literature survey, there is not any information about the micro-hole configurations on the CFRP surfaces for mechanical interlocking. This study focuses about the effect of the micro-holes which are created on the CFRP surfaces on the adhesive bonding of CFRP composites. Four different micro-hole configurations (functional 309 micro-holes, 309 micro-holes, 625 micro-holes and 914 micro-holes) were applied on CFRP surfaces by CO_2 laser. After micro-holes are created for mechanical interlocking between CFRP samples, adhesive paste was applied to obtain the adhesive bonding. Single lap shear tests were done and the effect of micro-hole configurations on the adhesive joint shear strength of CFRP composites was examined. Also, after mechanical tests, fractured surfaces were illustrated and investigated for determining the damage mechanisms.

2. MATERIALS AND METHODS

In this study, unidirectional carbon fiber reinforced epoxy composite $[0]_{16}$ laminates (CFRP) were used. Before adhesive bonding, mechanical interlocking with micro-holes on the surface of CFRP was performed using pulsed CO_2 laser of 200 W maximum power. This laser operates 10.6 μm wavelength with pulse duration in range of 5-400 □s and repetition rate range between 5 kHz and 100 kHz. To deflect the laser beam a galvanometric system was used together with a 160 mm focal length F-Theta lens to focus the laser beam. Four different micro-hole configurations were selected as functional 309, 309, 625 and 914 and illustrated in Fig.1.

For creating all of the micro-hole configurations, 380 □m length of lines were created through the fiber directions due to the heat affected zone of epoxy matrix and the interface regions. For optimum depth of micro-holes, CO_2 laser was used 20 repetitions at the same surface of CFRP with 38 W laser power. The optimum micro-hole depth was approximately 100 □m. In addition, the width of the micro-holes was nearly 250 □m. The effect of the micro-hole configurations on the bonding strength of CFRP/CFRP adhesive bonding was investigated by using a lap shear strength test with ASTM D5868-01 standard. The samples were prepared according to ASTM D5868-01 standard (1.8 mm thick, 101mm x 25.4 mm dimensions). Epoxy based paste adhesive (Loctite EA 9396 AERO) was used. Curing temperature was 66 °C with curing duration as 60 minutes in an oven. Bondline thickness was selected as 50 □m. In order to obtain statistical results, five samples were prepared for each micro-hole configurations and average values were given.

Beside this, for determining the effect of the micro-hole configurations on the adhesive shear strength of CFRP/CFRP composites, adhesive shear strengths of both abraded and fully laser treated CFRP/CFRP composites were also given. Dartec universal test machine was used which had a capacity of 60 kN for determining the adhesive shear strength of different mechanical interlocking with micro-hole configurations at CFRP/CFRP adhesive bonding. Test speed was selected as 13 mm/min according to ASTM D5868-01 standard. After mechanical tests, digital camera was used to observe the damage mechanisms which were occurred at the surface of the CFRP/CFRP adhesive bonded samples.
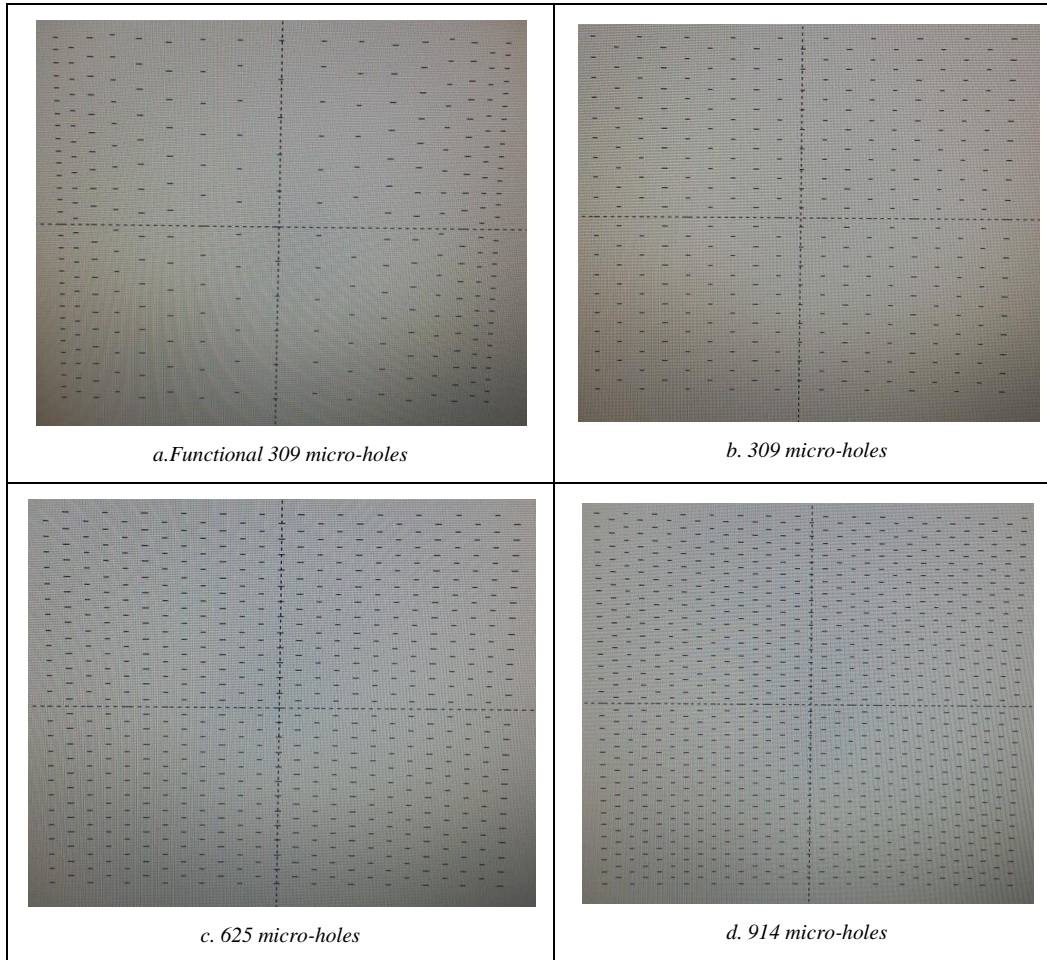
a.Functional 309 micro-holes

b. 309 micro-holes

c. 625 micro-holes

d. 914 micro-holes

Figure 1. Created micro-hole configurations on CFRP surfaces with CO_2 laser

3. RESULTS AND DISCUSSIONS

Typical geometry of the single lap joints and the application of forces during single lap shear tests are shown in Fig. 2 as stated in Ref.[8]. From Fig.2, the ideal force distribution along the bondline during single lap shear test of the CFRP/CFRP lap joint is not uniform owing to the differantial straining in the adherend. Therefore, the test gives a mean shear stress at failure or ''load divided by bond area''. It has long been recognized that the average shear stress bears little relationship to what is actually happening in the joint [10].
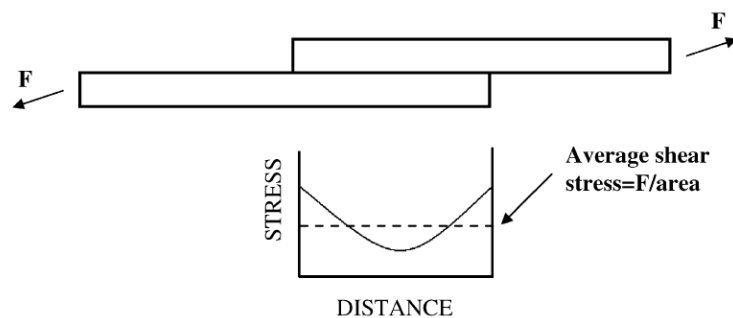

Figure 2. Typical single lap CFRP/CFRP sample geometry and force distribution during single lap shear test [8]

According Fig.2, the shear stresses concentrate at the edges of the adhesive bonding. By this way, more micro-holes are located at the edges of the CFRP/CFRP adhesive bonding as similar the curve of shear stress distribution which is stated in Fig.2 in this study (Fig.1-a). This type of micro-hole configuration is the functional 309 micro-holes. On the other hand, only the number of micro-holes is changed at the other three micro-hole configurations (309, 625 and 914) (Fig.1-b,c and d). By this way, the effect of micro-holes

number on the adhesive bonding strength of CFRP/CFRP adhesive bonding is also determined. Fig.3 shows the variation of adhesive joint shear strength due to the micro-hole configurations. From Fig.3, it is easily shown that mechanical interlocking with functional 309 micro-holes is provided. Beside this, it is thought that at higher micro-holes such as 914 micro-holes, shear strength values is decreased due to the reduction of adhesion area.
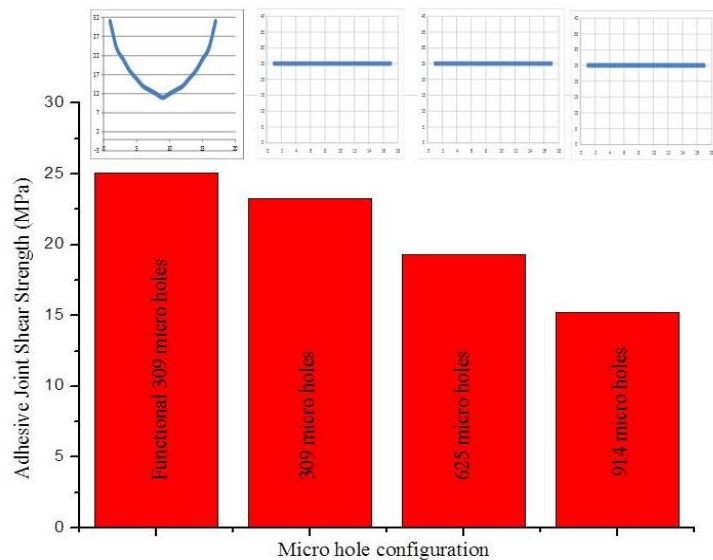

Figure 3. Variation of CFRP/CFRP adhesive joint shear strength due to the micro-hole configurations

For determining the existence of mechanical interlocking at CFRP/CFRP adhesive bonding, the adhesive shear strength of functional 309 micro-hole configurated CFRP/CFRP samples is compared to both abraded and fully laser treated CFRP/CFRP adhesive bonded samples. Fig.4 shows the variation of adhesive joint shear strengths according to surface treatment types. It is determined that the CFRP/CFRP adhesive bonded samples which include functional 309 micro-holes have the maximum shear strength values. By creating micro-holes with CO_2 laser, mechanical interlocking is increased the shear strength of the adhesive bonding. It is believed that epoxy based film adhesive fills the micro-holes and the applied shear load is damped at a higher adhesive surface area. Shear strengths of abraded sample and CO_2 laser surface treated samples are 22.72 MPa and 23.98 MPa, respectively. On the other hand, shear strength value is 25.02 MPa at CFRP/CFRP adhesive bonding with functional 309 micro-holes.
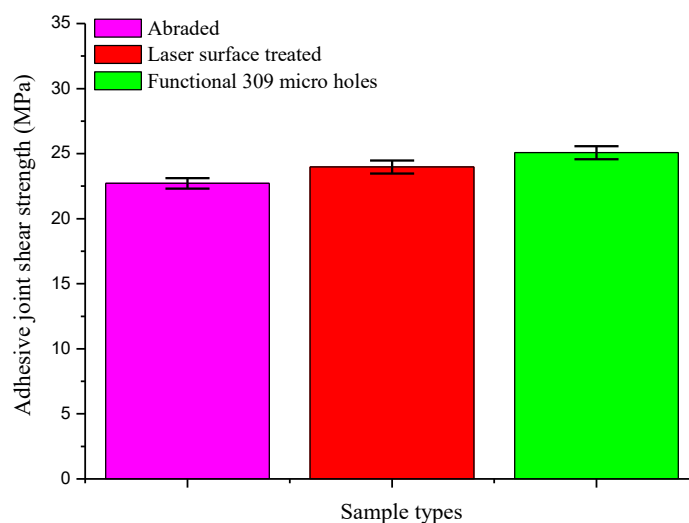

Figure 4. Variation of adhesive joint shear strengths according to surface treatment types

After single lap shear tests, digital camera observations are applied to determine the variation of damage mechanisms due to number of micro-holes and micro-hole configurations on the surface of CFRP/CFRP adhesive bondings. Fig.5 represents the fractured surfaces of CFRP/CFRP adhesive bondings. From Fig.5, the main damage mechanism is the cohesive failure for all the micro-hole configurations. But the intensity of the cohesive failure is increased by the unfilled micro-holes with the epoxy based film adhesive. On the other hand, the number of filled micro-holes is increased at functional 309 micro-holes and 309 micro-holes. The filling ratio is increased at lower number of micro-holes. Adhesive failure columns are also occurred due to the stitch regions of carbon fiber bundles. The epoxy based adhesive fills the area of stitch regions. At higher number of micro-holes, another damage mechanism is also occured as locally fiber tear failure. It is thought that if unfilled micro-holes are observed at the surface of the CFRP, the shear strength of the adhesive bonding decreases. By this way, the optimum number and the configuration is the functional 309 micro-holes. The damage mechanisms support the single lap shear test results.
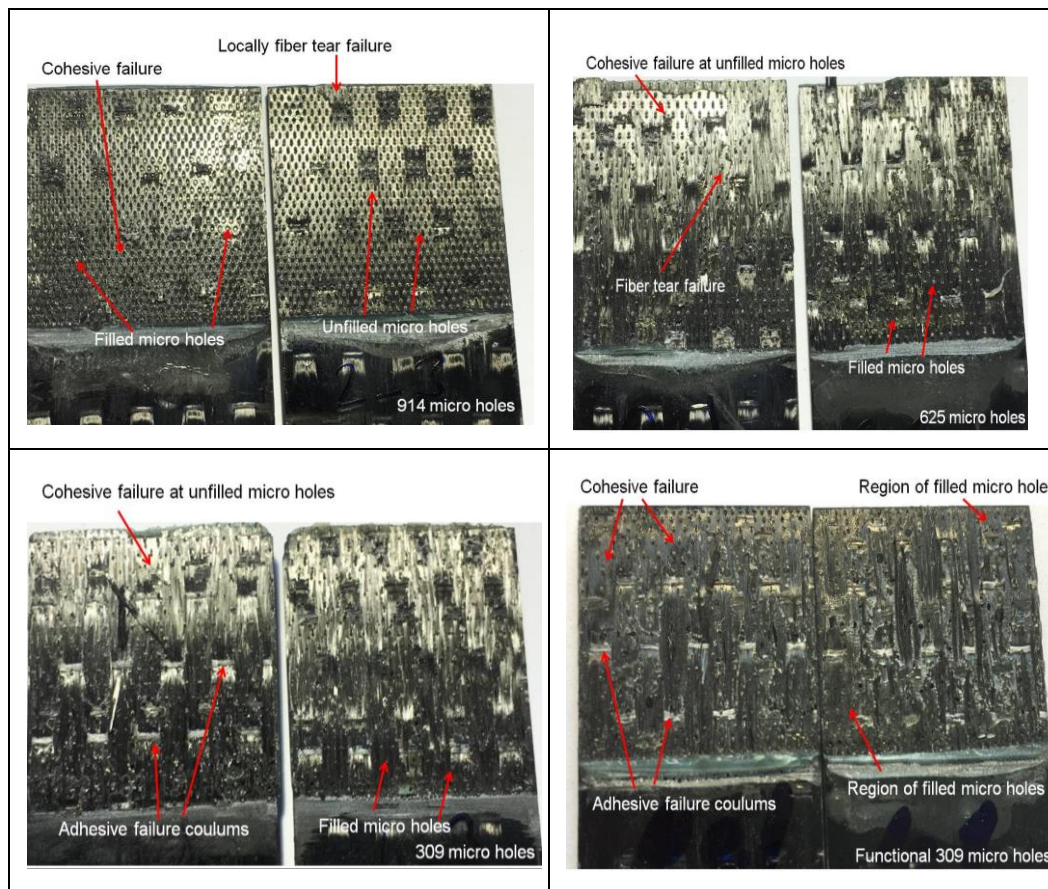

Figure 5. Damage mechanisms of various micro-hole configurated CFRP/CFRP adhesive bondings

4. CONCLUSIONS

The effect of the micro-holes configurations on the adhesive bonding of CFRP/CFRP was investigated by single lap shear tests. Obtained results are given below;

- From single lap shear tests, maximum shear strength was found as 25.02 MPa for functional 309 micro-holes. On the other hand, the shear strength values were decreased with the higher number of micro-holes at the surface of the CFRP samples.
- From digital camera observations, cohesive failure was the main damage mechanism for all the micro-hole configurations. But the intensity of this failure was increased due to the unfilled micro-holes. At higher micro-hole numbers, another damage mechanism was also found as fiber tear failure which caused the rapid reduction on the shear strength of CFRP/CFRP adhesive bonding. At last, number of filled micro-holes was increased with lower micro-hole numbers especially functional 309 micro-holes.

REFERENCES

[1] P. French, M. Naeem, A. Wolynski, and M. Sharp, "Fibre Laser Material Processing of Aerospace Composites", 339-346, 2015, [Online]. Available: http://www.spilasers.com/wp-content/uploads/2015/12/WHITE-PAPER-FIBER-LASER-MATERIAL-PROCESSING-OF-AEROSPACE-COMPOSITES.pdf

[2] H.C. Man, M. Li, and T.M. Yue, "Surface treatment of thermoplastic composites with an excimer laser", International Journal of Adhesion & Adhesives, 1998, 18, 151-157.

[3] Q. Benard, M. Fois, M. Grisel, and P. Laurens, "Surface treatment of carbon/epoxy and glass/epoxy composites with an excimer laser beam", International Journal of Adhesion & Adhesives, 2006, 26, 543–549.

[4] Sp. Pantelakis and K.I. Tserpes, "Adhesive bonding of composite aircraft structures: Challenges and recent developments", Science China Physics, Mechanics & Astronomy, 2014, 57-1, 2–11.

[5] P.N.B. Reis, J.M. Ferreira, and M.O.W. Richardson, "Effect of the Surface Preparation on PP Reinforced Glass Fiber Adhesive Lap Joints Strength", Journal of Thermoplastic Composite Materials, 2011, 25-1, 3-13.

[6] J.R.J. Wingfield, "Treatment of Composite Surfaces for Adhesive Bonding", International Journal of Adhesion and Adhesives, 1993, 13(3), 151–156.

[7] G. Wachinger, C. Thum, L. Llopart, A. Maier, H. Wehlan, and T. Stoven, "New trends in CFRP treatment and surface monitoring for automated structural adhesive bonding", In: Proceedings of ICCM-17, 17th International Conference on Composite Materials, 2009, 27-31.

[8] E.G. Baburaj, D. Starikov, J. Evans, G.A. Shafeev, and A. Bensaoula, "Enhancement of adhesive joint strength by laser surface modification", International Journal of Adhesion & Adhesives, 2007, 27, 268–276.

[9] Kim, W. S.; Lee, J. J. Interfacial fracture toughness measurement and improvement for composite/metal interfaces. KAIST, Korea.

[10] R.D. Adams, "Testing of bonded joints", In: Sadek MM, editor. Industrial applications of adhesive bonding. Amsterdam: Elsevier Applied Science, 1987, p. 80.

Design of an Adaptive Sliding Mode Controller with Optimal Coefficients and without Chattering for Coupled *Tanks System*

Metin Demirtas[1], Haris Calgan[2]*, Erdem Ilten[3]

Abstract

Sliding mode control is a non-linear control method. The method varies the dynamics of a nonlinear system by application of a high-frequency switching control. The structure of the control law changes according to the position of the state trajectory. The aim of this study is to design an adaptive sliding mode controller without chattering for liquid level control of coupled tanks system. Because, chattering problem in sliding mode control is one of the most important arguments in real-time applications. The goal is to obtain a robust adaptive sliding mode controller with respect to parameter variations and external disturbances. The sliding surface slope (λ) and the adaptation coefficient (α) of the controller is optimized by using Response Surface Methodology. Chattering of the control input in classical sliding mode control is eliminated by using adaptive control method. The effectiveness of the proposed controller is confirmed by the simulations of the dynamic model of the system by using LabVIEW software. The obtained results indicate that the chattering is eliminated.

Keywords: *Adaptive Sliding Mode Control, Level Control, Response Surface Method, Coupled Tanks System, LabVIEW, Chattering Problem*

1. INTRODUCTION

Liquids used in industrial systems often need to be transferred in the required amounts between storage tanks. To keep the amount or the liquid level in a storage tank at a desired value is one of the most requested features in such systems. In the case where the second tank's level cannot reaches the desired level, liquid flow from the first tank must be provided manually. Coupled tank system is an important plant model used for the representation of the fundamental problems that occur in this sector [1, 2]. Moreover, this model is an essential tool for performance analysis of designed control method.

An ideal Sliding Mode Controller (SMC) has a discrete switching function that holds the system on predefined sliding surface. In practice, this imperfect switching enhances undesired chattering problem which is the biggest drawback of SMC [3]. In literature, many researches have studied in order to avoid chattering problem of SMC. In reference [4], authors inspired by the classical bang-bang optimal control strategy and use second-order sliding mode controller to avoid of chattering. In reference [5], authors using discrete-time variable structure control systems ensure that the sliding motion is reached in finite time and chattering is eliminated. In reference [6], authors intend to use of sliding mode control for active and reactive power of double fed induction generator without chattering. Adaptive Sliding Mode Control (ASMC) can be convenient to resolve the chattering problem. Reaching the optimal value of the adaptation coefficient can increase tracking sensitivity.

Response surface methodology (RSM) is used for developing and optimization of complex processes by both statistical and mathematical techniques in common [7]. Evaluating multiple parameters and their interactions can be done by RSM with less number of experimental trials. Therefore, it is one of the most effective and precise method among many approaches [8, 9]. It is widely used in optimizing of tuning parameters of control systems [10, 11].

In this paper, liquid level control of nonlinear coupled tanks system with uncertain parameters is discussed. ASMC technique is handled with optimized adaptation coefficients by RSM in order to achieve accuracy of

---

[2]* *Corresponding author: Balikesir University, Department of Electrical-Electronics Engineering,Balikesir/Turkey .* *haris.calgan@balikesir.edu.tr*

[1,2,3] *Balikesir University, Department of Electrical-Electronics Engineering,Balikesir/Turkey.*

level tracking and to obtain low chattering. Evaluation of proposed control technique is carried out by creating LabVIEW simulation environment. In the second section, mathematical model of coupled tanks system is obtained. In the third section, Standard Sliding Mode Controller (SSMC) is designed. Fourth section includes operation of ASMC with optimized coefficients by RSM. Fifth section is information that includes simulation results. The obtained results are given in conclusion section.

2. DYNAMIC MODEL OF COUPLED TANKS SYSTEM

Coupled Tanks System as shown in Figure 1 consists of two cylindrical tanks connecting each other through an inner orifice. There is a variable speed inlet pump connected to first tank and supplements liquid. Coupling orifice allows the flow the liquid between two tanks. Furthermore, second tank has an outlet orifice that allows the flow of liquid out of the system. The aim of the control system is to maintain liquid level of the second tank $h_2(t)$ at the desired level h_{ref} by controlling the liquid replenishment speed of the first tank $q(t)$. Here, one of the most important point is that the pump of the first tank has the lack of an authority as to pump fluid out. Moreover, liquid flowing out of the second tank is entirely dependent on liquid pressure [12].
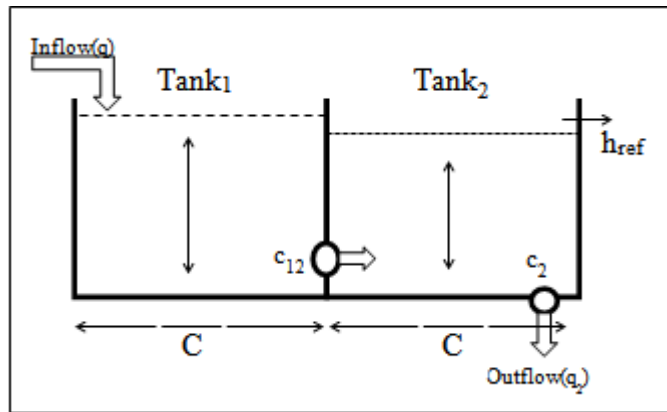

Figure 1. Model of coupled tank system

If input flow rate is chosen as input (q) and liquid level of Tank$_2$ is chosen as output (h_2), system can be described as Single Input Single Output (SISO). In this case, coupled tanks system can be modelled as:

$$\dot{h}_1 = -\frac{c_{12}}{C}\,\mathrm{sgn}(h_1 - h_2)\sqrt{2g\,|h_1 - h_2|} + \frac{q}{C} \tag{1}$$

$$\dot{h}_2 = \frac{c_{12}}{C}\,\mathrm{sgn}(h_1 - h_2)\sqrt{2g\,|h_1 - h_2|} - \frac{c_2}{C}\sqrt{2gh_2} \tag{2}$$

At equilibrium, in order to get constant liquid level set point, the derivate must be zero, i.e;

$$\dot{h}_1 = \dot{h}_2 = 0 \tag{3}$$

Hence, at equilibrium, from (1) and (2) following algebraic equations are obtained by using (3):

$$-k_1 sgn(h_1 - h_2)\sqrt{|h_1 - h_2|} + \frac{q}{C} = 0 \tag{4}$$

$$k_1 sgn(h_1 - h_2)\sqrt{|h_1 - h_2|} - k_2\sqrt{h_2} = 0 \tag{5}$$

Where the parameters k_1 and k_2 are defined by

$$k_1 = \frac{c_{12}\sqrt{2g}}{C}$$

$$k_2 = \frac{c_2\sqrt{2g}}{C} \tag{6}$$

From eq. (5) and (6), $k_1 sgn(h_1 - h_2) \geq 0$ should have been provided and $h_1 \geq h_2$ must be hold in order to satisfy the constraint $q \geq 0$. The output of the coupled tanks system is taken as the level of Tank$_2$. Therefore, according to this constraint, from (1), (2), (3), (4) and (5) dynamic model can be written as

$$\frac{dh_1}{dt} = k_1 \sqrt{h_1 - h_2} - k_2 \sqrt{h_2}$$

$$\frac{d(h_1 - h_2)}{dt} = k_2 \sqrt{h_2} - 2k_1 \sqrt{h_1 - h_2} + \frac{q}{C} \tag{7}$$

$$y = h_2$$

Applying the following conversion,

$$x_1 = h_2$$

$$x_2 = -k_2 \sqrt{h_2} + k_1 \sqrt{h_1 - h_2} \tag{8}$$

Specified in eq. (8) is written as follows:

$$\dot{x}_1 = x_2$$

$$\dot{x}_2 = f + bu \tag{9}$$

$$y = x_1$$

f and b in eq. (9) can be written as following form by using (1), (2), (8):

$$f = \frac{k_1 k_2}{2} \left(\frac{\sqrt{h_2}}{\sqrt{h_1 - h_2}} - \frac{\sqrt{h_1 - h_2}}{\sqrt{h_2}} \right) + \frac{k_2^2}{2} - k_1^2$$

$$b = \frac{k_1}{2C} \frac{1}{\sqrt{h_1 - h_2}} \tag{10}$$

3. SLIDING MODE CONTROL

The main idea of sliding mode control, in Figure 2, is firstly to force the states of the system to the previously selected area, and secondly, the system has to be kept in this region by properly designed control signal [1].

Determining the sliding surface of system given by Slotine and Li is the first step of designing controller. The form of general equation of sliding surface is given by [13]:

$$S(x) = (\frac{d}{dt} + \lambda)^{n-1} \cdot e \tag{11}$$

where desired output value is (h$_{ref}$), tracking error is (e), the order of the system is (n) and slope of sliding surface (λ) is positive. First order (n=2) sliding function presented in (12).
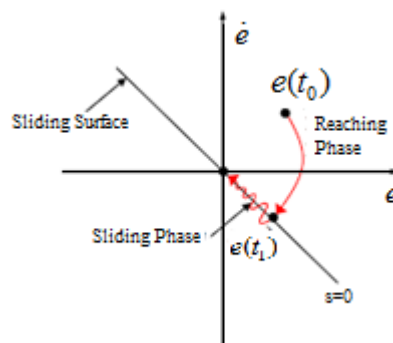

Figure 2. Principle of SMC

$$S = \dot{e} + \lambda e \tag{12}$$

$\lambda > 0$ denotes the slope of sliding surface, and tracking error (e) is obtained from $e = h_2 - h_{ref}$.

Sliding surface equations of desired coupled tanks system from (12) yields

$$s = \dot{e} + \lambda(h_2 - h_{ref}) \tag{13}$$

After obtaining sliding surface equation, the control law has to be defined by relation (14) which forces system to reach the reference point.

$$U(t) = U_0(t) + U_s(t) \tag{14}$$

U_0 is the continuous part and the equivalent control signal of SMC law. On the other hand, U_s is the switching control term effected by plant parameter variations and external disturbance. The continuous part of control signal $U_0(t)$ is calculated by equalizing the derivation of sliding surface eq. (11), (12) and (14) to the zero ($\dot{s} = 0$) presented in following form,

$$\dot{s} = \frac{k_1 k_2}{2}\left(\frac{\sqrt{h_2}}{\sqrt{h_1 - h_2}} - \frac{\sqrt{h_1 - h_2}}{\sqrt{h_2}}\right) + \frac{k_1^2}{2} - k_2^2 + \frac{k_2}{2C}\frac{1}{\sqrt{h_1 - h_2}}u + \lambda\left(-k_2\sqrt{h_2} + k_1\sqrt{h_1 - h_2}\right) \tag{15}$$

when $\dot{s} = 0$ and $u = U_0$ presented in following form;

$$U_0 = \frac{2C\sqrt{h_1 - h_2}}{k_2}\left[\begin{array}{c} -\dfrac{k_1 k_2}{2}\left(\dfrac{\sqrt{h_2}}{\sqrt{h_1 - h_2}} - \dfrac{\sqrt{h_1 - h_2}}{\sqrt{h_2}}\right) - \dfrac{k_1^2}{2} \\ -k_2^2 - \lambda\left(-k_2\sqrt{h_2} + k_1\sqrt{h_1 - h_2}\right) \end{array}\right] \tag{16}$$

The expression of U_0 is the function of output value h_2:

$$U_0(t) = f(h_1, h_2) \tag{17}$$

Discontinuous part U_s is switching term of control law and keeps the system around sliding surface presented in following equation,

$$U_s(t) = \beta sgn(s) \tag{18}$$

β is strictly positive constant. And signum function is defined as

$$sgn(s) = \begin{cases} +1 \text{ if s>0} \\ 0 \text{ if s=0} \\ -1 \text{ if s<0} \end{cases} \tag{19}$$

According to (15), (16) and (18), the control signal U(t) is calculated as

$$U(t) = \frac{2C\sqrt{h_1 - h_2}}{k_1}\left[\begin{array}{c} -\dfrac{k_1 k_2}{2}\left(\dfrac{\sqrt{h_2}}{\sqrt{h_1 - h_2}} - \dfrac{\sqrt{h_1 - h_2}}{\sqrt{h_2}}\right) - \dfrac{k_2^2}{2} \\ +k_1^2 - \lambda\left(-k_2\sqrt{h_2} + k_1\sqrt{h_1 - h_2}\right) \end{array}\right] + \beta\, sgn(s) \tag{20}$$

Chattering problem emerges in SSMC. ASMC method is one of the most popular technique which can accomplish the chattering problem is explained in the following section.

4. ADAPTIVE SLIDING MODE CONTROL METHOD

The main feature of SMC is the robustness against the parameter variations and external disturbances. Optimal value of β , in Standard SMC formula (19) and (20), cannot be achieved easily. Hence, in this section, the coefficient of the ASMC is adaptively adjusted.

When the modified control law is considered as $U_a(t)=U_{a0}(t)+U_{as}(t)$, which continuous part $U_{a0}(t)$ equals to $U_0(t)$, adaptive switching control term $U_{as}(t)$ can be arranged as,

$$U_{as}(t) = \eta\, sgn(s) \tag{21}$$

η denotes the adjustable positive gain and when the adaptation coefficient($\alpha > 0$), it is modified as;

$$\eta = \frac{1}{\alpha}|s|$$

(22)

The adaptation factor of η is adjusted by adaptation coefficient α which is strictly positive constant. Optimum α value ensures to avoid high frequency signals from the control input during the reaching reference point.

4.1. Optimization of λ and α Parameters with Response Surface Method

In this paper, RSM is applied for identifying the best combination of experimental parameters to get precise tracking performance. Experimental design of RSM by using Minitab program is carried out in order to optimize of adaptation coefficient α and sliding surface slope λ as shown in Figure 6.

↓	C1	C2	C3	C4
	λ	α	SettlingTime	Overshoot(%)
1	0,1	0,001	96	0
2	0,3	0,001	85	31
3	0,1	0,003	106	0
4	0,3	0,003	99	0
5	0,1	0,002	107	0
6	0,3	0,002	92	4
7	0,2	0,001	89	4
8	0,2	0,003	110	0
9	0,2	0,002	93	0

Figure 3. Experimental Design on Minitab

According to Experimental Design and RSM, application of the central composite design reduces the number of required experiments to 9. Optimum λ and α values are obtained 0.2051 and 0.0014 by using RSM. Effects of λ and α values to the system are shown in Figure 7, graphically. This graphic includes minimum and maximum values of λ and α, which is investigated during the experimental design. On the other hand, desired settling time and overshoot are given 0 second and 0%, respectively. d values on the graph shows the achievement in percent while getting that desired values.
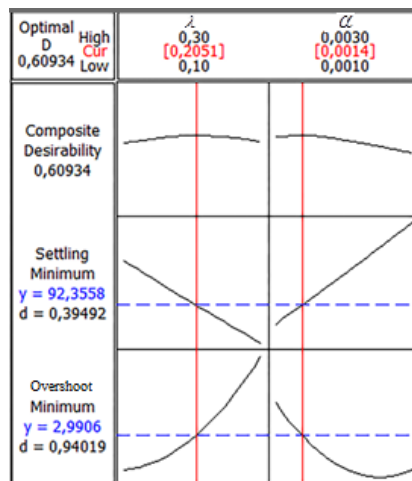

Figure 4. Response Surface Optimization Plot

5. SIMULATION RESULTS

Proposed control technique is performed on Coupled Tanks System which is simulated on LabVIEW. The results are given in the following graphs.

Values of plant parameters are given in Table 1 according to dynamic model of the Coupled Tanks System [14].

Table 51.Values of Plant Parameters

Parameter	Value
g	981 cm/s^2
C	208.2 cm^2
c_{12}	0.58 cm^2
c_2	0.24 cm^2
h_{ref}	5 cm

The input saturation $0\ cm^3/s \leq u \leq 50\ cm^3/s$ is used in the simulation to ensure value that the control signal always remains within the bound. The liquid level in the Tank$_2$ is the output signal y(t)=h$_2$(t) and the inflow to the Tank$_1$ is the control signal of coupled tanks system.

Parameters of SSMC λ and β values are adjusted to 0.045 and 15, respectively. λ and α parameters of ASMC are calculated 0.2051 and 0.0014 by using RSM, respectively (Figure 4). During the controlling liquid level of Tank$_2$, various unexpected external disturbances may affect the system. Under the stability, in order to show the response of both control technique against to that disturbances, experiments are carried out. At the 143th second, an amount of liquid was released from Tank$_2$, and at the 237th second some of the liquid was added. Figure 5 shows the control input signals comparison of each technique; also output signals are shown in Figure 6.
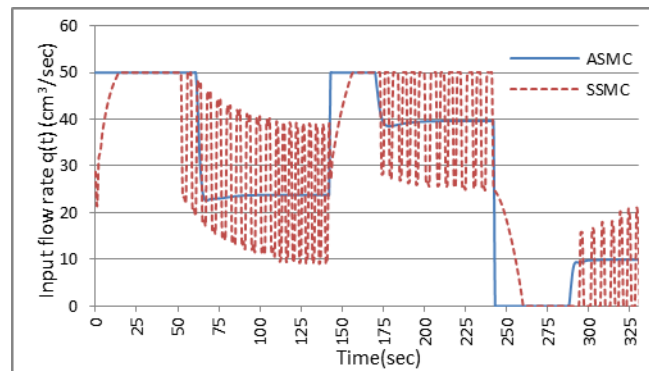

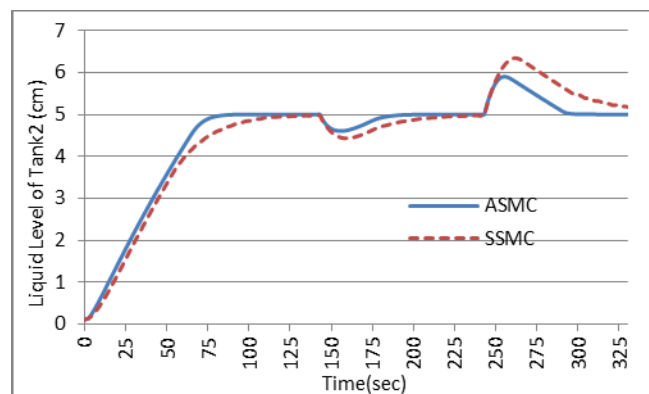*Figure 5. Input flow rate to Tank$_1$ under disturbances*

Figure 6. Liquid level in Tank$_2$ under disturbances

As shown in Figure 5, disturbance added to the system at 138th second and removed at 238th second. ASMC shows faster reaction against external disturbances. After the adding liquid to Tank$_2$ at the 238th second, SSMC reaches to reference value in 96 seconds. On the other hand, behavior of ASMC seems more sensitive. It reaches reference value in 54 seconds.
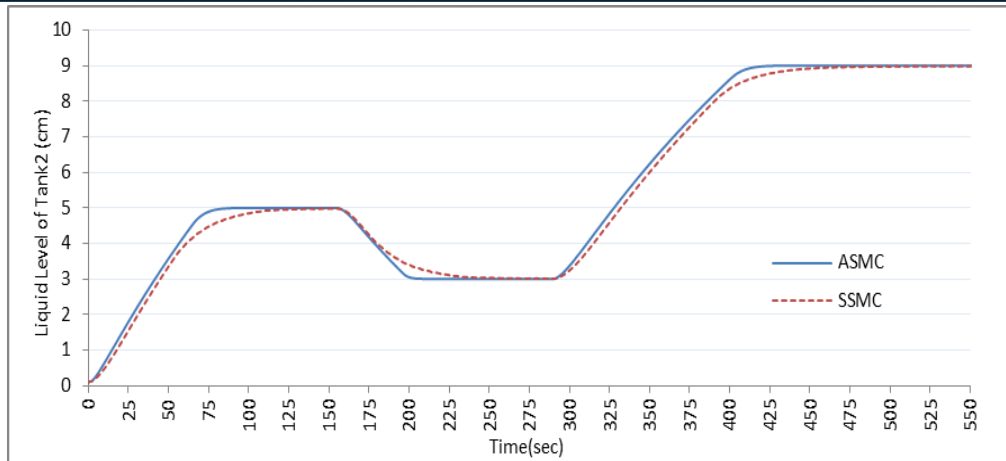
Figure 7. Liquid Level in Tank₂ in case of changing the desired reference

Desired reference liquid level value of Tank$_2$ has to be appropriate to set in industry. Therefore, the response of the controller in such cases must react quickly and effectively. Figure 7 shows the output signal of the system in case of decreasing reference level to 3 cm at the 153th second and increasing reference to 9 cm at the 287th second. Both control techniques' responses are illustrated. Fig. 8 shows the control signal of both techniques in the same case.
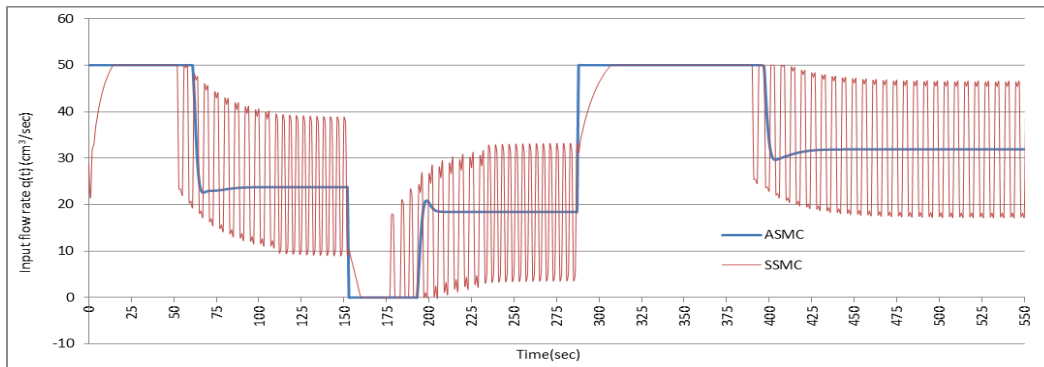

Figure 8. Input flow rate to Tank₁ in case of changing the desired reference

6. CONCLUSION

In this study, robust control design for coupled tanks system is investigated. The main objective is to propose an effective control method for elimination of chattering problem. On the other hand, tracking capacity is developed via optimization of parameters. Firstly, Standard Sliding Mode approach is used and linear sliding surface is presented. After that Adaptive SMC method is developed and adaptation parameters are optimized by using Response Surface Method. Furthermore, the performances of ASMC and SSMC are compared. Simulation results prove that ASMC has much better performance. Chattering problem substantially decreases by using Adaptive Sliding Mode Control as shown in Figure 5 and Figure 8.

ACKNOWLEDGMENT

REFERENCES

[1]. H. Abbas, S. Asghar, and S. Qamar, "Sliding mode control for coupled-tank liquid level control system," in Proc. 10th Int. Conf. FIT, Dec. 2012, pp. 325–330.

[2]. Cartes, David, and Lei Wu. "Experimental evaluation of adaptive three-tank level control." ISA transactions 44.2 (2005): 283-293.

[3]. Demirtas, Metin. "DSP-based sliding mode speed control of induction motor using neuro-genetic structure." Expert Systems with Applications 36.3 (2009): 5533-5540.

[4]. Bartolini, G., A. Ferrara, and E. Usani. "Chattering avoidance by second-order sliding mode control." IEEE transactions on Automatic Control 43.2 (1998): 241-246.

[5]. Golo, Goran, and Čedomir Milosavljević. "Robust discrete-time chattering free sliding mode control." Systems & Control Letters 41.1 (2000): 19-28.

[6]. CALGAN, Haris, and Metin DEMİRTAS. "An Adaptive Sliding Mode Controller Design for DFIG based Wind Turbine System on LabVIEW." (2016).

[7]. Sakar, Selcuk, et al. "Optimal design of single-tuned passive filters using response surface methodology." 2015 International School on Nonsinusoidal Currents and Compensation (ISNCC). IEEE, 2015.

[8]. Balci, Murat Erhan, and Aslan Deniz Karaoglan. "Optimal design of C-type passive filters based on response surface methodology for typical industrial power systems." Electric Power Components and Systems 41.7 (2013): 653-668.

[9]. Ilten, Erdem, and Metin Demirtas. "Off-Line Tuning of Fractional Order PI? Controller by Using Response Surface Method for Induction Motor Speed Control." Journal of Control Engineering and Applied Informatics 18.2 (2016): 20-27.

[10]. Ustun, Seydi Vakkas, and Metin Demirtas. "Optimal tuning of PI coefficients by using fuzzy-genetic for V/f controlled induction motor." Expert Systems with Applications 34.4 (2008): 2714-2720.

[11]. İskender, Beyza Billur, Necati Ozdemir, and Aslan Deniz Karaoglan. "Parameter Optimization of Fractional Order PI λ D μ Controller Using Response Surface Methodology." Discontinuity and Complexity in Nonlinear Physical Systems. Springer International Publishing, 2014. 91-105.

[12]. Alam M.T., Charam P., Alam Q., Purwar S., "Sliding Mode Control of Coupled Tanks System: Theory and an Application'' International Journal of Emerging Technology and Advanced Engineering, Vol. 3, No. 8, 2013, pp. 650-656.

[13]. Slotine, Jean-Jacques E. "Sliding controller design for non-linear systems." International Journal of control 40.2 (1984): 421-434.)

[14]. Almutairi, Naif B., and Mohamed Zribi. "Sliding mode control of coupled tanks."Mechatronics 16.7 (2006): 427-441.

Capacitive Power and Torque Estimation for Self-Excited Induction Generator with Elman Neural Network

Haris Calgan [1], Metin Demirtas [2], Murat Erhan Balci [2]

Abstract

This paper presents an attempt to estimate the excitation capacitive reactive power and torque requirements of Self Excited Induction Generator (SEIG) for maintaining under variable balanced resistive-inductive loading conditions using Elman Neural Network (ENN). Sets of data to train ENN and test data are obtained by using the well-known d-q model of induction machine in MATLAB/Simulink environment. After training, estimated power of the balanced excitation capacitor bank and the mechanical torque applied to the rotor shaft, which should maintain the desired frequency and magnitude of the SEIG's terminal voltage, are tested under various balanced loading conditions. The test results figure out that ENN can successfully be used as a tool for determination of the required excitation capacitor power and rotor shaft torque.

Keywords: *Elman neural network, SEIG, Capacitive reactive power*

1. INTRODUCTION

Self-excited induction generators have several advantages over traditional synchronous generators such as brushless construction (for squirrel-cage type induction generator), reduced size, reduced maintenance cost, good over-speed and short circuit protection capabilities, non-required synchronizing equipment and better transient performance [1], [2]. Due to these advantages, SEIGs can be employed with conventional energy sources as well as renewable energy sources (biogas, wind, small hydro heads...etc) in semi-isolated and isolated power systems. For self-excitation, the rotor of SEIG should be operated over synchronous speed, and a reactive power source should be connected across its stator terminals. For a reactive power source of SEIG, the switchable capacitor bank is widely preferred since it has the lowest cost and does not require complex control algorithms when compared to other reactive power compensators based on power electronic circuits [3].

The initiation of the excitation in the induction generator can be interpreted as a response of the resonant circuit, which consists of the generator and the capacitor bank connected to its terminals, and the magnitude and frequency of the voltage produced by SEIG depends on mechanical torque applied to its rotor shaft (or rotor speed), its loading ratio and the size of excitation capacitor bank [4]. Accordingly, under variable speed and loading conditions, the effective utilization of a SEIG require continuous optimization or adjustment of excitation capacitors to maintain an acceptable load voltage profile.

The per-phase steady state equivalent circuit of the SEIG is commonly considered as a model to calculate the minimum size of the capacitance [2], [5], [6], and it is analyzed by means of two different ways as the loop impedance [7]-[11] and nodal admittance [12]-[16] methods. Due to the fact that both methods need good initial guess, selection of proper search space and solution of nonlinear equations related with the real and imaginary parts of the loop impedance or nodal admittance, they are considerably time consuming. Therefore, in [17]-[19], genetic, particle swarm and artificial bee colony algorithms are implemented for time-efficient solution of the nonlinear equations in both approach.

In [20], the d-q model based method is used to provide a characteristic equation of operational impedance matrix of the SEIG, and the required excitation capacity is found by solving the characteristic equation. In [21], a minimum air-gap flux linkage is required to provide self-excitation, and the minimum value of

[1] *Corresponding author: Balikesir University, Department of Electrical-Electronics Engineering, Balikesir/Turkey . haris.calgan@balikesir.edu.tr*

[2,3] *Balikesir University, Department of Electrical-Electronics Engineering, Balikesir/Turkey*

excitation capacitance is found from the minimum air-gap flux linkage. In [22], [23], eigen value and eigen sensitivity based iterative technique combined with the d-q model of the induction machine is implemented to estimate the dynamic behavior and minimum/maximum capacitance requirement of SEIG.

On the other side, in [24], cascaded artificial neural networks (ANN) technique is implemented to analyze the steady state behavior of SEIG with varying terminal capacitance at rated speed with constant resistive load, and in [25] multilayer perceptron (MLP) ANN technique is implemented to estimate the excitation capacitance requirements to maintain constant airgap voltage of SEIG. Neural networks using in [24, 25] are static feedforward neural network type. The Elman neural network is a type of recurrent network model with a set of context nodes to store the internal states [26]. Therefore, ENN has certain dynamic characteristics over static neural network, such as MLP. On the basis of this advantage, it is widely used in adaptive control [27], systems identification [28] and prediction [29].

In this paper, under balanced variable loading conditions, the capacitive VAR and mechanical torque requirements of SEIG are estimated by using Elman neural network (ENN). Frequency and phase-to-phase rms value of the terminal voltage and active and reactive powers drawn by the supplied load are considered as inputs of ENN. The excitation capacitive reactive power and the rotor shaft torque, which are required to maintain the desired voltage and frequency regulation under the studied loading condition, are handled as outputs of ENN. The well-known d–q axis model of the induction machine is used to simulate SEIG suppling balanced resistive-inductive load in the MATLAB/Simulink environment, and the simulation results are obtained for training and testing of ENN. The test results show that proposed ENN based method can successfully be used as a tool for estimation of the required excitation capacitance power and rotor shaft torque values.

2. MODELLING OF SEIG

As mentioned in the introduction section, frequency (f) and phase-to-phase rms value (V_{eff}) of the terminal voltage generated by the SEIG vary with per rotor speed (w_r), power of excitation capacitance (Q_c), active and reactive powers drawn by the supplied load (P_L and Q_L) and the mechanical torque applied to the rotor shaft (T_m). In this study, f, V_{eff}, P_L and Q_L are considered as inputs of ENN. The Q_c and T_m values, which are required to maintain the desired voltage and frequency regulation under the studied loading condition, are handled as outputs of ENN. To provide the relations among these parameters via ENN, the training and test system will be provided in Matlab/Simulink environment, which is shown in Figure 1. The same figure shows that the system has the d-q model of the SEIG, the balanced excitation capacitor bank, the balanced three-phase variable load and measurement block used to collect the measurements of the torque applied to the rotor shaft, the powers drawn by the load and the capacity and the terminal phase-to-phase voltages.
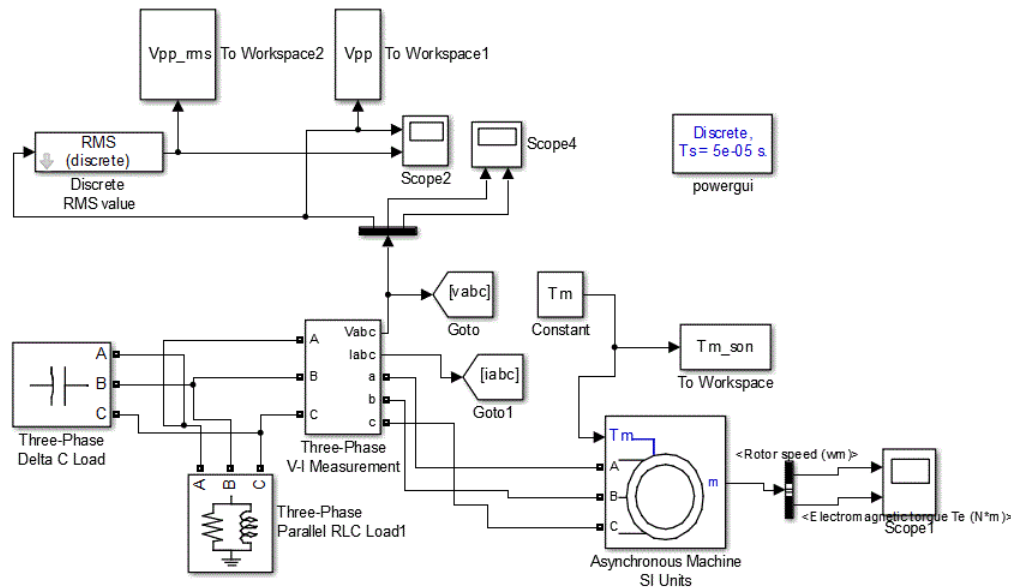
Figure 1. Simulink model of SEIG

Figure 2 shows ENN studied in this paper. It includes input layer with 4 inputs, hidden layer with 10 neurons and output layer with 3 neurons. It also has a feedback from output of the hidden layer to input of the hidden layer with context nodes. This feedback is useful for expressing nonlinear relations of the considered parameters of the SEIG. Activation functions of layers are 'logsig' and 'purelin', respectively. During the

training, backpropagation of error with Levenberg-Marquardt function is used to determine sensitivity of ENN. Table I shows the constraints of the input data used for training and test. Training data constraints are chosen according to used 4 kW induction machine. Minimum power factor is determined as 0.8 and inductive reactive power is chosen randomly according to determined power factor. Necessity capacitive reactive power is taken between 2500-5000 VAr. After training, to see the reliability of trained neural network, sets of test data are observed by using randomly inputs. Totally, 462 sets of training data and 40 sets of test data are obtained from simulation. During the training procedure, mean square errors reduce to 0.0013639 by 5000 iteration. Figure 3 shows the mean square errors of training versus iteration. It can be mentioned from Figure 3 that best training performance is reached nearly in 1500 iteration and network is trained almost perfectly.
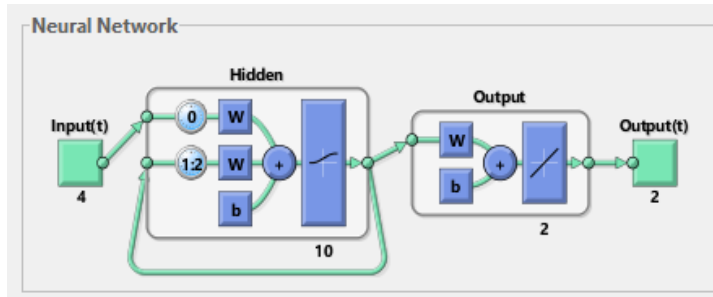

Figure 2. ENN structure

Table 52. Training data constraints

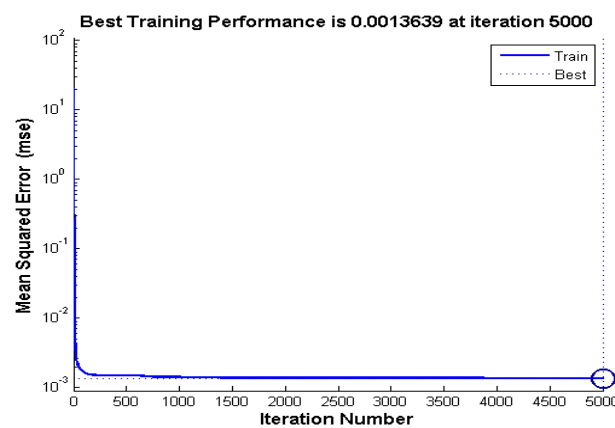| Name	Constraint	Increment
T_m (Nm)	[10,25]	3
Q_C (VAr)	[2500,5000]	250
P_L (W)	[1000,4000]	500
Q_L(VAr)	[0,3000]	Random

Figure 3. Mean square error of training procedure.

3. RESULTS AND DISCUSSION

The modeling of SEIG is tested using 40 samples of test data. Each sample includes f, V_{eff}, P_L, Q_L as ENN inputs, T_m and Q_c as ENN outputs. MATLAB/Simulink is used to obtain data and creating neural networks model. The reliability of ENN model was tested with obtained data mentioned in Section 3. For various training cases of the f, V_{eff}, P_L and Q_L, the variations of T_m and Q_c results obtained from Simulink and ENN models are shown in Figure 4 and 5. As shown in Figure 4, T_m provided by ENN and Matlab/Simulink models are very close to each other's. Figure 5 shows that the maximum value of the relative difference between Q_C values obtained by both models is well below 1%. These results point out that ENN is valid to estimate T_m and Q_c required for the maintaining of desired f and V_{eff} under the variable loading conditions. After well training of the ENN, under six different three-phase balanced load cases, it is employed to

determine T$_m$ and Q$_c$ values, which are required for maintain the terminal voltage with 400 V and 50 Hz. The results are presented in Table II.
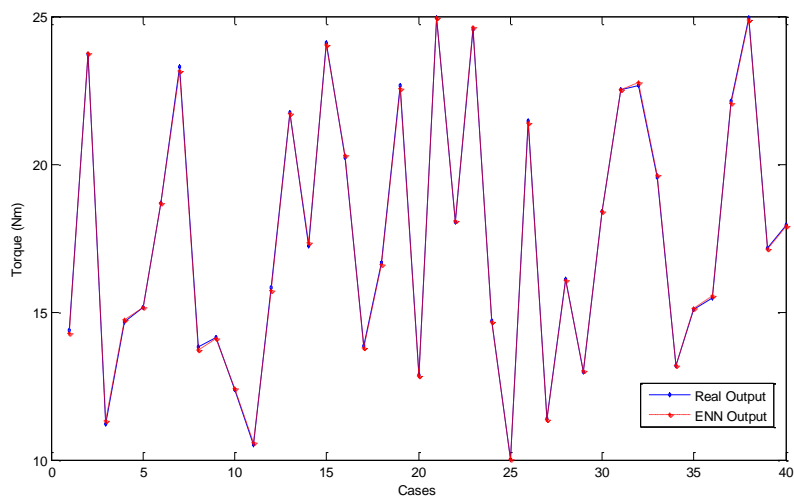
Figure 4. Variation of Torque for different load conditions.
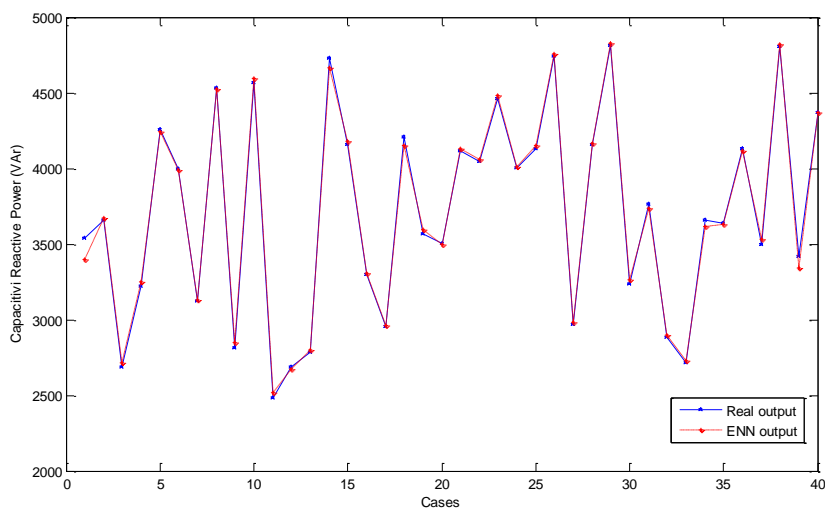
Figure 5. Capacitive reactive power change for different conditions.

Table II. Estimation of Tm and Q$_C$ with ANN.

Experiment	Desired V$_{eff}$ (V)	Desired f (Hz)	P$_L$ (W)	Q$_L$ (VAr)	Estimated Tm by ENN	Estimated Q$_c$ by ENN	Rated V$_{eff}$ (V)	Rated f (Hz)
1	400	50	3151	2061	21.66	5404	398	49.62
2	400	50	3860	1342	26.5	4753	401	50.12
3	400	50	1384	697	9.91	3689	400	49.87
4	400	50	2548	1512	17.65	4663	400	50.00
5	400	50	2971	970	20.49	4197	401	50.12
6	400	50	1652	1173	11.68	4178	401	50.13

It is clearly seen from Table II that the ENN predicts T_m and Q_c values to maintain f with the acceptable relative difference between -0.7% and 0.2%. The same table also shows that the T_m and Q_c values obtained by ENN provides V_{eff} around 400V.

4. CONCLUSION

SEIGs have various advantages such as brushless construction (for squirrel-cage type induction generator), reduced size, reduced maintenance cost, good over-speed and short circuit protection capabilities, non-required synchronizing equipment and better transient performance when compared to the traditional synchronous generators. As a results, today, they are widely employed with renewable energy sources such as biogas, wind, small hydro heads in semi-isolated and isolated power systems.

This paper employed Elman neural network (ENN) to estimate capacitive VAR requirement and rotor shaft torque of SEIG, which are required to maintain the desired voltage and frequency regulation under the variable three-phase balanced loading condition. Sets of data to train ENN and test data are obtained by using the well-known d-q model of induction machine in MATLAB/Simulink environment. Simulation results validates that ENN can successfully be used as a tool for determination of the required excitation capacitor power and rotor shaft torque values.

REFERENCES

[1]. G.K. Singh, "Self-excited induction generator research—a survey", Electric Power Systems Research, Volume 69, Issues 2–3, May 2004, Pages 107-114.

[2]. R. C. Bansal, "Three-phase self-excited induction generators: an overview," in *IEEE Transactions on Energy Conversion*, vol. 20, no. 2, pp. 292-299, June 2005.

[3]. M.H. Haque, Voltage regulation of a stand-alone induction generator using thyristor-switched capacitors, Proceedings of IEEE International Conference on Sustainable Energy Technologies, Singapore, 24–27 November (2008), pp. 44–49

[4]. E Levi, Y.W Liao, An experimental investigation of self-excitation in capacitor excited induction generators, Electric Power Systems Research, Volume 53, Issue 1, 5 January 2000, Pages 59-65

[5]. M. H. Haque, "Capacitance requirement in a three-phase SEIG under no-load and load conditions," *2012 IEEE International Conference on Power System Technology (POWERCON)*, Auckland, 2012, pp. 1-6.

[6]. Sunil Kumar Goyal, D.K. Palwalia, Analysis of performance parameters and estimation of optimum capacitance for asynchronous generator, Engineering Science and Technology, an International Journal, Volume 19, Issue 4, December 2016, Pages 1753-1762

[7]. N.H. Malik and A A Mazi, "Capacitor requirements for isolated self-excited induction generators", IEEE Trans. on Energy Conversion, Vol. 2, No. I, 1987, pp. 62-68.

[8]. A K. AI Jabri and AI. Alolah, "Capacitance requirement for isolated self-excited induction generator", IEE Proc., Part-B, Vol. 137, No. 3, 1990,pp.154-159.

[9]. B. Sawetsakulanond and V. Kinnares, "A simple approach to capacitance determination of self-excited induction generators for terminal voltage regulation", Proc. of the IEEE Power Electronics and Drive Systems Conference, pp. 1319-1327,27-30 Nov. 2007.

[10]. M.H. Haque, Comparison of steady state characteristics of shunt, short-shunt and long-shunt induction generators, Electric Power Systems Research, Volume 79, Issue 10, October 2009, Pages 1446-1453

[11]. M.F. Khan, M.R. Khan, Comprehensive analytical and experimental analysis of a self-excited induction generator for renewable energy application, Int. J. Renewable Energy Res. 5 (3) (2015) 746–756.

[12]. L. Quazene and G. Mc Pherson, "Analysis of the isolated induction generators", IEEE Trans. Power App. Syst., Vol. PA S-I 02, No.8, 1983, pp. 2793-2798.

[13]. T.F. Chan, "Capacitance requirements of self-excited induction generators", IEEE Trans. on Energy Conversion, Vol. 8, No. 2, 1993, pp.304-3II.

[14]. AM. Eltamaly, "New formula to determine the minimum capacitance required for self-excited induction generator", Proc. of the IEEE 23rd Power Electronics Specialist Conference, Vol. I, pp. 106-110, 23-27 June 2002.

[15]. Aissa Kheldoun, Larbi Refoufi, Djalal Eddine Khodja, Analysis of the self-excited induction generator steady state performance using a new efficient algorithm, Electric Power Systems Research, Volume 86, May 2012, Pages 61-67

[16]. M. Arjun, K. U. Rao and A. B. Raju, "A novel simplified approach for evaluation of performance characteristics of SEIG," *2014 International Conference on Advances in Energy Conversion Technologies (ICAECT)*, Manipal, 2014, pp. 31-36.

[17]. Y. K. Chauan, S. K. Jain, B. Singh, Genetic Algorithm-Based Optimum Performance of Compensated Self-Excited Induction Generator, International Journal of Modelling and Simulation, Vol. 31, No. 4, pp. 263-270, 2011.

[18]. Y. K. Chauhan, V. K. Yadav and B. Singh, "Optimum utilisation of self-excited induction generator," in *IET Electric Power Applications*, vol. 7, no. 9, pp. 680-692, November 2013.

[19]. D. K. Palwalia, A. K. Sharma, N. P. Patidar, G. Agnihotri, "Artificial Bee Colony Based Determination of Excitation Capacitance Requirements of Self-Excited Induction Generator", Ciência e Técnica Vitivinícola 29(6):313-336 · January 2014

[20]. C. Grantham, D. Sutanto, B. Mismail, "Steady-state and transient analysis of self-excited induction generators", IEE Proc. Part-B, Vol. 136, No.2, 1989, pp. 61-68.

[21]. O. Ojo, "Minimum airgap flux linkage requirement for self-excitation in stand-alone induction generators", IEEE Trans. on Energy Conversion, Vol. 10, No.3, 1995, pp. 484-492.

[22]. L. Wang, C.H. Lee, A novel analysis on the performance of an isolated self-excited induction generator, IEEE Trans. Energy Convers. 12 (2) (1997) 109–117.

[23]. Lee Ching-Huei, Wang Li. A novel analysis of parallel operated self-excited induction generator. IEEE Trans Energy Convers 1998; 13 (2): 117–23.

[24]. Khela, Raja Singh, et al. "Cascaded ANN for Evaluation of Frequency and Air-gap Voltage of SelfExcited Induction Generator." Inter Jour of Elect, Comp and Sys Eng 1.1 (2007): 57-63.

[25]. Khela, R.S. , Sandhu, K.S. 'ANN model for estimation of capacitance requirements to maintain constant air-gap voltage of self-excited induction generator with variable load'. International Journal of Computer Science & Technology, IJCST. 2011, 10–11, 2, 4.

[26]. Elman, Jeffrey L. "Finding structure in time." *Cognitive science* 14.2 (1990): 179-211.

[27]. Jon, Ryongho, et al. "Adaptive robust speed control based on recurrent elman neural network for sensorless PMSM servo drives." *Neurocomputing* (2016).

[28]. Gao, X. Z., X. M. Gao, and S. J. Ovaska. "A modified Elman neural network model with application to dynamical systems identification." *Systems, Man, and Cybernetics, 1996., IEEE International Conference on*. Vol. 2. IEEE, 1996.

[29]. Heydari, Azim, and Farshid Keynia. "Prediction of Wind Power Generation Through Combining Particle Swarm Optimization and Elman Neural Network (El-PSO)." *International Energy Journal* 15.2 (2015): 58-66.

Object Detection With RGB-D Data Using Depth Oriented Gradients

Erkut Arıcan[1], Tarkan Aydın[2]

Abstract

In this work, we present new descriptor for object detection using edge information and RGB-D's depth data. Histogram of Oriented Gradients algorithms is very popular for human detection and it is widely adapted in many object detection methods. Although edges include sufficient information to represent object boundaries, objects with high texture introduce edges that are incapable of describing the objects. We address this problem by including additional information from depth data obtained from RGB-D sensors readily available on the shelves. For object detection, we train and test our data using with multiclass support vector machines.

Keywords: *Histogram, Oriented, Gradients, HOG, RGB-D, Depth Data, Multiclass SVM*

1. INTRODUCTION

Nowadays, Computer vision takes a huge step thanks to technological development. As a result of these, there are many literature works about 2D object detection and recognition. There are also studies for 3D object detection.

Histogram of Oriented Gradients (HOG) [1] is very popular method for object detection. In our work, we modify HOG method. We will explain studies when we review in literature search in 2.1 and we explain our purpose in 2.2.

1.1. Literature Review

Firstly, we review edge detection methods. Mikolajczyk [2] and friends use edge-based local features and they use Scale Invariant Feature Transform (SIFT) [3] method. Other study which is using edge detection method is developed by Leordeanu [4] and friends. They use shape based object detection system. In literature, we found another study. This study developed by Ren and Li [5] and they combine HOG and edge information system.

Next step in literature search, we review some studies which are using HOG algorithm and compare their result with HOG algorithm. Shrivastava [6] and friends study to find visually similar images and they use mostly HOG algorithm. Stallkamp [7] and friends study with traffic sign. Their study includes HOG based algorithm and other algorithms at the same time determining traffic sign by humans. Malisiewicz [8] and friends' compare their study's results with other methods including Dalal's HOG algorithms.

In our work, we use RGB-D Depth Data. We search literature for RGB-D image sets and we examine 3 RGB-D datasets ([9], [10], [11]).

1.2. Purpose

In our study, our purpose is taking HOG algorithm as a base algorithm and combining RGB-D Depth data information to create a new descriptor. We use SUN3D [9] dataset to test our method.

We will continue this paper explaining basic techniques in section 2, our method in section 3 and showing test result in section 4.

---

[1] *Corresponding author: Bahcesehir University, Faculty of Engineering and Natural Sciences, Department of Computer Engineering, 34353, Besiktas/İstanbul, Turkey. erkut.arican@eng.bau.edu.tr*

[2] *Bahcesehir University, Faculty of Engineering and Natural Sciences, Department of Computer Engineering, 34353, Besiktas/İstanbul, Turkey, tarkan.aydin@eng.bau.edu.tr*

2. PROBLEM DEFINITION AND BASIC TECHNIQUES

Sometime using edge detection in RGB images, is not a good option for object detection because of the texture information on the object. When this situation is occurred object detection result will not be giving accurate output. We plan to use RGB-D Depth data for this problem and we expect to increase object detection results. In this work, we use Histogram of Oriented Gradients algorithm as a base algorithm and we do some modification on it. We combine RGB-D Depth data with HOG method and create a new descriptor. We will explain our method more detailly in section 3. Now we briefly explain HOG method.

2.1. Histogram of Oriented Gradients

In this section, we explain how to work Histogram of Oriented Gradient method simply. HOG method use some filters to extract edge information and using this information to calculate gradients. After some process and using histogram, it will create HOG descriptor.

3. METHOD

We described the problem in section 2 and our solution is combining RGB-D Depth data and HOG method. We define 4 step for our solution.

- 3D Image Dataset
- Adding Depth information to HOG algorithm
- Creating 3D Descriptor
- Learning

3.1. Image Datasets

We review 3 RGB-D image set and we select SUN3D [9] dataset to use in our project. You can see some example images from SUN3D dataset. Figure 1 shows us to RGB image and Figure 2 shows us to Depth images.

Figure 79 SUN3D Dataset RGB Image

Figure 80 SUN3D Dataset Depth Image

In SUN3D Dataset, there are many image sets taken from different places. Some image sets have got the object coordinates and label information. You can see depth image for an object from Maryland Hotel in Figure 3.

Figure 81 Depth Image for an Object

3.2. Depth Data & Histogram of Oriented Gradients

We will talk about HOG algorithm in section 2.1.

In gradient process, we have got a magnitude and direction values. We take magnitude values from RGB-D Depth image and we combine with RGB image's magnitude value. Before the combining magnitude values, we do some normalization in RGB-D Depth image's magnitude values using equation 1. We normalize biggest value to 1 inside the matrix. For Depth image magnitude matrix define "d" in equation.

$$d = \frac{d}{max(d)} \tag{1}$$

In Figure 4, there are some black parts, inside the black part there are no depth information. We need to eliminate these pixels inside our RGB-D depth object images so in the magnitude values we assign zero to all black pixels and their neighbor pixels.

$$r = r * d \tag{2}$$

In Equation 2, r means RGB's magnitude values and d means RGB-D Depth image magnitude values and we show combining RGB's magnitude values with RGB-D Depth image magnitude values. After all these calculation, we create new descriptor based on HOG algorithm.

3.3. Learning

After creating new descriptor, we use multi-SVM method use training and testing. We will show our test results in Section 4.

4. EXPERIMENTS

In SUN3D dataset we use 105 object and 26 unique labels from 2 image set. We have got 2 step in our experiments. Firstly, we use normal HOG algorithm to create descriptor using RGB and RGB-D Depth images. In table 1, you can see Multi-SVM and Multi-SVM with Cross Validation.

Table 53 Multi-SVM Errors using Unmodified HOG Algorithm

Normal HOG Algorithm	Multi SVM with Cross Validation (out-of-sample classification error)	Multi SVM without Cross Validation (in-sample classification error)
RGB	0,6762	0,1429
DEPTH	0,6381	0,2476

Our modified HOG algorithm create descriptor using with RGB and Depth images together. In table 2, you can see Multi-SVM and Multi-SVM with Cross Validation.

Table 54 Multi-SVM Errors using our Modified HOG Algorithm

Modified HOG Algorithm	Multi SVM with Cross Validation (out-of-sample classification error)	Multi SVM without Cross Validation (in-sample classification error)
RGB + DEPTH	0,6952	0,1429

In our work, we modified HOG algorithm using RGB-D Depth data. We share our new descriptor experiments result. We are planning to improve our code and improving result.

REFERENCES

[1]. N. Dalal and B. Triggs, "Histograms of Oriented Gradients for Human Detection," *IEEE Computer Society Conference on Computer Vision and Pattern Recognition (CVPR'05),* vol. 1., pp. 886–893, 2005.

[2]. K. Mikolajczyk, A. Zisserman, and C. Schmid, "Shape recognition with edge-based feactures," *Brit. Mach. Vis. Conf., Norwich,* pp. 1–10, 2003.

[3]. D. G. Lowe, "Object recognition from local scale-invariant features," *Proceedings of the Seventh IEEE International Conference on Computer Vision,* vol. 2, no. [8, pp. 1150–1157, 1999.

[4]. M. Leordeanu, M. Hebert, and R. Sukthankar, "Beyond local appearance: Category recognition from pairwise interactions of simple features," *Proceedings of the IEEE Computer Society Conference on Computer Vision and Pattern Recognition,* 2007.

[5]. H. Ren and L. Ze-Nian, "Object detection using edge histogram of oriented gradient," *IEEE International Conference on Image Processing (ICIP),* pp. 4057–4061, 2014.

[6]. A. Shrivastava, T. Malisiewicz, A. Gupta, and A. a. Efros, "Data-driven visual similarity for cross-domain image matching," ACM Transactions on Graphics, vol. 30, no. 6, p. 1, 2011.

[7]. J. Stallkamp, M. Schlipsing, J. Salmen, and C. Igel, "Man vs.˜Computer: {B}enchmarking Machine Learning Algorithms for Traffic Sign Recognition," *Neural Networks,* vol. 32, pp. 323–332, 2012.

[8]. T. Malisiewicz, A. Gupta, and A. A. Efros, "Ensemble of exemplar-SVMs for object detection and beyond," *Proceedings of the IEEE International Conference on Computer Vision,* pp. 89–96, 2011.

[9]. J. Xiao, A. Owens, and A. Torralba, "SUN3D: A database of big spaces reconstructed using SfM and object labels," *Proceedings of the IEEE International Conference on Computer Vision,* pp. 1625–1632, 2013.

[10]. K. Lai, L. Bo, X. Ren, and D. Fox, "A large-scale hierarchical multiview RGB-D object dataset," *Proceedings - IEEE International Conference on Robotics and Automation,* pp. 1817–1824, 2011.

[11]. N. Silberman, D. Hoiem, P. Kohli, and R. Fergus, "Indoor segmentation and support inference from RGBD images," *Lecture Notes in Computer Science (including subseries Lecture Notes in Artificial Intelligence and Lecture Notes in Bioinformatics),* vol. 7576 LNCS, no. PART 5, pp. 746–760, 2012.

A Study on the Grafting of Different Table Grape Varieties on Different Rootstocks

Sadettin GURSOZ[1], M. İlhan ODABASIOGLU[2], Bekir Erol AK[3]

Abstract

The use of new varieties in the newly established vineyard in the Sanliurfa province in recent years has increased significantly. Although saplings used in new vineyard were taken from different locations of Turkey, vineyards produced in nurseries in the Sanliurfa location is mostly preferred. This study was carried out in 2013 and it was aimed to determine the sapling combination performance of Red Globe, Honusu and Hatun Parmagi, which are used for table grape varieties and 99 R, 140 Ruggeri rootstocks vaccine sapling combinations. In the study, after callusing the shoots to create condition of the scion, the length of the shoots formed from the scion after callusing, level of root development, shoot development level, the site of graft's callus development level, coefficient of affinity, I. class sapling efficiency and total sapling efficiency was investigated. It was found that there was no difference between the rootstocks in terms of folding performance of the rootstock combinations examined in folding room. It has been determined that there is an inversely proportional relationship between root forming conditions in the rootstocks and decaying conditions in the rootstocks. Parallel results were obtained in terms of shoot development level and root development level. It was found that the best combination in terms of first class sapling production is 140 Ruggeri / Red Globe.

Keywords: *Grape rootstock, grafting, affinity level, first-class sapling*

1. INTRODUCTION

Annual vine sapling production in Turkey is 4 857 045. Grafted saplings takes nearly 85.9% of this production and 14.1% of them not grafted saplings. However, fluctuations are seen in this production over the years. The number of enterprises declaring that they produce vine saplings in Turkey is 31 as of 2011. A significant portion of these enterprises are located in Manisa province. Manisa is followed by Sanliurfa, Bursa and Bilecik provinces, respectively. Sanliurfa province provides 7.63% of Turkey's vine saplings production. Although the methods used by the sapling producers in Sanliurfa differ from each other, the varieties of grapes they produce vary from year to year according to the grape producers demands [1].

In the production of grafted vine saplings in Turkey, table grape varieties are produced more than wine and dried grape varieties [2]. The most produced variety in table grape varieties is Thomson Seedless. This variety is followed by Alphonse Lavallee, Superior Seedless and Horoz Karasi varieties respectively. In addition, Cilores, Italia, Crimson Seedless, Kabarcik, Trakya Ilkeren, Royal and Hatun Parmagi varieties are also produced in significant quantities. The production values of grafted vine saplings in Turkiye also reveal the variety preferences of producers engaged in viticulture and grape consumers, in recent years.

Nowadays, it is possible to select grape rootstocks resistant to soil-borne diseases and pests and to produce grafted vine saplings, but the affinity of these rootstocks with grape varieties to be grafted on varies. For this reason, it is important to previously know the affinity and performance of the rootstock / variety combination in the production of grafted vine saplings in terms of sapling producers. Increasing the affinity rate and sapling yield in the enterprises that produce grafted vine saplings directly affects the income from sapling production [3]. There are many factors that increase affinity and yield of sapling in the production of grafted vine saplings. These factors are; the times of receipt of the scion, the development conditions of the vines and the bough to be taken by the scion, the characteristics of the one year old boughs and vines, sustained storage conditions up to the time of grafting of the scions, the period of grafting, grafting method which is preferred,

---

[1] Corresponding author: Harran University, Agriculture Faculty, Department of Horticulture, 63100, Sanliurfa-TURKEY. sado@harran.edu.tr

[2] Harran University, Agriculture Faculty, Department of Horticulture, 63100, Sanliurfa-TURKEY. milhanodabasioglu@gmail.com

[3] Harran University, Agriculture Faculty, Department of Horticulture, 63100, Sanliurfa-TURKEY. beak@harran.edu.tr

germinating room conditions and etc [4, 5, 6, 7, 8, 9, 10, 11]. These factors, which indicates themselves directly in the yield and quality of the sapling, are also of great importance in grapevine cultivation. As a matter of fact, it has been reported that the high yield and quality of the product obtained from the rootstock / varieties combinations in which no problem of affinity is observed in the vineyards established with grafted vine saplings [8, 12, 13, 14].

In this study, germinating room performance and sapling performances of combinations of Red Globe, Hatun Parmagi and Honusu varieties grafted on 99 R and 140 Ruggeri rootstocks which widely used in grape sapling production in Sanliurfa province, were examined.

2. MATERIALS AND METHODS

2.1. Materials

The research was carried out in Sanliurfa in 2013. The scions of the rootstocks (99R and 140 Ruggeri) used in the research were obtained from a stock vineyard in Akcakale, Sanliurfa in February 2013. Scions (Red Globe, Hatun Parmagi, Honusu) were obtained from Gaziantep in the same period. Scions obtained from rootstocks and varieties were kept in cold weather storage with 85-90% relative humidity at +4 C until the grafting period (March 15) [15, 18]. The climate data for the region where the research is conducted is given in the Figure 1 [19].
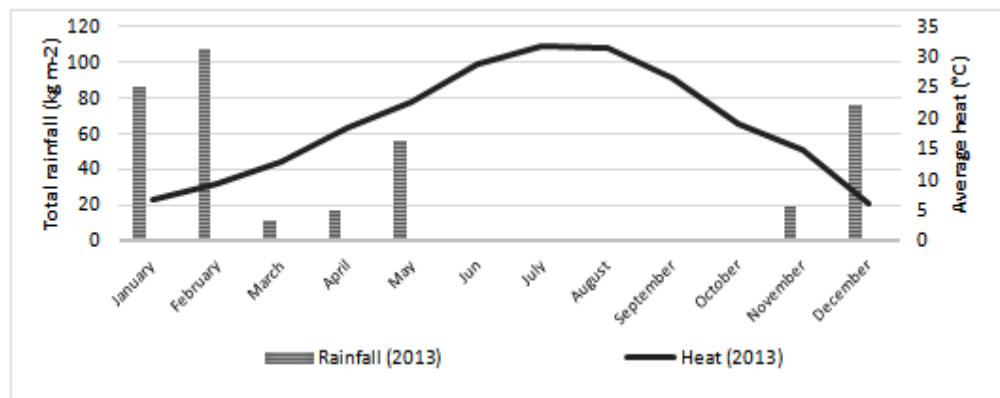

Figure 1. Climatic data of research area.

2.2. Methods

The research was set up in 3 renewal with randomized blocks in split parcel trial design. There were 20 grafted scions used in each renewal. At grafting, omega type desktop grafting machines were used. After grafting, the grafted scions were immersed in liquid paraffin at 80 ° C for 3-5 seconds, then immersed in water which was at 23 ° C temperature, to cool and solidify the paraffin. Then the grafted steels were transferred in the wooden boxes and were filled with semi humid sawdust. The sawdust was sprayed with captain fungicide before use.

Germinating (callusing) room conditions were kept at 26-28 °C and 80-85% humidity in the first week, 24-26 °C and 80-82% humidity in the second week, 22-24 °C and 75-80% humidity in the third week. The grafted scions were transferred after 22-26 days from the germinating room to acclimating room and kept about one week at there [11]. The grafted scions's shoots shortened by hand and were secondly immersed to liquid paraffin and planted in the nursery [10]. The saplings were removed from the nursery at the defoliation period (end of the November) for analyses.

When grafted scions are removed from the germinating room to acclimation room, some bud eyes forms shoots. In this study, it was determined whether or not shoots were formed at the grafted scions during the acclimation room period, and the ratio of the shoot-forming scions to the total grafted scions was expressed as percentage. When the grafted scions were taken into the germinating room, the lengths of the shoots were measured by the digital caliper. The shoot lengths of the scions which do not form shoots but whose bud eyes were still alive, were taken as "0" mm.

Some grape rootstocks tend to early form roots. So root formation is observed at the bottom of the some grafted scions (rootstock side) at the period when they are taken into the acclimating room. However, these roots usually getting dry after the planting while new ones occur. For this reason, these roots which forms during germination room period, cut before the planting. However, the formation of these roots may show carbohydrate accumulation and root formation ability of the rootstock which is used. In this study, the ratio of

the root forming scions to the total scions was determined as root formation after germinating and expressed as percentage.

When the grafted scions are transferred from the germinating to the acclimating room, decaying can be seen at the bottom of some rootstocks. However, these decaying, sometimes seen at the bottom of the rootstocks, is an undesirable condition and often prevents root formation after planting. In this study, the ratio (%) of the decaying scions to the total scions which were taken into acclimating room, was determined to be the decay of the bottom of the rootstock after germinating.

The level of callus development at the grafting site was assessed by modifying Reference [20]'s method. According to this, the callus development level is divided into 5 groups (0-25-50-75-100%) according to the proportion of the callusing to the whole grafting side. During the callusing, the level of callus formation at the bottom of the grafted scions (bottom of the rootstocks) was evaluated in a similar way.

The level of shoot development was made after the defoliation according to Reference [4]. The root development level was determined according to Reference [21] during the period when the saplings were removed from the nursery (during the winter period). In this study, the affinity coefficient was determined by using Perreudine method which Reference [22] used.

First class sapling means; saplings which have the characteristics specified in TSE (Turkish Standards Institute) 3981 in the rooted grape saplings [23]. The I class sapling efficiency was determined by expressing as percentage of the transplanted grafted scions that were transformed into the saplings that meet the standards. I. class sapling efficiency analyses were carried out during the period when the saplings were removed from the nursery (winter rest period). Total sapling efficiency determined with percentage of those converted from grafted scions to saplings.

3. RESULTS AND DISCUSSIONS

In our research, in terms of the formation of shoots 140Ru/Red Globe combination has the highest ratio (33.3%) when scions taken out from the germinating room (Table 1). However, after callusing, it was determined that there was no effect of rootstocks and varieties in terms of shoot formation. The longest shoots were obtained from the combination of 140 Ruggeri/Red Globe (17 mm). When rootstocks were compared to shoot lengths of grafted variety scions, it was determined that the shoots formed in the items of the grafted varieties on the 140 Ruggeri rootstock had higher values than those grafted on the 99 R rootstock. When the same comparison was made on grape varieties, it was seen that the Red Globe grape variety scions produced longer shoots (9.0 mm) than the other variety scions.

Table 1. After callusing (after germinating room period) grafted scion's shoot forming and shoot length.

Rootstock	Variety	Shoot forming (%)	Shoot length (mm)
99 R	Honusu	10.0 a	3.0 b
	Red Globe	10.0 a	1.0 b
	Hatun Parmagi	16.7 a	3.0 b
140 Ruggeri	Honusu	20.0 a	10.0 ab
	Red Globe	33.3 a	17.0 a
	Hatun Parmagi	6.7 a	2.0 b
99 R Average		12.2 A	2.0 B
140 Ruggeri Average		20.0 A	10.0 A

Means shown with the same column (vertical) are not significantly differently at p = 0.05 probability level.

In the combinations which used in 140 Ruggeri, about 80.0% of the grafted scions presented roots , while in 99 R this remained 60.0%. Varieties were determined to have no effect on the root formation of rootstocks during folding. 99 R/Red Globe combination was determined as the highest rate combination with the 16.7% in terms of decaying at the bottom part of the scions (Figure 2). The fact that the same combination has a low root formation level also indicates that the findings are parallel to each other. However, it has been

determined that there is no difference in the level of decaying at the bottom of the grafted scions which 140 Ruggeri and 99 R rootstocks are used.
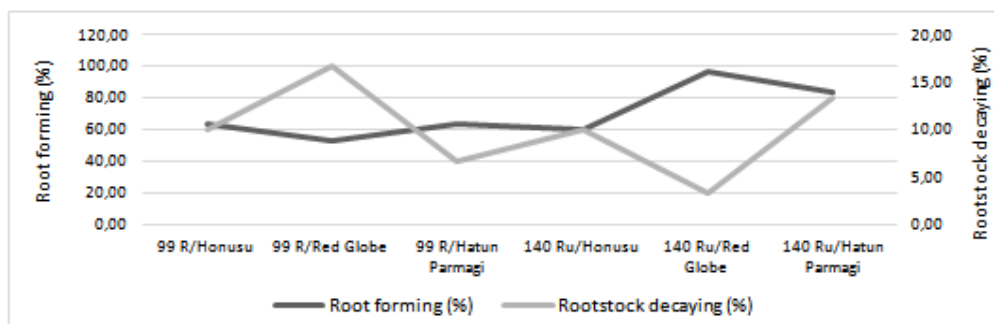

Figure 2. Relationship between root forming and decaying of bottom of rootstock.

The most successful combination of callus formation level at the grafting site was obtained in the Red Globe variety scions grafted on 140 Ruggeri rootstock. In addition, it has been found that the combinations of 140 Ruggeri/Honusu and 99 R/Hatun Parmagi do not significantly differ in terms of callus formation at the grafting site. When the rootstocks were compared in terms of callus development level at the grafting site, it was determined that 140Ruggeri (57.2%) had more callus forming than 99R (40.8%). In a similar manner, 140 Ruggeri were found superior to the 99R in terms of their ability to form calluses at the base of the grafted scions (Table 2.).

Table 2. Callus development level of grafted scions after germinating room period.

Rootstock	Variety	Callus development level at the grafting site	Callus development level at the bottom of the rootstock
99 R	Honusu	60.8 a	42.5 ab
	Red Globe	25.0 b	33.3 ab
	Hatun Parmagi	36.7 ab	29.2 b
140 Ruggeri	Honusu	46.7 ab	50.0 a
	Red Globe	64.2 a	40.0 ab
	Hatun Parmagi	60.8 a	40.0 ab
99 R Average		40.8 B	35.0 B
140 Ruggeri Average		57.2 A	43.3 A

Means shown with the same column (vertical) are not significantly differently at p = 0.05 probability level.

From the grafting combinations examined, the best shoot development level and best root development level was achieved in of Red Globe and Hatun Parmagi varieties which grafted on 140 Ruggeri rootstock (Figure 3). In addition, it was determined that there is a positive linear relationship between shoot development and root development. This may indicate that the storage carbohydrates present in the grafted scions are used equally for shoot and root formation at the germinating period.
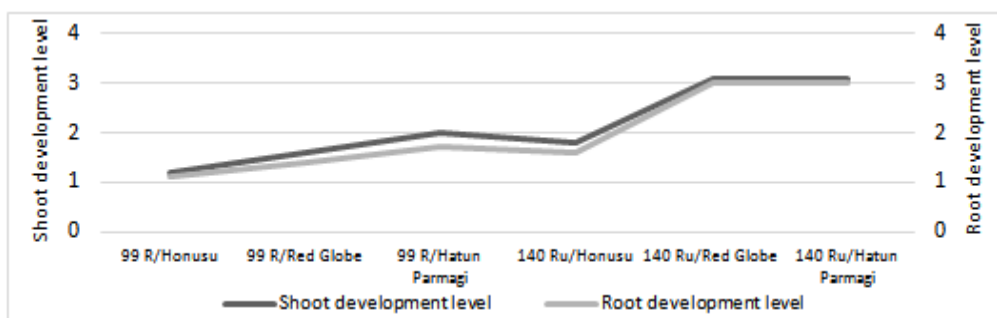

Figure 3. Relationship between shoot development level and root development level.

The highest affinity coefficient (11.5) was obtained from the combinations of grafting using Red Globe grape variety. In addition, the lowest affinity coefficients (10.2 and 10.3) were obtained from the grafting combinations which Honusu scions used. However, this study showed that the affects on the affinity coefficient of rootstocks were close to each other. It was determined that the best combination was the 140 Ruggeri/Red Globe in terms of both first class sapling yield and total sapling yield and 99R/Honusu grafting combination was the worst. There is no significant difference between the rootstocks in terms of the I class sapling efficiency and total sapling efficiency (Table 3).

Table 3. Affinity coefficient and sapling efficiency of rootstock-grape variety combinations.

Rootstock	Variety	Affinity coefficient	I class sapling efficiency (%)	Total sapling efficiency (%)
99 R	Honusu	10.3 ab	31.7 b	66.7 b
	Red Globe	11.5 a	46.7 ab	78.3 ab
	Hatun Parmagi	11.3 ab	53.3 ab	80.0 ab
140 Ruggeri	Honusu	10.2 b	35.0 ab	71.7 ab
	Red Globe	11.5 a	55.0 a	88.3 a
	Hatun Parmagi	11.2 ab	50.0 ab	83.3 ab
99 R Average		11.1 A	43.9 A	75.0 A
140 Ruggeri Average		10.9 A	46.7 A	81.1 A

Means shown with the same column (vertical) are not significantly differently at p = 0.05 probability level.

4. CONCLUSIONS

After germinating, it was determined that there was no difference between rootstocks in terms of shoot forming on the bud eyes. In addition, it was determined that the grape variety characteristics did not affect the after germinating period shoot forming of the bud eyes. It has been determined that in germinating room period there is an inversely proportional relationship between root forming in rootstocks and decaying of rootstock bottom. The effect of both rootstocks and varieties was not clearly determined in terms of decay at the bottom of the rootstocks of the grafted scions.

The level of development of callus tissue formed at both the grafting point and the bottom of the rootstock of the grafting combinations was examined and it was found that the rootstocks had similar responses in terms of both characteristics. Parallel results were obtained in terms of shoot development level and root development level. Both the shoot and root development levels of the combinations formed with 140 Ruggeri in the examined varieties were found to be better than the combination with the 99 R. It was determined that the effects of the rootstocks were close to each other in the combinations examined for the affinity coefficient but Honusu variety had a very low affinity coefficient.

REFERENCES

[1]   Bilgic, C., Bekisli, M.İ. and S. Gursoz, 2015. The Study On Grapevine Saplings Production And Irrigation In Nursery Enterprises. Selcuk Journal of Agriculture and Food Science-A, 27: 193-198.
[2]   Celik, H., 2012. Turkiye Bagcılıgı ve Asma Fidanı Uretimi-Dıs Ticareti İle İlgili Stratejik Bir Degerlendirme. Turk Tohumcular Birligi (TURKTOB) Dergisi, 4:10-16. (In Turkish).
[3]   Savas, Y., 2013. Economic Analysis of Grapevine Nurseries and Evaluation of Those Farms' Efficiencies: The Case Study of Manisa. Adnan Menderes University, Graduate School of Natural and Applied Sciences, Department of Agricultural Economics , Master Thesis, 53s, Aydın.
[4]   Celik, H., 1982. Kalecik Karası/41B Ası kombinasyonu icin Sera Kosullarında Yapılan Asılı Koklü Fidan Üretiminde Degisik Koklenme Ortamları ve NAA Uygulamalarının Etkileri. Ankara Üniv. Ziraat Fak. (In Turkish), 74s.
[5]   Celik, H., 1985. Asılı Koklü Asma Fidanı Üretiminde Basarıyı Etkileyen Etmenler. Türkiye 1. Bagcılık Sempozyumu Bildirileri. s139-153, Ankara. (In Turkish).
[6]   Celik, S., 1988. Bagcılık (Ampeloloji) Cilt 1. Anadolu Matbaa San. ve Tic. Ltd. Sti., Tekirdag, 428s. (In Turkish).
[7]   Kelen, M., 1994. Bazı Uygulamaların Asılı Koklü Asma Fidanı Üretiminde Kalite ve Randıman Üzerine Etkileri ile Ası Kaynasmasının Anatomik ve Histolojik Olarak İncelenmesi Üzerine Arastırmalar. YYÜ, Fen Bilimleri Enstitüsü, Bahce Bitkileri Anabilim Dalı, Doktora Tezi. 34s, Van. (In Turkish).

[8] Celik, H., Agaoglu, Y.S., Fidan, Y., Marasali, B. and. G. Soylemezoglu, 1998. Genel Bagcılık. Sunfidan A.S. Mesleki Kitaplar Serisi. 1: s253, Ankara. (In Turkish).

[9] Baydar, N.G. and M. Ece, 2005. Comparation of Different Scion/Rootstock Combinations in the Production of Grafted Grapevines in Isparta Condition. Süleyman Demirel University Journal of Natural and Applied Sciences, 9(3).

[10] Aslan, K.A., Ozcan, S., Kosetürkmen, S., Yagci, A., Sakar, E., Bekisli, M.İ. and D. Kilic, 2015. Comparison Of Different Grape Variety-Rootstock Combinations For Production Of Grape Sapling In The City Of Gaziantep. Selcuk Journal of Agriculture and Food Science-A, 27: 210-216.

[11] Bekisli, M.İ., Gürsoz, S. and C. Bilgic, 2015. Investigation of The Production of Grafted Grapevine Sapling in the Some Variety-Rootstocks Combinations Germinate Room Performance. Harran Journal of Agricultural and Food Science, 19 (1): 24-37.

[12] Oraman, M.N.: 1965. Yeni Bagcılık. Ankara Üniversitesi Ziraat Fakültesi Yayınları, Yayın No:253, Ders Kitabı No:89, Ankara, 347s. (In Turkish).

[13] Celik, H., 1996. Rootstocks used in viticulture and their importance for grape growing. Anadolu Journal of Agricultural Sciences, 6(2): 127-148.

[14] İnal, S., 1985. Bagcılıkta Kullanılan Amerikan Asma Anacları, Adaptasyon Durumları ve Bunların Bazı Üzüm Cesitleri ile Affiniteleri Üzerinde Arastırmalar. Türkiye 1. Bagcılık Sempozyumu, Ankara, s.123-138. (In Turkish).

[15] Becker, H., 1971. Neure Ergebnisse aus Untersuchungen Über die Techonologie der Lagerung van Rebenvermehrunsut. Probleme der Rebenveredlung, Heft 8,29-48. (In German).

[16] Gerhardt, R., Cheng-Yung, C. and F. Schneider, 1971. Probleme der Rebenveredlung. Hett 8,9-27. (In German).

[17] Sievers, E., 1971. Neue Wege bei der Versongang der Rebenveredlung mit Edelreis material. Weinberg und Keller, 18,253-279. (In German).

[18] Agaoglu, Y. and H. Celik, 1978. Bazı Amerikan Asma Anaclarında Ethrel Uygulamaları ve Dikim Sekillerinin Koklenme Üzerine Etkileri. Ankara Üniversitesi Ziraat Fakültesi Yıllıgı, Cilt:27, Fasikül l'den Ayrı Basım. (In Turkish).

[19] Turkish State Meteorological Service, 2014. Sanliurfa Climate Data.

[20] Damborska, M., 1981. Results of Investigations on the Callus Formation on Rootstock and Scion of Vines. Vinohrad, Bratislava, 19:8-9.

[21] İnal, S. and Y. Demirbüker, 1975. Bazı Sofralık ve Saraplık Üzüm Cesitlerinde Affinite Denemesi. Bagcılık Arastırma Ülkesel Projesi Sonuc Raporları, Tekirdag Bagcılık Arastırma Enstitüsü, Cilt:1, Sayı:1, Tekirdag. (In Turkish).

[22] Fidan, Y. and S. Can, 1984. Amerikan Asma Anaclarının Seciminde Etki Eden Baslıca Faktorler. Cumhuriyet Üniversitesi Tokat Ziraat Fakültesi. Tokat Bagcılıgı Sempozyumu, Tokat. (In Turkish).

[23] Turkish Standards Instıtution, 2006. Grafted Grape Sapling Standards. (In Turkish).

Utilization Of Some Elements Of Grape And Pistachio Cultivars Grown As Interplanted Orchard II

Bekir Erol AK[1]*, Sadettin GURSOZ[1], Sedat GOKOGLU[1]

Abstract

Most of the orchards are mixed with pistachio, olive and grape at Southeast Anatolia of Turkey. They can grow dry conditions. It was recommended generally pistachio and vineyard mixture. Mixture of pistachio and olive are not recommended because of the pollination problem. In this experiment, the amount of mineral nutrition uptake of Honusu grape and Kirmizi pistachio cultivars which are commonly grown in the same area was determined. Also, the influences on mineral nutrition uptake of these plants each other grown in the same conditions was compared. In mixed plant orchard, depending on mineral nutrition content of the soil, the amount of N uptake of grape and pistachio changed each other.

The leaf mineral nutrients of pistachio trees were determined such as; N 0,91 %; P 0,05 %; K 0,47 %; Ca 1,37 %; Mg 0,53 %; Fe 238,67 ppm; Zn 19,67 ppm; Cu 11,00 ppm; Mn 18,27 ppm. Although soil of the orchard has sufficient amount of K and Ca, it was determined that Honusu grape cultivar and Kirmizi pistachio cultivars could not have enough benefit from K and Ca mineral nutrition. Depend upon Mg content of the soil, Honusu grape cultivar was also uptake and had more benefit from Mg mineral nutrition compared to Kirmizi pistachio cultivar.

Keywords: *Grape, Pistachio, Macro, Micro Elements, Interplanting*

1. INTRODUCTION

Pistachio and grape are very imported two crops for South East Anatolia region of Turkey. They are growing together. In fact main crop is pistachio tree. It has very long juvenile period under non-irrigated soil conditions. Grape is very short time bearer crop. Farmers prefer them together because of the income starts early from grape then long time passes for pistachio. Pistachio and grape can be grown under high lime content soil conditions and big advantage high temperature, Low relative humidity and long summer period.

Nutrition statutes of soil and leaf should be known to prepare correct fertilization programmed. Then elements are determined need of plant which one is sufficient or deficit. The amount of elements is very important as well as soil pH. Because some elements opposite to another elements. That means if some elements are high in soil, another one is not uptaken by the plants. There are antagonism between the elements which is vital important for plant. For example; excessive of Ca causes the Fe deficiency, excessive of P, causes the Zn deficiency etc. Leaf and soil analysis should be done to make correct fertilization programme for plants. It should be kept in mind the antagonism between the elements [1].

There is a strong reproductive demand for nitrogen and carbohydrates in on-years, significant removal of nitrogen in the fruit at harvest, reduced recovery of January applied labeled fertilizer N than off-year trees in pistachio [2].

Fertilization is very important factor to get high quality and yield from the trees. But pistachio trees suffer from salinity and alkalinity. Fertilization depends on irrigation and pH of soil. Some elements can not be translocated because of high pH. The availabity of nutrients are changed to pH critical levels [3, 4]

The aim of this experiment, determination of (I) mineral nutrition content in the leaves of Commonly grown as interplanted plants grape (honusu cv.) and pistachio (kirmizi cv.) at the province Gazianatep. (ii) what about deficiencies of macro and micro nutrients (iii). to make comparison which one successful to uptake of elements under same soil and rain fed conditions.

---

[1] Corresponding author: Department of Horticulture, Faculty of Agriculture, Harran University, Sanlurfa, Turkey. beak@harran.edu.tr

2. MATERIAL AND METHODS

This work was carried out in the pistachio and grape orchards in Gaziantep province. The soil and leaf analysis was done at the laboratory of Pistachio Research Institute in Gaziantep. This orchard is growing under rainfed conditions.

The pistachio trees (Kirmizi cultivar) are planted 10 m x 10 m., 30 years old and vineyard is established between the pistachio trees. The Grape Cultivar was Honusu. Soil sampling was done different Depth such as 0-20 cm, 20-40 cm, 40-60 cm from ground level. To analysis were determined physical and chemical content of soil (Table 1, 2). Leaf sampling from grape was taken two times in a vegetation period. The first time was blooming time second was veraison (onset of rapid maturation or near harvest) [5]. Leaf of pistachio samples were taken 16-31 July (before fruit shell became red) [6]. Macro and micro elements were determined according to leaf samples.

Table 1. Soil physical traits and organic matter content of the experimental orchard.

Soil Depth (cm)	Soil attribute				
	pH (Soluble in Water)	Salt (%)	Lime (%)	Texture (%)	Organic matter (%)
0-30	7.90*	0.03	55.70	Loam (50)	2.30
30-60	8.00	0.02	68.80	Loam (50)	1.60
60-90	8.10	0.02	61.90	Loam (50)	1.30
Average	8.00	0.02	59.47	Loam (50)	1.73

* Each number is average of three different part of orchard of soil samples.

Table 2. Macro- and microelemental content of the soil in the experimental orchard.

Soil Depth	Nutritional content of the soil							
	P (ppm)	K (ppm)	Ca (ppm)	Mg (ppm)	Fe (ppm)	Zn (ppm)	Cu (ppm)	Mn (ppm)
0-30	4.70	278.00	5748.0	357.00	4.40	0.28	1.20	0.80
30-60	6.00	263.70	5187.0	197.00	3.80	0.22	0.10	0.60
60-90	8.40	234.30	4296.0	124.00	2.80	1.00	0.10	0.10
Average	6.37	258.67	5077.0	226.00	3.67	0.50	0.47	0.50

3. RESULTS AND DISCUSSION

The some macro and micro element contents of leaf of Grape and pistachio was given Table 3. According to Table 3 some elements are not taken because of high pH of soil. But especially Fe and Cu contents of leaves were very high although the soil condition is not suitable for uptake of these elements. This may be because of the spraying of this element for some diseases.

The elements content of pistachio leaves were compared with the normally maximum and minimum critical levels which was determined by Tekin [7]. As it was seen Table 3, nitrogen, potassium, Phosphoros, calcium and manganese levels were under minimum critical levels. However, magnesium, Iron zinc and copper were sufficient. Because Tekin [8], is reported that Mg content of pistachio leaves, which were taken Gaziantep province, were changed between 0.59 % to 0.83 %. He has determined that this critical level include in limits. But when it decrease from 0.50 % deficiency symptoms will start.

The elements content of grape leaves were compared with the normally maximum and minumum critical levels which was determined by Ibrikci et al., [9]. As it was seen Table 3 nitrogen, potassium, phosporos, calcium, zinc, and manganese levels were under minimum critical levels. However, magnesium, Iron and copper were sufficient. Magnesium content of leaves are upper critical level. As a summary of this experiment, very high pH some elements such as Iron were taken from soil because of their root systems.

Table 3. Some macro and micro element content of grape and pistachio leaves and comparison with critical level of pistachio.

ELEMENTS	GRAPE		PISTACHIO		
	Blooming Time	Ibrikci et al. (2004) (Blooming Time)	At Veraison		Tekin (2002) before fruit shell became red
N (%)	1,24	2.30-2.80	0,83	0,91	1.80-2.20
P (%)	0,13	0.25-0.45	0,09	0,05	0.06-0.14
K (%)	0,79	1.20-1.60	0,49	0,47	0.80-1.20
Ca (%)	1,07	1.50-2.50	1,50	1,37	2.20-3.70
Mg (%)	0,60	0.25-0.60	0,61	0,53	0.50-0.90
Fe ppm	87,00	60-175*	35,33	238,67	43-170
Zn ppm	6,23	20-70	9,53	19,67	10-25
Cu ppm	28,00	6-12	30,67	11,00	6-90
Mn ppm	6,13	30-100	91,67	18,27	20-50

*(Jones et al., 1991)

As it is well known zinc is one of the very important element for both species. When Zinc is compared between two plant, although they are growing same soil conditions, were enough uptaken by pistachio trees but grape. This situation shows that Zn is problem for vineyard each crops should be considered one by one to use as leaf fertilizer

4. CONCLUSIONS

South East Anatolia part of Turkey very dry and high temperature in summer time or growing period of plants. This part is very calcareous and very low rain conditions. The plant which are resistant to dry conditions, were grown without irrigation facilities long time. Now some suitable areas are irrigating due to Ataturk dam. The orchard that this experiment were run, is not irrigated so far. Soil is very high lime content and very low organic matter because of less rain and high temperature. Some of elements are not up taken by plants because of high pH conditions. But farmers know that no other plant or fruit trees can be grown in this soil conditions. Besides of these two crops olive is growing such a difficult conditions. Deficiency of element causes for low yield and quality. It became strong alternate bearing habit for pistachio nut.

The nutrients available to plant roots depend upon many factors, among which are climate, plant species, rootstock type, soil type, total nutrients in the soil, soil moisture, soil oxygen content, humus content, soil pH, and base saturation [4]. Depend upon the to soil nutrient, N availability was changed either pistachio or grape but there was no any problem with potassium and Manganese up taking although they were grown as interplanting or mixed growing system. According to results, such elements N, K, Ca, Mg to pistachio trees, N, P, K, Ca, Zn, Mn are deficit to Grape. This results shows that such a bad soil and climate conditions pistachio trees are benefit elements from soil better than grape.

ACKNOWLEDGEMENTS

REFERENCES

[1]. S. Ozbek, Genel Meyvecilik. Cukurova Universitesi, Ziraat Fakultesi yayınları: 111, . Ders Kitabı. No:6, 386 s. 1977.
[2]. S. Weinbaum, Picchioni, G., Muraoka, T., Ferguson, L. and Brown, P., Fertilizer nitrogen and boron uptake, storage, and allocation vary during the alternatebearing cycle. J. Amer. Soc. Hort. Sci. 119:24-31. 1994.
[3]. B. E. Ak, and H. Parlakci, The low yield reasons and solution of pistachio nut in Turkey. Nucis, 13:37-40, 2006.
[4]. M.N. Westwood, Temperate zone Pomology. W.H. Freeman and company, San Francisco, 404 p. 1978.
[5]. J.F. Levy, L'application du diagnostic Foliaire ala determination de besoins alimentaires des vignes. Le controle de la fertilisation des plantes cultivees. 295-305 p. 1968.

[6]. H. Tekin, G. Caglar., C. Kuru and F. Akkok, Determination of Nutrients for Pistachio trees and the best leaf samples collection periods. (in Turkish with an English summary). First National Symposium on Pistachio Nut, 11-12 September 1990, 120-138. 1990.

[7]. H. Tekin, Deficiencies of nutrients and fertilization in pistachio. (in Turkish), Pistachio Research Institute Publication No:14, 33 p. 2002.

[8]. H. Tekin, Gaziantep Yoresinde Topraktan ve Yapraktan Yapılan Farklı Gubre Uygulamalarının Antepfıstığının Yaprak Bilesimi, Gelisme, Verim ve Urun Kalitesine Etkilerinin Arastırılması. (Tez). C.U.Zir.Fak. Fen Bilimleri Enstitusu Adana, 1992.

ALTERNATIVE OIL PLANT: Styrax(Styrax Officinalis L.)

Cuneyt Cesur[1], Belgin Cosge Senkal[2],Tansu Uskutoglu[3], Hulya Dogan[4]

Abstract

Styrax (Styrax Officinalis L.) is deciduous, shrubby perennial plant which is grow Southeastern Anatolia, Mediterranean, Aegean, Marmara region and central black sea in Turkey. Regional name of Styrax is "Tesbi". Plant can grow in large area of Turkey where is mostly have bad soil structure and also unsuitable for agricultural production. It prefers dry rocky slopes, under the trees of the forest an elevation up to 1,500 metres (4,900 ft) above sea level. Grown under these conditions plant grains contain fatty oil up to %47.04. Different civilizations was used for various purposes such as spice and household appliances but now use for animal feed from tesbi shrubs and utilized as fuel in rural areas. Non-Edible fatty is not suitable for human consumption but it can be assert on industrial uses. Because of ever-growing human population in world, vegetable oil is necessary not only for human consumption but also in industrial uses. Tesbi shrubs can be imagine for unsuitable agriculture areas and its growing cost is too low when compared with other oil plants. If this plant insert on plant pattern, it will bring great benefit such as employment, cheap vegetable crude oil, environmental improvement and prevention for global warming.

Keywords: *Oil Plant, Styrax, Tesbi*

1. INTRODUCTION

Tesbi (Styrax Officinalis) is deciduous perennial shrub which is member of Styracaceae. It can grow in central America, Mexico, southernwestern Europe, southeastern Asia and middle east [1]. In the future, humankinds biggest problem will be waterborne problems because of global warming and increasing population moreover people are facing to irrigation problem in agricultural land [2], [3], [4]. For this reasons, farmers should take precautions in agricultural activities and one of the most important is minimizing irrigation [5], [6]. Tesbi shrub is important because it can grow in marginal forestry land where other plant can't grow easily or unsuitable for cultivation [7]. According to 2012 statistic, total Turkey's forestry lands are 22 million hectare and 53% of them is corrupt coppice forest [8]. This corrupt lands have big risks for biodiversity and erosion. As seen on picture 1a, Tesbi shrubs can be used for fighting with erosion because ıt can grow easily in slope. As seen on picture 1b,Turkey's South Mediterranean area Tesbi shrub blooming in April and its flower is using for bee cultivation.

Tesbi shrub finds place except for agriculture and forestry area because it is seen as uneconomic but this plant have been cutting for feeding animal and bio fuel because of high oil rate. Thus, plant faced to danger of extinction. This plant should protect for Biodiversity and sustainability. If we obtain economic benefit, ıt will be protected easy and faster. Tesbi shrub can be used in biodiesel industry because of seed oil. Biodiesel is an alternative renewable and green energy resource which is increasingly interest in recent years [9], [10], [11].

[1] *Corresponding author: Bozok University, Department of Crop Fields in Agriculture Faculty, Yozgat, Turkey. cuneyt.cesur@bozok.edu.tr*

[2] *Bozok University, Department of Crop Fields in Agriculture Faculty, Yozgat, Turkey. belgin.senkal@bozok.edu.tr*

[3] *Bozok University, Department of Crop Fields in Agriculture Faculty, Yozgat, Turkey. tansu.uskutoglu@bozok.edu.tr*

[4]*Bozok University, Vocational High School, Department of Plant and Animal Production, hulya.dogan@bozok.edu.tr*
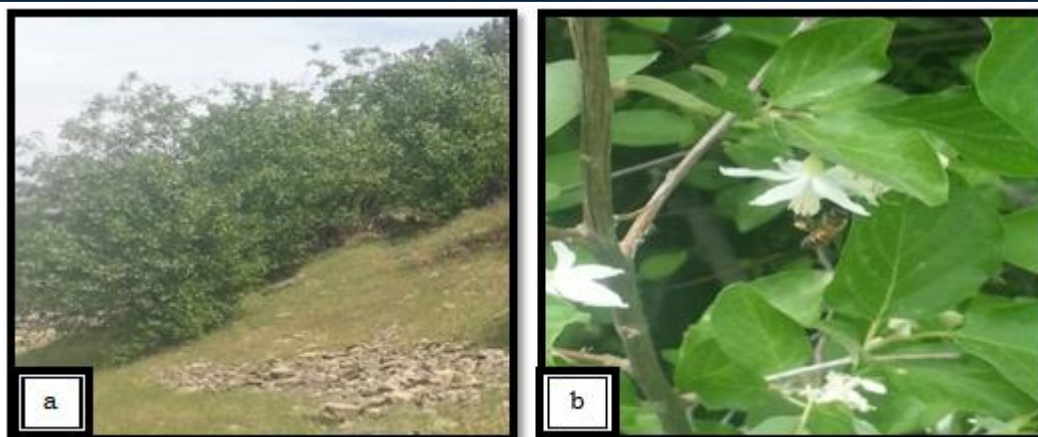
Figure 1. (a,b) During different grow period of tesbi shrubs

Particularly, developed countries are using biofuels at the moment and according to future predict of scientist, it is going to increase rate of using biofuels in developed countries. While Sweden is going to forbidden fossil fuel in 2020, E.U countries plan to increase rate of biofuel use up to 30% in 2030. Moreover, these countries aren't take tax on biofuels. Chinese, Indian, Taiwan, Malaysia, Philippines are given important for biodiesel production [12], [13], [14]. According to FAO and OECD's projection, from 2013 to 2022 15% of oil seed production is going to use as biofuels. In addition, ethanol and biodiesel uses will rise to %70.

2. TESBI SHRUBS MORPHOLOGY

Styrax officinalis L. is belong to Styracaceae family, deciduous perennial shrubs [15]. Plant local name is "Tesbi" in Southeast Anatolia and Mediterranean area in Turkey. At the same time, Tesbi known as aphid. Because of high sap ratio which aphid loves it, people named as Tesbi shrubs.
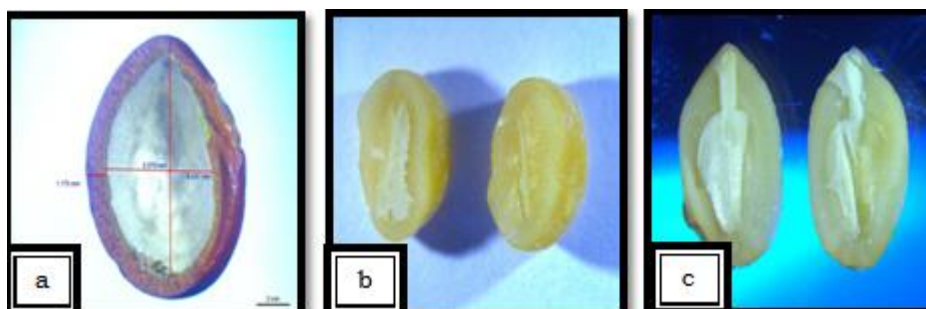

Figure 2. Styrax Officinalis a-) Seed Coat b-) seed horizontal section c-) seed vertical section

Styrax family include 8 genus and 120 species. It occurs non-continuous and represent 1 genus and 1 species in Turkey. Styrax officinalis occurs usually in south, southeast and intertropical America, tropical Africa, east Asya, Malaysia, Mediterranean and north coast of Turkey [16]. Styrax has a simple, relaxed form, with very thin elliptical leaves. Styrax shrubs is oilseed plant in forestry. It is deciduous which can grow up 2 to 6 m. It is grow into Pinus brutia-Pinus pinea forest in west and south Anatolia [17]. Flowers are bunch shape and actinomorphic, hermaphrodite, rarely monoecious, sometimes dimorphic and pentad structure. Flower colors are white and connected to stalk with petiole. Sepals are usually free, small and partially gamosepalous in Calyx. Sepals are blunt cup shaped. Petals are 3-5 lob. Stamens are epipetalous, variation between 8 and 13. Ovary starts with 3 cell and each of this cells contain many ovule. Fruit is thick-walled or dry capsule and winged form. Seed have endosperm. Embryo is flat or slightly curve. Cotyledons are notably big. When it dry thick-walled part is cracking irregularly. Seeds are single, big brownish and spherical [15], [18]. When seeds are ripening, it is drop in ground and easy to collect dry fruits. Harvest time is September. After flowering, its needed to 14 week for ripening.
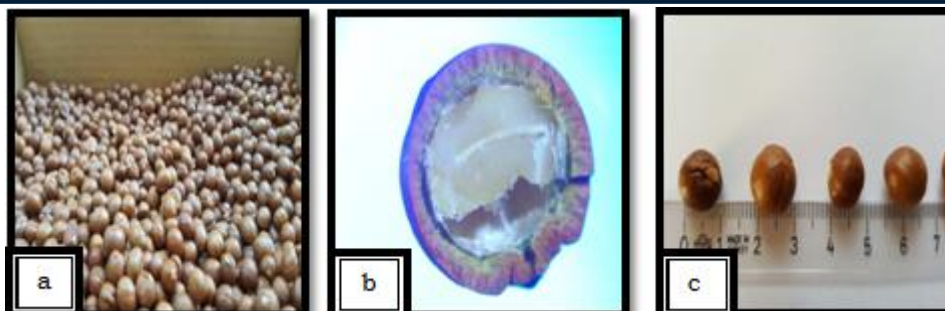
Figure 3. Different view of Styrax Oficinalis L a) seeds b) horizontal view of Styrax seeds. c) average seed size

3. TESBI SHRUBS' AREAS OF USAGE AND DEVELOPMENT OF AGRICULTURAL

According to figure 4, Tesbi shrubs occurs Southeast, Mediterranean, Aegean, Marmara and middle black sea region in Turkey.
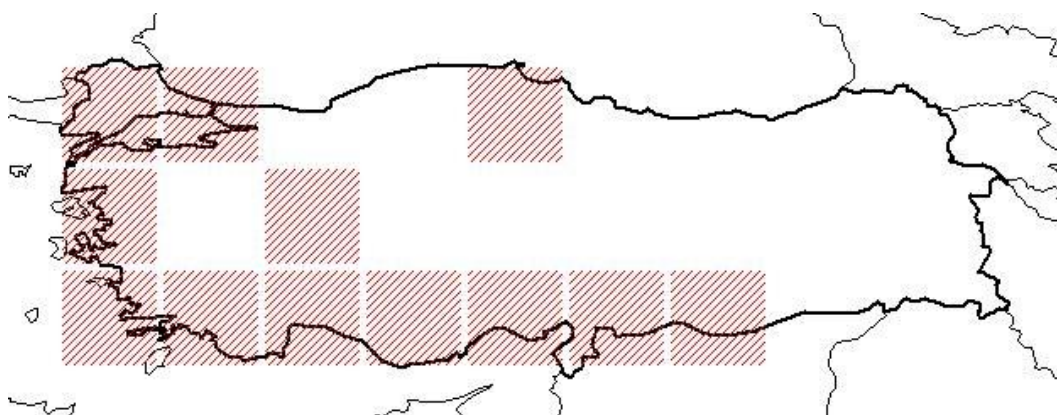

Figure 4. Distrubition of Styrax Oficinalis L. in Turkey

Tesbi shrubs mostly grows in forestry. its not agricultural appreciate but it have different usage in traditional life such as feeding of goat and solid fuel. It is also use as condiment, crude oil. It have antioxidant, antimicrobial, antifungal properties in medical treatment. Trunk and branch parts using for making wood materials [19], [20], [21]. In reference to [22], Natural insecticide is going to obtain from plant sap. For protect forest, necessary measure should be taken on timely. This plant is endangered species which is unprotected because of using for solid fuel and animal feeding.

3.1. Tesbi Seed Oil Compare with Other Important Oil Plants

Tesbi seeds are collected in Andırın town (37° 30' 09.70K, 36° 15' 46.04''D) which is Kahramanmaras province in Southeast Mediterranean of Turkey. Seeds are collected 440 m in October of 2015. Seed crude oil is determined 47% in Bozok University, Agriculture faculty Laboratory.

Figure 5. Locality of collected Tesbi seeds.

Tesbi seed oil is compared to some other important oil seed plants. As seen on Table 1, while vegetable oil rates are change from 20% to 50%, tesbi seed oil is 47.04%. This oil rate show that tesbi shrub seed have big potential. If this plant enter to plant production design, it will be provide very important benefit.

Table 1. Tesbi seed oil compare with other important oil plants

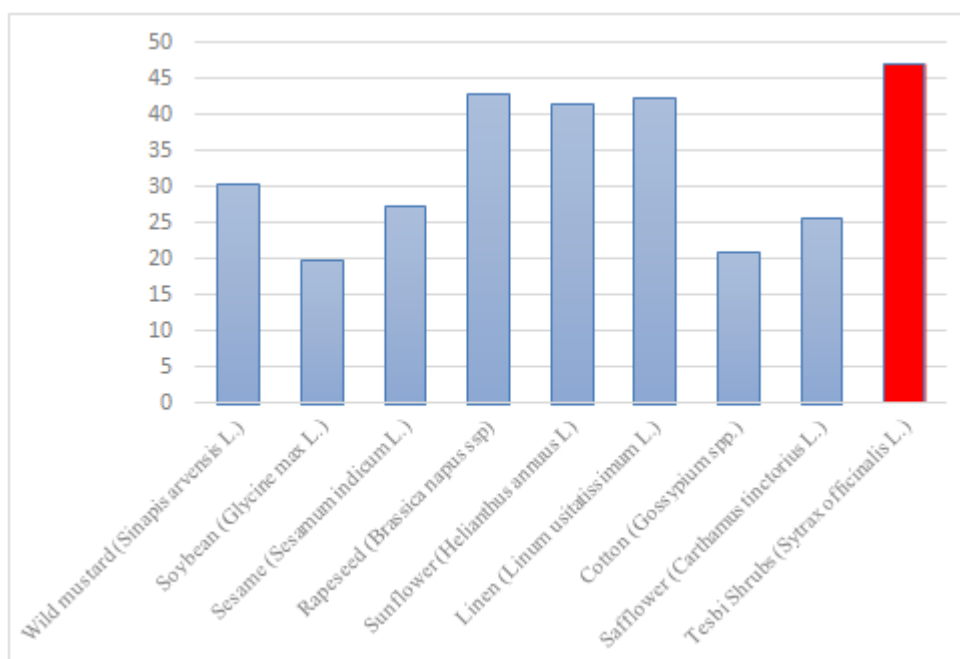| Plant	Crude oil (%)	Reference
Wild mustard (*Sinapis arvensis* L.)	30.45	[11]
Soybean (*Glycine max* L.)	20	[29]
Sesame (*Sesamum indicum* L.)	27.5	[30]
Rapeseed (*Brassica napus* ssp)	36-50	[31]
Sunflower (*Helianthus annuus* L)	33-50	[32]
Linen (*Linum usitatissimum* L.)	35–50	[33]
Cotton (*Gossypium spp.*)	21	[34]
Safflower (*Carthamus tinctorius* L.)	25.65	[11]
Tesbi Shrubs (*Sytrax officinalis* L.)	47.04	

Figure 6. Tesbi seed oil compare with other important oil plants

Countries which are making investigate in biodiesel industries preference marginal land for biodiesel production [23], [24]. Turkey which is have massive land and biodiversity find opportunity biodiesel production in the upcoming years. Thus, development of rural area and employment will accelerate. Moreover, increase the value of marginal land supply raw material for industrial production [25], [26]. Because of natural growing, tesbi shrubs are very important plant.

Erosion is the most important ecological issue which is control natural resource. Tesbi shrubs is growing broad and shallow and it have strong root structure. Because of this properties, plant can reduce rain drops and it protect soil from erosion. Also, tesbi shrubs can use dam catchment area for rehabilitation and it can extend economic life [27]. Tesbi shrubs can use many area such as recovery of environmental, using ornamental plant and plantation areas, wildlife protection areas, prevention of noise pollution. Styrax officinalis occurs dense in south of turkey and in provinence of Mersin which name is Gozne people are

making delicious jam from tesbi flower. This jam also show us that, plant can use for human comsumption [28].

4. CONCLUSION

Tesbi shrub seeds have 47.04% oil and plant can grow in marginal field which hasn't irrigation, bad soil condition. This plant can easily grow under forest and unfavorable conditons. If tesbi make fit for cultivation, it can gain favor such as obtaining industrial raw material, employment, improvement of biodiversity, prevention of erosion, global warming and put marginal land and unfavorable forest to good use.

ACKNOWLEDGMENT

REFERENCES

[1]. P. H. Davis, *Flora of Turkey and The East Aegean Islands*, 4nd ed, Edinburg, Scotland: Edinburgh University Press, 1972.
[2]. (2013) Climatevolenteers. [Online]. Available: http://www.climatevolunteers.com/?page=ilklimdegisikligi
[3]. R. Daghrir and P. Drogui, "Coupled electrocoagulation–electro-Fenton for efficient domestic wastewater treatment," *Environmental Chemistry Letters,* Vol.11, pp.151-156, June 2013.
[4]. C. Lorz, F. Makeschin and H. Weiss, *Integrated water resource management in Brazil* IWA Publishing, London, England, (eds., 2014) p. 134.
[5]. L. Brennan and P. Owende, "Biofuels from microalgae—A review of technologies for production, processing, and extractions of biofuels and co-products," *Renewable and Sustainable Energy Reviews,* Vol. 14 pp. 557–577, 2010.
[6]. M. Okcu, Z. Okcu, ve O, "Kalkısım, Atık Suların Tarımda Degerlendirilmesi ve Etkileri," Gumushane Üniversitesi Uluslararası katılımlı Cevre sempozyumu, 2013, s.385.
[7]. Y. Wang, X. Nie and Z. Liu, "Biodiesel Synthesis from Styrax confusus Hemsl Catalyzed by S2O8 2−/ZrO2‑TiO2‑Fe3O4," *J Am Oil Chem Soc* (2015) 92:813–820 (2015)
[8]. (2012) The OGM website. [Online]. Available: http://www.ogm.gov.tr/ekutuphane/Sayfalar/IstatistiklerAnonim
[9]. S. Jaichandar and K. Annamalai, "Emission and combustion characteristics of Pongamia oil methyl ester and its diesel blends in a CI engine," *Energy Sources Part A,* vol. 37 pp. 1473-1478, 2015.
[10]. T. Eryılmaz, and M.K. Yesilyurt "Influence of blending ratio on the physicochemical properties of safflower oil methyl ester-safflower oil, safflower oil methyl esterdiesel and safflower oil-diesel," *Renewable Energy,* vol. 95, pp. 233 – 247, 2016.
[11]. T. Eryılmaz, M.K. Yesilyurt, C. Cesur and O. Gokdogan, "Biodiesel production potential from oil seeds in Turkey," *Renewable and Sustainable Energy Reviews*, vol. 58, pp. 842-851, 2016.
[12]. T. Afacan, "Petrol Piyasası mı? Biyoyakıt yasası mı? Biyoyakıt Dünyası," Biyoyakitlar ve biyoyakıt teknolojileri sempozyumu, 2007, Sayı 12, s.34.
[13]. M. Cetin, and H. Kus, "Erzincan'ın Biyodizel Yakıt Amaclı Tarımsal üretim Potansiyeli," V. Yenilenebilir Enerji Kaynakları Sempozyumu 2009.
[14]. H. Oguz, H. Ogüt and O. Gokdogan, "Türkiye tarım havzaları üretim ve destekleme modelinin biyodizel sektörüne etkisinin incelenmesi," *Igdır Üniversitesi Fen Bilimleri Enstitüsü Dergisi*, vol. 2, pp. 77 – 84, 2012.
[15]. F. Yaltırık, *Flora of Turkey and East Aegean Island*, Ed.PH. Davis. Edinburg, Scotland: Edinburgh at the university, 1972.
[16]. Fritsch, P. W. 1996. Isozyme analysis of intercontinental disjuncts within Styrax (Styracaceae): Implications for the Madrean-Tethyan hypothesis. Amer. J. Bot. 83: 342–355.
[17]. T. Mataracı, *Agaclar, doga severler icin rehber kitap*, *Marmara Bolgesi dogal egzotik agac ve calıları*, İstanbul, Turkey: TEMA Vakfı, Yayın, 2002.
[18]. Y. Akman, O. Ketenoglu, L. Kurt, K. Güney, E. Hamzaoglu, and N. Tug, *Angiospermae (kapalı tohumlular)*, Ankara, Turkey: Palmiye Yayınları, 2007.
[19]. C. Proestos, I.S. Boziaris, G-J.E. Nychaqs and M. Komaitis, "Analysis of flavonoids and phenolic acids in Grek aromatic plants: Investigation of their antioxidant capacity and antimicrobial activity," *Food Chem.* Vol. 95, pp. 664-671, 2006.
[20]. P.M. Guarrera and L.M. Lucia, "Ethnobotanical Remarks on Central and Southern Italy," *J. Ethnobiol. Ethnomedicine*, vol. 3, pp.23, 2006.
[21]. C. Yücedag, "Effect oc Cracking and Sowing Time on Germination of Sytrax officinalis L. seeds," *African Journal of Biotechnology*, Vol. 10(73), pp. 16448 – 16451, 2011.
[22]. K. Dayıoglu, "Bazı Bitki (Melia azederach L., Sytrax officinalis L.,Quercus ssp.)Tohumlarından Elde Edilen Ekstraktların Cam Kesebocegi, Thaumetopoea pityocampa (Schiff.), Larvalarına Karsı Kullanılması," K.S.Ü Fenbilimleri Enstitüsü Orman Mühendisligi ana Bilim Dalı, Kahramanmaras, Turkey, 2008.
[23]. H. Sanlı, E. Alptekin and M. Canaklı, "Biyodizel Harmanlama Zorunlulugu – Türkiye Yaglı Tohum Sektorü – Biyodizel Hammaddesi Olarak Atık Bitkisel ve Hayvansal Yaglar, Ekoloji," Sempozyumu Bildiri Ozetleri Kitabı, 2013, s.26.

[24]. O. Gokdogan and M.F. Baran, M. F., "The energy balance of the sesame (Sesamum indicum L.) oil," *Energy Education Science and Technology Part A*: *Energy Science and Research*, vol. 32(6), pp. 7083-7086, 2014.

[25]. A. Karabulut, O. Sahin, S. Yapıcı and M.S., "Ezgi, Pamuk Yagında Biodizel Üretimine Cesitli Katalizorlerin EtkisininVizkozite ve İletkenlikle Takip edilmesi," VII. Ulusal Temiz Enerji Sempozyumu, UTES', 2008.

[26]. F. Gao, L. Zhaob and X. Wanga, "The Research Review About The Effect Of Bio-Fuel Development On Agricultural Market And Agriculture," *Agriculture and Agricultural Science Procedia*, vol. 1, pp. 488–494, 2010.

[27]. I. Ghawi and A. Battikhi, "Water melon production under mulch and trickle irrigation in the Jordan valley," *Journal of Agronomy and Crop Science*, vol. 157, pp. 145-155, 1986.

[28]. S. Oflas. (2016) Batı Anadolu'da Styrax officinalis'in yayılısı ile ilgili on müsahedeler. [Online] Available: http://biyolojikongreleri.org/pdf/UBK6_SZ_29.pdf.

[29]. R.F. Wilson, "Seed composition. In: H.R. Boerma and J.E. Specht, editors, Soybean: Improvement, production, and uses," *Agron. Monogr.* Vol. 16, pp.621–677, 2004.

[30]. O. Gokdogan and M.F. Baran, "The energy balance of the sesame (Sesamum indicum L.) oil," *Energy Education Science and Technology Part A: Energy Science and Research*, 2014 Vol. 32(6), pp. 7083-7086, 2014.

[31]. D. K. Salunkhe, J.K. Chavan, R.N. Adsule and S.S. Kadam, S. S., *World oilseeds: chemistry, technology, and utilization*, New York: America: Van Nostrand. Reinhold, 1992.

[32]. A.Y. Panchenco, "Sunflower production and breeding in the USSR." In: Proc. 2nd Int. Sunflower Conf. Morden, Manitoba, 1966, p. 15–29.

[33]. (2016) Canadian Grain Commission website. [Online]. Available: https://www.grainscanada.gc.ca/index-eng.htm.

[34]. E. Lukonge, M.T. Labuschagne and A. Hugo, "The evaluation of oil and fatty acid composition in seed of cotton accessions from various countries," *J. Sci. Food. Agric.*, vol. 87, pp. 340–347, 2007.

Numerical Investigation Of The Effect Of Twisted Tape In A Tube Using Water-Tio2 Nanofluid On Heat Transfer Enhancement

Toygun Dagdevir[1], Orhan Keklikcioglu[2]and Veysel Ozceyhan[3]

Abstract

In this study, effects of inserting twisted tape into a horizontal tube and adding TiO2 nanoparticle to water on heat transfer enhancement performance and pressure drop penalty are investigated with using CFD program. Analyses are carried out with Reynolds number of in range from 7860 to 15860, and constant heat flux of $50kW/m^2K$ is applied to wall of the tube. In order to simulate turbulent nanofluid flow k-ω standard turbulent model is applied for all cases. TiO2 particles with diameter of 10 nm dispersed in water with volume fraction of 0.2% - 2.0% are used as the working fluid. In order to create swirl flow and enhance heat transfer, the twisted tape (constant twist ratio is y/W=3.0) is used in this study. The results show that adding nanoparticle to water causes to get more convective heat transfer coefficient as from 6% (for 0.2% vol. fract.) to 11% (for 2.0% vol. fract.) in a smooth tube. Furthermore, both adding nanoparticle to water and inserting the twisted tape to the smooth tube causes to 1.44 times greater convective heat transfer coefficient than case of smooth tube and water. In addition to heat transfer performance, pressure drop penalty is investigated in this study. Increasing nanoparticles in the water increase pressure drop penalty slightly, but using twisted tape in the smooth tube increases pressure drop penalty as about 6.5 times more.

Keywords: *CFD, nanofluid, twisted tape, heat transfer, pressure drop*

1. INTRODUCTION

At last decade, energy costs dramatically rise up day by day, since human population increase and energy sources are consumed. Using the energy efficiently is significantly important for countries that import energy, especially. Heating or cooling systems need so much energy input such as pumping power and electrical resistant for heating, and compressor power for cooling. Within this scope, heat transfer enhanced methods are used and investigated methods. In recent years, nanofluid is used as working fluid for heat transfer devices. Choi [1] is probably the first researcher about the use of particles in nano dimension. Many researchers experimentally studied on this field and reported that nano-particles in the fluids augment heat transfer performance depends on concentration amount, particle size and Reynolds number at last three decades [2-10]. Main reason of using nanofluid is that thermal conductivity property is greater than conventional fluid. Thus, heat transfer performance enhances in comparison with using conventional fluid. The heat transfer enhanced investigations are carried out experimentally and numerically, or both of them.

Moghadassi et al. [11] investigated numerically the effect of water based Al2O3 and Al2O3-CuO hybrid nanofluid on forced convective heat transfer. The nanofluid with 0.1 % volume fraction and average particle size of 15nm was considered. Their results showed that higher convective heat transfer coefficient was obtained for Al2O3-CuO nanofluid. And they reported that average Nusselt number increase was 4.73% and 13.46% in comparison with Al2O3-water and distilled water, respectively. Celen et al. [12] numerically carried out an investigation for TiO2-water nanofluids in order to observe average temperature, pressure and velocity distribution inside pipe. They used an experimental study data to validate accuracy of numerical methodology. Their results were tolerably as similar as experimental results. Demir et al.[13] searched numerically forced convection flows of nanofluids consisting of water with Al2O3 and TiO2 nanoparticles in a horizontal tube with constant wall temperature used of a single-phase model. Dawood et al.[14] numerically

---

investigated the effect of nanoparticles on heat transfer enhancement in an elliptic annulus, unlike circular pipe. Al2O3, CuO, SiO2 and ZnO were employed as nanoparticles and volume fraction and Reynolds number respectively was ranging from 0.5% to 4% and 4,000 to 10,000. Their numerical results showed that the best heat transfer was obtained for gyliserin-SiO2 mixture that was volume fraction of 4% and Reynolds number of 10,000.

2. NUMERICAL INVESTIGATION

2.1. Solution Domain

In this study, thermal performance of twisted tape inserted in a horizontal straight tube under constant heat flux is numerically investigated via a CFD program. Working fluid is selected as water and, in addition to twisted tape insert, TiO2 nanoparticle is added to water. In order to model the solution domain 3D geometry is described as in Fig. 1. Smooth tube (ST) and twisted tape inserted tube (TTIT) are illustrated in Fig 2. The twisted tape has y/w ratio of 3.0. y and w represent the pitch length of twisted tape and width of the tape, respectively.
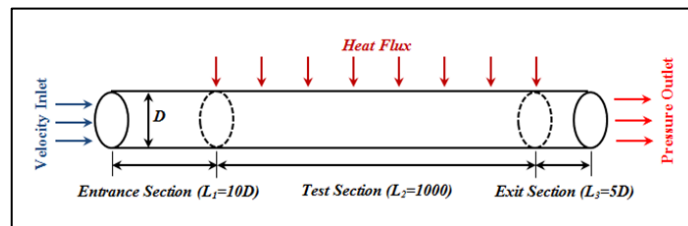

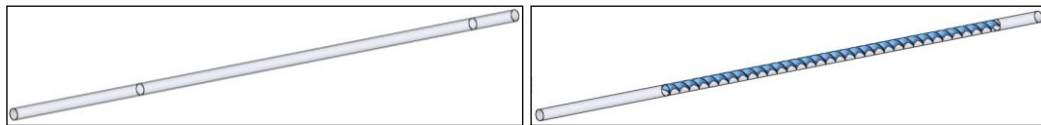*Figure 1. Solution domain and boundary condition types*

Figure 2. (a) Smooth tube (ST)   *(b) twisted tape inserted tube (TTIT)*

The test tube material is aluminium and selected as 19 mm diameter and an entrance section (L1) is taken as a 10D to supply fully developed flow at the inlet of the test region, test section L2 is considered as 1m and exit section (L3) is chosen as 5D to defect the reverse flow. The boundary condition and definition are given in Table 1. Polyhedral mesh structure and boundary layer mesh are created both smooth tube and twisted tape as illustrated in Fig 3.
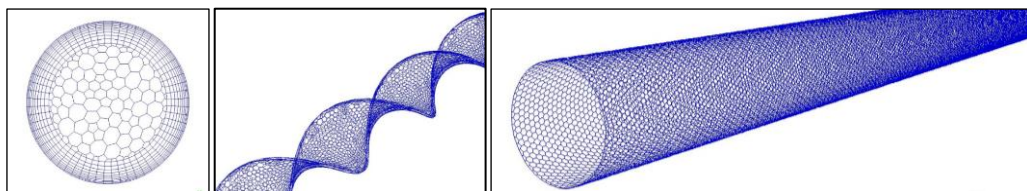

Figure 3. Mesh structure of cross sectional view of (a) the tube at inlet and outlet,(b) outer surface of twisted tape (c) outer surface of tube.

Table 1. Boundary condition definitions and values

	Definition	Value
D [mm]	Diameter	19
L_1 [mm]	Entrance Section	10D
L_2 [mm]	Test Section	1000
L_3 [mm]	Exit Section	5D
q'' [kW/m^{2}K]	Constant Heat Flux	50
Inlet Velocity magnitude [m/s]	Velocity Inlet	Calculated depends on Re
Gauge Pressure [Pa]	Pressure Outlet	0

2.2. Data Reduction and Thermo-Physical Properties of Nanofluid

The CFD program uses differential equation to simulate and calculate flow characteristic and thermal occurrences. Used conversation equations in CFD program are as follows:

Conservation of mass equation [15]*:*

$$\frac{\partial \rho}{\partial t} + \nabla.(\rho u) = 0 \tag{1}$$

Conservation of momentum equation [15]:

$$\frac{\partial}{\partial t}(\rho \vec{v}) + \nabla(\rho \vec{v}\vec{v}) = -\nabla P + \nabla(\bar{\bar{\tau}}) + \rho \vec{g} + \vec{F} \tag{2}$$

Energy equation [15]:

$$\frac{\partial}{\partial t}(\rho E) + \nabla(\vec{v}(\rho E + p)) = \nabla(k_{eff}\nabla T - \sum_j h_j \vec{J}_i + (\bar{\bar{\tau}}_{eff}.\vec{v})) + S_h \tag{3}$$

The results were compared with S. Eimsa-ard [16] et al. and commonly used equations that are Gnielinski Eq. (6) and Blasius Eq. (7) in terms of Nusselt number (4) and friction factor (5), respectively.

Gnielinski Equation [17]:

$$Nu = \frac{hD}{k} \tag{4}$$

$$f = \frac{\Delta P}{\frac{1}{2}\rho V^2 \frac{L}{D}} \tag{5}$$

$$Nu = \frac{\left(\frac{f}{8}\right)(Re-1000)Pr}{1 + \left[12.7\left(\frac{f}{8}\right)^{0.5}(Pr^{2/3}-1)\right]} \tag{6}$$

Blaisus Eq. [18]:

$$f = 0.316 Re^{-0.25} \tag{7}$$

2.3. Validation of the numerical methodology

In order to ensure validation of the numerical methodology, especially including fluid mechanics problems turbulence model should be determined, and experimental results or empirical correlations can be used for comparing numerical results. In this context, different turbulence models are tested and k-w standard model is most matching model with reference results. Validation of the numerical study for smooth tube and water is given in Fig 4 and 5 in terms of Nusselt number and friction factor, respectively. As can be seen in these figures, a good agreement is ensured for proving accuracy of numerical methodology.
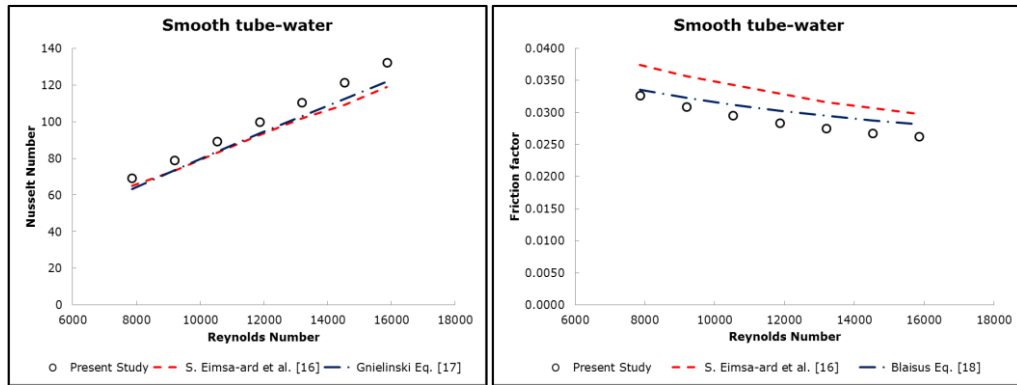
Figure 4. Numerical results for smooth tube and water in terms of (a) Nusselt number (b) friction factor

Mixture approach is employed to model nanofluids, and properties of fluid are applied as independent in temperature. Validation of nanofluid with different fraction (φ=0.002, 0.006, 0.01 and 0.02) and different nanoparticles is illustrated in Fig. 5. Good agreement is observed between the result of present study and the other studies. Thermo-physical properties of nanofluid is calculated with following equations:

Density of nanofluid:

$$\rho_{nf} = (1 - \varphi)\rho_{bf} + \varphi\rho_{np} \tag{8}$$

Specific heat of nanofluid:

$$Cp_{nf} = \frac{(1-\varphi)(\rho_{bf})(cp_{bf})+(\varphi\rho_{np})(cp_{np})}{\rho_{nf}} \tag{9}$$

Thermal conductivity:

$$k_{nf} = k_{bf} \frac{[k_{np}+(n-1)k_{bf}-(n-1)\varphi(k_{bf}-k_{np})]}{[k_{np}+(n-1)k_{bf}+\varphi(k_{bf}-k_{np})]} \tag{10}$$

$$n = 3/\psi \tag{11}$$

where n is the empirical shape factor and ψ is the sphericity, defined as the ratio of the surface area of a sphere to the surface area of the particle (Eq. 11), as stated by Duangthongsuk and Wongwises [19]. The sphericity value assumed as 1. Expressions of knf, knp and kbf are the thermal conductivity of nanofluid, nanoparticle and base fluid, respectively. Dynamic viscosity of hybrid nanofluid does not need to calculate again due not to including expect of volume fraction (φ) in the formula.

Dynamic viscosity:

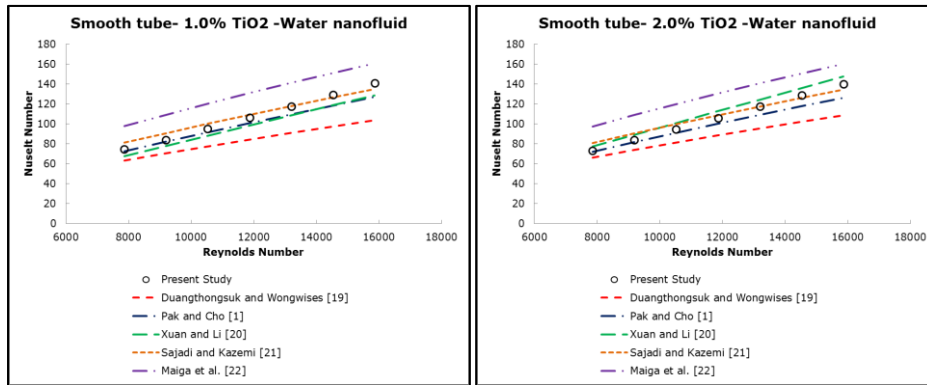$$\mu_{nf} = \mu_{bf}(123\varphi^2 + 7.3\varphi + 1) \tag{12}$$
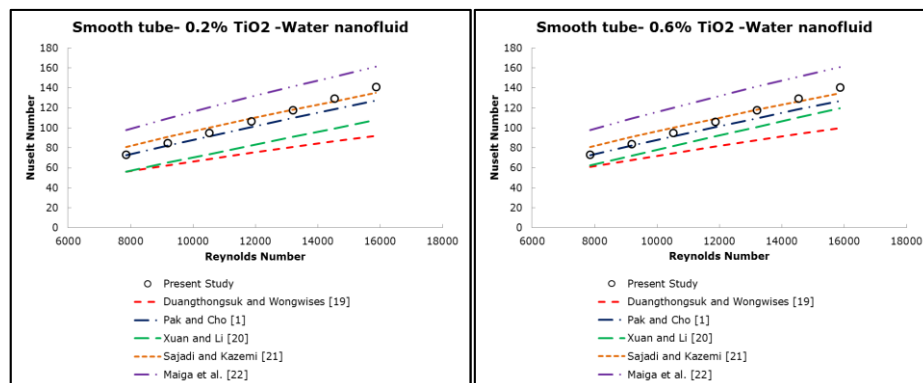
Figure 5. Validation of numerical results for smooth tube and TiO2-water nanofluid in terms of Nusselt number versus Reynolds Number.

In addition to nanofluid investigation, twisted tape effect is investigated in this study, and twisted tape for water validation is ensured as illustrated in Figure 6.
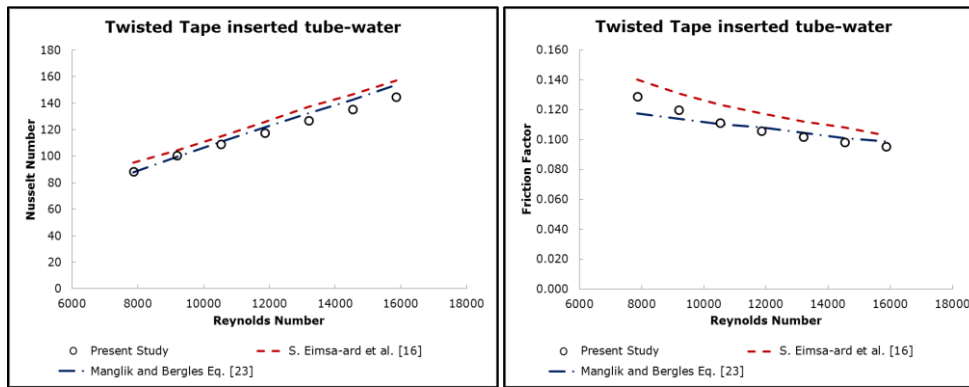

Figure 6. (a) Nusselt number results for TTIT   *(b) Friction factor results for TTIT*

3. RESULTS AND DISCUSSIONS

In this study, numerical investigation of effects of both TiO2-water nanofluid and twisted tape on thermal and hydraulic performance is carried out by using a CFD program. The nanofluid volume fraction is considered in range from 0.002 to 0.02. With developing nano technology, nanofluids have been used in heat transfer mechanisms. Because thermal conductivity of working fluid increases, heat transfer enhances for this systems. Numerical results of TiO2-water nanofluid through the smooth tube are given in terms of heat transfer coefficient and pressure drop in Fig 7 and 8, respectively. With increment of nanoparticle into water, heat transfer coefficient increases for increment of Reynolds number. Pressure drop increases with increment of nanoparticle into water, due to viscosity and density of the fluid increase.
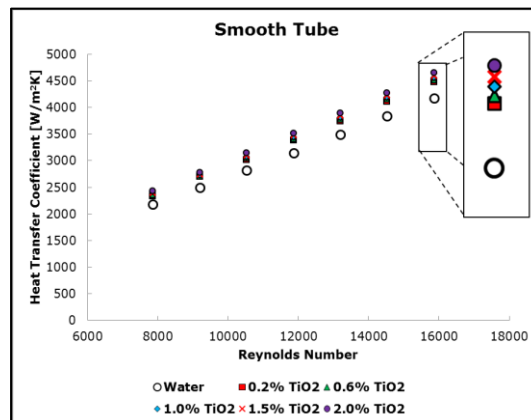

Figure 7. Results of TiO2-water nanofluid through the smooth tube in terms of heat transfer coefficient versus Reynolds number.
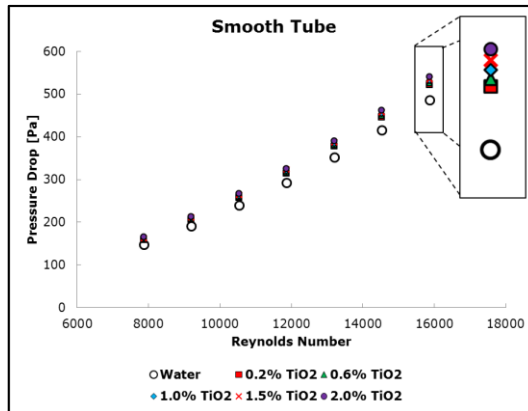
Figure 8. Results of TiO2-water nanofluid through the smooth tube in terms of pressure drop versus Reynolds number

In order to enhance heat transfer performance, turbulators like twisted tape insert are widely used. The twisted tape physically enhanced heat transfer by destructing thermal and hydraulic boundary layer near the inner surface of the tube. The effect of twisted tape in terms of heat transfer coefficient and pressure drop is given in Fig 9 and 10. The twisted tape inserts in tube create swirl flow, and because of that secondary flow occurs. With occurrence of the secondary flow, the fluid more contacts with heated wall and spends more time until leave the tube. The swirl flow and secondary flow is depicted in Figure 11 and 12, respectively. In other hand, inserting twisted tape cause to increase pressure drop penalty. It is expected result, because the flow counters with an obstacle surface in the flow direction.
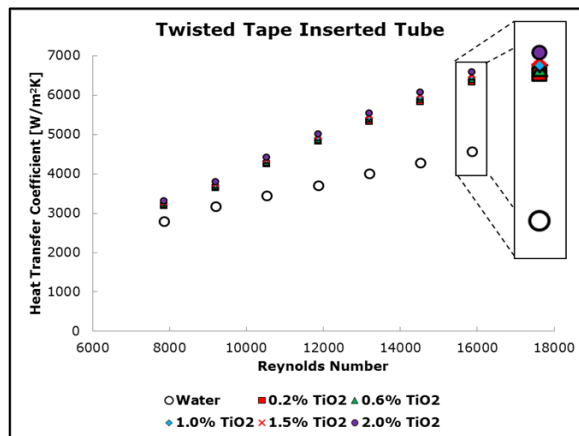

Figure 9. Results of TiO2-water nanofluid through the twisted tape inserted tube in terms of heat transfer coefficient versus Reynolds number.
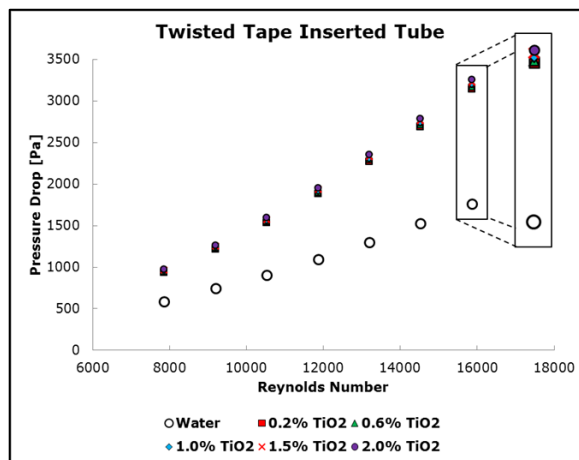

Figure 10. Results of TiO2-water nanofluid through the twisted tape inserted tube in terms of pressure drop versus Reynolds number.
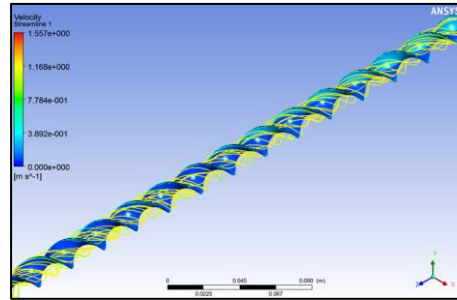
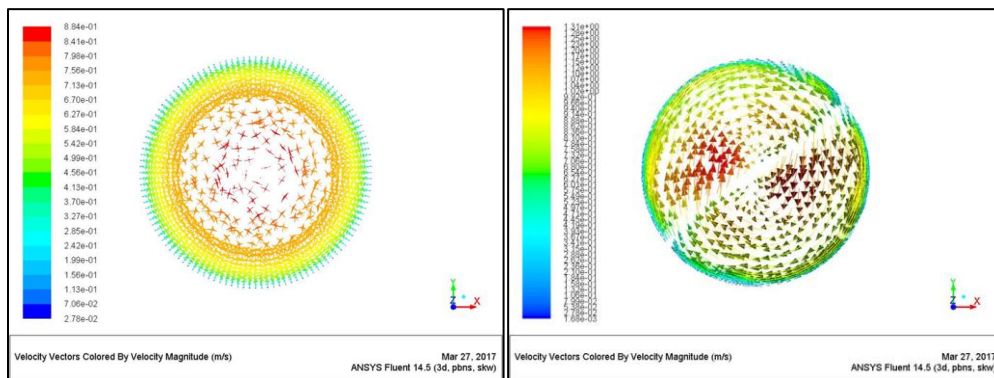*Figure 11. Swirl flow due to twisted tape through the tube.*

Figure 12. (a) Velocity vector contour of the smooth tube   *(b) Velocity vector contour twisted tape inserted tube.*

4. CONCLUSION

In this study, effect of TiO2-water nanofluid and twisted tape insert on heat transfer and pressure drop is numerically investigated by using mixture phase model. Results showed that convective heat transfer enhances for all considered volume fraction of TiO2 nanofluid with increasing Reynolds number. Major reason of the heat transfer enhancement is that thermal conductivity of the nanofluid is so greater than distilled water. Furthermore, with inserting twisted tape into smooth tube, it is purposed generating secondary flow. Maximum heat transfer coefficient is obtained as 6593 W/m^{2}K for the case of twisted tape inserted tube volume fraction 2.0, Reynolds number of 15,860. This value is 1.44 times greater than smooth tube for same Reynolds number.

The main findings can be summarized as physical (inserting twisted tape) and chemical (adding nanoparticle) reasons at below:

In terms of physical reasons

- ✓ Inserting a twisted tape in a tube increases heat transfer and pressure drop.
- ✓ The main reason of increasing heat transfer is destructing the boundary layer and occurring secondary flow.
- ✓ Maximum heat transfer coefficient is obtained as 6593 W/m^{2}K for Reynolds number of 15860. This value is 1.44 times greater than smooth tube for same Reynolds number.
- ✓ The main reason of increasing pressure drop is that flow encounter with an obstacle surface, and increasing static pressure through the tube.

In terms of chemical reasons

- ✓ Adding nanoparticle up to volume fraction of 2.0% into water, increases the heat transfer, as well. The main reason of this result is that thermal conductivity of the nanofluid increases, and because of that, heat transfer occurs more effectively between the molecules.
- ✓ Adding nanoparticle into water slightly increase the pressure drop in comparison with heat transfer. The reason of increasing pressure drop is related with increasing viscosity and density of the nanofluid.

REFERENCES

[1]. B.C. Pak and Y.I. Choi, "Hydrodynamic and Heat Transfer Study of Dispersed Fluids with Submicron Metallic Oxide Particles" *Exp. Heat Transfer*, vol. 11, pp. 151–170, August 2016.

[2]. S. Eimsa-ard, P. Promvonge, Numerical study on heat transfer of turbulent channel flow over periodic grooves, *International Communications in Heat and Mass* Transfer 35 (2008) 844-852.

[3]. A. Azari, M. Lalbasi, M. Derakhshandeh and M. Rahimi, An experimental study on Nanofluids convective heat transfer through a straight tube under constant heat flux, *Fluid Dynamics and Transport Phenomena* 21 (2013) 1082-1088.

[4]. S. Z. Heris, S. Gh. Etemad and M. N. Esfahany, Experimental investigation of oxide nanofluids laminar flow convective heat transfer, *International Communications in Heat and Mass Transfer* 33 (2006) 529-535.

[5]. S. Suresh, K. P. Venkitaraj, P. Selvakumar and M. Chandrasekar, Effect of Al2O3-Cu/water hybrid nanofluid in heat transfer, *Experimental Thermal and Fluid Science*. 38 (2012) 54-60.

[6]. M. M. Heyhat, F. Kowsary, A. M. Rashidi, S. A. V. Esfehani, A. Amrollahi, Experimental investigation of turbulent flow and convective heat transfer characteristics of alumina water nanofluids in fully developed flow regime, *International Communications in Heat and Mass Transfer* 39 (2012) 1272-1278.

[7]. D. Wen and Y. Ding, Experimental investigation into convective heat transfer of nanofluids at the entrance region under laminar flow conditions, *International Communications in Heat and Mass Transfer* 47 (2004) 5181-5188.

[8]. B. Sahin, G. G. Gültekin, E. Manay, S. Karagoz, Experimental investigation of heat transfer and pressure drop characteristics of Al2O3-water nanofluid, *Experimental Thermal and Fluid Science* 50 (2013) 21-28.

[9]. M. H. Esfe, S. Saedodin, M. Mahmoodi, Experimantal studies on the convective heat transfer performance and thermo physical properties of MgOwater nanofluid under turbulent flow, *Experimental Thermal and Fluid Science* 52 (2014) 68-78.

[10]. V. Trisaksri, S. Wongwises, Critical review of heat transfer characteristics of nanofluids, *Renewable and Sustainable Energy Reviews* 11 (2007) 512-523.

[11]. A. Moghadassi, E. Ghomi, F. Parvizian, "A Numerical Study of water based Al2O3 and Al2O3-Cu Hybrid Nanofluid Effect on Forced Convective Heat Transfer" *Int. Journal of Thermal Sciences*, 2015; 92: 50-57.

[12]. A. Celen, N. Kayaci, A. Cebi, H. Demir, A. S. Dalkilic, S. Wongwises "Numerical Study on Application of CuO-water Nanofluid in Automotive Diesel Engine Radiator" *Modern Mechanical Engineering*, 2012; 2: 130-136

[13]. H. Demir, A. S. Dalkilic, N. A. Kürekci, W. Duangthongsuk, S. Wongwises, Numerical investigation on the single phase forced convection heat transfer characteristics of TiO2 nanofluids in a double-tube counter flow heat exchanger, *International Communications in Heat and Mass Transfer* 38 (2011) 218-228

[14]. H. K. Dawood, H. A. Mohammed, N. A. C. Sidik, K. M. Munisamy, Numerical investigation on heat transfer and friction factor characteristics of laminar and turbulent flow in an elliptic annulus utilizing nanofluid, *International Communications in Heat and Mass Transfer* 66 (2015) 148-157.

[15]. *Fluent v.6.3 User Guide*, Fluent Corporation, Lebanon, New Hampshire, 2006.

[16]. S. Eimsa-ard, P. Seemawute, K. Wongcharee, Influences of peripherally-cut twisted tape insert on heat transfer and thermal performance characteristics in laminar and turbulent tube flows, Experimental Thermal and Fluid Science, 2010, vol. 34, pp. 711-719.

[17]. F.P. Incropera, P.D. Witt, T.L. Bergman, A.S. Lavine, *Fundamental of Heat and Mass Transfer*, John-Wiley & Sons, 2006.

[18]. Petukhov BS: Heat transfer and friction in turbulent pipe flow with variable physical properties. *In Advances in Heat Transfer*. Edited by: Hartnett JP, Irvine TS. New York: Academic Press; 1970.

[19]. W. Duangthongsuk and S. Wongwises, An experimental study on the heat transfer performance and pressure drop of TiO2-water nanofluids flowing under a turbulent flow regime, *International Journal of Heat and Mass Transfer*, 2010, vol. 53, pp. 334-344.

[20]. Y. Xuan, Q. Li, Investigation on convective heat transfer and flow features of nanofluids, *ASME J. Heat Transfer*, 2003, vol. 125, pp. 151-155.

[21]. A. R. Sajadi and M.H. Kazemi, Investigation of turbulent convective heat transfer and pressure drop of TiO2/water nanofluid in circular tube, *International Communications in Heat and Mass Transfer*, 2011, vol. 38, pp. 1474-1478.

[22]. M. S.E.B. Maiga, C.T. Nguyen, N. Galanis, G. Roy, T. Mare, M. Coqueux, Heat transfer enhancement in turbulent tube flow using Al2O3 nanoparticle suspension, *International Journal of Numerical Methods for Heat and Fluid Flow*, 2006, vol. 16, pp. 275-292.

Effects of Promalin (GA$_{4+7}$ + BA) Applications on Yield and some Nut Quality Characteristics of Pistachio

İzzet Acar[1]*, Niyazi SOGUT[2], Bekir Erol AK[1]

Abstract

Pistachio cultivation is more concentrated in the Southeastern Anatolia Region in our country. Pistachio production is increasing in Turkey from 30 thousand tons in 2001, increased to 144 thousand tons in 2015. Fruit size and yield are influenced by genetic factors, cultural practices and environmental factors. These factors are primarily affect cell number and cell size directly or indirectly. Gibberellins and auxins are controlling cell division and thus starting fruit size by affecting cell division. Promalin containing gibberellins and cytokinin promotes both cell division and cell enlargement. The aim of this study is to determine the effects of different doses of Promalin (GA$_{4+7}$+BA) on yield and quality characteristics of Kırmızı pistachio cultivar which widely grown in Turkey. For this purpose, Promalin had been sprayed to pistachio trees at the small fruit stage and beginning of kernel development stage, and its effects were determined on yield and quality of pistachio.

Finally, 25 ppm Promalin treatment had the highest fruit weight and yield value in Kırmızı cultivar. The highest fruit set and the lowest blank nut rate were obtained from 100 ppm while the best yield obtained from 50 ppm Promalin.

Keywords: *Pistachio, Fruit Quality, Promalin, Yield*

1. INTRODUCTION

Pistacia genus is a member of the Anacardiaceae family and contains at least 11 species [1], including *Pistacia vera* L., the cultivated pistachio. Pistachios have been grown in Turkey for over 1000 years, and the country has one of the largest pistachio germplasm collections in the world [2]. Turkey is also the third highest producer of pistachios in the world, after Iran and the USA [3].

Pistachio grows in the appropriate microclimate of the northern and southern hemisphere between 30-45° parallel of the world. Turkey is on the gene center of pistachio in the northern hemisphere; in particular, the Southeastern Anatolia Region has an important place in the pistachio cultivation [4].

Pistachio cultivation is concentrated in the Southeastern Anatolia Region of Turkey. Turkey is third in the world after Iran and the USA with 300.000 ha pistachio plantation area and 144.000 tons pistachio production [5]. Currently, over 95% of the pistachio orchards in Turkey are grown under rainfed (i.e. non-irrigated) conditions.

In the fruit trees, fruit size and yield are influenced by genetic factors, cultural practices and environmental factors. These factors affect cell number and cell size, directly or indirectly. Promalin which containing gibberellins and cytokinin promotes both cell division and cell elongation.

Exogenous application of plant bio-regulators (PBRs) has been reported to improve the endogenous levels of phytohormones [6], mineral nutrients [7], flowering and fruiting of different fruit crops [6].

By the use of plant bio-regulators; higher yield and improved fruit quality has been reported in mango [8], citrus [9], apple [10] and other fruits.

---

[1] *Corresponding author: Department of Horticulture, Faculty of Agriculture, Harran University, Sanlıurfa, Turkey. izzetacar@harran.edu.tr*

[2] *Department of Horticulture, Institute of Natural and Applied Sciences, Harran University, Sanlıurfa, Turkey.*

Exogenous application of Promalin has effective role on improving the yield, productivity and fruit quality in apple and pear [11]. One of the techniques to improve fruit size and shape in apple is Benzyladenine (BA) alone or in combination with Gibberellins (GA_{4+7}) applications [12].

Promalin has two ingredients. The first is a mixture of two natural gibberellins commonly found in plants which are Gibberellins 4 and Gibberellins 7. The second is a compound also found in nature classified as a cytokinin, 6-Benzyladenine. Gibberellins and cytokinins are growth regulators specific to plants. The two ingredients in Promalin contribute to increase fruit size; 6-BA stimulates cell division, and GA_{4+7} causes cell expansion. These effects only take place in plant tissues and only during the very early development of the fruitlet. The result is a larger fruit with more cells and larger cells. In addition, the gibberellins help reduce fruit russet and improve overall fruit finish [13].

The aim of this study was to determine the effects of different doses of promalin (GA_{4+7} plus BA) on yield and some quality characteristics of Kırmızı pistachio cultivar widely grown in Turkey.

2. MATERIAL AND METHODS

This study was carried out on 30-year-old pistachio trees of Kırmızı cultivar at Nizip District of Gaziantep province in Turkey in 2015. These trees were grown under nonirrigated conditions at a planting density of 180 trees/ha. Trees were selected on the basis of their uniformity of growth and fruit yield. Promalin, containing 50% Gibberellins and 50% Benzyladenine, was applied to the pistachio trees. The foliar application of Promalin (0 ppm, 25 ppm, 50 ppm, 100 ppm and 200 ppm) was conducted twice in year (once in beginning of May at the 'small fruit' stage and again in mid-June at the 'beginning of kernel development' stage) using a tractor-mounted sprayer.

Number of nuts per cluster were counted on the 12 fruit clusters randomly selected from each side of trees to determine the fruit set.

Mature nuts of the 'Kırmızı' cultivar were hand-harvested at the beginning of September in 2015, and fresh yield was measured in the orchard using a scale. A 1-kg sample of fresh nuts from each tree was left to dry for 5-6 days, allowing the fresh yield of each tree to be converted to dry yield (kg dry nut weight per tree) using the dry/fresh weight ratio of the nut samples.

Yield was evaluated at the harvest as kg fruit per tree and as yield per trunk cross-sectional area as g/cm^2. Quality characteristics were analyzed for blank nut rate (%), 100 nut weight (g), split nut rate (%) and kernel ratio (%, kernel weight / nut weight x 100).

The experiment was set up in a randomized block design with five replicates per treatment. The data were analyzed by ANOVA test from the statistical package MSTAT and differences between means were separated with the Fischer's Least Significant Difference (LSD) calculated with $p \leq 0.05$.

3. RESULTS AND DISCUSSION

3.1. Effect of Promalin on fruit set of pistachio trees

Promalin applications affected fruit set by counting number of nuts per cluster. The highest number of nuts was obtained from 100 ppm and the lowest obtained from 0 ppm (control); and 100 ppm Promalin increased fruit set 16.2% when compared with control (Table 1).

The highest fruit set obtained from 60 ppm Promalin in Starking Delicious apple [14].

3.2. Effect of Promalin on Yield per tree and yield per trunk cross sectional area

The highest yield per tree was obtained from 25 ppm and 50 ppm Promalin applications, and the lowest was from control (Table 1). 25 ppm and 50 ppm Promalin increased yield per tree 20.4% and 17.8% as to control, respectively.

Similarly, the highest value of yield per trunk cross sectional area was observed on 25 ppm and 50 ppm, and the lowest on 200 ppm and 100 ppm Promalin (Table 1). Yield per tree couldn't always confirm yield per trunk cross sectional area, because of growth differences between the trees.

Cytokinin applications increased yield, growth and Fe and Zn content of leaves in sweet cherries [15]. GA_{4+7} application increased yield of orange trees as 21%, and not only gibberellin applications, but combinations of GA+PCPA+2,4,5-T also could proposed for citrus fruits trees [16]. Foliar application of 25 ppm benzyladenine + 0.25% urea combination provided the highest yield in 'Uzun' pistachio cultivar [17].

Table 1. Effect of different Promalin doses on number of nuts, yield per tree and yield per trunk cross sectional area.

Promalin doses (ppm)	Number of nuts per cluster		Yield per tree		Yield per trunk cross sectional area	
	Number	Increase / decrease %	kg/tree	Increase / decrease %	g/cm^2	Increase / decrease %
0 (control)	42.44 b	0.0	6.70 b	0.0	447.94 b	0.0
25	45.83 ab	+8.0	8.07 a	+ 20.4	592.52 a	+ 32.3
50	44.44 ab	+4.7	7.89 a	+ 17.8	539.26 a	+ 20.4
100	49.33 a	+16.2	7.77 ab	+ 16.0	446.30 b	-0.4
200	48.25 ab	+13.7	7.00 ab	+ 4.5	439.40 b	-1.9

3.3. Effect of Promalin on nut quality characteristics of pistachio

3.3.1. Blank nut rate (%)

All Promalin doses decreased the blank nut rate in pistachio trees. The lowest blank nut rate was obtained from 100 ppm Promalin with 71.4% decrease when compared with control (Table 2).

The blank nut ratios were determined as 11.4% in Siirt, 11.9% in Kırmızı and 12.4% in Ohadi pistachio cultivars [18].

Blank nut formation could be at 2 different stages of fruit development in pistachio which are fruit set and fruit filling stages. The most important factors affecting blank fruit formation are; the lack of male trees in the orchard, deficiency of flowering coincidence between male and female trees and nutritional and hormonal deficiencies in trees [19].

Table 2. Effect of different Promalin doses on nut quality characteristics of pistachio

Promalin doses (ppm)	Blank nut rate %		100 nut weight g		Split nut rate %		Kernel ratio %	
	%	Increase / decrease %	g	Increase / decrease %	%	Increase / decrease %	%	Increase / decrease %
0 (control)	6.3 a	0.0	85.3 b	0.0	51.3 b	0.0	45.6 b	0.0
25	4.5 ab	-28.6	89.2 a	+4.6	66.0 a	+28.7	47.5 ab	+4.2
50	2.5 b	-60.3	89.2 a	+4.6	68.7 a	+33.9	49.3 a	+8.1
100	1.8 b	-71.4	87.5 ab	+2.6	47.0 bc	-8.4	45.7 b	+0.2
200	4.5 ab	-28.6	86.2 b	+1.1	42.0 c	-18.1	46.6 b	+2.2

3.3.2. 100 nut weight (g)

Nut weight is an important quality characteristic for pistachio. All promalin doses positively affected the 100 nut weight, and the highest value was observed for 25 and 50 ppm (Table 2).

25 ppm Promalin provided fruit set and fruit weight in Golden Delicious apples[16]. The 100 nut weight of pistachio cultivars were 78.7 g for Kırmızı, 105.1 g for Siirt and 107.6 g for Ohadi cultivars [20]. Irrigation, fertilization, soil and climatic conditions can affect nut weight of pistachio.

3.3.3. Split nut rate (%)

The highest split nuts were obtained from 50 and 25 ppm Promalin with 33.9% and 28.7% increase, respectively. 200 and 100 ppm Promalin had a negative effect on splitting rate of Kırmızı pistachio cultivar. The lowest value was obtained from 200 ppm Promalin application.

Split nut rates were 67% in Kırmızı, 86% in Siirt and 95% in Ohadi pistachio cultivars in Gaziantep conditions [21]. In Ceylanpınar climatic conditions, splitting rates were 43.8%, 66.5% and 47.0% for Kırmızı, Siirt and Ohadi, respectively [18].

Splitting rate was also affected by soil and climatic conditions, and cultural practices for pistachio trees.

3.3.4. Kernel ratio (%)

Kernel ratio was an important quality characteristic not only for pistachio, but also for walnut, hazelnut, pecan, chestnut and almond. Kernel ratio varied between 45.6% and 49.3%. The highest kernel ratio was observed on 50 ppm Promalin and the lowest was on control (Table 2).

Kernel ratios were between 43.24% and 45.10% for Siirt; 43.85% and 46.07% for Ohadi and 47.12% and 49.38% for Kırmızı pistachio cultivars [22].

The results of our study showed that Promalin has positive effects on pistachio trees. Finally, the highest nut weight was obtained from 25 and 50 ppm Promalin; the highest yield obtained from 25 ppm Promalin; the highest splitting and kernel ratio obtained from 50 ppm Promalin. On the other hand, 100 ppm Promalin both increased fruit set and decreased blank nut ratio in Kırmızı pistachio cultivar.

ACKNOWLEDGMENT

REFERENCES

[1]. M. Zohary, A monographical study of the genus Pistacia. Palestine J. Bot. Jerusalem Ser. 5:187. 1952.
[2]. N. Kaska, Pistachio research and development in the Near East, North Africa and Southern Europe. Nut Production Industry in Europe, Near East and North Africa. Reur Technical Series 13, 133-160. 1990.
[3]. Anonymous, FAOSTAT. http://faostat3.fao.org/download/Q/QC/E. April 2017. 2015.
[4]. H. Tekin, S. Arpaci, H. S. Atli, I. Acar, S. Karadag, Y. Yukceken and A. Yaman, Pistachio production. Pistachio Research Inst. Press No:13, Gaziantep (in Turkish). 2001.
[5]. Anonymous, TUIK Statistics. https://biruni.tuik.gov.tr/bitkiselapp/bitkisel.zul. April 2017. 2016.
[6]. J. A. Al-Duljaili, M.A. Al-Khafaji and K.H. Al-Juboory, The effect of localized GA3 application on the yield and quality of "Thompson Seedless" grape (Vitis venifera L.). Iraqi J. Agril. Sci., 5: 51-57. 1987.
[7]. L. D. Bist, Influence of PP333, Alar, CCC and Promalin on macronutrient status of pear leaf. Acta Hort., 274: 43-50. 1990.
[8]. M. T. Wahdan, S.E. Habib, M.A. Bassal and E.M. Qaoud, Effect of some chemicals on growth, fruiting, yield and fruit quality of "Succary Abiad" mango cv. J. Amer. Sci., 7(2): 651-658. 2011.
[9]. J. L. Gonzales and C.B. Borroto, Use of plant growth regulators to control fl owering in citrus. Biologia Plantarum, 29: 342-349. 1987.
[10]. B. A. Turk, and M. Stopar, Effect of 6-benzyladenine application time on apple thining of cv 'Golden Delicious' and cv 'Idared'. Acta Agril. Slovenica, 95 (1): 67-73. 2010.
[11]. P. Montalti, B. Cristofferi and S. Sansavini, Effect of GA4+7 and shoot pinching on hortinal levels in conference pear. Acta Hort., 161: 163-170. 1984.
[12]. D. W. Greene and W. R. Autio Vegetative Responses of Apple Trees Following Benzyladenine and Growth Regulator Sparys. Journal of the American Society for Horticultural Science, 115 (3):400-404. 1990.
[13]. Anonymous, Promalin. Valent Biosciences. www.valentbiosciences.com April 2017. 2017.
[14]. K. K. Jindal, S. Pal, P. S. Chauhan and M. S. Mankotia, Effect of promalin and mixtatol on fruit growth, yield efficiency and quality of Starking Delicious apple. In XXVI International Horticultural Congress: Key Processes in the Growth and Cropping of Deciduous Fruit and Nut Trees 636: 533-536. 2002.
[15]. A. Esitken, S. Ercisli, H. Karlıdag and F. Sahin Potential use of plant growth promoting rhizobacteria (PGPR) in organic apricot production, Proc. Int. Sci. Conf. Environmentally Friendly Fruit Growing. 7-9 September 2005. Tartu–Estonia, 90-97. 2005.
[16]. A. I. Ozguven, The use of Gibberellins in horticultural crops. Derim 11(2): 72-85 (in Turkish). 1994.
[17]. I. Acar, S. A. Tahtaci, S. Arpaci, Y. Aydin and S. Karadag, Determination of effects of plant growth regulator applications on alternate bearing in pistachios under suitable growing conditions. 4th International Symposium on Pistachios and Almonds. 22-25 May 2005, Tehran, Iran. Acta Horticulturae, 726:539-544. 2005.
[18]. B. E. Ak, The yield and fruit quality of Pistacia vera cv. Siirt grown at the Ceylanpinar State Farm. Second International Symposium on Pistachio and Almond. August 24-29, 1997, California (Davis), USA, ACTA Horticulturae, 470: 294-299. 1998.

[19]. M. Ayfer, The past, present and future of pistachio. First Pistachio Symposium in Turkey. 11-12 September 1990, Gaziantep, Turkey p:14-23 (in Turkish). 1990.

[20]. B. E. Ak, Effects of pollen of diffent *Pistacia* species on fruit set and fruit quality of pistachio PhD thesis. Cukurova Univ., Adana, Turkey. 1992.

[21]. R. Karaca and A. Nizamoglu, Quality characteristics of Turkey and Iranian pistachio cultivars grown in Gaziantep. First International Symposium on Pistachio Nut, Adana, Turkey, 20-24 Sept. 1994. Acta Hort. 419:307-312. 1995.

[22]. I. Acar and S. Eti, Abscission of pistachio flowers and fruits as affected by different pollinators. Pak. J. Biol. Sci. 10 (17):2920-2924, 2007.

Reinforcement of Silty Soil by using Basalt Fibers

Cyrille Prosper Ndepete[1], Sedat Sert[2]

Abstract

The use of fibers and chemical products in order to enhance the soil and concrete properties is not a new technique. But with environmental problems, natural fibers have been the most desired to be used in recent years to strengthen the physical and mechanical properties of soils. Many of the studies conducted on concrete show that basalt fibers are one of the preferred fibers and non-polluting. But it is difficult to find researches in the literature on the strengthening of soils by using basalt fibers. It is in this context that this study is oriented on the study of mechanical behavior of consolidated saturated silty soils reinforced by basalt fibers. This study is performed by using basalt fibers that are a natural and non-polluting material to improve the mechanical and physical properties of the soil by providing additional resistance to the shear strength. The study consists of gradually adding basalt fibers of different lengths of 6 mm, 12 mm and 24 mm to the silty soil. For this study, 40 undrained-unconsolidated triaxial tests (UU) were carried out on saturated soil samples which were firstly consolidated for 5 days under a load of 300 kPa. The results of these tests show that the inclusion of basalt fibers has indeed improved the soil shear strength used in this study. The improvement was observed for all soil samples enhanced with basalt fibers. This improvement is expressed by a contribution of forces opposed to breaks in soil during shearing.

Keywords: Consolidated Saturated Silty Soil, Soil Improvement, Basalt Fiber, Triaxial Compression Strength

1. INTRODUCTION

The soil reinforcement is an efficient and reliable method to enhance its strength and resistance. Fine grained soils may present a low bearing capacity and the problems of stability in the field of construction. To remedy these problems, chemicals, synthetic and natural fibers have begun to be used [1]. The most commonly used fibers today are those with the characteristics of tensile strength, acid, alkali and anticracking resistance. However these fibers being synthetic pose some environmental problems. Basalt fiber is a natural inorganic fiber. Having a compatibility with the environment, it has excellent mechanical properties and has good resistance to acids and alkalis. Compared to other fibers, basalt fiber has a significantly lower price.

Chao et al. [2] approved the inclusion of fibers as reinforcements have many advantages over the mechanical behavior of soils compared to planar geosynthetic materials. The fibers have a simple use methodology; they can be simply added and mixed with soil in the same way as cement, lime and other additives. The random arrangement of the fibers in the soil can reduce the potential weakness that may occur parallel to the vector oriented reinforcement and provide an isotropic increase in the resistance of the soil composite.

The effects of inclusion of random fibers can be distinguished by their material; in fact, different types of fibers have been used by researchers to reinforce fine and granular soils, such as PP fibers [2-3], plant fibers [4], PET fibers [5], flax fibers [6] and glass fibers [7].

In order to study the behavior of geotextiles-reinforced clay soils, unconfined compression tests were performed on reinforced and unreinforced soils. The variables used are the water content and the geotextile layer numbers. The results of the work show that increasing the water content decreases the unconfined compressive strength of the samples of reinforced and unreinforced soils whereas the increase of geotextile layers increases the unconfined compressive strength [8].

Eskisar and Altun [9] studied the mechanical properties of fine grained soils mixed with composite fibers (PP) using a series of unconfined undrained compression tests. The fibers of 6 mm - 12 mm and percentages

---
[1]*Corresponding author: Sakarya University, Institute of Natural Sciences, Sakarya-Turkey, ndepetecyrille@gmail.com*

[2]*Sakarya University, Department of Civil Engineering, Sakarya, Turkey, sert@sakarya.edu.tr*

of 0.1% - 0.5% and 0.75% were used. The results of their work indicate that the increases of percentage and length of fiber have improved also the compressive strength of the soil. But the percentage increase is a dominant factor affecting the compressive strength of the soil.

In order to produce composite building materials, which is durable and non-toxic, a search was conducted by using natural polymers and fibers. Mechanical tests were carried out on clay soil. The alginate which is a natural polymer from the cell walls of brown algae was used as an adhesive in the composite. Sheep wool was used as reinforcement. The results of the tests show that the inclusion of alginate alone increases the compressive strength from 2.23 to 3.77 MPa, and the addition of wool fibers increases the compressive strength to 37%. The combination of alginate with wool fiber doubles the compressive strength of the soil [10].

A series of unconfined compression tests and freeze-thaw tests were performed on clay soil (CH) reinforced with chicken feathers. A series of unconfined compression tests and freeze-thaw tests were performed on clay soil (CH) reinforced with chicken feathers. The prepared samples were exposed to 5 and 10 freeze-thaw cycles. The test results show that the inclusion of chicken feathers increases the unconfined compressive clay soil [11].

To study the effect of basalt fibers on the shear strength of compacted unsaturated silt soil, undrained unconsolidated triaxial tests (UU) were carried out firstly on natural silty soils and then on improved soils with basalt fibers of 6, 12 and 24 mm long with percentages of 1% - 1.5% and 2%. The results of these tests show that the inclusion of 24 mm long fibers in the soil gives a maximum improvement of strength and the optimum fiber content by dry weight of soil is 1.5% [12- 13].

2. MATERIALS AND EXPERIMENTAL PROCEDURE

2.1. Materials

The soil used in this study was collected in Adapazarı (Turkey) from a depth of 2 to 3 meters (Figure 1 and 2). Its physical properties are listed in Table 1. The fibers used are basalt fibers of different dimensions (6 mm - 12 mm and 24 mm) (Figure 3). The physical parameters of these basalt fibers are shown in Table 2.
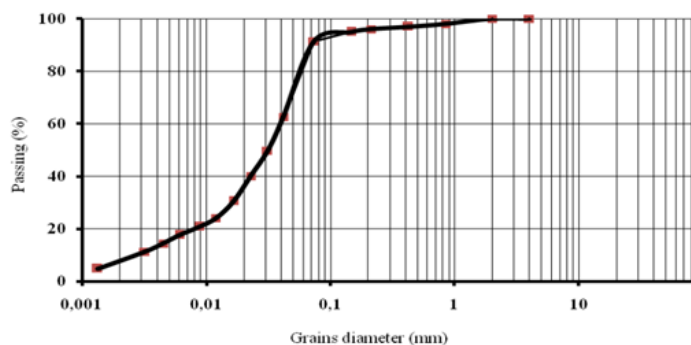

Figure 1. Silty soil sample

Figure 2. Grain size distribution curve of silt soil.

Table 1. Physical properties of silt soil samples.

Silt Soil		
Characteristics	Values	Units
-No200	92	%
Liquid Limit (LL)	32	%
Plastic Limit (PL)	23,27	%
Plasticity Index (IP)	8,73	%
Water content (w)	31	%
Soil classification: (ML)		

Using the USCS classification the soil sample is a silt soil of low plasticity (ML).

Figure 3. Basalt fibers; (a) unseparated fibers, (b) separate fibers

Table 2. Physical properties of basalt fiber

Basalt fiber		
Characteristics	Values	Units
Specific weight	2.60-2.65	g / cm^3
Modulus of elasticity	70-90	GPa
Tensile strength	2800-3000	MPa
Breaking limit	3.1	%
Diameter	6 - 25	μ
Temperature of application	450-550	^{0}C
Melting point	1350	^{0}C
Price	6	USD/kg

2.2. Test procedures

In order to study the effect of the content and the length of the basalt fibers on the UU strength of the saturated silt soil, basalt fibers of 6 mm - 12 mm - 24 mm and the percentages of 1% - 1.5% and 2% were used by dry weight of soil. Two categories of soil were used; one natural and the other enhanced.

2.3. Preparation of soil samples

For all lengths, some percentages (1% - 1.5% and 2%) of the basalt fibers were mixed with oven dried soil firstly. Next, for 2 kg of the dry soil sample, 40% of water was used in order to make the soil saturated and

911

then the wet soil sample was deposited for 1 hour in the desiccator in order to extract the air bubbles. Once the extraction of the air bubbles is complete, the soil sample was filled in the cell of 15 cm long and 10 cm of diameter and then submits to a uniaxial consolidation during 5 days under a load of 300 kPa (Figure 4).
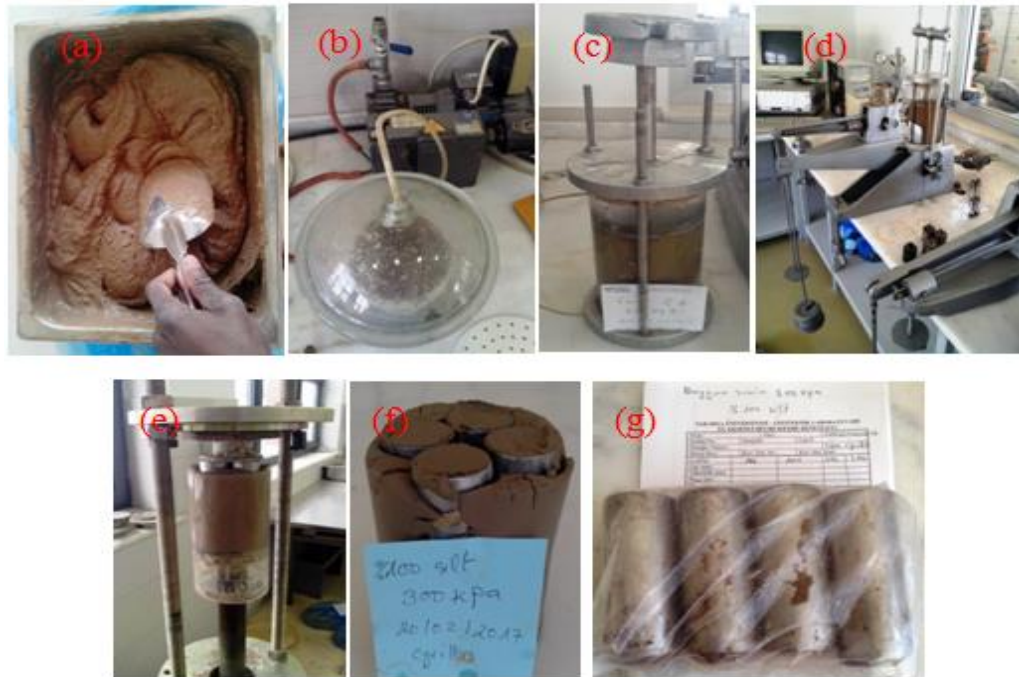

Figure 4. Soil sample preparation; (a) saturated soil, (b) extraction of air by the desiccator, (c and d) consolidation phase, (e, f and g) extraction of the soil sample.

2.4. UU Triaxial Test Procedures

After the consolidation phase, 4 saturated soil samples were collected by using the tubes of 7 cm long and 3.5 cm of diameter and then submit to unconsolidated undrained triaxial tests (UU). Figure 5 below shows the undrained unconsolidated test procedures (UU).
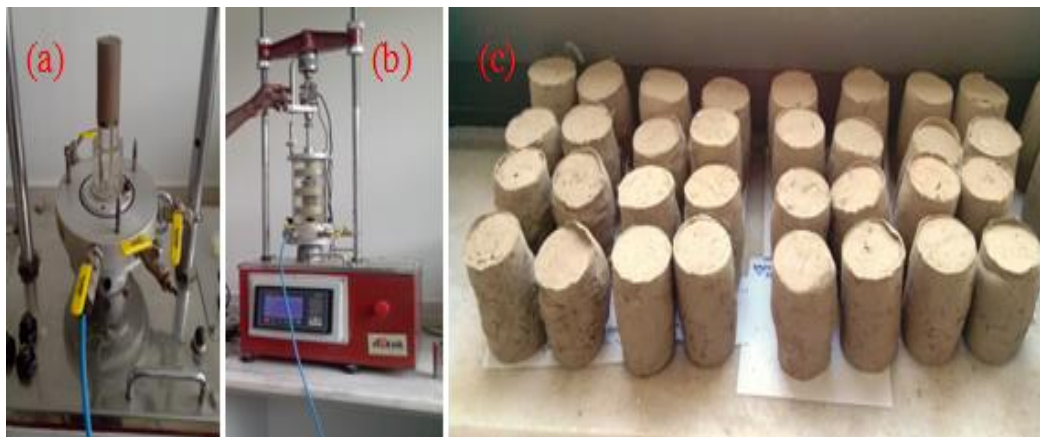

Figure 5. Triaxial test (UU), (a, b) UU triaxial test procedure, (c) soil samples after the triaxial tests.

The undrained unconsolidated triaxial tests were carried out according to Turkish Standard Norm (TS1900-2) with σ_3 pressures from 100 kPa to 400 kPa.

3. RESULTS AND ANALYSES

The results of the undrained unconsolidated triaxial tests are compiled in the Table 3 and in the Figures 6, 7 and 8 below.

Table 3. Maximum deviatoric stress as a function of the percentages and the length of the basalt fibers

Fiber length (mm)	% of fiber	100 kPa	200 kPa	300 kPa	400 kPa
		$\sigma_{d, max}$ (kPa)	$\sigma_{d, max}$ (kPa)	$\sigma_{d, max}$ (kPa)	$\sigma_{d, max}$ (kPa)
Soil	0	99,62	111,74	122,70	132,19
6	1	136,92	149,39	161,16	168,09
6	1,5	**141,09**	**166,54**	**174,70**	**188,68**
6	2	139,50	164,00	173,87	177,29
12	1	146,05	158,18	165,30	175,23
12	1,5	**171,44**	**175,85**	**179,80**	**192,00**
12	2	153,86	164,12	176,99	180,25
24	1	153,88	160,89	171,58	182,31
24	1,5	**163,08**	**177,20**	**181,16**	**193,01**
24	2	156,40	167,81	173,95	183,88

Figures 6 and 7 show the effect of the basalt fiber content on the UU strength of the silty soil samples. It is noted that all the samples improved by the basalt fibers have a variation of the UUS. Firstly, soil UUS tends to increase until reaching an optimum and then start to decrease when the fiber content reaches 2%. This phenomenon is explained by an interfacial reaction that occurs between soil particles and basalt fibers during the shearing of the soil. More than the fiber content increases, basalt fibers tend to attach to each other and not to the soil particles. The best improvement was obtained for the value of 1.5%.

Figure 8 shows the effect of the length of basalt fibers on the UUS of the silty soil samples. It is noted that the dimensions of basalt fibers play an important role in improving soil UUS. When the basalt fiber is long, there is a high probability that several breaking points are prevented during shearing. The best improvement was obtained for the 24 mm fibers.
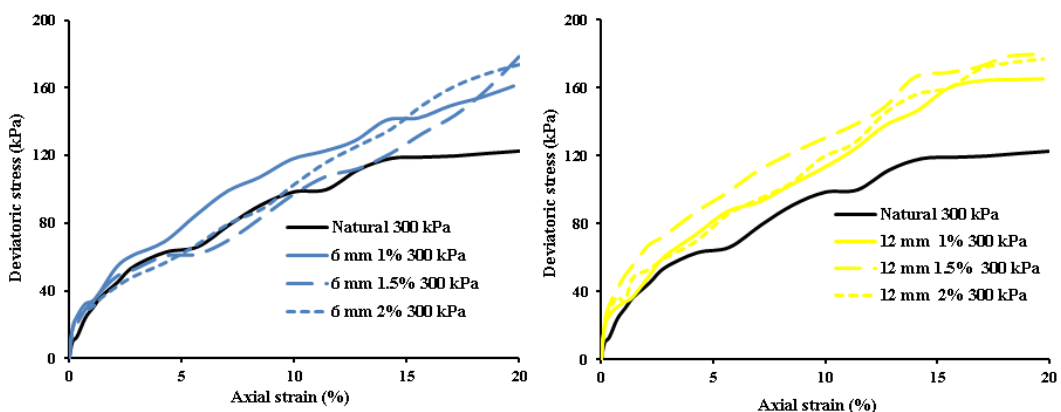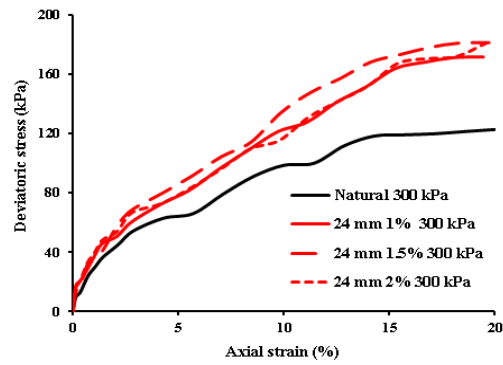
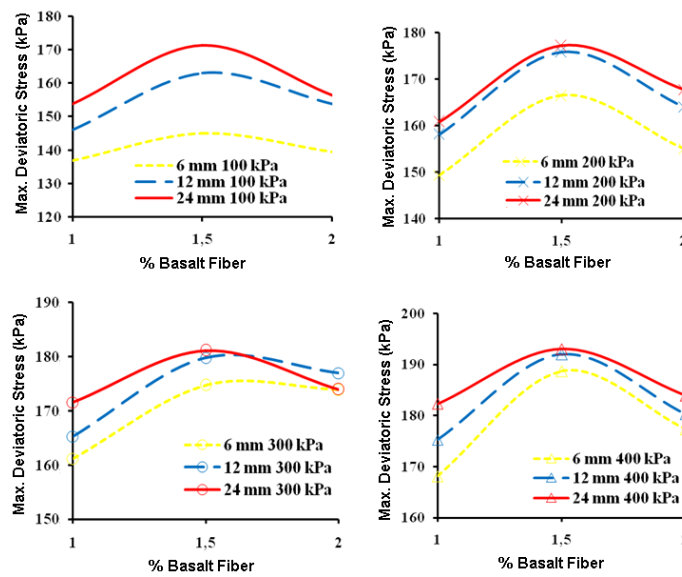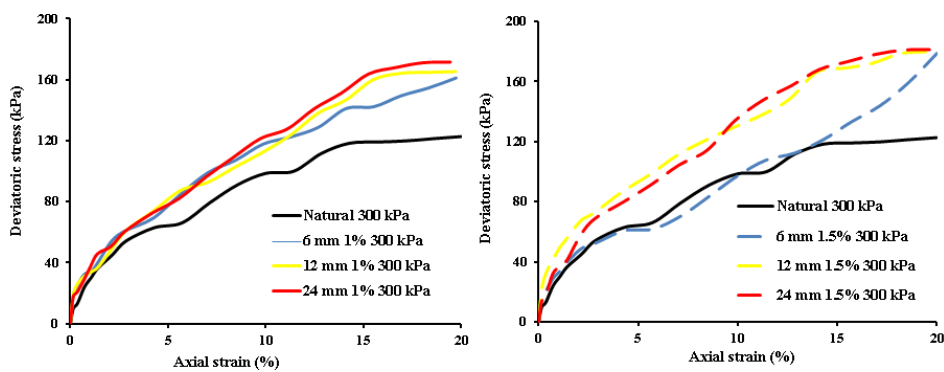*Figure 6. Stress-strain curves of the UUS; estimation based on percentage of basalt fiber ($\sigma_3=300$ kPa).*

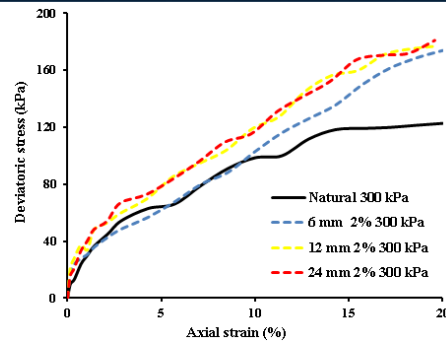*Figure 7. Max deviatoric stress - % of BF curves of the UUS.*

Figure 8. Stress-strain curves of the UUS; estimation based on the length of basalt fiber

Figure 9 shows the view of the reinforced and unreinforced silty soil samples after the triaxial test. Unreinforced soil samples present a visible rupture zones whereas the reinforced soil samples present any rupture zone. Mechanically, basalt fibers constitute a barrier in the soil during the shear phase.
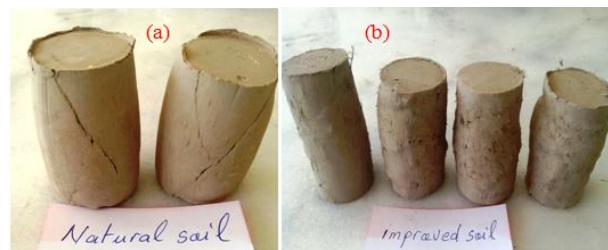

Figure 9. Examples of the soil samples after the triaxial test (UU); (a) natural soil, (b) improved soil

4. CONCLUSION

The effects of inclusion of basalt fibers on the silty soil UUS were studied in this paper. Basalt fibers of different dimensions (6 mm - 12 mm and 24 mm) were randomly distributed at various concentrations (1% -1.5% and 2%) and mixed with the silty soil samples. The results of this study can be summarized as follows:

The inclusion of basalt fibers contributes to the strengthening of the silt soil samples. The mechanical behaviors of silt soil were improved by the incorporation of basalt fibers. These fibers constitute a barrier to breaks in the soil.

The optimum fiber content corresponding to maximum improvement in strength is found to be 1.5% for all basalt fibers.

The further addition of basalt fibers decreases UUS of silt soil samples. When the percentage of basalt fiber exceeds 1.5%, the basalt fibers try to group together. It will not have a good interaction between the fibers and the soil particles. It will not have homogeneity in the soil sample.

The fibers length and the fibers content have a significant effect on the undrained shear strength of silty soils. The inclusions of basalt fibers 24 mm long and 1.5% produce a good result compared to fibers of 6 mm and 12 mm.

REFERENCES

[1] L. Gao, G. Hu, N. Xu, J. Fu, C. Xiang and C. Yang, "Experimental study on unconfined compressive strength of basalt fiber reinforced clay soil", Advances in Materials Science and Engineering, Vol. 2015, Article ID 561293, 8 pages.
[2] C.-S. Tang, B. Shi, L.-Z. Zhao, "Interfacial shear strength of fiber reinforced soil", Geotextiles and Geomembranes, vol. 28, pp. 54–62, 2010.
[3] E. Ibraim, A. Diambra, A.R. Russell, D. Muir Wood. Assessment of laboratory sample preparation for fiber reinforced sands. Geotextiles and Geomembranes, vol. 34, pp. 69-79, 2012.
[4] J. Maity, B.C. Chattopadhyay, S.P. Mukherjee, "Behaviour of different types of sand randomly mixing with various natural fibers", J. Inst. Eng. India Ser. A, vol. 93, no. 2, pp. 97–104, 2012.

[5] E. Botero, A. Ossa, G. Sherwell, E. Ovando-Shelley, "Stress-strain behavior of a silty soil reinforced with polyethylene terephthalate (PET)", Geotextiles and Geomembranes, vol. 43, pp. 363-369, 2015.

[6] S. V. Krishna Rao, A. M. A. Nasr, "Laboratory study on the relative performance of silty-sand soils reinforced with linen fiber, Geotech Geol Eng, vol. 30, pp. 63-74, 2012.

[7] A. Ates, "Mechanical properties of sandy soils reinforced with cement and randomly distributed glass fibers (GRC)", Composites Part B, vol. 96, pp. 295-304, 2016.

[8] E. Karkan, A. Okucu, B. Yagcı, "Investigation of stress-strain relationship and strength characteristic of geotextile reinforced clay (in Turkish)", 6th Geotechnical Symposium, pp. 573-583, Cukurova University, Adana, 2015.

[9] T. Eskisar, S. Altun, "Experimental investigation on mechanical behavior of fiber reinforced fine grained soils by unconfined compression test (in Turkish)", 6th Geotechnical Symposium, pp. 604-615, Cukurova University, Adana, 2015.

[10] F. Isık, R. K. Akbulut, A. S. Zaimoğlu and S. Arasan, "The usability of waste natural fibers in soil improvement of clayey soils (in Turkish)", 6th Geotechnical Symposium, pp. 688-698, Cukurova University, Adana, 2015.

[11] S. Sert, C. P. Ndepete, A. Beycioglu, "Estimation of undrained shear strength of basalt fiber reinforced silty soils by using fuzzy logic approach" 2nd International Conference on Computational and Experimental Science and Engineering (ICCESEN-2015), Abstract book, p. 369, Antalya, 2015.

[12] C.P. Ndepete and S. Sert, "Use of basalt fibers for soil improvement", Acta Physica Polonica A, vol. 130, pp. 355-356, 2016.

Slope Design for Excavations and Embankments at a Waste Deposit Area

Ertan Bol[1], Sedat Sert[2], Askın Ozocak[3]

Abstract

In this study, the stability of excavations and embankments have been investigated for a planned waste deposit area. Six borings, which total depth is 121 meters, have been conducted. In almost all of the soundings, red sandstones are encountered at the surface. In two borings, the average thickness of topsoil is 3 meters. These red sandstones belong to the Cakraz Formation (PTRc), which is characterized by reddish brown, granular-partly-broken, weak strength, middle-heavy weathered sandstones.

There are two different approaches in the design of rock engineering structures. These are empirical and numerical design approaches. Numerical solutions, which are developed mathematical approaches, are generally capable of solving stability by using the mechanical properties of rock materials (such as E, v, c, ϕ, σ_c). Empirical approaches generally use charts which are developed with observations or engineering experience. The input parameters required for both approaches are determined by rock mechanical tests and geotechnical studies carried out on rock masses encountered at the site. The integrative approaches, expressing rock mass parameters in a numerical form, are called rock mass classification systems. The input parameters required for these systems are generally determined from drillings conducted insitu. RMR (Bieniawski, 1973) and Q (Barton et al., 1974) classification systems, which are the famous ones, are mainly used for determining the required supports in tunnels, mines and underground spaces. On the other hand, the Geological Strength Index (GSI) proposed by Hoek and Brown (1997) can classify rock mass for general engineering problems. This work of Hoek and Brown was revised in 2002 (Hoek et al., 2002) and during this study, new criteria were applied to solve the problem.

In this study, classification of rock mass was made according to GSI and preliminary parameters which could be used to design slope geometry were determined. Limit equilibrium methods have been used as well and the comparison of the two methods results show similar tendency. According to analyzes made; there is no problem in terms of stability in excavations with 1 horizontal / 1 vertical ratio. Stability analysis on embankments were performed only by using limit equilibrium methods. It has been understood that there will be no stability problem for the slope geometry to be performed at 3 H/ 2V ratio for the embankments.

Keywords: *Slope Stability, Solid Waste Deposit, Excavations, Embankments, Geotechnics of Solid Waste Landfills*

1. INTRODUCTION

Landfills have been recognized as the cheapest form for the final disposal of municipal solid waste. Landfill method has been the most used method in the World. But growing population and industry bring together large volume of solid waste fill areas. To create large volume capacity deposit areas, excavations and embankments can be done. The main problems of a solid waste area in respect of Geotechnical Engineering are: Stability, Settlement and Permeability. In this study, the stability of excavations and embankments have been investigated for a solid waste deposit area. Study area location have been shown in the Figure 1. The study area is in the north of the city center Adapazarı, Turkey.

---

[1] Corresponding author: Sakarya University, Department of Civil Engineering, Serdivan/Sakarya, Turkey, ebol@sakarya.edu.tr

[2] Sakarya University, Department of Civil Engineering, Serdivan/Sakarya, Turkey, sert@sakarya.edu.tr

[3] Sakarya University, Department of Civil Engineering, Serdivan/Sakarya, Turkey, ozocak@sakarya.edu.tr
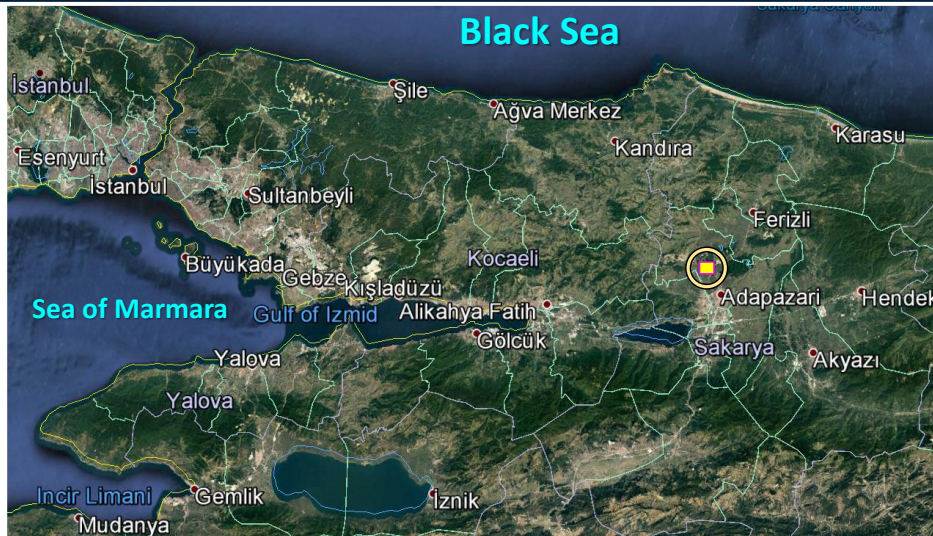
Figure 1. Location of Study Area (Adapazari, Turkey)

Six rotary drilling have been done in the study area. Almost all of the soundings are entered from the surface to the Cakraz Formation (*PTRc*) sandstones, which are characterized as reddish brown, very cracked, weakly resistant, very - medium weathered. In the two soundings, there is a top soil layer.

There are two different approaches in the design of rock engineering structures. These are empirical and numerical design approaches. Numerical solutions, which are developed mathematical approaches, are generally capable of solving stability by using the mechanical properties of rock materials (such as E, υ, c, ϕ, σ_c). Empirical approaches generally use charts which are developed with observations or engineering experience. The input parameters required for both approaches are determined by rock mechanical tests and geotechnical studies carried out on rock masses encountered at the site. The integrative approaches, expressing rock mass parameters in a numerical form, are called rock mass classification systems. The input parameters required for these systems are generally determined from drillings conducted in-situ. RMR [1] (Bieniawski, 1973) and Q (Barton et al., 1974) [2] classification systems, which are the famous ones, are mainly used for determining the required supports in tunnels, mines and underground spaces. On the other hand, the Geological Strength Index (GSI) proposed by Hoek and Brown (1997) [3] can classify rock mass for general engineering problems [3, 4]. This work of Hoek and Brown was revised in 2002 (Hoek et al., 2002) [5] and during this study, new criteria were applied to solve the problem.

2. GEOLOGY OF THE STUDY AREA

General geology of area is formed by Cakraz formation (*PTRc*), Akveren formation, Orencik formation and alluviums. The Cakraz formation cover the study area. Cakraz formation is Permian and Triassic aged.

These sandstones belonging to Cakraz formation (*PTRc*) form in northwest and north part of Adapazarı plain. The thickness of the residual soils ranges from 0.5 to 1.5 meters in areas where vegetation cover is common. The sandstones are reddish, purple yellowish gray colored, medium grain-sized, medium-poorly sorted, thin-thick layers. Sandstone levels are very blocky. The mudstones layered with sandstones are red-brown-purple colored, thin-layered. Figure 2 shows the geological map of the study area and the cross section lines used in the analyses.

3. IN-SITU AND LABORATORY RESEARCHES

Six rotary drilling which have total depth is 121 m have been conducted in the study area. Boring locations can be seen in the Figure 2. In almost all of the drillings, red sandstones are entered from the surface. In the two soundings, there is topsoil layer with an average thickness of 3 meters. Reddish brown, closely jointed, weakly strength, moderately and very weathered sandstones belongs to Cakraz Formation (Figure 3). There was no information on depth of groundwater in the drilling logs, so the study area was considered dry. The results of uniaxial compression strength tests on samples from borings of the study area are given in Table 1.
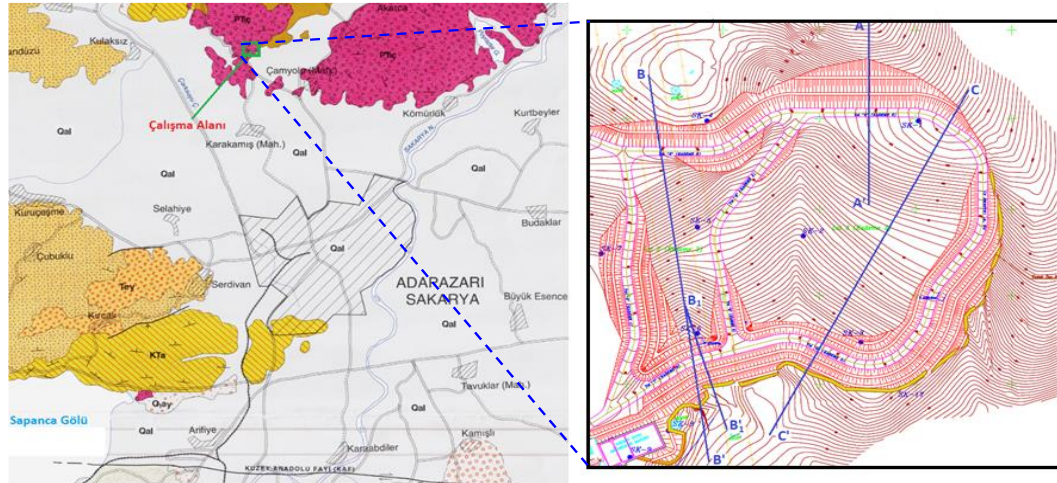
Figure 2.Geological map of the study area and the cross section lines

Table 1. Uniaxial strength test results

Sample No	Color	Diameter (cm)	Height (cm)	M (gr)	ρ_n (kN/m^3)	Uniaxial Load (kN)	σ_c (MPa)
1	Reddish Brown	4.82	9.11	431.31	25.45	77.63	42.55
2	Reddish Brown	4.80	9.54	462.38	26.28	55.53	30.69
3	Reddish Brown	4.81	9.23	437.03	25.56	29.61	16.29
4	Reddish Brown	4.82	9.64	471.03	26.27	30.97	16.97

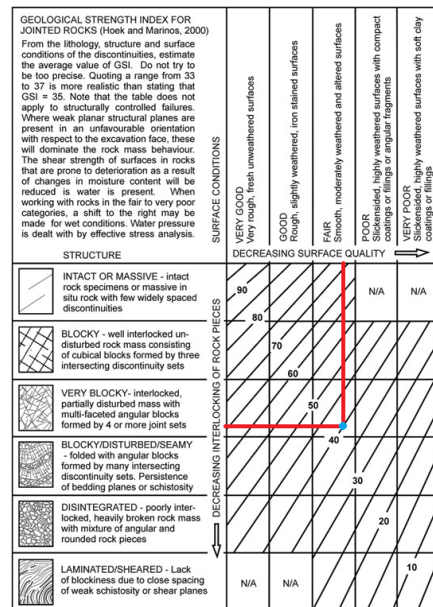*Figure 3. Reddish-brown sandstones on the study are   a*

Figure 4.GSI classification of the study area.

4. ROCK MASS CLASSIFICATION

There are some method to characterize of rock mass properties. One of them is geological strength index (GSI). The geological strength index (GSI) is a system of rock-mass characterization. It has been developed

in engineering rock mechanics to meet the need for reliable input data. These data particularly related to rock-mass properties required as inputs into numerical analysis for designing tunnels, slopes or foundations in rocks. A careful engineering geology description is the heart of the GSI classification [6].

GSI classification chart which can be seen in Figure 4 can be used by entering structure characteristics and surface conditions. On the other words; the first step in this classification is to determine the structure and surface conditions of the rock mass. It is seen from Figure 3 that rocks especially close to the surface on the study area are very blocky. According to in-situ observations, it has been understood that there are four joint systems. Joint surfaces are smooth, moderately weathered and altered. Therefore it can be selected from chart that, structure conditions is very blocky and surface conditions is fair. According to the chart that these evaluations gives GSI number as 40.

In order to determine the engineering parameters of the rock mass with GSI, it is necessary to measure or estimate the uniaxial strength and m_i which is the material constant of the intact rock. There are several tables available to determine the value of the m_i constant at various rocks [7] Hoek and Brown (1980a). It is understood from this research that, m_i can be taken 6 ± 2 for shales and 17 ± 4 for sandstones. According to this; m_i has been taken as an average of 15 in the reddish sandstones in the study area.

The relationship between the major and minor principal stresses in the Hoek-Brown [4] general failure criterion is given by,

$$\sigma'_1 = \sigma'_3 + \sigma_{ci} \left(m_b \frac{\sigma'_3}{\sigma'_{ci}} + s \right)^a \tag{1}$$

where σ'_1 ve σ'_3 are the maximum and minimum principal stresses at the failure. m_b is the Hoek-Brown constant of the rock mass. At the same time, Where m_b is the reduced value of m_i, which is the material constant for the intact rock and it can be calculated from [4] (Hoek et al., 2002).

$$m_b = m_i + exp\left(\frac{GSI-100}{28-14D}\right) \tag{2}$$

Where D is disturbance factor. In this study, D is 0.70 because of slopes to be mechanically excavated. So we can be calculated m_b=2.85. s ve a are constants depending on the characteristics of the rock mass. These constats can be calculated by [4] (Hoek et al., 2002).

$$s = exp\left(\frac{GSI-100}{9-3D}\right) \quad ve \quad a = \frac{1}{2} + \frac{1}{6}\left(e^{-GSI/15} - e^{-20/3}\right) \tag{3}$$

In this case, s = 0.0002 and a = 0.512 are calculated.

In Table 1, the lowest compressive strength is chosen as σ_{ci} =16 MPa, while staying on the safe side. The uniaxial compressive strength of the rock mass can be calculated as follows by equalizing σ'_3 is zero.

$$\sigma_c = \sigma_{ci}.s^a \tag{4}$$

Thus, the uniaxial compressive strength of the rock mass is calculated to be σ_c=0.187 MPa.

The tensile strength (σ'_t) is as follows;

$$\sigma_t = -\frac{s \cdot \sigma_{ci}}{m_b} \tag{5}$$

Thus, the tensile strength of the rock mass is σ'_{tm}=-0.005 MPa. However, when the situation is considered as three dimensions, the value of σ_c calculated above by the effect of earth pressure is calculated as σ_{cm}=1.506 MPa using the following formula to find the strength of the whole rock.

$$\sigma'_{cm} = \sigma_{ci} \frac{(m_b+4s-a(m_b-8s))\left(\frac{m_b}{4}+s\right)^{a-1}}{2(1+a)(2+a)} \tag{5}$$

The Hoek-Brown failure criterion allows the deformation modulus of the rock mass to be calculated as [4] (Hoek ve dig., 2002);

$$E_m(GPa) = \left(1 - \frac{D}{2}\right)\sqrt{\frac{\sigma_{ci}}{100}}.10^{((GSI-10)/40)} \tag{6}$$

E_m=1.462 GPa with the help of this formula. An Excel sheet was created for the calculation of the mentioned parameters and the summary of the results obtained is presented in Table 2. With the Hoek-Brown criterion it is possible to reveal Mohr envelope relations with large and small principal stresses. Shear strength parameters acoording to Mohr- Cloumb criterion are necessary for slope stability analysis, so chesion and internal friction angle should be obtained. The cohesion of the rock mass is calculated to be c=200 kPa and the friction angle ϕ=32 degrees.

Tablo 2. Rock Mass Properties according to Hoek-Brown [4] criteria

GSI	σ_{ci}	m_i	D	m_b	s	a	σ_c (MPa)	σ_{cm} (MPa)	σ_{tm} (MPa)	E_m (GPa)
40	16	15	0.7	0.555	0.0002	0.512	0.187	1.506	-0.005	1.462

5. STABILITY ANALYSIS

The area slopes to be used as the landfill are from north to south. It is considered to form the cuts of 30-40 meters in height to store solid waste. In Figure 1, as the line A-A shows, the greater the slope height, the greater the waste storage volume will be. For this reason, analyzes were made for both 30 meter and 40 meter cuts. The stability analyzes were carried out by Hoek & Bray (1977) [8] proposed method for the very jointed rock mass. These results compared the Simplified Bishop solutions that solve for the circular slip surface and use the limit equilibrium method.

5.1. Stability Analysis of Excavations

The northern cut of the waste area represents the critical slope. Figure 1 shows the cross-section line (A-A'). In the first design, the excavation is thought to be 30 meters. Within the scope of this research, the performance of the excavation of 40 meters has also been examined. In this study, the stability charts developed by Hoek&Bray (1977) [8] for very jointly rock slopes were used. According to boring logs there is no groundwater in the area foundations. Because of this Stability Chart N0: 1 [8] has been used (Figure 5) to analyze excavation slopes.
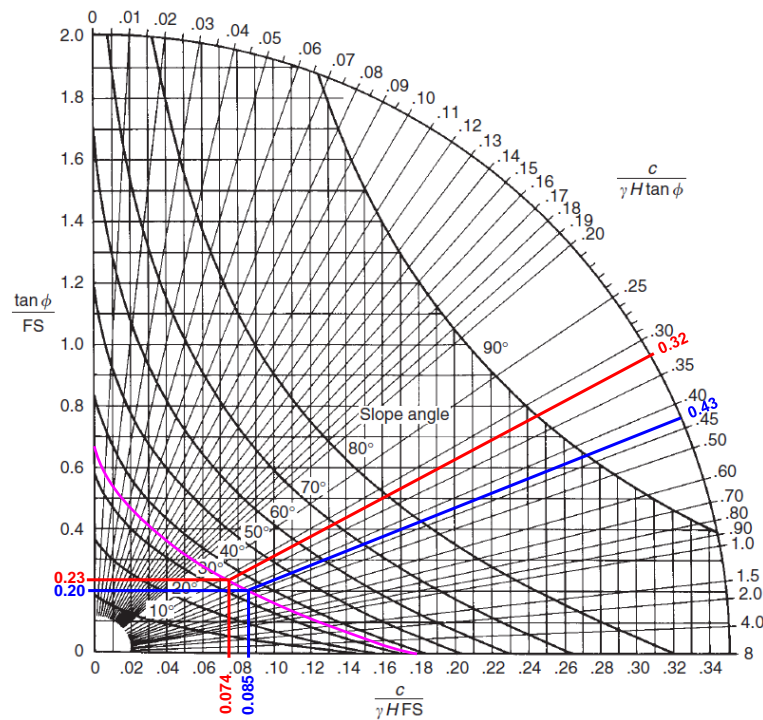

Figure 5a. Hoek&Bray [7] Stability Chart No 1 (for dry slopes), Slope Ratio: 3 horizontal-2 vertical

If the cohesion of the rock mass is taken as c=200 kPa kPa and the friction angle ϕ=32 degrees; for H=30 m cut height and 3 Horizontal – 2 Vertical ($\beta\approx34^0$) slope ratio, dimensionless value can be calculated as $\frac{c}{\rho.H.\tan\varphi} \approx 0.43$ (Sekil 4a blue lines). If this value is intersected on the graph with a slope angle of 34^0; $\frac{\tan\varphi}{GS_\varphi} = 0.20$ and $\frac{c}{\rho.H.GS_c} = 0.085$ values can be obtained. According to these calculations, factors of safety were found to be GS_ϕ=3.12 and GS_c=3.14. On the other hand, for H=40 m cut height and 3 Horizontal – 2 Vertical ($\beta\approx34^0$) slope ratio, dimensionless value can be calculated as $\frac{c}{\rho.H.\tan\varphi} \approx 0.32$ (Sekil 4a red lines). If this value is intersected on the graph with a slope angle of 34^0; $\frac{\tan\varphi}{GS_\varphi} = 0.23$ and $\frac{c}{\rho.H.GS_c} = 0.074$ values can be obtained. According to these calculations, factors of safety were found to be GS_ϕ=2.72 and GS_c=2.70.

The same calculations were repeated for 1 horizontal-1 vertical slope ratio. These results can be seen form Figure 5b. If the cohesion of the rock mass is taken as c=200 kPa kPa and the friction angle ϕ=32 degrees; for H=30 m cut height and 1 Horizontal–1 Vertical ($\beta\approx45^0$) slope ratio, dimensionless value can be calculated as $\frac{c}{\rho.H.\tan\varphi} \approx 0.43$ (Sekil 4b blue lines). If this value is intersected on the graph with a slope angle of 45^0; $\frac{\tan\varphi}{GS_\varphi} = 0.24$ and $\frac{c}{\rho.H.GS_c} = 0.102$ values can be obtained. According to these calculations, factors of safety were found to be GS_φ=2.604 and GS_c=2.614. On the other hand, for H=40 m cut height and 1 Horizontal – 1 Vertical ($\beta\approx45^0$) slope ratio, dimensionless value can be calculated as $\frac{c}{\rho.H.\tan\varphi} \approx 0.32$ (Sekil 4a red lines). If this value is intersected on the graph with a slope angle of 45^0; $\frac{\tan\varphi}{GS_\varphi} = 0.28$ and $\frac{c}{\rho.H.GS_c} = 0.09$ values can be obtained. According to these calculations, factors of safety were found to be GS_φ=2.23 and GS_c=2.22.
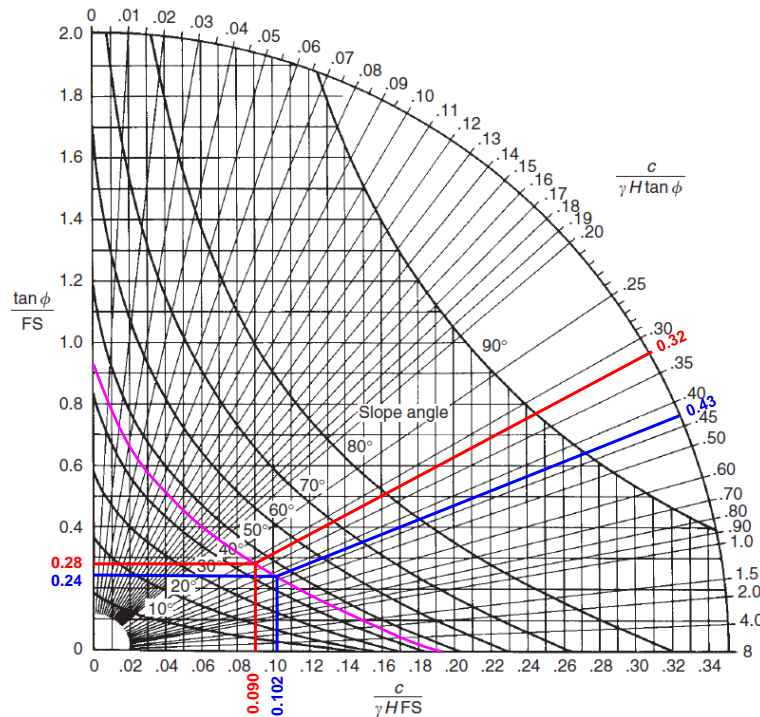

Figure 5b. Hoek&Bray [7] Stability Chart No 1 (for dry slopes), Slope Ratio: 1 horizontal-1 vertical

In addition to above evaluations, the excavation which have 30 meter height and 3H/2V slope ratio have been analyzed with a software which is using Simplified Bishop Method. Factor of safety was found 3.194 by taking shear strength parameters as the same with above calculations (c=200 kPa and ϕ=32^0) (Figure 6a). This value is almost the same with result of Hoek & Bray. On the other hand, safety factor of 40 meter excavation and 3H/2V slope ratio analyzed Simplified Bishop Method have been found almost the same (FS=2.857) with found by using stability chart above (Figure 6b).

Figure 6. Stability analysis of slopes with 3H-2V slope ratio (Simplified Bishop) a) 30 meter b) 40 meter

The excavation which have 30 meter height and 1H/1V slope ratio have been analyzed with a software which is using Simplified Bishop Method. Factor of safety was found 2.582 by taking shear strength parameters as the same with above calculations (c=200 kPa and ϕ=32^0) (Figure 7a). This value is almost the same with

result of Hoek & Bray. On the other hand, safety factor of 40 meter excavation and 1H/1V slope ratio analyzed Simplified Bishop Method have been found almost the same (FS=2.209) with found by using stability chart above (Figure 7b).
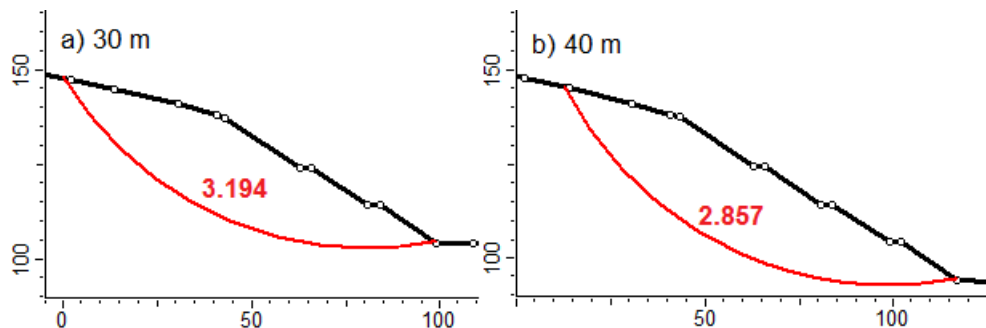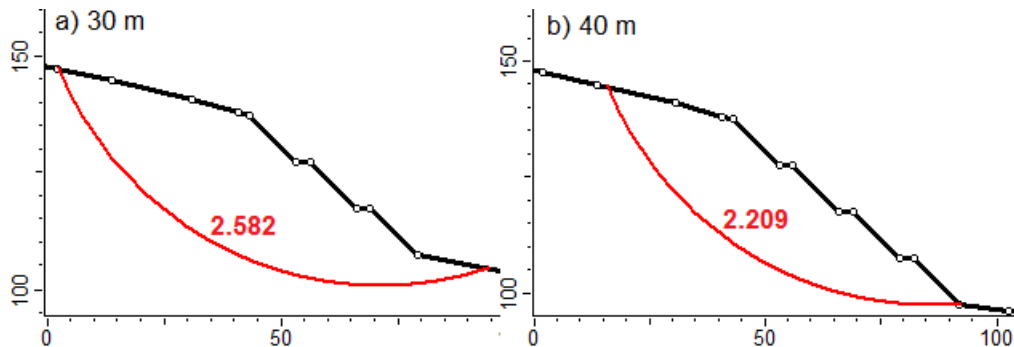

Figure 7. Stability analysis of slopes with 1H/1V slope ratio (Simplified Bishop) a) 30 meter b) 40 meter

5.2. Stability Analysis of Embankments

One of the structural elements that need to be questioned regarding the stability in the solid waste area is the embankments which will be constructed in the south and south-east of the storage area. Cross section lines representing the highest parts of these fillings and including the traces behind them were selected as lines B-B and C-C shown in Figure 1. The material to be obtained from the excavations to be carried out on the northern slopes of the deposit area will be used in these fillings. Shear box test have been conducted on these materials in the SAU Geotechnical Laboratory to evaluate shear resistance parameters of the fillings. Summary test results have been given in Table 3. Thus, it was decided that the cohesion should be c = 27 kPa and the friction angle should be $\phi = 28$ degrees in the stability analyzes.

Table 3. Shear Box Test Results

Sample No	Depth (m)	Color	$\rho\,(kN/m^3)$	e	$c\,(kPa)$	ϕ
1	Surface	Reddish Brown	18.91	0.53	27	28^0

In the stability analysis for the B-B' section in the dry state, the factor of safety for the static case was 1.866 and for the earthquake condition ($k_h=0.2g$) was found to be 1.251. Same way, in the stability analysis for the C-C' section in the dry state, the factor of safety for the static case was 1.911 and for the earthquake condition ($k_h=0.2g$) was found to be 1.289.
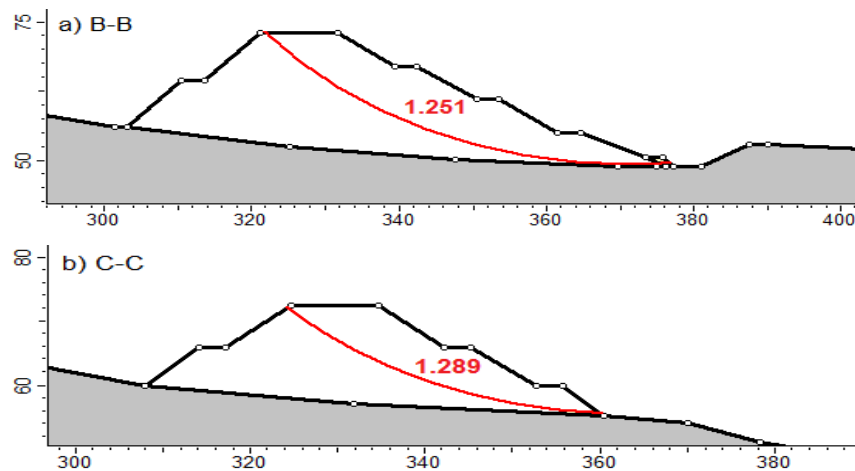

Figure 8. Stability analysis of embankments (Simplified Bishop) (kh=0.20g) a) B-B' Section b) C-C' Section

6. CONCLUSIONS

In very cracked, fragmented and heavily weathered rock environments, the slip surface doesn't follow to planar rock surfaces. In this type of weathered rocks behaves as a soil, circular slip occurs and there is no sign of intact rock. The shear resistance parameters (c and ϕ) that can be expressed for the entire blocky rock can be made using the rock mass classifications in the literature. GSI is a convenient way to describe these environments.

In this study, the stability of the embankments and excavations to be made in a selected area as the solid waste deposit area was examined. According to the drilling logs and in-situ observations, red sandstones are entered from the surface. Reddish brown, closely jointed, weakly strength, moderately and very weathered sandstones belongs to Cakraz Formation. There are four joint systems, joint surfaces are smooth, moderately weathered and altered. Therefore it can be selected from chart that, structure conditions is very blocky and surface conditions is fair. This evaluations gives GSI number as 40. It was decided that, the cohesion of the rock mass is 200 kPa and the friction angle is 32 degrees. Hoek&Bray stability chart and limit equilibrium methods have been used as well and the comparison of the two methods results show similar tendency. According to analyzes made; there is no problem in terms of stability in excavations with 1 horizontal / 1 vertical ratio. Stability analysis on embankments were performed only by using limit equilibrium methods. It has been understood that there will be no stability problem for the slope geometry to be performed at 3 H/ 2V ratio for the embankments.

REFERENCES

[1]. Z.T. Bieniawski, *Engineering classification of jointed rock masses,* Trans S Afr Inst Civ Eng 15:335–344, 1973.
[2]. N. Barton, R. Lien and J. Lunde, *Engineering classification of rock masses for the design of tunnel support*, Rock Mech 6(4):189–236, 1974.
[3]. E. Hoek and E.T. Brown, *Practical estimates of rock mass strength*, Int J Rock Mech Min Sci Geomech Abstr 34:1165–1186, 1997.
[4]. E. Hoek, P. Marinos and M. Benissi, *Applicability of the Geological Strength Index (GSI) classification for very weak and sheared rock masses*, The case of the Athens Schist Formation: Bulletin of Engineering Geology and the Environment v. 57, p. 151-160, 1998.
[5]. E. Hoek, C. Carranza-Torres and B. Corkum, *Hoek-Brown failure criterion - 2002 Edition*, in Hammah, R., Bawden, W., Curran, J., and Telesnicki, M., eds., Mining and Tunnelling Innovation and Opportunity, 2002.
[6]. V. Marinos, P. Marinos and E. Hoek, The geological strength index: applications and limitations, Bull Eng Geol Environ, 64: 55–65, 2005.
[7]. E. Hoek, and E.T. Brown, *Empirical strength criterion for rock masses*, J. Geotechnical Engineering Division ASCE: 1013–1025, 1980.
[8]. E. Hoek and J. Bray, *Rock Slope Engineering*, 1st ed., IMM, London, 1977.
[9]. Rocscience, Inc., R*ocLab v1.0: rock mass strength analysis using the generalized Hoek-Brown failure criterion*. [http://www.rocscience.com/products/RocLab.asp]. Date accessed: April 2007.

Exergy Loss Analysis of a Tube with Coiled Wire Inserts

Orhan Keklikcioglu[1], Toygun Dagdevir[2],Veysel Ozceyhan[3]

Abstract

In this study, the effect of coiled wire inserts on exergy loss inside a tube was experimentally investigated. The wire inserts were manufactured with an equilateral triangular cross-section and were coiled using a method so that an edge of the triangle is oriented to face the flow direction. Three different triangle side length of 4, 5 and 6 mm were chosen for the experiment. The coiled-wire inserts installed with 1 separation from the inner tube wall and coiled with three different pitch-to-diameter ratios: P/D= 1, P/D= 2 and P/D= 3. A specific method was employed to coil the wires so that an edge of the triangle was oriented to face the incoming air flow. A uniform heat flux was applied to the outer surface of the tube. Experiments were performed for a range of Reynolds numbers from 2851 to 27,732. The experimental results indicated that the Nusselt number increased and the friction factor decreased with decreasing pitch ratio and increasing Reynolds number and wire thickness. The exergy loss values were obtained with using coiled-wire at low Reynolds numbers. The results of the experiments were compared and presented graphically.

Keywords: *Exergy Loss, Heat Transfer, Pressure Drop, Coiled Wire*

1. INTRODUCTION

The thermal efficiency of the heat exchanger is one of the most significant problems in the heat transfer process. To save more energy and costs, the technology of heat exchangers needs to be improved. Many methods are used in heat transfer applications to enhance the heat transfer rate. To enhance the thermal performance of the heat exchangers, passive, active and conjugate methods can be used. Active methods require external power input for the process, in contrast passive methods do not require any additional energy to improve the thermo-hydraulic performance of the system.

Design parameter of thermal systems relates with not only heat transfer enhancement but also the amount of power input and in the systems. Therefore, the determining of the optimal consistence between the heat transfer rate and requirement of power input becomes main purpose of the design evaluations of a thermal systems. Exergy analyses has been conducted by many researchers to determine the optimal model of the thermal systems. There are several investigations on entropy generation and heat transfer analyses of thermal systems.

Paisarn Naphon [1] presented an experimental study on the exergy loss of the horizontal concentric micro-fin tube heat exchanger. Florez-Orrego et al. [2] evaluated the exergy cost and CO2 emission cost allocation for an integrated syngas and ammonia production plant. Martinaitis et al. [3] presented a methodology and algorithm for exergy analysis for heat recovery exchanger. They concluded that the developed methodology and algorithm can be used to solve the problem of net exergy efficiency of thermodynamic systems. Dizaji et al. [4] experimentally investigated the effect of shell corrugations on dimensionless exergy loss for shell and tube heat exchanger. They reported that the corrugation of tube and shell increased the dimensionless exergy loss. Amirahmedi et al. [5] carried out a numerical analysis about the effects of vortex generator and Reynolds number on the heat transfer and exergy loss in a trapezoidal duct. E et al. [6] numerically investigated the effects of inlet pressure on wall temperature and exergy efficiency of the micro-cylindrical combustor. Ko and Wu [7] analysed the entropy generation induced by turbulent forced convection in a curved rectangular duct with external heating by numerical methods. Huminic and Huminic [8] studied the heat transfer and entropy generation inside a helically coiled tube in tube heat exchanger in laminar flow

---

[1] *Corresponding author: Erciyes University, Department of Mechanical Engineering, 38039, Melikgazi/Kayseri, Turkey. keklikcioglu@erciyes.edu.tr.*

[2] *Erciyes University, Department of Mechanical Engineering, 38039, Melikgazi/Kayseri, Turkey, toygun@erciyes.edu.tr.*

[3] *Erciyes University, Department of Mechanical Engineering, 38039, Melikgazi/Kayseri, Turkey, ozceyhan@erciyes.edu.tr.*

regime using two different types of nanofluids. The increase of nanoparticles volume concentration leads to the reduction of the entropy generation. Ventsislav Zimparov [9] conducted an experimental investigation on heat transfer enhancement and entropy generation of three start spirally corrugated tubes with a twisted tape. Kurtbas et al. [10] studied the effects of propeller type turbulators located in the inner tube of co-axial heat exchanger were investigated on entropy generation rate and exergy loss rate. Another investigation of Yakut and Sahin [11] effect of coiled wire inserts on heat transfer enhancement and the entropy generation rate were investigated. Ching Chang Cho [12] investigated the heat transfer performance and entropy generation of natural convection in a partially heated wavy wall square cavity filled with Al2O3-water nanofluid.

From the literature cited above, several passive techniques have been applied in thermal systems to investigate the heat transfer and the exergy loss. In the present study, the exergy loss in a circular tube with coiled-wire inserts is investigated, experimentally. The wire inserts are manufactured with an equilateral triangular cross-section having 4, 5 and 6 mm side length and are coiled using a method so that a vertex of the triangle is oriented to face the flow direction. The coiled-wire inserts are installed with 1 mm separation from the inner tube wall and coiled with three different pitch-to-diameter ratios: P/D= 1, P/D= 2 and P/D= 3. Experiments are performed for a range of Reynolds numbers from 2851 to 27,732.

2. EXPERIMENTAL METHOD

2.1. Experimental apparatus

The test tube has 56 mm inner diameter (D1), 60 mm outer diameter (D2), and 2 mm thickness. The details of test tube fitted with coiled wire insert are shown in Fig.1.

Figure 82. The equilateral triangle cross section coiled-wire inserted in a tube with a separation from the inner wall of the tube.

All tests were carried out with experimental equipments as shown in Fig. 3. The test section composed a bell-mouth that used to supply uniform air inlet to the pipe, two current flaps for applying the heat flux, a tube to improve the air flow hydro-dynamically and a test tube, in length of 6000 mm and 2600 mm, respectively.

The test tube was subjugated uniform heat flux that was supplied by a variac transformer and isolated firmly with glass wool from the external surface. The wire coiled with three different pitch-to-diameter ratios and placed into the tube with 1 and 2 mm seperation by using teflon rings in Fig.1. Temperatures were measured by using 26 piece temperature sensors, they were applied on the external surface of the test tube as in Fig.2.
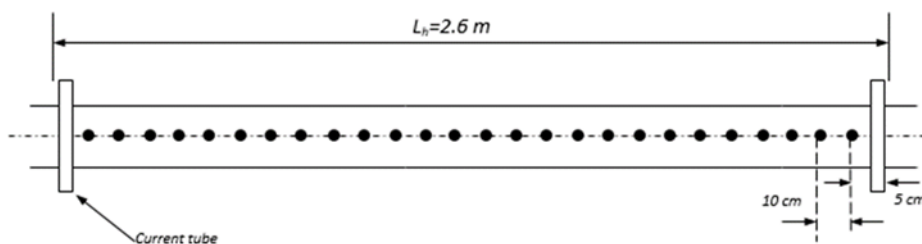
Figure 2. Temperature measuring method

Also, the inlet and the outlet temperatures of the bulk air were measured by two different sensors at certain points. The sensors measure the temperatures within ±0.2 °C accuracy rating according to the calibration test result. A blower that has the power of 3 kW is used to vacuum air into the test section and the blower is controlled by an inverter. To establish the pressure drop, a differential pressure gauge was used. The volumetric flow rate was determined by using flow meter in to the flow field.

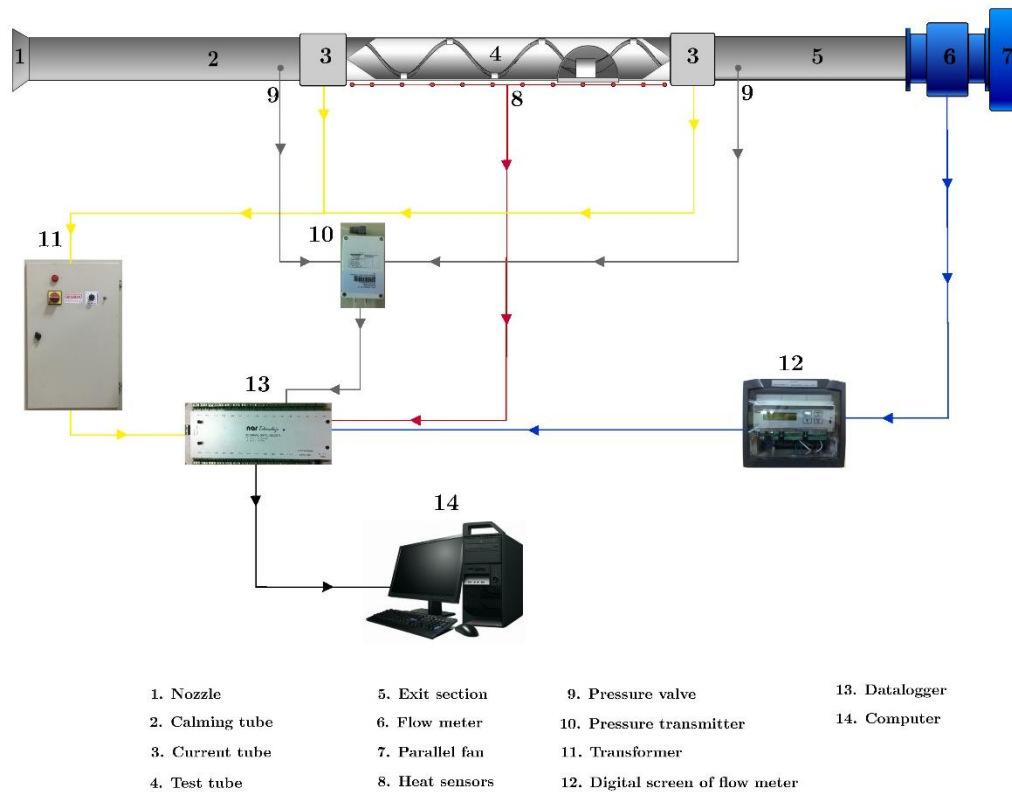| 1. Nozzle | 5. Exit section | 9. Pressure valve | 13. Datalogger |
2. Calming tube	6. Flow meter	10. Pressure transmitter	14. Computer
3. Current tube	7. Parallel fan	11. Transformer	
4. Test tube	8. Heat sensors	12. Digital screen of flow meter	

Figure 3. The details of experimental apparatus.

Different flow rate and electrical power values were tested in the experiments. The numeric data of temperature, the decrease of pressure, volumetric flow rate of the bulk air and electrical output were saved by a data logger and transmitted the computer via the data logger after the system reached the steady state condition. The experiments were carried out at the Reynolds number ranges from 3429 to 26,663. The Nusselt and Reynolds numbers, friction factor, heat transfer enhancement and the other data of the system were calculated by using software in the FORTRAN language.

2.2. Calculation of heat transfer and friction factor

The heat given by the air from the test tube is calculated by;

$$Q_{air} = mC_{p,air}(T_0 - T_i) = \Delta VI - Q_{loss} \qquad (1)$$

As a consequence, the heat flux subjected on to the experiment tube can be described as:

$$q = \frac{Q_{air}}{\pi D_2 L} \qquad (2)$$

The coefficient of local heat transfer for the experiment tube is represented as;

$$h(x) = \frac{q}{T_{iw}(x) - T_b(x)} \qquad (3)$$

In Eq.3, and represent the local inner wall temperature of the heated test tube and local bulk temperature of the fluid, respectively.

The local Nusselt Numbers were acquired by Eq.4,

$$Nu(x) = \frac{h(x)D}{k} \qquad (4)$$

For the air, the Reynolds number is

$$\mathrm{Re} = \frac{UD}{\nu} \tag{5}$$

The friction factor, f is calculated as follows, for the fully developed isothermal flow;

$$f = \frac{\Delta P}{\frac{1}{2}\rho.U^2 \frac{L}{D}} \tag{6}$$

where U represents the mean fluid velocity in the tube.

The heat transfer rate and friction factor of the smooth tube and tube fitted with coiled wire inserts are evaluated under the same pumping power as below [13];

$$(\dot{V}\,\Delta P)_s = (\dot{V}\,\Delta P)_c \tag{7}$$

$$(f\,\mathrm{Re}^3)_s = (f\,\mathrm{Re}^3)_c \tag{8}$$

$$\mathrm{Re}_s = \mathrm{Re}_c (f_c / f_s)^{1/3} \tag{9}$$

The enhancement efficiency is presented as follows [13]:

$$\eta = \frac{h_c}{h_s}\Big|_{pp} = \frac{Nu_c}{Nu_s}\Big|_{pp} = \left(\frac{Nu_c}{Nu_s}\right)\left(\frac{f_s}{f_c}\right)^{1/3} \tag{10}$$

2.3. Calculation of exergy destruction

The general exergy balance in steady state fluid flow is given [14] by:

$$Ex_{heat} - Ex_{work} + Ex_{mass,in} - Ex_{mass,out} = Ex_{des} \tag{11}$$

The rate form of general exergy balance can be expressed by Eq. 12:

$$\left(1 - \frac{T_0}{T}\right)Q_w - W + m_{in}\psi_{in} - m_{out}\psi_{out} = Ex_{des} \tag{12}$$

The flow exergy is computed as:

$$\psi = (h - h_0) - T_0(s - s_0) \tag{13}$$

where h, s and subscript zero are respectively enthalpy, entropy and properties at the restricted dead state (T_0 and P_0). The entropy and enthalpy deviations and heat transfer rate can be obtained as:

$$\Delta s = s_{out} - s_{in} = C_p \ln\left(\frac{T_{out}}{T_{in}}\right) - R\ln\left(\frac{P_{out}}{P_{in}}\right) \tag{15}$$

$$\Delta h = h_{out} - h_{in} = C_p(T_{out} - T_{in}) \tag{16}$$

$$Q_w = mC_p(T_{out} - T_{in}) \tag{17}$$

If the Eq. 12 rewritten with using given Eq. 15, 16 and 17:

$$Ex_{des} = mC_pT_0\left[\frac{T_{out}-T_{in}}{T_0} - \ln\left(\frac{T_{out}}{T_{in}}\right) + \frac{\Delta P}{\rho C_p T_0}\right] \tag{18}$$

Dimensionless form of Eq. 18 can be expressed as:

$$e_{des} = \left[\frac{T_{out}-T_{in}}{T_0} - \ln\left(\frac{T_{out}}{T_{in}}\right)\right] + \left[\frac{\Delta P}{\rho C_p T_0}\right] = e_{des,\Delta T} + e_{des,\Delta P} \tag{19}$$

3. EXPERIMENTAL RESULTS

3.1. Validation method

In this present work, in order to demonstrate the accuracy of the experimental results on Nusselt number and friction factor in smooth tube were compared with equations of Gnielinski [15] and Petukhov [16], as shown in Figs. 4 and 5, respectively. Both Nusselt number and friction factor values were validated in the turbulance flow conditions.
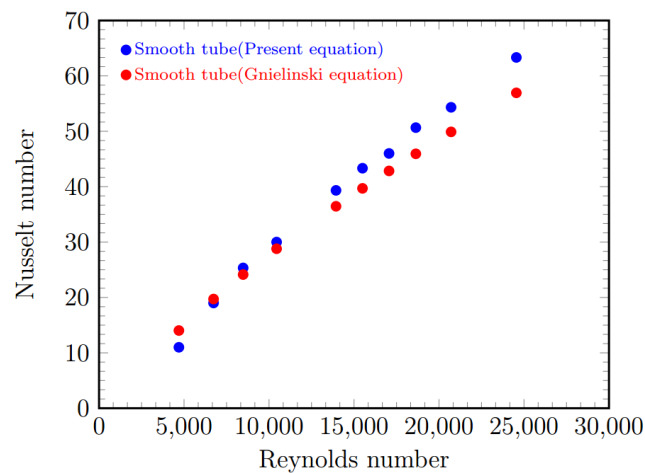

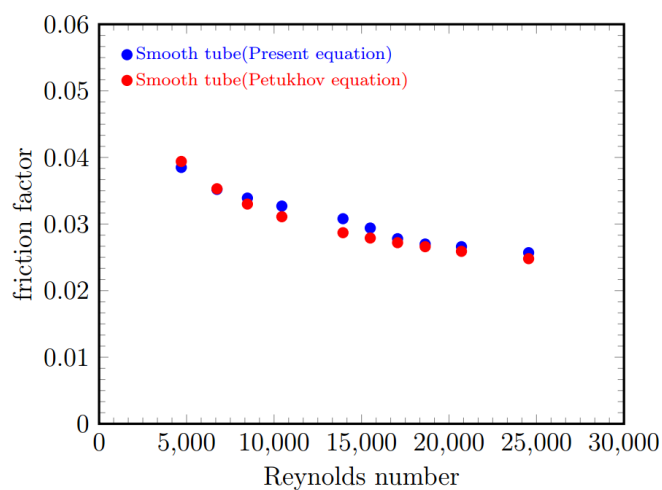Figure 4. Validation of Nusselt number in the smooth tube.

Figure 5. Validation of friction factor in the smooth tube.

As shown in figures, Nusselt number and friction factor values coincide with the previous equations.

3.2. The evaluation of Exergy loss

Thermal performance of the tube with the coiled-wire inserts placed into the flow region is related with the Nusselt number and friction factor . The coiled-wire inserts in the tube cause not only an increase in Nusselt number but also an increase in the friction factor. Therefore, the conversion of the Nusselt number and the friction factor should be investigated. In Figs. 6 and 7, the variation in the Nusselt number and friction factor are presented for all configurations.
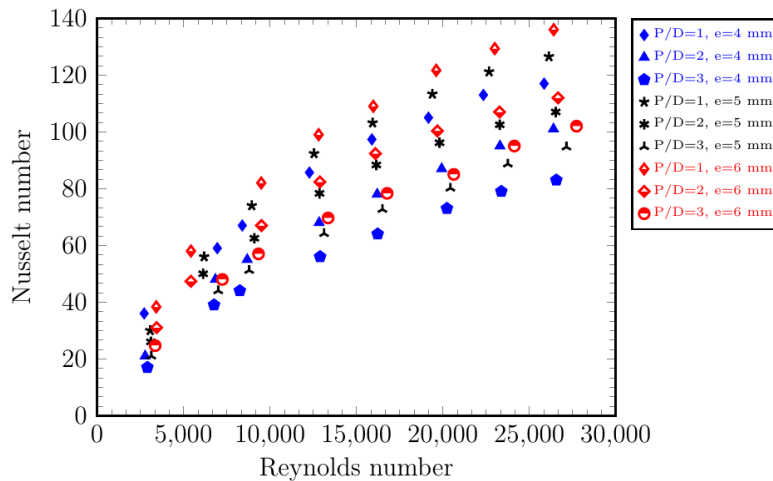

Figure 6. Variation of Nusselt number versus Reynolds number for all configurations.

Figure 6 depicts the Nusselt number increases with increasing triangle side length and decreasing pitch ratio. This suggests that the heat transfer has been enhanced in the tube related with the coil count and triangle thickness. As seen on from the Fig. 6 the increase rate of Nusselt number values for e=6 mm more significant than those for s=5 and s=4 mm side length.
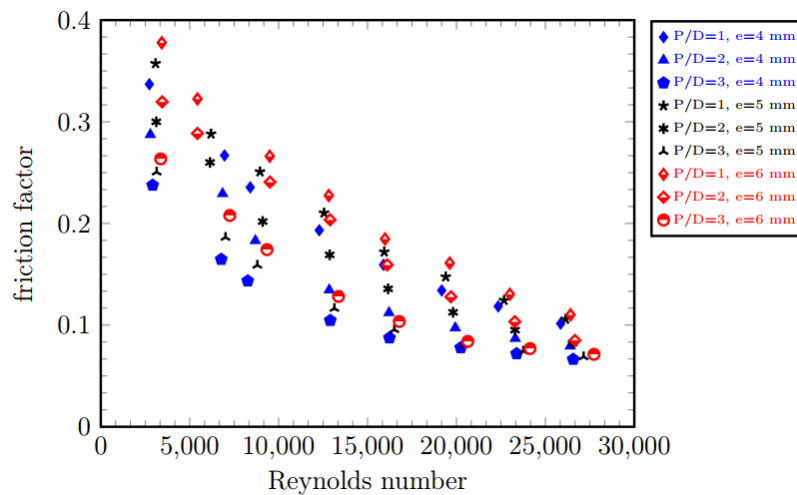
Figure 7. Variation of friction factor versus Reynolds number for all confugurations.

It is clear from the Fig. 7 that the use of coiled-wire inserts caused a significant increase in friction factor. The friction factor shows ascending trend when the coil pitch decreased and side length of triangle increased. The lowest friction factor has been determined for the model P/D=3 and e=4 mm at Reynolds numbers of 26,663.

Heat transfer enhancement techniques, especially passive methods increase the heat transfer rate but they also increase the friction factor. The primal aim of this study evaluate exergy loss for a circular tube with coiled wire inserts. Dimensionless exergy loss values versus Reynolds number for different configurations presented in Figs. 8, 9.

Figure 8. Variation of dimensionless exergy destruction versus Reynolds number for three different pitch ratio at e=6 mm..

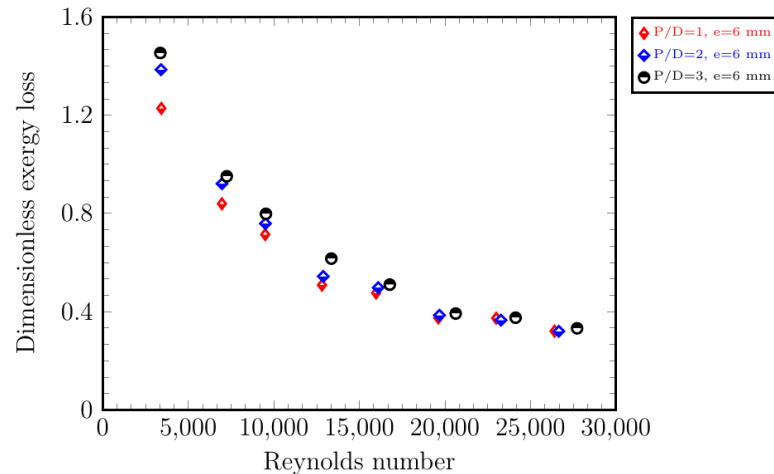Figure 8 represents the comparison of the dimensionless exergy destruction for the various Reynolds number with three different pitch ratios at a constant side length of e=6 mm. The dimensionless exergy destruction shows descending trend with the increment of Reynolds number. The highest exergy destruction achieved for the model of P/D=3 at Reynolds number of 2851.
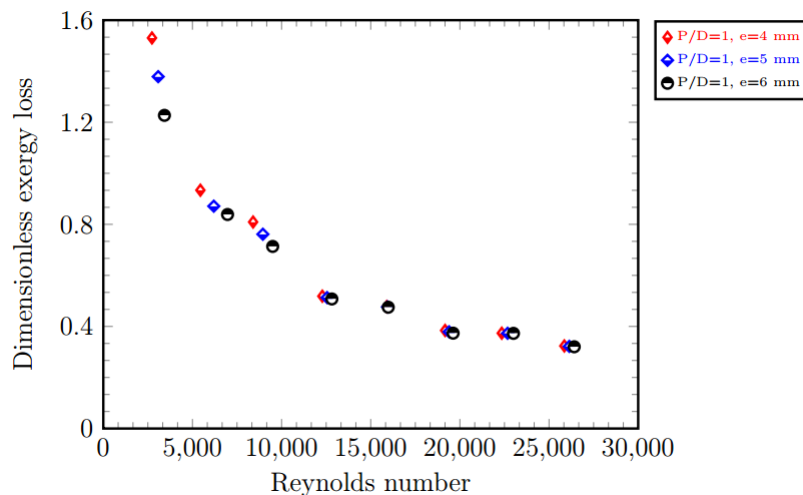

Figure 9. Variation of dimensionless exergy destruction versus Reynolds number for s=2 mm.

Figure 9 represents the dimensionless exergy loss for the various Reynolds number for P/D=1 mm with three different pitch ratios at a constant clearance. Exergy loss decreases with increasing side length. The lowest dimensionless exergy loss of 0.372 observed for P/D=1, e=6 mm model at highest Reynolds number as expected.

4. CONCLUSIONS

The investigations were conducted for a range of Reynolds numbers from 2851 to 27,792. The triangle side length of 4, 5, 6 mm were chosen for the experiments. The coiled-wire inserts installed with 1 mm separation from the inner tube wall and coiled with three different pitch-to-diameter ratios: P/D= 1, P/D= 2 and P/D= 3. Heat transfer rates increased with decreasing pitch ratio and with increasing triangle side length in the experiments. The experimental results revealed that dimensionless exergy loss decreases with increasing of Reynolds number and increases with increasing pitch ratio. It was also obtained that pitch ratio has significant effect on entropy generation number. The shorter side length configuration's dimensionless exergy losses were higher than the other models. Especially at low Reynolds numbers, the system achieves higher exergy loss. The lowest dimensionless exergy loss of 0.372 observed for P/D=1, e=6 mm model at highest Reynolds number as expected.

REFERENCES

[1]. P. Naphon, Study on the exergy loss of the horizontal concentric microfin tube heat exchanger, *International Communications in Heat and Mass Transfer*, vol. 38, pp. 229 – 235, 2011.

[2]. .D. Florez-Orrego, S. de Oliveira Junior, On the efficiency, exergy costs and CO2 emission cost allocation for an integrated syngas and ammonia production plant, *Energy*, vol. 117-2, pp. 341 – 360, 2016.

[3]. V. Martinaitis, G. Streckien, D. Bieka, J. Bielskus, The exergy efficiency assessment of heat recovery exchanger for air handling units, using a state property coenthalpy, *Applied Thermal Engineering*, vol. 108, pp. 388 – 397, 2016.

[4]. H. S. Dizaji, S. Jafarmadar, S. Asaadi, Experimental exergy analysis for shell and tube heat exchanger made of corrugated shell and corrugated tube, *Experimental Thermal and Fluid Science*, vol. 81, pp. 475 – 481, 2017.

[5]. S. Amirahmadi, S. Rashidi, J. A. Esfahani, Minimization of exergy losses in a trapezoidal duct with turbulator, roughness and beveled corners, *Applied Thermal Engineering*, vol. 107, pp. 533 – 543, 2016.

[6]. J. E, W. Zuo, X. Liu, Q. Peng, Y. Deng, H. Zhu, Effects of inlet pressure on wall temperature and exergy efficiency of the microcylindrical combustor with a step, *Applied Energy*, vol. 175, pp. 337 – 345, 2016.

[7]. T.H. Ko, C.P. Wu, A numerical study on entropy generation induced by turbulent forced convection in curved rectangular ducts with various aspect ratios, *International Communications in Heat and Mass Transfer*, vol. 36, pp. 25-31, 2009.

[8]. Gabriela Huminic, Angel Huminic, Heat transfer and entropy generation analyses of nanofluids in helically coiled tube-in-tube heat exchangers, *International Communications in Heat and Mass Transfer*, vol. 71, pp. 118-125, 2016.

[9]. Ventsislav Zimparov, Enhancement of heat transfer by a combination of three-start spirally corrugated tubes with a twisted tape, *International Journal of Heat and Mass Transfer*, vol. 44, pp. 551-574, 2001.

[10]. I. Kurtbas, A. Durmus, H. Eren, E. Turgut, Effect of propeller type swirl generators on the entropy generation and efficiency of heat exchangers*, International Journal of Thermal Sciences*, vol. 46, pp. 300 – 307, 2007.

[11]. Kenan Yakut, Bayram Sahin, The effects of vortex characteristics on performance of coiled wire turbulators used for heat transfer augmentation, *Applied Thermal Engineering*, vol. 24, pp. 2427-2438, 2004.

[12]. Ching-Chang Cho, Heat transfer and entropy generation of natural convection in nanofluid-filled square cavity with partially-heated wavy surface, *International Journal of Heat and Mass Transfer*, vol. 77, pp. 818–827, 2014.

[13]. R.L. Webb, Performance evaluation criteria for use of enhanced heat transfer surfaces in heat exchanger design, *International Journal of Heat and Mass Transfer*, vol. 24, pp. 715-26, 1981.

[14]. A.Felahat, M. Shabani, M. Maleki, , The exergy efficiency and pumping power of nanofluid through a helically coiled tube heat exchanger under turbulent flow , *Journal of Mechanical Engineering and Technology*, vol. 7, pp. 75-92, 2015.

[15]. V. Gnielinski, New equations for heat and mass transfer in turbulent pipe flow and channel flow, *Int. Chem. Eng.*, vol. 16, pp. 359-368, 1976.

[16]. B.S. Petukhov, Heat transfer in turbulent pipe flow with variable physical properties, J. P. Harnett (Eds.), *Advances in Heat Transfer*, Academic Press, New York, vol. 6, pp. 504-564, 1970.

Effect of the Coulomb Thermal Conduction on the Gyroviscous Magnetorotational Instability

Ebru Devlen[1], Ahmet Devlen[1]

Abstract

In this study, the physical instability defining the expected turbulence in Radiatively Inefficient Accretion Flows (RIAFs) around the supermassive black holes (e.g., Sagittarius A* in the center of our Galaxy) is discussed. These flows, with a high probability, include weakly collisional hot, optically thin and dilute plasmas. Within these flows, gravitational potential energy brought about by turbulent stresses is trapped as heat energy. Thus, in order accretion to be realized, outward transport of heat as well as angular momentum is required. This outward heat transport may reduce the mass inflow rate on black hole. MHD equations including tensor structure of Coulombic thermal conductivity coefficient in the heat flux term in the conservation of energy equation are solved. A result of the linear stability analysis, the dispersion relation is derived and the growth rates of instability are estimated. According to the various values of temperature gradient, the status of the Gyroviscous Magnetorotational Instability (GvMRI) is discussed.

Keywords: *accretion disk/flow, instability, MHD, waves*

1. INTRODUCTION

Accretion refers to the accumulation of matter onto a massive central body. Release of gravitational binding energy is a dynamic necessity for accretion to occur and a powerful source of luminosity. Accretion disks can be separated into three categories:

a) Protostellar disks, from whence stars and planets are born;

b) Disks formed by mass transfer in binary systems;

c) Disks/flows around the supermassive black holes thought to be the most luminous sources in the universe.

Most galaxies have at least one black hole in residence in their central regions. Even our home galaxy, the Milky Way, has a four million solar mass black hole located at its center, about 27 000 light years from Earth. Black holes are most often detected by the radiation produced when they gravitationally pull in surrounding gas.

In this work the physical instability defining the expected turbulence in Radiatively Inefficient Accretion Flows (RIAFs) around the supermassive black holes (e.g., Sagittarius A* in the center of our Galaxy) is studied. These flows, with a high probability, include weakly collisional hot, optically thin and dilute plasmas. Within these flows, gravitational potential energy brought about by turbulent stresses is trapped as heat energy. Thus, in order accretion to be realized, outward transport of heat as well as angular momentum is required. The presence of instability provides the transfer of angular momentum and heat.

In the dilute plasma, ion gyroradius is much smaller than the ion collision mean free path, i.e. $r_{Li} \Box \lambda_i$.

Conventional MHD theory assumes that plasma pressure is isotropic for simplicity. However, the one that want to make a more accurate model of plasma must take into consideration anisotropy in the pressure. The anisotropy in the pressure can be due to the presence of a strong magnetic field under laboratory conditions, but under the astrophysical conditions, the plasma may have a tensorial character even in the presence of a weak magnetic field, the resulting anisotropy being determined by the Larmor frequencies and the macroscopic velocity gradients of the constituents of the plasma. Under this condition, MHD equations

describing the plasma dynamics should include the anisotropic transport terms arising from the free flow of the particles along the magnetic field lines [1]. In order to take into account the arbitrarily high-order FLR effects the MHD equations should contain collisionless viscous tensor. Reference [2] considered viscous tensor in MHD equations and showed that the novel linear instability (Gyroviscous Magnetorotational Instability) is more powerful and greater than the ideal magnetothermal instability (MTI) and ideal magnetorotational instability (MRI) in the dilute astrophysical plasmas.

However in such plasmas diffusion of heat is mediated by charged particles that are confined to flow along magnetic field lines. The Coulombic heat flux is given by $\mathbf{Q} = -\chi \mathbf{bb} \cdot \nabla T = -\mathbf{X} \cdot \nabla T$ where χ is the conductivity along field lines which lie in the direction $\mathbf{B}/B = \mathbf{b}$ and $\mathbf{X} = \mathbf{X}(\chi, \mathbf{b})$ is the thermal conductivity tensor [3]. In this work, we extend our previous study by considering the thermal conductivity tensor.

2. FUNDAMENTAL EQUATIONS

In an attempt to investigate viscosity, and heat flux in a dilute plasma, one should consider the two-fluid equations. Below are the standard extended MHD equations that are obtained by using two-fluid equations including stress tensor $\mathbf{\Pi}$ and the heat flux $\mathbf{Q}$:

$$\frac{d\rho}{dt} + \rho \nabla \cdot \mathbf{v} = 0 \tag{2}$$

$$\rho \frac{d\mathbf{v}}{dt} = -\nabla P - \nabla \cdot \mathbf{\Pi} + \frac{(\nabla \times \mathbf{B}) \times \mathbf{B}}{c} + \rho \mathbf{g} \tag{3}$$

$$\frac{\partial \mathbf{B}}{\partial t} = \nabla \times (\mathbf{v} \times \mathbf{B}) \tag{4}$$

$$\frac{dP}{dt} + \frac{5}{3} P (\nabla \cdot \mathbf{v}) = -\frac{2}{3} \nabla \cdot \mathbf{Q} \tag{5}$$

where ρ is the mass density, $\mathbf{v}$ is the fluid velocity, P is the scalar pressure, $\mathbf{\Pi}$ is the stress tensor, $\mathbf{B}$ is the magnetic field, $\mathbf{g}$ is the gravitational acceleration, $\mathbf{Q}$ is the heat flux, and $d/dt = \partial/\partial t + \mathbf{v} \cdot \nabla$ is a Lagrangian derivative. Stress tensors have three components: parallel, perpendicular and the gyroviscous [1]. Perpendicular viscosity is greater than parallel viscosity by a factor of $(r_L / \lambda)^2$ in a dilute plasma, and therefore it may not be taken into account. We use parallel and gyroviscous components of the stress tensor, which are given by:

$$\mathbf{\Pi}^{\parallel} = 0.96 \frac{P}{2\nu} (\mathbf{I} - 3\mathbf{bb})(\mathbf{b} \cdot \mathbf{W} \cdot \mathbf{b}) \tag{6}$$

$$\mathbf{\Pi}^{gv} = \frac{P}{4\omega_c} \left\{ \mathbf{b} \times \mathbf{W} \cdot (\mathbf{I} + 3\mathbf{bb}) + [\mathbf{b} \times \mathbf{W} \cdot (\mathbf{I} + 3\mathbf{bb})]^T \right\} \tag{7}$$

where $\mathbf{b} = \mathbf{B}/B$, $\omega_c = eB/mc$ are the unit vectors along the magnetic field and the cyclotron frequency, respectively, and $\mathbf{W} = \nabla \mathbf{v} + (\nabla \mathbf{v})^T - 2/3 \mathbf{I}(\nabla \cdot \mathbf{v})$ is the rate of strain tensor.

3. DISPERSION RELATION

We apply a standard Wentzel–Kramers–Brillouin (WKB) perturbation analysis on the equilibrium state. To this analysis, all the variables in the MHD equations are denoted by sums of an equilibrium value (denoted with a "0" subscript) and a small perturbed quantity (denoted with "δ"). We work in a cylindrical coordinate system, (R, ϕ, z). Space-time dependence of the axisymmetric perturbations is assumed to be of the form $\exp(ik\mathbf{z} - i\omega t)$. The weak magnetic field has a helical shape with $B_\phi = B_0 \cos\theta$ and $B_z = B_0 \sin\theta$, where $\theta = \tan^{-1}(B_z / B_\phi)$ is the angle between the magnetic field vector and the ϕ axis of the coordinate system. In the equilibrium state of the differentially rotating plasma with a Keplerian velocity profile, $v_0 = R\Omega(R)\hat{\phi}$, plasma pressure is assumed to be isotropic.

The dimensionless dispersion relation derived from the set of linearized equations is given below:

$$\sigma^5 + \sigma^4(a_4 + ib_4) + \sigma^3(a_3 + ib_3) + \sigma^2(a_2 + ib_2) + \sigma(a_1 + ib_1) + (a_0 + ib_0) = 0 \quad (8)$$

where

$$a_4 = \left(4s^2\tilde{V}_{ther}\sqrt{X}\frac{1}{\varepsilon M_A}\left(\frac{\partial \ln T}{\partial \ln z}\right)\right)$$

$$b_4 = \left(\tilde{V}_{ther}Xs^2 + \tilde{V}_{par}X6s^2\frac{k_\perp^2}{k^2}\right)$$

$$a_3 = -\left\{ 2s^2X + \frac{Y^2}{4}\frac{kz^2}{k^2}(2sy^2-A)^2 - \frac{kz^2}{k^2}\tilde{N}^2 + 4\frac{kz^2}{k^2} + \frac{kz^2}{k^2}\frac{d\ln\Omega^2}{d\ln R} \right.$$
$$\left. + \frac{Y}{2}\left(\frac{d\ln\Omega^2}{d\ln R}(H+G) + \frac{kz^2}{k^2}4(2sy^2-A)\right) + \tilde{V}_{par}\tilde{V}_{ther}X^2 6s^4\frac{k_\perp^2}{k^2} \right\}$$

$$b_3 = a_4 6s^2\tilde{V}_{par}X\frac{k_\perp^2}{k^2}$$

$$a_2 = -a_4\left\{ \frac{Y^2}{4}\frac{kz^2}{k^2}(2sy^2-A)^2 + \left(2s^2X + \frac{kz^2}{k^2}\tilde{\kappa}^2\right) + \frac{Y}{2}\left(\frac{d\ln\Omega^2}{d\ln R}(G+H) + \frac{kz^2}{k^2}4(2sy^2-A)\right) \right\}$$

$$b_2 = -\left\{ \frac{Y^2}{4}\frac{kz^2}{k^2}\frac{d\ln\Omega^2}{d\ln R}3yYD(2sy^2-A) \right.$$
$$+ \tilde{V}_{ther}Xs^2\left(\begin{array}{l} 2s^2X - \dfrac{kz^2}{k^2}\tilde{N}_T^2 + \dfrac{kz^2}{k^2}\tilde{\kappa}^2 + \dfrac{Y^2}{4}\dfrac{kz^2}{k^2}(2sy^2-A)^2 \\ + \dfrac{Y}{2}\left(\dfrac{d\ln\Omega^2}{d\ln R}(G+H) + \dfrac{kz^2}{k^2}4(2sy^2-A)\right) \end{array} \right)$$
$$\left. + \frac{Y}{2}\frac{d\ln\Omega^2}{d\ln R}3s^2\left[\tilde{V}_{par}XG\frac{k_\perp^2}{k^2} + \frac{kz^2}{k^2}y6c\right] + \tilde{V}_{par}X\left[X6s^4\frac{k_\perp^2}{k^2} + 2cD\frac{kz^2}{k^2}\frac{d\ln\Omega^2}{d\ln R} - 2cD\frac{kz^2}{k^2}\tilde{N}^2\right] \right\}$$

$$a_1 = \left\{ \begin{array}{l} \dfrac{Y^2}{4}\left(\left(\dfrac{d\ln\Omega^2}{d\ln R}\right)^2\dfrac{kz^2}{k^2}y^2 2YD^2\right) + \left[s^2X + \dfrac{Y}{4}\dfrac{d\ln\Omega^2}{d\ln R}(G+2H)\right]\left(s^2X + \dfrac{Y}{4}\dfrac{d\ln\Omega^2}{d\ln R}G + \dfrac{kz^2}{k^2}\dfrac{d\ln\Omega^2}{d\ln R} - \dfrac{kz^2}{k^2}\tilde{N}^2\right) \\ + s^2\tilde{V}_{ther}X\left[\begin{array}{l} \dfrac{Y^2}{4}\dfrac{d\ln\Omega^2}{d\ln R}3y\dfrac{kz^2}{k^2}D(2sy^2-A) + \dfrac{Y}{2}\dfrac{d\ln\Omega^2}{d\ln R}3s^2\left(\tilde{V}_{par}XG\dfrac{k_\perp^2}{k^2} + y\dfrac{kz^2}{k^2}3c\right) \\ + \tilde{V}_{par}X\left(X6s^4\dfrac{k_\perp^2}{k^2} + 2cD\dfrac{kz^2}{k^2}\dfrac{d\ln\Omega^2}{d\ln R} - 2cD\dfrac{kz^2}{k^2}\tilde{N}_T^2\right) \end{array} \right] \end{array} \right\}$$

$$b_1 = -a_4\left\{ \frac{kz^2}{k^2}\frac{d\ln\Omega^2}{d\ln R}\frac{Y^2}{4}3yD(2sy^2-A) \right.$$
$$\left. + \tilde{V}_{par}X\left[6s^4X\frac{k_\perp^2}{k^2} - 4cD\frac{kz^2}{k^2}\frac{1}{2}\frac{d\ln\Omega^2}{d\ln R}\right] + 3s^2\frac{d\ln\Omega^2}{d\ln R}\frac{Y}{2}\left[\tilde{V}_{par}XG\frac{k_\perp^2}{k^2} + \frac{kz^2}{k^2}2cy4\right] \right\}$$

$$a_0 = a_4\left\{ \left(\frac{d\ln\Omega^2}{d\ln R}\right)^2\frac{Y^2}{4}y^2\frac{kz^2}{k^2}(2D^2) + \left(s^2X + \frac{Y}{4}\frac{d\ln\Omega^2}{d\ln R}(G+2H)\right)\left(s^2X + \frac{kz^2}{k^2}\frac{d\ln\Omega^2}{d\ln R} + \frac{Y}{4}\frac{d\ln\Omega^2}{d\ln R}G\right) \right\}$$

$$b_0 = s^2\tilde{V}_{ther}X\left\{ \left(\frac{d\ln\Omega^2}{d\ln R}\right)^2\frac{Y^2}{4}y^2\frac{kz^2}{k^2}2D^2 \right.$$
$$\left. + \left(s^2X + \frac{Y}{4}\frac{d\ln\Omega^2}{d\ln R}(G+2H)\right)\left(s^2X + \frac{kz^2}{k^2}\frac{d\ln\Omega^2}{d\ln R} + \frac{Y}{4}\frac{d\ln\Omega^2}{d\ln R}G - \frac{kz^2}{k^2}\tilde{N}_T^2\right) \right\}$$

where $A = \sin\theta(1 - 3\cos 2\theta)$, $D = 3\sin^2\theta\cos\theta$, $G = \sin\theta(1 + 3\cos 2\theta)$, $H = 3\sin\theta\cos^2\theta$, $\varepsilon = z/R$, $X = k_z^2 v_A^2/\Omega^2$, $Y = k_z^2 v_D^2/\Omega^2$, $\sigma = \omega/\Omega$, $\tilde{N} = N/\Omega$, $y = k_R/k_z$, $\tilde{V}_{par} = 0.96 k_z^2 P/2\nu\rho\Omega X$, $\tilde{V}_{ther} = 2k_z^2\chi T/5P\Omega X$, $s = \sin\theta$, $c = \cos\theta$ and M_A is Alfvenic Mach number, $N^2 = -(3/5\rho)(\partial P/\partial R)(d\ln P\rho^{-5/3}/dR)$ is Brunt-Vaisala frequency, $v_D^2 = P\Omega/2\omega_c\rho$ and $v_A^2 = B^2/4\pi\rho$ are drift velocity and Alfven velocity, respectively.

4. NUMERICAL SOLUTIONS

Figures 1–2 show numerical solutions of the dimensionless dispersion relation in Equation (8) under the particular assumptions. All the figures are drawn as dimensionless growth rate versus wavenumber for the Keplerian rotational profile.

(a)

(b)

(c)

(d)

Figure 83. Growth rates of different unstable modes for negative or positive temperature gradient and $k_R = 0$.

As shown the figures for all the wavenumbers, there are at least four unstable modes. The maximum growth rates of instability are so large for all the cases. Figures clearly shows that modified GvMRI including the thermal conduction tensor is more powerful and greater an instability than an ideal GvMRI [2]. Also, the above analysis shows that, regardless of the sign of the temperature gradient, a weakly magnetized and convectively stable dilute plasma harboring the combined effects of gyroviscosity, parallel viscosity, and thermal conduction tensor is unstable due to the gyroviscous force. The growth rate of unstable mode depends sensitively on the radial wavenumber (k_R). Comparing Figure 1a and Figure 2a, it is clearly seen that the growth rate decreases very rapidly for the case of $k_R = k_z$. For other modes, the growth rate does not change too much with the radial wavenumber, but unstable regions are larger than those in the cases of $k_R = 0$.
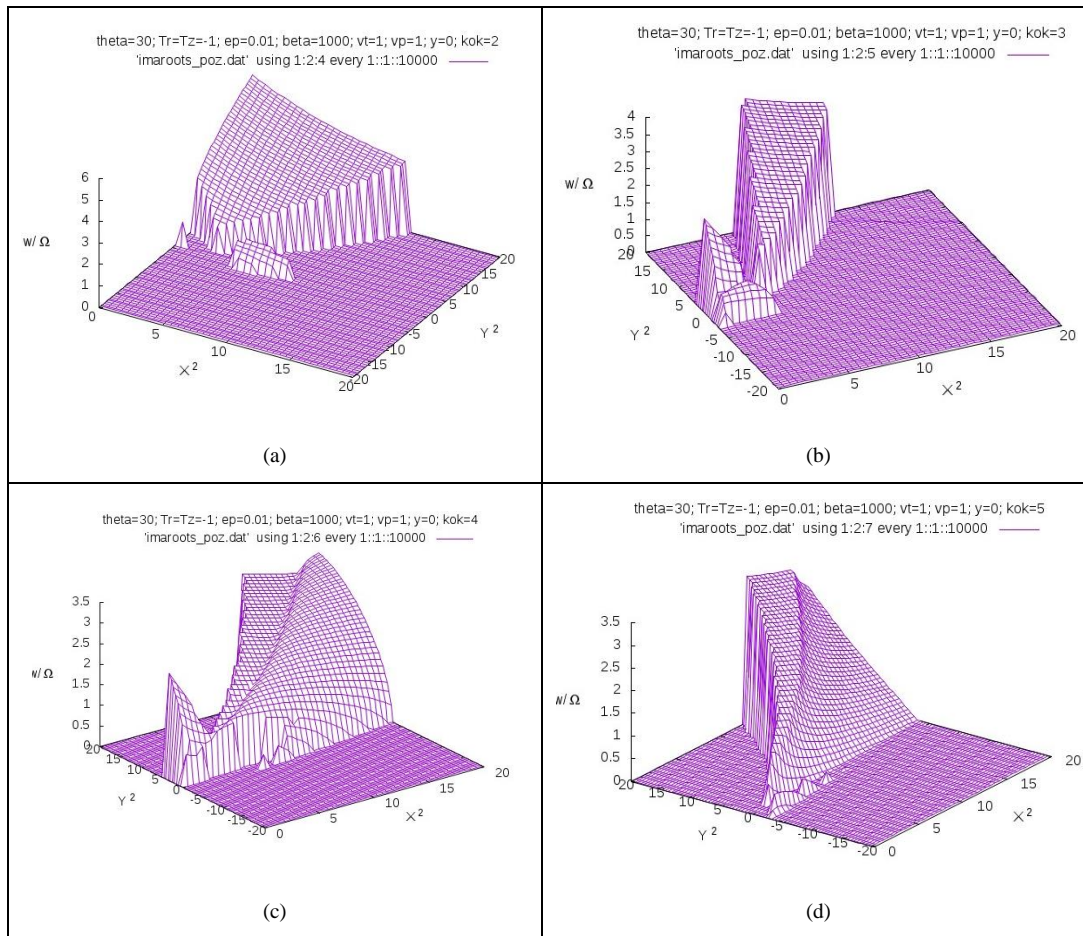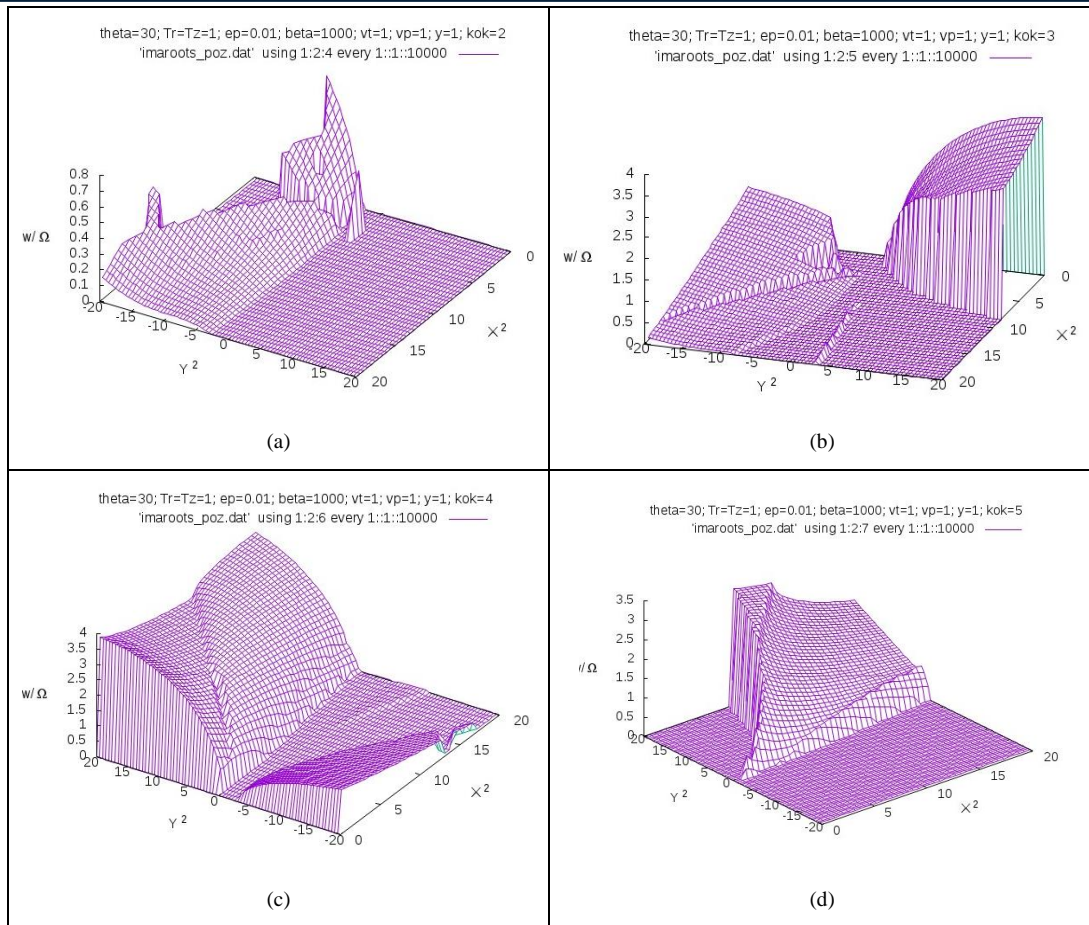
Figure2. Growth rates of different unstable modes for negative or positive temperature gradient and $k_R = 0$ *.*

This instability which is modified by thermal conductivity tensor may work for the accretion flows around the massive black holes and explain the expected turbulence in especially RIAFs.

ACKNOWLEDGMENT

REFERENCES

[1]   Braginskii, S. I., in Reviews of Plasma Physics, Vol. 1, ed. M. A. Leontovich (New York: Consultants Bureau); 1965; p.205.

[2]   Devlen, E. (2011) "The Anisotropic Transport Effects on Dilute Plasmas", The Astrophysical Journal, vol.731: 104, pp.1-16.

[3]   Socrates, A., Parrish, I.J., Stone, J. M., 2008, "Coulomb Bubbles: Overstable Driving Of Magnetoacoustic Waves Due To The Rapid And Anisotropic Diffusion Of Energy", ApJ, 675, 357.

A Novel, Fast and Improved Fox Hunting Optimization Algorithm (FHA) and Blur Kernel Estimation Application

Murat ONAY[1]*

Abstract

A Novel, fast and easy population-based search algorithm called the Improved Fox Hunting Algorithm (FHA) is presented here. FHA is a general-purpose algorithm. FHA can be applied to solve almost any optimization problem. There are lots of algorithms which mimic animal and plant behaviors in the literature. But human is the cleverest living creature in the world. The human uses the animals to benefit their superiority for hunting. The FHA algorithm mimics the fox hunting activity which is formed and improved since 16th century by the human. The algorithm performs some neighborhood searches combined with random search. It can be used for both combinatorial optimization and functional optimization. Also, as an application, FHA is applied to calculate the blur kernel of aerial images taken by our unmanned air vehicle.

Keywords: *Fox Hunting Algorithm, Functional Optimization, Swarm Intelligence, Optimization, Blur kernel, Image processing*

1. INTRODUCTION

Many complex multi-variable optimization problems that abound in the real world are usually hard works for classical methods. In order to overcome the deficiencies of traditional mathematical techniques, population based soft computing algorithms have been introduced over the last years. Several evolutionary or meta-heuristic algorithms have since been developed which combine rules and randomness mimicking natural behaviors of the animals. These behaviors include biological evolutionary processes (e.g., the evolutionary algorithm proposed by Fogel et al. [1], De Jong [2], and Koza [3] and the genetic algorithm (GA) proposed by Holland [4] and Goldberg [5]) and animal behaviors (e.g., the Ant Colony Optimization proposed by Dorigo et al. algorithm [6] and the Particle Swarm Optimization algorithm proposed by Eberthart and Kennedy [7], the Bees Algorithm proposed by Pham [8], Artificial Fish Swarm Algorithm proposed by Li [9]). These meta-heuristic algorithms based methods have been studied by many researchers to solve various optimization engineering problems.

In this paper a new, fast and improved Fox Hunting Algorithm (FHA) is presented here and applied to blur kernel estimation problem. This new meta-heuristic optimization algorithm simulates the fox hunting activity of the human beings. Fox hunting involves the tracking and chase of a fox. Horses are used to track the fox. Trained foxhounds and terriers are used to chase the fox [10]. Human beings use horses to go faster. They use foxhounds for tracking. Also they use terriers to deep search in holes and hives. Basic FHA mimics these all behaviors (see Ref. [11]). In this paper a modified FHA is introduced and applied to blur kernel estimation problem.

In recent years, digital images have been deeply integrated into the modern life. Movement or vibration of the camera is a common source of degradation in digital images. While the image is taken by an unmanned air vehicle (UAV) vibration is inevitable. In this work, we use our UAV [12] to take digital aerial images. Usually, blur kernel is used to reduce the taken image. Blur kernel means the map of camera shake while photo is taken. The recent years have witnessed significant advances in single image deblurring [13]. Estimating an unknown blur kernel from a single input blurred image is a severely ill-posed problem. Much

---

[1*] *Corresponding author Erciyes University, Faculty of Aeronautics and Astronautics, Turkey, e-mail: muratonay@erciyes.edu.tr*

success of the state-of the-art algorithms [14-20] can be attributed to the use of learned prior from natural images and the selection of salient edges for kernel estimation. Although numerous methods [14-18] have been proposed for motion deblurring, these priors are not still enough effective. So, in this work, we present a new method to estimate the blur kernel of aerial images. Here FHA is used to estimate the blur kernel. The procedure can be basically explained like in figure 1.
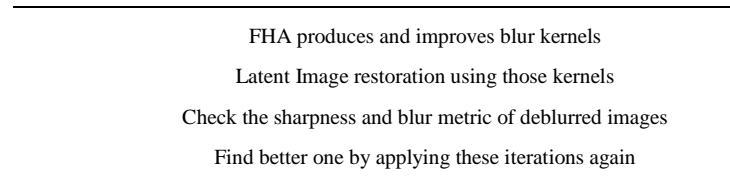

FHA produces and improves blur kernels

Latent Image restoration using those kernels

Check the sharpness and blur metric of deblurred images

Find better one by applying these iterations again

Figure 1. Basically pseudo code of blur kernel estimation procedure

After several iterations best blur kernel is found by FHA and applied to the aerial image. In the next sections fox hunting algorithm and blur kernel will be explained briefly.

2. FHA ALGORITHM

Optimization algorithms usually have two search mechanisms. The first one is a global search mechanism and the second one is a local search mechanism. By the experience researchers knows that the local search mechanism have to be modified while searching approaches to the solution. Because of that two search mechanisms are not efficient for real world problems. So FHA has three search mechanisms for searching in a more efficient way. The first one is a global search mechanism; the second one is a local search mechanism; the third one is the deeper local search mechanism. They are similar to the fox hunting activity in real world. Figure 2 shows a traditional Fox Hunting Activity. The first search with horses is like global search in the optimization process; it is fast and searches bigger areas with biggest steps in the whole search mechanism. The second one with trained foxhounds is like local search; it is slower than horses but searches the areas better. The third one with terriers is like deeper local search; it has the smallest steps but searches really deeply. So the solution can be found most closely to the global best position as fast as possible. For more information please see Ref. [11]. In this work we present a better mechanism to separate the local search and the deeper local search then earlier FHA [11]. We defined a flag called "flag of local search / deeper local search" (*fnsss*) to separate them. If *fnsss* is set to 0 then algorithm makes the local search. If *fnss* is set to 1 then algorithm makes the deeper local search. *fnsss* is modified automatically in the iteration. The flow chart of the modified FHA is shown in Figure 3.

Figure2.   Master of foxhounds leads the field from Powderham Castle in Devon, England, with the hounds in front [21].
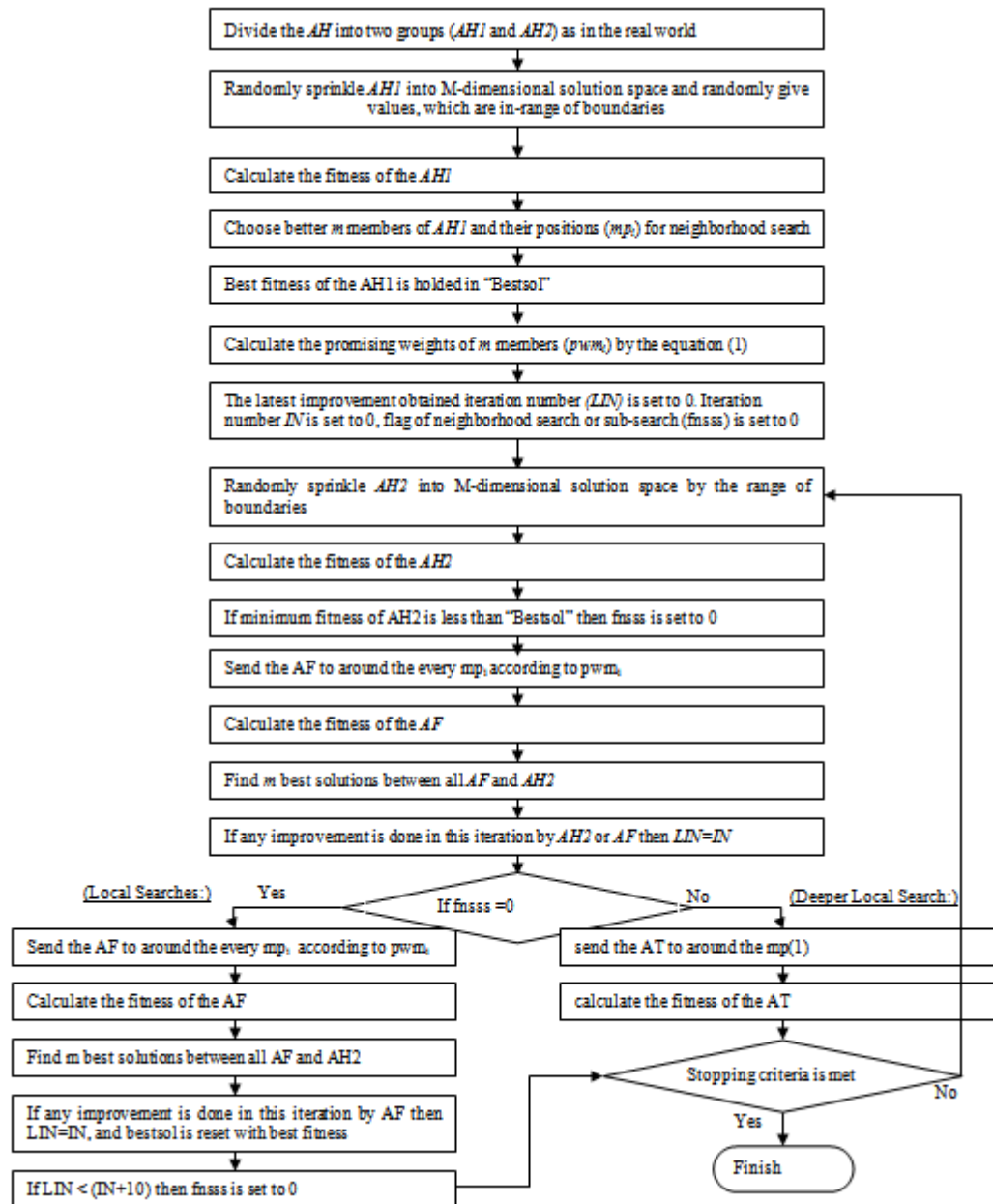
Divide the *AH* into two groups (*AH1* and *AH2*) as in the real world

Randomly sprinkle *AH1* into M-dimensional solution space and randomly give values, which are in-range of boundaries

Calculate the fitness of the *AH1*

Choose better *m* members of *AH1* and their positions (*mp_i*) for neighborhood search

Best fitness of the AH1 is holded in "Bestsol"

Calculate the promising weights of *m* members (*pwm_i*) by the equation (1)

The latest improvement obtained iteration number *(LIN)* is set to 0. Iteration number *IN* is set to 0, flag of neighborhood search or sub-search (fnsss) is set to 0

Randomly sprinkle *AH2* into M-dimensional solution space by the range of boundaries

Calculate the fitness of the *AH2*

If minimum fitness of AH2 is less than "Bestsol" then fnsss is set to 0

Send the AF to around the every mp_i according to pwm_i

Calculate the fitness of the *AF*

Find *m* best solutions between all *AF* and *AH2*

If any improvement is done in this iteration by *AH2* or *AF* then LIN=IN

(Local Searches:) Yes   If fnsss =0   No   (Deeper Local Search:)

Send the AF to around the every mp_i according to pwm_i | send the AT to around the mp(1)

Calculate the fitness of the AF | calculate the fitness of the AT

Find m best solutions between all AF and AH2 | Stopping criteria is met — No

If any improvement is done in this iteration by AF then LIN=IN, and bestsol is reset with best fitness | Yes

If LIN < (IN+10) then fnsss is set to 0 | Finish

Figure 3. Flow chart of the modified fox hunting algorithm

where *m* is number of promising solutions that are chosen from a group of solutions. mp_i is position of the *m* members where $i = 1, 2, …, m$. pwm_i is an array that determines how many *AF* members will send to every mp_i. pwm_i can be written as :

$$pwm_i = round\left(\frac{AF}{m} + \frac{AF}{10m}\left(round\left(\frac{m-2i}{2}\right)\right)\right) \text{ where } i = 1, 2,, m \qquad (1)$$

Here in Table 1 typical values of the parameters can be found. These parameters can be changed by experience on the problem and algorithm.

Table 1. Typical values of parameters for a search space between 0–20 (as example).

Scalers:	m	AH	AF	AT	AH Step size	AF Step size	AT Step size
Typical Values:	10	300	100	100	20	2	0,2

AH will be divided into two groups as been in the real world. First group, *AH1*, moves in the search area randomly at the beginning of the algorithm to find promising positions. Then *AH1* followed by *AF* to find the way to the solution. *AF* starts with the promising positions of *AH1*. While *AF* makes neighborhood search in the promising areas, the second group, *AH2*, moves all around the search space to find a more promising area. The search of *AH2* is like the global search in the optimization. Also search of *AF* is like the local search in the optimization. When *AF* can't find a better solution for about 10 iterations, *AF* gives his turn to *AT* by setting *fnsss*. *AT* makes deeper search with smaller steps than *AF*.

3. BLUR KERNEL ESTIMATION

The task of deblurring an image is image deconvolution; if the blur kernel is not known, then the problem is said to be "blind deconvolution". For a survey on the extensive literature in this area, see [22]. While doing the blind image deblurring blur kernel must be found from the blurred image. The camera shake or movement causes a movement on the image like shown in the Fig. 4.
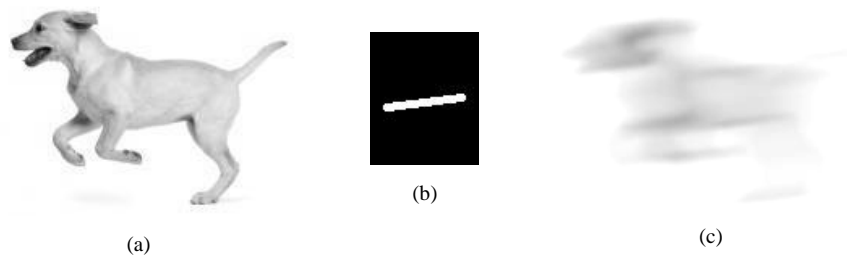

(b)

(a)

(c)

Figure 4. (a) Latent image, (b) blur kernel, (c) blurred image,

Fig. 5 shows the overview of our kernel estimation procedure. Given an observed blurred image, our proposed method iteratively estimates the latent image and refines the blur kernel until convergence. At the beginning the blur kernel is set randomly by FHA. Then it is modified by FHA in every iterations. The error is subtraction of sharpness from blur metric values.
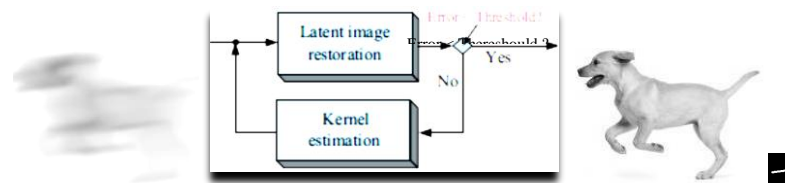

Figure 5. Overview of our kernel estimation procedure. Given an observed blurred image, our proposed method iteratively estimates the latent image and refines the blur kernel until convergence.

4. RESULT

Here one blurred aerial image is used to show the capability of the proposed method for kernel estimation. The image is taken by our UAV. The image is shown below. First image is taken aerial image by our UAV. Second one is deblurred image. Third one is computed blur kernel.
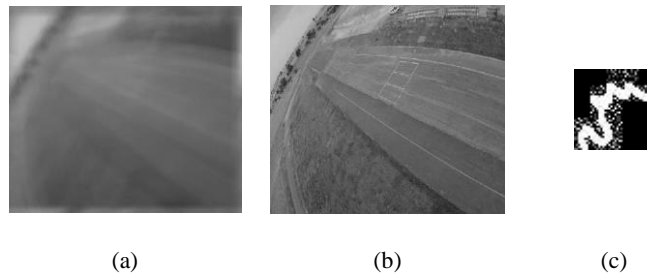
(a)	(b)	(c)

Figure 6.   (a) Aerial image taken by UAV, also input image, (b) Deblurred image (c) Computed blur kernel

5. CONCLUSION

The blur of aerial digital images taken by UAVs decreases the information quality of the images. To reduce the effect of blur on the image some algorithms have been published. Using blur kernel to reduce the degradation of aerial image is a good way. In this paper, a novel, fast and improved population-based search algorithm called the Fox Hunting Algorithm (FHA) is presented and used to calculate the blur kernel of aerial images taken by our UAV. The algorithm showed very good performance to estimate blur kernels as we expected.

ACKNOWLEDGEMENT

REFERENCES

[1] L.J. Fogel, A.J. Owens and M.J. Walsh, *Artificial Intelligence Through Simulated Evolution*, Chichester, UK, John Wiley, 1966.

[2] K. De Jong, *Analysis of the behavior of a class of genetic adaptive systems*, Ph.D. Thesis, Ann Arbor, MI, University of Michigan, 1975.

[3] J.R. Koza, *Genetic programming: a paradigm for genetically breeding populations of computer programs to solve problems*, Rep. No. STAN-CS-90-1314, Stanford University, CA, 1990.

[4] J.H. Holland, *Adaptation in Natural and Artificial Systems*, Ann Arbor, MI, University of Michigan Press, 1975.

[5] D.E. Goldberg, *Genetic Algorithms in Search, Optimization and Machine Learning*, Boston, MA, Addison Wesley, 1989.

[6] M. Dorigo, V. Maniezzo, A. Colorni, *Ant system: Optimization by a colony of cooperating agents*, IEEE Transactions on Systems, Man, and Cybernetics – part B: Cybernetics 26, pp. 29–41, 1996.

[7] R.C. Eberhart, and J. Kennedy, "A new optimizer using particle swarm theory," *Proceedings of the Sixth International Symposium on Micro Machine and Human Science*, Nagoya, Japan, pp. 39-43. Piscataway, NJ: IEEE Service Center, 1995.

[8] D.T., Pham, A. Ghanbarzadeh, E. Koc, S. Otri, S. Rahim, and M. Zaidi, "The bees algorithm - a novel tool for complex optimisation problems," *Proc 2nd Int Virtual Conf on Intelligent Production Machines and Systems (IPROMS 2006)*, Oxford, Elsevier, 2006.

[9] X.L. Li, *A New Intelligent Optimization-Artificial Fish Swarm Algorithm*, Doctor thesis, China, Zhejiang University of Zhejiang, 2003.

[10] Lord Burns, V. Edwards, J. Marsh, Lord M. Winter, *The Final Report of the Committee of Inquiry into Hunting with Dogs in England and Wales*, Her Majesty's Stationery Office, 2009.

[11] M. Onay, "A New and Fast Optimization Algorithm: Fox Hunting Algorithm (FHA)," in *Proc. International Conference on Applied Mathematics, Simulation and Modelling (AMSM 2016)*, 2016, pp. 153-156.

[12] T. Oktay, M. Konar, M. Onay, M. Aydin and M. M. Abdallah, "Simultaneous Small UAV and Autopilot System Design," *Aircraft Engineering and Aerospace Technology,* vol. 88, no. 6, pp. 818- 834, 2016.

[13] R. Kohler, M. Hirsch, B. J. Mohler, B. Sch¨olkopf, and S. Harmeling, "Recording and playback of camera shake: Benchmarking blind deconvolution with a real world database," *In ECCV*, pp. 27–40, 2012.

[14] R. Fergus, B. Singh, A. Hertzmann, S. T. Roweis, and W. T. Freeman, *Removing camera shake from a single photograph*, ACM Trans. Graph., 25(3): pp. 787–794, 2006.

[15] Q. Shan, J. Jia, and A. Agarwala, *High-quality motion deblurring from a single image*, ACM Trans. Graph., 27(3): pp. 73, 2008.

[16] A. Levin, Y.Weiss, F. Durand, and W. T. Freeman, "Efficient marginal likelihood optimization in blind deconvolution," *CVPR*, pp. 2657–2664, 2011.

[17] D. Krishnan, T. Tay, and R. Fergus, "Blind deconvolution using a normalized sparsity measure," *CVPR*, pp. 2657–2664, 2011.

[18] L. Xu, S. Zheng, and J. Jia, "Unnatural Lo sparse representation for natural image deblurring," *CVPR*, pp. 1107–1114, 2013.

[19] S. Cho and S. Lee, *Fast motion deblurring*, ACM Trans. Graph., 28(5): pp. 145, 2009.

[20] L. Xu and J. Jia, "Two-phase kernel estimation for robust motion deblurring," *ECCV*, pp. 157–170, 2010.

[21] Fox hunting, [Online]. Available: https://en.wikipedia.org/wiki/Fox_hunting, Retrieved 27.01.2016.

[22] D. Kundur, and D. Hatzınakos, *Blind image deconvolution*, IEEE Signal Processing Magazine 13, pp. 43-64, 3 May 1996.

Increasing Autonomous Performance of Unmanned Aerial Vehicle and Decreasing Motion Blur Effect on Aerial Images

Murat Onay[1]*, İ. Kurtulus Cıklaiblikci[2], Ziya Ozcelik[2], Omer Canga[2], F. Onur Sonmez[2],

Abstract

In this study, our unmanned aerial vehicle (UAV) flight parameters and position of camera are modified in order to decrease motion blur of aerial images. This modification is made by using "The Bees Algorithm". In addition, to show the performance of our improvement, same trajectory is tried to be tracked without modification and blur kernels of aerial images are compared. The blur kernel of images taken by modified autonomous flight has less vibration than non-modified autonomous flight. This study is gaining more importance with the increasing use of UAVs in the field of Photogrammetry and Remote Sensing.

Keywords: *Unmanned Air Vehicle, Autonomous Performance Improvement, Optimization,Bees Algorithm, Image Deblurring*

1. INTRODUCTION

The UAV is an acronym for Unmanned Aerial Vehicle, which is an aircraft with no pilot on board. UAVs can be remote controlled aircraft (e.g. flown by a pilot at a ground control station) or can fly autonomously based on pre-programmed flight plans or more complex dynamic automation systems.

In last decades mini UAVs are frequently used in the field of aerial photogrametry and remote sensing. One of the most important problems of aerial photogrametry and remote sensing is degradation of the taken images. If there is no vibration on the camera there will be no blur. But while the camera is on an UAV, there is no chance to take an image without vibration. In this situation, there is two way to take better images from UAV. The first way is decreasing the vibration of the UAV. The second way is deblurring of the taken images. Using one of them usually does not give good results. So in this study both of them are used together.

In this study our UAV is flied autonomously. Our UAV is shown in Fig. 1. Flight parameters and position of camera are modified to decrease the vibration. Modified autonomous flight and non-modified autonomous flight characteristics are compared using blur kernels of aerial images for both flights. Blur kernel means the map of camera shake while photo is taken. We estimated blur kernels of modified flight and non-modified flight aerial images by using our earlier blur kernel estimation method (see Ref. [1]). We compared them to show the performance of our improvement. Comparison shows that modified flight performance is better than non-modified flight performance. Flight parameters and position of camera theory will be explained briefly in the next section. Then the blur kernel will be explained shortly.
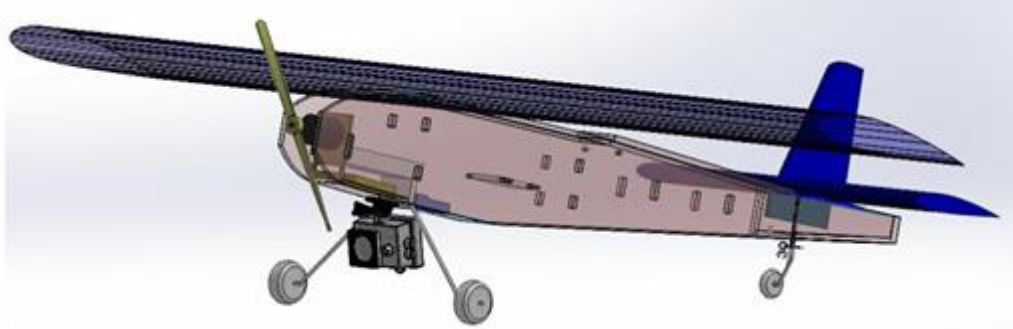
Figure84. Our UAV design used in this paper

2. THE UAV DESIGN FLIGHT PARAMETERS AND POSITION OF THE CAMERA THEORY

In order to model dynamics of our UAV, first the state-space models of it are required. Longitudinal and lateral linearized state-space models of any fixed-wing aircraft UAV are given in equation (1) and (2), respectively (see Ref. [2]).

$$
\begin{bmatrix} \Delta \dot{u} \\ \Delta \dot{w} \\ \Delta \dot{q} \\ \Delta \dot{\theta} \end{bmatrix} = \begin{bmatrix} X_u & X_w & 0 & -g \\ Z_u & Z_w & u_0 & 0 \\ M_u + M_w Z_w & M_w + M_w Z_w & M_q + M_w u_0 & 0 \\ 0 & 0 & 1 & 0 \end{bmatrix} \begin{bmatrix} \Delta u \\ \Delta w \\ \Delta q \\ \Delta \theta \end{bmatrix} + \begin{bmatrix} X_{\delta_T} & X_{\delta_e} \\ Z_{\delta_T} & Z_{\delta_e} \\ M_{\delta_T} + M_w Z_{\delta_T} & M_{\delta_e} + M_w Z_{\delta_e} \\ 0 & 0 \end{bmatrix} \begin{bmatrix} \Delta \delta_T \\ \Delta \delta_e \end{bmatrix} \tag{1}
$$

$$
\begin{bmatrix} \Delta \dot{v} \\ \Delta \dot{p} \\ \Delta \dot{r} \\ \Delta \dot{\phi} \end{bmatrix} = \begin{bmatrix} Y_v & Y_p & -(u_0 - Y_r) & -g\cos(\theta_0) \\ L_v^* + \frac{I_{xz}}{I_x} N_v^* & L_p^* + \frac{I_{xz}}{I_x} N_p^* & L_r^* + \frac{I_{xz}}{I_x} N_r^* & 0 \\ N_v^* + \frac{I_{xz}}{I_z} L_v^* & N_p^* + \frac{I_{xz}}{I_z} L_p^* & N_r^* + \frac{I_{xz}}{I_z} L_r^* & 0 \\ 0 & 1 & 0 & 0 \end{bmatrix} \begin{bmatrix} \Delta v \\ \Delta p \\ \Delta r \\ \Delta \phi \end{bmatrix} + \begin{bmatrix} 0 & Y_{\delta_r} \\ L_{\delta_a}^* + \frac{I_{xz}}{I_x} N_{\delta_a}^* & L_{\delta_r}^* + \frac{I_{xz}}{I_x} N_{\delta_r}^* \\ N_{\delta_a}^* + \frac{I_{xz}}{I_z} L_{\delta_a}^* & N_{\delta_r}^* + \frac{I_{xz}}{I_z} L_{\delta_r}^* \\ 0 & 0 \end{bmatrix} \begin{bmatrix} \Delta \delta_a \\ \Delta \delta_r \end{bmatrix} \tag{2}
$$

After using geometrical data of our UAV (see Ref. [3]), the numerical state-space models are obtained for 60 km/h flight condition and also some different flight conditions. Using them, flight dynamics modes of the UAV are obtained. These results are validated by using the existing data in related literature. There were qualitative and quantitative match between our modes and their modes (see Refs. [4, 5]). Therefore, our modelling procedure is correct.

The main superiorities of our UAV with respect to the similar ones are that it is able to passively morph. Morph is meaning that its geometry may change before flight in order to increase autonomous flight performance. For this purpose its wing and tailplate can assemble to fuselage from different points independently in a prescribed interval. Moreover, camera of it can also be assembled to fuselage from different points in a prescribed interval. In Fig. 2, passive morphing mechanisms for the UAV are illustrated.

The autopilot system we applied has a hierarchical structure. It's general and detailed block diagram is given in Fig 3. Any hierarchical autopilot system has three layers (i.e. outer, middle and inner). Control signals (e.g. aileron angle) are determined in inner layer. This autopilot system has six PID controllers inside. Using it three reference inputs (i.e. altitude, speed and heading angle) can be tracked. Before passing real time the position of wing, tailplane and camera and also autopilot parameters are simultaneously designed by using an Bees Algorithm (BA) (see Refs. [7-10] for more details) optimization method. Cost function (C) of the optimization is given in equation (2)

$$
C = \min_{x,y,z} f\,(ST, MOS, SSE) \tag{2}
$$

where *ST,MOS* and *SSE* are *settling time,maximum overshoot* and *steady-state error* respectively. *x*, *y* and *z* are *wing position*, *tailplane position* and *camera position* respectively also shown in Fig. 2. The optimal solution of cost function is obtained by using the BA. After obtaining optimal solution, it is used in real-time flights. These flights are modified autonomous flights. In Fig 4 modified autonomous flight and non-modified autonomous flight trajectory trackings are shown. It is clear from the figure modified autonomous flight trajectory is better than non-modified one. In Fig 5 rolling trajectory tracking for pitching angle of a modified autonomous flight with atmospheric turbulence is shown to show the performance of our improvement.

(a)   *(b)*

(c)   *(d)*

(e)   *(f)*

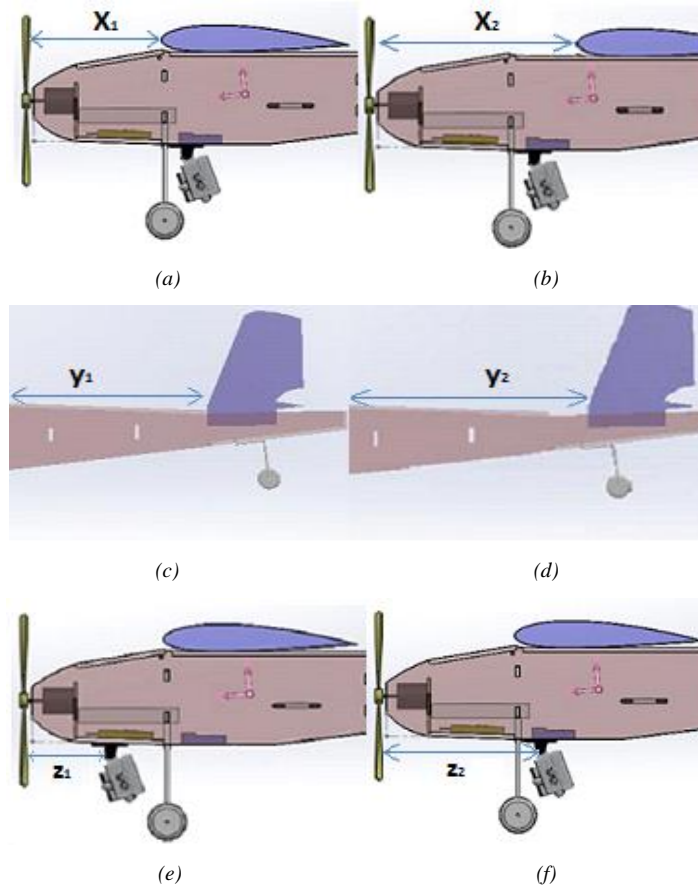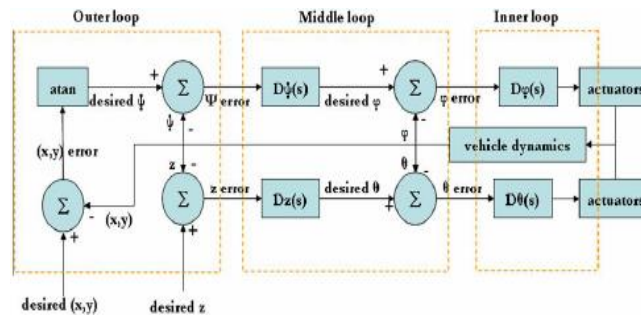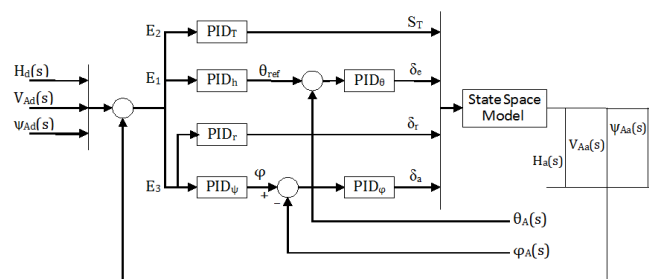*Figure 2. (a) UAV equipped with wing from front point, (b) UAV equipped with wing from rear point, (c) UAV equipped with tailplane from front point, (d) UAV equipped with tailplane from rear point, (e) UAV equipped with camera from front point, (f) UAV equipped with camera from rear point*

(a)

(b)

Figure 3. (a) General hierarchical autopilot system (taken from Ref. [11]) (b) PID based autopilot structure
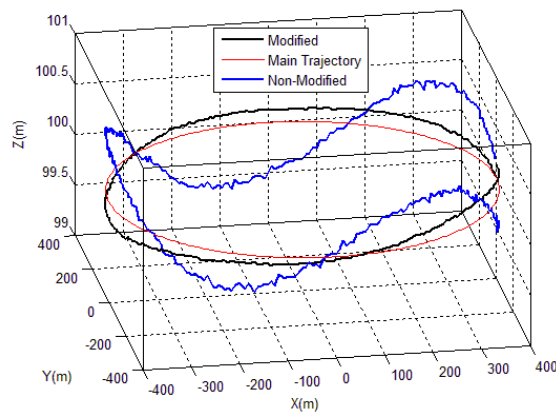
Figure 4. Zoomed rolling trajectory trackingfor pitching angle with atmospheric turbulence of modified Autonomous flight, Non-modified autonomous flight. Main trajectory is desired trajectory.

(a)   *(b)*
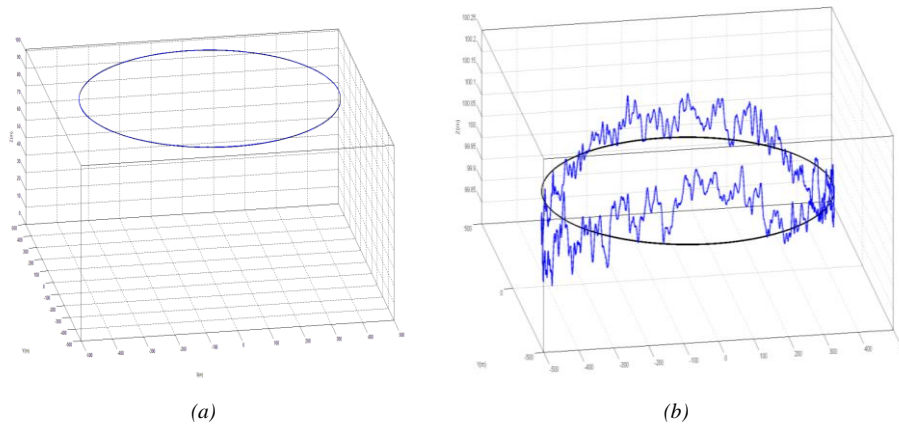
Figure 5. Rolling trajectory tracking for pitching angle of modified autonomous flight with atmospheric turbulence (a) Trajectory tracking of a modified flight (b) Zoomed trajectory tracking of the modified flight.

3. BLUR KERNEL

The blur on the taken image is caused by the camera shake movement. Deblurring of an image is made by image deconvolution. If the blur kernel is not known, then the problem is said to be "blind deblurring". For a survey on the extensive literature in this area, see Ref. [12]. While doing the blind image deblurring blur kernel must be found from the blurred image. Camera axis, camera movements and kernel results are shown in Fig. 6. The camera shake causes a movement on the image like shown in Fig. 7.

(a)   (b)

(c)   (d)
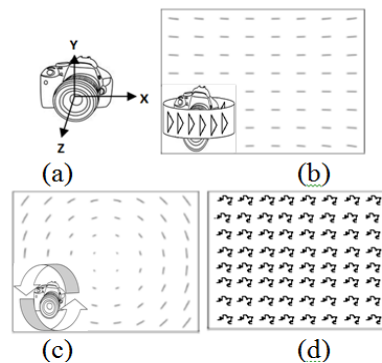
Figure 6. (a) Angles of the camera, (b) Blur kernel of the movement on Y axis, (c) Blur kernel of the movement on Z axis, (b) Blur kernel of the random movement

Figure 7. (a) Latent image, (b) Camera movement, (c) Blurred image.

The recent years have witnessed significant advances in single image deblurring [13]. Estimating an unknown blur kernel from a single input blurred image is a severely ill-posed problem. Much success of the state-of-the-art algorithms [14-20] can be attributed to the use of learned prior from natural images and the selection of salient edges for kernel estimation. Although numerous methods [14-18] have been proposed for motion deblurring, these priors are not still enough effective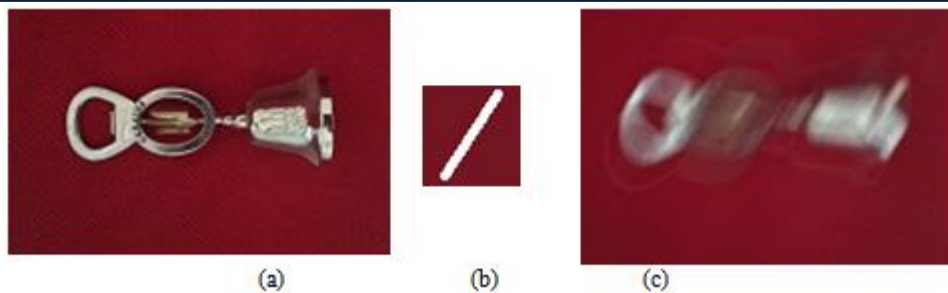. Deblurring with an unknown blur kernel is called blind image deblurring. Blind image deblurring has gained considerable attention and achieved great success in recent years. The formation process of image blur is usually modelled as:

$$B = I * k + n, \qquad\qquad (1)$$

where *B, I, k* and *n* represent the blurred image, latent image, blur kernel, and the additive noise, respectively. * denotes the convolution operator. It is a well-known ill-posed inverse problem, which requires regularization in order to obtain a high quality latent image. Here we used our earlier blur kernel estimation approach (see Ref. [1]).We estimate blur kernels of images for non-modified and modified autonomous flights to compare. In Fig.8 blur kernel estimation and deblurring for non-modified autonomous flight is shown. Also in Fig. 9 blur kernel estimation and deblurring for modified autonomous flight is shown. From the comparison of the both blur kernels in both figureit is clear that modified autonomous flight has less vibration than non-modified one. So that proves our improvement has good ability on aerial imaging.

Figure 8. Blur kernel estimation and deblurring for non-modified autonomous flight (a) Taken aerial image, (b) Calculated blur kernel, (c) Deblurred image.

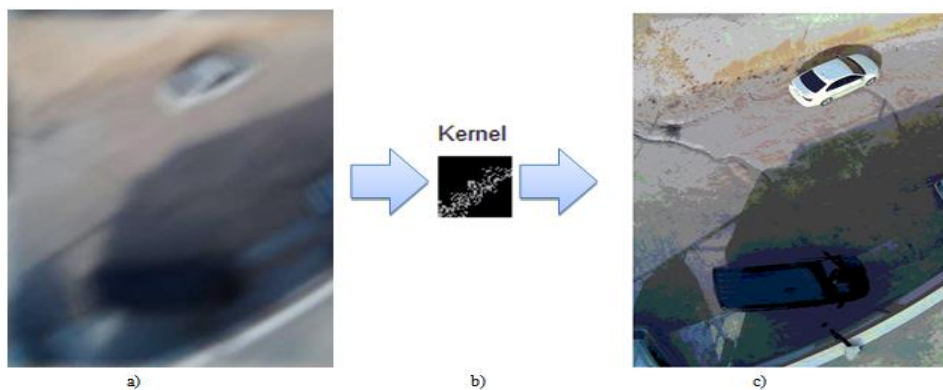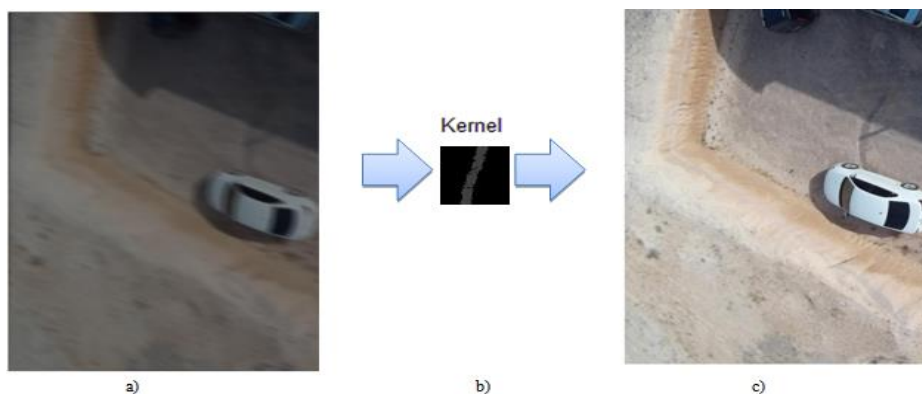*Figure 9.Blur Kernel Estimation and Deblurring for Modified Autonomous Flight (a) Taken Aerial Image, (b) Calculated Blur Kernel, (c) Deblurred Image.*

948

4. CONCLUSIONS

In this study our UAV is flied autonomously. Flight parameters and position of camera are modified. Vibrations of modified and non-modified autonomous flights are compared using blur kernels of aerial images. We compared them to show the performance of our improvement. Comparison is shown that modified flight has less vibration so improvement has good ability on aerial imaging.

ACKNOWLEDGEMENT

REFERENCES

[1] Onay M., "Blur Kernel Estimation by Using Bees Algorithm", *International Journal of System Modelling and Simulation*, vol.1, no.2, pp.8-11, 2016.

[2] R. C. Nelson, *Flight Stability and Automatic Control*, 2nd ed., New York: McGraw-Hill, 2007.

[3] T. Oktay, M. Konar, M. Onay, M. Aydin and M. M. Abdallah, "Simultaneous Small UAV and Autopilot System Design," *Aircraft Engineering and Aerospace Technology,* vol. 88, no. 6, pp. 818- 834, 2016.

[4] "Zagi-The original R/C EPP foam wing homepage," 2015. [Online]. Available: https://zagi.com/

[5] C. Hajiyev and S. Y. Vural, "LQR controller with Kalman estimator applied to UAV longitudinal dynamics," *Positioning,* vol. 4, no. 1, p. 36, 2013.

[6] P. Sadegh and J. C. Spall, "Optimal random perturbations for stochastic approximation using a simultaneous perturbation gradient approximation," *Automatic Control, IEEE Transactions on,* vol. 43, no. 10, pp. 1480-1484, 1998.

[7] Pham, D.T., S. Otri, A. Ghanbarzadeh, and E. Koc, "Application of the bees algorithm to the training of learning vector quantisation networks for control chart pattern recognition," *Information and Communication Technologies (ICTTA'06)*, Vol. 1, pp. 1624-1629, April 24-28, 2006.

[8] Pham, D.T., A. Ghanbarzadeh, E. Koc, S. Otri, S. Rahim, and M. Zaidi, "The bees algorithm - a novel tool for complex optimisation problems," in *Proc. 2nd Int Virtual Conf on Intelligent Production Machines and Systems (IPROMS 2006)*, Oxford, Elsevier, 2006.

[9] Pham, D.T., A.J. Soroka, A. Ghanbarzadeh, E. Koc, S. Otri, and M. Packianather, "Optimising neural networks for identification of wood defects using the bees algorithm," in *Proc. IEEE International Conference on Industrial Informatics*, Singapore, pp. 1346-1351, Aug., 2006.

[10] Pham, D.T., E. Koc, A. Ghanbarzadeh, and S. Otri, "Optimisation of the weights of multi-layered perceptrons using the bees algorithm," in *Proc. 5th International Symposium on Intelligent Manufacturing Systems*, Sakarya University, Turkey, pp. 38-46, May 29-31, 2006.

[11] H. Chao, Y. Cao and Y. Chen, "Autopilots for small unmanned aerial vehicles: a survey," *International Journal of Control, Automation and Systems,* vol. 8, no. 1, pp. 36-44, 2010.

[12] D. Kundur, and D. Hatzınakos, "Blind image deconvolution," *IEEE Signal Processing Magazine* vol. 13, 3 (May), pp. 43-64, 1996.

[13] R. Kohler, M. Hirsch, B. J. Mohler, B. Sch¨olkopf, and S. Harmeling, "Recording and playback of camera shake: Benchmarking blind deconvolution with a realworld database", in *Proc. ECCV*, pp. 27–40, 2012.

[14] R. Fergus, B. Singh, A. Hertzmann, S. T. Roweis, and W. T. Freeman, "Removing camera shake from a single photograph", *ACM Trans. Graph.*, Vol. 25(3), pp. 787–794, 2006.

[15] Q. Shan, J. Jia, and A. Agarwala, "High-quality motion deblurring from a single image", *ACM Trans. Graph.*, Vol. 27(3):73, 2008.

[16] A. Levin, Y.Weiss, F. Durand, and W. T. Freeman, "Efficient marginal likelihood optimization in blind deconvolution", in *Proc. CVPR*, pp. 2657–2664, 2011.

[17] D. Krishnan, T. Tay, and R. Fergus, "Blind deconvolution using a normalized sparsity measure", in *Proc. CVPR*, pp. 2657–2664, 2011.

[18] L. Xu, S. Zheng, and J. Jia, "Unnatural Lo sparse representation for natural image deblurring", in *Proc. CVPR*, pp. 1107–1114, 2013.

[19] S. Cho and S. Lee, "Fast motion deblurring", *ACM Trans. Graph.*, Vol. 28(5):145, 2009.

[20] L. Xu and J. Jia,."Two-phase kernel estimation for robust motion deblurring", in *Proc. ECCV*, pp. 157–170, 2010.

Investigation Of Silica Aerogels Effect On Paints Characteristics

Rana Aksu[1]

Abstract

New methods of energy saving are being researched by many scientists. An important research area in these studies are insulating paints. Silica aerogels are one of nanostructured insulating materials with low thermal conductivity, high surface area and low density. The main aim of this project is to study on alternative paint insulator by producing silica aerogel. In this research, Na_2SiO_3 and H_2SO_4 solution were used for synthesis of aerogels by using the sol-gel method. Acetonitrile and methanol:hexane solution was used for solvent exchange and surface modification. The effects of the process parameters such as the reaction temperature ($35-55^oC$), the solution amount (150-180ml), the aging temperature ($70-90^oC$) and the drying temperature ($50-70^oC$) were studied. Depends on the reaction parameters, three different kinds of aerogels were synthesized (aerogel1(A1), aerogel2(A2) and aerogel3(A3)). After that production progress, silica aerogels were added to two different kinds of paints (water and solvent-based). Aerogel amounts (%1-%3) and aerojel types were chosen as experiment factors. Properties of these samples, such as viscosity, hydrophobicity and adhesivity were measured. The viscosity measurements showed that the viscosity increase with the increasing amount of aerogel in both types of paint. When compared, the hydrophobic properties, best results were obtained in the using of A2 for water-based paint and using of A1 for the solvent-based paint. For the adhesivity, it can be said that it has an improving effect for all aerogel and paint types . In conclusion, the result of experiments demonstrated that silica aerogels have a positive effect on paint characteristics.

Keywords: *Aerogel, Insulation materials for paints, Energy saving*

1. INTRODUCTION

Aerogels are nanoporous materials usually synthesized from silica, with a high porosity, high specific surface area area ($500-1200m^2.g^{-1}$), high porosity (80–99.8%), low density ($\sim0.003-0.5g.cm^{-3}$), low thermal conductivity (0.005–0.1W/mK), low refractive index (~1.05) [1]. First aerogel was produced by S. Kistler in 1930's. He defined the aerogels as a material which is produced by replacing the solvents in the gel by air without substantially altering the network structure or the volume of the gel body [2].

Aerogels can be synthesized from various raw materials such as Tetramethylorthosilicate (TMOS), Tetraethylortosilicate (TEOS) and sodium silicate. There are lots of production methods to produce aerogels. Co-precursor method, derivatization method and sol-gel can be given as examples. In these several kinds of methods, sol-gel method is the best appropriate method in laboratory conditions. The applications of the method in large scale production increased in recent years [3].

The unique properties of aerogels make them great canditates for many applications. In recent years so much attention has been given to silica aerogels in several technological applications. Chemistry, aerospace, electronics, energy, agriculture and insulation can be given as an examples of the some applications areas [4].

In the present work, the role of different process conditions, such as reaction temperature, the solution amount, the aging temperature and the drying temperature was analyzed. Sol-gel method was chosen for the aerogel production. After the aerogel production has been done, these samples were used as paint additives. In this research, two kinds of paint were chosen; solvent and water based paints. Finally, for the investigation of the aerogels effect on paints, some paint analyses were done.

[1] Corresponding author: Yildiz Technical University, Department of Chemical and Metallurgical Engineering, 34220, Esenler/İstanbul, Turkey. ranaaksu@yandex.com

2. MATERIALS AND METHODS

2.1. Synthesis Of Aerogels

Sol-gel polymerization is the commonly employed method for the preparation of the aerogels. In this study, Na_2SiO_3 and H_2SO_4 solution were used for synthesis of aerogels by using the sol-gel method. Three different kinds of aerogels were obtained in the end of the polymerization. Sodium silicate solution amounts were determined as 150 ml,180 ml and 160 ml and also the other reaction parameters such as the drying temperature (70 ºC ,70 ºC and 50 ºC), the aging temperature (70 ºC, 90 ºC and 90 ºC), the reaction temperature (45 ºC, 55 ºC and 35 ºC) were worked on. The mixing rate was 240 rpm for every mixture. Depends on these reaction parameters, three different kinds of aerogels were synthesized (aerogel 1, aerogel 2 and aerogel 3, respectively). In the end of the reaction, the gelation was obtained which is shown in figure 1. After gelation, samples were sent to the oven to aging step at different temperatures for 3 hours. The aging step is shown in figure 2. The aging step to remove the Na+ ions from the samples, they were washed with distilled water for 24 h. Distilled water was changed at every 6 h of the day. The washing step is shown in figure 3. Acetonitrile was used for solvent exchange and methanol:hexane solution (molar ratio 1:1) was used for surface modification. Finally, the samples were dried at different temperatures for 24 h. The drying step is shown in figure 4.

Figure 2. The aging step at different temperatures for 3 hours.

Figure 1. The gelation was occured after the polymerization step.

Figure 3. The washing step was done for removing sodium ions.

Figure 4. The drying process at different temperatures for 24 h.

2.2. The Preparation Of The Paint Samples

After the production progress, silica aerogels were added to two different kinds of paints; water and solvent based. Aerogel amounts (%1, %2 ve %3) and aerojel types were chosen as experiment factors. For these two different kinds of paints, paint amounts were determined as 75 g and due to these ratio 0.75 g, 1.5 g and 2.25 g aerogels were used respectively. As the preparation of the samples Design Expert 7 optimization program was used.

3. RESULTS AND DISCUSSION

After the addition of the aerogels to paints, firstly viscosity measurements were done. Then the hydrophobicity of the samples were investigated and for the each sample, water flowing velocities on the surfaces were measured. For the investigation of the adhesivity, cross-cut tests were applied.

3.1. Viscosity Measurements

Viscosity is the resistance of a liquid material with homogeneous structure to flow. Liquids with lower viscosity under the same conditions flow faster than those with higher viscosity.

3.1.1. The Analysing Of The Viscosity Graphics For Water Based Paint

The viscosity graphics were created by using Design Expert 7 optimization program. The effect of aerogel types and aerogel amounts on viscosity are shown in Figure 5 and Figure 6.
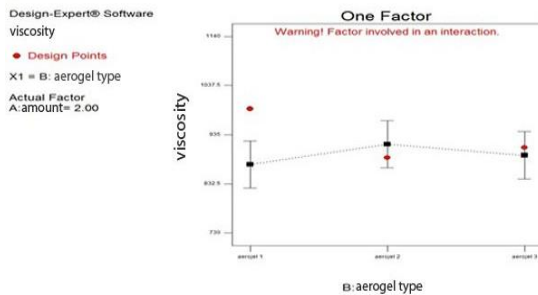
Figure 5.Viscosity vs. aerogel types graphic for the water based paint
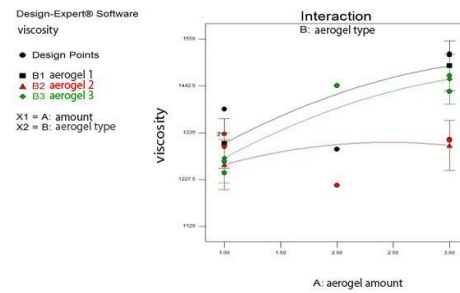
Figure 6. Viscosity vs. aerogel amounts graphic for the water based paint

These graphics demonsrated that the highest viscosity were reached by using aerogel type 2 and the least viscosity were reached by using aerogel type 1. For all the types, it was observed that the viscosity increases with the increasing amount of the aerogel.

3.1.2. The Analysing Of The Viscosity Graphics For Solvent-Based Paint

The effect of aerogel types and aerogel amounts on viscosity for the solvent based paint are shown in Figure 7 and Figure 8.

Figure 7. Viscosity vs. aerogel types graphic for the solvent based paint
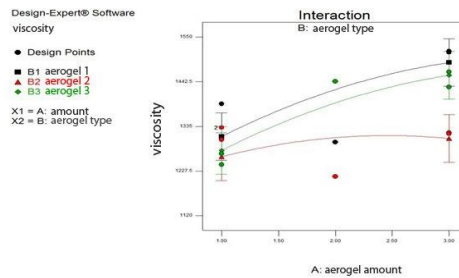
Figure 8. Viscosity vs. aerogel amounts graphic for solvent based paint

The graphics showed that the maximum viscosity were achieved by using aerogel type 1 and the minimum viscosity were achieved by using aerogel type 2. For all the types, it can be said that the viscosity increase with the increasing amount of the aerogel. When compared the behaviour of the solvent and water based paints, it can be seen that there is a similitiary in terms of the increasing viscosity with increasing amount of the aerogels.

3.2. Hydrophobicity Measurements

Contact angle is a measure of static hydrophobicity. When a pipette injects a liquid into a solid, the liquid will form some contact angle. Contact angle is higher than 90° for hydrophobic surfaces. In this present work, flow appearances and flow velocities of the samples were compared with control samples which includes no aerogels. The results of some samples are given below:
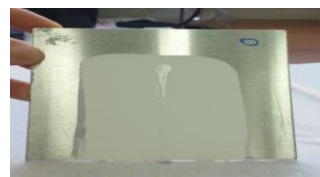
Figure 9. Control sample of water based paint

Figure 10.Flow appearance of control sample for water based paint

Figure 11. Sample with aerogel as a paint additive for water based paint

Figure 12. Flow appearance of sample with aerogel as a paint additive for water based paint

Figure 13. Control sample of solvent based paint

Figure 14. Flow appearance of control sample for solvent based paint

Fıgure 15. Sample with aerogel as a paint additive for solvent based paint

Figure 16. Flow appearance of sample with aerogel as a paint additive for water based paint

3.2.1. The analysing Of The Hydrophobicity Graphics For Water Based Paint

The effect of aerogel types and aerogel amounts on hydrophobicity for the water based paint are shown in Figure 17 and Figure 18.
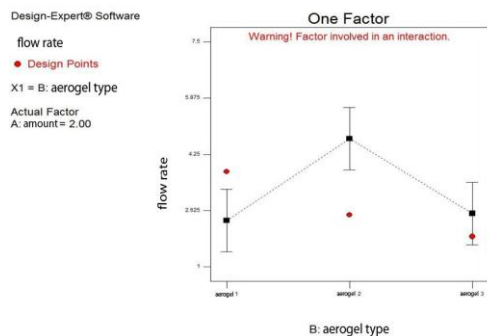
Figure 17. Aerogel type vs flow rate graphic for the water based paint
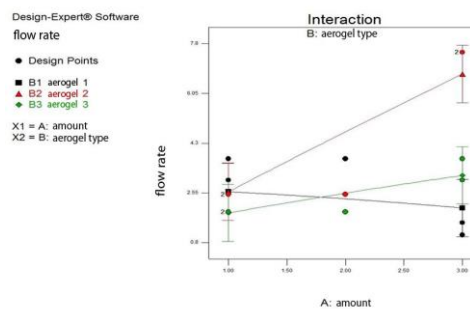
Figure 18. Aerogel amount vs. flow rate graphic for the water based paint

The graphics demonstrated that the maximum hydrophobicity were achieved by using aerogel type 2 and the minimum hydrophobicity were achieved by using aerogel type 1. For aerogel 2 and aerogel 3, hydrophobicity increased with the increasing amount of aerogel. On the other hand, for the aerogel 1, hydrophobicity decreased with the increasing amount of the aerogel.

3.2.2. The analysing of the hydrophobicity graphics for solvent based paint

The effect of aerogel types and aerogel amounts on hydrophobicity for the solvent based paint are shown in Figure 19 and Figure 20.
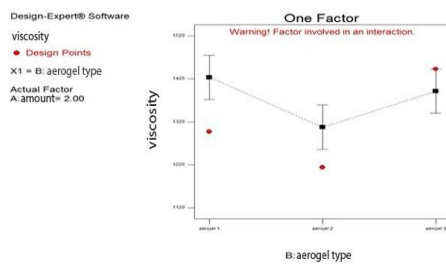

*Figure 19. Aerogel type vs. flow rate graphic for the solvent based paint*
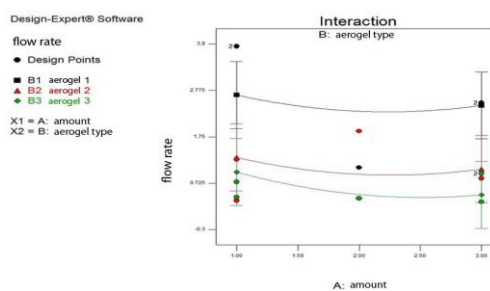
Figure 20. Aerogel amount vs. flow rate graphic for the solvent based paint

The graphics showed that for the solvent based paint, the best results were obtained by using of aerogel type 1. Minimum hydrophobicity was observed in case of using aerogel type 3. For all aerogel types it can be said that hydrophobicity decrease with the increasing amount of aerogels.

3.3. Adhesivity Measurements

For the investigation of the adhesivity, cross-cut tests were applied. This test is a method for measuring the resistance of paints and coatings to separation from surfaces when a right angle cross pattern is cut into the coating, penetrating through to the surface.

Figure 21. Water based paint without aerogel as a paint additive
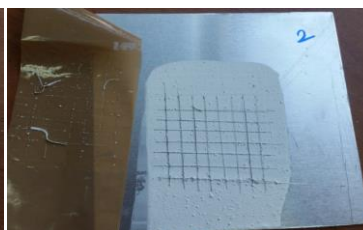
Figure 22. Water based paint with aerogel as a paint additive
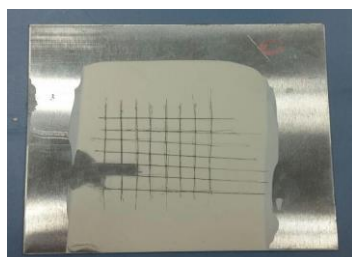
Figure 23. Solvent based paint without aerogel as a paint additive
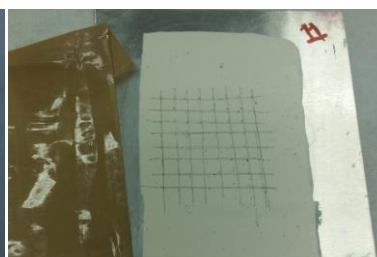
Figure 24. Solvent based paint with aerogel as a paint additive

3.3.1. The analysing of the adhesivity graphics for water based paint

The effect of aerogel types and aerogel amounts on adhesivity for the water based paint are shown in Figure 25 and Figure 26.
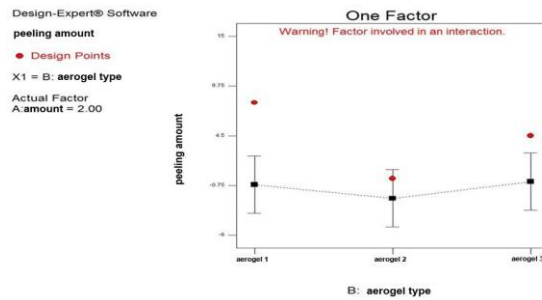
Figure 25. Aerogel type vs. peeling amount graphic for the water based paint
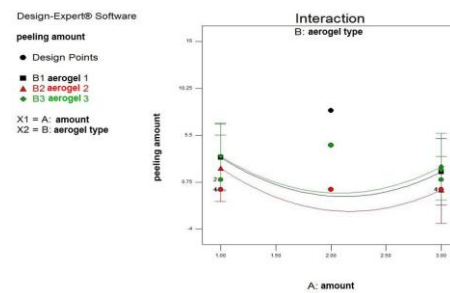
Figure 26. Aerogel amount vs. peeling amount graphic for the water based paint

The graphics showed that the maximum adhesivity was obtained in case of using aerogel type 3 as a paint additive and the minimum adhesivity was obtained with the utilization of aerogel type 2. In addition to this, it has been observed that peeling amount decrease with the increasing amount of aerogel utilization.

3.3.2. The analysing of the adhesivity graphics for solvent based paint

The effect of aerogel types and aerogel amounts on adhesivity for the solvent based paint are shown in Figure 27 and Figure 28.
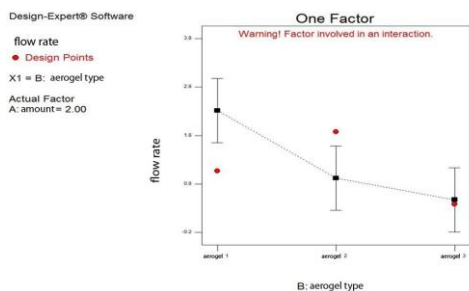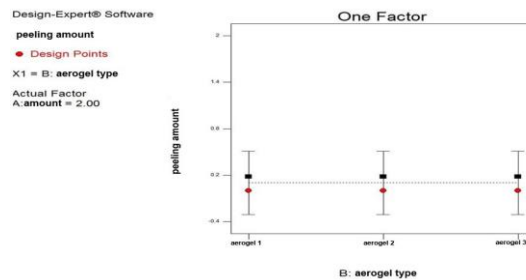

Figure 27. Aerogel type vs. peeling amount graphic for the solvent based paint
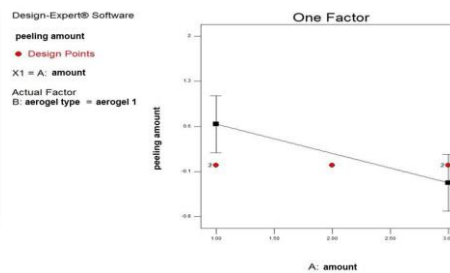
Figure 28. Aerogel amount vs. peeling amount graphic for the solvent based paint

The graphics demonstrated that as a parameter, aerogel type cannot be compared with each other. Because in case of utilization of all types of aerogel as a paint additive, the solvent based paint wasn't peeled. On the other hand, it can be said that aerogel utilization with increasing amount, decrease the peeling amount for the all types of aerogel.

4. CONCLUSION

In this study, experimental and numerical work were performed to investigate the silica aerogels effect on the paints characteristics. Based on the experimental and numerical studies, conclusions can be drawn as follows:

The viscosity measurements show that the best results were reached in case of using of the aerogel 1 for solvent-based paint and aerogel 2 for water-based paint. It has been observed that the viscosity increase with the increasing amount of aerogel in both types of paint.

When compared, the hydrophobic properties, the best results were obtained in the using of aerogel 2 for water-based paint and using of aerogel 1 for the solvent-based paint.

For the adhesivity, it can be said that it has an improving effect of all aerogel types for solvent based paint. For water based paint, the best results are obtained in aerogel 3, and in general, the amount of peeling is reduced as the amount of aerogel increases in all aerogel types.

The result of experiments demonstrated that silica aerogels have a positive effect on paint characteristics. This study is going to continue with the thermal conductivity measurements of the samples.

REFERENCES

[1] Sarawade, P.B., Quang, D.V., Hilonga, A., Jeon, S.J., Kim, H.T., (2012), Synthesis and characterization of micrometer-sized silica aerogel nanoporous beads'', Materials Letters 81: 37-40.
[2] S. Kistler, (1931), Coherent expanded aerogels and jellies", Nature, 127: 741-741.
[3] Dorcheh, A., S., Abbasi, M., H. (2008), Silica Aerogel; Synthesis, Properties and Characterization'', Journal of Materials Processing Technology, 199: 10-26.
[4] Bi, C., Tang, G. H., Hu, Z. J., (2014), Heat conduction modeling in 3-D ordered structures for prediction of aerogel thermal conductivity ",International Journal of Heat and Mass Transfer, 73: 103-109.

Comparison of Electricity Generation Technologies Using Life Cycle Assessment

Gulsah Yılan[1], Gokcen A. Ciftcioglu[1], M. A. Neset Kadırgan[1]*

Abstract

Fossil fuel related environmental impacts draw attention to emerging climate change mitigation problems for the last decades. As a consequence of debates in the United Nations Conference on Climate Change (COP 21, Paris), about 200 countries including Turkey have adopted the ground breaking Paris Agreement to take measures against climate change mitigation by reducing fossil fuel consumption. In order to accomplish this mission, conducting comprehensive analyses and developing down-to-earth plans are crucial in decision making processes for sustainable energy systems. This study aims to indicate the environmental impacts owing to electricity generation in Turkey for year 2014 and also estimate the course of change in impacts with future projections for 2023 and 2030. The computation results are expected to assist decision-makers for building more sustainable energy policies for the future. Life cycle assessment (LCA) methodology is used with the single issue cumulative energy demand (CED) method as well as the mid-point CML 2 baseline 2000 method. CED results reveal that minimum energy demands are attained when the share of renewable energy technologies increases. Nevertheless, most impacts remain the same with 2014 if renewable development pathway is put into practice according to the CML 2 baseline 2000 results. The combined results indicate that the environmental impacts are kept under control only if a shift from fossil fuel to renewable energy technologies is employed.

Keywords: *Cumulative Energy Demand, Electricity Generation, Life Cycle Assessment, Turkey.*

1. INTRODUCTION

As societies start to observe the consequences of their acts, the awareness of environmental problems at global scale has raised, recently. Ozone layer depletion, glacier melting, global warming, fossil fuel depletion, and climate change are the most dramatic examples of these consequences. In order to reduce the impacts of human acts on environment, sustainability concept has the key role. Sustainability is by definition "meeting the needs of the present without compromising the ability of future generations to meet their own needs" [1].

As energy sector is the main contributor to abovementioned consequences of human acts, measures are to be made primarily in this sector via sustainable energy policies. Energy policies are certainly a balancing act of many diverse factors such as economic, political, legal, technical, social, environmental and scientific issues. In fact, energy policies are also a combination of all of these factors [2]. Previously, technical and economic issues dominate the energy policy considerations; but as the impacts become inevitably problematic, the significance of environmental factors is realized, gradually.

The environmental impacts associated with energy sector are directly related to fuels used to meet the increasing demand correlated with the growth of populations. Especially fossil fuels have drawn great attention since their adverse effect on climate change. Replacing fossil fuel technologies with renewable energy alternatives is the main challenge in sustainable decision making process of the energy sector.

In 2015, the United Nations Conference on Climate Change (COP 21) is held in Paris and about 200 countries including Turkey have adopted the Paris Agreement to take measures against climate change mitigation by reducing fossil fuel consumption. In order to accomplish this mission, conducting comprehensive analyses and developing down-to-earth plans are crucial in decision making processes for sustainable energy systems.

According to the statistics published by Turkish Electricity Transmission Company, electricity generation mix in 2014 is dominated by fossil fuels which have a total share of 78% [3]. However, Turkey has very abundant potential in renewable energy sources like wind, geothermal and solar. The fossil fuel dependency

---

[1]* *Corresponding author: Marmara University, Department of Chemical Engineering, 34722, Kadıköy/İstanbul, Turkey. gulsah.yilan@marmara.edu.tr.*

[1] *Marmara University, Department of Chemical Engineering, 34722, Kadıköy/İstanbul, Turkey.*

problem of Turkey may be solved via diversification of the electricity generation technologies from a sustainable point of view, namely introducing renewables into the national system [4].

This study aims to indicate the environmental impacts owing to electricity generation in Turkey for year 2014 and also estimate the course of change in impacts with future projections for 2023 and 2030. The computation results are expected to assist decision-makers for building more sustainable energy policies for the future. In order to calculate the environmental impacts Life Cycle Assessment (LCA) methodology is used with cumulative energy demand (CED) method and the mid-point CML 2 baseline 2000 method.

2. MATERIALS AND METHODS

The environmental impacts associated with the electricity generated and supplied in Turkey are evaluated using a process-based LCA methodology following the ISO 14040/14044 guidelines [5, 6]. According to the ISO 14040, LCA consists of four phases: (i) Goal and Scope Definition, (ii) Inventory Analysis, (iii) Impact Assessment, and (iv) Interpretation (.
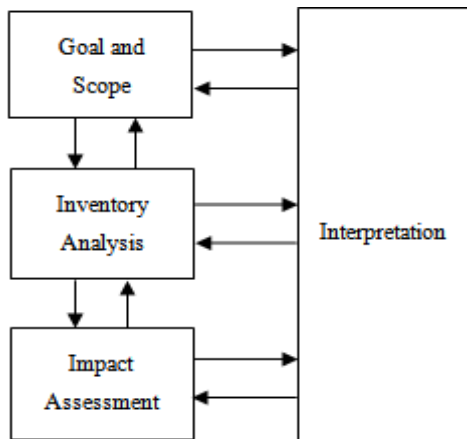
Figure 85) [7]. Environmental impacts of electricity generation technologies in 2014 in addition with three different scenarios for both 2023 and 2030 are computed via SimaPro 8.2.0.0 PhD software package.
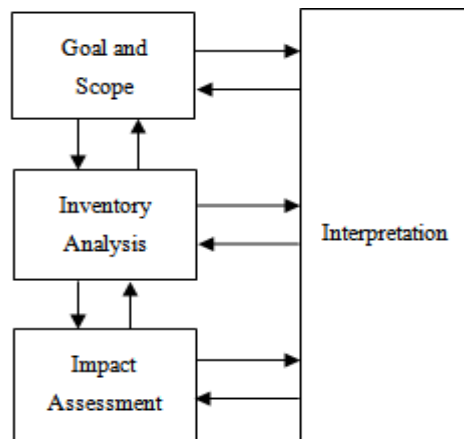
Figure 85. Life Cycle Assessment framework

2.1. Goal and Scope Definition

The goal of the study is to estimate the life cycle environmental impacts of electricity generated in 2014, 2023, and 2030 in Turkey. The functional unit is selected as the total electricity generated during the year from available technologies. The scope of this study is "cradle-to-gate" including extraction, processing and transport of fuels; operation of the power plants along with power plant construction. Since the functional units are related to the generation rather than supply of electricity, its distribution and consumption are out of the system boundary.

2.2. Inventory Analysis

The model used in this study is an example of *attributional modeling* since it examines the environmental impacts of the main electricity generation technologies and compares the impacts of these technologies with the same functional unit.

The main technologies of electricity generation in Turkey by the year 2014 are given in Figure 86 [3]. Background data is obtained from ecoinvent v3.01 database. Total electricity generated in 2014 is gathered from Turkish Electricity Transmission Company (TEİAS) statistics. Lignite and hard coal data is gathered from Turkish Statistical Institute (TUİK) and Turkish Coal Enterprises (TKİ). Natural gas data is gathered from Turkish Petroleum (TP). Transport of fuels is obtained by online mapping. Pipeline distances are gathered from the reports published by Republic of Turkey Ministry of Energy and Natural Resources (ETKB) and Republic of Turkey Ministry of Transport, Maritime Affairs and Communications (UDHK).

Future energy mix decisions are dominated by the following factors: meeting the increasing electricity demand and reducing the high dependence on imported fuels. In order to reflect the possible future electricity generation alternatives, three different scenarios are introduced for both years 2023 and 2030. Future scenarios are based on the publication by World Wide Fund for Nature (WWF-Turkey) supported by European Climate Foundation and collaborated with Bloomberg New Energy Finance (BNEF). Official plans (OP) is the scenario decision-makers are planning to apply; business-as-usual (BAU) scenario is a modified version of OP with more relevant targets; renewables development pathway (RDP) is the scenario offered for keeping environmental impacts close to 2014 levels for a sustainable future [8].
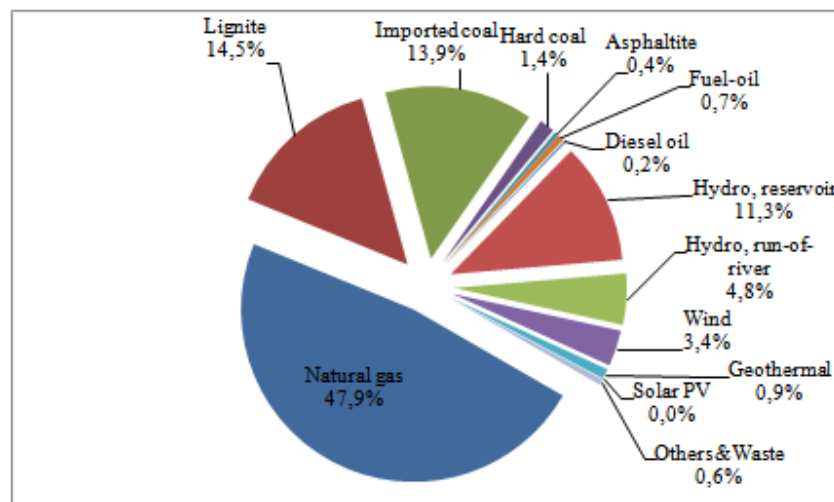
Figure 86. Electricity generation mix in 2014

2.3. Impact Assessment

Life cycle impact assessment (LCIA) methods used in this study are the single issue cumulative energy demand (CED) method [9] and the mid-point CML 2 baseline 2000 method [10]. Cumulative non-renewable fossil, non-renewable nuclear, non-renewable biomass, renewable biomass, renewable wind, solar, geothermal and renewable water demand impact categories are selected for CED method. Abiotic depletion, global warming (GWP100a), ozone layer depletion (ODP), human toxicity, fresh water aquatic ecotoxicity, marine aquatic ecotoxicity, terrestrial ecotoxicity, photochemical oxidation, acidification, and eutrophication are selected as the impact categories of CML 2 baseline 2000 method.

2.4. Interpretation

The last phase of LCA includes the evaluation of the results from either inventory analysis or impact assessment in comparison with the goal of the study defined in the first phase, the proposal of recommendations, and the final reporting of the results.

3. RESULTS AND DISCUSSION

3.1. Inventory Analysis and Interpretation

The most challenging part of an LCA study is inventory analysis since it is very critical to find adequate data to construct the model for selected generation technologies. First a general scheme of electricity generation

profile is drawn for both total generation levels (Figure 87) and for generation technology shares (Figure 88). As clearly seen in the figures, Turkey electricity sector is highly dependent on fossil fuel technologies. But this trend is about to change thanks to Paris Agreement (2015) taking measures against climate change mitigation by reducing fossil fuel consumption. In order to accomplish this mission, conducting comprehensive analyses and developing down-to-earth plans are crucial in decision making processes for sustainable energy systems. For this purpose, future scenarios are investigated from an environmental point of view. Total energy demand projections tend to increase by 2023 and 2030 in agreement with the population growth and increase in the level of welfare (Figure 89). Also the shares of electricity generation technologies in the future scenarios are presented (Figure 90).
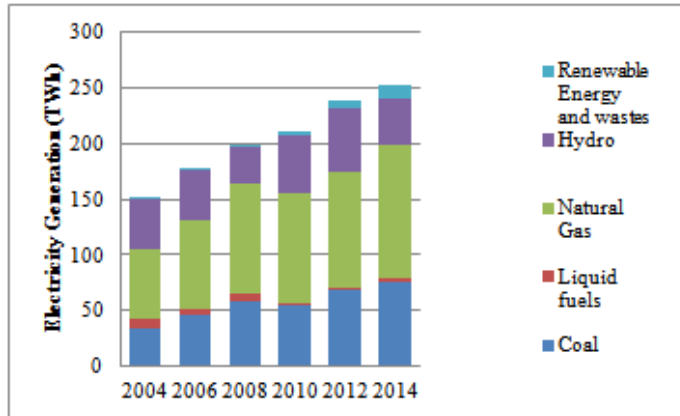
Figure 87. Electricity generation profile in Turkey (2004 - 2014)
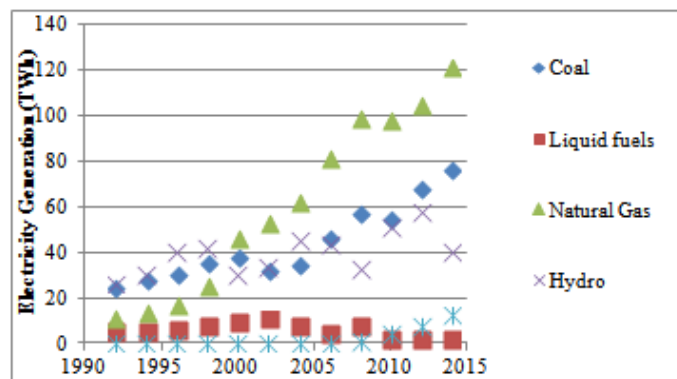
Figure 88. Electricity generation from primary energy sources
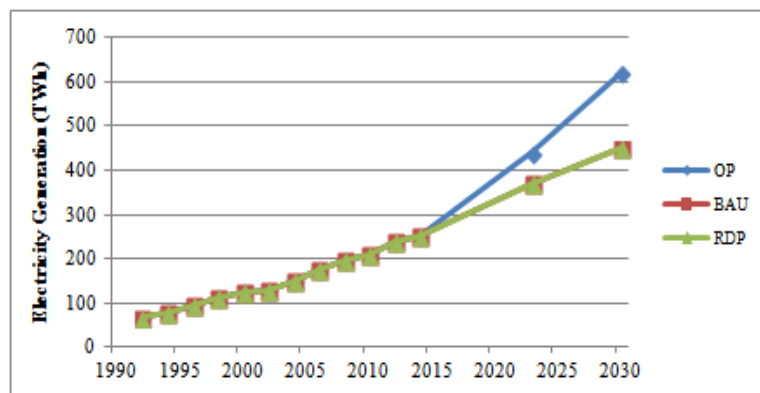
Figure 89. Electricity generation projections according to future scenarios

960
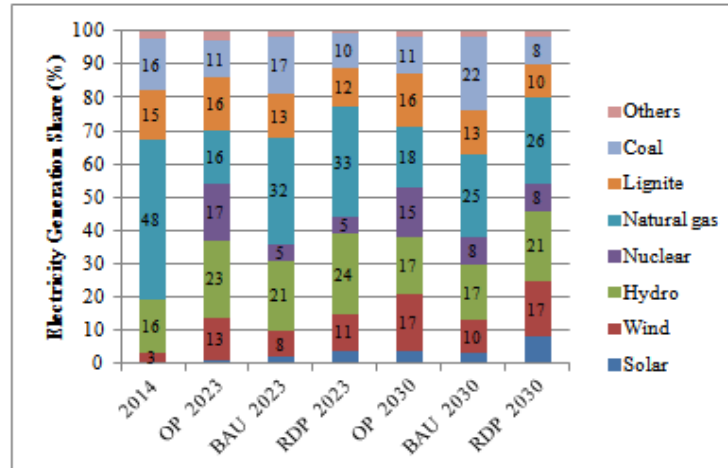
Figure 90. Electricity generation mix projections according to future scenarios.

3.2. Impact Assessment and Interpretation

The reduction of energy consumption is one of the most important criteria for sustainable development plans. As several environmental problems like climate change are directly associated with the energy use, cumulative energy demand is a very advantageous measure for making improvements. It is also easy to comprehend for decision-makers such as consumers, politicians or managers. Thus, CED method is useful to get a general view of the energy related environmental impacts in a life cycle and to make a comparison between different generation options.

The total energy use in a country is a good benchmark to measure and control the success of policy measures that aim to reduce the energy use. Since diverging concepts exist and the characterization of the different primary energy carriers has unclear basis, the CED-indicator is divided into eight categories for the ecoinvent database and no aggregated value is presented. Common to all categories is the basis that all energy carriers have an intrinsic value. This intrinsic value is determined by the amount of energy withdrawn from nature [9].

According to the CED results, non-renewable fossil energy demand increases business-as-usual and official plans scenarios since they highly depend on fossil fuel technologies. Non-renewable fossil energy demand can only be kept in 2014 levels if the renewables development pathway is applied (Figure 91a). Non-renewable nuclear energy demand has higher scores for official plans since it proposes a high level of nuclear share in the electricity generation (Figure 91b). Non-renewable and renewable biomass energy demand shows the same tendency for 2023 and 2030 scenarios (Figure 91c,d). Renewable wind, solar and geothermal energy demands increase in all future scenarios since the renewable share is expected to rise in all cases (Figure 91e). Renewable water energy, namely run-of-river and reservoir hydro power, demand also increase in all scenarios due to the shift to renewable energy technologies (Figure 91f).

However, energy use does not give a full picture for all environmental impacts in the life cycle of electricity generation. For example, eutrophication caused by intensive animal production is one problem that is not recorded by the energy use. Also the environmental impacts vary among different energy resources. The impacts of coal use concerning the energy content are normally more severe than these due to using natural gas. Thus, cumulative energy demand analysis cannot be the one and only method for evaluating the environmental impacts of a good or service. For this reason, CML 2 baseline 2000 impact assessment method is applied to get a full understanding of all impacts associated with generation technologies.

(a) *(b)* *(c)* *(d)* *(e)* *(f)*
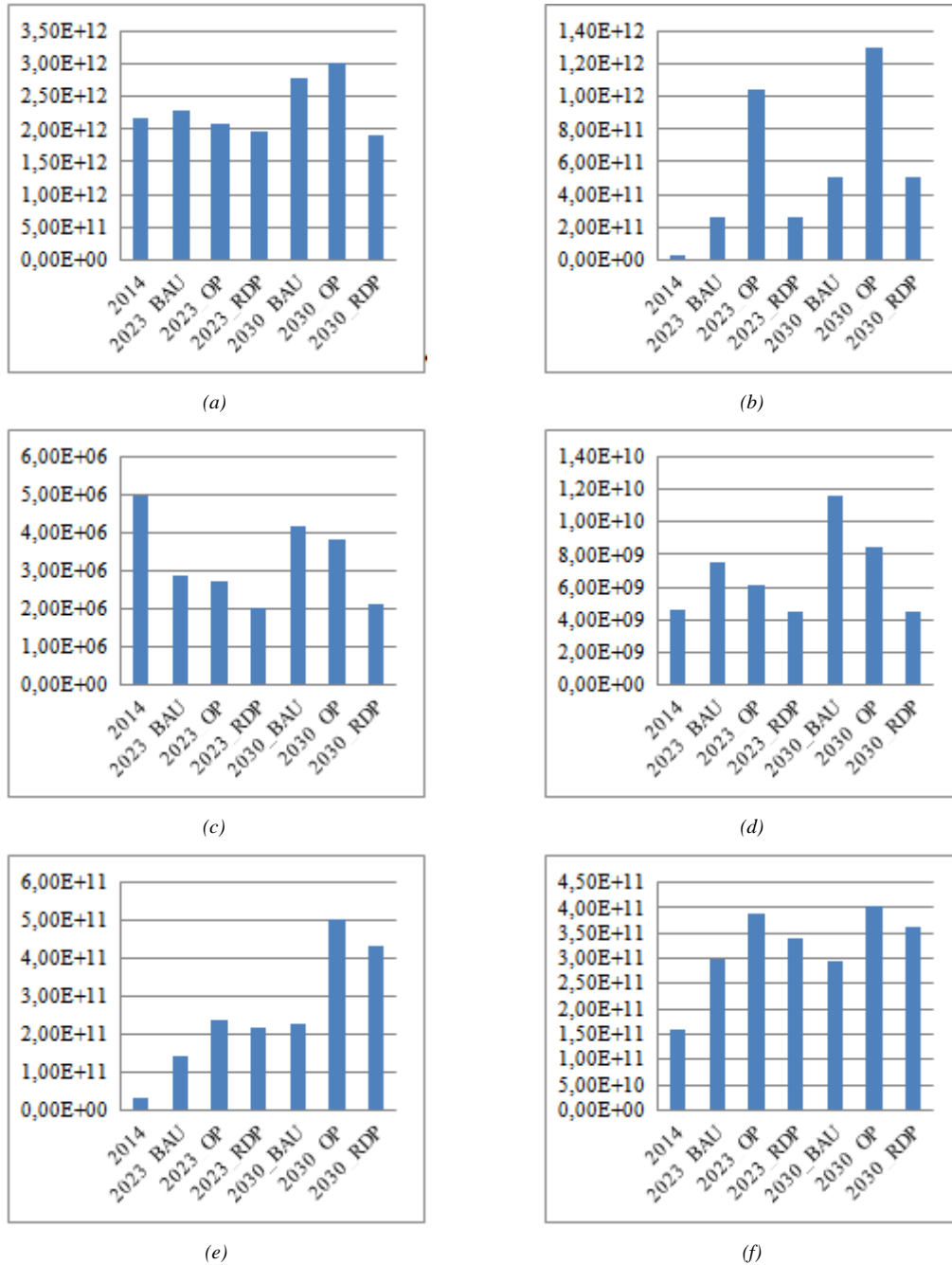
Figure 91. Cumulative energy demand (CED) results: (a) Non-renewable, fossil; (b) Non-renewable, nuclear; (c) Non-renewable, biomass; (d) Renewable, biomass; (e) Renewable, wind, solar, geothermal; (f) Renewable water

CML 2 baseline 2000 impact assessment method provides a measure for the potential environmental damage of airborne, liquid and solid emissions by means of appropriate equivalence factors to selected reference compounds for several impact categories [10]. CML 2 baseline 2000 impact assessment results are expressed in eleven categories: Abiotic depletion (mineral), abiotic depletion (fossil fuels), global warming (GWP100a), ozone layer depletion (ODP), human toxicity, fresh water aquatic ecotoxicity, marine aquatic ecotoxicity, terrestrial ecotoxicity, photochemical oxidation, acidification, and eutrophication.

All of the eleven categories have higher scores for the business-as-usual and official plans scenarios due to their high dependency of fossil fuel technologies and all of them also have lower scores for the renewables development pathway scenarios since they depend on replacing fossil fuel technologies with renewable technologies.
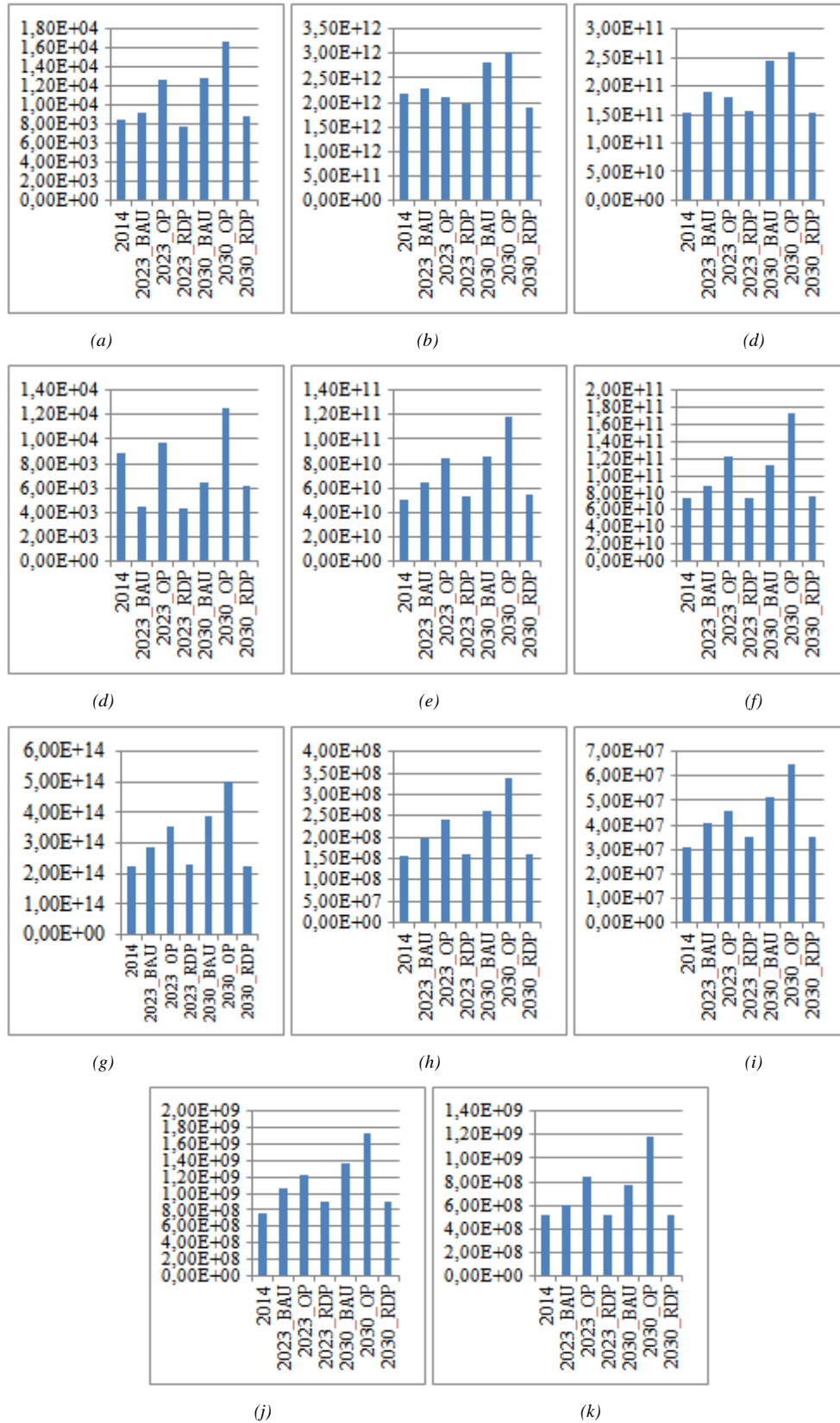
Figure 92. CML 2 baseline 2000 method results: (a) Abiotic depletion, minerals; (b) Abiotic depletion, fossil fuels; (c) Global warming (GWP100a); (d) Ozone layer depletion (ODP); (e) Human toxicity; (f) Fresh water aquatic ecotoxicity; (g) Marine aquatic ecotoxicity; (h) Terrestrial ecotoxicity; (i) Photochemical oxidation; (j) Acidification; (k) Eutrophication

4. CONCLUSIONS

Fossil fuel related environmental impacts draw attention to emerging climate change mitigation problems for the last decades. Electricity generation is one of the main contributors to climate change problem. This study aims to indicate the environmental impacts related to electricity generation in Turkey for year 2014 and also estimate the impacts with future projections for 2023 and 2030. The computation results are expected to assist decision-makers for building more sustainable energy policies for the future.

CED results reveal that minimum energy demands are attained when the share of renewable energy technologies increases. Nevertheless, most impacts remain the same as 2014 if renewable development pathway is put into practice according to the CML 2 baseline 2000 results. The combined results indicate that the environmental impacts are kept under control only if a shift from fossil fuel to renewable energy technologies is employed. Thus, this study indicates the necessity of renewable energy technologies for sustainable future scenarios.

ACKNOWLEDGEMENT

BIOGRAPHY

Gulsah YILAN received her Bachelor of Science degree from Chemical Engineering in 2008 and Master of Science degree from Bioengineering in 2011, both degrees are taken from Marmara University. She is a Doctor of Philosophy student and research assistant in Chemical Engineering Department in the same university. Interest areas are renewable energy technologies, electricity generation technologies, sustainability assessment methods, life cycle assessment and multi-criteria decision analysis.

REFERENCES

[1] WCED, *Our Common Future, London.* 1987.
[2] Talinli, I., E. Topuz, and M. Uygar Akbay, *Comparative analysis for energy production processes (EPPs): Sustainable energy futures for Turkey.* Energy Policy, 2010. **38**(8): p. 4479-4488.
[3] *TETC, Electricity Generation - Transmission Statistics of Turkey* 2014.
[4] Balat, M., *Security of energy supply in Turkey: Challenges and solutions.* Energy Conversion and Management, 2010. **51**(10): p. 1998-2011.
[5] ISO, *Environmental management - Life cycle assessment - Principles and framework. ISO 14040.* 2006.
[6] ISO, *Environmental management - Life cycle assessment - Requirements and guidelines. ISO 14044.* 2006.
[7] UNEP, *Evaluation of Environmental Impacts in Life Cycle Assessment*. 2003.
[8] *BNEF, Turkey's Renewable Power.* 2014.
[9] Frischknecht, R., et al., *Implementation of Life Cycle Impact Assessment Methods Data v2.0*, in *ecoinvent report No. 3*. 2007.
[10] Guinée, J.B.G., M.; Heijungs, R.; Huppes, G.; Kleijn, R.; Koning, A. de; Oers, L. van; Wegener Sleeswijk, and S.U.d.H. A.; Suh, H.A.; Bruijn, H. de; Duin, R. van; Huijbregts, M.A.J, *Handbook on life cycle assessment. Operational guide to the ISO standards. I: LCA in perspective. IIa: Guide. IIb: Operational annex. III: Scientific background.* 2002, Kluwer Academic Publishers.

Effects Of Some Rootstocks On Phenological And Some Fruit Traits Of "Siirt" And "Ohadi" Pistachio Cultivars In Sanliurfa Turkey

Bekir Erol AK[1]*, Ahmet OZDEMIR[2], Izzet ACAR[1]

Abstract

This experiment was done at the orchard of Ceylanpinar State Farm which is a very big governmental farm in Sanliurfa at Southeast Anatolia Region. Four rootstocks (P.vera, L, P. khinjuk, Stocks. P. terebinthus .L.ve P. atlantica, Desf.) were selected that two cultivars (Siirt and Ohadi) budded on them were selected. In this experiment phenological observations in spring and pomological analyses were done harvested nuts. There are effectiveness of different rootstocks on flowering time and flowering period of cultivars. Generally the flowering period was obtained longer onto P. atlantica rootstock.

According to results of pomological analyses, the weight of fruits were higher at the cultivars budded on P. atlantica rootstock. The efectiveness rate of physical traits, such as splitting, blank and filled nuts, were changed either rootstocks or cultivars.

Keywords: *Pistachio, Rootstock, Phenology, Traits*

1. INTRODUCTION

P.vera seedlings are stronger and more homogenous than the other rootstocks. Budded trees on this rootstock grow slowly during the first year but growth becomes faster in the following years. There is no incompatibility in budding with cultivars of pistachio. In the budded trees the juvenility period lasts long; therefore, the trees bear fruit quite late. In arid zones the trees reach the bearing stage 15 to 20 years after planting. They can withstand drought, high lime content and salinity in the soil but are sensitive to high soil moisture. The trees of *P.terebinthus* are grown generally as bushes. The plant has a strong and deep root system. Therefore it can be grown in poor rocky and stony soils. It is a kind of dwarfing rootstock for *P.vera*, L. so the trees budded on this rootstock can be easily recognized. *P.terebinthus* is as hardy as *P.vera* but hardier than *P.atlantica.* Therefore it is preferred to *P.atlantica* in cold areas. In Turkey it can be grown successfully at elevations up to 1200 m. *P.terebinthus* is suitable for planting in calcareous soils along the Mediterranean coast. It grows very well in places where the annual precipitation is about 400 to 600 mm [1,2].

 P. vera seedlings are stronger and more homogenous than the other rootstocks. Budded trees on this rootstock grow slowly during the first year but growth becomes faster in the following years. There is no incompatibility in budding with cultivars of pistachio [3]. In the budded trees the juvenility period lasts long; because of this, the trees bear fruit quite late. In arid zones the trees reach the bearing stage 15 to 20 years after planting. They can withstand drought, high lime content and salinity in the soil but are sensitive to high soil moisture. The trees of *P. terebinthus* are grown generally as bushes. The plant has a strong and deep root system. Therefore it can be grown in poor rocky and stony soils. It is a kind of dwarfing rootstock for *P. vera*, L. so the trees budded on this rootstock can be easily recognized. *P. terebinthus* is as hardy as *P. vera* but hardier than *P. atlantica.* Therefore it is preferred to *P. atlantica* in cold areas. it can be grown successfully at elevations up to 1200 m. *P. terebinthus* is suitable for planting in calcareous soils along the Mediterranean coast. It grows very well in places where the annual precipitation is about 400 to 600 mm [1,4].

---

[1] *Corresponding author: Department of Horticulture, Faculty of Agriculture, Harran University, Sanlıurfa, Turkey. beak@harran.edu.tr*

[2] *Department of Horticulture, Institute of Natural and Applied Sciences, Harran University, Sanlıurfa, Turkey.*

In the U.S.A., *P.atlantica*, *P.terebinthus* and *P.* integerrima were used in last decade. The last years the hybrid of *P.* integerrima and *P. atlantica* has been used for Kerman pistachio cultivar. The main hybrid rootstocks using UCB=1 (P. *atlantica* x *P.* integerrima) and PG-Iİ (P. integerrima × *P. atlantica*) for their different features [5].

The aim of this study was to determine of effects of *P. vera, P. khinjuk* and *P. atlantica* and *P. terebinthus* rootstocks on phenolojgical and some physical traits of Siirt and Ohadi pistachio cultivars grown in Turkey.

2. MATERIAL AND METHODS

The Site: This experiment was conducted in Sanliurfa- Ceylanpinar state farm,, in Turkey. Altitude: 375 m. There is not irrigation

The Rootstocks: Pistacia vera, P. Khinjuk, P. atlantica and *P. terebinthus*

Cultivars: Siirt and Ohadi, 22 years old. *Distances:* 6 m x 6 m

The Phenological Observations; Bud Swelling, Bud Bursting, First Flowering, Full Flowering, End of Flowering

The Physical analyses: 100 fruits x 5 replications (Each cultivar 500 fruits were analyzed. Splitting rate (%), Blank nut rate (%), Total Filled Nuts Rate (%) were determined.

Experimental Design: There are 4 rootstocks x 3 trees x 2 Cultivars. Totally 24 trees were used. Statistical analysis of the values were done according to randomized plot design. The obtained average results compared with "Least Significant Difference (LSD)" 5 % [6].

3. RESULTS AND DISCUSSION

3.1. Phenological observations of the trees

Effect of rootstocks on pheneological stages (Bud swelling, bursting, start, full and end of flowering) were determined for two cultivars Ohadi and Siirt. The obtained results are given in Table 1 and Figure 1. As seen in Table 1, the stages of flowering were earlier in Siirt than Ohadi. It is also clearly seen in Figure 1.

The spring temperatures are always important for all fruit trees. Because bud bursting or spring dormancy should be finished before flowers can open. After winter dormancy flowers are ready to open their flowers but environmental conditions are not suitable to start bursting [2]. Enough warmth is necessary to accumulate heat for the opening of flowers and vegetative growth. The flowering period can be changed according to temperature during flowering time. If the temperature is low or undulating by night and day, the period of flowering will be extended when compared with high temperatures.

3.2. Some physical traits of pistachio cultivars

Splitting of pistachio nut depents on cultural practices such as irrigation, fertilization and soil cultivation. But it is a genetical character. Generally it depends on kernel development. Rootstock is also one of the effective factor on splitting rate of pistachio nut [4].

Effects of some pistachio rootstocks on shell splitting rate of Siirt and Ohadi cultivars were given Table2. According to obtained data, shell splitting rate of Siirt (85.59 %) Cultivar better than Ohadi (61.71 %) cultivar. According to cultivars *Pistacia khinjuk* is better (87,02) in Siirt. In Ohadi cultivar *P. atlantica* and *P. terebinthus* are better. (Table 2).

Table 1. Phenological observations of the two pistachio cultivars budded on different rootstocks.

Cultivars	Rootstocks	Bud swelling	Bud bursting	Begining of Flowering	Full of flowering	End of flowering	Flowering period (day)
Ohadi	P. vera	18 Feb.	28 March	06 Apr.	12 Apr.	16 Apr.	10
	P. khinjuk	06 March	31 March	07 Apr.	11 Apr.	15 Apr.	08
	P. atlantica	07 March	02 Apr.	06 Apr.	10 Apr.	13 Apr.	07
	P.terebinth	06 March	30 March	02 Apr.	08 Apr.	13 Apr.	11

Siirt	P. vera	17 Feb.	24 March	03 Apr.	08 Apr.	11 Apr.	08
	P. khinjuk	05 March	29 March	01 Apr.	04 Apr.	09 Apr.	08
	P. atlantica	05 March	30 March	04 Apr.	09 Apr.	13 Apr.	09
	P.terebinth	02 Mart	26 Mart	31 Mart	03 Nisan	08 Nisan	09

Effects of some pistachio rootstocks on total filled nuts rate of Siirt and Ohadi cultivars were given Table 2. According to data total filled nut rate the highest value (87.89 %) obtained from Siirt cultivar as Ohadi was 76.18 % in Ohadi. Rootstocks are also effects of total filled nuts rate.

4. CONCLUSION

In this research, the effects of four different pistachio rootstocks (*P. vera*, *P. khinjuk*, *P. terebinthus* and *P. atlantica*) on Phenological stage, shell splitting, total filled nut and empty or blank fruits of two different cultivars (Siirt and Ohadi) were investigated. Siirt cultivar is earlier than Ohadi. The rootstocks are different strongest. Dwarf rootstocks is earlier than strong ones on flowering time. In shell splitting is compared between the cultivars. Siirt is better than Ohadi cultivar. This situation can be formullized such as follows; Siirt > Ohadi and *P.khinjuk*> *P.vera*= *P.atlantica* = *P. terebinthus*

Generally, In shell splitting rate and Total Filled Nuts rate (%)between the cultivars, Siirt was better then Ohadi (Siirt > Ohadi). Total filled nuts are formulized; Siirt > Ohadi and P.khinjuk> P.vera> P.atlantica = P. terebinthus.Among the rootstocks *P. atlantica* more effective then the other ones. (*P.atlantica*> *P.vera*> *P.khinjuk).* Blank or empty nut rates also was changed between the cultivars and rootstocks uch as Siirt < Ohadi and *P.atlantica* (18.58 %) < *P.vera* ((24.29 %) < *P. khinjuk,* (33.22 %).

Generally empty or blank fruits are falling down during June drop period. But this rootstock keeps all the fruits on the branches. Because of this reason, harvest time blank nut rate is higher then the others. It can be formulized such as; Siirt < Ohadi and *P.khinjuk < P.atlantica, P.vera* and *P. terebinthus.* These results shows that either phenological time or physical traits can be changed by cultivars also rootstocks affects these traits.

Table 2. Some physical traits of different pistachio cultivars budded on some Pistacia rootstocks (%)

Cultivars	Rootstocks	Splitted nuts (%)	Unsplitted nuts (%)	Unsplitted but filled nuts (%)	Blank Nuts (%)	Totally filled nuts (%)
Siirt	*Pistacia vera*	85,00	15,00	2,56	12,44	87,56
	Pistacia atlantica	85,34	14,66	1,36	13,30	86,70
	Pistacia khinjuk	87,02	12,98	3,53	9,45	90,55
	Pistacia terebintus	85,00	15,00	1,75	13,25	86,75
	Average	**85,59**	**14,41**	**2,30**	**12,11**	**87,89**
Ohadi	*Pistacia vera*	55,72	44,28	17,88	26,40	73,60
	Pistacia atlantica	70,26	29,74	4,50	25,24	74,76
	Pistacia khinjuk	50,60	49,40	27,94	21,46	78,54
	Pistacia terebintus	70,26	29,74	7,56	22,18	77,82
	Average	**61,71**	**38,29**	**14,47**	**23,82**	**76,18**

ACKNOWLEDGEMENTS

REFERENCES

[1]. Kaska, N., (1995). Pistachio nut production growing in Turkey. Acta Horticulturae, 419: 161-164.
[2]. N. Kaska, Pistachio research and development in the Near East, North Africa and Southern Europe. Nut Production Industry in Europe, Near East and North Africa. Reur Technical Series 13, 133-160. 1990.
[3]. Ayfer, M. 1964. Pistachio nut culture and its problems with special reference to Turkey. Univ. of Ankara Fac.of Agr. Yearbook, 189-217.
[4]. Ak, B.E., 1992. Effects of different *Pistacia* spp pollens on the fruit set and quality of Pistachios. (In Turkish with an English summary) Cukurova University Institute of Natural and Applied Science.Department of Horticulture, PhD. Thesis, Adana, 210 p.
[5]. Krueger, B. and. Ferguson, L. (1995). Pistachio rootstocks. The orchard: 41-42.
[6]. Bek, Y., (1983). Arastırma ve Deneme Metotları. C.U. Ziraat Fakultesi Ders notu yayınları : 92, 283 s.

Figure 1. Phenological stages of cultivars

CULTIVAR	ROOTSTOCKS	March				April																	
		28	29	30	31	01	02	03	04	05	06	07	08	09	10	11	12	13	14	15	16	17	
SİİRT	*P. vera*							�	▮	▮	▮	▮	▮	▮	▮	▮							8
	P. khinjuk					🟨	🟨	🟨	🟨	🟨	🟨	🟨	🟨										8
	P. atlantica								🟦	🟦	🟦	🟦	🟦	🟦	🟦	🟦							9
	P. terebinth.				🟩	🟩	🟩	🟩	🟩	🟩	🟩	🟩	🟩										9
OHADI	*P. vera*										🟥	🟥	🟥	🟥	🟥	🟥	🟥	🟥	🟥				9
	P. khinjuk											🟨	🟨	🟨	🟨	🟨	🟨	🟨	🟨	🟨			11
	P. atlantica											🟦	🟦	🟦	🟦	🟦	🟦	🟦					9
	P. terebint.						🟩	🟩	🟩	🟩	🟩	🟩	🟩	🟩	🟩	🟩	🟩						11

Effect of Inflation on Food and Producer Prices

Osman YILDIZ[1]

Abstract

In this study, the effect of changes in food and producer prices on inflation was investigated. Food and agricultural products included in the inflation basket have been taken into consideration. In particular, price and weight changes in underwear products that are effective in winter are considered important. Calculations have been made taking into account the price volatility in seasonal products and the changes resulting from the weight of these products. It is accepted that only underground production is effective for the first three months of 2017 (January, February, March). If product prices do not change due to seasonality, monthly change is predicted. It is accepted that each month different goods will enter the market with different volume values. Estimated figures are used because there are no monthly sales figures of agricultural products in the basket. Monthly consumption figures are calculated by considering the population. The relationship between CPI, D-PPI and Agricultural PPI was evaluated. Since the weight of agricultural products in the basket is high, inflation has a negative or positive effect. Despite very low consumption in the relevant months, inflation has been seen to have a high impact. Although the monthly prices did not change, it was seen that the price changed due to monthly changes in product weights. Although the weight of tomatoes, peppers, cucumber, eggplant, fresh beans and squash in the food was 6.63%, the effect on food inflation was 66,96%. Monthly variable weights in seasonal products found monthly changes due to weight, even if product prices did not change.

Keywords: *Inflation, Index, Producer prices, Consumer prices*

1. INTRODUCTION

Inflation has showing the change in the prices of goods and services for consumption of the dwellings over time period. While inflation has showing the state of the country's economy, there is an important economic indicator that shows how citizens are influenced by buying time, what money in the pocket can take and what not to buy over time. Therefore the buying power of the money is important as much as infilation.

There are many factors that affect price change. Food prices that are indispensable for society and change in producer prices is also important in terms of direct impact on inflation. The change in the prices of agricultural products and industrial products within the scope of producer prices should be monitored at what scale it is reflected in consumer prices.

Price indices, which are mathematical calculations, show the actual price changes as well as the artificial price changes due to the weight of the items in the basket. In particular, the food prices, which are of total spending groups and have an average 24.86% weight (21.77% by weight for 2017) [1]in the basket, varying with years is affecting inflation either positively or negatively. Nevertheless, it is observed that the price changes of producer agricultural products and industrial products are different from the consumer prices from time to time.

Structural problems in the producer and consumer chains disrupt the relationship between producer prices and consumer prices and increase the size of fluctuations in prices.

The Harmonised Index of Consumer Prices (HICP) gives comparable measures of inflation for the countries and country groups for which they are produced. They are economic indicators that measure the change over time of the prices of consumer goods and services acquired by households. In other words, they are a set of consumer price indices (CPI) calculated according to a harmonised approach and a single set of definitions. The HICP is a consumer price index, that is, it covers the consumption expenditure of the household sector [3].

---
[1] *Industrial Engineering Department, Faculty of Engineering, Karabuk University, 78050, Karabuk, Turkey. osmanyildiz@karabuk.edu.tr*

Consumer Price Index (CPI) measures the changes of the current retail prices of goods and services purchased by consumers over a given time period. While the index was calculated by TurkStat, 414 products was used in the compilation of the index in 2017. There are no important differences between TurkStat methodology reported in the Eurostat and relevant international [2].

Strict annual weight approach is used for seasonal items. Price coverage of index is constituted of purchasing prices. The prices of goods and services included within the index are retail. Item baskets and the weights are updated at the end of every year and chained with the Laspeyres formulation. Index is calculated by dividing current prices to the prices of previous December, which is "new price reference period (Po)", and then chained by multiplying it with the index numbers of December [1].

$$I = w.P_t/ P_o \text{ (Laspeyres formulation)} \tag{1}$$

(I = index, p = price, w = weight)

Sub indicators which represent time values of variables:

t = current year   o = base year

Prices of fresh fruit and vegetables are collected once a week in each month between 1 and 25 days.

Producer Prices Index of Agricultural Products (A-PPI)

PPI index is computed to measure the changes through time in the prices of agricultural products, which farmers produce and sale, at the first point of sale. There is no significant difference between TurkStat methodology and Eurostat and related international [1][10].

Selling prices of farmers to the marketing channels in each month between 1 and 31 days. It seems that the price collection time is different from the CPI.

Formulation of Laspeyres was used for the calculation of PPI for Turkey depending upon variables which are given below. Variables which are used for calculation of PPI for Agriculture:

$$I = w.P_t/ P_o \text{ (Laspeyres formulation)} \tag{2}$$

I = index   p = price   w = weight

Sub indicators which represent time values of variables: t = current year   o = base year

Domestic Producer Price Index (D-PPI) measures the change in the prices goods and services sold as output by domestic producers over a given time period [9].

Index formula is Laspeyres. Reference period is 2003. Frequency of weight updates is Every year and Period of current index weight is t-2 [1]

As of January 2013, the food and non-alcoholic beverages sector's price increase is increasingly rising and above the general inflation increase. The rise in price seems to have a direct impact on a significant part of the economy.

The Central Bank says that the increase in food prices - when considered in other sectors indirectly and directly affected by the sector - is about 30 percent of the overall inflation rate. Inflation affects lower and middle-income groups, which spend a large part of their income on food expenditures. On the other hand, in the foreign markets, the competitiveness of the food products with high export potential is decreasing and it shows that the policies applied for the elimination of these problems and the support payments made have not reached their targets. Factors that may lead to food prices inflation and / or chronic it in Turkey; Increasing production costs, supply shortages, export supply (fresh vegetables and fruits), isolation from world markets, and missing and clumsy organizations in product chains.

The most important export of Turkey is fresh fruit and vegetables. There is a constant external demand and a sustainable supply in this sector. However, when it comes to food inflation, the first product group is fresh fruit and vegetable, but the excess supply is not being used to offset price fluctuations in the domestic market. In recent years, the rise in food prices has triggered inflation, but no concrete proposals

have been made as to whether the impact rate reflects reality and why food prices are rising. This issue has been a topic of research in recent times and efforts are being made to prevent the rise in food prices.

TurkStat is the officially calculating and explaining the results of CPI, D-PPI and Agriculture PPI. Although studies have been conducted on why food prices are rising, is the increase in food prices the main effect of inflation in reality? No work has been done in this study yet. In this study, the factors affecting the increase of food prices, the calculation methods, the contribution of product basket and weights of D-PPI and Agricultural PPI affecting inflation, and the index formula and weighted factors are examined.

2. MATERIALS AND METHODS

In the study, monthly rate of change in CPI, D-PPI and Agriculture PPI general and food products were compared. Agricultural and food products that directly affect inflation have been identified. The effect of prices and weights of 33 products, which are located in Agricultural PPI and directly affecting CPI, is calculated. Especially in winter, tomatoes, peppers, cucumbers, fresh beans, squash and eggplant focused on. It is important that these products are uncovered products. Monthly sales quantities of food and agricultural products have been determined, the relationship between product weights and the effect of inflation has been established. Per capita and monthly consumption / sales figures of fruits and vegetables were calculated by considering the population of the country. Monthly effects of the products in the seasonal property were calculated. Because there are no monthly sales quantities of uncovered products, they are estimated using the marketing halls sale rates. Compared to the population of the country, per capita consumption and sales volumes were found. The effect on product weights in the inflation basket was calculated.

The following assumptions were made in the study:

It is accepted that only underground production is effective for the first three months of 2017 (January, February, March).

Even if product prices do not change, it is predicted that monthly changes will occur due to product weights.

It is predicted that each month different products will enter the market with different volume values.

The chain laspeyres price index formula is used. (by TurkStat).

Estimated figures are used because there is no monthly sales figures for agricultural products in the basket. It is assumed that the production amount of the uncovered products in the basket is supplied completely to the market. Monthly and per capita consumption values are taken into consideration by considering the population of the country.

$$\text{Estimated consumption per capita} = \text{Production quantity} / \text{Population} \qquad (3)$$

$$\text{Estimated monthly sales amount} = \text{Uncovered quantity} / 12 \text{ months} \qquad (4)$$

$$\text{For index calculations; Laspeyres index formula } I = w.P_t / P_o \qquad (5)$$
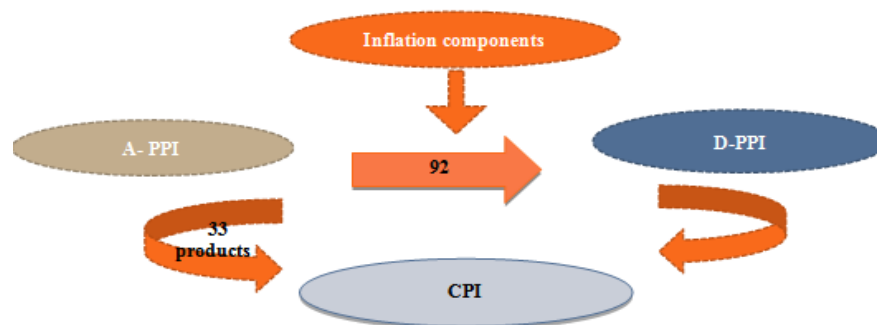

Figure 1. Inflation components

A-PPI has 33 products that directly affect the CPI. APPI has 92 products that directly affect D-PPI. All of the D-PPI's are affecting the CPI.
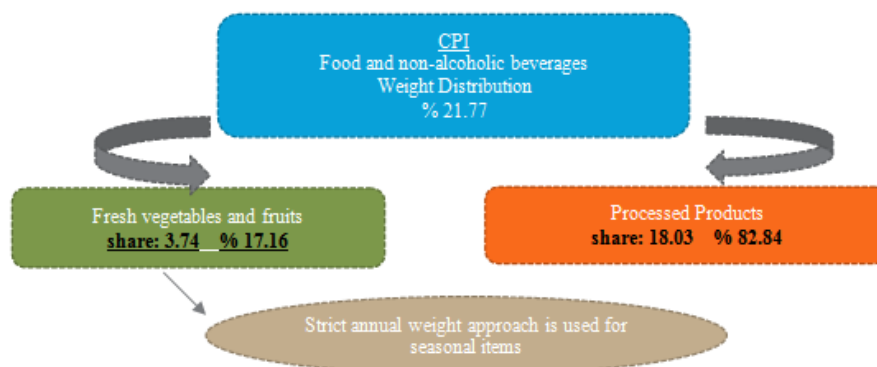

Figure 2. Weight Distribution.

The weights shown in Fig. 2 are used in the calculations. Food and non-alcoholic beverages constitute 21.77% of the total weight. Fresh vegetables and fruits have a share of 17.16% in food and non-alcoholic beverages [1].

Figure 3. D-PPI Weight Distribution.

88.79% of the total weight is in the manufacturing sector, of which 16.23% is food products [1].

Table 1. Vegetable production for land under protective cover and total, 2012-2016 (Tonnes)					
Products	2012	2013	2014	2015	2016
Pepper (Bell) UPC	80 891	94 173	90 414	94 598	103 413
Pepper (Bell)	383 213	398 470	391 009	393 109	418 435
Pepper (Green) UPC	387 459	384 171	387 006	385 548	414 058
Pepper (Green)	910 725	946 506	907 126	919 004	967 466
Pepper (Banana) UPC	-	-	32 563	47 909	52 883
Pepper (Banana)			104 364	115 568	114 891
Tomatoes UPC	3 096 349	3 200 930	3 285 570	3 394 447	3 614 472
Tomatoes	11 350 000	11 820 000	11 850 000	12 615 000	12 600 000
Bean (fresh) UPC	34 153	42 646	46 008	39 049	45 879
Bean (fresh)	621 036	632 301	638 469	640 836	638 532
Cucumber UPC	1 028 122	1 001 940	1 030 349	1 080 213	1 077 783
Cucumber	1 741 878	1 754 613	1 780 472	1 822 636	1 811 681
Eggplant UPC	241 969	252 396	261 874	250 311	291 314
Eggplant	799 285	826 941	827 380	805 259	854 049

Source: TurkStat

UPC:Under Protective Cover

As seen in Table 2, per capita consumption per capita and annual total sales quantities were calculated for the undercover products selected in the calculations.The total population and production figures were used when consumption and sales volumes were calculated.Since there is no monthly product sales, it is assumed that the same quantity is sold every month. In addition, monthly sales figures are calculated according to the transaction amount in the marketing hall. However, only monthly fixed sales are considered during the evaluation phase.It should be noted that the per capita consumption figures are very low as seen in Table 2.

Table 2. Vegetable consumption for land under protective cover and total, 2012-2016									
	Kg / person	Kg / person	Kg / person	Kg / person	Kg / person	Ton / Month*	According to Wholesale rate (2016)		
Products	2012	2013	2014	2015	2016	2016	January	February	March
Pepper (Bell) UPC	1,07	1,23	1,16	1,20	1,30	8.618	6.781	3.527	4.070
Pepper (Bell)	5,07	5,20	5,03	4,99	5,24	34.870			
Pepper (Green) UPC	5,12	5,01	4,98	4,90	5,19	34.505	27.150	14.121	16.297
Pepper (Green)	12,04	12,35	11,68	11,67	12,12	80.622			
Pepper (Banana) UPC	-	-	0,42	0,61	0,66	4.407	3.468	1.804	2.081
Pepper (Banana)	0,00	0,00	1,34	1,47	1,44	9.574			
Tomatoes UPC	40,94	41,75	42,29	43,11	45,29	301.206	434.012	158.162	230.864
Tomatoes	150,08	154,17	152,52	160,21	157,87	1.050.000			
Bean (fresh) UPC	0,45	0,56	0,59	0,50	0,57	3.823	397	178	442
Bean (fresh)	8,21	8,25	8,22	8,14	8,00	53.211			
Cucumber UPC	13,59	13,07	13,26	13,72	13,50	89.815	33.852	22.886	51.405
Cucumber	23,03	22,89	22,92	23,15	22,70	150.973			
Eggplant UPC	3,20	3,29	3,37	3,18	3,65	24.276	25.142	7.230	8.916
Eggplant	10,57	10,79	10,65	10,23	10,70	71.171			

UPC:Under Protective Cover

*Accepted 12 months equally sold.

Table 3. Population by years

Years	Population
2012	75 627 384
2013	76 667 864
2014	77 695 904
2015	78 741 053
2015	79 814 871

Sourse: TurkStat

Table 4. Monthly fixed prices (TL)

Products	Price Po	Price Jan.	Price Feb.	Price Mar.	Price Apr.	Price May	Price June	Price July	Price Aug.	Price Sep.	Price Oct.	Price Nov.	Price Dec.
Tomato	1,41	1,38	1,38	1,38	1,38	1,38	1,38	1,38	1,38	1,38	1,38	1,38	1,38
Cucumber	0,88	1,24	1,24	1,24	1,24	1,24	1,24	1,24	1,24	1,24	1,24	1,24	1,24
Pepper (green)	1,35	1,39	1,39	1,39	1,39	1,39	1,39	1,39	1,39	1,39	1,39	1,39	1,39
Eggplant	1,18	1,66	1,66	1,66	1,66	1,66	1,66	1,66	1,66	1,66	1,66	1,66	1,66

Table 5. Monthly variable prices (TL)

Products	Price Po	Price Jan.	Price Feb.	Price Mar.	Price Apr.	Price May	Price June	Price July	Price Aug.	Price Sep.	Price Oct.	Price Nov.	Price Dec.
Tomato	1,41	1,81	1,67	1,67	2,08	1,31	1,02	1,04	0,95	0,99	1,08	1,66	1,96
Cucumber	0,88	1,49	1,68	1,24	0,97	0,75	0,89	0,87	0,97	0,99	1,03	0,95	1,15
Pepper (green)	1,35	2,38	2,96	4,29	2,26	1,40	1,46	1,52	1,43	1,44	1,43	1,91	2,25
Eggplant	1,18	2,75	3,11	2,80	1,94	1,19	1,21	1,12	1,06	1,10	1,20	1,55	1,94

Table 6. Monthly variable weights

Products	Jan. Weight	Feb. Weight	Mar. Weight	Apr. Weight	May Weight	June Weight	July Weight	Aug. Weight	Sep. Weight	Oct. Weight	Nov. Weight	Dec. Weight
Tomato	71,72	64,27	62,91	67,03	69,82	54,78	50,56	53,96	57,89	58,12	57,64	60,01
Cucumber	6,73	11,47	13,41	15,52	13,77	13,84	18,39	16,30	15,93	16,48	17,16	16,73
Pepper (green)	8,95	14,39	13,98	9,23	8,66	17,92	18,78	15,20	13,68	12,81	13,52	12,62
Eggplant	12,60	9,87	9,70	8,22	7,75	13,46	12,26	14,55	12,50	12,59	11,67	10,64

Table 7. Index and price changes %

Products	İNDEX Dec.	İNDEX Jan.	İNDEX Feb.	İNDEX Mar.	İNDEX Apr.	İNDEX May	İNDEX June	İNDEX July	İNDEX Aug.	İNDEX Sep.	İNDEX Oct.	İNDEX Nov.	İNDEX Dec.
Other vegetables grown for fruit juice	110,17	106,59	107,72	108,45	108,46	107,49	110,43	111,89	111,78	110,68	110,91	110,84	110,17
% Change when monthly price does not		-3,25	1,06	0,67	0,01	-0,89	2,73	1,32	-0,09	-0,98	0,20	-0,06	-0,60
Tomato	97,95	97,95	97,95	97,95	97,95	97,95	97,95	97,95	97,95	97,95	97,95	97,95	97,95
Cucumber	140,13	140,13	140,13	140,13	140,13	140,13	140,13	140,13	140,13	140,13	140,13	140,13	140,13
Pepper (green)	103,21	103,21	103,21	103,21	103,21	103,21	103,21	103,21	103,21	103,21	103,21	103,21	103,21
Eggplant	140,28	140,28	140,28	140,28	140,28	140,28	140,28	140,28	140,28	140,28	140,28	140,28	140,28
% Change when monthly price changes		34,63	4,87	3,37	-9,88	-35,63	-6,79	1,28	-5,16	1,63	6,13	34,15	19,19

In order to measure the effect of product weights on the monthly price change, both the index values resulting from the changes in the monthly prices and the time index values in which the monthly prices did not change were calculated. Thus, the weights of the products in the basket were affected by monthly price changes. For these calculations, the prices in Tables 4 and 5 and the product weights in Table 6 are used. The data in the table are estimated product weights and monthly prices used for example.

3. RESULTS AND DISCUSSION

It has been determined that price changes of all three indices vary from time to time, and the price increase in agricultural products and industrial products affects the inflation rate. Because of the monthly variable weights in seasonal products, monthly price changes are seen even though product prices do not change. Since fixed weight is used for seasonal products, it is seen that the increase in the price of products with very low consumption increases inflation. Due to its weight in the CPI, it is seen that it primarily increases food inflation, which in turn triggers a general inflation change, even though the seasonal products are consumed or sold in small quantities. Factors that cause food prices to increase; Cost, stocking problems, problems in supply chain, marketing chain between producer and consumer etc.
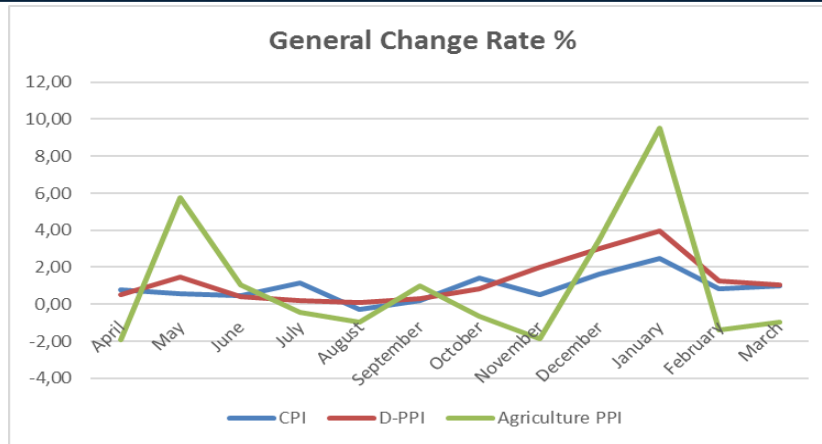
*Sourse: Calculated using TurkStat 2016-2017 data.*

Figure 4. Monthly changes in CPI, D-PPI and A-PPI (2016-2017)

Normally, the three indices should be parallel. But it does not seem like it. The index of agriculture has changed significantly over the past few months. This is not reflected in the CPI index.
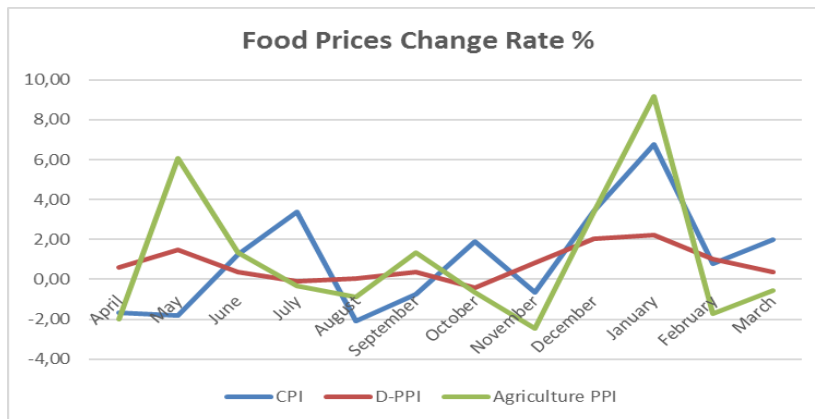
Sourse: Calculated using TurkStat 2016-2017 data.

Figure 4. Monthly changes in CPI, D-PPI and A-PPI for Food Prices (2016-2017)
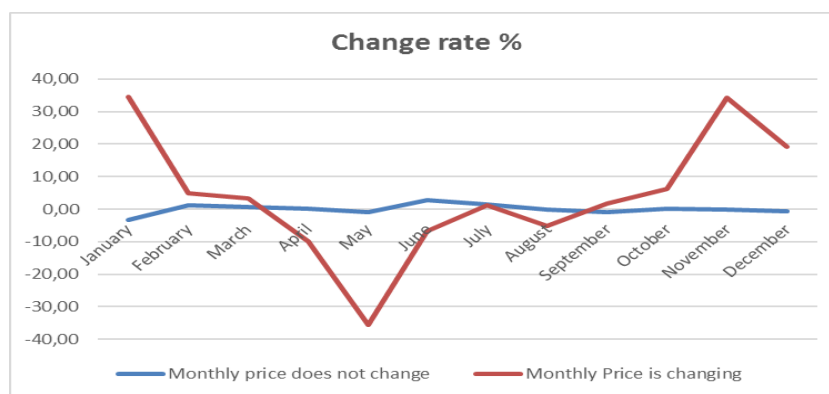
Sourse: Calculated using Table 7.

Figure 4. Example of monthly changes in A-PPI.

As shown in Figure 4, from January 2017 to December 2017, we see monthly price changes when products do not change prices. Due to the seasonality feature, it is seen how the price increases are realized.

974

Table 8. Consumer price index (2003=100) item basket and average prices (Turkey)

Products	Prices (TL)				Change rate %			Weight	Monthly Effect (2017)		
	2016 December	2017 January	2017 February	2017 March	January	February	March	%	January	February	March
Turkey					**2,46**	**0,81**	**1,02**		**2,46**	**0,81**	**1,02**
Food and non-alcoholic beverages					**6,37**	**0,84**	**1,93**	**21,77**	**1,39**	**0,18**	**0,42**
Sweet green pepper	3,9	6,6	6,4	7,0	69,5	-3,1	9,0	**0,04**	0,03	0,00	0,01
Stuff pepper	3,9	6,5	6,7	8,0	67,7	2,9	19,6	**0,04**	0,03	0,00	0,01
Green pepper	4,2	6,9	6,8	8,5	63,8	-1,5	26,1	**0,15**	0,10	0,00	0,06
Tomato	2,2	3,5	2,7	2,5	57,6	-22,3	-5,7	**0,67**	0,41	-0,15	-0,06
Green bean	-	8,6	11,5	13,9	-	34,4	20,6	**0,12**	-	0,04	0,04
Zucchini	3,2	6,2	5,4	4,1	93,3	-12,7	-24,3	**0,05**	0,04	-0,01	-0,02
Eggplant	3,5	6,4	5,2	5,3	79,4	-18,0	1,3	**0,15**	0,13	-0,03	0,00
Cucumber	2,7	4,7	5,2	4,7	74,7	10,2	-9,1	**0,24**	0,19	0,02	-0,03
Total	-	-	-	-	-	-	-	**1,44**	**0,93**	**-0,12**	**0,01**
%	-	-	-	-	-	-	-	**6,63**	**66,96**	-	-

Sourse: Calculated using TurkStat 2016-2017 data.

It has been shown that although the consumption of under protective cover such as tomatoes, peppers, eggplant, cucumber, fresh beans is low, it affects food inflation. The impact on food inflation was 66.96%, even though the weight of non-food products in table was 6.63%.

Factors Affecting Agricultural Price Change;

- Agricultural Production Quantity (Production Planning, Natural Conditions (drought, frost, heavy rainfall and other natural disasters etc.)

- Supporting policy, (modified, price threshold application)

- Marketing Channels (Direct sales, Indirect sales

- Supply-Demand Balance,

- Export-Import,

- Stocks,

- Input prices (major factor): The increase in production costs is mainly due to several different factors. The most important of these is import dependency in the use of agricultural inputs. (Such as; Diesel, pesticide, Fertilizer, Seed, Feed, Labor, etc)

4. CONCLUSIONS

In this study, the effect of changes in food and producer prices on inflation was investigated. Food and agricultural products included in the inflation basket have been taken into consideration. In particular, price and weight changes in under protective products that are effective in winter are considered important. Calculations was made taking into account the price volatility in seasonal products and the changes resulting from the weight of these products. It was accepted that only underground production is effective for the first three months of 2017 (January, February, March). Monthly prices were found to change monthly if they did not change. Since the weight of agricultural products in the basket is high, these products have a positive or negative influence on inflation. Despite very low consumption in the relevant months, inflation was found to have a high impact. Although the monthly prices did not change, it was seen that the price changed due to monthly changes in product weights. Although the weight of tomatoes, peppers, cucumber, eggplant, fresh beans and squash in the food was 6.63%, the effect on food inflation was 66,96%. The fact that the data compilation times of all three indices are different shows that comparison is not healthy. The use of fixed weights in seasonal products has caused unrealistic price increases in food inflation for products with monthly variability. The increase in food prices was not due to the increase in producer prices, but was attributed to subsequent marketing channels from the manufacturer.

Other factors effecting inflation; Supply chain, Marketing channels, Logistic support, Stock control, Production planning.

Factors affecting price change;

From the weight of the article, Time-sourced, Based on data quality, Product quality, Classification Measurement unit, Marketing process originated (Retail, Wholesale), Cost-based, (Fuel, etc.), Quantity-sourced, Sources of natural causes,

According to the results obtained, the weight of the food basket needs to be re-examined. In particular, it is necessary to re-weight the uncovered products considering the monthly consumption and considering the monthly sales figures. It is unacceptable that agricultural products in the basket of food have a great influence on the country's economy with such low consumption. In addition, agricultural product prices are not the only factor triggering inflation, but are also caused by problems in the supply chain from producer prices. It is to be ensured that the data collection times of all three indices and the index base years are the same.

ACKNOWLEDGMENT

REFERENCES

[1]. www.turkstat.gov.tr
[2]. www.tcmb.gov.tr
[3]. http://ec.europa.eu/eurostat.
[4]. Harmonised index of consumer prices (HICP) (prc_hicp),Reference Metadata in Euro SDMX Metadata Structure (ESMS),Compiling agency: Eurostat, the statistical office of the European Union, 2016.
[5]. Regulation (EU) 2016/792 of the European Parliament and of the Council of 11 May 2016 on harmonised indices of consumer prices and the house price index, and repealing Council Regulation (EC) No 2494/95 (Text with EEA relevance**)**, 2016.
[6]. Commission Regulation (EC) No 1334/2007 of 14 November 2007 amending Regulation (EC) No 1749/96 on initial implementing measures for Council Regulation (EC) No 2494/95 concerning harmonised indices of consumer prices (Text with EEA relevance), Official Journal of the European Union, 2007.
[7]. Commission Regulation (EC) No 330/2009 of 22 April 2009 laying down detailed rules for the implementation of Council Regulation (EC) No 2494/95 as regards minimum standards for the treatment of seasonal products in the Harmonised Indices of Consumer Prices (HICP) (Text with EEA relevance), Official Journal of the European Union, 2009.
[8]. Commission Regulation (EU) No 1114/2010 of 1 December 2010 laying down detailed rules for the implementation of Council Regulation (EC) No 2494/95 as regards minimum standards for the quality of HICP weightings and repealing Commission Regulation (EC) No 2454/97 (Text with EEA relevance), Official Journal of the European Union, 2010.
[9]. Handbook on industrial producer price indices (PPI), Eurostat, 2012.
[10]. Handbook for EU Agricultural Price Statistics, Eurostat, 2002.

BIOGRAPHY

Osman YILDIZ is an Assistant professor of Industrial Engineering Department at Karabuk University, Turkey. He is active in both teaching and research in the area of Quality engineering and engineering economy. Also, he is interested in Quality index and productivity, price and cost indices, management information systems.

Generation of a Multi-Layered Diffusion Coating on an Interstitial-Free Steel

Fikri Erdem Sesen[1], Omer Serdar Ozgen[2]

Abstract

Boronizing and titanium diffusion were applied to an interstitial-free steel substrate separately and one after another. Boronizing was carried out in a liquid environment by applying an electric current, but titanium diffusion was performed in a closed chamber containing solid chemicals. The generated single-layered and multi-layered diffusion coatings were characterised by utilising an optical microscope, a scanning electron microscope equipped with an energy dispersive spectrometer, and a Vickers microhardness tester. Phase analysis was carried out by an x rays diffractometer. Some chemical reactions were supposed to occur regarding titanium diffusion process and the standard formation enthalpies of these reactions were calculated by using a database. Microstructural investigations revealed that titanium diffusion was able to be applied after boronizing, causing the formation of a titanium based diffusion layer over the previously generated boride layer. On the other hand, when a titanium diffused substrate was boronized, the titanium based diffusion layer acted as a diffusion barrier to the introduced boron atoms, preventing the formation of a boride layer. However, if boronizing duration and the current density applied during boronizing were increased to a certain degree, boron atoms could surpass this barrier in small quantities and form small discontinuous regions. It was observed that the hardness of a phase which was formed within the titanium based diffusion layer was more than 4000 HV in some regions when titanium diffusion was applied after boronizing. The standard formation enthalpies of the six assumed chemical reactions were negative, indicating that these can occur at 1000 °C at which titanium diffusion was applied. Moreover, most of the products of these reactions were detected in x rays diffraction analyses.

Keywords: *Boronizing, Interstitial-Free Steel, Titanium Diffusion.*

1. INTRODUCTION

Surface modification techniques in several types are applied to steels in order to improve their hardness, mechanical strength, corrosion resistivity, resistivity to high temperature, etc. A group of these surface modification techniques involves the formation of an outer protective layer while another group is applied by diffusing an element through the cross-section of the substrate in a certain depth. The increase of the thickness is negligible in treatments related to diffusion. Boronizing (boron diffusion) is a type of latter-mentioned group of techniques. Boronizing is performed by diffusing elemental boron on to the substrate surrounded by a boronizing agent (source) which can be in solid, liquid, gaseous or even plasma state. Boronizing can be applied to almost all types of steels, titanium alloys and refractory metal alloys [1], [2].

Elemental titanium can be applied on to steel surface either as a protective coating or by diffusion. Titanium diffusion is generally performed before or after another surface treatment or as an intermediate stage between two different treatments [3].

Interstitial-free steel is a special type of steel possessing very little amount of alloying elements. Interstitials (carbon and nitrogen) are removed from solid solution through precipitation hardening. It is extensively used in cases where high ductility is desired [4].

This study aimed to investigate the resultant microstructure, phases and hardness that are achieved via boronizing and titanium diffusion applied separately or one after another. Moreover, some chemical reactions were introduced related to titanium diffusion process by the help of the x rays diffraction analysis results and the standard formation enthalpies of these reactions were calculated by using a database.

---

[1] *Corresponding author: Istanbul Technical University, Faculty of Chemistry-Metallurgy, Department of Metallurgical and Materials Engineering, 34469, Istanbul, Turkey. sesen@itu.edu.tr*

[2] *Istanbul Technical University, Faculty of Chemistry-Metallurgy, Department of Metallurgical and Materials Engineering, 34469, Istanbul, Turkey. sozgen@itu.edu.tr*

2. EXPERIMENTAL PROCEDURE

2.1. Samples

An interstitial-free steel was used as the substrate material. The chemical composition of the interstitial-free steel is given in Table 1. The steel plates were obtained after cold-rolling during the intermediate stages of the production held at Eregli Iron and Steel Works Co. (ERDEMİR) in Zonguldak, Turkey. The steel plates, having a thickness of 4 mm, were cut in to 50×23 mm dimensions and their surfaces were ground in order to eliminate any undesired matter before the diffusion coating processes.

Table 1. Chemical composition of the interstitial-free substrate.

Element	C	Si	Mn	P	S	Cr	Ni	Mo	Al	Ti	V	B
wt. %	0.0088	0.0110	0.2130	0.0136	0.0089	0.0250	0.0470	0.0010	0.0286	0.0597	0.0083	0.0004

2.2. Diffusion Coating Processes

Boronizing was performed electrothermochemically in a bath containing 100% dehydrated sodium borax which was melt in a chamotte crucible placed in a pit-type furnace which was heated to 900 °C. An electric current having a density of 0.10 or 0.40 A/cm^2 was applied during boronizing which lasted 45 or 120 minutes.

Titanium diffusion was carried out thermochemically in a one-use closed cylindrical chamber that contained micro-sized titanium particles, ammonium chloride and aluminium oxide. The chamber was heated in an electric-resistant furnace to 1000 °C and kept at this temperature for 2 hours. After that, it was left to cool down to room temperature.

2.3. Characterisation

Microstructural investigation was done by using an Olympus GX71 Optical Microscope and a Jeol JSM-7000F Field Emission Scanning Electron Microscope equipped with an energy dispersive spectrometer. The samples were metallographically prepared in a standard manner before the examinations. They were chemically etched with Nital3 solution before the optical investigations while coated with platinum and painted with silver chloride to be prepared for scanning electron microscope work. The phase analysis was carried out by utilising a Philips Pan Analytical X'Pert Professional type x rays diffractometer supplying CuKα radiation. The scanning was performed between 20 and 90 2θ values at a rate of 1° per min. The peaks on the patterns were identified manually by matching the related d values with the ones in the relevant indexes. A Future Tech FM 500 hardness tester was used in order to evaluate the hardness of the generated diffusion layers. A 50 gF load was applied for a dwelling time of 10 seconds. The standard formation enthalpies of the chemical reactions introduced about titanium diffusion process were calculated by using database HSC Chemistry Software v 6.12.

3. EXPERIMENTAL RESULTS

3.1. Results of Microstructural Investigations

A scanning electron microscope image showing the surface of the interstitial-free steel boronized at 900 °C for 45 minutes by applying a current density of 0.10 A/cm^2 is given in Figure 1. The stable boride phases of Fe_2B and FeB are visualised clearly in the image. Semi-quantitative chemical analysis values detected in the selected regions on the scanning electron microscope image are given in Table 2 in weight per cent.
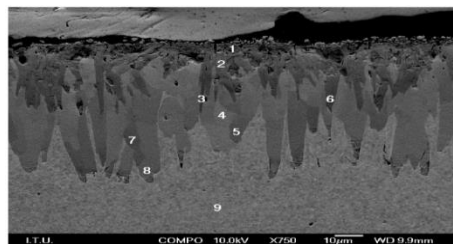

Figure 1. Scanning electron microscope image showing the surface of the interstitial-free steel boronized at 900 °C for 45 min by applying a current density of 0.10 A/cm2.

Table 2. Semi-quantitative weight per cent chemical analysis values detected in the selected regions numbered between 1 and 9.

Region	1	2	3	4	5	6	7	8	9
B% wt.	17.50	18.22	18.94	11.69	9.97	18.48	10.70	9.73	-
Fe% wt.	82.50	81.78	81.06	88.31	90.03	81.52	89.30	90.27	98.95
C% wt.	-	-	-	-	-	-	-	-	1.05

Another scanning electron microscope image showing the surface of the titanium diffused interstitial-free steel is given in Figure 2. Semi-quantitative chemical analysis values detected in the selected regions on the scanning electron microscope image are given in Table 3 in weight per cent.
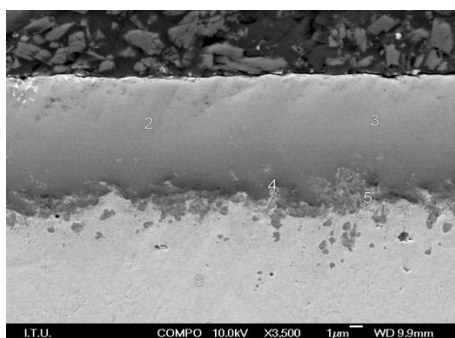

Figure 2. Scanning electron microscope image showing the surface of the interstitial-free steel titanium diffused at 1000 °C for 2 hours.

Table 3. Semi-quantitative weight per cent chemical analysis values detected in the selected regions numbered between 1 and 6.

Region	1	2	3	4	5	6
Al% wt.	7.08	1.30	-	2.85	2.32	-
Ti% wt.	46.88	98.70	100.00	72.03	71.53	-
Fe% wt.	46.05	-	-	25.12	26.15	100.00

The surface of the interstitial-free steel first boronized at 900 °C for 45 minutes by applying a current density of 0.10 A/cm^2 and then titanium diffused at 1000 °C for 2 hours can be viewed in another scanning electron microscope image given in Figure 3. Semi-quantitative chemical analysis values detected in the selected regions on the scanning electron microscope image are given in Table 4 in weight per cent.
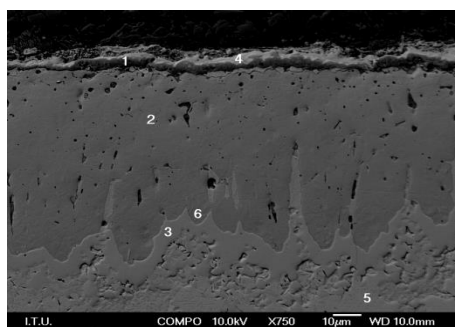

Figure 3. Scanning electron microscope image showing the surface of the interstitial-free steel first boronized at 900 °C for 45 min by applying a current density of 0.10 A/cm^2 and then titanium diffused at 1000 °C for 2 hours.

Table 4. Semi-quantitative weight per cent chemical analysis values detected in the selected regions numbered between 1 and 6.

Region	B% wt.	O% wt.	Al% wt.	Si% wt.	S% wt.	Ca% wt.	Ti% wt.	Mn% wt.	Fe% wt.	Ni% wt.
1	-	23.56	11.08	-	0.29	-	54.07	-	11.00	
2	6.70	-	-	-	-	-	-	2.32	90.99	
3	-	-	-	-	-	-	-	2.24	97.76	
4	-	6.19	2.44	0.92	-	1.21	72.98	-	7.45	8.80
5	-	-	-	-	-	-	-	1.92	98.08	
6	-	-	-	-	-	-	-	2.75	97.25	

The outer layer of the surface of the interstitial-free steel first boronized and then titanium diffused, by applying the above-mentioned parameters, can be visualised in more detail in the scanning electron microscope image given in Figure 4. Semi-quantitative chemical analysis values detected in the selected regions on the scanning electron microscope image are given in Table 5 in weight per cent.
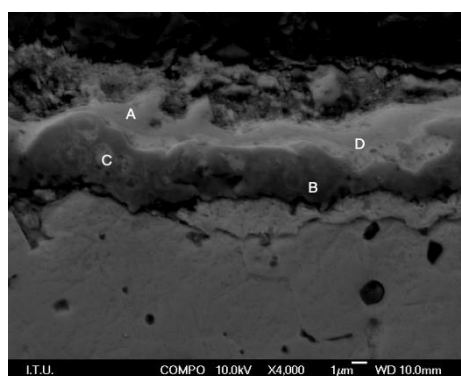

Figure 4. Scanning electron microscope image focusing on the outer surface (titanium based diffusion layer) of the interstitial-free steel first boronized at 900 °C for 45 minutes by applying a current density of 0.10 A/cm^2 and then titanium diffused at 1000 °C for 2 hours.

Table 5. Semi-quantitative weight per cent chemical analysis values detected in the selected regions named A-D.

Region	B% wt.	O% wt.	Al% wt.	Si% wt.	P% wt.	Ca% wt.	Ti% wt.	Fe% wt.	Ni% wt.
A	-	10.90	5.79	0.95	-	1.94	69.69	6.83	3.89
B	23.61	-	2.98	-	-	-	59.85	13.56	-
C	-	-	-	-	22.44	-	33.52	36.44	7.44
D	-	5.59	4.13	1.05	-	0.99	65.91	10.52	11.81

Another optical micrograph presenting the microstructure of the surface of the interstitial-free steel which was first titanium diffused at the above-mentioned parameters and then boronized at 900 °C for 45 minutes by applying a current density of 0.10 A/cm^2 is given in Figure 5. As can be seen in the micrograph, boronizing could not be accomplished after titanium diffusion.

Figure 5. Optical micrograph showing the surface of the interstitial-free steel first titanium diffused at 1000 °C for 2 hours and then boronized at 900 °C for 45 min by applying a current density of 0.10 A/cm² (Scale length: 10 µm).

The inhibiting effect of titanium based diffusion layer is visualised more clearly in Figure 6 where an optical migrograph showing two different surfaces of the interstitial-free steel which was first titanium diffused, then one surface cropped and finally boronized is given.
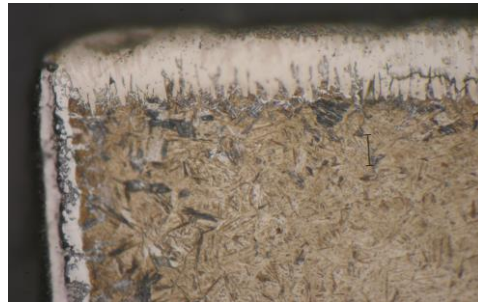
Figure 6. Optical micrograph of the interstitial-free steel showing the horizontal surface which was only boronized and the vertical surface which was first titanium diffused and then boronized (Scale length: 20 µm).

When the boronizing duration and the current density applied during boronizing carried out after titanium diffusion were increased to a certain degree, boron atoms were able to surpass the already generated titanium based diffusion layer. This phenomenon is visualised in an optical micrograph given in Figure 7 and a scanning electron microscope image given in Figure 8. Semi-quantitative chemical analysis values detected in the selected regions on the scanning electron microscope image are given in Table 6 in weight per cent.
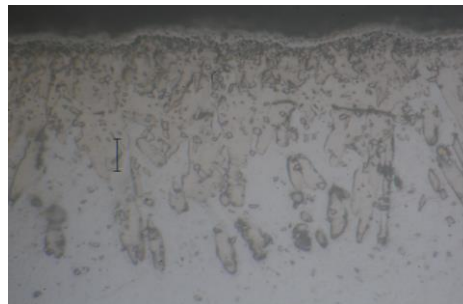

Figure 7. Optical micrograph of the surface of the interstitial-free steel titanium diffused at 1000 °C for 2 hours and then boronized at 900 °C for 120 min by applying a current density of 0.40 A/cm² (Scale length: 10 µm).
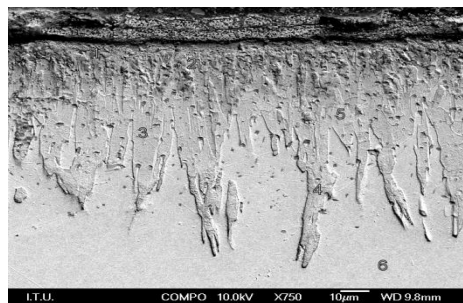

Figure 8. Scanning electron microscope image of the surface of the interstitial-free steel first titanium diffused at 1000 °C for 2 hours and then boronized at 900 °C for 120 min by applying a current density of 0.40 A/cm².

Table 6. Semi-quantitative weight per cent chemical analysis values detected in the selected regions numbered between 1 and 6.

Region	1	2	3	4	5	6
B% wt.	31.22	2.11	-	-	-	-
Al% wt.	0.51	-	-	0.29	0.38	-
Ti% wt.	48.13	0.34	0.20	0.56	0.37	-
Fe% wt.	20.15	97.55	99.80	99.16	99.25	100.00

3.2. Results of X Rays Diffraction Analyses

The pattern of the x rays diffraction analysis, obtained by scanning the diffusion layer formed on the surface of the interstitial-free steel that was boronized at 900 °C for 45 minutes by applying a current density of 0.10 A/cm^2, is shown in Figure 9. Stable boride phases of Fe$_2$B and FeB were detected on the scan as well as a metastable boride phase of Fe$_3$B. The pattern of the x rays diffraction analysis, obtained by scanning the diffusion layer formed on the surface of the interstitial-free steel that was titanium diffused at 1000 °C for 2 hours, is given in Figure 10. Phases of titanium iron, iron nitride and titanium nitride were detected in the scan in different stoichiometric ratios. The pattern of the x rays diffraction analysis, obtained by scanning the diffusion layer formed on the surface of the interstitial-free steel that was first boronized at 900 °C for 45 minutes by applying a current density of 0.10 A/cm^2 and then titanium diffused at 1000 °C for 2 hours, is presented in Figure 11. Stable boride phases of Fe$_2$B and FeB, iron nitride, titanium iron, titanium nitride and boron nitride were detected in the scan. Finally, the pattern of the x rays diffraction analysis, obtained by scanning the diffusion layer formed on the surface of the interstitial-free steel that was first titanium diffused at 1000 °C for 2 hours and then boronized at 900 °C for 120 minutes by applying a current density of 0.40 A/cm^2, is given in Figure 12. Stable boride phases of Fe$_2$B and FeB, metastable boride phase of Fe$_3$B, boron nitride, titanium diboride, titanium nitride and iron nitride in three different stoichiometric ratios were detected in the scan.
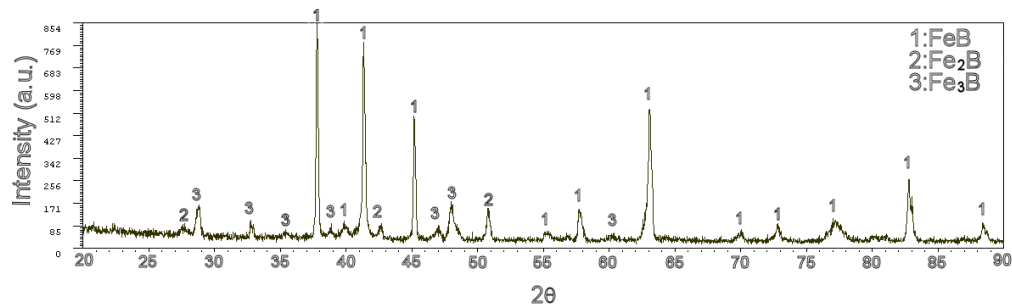

Figure 9. X rays diffraction pattern of the surface of the interstitial-free steel boronized at 900 °C for 45 min by applying a current density of 0.10 A/cm^2.
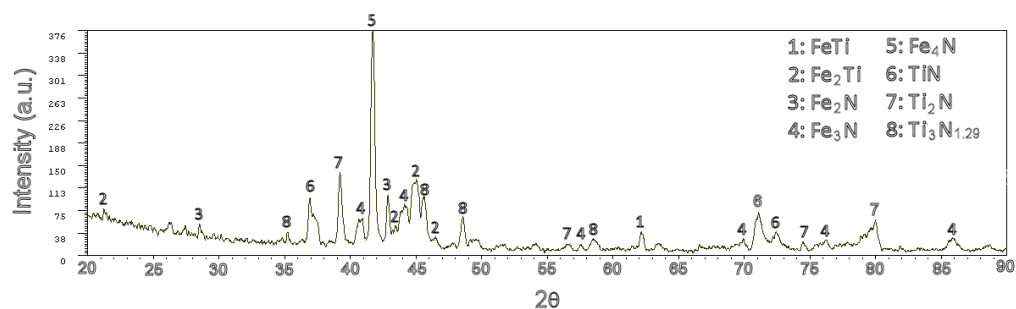

Figure 10. X rays diffraction pattern of the surface of the interstitial-free steel titanium diffused at 1000 °C for 2 hours.
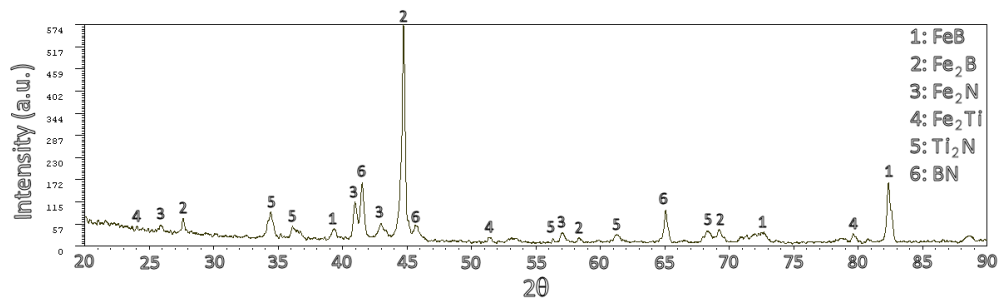
Figure 11. X rays diffraction pattern of the surface of the interstitial-free steel first boronized at 900 °C for 45 min by applying a current density of 0.10 A/cm^2 and then titanium diffused at 1000 °C for 2 hours.
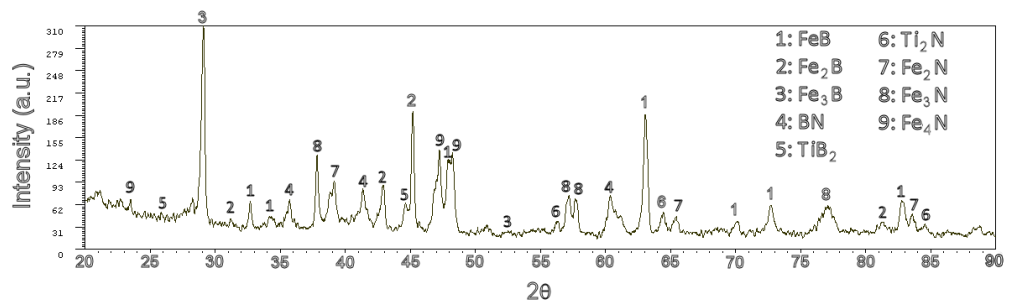

Figure 12. X rays diffraction pattern of the surface of the interstitial-free steel first titanium diffused at 1000 °C for 2 hours and then boronized at 900 °C for 120 min by applying a current density of 0.40 A/cm^2.

3.3. Results of Hardness Measurements

Figure 13. Optical micrograph presenting the difference of hardness between the substrate and the boride layer generated as a result of boronizing (Scale length: 20 μm).

An optical micrograph showing the boride layer generated as a result of boronizing after which Vickers hardness testing was applied is given in Figure 13 in order to present the hardness difference between the boride layer and the substrate considering the size of the indentation traces. The diagram shown in Figure 14 presents the change of hardness with respect to the distance from surface and the applied current density. Two other optical micrographs showing the outer layer of the diffusion coating on the surface of the sample which was first boronized and then titanium diffused are given in Figures 15 (a) and 15 (b). The size of the indentation traces indicates the extremely high hardness of a phase within the titanium based diffusion layer, which was formed as a result of titanium diffusion carried out after boronizing. Hardness values over 4000 HV were detected in this phase.
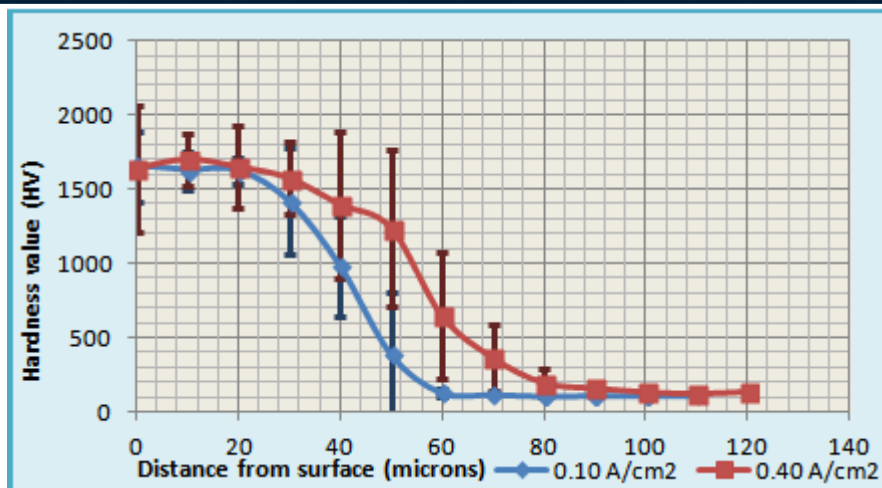
Figure 14. Change of hardness with respect to the distance from surface and the applied current density in case of merely boronizing at 900 °C for 45 min.

(a)   (b)
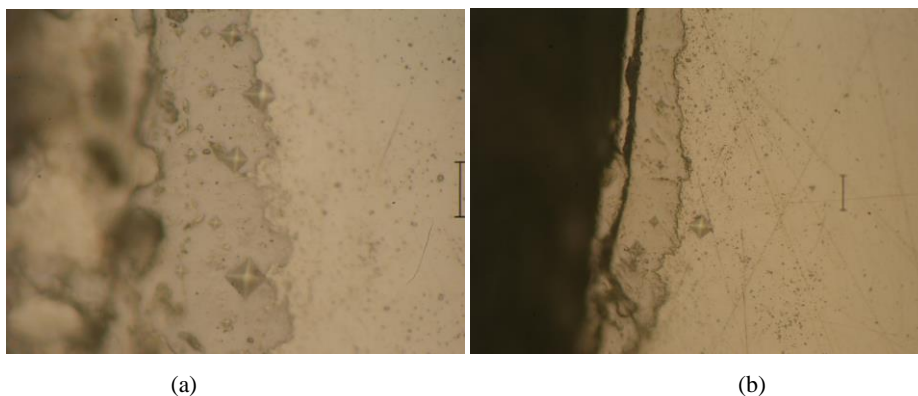
Figure 15. The outer layer of the diffusion coating generated as a result of first boronizing and then titanium diffusion. The size of the indentation traces indicates the abundance of a very hard phase within the titanium based diffusion layer (Scale length: 20 μm).

3.4. Results of Thermodynamic Calculations

Six chemical reactions were supposed to occur related to titanium diffusion process. They are written on the right side of Figure 16 and the standard formation enthalpies of five of them with respect to temperature are presented in a diagram on the left side of Figure 16. It is already known that the standard formation enthalpy of the first chemical reaction is negative over approximately 380 °C indicating that ammonium chloride decomposes into ammonia and hydrochloric acid [5]. It is concluded that, at normal atmospheric pressure, all of these six chemical reactions can occur at 1000 °C at which titanium diffusion was performed.

$$4Fe+2NH_{3(gas)}=2Fe_2N+3H_{2(gas)} \quad (5)$$
$$2NH_{3(gas)}=N_{2(gas)}+3H_{2(gas)} \quad (3)$$
$$2Fe_2N+4Ti=4FeTi+N_{2(gas)} \quad (6)$$
$$2Ti+2NH_{3(gas)}=2TiN+3H_{2(gas)} \quad (2)$$
$$2Fe_2N+4Ti=4FeTi+N_{2(gas)} \quad (4)$$
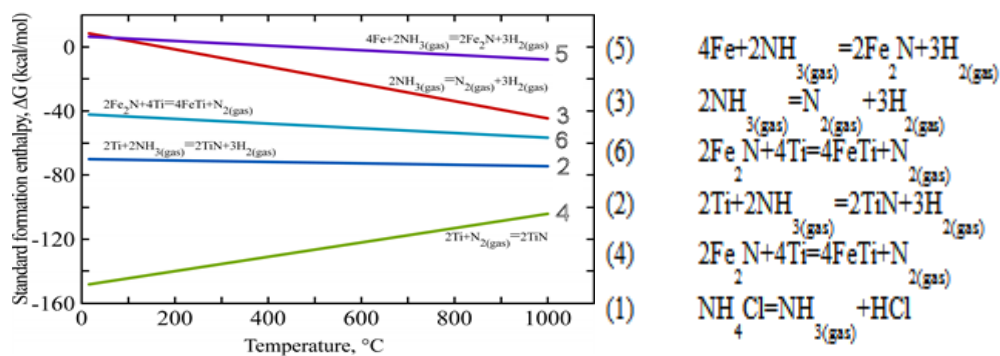$$NH_4Cl=NH_{3(gas)}+HCl \quad (1)$$

Figure 16. Six chemical reactions assumed to occur during titanium diffusion process and the standard formation enthalpies of five of them with respect to temperature.

4. CONCLUSION

In this study, multi-layered diffusion coatings were generated via diffusion of boron and titanium on an interstitial-free steel and the mechanism of titanium diffusion was tried to be revealed by introducing six chemical reactions. Titanium was easily diffused over the already generated boride layer in case of first boronizing and then titanium diffusion, but boron atoms could surpass the already formed titanium based diffusion layer in small quantities only if boronizing duration and the current density applied during boronizing were increased. A metastable phase of Fe_3B was detected in the boride layer, as well as the stable phases of Fe_2B and FeB. Abundance of a very hard phase with a hardness degree of over 4000 HV was determined within the titanium based diffusion layer that was generated over the boride layer.

REFERENCES

[1] A. K. Sinha, *Heat Treating: Boriding (Boronizing) of Steels*, ser. ASM Materials Handbook. Materials Park, OH, USA: ASM Int., vol. 4, pp. 978-997, 1995.

[2] J. R. Davis, *Surface Hardening of Steel: Understanding the Basics*: Boriding. Materials Park, OH, USA: ASM Int., pp. 213-226, 2002.

[3] N. Gidikova, "Thermodiffusion Treatment of Steel with Ti Thermodynamics and Phase Composition," *Mater. Sci. & Eng. A*, vol. 222, pp. 84-90, 1997.

[4] K. Dutta and K. K. Ray, "Ratcheting Strain in Interstitial Free Steel," *Mater. Sci. & Eng. A*, vol. 575, pp. 127-135, 2013.

[5] "ID: C1-103 Material Safety Data Sheet: Ammonium Chloride," Chem. One, Houston, TX, USA, 2010.

The Effect of Ultrasound Intensity on Polyethylene Oxide Chain Scission

Onur İnan[1], Ali Akyuz[1], Omer Aydogan[2]

Abstract

Ultrasound has various usage areas in the polymer industry. In academic means, polymer chain scission is the most important in these areas. When ultrasound is applied to the polymer solutions, cavitation bubbles are produced in the solution and the resulting hydrodynamic forces cause the polymer chains to scission and thus reduce the viscosity. Polyethylene oxide is a water-soluble and non-ionic polymer. Generally it is used as a rheological control agent in solutions and drug release-protein adsorption in biomedical applications. Molecular weight is an important parameter in these applications. In this study, the effect of ultrasound intensity on the solution of polyethylene oxide (Mw = 1000000 g / mol) has been investigated. The ultrasound frequency (20 kHz), temperature (25 ^{0} C), polymer concentration (0.001 g / mL) have been kept constant and the ultrasonic amplitude has been changed to 20,50,80,100 %. The polyethylene oxide chain scission has been characterized by the time-dependent change in specific viscosity of the solution. The results have also been analyzed with the theoretical Giz model.

Keywords: *Ultrasound, Polyethylene Oxide, Chain Scission*

1. INTRODUCTION

The ultrasound has a frequency range from 20 kHz to 10 MHz that the human ear can not hear. Ultrasound has two different fields of use: high frequency / low intensity and low frequency / high intensity according to frequency and intensity values. Low intensity ultrasound does not cause any change in materials and is used as an analytical technique in researches. High-intensity ultrasound can cause physical and chemical changes in a material. This type of use is called sonochemistry in the literature. Sonochemistry is used in a wide range of both academic and industrial sense, such as physics and various fields of chemistry, material science, food engineering. When a low-frequency high-intensity ultrasound passes through a liquid medium and a sufficiently strong negative pressure is applied during the expansion phase, the critical distance between the liquid molecules is exceeded and bubbles form in the liquid and collapse severely at one point. This event is called the cavitation phenomenon. [1-5]

The first effect of ultrasound application (sonication) on polymer solutions is polymer chain scission (polymer degradation). In the classical term, the degradation is the alteration of the chemical structure. In polymer technology it means a decrease in molecular weight or a decrease in the viscosity of the polymer solution. How the polymer chains in the solution break down during the sonication process is a debate among investigators in this issue. However, in recent years it has been concluded that chain breaking occurs due to ultrasonic cavitation and hydrodynamic forces [6-8].

Unlike chemical, thermal, enzymatic and photo polymer degradation methods, the scission of polymer chains by ultrasound is a non-random mechanism. The polymer chains in the solution (if there is a relatively weaker bond in the chain) are broken off from adjacent bonds to middle of the chain. In the initial stages of the sonication, long polymer chains are broken and chain breakage is rapid, then it slows down and approaches a limit value (limit molecular weight). The existence of this limit value indicates that chain breakage does not occur after this value. Ultrasonic chain scission does not result in monomer and oligomer formation, i.e. the polymer obtained at any moment of breaking is similar to the starting polymer, but the chain is shorter and the side chain reactions do not occur, provide various advantages according to their usage areas.

Polyethylene oxide is named as polyethylene glycol or polyoxyethylene. In general, the lower molecular weight one is defined as polyethylene glycol and those of high molecular weight are also referred to as

polyethylene oxide. Polyethylene oxide is generally a polymer used for drug release in solution and in the pharmaceutical and cosmetics industries [9]. In the pharmaceutical sector, polyethylene oxide sonication is frequently performed [10]. Vijayalakshmi and Madras (2005) investigated the initial molecular weight and solvent effect at constant temperature-concentration to polyethylene oxide chain scission [11]. Mehrdad , Rostami (2007) and Akyuz (2017) studied the effect of temperature and concentration on ultrasonic polyethylene degradation [8, 12]. Mehrdad (2008) reported the effect of HCl concentration on ultrasonic polyethylene oxide chain scission [13].

The ultrasonic chain scission of polymers influenced by several variables like temperature, frequency, solution concentration, molecular weight, solvent characteristics and ultrasound intensity [2-4,6,7].

To the best of our knowledge, no detailed study of investigating the effect of ultrasound intensity on polyetyhlene oxide degradation. In this study, the known initial molecular weight of polyethylene oxide in aqueous solution was sonicated at fixed concentration of 0.001 g / mL at 25 ° C for four different ultrasound intensities. So the effect of intensity on polyethylene oxide chain scission was investigated. The majority of degradation researches in the literature have been carried out the removal of samples from the sonication medium and determining their molecular weights. It was considered that the volume change could be important parameter instead of sampling from the sonication medium and individual sonication was applied to the polyethylene oxide solutions. The kinetic analysis of scission has been characterized by the change in specific viscosity of the samples. The specific viscosity data also have been analyzed on the basis of the theoretical Giz model [7].

2. MATERIALS and METHODS

Commercial Polyetyhylene Oxide (Mw = 1000000 g/mol, Sigma-Aldrich) and distilled water were used in this study. Distilled water was filtered by 0.45 µm econo-filters. A 50 mL round-bottom flask was selected as the sonication cell. The temperature was kept constant at 25 ^{0}C and polymer concentration was arranged 0.001 g/mL for all sonication experiments. Sonication was carried out using Sonopuls Ultrasonic Homogenizer GM-3100 Bandelin Sonopuls at a nominal frequency of 20 kHz. Ultrasound probe was immersed to 2 cm into the solution. On supplier information, for micro-tip MS 73 probe pressure amplitude arranged at 100% leads to an amplitude of 245 µm for the highest power output. Four amplitudes 20 % (49 µm) , 50% (122.5 µm), 80% (196 µm), 100% (245 µm) were selected in this study. For these amplitudes, the ultrasound intensities (I) were determined calorimetrically based on approach (equation 1) presented by Price [3]. In equation m = 50 g is the sample mass, c= 4.18 J/g 0C is the heat capacity of the solution, (dT/dt) is the time-dependent change of sample temperature, and r = 0.003 m is the radius of MS 73 probe. The intensity values obtained from equation (1) are 19.20, 25.94, 31.57, 34.60 W/cm2, respectively.

$$I = \frac{mc}{\pi r^2}\left[\frac{dT}{dt}\right] \tag{1}$$

Samples were subjected to sonication at 5-15-30-45-60-75-90-105-120-135-150 minutes to avoid volume change instead of withdraw sample from reaction medium. It is thought that the volume change can affect the sonication environment and the results.

For specific viscosity measurements, a capillary with a length of 20 cm and a radius of 0.025 cm connected to a Validyne Engineering DP15-28 pressure transducer was used. The voltage output of the converter is proportional to the pressure change. The detailed technique of specific viscosity measurement has been described in reference 7.

3. RESULTS and DISCUSSION

Various mechanisms and mathematical models have been developed to explain how ultrasound breaks down the polymer chains in solution. At the beginning of the sonication, the polymer chain breaks fast, then decelerates to a limit value in general, common in these models. The polymer that reaches the limit molecular weight value will no longer be affected by the ultrasound effect. Another important parameter that defines polymer chain scission is scission constant. This constant gives information about the effect of chain scission. According to Giz model, ultrasonic chain scission has heterogeneous nature. First, the long chains begin to break quickly and then the degradation is slowed down to a limit value. The degradation process has a variety of time constants. This variation is described in the form of the stretched exponential (equation 2).

$$\eta_{sp,t} = \eta_{sp,lim} + \left(\eta_{sp,in} - \eta_{sp,lim}\right)e^{-(k_G t)^\beta} \tag{2}$$

Here $\eta_{sp,t}$ is the specific viscosity at sonication time t, the initial specific viscosity is denoted as $\eta_{sp,in}$ and the limit specific viscosity as $\eta_{sp,lim}$. The scission constant for the Giz model is denoted by k_G and stretch factor is β.

Specific viscosity changes in ultrasonic polyethylene oxide scission experiments are given in Figure 1. Initial specific viscosity was determined to be 0.45 for 1×10^{-3} g / mL. Viscosities appear to decrease rapidly in the initial phases of the sonication in four different ultrasound intensity and then approach the limit values.
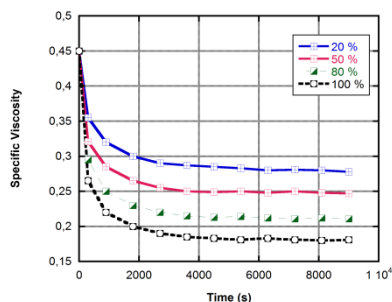

Figure 93. Specific viscosity evolution data for all experiments.

Figures 2, 3 and 4 show that the viscosity values are compared with the Giz model using the nonlinear curve fitting method, respectively. $R^2 = 0.998$ for 19.20 W/cm^2, $R^2 = 0.998$ for 25.94 W/cm^2, $R^2 = 0.997$ for 31.57 W/cm^2 and $R^2 = 0.998$ for 34.60 W/cm^2. As can be seen from the R^2 values, it is consistent with the experimental data of the Giz model.

Figure 2. The prediction of the Giz model and experimental data for I=19.20 W/cm².

Figure 3. The prediction of the Giz model and experimental data for I=25.94 W/cm².

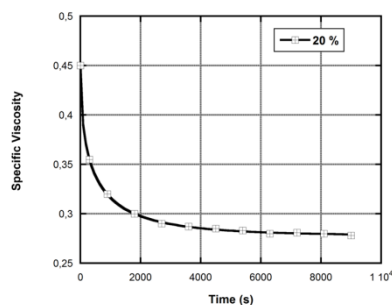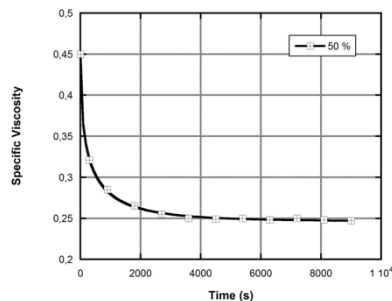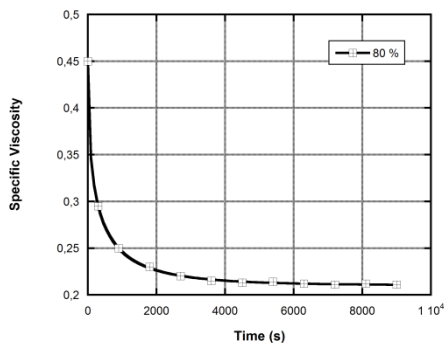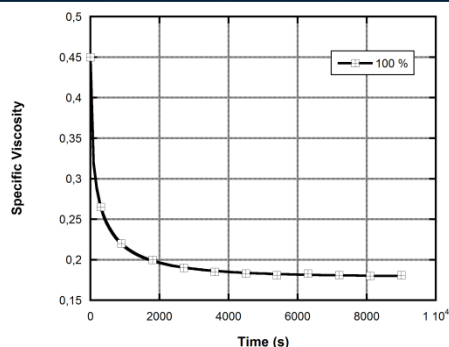*Figure 4. The prediction of the Giz model and experimental data for I=31.57 W/cm².*

Figure 5. The prediction of the Giz model and experimental data for I=34.60 W/cm².

In the Giz model, limit specific viscosities of 0.277, 0.246, 0.209 and 0.178 were reached, respectively. In addition, the Giz scission constants were found to be 0.00216, 0.00325, 0.00356, 0.00444 s^{-1}.

Figure 6 shows the variation of scission constants according to ultrasonic intensity obtained from Giz model. The highest scission constant for 34.60 W/cm^2 ultrasound intensity was obtained and the lowest scission constant for 19.20 W/cm^2 was obtained. As it is definitely predicted, a higher intensity of ultrasound gives rapid degradation including a lower limiting viscosity. A representation of this situation is shown in Figure 7. The limit viscosity is a linear function of the ultrasound intensity with the expression $\eta_{lim} = 0.402-0.0062xI$, $R^2 = 0.975$.
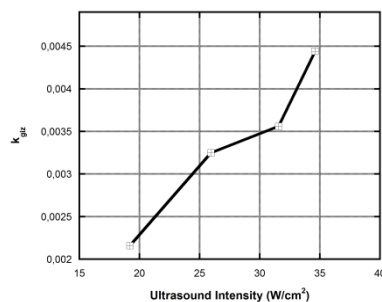
Figure 6. The scission constants for Giz model versus ultrasound intensity.
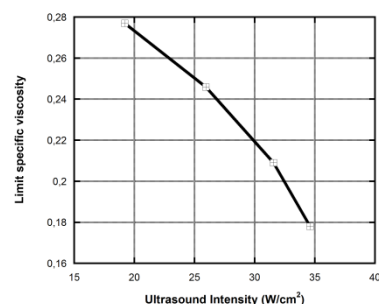
Figure 7. The limit specific viscosities for Giz model versus ultrasound intensity.

4. CONCLUSIONS

The effect of ultrasound intensity on the chain scission of polyethylene oxide is presented in this study. It can be concluded that the extent of chain scission and the specific viscosity reduction are affected by changing of intensity. The ultrasound converts electrical energy into mechanical energy. This energy is next to transferred into polymer solution. If ultrasound intensity is increased, the cavitation bubbles in polymer solution grow in size and also the number density of bubbles increase. In this way the hydrodynamic forces on polymer chains increase so that the chain scission becomes more faster. The scission rate has been found to be higher for 34.60 W/cm^2 intensity as compared to 19.20 W/cm^2 intensity about two times. The experiments also shows that the limit specific viscosity is found to be reasonably sensitive to ultrasound intensity.

REFERENCES

[1].   M.Schaefer, B. Icli, C. Weder, M.Lattuada, A. F. M. Kilbinger and Y. C. Simon, "The role of mass and length in the sonochemistry of polymers," *Macromolecules*, vol. 49, pp.1630-1636, Feb. 2016.

[2].   T. Wu, S. Ziwanovic, D. G. Hayes and J. Weiss, "Efficient reduction of chitosan molecular weight by high-intensity ultrasound: underlying mechanism and effect of process parameters," *J. Agric. Food. Chem.*, vol. 56, pp.5112-5119, June 2008.

[3].   M. R. Kasai, "Input power-mechanism relationship for ultrasonic irradiation: food and polymer applications," *Natural Science*, vol.5, pp.14-22, July 2013.

[4].   S. Koda, K. Taguchi, K. Futamura. "Effect of frequency and a radical scavenger on ultrasonic degradation watersoluble polymers," *Ultrason. Sonochem.*, vol. 18, pp. 276-281, June 2011.

[5].   A. Akyüz, H. Giz and A. Giz, "Kinetics of ultrasonic polymer degradation: Comparison of theoretical models with on-line data," *Macromol. Chem. Phys.*, vol. 209, pp. 801-809, Apr. 2008.

[6].   A. Akyüz, H. Giz and A. Giz, "Effect of solvent characteristics on the ultrasonic degradation of poly(vinylpyrrolidone) studied by on-line monitoring," *Macromol. Chem. Phys.,* vol. 210, pp. 1331-1338, Aug. 2009.

[7].   A. Akyüz, O. Kamer and A. Giz, "Online viscometric monitoring of ultrasonic sodium poly(styrene sulfonate) scission,"*J. Macromol. Sci., Pure Appl. Chem.*, vol. 50, pp. 535-540, Apr. 2013.

[8].   A. Akyüz, "Polietilen Oksitin Ultrasonik Zincir Kırılması: Konsantrasyon ve Sıcaklık Etkisi", *AKU Femubid*, vol. 17, pp. 109-106, Feb. 2017.

[9].   S. C. Smolinske, *Handbook of Food, Drug and Cosmetic Excipients*, Denver, USA: CRC Press, 1992.

[10].   V. S Murali, R. Wang, C. A. Mikoryak, P. Pantano, R. Draper "Rapid detection of polyethylene glycol sonolysis upon functionalization of carbon nanomaterials," *Exp. Bio. Med.* , vol. 240, pp. 1147-1151, 2015.

[11].   S. P. Vijayalakkshmi   and G. Madras "Effect of initial molecular weight and solvents on the ultrasonic degradation of polyethylene oxide," *Polym. Degrad. Stab.*, vol. 90, 116-122, Oct. 2005.

[12].   A. Mehrdad and M. R. Rostami "Effect of temperature and solution concentration on the ultrasonic degradation of the aqueous solutions of polyethylene oxide*," Iran. Polym. J.*, vol. 16, pp. 795-801. Nov. 2007.

[13].   A. Mehrdad, "Effect of HCl and solution concentration on the ultrasonic degradation of aqueous solutions of polyethylene oxide," *J. Polym. Eng.*, vol. 28, pp. 597-610, Dec. 2008.

[14].   M. Duval and E. Gross, "Degradation of polyethylene oxide in aqueous solutions by ultrasonic waves," *Macromolecules*, vol. 46, pp. 4972-4977, June 2013.

[15].   F. Kanwal, and R. A. Pethrick, "Ultrasonic degradation studies of poly(ethylene oxide), poly(ethylene adipate) and poly(dimethyllsiloxane)," *Polym. Degrad. Stab.*, vol. 84, pp. 1-6, Apr. 2004.

[16].   S. P. Vijayalakkshmi and G. Madras, "Effect of temperature on the ultrasonic degradation of polyacrylamide and polyethylene oxide," *Polym. Degrad. Stab.*, vol. 84, pp. 341-344, May 2004.

The Heavy Metal Effects of Mineralization and Alteration Areas with Buried Ore Deposits Potential on the Surface Waters

Alaaddin Vural[1], Ali Gundogdu[2]; Fatih Saka[3]; Volkan Numan Bulut[4]; Selcuk Alemdag[1], Mustafa Soylak[5]

Abstract

This paper aims at elucidating the potential environmental risks associated with ore deposits and alteration areas related to these mineralizations by quantifying contamination in stream waters in the areas. For this purposes, 21 surface water samples were collected the streams and analyzed for heavy metals. Concentrations of heavy metals in surface waters reached 160 μg/L for Al, 2886,4 μg/L for Mn, 13147 μg/L for Fe, 58,18 μg/L for Co, 1644 μg/L for Zn, 100 μg/L for Cu, 2376 μg/L for Sr, 770 μg/L for Ba and 96,70 μg/L for Pb. In addition, a high arsenic, cobalt, cadmium values were detected in some locations. Some other heavy metals are below the limit of detection.

As a result of the study done, alteration areas with buried ore deposits potential and ore deposit areas have been found to cause heavy metal contamination in the surface waters around these environments, therefore, more detailed studies should be done on such fields and necessary precautions should be taken in order to avert the dispersal of contamination sourced that areas.

Keywords: *Heavy metal contamination, alteration area, surface water, Gumushane*

1. INTRODUCTION

The Arzular-Kabakoy, Kaletas, Dolek and its surrounding areas are either mineral deposits or alteration areas with buried mineralization potential. All these areas have intense alteration and are situated at the east of the Gumushane city (NE Blacksea Region) (Fig. 1). The area is located at the southern zone of the Black Sea Tectonic Unit. In the area, it can be observed all stratigraphic units of the region. If the general geology of the site is mentioned, the basement geological unit of the area consists of pre-Jurassic metamorphic rocks [1] and unmetamorphosed granitoids [2]–[4]. These basement units are unconformably overlain by an early to middle Jurassic volcani-clastic unit which passes upward to the late Jurassic and early Cretaceous carbonate rocks. In the area late Cretaceous clastic unit begins with sandy limestones at the bottom and grades upward to red pelagic limestone and then to a turbiditic series which conformably overlie carbonates. All these units - outside of the study area- were cross cut by late Cretaceous intrusions [5]. The Eocene volcanic and volcaniclastic rocks overlie the late Cretaceous volcanic and/or sedimentary rocks with an angular unconformity [6], and intruded by calc-alkaline granitoids of same age [7]–[9]. In the study area, dominantly Eocene volcanic-clastic rocks are outcrop and these unit is intense altered and host some epithermal ore deposits such as Arzular gold deposits.

[1] *Corresponding author: Gümüshane University, Department of Geological Engineering, 29000, Baglarbası/Gümüshane, Turkey. alaaddinvural@hotmail.com*

[2] *Gümüshane University, Department of Food Engineering, 29000, Baglarbası/Gümüshane, Turkey*

[3] *Gümüshane University, Department of Civil Engineering, 29000, Baglarbası/Gümüshane, Turkey*

[4] *Karadeniz Technical University,*

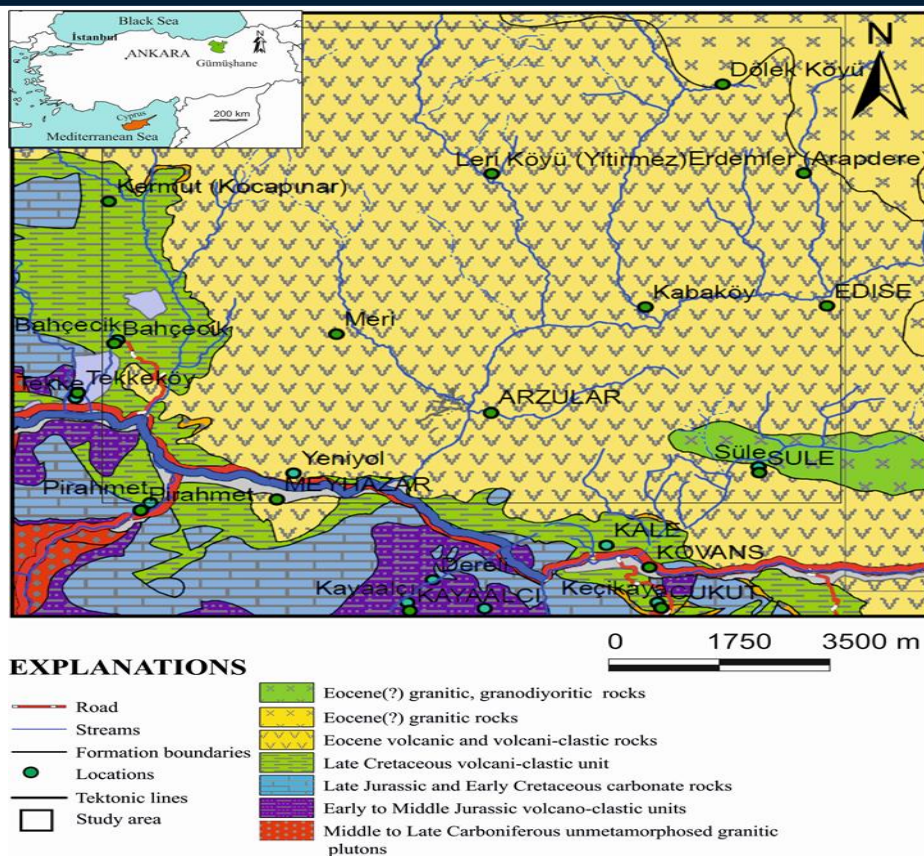[5] *Erciyes University, Faculty of Science, Chemistry.*

Figure 1. Geological and location map of the study area (after Guven [10]).

Mineral/ore deposits are important for development of countries but also they have contamination or pollution risk for remote areas as far as the surrounding areas.

The aim of the study is to assess of the effects of Arzular-Kabakoy, Kaletas, Dolek and its surrounding areas - which are either mineral deposits or alteration areas with buried mineralization potential- on the surface waters of the area.

2. MATERIAL AND METHOD

2.1. Sampling and Analysis

For elucidating the potential environmental risks associated with mineralization and alteration areas with buried ore deposits potential by quantifying contamination in stream waters in the areas, 21 surface water samples were collected the streams (Fig. 2) and analyzed for heavy metals by Inductively Coupled Plasma-Mass Spectrometry (ICP-MS) at Gumushane University Central Research Laboratory, Gumushane, Turkey. Water pH measurements were also performed on the area.

Surface water samples were taken using plastic bottles with a volume of 500 mL and then bottles were labeled and brought to the laboratory. As soon as the water samples were taken for metal analysis, it was acidified with ultrapure HNO_3 to 1 mL of concentrated acid. The water samples were also purified from the dust-soil-sludge using 0.45 μm nitrocellulose membrane in the laboratory.
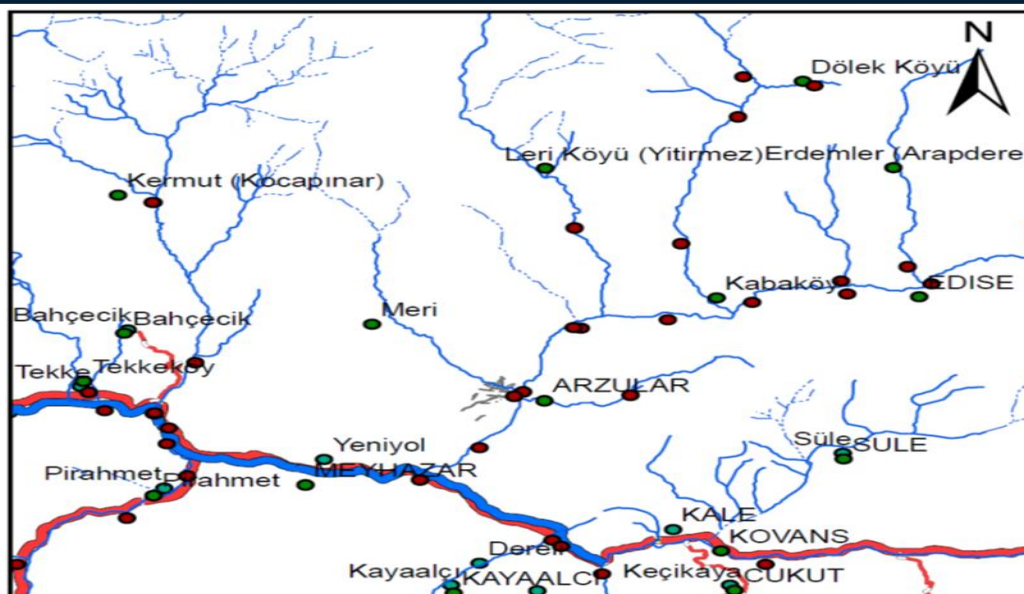
Figure 2. Water sampling locations (Purple circles are sampling locations)

After the samples were prepared for analysis, they were analyzed for some heavy metal/trace elements (HMTEs) using ICP-MS at Gumushane University Central Laboratory.

3. RESULT AND DISCUSSION

It has been found that the pH values of the waters vary between 7,02 to 8,68. According to this values, waters are between slightly neutral and generally basic but some of them are near acidic in especially intense altered areas such as Lerikoy etc.

Surface water element contents range from (as µg/L) 33 to 2886 for Mn, 89 to 13147 for Fe, 36 to 2032 for K, 13,9 to 100,2 for Cu, 226 to 1644 for Zn, 659 to 2376 for Sr, 9,9 to 16,1 for Rb, 13,8 to 770,4 for Ba, 10,10 to 96,7 for Pb, 7,20 to 137,90 for As, 6,60 to 6,70 only in 3 samples for Cd and 10,20 to 24,40 only 4 samples for Ni and 13,57 to 58,18 only in 3 samples for Co (Table 1, Fig. 3). Hg content of the waters were detected below the limit of detection.

The parameters of surface waters are compared with EPA water quality standards (Table 2). The surface water's pH values are within the standards but some HMTEs were above the EPA's standards. Mn values were found to be higher than EPA standards, especially at Dolek village alteration zone. As to Fe, those values are generally high in whole area. Co values were determined at only three points and these values were relatively high. Cd values were also determined at only three points. These values were close to the upper limit of the standard values. As values were determined at seven points in the area and all of these values are above the standard values. Pb values were close to upper limit of the EPA standards. The content of major elements such as Na, K, Ca, Mg and Al in water were determined within the limit values of EPA's surface water standards. Values of some HMTEs in surface waters such as Ni, Cu, Zn, Ba were also found within the limit values of EPA's.

Table 1. Descriptive statistics of the surface water samples

|	pH	Na	Mg	Al	K	Ca	V	Cr	Mn	Fe	Co	Ni	Cu	Zn	As	Rb	Sr	Cd	Ba	Pb
Mea.	8,02	7435,1	8452, 9	47,16	979,8	5407,96	26,36	20,70	392,30	1698,09	43,05	17,38	43,06	654,96	27,84	12,09	1249,96	6,63	279,47	50,19
Med.	8,07	6875	7337	25,30	1221,5	5736	13,45	20,7	114,60	473,00	57,41	17,45	32,50	501,00	7,80	11,40	1076,00	6,60	252,50	45,40
S.Dev.	0,43	3991,54	4010,85	48,35	542,4	3352,95	30,14	13,44	794,61	3721,30	25,54	7,89	24,03	346,04	48,62	2,07	483,15	0,06	191,42	32,75
Min	7,02	107	133	12,20	36	145	9,30	11,2	33,20	89,00	13,57	10,20	13,90	226,00	7,20	9,90	659,00	6,60	13,80	10,10
Max	8,68	16038	15042	160,00	2032	10153	115,40	30,20	2886,40	13147,00	58,18	24,40	100,20	1644,00	137,90	16,10	2376,00	6,70	770,40	96,70
Number	22	20	19	13	18	23	14	2	23	22	3	4	23	23	7	7	23	3	22	16
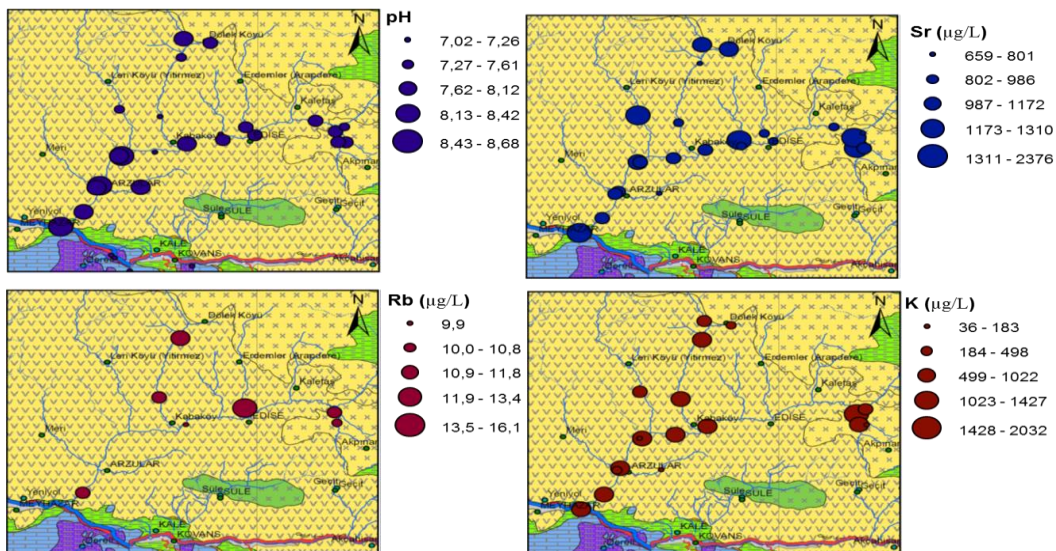
Figure 3. Dot distribution map of HMTEs
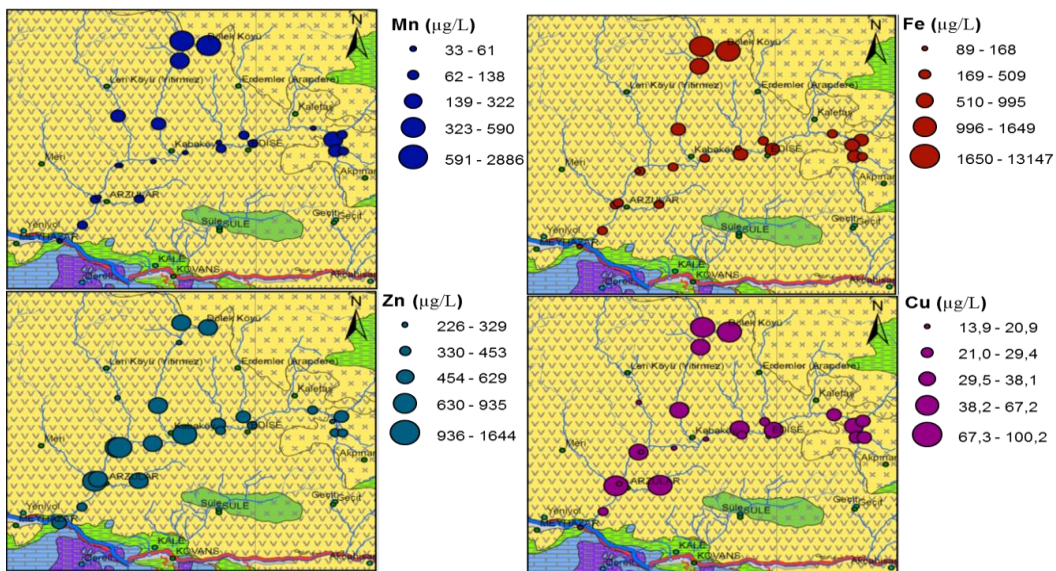
Figure 3 (continue)

Figure 3 (continue)

Table 2. EPA Water Quality Standards for some elements

		Drinking water	Surface water		
			A1	A2	A3
Al	µg/L	200	-	-	
As	mg/L		0,05	0,05	0,1
Ba	mg/L		0,1	1	1
Cd	mg/L		0,005	0,005	0,005
Ca	mg/L		-	-	-
Cr	mg/L		0,05	0,05	0,05
Co	mg/L		-	-	-
Cu	mg/L		0,05	0,1	1
Fe	mg/L	0,2	0,2	2	2
Pb	mg/L		0,05	0,05	0,05
Mg	mg/L		-	-	-
Mn	mg/L	0,05	0,05	0,3	1
Hg	µg/L	1	1	1	1
Mo	µg/L	-	-	-	-
Ni	µg/L	20	-	-	-
pH		6.5-9.0	5.5-8.5	5.5-9.0	5.5-9.0
K	mg/L	-	-	-	-
Se	mg/L	0,01	0,01	0,01	0,01
Na	mg/L	200	-	-	-
Sn	mg/L	-	-	-	-
Zn	mg/L	-	3	5	5

As a results, these findings point out that the surface waters in the Arzular-Kabakoy, Kaletas, Dolek and its surrounding areas were effected by some HMTEs such as Mn, Fe, Cd, Co and Pb. So ore deposit sites and related alteration areas with buried ore deposits potential have been found to cause heavy metal contamination in the surface waters around these environments, therefore, more detailed studies should be done on such fields and necessary precautions should be taken in order to avert the dispersal of contamination sourced that areas.

Studies on water quality parameters and other physical properties in the region are continuing. These data are the first to be obtained, when other data are obtained then they will be evaluated separately.

ACKNOWLEDGMENT

REFERENCES

[1]   G. Topuz, R. Altherr, W. H. Schwarz, A. Dokuz, and H. P. Meyer, "Variscan amphibolite-facies rocks from the Kurtoğlu metamorphic complex (Gumushane area, Eastern Pontides, Turkey)," Int. J. Earth Sci., vol. 96, no. 5, pp. 861–873, 2007.
[2]   Y. Yılmaz, "Petrology ancj structure of the Gumushane granite and surrounding rocks, NE Anatolia," 1972.

[3] G. Topuz, R. Altherr, W. Siebel, W. H. Schwarz, T. Zack, A. Has??zbek, M. Barth, M. Satir, and C. ??en, "Carboniferous high-potassium I-type granitoid magmatism in the Eastern Pontides: The Gumüshane pluton (NE Turkey)," *Lithos*, vol. 116, no. 1–2, pp. 92–110, 2010.

[4] A. Dokuz, "A slab detachment and delamination model for the generation of Carboniferous high-potassium I-type magmatism in the Eastern Pontides, NE Turkey: The Kose composite pluton," *Gondwana Res.*, vol. 19, no. 4, pp. 926–944, 2011.

[5] A. Kaygusuz, W. Siebel, C. Sen, and M. Satir, "Petrochemistry and petrology of I-type granitoids in an arc setting: The composite Torul pluton, Eastern Pontides, NE Turkey," *Int. J. Earth Sci.*, vol. 97, no. 4, pp. 739–764, 2008.

[6] M. Arslan and I. Aliyazicioglu, "Geochemical and petrological characteristics of the Kale (Gümüshane) volcanic rocks: Implications for the Eocene evolution of eastern Pontide arc volcanism, northeast Turkey," *Int. Geol. Rev.*, vol. 43, no. 7, pp. 595–610, 2001.

[7] O. Karsli, B. Chen, F. Aydin, and C. Sen, "Geochemical and Sr-Nd-Pb isotopic compositions of the Eocene Dolek and Saricicek Plutons, Eastern Turkey: Implications for magma interaction in the genesis of high-K calc-alkaline granitoids in a post-collision extensional setting," *Lithos*, vol. 98, no. 1–4, pp. 67–96, 2007.

[8] O. Karsli, A. Dokuz, I. Uysal, F. Aydın, R. Kandemir, and J. Wijbrans, "Generation of the Early Cenozoic adakitic volcanism by partial melting of Mafic Lower Crust, Eastern Turkey: implications for crustal thickening to delamination," *Lithos*, vol. 114, pp. 109–120, 2010.

[9] Y. Eyuboglu, M. Santosh, and S. L. Chung, "Crystal fractionation of adakitic magmas in the crust-mantle transition zone: Petrology, geochemistry and U-Pb zircon chronology of the Seme adakites, eastern Pontides, NE Turkey," *Lithos*, vol. 121, no. 1–4, pp. 151–166, 2011.

[10] İ. Güven, *Dogu Pontidlerin 1/25000 Olcekli Kompilasyonu*. Ankara: MTA Genel Müdürlügü, 1993.

BIOGRAPHY

Alaaddin Vural is an Associated Professor of Ore Deposits and Geochemistry at Gumushane University, Faculty of Engineering and Natural Sciences, Department of Geology Engineering. His work focuses specifically on the environmental geochemistry. His favorite place to do research is especially Gumushane Province which hosts a lot of ore deposits and alteration areas related to ore deposits and also has extended experience about west of Turkey's geology and ore deposits.

Selcuk Alemdag was born in 1979, in Trabzon. He is a Assist. Professor in Department of Geological Engineering of Faculty of Engineering at the University of Gumushane. His main area of interest are engineering geology, landslides, rock falls, dam site investigations, underground waters and waste landfills. He currently works on studying the body and reservoir area of waste dams and groundwater contamination.

The Heavy Metal Effects Of Alteration Fields On The Surface Waters: Saricicek (Gumushane-Turkey) And Its Near Vicinity

Alaaddin Vural[1], Ali Gündoğdu[2]; Fatih Saka[3]; Volkan Numan Bulut[4]; Selçuk Alemdağ[1], Mustafa Soylak[5]

Abstract

The objective of this study was to determine the potential heavy metal risks of the Sarıçiçek and its near vicinity (Gümüşhane in northeast Turkey) alteration area on the surface waters. The alteration area is situated at the east of the Gümüşhane City. In this study, 28 water samples collected from surface waters flowing through the alteration area were analyzed for contents of some main heavy metal including lead (Pb), copper (Cu), zinc (Zn), cadmium (Cd), cobalt (Co), manganese (Mn), nickel (Ni), mercury (Hg), barium (Ba), stronsium (Sr) and arsenic (As). Obtained data points out that the surface water flowing through the area was effected by some heavy metals such as Mn, Fe, As and Pb etc. So more attention should be paid to heavy metal contamination of the alteration areas on surface waters. Alteration areas are important target fields for ore deposit exploration, while also posing risks of heavy metal contamination.

Keywords: *Heavy metal contamination, alteration area, surface water, Gümüşhane*

1. INTRODUTION

The Saricicek alteration area and its near vicinity are located at the Black Sea Tectonic Unit in northeast Turkey. This belt hosts a lot of ore deposits, including, intensely altered Saricicek area (Fig. 1). While alteration areas are important targets for mineral exploration, these areas have a risk for environmental pollution [1]–[3]. Mining activities result in serious environmental impacts. In addition to local dispersion in soil profiles, they also cause extensive contamination of soils and plants, streams and increase in concentrations of toxic metals [4]. Many studies on mining areas during the last decade have focused on concentration, distribution and source identification of heavy metal/trace elements (HMTEs). But there is almost no study on the impact of alteration areas on environment, such as terrestrial and aquatic.

The aim of the study is to assess of the effects of Saricicek alteration field and its near vicitiny on the surface waters of the area. The area covers Saricicek village and its near vicinity near which is 55 km east of the city of Gümüşhane in northern Turkey. The study area is located at the southern zone of the Black Sea Tectonic Unit (Eastern Pontides). The basement of the tectonic unit of the area consists of pre-Jurassic metamorphic rocks [5] and unmetamorphosed granitic plutons [6]–[8].

---

[1] *Corresponding author: Gümüşhane University, Department of Geological Engineering, 29000, Bağlarbaşı/Gümüşhane, Turkey. alaaddinvural@hotmail.com*

[2] *Gümüşhane University, Department of Food Engineering, 29000, Bağlarbaşı/Gümüşhane, Turkey*

[3] *Gümüşhane University, Department of Civil Engineering, 29000, Bağlarbaşı/Gümüşhane, Turkey*

[4] *Karadeniz Technical University,*

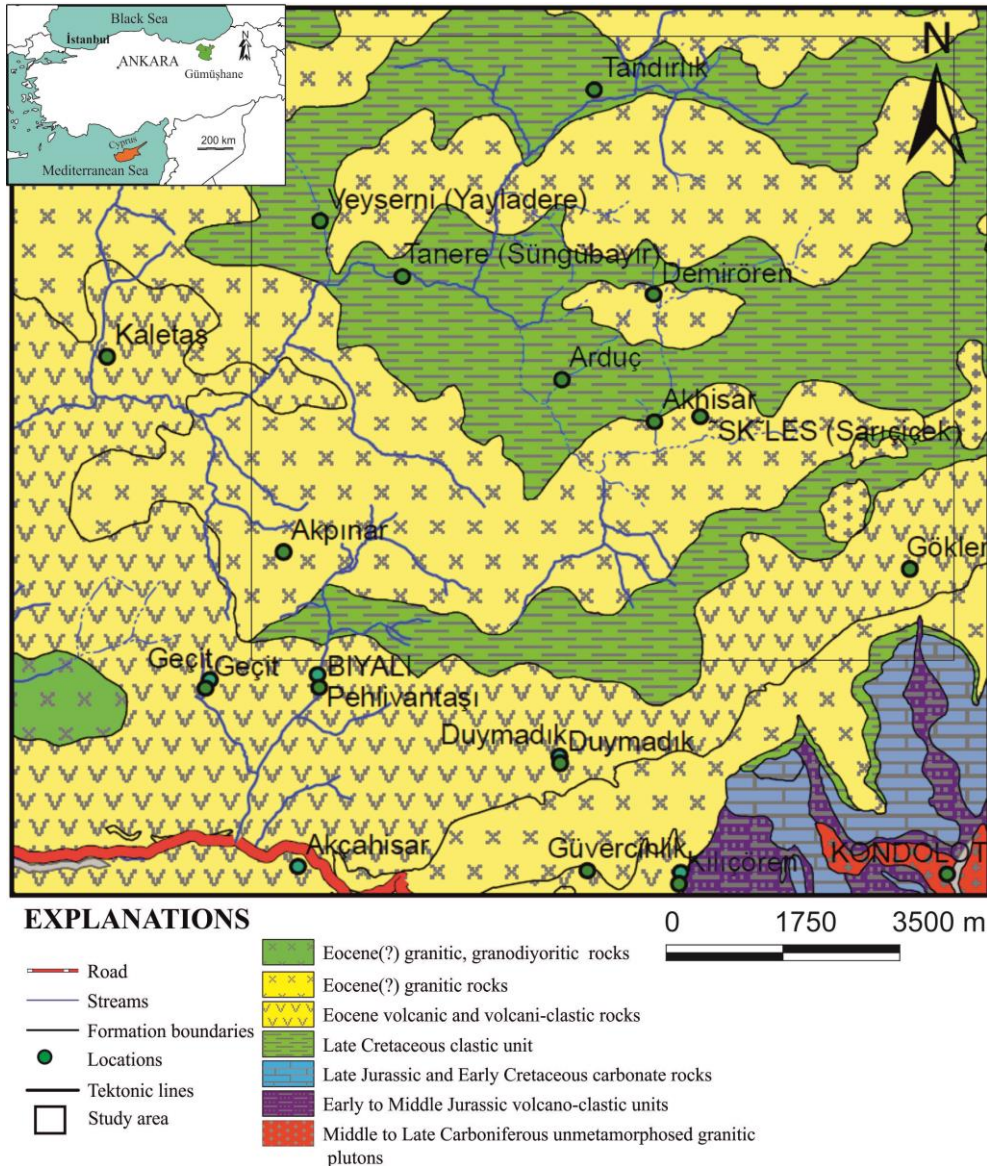[5] *Erciyes University, Faculty of Science, Chemistry*

Figure 1. Geological map of the study area (after Güven [9]).

These basement rocks are unconformably overlain by an early to middle Jurassic volcano-clastic unit which passes upward to the late Jurassic and early Cretaceous carbonate rocks. The late Cretaceous clastic unit begins with sandy limestones at the bottom and grades upward to red pelagic limestone and then to a turbiditic series consisting of sandstone, siltstone, marl and limestone which conformably overlie carbonates. All these units were cross cut by late Cretaceous intrusions [10]. The Eocene volcanic and volcaniclastic rocks overlie the late Cretaceous volcanic and/or sedimentary rocks with an angular unconformity [11], and intruded by calc-alkaline granitoids of same age [12]–[14]. The upper Cretaceous, southern and northern zones of the Black Sea Tectonic unit were dominated by different lithologies. During that time the northern zone was subjected to intense magmatic activity, the southern zone was invaded by turbiditic deposits. All these units start with conglomerate and nummulite bearing limestones and change to andesite basalt and pyroclastics and unconformably overlain by the Eocene units.

2. MATERIAL AND METHOD

2.1. Sampling and Analysis

In order to investigate the effect of the alteration zone on the surface waters, 28 water samples were collected from streams in the area (Fig. 2). pH measurements were also performed on site.Water samples from the streams were taken using plastic bottles with a volume of 500 mL and bottles were labeled and brought to the laboratory. As soon as the water samples were taken for metal analysis, it was acidified with ultrapure HNO_3 to 1 mL of concentrated acid. The water samples taken from the laboratory were also purified from the dust-soil-sludge using 0.45 μm nitrocellulose membrane and then analyzed.
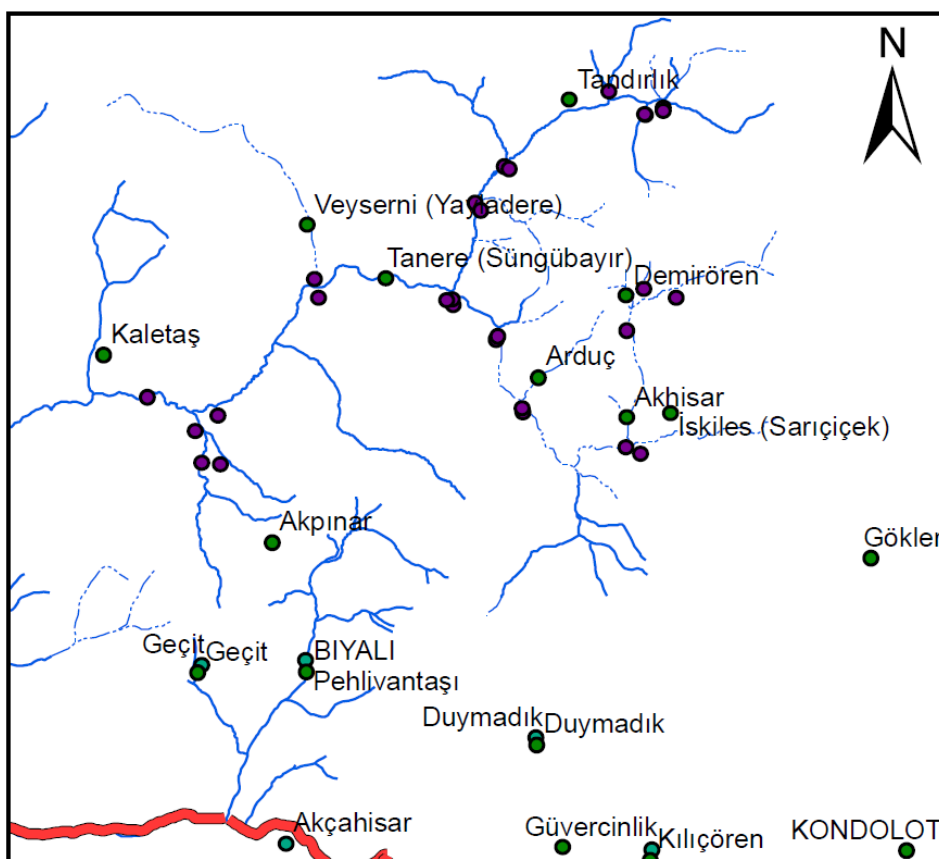

Figure 2. Water sampling locations (Purple circles are sampling locations)

After the samples were prepared for analysis, they were analyzed for some HMTEs using ICP-MS at Gümüşhane University Central Laboratory.

3. RESULT AND DISCUSSION

The pH values of the waters range from 6.85 to 8.45. According to this values, waters are between neutral and slightly basic. HMTEs contents range from (as μg/L) 11 to 2779 for Mn, 39 to 11976 for Fe, 10,80 to 538,4 for Ni, 10,80 to 103,60 for Cu, 101 to 4246 for Zn, 148 to 1334 for Sr, 84,1 to 728,6 for Ba, 11,6 to 192,6 for Pb, 21,3 only in one sample for As (Table 1, Fig. 3). Hg and Cd content of the waters were detected below the limit of detection.

When the element contents of surface waters are compared with EPA water quality standards; with the water pH values within the standards, Al values were higher in some points than EPA's surface water standards. Mn and Fe values of surface waters in the area have been determined above the standard limits especially in the A1 and A2 class surface waters and, to a lesser extent, in the A3 class surface waters. Ni values in surface waters are also found to be remarkably high. Cu and Zn values were measured at some points above the limit values. Pb is an important contaminant element for nature and has been found to reach quite high values at some points in the area.

Table 1. Descriptive statistics of the surface water samples

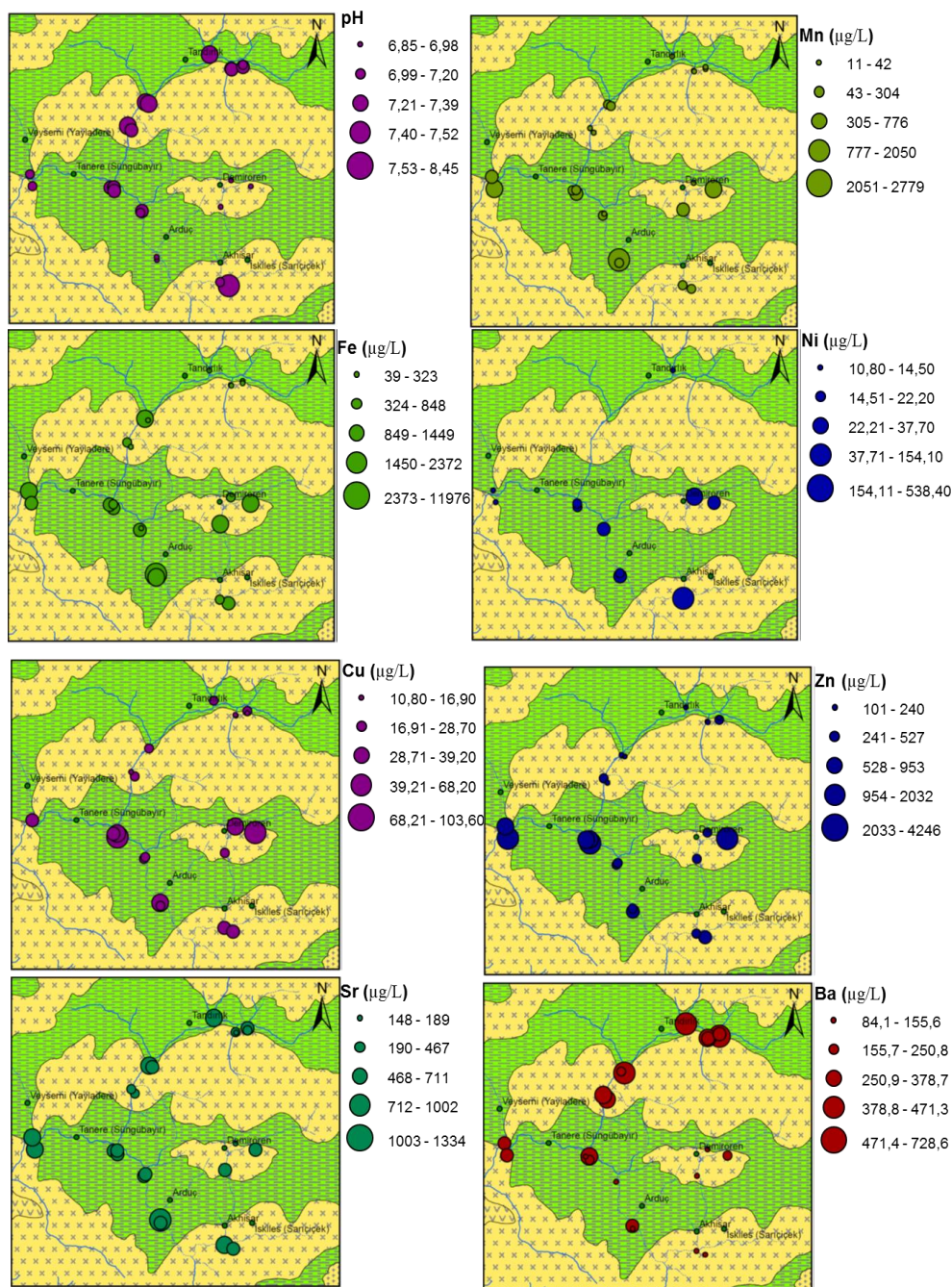|	pH	Na	Mg	Al	K	Ca	V	Mn	Fe		Co	Ni	Cu	Zn	As	Rb	Sr	Sn	Ba	Pb
Mea.	7,27	3947,27	3620,64	86,34	1842,15	2792,74	9,77	414,76	1361		15,25	80,84	35,58	1035,30	21,30	16,40	620,35	0,86	317,07	50,14
Med.	7,32	3839,50	3547,00	67,10	631,50	2858,00	10,10	151,60	848		15,25	22,20	28,00	378,00	21,30	11,10	624,00	0,77	322,80	23,35
S.Dev.	0,33	1863,96	969,80	88,98	4305,07	840,58	0,67	713,94	2412			157,07	23,52	1332,80		10,51	249,01	0,63	190,14	57,65
Min	6,85	1659,00	1844,00	11,80	86,00	1156,00	9,00	11,30	39		15,25	10,80	10,80	101,00	21,30	9,60	148,00	0,22	84,10	11,60
Max	8,45	10776,00	6351,00	333,30	19002,00	4828,00	10,20	2778,60	11976		15,25	538,40	103,60	4246,00	21,30	28,50	1334,00	1,89	728,60	192,60
Number	23	22	22	14	20	23	3	23	23		1	11	21	23	1	3	23	6	22	10

Figure 3. Dot distribution map of HMTEs

Figure 3 (continue)

Table 2. EPA Water Quality Standards for some elements

		Drinking water	Surface water		
			A1	A2	A3
Al	µg/L	200	-	-	
As	mg/L		0,05	0,05	0,1
Ba	mg/L		0,1	1	1
Cd	mg/L		0,005	0,005	0,005
Ca	mg/L		-	-	-
Cr	mg/L		0,05	0,05	0,05
Co	mg/L		-	-	-
Cu	mg/L		0,05	0,1	1
Fe	mg/L	0,2	0,2	2	2
Pb	mg/L		0,05	0,05	0,05
Mg	mg/L		-	-	-
Mn	mg/L	0,05	0,05	0,3	1
Hg	µg/L	1	1	1	1
Mo	µg/L	-	-	-	-
Ni	µg/L	20	-	-	-
pH		6.5-9.0	5.5-8.5	5.5-9.0	5.5-9.0
K	mg/L	-	-	-	-
Se	mg/L	0,01	0,01	0,01	0,01
Na	mg/L	200	-	-	-
Sn	mg/L	-	-	-	-
Zn	mg/L	-	3	5	5

As a results, these findings point out that the surface water flowing through the area was effected by some heavy metals such as Al, Fe, Mn, Ni, Cu, Zn and Pb. So more attention should be paid to HMTEs contamination of the alteration areas on surface waters. Alteration areas are important target fields for ore deposit exploration, while also posing risks of HMTEs contamination.

Studies on water quality parameters and other physical properties are continuing. These data are the first to be obtained, when other data are obtained then they will be evaluated separately.

ACKNOWLEDGEMENT

REFERENCES

[1]. S. B. El Kheir, J. Oubbih, N. Saidi, and A. Bouabdli, "Uptake and fixation of Zn, Pb, and Cd by thlaspi caerulescens: Application in the cases of old mines of mibladen and zaida (west of morocco)," *Arab. J. Geosci.*, vol. 1, no. 2, pp. 87–95, 2015.

[2]. T. N. Nganje, C. I. Adamu, A. N. Ugbaja, E. Ebieme, and G. U. Sikakwe, "Environmental contamination of trace elements in the vicinity of okpara coal mine, enugu, southeastern Nigeria," *Arab. J. Geosci.*, vol. 4, no. 1–2, pp. 199–205, 2011.

[3]. A. Vural, "Assessment of Heavy Metal Accumulation in the Roadside Soil and Plants of Robinia pseudoacacia, in Gumushane, Northeastern Turkey," *Ekoloji*, vol. 10, pp. 1–10, 2013.

[4]. A. Vural, "Biogeochemical characteristics of Rosa canina grown in hydrothermally contaminated soils of the Gümüşhane Province, Northeast Turkey," *Environ. Monit. Assess.*, vol. 187, no. 8, p. 486, 2015.

[5]. G. Topuz, R. Altherr, W. H. Schwarz, A. Dokuz, and H. P. Meyer, "Variscan amphibolite-facies rocks from the Kurtoğlu metamorphic complex (Gümüşhane area, Eastern Pontides, Turkey)," *Int. J. Earth Sci.*, vol. 96, no. 5, pp. 861–873, 2007.

[6]. Y. Yılmaz, "Petrology ancj structure of the Gümüşhane granite and surrounding rocks, NE Anatolia," 1972.

[7]. G. Topuz, R. Altherr, W. Siebel, W. H. Schwarz, T. Zack, A. Has??zbek, M. Barth, M. Satir, and C. ??en, "Carboniferous high-potassium I-type granitoid magmatism in the Eastern Pontides: The Gümüşhane pluton (NE Turkey)," *Lithos*, vol. 116, no. 1–2, pp. 92–110, 2010.

[8]. A. Dokuz, "A slab detachment and delamination model for the generation of Carboniferous high-potassium I-type magmatism in the Eastern Pontides, NE Turkey: The KOse composite pluton," *Gondwana Res.*, vol. 19, no. 4, pp. 926–944, 2011.

[9]. İ. Güven, *Doğu Pontidlerin 1/25000 Ölçekli Kompilasyonu*. Ankara: MTA Genel Müdürlüğü, 1993.

[10]. A. Kaygusuz, W. Siebel, C. Şen, and M. Satir, "Petrochemistry and petrology of I-type granitoids in an arc setting: The composite Torul pluton, Eastern Pontides, NE Turkey," *Int. J. Earth Sci.*, vol. 97, no. 4, pp. 739–764, 2008.

[11]. M. Arslan and I. Aliyazicioglu, "Geochemical and petrological characteristics of the Kale (Gümüşhane) volcanic rocks: Implications for the Eocene evolution of eastern Pontide arc volcanism, northeast Turkey," *Int. Geol. Rev.*, vol. 43, no. 7, pp. 595–610, 2001.

[12]. O. Karsli, B. Chen, F. Aydin, and C. Şen, "Geochemical and Sr-Nd-Pb isotopic compositions of the Eocene DOlek and Sariçiçek Plutons, Eastern Turkey: Implications for magma interaction in the genesis of high-K calc-alkaline granitoids in a post-collision extensional setting," *Lithos*, vol. 98, no. 1–4, pp. 67–96, 2007.

[13]. O. Karsli, A. Dokuz, I. Uysal, F. Aydın, R. Kandemir, and J. Wijbrans, "Generation of the Early Cenozoic adakitic volcanism by partial melting of Mafic Lower Crust, Eastern Turkey: implications for crustal thickening to delamination," *Lithos*, vol. 114, pp. 109–120, 2010.

[14]. Y. Eyuboglu, M. Santosh, and S. L. Chung, "Crystal fractionation of adakitic magmas in the crust-mantle transition zone: Petrology, geochemistry and U-Pb zircon chronology of the Seme adakites, eastern Pontides, NE Turkey," *Lithos*, vol. 121, no. 1–4, pp. 151–166, 2011.

BIOGRAPHY

Alaaddin Vural is an Associated Professor of Ore Deposits and Geochemistry at Gümüşhane University, Faculty of Engineering and Natural Sciences, Department of Geology Engineering. His work focuses specifically on the environmental geochemistry. His favorite place to do research is especially Gümüşhane Province which hosts a lot of ore deposits and alteration areas related to ore deposits and also has extended experience about west of Turkey's geology and ore deposits.

Selçuk Alemdağ was born in 1979, in Trabzon. He is a Assist. Professor in Department of Geological Engineering of Faculty of Engineering at the University of Gumushane. His main area of interest are engineering geology, landslides, rock falls, dam site investigations, underground waters and waste landfills. He currently works on studying the body and reservoir area of waste dams and groundwater contamination.

Estimation of Turkey's Electricity Consumption for 2023 by using Support Vector Machines Regression Algorithm

Semiha Durgun[1], Ali Osman Ozkan[2]

Abstract

In this study, the demand for 2023 Turkey's electrical energy consumption has been estimated by using the support vector machine sequential minimal optimization algorithm. For this aim, various variable such as Gross Domestic Product (GDP) between the years of 1980-2015, population and meteorological data were used in the prediction model. By using the model, Turkey's electrical energy consumption between the years of 2016-2023 was estimated.

Keywords: *Electrical energy consumption, Sequential Minimal Optimization (SMO) regression, Support Vector Machines (SVM)*

1. INTRODUCTION

Energy is a intersecting resource for the sustainability of the today's world culture. Energy demand represents the energy that is to be consumed in individual and institutional dimensions for economic activities to be performed. Urbanization process, economic growth and development, population, technological improvements, economic activity and efficiency are the improvement factors that influence energy demand. Accurate electricity consumption prediction has primary importance in the energy planning of the developing countries.

During the last decade several new techniques are being used for electricity consumption planning to exactly predict the future electricity consumption needs. Support Vector Machines (SVM) is new techniques being adopted for energy consumption prediction [1].

In this study, the SVM is implemented for the prediction of electricity energy consumption of Turkey. In the models, Gross Domestic Product (GDP), population and meteorological data are used as independent variables using historical data from 1980 to 2015. Long term electricity consumption prediction is the basis for energy investment planning and plays an essential role in developing countries for authority [2].

Over prediction of the consumption would contribute to unnecessary unemployed capacity which means wasted financial resources, whereas under prediction would lead the higher action costs for energy supplier and would cause potential energy outages [1].

Consequently, modeling electricity consumption with good accuracy becomes vital in order to withdraw costly mistakes. Electricity prediction models are developed specific to a nation or utility depending on market conditions prevailing [1].

Electricity market in Turkey has a quickly developing structure due to industrialization, fast urbanization and growing population for last three decades. The average annual (2015) increase in total electricity consumption in Turkey is about 27 %, which is far above the average of many countries in Europe and throughout the world.

However, energy sources in Turkey are quite scarce. Turkey's extensive dependence on import sources for its energy supply creates some economic and political negative effects, making authorities necessary to estimate future electricity consumption accurately by using the accurate models [2].

---

[1] Semiha Durgun, Necmettin Erbakan University, Department of Energy System Engineering, Konya/Turkey
semihadurgun@gmail.com
[2] Ali Osman Özkan, Necmettin Erbakan University, Department of Electrical and Electronic Engineering, Konya/Turkey
alozkan@konya.edu.tr

Many methods of predicting loads have been developed and transferred to practice in order to reach the correct prediction. Some of these; Ogurlu (2011), in his dissertation he estimated Turkey's annual total energy consumption and peak load (the time interval when the consumption of electricity energy is highest) between 2010 and 2025 [3]. Balcı et al. (2012), in their study short-term load estimation using regression analysis and least-squares method. Daily load estimates were made and compared with real values between the years of 2004-2010 [4].

2. MATERIALS AND METHODS

Regression is one of the most important tasks in machine learning and data mining. Different from classification, regression is used to predict numeric target values. In regression, a model is built from a set of training instances with numeric target values and is typically measured by its relative mean absolute error on the test instances.

Support Vector Machine (SVM) is an excellent model for solving the regression problems [5]. Smola and Scholkopf proposed an iterative algorithm called Sequential Minimal Optimization (SMO), for solving the regression problems using SVM. This algorithm is an extension of the SMO algorithm proposed by Platt for SVM classifier design [6]. In order to address the classification problems, Keerthi and Shevade present an improve version of Platt's SMO algorithm [7].

After this, Shevade et al. are successful in extending Keerthi and Shevade's improved ideas to Smola and Scholkopf's SMO algorithm for solving regression problem, simply named SMOreg [8]. SMOreg overcomes an important source of confusion and inefficiency caused by the way SMO maintains a single threshold value. Getting clues from criteria associated with the dual problem, SMOreg use two threshold parameters and devise two modified versions of SMO for regression [8]. Their experiments show that: SMOreg enhances the value of SMO for regression even further; SMOreg is much more efficient than the original SMO and SMOreg performs significantly better than the original SMO [8].

Our data set used in this study is as follows:

- Year (1980-2015),
- Gross Domestic Product (GDP) (Billion TL),
- Population (x1000 persons),
- Rainfall (mm),
- Moisture (%),
- Temperature (˚C),
- Wind (m/s),

Electricity Consumption (GWh)

Table 1 shows data set used in the study between 1980 and 2015 of Turkey.

Table 1. Data set used in the study between 1980 and 2015 of Turkey

YEAR	GDP	POPULATION	RAINFALL	MOISTURE	TEMPERATURE	WIND	ELECTICITY CONSUMPTION
	BILLION TL	X 1000 PEOPLE	mm	%	^{0}C	m/s	GWh
1980	0,005	44438	639,5	63,9	12,7	2,1	20398
1981	0,008	45540	751,3	64	13,3	2,2	22030
1982	0,01	46688	546,8	63,5	12,1	2,1	23587
1983	0,014	47864	657,8	64,9	12,3	2,1	24465
1984	0,022	49070	560,3	64,2	12,8	2	27635

⋮	⋮	⋮	⋮	⋮	⋮	⋮	⋮
2011	1297,713	74224	642,2	63,1	12,8	2	186100
2012	1416,798	75176	695,2	62,1	13,8	2	194923
2013	1567,289	76055	547	59,6	13,8	1,9	198045
2014	1748,168	76903	641,6	62,6	14,5	1,9	207375
2015	1952,638	77738	637,8	62,4	13,8	1,9	263828

WEKA (Waikato Environment for Knowledge Analysis), developed by the University of Waikato in New Zealand [9]. Weka is an open source data mining tool developed in Java. It is used for research, education, and applications. It can be run on Windows, Linux and Mac [9].

WEKA is a collection of machine learning algorithms for data mining tasks. WEKA contains tools for data pre-processing, classification, regression, forecasting, clustering, association rules, and visualization. It is also well-suited for developing new machine learning schemes. The most popular data input format of WEKA is attribute relation file format (arff) [9].

WEKA is a state-of-the-art tool for developing machine learning techniques and their application to real-world data mining problems. It is a collection of machine learning algorithms for data mining tasks. The new machine learning algorithms can be used with it and existing algorithms can also be extended with this tool [9].

Table-2 shows the estimated values of the SMO regression algorithm for the years between 2016 and 2023.

Table 2. Estimated values of the SMO regression algorithm for the years between 2016 and 2023.

YEAR	GDP	POPULATION	RAINFALL	MOISTURE	TEMPERATURE	WIND	ELECTICITY CONSUMPTION
	BILLION TL	X 1000 PEOPLE	mm	%	^{0}C	m/s	GWh
2016	2171,998	78802	704,1	61,6	12,99	1,97	250587
2017	2311,61	79822	708,8	60,9	14,66	1,83	252689
2018	2521,078	80844	704,9	60,1	15,27	1,82	262818
2019	2826,653	81879	734,6	61,1	15,1	1,86	284349
2020	3165,939	82929	740,8	60,2	14,3	1,84	299854
2021	3490,863	83992	716,6	58,9	14,33	1,82	313848
2022	3880,702	85066	678,5	58,1	15,24	1,83	331540
2023	4321,99	86154	669,2	58,1	15,09	1,86	357478

The estimated annual electricity consumption of Turkey between 2016 and 2023 is shown in Figure 1.

Figure 1. Turkey's annual electricity consumption between 2016 and 2023.

3. CONCLUSION

Electricity generation, transmission and distribution facilities require an investment of billions of dollars. Therefore, forecasting electricity consumption is very important for the investors and companies. Adequate capacity planning requires accurate forecasts of the future demand variations and timing of electricity demand.

It is necessary to use reliable methodologies and to develop new and alternative techniques for the estimation of future electricity consumption in Turkey properly. The analyzed results indicate that the SMOreg model can be used effectively for Turkey's long-term net electricity consumption forecast. Therefore, the recommendations presented in this article are useful for energy planners.

On the basis of the results, it is seen that the electricity consumption of Turkey in 2023 is estimated as 357478 GWh. In addition, the estimated GDP and the population of Turkey in 2023 are about 4322 Billion TL and 86 million 154 thousand people, respectively.

Accurate consumption models are needed immediately in Turkey. For this purpose, in this manuscript, the SMOreg model is recommended for alternative and successful estimation of electricity consumption of Turkey.

REFERENCES

[1] Kaytez F., Taplamacioglu M. C., Cam E., Hardalac F., 2014 Forecasting electricity consumption: A comparison of regression analysis, neural networks and least squares support vector machines, International Journal of Electrical Power & Energy Systems, pp. 431–438, May 2015.
[2] G. Ceylan, A. Demiroren, "Estimation of short-term load of artificial neural networks and Golbası region", Istanbul Technical University Faculty of Electrical and Electronics Engineering Publications, Istanbul, 1-2 , 2004.
[3] H. Ogurlu "Long Term Electricity Prediction of Turkey Using Mathematical Modeling", M. Eng. thesis, The Graduate School of Natural and Applied Science of Selcuk University, Department of Electrical and Electronics Engineering, Konya, Turkey,2011.
[4] H. Balcı, İ. I. Esener, and M. Kurban, "Short Term Load Estimation Using Regression Analysis", ELECO2012 Electrical - Electronics and Computer Engineering Symposium, Bursa, Turkey, November 29 - December 01 2012., pp. 796-801.
[5] J. C. Platt, "Fast training of support vector machines using sequential minimal optimization, in B. Scholkopf, C. Burges, A. Smola. Advances in Kernel Methods: Support Vector Machines, MIT Press, Cambridge, MA, December 1998.
[6] A. J. Smola and B. Scholkopf, " A tutorial on support vector regression" NeuroCOLT Technical Report TR 1998-030, Royal Holloway College, London, UK, 1998.
[7] S.S. Keerthi, S.K. Shevade, C. Bhattacharyya and K. R. K. Murthy, "Improvements to SMO Algorithm for SVM Regression" *Technical Report , CD-99-16,* 1999.
[8] L. Chaogun and J. Liangxiao, "Using Locally Weighted Learning to Improve SMOreg for Regression", PRICAI 2006: Trends in Artificial Intelligence, 9th Pacific Rim International Conference on Artificial Intelligence, Guilin, China, August 7-11, 2006, Proceedings. Springer
[9] [Online]. Available: http://www.cs.waikato.ac.nz/ml/weka/

Determining of The Recreational Motivations in Protected Areas with Gap Analyses Method: A Case Study on Uludag National Park

Sertac KAYA[1], Gamze KURKUT[1], Fırat Caglar YILMAZ[2], Haldun MUDERRİSOGLU[1]

Abstract

Recreation which is the essential requirement of quality life today has diversifying its sources gradually. However, increasing urbanization and industrialization cause recreational preferences to concentrate in natural areas. At this point, protected areas such as National Parks, Nature Parks appear to be most important natural resources for recreation. This study was carried out in Uludag National Park which is one of the most important protected area in Turkey. The aim of the study is to determine the recreational motivations that affect the users. In this respect, the effects of motivations on general field satisfaction are investigated. In addition, there has been identified the relationship with user characteristics to explain motivations. Within the scope of this study 20 criteria are assessed to determine the effect of motivation on involvement. Factor Analysis has been used to explain this criterias. As a result of the analysis, criterias seperate to factor groups. Along with these determined motivational factors, motivation criterias without experience the field and after the experiment have been assesed by the users. Moreover the effects of motivations that have a significant difference between them to the general satisfaction have been examined. As a result of the study, a significant relationship between the expectations before the field experience and the case of later the field experience has been determined.

Keywords: *GAP Analyses, motivation, protected area, recreation, satisfaction*

1. INTRODUCTION

Protected areas are places that offer the opportunity of recreation and spending time in a natural environment for urban residents living an intensive urban life. Today, such areas may confront an intensive usage potential due to their abovementioned Features [1].

In recent years, recreation, one of the basic requirements of quality life, is increasingly diversifying its resources. However, with increasing urbanization and industrialization, people are directed to natural areas.

Forests and the areas which can preserve nature quality (National Park, Nature Reserve, Nature Park, Nature Monument, Special Environmental Protection Area etc.) are the most important natural resources that meet the demand of outdoor recreation which is the result of releationships between people and nature to spiritual and physical renewal.

The most common natural areas where outdoor recreational activities are carried out are national parks and the foundation of these areas is that natural beauty and cultural features are protected in their natural conditions and opened to human benefit with social, cultural and touristic purposes.

Participation to outdoor recreational activities provides various benefits to the individuals. Therefore, in the areas where such activities are carried out, factors that encourage users to come to the area should be identified in order to increase the satisfaction of the users. In this context, determining the motivations that affect their involvement in recreational activities is an important issue. Scott et al. (1995) stated that the user experience in National Parks or Protected Areas will increase satisfaction [2]. In their study of Hull and

---

Michael (1995), they point out that in the outdoor, people have experienced significant changes in their mood with their entertainment experiences, especially stress is reduced [3].

With an effective visitor management, it will enhance the recreational qualities of user experiences and the diversity of recreation possibilities and the correctness of field use decisions will be questionable [4].

The aim of the study is to determine the recreational motivations that affect the users. In this respect, the effects of motivations on general field satisfaction are investigated. In addition, there has been identified the relationship with user characteristics to explain motivations.

Assumption 1: Uludag National Park does not meet expectations in terms of motivation criterias.

Assumption 2: Motivation factors from Uludag National Park are changing with user characteristics.

2. MATERIALS AND METHODS

Uludag National Park is the main material of the study. The study area was declared as a national park in 1961 that it consist of 12.762 hectares and its peak point is 2.543 meters [5]. It is located in just south-east of Bursa city center. (Figure 1). Uludag National Park which has rich potential in terms of natural areas is one of the most important tourism areas. It has been chosen as a study area because it has a rich recreational use especially in the winter months, a rich variety of flora and fauna, and a user population from almost every region of Turkey, not just from its immediate surroundings.

Within the scope of the study, a questionnaire study was applied to the user group of Uludag National Park. The questionnaire study that participants were randomly selected applied to 100 people by interview method. Confer et al. (1996), Todd et al. (2001), Graefe et al. (1999), Muderrisoglu et al. (2005) and Muderrisoglu et al. (2010)'s studies have been utilized to design the survey questions [6], [7], [8], [9], [10].

In the first part of the questionnaire prepared to determine user satisfaction and recreational motivations, frequency analysis was applied to determine socio-economic status and area usage habits of users.

In the second part, 20 questions about the motivation factors of participants have been asked according to the situation before and after experiment of area. The five-point Likert scale was used to measure the degree of motivation. Accordingly, 1 "very ineffective" and 5 "very effective" have been determined. In line with the participants' assessment after the experiment of the field; Factor analysis was done by Varimax Rotation method for motivation criterias. Cronbach's Alpha Reliabilitiy analysis was carried out to measure the reliability of the factors. Correlation analysis was applied to determine the relationship between the detected factors and user characteristics.

In the third part, GAP analysis was applied to measure the difference between the users' expectations without experience the field and their opinion after the experiment of field. Afterwards the general satisfaction level of the users who experience the area was determined. And the second correlation analysis of this study was applied to analyze the impact level of motivation criteria which has significant differences on general satisfaction.

In the last part of the study, proposals related to the area were brought forwards as a result of the findings.
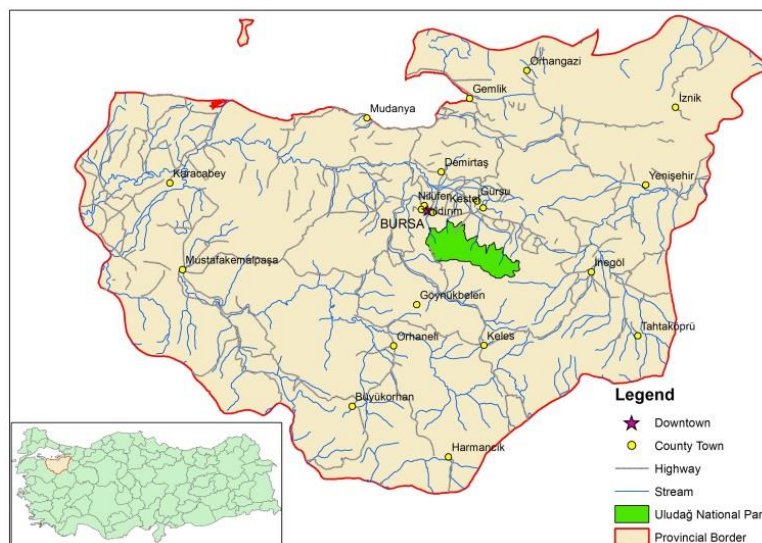

Figure 1. The location of study area

3. RESULTS AND DISCUSSIONS

3.1. Users Features and General Satisfaction Conditions

In this study, a questionnaire was applied to 100 people in Uludag National Park. 68% of the respondents are male, 32% are female. In terms of marital status, 20% are married while 80% are single. The ages of the respondents: 68% are 15-24, 24% are 25-35, 6% are 36-50, 2% are 51 and over. With regards to their education, 15% of the users have M.S or PhD degree, 75% are gratuated from university, 8% are high school and while 2% are elementary school. When monthly income status of the users is considered, 6% is less than 1000 TL, 35.4% is between 1000 - 3000 TL, 32.3% is between 3000-5000 TL and 26.3% is 5000 TL and over. While 15% of the respondents live in Bursa, 85% live in other cities. 24% of the respondents are in the private sector, 5% are public enterprises, 1% are housewives, 2% are retired and 68% are students (Table 1).

Table 1. Demographic Features of Uludag National Park Visitors

DEMOGRAPHIC FEATURES OF ULUDAG NATIONAL PARK VISITORS (N= 100)			
Gender	**Percent (%)**	**Marital Status**	**Percent (%)**
Male	68	Married	20
Female	32	Single	80
Residence	**Percent (%)**	**Age**	**Percent (%)**
Bursa	15	15-24	68
Other	85	25-35	24
Education	**Percent (%)**	36-50	6
Elementary School	2	51-65	2
High School	8	**Occupation**	**Percent (%)**
University (B.S)	75	Private sector	24
M.S or Ph.D.	15	Public enterprise	5
Income	**Percent (%)**		
<1000 TL	6	Housewife	1
1000-3000 TL	35,4		
3000-5000 TL	32,3	Retired	2
>5000 TL	26,3	Student	68

3.2. Visiting Frequency and Expectation Status

60% of the visitors reported that they had already visited the field and 40% reported that they were visiting first. In terms of previous visit numbers, 51.7% are more than one and 48.3% are only one time. While 29% of respondents selected safety for the priority expectation, 56% are entertainment and 15% are cheapness. Moreover, the order of these expectations which were obtained from the arithmetic mean is shown in Figure 2. Here, there is an inverse proportion between the order of preference and numerical values.
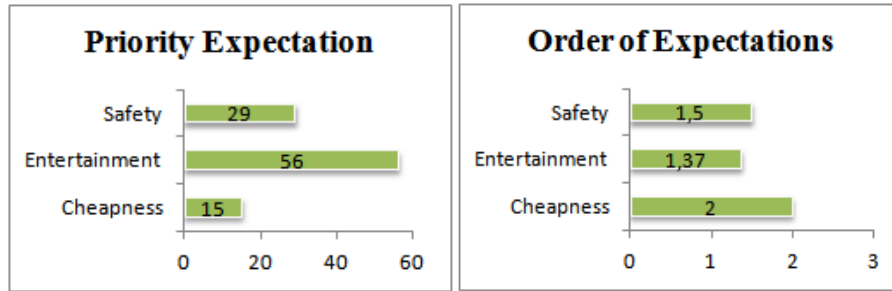
Figure 2. (a) Priority expectation of users   (b) Order of expectations

3.3. Motivation Criteria and Factor Analysis

In this study, 20 motivation criteria were assessed. The users were asked for each criteria to determine their expectations without experience the field and after the experiment. The most effective ones in terms of the expectations without experience the field are; good attitudes of park staff, good safety and security in the areas and availibity of appropriate activities. On the other hand the least effective ones are; the cheapness of the facilities, easy parking and less money to pay for activities. The most effective ones with regards to after the experiment are; crowdness of the area, easy access and notification about the history of areas. The least effective ones are; less money to pay for activities, hygienic condition of the toilets and easy parking.

In the study, factor analysis was done based on the data acquired from the users' observations after the experience of field. As seen in Table 3, 4 factors were determined according to the motivation criteria for Uludag National Park. Factor I is explained with a variance of 7,19% and Cronbach's alpha is 0.85. Calculated alpha value indicates that this factor is highly reliable. Factor I contains 6 motivation criteria. The common trait of these motivation criteria are that they are grouped under the heading "resources". Factor II is explained with a variance of 43,62% and Cronbach's alpha is 0.84. Calculated alpha value indicates that this factor is highly reliable. Factor II contains 6 motivation criteria at all. The common trait of these motivation criteria are that they are grouped under the heading "management". Factor III is explained with a variance of 8.04% and Cronbach's alpha is 0.89. Calculated alpha value indicates that this factor is highly reliable. Factor III consist of 5 motivation criteria. The common trait of these motivation criteria are that they are grouped under the heading "information". Factor IV is explained with a variance of 6.81% and Cronbach's alpha is 0.74. Accordingly, Factor IV is very reliable. The common trait of these motivation criteria are that they are grouped under the heading "experience". The most effective of these motivational factors is Factor III, which is collected under the heading of information.

Table 3. Motivation factor groups and arithmetic mean

	MFI	MFII	MFIII	MFIV
Easy access	,630	-	-	-
Lots of entertainment areas	,562	-	-	-
The cheapness of the facilities	,780	-	-	-
Less money to pay for activities	,789	-	-	-
Easy parking	,536	-	-	-
Availability of park staff who can answer the questions	,633	-	-	-
Fast access to park staff	-	,642	-	-
Good safety and security in the areas	-	,636	-	-
Good attitudes of park staff	-	,681	-	-
The presence of staff to reach your suggestions and complaints	-	,713	-	-
The adequate amount of security staff	-	,740	-	-
General information about the field	-	-	,581	-
Notification about the history of areas	-	-	,738	-
Notification about the security of the area	-	-	,743	-

Criteria				
Easy access to information	-	-	,857	-
Availibity of current and correct information	-	-	,715	-
Hygienic condition of the toilets	-	-	-	,729
Esthetic quality and maintenance of the area	-	-	-	,813
Crowdness of the area	-	-	-	,631
Availibity of appropriate activities	-	,580	-	-
VARYANS	7,19	43,62	8,04	6,81
ALFA	0,85	0,84	0,89	0,74
ARITHMETIC MEAN	3,27	3,47	3,50	3,50

*MF: Motivation Factor MFI: Resources, MFII: Management, MFIII: Information, MFIV: Experience

3.4. GAP Analysis

As seen in Table 4, the variation between the users expectations without experience the field and the situation after the experiment are significant for 15 motivation criteria. Generally the analysis results are as follows: the lack of recreational areas as much as users expect, the fact that facility and activity fees are above expectation, the number and quality of the staff to be cared about users are below expectation, the area can not meet security expectations, the information about the area is below expectation and general hygienic conditions can not meet expectation.

Table 4. GAP Analysis

FACTOR	Criteria	GAP	Expectation	After experience
		Mean Value Difference	Mean	
RESOURCES	Easy access	0,21	3,84	3,63
	Lots of entertainment areas	**0,38***	3,88	3,50
	The cheapness of the facilities	**0,72***	3,59	2,87
	Less money to pay for activities	**0,71***	3,63	2,92
	Easy parking	0,3	3,61	3,31
	Availability of park staff who can answer the questions	**0,52***	3,92	3,40
MANAGEMENT	Fast access to park staff	**0,46***	4,00	3,54
	Good safety and security in the areas	**0,42***	3,85	3,43
	Good attitudes of park staff	**0,54***	4,09	3,55
	The presence of staff to reach your suggestions and complaints	**0,59***	4,12	3,53
	The adequate amount of security staff	**0,48***	3,90	3,42
	General information about the field	**0,56***	3,95	3,39
INFORMATION	Notification about the history of areas	**0,53***	3,98	3,45
	Notification about the security of the area	0,27	3,87	3,60
	Easy access to information	**0,42***	3,78	3,36
	Availibity of current and correct information	0,2	3,78	3,58
	Hygienic condition of the toilets	**0,31***	3,85	3,54
EXPERIENCE	Esthetic quality and maintenance of the area	**0,44***	3,72	3,28
	Crowdness of the area	**0,37***	3,86	3,49
	Availibity of appropriate activities	0,17	3,90	3,73

* (p<0,05) Degree of motivation influence: 1 (not satisfied), 5 (very satisfied)

Figure 3. General Satisfaction Level of Uludag National Park.
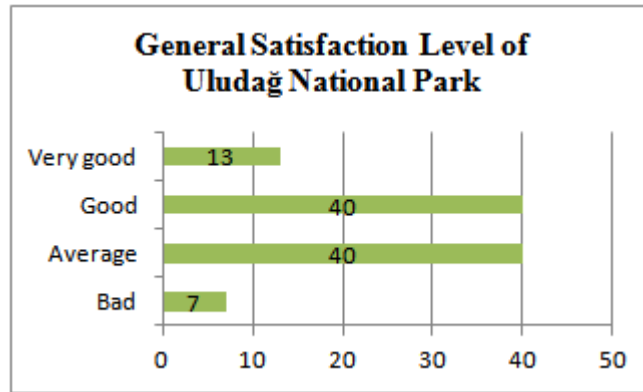
General satisfaction level from Uludag National Park's users is 13% very good, 40% good, 40% average good and 7% bad.

Uludag Milli Parkından memnuniyet duzeyini kullanıcıların %13'u cok iyi, %40'ı iyi, %40'ı orta iyi, %7'si ise kotu olarak bildirmislerdir. As it is seen, the users are satisfied with the national park generally (Figure 2).

3.5. Relationship between Motivation Criteria and General Satisfaction

Correlation analysis was applied in order to analyze the impact level of the motivational criteria which has significant variation on general satisfaction. When the results obtained in this context are examined; it can be seen that the strongest relationship is in the criteria of "getting general information about the field" and "getting information about the security of the field" (Table 6). In other respects, the weakest relationship is determined in the criteria that "there are sufficient staff to answer your questions" and "the behavior of the staff is good".

Table 6. Relationship between motivation criteria and general satisfaction

Criterias	General Satitsfaction Level
Lots of entertainment areas	,535**
The cheapness of the facilities	,413**
Less money to pay for activities	,438**
Availability of park staff who can answer the questions	,352**
Fast access to park staff	,437**
Good safety and security in the areas	,494**
Good attitudes of park staff	,367**
The presence of staff to reach your suggestions and complaints	,536**
The adequate amount of security staff	,593**
General information about the field	,623**
Notification about the security of the area	,636**
Availibity of current and correct information	,518**
Hygienic condition of the toilets	,552**
Esthetic quality and maintenance of the area	,583**
Availibity of appropriate activities	,536**

* p<0,05, **p<0,01, ***p<0,001

3.6. Relationship between motivation factors and user characteristics

Resources, information and experience among motivational factors vary according to user characteristics (Table 7). Users who have come from other cities and have never visited the field before are more satisfied with the resources factor. Low-educated users are more satisfied with the information factor. Users who have come from other cities seem to be more satisfied from experience factor. Moreover, there is no releation between management factor and user characteristics.

Table 7. Relationship between motivation factors and user characteristics

	Gender	Marital Status	Age	Residence	Income	Education	Whether or not to visit status of area
MFI: Resources	,015	,092	-,155	,252*	-,136	-,159	,201*
MFII: Management	,019	,010	-,008	,105	-,051	-,109	-,045
MFIII: Information	,025	-,035	,034	,104	-,119	-,221*	,103
MFIV: Experience	-,108	-,017	-,064	,294**	,132	-,122	-,079

* p<0,05, **p<0,01, ***p<0,001

4. DISCUSSION

In Uludag National Park, it has assigned that the majority of the subjects are male, 15-24 years old, university graduate and people come from outside the Bursa. Uludag National Park motivation factors vary with user characteristics at the least. The user characteristic that has the most impact on motivation factors is the place of residence. As the number of users from outside the province of Bursa increases, satisfaction factors related to resources and information increase. This is because; from the point of view of the information factor, it is possible that people come from outside Bursa are not provided with information as far as Bursa citizens, so they take more pleasure than others. From the point of view of the resources factor, it can be said that people come from outside Bursa do not have reference information which they can compare. Interpretation of the relationship between user characteristics and satisfaction factors through such and such inferences has the potential to provide important data for planning decisions.

On the other hand, not meeting the expectetions for 20 satisfaction criteria in the field reveals the necessity of reconsideration of recreational use and tourism sustainability in Uludag National Park. In this context; any improvements which are related to criteria in the factor group of information make a great contribution compared to other groups due to having strong impact level.

In accordance with all these results the assumptions of the research are explained as follows:

Assumption 1: It has been largely verified in this study. Only 5 of the 20 criteria were not examined because they did not show any significant varience.

Assumption 2: In this study, it has been partly confirmed that the satisfaction factors of Uludag National Park change with user characteristics. There are correlations between satisfaction factors and user characteristics, such as the place of residence, the level of education, and whether or not to experience the field earlier.

REFERENCES

[1]. Asıkkutlu S., 2013. Yedigoller Milli Parkı'nın Rekreasyonel Yonetim Planının Olusturulması, Duzce Universitesi Fen Bilimleri Enstitusü, Doktora Tezi, Düzce.
[2]. Scott D., Tian S., Wang P., Munson W., 1995. Tourism satisfaction and the cumulative nature of tourists'experiences, *Leisure Research Symposium*, San Antanio Texas.
[3]. Hull, R.B. and Michael, S.E., (1995). Nature-based Recreation, Mood Change, and Stress Restoration. Leisure Sciences, Volume:17, Number:1, pp:1-14.
[4]. Eagles, P. F. J. and S. F. McCool, 2002. Tourism in National Parks and Protected Areas: Planning and Mangement, USA. http://site.ebrary.com/lib/referans tarihi:02.10.2006.

[5]. Erten, S. ve Gündüz, S., 2011. Peyzaj Planlama ve Kentsel Tasarımda Koruma-Kullanma İçin Yeni Bir Sistem Yaklasımı Onerisi: Uludag Milli Parkı ve "Rejenerasyon". Megaron Journal, 6(2), 109-122.

[6]. Confer, J. J., H. Vogelsong, A. R. Graefe, D. S. Solan and J. K. Kramp, 1996. Relationships between motivations and recreation activity preferences among Delaware State Park visitors: an exploratory analysis. Proceedings of the 1996 Northeastern Recreation Research Symposium. New York. 146-153.

[7]. Todd, S.L., Graefe, A.R., Mann, W., 2001. Differences in scuba diver motivations based on level of development. Proceedings of the 2001 Northeastern Recreation Research Symposium. New York. 107-117.

[8]. Graefe, A.R., Thapa, B., Confer, J.J., Absher, J.D., 1999 Relationships between trip motivations and selected variables among Allegheny National Forest Visitors. Widerness Science in a Time of Change Conference, Montana. Volum 4, 107-112.

[9]. Müderrisoglu, H., Kutay, E. L. ve Ornekci Esen, S. 2005. Kırsal Rekreasyonel Faaliyetlerde Kısıtlayıcılar, Ankara Üniversitesi Tarım Bilimleri Dergisi. Cilt:11 Sayı:1, sf 40–44. Düzce.

[10]. Uzun S., Müderrisoglu H., 2010. Kırsal Rekreasyonel Alanlarında Kullanıcı Memnuniyeti: Bolu Golcük Ormanici Dinlenme Yeri Ornegi, Süleyman Demirel Üniversitesi Orman Fakültesi Dergisi, Seri: A, Sayı: 1, 67-82.

Robotic Applications on Military

Yesim Kalkan[1]

Abstract

Robots are re-programmable electro-mechanical systems and they may various equipment or part according to their special usage purposes. The main aim of the robotic technology is producing talented robots which have skills similar to human abilities. These talents are physical and mental abilities. Robots are frequently used in many areas which are automatic systems, industrial, medical, military, and research and rescue, etc. Usage of robots for the military purpose increases day by day. Moreover, ever-growing unmanned vehicle technology points out that in the future possible war will be managed by mobile robots which are equipped with heavy weapons. Serves for military purpose of autonomous and semi-autonomous combat robots are used under different environmental conditions which are air, marine and land. In this review will be mentioned about robot soldiers and their usage of military equipments, advantages from the point of tactics and financial of widespread robots which are spy and Logistics, transportation robots, disposal, bomb and mines robots, technical and mechanical properties of the monitor and reconnaissance robots with marine robots.

Keywords: *Military; Robot; Land; Air; Marine;Unmanned Systems,Robotic, , Automation Systems.*

1. INRODUCTION

The robot is a re-programmable electromechanic machine. It may have equipment according to functions of machine. [1].

Isaac Asimov, who is a well-known science-fiction writer, imagined the robot is an automatic machine and its appearance like a human being. For this purpose programmable robots have been directed by Positronic brain. In 1940's, robotic terms were used with three main laws, firstly by Isaac Asimov [1].

These laws;

1. A robot may no damage a human or it does not lead to hurt because of careless behave on it.

2. A robot must bey the commands which are given by human beings except contradiction between any orders and first law [2].

3. If there is not any conflict between first rule and the second rule, a robot must protect its own existence[2].

4. The main aim of robotic technology, producing devices that have physical skills and emotions such as a human being.

Development in science and technology has an important effect on improving of countries. The developing technology comes with a lot of amenities. Nowadays, keeping up with developed technology is a necessity, not an option. For this reason,countries examine their available systems of technological compliance and they make new plans for adoption of their substructure very well.

Nowadays, robots are used in many areas such as ındustrıal, medical, operational, search and rescue.

Industrıal robots are used in automation systems. Japan is the firstly country to use industrial robots. When the beginning of robot usage, people have reacted negatively because of their negatory beliefs that taskmasters would prefer the robots instead of people so workmen would encounter with unemployment [3]. Many things which are not carried by people, but they can be carried easily by robots. Spreading such application, it turns out that robots will be useful and use of robot is increased in the applications [4]. Industrıal robot has common usage in many sectors such as automotive, electrical, electronic and mechanic [5].

The usage of robots in the medical field is seen orthopedics and surgical interventions. The current robot systems, provide 10 times bigger and three dimensional image during surgical operations. These robots have

---

[1] Military Electronic Systems Engineering, Ankara University, Ankara/Türkiye, {yesim_2688}@hotmail.com

flexibility and move fast instruments so operator perform a medical intervention hard to reach in deep and narrow areas easily. Thus, in the medical fields, robots provide a great comfort and convenience both doctor and their patients [6].

In operational field, robots are used mostly commonly in various places which are not suitable life of people, have a high-incidence of radiation, craters and underwater environment. For example, Pathfinder Doppler and range measurement made using its radio communication system to transmit the difference data between motion and rotation rate on the poles of Mars [7].

In search and rescue field, people apply robots to detect victim during the emergency situations such as land-slip and collapse because of natural disaster of fire. Additionally, the robots are practical machine to detect the leakage in the pipelines [33].

The usage of robots is gradually increasing in military application. Moreover, ever-growing unmanned vehicle technology points out that in the future possible war will be managed by mobile robots which are equipped with heavy weapons.

In this review, the use of robot for military purpose will be discussed with supporting examples.

2. ROBOTS ARE USED FOR MILITARY PURPOSE

Todays the advanced electronic and mechanical technology has lots of contributions to devices which are used for military aims. One of them is an enhancement variety of military devices, the other one is the development of technology of them.

Using robots as a soldier and military vehicle is an annular factor with tactic and financial advantages. The reason of preferring robot for military boosts the power of army efficiency and avoid from loss of life and property [34].

Autonomous and semi-autonomous robots are able to work in three environments that are air,land and underwater.

2.1. Land Robot

Work on the unmanned land vehicle can be divided two main groups. One of them is able to use instead of the available military team and they act strategically and tactically. The other group is, unmanned land vehicle that helps association in all kinds of environment that can be tough land and weather conditions. The most important factor of all types of operation is taken and interpret of ally and opponent operative tactic, tactic and technical security intelligence as a rapidly and precisely. The role of this information to be acted upon with the accuracy of this interpreted security intelligence is a very important factor during winning or losing of war or conflict [8].If the current system has early warning system against the possible attack, taking required precaution profitably and removing the threat effectively by soldier [9]. The some problems may arise in the devices that used during conflict are detected and revise necessary operation in the vehicles. So, the robots will able to respond appropriately land able to answer more conveniently demands of soldiers [9].

Some problems mayarise inthe robots which ae used in combat. These problems are identified and necessary revision procuders are made in the robots, so these robots will be more appropriately according to demands. In this way, the use f robot for military purpose will be widespread [10].

2.1.1. Spy Robots

Spy robots are able to reach easily the places where are hard going or difficult taking information by soldiers. These robots control as a teleoperation or remote. When we look pragmatically, these robots have a life saving function. Spy robots have their own protective equipment on them.When the solder life, or its own security in danger,spy robots act to protect the life of soldiers and its security without any hesitation [11].

VIPeR is a sort of robot that is used in the military as a spy. It's small and light structure allow to access to anywhere with ease and rapidly [12]. PLC (Programmable Logic Circuit) HMI (Human Machine Interface) are used together in the VIPeR. Otherwise, it can show its problem on the screen thanks to EDFFS (Electronic Diagnostic Fult Security System). The communication protocol of VIPeR is RS232 and USB. It has various sensors which related to the identification of its position, stagger and rolling. It can take pictures with its camera and it's able to process this taken image with Hough Transformation [13].

2.1.2. Logistic Transportation Robot

Transportation robots help by carrying necessary ammunition, food and medical equipment of soldiers [14; 15].

These robots can overcome with the remote control the long distance and anywhere the dangerous for soldier successfully. Independent of each other wheels helps to rotate how it wants and protect its balance. For this reason, independent of each other wheels have a very important role in its direction and balance and these wheels convert to the robot to suitable machine for rough terrain [14].

2.1.3. Mine Disposal Robot and Bomb Disposal Robot

All around the world, land mine and bomb are used in order to damage the enemies, reduce to mobility and provide to regression of the enemy. Mine and bomb damage both people and devices besides environment seriously. For this reason, they constitute a great danger for civil and soldiers during combat and terrorist attack [16].

There are various works about mine scanning and bomb disposal short-range communication protocols such as RF (radio frequency) and infrared are preferred the robot that is used in work [17,18]. The robot is directed to differentiate which are manual, sound, light and following line.[16].

In general, palette wheels are used in bomb and mine disposal robot for moving easily in rough terrain. In addition, equipment of robot arms is on the robot for annihilation danger.

MIR (Micropower Impulse Radar) technology is chosen for mine detection. In 1990's, this technology was developed by Lawrence Livemore in a national laboratory in America [19]. Wide-band signals spread two billion rates thanks to the transmitter of MIR. This rate converts to ransom by noise filter. So, to echo of objects can be noticed only from a few centimeters to meters [20].

KAPLAN, is produced by Aselsan, can exemplify one of the bomb disposal robot. Robot arms on the KAPLAN interferes the bomb and it moves with ease on though terrain thanks to its pallets [21].

2.2. Aerial Robot

Unmanned aerial vehicle technology began to develop in the early 2000's. Aerial defense achieves a new size in the fields of reconnaaissance, observation and intelligence security thanks to unmanned aerial [22].

Unmanned aerial vehicles with weapons on them convert to more beneficial robots to provide military aerial security. The first unmanned aerial vehicle was used in Bekan Aerial Combat by Israel in 1982 [23]. IHA-X1,as the first unmanned aerial vehicle in Turkey, was designed and produced by TUSAS in 1990 [22].

Low-visibility, protect themselves, safe communication, volatilizable high altitude, co-operative with other devices are needed properties of unmanned aerial vehicles. Besides, it must not defuse easily by other counties with a defensive power above a certain level. For instance RQ-170, was belonged to the USA Airforce,was deceived its GPS system and was captured by Iran in 2011. Otherwise, Global Haw Unmanned Aerial Vehicle was dropped in Chinese air space [24]. Owing to these examples, unmanned aerial vehicles should be designed to more conservative and invisible in order to prevent such unwanted events.

2.2.1. Exploration and Observation Robots

Skylark, one of the exploration and observation unmanned aerial vehicle. It's small and it has high invisibility. Micro camera links with a USB on the battery. Taken photographs that are panoramic images are sent to ground center simultaneously. Wings control which has moved into the piezoelectric property is a rocket, descent motion is achieved like dron by spirally [25]. Skylark is a more practical robot. One of the reasons of it, it can be carried in a bag, and separated parts of Skylark are combined ready to use as manual with ease [26].

2.3. Underwater Robots

UUVs (Unmanned Underwater Vehicles), ROVs (Remote Operate Vehicles), AUVs (Automatic Underwater Vehicles) have a privileged place in the military due to investigation of underwater changes,searching and mine identification [1].

The first recorded submarine was designed as torpedo by Luppis While Head in 1864. Studies about the technology of underwater vehicle were continued by the First World War and Second World War. In 1946, the American produced unmanned underwater vehicle, which was suitable for military usage. So, a new robot was added for use of soldier. This robot as used in order to clean up radioactive water by the American Navy. Thus, the American army has not been exposed to danger and the designed vehicle has completed own mission successfully [28].

2.3.1. Compass Robots

In 1985 International Robotic System was designed jet-sky based around the "The-owl". "The-owl"was an unmanned submarine vehicle and it was suitable for military purpose [29]. In 1995, MRII vehicle was developed by Naavtec Inc. Completely autonomous navigation system was designed with usage of radar-based obstacle avoidance, GPS and compass. In 2004, Springer vehicle was developed by Plymonth University like MKI. The difference of it was having an automatic pilot system [30].

2.3.2. Mine Detecting and Disposal Robots

The buried mines under the ground led to the most important damage during the wars in the sea. The mines, that are buried previously, must be destroyed in order to prevent its damage. So, soldiers apply unmanned underwater systems for disposal in order to protect their safety of life and property. Talisman is one of the robot which is used by military and it is suitable for this military purpose. It can determine mines and overcome semi-automatically with the help of robot arms which are mounted on it. Thus, navy can pass in the most dangerous place on their route in safe [31].

2.3.3. Marine Robots

"Protector" is a leader of marine robot. It has thermal and infrared camera, communication hardware, and changeable, and portable weapons depend on usage aim. It has autonomous structures. So, when it is sent to the danger zone, image of suspicious things is sent to the center as a live broadcast. In addition, it has examination systems. In doubt, soldiers can direct the robot with remote control and it can remove the danger with mounted gun by itself [32].

3. RESULTS

Lot of military gets easier with the development of robot technology. Robot application in the military, prevents very much robot technology. The Robot has lots of function such as acquisition security intelligence, overcoming different dangers, taking precaution against to mines and bomb explosions.

With the development of new generation robots which will be more complex and will have more protected communication systems rather than the current robots which are given in the examples. In future, the classical combat strategies give place to more technological battle in which robots take role actively.

REFERENCES

[15]. Kyrinkopoulos, KastajJ., and Savvas G.Lozious. 2006. Section 2.4. Robottic:Fundementals and prospects, pp.93-107,oChapter2CIGR Handbookof Agricultural Engineering Volume VI Information Technology //Smith, J. O. and Abel, J. S., ``Bark and ERB Bilinear Transforms'', *IEEE Trans. Speech and Audio Proc*., 7(6):697-708, 1999.

[16]. Albayrak M.,Yüksel Y.G.,8051 Mikrodenetleyici Bir Sumo Robot Tasarımı ve Uygulaması,Süleyman Demirel Üniversitesi Fen Bilimleri Enstitüsü Dergisi.

[17]. Peskircioglu N., "Otomasyon ve Entegre Kalite Kontrolu", Verimlilik Dergisi, Sayı 15,Mayıs,s.19-40.

[18]. Cengelci B. Cizel H., Endüstriyel Robotları, Afyon Kocatepe Üniversitesi, Teknik Egitim Fakültesi, Makine Teknolojileri Elektronik Dergisi,2005.

[19]. Browne et al.,1988, I.WA, et al 1988 MNRAS 293, 257 Interferometer Phase Calibration Sources-II.

[20]. Kuthan K., Gürkok S., Sapmaz E., Karatas O., Gozübüyük A.,Benign Mediastimal Lezyonlara Robotik Yaklasım, Gülhane Askeri Tıp Akademisi Gogüs Cerrahisi Anabilim Dalı,Ankara.

[21]. Folkrer W.n., Yoder C.F., Yuan D.N., Standish E.M., Preston R.A., Interior Structure and sensonal Mass From Radio Technology of Mars Pathfinder,18 Mayıs,2016.

[22]. Aksoy R., Kurnaz S., İnsansız Kara Araclarının ve Muhabere Gereksinimleri, Ocak 2009, Havacılık Uzay Teknolojileri Dergisi, Ocak 2009, Cilt 4 Sayı1(1-10).

[23]. Ucuzal Levent., "Komuta Kontrol Bilgi Sistemlerinde(KKBS) Cografi Bilgi Sistemlerinin(CBS) Veri ile Natove TSK'de Bu Baglamda Yapılan Calısmalar ve Ar-Ge icerisinde onemi", SAVTEK 2002,Savunma Teknolojileri Kongresi, Orta Dogu Teknik Üniversitesi- Kara Harp Okulu, Ankara, ekim 2002, pp.398-399.

[24]. İrfan H., " Ulusal Tank ve Zırhlı Arac Tasarımlara Yonelik Silah Sistemleri Mühendisligi Yaklasımları", SAVTEK 2006, 3. Savunma Teknolojileri Kongresi, Orta Dogu Teknik Üniversitesi, Ankara, Haziran 2006,pp137-143.

[25]. Norma M.K.,Soldier and Robot Interact in Combat Environment, Oklahama 2012, A Dissetaion Submitted to the Graduate Facult in Partial Fuldiment of the Require fort he Degree of Doctor of Philasophy, pp.12.

[26]. Dave P.N, Kushare B.E., Modeling& Controlling of Unmanned Vehicle, pp 189, International Conferance on Multidisciplinar Research& Practice.

[27]. Givental G., Munie P., Ellison S., Bell B., Stevens D., Sierra A., Richards A., Gray J., Laurance Technology University Viper,IGVC 2008,AutonomousVehicle,MULE.

[28]. Spaty P.S., Military Robotics:LAtest Trends and Spital Grasp Solutions.(IJARAI),International Journal of Advanced Research in Artifical Intelligence, Vol.4., No.4,2015.

[29]. "LS3-LEGGEDSquad Support Systems" Boston Dynamics "Https://www.bostondynamics.com/robot-cheetan.html.

[30]. Yıldırım Y., Yüzgec U., Keser M., Mayın Algılama.

[31]. Saltabas İ:H., Kablosuz Haberlesme Yontemleri IEE802.16 Protokolü Yüksek Lisans Tezi, Sakarya ÜniversitesiFen Bilimleri Enstitüsü,Sakarya,2007.

[32]. Cora A., Taflan N., Sarac B., Ozdemir Y., Telsiz Bomba İmha Robotun Tasarmı ve Gerceklestirilmesi, Eleco 2014 elektrik-Elektronik Mühendisligi Sempozyumu,27-29 Kasım 2014.

[33]. Dutta P.K., Defense Advanced Research Project Agency(DARPA) contract OSU-RF.

[34]. Sümbül H., Coskun A., Mayın Tarama ve Bomba İmha Sistemlerinin Tek Robot Üzerinde Modernitasyonu.

[35]. www.aselsan.com.tr/tr-tr/ cozümlerimiz/ insansız-sistemelr/insansız-araclar/ kaplan-bomba-imha-robotu.

[36]. Karaagac C., Ucan Robotlar:Gelecegin Askeri Harekat Ortamında İnsansız hava Aracı Sistemleri, STM.

[37]. Savunma Sanayi Müstesarlıgı, "İHA Sistemleri Yol Haritası (2011-2030)", 2012.

[38]. Gerts B., "Inside the Ring:Here Come the Drones", The Washington Times, 23 Ekim 2013, http://www.wahingtontimes.com/new/2013/oct/23/inside-the-ring-here-core-the-drones/?page=all=#pagebreak, (14 Mayıs 2014).

[39]. Panaıt A.M., Skylark-Acrossbo- Launched Micro Scale Cheap UAV for close aerial surveillance UNCAS Bulletin Volume 4, Issıue 1/2012, pp 61-66.

[40]. McEvory J.F., Hall G.p., Mcdonald P.G., Evolution of Unmanned Aerial Vehicle Shape,Filght, Pat and Curera Type For Waterflowsurveys;disturbance effects and species recognisition.

[41]. Yıldız O., Yılmaz A., Gokalp B., "State of The Art System Solutions for Underwater Vehicles",Raioengineering,Cılt 18, Sayı4, p.590-600,Aralık 2009.

[42]. Daglı E., Civan C., Sohmelioglu S., Edis E., Tükel D., Dogus-USV İnsansız Deniz Aracu Streo Gorüs ile Haritalandırma.

[43]. OWLMKII https:// www.amilans.com/project/index.php.

[44]. Springr:The Unmmandder Surface Vehicl, Plymouth University,UK, www.springer-usv.com

[45]. Westwod D., Unmanned Vehicles for Shallow and coastal waters

[46]. Yan R., Pans S., Sun H., Pang Y., Development ad Missions of Unmanned Surface Vehicle,Harbiin Enginnering University, Herbin 150001,China.

[47]. Borekci İ., Kanlı O., The Development of Gas Detection, Adana Menderes Universitesi, Fen Bilimleri Enstitüsü, 2016.

[48]. Aksoy R., Kurnaz S., İnsansı Kara Aracları ve Muhabere Gereksinimleri, Havacılık ve Uzay Teknolojileri Dergisi, Cilt 4, Sayı 1, p.1-10, Ocak 2009.

Numerical Investigation on Determining the Effect of D/L Ratio on Thermal Performance of the Horizontal Mantled Hot Water Tank

Dogan Erdemir[2], Necdet Altuntop[1,2,] Nazmiye İsbulan[2]*

Abstract

The aim of present study is to investigate numerically thermal performance of the horizontal mantled hot water tank, which are used commonly in solar domestic hot water system. The effect of the tank diameter and tank length on thermal performance of the tank was investigated. Three different cases were studied, which are D/L=0.25, 0.50 and 0.85. Water volume was taken constant and 196 lt. This water capacity is a common volume for small solar domestic hot water systems. Performance evaluation was performed in the terms of temperature distribution inside tank, main outlet temperature and mantle outlet temperature. At the end of study, it was found that thermal performance of the tank reduced with increased D/L. For case D/L=0.25, main outlet temperature was 45 °C and mantle outlet temperature was 59 °C..

Keywords: *Horizontal mantled hot water tank, solar domestic hot water system, Sensible thermal energy storage, Thermal stratification*

1. INTRODUCTION

Energy storage can be defined as storing energy for later usage for a while. Renewable energy sources aren't available perpetually because of their nature. Energy storage is an important tool for utilizing the renewable energy sources when energy source is not active. For instance, solar energy can be stored for night or winter usage. Although, there are many energy storage types, thermal energy storage is the one of the most developed and matured type among the energy storage systems. Thermal energy storage systems divide into two main sections, which are sensible, and latent thermal energy storage systems. Sensible thermal energy storage systems are widely used for short duration storage and solar domestic hot water systems. Hot water storage tanks are used in solar domestic hot water systems.

Hot water tanks, which are used in solar domestic hot water systems, have two main type, which are horizontal and vertical tank. The most important performance parameter for hot water tanks is the thermal stratification. Better thermal stratification increases the efficiencies of system equipment, main outlet temperature and flow rate of the natural cycle. So it is investigated by many researchers and tried to enhance. Vertical hot water tanks show better thermal performance than horizontal tanks. Therefore, they are used in many applications from past to now. In recent years, the usage of horizontal hot water tanks increases, since usage of the vacuum tube solar collectors increase and they supply better visual according to horizontal hot water tank. However, there are few studies related to horizontal hot water tank. Alizadeh [1] performed experimental study in order to determine thermal behavior of the horizontal cylindrical hot water tanks. Andres and Lopez [2] developed a TRNSYS model for horizontal mantled hot water tank. Morrison et al. [3] studied experimentally the using of horizontal mantled hot water tank in solar water heating system. Jannatabadi and Taherian [4] investigated the thermal characteristic of horizontal mantled hot water tank. Helva et al. [5] performed an experimental study in order to determine the thermal stratification of horizontal hot water tank. Madhlopa et al. [6] researched to the geometry of double horizontal hot water tanks. Morrison et al. [7] investigated to using of the horizontal mantled hot water tank in the solar water heating systems. Khalifa and Mehdi [8] performed experimental and numerical studies for investigating the performance of horizontal hot water tank. Jannatabadi [9] researched the mixing effects on thermal performance in horizontal hot water tank. Youngand and Baughn [10] investigated to thermal behaviors of the horizontal hot water

---

tanks. Rosengarten et al. [11] defined the theoretical model in order to determine the thermal performance of horizontal mantled hot water tank. Rosengarten et al. [12] applied to PIV technique for investigating to flow line in mantle gap.

There are many studies in literature related to vertical hot water tanks. However, there is a limited number of works related to horizontal hot water tanks. In this study, the thermal performance of horizontal mantled hot water tank, which is widely used in solar domestic hot water systems, is investigated numerically. The most important design parameters are the diameter and length of tank. In this study, the effect of D/L ratio on the thermal performance in the horizontal mantled hot water tank was investigated numerically. There different D/L ratios, which are D/L=0.25, 0.50 and 0.85, were examined.

2. MATERIAL AND METHOD

In this section, the horizontal mantled hot water tank, which is used in present study, is descripted. Also, the methods used in this study are expressed.

2.1. Studied Horizontal Mantled Hot Water Tank

In this study, a horizontal and mantled hot water tanks were used. The schematic view of horizontal mantled hot water tank, which is used in this study, is seen in Fig. 1.
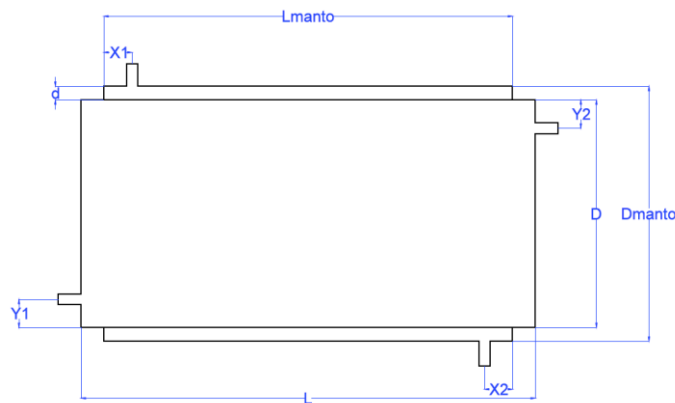
Figure 1. The schematic view of the horizontal mantled hot water tank used in this study

Table 55. Design parameters for the horizontal mantled hot water tank used in the present study

Parameter	Symbol	Value
Mantle diameter	D_m	See Table 2
Mantle gap	d	15 mm
Mantle length	L_m	See Table 2
Mantle inlet position	X_1	50 mm
Mantle outlet position	X_2	50 mm
Main inlet position	Y_1	50 mm
Main outlet position	Y_2	50 mm

Table 2. D/L ratios in constant volume, 196 l

D/L	D (mm)	L (mm)	V (l)
0.25	400	1560	196.35
0.50	500	1000	196.03
0.85	600	695	196.50

Three different D/L ratios were investigated. The tank volume was considered 196 *l* and it is taken same for all three cases. The dimensions and parameters used in this study is given in Table 2. As seen from Table 2, the tank diameter and length were changed. All other parameters were considered as constant. Mantle gap was 15 mm. This mantle gap value is commonly used in commercial applications. Also, it was considered that mantle covered to all inner tank ($L=L_m$). The D/L ratios, which were used in this study, are given in Table 2.

2.2. Numerical Model and Procedure

The horizontal mantled tank, which is seen schematically in Fig. 1 and given details in Table 1 and 2, is shown in Fig. 2. SolidWORKS 2018 [13] was used for modelling. As seen from Fig. 2, the solid sections of tank weren't modelled. Because hot water tanks are produced in thin metal sheet metal. Wall thickness doesn't have significant effect on heat transfer between mantle and inner tank.
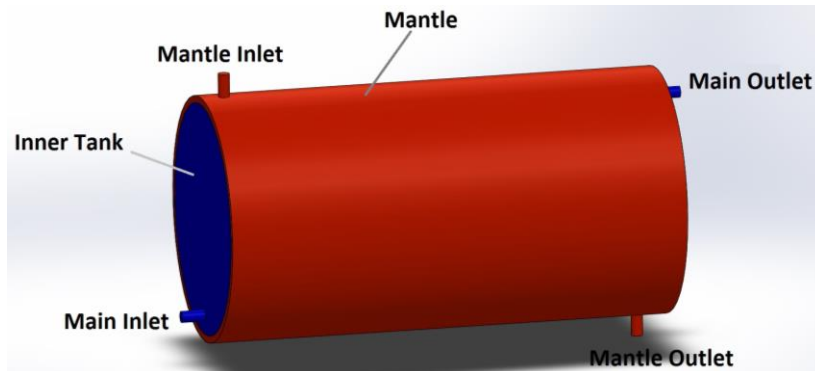
Figure 2. Solid model for the selected case, which is D/L=0.50

Ansys Workbench 18 Mesh software was used for obtaining the numerical model. Fluid volumes were divided into finite volume elements. Mesh structure for D/L=0.50 is seen in Figure 3. Smaller mesh size was used in mantle and inner tank contact surface in order to obtain more sensitive solution for heat transfer and fluid flow in contact surfaces between mantle and inner tank. Different mesh sizes were tried for suppling grip independency from larger size mesh to smaller size mesh. Also, the boundary conditions in inlets and outlets of the tank were defined. Numerical model, which was obtained by Mesh software, was solved by using FLUENT 18 [14]. k-ε turbulence model was used for determining to turbulence effects.
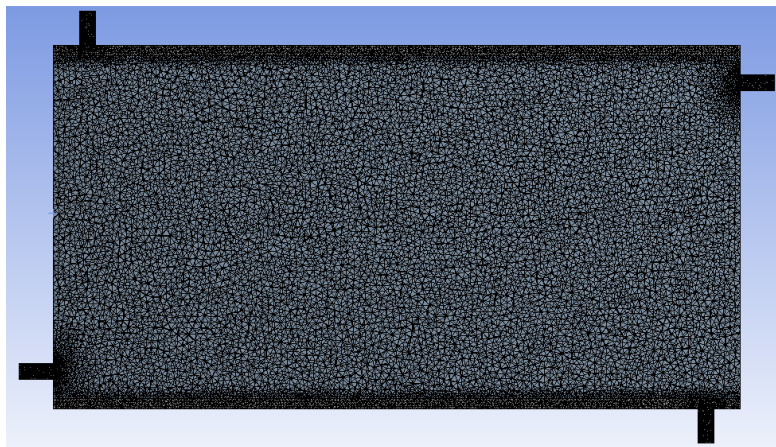
Figure 3. Mesh structure for D/L=0.50.

Mantle inlet temperature and velocity were taken as 350 K and 0.15 m/s, respectively. Main inlet temperature and velocity were taken as 293 K and 0.1 m/s, respectively. The first order upwind numerical schema and Simple algorithm were used to discretize the governing equations. Presto model was used for determining to pressure solving inside the tank. Transient analysis was performed for 120 minutes. Different time steps were used for suppling time step independency. The numerical simulations were conducted in three-dimensional domain. The analysis was based on transient, three-dimensional continuity, momentum and energy equations.

The continuity equation is:

$$\frac{\partial \rho}{\partial t} + \rho\left[\frac{1}{r}\frac{\partial (rV_r)}{\partial r} + \frac{1}{r}\frac{\partial V_\theta}{\partial \theta} + \frac{\partial V_z}{\partial z} = 0\right] \tag{1}$$
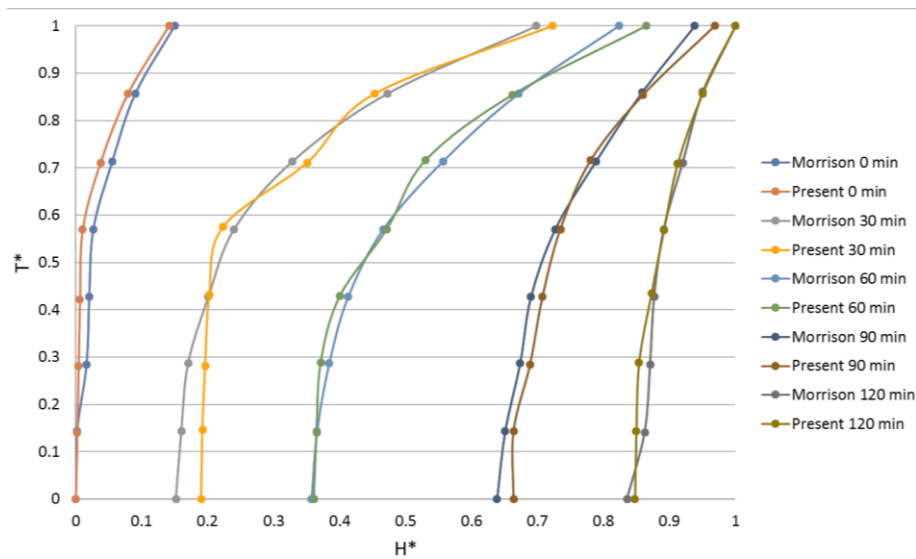

Figure 4. Comparison of the results of numerical and experimental studies

Momentum conservation equations are given in radial, axial and tangential axes, respectively.

$$\rho\frac{\partial V_r}{\partial t} + \frac{1}{r}\frac{\partial (r\rho V_r V_r)}{\partial r} + \frac{\rho}{r}\frac{\partial (V_\theta V_r)}{\partial \theta} + \rho\frac{\partial (V_z V_r)}{\partial z} = -\frac{\partial P}{\partial r} + \mu\left[\frac{\partial}{\partial r}(\frac{1}{r}\frac{\partial (rV_r)}{\partial r})\right] + \mu\left[\frac{1}{r^2}\frac{\partial^2 V_r}{\partial \theta^2} + \frac{\partial^2 V_r}{\partial z^2}\right]$$

$$+ \mu\left[-\frac{2}{r^2}\frac{\partial V_\theta}{\partial \theta}\right] + \frac{\rho V_\theta^2}{r} + \rho g_r\,\beta\,\Delta T \tag{2}$$

$$\rho\frac{\partial V_\theta}{\partial t} + \frac{\rho}{r}\frac{\partial (rV_r V_\theta)}{\partial r} + \frac{\rho}{r}\frac{\partial (V_\theta V_\theta)}{\partial \theta} + \rho\frac{\partial (V_z V_\theta)}{\partial z} = -\frac{1}{r}\frac{\partial P}{\partial \theta} + \mu\left[\frac{\partial}{\partial r}\frac{1}{r}\frac{\partial (rV_\theta)}{\partial r})\right] +$$

$$\mu\left[\frac{1}{r^2}\frac{\partial^2 V_\theta}{\partial \theta^2} + \frac{\partial^2 V_\theta}{\partial z^2}\right] + \mu\left[\frac{2}{r^2}\frac{\partial V_r}{\partial \theta}\right] - \frac{\rho.V_r V_\theta}{r} + \rho g_\theta\,\beta\,\Delta T \tag{3}$$

$$\rho\frac{\partial V_z}{\partial t} + \frac{\rho}{r}\frac{\partial (rV_r V_z)}{\partial r} + \frac{\rho}{r}\frac{\partial (V_\theta V_z)}{\partial \theta} + \rho\frac{\partial (V_z V_z)}{\partial z} = -\frac{\partial P}{\partial z} + \mu\left[\frac{\partial}{\partial r}(\frac{1}{r}\frac{\partial (rV_z)}{\partial r})\right] +$$

$$\mu\left[\frac{1}{r^2}\frac{\partial^2 V_z}{\partial \theta^2} + \frac{\partial^2 V_z}{\partial z^2}\right] + \rho g_z\,\beta\,\Delta T \tag{4}$$

Energy equation is:

$$\rho c_p\frac{\partial T}{\partial t} + V_r\frac{\partial T}{\partial r} + \frac{V_\theta}{r}\frac{\partial T}{\partial \theta} + V_z\frac{\partial T}{\partial z} = k\left[\frac{1}{r}\frac{\partial}{\partial r}\left(r\frac{\partial T}{\partial r}\right) + \frac{1}{r^2}\frac{\partial^2 T}{\partial \theta^2} + \frac{\partial^2 T}{\partial z^2}\right] + \mu\Phi \tag{5}$$

3. RESULTS AND DISCUSSION

3.1. Validation of the Numerical Model and Procedure

Numerical model and procedure were validated with Morrison et al.'s [7] study. Present numerical model was performed with Morrison et al.'s experimental conditions. Numerical results and Morrison et al.'s experimental results were compared. Dimensionless temperature and dimensionless position were used for comparing the results. Dimensionless temperature and position were calculated as follows:

$$T^* = \frac{T_{actual} - T_{min}}{T_{max} - T_{min}} \tag{6}$$

$$H^* = \frac{h}{D} \tag{7}$$

In numerical model, five different mesh sizes were used which are 2.8 million, 3.7 million, 4.8 million, 5.5 million and 6.2 million mesh. After 5.5 million mesh, there is no significant difference between the results. In addition to grid independence, three different time steps (3, 1 and 0.5 s) were tried for time step independency. Since the results weren't changed significantly after 1 s, time step for transient analyses is taken as 1 s. Comparison of the numerical and experimental studies is seen in Fig. 4. As seen from Fig. 4, the result of numerical solution and the result of experimental study [7] shown good agreement.

3.2. The Effect of D/L Ratio

Temperature distributions at the end of 120 minutes for all cases are seen in Fig. 5. As seen from Fig. 5, D/L=0.25 was shown better performance than order cases. Temperature gradient between inlet and outlet of the inner tank was better in D/L=0.25 case.

(a)

(b)
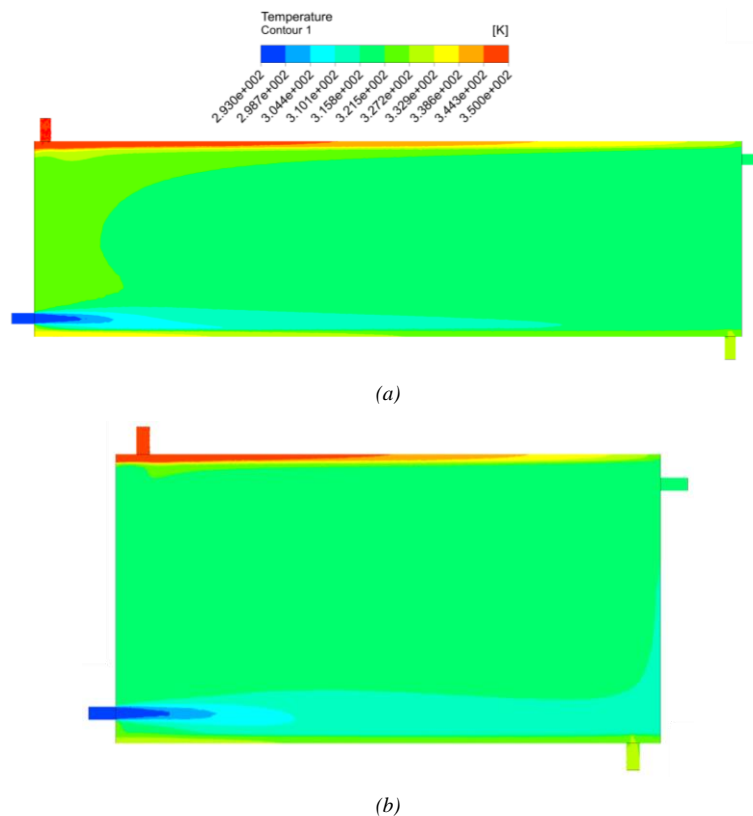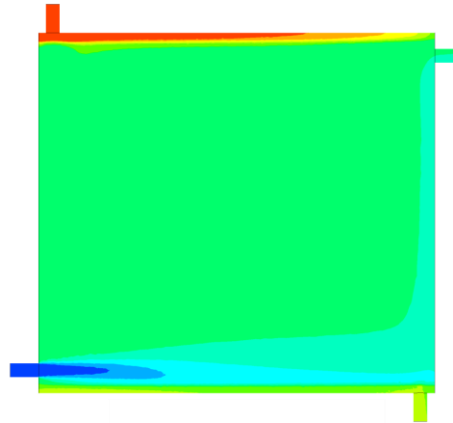
(c)

Figure 5. Temperature distribution for all cases at the end of 120 minutes: a) D/L=0.25, b) D/L=0.50 and c) D/L=0.85

Temperature gradient development for the D/L=0.25 is seen in Fig. 6. In Fig. 6, temperature distribution for D/L=0.25 for t=600, 1800, 3000, 4200, 5400 and 7200 s are shown. This temperature gradient development is compatible with Morrison et al.'s [7] study. When D/L ratio decreased, inlet water jet effect increased because of increasing tank length.
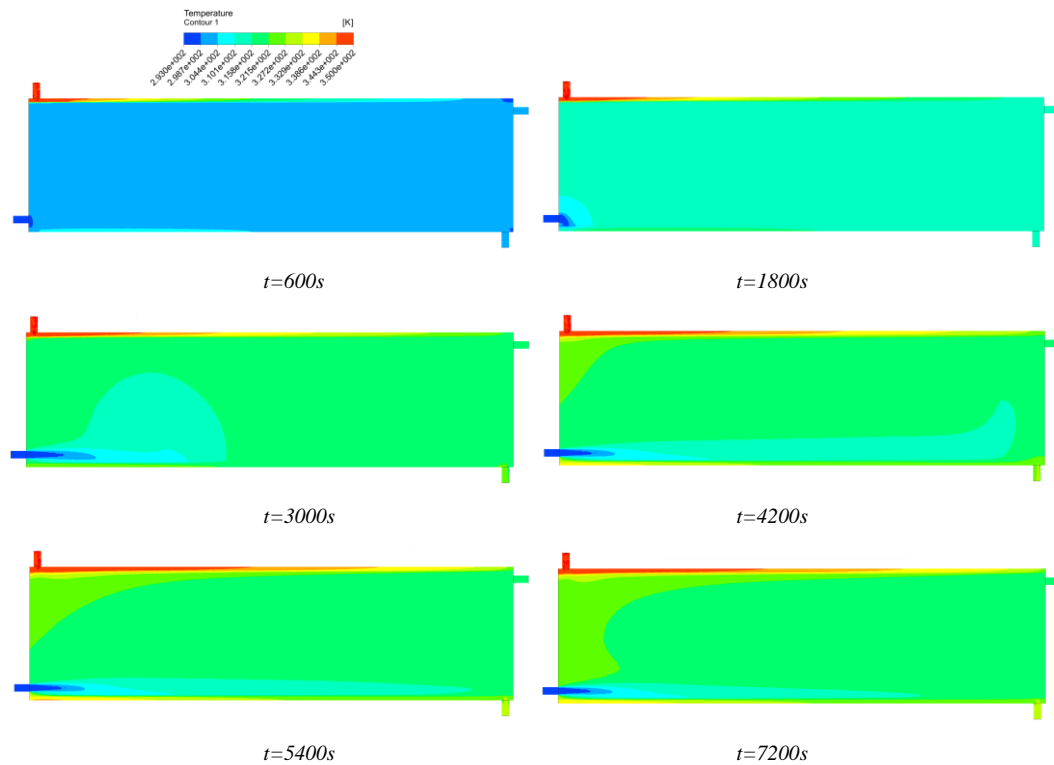

t=600s *t=1800s*

t=3000s *t=4200s*

t=5400s *t=7200s*

Figure 6. Temperature gradient development for the case D/L=0.25

Mantle outlet temperature and main outlet temperature are important for the system performance. Mantle outlet temperature is significant for the collector efficiency and also system efficiency. Mantle outlet temperature is desired as much as lower. Main outlet temperature is important for users. Because solar domestic hot water users desired much volume and higher temperature water. So, main outlet temperature is desired as much as higher. Mantle outlet and main outlet temperatures and their changings with the time are seen in Fig. 7. As seen Fig. 7, mantle outlet temperature was the lowest in D/L=0.25. Additionally, main outlet temperature was the highest in D/L=0.25.

As seen from these results (Fig.5, 6 and 7), the best thermal performance was seen in D/L=0.25. However, heat transfer surface area between mantle and inner tank should be consider. Heat transfer surface area were 1.96, 1.57 and 1.31 m^2 for D/L=0.25, 0.50 and 0.85 for respectively. Larger heat transfer surface area

supplied higher heat transfer amount from mantle to inner tank. So, D/L=0.25 showed the best thermal performance. In this study, the tank volume considered as constant for all cases. When equal heat transfer surface area considered, the results can be different.
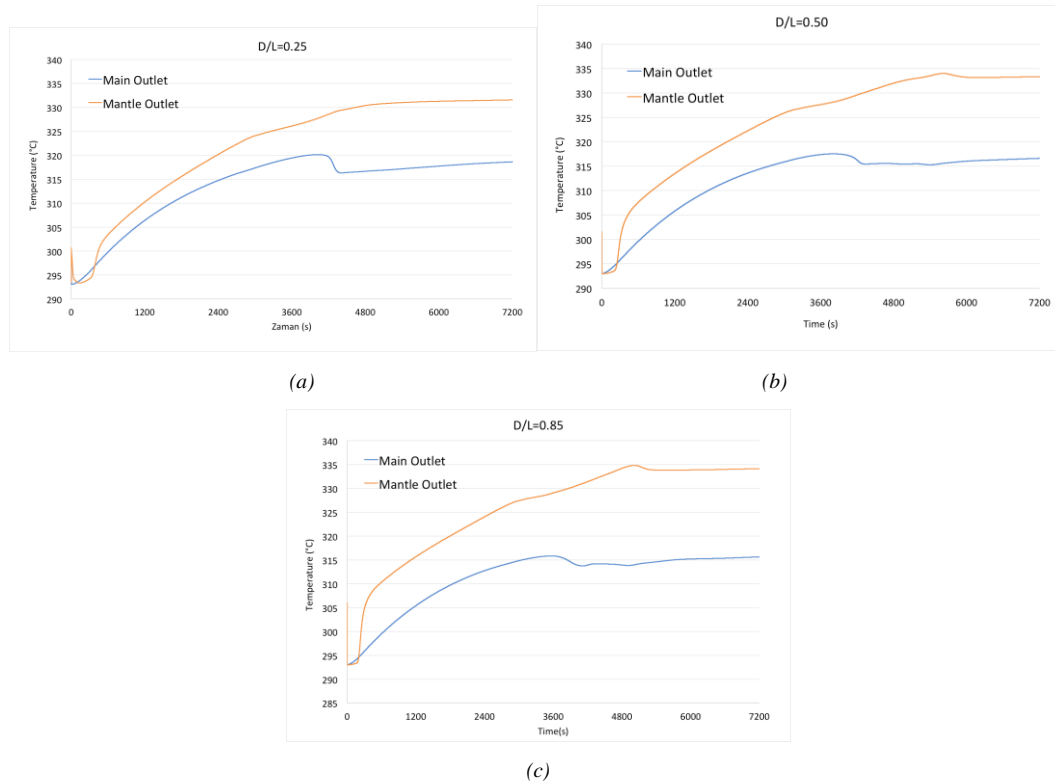

(a)

(b)

(c)

Figure 7. Main and mantle outlet temperature for all cases, a) D/L=0.25, b) D/L=0.50 and c) D/L=0.85

4. CONCLUSIONS

The following concluding remarks can be drawn from the present study:

- When constant tank volume considered, thermal performance of the system increased with decreasing D/L ratio. Because, heat transfer surface area increased with decreasing D/L ratio. So, heat transfer amount increased with decreasing D/L ratio.

- Tank length decreased with increasing D/L ratio. Decreasing length caused to inlet water jet. This situation affected to the tank negatively in the term of thermal performance.

- Mantle outlet temperature decreased with decreasing D/L ratio. Decreasing mantle outlet temperature supplied higher thermal efficiency for the system.

- Main outlet temperature increased with decreasing D/L ratio. Higher main outlet temperature supplied better system performance for system users.

- Mantle hot water tank is also a heat exchanger. Lower mantle outlet temperature and higher main outlet temperature increased the efficiency of heat exchanger. Because logarithmic mean temperature increased with lower mantle outlet and higher main outlet temperatures.

- The situation, which has constant heat transfer surface area for different D/L ratio, should be studied for determining the system performance in the term of the effect of D/L ratio on tank performance.

REFERENCES

[1]. Alizadeh, S. 1999. "An experimental and numerical study of thermal stratification in a horizontal cylindrical solar storage tank", Solar Energy, 66 (6), 409-421.
[2]. Andres A.C., Lopez M.C. 2002. "TRNSYS model of a thermosiphon solar domestic water heater with a horizontal storage and mantle heat exchanger", Solar Energy, 72 (2), 89-98.
[3]. Morrison G.L., Nasr, A., Behnia, M., Rosengarthen, G. 1998. "Analysis of horizontal mantle heat exchangers in solar water heating systems", Solar Energy, 64, 19-31.

[4]. Jannatabadi, M. 2012. "An experimental study of hot water consumption on the thermal performance of a horizontal mantle tank", 19 (9), 1332-1326.

[5]. Helwa, N.H., Mobarak A.M., ESallak M.S., EGhetany H.H. 1995. "Effect of hot-water consumption on temperature distribution in a horizontal solar water storage tank", Applied Energy, 52, 185-197.

[6]. Madhlopa, A., Mgawi, R., Taulo, J. 2005. "Experimental study of temperature stratification in an integrated collector-storage olar water heater with two horizontal tanks", 80, 989-1002.

[7]. Morrison, G.L., Rosengarthen, G., Behnia, M. 1999. "Mantle heat exchangers for horizontal tank thermosyphon solar water heaters", Solar Energy, 67, 53-64.

[8]. Khalifa A.N., Mehdi, M.M. 1999. "On the verification of one dimensional heat flow in a horizontal thermosyphon storage tank", Energy Conversion and Management, 40, 961-974.

[9]. Jannatabadi, M., Taherian, H. 2012. "An experimental study of influence of hot water consumption rate on the thermal stratification inside a horizontal mantle storage tank", 48, 1103-1112.

[10]. Young, M.F., Baughn, J.W. 1981. "An investigation of thermal stratification in horizontal storage tanks", 103, 286-290.

[11]. Rosengarten, G., Morrison, G.L., Behnia, M. 2001. "Mixed convection in a narrow rectangular cavity with bottom inlet and outlet", Heat and Fluid Flow, 22, 168-179.

[12]. Rosengarten, G., Behnia, M., Morrison, G. 1999. "Some aspects concerning modelling the flow and heat transfer in horizontal mantle heat exchangers in solar water heaters", International Journal of Energy Research, 23, 1007-1016.

[13]. SolidWORKS Premium 2018.

[14]. ANSYS Fluent 18.0.

A CFD Based Thermo-Hydraulic Performance Analyses of Different Spherical Capsules Using in Ice Thermal Storage System

Dogan Erdemir[1],*, Necdet Altuntop[1,2] Ali Jasim Al-Bayati[3]

Abstract

This study presents the performance analyses for ice capsules, which are used in encapsulated ice thermal storage system. Capsule shape has great impact on the system performance. Charging time can be decreased or more energy can be stored with the enhanced capsule shapes. Thus, the amount of energy stored in per unit time can be increased. In this study, five different capsule shapes have been investigated numerically and they have been compared with the ordinary sphere ice capsule. In numerical analyses, charging period has been considered. At the end of the study, it is found that modified capsuled have shown better performance according to the ordinary sphere capsule. Also, the capsules, which have surface extension toward to the capsule inside, have supplied shorter charging time. While the full freezing time for ordinary sphere is 2290 s, the freezing time for the modified capsules have varied from 1754 to 2201 s. Ultimately, the numerical model has been validated with experimental study in the literature for ordinary sphere.

Keywords: *Ice thermal energy storage, ITES, Off-peak cooling, Peak load, Solidification modeling*

1. INTRODUCTION

Ice thermal energy storage (ITES) systems are widely used for storing cold capacity, in order to decrease electricity consumption cost and/or chiller capacity. Ice storage systems are divided into static or dynamic systems according to the way ice is delivered to the storage tank. There are two types of ITES, which are static and dynamic. In static system, the ice is produced inside tank storage tank (encapsulated, ice-on-tube, ice-in-coil). In dynamic system, the ice is produced outside of the tank (ice slurry). Encapsulated ITES system is used in many commercial applications.

Ismail and Henriquez [1], investigated spherical encapsulated ITES. They used 1-D numerical model and validated their result with experimental study. They used different capsule materials. At the end of their study PVC is the most suitable material for capsule in the terms of heat transfer and production cost. Kousksou et al. [2] researched tank position. They emphasized that tank should be vertical for better performance. MacPhee et al. [3] researched different capsule geometry. Sphere capsule supplied better performance. Chaichana et al. [4] investigated the economic performance of ice-on-coil systems. ITES system saved 55 % in full storage, 15 % in partial storage. Cho and Choi [5], used paraffin instead of water inside the capsule. Erek and Dincer [6], investigated temperature changing through the flow direction. They emphasized that heat transfer coefficient decreased through the flow direction. Ezan et al. [7], developed thermal resistant mesh model for heat transfer analysis. Ismail et al. [8], used finite difference model for spherical encapsulated ITES. Chen and Yue [9-10] applied porous medium equation into encapsulated ITES. Ryu et al. [11] investigated super-cooling effect in ITES. Super-cooling was seen in inlet and outlet of the tank. Calvet et al. [12] added graphite inside the capsule. Amin et al. [13] developed a new model consists buoyancy forces and density changing with the temperature. ElGhnam et al. [14] studied the freezing and melting of water inside a spheriacal capsule of the often found in the beds of ITES systems.

There are many study related to encapsulated ITES in literature. Also, there are some studies investigated to capsule shapes, too. At the end of these studies, it is found that the spherical capsules show better thermal performance than cylindrical and rectangular capsules. In addition, there are many modified capsules in commercial application. However, there is no clear study about to investigate the thermal performance of modified capsules. The main goal of the present study is to determine the thermal performance of modified spherical capsules and also to compare with ordinary spherical capsule during the charging period.

2. MATERIAL AND METHOD

2.1. The Ice Capsules

Five modified different ice capsules have been investigated numerically. The studied ice capsules are seen in Fig.1. Capsules are named as Capsule A, B, C, D, E and F. As seen from Figure 1, Capsule A is an ordinary sphere capsule. Capsule B and C have extended surface into the capsule inside. Capsule E and F have extended surface into the capsule outside and Capsule D has with hole thought the diameter. Two main objectives of the modifying the capsule are to extent capsule surface area and to increase turbulent effects over the capsule. Heat transfer rate from heat transfer fluid (HTF) and capsule increases with the increasing surface area and turbulent effect. The diameters of capsules are different for each capsule due to supply equal water volume inside the capsules. The diameter differences among the studied capsules are approximately -1.2% and +1.5%. These differences don't have significant effect on the HTF flow and heat transfer between HFT and capsule. Capsule thickness hasn't been modeled. The capsule thickness and materials have been entered during the numerical analysis.
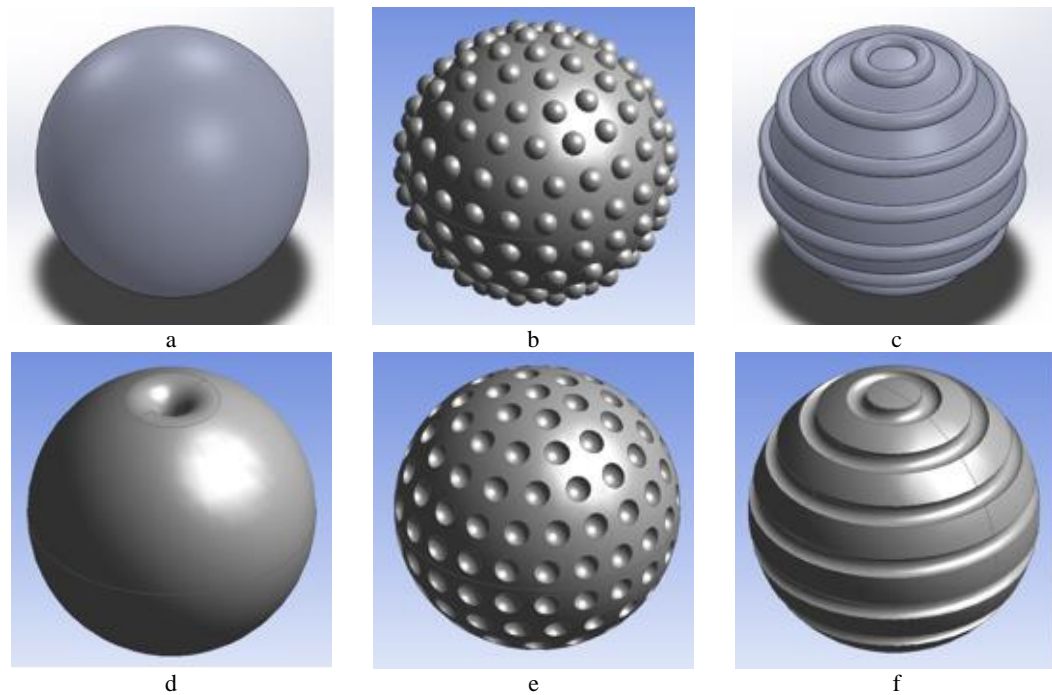
Figure 94. The studied capsules a) Capsule A b) Capsule B c) Capsule C d) Capsule D e) Capsule E f) Capsule F

2.2. Numerical Model and Procedure for Ice Capsules

Schematic view of the numerical system is shown in Figure 2. Numerical model has been built up base on the ElGhanam et al.'s [14] study. They performed an experimental study in order to determine the effect of the capsule material, capsule diameter, inlet temperature of HTF and flow rate of HTF on thermal performance for ice capsule. The dimensions of present numerical model and ElGhanam et al.'s study are also seen in Figure 2. Solid sections haven't been modeled in numerical model. Grid construction for ordinary sphere capsule and Capsule B are seen in Figure 3. This figure has been taken from mid-plane. In order to enhance heat transfer model, the smaller mesh size has been used in contact surfaces. Workbench 18 has been used for built up to numerical model. Different mesh sizes have been used for gathering grid independency.

Table 56. Physical features for HTF, water and ice.

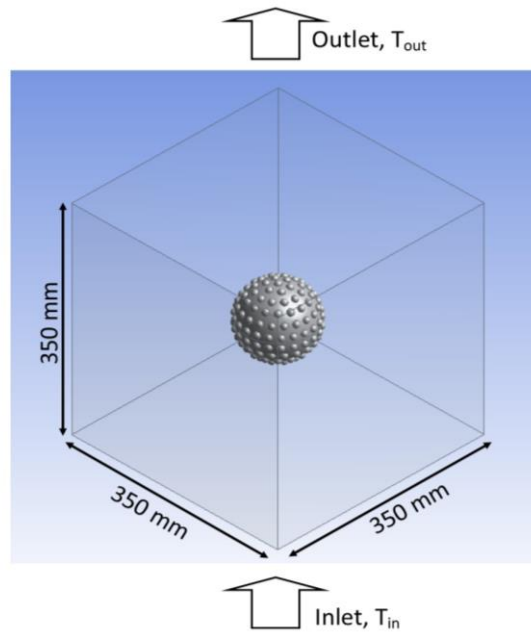| Material	Density	Specific Heat	Conductivity	Viscosity
	kg/m^3	J/kg K	W/m K	kg/m s
HTF	1058	3605	0.465	0.0085
Water	998.2	4182	0.6	0.001003
Ice	915	2200	0.0454	1.72×10^{-5}

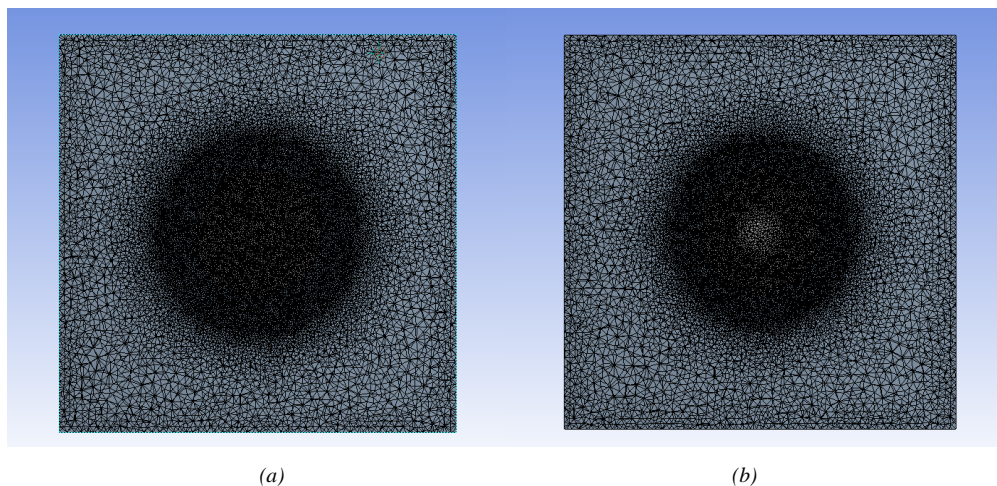*Figure 2. Numerical model of the system (Capsule B).*

(a)   *(b)*

Figure 3. Numerical models for a) ordinary sphere capsule, Capsule A and b) Capsule B
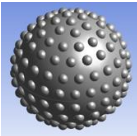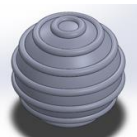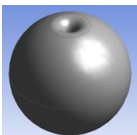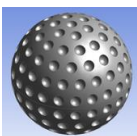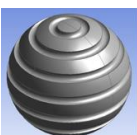
Fluent 18 [15] has been used for the numerical analyses. 3-D and transient numerical analyses have been performed. Solidification&Melting option has been used for modeling to freezing. Also, different turbulence models have been tried to get better solution. Additionally, different time steps have been performed in order to supply solution independency in the terms of time step. Specific features for the HTF, water and ice have been considered temperature independent (Table 1). 30% glycol-ethylene has been used as HTF. Latent heat

for water/ice phase changing has been taken as 333,5 kJ/kg. Solidification temperature has been set as 273.15 K. Coupled algorithm scheme has been used during the calculation for pressure-velocity coupling. PRESTO method has been used for pressure solutions. HTF inlet temperature and velocity have been taken as 263 K and 0.01 m/s, respectively. Numerical analyses have been performed until all water volume freezing. Analyses have run for charging period.

3. RESULT AND DISCUSSIONS

In this study, six different ice capsules have been investigated numerically. The performance of the ice capsules has been evaluated in the terms of charging time. Because the charging time is an important issue for ITES system. Lower charging time increased the system performance. Charging times of the studied capsules are given in Table 2.

Table 2. Charging time of the studied capsules.

Capsule Name	View of the Capsule	Charging Time (s)
Capsule A		2290 s
Capsule B		2094 s
Capsule C		2201 s
Capsule D		1929 s
Capsule E		1754 s
Capsule F		1772 s

As seen from Table 1, the modified capsules have reduced charging time. Because modified capsules have caused to increasing to turbulent effects over the capsule. Heat transfer rate has increased with the increasing turbulent effects. Most importantly, inward extended surfaces (Capsule E and F) have performed better than outward extended surfaces (Capsule B and D). Because, inward extended surface has supplied better thermal gradient according to outward extended surfaces. Also, Capsule D has also shown a good performance in terms of charging time. However, it should be considered that HTF flow has occurred along the hole. In fact, there are many capsules in the tank and it is not possible to adjust the positions of the capsules. So, Capsule D behavior can be different in real applications.

Temperature and velocity contour for all capsules are seen in Fig. 4. As seen from Fig. 4, the capsules, which supply shorter charging time, have better temperature distribution over the capsule. Temperature gradient layer is thicker than ordinary capsule (Capsule A). Also, turbulent effects for the modified capsules are clearly seen in Fig.4.
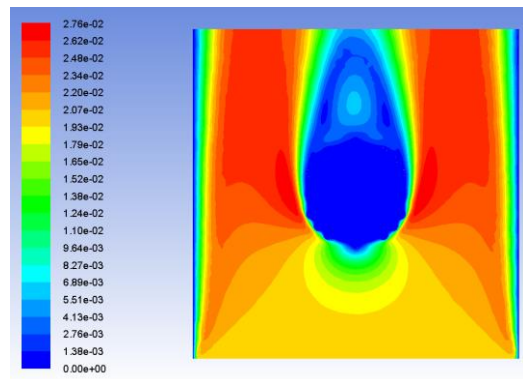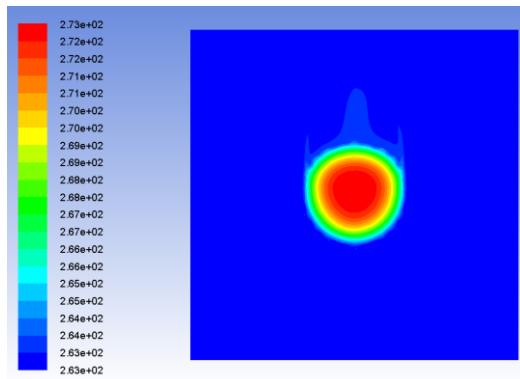
Temperature Contour
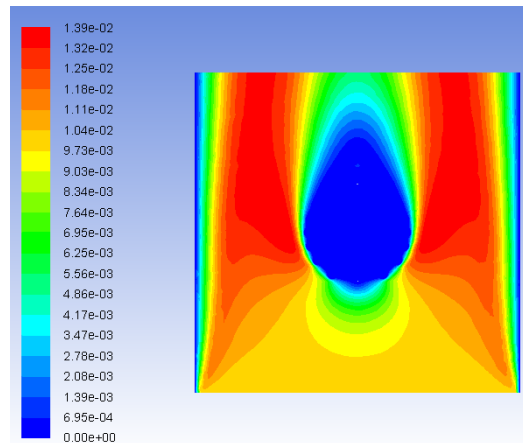Velocity Contour
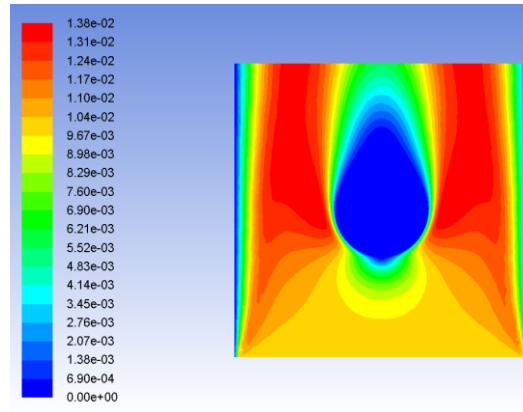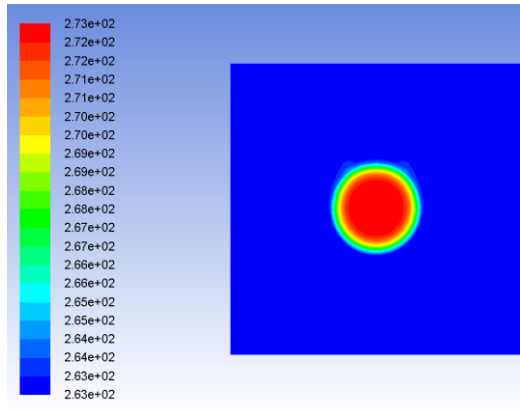
Capsule A
Capsule A

(a)

Capsule B
Capsule B

(b)

Capsule C
Capsule C

(c)

Capsule D   *Capsule D*

(d)
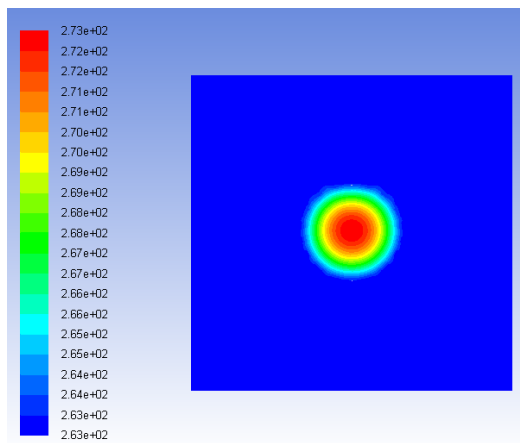

Capsule E   *Capsule E*

(e)

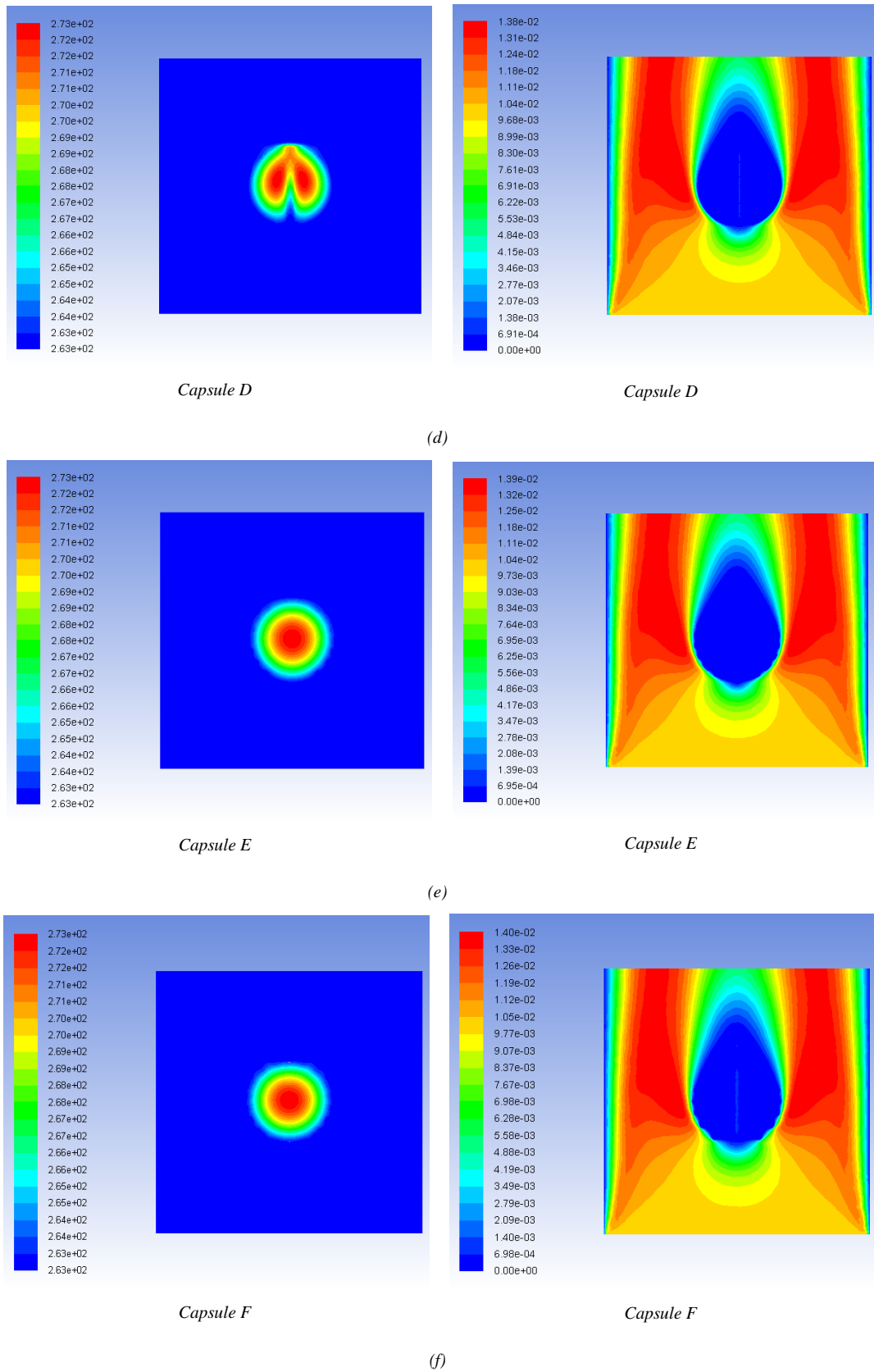*Capsule F*   *Capsule F*

(f)

Figure 4. Temperature and velocity contours for all studied capsules a) Capsule A, b) Capsule B, c) Capsule C, d) Capsule D, d) Capsule E and Capsule F

4. CONCLUSIONS

The following concluding remarks can be drawn from the present study:

- Modified ice capsules have shown better thermal performance according to ordinary sphere capsule.

- The capsules, which have inward extended surfaces, have shown better thermal performance than the capsules, which have outward extended surfaces.

- Modified capsules have increased temperature boundary layer thickness and turbulent effects. So they supply shorter charging time.

- Different capsule geometries and combine configurations should be studied.

- Discharging performance of the capsules should be studied.

- Thermal stress should be considered and studied for all cases. Because, although inward extended surfaces have supplied shorter charging time, it may become damaged and become unusable in a shorter time.

ACKNOWLEDGMENT

REFERENCES

[15]. Ismail, K.A.R., Henriquez, J.R., 2002. Numerical and Experimental Study if Spherical Capsules Packed Bed Latent Heat Storage System. Applied Thermal Engineering, 22: 1705-1716.
[16]. Kousksou, T., Bedecarrats, J.P., Dumas, J.P., Mimet, A., 2005. Dynamic Modelling of the Storage of an Encapsulated Ice Tank, 25: 1534-1548.
[17]. MacPhee, D., Dincer, I., Beyene, A., 2012. Numerical Simulation and Exergetic Performance Assessment of Charging Process in Encapsulated Ice Thermal Energy Storage System. Energy, 41: 491 – 498.
[18]. Chaichana, C., Charters W.W.S., Aye, L., 2001. An Ice Thermal Energy Storage Computer Model. Applied Thermal Engineering, 21: 1769 – 1778.
[19]. Cho, K., Choi, S.H., 2000. Thermal Characterictics of Paraffin in a Shperical Capsule During Freezing and Melting Processes. International Journal of Heat and Mass Transfer, 43: 3183 – 3196.
[20]. Erek, A., Dincer I., 2009. Numerical Heat Transfer Analysis of Encapsulated Ice Thermal Energy Storage Systems with Variable Heat Transfer Coefficient in Downstream. International Journal of Heat and Mass Transfer, 52: 851 – 859.
[21]. Ezan, M.A., Erek, A., Dincer, I., 2011. Energy and Exergy Analyses of an Ice-on-Coil Thermal Energy Storage System. Energy 36: 6375 - 6386.
[22]. Ismail, K.A.R., Henquez, J.R., da Silva, T.M., 2003. A parametric study on ice formation inside a spherical capsule. International Journal of Thermal Sciences 42: 881-887.
[23]. Chen, S.L., Yue, J.S., 1991. Thermal performance of cool storage in packed capsuled for air conditioning. Heat Recovery Systems and CHP, 11: 551-531.
[24]. Chen, S.L., Yue, J.S., 1991. A simplified analysis for cold storage in porous capsules with solidification. Energy Resources, 113: 108-116.
[25]. Ryu, H.W., Hong, S.A., Shin, B.C., Kim, A.D., 1991. Heat transfer characterictics of cool-thermal storage systems. Energy 16: 727-737.
[26]. Calvet, N., Py, X., Olives, R., Bedecarrats, J.P., Dumas, J.P., Jay, F., 2013. Enhanced performances of macro-encapsulated phase change materials (PCMs) by intensification of the internal effective thermal conductivity. Energy 55: 956-964.
[27]. Amin, N.A.M., Bruno, F., Belusko, M., 2014. Effective thermal conductivity for melting in PCM encapsulated in a sphere. Applied Energy 122: 280-287.
[28]. ElGhnam R.I., Abdelaziz R.A., Sakr M.H., Abdelrhman H.E., 2011. An experimental study of freezing and melting of water inside spherical capsules used in thermal energy storage systems.
[29]. ANSYS® Academic Research, Release 18.0, Help System, Solidification and Melting Analysis Guide, ANSYS, Inc.

Prediction of Temperature Decreasing on a Green Roof by Using ANN: Budapest Example

Dogan Erdemir[1], Necdet Altuntop[1,2]

Abstract

This study presents an artificial neural network (ANN) model to predict temperature decreasing on a green roof for Budapest, Hungary. The ANN model has been created by MATLAB Neural Network Toolbox. Training, test and validation data of the ANN model have been taken from nine different cities around the world. Meteorological data sets and temperature decreasing values on the green roof for these nine cities have been obtained from the study, which is situated in literature. ANN model has indicated sufficient results with 0.3982% RMSE and 99.05% R^2. This ANN model has been used for estimating the temperature decreasing on the green roof for Budapest, Hungary. At the end of this study, green roof has decreased the roof temperature up to 31 °C. The highest temperature decreasing has been observed at 18:30. The reduced roof temperature helps to decrease the air conditioning capacity and also electricity consumption for air conditioning.

Keywords: *Green roof, temperature decreasing, thermal comfort, artificial neural network, roof cooling*

1. INTRODUCTION

A green roof or living roof is a roof, which is covered a layer of soil on the roof area to grow plant. The roof of a building is completely or partially covered with vegetation and a growing medium, planted over a waterproofing membrane. The history of green roof is very ancient. In ancient times, the use of green roofs has begun in natural ways [1]. However, today, green roof system is a commercial application. Since green roof is used as commercial application, the determining of performance of the green roof is important for researchers. Green roof has two significant effects. These are the effect of decreasing roof surface temperature and the effect of heat insulation. Therefore green roof supplies better thermal comfort condition; better indoors air quality and energy savings [2], [3].

In many studies, green roof systems are compared with ordinary roofs. The comparisons are made on the basis of the temperature decreasing or the heat gain from the roof. These studies show that green roof has great impact on roof surface temperature. These comparing gives different results according to different geographic regions and climatic conditions. These studies show that green roof is an effective tool in all climatic conditions to reduce the temperature on the roof surface [4]-[6]. Heat gains from roof surface in summer season and heat loss from roof surface in winter season do not desire. The effect of green roof on heat gain and loss for a residential building has been experimentally researched in many studies [7]-[10]. These studies show that green roof decreases heat gain from roof surface up to 40% in summer. Also, it supplies heat gain instead of heat loss in winter.

There many experimental studies in literature related to green roof and its performance. Experimental studies are either small-scale studies in the laboratory or real-world studies [11]-[14]. Small-scale laboratory work requires high-cost equipment. In addition to this, the experimental works carried out under real conditions are long-term studies. Expensive or long experimental studies have encouraged researchers to use numerical modeling and estimation methods. Since there are many studies about green roof application, it is possible to reach many experimental data. Thus, different theoretical and numerical methods have been appeared. Cooling potential for Ujjain city has been trained and tested with ANN by taking data from experimental

---

[1] Corresponding author: Erciyes University, Department of Mechanical Engineering, 38039, Melikgazi, Kayseri, Turkey. erdemir@erciyes.edu.tr

[2] Erciyes University, Energy Conversion Research and Application Center, 38039, Melikgazi, Kayseri, Turkey. altuntop@erciyes.edu.tr

studies. In that study, experimental results and ANN result have been compared. Experimental and ANN results show good agreement to each other [15], [16]. The efficiency of green roof in some cities in Europe has been investigated traditionally in the terms of traditional and green roof temperature [17]. Also, there are some studies about ANN usage for green roof efficiency comparing [18]. Evaluation of green roof in the terms of energy is summarized in [19]. Investigation of convenience of the green roofs for a region requires both a few years study duration and expensive open area experiments [4], [20], [21]. In addition to this, there are some empirical equations gathering from experimental studies to determine green roof efficiency [7], [22].

In this study, it is addressed that the temperature decreasing arising from green roof has been investigated by using ANN in Budapest, Hungary. Climatic conditions and temperature decreasing values of the green roof for different cities around the world have been used as training data for ANN [6]. This developed ANN model has been used for estimating the temperature decreasing at the green roof in Budapest.

2. MATERIAL AND METHOD

2.1. Training, Test and Validation Data for ANN

In this study, the training, test and validation data have been taken from the Alexsandri and Jones's [2] study. Nine different cities from different climatic condition around the World have been used. These cities and their climatic features are given in Tab.1. Total solar radiation, temperature, wind speed and relative humidity were used as climate data for inputs of the ANN. Temperature decreasing values have been used as outputs of the ANN. Table 57. Nine different world cities used in the ANN modeling and their climatic characteristics

Table 58. Nine cities, which are used in ANN training and test data

City	Climate
London, England	Temperate
Montreal, Canada	Subarctic
Moscow, Russia	Continental, cool summer
Athens, Greece	Mediterranean
Beijing, China	Steppe
Riyadh, Saudi Arabia	Desert
Hong Kong, China	Humid, subtropical
Mumbai, India	Rain forest
Brasilia, Brazil	Savanna

Hourly total solar radiation, air temperature, wind velocity and relative humidity for the nine World cities are seen in Fig. 1. As seen from Fig. 1, training the data used in ANN training addresses a very large climatic range. Hourly climatic data has been derived from METEONORM [23]. These values are the average of 24 hours of the hottest month of the year for each city. Temperature decreasing values getting above 1 m from the green roof surface have been taken from Alexsandri and Jones's study [2]. Temperature decreasing values are seen in Fig. 2.

2.2. ANN Model

ANN is a computational model composed of neurons, which are used for solving complex functions. A neural network consists of three layers. These are the input layer, hidden layer and output layer. The input layer consist all the input factors considered in study (hour, total solar radiation, air temperature, wind velocity and relative humidity). Input parameters are processed according to neuron weights in hidden layer. Output value is calculated with its weight in the output layer. Generally, the hidden and output layers have an activation function. ANN modeling consists of three stages, which are the training, test and validation. In training step, the inputs are introduced to the network together with desired outputs. The weights and bias values are initially chosen randomly. The weights of neurons are adjusted during the training step. The purpose of

training algorithm is to minimize the global error level. When a satisfactory level of performance is reached the training is ended and the network uses weights to make decisions.
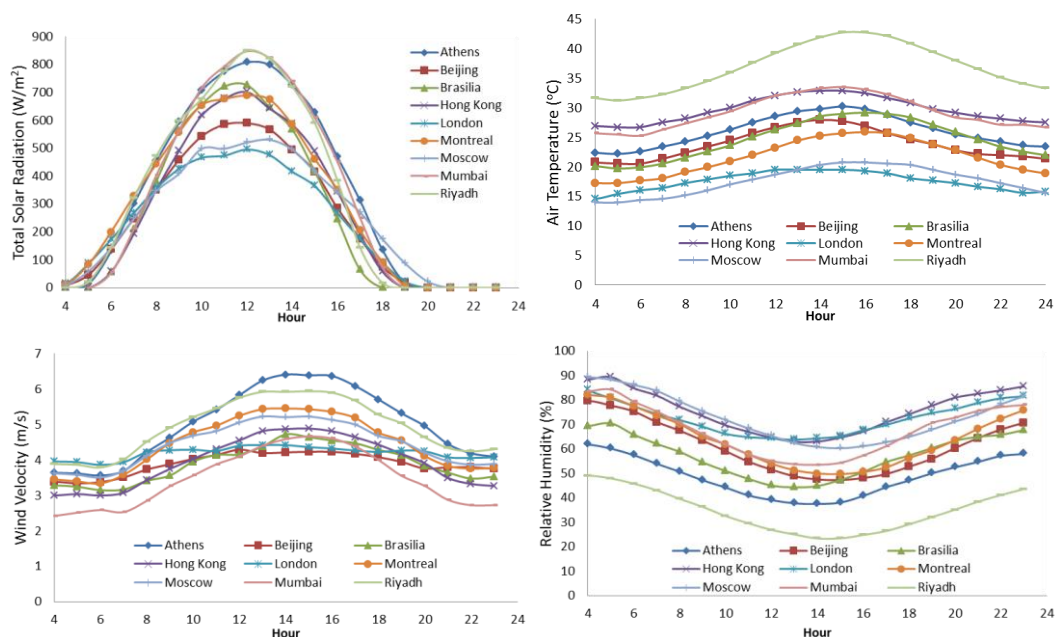

Figure 1. Hourly total radiation, air temperature, wind velocity and relative humidity for nine World cities.
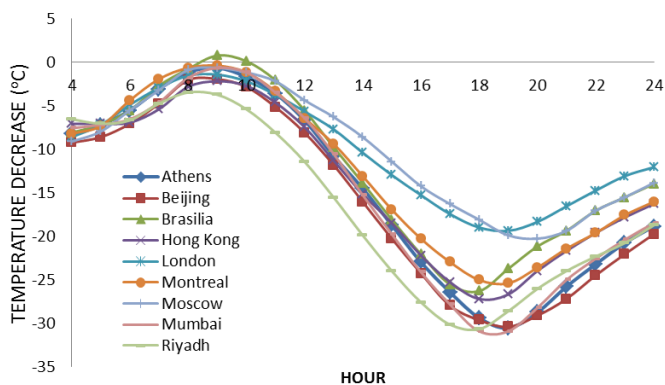

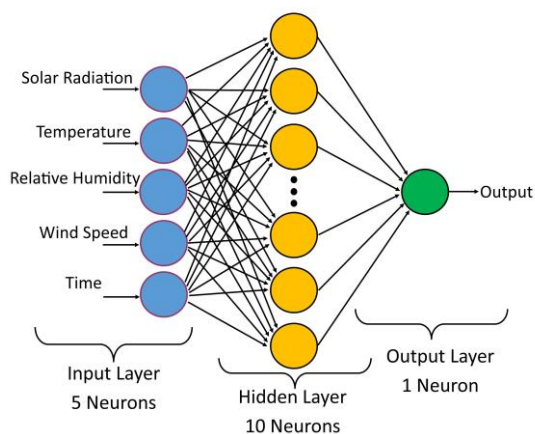*Figure 2. Hourly temperature decreasing values for nine World cities.*

Figure 3. The schematic view of ANN model considered in the present study.

Matlab Neural Network Toolbox [24] has been used for build up the ANN model. The schematic view of ANN model is given in Fig. 3. ANN model has three layers, which are input, hidden and output layers. The input layer has five neurons and the output layer has just one layer. The amount of neuron in hidden layer has important effect on the ANN model performance. Because of this reason, different neuron numbers have been tried. Also, different ANN training algorithms have been applied the model to obtain minimum error value.

3. RESULTS AND DISCUSSION

In this study, the effect of green roof on temperature decreasing on the roof surface has been investigated by using the ANN for Budapest. Hourly total solar radiation, air temperature, relative humidity and wind speed have taken from METEONORM [23]. During the ANN training process, different training algorithms and hidden layer neuron counts have been tried. Hidden layer neuron count is significant for the ANN performance. So, different neuron counts have been tries from 5 to 20. ANN performance has not changed after 10 neurons. Therefore, neuron count in hidden layer has been taken as 10. Three different training algorithm have been applied to the ANN. Training algorithms and their performances have been seen in Tab. 2. As can be seen from Tab.2, Levenberg-Marquardt back propagation algorithm has shown the best performance. So, Levenberg-Marquardt back propagation has been selected for training algorithm.

Table 2. The performance of training algorithms

Algorithm	Train	Test
Levenberg-Marquardt	0.99777	0.98854
Bayesian Regulation	0.99105	0.98189
Scaled Conjugate	0.98708	0.97689

In order to validate the ANN, temperature decreasing in World cities, which are used in training, has been estimated and compared. In Fig. 4, the estimated temperature decreasing data and the calculated temperature decreasing values, which are gather from Alexsandri and Jones's study [2]. As seen from Fig. 4, the ANN model has successfully predicted to temperature decreasing. There is little difference between the estimated and calculated temperature decreasing values.
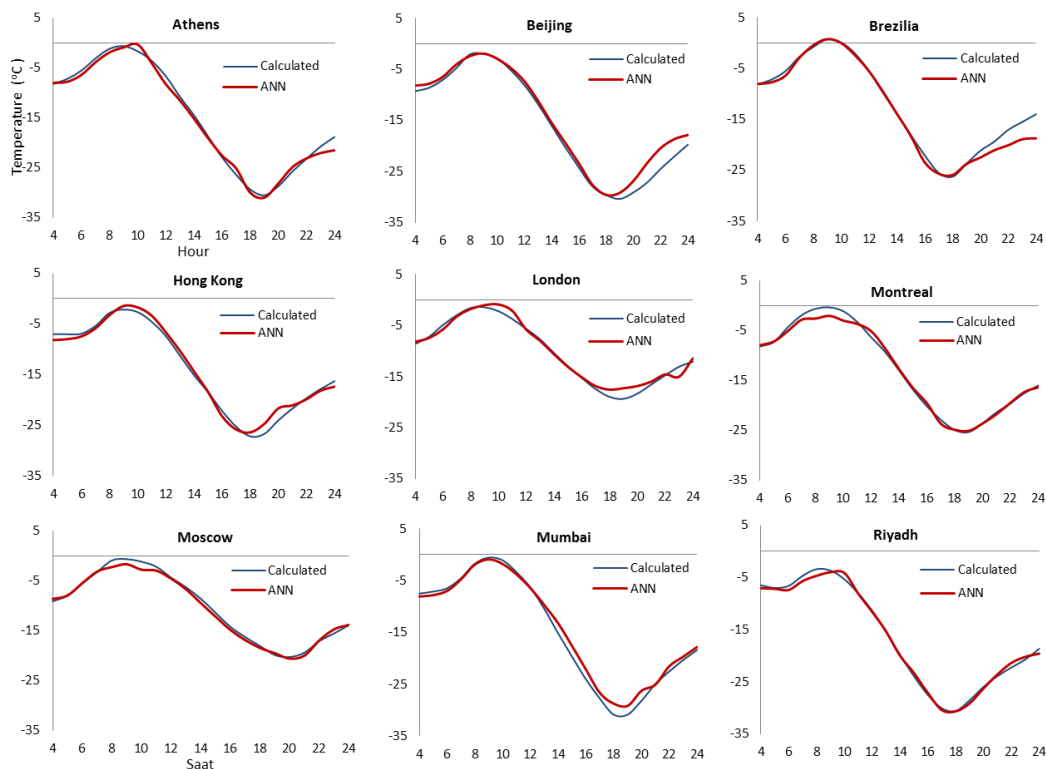

Figure 4. Comparing the calculated and estimated hourly temperature decreasing values for nine World cities.

Temperature decreasing values for Budapest is seen in Fig. 5. As can be seen from Fig. 5, the highest temperature decreasing is between 18:00 and 19:00. Even in the hottest hours of the day, green roof reduces the roof temperature on the roof surface. Temperature decreasing in Budapest is similar to the temperature decreasing in Athens and Beijing. Because relative humidity and solar radiation have important effect on temperature decreasing over the roof surface. So, temperature decreasing value is similar in these cities.

These results show that green roof can be good issue for the Budapest in order to decreased cooling load of the buildings. With decreasing cooling load, energy consumption can be reduced. Therefore, carbon emission and global warming effects can be decreased.
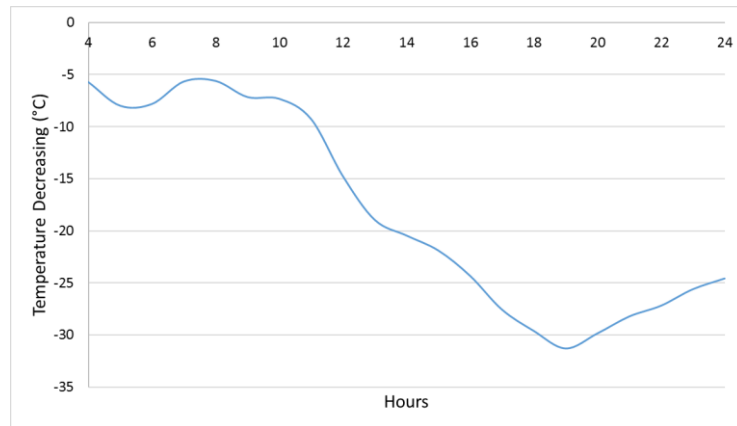

Figure 5. Temperature decreasing values for Budapest.

4. CONCLUSION

This study presents the effect of green roof utilization on temperature decreasing for Budapest, Hungary. An ANN model has been built up for estimating to temperature decreasing. Training data for the ANN has been taken from the study situated in literature. After the ANN training, it is determined that the ANN model has given sufficient result with 2.2894% RMSE and 94.01% R^2. This result shows that ANN model is a good tool for estimating to the performance of green roof. Budapest has a favorable climate in terms of green rood. The maximum temperature decreasing value has seen at 18:00 with 31.28 °C. During the day, green roof has decreased the roof temperature. With the use of the green roof in Budapest, the heat gain can be significantly reduced. Thus, the thermal comfort of buildings is ensured while less energy is consumed.

REFERENCES

[1]. (2016) Available: http://www.roofportland.com/guide-to-living-roofs-embracing-green-roof-systems-in-portland-2/

[2]. E. Alexandri and P. Jones, Developing a one-dimensional heat and mass transfer algorithm for describing the effect of green roofs on the built environment: comparison with experimental results, Building and Environment, vol. 42, pp.2835-2849, 2007.

[3]. ROOFSOL: Roof Solutions for natural cooling. Contract No. JOR3CT960074, Commission of the European Communities, DG XII Science, Research and Development.

[4]. T. Ayata, P. C. Tabarez-Velasco, J Srebric, An investigation of sensible heat fluxes at a green roof in a laboratory setup, *Building and Environment*, 46, 1851–1861, 2001.

[5]. S. Gaffin, C. Rosenzweig, L. Parshall, D. Beattie, R. Berghage, G. O'keeffe, D. Braman, Energy Balance Modeling Applied To A Comparison Of White And Green Roof Cooling Efficiency, Center For Climate Systems Research, Columbia University, 2880 Broadway, New York, Ny, 10025 / 2, Penn State Center For Green Roof Research, Department Of Horticulture, Penn State University, 301 Tyson Building, University Park, Pa, 16802

[6]. E. Alexandri, P. Jones, Temperature decreases in an urban canyon due to green walls and green roofs in diverse climates, *Building and Environment*, Volume 43, Issue 4, Pages 480-493, 2008.

[7]. D. J. Sailor, A green roof model for building energy simulation programs, Energy and Buildings 40, 1466–1478, 2008.

[8]. P. C. Tabares-Velasco, Predictive heat and mass transfer model of plant-based roofing materials for assessment of energy savings, *The Pennsylvania State University*, 180 pages; 3399713, 2009.

[9]. D. Kolokotsa, M. Santamouris, S. C. Zerefos, Green and cool roofs' urban heat island mitigation potential in European climates for office buildings under free floating conditions, *Solar Energy*, vol.95, pp.118–130, 2013.

[10]. A. F. Speak, J.J. Rothwell, S.J. Lindley, C.L. Smith, Reduction of the urban cooling effects of an intensive green roof due to vegetation damage, *Urban Climate*, 3, 40–55, 2013.

[11]. S. N. Ondimu, H. Murase, Combining Galerkin Methods and Neural Network Analysis to Inversely determine Thermal Conductivity of Living Green Roof Materials, *Biosystems Engineering,* vol.96, pp.541–550, 2007.

[12]. R. N. Hilten, T. M. Lawrence, E. W. Tollner, Modeling stormwater runoff from green roofs with HYDRUS-1D, *Journal of Hydrology*, vol.358, pp.288– 293, 2008.

[13]. S. W. Tsang, C. Y. Jim, Theoretical evaluation of thermal and energy performance of tropical green roofs, *Energy*, 36, 3590-3598, 2011.

[14]. I. Jaffal, S. Ouldboukhitine, R. Belarbi, A comprehensive study of the impact of green roofs on building energy performance, *Renewable Energy*, 43, 157-164, 2012.

[15]. S. Pandey, D. A. Hindoliya, R. Mod, Artificial neural networks for predicting indoor temperature using roof passive cooling techniques in buildings in different climatic conditions, Applied Soft Computing, Volume 12, Pages 1214-1226, 2012.

[16]. S. Pandey, D.A. Hindoliya, R. Mod, Artificial neural network for predation of cooling load reduction using green roof over building in Sustainable City, Sustainable Cities and Society, Volume 3, Pages 37– 45, 2012

[17]. F. Ascione, N. Bianco, F. de' Rossi, G. Turni, G. P. Vanoli, Green roofs in European climates are effective solutions for the energy savings in air-conditioning?, Applied Energy, Volume:104, Pages: 845–859, 2013.

[18]. A. Ashtiani, P. A. Mirzaei, F. Haghighat, Indoor thermal condition in urban heat island: Comparison of theartificial neural network and regression methods prediction, Energy and Buildings, 76, 597–604, 2014.

[19]. O. Saadatian, K. Sopian, E. Salleh, C. H .Lim, S. Riffat, E. Saadatian, A. Toudeshki, M .Y. Sulaiman, A review of energy aspects of green roofs, Renewable and Sustainable Energy Reviews, 23, 155–168, 2013.

[20]. P. C. Tabares-Velasco, and J. Srebric, The Role of Plants in the Reduction of Heat Flux through Green Roofs: Laboratory Experiments, ASHRAE Transactions, 115(2) 2009.

[21]. T. G. Theodosiou, Summer period analysis of the performance of a planted roof as a passive cooling technique, Energy and Buildings 35, 909–917, 2003

[22]. J. W. Deardorff, Efficient prediction of ground surface temperature and moisture, with inclusion of a layer of vegetation, Journal of Geophysical Research 83, 1889–1903, 1978.

[23]. J. Remund, R. Lang, S. Kunz, Meteonorm, version 3.0, Meteotest, Bern, 1997.

SIMULATION of DRAINAGE PROCESS in SPORT FIELDS SUBJECT to VARIOUS RAINFALL INTENSITIES and VARIOUS DRAINAGE LAYER ORIENTATIONS

Ahmet Dogan[1], Emmanuel Rukundo[2], Hayrullah Agaccıoglu[3], Erdal Kesgin[4]

Abstract

The simulation of water transport and drainage in unsaturated layered soils is challenging due to the contrast of hydraulic properties and the dependence of hydraulic conductivity on saturation. This study deals with the simulation of soil water dynamics, retention and drainage process in a sport field under various rainfall intensities. The experimental setup of coarse layered soils and root zone layer covered by grass was subjected to the rainfall simulators. Matrix water potential sensors (MPS-6) and soil moisture sensors (10 HS) were installed into the soil layers in order to accurately measure the water potential and volumetric water content respectively during the infiltration and drainage process. The nonlinearity problem of water flow in unsaturated soil was settled by Richards' equation through the HYDRUS model. The hydraulic properties were estimated by laboratory means and inserted into HYDRUS and the modelled soil water retention curves were described by using the Van Genuchten model. The HYDRUS model realistically simulated soil water content throughout the water flow in unsaturated soil and drainage period. The model results and experimental measurements were compared for various rainfall rates and various drainage layer orientations. The outcomes of this study yields important insights into comprehension of water dynamics in unsaturated coarse soils and quick drainage of a field sport. The model results help decision makers to understand up to what rainfall intensities football can be played without any hassle due to undrained or slow-drained rainfall waters.

Keywords: *Drainage, Unsaturated Flow, Richards Equation, Hydrus.*

1. INTRODUCTION

Soil water dynamics is the key variable in land-surface and subsurface hydrology and the simulation of soil water drainage is essential for effective water and soil management. Soil water dynamics include soil water retention, soil water flow and drainage process. Simulating water distribution and motion in unsaturated soils requires understanding of hydraulic properties of soil such as water retention curve which relates the matric pressure head to the water retained in the soil. This function establishes a link that involves a capacity factor (water content) to un intensity factor (the energy state of the soil moisture) well known as suction or matric potential. The water retention curve is largely dependent upon the soil texture referred to as the distribution of the soil particles size and the soil structure known in many literatures as arrangement of the soil particles [1],[2]. The water retention curves are mostly applied in the prediction of the water transport in the unsaturated soils and are very useful as the fundamental part of identifying the hydraulics parameters of soil [3].

Several researchers have focused on soil water dynamics and drainage processes in line of understanding the mechanism of water and solute movement in layered soils [4], [5]. Other researchers have been interested in the development of water movement barriers with purpose of rising the soil storage capacity and decreasing infiltration which is a significant part and needed to be applied in liquid waste management [6]. Other many

---

[1] *Corresponding author: Yildiz Technical University, Department of civil engineering, 34220, Esenler/İstanbul, Turkey. ahmet@yildiz.edu.tr*

[2] *Yildiz Technical University, Department of Civil Engineering, 34220, Esenler/İstanbul, Turkey.emmyruk7bc@gmail.com*

[3] *Yildiz Technical University, Department of Civil Engineering, 34220, Esenler/İstanbul, Turkey.agacci@yildiz.edu.tr*

[4] *Yildiz Technical University, Department of Civil Engineering, 34220, Esenler/İstanbul, Turkey.ekesgin@yildiz.edu.tr*

studies focused on generating the numerical methododologies to evaluate accurately the hydraulics variables in layered soils[7].

Modeling the water movement in the layered coarse soils is challenging due to the complexity of hydraulic properties of the soil under various moisture contents and the dependence of hydraulic conductivity on water content. Nowadays various empirical, analytical and numerical methods are accessible for modeling soil water dynamics[8],[9],[10]. Owing to the computer advance in technologies, the numerical procedures have been adopted by many researchers in simulating the soil water movement and solute transport [11] [12] [13] [14]. HYDRUS program is a well known windows-based model for studying the soil water and solute transport in unsaturated medium[11]. Water movement, in unsaturated soil, has complications due to the dependence of flow parameters on saturation of the media and leading to the nonlinear problem. This particular nonlinear problem can be solved by Richards equation [15] based on finite element technics through HYDRUS [13].

The main objective of this study is to investigate the drainage process of a sport field subjected to various rainfall intensities and various layer orientations.

2. MATERIAL AND METHODS

2.1. Laboratory experiment

The study's experiments were conducted in hydraulic laboratory of Yildiz Technical University. The soil rectangular container with the dimensions of Lx=150 cm, Ly=130 cm, Lz=45 cm were filled with 3 different types of soil in layer such as root zone with grasses at the top, sand (0.6-1.2 mm or 1.2-1.5 mm) in the middle, and course sand (5-8 mm) at bottom of the container (Table 1 and Table 2). The soil sensors were installed at several depths (in the middle of each type of soil) for measuring the volumetric water content and matrix potential. The MPS-6 sensors provide for long period of time, soil water potential and temperature records at selected location in soil. Its range varies from field capacity to air dry. The 10 HS sensors are soil moisture sensor enables to monitor accurately volumetric water content over a long period of time. The soil container was left open at the top and subjected to rainfall simulators which supplies various intensity of rainfall and for this study, two type of rainfall intensities were used (Figure 2). The saturated hydraulic conductivity Ks which is described as the property of water flow through saturated medium, for different type of the soils was experimentally determined by laboratory test and the results are presented in Table 1 and Table 2.
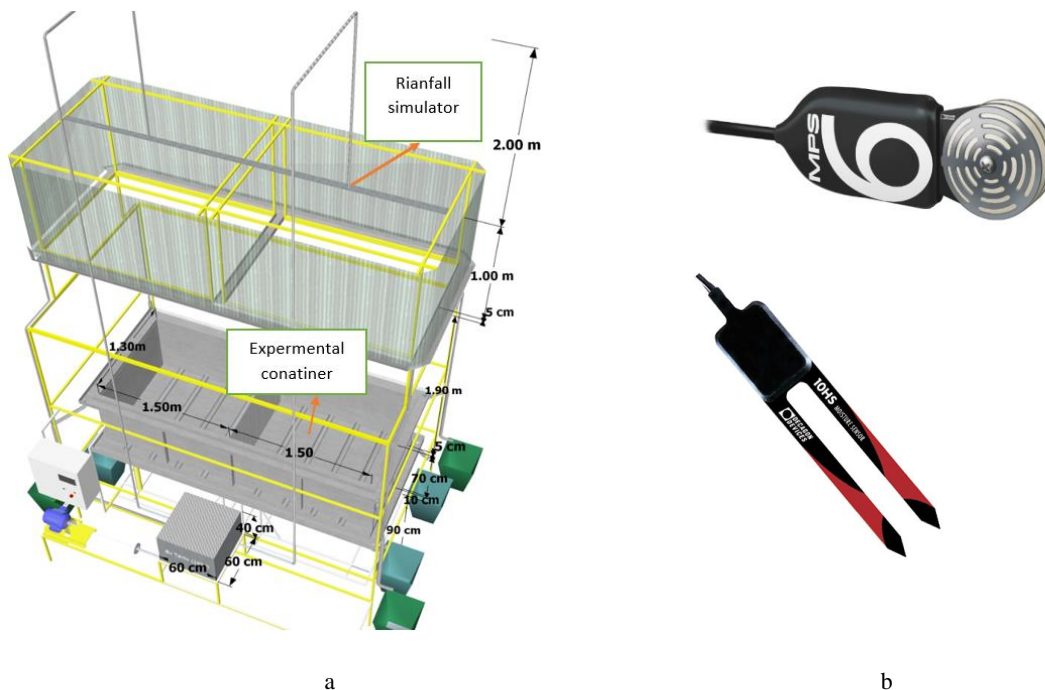

a   b
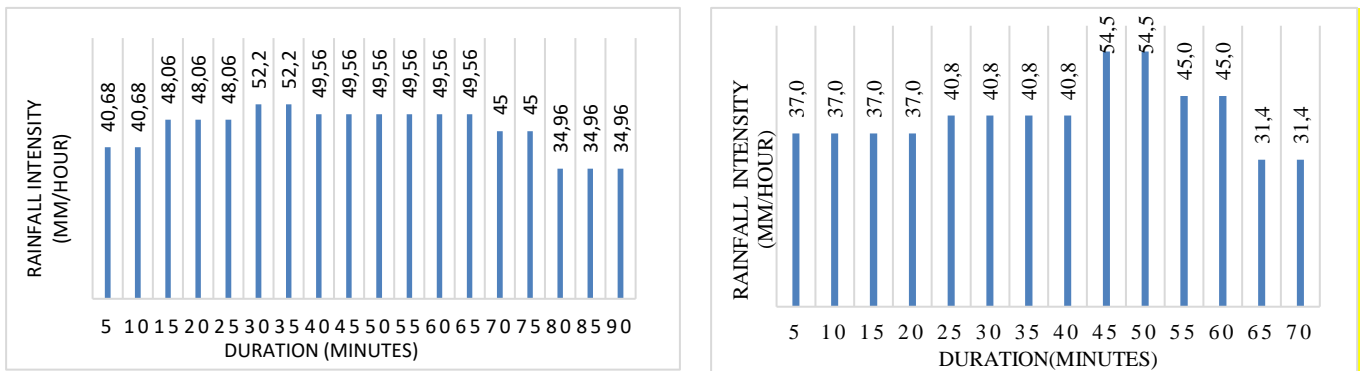
Figure1. (a)Experimental setup and (b)Sensors

Figure2. Rainfall intensities supplied by rainfall-simulators

Table1. Material Properties for experiment 1

Soil depth(cm)	Material	θ_r (cm³/cm³)	θ_s (cm³/cm³)	α[cm⁻¹]	n[-]	Ks(cm/min)	l
0-15	Root layer	0.1273	0.428	0.036	1.56	0.165	0.5
15-30	0.6-1.2 mm	0.0003	0.463	0.124	2.28	0.435	0.5
30-45	5-8 mm	0.0002	0.388	0.145	2.68	59.1	0.5

Table 2. Material Properties for experiment 2

Soil depth(cm)	Material	θ_r (cm³/cm³)	θ_s (cm³/cm³)	α[cm⁻¹]	n[-]	Ks(cm/min)	l
0-15	Root layer	0.1273	0.428	0.036	1.56	0.0173333	0.5
15-30	1.2-1.5 mm	0.00025	0.413	0.124	2.28	0.549	0.5
30-45	5-8 mm	0.0002	0.388	0.145	2.68	59.1	0.5

Where θ_r: Residual moisture parameter obtained from the experimental retention curve at wilting point, θ_s: Saturated volumetric moisture content, it referred to as porosity in this study, Ks: Saturated hydraulic conductivity, l: pore-connectivity property, α and n are empirical values of equation which affect the shape of hydraulic functions.

2.2. Governing Water Transport Equation and HYDRUS Model

The Richards equation was solved analitically in HYDRUS model as the governing water flow equation. The dimensional uniform water transport in unsaturated soil is expressed as:

$$\frac{\partial \theta}{\partial t} = \frac{\partial}{\partial z}\left[K\left(\frac{\partial h}{\partial z} + \cos \alpha\right)\right] - S \qquad (1)$$

Where K represents unsaturated hydraulic conductivity [LT⁻¹], h is the matric head induced by capillary action [L], θ is the volumetric water content [L³L⁻³], z is the spatial coordinate S stands for the sink term [L³L⁻³T⁻¹], t is time and α is the angle between the flow direction and vertical axis, 0°< α < 90°.

HYDRUS model applies the Galerkin finite element method to find a numerical solution to the governing water movement equation. The transport domain related to this experiment container is a rectangular : Lx=150 cm, Ly=130 cm, Lz=45 cm (Figure 3) and the initial conditions to the model were provided in terms of volumetric moisture content where at the beginning of the experiment, the soils were almost dry.
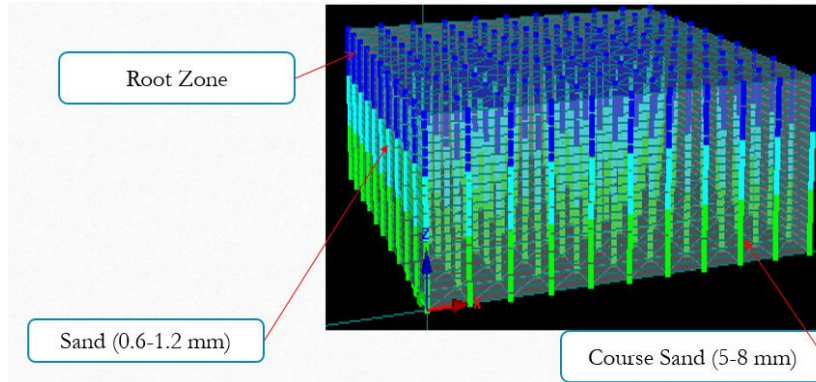
Figure3. presentation of soil types in HYDRUS model

2.3. Unsaturated soil hydraulic parameters

In this study, the soil hydraulic properties were defined by the Van Genuchten expression [16].

$$\theta(h) = \theta_r + (\theta_s - \theta_r)[1 + (\alpha h)^n]^{-m}, h < 0. \tag{2}$$

$$(h) = \theta_s, h \geq 0. \tag{3}$$

$$K(h) = K_s S_e^l \left[1 - \left(1 - S_e^{1/m}\right)^m\right]^2 \tag{4}$$

$$S_e = \frac{\theta - \theta_r}{\theta_s - \theta_r} \tag{5}$$

where, θ is the volumetric water content[L^3L^{-3}]; θs and θr stand for the saturated and residual water contents[L^3L^{-3}] respectively, h represents the matric head(kPa); α is a scale parameter, the inverse of air entry pressure[L^{-1}], n and m are empirical shape parameters that govern the shape of fitted water retention curve, m=1-1/n and 0<m<1, Ks is the saturated hydraulic conductivity [$L \, T^{-1}$] and Se is effective water content.

The Van Genuchten equation have 4 independent parameters ($\theta_r, \theta_s, \alpha$ and n) which were determined from observed soil water retention curve and were used as entry data into HDRUS model. The residual water contents (θ_r), for various layers of soil profile, was estimated by determining the water content on very dry soil. The θ_r is expressed as the volumetric water content when $\frac{d\theta}{dh}$ tends to zero, at high matric head or permanent wilting point. The change in shape parameter n may cause considerable change in water retention curve. For a given type of soil, if n value is high(low) the slope of the water retention curve will be big (small).
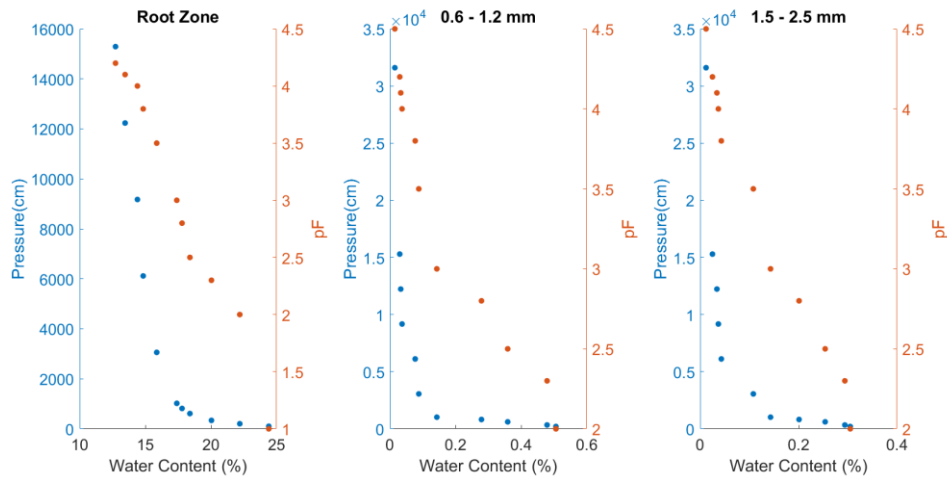
1044

3. RESULTS

3.1. Laboratory results

Figure4. water retention curves obtained experimentally

The form of a water retention curves, obtained experimentally, is presented in the figure 4. The volumetric water content is drawn against the matric pressure (cm) and pF Logarithmic function (pF= log (matric pressure(cm)). When matric pressure is near to zero, the soil is near to saturation, and water is retained or stored in the soil by capillary action. As the water content becomes lesser (when soil drains), binding of the water, in the soil pores, begins to be stronger, and at high water pressure head (at wilting point) the water is strongly bound in the smallest of pores and from this point we get residual water content. From the Figure 4, it can be observed that at the wilting point of the soil types: the root zone, 0.6—1.2 mm, and 1.5-2.5 mm, the residual water contents reach12.73%, 0.030 % and 0.025% respectively.

Sandy soils (0.6-1.2 mm and 1.2-1.5 mm) include mostly capillary binding force, and will therefore deliver majority of the water at low matric pressure, while root zone soil release water at high matric pressure. Root zone soil holds more water than sandy soils (0.6-1.2 mm and 1.2-1.5 mm). The maximum water retaining capacity is referred to as the porosity and was used as saturated water content in HYDRUS.

3.2. Model Results

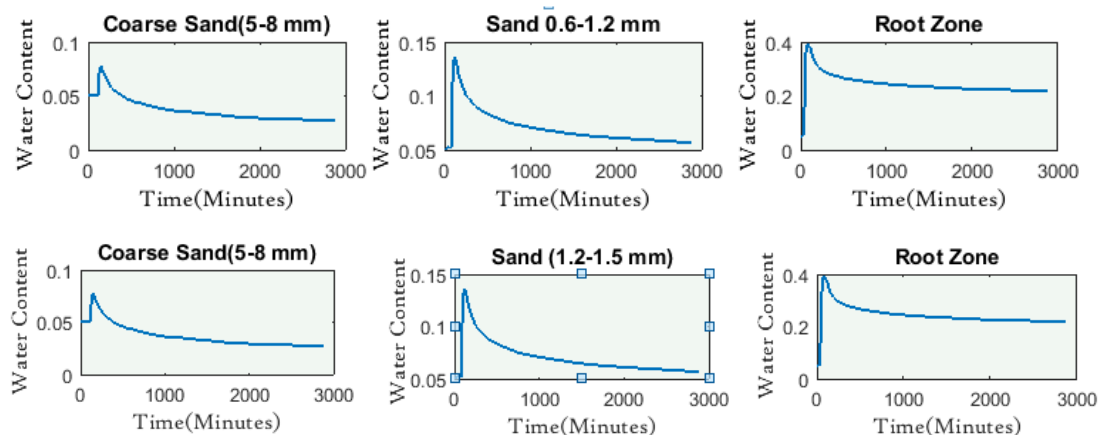Time histories of Infiltration Process

Figure5. Time histories of the volumetric water content

The Figure 5 presents the time histories of volumetriv water content at each of soil' middle point, it can be seen that the initial water content, for the different types of soil used during this study, are close to 0 m^3/m^3 as the soils were nearly to dry condition. When the applied rainfall reaches the soil surface (at time t = 0 minute), the water starts to be stored in the soil and the volumetric water content stars to increase in the top soil (Root zone soil). As the infiltration process continue to happen, the increase in water content continue to happen along the entire depth (in sand(0.6-1.2) and in course sand(5-8).
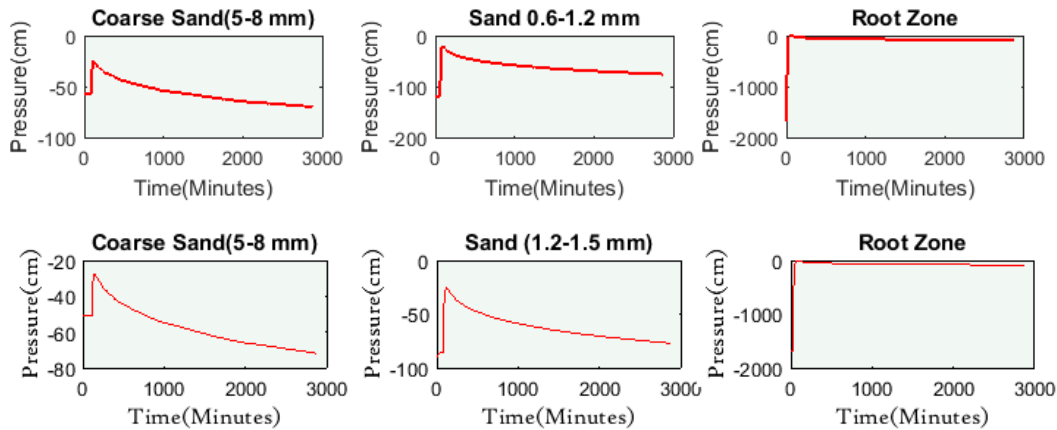

Figure6. Time histories of the pressure

The infiltration process is shown by the pore water pressure responses presented in Figure 6. it is observed that when the rainfall reaches the top soil (Root zone soil) at t=0 s, water starts to infiltrate the root zone, and a few minutes later, the rapid change in pressure (reduction of suction) is observed and the pressure comes from dry state to near zero (nearly saturation). As water continue to infiltrate and reach other layers, as well the pore pressure in the soil is quickly increased to near but not zero, as sand and course sand did not reach the saturation.
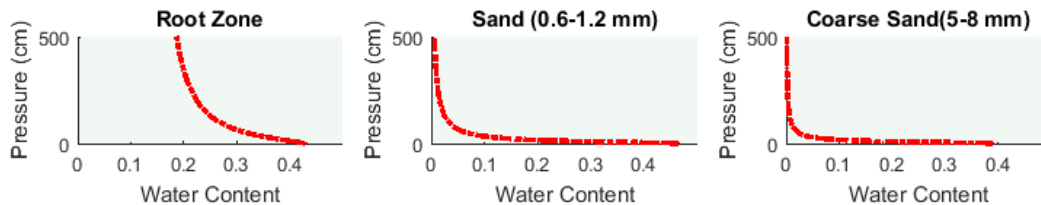
Figure7. water retention curves obtained from the HYDRUS Model (experiment 1)
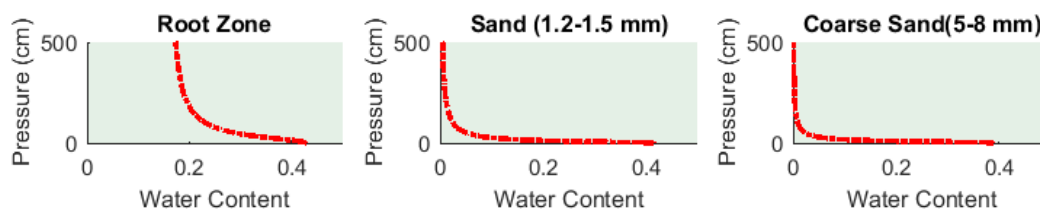

Figure8. water retention curves obtained from the HYDRUS Model (experiment 2)

It can be observed from the figure 7 and 8 that for sandy soil: sand (0.6-1.2 and 1.2 -1.5 mm) and course sand (5-8 mm)have not the same drainage behavior as the root zone soil, they do not strongly retain as much water as root zone soil and will become completely dry more quickly.

4. DISCUSSION AND CONCLUSIONS

This study presented the both infiltration experiment and its HYDRUS simulation of water flow in unsaturated layered soils. An infiltration experiment was carried out in the experimental set up with dimensions of 150x130x45cm with 3 drainage orientation soils. The Richards equation through HYDRUS model was analytically used to describe the water flow in unsaturated soil. The Van Genutchen model was applied to characterize the shape of water retentions curves of different type of soils used in this study. The Van Genuchten parameters (θ_r, θ_s) were determined from observed soil water retention curves and were used as entry data in HDRUS. The α and n parameters were estimated based on calibration of Hydrus model by referring to the retained water curves obtained experimentally.

The experimental results reveal that the residual water content at the wilting point for the root zone, 0.6—1.2 mm and 1.2-1.5 mm are 12.73%, 0.030 % and 0.025% respectively. Sandy soils (0.6-1.2 mm and 1.5-2.5 mm) show the most capillary binding force therefore they deliver majority of the pressure head, while root zone soil, with adhesive and osmotic binding, release water at more negative pressure. It has been seen that the root zone soil holds more water than sandy soils (0.6-1.2 mm and 1.5-2.5 mm). The maximum water retaining capacity is referred to as the porosity and was used as saturation water content in HYDRUS.

The simulation of water flow by HYDRUS model were in good agreement with experimental obtained results. The outcomes of this study yields important insights into comprehension of water dynamics in unsaturated coarse soils and its drainage. The study results help decision makers to understand up to what rainfall intensities football can be played without any hassle due to undrained or slow-drained rainfall waters.

REFERENCES

[1]. P.J.Salter and J.B. Williams, "The influence of texture on the moisture characteristics of soils. Part I: A critical comparison of techniques for determining the available water capacity and moisture characteristic curve of a soil," J. *Soil Sci.* vol. 16 pp. 1–15, 1965.

[2]. L.A. Richards and L.R. Weaver, "Moisture retention by some irrigated soils related to soil moisture retention," *J. Agric. Res*. Vol. 69 pp. 215–235, 1944.

[3]. A. Klute, *Water retention: Laboratory methods. p. 635–662. In A. Klute (ed.). Methods of soil analysis. Part 1,* 2nd ed. Agron. Monogr. 9. ASA and SSSA, Madison, WI, 1986.

[4]. E. Alfnes, W. Kinzelbach and P. Aagaard, "Investigation of hydrogeologic processes in a dipping layer structure: 1. The flow barrier effect," *J. Contam. Hydrol*. vol. 69: pp. 157-172, 2004.

[5]. M. Huang, S. L. Barbour, A.E. lshorbagy, J. D. Zettland B. C. Si, "Infiltration and drainage processes in multilayered coarse soils," *Can. J. Soil Sci.* vol. 91: pp. 169-183, 2011.

[6]. M. V. Khire, C. H. Benson and P. J. Bosscher, "Capillary barriers: design variables and water balance," J. *Geotechnol. Geoenviron. Eng*., vol. 126 pp. 695-708, 2000.

[7]. N.Romano, B. Brunone and , A. Santini, "Numerical analysis of one-dimensional unsaturated flow in layered soils," *Adv. Water Resour*. vol. 21 pp. 315-324, 1998

[8]. F.J. Cook, P.J. Thornburg, P. Fitch, K.L. Bristow, "WetUp: a software tool to display approximate wetting pattern from drippers," *Irrig. Sci*. vol. 22, pp. 129–134, 2003,

[9]. X. Chu, M.A. Marino, "Determination of ponding condition and infiltration into layered soils under unsteady rainfall," *Journal of Hydrology*, vol. 313, pp. 195–207, 2005.

[10]. J. Liu, J.Zhang and J. Feng, "Green–Ampt model for layered soils with no uniform initial water content under unsteady infiltration," *Soil Science Society of American Journal,* vol. 72 (4), pp. 1041–1047, 2008.

[11]. J. Simunek, M. Sejna, M.Th. van Genuchten, "The HYDRUS-2D software package for simulating two-dimensional movement of water, heat and multiple solutes in variably saturated media, version 2.0," Rep. IGCWMC-TPS-53, *Int. Ground Water Model. Cent., Colo. Sch. of Mines, Golden, CO*, p. 251, 1999.

[12]. C.M. Cote, K.L. Bristow, P.B. Charlesworth, F.J. Cook and P.J. Thorburn, "Analysis of soil wetting and solute transport in subsurface trickle irrigation," *Irrig. Sci.* vol. 22, pp. 143–156, 2003.

[13]. J. Simunek, M.Th. van Genuchten and M. Sejna, *The HYDRUS-1D Software Package for Simulating the One-Dimensional Movement of Water, Heat and Multiple Solutes in Variably-saturated Media, Version 3.0,* Department of Environmental Sciences, University of California Riverside, Riverside, California, USA, 2005.

[14]. G. Provenzano, "Using HYDRUS-2D simulation model to evaluate wetted soil volume in subsurface drip irrigation systems," *J. Irrig. Drain. Eng.* Vol.133 (4), pp. 342–349, 2007.

[15]. Z. Lei, S. Yang and S. Xie, *Soil Water Dynamics*. Tsinghua University Press, Beijing, 1988.

[16]. M.T. van Genuchten, "A Closed-Form Equation for Predicting the Hydraulic Conductivity of Unsaturated Soils," *Soil Science Society of America Journal.,* vol. **44**, pp. 892-898, 1980.

Tectonically Driven Uplift and Seismicity of the Eastern Pontides (Trabzon-Rize/Turkey and Its Vicinity)

Mustafa SOFTA[12], Tahir EMRE[1], Hasan SOZBILIR[1], Joel Q.G. SPENCER[2], Mehmet TURAN[3]

Abstract

The Eastern Pontides has undergone active and progressive uplifting at rates ranging from 0.59–1.00 mm/years during the Quaternary-Holocene period because of active deformations caused by Eurasia in the north and the Arabic platforms in the South. A total of 308 earthquakes that were greater than a magnitude of 3 were detected using catalogs of instrumental and historical earthquakes between 1852 and 2017. Twenty of these earthquakes were greater than a magnitude of 5. Lineation analysis from aerial photos and field studies show that there has been extensive earthquake activity in the Eastern Pontides since the historical period and the dominant direction was identified as different sets of WNW-ESE, E-W, and ENE-WSW. The linearity overlaps for the earthquakes that occur on the land and in the Black Sea. These lineations were infilled with obsidians during the Pleistocene age. During seismic studies performed in the Eastern Black Sea, the Eastern Black Sea fault, the Trabzon-Rize fault and the northern dipping normal faults are defined in the Rize region. Previous seismic profiles have also shown that the eastern part of the Eastern Pontides is more active than the western part because these faults cut Quaternary sediments. Additionally, we suggest that the Eastern Black Sea Fault, which limits the south of the Black Sea, may be active today because of the oblique reverse fault that was observed during the focal mechanisms solution of the earthquakes at M_w: 6.2 in 1959 and M_s: 5.8 in 2012 in the nearest Batum. To date, our findings indicate that: (i) the eastern part of the Eastern Pontides mountain range that rises between 0.59 mm/year and 1.00 mm/year is more active than the western part; (ii) linearity can be an active fault based on the fission track studies of the obsidians and the intense earthquake activity on these lineaments in Eastern Pontides; and (iii) earthquakes of at least a magnitude of 5 have occurred in the Eastern Pontides within 200 years, based on both the historical and instrumental earthquake records and the fault type, length, and kinematic characteristics.

Keywords: *Uplift Rate, Eastern Pontides, Earthquake, Active Fault, Black Sea*

1. INTRODUCTION

Active deformation zones are the sites of intense earthquake activity linked with rapid vertical movement. Eastern Pontides orogenic belts is valuable and virtually unstudied area concerned with neotectonic studies in Alpine-Himalayan deformation zone. Eastern Pontides (NE Turkey) orogenic belt, which extends along the southeastern coast of the Black Sea region (Fig. 1). Active deformation zones in the eastern Pontides leads to three different subgroups from north to south, depending on lithological assemblages and facies [3], [6]. Each zone is not only separated by E–W-, NE–SW- and NW–SE-trending fault zones, but it also gives the entire belt a block-faulted structural architecture [4], [6], (Fig. 2). During seismic and gravity studies performed in the Eastern Black Sea, the Eastern Black Sea fault (which is a southward-dipping reverse fault), the Trabzon-Rize faults (which are a strike-slip faults), and the northern dipping normal faults are defined in the Rize region (Fig. 3A). Direction of these fault systems are nearly parallel to right-lateral North Anatolian Fault and left-lateral Northeast Anatolian Fault. The linearity overlaps for the historical and instrumental earthquakes that occur on the land and in the Black Sea (Fig. 2). Vertical movement of the eastern Pontides has been confined to limited ESR dating method using the chronology of marine terraces, but some of these dates are considered unreliable due to possible contamination by flooding. In this paper, we aimed to decipher

Quaternary tectonic deformations and earthquake activity within coast of Eastern Pontides by using uplifted marine terraces and previous seismic profiles with bouger anomalies map also new geochronological data (OSL dating) in order to address the age of the marine terraces in the region.
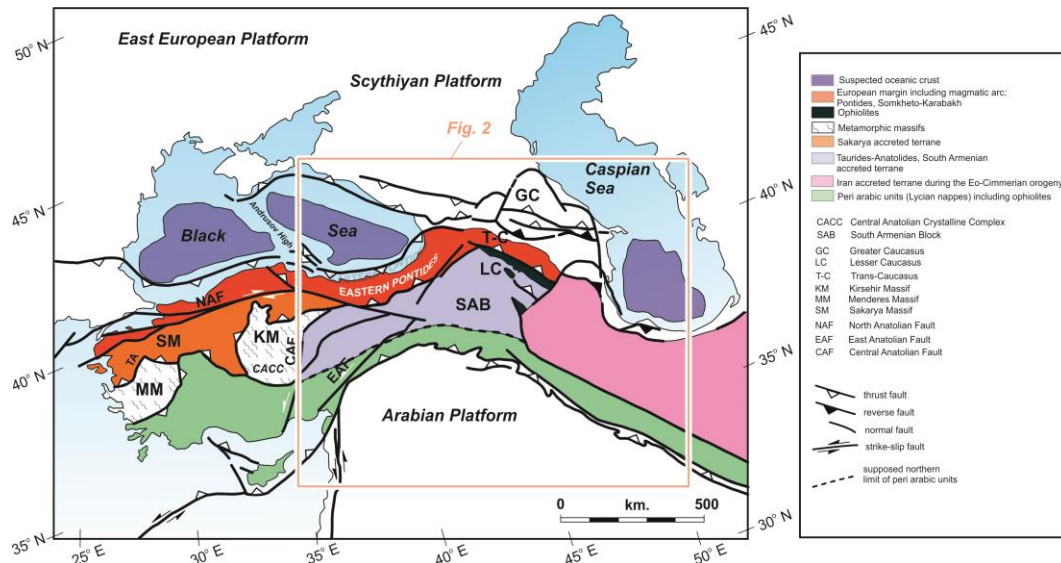
Figure 1. General geological map of the Eastern Pontides – Caucasus region, after [8], [9] with modifications.

2. MATERIAL AND METHODS

In this study, in order to determine the uplift rate of the eastern Pontides, Optical Stimulated Luminescence (OSL) dating analyses of quartz's mineral extracted from marine terrace formation samples, from different levels, were performed in the Luminescence Dating Laboratory, Dept. of. Geology, Kansas State University. In seismicity section, we used to both earthquake catalogs for the eastern Pontides (Trabzon-Rize cities and vicinity) and previous seismic profiles and bouger gravity anomalies maps.

Based on the accurate geochronological datas and in conjunction with the earthquake catalaogs, previous seismic profiles-bouger anomalies maps and field studies with aerial photos, we interpreted a revised a neotectonic study to explain the earthquakes linked with active faults in the eastern Pontides (Fig. 2 and 3).

Figure 2. Simplified neotectonic map of E. Turkey (after [1]). Rectangles indicates uplift rates for the Black Sea basin. 1: Major strike–slip faults. 2: Major thrust faults. 3: Relative motion of blocks w.r.t. to Eurasia. 4: Focal mechanisms of M_w. 4.8 earthquake (CMT Harvard). 5: Instrumental seismicity of greater than 3, (USGS-NEIC). Ar, Armenia; D, Dagestan; T, Talish; E.A.F., East Anatolian fault; N.A.F., North Anatolian fault; P.S.S.F., Pambak –Sevan-Sunik fault, Z.F., Zagros fault; N.T.F., North Tebriz fault; G.S.F, Geltarechka-Sarikamis fault.
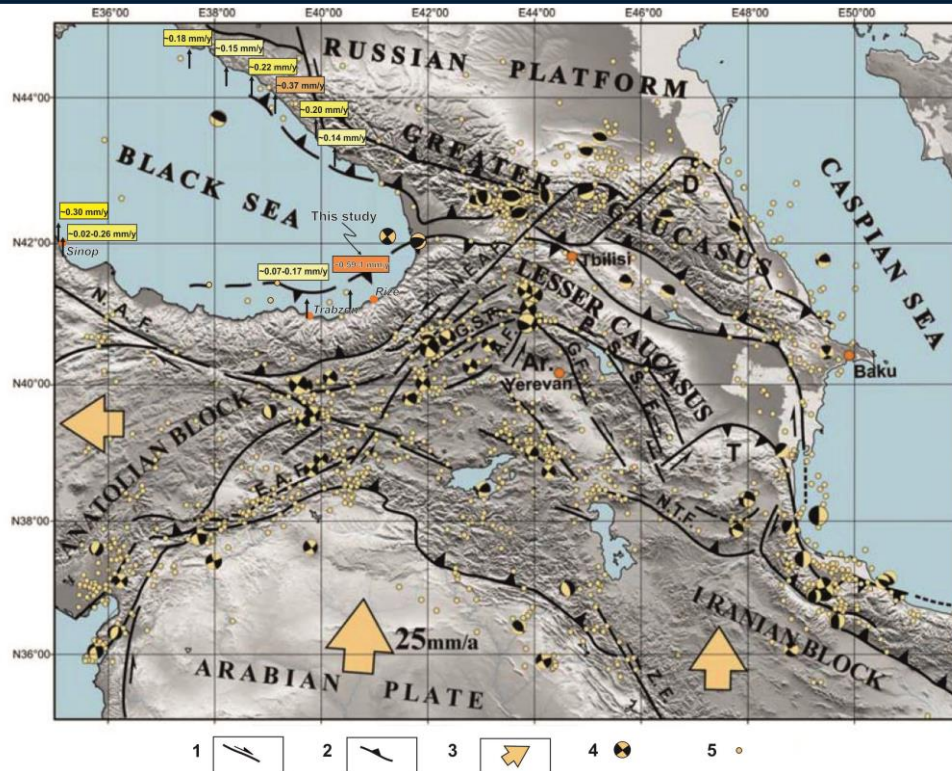
3. RESULT AND DISCUSSION

The main findings of this study, which focuses on the earthquake activity and neotectonic settings of coastal of eastern Pontides Orogenic Belt, are as follows:

Main tectonic lines of Eastern Pontides are the Eastern Black Sea fault which is a southward-dipping reverse fault, the Trabzon-Rize faults which are a strike-slip faults and the northern dipping normal faults are defined in the Rize region. Lineation analysis from the aerial photos was made for Eastern Pontides and the dominant direction were identified as different sets of WNW-ESE, E-W, ENE-WSW (Fig. 2). According to the existing literature, this lineations were infilled with obsidians during the Pleistocene age. Obtained accurate age data and sea level curves allowed us to determine a global sea level of MIS 1, MIS 3 and MISs 5a, respectively. There might be possible Quaternary faults or lineations according to the active fault classification of [5] and [7], based on the fission track studies on the obsidians. The apparent vertical movement is ranging from 1.0 mm/yr to 0.59 mm/yr during the Quaternary-Holocene time interval (Fig. 2). Previous seismic profiles have also shown that the eastern part of the Eastern Pontides is more active than the western part because these faults cut Quaternary sediments (Fig 3C). Additionally, we suggest that the Eastern Black Sea Fault, which limits the south of the Black Sea, might be active today because of the oblique reverse fault that was observed during the focal mechanisms solution of the earthquakes at M_w: 6.2 in 1959 and M_s: 5.8 in 2012 in the nearest Batum (Fig. 2). Based on both the historical and instrumental earthquake records and the fault type, length, and kinematic characteristics, earthquakes of at least a magnitude of 5 have occurred in the Eastern Pontides within 200 years.
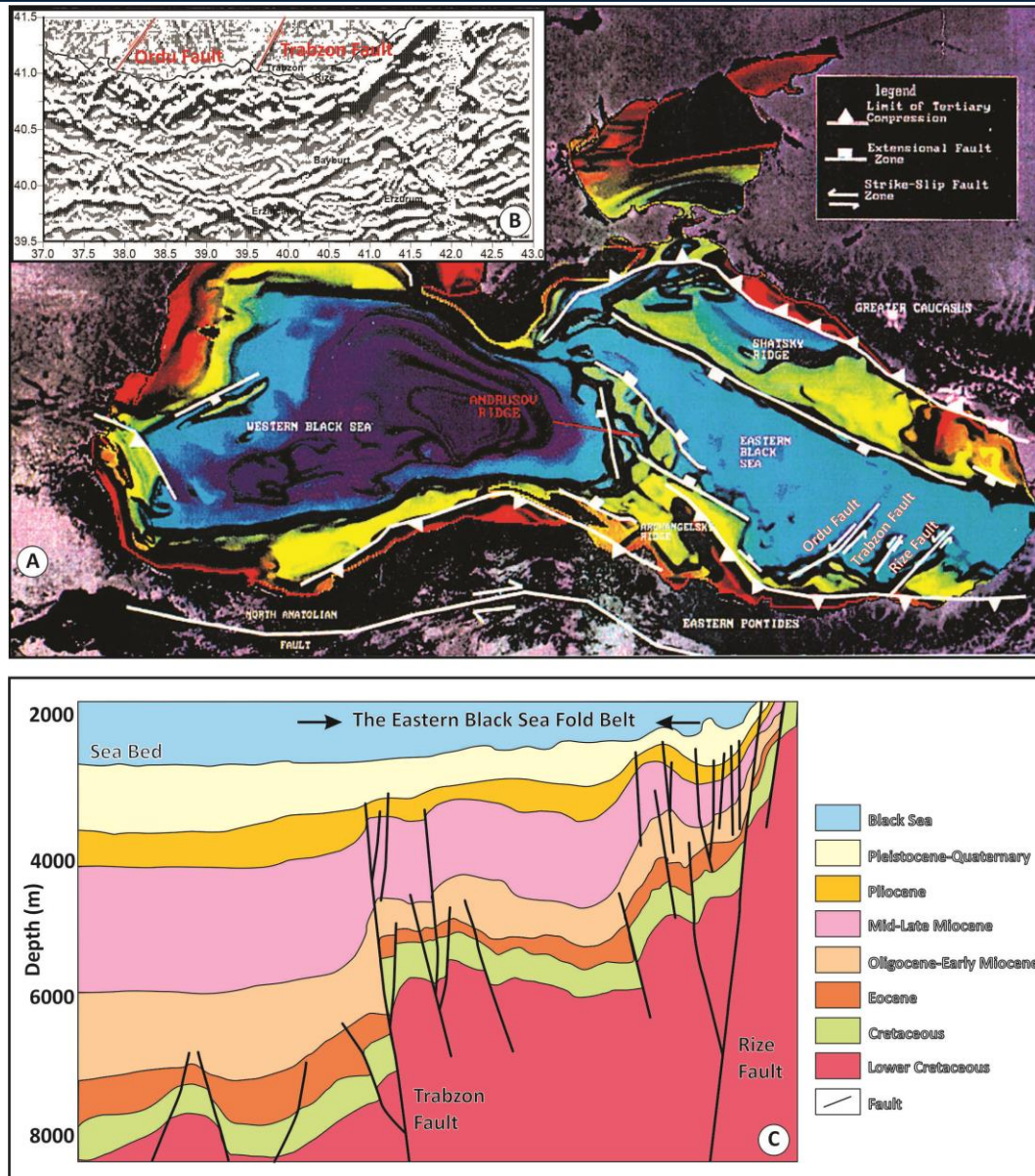
Figure 3. A) Tectonic map of the Black Sea and its vicinity (after [10]) B) Bouger gravity anomalies map of the eastern Pontides (After [2]). C) Seismic section of the eastern Black Sea (after [10]).

ACKNOWLEDGMENT

REFERENCES

[1]. A. Avagyan, M. Sosson, A. Karakhanian, H. Philip, S. Rebai, Y, Rolland, R. Melkonyan, V. Davtyan, "Recent tectonic stress evolution in the Lesser Caucasus and adjacent regions". *Geological Society of London*, Special Publications, 340, pp. 393-408, 2000.

[2]. Y. Bayrak, and N. Maden, "Dogu Karadeniz ve Civarının Depremselligi," in *Proc. of Dogu Karadeniz Bolgesi Afetleri, Yer Arastırmaları ve Yer Secimi Toplantısı*, 2001, paper 2, pp. 15-23 (in Turkish).

[3]. O. Bektas, C. Yılmaz, K. Taslı, K. Akdag, and S. Ozgur, "Cretaceous, Rifting of the Eastern Pontide Carbonate Platform (NE Turkey); The Formation of Carbonate Breccias and Turbidites as Evidence of a Drowned Platform", *Giornale di Geologia*, vol. 57(1-2), pp. 233-244, 1995.

[4]. O. Bektas, and S. Capkınoglu, "Dogu Pontid magmatik arkında (KD Türkiye) neptünyen dayklar ve blok tektonigi", *Geosound,* vol. 30, pp. 451-463, 1997.

[5]. O. Emre, T.Y. Duman, S. Ozalp, H. Elmacı, S. Olgun, and F. Saroglu, "Active Fault Map of Turkey with and Explanatory Text". General Directorate of Mineral Research and Exploration, Special Publication Series-30. 2013.

[6]. Y. Eyuboglu, "Description and geotectonic important of the Alaskan-Type mafic-ultramafic Rocks in the Eastern Pontide Magmatic Arc (NE Turkey)", Ph.D. Turkish Thesis, Karadeniz Technical University, Trabzon, Turkey, 2006.

[7]. C.W. Jennings, "Fault activity map of California and adjacent areas with locations and ages of recent volcanic eruptions: California Department of Conservation", Division of Mines and Geology Data Map Series No. 6, 92 p., 2 plates, map scale 1:750,000, 1994.

[8]. Y. Rolland, M. Hassig, D. Bosch, M.J.M. Meijers, M. Sosson, O. Bruguier, Sh. Adamia, N. Sadradze, "A review of the plate convergence history of the East Anatolia-Transcaucasus region during theVariscan: insights from the Georgian basement and its connection to the Eastern Pontides," *Journal of Geodynamics.* http://dx.doi.org/10.1016/j.jog.2016.03.003.

[9]. M. Sosson, Y. Rolland, T. Danelian, C. Muller, R. Melkonyan, S. Adamia, T. Kangarli, A. Avagyan, G. Galoyan, "Subductions, obduction and collision in the Lesser Caucasus (Armenia, Azerbaijan, Georgia), new insights," *Geological Society of London*, Special Publications, 340, 2010, pp. 329-352.

[10]. (1997) The Turkish Petroleum Corporation website. [Online]. Available: http://www.tpao.gov.tr/tp5/

A Small – Size RF Measurement System

Sebnem Seckin Ugurlu[1], Ahmet Ozkurt[2]

Abstract

The effects of electromagnetic sources on devices and public are very important topics. The measurements of radiated emission from devices, electromagnetic compatibility (EMC) and electromagnetic interference (EMI) tests for products, shielding effectiveness of materials must be done in accredited laboratories. However, in the evaluation and prototyping processes, these tests are needed to be done several times. In this study, a small-sized, low cost RF measurement system including a portable RF anechoic chamber that can be used between 700 – 3000 MHz is proposed. The radiated emission levels from two different commercial cellular phones at 900 MHz GSM, 1800 MHz GSM, 2100 MHz 3G and 2400 MHz Wi-Fi frequencies are measured with this system as an application example and they are discussed to the International Commission on Non-Ionizing Radiation Protection (ICNRP) Guidelines. In the light of this study, more complex and specific measurements can be carried out.

Keywords: *Anechoic Chambers, Cell Phone Emission, Rf Measurements*

1. INTRODUCTION

The rapid development in the radio frequency technology lead us to an environment with additional electromagnetic sources. Smart phones, base stations, access points, personal computers and portable devices employing wireless technologies, hand-set telephones, smart watches and wearable devices are primary sources of these electromagnetic fields. These kind of devices operate generally in the frequency band of 700 – 3000 MHz. This frequency range tends to increase as new generation communication technologies are developed. It is necessary to increase the frequency above 3GHz in order to meet the bandwidth requirements of fifth generation (5G) devices [1-3]. Yet, the discussion on the possible effects of this increased exposure to electromagnetic fields still continues. The controversy raised as the World Health Organization (WHO) classified the electromagnetic fields radiated from mobile devices as "possibly carcinogenic" [4].

Recent studies on both human and animal subjects uncovers different effects of electromagnetic exposure for different exposure durations. Studies of Meo et.al. [5] on 159 students of age 12-16 who are exposed to RF fields at 925 MHz for a duration of 6 hours for five days a week shows that the mean HbA1c levels, which is associated with risk of type 2 diabetes mellitus, of students who are exposed to higher levels of RF fields are significantly higher than the students who are exposed to low level of RF fields. Kesari, Kumar and Behari find that Wistar rats that are exposed to mobile phone RF fields for 2 hours per day for a duration of 45 days with a SAR of 0.9 W/kg show a change antioxidative enzyme activities, protein kinase C, melatonin, caspase 3, and creatine kinase which are related to the overproduction of reactive oxygen species [6]. Khalid et.al. suggest that even for the worst case scenario for Wi-Fi devices operating in schools, the personal exposure in a classroom where 30 laptops and 1 access point operate in full duty cycle would not exceed the ICNIRP international guideline reference level of 10 W m^{-2} [7]. However, the effects of such a limited SAR for longer durations are not considered. The accurate measurement of the radiation from such devices is very important.

Preventing unwanted RF fields has become a popular topic because of all these health concerns stated before. These prevention methods are can be applied to houses, medical facilities, offices or even in nursery rooms. These kind of materials are defined as shielding materials. Thus, it is important to identify the electromagnetic behaviors of such materials accurately. Also, every electronic consumer product need to be tested for their immunity to the outer electromagnetic sources (EMI) and the fields they produce when they are working. These field levels should be within specified limits. These measurements should be carried in

---

[1] Corresponding author: Dokuz Eylul University, Graduate School of Natural and Applied Sciences, 35400, Buca/İzmir, Turkey. sebnem.seckin@deu.edu.tr

[2] Dokuz Eylul University, Department of Electrical and Electronics Engineering, 35400, Buca/İzmir, Turkey. ahmet.ozkurt@deu.edu.tr

accredited laboratories. If the device fails these tests, the design should be reconsidered and new test should be done.

In this study, the implementation and measurement results of a small sized, low-cost electromagnetic measurement system involving an RF anechoic chamber which can be used in the frequency range of 700-3000 MHz is given. This compact and portable system gives the opportunity to make preliminary measurements of many RF radiation properties such as electromagnetic interference (EMI), electromagnetic compatibility (EMC), shielding effectiveness of materials, radiation levels from wireless devices operating at the given frequency limits. The reason to implement a measurement system in this frequency range is 900 MHz GSM, 1800 MHz GSM, 2100 MHz third generation (3G) band, public ISM bands, 2400 MHz Wi-Fi and Bluetooth as well as digital enhanced cordless telecommunications (DECT) phones operate in this frequency band. Research institutes, universities, companies can easily construct this system and make their preliminary measurements before applying for an accredited laboratory which can be a huge budget.

2. MATERIALS AND METHODS

Until 1970s RF measurements were used to hold in open areas. However, it is known that such a system can be affected from other sources. It is sometimes can be obligatory to separate all other sources but to investigate one specific source. RF anechoic chambers are used in such situations. An RF anechoic chamber is a box which is shielded with very good conductors to prevent outer RF sources to interfere the ongoing measurement. Interior of the chamber is covered with absorber materials which decrease the reflections inside the chamber for the desired frequency range. Simmons [8] proposed an RF anechoic chamber with such absorbers. The dimensions of RF anechoic chambers depend on the measurements that are held in the chambers. Some of these chambers are as large as 21m x 13.5 m x 8.5 m. Such a chamber can be used from 150 kHz up to 18 GHz [9].

2.1. Determining Chamber Sizes

It is obligatory that the RF fields inside the anechoic box to be plane waves. This can be ensured to place the antennas with a distance of at least far-field of the antennas used [10]. Also, the designed or bought antennas' radiation patterns are calculated in the far-field zone. With a distance smaller than the far-field, these anticipated radiation patterns are not accurate. The far field of the antenna is proportional to square of its largest dimension and inversely proportional to the wavelength. Thus, the antenna selection is the most important step for designing such a chamber.
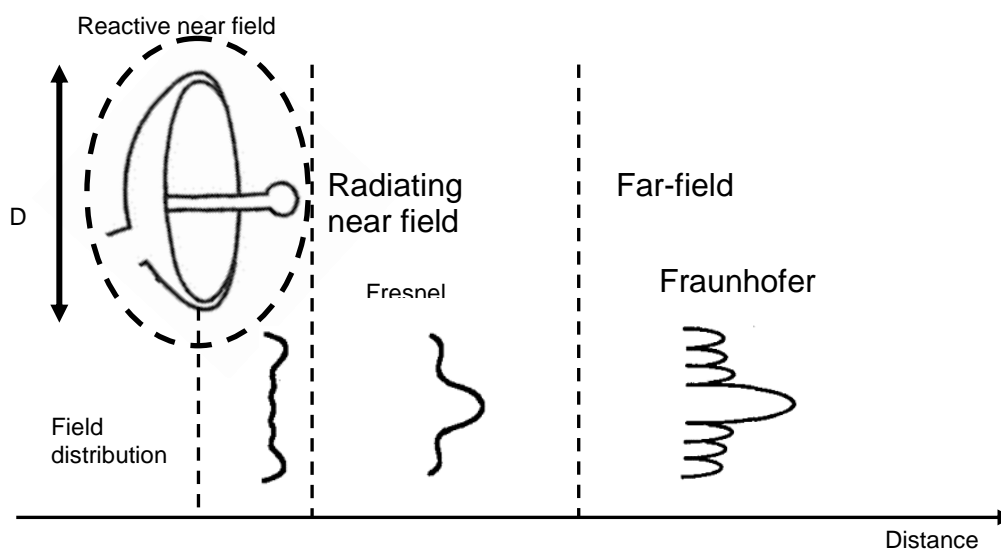
Figure 95 The change in the radiation pattern of the antenna with distance (Rahmat-Samii, et.al. [10])

The receiver and transmitter antennas are preferred to be directional antennas. Also, for a fast and accurate measurement, an antenna that covers the whole frequency band of interest is needed. Two log periodic antennas from Gigahertz Solutions are preferred for our system. In[10], VSWR of the preferred antenna can be seen. The VSWR is below 2.5 GHz for most of the frequency band of interest. The maximum dimension of the antenna is 17 cm. The calculated far-field for this antenna is 58cm for 3GHz and 14cm for 700 MHz. In order to keep the chamber dimensions at its minimum, flat laminate absorbers are preferred. This kind of

absorbers have less absorption but they are smaller in size compared to the high performance pyramidal absorbers. ETS-Lingdren FL-4500CL (-25 dB average absorption at 455 MHz and above), FL-2250CL series absorbers (-30 dB average absorption at 940 MHz and above) are chosen for this purpose. The outer conductor is stainless steel. The whole structure is mounted on wheels to provide mobility. The doors are sealed with conductive gaskets in order to prevent electromagnetic leakage.
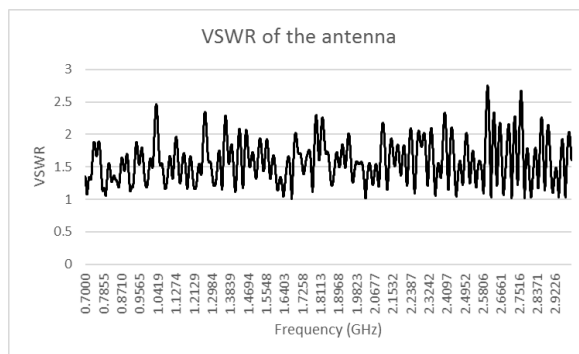
Figure 96. VSWR of Gigahertz solutions antenna between 0.7-3 GHz

The total dimension of the chamber is 1m x 1.5m x 1m as seen in [11]. Anritsu MS2711D Handheld Spectrum Analyzer or Anritsu Vector Star Network analyzer.
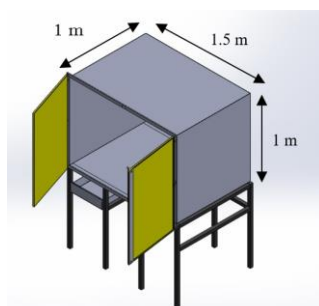
Figure 97. Final design of the chamber

(a)   (b)

Figure 98. Closed view and (b) open view of RF anechoic chamber

2.2. Available Measurements

Many of RF radiation measurements require a receiver and transmitter antenna. The main idea is to either measure the radiated emission from a device or transmit some energy to the device/material under test and measure the transmitted field from it. In [11] the measurement set-up can be seen. This set-up can be used for shielding effectiveness measurement.
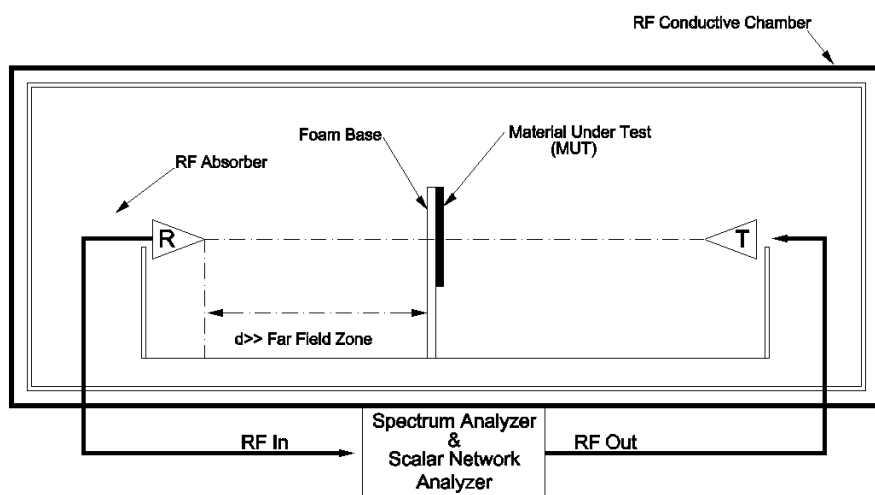
Figure 99. Measurement set-up for shielding effectiveness measurement.

Shielding effectiveness is a term that defines the amount of shielded field for a specific frequency or frequency range [11].

$$SE_{dB} = 10 \log \frac{P_i}{P_t} \qquad (1)$$

The mathematical definition of shielding effectiveness is given in Equation [12] where Pi is the incident field on a planar material and Pt is the transmitted power from this material. There are some proposed methods in literature to measure this parameter. ASTM D4935-10 is most widely used method to measure shielding effectiveness of a planar material [12]. In this method, a large coaxial specimen holder is used. But as the standard suggest, this method is valid for the frequency range of 30 MHz – 1.5 GHz which does not cover 1800 MHz GSM, 2100 MHz 3G and 2400 Wi-Fi bands. There are studies to extend the applicable frequency range of this system [13]. However, the proposed system's valid frequency band depends on the bandwidth of the antenna used and its dimensions. To calculate the shielding effectiveness of the material under test (MUT), first the received field values are taken without any material between the antennas. Then, the material is placed in the middle of two antennas and received field values are noted. The difference between them gives the shielding effectiveness.
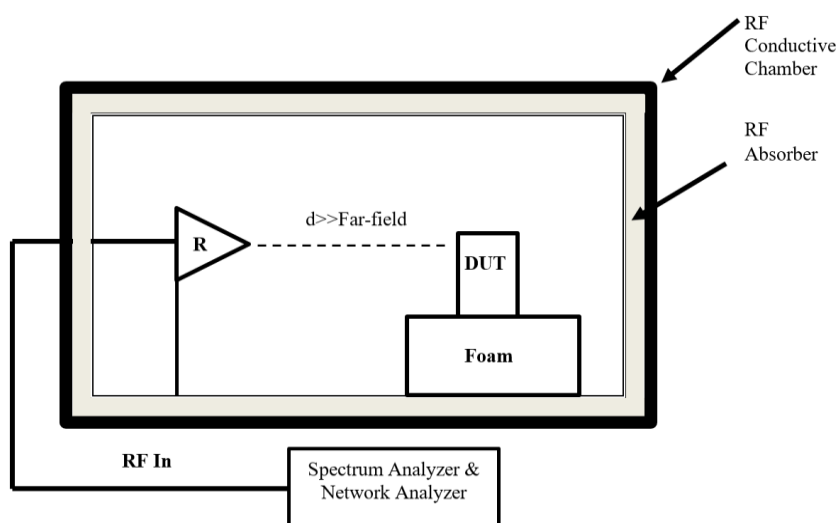
Figure 100. Electromagnetic radiated emission measurement.

The measurement set-up seen in [13] is used for measurement of the electromagnetic radiated emission from devices. Such a set-up can be used determine the radiated electric and magnetic fields from wireless devices such as cellular phones, DECT phones, Wi-Fi access points, laptops, tablet devices and any other devices that operates in the 700 - 3000 MHz frequency range.

3. RESULTS AND DISCUSSION

The proposed measurement system and RF anechoic chamber to be used in the 700 – 3000 MHz frequency range is designed and implemented. Many electromagnetic measurements such as EMC/EMI, shielding effectiveness, antenna characterization and radiated emissions are held in this chamber. In this study radiated emission from two commercial cellular phones are measured. One of these cellular phones operates at 900 MHz, has 3G property and the other one operates at 1800 MHz as well as 2100 MHz 3G. Both phones' radiated emission is measured at transmitting mode (calling another device) at 2G and 3G frequencies, receiver mode (receiving call from another device) at 2G and 3G frequencies, Wi-Fi access point mode. Multiple measurements are taken from close range (10cm) and from far range (30cm) to investigate the effect of the distance. In order to simulate the worst case scenario, the devices operated with minimum coverage which was achieved by slightly closing the doors of the anechoic chamber. The doors cannot be fully closed as this will cause the loss of the connection between the device under test (DUT) and the base station. The measurements are taken with "hold" option which ensures to save the maximum received value.

In Figure 101, the received power when the DUT operates in 2G mode (3G option is disabled) for the whole frequency span for a distance of 30 cm. The received power is -34 dBm maximum at 913 MHz. In the no call mode, communication with the base station continues and this leads to an emission of -24.42 dBm maximum 909 MHz. This is a greater maximum value than receiving mode which shows that the emission happens even if there is no call and the RF effects of the cellular phone continue. When the distance is reduced to 10 cm with DUT in the receiver mode, the received power is -31 dBm at 910 MHz. The radiated emission levels from DUT for the transmitter mode when the distance is 10 increases to -10dBm at 909 MHz which is 100 times more than the receiver mode of the DUT.
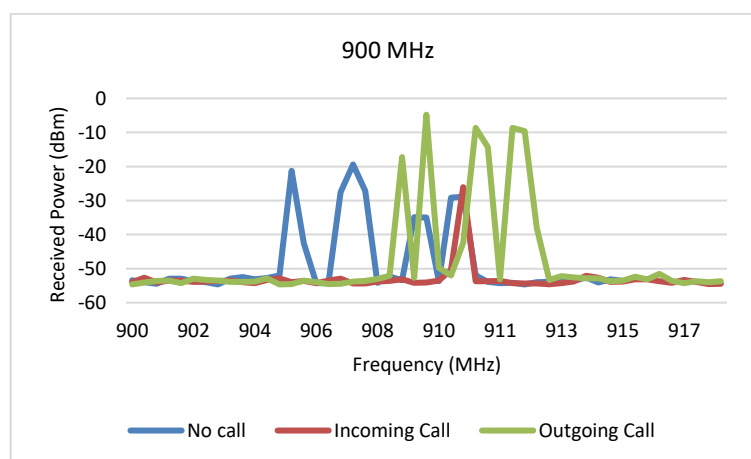
Figure 101. Received power for no call, incoming call and outgoing call between 900-920 MHz (distance=30 and 10 cm)

The radiated emissions from a second commercial cellular phone which operates at 1800 MHz GSM are investigated. It is known that as the frequency increases the reduction in the signal increases. Thus, devices tend to operate at higher power levels in this frequency. In Figure 102, the DUT is in the receiver mode and the receiver antenna is positioned at a distance of 10 cm from DUT. The maximum received power is -17 dBm at 1725 MHz. When DUT is in the transmitter mode the received powers are -24dBm at 1717 and 1721 MHz.
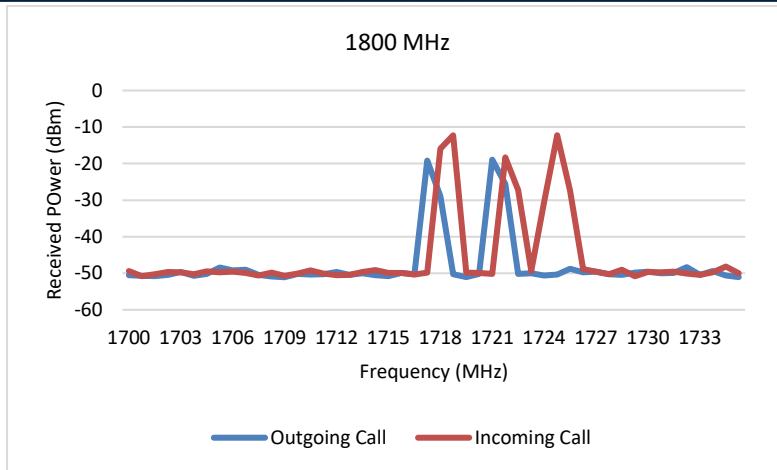
Figure 102. Received power for incoming call and outgoing call between 1700 - 1750 MHz (distance=10 cm)

When DUT is set up as a Wi-Fi access router, it uses 3G band in the receiver mode and transmits Wi-Fi data at 2400 MHz. In Figure 103, the received power from DUT is seen for the frequency range of 2000-2450 MHz. In this range, both 3G transmission and Wi-Fi transmission can be seen. The average of 2100 MHz band is -47 dBm with a peak value of -45 dBm at 2050 MHz. The Wi-Fi emission is -47 dBm at 2439 MHz. The received power levels are very low compared to the 2G and 3G transmissions. When the distance is increased to 30 cm, the radiated emission level goes down to -51 dBm at 2435 MHz (Figure 104).
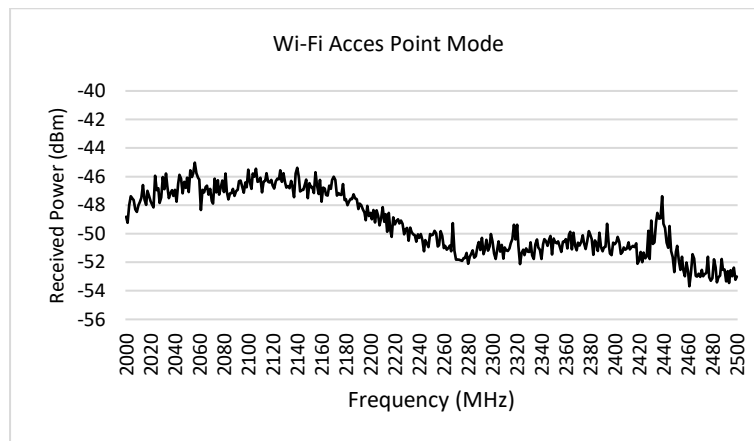
Figure 103. Wi-Fi Access Point Mode (distance = 10 cm)
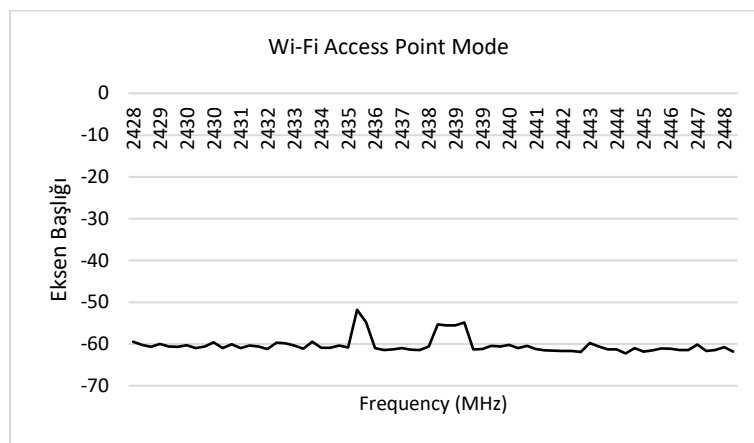
Figure 104. Wi-Fi Access Point Mode (distance = 30 cm)

These radiated emission values must also be considered in terms of field values and corresponding International Commission on Non-Ionizing Radiation Protection Guidelines [14]. These values are shown in Table 59.

Table 59. Maximum electromagnetic field levels and corresponding ICNRP limits

Mode	Distance (cm)	Frequency (MHz)	Maximum Electric Field (V/m)	ICNRP limit (V/m)	Maximum Magnetic Field (A/m)	ICNRP limit (A/m)
Receiver	10	910	0.184872	41	0.000490	0.111000
Receiver	30	913	0.133617	41	0.000354	0.111000
Transmitter	10	909	2.139612	41	0.005675	0.111000
No call	30	909	0.396934	41	0.001053	0.111000
Receiver	10	1725	1.721395	58	0.004566	0.160000
Transmitter	10	1721	0.795125	58	0.002109	0.160000
Transmitter	10	2438	0.030281	61	0.000083	0.160000
Receiver	10	2106	0.081689	61	0.000217	0.160000

4. CONCLUSIONS

In this study, a compact, low-cost and portable electromagnetic test system that can be used in the frequency range of 700 – 3000 MHz is given. The main reason to develop such a system this frequency range covers many of the mostly used the industrial, scientific and medical (ISM) radio bands which are also investigated for their effects on health. With this system the radiated emission from devices can be measured while bypassing the contribution of other RF sources. While these measurements can already be done in large anechoic chambers, they are too expensive and large in dimensions. However, the proposed system is small and very low-cost compared to those chambers. Thus, it can be used by research facilities, universities and companies on tight budgets. This knowledge of the radiated emission can be a preliminary view of EMI/EMC measurements, antenna characterizations before applying for accredited laboratories. It is also possible to measure SAR values effectively with an addition of a proper phantom since the system makes it possible to distinguish different sources.

The radiated emission from two commercial cellular phones are measured with the proposed system. These measurements are taken for 900 MHz GSM, 1800 MHz GSM, 2100 MHz 3G and 2400 Wi-Fi bands because these bands are the mostly occupied bands due to the increasing use of wireless devices. The measurements are taken at 10 cm and 30 cm to investigate the effect of the distance. The tests are to determine the radiated fields from cellular phones only. The effect of radiation from base stations are not included in the measurements by placing the DUT in an anechoic chamber. Also, these results show the worst case scenario because the DUTs operate with least coverage.

It is observed that maximum field levels determined by the guidelines of ICNRP for public are never exceeded. However, this conclusion doesn't mean cellular phones are safe to carry as the discussion of reducing these limits continues. Also, the measurements are taken at a distance to ensure the far-field conditions. When it is considered that devices are used at a very close distance, these near field measurements must be done with near-field probes for accurate results. This implemented system can be adapted to higher frequency measurements with proper antenna system.

ACKNOWLEDGMENT

REFERENCES

[1]. Y. Okumura, "5G mobile radio access system using SHF/EHF bands," in *Microwave Conference (APMC)*, 2014, pp. 908-910.

[2]. W. Yi, et al., "5G Mobile: Spectrum broadening to higher-frequency bands to support high data rates," *IEEE Vehicular Technology Magazine*, vol 9(3), pp. 39-46, 2014.

[3]. J. Gozalvez, "5G tests and demonstrations [mobile radio]," *IEEE Vehicular Technology Magazine*, vol. 10(2), pp. 16-25, 2015.

[4]. R. Baan, et al., "Carcinogenicity of radiofrequency electromagnetic fields," *Lancet Oncology*, vol. 12(7), pp. 624-626, 2011.

[5]. S. A. Meo, et al., "Association of exposure to radio-frequency electromagnetic field radiation (RF-EMFR) generated by mobile phone base stations with glycated hemoglobin (HbA1c) and risk of type 2 diabetes mellitus," *International Journal of Environmental Research and Public Health*, vol 12(11), pp. 14519-14528, 2015.

[6]. K.K Kesari, S. Kumar, and J. Behari, "900-MHz microwave radiation promotes oxidation in rat brain," *Electromagnetic Biology and Medicine*, vol. 30(4), pp. 219-234, 2011.

[7]. M. Khalid, M et al., "Exposure to radio frequency electromagnetic fields from wireless computer networks: Duty factors of Wi-Fi devices operating in schools," *Progress in Biophysics & Molecular Biology*, vol. 107(3), pp. 412-420, 2011.

[8]. A. Simmons and W. Emerson. "An anechoic chamber making use of a new broadband absorbing material," in *1958 IRE International Convention Record.*, 1953, pp. 34-41.

[9]. (2002) NEC/TOKIN website. [Online]. Available: http://www.tee.tokin.jp/eng/pdf/ANECHOIC_CHAMBERS.pdf.

[10]. Y. Rahmat-Samii, L.I. Williams and R.G. Yaccarino, "The UCLA bi-polar planar-near-field antenna-measurement and diagnostics range," *IEEE Antennas and Propagation Magazine*, vol. 37(6), pp. 16-35, 1995.

[11]. *IEEE Standart Method for Measuring the Effectiveness of Electromagnetic Shielding Enclosures*, IEEE Std., 2006.

[12]. *Standart Test Method for Measuring the Electromagnetic Shielding Effectiveness of Planar Materials*, ASTM, 2010.

[13]. T. W. Więckowski and J.M. Janukiewicz, "Methods for evaluating the shielding effectiveness of textiles. *FIBRES & TEXTILES in Eastern Europe*, vol. 14(5), pp. 18-22, 2006.

[14]. *Guidelines on Exposures*, ICNRP, 2010.

BIOGRAPHY

Sebnem SECKİN UGURLU: She received her bachelor's degree and master's degree from Dokuz Eylul University, Department of Electrical and Electronics Engineering in 2007 and 2011 respectively. She has been working as an assistant researcher in the same department since 2008. She is also a PhD candidate studying in the fields of numerical methods in electromagnetics. Her research interests are TLM, FDTD, antenna design, electromagnetic simulations.

Ahmet OZKURT: He got his bachelors' degree, master's degree and PhD degree from Dokuz Eylul University Electrical – Electronics Engineering Department, Izmir in 1991, 1995 and 2001 respectively. He had worked as research assistant from 1993 to 2000 and as lecturer from 2000 to 2003. He has been working as Assistant Professor in the same department in Electromagnetic waves and microwave technique branch since 2003. His areas of interests include applied microwave, electromagnetic shielding, electromagnetic measurements, mechatronic systems, robotics and virtual reality.

Potential Effects of Air Pollution on Greenhouse Production Activities

Sedat Karaman[1], Zeki Gokalp[2]

Abstract

Greenhouses are off-season production facilities and thus it is quite significant to bring climate parameters into desired levels. Air pollution in greenhouse production sites has significant impacts on greenhouse plants. Existence of phytotoxic gases like ozone, nitrogen peroxide, ethylene, Sulphur dioxide, fluorine and mercury vapors, herbicide and insecticide vapors and the chemical gases used in soil fumigation seriously affect plant growth and development and greatly alters plant quality. Impact levels of toxic gases are closely related to climate of the surrounding environment. The greenhouses located in crowded cities or close to intensive industrial regions are greatly exposed to ozone and other oxides. Industrial facilities release serious quantities of Sulphur dioxide to environment. In present study, potential effects of air pollution on greenhouse production activities were assessed and measures to be taken to minimize such effects of hazardous gases on plant growth and development were provided.

Keywords: *Greenhouse, air pollution, plant growth*

1. INTRODUCTION

Air pollution in greenhouses farming sites has serious negative impacts on plants in greenhouses. Hazardous gases in greenhouse environments mostly come from the plants themselves (ethylene), photochemical reactions, fuels burn inside the greenhouses, fungicides-pesticides used in plant protection practices, chemicals used to preserve wooden components of the greenhouses. The pollutants with detrimental impacts on greenhouse plants are classified as ozone, nitrogen peroxide, ethylene, sulphur dioxide, fluorine, mercury vapor, phenols, herbicide and insecticide vapors, chemical gases released by soil chemicals, and the gases in ambient air inside and around the greenhouse. All these pollutants alter plant quality and may reduce the yields. Ventilation is the best way to minimize detrimental impacts of such gases on greenhouse plants. Existence of hazardous gases and their level of impact are closely related to climate pattern of the region where greenhouses activities were practiced. The greenhouses constructed in crowded cities or intense industrial activities are quite nested with ozone and other oxides. Besides various other phytotoxic gases, industrial facilities release serious amounts of sulphur dioxide to atmosphere. Then, such oxides released to atmosphere exert serious threats on all plants. These pollutants create a smoky and hazy appearance in the air and they may reach to vital levels when they compounded with fog, exhaust and chimney gases.

Nitrogen oxides: Nitrogen oxides (N_2O) are quite effective on plants. They compound with oxygen with the impact of solar rays and create ozone gas. When the ozone gas concentration in atmosphere reached to certain levels (0,3-0,6 ppm), especially the tip shoots are damaged. In later phases, yellowing is seen in leaves, chlorophyll and starch is degraded and carotenoids are broken down. Excess nitrogenous fertilizer uses reduce the harmful effects of oxides in the air. Thusly, high temperatures reduce the plant resistance to oxides. Improper burning of hydrocarbons in crowded cities and industrial localities result in excessive release of phytotoxic compounds to atmosphere. Also, vehicle exhausts, open garbage and other waste burns, home chimneys are the other sources polluting and poisoning the atmosphere [1; 2].

Ethylene: Ethylene (C2H4) occurs in trace amounts in gasoline and natural gas and is produced when these substances are burned. It also is present in wood and tobacco smoke. Ethylene is a plant hormone produced by plants during their growth and development. However, ethylene produced through defective heating equipment can be detrimental to greenhouse crops, because it is produced in greater quantities. Ethylene pollution influences the activities of plant hormones and growth regulators, which affect developing tissues and normal organ development, many times without causing leaf-tissue damage. Injury to broad-leaf plants

---

[1] *Corresponding author: Gaziosmanpasa University, Department of Biosystem Engineering, 60250, Tokat, Turkey. sedat.karaman@gop.edu.tr*

[2] *Erciyes University, Department of Biosystem Engineering, 38039, Kayseri, Turkey. zgokalp@erciyes.edu.tr*

occurs as a downward curling of the leaves and shoots (epinasty), followed by a stunting of growth. Other symptoms of excess ethylene exposure include the abscission of flower buds, petals or leaves; water-soaking of older leaves; chlorosis; and wilting of flowers. Crops vary in their sensitivity and response to ethylene toxicity. The degree to which a crop is affected depends on the variety, temperature, ethylene concentration, and the duration of exposure. High temperatures and high light levels will increase the severity of ethylene damage. In high tunnels that burn propane, kerosene or use motors that burn gasoline and have poor or no ventilation, even minute amounts of this pollutant can cause severe damage to tomatoes. Unvented unit heaters in greenhouses can at times also cause problems. These problems tend to increase in very tight greenhouse structures, i.e., those that have little exchange with the outside air. Symptoms of ethylene damage can be very subtle, especially if there are no plants grown in clean air available for comparison [3].

Proper heating system installation and maintenance are the best ways to prevent problems. A maintenance plan should include cleaning the unit heater and fuel orifice twice a year. Propane flames should have a small yellow tip when properly adjusted and natural gas flames should be a soft blue with a well-defined inner cone. To ensure proper combustion, heater units should have a clean air intake and should be vented to the outside with a stack, which keeps exhaust gas from being drawn back into the greenhouse through the ventilation system [3].

Sulphur dioxide (SO₂): During the combustion process, sulfur in fuel sources is converted to sulfur dioxide. If this leaks into the greenhouse and combines with the moisture there, sulfuric acid is formed. Low levels of sulfur dioxide may result in flecking and premature leaf drop. Higher levels can cause severe leaf burn, especially on young leaves [4].

Sulphur dioxide concentrations over 0,5-0,7 mg/m^3 may have poisonous effects on plants. High sulphur dioxide concentrations result in necrotic symptoms on leaves. The sulphur dioxide absorbed by plant leaves dissolved in moist surfaces of mesophyll cells in pores of stomas. In monocotyledonous plants, initially leaves wrinkled from the tips and then a general wrinkle is observed in plants. In dicotyledonous plants, initially red, yellow and brown stains are observed in leaves and then leaves are twisted, dry and defoliate. The change in color of perennial plants starts from the tip of the plant. The greatest damage in plants is observed in tissues rich in chlorophyll around the stomas. In annual plants, the youngest leaves are the most resistant sections of the plants; mid-age leaves are the most sensitive sections. In microscopic images of leaves with sulphur dioxide damage, chlorophyll break downs, inexistence of tannin substances, plasm degradation, inexistence of cell intra lamellas due to pectin dissolve are observed. The greatest damage is usually observed in chlorophyll-rich tissues around the stomas [5, 2].

Sulphur dioxide damage decrease with increasing moisture levels inside the greenhouse. The damage increases as the indoor air get drier. Moisture levels in greenhouses decreases especially day hours and increase through evening hours and reaches to maximum levels at night hours.

The exposure of succulent, broad-leaved plants to sulfur dioxide (SO₂) and its by-product sulfuric acid usually results in dry, papery blotches that are generally white, tan, or straw-colored and marginal or interveinal damages on some species, chronic injury causes brown to reddish brown or black blotches. Both the upper and lower leaf surfaces are affected. The leaf veins normally remain green. Chlorosis (yellowing) and a gradual bleaching of the surrounding tissues are fairly common. Injured grass blades develop light tan to white streaks on either side of the mid-vein. A tan to reddish brown dieback or banding occurs on conifer leaves, with adjacent chlorotic areas. Growth suppression, reduction in yield, and heavy defoliation may also occur. Middle-aged leaves and young plants are most susceptible to sulfur dioxide [6].

Mercury vapor: Mercury is used in agriculture as fungicide and such uses constitute about 5% of total industrial use of mercury. The fungicides used in agriculture are the greatest sources of mercury released to environment and vaporization of metallic mercury is the greatest atmospheric pollutant [2].

Mercury vapor has instant impacts of plants. Such impacts are also closely related with greenhouse indoor temperatures. Mercury vapor has greater impacts at high indoor temperatures than low temperatures. High temperatures speed p vaporization process from the source and thus mercury vapor then occupy larger areas. Mercury vapor in air generally is taken up by and accumulated in bud leaves. Therefore, the plants sensitive to mercury vapor, like tomato and lettuce, should not be grown in places with intense mercury vapor, or the plants grown in such places should not be allowed to be sold in markets. In greenhouses, special attention should be paid while using paints containing metallic mercury and fungicides containing organic mercury. Such substances may increase mercury vapor inside the greenhouses. Mercury-containing substances should not be used in any greenhouses, except for flower greenhouses. In flower greenhouses however, mercury vapor may result in faded leaves, purple, blue greenish white leaves, closed buds, leaned leaves, yellowish or brownish leaf veins. Mercury vapor slows down plant growth, hardens branches and reduce flower formation [1].

Atmospheric fluorine gases: Hydrogen fluoride gas intensified around the plants has phytotoxic impacts on plants. Effects of fluorine on plants are closely related to moisture content of the ambient air. There is a positive relationship between increasing moisture contents and plant fluorine uptake. Necrosis over leaf tips and edges are the initial symptoms of fluorine damage. In monocotyledons, changes in leaf color starts from the tip and extends throughout the leaf. In dicotyledonous plants, dry outs are observed over the leaf edges, necrosis and cracks are observed over the fruits. It is impossible to distinguish fluorine damages from sulphur damages. With regard to physiological impacts of fluorine, inactivity of enzymes related to carbohydrate metabolism is the greatest issue. The damage created by fluorine and fluoro-hydrogen depend on fluorine concentration in the air, exposure duration, amount of fluorine exerted on plant, plant individual sensitivity and various other edaphic and climate factors. While 15-20 ppm fluorine does not create necrosis in several plants, occurrence of necrosis is totally dependent on wind and moisture conditions until fluorine levels of 105 ppm. Over this concentration, plants are damaged. Only some tolerant species can resist up to a concentration of 500 ppm [5, 1]

Fluorides absorbed by leaves are conducted towards the margins of broad leaves and to the tips of monocotyledonous leaves. Little injury takes place at the site of absorption, whereas the margins or the tips of the leaves build up injurious concentrations. The injury starts as a gray or light-green water-soaked lesion, which turns tan to reddish-brown. With continued exposure the necrotic areas increase in size, spreading inward to the midrib on broad leaves and downward on monocotyledonous leaves [6].

Hydrogen sulfide: Hydrogen sulfide is less harmful than fluorine gases and sulphur dioxide. It can create damages on young and fast-growing shoots. Sulfurous chemical applications inside the greenhouse increase sulphur concentrations. The existence of the gas can be identified with scant smell of the gas [1]. Wrinkles are the initial symptoms on plants. There is no color change but stains can be formed over the leaves of some species. Microscopic assessments revealed decolonization of chloroplasts and thickened protoplasm [5]. In general, sulfide concentrations below 10 mg/m^3 do not influence respiration in plants, but a concentration of over 500 mg/m^3 terminates respiration [2].

Ammonia gas: Conversion of fertilizer nitrogen into ammonia creates an atmospheric pollution. In greenhouses, when the nitrogenous fertilizers are applied in ammonia or urea forms, there will be more nitrogen losses [2]. Subsequent and excessive manure applications to greenhouse soils may also increase ammonia concentrations inside the greenhouses. With increasing indoor ammonia concentrations, plants start to lose their green colors and get brown color and dry appearance. All the young and old leaves and shoots are equally influenced from ammonia gas. In case of quite high ammonia concentrations for a long time inside the greenhouses, entire green herbage of the plants are damaged and leaves change their colors and ultimately defoliate [1].

High ammonia concentrations have toxic impacts on both plants and soil microorganisms. Slowdown in nitrification process is the initial indicator of such impacts [7]. Previous researches revealed that when cabbage, sunflower and tomato leaves were exposed to 40 ppm ammonia concentration for an hour, negative effects were observed [8]. Although natural ammonia concentrations do not create any damages on plants, 16,6 ppm or 11,62 mg NH_3/m^3 levels might have quite toxic impacts when the plants were subjected to these concentrations for 4 hours. The sensitivity to NH_3 toxicity varies based on plant species and varieties. NH_3 terminates assimilation. Reversible assimilation depressions can be observed even at low NH_3 concentrations (2:7500) in plants without extreme acid cellular juice. Acid cellular juice form salt with NH_3 and prevents pH changes as such creating protein disintegration or deposit. Carbohydrate deficits in plants reduce plant resistance against ammonia damage [5].

When plants take up nitrogen, they may absorb more than they need to support current growth. Extra nitrogen is stored in case fertilizer levels become lower later on. Nitrate can be safely stored by the plant, but when plants take up and store too much ammonium, it can cause damage to cells. Toxicity occurs when ammonium has built up to excessive levels in the substrate, ammonia nitrogen forms are converted to nitrate by naturally occurring bacteria called nitrifies. In this case there is little worry about ammonium building up in the substrate unless the grower supplies very excessive amounts of a high ammonia fertilizer. However certain growing conditions, such us low temperature (less than 60F/15 °C average daily temperature), wet or low oxygen soils, and low media pH will suppress function of nitrifying bacteria and cause ammonium to build up to toxic levels in the substrate. That is, under cool wet conditions typical in winter and early spring, ammonium toxicity has the highest likelihood of occurring. In bedding plants and plugs, symptoms appear first in younger leaves. Leaves exhibit yellowing (chlorosis) between the veins. This can progress to scattered brown (necrotic) spots. On more mature crops, mid to older leaves are affected. Depending on plant species, the edges of leaves may curl upward or downward. Root growth is impeded and root tips may die, which becomes an entry point for root diseases [9].

Carbon monoxide: Carbon monoxide is a poisonous gas and it is a product of coal burning with limited air and it is converted into carbon dioxide in the atmosphere. Carbon monoxide release is minimized with the optimum burning. This gas is not disappeared easily in the atmosphere and amount of CO released to atmosphere depend on air quantities included into the burning process. Carbon monoxide also gets into the greenhouses from the roods within close vicinity of the greenhouses.

Carbon monoxide has significant effects on plants. Leaves have yellow color and then defoliate. Growth is inhibited in leaves and shoots. The motor-operated devices inside the greenhouses may increase carbon monoxide concentrations if the ventilation is not performed [1]. Plants are more resistant to carbon monoxide than animals and humans. Therefore, they get damaged only at quite high concentrations. Typical microscopic damages are observed at high carbon monoxide concentrations [5].

Chlorine gas: The chlorinated cleaning liquids may increase chlorine concentration of ambient air. Continuous irrigations with chlorinated municipal water may also increase indoor chlorine concentrations. When the chlorinated water is sprayed to plants increases chlorine concentrations even more. In general, chlorine damages are initially observed in mid-age leaves, then old leaves. Young leaves are more resistant to chlorine damages and they influenced from the chlorine gas as they grow up [1].

Injury caused by chlorine (Cl_2) is somewhat similar to that caused by sulfur dioxide and fluorides, in that it is marginal and interveinal. On broad-leaved plants, necrotic, bleached, or tan to brown areas tend to be near the leaf margins, tips, and between the principal veins. Injured grass blades develop progressive streaking toward the main vein in the region between the tip and the point where the grass blade bends. The streaking usually occurs alongside the veins. Middle-aged leaves or older ones are often more susceptible than the young ones. Bleaching and tissue collapse can occur. Conifers may show tip-burn on the current season's needles [6].

Herbicides: Misuse use of any herbicides inside or around the greenhouses may create significant damages on plants. Especially 2,4-D like hormonal herbicides exert the greatest hazards in greenhouses. Such herbicides should be used neither inside nor around the greenhouses. Even e vapor released from 2,4-D compounds released from the containers stored around the greenhouses ay have detrimental impacts on plants. A pulverizator used in spraying herbicides should not be used in other chemical applications even after cleaning. The best way to eliminate such hazards, it is better to keep a separate pulverizator for herbicide treatments [1].

Herbicides are chemicals used to keep weeds from interfering with the growth of greenhouse crops. Weeds indicate poor cultural practices, and compete with desirable plants for water, carbon dioxide, light and nutrients. They also are a reservoir for diseases and insects especially white flies and spider mites. Herbicide damage on non-target plants may cause slight to serious injury symptoms and can occasionally cause economic damage as well. Herbicide chemistry and physical properties usually determine how herbicides interact with the biological and physical systems of the plant. Factors determining herbicide efficacy and crop safety are complex and include plant species, plant size, stage of growth, soil chemical and physical properties, soil moisture, temperature, and relative humidity. Post-emergence herbicide uptake and efficacy can be affected by spray additives that enhance the performance of the herbicide but may also increase the risk of crop injury [10].

Herbicides can injure foliage, shoots, flowers, and fruits. If injury is severe enough, either from one incident or repeated exposure, it may reduce yield, produce poor fruit quality, distort ornamental or nursery plants, and occasionally cause plant death. Herbicide symptoms may be visible for a few days to several years depending on the herbicide involved, plant species, stage and rate of growth, environmental and soil conditions, and cultural practices. In addition, herbicides may reduce non-target plant vigor, increase susceptibility to disease, and shorten the life cycle of a plant. Herbicide injury to non-target plants also may result in illegal residues on the exposed crop. In ornamental nursery plants even slight herbicide symptoms may affect the marketability of damaged plants. Several herbicide injury symptoms, such as general and interveinal chlorosis, mottled chlorosis, yellow spotting, purpling of the leaves, necrosis, and stem dieback, may result from causes other than herbicide exposure. If herbicide damage is suspected, the progression of symptoms and the study of herbicide symptomology in its entirety are critical [10].

Soil fumigants: Formaldehyde, chlorokiprine and methyl bromide are the most common fumigants used to prevent soil-born diseases. Formaldehyde and chlorokiptine vapor has poisonous effects on plants. Therefore, such fumigants should be applied only when the greenhouse was fully empty. Only the methyl bromide should be applied in case of obligatory cases when there were plants inside the greenhouse [1].

REFERENCES

[1]. B. Kılıc, Sera ortamında cevre ozellikleri, kirleticiler ve etkileri. Ziraat Derg., Sayı 45. 1988.
[2]. M.T . Topbas, R. Brohi, M.R. Karaman, *Cevre Kirliligi. T.C. Cevre Bakanlıgı Yayınları*, Ankara, 1998.

[3]. J. Brust, Greenhouse *"Air Pollution" Caused by Ethylene, WCU*, University of Delaware :Cooperative Extension, April 24th, 17:6, 2009

[4]. G. Johnson, *Air Pollution Damage to Transplants in the Greenhouse, WCU*, University of Delaware :Cooperative Extension, WCU 20 (7), May 4, 2012.

[5]. K. Haktanır, and S. Arcak, *Cevre Kirliligi. Ankara Üniv. Ziraat Fak.* Yayın No: 1503, Ders Kitabı: 457, Ankara, 1998

[6]. E. J. Sikora, and A.H. Chappelka, Air Pollution Damage to Plants, Alabama A &M and Auburn Universites, ANR-913 p.1-5. 1987.

[7]. N. Güzel, *Toprak verimliligi ve gübreler. C.Ü. Ziraat Fak. Yay.*, No: 168, Ders Kitabı No: 13, Adana. 1982.

[8]. Anonymous, *Hazardous Properties of Ammonia, IFA*, 28, F-76008, Paris. 1990.

[9]. N. Matson, Ammonium Toxicity: Avoid Getting Burned This Winter. Cultures Notes, Growertalks, October 11 p36. 2011.

[10]. K. Al-Khatib, Herbicide Damage, Herbicide Symptoms, UC IPM, University of California Division of Agriculture and Natural Resources, 2017.

Solar Energy Use in Greenhouses

Sedat Karaman[1], Zeki Gokalp[2]

Abstract

Greenhouses provide the best conditions for plant growth and development in off-seasons. Heating is required in cold regions to provide these optimum conditions. However, heating costs constitute the greater portion of total production costs even in mild climates. Therefore, natural energy resources should be preferred in greenhouse heating in regions with available resources. Solar energy is quite available in almost everywhere and it is a free source. However, several technical and economic problems may be experienced in using solar energy for greenhouse heating. For solar energy to be used in greenhouse heating, solar radiation should be converted into heat energy and then this energy should be stored in somewhere for heating. In present study, potential use of solar energy in greenhouse heating was assessed, problems were put forth and possible solutions were provided for these problems.

Keywords: *Solar Energy, Greenhouse, Solar Radiation, Heating*

1. INTRODUCTION

Greenhouses allow all year-long production with adjusted climate parameters. In outdoor production activities, climate conditions are not always available. Therefore, greenhouses are constructed to get year-long yields from plant production activities.

The primary target in under-cover production is to keep indoor temperatures at optimum levels. Greenhouses should be heated to get maximum yields when the outdoor temperatures get too low. Heating constitutes the greatest cost item (almost 60-70% of total production costs) in cold-region greenhouses. In Mediterranean ecological zone, greenhouses are heated only during the coldest times of the year. But, sufficient attention is not paid in heating of greenhouses even in Mediterranean climate zone. Then, various problems are experienced with regard to yields, quality and harvest times. Usually the cheapest energy source is preferred in greenhouse heating.

Recent studies have focused on alternative, renewable and cheap energy sources in greenhouse heating rather than commonly used fossil fuels. The primary target is to improve heating efficiency and reduce heating costs. Solar energy is among those renewable and cheap energy sources and there is an ever-increasing interest in solar energy. With the use of solar energy, greenhouse heating costs and thus the total production costs can significantly be reduced.

Sunlight is generally considered as a plentiful resource; the exceptions highlight the importance of solar energy to agriculture. Agriculture and horticulture seek to optimize the capture of solar energy in order to optimize the productivity of plants. Greenhouses convert solar light to heat, enabling year-round production and the growth of specialty crops and other plants not naturally suited to the local climate. Various strategies are commonly used to extend the spring and fall growing seasons by a few weeks. An energy-efficient solar-heated greenhouse can provide an inexpensive and successful tool to fill the gap for farmers with winter garden-envy. A variety of cold-hardy species, including vegetables, salad crops, restaurant garnishes, and fresh cut flowers can be successfully and economically cultivated in a properly designed solar-heated winter greenhouse with little or no added heat. Of course, one could preserve summer crops by canning and drying, but fresh vegetables in winter months would make a healthy diet more likely [1].

Commercial greenhouses typically rely on the sun to supply their lighting needs, but are not designed to use the sun for heating. They rely on gas or oil heaters to maintain the temperatures necessary to grow plants in the colder months. Solar greenhouse, however are designed to utilize solar energy both for heating and lighting [2].

---

[1] Corresponding author: Gaziosmanpasa University, Department of Biosystem Engineering, 60250, Tokat, Turkey. sedat.karaman@gop.edu.tr

[2] Erciyes University, Department of Biosystem Engineering, 38039, Kayseri, Turkey. zgokalp@erciyes.edu.tr

Greenhouse is one of the most commonly passive solar energy applications. Greenhouses provide opportunities in cold climates to grow food and horticultural products near to market, reducing the cost and fossil fuel use associated with shipping. A greenhouse could be as simple as plastic films supported by wires, and yet it could help to raise the inner temperature. Also in commercial applications, greenhouse technology has been proven to be economical and efficient in construction and operation [3; 1].

2. SOLAR HEATING SYSTEMS USED IN GREENHOUSES

The conventional greenhouse, designed primarily to capture light, tends to overheat on sunny days, lose more heat than it gains on cloudy, windy or cold days, and lose heat rapidly each day after sundown. Solar greenhouses differ from conventional greenhouses in that they are designed to both collect and retain solar energy, and thus reduce the use of fossil fuels for heating. If improperly ventilated, any greenhouse will overheat. Solar energy reaches the Earth's surface by direct radiation and by diffuse sky radiation, reflected from clouds and atmospheric dust. Diffuse radiation also includes radiation reflected from adjacent ground or building surfaces. The relative proportion of total radiation from these sources varies widely in each climate. Hot-dry climates with clear skies enable a large percentage of direct radiation to reach a building while up to 40 percent of the total radiation received may be diffuse in temperate and humid climates. In northern areas, low winter sun reflection off snow may result in a greater amount of incident radiation on vertical walls than in warmer, but cloudier, areas. Because of different types and amounts of radiation and different heating demands, the design of optimum solar heating components will vary in each locale, and with the particular use of the greenhouse [4].

Natural energy sources to be used in greenhouse heating may reduce heating costs significantly, thus reduce total production costs, too, since heating constitutes the greatest cost item in greenhouse production activities. Among various renewable energy sources, solar energy, geothermal energy and biomass have already been used for heating greenhouses. Solar energy has been used mainly with passive systems and energy storage [5].

Passive solar greenhouses are often good choices for small growers, because they are a cost-efficient way for farmers to extend the growing season. In colder climates or in areas with long periods of cloudy weather, solar heating may need to be supplemented with a gas or electric heating system to protect plants against extreme cold. Active solar greenhouses use supplemental energy to move solar heated air or water from storage or collection areas to other regions of the greenhouse [6].

The cleanliness and abundance of solar energy has made it an attractive option for non-fossil fuel based heating systems. A greenhouse by nature is designed to capture and utilize this energy, so when it comes to finding ways to increase the efficiency of greenhouses, it is natural that finding a way to further utilize the sun's energy is the first thing that comes to mind. One way of doing this is through solar thermal heating systems, which involve collecting and storing the sun's heat through a variety of methods in order to redistribute it as needed (these systems differ from solar electricity, such as photovoltaic cells, which implies the direct conversion of solar energy into electricity). There are passive solar thermal systems, which complete this process without the use of mechanical inputs, and active systems, which increase their heating capabilities through mechanical components such as fans and pumps. Contrary to popular belief, solar thermal systems do not just provide heat – they can provide cooling and ventilation services as well, making them an extremely versatile investment [7].

3. ACTIVE AND PASSIVE SOLAR HEATING SYSTEMS

Greenhouses are heated by passive solar heat. In this system the greenhouse acts as the collector and heat is stored in an internal water or rock storage. The main advantages of the passive systems are their simplicity of construction, low maintenance, and appreciably lower first costs [4].

Not surprisingly, greenhouses use a phenomenon called the greenhouse effect. Despite its negative connotation due to global warming, the greenhouse effect is useful for controlling climates indoors without burning fuels to maintain temperature. This effect works by allowing light to enter a structure by penetrating a transparent layer. When light enters, it refracts and is absorbed as it hits objects (Figure 1). Some of the energy in the light is converted into infrared thermal energy, which is trapped as heat inside the building. Here is an abridged version of the process [8].

- Light penetrates a transparent layer, and the rays refract

- Some light energy is converted to infrared thermal energy as it is absorbed and reradiated from objects (thermal mass)

- Warm air rises, heating the greenhouse

- Re-radiated wavelengths longer than infrared rays pass through the greenhouse "glass" into the atmosphere.

The problem with regular greenhouses is that once the sun goes down the building needs supplemental energy to maintain the climate. This usually involves burning large amounts of expensive fossil fuels which releases emissions and harms the environment.
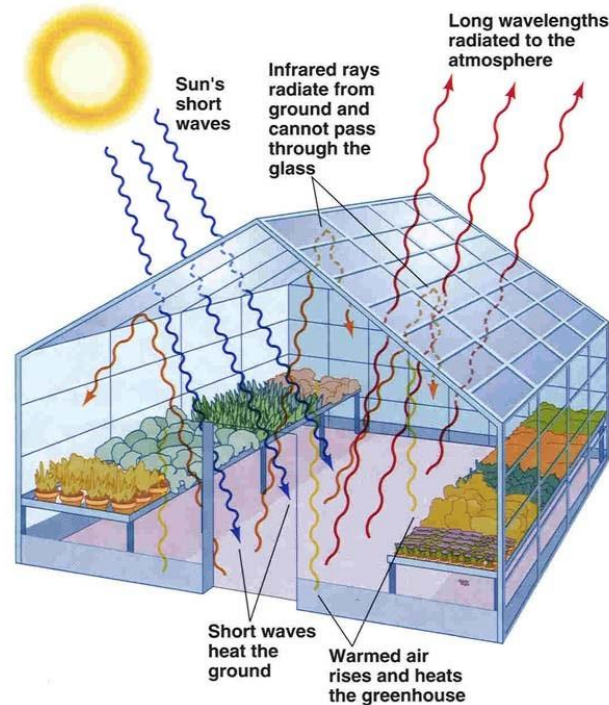

Figure 1. Passive solar system

In a passive system the building and its components collect and store the solar energy. No blowers, pumps or electrical equipment are used. This is usually the most cost effective way to use energy from the sun. Water barrels or rock walls typically store heat for a passive system used in greenhouses [4].

Heat collected is normally stored for later use by warming a material such as a brick or concrete wall, water, small stones, or a material that changes phase. Pound for pound, water can store more heat than any commonly available material. One Btu of heat will raise the temperature of a pound of water 1°F. This value is called specific heat. Rock, iron, or aluminum have specific heats of about 0.2   Btu or less per pound of material per °F temperature rise [4].

Glass and plastic are poor insulators, losing more than ten times as much heat as a well-insulated wall. Areas of the greenhouse that don't receive direct sunlight, such as the north wall and roof, and foundation, can be insulated to retain heat. Insulated interior walls and framing members are painted white to reflect light. A large thermal mass, usually water or rock, is placed in the greenhouse to absorb and store the excess day heat; at night, this heat emanates from the storage into the greenhouse. Night insulation systems using blankets, panels or shutters are often provided to reduce heat loss through the glazing [4].

Although from the technological point of view greenhouses are well covered, they have to cope with the continuously increasing costs of the energy. Their main asset, the direct use of the solar energy, is not able to constantly ensure the temperature constraints demanded by plants, because of the hardly predictable weather conditions. That is why most greenhouses have to be connected to conventional energetic infrastructures: electricity, gas, warmed water, etc. Our purpose is to investigate a fundamental improvement of the greenhouse concept, with a huge potential to improve our lives: the Passive Greenhouses [9].

In active solar heating systems, a heat collection and storage units apart from main greenhouse building are used. The heat energy collected through greenhouse cover and the heat energy stored in active heating system are used to meet heating requirement of the greenhouse. In these systems, heat collection units cover large areas, initial investment and operational costs are high, input costs are also high, thus economical use of such systems are quite limited [10].

Significantly more expensive and complex active solar heating systems are rarely used. They have external solar collectors and fans or pumps to move the heated fluid or air into the greenhouse or into a storage [4].

Active solar systems typically have separate solar collectors and either pumps or blowers to transfer heat via liquid or air from the collectors to a separate storage. The same or additional pumps or blowers may be needed to remove the heat from storage and distribute it within the greenhouse. A blower and duct system that transfers heat from the ridge of the greenhouse to a rock bed is an example of an active system [4].

An active method for solar heating greenhouses uses "subterranean heating" or "earth thermal storage solar heating". This method involves forcing solar heated air, water, or phase change materials through pipes buried in the floor. If hot air is used for subsurface heating, inexpensive flexible drainage or sewage piping about 10 centimeters (4 inches) in diameter can be used for the piping. Although more expensive, corrugated drainage tubing provides more effective heating than smooth tubing, since it allows for greater interaction between the heat in the tube and the ground. The surface area of the piping should be equal to the surface area of the floor of the greenhouse. Once installed, these pipes should be covered with a porous flooring material that allows for water to enter into the soil around them, since moist soil conducts heat more effectively than dry soil. The system works by drawing hot air collected in the peak of the roof down through pipes and into the buried tubing. The hot air in the tubes warms the soil during the day. At night, cool air from the greenhouse is pumped through the same tubing, causing the warm soil to heat this air, which then heats the greenhouse [11; 12; 1].

Solar greenhouses are designed not only to collect solar energy during sunny days but also to store heat for use at night or during periods when it is cloudy. They can either stand alone or be attached to houses or barns. A solar greenhouse may be an underground pit, a shed-type structure, or a Quonset hut. Large-scale producers use freestanding solar greenhouses, while attached structures are primarily used by home-scale growers. Passive solar greenhouses are often good choices for small growers, because they are a cost-efficient way for farmers to extend the growing season. In colder climates or in areas with long periods of cloudy weather, solar heating may need to be supplemented with a gas or electric heating system to protect plants against extreme cold. Active solar greenhouses use supplemental energy to move solar heated air or water from storage or collection areas to other regions of the greenhouse [13; 1].

Solar greenhouses differ from conventional greenhouses in the following four ways [14; 1].

- Have glazing oriented to receive maximum solar heat during the winter;

- Use heat storing materials to retain solar heat;

- Have large amounts of insulation where there is little or no direct sunlight;

- Use glazing material and glazing installation methods that minimize heat loss;

- Rely primarily on natural ventilation for summer cooling.

Many types of passive solar systems have been used for heating greenhouses (Santamouris et.al, 1994). According to the characteristics of the heat storage system they are categorized as greenhouses with:

   a) Heat stored in water

   b) Heat stored as latent heat in various materials

   c) Heat stored in rock bed

   d) Heat stored in buried pipes

An alternate route to producing heat at night is to store heat during the day, and release it when needed. This is where the idea of a *passive solar* greenhouse comes in. Passive solar essentially means that the greenhouse inactively benefits from the sun's power (Figure 2). This is accomplished through the use of special insulation in strategic locations such as the north wall and parts of the east and west walls [8; 15].

Another, more advanced technique is the use of a Ground to Air Heat Transfer system, or GAHT system. This system usually lays in the soil below the greenhouse, and is able to build up heat throughout the day using warm air from the greenhouse. As temperatures drop at night, thermal energy is slowly circulated into the greenhouse using warmed air from underground. While up front expenses are higher, the benefits of a passive solar greenhouse pay for them over time [8; 15].
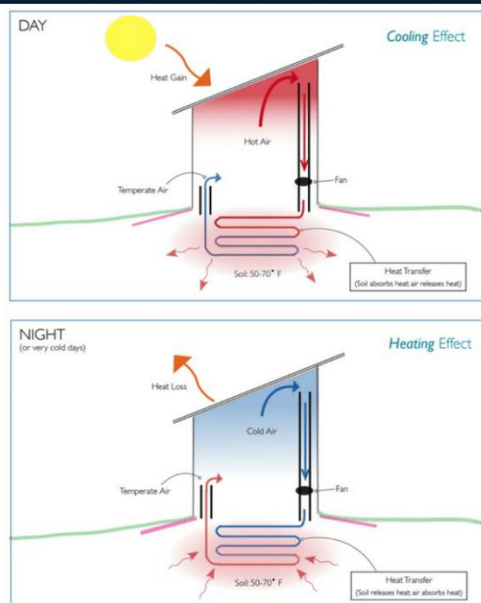
Figure 2. Ground to air heat transfer (GAHT) system

The orientation of the greenhouse can also increase the absorption of solar energy. A walk-in tunnel orientated east-west will absorb substantially more energy than a similar structure orientated north-south. Placement of the self-supported vertical water tubes on the north side as a "wall of water" increases energy absorption and storage therefore raising greenhouse night temperatures up to 16 C0 in Israel, depending on local radiation and climatic conditions. Losses of energy to the surrounding is reduced by covering the greenhouse with a double layer of plastic sheets with IR blockage, with a gap of air between the sheets or by the use of thermal screens or insulation blankets. From sunset when there is no more accumulation of heat, the water tubes and the soil release heat energy in to the volume of the greenhouse. Similar practical applications of these principles are used elsewhere in the world. In parts of China solar energy is stored in a thick wall made from mud or clay bricks. In Israel we have applied these principles in walk-in tunnels for the growing of basil. The combination of these components have allowed us to grow basil (a summer crop) in the winter, while increasing production, preventing plant diseases, and improving quality while reducing costs and emission of greenhouses gases [16].
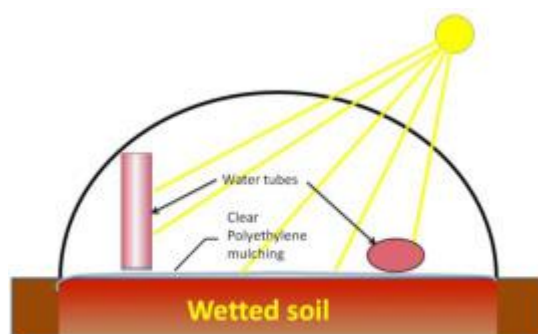
Figure 3: Absorption and storage of energy from the sun

Using horizontal water tubes (fig. 2) is not a new method for it was tried years ago. Even though the horizontal tubes have some contribution to warming the greenhouse, they are located in the worst place in the greenhouse, the coldest and most shaded place, and they are exposed to mechanical damage. A unique solution of arranging the water tubes vertically (fig. 3) is a good and effective solution to the problems of the horizontal water tubes. They stand independently they are not supported by the greenhouse structure. They have a rigid frame made out of a metal sheet sleeve, or are supported by using a sleeve made from a metal wire mesh. The vertical tubes are exposed to the sun and they are not in the way of the workers in the greenhouse. It is possible to store a much greater volume of water in the greenhouse to enable greater storing

of heat energy. Positioning the vertical tubes correctly reduces shading problems and is suitable for multi-span greenhouses and north-south orientations in walk-in tunnels *[16]*.

A similar, albeit more complex, concept to thermal mass is utilized by passive solar thermal systems. In a solar thermal system, heat is absorbed above ground during the day using a heat-transfer medium - often water or an engineered working fluid but air can also be used. The heat transfer medium is then pumped through pipes underground, where the radiant heat warms the soil during the night. At night, fluid is cooled and stored, and can then be released during the day to keep the house cool

One of the most important components of the solar thermal system is the solar collector, a device that absorbs the sun's radiation and transfers it to a working fluid. From there, the fluid is either pumped into a storage tank where it can be drawn on for colder or cloudy days, or directly into the heating system [7].

There are three types of stationary solar collectors: conventional flat plate collectors, evacuated tube collectors, and compound parabolic collectors. In a flat plate collector, solar radiation passes through a flat glazed surface and is absorbed by a transport medium. Compound parabolic collectors utilize a trough of reflective material to focus solar radiation into a heat absorber [7].

REFERENCES

[1]. S. Gorjian, S, T. T. Tavakkoli, B. Ghobadian, *Solar Powered Greenhouses, SET2011*, 10th International Conference on Sustainable Energy Technologies, Istanbul, TÜRKİYE, 4-7, p.5, Sep. 2011.

[2]. J. Chikaire, F. N. Nnadi,,R. N. Nwakwasi, N.O. Anyoha, O. O. Aja, P.A. Onoh, C. A. Nwachukwu, *Solar Energy Applıcatıons for Agrıculture, Journal of Agricultural and Veterinary Sciences, Cenresin Publications* (2), p. 58-62, 2010.

[3]. Y. Dov Strauch Y, *Test of Technologies for Affordable Solar Greenhouses*, M.Sc Thesis, Department of Thecnology, Appalachian State University, Boone, North Carolina, 2008.

[4]. J. W. Bartok, J. White, T W. J. Roberts, N J R. A. Aldrich, R. A. Parsons, *Solar greenhouse fort the home, Cooperative Extension Northeast Regional Agricultural Engineering Service*, NRAES-2, p.60, 1984.

[5]. M. Santamouris, A. Argiriou, M. Vallindras, *Design and operation of a low energy consumption passive solar agricultural greenhouse, Solar Energy*, 52, 371-378, 1994.

[6]. C. Svejkovsky, *Renewable Energy Opportunities on the Farm. A Publication of ATTRO-National Sustainable Agriculture Information Service*, U.S.A. Available at www.attra.necat.org. 2006.

[7]. P. Croker, K. Fink, K. McDonald, D. Peters, D, *Alternative Heating Sources in Vermont Greenhouses, http://www.middlebury.edu/system/files/media/GreenhouseFINAL.pdf*, 2017.

[8]. http://helios.pomfretschool.org 2017.

[9]. M. Balas, C. Musca and S. Musca, *The Passive Greenhouses, Chapter 5, Paths to sustainable energy (Ed: Nathwani, J and Artie W. Ng.), Published by InTech*, p.75-92, Rijeka, Croatia, 2010.

[10]. H. Oztürk, A. Bascetincelik, C. Karaca, *Sera Isıtması icin Güneş Enerjili Aktif Isıtma Sistemleri. 6. Seracılık Sempozyumu Bildiriler Kitabı*, s.49-54, 5-7 Eylül 2001, Fethiye-Mugla, 2001.

[11]. G.J . Monk, D. H.Thomas, J. M. Molnar, L. M. Staley, *Solar Greenhouses for Commercial Growers. Publication 1816. Agriculture Canada*. Ottawa, Canada, 1987.

[12]. V. M. Puri, C. A. Suritz, *Feasibility of subsurface latent heat storage for plant root zone and greenhouse heating. American Society of Agricultural Engineers (Microfiche collection)* 20 p., 1985.

[13]. A. Ron, A. Shapiro, *Low-Cost Passive Solar Greenhouses. National Center for Appropriate Technology, Butte, MT*, 173 p. 1981.

[14]. Anonymous, *Illinois Solar Energy Association, Solar Greenhouse. ISEA,* Fact Sheet #9. Accessed at: www.illinoissolar.org. 2002.

[15]. http://www.ceresgs.com 2017.

[16]. D. Shapiroa, T. Dekoa, S. Itshaka, D. Silvermanb, M. Sacksb, U. Adlerc, I. Esquirec,Y. Stiglizd, *An Innovative Way For Heating Greenhouses Using Solar Energy During The Winter For Summer Crop Production,* http://www.ginegar.com/2017.

Effect of Bondline Thickness on Adhesive Bonding of Laser Treated Carbon Fiber Reinforced Composites

Erhan Akman,[1,4], Yalcın Erdogan[2], M. Ozgur Bora[1], Onur Coban[1], Belgin Genc Oztoprak[1,4], Arif Demir[3,4]

Abstract

Many industries such as automotive, aerospace and maritime showing a growing interest in carbon fiber reinforced polymer (CFRP) composites due to their advantages such as; excellent mechanical and chemical durability and relatively high specific strength. But the traditional joining methods for instance rivets or bolts do not allow to exhibit the advantages properly. So it seems that adhesive bonding is the most promising method for joining the CFRP composite structures. In adhesive bonding there are lots of parameters affecting the strength of the joint such as surface energy, curing cycle and so the thickness of the adhesive layer. In this study effect of the bondline thickness on the adhesion strength of CO_2 laser ablated CFRP composite structures have been investigated by single lap shear tests. Surface treatments have been realized without damaging the load-carrying fibers. Surface treated CFRP samples have been adhesive bonded with the bondline thicknesses ranging between 30-500µm. Bondline thicknesses have been observed by optic microscopy. Single lap shear tests have been performed according to ASTM D5868-01 with 60 kN DARTEC universal test machine.

Keywords: Carbon Fiber Reinforced Polymer, Laser Treatment, Adhesive Bonding, Bondline Thickness

1. INTRODUCTION

While many features of conventional materials are not sufficient for the needs of the developing technology, production of composite materials with superior properties has started and a rapid development process has introduced in this regard. The primary advantages of composite materials are their high strength, relatively low weight, and corrosion resistance. If the application of the composite parts is large and complex, the structures are usually produced by combining several parts. Joints are naturally the weakest parts of the structure, so the manufacture of joints is very important. Conventional methods such as rivets and screws used in the joining process require holes which lead to major stress concentrations and also damage to the fibers that are responsible for carrying the load in the composite materials [1]. In addition, the rivets and screws in use reduce the lightness advantage of composite materials [1]. Adhesive bonding is an alternative method that provides full use of the advantages offered by composite materials [2]. Adhesive bonding is a material joining process in which bonding is provided with an adhesive which placed between the adherend surfaces [2]. However, in order for the bonding technique to be used in production, it is necessary for the bond to achieve the desired strength values. There are lots of parameters that affect the strength and durability of the adhesive bonding such as nature of the adhesive and the adherend material, bondline thickness, contamination, stress and environmental factors, and mostly improper surface treatment of adherend [3]. The problem of adhesion between the adhesive and the adherend usually arises from chemicals such as mold release agents that cause surface contamination [1]. Pretreatment on the surfaces removes the weak boundary layers on the surface, change the surface energy and improve the microphotographic properties of the surface [3]. There are different surface treatment methods which can be used for pretreatment of the composite surface for adhesive joint such as sand-blasting, abrading, peel ply and plasma etc. [4]. In addition to

---

[1] *,*Corresponding author: Kocaeli University, Faculty of Aeronautics and Astronautics, Aircraft Material Research and Development Laboratory, 41285, Kartepe/Kocaeli, Turkey, E-mail: erhan.akman@kocaeli.edu.tr.*

[2] *Electro Optic System Engineering. Kocaeli University, Kocaeli, Turkey.*

[3] *Department of Physics, Kocaeli University, Kocaeli, Turkey.*

[4] *BEAM Ar-Ge Optics, Laser and Spectroscopy, KOU Technopark, Kocaeli, 41275, Turkey.*

traditional methods, laser is an alternative method that can be used for surface treatment [5]. Precision control of the energy transferred to the material can be achieved during the laser surface treatment. Using laser as an ablation source selective removal of the resin without any degradation of fibre reinforcement is possible [6].

Another important parameter that affects the shear strength is the bondline thickness. While experimental studies show opposite, the strength increases with the adhesive thickness according to the classical elastic analyses [7]. According to Adams et. al [8] thicker bondline thickness includes more voids and microcracks. Gleich et. al [9] and Silva et al. [10] have explained this situation as interface stresses have been higher for thicker bondlines.

In this study effect of the bondline thickness on the adhesion strength of CO2 laser ablated CFRP composite structures was investigated by single lap shear tests. Surface treatments were realized without damaging the load-carrying fibers. Surface treated CFRP samples were adhesive bonded with the bondline thicknesses ranging between 30-500µm.

2. MATERIALS AND METHODS

Surface treatment process of the carbon fiber reinforced polymer laminates was performed using pulsed CO2 laser of 200 W maximum power. This laser operates 10.6 μm wavelength with pulse duration in range of 5-400 μs and repetition rate range between 5 kHz and 100 kHz. To deflect the laser beam a galvanometric system was used together with a 160 mm focal length F-Theta lens to focus the laser beam. During surface treatment, plates were fixed at the focal point of the F-Theta lens (line width of the laser beam on the surface is approximately 200 μm under these circumstances). The position of the samples at the z axis was aligned using a manual stage. On the samples, an area of 25.4 mm x 25.4 mm was irradiated in air by scanning the surface line by line with parallel laser beam traces.

The effect of the bondline thickness on the bonding strength of CFRP-CFRP bonding has been investigated by using a lap shear strength test (ASTM D5868-01). The sample has been prepared according to ASTM standards (1.8 mm thick, 101mm x 25.4 mm dimensions). Paste adhesive (Loctite EA 9396 AERO) was used as adhesives. Curing temperature and curing duration were 66 °C and 60 minutes respectively. In order to obtain statistical results, five samples were prepared for each examined parameter. A pre-study was carried out to determine the optimum laser fluence.

In the study, bondline thickness of the samples were changed between 30-500µm. A fixture consisting of three axis linear translation stages was prepared to provide precision control of the bondline as seen Figure 1. The bondline tolerance of the samples using this fixture is ±10µm. A dimensional verification was carried out using the cross sectional microscope images (see Figure 1b) and the tensile test was conducted after test.
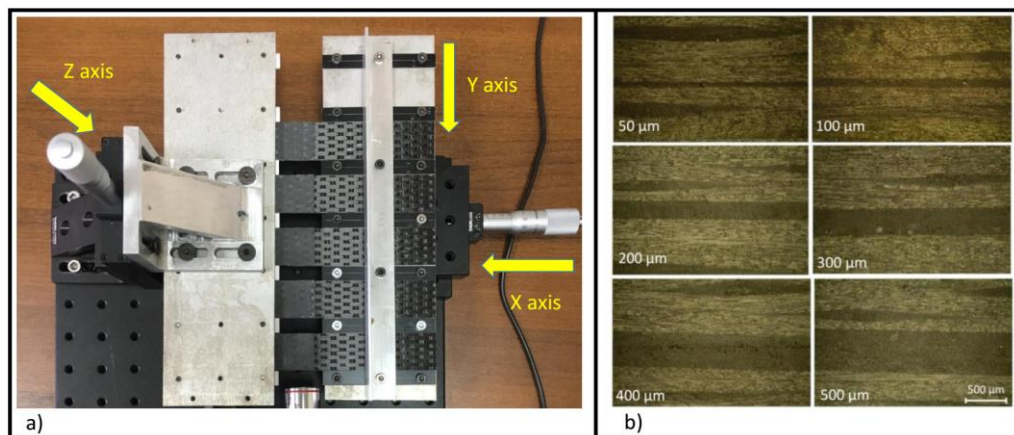
Figure 1. Image of the fixture used for the precision control of the bondline thickness.

3. RESULTS AND DISCUSSIONS

The main purpose of laser material processing is to make the desired changes in the controlled manner by using the power of the intensified electromagnetic radiation [11]. In this process achieving the desired result depends on the parameters of the material, laser and application method. The most important parameter to be optimized is the laser fluence, which is defined as the laser energy in the unit area. Too much increase in the laser fluence can cause delimitation errors and damage to the resin which holds the fiber layers near the surface [3]. In our experiment, pre-studies were shown that the most suitable laser fluence was $9j/cm^2$ for the

adhesive joint of the CFRP laminates (see in Figure 2a). So, all samples used for determining the bondline were treated with 9 j/cm² laser fluence. Optical microscope image and the surface profile of the laser treated surface is shown in the Figure 2a and 2b. The surface roughness of untreated CFRP laminates 1.4µm was increased to 1.92 µm after laser surface treatment.
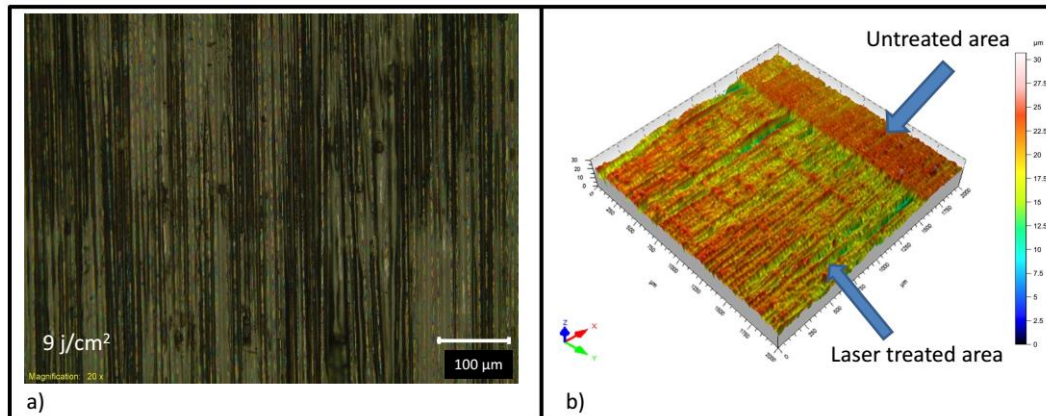

Figure 2. a) optical microscope image and b) surface profile of the laser treated CFRP surface.

Adhesive joint strength versus adhesive thickness has been plotted in Fig 3. for CFRP joints bonded paste adhesive. Adhesive thickness ranging from 30µm to 500µm has been investigated. The highest single-lap strength was obtained in 50µm bondline thickness as seen in Fig 3. As seen in the plot there is a general trend of decrease in single-lap adhesive joint shear strength with adhesive thickness. While the variation of the single-lap strength was not too much between 30µm and 100µm bondline thickness, a rapid decrease on the strength was observed when the thickness was increased 300 µm and more. Increase of adhesive thickness from 50µm to 500µm resulted in a decrease of about 50–55% in adhesive joint shear strength. When the bondline thickness was decreased to 30µm a decrease was also observed in single-lap strength as seen in Fig 3.
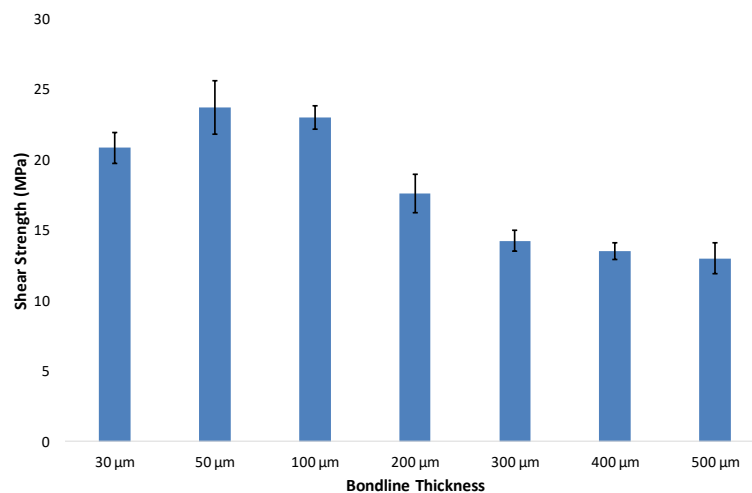
Figure 3. A plot of adhesive joint strength vs. adhesive thickness.

After single lap shear tests, digital camera observations have been applied in order to determine the variation of damage mechanisms due to bondline thickness on the surface of CFRP/CFRP adhesive bondings as seen in Fig. 4. From Fig.4, it can be seen that the main damage mechanism is the cohesive failure for all bondline thickness. In addition, local fiber tear failure is also observed due to higher bondline thickness. At higher bondline thickness, more adhesive paste penetrates the CO_2 laser treated surfaces. During single lap shear tests, applied load is supported by both adhesive paste regions (cohesive failure) and interface regions (adhesive paste with fiber bundles). By this way, fiber tear failure occurs. For a better adhesive bonding, it is suggested that adhesive bonded CFRP/CFRP adhesive bonding only damages as cohesive failure.

Figure 4. Damage mechanisms of different bondline thickness of CFRP/CFRP adhesive bondings.

4. CONCLUSIONS

The effect of the bondline thickness on the adhesive bonding of laser treated CFRP surfaces were investigated by single lap shear tests. According to experimental results;

The variation of the strength is very sensitive to the bondline thickness. From single lap shear tests, maximum shear strength was found as 23.72 MPa at the 50μm bondline thickness. When the bondline thickness has been increased or decreased, shear strength decreases.

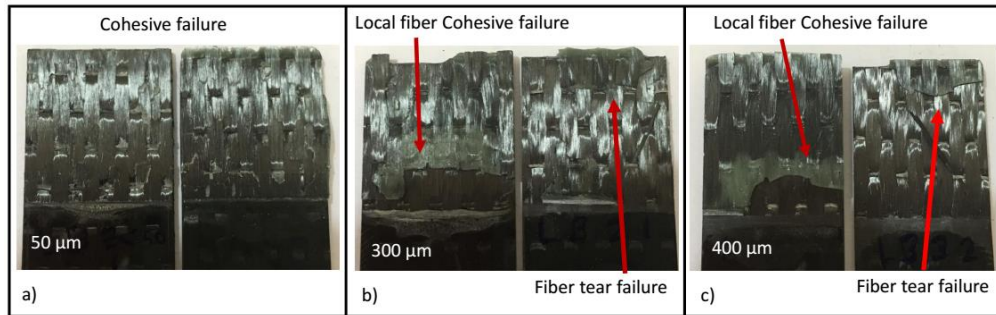From digital observations, cohesive failure is the main damage mechanism which is observed for all bondline thickness. In addition, at higher bondline thicknesses, fiber tear failure which causes to decrease the shear strength of CFRP/CFRP adhesive bonding is also observed.

ACKNOWLEDGMENTS

REFERENCES

[1]   S. Kreling, F. Fischer, R. Delmdahl, F. Gäbler, K. Dilger, "Analytical characterization of CFRP laser treated by excimer laser radiation", Physics Procedia 41 (2013) 282 – 290.

[2]   M D Banea, LFM da Silva, "Adhesively bonded joints in composite materials: an overview", Proc. IMechE Vol. 223 Part L: J. Materials: Design and Applications.

[3]   K.L. Mittal and Tomas Bahners, "Laser Surface Modifcation and Adhesion", Wiley 2015.

[4]   Tomohiro Yokozeki, Masaru Ishibashi, Yayoi Kobayashi, Hideyasu Shamoto, Yutaka Iwahori, "Evaluation of adhesively bonded joint strength of CFRP with laser treatment, Advanced Composite Materials", Vol. 25, No. 4, 317–327, 2016.

[5]   F. Fischer, S. Kreling, P.Jaschke, M. Frauenhofer, D. Kracht, K. Dilger, "Laser Surface Pre-Treatment of CFRP for Adhesive Bonding in Consideration of the Absorption Behaviour", The Journal of Adhesion, 88:350–363, 2012.

[6]   Q. Bénard, M. Fois, M. Grisel, P. Laurens, "Surface treatment of carbon/epoxy and glass/epoxy composites with an excimer laser beam, International Journal of Adhesion and Adhesives", Vol. 26, No. 7, 2006, pp. 543-549.

[7]   Jose M. Arenas, Julian J. Narbon, Cristina Alıa, "Optimum adhesive thickness in structural adhesives joints using statistical techniques based on Weibull distribution", International Journal of Adhesion & Adhesives 30 (2010) 160–165.

[8]   Adams RD, Peppiatt NA. "Stress analysis of adhesively bonded lap joints". J Strain Anal Eng 1974;9:185–96.

[9]   Gleich DM, van Tooren MJL, Beukers A. "Analysis and evaluation of bondline thickness effects on failure load in adhesively bonded structures". J Adhes SciTechnol 2001;15(9):1091–101.

[10] Da Silva LFM, Rodrigues TNSS, Figueiredo MAV, de Moura MFSF, Chousal JAG,."Effect of Adhesive Type and Thickness on the Lap Shear Strength. J Adhes 2006;82(11):1091–115.

[11] Sugioka, K., Meunier, M., Pique, A., "Laser Precision Microfabrication", 135, Springer, New york, 90-95, 2010.

Investigation of Laser Induced Line Pattern Surface Structuring Effect on Adhesive Bonding of CFRP Aircraft Composites

Onur Coban[1], Erhan Akman[1,3], M.Ozgur Bora[1], Belgin GencOztoprak[1,3], Arif Demir[2,3]

Abstract

Adhesion can be greatly improved by the correct surface preparation techniques. One of the most common and useful technique is specific surface structuring which leads mechanical interlocking and greater adhesion. This work describes the effect of laser induced line pattern surface structuring on adhesive bonding of carbon fiber reinforced polymer (CFRP) composites. Surface patterns with vertical lines in different thicknesses and distances were obtained by CO_2 laser treatment. Laser treated surfaces were analyzed by optical microscopy. Surface treated CFRP samples have been adhesively bonded and then adhesive strength of bonded CFRP samples with different line patterns was determined by single lap shear tests according to ASTM D5868-01. After destructive tests, damaged surfaces were analyzed for the failure mechanisms. It was found that the strength of adhesive bonding depends on different line patterned surface types.

Keywords: *CFRP, Laser Surface Structuring, Adhesive Bonding, Mechanical Interlocking*

1. INTRODUCTION

Composite materials are increasingly used in aircraft composites due to their superior weight to strength ratio. This tendency becomes evident with the composite usage for commercial aircrafts exceeding 50 wt.% and so it is important to develop bonding techniques for composite structures [1, 2]. Traditional mechanical joints such as bolted or riveted are being replaced by adhesively bonded joints partially for the advantages of corrosion resistance, lower weight increment, damping, good insulation performance, good smooth aerodynamic shape and more uniform load stress distribution [1-5]. For civil aircraft, bonding of composites is well-established for various secondary joints; such as in the rear pressure bulkhead, the ailerons, the vertical tail plane and the radome as shown in Fig. 1. [1, 6]. The term adhesion means both the establishment of interfacial bonds and the mechanical load required to break an assembly. One of the main difficulties in the study of adhesion mechanisms lies in the fact that the subject is at the boundary of several scientific fields, including macromolecular science, physical chemistry of surfaces and interfaces, material science and mechanics of fracture.

Therefore many theoretical models of adhesion have been proposed: Mechanical interlocking, electrostatic theory, theory of boundary layers and interphases, physical absorption theory, diffusion theory and chemical bonding theory. It is well known that, ''mechanical interlocking'' has a significant role in the bonding process that the adhesive in its liquid state will penetrate into the obtained patterns and so there is a degree of mechanical interlocking. So, one of the most important conditions is the pretreatment of the surface, especially due to the low surface energy and wettability exhibited by polymers [7]. Many researchers have studied the modification of composite surfaces by means of solvent cleaning [8], abrasion, peel-ply [9], tear-ply, acid chemical etching [10, 11] or plasma treatments [12, 13]. Laser surface treatment is also applied for surface cleaning and for removal of coating [14]. All these surface preparation methods focused on random surface roughening. However, there is not any effort for preparing regularly oriented surface roughness to gain mechanical interlocking in adhesive bonding of polymer composites. Therefore, in this study laser

[1] ,* Corresponding author: Kocaeli University, Faculty of Aeronautics and Astronautics, Aircraft Material Research and Development Laboratory, 41285, Kartepe/Kocaeli, Turkey. onur.coban@kocaeli.edu.tr

[2] Kocaeli University, Department of Physics, 41380, Umuttepe/Kocaeli, Turkey.

[3] BEAM Ar-Ge Optics, Laser and Spectroscopy, Kocaeli University-Technopark, 41275, Yeniköy/Kocaeli, Turkey.

induced line patterns (laser scribes) were regularly oriented on the carbon fiber reinforced polymer (CFRP) composites to possess mechanical interlocking in adhesive bonding.

2. MATERIALS AND METHODS

The adherend composite laminate is unidirectional carbon/epoxy and the thickness is 1,8 mm. The two component structural liquid adhesive ''Hysol® EA 9396TM'' was selected to bond the CFRP adherends together. Hysol EA 9396 is a low viscosity adhesive and its mixed density is 1.14 g/ml. Treatments were carried out at atmospheric pressure. The laser beam deflection realized using galvo scanner system. The laser system and the parameters were given in Fig. 1. Laser treated surface roughness topography of CFRP samples were obtained by Nanovea PS50 non-contact 3D laser profilometer.

Max. Average Power	200 W
Peka Power	200 - 480 W
Pulse duration	5 – 400 μs
Pulse energy	2,5 – 190 mJ
Repetition rate	0-100 kHz
Laser beam diameter	8.0 ± 0,5 mm
Lazer beam divergence	< 2 mrad
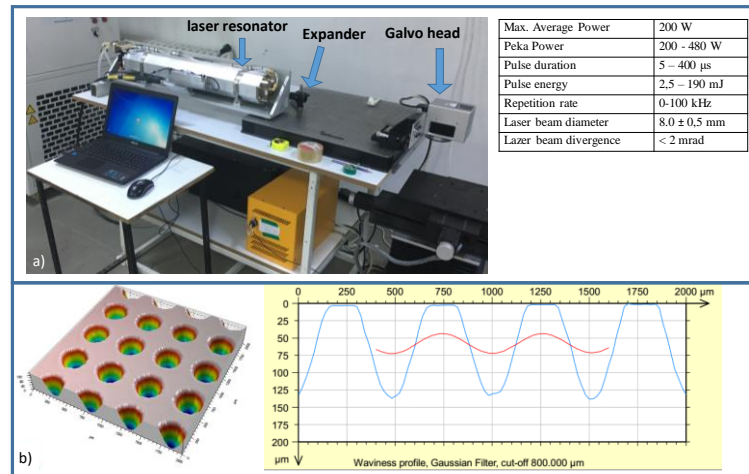
Figure 1. Laser system and its parameters.

2.1. Effect of laser induced line scribe depth on mechanical interlocking and shear strength of adhesive bonded CFRPs

Various scribe depths were obtained by selected laser parameters as given in Table 1. In this table sample types were abbreviated from "laser scribe pattern 1-5" to "LSP1-5". In LSP1-3; 127 scribes were created regularly as shown in Fig. 2. Additionally, optical microscopy images and topography results were also given in Fig. 2. With the increment of laser accumulated fluence values from 18 J/cm2 to 1700 J/cm2, roughness values were obtained as 6,8 μm, 20,2 μm and 25,5 μm; respectively for LSP1, LSP2 and LSP3. It is clear that laser accumulated fluence increment caused an increment of scribe depth. So, the first section of this study was performed for the investigation of the scribe depth effect on mechanical interlocking and shear strength of adhesive bonded CFRPs.

Table 1: Laser parameters for various scribe depths

Sample type	Power (W)	Velocity (mm/s)	Laser accumulated fluence (J/cm^2)
LSP1 (127 scribes with 1 shot laser)	2	100	1x18=18
LSP2 (127 scribes with 5 shots laser)	38	200	5x170=850
LSP3 (127 scribes with 10 shots laser)	38	200	10x170=1700
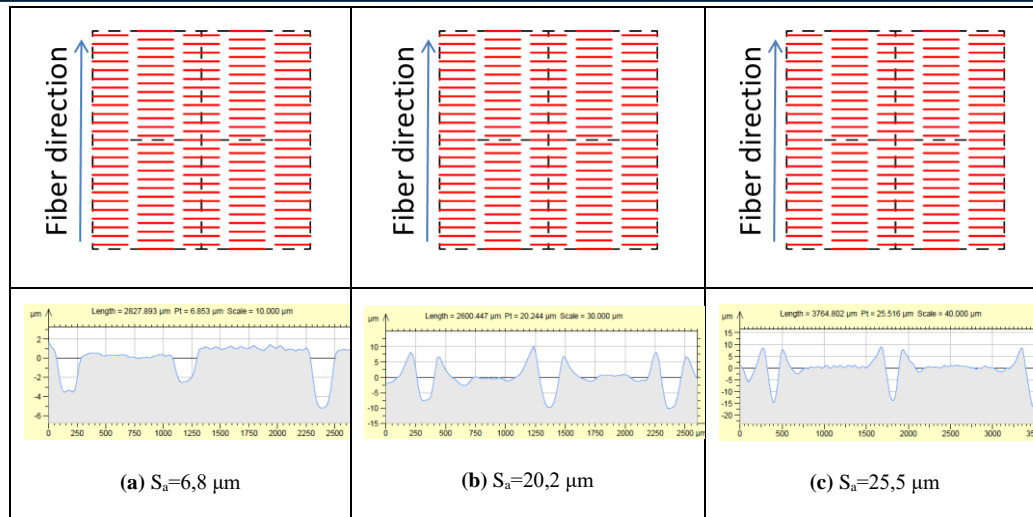
Figure 2. Optical microscopy and topography analysis of laser scribe patterns; (a) LSP1, (b) LSP2 and (c) LSP3

2.2. Effect of number of laser induced line scribes on mechanical interlocking and shear strength of adhesive bonded CFRPs

After optimizing the scribe depth effect in first section of this study, an addition investigation was performed for the effect of scribe amount on mechanical interlocking and on shear strength of adhesive bonded CFRPs. Various amounts of scribes were created such as 127, 72 and 33. Laser scribe patterns were abbreviated as LSP3-5. Laser parameters were same as with the LSP3 as given in Table 1. Laser scribe patterns, optical images and topography results were illustrated in Fig. 3. All roughness values were same such as 25,5 µm. Only the number of scribes was changed and so this effect on mechanical interlocking and shear strength of adhesive bonded CFRPs was investigated in this second section.
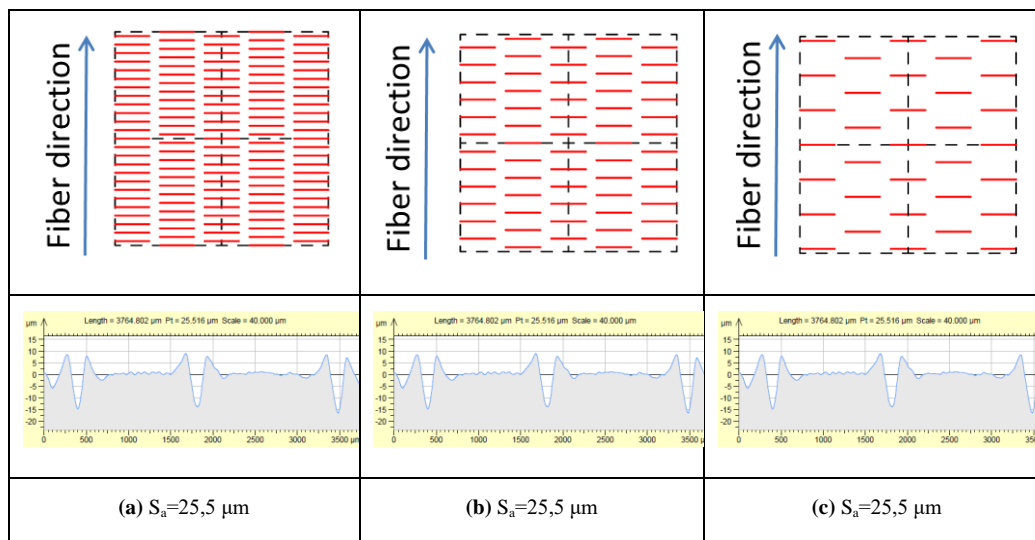
Figure 3. Optical microscopy and topography analysis of laser scribe patterns; (a) LSP3, (b) LSP4 and (c) LSP5

2.3. Sample Preparation

Single lap joint specimens were adhesively bonded according to the ASTM D5868-01 as illustrated in Fig. 4 with the adhesive bondline thickness of 50 µm [15]. At least 5 coupons were prepared at the same time by a manually stage micrometer controlled apparatus. All adhesive bonded samples were cured at 66°C for 1h.

Figure 4. Single lap shear overlay [15]

2.4. Single lap shear test
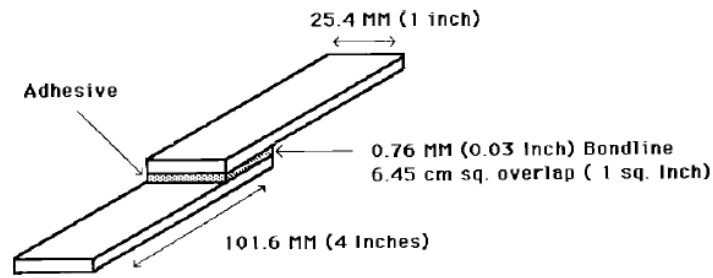
Test coupons were prepared with doublers for not to cause eccentric. Tests were performed according to ASTM D5868-01 with the crosshead speed of 13mm/min by an Dartec® universal test machine equipped with a 60000 N load cell.

3. RESULTS AND DISCUSSION

Single lap shear test results as shear strength values of adhesive bonded CFRPs with LSP1-3 were shown in Fig. 5. It is clear that scribe depth has a significant effect on shear strength. Because of the increment of scribe depth from 6,8 μm to 20,2 μm, shear strength was increased from approximately 19 MPa to 23 MPa. However, this shear strength increment was then decreased again to 19 MPa levels with further increment of scribe depth. So, it should be noted that laser induced line scribe depth should be optimized for the best mechanical interlocking and shear strength of adhesive bonded CFRPs.

Figure 5. Scribe depth effect on shear strength of adhesive bonded CFRPs with LSP1-3

After single lap shear tests, SEM images of damaged surfaces of adhesive bonded CFRP samples were illustrated in Fig. 6. It can be seen for LSP1 that, adhesive failure with weaker adherends was determined. This result was depicted from glossy fiber bundles that there is not any evidence of strong adhesion. Shear strength result of LSP1 was obtained as low value, so this could be attributed to the adhesive failure of weak adhesive bonded LSP1 adherends. SEM images of damaged surfaces for LSP2 showed a cohesive failure mode. There are amount of regular adhesive traces that can be seen clearly in Fig. 6-b. This result supports the achieved highest shear strength that belongs to LSP2 with highest scribe depth. It could be noted that with this LSP mechanical interlocking was worked successfully. On the other hand with further increment of scribe depth, shear strength value was decrease because of adhesive failure mode as can be seen in Fig. 6-c. It is important that, penetrated liquid adhesive into the much higher scribe depth caused much more shear stress and moments.
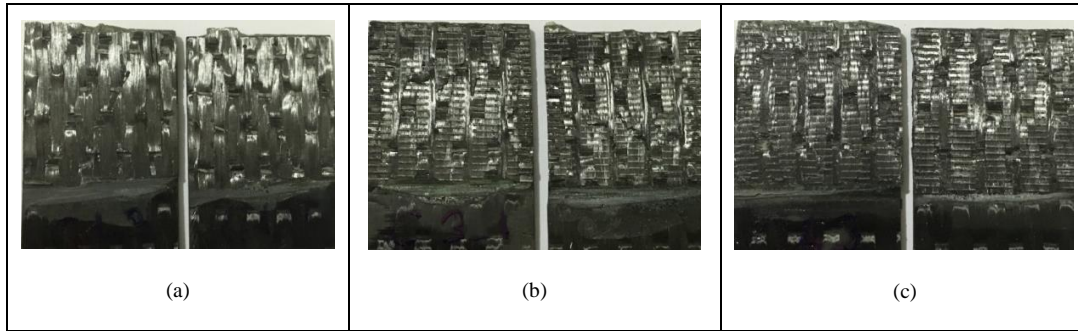
Figure 6. SEM images of damaged CFRP surfaces after single lap shear tests; (a) LSP1, (b) LSP2 and (c) LSP3

Single lap shear test results as shear strength values of adhesive bonded CFRPs with LSP3-5 were shown in Fig. 7. Amount of laser induced line scribe has also significant effect on shear strength of adhesive bonded CFRPs. It is clear that higher shear strength values were achieved with the decrement of scribe amount. Shear strength value of LSP3 with 127 scribes was obtained as 19 MPa, and with the decrement of scribe amount from 127 to 72 this value was increased to 20 MPa and then further decrement of scribe amount to 33, shear strength value was achieved as 23 MPa.
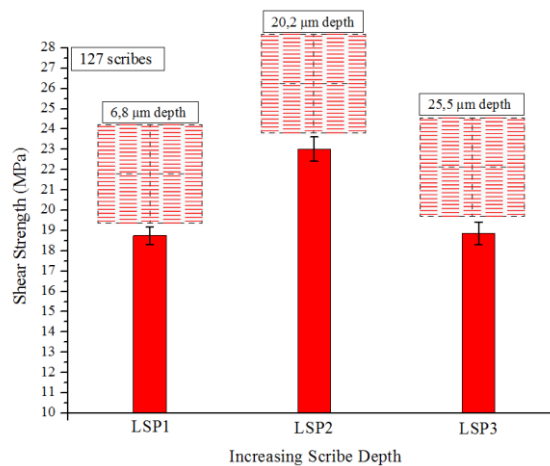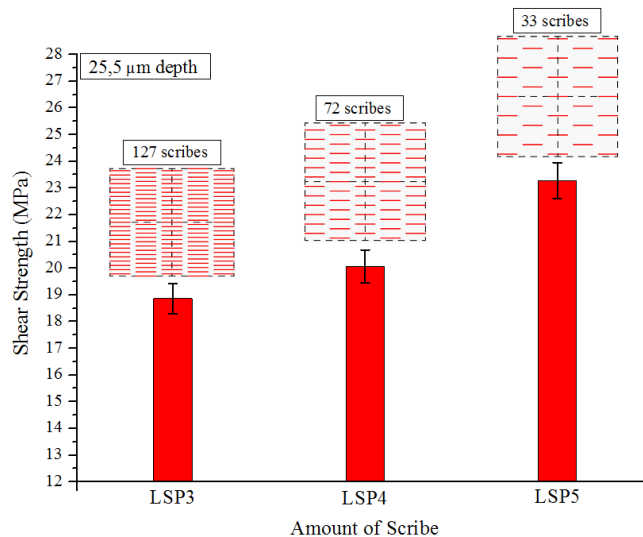

Figure 7. Scribe depth effect on shear strength of adhesive bonded CFRPs with LSP1-3

After single lap shear tests, SEM images of damaged surfaces of adhesive bonded CFRP samples were illustrated in Fig. 8. Damaged surface analysis of LSP3 sample was mentioned above, adhesive failure mode was negatively affected the shear strength of adhesive bonding. However, with the scribe amount decrement, adhesive failure mode was changed step by step to cohesive failure mode. The increment of shear strength of adhesive bonded CFRPs with the decrement of scribe amount can be attributed to this aforementioned phenomenon of failure mode development.
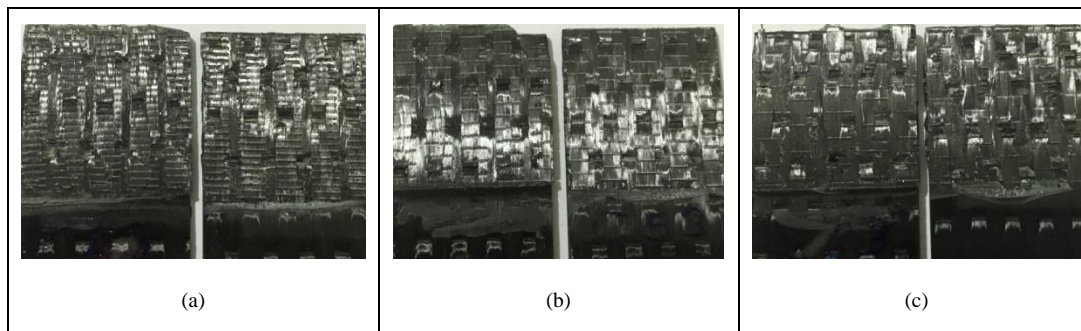
Figure 8. SEM images of damaged CFRP surfaces after single lap shear tests; (a) LSP3, (b) LSP4 and (c) LSP5

4. CONCLUSIONS

Laser induced line pattern surface structuring effect on adhesive bonding of CFRP aircraft composites were investigated by single lap shear tests. According to experimental results following conclusions were derived:

Laser induced line scribe depth has a significant effect on mechanical interlocking induced shear strength of adhesive bonded CFRPs.

Laser induced line scribe amount with the same depth has also a significant effect. The decrement of this scribe amount caused higher shear strength of adhesive bonded CFRPs.

It is suggested that, adhesive bonding strength of CFRPs can be enhanced with optimum laser induced line patterns that had a significant effect on mechanical interlocking phenomenon.

REFERENCES

[1] T. Lobel, D. Holzhuter, M. Sinapius, C. Huhne, "A hybrid bondline concept for bonded composite joints", International Journal of Adhesion&Adhesives 68 (2016) 229–238.

[2] E. M. Moya-Sanz, I. Ivañez, S. K. Garcia-Castillo, "Effect of the geometry in the strength of single-lap adhesive joints of composite laminates under uniaxial tensile load", International Journal of Adhesion & Adhesives 72 (2017) 23–29.

[3] S. Liu, X. Cheng, Q. Zhang, J. Zhang, J. Bao, X. Guo, "An investigation of hygrothermal effects on adhesive materials and double lap shear joints of CFRP composite laminates", Composites Part B 91 (2016) 431-440.

[4] H. Luo, Y. Yan, T. Zhang and Z. Liang, "Progressive failure and experimental study of adhesively bonded composite single-lap joints subjected to axial tensile loads", Journal of Adhesion Science and Technology, 2016 Vol: 30, No: 8, 894–914.

[5] X. Guo, Zhi-dong Guan, Heng-chang Nie, Ri-ming Tan & Zeng-shan Li, "Damage tolerance analysis of adhesively bonded composite single lap joints containing a debond flaw", THE JOURNAL OF ADHESION 2017, Vol: 93, No: 3, 216–234.

[6] D.N. Markatos, K.I. Tserpes, E. Rau, S. Markus, B. Ehrhart, S. Pantelakis, "The effects of manufacturing-induced and in-service related bonding quality reduction on the mode-I fracture toughness of composite bonded joints for aeronautical use", Compos. Part B 2013; 45: 556–64.

[7] N. Encinas, B.R. Oakley, M.A. Belcher, K.Y. Blohowiak, R.G. Dillingham, J. Abenojar, M.A. Martínez, "Surface modification of aircraft used composites for adhesive bonding", International Journal of Adhesion&Adhesives, 50 (2014) 157–163.

[8] A.J. Kinloch, Adhesion and adhesives, London: Chapman&Hall;1987;123–7.

[9] J.L. Cotter, A. Mahoon, Int. J. Adhes. Adhes., 1982;2:47–52.

[10] G.M. Wu, Y.T. Shyng, S.F. Kung, C.F. Wu, Vacuum, 2009; 83:S271–4.

[11] B.R.K. Blackman,A.J. Kinloch, J.F. Watts, Composites, 1994;25(5):332–41.

[12] J.M. Hill, E. Karbashewski, A. Lin, J. Adhes. Sci. Technol., 1995; 9(12):1575.

[13] H. Li, H Liang, F. He, Y. Huang, Y. Wan, Surf. Coat. Technol., 2009; 203:1317–21.

[14] T. Yokozekia, M. Ishibashi, Y. Kobayashi, H. Shamotoc and Y. Iwahori, "Evaluation of adhesively bonded joint strength of CFRP with laser treatment", Advanced Composite Materials, 2016, Vol. 25, No. 4, 317–327.

[15] ASTM International Designation: D5868-01, Standard Test Method for Lap Shear Adhesion for Fiber Reinforced Plastic (FRP) Bonding, Reapproved 2014.

Determination of Appropriate Axial Vibration Dampers for a Naval Vessel Driven by CODAG Propulsion

Abdullah Gokturk[1,2], Osman Azmi Ozsoysal[3]

Abstract

The objective of this study is to reduce the vibration oscillations on a naval vessel propulsion system driven by CODAG. Within vibration analysis of the system firstly; physical model of the naval ship's propulsion system consist of mass, spring and damping elements developed properly and the effects of dynamic forces, which are consisted of main engine stresses, and the hydrodynamic forces that come from water effect are also taken into consideration. Afterwards, equation of motions derived for each mass and consequently by solving these equations, employing matrix approach, natural frequencies and modes of the axial vibration obtained. Finally, a model for propulsion system formed in Matlab/Simulink program. The axial vibrations caused by internal and external forces that excite the system examined and illustrated with graphs how the model respond in the face of undamped and under different axial damping ratios. Then which is also our goal; axial damping ratios that can absorb vibrational motions of the system successfully determined.

Keywords: *Naval vessel, vibration, Codag propulsion, axial dampers*

1. INTRODUCTION

Recent advances in ship design has led to build greater in size and more flexible vessels employ more powerful diesel engines with larger strokes. Flexibility in these structures brings about vibration problems. The main sources of ship vibration can be classified into two major groups; internal and external sources. Internal sources are main & auxilary machines and propulsion system components and the external sources are hydrodinamic loadings by direct action or induced by the ship motions.

Vibration aboard ship may result in fatigue failure of local structural members or major machinery components, adversly effect the performance of vital shipboard equipment, increase maintenance costs and greatly increase discomfort or annoyyance to passengers and crew. These all are why excessive ship vibrations must be taken under control. However, when ship is sailing, corrections on the vessel to decrease vibration problems is too difficult and couses great costs. Therefore, it is very important to identify and make corrections of vibration problems in design stage[1].

Antonides [2], made measurements on the propulsion system of the USS Simon Lake (AS-33) as a part of a program to improve analysis procedures used by the navy for predicting the longitudinal vibration of shaft propulsion system. The objective was to find the axial exciting forces and damping associated with the propulsion system of the ship, as well as to determine how the gear case, turbines, condenser, and machinery foundation effect longitudinal vibration. Alternating thrust in the shaft and longitudinal displacement of the gear case, low-pressure turbine condenser and machinery foundation was measured. A resonance was found to exist in the operating range, but is not considered detrimental. The gear case, turbines and condenser move essentially as one unit. A mass-elastic system derived from measured data includes a level effect acting on the foundation mass. The exciting forces were lower than usual, except at or near full power.

[1]Corresponding author: Istanbul Technical University, Department of Naval Architecture and Marine Engineering, 31200, Sariyer/Istanbul, Turkey. gokturka@itu.edu.tr

[2] Corresponding author: Iskenderun Technical University (İSTE), Department of Naval Architecture and Marine Engineering, 34467, İskenderun/Hatay, Turkey. gokturka@itu.edu.tr

[3] Istanbul Technical University, Department of Naval Architecture and Marine Engineering, 31200, Sariyer/Istanbul, Turkey. ozsoysal@itu.edu.tr

Alarcin at al. [3], on their study were concern with to decrease of vibration oscillations on ship main engine shaft system. The mathematics model of system was composed by Lagrange method and the effect of dynamics forces, which are consisted of main engine stresses, and the hydrodynamic forces that come from water effect were taken into consideration. The axial and torsional vibration are the factors during the analyze. Matlab–Simulink was used to obtain the oscillation of axial and torsional vibrations and to make these oscillations less different types of damping coefficient effects were investigated.

Zhang at al.[4] by modelling of the propeller shaft crankshaft with piston under the influence of angular and axial forces acting on the propeller was investigated. Between propeller and 1st order crankshaft journal, 5th and 6th order piston-crank journal's shaft torsional vibrations have been observed frequency change. Axial vibrations, except for the amplitude, a change of frequency components are expressed almost the same. Considering of coupled vibrations a nonlinear behavior effect was observed. They determined that when the propeller crankshaft vibration analysis approaches to linearity, a large error would be experienced.

Jiang at al. [5] studied the vibration performance of the propulsion shaft introduced by the coupling effect of the propeller and diesel engine. Firstly, the empirical formulas of the exciting force introduced by the diesel and propeller were given. Then a finite element model of propulsion shaft was established with ANSYS. Meanwhile the dynamic responses of the shaft introduced by the diesel excitation, the propeller excitation and the coupling effect of the two excitation were obtained respectively. The research results show that well matched diesel-propeller contributes to the vibration reduction of the propulsion shaft.

Several operations can be done at the ship design stage to reduce the excessive ship vibrations:

reducing exciting forces amplitude,

increasing stiffness,

avoid values of frequency ratio near resonant condition and

increasing damping ratios.

Avoiding vibrations by increasing damping ratios is the main objective of this study.

2. CODAG PROPULSION SYSTEM VIBRATION MODELING

The main sources of axial vibrations in ship propulsion systems are the diesel engine crank mechanism, which produces the power needed for propeller propulsion and propulsion systems. Therefore, when axial vibration analysis is carried out, propeller characteristics, thrust generated and diesel engine characteristics must be well determined.

CODAG (Combined Diesel and Gas) is a type of propulsion system for ships which need a maximum speed that is considerably faster than their cruise speed, particularly warships like modern frigates or corvettes. It consists of diesel engines for cruising and gas turbines that can be switched on for high-speed transits. In figure 1, a simplified 3D model for CODAG propulsion system is represented and relevant to this model, idealized mass, spring and damping system for axial vibration analysis is shown in figure 2.
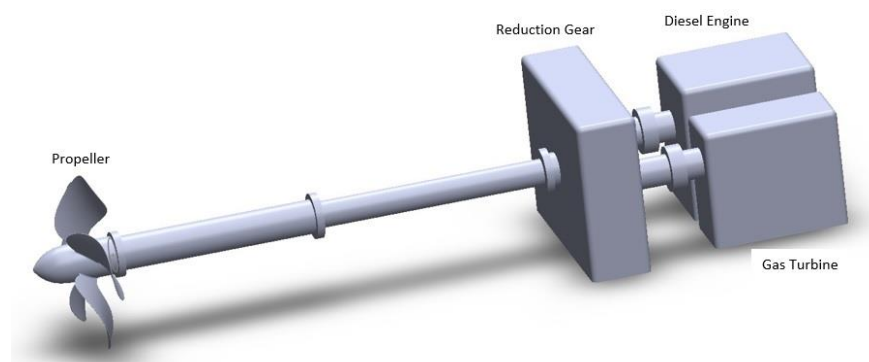

Figure 105. CODAG propulsion system simplified 3D model.
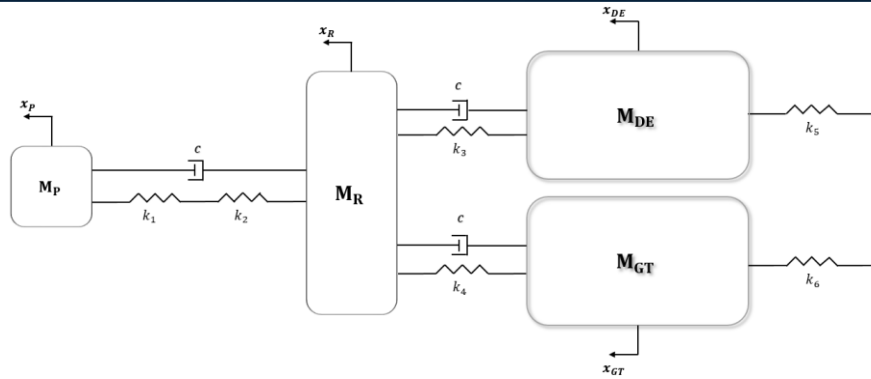
Figure 106. Idealized mass, spring damping system.

Equations of motion for the system derived from mass spring damping system, as shown below:

$$M_P\ddot{x}_P + c(\dot{x}_P - \dot{x}_R) + k_e(x_P - x_R) = T$$
$$M_R\ddot{x}_R - c(\dot{x}_P - \dot{x}_R) + c(\dot{x}_R - \dot{x}_{DE}) + c(\dot{x}_R - \dot{x}_{GT}) - k_e(x_P - x_R) +$$
$$+k_3(x_R - x_{DE}) + k_4(x_R - x_{GT}) = F_R \tag{1}$$
$$M_{DE}\ddot{x}_{DE} - c(\dot{x}_R - \dot{x}_{DE}) - k_3(x_R - x_{DE}) + k_5 x_{DE} = 0$$
$$M_{GT}\ddot{x}_{GT} - c(\dot{x}_R - \dot{x}_{GT}) - k_4(x_R - x_{GT}) + k_6 x_{GT} = 0$$

In order to write differential equations expressing the dynamic behavior of the system in matrix form, it is necessary to specify the mass, damping and stiffness matrices of these equations. The matrix expression for the equations of motion is:

$$
\begin{bmatrix} M_P & 0 & 0 & 0 \\ 0 & M_R & 0 & 0 \\ 0 & 0 & M_{DE} & 0 \\ 0 & 0 & 0 & M_{GT} \end{bmatrix}
\begin{Bmatrix} \ddot{x}_P \\ \ddot{x}_R \\ \ddot{x}_{DE} \\ \ddot{x}_{GT} \end{Bmatrix}
+
\begin{bmatrix} c & -c & 0 & 0 \\ -c & 3c & -c & -c \\ 0 & -c & c & 0 \\ 0 & -c & 0 & c \end{bmatrix}
\begin{Bmatrix} \dot{x}_P \\ \dot{x}_R \\ \dot{x}_{DE} \\ \dot{x}_{GT} \end{Bmatrix}
$$
$$
\begin{bmatrix} k_e & -k_e & 0 & 0 \\ -k_e & k_e+k_3+k_4 & -k_3 & -k_4 \\ 0 & -k_3 & k_3+k_5 & 0 \\ 0 & -k_4 & 0 & k_4+k_6 \end{bmatrix}
\begin{Bmatrix} x_P \\ x_R \\ x_{DE} \\ x_{GT} \end{Bmatrix}
=
\begin{Bmatrix} T \\ F_R \\ 0 \\ 0 \end{Bmatrix}
$$

T is the thrust, which obtained at maximum power in the case of attaching to a fixed point. F_R is the force generated by the reduction gear. The natural frequency is a value that depends on its own mass and rigidity. Therefore, these values are not taken into account since there is no effect of force and damping on calculation of natural frequency.

$$
\begin{bmatrix} M_P & 0 & 0 & 0 \\ 0 & M_R & 0 & 0 \\ 0 & 0 & M_{DE} & 0 \\ 0 & 0 & 0 & M_{GT} \end{bmatrix}
\begin{Bmatrix} \ddot{x}_P \\ \ddot{x}_R \\ \ddot{x}_{DE} \\ \ddot{x}_{GT} \end{Bmatrix}
+
\begin{bmatrix} k_e & -k_e & 0 & 0 \\ -k_e & k_e+k_3+k_4 & -k_3 & -k_4 \\ 0 & -k_3 & k_3+k_5 & 0 \\ 0 & -k_4 & 0 & k_4+k_6 \end{bmatrix}
\begin{Bmatrix} x_P \\ x_R \\ x_{DE} \\ x_{GT} \end{Bmatrix}
=
\begin{Bmatrix} 0 \\ 0 \\ 0 \\ 0 \end{Bmatrix}
$$

In order to calculate natural frequency we should solve the eigenvalue problem for the system.

$$\left|[K] - w^2[M]\right| = 0 \qquad (2)$$

$$\left|\begin{bmatrix} k_e & -k_e & 0 & 0 \\ -k_e & k_e + k_3 + k_4 & -k_3 & -k_4 \\ 0 & -k_3 & k_3 + k_5 & 0 \\ 0 & -k_4 & 0 & k_4 + k_6 \end{bmatrix} - w^2 \begin{bmatrix} M_P & 0 & 0 & 0 \\ 0 & M_R & 0 & 0 \\ 0 & 0 & M_{DE} & 0 \\ 0 & 0 & 0 & M_{GT} \end{bmatrix}\right| = \begin{Bmatrix} 0 \\ 0 \\ 0 \\ 0 \end{Bmatrix}$$

We need the values of parameters to solve eq. (2) and find natural frequencies for the system. Table 1 represents shaft characteristics for the propulsion system and there is mass and force values shown in Table 2. Additionally, shaft rigidity values (k) are calculated based on shaft properties and shown in Table 2.

Table 60. Shaft Dimensions [6]

Shaft Type	Shaft Diameter(mm)	Shaft Length(mm)
Propeller shaft	480	14250
Intermediate shaft	420	14900
Diesel Engine thrust shaft	400	3600
Gas Turbine thrust shaft	400	3600

Table 2. Mass, spring system parameters.

M_P	M_R	M_{DE}	M_{GT}	T	F_R	k_e
13400	32300	13400	15000	197137	2.67×10^9	1.13×10^9
kg	kg	kg	kg	N	N/m	N/m

k_1	k_2	k_3	k_4	k_5	k_6
2.67×10^9	1.95×10^9	7.33×10^9	7.33×10^9	1.29×10^9	1.87×10^9
N/m	N/m	N/m	N/m	N/m	N/m

By solving the eq. (2), frequencies of the system is found and shown in Table 3.

Table 2. Natural frequencies of the system.

	Frequency (Hz)
w_1	2.306
w_2	14.592
w_3	468.792
w_4	1256.433

3. SIMULATION

The vibrations of the CODAG propulsion system components in axial directions are analyzed by simulating various damping values with m-file and Simulink model files created in Matlab/Simulink program as shown in Figure 3.
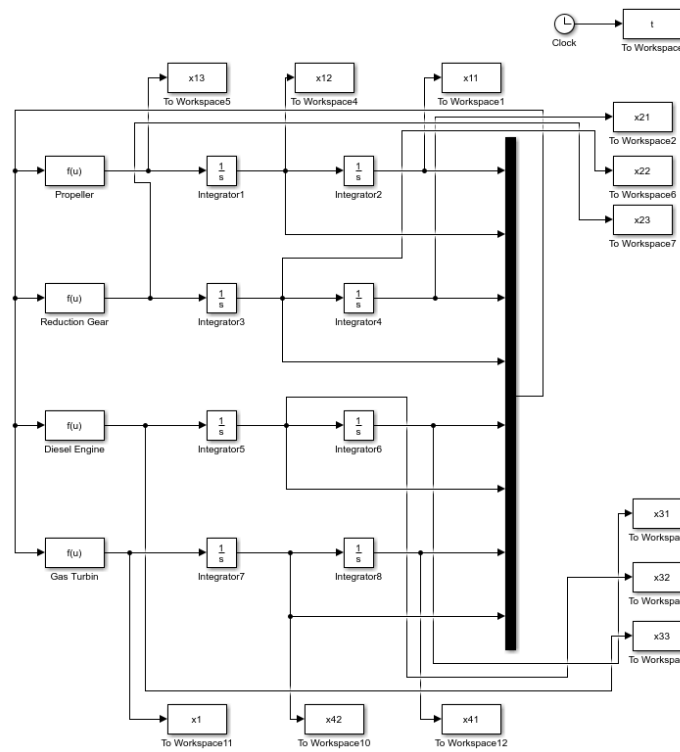
Figure 3. CODAG propulsion system Simulink model.

As a result of the analysis of the axial vibrations of the CODAG propulsion system elements at undamped and different damping ratios, the amplitude variations of axial displacements and the velocities of the propeller, reduction gear, diesel engine and gas turbine are illustrated in graphs respectively.
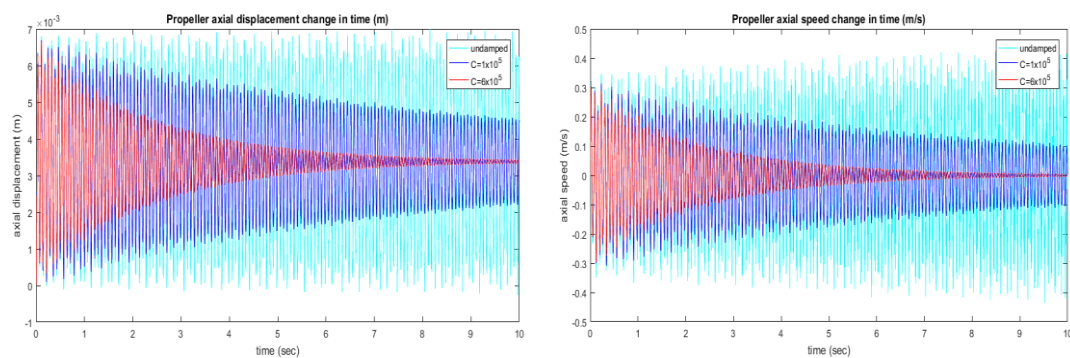
Figure 4. (a) Propeller axial displacement change in time(m)

(b) Propeller axial speed change in time (m/sec).
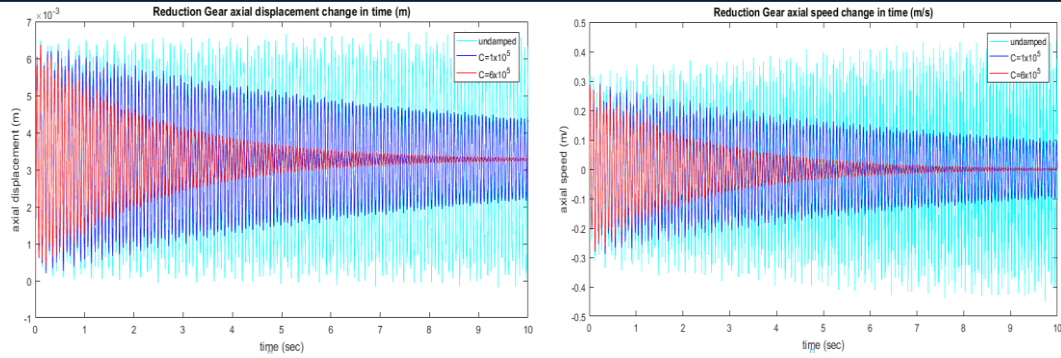
Figure 5. (a) Reduction Gear axial displacement change in time (m).

(b) Reduction Gear axial speed change in time (m/sec).
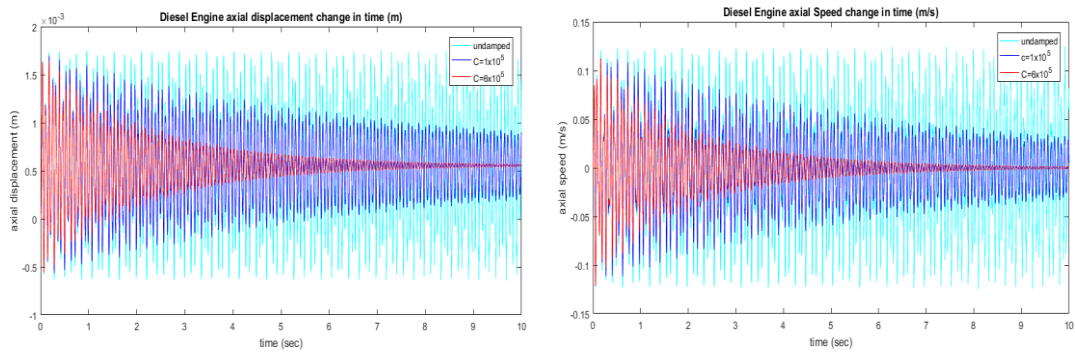
Figure 6. (a Diesel Engine axial displacement change in time(m).

(b) Diesel Engine axial speed change in time (m/sec).
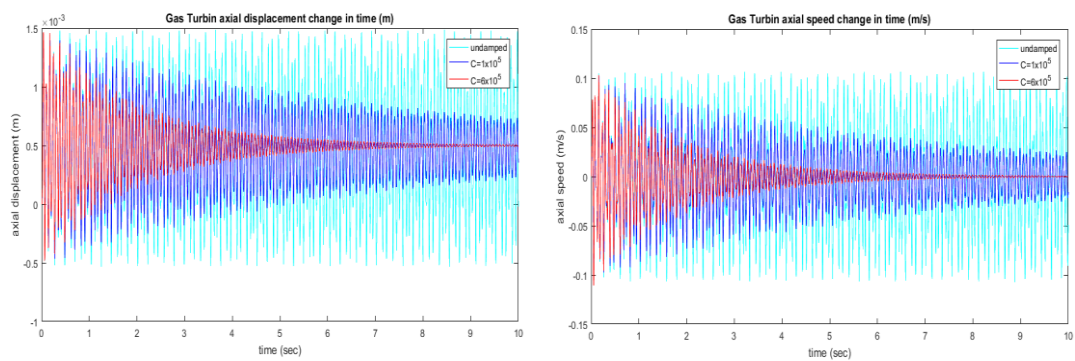
Figure 7. (a) Gas Turbin axial displacement change in time (m).

(b) Gas Turbin axial speed change in time (m/sec).

Considering the simulation, by applying the axial damping coefficients from $1x10^5$ Ns/m to $6x10^5$ Ns/m, the damping ratios changes from 27.34% to 45.46% for propeller axial displacement, and changes from 76.2% to 88.3%.for propeller axial velocity. Damping ratios for reduction gear axial displacement, changes from 30.7% to 47.2% and for reduction gear axial velocity, changes from 77.3% to 89.7%. Damping ratios for diesel engine axial displacement, changes from 36.7% to 55.3% and for diesel engine axial velocity, changes from 79.4% to 93.6%. Damping ratios for diesel engine axial displacement, changes from 39.8% to 56.7% and for diesel engine axial velocity, changes from 81.2% to 94.9%.

4. CONCLUSION

In this study, the propulsion system vibrations of a naval vessel driven by CODAG are investigated. Firstly, the propulsion system is modeled separately as mass-spring-damping element, equations of motion for each mass are obtained and dynamic behavior of the system in nature is observed by neglecting the effect of force and damping elements. The system is also modeled using Matlab/Simulink program for the case when the system is in operation, that is, the system is under the influence of excitations and damping elements. Axial vibrations due to internal and external forces acting on the system are analyzed and how the model responds

to undamped and different damping conditions is illustrated. The axial damping coefficient, $C = 6 \times 10^5$ Ns/m, that can successfully absorb the oscillatory motion of the system in the axial direction has been determined.

REFERENCES

[1]. American Bureau of Shipping, "Guidance Notes on Ship Vibration." 2006.

[2]. G. Antonides, "Longitudinal vibration of propulsion system on USS Simon Lake (AS-33)." *Acoustics and Vibration Laboratory Research and Development Report*, Report 2147, S-F0131108 Task 01351, 1966.

[3]. F. Alarcin and F.C. Korkmaz "Vibration analysis of ship main engine and shaft system," *Journal of Engineering and Natural Sciences, Sigma 3,* 2012, pp.310-319.

[4]. G. Zhang, Y. Zhao, T. Li, and X. Zhu, "Propeller excitation of longitudinal vibration characteristics of marine propulsion shafting system," *Hindawi Publishing Corporation Shock and Vibration*, 2014, Article ID 413592, 19 pages.

[5]. X. Jiang, X. Zhou and K. Chen, "Vibration characteristics of a marine propulsion shaft excited by the effect of propeller and diesel," *Transportation Information and Safety (ICTIS, International Conference on, Whuan*, 2015, pp. 893-897.

[6]. MTU, "Technical Sales Documentations," Friedrichshafen, Germany, 2011.

Prediction of Daily Groundwater Level in Arcadia, Florida Using Support Vector Machines

Ada YILMAZ[1], Fatih UNES[1], Mustafa DEMİRCİ[1], Bestami TASAR[1], Yunus Ziya KAYA[2]

Abstract

Groundwater is commonly used in irrigation, domestic and industrial activities. Due to large population growth and overuse of groundwater source, groundwater management has become more important issue in recent years. Determination of groundwater level is the most difficult task in the groundwater management. In this study, Support Vector Machines (SVM) method was used to predict daily groundwater level from daily air temperature, precipitation, evapotranspiration and lag time series of groundwater level. SVM model results were compared with Multi Linear Regression (MLR) model results and prediction ability of models were investigated.

Keywords: *Groundwater Level, Forecasting, Support Vector Machines*

1. INTRODUCTION

Groundwater is one of the most important fresh water source used in all human activities. It is often used in irrigation, industry and domestic needs. However, huge population growths, overuse of sources and climate changing have threatened groundwater sources. The threats of sources have made groundwater management compulsory.

To have an effective groundwater management plan, it is essential to model groundwater fluctuations. Modeling its fluctuation using physically-based methods is difficult due to have many independent variables. Because of these difficulties, soft computing methods have been often used to prediction of groundwater level.

Support vector machines (SVM), which were introduced by Vapnik [1], are a relatively new structure in the data-driven prediction field. The SVM is based on the structural risk minimization (SRM), instead of the empirical risk minimization (ERM) of ANNs, which can cause the solution to be captured in a local minimum and the network over fitted. The SRM minimizes the empirical error and model complexity simultaneously, which can improve the generalization ability of the SVM for classification or regression problems in many disciplines [2]. Many researchers used SWM method to predict groundwater level [2] and lake water level [3], [4], [5].

In this study, SVM and MLR models were used to predict daily groundwater level from daily air temperature, precipitation, evapotranspiration and lag time step of groundwater level.

2. STUDY AREA

Daily air temperature (T), precipitation (P) and evapotranspiration (EV) data were taken from Desoto Country near of Arcadia, Florida which is located 27°10'42"N latitude and 81°46'23"W longitude (Fig. 1). The county has a total area of 1,660 km^2, of which 1,650 km^2 is land and 6.2 km^2 (0.4%) is water [6]. Average annual temperature is 72.05°F and average annual precipitation is 52.28 inch in study area.

Daily groundwater level (GWL) data were taken from Desoto Country near of Arcadia, Florida which is located 27°15'40.1"N latitude and 82°00'18.8"W longitude.

[1,] *Corresponding author: Iskenderun Technical University Civil Engineering Department,. 31200,İskenderun / Hatay – TURKEY. ada.yilmaz@iste.edu.tr, faith.unes@iste.edu.tr, mustafa.demirci@iste.edu.tr, bestami.tasar@iste.edu.tr*

[2] *Engineering Department, Osmaniye Korkut Ata University, Osmaniye, TURKEY. yunuszkaya@osmaniye.edu.tr.*
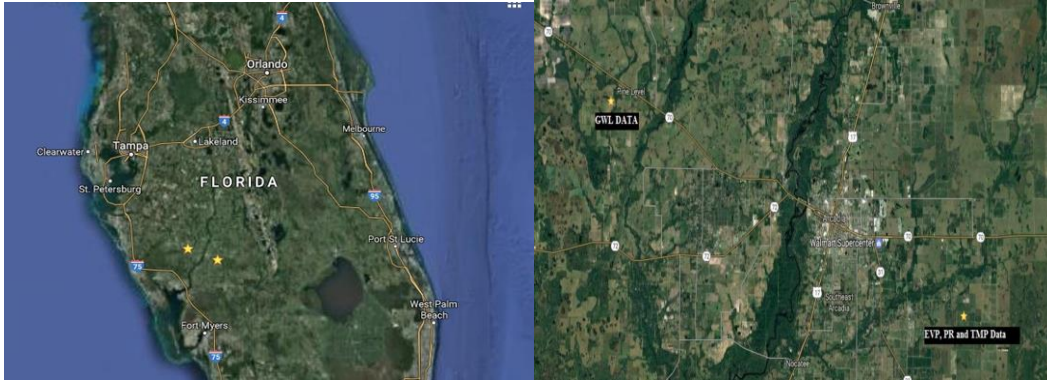
Figure 1. Study Area

3. MODELS

3.1. Support Vector Machines (SVM) Model

Support Vector Machine (SVM) model become popular due to their many attractive features and promising empirical performance. Their formulation embodies the structural risk minimization (SRM) principle, which has been shown to be superior to the more traditional empirical risk minimization (ERM) principle employed by many of the other modeling techniques [7], [8]. It is difference that provides SVM with a greater ability to generalize, which is the goal in statistical learning.

The idea behind SVM is to find a hyper plane that separates two classes in the transformed feature (input) space with a maximum distance. SVR aims to find the optimal regression hyperplane, that all training samples lie within an ε-margin around it and is also as flat as possible [9]. Network architecture of SVM, adapted from [10] is shown in Fig 2.
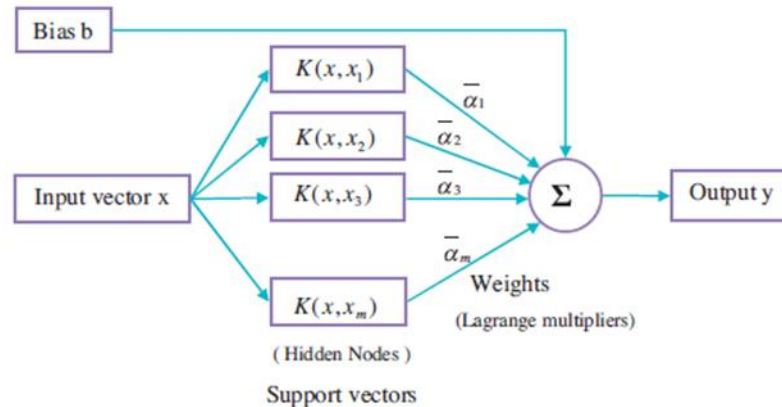
Fig. 2. Network Architecture of SVM. Adapted from [10].

3.2. Multi Linear Regression (MLR) Model

The MLR technique occurs with the relationship between two or more independent variables and a dependent variable by fitting a linear equation to the observed data. The generic form of an MLR model is as follows [11]:

$$Y_i = \beta_0 + \beta_1 X_1 + \beta_2 X_2 + \cdots + \beta_k X_k + \varepsilon_i \tag{1}$$

where Yi represents the observation of the dependent variable Y; X_{1i}, X_{2i}, ……., X_{ki} represent the observations of each of the independent variables X_1, X_2,…, X_k respectively; β_0, β_1, β_2........, β_k are fixed but unknown parameters; and εi is a random variable that is normally distributed.

The task of MLR modeling is to determine the unknown parameters (β_0, β_1, β_2........, β_k) of an MLR model (Eq. 1).

4. RESULTS

In models, total 2286 data derived two parts, 2000 data for training and 286 data for testing. As input data, combinations of daily air temperature (T), precipitation (P), evapotranspiration (EV) and groundwater level in one lag time step (GWL$_{t-1}$) were used.

SVM and MLR model results, calculated using T, P and EV inputs, provided similar low correlation coefficient value. The distribution and scatter graphs are shown Figure 3 and Figure 4.
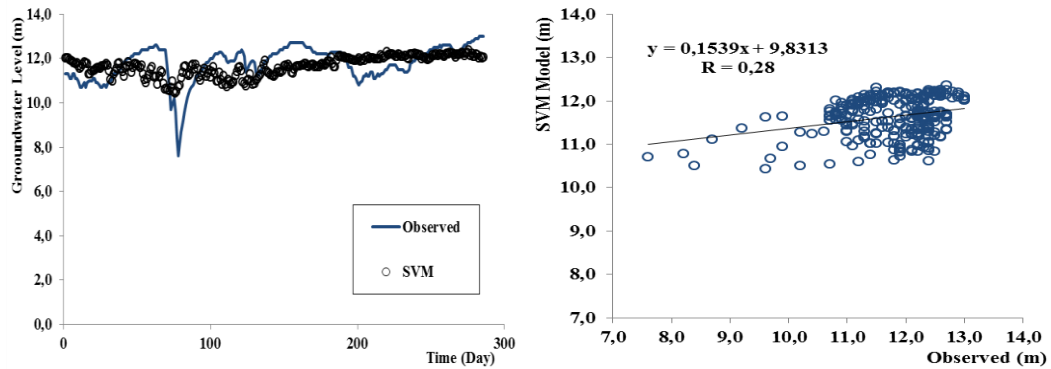
Figure 3. SVM model result calculated using T, P and EV inputs.
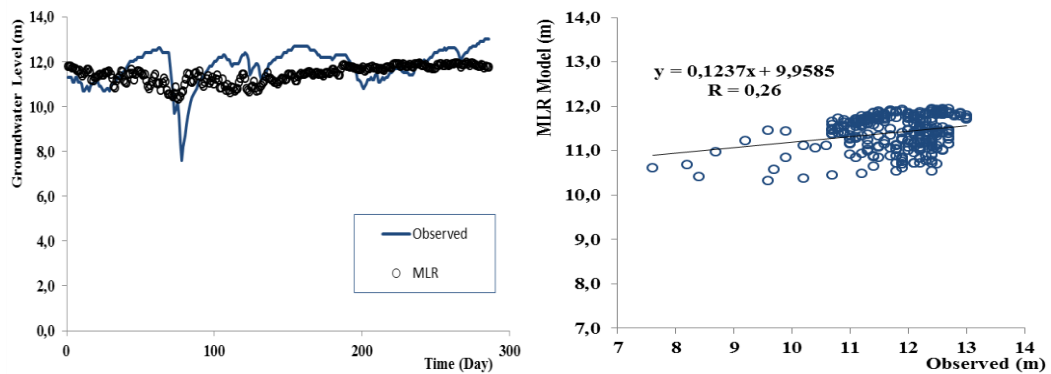
Figure 4. MLR model result calculated using T, P and EV inputs.

SVM and MLR model results, calculated using T, P, EV and GWL$_{(t-1)}$ inputs, provided similar high correlation coefficient value. The distribution and scatter graphs are shown Figure 5 and Figure 6.
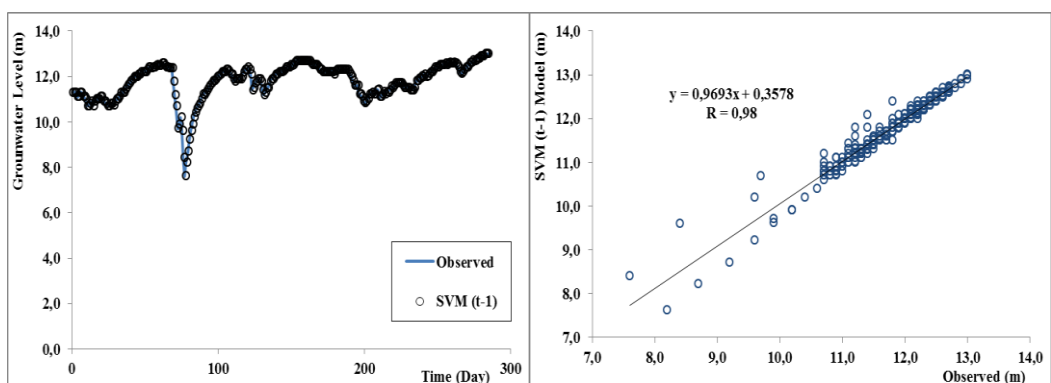
Figure 5. SVM model result calculated using T, P, EV and GWL$_{(t-1)}$ inputs
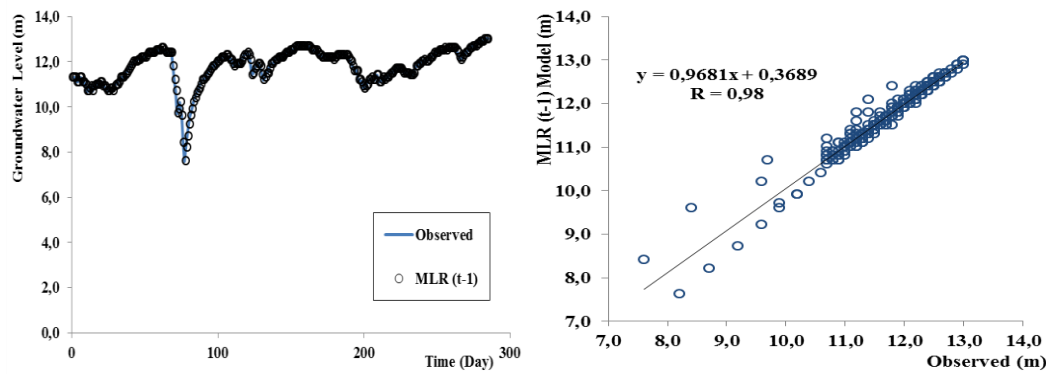
Figure 6. MLR model result calculated using T, P, EV and GWL$_{(t-1)}$ inputs

Mean square error (MSE) and absolute mean error (MAE) for the performance evaluation of the SWM and MLR models were calculated as follows;

$$MSE = \frac{1}{N}\sum_{i=1}^{N}\left(Yi_{observed} - Yi_{forecast}\right)^2 \tag{2}$$

$$MAE = \frac{1}{N}\sum_{i=1}^{N}\left|Yi_{observed} - Yi_{forecast}\right| \tag{3}$$

where, N and Yi denote the number of data sets and groundwater level, respectively.

SVM and MLR model results were compared using R, MSE and MAE values and are shown Table 1. SVM and MLR models gave results at similar accuracy.

SVM$_{(t-1)}$ and MLR$_{(t-1)}$ models which used T, P, EV, GWL$_{(t-1)}$ data as input provided high correlation value than SVM and MLR models which used T, P and EV data as input.

Table 1. Comparing Performances of SVM and MLR Models

Method	Inputs	MSE	MAE	R
SVM	T, P, EV	0.82	0.69	0.28
	T, P, EV, GWL$_{t-1}$	0.176	0.096	0.98
MLR	T, P, EV	0.88	0.75	0.26
	T, P, EV, GWL$_{t-1}$	0.177	0.097	0.98

5. CONCLUSION

In this study, Support Vector Machines model was used to predict daily groundwater level using input combinations that consist of temperature, precipitation, evapotranspiration and one lag time step of groundwater level. SVM model results were compared with Multi Linear Regression (MLR) model results and prediction ability of models were investigated.

SVM and MLR models did not reach the desired accuracy in the problem and they could not provide a good prediction for groundwater level using daily precipitation, air temperature and evapotranspiration as inputs.

When groundwater level data which lagged of 1 time step were added to inputs, it was seen that SVM and MLR reached desired predictions.

REFERENCES

[1]. Vapnik, V.N., 1995. The Nature of Statistical Learning Theory. Springer-Verlag, New York, USA. 314 p.

[2]. H. Yoon, S. C. Jun, Y. Hyun, G. O. Bae, K. K. Lee, A comparative study of artificial neural networks and support vector machines for predicting groundwater levels in a coastal aquifer, Journal of Hydrology, Volume 396, Issues 1–2, 5 January 2011, Pages 128–138.

[3]. T. Asefa, M. Kemblowski, U. Lall, G. Urroz, Support vector machines for nonlinear state space reconstruction: application to the Great Salt Lake time series, Water Resour. Res., 41 (2005), p. W12422, http://dx.doi.org/10.1029/2004WR003785.

[4]. A.F. Khalil, M. McKee, M. Kemblowski, T. Asefa, L. Bastidas, Multiobjective analysis of chaotic dynamic systems with sparse learning machines , Adv. Water Resour., 29 (2006), pp. 72–88

[5]. M.S. Khan, P. Coulibaly, Application of support vector machine in lake water level prediction, J. Hydrol. Eng., 11 (2006), pp. 199–205

[6]. "US Gazetteer files: 2010, 2000, and 1990", United States Census Bureau, 2011-02-12, Retrieved 2011-04-23.

[7]. Osuna, E., Freund, R. and Girosi, F., An improved training algorithm for support vectormachines, In Proc. of the IEEE Workshop on Neural Networks for Signal ProcessingVII, pp. 276-285, New York, 1997.

[8]. Gunn, S., Support Vector Machines for Classification and Regression, ISIS TechnicalReport, 1998.

[9]. Scholkopf B., Smola A.J. 2002. Learning with Kernels. MIT Press.

[10]. Chen S.T., Yu P.S. 2007. Real-time probabilistic forecasting of flood stages, Journal of Hydrology 340 (1–2), 63–77.

[11]. Makridakis S, Wheelwright SC, Hyndman RJ (2008) Forecasting methods and applications, 3rd edn. Wiley, Singapore, 656 pp.

Platform Development for Parallel Operations of Single Board

Kubra Karadag[1], Ozgur Tamer[2]

Abstract

Recent developing technology requires affordable, scalable, efficient and flexible solutions as high performance computing and parallel programming to solve large-scale, data-rich programs.

In this work, we present a scalable cluster consisting of single board computers (SBC) and evaluate its performance. The cluster, will be taken by solving problem of massive size on different number of nodes and the results are evaluated.

We prefer a SBC called Super Pi as the nodes of the cluster. Super Pi is equipped with 1 GB shared DDR3 and dual-core (ARM Cortex-A7) processor. The clusters performance was evaluated for different number of nodes up to 17. The cluster nodes were connected over a gigabit ethernet switch.

A master SBC was reconfigured for the forthcoming operations. The workload program was also written by using Python programming language. The MPICH which is an implementation of the Message Passing Interface standard, was installed on nodes for performing parallelization of the workload program. The program was tested by solving parallel with each of 1-2-4-8-16-24 node lines.

Consequently, considerable reductions at runtime for every node that is added to parallel computing which was the expected result of the project were reached.

Keywords: *Single Board Computer, Parallel Computing, Cluster Computing*

1. INTRODUCTION

Nowadays technological development requires a fast, affordable, scalable, effective and portable platform for computational operation of massive work loaded problems. Parallel computing on high performance computers have used for a long time to satisfy these needs.

This project essentially scopes on parallel computing. Because of this, parallel computing, must be well understood for next steps.

In the simplest sense, parallel computing is the simultaneous use of multiple compute resources to solve a computational problem:

- A problem is broken into discrete parts that can be solved concurrently

- Each part is further broken down to a series of instructions

- Instructions from each part execute simultaneously on different processors

- An overall control/coordination mechanism is employed

The compute resources are typically; a single computer with multiple processors/cores or an arbitrary number of such computers connected by a network [1]. If to do a more in-depth review is needed, Flynn's Taxonomy can be meet it.

Flynn's taxonomy classified the computer architecture which has multi-processors. Classfication is made along to the two factors which are instruction stream and data stream.

Flynn's taxonomy divides architecture mainly as;

---

[1] *Corresponding author: Dokuz Eylul Universty, Department of Mechatronics Engineering, Kaynaklar/İzmir, Turkey, kubra.karadag@deu.edu.tr*

[2]*Dokuz Eylul Universty, Department of Mechatronics Engineering, Kaynaklar/İzmir, Turkey, ozgur.tamer@deu.edu.tr*

- SISD single instruction, single data

- SIMD single instruction, multiple data.

- MISD multiple instruction, single data

- MIMD multipleks instruction, multiple data

Besides of architecture, for effective parallel computing, the parallel programming structure is extremely important too. Parallel programing is a software part of parallel computing. The problem type and computer architecture structure must be considered for proper computing.

Parallel programing models divide into many types which are shared memory, threads, distributed memory / message passing, data parallel, hybrid, single program multiple data (SPMD), multiple program multiple data (MPMD).

In this work, main aim was creating a platform as a Beowulf cluster which is known as main architecture of high performance computers. The Beowulf clusters' working logic is simply depends on master-slave relationship. Master works as a server and slave works as a processor. Generally, there is a one master on a cluster and it distributes workload to the slaves. After processing was done by slaves, the results send back to the master. For this project, Super Pi single board computer was selected to execute these missions. A similar work is presented by Joshua Kiepert and named as "Creating A Raspberry Pi-Based Beowulf Cluster" [2]. In Kiepert's project Raspberry Pi SBCs used as node of the cluster.

A single-board computer (SBC) is a complete computer built on a single circuit board, with microprocessor, memory, input/output (I/O) and other features required of a functional computer. Single-board computers were made as demonstration or development systems, for educational systems, or for use as embedded computer controllers [3].

Single board computers were made possible by increasing density of integrated circuits. A single-board configuration reduces a system's overall cost, by reducing the number of circuit boards required, and by eliminating connectors and bus driver circuits that would otherwise be used. By putting all the functions on one board, a smaller overall system can be obtained, for example, as in notebook computers. Connectors are a frequent source of reliability problems, so a single-board system eliminates these problems [4].

According all of these architectures and models, once computing tremendous workload, there are many performance criterias should be satisfied. For example; cycle time calculation, speedup, efficiency, scalability. In this project, performance was evaluated from speedup. For this reason, Amdahl's Law was prefered for speed up calculation.

1.1. Amdahl's Law

Amdahl's law can be used to calculate how much a computation can be speed up by running part of it in parallel.

Introducing the number of processors performing the parallel fraction of work, the relationship can be modelled by:

$$\text{speedup} = \frac{1}{\frac{P}{N}+S} \qquad (1)$$

- P= parallel fraction

- N= number of processors

- S= serial fraction

In the next section, the method will be explained in Part 2. The hardware of the project will be expressed in the part 2.1. The software of the project will be expressed in part 2.2. After giving information about the platform's hardware and software and project's method, in part3, the results will be given. Finally, in part 4, conclusions will be discussed.

2. METHOD

2.1. Hardware

In this project 17 single board computers, 1 gigabits ethernet switch, 17 power adapters for each single board computers, 17 memory cards, 17 memory cards adapters, ethernet cables and a modem have used for building the cluster.

The most remarkable equipment is single board computer for sure. In this project, single board computer which could have called as a node of Beowulf cluster, is performing like a real computer.

In this work, a SBC called Super Pi used as the nodes of the cluster. Producer company The Foxconn launched Super Pi as a redesign of Banana Pi. The overall design shows clear relationship with the Banana Pi but PCB design and onboard connector positions are mostly different [5]. Super Pi is equipped with 1 GB shared DDR3 and dual-core (ARM Cortex-A7).
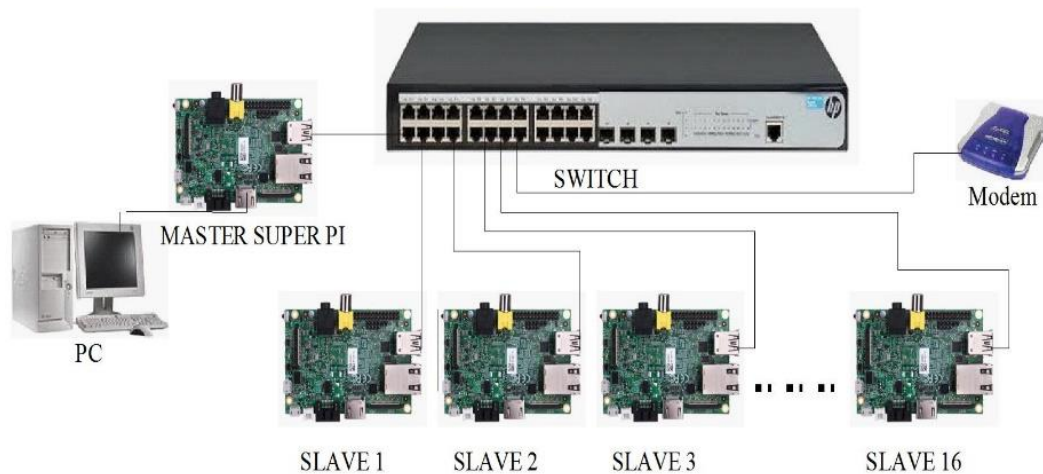
Figure 1. Super Pi Cluster Scheme

The single board computers used as node of the cluster. SBCs did a computational works as processors. As seen at the figure, SBCs divided into two, one of them is master which is controller and distributer and the others called as slaves are making computing the workload as processers.

The switch used for communication provider. The SBCs directly plug into the switch via ethernet cables and reach to the others thanks to it.

Modem used for IP address distributing. This helps to create a proper traffic infrastructure easily. All SBCs on the cluster get a unique IP address from the modem. Modem and switch give the communication infrastructure to single board computer for parallel operations or data sharing.

Memory cards and adapters are used for booting and data storing so the operating system installed on memory cards and conducted through memory card adapters.

The other equipment used as complement to connecting each members of platform to other.

2.2. Software

In this work, due to the fact Super Pi single board computers' resemblance of Banana Pi, Raspbian for Banana Pi operating system which is based on Linux, has been installed.

Python programming language was preferred to create the test program.

For parallel operation, the platform needs special programs. Message Passing Interface (MPI) and Message Passing Interface for Python (Mpi4py) are examples of these programs which used for conducting to parallel operations.

MPI is a specification for the developers and users of message passing libraries. MPI primarily addresses the message-passing parallel programming model: data is moved from the address space of one process to that of another process through cooperative operations on each process [6].

MPI invested for designing parallel programs in C or Fortran on distributed memory platform but nowadays it can be used properly and efficiently on any architecture whether distributed memory, shared memory or hybrid.

Mpi4py provides bindings of the MPI standard for the Python programming language, allowing any Python program to exploit multiple processors [7].

For the first step of setting up node Raspbian for Banana Pi operating system was downloaded and has installed on memory card.

At the first time boot up operations, basic configurations which contain storage configurations, SSH activation, password and hostnames changing must be performed. For realizing to these operations, access was provided to the software configuration tool.

Mpi and Mpi4py programs were downloaded and were Installed on single board computer for parallel operations.

The first configured computer memory card was ready to be cloned as a basic configured card to all cluster nodes.

Then for individualization to each slave nodes, static IPs and hostnames assignment were arranged.

The proper login credentials were entered to the master node for making a not encrypted connection to the slave nodes as needed.

The ssh-copy-id operation was done to ensure that all nodes are in not encrypted contact with the master node.

A test program for parallel operation was written to evaluate cluster performance. In this program, the master node creates a massive random array and divide this array into the size of slave nodes number. Then it sends divided array parts to the slaves for computing. After slaves have accomplish their tasks, all results are sent to the master. The defined jobs are;

- Slaves compute the square of elements of divided array.
- Master does distributing and monitoring only.

First of all, the test program was run for only one single board computer. Then program was run for 1 master with 2, 4, 8, 16 single board computer slaves respectively.

3. RESULTS

When single board computers work, there are lots of processing behind the scene. At the embedded system, detection or avoiding this kind of processes are not easy when special processing keeps going.

Due to these reasons, to minimize these effects and evaluate proper results, every step was repeated for 50 times. After, means of results were calculated

As seen the graphic on below, there is a recognizable decrease on processing time and noticeable speed up which is proportional to number of slaves.
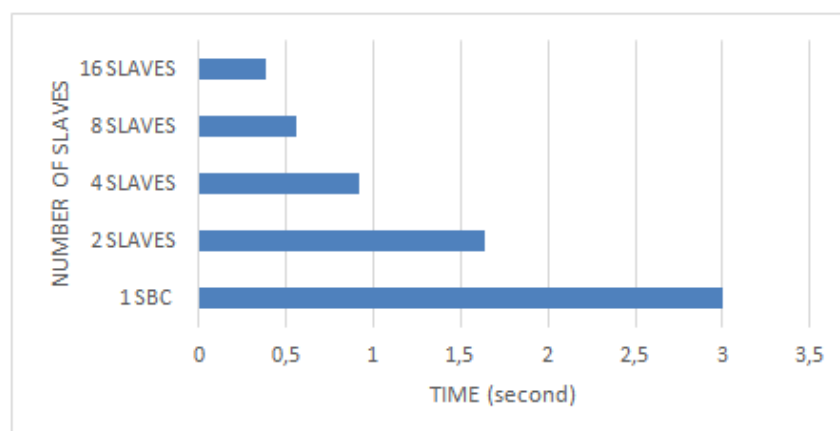
Figure 2. Execution time reduction

In this project, in scope of written test program parallel fraction is evaluated as % 93 and serial fraction is % 7.

When Amdahl's Law was conducted for this proportions for all of cluster sizes. The comparison table and graphic were presented in table below.

As seen on below at table and comparison graphic, calculated and measured result nearly meet each other.

Table 1. Comparison time of results

	2 SLAVES	4 SLAVES	8 SLAVES	16 SLAVES
AMDAHL'S LAW	1,87	3,31	5,37	7,8
TEST RESULTS	1,83	3,26	5,31	7,74
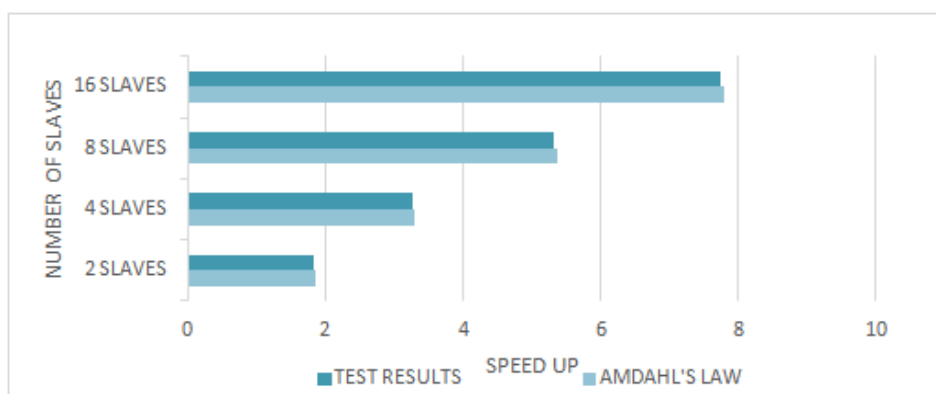
Figure 2. Comparison time of results

4. CONCLUSION

Consequently, we can see the expected result of the Project which is a considerable reduction at runtime for every node that is added to parallel computing.

Changes in runtime are nearly proportional to the number of nodes. That shows measurable parallelism. In this context, the cluster can be considered as a scalable platform. As seen, for each added node has contributed almost a proportionally speed up. This feature gives a clue about the relationship between size of the cluster and performance of the cluster.

This project results shows that extremely cheap single board computer as Super Pi can be used as a processor in cluster and it can be give a successful performance results.

This low costed platform can be used like a high-performance computer in many needed field for experimental parallel computing platform at schools, HPC for project which has shoestring budget or hobby material for who interests. In any event, we foresee that, this kind of platforms will become much more popular into the near future.

REFERENCES

[1]. B. Barney. (2016) Parallel Computing webpage on computing. [Online]. Available: https://computing.llnl.gov/tutorials/parallel_comp/

[2]. J. Kiepert. (2013) Creating a Raspberry Pi-Based Beowulf Cluster webpage on coen.boisestate [online]. Available: http://coen.boisestate.edu/ece/files/2013/05/Creating.a.Raspberry.Pi-Based.Beowulf.Cluster_v2.pdf

[3]. Diamond Systems Corp. (2016) COM - Based SBCs: The Superior Architecture for Small Form Factor Embedded System webpage on whitepaper [online]. Available: http://whitepaper.opsy.st/WhitePaper.diamondsys-combased-sbcs-wpfinal-.pdf

[4]. W. Rosch, *Hardware Bible*,5th Ed., Indianapolis, Indiana: Que, 1999.

[5]. (2017) SUNXI website. [Online]. Available: http://linux-sunxi.org/Foxconn_Super_Pi

[6]. B. Barney (2016) Message Passing Interface (MPI) webpage on computing. [Online]. Available: https://computing.llnl.gov/tutorials/mpi/#What

[7]. L. Dalcin. (2017) The MPI for Python webpage on mpi4py. [Online]. Available: https://mpi4py.readthedocs.io/en/stable/

BIOGRAPHY

Kubra Karadag: received the bachelor degree in Mechanical Engineering from Celal Bayar University in 2013. Now, she is doing M.Sc. in The Graduate School of Natural and Applied Sciences Department of Mechatronics Engineering, Dokuz Eylul University. Currently she is research assistant at İzmir Katip Celebi University Mechatronics Engineering Department. Her research interests are in the parallel programming and computational tools and platforms.

Ozgur Tamer: is assistant professor of Dokuz Eylul Universty, Electrical and Electronics Engineering Department and Mechatronics Engineering Department. He received the bachelor, M.Sc., and Ph Degrees in Electrical and Electronics Engineering Department from Dokuz Eylul University. He worked as postdoctoral researcher at Norwegian University of Science and Technology (NTNU) Department of Telematics in 2010-2011. His research interests are in field programmable gate arrays (fpga), SystemC and intelligent antenna systems for mobile communication.

Groundwater Level Forecasting Using Artificial Neural Network and Autoregressive Moving Average Models; A Case Study

Ada YILMAZ[1], Fatih UNES[1], Mustafa DEMİRCİ[1], Bestami TASAR[1], Yunus Ziya KAYA[2]

Abstract

Groundwater is the one of the most significant fresh water source in the world. But, sources have been under threat due to population growth, overuse of sources and climate changing. These threats have made groundwater management necessary. Prediction of groundwater level has great importance to prepare an effective groundwater management plan. Although, there are many physically-based methods developed to predict groundwater level, they are limited and unpractical. In recent years, as an alternative way to physically-based methods, empiric models have been started to use in hydrological problems. In this paper, Artificial Neural Network (ANN) and Autoregressive-Moving-Average Model (ARMA) were used to predict groundwater level from lagged time series of groundwater level and model results were compared.

Keywords: *Groundwater Level, Forecasting, Artificial Neural Network, Autoregressive Moving Average*

1. INTRODUCTION

Groundwater is one of the most used fresh water resource in the world. It is often used for many basic human needs like irrigation, domestic and industrial needs. Although groundwater has a great importance in our lives, sources have been threatened by population growth, climate changing and overuse of sources. To protect groundwater sources, fluctuations of groundwater level should be well monitored and effective management plan should be prepared.

Accurate prediction of groundwater level makes possible to develop water management plan. But, determination of groundwater level is a difficult task because of many different variables that effect groundwater level. Although physically-based methods were developed for determination of groundwater level, they have practical limitations. In recent years, empirical models have been often used as alternative way to physically-based models for determination of hydrological variables and have provided successful predictions.

Two of those models, Artificial Neural Network (ANN) and Autoregressive Moving Average (ARMA) have been used for determination of variables in the water resources engineering and many different disciplines. Recently, the use of artificial intelligence methods such as artificial neural networks (ANNs) has been accepted as an appropriate tool for modeling complex nonlinear phenomena in hydrology and water resources systems, leading to widening of their applications. Daliakopoulos et al. [1] used various ANN structures to forecast groundwater level. Many researchers [2], [3], [4], [5], [6] used ANN to solve various water resource problems including time-series forecasting. Unes [7] used ANN model for predicting reservoir level fluctuation. Unes [8] predicted plunging depth of density flow in dam reservoir using the ANN technique. Unes et al. [9] used ARMA model to predict daily reservoir level by different lag time steps. Shirmohammadi et al. [10] used several data-driven techniques including ARMA to predict groundwater level.

In this study, ANN and ARMA models were used to predict daily groundwater level in Arcadia, Florida in USA. As input, groundwater levels in different lag time steps were used. Model results are compared and prediction ability of models was investigated.

[1.] *Corresponding author: Iskenderun Technical University Civil Engineering Department,. 31200, İskenderun / Hatay – TURKEY. ada.yilmaz@iste.edu.tr, faith.unes@iste.edu.tr, mustafa.demirci@iste.edu.tr, bestami.tasar@iste.edu.tr*

[2] *Engineering Department, Osmaniye Korkut Ata University, Osmaniye, TURKEY. yunuszkaya@osmaniye.edu.tr.*

2. STUDY AREA

Daily groundwater level data were taken from the station in Desoto Country near of Arcadia, Florida. The station is located at 27°15'40.1"N latitude and 82°00'18.8"W longitude (Fig. 1). The county has a total area of 1,660 km^2, of which 1,650 km^2 is land and 6.2 km^2 is water [11]. Average annual temperature is 72.05°F and average annual precipitation is 52.28 inch in study area.

All of daily groundwater level data used in this study were obtained from USGS (United States Geological Survey) web site. They consist of 2286 daily groundwater level data which are divided two parts as training (2000) and testing (286).
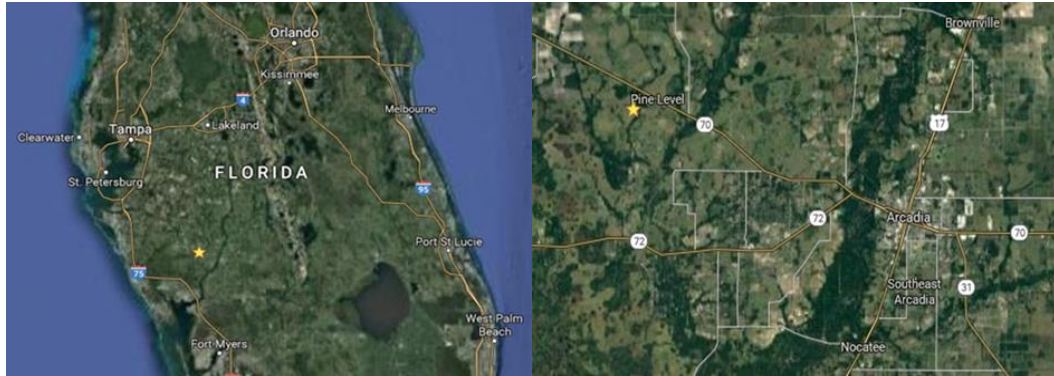
Figure 1. Study Area

3. MODELS

3.1. Artificial Neural Network (ANN) Model

The ANN is derived from the parallel information architectures found in the brain neuron systems. It has been widely used in various field of science including time series forecasting. One specific advantage of ANNs compared to traditional methods is that they are not dependent on the complexity or the structure of phenomenon. Therefore, ANN can be used to solve complex non-linear problems that have a lot of different input parameters and varying scale and boundary conditions.

An ANN model consists of input, hidden and output layers with their nodes (Fig. 2). Multilayer perceptrons (MLP) are feed-forward networks with one hidden layer and back-propagation algorithm (BPA). Units in hidden and output layers are linked to all units in preceding layer. Each connection has a weighting factor. MLP can occur on more than one hidden layer, but theoretical works have shown that a single hidden layer is sufficient for an ANN to approximate any complex nonlinear function [12], [13].
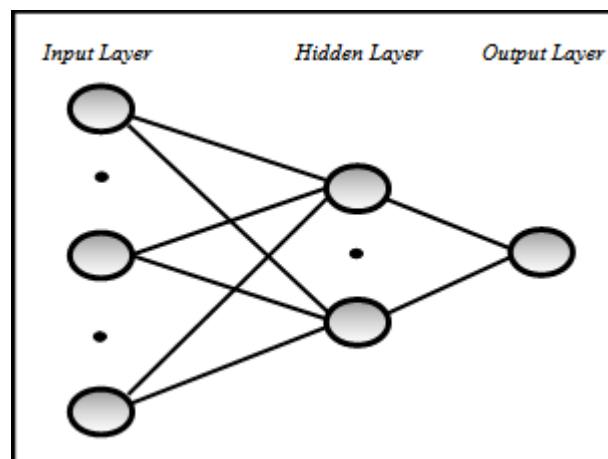
Figure 2. General ANN Structure

3.2. Autoregressive Moving Average (ARMA) Model

Sums or differences of purely random numbers are the basis for ARMA models of the processes by which many kinds of time series are assumed to be generated and thus form the basis for recent suggestions for

analysis, forecasting and controlling of the Autoregressive (AR), the Moving Average (MA) and the mixed Autoregressive Moving Average (ARMA) models. These models will help us attempt to capture or "explain" more of the serial correlation present within an instrument. Ultimately they will provide us with a means of forecasting the future values.

ARMA [p; q] models (Box and Jenkins [14]) use a weighted linear combination of previous values and shocks which can be written as:

$$y_t = \varphi_1 y_{t-1} + \varphi_2 y_{t-2} + \cdots + \varphi_{t-p} y_{t-p} + \cdots + a_t + \theta_1 a_{t-1} + \theta_2 a_{t-2} + \cdots + \theta_{t-p} a_{t-p} \qquad (1)$$

where y_t is the predicted value, a_i's are the residuals, and φ_i's and θ_i's are the weights associated with each previous observation and shock respectively.

4. RESULTS

In models, total 2286 data derived two parts, 2000 data for training and 286 data for testing. As input data, groundwater levels in one (GWL_{t-1}) and two (GWL_{t-2}) lag time steps were used and model results were compared.

4.1. ARMA Model Results

ARMA(1-1) model which used groundwater level in one lag time step as input provided higher correlation coefficient value (R=0.94) than ARMA (2-2) (R=0,89) model. The distribution and scatter graphs are shown Figure 3 and Figure 4.
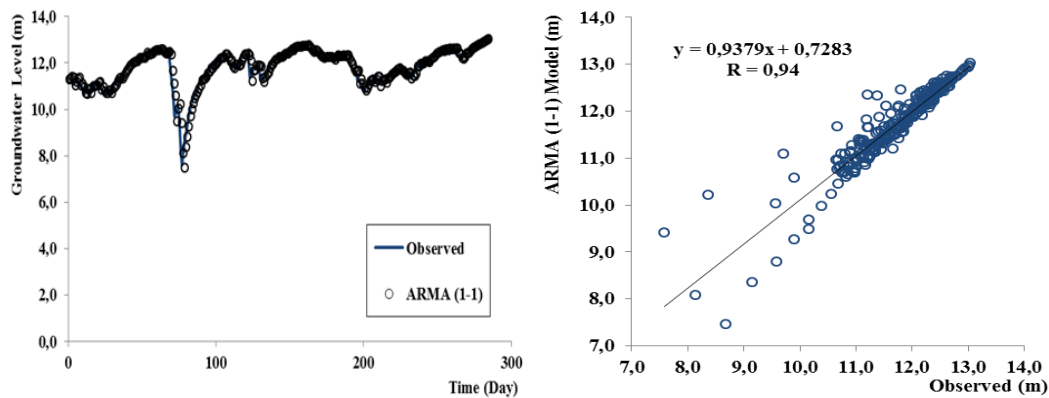
Figure 3. Observed and predicted groundwater level in test period ARMA (1-1)
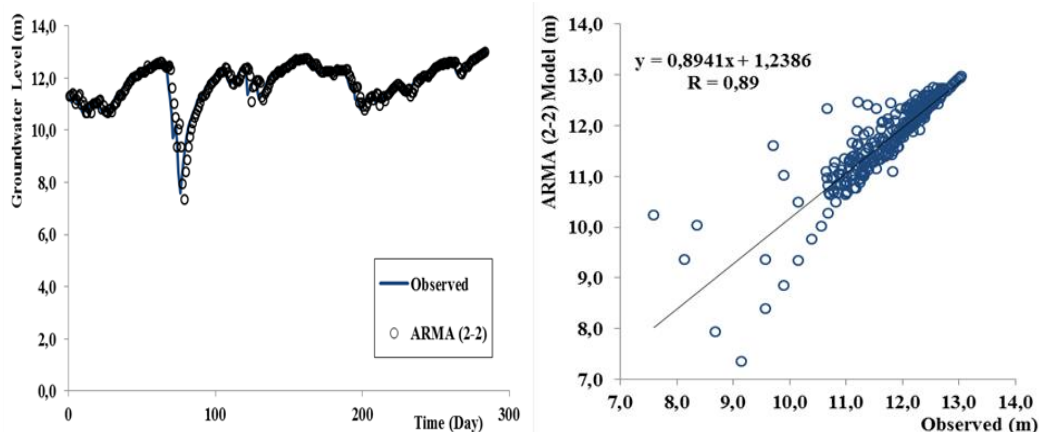
Figure 4. Observed and predicted groundwater level in test period ARMA (2-2).

4.2. ANN Model Results

ANN1 and ANN2 models provided similar correlation coefficient value in both of lag time steps. The distribution and scatter graphs are shown Figure 5 and Figure 6.
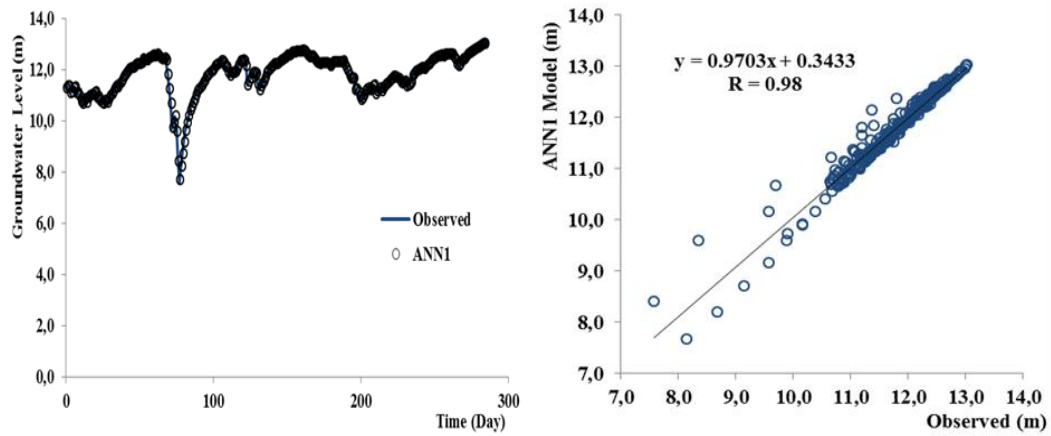
Figure 5. Observed and predicted groundwater level in test period ANN1
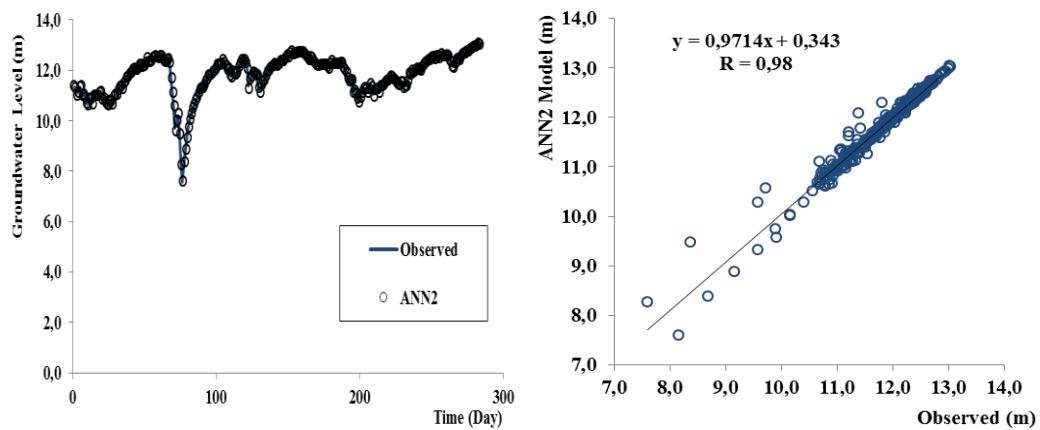
Figure 6. Observed and predicted groundwater level in test period ANN2

5. GENERAL EVULUATION

The correlation coefficient (R), mean square error (MSE) and absolute mean error (MAE) for the performance evaluation of the ARMA and ANN models were calculated. For both of two models, mean square error (MSE) and mean absolute error (MAE) were computed as follows;

$$MSE = \frac{1}{N}\sum_{i=1}^{N}\left(Yi_{observed} - Yi_{forecast}\right)^2 \tag{2}$$

$$MAE = \frac{1}{N}\sum_{i=1}^{N}\left|Yi_{observed} - Yi_{forecast}\right| \tag{3}$$

where, N and Yi denote the number of data sets and groundwater level, respectively.

Results are compared using R, MSE and MAE values and are shown Table 1. It was seen that ANN model gave better results than ARMA model in both of two lagged time steps.

Table 1. Comparing performances of ANN and ARMA models

Method	Input Combinations	MSE	MAE	R
ANN	GWL_{t-1}	0,00966	0,03191	0,977
	GWL_{t-2}	0,00758	0,02590	0,982
ARMA	GWL_{t-1}	0,02891	0,05707	0,938
	GWL_{t-2}	0,05065	0,07792	0,892

6. CONCLUSION

Forecasting of groundwater level fluctuations has important role in management of groundwater sources. In this study, Artificial Neural Network (ANN) and Autoregressive Moving Average (ARMA) models were used to predict daily groundwater level in Arcadia, Florida in USA. As input, groundwater level in one and two lag time steps were used and results of ANN and ARMA models were compared.

Artificial Neural Network (ANN) model provided better estimates of daily groundwater level than Autoregressive Moving Average (ARMA) model at both of lag time series. Advantages of ANN model can be explained by that ANN can correctly adapt nonlinear behavior of problem than ARMA model.

Finally, the results showed that ANN model is useful alternative method to predict daily groundwater level.

REFERENCES

[1]. I.N. Daliakopoulos, P. Coulibaly, I.K. Tsanis, ''Groundwater level forecasting using artificial neural networks'', Journal of Hydrology 309 (2005), pp. 229–240   J.
[2]. C.M. Zealand, D.H. Burn, S.P. Simonovic, ''Short-term streamflow forecasting using artificial neural networks'', J. Hydrol., 214 (1999), pp. 32–48S.
[3]. K.P. Sudheer, A.K. Gosain, K.S. Ramasastri, ''A data-driven algorithm for constructing artificial neural network rainfall–runoff models'', Hydrol. Process., 16 (2002), pp. 1325–1330.
[4]. H.K. Cigizoglu, ''Estimation, forecasting and extrapolation of river flows by artificial neural networks'', Hydrol. Sci. J., 48 (2003), pp. 349–361.
[5]. M.N. Almasri, J.J. Kaluarachchi, ''Modular neural networks to predict the nitrate distribution in ground water using the on-ground nitrate loading and recharge data'', Environ. Modell. Software, 20 (2005), pp. 851–871.
[6]. P.S. Yu, S.T. Chen, I.F. Chang, ''Support vector regression for real-time flood stage forecasting'', J. Hydrol., 328 (2006), pp. 704–716.
[7]. Unes F., Dam reservoir level modelıng by neural network approach. A casestudy, Neural Network World, 4(10), (2010), 461–474.
[8]. Unes F., Prediction of Density Flow Plunging Depth in Dam Reservoirs: An Artificial Neural Network Approach, CLEAN - Soil, Air, Water, 38(3),(2010), 296–308, DOI 10.1002/clen.200900238.
[9]. F. Unes, M. Demirci, O. Kisi, ''Prediction of Millers Ferry Dam Reservoir Level in USA Using Artificial Neural Network'', Periodica Polytechnica Civil Engineering, 2005, pp. 309-318.
[10]. B. Shirmohammadi, M. Vafakhah, V. Moosavi, A. Moghaddamnia, ''Application of Several Data-Driven Techniques for Predicting Groundwater Level'', Water Resources Management, 2013, Volume 27, Issue 2, pp 419–432.
[11]. "US Gazetteer files: 2010, 2000, and 1990", United States Census Bureau, 2011-02-12, Retrieved 2011-04-23.
[12]. G. Cybenco, ''Approximation by superposition of a sigmoidal function. Mathematics of Control'', Signals and Systems, 2, 1989, pp. 303-314.
[13]. K. Hornik, M. Stinchcombe, H. White, ''Multilayer feedforward networks are universal approximators'', Neural Networks, 2, 1989, pp. 359-366.
[14]. Box G, Jenkins G, Time Series Analysis, Forecasting and Control, HoldenDay, San Francisco, USA, 1970.

An Implementation of DNA based Security Model in Medical Data

Rukiye Karakıs[1], Kali Gurkahraman[2]

Abstract

Digital Imaging and Communications in Medicine (DICOM) standard handles, stores, prints, and transmits the medical images. The DICOM file format includes a metadata header that contains image and patient information, modality, acquisition parameters, physician, and health center information etc. Hence, patient information in DICOM file must be secured to prevent tampering, patient privacy leaks, and to illegal copying according to medical health standards. This study aims to increase medical images security with using image steganography techniques. Magnetic resonance (MR) images are used as the cover image. The doctor's comments are combined with information about patient (name, ID, birth date, gender, age, weight, address), study (date, time, ID, modality, description), and acquisition series (date, time, and description) in the file header of MR images to compose message. The similarity gray level values of each pixel is measured by Euclid distance to its 8 neighbors. The message are hidden non-sequentially in the Least Significant Bits (LSBs) of pixels according to the similar values. The message is encoded according to DNA structure, and it is compressed by using Huffman algorithm. After embedding message, the header of DICOM image does not contain any personal information. The quality measurement of stego system is measured by peak signal-to-noise ratio (PSNR), structural similarity measure (SSIM), universal quality index (UQI), and correlation coefficient (R). According to the obtained results, proposed method ensures the confidentiality of the patient information in DICOM images.

Keywords: *steganography, medical data security, DNA encoding, Huffman compression, similarity.*

1. INTRODUCTION

Today, many attacks are performed to capture medical data. All patients' records such as patient demographics, past medical history, vital signs, laboratory data, medical images and radiology reports must be protected according to medical health standards [1]-[2].

Digital Imaging and Communications in Medicine (DICOM) is the international standard for medical devices and medical images which includes ultrasound, X-ray, computed tomography (CT), magnetic resonance (MR) imaging etc. The DICOM file format includes a metadata header that contains image and patient information, modality, acquisition parameters, physician, and health center information. Hence, patient information in DICOM file must be secured to prevent tampering, patient privacy leaks, and to illegal copying according to medical health standards [1]-[2]-[3]-[4].

Encryption is frequently used to provide data security. However, encryption does not assure the confidentiality of data and it also boosts computational time and costs. In recent years, steganography techniques have been used to protect medical data [1].

Steganography is the science of concealing a file, message, image, or video within another text, image or video file. In literature, steganography methods can be performed in spatial domain or transform domain [4]. Spatial domain techniques operate more rapidly and they are simple. Transform domain techniques are also complex and they have high computational complexity and time. Furthermore, spatial domain techniques are vulnerable against many geometric distortions, filtering and compression. Transform domain techniques are also robust about same attacks.

In the literature, many studies were performed to secure the patients' medical image information (name, ID, birth date, gender, age, weight, address) with different image modalities such as MR, CT, X-ray, etc. [1]-[5]-

[6]-[7]-[8]. DNA has many advantages for storing digital data. DNA-based steganography can be used to qualify the methods as essentially unbreakable [9]-[10].

This study aims to increase medical images security with using steganography technique based on DNA encoding and Huffman compression. In proposed stego system, 27 MR images are used as the cover image. The doctor's comments are combined with information about patient (name, ID, birth date, gender, age, weight, address), study (date, time, ID, modality, description), and acquisition series (date, time, and description) in the file header of MR images to compose message.

The remainder of the study is organized as follows. Section 2 presents materials and methods, Section 3 includes the results and discussion. Finally, Section 4 gives the conclusion.

2. MATERIALS AND METHOD

In this study, 27 MR images with 256x256 size and 16 bit were used as cover images to test the proposed stego system. The images were obtained from *Micro Dicom Viewer* software website [11]. The embedded message was combined with doctor's comments (234 byte) and the patient's information (252 byte). The patient's information (name, ID, birth date, gender, age, weight, address of patients, date, time, ID, modality, description of study, and date, time, description of series) were selected from the meta headers of DICOM files. Secret message capacity is 498 byte and after DNA encoding its capacity is 7921 byte.

This study has two stages: embedding and extracting. In the embedding stage, the patient's information is collected from the header of MR images and it is combined with doctor's comments, as it can be seen Figure 1. The message is encoded according to DNA structure with using 128-bit doctor's stego-key, and it is compressed by using Huffman algorithm. The message are hidden non-sequentially in the Least Significant Bits (LSBs) of pixels according to the similar gray values. The similarity gray level values of each pixel is measured by Euclid distance to its 8 neighbors. After embedding message, the headers of stego DICOM images do not contain any personal information. These information can be shown by expert doctors with 128 bit stego-key.
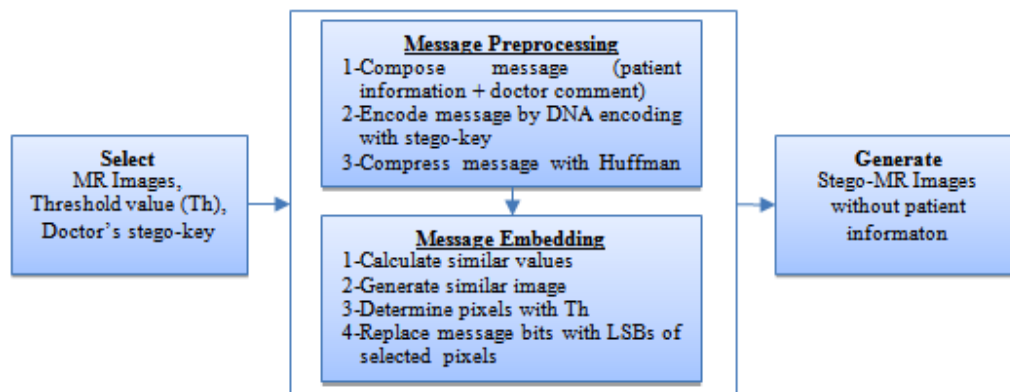
Figure 1. Message embedding stage

In the extracting message stage, similarity gray values are calculated from stego MR images and pixels which have a hidden message are determined in Figure 2. Obtained message is decompressed by Huffman and deciphered by DNA decoding.

The quality of stego system is measured by peak signal-to-noise ratio (PSNR), structural similarity measure (SSIM), universal quality index (UQI), and correlation coefficient (R). The details of performance methods can be found in [1]. The code and analysis of the study are executed in Microsoft Visual Studio .Net and MATLAB.
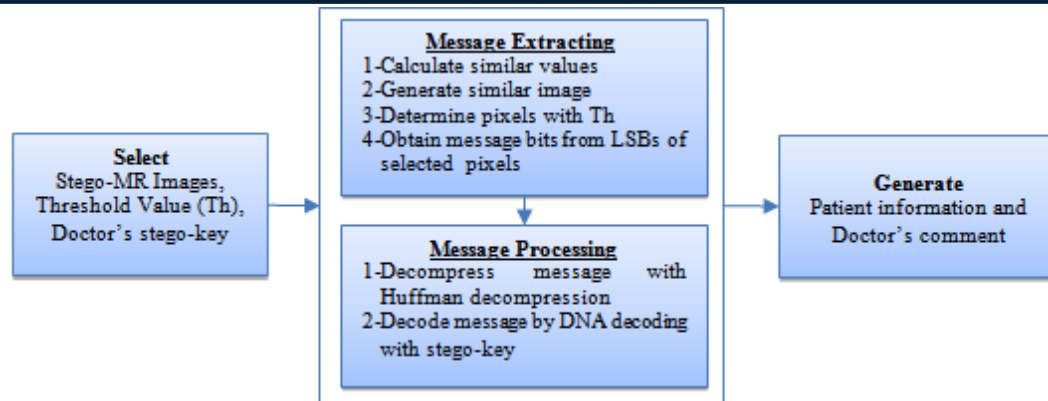
Figure 2. Message extracting stage

2.1. Similarity-Based LSB

LSB method embeds the secret message' bits in the least significant bits of pixel values of the cover image. It is simple and fast strategy. LSB method has high imperceptibility and embedding capability. However it is vulnerable against many geometric distortions and compression attacks. For this reason, this study used a similarity-based LSB technique whose details can be found in [1].

This techniques generates a new image which has similar values of each pixel. The similarity gray level values of each pixel is measured by Euclid distance to its 8 neighbors with respect to the gray level differences of each color component. The message are hidden non-sequentially in the LSBs of pixels according to the similar values. If these similar values of pixels are higher than the threshold, they hides the message's bits. In this study, threshold value was determined as 0.5.

2.2. DNA Encoding

Today, data storage is a big problem for digital world. A single gram of DNA can store terabytes data. For this reason, DNA has many advantages for storing digital data. A DNA molecule is composed of two DNA strands held together by hydrogen bonds between the paired bases which are adenine (A), cytosine (C), guanine (G), and thymine (T). A always pairs with T, and G with C with the hydrogen bond between them [9]-[10]-[14].

In this study, DNA encoding is used to increase the security of hidden message. Initially, hidden message is converted to ASCII code. Bit values of ASCII codes is encoded as A (00), T (01), C (10) and G (11). Secondly one time pad (OTP) key is determined by using expert doctor key. For each bit in the binary message, a key length of 10 bits is generated (*TATGAGTTTG, CCGAGACCTC, GTCGATCTCT, ...*). OTP key is converted to DNA bases. Finally, the hidden message's bits are encrypted by OTP key with using DNA Hybridization. If the binary data is '0', last 10 bases of OTP key for this binary data is transferred without changing in the encoded message. For example, OTP key is *TTTGAATCAC,* the encrypted message is *TTTGAATCAC.* If the binary data is '1', last 10 bases of OTP key for this binary data is changed in the encoded message. For example, OTP key is *TTTGAATCAC,* the encrypted message is *AAACTTAGTG* [9]-[10].

In DNA decoding, encrypted message is converted to DNA bases. OTP key is generated as DNA bases according to the encrypted message length. Finally, the encrypted message is compared with the OTP key to obtain the decrypted message. If the first 10 bases of the encrypted message is *TTTGAATCAC* and the last 10 bases of the OTP key is *TTTCAATGAC*, the binary data of decrypted message is assigned as 0. If the encrypted message is complementary to the OTP key, the binary data of decrypted message is produced as 1 [9]-[10].

DNA encoding with hybridization is not advantageous because of its high capacity. For this reason, Huffman lossless compression method was used to solve this capacity problem in this study. Huffman compression algorithm's detail can be found in [12]-[13].

3. RESULTS AND DISCUSSION

Figure 3 and Figure 4 show the differences between cover and stego MR images. After message embedding, stego images does not include any patient information, as it can be seen Figure 3 and Figure 4. The patient information can be only shown by authority person. There are little differences in the histograms of the cover and stego images.
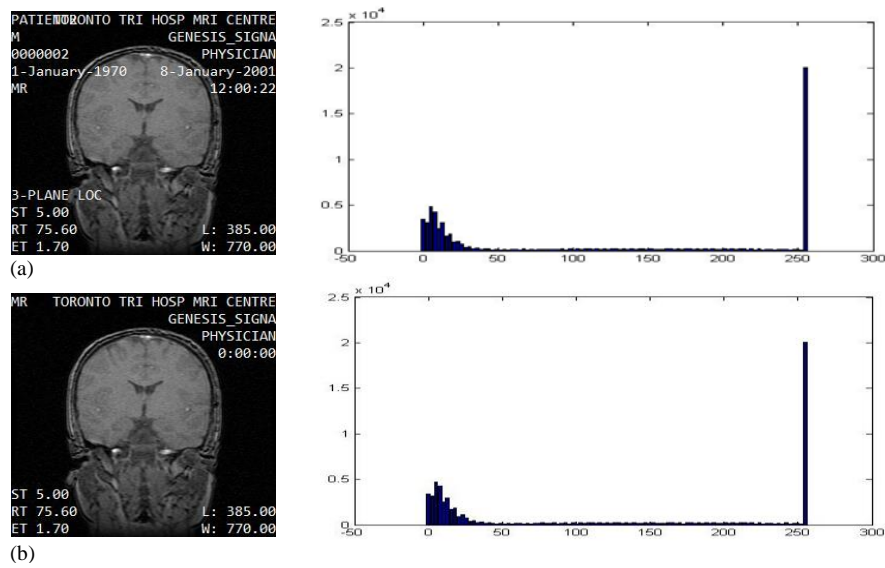
Figure 3. (a) Cover image and its histogram (b)Stego image and its histogram
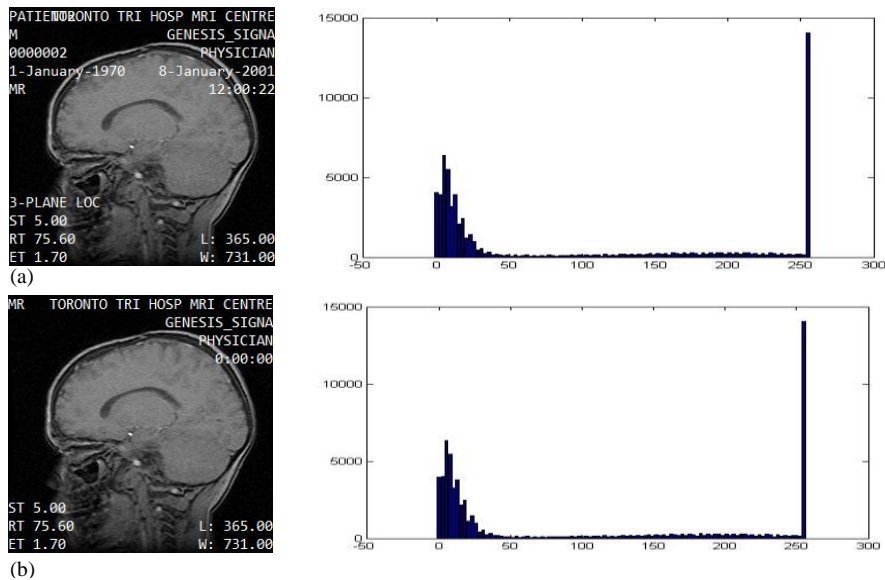
Figure 4. (a) Cover image and its histogram (b)Stego image and its histogram.

In Table 1, the performances of methods were evaluated by PSNR, SSIM, UQI, and R values. The name of proposed method is symbolized as Similarity+DNA+Huffman in Table 1. The mean PSNR values of the proposed method with 27 MR images was found as 55.3992 dB. The mean of the obtained SSIM values and UQI values were 0.9954 and 0.9999, respectively. The mean correlation coefficient (R) values was 0.9983. Similarity based LSB method was achieved the best performance result in Table 1. Similarity based LSB (Similarity), similarity based LSB with Huffman compression (Similarity+Huffman) and LSB methods embed the message without encryption. Hence, hidden message is vulnerable to attacks in these methods.

Table 61. Performance comparison between stego and cover MR images

Algorithms	PSNR	SSIM	UQI	R
Similarity+DNA+Huffman	55.3992	0.9954	0.9999	0.9983
Similarity	69.8010	0.9998	0.9999	1.0000
Similarity+Huffman	65.4471	1.0000	0.9999	1.0000
LSB	67.4983	0.9996	0.9999	1.0000

The capacity comparison between proposed method and other methods is given in Table 2. As it can be seen Table 2, DNA encryption increased the message capacity, so it effects the performance result in Table 1. Huffman lossless compression also ensured to decrease the message capacity.

Table 2. Capacity comparison

Algorithms	Patient Information	Doctor Comments	Message*
Similarity+DNA+Huffman	252 byte	234 byte	**7921 byte**
Similarity	252 byte	234 byte	490 byte
Similarity+Huffman	252 byte	234 byte	156 byte
LSB	252 byte	234 byte	490 byte
* hidden message includes the message length information as 4 byte			

Figure 5 shows the PSNR values between proposed method and other methods. The PSNR values of 27 MR images ranged between 53.4572 dB and 59.2004 dB ± 1.0571. These values were lower than the other methods results. Because, the message capacity was so high in the proposed method with DNA encryption. Nevertheless, The PSNR values were much higher than the lower limit of 35 dB in literature.
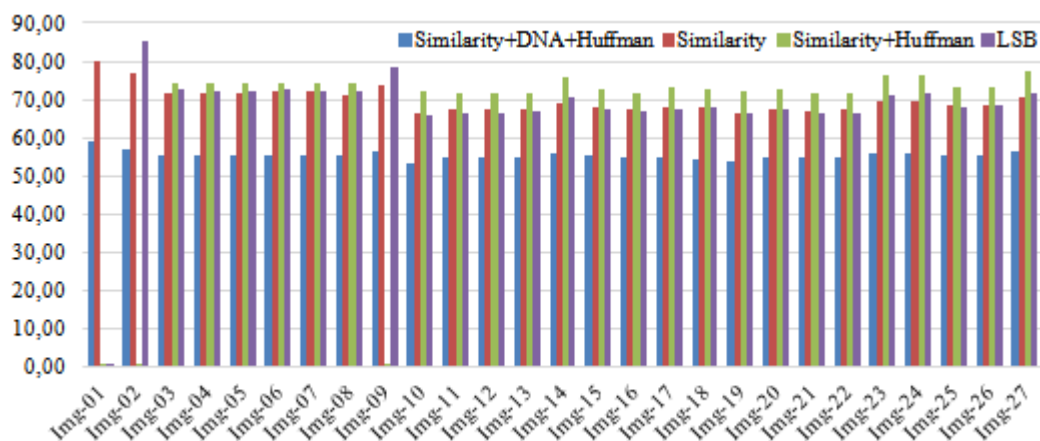
Figure 5. PSNR values between stego and cover MR images.

4. CONCLUSION

Today, medical data security is frequently ensured by cryptology and steganography. For this reason, this study propose a DNA based steganography model to secure medical images. 27 MR images are used to test the proposed model. The hidden message is composed of doctor's comment, and patient information in the file header of DICOM images. Similarity based LSB algorithm selects non-sequential LSB pixels to hide the message. The message is secured by using DNA encryption and Huffman lossless compression algorithms.

According to obtained performance result, DNA encryption algorithm can be used in steganography. However, DNA encryption algorithm with hybridization increases the message capacity. For this reason, lossless compression method should be used.

REFERENCES

[1]. R. Karakıs, R., İ. Guler, İ. Capraz, E. Bilir, "A Novel Fuzzy Logic-Based Image Steganography Method to Ensure Medical Data Security", *Computers in Biology and Medicine*, vol. 67, pp. 172–183, 2015.
[2]. R. Karakıs, R., İ. Guler, İ. Capraz, E. Bilir, "Medikal Sinyaller icin Benzerlik Tabanlı Goruntu Steganografi Uygulaması", *Akademik Bilisim 2015*, http://ab.org.tr/ab15/bildiri/188.pdf, 2015.
[3]. M. Haidekker, "Image Storage, Transport, and Compression", *Wiley-IEEE Press*, Edition: 1, pp. 386-412, 2011.
[4]. A. Cheddad, J. Condell, K. Curran, P. McKevitt, "Digital image steganography: Survey and analysis of current methods". *Signal Processing*, vol. 90, pp. 727–752, 2010.

[5]. L.-Q. Kuang, Y. Zhang, X. Han, "Watermarking Image Authentication in Hospital Information System", *Information Engineering and Computer Science, 2009. ICIECS 2009*, pp. 1-4, 2009.

[6]. H. Nyeem, W. Wageeh Boles, C. Colin Boyd, "A Review of Medical Image Watermarking Requirements for Teleradiology", *J. Digit. Imaging*, vol. 26, pp. 326-343, 2013.

[7]. G. Coatrieux, L. Lecornu, B. Sankur, C. Roux, "A Review of Image Watermarking Applications in Healthcare, Engineering in Medicine and Biology Society", *2006. EMBS '06. 28th Annual International Conference of the IEEE*, pp. 4691-4694, 2006.

[8]. K. A. Navas, M. Sasikumar, "Survey of Medical Image Watermarking Algorithms", *SETIT 2007 4rth International Conference: Sciences of Electronic, Technologies of Information and Telecommunications, TUNISIA*, pp. 1-6, 2007.

[9]. Z. Wang, X. Zhao, H. Wang, G. Cui, "Information hiding based on DNA steganography", *2013 IEEE 4th International Conference on Software Engineering and Service Science*, pp. 946- 949, 2013.

[10]. A.P. Thiruthuvadoss, "Comparison and Performance Evaluation of Modern Cryptography and DNA Cryptography", Royal Institute of Technology, Masters of Science, 2012.

[11]. Micro Dicom Viewer Software Website. [0nline]. Available: http://www.microdicom.com/component/jdownloads/send/2-images/1-mr.html

[12]. Huffman, D., "A Method for the Construction of Minimum-Redundancy Codes, Proceedings of the IRE, vol. 40 (9), pp. 1098–1101, http://compression.ru/download/articles/huff/huffman_1952_minimum-redundancy-codes.pdf, 1952.

[13]. Huffman Coding. [0nline]. Available: http://en.wikipedia.org/wiki/Huffman_coding.

[14]. B. Alberts, A. Johnson, J. Lewis and et al. "The Structure and Function of DNA", *Molecular Biology of the Cell. 4th edition. New York: Garland Science*, 2002 [Online]. Available: https://www.ncbi.nlm.nih.gov/books/NBK26821/.

Comparison of Three Different Wave Climate Studies Along the South Western Black Sea Coasts

Recep Emre Cakmak[1], Bilal Bingolbali[2], Halid Jafali[2], Adem Akpınar[2]

Abstract

Turkey has long shorelines experiencing excessive coastal and marine activities. In the planning and design of coastal and offshore structures, as well as other marine activities, accurate information on wave conditions is needed. Unfortunately for Turkey, there are no real-time wave monitoring stations around its seas and coasts except a few short-term measurements made within some scientific research projects (e.g. NATO TU-WAVES). Therefore, wave climate studies are done with the help of numerical wave hindcast models (e.g. WAM, SWAN, and WWIII etc.) that generate waves using the archived wind data (e.g. ERA Interim, MERRA, CFSR etc.). There are a few wave climate studies conducted using different wave models so far developed for the southwestern Black Sea such as Ozhan & Abdalla (1999) and Saracoglu (2011). In the present study, we aim to compare results from both the above mentioned works with the SWAN model's results from our previous study (Akpınar et al., 2015) where a nested model was forced with the CFSR winds together with a calibrated whitecapping coefficient including the best wind growth and whitecapping combination determined for the southwestern Black Sea. In this regard, the main goal of this study is to reveal wave climate differences among these three studies. For this purpose, wave roses, plots of mean wave period (T_m) versus significant wave height (H_s) and extreme value estimates with different return periods at some locations in the southwestern Black Sea are compared and differences in the three wave climate studies are assessed. Examination of the degree of consistency in results of the three models is believed to help provide an insight for future studies in the region.

Keywords: *Swan, Wave Climate, Wave Rose, Extreme Waves, Black Sea*

1. INTRODUCTION

Being a country of which three sides are surrounded by seas, Turkey has profoundly long shorelines experiencing excessive coastal and marine activities. In the planning and design of coastal and offshore structures, as well as other marine activities such as shipping, coastal engineering, fishing, navigation and recreation, optimal sitting of both wind and wave energy farms, and even tourism, accurate information on wind and wave conditions is needed. Unfortunately for Turkey, there are, at the moment, no real-time wave monitoring stations around the seas and coasts surrounding Turkey. However, a few short-term wave measurements have been made within some scientific research projects (such as NATO TU-WAVES). For this reason, wave climate studies are done with the help of numerical wave hindcast models (such as WAM, SWAN, and WWIII etc.) that generate waves using the archived wind data (such as ERA Interim, MERRA, and CFSR etc.). There are a few wave climate studies conducted using different wave models that have so far been developed for the south western Black Sea. The first, Wind and Deep Sea Wave Atlas of Turkish Coasts, is a product of a study carried out by Ozhan and Abdalla (1999). The second study was performed by Saracoglu (2011) that he revealed wind and wave climate with the MIKE 21 SW forcing with ECMWF ERA analysis wind data for several points in the above mentioned atlas and compared the results of both the studies. In the present study, we aim to compare the results from both works (Ozhan and Abdalla, 1999; and Saracoglu, 2011) with the SWAN model's results developed in our previous study (Akpınar et al., 2015) where a nested model was forced with the CFSR winds together with the calibrated whitecapping coefficient including the best wind growth and whitecapping combination determined for the south western Black Sea. In this regard, the aim of the study is to compare three different wave climate studies developed for the Black sea. This study particularly focuses on the south western Black Sea coasts. For this purpose, wave roses, the

---

[1] *Corresponding author: Uludag University, Department of Civil Engineering, 16059, Görükle/Bursa, Turkey.*
remrecakmak@uludag.edu.tr

[2] *Uludag University, Department of Civil Engineering, 16059, Görükle/Bursa, Turkey*

plots of mean wave period (Tm) versus significant wave height (Hs) and extreme value estimates with different return periods at some locations in the south western Black Sea are compared and differences at three wave climate studies are assessed.

2. STUDY AREA

Results from the mentioned numerical models are compared with the ones in selected atlas points from the points in the southwestern Black Sea region. A general view of the study area and locations of selected points are given in Figure 1.
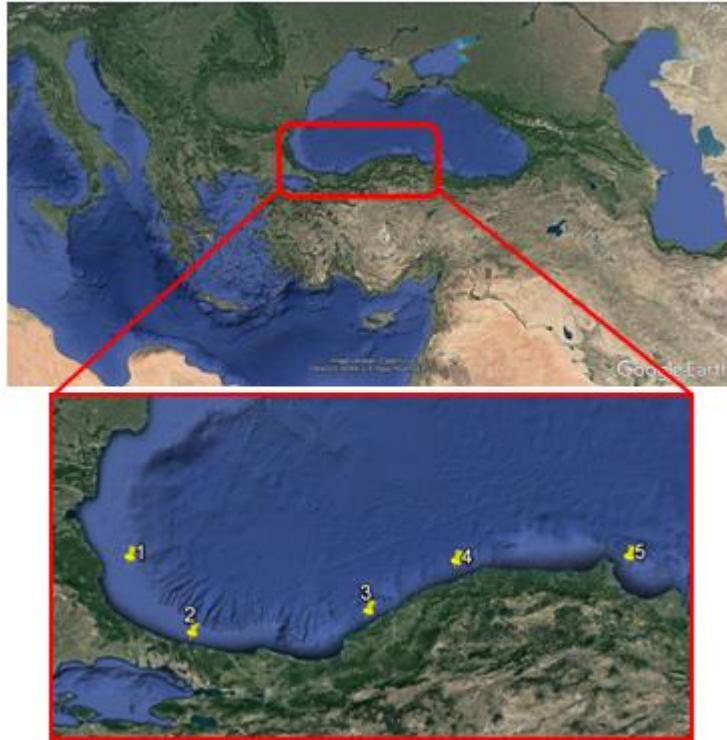
Figure 1. The study area and locations of the selected points.

Coordinates of the points shown in the figure are presented in Table 1.

Table 1. Coordinates of the selected points.

Locations	1	2	3	4	5
Coordinates	42.00 N 28.40 E	41.25 N 29.30 E	41.50 N 31.70 E	42.00 N 32.90 E	42.00 N 35.30 E

3. MATERIALS AND METHODS

The Wind and Deep Sea Wave Atlas of Turkish Coasts developed by Ozhan and Abdalla (1999) made use of the WAM model developed by the WAMDI group in 1988. As for the wind data source, the model was forced with analysis wind fields produced by the ECMWF (European Centre for Medium Range Weather Forecast). However, the good-quality data set only covered a period of 8 years at the time from 1991-1999 and for this reason, wind fields predicted from synoptic maps were used to compliment the data required for the analysis of the extreme wave analysis.

ECMWF ERA Analysis wind data source were used as an input in the MIKE 21 SW wave model by Saracoglu (2011). The calibration of the model was conducted using wave parameters from measurement

stations found at Gelendhzik, Hopa, Sinop, Filyos and Karaburun in the Black Sea as well as Ambarli in the Marmara Sea. The model simulations were for a period from 1996 to 2008 (12 years).

In the model developed by Akpınar et al. (2015) under funding from the Tubitak Project (Since 2015), SWAN model developed at Delft University of Technology was used. The model used CFSR wind data source produced by NOAA as an input and a simulation covering a period of 31 years was achieved.

4. RESULTS

4.1. Wave roses

The wave roses of all models for all points are presented in Figure 2. Directional distributions of waves from all three wave climate studies are almost similar at locations 1 and 2. Waves are coming from a direction sector between North North-east (NNE) and East North-east (ENE) at these two locations as these three wave climate studies. However, at these two locations, dominant direction is deviated 22.5° eastward with respect to the atlas produced by Ozhan and Abdalla (1999), which agree with our results by Akpınar et al. (2015), in the MIKE model's results by Saracoglu (2011). The dominant direction in the atlas produced by Ozhan and Abdalla (1999) at location 3 is N, but this direction is around NNE in the other two wave climate studies. At location 4 wave rose of the atlas produced by Ozhan and Abdalla (1999) and MIKE model's results by Saracoglu (2011) show closer directional distribution. Here, the dominant waves around the NNW direction are not seen in our SWAN model results. The dominant wave direction deviates according to the wave atlas produced by Ozhan and Abdalla (1999) 22.5° and 45° northward in MIKE and SWAN model' results, respectively, at location 5.

4.2. Hs – Tm graphs

Examining the graphs plotted for significant wave height (x-axis) against average wave period (y-axis), evaluation on how the models predict period of similar wave heights was conducted. For each of the three studies, Hs - Tm plots representing each location are given in Figure 3. In SWAN model, three different periods (T_{m01}, T_{m02} and T_{m-1}) are taken into consideration. Other two studies present the results based on only one period where it was mentioned as mean wave period. Therefore, we guess that they presented the results for T_{m02}. The wave period corresponding to frequently seen wave height in each model was also investigated. These values were determined for waves at 2 m for points 1 and 2 and 1 m for the other points. Comparison of corresponding mean wave period values against certain wave heights is presented in Table 2. As seen in the table, the mean wave period (T_{m02}) values corresponding to the same wave heights in our SWAN model results by Akpınar et al. (2015) are lower than in the other two models at locations 1, 4, and 5. At locations 2 and 3, it is higher than in the MIKE model results by Saracoglu (2011) but lower than in the atlas produced by Ozhan and Abdalla (1999).

Table 2. Wave period values against frequent wave heights

Location	Frequently seen H_{m0}	Corresponding mean wave periods		
		Ozhan and Abdalla (1999)	Saracoglu (2011)	Akpınar et al. (2015)
1	2 m	6.5 s	5.5 s	4 s for T_{m01} and T_{m02} and 5 s for T_{m-1}
2	2 m	6.5 s	5 s	5 s for T_{m01}, 6 s for T_{m02} and 6.5 s for T_{m-1}
3	1 m	5.5 s	4.5 s	5.5 s for T_{m01}, 5 s for T_{m02} and 6 s for T_{m-1}
4	1 m	5 s	4.5 s	4.5 s for T_{m01}, 4 s for T_{m02} and 5 s for T_{m-1}
5	1 m	5 s	4.5 s	4.5 s for T_{m01}, 4 s for T_{m02} and 5.5 s for T_{m-1}

Figure 2. Wave roses from three wave climate studies (from Ozhan and Abdalla (1999) in upper panel, Saracoglu, (2011) in middle panel, and Akpınar et al., (2015) in the bottom panel) at all points from 1 to 5 (left to right).
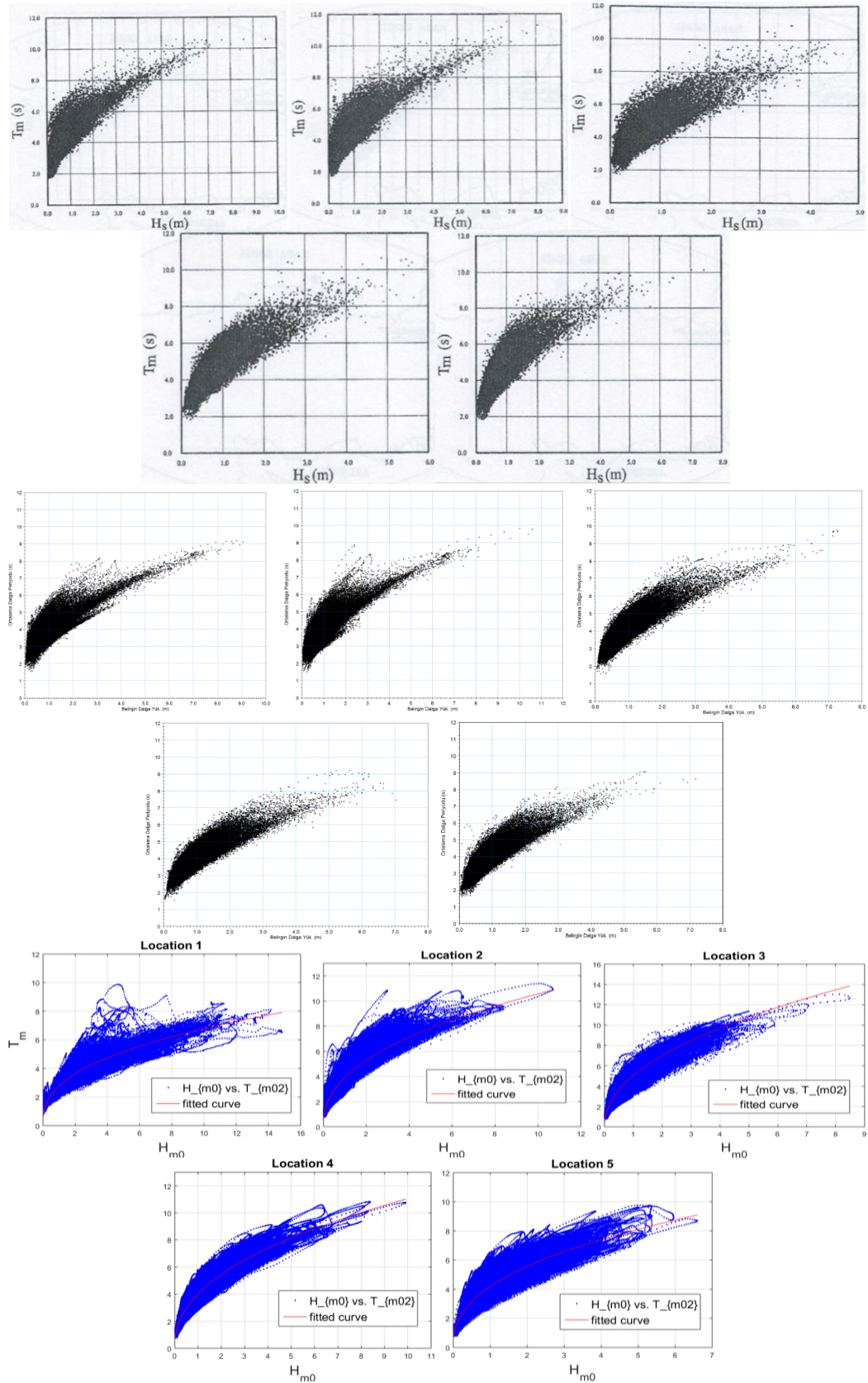
Figure 3. H_{m0} - T_m plots from three wave climate studies (from Ozhan and Abdalla (1999) in upper panel, Saracoglu, (2011) in middle panel, and Akpınar et al., (2015) in the bottom panel) at all points from 1 to 5 (left to right).

4.3. Extreme wave height

Extreme value plots obtained using the annual maximum wave height data over the years covered by each study, are presented in Figure 4. The values of 10-year and 100-year recurrence period (Rp) from these graphs are summarized in Table 3. In the MIKE model results of Saracoglu (2011), extremes of 100 years at some points cannot be determined from the presented graphs. From the graphs and the summary table, our SWAN model results by Akpınar et al. (2015) gave higher extreme wave heights in the western part of the study area. Except for location 4, the atlas produced by Ozhan and Abdalla (1999) predicted larger extreme wave heights in the eastern side. The same is the case with the MIKE model results of Saracoglu (2011), however it estimated extreme wave heights closer to the atlas produced by Ozhan and Abdalla (1999) in the eastern part.

Table 3. Extreme wave heights for all studies at each stations

Locations	Rp: 10 years			Rp: 100 years		
	Ozhan and Abdalla (1999)	Saracoglu (2011)	Akpınar et al. (2015)	Ozhan and Abdalla (1999)	Saracoglu (2011)	Akpınar et al. (2015)
1	7.8 m	9.8 m	12.5 m	10.8 m	-	16.2 m
2	7 m	10.5 m	8.5 m	9.5 m	-	10.5 m
3	6.5 m	7 m	6.8 m	8.5 m	8.5 m	8.5 m
4	7 m	7.5 m	9.4 m	9 m	9 m	12.1 m
5	6.2 m	6.8 m	6.2 m	8.6 m	8.2 m	7.8 m

5. CONCLUSION

The general conclusions reached as a result of the study are given here:

✓ Waves generally come from a similar direction sectors as three wave climate studies. But they show some differences on dominant wave directions at some locations.

✓ The mean wave period (T_{m02}) values corresponding to the same wave heights are different at different locations. At some locations SWAN model results by Akpınar et al. (2015) are lower than in the other two wave climate studies but at other locations they are higher.

✓ In the western part of the study area, the SWAN model results by Akpınar et al. (2015) gave higher extreme values, and it is lower around Sinop.

✓ For future works, the discrepancies between these three wave climate studies can be examined using more up-to-date wave data for more locations and reasons of these discrepancies can be investigated.

ACKNOWLEDGEMENT

REFERENCES

[1]. A. Akpınar, S. Bekiroglu, GPh. VanVledder, B. Bingolbali, H. Jafali, "Temporal and Spatial Analysis of Wave Energy Potential Along the Southern west Coasts of the Black Sea," Project Number: 214M436, TUBITAK Project, 2005 (In Progress).

[2]. E. Ozhan, and S. Abdalla, "Turkish Coast Wind and Deep Water Wave Atlas, Applied Project Report, Middle East Technical University, Civil Engineering Department, Ocean Engineering Research Center, Ankara, Turkey, 1999.

[3]. K. E. Saracoglu, "The wave modelling and analysis of the Black Sea and the Sea of Marmara," Yıldız Tecnical University, İstanbul, Master Thesis, 2011.

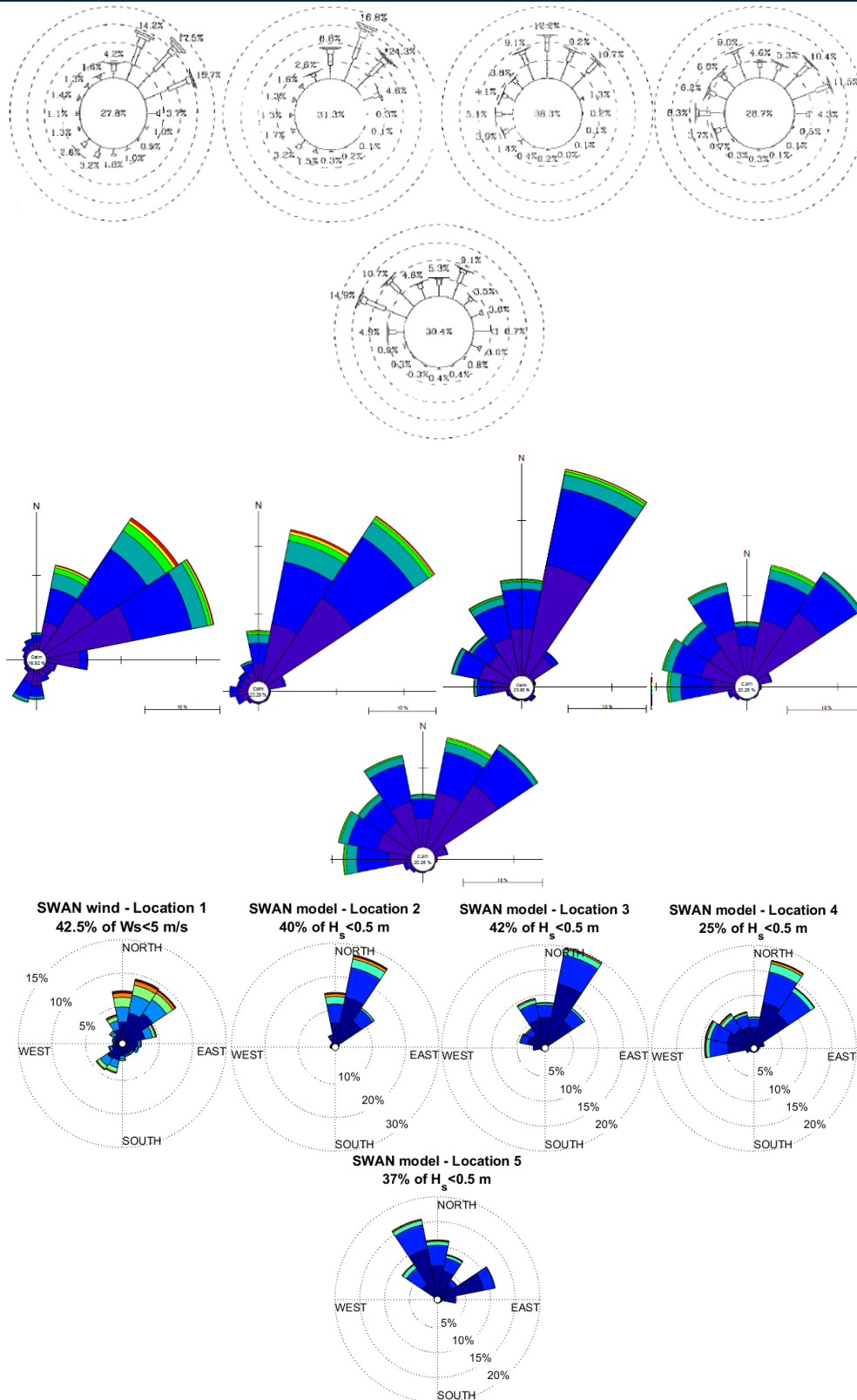*Figure 4. Extreme value plots from three wave climate studies (from Ozhan and Abdalla (1999) in upper panel, Saracoglu, (2011) in middle panel, and Akpınar et al., (2015) in the bottom panel) at all points from 1 to 5 (left to right)*
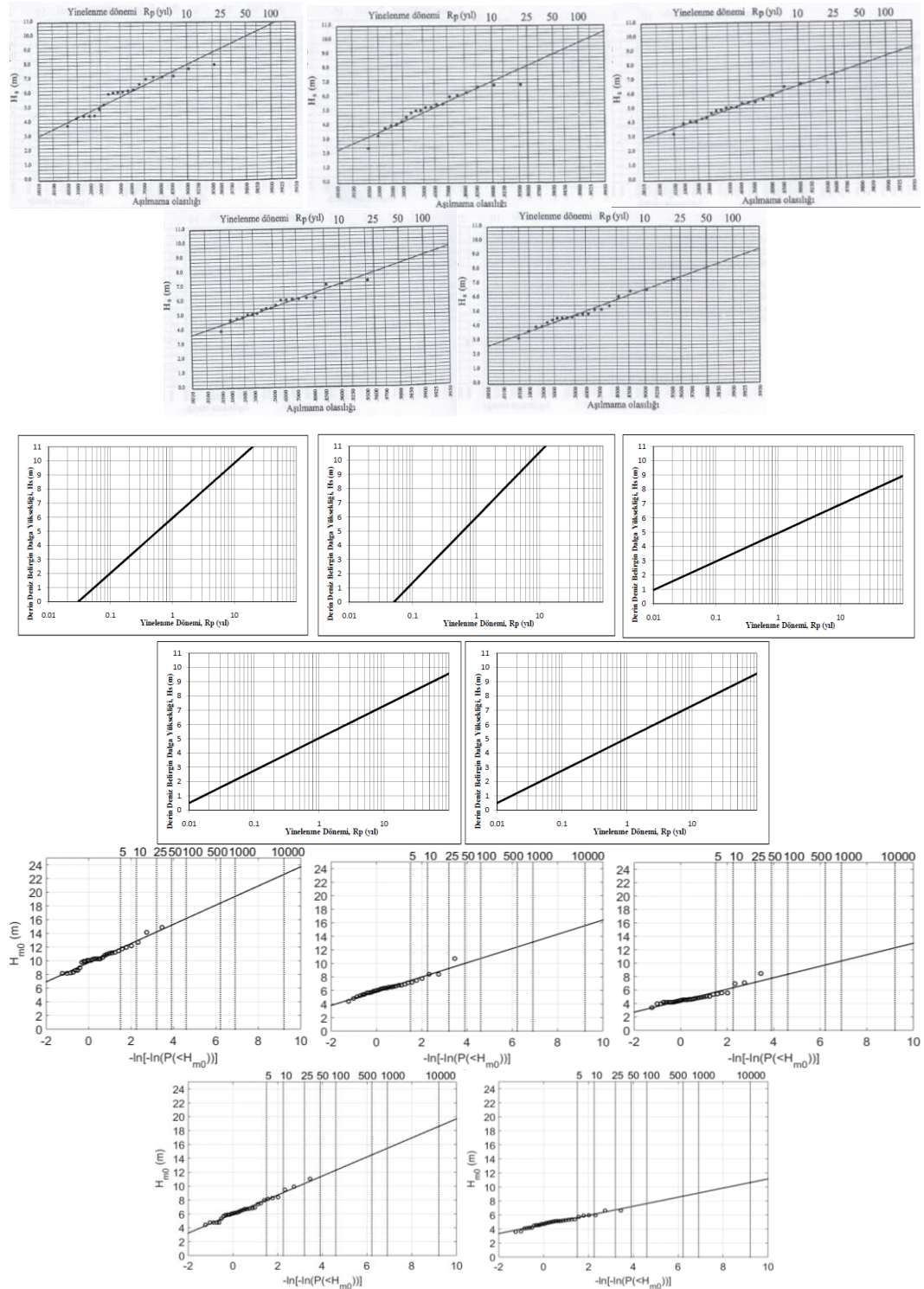
Effect of Elicitation on Biomass Production With Using Different Explant Sources on Sweet Violet (*Viola odorata* Linn)

Didem Tastekin[1], Begum Akyol[1], Aynur Gurel[1]

Abstract

Viola odorata L., which is also known as sweet violet, is an important ornamental plant with high seconder metabolite content in pharmaceutical area. In this study, it has been aid to specify appropriate sterilization procedure on petiole and leaf explants, establish callus regeneration protocol and determine effect of some elicitor treatments such as salicylic acid and salt on growth curve obtained through cell suspension culture under in vitro conditions. The different sterilization methods and medium composition have been used for callus culture. The most effective sterilization procedures were 1 min ethanol (70%), 5 min NaOCl (60%) for leaf explants; 1 min ethanol (70%), 10 min NaOCl (60%) for petiole explants. The sterilization success had been observed as 100% with these sterilization methods for both explants. The highest callus regeneration percentage (100%) was obtained on MS (Murashige and Skoog, 1962) medium supplemented with 2.5 mg/L BAP and 1.5 mg/L 2,4-D for both explant type. This callus medium was used for cell suspension culture. For elicitor treatments, NaCl (0, 15 g/L and 30 g/L) and salicylic acid (15 and 30 mg/L) were added to culture medium to make growth curves. 30 mg/L salicylic acid dose was determined as the most effective protocol for biomass production and the highest SCV was obtained in 17 culture days. This study is unique and these results will be instructive for some studies related with production of high seconder metabolite quantity.

Keywords: *Viola odorata, biomass, callus regeneration, cell suspension culture, elicitor*

1. INTRODUCTION

Viola odorata Linn., which is commonly known as "Sweet Violet", "English Violet", "Common Violet" or "Garden Violet", belongs to the Violaceae family and is a herb with stout rootstocks ([1], [2], [3]). The Violaceae family contains about 500 species and the most important medicinal plants of this family are Viola tricolor, Viola arvensis and *Viola odorata* [1]. *Viola odorata* Linn's natural habitat are Asia, North Africa and Europe [2]. This plant is a well known medicinal, edible and ornamental plant which blooms with purple flowers of attractive scent early in the spring. It grows in places exposed to sun, alongside hedges, river banks, on the edges of deciduous forests [4].

The uses of *V. odorata* L.for therapeutic purpose, dates back as far as 500 BC [2]. The leaves and flowers of this plant are employed in perfume industry. *V. odorata* L. has different essential oils such as citronella, geraniol, salicylaldehyde, linalool and these secondary metabolites are used as anti-inflammatory, healing and soothing agents. In traditional medicine, this plant had been used treatment of different disease such as anxiety, insomnia, bronchitis, cystitis, rheumatism and lower blood pressure ([1], [2])

Plant tissue and cell suspension cultures are investigated by biotechnological methods and provide a promising bioproduction platform for desired natural products [5]. Because of their capacity for active continuous growth and easy scale-up in large culture volumes, undifferentiated plant cell suspension cultures can be a convenient alternative for secondary metabolite production [6]. Even though all the advantages of plant cell culture, there are some limitation too. Therefore various tissue culture techniques are developed to enhance the yield of secondary metabolites, such as the use of elicitors. Elicitors are biotic or abiotic compounds which can enhance the secondary metabolite and biomass production in *in vitro* cultures [7].

The aim of this research, were develop a sterilization protocol for petiole and leaf explant, establish the best callus induction medium and determine the effect of NaCl and salicylic acid elicitors on growth curve.

---

[1]* Corresponding author: Ege University, Department of Bioengineering, 35100, Bornova/Izmir, Turkey, begumakyol.ege@gmail.com

2. MATERIALS AND METHODS

2.1. Plant Material and Sterilization

V. odorata L. plants were used as the initial explant source for this study. Leaves and petiole explants were obtain from these parent plants (Figure 1). Under aseptic conditions, all explants were surface sterilized with 70% ethanol (v/v) for 1 min, followed by different duration in 60% (v/v) sodium hypochlorite (Table 1), and subsequently, rinsed three times with distilled-sterile water. Pre-treatment wasn't applied at "1st sterilization". All explants soaked some water with 2-3 drop detergent for 5 min and rinsed with tap water for 10 min at other treatments.
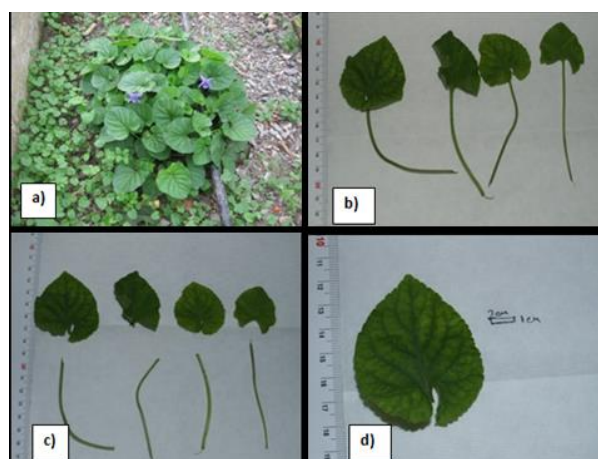
Figure 1. Viola odorata L. plant, a) General view of the natural environment of Viola odorata L. plant. b) Viola odorata L. plant explants. c) Viola odorata L. leaf and petiole parts. d) Leaf explant which aparted from petiole part

Table 1. Sterilization treatments for leaf and petiole explant

	Duration at 70% EtOH (leaf and petiole)	Duration at 60%(v/v) NaOH
1st treatment*	1 min	5 min (leaf), 10 min (petiole) **
2nd treatment	1 min	10 min (leaf), 15 min (petiole)
3rd treatment	1 min	5 min (leaf), 10 min (petiole)

* Pre-treatment was applied
** A drop of Tween 20 added to NaOH solution.

2.2. Callus Culture

MS [8] and ½ MS basal medium which including different concentration BAP (6-Benzylaminopurine) and 2,4-D (2,4-Dichlorophenoxyacetic acid)/NAA (Naphthaleneacetic acid)/IAA (Indole-3-acetic acid) as plant growth regulator (Table 2). 60 g/L sucrose as carbon source and 3 g/L gelrite as gellint agent were added to the culture medium (pH:5,8). To promoto the callus initiation, leaf explants was cut into 2 cm^2 sections, petiole explants were injured and transferred to the culture medium. different sterilization techniques and medium compositions were combined for to obtained best callus regeneration percentage from both two type of explant (Table 3).

For callus initiation, "1st treatment" and "2nd treatment" were used for sterilization protocol and explants were cultured on 1 medium compositions. Because of results of these treatment isn't enough, "3rd sterilization" protocol used for sterilization and 3 medium compositions used for callus initiation.

Table 2. *Culture media tested for callus initiation*

No	Basal medium	BAP (mg/L)	2,4-D/NAA/IAA (mg/L)
1	½ MS	2,5	0,15 (2,4-D)
2	MS	2,5	0,75 (2,4-D)
3	MS	2,5	1,5 (2,4-D)
4*	MS	2,5	1,5 (NAA)
5*	MS	2,5	1,5 (IAA)

* These medium were just used for sloven callus.

Table 3. *Sterilization and medium composition combination for callus initiation*

Application	Medium	Sterilization
A	1	1st treatment
B	1	2nd treatment
C	2	3rd treatment
D	3	3rd treatment

2.3. Cell Suspension Culture

3rd medium composition (MS+2,5 mg/L BAP+1,5 mg/L 2,4-D) used for cell suspension culture. 0,5 g callus (fresh weight) were transferred into a 250-mL Erlenmeyer containing 50 ml 3rd medium. The culture vessels were placed on an orbital shaker at 100 rpm under dark culture conditions at 24± 2°C. Some round cell aggregates were formed after culturing 45 days. Culturs were filtered and cell aggregates were collected and transferred to semi-solid medium (4th and 5th medium). Cell suspension culture were subcultured in the 4th medium (MS+2,5 mg/L BAP+1,5 mg/L NAA), because plant cells didn't disperse enough. NaCl (0, 15 g/L and 30 g/L) and salicylic acid (0, 15 and 30 mg/L) are added to the cell suspension culture as elicitors through sterilized with syringe filter (0,2 μm pore size). To prepare a growth curve of diving cells,   the cell suspension culture were harvested every 3-4 days intervals for 21 days and analyzed. Fresh weight was measured after removing culture medium by suction filtration. The cells were dried at room temperature until a constant weight for dry weight determination. To determine the SCV (Settled cell volume) 1 ml sample transferred to the centrifuge tube and the high of cell aggregates were measured after 5 min.

2.4. Culture Conditions

The pH of all the media was adjusted to 5.8 with 1 N HCl or 1 N NaOH and they were autoclaved at 121 ºC at 1.04 kg.cm^{-2} for 15 min. All semi-solid cultures were incubated under a 16-h light photoperiod (50 μmol m^{-2}.s^{-1}) provided by cool-white fluorescent light at 24±2°C and cell suspension cultures were incubated under dark conditions.

3. RESULTS AND DISCUSSION

Different protocols for sterilization treatment has been experimented on petiole and leaf explants and results were obtained from 5-7 days of cultures (Table 4). The best sterilization percentage (%100) were obtained from "3rd treatment" for both explant type (Figure 2).

Table 4*. Sterilization percentage for different explants*

	Sterilization Percentage (%)	
Sterilization	**Leaf Explant**	**Petiole Explant**
1st treatment	20,52	65
2nd treatment	63,33	72,73
3rd treatment	100	100
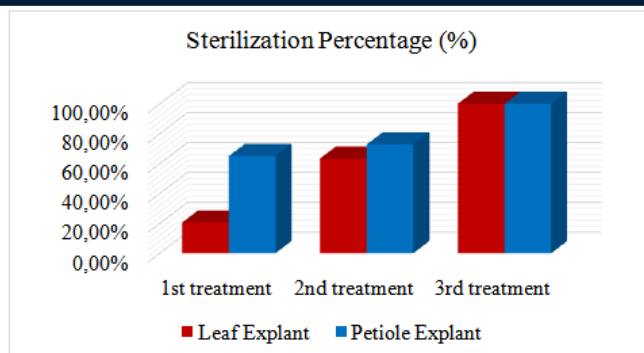
Figure 2. *Sterilization percentage of different explant (%)*

Different explants have gave different responses to the medium compositions and sterilization protocol combinations. While explant type and sterilization method were found as effective factors separately, it was determined that they did not have any effect together. In the study, the percentage of contamination in leaf explants was higher (62 %), and lower contamination in petiole explants (47.67 %) was observed. When the samples were compared in their own intakes, contamination was observed at a higher rate (77.5 %) in the first experiment and 0% in the 3rd and 4th experiment (Table 5).

Table 5. *Contamination percentage (%) which obtained from experiments using different sterilization methods and explant resources*

Application	Leaf			Petiole			Average
	R1	R2	R3	R1	R2	R3	
A	84,61	84,61	92,30	66,66	66,67	69,23	77,5 a
B	40	30	40	28,57	28,57	25	32,17 b
C	0	0	0	0	0	0	0 c
D	0	0	0	0	0	0	0 c
Average	62 a			47,67 b			

*LSD=14,107 (R=Replicate)

Callus regeneration was observed with different percentage according to explant type and applications (Figure 4). All explants gave callus with different colors with different densities. According to the obtained results, the best sterilization protocol was determined as application C and the best callus regeneration protocol was observed as application D. Compact callus clusters which has cream, green and brown tones were regenerated from leaf explants during 35 days of culture. The amount of callus which were obtained from petiole explants was less than leaf explants, however these callus clusters were cream and more friable than others (Figure 3).
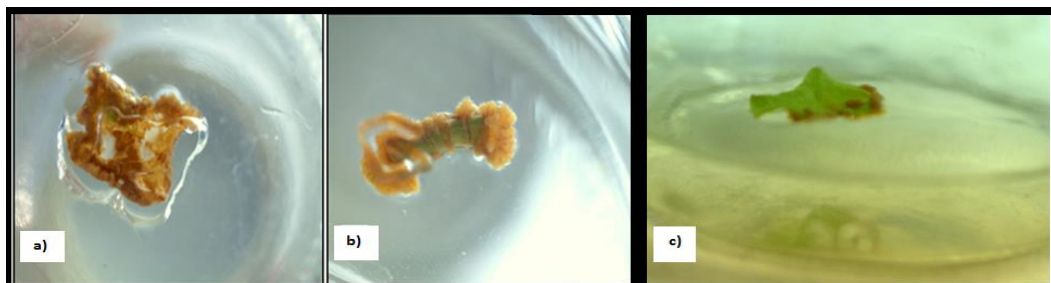
Figure 3. *Callus regeneration a) on leaf explant, b) on petiole explant. c) Callus initiation on leaf explant.*
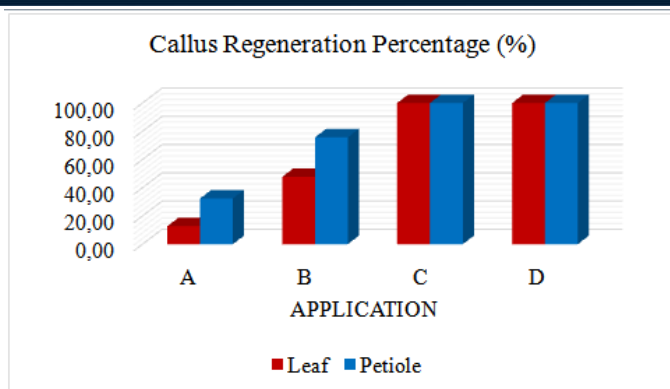
Figure 4. *Callus regeneration percentages of different explant (%)*

On the first cell suspension culture, callus had gave compact clusters which have nearby 1 cm diameter and globular embryo regeneration had shown. After the filtration of culture, these clusters were transferred to the semi-solid medium and root formation was obtained with low frequency. 10 days after the subculturing the suspension culture, elicitors were applied (Figure 5).
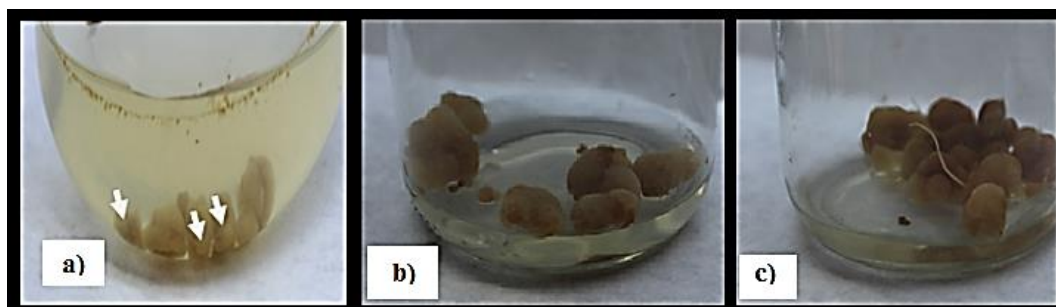
Figure 5. *a) Callus clusters and embryo regenerations on cell suspension culture, b) Callus clusters on semi-solid medium, c) Root formation on semi-solid medium.*

The highest biomass was obtained from 30 mg/L salicyclic acid elicitation on 17th day of culture (Figure 6). If the dry weight values are compared, the best result was gained from control, however viability of control group weren't stay long (Figure 7). When SCV ratios examined, as well as there wasn't any meaningful releationship between elicitors, the best result was obtained from 15 mg/L salicyclic acid elicitation (Figure 8). Because of control group gave the lowest ratio, it can say that elicitation was effective for this process (Table 6).

Table 6. *Biomass values from different elicitors on different days*

Elicitor	Day	Fresh wieght (g)	Dry weight (g)	SCV (%)
NaCl (15 g/L)	0	0,016	0,018	1
	4	0,013	0,004	6
	7	0,035	0,001	5
	18	0,062	0,006	5
	21	0,043	0,005	6
NaCl (30 g/L)	0	-0,019	0,019	1
	4	0,035	0,003	4,5
	7	0,028	0,002	4,5
	18	0,057	0,006	5
	21	0,043	0,005	5

	0	0,036	0,004	7,5
Salicyclic Acid (15 mg/L)	3	0,039	0,002	7
	14	0,062	0,006	7,5
	17	0,05	0,004	6,5
Salicyclic Acid (30 mg/L)	0	0,037	0,004	5,5
	3	0,038	0,002	6,5
	14	0,072	0,007	5,5
	17	0,082	0,005	5,5
Control	0	0,059	0,007	2
	3	0,005	0,001	3
	14	0,064	0,008	2
	17	0,052	0,005	2
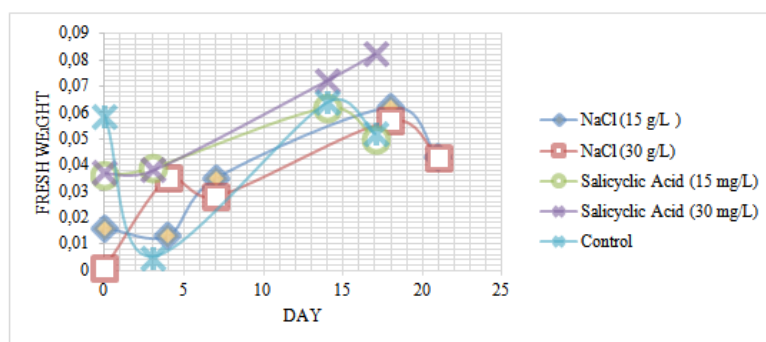
Figure 6. *Fresh weight values which obtained from elicitation treatment*
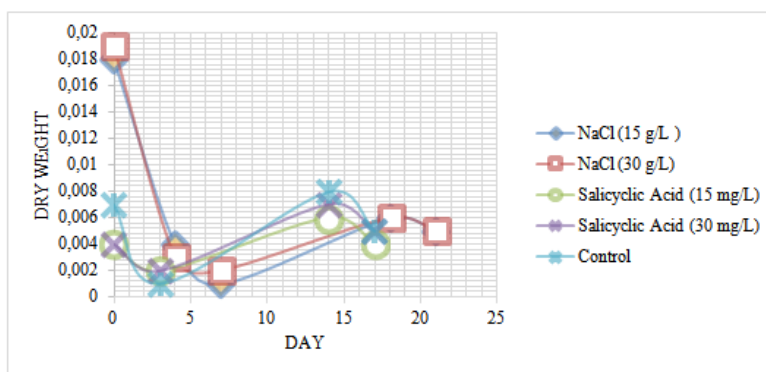
Figure 7. *Dry weight values which obtained from elicitation treatment*
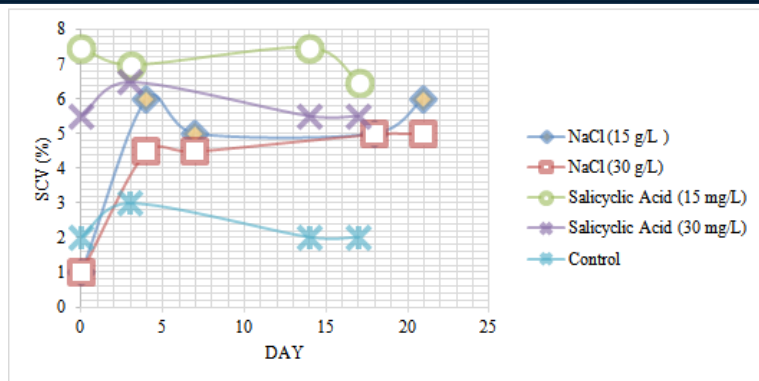
Figure 8. *SCV values which obtained from elicitation treatment*

In this study, with using application D, the best callus regeneration percentage (%100) was obtained. In the experiment to increase biomass in cell suspension cultures, the highest biomass production observed at 30 mg/L salicyclic acid elicitation on 17th day of culture. While the study's sterilization and callus regeneration steps provide a more effective protocol in a shorter time than the studies performed so far, no cell suspension cultures and elucidation studies have been performed, so that the obtained data will be the first data and will be used as a guideline.

4. CONCLUSION

In this study, callus cultures were established after formation of sterilization protocols for different explant types (petiole and leaf) and cell suspension cultures were obtained with obtained calluses. In addition, different elicitors examined to increase the efficiency of biomass by testing different elicitation methods. In this way, a protocol which allows higher biomass production in a shorter time has been identified. This protocol will provide guidance in large-scale studies aimed at increasing the amount of secondary metabolite in subsequent cell suspension cultures. Until now, no work has been done in this area, this is the only work in the field of work and makes it important to increase.

5. ACKNOWLEDGE

REFERENCES

[1]. M. Akhbari, H. Batooli and F.J. Kashi, Composition of essential oil and biological activity of extracts of Viola odorata L. from central Iran. Natural Product Research, Vol. 26, No. 9, 2012

[2]. H.S. Siddiqi, M. H. Mehmood, N.U. Rehman and A.H.Gilami, Studies on the antihypertensive and antidyslipidemic activities of Viola odorata leaves extract, Lipids in Health and Disease, 11:6, 2012.

[3]. M. E. Beyrouthy, M. Kafrouny, N. A. Apostolides, A. El-Hejin, L. Siddig, E. Azhar and A. M. A. Nour, Macroscopic, Microscopic and DNA Fingerprinting to Fight Adulteration of Banafsaj (Viola Odorata L) Sold at the Lebanese Herbal Shops, European Journal of Scientific Research, Vol. 104, 2013.

[4]. R. Erhatić, V. Židovec, M. H. Čustić, Z. Lončarić, M. Vukobratović, Š. Ščetarić, The Impact of Substrate and Fertilization on Growth and Development of Viola odorata L. 25th International Scientific-Experts Congress on Agriculture and Food Industry, Izmir 2014

[5]. W. Yue, Q. L. Ming, B. Lin, K. Rahman, C. J. Zheng, T. Han and L. P. Qin, Medicinal plant cell suspension cultures: pharmaceutical applications and high-yielding strategies for the desired secondary metabolites. Journal Critical Reviews in Biotechnology, Volume 36, 2016.

[6]. D. Hidalgo, A. M. Márquez, R. Cusidó, R. B. Martínez, J. Palazon and P. Corchete, Silybum marianum cell cultures stably transformed with Vitis vinifera stilbene synthase accumulate t-resveratrol in the extracellular medium after elicitation with methyl jasmonate or methylated β-cyclodextrins. Engineering in Life Sciences, 2017

[7]. M. Bayraktar, E. Naziri, I. H. Akgun, F, Karabey, E. Ilhan, B. Akyol, E. Bedir, A. Gurel, Elicitor induced stevioside production, in vitro shoot growth, and biomass accumulation in micropropagated Stevia rebaudiana, Plant Cell Tissus and Organ Culture, 2016J. Padhye, V. Firoiu, and D. Towsley, "A stochastic model of TCP Reno congestion avoidance and control," Univ. of Massachusetts, Amherst, MA, CMPSCI Tech. Rep. 99-02, 1999.

[8]. T. Murashige, F.Skoog, A revised medium for rapid growth and bioassay with tobacco tissue cultures. Physiol. Plant, 1962.

In Vitro Sterilization And Multiplication Protocol Of Prickly Pear Cactus (Opuntia Ficus Indica)

Merve Sezen¹*, Begum Akyol¹, Aynur Gurel¹

Abstract

Opuntia ficus indica, has been used as human food, forage, mineral source and a cure for several illnesses for ages. This genus have became more favoured fruit in the market because of its high contents of minerals and antioxidant property. Opuntia ficus indica provides an opportunity to study with different methods such as; micropropagation by organogenesis or somatic embryogenesis in in vitro and micrografting and. The aim of this study was to determine the most suitable surface sterilization protocol and medium composition for micropropagation for Opuntia ficus indica. In accordance with this purpose, 1 cm of shoot tips and 1 cm² cladode explants were cultured in Murashige and Skoog (Murashige and Skoog, 1962) basal medium supported with different doses of 6-Benzylaminopurine (BAP) (0.5, 1 and 2 mg/L). For sterilization treatments, 50 % NaOCl solution for different duration periods (3, 5 and 7 min) were tested. The most effective sterilization procedure was obtained with 3 min NaOCl treatment and shoot tip explants were more convenient for micropropagation while shoot number per explant was increased approximately 10-fold by MS medium which including 1 mg/L BAP. At the same time, this medium composition gave the highest survival ratio (66%) and had shown 25.9% rooting ratio. With this research, surface sterilization problems were minimized, percentage of explant viability and multiple shoot regeneration were increased according to beginning material.

Keywords: *Opuntia, ficus, indica, sterilization, multiple shoot regeneration, rooting, micropropagation*

1. INTRODUCTION

Opuntia ficus-indica is a species of the genus Opuntia, which belongs to the Cactaceae family. The plant which commonly called indian fig or barbary fig is one of the members of Caryophyllales order. The number of recorded species of Opuntia genus is between 160 and 250 [Fig. 1][1][2].

---

¹ *Department of Bioengineering, Ege University, Bornova-Izmir/ Turkey
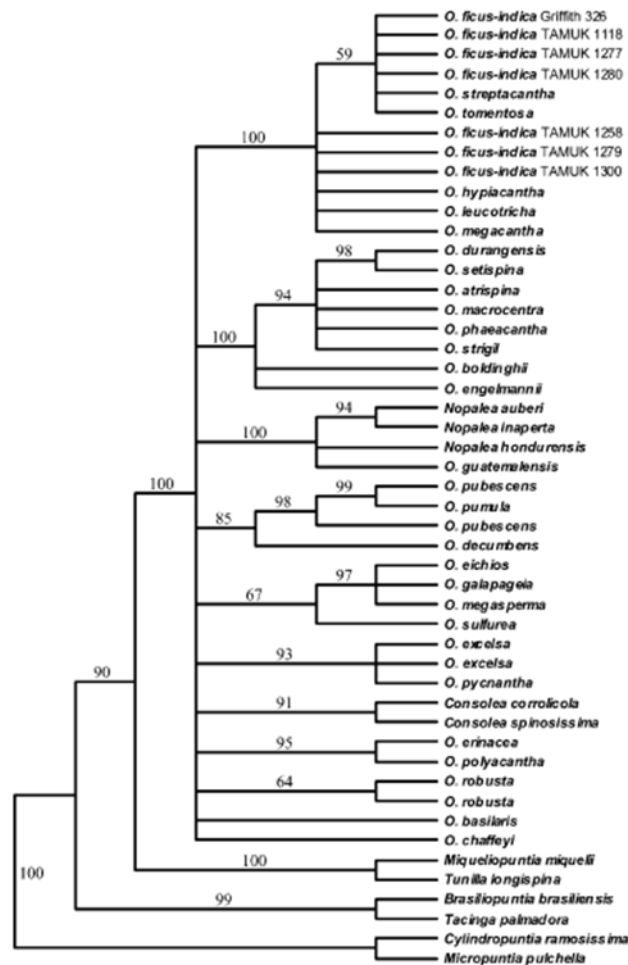
Figure 1: Phylogenetic analysis of Opuntia ficus-indica and related taxa. (M. Patrick Griffith,2004)

In the history of the cactus, there are some evidendences which show ancient people used this cacti as food source about 12000 years ago, long before cultivation. It is believed that during the discover of America continent, Colombus took the cacti along with him while returning to Lisbon in 1493 and this event became the beginning of spreading of ficus indica to the rest of the World. First, the cacti is placed in the Caribbean by the late 1400s, then started to cultivation in the 1519, Tlaxcala, Mexico. In the late 15th century, sailors stored this plant to use against scurvy in their stores and helped to spread it around the Europe. In the present, *O. ficus indica* is commonly located in Mexico, Latin America, South Africa and Mediterranean area. [3][4][5]

Opuntia genus is accepted as one of the most ideal crops in arid and semi-arid regions because of its high efficiency of converting water as biomass. *Opuntia ficus-indica*, one of several long-domesticated cactus species, is the most widespread and economically important of these cactus crops, as important as corn and tequila agave in the agricultural economy of modern Mexico. In Morocco the prickly pear is used as hedges of demarcation, to prevent the erosion and also for the fruits consumption. Recently, in some countries as Mexico, Italy and South Africa, the Prickly pear is cultivated on considerable surfaces for industrial ends in Mexico, its culture stretches on a surface of 300,000 ha, while to Morocco, the surface of the culture of the Prickly pear is of about 120,000 ha. [6][7]

The cacti yields an edible fruit which is juicy and sweet, with a thorny peel and a large number of small and hard seeds and is called prickly pear, indian fig or barbary fig. Recently, the production of this fruit started to increase because of its high mineral such as Ca, Na, Mg, Zn, Fe and polyphenol content which is effective against patogenic bacteria and radiation UV. Also its flower has important amount of fiber and protein for animal use. [7][8][9]

Opuntia ficus indica is one of the many plants which are used as cure for scars and ilnesses by ancient civilizations. Its cladods are used for stomach ulcer; fruits for ovarian cancer and dried flowers for prostate cancer in modern medicine. [10]

Due to its many benefits, the number of studies have increased for *in vitro* propagation of *Opuntia ficus indica.* In one of these studies, Finti et. al. used adenine sulfate (40 mg/L), monosodium fosfate (50 mg/L), sucrose (50 mg/L), phytagel (0.3%), benzyladenine (2.2 µM) and 0.5 mg/L IBA or IAA with MS medium for *in vitro* propagation. Then, the growing shoot subcultured in 5 mg/L BA based MS medium. As a result, they recorded best rooting in IBA and best success in acclimatization. [11]

Angulo-Bejarano and Paredes-López used indirect organogenesis method and cultured explants of 1 cm^2 in 20 different combinations of 2,4 diphenoxyn and benzyladenine based MS medium. Best results were obtained in media which contain 2.26 µM 2,4-D and 2.21 µM BA. [12]

In another study, Gomes et. al. cultured tips of shoots in 4-amino 3,5,6-tricloropicolinic acid (4 mg/L) based semi-solid MS medium for direct somatic embryogenesis micropropagation. As results, closed vascular system in the developing embryos and the absence of a vascular connection between the somatic embryos were recorded in explants [13].

Lopez et.al. analyzed 3 different Opuntia genus (*Opuntia ficus indica, Opuntia undulata, Opuntia stricta)* to determine the antioxidant amount of each of their fruits and came to conclusion *Opuntia ficus indica* has the most powerful antioxidant capacity and highest taurine content. [14]

2. MATERIALS AND METHODS

2.1. Sample Collection and Preparation

The *Opuntia ficus indica* materials with many cladods were provided from Ege University Botanic Garden [Fig 2]., First (young), second and third cladods from top to bottom were excised as explants.
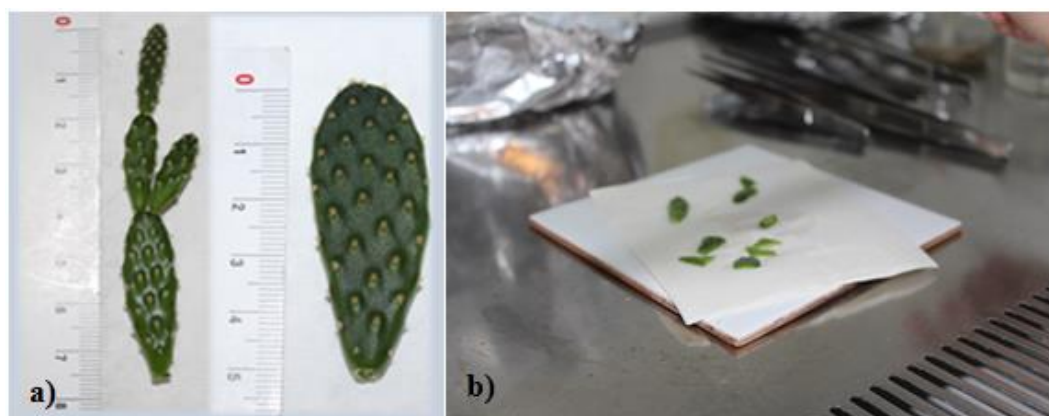
Figure 2: a) Young shoots collected from botanic garden. b) Size of cultured explants

2.2. Sterilization Protocol

Pre-treatment was applied on the collected material. The samples were exposed to 9-10 drop of detergent with water for 15 minutes and then held under running water for 45 minutes. 100 ml 50 % (v/v) NaOCl solution, 100 ml 70% (v/v) ethanol and 3 of 100 ml sterile water were used for sterilization which made inside of the laminar flow cabinet. First, the explants exposed to ethanol for 1 minute and followed by different duration periods as 3-5-7 minutes into NaOCl solution and purified from NaOCl by soaked into 3 sterile waters for 1 minute for each [Table 1].

Table 1: Surface sterilization treatments in Opuntia ficus indica

	Duration at 70% EtOH	Duration at 50%(v/v) NaOCl
1st treatment	1 min	3 min
2nd treatment	1 min	5 min
3rd treatment	1 min	7 min

2.3. Culture media Preparation

Three different medium compositions were prepared with 6-Benzylaminopurine (BAP) based MS medium. Media were supplemented with 1.9 g/l KNO_3, 0.1 g/l myo-inositol, 30 g/l sucrose and 3 g/l gelrite. BAP doses were decided as 0.5-1 and 2 mg/l by considering previous studies about mentioned cactus [Table 2]. 1 mg/l BAP based MS medium to find sterilization protocol and after that MS media with different BAP contents to determine the most suitable BAP doses were used. The prepared media poured into glass tubes as 10 ml each (pH:5.8).

Table 2: Culture media with different BAP doses for shoot regeneration

	Basal Medium	BAP (mg/L)
K1	MS	0.5
K2	MS	1
K3	MS	2

2.4. Cultivation Process

Explants were cultured as 1 cm pieces only from the tip of cladods and also 1 cm^2 longitudinal pieces. It has been careful to have as many as possible spines in explants [Fig 2]. The cutted explants were placed as one explant per tube. The culture tubes were maintained in culture room having 24±2°C temperature and 16-h light photoperiod (3500 lux). Treatments were set up as 3 repetitions, according to randomly plot experiment design

3. RESULTS AND DISCUSSION

In order to determine relation between explant age according to young- new regenerated cladod situation and success of cultivation, most suitable sterilization protocol of NaOCl and convenient doses of BAP in MS media were examined. In the experiment to find the most effective sterilization protocol, contamination ratio recorded as 0% at 3 min of NaOCl treatment while the highest vitrification has seen at 5 min of NaOCl [Fig 3]. As the duration in NaOCl got longer, the explants were more damaged physically and went through morphological change which effected regeneration of explants adversely.

The youngest explants which were tips of cladods showed the highest number of shoots and survival. The older explants had less chance to survive. The oldest explants experienced vitrification. Vitrification, also formerly called hyperhydricity is morphological, anatomical and physiological disorder encountered during *in vitro* culture periods of herbaceous and woody plants.

These results explained the best sterilization method for *Opuntia ficus indica* is 1 min in 70% (v/v) ethanol and 3 min in NaOCl after pre-treatment considering sterilization and vitrification ratios [Fig 4].
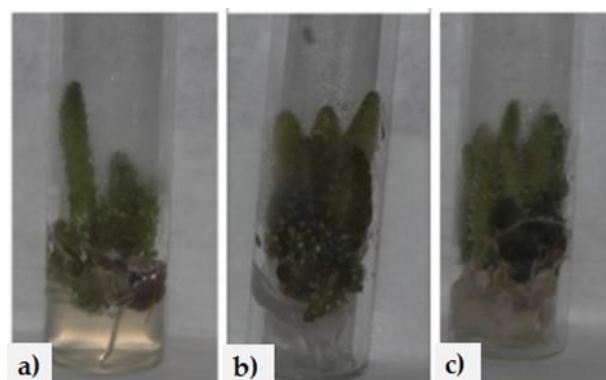
Figure 3: Vitrification after surface sterilization in NaOCl for a) 3 min. b) 5 min. c) 7min.
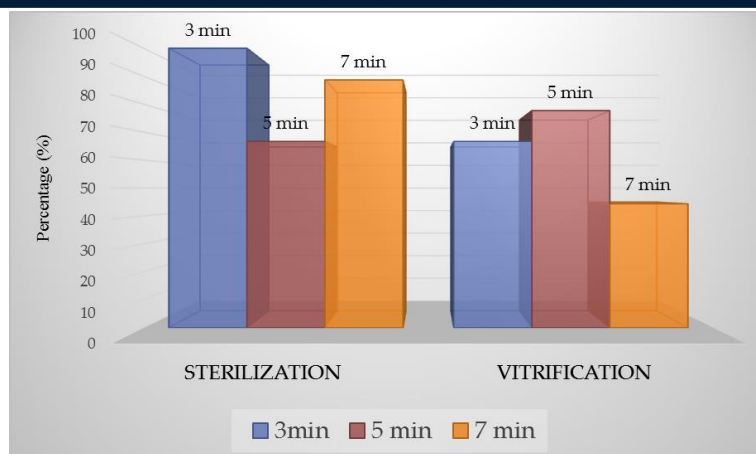
Figure 4. Sterilization and vitrification percentages according to NaOCl treatments

Table 3: Resuts of different sterilization protocols

	Sterilization (%)	Vitrification (%)
3 min	100	66.7
5 min	66.7	77.7
7 min	88.7	44.3

In the experiment to determine the best BAP combination as growth regulator, the highest shoot regeneration capacity was obtained in MS medium including 1 mg/l BAP concentration with 10 shoots per explant. At other combinations, 9 shoots per explant in 0.5 mg/l BAP and 8 shoots per explant in 2 mg/l were recorded. Morphological change has seen at all ratios of BAP as an effect of explants age. Vitrification problem was in highest level in 2 mg/l BAP concentration. At this concentration, shoots grew in an irregular order [Fig 5] and rooting ratio was the lowest of them all [Fig 6]
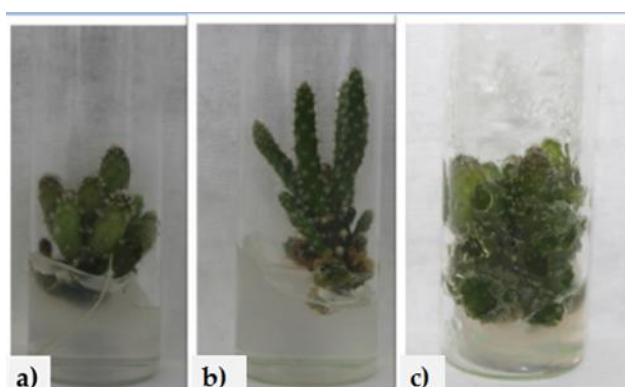
*Figure 5: Treatment of BAP as **a**) 0.5 mg/l **b**) 1 mg/l   **c**) 2 mg/l*
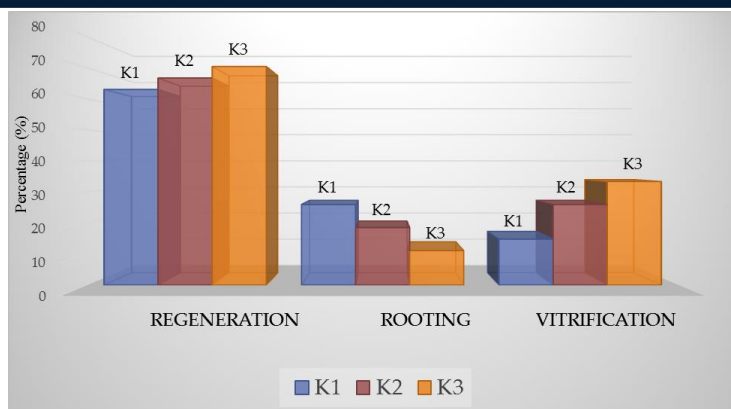
Figure 6. Shoot regeneration, rooting and vitrification percentages

Table 4: Result ratios of medium compositions with BAP

	Regeneration (%)	Rooting (%)	Vitrification (%)
K1	62. 9	25.9	14.8
K2	66.7	18.5	25.9
K3	70.4	11.1	33.3

4. CONCLUSION

Plant tissue culture techniques are alternative production methods which provide more rapid, time saving and effective protocols. Because of that reason, nowadays production of cactus plants with micropropagation techniques are popular research areas.

We came to conclusion that the best sterilization protocol in 3 min of NaOCl (50%) and the most optimum concentration of BAP is 1 mg/l as cladod number and survival ratios are considered. This research provided a useful protocol on regeneration for *Opuntia ficus indica* and these methods can be adapted for a commercial production.

REFERENCES

[1]   T. Nharingo, M. Moyo, Application of Opuntia ficus-indica in bioremediation of wastewaters, Journal of Environmental Management, 166 (2016) 55-72.
[2]   I. Ganopoulos, A. Kalivas , N. Kavroulakis, A. Xanthopoulou, A. Mastrogianni, G. Koubouris, P. Madesis, Genetic diversity of Barbary fig (Opuntia ficus-indica) collection in Greece with ISSR molecular markers, Plant Gene 2 (2015) 29–33.
[3]   B. Adli, A. Boutekrabt , M. Touati, T. Bakria, A. Touati, E. Bezini, Phenotypic diversity of Opuntia ficus indica (L.) MILL. in the Algerian steppe, South African Journal of Botany 109 (2017) 66–74.
[4]   N. Bayara, M. Kriaaa, R. Kammoun, Extraction and Characterization of Three Polysaccharides Extracted from Opuntia Ficus Indica Cladodes, International Journal of Biological Macromolecules S0141-8130(16)30852-2.
[5]   D. Butera, L. Tesorıere, F. Dı Gaudıo, A. Bongıorno, M. Allegra, A. M. Pıntaudı, R. Kohen, M. A. Lıvrea, Antioxidant Activities of Sicilian Prickly Pear (Opuntia ficus indica) Fruit Extracts and Reducing Properties of Its Betalains: Betanin and Indicaxanthin, J. Agric. Food Chem. 2002, 50, 6895−6901.
[6]   M. Patrick Griffith, The Orıgıns Of An Important Cactus Crop, Opuntıa Fıcus-Indıca (Cactaceae): New Molecular Evıdence, American Journal of Botany 91(11): 1915–1921. 2004.
[7]   O. Khatabia, H. Haninea, D. Elothmanib, A. Hasib, Extraction and determination of polyphenols and betalain pigments in the Moroccan Prickly pear fruits (Opuntia ficus indica), Arabian Journal of Chemistry Volume 9, Supplement 1, September 2016, Pages S278–S281.
[8]   E. M. Galatı, M. R. Mondello, D. Gıuffrıda, G. Dugo, N. Mıcelı, S. Pergolızzı, M. F. Tavıano, Chemical Characterization and Biological Effects of Sicilian Opuntia ficus indica (L.) Mill. Fruit Juice: Antioxidant and Antiulcerogenic Activity, J. Agric. Food Chem. 2003, 51, 4903−4908.
[9]   I. Ammara, M. Ennouria, O. Balia, H. Attia, Characterization of two prickly pear species flowers growing in Tunisia at four flowering stages, LWT - Food Science and Technology Volume 59, Issue 1, November 2014, Pages 448–454.

[10] Y. S. Coria Cayupána, M. J. Ochoab, M. A. Nazarenoa, Health-promoting substances and antioxidant properties of Opuntia sp. fruits. Changes in bioactive-compound contents during ripening process, Food Chemistry Volume 126, Issue 2, 15 May 2011, Pages 514–519.

[11] A. El Finti, R. El Boullani, F. El Ayadi, N. Ait Aabd, A. El Mousadik, Micropropagation in vitro of Opuntia Ficus-Indica in south of Morocco, International Journal of Chemical and Biochemical Sciences, 1(2012):6-10.

[12] P. I. Angulo-Bejarano, O. Paredes-López, Development of a Regeneration Protocol through Indirect Organogenesis in Prickly Pear Cactus (Opuntia ficus-indica (L.) Mill), Scientia Horticulturae 128 (2011) 283-288.

[13] F. L. A. F. Gomes, F. F. Heredia, P. B. Silva, O. Faco, F. A. P. Campos, Somatic Embryogenesis and Plant Regeneration in Opuntia ficus-indica (L.) Mill (Cactaceae), Scientia Horticulturae 108 (2006) 15-21.

[14] J. A. Fernández-López, L. Almela, J. M. Obón, R. Castellar, Determination of Antioxidant Constituents in Cactus Pear Fruits, Plant Foods for Human Nutrition, September 2010, Volume 65, Issue 3, pp 253–259.

Waste Heat Energy Recovery in the Iron-steel Industry Using Organic Rankine Cycle (ORC)

Semih Akın[1], Yusuf A. Kara[2]

Abstract

The iron-steel industry is one of the most energy-intensive industries, and it is responsible for almost 5% of total world energy consumption. The molten slag, a by-product of iron-steel making processes, is exhausted with the critically high temperature of about 1450℃-1550℃. Thanks to this remarkable high temperature of the molten slag, it is seen as a potential source of energy and raw material. Nowadays, dry granulation method is generally used to increase the heat transfer surface of the molten slag and then waste heat energy recovery processes are implemented by using the fluidized bed technology. However, the granulated molten slag is discharged from the fluidized bed at the relatively high temperature of about 650℃-700℃ and this high- temperature granulated slag is generally not used for energy recovery. In this study, a waste heat energy recovery system is proposed using Organic Rankine Cycle (ORC) in order to benefit from the critically high temperature of the slag particles after it is discharged from the fluidized bed. The theoretical results show that the designed system allows obtaining 104.49 kWh energy production for the mass flow rate of slag of 1.67 kg/s.

Keywords: *molten slag, organic rankine cycle, the iron-steel industry, waste heat energy recovery*

1. INTRODUCTION

The iron-steel industry is the leading industry of the global economy, and the iron-steel industry has developed significantly over the past two decades in terms of its production processes. According to the report published by the World Steel Association, world crude steel production has reached 1,621 million tons in 2015 [1]. However, the iron-steel industry is the most energy consuming industry all around the world, and it is responsible for almost 5% of total world energy consumption [2].The iron-steel industry is also the leading industry where most energy efficiency studies take place, and the number of these studies has been increasing each passing year so as to raise energy efficiency in the iron-steel sector. High temperature waste heat energy is mainly stored in the products, molten slag, and waste gases. As shown in Figure 1, the significant amount of the waste heat energy is stored into molten slag, which is equal to 35% of total waste heat energy [2].Molten slag is a kind of by-product formed during steel production processes, and it is exhausted with the critically high temperature of about 1450℃-1550℃ [2].Thanks to this high temperature, molten slag carries a sensible amount of heat energy, and this feature of molten slag attracts the researchers to develop new techniques for recovering waste heat energy from iron and steel slag. Nowadays, fluidized bed technology is widely used for a large variety of waste heat energy recovery processes including, heat energy recovery from molten slag. However, after granulation process, solid slag particles are discharged from fluidized bed with a sensible temperature of about 650℃-700℃, and then these slag particles are used as a kind of raw materials of Portland cement, asphaltic concrete, and roadbed material without implementing any additional waste heat recovery processes [2]. In this context, ORC, one of the most economic and efficient ways to convert low-grade thermal energy to electricity, has drawn increasing attention in recent years since it can be used easily for small scale applications [3].

[1] Corresponding author: University of Georgia, 30605 Athens/Georgia, USA. semih.akin@uga.edu

[2] Yusuf A.Kara, Bursa Technical University, Faculty of Natural Sciences, Architecture and Engineering, 16330 Yıldırım/Bursa, Turkey. yusufali.kara@btu.edu.tr
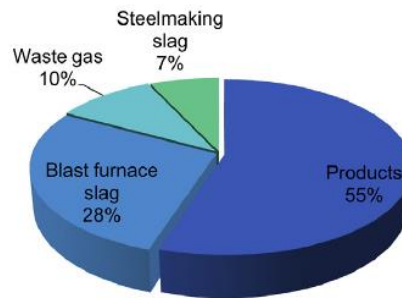
Figure 1.Distribution of high-temperature waste heat in steel industry [2]

In the present study, a waste heat energy recovery system for 1.67 kg/s mass flow rate of molten slag is proposed by using ORC to utilize the waste energy of slag particles. In addition, the system components are defined, the system efficiency is calculated, and feasibility of the system is discussed.

2. MATERIALS AND METHODS

The researches related to waste heat recovery has drawn significant attention in recent years. Waste heat recovery studies not only help to reduce the demand for the fossil fuels, but also provide an important contribution to the environment by reducing CO_2 emission. However, most of the waste heat recovery applications are carried out low-grade, and hereby ORC seems to be a suitable method to recover energy from a low-grade heat source [3]. ORC has been widely used to most of the low-temperature heat sources including solar energy, biomass energy, geothermal energy, and waste heat energy. In this study, ORC is used as a waste heat energy application for the iron-steel industry. The schematic diagram of the proposed waste heat energy recovery system is given in Figure 2. R134a is selected as the working fluid for the system since it is cheap, non-toxic, non-flammable, and environment-friendly [4]. In this system, firstly the slag particles exposed to first recovery operations are carried to second fluidized bed, and here the air is blown on the slag particles by using the fans. Therefore, a certain amount of heat is transferred to the air. Second, the obtained hot air is sent to the boiler for evaporating R134a, and then before leaving the system the air is carried to the heat recovery steam generator (HRSG) in order to be used for increasing the temperature of the working fluid. Third, the working fluid leaves the boiler as the superheated vapor at 2 MPa and 150 ℃, and then it enters the steam turbine to generate mechanical power. In the fourth step, the expanded working fluid moves to the recuperator, and thus the temperature of the pumped R134a is increased here by heat transfer with the R134a discharged from the turbine. Then, the working fluid comes into the condenser at 1 atm and 15 ℃, and leaves the condenser as the saturated liquid. Finally, the saturated R134a is pumped to the recuperator, and the cycle begins again.
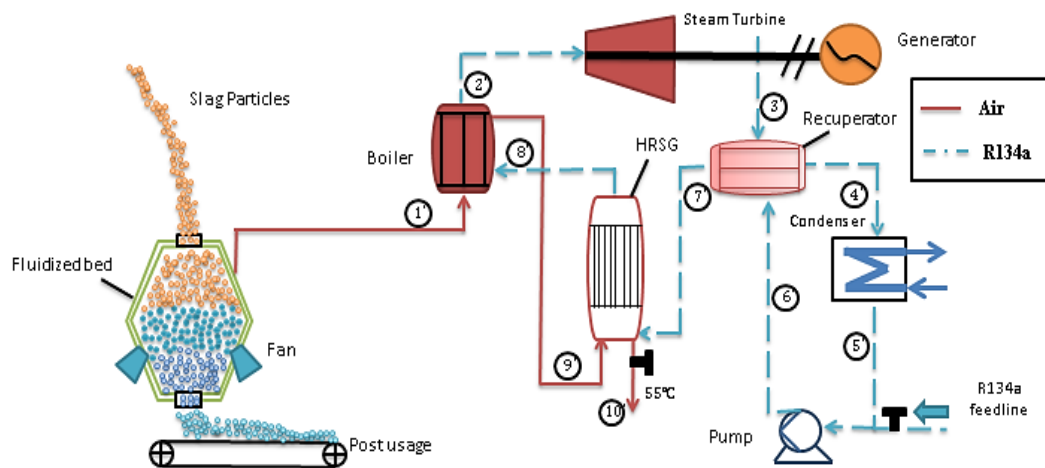
Figure 2.Schematic diagram of the ORC system

2.1. Thermodynamic analysis of the ORC system

First, slag particles enter the fluidized bed with the mass flow rate of 1.67 kg/s at 606 °C, and then the air is blown by the fans on the slag particles. The energy conversation in a slag droplet is defined by Eq. 1, where c_p is the specific heat of the slag, ε the emissivity, A_d cross-sectional area of slag droplet, σ the Stephan-Boltzman constant, h the convective heat transfer coefficient, and V_d is the volume of the slag particle [5].

$$-hA_d \left(T_1 - T_0 \right) - A_d \varepsilon \sigma \left(T^4 - T_0^4 \right) = V_d \rho_d c_p \frac{dT}{dt} \tag{1}$$

The value of the temperature difference between inside the fluidized bed and its walls is expected to be rather small, and that is why radiative heat transfer was omitted for calculations. When this differential equation is solved, Eq. 2 is obtained where Δt is the time difference, T_2 the outlet temperature of slag particle, T_o the air temperature, and T_1 inlet temperature of the slag particles respectively.

$$-\Delta t = \frac{V_d \rho_d c_p}{hA_d} \ln \left| \frac{T_2 - T_0}{T_1 - T_0} \right| \tag{2}$$

The convective heat transfer coefficient between the slag particles and the air can be estimated by the following empirical equation, where K_g is the thermal conductivity of the air, Re the Reynolds number, Pr the Prandtl number, and d diameter of the slag particle [5]. Next, the outlet temperature of the slag particles is calculated by putting the heat transfer coefficient into the Eq. 2.

$$h = \frac{K_g}{d} \left(2 + 0.6\sqrt{\text{Re}} \sqrt[3]{\text{Pr}} \right) \ (W/m^2 K) \tag{3}$$

Finally, the heat transfer between the slag particles and the air can be calculated by Eq. 4, where Q is the amount of the heat transfer, $\dot{m}$ the flow rate of the slag particle, c_p the specific heat of the slag particle, T_1 the initial temperature of the particles, and T_2 the outlet temperature of the slag particles.

$$Q = \dot{m} c_p \left(T_1 - T_2 \right) \qquad (kW) \tag{4}$$

The amount of heat transfer between the slag particles and the air is also equal to the energy change of the air. Thus, the outlet temperature of the air can be calculated by using Eq. 5, where $\dot{m}_a$ is the flow rate of the air, c_{pa} the specific heat of the air, T_{a1} the outlet temperature of the air, and T_0 the inlet temperature of the air.

$$Q_a = \dot{m}_a c_{pa} \left(T_{a1} - T_0 \right) \qquad (kW) \tag{5}$$

2.1.1. Heat Exchanger Design

The heat exchangers in the system including boiler, condenser, HRSG, and recuperator are designed as shell-tube heat exchangers with 25% segmental baffles. The calculations were performed under the conditions that cycle is continuous, the working fluid is incompressible, the ambient temperature is 25 °C, another properties such as Re, Pr number are calculated at average temperature. To determine the tube-side heat transfer coefficient of the heat exchangers Petukhov-Kirillov correlation given by Eq. 6 was used. In this equation, Nu is the Nusselt number, f is the Filonenko's friction factor [6].

$$Nu = \frac{(f/2) \times \text{Re} \times \text{Pr}}{1.07 + 12.7(f/2)^{1/2} \left(\text{Pr}^{2/3} - 1 \right)} \tag{6}$$

$$f = \left(1.58 \ln \text{Re} - 3.28 \right)^{-2} \tag{7}$$

The Kern method was used to determine the shell-side heat transfer coefficient. The Kern relation is given by Eq. 8, where k is the heat transfer coefficient, $j_{h,k}$ the dimensionless heat coefficient, μ the shell fluid dynamic viscosity at average temperature, μ_0 the tube fluid dynamic viscosity at average temperature [6].

$$Nu = \frac{h_g D_e}{k} = j_{h,k} \ \text{Re} \ \text{Pr}^{1/3} \left(\frac{\mu}{\mu_0} \right)^{0.4} \tag{8}$$

The shell-side velocity of the HRSG was calculated pretty low although there is no segmental baffle inside the HRSG. That is why the shell-side heat transfer coefficient was calculated by applying the Churchill-Chu correlation since it is used for the natural convection along the vertical part of the tube. The Churchill-Chu correlation is represented by Eq. 9, where Gr is the Grashof number and Re the Reynolds number respectively [7]. If the value of this equation is rather bigger than 1, then forced convection effect can be neglected [8].

$$\frac{Gr}{Re^2} \gg 1 \tag{9}$$

Reynolds number for the shell-side of the HRSG is given by Eq. 10, where u is the fluid mean velocity inside the heat exchanger, d_e tube diameter, and v kinematic viscosity. The Reynolds number calculated from Eq. 10 is smaller comparing to Grashof number since u is pretty small because of large shell diameter. As a result, the Churchill-Chu correlation is valid for this type of HRSG application, and the shell-side heat transfer coefficient can be calculated as for natural convection heat transfer process.

$$Re = \frac{ud_e}{v} \tag{10}$$

2.1.2. Pressure Drops in the Components

Pressure drops occurred in the component should be calculated to find the amount of energy consumption by the fans. The pressure drop in the fluidized bed was calculated by Eq 11 given below, where ΔP is the pressure drop, H the height of the fluidized bed, ε_{ma} the bed voidage at minimum fluidization, ρ_p the density of the particle, ρ_g the density of the gas [9].

$$\Delta P = H\left(1 - \varepsilon_{ma}\right)\left(\rho_p - \rho_g\right) \qquad (Pa) \tag{11}$$

Pressure drops in the heat exchanger were obtained by using Kern method. The Kern correlation to determine the pressure drop in the tube-side is given by Eq 12, where $\Delta P_{k,pipe}$ the amount of the pressure drop in the tube-side, n_p the number of the tube passes, λ_f the fraction coefficient, L the tube length, d_i the inner diameter of the tubes, μ the dynamic viscosity at average temperature, μ_0 the dynamic viscosity at wall temperature, ρ the fluid density, and U the fluid flow velocity,

$$\Delta P_{k,pipe} = n_p \left[\lambda_f \frac{L}{d_i}\left(\frac{\mu}{\mu_0}\right)^{-m} + 2.5\right]\rho \frac{U^2}{2} \qquad (Pa) \tag{12}$$

After the pressure drops are calculated, the fans power can be calculated by Eq 13, where W_{fan} the fan power, $\dot{Q}$ the volumetric flow rate of the air, ΔP_k the overall pressure drop occurred in the components.

$$W_{fan} = \dot{Q}\,\Delta P_k \qquad (kW) \tag{13}$$

2.1.3. Steam Turbine Calculation

According to the performed calculations, the working fluid enters the steam turbine at 2MPa and 150 ℃, and leaves the turbine at 1 atm and 60℃ as shown in Figure 3. The isentropic efficiency of the turbine was calculated by Eq 14 as 86%.

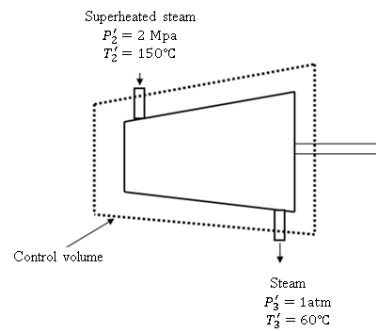$$\eta = \frac{h_{2'} - h_{3'}}{h_{2'} - h_{3s}} \tag{14}$$

Figure 3.Inlet and outlet conditions of the steam turbine.

The power generation by the steam turbine was calculated as 160.16 kW by Eq 15, where W_t is the turbine power, $\dot{m}_{R134a}$ the mass flow rate of the working fluid, and h is the enthalpy respectively. Net power generation was calculated as 104.49 kW, after the fan power, and the pump power were subtracted from the power generation by the steam turbine. The system efficiency was also calculated as 23%.

$$\dot{W}_t = \dot{m}_{R134a} \times \left(h_{2'} - h_{3'} \right) \qquad\qquad (kW) \qquad (15)$$

3. RESULTS AND DISCUSSIONS

Some approximations are employed in the calculations of the components during the design processes of the ORC system. One approximation is that the flow was modeled as the frictionless flow, and all calculations are performed under the incompressible flow condition. This situation affects the pressure drops in the components, and it will necessitate a higher-capacity pump and fan. Another approximation is that the flow is uniform in the fluidized bed, and the necessary parameters for the calculations such as the specific heat, coefficient of thermal conductivity are selected at average temperatures. Additionally, the pressure drops in the pipeline were not calculated since the exact length of the pipeline could vary depending on which alignment is chosen. In addition, the condenser was designed as a finned-tube heat exchanger, but the pressure drop in the condenser was not included in the overall pressure drop. Friction losses in the pipes and the turbine were also not taken into account in the calculations. The study also needs a cost analysis to determine the economic feasibility of the system. If these assumptions and approximations had not been done, more accurate results would have been obtained for the ORC system.

4. CONCLUSIONS

In this study, a waste heat energy recovery system was proposed by using ORC to utilize the critically high temperature of the slag, followed by an initial heat recovery process. The theoretical results show that the designed ORC system allows obtaining 104.49 kWh energy generation for the mass flow rate of the slag of 1.67 kg/s. The aim of this study is to show that the designed ORC system might be used to utilize waste heat energy in the iron-steel industry, and the design of this system might also be adapted to other applications.

REFERENCES

[1].   (2017) The WSA website. [Online]. Available: https://www.worldsteel.org/en/dam/jcr:1568363d-f735-4c2c-a1da-e5172d8341dd/World+Steel+in+Figures+2016.pdf
[2].   H. Zhang, H. Wang, X. Zhu, Y.-J. Qiu, K. Li, R. Chen, and Q. Liao, "A review of waste heat recovery technologies towards molten slag in steel industry," *Applied Energy,* vol. 112, pp. 956-966, 2013.
[3].   W. Pu, C. Yue, D. Han, W. He, X. Liu, Q. Zhan, Y.Chen, "Experimental study on Organic Rankine cycle for low-grade thermal energy recovery", *Applied Thermal Engineering,* vol. 94, pp. 221-227, 2016.
[4].   S.Masheiti, B.Agnew, S.Walker, "An evaluation of R134a and R245fa as the working fluid in an Organic Rankine Cycle Energized from a Low Temperature Geothermal Energy Source", *Journal of Energy and Power Engineering,* vol. 5, pp. 392-402, 2011
[5].   Q. Yuelin, L. Xuewei, B. Chenguang, C. Pan, Q. Guibao, and Z. Jie, "Mechanism of Dry Molten Slag Granulation Using a Rotating Multi-Nozzle Cup Atomizer," ste*el research international, vo*l. 85, no. 1, pp. 44-52, 2014.
[6].   S.Kakac, H. Liu, A.Pramuanjaroenkij, *Heat Exchangers- Selection, Rating, and Thermal Design*, 3rd ed., Newyork, USA, CRC Press- Taylor &Francis Group, 2012.
[7].   Churchill, S.W., Chu, H.H., "Correlating equations for laminar and turbulent free convection from a vertical plate", Int. J. Heat Mass Transf. 18 (11), 1323–1329, 1975.
[8].   Y.A.Kara, C.Arslanturk, "Modeling of central domestic water heater for buildings", *Applied Thermal Engineering*, vol 24, pp. 269-279, 2004.
[9].   B. Prabir, *Circulating Fluidized Bed Boilers,* 1st ed., Switzerland, Springer, 2015.
[10].   R.K Shah, D.P. Sekulic, *Fundamentals of Heat Exchanger Design,* 1st ed., USA, Wiley, 2002.

BIOGRAPHY

Semih Akın was born in İstanbul, Turkey. He received his bachelor's degree from the Department of Mechanical Engineering and the Department of Industrial Engineering (Double Major) at Uludag University, Bursa, Turkey in 2013. He also obtained his M.S. from the Department of Mechanical Engineering at Bursa Technical University in 2016. From 2014 to 2016, he worked as Research and Teaching Assistant at Bursa Technical University. Mr. Akın's major fields of study are renewable energy technologies and energy efficiency. He is currently an IEP student at the University of Georgia in Athens, USA.

Yusuf Ali Kara is a Professor in the Department of Mechanical Engineering at Bursa Technical University, Turkey. He received his Ph.D. degree in 1999 from Ataturk University, Erzurum, Turkey. His main research interests are heat pumps, heat exchangers, and renewable energy. He has published sixteen articles in the international journals.

CH₄ Emissions From Solid Waste in Karabuk Province

Ali CAN[1]

Abstract

The waste disposal sites are one of the important CH_4 emission sources according to the Intergovernmental Panel on Climate Change (IPCC) methodology. And decaying of organic compounds by anaerobic bacteria, especially by methanogenesis creates CH_4. According to the many research, it can be concluded that the decaying is continuous during 15-20 years and then it is decreasing over the following decades. The monitoring mechanism and techniques have to be developed for collection processes of CH_4; because, the collected CH_4 can be used as biogases. Therefore the managed landfill sites are important for high efficient recovery of CH_4

In many countries, the waste is not defined as garbage and it is evaluated as money. The biogas production from waste disposal sites is also encouraged by UNFCCC. It means it gives a great opportunity for countries to tackle with climate change problems, not only by decreasing during recovery process but also using as fuel for clean energy purposes.

In this study, the general aim is to determine the potential CH_4 emissions from solid waste disposal sites in Karabuk Province. Although the scale is province level, the study is being extended to regional and country scale. Because, the potential of producing biogas from waste disposal sites in Turkey is very high.

In Karabuk province, the tackling with waste disposal sites, decrease the CH_4 emission approximately 0.2% in Turkey's total GHGs emissions. Using this methane again as clean biogases fuel will also decrease an extra 0.5% emission, because the usage of these produced gases is decreasing other fuel consumptions and it is not necessary for countries to calculate CO_2 emission from biogases for UNFCCC submissions.

Keywords: *IPCC methods, CH4 emission, Solid Waste, Biogas*

1. INTRODUCTION

The portion of renewable energy sources in total energy consumption is increasing considerably due to the potential lack of some nonrenewable energy source in the future. This situation creates many positive effects not only today's but also future life of peoples. The climate is changing and the people impact on climate is more intensely felt every day. It means that the negative effects of people on environmental vital elements need to be reduced. The most important reason for climate change is human generated or anthropogenic emission sources. In particular, direct greenhouse gases (GHGs) emissions increase this adverse effect. The emission sources are present in a wide variety and the effects of these sources are different due to their different emissions. However, their total impacts are projected as disastrous [9], [10]. For that reason, the emission sources have to be considered as carefully. The emission sources have be studied on a local basis. Because, the potential affect is changing with many factors such as wind, air temperatures, air humidity, local sinks and geographical aspects. The main emission sources are categorized into waste, energy, industry and agriculture [6].

Disposal of municipal wastes is producing most of the GHGs. However, waste is considered as an economical matter and quite valuable because it has an potential to be recycled, burned for energy, and degraded organics into CH_4 to get biogases [1], [2], [11]. In many countries, the waste is not defined as garbage and it is evaluated as money.

Landfill gas consist of approximately 50 percent CO_2 and 50 percent CH_4 by volume. However, the percentage of CO_2 in landfill gas may be smaller because of decomposition of subtracts with a high hydrogen/oxygen ratio (e.g. fats, hemicellulose) and because some of the CO_2 dissolves in water within the site [6]. In waste disposal sites, the degradable organic compounds (DOC), the atmospheric moisture and air

---

[1]*Corresponding author: Karabuk University, Engineering Faculty, Mechanical Engineering Department, Balıklar Kayası Mevkii, Karabük, 78100, Turkey. alican@karabuk.edu.tr*

temperature are important factors for CH_4 production. The DOC values are reflected by the waste composition. And some fractions are converted to the landfill gas that is determined by kinetic methodologies [6], [11].

Waste disposal sites have shown that the decaying organics has a great potential to produce CH_4. Although, there is some uncertainty in producing biogases from organic decaying, this remain low in the long term CH_4 collecting in managed disposal sites [7]. The biogas production from waste disposal sites is also encouraged by UNFCCC. It means it gives a great opportunity for countries to tackle with climate change problems, not only by decreasing during recovery process but also using as fuel for clean energy purposes [6], [7], [4], [5] .

Turkey has been a party for United Nations Climate Framework Convention on Climate Change since 2004 and ratified Kyoto Protocol in 2009 without any commitment. It means Turkey has to deal with climate change problems [14], [16]. In Turkey, according to the energy balance tables, total 2.7 million tonnes of oil equivalent (TOE) energy were obtained from biogases and wastes in 2015 [8]. In order to decrease the GHGs emissions in the future, Turkey could use wastes as a fuel to obtain a clean energy. Moreover, it is not necessary to calculate CO_2 emission from biogas burning for UNFCCC submissions. Therefore, this potential can be used for mitigation purposes of GHGs in the atmosphere.

The main purpose of this study was to investigate the effect of wastes on air emission and possible production capacity of biogases in province Karabuk by using IPCC methodology. The municipal waste data were obtained on the web site of State Institute of Statistics [15] and the energy balance tables are gathered from Ministry of Energy and Natural Resources [8]. The CH_4 and emissions were calculated by using the IPCC-Tier 1 method [6], [7], [4].

2. METHODOLOGY

The total municipal waste data of Karabuk provinces for the years between 2001 and 2014 were obtained on the web site of State Institute of Statistics [15]. However, this data contains many missing years for the series. Therefore, the lack data are estimated by using trend analysis.

The best fit linear and polynomial regression models are studied and the closest R-squared values to the "1" was accepted as the best fit line to the series, The series equation was also used for projecting the future municipal solid waste until year 2020. The linear, second order and third order polynomial trendline are given as;

A linear regression model is described by the following formula (1) [3]:

$$y = mx + b \tag{1}$$

m   : the slope

b   : the intercept

y & x   : estimated and known variables

A polynomial regression model is described by the following formula (2):

$$y = b + c_1 X + c_2 X^2 + c_3 X^3 + \cdots + c_n X^n \tag{2}$$

b   : constant

$c_1,,,c_n$: constant

y & x   : estimated and known variables

And the R-squared value which is a statistical measure of how close the variables are fitted to the regression model. R-squared is also known as the coefficient of determination and it is calculated as (3):

$$R^2 = 1 - \frac{SSE}{SST} \ ; \ \text{where} \ \ SSE = \sum(Y_i - \hat{Y}_i)^2 \ \text{and} \ SST = (\sum Y_i^2) - \frac{(\sum Y_i)^2}{n} \tag{3}$$

R^2 : R squared value

SSE   : sum of squares of the residual error

SST   : treatment sum of squares

n   : degrees of freedom

And finally, the biased results have to be checked for goodness of fit by residual plotting.

To calculate the CH_4 emissions, the (IPCC - Tier 1) methodology was used as given in the below formulas (4) [6], [7].

$$CH_4 \ Emission = (MSWT * MSWF * MCF * DOC * DOCF * F * 16/12 - R) \cdot (1-OX) \tag{4}$$

1139

MSW_T : Total Municipal Solid Waste (tonnes/year)

MSW_F : Solid waste fraction in municipal solid waste disposal sites (default value is 1)

MCF : Methane correction factor (fraction) (for unmanaged disposal sites DF is 0.6)

DOC : Biodegradable decomposition of organic carbon (fraction) (0.10-0.21)

DOC_F : Degradable Organic Compound Fraction (DF is 0.77)

F : CH_4 fraction in storage gases (DF is 0.5)

R : Recycled CH_4 (tonnes/year)

OX : Oxidation Factor (Fraction – DF is 0)

3. RESULTS AND DISCUSSION

The results have shown that there is a big capacity for producing electricity from the solid waste disposal in Karabuk provinces. In this study, the potential energy producing projections are also estimated to help the local authorities for future planning. This potential is determined from simple quantity of municipal solid wastes. The annual municipal solid waste data for the years between 2001 and 2015 are gathered from TurkStat web pages [15], [16]. However, the data is not as time series and the data of years 2005, 2007, 2009, 2011 and 2013 are missing. For that reason, the missing data is estimated by using best fitted regression model. The linear and polynomial regression model was considered as seen in the following Figure1. The highest R-squared value was observed in third order polynomial regression model as seen in the figures.
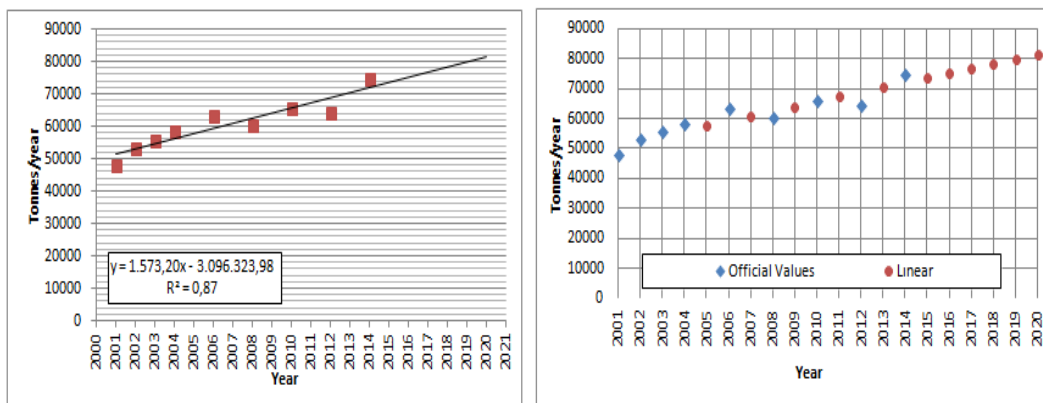
Figure 1. Linear Trendline Model Results
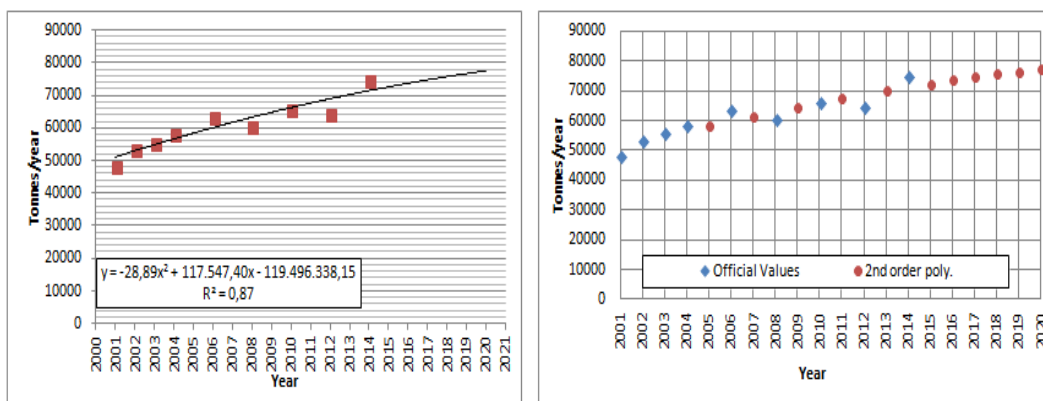
Figure 2. 2nd order Trendline Model Results
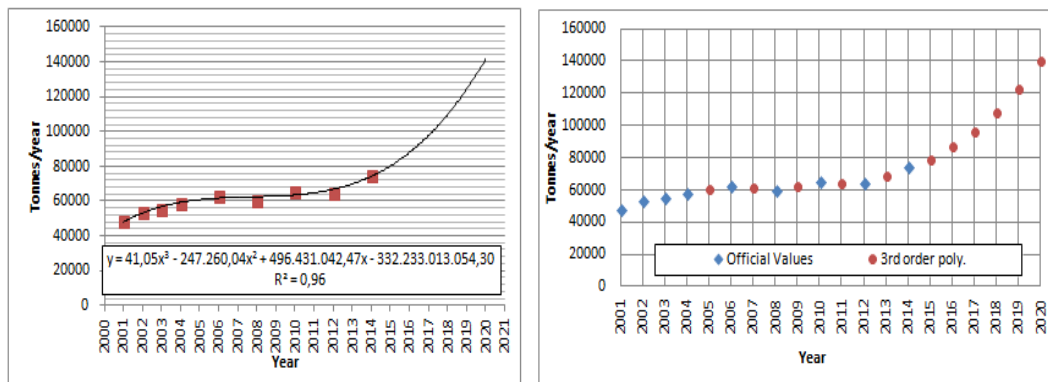
Figure 3. 3rd order Trendline Model Results

It has to be noted that the highest R squared value does not mean that the best fitted value. The biased results have to be checked for goodness of fit by residual plotting as seen in the Figure 4. According to this plotting, the 3rd order polynomial regression is biased with estimated results. Therefore, the 3rd order polynomial model is decided to be used for future CH_4 emission estimation.
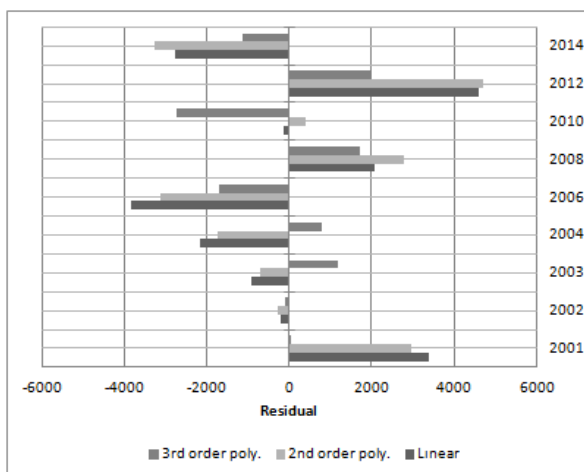
Figure 4. The models residual plotting

The missing years municipal solid waste quantity and the possible solid waste disposal until year 2020 was estimated by highest R squared value and goodness of fit model, which is third order polynomial model. By using this model, the projected solid waste quantity is determined as 140,76 Gg in 2020. And the CH_4 emission from this projection is calculated as 6.5 Gg CH_4 emissions by using IPCC approaches. Through the years the methane emission is increasing and it is approximately increasing 191.5 % in 20 years. The trend of CH_4 emission from solid waste disposal sites was seen in the following Figures 5.
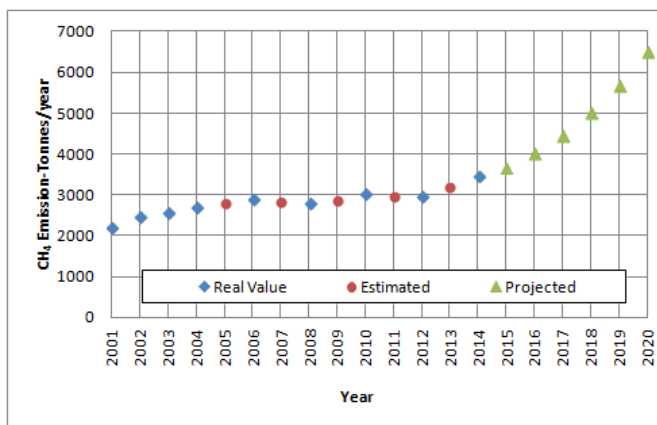
Figure 5. The CH4 emission between the years 2001 and 2020

According to the highest CH_4 production capacity, 29265 MW electricity can be produced from the solid waste disposal sites. Approximately, 1 Gg CH_4 is producing 4500 MW electricity depending on the heating values [7], [12], [13]. But the CH_4/CO_2 ratio is critical for producing biogases from the solid waste disposal sites [11]. The highest electricity production capacity of Karabuk province is observed in Figure 6.
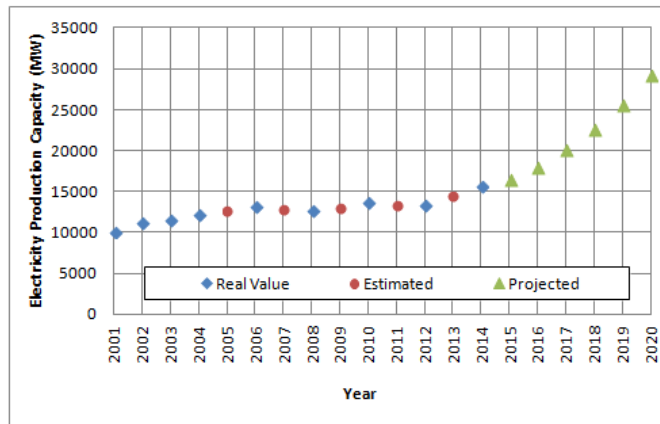
Figure 6. The Electricity production capacity of solid waste disposal sides in Karabuk Province

The CH_4 emission from waste is used as fuel by increasing number of municipalities and private sectors. In order to tackle with climate change and to decrease the emissions in the future, Turkey could use wastes as a fuel to obtain a clean energy. The realization of this possibility will decrease the CH_4 emission in the atmosphere considerably. Although Turkey is a party for United Nations Climate Framework Convention on Climate Change and Kyoto Protocol, it has to be deal with this severe problem. In Karabuk province, the tackling with waste disposal sites, decrease the CH_4 emission approximately 0.2 % in Turkey's total GHGs emissions. Using this methane again as clean biogases fuel will also decrease an extra 0.5% emission, because the usage of these produced gases is decreasing other fuel consumptions and it is not necessary for countries to calculate CO_2 emission from biogases for UNFCCC submissions. In order to tackle with climate change and to decrease the emissions in the future, Turkey could use wastes as a fuel to obtain a clean energy.

4. CONCLUSION

The study has shown that the possibilities of using methane gases from solid waste disposal sites are considerable decreasing the CO_2 equivalent emissions in the atmosphere. In Karabuk province, the tackling with waste disposal sites, decrease the CH_4 emission approximately 0.2 % in Turkey's total GHGs emissions. Using this methane again as clean biogases fuel will also decrease an extra 0.5% emission, because the usage of these produced gases is decreasing other fuel consumptions and it is not necessary for countries to calculate CO_2 emission from biogases for UNFCCC submissions.

REFERENCES

[1]. Aitchison E., 1995. **IEA bioenergy agreement task XI. Municipal Solid Waste Conversion to energy and end task review**. Original research Article Biomass and Bioenergy. Vol.9. p.343-349.

[2]. Aitchison E., 1996. **Methane generation from UK Landfill Sites and its use as and energy resources.** Energy Conversion and Management. Vol.37. p. 1111-1116.

[3]. Draper N.R., Smith H.,1966. **Apllied Regression Analysis**. P.1-70.

[4]. Eurostat, 2016. **Greenhouse gas emission from waste disposal**. [Online]. Available: http://ec.europa.eu/eurostat/statistics-explained/index.php/Archive:Greenhouse_gas_emissions_from_waste_disposal date: 12.12.2016.

[5]. EEA, 2017. EEA greenhouse gas - data viewer. [Online]. Available: http://www.eea.europa.eu/data-and-maps/data/data-viewers/greenhouse-gases-viewer date: 12.01.2017.

[6]. IPCC Greenhouse Gas Inventory Reference Manual – **Revised 1996 IPCC Guidelines for National Greenhouse Gas Inventories** – Volume 3 – Intergovernmental Panel on Climate Change – Edited by Houghton J.T., et al. 1996.

[7]. IPCC Greenhouse Gas Inventory Reference Manual – **IPCC Guidelines for National Greenhouse Gas Inventories** - Intergovernmental Panel on Climate Change, 2006.

[8]. MENR - **The annual Energy and Petroleum Balance Sheets 1970-2015**, Ministry of Energy and Natural Resources, 2015.

[9]. OECD, 2015. **Climate Change Risks and Adaptation**: Linking Policy and Economic, OECD Publishing, Paris. p.13-35.

[10]. OECD 2015. **Climate Change Mitigation: Policies and Progress**, OECD Publishing, Paris. p.17-53.

[11]. Poulsen T.J., Adelard L., Wells M., 2017. **Improvement in CH_4/CO_2 ratio and CH4 yield as related to biomass mix composition during anaerobic co-digestion**. Waste Management. Vol 61. p.179-187

[12]. Rajaeifara M.A, Ghanavatib H., Dashtid B.B., Heijungse R., Aghbashlof M., Tabatabaeib M. 2017. **Electricity generation and GHG emission reduction potentials through different municipal solid waste management technologies: A comparative review**. Renewable and Sustainable Energy Reviews Vol 79. p 414–439.

[13]. Rios M., Kaltschmitt M., 2016. **Electricity generation potential from biogas produced from organic waste in Mexico**. Renewable and Sustainable Energy Reviews Vol 54. p. 384-395.

[14]. TurkStat, **National Greenhouse Gas Inventory Report, 1990-2015**. Annual Report submission under the "Framework Convention on Climate Change, 2015.

[15]. TurkStat, Municipal Waste Statistics, [Online]. Available: https://biruni.tuik.gov.tr/medas/?kn=119&_locale=en. date: 23.04.2017

[16]. UNFCCC, 2017. The UNFCCC website, **National Inventory Submissions**. [Online]. Available: http://unfccc.int/national_reports/annex_i_ghg_inventories/national_inventories_submissions/items/10116.php. date: 20.04.2017.

CFD Analysis of CuO-Water Nanofluid Flow in a Square Cross-Sectioned Duct under Turbulent Flow Condition

Mutlu Tekir[1], Kamil Arslan[2]

Abstract

Day by day nanofluids are finding place more usage areas. It is used in nuclear reactor cooling, electronic chip cooling, and heat exchangers to increase convective heat transfer and efficiency. Convective heat transfer coefficient is examined in this study for three different k-ε turbulence model types. The study was conducted between 10.000-100.000 Reynolds numbers. This study focuses on numerical investigation of forced convection nanofluid flow in a square cross-section duct under turbulent flow regime.

Keywords: *Cfd, Turbulent Flow, Cuo-Water Nanofluid*

1. INTRODUCTION

Heat transfer enhancements have reached its limits with traditional technologies like fins and microchannels, because of the fact that traditional heat transfer fluids have low thermal conductivity. Therefore, new methods were being searched. One of these new methods is by adding metallic or non-metallic nanoparticles to the heat transfer fluid [1]. It is a fact that many fluids like water, ethylene glycol and oil have low thermal conductivity. Nanometer size metallic nanoparticles like copper, silver, gold, titanium, their oxides, and carbon are used to enhance the heat transfer coefficient in heat transfer fluids. Nanofluids can be used in nuclear reactor cooling, car electronics cooling, cancer treatment, and they can be implemented for safer surgery. Buongiorno and Hu proved that nanofluids are the best candidate for backup safety system as emergency nuclear core cooling, and for waste heat removal system [2].

Two different models are being used to analyze nanofluid flow numerically. In single phase model, nanoparticles are assumed to be distributed homogenously inside the base fluid, and to show uniform properties across the base fluid. On the other hand in the multiphase model, equations are solved separately for these two different phases. Multiphase models can be solved by Eulerian-Eulerian Model, and Eulerian-Langrangian Model approaches [3].

Arslan [4] compared the turbulence models which can be used for analysis of internal flow in a semicircular duct. It was realized that k-ε turbulence models give more precise solutions than the others. Kaya [5] studied numerically on the topic of nanofluid turbulent flow in a square duct which there was not many researches about. Using correlations to find the physical and thermal properties of nanofluid, it was analyzed the Al_2O_3-water single phase nanofluid turbulent flow by using k-ε RNG turbulence model, and temperature dependent thermal, and physical properties on Ansys Fluent software. It was applied 500 kW/m^2 heat flux on the duct wall. After that, the results were compared with other correlations determined from other experimental studies. Goktepe et al. [3, 6] studied laminar internal flow with forced convective heat transfer. The results were compared for different models with using Al_2O_3-water nanofluid: Eulerian-Eulerian, Eulerian-Mixture, Single Phase Dispersion, and Single Phase Homogenous models. Single Phase Dispersion model has been given the most successful results. Saghir et al. [7] analyzed the laminar nanofluid flow using Single Phase and Eulerian-Eulerian Mixture model. The results were compared with the experimental data. They found that thermal and physical properties of Al_2O_3-water nanofluid were the same as using previously published correlations. They realized that results from using Single Phase model was the closest to the experimental

---

[1]*Corresponding author: Karabük University, Department of Mechanical Engineering, 78050, Karabük, Turkey. mutlutekir@karabuk.edu.tr*

[2]*Karabük University, Department of Mechanical Engineering, 78050, Karabük, Turkey. kamilarslan@karabuk.edu.tr*

results. Esmaeilnejad et al. [8] researched the Al_2O_3-water and CuO-water nanofluids numerically in microchannel flow, and it was found that increasing nanoparticle volume concentration also increases heat transfer rate and pressure drop. They realized that the results found from temperature dependent thermal and physical properties approximate to the results found from constant thermal and physical properties.

Considering the literature review about nanofluids, the aim of this work is to investigate numerically the heat transfer enhancement of CuO-water nanofluid through a square cross-section duct under the turbulent flow regime for constant heat flux boundary condition. The turbulence models are compared with the experimental results from literature.

2. PROBLEM DESCRIPTION AND GOVERNING EQUATIONS

In this study, flow and heat transfer characteristics of CuO-water nanofluid flow in a 0.01 m x 0.01 m square cross-section and 3 m long straight duct. The numerical analyses were conducted using Ansys Fluent 17.0 software.

The convective heat transfer coefficient and Nusselt number are fundamental parameters to find out thermal performance of the nanofluid and are defined by the following equations;

$$h_{nf} = \frac{q''}{(T_w - T_b)_{avg}} \tag{1}$$

$$T_b = \frac{T_{in,nf} + T_{out,nf}}{2} \tag{2}$$

$$Nu_{nf} = \frac{h_{nf} \cdot D_h}{k_{nf}} \tag{3}$$

where $(T_w - T_b)_{avg}$ is the linear mean temperature difference of wall and the bulk at the inlet and the outlet sections of the duct, h is the convective heat transfer, D_h is hydraulic diameter, k is thermal conductivity, nf represent the nanofluid, q'' is heat flux. Calculated Nusselt number from the equation above compared with three different theoretical Nusselt number correlations: Dittus-Boelter, Gnielinski and Sieder-Tate correlations [9].

f is the friction coefficient that is found by Darcy-Weisbach equation given below [9]:

$$f = \frac{\Delta P}{\left(\frac{L}{D_h}\right) \cdot \left(\frac{\rho \cdot V^2}{2}\right)} \tag{4}$$

and calculated friction coefficient can be compared with Blausius correlation [9]:

$$f = 0.316 Re^{-1/4} \tag{5}$$

Numerical nanofluid analyses are made with three different approaches: Single Phase Model, Euler-Euler Approach, Euler-Lagrange Approach. In this study Single Phase Model was used. All these models have advantages and disadvantages. Single Phase Model offers low computational cost and reasonable accuracy. Physical properties of the nanofluids are calculated from water and nanoparticle characteristics at the mean temperature using the following equations [10, 11]:

$$\rho_{nf} = (1 - \varphi)\rho_{bf} + \varphi\rho_{np} \tag{6}$$

$$(\rho C_p)_{nf} = (1 - \varphi)(\rho C_p)_{bf} + \varphi(\rho C_p)_{np} \tag{7}$$

$$\frac{k_{nf}}{k_f} = \frac{k_{np} + 2k_{bf} - 2\varphi(k_{bf} - k_{np})}{k_{np} + 2k_{bf} + \varphi(k_{bf} - k_{np})} \tag{8}$$

$$\mu_{nf} = \frac{\mu_{bf}}{(1 - \varphi)^{2.5}} \tag{9}$$

where bf represents base fluid, np represents nanoparticle, ρ is density, φ is nanofluid volume concentration, C_p is thermal capacity, and μ is the dynamic viscosity.

The thermophysical properties of pure water and CuO nanoparticle are given in Table 1 at the bulk temperature [14].

Table 1. Thermophysical Properties of water and CuO nanoparticle.

Material	Water	CuO
Density (kg/m3)	995.7	6400
Thermal conductivity (W/m K)	0.615	20
Specific Heat (J/kg*K)	4178	533
Viscousity (kg/m*s)	0.798	-

Reynolds and Prandtl numbers are calculated by the eq. (10) and eq. (11), respectively [9]:

$$Re_D = \frac{\rho \cdot V \cdot D_h}{\mu} \tag{10}$$

$$Pr_{nf} = \frac{C_{p_{nf}} \mu_{nf}}{k_{nf}} \tag{11}$$

For incompressible, steady-state flows, continuity, momentum, and energy equations are given in eq. (12) – (14) [12];

$$\vec{\nabla} \cdot \vec{V} = 0 \tag{12}$$

$$\rho \frac{D\vec{V}}{Dt} = -\Delta p + \mu \nabla^2 \vec{V} \tag{13}$$

$$\rho c_p \frac{DT}{Dt} = k \nabla^2 T \tag{14}$$

Turbulence models play important role in these analyses. The k-ε turbulence model was used in numerical calculations. Turbulent kinetic energy k and its dissipation rate ε are calculated from the transport equations:

$$\frac{\partial}{\partial t}(\rho k) + \frac{\partial}{\partial x_i}(\rho k u_i) = \frac{\partial}{\partial x_j}\left(\left(\mu + \frac{\mu_t}{\sigma_k}\right)\frac{\partial k}{\partial x_j}\right) + G_k + G_b - \rho\varepsilon - Y_M + S_k \tag{15}$$

$$\frac{\partial}{\partial t}(\rho \varepsilon) + \frac{\partial}{\partial x_i}(\rho \varepsilon u_i) = \frac{\partial}{\partial x_j}\left(\left(\mu + \frac{\mu_t}{\sigma_\varepsilon}\right)\frac{\partial \varepsilon}{\partial x_j}\right) + C_{1\varepsilon}\frac{\varepsilon}{k}(G_k + C_{3\varepsilon}G_b) - C_{2\varepsilon}\rho\frac{\varepsilon^2}{k} - S_\varepsilon \tag{16}$$

Eddy viscosity is calculated from the eq. (17).

$$\mu_t = \rho C_\mu \frac{k^2}{\varepsilon} \tag{17}$$

where G_k is the generation of turbulent kinetic energy due to mean velocity gradients, G_b is the generation of turbulent kinetic energy due to buoyance, Y_M is the contribution of the fluctuating dilatation in compressible turbulence to the overall dissipation rate, $C_{1\varepsilon}$, $C_{2\varepsilon}$, and $C_{3\varepsilon}$ are constants, σ_k and σ_ε are the turbulent Prandtl numbers for k and ε, S_k and S_ε are user-defined source terms.

The constants for turbulence models are given in eq. (18) – eq. (20) [12, 13]:

k-ε Standard:

$$C_{1\varepsilon} = 1.44, \quad C_{2\varepsilon} = 1.92, \quad C_\mu = 0.09, \quad \sigma_k = 1.0, \quad \sigma_\varepsilon = 1.3 \tag{18}$$

k-ε RNG:

$$C_{\varepsilon 1} = 1.42, \quad C_{\varepsilon 2} = 1.68, \quad C_\mu = 0.0845, \quad \sigma_k = 0.7194, \quad \sigma_\varepsilon = 0.7194, \quad \eta_0 = 4.38 \quad \beta = 0.012 \tag{19}$$

k-ε Realizable:

$$C_{1\varepsilon} = 1.44, \quad C_{2\varepsilon} = 1.9, \quad \sigma_k = 1.0, \quad \sigma_\varepsilon = 1.2 \tag{20}$$

In solving the numerical model, uniform axial velocity, temperature, turbulent intensity, and hydraulic diameter were given at the inlet of the duct. Turbulent intensity is as follows;

$$I = 0.16 Re_D^{-1/8} \tag{21}$$

Because of the uniform axial velocity at the inlet, 3 m length was chosen to obtain the hydrodynamically and thermally fully developed flow. Inlet temperature was 300 K, and outlet pressure was atmospheric pressure condition. The heat flux from wall was 20 kW/m², and no-slip condition was applied for nanofluid flow.

Numerical simulations were performed for the CuO-water nanofluids in the turbulent regime with the Reynolds numbers ranging from 10^4 to 10^5. Furthermore, simulations were carried out for different nanoparticle volume concentrations (0-4%).

3. NUMERICAL COMPUTATION

In the analysis, commercial CFD software Ansys 17.0 was used. This software uses the finite-volume method to perform numerical calculations by solving governing equations along with the boundary conditions. The convection terms in continuity, momentum, and energy equations were discretized using second order upwind scheme. For discretization of pressure the standard scheme was used, and for pressure-velocity coupling SIMPLE algorithm was used. Least square cell based method was applied for the discretization of the equations. For convergence, iterations were continued until the residuals reached 10^{-6}. As shown in Figure 1, hexahedral mesh was used for the square cross-section duct, and mesh intensity was increased near the wall to enhance the accuracy and to simulate better thermal convection and flow in the viscous layer, so y+ was maintained below 1.
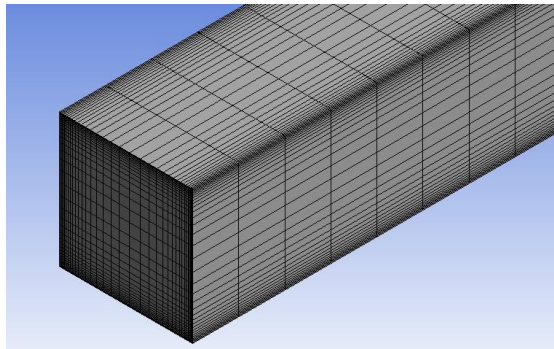
Figure 1. Mesh distribution of the computational domain.

Essential factor that affects the accuracy of results is quality and cell number of mesh. Poor quality mesh or smaller mesh number causes to decrease accuracy of results, while higher mesh number increases computational time. Therefore mesh study is very crucial to reach reasonable accuracy of results within reasonable computational time.

As seen in Figure 2, while mesh number increases, Nusselt number and Darcy friction factor repeat themselves after the specific mesh number. After a certain value, error rate decreases, but increasing mesh number can significantly increase computational time. Therefore Case Study 8 with 2.890.000 mesh number has been used as a base for other analyses that are going to be performed.

(a)   *(b)*
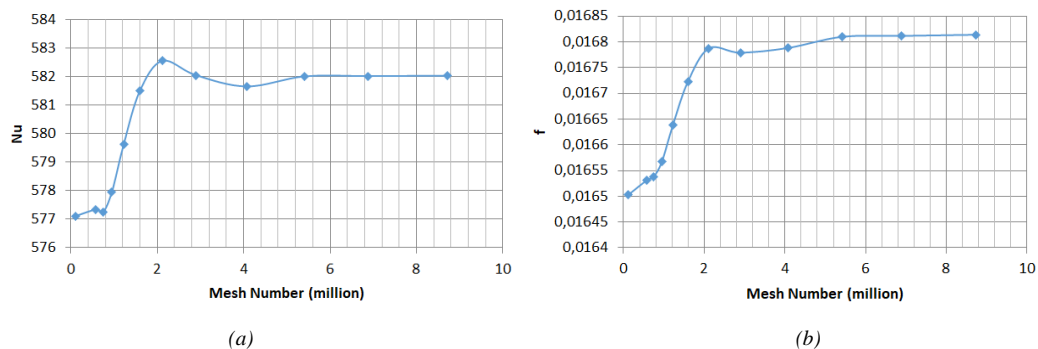
Figure 2. Variation of Nusselt number (a) and Darcy friction factor (b) with mesh number

After determining the optimum mesh number, k-ε turbulence models have been compared with well-known correlations of Gnielinski, Sieder-Tate, Dittus-Boelter, and Blausius correlations [9]. It can be seen in the Figure 3 that the Standard *k-ε* turbulence model is the most suitable model for this study.
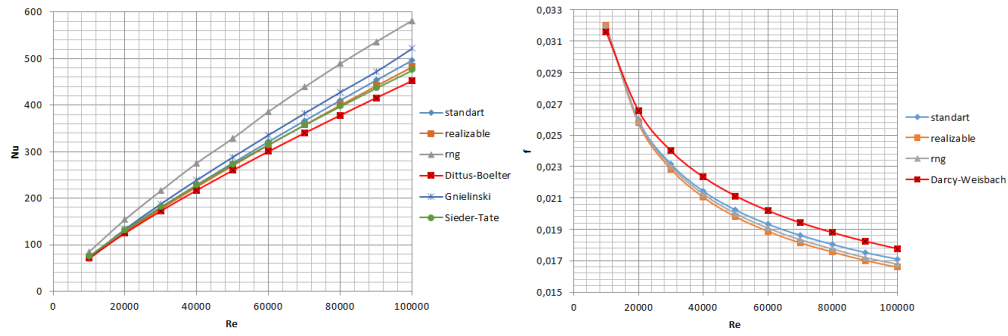
Figure 3. Variation of Nusselt number (a) and Darcy friction factor (b)
for different turbulence models and comparison with literature

4. RESULTS

Variation of convective heat transfer coefficient with Reynolds number for different nanofluid volume concentrations are given in Figure 4. Increasing nanofluid volume concentration increases the convective heat transfer coefficient and also the rate of convective heat transfer inside the duct. Furthermore; highest increase of convective heat transfer occurs on lowest Reynolds numbers.
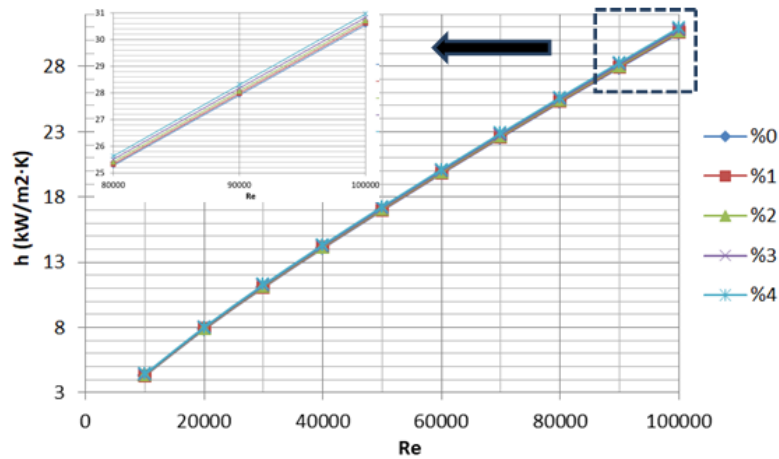
Figure 4. Variation of convective heat transfer coefficient according to Reynolds number for different nanofluid volume concentrations.

h_{nf}/h_{bf} ratio for different nanofluid volume concentrations can be seen in Table 2. h_{nf}/h_{bf} ratio is important factor on determining the performance of nanofluid.

Table 2. Calculated h_{nf}/h_{bf} ratio for different nanofluid volume concentrations.

Re/φ%	0	1	2	3	4
10000	1	1,006	1,012	1,019	1,027
20000	1	1,004	1,009	1,014	1,021
30000	1	1,003	1,008	1,013	1,019
40000	1	1,003	1,007	1,012	1,017
50000	1	1,003	1,006	1,011	1,016
60000	1	1,003	1,006	1,010	1,015
70000	1	1,002	1,006	1,010	1,015
80000	1	1,002	1,005	1,009	1,014
90000	1	1,002	1,005	1,009	1,014
100000	1	1,002	1,005	1,009	1,014
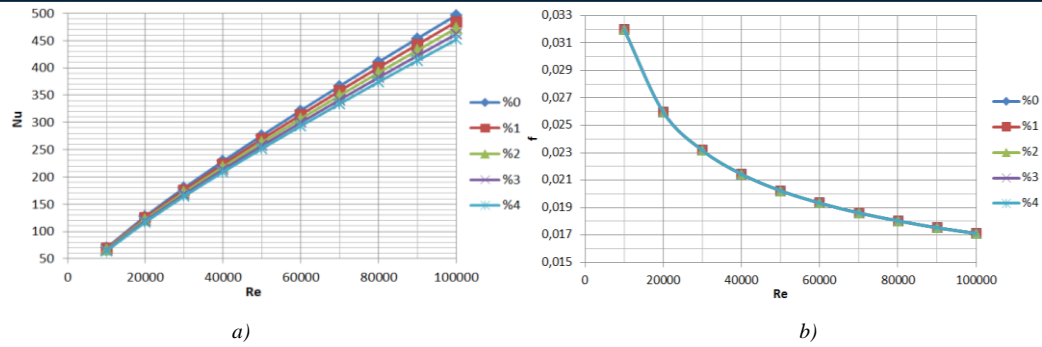
*Figure 5. Change of Nusselt number (**a**) and change of friction factor (**b**) according to Reynolds number at different nanofluid volume concentrations.*

For all volume concentrations Nusselt number increases with increasing Reynolds number. Nusselt number decreases with increasing nanofluid volume concentration for fixed Reynolds numbers. For turbulent regime forced heat transfer studies, the turbulence and vortices have more determinative role in heat transfer mechanism than diffusion mechanism. Thus increment of the nanofluid volume concentration has no increasing effect on Nusselt number, despite it causes increased thermal conductivity.

On the other hand the friction factor decreases with increasing Reynolds number. The boundary layer thickness decreases by increasing Reynolds number, so frictional effects and friction factor decrease too. Friction factor increases with increasing volume concentration, because increasing volume concentration also increases viscosity. To put in a nutshell increasing nanofluid volume concentration has barely effect on friction factor, so much more convective heat transfer values can be reached without further power input. These results are in common with the results Aghaei et al.[16]. They also realized in their numerical study that increasing nanofluid volume concentration causes to reduce in the Nusselt number [16].

As can be seen in Figure 6, the present numerical analyses were compared with correlations obtained from experimental data of Pak and Cho [17] and Maiga and Nguyen et al. [18]. It can be obtained that the deviation of Maiga et al. [18] correlation from the present study is bigger than the deviation of Pak and Cho's [17] correlation.

5. CONCLUSION

In this present study, steady state turbulent forced convection of water-CuO nanofluid inside a square cross-section duct was numerically researched by means of finite volume method. Single phase, constant thermophysical properties were taken into account. Results showed that useful contribution to the convective heat transfer provided by addition of CuO nanoparticles into the pure water comparing the case with just the base fluid. Heat transfer increased with increasing nanofluid volume concentration and Reynolds number.
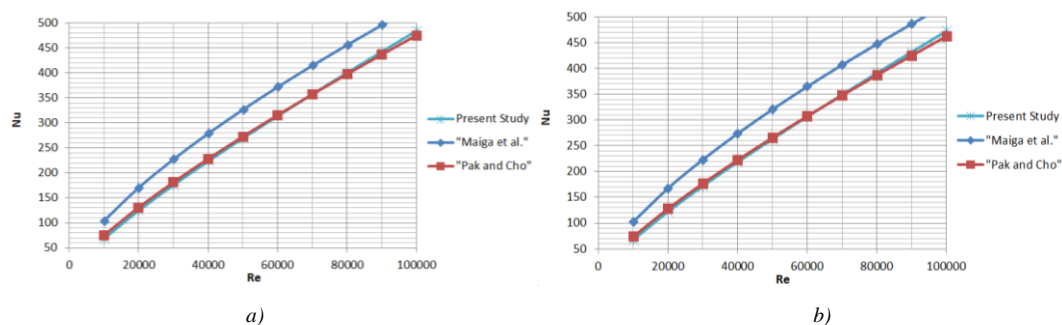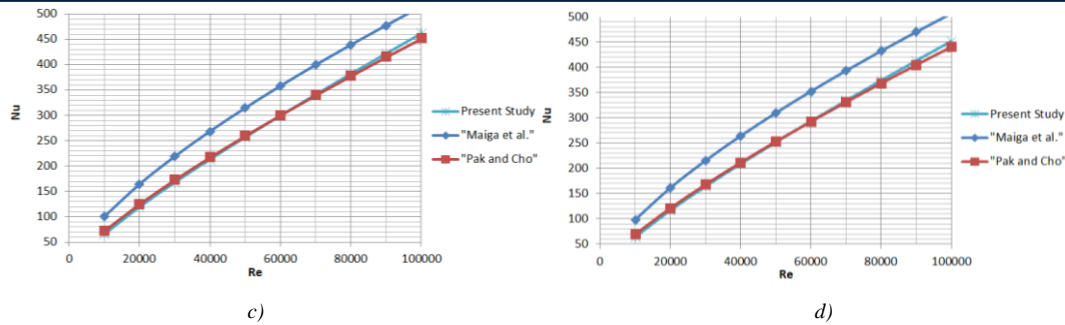
Figure 6. Change of Nusselt number according to Reynolds number for different nanofluid volume concentrations: **(a)** 1.0%, **(b)** 2.0%, **(c)** 3.0%, **(d)** 4.0%.

REFERENCES

[1]. M'Hamed, B., Sidik, N. A. C., Yazid, M. N. A. D. M., Mamat, R., Najafi, G., Kefayati, G. H. R., A review on why researchers apply external magnetic field on nanofluids, International Communications in Heat and Mass Transfer, Vol 78, pp 60-67, 2016.

[2]. Buongiorno, J., Hu, W., "Nanofluid Coolants for Advanced Nuclear Power Plants," Proceedings of ICAPP'05, Seoul, pp. 15-19,2005.

[3]. Goktepe, S., Atalık, K., Ertürk, H., Comparison of Single and Two-Phase Models for Nanofluid Convection at the Entrance of a Uniformly Heated Tube, International Journal of Thermal Sciences, Vol 80, pp. 83-92, 2014.

[4]. Arslan, K., Three-Dimensional Numerical Investigation of Turbulent Flow And Heat Transfer Inside a Horizontal Semi-Circular Cross-Sectioned Duct, Thermal Science, Vol 18, No 4, pp. 1145-1158, 2014.

[5]. Kaya, O., Numerical Study of Turbulent Flow and Heat Transfer of Al_2O_3-Water Mixture in a Square Duct with Uniform Heat Flux, Heat and Mass Transfer, Vol 49, No 11, pp.1549-1563, 2013.

[6]. Mokmeli, A., Saffar-Avval, M., Prediction of Nanofluid Convective Heat Transfer Using the Dispersion Model, International Journal of Thermal Sciences, Vol 49, pp. 471-478, 2010.

[7]. Saghir, M. Z., Ahadi, A., Yousefi, T., Farahbakhsh, B., Two-Phase and Single Phase Models of Flow of Nanofluid in a Square Cavity: Comparison with Experimental Results, International Journal of Thermal Sciences, Vol 100, pp. 372-380, 2016.

[8]. Esmaeilnejad, A., Aminfar, H., Neistanak, M. S., Numerical Investigation of Forced Convection Heat Transfer Through Microchannels with Non-Newtonian Nanofluids, International Journal of Thermal Sciences, Vol 75, pp. 76-86, 2014.

[9]. Incropera, Frank P., DeWitt, David P., Fundamentals of Heat and Mass Transfer (6th ed.). Hoboken: Wiley, 2007.

[10]. Brinkman, H.C., The Viscosity of Concentrated Suspensions and Solutions, J. Chem. Phys., Vol. 20, No. 4, pp. 571, 1952.

[11]. Maxwell, J. C., A Treatise on Electricity And Magnetism. UK: Clarendon, 1973.

[12]. Fluent Theory Guide, Ansys Fluent Inc.

[13]. Tekir, M., Gedik, E., Arcaklıoglu, E., Calapkulu, M., Kasap, C., CFD Analyses of a Two-Stage Natural Gas Pressure Regulator, Mugla Journal of Science and Technology, Vol. 2, No. 1, pp. 14-19, 2016.

[14]. Lide David, Frederikse HPR, editors, CRC Handbook of Chemistry and Physics.Cleveland, Ohio: CRC Press; 1978.

[15]. Zhu, H. T., Zhang, C. Y., Tang, Y. M., Wang, J. X., Novel Synthesis and Thermal Conductivity of CuO Nanofluid, The Journal of Physical Chemistry C, Vol. 111, pp. 1646-1650, 2007.

[16]. Aghaei, A., Sheikhzahed, G. A., Dastmalchi, M., Forozande, H., Numerical Investigation of Turbulent Forced-Convective Heat Transfer of Al2O3–Water Nanofluid with Variable Properties in Tube, Ain Shams Engineering Journal Vol. 6, pp. 577–585, 2015.

[17]. Pak, B. C., Cho, Y. I., Hydrodynamic and Heat Transfer Study of Dispersed Fluids with Submicron Metallic Oxide Particles, Experimental Heat Transfer, Vol. 11, 151–170, 1998.

[18]. Maiga, S. B., Nguyen, C. T., Galanis, N., Roy, G., Mare, T., Coqueux, M., Heat Transfer Enhancement in Turbulent Tube Flow Using Al2O3 Nanoparticle Suspension, International Journal of Numerical Methods for Heat & Fluid Flow, Vol. 16, pp. 275–292, 2006.

Households' Fuel Consumption Effects on Climate Change Problem in Turkey

Ali CAN[1]

Abstract

The climate system of earth is changing due to high portion anthropogenic greenhouse gases (GHG) emissions from many sources. The sources can be categorized as: energy, industries, solvent and other product use, agriculture and waste. All these sources are continuously emitting emissions and pollute the atmosphere. Approximately 80% of GHG emission is originated from energy consumption. The economy is always showing parallel behavior with energy consumption. Human well-being is also explained by high portion efficient energy usage. Energy is needed for heating, processing, transporting, constructing and so on. Therefore, the energy effects on climate change are unavoidable. The consumption of fuels in households for heating purposes is also emitting considerable GHGs emissions to the atmosphere. In the consideration of climate change problems, households are one of the main sources that affect the atmosphere.

Turkey has started to work on National emission inventories after the ratification of United Nations Framework Convention on Climate Change (UNFCCC) in 2004 and improved the studies on climate change after the ratification of Kyoto Protocol (KP) in 2009. The effect of climate change in Turkey is an important subject after being Annex I country to the protocol. Although Turkey has not any obligation for the protocol, Turkey has to deal with emission sources and try to decrease their emission levels for national purposes.

In this study, the main aim is to determine the direct GHGs emissions from provincial households' fuel consumption and to conclude their effect on climate change. For local studies, these kinds of studies are very valuable and helping local authorities to tackle with this important problem.

The highest CO_2 equivalent direct GHGs emission decreasing between 2007 and 2015 is observed in capital city of Turkey with a value of 0.24 million tones. Ankara is followed with Sivas, İzmir, Konya, Balıkesir, Kayseri, Manisa and İstanbul with respective annual values of 0.134, 0.127, 0.123, 0.120, 0.114, 0.113 and 0.10 million tones. The only direct GHGs emission increase is observed in Urfa and Antalya with 0.001 and 0.011 CO_2 equu. million tonnes due to the high population increase rate 27% and 30% respectively and regional fuel consumption characteristic. The consumption of the fuels in households totaly emits 0.59 million tonnes CH_4 and 597 tonnes N_2O in 2015. The highest portion of households' CH_4 and N_2O are emitted from İstanbul, İzmir and Ankara provinces. Throughout the years, approximately 36% of CH_4 emission and 40% of N_2O emission are created by these three provinces.

The total tones of oil equivalent (TOE) are not changing. However the coal usage in the households is shifted to the natural gas and the usage of the natural gas is considerable decreasing the household's GHGs emission in Turkey provinces.

Keywords: *GHG Emissions, Ipcc Methods, Co_2 Equivalent, Co_2, Ch_4 And N_2o Emission*

1. INTRODUCTION

The climate change studies have shown that the GHGs are emitted continuously by human beings and it will not stop due to some economical considerations of countries. However, the Paris Agreement builds upon the Convention and brings all nations into a common cause to undertake ambitious efforts to combat climate change and adapt to its effects, with enhanced support to assist developing countries to tackle with this problem [15]. If the countries do not find a solution for this ambitious problem, the future of earth is giving a signal not to reverse these severe impacts [10]. The effect of climate change is felt tremendously: average temperature is increasing, precipitation patterns in different regions of the earth are changing, arctic ice is melting, sea level is rising, flora and fauna diversity is decreasing.

---

[1]*Corresponding author: Karabuk University, Engineering Faculty, Mechanical Engineering Department, Balıklar Kayası Mevkii, Karabük, 78100, Turkey. alican@karabuk.edu.tr*

Extensive studies on residential energy consumption have been carried out and the GHGs related to this consumption are forcing to improve low carbon emissions with application of new technologies and equipments. The total number of households is increasing; however total energy consumption is decreasing. The increase the portion of renewable energy consumption and increase in energy efficiency in the households are the solutions for the mitigation of climate change affects in residents. Moreover, the coal consumption has also decreased in the households. The usage of clean energy such as Natural Gases was increased in the earth [4].

Countries are struggling with climate change problem. But, there are many uncertainties in the problem definitions, mostly created by unpredictable risks. The best description is made with national GHGs emission inventories and their concentrations in the atmosphere. The emission source description and source data collection is very sensitive for the accurate emission estimation. And it is the best way to show the mitigation progress. Households have to provide a strong encouragement to manage these risks. Maybe household is not a highest portion emission sources. However, its indirect responsive affect in mitigation scenarios cannot be ignored [10]. In some European countries, the household's consume considerable primary energy and depending on this consumption, the households significant contribution, around 30%, to the CO_2 equivalent emission to the atmosphere. The (European Union) EU has ambitious goals related to the increase in energy efficiency in buildings including households to tackle with climate change problems [2], [3].

The Kyoto Protocol, signed in 1997, set out emission reduction commitments for annex I Parties that had ratified the UNFCCC at the time of negotiating the Kyoto Protocol (i.e. all except Turkey). The first commitment period ran from 2008-12 and the second commitment period runs from 2013-20. Commitments under the Kyoto Protocol are expressed in the form of emission budgets over a period. Countries can meet their commitments by reducing GHG emissions domestically [11].

Turkey has started to work on National emission inventories after the ratification of United Nations Framework Convention on Climate Change (UNFCCC) in 2004 and improved the studies on climate change after the ratification of Kyoto Protocol (KP) in 2009. The effect of climate change in Turkey is an important subject after being Annex I country to the protocol. Although Turkey has not any obligation for the protocol, Turkey has to deal with emission sources and try to decrease their emission levels for national purposes [13].

The main purpose of this study was to investigate the effect of provincial households' GHGs emissions in Turkey. The CO_2, CH_4 and N_2O emissions were calculated due to household's fuel consumption data by using the IPCC-Tier 1 method [6], [7]. The province basis data was calculated according to the population census. The mid-year population value and total number of households was used for estimating household base GHGs emissions for the period 2007-2015. And energy consumption data were estimated according to the Common Reporting Tables of Turkey's Emission Inventory on UNFCCC web page [16] and energy balance tables of Ministry of Energy and Natural Resource [9].

2. METHODOLOGY

The main source of GHGs emission from households is considered as the fuel consumption for heating purposes. For that reason, the results of TurkStat survey "Energy Consumption in Residence" in selected provinces in 7 regions are used [12]. The household heating purposes fuel consumption characteristic and the regional households' fuel used factors were main approaches to determine the total consumption of fuels in each province's households as explained in a study by Can [1].

The approach is bottom-up approaches and the final results have to be adjusted according to the energy balance tables. The household behavior, meteorological condition, severe winter and regional fuel consumption are affecting emission calculations. As seen in Figure 1, Turkstat National Emission Inventory (EI) results are calculated according to the total household's fuel consumption and methodology is IPCC approaches. However, the results are not province basis. In our study, the province base emission is calculated and then according to the Figure 2, total GHGs emission is corrected in province basis.

1152
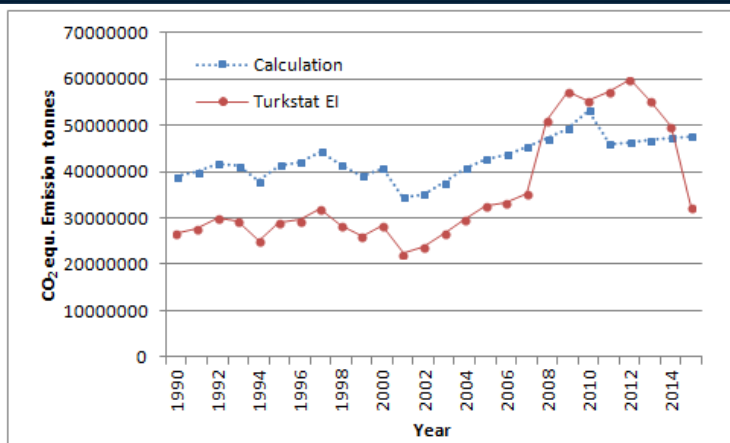
Figure 1. Consideration of household CO_2 equivalent emissions calculations with Turkstat EI
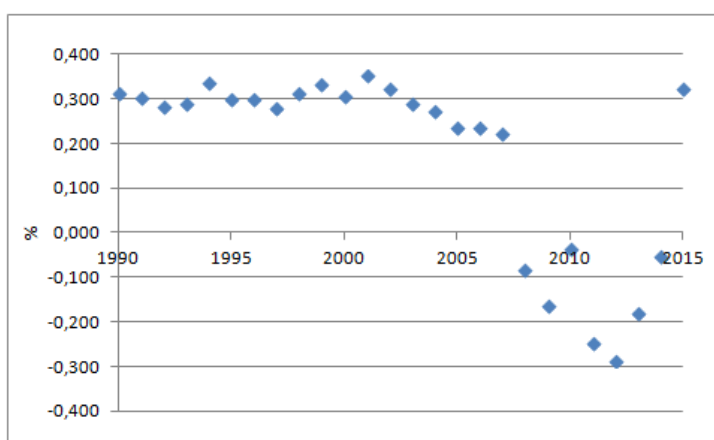
Figure 2. Annual correction factors due to TOE values of Energy Balance tables

In calculating the CO_2, CH_4 and N_2O emissions, the (IPCC - Tier 1) methodology was used as given in the below formulas (1), (2). The general formula (1) for the CO_2 emission is given as [6], [7].

$$CO_2 \; Emiss. = \sum(U_n + I_n - HI_n - IB \pm SC) * EF * CF * E * C\text{-}CO_2 \qquad (1)$$

U_n	: The fuel production quantity
I_n	: Imported fuel quantity
HI_n	: Exported fuel quantity
IB	: International Bunkers
SC	: Stock changes
CF	: Conversion Factor
N	: Fuel type
EF	: Emission Factor (IPCC value)
E	: Efficiency (99%)
$C\text{-}CO_2$	: Carbon to CO_2 emission

And the general formula (2) for the CH_4 and N_2O emissions is given by IPCC Guidelines [6], [7].

$$\textbf{Non-}CO_2 \; \textbf{Emiss.} = \sum(U_n + I_n - HI_n - IB \pm SC) * EF * CF \qquad (2)$$

For the GHGs emission calculations, the following steps are considered: The energy units are converted into Net Calorific Values (NCV) and the fuel data consumption of household in provinces are estimated according to the Can [1] studies.

The other necessary data (TOE values and energy balance tables are gathered from Ministry of Energy and Natural Resources (Figure 3), the fuel used data, source emissions, Country Specific Emission Factors (EF) and Implied Emission factors (IEF) are gathered from CRF tables given on UNFCCC web page [16], households number and mid-year population are gathered from TurkStat web page [14].
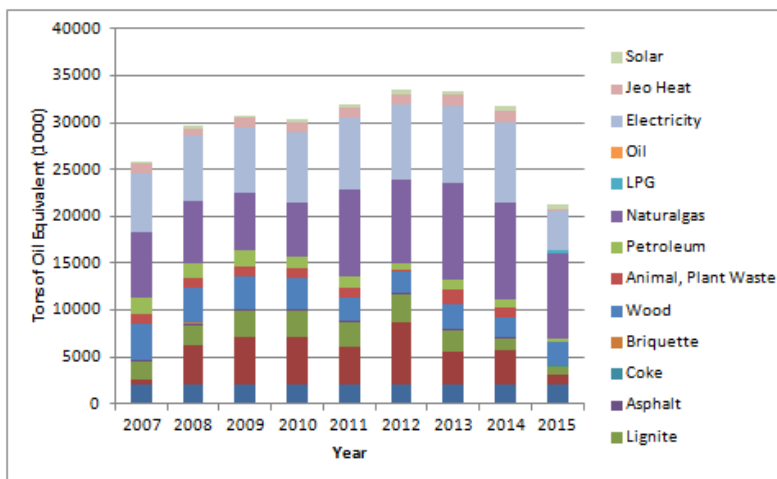
Figure 3. Household fuel consumptions for the years 2007-2015.

After calculating province base GHGs emission data, the results are represented by Geographic Information System (GIS) techniques [8]. For the consideration, the CH_4 and N_2O are converted to CO_2 equivalent emissions. The CH_4 is multiplied by 21 and N_2O is multiplied by 310 and the obtained global warming potential values of direct GHGs are gathered to reach CO_2 equivalent emissions [5]

3. RESULTS AND DISCUSSION

The results of this study have shown that the usage of the natural gas is considerable decreasing the household's GHGs emission in Turkey provinces. The coal usage in households is decreased and the total tone of oil equivalent (TOE) is not changing considerably until year 2015. But in this year, just related to air temperatures, the consumption of fuels is decreased to 19.1 million TOE energy. Related to this consumption, the provincial GHGs emission was also decreased to the 32.2 million tones CO_2 equivalent emission from household heating purposes fuel consumption. This value is similar to the TurkStat National EI value.
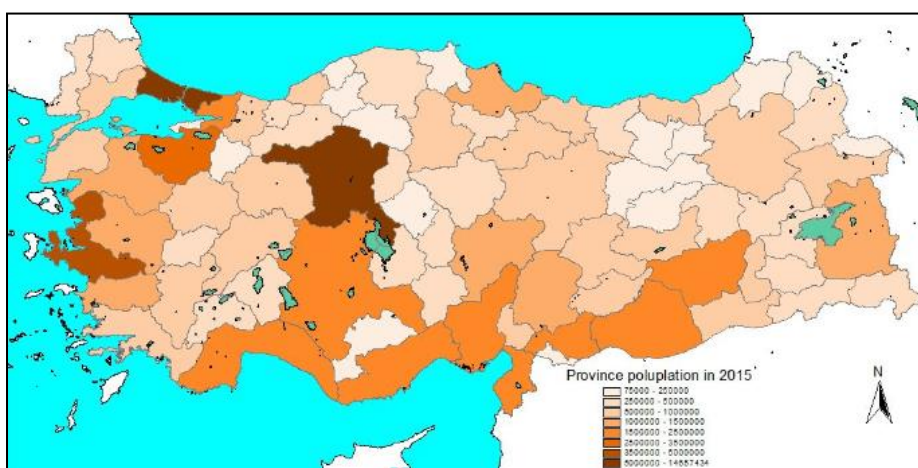
Figure 4. Midyear population of provinces in 2015
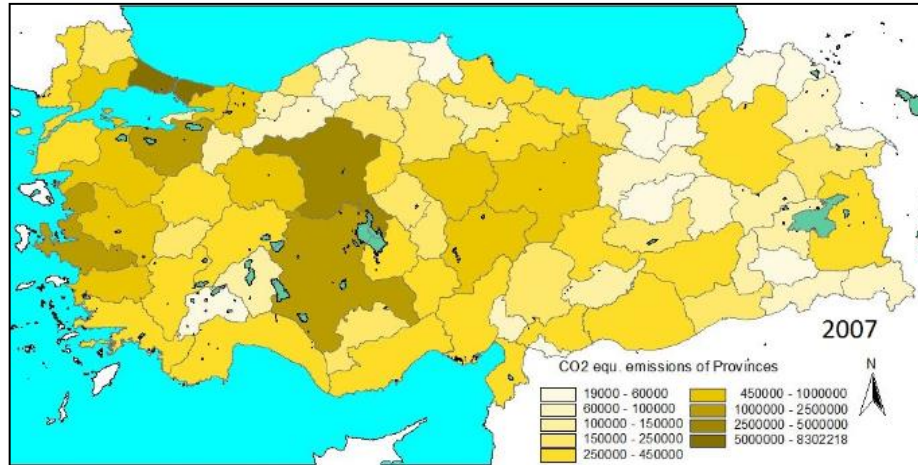
Figure 5. CO_2 egu. emission of provinces in 2015 in unit tonnes
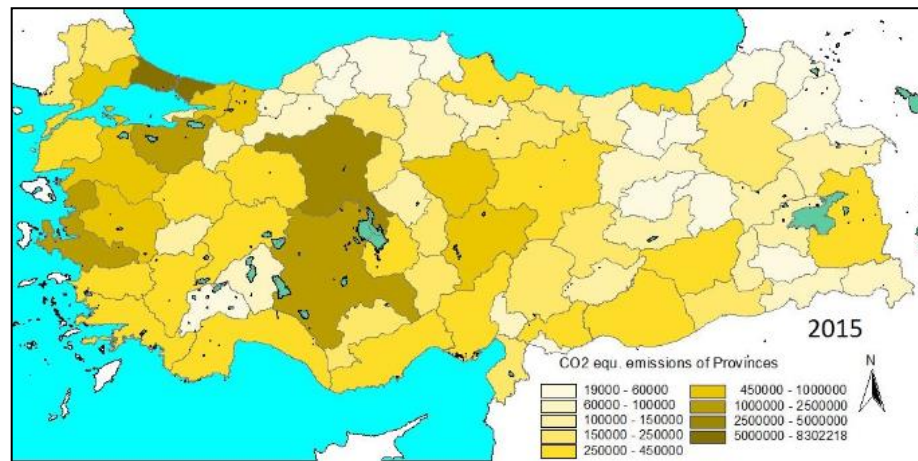
Figure 6. CO_2 egu. emission of provinces in 2015 in unit tonnes

The provincial GHGs emission is partially depending on provincial population (See Figure 4). However, the regional fuel consumption ratio is also effective for the final estimation of GHGs emissions. The climate and meteorological aspects are also affecting final fuel usage in the provinces. The annual emissions in provinces are considerably changing as seen in figure 5 and Figure 6. According to the figure 5 and Figure 6, the highest CO_2 equivalent direct GHGs emission decreasing between 2007 and 2015 is observed in capital city of Turkey with a value of 0.24 million tones. Ankara is followed with Sivas, İzmir, Konya, Balıkesir, Kayseri, Manisa and İstanbul with respective values of 0.134, 0.127, 0.123, 0.120, 0.114, 0.113 and 0.10 million tones.

The only direct GHGs emission increase is observed in Urfa and Antalya with 0.001 and 0.011 CO_2 equ. million tonnes due to the high population increase rate 27% and 30% respectively and due to the regional fuel consumption characteristic. The detail differences are also given in figure 7. As seen in figure, the direct GHGs emission was decreasing considerably in most of the provinces of Turkey. Therefore, the total CO_2 equ. emission is decreased from 48 to 32 million tonnes.
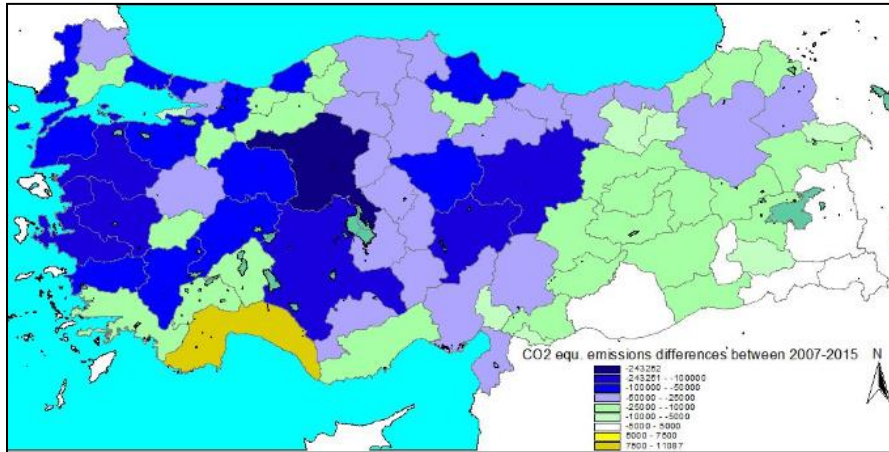
Figure 7. CO_2 egu. emission differences between 2007 and 2015 in units tonnes

Figure 8. CH_4 emission in 2015 in units tones

Figure 9. N_2O emission in 2015 in units tones

The consumption of the fuels in households totaly emits 0.59 million tonnes CH_4 and 597 tonnes N_2O in 2015. The highest portion of CH_4 and N_2O are emitted from İstanbul, İzmir and Ankara provinces. Throughout the years, approximately 36% of CH_4 emission and 40% of N_2O emission are created by these three provinces.

4. CONCLUSION

The study has shown that the usage of the natural gas is considerable decreasing the household's GHGs emission to the 32.2 million tones CO_2 equivalent value in 2015. The regional fuel consumption ratio is

highly affected by population, number of households and meteorological aspects of provinces. The emissions in some provinces are considerably changing. The highest CO_2 equivalent direct GHGs emission decreasing between 2007 and 2015 is observed in capital city of Turkey with a value of 0.24 million tones. Ankara is followed with Sivas, İzmir, Konya, Balıkesir, Kayseri, Manisa and İstanbul with respective values of 0.134, 0.127, 0.123, 0.120, 0.114, 0.113 and 0.10 million tones. The consumption of the fuels in households totaly emits 30.77 million tones CO_2, 0.59 million tonnes CH_4 and 597 tonnes N_2O in 2015. For this year, the CO_2 equ. emission value is around 32.2 million tones. However, this value is decreased with 8.8% with changing characteristic of fuel consumption in households between study periods. The natural gases is important fuel for climate change mitigation purposes.

ACKNOWLEDGeMENT

REFERENCES

[1]. Can A., 2006. **Investigation of Turkey's Carbon Dioxide Problem by Numerical Modeling**. (Ph.D.Thesis) – METU.

[2]. **Directive 2010/31/EU of the European Parliament and of the Council of 19, May 2010 on the energy performance of buildings** [Online]. Available: http://www.buildup.eu/en/practices/publications/directive-201031eu-energy-performance-buildings-recast-19-may-2010 date: 12.03.2017.

[3]. **Directive 2012/27/EU of the European Parliament and of the Council of 25 October 2012 on energy efficiency** [Online]. Available: http://www.buildup.eu/en/practices/publications/directive-201227eu-european-parliament-and-council-25-october-2012-energy date: 12.03.2017.

[4]. EIA, 2016. **Residential Energy Consumption Survey** (RECS). Energy Information Agency, U.S. [Online]. Available: https://www.eia.gov/consumption/residential/ date: 16.12.2016.

[5]. IPCC 1995. **Summary for Policymakers and Technical Summary of the Working Group I Report** - A report of the Intergovernmental Panel on Climate Change. P.22.

[6]. IPCC 1996. Greenhouse Gas Inventory Reference Manual – **Revised 1996 IPCC Guidelines for National Greenhouse Gas Inventories** – Volume 3 – Intergovernmental Panel on Climate Change – Edited by Houghton J.T., et al. 1996.

[7]. IPCC 2006. Greenhouse Gas Inventory Reference Manual – **IPCC Guidelines for National Greenhouse Gas Inventories** - Intergovernmental Panel on Climate Change, 2006.

[8]. Martin D. 1996; Geographic Information Systems – Second Edition – Socio economic applications.p.71-161.

[9]. MENR - **The annual Energy and Petroleum Balance Sheets 1970-2015**, Ministry of Energy and Natural Resources, 2015.

[10]. OECD, 2015. **Climate Change Risks and Adaptation**: Linking Policy and Economic, OECD Publishing, Paris. p.13-35.

[11]. OECD 2015, **Climate Change Mitigation: Policies and Progress**, OECD Publishing, Paris. p.17-53.

[12]. SIS - Energy Consumption in Residence – State Institute of Statistics-Prime Ministry Republic of Turkey.p.56-57, 99-109., 1998.

[13]. TurkStat, **National Greenhouse Gas Inventory Report, 1990-2015**. Annual Report submission under the "Framework Convention on Climate Change, 2015.

[14]. TurkStat, **Adress based population registration system results**. [Online]. Available: https://biruni.tuik.gov.tr/medas/?kn=95&locale=en date:18.12.2016

[15]. UNFFFC, 2016. The UNFCCC website, **Paris Agreement Essential Elements**. [Online]. Available: http://unfccc.int/paris_agreement/items/9485.php date: 18.12.2016.

[16]. UNFCCC, 2017. 2017The UNFCCC website, **National Inventory Submissions**. [Online]. Available: http://unfccc.int/national_reports/annex_i_ghg_inventories/national_inventories_submissions/items/10116.php. date: 20.04.2017.

Determination of Carbon Footprint for Fuels Used for Domestic Heating in Denizli, Turkey

Sibel Cukurluoglu[1]

Abstract

Carbon footprint is a measure of the environmental impact of human activities in terms of the amount of greenhouse gas produced, measured in units of carbon dioxide. Carbon dioxide is among the greenhouse gases that cause global warming. The greenhouse gas, which has the largest share among greenhouse gases, is carbon dioxide. Carbon dioxide is formed during the use of fossil fuels. Therefore fossil fuel type and usage amount are important. In this study, the amounts of carbon dioxide per person and carbon footprints were calculated by taking into account the parameters of natural gas and coal used for domestic heating and personal consumption habits in 2010-2014 period in Denizli province center, Turkey. It has been determined that the amount of carbon dioxide per person sourcing from the use of coal is higher than the amount of carbon dioxide per person originating from the use of natural gas. Although the amount of personal carbon footprint in Denizli is lower than the average in Turkey, it is seen that there is a very high amount of carbon footprint in the world target.

Keywords: *Carbon footprint, carbon dioxide, fossil fuel, global warming, greenhouse gas.*

1. INTRODUCTION

First of all, the increase of the consumption of developed countries and all other societies is at the risk of the future of natural ecosystems and ecological life cycle. Every product produced leaves traces of ecological life in the process from raw material extraction to processing, processing and conversion to final product in the production band. Work is being done to keep these traces under control and to reduce them. The phrase "footprint" developed by scientists in recent years expresses how much natural resources are used by humans in quantities. The ecological footprint is called the footprint of the people they leave ecological imagination. Ecological footprint measures the ecological assets that a given population requires to produce the natural resources it consumes (including plant-based food and fiber products, livestock and fish products, timber and other forest products, space for urban infrastructure) and to absorb its waste, especially carbon emissions.

The global hectare, the criterion for ecological footprint and biological capacity, refers to the production capacity of 1 hectare of land over average productivity. Thus, the total amount of resources provided from various land types over a certain period of time and the demand for these resources are expressed in numerical form by being converted into a common unit. Biogeographically productive areas, cultivated areas, forests and areas with fish hunting. These areas do not include deserts, glaciers and open ocean [1].

The most important component among ecological footprint components is carbon footprint. Ever since, ecological footprints have increased the continuous rate within its components. Carbon footprint, which is the measure of the natural carbon, is expressed as the amount of carbon dioxide released by an energy-consuming activity.

The gases forming the carbon footprint have a significant share of the greenhouse effect. The release of gases such as methane (CH_4), carbon dioxide (CO_2), hydrochlorofluorocarbons ($HFCF_s$), perfluorocarbons (PFC_s) into the environment increases the amount of carbon in the environment. Among these gases, the largest share of carbon footprints is carbon dioxide [2].

Among greenhouse effect gases, CO_2 has a 50% share in global warming. This is caused by the fact that the CO_2 molecules in the air are 50-100 years old. At the beginning of measures to prevent global warming is to reduce the amount of CO_2 given to the atmosphere [3].

[1] Corresponding author: Pamukkale University, Faculty of Engineering, Department of Environmental Engineering, Denizli, 20070, Turkey. scukurluoglu@pau.edu.tr

Turkey is an ecologically indebted country all over the world because it consumes its consumed resources more rapidly than during the renewal period. One of the major reasons for this biological inactivity is rapid population growth. The ecological footprint of consumption for the first time exceeded the biological capacity in 1974, doubling the biological capacity in 2007. The total ecological footprint of the production exceeded the biological capacity for the first time in 1972 and in 2007 the ecological footprint reached 1.6 times the biological capacity. This suggests that resource consumption in the country is not sustainable at the national level and that imports of biological capacity from other countries are needed [4].

The component which has the biggest share among ecological footprint components in Turkey is carbon footprint with 46%. The electricity sector is the 26% with the largest share of carbon footprint CO_2 emissions. Manufacturing industry and construction is second in the order of 22%. Imports are 16%, transportation is 15%, non-electrical housing and services are 12% and transportation, agriculture and so on. It has been determined that emissions have a share of 8% [5].

Increasing use of fossil fuels, destruction of forests, increase in population and increase in consumption have caused carbon dioxide, methane and nitrous oxide gases to release and accumulate in the atmosphere. Accumulating these gases, radiation from the sun is reflected back to earth by multiplying and causing the earth's temperature to rise. Reducing the carbon footprint is a great way to prevent global warming.

The carbon footprint is divided into two classes as primary and secondary footprints. The primary footprint is a measure of CO_2 emissions from fossil fuel use for energy consumption and transport activities. The secondary footprint is a measure of the CO_2 emissions that occur during the life cycle of the commodities used, from production to consumption.

In this study amounts of the natural gas and coal used in domestic heating were determined and the amount of carbon footprint in Denizli in 2010-2014 was calculated.

2. MATERIALS AND METHODS

Carbon dioxide is the most important gas forming the carbon footprint. Various methods are used to calculate the carbon footprint. Carbon footprints resulting from fuel consumption were calculated using a virtual calculator based on programming. In this calculator, the amount of carbon dioxide and carbon footprint are calculated by inputting basic information such as the type and amount of fuel used for domestic heating, as well as personal habits such as driving status, travel by airplane, and food consumption habits.

2.1. Study Site

This study was carried out to determine the amounts of carbon dioxide and carbon footprints in Denizli, Turkey (Figure 1).

Figure 1. The location of study site Denizli, Turkey

2.2. Fuel Consumption Amounts

The amount of carbon dioxide released to the atmosphere per person and carbon footprints were calculated in the province of Denizli in 2010-2014 depending on the consumption of natural gas and coal used for domestic heating purposes. Natural gas consumption amounts for 2010-2014 were obtained from Enerya Denizli Natural Gas Distribution Corporation. The amounts of coal consumption were provided by the Provincial Directorate of Environment and Urban Planning in Denizli.

The calculation program requires the amount of per person fuel consumption to calculate the carbon dioxide values that a person makes. In order to calculate natural gas and coal consumption amounts per person, natural gas and coal usage rates were related to population. Unit changes related to fuel types have been carried out. Natural gas and coal usage rates for the years 2010-2014 in Denizli province center were shown in Table 1. As of 2010, 30% of the population uses natural gas. In 2014, this ratio has reached 70%. With the widespread use of natural gas, the rate of coal use has decreased.

Table 62. The fuel usage rates by years

Year	Natural Gas Use Rate (%)	Coal Use Rate (%)
2010	30	70
2011	45	55
2012	50	50
2013	60	40
2014	70	30

2.3. Calculation of Carbon Footprints

Amounts of CO_2 originating from the fossil fuels used for domestic heating purposes in Denizli city center as well as the amounts of CO_2 generated by considering the general consumption habits and usage of the people living in the region were determined and carbon footprints were calculated. Carbon footprints, which are based on fuel consumption, were calculated using a virtual calculator based on programming.

3. RESULTS AND DISCUSSION

3.1. Fuel Usage for Domestic Heating in Denizli

Fuel types used in domestic heating in Denizli city center are mostly natural gas and coal. The use of natural gas with domestic heating started in 2006.

In Figure 2, total natural gas consumption amounts used in domestic heating in Denizli since 2010 were given. The amount of natural gas consumption in 2011 is almost double the amount of natural gas consumption in 2010. It is observed that natural gas consumption amounts continue to increase in the following years.
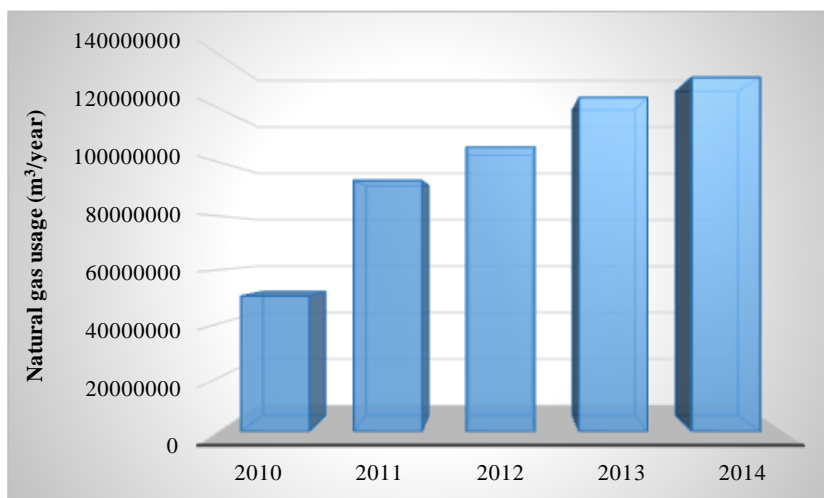
Figure 2. Natural gas consumption amounts in Denizli period of 2010-2014

The consumption of coal used in domestic heating in Denizli showed a tendency to decrease after 2010 due to the increase of natural gas usage (Figure 3).
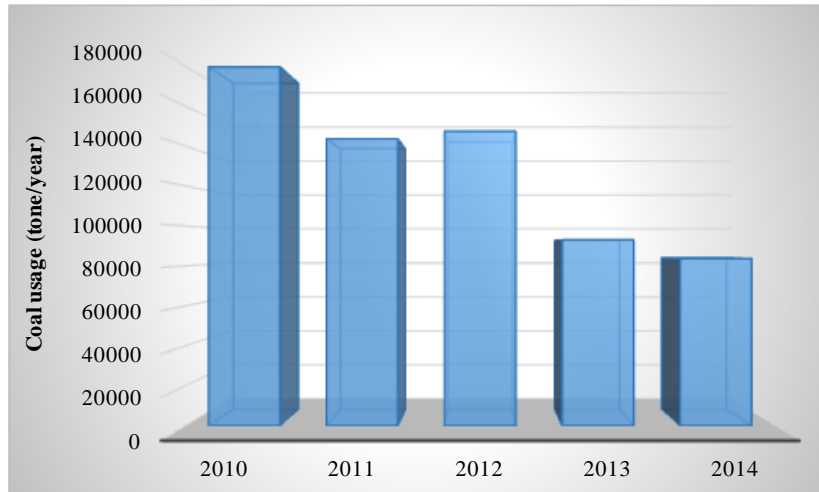
Figure 3. Coal consumption amounts in Denizli period of 2010-2014

Figures 4 and 5 presents the fuel consumption amounts per person used in domestic heating in Denizli for five years period starting from 2010 for natural gas and coal, respectively. It is seen that fuel consumption per person differs according to years. The reasons for the difference can be expressed as changes in fuel usage habits and seasonal changes.
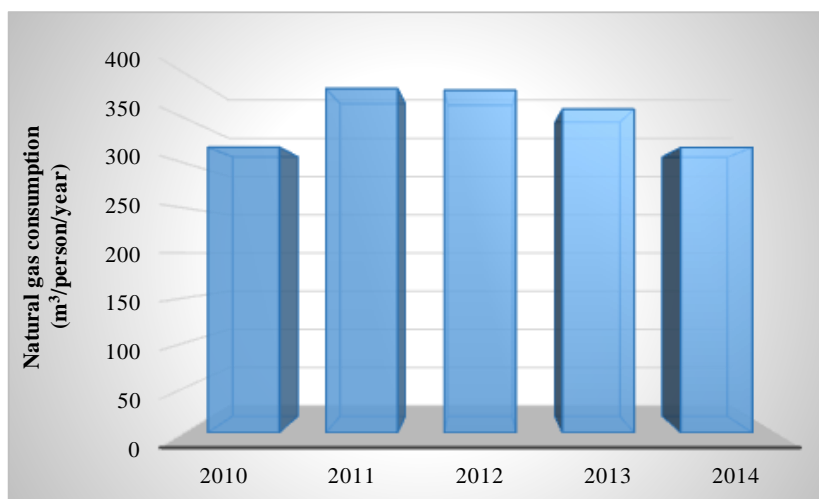
Figure 4. Natural gas consumption amounts per person in Denizli
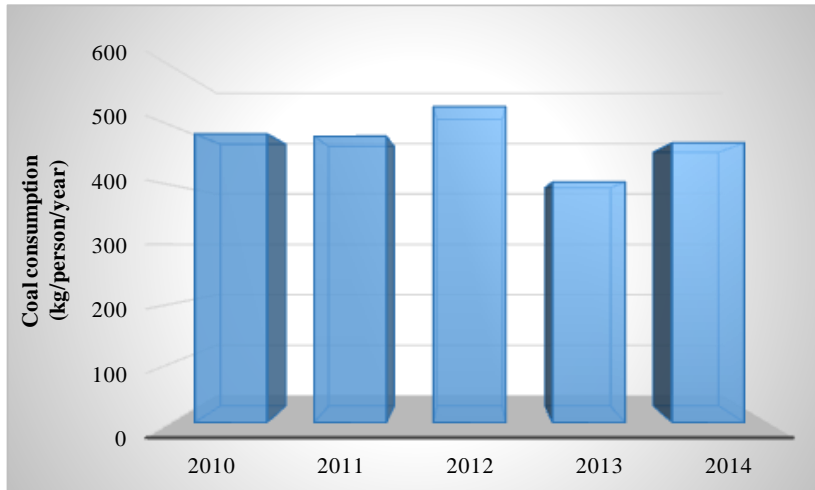
Figure 5. Coal consumption amounts per person in Denizli

3.2. Carbon Dioxide Emissions from Fuel Used for Domestic Heating in Denizli

The amounts of CO_2 per person resulting from the use of natural gas and coal for heating in Denizli during 2010-2014 were given in Figures 6 and Figure 7, respectively. The amount of CO_2 resulting from the use of natural gas per person have begun to decline after 2011.
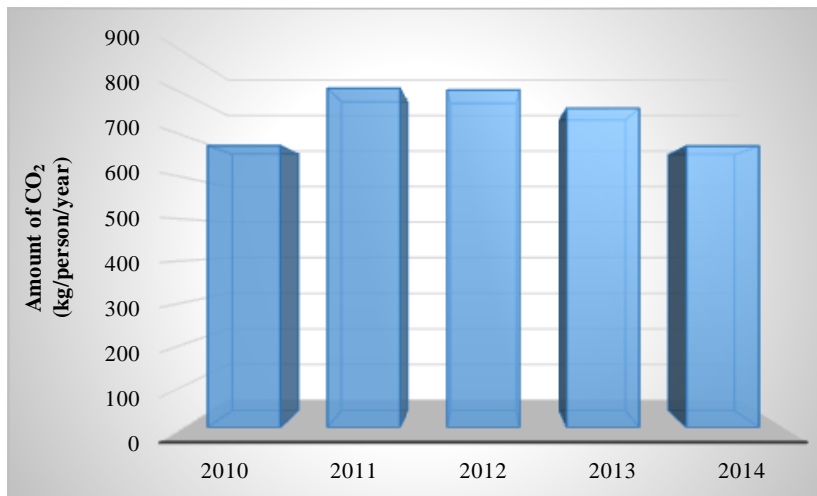
Figure 6. Amount of CO_2 per person resulting from the use of natural gas in Denizli

The amount of CO_2 per person originating from the use of coal varies, and this variability is due to such as different trends in the amount of coal consumption, uncertainties in new areas of natural gas use.
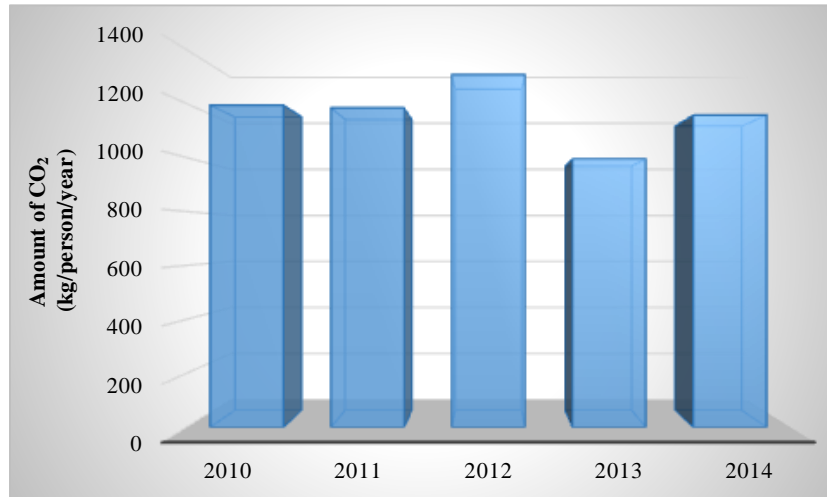
Figure 7. Amount of CO_2 per person resulting from the use of coal in Denizli

In Figure 8, the amounts of CO_2 per person from the use of coal and natural gas for heating purposes in Denizli in 2010-2014 were given. It has been observed that the amount of CO_2 per person resulting from the use of coal is greater than the amount of CO_2 per person resulting from the use of natural gas. It has been determined that in 2010 and 2014, a coal-using person in domestic heating would cause approximately twice as much CO_2 emissions as a natural gas user.
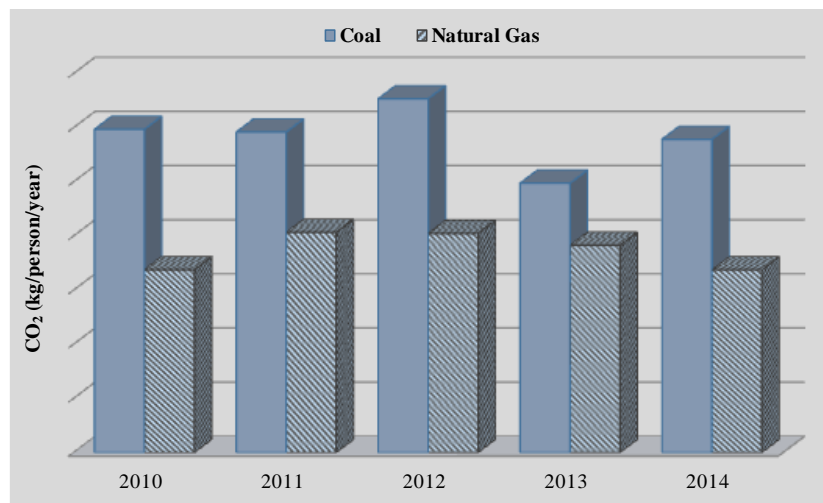
Figure 8. Amounts of CO_2 per person resulting from the use of coal and natural gas in Denizli

Total amount of CO_2 in Denizli in 2010-2014 is shown in Figure 9. Total CO_2 amounts have been determined to increase by 2012 when evaluated on a yearly basis. However, after 2012, the total amount of CO_2 has tended to decrease. As of 2012, there is a decrease in the coal use rate and annual total CO_2 amount.
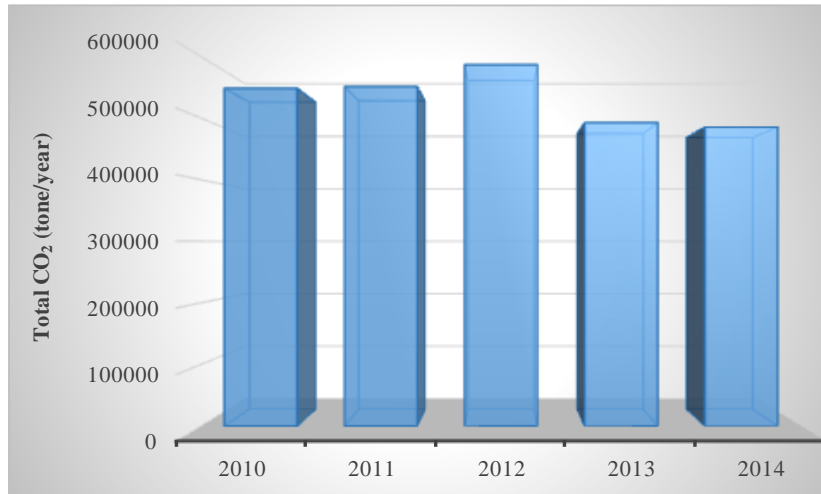
Figure 9. Total CO$_2$ amounts sourced from the use of coal and natural gas in Denizli

3.3. Carbon Footprints in Denizli

Figure 10 shows the individual carbon footprint quantities determined by taking into account the CO$_2$ emission factors related to the use of natural gas for domestic heating purposes in 2010-2014 in Denizli, the Turkey's average and the world target. The individual carbon footprint quantities related to the use of coal in Denizli, the Turkey's average and the world target are shown in Figure 11.

The population using natural gas seems to have less carbon footprint than the population using coal. According to 2010 data, Turkey's carbon footprint averages 4.1 tones. While the amount of carbon footprint of the population using natural gas remained below this average, the amount of carbon footprint for the coal-using population was slightly above the average. It has been determined that the carbon footprint of Denizli in 2010-2014 as a result of the use of natural gas and coal for heating purposes is far from the world target.
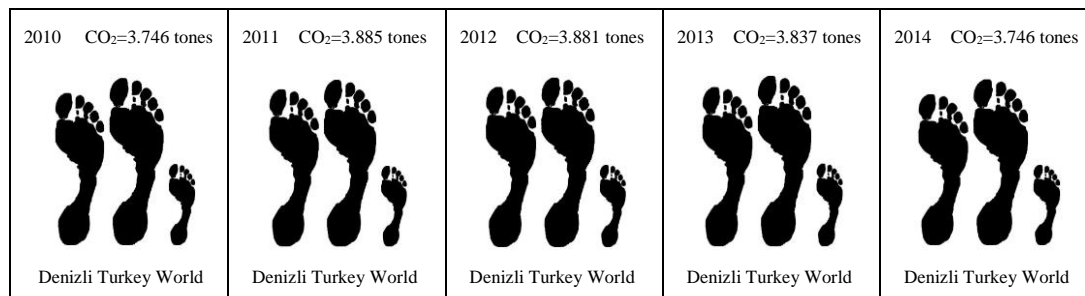
Figure 10. Natural gas based carbon footprint quantities per person in Denizli in 2010-2014
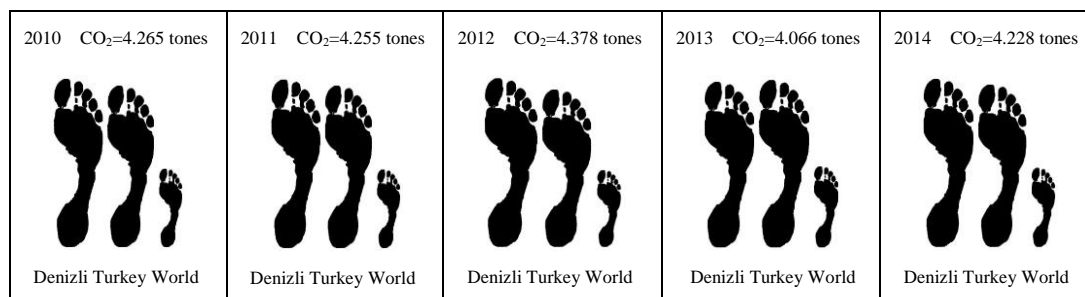
Figure 11. Coal based carbon footprint quantities per person in Denizli in 2010-2014

1164

4. CONCLUSIONS

The amounts of carbon footprints were calculated by taking into account the parameters of natural gas and coal used for domestic heating and personal consumption habits in 2010-2014 in Denizli, Turkey in this study. It has been determined that the carbon footprint of Denizli in 2010-2014 as a result of the use of natural gas and coal for heating purposes is far from the world target.

Natural gas contributes to the reduction of carbon footprint, but it is not possible to bring the carbon footprint closer to the world target, just by disseminating the use of natural gas. In order to reduce the carbon footprint, many measures must be taken such as changing the consumption habits to produce less carbon footprint, choosing alternatives that do not create a carbon footprint in transportation, or using public transportation, and heat insulation of houses to consume less fuel in domestic heating.

REFERENCES

[1]. J. Bowyer, K. Fernholz, J. Howe, and S. Bratkovich, "Comparing the ecological footprints of the U.S. and the E.U.," Dovetail Partners, Inc., Tech. Rep., 2009.
[2]. B. Ozlem, "Determination of carbon footprint in a selected paper fabric," Istanbul Technical University Institute of Science and Technology Environmental Engineering Department, 2013, in Turkish.
[3]. L. Topcu, "The effect of public transportation systems on greenhouse gas emissions," M. Eng. Thesis, Istanbul Technical University Institute of Science and Technology Mechanical Engineering Department, 2008, in Turkish.
[4]. WWF, 2012, Ecological footprint report of Turkey. Available: http://www.wwf.org.tr/?1412.
[5]. C. E. Ozsoy, "Low carbon economy and Turkey's carbon footprint," *HAK-IS International Labor and Society Journal*, vol. 4, 4, 9, 199-215, 2015, in Turkish.

BIOGRAPHY

Sibel Cukurluoglu is an Assistant Professor at Pamukkale University, Faculty of Engineering, Environmental Engineering Department, Denizli, Turkey. Her research interests include air quality management, air pollution control and air quality modelling.

Recommendations for xDSL Technologies and Applications

Esra SOGUT[1],Saadin OYUCU[2], O. Ayhan ERDEM[3], Huseyin POLAT[4]

Abstract

All kinds of data such as audio, video and text are transmitted without errors, quickly and easily in media such as fiber, radio or copper cable. The transmission environments used must be user-supported, highly usable, portable and qualified. DSL (Digital Subscriber Line) technology is used in order to enable users to transmit and process the data quickly and securely on advanced systems and to handle this data, apart from modem technology. DSL technology is examined in this study; xDSL technology is explained in terms of usage areas, distance and speed relationships. DSL varieties called xDSLs are handled separately and compared in terms of data transmission speeds (download / upload), structures (symmetric / asymmetric) and transmission distances. And it is presented in detail. According to the researchers made, it has been suggested which xDSL technology model is more suitable for which application or system. Thus, the advantages of DSL technology for institutions, organizations or individual users are mentioned.

Keywords: *ADSL, DSL Technologies, xDSL, xDSL Applications*

1. INTRODUCTION

Today, usage area of computers and internet is getting bigger. The amount of data that are used and stored is also increasing, and transmitting of these data is becoming a huge problem. It is vital that the data exchange should be fast and error-free. Day by day, the technologies that are used are getting better. Any type of data(voice, image, text, video, etc.) can be created at any time so it is a necessary that transmission medium should be convenient to use, suitable for carrying, multi-user provided, and qualified.

Other than a modem, DSL(Digital Subscriber Line) technology is also using in order to transmit and processing of data fastly and securely. DSL as a technology performs remote connection and transmitting of high dimensional data successfully. In addition, it provides fast, economical, and easy process.

In this study, DSL technology is examined in terms of usage area, distance, and speed relations. Each DSL type (xDSL) is analyzed and compared to the data transmission speed (upload, download), structure (symmetry, asymmetry), and transmission distance. We provide suggestions about which xDSL technology is more convenient to a specific application. Possible benefits that the DSL technology can provide is also mentioned. It is observed that the DSL technology can work with different type of applications integrated and the efficiency can be increased.

2. DSL TECHNOLOGY

DSL has been developed for compressing a large number of data in a fast way across the line. This technology aims to provide faster access for people, higher communication speed, and services for advanced data.

---

[1] Corresponding author: Gazi University, Department of Computer Engineering, Faculty of Technology, 06500, Teknikokullar/Ankara, Turkey. *esrasogut@gazi.edu.tr*

[2] Gazi University, Department of Computer Engineering, Faculty of Technology, 06500, Teknikokullar/Ankara, Turkey. *saadinoyucu@gazi.edu.tr*

[3] Gazi University, Department of Computer Engineering, Faculty of Technology, 06500, Teknikokullar/Ankara, Turkey. *ayerdem@gazi.edu.tr*

[4] Gazi University, Department of Computer Engineering, Faculty of Technology, 06500, Teknikokullar/Ankara, Turkey. *polath@gazi.edu.tr*

DSL is also shown as a technology that transmits signals to user devices on a unit-time basis. In general, a DSL consists of a pair of modems connected to the end of a copper line. It is used to compress high speed data going from point A to point B along the copper wire. In other words, a modem pair connected to a line forms a digital subscriber line. In short, DSL is not a line but a modem. Two-way data is sent with DSL modems. In other words, depending on the technology used, the data flow is inversely proportional to the distance [1].

Digital subscriber lines are divided into two: symmetric and asymmetric. The symmetry of a line means that during data transmission over that line, the data can reach the network at the highest speed in the same way from the user to the network or from the network to the user. On an asymmetric line, the highest speeds that can be reached during these two data streams are different.

Because DSL technology uses a wide frequency range, it is possible to have voice and data at the same time with the use of a single copper connection. The voice call will normally be sent over the 0-40 kHz spectrum and the data will be sent using higher frequencies. In a unique way, data will be sent over a LAN / WAN connection. Certainly, this sharing of copper can reveal some problems. In particular, most phones can interfere with the DSL data stream and cause interference on the handset.

The data capacity of xDSL on a physical network is based on many factors. Factors affecting data capacity: signal attenuation in copper pairs, interference with other copper pairs in use, other noise sources on the network, and airborne transmissions.

3. TYPES OF DSL TECHNOLOGY (XDSL)

DSL variants include ADSL, RADSL, HDSL, SDSL and VDSL. The abbreviation xDSL defines the technology as a whole. The view of xDSL family tree prepared by Teleconnect Company is given in Annex-1. They are separated by features such as technique, distance, number of used pairs of wires, download-upload, bandwidth, speed.

3.1. ADSL (Asymmetric Digital Subscriber Line)

ADSL is initially designed to deliver custom video at 8Mbps download and 640Kbps upload speeds. Today, ADSL is especially used as a form of high-speed internet access [1]. ADSL is intended for home and small businesses. It is a standardized technology in 1995. It is used to send a large amount of data in one direction and a small amount of data in the other direction using a copper cable. Due to its asymmetrical structure, data transmission is done to the user fast. The data transmission is done the reverse direction slowly. Table 1 shows the speed distance relation in ADSL technology. ADSL also provides simultaneous phone calls to users [2].

Table 2. Speed Distance Relation in ADSL

Distance	Speed
5.5 Km	1.544 Mbps
4.8 Km	2.048 Mbps
3.6 Km	6.312 Mbps
2.7 Km	8.448 Mbps

3.2. ADSL-Lite / DSL.Lite / UADSL/ UDSL/ G.Lite

ADSL-Lite technology is easy to use. It provides high data transmission speeds for Internet access. It also offers long transmission distance, flexible data rate options, compatibility with ADSL [3]. G.Lite, also known as universal ADSL, makes it possible to establish an internet connection to home and business computers up to 1.5Mb / s via regular telephone lines.

3.3. HDSL (High bit rate Digital Subscriber Line)

Interest in modulation techniques that provide full Duplex transmission of approximately 1.6 Mb / s is increasing in recent times. This technology is the antithesis of HDSL. This technology will enable digital services to be procured at low cost and quickly [4]. HDSL is the oldest of xDSL technology and standardized in 1992. It can transmit symmetrically up to 2 Mbit / s. It transmits and receives data at the same rate and uses

3.4. SDSL (Symmetric Digital Subscriber Line)

In SDSL technology, digital data is transferred on one line and in two directions at the same time. The same bit rate exists in both directions because it has a symmetrical structure. SDSL connections generally provide 6 Mbit / s transmission in both directions and require a 4-wire connection [1]. This is generally more expensive than ADSL and is provided by commercial telephone companies. However, SDSL is more suitable for home users with a single phone line compared to HDSL. SDSL is suitable for phone, data and multimedia data [7].

3.5. VDSL (Very High-bit-rate Digital Subscriber Line)

VDSL uses a copper wire pair as the physical medium. This is a numeric data transfer technology limited by the medium. Symmetric and asymmetric data streams are supported to provide more flexibility in the implementation of certain applications [1]. Another advantage of the VDSL architecture is the security approach provided by point-to-point connections. This is a significant advantage over technologies based on bus architecture.

This technology provides higher bandwidth compared to ADSL and DSL. VDSL is usually associated with a bundle of packets. Like existing xDSLs, it can provide high speed internet access and voice services. Due to the increased bandwidth requirement, VDSL provides faster internet access. It can also carry more audio channels and digitally encoded videos at the same time. Symmetrically 20 Mbit / s and asymmetric 52 Mbit / s can be achieved [8]. This can provide both short-reach symmetric and long-reach asymmetric operation. VDSL was announced by ETSI in 1995. The VDSL speed distance relationship is shown in Table 2.

Table 2. Speed Distance Relation in VDSL

Distance	Speed
12.96 Mbps	1.4 Km
25.82 Mbps	900 m
51.84 Mbps	300 m

3.6. VoDSL (Voice over DSL)

VoDSL technology has emerged as a result of the rapid increase of network capacity due to the combination of voice and data. VoDSL offers quality voice services. It also supports a wide range of data applications over the existing line in the area where the user is located and uses copper infrastructure. It simultaneously provides data information and multiple audio information (including fax transmission) on the high-speed digital line offered by ADSL. At the DSL Forum Technical Committee Meeting in 2001, VoDSL technology was taken into consideration.

VoDSL allows the transmission of data and multiple voices call over a single copper pair. It offers high speed internet access to users on a single DSL copper line. It also provides local and long distance telephone service [9]-[11].

3.7. SHDSL/ G.SHDSL (Single-line High Speed DSL/ Symmetrical high-bit-rate DSL)

SHDSL is based on HDSL and is recommended by ITU. Currently, SHDSL can operate at data rates with higher ratios, ranging from 192 kbps to 2.312 Mbps (in 2-wire mode) and 384 Kbps to 4.624 Mbps (in 4-wire mode) [4]. It has compatible with all other DSL technologies. It can be used for multi-audio channels and video conferencing applications. SHDSL is the best choice for high flow bit rates in medium and long lines. It also includes a convergence similar to VDSL for packet transmission [12]-[14].

3.8. RADSL (Rate Adaptive Digital Subscriber Line)

RADSL is an ADSL-based technology developed by Westell. It is possible to set the data rate according to the status of the line via software. It is possible to exceed the maximum speeds that ADSL can reach. The advantage of RADSL is that it can automatically adjust the speed of the line to reach the proper speed. This

technology allows users to make phone calls and transmit data over a single copper pair [15], [16]. RADSL allows different data types such as voice, data, and multimedia depending on the communication type.

This technology adjusts the internet connection speed depending on the length and quality of the local loop. In addition, it increases connection speeds for the remote users from the telephone exchange. It extends the broadband area from 3.5 to 5.5 km [17].

3.9. IDSL/ G.SHDSL (Single-line High Speed DSL/ Symmetrical high-bit-rate DSL)

ADSL technology is adapted to work with existing technologies. IDSL technology has been developed for this. IDSL technology provides a full 128 Kbps ISDN connection to users at home or at work. It is only a data connection, so it does not carry audio information [18], [19].

3.10. Comparision of xDSL Technologies

The types of xDSL technology are compared with the specified features and presented in table form in Annex-2 [2], [3], [14], [17]-[20]. The features used when making comparisons are important for these technologies. For example, download / upload speeds, distances.

4. BENEFITS OF XDSL TECHNOLOGY

DSL supports voice and data transmission and provides a permanent connection. ADSL connections will increase the number of interactive internet services since sending a message, setting up the appropriate environment for starting a phone call or video call. Also;

- Offers a low price option for internet access and transportation,
- It provides very high bandwidth for data transmission,
- Configures for each subscriber of the cable network and provides high security
- It is easy to adapt and provides convenience with interface,
- It offers the possibility of using the Internet and telephone line at the same time,
- Service providers offer DSL modems,
- It is cheaper than cable connections,
- Use copper bottom for telephone use,
- It does not require extra infrastructure investment,
- It is possible to implement existing and new methods used in communication technology on DSL,
- Symmetric and asymmetric data transfer is possible.

5. CONCLUSION AND SUGGESTIONS

xDSL technology, widely used around the world, has given new insights to communication systems. Particularly the most important feature is the use of copper bottom for telephone use and the lack of extra infrastructure investment. The high speed of data transmission, the sufficient bandwidth, the lack of compliance problems and the economic suitability make this technology preferable. It will be integrated with many applications in the future to make it even more useful and productive.

REFERENCES

[1]. M. Alkan, H. Tekedere, A. Polat, " DSL Teknolojisinin İletisime Sundugu Genis Bant İmkanları." in *Proc. INET-TR*, 2001, paper 12, p. 5..
[2]. M. K. Cantekinler, A. D. Caycı, O. Dasdemir, F. Yayla, R. Yılmaz, "Teknoloji, Hizmetler, Düzenleme ve Dünyadaki Gelismelerle Genisbant Raporu," Telekomünikasyon Kurumu, Sektorel Arastırma ve Stratejiler Dairesi Baskanlıgı, Tech. Rep. 1-50, 2008.
[3]. A. Johansson, "ADSL Lite-The Broadband Enabler For The Mass Market," Ericsson Tech. Rep. 4, 1998.
[4]. S. Gorshe, A. Raghavan, T. Starr, S. Galli, *Broadband Access: Wireline and Wireless - Alternatives for Internet Services,* Ed. ABD: John Wiley & Sons, 2014.
[5]. J. J. Werner, "The HDSL Environment," *IEEE Journal on Selected Areas in Communications*, vol. 9, pp. 6, 1991.
[6]. G. Pottie, M. V. Eyuboglu, "Combined Coding and Precoding for PAM and QAM HDSL Systems," *IEEE Journal on Selected Areas in Communıcatıons*, vol. 9, pp. 6, 1991.

[7]. "Guide to Broadband, DSL, SDSL, ADSL and ADSL 2+", M. Clark, 2006.

[8]. Digital Subscriber Line Forum, "DSL Forum Technical Report TR-040: Aspects of VDSL Evolution," Digital Subscriber Line Forum, Tech. Rep. 5-20, 2001.

[9]. S. M. Musa, C. M. Akujuobi, N. F. Mir, "VoDSL Information Management for Broadband Communication Network Access," *Journal of Computing and Information Technology*, vol. 15, pp. 17-24, 2007.

[10]. S. M. Musa, E. U. Opara, M. A. Shayib, M. A. El-Aasser, "Statistical Analysis of VoDSL Technology for the Efficiency of Listening Quality of 640k/640k," *Journal of International Technology and Information Management*, vol. 19, pp. 4, 2010.

[11]. W. Afric, N. Matogif, R. Svalina, "Voice over Digital Subscriber Line Application in Croatian Network," in *Proc. 47th International Symposium El-M*, 2005, paper 2, page 15.

[12]. C. Hellberg, T. Boyes, D. Greene, *Broadband Network Architectures: Designing and Deploying Triple-Play Services,* Ed. Germany: Pearson Education, 2007.

[13]. *Cisco Public Information about G.SHDSL*, Cisco Systems, 1996.

[14]. Digital Subscriber Line Forum, "Symmetric DSL White Paper," Digital Subscriber Line Forum, Tech. Rep.1-14, 2002.

[15]. I. A. Dhotre, V. S. Bagad, *Data Communication and Networking*. Ed. Pune: Technical Publications, 2006.

[16]. T. D. Stefano, R. Kneller, J. Timmis,, "Information Communication Technologies and Firm Performance: Evidence for UK Firms," The University of Nottingham, United Kingdom, China and Malaysia Discussion Papers in Economics, Tech. Rep. 5-12, 2016 .

[17]. M. Gagnaire, "An Overview of Broad-Band Access Technologies," *IEEE*, vol. 85, pp. 12, 1997.

[18]. D. Smith, "xDSL: The Solution for Todays Bandwidth Demands," *New Telecom Quarterly- Technology Futures*, vol. 5, pp. 33-37, 1997.

[19]. V. Krsti, M. Stojanovi, "Dıgıtal Subscrıber Lıne Technology: Network Architecture, Deployment Problems and Technical Solutions," in *Proc. 8th Telecommunications Forum TELFOR*, 2000, paper 3, p. 10.

[20]. T. Starr, *DSL Advances,* Ed. New Jersey: Prentice Hall Professional, 2003.

APPX-1. ILLUSTRATİON OF XDSL FAMİLY TREE

APPX-2. Comparisiosn of xDSL Teknologies [2], [3], [14], [17]-[20]

Types of xDSL	Data path download/upload	Distance	Scope of applications
ADSL	1.5-9 Mbps 64 Kbps-900Kbps	5.5 km	It is used for internet, web access, motion picture, video on demand and remote local network access. It needs a splitter. It is asymmetrical. It uses a pair of copper wires (two wires). It is suitable for small and medium sized home and businesses.
ADSL.Lite	256 Kbps-1.544 Mbps 512 Kbps	5.5 km	Can be used by ADSL users. It does not need a splitter. It is asymmetrical.
HDSL	1.544 Mbps 2.048 Mbps	3-4 km	Service between the server and the telephone company. Used for WAN, LAN, server access. It is symmetrical. Two double copper wires (4 wires).
SDSL	256 Kbps-2.3 Mbps 256 Kbps-2.3 Mbps	4-5 km	Suitable for businesses. It is symmetrical. A pair of copper wires (two wires).
VDSL	13 Mbps-52 Mbp 6 Mbps-26 Mbps	300m-1 km	It is used in applications where very high speed is required. Ex: TV broadcast, HDTV. It is symmetrical.
SHDSL	2.31 Mbps-4.6 Mbps 2.31 Mbps-4.6 Mbps	6 km	Same as HDSL but only needs one twisted line. It is symmetrical. A pair of copper wires (two wires).
RADSL	32 Kbps-9 Mbps 32 Kbps-1.5 Mbps	3.5-5.5 km	It is used for internet access, video broadcast, LAN access. Similar to ADSL. He needs a splitter. This technology is compatible with the line. It is asymmetrical. A pair of copper wires (two wires). Audio, data, multimedia, custom video.
IDSL	128 Kbps-144 Kbps 128 Kbps-144 Kbps	5.5 km	This only allows data transmission. Voice conversation can not be made on the same line. It is symmetrical. Suitable for home and small-scale businesses.

BIOGRAPHY

Esra SOGUT

She was born in Eskisehir, Turkey. She finished her BSc in Eskisehir Osmangazi University, Department of Computer Engineering in 2012 and MSc in Gazi University, Department of Computer Engineering in 2016, Turkey. Since 2016, she has made her Ph.D. in Gazi University, Department of Computer Engineering. Her area of study is Cyber Security, Computer Networks, and Software. Her profession currently is a research assistant at Department of Computer Engineering, Faculty of Technology, Gazi University, Ankara, Turkey.

E-Mail: esrasogut@gazi.edu.tr

Saadin OYUCU

He was born in Gaziantep, Turkey. He graduated from Gazi University, Department of Electronics and Computer Education in 2012, Turkey. He received his M.Sc. in Computer Engineering in 2015. He began Ph.D. in Computer Engineering 2015. He is doing research in the in the fields of Computer Networks, M2M, Internet of Things, Web Services, Software and NoSQL Databases. Saadin Oyucu is currently working as research assistant at Department of Computer Engineering, Faculty of Technology, Gazi University, Ankara, Turkey.

E-Mail: saadinoyucu@gazi.edu.tr

Prof. Dr. O. Ayhan ERDEM

He was born in Ankara, Turkey. He received his M.Sc. in 1989 and a Ph.D. degree in 2001 both from Gazi University. In 1990 he attended to English Language Education Program of Indiana University, USA. He finished Computer of Technology at Purdue University. He has books and papers about, also he is doing research in the fields of Computer Networks, Programming Languages, IT, Computer Systems. He still is a Professor at Department of Computer Engineering, Faculty of Technology, Gazi University, Ankara, Turkey.

E-Mail: ayerdem@gazi.edu.tr

Assist. Prof. Dr. Huseyin Polat

He was born in Adana, Turkey. He graduated from Black Sea Technical University, Department of Electrical-Electronic Engineering in 1993, Turkey. He received his M.Sc. in Electric Education in 1999 and Ph.D. degree in Electronic and Computer Education from Gazi University in 2006. He is doing research in the in the fields of Data Acquisition, Digital Signal Processing, Computer Networks, M2M, Internet of Things and Artificial Neural Network. Dr. Huseyin Polat is currently working as assistant professor at Department of Computer Engineering, Faculty of Technology, Gazi University, Ankara, Turkey.

E-Mail: polath@gazi.edu.tr

Antioxidant Activities of Natural Honey Samples from Hakkari and Mus Regions (Turkey)

Tulin Eker[1], Adnan Bozdogan[2], Zeynep Ulukanlı[3]

Abstract

Hakkari and Mus are the reputable two regions which contribute the honey production in Turkey. The natural habitats of these regions are very convenient for beekeepers. In the present study, honey samples obtained from beekeepers from Hakkari and Mus regions were analyzed to determine the total phenolic (TPC), flavonoid (TF), ascorbic acid (AAC), carotenoid (TCC) contents as well as their antioxidant activities such as DPPH scavenging activity (2-diphenyl-1-picrylhydrazyl), Reducing Power (RP) and Ferric-Reducing antioxidant power (FRAP). The present results indicated that there were no significant differences among the total phenolic contents of honey samples. The highest total flavonoid content was found in a honey sample from Mus-2 (9.5 mg of quercetin /100 g of honey). The lowest ascorbic acid content was found in a sample from Mus-2 (0.93 mg/100 g of honey), and two samples from Hakkari-2 (0.99 mg/100 g of honey) and Hakkari-4 (0.81 mg/kg of honey). The highest carotenoid content was found in a honey sample from Hakkari-2 (1.00 β-carotene mg/kg of honey). Three concentrations ranging from 12.5 to 50 mg/mL of the honey samples were used for antioxidant assays. BHT was used as the synthetic antioxidant to compare results. In the experiments, BHT had the highest DPPH scavenging activity at all concentrations (12.5, 25 and 50 mg/mL). At 12.5 mg/ml, reducing power and FRAP (0.22 Fe^{+2} mmol/L) values were the highest in a sample from Mus-2 and Hakkari-3, respectively. A positive and significant correlation were determined between the reducing power value and total flavonoid content ($R^2=0,793$).

Keywords: *Hakkari, Mus, honey, antioxidant activity, physicochemical properties, Turkey*

1. INTRODUCTION

The apiculture is a cultivation branch that can be carried out with various branches of agriculture. Turkey has very suitable conditions for beekeeping in terms of its climatic characteristics. Honey is one of the most known bee products [1].

Honey is a natural sweet substance that produced by honey bees from the nectar of flowers that was transformed by combining with specific substances of their own. The composition of honey is variable, based on the plant types, climate, environmental conditions, and contribution of the beekeeper [2].

Honey has been asserted to involve about 200 substances. The carbohydrates contain about 95% of a honey's dry weight. Fructose and glucose are the primary carbohydrates. Besides, honey contains certain minor constituents such as proteins, free amino acids, organics acids, phenol compounds, vitamins, and traces minerals that are responsible for several therapeutic features (antioxidant, anti-inflammatory, anticancer, antimutagenic, antibacterial, antifungal, and antiviral activities) [3], [4]. Plants are source of polyphenolic substances with plenty of diversity and complexity. These bioactive compounds may be passed to honey by nectar or honeydew that collected by bees from plants [5]. The main quality of honey is linked with the availability, variety and concentrations of bioactive compounds in, and this again based on the geographic and floral structure of the area [3].

[1] *Corresponding author: Osmaniye Korkut Ata University, Department of Food Engineering, Faculty of Engineering, , Karacaoglan Campus 80000, Osmaniye, Turkey. tulinsahin@osmaniye.edu.tr*

[2] *Osmaniye Korkut Ata University, Department of Food Engineering, Faculty of Engineering, Karacaoglan Campus 80000, Osmaniye, Turkey bozdogan@osmaniye.edu.tr*

[2] *Osmaniye Korkut Ata University, Department of Biology, Faculty of Arts and Science, Karacaoglan Campus 80000, Osmaniye, Turkey zeynepulukanli@osmaniye.edu.tr*

Phenolic compounds -especially flavonoids-in honeys assigned as an important group for functional properties and therapeutic significance. There are several studies that have reported that antioxidant and antibacterial activities of honeys were strongly correlated with concentrations of phenolic compounds in honeys [2], [4], [6]-[8].

Turkey, is the home for the plenty of nectar and honeydew honey types. Therefore, apiculture is a traditional agricultural activity in almost every region of Turkey. The main goal of this study was to monitor the concentration of bioactive components and antioxidant activities of seven samples of honeys from Hakkari and Mus region of Turkey. The correlation analysis was carried out to find the relationship between the antioxidant activities.

2. MATERIAL AND METHODS

2.1. Honey samples

A total number of 7 natural honey samples were obtained from beekeepers in Mus (Mus 1 (M1) and Mus 2 (M2)) and Hakkari locations (Hakkari 1-5 (H1-5)). All samples were collected in their original packages and then transferred to the laboratory and kept at 4 ºC until analysis.

2.2. Determination of total phenolic content

The Folin–Ciocalteu method was used to determine total phenolic content [9]. A 5 g of honey sample was diluted to 50 ml with distilled water and then filtered. This solution (0.5 ml) was mixed with 2.5 ml of 0.2 N Folin–Ciocalteu reagent. After incubation for 5 min., sodium carbonate (2 mL, 75 g/l) was added. The solution was left for incubation at room temperature for 2 h in a dark place. After incubation, the absorbance of the reaction mixture was measured at 760 nm (UV 1800 Shimadzu) against a methanol blank. The calibration curve was produced by using gallic acid (0–200 mg/l) as standard. The total phenolic content was expressed in mg of gallic acid equivalents (GAE)/100 g of honey [10].

2.3. Determination of total flavonoid content

The Dowd method adapted Meda et al. [10], was used to determine total flavonoid content. The diluted honey samples (5 mL) for previous method (TPC) was mixed with $AlCl_3$ (1 mL, %2). Absorption readings at 415 nm (UV 1800 Shimadzu) were taken after 10 min. against a blank sample prepared with a 5-ml honey solution and 5 ml methanol without $AlCl_3$. The total flavonoid content was determined using a standard curve with quercetin (0–50 mg/l) as the standard and results expressed as mg of quercetin equivalents (QE)/100 g of honey.

2.4. Determination of total carotenoid content

Total carotenoid content was carried out as previously reported Alvarez-Suarez et al. [11]. The honey sample (1 g) was vigorously shaken with n-hexane:acetone mixture (10 mL, 6:4, *v/v*) for 10 min at room temperature. The solution was filtered and the absorbance of the filtrate was measured at 450 nm (UV 1800 Shimadzu) against a blank using a spectrophotometer. β-carotene was used for the calibration curve (1-6 mg/L) and total carotenoid content was expressed as mg of β-carotene equivalents.

2.5. Ascorbic acid content

Ascorbic acid determination was carried out as reported by Cemereoglu [12]. Honey sample (100 ml) was mixed with 100 ml meta-phosporic acid. The solution was vigorously shaken and then filtered. The filtrate (5 mL), acetate buffer (5 mL) and 2,6-diklorofenolindofenol solution (1 mL, 25 mg/200 mL) were mixed and then shaken gently. Then, 10 mL of xylene was added and the sample was centrifuged. The absorbance of the upper phase was read at 500 nm against xylene. Ascorbic acid contents of honey samples were calculated using a standard curve for ascorbic acid, and was expressed in mg/kg.

2.6. Reducing power assay

The reducing power was determined according to the method of Oyaizu [13]. Various concentrations of honey methanolic extracts (2.5 mL) was mixed with 0.2 M sodium phosphate buffer (2.5 mL, pH 6.6) and potassium ferricyanide (2.5 mL, 1%). After incubation at 50 °C for 20 min, trichloro acetic acid (2.5 mL, 10%, *w/v*) was added and the mixture was centrifuged at 1000 rpm for 8 min. The upper layer (2.5 mL) was mixed with deionized water (2.5 mL) and ferric chloride (1mL, 0.1%). The absorbance of samples was measured spectrophotometrically (UV 1800 Shimadzu) at 700nm. BHT was used as standard.

2.7. DPPH (1,1-diphenyl-2-picrylhydrazyl) assay

2,2-diphenyl-1-picrylhydrazyl (DPPH) free radical was monitored according to a method reported previous [14]. Various concentrations of honey extracts were mixed with methanolic solution of DPPH radical (2.7 mL, 6×10^{-5} M). Each mixture was shaken vigorously and incubated in a dark place for 30 minutes at room temperature. The absorbance of samples was measured spectrophotometrically (UV 1800 Shimadzu) at 517 nm. DPPH scavenging activity was calculated as percentage of DPPH discoloration using the formula where A_{sample} is the absorbance of the solution and $A_{control}$ is the absorbance of the pure DPPH solution.

$$Scavenging\ DPPH\ \% = (A_{control} - A_{sample})/(A_{control}) \times 100 \qquad (1)$$

2.8. Ferric Reducing Ability Antioxidant Power (FRAP)

The FRAP method was conducted according to Benzie and Strain [15]. The FRAP reagent contained 10 mmol/L TPTZ solution in 40 mmol/L HCl, 20 mmol/L $FeCl_3$ and 0.1 mol/L acetate buffer (pH 3.6), [1:1:10] was prepared freshly and incubated at 37 °C for 10 min. Then, methanolic extracts of honey samples (0.3 mL) and FRAP reagent (2 mL) were mixed in a volumetric flask (10 mL) and made up to volume with distilled water. The blue colored solutions were left for incubation at room temperature for 10 min. The absorbance was measured spectrophotometrically at 593 nm against a blank contained FRAP reagent (2 mL) and distilled water (8 mL). Calibration curve was performed using working solutions of $FeSO_4.7H_2O$ (0.2-2 mmol/L) for FRAP methods.

3. RESULTS AND DISSCUSSION

3.1. Total phenolic content

Most plants contain extensive number of polyphenols and flavonoids and each plant tends to have a distinctive profile. The amount and type of polyphenolics that are main factors for biological activities, including antioxidant, antimicrobial, antiviral, and anticancer activities. are related to floral origin of honey Honey involves diversified phenolics which makes it a good source of antioxidants [2]. Total phenolic content (mg of GAE/100 g of honey) varied from 19.22 to 28.35 using the standard curve of gallic acid. The highest phenolic content was observed in H1, although no significant differences exist between TPC contents of honey samples. Several investigators have found phenolic compounds in honey [2], [10], [11], [16]-[22]. In previous multifloral honey reports, TPC (mg/100 g) was found between 0.323 and 0.149 in Spain [23], 32.59-93.66 in Burkinian honeys [10], 8.36-14.693 in Czechoslovakia honeys, 198 in honeys from Black Sea region of Turkey and 35.3-1961 in honeys from Central Anatolia cities of Turkey [24]. The phenolic content of the 7 honey samples that we analyzed are lower than previous reports except values obtained by Soria et al. [23] and Lanchman et al. [25].

3.2. Total flavonoid content

Using the standard curve generated by quercetin, the total flavonoid content of honey samples (mg of QE/100 g) varied from 7.98 to 9.50 with a mean value of 8.59. The differences between honey samples were the significant. The highest TF content was observed in M2 (9.50 mg/100 g) that had the highest TPC value. The mean value for total flavonoid in present study is higher than Burkinian honeys (0.41-8.37 mg QE/100 g) [10]. TF contents of honeys (5.38-26.75 mg QE/100 g) from Central Anatolian cities in Turkey were higher than our values [24].
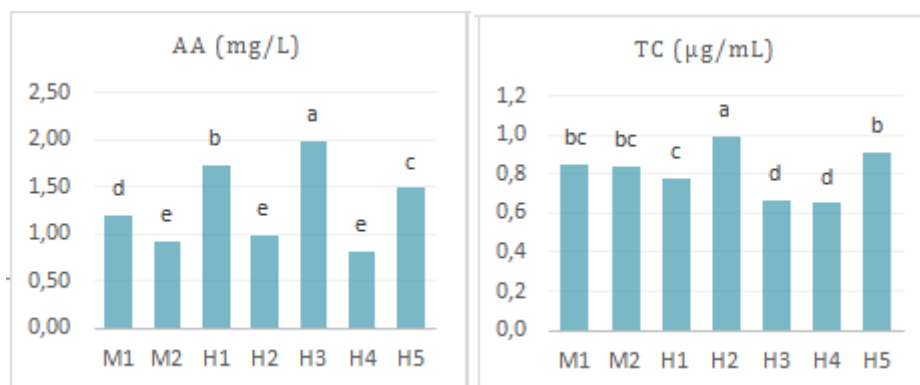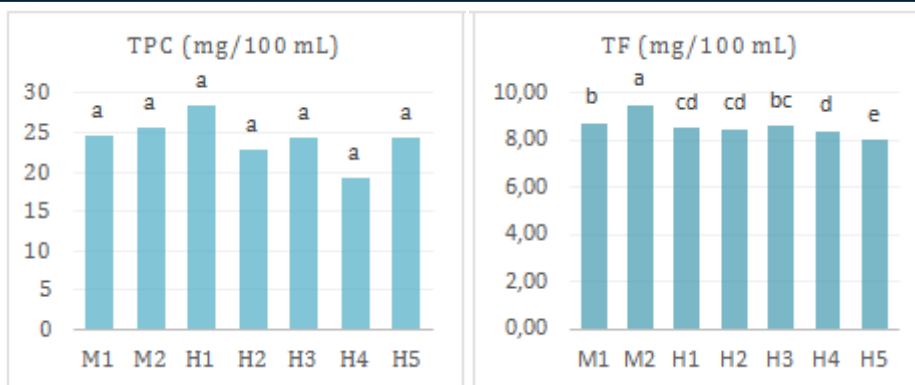
Figure 1. *Total phenolic content (TPC), total flavanoid (TF), ascorbic acid (AA), total carotenoid (TC) contents of honey samples. Bars with different letters are significantly different among means at P≤0.05 (ANOVA followed by LSD test).*

3.3. Total carotenoid content (TC)

Total carotenoids are shown in Table. H2 has the highest carotenoid content (1.00 ±βcarotE/kg of honey) whereas the lowest contents were measured in H3 (0.67 ±mg βcarotE/kg of honey) and H4 (0.65 ±βcarotE/kg of honey). TC content (mg βcarotE/kg of honey) of multifloral honeys in Saudi Arabia was between 50.24 and 64.84 [18], Cuban honeys was between 1.17 and 5.57 [14], honeys in the arid and not arid region of the United Arab Emirates ranged from 0.173 to 0.820, and 0.067 to 0.113 [26].

3.4. Ascorbic acid content (AA)

Ascorbic acid in honey acts as antioxidants [11]. In present study, ascorbic acid content was monitored spectrophotometrically. Ascorbic acid content of honeys from Hakkari-Mus region ranged from 1.20 mg/kg to 1.99 mg/kg. While H3 had the highest ascorbic acid content, M2, H2, and H4 had the lowest.

In a previous study, the amount of ascorbic acid (mg/kg) in branded and unbranded balls ranged from 1 to 17.7 and 1.4 to 13.5 mg/kg, respectively [27]. Moniruzzaman et al. [20], indicated that the ascorbic acid content was 140.14 mg/kg in acacia honey, 140 mg/kg in ananas honey, 145 mg/kg in Borneo honey and 140.14 mg/kg in Tualang honey. The results of the present study were in accordance with Rahman et al. [27], in relation to ascorbic acid content; however, the values of ascorbic acid contents (mg/kg) reported by Moniruzzaman et al. [20] were higher than our results. As it was indicated in previous studies, it was observed that the ascorbic acid content of honeys change depending on the flora source.
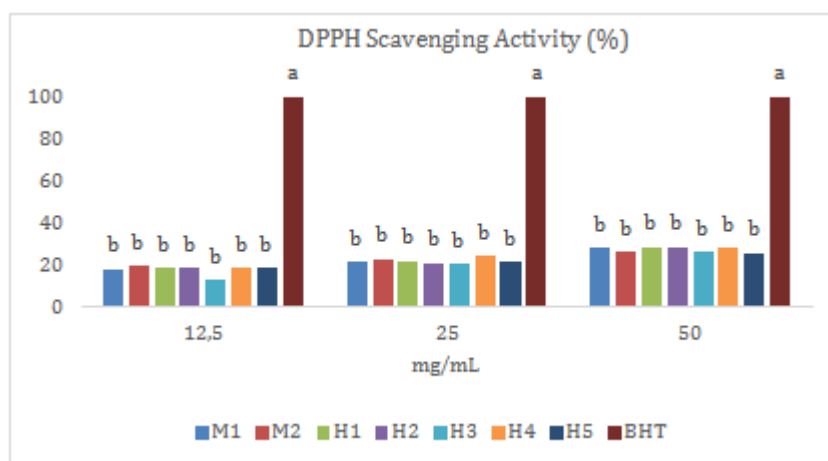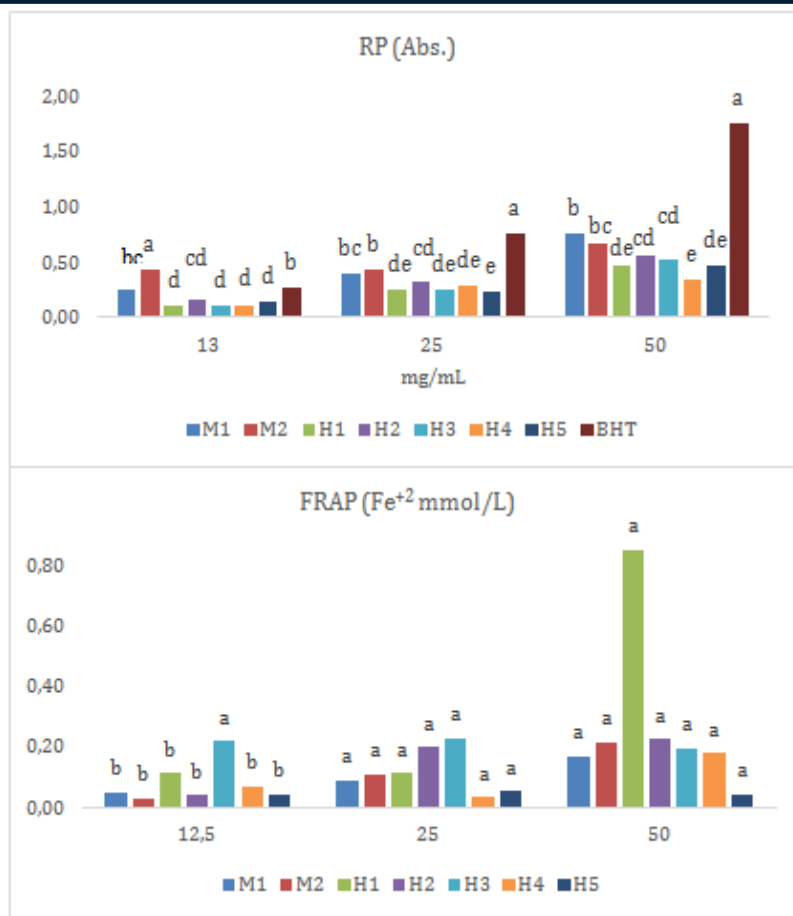
Figure 2. *Antioxidant activities of honey methanolic extracts. Bars with different letters are significantly different among concentrations at P≤0.05 (ANOVA followed by LSD test). Abs: Absorbance, BHT: Butylated hydroxytoluene.*

3.5. DPPH Scavenging Activity

The results of DPPH scavenging activity indicated that the active radical scavengers were similar in all honeys. The BHT, is a synthetic antioxidant, that was used as a standard and its activity was 100% at all concentrations.

3.6. Reducing Power Activity

Reducing power (RP) activities of the honey samples were measured on the method suggested by Oyaizu [13]. The presence of reducing agents in the honey reduced the ferric ions to ferrous ions. This reduction was determined at 700 nm against a blank. An increase in absorbance indicates a high reducing power [28]. The RP of the honey samples at 12.5, 25 and 50 mg/mL increased with concentration when compared with BHT as the control. The average RP values of samples were 0.19 at 12.5 mg/mL, 0.31 at 25 mg/mL and 0.54 mg/mL at 50 mg/mL, respectively. The M2 sample showed the highest reducing power activity after BHT as standard. The total reducing power is the sum of the reducing powers of individual compounds present in a sample. The results of the total reducing power assays correlated well with total flavonoid contents (R^2: 0.793). Different RP activities in honey samples may be related to amounts of individual redactor compounds that react with free radicals.

3.7. Ferric-Reducing antioxidant power (FRAP).

FRAP average values of honey samples were ranged from 0.05 to 0.36 mM Fe^{+2}. H1 showed the highest average value. In previous studies, lower and higher FRAP values were reported in the unifloral honeys. It was reported that FRAP values ranged from 0.054 to 0.1967 mM Fe^{+2} in Cuban honeys [11], 0.087 to 0.576 in African honeys [20] and 0.053 to 1.759 in Portuguese honeys [14].

4. CONCLUSION

The seven Turkish honeys were studied in present study. Three antioxidant test systems were utilized to evaluate the antioxidant properties of honeys. The antioxidant activity showed a linear positive relationship with the honey concentration (12.5, 25 and 50 mg/mL) in all samples. The results of antioxidant assays changed in relation to the order of antioxidant capacity of the honeys. Current analysis showed that honey samples from regions of Hakkari and Mus region of Turkey had important potential in combating with oxidant damage. In addition, further investigation is required to determine of their individual biologically active components.

REFERENCES

[1]   F. Karadal, Y. Yildirim, "Balın kalite nitelikleri, beslenme ve saglık acısından onemi", Erciyes Universitesi Veterinerlik Fakültesi Dergisi, vol 9(3) pp. 197-209, 2012.
[2]   M. Kücük, S. Kolayli, S. Karaoğlu, E. Ulusoy, C. Baltaci, F, Candan," Biological activities and chemical composition of three honeys of different types from Anatolia", Food Chemistry, vol 100(2), pp. 526–534, 2007. Available: http://doi.org/10.1016/j.foodchem.2005.10.010.
[3]   O. Escuredo, M. Míguez, M. Fernández-González, M. Carmen Seijo, "Nutritional value and antioxidant activity of honeys produced in a European Atlantic area", Food Chemistry, vol 138(2-3), pp. 851–856, 2013. Available: http://doi.org/10.1016/j.foodchem.2012.11.015.
[4]   R. El-Haskoury, W. Kriaa, B. Lyoussi, M. Makni, "Ceratonia siliqua honeys from Morocco: Physicochemical properties, mineral contents, and antioxidant activities", Journal of Food and Drug Analysis, pp. 7–13, 2017. Available: http://doi.org/10.1016/j.jfda.2016.11.016.
[5]   S. Silici, O. Sagdic, L. Ekici, "Total phenolic content, antiradical, antioxidant and antimicrobial activities of Rhododendron honeys", Food Chemistry, vol 121, pp. 238–243, 2010.
[6]   Z. Can, O. Yildiz, H. Sahin, E. Akyuz Turumtay, S. Silici, S. Kolayli, "An investigation of Turkish honeys: their physico-chemical properties, antioxidant capacities and phenolic profiles", Food Chemistry, vol 180, pp. 133–141, 2015. Available: http://doi.org/10.1016/j.foodchem.2015.02.024.
[7]   F. M. Bueno-Costa, R. C. Zambiazi, B. W. Bohmer, F. C. Chaves, W. P. da Silva, J. T. Zanusso, I. Dutra, "Antibacterial and antioxidant activity of honeys from the state of Rio Grande do Sul, Brazil", LWT - Food Science and Technology, vol 65, pp. 333–340, 2016. Available: http://doi.org/10.1016/j.lwt.2015.08.018.
[8]   S. Ayoub Meo, S. Ahmad Al-Asiri, A. Latief Mahesar, M. Javed Ansari, "Role of Honey in Modern Medicine", Saudi Journal of Biological Sciences, In Press, 2017.
[9]   V. L. Singleton, J. A. Rossi, "Colorimetry of total phenolics with phosphomolybdic- phosphotungstic acid reagents", American Journal of Enology and Viticulture, vol 16, pp.144–158, 1965.
[10]   A. Meda, C. E. Lamien, M. Romito, J. Millogo, Nacoulma, O. G. "Determination of the total phenolic, flavonoid and proline contents in Burkina Fasan honey, as well as their radical scavenging activity" Food Chemistry, vol 91(3), pp. 571-577, 2005.
[11]   J. M. Alvarez-Suarez, S. Tulipani, D. Díaz, Y. Estevez, S. Romandini, F. Giampieri M. Battino, "Antioxidant and antimicrobial capacity of several monofloral Cuban honeys and their correlation with color, polyphenol content and other chemical compounds", Food and Chemical Toxicology, vol 48, pp. 2490–2499, 2010.
[12]   B. Cemeroglu, 2010. Gıdalara uygulanan bazı ozel analiz yontemleri, Gıda Teknolojisi Dernegi Yayınları No:34., Bizimgrup Basımevi, Kızılay, Ankara, Türkiye.
[13]   M. Oyaizu, "Studies on products of browning reactions: Anti- oxidative activities of products of browning reaction prepared from glucosamine", Japanese Journal of Nutrition, vol 44, pp. 307–315, 1986.
[14]   A. Alves, R. Ramos, M. Goncalves, M. Bernardo, B. Mendes, "Antioxidant activity, quality parameters and mineral content of Portuguese monofloral honeys", Journal of Food Composition and Analysis, vol 30, pp. 130-138, 2013.
[15]   I. F. F. Benzie, J. J. Strain, "The ferric reducing ability of plasma (FRAP) as a measure of "antioxidant power": the FRAP assay", Analytical Biochemistry, vol 239, pp. 70–7, 1996.
[16]   M.L. Al, D. Daniel, A. Moise, O. Bobis, L. Lasio, S. Bogdanov, "Physico-chemical and bioactive properties of different floral origin honeys from Romania", Food Chemistry, vol 112, pp. 863-867, 2009.
[17]   M. I. Isla, A. Craig, R. Ordonez, C. Zampini, J. Sayago, E. Bedascarrasbure, A. Alvarez, V. Solomon, L. Maldonado, "Physicochemical and bioactive properties of honeys from Northwestern Argentina", LWT-Food Science and Technology, vol 44, pp. 1922-1930, 2011.
[18]   A.S. Alqarni, A.O. Owayss, A.A. Mahmooud, "Physico-chemical characteristics, total phenols and pigments of national and international honeys in Saudi Arabia", Arabian Journal of Chemistry, vol 9(1), pp. 114-120, 2012.
[19]   J. C. Serem, M. J. Bester, "Physicochemical properties, antioxidant activity and cellular protective effects of honeys from southern Africa", Food Chemistry, vol 133, pp. 1544-1550, 2012.
[20]   M. Moniruzzaman, M. I. Khalil, S. A. Sulaiman, S. H. Gan, "Physico-chemical and antioxidant properties of Malaysian honeys produced by Apis cerana, Apis dorsata and Apis mellifera", BMC Complementary and Alternative Medicine, vol 13(43), pp. 2013.Available: http://biomedcentral.com/1472-6882/13/43.
[21]   I. A. A. A. Da Silva, T. M. S. Da Silva, C. A. Camara, N. Queiroz, M. Magnani, J. S. De Novais, L. E. B. Soledade, E. O. Lima, A. L. De Souza, A. G. De Souza, "Phenolic profile, antioxidant activity and palynological analysis of stingless bee honey from Amazonas, Northern Brazil", Food Chemistry, vol 14, pp. 3552-3558, 2013.
[22]   A. Boussaid, M. Chouaibi, L. Rezig, R. Hellal, F. Donsi, G. Ferrari, S. Hamdi, "Characterization of Coffea arabica monofloral honey from Espírito Santo, Brazil", Arabian Journal of Chemistry, 2014. Available: http://dx.doi.org/10.1016/j.arabjc.2014.08.011.

[23] A. C. Soria, M. Gonzalez, C. de Lorenzo, I. Martinez-Castro, I. Sanz, "Characterization of artisanal honeys from Madrid (Central Spain) on the basis of their melissopalynological, physicochemical and volatile composition data", Food Chemistry, vol 85, pp. 121-130, 2004.

[24] F. Tornuk, S. Karaman, I. Ozturk, O. S. Toker, B. Tastemur, O. Sagdıc, M. Dogan, A. Kayacier, "Quality characterization of artisanal and retail Turkish blossom honeys: Determination of physicochemical, microbiological, bioactive properties and aroma profile", Industrial Crops and Products, vol 46, pp. 124-131, 2013.

[25] J. Lachman, M. Orsak, A. Hejtmankova, E. Kovarova, "Evaluation of antioxidant activity and total phenolics of selected Czech honeys", LWT-Food Science and Technology, vol 43, pp. 52-58, 2010.

[26] H. M. Habib, F. T. Al Meqbali, H. Kamal, U. D. Souka, W. H. Ibrahim, "Physicochemical and biochemical properties of honeys from arid regions", Food Chemistry, vol 153, pp 35-43, 2014.

[27] K. Rahman, A., Hussain, S. Ullah, I. U. M. Zai, "Phytochemical analysis and chemical composition of different branded and unbranded honey samples", International Journal of Microbiological Research, vol 4(2), pp. 132-137, 2013.

[28] G. K. Eaton, M. P. Ayres, "Plasticity and constraint in growth and protein mineralization of ectomycorrhizal fungi under simulated nitrogen deposition", Mycologia, vol 94 (6), pp. 921-932, 2002.

The Physicochemical Properties and Antioxidant Activities of Honey From Kars (Turkey)

Tulin Eker[1], Adnan Bozdogan[2], Zeynep Ulukanlı[3]

Abstract

This study investigated some physicochemical and biochemical properties and antioxidant activities of different honeys collected from beekeepers from Kars regions of Turkey. Seven honey samples from the regions of Centre, Kagızman, Digor, Selim, Sarıkamıs, Susuz and Arpacay were examined. Electrical conductivity, moisture, pH, brix, refractive index, total acidity, and color values (L, a and b) analyses of the honey samples were assessed for the determination of the physiochemical characteristics. Total phenolic compounds, total flavonoids and antioxidant activity were measured. The findings of the present study confirm that honey sample from the region of Selim showed the highest pH (3.47±0.02), total acidity (30.0±2.80 meq/kg), moisture (19.41±0.02%) and L (64.50±7.80) values. The results for total phenolic content (13.11–35.06 mg GAE/100 g), total flavonoid content (4.31-7.97 mg QE/100 g) and the antioxidant assays revealed that honey samples from the region of Kars have high level of antioxidant activity.

Keywords: *Kars, honey, antioxidant activity, physicochemical properties, Turkey*

1. INTRODUCTION

Honey is a natural sweet food that produced by honey bees from the nectar of flowers. The compounds in honey is changeable, based on the variances in flower type, climate, environmental conditions, and contribution of the beekeeper [1].

Honey has been asserted to involve about 200 substances of which, carbohydrates contain about 95% of a honey's dry weight. Fructose and glucose are the primary carbohydrates [2], [3].

Phenolic compounds -especially flavonoids-in honeys assigned an important group for functional properties and scientific and therapeutic significance of honeys. There are several studies that have reported that antioxidant and antibacterial activities of honeys were strongly correlated with concentrations of phenolic compounds in honeys [1], [4]-[7].

The production of honey is of economical significance in both different regions as well as rural areas of many countries. Consumers living in densely populated areas tend to buy honey from rural areas because of the quality and spesific properties inconcern. In many countries, the regional and international criteria have been available for defining the honey quality including sensory, chemical, physical and microbiological characteristics [8].

Turkey–is home to plenty of nectar and honeydew honey types, is very rich regarding production and variety of honey. Therefore, apiculture is a traditional agricultural activity in almost every region in Turkey. The main goal of this study was to monitor the physicochemical properties and total phenolic, total flavonoid and antioxidant activities of seven samples from Kars region.

---

[1] Corresponding author: Osmaniye Korkut Ata University, Department of Food Engineering, Faculty of Engineering, , Karacaoglan Campus 80000, Osmaniye, Turkey. tulinsahin@osmaniye.edu.tr

[2] Osmaniye Korkut Ata University, Department of Food Engineering, Faculty of Engineering, Karacaoglan Campus 80000, Osmaniye, Turkey bozdogan@osmaniye.edu.tr

[2] Osmaniye Korkut Ata University, Department of Biology, Faculty of Arts and Science, Karacaoglan Campus 80000, Osmaniye, Turkey zeynepulukanli@osmaniye.edu.tr

2. MATERIAL AND METHODS

2.1. Material

The total numbers of 7 natural honey samples were obtained from beekeepers in Kars locations (Centre, Kagızman, Digor, Selim, Sarıkamış, Susuz and Arpacay). All samples were collected in their original packages and were transferred to the laboratory and kept at 4-5 ºC in a dark place until analysis.

2.2. Methods

2.2.1. Determination Of Physicochemical Analyses

The pH of honey solution (10%, *w/v*) was recorded with a pH meter (Thermo scientific, Singapore) [9]. A titrimetric method was used for the total acidity measurement of each honey specimen [9]. The content of the total soluble solids (°Brix) was measured using a digital refractometer at 20°C (Kruss Optronic, Germany). A conductivity meter (Hanna EC 215 model Hanna Instruments, USA) was employed for the determination of the electrical conductivity [10]. A digital refractometer (Kruss Optronic, Germany) was used for determining the refractive index at 20 °C. The moisture content (%) was based on the interaction between refractive index and water content [9]. A Conica Minolta colorimeter (Chroma Meter CR-400 Japan) was used for the color of each honey sample (L, a and b) [11].

2.2.2. Determination of total phenolic, total flavonoid content and antioxidant activity

The Folin–Ciocalteu method was used to determine total phenolic content (TPC) [12]. A 5 g of honey sample was diluted to 50 ml with distilled water then filtered. This solution (0.5 ml) was mixed with 2.5 ml of 0.2 N Folin–Ciocalteu reagent. After incubation for 5 min., sodium carbonate (2 mL, 75 g/l) was added. The solution was left incubation at room temperature for 2 h in a dark place. After incubation, the absorbance of the reaction mixture was measured at 760 nm (UV 1800 Shimadzu) against a methanol blank. The calibration curve was produced by using gallic acid (0–200 mg/l) as standard. The total phenolic content was expressed in mg of gallic acid equivalents (GAE)/100 g of honey [13].

The Dowd method adapted Meda et al. [13], was used to determine total flavonoid (TF) content. The diluted honey samples (5 mL) for previous method (TPC) was mixed with $AlCl_3$ (1 mL, %2). Absorption readings at 415 nm (UV 1800 Shimadzu) were taken after 10 min. against a blank sample prepared with a 5-ml honey solution and 5 ml methanol without AlCl3. The total flavonoid content was determined using a standard curve with quercetin (0–50 mg/l) as the standard and results expressed as mg of quercetin equivalents (QE)/100 g of honey.

The antioxidant activities of honeys were monitored according to a method reported previous [14]. Various concentrations of honey extracts were mixed with methanolic solution of DPPH radical (2.7 mL, 6×10^{-5} M). Each mixture was shaken vigorously and incubated in a dark place for 30 minutes at room temperature. The absorbance of samples was measured spectrophotometrically (UV 1800 Shimadzu) at 517 nm. DPPH scavenging activity was calculated as percentage of DPPH discoloration using the formula where A_{sample} is the absorbance of the solution and $A_{control}$ is the absorbance of the pure DPPH solution.

$$Scavenging\ DPPH\ \% = (A_{control} - A_{sample})/(A_{control}) \times 100 \qquad (1)$$

3. RESULTS AND DISSCUSSION

Physicochemical characteristics of honey samples are presented in Table 1. The pH values of honey samples were similar to those previously reported in Algerian, Turkey and Malaysian honeys varied between 3.19-4.43 [15]-[18]. The low pH value was prevented the presence and growth of microorganisms.The low pH value was prevented the presence and growth of microorganisms. This parameter is important that they influence honey texture, stability and shelf life [17], [18].

The acidity values for honey samples were within the required limits (below 50 meq/kg, The Council of the European Union, 2002) prevented the undesirable fermentation. The honey acidity contributes its stability against microorganisms and to flavor. The differences of TA value could be related to the season and the species of the plant where honeybee collect the nectar [15], [19].

Soluble solids content (Brix) and refractive index values in Kars honey samples ranged with significant differences between honey samples. Algarni et al. [20] recorded 70-84 % soluble solid content of Saudi Arabia honeys. The present results, are similar to those previous reports of total soluble solids content (Brix) of honey samples [20], [24]. It is reported that refractive index varies from 1.4889 to 1.4999 by Quchemoukh et al. [16], and from 1.4745 to 1.5067 by Algarni et al. [20] respectively.

Moisture values were all below 20 %, the maximum value established by European Communitiy Directive (The Council of the European Union, 2002). Electrical conductivity is a good criterian related to botanical origin of honey control (Yucel and Sultanoglu, 2013; Belay et al. 2013). Electrical conductivity in honey samples varied in the ranged 0.15-0.75 mS cm^{-1}. Samples were below the permitted levels by the European Communitiy Directive (The Council of the European Union, 2002). The color of honey is related to content of phenolic, polen, HMF and minerals [25].

There was a significant difference between color values of honey samples due to location. Sarıkamıs had the lowest L (lightness) value so it was the darkest honey among locations. Honey includes various phenolics which makes honey a good source of bioactive compounds [1]. Total phenolic content (mg of GAE/100 g of honey) varied from 19,22 to 28,35 using the standard curve of gallic acid. The highest phenolic content was observed in Sarıkamıs and Arpacay honeys. Several investigators have found phenolic compounds in honey [1], [13], [26]-[32]. In previous multifloral honey reports, TPC (mg/100 g) was found between 0,323-0,149 in Spain [33], 32,59-93,66 in Burkinian honeys [13], 198 in honeys from Black Sea region of Turkey and 35,3-1961 in honeys from Central Anatolia cities of Turkey [19]. The phenolic content of the 7 honey samples that we analyzed are lower except values obtained by Soria et al. [33] and Lanchman et al. [34]. Most plants contain an extensive number of polyphenols and flavonoids and each plant tends to have a distinctive profile. The amount and type of polyphenolics that are main factors responsible for biological activities, including antioxidant, antimicrobial, antiviral, and anticancer activities. are related to floral origin of honeyHoney sample from Sarıkamıs region had the highest total phenolic (35.06 mg of GAE/100 g of honey), total flavonoid (7.97 mg of Quarcetin/100 g honey) content and total antioxidant activity (63.59%).

Tablo 3 Physicochemical characteristics of honey sample

Parametres	Centre	Kagızman	Digor	Selim	Sarıkamıs	Susuz	Arpacay
pH	3.71^b±0.01	3.61^b±0.01	3.65^b±0.02	3.47^a±0.02	3.60^b±0.01	3.70^b±0.02	3.68^b±0.05
Total acidity*	20.0^b±1.4	24.0^{ab}±1.4	18.0^b±1.0	30.0^a±2.80	22.0^b±2.0	20.0^b±1.4	20.0^b±2.80
°Brix (%mass)	83.6±1.40	84.90±1.0	81.8±0.8	79.40±1.0	80.60±01.4	82.60±2.8	82.80±1.0
Refractive index	1.4999^b±0.0	1.5029^a±0.0	1.4949^e±0.0	1.4880^g±0.0	1.4918^f±0.0	1.4965^d±0.0	1.4975^c±0.0
Moisture (%)	14.70^f±0.3	13.51^g±0.02	16.68^c±0.11	19.41^a±0.02	18.02^b±0.2	16.05^d±0.02	15.65^e±0.04
Conductivity**	0.26^a±0.0	0.09^{de}±0.0	0.17^b±0.0	0.09^{de}±0.0	0.15^{bc}±0.01	0.08^f±0.01	0.12^{cd}±0.01
L (Lightness)	60.47^{ab}±2.1	59.99^{ab}±4.7	56.05^{ab}±7.6	64.50^a±7.80	46.12^b±0.4	66.62^a±1.88	66.17^a±1.4
a (red)	-0.81^c±0.12	-0.81^c±0.36	-0.27^{abc}±0.3	-0.44^{bc}±0.28	-0.51^{bc}±0.07	0.36^a±0.08	-0.30^{ab}±0.0
b (yellow)	6.17^b±0.84	4.76^{bc}±0.5	4.63^{bc}±1.1	3.43^{cd}±0.1	10.30^a±1.2	-0.58^e±0.1	1.76^d±0.1

The letters represents which honeys are different by Tukey test with significance (p<0.05) *meq/kg,**mS/cm
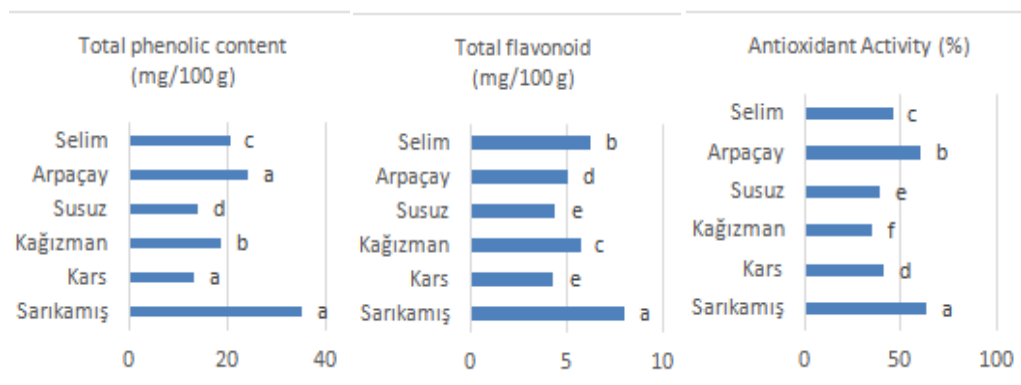

Figure 107Total phenolic, total flavanonoid and antioxidant activity. The letters represents which honeys are different by Tukey test with significance (p<0.05)

4. CONCLUSION

In conclusion, several methods were utilized in order to evaluate the biological and physicochemical properties of Turkish honeys of Kars locations. Moisture content, total acidity, electrical conductivty of honey samples in all locations of Kars were under permitted levels by the European Communitiy Directive (The Council of the European Union, 2002). Sarıkamıs honey was found to have highest TPC, TF and TAA values. The results of the physicochemical parameters as well as their antioxidant potential could suggest the consumption of honey from Kars region as a rich source of natural product.

REFERENCES

[1] M. Kucük, S. Kolayli, S. Karaoğlu, E. Ulusoy, C. Baltaci, F, Candan," Biological activities and chemical composition of three honeys of different types from Anatolia", Food Chemistry, vol 100(2), pp. 526–534, 2007. Available: http://doi.org/10.1016/j.foodchem.2005.10.010.

[2] O. Escuredo, M. Míguez, M. Fernández-González, M. Carmen Seijo, "Nutritional value and antioxidant activity of honeys produced in a European Atlantic area", Food Chemistry, vol 138(2-3), pp. 851–856, 2013. Available: http://doi.org/10.1016/j.foodchem.2012.11.015.

[3] R.W. El-Haskoury, B. Kriaa Lyoussi, M. Makni, "Ceratonia siliqua honeys from Morocco: Physicochemical properties, mineral contents, and antioxidant activities", Journal of Food and Drug Analysis, vol 7–13, 2016.

[4] Z. Can, O. Yildiz, H. Sahin, E. Akyuz Turumtay, S. Silici, S. Kolayli, "An investigation of Turkish honeys: their physico-chemical properties, antioxidant capacities and phenolic profiles", Food Chemistry, vol 180, pp. 133–141, 2015. Available: http://doi.org/10.1016/j.foodchem.2015.02.024.

[5] F. M. Bueno-Costa, R. C. Zambiazi, B. W. Bohmer, F. C. Chaves, W. P. da Silva, J. T. Zanusso, I. Dutra, "Antibacterial and antioxidant activity of honeys from the state of Rio Grande do Sul, Brazil", LWT-Food Science and Technology, vol 65, pp. 333–340, 2016. Available: http://doi.org/10.1016/j.lwt.2015.08.018.

[6] Haskoury et al. 2017;

[7] S. Ayoub Meo, S. Ahmad Al-Asiri, A. Latief Mahesar, M. Javed Ansari, "Role of Honey in Modern Medicine", Saudi Journal of Biological Sciences, In Press, 2017.

[8] M. Cenet, Z. Ulukanli, A. Bozdogan, G. Sezer, E. Memis, "The authentication of the botanical origin, physicochemical properties, antioxidant and antimicrobial activities of East Mediterranean honey", Biointerface Research in Applied Chemistry, vol 6(6), 2016.

[9] AOAC. In K. Helrich (Ed.), VA: Association of Official Analytical Chemists; 1990; 15th edn, 1990.

[10] S.L.G. Gomes Dias, L.L.P. Moreira Rodrigues, L. Estevinho, "Physicochemical, microbiological and antimicrobial propertiesof commercial honeys from Portugal", Food and Chemical Toxicology, vol 48, pp. 544-548, 2010.

[11] J. Bertoncelj, U. Dobers, M. Jamnik, T. Golob, "Evaluation of the phenolic content, antioxidant activity and colour of Slovenian honey", Food Chemistry, vol 105, pp. 822–828, 2007.

[12] V. L. Singleton, J. A. Rossi, "Colorimetry of total phenolics with phosphomolybdic- phosphotungstic acid reagents", American Journal of Enology and Viticulture, vol 16, pp.144–158, 1965.

[13] A. Meda, C. E. Lamien, M. Romito, J. Millogo, Nacoulma, O. G. "Determination of the total phenolic, flavonoid and proline contents in Burkina Fasan honey, as well as their radical scavenging activity" Food Chemistry, vol 91(3), pp. 571-577, 2005.

[14] L. Estevinho, A. Pereira, P., Moreira, L., Dias, L.G.E. Pereira, "Antioxidant and antimicrobial effects of phenolic compounds extracts of Northeast Portugal honey", Food and Chemical Toxicology, vol 46(12), pp. 3774-3779, 2008.

[15] N. Malika, F. Mohammed, E.A. Chakib, "Microbiological and physicochemical properties of Moroccan honey", International Journal of Agriculture and Biology, vol 7 (5), pp. 773-776, 2005.

[16] S. Ouchemoukh, H. Louaileche, P. Schweitzer, "Physicochemical characteristics and pollen spectrum of some Algerian honeys", Food Control, vol 18(1), pp. 52-58, 2007.

[17] Y. Yücel, P. Sultanoglu, "Characterisation of honeys from Hatay Region by their physicochemical properties combined with chemometrics", Food Bioscience, vol 1, pp. 16-25, 2013.

[18] M. Moniruzzaman, M. I. Khalil, S.A. Sulaiman, S.H. Gan, "Physico-chemical and antioxidant properties of Malaysian honeys produced by Apis cerana, Apis dorsata and Apis mellifera", BMC Complementary and Alternative Medicine, vol 13(1),pp. 43, 2013.

[19] F. Tornuk, S. Karaman, I. Ozturk, O.S. Toker, B. Tastemur, O. Sagdıc, M. Dogan, A. Kayacier, "Quality characterization of artisanal and retail Turkish blossom honeys: Determination of physicochemical, microbiological, bioactive properties and aroma profile", Industrial Crops and Products, vol 46, pp. 124-131, 2013.

[20] A.S. Alqarni, A.O. Owayss, A.A. Mahmooud, "Physicochemical characterics total phenols and pigments of national and international honeys in Saudi Arabia", Arabian Journal of Chemistry, vol 9(1), pp. 114-120, 2012.

[21] L.R. Silva, R. Videira, A.P. Monteiro, P. Valentao, P.B. Andrade, "Honey from Luso region (Portugal): Physicochemical characteristics and mineral contents", Microchemical Journal, vol 93, pp. 73-77, 2009.

[22] A. Batu, E. Kücük, M. Cimen, "Dogu Anadolu ve Dogu Karadeniz bolgeleri cicek ballarının fizikokimyasal ve biyokimyasal degerlerinin belirlenmesi", Gıda Teknolojileri Elektronik Dergisi, vol 8(1), pp. 52-65, 2013.

[23] D. Anupama, K.K. Bhat, V.K. Sapna, "Sensory and physicochemical properties of commercial samples of honey", Food Research International, vol 36, pp. 183-191, 2003.

[24] H.M. Habib, F.T. Al Meqbali, H. Kamal, U.D. Souka, W.H. Ibrahim, "Physicochemical and biochemical properties of honeys from arid regions", Food Chemistry, vol 153, pp. 35-43, 2014.

[25]   R.A. Perez, M.M. Gonzales, M.T. Iglesias, E. Pueyo, C. Lorenzo, "Analytical, Sensory and Biological Features of Spanish Honeydew Honeys", In 1st World Honeydew Honey Symposium pp. 16-17, 2008.

[26]   J.M. Alvarez-Suarez, S. Tulipani, D. Díaz, Y. Estevez, S. Romandini, F. Giampieri, M. Battino, "Antioxidant and antimicrobial capacity of several monofloral Cuban honeys and their correlation with color, polyphenol content and other chemical compounds", Food and Chemical Toxicology, vol 48(8), pp. 2490-2499, 2010.

[27]   M.I. Isla, A. Craig, R. Ordoñez, C. Zampini, J. Sayago, E. Bedascarrasbure, L. Maldonado, "Physico chemical and bioactive properties of honeys from Northwestern Argentina", LWT-Food Science and Technology, vol 44(9), pp. 1922-1930, 2011.

[28]   A.S. Alqarni, A.A. Owayss, A.A. Mahmoud, "Physicochemical characteristics, total phenols and pigments of national and international honeys in Saudi Arabia", Arabian Journal of Chemistry, vol 9(1), pp. 114-120, 2016.

[29]   J.C. Serem, M.J. Bester, "Physicochemical properties, antioxidant activity and cellular protective effects of honeys from southern Africa", Food Chemistry, vol 133, pp. 1544-1550, 2012.

[30]   M. Moniruzzaman, M. I. Khalil, S. A. Sulaiman, S. H. Gan, "Physico-chemical and antioxidant properties of Malaysian honeys produced by Apis cerana, Apis dorsata and Apis mellifera", BMC Complementary and Alternative Medicine, vol 13(43), pp. 2013. Available: http://biomedcentral.com/1472-6882/13/43.

[31]   I. A. A. A. Da Silva, T. M. S. Da Silva, C. A. Camara, N. Queiroz, M. Magnani, J. S. De Novais, L. E. B. Soledade, E. O. Lima, A. L. De Souza, A. G. De Souza, "Phenolic profile, antioxidant activity and palynological analysis of stingless bee honey from Amazonas, Northern Brazil", Food Chemistry, vol 14, pp. 3552-3558, 2013.

[32]   A. Boussaid, M. Chouaibi, L. Rezig, R. Hellal, F. Donsi, G. Ferrari, S. Hamdi, "Characterization of Coffea arabica monofloral honey from Espírito Santo, Brazil", Arabian Journal of Chemistry, 2014. Available: http://dx.doi.org/10.1016/j.arabjc.2014.08.011.

[33]   A. C. Soria, M. Gonzalez, C. de Lorenzo, I. Martinez-Castro, I. Sanz, "Characterization of artisanal honeys from Madrid (Central Spain) on the basis of their melissopalynological, physicochemical and volatile composition data", Food Chemistry, vol 85, pp. 121-130, 2004.

[34]   J. Lachman, M. Orsak, A. Hejtmankova, E. Kovarova, "Evaluation of antioxidant activity and total phenolics of selected Czech honeys", LWT-Food Science and Technology, vol 43, pp. 52-58, 2010.

Mining Association Rules for Quality Improvement of the Examination Guidance in Hospitals

Esra Satır[1]*, Ufuk Karacaylı[1], Gamze Karaduman[1]

Abstract

People suffer various diseases each of which diagnosis may not be certain in the beginning due to the problems like misdirection, miscommunication and etc. Generally, detection of true departments in hospitals for diagnosis and treatment may be difficult at the first stage. Therefore, the aim of this study is to set up a system linked to Knowledge Discovery in Databases for directing the patient, efficiently. The procedure is to choose and perform the appropriate algorithm by considering the parameters in the handled data set. Accordingly, association rules are preferred where data can be described in rules of multiple granularities. These rules can be effective in uncovering unknown relationships and provide some results that can be basis for forecasting and decision making. Apriori algorithm is regarded as a well-known association rule learning algorithm in computer science. Apriori algorithm has been successfully applied to various problem domains such as manufacturing, marketing, logistics, medicine and many others. This study focuses on directing the patients efficiently by considering the previously appealed departments in the employed data set. Similar situations in the data set will be considered during the queries for decision making by using association rules. Implementation of this study has been carried out via a program developed with C# programming language. The employed data set has been obtained from Duzce University Medical Faculty. The experiments in the scope of this study have been performed by testing various support and confidence values. Thus, an effective guidance has been aimed for the patients without losing any time and without causing any misunderstanding.

Keywords*: Data mining, Association rules, Apriorialgorithm*

1. INTRODUCTION

People suffer various diseases each of which diagnosis may not be certain in the beginning due to the problems which originate both from the patient and the concerning personnel. These problems can occur due to lack of information, misdirection, miscommunication and etc. Generally, detection of true departments in hospitals for diagnosis and treatment is a big problem and it may be difficult at the first stage because of the mentioned problems. Therefore, the aim of this study is to set up a system linked to Knowledge Discovery in Databases (KDD) for directing the patient, efficiently. KDD has become one of the fastest growing research topics in mathematics and computer science, because the ability to continually change and acquire new understanding is a driving force for its applications. For example data mining have served in the search and retrieval of computer-aided design elements. The KDD process, specifically data mining techniques, is used to characteristically discover knowledge from data. The data mining process extracts knowledge from an existing data set and transforms it into a human-understandable structure for further use. Besides, data mining applications are very suitable for quality improvement programs [1].

In this study, the procedure is to choose and perform the appropriate algorithm by considering the parameters in the handled data set. Accordingly, association rules are preferred where data can be described in rules of multiple granularities. Association rule mining is a data mining technique used to find out useful and invaluable information from huge databases. It is employed to discover interesting relations between the variables in large databases. This dependency modelling analyses strong rules discovered in databases using different measures of interestingness [1]. These mined rules can be effective for uncovering unknown relationships and provide some results that can be basis for forecasting and decision making in the proposed study. Accordingly, Apriori algorithm is regarded as a well-known association rule learning algorithm in computer science.

---

[1]* Corresponding Author, Department of Computer Engineering, Düzce University, Düzce, Turkey.

The rest of this paper has been organized as four sections. In section 2, the related methods on different practical problems in the literature have been explained. In section 3, the employed method, Apriori algorithm, has been mentioned. In section 4, obtained results have been presented. Finally, a general outcome has been provided in section 5.

2. MATERIALS AND METHODS

Computational intelligence concepts have recently been used in discovering the relationships between different diseases and patient attributes [2]. Among the new techniques developed, data mining is the process of discovering significant knowledge, such as patterns, associations, changes, anomalies and significant structures, from large amounts of data stored in databases [3]. Apriori algorithm has been successfully applied to various problem domains such as manufacturing, marketing, logistics, medicine and many others.

In 2008, Liao and Lin proposed a study where a two-stage data mining approach has been implemented to investigate stock market investment in the Taiwan. First, they employed Apriori algorithm for mining the knowledge from historical data and this knowledge has been illustrated as knowledge patterns and rules in order to propose stock category association and possible stock investment collections. Then, K-means algorithm, a methodology of cluster analysis, has been employed for clustering of stock in order to mine the information for investment. Thus, using two different data mining approaches, they provided two aspects of data mining results in terms of presenting possible investment portfolio with stock market association and cluster knowledge [4].

In 2011, Liao and You investigated the following research issues related to the co-movement between exchange rates and categorical stock indexes in the Taiwan financial capital market: (1) the study of the changes of 13 foreign currency exchange rates indexes by association rules to find a similar trend in foreign currency change, and but also to identify the co-movement of foreign currency; (2) the use association rules to understand the co-movement between 13 international exchange rates and 30 categorical stock indexes in Taiwan; (3) the 13 subjects of the study will be stalls in foreign currency in accordance with their national and regional classification. When compared to exploring the same geographical area, the financial trading environment of countries was similar to changes foreign currency exchange rates; (4) to provide an opportunity for the foreign exchange market and stock market investors to invest in the Taiwan market with a different direction and a new way of thinking [5].

In 2012, Carmona et al. prpoposed a methodology for extracting useful information from web usage data acquired using Google Analytics in the website www.OrOliveSur.com. The concening website has been devoted to the national and international sales of extra virgin olive oil and derivatived products from the south region of Spain, Andalusia. They employed clustering, association rules and subgroup discovery techniques because we needed to describe the user behaviours in the website with respect to several properties [6].

In 2013, Nahar et al. investigated the sick and healthy factors which contribute to heart disease for males and females. In the concerning study, association rule mining, a computational intelligence approach, has been used to identify these factors and the UCI Cleveland dataset, a biological database, has been considered. They founded that females had been seen to have less chance of coronary heart disease then males by analyzing the information available on sick and healthy individuals and taking confidence as an indicator. Also, the attributes indicating healthy and sick conditions have been identified [2].

In 2014, Verma et al proposed a study that aims to find out the patterns of incidents in a steel plant in India. Occupational incidents occur in steel plant mainly in form of injury, near miss, and property damage or in combination. Different factors are responsible for such incidents to occur. They proposed an incident investigation scheme. In the concerning study, association rule mining approach has been used to discover cause-and-affect patterns (rules) using 843 incidents. Thirty-five meaningful association rules have been extracted using three criteria, support (S), con- fidence (C) and lift (L) [7].

In 2016, J. Deshmukha and Bhosleb proposed a stdy employing association rules for imge mining on medical image datasets. They presented the concept of data mining for discovering frequent image patterns in mammogram images using association rule. The proposed method has two phases. First phase is segmentation of digital mammogram to find region of interest (ROI) consisting of median filtering for noise removal, morphological processing for removing the background and suppressing artifacts, image enhancement techniques to improve image quality followed by region growing algorithm for complete removal of pectoral muscle. Second phase is image mining to find frequent image patterns present in mammogram images using Association rule. It consists of feature extraction, optimization by selecting most discriminating features among them, discretization of selected features and generation of transaction representation of input images. This has been given as input to Apriori algorithm to generate association rules. Result showed that image mining was feasible and gave strong association rules [8].

3. THEORY AND CALCULATION

Association rules algorithm is used mainly to determine the relationships between items or features that occur synchronously in the database. For instance, if people who buy item X also buy item Y, there is a relationship between item X and item Y, and this information is useful for decision makers. Therefore, the main purpose of implementing the association rules algorithm is to find synchronous relationships by analyzing the random data and to use these relationships as a reference during decision-making.

Make $I = \{i_1, i_2, …, i_m\}$ as the item set, where each item represents a specific literal. D stands for a set of transactions in a database in which each transaction T represents an item set such that T $T \subseteq I$. That is, each item set T is a non-empty sub-item set of I. The association rules are an implication of the form X → Y, where $X \subset I,\ Y \subset I$ and $X \cap Y = \emptyset$. The rule X → Y holds in the transaction set D according to two measure standards – support and confidence. Support (denoted as $Sup(X,\ D)$) to represent the rate of transactions in D containing the item set X. Support is used to evaluate the statistical importance of D, and the higher its value, the more important the transaction set D is. Therefore, the rule X → Y has support $Sup(X \cup Y,\ D)$ represents the rate of transactions in D containing X $\cup$ Y. Each rule X → Y also has the other measuring standard called Confidence (denoted as $Conf(X \to Y)$), representing the rate of transactions in D that contain X and also Y. That is,

$$\text{Conf}(X \to Y) = \text{Sup}(X \cap Y)/\text{Sup}(X,D) \qquad (1)$$

In this case, Conf(X → Y) denotes that if the transaction includes X, the chance that transaction also contains Y is relatively high. The measure confidence is then used to evaluate the level of confidence about the association rules X → Y. Given a set of transactions D, the problem of mining association rules is to generate all transaction rules that have certain user-specified minimum support (called *Minsup*) and confidence (called *Minconf*). The problem of mining association rules can be decomposed into two steps. The first step is to detect a large item set whose support is greater than Minsup and the second step is to generate association rules, using the large item set. Such rules must satisfy two conditions:

1. $Sup(X \cup Y,\ D) \geq Minsup$

2. $Conf(X \to Y) \geq Minconf$

To explore the association rules, many researchers use the Apriori algorithm. In order to reduce the possible biases incurred when using these measure standards, the simplest way to judge the standard is to use the lift judgment. Lift is defined as follows [4]:

$$\text{Lift} = \text{Confidence}(X \to Y)/\text{Sup}(Y) \qquad (2)$$

4. EXPERIMENTAL RESULTS AND DISCUSSIONS

Implementation of this study has been carried out via a program developed with C# programming language. The employed data set has been obtained from Duzce University Medical Faculty. Data are collected by observing the departmens where each patient consulted. The consulted departments by the patiens have been provided in Table 1.

Table 63. Outpatienl clinics consulted by the patiens

Outpatient Clinic	Abbreviation	Outpatient Clinic	Abbreviation
Brain Surgery	BR	Ophthalmology	OPH
General Surgery	GEN	Urology	URO
Emergency	EM	Nephrology	NEP
Psychiatry	PSI	Orthopedics	ORT
Chest Diseases	CHE	Diabetes	DIA
Neurology	NEU	Infectious diseases	IND
Physical medicine and rehabilitation	PMR	Cardiology	CAR
Family Medicine	FAM	Cardiovascular diseases	CAD
Otorhinolaryngology	OTO	Gynaecology	GYN
Endocrinology	END	Hypertension	HYP
Oncology	ONC	Legal medicine	LEM
Child endocrinology	CEN	Dermatology	DER
Pediatry	PED	Pregnancy	PRE
Internal Medicine	INM		

The experiments in the scope of this study have been performed by testing various support and confidence values. Thus, an unbiased evaluation has been aimed for effective guidance of the patients without losing any time and without causing any misunderstanding. The employed parameters for the performed experiments and the mined association rules have been provided in Table 2.

Table 2. Parameters for the experiments and mined association rules

Support	Confidence	Percentage	Association Rule
3	55	93%	BR=NO & GEN=NO & EM=NO & PSI=NO & CHE=NO
		100%	BR =NO & GEN=YES & EM =NO & PSI=NO & CHE =NO
		92%	BR =NO & GEN=NO & EM =YES & PSI=NO & CHE =NO
4	55	93%	BR =NO & GEN=NO & EM =NO & PSI=NO & CHE =NO
		100%	BR =NO & GEN=YES & EM =NO & PSI=NO & CHE =NO
		92%	BR =NO & GEN=NO & EM =YES & PSI=NO & CHE =NO
5	55	87%	BR =NO & GEN=YES & EM =NO & PSI=NO
		93%	BR =NO & GEN=NO & PSI=NO & CHE =NO
		100%	BR =NO & GEN=YES & PSI=NO & CHE =NO
		94%	BR =NO & EM =NO & PSI=NO & CHE =NO
		92%	BR =NO & EM =YES & PSI=NO & CHE =NO
		94%	GEN=NO & EM =NO & PSI=NO & CHE =NO
		100%	GEN=YES & EM =NO & PSI=NO & CHE =NO
		92%	GEN=NO & EM =YES & PSI=NO & CHE =NO
6	55	87%	BR =NO & GEN=YES & EM=NO & PSI=NO
		93%	BR =NO & GEN=NO & EM=NO & CHE =NO
		100%	BR =NO & GEN=YES & PSI=NO & CHE =NO
		94%	BR =NO & EM =NO & PSI=NO & CHE =NO
		92%	BR =NO & EM =YES & PSI=NO & CHE =NO
		94%	GEN=NO & EM =NO & PSI=NO & CHE =NO
		100%	GEN=YES & EM =NO & PSI=NO & CHE =NO
		92%	GEN=NO & EM =YES & PSI=NO & CHE =NO
7	55	93%	BR =NO & GEN=NO & PSI=NO & CHE =NO
		100%	BR =NO & GEN=YES & PSI=NO & CHE =NO
		94%	BR =NO & EM =NO & PSI=NO & CHE =NO
		92%	BR =NO & EM =YES & PSI=NO & CHE =NO
		94%	GEN=NO & EM =NO & PSI=NO & CHE =NO
		100%	GEN=YES & EM =NO & PSI=NO & CHE =NO
		92%	GEN=NO & EM =YES & PSI=NO & CHE =NO

As seen in Table 2, the percentages of the rules changesu between 87% and 100%. We can claim that these values are relevant for directing the patients efficiently since they indicate the accuracy of each rule. Besides, 4 itemset rules with percentages changing between 92% and 100% have been obtained in the performed experiments. For instance, let's interpret the following rule:

BR =NO & GEN=YES & EM =NO & PSI=NO & CHE =NO

A patient who didn't consult Brain Surgery, consulted General Surgery, didn't consult Emergency, Psychiatry and Chest Diseases. Thus, incoming patients in the similar situations can be guided by considering this rule not to loose time. This rule has the support value 3, and confidence value 55. By investigating Table 2, it can be said that the greater the support values are be, the shorter the rules are.

5. CONCLUSION

In this study, association rules are mined via Apriori algorithm for directing the patient efficiently in order to prevent the problems due to the lack of information in terms of both patient and the personnel. The contribution of this study is appltying the Apriori algorithm to a novel practical field. However, there are still some operations in order to render this study more efficient. There is a critical issue about Apriori algorithm in case of processing large data set. For this purpose and at the same time for increasing the accuracy of the algorithm, some auxiliary methods in the scope of optimization can be employed. This will increase the performance both in terms of time and accuracy while rule mining.

REFERENCES

[1] B. Kamsu-Foguem, F. Rigal, F. Mauget, "Mining association rules for the quality improvement of the production process", *Expert Systems with Applications*, vol. 40, pp. 1034–1045, 2013.

[2] J. Nahar, T. Imam, K. S. Tickle, Y. P. P. Chen, "Association rule mining to detect factors which contribute to heart disease in males and females", *Expert Systems with Applications*, vol. 40, pp. 1086–1093, 2013.

[3] S. H. Liao, W. J. Chang, C. C. Lee, "Mining marketing maps for business alliances", *Expert Systems with Applications*, vol. 35, pp. 1338–1350, 2008.

[4] S. H. Liao, H. H. Ho, H. W. Lin, "Mining stock category association and cluster on Taiwan stock market", *Expert Systems with Applications*, vol. 35, pp.19–29, 2008.

[5] S. H. Liao, P. H. Chu, Y. L. You, "Mining the co-movement between foreign exchange rates and category stock indexes in the Taiwan financial capital market", *Expert Systems with Applications*, vol. 38, pp. 4608–4617, 2011.

[6] C.J. Carmona, S. Ramírez-Gallego, F. Torres, E. Bernal, M.J. del Jesus, S. García, "Web usage mining to improve the design of an e-commerce website: OrOliveSur.com", *Expert Systems with Applications*, vol. 39, pp. 11243–11249, 2012.

[7] A. Verma , S. D. Khan, J. Maiti, O.B. Krishna, "Identifying patterns of safety related incidents in a steel plant using association rule mining of incident investigation reports", *Safety Science*, vol. 70, pp. 89–98, 2014.

[8] J. Deshmukha, U. Bhosleb, "Image Mining using Association Rule for Medical Image dataset ", *Procedia Computer Science*, vol. 85, pp. 117 – 124, 2016.

COMPARISON OF NATURAL WASTEWATER TREATMENT SYSTEMS

Zeki GOKALP[1], Sedat KARAMAN[2]

Abstract

Natural wastewater treatment systems are constructed for domestic, industrial and agricultural wastewaters in specially design basins filled with graded substrate material and planted with aquatic plants. The treatment processes naturally encountered in natural wetlands are imitated in these systems. Natural treatment systems can be constructed either as surface flow systems or sub-surface flow systems (either horizontal or vertical flow). Each system has special advantages and disadvantages over one another. In Turkey, mostly sub-surface horizontal flow natural treatment systems are preferred. In present study, initially some design criteria for different natural wastewater treatment systems are provided. Then, different systems were compared based on both design criteria, operational and maintenance practices. Finally, a system recommendation was provided for central Anatolia provinces.

Keywords: *Natural treatment, wastewater, surface flow, subsurface flow, central Anatolia*

1. INTRODUCTION

Ever-increasing water and food demands with rapidly increasing world population exert an increased stress on limited fresh water resources. The agricultural, domestic and industrial sectors are in continuous competition for limited water resources. Continuously polluted waters, decreasing water resources due to global warming and climate chance, increasing labor and energy costs all brought the water and treatment technologies into the first place of the world's agenda. To overcome the water-related problems, water losses in agricultural, domestic and industrial uses should be prevented, effective and efficient water use should be provided and possible use of wastewater and treated water should be investigated [1].

Effluent wastewaters are most of the time discharged into seas, rivers and other water bodies without any treatments due to high treatment costs both in Turkey and throughout the world. There are 3225 municipalities in Turkey. Of these municipalities, 2421 have a sewage system and 44.7% of 3.26 billion m³ wastewater are discharged into sea, 43.1% into rivers, 3.5% into dams, 2.1% into lakes, 1.5% into lands and 5.1% into other receiving bodies. About 69% of discharged wastewater is treated with 236 treatment facilities serving to 442 municipalities. Of these treatment facilities, 29 are physical, 158 are biological, 32 are advanced and 17 are natural treatment facilities [2].

Natural treatment systems, so called as constructed wetlands, are treatment systems used as an alternative to conventional treatment systems because of their low construction, operation and maintenance costs, energy demands, easy operation and low sludge generation [3, 4]. Constructed wetlands with their cheaper and easy construction, low energy and labor costs, easy operation, maintenance and monitoring were also specified as the primary issue in rural development strategy document of State Planning Organization of Turkey [5]. These systems are specially designed systems imitating the natural wetlands and include soil, plant and microorganisms to remove the pollutants from wastewaters. An excavated constructed wetland basin is lined with compacted clay or synthetic membrane and filled with graded sand-gravel substrate [6]. Today, constructed wetlands are widely used to treat domestic wastewaters [7], agricultural wastewaters [8], industrial wastewater and runoff waters [9].

These systems can be constructed either as surface flow systems or sub-surface flow systems (either horizontal or vertical flow). Each system has special advantages and disadvantages over one another. In Turkey, mostly sub-surface horizontal flow natural treatment systems are preferred. In present study, initially

---

[1] *Corresponding author: Erciyes University, Agricultural Faculty, Department of Biosystems Engineering, 38039, Melikgazi/Kayseri, Turkey. zekigokalp@yahoo.com*

[2] *Gaziosmanpasa University, Agricultural Faculty, Department of Biosystems Engineering, 60060, Taslıciftlik/Tokat,Turkey, skaraman@gop.edu.tr*

some design criteria for different natural wastewater treatment systems are provided. Then, different systems were compared based on both design criteria, operational and maintenance practices. Finally, a system recommendation was provided for central Anatolia provinces.

2. NATURAL WETLANDS

The natural wetlands are defined as the transition zones between lands and water bodies and include the sites with specific flora and fauna adapted to these regions and characterized with their high water tables and high organic matter contents [10]. They usually have water depths less than 6 meters and include the sites of flood plains, shallow shores, lagoons, estuaries, sluggish sections of rivers, lakes with fresh, bitter or salt water [11]. Nutrient inflow to wetlands supports the growth of vegetation and such vegetation constitute the primary component of wetland food-chain and converts inorganic materials into organic materials [12]. Wetlands are the natural heritages of the world with their biologic diversity and provide the following functions [13];

Wetlands provide a habitat for a rich flora and fauna,

Wetlands are the ecosystems with the highest biological production like tropical rainforests

Wetlands stabilize the water regimes of the regions where they are located through charging or discharging groundwater tables, storing floodwater, controlling floods, preventing see water intrusion,

Wetlands purify waters through retaining residues and poisonous materials or using nutrients (nitrogen, phosphorus).

Wetlands have a high economic value with their supports provided in fishery, agriculture, livestock, reed production and tourism,

Wetlands raise the humidity of the region where they are located and have positive impacts primarily on local climate parameters such as precipitation and temperature.

Wetlands are the ecosystems with the highest biological production like tropical rainforests.

Natural treatment systems purify waters and such functions bring the preservation of such sites into consideration. Although researches indicated high waste water treatment performance of natural wetlands [14, 15], such implementations may have some adverse effects with regard to preservation of these sites (Figure 1). Toxic elements in wastewaters, negative impacts of pathogens and additional hydraulic loading and nutrients can cause long-term degradations in these natural systems. Therefore, constructed wetland technologies have been developed instead of natural ones for wastewater treatment purposes.

Figure 1. Natural wetland

3. CONSTRUCTED WETLANDS

Constructed wetlands emulate the natural systems and contain soil, plant and microorganisms, commonly encountered in natural ones, within specially-designed and constructed basins to remove pollutants from wastewaters [14]. These systems are commonly composed of a compacted clay or synthetic liner overlaid with graded sand and gravel substrate material, reeds like aquatic plants and the other engineering structures adjusting hydraulic loading rates, retention times and water levels within the basin (Figure 2). Constructed wetlands, also called natural treatments systems, today are used for treatment of various wastewater resources.

Natural treatment systems have some advantages over conventional treatments systems. They are cheaper and easier to construct, require low energy and operational costs, do not require expert personnel, environment-compatible systems and provide habitat for various wetland organisms. Beside these advantages, they have

also some disadvantages. They require larger areas and system performance is less stable and easily be altered by changing climate conditions [15].

A successful constructed wetland design should take the following general criteria into consideration [15]:

The design should be kept as simple as possible and complex technological approaches should be avoided to prevent possible failures.

The wastewater flow should be supplied through gravitational flow,

The design should be so performed as to require the least maintenance,

The design should comply with the natural landscape and topography,

Extreme weather and climate conditions should be considered in design,

The systems should be allowed time to reach the desired performance values.
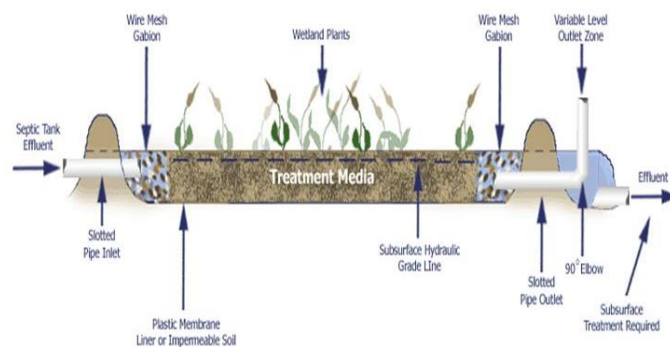

Figure 2. Constructed wetland components [6]

Constructed wetlands can either be designed as the primary treatment unit or integrated into multi-stage treatment systems. They are commonly designed as surface flow and sub-surface flow constructed wetlands. Based on flow regime, sub-surface flow wetlands are also classified as vertical and horizontal flow constructed wetlands.

3.1. Surface Flow Constructed Wetlands

The surface flow constructed wetland systems are typically composed of a bed or canal, a compacted impervious layer, soil or another media for plant rooting and relatively low water level flowing through the system (Figure 3). Water surface is above the filtrate or fill material. These systems resemble the natural wetlands and provide various benefits for wild life beside water treatment [16]. While the sections closer to surface are aerobic, deeper sections and substrate material are anaerobic. The primary advantage of these systems are their low investment, operation and maintenance costs, easy construction and operation and the basic disadvantage is the land requirement to construct such systems since they require significantly larger areas than the other constructed wetland or conventional treatment systems.
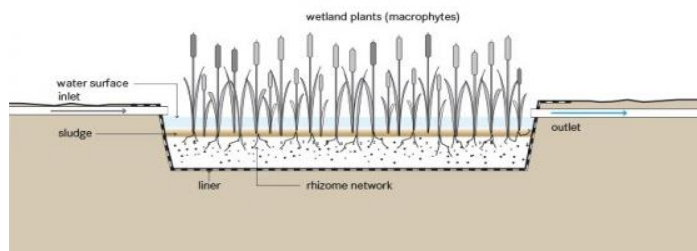

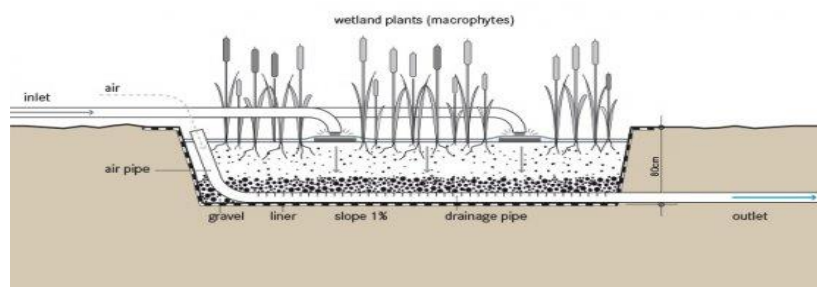*Figure 3. Surface flow constructed wetlands*

1192

In system design, biological oxygen demand (BOD), total suspended solids (TSS), nitrogen (total Kjeldahl nitrogen, denitrification and ammonium nitrogen), phosphorus, coliform bacteria, metal and other particulate pollutant performances are taken into consideration. Some recommended design criteria for optimum performance from surface flow constructed wetlands are provided in Table 1 [17].

Table 1. Design parameters for surface flow constructed wetlands

Parameter	Design Criteria
Influent quality	BOD $\leq 20 - 30$ mg L^{-1} TSS $\leq 20 - 30$ mg L^{-1}
Pre-treatment	Oxidation basins
Design flows	Q_{max} (maximum monthly flow) Q_{ave} (average flow)
Maximum BOD loading	20 mg L^{-1} : 45 kg ha^{-1} day^{-1} 30 mg L^{-1} : 50 kg/ha^{-1} day^{-1}
Maximum TSS loading	20 mg L^{-1}: 45 kg ha^{-1} day^{-1} 30 mg L^{-1}: 50 kg ha^{-1} day^{-1}
Water depth	0.6 – 0.9 m (full plant cover sections) 1.2 – 1.5 m (Open water surfaces) 1.0m (Inlet settling section)
Maximum HRT	2 days (full plant cover sections) 2 – 3 days (Open water surfaces)
Basin geometry	Optimum 3:1 – 5:1
Inlet settling section	In case of failed pretreatment in settling
Inlet	Uniform influent distribution in inlet
Outlet	Uniform effluent collection in outlet

3.2. Sub-surface flow constructed wetlands

Subsurface flow constructed wetlands are composed of a compacted clay or synthetic impermeable liner overlaid by graded gravel and sand substrate material planted with aquatic plants and water level control structures (Figure 4). They are designed in either horizontal flow or vertical flow and can be used with and without emergent plants [18]. Contrary to surface flow systems, water does not come out to surface in these systems and flows through a substrate material and reaches to outlet. Same parameters are considered in design and recommended design criteria are provided in Table 2 [17].
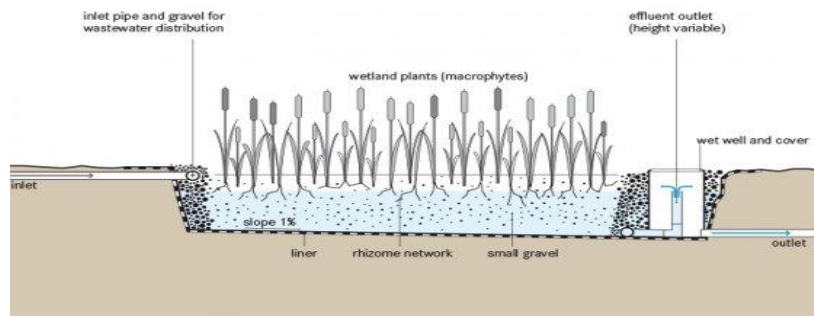
Figure 4. Vertical and horizontal flow sub-surface constructed wetlands

The most significant component of these systems is the substrate material filtering the wastewater. The material both provides a medium for rooting of aquatic plants and distributes influent, directs and collects effluent, provides surface area for microbial activity and filters suspended solids. Although various size and composition of substrate materials have been tried, there are not any concrete evidences about which size or type of material is the best. The basic criterion is not to allow small particles settle into the pores of coarser ones. Substrate upper surface should be leveled and about 1% slope should be provided at bottom surface. Inlet pipes should be so arranged to prevent short-circuit and substrate clogging and provide an equal flow. Outlet pipes should also prevent short-circuits, provide equal water collection and allow the operators to arrange the water level and effluent drainage.

Table 2. Design parameters for sub-surface flow constructed wetlands

Parameter	Design Criteria
BOD	6 g m^{-2} day^{-1} – 30 mg L^{-1} for inlet
TSS	20 g m^{-2} day^{-1} – 30 mg L^{-1} for inlet
Depth	Substrate: 0.5-0.6 m Water 0.4-0.5 m
Length	Minimum 15 m
Width	Maximum 61 m
Bed bottom slope	0.5 – 1%
Bed surface slope	Flat or almost flat
Hydraulic conductivity	1000 m day^{-1} for the first 30% of length
Substrate	Inlet section: 40-80 mm

In Turkey, sub-surface horizontal flow constructed wetlands are commonly used for domestic wastewater treatment in rural parts, especially in villages. Usually the type-projects designed by Special Provincial Administrations just by taking the total population to be served into consideration are implemented (Figure 4). Most of the time, local conditions, influent quality parameters, hydraulic loading rates, retention times and site-specific characteristics are not taken into consideration. Therefore, various failures 1194cur because of such design errors and most of the already constructed systems are not either well-operating or not-operating at all [19]. The common failures are classified as: failures in site selection, inlet clogging, substrate clogging and consequent water poundings over the surface, outlet clogging, leakage through slopes, plantation failures, failures in operation and maintenance [20]. Effluents of properly operating systems can also be used for irrigation purposes. However, irrigation water quality parameters should definitely be taken into consideration before using treated effluents.

4. CONCLUSION

Natural treatments systems, also called constructed wetlands, can reliably be implemented in sites with low land costs and limited labor force. They are getting common in rural parts of Turkey, especially in villages to treat domestic wastewater. Such implementations were also specified as the primary issue in rural development strategy document of State Planning Organization. Sub-surface horizontal flow constructed wetlands are common in practice. However, most of the already constructed systems are not either well-

operating or not operating at all just because of errors and mistakes made in their design, operation and maintenance processes. Such errors must urgently be corrected to prevent the waste of investment made on these systems. Re-use of treated effluent for irrigation purposes is also a critical issue to be considered. Almost 70% of renewable water resources are allocated to irrigations and re-use of constructed wetland effluents may provide significant water savings in irrigated agriculture. But, irrigation water quality parameters must be taken into consideration before the re-use of treated effluents. As to conclude, constructed wetlands are the significant systems to prevent water resources pollution since the wastewater previously was being discharged into receiving bodies without any treatments. Now, treated effluents are discharged into water bodies with these systems and consequently both water quality and aquatic life are preserved against the toxic and hazardous impacts of untreated sewage. Since central Anatolian provinces have terrestrial climate with harsh winters, sub-surface flow systems, especially horizontal flow sub-surface constructed wetlands are recommended.

REFERENCES

[1]. T. Akuzum, B. Cakmak, Z. Gokalp, "Türkiye'de su kaynakları yonetiminin degerlendirilmesi", 1. Ulusal Su Kaynkaları Yonetimi Sempozyumu, 20-22 Ekim 2010, Karaman.
[2]. Anonymous, "Belediye Atıksu İstatiskileri", 2008. TUIK Haber Bülteni, Sayı 74.
[3]. D.A. Hammer, R.X. Bastian, "Wetlands ecosystems: Natural water purifiers". In: D.A. Hammer, (Ed.), "Constructed Wetlands for Wastewater Treatment". Chelsea, Lewis, pp. 5–19, 1989.
[4]. H.R. Kadlec, R.L. Knight, "Treatment Wetlands". Lewis, Boca Raton, New York, London, Tokyo, p. 893, 1996.
[5]. Anonymous, "Ulusal Kalkınma Stratejisi", Devlet Planlama Teskilatı, 2006, http://sgb.tarim.gov.tr
[6]. Anonymous, "What are constructed wetlands in Treatment of Agricultural Waste by use of Constructed Reed-bed Wetlands", 2011, http://pgoforth.myweb.uga.edu/page3.html.
[7]. P. Cooper, M. Smith, H. Maynard, "The design and performance of a nitrifying vertical-low reed bed treatment system", Wat. Sci. Tech. 35, 215–221, 1997.
[8]. R. Rivera, A. Warren, C.R. Curds, E. Robles, A. Gutierrez, E. Gallegos, A. Caldeffin, "The application of the root zone method for the treatment and reuse of high strength abattoir waste in Mexico". Wat. Sci. Tech. 35, 271–278, 1997.
[9]. J.X. Dombush, "Natural renovation of leachate-degraded groundwater in excavated ponds at a refuse landfill", In: D.A. Hammer (Ed.), "Constructed Wetlands for Wastewater Treatment". Chelsea, Lewis, pp. 743–752, 1989.
[10]. H. Ciftci, S. Kaplan, H. Koseoglu, E. Karakaya, M. Kitis, "Yapay Sulak alanlarda Atıksu Arıtımı ve Ekolojik Yasam", Erciyes Üniv. Fen Bilimleri Enstitüsü Dergisi 23 (1) 149-160, 2007.
[11]. S. Cirik, "Sulak Alanlar", Ekoloji Dergisi, Nisan-Mayıs-Haziran, Sayı 7, s.50-51, 1993.
[12]. Hammer, D.A., Bastian, RX. (1989). Wetlands ecosystems: Natural water purifiers. In: Hammer, D.A. (Ed.), Constructed Wetlands for Wastewater Treatment. Chelsea, Lewis, pp. 5–19.
[13]. Z. Ayvaz, "Dogal Zenginlik Müzeleri Sulak Alanlar", Ekoloji Magazin, Nisan-Haziran, Sayı 6, 2005.
[14]. EPA, "Constructed wetlands for wastewater treatment and wild life habitat: 17 Case Studies". EPA832-R-93-005, 1993.
[15]. EPA, "A Handbook of Constructed Wetlands", Volume 1: General Considerations, USEPA Region III with USDA, NRCS, ISBN 0-16-052999-9, 1995.
[16]. R.B.E. Shutes, M. Revitt, M. Forshaw, B. Winter, "Constructed Wetland Monitoring and Management for Urban Runoff Management". In : Editors : Mansor, M., Eng, L.P. and Shutes, R.B.E. *Constructed Wetlands : Design, Management and Education*. Universiti Sains Malaysia Publisher, Malaysia, 2002.
[17]. EPA, "Manual, Constructed Wetlands Treatment of Municipal Wasterwaters", EPA/625/R-99/010, U.S. Environmental Protection Acency, Cincinnati, Ohio, USA, 1999.
[18]. T.C. Young, A.G. Collins, T.L. Theis, "Subsurface flow wetland for wastewater treatment at Minoa, NY". Report to NYSERDA and USEPA, Clarkson University, NY, 2000.
[19]. Z. Gokalp, B. Cakmak, "Dogal Arıtma Sistemlerinde Karsılasılan Problemler ve Cozüm Onerileri", 3. Uluslararası Bursa Su Kongresi, Cilt 1, s.119-126, 2013.
[20]. Z. Gokalp, O, Uzun, Y. Calıs, "Common Failures of the Natural Treatment Systems (Constructed Wetlands) of Kayseri", Turkey. Ekoloji 23(92):38-44, 2014.

Failures In Constructed Wetlands (Natural Wastewater Treatment Systems)

Zeki GOKALP[1], Sedat KARAMAN[2]

Abstract

Natural treatment systems, so called as "constructed wetlands" are artificial domestic wastewater treatments systems commonly used in rural sections of the country. Constructed wetlands with their low construction, operation and maintenance costs, low energy demands, simple operation and low sludge generation are preferred as an alternative to conventional treatment systems. These systems imitate natural wetlands in specially designed basins including soil, plant and microorganisms to remove the pollutants from wastewaters. These systems are designed and constructed based on various criteria. However, failures are also common in these systems when the design principles were not obeyed fully. Failures are usually observed because of improper site selection, substrate clogging, leakage through the compacted clay liner and sloped sides and various other improper design practices. In present study, common failures in constructed wetlands were assessed and solutions were proposed to overcome such failures.

Keywords: *Constructed wetland, water treatment, wastewater, failure, leakage*

1. INTRODUCTION

Today, world population reached to 7.5 billion and there is an ever-growing demand for food and water resources to feed this huge and continuously increasing population. There is an increasing pressure exerted over available water resources since agricultural, industrial and domestic water users are in a challenging competition for limited fresh water resources. Besides, current global warming and climate change aggravate this pressure over water resources. Thus, world countries have put water resources and water-related problems into first place in their agendas and assigned uppermost significance to water resources.

Agriculture is the greatest water user sector especially in developing countries. Therefore, initially agricultural water use should be handled to overcome water-related problems, then the problems in other water using sectors should be taken into consideration. Water losses and wastes in all sectors should be prevented, efficient water use should be provided and possible use of wastewater and treated water should be investigated [1].

According to the results of Municipal Wastewater Statistics Survey, which was applied to all municipalities, 1,309 municipalities out of 1,396 municipalities were served by sewerage systems in 2014 in Turkey. Out of 4.3 billion m^3 of wastewater collected by sewerage systems, 44.6% was discharged into sea, 44.2% was discharged into river, 2.8% into dam, 2.2% into lake and artificial lake, 0.4% onto land, and 5.8% to other receiving bodies. Out of 4.3 billion m^3 of wastewater discharged via sewerage system, 3.5 billion m^3 was treated in wastewater treatment plants. It means treatment was applied to 81% of discharged wastewater. The rate of advanced treatment was 41.6%, while the rate of biological treatment was 33.2%, the rate of physical treatment was 25.0% and the rate of natural treatment was 0.2%. About 50.5% of the treated wastewater was discharged into sea, 40.5% was discharged into river, 1.8% was discharged into dam, 1.4% was discharged into lake and artificial lake, 0.2% was discharged onto land and 5.6% was discharged into other receiving bodies. It is determined that, in 2014, population served by sewerage systems has a share of 84% in Turkey's population and a share of 90% in total municipal population. Rate of population served by wastewater treatment plants was 64% in Turkey's population, and 68% in total municipal population. Average amount wastewater discharged from municipal sewerage systems per capita per day was calculated as 181 liters.

[1] Corresponding author: Erciyes University, Agricultural Faculty, Department of Biosystems Engineering, 38039, Melikgazi/Kayseri, Turkey. zekigokalp@yahoo.com

[2] Gaziosmanpasa University, Agricultural Faculty, Department of Biosystems Engineering, 60060, Taslıciftlik/Tokat,Turkey, skaraman@gop.edu.tr

Considering the three largest cities, average amount of wastewater discharged per capita per day was 230 liters for Istanbul, 183 liters for Ankara, and 214 liters for Izmir [2].

Constructed wetlands, also called natural treatment systems with their cheaper and easy construction, low energy and labor costs, easy operation, maintenance and monitoring were specified as the primary issue in rural development strategy document of State Planning Organization of Turkey (Anonymous, 2006). Natural and constructed wetlands are treatment systems employed as an alternative to conventional treatment systems because of their low construction, operation and maintenance costs, low energy demands, simple operation and low sludge generation [3, 4]. These systems are specially designed systems imitating the natural wetlands and include soil, plant and microorganisms to remove the pollutants from wastewaters. An excavated constructed wetland basin is lined with compacted clay or synthetic membrane and filled with graded sand-gravel substrate [5]. Today, constructed wetlands are widely used to treat domestic wastewaters, agricultural wastewaters, industrial wastewater and runoff waters. Treated effluent water can be used for irrigation and other water recycling purposes.

In present study, initially brief information was provided about the natural wetlands to present an insight into natural treatment systems. Then, possible use of constructed wetlands imitating these natural wetlands for waste water treatment in rural parts of Turkey, especially in villages, was assessed. Brief information was also provided about potential drawbacks and problems observed in construction, operation and maintenance of these systems.

2. CONSTRUCTED WETLANDS

Many terms are used to denote constructed wetlands, such as reed beds, soil infiltration beds, constructed treatment wetlands, treatment wetlands, etc. Beside "engineered" wetlands, the terms of "man-made" or "artificial" wetlands are often found as well [6]. Constructed wetlands imitate the natural wetlands in treatment of domestic wastewaters. They are also called natural treatment systems and contain soil, plant and microorganisms within specially-designed and constructed basins to remove pollutants from wastewaters [7]. These systems are commonly composed of a compacted clay or synthetic liner overlaid with graded sand and gravel substrate material, reed like aquatic plants and the other engineering structures adjusting hydraulic loading rates, hydraulic retention times and water levels within the basin (Fig. 1). Constructed wetlands are engineered systems that use natural functions of vegetation, soil, and organisms to treat different water streams. Depending on the type of wastewater that has to be treated the system has to be adjusted accordingly which means that pre- or post-treatments might be necessary.

Constructed wetlands have several advantages over the conventional treatment systems. The primary advantage is their low costs and easy construction. They require quite low or even zero-energy for operation and have significantly lower operational costs than the conventional ones. Constructed wetlands are environment-friendly systems and provide habitat for various wetland plants and organisms. Beside these advantages, they have also some disadvantages. They require larger construction areas than regular and conventional treatment systems to treat the same capacity wastewater influent. The system performance is less stable, dominantly depend on wastewater characteristics and can easily be altered by changing climate conditions[8].

A successful constructed wetland design should take the following general criteria into consideration [8]:

- The design should comply with the natural landscape and topography.

- The design should be kept as simple as possible.

- Extreme weather and climate conditions should be considered in design.

- The design should be so performed as to require the least maintenance.

- The wastewater flow should be supplied through gravitational flow.

- The systems should be allowed time to reach the desired performance values.

Constructed wetlands are commonly designed as surface flow and sub-surface flow constructed wetlands. Based on flow regime, sub-surface flow wetlands are also classified as vertical and horizontal flow constructed wetlands. In Turkey, mostly sub-surface horizontal flow constructed wetland systems are used for domestic wastewater treatment in rural sections of the country. Thus, brief information was provided about surface flow systems and then sub-surface horizontal flow systems were explained in detail.
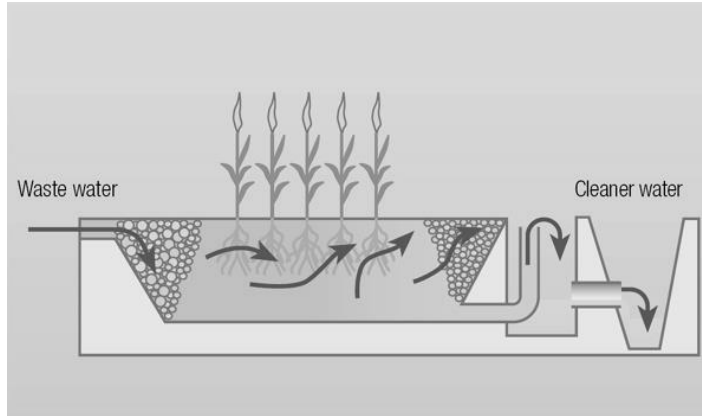
Figure 1. Constructed wetland components [9]

2.1. Surface Flow Constructed Wetlands

Surface flow constructed wetland systems are composed of a natural or excavated bed or canal, a compacted impervious layer at the bottom, soil or another substrate media for plant rooting and relatively low water level flowing through the system (Fig. 2). Water surface is open to atmosphere and above the filtrate or substrate material. These systems look more like the natural wetlands and provide various benefits for wild life beside water treatment [10]. The primary advantage of these systems are their low investment, operation and maintenance costs, easy construction and operation and the basic disadvantage is the land requirement to construct such systems since they require significantly larger areas than the other constructed wetland or conventional treatment systems [11].
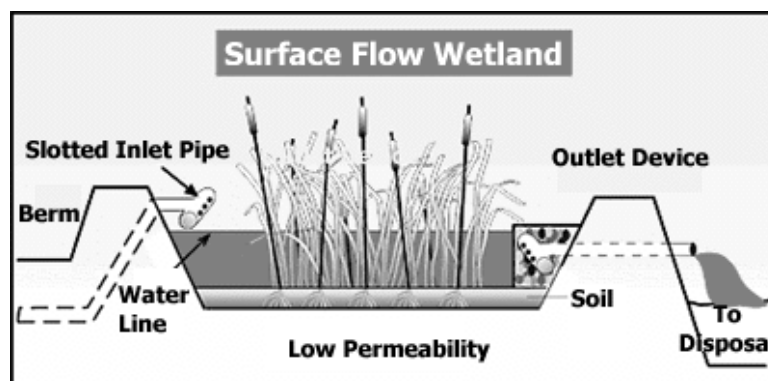

Figure 2. *Surface flow constructed wetlands [12]*

2.2. Sub-Surface Flow Constructed Wetlands

Contrary to surface flow systems, water does not come out to surface in sub-surface flow constructed wetland systems, in other words, water level is not open to atmosphere and flows through a substrate material and reaches to outlet. Sub-surface flow constructed wetlands are usually composed of an excavated basin, a compacted clay or synthetic impermeable liner overlaid by graded gravel and sand substrate material planted with aquatic plants and water level control structures (Fig. 3). Based on flow regime, they are designed in either horizontal flow or vertical flow and can be used with and without emergent plants [13]. Certain parameters should be taken into consideration in design of these systems and recommended design criteria are provided in Table 2 [11].
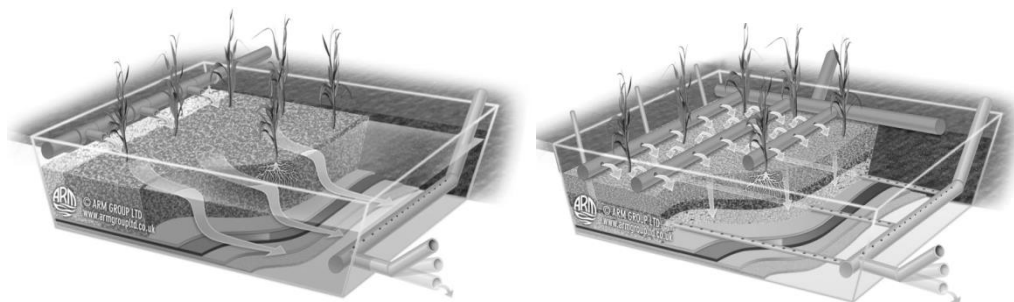
Figure 3. Horizontal and vertical flow sub-surface constructed wetlands [14]

Table 2. Design parameters for sub-surface flow constructed wetlands

Parameter	Design Criteria
BOD	6 g m^{-2} day^{-1} – 30 mg L^{-1} for inlet
TSS	20 g m^{-2} day^{-1} – 30 mg L^{-1} for inlet
Depth	Substrate: 0.5-0.6 m
	Water 0.4-0.5 m
Length	Minimum 15 m
Width	Maximum 61 m
Bed bottom slope	0.5 – 1%
Bed surface slope	Flat or almost flat
Hydraulic conductivity	1000 m day^{-1} for the first 30% of length
	10000 m day^{-1} for the last 70% of length
Substrate	Inlet section: 40-80 mm
	Process section: 20-30 mm
	Outlet section: 40-80 mm
	Planting section: 5-20 mm

Commonly sub-surface horizontal flow constructed wetlands are used for domestic wastewater treatment in rural parts, especially in villages of Turkey. Municipal waste water administrations or special provincial administrations are responsible for the construction of these systems. However, most of them have already been constructed by special provincial administrations. The administrations usually use type-projects designed to serve certain populations. Since these systems are constructed in villages, they are commonly designed for 250, 500, 750 and 1000 people. A type project designed for a population of 750 people is presented in Fig 4. Concrete septic tanks (usually with 4 cells) are constructed in front of constructed wetland systems to provide a pre-treatment for influent. Suspended soils are mostly settled in septic tanks.

About 1.0 m deep basin is excavated with construction machinery just by taking the population into consideration. Usually about 1 m^2 base area was considered for each person. An aspect ratio (L:W) of about 5:1 is generally used in sub-surface flow constructed wetland systems in Turkey. Excavation of slopes usually performed at a ratio of 1H:2V. Once the basin was excavated, about 10 cm clay liner is placed over the bottom and slopes and the liner is then compacted. Instead of using geotextile or synthetic liners, compacted clay is generally used in Turkey to provide bottom lining and to prevent possible seepage through the bottom and slopes.

The most significant component of these systems is the substrate material filtering the wastewater. The material both provides a medium for rooting of aquatic plants and distributes influent, directs and collects effluent, provides surface area for microbial activity and filters suspended solids. Although various size and composition of substrate materials have been tried, there are not any concrete evidences about which size or type of material is the best. The basic criterion is not to allow small particles settle into the pores of coarser ones. About 15 cm agricultural soil is placed over the clay liner for rooting of aquatic plants to be planted later on. Over the soil, about 25-30 cm medium gravel (1.0-1.5 cm diameter) layer is placed and over that layer, about 20 cm sand (2.0 mm) layer is placed. Substrate upper surface is leveled and about 1% slope is provided at bottom surface. Coarse gravel (4.0-6.0 cm diameter) is placed at the influent entrance and effluent outlet sections to provide easy influent flow into substrate material through the perforated pipe placed around the top of coarse gravel and easy discharge of effluent through perforated drainage pipe placed beneath the coarse gravel.
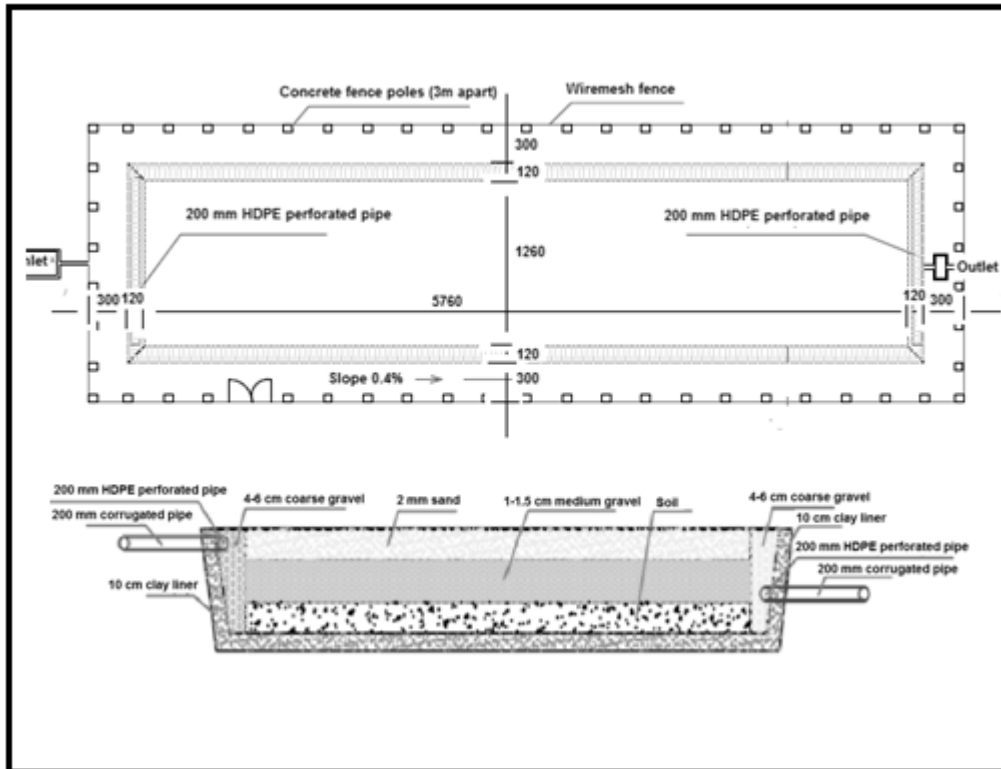

Figure 4. A pilot project designed for a population of 500 people

Side berms are slightly elevated from the substrate surface to prevent runoffs and erosion of fine materials into the reed bed. Usually common reed (*phragmites australis*) is used for surface plantation of constructed wetlands in Turkey. A usual density is taken as 3-5 plants (rhizomes) per square meter. Finally entire red bed is surrounded with wire-mesh fences to prevent access to reed bed. The system is then handed over to local administration (village administration) for operation.

In Turkey, only the population to be served was taken into consideration while designing horizontal flow sub-surface constructed wetlands. Local topography, climate conditions, influent wastewater characteristics, hydraulic loading rates, hydraulic retention times, site-specific characteristics, discharge criteria and most important of all standard design procedures are not taken into consideration. Thus, various failures are experienced because of such design errors and majority of already constructed systems are not either well-operating or not-operating at all [15].

The common failures are classified as: failures in site selection, inlet clogging, substrate clogging and consequent water ponding over the surface, outlet clogging, leakage through slopes, plantation failures, failures in operation and maintenance [16]. Site selection is a failure observed in some cases where reed bed was constructed just by small streams adjacent to high slopes (Fig. 5a). While design manuals for sub-surface systems recommend 5 m^2 basin surface area per capita, or at least 3-5 m^2 in case of limited land resource, the systems constructed in Turkey usually allocate about 1 m^2 basin surface area per capita. Then clogging is experienced at the influent input section because of excessive loading (Fig. 5b, c).

Seepage is another problem in constructed wetlands of Turkey. Commonly clay liners are used to prevent possible seepage. It is easy to compact clay liner over the bottom, but compaction is quite difficult over the sloped surfaces. Therefore, seepage commonly is observed from the sloped surfaces of reed beds. A regular and well-developed plant cover is not established in majority of the systems. Reed beds just turned into 'weed beds' because of improper and insufficient plantation (Fig. 5d). The constructed wetland systems should be properly operated, maintained and monitored. System performance should regularly be assessed through routine analyses for different pollution parameters to see if the system performance meets the relevant discharge criteria. In Turkey, none of these post-construction implementations are performed.

(a)   **(b)**   **(c)**   **(d)**

Figure 5. Common failures experienced in practice (Gokalp et al., 2014)

3. CONCLUSION

As long as appropriate design criteria were taken into consideration, constructed wetlands, also called natural treatment systems, can reliably be implemented in sites with low land costs and limited labor force. These systems, especially sub-surface horizontal flow constructed wetland systems, are getting common in rural parts of Turkey, especially in villages to treat domestic wastewater. Such implementations were also specified as the primary issue in rural development strategy document of State Planning Organization of Turkey. However, most of the already constructed systems are not either well-operating or not operating at all just because of errors and mistakes made in their design, operation and maintenance processes. Such errors must urgently be corrected to prevent the waste of investment made on these systems. Valid design specifications, site-specific conditions, local climate conditions and extreme values, influent wastewater characteristics, hydraulic loading rates and retention times should all be taken into consideration while designing a natural treatment system for a specific location. As to conclude, constructed wetlands are the significant systems to prevent water resources pollution since the wastewater previously was being discharged into receiving bodies without any treatments. Now, treated effluents are discharged into water bodies with these systems and consequently both water quality and aquatic life are preserved against the toxic and hazardous impacts of untreated sewage. Re-use of treated effluent for irrigation purposes is also a critical issue to be considered. Almost 70% of renewable water resources are allocated to irrigations and re-use of constructed wetland effluents may provide significant water savings in irrigated agriculture. But, irrigation water quality parameters must be taken into consideration before the re-use of treated effluents.

REFERENCES

[1] T. Aküzüm, B. Cakmak, Z. Gokalp, "Türkiye'de su kaynakları yonetiminin degerlendirilmesi", 1. Ulusal Su Kaynkaları Yonetimi Sempozyumu, 20-22 Ekim 2010, Karaman.

[2] Anonymous 2015a. Municipal Waste Water Statistics 2014, *Turkish Statistical Institute,* No:18778, 22 December 2015.

[3] Kadlec, H.R., Knight, R.L. 1996. Treatment Wetlands. Lewis, Boca Raton, New York, London, Tokyo, p. 893.

[4] H.R. Kadlec, R.L. Knight, "Treatment Wetlands". Lewis, Boca Raton, New York, London, Tokyo, p. 893, 1996.

[5] Anonymous, "What are constructed wetlands in Treatment of Agricultural Waste by use of Constructed Reed-bed Wetlands", http://pgoforth.myweb.uga.edu/page3.html. Accessed 29.01.2015.

[6] H. Hoffmann, C. Platzer, E. von Münch, M. Winker, "Technology review of constructed wetlands - Subsurface flow constructed wetlands for greywater and domestic wastewater treatment". Deutsche Gesellschaft für Internationale Zusammenarbeit (GIZ) GmbH, Eschborn, Germany, 2011.

[7] EPA, "Constructed wetlands for wastewater treatment and wild life habitat: 17 Case Studies". EPA832-R-93-005, 1993.

[8] EPA, "A Handbook of Constructed Wetlands", Volume 1: General Considerations, USEPA Region III with USDA, NRCS, ISBN 0-16-052999-9, 1995.

[9] Anonymous, *http://www.unep.org/yearbook/2003/070.htm.* Accessed 30.01.2016.

[10] R.B.E. Shutes, M. Revitt, M. Forshaw, M. and B. Winter, "Constructed Wetland Monitoring and Management for Urban Runoff Management". In : Editors : Mansor, M., Eng, L.P. and Shutes, R.B.E. *Constructed Wetlands : Design, Management and Education*. Universiti Sains Malaysia Publisher, Malaysia, 2002.

[11] EPA, "Manual, Constructed Wetlands Treatment of Municipal Wasterwaters", EPA/625/R-99/010, U.S. Environmental Protection Acency, Cincinnati, Ohio, USA, 1999.

[12] Anonymous, *http://www.wateronline.com/doc/surface-flow-systems-work-like-natural-wetlan-0001.* Accessed 30.01.2016.

[13] T.C. Young, A.G. Collins, and T.L. Theis. "Subsurface flow wetland for wastewater treatment at Minoa", NY. Report to NYSERDA and USEPA, Clarkson University, NY, 2000.

[14] Anonymous, *http://www.armreedbeds.co.uk/resources/constructed-wetlands/horizontal-subsurface-flow/.* Accessed 31.01.2016.

[15] Z. Gokalp, B. Cakmak, "Dogal Arıtma Sistemlerinde Karsılasılan Problemler ve Cozüm Onerileri", 3. Uluslararası Bursa Su Kongresi, Cilt 1, s.119-126, 2013.

[16] Z. Gokalp, O, Uzun, Y. Calıs, "Common Failures of the Natural Treatment Systems (Constructed Wetlands) of Kayseri", Turkey. Ekoloji 23(92):38-44, 2014.

Solving Constrained Optimization Problems with Sine-Cosine Algorithm

Simge Ekiz[1], Pakize Erdogmus[2], Busra Ozgur[3]

Abstract

Optimization algorithms aim to find the optimum values that give the maximum or minimum result of a function under given circumstance.

There are many approaches to solve optimization problems. Stochastic population-based optimization approaches tend to give the best results in a reasonable time. Two of the state-of-art stochastic optimization algorithms are Genetic Algorithms (GA) and Particle Swarm Optimization(PSO). In addition, Sine-Cosine Algorithm is one of the recently developed stochastic population-based optimization algorithms. It is claimed that Sine-Cosine has a higher speed than the counterparts of it. Moreover, Sine-Cosine Algorithm occasionally outperforms other optimization algorithms including GA and PSO. This algorithm is successful because it can balance exploration and exploitation smoothly.

In the previous studies, the above-mentioned algorithms were evaluated and compared to each other for the unconstrained optimization test functions. But there is no study on constrained optimization test problems. In this study, we aim to show the performance of Sine-Cosine Algorithm on constrained optimization problems. In order to achieve this, we are going to compare the performances by using well-known constrained test functions.

Keywords: *Sine-Cosine Optimization Algorithm, Constrained Optimization Problems, Penalty Method*

1. INTRODUCTION

Optimization can be defined as finding the most effective and highest achievable performance under the given limitations. Mathematically speaking, Optimization is finding the minimum or maximum of a function subject to the constraints. A set of values that satisfies all the constraints of an optimization problem creates a feasible solution. The optimization technique tries to find the optimum solution from all of these feasible solutions [1].

Optimization problems can be found in every area of life because all living things tend to do the best. For example, Birds fly in 'V' shape to reduce the energy consumption, another example fish moves in flocks to benefit from defense against predators [2]. Optimization problems have been a topic since 1960's. In these years optimization problems have been tried to solve by classical mathematical methods. Deterministic methods have a great advantage that they find global optima. Unfortunately, they cannot solve all nonlinear problems. With classical optimization, only limited problems can be solved. The inadequacy of classical methods has forced scientists to search for new methods. To find the optimum, solution stochastic algorithms are developed. These algorithms sample the search space without exploring it thoroughly. Stochastic computation techniques have received a great deal of attention regarding their potential as optimization techniques for complex problems. As a result, the development of stochastic algorithms has begun.

It is impossible to develop one way to solve all the nonlinear problems. There are a lot of methods proposed. Stochastic algorithms can find promising solutions for difficult optimization problems, but there is no guarantee that optimal solutions can be reached all the time. Stochastic algorithms are good at solving most of the real world problems which are nonlinear and multimodal[1].

The general nonlinear programming problem is defined as follows[3];

---

[1] *Corresponding author: Duzce University, Department of Computer Engineering, Duzce, Turkey. simgeekiz@duzce.edu.tr*

[2] *Duzce University, Department of Computer Engineering, Duzce, Turkey. pakizeerdogmus@duzce.edu.tr*

[3] *Duzce University, Department of Computer Engineering, Duzce, Turkey. busratakgil@duzce.edu.tr*

Minimize $\quad\quad f(x), \quad x = (x_1, \dots, x_n) \in R^n$

Subject to the constraints $g_i(X) \geq 0$

$$h_i(X) = 0$$

Where $g_i(X)$ and $h_i(X)$ are constraints that are required to be satisfied.

The optimization problem is based on finding the optimum value of the objective function, and if there are no constraints on the variables, these problems are called unconstrained optimization problems. The solution of unconstrained optimization problems is easier than the constrained ones. However, most real-life problems are constrained. It is necessary to find the best value of a constraint optimization problem such as resource constraint, time constraint, cost constraint, design constraint according to these conditions.

1.1. Related Works

In 1994 Joines and Houck solve four test cases of constrained optimization problems with the genetic algorithm. They transform constrained optimization problems to the unconstraint optimization by using the penalty method. They aim at reaching the feasible solution of genetic algorithm by giving appropriate value according to the number of generations[4]. In 1996 Michalewicz and Schoenauer present several constraint-handling techniques for optimization problems. The first one based on feasibility of solutions, the second one is penalty based, the third method makes a clear distinction between feasible and infeasible and fourthly hybrid methods. Moreover, they provide 11 test cases which we use in this study to make our experiments[3]. In 2002 Hu and Eberhart applied one of the constraint handling methods which based on preserving feasibility of solutions. They test particle swarm optimization algorithm on the same test cases[5]. In 2005 Yeniay go over all constraint handling penalty based techniques for the genetic algorithm. He mentions their advantages and disadvantages. He emphasizes the importance of setting appropriate values of the penalty parameters[6].

1.2. Dealing with constraints

All the stochastic algorithms are directly suited to unconstrained optimization problems. Applying these algorithms to constrained optimization problems has always been a problem. In real life problems such as engineering design problems are constrained optimization problems and constraints has a great effect on the optimization performance[7]. Fortunately, many constrained optimization algorithms can be transformed to the unconstrained case, often with the use of a penalty method.

Penalty function method is common because of its simple principle and easy implementation. We modify the objective function in such a way that it penalizes any violation of the constraints.

Penalty function method can be formulated as follows[8];

Minimize $\quad\quad f(x)$

Subject to the constraints $g_i(X) \geq 0 \quad\quad i = 1,2,3,\dots\dots m$

The equivalent unconstrained optimization problem can be stated as;

Minimize $\quad\quad F(x) = f(x) + P(x)$

Maximize $\quad\quad f(x)$

Subject to the constraints $\ g_i(X) \geq 0 \quad\quad i = 1,2,3,\dots\dots m$

The equivalent unconstrained optimization problem can be stated as;

Maximize $\quad\quad F(x) = f(x) - P(x)$

In minimization problems, we include the penalty function which adds a high cost to the objective function. In maximization problems, we subtract the penalty function from the objective function.

In this study, we implement two of the state-of-art algorithms that we mentioned to the well-known constraint test cases. In addition to these algorithms, we also implement Sine Cosine Algorithm that developed in 2016[9]. The above-mentioned algorithms were directly suited to unconstrained optimization test functions. To deal with constraints we use the penalty function method due to its popularity and easy implementation [7]. Penalty method adds the penalty term to the objective function for any violation of the constraints [8], [10]. We aim to show the performance of Sine-Cosine Algorithm on constrained optimization problem and compare results with genetic algorithm and particle swarm optimization algorithm.

2. BACKGROUND THEORIES

2.1. Genetic Algorithm (GA)

Pseudo code for Genetic Algorithm;
Begin
t ← 0;
InitializePopulation[P(t)];
EvaluatePopulation[P(t)];
while not termination **do**
P'(t) ← Selection[P(t)];
P(t+1) ← ApplyGeneticOperators[P'(t)uQ];
EvaluatePopulation[P(t+1)];
t ← t+1;
end while
return BestSolution
end

Genetic algorithm mimics the biological evaluation. It starts with creating a population randomly. And population can be described as a group of individual solutions. In each iteration, the algorithm chooses some solutions from the current population as parents according to their fitness values to form a new generation. The new generation is created by applying genetic operators such as crossover and mutation. Next, these new generations are evaluated, and this process is going on until the termination condition is met. And the population evolves toward an optimal solution.

2.2. Particle Swarm Optimization Algorithm (PSO)

Pseudo code for Particle Swarm Optimization Algorithm;
Begin
t ← 0;
InitializeParticles[P(t)];
EvaluateParticles [P(t)];
while not termination **do**
t ← t+1;
Select pBest for each Particle;
Select gBest from P(t-1);
CalculateParticleVelocity[P(t)];
UpdateParticlePosition[P(t)];
EvaluateParticles [P(t)];
end while
return BestSolution
end

Particle Swarm Optimization is another population optimization technique developed by Eberhart and Kennedy in 1995. It starts with initializing the population of random solutions called particles. In PSO the particles have velocity values alongside the fitness values. In every iteration, gbest and pbest are selected. Pbest is the best solution has achieved so far by a particle. Gbest is the best value obtained so far by any particle in the population. Next, the velocities of the particles are calculated using pbest and gbest values. Then particle positions are updated based on the velocities. Thus, the particles follows the best particle in the search space.[11]

2.3. Sine Cosine Algorithm (SCA)

Pseudo code for Sine Cosine Algorithm;

```
begin
    InitializeSearchAgents[X];
    while t<maximum number of iterations do
            EvaluateSearchAgents[X];
            UpdateBestSolution(P=X*);
            Update r₁r₂r₃r₄ ;
            UpdateSearchAgentPosition;
    end while
return BestSolution
end
```

Sine cosine algorithm can be described as the following formula;

$$X_i^{t+1} = \begin{cases} X_i^t + r_1 * \sin(r_2) * |r_3 P_i^t - X_i^t|, & r_4 < 0.5 \\ X_i^t + r_1 * \cos(r_2) * |r_3 P_i^t - X_i^t|, & r_4 \geq 0.5 \end{cases}$$

As another population-based optimization algorithm sine cosine algorithm also starts with initializing random solutions called search agents. Sine cosine algorithm uses 4 variables to tune. These are r variables. r_1 decides that search agent is going to do whether exploration or exploitation. All stochastic algorithms are both exploration and exploitation but it is important to balance these. r_2 decides how far the solution's movement should be. r_3 assign a random weight and r_4 decided whether sine or cosine formula is going to be used.

In every iteration, the solutions are evaluated by using the fitness function and the algorithm assigns the best solution obtained so far as the destination point. Next, the r variables are updated.

Search agent positions are updated based on the r variables and the best solution. Thus the potential solutions follow the best solution in the search space [9].

3. EXPERIMENTS

We use global optimization toolbox in Matlab© which includes both genetic algorithm and particle swarm optimization algorithms with default values. And we implement Sine cosine algorithm with 30 search agents and 1000 iterations. The algorithms are run 30 times on the popular constraint optimization test problems that Michalewicz and Schoenauer first presented. We get these test problems from Kyoto University global optimization test problems web site[13]. We implement penalty method to these test cases.

The test problems are given below;

G1	Min $f(x) = \sum_{i=1}^{4} x_i - 5\sum_{i=1}^{4} x_i^2 - 5\sum_{i=5}^{13} x_i$
G2	Max $f(x) = \left\|\dfrac{\sum_{i=1}^{n} \cos^4(x_i) - 2\prod_{i=1}^{n} \cos^4(x_i)}{\sqrt{\sum_{i=1}^{n} i x_i^2}}\right\|$
G4	Min $f(x) = 5.3578547 x_3^2 + 0.8356892 x_1 x_5 + 37.293239 x_1 - 40792.141$
G5	Min $f(x) = 3x_1 + 10^{-6} x_1^3 + 2x_2 + \frac{2}{3} * 10^{-6} x_2^3$
G6	Min $f(x) = (x_1 - 10)^3 + (x_2 - 20)^3$
G7	Min $f(x) = x_1^2 + x_2^2 + x_1 x_2 - 14x_1 - 16x_2 + (x_3 - 10)^2 + 4(x_4 - 5)^2 + (x_5 - 3)^2$ $+2(x_6 - 1)^2 + 5x_7^2 + 7(x_8 - 11)^2 + 2(x_9 - 10)^2 + (x_{10} - 7)^2 + 45$

G8	$\text{Max } f(x) = \frac{\sin^3(2\pi x_1)\sin(2\pi x_2)}{x_1^3(x_1+x_2)}$
G9	$\text{Min } f(x) = (x_1 - 10)^2 + 5(x_2 - 12)^2 + x_3^4 + 3(x_4 - 11)^2 + 10x_5^6 + 7x_6^2 + x_7^4$ $-4x_6x_7 - 10x_6 - 8x_7$
G10	$\text{Min } f(x) = x_1 + x_2 + x_3$
G11	$\text{Min } f(x) = x_1^2 + (x_2 - 1)^2$
G13	$\text{Min } f(x) = e^{x_1x_2x_3x_4x_5}$

4. EXPERIMENTAL RESULTS

Results are shown in figures. The red lines represent the best-known values gathered in Kyoto University Global Optimization Website.

Sine cosine algorithm, genetic algorithm, and particle swarm optimization algorithm are represented by respectively by orange, pink and blue bars. In terms of accuracy mostly genetic algorithm gives the best results. SCA algorithm is outperformed by the others or results as the same.
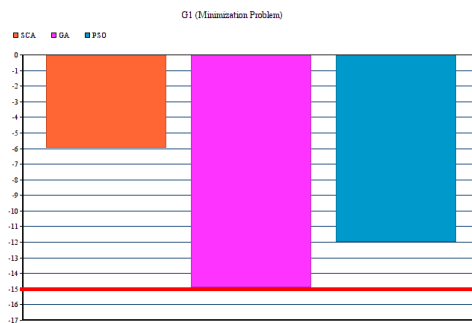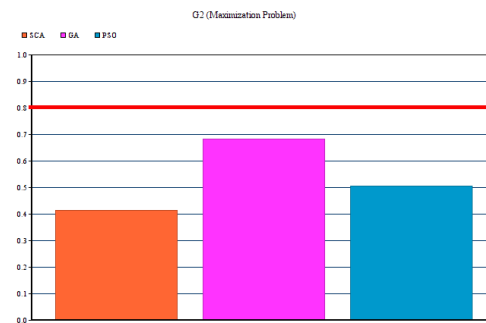

Figure 1. G1 Test Function(Minimization)

Figure 2. G2 Test Function(Maximization)

In G1 global optimization test case, genetic algorithm outperforms the other two algorithms. G1 is minimization problem and GA reaches the minimum value which is -15.

In G2 is maximization problem and in these experiments, any of the algorithms reach the maximum value gathered in Kyoto University Global Optimization Website so far.
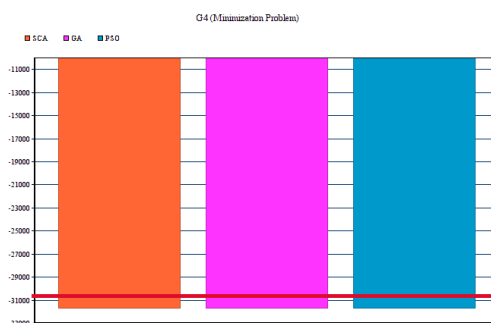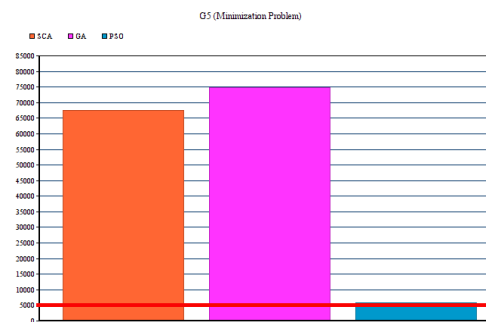

Figure 3. G4 Test Function(Minimization)

Figure 4. G5 Test Function(Minimization)

All the algorithms find the optimum value in G4 and G11 test cases. Like in these situations it is better to choose the algorithm which takes a shorter time. In G5 only PSO find the minimum optimal value. In G6, SCA and GA are both find the minimum value which updates the minimum value found up to now. Moreover, SCA is not good at solving problems like G7 but in the G8 test case, SCA outperforms both GA and PSO. In G9, G10, G13 test cases SCA is outperformed by the others.
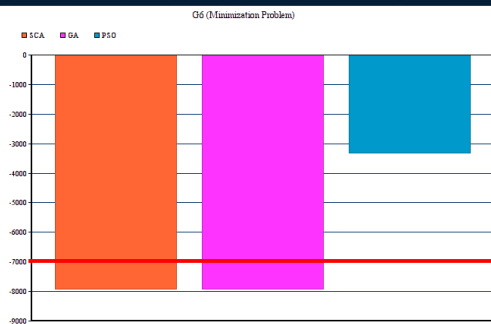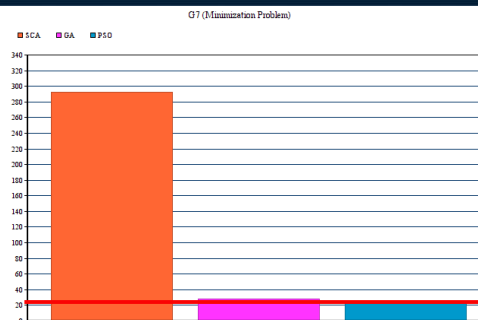
Figure 5. G6 Test Function(Minimization)

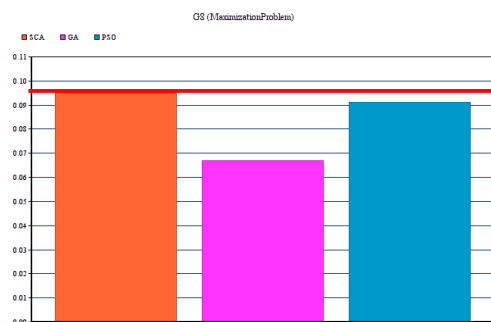*Figure 6. G7 Test Function(Minimization)*

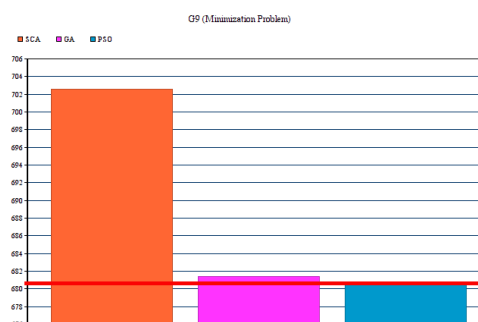*Figure 7. G8 Test Function(Maximization)*
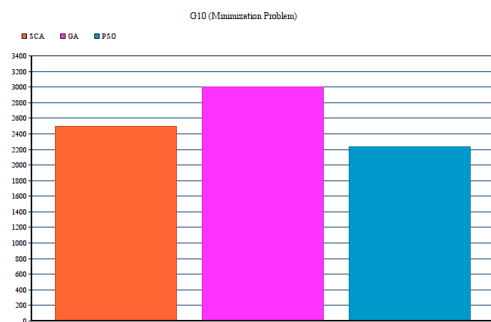

Figure 8. G9 Test Function(Minimization)

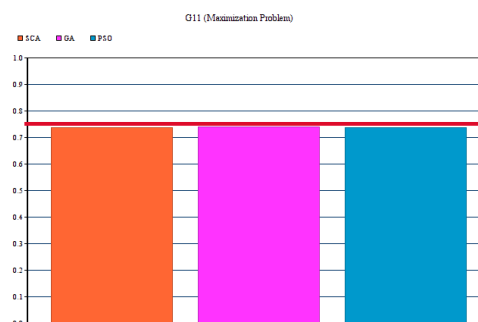*Figure 9. G10 Test Function(Minimization)*

Figure 10. G11 Test Function(Maximization)
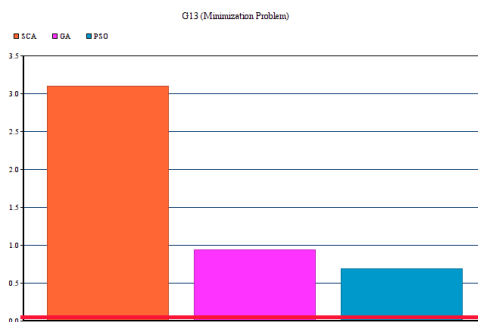

Figure 5. G13 Test Function(Minimization)
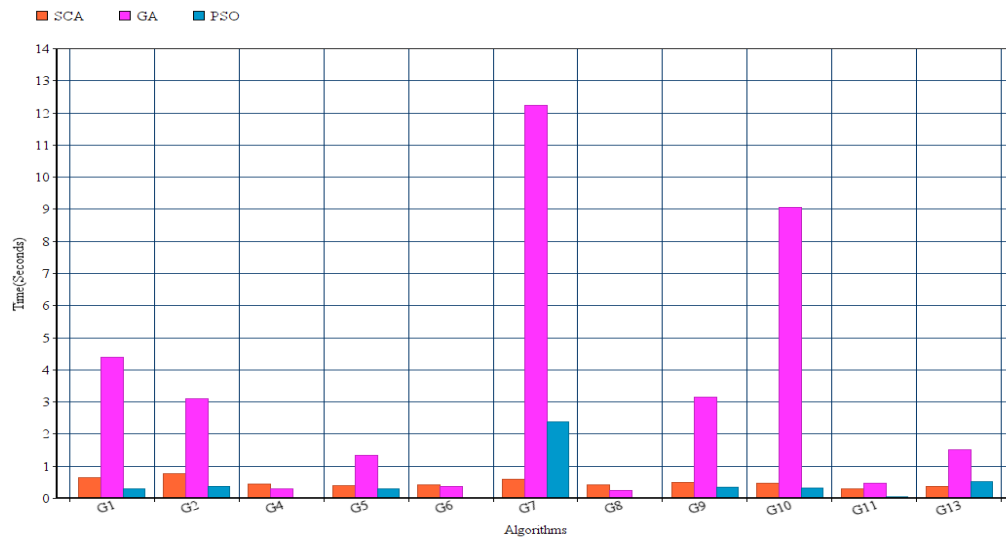
Algorithms Time Chart

Figure 108. The time taken by the algorithms for each test case

This graph demonstrates the time taken by the algorithm for each problem. In most of the cases, the slowest algorithm is a genetic algorithm. Except two of the cases, PSO is the fastest one. And SCA takes slightly more time than the PSO. Mostly both PSO and SCA finish under a second.

5. CONCLUSIONS AND DISCUSSION

In this study, we optimized well known constrained optimization problems with using the recently developed sine cosine algorithm. We deal with constraints with the help of penalty method. Then we compared SCA algorithm results with GA and PSO. In terms of accuracy GA gives the best results but in terms of speed PSO and SCA are faster. Although SCA gives better result in unconstrained optimization problems, it does not perform well on constrained optimization problems. But SCA is a new algorithm and it might give better results by making further improvement in the algorithm. Also, it might give better results when we change the method of handling constraints.

REFERENCES

[1] A. Askarzadeh, "A novel metaheuristic method for solving constrained engineering optimization problems: Crow search algorithm," *Comput. Struct.*, vol. 169, pp. 1–12, 2016.

[2] "Swarm Behaviour." [Online]. Available: https://en.wikipedia.org/wiki/Swarm_behaviour.

[3] Z. Michalewicz and M. Schoenauer, "Evolutionary Algorithms for Constrained Parameter Optimization Problems," *Evol. Comput.*, vol. 4, no. 1, pp. 1–32, 1996.

[4] J. A. Joines and C. R. Houck, "On the use of non-stationary penalty functions to solve nonlinear constrained optimization problems with GA's," in *Evolutionary Computation, 1994. IEEE World Congress on Computational Intelligence., Proceedings of the First IEEE Conference on*, 1994, pp. 579–584.

[5] X. Hu and R. Eberhart, "Solving Constrained Nonlinear Optimization Problems with Particle Swarm Optimization," *Optimization*, vol. 2, no. 1, pp. 1677–1681, 2002.

[6] O. Yeniay, "Penalty function methods for constrained optimization with genetic algorithms," *Math. Comput. Appl.*, vol. 10, no. 1, pp. 45–56, 2005.

[7] Q. He and L. Wang, "An effective co-evolutionary particle swarm optimization for constrained engineering design problems," *Eng. Appl. Artif. Intell.*, vol. 20, no. 1, pp. 89–99, 2007.

[8] A. Homaifar, C. X. Qi, and S. H. Lai, "Constrained Optimization Via Genetic Algorithms," *Simulation*, vol. 62, no. 4, pp. 242–253, 1994.

[9] S. Mirjalili, "SCA: A Sine Cosine Algorithm for solving optimization problems," *Knowledge-Based Syst.*, vol. 96, pp. 120–133, 2016.

[10] R. Courant, "Variational methods for the solution of problems of equilibrium and vibrations," *Bull. Am. Math. Soc.*, vol. 49, no. 1, pp. 1–24, 1943.

[11] J. Kennedy and R. Eberhart, "Particle swarm optimization," *Neural Networks, 1995. Proceedings., IEEE Int. Conf.*, vol. 4, pp. 1942–1948 vol.4, 1995.

[12] J. Brownlee, "Particle Swarm Optimization." [Online]. Available: http://www.cleveralgorithms.com/nature-inspired/swarm/pso.html. [Accessed: 26-Apr-2017].

[13] A. R. Hedar, "Global Optimization Test Problems." [Online]. Available: http://www-optima.amp.i.kyoto-u.ac.jp/member/student/hedar/Hedar_files/TestGO.htm.

Designing Autonomous Vehicle Parking System with Embedded Trajectories

Bunyamin Esiyok[1], Anil Can Turkmen[2], Ozgur Kaplan[2], Cenk Celik[2]

Abstract

In this study, there is an algorithm which offers a solution to parking problem for vehicles. Parallel parking type is chosen for an algorithm. The system works after finding an enough parking space then use implemented trajectories for suitable parking. Matlab-Simulink is used for simulation process.

Keywords: *Autonomous vehicle, Trajectory, Parallel parking, Ultrasonic sensor, Path planning*

1. INTRODUCTION

Automotive companies are in a big technology war as the other industries. Automotive technology was just mechanical in early times but today electronics part has a big part of the industry. New technologies and solutions are generally in an electronic way and also electrical cars are used in daily life. Intelligent driver assistant systems are playing an important role in the automotive industry. In the last decade, researchers spend their times for perfect parking process more than the other innovations for vehicles. Due to making a fully autonomous car, autonomous parking is a key part of the system.

Except autonomous driving, autonomous parking system suggests enjoyable driving experiences. According to researches, especially novice drivers have a problem with parking process. Also, crowded cities are getting bigger and bigger every day which means drivers have a problem with the number of parking areas.[1]

The goal of the park assistant system is to help the drivers have more enjoyable and more productive driving experiences. Also, another aim is decreasing damages during the parking operation. Parking damages have very bad effect on World's economy. Because countries and insurance companies pay money for simple parking damages and also owners of the cars' sell their cars below its value because of damage history.

In the system, ultrasonic sensors are used for scanning the area. Sensors are located on the corners of the car. After scanning the area, the system chooses the suitable trajectory for parking process.

2. AUTONOMOUS DRIVING LEVELS

Level 0: Driving process is completely controlled by human driver.

Level 1: A specific driver assistant system helps driver such as automatic brake systems.

Level 2: In this level, at least two tasks are controlled by a system.

Level 3: In this level, still driver is the most importantly competent. There are some systems as line tracking or distance tracking. Nowadays car companies produce their cars in this level

Level 4: This level is like the fully-autonomous system but one difference. The driver sits in the driver seat and generally interested in the environment. The vehicle starts self-driving in highways.

Level 5: This is a fully-autonomous system which driver can sit in the back seat.

Autonomous levels are generally accepted in that scale. Autonomous parking system has a key role for autonomous driving. And also autonomous parking system is a very big innovation for stepping up from level three to four.

---

[1] Corresponding author: Yildiz Technical University, Department of Environmental Engineering, 34220, Esenler/İstanbul, Turkey. ocinar@yildiz.edu.tr

[2] Zenith Group, Sarajevo, Bosnia and Herzegovina, mkose@zenithgroup.ba

3. LITERATURE SURVEY

In recent years, parking assistance systems were improved in the automotive industry to make perfect movements for perfect parking instead of drivers. Path planning is one of the important problems for parking operation. For this reason, trajectory planning algorithm needs to be good and creative for a collision-free path starting from the first point to the last position, which is described as a parking area. Of course, this trajectory needs to satisfy all kinematic conditions and limitations of the car model. This kind of problem belongs to the most frequently considered examples in robotics literature, where various solution approaches are available, e.g. planning based on neural networks, fuzzy-techniques, dynamic programming, numerical continuation methods and two-step algorithms making use of small-time controllability. In any case, rather experimental techniques are connected for this assignment in the application. One reason might be that lots of authors analyzed the case of full autonomous-maneuvering, though most versions of assistant systems just control the steering system of the car, driver still needs to control the velocity. One more issue of the systematic technique is that frequently complicated calculations are included which are difficult to achieve progressively. Besides, some of the features required by the automotive industry, like that the path founded by the car should be same as the behavior of a real driver or that steering at standstill should be avoided, are rather difficult to integrate into the systematic-frameworks.

In this contribution, a usable type of an algorithm is developed and this algorithm ensures the requirements for some real-life applications. Besides, the methodology is based on a strong hypothesis guaranteeing that a solution is always found provided that one exists. In principle, the proposed strategy is a combination of the crash-free planned path algorithm created in and the path planner for a vehicle presented in. Parking operation has special requirements such as velocity controlling, steering controlling, trajectory finding etc. These processes have to be in progress together and final position of the vehicle should be where it is demanded. Besides, it is indicated how sensible calculation times can be accomplished by performing real parts of required costly figuring offline. In this setting, some point of interest on a keen usage structure of the algorithm is given. In the following section, a suitable dynamic model of a vehicle is presented and the considered trajectory planning issue is defined all the more definitely. Besides, some essential outcomes coming about because of the uncommon structure and basic properties of the vehicle model are expressed. [2]

4. PREVIOUS PARKING ALGORITHMS

In 1999, M. Wada, K. Yoon, H. Hashimoto, and S. Matsuda proposed a paper in an International Conference named "Development of advanced parking system using human guidance". This paper offers not only parallel but also vertical parking with an increased complexity in maneuvers and numerous direction changes. In this solution, parking time lasts longer and needs parking space around 1.55 times of the vehicle length for the parking process. [3]

In 2001, F. Gomez-Bravo, F. Cuesta and A. Ollero, proposed a paper named "Parallel and diagonal parking in nonholonomic autonomous vehicles". This study presents collision-free trajectories from an initial position to final position. There are several trajectories determined before and the algorithm based on a fuzzy logic controller. Researchers tested that method in a small electrically powered car model. But testing with a real car model was unsuccessful because of the less ability of parking the car in small distance areas. Real car kinematics is not appropriate for this method. [4]

In 2008, T.-H. Hsu, J.-F. Liu, P.-N. Yu, W.-S. Lee proposed a paper named "Development of an automatic parking system for vehicle," in Vehicle Power and Propulsion Conference. This paper focuses on steering motor controller. In the project, the main idea is parking the car with the path which has the minimum length from the possible trajectories. This parking system just working for the back parking process. [5]

In 2006, I. Song, K. Gowan, J. Nery, H. Han, T. Sheng, H. Li, and F. Karray proposed a paper "Intelligent parking system design using FPGA" in an international conference which is also a fuzzy control based solution. This study concentrates on initial and final positions of the trajectories and does not care about the comfortable drive. But instead of comfortable drive, that study presents fast car parking for the drivers. [6]

In 2000, J. Xu, G. Chen, and M. Xie proposed a vision guided automatic parking paper named "Vision-guided automatic parking for smart car" in Intelligent Vehicles Symposium. In this system video data needed to find a space and calculate a collision-free parking path. Neural network and hybrid fuzzy logic algorithms are used to find solution. This parking operation is useful for parallel parking operation. [7]

In 2012, N.Scicluna, E.Gatt, O.Casha, I.Grech, and J.Micallef proposed a paper for autonomous parking using fuzzy logic control in International conference named "FPGA-based autonomous parking of a car-like robot using fuzzy logic control" [8]

After having knowledge about these algorithms, generally, systems need parking space more than 1.4 times of the vehicle length for the parking process. [9]

5. PARKING PROBLEM

Parking is the process that leaving the car temporarily in a parking area until it required. Parking process seems easy but it has some difficulties especially for novice drivers. There are a lot of factors that effect on parking process. For example; length of the car, steering angle, size of the tires, angle of the road etc. Also, there is a problem about the parking area, because parking could be between two cars, by the side of the road, or in a parking space between poles etc. There is no standard parking space set in the world. Every country and local governments have their rules. This problem starts from that, not every car has the same length. That's why there is no standard variable for parking. Sometimes it's not easy to park these places even for experienced drivers.

6. VEHICLE MODEL

6.1. Bicycle Model

Bicycle model is widely used in this kind of research as autonomous systems. This model can be modified to four-wheel car.
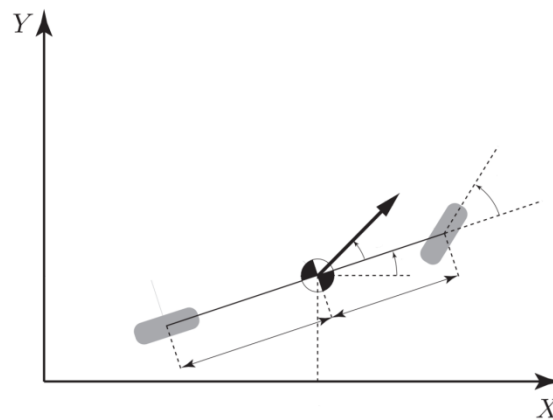

Figure 109. An example of a bicycle model. [10]

Center of gravity is one of the important points for automotive engineering. Bicycle model is flexible and realistic. Any model can be built up to this dynamic. A usable car which has a great load distribution between front and rear wheels is found for this study.

In this study, car variables are presented in the following:

Length: 4491 mm

Width: 1852 mm, with mirrors: 1978 mm

Drag coefficient: 0.30

Turning circle diameter: 11100 mm

Wheelbase: 2450 mm

Steering Ratio: 12.55:1 – 16.3:1

In figure 2, dynamics blocks of the car presented.

This model has the blocks which car needs when it is parking itself. They are;

1-Sensor Data

2-Hand Brake

3-Steering Selection System

4-X and Y position

5-Heading Angle

6-Timer

7-Shift Changer

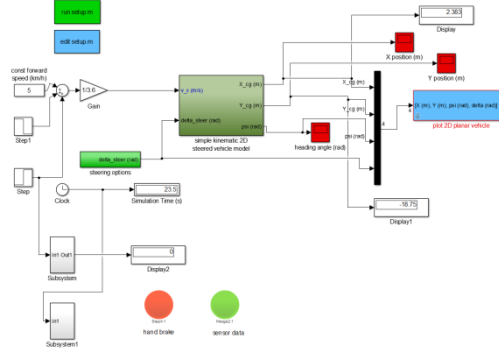8-Throttle pedal

9-Brake pedal

Figure 2. Dynamic model blocks

In the following figure, subsystem of the model presented for steering selection.
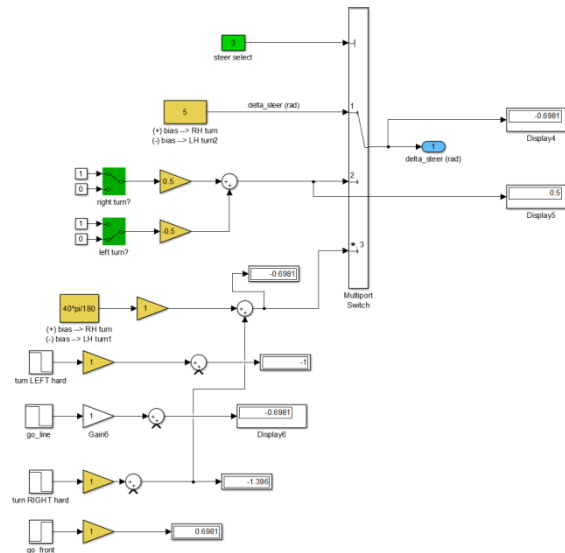
Figure 3. Subsystem of steering option selection

7. RESULT AND DISCUSSION

During simulations, parking process tested in different situations. Assumptions were set as 0.57, 1.416 and 2.262 meters for the distance between autonomous car and parking line (parking area or parked car). With these assumptions, 24 different trajectories were tested successfully. The study could be contributed with the numerous trajectories to use this algorithm in real life.

In this system, motivation is parking the car with less maneuvering with no crash. Firstly, less maneuvering decreases the fault possibility during parking process. Secondly less maneuvering gives the possibility of parking the car in a shorter time.

In the following figures, displacement of car presented for X and Y axes. These data are taken from the blocks which are the parts of car's dynamic model.

Figure 4. Displacement on X-axis

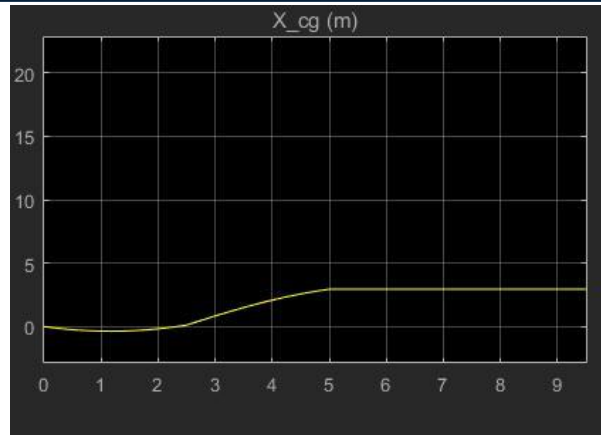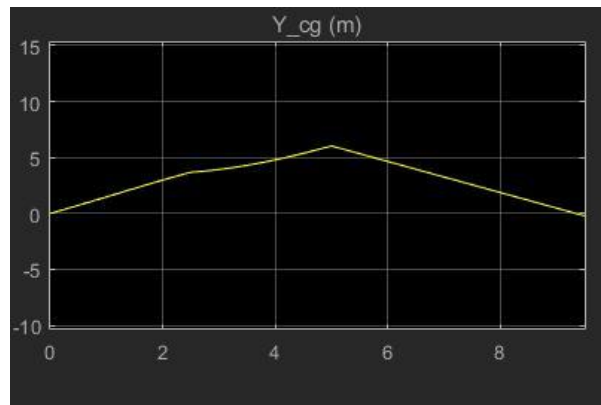*Figure 5. Displacement on Y-axis*

8. CONCLUSION

Due to driver does not control anything, this system is much more comfortable comparing to other parking assistance systems.

System dynamics could be integrated any car model in the future.

In the system required parking area is found as 7.2 meters which are 1.6 times of the vehicle length. If distance between autonomous car and parking line decreases, needed parking are becoming longer.

In the system, required free space for parking area is optimum for a comfortable parking space. Because car can leave the parking area with one move and other cars' drivers do not have any potential problem. Due to less maneuvering, possibility of crashing into a car or an object is less and system reduces the possibility of making mistake.

In the world general, people parks the car just the right side. But in some countries such as Turkey, people allowed to park the car on the left side so system modified also for left side parking. After modifying for the left side parking, 24 different situations were tested successfully.

REFERENCES

[1] Rafique, M.U. and Faraz, K., "Guidance Based Autonomous Parking Assistant", *2nd International Conference on Industrial Mechatronics and Automation*, Wuhan-China, 30 May-31 May 2010, pp. 320-324, China, 2010.

[2] Muller, B., Deutscher J. and Grodde S., "Continuous Curvature Trajectory Design and Feedforward Control for Parking a Car", *IEEE Transactions on Control Systems Technology, Vol. 15, No.3*, May 2007, pp. 541-553.

[3] M. Wada, K. Yoon, H. Hashimoto, and S. Matsuda, "Development of advanced parking assistance system using human guidance," in Advanced Intelligent Mechatronics, 1999. Proceedings. 1999 IEEE/ASME International Conference on, 1999, pp. 997–1002.

[4]   F. Gomez-Bravo, F. Cuesta, and A. Ollero, "Parallel and diagonal parking in nonholonomic autonomous vehicles," Engineering Applications of Artificial Intelligence, vol. 14, no. 4, pp. 419 – 434, 2001.

[5]   T.-H. Hsu, J.-F. Liu, P.-N. Yu, W.-S. Lee, and J.-S. Hsu, "Development of an automatic parking system for vehicle," in Vehicle Power and Propulsion Conference, 2008. VPPC '08. IEEE, 2008, pp. 1–6.

[6]   I. Song, K. Gowan, J. Nery, H. Han, T. Sheng, H. Li, and F. Karray, "Intelligent parking system design using FPGA," in Field Programmable Logic and Applications, 2006. FPL '06. International Conference on, 2006, pp. 1–6.

[7]   J. Xu, G. Chen, and M. Xie, "Vision-guided automatic parking for smart car," in Intelligent Vehicles Symposium, 2000. IV 2000. Proceedings of the IEEE, 2000, pp. 725–730.

[8]   N. Scicluna, E. Gatt, O. Casha, I. Grech, and J. Micallef, "FPGA-based autonomous parking of a car-like robot using fuzzy logic control," in Electronics, Circuits, and Systems (ICECS), 2012 19th IEEE International Conference on, 2012, pp. 229–232.

[9]   Ertugrul, H., "An FPGA Implementation of two-step Trajectory Planning for Automatic Parking", Middle East Technical University, Sept 2013, pp. 6-7.

[10] Rajamani, R., Vehicle Dynamics, and Control, ser. Mechanical Engineering Series. Springer, 2011 pp. 26.

[11] https://www.mathworks.com/ , last accessed in April 2016.

Performance Evaluation of MPLS Networks with Traffic Engineering

Ali Gezer[1]

Abstract

Multi-Protocol Label Switching (MPLS) technology becomes an efficient solution for Internet Service Providers backbone network which includes the traffic engineering specifications of ATM and scalability of IP networks. MPLS nodes route packets from one hop to another in MPLS cloud using short path labels in comparison to IP routers which decides next hop via looking complex routing tables. MPLS establishes connection oriented paths over a connectionless IP network. MPLS also provides many services such as Layer 2 VPN, layer 3 VPN and traffic engineering. It works well with many data link layer protocols such as IP, ATM, Frame Relay etc. In this paper, we take into consideration traffic engineering capabilities of MPLS routing technology. We evaluate the performance of MPLS network using dynamic and static label switched paths. A quite heavy traffic load is applied to designed networks which include video conferencing voice, web, ftp, Email, file print and database traffic. Traffic received and sent, voice jitter, hop counts and delay performance metrics are obtained to compare the performance of two path models. Most of the time, dynamic LSPs give better performance results.

Keywords: *Multi-Protocol Label Switching (MPLS), Opnet Simulator, Performance Evaluation, Traffic Engineering*

1. INTRODUCTION

Multi-Protocol Label (MPLS) is a new technology which generally works in the backbone of ISPs to connect the network of service providers to the outside world. It's called multi-protocol because it works with multiple protocols including IP, ATM and FR. The most prominent feature of MPLS technology which is superior to conventional technologies in many ways is to be fully compatible with the Internet Protocol. Therefore, there is no need to change any other components of the network unlike ATM technologies [1].

MPLS plays a key role in next generation networks by delivering QoS and traffic engineering features [2]. MPLS technology shows its advantages in managing traffic in the case of some links or paths are under or over utilized [2]. MPLS, Traffic engineering mechanisms are mostly deployed by ISPs to guarantee Quality of Service (QoS) and efficiently utilize network resources such as link bandwidth [3].

For some specific traffic type such as voice traffic which is considered as delay sensitive traffic, MPLS technology could minimize the delay. In [4], it is explained by performing experiments on real environment that MPLS based network provide better Quality of Services (QoS) as compared to conventional networks for voice and other traffics in terms of packet loss and end to end delay. In the mentioned study, an MPLS based network is implemented to reduce propagation delay and avoid packet loss in order to improve Mean Opinion Score (MOS) for VOIP networks [4].

In IP routing when a packet reaches a router, the router process the packet then forward the packet to the next hope [5]. But MPLS routing is deployed in order to cope with processing delay. Therefore, it provides better solution for the delay sensitive traffics, such as audio and video, to switch the packets in fastest way [6].

In this study, we design two network scenarios with using MPLS static paths and dynamic paths to reveal the advantages and performance results of two routing strategies. Traffic load for the designed network includes HTTP traffic, e-mail, FTP, database applications, VoIP and video conferencing. The rest of the paper is organized as follows. Section II presents the background information about MPLS technology. In Section III, we give the details of designed networks via Opnet 14.5. Section III presents the obtained simulation results.

---

[1] *Corresponding author: Erciyes University, Department of Electronic and Automation, 38039, Kayseri, Turkey. aligezerr@hotmail.com*

2. MPLS OVERVIEW

MPLS is a packet forwarding technology that uses labels to make packet forwarding decisions. It establishes connection-oriented paths over a connectionless IP network. As stated in its name, it is multi-protocol because it will work with IP, ATM or Frame Relay. The underlying routing infrastructure behind MPLS may be provided by any Internet gateway protocol such as RIP, OSPF, etc. Also it's called the layer 2.5 because it is located between the layer 2 and layer 3 in Open System Interconnection (OSI) model.
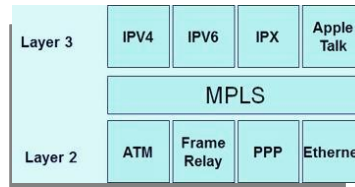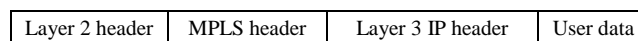

Figure 1. MPLS layer

Layer 2 header	MPLS header	Layer 3 IP header	User data

Figure 2. The location of MPLS header

MPLS header consists of 32-bit. It includes label, CoS, S, TTL fields as shown in Fig. 3.

20 bits	3bits	1bit	8 bits
Label	CoS	S	TTL

Figure 3. MPLS header

Label - Label Value is 20 bits long which is used to identify Label Switched Paths (LSP).

CoS - It is seperated for the determination of Quality of Service (QoS) needs and 3 bits long.

S - Bottom of Stack, 1 bit, which is used to indicate the bottom of label stack.

TTL - Time to Live field is 8 bit long. MPLS TTL field has similar function as that of IP header TTL field.

2.1. MPLS TERMINOLOGY

Label Switched Path (LSP): It is the path that exists inside MPLS network which direct packets in the network to pass it through the LSR routers and ends at LER routers. It is used as a specific path followed by a selected sequence of packets.

Forwarding Equivalence Class (FEC): FEC is a group of IP packets that will be forwarded in the same manner over the same path. All packets which belong to a particular FEC will follow the same LSP. FECs are defined based on any of the IP header fields.

Label Switch Router (LSR): This type of router located in the center of MPLS network. It is responsible to examine packets for transferring them to the next node in the network. LSR also gives new label to the header and removes old one.

Label Edge Router (LER): This type of router located at the output side of an MPLS network. It is responsible to remove or add label to the packets when enter or exit MPLS domain.

3. NETWORK DESIGN WITH OPNET 14.5

Opnet 14.5 Network simulator is used to simulate IP/MPLS network with static MPLS paths and dynamic MPLS paths.

Our network model consists of 12 MPLS routers, 7 point to point workstations and one point to point server. 5 of the routers are LER ones and the rest are LSR routers. PPP Sonet OC3 links are used to connect each router to others and also PPP workstations and server are connected to related router with these links. The data rate of OC3 link is 148.61 Mbps available to user after accounting for the SONET overhead. RIP protocol is chosen for preparing routing table in routers. Web, video, VoIP, FTP, database, e-mail and File Print traffic are applied to the networks in both scenarios. MPLS definition attribute is used for establishing LSPs and controlling how packets are labeled and directed in the network. The two important MPLS configuration attributes are Forwarding Equivalence Class (FEC) and traffic trunk. FEC is responsible for

classification of all the packets and directing them in the same way. Traffic trunks are responsible for capturing traffic characteristics such as peak rate, average rate to perform tasks properly.

In the first scenario, LSP static paths are established between end points. Static LSPs are deployed by manually defining fixed paths between end points. In real environment, all transit routers must be configured with labels and label actions. For static LSPs, dynamic signaling protocols are not required. The designed network with Static path is shown in Figure 4.
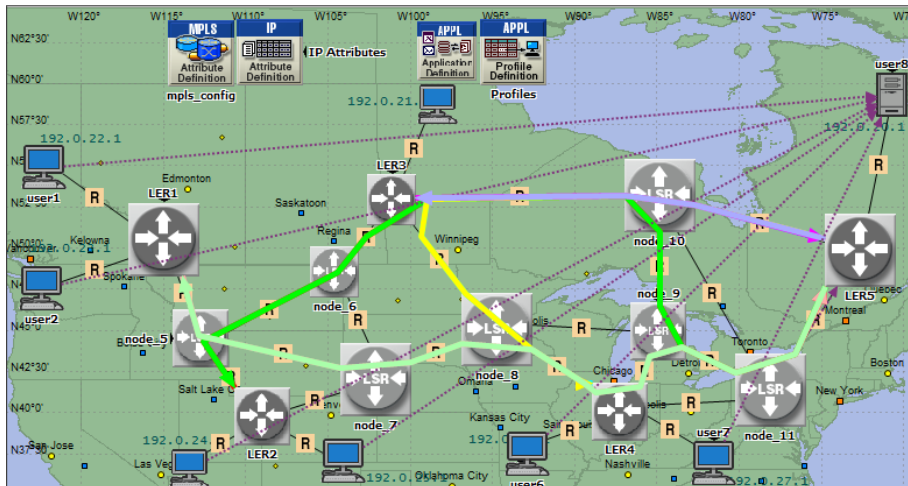

Figure 4. First Scenario. MPLS network with static paths.

In the second scenario, static LSPs are replaced with dynamic counterparts. Label switched paths are created by distributing labels for them. Different label distribution protocols are used for different applications. Default traffic engineering parameters are chosen for this scenario. Signaling protocols are used to define specific route to setup LSPs. IGP routing is a necessity for dynamic label signaling exchange. In real environment operators are required to configure the MPLS routers with selected label signaling types.
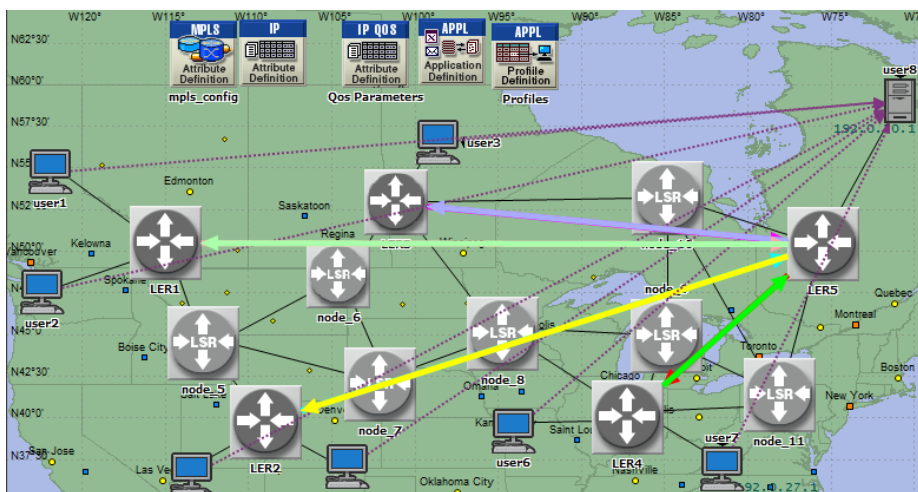
Figure 5. Second Scenario. MPLS network with dynamic paths

Application definition attribute and profile definition attributes are used for defining Web, Video and VoIP applications and related profiles. The VoIP application uses G.711 encoder scheme and VoIP service is used for establishing the VoIP calls.

4. SIMULATION RESULTS

The total time for running each simulation is 40 minutes. First of all, e-mail sent and received traffic is evaluated. While e-mail sent traffic is lower for Dynamic LSPs, the received Email traffic gives high ratio. So, it is obvious that the throughput of Email traffic is better in terms of LSP dynamic paths.
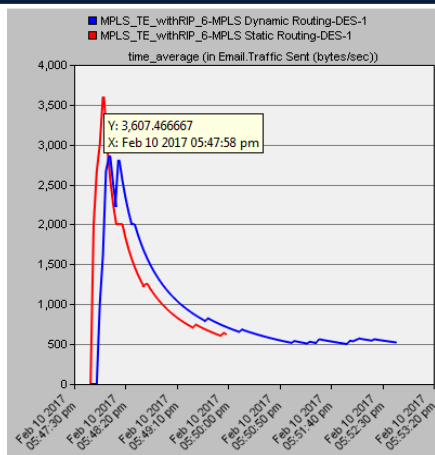
Figure 6. Email Traffic Sent   *Figure7. Email Traffic Received*
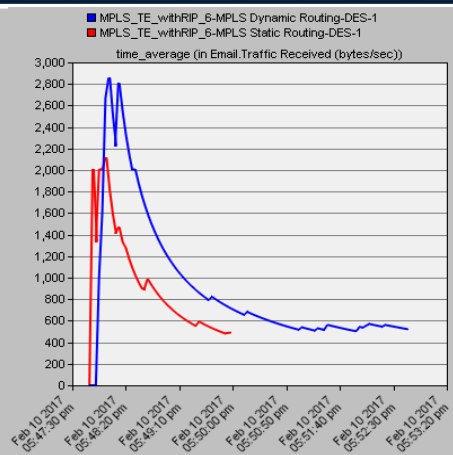
Second, download response time of FTP traffic is considered. As could be seen in Figure 8, the download response time of FTP traffic is lower for LSP dynamic paths. It is approximately 0.5 second. End to end delay variation of VoIP packets are shown in Figure 9. Jitter in Voice traffic for Static routing is higher at the beginning but after some time it gets synchronized.
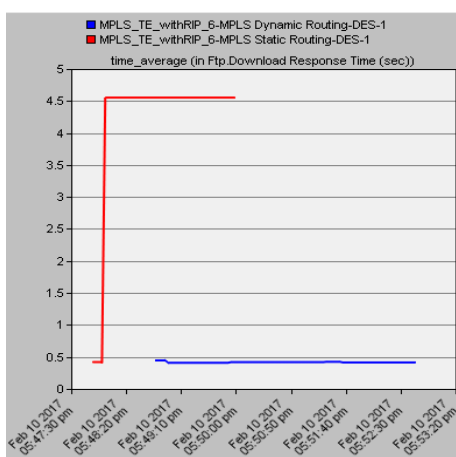
Figure 8. FTP Download Response Time   *Figure 9. Voice Jitter*

In Figure 10, it could be seen that average number of hops that packets traversed in MPLS domain for dynamic routing is much better. This result is due to the dynamic routing determines the best way via a chosen IGP protocol. Static LSPs give better result in terms of IP packet dropped as presented in Figure 11.
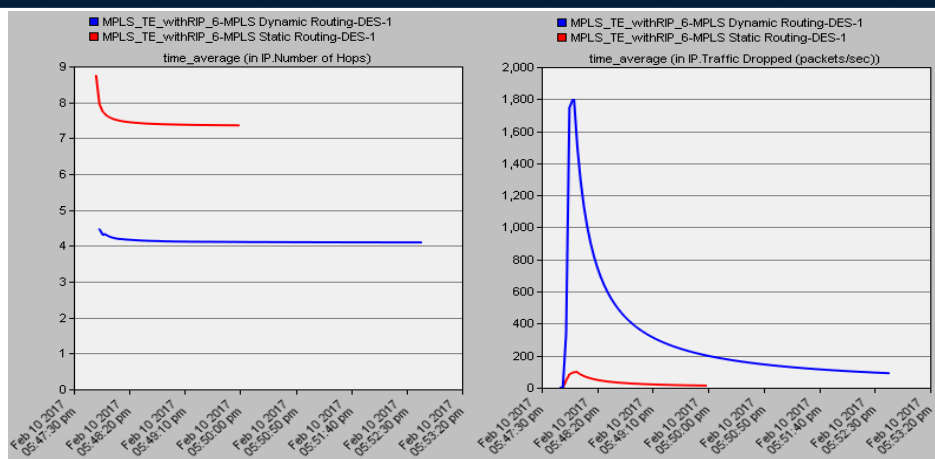
Figure 10. Average Number of Hops   Figure 11. IP Packet Dropped

5. CONCLUSIONS

MPLS is a new network technology which uses label switching for packet forwarding. MPLS combines traffic engineering features of ATM and scalability of IP networks. It is mostly used in Internet Service Provider's backbones due to its support for Layer 2 VPN, Layer 3 VPN, Quality of Service and traffic engineering. The most prominent feature of MPLS is to allow routing traffic efficiently, reduce network congestion and hence improve network performance and efficiency of the Internet.

According to simulation results, Dynamic LSPs gives better performance results in terms of Email traffic throughput, FTP downlad response time, voice jitter and average number of hops. Static LSPs gives low IP packet dropped value compared to dynamic LSPs.

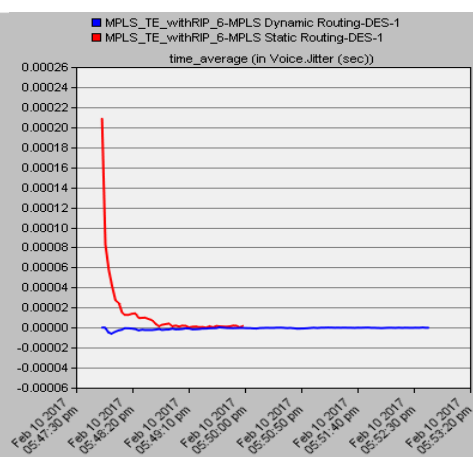## REFERENCES

[1]   A. Gezer, M. Khaleel, "Performance Comparison Between IP and MPLS Networks Using Opnet Modeller," *International Conference on Advanced Technology & Sciences (ICAT'17),* 9-12 May 2017, pp. 173.
[2]   M.K. Porwal, A. Yadaw, S.V. Charhate, "Traffic Analysis of MPLS and non MPLS Network including MPLS signaling protocols and traffic distribution in OSPF and MPLS," *Emerging Trends in Engineering and Technology, 2008 ICETET '08*, 2008.
[3]   I. Hussain, "Overview of MPLS Technology and Traffic Engineering Applications," *International Conference on Networking and Communication (INNC),* 2004, pp. 1-9.
[4]   J. Tahir, M. Zain Siddiqi, S. Arif, "Performance analysis of MPLS based networks with conventional networks," *2017 2nd Workshop on Recent Trends in Telecommunications Research (RTTR)*, 2017.
[5]   K. P. Mahesh, A. Yadav and S. V. Charhate, "Traffic Analysis of MPLS and Non MPLS Network including MPLS Signaling Protocols and Traffic Distribution in OSPF and MPLS," *In Proc of Int. Conf. on Emerging Trends in Engineering and Technology(ICETET)*, pp. 9-14, 2008.
[6]   N. Rikli and S. Almogari, "Efficient Priority Schemes for the Provision of End-to-End Quality of Service for Multimedia Traffic over MPLS VPN networks," *Journal of Computer and Information Sciences-King Saud University* pp. 89-98, vol. no. 25, 2013.

Forecasting of Daily Evapotranspiration Using Artificial Neural Networks Technique

Bestami TASAR[1], Fatih UNES[2], Mustafa DEMİRCİ[3], Ada YILMAZ[4], Yunus Ziya KAYA[5]

Abstract

Evapotranspiration estimation has significant roles in irrigation management and hydraulic designs in arid seasons and area. In this paper, evapotranspiration forecast was tried to assess the performances of artificial neural networks (ANN) and empirical equations (classical methods) such as Hargreaves-Samani and Ritchie equation. Study area was chosen Massachusett, U.S.A (Cambridge reservoir). Mean daily air temperature (AT), wind speed (WS), solar radiation (SR) and, relative humidity (RH) were used for forecasting mean daily evapotranspiration. All daily data are divided as training and test data. The evaluation of the method results was made according to the statistical parameters such as determination coefficient and error calculations. Based on comparison of the results, it is found that the ANN model gives better estimates than the other techniques.

Keywords: Hargreaves-Samani Equation, Artificial Neural Networks, Evapotranspiration, Estimation

1. INTRODUCTION

Evapotranspiration (ET) estimation has significant roles in irrigation management and hydraulic designs in arid seasons and area. ET is the phenomenon of evaporation and transpiration at the same time and ET is the basic component of the hydrological cycle. It depends on factors like solar radiation, air temperature, wind speed, relative humidity and environmental conditions. Because ET depends on too many parameters, the correct estimation is difficult and important

In the past decades, researchers benefited from artificial intelligence techniques during ET prediction [1] [2].

Kisi [3] studied to predict ET which gauged at four stations (Adana, Antalya, Isparta, and Mersin) in Turkey. He researched to predict ET with empirical equations: Valiantzas, Copais, Turc, Hargreaves-Samani, Hargreaves, Ritchie, and Irmak. At the end of the his study, his results showed that prediction with Valiantzas equation had a best ET results. Turc equation prediction had worst results.

Recently, the use of artificial intelligence methods such as artificial neural networks (ANN) has been accepted as an appropriate tool for modeling complex nonlinear phenomena in hydrology and water resources systems, leading to widening of their applications. Unes [4] used ANN model for predicting reservoir level fluctation. Unes [5] predicted plunging depth of density flow in dam reservoir using the ANN technique.

Kisi [6] tried to forecast ET in Iran. In their study, they used Artificial Neural Networks (ANN), Adaptive Neuro-Fuzzy Inference System (ANFIS), Support Vector Machine (SVM) and Gene Expression Programming (GEP) approaches and empricial methods such as Hargreaves–Samani (HS), Makkink (MK), Priestley–Taylor (PT), Turc (T) for prediction ET. Comparison of the results, GEP and HS techniques results more reasonably than other techniques.

Kaya et al. [7] studied to estimate of ET amount. They used for prediction with M5T and Turc empirical method. They found that M5T data mining method had better performance than Turc empirical method.

Purpose of this academic work is to research the effectiveness and applicability of classical evapotranspiration methods and artificial intelligence such as, ANN. Daily datas are taken from a meteorological station in Massachusett, U.S.A..

[1,2,3,4]*Corresponding author: Iskenderun Technical University Civil Engineering Department,.31200,İskenderun Hatay/TURKEY, bestami.tasar@iste.edu.tr, fatih.unes@iste.edu.tr, mustafa.demirci@iste.edu.tr, ada.yilmaz@iste.edu.tr*

[5]*Civil Engineering Department, Osmaniye Korkut Ata University, Osmaniye, TURKEY, yunuszkaya@osmaniye.edu.tr*

2. METHODS

In this paper, evapotranspiration forecast was tried to assess the performances of empirical equations (classical methods) such as Hargreaves-Samani and Ritchie equation, artificial neural networks (ANN).

2.1. Hargreaves-Samani Equation

Hargreaves and Samani [8] studied experimentally to find ET. In Hargreaves-Samani equation; solar radiation(R_s), daily mean temperature (T_{mean}).

daily maximum temperature (T_{max}) daily minimum temperature (T_{min}) parameters used. It was given below;

$$ET = 0,0135R_S \cdot 0,408(T_{mean} + 17,8) \tag{1}$$

Relationship between the solar radiation and extraterrestrial solar radiation is below;

$$R_S = 0,16R_a(\sqrt{T_{max} + T_{min}}) \tag{2}$$

Here, R_a : extraterrestrial solar radiation, if we determine (1) equation using R_a, then the equation becomes

$$ET = 0,0023R_a \cdot 0,408(T + 17,8)(\sqrt{T_{max} + T_{min}}) \tag{3}$$

2.2. Ritchie Equation

The Ritchie method that introduced by Jones and Ritchie [9]. Equation is:

$$ET = \alpha_1[3,8710^{-3} \cdot R_S \cdot (0,6T_{max} + 0,4T_{min} + 29)] \tag{4}$$

In Ritchie equation, solar radiation(R_s), daily maximum temperature (T_{max}) daily minimum temperature (T_{min}) parameters and α (coefficient) used. Coefficient of α is dependent on T_{max} ;

$$T_{max} < 5°C \qquad \alpha_1 = 0,01\exp[0,18(T_{max} + 20)]$$

$$5 < T_{max} < 35°C \quad \alpha_1 = 1,1$$

$$T_{max} > 35°C \qquad \alpha_1 = 1,1 + 0,05(T_{max} - 35) \tag{5}$$

2.3. Artificial Neural Networks (ANN)

Artificial neural networks, inspired by the structure of nerve cells in the human brain, are dense parallel systems consisting of many process elements connected with each other with different weights. The most widely used method among the ANN methods is the feed-forward-back-propagation ANN model, which operates according to the principle of back propagation of errors. In this model, an artificial neural network consists of five main parts: the input layer, the variable weight factors, the total function, the activation function and the output layer. In Fig. 1 , A three-layers artificial neural network structures are given.
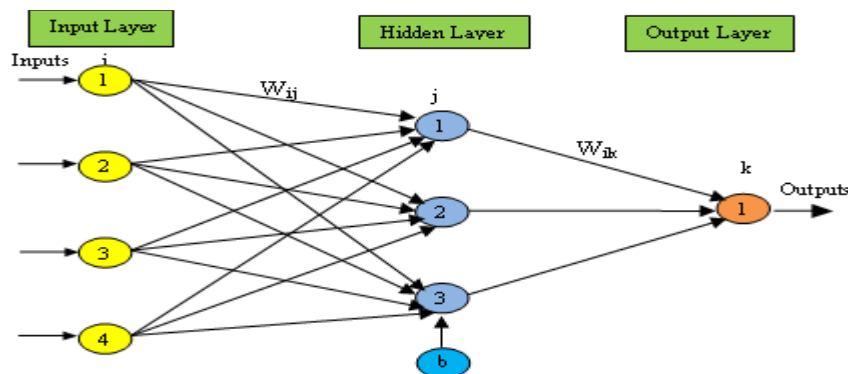
Fig. 1. ANN Structures with three layers (input, hidden and output layers) used in ET estimation

According to Fig. 1, W_{ij}; Is the connection weights between the input and the hidden layer and W_{jk} is the connection weights between the hidden layer and the output layer. These W_{ij} and W_{jk} values are coefficient values that express the effect of the previous input data on the processed element. These coefficients, which initially receive random weight values, change constantly by comparing the actual output values with the

outputs estimated in the training process. Errors until they reach their minimum link weight values, errors propagated backwards.

Each cell in the hidden and output layers in Fig.1. allows the data from the previous layer to enter the total function (net). This function calculates the net input to the cell and determines the following equation.

$$net_{pj} = \sum_{i=1}^{N} W_{ij} X_{pi} + b_j \qquad (6)$$

In equation (6), N is the size of input vector, b_j is the bias term, W_{ij} is the set of weights between i and j layers, X_i is the input set of the i-th layer for the p-th instance. The activation function generates the output f (net) by passing the net value through a nonlinear identification function in each cell of the j and k layers. One of the most commonly used identification functions is Sigmoid function. Sigmoid function is used in this study and is expressed as in equation (7).

$$f(net) = \frac{1}{1 + e^{-net}} \qquad (7)$$

3. METHOD RESULTS

In this study, it was investigated which model performed better to predict ET and datas taken from Cambridge Resorvoir in USA. As data, United States Geological Survey (USGS) [10] measurement data was used. A total of 1081 days of 3 years (2014-2017) was used for estimation. In the study, some of the data (75%) are used for training and the remaining part (25%) is divided into two parts to test the obtained models. That is, 1081 data in 3 water years were used to training and 811 data models and 270 data were used to test models.

3.1. Hargreaves-Samani Equation (HSE) Results

For the HSE analysis, daily air temperature (AT), solar radiation (SR) were used as input values. HSE model were evaluated, and in the graphs below, the distribution of the test estimates is shown in Fig. 2. The scatter plot is shown in Fig. 3.

Fig. 2. *Hargreaves-Samani equation distribution graph*

Fig. 3. Scatter chart of Hargreaves-Samani equation and observed values

The determination coefficient $R^2 = 0.985$ was obtained for the graph generated for the test with the HSE results. The HSE estimates at the test phase show good results values for the observed daily real-time ET.

3.2. Ritchie Equation (RE) Results

For the RE analysis, daily air temperature (AT), solar radiation (SR) were used as input values. RE model was evaluated, and in the graphs below, the distribution of the test estimates is shown in Fig. 4. The scatter plot is shown in Fig. 5.
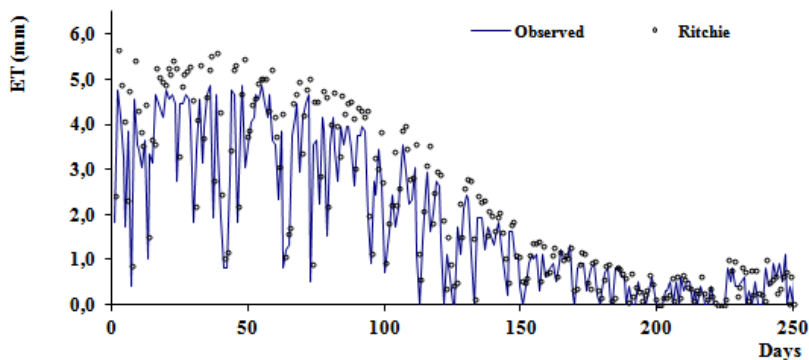
Fig. 4. Ritchie equation distribution graph.
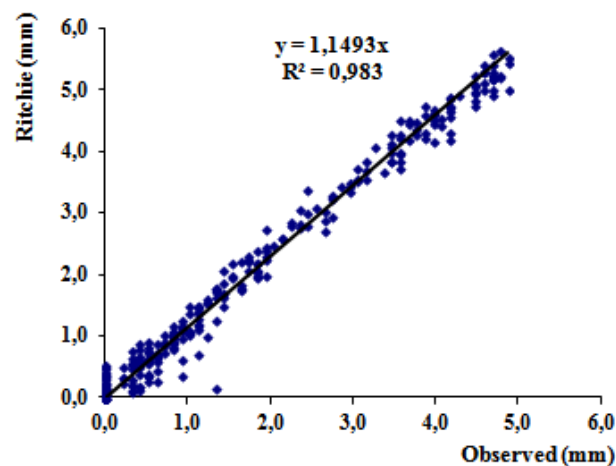
Fig. 5. Scatter chart of Ritchie equation and observed values.

The determination coefficient $R^2 = 0.983$ was obtained for the graph generated for the test with the Ritchie equation results. The RE estimates at the test phase show good results values for the observed daily real-time ET but The RE estimates at the test phase show worse results than the HSE model values.

3.3. Artificial Neural Networks (ANN) Results

For the ANN model analysis, daily air temperature (AT), wind speed (WS), solar radiation (SR) and, relative humidity (RH) were used as input values. For the ANN model analysis, ANN model was evaluated, and in the graphs below, the distribution of the test estimates is shown in Fig. 6. The scatter plot is shown in Fig. 7.
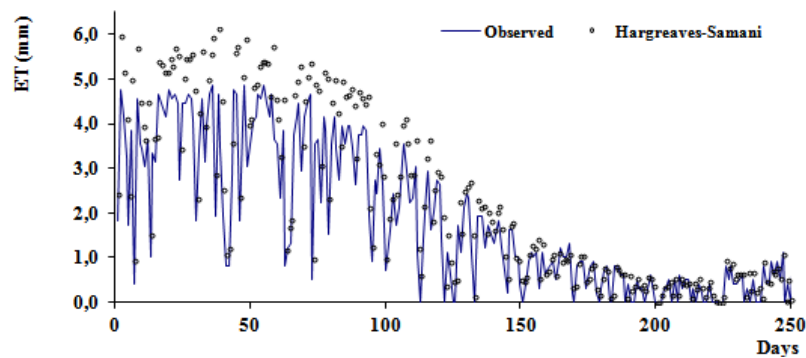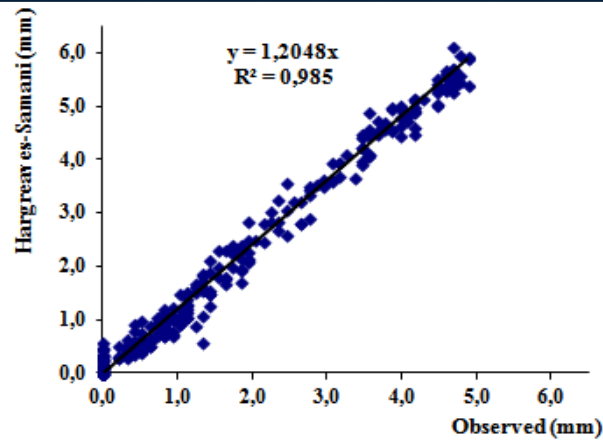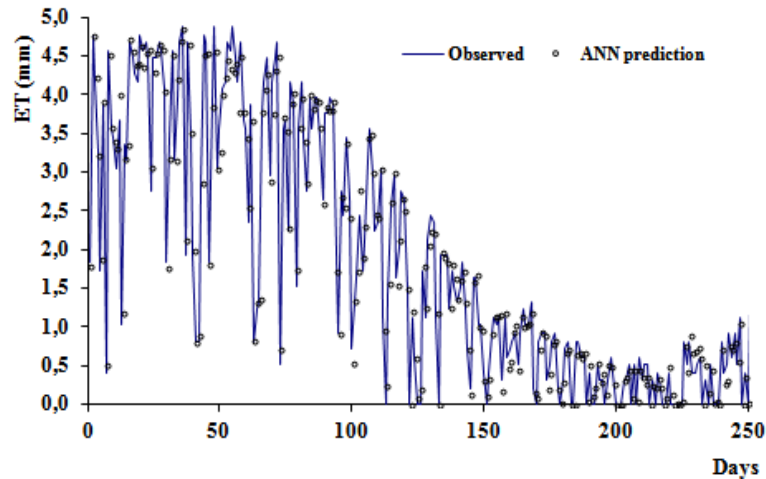

Fig. 6. ANN distribution graph
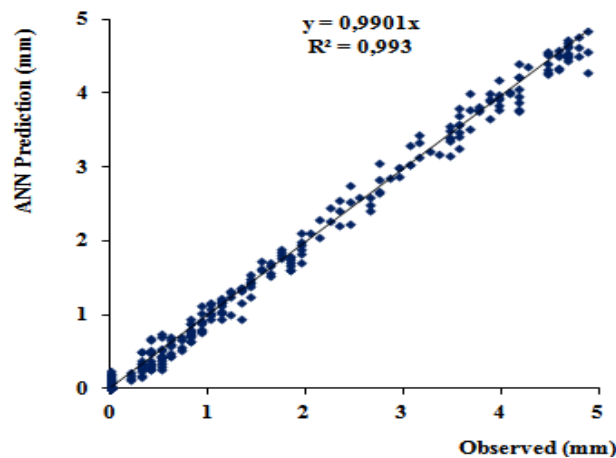
Fig. 7. Scatter chart of ANN and observed values

The determination coefficient $R^2 = 0.993$ was obtained for the graph generated for the test with the ANN model results. The ANN estimates at the test phase show good results values. The ANN estimates at the test phase show better results than the other model values for the observed daily ET.

3.4. Evaluation of Estimation Results

The results of HSE, RE and ANN for the models generated for 3 years data are as follows. For each model, the mean square error (MSE), the mean absolute error (MAE), and the determination coefficients (R^2) between the model estimates and observations. MSE and MAE were determined as follows. the observed values are calculated. The results are also used to compare the performance of model estimates and the observed values are calculated. The MSE, MAE and R are also used to compare the performance of model estimates and observations. MSE and MAE were determined as follows.

$$MSE = \frac{1}{N}\left(\sum_{i=1}^{N} Y_{i\,observed} - Y_{i\,estimate}\right)^2 \qquad (8)$$

$$MAE = \frac{1}{N}\sum_{i=1}^{N}\left|Y_{i\,observed} - Y_{i\,estimate}\right| \qquad (9)$$

Here, N represents data numbers and Y_i ET datas.

ET amounts from 811-day observations used in the training of the all model were also trained for ANN model as input. Models created in the second step were applied to the inputs of the test data generated from 270 day observations and the results obtained with the model were compared with the measured values. The results obtained from these studies are given in Table 2. below.

Table 2. *Cambridge Resorvoir in USA comparison of performances of models for 5 years data*

Models	Model Inputs	MSE	MAE	R^2
HSE	AT-SR	0,542	0,418	0,985
RE	AT-SR	0,427	0,355	0,983
ANN	**AT-SR-WS-RH**	**0,101**	**0,135**	**0,993**

MSE: Mean square error; MAE: Mean absolute error R^2: Determination coefficients.

The model with the best result according to Table 2. is MSE, MAE is the smallest, R is the model with the largest value. According to MSE, MAE and R^2, The ANN (0,101-0,135-0,993) model was found to perform better than the other models at all performance evaluations.

The ANN method gives better results compared to the emprical methods in test period. The ANN predictions for the training and testing period in the same form are given in Figs. 6 and 7, respectively. The data in Figs. 6 and 7 shows that ANN models provide good predictions during the training and test data phases. A compromise can be defined between the training and test results and experimental measurements. It can be understood from these results that the ANN model estimates are less scattered, resulting in lower MSE, MAE and higher R^2 values.

Although, in reality, the evapotranspiration phenomenon involves nonlinear and unsteady conditions, the ANN model provides the best performance correlations for the test and training data sets.

4. CONCLUSIONS

In this study, authors study on evapotranspiration (ET) prediction using ANN model for Massachusett, U.S.A (Cambridge reservoir) region. ANN model is built up to estimate daily ET using daily air temperature (AT), wind speed (WS), solar radiation (SR) and, relative humidity (RH) parameters. It is understood that ANN technique gives quite close results to Hargreaves-Samani and Ritchie empirical equations results. Determination coefficients (R^2) calculations present that all methods gave good ET prediction results, but according to the error calculations (MSE and MAE) it is clear that ANN method results are better than empirical equation results.

When an ANN model is developed for a specific region, the model can be quite helpful in the water resources management studies. The daily ET estimations can be quite informative for the determination of the periodic water supply strategies, the hydraulic designs and irrigation management studies. Finally, these results show that ANN is a useful alternative method for ET prediction.

Although the evapotranspiration in the dam reservoir is a complicated problem that actually affects a large number of parameters, the ANN model can obtain a solution with a fairly accurate result.

REFERENCES

[1] Y. Fenga, N. Cuib, L. Zhaob, X. Hud, Daozhi Gonga, "Comparison of ELM, GANN, WNN and empirical models for estimating reference evapotranspiration in humid region of Southwest China", Journal of Hydrology, Volume 536, Pages 376–383, May 2016.

[2] T. Partal, "Comparison of wavelet based hybrid models for daily evapotranspiration estimation using meteorological data", KSCE Journal of Civil Engineering, Volume 20, Issue 5, pp 2050–2058, July 2016.

[3] O. Kisi, "Comparison of Different Empirical Methods for Estimating Daily Reference Evapotranspiration in Mediterranean Climate", Journal of Irrigation and Drainage Engineering, Volume 140 Issue 1, January 2014.

[4] F. Unes, "Dam reservoir level modelıng by neural network approach. A casestudy", Neural Network World, 4(10), 461–474, 2010.

[5] F. Unes, "Prediction of Density Flow Plunging Depth in Dam Reservoirs: An Artificial Neural Network Approach", CLEAN - Soil, Air, Water, 38(3), 296–308, DOI 10.1002/clen.200900238, 2010.

[6] O. Kisi, "Daily river flow forecasting using artificial neural networks and autoregressive models", Turk J Eng Environ Sci ;29:9–20, 2005.

[7] Y.Z. Kaya, M. Mamak, F, Unes, "Evapotranspiration Prediction Using M5T Data Mining Method", International Journal of Advanced Engineering Research and Science (IJAERS), Vol-3, Issue-12, 2016.

[8] G.H. Hargreaves, Z.A. Samani, "Reference crop evapotranspiration from temperature", Applied Engineering. in Agric. 1:96-99, 1985.

[9] J.W. Jones, & J.T. Ritchie, "Crop growth models. Management of Farm Irrigation Systems" (ed. by G. J. Hoffman, T. A. Howel & K. H. Solomon), 63–89. ASAE Monograph no.9, ASAE, St Joseph, Michigan, USA, 1990.

[10] USGS.gov | Science for a changing world [WWW Document], n.d. URL https://www.usgs.gov/

Prediction of Daily Suspended Sediment Load Using Support Vector Machine

Bestami TASAR[1], Fatih UNES[2], Mustafa DEMİRCİ[3], Ada YILMAZ[4], Yunus Ziya KAYA[5]

Abstract

Prediction the amount of suspended sediment being transported by a river is correctly important due to the adverse impacts of hydraulic structures such as dam, bridge. In this paper, support vector machine (SVM) and adaptive Neuro-fuzzy (NF) techniques are used for forecasting daily suspended sediment concentration from daily temperature of water and streamflow in the river. As a study area, the Augusta station of Skunk river, in U.S.A., was chosen as. NF and SVM models are compared to each other according to three statistical criteria, namely, mean square errors (MSE), mean absolute relative error (MAE) and correlation coefficient (R). These criteria were used to evaluate the performance of the models. NF model shows better predictions than the SVM model according to obtained model and measurement results.

Keywords: *Support Vector Machine, Neuro-Fuzzy, Suspended Sediment, Prediction, Model*

1. INTRODUCTION

Prediction the amount of suspended sediment (SS) being transported by a river is correctly important due to the adverse impacts of hydraulic structures such as dam, bridge. In particular, the sediment that accumulates in the water storage structures such as dam reservoir reduces the reservoir capacity. Decrease of reservoir capacity causes shortening of economic life of facilities. In order to prevent or even delay these damages, a passive storage called dead storage is determined in the dam reservoir. It is designed to remain under the water intake structure. The service life of a dam, namely its useful life, depends on the amount of storage. So, it is important to accurately forecast the type and amount of sediments in dam projects.

Determination of suspended sediments by measurements is the most accurate method. However, this method takes time and is costly. In addition, there is no measurement of the amount of sediments in many observation stations, although water flow is measured. It is especially difficult to measure the amount of sediments in the stations in case of flooding.

The movement of sediments in the rivers is a complicated and difficult problem. In the past, many researchers applied artificial intelligence methods and obtained different results in order to explain this problem and provide correct solutions.

Buyukyildiz and Kumcu [1] studied to predict sediment load which gauged at Ispir Bridge station, Coruh River in Turkey. They examined artificial intelligence methods such as Support Vector Machine (SVM), Artificial Neural Network (ANN) and Adaptive Neural Fuzzy Inference System (ANFIS). Based on the model results; SVM, ANN and ANFIS have a good results in test phase.

SVM has been used successfully for prediction of suspended sediment during recent studies ([2]; [3]; [4]). Cimen [5] used SVM for predicting suspended sediment load in two rivers in U.S.A.. He revealed that SVM regression's results have a good accuracy in testing period.

Kisi and Zounemat-Kermani [6] conducted studies to estimate the amount of SS in the two stations on the Muddy River in the USA. They used the daily flow rate and the amount of solids concentration data in the study. ANN, NF, SRC (Sediment Rating Curves), and CNF models (Clustered Neuro-Fuzzy model, SVM has been used successfully for prediction of suspended sediment during recent studies ([2]; [3]; [4]). Cimen [5]

[1,2,3,4]*Corresponding author: Iskenderun Technical University Civil Engineering Department,.31200,İskenderun Hatay/TURKEY,* bestami.tasar@iste.edu.tr, fatih.unes@iste.edu.tr, mustafa.demirci@iste.edu.tr, ada.yilmaz@iste.edu.tr

[5]*Civil Engineering Department, Osmaniye Korkut Ata University, Osmaniye, TURKEY,* yunuszkaya@osmaniye.edu.tr

used SVM for predicting suspended sediment load in two rivers in U.S.A.. He revealed that SVM regression's results have a good accuracy in testing period.

Kisi and Zounemat-Kermani [6] conducted studies to estimate the amount of SS in the two stations on the Muddy River in the USA. They used the daily flow rate and the amount of solids concentration data in the study. ANN, NF, SRC (Sediment Rating Curves), and CNF models (Clustered Neuro-Fuzzy model, developed from classic NF). The CNF method has shown that it provides better SS estimations results than others in rivers. CNF method can be presented as an alternative to ANN, NF, SRC methods in SS prediction.

Rajaee et al.[7] tried to estimate sediment load of Khaivchay River. Comparison of the models' results, NF technique results more reasonably forecast suspended sediment load than other techniques. Demirci and Baltaci [8] investigated the performance of the sediment rating curves (SRC), multiple linear regression (MLR) and fuzzy logic (FL) methods in estimating SS concentration. They used to forecast the concentration of sediment concentration from average temperature and daily real time flow. According to the their models estimation results, NF model has shown good results in comparisons for both 5-year and 50-year sediment estimation. Tasar [9] used Fuzzy Logic (FL) for forecasting daily suspended sediment at Skunk River, US.

2. METHODS

In this paper, support vector machine (SVM) and adaptive Neuro-fuzzy (NF) techniques are used for forecasting daily suspended sediment concentration from daily temperature of water and streamflow in the river.

2.1. Neuro-Fuzzy (NF)

Neuro-fuzzy, first described by Zadeh [10], is based on fuzzy cluster logic. NF system, works by a learning algorithm derived from neural network functional rules. The parameters of the fuzzy inference system are determined by the neural network learning algorithms In a fuzzy rule-based system, different analysis methods such as Sugeno can be applied. NF with Sugeno type works according to "If-Then" rule and The NF structure uses the Sugeno-Fuzzy rules. It is possible to introduce fuzzy systems that logical models which is consisted of "If-Then" rules and membership functions.

2.2. Support Vector Machine (SVM)

SVM is a method of learning found by Cortes and Vapnik [11] for solving the classification and regression problems. It is likely that classification of variables on a plane by drawing a boundary between them. The boundary which is drawn between variables must be as far as possible to each variable. SVM provides to defines how to draw this boundary between variables group The network structure of SVM is given in Fig.1.
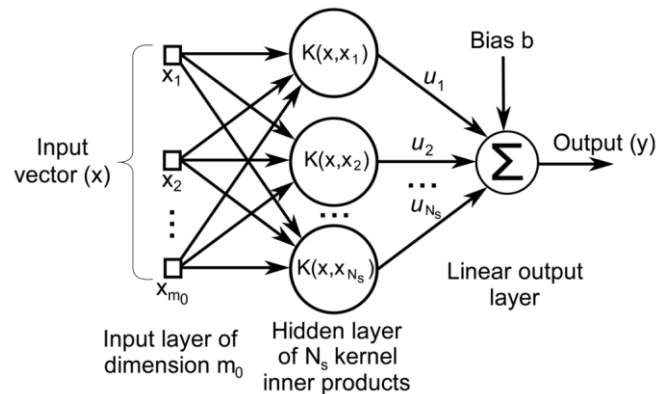
Fig. 1. Architecture of a SVM by Gonzalez et al.[12].

3. APPLICATION AREA AND MODEL RESULTS

3.1. Application Area

In this study, Des Moines County area (Hydrologic Unit No: 18020109) in Iowa, United States was selected as the application field for estimating suspended sediment concentration amount. The Augusta station on the Skunk River has been studied (USGS Station No: 05474000). Datum indicator at sea level Gage Datum: about 160 m (NGVD29 National Geodesy Vertical Datum) In addition, as data in this study, 5 water

belonging to Augusta station year datas were taken from the USGS (United States Geological Survey) website. The overviews of the Augusta station on the USGS Skunk River are shown in Fig. 2.

Fig. 2. USGS Augusta station overviews on Skunk River

3.2. Model Results

In this study, it was investigated which model performed better using daily average water temperature, real time streamflow and sediment concentration data from Augusta Station on Skunk River in USA. As data, American Geological Research Survey (USGS) measurement data was used for five water years of Augusta station. A total of 1580 days of five years (2005-2009) was used for estimation. In the study, some of the data (70%) are used for training and the remaining part (30%) is divided into two parts to test the obtained models. That is, 1580 data in 5 water years were used to training and 1100 data models and 480 data were used to test models.

All statistical parameter changes of Augusta station, statistical parameter changes for training and statistical parameter changes for test are shown in Table 1. In Table 1., x_{max}, x_{min}, x_{mean} represent the maximum, minimum, mean values of the data respectively. S_x, c_{sx} represents the standard deviation and the skewness coefficient, respectively.

Table 1. Augusta station training and test statistical parameter changes.

	Variables	T_{mean} (°C)	Q (m³/s)	S (mg/L)
	x_{max}	35	1217,6	3040
Training	x_{min}	0	3,1	7
Datas	x_{mean}	14,7	116,6	242
	s_x	9,7	159,5	345,2
	c_{sx}	0,1	2,7	3,4
	x_{max}	30	1245,9	3410
Test	x_{min}	0	21,6	14
Datas	x_{mean}	16,6	289,1	348,1
	s_x	8,8	253,5	392,3
	c_{sx}	-0,3	1,4	3,4

T_{mean}: Mean temperature; Q: Streamflow; S: Sediment concentration

3.2.1. Neuro-Fuzzy (NF) Model

For the NF model, as in other model, the 5-year data are divided into training and test data. The mean temperature (T_{mean}), the streamflow (Q) and the lagged time sediment concentration (S_{t-1}) at time t-1 were used as input values for the NF model analysis.

As in the case of 5 years of training, the data divided into two parts as training and test are entered into the Matlab Fuzzy Logic section as three inputs one output and the results are taken according to the rules established. The results are obtained by establishing the rules between temperature and current and sediment concentration. For the 5-year data generated, NF models were evaluated, and in the graphs below, the distribution of the test estimates is shown in Fig. 3. The scatter plot is shown in Fig. 4.

Fig. 3. *Measurement and NF distribution graph for 5 years test data*

Fig. 4. *Measurement and NF scatter graph for 5 years test data*

The correlation coefficient R = 0.80 was obtained for the graph generated for the test with the NF model results. The NF estimates at the test phase show good results values for the observed daily real-time sediment concentrations.

3.2.2. Support Vector Machine (SVM) Model

For the SVM model analysis, as in NF, the 5-year data are divided into training and test data. T_{mean}, Q and S_{t-1} were used as input values. In SVM model, The 5-year forecast data is used as it is in the fuzzy logic model. For the 5-year data generated, SVM model was evaluated, and in the graphs below, the distribution of the test estimates is shown in Fig. 5. The scatter plot is shown in Fig. 6.
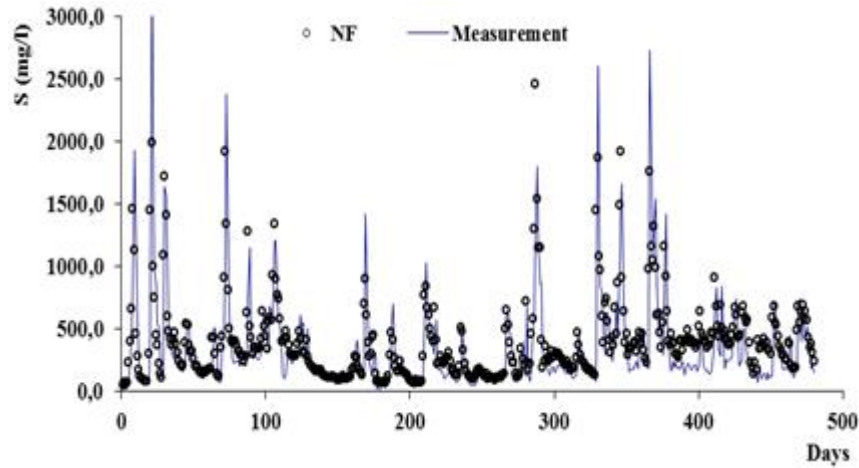
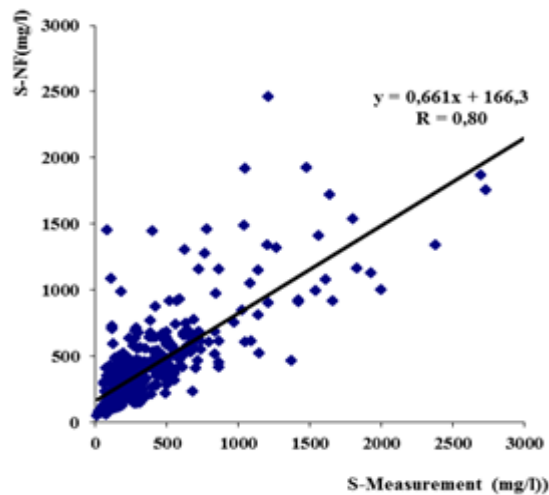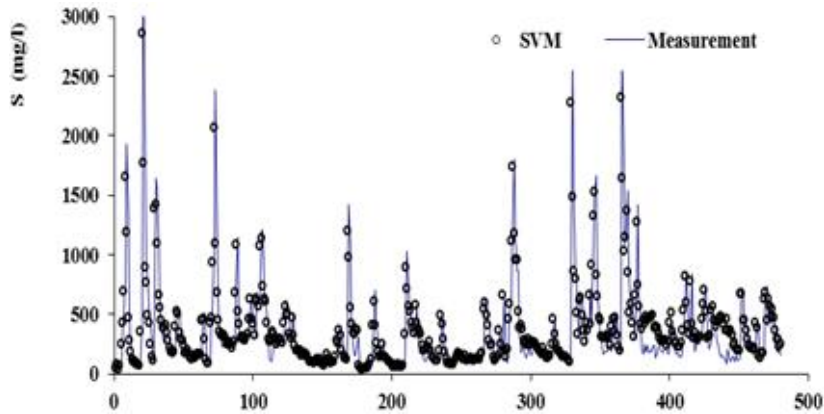**Fig. 5.** *Measurement and SVM distribution graph for 5 years test data*
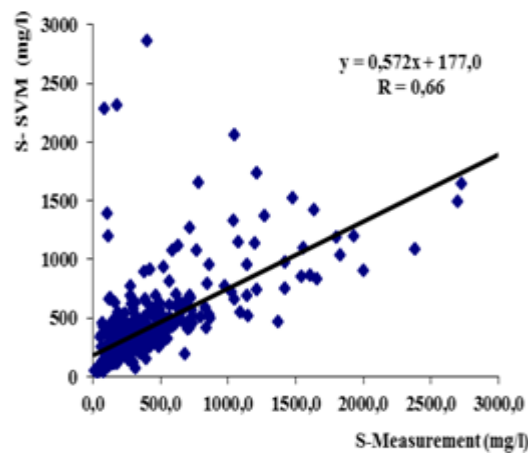
Fig. 6. *Measurement and SVM scatter graph for 5 years test data.*

The correlation coefficient R = 0.66 was obtained for the graph generated for the test with the SVM model results. The SVM estimates at the test phase show worse results than the FL model values for the observed daily real-time sediment concentrations.

3.3. Model Results and Analysis

The results of NF and SVM for the models generated for 5 years data are as follows. For each model, the mean square error (MSE), the mean absolute error (MAE), and the correlation coefficients (R) between the model estimates and observations. MSE and MAE were determined as follows. the observed values are calculated. The results are also used to compare the performance of model estimates and the observed values are calculated. The MSE, MAE and R are also used to compare the performance of model estimates and observations. MSE and MAE were determined as follows.

$$MSE = \frac{1}{N}\left(\sum_{i=1}^{N} Y_{i\,observed} - Y_{i\,estimate}\right)^2 \qquad (1)$$

$$MAE = \frac{1}{N}\sum_{i=1}^{N}\left|Y_{i\,observed} - Y_{i\,estimate}\right| \qquad (2)$$

Here, N represents data numbers and Y_i sediment concentration datas.

Sediment amounts from 1100-day observations used in the training of the SVM model were also trained for NF model as input. Models created in the second step were applied to the inputs of the test data generated from 480 day observations and the results obtained with the model were compared with the measured values. The results obtained from these studies are given in Table 2. below.

1232

Table 2. Skunk River Augusta station comparison of performances of models for 5 years data

Models	Model Inputs	MSE	MAE	R
NF	Q,T, S_{t-1}	58204	147	0,80
SVM	Q,T, S_{t-1}	94085	153	0,66

MSE: Mean square error; MAE: Mean absolute error R: Correlation coefficients.

The model with the best result according to Table 2. is MSE, MAE is the smallest, R is the model with the largest value. According to MSE, MAE and R, the SVM model (94085-153-0,66) has the lowest success rate. The NF (58204-147-0,80) model was found to perform better than the SVM model at all performance evaluations.

The predictions of suspended sediment show that the model accuracy increases with different input combinations. Fig. 4 provides the scatter plots of the observed and predicted sediment amount during the NF test periods. As seen from Table 2, NF model has the smallest MSE- MAE and the highest R for three-input combination during the test period. According to the entire model results, NF singles out as having small MSE, MAE and high R values for the same input combination.

4. CONCLUSIONS

In this study, the performances of Neuro-Fuzzy (NF) and Support Vector Machines (SVM) methods in estimating the sediment concentration were investigated. Mean temperature, daily real-time flow rate, sediment concentration, 5-year data from the Skunk River Augusta station in the US were used. For the 5-year data, the best results according to the MSE, MAE and R criteria were obtained in the NF model.

 Although all present model approaches are quite helpful and important in the water resources management studies, but it is shown in this paper that the NF can be a viable alternative for river sediment prediction in future research.

NF model applications developed for a specific region can be used as a very useful method for predicting sediment concentration from other methods, both in terms of the level of error and the proximity of estimates to observed values.

REFERENCES

[1]   M. Buyukyildiz, S. Y. Kumcu, "An Estimation of the Suspended Sediment Load Using Adaptive Network Based Fuzzy Inference System, Support Vector Machine and Artificial Neural Network Models, Water Resources Manage, 31:1343–13592017.

[2]   B. Bharti, A. Pandey, S. K. Tripathi, D. Kumar, "Modelling of runoff and sediment yield using ANN, LS-SVR, REPTree and M5 models", Journal of Hydrology Research, Volume 48,issue 2.

[3]   R. M. Adnan, X. Yuan, O. Kisi, Y. Yuan, "Streamflow Forecasting Using Artificial Neural Network and Support Vector Machine Models" American Scientific Research Journal for Engineering, Technology, and Sciences (ASRJETS), ISSN (Print) 2313-4410.

[4]   O. Kisi, "Daily river flow forecasting using artificial neural networks and autoregressive models", Turk J Eng Environ Sci ;29:9–20, 2005.

[5]   M. Cimen,   "Estimation of daily suspended sediments using support vector machines" Hydrological Sciences Journal, 53:3, 656-666.

[6]   O. Kisi, M. Zounemat-Kermani, "Suspended sediment modeling using neuro-fuzzy embedded fuzzy c-means clustering technique". Water Resources Management, 30, 3979-3994, 2016.

[7]   T. Rajaee, S. A. Mirbagheri, M. Zounemat-Kermani, V. Nourani, "Daily suspended sediment concentration simulation using ANN and neuro-fuzzy models". Science of the Total Environment 407 4916–4927, 2009.

[8]   M. Demirci, A. Baltaci,. "Prediction of suspended sediment in river using fuzzy logic and multilinear regression approaches". Neural Computing Applications, 23, 145-151, 2013.

[9]   B. Tasar, "Using fuzzy logic modelling suspended sediment estimation in river". Master's thesis, Iskenderun Technical University,2016

[10]   L.A. Zadeh,. "Fuzzy Sets. Journal of Information Control", 8(3), 338-353, 1965.

[11]   C.Cortes, V. Vapnik, "Support vector networks, Machine Learning", 20,1-25, 1995.

[12]   R. R.Gonzalez, J. G.Gil, F.J.G.Gil 2 and V. M.Martínez, "An SVM-Based Classifier for Estimating the State of Various Rotating Components in Agro-Industrial Machinery with a Vibration Signal Acquired from a Single Point on the Machine Chassis", Sensors 2014, 14(11), 20713-20735; doi:10.3390/s141120713.

Environmental Applications and Impact of Nanotechnology

Sakine UGURLU KARAAGAC[1]

Abstract

Environmental pollution caused by different sources is becoming a serious problem throughout the world in todays. To solve this problem different technologies can be used in environmental science. One of these technologies is nanotechnology in recent years. Nanotechnology is a field of applied science, focused on the design, synthesis, characterization and application of materials and devices on the nanoscale in different areas. It plays an important role in the development of innovative methods to produce new products and to reformulate of new materials and chemicals with improved performance resulting in less consumption of energy and materials. Thus, reduced harm are provided for the environment. There are great potentials for environmental engineering application and cleaner energy generation. We can use nanotechnology in environmental applications, such as ultrafiltration in most membrane separation processes, wastewater treatment and desalination via reverse osmosis, removal of organic pollutants from industrial waste water, nanosensors to detect toxic gas leaks at extremely low concentrations and filtration techniques in buildings to purify indoor air volumes, etc. Environmental applications of nanotechnology can provide the development of solutions to the existing environmental problems and preventive measures for future problems.

The environmental impact of nanotechnology is some possible effects on the environment. It can be divided into two aspects: the potential for nanotechnological innovations to help improve the environment, and the possibly novel type of pollution that nanotechnological materials might cause if released into the environment.

Key Words: _Nanotechnology, environment, application, environmental impact_

1. INTRODUCTION

Environmental pollution caused by different sources is becoming a serious problem throughout the world in todays. To solve this problem different technologies can be used in environmental science. One of these technologies is nanotechnology in recent years. Nanotechnology is a field of applied science, focused on the design, synthesis, characterization and application of materials and devices on the nanoscale in different areas. Nanotechnology is the study of the controlling of matter on an atomic and molecular scale. Generally nanotechnology deals with structures sized between 1 to 100 nanometer in at least one dimension, and involves developing or modifying materials or devices within that size.

While many definitions for nanotechnology exist, it can be called "nanotechnology" only if it involves all of the following:

- 1- Research and technology development at the atomic, molecular or macromolecular levels, in the length scale of approximately 1 - 100 nanometer range.

- 2- Creating and using structures, devices and systems that have novel properties and functions because of their small and/or intermediate size.

- 3. Ability to control or manipulate on the atomic scale.

Nanotechnology is already making **today's** products: Lighter, stronger, faster and smaller and more durable.

---

[1] XXXYYYZZZ
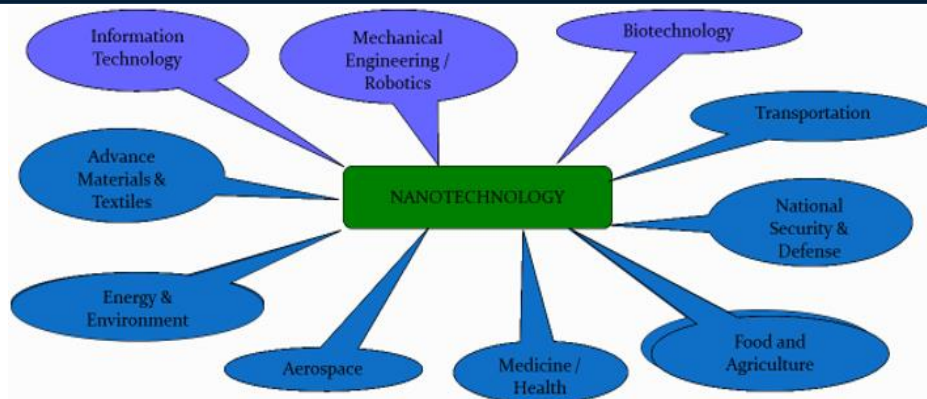
Fig.1. Nanotechnology spans many areas.

It plays an important role in the development of innovative methods to produce new products and to reformulate of new materials and chemicals with improved performance resulting in less consumption of energy and materials. Thus, reduced harm are provided for the environment. There are great potentials for environmental engineering application and cleaner energy generation.

2. ENVIRONMENTAL APPLICATIONS

Nanotechnology can be used in environmental applications, such as;

-Nanosensors to detect toxic gas leaks at extremely low concentrations,

-Filtration techniques in buildings to purify indoor air volumes,

-Ultrafiltration in most membrane separation processes,

-Wastewater treatment and desalination via reverse osmosis,

-Remediation of contaminated groundwater using nanoparticles containing zero-valent iron,-

-Removal of organic pollutants from industrial waste water, etc.

Environmental applications of nanotechnology can provide the development of solutions to the existing environmental problems and preventive measures for future problems. The environmental impact of nanotechnology is some possible effects on the environment. It can be divided into two aspects: the potential for nanotechnological innovations to help improve the environment, and the possibly novel type of pollution that nanotechnological materials might cause some toxic effects if released into the environment.

Table 1. Environmental applications

Application	Examples
Carbon capture	Photocatalyst consisting of silica Nanosprings coated with a combination of titanium dioxide
Sensors	Pollutants sensors that able to detect lower limits with low cost
Remediation (decontamination, oil spill management)	Heavy metal decontaminant removes heavy metals such as lead, cadmium, nickel, zinc, copper, manganese and cobalt in a neutral pH environment without using any form of sulphur
Wastewater treatment	Ceramic membrane modules, utilizing the CeraMem technology platform, can be supplied with a variety of inorganic microfiltration and ultrafiltration membranes.
Energy	Heat distribution e.g. ceramic-like materials that provide sufficient reliability and durability of the entire structure
Drinking water purification	

3. POSITIVE EFFECTS ON ENVIRONMENT

Nanotechnology offers potential economic, societal and environment benefits. It also has the potential to help reduce the human footprint on the environment by providing solutions for energy consumption, pollution, and green gas emissions. Nanotechnology offers the potential for significant environmental benefits, including cleaner, more efficient industrial processes. Improved ability to detect and eliminate pollution by improving air, water, and soil quality. High precision manufacturing by reducing amount of waste. Clean abundant power via more efficient solar cells. Removal of greenhouse gases and other pollutants from the atmosphere. Decreased need for large industrial plants. Remediating environmental damages.

4. NEGATIVE EFFECTS ON ENVIRONMENT

Understanding of the environmental effects and risks associated with nanotechnology is very limited and inconsistent.

The potential environmental harm through nanotechnology can be summarized as follows:

-High energy requirements for synthesizing nanoparticles causing high energy demand,

-Dissemination of toxic, persistent nanosubstances originating environmental harm,

-Environmental implications of other life cycle stages also not clear,

-Lack of trained engineers and workers causing further concerns,

-Lower recovery and recycling rates.

5. CONCLUSION

There is no doubt that nanotechnology will continue to be develop, be a benefit to society and improve the environment in various ways. Nanoscale materials will make the products better in terms of functionality, weight savings, less energy consumption and a cleaner environment. Nanomaterial may help clean certain environmental wastes, but contaminate environment in other ways.

Choosing the right nanoscale materials is one of the key parameters for the future direction of nanotechnology. Engineering ethics need to be defined before the commercial use of nanotechnology. Risk assessment on new nanomaterial based application is important to evaluate potential risk to our environment when the products are in use. Full life cycle evaluation and analysis for all difference applications should be conducted with constant attention.

Nanotechnology has great potential for improving environmental quality, reducing consumption of resources and energy, and allowing environmentally beneficial economic development.

However, rapid development and expanding use and disposal of nanoproducts very likely poses complex risks to the environment and biological systems due to the tiny size and high surface area of nanoparticles.

ACKNOWLEDGEMENTS

REFERENCES

[1] Zhang, B., Misak, H., Dhanasekaran, P.S., Kalla, D. and Asmatulu, R., 2011. Environmental Impacts of Nanotechnology and Its Products. Proceedings of the 2011 Midwest Section Conference of the American Society for Engineering Education (2011).

[2] Mansoori, G.A., Rohani, T., Bastami, A., Ahmadpour, Z. and Eshaghi, (2008). B Envıronmental application of nanotechnology. Annual Review of Nano Research, Vol.2, Chap.2, 2008.

[3] Ibrahim, R.K., Hayyan, M., Al Saadi, M.A., Hayyan, A. and Ibrahim, S. (2016). Environmental application of nanotechnology: air, soil, and water. Environ Sci Pollut Res (2016) 23:13754–13788.

Usability of Blast Furnace Flue Dust in Reduction of Manganese Ore Concentrate

Fikri Erdem Sesen[1], İbrahim Ozdemir[2], Mustafa Kelami Sesen[3]

Abstract

Blast furnace flue dust is an important source of iron and carbon. Depending on the blast furnace practice, its carbon content varies roughly between 20 and 50 % while its iron content can exceed 50 % if iron oxides are considered. It is traditionally recycled by adding in to the sintering blend. However, it can be used as a reductant since it is a carbon-bearing by-product. This study aims to investigate the utilisation of blast furnace flue dust as a reductant and iron source in ferromanganese production. For this reason, two blends were prepared: Manganese ore concentrate + coke + mill scale (1) and manganese ore concentrate + coke + blast furnace flue dust (2) were blended in a ratio that was calculated for providing 200 % of the theoretical carbon content. The blends were heated in a furnace at 1200 °C for 2 hours to achieve the reduction. The reduction degree of 68.35 % achieved by the reduction of the second blend was considerably higher than the reduction degree of 60.97 % achieved by the reduction of the first blend. After that, a new blend was prepared by the addition of lime having a CaO content equal to the SiO2 content in order to adjust the basicity ratio as 1 and CaF2 in order to obtain fluidity. This new blend was heated in the furnace at 1600 °C for 90 minutes to achieve ferromanganese production via reduction-melting.

Keywords: *Blast Furnace Flue Dust, Ferromanganese, Recycling, Reduction-Melting*

1. INTRODUCTION

Perhaps all of the industrial production processes face problems related to high set up and management costs, raw material abundance, energy requirements and environmental effects. Since population and industrial production are continuously growing, the requirements of storage or disposal of waste materials are increasing. Therefore, industry, in general, has begun to search for alternative production methods in which recycling is a significant aspect. No exception can be mentioned about iron-steel industry since it is responsible for consumption of raw material and energy in vast amounts and is the cause of environmental pollution in a large scale. Because of these reasons, types of materials which come out during iron-steel production processes were used to be called "waste", but they are called "residue" or even "by-product" nowadays and many of them are re-used in the flow chart.

With negligible exceptions, steel is being produced by two main methods in the current iron-steel industry. One of these is steel production derived from iron ore in integrated plants while the other is production in electric arc furnaces by using steel scrap. About 70% of the world's steel production is carried out in integrated plants [1]. Blast furnace process is the most important production stage in integrated plants. During the production of molten pig iron, about two tons of waste is generated per ton of material obtained. The primary by-products generated during the production of molten pig iron include blast furnace gas, slag, dust and sludge from top gas cleaning. The recovery and re-use of these wastes within the same production unit or by different industrial installation are essential for both protecting the environment and conserving metals and mineral resources. For this reason, the individual units in an integrated steelmaking plant are connected both in terms of product flows and internal flows of residues (mill scale, fly dusts and sludges, furnace gas, etc.). These interdependencies have been installed in order to minimise emissions, optimise productivity and reduce costs. Dust and sludge typically constitute 4 to 7% of the produced hot metal with an iron content of 15-40%, carbon content of 25-40% and SiO_2 content of 7-10% [2].

[1] Corresponding author: Istanbul Technical University, Faculty of Chemistry-Metallurgy, Department of Metallurgical and Materials Engineering, 34469, İstanbul, Turkey. sesen@itu.edu.tr

[2] Istanbul Technical University, Faculty of Chemistry-Metallurgy, Department of Metallurgical and Materials Engineering, 34469, İstanbul, Turkey. ozdemir.ibrahim@hotmail.com.tr

[3] Istanbul Technical University, Faculty of Chemistry-Metallurgy, Department of Metallurgical and Materials Engineering, 34469, İstanbul, Turkey, mksesen@itu.edu.tr

While recycling of blast furnace flue dust which is formed as a result of production of molten pig iron is important, manganese is another important material for steel production. 90-95% of the produced manganese ore is used in iron-steel production for several aims. Manganese is added to steel as an alloying element in order to increase its strength, toughness and hardness. It also forms sulphides with sulphur in the steel and controls sulphur compounds by this way. The generated manganese sulphide compound prevents the formation of iron sulphide microstructure, which causes hot tearing. Another reason for manganese usage is related to the deoxidation duty of manganese in steel. Manganese is the third important deoxidizer after aluminium and silicon. Manganese plays an important role in clean steel production because of these reasons. Additionally, manganese is used as a ferroalloy [3]. In this work, which was carried out because of these reasons, studies and investigations were performed towards the usage of blast furnace flue dust in ferromanganese production. Recyclability of iron and reductiveness of carbon in the composition of blast furnace flue dust were investigated on the basis of using it in ferromanganese production. Before the experimental work, thermodynamic conditions of the process were revealed by performing calculations about chemical reactions that are supposed to occur and studying related phase diagrams. The theoretical carbon content which is required for the solid-state reduction to occur was determined by this way. Sieve analyses, chemical composition analyses and x rays diffraction analyses were applied to the raw materials before reduction treatments whereas chemical composition analyses and x rays diffraction analyses were applied to the treated samples. As a final stage of the experimental work, reduction-melting was tried to be performed in order to achieve ferromanganese production. The product was characterised by utilising an optical microscope, a scanning electron microscope equipped with an energy dispersive spectrometer, and a Vickers microhardness tester.

2. EXPERIMENTAL DETAILS

2.1. Raw Materials

Manganese ore concentrate, coke, mill scale, blast furnace flue dust, bentonite, lime and calcium difluoride were used as raw materials during experimental work. Chemical compositions of the as-received manganese ore concentrate, the coke, the mill scale and the blast furnace flue dust are given in Tables 1, 2, 3 and 4 respectively. X rays diffraction analysis pattern of the as-received manganese ore concentrate is given in Figure 1 and the chemical composition of the coke ash, which is a constituent of the coke, is given in Table 5.

Table 1. The chemical composition of the as-received manganese ore concentrate.

Component	Mn	SiO_2	Al_2O_3	CaO	Fe	Na_2O	K_2O	C	MgO	S
wt. %	50.230	16.560	1.070	0.410	0.320	0.260	0.240	0.110	0.081	0.023

Table 2. The chemical composition of the coke.

Component	Fixed carbon	Ash	Volatile matter
wt. %	83.49	14.83	1.68

Table 3. The chemical composition of the mill scale.

Component	Iron oxide	MnO	SiO_2	Cu_2O	Cr_2O_3	balance
wt. %	~98.33	0.58	0.21	0.24	0.29	~0.15

Table 4. The chemical composition of the blast furnace flue dust.

Component	Fe_2O_3	C	SiO_2	Al_2O_3	CaO	MgO	K_2O	MnO	ZnO	S
wt. %	34.64	23.23	9.13	2.06	9.99	1.29	0.27	0.51	0.30	0.34

Table 5. The chemical composition of the coke ash.

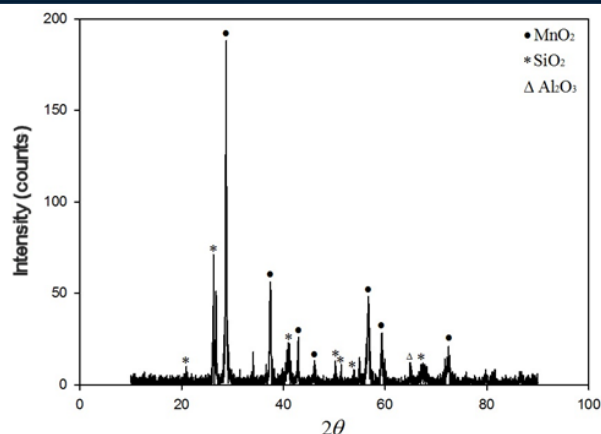| Component	SiO_2	Al_2O_3	SO_3	P_2O_5	CaO	MgO	K_2O	Fe_2O_3	TiO_2	Na_2O
wt. %	46.53	23.49	2.71	0.98	4.66	1.92	2.64	14.88	1.15	0.39

Figure 1. X rays diffraction analysis pattern of the as-received manganese ore concentrate.

Coke was used as a reductant, bentonite was used as a binder, mill scale was used as an iron source and blast furnace flue dust was used as a source of both iron and carbon. Lime was used to adjust the basicity ratio as 1 and calcium difluoride was used to obtain the fluidity prior to reduction-melting.

2.2. Experimental Work and Characterisation

At first, two blends were prepared. The mixture of manganese ore concentrate-coke was blended with mill scale for one and with blast furnace flue dust for the other. The coke amount of the blend containing mill scale was adjusted to provide 100, 150 and 200% of the stoichiometric carbon content calculated according to the theoretical reduction reaction. Samples of 25 g were taken from the three mentioned blends for each reduction experiment. The samples were charged into a tube-type furnace, hold in this furnace at 1100, 1200, 1250 and 1300 °C for 1, 2, 3 and 4 hours and then they were left to cool down in the furnace. The samples were weighted after the reduction treatment in order to calculate the theoretical reduction degree regarding each reduction experiment. Analyses of x rays diffraction and chemical composition were also applied to the samples for the aim of understanding the remaining and generated phases. As a result of these initial stage reduction treatments, the most suitable experimental parameters of temperature, duration and stoichiometric carbon content were determined. After that, the reduction experiments were applied to the blend containing blast furnace flue dust, which is a source of iron and carbon, with these determined parameters. The treated samples were characterised by using the methods mentioned above.

As a final stage of the experimental work, reduction-melting was tried to be performed in order to achieve ferromanganese production. For this experiment, a new blend was prepared by addition of lime having a CaO content equal to the SiO_2 content in order to adjust the basicity ratio as 1 and CaF_2 to obtain fluidity. This new blend was heated in the furnace at 1600 °C for 90 minutes to achieve ferromanganese production via reduction-melting. The product was characterised by using an optical microscope, a scanning electron microscope equipped with an energy dispersive spectrometer, a Vickers microhardness tester and by applying analyses of x rays diffraction and chemical composition.

3. EXPERIMENTAL RESULTS

3.1. Results of Solid-state Reduction Experiments

The parameters applied during solid-state reduction of the samples containing mill scale is shown in Table 6 together with the calculated theoretical reduction degrees. As a result of the reduction treatments that were carried out at 1300 °C for 1 hour and at 1250 °C for 2 hours, high reduction degrees such as 81.57 and 70.08 were achieved. During these treatments, however, partial melting of the blend, which is an undesired phenomenon, was observed. Thus, the optimum experimental parameters were determined as 1200 °C temperature, 2 hours duration and a stoichiometric carbon content of 200%. As a result of substituting mill scale with blast furnace flue dust, reduction degrees of 68.35 and 67.10%, which are considerably higher than the one achieved with mill scale (60.97%), were reached. The comparison of the x rays diffraction analysis pattern of the reduced sample containing mill scale with that of the reduced sample containing blast furnace flue dust is given in Figure 2. It can be understood from the figure that if blast furnace flue dust is used in the blend instead of mill scale, the peaks that resemble iron oxide and manganese oxide become shorter while some peaks that resemble elemental manganese appear as a result of the reduction treatment. This result is considered to be caused by the significant carbon content of blast furnace flue dust, which benefits reduction.

Table 6. The parameters applied during the initial stage reduction experiments performed with mill scale and the related calculated theoretical reduction degrees.

Experiment number	Temperature (°C)	Duration (hours)	Theoretical carbon content (%)	Reduction degree (%)
1	1100	1	150	45.46
2	1200	1	150	56.08
3	1250	1	150	64.58
4	1300	1	150	81.57
5	1250	2	150	70.08
6	1200	2	150	57.14
7	1200	3	150	58.20
8	1200	4	150	62.45
9	1200	2	100	52.04
10	1200	2	200	60.97
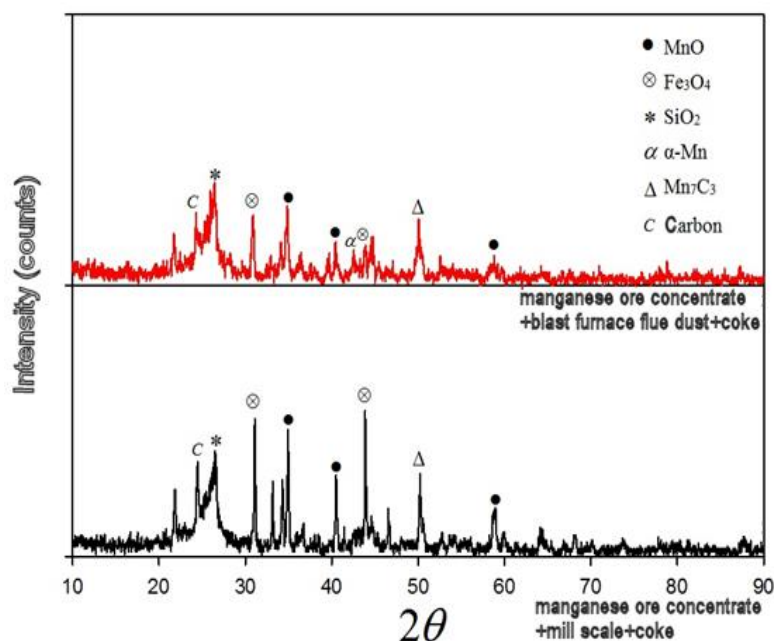
Figure 2. X rays diffraction analysis pattern of the reduced sample containing blast furnace flue dust (above) and mill scale (below).

The Boudouard reaction can be written simply as follows:

$$2CO_{(gas)} = C_{(solid)} + CO_{2(gas)} \tag{1}$$

If the pressure is increased, the reaction thermodynamically proceeds to the right in order to decrease the pressure. Thus, if the blast furnace top pressure is increased, more carbon is produced as a constituent of fly ash. Carbon supplied from the fly ash is more reactive, i.e. a better reductant, than carbon in the coke [4].

3.2. Results of Reduction-melting Experiment

Two optical micrographs presenting the phases and indentation traces related to the product obtained as a result of the reduction-melting experiment are given in Figure 3 (a) and 3 (b). The average hardness value of the darker region was about 1000 HV, while that of the lighter region was 790 HV. Darker regions resemble manganese carbide while lighter regions resemble iron carbide in different stoichiometric ratios. A metallisation degree of 74% was achieved as a result of the reduction-melting treatment.

(a)	(b)
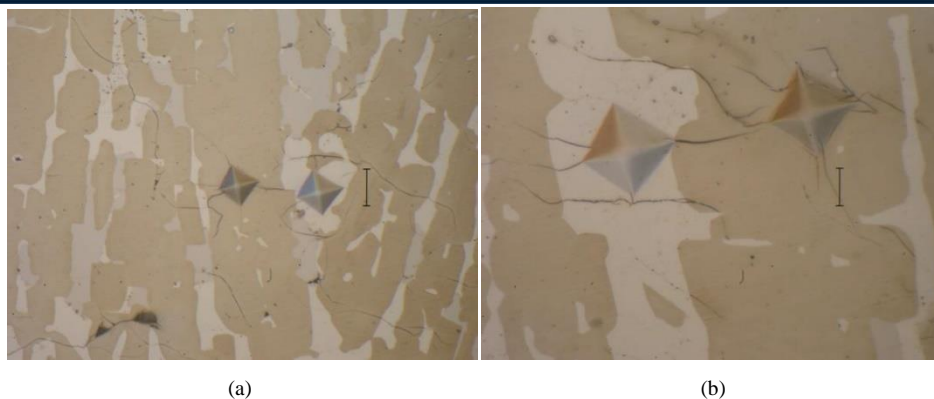
Figure 3. Optical micrographs showing the resultant view of the sample after the reduction-melting treatment (Scale length: 20 µm (a), 10 µm (b)).

A scanning electron microscope image showing the metallic phases obtained as a result of the reduction-melting treatment is given in Figure 4. The related energy dispersive spectrometric analysis results are given in Table 7 in weight per cent.
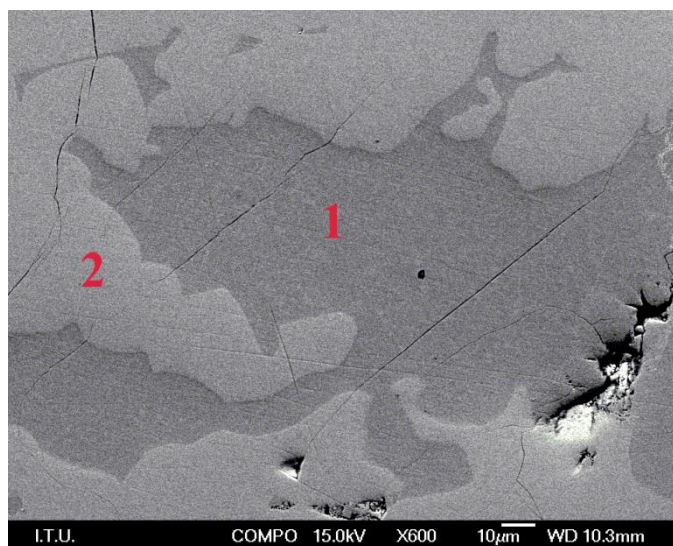
Figure 4. Scanning electron microscope image in which the metallic phases obtained as a result of the reduction-melting treatment is viewed.

Table 7. Semi-quantitative weight per cent chemical analysis values detected by energy dispersive spectrometer.

Region	Mn% wt.	Fe% wt.	Si% wt.	C% wt.
1	53.20	29.20	14.24	3.36
2	66.16	18.01	9.69	6.14

The hardness of the second region was thought to be higher since its manganese and carbon content were higher than that of the first region.

4. CONCLUSION

This work reveals that recycling of iron in blast furnace flue dust can be achieved. The reduction degree reached in case of using blast furnace flue dust is considerably (~12%) higher than that reached in case of using mill scale. The primary result of this situation must be the significant carbon content of blast furnace flue dust. Moreover, carbon supplied from blast furnace flue dust is more reactive (a better reductant) than carbon in the coke. It was understood that blast furnace flue dust could be utilised in ferromanganese production in certain experimental conditions including reduction-melting.

REFERENCES

[1] R. Remus, M. A. A. Monsonet, S. Roudier and L. D. Sancho, *Best Available Techniques Reference Document for Iron and Steel Production*, Joint Research Centre, the European Comission, Publications Office of the European Union, Luxembourg, 2013.

[2] N. C. C. Lobato, E. A. Villegas and M. B. Mansur, "Management of Solid Wastes from Steelmaking and Galvanizing Processes: A Brief Review," *Resour. Conserv. Recycl.*, vol. 102, pp. 49-57, 2015.

[3] M. Gasik, *Handbook of Ferroalloys Theory and Technology*, Elsevier, USA, 2013.

[4] Y. Yamazaki, Chapter 3: *Gasification Reactions of Metallurgical Coke and its Application – Improvement of Carbon Use Efficiency in Blast Furnace*, ser. Y. Yun, Ed., Gasification for Practical Applications, InTech, 2012.

Wi-Fi Based and Time-Limited Secure Control System Design for Door Locks

İsmail KIRBAŞ[1]

Abstract

The proposed system provides authorized control of Wi-Fi based door lock mechanisms from a certain control center via internet connection and recording the input and output operations. A secure random key-token mechanism has been developed to make data exchange transactions over the Internet more secure. Thus, when a user name and key information are entered using a smartphone, tablet or computer capable of connecting to a wireless network, control of the door locks by a central system and control of input / output operations are provided within the scope of user permissions.

Keywords: *Internet of Things, Key-Token Security Mechanism, Remote Door Control, Time-Limited Access, Wi-Fi Based Secure Control Application*

1. INTRODUCTION

Today, design and production of remote controlled devices that can be connected to computer networks using wireless communication systems are constantly increasing. Home and office applications are the leading application areas in remote control sector [1]–[3]. Its main activities are electronic lock mechanisms for intelligent home and office automation and access control systems developed for hotels [4].

When the recent studies in the literature are examined, it is frequently seen that there are many paper related to internet of things, GSM, android and cloud based home security projects [5]–[7].Ismail at al,. developed an android-based home door locks application via Bluetooth for disabled people [8], Arslan and Kirbas suggested a wireless sensor/actuator node prototype for Internet of Things [9], Hwang and Baek proposed a wireless access monitoring and control system based on digital door lock [10]. Choudhury at al, introduced an SMS based home security system [11]. Pramanik at al, suggested an GSM based smart home and digital notice board [12]. Kirbas developed an actuator sensor node prototype for Internet of Things applications [13].

Such systems are typically designed to be controlled over a wireless communication system such as Bluetooth or Wi-Fi. As a user interface, smart devices are generally used which do not require special interface equipment such as smartphones or tablets.

In this paper, our main goal is to control the Wi-Fi based door lock mechanisms safely from a certain authorization center via internet connection and record all input and output operations. For this purpose, a random key-token mechanism has been developed to make data exchange transactions over the Internet more secure. Thus, using a smartphone, a tablet or a computer connected to a wireless network, control of the door locks by a central system and monitor of input-output operations are provided within the scope of user permission including user name and secure key information.

2. PROPOSED SYSTEM ARCHITECTURE

The scheme of the developed control mechanism is given in Figure 1. The control mechanism basically consists of three components. First component is an interface tool or a hardware that can access to the authorization page, which can connect to the wireless network, such as smartphone, tablet or laptop computer belonging to the user.

---

[1] *Corresponding author: Mehmet Akif Ersoy University, Department of Computer Engineering, 15100,Istiklal Campus/Burdur, Turkey. ismailkirbas@mehmetakif.edu.tr*
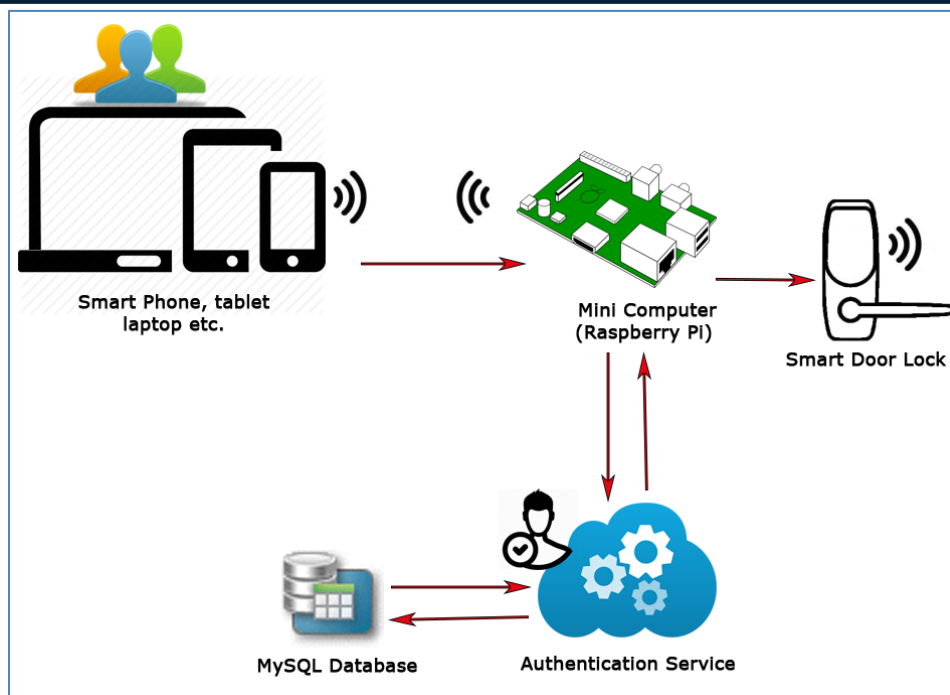
Figure 1. Architecture of the proposed communication system.

The second component is a low-cost and card-size computer (Raspberry Pi 3) [14], which is connected to the door lock so that it can send a direct electrical opening command and runs a web server software. The mini-computer must be directly connected to the wireless network and has a static IP address on this network.

Each user has a different username and secret key. When a registered user wants to pass through a door, he/she should access the web server running on the minicomputer via wireless network or internet and submits his/her user name and secret key information on the login page. At this stage, the control software running on the mini-computer connects to the Authentication Service (AS) and investigate whether the user has a permission to enter or not at that time.

Figure 2 shows the secure login page of the door lock authorization application used by smart devices. The connection is made by entering the static IP address of the minicomputer using the browser on the smart device. Then enter the user name and secret key and click "Open The Door" button.

Figure 2. Application screenshot on an android smartphone.

If the user is allowed to unlock the door, the AS produces and sends 32-byte token to the minicomputer. After checking the validity of the token, the mini-computer sends an electrical signal to the lock mechanism to open the door.

At the same time, the authorization service also records the user name and the gate number of the mini computer and the query time in a MySQL database located on the web server. Thus, all input and output operations are recorded on a web server. Detailed reports of input-output operations can be generated through a web interface located on the authentication server.

3. HARDWARE AND SOFTWARE DESIGN

Electrically controlled door mechanisms are inevitable and important part of the remote control system. Today, there are many electronic door lock mechanisms that can work with battery and have low electricity consumption values.

In this project, we preferred Raspberry Pi 3 minicomputer because of its low cost and high performance. The Raspberry Pi 3 has a 64 bit ARMv7 BCM 2837 microprocessor running at 1.2 Ghz, 1 GB of RAM and a 400 MHz VideoCore IV graphics processor. It has Bluetooth 4.1 (Bluetooth Low Energy) support and has Wi-Fi adapter with 802.11n support for wireless communication. There are 4 USB 2.0 ports, 1 Full HDMI output, 40 general-purpose input-output pins, 4-pin stereo output and composite video output. It has CSI camera port for camera connection and DSI display port for touch screen applications. There is a Micro SD card input for loading operating system and storing data. As an operating system, Raspbian Jessie kernel 4.4 was installed.

Apache version 2 is integrated for the web server software, PHP 5 as PHP interpreter, MySQL and PhpMyAdmin applications are preferred as database management software. The wiringPi software [15] and the PHP interpreter cURL module [16] have been installed to access the general purpose input / output pins of the minicomputer. Figure 2 depicts a photograph of the first prototype. The minicomputer drives an optocoupler through a digital output pin, and the relay connected to the optocoupler is connected to the door lock mechanism.

Figure 3 shows the developed hardware prototype and breadboard for the proposed application.
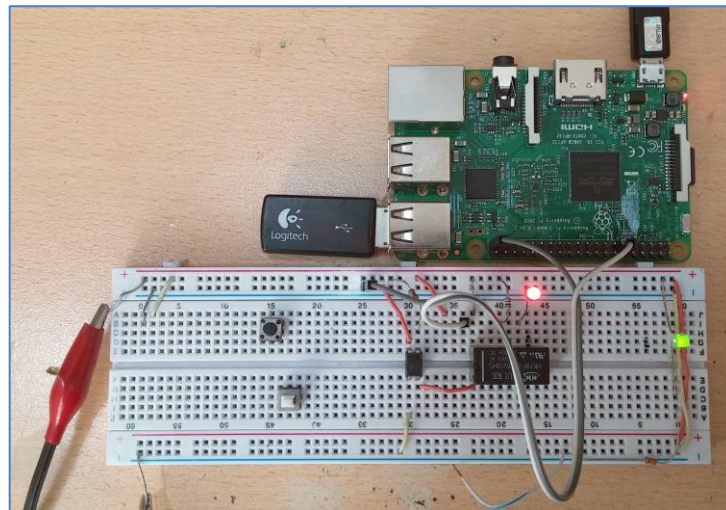
Figure 3. The developed hardware prototype.

The authorization service software in minicomputer, performs an inquiry and if the user has permission, the door lock is unlocked and all operations are recorded.

4. RANDOM KEY-TOKEN MECHANISM FOR SECURE COMMUNICATION

Security in door control mechanisms is the most important parameter. In order to perform secure data exchange between the authorization service and the minicomputer a random key-token mechanism has been developed.

Figure 4 demonstrates the developed secure and time-limited random key-token mechanism and data flow.
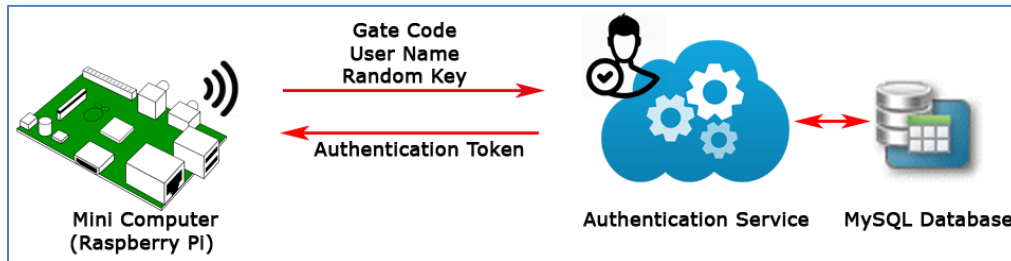
Figure 4. Secret key-token mechanism used for secure communication.

When a registered user wishes to open the door, it is connected via the static IP address of the minicomputer that manages the door. The minicomputer generates a random key and a token corresponding to this key for querying authority, but sends only the randomly generated key to the authorization service, the username and the gate code number of the mini computer.

The Authentication Service (AS) queries the MySQL database on the web server to determine whether the user has permission to access. If the user authorized, AS produces the same token generated by minicomputer and sends to the minicomputer. The minicomputer compares the generated and received tokens. If the tokens do not match, the locking mechanism stays locked otherwise unlocked. The minicomputer generates a unique random key-token pair for each entrance and each of them can be used only once [17].

Data communication between the authorization service and the mini computer is done in JSON format. Figure 5 shows sample data sent from the minicomputer to the authorization service.

```
{
    "UserName": "Ismail Kirbas",
    "GateCode": "1245",
    "RandomKey": "25860882"
}
```

Figure 2. The user query in JSON format.

Figure 6 contains sample data containing the authorization token generated by the authorization service.

```
{
    "GateCode": "1245",
    "RandomKey": "25860882",
    "AuthorizationToken": "2c4b55635099ba586ddcf29d394bd8db"
}
```

Figure 3. An example response from the Authorization Service to minicomputer in JSON format.

When minicomputer generates a random key, a counter begins to count down from a certain value in seconds or minutes. If AS cannot send the right token value within a certain period of time, minicomputer consider the random key and token pair is invalid. Thus, the attempting request to open the door is rejected. The counter's starting value is a time limit for a valid connection.

The Authorization Service and all minicomputers should have static IP addresses to reach each other directly.

If it is desired to restrict input / output time for users or doors, individual timelines can be prepared for each user or door using the Authorization Service software. Thus, within a user's authority, more than one door becomes controllable according to a timetable and all user activities can be logged on a web service.

5. CONCLUSION

This work includes a Wi-Fi and web based time and user-restricted remote control application. The use of mobile devices such as smartphones and tablets is envisaged as a user interface. In addition, a web-based control mechanism is used regardless of the operating system running on the intelligent devices. This is intended to be independent of the hardware and operating system.

It acts as a server authorization service on the Internet, and it is decided whether or not users will be able to log in, taking into account user authority and time constraints. A low-cost minicomputer (Raspberry Pi 3) with a web server software is connected to the door lock mechanism and the user's access through this computer's internet connection is controlled.

In order to increase the reliability of the communication, a random key and time limited token mechanism has been developed. The proposed application approach can be employed in hotels, firms, site entrance and offices.

For future studies, android and IOS applications also can be developed for the proposed system to provide the users more customized interfaces. Along with that, new biometric security features can be integrated to improve the existing security mechanism.

REFERENCES

[1]. Y. T. Park, P. Sthapit, and J. Y. Pyun, "Smart digital door lock for the home automation," in *TENCON 2009 - 2009 IEEE Region 10 Conference*, 2009, pp. 1–6.

[2]. C. H. Hung, Y. W. Bai, and J. H. Ren, "Design and implementation of a single button operation for a door lock control system based on a near field communication of a smartphone," in *Consumer Electronics - Berlin (ICCE-Berlin), 2015 IEEE 5th International Conference on*, 2015, pp. 260–261.

[3]. J. Rui and S. Danpeng, "Architecture Design of the Internet of Things Based on Cloud Computing," in *2015 Seventh International Conference on Measuring Technology and Mechatronics Automation*, 2015, pp. 206–209.

[4]. A. Abloy, "Vingcard elsafe - electronic hotel locks." Assa Abloy, 2015.

[5]. S. Rajadurai, P. P. Nehru, and R. Selvarasu, "Android mobile based home security and device control using GSM," in *Innovations in Information, Embedded and Communication Systems (ICIIECS), 2015 International Conference on*, 2015, pp. 1–5.

[6]. A. Zimmermann, R. Schmidt, K. Sandkuhl, M. Wißotzki, D. Jugel, and M. MOhring, "Digital Enterprise Architecture - Transformation for the Internet of Things," in *2015 IEEE 19th International Enterprise Distributed Object Computing Workshop*, 2015, pp. 130–138.

[7]. İ. Kirbaş and M. E. Yüksel, "An Open Source Cloud Computing Application for the ARM Based Embedded Systems: mbed Platform," *J. Grad. Sch. Nat. Appl. Sci. Mehmet Akif Ersoy Univ.*, vol. 6, no. 2, pp. 74–81, 2015.

[8]. N. H. Ismail, Z. Tukiran, N. N. Shamsuddin, and E. I. S. Saadon, "Android-based home door locks application via Bluetooth for disabled people," in *Control System, Computing and Engineering (ICCSCE), 2014 IEEE International Conference on*, 2014, pp. 227–231.

[9]. K. Arslan and İ. Kırbaş, "Developing Wireless Sensor/Actuator Node Prototype for Internet of Things Applications," *J. Grad. Sch. Nat. Appl. Sci. Mehmet Akif Ersoy Univ.*, vol. Special Issiue 1, no. 7, pp. 35–43, 2016.

[10]. I. K. Hwang and J. W. Baek, "Wireless access monitoring and control system based on digital door lock," *IEEE Trans. Consum. Electron.*, vol. 53, no. 4, pp. 1724–1730, Nov. 2007.

[11]. B. Choudhury, T. S. Choudhury, A. Pramanik, W. Arif, and J. Mehedi, "Design and implementation of an SMS based home security system," in *Electrical, Computer and Communication Technologies (ICECCT), 2015 IEEE International Conference on*, 2015, pp. 1–7.

[12]. A. Pramanik, Rishikesh, V. Nagar, S. Dwivedi, and B. Choudhury, "GSM based Smart home and digital notice board," in *2016 International Conference on Computational Techniques in Information and Communication Technologies (ICCTICT)*, 2016, pp. 41–46.

[13]. İ. Kirbaş, "An Actuator Sensor Node Prototype For Internet of Things Applications," presented at the International Science and Technology Conference, Vienna, Austria, 2016, vol. 1, p. 92.

[14]. R. P. Foundation, "Raspberry Pi," *Teach, Learn, and Make with Raspberry Pi*. [Online]. Available: https://www.raspberrypi.org. [Accessed: 04-May-2017].

[15]. G. Henderson, "Wiring Pi," *GPIO Interface library for the Raspberry Pi*. [Online]. Available: http://wiringpi.com/. [Accessed: 03-Mar-2017].

[16]. D. Stenberg, "cURL," *Command line tool and library for transferring data with URLs*. [Online]. Available: https://curl.haxx.se. [Accessed: 03-Mar-2017].

[17]. I. Kirbas, "Developing and Remote Controlling a Multi-Zone Cooling Plant using Web Services and a Secure Token Mechanism," *Meas. Control*, vol. 48, no. 9, pp. 278–284, 2015.

BIOGRAPHY

İsmail KIRBAŞ, got his bachelors' degree in the Computer Education Department in Technical Education Faculty at Kocaeli University, Kocaeli/Turkey in 2000, his master degree in the Electronics and Computer Education at Kocaeli University in 2008, PhD degree in Electronics and Computer Education Department at Sakarya University in 2013. He is still an academic member of the Computer Engineering Department at Burdur Mehmet Akif Ersoy University. His major areas of interests are: Wireless Sensor Networks, Embedded Systems, Design of Experiments, Time Series Predictions and Mobile Programming.

An Image-Based Recommender System Based on Image Annotation

Kemal Ozkan[1], Zuhal Kurt[2], Erol Seke[3]

Abstract

Recommender system is a software that analyzes available data to make recommendations about various products and services to their users might be interested in. These systems must perform efficient for both users and the e-commerce sites benefiting from such systems. Ensuring proper and reliable recommendations increases user satisfaction that results selling more products and services. Collaborative filtering, content-based, and hybrid techniques are type of methods for recommender systems. Content-based recommender systems are usually text-based systems, but image-based recommender systems have become increasingly in favour for the content-based recommender systems in recent years.

The process of an image based recommender system is to match a users' image with the most similar image and recommend it. The recommendation images are the most likely images uploaded and widely acclaimed from the users. The most challenging problem in image-based recommneder systems is to match an image with the most similar visual words or classes based on the image's visual content. In this study, we are planning to solve this problem using Bag of words model, which is an effective model in computer vision, and also features are extracted with commonly used descriptors.

Keywords: *Bag of words model, descriptor, cosine similarity, Image-based recommender system, label.*

1. INTRODUCTION

The major aims of recommender systems are help customers to find products to that they seek, the other one is increasing sales ratios for sellers. Therefore, success of recommender systems is imperative for both users and the e-commerce sites utilizing such systems. Providing accurate and dependable recommendations increases user satisfaction that results selling more products and services. On the other hand, inaccurate recommendations make users to search alternative sites for shopping. Recommender systems can be grouped as collaborative filtering, content-based, and hybrid recommender systems. Collaborative filtering is a common recommender system. In addition to collaborative filtering algorithms, content-based and hybrid recommender systems are increasingly becoming popular due to widespread use of social media. Content-based recommender systems are usually text-based systems. Image-based recommender systems are receiving increasing attention in the recent years.

Although there are studies focusing on image-based recommender systems, such systems are still challenging research field with some unresolved problems. These systems are based on images uploaded by users. They first determine the most similar users based on the images they upload to the system. They then return the most likely image to the users based on the images liked by the neighbors. The most difficult problem in image-based recommender systems is to match an image with the most similar visual words or classes based on the image's visual content. In this paper, we are planning to solve this problem using common image annotation techniques, which is an effective method in computer vision. Another challenging problem in image-based recommender systems is the online computation time caused by the large amount of data in real life applications.

---

[1] Corresponding author: Eskişehir Osmangazi University, Department of Computer Engineering, 26480, ESOGU Meşelik Yerleşkesi /Eskişehir, Turkey. kozkan@ogu.edu.tr

[2] Eskişehir Osmangazi University, Department of Mathematics and Computer Science, 26480, ESOGU Meşelik Yerleşkesi /Eskişehir, Turkey. zkurt@ogu.edu.tr

[3] Eskişehir Osmangazi University, Department of Electrical and Electronics Engineering, 26480, ESOGU Meşelik Yerleşkesi /Eskişehir, Turkey. eseke@ogu.edu.tr

Pliakos and Kotropoulos (2015) are proposed an image recommender system using some known image annotation techniques to achieve these problems. This system work with large collections of touristic images and the structure of their system is based on clustering and classification algorithms. Tourism related images have been annotated geographically, semantically, and visually, utilizing visual features and text data, finally this system is recommend touristic place of interest of user's, [1].

A novel framework called JustClick [3] is a personalized image recommendation system working with large-scale collections of manually annotated Flickr images. The procedure of this system is based on topic networks, that are automatically produced for outlining large-scale collections of manually annotated Flickr images at a semantic level. They used hyperbolic visualization method to enable interactive navigation and exploration of the topic network, so that users can find out the large-scale image collections at the first glance, build up their mental query models interactively and specify their image needs more precisely by selecting the image topics on the topic network directly and also can assess the relevance between the recommended images and their real query intentions interactively. An implementation of this system is allowing users to express their time-varying query intentions and to direct the system to more relevant images according to their personal preferences [3].

A personalized recommender system model that is based on analysis of colour features of product images is proposed in, [2]. Algorithm of this system is based on extraction of colour- features of images in order to demonstrate impressions related to the human perception of images. This system retrieves and ranks the images corresponding to the desired impressions, with using extracted colour features. The structure of this model is based on service-oriented architecture in order to promote its exibility and reuse, which is important when applying the model to existing recommender system environments, [2].

A profile based image recommender system for is proposed in [4,5], and this system is able to reach user for retrieval of images from profile based search engines by using smartphone. All users of this system have his/her own profile and semantic signature of each user search is stored individually. This approach improves the performance of search result as it is refering individual profile to know users search intension. The images are reranked using keyword expansion to provide better efficiency and effectiveness by using semantic signature for more precise output [4].

The feature extraction techniques are used in order to image annotation, the Color / Scale Invariant Feature Transform (SIFT / C-SIFT) [6,7], Speeded-Up Robust Features [8], Maximally Stable Extremal Regions(MSER) [9] and Local Binary Pattern (LBP) [10] frequently used descriptors, and also new approaches available in the literature. In this paper, we develop an image recommender system, to design this system, we are going to use novel image annotation approaches. Our proposed system needs to uploaded image from user, these images become query images for our system, then annotate these images to understand users' preferences. Outputs of the proposed system are recommendation images that are suitable for user pleasurement. The algorithm of the proposed method and the experimental results will be given in order of the second part and the third part of the study. Finally, the conclusion and future work will be given in section 4.

2. MATERIALS AND METHODS

There are two problems that might affect the overall success of recommender systems. These problems are known as sparsity and accuracy problems. To solve the sparsity problem, we are going to use image annotation techniques to get the image labels, and to construct visual vocabulary. Furthermore, the visual words help the image based recommender system to collect data about the users, which might improve the accuracy of our recommender system. Contemporary recommender systems utilize GPS data and the labelled data of the collected images to provide recommendations. However, we design our system in such a way so that it will also use unlabeled data to estimate recommendations. At the end, the design of proposed image-based recommender system is based on visual words among images. To design the proposed image-based recommender system, we are going to use novel approaches such as popular feature extraction techniques. Overall performance of the proposed system is evaluated in terms of accuracy and evaluated with using popular data-based experiments. The algorithm of the proposed recommender system is given under below.

- Firstly, the user is prompted to upload the users' image to the proposed system, that is returned the recommendation images.

- The commonly known feature extraction methods and the bag of Words (BoW) model are used in the proposed system.

- To extract features from the images, the popular SIFT, SURF and LBP descriptors are used, and the training set is obtained.

- In this proposed system, the same feature extraction techniques is applied to users' images, and these images are accepted as test set. Each extracted features from test images is compared to final image feature histogram vector, then we recommend top N-10 images to the user.

- The selection opportunity of the best recommendation from the recommendation images is given to user.

- The proposed system is used on the Yahoo! shoes database, that is created by Yahoo! Research Lab in 2012.

3. RESULTS AND DISCUSSION

The proposed system is implemented on the challenging Yahoo! Shopping Shoe dataset, [11]. As stated in [11], this dataset provides a new benchmark which contains a diverse collection of types of shoe photos. Object recognition algorithms aim to identify if there is a pair of shoe and the type of shoes (clogs or high heels) appear in a photo automatically. Yahoo! Shopping is the best place to read user reviews, explore great products and buy online. Dataset is collected from a small subset of product from Yahoo! Shopping to reflect the interesting real-world problem of fine-grained object recognition. This dataset contains a small sample of the Yahoo! Shopping shoe photos. This dataset contains 107 folders, each corresponding to a type and brand of shoe. Also included is a .mat file (shoe_annos.mat), which contains a bounding box for each shoe image.

We use shoe annotation file to read images from Yahoo! Shopping Shoe database. This file (shoe_annos.mat), contains 4513 image file and a bounding box for each shoe image. For example, the image at classes/Iowa_hiking/757550203 640.jpg, has the bounding box: $(x1, y1, x2, y2) = (143, 55, 501, 417)$. We apply boundary box property to all shoe images and create a new annotated dataset.

We use SURF, LBP and SIFT descriptor for feature extraction from each images of Yahoo! Shoes Dataset. We select 9 images from each shoe classes to create a training image set, hence the test set is included 21 images from each shoe classes. The descriptors obtained from training images are clustered by k-means clustering method. Clustering centers are considered as visual words that form visual words. To create image representation, each extracted descriptor is compared to the visual words and associated to the closest word. Finally, image feature histogram vector is obtained. We select randomly 9 images from each class in Yahoo dataset. These 9 images called user's images, we use them as part of test images in our system. The features are extracted from 9 test images with using SIFT, SURF and LBP descriptors. Each extracted features from test images is compared to final image feature histogram vector, then we recommend images which are similar with user's image.The similarity of user images with recommendation images is found with k-nn algorithm.The accuracy of recommendation rates for SIFT, Surf, LBP descriptors are respectively %69, %71 and %62. Also, the accuracy of recommendation rates for each class in Yahoo! Shoe dataset is given in Table 1.

We select 10 random images from 7 different heel shoe classes, then we define these images as user-uploaded images. We offer 10 shoe images to user, after this recommendation level the user should select a shoe image, which is wanted to bought by user. An example of our proposed system process is given in Fig. 1, for this example 10 random images from 7 different heel classes are called query images, shown Fig. 1.a). Our system is offer recommendation images to user for a consideration query images, that images are shown in Fig. 1.b).

a-Query Images

b-Recommendation images

Figure 1. Images are selected from 7 different heel shoe classes as user-uploaded images a) query images, b) Recommendation images that have user's appreciation.

4. CONCLUSIONS

The user is leaving information on the site when on the move, and recommender systems are used this information to recommend products as user's appreciation. Text-based and rate-based recommendation systems attempt to find and offer items to user, in contemporary studies. In this study, an image-based recommender system is examined in addition to these systems. Recently, the number of shopping on the Web

is expressed in millions, hence recommender systems are need effective methods to recommend item that user likes or has previously purchased. In this paper, a system has been developed that returns the recommendation images from the users' uploaded images. After the user upload images to the system, image annotation techniques are used for extracting features from this images, and system is recommend images that have same features with the users' image. It is planned to use multi-label image annotation technique to improve this proposed recommender system.

Table 1. Accuracy of recommendation rates for each class in Yahoo! Shoe dataset.

american eagle sandals	ariat western boots	badgley mischka high heels	betsey johnson platform high heels	birkenstock sandals	clarks sandals	cobian sandals
0,85	0,75	0,9	0,95	0,75	0,8	0,7
1	0,95	0,9	0,8	0,9	0,75	0,8
0,9	0,6	0,95	0,95	0,6	0,8	0,7

corso como flats	creative recreation sneakers	crocs clogs	crocs sandals	crocs slipons	cushe sandals	cushe slipons
0,6	0,6	0,35	0,8	0,2	0,85	0,55
0,75	0,7	0,3	0,9	0,35	0,65	0,65
0,8	0,7	0,4	0,8	0,3	0,7	0,2

ecco laced	ecco slipons	ed hardy sneakers	finn comfort sandals	fitflop sandals	frye laced	grazie sandals
0,3	0,4	0,8	0,9	0,75	0,25	1
0,35	0,4	0,95	0,95	0,9	0,8	0,9
0,05	0,5	0,5	0,75	0,9	0,4	0,9

havaianas sandals	irish setter boots	keen hiking	keen sandals	keen slipons	lacoste slipons	lacoste sneakers
0,75	0,85	0,7	0,7	0,35	0,6	0,35
0,9	0,85	0,45	0,65	0,5	0,65	0,75
0,95	0,6	0,3	0,65	0,25	0,4	0,5

le chameau rain boots	lowa hiking	manolo blahnik high heels	mephisto sandals	mephisto slipons	merrell sandals	merrell slipons
1	0,55	0,9	0,7	0,4	0,85	0,6
1	0,45	0,9	0,9	0,3	0,7	0,5
1	0,25	0,95	0,25	0,2	0,6	0,35

michael kors high heels	nike sandals	oakley sandals	pleaser usa high heels	pleaser usa platform high heels	polo sneakers	puma sneakers
0,8	0,65	0,8	1	0,8	0,5	0,8
0,8	0,8	0,8	1	0,9	0,6	0,7
0,7	0,8	0,95	0,95	0,6	0,4	0,4

quiksilver sandals	ralph lauren sandals	reebok sneakers	reef flip-flops	rider sandals	roxy sandals	sam edelman sandals
0,9	0,8	0,35	0	0,9	0,85	0,8
0,75	0,85	0,55	0,1	0,9	0,9	0,8
0,8	0,75	0,3	0	1	0,8	0,75

sanita clogs	sanuk sandals	sanuk slipons	sebago boat shoes	shiekh sandals	skechers sandals	skechers slipons
0,65	0,95	0,35	0,6	0,95	0,65	0,6
0,5	0,85	0,3	0,5	1	0,75	0,35
0,25	0,7	0,4	0,45	1	0,75	0,15

skechers sneakers	sorel boots	sperry boat shoes	sperry sandals	stuart weitzman high heels	superga sneakers	teva sandals
0,2	0,75	0,6	0,9	0,9	0,7	0,8
0,15	0,65	0,45	0,9	0,858	0,75	0,8
0,45	0,5	0,15	0,7	0,9	0,6	0,65

timberland boots	toms slipons	tory burch sandals	tretorn rain boots	volatile sandals	volcom sandals	yellow box sandals
0,65	0,65	0,8	0,8	0,85	0,75	0,85
0,5	0,8	0,75	0,85	0,8	0,75	0,75
0,4	0,75	0,7	1	0,9	0,85	0,75

ACKNOWLEDGEMENT

REFERENCES

[1]. K. Pliakos, and C. Kotropoulos, "Building an image annotation and tourism recommender system", *Int. J. Artif. Intell. Tools*, 24 (5), 2015.

[2]. A. Sasa, M. Krisper, Y. Kiyoki, and X. Chen, "A personalized recommender system model using colour-impression-based image retrieval and ranking method", *ICIW 2011 : The Sixth International Conference on Internet and Web Applications and Services*, 124-130, 2011.

[3]. J. Fan, D.A. Keim, Y. Gao, H. Luo, and Z. Li, "JustClick: Personalized image recommendation via exploratory search from large-scale flickr image collections", *IEEE Trans. Circuits Syst. Video Technol.*, 19 (2): 273-288, 2008.

[4].   P. Bhagat, N. Mahakalkar, R. Chaudhari, and A. Gotmare, "A survey paper on profile- based image recommender system for smartphone", *In International Journal of Engineering Research and Technology*, vol(3), ESRSA Publications, 2014.

[5].   L. Cao, J. Luo, A. Gallagher, X. Jin, J. Han, and T.S. Huan, "A worldwide tourism recommendation system based on geotaggedweb photos", *IEEE International Conference on Acoustics Speech and Signal Processing (ICASSP),* 2274-2277, 2010.

[6].   D. G. Lowe, "Distinctive image features from scale-invariant keypoints", *Int. J.Comput. Vision*, 60: 91-110, 2004.

[7].   S. Van de, E.A. Koen, T. Gevers, and G. M.C. Snoek, "Evaluating color descriptors for object and scene recognition", *IEEE T. Pattern Anal.*, 32 (9):1582-1596, 2010.

[8].   H. Bay, T. Tuytelaars, and L.V. Gool, "SURF: Speeded up robust features", *In ECCV*, (1): 404-417, 2006.

[9].   J. Matas, O. Chum, M. Urban, and T. Pajdla, "Robust wide baseline stereo from maximally stable extremal regions", *Proc. of British Machine Vision Conference*, 384-396, 2002.

[10].   M. Heikkila, M. Pietikainen, and C. Schmid, "Description of interest regions with local binary patterns", *Pattern Recogn.* , 42: 425-436, 2009.

[11].   https://webscope.sandbox.yahoo.com/catalog.php?datatype=i.

Shape Features Based Conic Arcs for Unclassified Wheat Identification

Ahmet Okan Onarcan[1], Kemal Ozkan[2], Erol Seke[3] , Murat Olgun[4]

Abstract

Wheat is one of the main nutrients used in the world. Consumption of foodstuff produced from quality wheat is of great importance for healthy generations. It is necessary to separate the high and low quality wheat. In this paper, a new recognition method for quality wheat and unclassified wheat is presented. The most distinctive feature for determination of wheat quality is its shape. In this study, objects are first represented by a few descriptive points on their contours obtained from their images. Neighboring points are connected by linear or conical curve fitting. The objects are then represented by an attribute vector constructed from parameters of the curves. Finally, these vectors are used to classify objects (wheat) using support vector machines (svm). Performance is improved with cross validation for each class.

Keywords: *Feature Extraction; Wheat; Unclassified Wheat; Shape Descriptor.*

1. INTRODUCTION

Here we are recognizing quality wheat and unclassified wheat. In computer vision shape is a distinctive feature for object recognition. The presence of curvature and straight lines and soft and sharp transitions, helps us visually identify and analyze the object more easily. Therefore, there are many studies in literature related to shape-based descriptors. A good descriptor should be robust, fast running, distinctive against noise and geometric transformations with few attributes. Shape-based descriptors are generally divided into regional and contour based representatives. Contour based descriptors first extract the outer line of the object in binary format and try to identify the object through this line. Sometimes it is too complicated to describe large images. Especially on large shapes when there is occlusion, and overlapping with each other is one of the problems encountered in recognition performance. In order to get rid of them we can make meaningful interpretations of the whole shape by separating small parts. On the contrary, we can construct a whole shape by adding the vertices and curves from specific dominant points. These dominant points are mostly the corner points on the boundary (Figure 1). The points where the curvature is broken by other expressions are referred to by such terms as dominant point, interesting point, corner point.
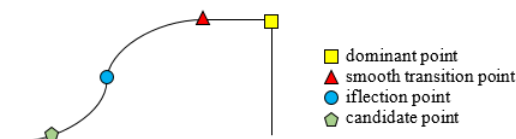

- □ dominant point
- ▲ smooth transition point
- ● iflection point
- ⬠ candidate point

Figure 1. dominant, smooth transition, inflection and candidate points

The dominant point extraction is usually achieved by two basic methods; polygonal approach methods and direct methods (corner detection algorithms). The main idea in the polygonal approach is to determine meaningful points on the contour of the shape. The polygonal approach is applied in two different ways by joining or separating the parts of the shape. During joining process; small changes are eliminated by trying to express the shape by curves and straight lines. In separating process, is made by fitting the curves and lines

---

[1] *Anadolu University, School of Foreign Languages, 26555, Eskişehir, Turkey. aoonarcan@anadolu.edu.tr*

[2] *Corresponding author: Eskişehir Osmangazi University, Faculty of Engineering and Architecture, Computer Engineering Department, 26480, Eskişehir, Turkey. kozkan@ogu.edu.tr*

[3] *Eskişehir Osmangazi University, Department of Electrical and Electronics Engineering, 26480, ESOGU Meşelik Yerleşkesi /Eskişehir, Turkey. eseke@ogu.edu.tr*

[3] *Eskişehir Osmangazi University, Faculty of Agriculture, Department of Field Crops, 26480, ESOGU Meşelik Yerleşkesi /Eskişehir, Turkey. molgun@ogu.edu.tr*

between points. In direct methods, the points which have the highest values are generally determined as the dominant point. At later stages, curvature correction can be achieved in a variety of ways [1,2,3]. To find the dominant points, Wu proposed the adaptive inflection value for each point on the boundaries of the shape, and determined the dominant points depending on this measure [4]. In another study, an algorithm is developed to eliminate contiguous points on the same line on the contour [5]. The area to the right and left of the dominant points is called the support region [1]. At that study, to find the support region, a ratio was developed to find the distance between each point to its beam [1]. In another method, the k-cosine [3] measurement was used to calculate the support region [6]. In [7], Z. Kurt and et al proposed a method based on the difference of the absolute angle between the support points on the right and left side of the candidate point on the contour. They used Principle Component Analysis (PCA) to calculate the support regions.

This work has been done with an object-based identifier and object parsing [7,8]. In the second section, the method used is mentioned, in the third section the experiences are explained and in the fourth section the result is explained.

2. METHOD

Here we use the progressively developed method [8]. In the method, as expresssed in Figure 2, the contour of the shape is extracted by an edge detection algorithm. Each point on the contour is determined as a candidate point and tried to find which one is more important (Figure 1). The meaningful points are fitted by line and curve. In this way, the contour have been tried to be described in the most obvious way.
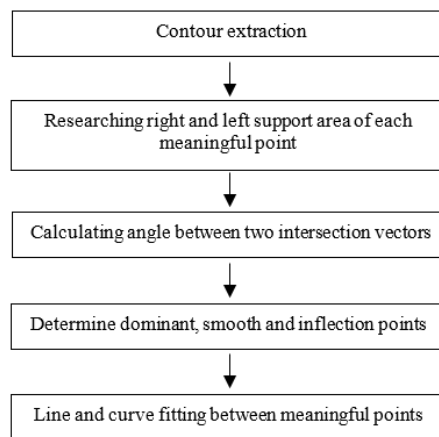

Figure 2. Block diagram of shape description

First Canny edge detector is used to find the contour of the shape (Figure 4.a.). Each of the points p_i, on the contour is treated as the candidate point. Then on the candidate meaningful points, the right and left support regions are calculated by Principal Component Analysis (PCA) method [7].
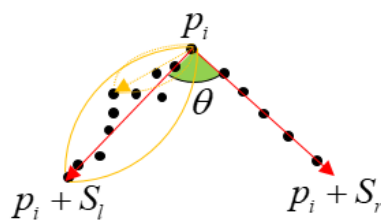

Figure 3. Researching right and left support regions

Here, the neighboring pixels in the vicinity of the candidate point are searched for the presence of the support region (Figure 3). The direction of the eigenvector gives us the support region which is the largest eigenvalue of the covariance matrix of the data. At the beginning, PCA is applied by taking three points and the angle that the largest eigenvalue is made with the coordinate axis is calculated. The operation is performed by increasing the number of the points. The obtained angle is compared with the previous ones. This process continues until the angle reaches a sifnificant threshold value. This process is applied to both the right and left sides of the candidate point. In this way, the right S_r and left S_l support regions are calculated (Figure 3).

Meaningful points are found by the means of right and left support regions of the candidate point. The angle θ between the distribution directions of the support regions is calculated (Figure 3). This angle θ is called a

certain meaningful point when it is greater than a first threshold angle: $\theta > T_1$. It is called a weak meaningful when it is between first and second threshold angles: $T_1 > \theta > T_2$. If the angle is less than the second threshold value $\theta < T_2$, it is not a meaningful point and deleted from the list.

When the shape is describing by the polygonal approximation, at first straight lines and circular arcs are used between certain points [7,9]. First break points described as c, the corner points and as s the smooth transition points (Figure 1), as l lines and as a arcs [10]. These are 5 types including: c-ll:line-corner-line, c-la:line-corner-arc, c-aa:arc-corner-arc and s-la:line-smooth transition point-arc and s-aa:arc-smooth transition point-arc.

These types are then expanded to 29 types by adding arcs respectively c:circle, e:ellipse, p:parabola and h:hyperbola [11]. These are c-ll, c-lc, c-le, c-lp, c-lh, c-cc, c-ce, c-cp, c-ch, c-ee, c-ep, c-eh, c-pp, c-ph, c-hh, s-lc, s-le, slp, s-lh, c-cc, s-ce, s-cp, s-ch, s-ee, s-ep, s-eh, s-pp, s-ph, s-hh.
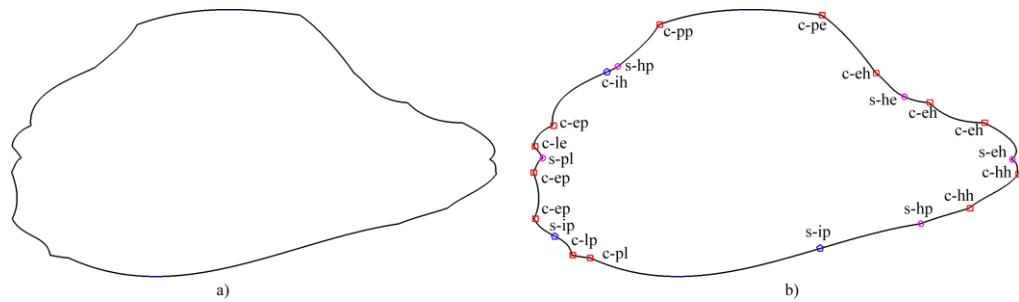

Figure 4. a) Contour of the image, b) line/arc fitted image.

With considering the inflection points, Z. Kurt and et al expanded the types to 43 types [7]. Inflection point is the point at which the curve changes its direction. Which is the solution points of the equation: $f'(x).f''(x) = 0$. Thus, meaningful points are defined as certain, weak and inflection points. In this study, because circle is the special form of the ellipse, the circle was removed and types is reduced to 26 types [8]. In this way, the shape was tried to be described with the most accurate and least lines and arcs (Figure 4.b.). Finally, number of the lines and arcs are counted to create the feature vector (Table 1).

Table 64. Feature representation of a shape

type	s-ll	s-lp	s-le	s-lh	s-pp	s-pe	s-ph	s-ee	s-eh	s-hh	c-ll	c-lp	c-le
count	0	1	0	0	0	0	2	0	2	0	0	2	1
type	c-lh	c-pp	c-pe	c-ph	c-ee	c-eh	c-hh	c-ie	c-ip	c-ih	s-ie	s-ip	s-ih
count	0	1	4	0	0	3	2	0	0	1	0	2	0

3. EXPERIMENTS AND RESULTS

The dataset used is consists of two classes. 60 of them are quality wheat images and 60 of them are of unclassified wheat images, totally 120 piece of Turkish Aldane class wheat images (Figure 5). Wheat images lying face down, supine, or side-lying. Size of the images are 800×1600 pixels. The pictures are taken under the same conditions: illuminance, distance. Under these condition scaling factor is elaminated and didn't need to use a scaling filter like Gaussian low pass [8].

Figure 5. Top side: quality wheat, bottom side: unclassified wheat images.

The application is implemented with MATLAB software. Feature vectors are finally classified with Support Vector Machines (SVM) [12]. In the SVM classifier, the C parameter was selected 1.0 and the kernel 2.0 for high performance. İmages are divided as training and test clusters. As a result of the randomly chosen pictures, the classes were separated by a performance ratio of 70.83%.

4. CONCLUSION

The method used is a recent shape-based descriptor. Instead of a whole shape, it represents shapes, by dividing them into lines and arcs is an advantage, especially in case of occlusion. With this way, the synchronization speed is also increasing. It is obvious to improve meaningful points and calculating support regions which are referenced in the creation of the feature vector. Different variations can have better results depending on the type of data set. In the next phase of the study, different classifiers are planned in order to increase the recognition performance and the result will be examined.

ACKNOWLEDGEMENT

REFERENCES

[1]. C.H. Teh, R.T. Chin, "*On the detection of dominant points on digital curves*", IEEE Transactions 0/ Pattern Analysis and Machine intelligence 11 (1989) 859-872.
[2]. B. Kerautret, J.-O. Lachaud, B. Naegel, Comparison of discrete curvature estimators and application to corner detection, in:ISVC (1), Vol. 5358 of LNCS, 2008, pp. 710-719.
[3]. A. Rosenfeld, E. Johnston, Angle detection on digital curves, IEEE Trans. Comput. 22 (1973) 940-941.
[4]. Wen-Yen Wu, "Dominant point detection using adaptive bending value", Image and Vision Computing 21 (2003) 517-525
[5]. M. Marji, P. Siy, "Polygonal representation of digital planar curves through dominant point detection - a nonparametrie algorithm", Pattern Recognition 37 (2004) 2113-2130.
[6]. B.K. Ray, K.S. Ray, "Detection of significant points and polygonal aproximation of digitized curves", Pattern Recognition Letters 22 (1992) 443-452.
[7]. Z. Kurt, K. Ozkan, "Description of Contour with Meaningful Points", SIU 2013 Semposium, Cyprus – Girne (2013).
[8]. T. Avcı, G. Kokdemir, Z. Kurt, K. Ozkan, "Shape Features Based Conic Arcs for Leaf Recognition", IEEE 22nd Signal Processing and Communications Applications Conference (SIU 2014), Trabzon, Turkey. 2014 22nd Signal Processing and Communications Applications Conference (SIU).
[9]. D. Cremers, M. Rousson and R. Deriche, "A Review of Statistical Approaches to Level Set Segmentation: Integrating Color, Texture, Motion and Shape", International Journal of Computer Vision Vol. 72, no. 2, (2007) 195-215.
[10]. H.T. Sheu, W.c. Hu, "Multiprimitive segmentation of planar curves- A two-level breakpoint classification and tuning approach", IEEE Transactions on Pattern Analysis and Machine Intelligence 21 (1999) 791-797.
[11]. Wu-Chih Hu, "Multiprimitive segmentation based on meaningful breakpoints for fitting digital planar curves with line segments and conic ares", Image and Vision Computing 23 (2005) 783-789.
[12]. Hsu, Chih-Wei; Chang, Chih-Chung & Lin, Chih-Jen, "A Practical Guide to Support Vector Classification", Department of Computer Science and Information Engineering, National Taiwan University (2003).

ICENS

3RD INTERNATIONAL CONFERENCE ON
ENGINEERING AND NATURAL SCIENCES

WWW.ICENS.EU